Guangxi Yue
Hai Zhang
Changsui Zhao
Zhongyang Luo
Editors

Proceedings of the 20th International Conference on Fluidized Bed Combustion

TSINGHUA UNIVERSITY PRESS

Springer

Guangxi Yue
Hai Zhang
Changsui Zhao
Zhongyang Luo

Proceedings of the 20th International Conference on Fluidized Bed Combustion

Guangxi Yue
Hai Zhang
Changsui Zhao
Zhongyang Luo

Proceedings of the 20th International Conference on Fluidized Bed Combustion

With 1280 figures

TSINGHUA UNIVERSITY PRESS

Springer

Editors
Guangxi Yue
Department of Thermal Engineering
Tsinghua University
Beijing, 100084, China
Email: ygx-dte@tsinghua.edu.cn

Hai Zhang
Department of Thermal Engineering
Tsinghua University
Beijing, 100084, China
Email: haizhang@tsinghua.edu.cn

Changsui Zhao
School of Energy and Environment
Southeast University
Nanjing, 210096, China
Email: cszhao@seu.edu.cn

Zhongyang Luo
Institute for Thermal Power Engineering
Zhejiang University
Hangzhou, 310027, China
Email: zyluo@cmee.zju.edu.cn

ISBN 978-7-302-20146-5
Tsinghua University Press, Beijing

ISBN 978-3-642-02681-2
Springer Dordrecht Heidelberg London New York

e-ISBN 978-3-642-02682-9

Library of Congress Control Number: pending

Cover design: Frido Steinen-Broo, EStudio Calamar, Spain

Printed on acid-free paper

Springer is a part of Springer Science+Business Media (www.springer.com)

PREFACE

The proceedings of the 20th International Conference on Fluidized Bed Combustion (FBC) collect 9 plenary lectures and 175 peer-reviewed technical papers presented in the conference held in Xi'an China in May 18-21, 2009. The conference was the 20th conference in a series, covering the latest fundamental research results, as well as the application experience from pilot plants, demonstrations and industrial units regarding to the FBC science and technology. It was co-hosted by Tsinghua University, Southeast University, Zhejiang University, China Electricity Council and Chinese Machinery Industry Federation.

A particular feature of the proceedings is the balance between the papers submitted by experts from industry and the papers submitted by academic researchers, aiming to bring academic knowledge to application as well as to define new areas for research.

The authors of the proceedings are the most active researchers, technology developers, experienced and representative facility operators and manufacturers. They presented the latest research results, state-of-the-art development and projects, and the useful experience.

The proceedings are divided into following sections:

- CFB Boiler Technology, Operation and Design
- Fundamental Research on Fluidization and Fluidized Combustion
- CO2 Capture and Chemical Looping
- Gasification
- Modeling and Simulation on FBC Technology
- Environments and Pollutant Control
- Sustainable Fuels

The proceedings can be served as idea references for researchers, engineers, academia and graduate students, plant operators, boiler manufacturers, component suppliers, and technical managers who work on FBC fundamental research, technology development and industrial application.

The editors would like to take this opportunity to thank our FBC colleagues around the world who devoted much of their time to review the manuscripts to keep the scientific standard of the proceedings.

Xi'an, China
May 2009
Guangxi YUE
Hai ZHANG
Changsui ZHAO
Zhongyang LUO

Steering Committee Members:

Anthony, J. Edward	CETC-O,Natural Resources, Canada
Basu, Prabir	Dalhousie University, Canada
Bonk, L. Donald	National Energy Technology Laboratory, USA
Bulewicz, M. Elzbieta.	Cracow University of Technology, Poland
Cabanillas, Andres	CIEMAT, Spain
Chen, Hanping	Huazhong Science and Technology University, China
Chyang, Chien-Song	Chung Yuan Christian University, Taiwan, China
DeLallo, R. Michael	Parsons Infrastructure & Technology Group,Inc., USA
Grace, John	University of British Columbia, Canada
Gulyurtlu, Ibrahim	INETI, Portugal
Horio, Masayuki	Tokyo University of Agriculture & Technology, Japan
Hotta, Arto	Foster Wheeler Power Group, Inc., Finland
Hrdlicka, Frantisek	CVUT Prague, Czech Republic
Hupa, Mikko	Abo Akademi University, Finland
Jaud, Philippe	R&D Division EDF, France
Jia, Lufei	CETC-O,Natural Resources, Canada
Kim, Sang Done	Korea Advanced Institute of Science and Technology, South Korea
Leckner, Bo	Chalmers University of Technology, Sweden
Luo, Zhongyang	ZhejiangUniversity, China
Maryamchik, Mikhail	Babcock & Wilcox, USA
Miccio, Michele	University of Salerno, Italy
Mustonen, John	Stone & Webster Consultants, USA
Newby, A. Richard	Siemens-Westinghouse Power Corp., USA
Nowak Wojciech	Czestochowa University of Technology , Poland
Pham, Hoang Luong	Hanoi Univeristy of Technology, Vietnam
Preto, Fernando	CETC-O,Natural Resources, Canada
Rozelle, Peter	Department of Energy, USA
Rubow, N. Lynn	Parsons Energy and Chemicals Group, USA
Selcuk, Nevin	Middle East Technical University, Turkey
Skowyra, Richard	Alstom Power, USA
Wedel, von George	Lurgi Energie und Entsorgung, Germany
Werther, Joachim	Technical University Hamburg-Harburg, Germany
Wietzke, L. Donald	Babcock & Wilcock Company, USA
Winter, Franz	Vienna University of Technology, Austria
Yue, Guangxi	Tsinghua University, China
Zhao, Changsui	Southeast University, China

Sponsors

China National Machinery & Equipment Import & Export Corporation

China Power Investment Corporation

Dongfang Electric Corporation

Foster Wheeler Corporation

Harbin Electric Corporation

Shanghai Electric Corporation

Qingdao Songling Power Environmental Equipment Co., Ltd

Taiyuan Boiler Works

Wuxi Boiler Works

Yixin High Alumina Bricks Company

National Nature Science Foundation of China

CONTENTS

Keynotes

CFB Boiler Technology, Operation and Design

Fundamental Research on Fluidization and Fludized Combustion

CO_2 Capture and Chemical Looping

Gasification

Modling and Simulation

Environmentals and Pollution Control

Sustainable Fuels-Combustion and New Concept

Keynotes

LATEST DEVELOPMENT OF CFB BOILERS IN CHINA

G. X. Yue, H. R. Yang, J. F. Lu, H. Zhang

Key Laboratory for Thermal Science and Power Engineering of Ministry of Education
Department of Thermal Engineering, Tsinghua University, Beijing, 100084, China

Abstract: The circulating fluidized bed (CFB) coal-fired boiler has being rapidly developed in China since 1980s and becomes a key clean coal technology used in thermal and power generation. In this paper, the development history and development status of the CFB boiler in China are introduced. The development history of the CFB boiler in China is divided into four periods and the important features of each period are given. Some latest research activities and important results on CFB boilers, and the typical achievements and newest development of the CFB boiler in China are also introduced. In addition, a few challenges and development directions including the capacity scaling up, SO_2 removal and energy saving are discussed.
Keywords: CFB boiler, development, summary, status

INTRODUCTION

The power demand has been kept increasing rapidly with the economic growth in the past three decades in China. Though the installation capacity for power generation in hydro, nuclear and renewable energy grows significantly, coal keeps dominant in the energy reserve structure and thereby dominant in power generation. Even in the year of 2020, it is expected that coal will remain 75% in power generation (Ni, 2005). Consequently, clean coal technology (CCT) development and implementation will still be the most important strategies for Chinese energy development in the foreseeable future.

Compared with other CCTs, such as IGCC, circulating fluidized bed (CFB) coal combustion is unique in wide fuel flexibility, cost-effective emission control, and rather high efficiency. Particularly, it is most suitable combustion technologies for high ash, high sulfur or low volatile content coals. This feature perfectly fits the Chinese coal reserve structure, in which a great portion of coal is with high ash, high sulfur, low volatile content, and low heating value. Besides, CFB and fluidized bed boilers are regarded available devices to burn the millions tons of coal waste generated by the coal mining industries every year in China.

Upon the above background, CFB coal combustion technology has being developed rapidly in the last two decades (Luo and Cen, 2005; Yue et al., 2005). Today, it dominates the boiler market in thermal generation and penetrates into the market of the utility boilers.

In this paper, the development history of CFB boiler in China will be introduced first, followed by the research activities, and then some challenges will be discussed.

CFB BOILER DEVELOPMENT HISTORY IN CHINA

The history of CFB boiler development in China is the extension of that of fluidized bed combustion (FBC) boiler development, which began in 1960s on bubbling fluidized bed (BFB) boiler. By 1980, the number of operating BFB in China was over 3000, largest unit population in the world. Encouraged by the success of first commercial CFB boiler in former Lurgi Company, Germany (Feng, 2005), Chinese researchers and engineers imitated the R&D on CFB boiler in 1982, and have kept paying a great effort since then. Generally, the development history of CFB boiler in China can be divided in fourth periods: 1980-1990, 1990-2000, 2000-2005 and after 2005.

The first period was in the 1980s. It was the beginning and learning period, featured with strong influence of FBC boiler. In that period, a CFB boiler was even regarded as a BFB boiler with an extended furnace plus a separator in China and international wide. One of the main focuses was on the gas-solid separators. The typical Chinese CFB technologies included the CFB boiler with S-shaped planar flow separators invented by Tsinghua University (Zhang et al., 1988), the CFB boiler with louver type separators invented by the Institute of Engineering Thermophysics of Chinese Academy of Science (IET-CAS) (Wang, 1995). The capacity of the CFB boiler was below 75t/h, most in 35-75t/h. Because the collection efficiency of the separators was too low to satisfy the material balance of circulating system, those CFB boilers, in fact, could only operating in BFB or turbulent bed condition with certain amount of fly ash recirculation. The upper furnace was not in fast fluidized bed and thus the heat transfer was too weak. Consequently, the boilers often failed to reach full designated load. Some other severe problems often occurred included the over high temperature in dense bed, and severe erosion in furnace and in second pass.

The second period was in the 1990s. It was featured with improvement and progress. In that period, supported by the government, Chinese researchers conducted vast amount fundamental studies on the gas- solid, two phase flow, heat transfer and combustion in CFB boiler and grasped the key knowledge and know-how of CFB boiler, rather than using the out-of-date BFB ones. Most CFB boilers developed in the 1st period were successfully adjusted or retrofitted to reach the full designated output. Along with the economic blooming, more than one hundred CFB boiler with improved deign with capacity of 75-130t/h were also put into operation in China. The gas-solid separators with low collection efficiency were not used anymore. Instead, different types of cyclones with high collection efficiency were used, including the hot round cyclone, the water-cooled round cyclone and the square-shaped water-cooled cyclone (Yue et al., 1997).

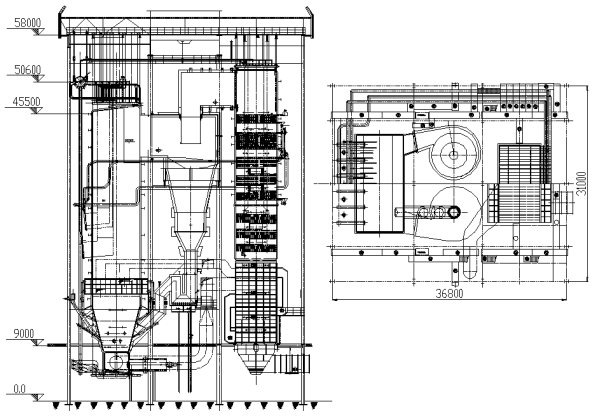

Fig. 1 200MWe CFB boiler with swirl cyclone co-developed by Institute of Engineering Thermophysics, ACS, and Shanghai Boiler Work, China

The third period was in 2000-2005, the early five years of this century. In the period, CFB boilers became rather mature, dominating heat power co-generation plants and emerging in utility boiler market in China. However, the development of domestic CFB combustion technology still lagged than the requirements of the power industry to build CFB power plants with the unit capacity over 100MWe and power generation efficiency over 35%. Thus, on one hand, the major Chinese boiler works urgently import the advanced foreign technologies by licensing or technical transfer. For example, Harbin Boiler Works Company got license of 100-150MWe reheat CFB from EVT, and Shanghai Boiler Works got license of reheat CFB boiler from former Alstom CE. On the other hand, during this period, Chinese researchers independently developed their own reheat CFB boilers based on the experience accumulated in smaller capacity CFB boiler development in the first two periods, and improved some foreign technologies that were found not fully suitable for Chinese local coals. The typical achievements were: (1) 135-200MW CFB boilers with swirl cyclones co-developed by IET-CAS - Shanghai Boiler Works (Liu, 2008), shown in Fig. 1; (2) 135-150MW CFB boilers with steam cooled cyclone co-developed by Dongfang Boiler Works (Wang P. et al., 2007); (3) 135-200MW CFB boilers with hot cyclone and fluidization status reformed co-developed by Tsinghua-Harbin Boiler Works (Lu et al., 2002a; Jiang et al. 2004); (4) 200MW CFB with pneumatic control EHE co-developed by TPRI-Harbin boiler (Sun et al., 2005), shown in Fig. 2.

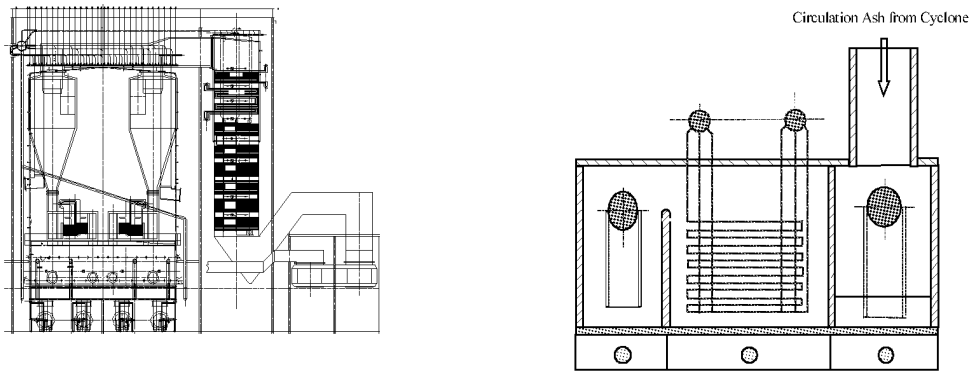

Fig. 2 200MW CFB boiler co-developed by TPRI and Harbin Boiler Works (a) boiler island; (b) pneumatic control EHE

The fourth period began in 2006 and featured by the quick spread of the 300MW sub-critical CFB boiler and the development of the 600MW supercritical CFB. In order to increase the power generation efficiency of CFB boiler, supported by State Development and Reforming Commission (SDRC), three largest boiler works in China obtained technical license of 300MW CFB boiler from Alstom Company in the late 1990s. The first demonstration in Baima Power Plant, Sichuan Provice (burning anthracite) operated in April 2006 followed by Qinhuangdao Power Plant, Hebei Province (burning bituminous) in June, 2006, Honghe Power and Xiaolongtan Power Plant in Yunnan Province (burning lignite) in October 2006.

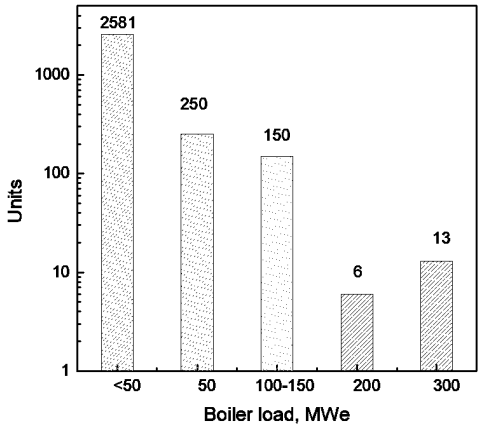

Fig. 3 The market of CFB boiler in China by end of 2008

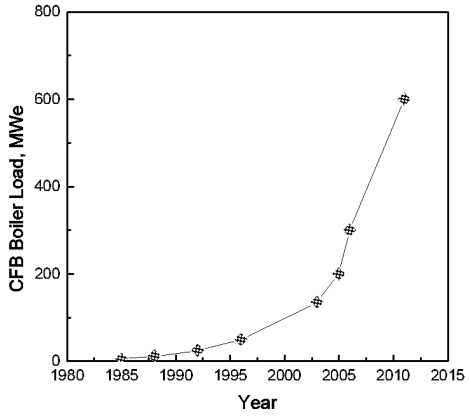

Fig. 4 CFB boiler scaling history in unit capacity in China

The first 300MWe CFB boiler with single furnace and without EHE co-developed by Tsinghua-Dongfang Boiler Works operated in 2008. So far, the total number of 300MWe CFB boilers in operation is 13 units. The initiation of 600MW supercritical CFB demonstration was an important event in this period. Chinese researchers started the investigation of supercritical CFB under the support of Ministry of Science and Technology (MOST) in the Tenth Five Year Plan (2001-2006) and finalized the conceptual design by the end of 2005. Then the SDRC supported the demonstration of 600MW supercritical CFB project in Baima Power Plant in 2007. The commissioning of the boiler is set by the end of 2011.

By 2008, the total power capacity of CFB boiler in China is around 63000MWe that is more than 10% of total Chinese coal fire power installation. Among these boilers, about 150 units are 100-150MWe, and 13 units are in 300MWe class. During the Eleventh Five Year Plan (2007-2011), approved by SDRC, 50 units of 300MWe CFB boilers are to be built and more CFB boilers burning coal waste with total capacity of 2000MWe are under approval.

SOME IMPORTANT RESEACHE ACTIVITIES AND RESULTS

Over two decades, Chinese researchers and engineers conducted vast amount of fundamental researches on CFB combustion, targeting the design of CFB boilers. The research topics cover fluidization, fluid mechanics, heat transfer, combustion, emission control and other aspects in the CFB boiler. Some important results were obtained.

Bed material balance

First, it was found that bed material balance is important for heat transfer and combustion performance. Solid particles with respect to size distribution should be kept in balance during the stable operation. Although the size of feeding particles into a CFB boiler is widely distributed, the size distribution of the recycling ash is rather narrow as the system behaves like size selection machine. The average size of bed inventory (bed quality) and the circulating rate of ash depend on the performance of separator and bed ash drain characteristics (Yang et al., 2005), besides the superficial velocity and ash formation characteristics of coal and limestone.

Moreover, the overall system efficiency, especially the efficiency for circulating ash (near the d_{99} of separator) strongly impacts the circulating rate G_s, which is typically three order larger than the feeding rate of such size particles. The design of cyclone separator and bed ash drainage should keep the efficiency for circulating ash over 99.7% (Yang et al., 2005). In engineering practice, sometimes, ash cooler with size classification are needed to keep fine circulating ash in bed. Mathematical modeling, considering the coal ash formation and attrition characteristics, the particle segregation in dense bed, is suggested to be used.

Axial and peripheral distributions of heat transfer coefficient and heat flux

The heat transfer coefficient and heat flux, and their distribution in the furnace are important for the design

of heating surfaces. Due to significant difference in gas-solid hydrodynamics between the practical CFB boilers and the laboratory CFB risers, the field measurements in commercial CFB boilers were conducted directly. The results confirmed that the overall heat transfer coefficient between two phase flow and the water wall, α_b, is mainly composed of particle suspension convective heat transfer coefficient α_c and particle suspension radiative heat transfer coefficient α_r (Andersson and Leckner, 1993). Along the furnace height, α_b is directly proportional to the certain power of solid suspension density. Furthermore, it was found that peripheral heat transfer coefficient and heat flux distribution is not even(Zhang H et al., 2005), and influenced by the heating surface arrange in the top furnace (Zhang P et al., 2009). The deviation of the peak and least value could be 6-8%. Based on the field data, more practical model was developed and empirical correlations were provided and accepted by boiler design companies.

Axial profile of heat release fraction

Heat release fraction, namely the burning fraction of coal particles in a specific section of the furnace was introduce to guide the CFB boiler design, e.g., to arrange heating surfaces in furnace and set flowrate ratio of primary air to secondary air (Jin et al., 1999; Yue et al., 2005). Both laboratory experiments and field measurement found that heat release fraction in dense bed of a CFB is much less than that of a bubbling bed, and a remarkable amount of CO is produced in the dense bed even with high O_2 concentration, confirming that the dense bed of a CFB is in a reducing atmosphere. It was also found that the coal particle size plays an important role in the axial profile of the amount of heat release in the CFB. For large coal particles, combustion mainly happens in the dense bed; for small coal particles, combustion mainly happens in the freeboard section. Heat release fraction profile is strongly influenced by the size distribution of coal particles, and their fragmentation and attribution characteristics during the combustion.

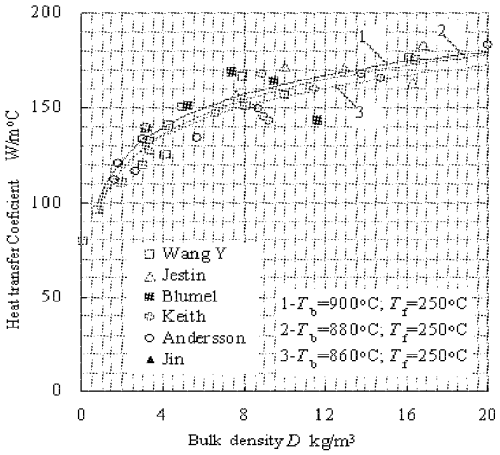

Fig. 5 Variation of heat transfer coefficient with bulk density in a 135MWe CFB boiler (Wang, 2005)

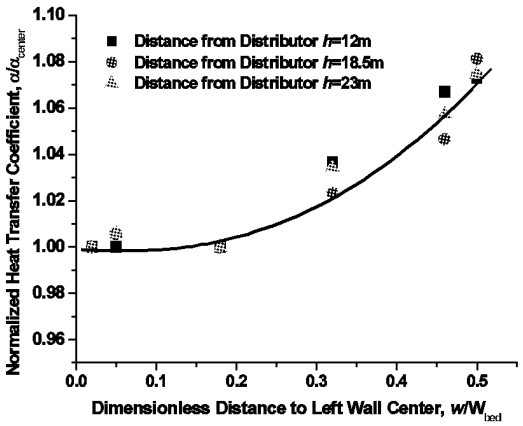

Fig. 6 Peripheral distributions of heat transfer coefficient on front wall side in 1a 135MWe CFB boiler (Zhang H et al., 2005)

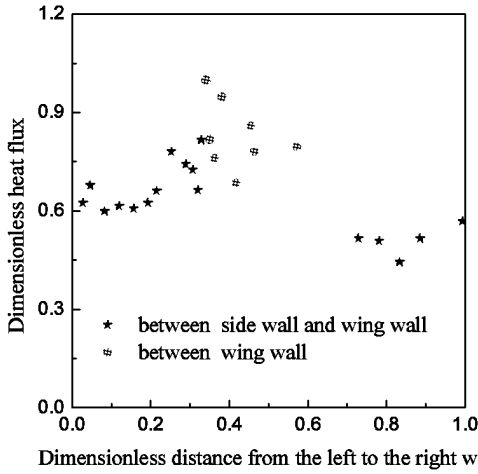

Fig. 7 Distributions of dimensionless heat flux along the side wall in a 300MWe CFB boiler (Zhang P et al., 2005)

Feasibility study on N_2O removal

Nitrous oxide (N_2O) is a typical pollutant emitting from CFB boilers. The development of an effective and cost-effective technology to reduce the N_2O emission from CFB boilers is of significance. The experiments showed that circulating ashes may possess remarkable catalytic effect on N_2O reduction and the intensity of the catalytic effect strongly depends on operational parameters such as reaction temperature and O_2 concentration (Loffer et al., 2002; Hou et al., 2007). It is feasible to inject NH_3 at the cyclone entrance of CFB boiler to form a selective catalytic reduction (SCR) process for N_2O emission without using extra catalyst.

Post combustion in the cyclone

Remarkable post combustion of the gas and solid combustibles in the cyclone of CFB boilers was reported by the CFB power plant. This phenomenon increased flue gas temperature of about 30-50oC, and the heat release fraction in the cyclone about 5-8% of the total heat release in the boiler (Yue et al., 2005; Li et al., 2009). Without well understanding such a phenomenon, overheating of reheated and superheated steam and extra heat loss of exhaust flue gas could be introduced. Post combustion could play a more important role as the unit capacity of the boiler, and often the dimension of the cyclone increases. Recently experimental and modeling studies on post combustion were conducted. It was found that post combustion post combustion is sensitive to coal type, and it is most severe in a CFB boiler burning low volatile anthracite coal. It is also impacted by fuel size distribution, the overall fluidizing air flow rate, and the primary/secondary air ratio. The main reason is that the coal type and feeding coal size, and the operating parameter, differ from the design values. To overcome the post combustion in the cyclones of existing CFB boilers, the feasible solution is to change the operational state back to the designate state by adjusting the bed inventory and feeding coal size based on material balance calculation and heat release fraction distribution. For the anthracite burning CFB boiler with thermal insulated cyclones, post combustion is needed to be carefully considered in the design phase.

Misdistribution of hydrodynamics in a CFB boiler with multiple cyclones

As the unit capacity of the CFB boiler becomes large, multiple cyclones are used at the same time. Multiple enclosed circulation loops of the two-phase flow exist and each loop consists of the furnace and the set of external components including a cyclone, a standpipe and a solid recycle valve. Some experiments were conducted to simulate the fluid dynamics in the 300MWe and 600MWe CFB boilers with multiple cyclones (Yue et al., 2008). The results confirmed the polymorphism of flow non-uniformity and thereby the fluid dynamic characteristics in each loop are not necessary to be the same. In the furnace the lateral difference of the axial pressure profiles corresponding to the cyclone location is little, indicating that the transverse material concentration distribution in the furnace is unbiased. However, the solid flow rate and the material distribution in one loop could be remarkable different from the others. Under present experimental condition, the circulating rate in the middle loop is about 10% larger than that in the side loops.

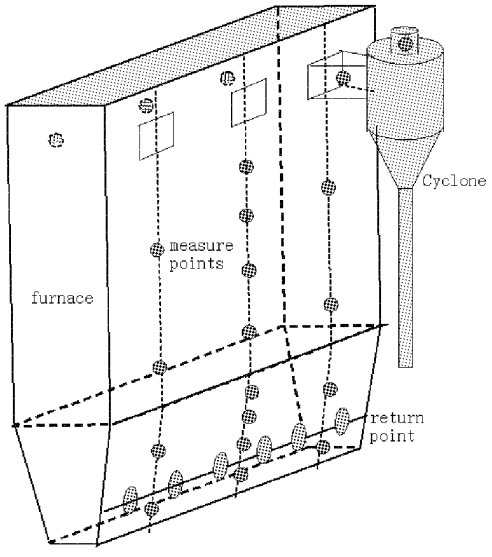

Fig. 8 Schematic diagram of CFB boilers with multiple cyclones (Yue et al., 2008)

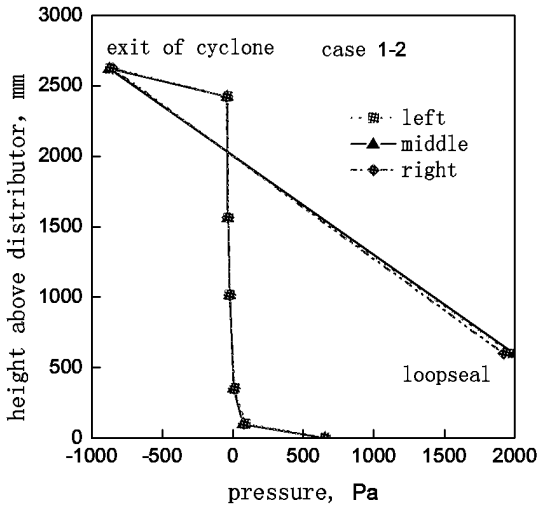

Fig.9 Pressure profile in the different enclosed loops in a CFB with three cyclones(U_g=1.08m/s, I=50kg)(Yang et al., 2009)

Design Theory for CFB Boilers

One of the most important research achievements is the State Specification Design Theory of the CFB boilers, which was partially published at the 18th FBC conference 2005 in Toronto, Canada (Yue et al., 2005).

It was found that a CFB boiler can be generally described as the superposition of a fast bed in the upper part with a bubbling bed or turbulent bed in the bottom furnace. The CFB boiler as an opening fluidization system with fast bed in the upper furnace can be operated at multiple states and each state is "specified" by U_g and G_s (Li and Kwauk, 1980). Moreover, a CFB boiler can operate at different states while keeping the upper furnace in fast bed regime with a given U_g and dependent G_s by adjusting M and bed quality. As the upper furnace is in fast bed fluidization, the state of a CFB boiler can be "specified" by U_g and G_s or bed voidage. That means a CFB boiler operates at specific U_g at designated load, while G_s depends on the material balance. Any changes in material balance shall change the fast bed state. This is not acceptable by the designer and operator. Therefore, it is suggested that during the design of a CFB boiler, the state in fast bed regime is pre-selected. When the state is fixed, the heat transfer coefficient profile along the furnace height is also fixed. The operator should keep the CFB boiler operating around the pre-selected state by controlling the bed inventory (the amount and size distribution).

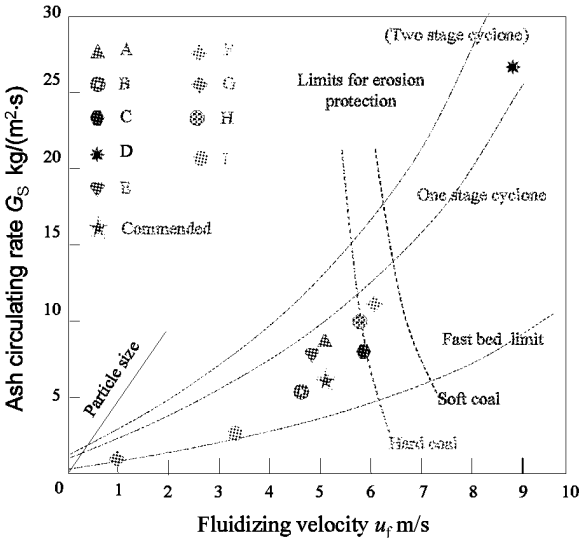

Fig. 10 Guide map of fast bed status in CFB boiler(Yue et al., 2005)

Based on the summary all types of CFB technologies in the world, a guide map for the fluidization state selection, especially when a Chinese coal is burnt, is obtained and shown in Fig. 10. The guide map distinguishes BFB and CFB by G_s. It also shows the maximum G_s determined by material balance. Furthermore, the map gives the warning line for erosion. Shown in the map, possible design state should only locate in a limited triangle area. Guided by this map, some domestic boiler works re-selected the fluidization state in CFB boiler design. As a result, the performance of the boiler was improved. The guide map also provided a guild line for the retrofitting of some foreign technologies.

CHALLENGES AND NEAR-FUTURE DEVELOPMENTS

Although CFB technology is rather mature in China, it is still facing challenges in three aspects. As it enters the utility boiler market, CFB boiler is expected to have compatible availability, power generation efficiency as the pulverized coal fired (PC) boilers with the same capacity. Besides, the sulfur capture efficiency of a CFB boiler should compatible with that of FGD used in a PC boiler.

Capacity scaling up for efficiency improvement

Increasing the unit capacity and steam parameters of a CFB boiler is a direct measure for power generation efficiency improvement. For this purpose, China imported Alstom's 300MW sub-critical CFB boiler technology (17.5MPa,540/540) in 2003. Since then, sub-critical 300MW CFB boilers has quickly spread out in China. The overall power generation efficiency increased around 5% compared with that of high pressure (12.7MPa, 535/535) CFB boilers. Based on the increasing experience from Alstrom technology, Chinese engineers and researchers simplified the Alstrom process to meet the market potential. The pioneer work was done by Dongfang Boiler Works. A conceptual design with simpler process was suggested. It is featured by single furnace, three cyclones, M shape arrangement, in-furnace reheater and superheater panel, partition in second pass and no external heat exchanger (Nie et al., 2007). The schematic is shown in Fig. 11. The conceptual design was investigated and approved by cold test in Tsinghua University (Yue et al., 2008). The first demonstration of this boiler was successfully put in commercial operation in 2008. By now, over 40 units are thereafter ordered, because of its reliable, simple operation and less price. Similar process was also adopted by Shanghai Boiler Works and Harbin Boilers Works (Zhang Y et al., 2008).

Another 330MW CFB demonstration was undertaken with the design of TPRI and Harbin Boiler Works (Jiang et al., 2007). The boiler was of single furnace with superheater panels, pneumatic control EHE, single

second pass. The boiler was put in commercial operation in the end of 2008. Fig. 12 shows the schematic of the boiler structure and Fig. 13 shows a picture of the layout of the boiler.

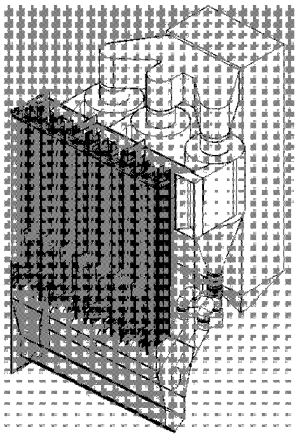

Fig. 11 Schematic of 300MW CFB without EHE

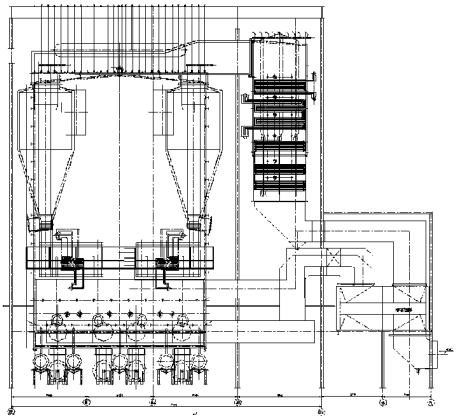

Fig. 12 330MW CFB boiler with pneumatic control EHE

To further improve power generation efficiency, the next step is clearly to go supercritical. Chinese researchers finished the conceptual design of the supercritical CFB (SCFB) boiler in the end of 2005 (Lu et al., 2002b; Liu, 2003; Wu et al., 2004). Then SDRC proved the demonstration project of 600MWe SCFB in Baima Power Plant in 2007. Dongfang Boiler was selected as the boiler supplier. The designate parameters of the SCFB boiler are: steam temperature: 571℃/569℃; stream pressure: 25.4MPa; main steam flowrate: 1900t/h; boiler efficiency: 92%; SO_2: <300mg/Nm^3; NO_x: <200mg/Nm^3; and power generation efficiency: 42% (Nie et al., 2007; Li Y. et al. 2009).

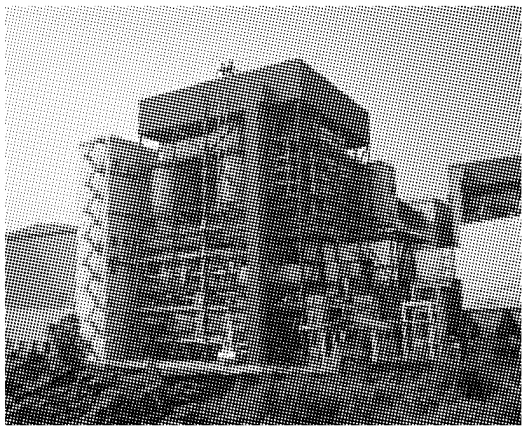

Fig. 13 Picture of 300MW CFB boiler with pneumatic control EHE

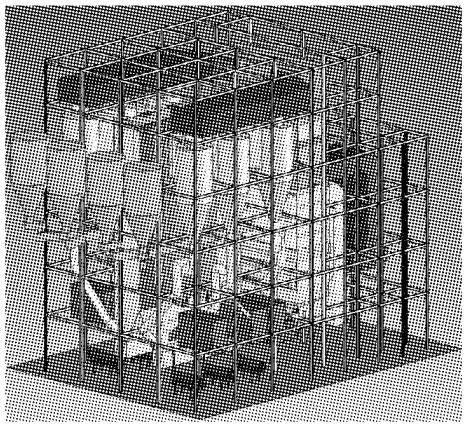

Fig. 14 3-D schematic of 600MW supercritical CFB boiler

The boiler is of twin furnace (with total cross section 15×28m^2 and 55 m height) divided by a partition waterwall and two air distributors. Six cyclones with inner diameter 9m are located outside furnace, each connected with individual external heat exchanger (EHE). 12 superheater panels are inserted in furnaces. The high temperature superheater and low temperature reheater are located in the second pass. The high temperature reheater, the first and high temperature superheaters are located in EHSs. There are two options for the cyclone selection. One is the steam-cooled cyclone used as the low temperature superheater. The other is the refractory lined cyclone. The flow chart of water and steam can be seen in Fig. 15 and 16. Water jacketed rotary ash cooler is used instead of fluidized bed ash cooler because of its worse experience for Chinese coal. The demonstration in Baima shall be in commissioning in 2010 or 2011.

SO_2 Removal in a CFB boiler

The in-furnace de-SOx (desulphurization) in a CFB boiler used be and still is a problem in China. The original purpose of fluidized bed combustion technology was for coal waste utilization in China. Thus, not much research was done on limestone additives in fluidized bed. Even CFB combustion has practiced in China

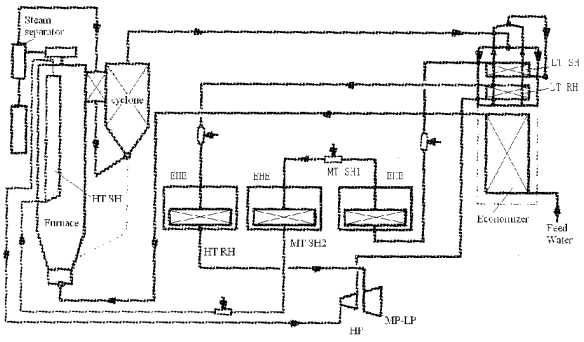

Fig. 15 Flow diagram of 600MW SCFB boiler with steam cool cyclone

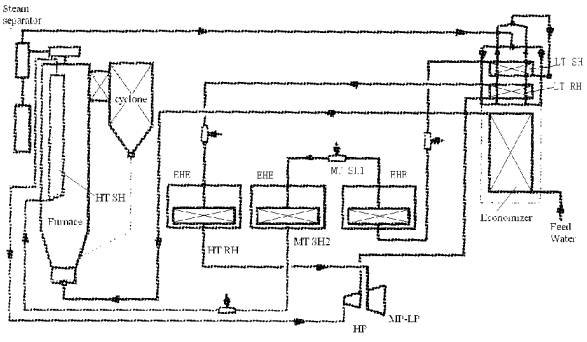

Fig. 16 Flow diagram of 600MW SCFB boiler with hot cyclone

widely since the early 1980s, only a few power plants did regularly use limestone for de-SOx in the CFB boiler. In addition, the limestone crushing, feeding system was not well designed and installed. As a result, the de-SOx efficiency was rather low, gave the people a wrong impression that CFB de-Sox efficiency is only 80-85%.

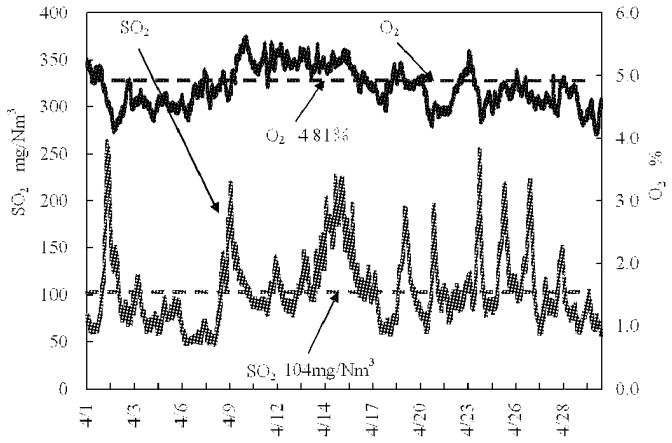

Fig. 17 SO_2 emission record for a 135MW CFB boiler

In recent years, the state emission standard becomes more stringent, so that the environmental protection bureau even forced the owners of CFB to install the wet FGD for CFB boiler. Now more and more CFB owners paid more attention on the de-SOx process of CFB boilers. For example, Shandong Huasheng Power Plant, with the help of Xian TPRI carefully selected the most active limestone, and optimized the limestone size and improved the limestone feeding system for a 135MW CFB boiler. The average SO_x emission over one month operation was 104mg/Nm^3 when Ca/S=2.2, burning a coal with sulfur content of 2.11%. They compared the operational cost of de-SOx in a CFB boiler and a wet FGD used in a PC boiler with the same capacity. It was found that the cost for a CFB boiler is 0.008￥/kWh and that for the FGD is over 0.02￥/kWh, 1.5 times higher. While the compensation for de-SOx from Power Grid is 0.015￥/kWh. Many Chinese CFB boiler power plants, are encouraged by above experience are taking action to implement in-furnace de-SOx.

Energy saving CFB process

Recently, Chinese researchers are working on the new idea for improving both the availability and the energy-saving for CFB combustion. Erosion in furnace wall has the major impact on the availability of CFB boilers because the splashing on the surface of dense bed in CFB furnace (Li et al., 2009a, 2009b). Besides, high bed inventory in furnace needs a high pressure draft fan for fluidization, introducing high power consumption for the primary draft fan.

Based on the State Specification Design Theory of CFB boilers, Tsinghua University proposed a novel CFB technology by reconstructing the fluidization state in the furnace by adjusting the bed inventory and bed quality (Yang H R et al., 2009). A patent for energy saving CFB process has already been approved by Chinese patent Bureau. The patent application in EU and US is also in processing.

The first validation of the concept was successfully done on a 75t/h CFB boiler in Shanxi Province, China, burning bituminous washing waste with heating value 18.34MJ/kg (received base) and ash content 38.42%.

The size distribution of coal and ash formatio are shown in Fig. 18.

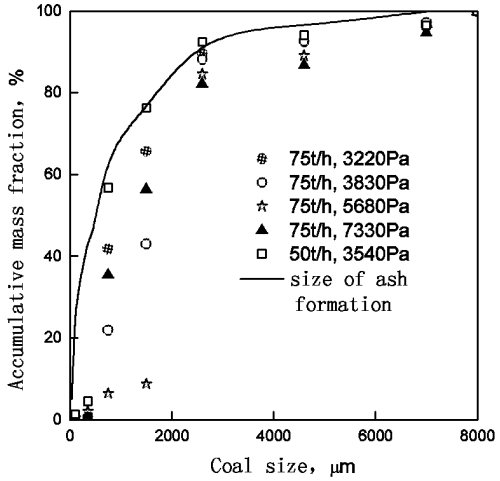

Fig. 18 Size distribution of feeding coal for the tested low bed inventory CFB boiler (Yang H R et al., 2009)

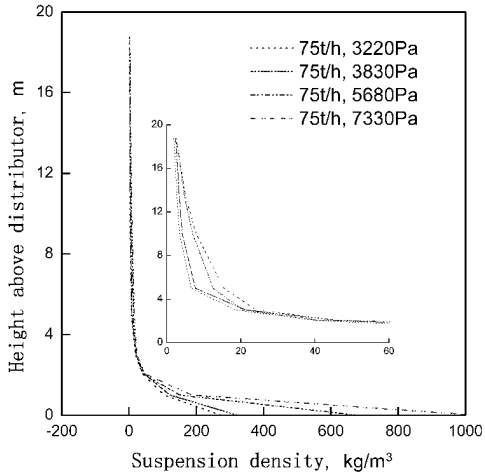

Fig. 19 Bulk density distribution for different bed inventory (Yang H R et al., 2009)

The bed pressure drop in the furnace was adjusted to 3.2, 3.8, 5.6 or 7.3 kPa by controlling the discharges of bottom ash and circulating ash. Fig. 19 shows the bulk density distribution along the height of furnace and corresponding bed inventory. As we decrease the bed inventory of a fast bed, the bottom dense bed shrinks faster than upper lean phase. The field tests shown that the boiler could operate steadily with a bed pressure drop as low as 3.1kPa, much lower than the conventional value. At the same time, the temperature in the furnace only changed slightly (around 14°C), as shown in Fig. 20. The tests also show an obvious impact of bed inventory on the combustion efficiency.

Theoretical analyses and practical applications showed that reconstruction of the fluidization state can be done by decreasing the bed inventory at a value much lower than normal experience. To do this, we have to carefully evaluate the performance of circulating system of the CFB boiler to make material balance towards more fine particles. Both size distribution of feeding coal and the ash size formation characteristic of feeding coal should be considered

A long term operation test was done for three CFB boilers in Shanxi. It was estimated that with the novel technology, around 5 million kWh electricity were save in one year. Besides, there was barely any erosion in furnace water wall.

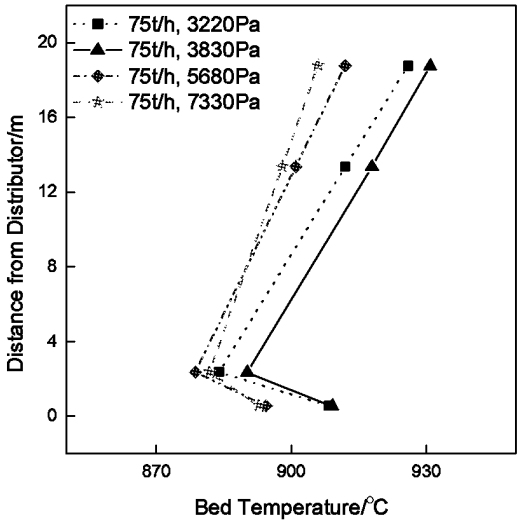

Fig. 20 Temperature in furnace for different bed inventory (Yang H R et al., 2009)

Encouraged by the achievement, the boiler manufacturer expanded the technology to burn other coals such as sub-bituminous, anthracite and lignite, and larger CFB boilers with capacities of 150t/h and 220t/h (Su et al., 2007).

CONCLUDING REMARKS

China is the biggest market of CFB boilers. Today, in China CFB boilers are no longer limited to be industrial boiler used only for thermal generation. They are playing more and more important role in the electrical power generation. During the near three-decade's development of CFB boiler in China, Chinese boiler works are capable to manufacture the 600MWe class supercritical boiler, the largest one in world. The engineers are experienced in boiler operation and maintenance. The researchers also mastered and developed the CFB boiler design theory. However, challenges and problems still remain, such as capacity scaling up, service power reduction, and SO_2 capture.

It is expected with the resolve of the challenges and problems, the CFB boiler will more mature and prevailing in power generation in the foreseeable future.

ACKNOWLEDGEMENTS

Financial supports of this work by Key Project of the National Eleventh-Five Year Research Program of China (2006BAA03B02) and National Science Fund Committee (50406002) are gratefully acknowledged.

REFRENCES

Anderssen, B A., Leckner, B., Int. J. Heat Transfer, (1992), 35, 3353-3362.
Feng, J. K. Proceedings of the 5th International Symposium on Coal Combustion, (2003) 209-212.
Hou, X. S., Zhang, H., Yue, G. X, et al., Reduction of N_2O and NO by NH3 on Circulating Ashes: The Effect of O_2 Concentration, 19th International Fluidized Bed Combustion Conference, Austria, Vienna, 2006.
Jiang, M. H., Sun ,X. B. Proceeding of the CSEEE, (2007), 27(23), 1-6.
Jiang, Y. D, Yu, L., Zuo, G. et al. Thermal Power Generation, (2004),12, 29-33.
Jin, X, Lu, J. F., Qiao, R, et al. Clean Coal Technology, (1999), 5(1): 20-23.
Li, J. F, Yang, S, Hao, J. H, et al. Operational Status of 135MWe Circulating Fluidized Bed Boilers in China, 20th International Conference on Fluidized Bed Combustion, Xi'an China, 2009a.
Li, J. F, Mi, J. H., Hoa, J. H, , et al. Operational Status of 300MWe Circulating Fluidized Bed Boilers in China, 20th International Conference on Fluidized Bed Combustion, Xi'an China, 2009b.
Li, S. H., Yang, H. R., Zhang, H. et al., Combustion Model for a CFB Boiler with Consideration of Post-Combustion in the Cyclone, 20th International Conference on Fluidized Bed Combustion, Xi'an China, 2009.
Li, Y., Nie, L., Hu, X. et al. Structure and Performance of a 600mwe Supercritical CFB Boiler with Water Cooled Panels, 20th International Conference on Fluidized Bed Combustion, Xi'an China, 2009.
Li, Y. C., Kwauk, M. The Dynamics of Fast Fluidization. In: Kunii D, Matsen J M eds. Fluidization IV, Plenum Press, New York and London, 1980: 537-544.
Liu, J., Wang Q. H., Luo Z. Y. et al. Power Engineering, 2003, 23(1), 2179-2204.
Liu, X. Boiler Technology, 2008, 39(6), 36-41.
Löffler, G., Wartha, C., Winter, F., and Hofbauer, H. Energy & Fuel, (2002)12:1024-1032.
Lu, J. F., Lin, X.,Yu, L., et al., Boiler Manufacturing, (2002a), 3, 1-5.
Lu, J. F, Yue, G. X., Zhang, J. S. et al. Boiler Manufacturing, (2002b), 4, 1-5.
Luo, Z.Y., Cen, K.F., Research and Development on Circulating Fluidized Bed Combustion Technology in China, in: Eds: Cen, K, 8th Circulating Fluidized Bed Technology, May 10-13, 2005, Hangzhou, China.
Ni, W. D., Current Status and Development of China's Energy, China-Japan Forum for Energy Partnership Workshop for Clean Coal Technology, June 2005, Beijing, China.
Nie, L. Wang, P., Huo, S. et al. Dongfang Electric Review, (2007),21(2), 33-42.
Nie, L., Wang, P., Peng, L., et al. Journal of Power Engineering, (2008), 28(5), 701-706.
Su, J. She, J., Zhao, X. X, et al. The Design and Its Operation of The Lower Energy Consumption Circulating Fluidized Bed Boiler, 1st Chinese National Conference on CFB Boilers, 2007, Hainan, China.
Sun, X. B, Yu, L., Wang, Z.W, International Power for China, (2005), 9(1), 19-22.
Wang D. Z, Zhang Y., Pan Z, et al. Journal of Combustion Science and Technology, (1995), 1(1), 49-53.
Wang, P., Nie, L., Huo, S. et al. Dongfang Electric Review, (2007), 21(1), 5-10.
Wu, Y. X., Lu, J. F, Zhang, J. S. et al., Boiler Technology, (2004), 35(3), 1-6.
Wang, Y. Measurement of Heat Transfer in a 465t/h Circulating Fluidized Bed Boiler, Thesis, Tsinghua University, 2005.
Yang, H. R, Yue, G. X., Wang, Y., Journal of Engineering for Thermal Energy and Power, (2005),20(3),291-295.
Yang, H. R, Zhang, H., Lu, J. F. et al. Novel CFB technology by Reconsideration of Fluidization State, 20th International Conference on Fluidized Bed Combustion, Xi'an China, 2009.
Yang, S., Yang, H. R. Liu, Q. et al. Research On Flow Non-Uniformity in Main Circulation Loop of a CFB Boiler with Multiple Cyclones, 20th International Conference on Fluidized Bed Combustion, Xi'an China, 2009.
Yue, G.X., Li, Y., Lu, X. M. et al. The First Pilot Compact CFB Boiler with Water Cooled Separator in China, 14th International Conference on Fluidized Bed Combustion, Canada, 1997.
Yue, G. X., Lu, J. F., Zhang, H, et al. Design Theory of Circulating Fluidized Bed Boilers, 18th International Fluidized Bed Combustion Conference, May 18-21, 2005, Toronto Canada.
Yue, G. X., Yang, H. R., Zhang, H. et al, Post Combustion in Circulating Fluidized Bed Boilers, 19th Fluidized bed conference, Austria, Vienna, 2006.
Yue, G. X., Yang, H. R., Nie L. et al. Hydrodynamics of 300MWe and 600MWe CFB Boilers with Asymmetric Cyclone Layout, 9th Circulating Fluidized Bed Technology, May 2008, Hamburg, Germany.
Zhang, H., Lu, J.F.; Yang, H. R.; et al. in: Eds: Cen, K, 8th Circulating Fluidized Bed Technology, (2005), 254-260.
Zhang, P., Lu, J.F.; Yang, H. R. et al. Heat Transfer Coefficient Distribution in the Furnace of a 300MWe CFB boiler, 20th International Conference on Fluidized Bed Combustion, Xi'an, China, 2009.
Zhang, X. Y., Zheng, Q.Y, Yue G. X. Proceedings of the 1st International Symposium on Coal Combustion, Eds. Feng J., (1988), 527-533.
Zhang, Y., Wang, F., Jiang, X., Boiler Manufacturing, (2008), 3, 1-3.

GASIFICATION OF BIOMASS IN FLUIDISED BED: REVIEW OF MODELLING

A. Gómez-Barea[1], B. Leckner[2]

1 Department of Chemical and Environmental Engineering. University of Seville, Seville, Spain
2 Department of Energy and Environment, Chalmers University of Technology, Göteborg, Sweden

Abstract: Modelling of biomass gasification in bubbling and circulating fluidised bed (FB) is reviewed. The focus is on comprehensive fluidisation models, where semi-empirical correlations are employed to simplify the fluid-dynamics of the FB. The conversion of single fuel particles, char and gas reaction kinetics are dealt with, outlining the key phenomena that should be included in gasification models. An assessment of published models is presented and the need of further investigation is identified.
Keywords: fluidized bed, gasification, modeling, biomass, review

INTRODUCTION

Mathematical modelling of fuel conversion reactors is based on balances of mass, species, energy and momentum within the domain concerned (reactor and fuel particle) with its boundary conditions and source terms. The chemical conversion is expressed by the source terms, which couple the reactor model with the conversion models. Computerised reactor models based on CFD technique follow most closely the fundamental partial differential equations, but in fluidised bed reactors, when chemical conversion is included, the model solution through numerical methods tend to become too extensive, and simplifications are introduced based on empirical or semi-empirical relationships. These simplified approaches are the most common ones so far in fluidised bed gasification (FBG) modelling. They are the focus of the present survey that deals with reactor modelling as well as with modelling of reactions, both homogeneous and heterogeneous, applied to biomass and waste gasification in a fluidised bed (FB).

Modelling of combustion and gasification in FB is similar in many respects, for instance, in the case of fluid-dynamics, devolatilisation, oxidation of volatiles, char conversion and comminution processes. There are differences, though, such as in the mode of conversion of char and in issues related to heat transfer to surfaces. With caution, therefore, many of the model elements from FB combustor models can be utilised in FBG models. Relevant reviews of coal combustion in FB are available (La Nauze, 1985; Hannes 1996; Eaton et al., 1999; Ravelli et al., 2008). Despite the different physical and chemical properties of biomass and coal, there are no conceptual differences between the fuels with respect to model structure and mathematical description of the process. Reviews on modelling of gasification in FB for coal (Gururajan et al., 1992; Moreea-Taha, 2000) are useful also for biomass. Past reviews specifically devoted to modelling of biomass gasification in FB include those of Buekens and Schoeters (1985), Hamel (2001), and Newstov and Zabaniotou (2008). An updated survey of the main mathematical reactor models for biomass and waste gasification in FB is presented here.

FLUID DYNAMICS

Figure 1 presents typical flow patterns in FBG units, valid for bubbling (stationary) or circulating beds. Graph (b) shows quantitatively the concentration of solids in different parts of a reactor. Two main zones are distinguished: a bottom zone and a freeboard (or riser in the CFB case). The bottom bed is a bubbling fluidised bed. The freeboard is a more dilute zone, where the solids are carried away upwards from the bed. There is a splash region between the two zones, characterised by the return of the solids that were thrown up from the bed's surface. The flow structure in the freeboard is not qualitatively different in the two types of bed: there is a clustered particle flow moving upwards and a thin layer of separated particles moving down at the walls. Since the momentum equation is not solved in fluidisation models, the flow pattern has to be specified by relations based on measurements.

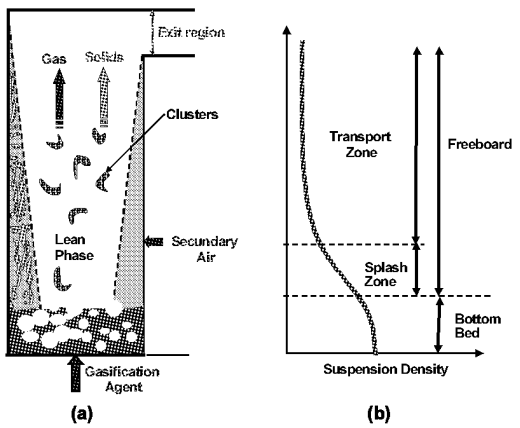

Fig. 1 The flow pattern in an FB

The following key parameters define the flow pattern in an FB: (a) in the bottom zone: the (volume) fraction occupied by gas ε, the fraction occupied by bubbles ε_b, the fraction of gas in the emulsion phase, ε_e, the velocity of gas in the emulsion u_e, the bubble velocity u_b and bubble size d_b. (b) In the freeboard the corresponding voidage is ε_F, and 1- ε_F is the solids flow. Other variables necessary for the solution of the conservation equations can be obtained from the quantities mentioned.

Modelling of the bottom zone

Despite the observation of different time-averaged bottom bed voidages in bubbling and circulating beds, the modelling of the two types of FB is similar for fuel conversion devices employing sufficiently wide beds of Group B particles, provided that the correlations used are within their ranges of validity (Pallarès and Johnsson, 2006). At every height h, a part of the gas flows through the emulsion phase and the rest forms bubbles. The overall voidage is

$$\varepsilon = \varepsilon_b + (1-\varepsilon_b)\varepsilon_e \tag{1}$$

The bubble size can be calculated by correlations, for instance the one of Mori and Wen (1985) or other alternative equations found in Kunii and Levenspiel (1991) and Souza-Santos (2004). The bubble velocity can be estimated by Davidson and Harrison (1963) as $u_b=u_v+u_{br}$, where u_{br} is the single bubble velocity and u_v is the visible bubble flow defined as $u_v=\varepsilon_b u_b$, which, according to the original two-phase theory is $u_v=u_0-u_{mf}$. The porosity and velocity at minimum fluidisation is given by correlations (Kunii and Levenspiel, 1991). The average voidage ε is calculated by a bed expansion factor

$$f_{bex} = \frac{1-\varepsilon_e}{1-\varepsilon} \tag{2}$$

f_{bex} depends on the height above the bottom h and is calculated by empirical correlations, such as those of Babu et al. (1978) obtained by fitting measurements from commercial BFB coal gasifiers. Equation (2), together with a correlation for f_{bex}, yields a relationship for ε and ε_e. Some authors assume $\varepsilon_e = \varepsilon_{mf}$. Then ε can be directly estimated by Eq. (2), and Eq. (1) is used to obtain ε_b. The two-phase theory of fluidisation determines the gas split near the distributor (h=0) as an initial condition, but this theory is abandoned for positions above the distributor to allow for gas generation and temperature variation with height. The coefficient of mass exchange between bubble and emulsion, k_{be}, can be calculated with the correlation of Sit and Grace (1981), who used previous experimental studies to suggest a combination of convection and diffusion processes where the clouds around the bubbles were included as part of the emulsion. Models and correlations of the parameters discussed have been surveyed by Yates (1983), Kunii and Levenspiel (1991), Oka (2004) and Souza-Santos (2004).

Modelling of the freeboard

The key concept of freeboard modelling is the quantification of the entrainment of particles from the bubbling bottom zone and the steady solids flow through a circulation loop back to the bed. Particles are thrown out of the bottom bed by the bubble eruptions and/or carried away by the gases. The bubble eruptions form a splash zone with a high back-mixing of particles. Above the splash zone, sufficiently small particles are carried away by the flow of gas, and the clustering back-mixing in the core of the transport zone is small. Instead, particles are transported from the core into the wall layers, where the gas velocity is smaller and they fall downwards. This second mechanism is dominant far away from the splash zone. The upward flow of particles in the transport zone is $F_c=G_cA_c$ where A_c the cross-section area of the core (index c) and G_c is the particle flux given by

$$G_c = G_{co}\exp(-K(h-H)) \tag{3}$$

that takes into account the transfer of particles between the core and the wall layer, and K is a "decay" constant correlated experimentally. G_{co} is measured or calculated at the exit of the riser as $G_{co}=\rho_{co}(u_0-u_t)$ based on the assumption that the flow in the transport zone is rather dilute. At any height the balance $F_w+F_c=F_{wo}+F_{co}=AG$ holds, so the downward flow at the wall can now be written as

$$F_w = AG\left[1-(1+k_b)\exp(-K(h-H))\right] \tag{4}$$

k_b describing the backflow from the top of the riser is estimated by measurements (Johnsson et al., 1995). The suspension density in the transport zone can be obtained from

$$\rho = \rho_o \exp(-K(h-H)) \tag{5}$$

with ρ_o being the average density at the top. Close to the bottom bed, the particle concentration is not only affected by the drag from the gas but also by the ejection of particles by the bubbles, which induces a ballistic mechanism of solids transport, characterised by backflow of coarser particles. The corresponding density generated by this mechanism must be added to that of the transported flux of particles. Therefore, in the modelling of average axial density profiles through the splash zone down to the surface of the bottom bed, both

mechanisms are accounted for:

$$\rho = \rho_{Bx} \exp(-a(h - H_x)) + \rho_o \exp(-K(h - H)) \quad (6)$$

Figure 2 shows how ρ is the sum of the two contributions. The value of ρ_{Bx} is obtained by the following consideration: at the bed surface $h=H_x$, $\rho=\rho_x$; since the two components of particle density are assumed to coexist at the surface, it holds: $\rho_x=\rho_{Bx}+\rho_{ox}$ so that $\rho_{Bx}=\rho_x-\rho_{ox}$., where ρ_{ox} is given by applying Eq. (6) at $h = H_x$. The first part of Eq. (6) represents the contribution of the splash zone, caused by the particles thrown up by the movement of the bed, similar to the classical form proposed by Lewis and others, typical for the bubbling bed. The decay constants a and K have been determined empirically (Kunii and Levenspiel (1991) and Johansson et al. (2007)) by, for instance, $a=4u_t/u_0$ and $K=0.23/(u_0-u_t)$. To apply the present model, the suspension density at the top of the riser ρ_o is the most uncertain parameter. It can be estimated, though, from the circulating flux G, $\rho_{co} = (u_0 - u_t)/G_{co}$ if G is measured. Alternatively, an estimate of ρ_o is obtained from pressure measurements along the riser. Clearly this latter equation is not valid at the walls where $u<u_t$ and the particles fall down. This means that $dp/dh = -\rho g$ is difficult to interpret, and so, it is uncertain to determine ρ from pressure drop measurements. However, in a large riser this seems to be of minor importance. Finally, in the equations, the bottom bed parameters ρ_x and H_x are obtained by the bottom bed model presented above or by direct measurements. From the densities, the freeboard voidage $\varepsilon_F = (1-\rho/\rho_s)$ can be calculated.

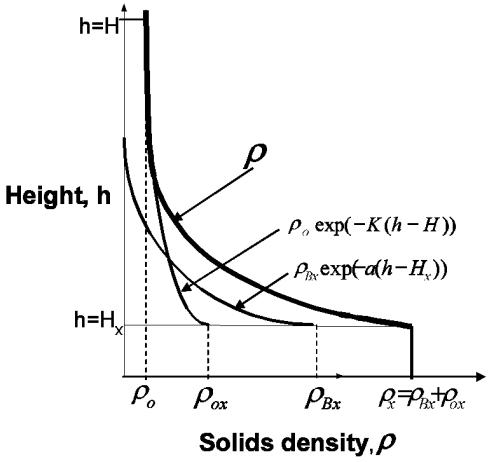

Fig. 2 Solids density profiles in an FB

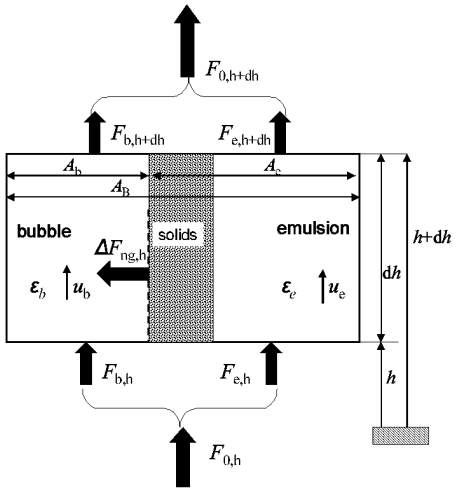

Fig. 3 Definitions of fluid-dynamic parameters in a control volume of the bottom bed

MASS BALANCES

Once the fluid-dynamic variables of the various regions in the FB have been defined, the conservation equations can be formulated. Figure 3 shows the geometry of a differential volume in the bottom zone with the main fluid-dynamic parameters used. In the bottom bed, the mass conservation balances for gas species in the bubble and emulsion at height h are written as

$$\frac{1}{A_B}\frac{dF_{i,b}}{dh} = \varepsilon_b R^b_{gg,i} - \varepsilon_b a_b k_{be,i}(\rho_{i,b} - \rho_{i,e}) + \Delta F_{ng,i} \quad (7)$$

$$\frac{1}{A_B}\frac{dF_{i,e}}{dh} = \varepsilon_e(1-\varepsilon_b)R^e_{gg,i} + \sum_m (1-\varepsilon_e)(1-\varepsilon_b)\sigma_m R^e_{gs,m,i} + \varepsilon_b a_b k_{be,i}(\rho_{i,b} - \rho_{i,e}) - \Delta F_{ng,i} \quad (8)$$

The mass flow rates of gas i in the bubble and emulsion are given by $F_{i,b}=u_b\rho_{i,b}A_b$ and $F_{i,e}=u_e\rho_{i,e}A_e$. The cross section areas in the bubble phase, A_b, and the emulsion, A_e, are related to the cross section of the reactor (bottom zone "B"), A_B, by: $A_B=A_b+A_e$. The chemical reaction terms $R^{b/e}_{gg,i}$ and $R^{b/e}_{gs,m,i}$ are given by

$$R^{b/e}_{gg,i} = \sum_{j=1}^{n_{ggr}} r^{b/e}_{j,i}\, \nu_{i,j} MM_i \qquad R^e_{gs,m,i} = \sum_{j=1}^{n_{gs}} r^e_{j,m,i}\, \nu_{i,j} MM_i \quad (9)$$

All solids are assumed to be in the emulsion phase (and so, heterogeneous gas-solid reactions take place). The main homogeneous reactions are the oxidation of volatiles, the water-gas-shift reaction and the reforming of hydrocarbons. The main heterogeneous reactions are the devolatilisation and char-gas (mainly O_2, CO_2 and H_2O) reactions. As a result of fuel devolatilisation and gas-char reactions in the emulsion, as well as of the

increase in molar volume due to the homogeneous reactions, there is a net generation of gas in the emulsion phase. This gas is assumed to be instantaneously transferred to the existing bubbles (exogenous bubbles) or it directly forms new bubbles, i.e. endogenous bubbles. Figure 3 illustrates this by the arrow representing the net flow, ΔF_{ng}, from the reacting solids in the emulsion to the bubble phase. The expression for ΔF_{ng} is:

$$\Delta F_{ng} = (1-\varepsilon_b)\sum_{i=1}^{n_{sp}}\left((1-\varepsilon_e)\sum_m \sigma_m R^e_{gs,m,i} + \varepsilon_e R^e_{gg,i}\right) \tag{10}$$

Several solids m whose volume fraction is σ_m can be part of the bed: inert bed material, char and catalyst. The term $R^e_{gs,m,i}$ takes into account the generation of the gaseous species i by reaction with solid m. The contribution of each individual species i to the net flow is $\Delta F_{ng,i}$ given by:

$$\Delta F_{ng,i} = \Delta F_{ng}\frac{c_{i,e}}{c_{T,e}} \tag{11}$$

At any height h, the total gas flow rate $F_{0,h}$ must be updated to incorporate the increments in the flow given at this height h, $\Delta F_{ng,h}$. By mass balances at height h (see Fig. 3) one can write:

$$F_{0,h+dh} = F_{0,h} + \Delta F_{ng,h} = (F_{e,h} + F_{b,h}) + \Delta F_{ng,h} = F_{e,h+dh} + F_{b,h+dh} \tag{12}$$

In the mass conservation equations of the gaseous species in the freeboard a single-phase model is often assumed for the gas (plug flow) and an axial distribution for the solids, $\varepsilon_F(h)$:

$$\frac{1}{A_F}\frac{dF_{i,F}}{dh} = \varepsilon_F R^F_{gg,i} + \sum_m (1-\varepsilon_F)\sigma_m R^F_{gs,m,i} \tag{13}$$

In Eq. (13) the solids and gas are lumped into a single phase (index F). The mass conservation balances for the solids m in the perfectly mixed bottom bed are

$$F_{m,in,B} - F_{m,out,B} = A_B \int_o^{H_s} (1-\varepsilon_e)(1-\varepsilon_b) R^e_{gs,m}\, dh \tag{14}$$

The flow of solids m entering the bed, $F_{m,in,B}$ consists of the solids fed and the recycling flow, if there is one. The flow of solids leaving the bed, $F_{m,out,B}$ is to the drainage (continuous overflow or batch-wise mechanical removal) and the flow to the freeboard. A similar equation is formulated in the freeboard, accounting for the variation with height. The boundary conditions are given by the composition and flow rates of the fluidisation agent and the solids fed to the reactor. The reaction terms R_{gg} and R_{gs} may vary with h and, therefore, the spatial distribution of particles involved in the calculations of these quantities, mainly char and devolatilising particles, has to be known. However, the char is well mixed, so a volumetric source equally distributed through the bed can be defined.

In addition to the spatial distribution of solids, in an FBG there is a particle size distribution (PSD) of solids. Several phenomena contribute to changing the original PSD of the feed: gas-solid reactions, entrainment, fragmentation and generation of fines by attrition. The most common solids in FBG are inert bed material, fuel, and catalyst for tar removal, such as dolomite, lime or other. Let a particle of kind m and of size l be named as a particle of the m,l class. The flux and density relationships defined above for the freeboard at h can be used for a particle of m,l class at height h, provided that the mass fraction of the particle, $x_{m,l}$, of the m,l class at height h is known. For instance: $G_{m,l}=Gx_{m,l}$, $\rho_{m,l}=\rho x_{m,l}$, etc. Therefore, the model developed is directly applicable if the decay constant and boundary conditions at the surface of the bottom bed and at the top of the freeboard are formulated for a particle of the m,l class. To calculate the mass fraction of a particle of the m,l class at steady state in the bottom bed, a population balance for each solid m should be formulated (losses=gains):

$$F_{m,l,in} + \Gamma_{m,l,gain} = F_{m,l,out} + \Gamma_{m,l,loss} + \Re_{m,l} \tag{15}$$

The sum of Eq. (15) for all sizes l yields Eq. (14). The term $F_{m,l,in}$ represents the contribution from the feed and recirculation streams. The term $F_{m,l,out}$ is the loss due to forced withdrawals and by entrainment at the surface of the bed $F_{m,l,ent}$. The fraction m,l of particles in the withdrawal streams is equal to that in the bottom bed $x_{m,l,B}$ if the bed is perfectly mixed. The corresponding net entrainment at the bed's surface is:

$$F_{m,l,ent} = x_{m,l,c}F_{c,x} - x_{m,l,w}F_{w,x} \tag{16}$$

where a distinction is made between the solids in the wall layer and in the core (indices c and w), because their may differ. The terms $\Gamma_{m,l,gain}$ and $\Gamma_{m,l,loss}$ represent the gain of particles of the m,l class due to the attrition and fragmentation of particles from superior levels (size $>l$) and the loss of particles of the m,l class to inferior levels (size $<l$). The term $\Re_{m,l}$ represents the consumption by chemical reaction of particles of the m,l class. The recycling stream depends on the efficiency of the particle separator (cyclone). A simple method for

estimation of the cyclone efficiency as a function of its main geometry parameters and temperature was given by Leith and Metha (1973). For CFB, the semi-empirical model developed by Zhang and Basu (2004) can be used. A summary of more sophisticated methods has been published by Cortés and Gil (2007).

ENERGY BALANCE

Heat balances can be formulated, depending on the aim: (1) overall heat balance over the reactor (Yan et al., 1999), (2) overall heat balances over regions, such as bed, secondary air injection zone, and freeboard, (Corella and Sanz, 2005) (3) heat balances over the various regions without distinction of phases (Jiang and Morey, 1992), and (4) heat balances over the phases and along the zones of the reactor, including heat and mass transfer between bubble and emulsion, gas and solid particles and heat transfer across the external surface (heat losses) (Souza-Santos, 1987, 1989; Jennen et al., 1999; Hamel, 2001; Ross et al., 2005). A model of Type 1 can be formulated as heat input=heat outlet+heat loss:

$$\sum_{k=1}^{n_{fs}}\sum_{i=1}^{n_{sp}} F_{i,k}H_{i,k} = \sum_{k=1}^{n_{os}}\sum_{i=1}^{n_{sp}} F_{i,k}H_{i,k} + Q_{loss} \tag{17}$$

The left-hand side is the total sum of energy entering the bed: species i in the feed streams k, including m solids: fuel, catalyst, inert, etc., and the gas feed streams: fluidisation agent, secondary injection of air or oxygen, produced gas recirculation, etc. n_{fs}, n_{os} and n_{sp} are, respectively, the number of feed and outlet streams and the total number of species in the system. The recirculation stream is internal and not included in Eq. (17). The right-hand side represents the energy carried by gas and solid products leaving the bed and the net heat loss from the fluidised bed to the surroundings Q_{loss}. The latter can be treated as an input parameter (Yan et al., 1999)), or alternatively, it can be calculated on the basis of reactor temperature, type and thickness of insulation and dimensions of the reactor.

A model of Type 4, a 1D isothermal model of the phases, can be formulated as the heat balance over a differential volume of height dh, yielding for the gas in the bubble and emulsion phases of the bottom bed:

$$\frac{1}{A_B}\frac{d\left(F_b H_b\right)}{dh} = \varepsilon_b h_{be} a_b (T_e - T_b) + \Delta F_{ng}\overline{c}_{p,ng}(T_e - T_b) \tag{18}$$

$$\begin{aligned}\frac{1}{A_B}\frac{d\left(F_e H_e\right)}{dh} = &\sum_m (1-\varepsilon_e)(1-\varepsilon_b)\sigma_m h_{gs,m}(T_{s,m} - T_e) + \varepsilon_b a_b h_{be}(T_b - T_e) \\ &- \Delta F_{ng}\overline{c}_{p,ng}(T_e - T_b) + U_w(T_e - T_{ext})\end{aligned} \tag{19}$$

H_e and H_b are enthalpies accounting for of all the species in the respective phase.

$$H_{b/e} = \sum_i^{n_{sp}} x_{i,b/e} H_i \tag{20}$$

H_i is the enthalpy of the i species including sensible heat and chemical energy, hence, taking into account the changes in temperature and chemical reaction. For the gas in the bubble phase, Eq. (18) expresses the change in enthalpy due to the net rate of heat transfer from the emulsion by convection (with coefficient h_{be}) and to the accompanying net flow ΔF_{ng}. In the emulsion, Eq. (20), the enthalpy changes by the net rate of heat transfer from the solid particles (by convection with coefficient h_{gs}), the bubbles (by convection with coefficient h_{be} and by the net flow) and by exchange with the surroundings (with the overall heat-transfer coefficient U_w). U_w contains three mechanisms of heat transfer in series: bed to wall (with film transfer coefficient h_{bw}), conduction through the solid insulation blanket and free convection caused by the environment (at T_{ext}). Correlations for h_{be}, h_{gs} and h_{bw} can be found in Kunii and Levenspiel (1991) and Souza-Santos (2004). Boundary conditions necessary for Eqs. (18) and (19) are simply formulated from the heat input with the gas and solids feed streams and are not explicitly written here. The boundary condition for the gas temperature above the distributor (h=0) is more complex and can be found in Souza-Santos (2004).

The heat balance for a particle of type m is:

$$\left(F H\right)_{m,in,B} - \left(F H\right)_{m,out,B} = A_B \int_o^{H_x} \left\{(1-\varepsilon_e)(1-\varepsilon_b)\sigma_m h_{gs,m}(T_{s,m} - T_e)\right\} dh \tag{21}$$

For the freeboard, the heat balance formulation is:

$$\frac{1}{A_F}\frac{d(F_F H_F)}{dh} = U_w(T_F - T_{ext}) \tag{22}$$

Eq. (22) considers the solids and the gas in the freeboard as one isothermal phase, similar to the mass conservation equation, Eq. (13), where solids and gas are lumped. As a result, the flow F_F and enthalpy H_F are

the sum of the heat contents of species in the gas and in the solids at height h. The boundary condition for Eq. (22) is obtained by flux and temperature coupled to the bottom bed model at $h=H_x$.

SOURCE TERMS

Figure 4 presents the main conversion processes in an FBG. A biomass particle undergoes a series of conversion processes: initial drying and devolatilisation, subsequent oxidation and reforming of volatiles, and gasification of char. Fuel and char particles are affected by fragmentation and attrition that take place together with chemical conversion. We review these processes and the way they have been treated in published models.

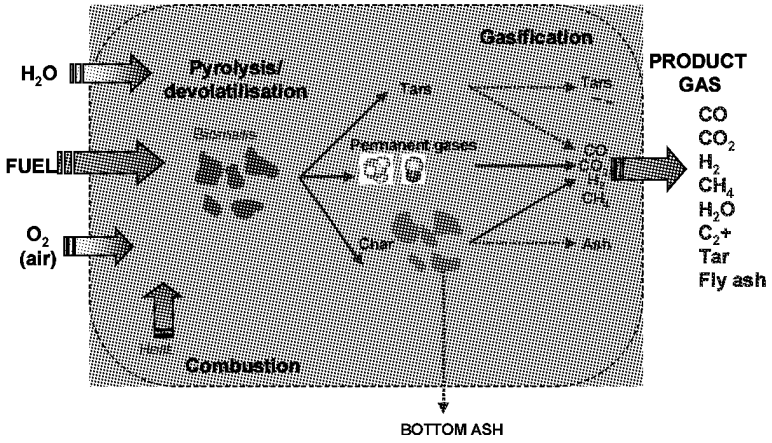

Fig. 4 The main conversion processes in an FBG

Mass and heat transport at particle scale in FBG

The rate of transport of heat and mass from the bulk gas (in the emulsion of an FB) to the surface of a particle is calculated from the outside gradient of gas at the particle's surface ($+s$)

$$\left.\frac{\partial\theta}{\partial X}\right|_{+s} = \mathrm{Nu} \qquad \text{and} \qquad \left.\frac{\partial C_i}{\partial X}\right|_{+s} = \mathrm{Sh} \tag{23}$$

where $X=x/x_o$, $\theta = (T-T_s)/(T_s-T_{g\infty})$ and $C_i = (c_i - c_{gi\infty})/(c_{si}-c_{gi\infty})$ are the dimensionless size, temperature, and concentration of species i. Nu and Sh are the Nusselt and Sherwood numbers defined as $\mathrm{Nu}= hx_o/\lambda_g$ and $\mathrm{Sh}=h_m x_o/D_{g,i}$. The temperature and concentration of the gas far from the particle are $T_{g\infty}$ and $c_{gi\infty}$ and at its surface T_s, and c_{si}. Heat and mass transfer coefficients (Nu and Sh) for a fuel particle in an FB of inert particles have been summarized by Leckner (2006).

Eq. (23) can be formulated as gradients of T and c_i at the internal face of the particle surface (-s),

$$\left.\frac{\partial\theta}{\partial X}\right|_{-s} = \mathrm{Bi_h} \qquad \left.\frac{\partial C_i}{\partial X}\right|_{-s} = \mathrm{Bi_m} \tag{24}$$

$\mathrm{Bi_h}$ and $\mathrm{Bi_m}$ are Biot moduli for heat and mass transport, defined as $\mathrm{Bi_h} = hx_o/\lambda_s$ and $\mathrm{Bi_m} = h_m x_o/D_{s,i}$. If $\mathrm{Bi_h}$ and $\mathrm{Bi_m}$ are $>>1$, the external mass and heat process are rapid enough not to limit the rate of supply of mass and heat to the particles. In this case $T_{g\infty}$ and $c_{gi\infty}$ equals T_s, and c_{si} and the rate is calculated by modelling the internal process in detail. When $\mathrm{Bi_h}$ and $\mathrm{Bi_m}$ are $<<1$, the opposite holds, the external rate of mass and heat transport determines the rate, so the accurate calculation of h and h_m is important. In the intermediate case, when $\mathrm{Bi_h}$ and $\mathrm{Bi_m}\approx 1$, both external and internal processes must be taken into account.

In FBG or FBC, devolatilisation of fuel particles is caused by thermal degradation and heat supply plays a fundamental role, whilst the transport of mass is of secondary importance. The essential external film coefficient to determine is then h. In contrast, transport of the gas component i in the emulsion into a char particle is the relevant process for gasification of char; in this case heat transfer plays a secondary role, since the thermal gradients at particle scale are smooth. Therefore, the external film coefficient to determine is h_m. Fuel particles are relatively large, so intraparticle diffusion is often the rate-limiting process for mass transfer. On the other hand, the conversion of fine char particles by gasification in an FBG is limited by both intraparticle and external mass transport.

Drying and devolatilisation

Extensive surveys on pyrolysis chemistry and its kinetics are available (Roberts, 1970; Agarwal and La

Nauze, 1989; Moghtaderi, 2006; Di Blasi, 2008). Several reaction schemes are formulated: one-step, or competing reactions, including secondary reactions (Di Blasi, 2008). Due to the complexity of reaction paths and generation of products the detailed kinetics are not yet clearly known. Experimental kinetic data vary widely, even for a given biomass such as wood, as realised early by Roberts (1970).

Pyle and Zaror (1984) classified the regimes of pyrolysis in terms of $Bi_h = hR/\lambda_s$ and an inverse Damköhler number that they called Pyrolysis number, Py, defined as the ratio of the rates of heat conduction in the particle and devolatilisation $Py=\lambda_s/(k_p R^2 \rho_s c_{ps})$. For thermally large particles, pyrolysis is controlled by internal heat conduction, $Bi_h>>1$ (say $Bi_h > 50$) and $Py<<1$ (say $Py < 10^{-3}$). A thin reaction zone (a char/wood front) penetrates into the virgin solid with a rate completely controlled by the internal heat transfer. When $Bi_h<< 1$ intra-particle gradients are negligible. This is the regime of thermally small particles; two extreme types of behaviour may occur in this situation depending on the product $Bi_h Py=h/(k_p R\ \rho_s c_{ps})$. On the one hand, for $Bi_h Py<< 1$ external heat transfer to the surface of a particle controls pyrolysis. In this case the devolatilisation kinetics is so fast that carbonisation is uniform throughout the particle. On the other hand, $Bi_h Py>>1$ corresponds to pure kinetic control. For intermediate values and when all parameters are large, a more complex description is necessary and all processes should be taken into account to describe the pyrolysis by formulation of advanced particle models (Chan et al., 1985; Miller and Bellan, 1997). In an FBBG fed with relatively large fuel particles, the situation is roughly $Bi_h > 20$ and $Py \approx 0.1$, so the situation is close to be controlled by internal heat conduction, although kinetics and heat transfer to the particles' surface still have some effect. When gasifying wet fuel particles, the devolatilisation times can be delayed significantly by the presence of water. In general, devolatilisation and drying occur sequentially for small particles and in parallel for larger particles. Several studies have established limits to quantify this. Various extreme regimes can be distinguished by another dimensionless number, the Drying number, Dr (Thunman et al., 2004).

The time of devolatilisation, including drying, is measured for the type of fuel and range of particle size of interest and evaluated by a correlation, containing two coefficients a_1 and a_2 together with the characteristic dimension d of the fuel particle, $t = a_1 d^{a2}$ (Ross et al., 2000; de Diego et al., 2003; Sreekanth et al., 2008). The constants have some physical meaning as can be seen from a derivation of the times for drying and devolatilisation of thermally small particles or thermally large particles. The first constant, a_1, is related to the specific fuel and the second constant, a_2, to the physical process. Theoretically, a_2 approaches unity if the process is limited by the thermal process. If the process is controlled by the kinetics of devolatilisation,, a_2 approaches zero. For thermally large particles a_2 approaches two. These numbers are approximate because other processes are also present, such as swelling or shrinkage of the particle, temperature dependence of the physical data, and convective flows within the fuel particle. However, according to empirical experience for most fuels in combustion or gasification devices, the constant a_2 ends up in the region of 1.5 to 2.

Particle models predicting theoretically the time of devolatilisation, the yields of char, gas and tar, are available (Chan et al., 1985; Miller and Bellan, 1997; Peters and Bruch, 2003; Sreekanth et al., 2008). In FBBG modelling, however, empirical correlations or experimental data are employed to characterise the devolatilisation step. This is probably because particle models are complex and time-consuming and need a great amount of input data, and because they do not predict the composition of the products released. Then, simplified approaches based on experimental information have been applied for modelling and simulation of FBBG, where the fractions of char, tar and gas (and the composition of main species in the gas) are estimated (Radmanesh et al., 2006; Souza-Santos, 1987, 1989, 2004). Sometimes prediction is made on the instantaneous yield of gas and its composition, but most cases estimate the final (accumulated) value of these quantities. Kinetic models and measurements are available for various biomasses, especially for woody biomasses (Hajaligol et al. (1982), Nunn et al. (1985), Boroson et al. (1989), Rath et al. (2002), Jand and Foscolo (2005)). Some FBBG models have assumed even simpler devolatilisation models, assuming that the gas is in equilibrium (Bilodeau et al. (1993)), an approach that does not seem to be realistic under FBG conditions. Other authors (Sadaka et al. 2002) developed empirical models to predict the composition of the gas released from the pyrolysis zone. These models are simple enough, but the empirical data selected to close the balances seem very case-specific. Thunman et al. (2001) formulated a lumped particle model with three adjustable empirical relations dedicated to both FB and fixed bed conditions.

Chemical conversion of char

The rate of char conversion in an FBG is influenced by a number of variables: char temperature, partial pressure of the reactants and the products, particle size, porosity, mineral content of the char, etc, some of which vary with time due to chemical conversion and attrition. Therefore, char reactivity depends on the parent fuel from which the char is obtained and on the form of preparation, especially the heating rate and peak temperature (Buekens and Schoeters, 1985).

To estimate char conversion in an FBG, three main aspects have to be taken into account: the intrinsic

reactivity of the char, the reactivity of a char particle of finite size and the distribution of char particles in the bed having different extent of conversion. The reactivity of a char sample at time t is defined as:

$$r_m = -\frac{1}{m_c}\frac{dm_c}{dt} = \frac{1}{(1-x_c)}\frac{dx_c}{dt} \tag{25}$$

By varying the concentration c of the reactant gas (O_2, H_2O, CO_2 or H_2) and the temperature T, the rate of the char–gas reaction is fitted against measurements by assuming a kinetic law, often of n_{th} order, $r_m=k_m c^n$, where k_m is a kinetic coefficient. The reactivity can also be defined per unit of reacting surface, $r_A=k_A c^n$. The rate coefficient k_A (as well as k_m) is related to temperature via an Arrhenius expression. To relate r_m and r_A, the total reacting surface area per unit of mass A_g is introduced, $r_m=A_g r_A$. A distinction is sometimes made between the internal (A_i) and external (A_e) areas of a particle, so that $A_g = A_i+A_e$. The change in reactivity during conversion is described by the variation of A_g, while k_A is assumed to depend on temperature and concentration only. A practical way to describe this effect is to relate A_g to a reference state of conversion ("0"), using a structural profile $f(X)$, $A_g = A_{g0} f(X)$.

Most char particles in an FBG have a macroscopic size, typically from 0.5 to 5 mm, so a model is required to obtain the overall reactivity of the particle $r_{v,p}$ from the intrinsic reactivity, taking into account the reactivity at position z within the char particle. For a spherical char particle of radius R, $r_{v,p}$ can be computed as:

$$r_{v,p} = \frac{3}{R^3}\int_0^{R(t)} r_v(t,z)z^2 dz = \frac{3\rho_{c0}A_{g0}}{R^3}\int_0^{R(t)} k_A c^n (1-X) f(X) z^2 dz \tag{26}$$

where the intrinsic reactivity used in Eq. (26) is expressed per unit of volume, that is $r_v=\rho_c r_m = \rho_c r_A A_g$. To obtain the local concentration $c(z,t)$, the temperature $T(z,t)$, and the conversion $X(z,t)$, the conservation equations for the gas species and temperature, together with the solid carbon balance have to be solved for the char particle including the boundary layer surrounding the particle.

According to the classical plot of r vs. $1/T$, various regimes (Regimes I, II, III) for conversion of char can be distinguished (Laurendeau, 1978). Representations of the conversion of char are shown in Fig. 5. A spherical particle has been assumed for simplicity. Case (a) is the uniform conversion model (UCM) where the reaction takes place throughout the char particle. This is Regime I when the rate of gasification of a single char particle can be calculated from the intrinsic reactivity evaluated for emulsion conditions $r_{v,p}=r_{v,e}$. In the surface reaction

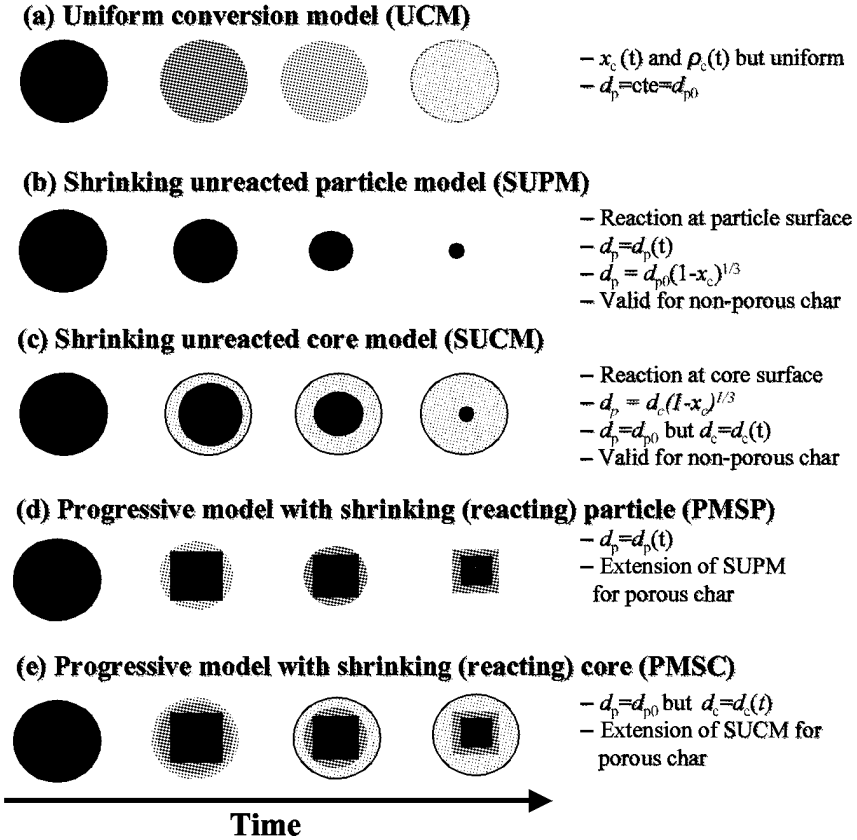

Fig. 5 Single char-particle conversion models

models (Cases (b) and (c), Regime III) the reaction takes place on the external surface of the particle. The useful kinetic coefficient is k_A, and there is no need for a complex description of the development of the internal area: the reaction surface is A_e. Two cases are distinguished according to the ash behaviour during conversion: the shrinking unreacted particle model (SUPM (Case (b)), where the ash formed peels off instantaneously, and the shrinking unreacted core model (SUCM, Case (c)), where the ash formed remains attached to the particle. Extension to porous chars can be handled with progressive models (PM) with shrinking particle (PMSP) and with shrinking core (PMSC), shown as Cases (d) and (e) in Fig 5. In these two models the reaction takes place in a reaction zone, which grows inwards during the progress of reaction. The difference between the two models is in the behaviour of the ash, which is removed in the case of the PMSP, whereas it is maintained in the PMSC.

The char in an FBBG is not much converted by oxygen because this is rapidly consumed by the volatile gases, and the contribution of combustion to the overall char conversion is small. The combustion of char is controlled by external diffusion (Regime III) and the reactivity of a particle is $r_{m,p}=A_e h_m \rho_e$. The reaction takes place in a very thin layer in the particle close to the external surface. Therefore, in char combustion sharp-interface reaction models are often adopted (Cases (b) and (c) in Fig. 5). This greatly simplifies the solution, since A_e can be directly correlated with the conversion x_c as indicated in Fig.5. A description of the internal surface and the pore development during conversion is not necessary in any of these cases. In contrast, during the reactions with CO_2 and H_2O, the reaction zone occupies most of the char particle, and the interior surface changes significantly (internal area and catalytic effects). The intermediate regime, Regime II, is most likely to occur during gasification. To handle this case, a model accounting for the local degree of carbon conversion, reaction area, gas concentration, and temperature is essential. A procedure to estimate the gasification of single char particles has been published by Gómez-Barea et al. (2007, 2008).

The calculation of the overall reactivity in the bed, $r_{m,B}$ has to take into account the distribution of char particles in the bed, each having the reactivity $r_{m,p}(x_c)$. Most FBG models assume that $r_{m,B}$ can be approximated by the reactivity evaluated at the average conversion in the bed, $x_{c,B}$. To assess this approximation, a factor Ω is introduced as $\Omega= r_{m,B}/ r_{m,p}(x_{c,B})$. Ω indicates the error made by using $x_{c,B}$ to evaluate $r_{m,p}$ instead of the actual one in the bed $r_{m,B}$.When $\Omega\sim1$, the distribution of conversion has a small impact on the average reactivity in the bed, and a population balance is not necessary. The simplification $\Omega\sim1$ has been investigated by Heesenk et al. (1994), Caram and Amundson (1978) and Gómez-Barea et al. (2008). In general, Ω depends on $(1-X)f(X)$ and η_p, the latter being an effectiveness factor accounting for the impact of diffusion and the change in porous structure on the reactivity. The effect of Ω, while applying a variety of $(1-X)f(X)$ expressions for char gasification, has been analysed by Gómez-Barea et al. (2008). The general conclusion is that a population balance is not necessary at low conversion, and so, it seems not to be necessary for the modelling of a hypothetical char combustion zone with a distribution of char particles. However, it may be necessary for the evaluation of the overall char gasification rate for some chars, if relatively high conversion is attained in the reactor.

Comminution of solid particles

Fuel size is reduced by shrinkage during devolatilisation, primary fragmentation, secondary and percolative fragmentation of char, and fines generation by abrasion. The attrition behaviour can be different from one fuel to another. It is difficult to infer attritability from fuel properties, so it has to be characterised by experiments (Chirone et al., 1991). Inclusion of attrition in the population mass-balances given above is rather complex, demanding detailed knowledge of the mass-flow rates from each particle-size class to all of the other classes of the actual fuel-particle size, i.e. models of the terms $\Gamma_{m,l}$ in Eq. (15). For inert material and catalysts, attrition can be characterised by abrasion, and the description of this mechanism has also to be considered.

Due to the complexity, the description of comminuition in general is out of the scope of this review. Here, a qualitative description is given of the key quantities, showing the essentials of attrition modelling and the type of input necessary for first estimates. The simplified treatment of FB combustion of coal char by Arena et al. (1995) and of biomass char by Scala et al. (2006) is extended to FB gasification. Primary fragmentation and particle shrinkage, considered to be instantaneous, affect the size distribution of char and reduce the average diameter. The relationship between the original fuel size, d_f and the average size of the fragments of char after devolatilisation, $d_{ch,0}$, can be formulated as $d_{ch,0}/d_f\approx (\varphi/n_1)^{1/3}$, φ being a shrinkage factor, defined as $\varphi=\rho_f Y_{ch}/\rho_{ch}$, and n_1 is the number of fragments after primary fragmentation (immediately after devolatilisation) (Scala et al., 2006). ρ_f and ρ_{ch} are the density of the initial fuel and that of the resulting char, and Y_{ch} is the fixed carbon fraction of the fuel. The average diameter of the char in the bed, $d_{ch,B}$., is assumed to be the result of two independent processes, one accounting for chemical reaction and the other for fragmentation by the approximate relation:

$$d_{ch,B} / d_f \approx \left(\varphi/(n_1 n_{2,m})\right)^{\frac{1}{3}} \sigma \quad (27)$$

σ is a factor that depends on the mode of combustion and $n_{2,m}=(1+n_2)/2$, n_2 being the number of fragments during secondary fragmentation experimentally determined (Scala et al., 2006). In the calculations, the change in size caused by generation of fines by attrition can be neglected because peripheral percolative fragmentation dominates rather than mechanical attrition during biomass char conversion in FBG. The fines generation is then neglected for the estimation of the char diameter in the bed, but the rate of conversion (Scala et al., 2006) is enhanced, and this is accounted for by an enhancement factor $(1+\alpha)$ that can be determined by measurements under the operating conditions of interest. σ in Eq. (27) should be estimated according to the mode of conversion of the particle by a simple solids population balance. For combustion according to the shrinking core model controlled by gas-film diffusion, σ ranges between 0.78 and 0.80 (Arena et al., 1995). For char conversion in gasification reactors, σ can vary more, depending of the reaction order and intraparticle mass transfer effects. To sum up, for the estimation of the average particle size in the bed, $d_{ch,B}$, one has to measure n_1, n_2, φ. It is expected that n_1 and φ do not change from combustion to gasification due to the difficulty of oxygen to penetrate the front created by volatiles during devolatilisation. In contrast, $n_{2,m}$, can be different under oxidising conditions due to the possible enhancement of fragmentation and attrition by oxygen.

Kinetics of homogeneous reactions

Homogeneous combustion of volatile species (HVC) and the water-gas-shift reaction (WGSR) may have a great impact on the outlet gas composition, carbon conversion and gasification efficiency. On the one hand, HVC determines the behaviour in the so called flaming pyrolysis zone, a high temperature zone where the biomass is rapidly devolatilised and oxidised, yielding char and volatiles (light gases and tars). On the other hand, the WGSR together with the heterogeneous conversion of char with CO_2 and H_2O determine the final gas composition and carbon conversion. Therefore, both HVC and WGSR are key steps in biomass conversion that should be properly modelled. The rate of HVC has a strong impact on FBG of high-volatile fuels, such as low-rank coals and biomasses and wastes (Yan and Zhang, 1999).

One could imagine that the reaction rate and the kinetics of the homogeneous reactions are well known, but this is not the case. The reactions between the stable chemical species involved in the homogeneous reactions are a complex combination of several elementary reactions, so they have been determined experimentally. However, there is a great variation between the expressions for the same reaction, and therefore a preliminary screening of the various kinetics of the HVC is needed in the modelling of FBBG, especially the oxidation of CO and H_2. No publication has been found that assesses the effect of this choice of kinetics on the final performance of the FBBG. The uncertainty in the choice of the WGSR kinetics is of less concern than those of the HVC. Other homogeneous reactions, such as (non-catalytic) steam reforming of methane are slow under normal conditions in FBBG and the choice of kinetics seems to play a minor role. Other homogeneous reactions involving tar species are discussed below.

Conversion of tar

Tar is a large number of hydrocarbon species, usually heavier than benzene, whose properties differ widely among each other. Operational factors like the ratios of air/oxygen, steam/biomass, catalyst/biomass, and design details like bed and freeboard height, have major effects on the amount and composition of the tar compounds (Kinoshita et al., 1994; Milne et al., 1998; Brage et al., 2000). Other design data, such as point of introduction of fuel, staging of the gasification agent (for instance secondary injection), determine the effective contact time of the tar in the various zones of the FB and, thus, the final composition of the tar (Devi et al., 2002). Gómez-Barea and Leckner (2009) have summarised ways to determine the tar composition and concentration by modelling. Despite the great effort made to understand the reaction mechanisms of tar compounds, the complexity of the process makes it difficult to develop comprehensive models, and the tar conversion models are still quite empirical. To date it has not been possible to predict the composition of tar in the outlet gas. Only quantitative estimates of the overall tar concentration have been reasonably well achieved.

In practical operation of FBBG, the conversion of tar with oxygen is limited because tar competes with light gases and char for the oxygen, and the light gases are more reactive than tar. Then, in FBBG operation without catalysts in the bed, depending on temperature, thermal cracking partially converts the tar in the reactor. The kinetics reported in literature for thermal cracking vary widely, and the selection of kinetics is critical. With a catalyst present, the catalytic reactions are usually more rapid than thermal cracking, so a correct prediction of tar in the outlet gas is likely to depend on the accurate choice of the catalytic kinetics. The selection of kinetics for thermal cracking should not be essential in such a case. When diffusion effects within the catalyst particles are rate-controlling, detailed description of the heterogeneous model process at a particle level, i.e. a particle model, could be critical. In both cases, the kinetics, the type of biomass, and the conditions for which the

experimental data have been obtained, should be carefully analysed. The overall conclusion is the same as for homogeneous reactions: in developing and validation of reaction models, it is not enough to report the assumptions made and the kinetic expression used. All reactor models taking "external" kinetics or kinetics that have been obtained under conditions differing from those of the FBBG to be modelled, should include a sensitivity analysis to elucidate the degree of uncertainty in the tar concentration of the outlet gas. This is lacking in all FBBG models published up to date. A great deal of work is still needed in this area.

REVIEW OF LITERATURE FBBG MODELS

A detailed review of some selected FM of FBBG (Nikoo et al. (2008), Ramanadesh et al. (2006), Sadaka et al. (2002), Fiaschi and Michelini (2001), Bilodeau et al. (1993), Jiang and Morey (1992), van den Aarsen (1985) and Raman et al. (1981) for BFBBG and Corella and Sanz (2005), Petersen and Werther (2005), Liu and Gibbs (2003) and Jennen et al. (1999) for CFBBG), published up to date has been presented by Gómez-Barea and Leckner (2009). Based on that survey the sophistication and the hypotheses made by modellers can be assessed to provide an idea on the ability to predict measurements: (1) Most models are one dimensional and steady state, and the fluid-dynamics are based on the two-pase theory of fluidisation with some modifications. (2) The freeboard is not modelled in many BFBG models, but for CFBBG it is taken into account. (3) A common assumption is instantaneous devolatilisation of the fuel. The composition of volatile species is not clearly reported by some authors. In some cases correlations are used from other biomass materials or even from coal. (4) A majority of modellers have not paid sufficient attention to char conversion, neglecting the effects of mass transfer in the particle, the change in reactivity during char gasification, and the distribution of conversion in the bed. (5) Fragmentation and attrition of fuel and char have only been treated in one model. (6) Tar conversion is not usually modelled or modelled as one or two lumped species reacting by oxidation, thermal cracking or reforming with H_2O. (7) The effect of in-bed catalysts has been modelled by some authors, but not in a comprehensive way. (8) Most experiments are only validated by the temperature and composition of the outlet gas stream. (9) In general, models predict the main gaseous species reasonably well. However, only a few test runs (sometimes only one) have been used for validation. (10) All models have been validated in lab-scale FBs, where the fluid-dynamics can differ from full-scale gasifiers. Many fluid-dynamic correlations are taken from studies involving Geldart A particles (mainly from FCC catalyst) and can differ greatly from what is valid for Geldart B particles, normally employed in FB gasifiers. (11) In almost all models a valuable sensitivity analysis is made to study the effect of some variables. (12) Most models are learning models according to the classification of van Swaaij (1985). Development design-models are more rarely dealt with. The only model of this kind is the one of Petersen and Werther (2005). It is also possible that the model of Corella and Sanz (2005) could be used for design purposes, but the published details are not sufficient to assess this ability. The models of Hamel (2001) (HM) and Souza-Santos (1987, 1989, 2004, 2007, 2008a, 2008b) (SSM) have been developed in a general way and seem to be the most advanced FM developed up to date, although details of these models still need improvements (Gómez-Barea and Leckner, 2009).

From the data and analysis presented, the following main conclusions are outlined: (1) Pyrolysis or devolatilisation is a key step, affecting greatly the model results. To support a reliable model, measurements of the gas composition and yield of pyrolysis in laboratory scale at high heating rates with the biomass of interest are required, if such results are not available in literature. (2) Char and tar conversion are the processes whose modelling is least satisfactory. A great research effort is still needed to improve the tar chemistry. Char conversion chemistry is well known for biomass and coals, but published reactor models do not deal with this information: char conversion should be modelled in a more rigorous way. (3) Validation has not been sufficiently detailed. There are still uncertainties about the model structure. There is no validation against commercial-scale equipment. (4) The SSM and HM are the most advanced models published up to date for simulation. In the case of SSM, the modelling of CFBBG is still uncertain and further details should be reported. The HM seems to be valid for both BFBBG and CFBBG, especially for coal. (5) The reliability of these models for simulation of large-scale FBGs is as valid as the semi-empirical correlations used for the development of the fluid-dynamics.

CONCLUSIONS

The most relevant phenomena to be considered in modelling of FBBG were reviewed, including fluid-dynamics and chemical conversion processes. The fields where further research is needed were identified. Devolatilisation and conversion of tar and char are the processes that still require major modelling efforts. The survey of published mathematical reactor models for biomass and waste gasification in FB shows that most FBBG models fit reasonably well selected experiments, but there are few measurements available for detailed

comparison with the models. Validation of models with full-scale FBBG units is necessary. In addition, the scaling-up of results obtained in laboratory FBG to large-scale units and the consideration in the models of the specific characteristics of waste and biomass fuels have to be addressed in future models.

NOTATIONS

A	area, m^2
$A_{g/e/i}$	total/ext./intern. area density, $m^2\ kg^{-1}$
a_b	area to volume ratio in a bubble, m^{-1}
a	decay constant due to clustering flow, –
$Bi_{h/m}$	Biot modulus for heat and mass transport,
D	diffusivity or dispersion coeff., $m^2 s^{-1}$
d	diameter, m
d_b	bubble size, m
d_p	solid particle size, m
Da	Damköhler number, –
c	gas concentration, $kg\ m^{-3}$
C	dimensionless concentration, –
F	mass flow rate, $kg\ s^{-1}$
f_{bex}	bed expansion factor, –
f	structural profile,-
g	acceleration of gravity, $m\ s^{-2}$
G	mass flux, $kg\ m^{-2}\ s^{-1}$
H	riser height, m, specific enthalpy, $kJ\ kg^{-1}$
H_x	height of the bed surface, m
H_i	enthalpy of species i, $kJ\ kg^{-1}$
h	vertical coordinate along the riser, m
h	gas-solid heat transfer coeff., $Wm^{-2}\ s^{-1}$
h_m	gas-solid mass transfer coeff., $m\ s^{-1}$
h_{be}	bubble-emulsion heat coeff., $W\ m^{-2}\ s^{-1}$
h_{bw}	bed to wall heat transfer coeff., $W\ m^{-2}\ s^{-1}$
k_{be}	bubble-emulsion mass transfer coeff., s^{-1}
k_b	back-flow ratio, –
k	kinetics coefficient, (various units)
K	decay constant due to transport flow, –
m	mass
MM	molecular mass, $kg\ kmol^{-1}$
Nu	Nusselt number, Nu= hx_o/λ_g, –
n_{ggr}	number of gas-gas reactions
n_{rchar}	number of gas-char reactions
n_{fs}	number of fed streams
n_{ws}	number of withdrawal streams
n_{sp}	number of species
p	pressure, Pa
Py	Pyrolysis number, Py= $\lambda_s/(\rho c_p x_o^2 k_{pyr})$, –
Q_{loss}	heat loss rate, kJ s^{-1}
R	rate of reaction, $kg\ m^{-3}\ s^{-1}$
$R_{j,i}$	reaction rate of sp. i in reac. j, $kg\ m^{-3}\ s^{-1}$
r_m	char reactivity per unit mass, $kg\ s^{-1} kg^{-1}$
r_A	char reactivity per unit area, $kg\ s^{-1} m^{-2}$
r_v	char reactivity per unit volume, $kg\ s^{-1} m^{-3}$
Sh	Sherwood number, Sh=$h_m x_o/D_{g,i}$, –
t	time, s
T	temperature, K
U	fluidisation velocity, gas velocity, $m\ s^{-1}$
U	dimensionless velocity, –
U_w	bed-wall heat transfer coeff., $W\ m^{-2}\ s^{-1}$
V	volume, m^3
x_0	characteristic length, m
X	dimensionless distance, local conversion
x_c	conversion, total, X local, –
x	mass fraction, $kg\ kg^{-1}$
Y_{ch}	fixed carbon in the fuel, $kg\ kg^{-1}$
z	position in a particle

Greek letters

$\Gamma_{m,loss}$	attrition loss of m,l-class particle, $kg\ s^{-1}$
$\Gamma_{m,gain}$	attrition gain of m,l-class particle, $kg\ s^{-1}$
ΔF_{ng}	emulsion->bubble net gas flow, $kg\ m^{-3} s^{-1}$
$\Delta F_{ng,i}$	emulsion->bubble i-gas flow, $kg\ m^{-3}\ s^{-1}$
ε	volume concentration or porosity, $m^3\ m^{-3}$
φ	shrinking factor, –
$\nu_{i,j}$	stoichiometric coeff. i species, reaction j
Ω	factor to asses the distribution of conversion of char in the bed, –
ρ	mass concentration or density, $kg\ m^{-3}$
σ_m	volume fraction of solid m, $m^3\ m^{-3}$
$\Re_{m,l}$	reaction rate of m,l-particle, $kg\ m^{-3} s^{-1}$
θ	dimensionless temperature,–

Subscripts

A	area
b	bubble, back-flow
br	rising bubble
B	bed (bottom bed)
c	core
dev	devolatilisation
e	emulsion, effective, external
ext	external or exterior
ent	entrainment
F	freeboard
g	gas, total area
gg	gas-gas reaction
gs	gas-solid reaction
h	horizontal or radial
in	inlet, entering the system
i	type of gas, internal
l	size level of a PSD
m	type of solid, mass
mf	minimum fluidisation
o	at the top of the riser (out) (h=H_x)
out	outlet, leaving the system
pyr	pyrolysis
rec	recycling stream
s	solid
v	vertical or axial, visible (applied to velocity and flow), volatile matter, volume
t	terminal (applied to velocity)
T	total
x	at bed surface

0 superficial, initial, inlet
w wall
∞ gas bulk condition

Some abbreviations

CFB circulating fluidised bed
BFB bubbling fluidised bed
FB fluidised bed
FBG fluidised bed gasifier/gasification
FBBG fluidised bed biomass gasifier
FM fluidisation model
PSD particle size distribution

REFERENCES

Agarwal, P.K., La Nauze R.D.: Chem. Eng. Res. Des. 67 (1989), pp. 457–480.
Arena U., Chirone R., D'Amore M., Miccio M., Salatino P.: Powder Technol. 82 (1995), pp. 301–316.
Babu P., Shah B., Talwalker, A.: AIChE Symp. Series (1978), pp. 176–186.
Bilodeau, J.F., Thérien, N., Proulx, P., et al..: Canadian J. Chem. Engn. 71 (1993), pp. 549–577.
Boroson, M.L., Howard, J.B., Longwell, J.P., Peters, W.A.: AIChE J. 35 (1989), pp. 120–128.
Brage, C., Yu, Q., Chen, G., Sjöström, K.: Biomass and Bioenergy 18 (2000), pp. 87–91.
Buekens, A.G., Schoeters, J.G., in: R.P. Overend, T.A. Milne and K.L. Mudge, Eds, Fundamentals of Thermochemical Biomass Conversion, Elsevier Applied Science Publishers, London (1985), pp.619–689.
Caram, H. S., Amundson, N. R.: Ind. Eng. Chem. Proc. Des. Dev. 18 (1978), pp. 96–102.
Chan, W.-C., Kelbon, M., Krieger B.B.: Fuel 64 (1985), pp. 1505–1513.
Chirone, R., Massimilla, L., Salatino P.: Prog. Energy Combust. Sci. 17 (1991), pp. 297–326.
Corella, J., Sanz, A.; Fuel Processing Technology 86 (2005), pp. 1021–1053.
Cortés, C., Gil, A.: Progress in Energy and Combustion Science 33 (2007), pp. 409–452.
Davidson, J.F., Harrison, D.: Fluidised particles. Cambridge, 1963.
de Diego, L.F., García-Labiano, F., Abad, A., Gayán, P., Adánez, J.: Energy Fuels 17 (2003), pp. 285–290.
Devi, L., Ptasinski, K.J., Janssen, F. J. G.: Biomass & Bioenergy (2002), pp. 125–140.
Di Blasi, C.: Progress in Energy and Combustion Science 34 (2008), pp. 47–90.
Eaton, A.M., Smoot, L.D., Hill, S.C., Eatough, C.N.: Prog. Energy Combust. Sci. 25 (1999), pp. 387–436
Fiaschi, D., Michelini, M.: Biomass & Bioenergy 21 (2001), pp. 121–132.
Gómez-Barea, A., Ollero, P., Leckner, B.: Chem. Eng. Sci. 62 (2007), pp. 1477–1493.
Gómez-Barea, A., Leckner, B., Santana, D., Ollero, P.: Chem. Eng. Journ. 141 (2008), pp. 151–168.
Gómez-Barea, A., Leckner, B.: To be published (2009).
Gururajan, V.S., Agarwal, P.K., Agnew, J.B.: Trans IChemE, 70 (1992), pp. 211–238.
Hajaligol, M.R., Howard, J., Longwell, J.P. et al.: Ind. Eng. Chem. Proc. Des. Dev. 21 (1982), pp. 457–465.
Hamel, S.: Ph.D. Dissertation, Universität Siegen, 2001.
Hannes, J. P.: PhD. Thesis, RWTH Aachen, 1996.
Heesink, A.B.M., Klaus J., van Swaaij W.P.M.: Chem. Eng. Sci. 49 (1994), pp. 2243–2261.
Jand, N., Foscolo, P.H.: Ind. Engn. Chem. Res. 44 (2005), pp. 5079–5089.
Jennen, T., Hiller, R., Köneke, D., Weinspach, P.M.: Chem. Engn. Techn. 22 (1999), pp. 822–826.
Jiang, H., Morey, R. V.: Biomass and Bioenergy 3 (1992), pp. 431–447.
Johansson, A., Johnsson, F., Leckner, B.: Chem. Engng. Sc. 62 (2007), pp. 561–573
Johnsson, F., Zhang, W., Leckner, B., Proc.2nd Int. Conf. on Multiphase Flow, 1995. pp. 25–32.
Kinoshita, C.M., Wang, Y., Zhou, J.: Journal of Analytical and Applied Pyrolysis 29 (1994), pp. 169–181.
Kunii, D., Levenspiel, O.: Fluidization engineering, 2nd ed. Elsevier, Amsterdam, 1991.
Kurkela, E., Ståhlberg, P. Fuel Process. Technol. 31 (1992), pp. 1–21
La Nauze R.D.: Chem Eng Res Des 63 (1985), pp. 3–33.
Laurendeau, N.M.: Prog. Energy Combust. Sci. 4 (1978), pp. 221–270.
Leckner, B.: Heat and mass transfer in fluidized bed, Chapter 5.2 in: Crowe C. (Ed.), Multiphase flow handbook. CRC Press; ISBN 0-8493-1280-9, 2006.
Leith, J. and Metha, D: Atmospheric Environment 7 (1973), pp. 527–549.
Liu, H., Gibbs, B.M., Fuel 82 (2003), pp.1591–1604.
Miller, R.S., Bellan, J. Combust. Sci. and Tech. 126 (1997), pp. 97–137.
Milne, T.A., Evans, R.J., Abatzoglou, N.: NREL/TP-570-25357, 1998.
Moghtaderi, B.: Fire and Materials, 30 (2006), pp. 1–34.
Moreea-Taha, R.: IEA Greenhouse Gas R&D Programme: UK, 2000.
Newstov, D.A., Zabaniotou, A: Chem. Eng. J. 143 (2008), pp. 10–31.
Nikoo, M.B., Mahinpey, N.: Biomass and Bioenergy 32 (2008) , pp. 1245–1254.
Nunn, T.R., Howard, J.B., Longwell, J.P. et al.: Ind. Eng. Chem. Proc. Des. Dev. 24 (1985), pp. 836–844.
Oka S.O., Fluidised Bed Combustion, Marcel Dekker, New York, 2004.
Pallarès, D., Johnsson, F.: Prog. Energy Comb. Sci. 32 (2006), pp. 539–569.
Peters, B. and Bruch, C.: J Anal. Appl. Pyrol, 70 (2003), pp. 233–250.
Petersen, I., Werther, J.: Chemical Engineering and Processing 44 (2005), pp. 717–736.
Pyle, D.L., Zaror, C.A.: Chem Eng Sci. 39 (1984), pp. 147–158.
Radmanesh, R., Chaouki, J., Guy, C.: AIChE J., 52 (2006), pp. 4258–4272.
Raman, P., Walawender, W.P., Fan, L.T. et al.: Ind. Eng. Chem. Proc. Des. Dev. 20 (1981), pp. 686–692.
Rath, J., Steiner, G., Wolfinger, M.G. and Staudinger, G.: J. Anal. Appl. Pyrol. 62 (2002), pp. 83–92.

Ravelli, S., Perdichizzi, A., Barigom, G.: Progr. Energy and Comb. Sci. 34 (2008), pp. 224–253.
Roberts, A.F.: Combustion and Flame 14 (1970), pp. 261–272.
Ross, D.P., Heidenreich, C.A., Zhang, D.K.: Fuel 79 (2000), pp. 873–883.
Ross, D.P., Yan, H.M., Zhong, Z., Zhang, D.K.: Fuel 84 (2005), 1469–1481.
Sadaka, S.S., Ghaly, A.E., Sabbah, M.A.: Biomass & Bioenergy 22 (2002), pp. 439–462.
Scala, F., Chirone, R., Salatino, P.: Energy and Fuels 20 (2006), pp. 91–102.
Sit, S.P. and Grace, J.R.: Chem Eng Sci 36 (1981), pp. 327–335
Souza Santos, M. L.: Fuel 68 (1989), pp. 1507–1521.
Souza-Santos, M. L.: PhD Thesis, University of Heffield, UK, 1987.
Souza-Santos, M. L.: Solid Fuels Combustion and Gasification, Marcel Dekker, New York, 2004.
Souza-Santos, M.L.: Fuel (in Press, 2008a)
Souza-Santos, M.L.: The Open Chemical Engineering Journal 2 (2008b), pp. 106–118.
Souza-Santos, M.L.: Fuel 86 (2007), pp. 1684–1709.
Sreekanth, M., Sudhakar, D.R., Prasad, B.V.S.S.S., et al.: Fuel Proc. Technology 89 (2008), pp. 838–850.
Thunman, H., Davidsson, K. Leckner, B.: Combustion and Flame 137 (2004), pp. 242–250.
Thunman, H., Niklasson, F., Johnsson, F., Leckner, B.: Energy & Fuels 15 (2001), pp. 1488–1497.
van den Aarsen, F.G.: Ph.D. Dissertation, Twente University Publication, University of Twente, 1985.
van Swaaij W.P.M. in: J.F. Davidson et al. (Eds.), Fluidization, 2nd Ed., AP, London, 1985, pp. 595–629.
Yan, H.M., Heidenreich, C., Zhang, D.K.: Fuel 77 (1997), pp. 1067–1079.
Yan, H.M., Heidenreich, C., Zhang, D.K.: Fuel 78 (1999), pp. 1027–1047.
Yan, H.M., Zhang, D.K.: Chemical Engineering and Processing 39 (1999), pp. 229–237.
Yates, J.G.: Fundamentals of Fluidized-bed Chemical Processes, Butterworths. London, 1983
Zhang, R., Basu, P.: Powder Technology 147 (2004), pp. 86–93.

POTENTIALS OF BIOMASS CO-COMBUSTION IN COAL-FIRED BOILERS

J. Werther

Institute of Solids Process Engineering and Particle Technology
Hamburg University of Technology
D 21071 Hamburg, Germany

Abstract: The present work provides a survey on the potentials of co-combustion of biomass and biogenic wastes in large-scale coal-fired power plants. This allows an energetic utilization at a high level of efficiency which is not obtainable in small-scale dedicated biomass combustors. Co-firing at low percentages of the thermal power (typically below 5-10 %) avoids the characteristic operating problems of biomass combustion, i.e. ash sintering and fouling of heat transfer surfaces. Co-firing of biogenic wastes is already widely practiced in Germany, non-waste biomass like forest residues are for subsidy reasons combusted in small dedicated mono-combustion plants. A future increase of co-combustion may be associated with the upgrading of biogenic wastes with high water content to biofuels by drying. Such biofuels could substitute more expensive coal and save on CO_2 emission certificates. In the more distant future biomass co-combustion may help in the CO_2 scrubbing process by lowering the target level of CO_2 absorption efficiency.
Keywords: biomass, co-combustion, large boilers, biofuel

INTRODUCTION

In March 2007 the European Union (EU) summit endorsed the Commission's Renewable Energy Roadmap which sets a binding target of increasing the level of renewable energy in the EU's overall mix from below 7 % today to 20 % of the primary energy consumption in 2020[1]. In January 2008 the Commission presented a proposal for a directive to reach this target. The proposal is now forwarded to the EU Council and Parliament for approval. First half of 2009 is the target date for the adoption of the legislation and March 31, 2010 is the deadline for the EU member states to present National Action Plans (NAPs) on renewables. These are ambitious goals which will certainly undergo modification when the bargaining of the member countries starts.

In Germany the Government's goal is to increase the share of renewables in the electricity consumption to 12.5% by 2010 and to 20 % by 2020[2]. For 2007 a recent communication by the German Ministry of Environment[3] states that the share of renewables in the primary energy consumption was 6.7 %. Usage of renewable energies was reported to have avoided a CO_2-emission of 115 million tons in 2007[3]. The biggest contribution to primary energy supply was from solid biofuels which accounted for 34.6 % of the renewables' share.

These figures indicate that there is a strong political will to achieve a sustainable energy supply via renewable energies among which the energy from biomass plays a dominant role. Behind the term biomass is hidden a multitude of materials which can be converted to energy in a multitude of different ways. Fig. 1 which was taken from a book by Kaltschmitt et al.[4] gives a good illustration of this variety. Not all of these technological options are economically feasible. Moreover recent political developments have shown that the bioenergy pathway starting from energy crops is highly questionable because of its unavoidable collision with food production. Therefore, in the following energy crops and their energetic usage will not be discussed.

The present work is devoted to the very traditional combustion route, however, in a special application, namely the co-combustion with coal in large-scale power stations. The term "large scale" means here the range of power stations operated nowadays by utility companies, starting with the 100 MW thermal circulating fluidized bed boiler operated by a local utility for heat and power cogeneration and going up to the huge 1000 MW electric pulverized coal boiler. In the following the incentives for co-combustion of biomass with coal in large-scale power stations will be discussed first. Then, after examining the potential of biomass for co-combustion the characteristics of different types of biomass as fuels will be highlighted before mono-combustion vs. co-combustion will be treated.

Since the technologies for the energetic usage of biomass are largely dependent on political boundary conditions given by laws and subsidies the following work is focused on applications in Europe and more specifically, in Germany.

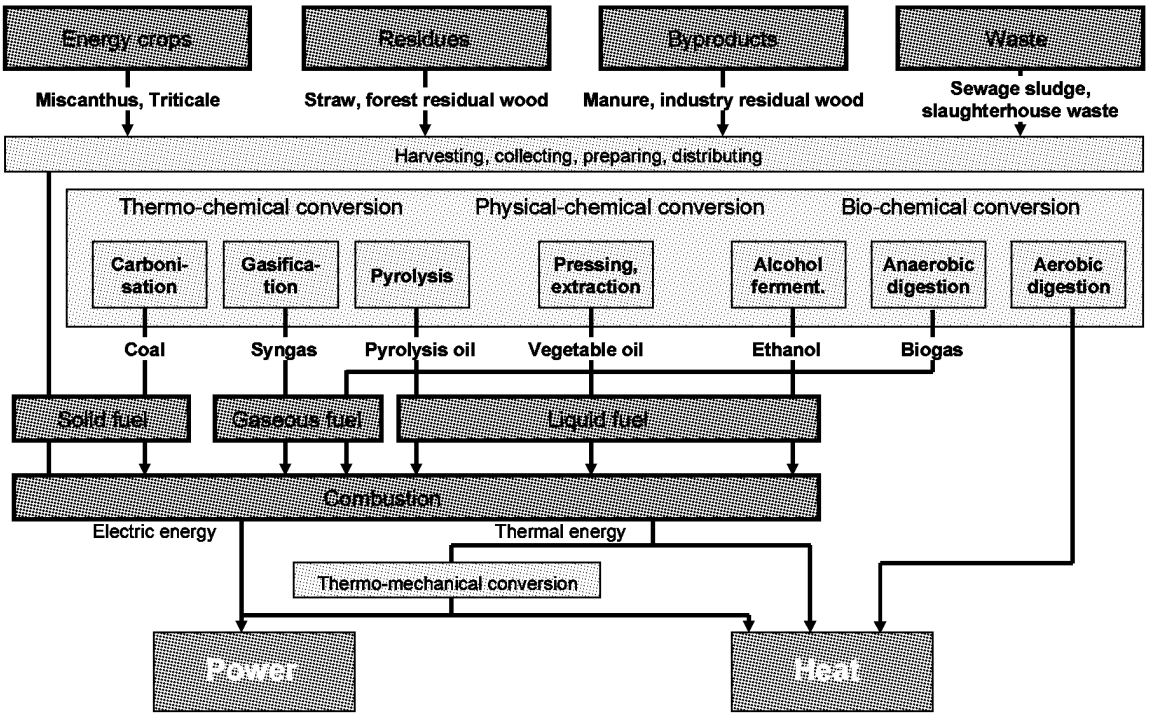

Fig. 1 Possibilities of energy provision from biomass (after[4])

INCENTIVES FOR CO-COMBUSTION

In 1997 the electricity market in Germany was liberalized by law. The former monopolistic structure with each utility being in charge for a well-defined supply area was suddenly no longer existing and competition started. As a consequence the interest of utilities to generate additional income or to lower the electricity generating costs increased drastically. Therefore, there is a strong incentive for using cheap fuels now which can substitute at least partially the base fuel coal. The best fuels in this sense are those which are available at negative costs, i.e. wastes which are taken for disposal. This economical incentive for co-combustion is still getting stronger because the price of coal is steadily increasing. For example, Basler[5] recently reported an increase of the coal price of over 70 % from 1999 to 2006. A further jump by a factor of nearly 2 has occurred in 2007 following the increase in oil prices.

The second incentive to use biomass for co-combustion is, of course, the sustainability aspect: recently generated C substitutes fossil C. The monetary side of this aspect is that the substitution of coal will reduce the number of CO_2-emission certificates which are required to operate the plant.

A third incentive is the plant efficiency. The large-scale coal-fired power stations have electrical efficiencies up to 40-44 % whereas the usually much smaller mono-combustion plants have efficiencies of at most 30 %. In this way by co-combustion significantly more electricity can be generated from a given amount of biomass.

Some biomasses like straw, for example, are available seasonally only. The advantage of co-combustion in the case of non-availability of the biomass is that switching back to the base fuel is easily possible.

A fourth incentive is the well-known economy of scale. The specific investment costs as well as the operating costs decrease with increasing size which is an economic advantage of co-combustion in a large boiler compared with mono-combustion in a small plant.

At present, it has to be admitted that it is mainly the first incentive of getting a cheap fuel which has prompted utilities to go into the business of co-combustion which in practice mostly means the co-combustion of waste materials[6].

POTENTIALS OF BIOMASS FOR CO-COMBUSTION

As has been stated above, energy crops will not be taken into account because of the risk of collisions with food production and it being unclear to what extent arable land is available. This leaves the biogenic waste material as the main resource of biomass for co-combustion.

Table 1 gives a summary of the different biogenic residues and wastes which in principle are available for co-combustion. A distinction is made between the theoretical potential and the technical one which considers

that it is not economically feasible to collect all the waste which is theoretically available. For example the usability of wood residues from forests depends on their accessibility. Furthermore there are ecological limits for the usage of agricultural residues. For a sustainable agricultural production it is considered to be necessary to leave up to 80 % of the straw on the field in order to keep the quality of the soil [9]. We see from Table 1 that the technical potential of biogenic residues and wastes is considerable.

Table 1 Theoretical and technical-ecological potentials of biogenic residues and wastes in Germany (after [7,8])

	Theoretical potential 10^6 t d.m./a	**Technical potential 10^6 t d.m./a**
Residues from forestry, timber and paper industry (sawdust, bark, waste wood, paper, paper sludge, forestry residues)	45.6	42
Agricultural residues (straw and other harvesting wastes, liquid manure)	66.7	32.7
Residues from flaying (abattoir refuse, meat and bone meal)	0.9	0.9
Residues from food industry (laitance, blackstrap molasses)	1.5	1.5
Waste industry (waste textiles, biogenic wastes)	6.0	5.7
Waste water treatment (sewage sludge)	2.3	2.2
Total	123	85

It is interesting to compare these figures with the annual consumption of coal in Germany. In 1996 189 million tons of lignite and 74 million tons of bituminous coals were consumed in power stations[10]. Comparing the total number of 263 million tons of coal with the technical potential of 85 million tons dry matter of biomass and considering the significantly higher heating value of the coals clearly shows that there is considerable space for co-combustion. In summary, there are both strong incentives and possibilities for co-combustion of biomass in coal-fired power stations.

CHARACTERISTICS OF BIOMASS AS FUELS

Characteristics of biomass as fuels are compared in Table 2 with those of coals. We see that the heating values are generally lower but of the same order of magnitude as for coals. Significant differences are observed in the content of volatiles: biofuels have higher volatiles contents, typically around 80 % based on the water-and-ash-free matter. Significant differences are also obvious with regard to the ash content: wood has a very low ash content whereas sewage sludge has an ash content in the water-free matter of around 50 %.

Table 2 Biomasses as fuels in comparison with coals (after [11], data for sewage sludge [12] and [13])

Fuel	**Lower calorific value MJ/kgwf***	**Ash content %wf***	**Volatiles %wf***	**Water content %raw**
Bituminous coal	29.7	8.3	34.7	5.1
Lignite	20.6	5.1	52.1	50.4
Spruce wood	18.8	0.6	82.9	10-65
Wheat straw	17.2	5.7	77.0	16
Sunflower straw	15.8	12.2	72.7	16
Miscanthus	17.6	3.9	77.6	
Digested sewage sludge				
- dried	14.6	51.0	45.4	13
- mechanically dewatered	13.5	51.8	44.4	76

* water-free substance

Table 3 gives elemental analyses of different biomass and coals and Table 4 provides further insight into the composition of ashes. Biomass is generally characterized by a lower content of carbon and a higher content of oxygen. The sulphur content is generally low with the exception of sewage sludge where the higher content is due to the dosage of S containing compounds in the sewage water treatment process. Striking are the low ash softening points of straw and miscanthus which may cause serious problems in the combustion process. These are generally attributed to the high content of alkalis, particularly potassium. Considerable progress has been

made in recent years in the understanding of the complex phenomena of bed sintering, superheater fouling and high temperature corrosion[14].

Table 3 Elemental analysis of biomass and coals (after [11], data for sewage sludge from [12])

Fuel	C	H	O	N	S	K	Ca	P	Cl	Ash softening point
	%wf*					%wf*				°C
Bituminous coal	72.5	5.6	11.1	1.3	0.94				<0,13	1250
Lignite	65.9	4.9	23.0	0.7	0.39				<0,1	1050
Spruce wood	49.8	6.3	43.2	0.13	0.015	0.13	0.70	0.03	0.005	1426
Wheat straw	45.6	5.8	42.4	0.48	0.082	1.01	0.31	0.10	0.19	998
Sunflower straw	42.5	5.1	39.1	1.11	0.15	5.00	1.90	0.20	0.81	839
Miscanthus	47.5	6.2	41.7	0.73	0.15	0.72	0.16	0.07	0.22	973
Digested sewage sludge	30.4	3.7	18.8	3.7	1.8					1200 (HT)**

*water-free substance, ** hemisphere temperature

Table 4 Elemental analysis of the laboratory ash (from [14], Abo Akademi data; the numbers give weight per cent of the elements expressed as their most common oxides)

Fuel	SiO_2	Al_2O_3	Fe_2O_3	TiO_2	MnO	$CaCO_3$	MgO	P_2O_5	Na_2O	K_2O	SUM, %
Forest residue	36.75	5.81	1.91	0.22	1.46	37.14	2.93	3.17	0.20	7.72	97.32
Straw	58.49	0.39	0.33	0.03	0.00	21.10	2.13	3.53	0.25	13.59	99.84
Rice straw	69.88	0.28	0.24	0.01	0.57	6.16	1.55	1.53	0.40	15.26	95.88
Almond shells	6.22	0.98	0.66	0.06	0.05	36.32	3.01	1.60	0.38	30.66	79.95
Olive residues	19.75	1.74	2.69	0.08	0.06	36.50	12.12	2.73	0.11	17.61	93.40
Sewage sludge	17.86	9.89	36.65	0.75	0.08	13.28	1.12	19.61	0.53	0.82	100.59
Coal	46.48	24.60	8.43	0.98	0.16	6.83	2.62	0.48	1.36	2.34	94.28

Hupa and his co-workers[15] have performed thermodynamic equilibrium calculations in order to elucidate the chemical composition of the forming fly ash. In figure 2 the composition of the ash under combustion conditions with an excess air ratio of 1.1 is shown as a function of temperature for the combustion of Salix, a fast growing willow tree. The calculation used as an input the elemental analysis of the fuel and the chemical composition of the flue gas. We see that above 900°C a liquid phase develops which consists of a mixture of potassium carbonate and potassium sulfate which is in general agreement with the observation of low melting ashes for some type of biomass.

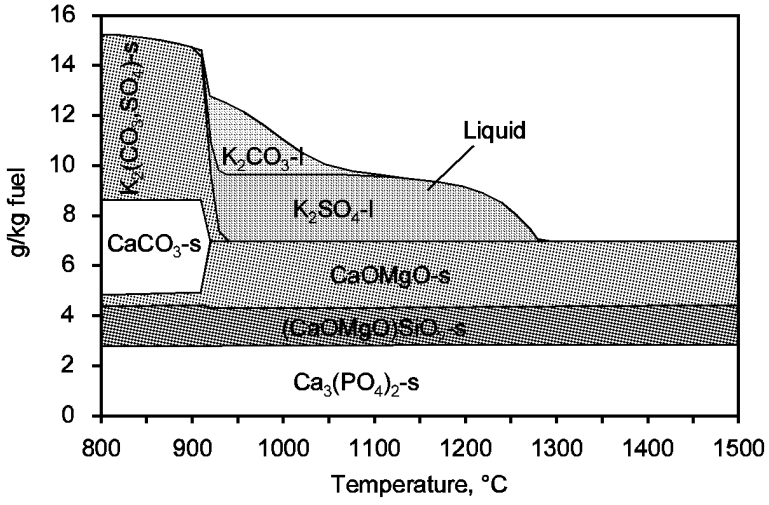

Fig. 2 Thermodynamic equilibrium calculation for the ash composition in presence of flue gas for the combustion of salix [15]

When biomass is combusted in fluidized beds of quartz sand particles sintering of the bed material has frequently been observed[17]. Zevenhoven-Onderwater et al.[16] have found that this effect is often connected to the formation of molten or glassy alkali silicates on the surface of the quartz particles as a result of the chemical interaction with the fly ash particles. As an example Fig. 3 shows a SEM picture of sections of bed particles from quartz sand after they had been exposed to the combustion of sawdust. The white surface layers consist of calcium and potassium silicates. The possible reaction at the quartz surface was described by

$$SiO_2\,(s) + 2\,KCl\,(g) + H_2O\,(g) \rightarrow K_2SiO_2\,(l) + 2\,HCl\,(g).$$

Fouling and corrosion of heating surfaces are frequently observed in biomass combustion. They are caused by the stickiness of the fly ash particles under high temperature conditions. Salt mixtures like the ones occurring in fly ashes melt in stages when heated. Fig. 4 shows a melting curve for a salt which consists of a mixture of sulfate and chloride of sodium and potassium[14]. The figure is based on the Abo Akademi thermodynamic multicomponent melt model which permits calculation of the percentage of liquid phase as a function of temperature for a given mixture of typical inorganic salts in biomass ashes[18,19], T_o is the temperature at which the first molten phase appears and which can be relevant for superheater corrosion. If the superheater tube metal temperature is higher than the first melting temperature T_o of the fly ash particles deposited on the tube, the tube metal will be exposed to some liquid phase of the salt deposit[14]. Figures 5 and 6 show some practical examples of deposits found in technical combustors. In Fig. 5 deposits are presented on the chill grid in the flue gas path of a circulating fluidized bed (CFB) boiler for waste wood operated in Hamburg by Vattenfall Europe[20]. Fig. 6 depicts deposits on an electrochemical probe in the flue gas path of a CFB boiler operated by RWE on their Berrenrath site[21].

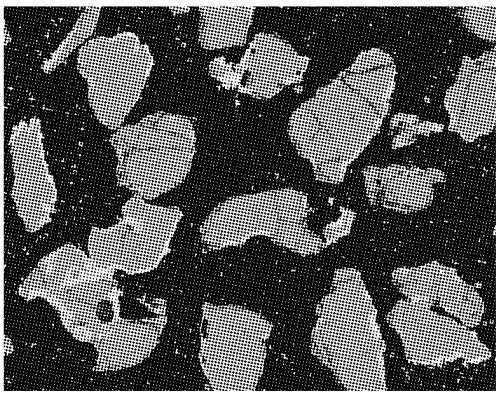

Fig. 3 Sintering of bed material during biomass combustion in the fluidized bed (combustion of saw dust in a fluidized bed of quartz sand particles[14,16])

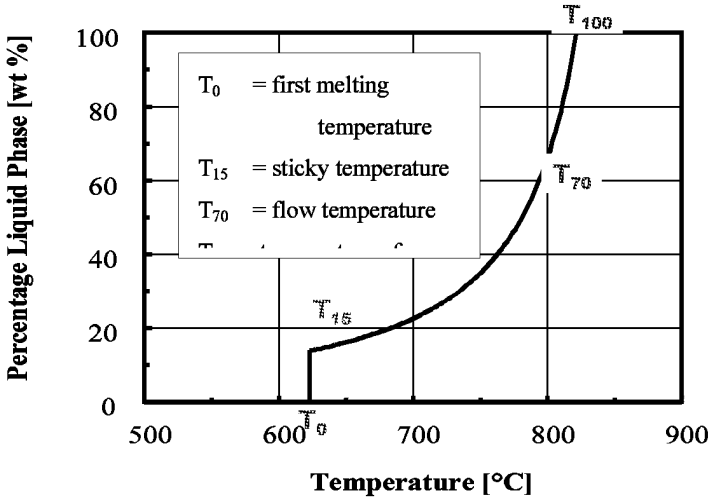

Fig. 4 Calculated melting curve for a mixture of sulfate and chloride of sodium and potassium[14,18,19]

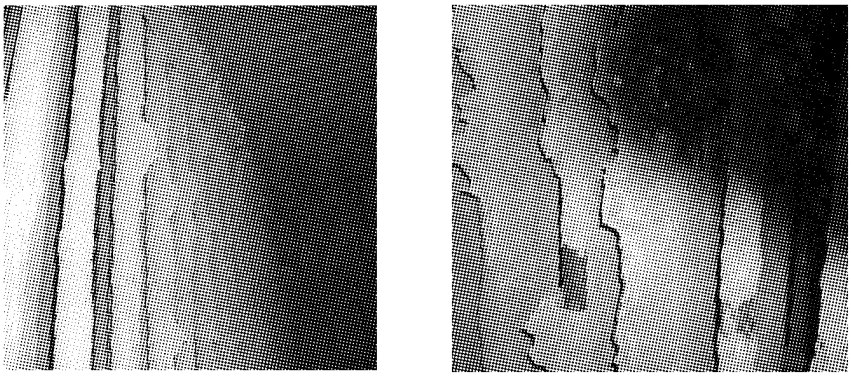

(a) after 2 months operation (b) after 9 months operation

Fig. 5 Deposits on the chill grid in the flue gas path of a circulating fluidized bed boiler for waste wood combustion[20]

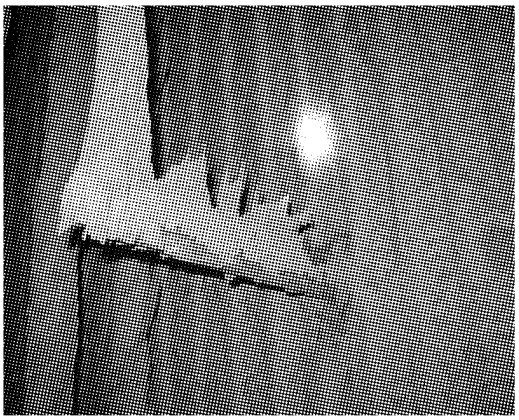

Fig. 6 Deposits on an electrochemical probe in the flue gas path of a CFB boiler after 6 months of co-combustion operation [21]

In summary it can be stated that each type of biomass has its special combustion characteristics. Some types of biomass tend to form low melting ashes which may cause severe problems in the combustion process.

MONO-COMBUSTION VS. CO-COMBUSTION OF BIOMASS

The straightforward way to combust biomass, of course, is to burn it in a plant which is especially designed for this purpose. Such a dedicated plant must, however, be adapted to the special characteristics of the fuel. In particular, the risks of high-temperature corrosion of heating surfaces have to be considered by keeping the metal surface temperatures at comparatively low levels. As a result the values of the steam parameters are generally kept below the levels used in modern coal-fired boilers. For example, in Hamburgs's recently built 20 MWe CFB power plant for biomass combustion the steam parameters are 90 bar and 500°C[22]. The erection of dedicated biomass-fired power plants is encouraged by the German government. Their Erneuerbare-Energien-Gesetz (EEG, Renewable Energies Law) subsidizes electricity generated in biomass-fired power plants up to a size of 20 MWe.

A simple way to avoid the problems caused by biomass in a mono-combustion plant is to mix the biomass to a small extent with the easier-to-operate fuel coal. The expectation is that if biomass ash is present at a low percentage in the coal ash only its negative effects will not be significant. This is the basic idea behind the co-combustion of biomass with coal in already existing large-scale power plants.

In this way the biomass combustion can make use of the high efficiency level of coal-fired power stations which is due to the significantly higher values of the steam parameters. For example, the recently built 261 MWe unit no.6 of Turow/Poland which is a lignite fired CFB boiler of the Foster Wheeler design has steam values of 196 bar and 565°C [23] and RWE's modern pulverized coal fired boilers with an overall efficiency of >43 % are characterized by 250 bar and 576 °C.

It should be noted, however, that in the case of co-combustion of biogenic wastes the power plant is subjected to the emission regulations set forth in the 17thBlmSchV of August 19, 2003 (17th Amendment to the Federal Immission Law) which is the German adoption of the European Union's Directive 2000/76/EC for waste incineration. The 17th BlmSchV is more stringent than the 13th BlmSchV which is normally valid for power stations. In particular, it sets limits for the emission of substances which are not regulated at all in normal power plant operation like mercury, cadmium and dioxins/furans. Whereas for co-combustion in the case of SO_2 a mixing rule is applied which weighs the contribution of the waste to the plant's thermal power, in the case of mercury, for example, independent of the share of waste in the feed the limit of 30 µg/Nm^3 is valid for the whole flue gas of the power plant. If this limit can only be kept by installing an additional flue gas cleaning system this can make the co-combustion commercially unattractive for the power plant.

However, the sum of the advantages – highly efficient combustion, cheap fuel replacing more expensive coal, CO_2-neutral fuel, fuel flexibility, use of existing plant and infrastructure – has in recent years established the co-combustion in several European countries with different applications which will be discussed in the two following sections.

EXAMPLES OF BIOMASS CO-COMBUSTION IN EUROPE

In the Netherlands waste wood is co-combusted in a 635 MWe pulverized coal fired boiler located in Nijmegen in a quantity of 60,000 t/a. The share of the biomass in the total thermal power is 4.5 %[11].

In Austria there exists in St. Andrä a pulverized coal fired boiler of 124 MWe where mainly bark is co-fired. The biomass contributes 10 MW thermal power which corresponds to 3 % of the total thermal power[11].

In England a total of 14 coal fired power stations (all pulverized coal) are practicing co-combustion. The cumulative renewable electricity from biomass co-firing to November 2006 amounted to 6.2 TWhe. Types of biomass used were dry granular or pelletized residues from palm oil and olive industries[25].

In Germany the situation is characterized by the presence of the EEG law which subsidizes the energetic use of biomass in small dedicated mono-combustion facilities with an electric power not exceeding 20 MWe. As a result no biomass which can be burnt in a so-called "EEG plant" will find its way to co-combustion. To a smaller extent animal meal is fired in the Duisburg co-generation plant[26], waste wood and RDF in RWE's Berrenrath boiler[21] and also RDF in Flensburg in CFB boilers[27]. It has, however, become quite popular in Germany to co-fire sewage sludge which will be discussed in the next section in detail.

CO-COMBUSTION OF SEWAGE SLUDGE IN GERMANY

Some general remarks

Sewage sludge is a biomass which is continuously produced and which has to be treated anyway. In 2006, in Germany about 2 million tons dry matter of sludge were produced from which a half went into combustion and the other half into landscaping and into farming where the sludge is used as a fertilizer[28]. Because of its content of contaminants the use on farmland is decreasing.

A distinction has to be made between raw and digested sludge. Normally, the raw sludge will be subjected to anaerobic digestion. In the digestion tower digester gas is produced which is subsequently burnt in a gas motor or gas turbine for electricity and heat generation. The digestion – although not absolutely necessary since, for example, in Berlin the raw sludge is directly combusted – has the beneficial effect that it stabilizes the sludge which enables storage (for a limited time) and transport. The digested sludge is normally dewatered in centrifuges to a dry matter content of roughly 30 %. In this form it is not a serviceable fuel because the raw matter has a lower calorific value of 1.1 MJ/kg only. If it is combusted it is simply a means of disposal. However, currently this is widely practiced in mono-combustion plants and with co-combustion.

An alternative is to thermally dry the digested and mechanically dewatered sludge to a dry matter content of about 45 to 50% which allows an autothermal combustion of the sludge. This is practiced for example in Hamburg's sludge incineration plant VERA[29]. Comparatively rare is the thermal drying of the sewage sludge to a residual water content <10 % which then leads to a useful fuel with a LCV of 13.8 MJ/kg. At present this method of complete drying is practiced in 31 plants which are all located on the sites of sewage water treatment plants[30].

Examples of power plants with co-combustion

As an example Fig. 7 shows the arrangement for the co-combustion of sewage sludge in the Heilbronn power plant. This PC fired power plant is owned by EnBW Kraftwerke AG and consumes 1.2 million t/a of bituminous coal as a regular fuel with 20,000 t/a of dry and 60,000 t/a of mechanically dewatered sludge being

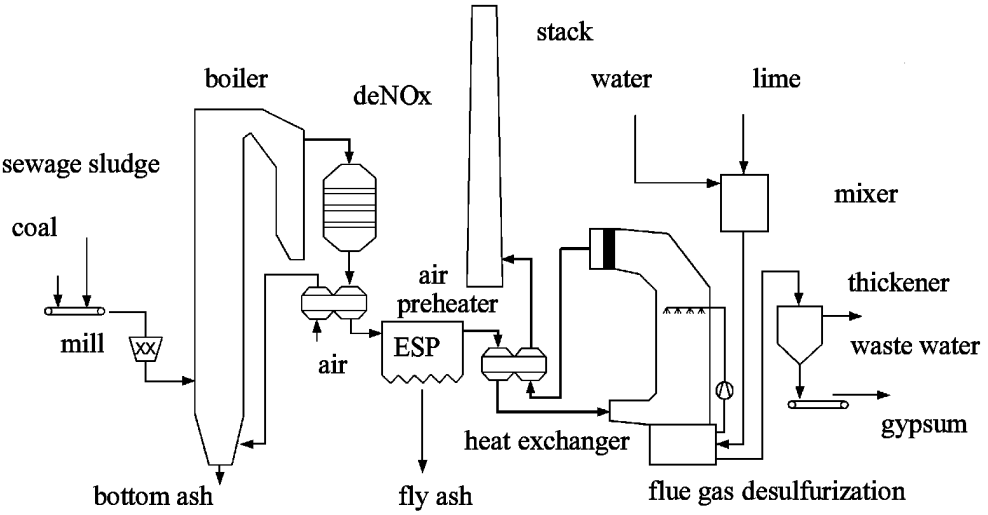

Fig. 7 Co-combustion of sewage sludge in the Heilbronn power station [31]

co-fired. As it is seen from the flowsheet the sewage sludge is fed together with the coal into the mills. No special treatment of the flue gas is necessary. However, a strict quality control limits the content of contaminants in the accepted sludges. For example, the Hg content is limited to 2 mg/kg d.m.

In Fig. 8 the flowsheet of the Berrenrath plant is shown which is owned by RWE Power AG. This is a CFB boiler which is operated on lignite. The sludge is introduced together with the coal into the return leg from the syphon to the combustion chamber which leads to an intense mixing with the bed material. In order to keep the limiting value of the 17thBlmSchV for Hg in the flue gas an additional gas cleaning turned out to be necessary. For this purpose an entrained flow adsorption with active coke was installed between the waste heat boiler and the electrostatic precipitator (ESP), which finally leads to a Hg concentration below 4 $\mu g/m^3$ in the cleaned flue gas[6].

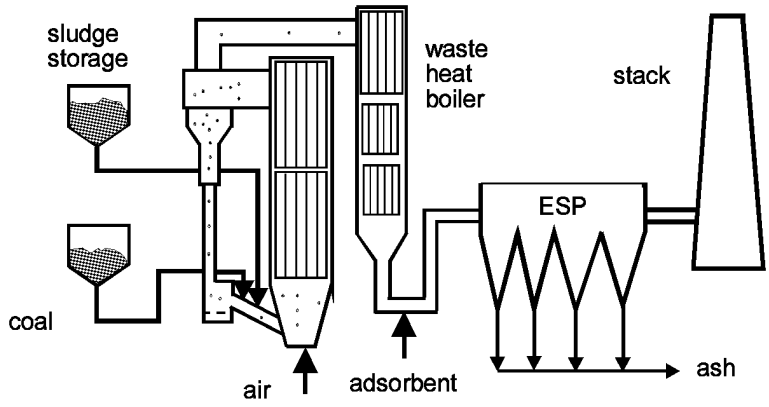

Fig. 8 Co-combustion of sewage sludge in the Berrenrath power station [6]

The relative ease of the co-combustion of sewage sludge has motivated a lot of power stations to step into this business. As a result the capacity for co-combustion of sewage sludge in coal-fired power stations has increased drastically within the last 10 years. Fig. 9 illustrates this development. At present, 18 hard-coal-fired and 8 brown-coal-fired power stations in Germany use this opportunity (Fig. 10).

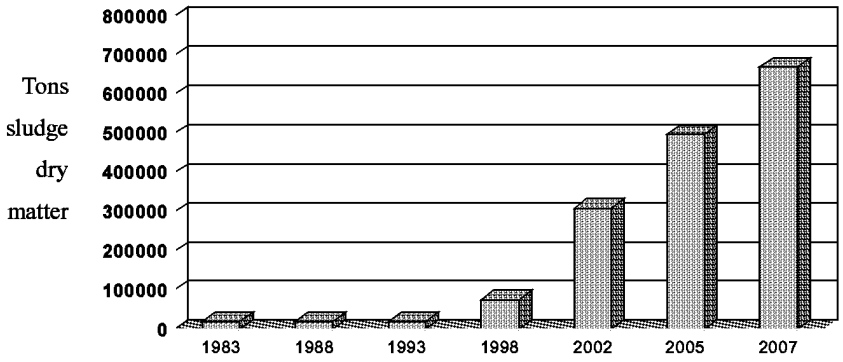

Fig. 9 Development with time of the capacity for co-combustion of sewage sludge in German coal-fired power stations (from [32])

A detailed investigation of co-combustion in the Duisburg power plant

A thorough investigation of co-combustion has been carried out jointly by the author's group and Stadtwerke Duisburg AG on their fluidized bed boiler [26]. In the framework of the EU-funded COPOWER project it was investigated whether co-firing of one or more biomass or waste materials could provide synergy effects which might affect the operating behavior of the plant in a positive way.

The Duisburg cogeneration plant was commissioned in 1985 as one of the first large-scale CFB boilers. It has a rated thermal power of 252 MW and a maximum electrical output of 105 MWe. Fig. 11 shows a flowsheet of this plant. In a measurement campaign over 12 days co-firing of bituminous coal from Colombia with mechanically dewatered municipal sewage sludge and wood pellets was tested. Table 5 gives a comparison of the fuel analyses. The sludge was pretreated with lime for stabilization which explains the high Ca content in its elemental analysis.

The campaign consisted of 4 test periods of 3 days each. In periods I and IV the plant was operated with coal alone. In period II the sludge was co-fired. It was pumped by a thick matter piston pump into the lower part of the combustion chamber. In period III wood pellets and sewage sludge together were co-fired with the coal. The wood pellets were pneumatically conveyed and blown directly into the lower part of the combustion chamber. The aim of test series IV was to check if the plant returned to the initial operating conditions and emissions of test period I. During all the tests the boiler was operated as close as possible to full load. Table 6 gives an overview on thermal power distribution and relevant mass flows in the different test periods.

Fig. 10 Locations of power stations with co-firing of sewage sludge (bituminous coal firing in black, lignite firing in grey; from [32])

In Fig. 12 the pressure drop of the combustion chamber Δp_{CFB} which is proportional to the solids inventory is plotted for the test periods I to III. During the co-combustion of wood with sewage sludge and coal a significant decrease in the solids hold-up of the combustion chamber can be noticed compared to the two previous test periods. This reduction by 15 % leads to the positive effect of a reduction of the fan power necessary for the fluidization of the bed material. In addition, the vertical distribution of the ash material is influenced by the fuels used as shown in Fig. 13 where the relative pressure drop, which compares the pressure drop $\Delta p_{transport}$ of the transport zone in the upper part of the combustion chamber with the total pressure drop Δp_{CFB} in the combustion chamber. An increase of this ratio indicates that relatively more ash material has been accumulated in the upper part of the combustor.

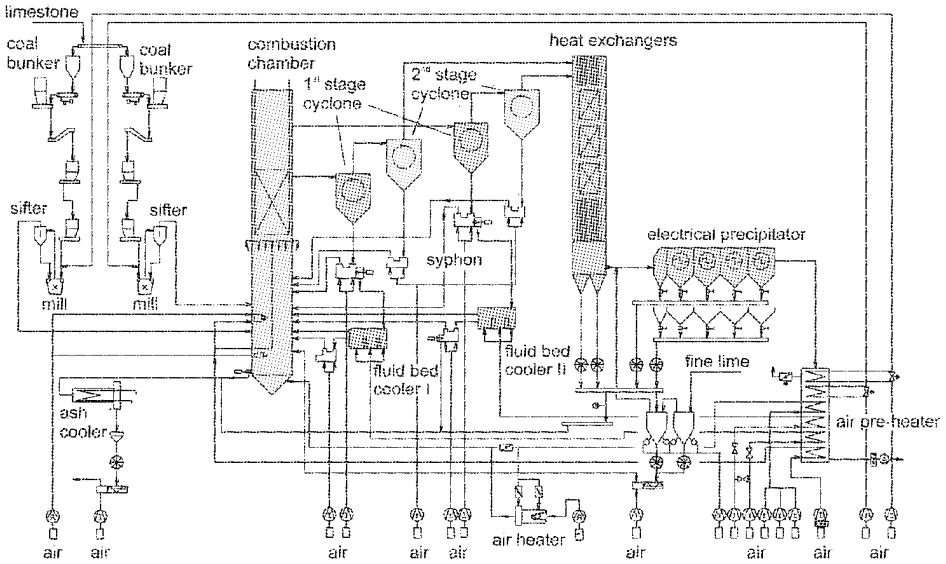

Fig. 11 Flow diagram of the Duisburg boiler

Figs. 12 and 13 taken together indicate that the addition of the wood changes the particle population inside the combustion chamber. The lightweight wood coke and ash particles are easily entrained and this increases the external solids circulation. The relatively increased solids holdup in the upper part of the combustion chamber indicates a finer mean particle size in the circulation loop which is beneficial for heat transfer particularly in the external fluid bed heat exchangers.

Table 5 Analysis of fuels used during the Duisburg tests

		coal 'El Cerrejon'	sewage sludge	wood pellets
LHV	MJ/kg(waf)	31.98	22.39	18.72
water	wt.-% (raw)	15.39	74.3	9.3
ash	wt.-% (wf)	10.3	44.8	0.5
volatiles	wt.-% (waf)	41.9	88.8	84.9
C	wt.-% (waf)	81.0	55.91	51.4
H	wt.-% (waf)	6.01	7.45	6.1
O	wt.-% (waf)	10.7 *	26.85 *	42.47 *
N	wt.-% (waf)	1.5 **	7.3 **	0.03
S	wt.-% (waf)	0.79	2.49	< 0.01
Ca	wt.-% (wf)	0.23	2.3	0.06

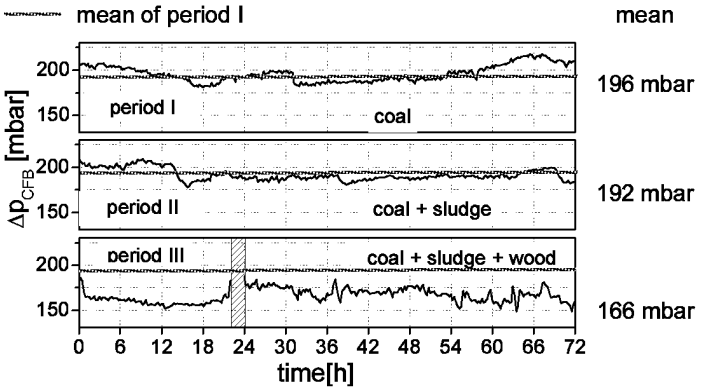

Fig. 12 Total pressure drop in the combustion chamber

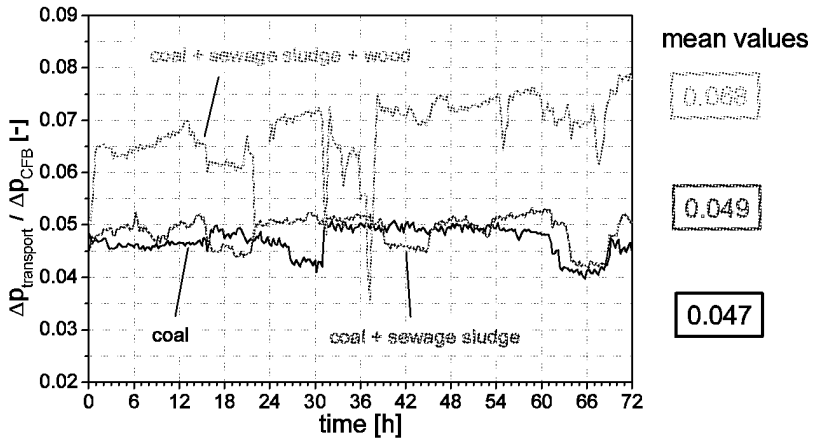

Fig. 13 The ratio of the pressure drop in the transport zone $\Delta p_{transport}$ which occupies the upper half of the combustion chamber to the total pressure drop Δp_{CFB}

In Fig. 14 the time dependence of the NOx emissions during the test periods is plotted. The level of concentrations is comparatively low for a CFBC. Since the Duisburg combustor is not equipped with heat exchanger tube walls a more homogeneous temperature profile is present, which is considered to be the reason for the level of concentrations.

A significant reduction of the NO_x emissions is observed for co-firing conditions with sewage sludge compared to pure coal firing although the N-in-fuel mass flow is increased (cf. Table 6). With an addition of wood to the coal and sewage sludge the level of NO_x emissions increases again. This is another synergy effect. The negative impact of the wood towards the NO_x emissions is compensated for by the positive effect of sewage sludge. The overall emissions remain at a level which does not exceed the level of pure coal firing. The decrease of NO_x emissions during the combustion of mechanically dewatered sewage sludge is a well known phenomenon[12]. However, the details about the mechanisms are not yet completely understood. The local release of ammonia from the wet sewage sludge seems to play an important role.

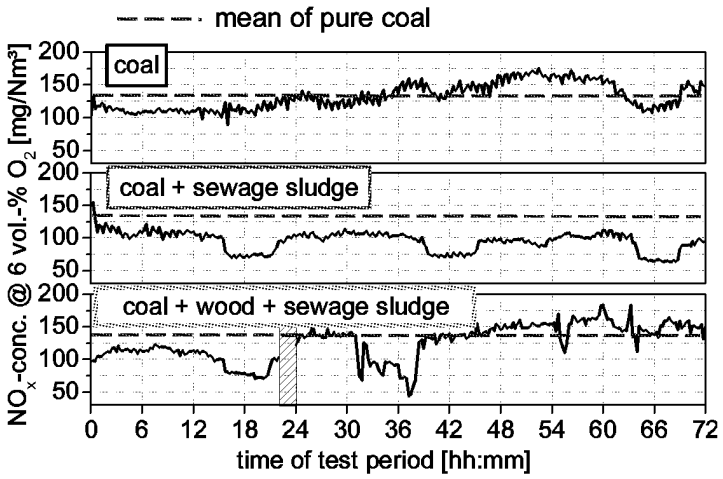

Fig. 14 NO_x emissions (calculated as NO_2 and based on 6 vol.-% O_2 in the flue gas)

Table 6 Comparison of flows in the different test periods (*estimated from previous analyses)

		coal	sewage sludge	wood pellets	sum
fuel mass flow (raw) [t/h]	period I + IV	37.6	-	-	37.6
	period II	36.9	4.1	-	41.0
	period III	31.3	4.3	7.3	42.9
thermal power [MW]	period I + IV	248	-	-	248
	period II	243	1.6	-	245
	period III	206	1.7	33.9	242
ash mass flow [t/h]	period I + IV	3.5	-	-	3.5
	period II	3.4	0.5	-	3.9
	period III	2.9	0.5	0.03	3.4
water-in-fuel mass flow [t/h]	period I + IV	5.8	-	-	5.8
	period II	5.7	3.1	-	8.8
	period III	4.8	3.2	0.7	8.7
sulphur-in-fuel mass flow [kg/h]	period I + IV	225	-	-	225
	period II	221	15	-	236
	period III	188	15	0	203
nitrogen-in-fuel mass flow [kg/h]	period I + IV	433*	-	-	433
	period II	425*	53*	-	478
	period III	360*	55*	2	417

The sulphur transported with the fuels forms SO_2 during combustion. In order to reduce the SO_2 emissions limestone is added to the combustion chamber. Limestone consists mainly of $CaCO_3$ and forms $CaSO_4$ when reacting with SO_2 (sulphation reaction). In that way sulphur is captured in a solid form. Fig. 15 compares the amount of sulphur captured as $CaSO_4$ with the amount of Ca fed in form of limestone. Since the amount of sulphur captured cannot directly be measured it has been calculated from the difference of the sulphur-in-fuel molar flow into the combustor and the sulphur flow out of the system with the flue gas.

When comparing pure coal firing with the co-combustion of sewage sludge and coal a positive effect induced by sewage sludge can be identified. The amount of sulphur contained in the fuels is higher for co-combustion of sewage sludge and coal (236 kg/h) compared to pure coal firing (225 kg/h) as shown in Table 6. Since the level of SO_2 emissions is kept nearly constant during the two test periods considered, the amount of $CaSO_4$ formed and thus of sulphur captured is increased for co-combustion of sewage sludge. As a consequence an increased limestone requirement could have been expected. However, the limestone requirement decreases. The reason is an additional supply of Ca with sewage sludge, which is based on its pre-treatment with lime for stabilization. The Ca/S ratio in the sewage sludge is 1.3 compared to that of coal of 0.3. Although the phosphates supplied with the sludge have the tendency to capture the Ca faster than sulphur does[33] the net effect is positive. In other words the limestone requirement is reduced under conditions of co-firing with sewage sludge. The comparison between pure coal firing and coal and sewage sludge co-combustion shows that an increase of 2.6 % of calcium-in-fuel dosage is associated with a reduction of 20.0 % of externally dosed calcium. These percentages are calculated on the basis of the overall amount of calcium input (externally dosed plus in-fuel calcium) during pure coal firing in test period I.

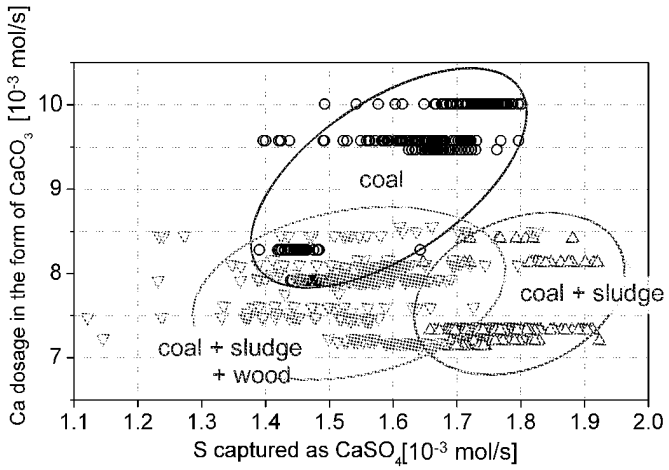

Fig. 15 Comparison of captured sulfur and Ca dosage in the form of $CaCO_3$

This beneficial effect of the sewage sludge is probably mainly attributable to the fact that sewage sludge produces a fine ash, so that the Ca containing compounds are also released from the fuel matrix in a finely divided form which offers a high volume specific surface for the sulphation reaction.

In summary, it can be concluded from the measurement campaign in Duisburg that co-combustion of biomass or waste is not always a burden. On the contrary, co-firing of a suitable mixture of biomass and waste can have positive effects on the gaseous emissions and on the operating behavior of coal-fired power plants. Of course, each application has to be examined carefully and the risk of high-temperature corrosion remains an issue which requires careful consideration.

PERSPECTIVES OF BIOMASS CO-COMBUSTION

It is not easy to predict what will happen with biomass co-combustion in large power plants in the future. The development will strongly depend on political actions. If, as it is the case in Germany, policy favors the utilization of biomass from forest residues or waste wood in small-scale combustion plants then these materials will not be available for co-combustion in large power plants in spite of its being more energy efficient (and due to the economy of scale also cheaper). If the generation of biofuels from biomass is subsidized sufficiently then biomass will go that way.

On the utility side the primary goal is to make money. This is at present mainly achieved by using cheap fuels and the cheapest fuels are those with negative prices, namely wastes. However, there are also tendencies which may make co-combustion of biomass and wastes with biogenic content more popular:

- the price of coal is increasing which is an incentive to substitute fuels
- CO_2 emission trading is coming; with prices for CO_2 emission certificates rising the incentive to use biogenic fuels is increasing.

In this sense it may be useful to "upgrade" water-containing biogenic wastes by drying them to biofuels in the heat-and-power network of large power stations. As an example of this idea Table 7 shows a cost calculation for the drying of mechanically dewatered sewage sludge with a water content of 70 % and a lower calorific value of 1.1 MJ/kg to a water content of 10 % and a LCV of 13.8 MJ/kg. This "biofuel" (which in the legal sense, of course, is still a waste) is then used to substitute bituminous coal in the power station.

The data and assumptions and calculations were made with the help of partners in industry. The total capacity of 300.000 t/a of wet sewage sludge is identical with the actual co-combustion capacity of the Lippendorf power plant [32]. Table 7 at first highlights the cost structure. An investment into a dryer has to be made which causes also costs of infrastructure. The dryer is operated with steam taken from the steam turbine and therefore this extraction of steam leads to a reduction in the electricity production which occurs in the costs of preparing the biofuel. On the other hand the power station has several earnings with using the thus generated fuel: the major contribution to earnings is the acceptance fee of the waste material. The second contribution is the substitution of the coal: the 100,000 t of dried sewage sludge are replacing 55.000 t of bituminous coal. The third contribution is the saving on CO_2 emission certificates due to the substitution of the coal by the biofuel. As a result of these various contributions the profit and loss statement yields a good profit of 11.6 million Euros per year.

This is impressive and the question is now: why is this on-site drying not widely practiced by power stations already? The calculation shown in Tab. 8 gives the answer. Here the cost-structure of the currently

Table 7 Production of a biofuel by drying of mechanically dewatered sludge in combination with a power station operating on bituminous coal

Basic design data:	
Throughput of mechanically dewatered sludge	300,000 t/a
Water content of the mechanically dewatered sludge	70 %
Water content in the dry product	10 %
Amount of water to be dried away	200,000 t/a
Amount of dry product	100,000 t/a
Lower heating value of the product	13.8 MJ/kg
Annual operating time	6,000 h/a
Design of the dryer:	
Specific water evaporation	33.3 t/h
Specific steam requirement for drying	1.2 t steam/t H_2O
Steam quality (saturated steam)	4 bar
Steam requirement	40 t/h
Spiral screw heat exchanger for drying:	
one screw evaporates 1.2 t water/h and costs 0.5 million €; for 33.3 t/h we need 28 screws which cost 14 million €; additional 5 million € are needed for construction work, piping, instrumentation, control etc	19 10^6 €
Infrastructure for sewage sludge supply: Receiving area, storage, conveying to dryer	7 10^6 €
Infrastructure for dryer plus conveying to boiler	2 10^6 €
Total costs of investment:	
Infrastructure for sewage sludge handling	7 10^6 €
Dryer	19 10^6 €
Infrastructure for dryer	2 10^6 €
total	28 10^6 €
Capital cost (amortization 10 years, 6 % interest rate, capital costs 13.6 %/a of invest)	3.81 10^6 €/a
maintenance costs (2 % of investment)	0.56 10^6 €/a
cost of personnel (2 jobs with shift system including provision for holidays and illness result in staff requirement of 10 workers; each workers costs 60,000€/a including social costs)	0.60 10^6 €/a
Revenues of the power plant are reduced because turbine steam is sent to the dryer:	
Specific electricity loss ca. 0.14 MWh/t steam: the 40 t/h steam consumption are equivalent to loss of 5.6 MWe. Price of base load electricity assumed with 70 €/MWh leads to reduction of revenues of 40x0.14x6,000x70	2.35 10^6 €/a
Summary of costs:	
Revenue reduction due to reduction of electricity production	2.35 10^6 €/a
Capital costs	3.81 10^6 €/a
maintenance costs	0.56 10^6 €/a
costs of personnel	0.60 10^6 €/a
total	7.32 10^6 €/a
Proceeds for the power station:	
The dewatered sewage sludge is accepted for a fee of 35 €/t, in total 300,000x35	10.50 10^6 €/a
Bituminous coal is substituted by the dried sewage sludge: The dried sewage sludge has a LCV of 13.8 MJ/kg, the coal's is 25 MJ/kg; the amount of 100,000 t/a biofuel replaces 100,000x13.8/25=55,000 t bituminous coal. The coal costs 100 €/t which means a saving on coal costs of	5.5 10^6 €/a
The biofuel saves on CO_2 emission certificates: The bituminous coal has an emission factor of 0.095 t CO_2/GJ which is equivalent to 0.095x25=2.38 t CO_2/t coal; in total the 55,000 t of coal saved are equivalent to a saving of 55,000x2.38=130,900 t CO_2. With an assumed value of 22,50 €/t CO_2 this is equivalent to a saving of	2.95 10^6 €/a
Total	18.95 10^6 €/a
Profit and loss statement:	
Total proceeds	18.95 10^6 €/a
Total costs	7.32 10^6 €/a
Total profit	11.63 10^6€/a

practiced co-combustion of mechanically dewatered sewage sludge in the coal-fired power plant is described. The earnings mainly consist of the fees for sludge acceptance and – to a minor part – of the savings on CO_2 emission certificates. But also the list of costs is much shorter. A relatively small investment for receiving, storing and dosing the sludge has to be made only. The major point is that the cost of the in-furnace drying of the sludge is not considered at all. The argument is that the coal milling devices of the PC boiler which combine grinding and drying have enough reserve capacity to cope with the small percentage of water coming with the sludge. In fact, the drying capacity in the mills is considered to be the limiting factor for the sludge throughput in a given plant.

If one accepts this view then the total profit turns out to be 9.8 million Euros per year. The difference to the 11.6 million profit for the sludge drying alternative is not big enough to outweigh the risks associated with this latter route.

Things may be different in the case of a fluidized bed boiler where no external milling and drying exists and they will be totally different in future PC fired power stations operating on predried brown coal as it is planned by RWE with their WTA-concept[34] since operating with predried brown coal requires also predrying of the co-fuel because mill drying is no longer available there.

Table 8 Co-combustion of mechanically dewatered sewage sludge in the coal-fired power station

Basic design data:	
Throughput of mechanically dewatered sludge	300,000 t/a
Lower heating value of the sludge	1.1 MJ/kg
Proceeds:	
1. The dewatered sludge is accepted for a fee of 35 €/t, in total 300,000×35	10.50 10^6 €/a
2. The utilization of the biogenic content of the sludge saves on CO_2 emission certificates: the bituminous coal emits 0.095 tCO_2/GJ; with the LCV of 1.1 GJ/t sludge it follows a saving on CO_2 emission of 0.095×1.1 = 0.10 tCO_2/t sludge; with the certificate price of 22.50 €/tCO_2 the saving on emission certificates is 300,000×0.1×22.50=	0.68 10^6 €/a
total proceeds	11.18 10^6 €/a
Costs:	
(infrastructure for sewage sludge reception, storage and dosage assumed to be an investment of 7×10^6 €)	
Capital costs (13.6 % of investment)	0.95 10^6 €/a
Maintenance (2 % of investment)	0.14 10^6 €/a
Costs of personnel (1 job, 5 workers, 60,000 €/a each including social costs)	0.30 10^6 €/a
Cost of in-furnace drying of the sewage sludge	----
total cost	1.39 10^6 €/a
Profit and loss statement:	
total proceeds	11.18 10^6 €/a
total cost	1.39 10^6 €/a
total profit	9.79 10^6 €/a

The development of coal-fired boilers is currently directed towards increasing the efficiency by increasing the values of the steam parameters. Under the keyword "700°C power station" efforts are made to develop and test materials which can be used at higher temperature levels. For such advanced materials the risk of corrosive attack will be higher and therefore operators will be reluctant to co-fire biogenic wastes.

In the more distant future the development will be towards the CO_2-free coal-fired power station with CO_2 sequestration. Among the three routes – pre-combustion, post combustion and oxyfuel – the post combustion route with CO_2 scrubbing from flue gas will certainly play an important role. In this context biomass co-firing could be interesting: if 10 % of the CO_2 in the flue gas are from biomass, then a 90 % efficiency of the scrubber is sufficient to make the power plant CO_2-free in the legal sense. The resulting reduction in requirement on scrubbing efficiency when compared to the combustion of coal without biomass will possibly reduce the cost of scrubbing significantly.

SUMMARY AND CONCLUSIONS

Co-firing of biomass and biogenic wastes in large-scale coal-fired power plants allows an energetic

utilization at a high level of efficiency which is not obtainable in small-scale dedicated biomass combustors.

Co-firing at low percentages of the thermal power (typically below 5-10 %) avoids the typical operating problems of biomass combustion, i.e. ash sintering and fouling of heat transfer surfaces.

Co-firing of biogenic wastes is already widely practiced in Germany, non-waste biomass like forest residues are for subsidy reasons combusted in small dedicated mono-combustion plants.

A future increase of co-combustion may be associated with the upgrading of biogenic wastes with high water content to biofuels by drying. Such biofuels could substitute more expensive coal and save on CO_2 emission certificates.

In the more distant future biomass co-combustion may help in the CO_2 scrubbing process by lowering the target level of CO_2 absorption efficiency.

ACKNOWLEDGEMENTS

The author expresses his sincere thanks to Harald Hanssen from Hamburg Wasser, Matthias Jasper from E.ON Kraftwerke and Hans Joachim Klutz and Uwe Peters from RWE Power for helpful and stimulating discussions.

REFERENCES

[1] http://www.bmu.de/erneuerbare_energien/kurzinfo/doc/3988.php.

[2] http://www.euractiv.com/en/energy/eu-renewable-energy-policy/article-117536.

[3] BMU: Entwicklung der erneuerbaren Energien in Deutschland im Jahr 2007. www.bmu.de.

[4] M. Kaltschmitt, W. Streicher, A. Wiese (eds.): Renewable Energy, Springer, Berlin 2007.

[5] M. Basler, First Foster Wheeler Boiler Days, Hamburg, April 24-25, 2007.

[6] B. Röper, First Foster Wheeler Boiler Days, Hamburg, April 24-25, 2007.

[7] Sachverständigenrat für Umweltfragen: Klimaschutz durch Biomasse. Sondergutachten. July 2007. www.bmu.de.

[8] F. Knappe et al.: Stoffstrommanagement vom Biomasseabfällen mit dem Ziel der Optimierung der Verwertung organischer Abfälle. Umweltbundesamt Berlin, UBA-Texte 04/07.

[9] U.R. Fritsche et al.: Stoffstromanalyse zur nachhaltigen energetischen Nutzung von Biomasse. Öko-Institut Darmstadt 2004.

[10] Bundeswirtschaftsministerium, Energiedaten '97/98.

[11] M. Kaltschmitt, H. Hartmann (eds.): Energie aus Biomasse. Springer, Berlin 2001.

[12] J. Werther, T. Ogada: Prog. in Energy and Combustion Science 25 (1999), 55-116.

[13] M. Sänger, PhD Dissertation, Technical University Hamburg-Harburg 2000.

[14] M. Hupa, in J. Werther, W. Nowak, K.-E. Wirth, E.-U. Hartge (eds.): Circulating Fluidized Bed Technology IX, TuTech Innovation GmbH, Hamburg 2008, p. 845-856.

[15] M. Hupa et al., Proc. ITIT Symposium on Effective Utilization of Low Grade Fuels by Fluidized Bed Technology, AIST-NIRE-NEDO, Tsukuba, Japan, December 1-2, 1999.

[16] M. Zevenhoven-Onderwater et al., Fuel 20 (2006), 818-824.

[17] J. Werther et al., Prog. in Energy and Combustion Science 26 (2000), 1-27.

[18] R. Backman et al., Tappi J. 70 (1987), 123-127.

[19] R. Backman et al. in R.P. Gupta, T. Wall, L. Baxter (eds.): Impact of Mineral Impurities in Solid Fuel Combustion. Kluwer Academic Publ., New York 1999, 405-416.

[20] M. Mineur, First Foster Wheeler Boiler Days, Hamburg, April 24-25, 2007.

[21] B. Röper, First Foster Wheeler Boiler Days, Hamburg, April 24-25, 2007.

[22] M. Mineur, in: J. Werther, W. Nowak, K.-E. Wirth, E.-U. Hartge (eds.): Circulating Fluidized Bed Technology IX, TuTech Innovation GmbH, Hamburg 2008, p. 1099-1104.

[23] W. Nowak et al., in J. Werther, W. Nowak, K.-E. Wirth, E.-U. Hartge (eds.): Circulating Fluidized Bed Technology IX, TuTech Innovation GmbH, Hamburg 2008, p. 1057-1062.

[25] ThermalNet Newsletter, Issue 05, September 2007, www.pyne.co.uk.

[26] R. Wischnewski, J. Werther, N. Heidenhof; VGB PowerTech 12 (2006), 63-70.

[27] W. Baar, D. Roschek, in: J. Werther, W. Nowak, K.-E. Wirth, E.-U. Hartge (eds.): Circulating Fluidized Bed Technology IX, TuTech Innovation GmbH, Hamburg 2008, 1111-1116.

[28] Statistisches Bundesamt, 2008.

[29] http://www.verahamburg.de.
[30] ATV-DVWK-M379 Klärschlammtrocknung, ATV-DVWK, Hennef 2003.
[31] P. Buck, Klärschlamm aktuell, ATV-DVWK, Hennef/Germany 2003, 469-479.
[32] H. Hanssen, presentation at the Symposium“ Fluidized Bed Technology – from Basic Research to the Industrial Application”, Hamburg University of Technology, April 18, 2008.
[33] L.-E. Amand, B. Leckner in: K. Cen, J. Yan, Y. Chi (eds.), Proc 3rd Int. Conf. on Combustion, Incineration/Pyrolysis and Emission Control, Hangzhou/China 2004.
[34] F. Schwendig, H.-J. Klutz, J. Ewers; VGB PowerTech 12 (2006), 51-57.p

Formation and Reduction of Pollutants in CFBC: From Heavy Metals, Particulates, Alkali, NO_x, N_2O, SO_x, HCl

Franz Winter

Institute of Chemical Engineering, Vienna University of Technology,
Getreidemarkt 9/166, 1060 Vienna, Austria, franz.winter@tuwien.ac.at

Abstract: Due to the advantages of fluidized bed combustors a wide range of different fuels is utilized. The fuels range from anthracite, medium and low rank coals to peat, wood residues, biomass waste, sewage sludge and other sludges to plastics and municipal solid waste. Because of this wide range of fuels pollutants such as heavy metals, particulates, alkali, NO, NO_2, N_2O, SO_2, SO_3 and HCl may be formed during the fuel conversion process depending on the fuel and operating conditions.
These pollutants may lead to difficulties in operation of the fluidized bed combustor e.g. because of slagging and fouling the heat transfer may decrease or the efficiency of the SCR catalyst. High concentrations in the flue gas may lead to health problems and pollution of the environment.
This work investigates the conversion routes of the pollutants from the fuel to the final flue gas. It is discussing the different chemistry of the pollutants and their possible interactions inside the combustor. Primary measures to avoid pollutant formation and reduction paths are demonstrated. Areas for further research are recommended.
Keywords: pollutants, heavy metals, particulates, NO_x, SO_2, HCl, alkali

INTRODUCTION

Fluidized bed combustors (FBC) are able to utilize a wide range of fuels. The fuels range from anthracite, medium and low rank coals to peat, wood residues, biomass waste, sewage sludge and other sludges to plastics and municipal solid waste. Because of this wide range of fuels pollutants such as heavy metals, particulates, carbon in ash, alkali, NO, NO_2, N_2O, SO_2, SO_3 and HCl may be formed during the fuel conversion process depending on the fuel and operating conditions.

This work gives an overview of the conversion routes of the pollutants from the fuel to the final flue gas. It is discussing the different chemistry of the pollutants and their possible interactions inside the combustor. Primary measures to avoid pollutant formation and reduction paths are demonstrated. An overview of state-of-the-art secondary measures is given. Areas for further research are recommended.

NITROGEN OXIDES NO, NO_2, N_2O

NO and NO_2, summarized as NO_x are harmful pollutants which may cause direct health injuries of the respiratory organs, form acid rain and ground-level ozone. NO is primarely formed in the combustion zone and further oxidized to NO_2. N_2O (nitrous oxide) is a 200 times more effective greenhouse gas as CO_2 because of its strong absorption in the infrared spectrum. In addition N_2O contributes to the destruction of the ozone layer in the stratosphere.

Because of the relatively low combustion temperature of about 850°C the nitrogen oxides are not formed from the molecular nitrogen (N_2) of the combustion air but from the nitrogen which is in the fuel, i.e. fuel – nitrogen during devolatilization and char combustion. In Table 1 typical nitrogen contents of a wide range of fuels is given.

Table 1 Typical carbon and nitrogen contents obtained from ultimate analysis on a dry and ash free basis from various fuels

Analysis (daf)	ANT	LVB	MVB	HVB	SUB	LIG	PT	WD	WPB	SEW	PE
carbon [w-%]	93	87	88	83	67	66	60	50	48	56	85
nitrogen [w-%]	1.2	1.8	1.6	1.5	1.3	1.2	1.5	0.18	2.77	6.3	0.07

ANT - anthracite, LVB - low volatile bituminous coal, MVB - medium volatile bituminous coal, HVB - high volatile bituminous coal, SUB - sub-bituminous coal, LIG - lignite, PT - peat, WD - wood, WPB - wooden pressboard, SEW - sewage sludge, PE - polyethylene.

However, it is interesting to see that a high content of nitrogen leads to low conversion rates to NO (refer to Fig. 1). This is attributed to intrinsic NO reduction by formed HCN and NH_3 intermediates (refer also to

Figure 2), see also Winter et al. 1999.

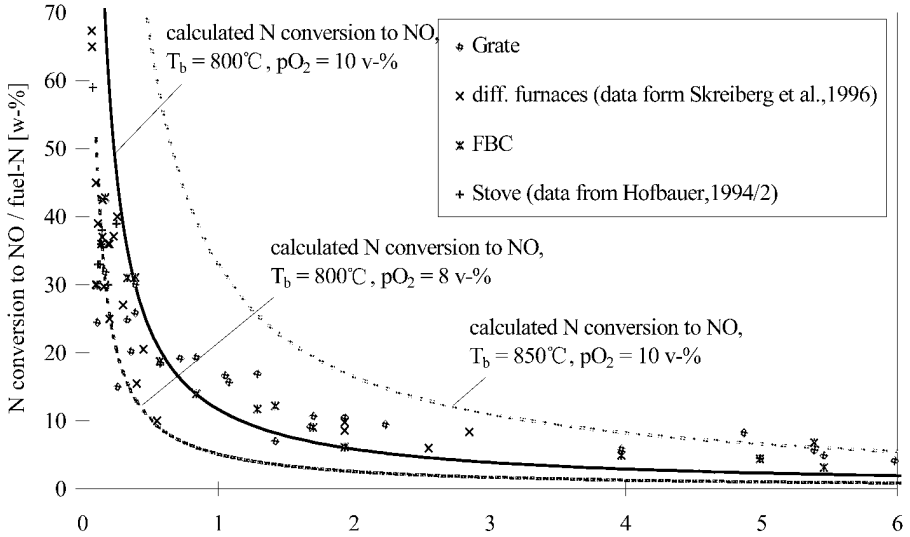

Fig. 1 Conversion of fuel-nitrogen to NO depending on the fuel-nitrogen content of the fuel burned (Wartha et al., 1997)

Figure 2 shows the main reaction paths during devolatilization and char combustion of an arbitrary fuel to NO, N_2O and N_2. During the early stage of devolatilization volatile nitrogen is released e.g. in the form of HCN or NH_3. Those intermediates are further oxidized to NO and N_2O. For HCN conversion refer e.g. to Dagout et al. 2008 and Molina et al. 2009. However during conversion intrinsic reduction may also take place depending on local operating conditions leading to N_2 (Winter et al. 1996).

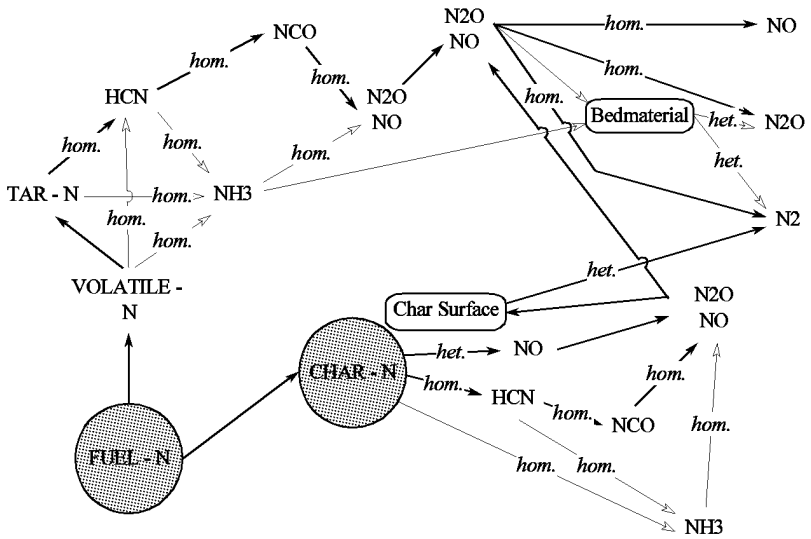

Fig. 2 The main reaction paths during devolatilization and char combustion of an arbitrary fuel to NO, N_2O and N_2

The effect of operating conditons on NO and N_2O is summarized in Table 2. An excellent primary measure to reduce NO and N_2O is severe air staging which is common practice in fluidized bed combustion. Usually selective non-catalytic reduction (SNCR) is not necessary however in certain cases it may be necessary. An increase in temperature e.g. above 850°C leads to a strong decrease in N_2O. However this interferes with optimum desulfurization.

Table 2 Summary of the main parameters influencing NO and N_2O emissions. Increasing parameters lead to increasing (↑) or decreasing (↓) NO, N_2O emissions

increasing parameters	NO emission	N_2O emission
Temperature	↑	↓
Volatile matter content	↓ (BFBC) ↑ (CFBC)	↓
Nitrogen content	↑	↑
Excess air	↑	↑
Air staging	↓	↓
Limestone addition	↑	↓
SO_2 concentration	↓	↑
SNCR	↓	↑

SULFUR OXIDES SO_2, SO_3

Sulfurdioxid (SO_2) is a poisonous gas and causes direct health injuries of the respiratory organs and forms acid rain. It can be further oxidized to sulfurtrioxid (SO_3) which acts in a similar way. They can be summarized as SO_x. SO_2 is formed by oxidation of the sulfur in the fuel (refer to Table 3) under combustion conditions and depends therefore on the sulfur content.

In fluidized bed combustion usually limestone ($CaCO_3$) is added which calcines (R1) and sulfation (R2) takes place, see Reactions 1-3. This in-situ desulfurization is a strong advantages of fluidized bed combustion technology e.g. in comparison to pulverized coal combustion where flue gas desulfurization has to be considered.

$CaCO_3 \Rightarrow CaO + CO_2$ R1 calcination

$CaO + SO_2 \Rightarrow CaSO_3$ R2 sulfation

$CaSO_3 + ½\ O_2 \Rightarrow CaSO_4$ R3 oxidation

A detailed discussion of the mechanism and review can be found in Anthony and Granatstein (2001).

Calciumsulfate forms tight shells due to its high molar volume inhibiting the CaO core to react further. Therefore the conversion is typically not more than 40% which is a major limitation of this technology. The optimum desulfurization temperature is about 850°C and commonly used in practice as operating temperature.

Figure 3 shows the $CaSO_4$ shell and the unreacted CaO core inside (Anthony and Granatstein, 2001).

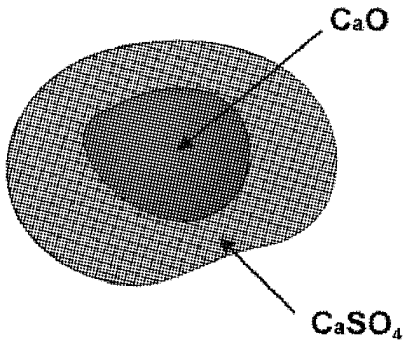

Fig. 3 The $CaSO_4$ shell and the unreacted CaO core inside

Table 3 Typical sulfur contents obtained from ultimate analysis on a dry and ash free basis

Analysis (daf)	anthracite	coals	lignite	peat	straw	wood	sewage sludge	tire waste	petroleum coke
sulfur [w-%]	1	1	0.5-3	0.5	0.1	0.02	0.8	1.5	5-7

HYDROCHLORIC ACID HCL, ALKALI, HEAVY METALS, DIOXINS

Hydrochloric acid (HCl) is a poisonous gas and causes direct health injuries of the respiratory organs and forms acid rain. It originates from the fuel by its conversion and depends therefore on the chlorine content of the fuel (refer to Table 4, refer also to Yudovich and Ketris 2006, Vassilev et al., 2000, Aho and Ferrer, 2005, Biobib, 1996, Kling et al., 2007, Mattenberger et al., 2008.).

Table 4 Typical chlorine contents on a dry fuel basis

Ulitmate Analysis (dry fuel)	hard coals	brown coals	peat	wheat straw	wood	sewage sludge ash	waste wood	Meat Bone Meal
chlorine [w-%]	0.01 – 0.2	0.005 – 0.1	0.01	0.5	<0.01	0.01	0.3	0.35

The fuel chlorine undergoes oxidation usually to HCl under combustion conditions however additional reactions may play a role and molecular chlorine (Cl_2) may be formed in small quantities:

$4HCl + O_2 \Rightarrow 2Cl_2 + 2H_2O$ R4 conversion to Cl_2 (Deacon reaction)

$MeCl + H_2O \Rightarrow HCl + MeOH$ R5 Me = Na, K interaction with alkali chemistry

$2MeCl + SO_2 + H_2O + ½\ O_2 \Rightarrow Me_2SO_4 + 2HCl$ R6 interaction with $CaCl_2$ and sulfur chemistry

$2MeCl + H_2O + ½\ O_2 \Rightarrow Me_2CO_3 + 2HCl$ R7 interaction with alkali-chlorides

$CaCl_2 + SO_2 + H_2O + ½\ O_2 \Rightarrow CaSO_4 + 2HCl$ R8 interaction with $CaCl_2$ and sulfur chemistry

$SO_2 + Cl_2 + H_2O \Rightarrow SO_3 + 2HCl$ R9 interaction with sulfur chemistry, formation of SO_3

$Al_2O_3.2SiO_2 + 2MeCl + H_2O \Rightarrow Me_2O.Al_2O_3.2SiO_2 + HCl$ R10 interaction with alumina silicates

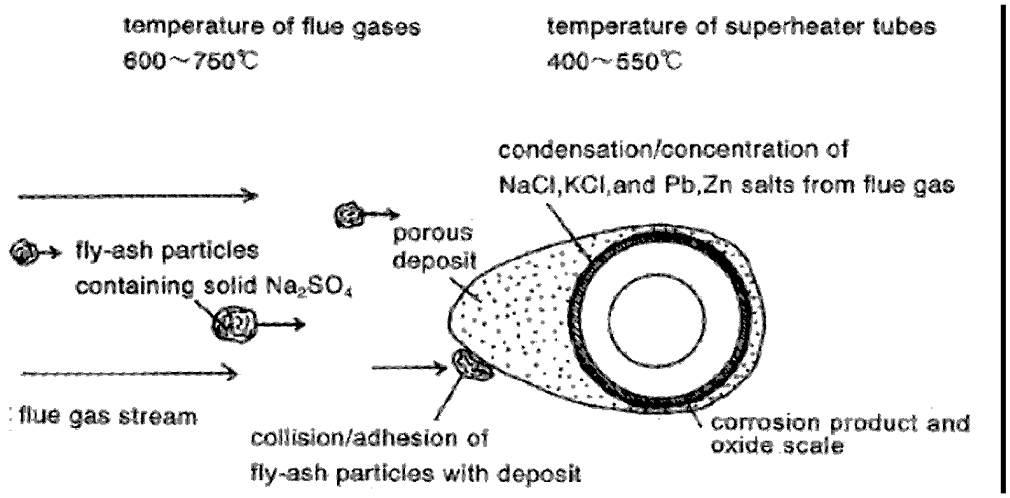

Fig. 4 The schematic corrosive salt formation on boiler tubes (Otsuka, 2008)

Reaction 5 shows the formation of HCl from alkali chlorides. Reactions 6, 8 and 9 show the interaction with the sulfur chemistry. Cofiring a biomass fuel which has a high chlorine content with a sulfur-containing fuel (e.g. lignite) may have benefical effects because instead of low melting alkali chlorides (MeCl) sulphates (Me_2SO_4) are formed and HCl is released (e.g. Gogebakan et al. 2009) refer also to Broström et al., 2007. A similar positive effect shows alumina silicates (meta-kaolinite) (e.g. Aho et al., 2005, Gogebakan et al., 2009).

Generally fuels with high chlorine contents lead to significant corrosion of the boiler tubes (e.g. Otsuka 2008, Skrifvars et al., 2008) and increases the propensity for bed agglomeration and deposit formation (refer e.g. to Zbogar et al., 2009).

Figure 5 shows the interaction of sulfur, alkali, chlorine and heavy metals (Pb, Zn) on the deposit chemistry (Otsuka, 2008).

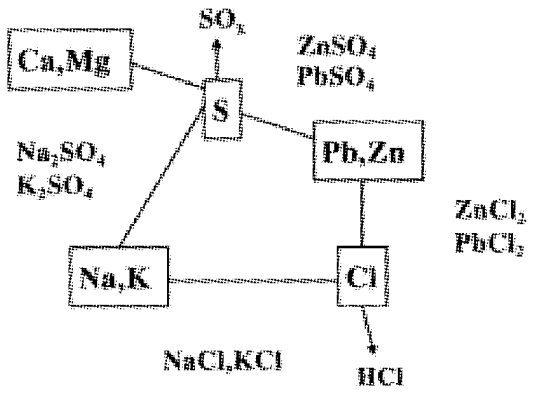

Fig. 5 The sulfur, alkali, chlorine and heavy metals (Pb, Zn) on the deposit chemistry

Chlorine and HCl may also be responsible for mercury oxidation in the flue gas. Knowledge of the mercury species (elemental mercury Hg^0, oxidized mercury Hg^{2+} or particle-bound mercury Hg_p) in the flue gas is very important because of its different physical and chemical behavior. Oxidized mercury can be captured in conventional wet scrubbers (refer also to Davidson, 2005).

Chlorine and especially Cl_2 have a propensity to the formation of polychlorinated dibenzo-dioxins (PCDDS) and polychlorinated dibenzo-furans (PCDFs) which have a high toxicity. Transition metals like Cu and Fe can catalyze PCDD/Fs formation. Small organic molecules can be adsorbed onto the fly ash from flue gases and may be subsequently converted to PCDD/Fs (refer also to Liu et al. 2000). Co-firing paper recycling residues, Scheidle et al. (1986), or municipal solid waste (MSW), Lindbauer et al. (1992), with coal drastically reduced the formation of PCDD/Fs. Also other studies have shown that the addition of coal, especially high sulfur coals to MSW decreases PCDD/Fs. This may be attributed to the shift of Cl_2 to HCl according :

$SO_2 + Cl_2 + H_2O \Rightarrow SO_3 + 2HCl$ R9 interaction with sulfur chemistry, formation of SO_3

PARTICULATES

Particulate matter (PM) is used for ultrafine solid particles and droplets in the air. PM2.5 refers to the particles which are 2.5 μm or smaller in size. PM10 to particles which are smaller than 10 μm, respectively. They are harmful to the respiratory system. Particles smaller than 2 μm are able to penetrate deep into the lung. Fine particulate formation may differ depending on coal or biomass combustion and operating conditions. A study on the formation of PM10 and PM2.5 in a laboratory-scale CFBC is given in Rajczyk and Nowak (2008) for biomass and coals. They found that biomass combustion particles eith the diameter larger than 1 μm are rich in calcium (Ca) whereas in the particles smaller than 1 μm potassium (K) is the dominant element.

Another effect of mainly alkali in ultra fine particles (below 100 nm, mainly potassium) in the flue gas was responsible for the deactivation of high-dust SCR catalysts used for NO_x reduction. A study has been done in three 100 MW scale boilers during biofuel and peat combustion (Kling et al., 2007).

CONCLUSIONS

This paper gives an overview of possible pollutants formed in fluidized bed combustors. As the fuel range used in CFBCs is large a wide range of potential pollutants may be formed. The fuel is the main source for pollutants formation e.g. NO_x, N_2O, SO_x, HCl, heavy metals and alkali.

These pollutants may lead to difficulties in operation of the fluidized bed combustor e.g. because of slagging and fouling the heat transfer may decrease or the efficiency of the high dust SCR catalyst. High concentrations in the flue gas may lead to health problems and pollution of the environment.

In this paper it has been shown that there is a strong interaction between the different pollutants' chemistries. The sulfur chemistry interacts with the chlorine chemistry and affects even deposit composition, mercury speciation and dioxin formation. Homogeneous reactions in the gas phase as well as heterogeneous and catalytic reactions on the solids' surfaces and even in the liquid phase may be of importance.

Now we are in the early stage of understanding the fundamental processes taking place in practical combustion systems like in CFBCs. However there is a significant lack of knowledge considering their interactions. The fluidized bed system is paramount for co-combustion of a wide range of fuels leading to an even closer interaction of pollutants' chemistries.

ACKNOWLEDGEMENTS

The author wants to acknowledge the very fruitful discussions within the International Energy Agency – Fluidized Bed Conversion research group and the Austrian Ministry for Transport, Innovation and Technology (BMVIT) for the financial support.

REFERENCES

Aho, M., Ferrer, E. (2005). Importance of Coal Ash Composition in Protecting the Boiler against Chlorine Deposition during Combustion of Chlorine-Rich Biomass, Fuel, 84 (2005), pp. 201-212.

Anthony, E.J., Granatstein, D.L., (2001). Sulfation Phenomena in Fluidized Bed Combustion Systems, Progress in Energy and Combustion Science, 27 (2001), pp. 215-236.

Biobib (1996), A Biomass Fuel Database, Institute of Chemical Engineering, Vienna University of Technology: http://www.vt.tuwien.ac.at/biobib/

Broström, M., Kassman, H., Helgesson, A., Berg, M., Andersson, C., Backman, R., Nordin, A. (2007). Sulfation of Corrosive Alkali Chlorides by Ammonium Sulfate in a Biomass Fired CFB Boiler, Fuel Processing Technology, 88 (2007), pp. 1171-1177.

Dagaut, P., Glarborg, P., Alzueta, M. U. (2008). The Oxidation of Hydrogen Cyanide and Related Chemistry, Progress in Energy and Combustion Science, 34 (2008), pp. 1-46.

Davidson, R.M. (2005). Chlorine in Coal Combustion and Cofiring, Report of the IEA Clean Coal Centre, London, UK.

Furimsky, E., Zheng, L., (2003). Qunatification of Chlorine and Alkali Emissions from Fluid Bed Combustion of Coal by Equilibrium Calculations, Fuel Processing Technology, 81 (2003), pp. 7-21.

Gogebakan, Z., Gogebakan, Y., Selcuk, N., Selcuk, E. (2009). Investigation of Ash Deposition in a Pilot-Scale Fluidized Bed Combustor Co-Firing Biomass with Lignite, Bioresource Technology, 100 (2009), pp. 1033-1036.

Kling, A., Anderssson, C., Myringer, A., Eskilsson, D., Järas, S. (2007). Alkali Deactivation of High-Dust SCR Catalyst used for NO_x Reduction Exposed to Flue Gas from 100 MW-scale Biofuel and Peat Fired Boilers: Influence of Flue Gas Composition, Applied Catalysis B: Environmental, 69 (2007), pp. 240-251.

Liu, K., Pan, W.-P., Riley, J.T. (2000). A Study of Chlorine Behavior in a Simulated Fluidized Bed Combustion System, Fuel, (2000), pp. 1115-1124.

Lindbauer, R.L., Wurst, F., Prey, T. (1992). Chemosphere (1992), p. 1409.

Mattenberger, H., Fraissler, G., Brunner, T., Herk, P., Hermann, L., Obernberger, I. (2008). Sewage Sludge Ash to Phosphorous

Fertiliser: Variables Influencing Heavy Metal Removal during Thermochemical Treatment, Waste Management, 28 (2008), pp. 2709-2722.

Molina, A., Murphy, J.J., Winter, F., Haynes, B.S., Blevins, L.G., Shaddix, C. (2009). Pathways for Conversion of Char Nitrogen to Nitric Oxide during Pulverized Coal Combustion, Combustion and Flame (2009) in press.

Otsuka, N. (2008). A Thermodynamic Approach on Vapor-Condensation of Corrosive Salts from Flue Gas on Boiler Tubes in Waste Incinerators, Corrosion Science, 50 (2008), pp. 1627-1636.

Rajczyk, R., Nowak, W. (2008). PM2.5 and PM10 Emission from Biomass Combustion in the Circulating Fluidized Bed, Proc. of Int. Conf. on Circulating Fluidized Beds, May 13-16, 2008, pp. 949-954.

Scheidle, K., Wurst, F., Kuna, R.P. (1986). Chemosphere (1986), p. 2089.

Skrifvars, B.-J., Backmann, R., Hupa, M., Salmenoja, K., Vakkilainen, E. (2008). Corrosion of Superheater Steel Materials under Alkali Salt deposits Part 1: The Effect of Salt Deposit Composition and Temperature, Corrosion Science, 50 (2008), pp. 1274-1282.

Vassilev, S.V., Eskenazy, G.M., Vassileva, C.G. (2000). Contents, Modes of Occurrence and Origin of Chlorine and Bromine in Coal, Fuel, 79 (2000), pp. 903-921.

Wartha, C., Reisinger, K., Winter, F., Gogolek, P., Hofbauer, H., (1997). The Importance of NO Formation Characteristics for the Prediction of NO - Emissions from Grade and Fluidized Bed Combustors, 4th Int. Conf. on Technologies and Combustion for a Clean Environment, July 7-10, 1997, Lisbon.

Winter, F., Wartha, C., Löffler, G., Hofbauer, H., (1996). The NO and N_2O Formation Mechanism during Devolatilization and Char Combustion under Fluidized Bed Conditions, Proc of 26th Int. Conf. on Combustion, The Combustion Institute, pp. 3325-3334.

Winter, F., Wartha, C., Hofbauer, H., (1999). NO and N_2O Formation during the Combustion of Wood, Straw, Malt Waste and Peat, Bioresource Technology, 70 (1999), pp. 39-49.

Yudovich, Y.E., Ketris, M.P., (2006). Chlorine in Coal: A Review, Int. Journal of Coal Geology, 67 (2006), pp. 127-144.

Zbogar, A., Frandsen, F., Jensen, P.A., Glarborg, P. (2009). Shedding of Ash Deposits, Progress in Energy and Combustion Science, 35 (2009), pp. 31-56.

LATEST EVOLUTION OF OXY-FUEL COMBUSTION TECHNOLOGY IN CIRCULATING FLUIDIZED BED

C .S. Zhao, L. B. Duan, X .P. Chen, C. Liang

School of Energy and Environment, Southeast University, Nanjing, 210096, China

Abstract: O_2/CO_2 combustion technology is considered as one of the most promising method to mitigate the greenhouse effect, and the O_2/CO_2 CFB combustion technology which combines O_2/CO_2 combustion technology with circulating fluidized bed (CFB) combustion technology will extend both their advantages. The latest research findings on O_2/CO_2 CFB combustion technology are reviewed, the combustion and pollutant emission characteristics are expatiated, its effects on the boiler design are analyzed, the techno-economic assessment are reported and the key issues are indicated in the paper. O_2/CO_2 CFB combustion technology has no insolvable bottleneck in its development and due to its economic superiority; it is one of the most important clean coal technologies.

Keywords: O_2/CO_2 CFB combustion technology, review, combustion characteristics, pollutant emission, techno-economic assessment

INTRODUCTION

The *Fourth Assessment Report* (IPCC. 2007) from Intergovernmental Panel on Climate Change (IPCC) presents that most of the observed increase in global average temperatures since the mid-20th century is very likely due to the observed increase in anthropogenic Green House Gas (GHG) concentrations. And carbon dioxide (CO_2) is the most important anthropogenic GHG. Its annual emissions have grown between 1970 and 2004 by about 80%, from 21 to 38 gigatonnes (Gt), and represented 76.7% of total anthropogenic GHG emissions in 2004. And 56.6% of them were from fossil fuel use, as shown in Fig.1. In China, coal is the major fossil fuel and is mainly used for power generation, so it is urgent and significant to find an efficient CO_2 reduction technology for the coal-fired power plants in China.

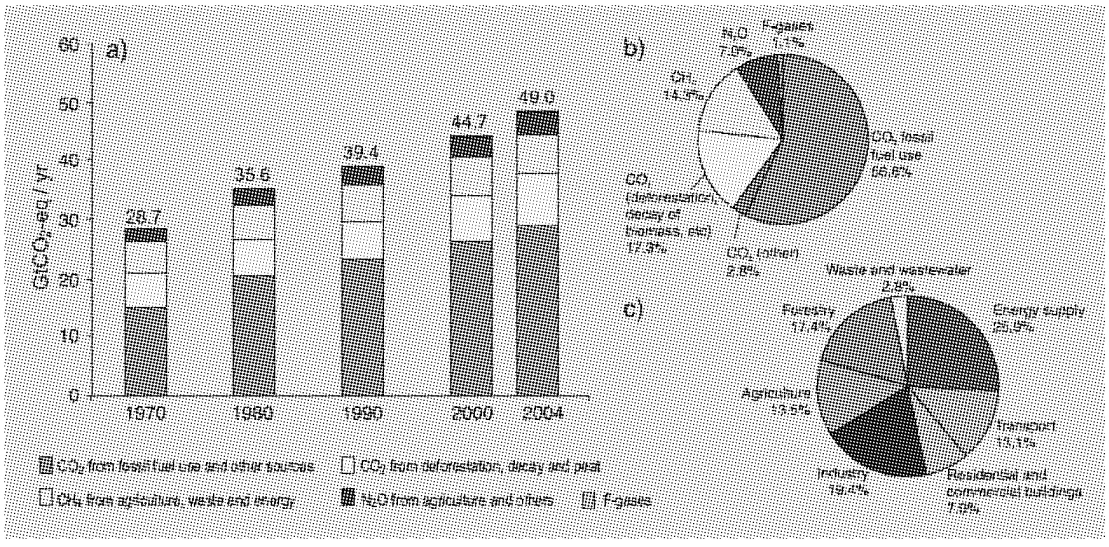

Fig.1 (a) Global annual emissions of anthropogenic GHGs from 1970 to 2004. (b) Share of different anthropogenic GHGs in total emissions in 2004 in terms of CO_2-eq. (c) Share of different sectors in total anthropogenic GHG emissions in 2004 in terms of CO_2-eq (Forestry includes deforestation.)

At present, several technologies are being developed for CO_2 capture and storage from coal-fired power plant that include (Buhre et al.2005; Yan et al., 2007; Abanades et al., 2002; Singh et al., 2003):

1) Post combustion capture by chemical absorption, usually mono-ethanolamine (MEA).
2) The integrated gasification combined cycle (IGCC).
3) Calcination/Carbonation cycles reactions of sorbents for CO_2 sorption.
4) Chemical looping combustion (CLC).
5) Membrane separation technology for CO_2 separation from the flue gas.
6) Oxy-fuel combustion. In this technology, pure O_2 and recycled flue gas (RFG) are fed into the furnace

for the combustion of the fuel. The RFG is used to control flame temperature and make up the volume of the missing N_2 to ensure the heat transfer in the boiler. Latest studies (Singh et al., 2003; Grainger et al. 2008; Klemes et al., 2007; Kay et al., 2006; Kay et al. 2007; Okawa et al., 1997) show that oxy-fuel technology has an advantage of simultaneous reduction of $CO_2/SO_2/NOx$, and oxy-fuel combustion is one of the most competitive technologies for both new boiler installation and old boiler retrofit.

Due to its good fuel flexibility, high boiler efficiency, low NOx emission, economical limestone desulfurization, and easy load adjusting, CFB combustion technology is quite meaningful for the mainly fossil fuel based power generation in China (Basu, 1999 and Gayan et al., 2004). At present, there are nearly 3,000 circulating fluidized bed (CFB) boilers installed in China, with total capacity reaching 65 millions kilowatts. Among them, more than one hundred and fifty 100MWe ~ 200MWe CFB units and thirteen 300MWe CFB units have been put into industrial operation. The unit number and the overall power generation capacity of CFB boilers in China share more than half of the total number and capacity in the world. Oxy-fuel CFB technology which can produce high CO_2 concentration flue gas from CFB boilers for storage or EOR was explored based on this background. It combines the two clean coal combustion technologies together and may play more multi-advantages. In the paper, the research findings on O_2/CO_2 CFB combustion technology are reviewed and summarized, the state of art of this technology is described and further studies needed are suggested.

OXY-FUEL CFB TECHNOLOGY DESCRIPTION

Oxy-fuel technology is the combination of oxy-fuel combustion technology and CFB combustion technology, and its schematic diagram is shown in Fig.2. Pure O_2 from ASU and RFG are fed into the furnace for the combustion of fuel. The RFG is used to control flame temperature and make up the volume of the missing N_2 to ensure there is enough gas to carry the heat through the boiler. Sorbents are fed into the boiler for SO_2 capture, and separated solid particles from the cyclone separator are fed back into the furnace to reburn. The exhaust flue gas with high CO_2 concentration (generally bigger than 95%) is transported for geological storage or enhanced oil recovery (EOR). The characteristics of oxy-fuel CFB combustion may include the following:

- Greater than 95% purity CO_2 can be reached in the exhaust gas;
- Good fuel flexibility, especially for low rank fuel as petroleum coke, MSW, etc. Possibility of negative CO_2 emission when firing biomass with CO_2 sequestration;
- Economical furnace desulfurization with sorbents;
- Improved desulfurization efficiency and calcium utilization;
- Lower NOx emission than conventional CFB boilers;
- High proportions of CO_2 and H_2O in the furnace gases result in higher gas emissivities;
- By recycled ash burning, the residence time of the particles in the furnace is prolonged, which can weak the long burnout time effect caused by high CO_2 concentration in the furnace;
- For flue gas recycled, the heat loss due to exhaust gas are largely reduced;
- Compared with oxy-fuel PC boilers, less flue gas needs to be recycled for heat, which can be removed by means of external solid heat exchangers.

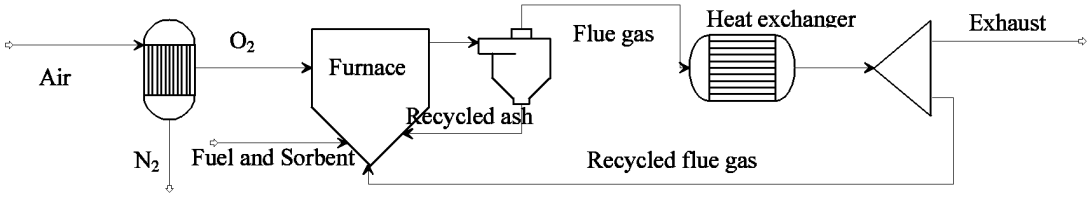

Fig. 2 Diagram of CFB O_2/CO_2 combustion technology

MAIN FINDINGS OF OXY-FUEL CFB TECHNOLOGY

The oxygen firing fluidized bed combustion was first explored by Zhejiang University in China. CANMET Energy Technology Centre in Canada has accomplished the mini-CFBC oxy-fuel combustion test and the commissioning of the 0.8MWth CFBC for oxy-fuel combustion is on going. ALSTOM has modified its 9.9 MM-Btu/hr Multiuse Test Facility (MTF) pilot plant to operate with O_2/CO_2 mixtures of up to 70 % O_2 by volume. Foster Wheeler/VTT is working on Oxy-fuel CFBC on a pilot scale facility. CERCHAR (SNET–French Utility) in France and Southeast University in China are planning to carry out pilot plant scale work.

Combustion characteristics of coal in O_2/CO_2 atmosphere

The latest researches on coal combustion characteristics focus mainly on ignition, burning rate, flame temperature, flame propagation speed, combustion stability and burnout characteristic, etc. TG study (Luo et al., 2004] on coal combustion in O_2/CO_2 atmosphere shows that as the O_2 content increases in the atmosphere, the ignition temperature of coal char decreases and the burnout time becomes shorter, the presence of CO_2 doesn't influence the char combustion reaction kinetics. Experiment in a combustion-driven laminar flow reactor (Molina and Shaddix, 2007) shows that the presence of CO_2 retards coal particle ignition but has no measurable effect on the duration of volatile combustion. For homogeneous ignition, as observed in the experiments, the effect of CO_2 can be explained by its higher specific molar heat and the effect of O_2 can be explained by its effect on mixture reactivity. In a microgravity combustion chamber (Kiga et al., 1997), the flame propagation speed of pulverized coal cloud was measured and results reveal that the flame propagation speed in O_2/CO_2 atmosphere is markedly lower than that in O_2/N_2 and O_2/Ar mixture and it can be improved by increasing oxygen concentration. Suda et al (2007) argued that reduction of flame stability in O_2/CO_2 combustion is mainly due to the larger heat capacity of CO_2 gas by both experimental and numerical analysis. Kimura et al (1995) observed the flame in O_2/CO_2 blown combustion was dark and unstable with high unburnt carbon. To match the adiabatic temperature in air-blown combustion, the O_2 concentration has to be raised to 42%. Tan et al (2006) found that the O_2/RFG flames are much less brighter and more compact than conventional combustion. 28%-35% O_2 concentration is proper to get the similar flame temperature and heat flux with air combustion. By numerical simulation, Liu et al (1999) concluded that the overall combustion rate of carbon particle in CO_2/O_2 (CO_2/O_2 mole ratio is 79/21) atmosphere is lower than air. With reducing of CO_2/O_2 mole ratio, the overall combustion rate increase obviously. On a laboratory scale CFB apparatus, Czakiet et al (2006) found that by elevating O_2 concentration, the carbon conversion ratio can be improved and increasing temperature of the reactor has no effect on the carbon conversion ratio between 973-1133K. ALSTOM operated their multi-use test facility successfully on coal and petroleum coke combustion with O_2/CO_2 mixture with up to 70% O_2 in the firing zone and there were no evidence of particle agglomeration or defluidization in the furnace.

There are quite little findings on oxy-fuel CFB combustion published in open literature. Due to the strong back-mixing of material, good mass and heat transfer, flyash reburning and additional cooling of recirculated solids, the problems which oxy-fuel combustion bring such as ignition delay, low burning rate and high carbon content in flyash can be overcame. It can be expected that oxy-fuel combustion is better applied to CFB boilers rather than PC boilers.

Pollutant emission characteristics

SO_2 emission characteristics

Many investigations on the desulphurization characteristics of sorbents in O_2/CO_2 atmosphere in CFB have been done, holding that atmosphere strongly affects the sulfur retention capability of sorbents. Recent reviews agreed that the calcination temperature of limestone depends on the CO_2 partial pressure, as shown in Fig.3. In the zone under the curve in the figure, limestone will be first calcined into calcium oxide (CaO) and then be sulfated to Calcium sulfate ($CaSO_4$), described by the following equations:

$$CaCO_3 \rightarrow CaO + CO_2 \quad (1)$$

$$CaO + SO_2 + 1/2O_2 \rightarrow CaSO_4 \quad (2)$$

In the zone above the curve, limestone will not decompose but be directly sulfated, as the following equation:

$$CaCO_3 + SO_2 + 0.5O_2 \rightarrow CaSO_4 + CO_2 \quad (3)$$

In the oxy-fuel CFB furnace, CO_2 partial pressure is usually above 0.7. And in the temperature range from 800℃ to 950℃, which is the main operation temperature zone of the CFB furnace, there exist two different desulfurization mechanisms. In the lower temperature zone, direct sulfation of limestone will take place. When the temperature is higher, calcination/sulfation reaction will take place. Due to the different mechanisms, the microstructure, calcium utilization and desulfurization efficiency are quite different. Studies (Snow et al., 1998; Liu et al., 2000; Fuertes et al., 1995 and 1994; Chen et al., 2007) showed that the calcium conversion under direct sulfation is usually higher than that under calcination/sulfation due to the porosity of the product layer. $CaSO_4$ is normally the final product in the O_2 containing sulfation atmosphere and it has a molar volume of 46 cm^3, which is 24.7% higher than the molar volume of $CaCO_3$. Despite the high molar volume of the product, the product layer formed by the direct sulfation reaction is more porous than that formed by calcination/sulfation. The direct sulfation reaction can often proceed at a fairly high rate even at high conversions. In the direct sulfation zone, elevating temperature can enhance the direct sulfation rate and improve the calcium conversion, while CO_2 partial pressure has negligible effect on calcium conversions, as

shown in Fig.4 and Fig.5. Czakiert et al (2006) investigated the sulfur conversion in a laboratory-scale CFB combustor and concluded that oxygen enrichment can improve the conversion of fuel sulfur to SO_2 because increasing temperature due to oxygen enrichment can weak the sulfur retention abilities of the mineral matter in the ash. Mao et al (2005) studied the SO_2 emission characteristics by a multi-function CFB setup and found that as the bed temperature increases and the O_2 content in the atmosphere increases, the desulfurization efficiency increases.

Although lots of work have been done, there are many uncertainties in the direct sulfation mechanism of limestone during the oxy-fuel combustion process. For example, the past studies all used not recycled flue gas but simulated gases to investigate the sulfation characteristics of limestone. In these cases, no vapor and ash were included, but vapor and ash had great influence on the sulfation behaviors. Also, in the actual CFB combustion condition, the differences may be bigger.

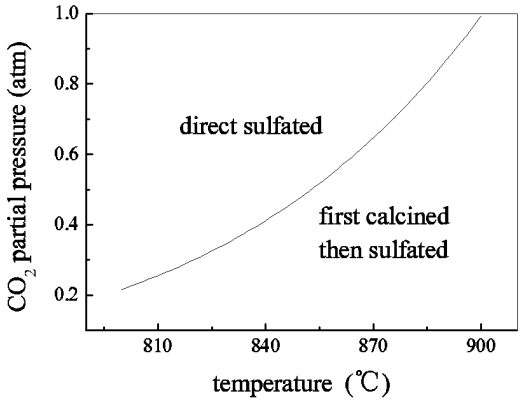

Fig.3 Effect of CO_2 partial pressure on calcination temperature of calcium carbonate

What attention should be paid is that when the combustion temperature is high and the calcination of the limestone still occurs in the oxy-fuel CFB furnace, the unreacted CaO will be carbonated when the ash cooled to the calcination temperature. And this phenomenon has the potential to cause fouling of the heat transfer surfaces in the back end of the boiler and to create serious operational difficulties. Wang et al (2008) found that both temperature and H_2O concentration play important roles in determining the reaction rate and extent of the carbonation. When the temperature is less than 400℃, no carbonation occurred without the presence of H_2O in the gas phase. However, with water vapor addition, carbonation will occur even at 250℃.

As can be predicted, the desulfurization efficiency of sorbents in oxy-fuel CFB combustor may be quite different from the laboratory-scale studies. And pilot-scale oxy-fuel CFB combustor with recycled flue gases is urgently needed. CANMET and Southeast University are carrying the on-going work.

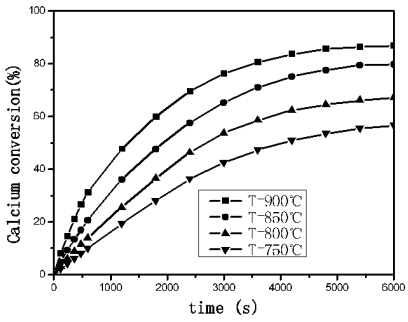

Fig. 4 Effect of temperature on calcium conversion ratio

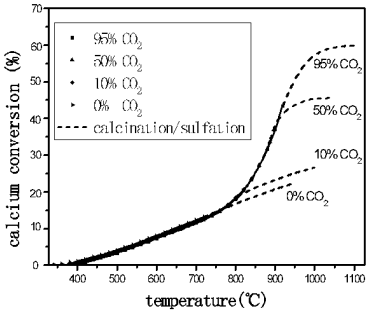

Fig. 5 Effect of CO_2 partial pressure on calcium conversion ratio

NOx emission characteristics

The NOx emission behavior during oxy-fuel coal combustion process has been studied using both O_2/RFG and O_2/CO_2 mixture in different apparatus. Kimura et al. (1995) reported a reduction of NOx in the exhaust to less than one-third of that exhausted with conventional air combustion. Okazaki et al. (1997) examined separately the effects of CO_2 concentration, reduction of recycled-NO in the flame, and interaction of fuel-N and recycled NOx on the decrease of the final NOx exhausted from the coal combustion system with the recycled CO_2. They concluded that the conversion ratio from the fuel-N to exhausted NOx is reduced to less than one-fourth of that with air combustion, and the effect of a reduction of recycled-NO in the furnace was dominant and amount to 50%-80%. Whatever, NOx emission during oxy-fuel combustion reduces largely, the reasons (Hu et al., 2001 and 2003; Chen et al., 2007) include the following:

1) without N_2 in the atmosphere, there is no thermal NOx and prompt NOx formation,
2) the interaction of fuel-N and recycled NOx,
3) the reduction of recycled NOx by the reducing radical in the flame,
4) the bigger tendency of NO/CO/Char reaction due to the higher CO concentration in oxy-fuel

combustion.

During the oxy-fuel combustion process in CFB, NOx reduction will be more due to the lower combustion temperature, air staging, higher CO concentration and the catalytic reduction of the calcium oxide (Czakiet et al., 2006; Francesco et al., 2001; Hughes et al., 2006; Kim et al., 2007). At present, the investigations concerning N_2O, another important GHG which has a large emission during CFB combustion process, have rarely been reported. But these kinds of study will be highlighted in future for the big environment damage and complex generation-disappearance mechanism of N_2O.

Minerals, particulate matter and heavy metals

During coal combustion, ash particles are formed from the inorganic matter presented in coal. The mechanisms of ash formation have been studied extensively in the literature, and are affected by the combustion conditions and the coal characteristics (Sheng and Li, 2008). The majority of inorganic matter presented in black coals occurs in the form of minerals of various types and sizes. These minerals can be closely associated with the organic matter (included minerals), or they occur excluded from the organic matter (excluded minerals). The majority of ash particles are formed from four formation mechanisms,

1) Included mineral coalescence,
2) Char fragmentation,
3) Excluded mineral fragmentation,
4) Vaporization and subsequent condensation of inorganic matter.

Krishnamoorthy and Veranth (2003) used a detailed char particle combustion model to study the effect of bulk gas composition (e.g. CO_2 concentration) on CO/CO_2 ratio inside a burning char particle. They indicated that increasing CO_2 in the bulk gas significantly changed the CO/CO_2 ratio in the particle which could affect the vaporization of refractory oxides, as the concentration of the reducing gas inside the particle increases.

A study by Sheng (2007) demonstrated, in comparison to air combustion, O_2/CO_2 combustion at the same O_2 concentration decreased the yields of the fine particles in both submicrometer and fine fragmentation regions, because it resulted in a lower particle combustion temperature, while increasing the O_2 concentration in the O_2/CO_2 mixture enhanced the formation of the fine particles in both regions. It was found that the O_2/CO_2 combustion resulted in the size of the submicrometer fume mode shifting to a smaller size.

Suriyawong and co-workers (2006 and 2008) investigated the effect of environment on PM. They found the mass, number concentration, and mean size of the submicrometer particles decrease when N_2 is replaced with CO_2, When N_2 is partially removed from the air stream, the mean particle size, mass, and number concentration increase with an increasing N_2/CO_2 ratio.

By equilibrium calculation, Zheng and Furimsky (2003) found that distribution of trace metals was unaffected when O_2 concentration in O_2/CO_2 mixture approaches that in air. The effect of O_2/CO_2 mixture on the distribution of chlorine- and alkali- containing compounds in the vapor phase was minor compared with that in air.

Little studies on heavy metals, trace elementals and PM emission in oxy-fuel CFB combustion were reported.

INFLUENCE OF OXY-FUEL COMBUSTION ON CFB BOILERS

The inconsistent characteristics on heat transfer, combustion and pollutant emissions between oxy-fuel and conventional air combustion necessitate the differences on boiler design and operation with oxy-fuel combustion.

Bed temperature

Bed temperature is one of the most important operation parameters for CFB boiler and proper temperature controlling can avoid agglomeration, reduce pollutant emission and guarantee heat exchange inside the CFB boilers. Generally, the bed temperature of a CFB boiler are controlled around 850℃ for optimum desulfurization temperature, and the optimum temperature may get up to 900℃ when firing anthracite coal and especially petroleum coke. Compared to PC boilers, CFB boilers have more ways to control bed temperature such as adjusting cyclone ash recirculating ratio, air staging and fly ash reinjection etc. For oxy-fuel combustion, RFG is used to moderate the bed temperature. In oxy-fuel CFB combustion, the O_2/RFG ratio can even be changed respectively in the primary and second gas supply to achieve the best temperature profiles and most pollutant reduction. Mao (2005) investigated the temperature profiles of a laboratory-scale CFB setup with inner diameter of 77mm and height of 2800mm under air and O_2/CO_2 atmosphere. Results in Fig.6 show that as the O_2 content in the air supply increases from 21% to 29%, the bed temperature increases by about 20℃.

1-demenisional model calculation (Saastamoinen et al, 2006) result indicated that temperature gradient in vertical direction is much higher with high O_2 concentration than with air combustion (Fig.7). For the solid temperature during coal combustion is not even, local high temperature zone may exist in the combustor, especially near the high O_2 concentration gas injection locations. This may cause the agglomeration problem during oxy-fuel CFB combustion. ALSTOM burned three fuels in their bubbling fluidized combustor under different atmospheres and found that at 50% O_2 in feed gas with Tri-star coal, there was agglomeration when the fluidization velocity was 0.52m/s, and when the velocity increased to 0.85m/s, the agglomeration disappeared.

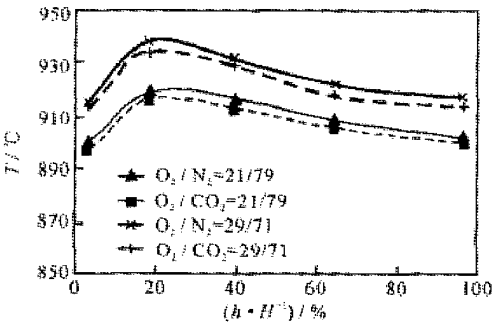

Fig. 6 Temperature profiles in vertical direction (experimental result)

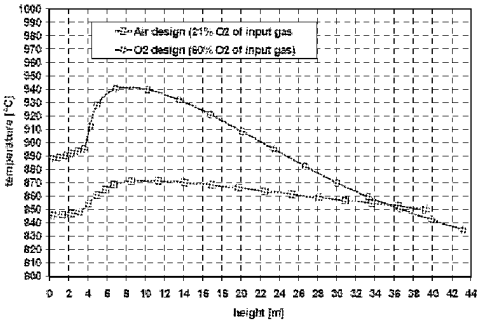

Fig. 7 Temperature gradient in vertical direction (calculated result)

Heat transfer and heating surface arrangement

CO_2 and H_2O have higher thermal capacities compared to N_2. The increase in thermal capacity increases the heat transfer in the convective sections of the boiler. However, the amount of gases passing through the boiler in the oxy-fuel case is lower and increased heat transfer in the radiative section of the boiler results in lower gas temperature entering the convective pass. Both of these factors will act to lower the heat transfer in the convective section of the boiler. The heat transfer in the radiative and convective sections of the boiler will need to be optimized to ensure efficient operation.

There are mainly three parts for heat transfer for a CFB boiler system: combustor, external heat exchanger and convective pass. Since the O_2 concentration in the feed gas is elevated, the total gas volume in the CFB furnace reduces to maintain the good combustion efficiency, and to get a good fluidization effect, the furnace size reduces a lot at the oxy-fuel combustion style. According to Saastamoinen's conclusion (2006), the volume of the furnace in 60% O_2 case will be 38% of that in 21% O_2 case. In the much smaller space, various heat exchanger options will be necessary to meet the heat duty distribution need. The heat duty distribution of the studied case is shown in Fig. 8. It can be seen that the convective pass and furnace wall heat duties are largely diminished for the O_2 design due to the reduced flue gas. And heat duties of INTREX superheating and wing-wall superheating are augmented to make up them. ALSTOM also studied the heat duty distribution of oxy-fuel combustion with 70% O_2 concentration comparing with air combustion, concluding that heat duty of external heat exchanger may exceed 70%.

ALSTOM also studied the CFB boiler general arrangement firstly, as shown in Fig. 9.

Separator efficiency and flyash reinjection

At the same O_2 concentration, the burnout temperature has been proven to be higher and burnout time to be longer than conventional air combustion. And for the CFB boilers in China, there is a common problem of high carbon content in flyash. So measures should be taken to reduce the unburnt carbon in flyash. Particle size of the feed fuel should be controlled more strictly. Cyclone separators with higher separation efficiency must be explored. And flyash recirculating may be used extensively in the oxy-fuel CFB boilers.

Sealing problems

One strong advantages of oxy-fuel combustion is the production of high CO_2 concentrated (normally over 95%) flue gas stream for EOR. For the existing CFB boilers, they are almost designed and operated under balance ventilation, and air leakage takes place at the micro-negative pressure locations such as the economizer, air preheater, tail duct, and so on. These may cause the CO_2 concentration in the flue gas to fall and increase the cost of flue gas treatment. Improving the sealing capability of the heat surface at the

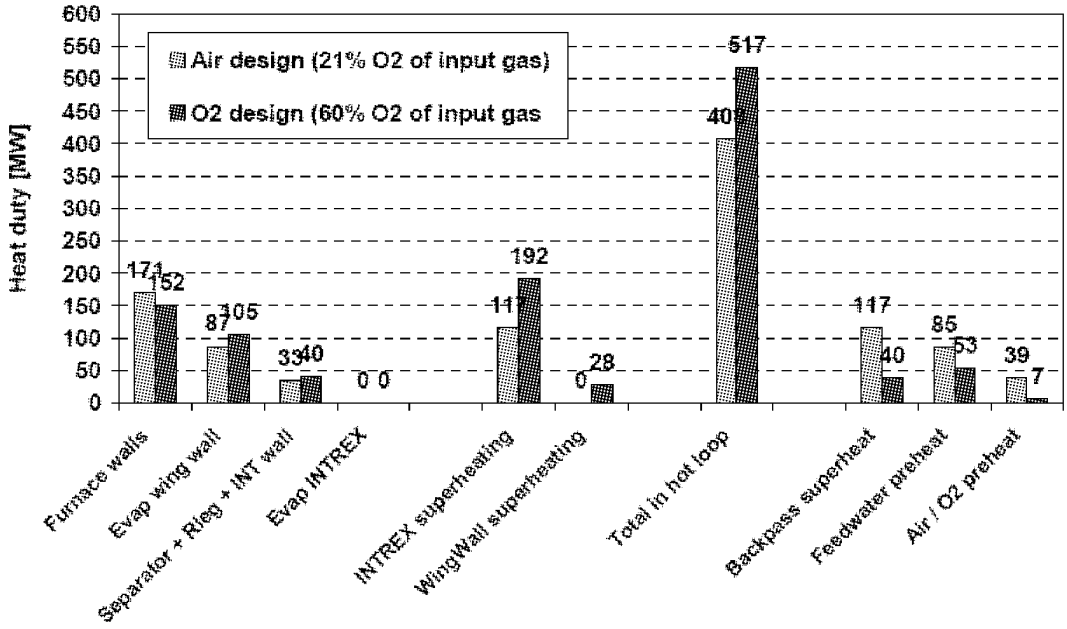

Fig. 8 The heat duty distribution of an oxy-fuel CFB boiler

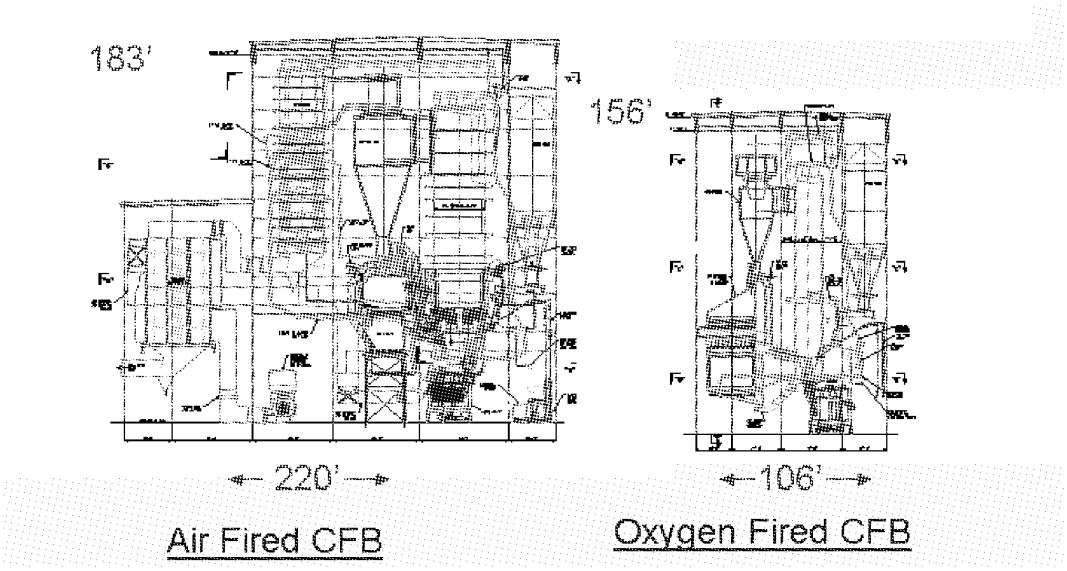

Fig. 9 CFB profiles with air fired and oxygen fired

tail is important if this ventilation mode remains. Also the boiler can be operated at the micro-positive pressure mode according the successful experience of the gas-fired and oil-fired boilers.

Erosion and abrasion

Flue gas recycle makes the acid gas such as SO_2 and NO_X concentrated in the furnace and augments the erosion of the water wall and heat surface of the furnace. With O2 enrichment, the furnace size reduces compared with air combustion which may cause more serious abrasion of furnace wall. So CFB boiler with oxy-fuel combustion brings higher requirement for material.

TECHNO-ECONOMIC STUDIES

The net efficiency reduction of oxy-fuel CFB power plant is mainly originated from the introduction of air separation unit (ASU) and CO_2 compression and purification system. The former studies indicate that oxy-fuel combustion has some economic advantages compared with other CCS technologies (Pierce et al., 1995; Akai et al., 1995; Gotlicher and Pruschek, 1995).

At present, the main air separation technologies (Rezvani et al, 2006) include cryogenic distillation,

pressure swing absorption, chemical looping combustion and membrane technology. And the only separation technology that can provide the O_2 flows required in the present application is cryogenic distillation. Andersson and Johnsson (2006) evaluate the power consumption and the investment cost of the ASU for an 865MWe lignite-fired oxy-fuel power plant. The specific power consumption of the ASU with a production capacity of 276900 Nm^3 to 5287000 Nm^3 ranges from 0.34kW/Nm^3 /h to 0.36kW/Nm^3 /h for produce O_2 of 99.6% purity. And the power consumption can be reduced if the O_2 purity decreases.

The flue gas treatment basically involves the removal of water and the non-condensable gases. Generally, the flue gas of an oxy-fuel CFB power plant before treatment contains 80%-90% CO_2, 10%-15% water and a little percent of SO_2. A complete dehydration of the flue gas is important, since it will reduce the mass flow and prohibit corrosion and hydrate precipitation. According to the destinations of the flue gas, the requirements of the flue gas composition are different. For example, storing SO_2 below the ground level may cause problems due to its sulfation behavior in contact with the calcium present in the storage environment. So it is better to remove the SO_2 if the flue gas is transported for geological storage. And CO_2 alone may cause corrosion of the transport duct in the presence of water. Therefore, the maximum water content in the flue gas prior to the compressor should not exceed 60-100mg/Nm^3. What should be mentioned is that the flue gas transport cost depends on the transport distance to a certain extent.

Andersson concluded the net electrical efficiency become 33.5% with oxy-fuel combustion, compared with 42.6% for the reference plant. ALSTOM performed the investment study of oxy-fuel CFB power plant. They separated the investment into 3 parts including traditional power plant equipment, ASU and gas processing system, as shown in Fig.10. The figure shows that the traditional power plant equipment investment reduces about 20% as a result of cost reduction in the boiler island. The improvement of updated O_2 fired power plant is mainly a small decreases in the specific plant cost and a small increase in the net plant output. They concluded the CO_2 mitigation price for original oxy-fired and updated oxy-fired power plants are about 40 and 37$/t of CO_2 avoided respectively. But for CANMET, the result is about 35$/t (Singh et al., 2003).

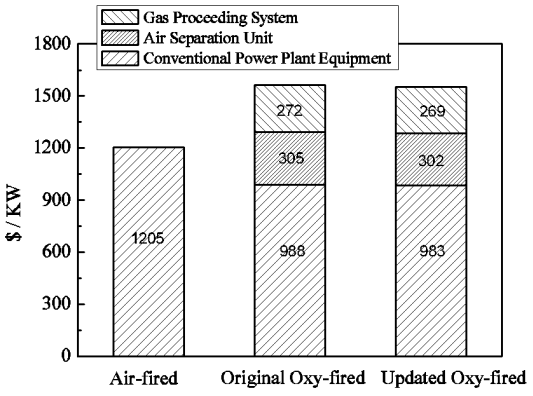

Fig. 10 Investment cost of O_2/CO_2 CFB power plan

IMPORTANT POINTS FOR CFB BOILERS WITH OXY-FUEL

The researches on oxy-fuel CFB combustion are all in laboratory or pilot scale, and many important points need to be further studied.

The selection of fluidization velocity

Fluidization velocity is one of the most important parameters for CFB design and operation, which affects the bed temperature distribution, heat flux, heat surface arrangement, agglomeration and abrasion, etc. At present, the fluidization velocity of CFB boilers with air combustion is about 5-7 m/s. With oxy-fuel combustion, the fluidization velocity may change due to the different radiative and convective heat transfer distribution.

Pollutant emission

During the oxy-fuel combustion process in CFB, the formation and emission mechanisms of gas pollutant as SO2 and NOx are still unclear. The effects of oxy-fuel combustion on trace elements emissions and on flyash size distribution have not yet been experimentally determined. The heavy metal transformation and volatile organic compounds emission characteristics have not been studied. As the growing awareness of environment protection, these areas will be recognized.

Hot or cool flue gas looping

Weather the flue gas needs to be cooled and dust-removed before recycle or not is quite important. Certainly, the clean gas without water vapor and dust is beneficial for the boiler operation safety, but will add the investment of equipment. Hot gas recycle can reduce the heat loss and make the unburnt carbon and

unreacted sorbents recirculated in the furnace, improving the combustion efficiency and calcium utilization efficiency. But hot gas recycle may cause corrosion and abrasion problems.

Numerical simulation of oxy-fuel CFB combustion

The comprehensive models which couple fluid dynamic, mass and heat transfer and combustion in an Oxy-fuel CFB boiler are rarely reported. This kind of models has great significance in saving experimental expense, solving theoretical difficulties and guiding design and operation.

Demonstration power plant

So far, there was not a demonstration oxy-fuel CFB power plant in the world. And it is the only road for this technology to commercial utilization.

CONCLUSIONS

Oxy-fuel CFB combustion is a promising technology for CO_2 reduction, which combined the advantages of CFB combustion and oxy-fuel combustion. Many investigations on oxy-fuel CFB combustion were carried out including combustion and pollutant emission characteristics of coal, heat transfer and boiler design and techno-economic study which indicated that there is no bottleneck for oxy-fuel CFB combustion in commercial application. But many important points such as desulfurization, NO_X emission, ash property, etc also need to be further studied. And the next important step is the construction of a demonstration power plant.

ACKNOWLEDGEMENTS

Financial supported by the Special Funds for Major State Basic Research Projects of China (2006CB705806); supported by the Foundation for Excellent Doctoral Dissertation of Southeast University. Many arguments in this paper are from the references and all the authors of the references are acknowledged.

REFERENCES

Abanades, J. C.: Chem. Eng. J. **90**(2002), pp.303-306.
Andersson, K. and Johnsson, F.: Energy Convers. Manage. **47**(2006), pp.3487-3498.
Akai, M., Kagajo,T., Inoue, M.: Energy Convers. Manage. **36**(1995), pp.801-804.
Basu, P.: Chem. Eng. Sci. **54**(1999), pp.5547-5557.
Buhre, B., Elliott, L. and Sheng, C.D.: Prog.Energy Combust. Sci. **31** (2005), pp.283-307.
Chen, C.M, Zhao,C.S, Liang, C., Pang, K.L.: Fuel Process.Techno. **88**(2007), pp.171-178.
Chen, J.C., Liu, Z.S., Huang, J.S.: J.Hazard. Mater. **142** (2007), pp.266-271.
Czakiert, T. Bis, Z., Muskala, W.: Fuel Process.Techno. **87**(2006), pp.531-538.
Francesco, M., Gerhard L., Verina J. W.: Fuel, **80**(2001), pp.1555-1566.
Fuertes, A.B., Velasco, G., Alvarez, T., Fernandez, M,J.: Thermochim. Acta, **254**(1995), pp.63-78.
Fuertes, A. B, Velasco, G., Fuente, T., Alvarez, T. Fuel Process.Techno. **38**(1994), pp.181-192.
Gayan, P., Adanez, Juan. and Luis F.: Fuel, **88**(2004), pp.277-286.
Gotlicher, R. and Pruschek. Energy Convers. Manage. **38** (1995), pp.173-178.
Grainger, D. and Hagg, M.B.: Fuel. **87**(2008), pp.14-24.
Hu,Y. Q., Kobayashi,N. and Hasatani, M.: Fuel, **80**(2001), pp.1851-1855.
Hu,Y.Q., Kobayashi,N. and Hasatani, M.: Energy Convers. Manage. **44**(2003), pp.2331-2340.
Hughes, R., Jia, L.F., Tan, Y.W.: 19th Int. FBC Conference.
Intergovernmental Panel on Climate Change: Climate change 2007: IPCC Fourth Assessment Report-Climate Change 2007.
Kay, D., Martijn, V.T. and Andre, F.: Prog. Energy Combust. Sci. **32** (2006), pp.215-246.
Kay, D., Martijn V.T. and Andre, F.: Prog. Energy Combust. Sci. **33**(2007), pp.580-609.
Kiga, T., Takano, S., Kimura, N.: Energy Convers. Manage. **38**(1997), pp.129 - 134.
Kim, H. K., Kim,Y., Sang, M.L.: Proceed. Combust. Instit. **31**(2007), pp.3377-3384.
Kimura, N., Omata, K., Kiga,T., and Takano, S.: Energy Convers Mgmt. **36**(1995), pp.805 - 808.
Klemes, J., Bulatov, I. and Cockerill, T.: Comput. Chem. Eng. **31**(2007), pp.445-455.
Krishnamoorthy, G., Veranth, J.M. Energy Fuels. **17**(2003), pp.1367 – 1371.
Liu, H., Katagiri, S., Kaneko, U.: Fuel, **79**(2000), pp.945-953.
Liu, Y.F., Yan, W.P., Song, Z.P.: J. Eng. Thermophysics.**20**(1999), pp.769-772 (in Chinese).
Luo, Z.Y., Mao, Y.R. and Wu X.C.: Thermal power generation, **6**(2004), pp.14-18. (in Chinese).
Mao, Y.R., Fang, M.X., Luo, Z.Y.: J. Combust. Sci. Techno.**11**(2005), pp.188-191 (in Chinese).
Molina, A., Shaddix C.: Proc. Combust. Inst. **31**(2007), pp.1905-1912.
Okawa, M., Kimura, N. and Kiga, T.: Energy Convers. Manage. **38**(1997), pp.123-127.
Okazaki, K., Ando, T.: Energy, **22**(1997), pp.207-215.
Pierce, W.F., Riemer, William, G., Ormerod.: Energy Convers. Manage. **36**(1995), pp.813-818.

Rezvani, S., Huang, Y., McIlveen, W.D., Hewitt, N., Wang, Y.D.: **86**(2007), pp.1034-1043.
Saastamoinen, J., Tourunen, A., Pikkarainen, T.: 19th Int. FBC Conference.
Sheng, C.D, Li, Y.: Fuel. **87**(2008), pp.1297-1305.
Sheng, C.D, Lu, Y.H, Gao, X.P.: Energy Fuels. **21**(2007), pp.435-440.
Singh, D., Croiset, E. and Douglas P.L.: Energy Convers. Manage. **44**(2003), pp.3073-3091.
Snow, M.J.H., Longwell, J.P. and Sarofim, A.F.: Industr. Eng. Chemist. Res. **27**(1988), pp.269-273.
Suda, T., Masuko, K., Sato, J.: Fuel, **66**(2007), pp. 2008-2015.
Suriyawong, A., Gamble, M., Lee, M.H.: Energy Fuels. **20**(2006), pp.2357–63.
Suriyawong, A., Christopher, J., Hogan, Jr. : Fuel. **87**(2008),pp.673-682.
Tan, Y.W, Croiset, E., Douglas, M.A.: Fuel, **85**(2006), pp.507–512.
Wang, C.B., Jia, L.F., Tan,Y.W.: Fuel, **87**(2008),pp.1108-1114.
Yan, S.P., Fang, M.X. and Zhang W.F.: Fuel Process. Techno. **88**(2007), pp.501-511.
Zheng, L. and Furimsky, E.: Fuel Process.Techno. **81**(2003), pp.23-34.

FOSTER WHEELER'S SOLUTIONS FOR LARGE SCALE CFB BOILER TECHNOLOGY: FEATURES AND OPERATIONAL PERFORMANCE OF ŁAGISZA 460 MWe CFB BOILER

Arto Hotta

Foster Wheeler Energia Oy, Finland

Abstract: During recent years, once-through supercritical (OTSC) CFB technology has been developed, enabling the CFB technology to proceed to medium-scale (500 MWe) utility projects such as Łagisza Power Plant in Poland owned by Poludniowy Koncern Energetyczny S.A. (PKE), with net efficiency nearly 44%. Łagisza power plant is currently under commissioning and has reached full load operation in March 2009. The initial operation shows very good performance and confirms, that the CFB process has no problems with the scaling up to this size. Also the once-through steam cycle utilizing Siemens' vertical tube Benson technology has performed as predicted in the CFB process. Foster Wheeler has developed the CFB design further up to 800 MWe with net efficiency of $\geqslant$45%.

Foster Wheeler's circulating fluidized bed (CFB) boiler technology meets today's market demand for utility-size boilers with capability to fire broad range of fuel qualities from low-grade high-ash fuels, good quality bituminous and anthracite coals to various biomass and waste fuels. The high efficiency CFB boilers are designed for firm emission performance and high reliability.

The proven high efficiency circulating fluidized-bed (CFB) technology offers a good solution for CO_2 reduction both in repowering of coal fired power plants and in greenfield power plants. CFB technology with its excellent fuel flexibility offers the opportunity to further reduce CO_2 emissions by co-combusting coal with biomass. FW has also developed CFB gasification technology for biomass applications. An example of this technology is gasification of biomass with a pressurized gasifier to produce syngas, which can be used for biodiesel production to address the reduction of CO_2 emissions from vehicles.

Carbon capture and storage (CCS) offers the potential for major cuts in CO_2 emissions of fossil fuel-based power generation in the fairly short term, provided that it gains public acceptance, the required regulatory framework is created and emission trading mechanisms or other incentives can provide solid return on the major investments required. Oxy-fuel combustion is one of the identified main CCS technology options, and Foster Wheeler is developing its CFB combustion technology for oxy fuel combustion to provide a CCS-ready solution. Foster Wheeler is currently developing Flexi-Burn™ CFB concept, which enables the plant to be operated either with or without carbon capture. This paper presents the existing status of CFB technology in respect of boiler efficiency and fuel flexibility. The main advantages of the CFB technology for oxyfuel combustion and a development plan for the Flexi-Burn™ CFB will be presented.

Keywords: large scale CFB boiler, Foster Wheeler, CO_2 reduction

INTRODUCTION

Foster Wheeler is a global engineering and construction contractor and a supplier of power equipment. Among other products, the company offers state-of-the-art boilers for heat and electricity generation based on circulating fluidized bed (CFB) technology. Boilers are offered for a variety of fuels and mixes, including fossil-derived fuels (e.g. coal, waste coal, petcoke), peat, biomass-derived fuels (e.g. wood, agricultural residue, bio-sludge), and waste fuels (e.g. contaminated wood, REF, TDF).

During the past 30 years Foster Wheeler has booked nearly 350 CFB boilers, of which almost 240 are designed for coal and wastes from the coal mining industry with total thermal capacity of 47,000 MWth (Fig. 1). All the boilers share the same circulating fluidization principle; however, depending on the quality of fuel, the boilers differ significantly in design and operation.

Power generation based on the combustion of solid fuels is expected to remain as mainstream technology for the foreseeable future. Fuel resources are abundant and widely distributed, which tends to provide price stability and security of supply. At modern power plants, the traditional pollutants are well under control. When

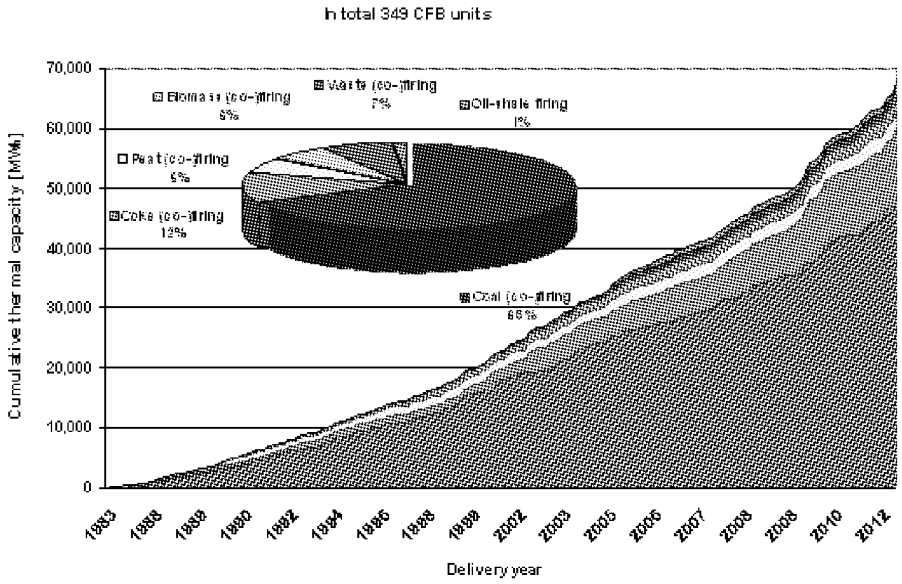

Fig. 1 Foster Wheeler's CFB references (as by 02.09.2008)

considering either new plants or repowering of old plants, efficiency and environmental performance are key issues. High efficiency means lower fuel requirements, and lower levels of ash and emissions, including CO_2. In the near future the main market for CFB in Europe will continue to be the replacement of existing old coal-fired units. Utilization of proven high efficiency CFB technology is an ideal solution both for repowering and for new plants. CFB technology has proven excellent fuel flexibility and also offer the option to co-combust of biofuels with different grades of coals, which can further reduce CO_2 emission (Jäntti T et al., 2006).

CFB technology is now proven at utility-scale. Plant sizes up to 300 MWe are in operation today. The net efficiency of those conventional sub-critical designs is approximately 38-40%, depending on fuel and condenser conditions. During recent years, once-through supercritical (OTSC) CFB technology has been developed, enabling the next stage in CFB development to proceed medium-scale (<500 MWe) utility projects such as Łagisza, with net efficiencies near 45%. Łagisza power plant is currently under commissioning and has reached full load operation in March 2009. The operation shows very good performance and confirms, that the CFB process has no problems with the scale-up up to this size. Additionally, the once-through steam cycle utilizing Siemens' Benson technology has performed as predicted in a CFB process. Foster Wheeler has developed the CFB design further up to 800 MWe with net efficiency of >45% to be commercial during 2009.

However, scaling up the technology further to utility scale (600-800 MWe) with net efficiency of 45-50% is needed to fulfill the future requirements of utility operators (Jäntti T et al., 2006).

FW is continuously working on improving the efficiency and co-combustion capability of its CFB boilers. Efficiency increases and co-firing of coal with CO_2-neutral fuels provide a technically and economically feasible solution to the CO_2 issue in the short and medium term, while major emission cuts possibly required in the future call for more powerful solutions. Post-combustion capture of CO_2 from power station flue gases is considered technically feasible, but in combustion with air, the flue gas volumes are large and CO_2 very much diluted with N2. Separation of CO_2 from such a stream is costly, and other options are being explored (Jäntti T et al., 2006).

In oxyfuel combustion systems, the fuel is burned in a mixture of pure O_2 and recirculated flue gas, instead of air. The absence of air nitrogen produces a flue gas stream with a high concentration of CO_2, making its much easier to separate the CO_2 CFB technology appears to be ideally-suited for oxyfuel combustion, and FW is developing its CFB for oxycombustion to provide the potential for nearly 100% reduction of CO_2 (Jäntti T et al., 2006). The main focus at the moment is in a Flexi-Burn™ concept, which enables the plant to be operated either with or without carbon capture, allowing more flexible operation and reduction of risks in plant operation.

HIGH EFFICIENCY & FUEL FLEXIBLE CFB NOW IN UTILITY SCALE PROVIDES SOLUTION TO REDUCE CO_2 EMISSIONS

Scale-up

Responding to an ever-growing demand for power generation, CFB boiler technology has developed to meet utility-scale requirements (Fig. 2). Today, the largest CFB units based on natural circulation are two 300 MWe CFB boilers at Jacksonville Energy Authority in Jacksonville, Florida, U.S.A. These boilers burn either 100% coal or 100% petroleum coke or any combination of the two. The largest units in terms of physical dimensions are three 262 MWe CFB boilers at Turow power plant in Poland. The fuel for these boilers is lignite with moisture content of 45% wt, which increases the flue gas flow considerably. The net efficiency of conventional sub-critical designs is approximately 38–40%, depending on fuel and condenser conditions.

During recent years, once-through supercritical (OTSC) CFB technology has been developed, enabling the next stage in CFB development to proceed to medium-scale (<500 MWe) commercial projects such as Łagisza, with net efficiencies near 45%. However, scaling up the technology further to utility size of 600- 800 MWe with net efficiency of 45–50% is needed to fulfill the future requirements of utility operators.

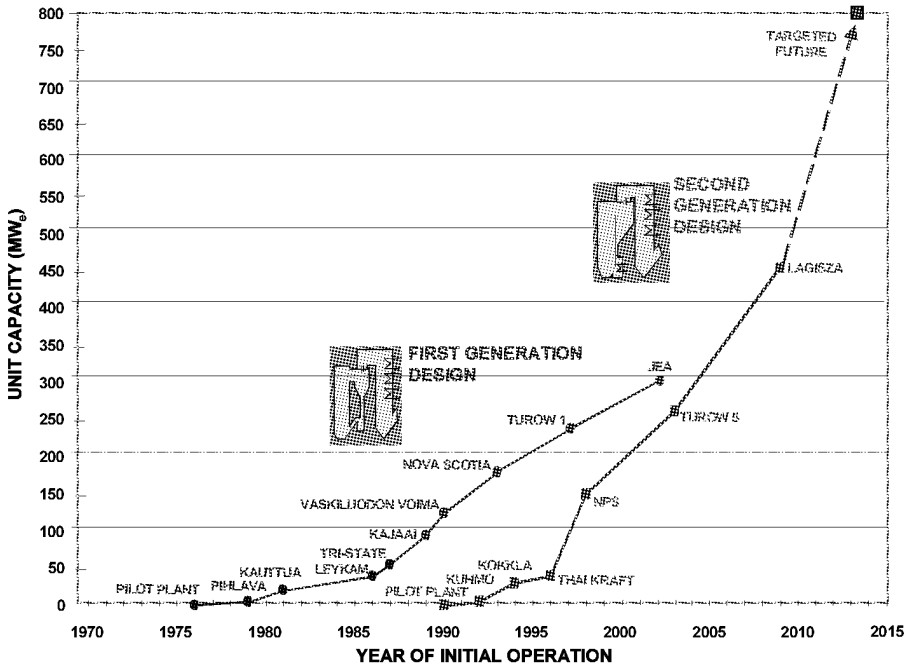

Fig. 2 Scaling-up of Foster Wheeler's CFB boilers

Scaling-up of Foster Wheler's CFB boiler technology has been achieved through development of a second-generation design. This design features integration of the separator for circulating solids and the furnace (Fig. 3(a)). A water/steam cooled separator replaced the hot cyclone with heavy refractory lining, which was distinctive for the first-generation design. This concept offers several advantages, such as:

- Less refractory in the system, thus reducing maintenance cost,
- Shorter start-up time due to less temperature sensitivity in the refractory,
- No expansion joints between the separator and the combustion chamber,
- Smaller foot-print of the boiler, which can be very important in re-powering schemes where the new boiler has to fit into an existing building or existing site.

The second-generation design was introduced in 1992, and in 1996 the design was enhanced with introduction of INTREX™ – integrated heat exchanger located in the furnace (Fig. 3b). INTREX™ extract heat from the hot circulating material that is returned from the separator, or solids are taken directly from the lower part of the furnace. Continuous flow of dense solids enables high heat-rate coefficients within a small physical space, and prevents formation of deposits on tube surfaces. No mechanical devices are needed and all required controls are performed by air fluidization. Superheaters and reheters of INTREX™ type are particularly effective in designs for fuels that can cause corrosion on conventional heat surfaces, and for

large-scale utility boilers.

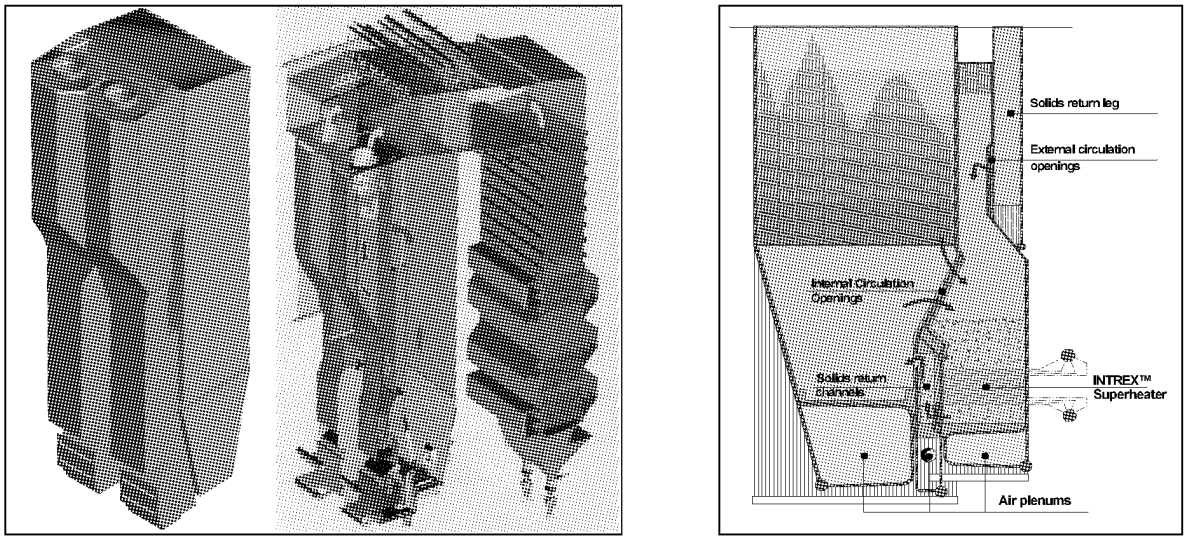

Fig. 3 Features of second-generation Foster Wheeler's CFB boiler design
(a) water/steam cooled integrated separator (1992-); (b) INTREXTMsuperheater (1996-)

Developing CFB technology to even larger sizes and higher plant efficiencies is an ongoing challenge. There is an increasing demand for boilers in the size range of 600 to 800 MWe, as existing power plants are aging and new replacement capacity has to be built. CFB technology is now emerging as an alternative plant of this size, thanks to the benefits it offers in terms of fuel flexibility and inherently low emissions. New, modern power plants need to have high efficiency for economic reasons and to minimize emissions, including CO_2. Plant net efficiency of approximately 45% (LHV) is expected. This calls for utilizing ultra supercritical steam parameters, together with an optimized power plant cycle and high boiler efficiency. Foster Wheeler develops design for 800 MWe CFB boiler with ultra-supercritical steam parameters. The scale-up of critical CFB components, such as the furnace, solids separators, and fluidized bed heat exchangers to 800 MWe is possible. The actual scale-up of the dimensions and size of plant components required is quite moderate, due to the modular approach adopted for the boiler design (Hotta A. et al., 2006).

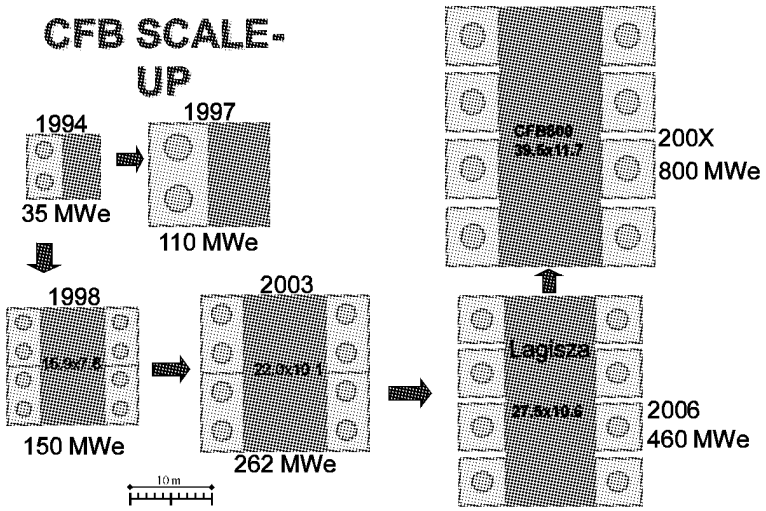

Fig. 4 CFB Scale up – modular approach

Reducing CO_2 emissions

Due to its economic advantage, abundance and shortage of alternatives, coal is expected to remain the dominant fuel for the foreseeable future, either for new power plants, or to replace older or inefficient units. A large number of coal-based plants will need to be built in Europe and worldwide in the next decade. However,

CO_2 emissions from fossil-fired power generation are a major contributor to climate change. As a result, modern power plants are expected to comply with high efficiency and firm environmental performance. When considering either new plant or repowering of old units, utilization of proven high efficiency CFB technology is an ideal solution. High efficiency leads to lower fuel requirements, and lower levels of ash and emissions, including CO_2. In addition, CFB technology has proven excellent in fuel flexibility and co-firing of CO_2-neutral fuels with different grades of coals, which can further reduce CO_2 emission.

Reduction of greenhouse gas emissions has become a major challenge for the energy producers and technology suppliers. Currently, the main approach to reducing emissions is to increase efficiency. When combined with other solutions, efficiency improvement has a direct impact on the consumption of natural resources, the generation of waste matter and the economics of production.

Scaling-up CFB processes		Turow #5	Lagisza	CFB800
Main steam flow	kg/s	196	360	589
Main steam pressure	MPa	17	27.5	30.9
Main steam temperature	°C	565	580	600
Reheat steam flow	kg/s	181	307	469
Reheat steam pressure	MPa	3.9	5.5	4.5
Reheat steam temperature	°C	568	580	620
Design capacity	MWe	262	460	760
Net electrical efficiency	-	39	44	>45
Boiler type	-	drum	OTSC	OTSC

Fig. 5 Scale up of steam parameters

Co-firing of solid fossil fuels with CO_2-neutral fuels in highly fuel-flexible CFB boilers provides a technically and economically feasible solution for CO_2 reduction up to certain degree, both in repowering and greenfield applications (Eriksson, T. et. al, 2007).

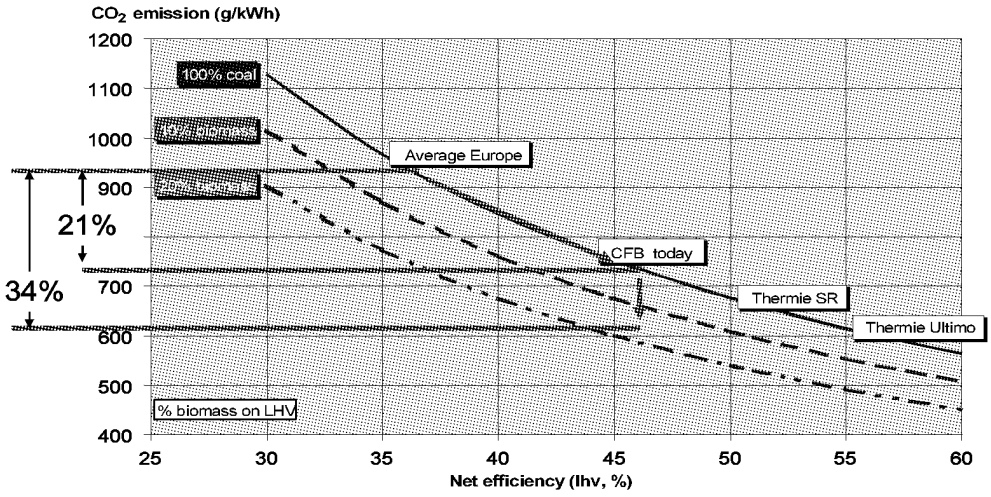

Fig. 6 Impact of efficiency improvement and biomass cofiring on CO_2 reduction

Advantages of CFB technology with emphasis on fuel flexibility

Circulating fluidized bed (CFB) process provides an ideal burning environment for a wide variety of fuels. The advantages of CFB technology can be summarized as follows:

— Fuel flexibility and multi-fuel firing,
— Low SO_2 emissions due to efficient sulfur capture with limestone in the furnace,
— Low NO_x emission due to low combustion temperature and air-staging,
— Low CO and CxHy due to turbulent conditions and good mixing,
— Secondary flue gas clean-up systems typically not needed,
— Stable operating conditions and good turn-down ratio,

— Support firing is not needed except during start-up periods,
— Increased capacity possible within the same footprint as old boilers,
— No need for fuel preparation (e.g. pulverizing).

One of the important advantages of CFB technology is the possibility of burning a diverse range of fuels alternately and/or simultaneously. Fuel flexibility includes both a wide range of heating values and the possibility of burning fuels with very different physical and chemical properties. The types of fuels used in CFB boilers include coal of various degrees of carbonification, waste coal, petroleum coke, peat, wood-derived fuels, agricultural and agro-industrial wastes, sludge, refuse derived fuels, tires, etc (see Fig. 7). Figure 8 compares chemical properties of few selected fuels used in commercial boilers.

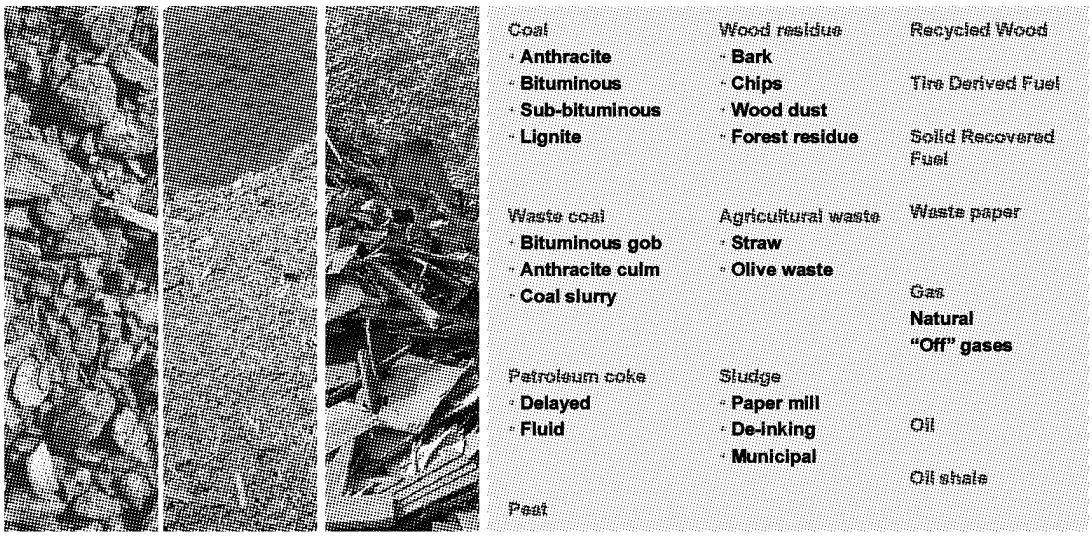

Fig. 7 Type of fuels (co-) fired in Foster Wheeler's CFB boilers

CFB boilers can effectively deal with wide variations in coal quality, which can exist even within coals from a single mine. In an attempt to minimize the operational costs, utilities seek possibilities to utilize cheaper, lower-grade coals with high moisture, ash and sulfur content (see also Fig. 8). Low-grade coals that have been already used in power production, especially in Poland, have been local lignite coals or lower-rank bituminous coals, which do not have an export market due to low quality. Utilization of these coals in old pulverized coal and stoker fired boilers - which usually were not equipped with neither desulphurisation, nor proper dust removal installations - have caused many environmental problems in the form of gaseous and dust emissions. However, low-grade coals have been used in environmentally sound way in a number of high efficiency CFB

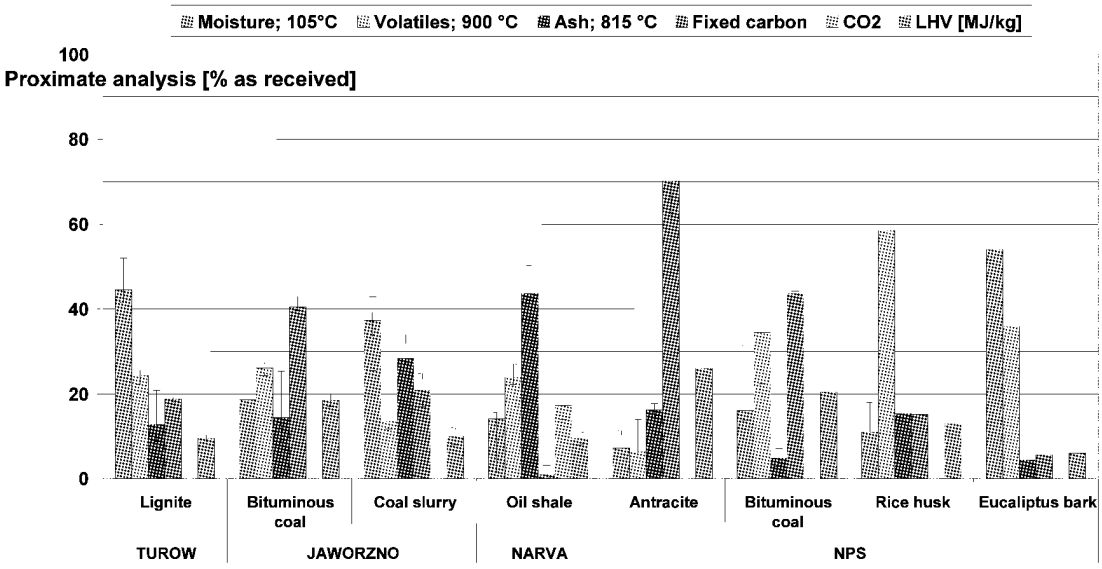

Fig. 8 Fuel properties (data from Foster Wheeler's fuel database)

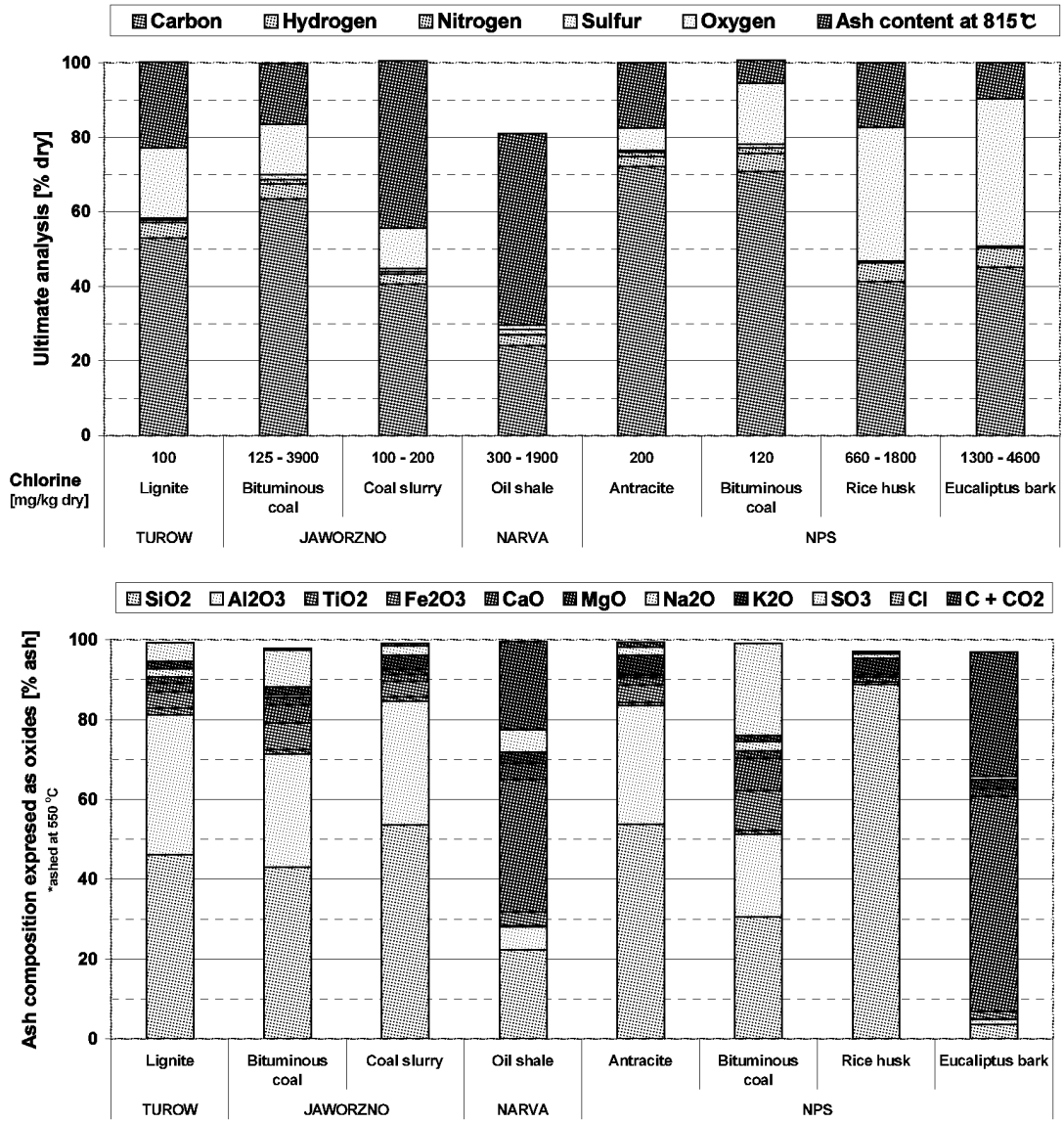

Fig. 8 (Continued)

boilers.

The possibility of using coal washery rejects in CFB boilers has proved particularly valuable in Poland; for example in power station Jaworzno. Modern CFB technology provides an efficient and profitable way to produce power from these wastes which otherwise would need to be disposed in a landfill, while also providing some profit from the waste coal rather than paying fees for its disposal.

At present, most CFB installations are designed for multi-fuel firing capability, i.e. for more than one solid fuel (Barišić, Hupa, 2007). Coal and peat are common fuels in multi-fuel CFB installations together with wood or wood-based fuel (Jäntti et al., 2006).

Utilization of biomass as a sustainable energy source is already seen as one of the key options in the short and medium term for mitigating CO_2 emissions. However, the physical and chemical characteristics of the diverse spectrum of biomass fuels vary widely (Phyllis). Utilization of biomass fuels in CFB boilers may cause operational problems, such as agglomeration, deposit formation, and corrosion (Hiltunen et al., 2008; Coda Zabetta et al., 2008). However, such problems can be limited with proper boiler design, suitable boiler operation, alternative bed materials or additives, and most effectively by co-combustion with coal or peat that can capture problematic elements from biomass/wastes. Coal co-combustion is applied for example in NPS utility, Thailand, to fire high shares of local biomass rice husk and eucalyptus bark.

REPOWERING WITH HIGH EFFICIENCY CFB

Over 60 % of existing coal-fired power plants throughout Europe are more than 20 years old, and many with modest efficiency (Jäntti, 2006). Consequently, this will results in a substantial need for new thermal power plants in the near future.

Depending on local, regional or country environmental performance standards, CFB's can often meet emission limits without any secondary flue gas cleaning systems, and plant owners do not need to be concerned about the costs or space requirements of flue gas desulfurization or selective catalytic reduction units. A CFB boiler can typically fit into an old boiler house. However, it is seldom possible to use the old steel structures or foundations, as the boiler loads differ from the original boiler. What is important, however, is that boiler output and efficiency can be increased. Foster Wheeler has wide experience in repowering projects in the scale of 200-300 MWe. Today's CFB technology can reach 45% efficiency when utilizing the supercritical steam parameters (Jäntti T et al., 2006).

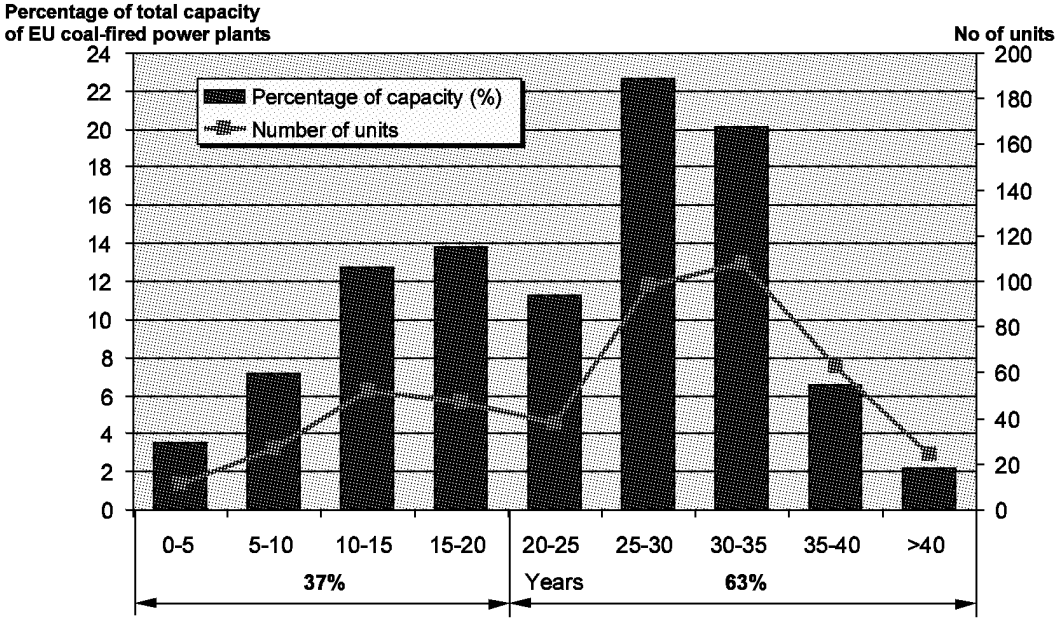

Fig. 9 Age structure of power plants in European countries (taken from Jäntti, 2006)

ŁAGISZA 460 MWe CFB BOILER

Features

CFB is not only suitable for hard-to-burn fuels, but the technology is also ideally suited for quality bituminous coal. Through a continuous scale-up and development process, CFB technology has now reached medium utility scale with once-through supercritical boiler technology.

Utilizing Siemens' BENSON low mass-flux vertical tubing technology offers some clear advantages for CFB technology, including a lower pressure drop over the furnace tubing, resulting in less power needed for feed water pumps and lower auxiliary power consumption. The combustion temperature in a CFB is homogenous both vertically and horizontally, which means that the heat flux is relatively uniform, and the risk of overheating is not present as it is in conventional technology with a heat flux that can be up to three times higher locally.

The first company to benefit from OTU CFB technology with supercritical steam parameters will be the Polish utility, Poludniowy Koncern Energetyczny S.A. (PKE). The new 460 MWe (gross) unit will replace old power blocks of Łagisza Power Plant. The existing blocks were erected in 1960's and consist of seven units (110-125 MWe each). Two of them will be shut down after the new 460 MWe unit is commissioned. The new boiler will be built adjacent to the old boilers and many of existing plant systems like coal handling and water treatment will be renovated and utilized for the new CFB unit.

Main fuel for the boiler is bituminous coal. The source of fuel consists of 10 local coal mines with wide range of coal parameters, proving once more the fuel flexibility of the CFB technology. Table 1 summarizes parameters of design fuel and overall fuel range. Boiler design is optimized with a possibility for combustion of

additional fuels. Main additional fuel is coal slurry that is available in large amounts in local coal mines. Due to CFB technology characteristics, wet coal slurry can be combusted with 30% share by fuel heat input. Coal washing rejects can also be burned in form of dry coal slurry granulates with a share up to 50% of heat input. Boiler is designed also to utilize biomass fuels up to 10% of fuel input. The biomass feeding equipment is included in the delivery as an option to be installed later.

The Łagisza CFB boiler is dimensioned according to data given in Table 2. The general boiler layout was based on the conventional in-line arrangement already applied for Units 4–6 of the Turów power plant. Figure 10 shows schematics of the boiler. Detailed description of the once-through boiler design and related aspects can be found in Venäläinen, Psik, 2004.

Table 1 Fuel properties for the Łagisza project

		Coal range	Coal slurry range (max 30% input)
Lower heat value	MJ/kg	18–23	7–17
Moisture content	%	6–23	27–45
Total ash content	%	10–25	28–65
Sulfur content	%	0.6–1.4	0.6–1.6

Table 2 Boiler data for the Łagisza 460 MWe CFB boiler

Maximum continuous flow	kg/s	359.8
Minimum continuous flow	kg/s	143.9
HP steam pressure at turbine inlet	MPa	27.50
HP steam temperature at turbine inlet	°C	560
Cold reheated steam flow	kg/s	306.9
Cold reheated steam pressure	MPa	5.46
Cold reheated steam temperature	°C	314.3
RH steam temperature at IP turbine inlet	°C	580
Feed water temperature	°C	289.7

The emission requirements for the Łagisza boiler are according to European Union directive for Large Combustion Plants, and considerable emission reduction is expected compared to existing PF unit. The emissions of sulfur dioxide are controlled with limestone feeding into the furnace. With the design coal a sulfur reduction of 94% is required, and that shall be achieved in the CFB with a calcium to sulfur molar ratio of 2.0–2.4. The nitrogen oxide emissions are controlled with low combustion temperature and staged combustion. There are also provisions made for a simple ammonia injection system (SNCR), however that is not required on design coals. Compared to original plants, NOx expected to be reduced by 71%, and CO2 by 28%. Particulate emissions are controlled by electrostatic precipitator. The plant efficiency is expected to be improved from 34.7% to nearly 44%.

Operational Performance

The Łagisza power plant achieved full load steam conditions on 100% coal on March 2009 running at the designed supercritical steam pressure and temperature. The boiler has been running in stable operation on coal from 25 to 100 % MCR and has shown to operate as designed and predicted. Since the official performance testing has not been made so far, more detailed performance figures are not shown in this paper. The emissions of SO_2, NO_x and CO are below guaranteed and permitted values. Also the combustion efficiency appears to be very good. The unburnt carbon in ash has remained well below 5% at all loads. The analyses of coal used during the commissioning is presented in Table 3.

The once-through steam cycle utilizing Siemens' Benson technology has performed as predicted by Foster Wheeler's 3D model for the CFB process and Siemens's prediction tools for the once-through steam cycle. The excessive dynamic modeling and simulation, which was done during the design and engineering of the boiler has now shown its merits. The boiler controls were applicable as they had been set based on control simulations,

and only minor tuning has been required during the actual operation. The overall operation of the large CFB has been very smooth and it has been easy to operate.

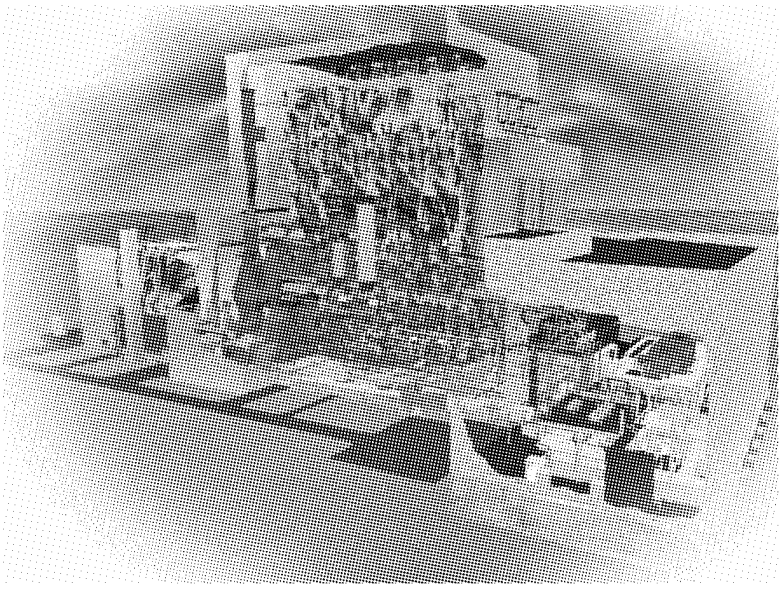

Fig. 10 The 460 MWe once-through CFB at PKE, Łagisza

Table 3 Analyses of the Ziemovit coal

Fuel		**Bituminous coal (Ziemowit, Poland)**
LHV	MJ/kg	19,8
LHV (dry)	MJ/kg	22,92
Moistute	%	12,3
Ash	%	26,4
Volatiles	%	28,6
Fixed carbon	%	45
C	%	58,2
H	%	3,8
S	%	1,16
N	%	0,97
O	%	9,5

One of the challenges in scaling up boilers is the mechanical design of the large constructions and the resulting large thermal expansions of the pressure parts. Plenty of attention was paid to mechanical details during the engineering of the Łagisza boiler. As a result, there have been no bigger mechanical problems encountered due to the scale-up during the initial operation of the plant.

FLEXI-BURN™ CFB – SOLUTION FOR CARBON CAPTURE

When bigger emission cuts are required, CCS offers potential for near zero emission power production from fossil fuels, though at the expense of efficiency and costs. FW is developing currently oxy fuel CFB-technology, which is seen to be the most feasible alternative for CCS at the moment.

Figure 11 shows a simplified process flow scheme of an oxycombustion power plant, which consists of an air separation unit (ASU), a power plant with O_2-blown combustion, and a CO_2 treatment unit. Oxygen is mixed with recirculated flue gases, which creates a mixture of primarily O_2 and CO_2 (and H_2O) used as oxidant in combustion instead of air. The absence of air nitrogen produces a flue gas stream with a high concentration of CO_2, making it much easier to separate the CO_2. CFB technology appears to be ideally suited for oxy fuel combustion, and as a longer term activity, FW is developing its CFB for oxycombustion to provide the potential for nearly 100% reduction of CO_2 (Eriksson, T. et. al, 2007).

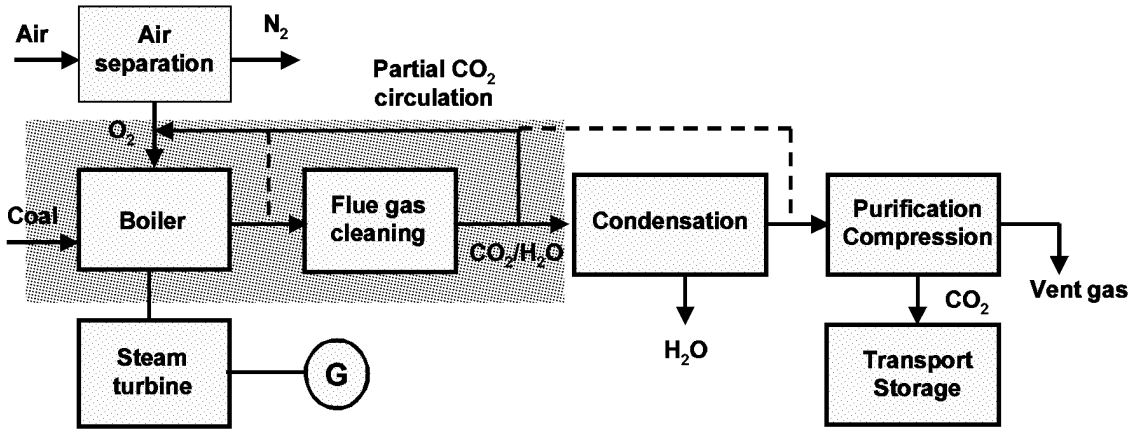

Fig. 11 Schematic of an Oxycombustion Power Plant

Oxy-CFB technology , the Flexi-Burn™ CFB, is being developed for existing boilers as a retrofit solution, for new "capture ready" boilers to be modified for CCS in the future, and for integrated greenfield power plants with CCS from the beginning. Designing an oxyfuel power plant calls for case-specific optimization of the performance and economics. Normal boiler designs with reasonable modifications can be applied, if the mixing ratio of oxygen and recycled flue gas ratio is chosen so that the adiabatic combustion temperature is close to that of air firing. Such a plant could even be operated either with or without carbon capture and thus with lower or higher output, for instance depending on the price of CO_2 allowances and electricity (Eriksson, T. et. Al., 2007).

The 460 MWe once-through supercritical, coal fired CFB boiler plant being designed and constructed by FW for the Polish utility PKE at Łagisza power plant has been used as a starting point and reference in an study that considers plant optimization items and aims to generate knowledge about boiler conversions for oxyfiring and design of new "capture ready" boiler plants. High-O_2 designs provide potential for cost savings and higher efficiency but require an entirely new boiler concept, and will be a subject of future studies (Eriksson, T. et. Al., 2007).

CONCLUSIONS

Circulating fluidized bed (CFB) boiler technology has developed to meet utility-scale requirements. Owning to high efficiency, excellent multi-fuel capability and low emissions of major pollutants (SO_2, NO_x, CO, CO_2, particulates etc.) the technology offers reliable solution for both repowering of old power plants or building a new plant. CFB technology has proved excellent with both low-grade fuels, such as lignite and low-grade bituminous coals, coal washery rejects, oil shale, and with good quality fuels. Co-combustion of various types of biomass and waste fuels in CFB boilers has proven as efficient and economic way to reduce CO_2 emissions.

The Łagisza power plant has reached full load operation and has been operating at the designed supercritical steam pressure and temperature. The boiler has been running in stable operation on coal from 25 to 100 % MCR and has shown to operate as designed and predicted. The positive results from Łagisza confirm, that the Foster Wheeler CFB technology can be commercially offered sizes up to 800 MWe with once-through supercritical technology.

Carbon capture and storage (CCS) offers the potential for major cuts in CO_2 emissions of fossil fuel-based power generation in the fairly short term. Oxy-fuel combustion is one of the identified main CCS technology options. Foster Wheeler Global Power Group (FW) is developing its Flexi-Burn™ CFB technology for oxycombustion to provide a CCS-ready solution.

REFERENCE

Barišić, V., Coda Zabetta, E., Hotta, A., Krztoń, B. Foster Wheeler Experience in Combustion of Low-Grade High-Ash Fuels in CFBs, Power Plants 2008 Vrnjačka Banja, Serbia, 29–31 October 2008.

Barišić, V.; Hupa M. On changes in bed-material particles from a 550 MWth CFB boiler burning coal, bark and peat. Fuel 86, 2007, 464–468.

Coda Zabetta, E.; Barišić, V.; Peltola, K.; Hotta, A. Foster Wheeler Experience with Biomass and Waste in CFBs. 33rd International Technical Conference on Coal Utilization & Fuel Systems, Clearwater, Florida, USA, 2008.

Eriksson T., Sippu O., Hotta A., Zhen Fan, Myöhänen K., Hyppänen T., Pikkarainen T.: Oxyfuel CFB Boiler as a Route to Near Zero CO2 Emission Coal Firing. POWER-GEN Europe 2007, June 26-28, 2007, Madrid, Spain.

Hiltunen, M.; Barišić, V.; Coda Zabetta, E. Combustion of Different Types of Biomass in CFB Boilers. 16th European Biomass Conference, 2008,Valencia, Spain.

Hotta, A.; Nuortimo, K.; Eriksson, T.; Palonen, J.; Kokki, S. CFB Technology Provides Solutions to Combat Climate Change. 9th International Conference on Circulating Fluidized Beds, 2008, Hamburg, Germany.

Hotta, A.; Uus, M.; Parkkonen, R. Enhanced Performance Using CFB Boilers to Fire Oil Shale Compared to PC Technology. POWER-GEN Europe 2005, Milan, Italy.

Hotta, A.; Venäläinen, I. Design and Scale-up Philosophy of One-through CFB Boilers with Supercritical Parameters. VGB PowerTech 4, 2006, 66–71.

Jäntti, T.; Eriksson, T.; Hotta, A.; Hyppänen, T.; Nuortimo, K. Circulating Fluidized-bed Technology – toward zero CO2 Emissions. POWER-GEN Europe 2006, Cologne, Germany.

Navarrete Fernández, E. Polish Operating Experience from Burning Coal, Coal Washery Reject and Brown Coal in Circulating Fluidized Bed Boilers. Enerji 2003, Istanbul, Turkey.

Psik, R.; Jablonski, J.; Wyszynski, J. Turów Rehabilitation Project – The World's Largest CFB Repowering Project, POWER-GEN Europe, 2005, Milan, Italy.

Pyykkönen, A.; Hotta, A. Foster Wheeler's 2*150 MWe CFB Boilers Started up Successfully in NPS Power Plant in Thailand. POWER-GEN Asia 2000, Bangkok, Thailand.

Phyllis: The Composition of Biomass and Waste; Energy Research Centre of Netherlands (ECN), Unit Biomass: Petten, The Netherlands (http://www.enc.nl.phyllis)

Venäläinen, I.; Psik, R. 460 MWe Supercritical CFB Boiler Design for Łagisza Power Plant. POWER-GEN Europe 2004, Barcelona, Spain.

FLUIDIZED COMBUSTION OF LIQUID FUELS: PIONEERING WORKS, PAST APPLICATIONS, TODAY'S KNOWLEDGE AND OPPORTUNITIES

M. Miccio[1], F. Miccio[2]

1 Dipartimento di Ingegneria Chimica ed Alimentare - Università di Salerno – Fisciano SA - ITALY
2 Istituto di Ricerche sulla Combustione - C.N.R., Napoli - ITALY

Abstract: The use of liquid fuels for fluidized bed (FB) combustion is gaining importance for co-firing, waste incineration, switch to renewable energy sources or during plant start-up.

The design of a suitable liquid injection system is a key requirement to ensure that all of heat is released within the bed of a bubbling fluidized combustor or the riser of a circulating system.

The scientific literature has revealed around 100 papers dealing with FB combustion of liquid fuels since the pioneering work in 1975. This paper conveys an effort to review the relevant aspects of FB combustion of liquid fuels, with the exclusion of mixtures of solid fuels in liquids, which were left out of this work. Following a logical path that goes from early investigations toward a more sound knowledge, it is organized in four sections: Fuels, Fuel Feeding, Combustion Results and Emissions. The Conclusions summarize the main aspects and draw prospective for future research and application of liquid fuel FB combustion.

Keywords: bubbling fluidized bed, circulating fluidized bed, liquid fuel, fuel injection, combustion efficiency, sulfur oxides , NO_x, carbon monoxide

INTRODUCTION

The use of liquid fuels for fluidized bed combustion (FBC) is gaining importance for application during co-firing and waste incineration or for plant start-up. In parallel, increasing interest in biomass- and waste-derived fuels, as a consequence of the Kyoto protocol and the need of optimal energy-source share, calls for innovative combustion solutions. Since the fluidized bed technology is effective for burning high-volatile fuels like biomass and solid opportunity fuels, the extension to liquid fuels is rather straightforward, in particular if benefits are obtained, for instance burning liquid wastes with medium heating value and raw vegetable oils without any preventive chemical treatment. These fuels can be reliably processed using fluidized bed combustion thanks to FBC robustness, flexibility and effectiveness.

The literature on FB combustion of liquid fuels is still sparse. A part of studies have a fundamental character for understanding the mechanism of liquid fuel FB combustion; a number of papers are available on different aspects as well as on different technical options. So far, both options of bubbling fluidized bed (BFB) and circulating fluidized bed (CFB) have been used for liquid fuel combustion.

The search of the scientific literature revealed around 100 papers dealing with FB combustion of liquid fuels, after the exclusion of mixtures or suspensions of solid fuels in liquids, which were left out of this work. Nevertheless, no dedicated reviews are available on this matter. Therefore, this paper represents a first effort in this direction by addressing relevant practical aspects and scientific issues in FB combustion of liquid fuels.

FUELS

Table 1 reports the list of the liquid fuels used in the research activities reviewed by the present paper.

Concerning nature and origin, the majority of the fuels is originated upon petroleum refining processes as valuable products (diesel fuel, kerosene, gasoline, fuel oil), by-products (pitch, heavy oil, mazut) and liquid wastes to be disposed (acid tar waste, waste oil). Orimulsion® is a bitumen-based water suspension that is very similar to a heavy fuel oil in its appearance. It is produced from Venezuelan bitumen deposits in the Orinoco region by direct extraction with steam from the underground reservoirs and a further addition of surfactants for its stabilization (Zlatar, 1989).

Concerning renewable fuels, pyrolysis oils are generated by dedicated processes of thermo-chemical conversion of biomass/wastes into liquid fractions. Sunflower oil, commonly used for cooking, is produced by milling, pressing and separating the oil fraction of sunflower seeds. Biodiesel is obtained via trans-esterification of rape oil for generating a fuel with rheological properties similar to those of a common diesel fuel.

Table 1 Petroleum-derived liquid fuels for FB combustion (in alphabetical order)

Fuel name	Brief description	Origin	Nature	LHV MJ kg^{-1}
Acid tar waste	By-products of oil-refining industry	Refinery	Fossil	20.0-30.0
Biodiesel	Bio fuel for automotive application	Chemical processing	Renewable	37.0
Diesel fuel	Standard fuel for automotive application	Refinery	Fossil	42.6
Fuel oil	Petroleum derived oil for heating	Refinery	Fossil	40.0-42.0
Gasoline	Standard fuel for automotive application	Refinery	Fossil	43.3
Heavy oil, mazut	Heavy oil from petroleum distillation	Refinery	Fossil	40.7
Kerosene	Standard fuel for aircraft application	Refinery	Fossil	43.1
Oil sludge	Residual oil from petroleum storage	Refinery, oil deposits	Fossil	30.0-40.0
Orimulsion®	Emulsion of natural bitumen in water	Steam assisted extraction	Fossil	39.7
Pitch	Petroleum pitch	Refinery	Fossil	30.0-40.0
Pyrolysis oil	Oil generated by pyrolysis of biomass/ wastes	Chemical processing	Fossil/renewable	20.0-30.0
Sunflower oil	Vegetable oil for food appliance	Agro-industry	Renewable	37.1
Waste oil	Waste oil from mechanical processes	Industry	Fossil	30.0-40.0

FUEL FEEDING

Fuel viscosity. One of first FBC tests with petroleum liquid fuels in a fluidized bed (Pillai and Elliot, 1976) showed besides the low combustion efficiency the problems of blockage of the feeding nozzle and agglomeration of the bed material. Among fuel properties, the viscosity is very important. In many papers related to liquid fuel combustion in fluidized beds, authors reported that several first trials failed, on account of problems in the feeding system. Very often the high fuel viscosity was the cause of feeding problems.

For improving feeding system and enabling appropriate pumping of viscous liquid fuels, the tanks of liquid fuels are usually heated up to a certain temperature. In that case the whole transport line from the tank till the fluidized bed furnace must be heated. The level of temperature for heating up of tanks and transportation lines depends on liquid fuel viscosity and thermal stability.

Barker and Beacham (1980) estimated that very viscous liquid fuels can be satisfactorily transported and dispersed through appropriate nozzles if their kinematic viscosity is around 150 – 350 mm^2/s. While for typical oil fuel in conventional burners it is 15 – 30 mm^2/s. Taking into account viscosity of different petroleum-based liquid fuel, it was necessary for acceptable feeding to heat up the whole feeding system at temperatures usually not above 150°C (Brereton et al., 1995; Kerr and Probert, 1990; Anthony and Lu, 2001; Barczus et al., 2001). One of rare examples with higher heating temperature is reported by Legros et al. (1989 and 1991). They used a pitch obtained from refinery hydrocracking unit and they had to heat up this fuel to 190°C. While Anthony and Lu (2001) reported that for three different petroleum-based liquid fuels (fuel oil, pitch and bitumen) the feeding system was heated up to 120°C only. At this temperature only for one of the investigated fuels, that is for bitumen, its viscosity was over the proposed value of 350 mm^2/s. Therefore the reported unsatisfactory combustion performance just for bitumen could be the too high viscosity for good dispersion in FB. In contrast, Orimulsion®, the bitumen-based emulsion, was rather successfully burnt in a fluidized bed furnace (Miccio et al., 1999) by carrying out its feeding at room temperature with a viscosity in the order of 500 mm^2/s.

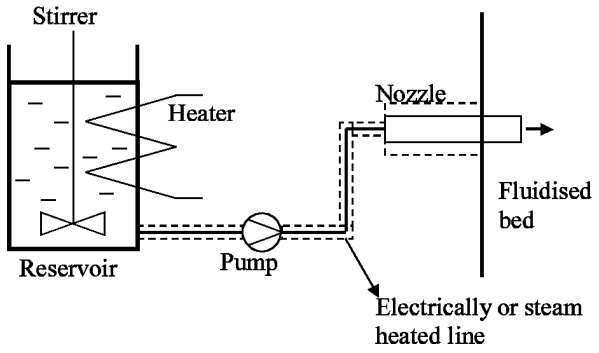

Fig. 1 Typical system for feeding viscous petroleum-based liquid fuels to FBC plants

Some refinery by-products, which were investigated for combustion in fluidized bed as liquid fuels, are actually in solid phase at room temperature. An example of that kind of material is asphalt. Wu et al. (2001) made experiments burning asphalt in CFB. The viscosity of this material at 170°C was reported to be 59650 mm^2/s. This value is by three orders of magnitude greater than viscosity of typical oil fuels for conventional boiler. Nevertheless this kind of hydrocarbons also can find application as a liquid fuel for fluidized bed combustion. The authors reported that the tank and transportation line had to be maintained at temperatures between 200 and 340°C. Acid tar wastes of petroleum origin were investigated for combustion in a FB facility by Kerr and Probert (1990). This fuel contained a relatively large amount of water and did not show tendency of depositing tarry material as a result of long standing. Based on some pumping tests, the authors recommended that these acid tar wastes should be heated up to 30°C at least.

Feeding system. A typical feeding system for viscous petroleum-based liquid fuels is shown in Fig. 1. It consists of a tank containing fuel, an agitator for stirring fuel, a heater for maintaining fuel in good flow conditions, a transportation line till the pump, and after that till the injection point and the nozzle. The transportation line is usually heated and heat insulated. The heating of the tanks and the transportation lines, reported mainly from research activities with relatively small fluidized units, was provided by electric heaters or by steam. If the required temperature for heating up was higher, then the preferable solution was by steam. In industrial applications the heating of fuel with steam may be the only reasonable solution.

Nozzles. The nozzle is a critical point of feeding system, since its inappropriate design usually cannot be overcome by adjustment of other operational parameters. In first attempts of research activities on FBC of liquid fuels, these were fed through nozzles without cooling. Consequently, the nozzles were heated up to high temperature, and then petroleum-based liquid usually cracked forming deposits on the inside nozzle wall. Finally, after a relatively short time, the nozzle became blocked (Pillai and Elliott, 1976). In general, it is enough to cool the nozzle with air stream. The air stream used for nozzle cooling also served as a medium for dispersing or atomization of liquid fuel. By this way the air stream was being heated up, and at the exit of the nozzle it dispersed the liquid fuel without decrease of the fuel temperature, which accelerated the subsequent fuel evaporation (Anthony and Lu, 2001; Legros et al., 1991).

As an easier design solution, in pilot or industrial facilities, the nozzles are usually horizontally inserted into the fluidized bed. Since nozzles have to give a relatively even distribution of liquid fuel across the fluidized bed, it is necessary that parts of nozzles that are inside the furnace are relatively long. It means that these relatively long parts of nozzles are exposed to high heat flux coming from the surrounding hot fluidized bed. Experiences show that in these cases it is necessary to cool the nozzles by water, since the air cooling rate was not high enough to prevent overheating and cracking of liquid fuel within the nozzles, and finally blockage of the nozzle (North et al., 1999; Barczus et al., 2001). In some research investigation, vertical injectors directly inserted in the air distributor were preferred.

Since agglomeration of fluidized bed particles was experienced, some attempts for avoiding it, like increasing the excess air, variation of the bed height and using support gas combustion did not bring remarkable success (Pillai and Elliott, 1976). The experimental research of Miccio et al. (1999) with a bitumen-based emulsion showed that in inert atmosphere this fuel practically does not have tendency to form deposits on inert particles which could cause agglomeration of the fluidized bed. The experiments were done at 850°C, and they practically excluded the onset of reducing/sub-stoichiometric conditions in the bed as one of reasons for agglomeration during combustion of liquid fuels. The main reasons for agglomeration of inert particles of fluidized bed during combustion of liquid fuel are insufficiently high bed temperature and weak mixing at the location where the fuel is introduced. A first measure for avoiding FB agglomeration was introducing liquid fuels into fluidized beds only if the bed temperature was over 750°C (Brereton et al., 1995; Legros et al., 1991). Moreover, enhancing the mixing of the fluidized bed at least in the region of the liquid fuel injection and dispersing viscous fuels in relatively fine droplets are also effective (Legros et al., 1991; Barker and Beacham, 1980). Apart from inadequate nozzle designs or operating parameters, the agglomeration of fluidized bed particles might be caused if the nozzle is positioned too low in the bed. In the lowest part of the fluidized bed there is a great temperature gradient, starting from the inlet temperature of fluidizing air to the nominal bed temperature. This temperature gradient exists in a relatively narrow zone of fluidized bed, but if the exit of the nozzle is located just close to this zone, temperature of that zone will be even lower. Since the temperature in the zone is lowered, the gas velocity decreases, while the mixing becomes weak. These conditions could provoke agglomeration of fluidized bed particles. Legros et al. (1991) suggested a narrowed bottom part of fluidized beds as a measure for improving mixing in the zone of fuel injection.

Nozzle position. In available literature there is some data about the height where the fuel is injected into fluidized beds. Concerning CFB, in one case it was at 39 cm above primary air distributor (Brereton et al., 1995), while in another paper the nozzle was only 12 cm above the bubble caps (Anthony and Lu, 2001).

Regarding BFB, the height of the nozzle location in the fluidized bed was given only by Miccio et al. (1999), that is 6.5 cm above the distributor level. All these examples are from research activities, and in all the cases the feeding was regarded as a successful one.

Location of fuel nozzles is a matter of optimization between the need to avoid agglomeration (shallow nozzle) and that of increasing the residence time of liquid fuel and its vapor (deep nozzle). In both early and recent research works, it was determined that for good feeding and dispersion of liquid fuel in a fluidized bed it is favorable to assist the liquid fuel injection with air or steam (Brereton et al., 1995; Anthony and Lu, 2001; Wu et al., 2001; Miccio et al., 1999). However, in the case of larger pilot facilities or industrial plants, according to the published papers, there was no need for air assisting dispersion of liquid fuel (North et al., 1999; Barczus et al., 2001).

Miccio et al. (1999) made tests with and without air assistance to dispersion of liquid fuel (bitumen-based emulsion). During the liquid fuel feeding without air assistance no operation problems were experienced and the authors found that the combustion efficiency and the emissions were not largely affected by air assisting. However, they concluded that higher ratio of air to fuel flow rate gave more regular operation of nozzle feeding. Anthony and Lu (2001) provided similar comments: air assistance is necessary for good atomization and most importantly for improving the mixing in the immediate vicinity of the nozzle. They also did not recommend high flow rate of assisting air, since they did not notice better operation performance with a remarkably increased air flow rate through the nozzle.

Nozzle number. Finally, the design approach for the number of nozzles per unit cross section of the fluidized bed for liquid fuel feeding could be the same as that for high volatile solid fuels (e.g., lignite or biomass). For small-scale units used in research activity, with a cross section up to 0.15 m^2, a single injector was always used. Hence, from these investigations an appropriate conclusion could be hardly drawn about the optimum number of injectors per square meter of the furnace cross-section. The paper by North et al. (1999) reported that in an industrial plant of about 20 MWth there were 6 injectors per 21 m^2 of bubbling fluidized bed cross section. On another side there are some recommendations that number of nozzles for liquid fuels should be similar to the number of feeding points for coal, i.e., one feeding point per square meter of furnace cross section (Stubington and Davidson, 1981). Since there are very few published papers about fluidized bed industrial plants fired with liquid fuel, the optimum number of feeding points still remains a questionable design parameter.

COMBUSTION RESULTS

Petroleum-derived fuels. One of first published investigations with combustion tests on liquid fuels in a fluidized bed combustor was done by Pillai and Elliot in 1976. They used commercial liquid fuels, i.e., diesel fuel and heavy fuel-oil and tested four different positions for introducing liquid fuels into the furnace; one of ports was overbed, more exactly 0.25 m above the bed surface. In spite of suitable variations of excess air, fluidization velocity and temperature, this overbed trial was treated as unsuccessful. The main disadvantage was a very low burn off in the bed, which was made evident by a luminous and sooty flame above the bed. The authors highlighted that only few percentages of the heat introduced with fuel were developed in the fluidized bed. But the change of nozzle position did not give much better results. Other positions of the nozzle were just at the level of fluidized bed surface and in the bed. The combustion efficiency with reference to the fluidized bed was slightly higher after the changes in nozzle position, but not yet satisfactory, being only 20% at maximum. The main reason was the shallow bed, only 150 mm high. As an attempt for increasing the combustion efficiency, their idea was to enable long enough residence time of fuel vapors within the bed and to improve mixing between fuel and air within the bed. They tried a two-stage combustion process in a single fluidized bed. The leading idea was to create two zones in one fluidized bed: the bottom zone with greater and heavier particles for liquid fuel gasification at lower temperature, and the upper zone with lighter particles for combustion at higher temperature. For that purpose the inert solids consisted of two different materials, with different density and particle size.

Almost the same idea of two-zone fluidized bed was applied by a group of pioneering Russian investigators (Keler and Berg, 1979; Berg et al., 1983). In the first experimental set-up they installed heat exchanger tubes in the upper zone of the bed, 100 mm above the fuel nozzle and 200 mm above the distributor plate. The main purpose of the embedded tubes was to prevent formation of great gas bubbles and to improve mass exchange between fuel vapor bubbles and emulsion. At a bed temperature of 930°C and 25% excess air the heat loss in unburned gases was 1.5%, whereas at 1050°C and 10% excess air a negligible heat loss was found. This temperature, however, was too high for efficient sulfur retention. For that reason the authors decided to use coarser solid particles in the lower part of the bed, with the idea that different temperatures could be obtained in the lower and upper part of the fluidized bed. The lower temperature is favorable for sulfur

retention, while the higher temperature for large combustion efficiency. As the next step, the same authors built a two-stage fluidized bed, by separating it along its height with a distributor plate. In the lower part of the bed the liquid fuel was vaporized and partly burnt, whereas the intermediate distributor plate allowed much better mixing between the fuel vapors and air entering the upper fluidized bed. This segmented fluidized bed was suitable for much quicker heat up of the equipment. The authors observed that above 600°C the liquid fuels burned without any external support.

In parallel, a pioneering experimental work was satisfactorily carried out on pressurized fluidized bed combustion of liquid fuel by Roberts et al. (1975). The experiments were carried out on a combustor with a plan area up to 0.7 m^2, operating at pressures up to 600 kPa. Combustion of heavy oil was surprisingly successful even at the lowest tested temperature, i.e., 800°C, the combustion efficiency being always greater than 99.8%. On the contrary, the combustion efficiency of parallel coal-fired tests dropped down to 97.5% when decreasing the bed temperature to 800°C. It is worth noting that a baffle system was used in the freeboard to reduce the extent of splashing zone and hence to improve the combustion efficiency in the bed. An important authors' recommendation was that of ensuring exceptionally uniform fuel and air distribution in the bed. In turn, this will reduce undesirable freeboard combustion and consequent drawbacks like difficult control of heat exchange duties, excessive freeboard temperature resulting in possible ash softening, alkali volatilization, etc., and hence fouling of surfaces downstream.

Beacham and Marshall (1979) reported a successful experience and combustion results of heavy fuel oil in an industrial fluidized bed boiler, that was reconstructed from a spreader stoker fired boiler. The heavy fuel oil was injected through several specially designed injectors, the so-called "climbing film" oil nozzles. In the same boiler they tested different types of coal, too. The same nominal steam output obtained with coal was also reached by burning the heavy fuel oil with 40% excess air. Combustion efficiency was 99.5%, whereas CO concentration in flue gases was below 100 ppm.

On the basis of accumulated experience from several different fluidized bed combustors and boilers, Barker and Beacham (1980) gave some kind of overview of petroleum-derived liquid fuel combustion results in UK. Liquid fuels, especially the more volatile ones, are very quickly transformed into vapors as a result of heating, but pass through the fluidized bed without being adequately mixed with air. This leads to poor in-bed combustion and high temperatures above the bed and along the freeboard. Even worse, fuels can leave the combustion system without being completely burnt. They reported about the attempts to improve the combustion process performance. For instance, the tests performed in a 300 mm ID combustor showed that generally the increase in the bed solids inventory was beneficial, but not beyond a bed height of 50 cm. For other fluidized boilers Barker and Beacham discussed about satisfactory liquid fuel combustion with a bed height in the range 0.5-0.7 m and fluidizing velocities in the range 1.5-3 m/s. As a successful example, they reported results from a fluidized bed boiler where the combustion efficiency was 99.9%, the unburned carbon in fly ash was 0.23%, the freeboard temperature was lower than the bed temperature (760 versus 840°C), with an excess air of 20%. In this case high combustion efficiency was accomplished at the optimal bed temperature for sulfur retention (about 850°C).

Enyakin et al. (1980) made combustion tests with heavy fuel oil in a pilot bubbling fluidized bed boiler, with the cross section of 0.5 m^2. The bed was relatively deep, 0.9 m, and as a consequence 90% of the fuel was able to burn within the bed, 6% in the splash zone and the rest in the convective sections of the freeboard. They were able of achieving a specific power output as high as 2.9 MW/m^2 (with ref. to the combustor cross section). In order to further decrease the extent of combustion above the bed with this heavy fuel oil they recommended a bed depth till to 1.5 m. They also reported visual and acoustic observations; in particular, they noticed appearance and explosion of fuel bubbles at the bed surface.

Along the same path, Borodulya et al. (1992) challenged the issue of estimating the optimum height of a bubbling fluidized bed burning conventional liquid fuels. They concluded that the optimum bed height linearly depends on the liquid fuel feed rate; further, they provided reference values about the optimal height, which should be from 0.55 till 0.85 m for a fuel feed rate per single nozzle from 1.2 to 1.8 kg/h.

Combustion and desulfurization tests of a high sulfur liquid fuel (Egyptian mazut) have been successfully carried out by Okasha et al. (2003) in a bubbling fluidized bed combustor with 300 mm ID and 3.3 m height, equipped with a purposely designed fuel injector in the bed region. Among operating variables, the focus was on the role played by the bed height, the injection air flow rate and the Ca/S ratio, in order to minimize the influence of segregation phenomena in the bed on combustion efficiency and sulfur retention. In particular, the rate of dispersion gas used for the fuel injection had the largest effect on bed mixing and higher values boosted both fuel conversion and desulfurization.

Fluidized combustion of Orimulsion® was investigated in a joint project by ENEL (I) and National Research Council of Italy. Combustion tests were performed by Miccio et al. (1999) in a bubbling fluidized bed

experimental facility with 370 mm ID and 4.6 m height. The bed temperature was constant at 850°C. The combustion efficiency of the Orimulsion® was always greater than 98.5%. A part of the fuel burnt in the freeboard and, therefore, a temperature over 1000°C was measured there. This finding was interpreted as the consequence of insufficient mixing between the fuel and air within the bed. As a confirmation of intensive combustion in the splash zone, the oxygen concentration profile showed a very sharp drop of about 4% just above the bed. The bed height was in the range 30-71 cm, and it was noticed that the increase of the bed height led to the decrease of temperature in the freeboard, on account of a greater residence time of the fuel in the bed. For the bed height of about 70 cm, the temperature in the freeboard exceeded the bed one by 100°C. The measurements by Miccio et al. (1999) showed very uneven gas concentration profile in radial direction in the splash zone. The gas probe was positioned above the bed surface and oxygen concentration ranged from 2% above the injection point till 10 % at the opposite side. This was the proof that even a bed as tall as 70 cm did not enable satisfactory mixing and residence time of fuel within the bed. This implies that lateral mixing could be a limitation for realizing efficient combustion of liquid fuel within large scale fluidized bed. In spite of this uneven gas concentration profile, the authors calculated that 80-95 % of the liquid fuel conversion occurred in the fluidized bed.

Miccio et al. (1999) carried out some injection tests under inert atmosphere and found that only less than 10% of carbon originally contained in Orimulsion® was converted into a solid carbon phase. This evidence implies that combustion of Orimulsion®, after evaporation of fuel droplets, can be treated as homogeneous combustion only.

Non-commercial liquid fuels. Kerr and Probert (1990) attempted co-combustion of acid tar, a by-product of oil-refining industry, with coal. They run a bubbling fluidized bed combustor of 1.2m x 1.2m cross section, with a total heat input of about 2 MW_{th}, the share of acid tar being about a half. The bed height was 0.75 m, the bed temperature constant and equal to 855°C, the primary to secondary air ratio around 2:1. Several tests were made ending in very successful results: a combustion efficiency as high as 99% was attained. The authors reported that, however, about 2/3 of the heat was developed in the fluidized bed and 1/3 above the bed during co-combustion. Since they did not present combustion results of sole coal, it is hard to estimate how much the acid tar burnt in the fluidized bed and how much above the bed.

Very extensive testing of pitch combustion has been carried out at the University of British Columbia (CDN). Combustion tests were performed in a 152 mm square cross-section circulating fluidized combustor with a height of 7.3 m. Different values of primary to secondary air ratio were used in order to obtain good mixing characteristics in the bottom part and in the upper part with appropriate temperature distribution along the riser. Typical temperatures in the riser were 850-900°C. The pitch material was fed into the riser through a nozzle at the same level of the solids return valve, only after the combustor temperature had reached the value of 750°C. The measured values of operating temperature at several places along the riser were in a relatively narrow range, i.e., only 20°C. In all tests the combustion efficiency was very high, always over 99%. It is worth mentioning that a temperature in the riser of about 760°C was enough high to enable high combustion efficiency of over 99.9% (Legros et al., 1991). Even at this temperature the emissions of hydrocarbons and CO were not larger than 30 ppm and 160 ppm at 3% O_2 in flue gases. The authors did not notice any effect of the air flow ratio on the combustion efficiency.

In combustion tests performed afterwards, with the main aim of obtaining high sulfur retention efficiency by limestone, Brereton et al. (1995) changed the operational parameters a little. The primary to secondary air ratio was increased to 2.5, the pitch feed rate was decreased with a consequence of higher excess air and oxygen concentration of 7% in flue gases. Again the combustion efficiency was very high, i.e., 99.7%. Since very high temperature was measured in the secondary cyclone, almost the same value as in the riser, it was concluded that cyclones played an important role in final stage of homogeneous combustion of CO and hydrocarbons. Also Lafanechere et al. (2001) considered pitch for co-combustion with two coals at an industrial CFB boiler of 60 MWth in Marseille (F). They were mainly concerned with the furnace temperature profile and the boiler heat transfer coefficients, with some benefits provided by pitch addition.

In a similar way, Wu et al. (2001) successfully tested asphalt in a pilot CFB combustor obtaining high combustion efficiency between 99 and 99.5%, while the temperature difference between the bottom bed and the top of the riser did not exceed 50°C. Differently from coal combustion in a circulating fluidized bed where there is a relatively sharp drop of oxygen concentration in the riser wall region rich in char and inert particles, during combustion of liquid fuel they measured relatively close values of oxygen concentrations near the wall and at the center of the riser cross section. This implies that in the case of liquid fuel combustion a more homogeneous gas concentration field establishes in the riser cross section.

At the same time, Barczus et al. (2001) tested a heavy oil in another pre-pilot CFB combustor. They concluded that temperature is not a critical parameter for highly efficient combustion. At a riser temperature of

850°C combustion efficiency was reported to be acceptably high and concentrations of CO and hydrocarbons in flue gases were very low, i.e., less than 30 ppm; at 915°C, unburned gaseous components were almost non-detectable.

Anthony and Lu (2001) equipped a pilot bubbling fluidized bed facility to burn three different petroleum-based liquid fuels: heavy oil, pitch and bitumen. Once a nozzle for good atomization of the liquid fuels was designed, an extensive program of experiments was carried out. The bed height ranged from 0.4 till 1 m. They found that the increase of bed height did not have effect on the temperature distributions along the furnace height and on the combustion efficiency. Secondary air was used, but there were no comments regarding the effect of the secondary air. The authors varied the fluidizing velocity from 1.3 till 2.8 m/s. They observed that fluidizing velocity affected the temperature in the freeboard. During combustion of the heavy oil with a lower fluidizing velocity, they measured lower temperatures in the freeboard, and it was explained by a longer residence time of fuel in the fluidized bed, and a greater part of the fuel burnt in the bed. However, during combustion of pitch, the opposite happened, i.e., the greater fluidizing velocity led to lower temperatures in the freeboard. This phenomenon was explained by an enhanced mixing in the bed. Comparing the measured values during combustion of different liquid fuels, they concluded that the type of liquid fuel did not significantly affect the temperature distributions along the height of the furnace. Much more influence on the temperature distributions had the nozzle type. Generally, the combustion efficiency was always higher than 98.5%.

One of very rare examples of industrial applications of bubbling fluidized bed for burning liquid fuel residues was given by North et al. (1999). In a boiler furnace of 21 m^2 cross section and 6 m height a high sulfur pitch was burnt with the addition of wastewater containing organic compounds. The authors reported an increase in the freeboard temperature up to 1200°C, which was 170°C over the bed temperature; therefore, they estimated that about 40% of the pitch burnt above the bed surface.

Recently, Miccio et al. (2008) burned two liquid biofuels, i.e., biodiesel and sunflower oil, in a lab-scale internal circulating fluidized bed reactor (ICFB) for co-gasification of biomass/waste fuels or incineration of liquid wastes. The fuel was fed to the inner column (riser), so the combustion of fuel vapors took place with a rather limited residence time. The study has been aimed at checking the occurrence of the micro-explosive behavior already observed in BFB combustion. The efficiency of combustion and the CO emissions slightly differ between biodiesel and sunflower oil, the biodiesel giving rise to a better combustion performance.

EMISSIONS

Sulfur oxides. Light petroleum-based liquid fuels have usually low content of sulfur and can be burnt in conventional burners with low emission. With combustion of heavy petroleum-based liquid fuels, one of main problems is the emission of sulfur oxides.

Roberts et al. (1975) carried out experiments on sulfur retention using dolomite and limestone at combustion pressures of 350-600 kPa and temperature of 800°C. The obtained results indicated that the sulfur retention efficiencies, both of heavy oil and coal, are similar. As expected, the sulfur retention was enhanced with Ca/S molar ratio, in particular, when using dolomite. For instance, sulfur retention increased from 72 % to 92% raising Ca/S ratio from 0.8 to 1.8 in the case of dolomite. On the other side, it increased from 65% to 77% raising Ca/S ratio from 1.8 to 2.8. They always found a modest improvement in sulfur retention with increase in bed temperature. The behavior is quite different from that at atmospheric pressure where sulfur retention falls sharply with a temperature increase above 800-850°C.

Beacham and Marshall (1979) reported a high sulfur retention in a FB boiler burning a heavy fuel oil containing 3% sulfur. About 95% SO_2 retention was achieved at the expense of a Ca/S ratio as high as 5.3.

Enjakin et al. (1980, 1985) performed combustion tests with commercial heavy fuel oil (mazut) containing 2.1% sulfur in a pilot plant with the fluidized bed cross section of 0.5 m^2. They made three trials, the first with dolomite, the second with limestone, and the third without adding any sorbent. In the latter case, the concentrations were 35 ppm SO_3 and 700 ppm SO_2. After adding sorbents the concentrations decreased to 6 ppm SO_3 and 210 ppm SO_2, at Ca/S ratio equal to 3. Further increase of the Ca/S ratio was not effective on further decreasing of the sulfur oxides concentrations. One of conclusions of the authors was that the measured concentration of SO_3 (6 ppm) was low enough and would not lead to dew-point corrosion of heat exchange surfaces. In fact, the major problem with SO_3 is related to lowering the acid dew-point of wet flue gases, which effects more rapid metal corrosion of heat exchangers. For instance, at 1 ppm SO_3 the acid dew-point is 110°C, while at 80 ppm SO_3 the acid dew-point is 150°C (Brereton et al., 1995).

In a further paper on petroleum-based liquid fuel combustion in fluidized bed, Barker and Beacham (1980) reported about concentrations of SO_3. The authors measured 6 ppm of SO_3 and 2640 ppm of SO_2 in combustion

tests without addition of limestone, while they did not detect any SO_3 in tests with limestone. In these combustion tests, similarly to findings of Enjakin et al. (1985), SO_2 did not show a remarkable tendency to SO_3 conversion at standard FBC temperature and with excess air of 20%.

Barker and Beacham (1980) noticed that the inert bed material of fluidized bed during combustion of petroleum based liquid fuel retained "a large proportion of the ash from liquid fuel". In their liquid fuel the main ash constituents were sodium and vanadium compounds. These metals created a surface layer on bed particles of relatively inert compounds. The authors reported that more than 90% of vanadium from the ash was retained on bed particles. The advantage of the layer is avoiding catalytic effects of vanadium in the stream of flue gases, in combination with SO_3, with extreme corrosion of the heat exchange surfaces. Furthermore, it was noticed by Barker and Beacham (1980), Enjakin et al. (1985), and Brereton at al. (1995) that the presence of limestone has positive effects and significantly lowers the SO_3 concentrations.

Typical molar ratio Ca/S for limestone added in FB combustors during combustion of liquid fuels was in a similar range as for coal combustion. That means the ratio was usually around 3, but some combustion tests were carried out with the molar ratio from 2 till 6.9 (Anthony and Lu, 2001).

Arthursson and Ostenberg (1979) reported about a demonstration bubbling fluidized bed boiler of 25 MWth for district heating. Since the fuel was high-sulfur residual oil, for accomplishing the high sulfur retention they used dolomite as the inert bed material. Using this bed material the Ca/S molar ratio could be as low as 1.5, while the emission of SO_2 was below the environmental requirements.

There is some difference in emission between combustion in bubbling and circulating fluidized beds. Generally liquid fuels leave very quickly the bubbling bed in BFBC or the dense bottom bed in CFBC, and tend to burn above the bed. For bubbling fluidized beds, this means that the formation of sulfur-oxides can occur to a great extent above the bed, and practically without contacts with particles of limestone in the bed. As a result the concentration of SO_2 can be very high. In circulating fluidized bed boilers, conditions for capturing SO_2 are better, since limestone particles circulate together with inert material, passing the whole riser height and having improved contact with gaseous sulfur oxides.

However, for optimal sulfur retention it is necessary that the liquid fuel burn off mainly occurs, if it cannot be completed at all, just in the dense fluidized bed. That means the emission of sulfur-oxides is affected by the quality of fuel distribution and dispersion, and also by positions of nozzles in the fluidized bed furnace. If design solutions of nozzles and fluidized bed boilers enable combustion mainly in the bed, sulfur oxides will be formed within the bed and, under controlled temperature conditions favorable to SO_2 capture, sulfur retention by limestone or dolomite particles will result much higher.

Wu et al. (2001) conducted tests with asphalt in a CFBC pilot plant. They found that, for the same other operating parameters, the use of steam instead of air for assistance to fuel injection led to higher SO_2 emission. They achieved a maximum sulfur capture efficiency of 94% with SO_2 emission of 110 ppm.

The sulfur retention in CFB units burning liquid fuel was less effective if compared with coal, while maintaining Ca/S ratio and other parameters the same. At a CFB plant of 60 MWth (Lafanechere et al., 2001) the emission of SO_2 was almost quadrupled when half of the heat input was switched from coal to petroleum pitch, while the sulfur content expressed per MJ of fuel heating value was about twice less in the petroleum pitch than in the coal. Similar relatively low sulfur capturing efficiencies were measured during combustion of petroleum liquid fuel in other CFB units (Zhang et al., 1991, Barczus et al., 2001). Zhang et al. (1991) carried out combustion tests also in bubbling fluidized bed units, using petroleum fuels and coal; their conclusion was that concerning liquid fuel the circulating fluidized bed gives a higher sulfur capturing efficiency than the bubbling one.

In an industrial bubbling fluidized bed of 20MWth burning high sulfur pitch the sulfur capture efficiency was 85%, with SO_2 emission of 400 ppm. In a very extensive investigation of Anthony and Lu (2001) three different petroleum liquid fuels were tested in a bubbling FB combustor. Although the sulfur retention was in the range 71–93%, the SO_2 emission was till 1600 ppm due to very high sulfur content.

Nitrogen oxides. Petroleum-based liquid fuels contain usually less nitrogen than coal on mass basis. If the nitrogen content in liquid fuels is recalculated on the basis of heating value, it becomes even less compared to coal. Therefore it seems that for reaching allowable emissions of nitrogen oxides it would not be necessary to apply any special measures.

Roberts et al. (1975) reported that the NO_x emissions from heavy oil (typically 130 ppm) are much lower than from coal (300-600 ppm) in the case of atmospheric combustion. However, in the case of pressurized combustion NO_x emissions become comparable (around 110 ppm), as a large part of the NO_x formed during coal combustion is reduced inside the bed thanks to the high residence time and contact with char. NO_x was found to increase with excess air as usual, but no consistent effect of temperature was observed.

Beacham and Marshall (1979) confirmed the low NO_x emissions of FBC burning heavy liquid fuels. NO_x

levels were typically below 140 ppm, but above 300 ppm when burning coal.

Keler and Berg (1979) reported that during mazut combustion in a laboratory bubbling fluidized bed the NO_x emission were in the range 150-400 mg/m^3 at excess air 1.25. Comparing this value with the EU regulations of that time (650 mg/m^3) it was below the limit. But comparing with the present regulation these emissions are somewhere across the limits (200-400 mg/m^3, depending on thermal capacity).

Enjakin et al. (1980, 1985) favorably compared the NO_x emissions during combustion of mazut in a pilot bubbling fluidized bed boiler with those from industrial plants with conventional burners. The emissions of NO_x from the industrial plants were between 135 and 155 ppm, whereas from the FB pilot boiler ranged between 90 and 110 ppm at the same value of excess air.

These good results obtained from the first research activities showed possibility for the fluidized bed technology to achieve low emission of nitrogen oxides during combustion of liquid fuels. Since the temperatures in combustion chamber of circulating or bubbling FB facilities are relatively low, the main part of NO_x originated from the nitrogen contained in the fuel. However, only a minor part of the fuel nitrogen is converted to NO_x. Barczus et al. (2001) found for a CFB unit that only 7% of the nitrogen from the used fuel was converted to NO_x. Anthony and Lu (2001) calculated that during experiments in their BFB combustor the conversion of nitrogen to NO_x was between 14 and 52%, whose range includes the value (19%) reported by North et al. (1999) for another industrial BFB facility.

More recent data were obtained in a pilot CFB unit by Barczus et al. (2001) with NO_x level very close to 100 ppm for two different operational temperatures (850 and 915°C). During these experiments N_2O was not detected, this result being attributed to presence of hydrogen radicals, formed during the hydrocarbon decomposition and active for reduction of N_2O.

At the previously mentioned CFB plant of 60 MWth (Lafanechere et al., 2001) replacing a half of the coal heat input by a petroleum pitch led to an increase of NO_x up to 25%, in spite of the fact that the petroleum pitch had a 4 times lower content of nitrogen. No information was reported on changes of temperature profiles in the combustor, but it was reported that during co-combustion the oxygen concentration was higher (39% expressed in relative number). Taking into account that in the case of co-combustion the content of char particles in the riser was smaller and the oxygen concentration was higher, it is likely that these factors led to higher concentrations of NO_x.

Investigating the effects of different types of assisting fluid in feeding of heavy petroleum residues, Wu et al. (2001) detected that for the same total excess air the use of steam as assisting medium for fuel injection, instead of air, led to considerably decreasing NO_x emission (260 ppm with air, 200 ppm with steam).

At bubbling fluidized bed facilities different values of NO_x emissions were measured. At an industrial unit of about 20 MWth (North et al., 1999), NO_x emissions in two tests were 200 and 140 ppm.

The influence of oxygen concentration changes on NO_x was presented in the work by Miccio et al. (1999) on Orimulsion®. The measured NO_x emissions ranged from 60 till 80 ppm at O_2 concentrations in flue gases below 3% and reached about 140 ppm at 5% O_2.

Carbon monoxide. The emission of CO is a consequence of the inefficiency of combustion process. In general, high concentrations of CO have been measured in the flue gases from some lab-scale or pilot experimental facilities burning petroleum-based liquid fuel. However, those findings cannot be considered representative of a general assessment of combustion process. A liquid fuel very quickly vaporizes and runs out the fluidized bed, burning above the fluidized bed as well. Therefore small height of experimental FB unit can give rise to great concentrations of CO because of a too short residence time.

With reference to bubbling fluidized beds, Miccio et al. (1999) reported CO emissions around 200 ppm (in some trials as low as 50 ppm) in a 370 mm ID, 4 m tall experimental BFB facility. In contrast, Anthony and Lu (2001) reported measured values of much higher CO emissions from their pilot combustor, ranging from 150 to more than 3000 ppm.

In CFB facilities the emissions of CO varied, but in general were lower than in bubbling fluidized bed. In the industrial plant Somedith (Lafanechere et al., 2001) the CO concentration was halved during co-combustion of pitch and coal compared to solely coal. In other pilot CFB units, at approximately the same conditions of temperature and excess air, the CO concentrations varied from 24 ppm (Barczus et al., 2001), over 150 ppm (Wu et al., 2001), till 270 ppm (Brereton et al., 1995).

Ash. Since the liquid fuels - even the heaviest of them like bitumen and asphalt - have mineral components not over 2% and very often below 1%, ash problems are generally not reported. It was noticed that some of heavy liquid fuels have very high concentrations of heavy metals. Therefore, there is necessity of taking care about this material: for instance Wu et al. (2001) reported the chemical analysis of asphalt ash leachate after a 24-hour treatment in an acetic acid solution, showing that the concentrations of heavy metals were a few orders of magnitude less than the permitted values.

Since the content of vanadium can be high in ash of liquid fuels (in some petroleum pitch V_2O_5 rates up to 25%), and it exerts a very strong catalytic effect, vanadium was separately analyzed in a few papers. Besides its role in creating aggressive species, it is important that vanadium and generally heavy metals are not emitted as vapor with flue gases. Legros et al. (1991) checked the mass balance on vanadium during FB combustion of liquid fuels; it was closed to 95% in one case and 129% in another case, confirming that all vanadium remained in solid phase.

Barker and Beacham (1980) commented on the fate of liquid fuel ash and fluidized bed material. Contrary to coal combustion where coal ash usually replaces the initial bed material, during combustion of liquid fuel the initial bed material practically does not change. Since they detected that the bed material retained some components from the liquid fuel ash, they emphasized that an appropriate bed material should be chosen during combustion of liquid fuel to retain the main and the most harmful ash components.

CONCLUSIONS

A general picture of phenomena occurring during the liquid fuel combustion process in a bubbling fluidized bed or in the bottom bed of a CBFC riser is available nowadays. They are fuel injection with air-assisted atomization or without it, fuel vaporization, fuel vapor bubble formation, fuel vapor pyrolysis and homogeneous oxidation, mixing of the fuel (and its products) by coalescence with the exogenous (air) bubbles, mass transfer between the fuel bubbles and the dense phase by convection and diffusion.

Combustion results of different liquid fuels obtained at different pilot and industrial fluidized bed facilities imply that, in order to achieve an efficient combustion process, the main operating variables, such as bed temperature, fluidizing velocity, bed height, excess air factor, primary-to-secondary air ratio, etc., must have practically the same values as those adopted for coal combustion. The most important issues for efficient combustion of liquid fuels are in relation to design and operation of the fuel feeding system.

A reasonable choice of fuel injection design and operation parameters is more critical in BFBC than in CFBC because it is just the bubbling bed and not the freeboard the place where mixing actions and mass transfer phenomena, which are required for efficient contacting and burning, are carried out.

Many investigators (Pillai and Elliot, 1976; Enyakin et al., 1980; Stubington and Davidson, 1981; Deguchi et al., 1984; Kerr et al., 1990; Miccio et al., 1999; Frassoldati et al., 2007) reported a temperature increase in the freeboard with respect to the bed (e.g., up to 200°C) and intense above-bed combustion. This was due to incomplete burn off of fuel vapors or pyrolysis products within the bed and/or their partial bypass as bubbles. In general, the extent of post-combustion was reduced by increasing bed temperature, bed height and fuel feed nozzle size; it was less sensitive to dispersing air velocity, whereas it was enhanced by use of secondary air.

As long as the operating bed temperature moves downward from the typical value for FBC of solid fuels, i.e., 850°C, more and more of fuel burn off is deferred from the bed to the freeboard. More importantly, the general combustion pattern becomes less smooth and predictable, with proven evidence of sudden light flashes in the splash zone, pressure spikes in the freeboard and detectable acoustic waves (Ferrante et al., 2008). The ensemble of these events was referred to as micro–explosion (Miccio et al., 2003), was typical of the liquid fuel combustion at low-temperature, i.e., 650-750°C, and made the fluidized combustion of liquid fuels quite similar to that of premixed gaseous fuels (Pre et al., 1998).

Taking into account the possibilities of adding sorbent particles, with the consequent *in situ* capture of SO_2, and of using catalytic particles as bed solids to retain or convert other harmful compounds, we can conclude that the fluidized bed technology is favorable compared to other conventional liquid fuel burning technologies, when the concept of *in situ* emissions control is preferred to that of post-processing of gaseous exhausts. This is especially true in the cases of high sulfur liquid fuels or dirty wastes.

A serious concern remains about the emissions of heavy metals and alkali species in the cases of heavy fuels or refinery wastes. Anyway, Barker and Beacham (1980) reported capture of Na (>75% of input) and Va (>90% of input) by bed particles.

Of course, the recently raised issue of nano-particulate emission remains open to questions and for sure deserves suitable investigations.

Combustion of petroleum-based liquid fuels in fluidized beds showed also that emission of nitrogen oxides can be lower than in conventional boilers. Since the earlier works low NO_x emissions were demonstrated in FBC of heavy liquid fuels. In bubbling FBC NO_x levels were typically below 140 ppm, whereas the levels were above 300 ppm when burning coal (Beacham and Marshall, 1979). The main part of NO_x originates from the nitrogen contained in the fuel, although only a minor part of the fuel nitrogen is converted to NO_x (e.g., between 14 and 52% according to Anthony and Lu, 2001).

Concerning N_2O, it was not detected in a reference set of experiments (Barczus et al., 2001).

Additional research work directed at improving liquid fuel distribution and dispersion will have a firm

fallout on the front of emissions. The resulting enhancement in contacting and mixing patterns will be reflected in diminishing emissions of CO and increasing SO_2 retention.

From the operation viewpoint, we may conclude that FB combustion of conventional liquid fuels (i.e., commercial products of oil refining) was demonstrated to be technically and environmentally feasible since the early works (Barker and Beacham, 1980). The most important aspects relevant to plant design, operation and performance refer to the fuel feeding system:

— number of nozzles or nozzle density per bed square cross section in large plants
— vertical location and arrangement of nozzles in the bed
— use of a secondary gaseous stream (e.g., air) for assistance to liquid fuel dispersion or atomization
— choice of an optimal dispersion velocity (referred to the nozzle exit section) for a suitable jet penetration inside the bed and a proper droplet size distribution of the dispersed liquid fuel
— choice of an optimal Air-to-Liquid fuel mass feed ratio for an appropriate fuel droplet size distribution

In general, bed design and operating conditions are to be preferred, under which the residence time of fuel-containing bubbles is prevailing on other characteristic times such as fuel vaporization. From an application point of view this can be achieved by deep underbed fuel feeding and air-assisted injection.

The above aspects have been studied at the lab scale and generally tested with success at the pilot scale. However, scale-up to industrial size application requires further consideration.

From the application viewpoint, we may conclude that FB combustion of conventional liquid fuels (i.e., commercial products of oil refining) is not competitive in the sector of utility or for process heat generation. It is not appealing from the viewpoint of fuel utilization and is not economically convenient from the viewpoint of investment and operation costs.

The situation changes when FB combustion is considered for non-commercial liquid fuels like high sulfur oil-derived fractions or dirty wastes or renewable liquid fuels. In the past, the FB combustion of high sulfur fuel oil was applied in some instances with the goal of attaining an effective desulfurization and a successful combustion at the same time (Barker and Beacham, 1980; Arthursson and Ostenberg, 1979). Renewable liquid fuels (e.g., vegetable oils) might be burned in FBC systems at small to medium scale for district heating or decentralized heat and power generation in developed countries or third-world regions where oily biomass is easily grown and processable. This option does not exclude the co-combustion with solid fuels or a dual fuel plant configuration with a switch between solid and liquid fuels, opening perspectives for both new investigations and applications.

Finally, a new possibility is envisaged for applications in which the released heat is directed at producing high temperature, high pressure fluid streams (e.g., for use in an external engine) taking advantage of the extremely high heat transfer coefficients in fluidized bed.

ACKNOWLEDGEMENTS

The authors gratefully acknowledge the financial support of the Italian Ministry of Foreign Affairs and of the University of Salerno for staff Mobility Projects. The authors are deeply thankful to Dr. M. Ilic and Prof. F. Okasha who took advantage of Mobility and collaborated to collection, classification and analysis of the papers useful for the present review.

REFERENCES

Anthony, E.J., Lu, D.Y., Proc. 16th FBC Conference (2001), FBC01-0093.
Arthursson, D.A.A., Oesterberg, H., J. Inst. Energy **42** (1979), p. 140-142.
Barczus, C., Henning, B., Blanke, T., Scherer, V., Proc. 16th FBC Conference (2001), FBC01-0152.
Barker, D., Beacham, B., Proceedings of the Inst. of Fuel Intern. Conf., London (1980), p. IA-3.
Beacham, B., Marshall, A.R., J. Inst. Energy **June** (1979), p. 59-64.
Berg, B. V., Keler, V. P., Podshivalov, V. G., Vasinov, E. A., Teploenergetika **8** (1983), p. 51-53.
Borodulya, V.A., Dikalenko, V.I., Dobkin, S.M., Markevich, I.I., Heat Transfer Res. **24** (1992), p. 832-839.
Brereton, C. M. H., Lim, C. J., Grace, J. R., Luckos, A., Zhu, J., Fuel **74** (1995), p. 1415-23.
Deguchi, A., Hosoda, H., Miura, M., Hirama, T., Nisizaki, H., Nenryo Kyokai ShiJ **63** (1984) p. 1066-1070.
Enyakin, Y.P., Zaitseva, M.P., Maidanic, M.N., Bozhevol'nova, E.V., Maslennekova, N.S., Pozhogina, A.N., Terzieva, V.F., Teploenegetika **12** (1980), p. 33-36.
Enyakin, Y. P., Zeger, K.E., Zaitseva, M.P., Teploenergetika 7 (1985), p. 45-48.
Ferrante, L., Miccio, M., Miccio, F., Solimene, R., Energy & Fuels, **22** (2008), p. 4213-4222.
Frassoldati, A, Faravelli, T, Miccio, F, Miccio, M., Ranzi, E., J. Energy Res. Techn. **129** (2007), p. 33-41.
Keler, V. R., Berg, B. V., Teploenergetika **10** (1979), p. 60-62.
Kerr, K., Probert, S.D., Applied Energy **35** (1990), p. 189-243.
Lafanechere, L., Thomas, P., Evrard, R., Briand, P., Proc. 16th FBC Conference (2001), FBC01-0067.

Legros, R., Brereton, C. M. H., Lim, C. J., Li, H., Grace, J. R., Anthony, E. J., Proc. 10th FBC Conference **2** (1989), p. 661-666.
Legros, R., Lim, C.J., Bretreton, C.M.H,. Grace, J.R., Fuel **70** (1991), p. 1465-1471.
Miccio, F., Miccio, M., Repetto, L., Traniello Gradassi, A., Proc. 15th FBC Conference (1999), p. 1354-1376.
Miccio, F., Miccio, M., Olivieri, G., Silvestre, A., Ind. Eng. Chem. Research **42** (2003), p. 3973-3981.
Miccio, F., Kalisz, S., Baxter, D., Svoboda, K., Chemical Engineering Journal **143** (2008), p. 172-179.
North, B., Eleftheriades, C., Engelbrecht, A., Proc. 15th FBC Conference (1999), Paper No. FBC99-0017.
Okasha, F.M., El-Emam, S. H., Mostafa, H. K., Exp. Thermal Fluid Science **27** (2003), p. 473-480.
Pillai, K. K., Elliott, D. E., J. Inst. Fuel, **49** (1976), p. 206-210.
Pre, P., Hemati, M., Marchand, B., Chem. Eng. Sc. **53** (1998), p. 2871-2883.
Roberts, A.G., Stantan, J. E., Wilkins, D. M., Beacham, B., Hoy, H. R., Inst. Fuel Symp. Ser. (London) (1975), D4 /1-D4 / 11.
Stubington, J.F., Davidson, J.F., AlChE Journal **27** (1981), No. 1, p. 59-65.
Wu, S., Sellakumar, K.M., Tuncay, J., Proc. 16th FBC Conference (2001), FBC01-0185.
Zhang, J. O., Jones, W. E., Lau, I. T., Friedrich, F. D, Proc. 11th FBC Conference **2** (1991), p. 639-648.
Zlatar, M., Financial Times Report, Financial Times, London, 1989.

DIRECT NUMERICAL SIMULATION OF VERTICAL PARTICULATE CHANNEL FLOW IN THE TURBULENT REGIME

M. Uhlmann[1], A. Pinelli[2]

1 Institute of Hydromechanics, Turbulent Flow Group, University of Karlsruhe, Germany
2 Energy Department, Simulation Unit, Ciemat Madrid, Spain

Abstract: We have conducted a DNS study of dilute turbulent particulate flow in a vertical plane channel, considering up to 8192 finite-size rigid particles with numerically resolved phase interfaces. The particle diameter corresponds to approximately 9 wall units and their terminal Reynolds number is set to 136. The fluid flow with bulk Reynolds number 2700 is directed upward, which maintains the particles suspended upon average. Two different density ratios were simulated, varying by a factor of 4.5. The corresponding Stokes numbers of the two particles were O(10) in the near-wall region and O(1) in the outer flow. We have observed the formation of large-scale elongated streak-like structures with streamwise dimensions of the order of 8 channel half-widths and cross-stream dimensions of the order of one half-width. At the same time, we have found no evidence of significant formation of particle clusters, which suggests that the large structures are due to an intrinsic instability of the flow, triggered by the presence of the particles. It was found that the mean flow velocity profile tends towards a concave shape, and the turbulence intensity as well as the normal stress anisotropy are strongly increased. The effect of varying the Stokes number while keeping the buoyancy, particle size and volume fraction constant was relatively weak. More details about part of this work can be found in Uhlmann (2008).

Keywords: particulate flow, turbulence, channel flow, DNS, immersed boundary method

INTRODUCTION

In the present study we are interested in the effect of solid heavy particles upon the structure of turbulent flow in a vertical plane channel. Past experimental studies of this configuration have revealed that the turbulence intensity can be substantially modified by the addition of particles (Tsuji el al., 1984; Kulick et al., 1994; Suzuki et al., 2000). Depending on the exact choice of the various parameters, either enhancement or attenuation can be achieved. However, the underlying mechanisms of the interaction between the two phases have so far not been elucidated in detail, especially in the regime where the smallest length scales of the turbulent flow are comparable to the particle diameter. Moreover, laboratory measurements can often not provide flow data with sufficient detail for the purpose of analyzing the dynamics of the interaction processes. Previous numerical simulations, on the other hand, have for the most part been limited to the point-particle regime, which loses its validity when the particle Reynolds number becomes appreciable and/or the size of the particles is not negligible compared to the smallest fluid scales (Elghobashi, 1994). More specifically, particle wakes cannot be represented in the framework of the point-particle approach. To our knowledge, the only previous direct numerical simulation (DNS) study of turbulent vertical channel flow with finite-size particles has been performed by Kajishima et al, (2001). However, these authors considered only a small number (Np=36) of relatively large particles (with a diameter corresponding to 32 wall units) and the angular particle motion was neglected. In the course of the present study we have performed interface-resolved DNS of turbulent flow in a vertical plane channel configuration involving up to 8192 spherical particles and integrating the equations of motion over O(100) bulk flow time units. In the following section the particular immersed boundary method used in our simulations is reviewed. We proceed by describing the specific conditions of the simulated flow cases as well as the initialization procedure, before turning to the presentation of the results. We discuss the Lagrangian correlation functions, the dispersion data, the spatial distribution of the dispersed phase, the structure of the carrier phase and finally the Eulerian statistics. The paper closes with a short summary and conclusion.

NUMERICAL METHOD

The Navier-Stokes equations for an incompressible fluid can be written as:

$$\partial_t \boldsymbol{u} + (\boldsymbol{u}\cdot\nabla)\boldsymbol{u} + \nabla p = \nu \nabla^2 \boldsymbol{u} + \boldsymbol{f} \tag{1a}$$

$$\nabla\cdot\boldsymbol{u} = 0 \tag{1b}$$

where $\boldsymbol{u}$ is the vector of fluid velocities, p the pressure normalized with the fluid density and $\boldsymbol{f}$ a volume force term. The basic idea of the immersed boundary method is to solve these equations in the entire domain Ω, including the space occupied by the solid particles, instead of only considering the interstitial fluid domain Ω_f. For this purpose, the force term $\boldsymbol{f}$ is introduced and formulated in such a way as to impose a rigid body motion upon the fluid at the locations of the solid particles. The main advantage of this approach lies in the possibility to use a fixed computational grid with a simple structure, allowing for efficient numerical solution techniques to be applied. In the following we will recall the essential points of our specific formulation of the immersed boundary method (Uhlmann, 2004). For this purpose, let us write the momentum equation in semi-discrete form:

$$\frac{\boldsymbol{u}^{n+1}-\boldsymbol{u}^{n}}{\Delta t}=\boldsymbol{rhs}^{n+1/2}+\boldsymbol{f}^{n+1/2} \tag{2}$$

where $\boldsymbol{rhs}$ regroups the convection term, the pressure gradient and the viscous term, the superscripts denoting the time level. The additional force in (2) can be expressed by simply rewriting the equation (Fadlun et al, 2000):

$$\boldsymbol{f}^{n+1/2}=\frac{\boldsymbol{u}^{(d)}-\boldsymbol{u}^{n}}{\Delta t}-\boldsymbol{rhs}^{n+1/2} \tag{3}$$

where $\boldsymbol{u}^{(d)}$ is the desired velocity at any grid point where forcing is to be applied (i.e., at a node inside a solid body). Formula (3) is characteristic for direct forcing methods (Fadlun et al., 2000; Kim et al., 2001), as opposed to formulations which rely on a feed-back mechanism (Lai and Peskin, 2000; Goldstein et al., 1993; Hoefler and Schwarzer, 2000). The drawback of the latter techniques is an often severe restriction of the time step, caused by the time scale of the feed-back law itself. Direct forcing methods, on the other hand, are free from this restriction. However, problems can arise in practice from the fact that the solid-fluid interface seldomly coincides with the Eulerian grid lines, meaning that interpolation needs to be performed in order to obtain an adequate representation of the interface. Inspired by Peskin's original immersed boundary method (Peskin, 1972; Peskin, 2002), we choose to compute the force term at Lagrangian positions attached to the surface of the particles, viz.

$$\boldsymbol{F}^{n+1/2}=\frac{\boldsymbol{U}^{(d)}-\boldsymbol{U}^{n}}{\Delta t}-\boldsymbol{RHS}^{n+1/2} \tag{4}$$

where upper-case letters indicate quantities evaluated at Lagrangian coordinates. Obviously, the velocity in the particle domain S is simply given by the solid-body motion,

$$\boldsymbol{U}^{(d)}=\boldsymbol{u}_c+\omega_c\times(\boldsymbol{X}-\boldsymbol{x}_c),\ \boldsymbol{X}\in S \tag{5}$$

as a function of the translational and rotational velocities of the particle, $\boldsymbol{u}_c$, Ω_c, and its center coordinates, $\boldsymbol{x}_c$ The two remaining terms on the right hand side of (4) can be collected as

$$\tilde{\boldsymbol{U}}=\boldsymbol{U}^{n}+\boldsymbol{RHS}^{n+1/2}\Delta t \tag{6}$$

which corresponds to a preliminary velocity obtained without applying a force term. Its Eulerian counterpart, is evaluated explicitly as:

$$\tilde{\boldsymbol{u}}=\boldsymbol{u}^{n}+\boldsymbol{rhs}^{n+1/2}\Delta t \tag{7}$$

The final element of our method is the transfer of the velocity (and *r.h.s.* forces) from Eulerian to Lagrangian positions as well as the inverse transfer of the forcing term to the Eulerian grid positions. For this purpose we define a Cartesian grid $\boldsymbol{x}_{ijk}$ with uniform mesh width x in all three directions. Furthermore, we distribute so-called discrete Lagrangian force points $\boldsymbol{Xl}$ (with $1\le l\le NL$) evenly on the particle surface. An *even* distribution of points on the surface of a sphere can be obtained in a pre-processing step by an iterative procedure (see Appendix A in Uhlmann, 2004). Using the regularized delta function formalism of Peskin (Peskin, 1972; Peskin, 2002), the Eulerian/Lagrangian transfer can be written as:

$$\tilde{\boldsymbol{U}}(\boldsymbol{X}_l)=\sum_{i,j,k}\tilde{\boldsymbol{u}}(\boldsymbol{x}_{i,j,k})\,\delta_h(\boldsymbol{x}_{i,j,k}-\boldsymbol{X}_l)\,\Delta x^3 \tag{8a}$$

$$\boldsymbol{f}(\boldsymbol{x}_{i,j,k})=\sum_{l}\boldsymbol{F}(\boldsymbol{X}_l)\,\delta_h(\boldsymbol{x}_{i,j,k}-\boldsymbol{X}_l)\,\Delta V_l \tag{8b}$$

where ΔV_l designates the forcing volume assigned to the l^{th} force point. We use a particular function δ_h which has the properties of continuous differentiability, second order accuracy, support of three grid nodes in each direction and consistency with basic properties of the Dirac delta function (Roma et al, 1999). It should be underlined that the force points are distributed on the interface between fluid and solid, and not throughout the whole solid domain. The reason for this is efficiency: the particle-related work currently scales as $D^2/(\Delta x)^2$ instead of $D^3/(\Delta x)^3$, where D is the particle diameter. The consequences for the efficiency of the forcing due to these two alternative placements of the forcing points have been discussed in a previous study (Uhlmann, 2005b). The above method has been implemented in a staggered finite-difference context, involving central, second-order accurate spatial operators, an implicit treatment of the viscous terms and a three-step Runge-Kutta procedure for the non-linear part. Continuity in the entire domain Ω is enforced by means of a projection

method. The particle motion is determined by the Runge-Kutta-discretized Newton equations for translational and rotational rigid-body motion, which are weakly coupled to the fluid equations. One step of our algorithm can be summed up as follows:

(1) compute the explicit velocity estimation $\tilde{\boldsymbol{u}}$

(2) transfer ũ to Lagrangian positions at the fluid-solid interfaces

(3) compute the force term $\boldsymbol{F}$

(4) transfer $\boldsymbol{F}$ back to Eulerian grid positions, obtaining $\boldsymbol{f}$

(5) perform one time step of the Navier-Stokes equations on the fixed grid with the force term $\boldsymbol{f}$

(6) advance the equations for particle motion, using the available force/torque.

The complete set of equations has been given in (Uhlmann, 2004). During the course of a simulation, particles can approach each other closely. However, very thin liquid inter-particle films cannot be resolved by a typical grid and therefore the correct build-up of repulsive pressure is not captured which in turn can lead to possible partial "overlap" of the particle positions in the numerical computation. In practice, we use the artificial repulsion potential of (Glowinski et al., 1999), relying upon a short-range repulsion force (with a range of $2\Delta x$), in order to prevent such non-physical situations. The stiffness parameter appearing in the definition of the repulsion force has been calibrated in simulations of two sedimenting particles and particle-wall interactions. The current algorithm has been coded for execution on parallel machines with distributed memory, using the MPI standard. For reasons of efficiency, the Helmholtz problems to be solved during the predictor step are simplified by second-order-accurate approximate factorization. The Poisson problem in the projection step is solved by a multi-grid technique. We use a domain decomposition approach for distributing the Eulerian nodes over a three-dimensional processor grid. Each processor treats the particles momentarily located in its sub-domain. Additionally, the neighbor processors need to contribute to the transfer operations (8) whenever particles happen to overlap sub-domains of the distributed Eulerian grid. The particle treatment can therefore be described as a "master-and-slave" technique. Our method has previously undergone extensive testing and validation with reference to available analytic, experimental and numerical data in what can be considered as standard "benchmark" cases. Detailed results can be found in (Uhlmann, 2004; Uhlmann, 2005a, 2006).

FLOW CONFIGURATION

We are considering particulate flow in a plane channel which is aligned along the vertical direction (Fig. 1). The fluid is driven in the positive x direction by a mean pressure gradient $<p_x><0$.

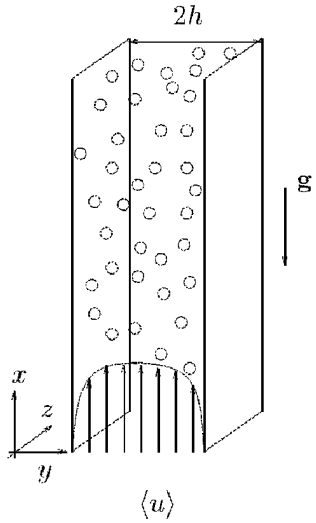

Fig. 1 Flow configuration

The bulk flow Reynolds number is maintained constant at a value of $Re_b=u_b h/\nu=2700$ (u_b, being the bulk velocity), which generates a turbulent flow with $Re_\tau=u_\tau h/\nu=172$ (u_τ being the wall shear velocity) in the absence of particles. The particle size is chosen as $D/h=1/20$, corresponding to $D+=8.6$ in wall units. This regime is of particular interest since the particles are of comparable size to the coherent structures typically found in the buffer layer of wall-bounded turbulent flow and a mutual interaction can therefore be expected. A spatial resolution of $D/\Delta x=12.8$ has been chosen, this value corresponds to a mesh width of $\Delta x/h=1/256$ (i.e., $Dx+=0.67$ in wall units). We have further imposed the equality between bulk fluid velocity (u_b) and terminal particle velocity ($u_{c\infty}$). This condition means that the average sedimentation velocity for a large number of particles will be close to zero, supposing that their spatial distribution is near uniform. In practice the average sedimentation velocity takes a slightly positive value. From the condition $u_{c\infty}=u_b$. it follows that the terminal particle Reynolds number (based upon the particle diameter and the relative velocity between phases) measures $Re_{D\,\infty}=136$. From the equality between buoyancy and drag forces acting upon an isolated particle, we can form the Archimedes number, which takes the following value:

$$Ar=(D/h)^3 Re_b^2 \frac{|\boldsymbol{g}|h}{u_b^2}\left(\frac{\rho_p}{\rho_f}-1\right)=13328 \tag{9}$$

where ρ_p/ρ_f is the density ratio between particle and fluid phase and $\boldsymbol{g}$ the gravitational acceleration. This leaves us with one parameter free to choose (ρ_p/ρ_f say), the other one being $\boldsymbol{g}\,h/u_b 2$ fixed by (9). We have analyzed two cases with parameter values as given in Table 1.

Table 1 Physical parameters in our simulations of particulate flow in a vertical plane channel. In all cases the particle diameter is chosen as $D=h/20$, the global solid volume fraction is set to $\phi_s = 0.0042$. B2 is a case with identical conditions as case B, except that the streamwise period of the domain was doubled

case	$\frac{\rho_p}{\rho_f}$	$\lvert\mathbf{g}\rvert h/u_b^2$	St^+	St_b	N_p	Ω
A	10	1.625	67	3.75	512	$4h\times 2h\times h$
B	2.21	12.108	15	0.83	4096	$8h\times 2h\times 4h$
B2	2.21	12.108	15	0.83	8192	$16h\times 2h\times 4h$

The relative particle density in case A is approximately *4.5* times higher than in case B, and the Stokes number (defined as the ratio between particle and fluid time scales) varies accordingly. In particular, we determine the particle time scale from the usual Stokes drag law $\tau_{SD}=D^2\rho_p/(18\ \nu\rho_f)$, and consider two time scales for the fluid motion: the near-wall scale $\tau^+=\nu u_\tau^2$ and the bulk flow scale $\tau_b=h/u_b$. Consequently, we can form two Stokes numbers, characterizing the ratio of time scales in the near-wall region, $St^+=\tau_{SD}/\tau^+$, and in the outer flow $St_b=\tau_{SD}/\tau_b$. Table 1 shows that the present particles have a relatively large response time with respect to the flow in the near-wall region ($St^+>10$), but both scales are comparable in the bulk of the flow ($St_b\approx O(1)$). The global solid volume fraction has been set to $\phi_s=0.0042$, which can be considered at the upper limit of the dilute regime. The two cases were run in computational domains of different sizes, the volume in case B being eight times larger. The number of particles in cases A, B is therefore $N_p=512$, $N_p=4096$, respectively. The domain used in case A represents evidently a smaller sample size per instantaneous flow field. However, it allows for simulations over longer time intervals which is of special interest for the computation of slowly evolving statistical quantities acquired along the particle paths. Table 2 shows the global grid size of the simulations, which exceeds 10^9 Eulerian nodes and 2×10^6 Lagrangian force points in case B, where the work is typically distributed over 512 processors of a PC cluster with fiberoptical interconnect. Finally, we have recently initiated a third case, B2, which is identical to case B, except that the streamwise period of the domain was doubled. We will briefly mention this run in the final discussion.

Table 2 Numerical parameters employed in our DNS. Ni is the number of grid nodes in the i^{th} direction, np is the number of processors, tobs is the observation interval in bulk flow time units after discarding the initial transient. The grid spacing in all cases is fixed at $\Delta x=h/256$, corresponding to $N_L=515$ Lagrangian force points per particle, and the time step at $\Delta t=0.00162\ h/U_b$

case	$N_x \times N_y \times N_z$	np	t_{obs}
A	$1024 \times 513 \times 256$	32	556
B	$2048 \times 513 \times 1024$	512	95
B2	$4096 \times 513 \times 1024$	1024	11

Initialization of the simulations

Particles are introduced into fully-developed turbulent single-phase flow at time t_0. The initial particle positions form a regular array covering the computational domain. Their initial velocities are matched with the fluid velocities found at t_0. at the respective center locations; the initial angular particle velocities are set to zero. During the first time step of the two-phase computation, the coupling algorithm solidifies the fluid occupying the volume of each particle and buoyancy forces set in. Figure 2(a) shows how the average vertical particle velocity $\langle u_p\rangle_p$ (the symbol $\langle\ \rangle_p$ indicates an average over all particles) drops from a value close to the bulk fluid velocity to almost zero over an initial interval of approximately 3 (1) bulk time units in case A (B). Let us mention that the long-time averaged mean upward drift of the particles amounts to $0.029u_b$ and $0.058\ u_b$ respectively. The data corresponding to the initial transient will not be considered in the following and, therefore, an initial interval of 17 bulk time units has been discarded. The length of the observation interval for the two cases is indicated in Table 2.

From Fig. 2(b) it can be seen that the friction velocity increases immediately after the addition of particles, leading to a sharp rise of Re_τ which then oscillates around a new mean value of approximately 225 in both cases. The amplitude and frequency of the oscillations is larger in case A due to the smaller box size. This higher friction velocity in the particulate cases reflects the modification of the mean fluid velocity profile as discussed below (Figures 13 and 15).

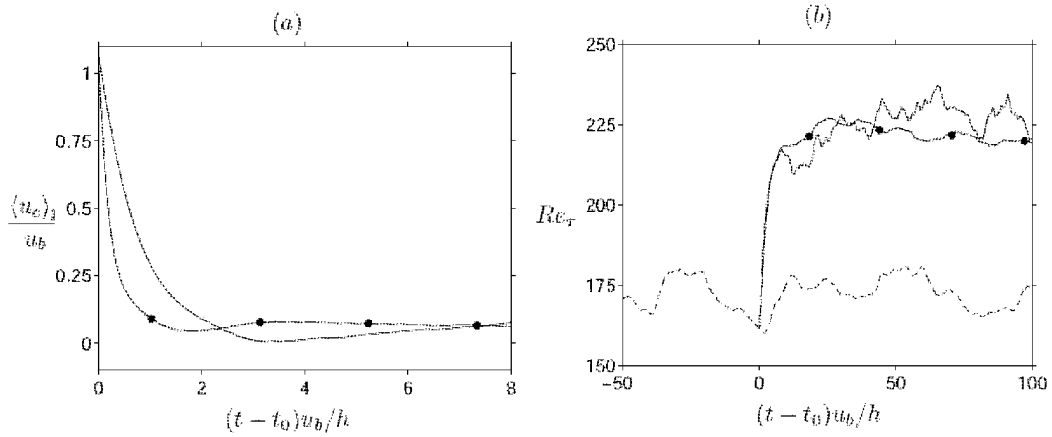

Fig. 2 (a) The average vertical particle velocity during start-up of the two-phase simulation. (b) The time evolution of the friction-velocity-based Reynolds number around the start-up time. Particles are added at t=t0 solid line, case A; - • -, case B; - - -,single-phase flow

Lagrangian correlations

Let us introduce the notation for the different averaging operations employed in the following $< x_i >_x$ refers to the streamwise average of any quantity x_i, $< x_i >_{xz}$ is the average over wall-parallel planes and $< x_i >_t$ temporal average (over the observation interval given in table 2, except where otherwise stated); the average over time and wall-parallel planes is denoted by $<< x_i >_{xz} >_t$; as mentioned above, $< x_i >_p$ refers to the average over all particles. The Eulerian space averages of quantities related to the dispersed phase are carried out for discrete 'bins' in the wall-normal direction, defined as $I_j=[j-1, j) \cdot 2h/N_{bin} \forall\, 1 \leqslant j \leqslant N_{bin}$. In practice a value of $N_{bin}=40$ was chosen, such that the width of each bin corresponds to one particle diameter. The time and planewise average of a particle-related quantity is then computed for each bin by the following formula:

$$\langle \eta \rangle (y_j) = \frac{\int_0^{t_{obs}} \sum_{i=1;\, x_{c,2}^{(i)} \in I_j}^{N_p} \eta_c^{(i)}(t)\, dt}{\int_0^{t_{obs}} \sum_{i=1;\, x_{c,2}^{(i)} \in I_j}^{N_p} 1\, dt} \tag{10}$$

where y_j is the coordinate of the center of the bin I_j. The Lagrangian auto-correlation of particle velocity components is defined as follows:

$$R_{Lp,\alpha}(\tau) = \frac{\left\langle \left\langle u'_{c,\alpha}(t) \cdot u'_{c,\alpha}(t+\tau) \right\rangle_p \right\rangle_t}{\left\langle \left\langle u'_{c,\alpha}(t)^2 \right\rangle_p \right\rangle_t} \tag{11}$$

where $u'^{(i)}_{c,\alpha}(t) = u^{(i)}_{c,\alpha}(t) - \langle uc \rangle\ (y_j\ | x_\omega 2^{(i)}(t) \in I_j)\ \delta_{\alpha 1}$ is the instantaneous velocity of the i^{th} particle in the α direction, from which the mean streamwise particle velocity at the corresponding bin y_j has been subtracted. As pointed out by Ahmed and Elgobashi (2001), eliminating the mean velocity contribution yields the Lagrangian correlations due to turbulence.

Our present results are shown in Fig. 3. First we observe that the initial decay of all components of the correlation function is faster in case B than in case A, as can be expected from the lower relative density in the former case. The first zero-crossing of components α=1,2,3 occurs approximately at 90,16,16 (50,3,2) bulk time units in case A (B). In both cases these values exhibit a large difference between the vertical and the two horizontal components, which resembles the strong anisotropy of the near-wall turbulent flow field, as evidenced e.g. by two-point fluid velocity autocorrelations for streamwise separations (Kim et al., 1987 and discussion below). A striking feature of the correlation functions in case B is what seems to be a damped oscillation around the exponentially decaying value, found in all three coordinate directions, with a period of roughly *8* bulk time units. A corresponding small "bump" can also be found in the curves for case A, approximately for the same time separation as the first local minimum in case B. It can be speculated that this oscillation is a signature of the large streamwise elongated flow structures which have been detected in the present case and which will be discussed below. The fact that this feature is more visible in case B is again a consequence of its lower particle inertia. The dispersion of particles (mean-square displacement) along the coordinate direction x_α starting from the particle position at time t_1 (coinciding with the beginning of the observation interval) is defined as:

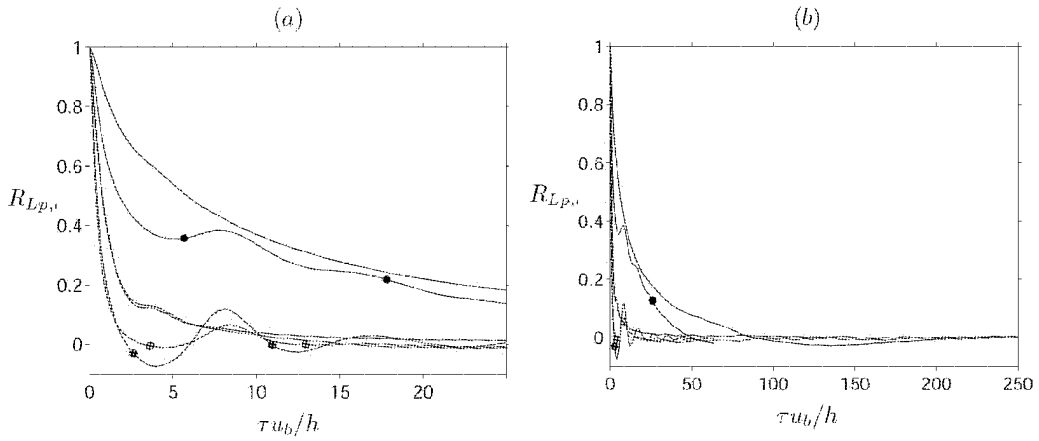

Fig. 3 Lagrangian particle velocity auto-correlations as a function of the time separation τ: (a) for short separations; (b) for long separations. Solid line, case A; - •-, case B. Colors indicate the velocity components: black α=1, red α=2 and blue α=4

$$M_{p,\alpha}=\frac{1}{N_p}\sum_{i=1}^{N_p}\left(x_{c,\alpha}^{(i)}(t)-x_{c,\alpha}^{(i)}(t_1)-dx_\alpha(y_j: x_{c,2}^{(i)}(t_1)\in I_j)\right)^2 \tag{12}$$

where the third term in the sum on the right-hand-side corresponds to the mean displacement of particles originating from wall distances pertaining to the same discrete bin as the i^{th} particle in the summation (see discussion in Ahmed and Elgobashi, 2001). Again, subtraction of the equivalent mean displacement yields the dispersion due to turbulence. The quantity $dx_\alpha(y_j)$ is computed analogously to (10), viz.

$$dx_\alpha(y_j)=\frac{\sum_{i=1;\,x_{c,2}(t)\in I_j}^{N_p} x_{c,\alpha}^{(i)}(t)-x_{c,\alpha}^{(i)}(t_1)}{\sum_{i=1;\,x_{c,2}(t)\in I_j}^{N_p} 1} \tag{13}$$

From Fig. 4 it can be seen that the dispersion of the particles is largest in the streamwise (vertical) direction and smallest in the spanwise direction. The figure also shows that the dispersion in case B in all three directions is greater than the counterpart in case A at all times. It is evident that the smaller size of the computational domain starts to affect the time evolution earlier in case A, with the curve for the streamwise component already leveling off after approximately 8 bulk time units. If we concentrate on case B, we observe that the dispersion in the vertical direction follows approximately a behavior proportional to t^2, whereas the two horizontal components grow with slopes intermediate between t and t^2.

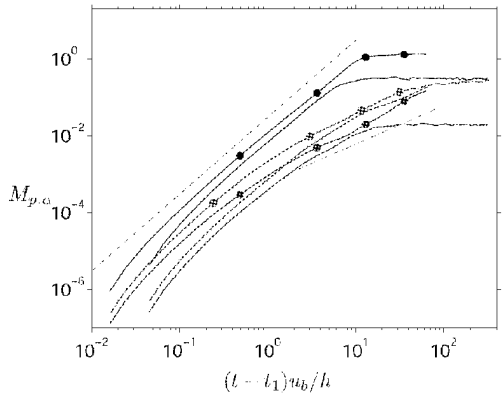

Fig. 4 Mean-square particle displacement for cases A,B as a function of elapsed time. Symbols and lines as in figure 3. The dashed line has a slope of 2, the dash-dotted line a slope of 1

Structure of the dispersed phase

The wall-normal profile of the mean solid volume fraction $<\phi_s>$, normalized by the global value ϕ_s, is shown in Fig. 5(a). The curves are nearly symmetric and very similar in both cases, the data in case B being considerably smoother due to the larger sample size. The distribution of particles is visibly inhomogeneous with a sharp peak located around y/h=0.1, corresponding to approximately 23 wall units. The position of the peak concentration coincides therefore with the location of the maximum intensity of streamwise fluid velocity fluctuations (cf. 16 below), commonly associated with the most probable position of buffer-layer streaks. It

should be pointed out that we do not observe an increase in the height of the peaks as the simulation proceeds further, indicating that a statistical equilibrium between 'outward' and 'inward' wall-normal particle motion has been reached. At the center of the channel, the mean solid volume fraction exhibits a third local maximum at about 70% of the amplitude of the main peaks. However, the variation of $<\phi_s>$ across the bulk flow region ($0.5 \leqslant y/h \leqslant 1$) is rather small.

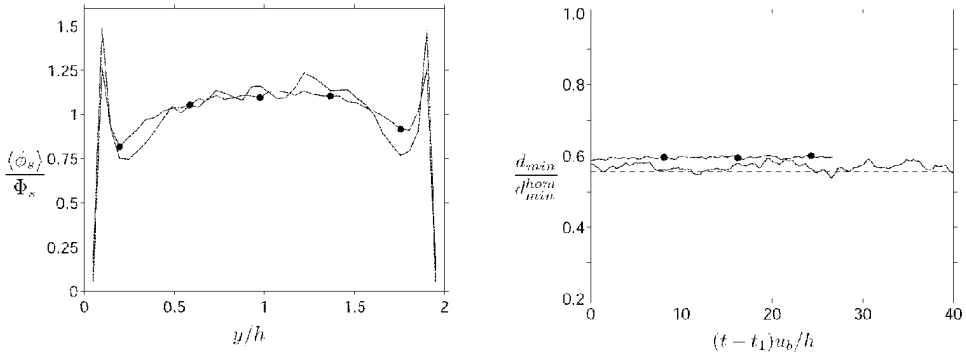

Fig. 5 (a) profiles of the mean solid volume fraction, normalized by the global value Φ_s. Solid line, case A; - • -, case B. (b) time evolution of the average distance to the nearest neighbor, normalized by the value for a homogeneous distribution. Symbols as in figure 3. The dashed line corresponds to the value for a random distribution with the same solid volume fraction

In order to gain further insight into the instantaneous spatial distribution of particles, we define the average distance to the nearest particle, viz

$$d_{min}=\frac{1}{N_p}\sum_{i=1}^{N_p} min_{j=1,j\neq i}^{N-p}(d_{i,j}) \tag{14}$$

where $d_{ij}=|xc^{(i)}-xc^{(j)}|$ is the distance between the centers of particles i and j. The time evolution of the quantity d_{min}, normalized by its value for a homogeneous distribution with the same solid volume fraction, $d_{min,hom}=(||\Omega||/N\_p)^{1/3}$, has been plotted in Fig. 5(b). The ratio is bounded by the values 0.2 (corresponding to each particle being in contact with at least one other particle) and 1.0. Actual values recorded during our simulations vary mildly between 0.5 and 0.6, which is in fact very close to the value of a random distribution (determined as approximately 0.555). It is interesting to note that simulations of pure sedimentation in triply periodic domains also yield average values of approximately 0.55 for the mean minimum inter-particle distance (Kajishima, 2004). An alternative way of characterizing the spatial structure of the dispersed phase is by searching directly for the presence of particle clusters. Here we define a cluster as a set of particles of which each member is within a distance l_c of at least one other member (Wylie and Koch, 2000). The cluster detection has been implemented according to the fast algorithm suggested by Melheim (2005). Figure 6(a) shows our results for case B (data for case A exhibits more noise, but essentially the same features). It can be seen that for two different cut-off lengths $l_c=2.5D$ and $4D$ the probability of finding clusters of a given size does not differ significantly from the corresponding probability found in random particle distributions. Since particles can interact over long distances via their wakes, the cluster definition was then modified in order to take the non-isotropic structure of the wakes into account. Instead of using a spherical cut-off radius, we define clusters through an ellipsoidal definition. More specifically, two particles i and j are considered as members of a cluster if their positions obey:

$$\frac{(x_{c,1}^{(i)}-x_{c,1}^{(j)})^2}{l_{cx}^2}+\frac{(x_{c,2}^{(i)}-x_{c,2}^{(j)})^2}{l_{cy}^2}+\frac{(x_{c,3}^{(i)}-x_{c,3}^{(j)})^2}{l_{cz}^2}\leq 1 \tag{15}$$

Figure 6(b) shows the probability of finding clusters with an elongation by a factor of 3 in the streamwise direction. The probability increases with respect to the spherical definition, but so does the result for the random particle distribution. It must therefore be concluded that the spatial distribution of particles in the present cases is not significantly different from a random distribution.

Structure of the carrier phase

Figure 7(a) shows isosurfaces of the fluctuations (with respect to the plane-average) of the streamwise velocity field for one snapshot of case B and for single-phase flow. The flow in the absence of particles exhibits the well-known streaky structures with streamwise characteristic lengths between 200 and 600 wall units. In the two-phase case the picture is radically different. First, a large number of particle wakes clutter the image,

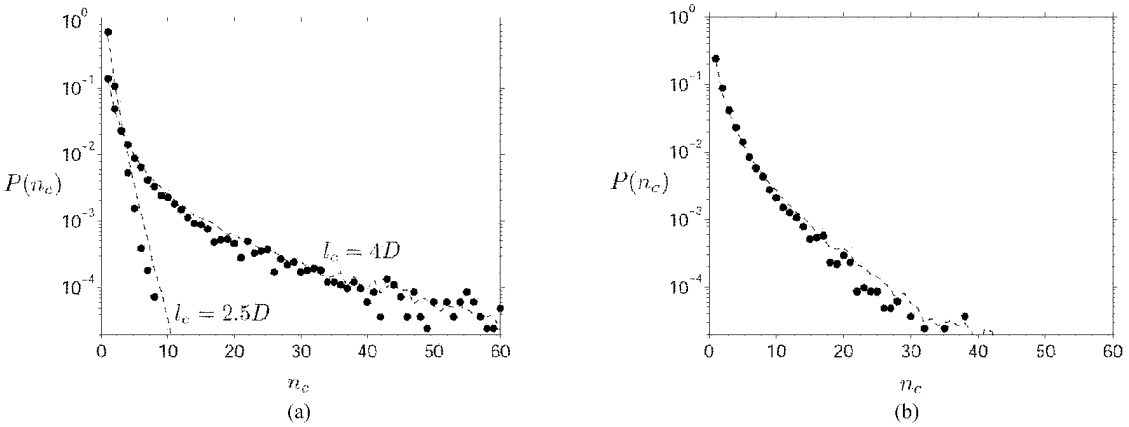

Fig. 6 Probability of finding a particle cluster with n_c members in case B (symbols). (a) Using two different spherical cut-off lengths of l_c=2.5D and 4D; (b) using an ellipsoidal cut-off with axes of length l_{cx}=7.5D, l_{cy}=l_{cz}=2.5D. The probability was evaluated from 20 instantaneous snapshots. The dashed lines correspond to the probability for a random particle distribution with the same solid volume fraction (evaluated from 100 realizations)

being recognizable as streamwise elongated surfaces with negative fluctuation values (due to fluid upflow and negative particle buoyancy). In addition, we can observe very large coherent structures of both signs, with streamwise dimensions of the order of the length of the current domain ($8h$). These structures are clearly induced by the addition of particles since they have no counterpart in single -phase flow. Figure 7(b) shows a short time sequence of plots of the streamwise-averaged x-component of the flow velocity from which the plane-average has been subtracted. The large structures are clearly visible in the cross-plane and their temporal coherence over the interval of 14 bulk time units can be verified. It can be observed that the wall-normal and spanwise dimensions are of the order of the channel half-width h.

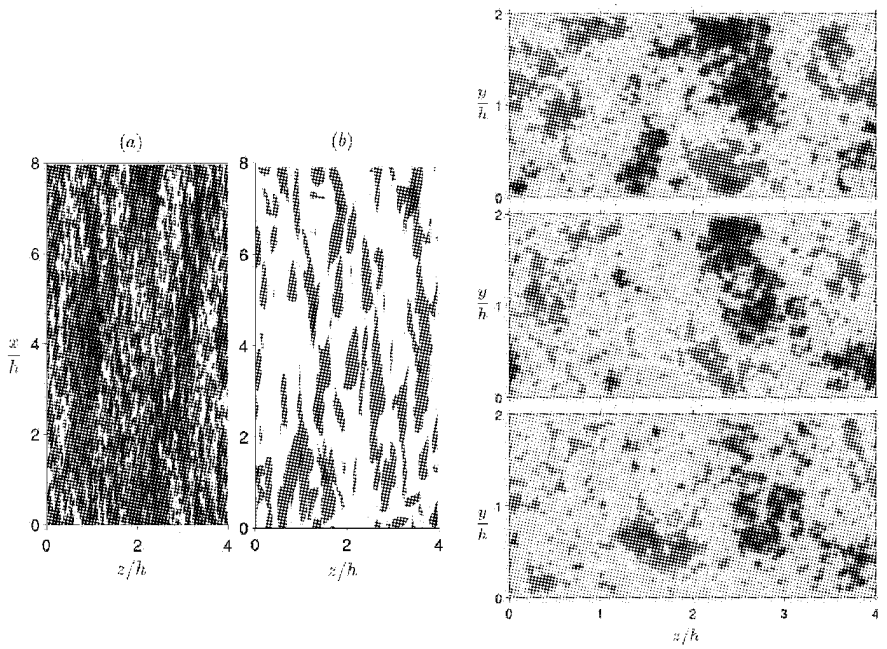

Fig. 7 (a) instantaneous three-dimensional isosurfaces of streamwise velocity fluctuations (with respect to the plane average) u -<u>$_x$=±3.6 u$_\tau$... Red (blue) surfaces correspond to the positive (negative) value. The view is directed towards the wall at y=0, and only the field in the lower half of the channel (0≤y/h≤1) is visualized for clarity. (a) Case B; (b) single phase flow at the same bulk Reynolds number. Right: instantaneous streamwise-averaged x-component of the flow velocity from which the plane-average has been subtracted, u"=< u >x < u>$_{xz}$, case B. The color code ranges from u"=-3.5 u$_\tau$. (blue) to u"=+3.5 u$_\tau$. (red). Time increases from top to bottom, with an increment of approximately 7 bulk flow time units

For the purpose of comparison, figure 8 shows a sequence of the same quantity for single-phase flow, where no flow structures of comparable dimensions can be found. Figure 9 shows two-point autocorrelations of velocity, $R_\alpha(r_x)$ and $R_\alpha(r_z)$, in wall-parallel planes located approximately 21 wall units above the wall. These quantities were computed from 9 instantaneous flow fields and using planes adjacent to both walls. It should

also be noted that the correlations were computed by Fourier transform of the composite flow field, i.e., containing the regions of the immersed solid particles (cf., discussion in the following section).

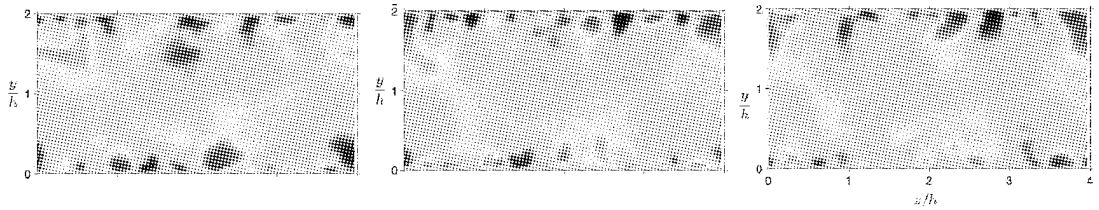

Fig. 8 Same as Fig. 7, but for single phase flow. Time from left to right

For small streamwise separations r_x^+ (Fig. 9(a)) all velocity components exhibit a faster decrease than the single-phase case. For streamwise separations over 200 wall units, however, the streamwise component in case B shows a larger correlation value, consistent with the observed large-scale elongated structures. Considering spanwise separations (Fig. 9(b)), it can be seen that the correlations in the particulate case still exhibit some of the features which are commonly believed to be the signatures of the buffer-layer coherent structures, i.e. a local minimum for separations of approximately 30 wall units for the wall-normal component. However, the correlation functions of the streamwise and spanwise components in the two-phase case do not take the usual negative values for $r_z^+ \approx 0$. Instead, the first zero-crossing takes place at around 150 wall units, and noticeable negative correlation values are found for R_1at separations as large as $r_z^+ \approx 300$. The evidence from the correlation functions shows that the structures which we have observed instantaneously have a large significance for the flow statistics, masking in part even the signatures of the streaks and streamwise vortices.

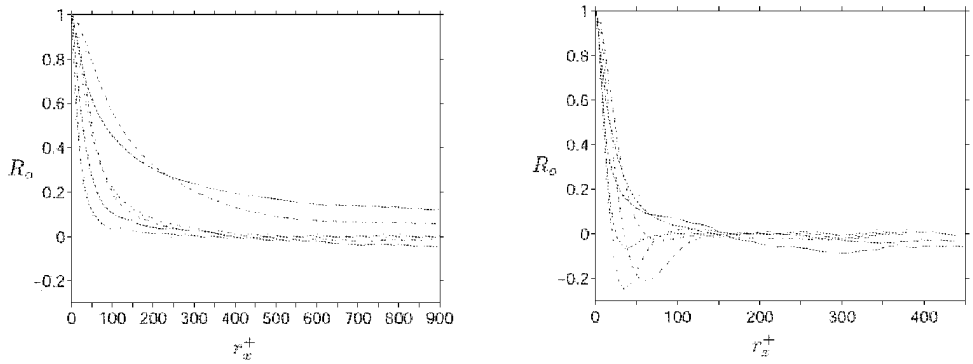

Fig. 9 Two-point autocorrelations of flow velocity fluctuations at a wall distance of y/h=0.094 ($y^+ \approx 21$) in case B. (a): for streamwise separations; (b): for spanwise separations. Colors indicate the components (black: α=1, red: α =2 and blue α =3). The correlations were obtained by averaging over 18 instantaneous data sets spanning a temporal interval of 45 bulk time units. The dashed lines correspond to single-phase flow of Kim (1987)

In order to conclude this section, we consider the effect of the large scale fluid structures upon the particle motion. A visualization of instantaneous particle positions and their velocities is presented in figure 10 for three snapshots corresponding to the sequence of flow fields of Fig. 8. Here particles with large positive (negative) streamwise velocity fluctuation with respect to the long-time average are highlighted by red (blue) color. Comparing figures 10 and 7, a strong spatial correlation between locally high (low) fluid velocity and high (low) particle velocity can be observed. Continuous animations of the three-dimensional particle motion of this case show that the particles indeed exhibit collective motion in form of streamwise-elongated patches over times of the order of 20 bulk units.

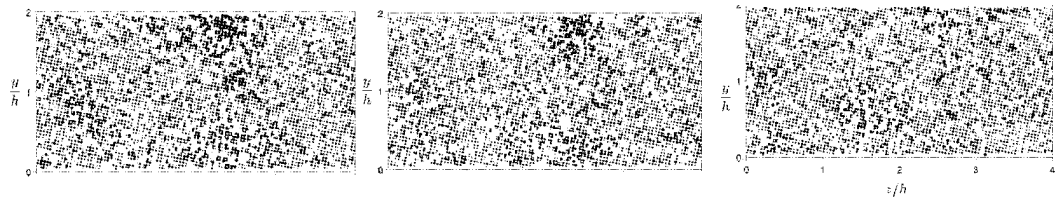

Fig. 10 Instantaneous particle positions projected upon the cross flow plane, corresponding to the flow fields in figure 7. The particles are colored according to their instantaneous vertical velocity fluctuations (with respect to the long-time average): u_c-<u_c>$\geqslant$0.18u_b red; u_c-<u_c>$\leqslant$-0.18u_b blue; else, gray

Eulerian statistics

Here we consider the Eulerian statistics which have been accumulated over time and wall-parallel planes, as indicated above. Concerning the computation of statistical quantities of the carrier phase, no distinction has been made between the fluid regions and the volume occupied by the solid particles, as already mentioned during the discussion of figure 9. This decision was taken in favor of computational efficiency. The difference between the present approach on the one hand and accumulation of statistics exclusively at grid nodes occupied by the fluid phase on the other hand has been evaluated from 5 instantaneous snapshots in case B. The differences were found to be insignificant, except for the r.m.s. of streamwise velocity fluctuations, where a maximum relative discrepancy of 6.3% was found. In fact, the current approximate evaluation of the statistics always overestimates the *r.m.s.* value of the streamwise fluid velocity fluctuations and slightly underestimates the mean streamwise fluid velocity. This is due to the fact that the average rigid body motion represents a negative velocity fluctuation with respect to the mean of the carrier phase at all wall distances. The usual check of the statistical convergence of low-order moments in plane channel flow includes a verification of linearity of the total shear stress $\tau_{tot} = \langle u'v' \rangle^+ - \partial_y \langle u \rangle^+$. However, integrating the streamwise momentum balance over the whole domain and time gives for the present case (assuming a statistically steady state):

$$\frac{1}{Re_\tau}\partial_{yy}(\langle u \rangle / u_\tau) - \partial_y \langle u'v' \rangle / u_\tau^2 + 1 = (\frac{\rho_p}{\rho_f} - 1)\frac{\Phi_s - \langle \phi_s \rangle}{Fr_\tau} \qquad (16)$$

Here, $\Phi_s - \langle \phi_s \rangle$ represents the local deviation from a homogeneous particle distribution, and we have defined a Froude number based upon the wall shear velocity, $Fr_\tau = u_\tau^2/(h|\boldsymbol{g}|)$. It can be seen from (16) that whenever the particle distribution is not uniform, the total shear stress does not vary linearly with y. Indeed the present profiles of τ_{tot} (not shown) are quite different from the usual straight line, especially due to the distinct peaks in solid volume fraction (Fig. 5(a)). Therefore, an alternative criterion for the convergence of statistics needs to be considered. Asymptotically, the profiles of the various first and second moments of the flow variables should attain symmetry (or anti-symmetry) about the centerline.

From Figures 11 (a) and 11(b), showing the mean velocities of the two phases, we can judge that this is not the case for the present observation interval (given in table 1). In both cases the profiles are biased towards one wall, this effect being more pronounced in case A which represents a somewhat smaller number of samples. Below we will therefore mostly consider data from case B. The fact that the low-order moments converge at such a slow rate can be attributed to several causes. First, the present suspension is relatively dilute, which means that it takes a very long time for a sufficient number of particles to visit each wall-normal bin. Secondly, the large-scale flow structures which were discovered in the preceding section impose a very long time scale. The relatively high mean particle velocities around *y/h=0.4* (figure 12 right) are a direct consequence of the slowly evolving high-speed flow structures observed in figures 8 and 11 at the corresponding locations. At the present time it does not seem feasible to continue the integration of these simulations for intervals which would allow the statistics t reach a truly asymptotic form. However, the statistical data accumulated up to the present date is still of considerable interest.

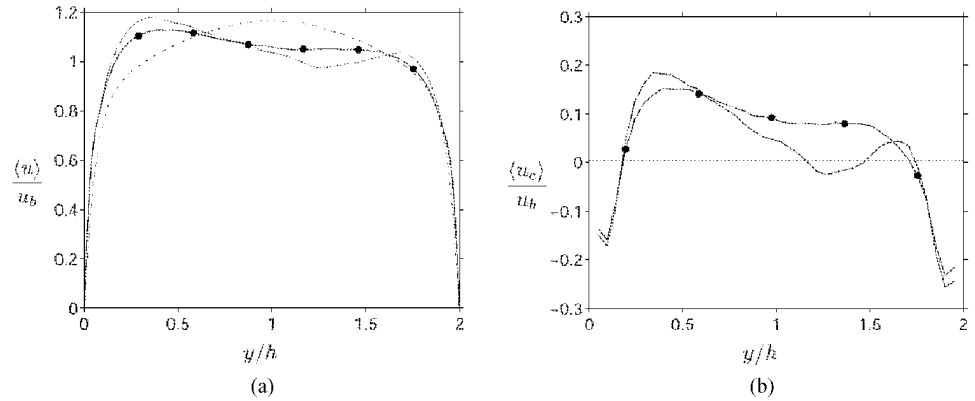

Fig. 11 (a) the mean flow velocity as a function of the wall-normal coordinate. (b) the mean streamwise particle velocity. Solid line, case A; - • -, case B; ---, single-phase flow (Kim, 1987)

Turning again to the mean velocity profiles for the two phases (figure 11) we note that there is a strong similarity in shape. As a consequence, the mean slip velocity $< u > - < u_c >$ is nearly constant across most of the channel width. Its value is approximately u_b, as estimated a priori from the equilibrium between buoyancy and drag acting on a single sphere in unperturbed flow. Concerning the mean fluid velocity in figure 11, we

observe a clear difference with respect to the single-phase case, characterized by a tendency to form a concave profile with larger gradients at the walls and a flat section near the centerline. Concave velocity profiles were previously observed by (Tsuji et al., 1984) in experiments on vertical particulate pipe flow, albeit at higher Reynolds numbers and much higher density ratios. The presently simulated cases are therefore situations where a strong two-way interaction takes place. Figure 12(a) shows the mean velocity profile of case B in wall scaling and semi-logarithmic representation. It can be seen that the logarithmic region is shorter than in single-phase flow and that the intercept of the logarithmic law is substantially decreased, similar to rough-wall turbulent flow. This behavior is consistent with the increase in the friction-velocity based Reynolds number observed in Fig. 2(b). The *r.m.s.* fluctuations of fluid velocities are shown in Fig. 12(b). The largest difference with respect to the single-phase data is obtained for the streamwise component which is practically constant in the range $0.25 \leqslant y/h \leqslant 1$. When normalized by wall units, the wall-normal and spanwise components are reduced in the particulate case across most of the channel width. The overall turbulence intensity is increased substantially, i.e. by a factor of approximately 6 at the centerline, and the anisotropy is strongly affected. The injection of energy into the streamwise fluctuations has two causes: the presence of wakes, and the formation of large-scale streamwise elongated flow structures. Both phenomena were visualized in fig. 7 (left). Experimental measurements of Suzuki et al. (2000) in more dilute downward vertical channel flow at comparable Reynolds numbers and similar values for the particle parameters have also revealed a substantial increase in streamwise fluid velocity fluctuation levels and anisotropy for $y^+>20$.

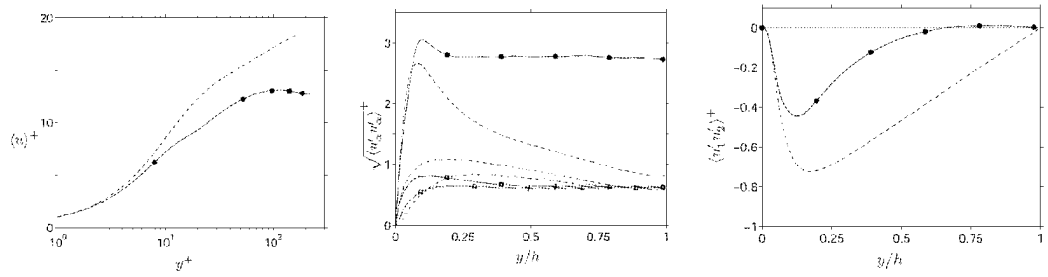

(a) (b) (c)

Fig. 12 (a) the mean flow velocity of case B in wall units. (b) The normal stresses of case B. Colors indicate the velocity components: α=1, black; α =2, red and α =3 blue. (c) the Reynolds stress of case B. In all the figures, the dashed lines correspond to the single-phase reference data of Kim et al. (1987)

The Reynolds stress profile (Fig. 12 on the right) exhibits an extensive region with values close to zero ($0.6 \leqslant y/h \leqslant 1$). In this outer region the presence of particles apparently causes a decorrelation between the turbulent motion in the streamwise and wall-normal direction, thereby suppressing the average Reynolds stress. Finally, let us turn to some Eulerian statistics pertaining to the dispersed phase. Figure 13(a) shows the r.m.s. of particle velocity fluctuations of case B. A similar trend as for the fluid velocities can be noted with a near-equality of the two horizontal components and a much larger intensity of the vertical component. Furthermore, all components exhibit a small peak at approximately y^+=34 and a visibly lower intensity around the common location of the buffer-layer streaks. Compared to the fluid counterpart, the intensity of the streamwise particle velocity fluctuations is approximately 25% lower across most of the channel, while it is slightly higher for the two horizontal components. Regarding this comparison between the two phases, Suzuki et al. (2000). have observed smaller intensities of the particle velocity fluctuation for all components above y^+=20 and the opposite behaviour for the streamwise and wall-normal components below this wall-distance. The profile of the mean angular particle velocity in the spanwise direction $<\omega_{c,z}>$ is shown in Fig. 13(b). Its absolute value has a maximum at a wall-distance of approximately *30* wall units and tends towards zero at the centerline and at the wall. The figure also includes a curve given by $-A\ \partial_y <u>$, which corresponds to the steady rotation of a cylinder in a simple shear flow, where A is positive and decreases with the shear Reynolds number (cf. Ding and Aidun, 2000; Zettner and Yoda, 2001). It can be seen that our data for case B is reasonably well represented when choosing A=0.1, except for the region y^+<30, where the damping effect of the wall presumably plays an important role. A similar conclusion is reached for the data of case A (not shown). Constrained simulations of single neutrally-buoyant particles in laminar pipe flow have likewise yielded a proportionality between the steady-state angular particle velocity and the wall-normal fluid velocity gradient over most of the pipe radius. For comparison see Fig. 3 in Yang et al. (2005).

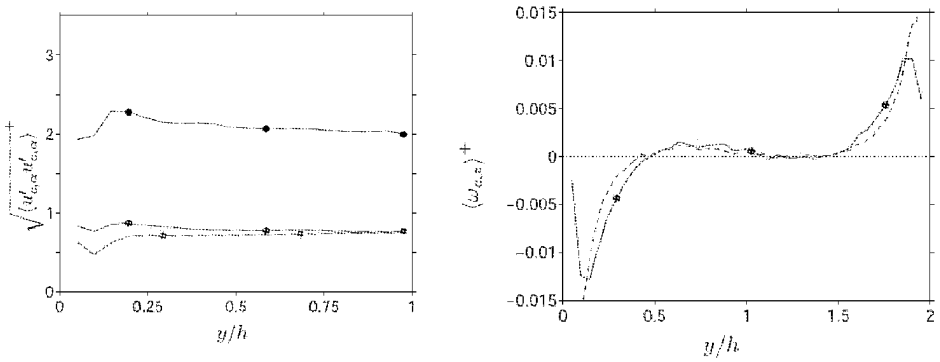

(a) (b)

Fig. 13 (a) the r.m.s. of particle velocities of case B. Color code as in figure 12-center. (b) the mean angular particle velocity with respect to the z axis in case B. The dashed line *corresponds to* -0.1 ∂_y < u>

CONCLUSIONS

We have conducted a DNS study of turbulent particulate channel flow in a vertical arrangement, considering finite-size rigid particles with numerically resolved phase interfaces. The immersed boundary simulations were performed for the dilute regime (0.42% solid volume fraction), allowing for an approximate treatment of direct particle encounters. Our simulations are for spherical heavy particles whose buoyancy is adjusted such that the terminal velocity matches the bulk flow velocity. For the present bulk Reynolds number of 2700 and particle size of 1/20 of the channel half-width (corresponding to approximately 9 wall units), this leads to a terminal particle Reynolds number of 136. Two different density ratios were considered, varying by a factor of 4.5. The corresponding Stokes numbers of the two particles were O(10) in the near-wall region and O(1) in the outer flow. We have presented Lagrangian autocorrelations of particle velocities, particle dispersion, particle distribution functions, flow visualizations, Eulerian two-point autocorrelation data and Eulerian one-point moments. The main findings can be summarized as follows:

(1) We observe the formation of large-scale elongated streak-like structures with streamwise dimensions of the order of 8 channel half-widths and cross-stream dimensions of the order of one half-width. Particle velocities are strongly affected by these structures, which in turn allows to follow their evolution over substantial time intervals. Moreover, the large particle-induced structures alter the fluid velocity auto-correlations substantially.

(2) We have found no evidence of significant cluster formation of the dispersed phase. This conclusion is based upon simple visualization, monitoring of the mean minimal pairwise particle distance, cluster detection with spherical and (streamwise elongated) elliptical cut-off.

(3) The presence of slowly-evolving large scales leads to a slow convergence of the Eulerian statistics, which is evidenced by the lack of symmetry of the profile of the mean fluid velocity, amongst others, even after a considerable observation interval (556 and 95 bulk time units in cases A and B, respectively).

(4) The presence of particles causes a strong modification of the mean flow, which tends towards a concave profile, as well as a substantial increase in turbulence intensity (by up to a factor of 6), mainly in terms of streamwise velocity fluctuations.

(5) The effect of varying the Stokes number while keeping the buoyancy, particle size and volume fraction constant was relatively weak. Only the Lagrangian correlations and the dispersion were significantly affected.

Vertically elongated structures have previously been detected in pure sedimentation flows by Kajishima and Takiguchi (2002), see also Kajishima (2004) and in grid-generated turbulence by Nishino and Matsushita (2004). However, in the aforementioned cases the main feature of the "structures" was a local accumulation of particles. This is not true in the present case, where we have been unable to detect the large structures by considering only the spatial distribution of particles. Instead we believe that the addition of particles to the turbulent wall-bounded flow triggers an inherent instability leading to the formation of streak-like structures of very large dimensions. This specific point should be further investigated in the future. One question which naturally arises in relation with the emergence of flow scales of the order of the streamwise period of the computational domain is whether the finite box size might play a decisive role. It should be mentioned that these largest scales are not clearly observed in the case with the smaller domain (case A). On the other hand, performing simulations with much larger domains than the one used in case B is a challenging task, since the simulations in case B are already on the limit of what we can afford with the present algorithm on the largest available hardware. Nevertheless, we have recently initiated a companion simulation B2 (Tables 1 and 2) with

twice the streamwise period as case B and otherwise identical conditions. The run was initialized with an exact periodic extension of a fully developed field of case B (towards the end of the observation interval). Up to the present date (after an elapsed time of 11 bulk time units), the results of this extended simulation have not significantly diverged from the original case B. It still remains to be seen how the large streak-like structures scale in the extended domain, once the simulation has sufficiently evolved from the initial condition.

NOTATIONS

N_p	number of particles
$\boldsymbol{u}$, p	fluid velocity and pressure
ν	fluid kinematic viscosity
ρ_p, ρ_f	particle and fluid densities
$\boldsymbol{f}$	volume force on the fluid
Ω	whole computational domain
Ω_f	computational domain occupied by fluid
$\boldsymbol{U}$	particle velocity
$\boldsymbol{F}$	force acting upon a particle
D	particle diameter
Δx	grid spacing
$x_{i,j,k}$	Eulerian coordinate
Re_b	bulk Reynolds number
Re_τ	skin friction Reynolds number
U_{c^∞}	terminal particle velocity
Ar	Archimedes number
St_b	Bulk Stoke's number
St^+	Wall units Stoke's number
U_g	fluidizing gas velocity, m/s
X_l	Lagrangian coordinate
$\boldsymbol{u}_c$	velocity of particle center of mass
ω_c	particle rotational velocity
δ_h	regularized Dirac's delta function
h	channel half height
$< >_\alpha$	average operator along direction
u_τ	skin friction velocity
$\boldsymbol{g}$	gravity acceleration
Re_{D^∞}	terminal particle Reynolds number
τ_{SD}	particle time scale
$R_{Lp,\alpha}(\tau)$	Lagrangian autocorrelation function
$M_{p,\alpha}$	mean square particles displacement
$dx_d(y)$	particle turbulence dispersion
d_{min}	average distance to closest particle
ϕ_s	solid volume fraction

ACKNOWLEDGEMENTS

This work was supported by the Spanish Ministry of Education and Science under grant ENE2005-09190-C04-04/CON. The authors thankfully acknowledges the computer resources, technical expertise and assistance provided by the Barcelona Supercomputing Center - Centro Nacional de Supercomputación.

This article is dedicated to our colleague Andrés Cabanillas struck by destiny last year.

REFERENCES

Ahmed, A.M. and Elgobashi, S.: Phys. Fluids **13(11)** (2001), pp.3346-3364.
Ding, E.J, and Aidun, C.K.: J. Fluid Mech **423** (2000), pp.317-344.
Elgobashi, S.: Appl. Sci. Res. **52** (1994), pp.309-329.
Fadlun, E.A., Verzicco, R., Orlandi, P. and Mohd-Yusof, J.: Comput. Phys. **161** (2000), pp. 35-60.
Glowinsky, R., Pan, T.W., Hesla, T.I. and Joseph, D.D.: Int. J. Multiphase Flow **25** (1999), pp. 755-794.
Goldstein, D., Handler, R. and Sirovich, L.: J. Comput. Phys. **105** (1993), pp. 354-366.
Höfler, K. and Schwarzer, S.: Phys. Rev. E. **61** (2000), pp 7146-7160.
Kajishima,T., Takiguchi, H., Hamasaki, H. and Miyake, Y.: JSME Int. J. Series B **44** (2001), pp.526-535.
Kajishima,T., and Takiguchi, H.: Int. J. Heat Fluid Flow **23** (2002), pp.639-646.
Kajishima, T. (2004). Numerical Investigation of Collective Behavior of Gravitationally Settling Particles in a Homogeneous Field. 5th Int. Conf. Multiphase Flows.
Kim, J., Kim, D. and Choi, H.: J. Comput. Phys. **171** (2001), pp. 132-150.
Kim, J., Moin, P. and Moser, R.: J. Fluid Mech. **177** (1987), pp.133-166.
Kulick, J.D. , Fessler, J. R. and Eaton, J. K.: J. Fluid. Mech. **277** (1994), pp.109-134.
Lai, M.-C., Peskin, C.S.: J. Comput. Phys. **160** (2000), pp. 705-719.
Melheim, J.A.: Comput. Phys. Commun. **171(3)** (2005), pp.155-161.
Nishino K. and Matsushita, H. (2004). Columnar Particle Accumulation in Homogenoeus Turbulence. 5th Int. Conf. Multiphase Flows.
Peskin, C.S.: Acta Numerica **11** (2002), pp. 479-517.
Peskin, C.S. (1972). Flow Patterns around Heart Valves. PhD Thesis, A. Einstein College of Medicine.
Roma, A.M., Peskin, C.S. and Berger, M.J.: J. Comput. Phys. **153** (1999), pp. 509-534.
Suzuki, Y., Ikenoya, M. and Kasagi, N.: **29** Experiments in Fluids .(2000), pp.S185-S193.
Tsuji, Y., Morikawa, Y. and Shiomi, H.: J. Fluid Mech. **139** (1984), pp.417-434.
Uhlmann, M. (2004). New Results on the Simulation of Particulate Flow. CIEMAT Tech. Report 1083.

Uhlmann, M.: J. Comput. Phys. **209(2)** (2005), pp. 448-476..
Uhlmann, M. (2005b). An Improved Solid Fluid Coupling Method for DNS of Particulate Flow on a Fixed Mesh. 11th Workshop Two-Phase Flows.
Uhlmann, M. (2006). Experience with DNS of Particulate Flow using a Variant of the Immersed Boundary Method. ECCOMAS CFD.
Uhlmann, M.: Phys. Fluids **20(05)** (2008), pp. 3305-3332.
Wylie, J.J. and Koch, D.L.: Phys. Fluids: **12(5)** (2000), pp.964-970.
Yang, B.H., Wang, J., Joseph, D.D., Hu, T., Pan, T.W. and Glowinski, R.: J. Fluid Mech. **540** (2005), pp.109-131.
Zettner, C.M. and Yoda, M.: J. Fluid Mech. **442** (2001), pp.241-266.

CFB Boiler Technology, Operation and Design

GASIFICATION IN FLUIDIZED BEDS – PRESENT STATUS & DESIGN

Prabir Basu[1], Bishnu Acharya[1], Animesh Dutta[2]

1 Dalhousie University, PO Box 1000, Halifax
2 NS College of Agriculture, Truro, Nova Scotia

Abstract: Biomass has made great in-roads in its use in energy and chemical industries. Gasification is one of the major means for its conversion. For thermo-chemical conversion of biomass three major gas-solid contacting processes, fixed bed, entrained bed and fluidized bed are used. Various versions of fixed bed gasifier (up-draft, down-draft, and side-draft) proved successful but primarily in small capacity units while entrained bed reactors found favour in very large capacity units. Fluidized bed gasifier fills the important intermediate size range. A review of the current commercial use of fluidized bed gasifier shows that it is yet to take the centre stage in the gasification market. This paper examines the issues preventing wider scale use of fluidized bed gasifier and what is the current state of research in those issues.
Keywords: biomass gasification, fluidized bed gasifier

INTRODUCTION

Status of gasification

The rise in the fuel prices and the environmental regulation has been the driving force for the growth of the gasification technology which in the past was considered less competitive than the traditional means of energy supply. Figure 1 shows the status of gasification and the application for which it is used for, showing its present and the planned capacities. So, at present the energy production from gasification is around 60 GWth. But in coming years, the energy production from gasification is set to grow rapidly reaching around 150 GWth, by 2014, which is 1.5 times more than that used at present,. The gasification technology in coming future will mainly be used for power production.

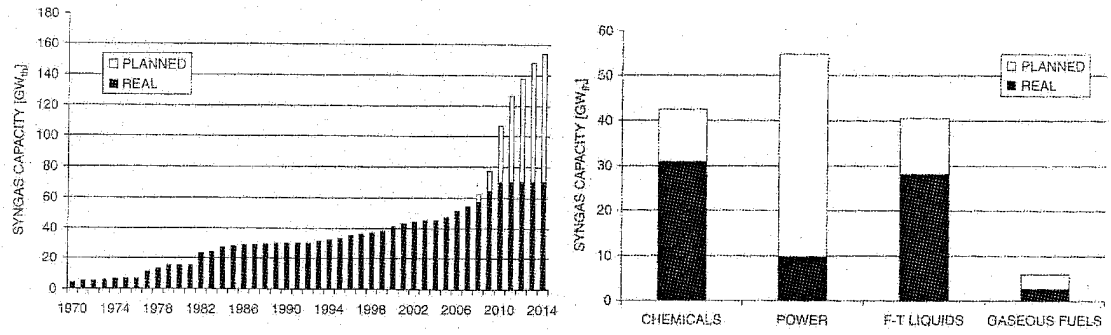

Fig. 1 Worldwide gasification capacity (Higman and Burgt, 2008)

Advantages of gasification process are explained elsewhere (Basu, 2006). So, it is not discussed here for brevity. These advantages propelled it to develop many major energy projects. Table 1 shows some of the commercial gasifier projects.

Although gasification has been around for more than a century, it did not make any major in-roads into the main stream energy or chemical industries. The growth in gasification industries seems to have been very slow because of incapability of meeting the following challenges, some of them are common to all gasifier and some specific to fluidized bed ones.

Technical challenges

(1) Availability is the most important factor that prevents the wide scale use of gasifiers in the main stream energy industries. Present day gasifiers have not reached the standard (>90%) expected in utility industries. The 140 MW high temperature Winkler gasifier of Rheinbrau started with a availability of 45% and rose to 89% in 1997 (Renzenbrink et al., 1997). This force EPC to specify a stand-by gasifier in order to meet the overall unit

availability matching the industry standard.

Table 1 Gasification Projects

Country	Projects	Type	Output (MWth)
Austria	Zeltweg BioCoComb Project	CFB	10
	Güssing	Dual CFB	8
	Pöls Bark Gasification Project	CFB	35
Brazil	Brazilian BIG-GT Demonstration Project	CFB	32 (MWe)
Denmark	Harboøre Project	Updraft	4
	Høgild Project	Co-current down draft	0.5
	Blære Project	Two stage gasification	0.25 (MWth) + 0.1 (MWe)
Finland	Lahti Kymijärvi Project	CFB	60
	ECOGAS Energy plant, Varkaus	BFB	50
Italy	Thermie Energy Farm Project	Lurgi CFB	14 (MW_e)
	SAFI SpA RDF Gasification Project	CFB	6.7 (MWe)
The Netherlands	KARA/BTG	Co-current Downdraft	0.15 (MWe)
	Amergas BV Project	Lurgi CFB	350 (MWth) + 600 (MWe)
Sweden	Gotaverken Project (Varo)	CFB	2
	Värnamo Project	IGCC	18
Switzerland	Pyroforce Gasification Plant	KHD pyroforce gasifier	0.2 (MWe)
United Kingdom	ARBRE Project	low pressure TPS gasifier	8 (MWe)
	Boughton Pumping Station CHP Project	Down draft	0.18 (MWth) + 0.1 (MWe)
	Blackwater Valley Museum Project	Down draft	0.4 (MWth) + 0.2 (MWe)
USA	Vermont Battelle/FERCO Project	Low pressure Battelle gasifier	15 (MWe)

(2) Complex operation due to large number ancillary equipment like oxygen separation unit (OSU), gas sweeteners etc.

(3) Beside the cost OSU is a major power consumer. For example of the 315 MW generated by the IGCC plant at Polk station 50 MW is consumed by OSU and 10 MW by the other auxiliaries. Such a high (20%) auxiliary power consumption reduces the attractiveness of gasification as a means for energy generation.

(4) Gasification of high alkali biomass (agglomeration problems), RDF, and waste (mercury removal problem)

(5) Tar control in order to avoid the problems in gas cooling and filtration as well as its removal without producing toxic waste water

(6) Poor carbon conversion is a major problem. It has been less than 90.5% (ref). High carbon in ash reduces the ash quality, and deprives the plant owners from the revenue expected from the sale of gasifier ash for their end-use. High carbon in ash imposes an additional burden of disposal cost.

Non technical challenges

Beside above technical challenges, several other challenges retarded the market penetration of gasification.

(1) Higher investment

(2) Fuel availability and price level for non-conventional fuels like biomass

(3) Subsidies available for biomass only plants but not for co-firing

(4) Economic competitiveness with steam cycles, co-firing etc

(5) Complicated and costly means for power production

(6) Small difference in efficiency compared to steam cycles

Over the year a large variety of gasifier has been developed, used and studied. A summary of those designs

is presented below.

Gasifier is essentially a gas-solid contacting reactor that facilitates gasification reactions. Based on the mode of gas-solid contacting, the gasifiers are categorized into three broad types: Moving bed, Fluidized bed and Entrained flow gasifier. The following table indicate some of the commercial technologies based on these processes.

Moving bed	Fluidized bed	Entrained flow
(1) Lurgi dry bottom gasifier (2) BGL slagging gasifier	(1) The Winkler Process (2) BHEL Gasifier (3) The KBR transport gasifier (4) Twin reactor gasifier (5) The EBARA gasifier (6) GTI membrane gasifier (7) Rotating Fluidized bed gasifier (8) Chemical Looping gasifier (9) Internal circulating gasifier (10)Foster Wheeler ACFB gasifier	(1) The Koppers-Totzek gasifier (2) The Siemens SFG gasifier (3) The E-Gas gasifier (4) The MHI gasifier (5) The EAGLE gasifier

BUBBLING FLUIDIZED BED GASIFIERS

Winkler gasifier

It is the oldest fluidized bed gasifier, and has been in commercial use for many years. The Winkler [1922] pulverized brown coal gasifier invented in the 1920's to produce synthesis gas (H_2, CO, CO_2) was probably the first to use fluidization on an industrial scale, starting from an initial model of 2m diameter 13m in height and producing some 2,000 m^3/h of gas, as shown in Figure 2 (not available), and improved to 5.5m diameter 23m in height processing some 700 t/d of coal. Modern version of Winkler gasifier could operate at either atmospheric or elevated pressures. The Low Temperature version of the works with a bubbling fluidized bed kept below 980°C to avoid ash melting. Crushed coal (<10 mm) is fed into the gasifier and ash is removed from its bottom by using screw conveyors. The high temperature newer version used steam & oxygen as the gasifying medium, which is introduced into the fluidized bed at different levels, as well as above the fluidized bed. The fluidized bed is maintained at a pressure of 10 bar; the temperature of the bed is maintained at above 900°C to minimize production of methane and other hydrocarbons (Basu, 2006).

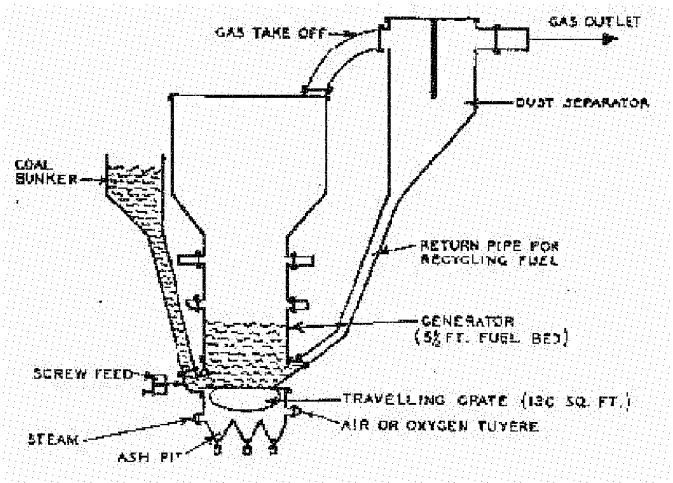

Fig. 2 Sketch of the original Fluidized bed gasifier developed by Winkler

EBARA's TwinRec process

Here differential fluidization velocity permits excellent mixing of the bed materials and the feed. The product gas is burnt in a cyclonic furnace where solids are separated. This gasifier is used primarily to recover recyclable materials by removing their organic components through gasification and combustion (Steiner C. et

al, 2002).

Gas Technology Institute membrane reactor

GTI is attempting to develop a fluidized bed using fluidized bed membrane reactor. Membrane selectively removes hydrogen from the product gas and if applied in the reaction site, it could continuously remove hydrogen as it is formed by the shift reaction. Thus it further favours the forward reaction. This could simplify the processing steps by reducing/eliminating the downstream shift reactor, separation and purification operations for the conventional gasification technologies (Doong S. et al, 2005).

Internally circulating fluidized bed gasifier

This bubbling fluidized bed reactor is divided into two chambers but connected by openings at the bottom. Higher fluidization velocity in one chamber force solids to move up and overflow into the second chamber fluidized at lower velocity. This arrangement provide more uniform distribution of biomass particles in the reactor with increase of gasification yield, reduction of tar formation, reduction of fine particles of mineral and carbonaceous nature elutriated in syngas (Freda C. et.al., 2008).

Spout fluid-bed gasifier

Spout-fluid bed gasifier is a combination of a fluidized bed and spouted bed by combining the fluid flow of the single central opening (spouted bed) with the auxiliary fluid flow through the distributor plate (fluidized bed). Spout-fluid bed reactors used for combustion or gasification are reported to overcome the limitation of spouted bed and fluidized bed by providing higher rate of mixing, better solid fluid contact, even fluid flow distribution resulting to the minimization of dead zones, improved mass and heat transfer characteristics. Recently, Thamavithya and Dutta (2008) studied MSW gasification in a spout-fluid bed reactor.

CIRCULATING FLUIDIZED BED (CFB) GASIFIERS

Foster wheeler atmospheric CFB heat gasifier

This air blown gasifier operates at atmospheric pressure in a circulating fluidized bed. Depending on the fuel and the application need it operates at a temperature within the range of 800-1000°C. The hot gas from the gasifier passes through a cyclone, which separates most of the solid particles associated with the gas and returns them to the bottom of the gasifier. An air preheater is located below the cyclone to raise the temperature of the gasification air and indirectly the temperature level inside the gasifier.

Chemical looping gasifier

This concept can separate the waste flue gas from the product gas, thus avoiding the nitrogen dilution of the product gas. It is based on the well studied chemical looping combustion (Mattisson T., 2007). Acharya, et al. (2008) proposed that biomass be fed into a fluidized bed gasifier with CaO as the bed material and steam as the fluidizing agent. The CaO will capture the CO_2 produced in the steam gasification reaction producing $CaCO_3$ that will flow into a calciner kept in fast fluidization by recycled CO_2 (Figure 3). Key feature of this process is its production of nitrogen free hydrogen. The CO_2 also being nitrogen free is amenable for easy sequestration. The generation and regeneration of CaO in batch fluidized bed is demonstrated in a batch reactor (Mahishi & Goswami, 2007).

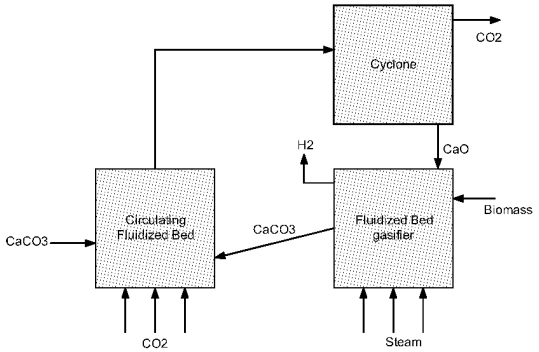

Fig. 3 Chemical looping gasification (Acharya B et al., 2008)

Twin Reactor system

In this system, the pyrolysis, gasification and combustion takes place in different reactors. In the combustion zone, the tar and gas produced during pyrolysis is combusted which will heat the inert bed material. The bed material is then circulated into the gasifier and the pyrolysis reactor to supply heat. The char and heat

carrier from pyrolyser is taken into gasifier. The gasification of char in presence of steam produces the product gas. The residual char and the heat carriers from gasifier are taken back into combustor. This system was developed to overcome the problem of tar: as it is combusted in combustor thus product gas free of tar can be obtained. The original concept of Battle involved two CFB risers, while the more recent version of the Technical University of Vienna operates the combustor in fast bed and the gasifier in a bubbling bed regime.

KBR (Kellogg Brown and Root) transport gasifier

It is a hybrid gasifier having characteristics of both entrained bed gasifier and fluidized bed reactor. The KBR gasifier operates at considerably higher circulation rates, velocities (11-18 m/s), and riser densities than a conventional circulating fluidized bed, resulting in higher throughput, better mixing, and higher mass and heat transfer rates. Solids transported are separated from the product gas in two stages and returned to the base of the riser. The gasifier operates at 900-1000℃ and 11-18 MPa (Higman & Burgt, 2008) Oxygen, when used gives higher heating value than when air is used as the gasifying medium.

DESIGN METHODS

Very little information on design of fluidized bed gasifier is available in published literature. Based on information scattered in literature the design methods are grouped into 4 broad groups:

(1) Stoichiometric equilibrium method
(2) Non-stoichiometric equilibrium method
(3) Residence time based method
(4) Kinetic model based method

Details are given in Basu (2009). They are not discussed here for brevity:

OPERATING PROBLEMS

Compared to boilers or furnaces, gasification is a relatively new technology. As such there is a dearth of information on its operation. Based on the information available from different sources including the review of Higman and Burgt (2008) major operating problems are as follows.

Refractory

Gasification being an endothermic process heat needs to be conserved in the reactor as much as possible and it is done by several layers of insulation and refractory. Refractory maintenance has been a major issue in many plants. The Polke station, for example had to change refractory after 451 days. Frequent fuel switch, start-up, shutdowns increases the frequency of refractory maintenance. A major practical issue is the long down-time required for refractory or any in-furnace maintenance. Owing to the thick layer of refractory a cool-down period of 30-36 hours is required for shut down and similar longer time for heat up. These adversely affect the revenue stream of the plant.

Temperature measurement

Thermocouples installed in the gasifier fail readily due to a combination of extreme temperature, reducing, corrosive and erosive environment in the gasifier. For large diameter commercial units it is necessary to accurately measure the temperature at the core of the gasifier, but it is very difficult to maintain a thermocouple long enough especially in a fluidized bed. The inability to directly measure the temperature slows the resolution of many operating problems, and product quality control.

Agglomerates

Agglomeration is a major problem in fluidized bed gasifiers. Alkali metals like potassium and chlorine found higher in agricultural and energy crops reduces the melting temperature of ash. The melting/sintering of ash interferes with the fluidization causing agglomeration of fluidized bed particles (Mettanant et al., 2008). Potassium and silica may form a mixture of alkali metal silicates, in presence of chlorine, which can melt at temperature below 800°C. Bed agglomeration can result in poor fluidization quality and therefore poor conversion efficiency. Severe cases may result in total defluidization result in shutting down of plants.

Tar

Tar formation, a major problem in gasifiers. Among different types of gasifier, fixed bed and fluidized bed are more vulnerable of tar while the entrained bed as it operates at high temperature so tar problem will be less. It must be controlled to prevent the problems such as: fouling and plugging of equipment, difficulty in handling the tar water mixture, contamination of waste stream. To reduce this one can: 1) use operating conditions that favour reduced formation of tar like use of bed materials like olivine and 2) apply down stream cleaning process. Higher operating temperature, moisture and higher residence time may lower the tar content of the product gas.

Corrosion

Corrosion is a major issue in gasifier due to its high temperature and reducing environment. It especially bad in biomass fed units. As reported by Perkins, (1993), experiment done in the atmosphere of oxygen blown fluidized bed gasifier on 88 different commercial alloy and coatings shows that most of the steel corroded at rate of 0.05mm/year at 650°C and the rate exceeds to 0.5 mm/year at temperature of 815°C. No materials were identified of having resistance on corrosion for long term at temperature above 650°C.

Synthesis gas cooling

In fluidized bed gasifier, the lime stone used for sulphur capture, may react with carbon dioxide and may form calcium carbonate at temperature below 950°C that may cause the fouling in the syngas cooler. The corrosion potential in syngas cooler is high especially when coal is used as the fuel. In the syngas cooler, the equilibrium favours the reverse of the Boudouard reaction. Iron or nickel of the cooler catalyze the reaction around 400-450°C, forming carbon which destroys the metal matrix. The surface metal is lost as the dust into gas phase.

CONCLUSIONS

A review of fluidized bed gasifier shows a wide range of gasifier designs with each having its distinct advantages with no single design as the best. Fluidized bed gasifiers are increasingly capturing the market for intermediate to large capacity gasifiers. It is especially been favoured for biomass. The wide-scale commercial use of fluidized bed gasifier is being impeded by a number of technical and non-technical issues. Poor availability on account of agglomeration, refractory maintenance and tar formation are some of the major operating problems. Technical challenge remains with high cost auxiliary power consumption of oxygen separation units.. There is a need for development of an alternative to oxygen for production of high heating value gas. Minimization of carbon loss is also a major technical challenge.

REFERENCES

Acharya, B., Dutta, A, Basu, P. (2008) "Chemical looping gasification of biomass for hydrogen enriched gas production with in-process carbon-dioxide capture" To be published.

Basu, P. 2009, Chapter 7 in "Gasification & Pyrolysis of Biomass: Design and Theory", Elsevier, New York.

Basu, P. 2006. "Combustion and Gasification in Fluidized Beds", Taylor and Francis. USA

Basu, P. Metanant, V, Goswami, P., (2009), "Corrosion Problems Associated with Biomass Fed Fluidized Bed Gasifiers and Combustors" To be published.

Doong S, Ong E, Atroshenko M, Lau F and Roberts M, (2006). "A Novel Membrane Reactor for Direct Hydrogen Production from Coal", Final Technical Report.

Freda C., Canneto G., Mariotti P., Fanelli E., Molino A. and Braccio G. (2008) "Cold model testing of an internal circulating fluid bed gasifier". Second international workshop "Biomass Gasification Technologies" in TUBITAK Marmara Research Center, Gebze Campus.

Guan. J, Wang. Q, Li. X, Luo. Z, & Cen. K (2007). Thermodynamic analysis of a biomass anaerobic gasification process for hydrogen production with sufficient CaO. Renewable Energy 32, 2502-2515.

Higman C and Burgt M. V. D, (2008). "Gasification", Elsevier Science: second edition.

Mahishia M. R. & Goswami, D.Y. (2007). An experimental study of hydrogen production by gasification of biomass in the presence of a CO2 sorbent. International Journal of Hydrogen Energy 32, 2803-2808.

Mattisson T, (2007). "Chemical-looping combustion using gaseous and solid fuel", 2nd workshop: International Oxy-Combustion

Research Network.

Mettanant, V, Basu, P., Butler, J. (2008), "Agglomeration in Biomass Fired Fluidized Bed Gasifier and Combustor" In Press, Journal of Canadian Society of Chemical Engineers.

Perkins .R, (1993)."Corrosion in coal gasification atmospheres", Journal De Physique IV, Volume 3.

Steiner C, Kameda O., Oshita T and Sato T, (2002). "EBARA's Fluidized Bed Gasification: Atmospheric 2×225 t/d for Shredding Residues Recycling and Two-stage Pressurized 30 t/d for Ammonia Synthesis from Waste Plastics", The 2nd International Symposium on Feedstock Recycling of Plastics.

Thamavithya, M., and Dutta, A. (2008), "An Investigation of MSW gasification in a spout-fluid bed reactor", in print Fuel Processing Technology.

Winkler, F., German patent, 437,970 (Dec. 2, 1922); U. S. patents, 1,582,718 (1928); 1,840,649 (Jan. 12, 1932).

CFB Boiler Technology, Operation and Design

RESEARCH AND DEVELOPMENT OF LARGE CAPACITY CFB BOILERS IN TPRI

Sun Xianbin, Jiang Minhua

Thermal Power Research Institute, Xi'an, 710032, China

Abstract: This paper presents an overview of advancements of circulating fluidized bed (CFB) technology in Thermal Power Research Institute（TPRI）,including technologies and configuration and progress of scaling up. For devoloping large CFB boiler, the CFB combustion test facilities have been established, the key technologies of large capacity CFB boiler have been research systematically, the 100MW~330MW CFB boiler have been developed and manufactured. The first domestically designed 100MW and 210MW CFB boiler have been put into commericial operation and have good operating performance. Domestic 330MW CFB boiler demonstration project also has been put into commericial operation,which is H type CFB boiler with Compact heat exchanger. This boiler is China's largest CFB boiler.The technical plan of domestic 600MW supercritical CFB boiler are also briefly introduced.

Keywords: circulating fluidized bed boiler, scaling up, supercritical CFB boiler

INTRODUCTION

In order to develop large CFB boilers with independent intellectual property, Thermal Power Research Institute(TPRI) established a laboratory with complete functions for the technical development of CFB boilers. This laboratory consists of a 1MW and 4MW CFB combustion test facilities and a laboratory for limestone desulphurization performance evaluation.It carried out tests on CFB combustion and desulphurization for Chinese typical coals and limestone and research on heat-transfer characteristics and key parts,and developed the first home-made 100MW and 210MW CFB boiler.Based on the experience of research and development, the laboratory further researched key techniques for enlarging Capacity systematically,and cooperating with Harbin Boiler Co.(HBC), developed the first domestic 330MW CFB boiler with independent intellectual property and put it into engineering demonstration,laying a solid foundation for the development of CFB boilers of even larger capacity.

KEY TECHNOLOGIES IN LARGE CFB BOILERS

Building calculation model for furnace heat transfer

The heat-transfer characteristic inside boiler furnace is one of important issues in large CFB boilers. the heat-transfer process inside furnace is of complicated mechanism, for it involves the heat exchange between the gas-solid particles of high mass concentration and heating surface. Translated into the fields of engineering design and application, the most noteworthy approach focuses on the calculation method for heat-transfer of water wall and superheater. Experimental researches on heat-transfer inside furnace were carried out on a 1MW CFB hot-state test facility and then an calculation model of furnace heat transfer was built as the following.

$$a_1 = k \times u_f^a \times t_b^\beta \tag{1}$$

Building calculation model of furnace height

For the furnace of large CFB boilers, a rational furnace height can be determined by the following calculation model.

$$H_f = 29.7 + k \ln C_b \tag{2}$$

Developing new external heat exchanger

External heat exchanger is the key technology of large CFB boilers. For this reason, TPRI did R&D work on a patent technology termed as compact ash-flow splitting and heat exchanger-CHE,and in addition, carried out an in-depth experimental research on a 4MW CFB hot-state test facility.The CHE uses pneumatic control principle to regulate the splitting proportion of circulating ash and has an integrated structure.

The structure of CHE is shown in Fig.1. It follows the working principles that the circulating ash coming from the separator is split into two parts in the ash distribution chamber. One serving as high-temperature circulating ash(890℃), flows into the ash returning tube and then back to the furnace, the other flows towards the heat exchange bed with heating surface, exchanging heat with the heat exchanger and then flows into the

low-temperature bed material returning chamber,then the low- temperature ash particles return to the furnace through the low- temperature ash returning tube.

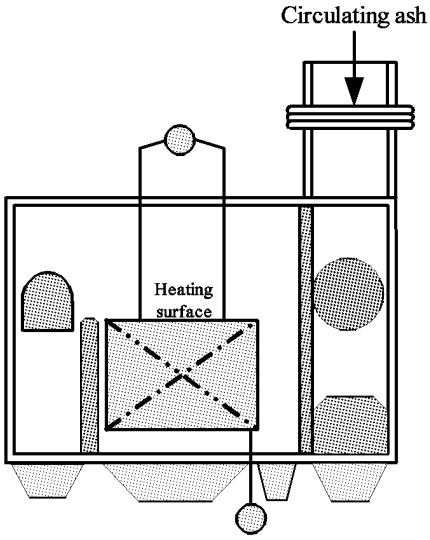

Fig. 1 Schematic diagram of CHE

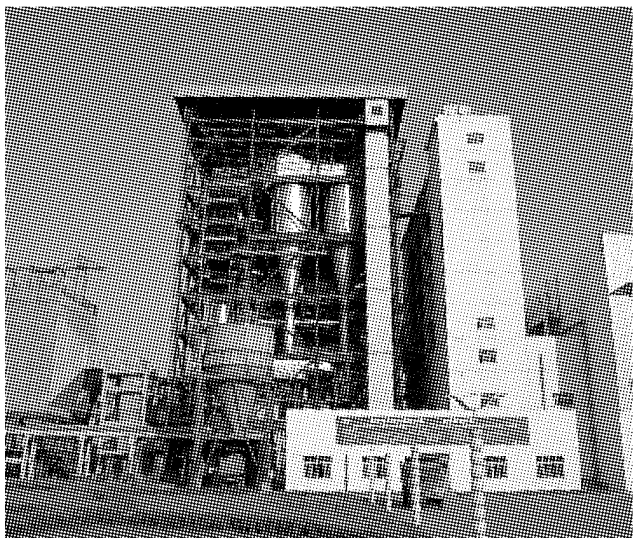

Fig.2 H-shaped domestic 100MW CFB Boiler

Building calculation model of heat transfer for external heat exchanger bed

For the low-speed fluidized heat-transfer process of fine particles inside the external heat exchanger bed,Experimental researches were made on the 4MW CFB hot-state test facility.A calculation model of heat transfer in the external heat exchanger bed was built.

$$a_{che} = \lambda \times t_b^{\nu} \tag{3}$$

ENGINEERING DEMONSTRATION OF DOMESTIC CFB BOILERS

100 MW CFB Boiler

Jointly developed by TPRI and HBC, The first home-made 100 MW CFB boiler is located at Jiangxi Fenyi Power Plant, referring to Fig.2 for its overall structure. The boiler is of H-shaped structure with four cyclone separators installed at the both sides of the furnace.The main design and operation parameters can be seen in Table 1.

The 100MW CFB boiler in Fenyi Power Plant was built and started on Nov.14, 2002, and put into commercial operation on Jun.19, 2003 after 96-hour trial operation. The practical operation experience is shown in the following aspects.

1) The main performance parameters and the output of the boiler reached or exceeded the designed values.when firing bituminous coal of 15-20MJ/kg low heat value,the boiler was in stable combustion at a furnace temperature of 920-930℃ and a main steam temperature of 535-540℃. The boiler thermal efficiency was 90.76% in case of firing design coal.

2) The pressure drop at the water side of economizer was 0.24MPa. The pressure drop at the steam side of superheater was 1.27MPa. They were lower than the designed values of 0.35MPa and 1.30MPa, respectively.

Table 1 Design and operation parameters of domestic 100 MW CFB Boiler

parameter	design value	Operation value
Main steam flow ($t \cdot h^{-1}$)	410	421
Main steam pressure (MPa)	9.8	9.8
Main steam temperature (℃)	540	540
Feed water temperature (℃)	215	233
Boiler thermal efficiency (%)	90.18	90.76
Furnace temperature (℃)	920	930
Exhaust gas temperature (℃)	135	137
Desulphurization efficiency(%)	85	90

(Continued)

parameter	design value	Operation value
Ca/S	2.2	2.1
Primary air temperature (℃)	200	213
Secondary air temperature (℃)	200	206
SO_2 emission (mg/m^3)	400	300
NOx emission (mg/m^3)	250	113
CO emission (mg/m^3)	250	173

3) The boiler was of favorable variable load characteristics with the maximum power output of 108MW, and could be in stable operation at 30% BRL(Boiler Rated load)without any oil support.

4) After 15000 hours of operation, the test on heating surface shows that the abrasion at tube wall was quite slight with the local maximum abrasion inside furnace less than 0.5mm.

5) The annual availability of the unit may reach 92.97%, and the auxiliary power consumption rate was 10.5%.

210 MW CFB Boiler

The overall layout of domestic H-shaped 210 MW CFB boiler can be seen in Fig.3, referring to Table 2 for the design and operation parameters. The diameter of boiler cyclone is 6.4m,and the sectional area of furnace is $160m^2$ with parts of superheater and reheater installed inside four CHEs.

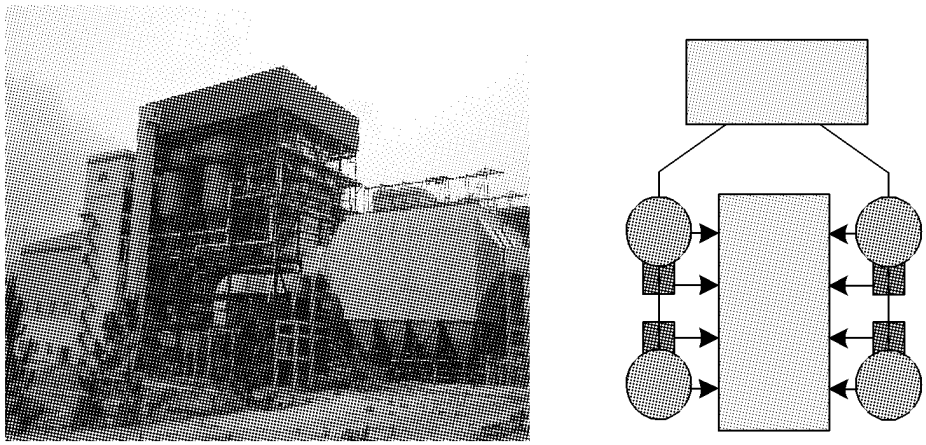

(a) (b)

Fig. 3 H-shaped domestic 210MW CFB Boiler
(a) stereotome; (b) tope view

The home-made 210MW CFB boiler, installed in Jiangxi Fenyi Power Plant,had experienced 96-hour trial operation successively up to July 7,2006, during which all performance parameters met the design requirements with the the maximum boiler output of 224MW and the continuous load rate of 94.6%.

Table 2 Design and operation parameters of domestic 210 MW CFB Boiler

parameter	design value	Operation value
Main steam flow ($t \cdot h^{-1}$)	670	690
Main steam pressure (MPa)	13.73	13.73
Main steam temperature (℃)	540	540
Reheat steam flow ($t \cdot h^{-1}$)	584	584
Inlet pressure of reheat steam (MPa)	2.56	2.36
Outlet pressure of reheat steam (MPa)	2.38	2.14
Inlet temperature of reheat steam (℃)	314	312
Outlet temperature of reheat steam (℃)	540	540
Feed water temperature (℃)	249	250
Boiler thermal efficiency (%)	89	89.04

(Continued)

parameter	design value	Operation value
Furnace temperature (℃)	920	930
Exhaust gas temperature (℃)	131	135.6
Primary air temperature (℃)	240	250
Secondary air temperature (℃)	240	250
SO_2 emission (mg/m^3)	390	271
NOx emission (mg/m^3)	150	80
BMLR (BMCR%)	30	25

The practical operation shows that the CHEs firstly applied in China are in stable operation and they can well regulate the bed temperature,superheating and reheating steam temperature during boiler load variation.

When the boiler was operating at a load of 50MW, thanks to the regulation of CHEs,the bed kept on normal operation with the bed temperature above 850℃. This is of great significance for this anthracite-fired CFB boiler, ensuring the combustion efficiency at low load and the optimal desulphurization temperature at variable load.

H-shaped 330MW and M-shaped 300MW CFB Boilers

For large CFB boilers of 200MW and above,a concept and design idea of compound boiler type was proposed for the first time in China.That means to arrange some platen superheaters inside the furnace, place the other superheaters and reheaters inside the CHE, which is superior to other type large CFB boilers in radiation space utilization, abrasion resistance,steam temperature features and power consumption of external heat exchangers.

Figure 4 shows the technical solution of H-shaped 330 MW CFB boiler designed by TPRI for Jiangxi Fenyi Power plant.Currently this demonstration project also has been put into commericial operation in January 2009. Figure 5 shows the technical solution of M-shaped 300 MW CFB boiler under development, which is equipped with three high-temperature cyclone separators of 8.8m in inside diameter and three sets of material separation and returning system in parallel.Its superheater Ⅱ is of wing wall structure and placed at the upper part of furnace;its superheater Ⅰ is arranged inside two CHEs.Reheater Ⅱ is installed inside another CHE,and reheater Ⅰ and superheater Ⅲ are installed at the back pass.

In light of the advantages such as less metal consumption and simple coal feeding system, M-shaped 300 MW CFB boiler is preferred for power units firing bituminite and lignite. H-shaped 330MW CFB boiler is favorable evenness and splitting performance for reliable coal feeding and ash returning, so it is practicable for difficult to burn coals,such as anthracite and lean coal.

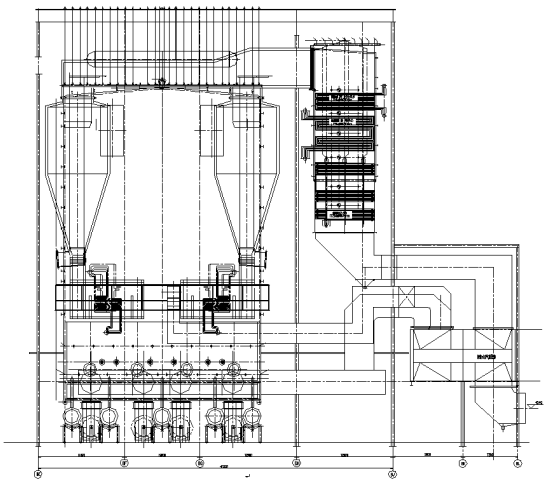

Fig. 4 H-shaped domestic330MW CFB Boiler

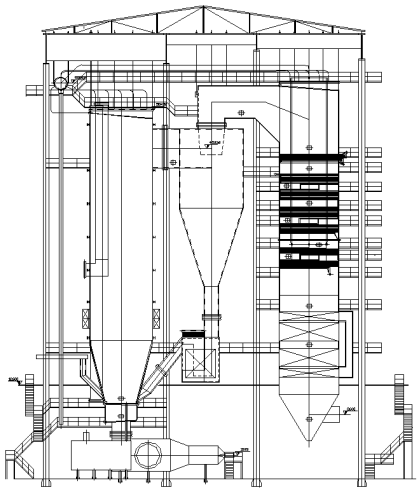

Fig.5 M-shaped domestic300MW CFB Boiler

DESIGNING 600MW SUPERCRITICAL CFB BOILER

Figure 6 shows the enlarging process of a CFB boiler from 50MW to 800MW. If the capacity is increased to 600 MW, It is inevitable to introduce H-shaped arrangement.Referring to Fig.7 for the completed design scheme of a 600MW supercritical CFB boiler,there are six separators(8.5m in diameter)placed on both sides of its furnace; the sectional area and height of the furnace are 405m^2 and 58m, respectively; in addition,the water wall has the structure of once rising vertical tubes equipped with six CHEs.

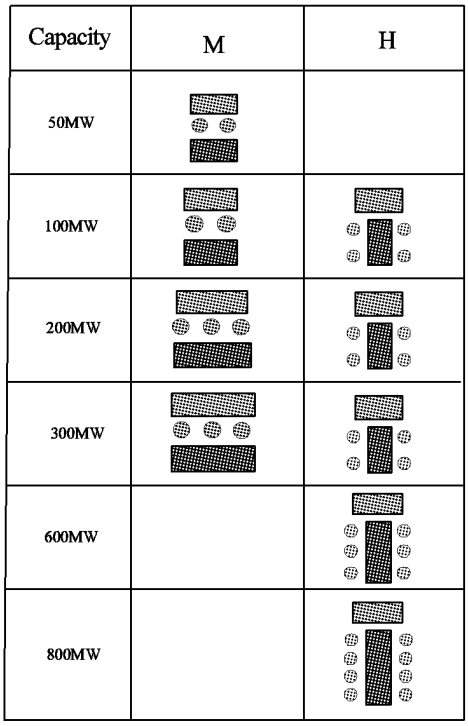

Fig. 6 Layout of domestic CFB boiler development

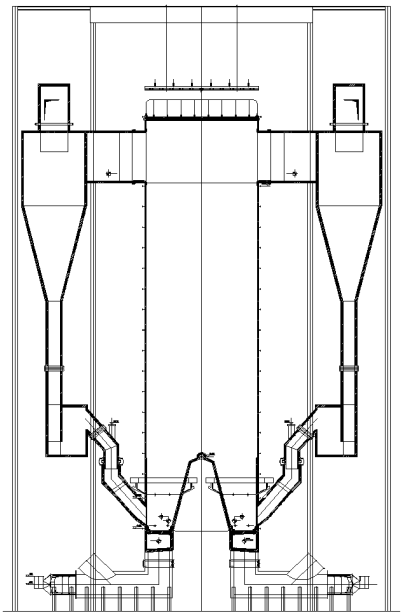

Fig.7 Design of 600MW supercritical CFB Boiler

For project use, it is essential to carry out in-depth research on several key technologies of 600 MW supercritical CFB boiler, shch as the distribution of heat flux density inside boiler, the heating surface protection in external heat exchanger under particular conditions, the evenness of gas-solid splitting in cyclones and the diffusion rules of coal particles flowing into furnace,etc.

NOTATIONS

α_1 heat-transfer coefficient inside furnace, W/(m^2℃)
u_f superficial gas velocity, m/s
t_b furnace temperature,℃
k characteristic coefficient of heat transfer
α ash concentration exponent
β temperature exponent
H_f total height of furnace, m
C_b burn-up index of coal
K furnace characteristic coefficient
α_{che} heat-transfer coefficient of external heat exchanger, W/(m^2℃)
t_b bed temperature of external heat exchanger, ℃
λ characteristic coefficient of heat transfer
v temperature exponent

ACKNOWLEDGEMENTS

Financial supports of this work by Key Project of the National eleventh-Five Year Research Program of China (2006BAA03B02-02) and National high technology research development plan(2007AA05Z302) are gratefully acknowledged.

REFERENCES

W.-Fr. Stab, V. Adamec. Difficult to burn fuels in mid-size to large CFB applications latest experience and outlook. Proceedings of

the 16th international conference on fluidized bed combustion. May 13-16,2001, Reno, Nevada. USA.

Robert A. Dyr, Jerry Hebb, Scott L. Darling. The JEA CFB Demonstration Project: An update. PowerGen-Europe, Helsinki, Finland, June 20-22,2000.

Steve Goidich. Integration of the BENSON vertical OTU technology and the compact CFB boiler. powerGen international Orlando, Florida, November 2000.

Sun X B, He W Q, Lv H A,*et al.*Study and test on heat transfer of CFB .Thermal Power Generation, 2000,29(1): 20-21,57.

Sun X B, Li G H, Jang M H. Study on several forward tasks in the technical sector of CFB boilers.Thermal Power Generation, 2005, 34(11): 1-5.

Sun X B, Li Z W, Shi Z H, *et al*. Experimental study on the compact splitting-type returning ash heat exchanger of CFB boilers. Electric Power , 2006, 39(7): 27-30.

Joachim Werther.Fluid dynamics temperature and concentration fields in large-scale CFB combustors.Proceedings of 8th International Conference on Circulating Fluidized Beds. May 10-13,2005, Hangzhou,China.

Sun X B,,Yu L, Zou S F *et al*. Design and operating experiences of indigenous 100 MW CFB boiler. Electrical Equipment,2004,5(12):7-9.

Sun X B,Yu L, Wang Z W, *et al*. Design and research of domestic 200 MW CFB boilers. International Electric Power for China, 2005,9(1)19-22.

Sun X B, Wang Z W, Jiang M H, *et al*. A study on the design of research domestic 300 MW CFB boilers. Thermal Power Generation, 2001, 30(6): 1-6.

Li Z W, Sun X B, Shi Z H. Hydrodynamic calculation of 600 MW supercritical CFB boiler. Thermal Power Generation, 2006, 35(12): 7-9.

EXPERIENCE FROM THE 300 MWe CFB DEMONSTRATION PLANT IN CHINA

P. Gauvillé, J.-C. Semedard, S. Darling

ALSTOM Power

Abstract: This paper will describe the background and current status of the 300MWe CFB Demonstration Project located at the Baima Power Plant in Sichuan Province. This project was the first 300MWe class CFB in China and the first project built under the Transfer of Technology from Alstom. The plant entered commercial operation in early 2006. The fuel is a high-ash anthracite which has presented significant challenges in terms of higher-than-expected ash content and top size. While this fuel has been problematic for the adjacent suspension-fired boilers, performance in the CFB boiler has been excellent, with low carbon content in the ash, low turndown and low emissions. Key boiler performance parameters will be described along with a comparison of design and actual performance and the operational experience will be addressed. Finally, the paper will describe Alstom' s process for scaling the CFB technology from 300MWe to 600MWe, and our supercritical CFB design.

Keywords: CFB, performances, anthracite, 300MWe

INTRODUCTION

Fluidized bed combustion plants have been in successful operation for many years in the capacity range from 50 to 350MWe. Steam generators with circulating fluidized bed (CFB) combustion have found acceptance throughout the world over the last few years, in particular for the power generation, but also as industrial power plant and combined heat and power station. The reason for this success was twofold: (1) they could meet the considerably stricter anti-pollution legislation without add-on equipment, and (2) fluidized bed combustion plants allow the use of a broad fuel range, including various sludges and production residues and different types of coal and biomass. CFB plants are also successful in China for the same reasons.

The increase in the energy consumption in China necessitates that new power stations are provided. As the Chinese fuel market includes a share of low-volatile and high-sulfur coals, the fluidized bed technology is an excellent technology for these fuels.

The construction of the 300MWe demonstration power plant Baima in the province of Sichuan is an important milestone in this respect. Following a detailed evaluation process in the years from 1998 to 2002 the delivery contract was awarded for the boiler scope at the beginning of 2003, making the Baima plant the first 300MWe CFB plant in China and one of the biggest worldwide.

The paper describes the project schedule and realization, focuses on the design and the basic principles applied for this boiler, and gives a status of operational feedback from the commissioning phase and the commercial operation of the plant. Furthermore, the paper will address the further increase in capacity up to 600MWe, which will further improve the economic efficiency of these plants in combination with the introduction of supercritical steam parameters and the once-through technology.

THE BAIMA PROJECT IN CHINA

Alstom Power Boilers was awarded the contract for supplying the first 300MWe CFB boiler in China, one of world's largest CFB boilers, burning an anthracite and built in Sichuan province. The Baima plant was constructed for Sichuan Baima CFB Demonstration Power Plant Co. Ltd., whose main shareholder is State Power Grid and Sichuan Bashu Development Company. The contract was signed in July 2002 and put into effect in April 2003. According to the contract, Alstom supplied the CFB boiler, with most of the manufacturing being done in China and subcontracted to Dongfang Boiler Group which took advantage of the proximity of its workshop from the site.

The Baima Project includes a Transfer of Technology agreement for CFB boilers between 200 and 350MWe from Alstom to three of China's boiler manufacturers and to the seven members of the Chinese Electric Power Design Institute.

The Baima CFB Demonstration Power Plant has been in commercial operation since April 2006 and test campaigns were conducted for optimizing performance such as limestone consumption or carbon burnout. In 2007 a particular program was launched for allowing the power plant to be operated in automatic mode under significant fluctuation of coal quality. Performance tests were conducted in May and June 2007.

One reason for selecting CFB technology for Baima was that the anthracite can be burnt without oil support even at low loads. The minimum load without oil support guaranteed for Baima was 35 %. Another reason was that post-capture equipment such as SO_2 scrubbers and SNCRs are avoided, thus positively impacting CFB investment cost and ease of operation, while still meeting environmental emissions requirements.

BOILER DESIGN

This 1025tonnes/hr natural circulation CFB boiler was designed to fire a Chinese anthracite coal at steam conditions as shown in Table 1. The anthracite coal is characterized by a relatively low volatile matter content (8.5 as received) and a high ash content (35 % as received). The lower calorific value is 4420 kcal/kg. The detailed analysis is given in Table 1.

Table 1 Baima CFB Boiler Main Data

Steam conditions at MCR	**Units**	
Main steam flow	t/h	1025
Main steam pressure	Bar	174
Main steam temperature	°C	540
RH steam flow	t/h	844
RH steam pressure	Bar	37
RH steam temperature	°C	540
Feed Water temperature	°C	281
Design coal analysis		
Carbon	% wt AR	49.2
Volatile matter	%	8.55
Sulfur	%	3.54 to 4.30
Ash	%	35.27
Moisture	%	7.69
Lower Heating Value	kcal/kg	4420
Emissions level		
SO_2	mg/Nm³ ≅ 6 % O_2	600
NO_X	mg/ Nm³ ≅ 6 % O_2	250
Particulates	mg/ Nm³	100

The emission requirements for the gases discharged at the stack are also shown in Table 1. No post-combustion cleaning equipment is required. The design utilizes the concepts developed and well proven by Alstom over several years of successful operation at the Provence and Red Hills plants, i.e. a dual grate (pant-leg) furnace, four high efficiency cyclones and four external fluidized bed heat exchangers (FBHEs) - two for bed temperature control and two for reheat steam temperature control [1]. The arrangement of the CFB boiler is shown in Fig. 1.

Potential (uncontrolled) sulfur dioxide levels in the flue gas are close to 10000 mg/Nm^3 (6% O_2 Dry Gas) for the design coal and 14000mg/Nm^3 for the higher sulfur coal. SO_2 emission must be lower than 600 mg/Nm^3 when burning the design coal so that the required sulfur capture efficiency is close to 94%. Sulfur capture is performed by injecting limestone into the furnace through four ports located in the return ducts from seal pots to furnace. Calcium carbonate ($CaCO_3$) content in the limestone is within 90 to 92%.

Two major challenges for the Baima project in terms of performance were the combustion efficiency and the limestone consumption. While the 250mg/Nm^3 NOx emission limit was relatively low, this had already been achieved at other Alstom units. Test campaigns with a low rank fuel had been conducted at the Provence 250MWel CFB power plant and had demonstrated the ability to manage the NOx emission below the limit by changing the combustion temperature and in particular the air staging.

To achieve the high required performance, Alstom held to the following basic design principles:

- Uniform furnace temperature within the range 880°C-900°C in which the limestone reactivity was demonstrated the highest and the carbon burnout near the expected figure.

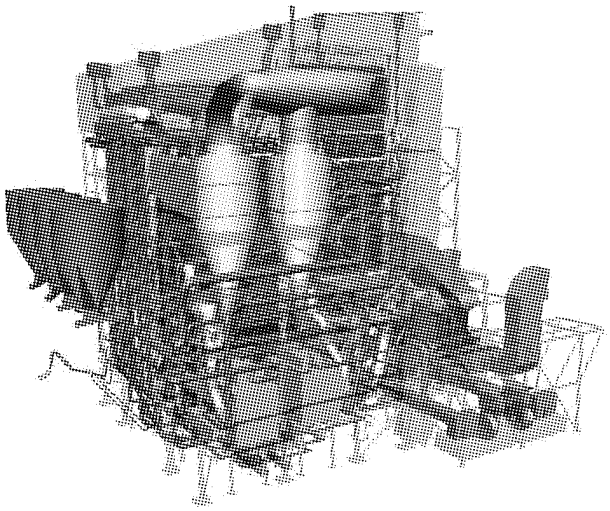

Fig. 1 Baima CFB Arrangement

- Besides the furnace water walls and the extended walls located in the furnace for complying with the required evaporative duty, heating surfaces for superheat or reheat duty were put into the external beds.
- The cyclone and the inlet duct were designed to achieve the highest possible capture efficiency. Several designs were tested on a cold flow model before choosing the final shape. This design was able to retain the fine particles of lime and carbon in the solid loop and hence improve the performances by increasing solids residence time. Furthermore high capture efficiency leads to an increase in the circulating ash flow, ensuring a high heat transfer and a uniform temperature in the furnace and good contact between CaO particles and SO_2 rich flue gas for optimum sulfur removal.
- Air staging in the bottom part was reviewed for burning anthracite based on Alstom's previous experience. The ratio of primary air rate flow to total air flow was increased and secondary air was properly distributed around the furnace enclosure and in the core of furnace through air ports located on the both sides of internal walls (pant-leg) and over two levels.
- Coal was injected with the limestone in the return ducts from seal pots to furnace for allowing a pre-mixing with the circulating ash before entering into the furnace. Return ducts were arranged for getting a circulating ash flow at the entrance into the furnace, onto the centre line of the fluidization grate. This arrangement takes advantage of the high momentum balance of circulating ash for achieving a good penetration and mixing of all the solids along the furnace grate. Uniform distribution of coal and limestone was reached and matched the air distribution.
- Bed inventory was also increased, compared to that from other CFBs commercial units burning higher rank fuel.

BREAKTHROUGH FURTHER TO BAIMA COMMISSIONING AND OPERATION

Many difficulties in the procurement of coal from Chinese market occurred from the beginning of the commissioning so that the quality of coal was worse than that of contractual technical specifications.

Whereas the contractual ash content was specified within 30 to 40%, the current ash content was very often higher than 50% bringing about troubles in the bottom ash removal system and the coal crushing system.

Figure 2 highlights the ash content over an operating period in July 2007 of seven consecutive days. Average ash content was close to 50% and sometimes exceeded 60%.

A large amount of stones in the raw coal brought about a very fast wearing of hammers in the secondary crusher so that the expected coal PSD, important for achieving the design conditions, has never been reached. 30% by wt of coal particles were larger than 3mm with a maximum size around 15 mm and a D50 of 1 to 2 mm. Hence, coarse particles had to be extracted from the Fluidized Bed Ash Coolers (FBAC's) but the high amount of ash including many oversized particles led to a coarse ash build up inside the tube bundles and lack of heat exchange. Excessive ash temperatures at the FBAC discharge were measured, so downstream mechanical ash conveyors tripped very often. Although modification of the FBACs would have probably been able to solve the problems, the owner decided to remove the FBACs and to replace them by Rotary Ash Coolers (RAC's). The replacement took place in September 2007. Since October 2007, when the four RACs were put into operation , there has been no trouble in the ash extraction system even though the thermal performance of the coolers was lower than expected. Cooler thermal capacity was improved during the plan outage in July 2008 by increasing RAC length approximately 20%.

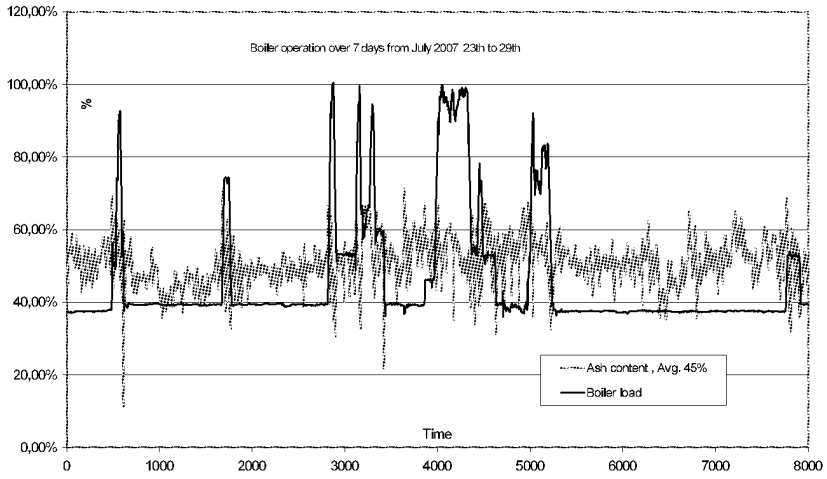

Fig. 2 Coal ash content vs time

Each RAC was installed in the place of an existing FBAC, which was dismantled. The inlet of the ash cooler was kept through the cone valve and a vent to the flue gas duct was installed. The water quality and pressure were taken into consideration and this led to a thick shell for the cooler. Figure 3 shows the design principle of the RAC. Such coolers are widely used in China.

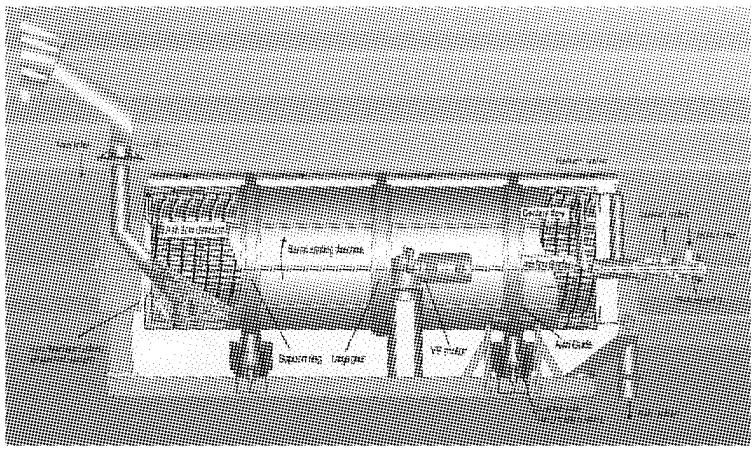

Fig. 3 Rotary Ash Coolet

The trial run was successfully passed on April 17th, 2006 and the boiler has been in commercial operation since then, following grid demand mainly between 160 and 300 MWel. Performance tests were carried out in June 2007 and demonstrated the outstanding combustion and emissions as reported in Table 2.

Table 2 Performance tests results

Baima performance tests	BECR Perf test 1	BECR Perf test 2	Design
date	26th June 2007	27th June 2007	BECR
Coal quality stability	good	good	good
Coal LHV MJ/kg	15,38	16,49	18,5
Ash %	43,5	40,5	35,3
LHV Boiler efficiency % (corr)	> 93	> 93	< 92
Added Ca/S (corr)	< 1,5	< 1.7	< 2,0
Sulfur capture %	> 95	> 94	> 94
SO_2 emission mg/Nm3 6%O_2 dry	< 600	< 600	600
CO emission mg/Nm3 6%O_2 dry	< 150	< 130	NA
NO_X emission mg/Nm3 6%O_2 dry	< 100	< 100	250

The combustion efficiency is also very good and the heat loss due to the unburned carbon is less than 3% on LHV basis. The auxiliary power consumption was close to 8600kW below the guaranteed value to 9500kW.

It was also demonstrated that the boiler was able to operate in steady condition at 35% load without any fuel oil support while keeping the rated steam temperatures at 540/540°C.

The bed temperature was controlled to the 880 °C average temperature set point by adjusting the heat pick-up in the external beds. At 35% load the heat-pick distribution between the furnace and the external beds is respectively 2/3 and 1/3 of the overall heat pick-up in the hot loop. A minimum flow rate of circulating ash is required for the feeding of external beds and hence for reaching the heat pick-up needed in the FBHEs. The flow rate of circulating ash can be calculated with the flue gas volume along with the ash concentration in the upper part of furnace which is derived from the difference of pressure equal to 0.24kPa at 35% load as shown in Fig. 4.

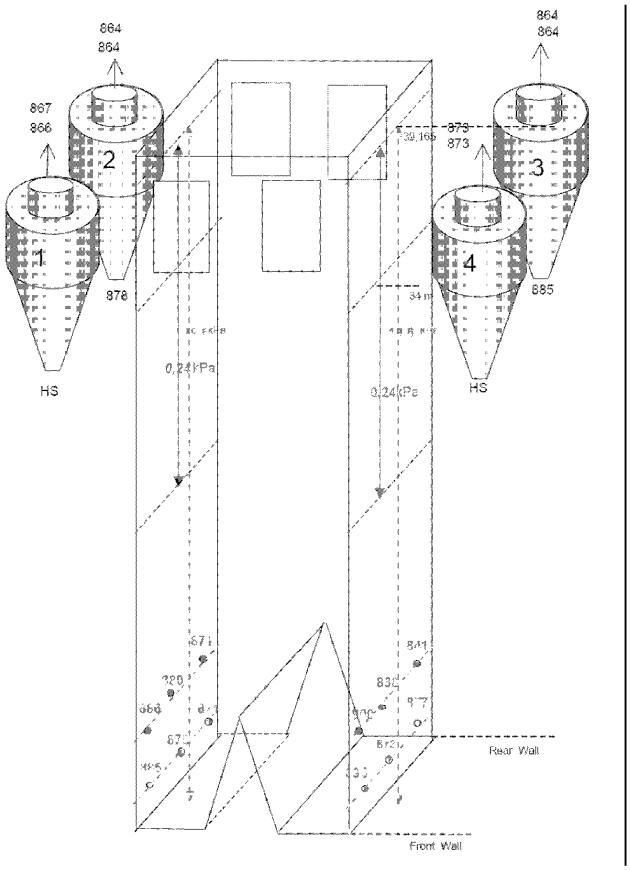

Fig. 4 35% Load – Bed temperature and pressure

The difference of temperature between the bottom part of the furnace and the cyclone outlets is less than 20°C.

CO emission was close to 50 mg/Nm^3 and NOx emission around 100mg/Nm^3 as shown in Fig. 5, even though excess air was increased up to 70%.

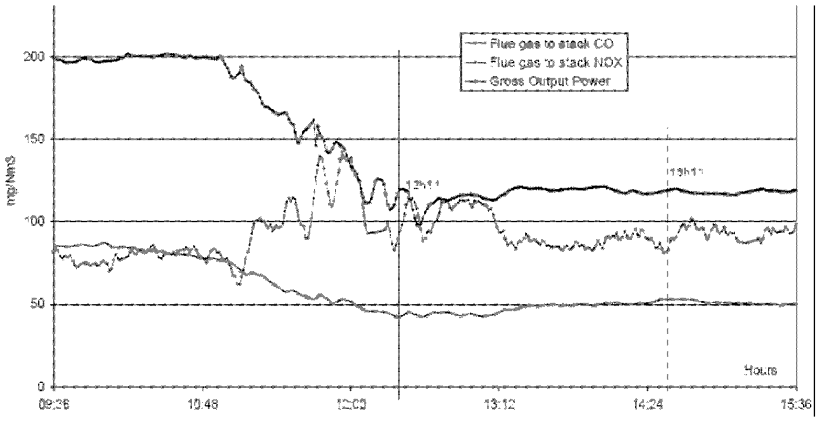

Fig. 5 CO and Nox emissions

The operation of the unit in automatic mode needed a real effort in the setting of control loops because of the variability of coal quality. Coal flow varied from 120 t/h up to 200 t/h for the same power output of 300MW over 1 hour as reported in the Fig. 6.

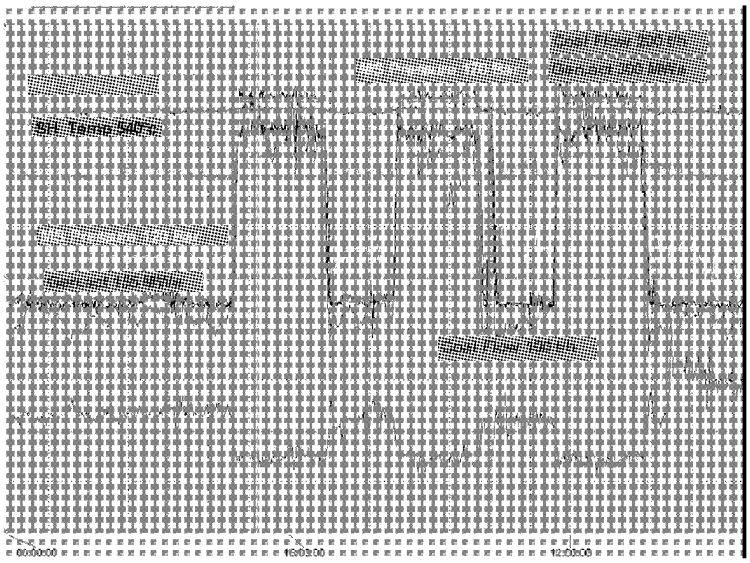

Fig. 6 Coal flow variation at constant power generation

If the unit is operated under boiler follow mode, main steam pressure is controlled by the coal feeders. Changes in electric power demand, acting simultaneously on the HP turbine throttle valves and on the boiler load demand through a feed-forward controller, required the operators to be very watchful because the unit was sensitive.

If the coal quality was fluctuating too much, the unit was operated under turbine follow mode.

In that case, the electric power demand acts on the speed of coal feeders and the main steam pressure is controlled by the HP turbine throttle valves.

The main steam temperature and the reheat steam temperature were able to be controlled at the rated temperatures as reported on figure 7 while the boiler was operated between 100% and 50% MCR and with a main steam pressure set point from 120 to 170 Bar.

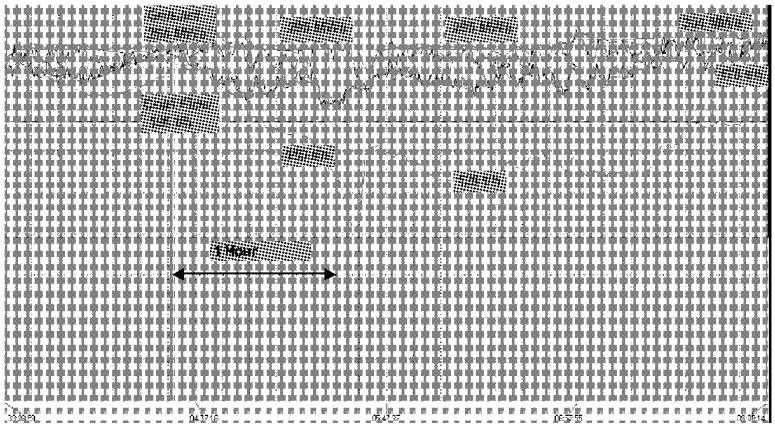

Fig. 7 Boiler load variation within 150 to 300 MWe

In spite of the obvious difficulty to optimize operation with such variable coal properties, the bed temperature was around 880 °C and good combustion was achieved.

Another area in the CFBs which requires careful quality control is the refractory in the furnace. Therefore, special care was taken in order to ensure high quality for the delivery and erection of the refractory, large portions of which were supplied directly from China. Those efforts included clear specifications during the design phase and close supervision and day-to-day quality control with on site replacement, if necessary, during erection. Dry out definition and supervision was also in Alstom's responsibility. Those efforts made during the engineering phase and the erection of refractory and the normal maintenance managed cautiously by the owner resulted in a very successful outcome. Fig. 8 shows the cleaning of joints and gives an idea of the excellent

refractory condition after 14000 hours of operation.

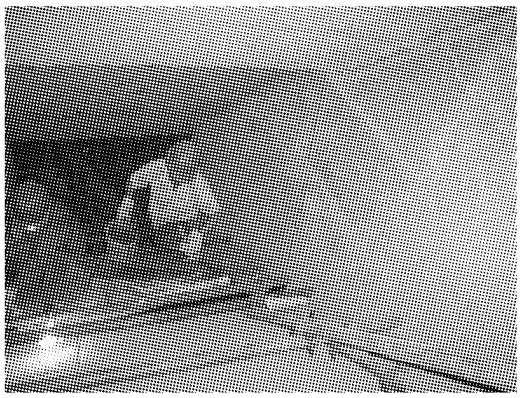

Fig. 8 Cleaning of joints after 14000 hours

FURTHER SCALE-UP AND SUPERCRITICAL DESIGN

The increase in CFB boiler capacity to 400 up to 600MWel is considered as the next feasible step with a mitigation of technical risk resulting from the significant experience that Alstom gained through the 300-350 MWel CFBs. This increase in capacity is to be combined with the introduction of supercritical technology that Alstom pioneered and has utilized for many years for pulverized coal (PC) boilers.

The increase in capacity and the introduction of supercritical steam parameters in CFB plants impact some key components such as the furnace, cyclones and FBHEs.

Furnace

For boiler sizes above 400MWe a concept with a dual grate (pant leg) is required in order to ensure proper air distribution and complete combustion. Two or three cyclones and up to three FBHEs are arranged on each side of the furnace. Figure 9 shows the overall arrangement of a six-cyclone boiler.

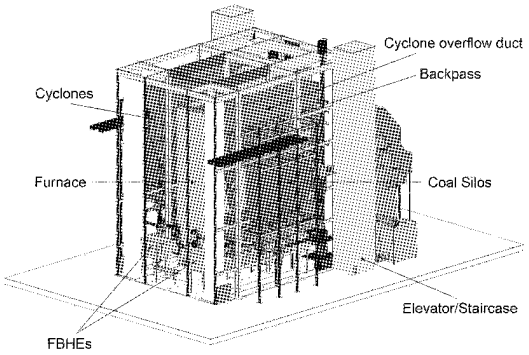

Fig. 9 Arrangement of a supercritical fluidized bed boiler for 600 MWe

- Besides having some impact on the size of buckstays, the furnace width is typically lower than for a 300 MWel single grate design.
- The furnace depth is designed in such a manner that the secondary air can penetrate deeply into the furnace. With the conventional single grate concept this requirement leads to widths of max. 10 m. In order to avoid this limitation for large furnaces, the dual grate concept was introduced.

A staging of the secondary air is especially effective for high reactive fuels. The more homogeneous the oxygen distribution, the less NO_X and SO_2 is produced and the more effective becomes the limestone consumption and fuel burnout. Each grate section of the dual grate is provided with separate fuel and air feeding points. The secondary air is injected from the enclosing wall and also from the interior furnace walls. The separate control of the primary and secondary air above each grate section helps to achieve a uniform fluidization, homogeneous stoichiometries and a uniform bed material inventory.

Cyclone

For supercritical steam parameters the cyclones plus inlet and outlet ducts are supplied with a tubed design and cooled by the superheated steam. This leads to a minimization of the refractory lining in the cyclone area.

Experience with the manufacturing and erection of tubed cyclones have already been gained with subcritical plants and nowadays the steam cooled cyclone is the common design for the majority of 300MW_{el} and larger CFBs .

FBHE

For the optimum utilization of the heat input to the furnace, FBHEs are used as a supplement to the heating surfaces in the furnace. In the FBHEs the circulating ashes with temperatures from 845 to 900 °C are cooled to approx. 600 °C, and the heating surfaces can be arranged as superheater, reheater or even as evaporator. The ash flow into the FBHE is controlled by an ash valve.

Besides the possibility of controlling the furnace and reheater temperature without spray attemperation, another advantage of the FBHE is the high heat transfer coefficient from the ash particles to the tube banks, which leads to compact heating surfaces. Modular design enables the increase of the thermal output without any modification of the design concept. Thus, the scale-up risks are avoided. With the increase of the plant capacity the number of the FBHEs is increased. The number of FBHEs can be at most equal to the number of the cyclones.

SUMMARY

In recent years, CFB plants have become established in the capacity range from 250 to 350 MWe. A further capacity increase up to 600 MWe is feasible. The introduction of supercritical steam parameters further improves efficiency and additionally allows the reduction of CO_2 emissions. In this context, CFB technology takes advantage of the design and operating experience of pulverized fuel firing plants. Particularly in the area of the materials and once-through technology the experience from pulverized fuel firing plants can be directly applied to the fluidized bed.

All the experience gained throughout the operational feedback of Baima CFB power plant as well as from the other CFBs in China and throughout the world, emphasizes the ability of the CFB technology to achieve high performances for a wide range of fuel and comply with strict emissions of pollutants.

In the meantime, the international community is pushing forward towards a drastic reduction of CO_2 emission. Many CO_2 capture technologies are being investigated and the first demonstration plants have just been in operation for a few months. CFB technology with oxygen firing is also a promising and competitive solution for commercial power plant addressing a wide range of fuels, including low grade coals and pet coke. The size of CFB boiler might be reduced compared to CFB boiler in Air fired. Alstom is developing Oxy CFB technology with the objective of constructing the first demonstration plant within the next two or three years.

REFERENCES

[1] Semedard, J.-C.; Skowyra, R. S.; Stamatelopoulos, G.-N.: Circulating fluidised bed technology applied to diverse fuels in Asia: Demonstrating successful Projects, Power-Gen Asia 2006, August 2006, Hong-Kong,

PROJECT MAXAU – FIRST APPLICATION OF HYBRID CFB TECHNOLOGY BY AUSTRIAN ENERGY & ENVIRONMENT

Kurt Kaufmann, Herbert Köberl, Thomas Zotter

AE&E Austria GmbH & CO KG, Graz, Austria

Abstract: As a worldwide supplier of fluidized bed combustion plants the reference list of Austrian Energy & Environment comprises more than 80 fluidised bed boilers over a wide capacitiy range with different kinds of fuel such as coal, biomass, sludges, RDF or various industrial wastes.

Actually two types of CFB Boilers were supplied by AE&E:

On the one hand the "classical", conventional **POWERFLUID®** CFB with cooled furnace, cyclone, cross-over duct or vertical convection pass to be employed for combustion of conventional fuels such as hard coal, lignite, biomass and sludge et al. The chlorine content of these fuels is as a rule lower than 0.1% in dry matter.

On the other hand the especially developed CFB for the combustion of refuse derived fuel (RDF) with the special features of an adiabatic primary loop with controlled heat extraction in an external bed material cooler, a toroid shaped adiabatic post combustion chamber downstream the primary cyclone. This combustion part is followed by a well known boiler concept of a classical waste incineration consisting of two radiation passes and a horizontal convection pass with hanging superheater and evaporation bundles.

Live steam temperatures up to 470°C (450°C) with fuel chlorine contents of 1.2% (1.5%) in dry matter can be accepted with this concept.

Market development in the last years showed a limited access to a particular segment with these two CFB concepts. This market segment consists of co - combustion plants firing biomass and / or conventional fuels with addition of RDF or production residues - in the majority of cases in the pulp and paper industry. The chlorine content in these fuel mixtures is typical around 0.2% in dry matter, with often missing sulphur content and the required live steam temperatures are between 500°C and 520°C.

Out of this AE&E developed a "combined" CFB-concept with the brand name **POWERFLUID®**-Hybrid.

The presentation will provide a detailed description of the special features of the Hybrid technology by means of the Maxau plant.

Keywords: RDF, Hybrid, Maxau

INTRODUCTION

Depending on special requirements of the various fuels and the size of the boiler different combustion systems like the bubbling bed or a circulating fluidized bed technology will be used.

All of these systems have been developed by AE&E and will allow maximum flexibility in the range of fuels. Beside environmentally sound combustion with low emissions, maximum boiler efficiency is the main target.

To reach the market for co-combustion plants firing a combination of biomass and/or conventional fuels together with RDF and other waste fuels a new concept was needed.

In addition the rules for the co - combustion of waste in the EC, stipulated in the Directive 200/76/EC, must be fulfilled. These are amongst others the requirement for a minimum residence time of 2 seconds for the flue gas at more than 850°C.

In the new developed CFB concept with the brand name **PowerFluid®**- Hybrid, which is in optimum accordance with these requirements, proven components of the two already established types were used and combined.

Table 1 Comparison of the different systems

The first implementation of this new CFB type for co-combustion of waste is on the way fulfilling a contract signed in spring 2008.

The order consists of CFB plant approved according to the 17th BImSchV of Germany in a paper mill located in Maxau, Germany. The plant is designed for a live steam capacity of 198 tons/h with 520°C and 95 barg.

Table 1 compares the different systems showing the main features

	Conventional POWERFLUID® Boiler	**Hybrid POWERFLUID® Boiler**	**RDF POWERFLUID® Boiler**
Fuels	Coal, Biomass, Sludge,	Coal, Biomass, Sludge, RDF, Rejects	RDF, Rejects, Coal, Biomass, Sludge,
Chlorine Content	< 0,1% in dry sub.	< 0,3% in dry sub.	< 1,5% (1,2%) in dry sub.
Max. Steam Output	max. 450 tphr/346 tphr	< 290 tphr	~ 180 tphr
Max. Steam Parameters Pressure/Temperature	145 bara / 560 °C	115 bara / 520 °C	70 bara / 450 °C (470 °C)
Max. Flue Gas Flow	< 530.000 Nm³/h	< 340.000 Nm³/h	< 260.000 Nm³/h
Fuel Heat Input	approx. 300 MW_{th}	approx. 220 MW_{th}	approx. 150 MW_{th}

COMBUSTION TECHNOLOGY

Starting from the "classic" CFB design with water-wall-cooled combustion chamber, one or more hot cyclones and backpass heating surfaces Austrian Energy & Environment developed a CFB design considering all the features of waste fuels. This design which can provide in total now more than 100.000 operating hours makes a clear difference between combustion and steam production. The combustion takes places in a complete adiabatic system consisting of combustion chamber, cyclone and post combustion chamber securing a nearly complete burnout as well as enough residence time for the flue gases at high temperature. The steam generator itself is based on the proved design of waste incineration boilers consisting of a horizontal tail-end pass and a vertical economizer pass. Final stage superheating of the steam is done in an external fluidized bed heat exchanger (bed material cooler). A flow sheet of such a system is shown in Fig. 1.

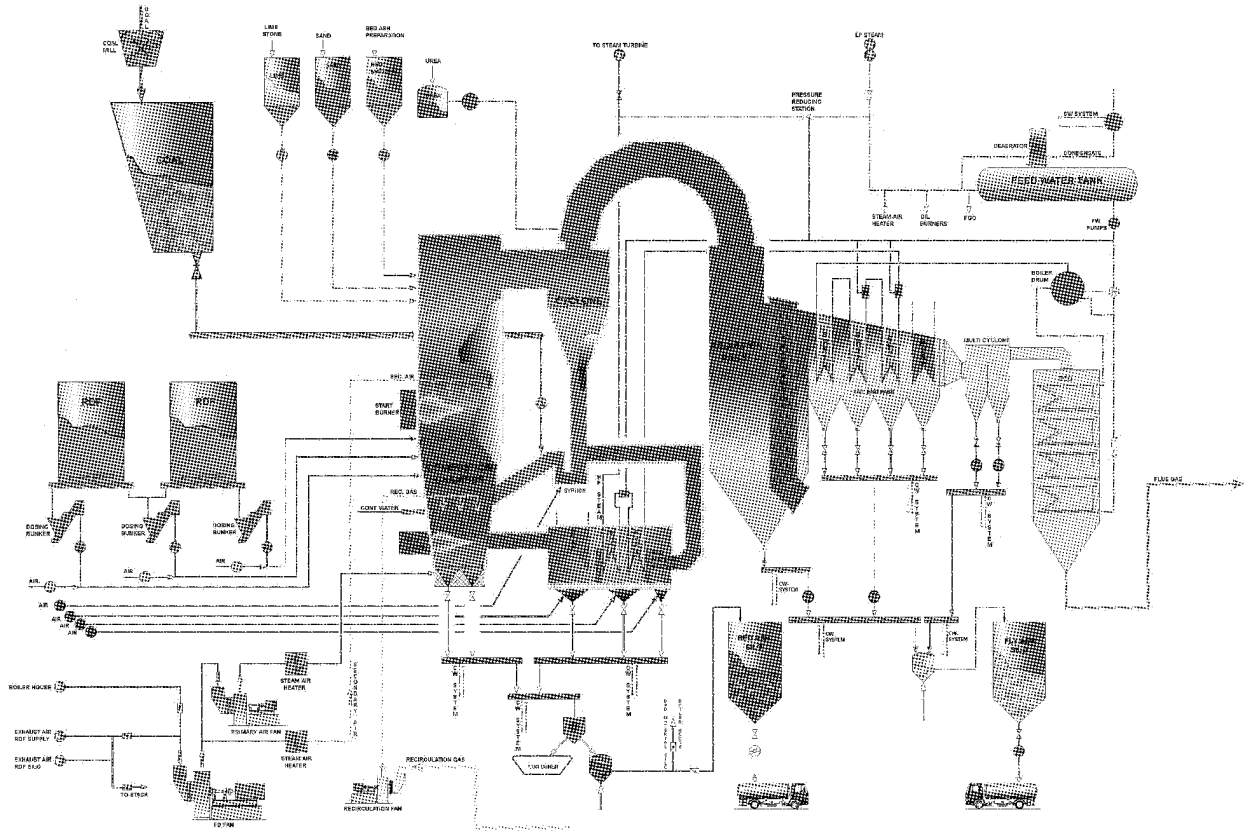

Fig. 1 Flow sheet of a waste fired CFB, System RDF-**PowerFluid®**

Recently the market required plants which are able to fire not only waste fuels. The usage of sludges, biomass, waste wood, rejects etc. in combination with conventional fuels should be possible. Additionally the plant efficiency became an important factor. Therefore the steam parameters had to be increased; also to open the possibility to incorporate a new boiler plant into steam systems of existing power plants.

Out of this a combination of these two solutions has been developed to use the advantages of both

technical concepts. This combined system - a so called "hybrid" - shows the following main features:

- Adiabatic refractory lined lower part of combustion chamber including all openings for fuel, air and inertial material for optimised combustion. The nozzle grid at the bottom is of an open type with air beams to allow coarse particles to be easily removed. This part is of round shape. The transition of round to rectangular cross section is in the refractory lined part of combustion chamber. In this adiabatic area the requirements of keeping 850 °C for at least two seconds (according to EU regulations 2000/76 for waste firing) can be ensured.
- Cooled area in the upper part of the combustion chamber
- Adiabatic refractory lined round cyclone. In addition to the excellent separation efficiency of the round cyclone, it works also like a post combustion chamber to ensure a very good burnout rate resulting in low CO- and TOC-emissions.
- Cross Over and vertical radiation pass with evaporator wing walls to reduce the flue gas temperature down to a reasonable level before entering the superheater 1
- Tail end pass with hanging superheater 1
- Vertical pass with hot air preheater and finned tube economiser
- Bed material heat exchanger containing only the final stage superheaters 2 and 3

The flow sheet of this Hybrid-System is shown in Fig. 2.

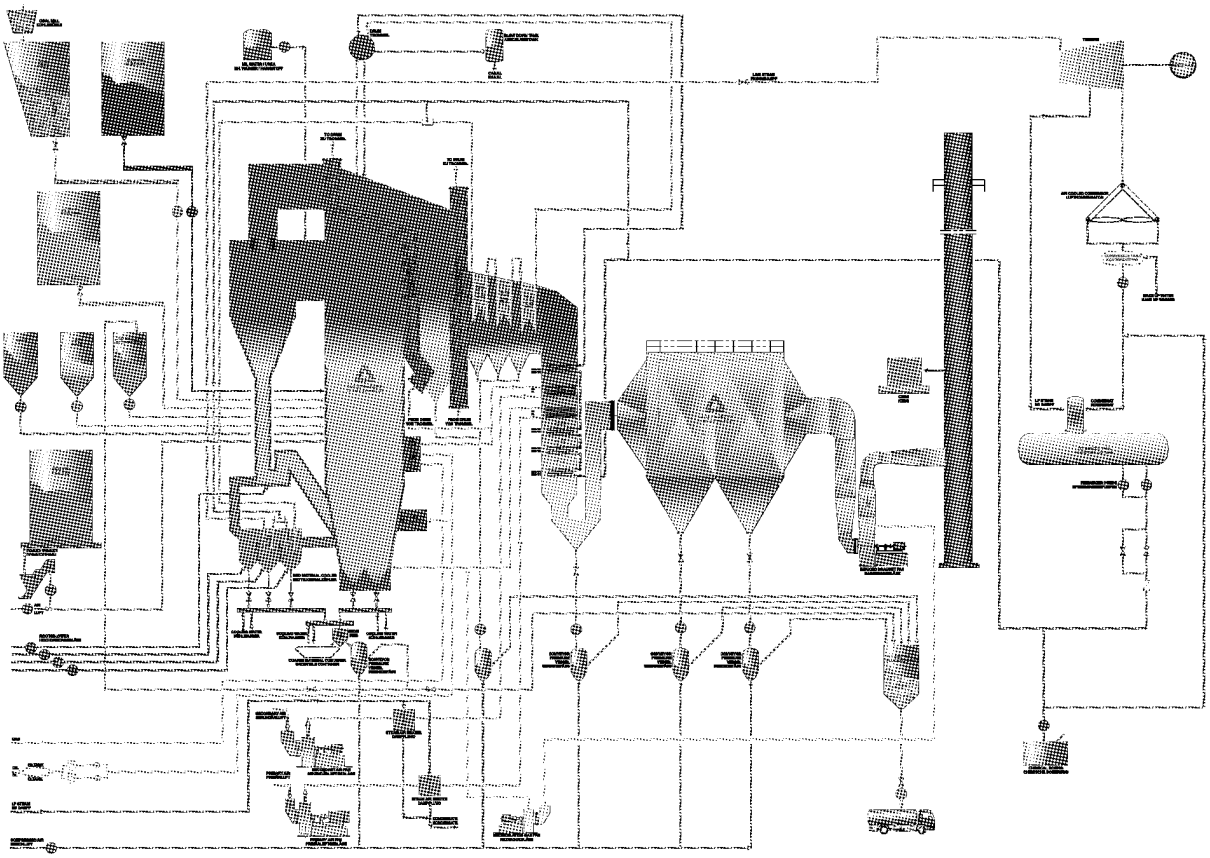

Fig. 2 Flow sheet, System Hybrid-**PowerFluid®**

PLANT DESCRIPTION

Maxau is located in Germany in the vicinity of Karlsruhe. The boiler plant will be built in the existing paper mill of Stora Enso.

The plant will be incorporated into the existing power plant consisting of three boilers, one gas turbine with HRSG and three steam turbines. A new steam turbine of 35 MWel will also be installed in the course of the overall project.

The general arrangement of the new boiler plant is shown in Fig. 3.

The fuels are coming from the waste paper treatment plant of the mill where three different kind of sludges (biological, deinking and fiber sludge) as well as the rejects are generated and have to be removed. Until now the removal has been done externally.

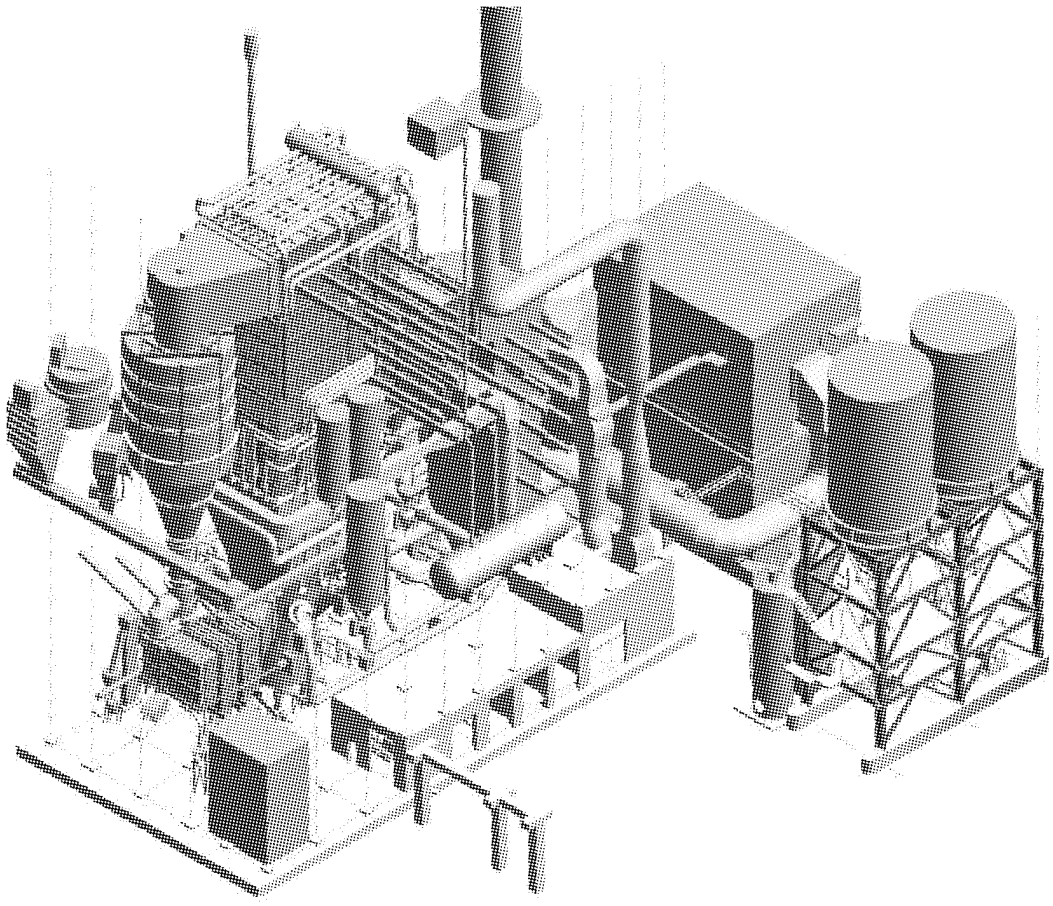

Fig. 3 General Arrangement

Coal and biomass are delivered by ship and train and a fuel transportation system directly to the power plant's fuel yard.

The project has been awarded in April 2008. The erection works on site will start in 2009 and the hand-over to Stora Enso is scheduled for October 2010.

TECHNICAL DATA

Steam Parameters

- Steam Capacity: 198 tphr
- Steam Pressure: 95 bara
- Steam Temperature: 520 °C

Fuels:

- 0 – 100% Biomass (Bark, Woodwaste II)
- 0 – 100% Coal
- 0 – 15% Sludge
- 0 – 10% Rejects

CONCLUSIONS

To correspond to the requirements of high efficiency plant combined with the capability of firing a wide range of fuels, Austrian Energy & Environment designed a new technical concept. This concept combines the advantages of the classic CFB-combustion with those of the RDF-fired CFBs developed by Austrian Energy & Environment during the last decade.

1300°F 800 MWe USC CFB BOILER DESIGN STUDY

Archie Robertson, Steve Goidich, Zhen Fan

Foster Wheeler North America Corp., R&D, Livingston, NJ 07039, USA

Abstract: Concern about air emissions and the effect on global warming is one of the key factors for developing and implementing new advanced energy production solutions today. One state-of-the-art solution is circulating fluidized bed (CFB) combustion technology combined with a high efficiency once-through steam cycle. Due to this extremely high efficiency, the proven CFB technology offers a good solution for CO_2 reduction. Its excellent fuel flexibility further reduces CO_2 emissions by co-firing coal with biomass. Development work is under way to offer CFB technology up to 800MWe capacities with ultra-supercritical (USC) steam parameters. In 2009 a 460MWe once-through supercritical (OTSC) CFB boiler designed and constructed by Foster Wheeler will start up. However, scaling up the technology further to 600-800MWe with net efficiency of 45-50% is needed to meet the future requirements of utility operators. To support the move to these larger sizes, an 800MWe CFB boiler conceptual design study was conducted and is reported on herein. The use of USC conditions (~1100°F steam) was studied and then the changes, that would enable the unit to generate 1300°F steam, were identified. The study has shown that by using INTREX™ heat exchangers in a unique internal-external solids circulation arrangement, Foster Wheeler's CFB boiler configuration can easily accommodate 1300°F steam and will not require a major increase in heat transfer surface areas.

Keywords: CFB, USC, INTREX

INTRODUCTION

Increased energy efficiency is needed to sustain robust economic growth, enhance national security, and protect environment and coal is expected to remain the leading fuel source for power generation for a long time. Efficiency and environmental performance are key issues when considering either repowering existing power plants or constructing new power plants. One of the main approaches to reduce emissions from power plants is to increase their efficiency. High efficiency means a lower fuel requirement, and results in lower ash discharge and gas emissions, including CO_2. The need for high efficiency is also important for CO_2 removal by oxy-combustion, because a reduction in fuel firing also means a lower O_2 requirement from its air separation unit, less CO_2 gas to be processed in downstream CO_2 compression and purification unit, and less storage volume for CO_2 sequestration.

With supercritical steam cycles providing high plant efficiencies, the interest is to pursue even more advanced steam conditions, such as 1300°F (700°C) to further increase efficiency and reduce emissions.

Circulating fluidized bed (CFB) combustion, with its well-known benefits of fuel flexibility, biomass co-firing capability, and low emissions, has established itself as a boiler technology suitable for utility-scale power generation. Interest in CFB combustion has been steadily increasing, 300 MWe plant sizes are in operation, and designs for larger boilers are being developed. As example, Foster Wheeler has designed and is constructing a 460 MWe SC CFB boiler for the Lagisza power station in Poland, a unit scheduled to start up in 2009 (Ref-5). Developing even larger size CFBs (600-800 MWe) with higher efficiencies is an ongoing challenge (Ref-1 to 4). A conceptual design study for an 800 MWe has been conducted to investigate the technical feasibility and economics of USC CFB boilers under U.S. Department of Energy (DOE) Cooperative Agreement No. DE-FC26-03NT41737. Foster Wheeler, together with a group of interested companies in Europe has completed a similar study for an 800 MWe power plant with USC CFB (Ref-1). Foster Wheeler has also started a boiler design with emphasis of configuration effect on part load performance of a 660 MWe SC CFB boiler at 620°C.

Table 1 Study Steam Cycle Conditions

	Case 2	Case 3
Unit Nominal Capacity, MWe	800	800
Main Steam Pressure, psia	4351	5076
Main Steam Temperature, °F	1112	1292
Reheat Inlet Temperature, °F	1148	1328
Condenser Back Pressure, "Hg	2.0	2.0

The USC steam cycle conditions used in the DOE study are listed in Table-1. In this study USC CFB boiler conceptual designs were developed for nominal plant outputs of 400 and 800MWe and then the changes to the latter that would generate 1300°F superheat and reheat steam, were identified. In Case-1 a nominal 400 MWe CFB boilers was conceptually designed for superheat and reheat steam temperatures of 1100°F, that are coming into use in the latest PC boilers. Case-2 investigated a move to a nominal 800MWe size with a modest increase in superheat and reheat temperatures (1112°F and 1148°F respectively). In Case-3 the nominal 800MWe CFB boiler was moved to more advanced steam conditions at 5061 psig and 1300°F steam temperatures for further gains in plant efficiency. The performance and cost of the 400MWe Case-1 plant were presented in an earlier paper, whereas, the performance and design aspects of the 800MWe CFB boilers are presented herein. With superheater/reheater tube metal temperatures typically running 100-200°F hotter than their steam, 1300°F steam will require a new generation of pressure part materials with high creep strength. These new materials are under development and test under other DOE contracts.

DESIGN AND SCALING UP

Preliminary studies show that the scaling-up to 800 MWe is possible for boiler components such as the furnace, solids separators, and fluidized bed heat exchangers (INTREX™). The actual scaling-up of the dimensions and size of plant components required is quite moderate due to Foster Wheeler's modular approach shown in Fig. 1.

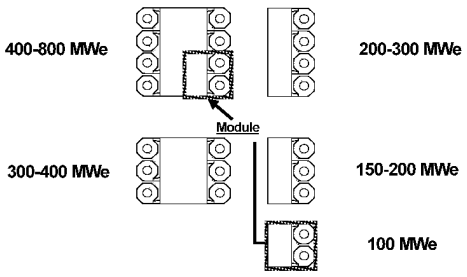

Fig. 1 Modular design of CFB boiler

The design of a CFB furnace involves a careful evaluation of fuel and sorbent characteristics followed by a selection of operating temperature, gas velocity, gas/solids residence times, and solids circulation rates. Furnace heights are typically below 165 feet to maximize the cost effectiveness of its heat transfer surfaces. Similar, the furnace depth (side wall to side wall distance) is typically limited to approximately 40 feet to insure distribution uniformly across the unit for fuel and secondary air injections. Primary air is admitted at the base of the unit and, to provide highly turbulent mixing of fuel, air, and sorbent, plus enhanced solids entrainment, Foster Wheeler narrows the furnace cross section at the base of the unit by slopping the side walls inward. With maximum allowable furnace heights and depths established, the main remaining variable in the scaling-up process is the width of the furnace. By using the Fig. 1 modular approach, the boiler cross sectional flow area can be increased to accommodate increased firing rates and enable flue gas velocities to be kept at normal levels.

The number of fuel feeding and limestone injection points required by large units will be based on the cross section feed areas (pounds per hour per square feet of bed area) proven in smaller units. The same applies also for air distribution and start-up burners. Other auxiliary equipment, such as fans, conveyors, feeders, air heaters, baghouse filters, etc. are similar to those used in large power plants, which means that there will be no scaling-up issues in the auxiliary systems.

Maintaining high collection efficiency in the CFB boiler's solids separators is a key to achieving high combustion efficiency, reduced limestone consumption, and high sulfur capture efficiency. Since the separation efficiency of these devices tends to decrease as physical sizes/diameters increase, large CFB boilers will use the separator sizes proven in smaller size units. Although a large CFB boiler will tend to require a larger number of separators, they will be of a proven size and design. By applying them in nominal 100MWe furnace-separator module building blocks (Fig. 1), scaling-up will not be an issue, especially since Foster Wheeler has already provided several CFB boilers with separators installed on opposing walls.

In addition to an increase in physical dimensions, the move to larger size, higher efficiency plants results in changes in boiler heat duty distributions; Table 3 shows the heat duty distributions of the Case 2 and Case 3 plants.

Foster Wheeler's cascading INTREX™ design, as an example, shown in Fig. 2 has been utilized to meet their needs. The INTREX™ fluidized bed heat exchangers are located under the solids separators. The solids collected by the separators pass through the INTREX™ cells (external solids circulation), after transferring heat to the immersed tube bundles, and return

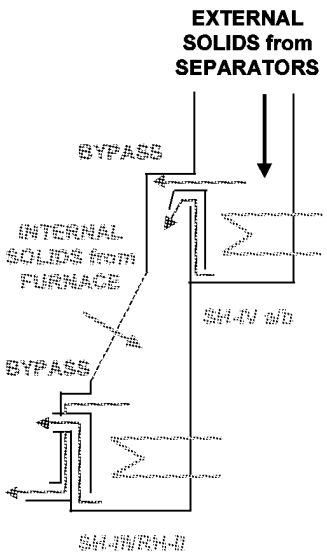

Fig. 2 Cascading INTREX™

to the furnace via aerated lift legs. Slots can be provided in the lower furnace walls adjacent to the INTREX™ cells to allow bed hot solids from the lower furnace to fall into the INTREX™ cells (internal solids circulation), which increases LMTD and heat duty for USC steam finish superheating. These exchangers provide a dense "package" of highly efficient heat transfer surfaces and have been utilized on several Foster Wheeler CFB boilers.

After passing through the furnace solids separators, the nominal 1600°F flue gas of a large CFB boiler will be cooled in a heat recovery area (HRA) consisting of convective tube bundles and walls used for steam superheating, reheating, and feedwater preheating; the arrangement will be typical of large PC boilers.

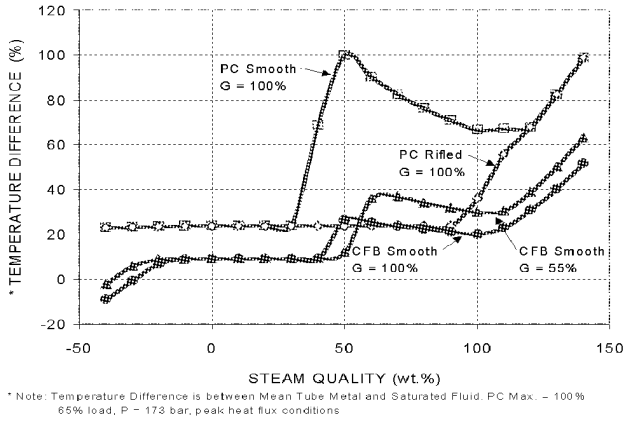

Fig. 3 Comparison of dry out

Because CFB furnace heat fluxes are relatively low and uniform, its tubes probably do not require internal rifling and they can operate with water mass flow rates lower than those of a PC furnace and still be protected from dry-out (Fig. 3). With the flow rate reduced, the tube friction loss is much smaller than the hydrostatic pressure effect. Although an increase in heat input still increases the friction loss, the increase is less than the reduction in hydrostatic pressure. With the tube total pressure loss now less than that of the average tube, the water flow rate to the tube will increase; this flow increase provides additional cooling that will help limit increases in tube metal temperatures. This is the desirable self-compensating characteristic wherein an excessively heated tube will experience an increase in flow that tends to limit over heating. Even though the furnace walls of a CFB will not require rifled tubing, evaporative tube surfaces that protrude into the furnace will be provided with normal rifling as, being heated from both sides, their heat fluxes are significantly higher than the one-side heated enclosure wall values. Compared with a SC PC boiler, a SC CFB boiler will operate with lower water mass flow rates that result in reduced pressure loss/pumping power.

PLANT PERFORMANCE

Full load heat and material balances were prepared for the nominal 800MWe plants. Both utilized a single reheat steam turbine and a single-pressure condenser operating at 2.0 inches Hg absolute, with feedwater heater trains consisting 3 HP and 5 LP units, and one deaerator. Table 2 summarizes the full load performance of the two plants. In order to clearly see the effects of higher steam temperatures, the CFB boilers have been designed to operate with essentially the same coal, limestone, air, and flue gas flow rates. The higher steam temperatures and pressures of the Case-3 plant result in both a higher plant efficiency and a higher power output. The Case-2 and Case-3 plants have net outputs of 740.5 MWe and 768.2MWe with efficiencies of 41.3% and 43.3% (HHV) respectively. These efficiencies are 15-20% higher than a comparable 36% efficient sub-critical pressure CFB plant. As a result, the USC plants operate with less coal flow and higher outputs than sub-critical plants and their emissions are proportionately reduced.

The operating conditions of the USC CFB boilers are also shown in Table 2. Both boilers operate with nominal 1560°F bed/furnace temperatures and combust 2.5% sulfur Illinois No. 6 coal with 20% excess air. The CFB operates with staged air injection to control NOx emissions, and limestone is injected into their furnaces at a Ca/S molar feed ratio of 2.4 to provide 96% sulfur capture. Table 3 lists the heat duties of the two boilers. The 1300°F Case-3 boiler, because of its higher feed water and combustion air inlet temperatures together with a ~4 % smaller steam flow, operates with a ~4% lower total duty; preheat, evaporation, and reheat duties are smaller, whereas, the total superheat duty is about 13 % higher.

Table 2 Operation Conditions

Case		**2**	**3**
Nominal USC Steam Temperatures		1,100F	1,300F
Plant Power Summary			
Gross Output, MWe		777.6	804.6
Auxiliary Load, Mwe*		37.2	36.4
Net Output, MWe		740.4	768.2
HHV Efficiency, %		41.3	43.3
Turbine Steam Conditions:			
Main Steam Flow Rate	Mlb/hr	4,514	4334
Main Steam Temperature	F	1,112	1292
Main Steam Pressure	psia	4,351	5076
Reheat Steam Flow Rate	Mlb/hr	3,867	3508
Reheat Steam Temperature	F	1,148	1328
Reheat Steam Pressure	psia	653	970
H&M Balance Parameters:			
Flow Rates:			
Combustion Air	Mlb/hr	5,446	5,389
Coal	Mlb/hr	524.5	518.8
Limestone	Mlb/hr	105.6	104.3
Total Ash	Mlb/hr	149.4	147.6
Stack Flue Gas	Mlb/hr	5,927	5,864
CO_2 in Flue Gas	Mlb/hr	1,250	1,236
CO_2 in Flue Gas	lb/MWeNet	1,688	1,607
Temperatures:			
Ambient	F	63	63
Combustion Air Entering CFB	F	535	625
CFB Furnace Exit	F	1,568	1,564
Flue Gas Entering Air Heater	F	625	800
Flue Gas Leaving Air Heater	F	267	268
Stack Flue Gas	F	286	287
CFB Bottom Ash	F	500	500
CFB Feedwater Inlet	F	553	629
Plant/CFB Excess Air	%	20	20
Steam Condenser Cooling Duty	MMBtu/hr	2,731	2,570
*Boiler Feed Pump Has Steam Turbine Drive			

Table 3 USC CFB Boiler Full Load Duties

Case		**2**	**3**
Nominal USC Steam Temperatures		1,100F	1,300F
Full Load Boiler Duties			
Preheat/Economizer	MMBtu/hr	461	330
Evaporation	MMBtu/hr	2032	1876
Superheat	MMBtu/hr	1710	1929
Reheat	MMBtu/hr	1214	1058
Total	MMBtu/hr	5417	5193

Table 4 lists the general features of the CFB boilers, all of which reflect conventional CFB design practices, and the 1300°F boiler is shown in side view in Fig. 4. Including silos, fans, and air heater, both nominal 800MWe units occupy an approximate 200 feet by 330 feet footprint and are top supported from structural steel approximately 250 feet above grade.

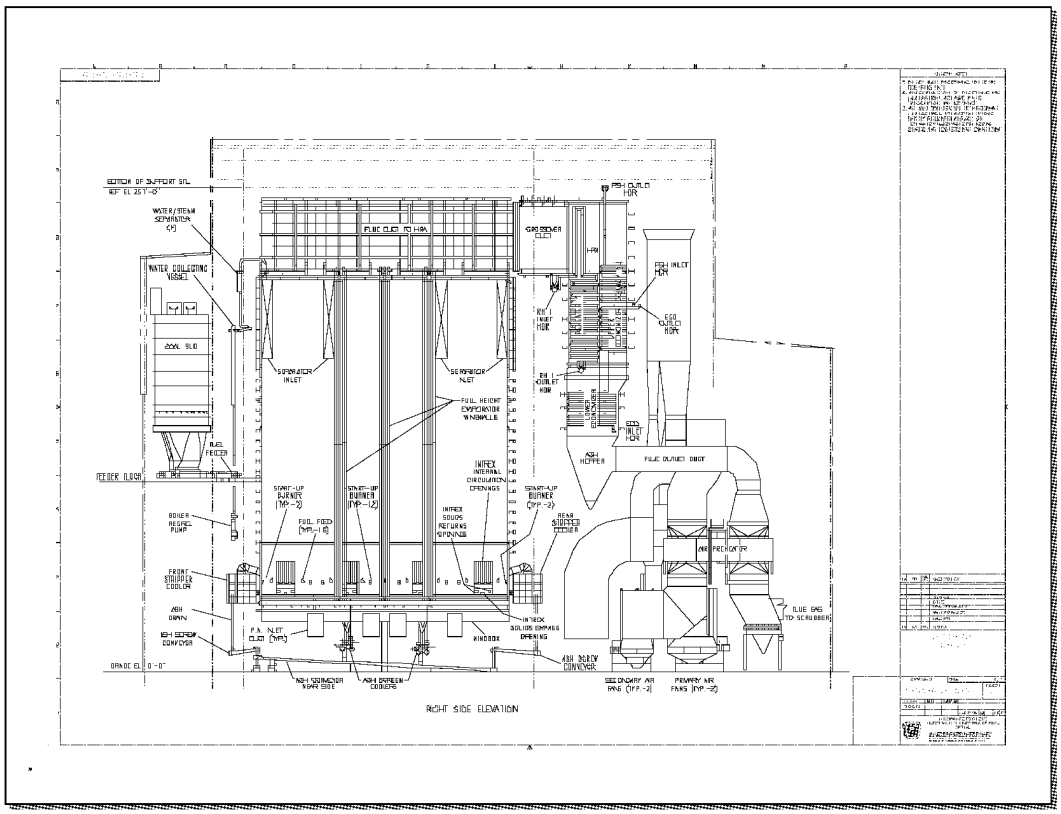

Fig. 4 Nominal 800 MWe Power Plant with 1300°F USC CFB Boiler – Side View

Table 4 USC CFB Boiler Features

Case		**2**	**3**
Nominal USC Steam Temperatures		1,100F	1,300F
Net Plant Output	MWe	740.4	768.2
Number of			
Coal Silos		4	4
Limestone Silos		1	1
Full Height Wing Walls		6	0
Pendant SHTR Panels0		1	0
Compact Separators		8	8
INTREXs		16	16
Btm Ash Stripper Coolers		2	2
Typeof Heat Recovery Area			ParallelPass ParallelPass

Table 5 presents CFB furnace dimensions along with INTREX™ arrangements and compares them to two other operating Foster Wheeler CFB boiler installations. As seen from the drawing and Tables 4 and 5, the nominal 800 MWe units reflect Foster Wheeler's modular building block approach to scale up and, as a result, are essentially conventional in configuration. The boilers operate with INTREX™ heat exchangers located under their Compact Solids Separators. The 800 MWe boilers have a large INTREX™ duty requirement and to keep their heat exchangers at commercially proven sizes they were divided into 16 units; to eliminate

equipment congestion along the sidewalls, they are provided in pairs in a stacked configuration, placed one above the other rather than side by side. Solids collected by the Compact Separators pass through the upper eight external circulating INTREX™ cells and, after cooling, cascade down into the lower eight INTREX™ cells for return to the furnace. The lower INTREX™ cells supplement their external solids circulation with internal solids circulation wherein nominal 1600°F solids flow directly into these cells from the furnace; this raises their hot side temperature and, with bed to steam log mean temperature differences (LMTD) increased, reduces their tube surface area requirements. Solids can also be bypassed around both upper and lower INTREX™ cells by controlling the aeration rate to their lift legs. As a result of the Figure 1 modular scale-up approach, the boilers reflect a conventional arrangement of proven components; although the approach of stacking of the INTREX™ heat exchangers is new, rather than side by side placement, there are no perceived development or scale-up issues.

Table 5 Comparison of Furnace Dimensions and INTREX™ Sizes

Operating Plant or Case	JEA 1-2	Turow 4-6	Case 2	Case 3
Nominal Gross Boiler Output, MWe	300	262	800	800
Steam Cycle Pressure	SubCrit	SubCrit	USC	USC
Furnace Dimensions, ft				
Depth	22.0	33.1	38.0	38.0
Width	85.3	72.2	129.7	129.7
Height	115.2	137.8	164.0	164.0
Solids Separators				
Total Number	3	4	8	8
Arrangement	In Line	Opposed	Opposed	Opposed
Number of INTREX Heat Exchangers	6	8	16	16

In a CFB boiler the air flow rate and, hence, fluidizing velocity varies with load/coal firing rate until a minimum, turn down design value is reached. Reduced flue gas velocities result in reduced solids circulation rates, reduced upper furnace temperatures, and reduced INTREX™ bed temperatures, especially in the lower level. To maintain both superheat and reheat temperatures with a cascading INTREX™ arrangement, the finishing superheater (SH-IVa/b) was placed in the upper INTREX™ level, and the intermediate superheater and finishing reheater were located in the lower level where internal circulation was used to augment their performance. By combining a stacked INTREX™ configuration with internal solids circulation and a parallel pass HRA, superheat and reheat temperatures can be maintained at full load values over the 45 to 100% load range.

As identified in Table 3 the move to 1300°F steam reduces the boiler's preheat, evaporation, and reheat duties but increases its superheat duty. The changes to the boiler to accommodate these new conditions are summarized as follows:

a) To reduce evaporation duty: Furnace height was reduced by approximately 6.5 feet; Full height evaporator wing-walls were removed; Less conductive, thicker refractory is used in the lower furnace;

b) To reduce economizer duty: Upper economizer surface increased (+18%), lower reduced (-63%); Air heater surface increased (+5%); adjustment required to achieve stack temperature with reduced economizer duty (shifts more heat into high temperature furnace solids circulation loop);

c) To increase superheat duty: In-furnace platen superheaters (10%) were added upstream of INTREX™ SH-III; A loop of tubing was added to upper INTREX™ SH-IV (now same number of tube elements in the upper and lower INTREX™ cells);

d) To meet reduced reheat duty: Convection reheater surface increased (+25%); addition required to compensate for reduced INTREX™ RH-III duty resulting from higher steam temperatures and increased INTREX™ RH-IV duty which lowers solids temperature to RH-III.

With these changes, the evaporator inlet water is sufficiently sub-cooled over the load range, maximum evaporator outlet superheat is about 86 Btu/lb, and full reheat steam temperature is maintained down to

approximately 45% load (1323°F at 40% load). These results show that a CFB boiler can achieve/operate with advanced USC steam conditions (5261 psig and 1300°F) in a conventional configuration provided materials, with sufficient strength, fire side corrosion resistance, and steam side oxidation resistance, are developed for these conditions.

SUMMARY

This study, as an example, has shown that CFB boilers can move to USC steam conditions in 800 MWe sizes; these units are expected to have performance and economics that are similar to those of comparably sized PC boilers while still offering greater fuel flexibility and ability of co-firing with biomass. In addition, their furnaces can be built from straight, self supporting, vertical tubes rather than complex spiral wall designs. Their lower pressure drop will enable them to operate with a self-compensating characteristic, that will limit tube overheating and failures. When advanced materials are developed with sufficient strength, outside corrosion resistance, and inside oxidation resistance, CFB boilers can accommodate steam temperatures as high as 1300°F while maintaining conventional, cost effective configurations.

REFERENCES

1. Arto Hotta, Kalle Nuortimo, Timo Eriksson, Juha Palonen, Sami Kokki, "CFB Technology Provides Solutions to combat Climate Change", VGB-KELI 2008 Conference, May 6-8, 2008, Hamburg, Germany
2. Z. Fan, S. Goidich, A. Robertson, S. Wu, "Ultra-Supercritical Pressure CFB Boiler Conceptual Design Study", final report (DE-FC26-03NT41737), Sept. 2006
3. Horst Hack, Arto Hotta, Ari Kettunen, Timo Eriksson, "Ultra-Supercritical CFB Technology to Meet the Challenge of Climate Change", Power-Gen 2008 Conference, Dec. 2-4, 2008, Orlando, USA
4. Z. Fan, S. Goidich, A. Robertson, "800 MWe CFB Boiler with 1300°F Supercritical Steam", The 33rd Int. Technical Conference on Coal Utilization & Fuel Systems, June 1-5, 2007, Clearwater, USA
5. Arto Hotta, "Features and Operation Performances of 460 MWe Supercritical CFB Boiler", The 20th FBC, Xi'an, China, May 18-20, 2009 (Keynote speech, Foster Wheeler Energia OY, Finland)

STRUCTURE AND PERFORMANCE OF A 600MWe SUPERCRITICAL CFB BOILER WITH WATER COOLED PANELS

Y. Li[1], L. Nie[2,3], X. K. Hu[2], G. X. Yue[1], W. K. Li[1], Y.X. Wu[1], J. F. Lu[1], D. F. Che[3]

1 Key Laboratory for Thermal Science and Power Engineering of Ministry of Education, Department of Thermal Engineering, Tsinghua University, Beijing, China
2 Dong Fang Boiler Group Co. Ltd., Zigong, China
3 Department of Thermal Engineering, School of Energy and Power Engineering, Xi'an Jiaotong University, Xi'an, China

Abstract: The circulating fluidized bed (CFB) combustion technology is one of the approved clean combustion technologies, and the power supply efficiency can be improved combining with the supercritical technology. A 600MWe supercritical CFB boiler is introduced in this paper. This boiler is designed based on the success of 300 MWe CFB boilers, which has a single furnace with three cyclones without external heat exchangers. There are twin furnaces and twin air distributors in the boiler. The water walls of the twin furnace above dense bed combines to a common fence wall with some channels to balance the pressure of the two furnaces. The smooth tubes are adopted in membrane water wall with mixing header. Six cyclones are located beside the furnace as well as six loopseals and six external heat exchangers. The hydrodynamic characteristic of water wall is available with the modeling prediction. And the performance of the 600MWe supercritical CFB boiler is also investigated.
Keywords: supercritical, 600MWe, CFB boiler, structure, performance

INTRODUCTION

Circulating fluidized bed (CFB) coal-fired boiler, a proven cost-effective and environmental-friendly way for coal utilization, is under rapid development. In order to increase its power supply efficiency of the CFB power plant, an important way is to increase its steam parameters. Supercritical CFB combines the advantages of low emission of traditional CFB and high efficiency of supercritical steam cycle (Ragner, et al., 2003), and have attracted much attention in these year (Ray, et al., 1996; Bursi, et al., 1999; Nowak, 1999). F The first supercritical CFB boiler of 460 MWe was designed by Foster Wheeler Company (FW), and will be put into operation soon in Poland (Kari, et al., 2003; Ilkka, et al., 2004; Stephen, et al., 2005).

More that ten 300MWe CFB boilers made with the technology introduced from Alstom or domestic have been put into operation in China (Yue, 2007; Guo et al., 2009). Based on the research results and application experience, the Chinese researchers and engineer have being working on the design of supercritical CFB (SCFB) boilers (e.g., Wu et al., 2004; Lu et al., 2007). The first SCFB boiler being demonstrated in China is of 600MWe. The project is financially supported by the national Ministry of Science and Technology (MOST).

THE DESIGN PRINCIPAL

A CFB boiler is obviously different from a pulverized coal fired boiler on the fuel, combustion method and heat flux distribution, etc. In furnace desulphurization using limestone is suitable for a CFB boiler.

Based on CFB boiler design theory (Yue, et al., 2005; Yue, 2007) and engineering experience, the fluidization and circulating quality could be determined by two key parameters: ash circulating rate G_s and fluidizing velocity u_f. In the CFB design, it is also important to consider the erosion of water wall in the furnace. If u_f is lower than a critical value for a certain coal, the erosion of water walls decreases effectively, as shown in Fig. 1. Furthermore, the supercritical boiler runs under both the supercritical and the sub-critical conditions during the application. Thus, the hydrodynamic stability and the thermal deviation of water wall must be considered carefully when the supercritical boiler is designed.

A once-through 600MWe SCFB boiler is designed according to the characteristic of the local fuel. The rated steam output of this boiler is 1900 t/h, with the main steam of 25.5 MPa in pressure and 571 °C in temperature, and the reheat steam 569°C in temperature. Once-through vertical membrane water walls are arranged in the furnace. Twin furnaces are combined to ensure the secondary air jet penetration depth. Shown in Fig. 2, six cyclones as well as six loopseals, six external heat exchangers (EHEs) under them are installed beside the furnace, three sets on each side. The secondary superheater and high temperature reheater are immersed in the EHEs, while the final superheater is the wing wall type hanging in the upper furnace.

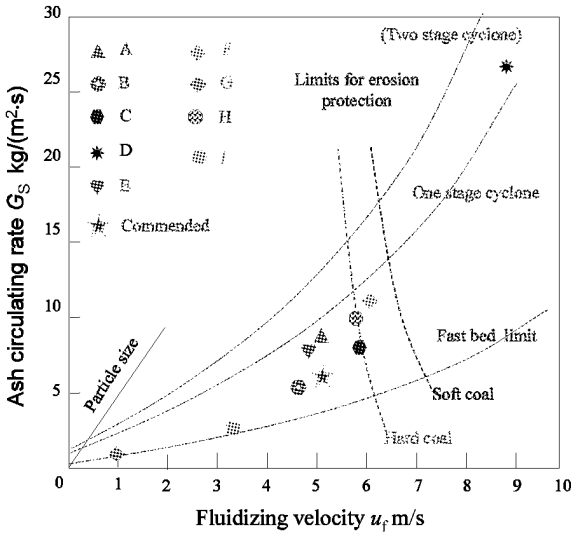

Fig. 1 State specification by several major CFB boiler manufacturers (Yue, et al., 2005)

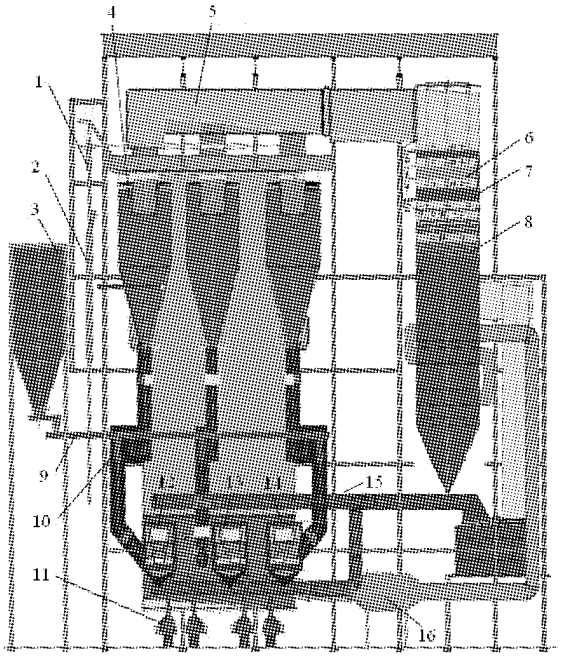

Fig. 2 Schematic diagram of the 600MWe supercritical CFB boiler

1-Steam-water separator	2-Water vessel	3-Coal bunker
4-Cyclone separator	5–Gas pass	6-Primary superheater
7-Primary reheater	8-Economizer	9-Coal feeder
10. Loopseal.	11-Bottom ash cooler	12-EHE (RH II)
13-EHE (SH II_1)	14-EHE (SH II_2)	15-Secondary air
16–Hot gas generator		

The fuel gas out of cyclones is collected, and introduced from two sides into the secondary pass. The primary superheater and the low temperature reheater are installed in line in the heat recover pass, which is packed by steam cooled membrane wall. Below it, the economizer and the air preheater are installed. During the period of boiler start-up and shut-down, a circulation pump is used to ensure minimum amount of water flow through the evaporator. When the boiler load exceeds 35% THA (Turbine Heat Acceptance), the steam exiting the evaporators is slightly superheated. At that moment, the circulation system can be shut down and the boiler is in once-through operation mode. In order to optimize the distribution of the water flow rate in the water walls, smooth tubes and the end into the inlet headers are carefully selected in size.

The solid particles escaping from the furnace with gas are collected by the high efficiency cyclones. Some of the particles are returned into the furnace directly through loopseals, others are introduced into EHEs to rise the steam temperature. Four EHEs are used for the secondary superheater. The secondary superheater is divided

into two parts (SHII_1 and SHII_2), between which a spraying desuperheater is designed. The material flow rate from loopseals into these EHEs can be controlled to accommodate the bed temperature of the furnace. Two EHEs are used for the high temperature reheater (RH II). The reheat steam temperature is controlled by the material flow rate from loopseal into these two EHEs. The water - steam system is shown in Fig. 3.

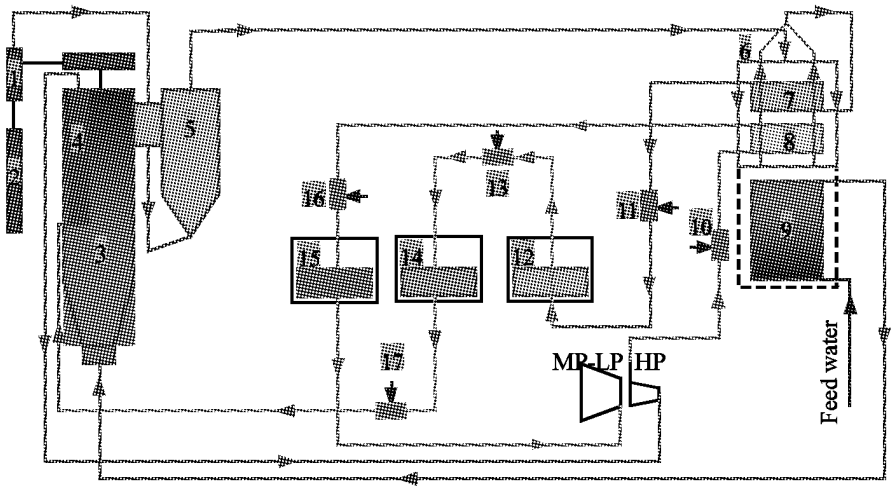

Fig. 3 Water - steam system of the 600 MWe supercritical CFB boiler

1-Steam-water separator
2-Water vessel
3-Furnace
4-EHE (SH III)
5-Cyclone
6-Steam cooled membrane
7-Primary superheater
8-low temperature reheater
9-Economizer
10-Desuperheater for reheater emergency
11-The first stage desuperheater
12-EHE for SH II_1
13-The second stage desuperheater
14-EHE for SH II_2
15-EHE for high temperature reheater
16-Desuperheater for reheater
17-The third stage desuperheater

THE MAIN STRUCTURES

Furnace

The main loop of the 600MWe CFB boiler is based on the success of the 300MWe CFB (Guo, et al., 2009). In the 300MWe CFB boiler, there is a single furnace and three cyclones in line without EHE. Shown in Fig. 4, the furnace of a 600MWe CFB boiler is regarded as the combination of the furnaces of two 300MWe CFB boilers, with a common water wall between. The bottom of the 600MWe furnace is made of two individual parts as same as that one of 300MWe CFB boiler. With such structure, the mixing of the secondary air with the solid particles in the furnace is improved. The water walls between the two furnaces are combined into the common header. In order to hang the bottoms of the furnace and the common header, a common water wall from the common header to the roof of the furnace is designed. There are some openings on the common water wall, through which the flue gas can be exchange and pressure balance between the two furnaces is realized. The hydrodynamic of the boiler was investigated by recent studies and some are based on the available heat flux model(Lu, et al., 2007; Li, et al., 2008a , Li, et al., 2009a; Li, et al., 2009b).

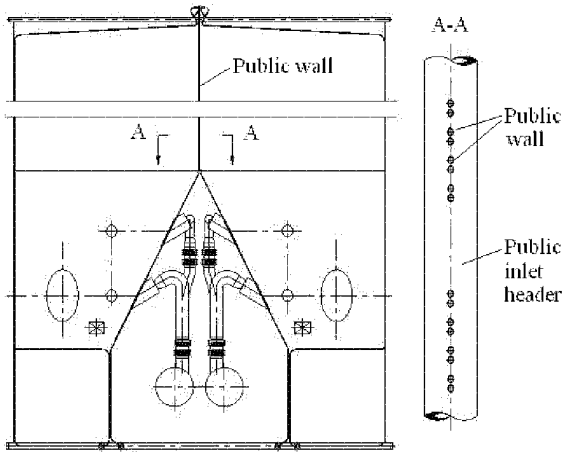

Fig. 4 Simplified structure of the furnace

The primary air heated by the air preheater, as well as the secondary air, is introduced to the furnace through the primary air wind box located below the bed. It is used to fluidize the material and fuel particles in the bed. And the fluidization air for the EHEs and the loopseals comes from the high pressure air fan. There are twelve coal feeders. Six coal feeders and six limestone feeders are connected with the return pipes through which the material collected by the cyclones are sent into furnace directly. The other six coal feeders are connected with the return pipes through which the low temperature material from EHEs are sent into the

furnace. Eight bottom ash coolers are symmetrically arranged at the both sides of the furnace.

Cyclone separators

As mentioned above, the performance of the cyclone is proved in the 300MWe CFB (Guo, et al. 2009). The cyclones used in the 600MWe SCFB boiler are of the same size as that used in 300MWe CFB boilers. They are with high collection efficiency and reasonable pressure drop. For this supercritical 600MWe CFB boiler, the six cyclone separators are arranged on the both sides of the furnace, three cyclones on each sides. After cleaned by the cyclones, the flue gas flows out from the cyclone into the back pass through the horizontal flue gas pass.

If the cyclones are arranged appropriately, the solid particle flow stream in each cyclone is rather even. Obviously, the three cyclones location is unsymmetrical. Thus the position of the furnace exit is a key. The experimental studies in the cold model show that for the 300 MWe sub-critical CFB boilers developed by Dongfang Boiler Company, the pressure drop of each cyclone in three parts of the furnace is much closed. The gas-solid flow is uniform, and the unbalance of the suspension density is lower (Yang, et al, 2009). It is also improved by the operation of the 300MWe CFB boilers. Consequently, the cyclone and its location design in the supercritical 600MWe CFB boiler are reliable.

External heat exchangers

The external heat exchanger (EHE) in large scale CFB boiler is necessary to arrange the high temperature heating surfaces. In this 600MWe CFB boiler, six EHEs are arranged at both sides of the furnace with the high temperature reheater in two EHEs and secondary superheater in four EHEs. The EHEs are the most important equipments to control the bed and the reheater steam temperature. By adjusting the flow rate of the circulating material passed through the EHEs, the heat absorbed by the immersed tubes in them can be changed. The size of EHEs scales up with the increasing of the boiler capacity. But the heat absorption percentage by the EHEs should be limited.

THE PERFORMANCE PREDICTION

It is necessary to study the performance of the boiler, especially its hydrodynamic characteristics and the flow deviation of the water walls in the furnace. Based on the hydrodynamic model, it is found that the outlet temperature deviation of water walls is small at varies load. The smooth tubes and inlet header with special size introducing pipes can be used in the 600 MWe supercritical CFB boiler, with which the water walls is safe and the hydrodynamic characteristics is stable.(Li et al., 2008; Li et al., 2009a)

The variation of the bed temperature and the average heat transfer coefficient of water wall in the furnace are predicted. Figure 5 shows that the bed temperature and the flow rate of gas solid two phase flow at the furnace outlet decrease with the decreasing of the load. The material circulating rate declines with the decreasing of the load, leading to the increasing of the combustion fraction in the lower furnace and the decreasing of the average heat transfer coefficient of water walls, as shown in Fig. 6. At the same time, the low temperature material from the EHEs to the furnace decrease with the heat absorption of the EHEs at lower loads. As a result, the bed temperature reduces with less extent.

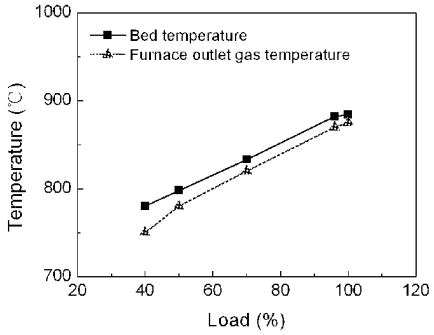

Fig. 5 Temperature of the bed and the gas solid two phase at the furnace outlet at different loads

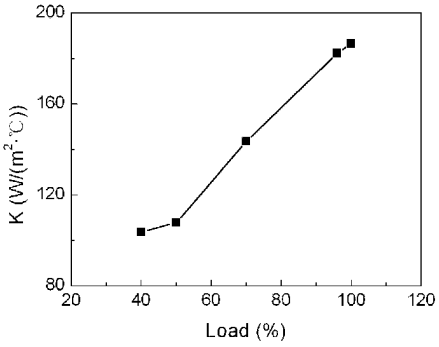

Fig. 6 Average total heat transfer coefficient of water walls at different loads

Temperature at the furnace outlet is affected by the heat absorption in furnace. The fluidization velocity and the circulating solid rate decrease with decreasing of the load. As a result, the suspension solid density decreases, and thereby the total heat transfer coefficient decreases. Consequently, the temperature at the furnace outlet decreases slightly with the decreasing of the load.

The temperature of the reheater steam and the bed is controlled by EHEs. The heat absorbing fraction of different heating surface at different loads is shown in Fig. 7. The flow rate of the circulating material passed through EHEs and the heat transfer coefficient of the immersed tubes in EHEs are the main factors affecting the material temperature at the outlet of EHEs. The fluidizing velocity affects strongly heat transfer coefficient of these immersed tubes. The heat absorbed by the immersed tubes in EHEs decreases with the decreasing of the load. Moreover, in case the load is lower than 50%, the heat absorption fraction in EHE should be higher due to the steam temperature control, as shown in Fig. 8.

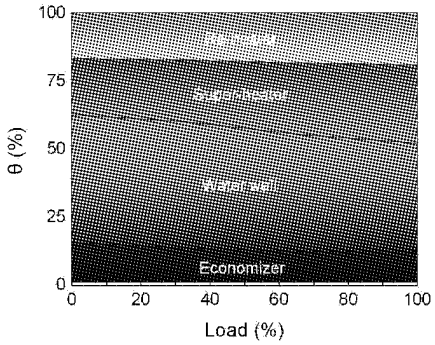

Fig. 7 Heat absorption fraction of different heating surfaces at different loads

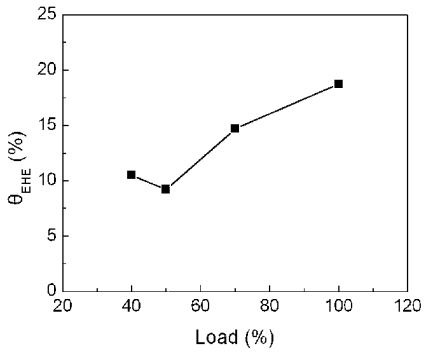

Fig. 8 Heat absorption fraction of EHE at different loads

CONCLUDING REMARKS

Supercritical CFB boiler combines the advantages of high efficiency of supercritical steam cycle and low emission of CFB combustion technology. The known knowledge shows that the SCFB boiler is easier in operation than the supercritical pulverized coal-fired one. It is expected the development of SCFB will be greatly faster shortly after the first 460MWe SCFB boiler designed by FW is put into operation. It is also expected that the 600MWe SCFB boiler developed in China will be successful. Since the boiler is based on the vast fundamental studies and application experience of design, commissioning, erection and operation for numerous sub-critical CFB boilers, especially the 300MWe ones in China. The structure of a 600 MWe SCFB boiler is reasonable, and the predicted performance is excellent. Validation of the design will be conducted in the near future after the SCFB boiler is put into commissioning, very possibly by the end of 2011.

ACKNOWLEDGEMENTS

Financial support by Key Project of the National Eleventh-Five Year Research Program of China (2006BAA03B02) and High Technology R&D (863) (2007AA05Z303) are gratefully acknowledged.

REFERENCES

Bursi, J.M., Lafanechere, L., Jestin, L.: Proceeding of 5th Inter. Conf. on CFB Technology. Germany, (1999), pp.913-916.
Guo, Q., Zheng, X.S., Zhou, Q., et al.: Proceeding of 20th Inter. Conf. on FBC. Xi'an: (2009).
Ilkka, V., Rafał, P.: Power-Gen Europe, (2004) Barcelona, Spain.
Kari, M., Timo, T., Jouni, M., et al.: Proceeding of the 17th Inter. Conf. on FBC. USA, (2003).
Li, Y., Li, W,K., Wu, Y,X., et al.: Proceedings of the CSEE, 28(2008), pp.1-5.
Li, Y., Li, W.K., Wu, Y.X., et al.: J of Tsinghua Univ (Sci & Tech), 49(2009a), pp,244-248.
Li, Y., Li, W.K., Wu, Y.X., et al.: Proceedings of the 20th Inter. Conf. on FBC. Xi'an: (2009b).
Lu, J.F., Yu, L., Yue, G.X., et al.: Journal of Power Engineering, 27(2007a), pp.336-340.
Lu, J.F., Yu, L., Zhang, Y.J., et al.: Journal of Power Engineering, 27(2007b), pp.497-501.
Nowak, W.B.Z., Laskawiec, J.: Proceedings of the 15th Inter. Conf. on FBC. Savannah: (1999), No. 0122.
Ragner, L., Rudolf, K., Pertti, K., et al.: Power-Gen Europe, (2003) Dusseldorf, Germany.
Ray, A., Bowman, H.F.: ASME J of Dynamic Systems, Measurement and Control, 13(1996), pp.332-339.
Stephen, J.G., Song, W., Zhen, F., et al.: Inter. Pittsburgh Coal Conference. (2005) Pittsburgh PA, USA.
Wu, Y.X., Lu, J.F., Zhang, J.S., et al.: Boiler technology, 35(2004), pp.1-5.
Yang, S., Yang, H.R., Zhang, H.: Proceedings of the 20th Inter. Conf. on FBC. Xi'an: (2009).
Yue G.X.: Proceeding of 1st conference on CFBC of China. Hannan, (2007): pp.2-30.
Yue, G..X., Lu, J.F., Zhang, H., et al.: Proceeding of 18th Inter. Conf. on FBC. Toronto: (2005) pp.135-146.

STARTUP, COMMISSIONING AND OPERATION OF FENYI 100MW CFB BOILER

Zhiwei Wang[1], Wugao Yu[2], Shi Bo[2]

1 Thermal Power Research Institute, Xi'an, 710032, China
2 Jiangxi Fenyi Power Plant, Fenyi, 430070, China

Abstract: The first 100MW CFB boiler, designed by the Thermal Power Research Institute and manufactured by Harbin Boiler Company Limited, has been successfully running in Jiangxi Fenyi Power Plant since 2003. Local high ash content anthracite and lean coal that are very difficult to burn out are used in the 100 MW CFB boiler. The results of the 100MW CFB boiler shows that the CFB boiler can run in 30% MCR and startup with two under bed burners, and the boiler efficiency higher than 88% can be got after the combustion modification test. The CFB boiler can be operated with full load and reaches design parameters. The emissions of NO, N_2O and CO are less than 70mg/m^3, 30mg/m^3, and 125mg/m^3, respectively, and SO_2 less than 400mg/m^3 after limestone injection. The bottom ash temperature from bed ash coolers is less than 120℃ after its modification. Coal blockage at the coal storage silo is the main problem influencing the CFB boiler continuous operation. The running experiences for 5 years proved that the CFB boiler performance is successful, and the results were applied in 210 MW and 330 MW CFB Boiler design of Fenyi Power Plant.

Key words: CFB boiler, commissioning, combustion efficiency

INTRODUCTION

To promote the utilization of the circulating fluidized bed (CFB) boiler in Chinese Clean Coal Combustion Project, the first 100MW CFB boiler with Chinese technology was installed in Jiangxi Fenyi Power Plant. As the State Economic and Trade Commission Demonstration Program, the Jiangxi Fenyi 100MW CFB boiler was approved in 1999, and its construction began in December 2000. Its initial startup was in November 2002, and it passed 72 + 24 hours trial operation on June 19, 2003 after near 6 moths alteration and optimization, with total accumulated operation time of 31703.4 hours and 26.16557×10^8 kWh by June 2008.

It is the first 100MW CFB boiler, which was designed by the Thermal Power Research Institute and manufactured by the Harbin Boiler Company Limited (Wang Zhiwei, Sun Xianbin et al. 2005; Lang Liping, 2003), reference with the operation experience of the Neijiang 100MW CFB boiler, especially taken in and overcoming the problems from the Neijiang 100MW CFB boiler.

The side view of Jiangxi Fenyi 100MW CFB boiler is shown in Fig. 1 and Fig. 2.

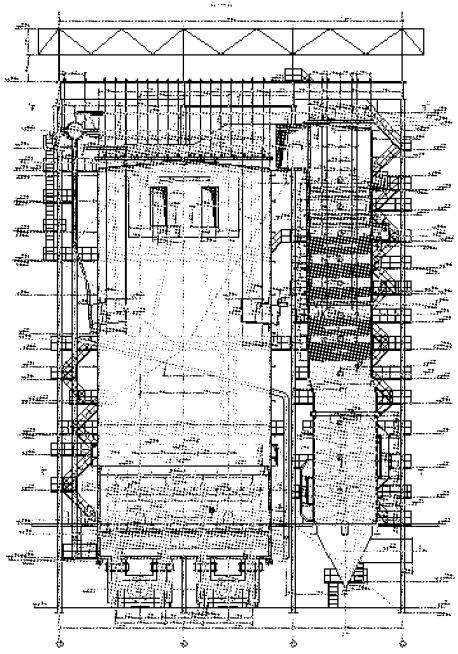

Fig. 1 Side view of 100MW CFB boiler

Fig. 2 View of 100MW CFB boiler in site

The design and check coal features is in Table 1.

Table 1 Ultimate and proximate analysis of coals

Item	Symbol	unit	Design coal	Check coal		Site coal
			Xicha	Pingxiang	Daguangshan	
Total moisture	M_t	%	3.2	6.78	4.4	6.0
Moisture(Air dried)	M_{ad}	%	2.79	0.63	3.40	1.59
Ash(as received)	A_{ar}	%	30.82	36.95	29.56	46.69
High heat value	$Q_{gr,var}$	MJ/kg	21.71	18.89	21.76	15.26
Low heat value	$Q_{net,v,ar}$	MJ/kg	21.39	18.21	21.57	14.82
Carbon(as received)	C_{ar}	%	61.71	48.51	62.28	40.25
Hydrogen(as received)	H_{ar}	%	1.20	2.57	0.43	1.49
Oxygen(as received)	O_{ar}	%	1.92	3.78	1.40	4.22
Nitrogen(as received)	N_{ar}	%	0.43	0.77	0.13	0.53
Sulfur(as received)	$S_{t,ar}$	%	0.72	0.64	1.80	0.82
Volatile(dried ash free)	V_{daf}	%	6.10	21.02	4.29	15.45
Deformation temperature	DT	℃	1485	1465	1160	>1500
Softening temperature	ST	℃	>1500	>1500	1340	>1500
Fusion temperature	FT	℃	>1500	>1500	1410	>1500

The four insulation cyclones are arranged on the two sides of the furnace, two on each side. Though two cyclones is enough safe for 100MW CFB boilers, the four cyclones structure of Fenyi 100MW CFB boiler are used and aimed at the larger CFB development of the 210MW and 330 MW CFB boiler, which were built in Fenyi Power Plant.

There is a lean oxygen zone in the center of the CFB furnace in Neijiang 100MW CFB boiler, the same phenomenon as reported and analyzed (Wang Zhiwei and Sun Baohong, 2001; Yu Long, et al. 2004). To promote the secondary air mixing ability and to increase oxygen concentration in the center of the furnace, the width of the furnace is 5.81m and the ratio of width to depth is 2.8, intend to assure the more secondary air mixing and higher combustion efficiency.

The design coal is Xicha anthracite, in order to increase stable operation under low load, some methods were carefully taken in design, such as increasing furnace height to 35.716m, designed furnace temperature 920℃, higher secondary air velocity more than 100 m/s (B-MCR), and low bed velocity of 5m/s (B-MCR).

OPERATION

Startup

During the startup, only the two under bed burner were used, because of the deformation of the four upper bed burners. The startup oil consumption decreased from 50 tons to 18 tons, with the optimization of turbine system and cold mode regulation (Wang Zhiwei1 and Zhao Min et al. 2006; Zhao min, 2003). The startup furnace temperature profiles are shown in Fig. 3.

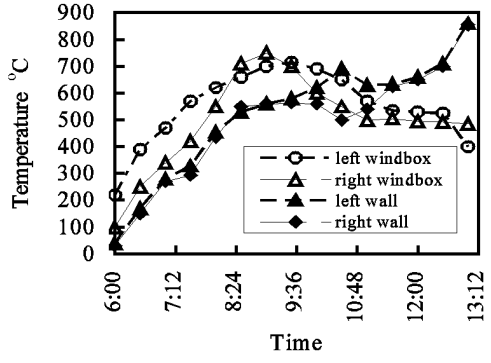

Fig. 3 Temperature profiles of the boiler startup

Boiler load

The design coal is Xicha anthracite, but in operation, the boiler uses local high ash content anthracite. The particle diameter analysis of coal after crash and bottom ash is in Table 2.

Table 2 Particle diameter analysis of coal after crash and bed ash

Diameter/μm	Accumulated mass/%	
	Local anthracite	bottom ash
25	100	100
87.5	99.58	96.17
139.5	91.77	80.62
217	90.81	77.1
495	84.79	66.29
855	69.63	46.27
2000	62.53	35.59
4000	36.28	13.68
5850	21.48	6.38
8350	19.00	5.10
11500	9.31	1.93
13000	1.67	0.38

Though the coal used on the boiler is quite different from the design coal (see table2), boiler can be continuously operated with 30% MCR without utilization of startup burners. The main steam temperature and pressure satisfy the design aims and full load can be got, but the size distribution of site coal is very difficulty to control the design sieved size distribution because of the coal variety, which caused some troubles for the bottom ash cooler. The high total moisture in coal sometime caused the blockage at the coal storage silo.

The boiler load can keep on within the range of ±2% when the coal is stable. Figure 4 is the boiler load profile on November 7, 2003, the load curve is preordered by power net.

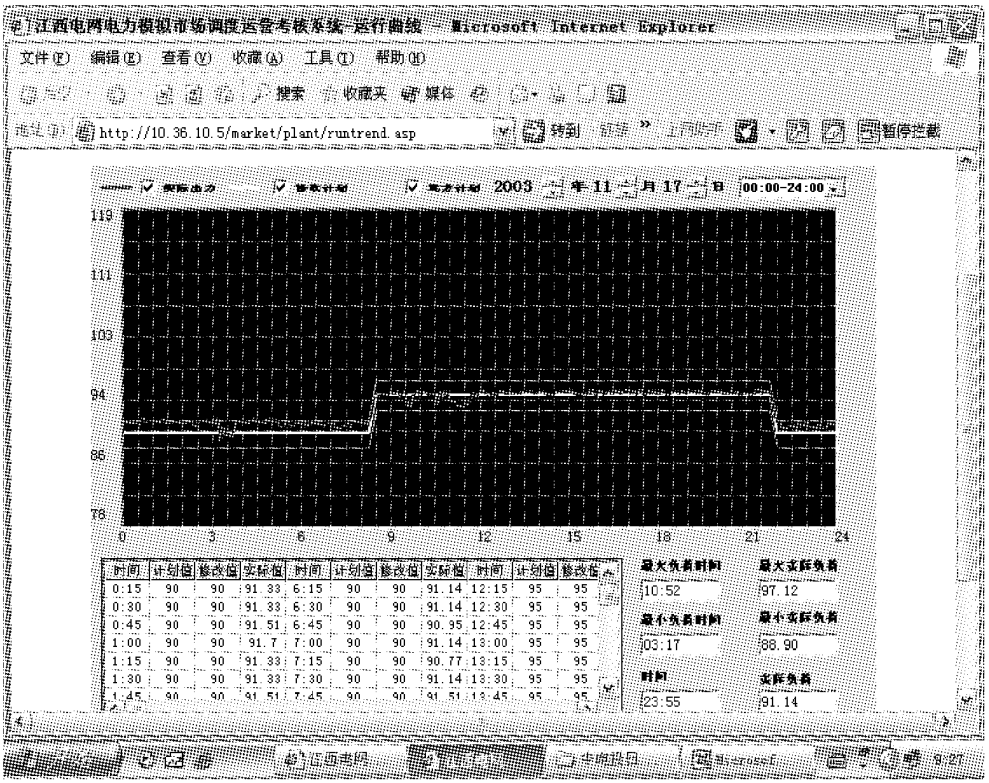

Fig. 4 Load profile of the boiler

Bed material balance

The bed material balance is one of the CFB boiler normal operation bases (Fen Junkai ,2000; Wang Zhiwei, 2003), and the CFB boiler run needs the basic balance of bed material or the least ash quantity (Wang Zhiwei, 2002). Through the analysis of bed material balance in CFB boiler, the ash content (Aar=46.69%) in the coal is enough to maintain the bed material balance for normal operation. The typical particle analysis of coal, bed ash, circulating ash and fly ash are shown in Fig. 5 and Fig. 6 (after combustion modification). The particle diameter of circulating ash is mainly in the range 0-0.3mm, with d_{50} 0.12mm.

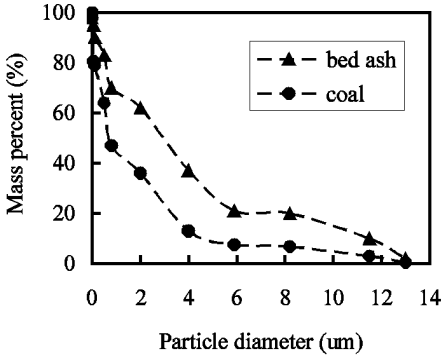

Fig. 5 Particle diameters of bed ash and coal

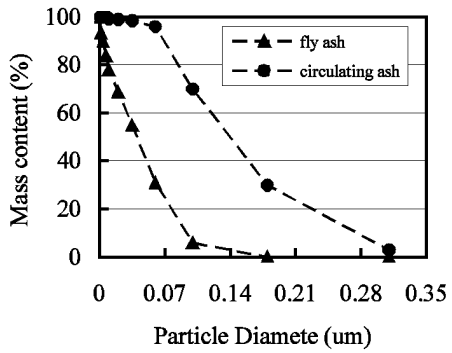

Fig. 6 Particle diameters of fly ash and circulating ash

The pressure profile is an important index to judge the suspension density of the furnace, and the upper suspension density should be a key for CFB material balance (Wang Zhiwei and Wu Xiaolin et al. 2002). To maintain the bed material balance, it is necessary to modify the operation parameters under the basis of cold mode test, and the technical level of the boiler operators is also very important for its normal operation. The furnace pressure profile under some loads is shown in Fig. 7 after the combustion modification (Wang Zhiwei and Shi Bo et al. 2004), the pressure more than 1200 Pa under 100MW load at 8.6 m level is proposed.

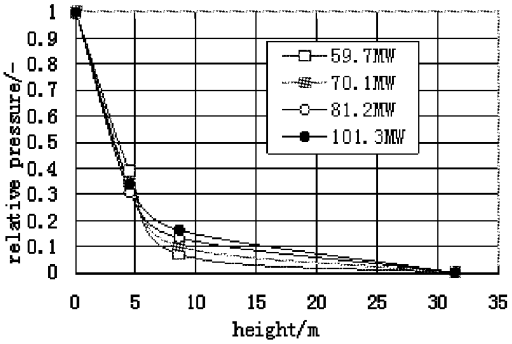

Fig. 7 Furnace pressure profile under different load

Control of the combustible content in the fly ash

In its initial operation, the combustible content in the fly ash was higher than 20% and the boiler efficiency was lower than 83%. Through primary modification, the d_{50} of the fly ash decreased to some extent, and the concentration of the combustible content in the fly ash decreased significantly, as in Fig. 8 and Fig. 9. The average combustible content in the fly ash is less than 9%, and the boiler efficiency is higher than 88%. It is believed that the combustible content in the fly ash can be reduced through addition modification.

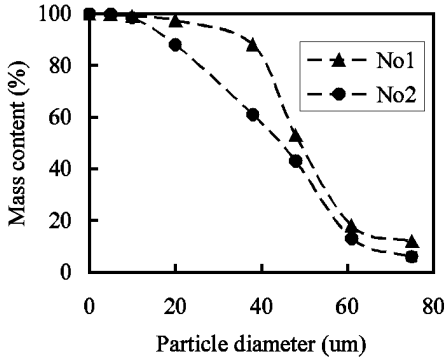

Fig. 8 Fly ash particle diameters

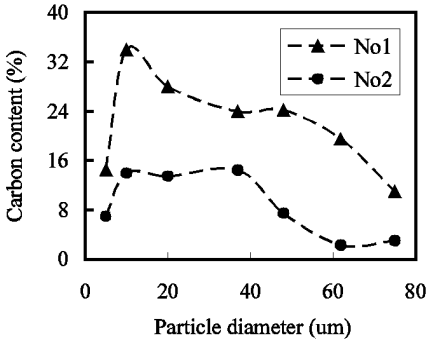

Fig. 9 Carbon content in fly ash

5 years running statistic

The 100 MW CFB boiler run since 2003, the main statistic is listed in Table 3.

Table 3 The main statistic for 5 years

Time	Power quantity	Self use electricity	Coal rate	Net Coal rate	Run time
year	$\times 10^4$ kWh	%	g/kWh	g/kWh	hour
2003	27380.81	10.62	399.46	446.93	3922.2
2004	53137.73	10.85	396.73	444.99	5672.883
2005	55430.07	10.77	390.58	437.71	6688.23
2006	55528	10.705	381.01	424.95	6852.2
2007	55449.2832	11.15	378.31	425.78	6647.15
To 2008.6.30	14729.789	12.922	381.495	438.108	1920.773

The maximum continual running time is 2600.78 hours (from 2006-10-22 16:58 to 2007-2-8 1:45). Two whole maintain were in 2004-5-8 and 2008-5-1, middle maintain happens every year.

Self use electricity increases from 2007 since some auxiliary equipment for the 210 MW CFB boiler uses the same communal system. The high self use electricity is a problem for larger CFB boiler compared with the pulverized coal boiler, how to decrease the self use electricity should be researched carefully.

AUXILIARY SYSTEMS

A lot of problem happened at Auxiliary systems on the early running (Sun Tao, 2006), the bottom ash cooler and the blockage of the coal silo were main problem to solve.

Because of the high ash content in the coal used in the 100MW CFB boiler, and the bottom ash removal rate is higher than 20t/h, which is much higher than the design max. value of 9t/h. In the beginning of the boiler commissioning, the temperature of the bed ash leaving from the cooler was high than 300℃, resulting in the broken of ash scraper. In addition, because of the frame problem of the cooler and the limited heating area of the cooler, the leakage of tube in the cooler occurred occasionally, and the bottom ash removal depended mainly by labors.

After the modification of bottom ash cooler (Sun Tao, 2005), it is in normal running, and the bottom ash temperature can be controlled under 120℃. There are four bottom ash coolers as designed, and the boiler can be operated with full load with two bottom ash coolers working.

Because the coal often changes in China and it is very difficult to control the coal particle size, the fluidized bottom ash cooler with wind and water is unfit. The rotator bottom ash coolers are used in the 210 MW CFB boiler of Fenyi power plant.

In the initial operating of the 100MW CFB boiler, the blockage of the coal silo occurred occasionally, which was the main problem influencing the boiler operation by now. To solve this problem, a vibrator and loosing device were installed in the coal silo, with a new transmission silo under the main coal silo. After modification, the coal silo blockage occurred much seldom (Sun Tao, 2004).

The coal does not pass through screen between the primary crusher and the secondary crusher, resulting in serious wearing of the secondary crusher. While the ash content in the coal increases, the coal particle diameter usually exceeds the design value, often leading to combustion and ash discharge problems.

The bottom ash is mechanically conveyed to the ash storage silo, the bottom ash conveying system includes scraper and clamshell unloader. Though the problem of clamshell is the main reason influencing the bottom ash system operation, which is successful in Jiangxi Fenyi 100MW CFB boiler compared with the pneumatically conveying equipment. Because the coal size usually exceeds the design value, leading to large bed ash particles, it is very difficult and serious tube abrasion to convey bed ash pneumatically. And direct conveying of bottom ash to discharge silo with the scrapper or clamshell unloader is recommended in China.

EMISSIONS

The emissions from Jiangxi Fenyi 100MW CFB boiler were tested and without limestone addition, the concentrations of NO, N_2O and CO are less than 70mg/m^3, 30mg/m^3, and 125mg/m^3, respectively, and SO_2 less than 2900mg/m^3 (dry, 6% O_2), and SO_2 less than 400mg/m^3 after limestone addition.

The N_2O concentration in the flue gas is very low, which might result from low fuel nitrogen content in the coal and the high furnace temperature which is more than 920℃.

The NO and CO concentrations in the flue gas are very low; as a result, increasing in furnace temperature to some extent is important for maintaining high boiler efficiency, stable operation and decreasing N_2O emissions.

CONCLUSIONS

The operation of the first 100MW CFB boiler with the Chinese technology indicates that it is successfully designed and manufactured. The boiler parameters satisfy the design value. It also provides experience for designing and constructing 210MW and 330MW CFB boiler.

REFERENCES

Fen Junkai: Factors to Keep Circulating Fluidized-Bed Combustion Boilers in Normal Operation. Energy Infor mation and Research. 16-1 (2000), pp. 1-6.

Lang Liping, Sun Xianbing, Wang Zhiwei: Design of Jiangxi Fenyi 410 t/h CFB Boiler. Boiler Manufacturing. -1(2003), pp. 10-12.

Sun Tao, Zhu He ping, Shi Bo et al.: Perfection Measures for Coal Feed System of 100MW CFB Boiler in Fenyi Power Plant. Thermal Power Generarion. 33-11(2004), pp. 77-78.

Sun Tao, Shi Bo, Zhu Heping, etal.: The System Transforms of Fen Yi Power Plant 100 MW CFBB Bottom Ash Cooler. Boiler Technology. 36-4(2005), pp. 65-67.

Sun Tao, Shi bo, Wang Zhiwei: Introduction of 100 MW CFB Boiler Operation in Fenyi Power Plant. Boiler Manufacturing. -1(2006), pp. 7-9.

Wang Zhiwei, Sun Baohong: Analys is of Carbon Monoxide Combustion in Circulating Fluidized Bed Boiler. Power Engineering, 21-5(2001), pp: 1396-1399.

Wang Zhiwei, Wu Xiaolin, Leng Hongchuan: Analysis of Material Distribution Characteristics about Circulating Fluidized Bed Boiler. Cogeneration Power Technology. -3(2002), pp: 7-9, 17.

Wang Zhiwei: Study on bed material balance of CFB boiler. Cogeneration Power Technology. -4(2002), pp: 9-12.

Wang Zhiwei: Balancing Analysis of Charges of Circulating Fluidized Bed Boilers. Power Equipment. -3(2003), pp. 20-23, 35.

Wang Zhiwei, Shi Bo, Sun Tao, etal.: The research on the pressure distribution in 100MW CFB boiler furnace. Power System Engineering. 20-6(2004), pp. 15-16.

Wang Zhiwei, Sun Xianbin, Zhang Min, etal.: Design of Fenyi 100MW CFB boiler. Proceedings of 8th International Conference on Circulating Fluidized Beds. Hangzhou, China, May 10-13, 2005, pp. 667-674.

Wang Zhiwei1, Zhao Min, Yu Wugao: Introduction on the hot igniting of 100MW CFB boiler Cogeneration Power Technology. -1(2006), pp: 6-7.

Yu Long, Li Junfu, Wang Zhiwei, etal.: Prospective Research Progress of Combustion Technology for Circulating Fluidized Beds. Journal of Engineering for Thermal Energy and Power. 19-4(2004), pp. 336-342.

Zhao min, Wang Zhiwei, Zou Shengfa, etal.: Introduction on the cold igniting of 100MW CFB boiler. Boiler Manufacturing. -4(2003), pp. 37-38.

DESIGN AND OPERATION OF LARGE SIZE CIRCULATING FLUIDIZED BED BOILER FIRED SLURRY AND GANGUE

Zhang Man[1,2], Bie Rushan[1], Wang Fengjun[2]

1 School Of Energy Science and Engineering, Harbin Institute Of Technology, Harbin, China
2 Design department, Harbin Boiler Company Limited, Harbin, China

Abstract: The way which burns slurry and gangue to generate electricity and provide heat has been always desired. If mixture of slurry and gangue are burnt by conventional combustion technology, it is difficult to be satisfied., but for circulating fluidized bed(CFB) boiler, it is flexible for fuels and it is easy to desulfurize and DeNox in the furnace of the boiler. There are lots of advantages to burning the mixture of slurry and gangue in CFB boiler. This technology has been researched and practiced for many years, it is mature now and has been used widely, by now, 50MW, 135MW and 300MW CFB boiler which burn the mixture of slurry and gangue have already been operated in China. In the paper, slurry characteristic and conveying is described, the design and operation of boilers mentioned above will be also introduced in detail.

Keywords: Circulating Fluidized Bed Boiler, slurry , gangue， mix combustion, application

INTRODUCTION

Both of the slurry and gangue are waste of washing coal, but they are different on physical configuration and characteristic. The gangue particle size is large, it is easy to dry and convey, and its configuration is sT when it is accumulated. The slurry is fine, high moisture, high viscosity and it is difficult to convey, it runs out if it meets water and it floats when it is dry. The slurry pollutes environment and it is difficult to deal with. It affects the normal work in washing coal plant, some washing coal plant is shut down because of this. So we try to find a way to burn slurry and gangue to generate electricity and provide heat. It will reduce the cost of power plants.

The feature of slurry and gangue mixture is high ash, high moisture and low heat value. Especially for slurry, its physical configuration and characteristic is very special. If they are used for conventional combustion technology, the performance is hard to be satisfied, but for circulating fluidized bed(CFB) boiler, it is flexible for fuels and it is easy to desulfurize and DeNox in the furnace of the boiler. There are lots of advantages to burn the mixture of slurry and gangue in CFB boiler. This technology is researched and practiced for many years, it is mature now and has been used widely.

By now, 50MW, 135MW and 300MW CFB boiler which burn the mixture of slurry and gangue have already been operated in China. Slurry characteristic and conveying is described and the design and operation of boilers mentioned above are introduced in this paper in detail.

CHARACTERISTIC OF THE SLURRY

Characteristic analysis of the slurry

Slurry is coal fine particle with high moisture and impurity which is separated during washing coal. Normally, the heat value of slurry is 14.65MJ/kg～18.32MJ/kg，the particle size is d50=0.03mm. Slurry is a fuel with high moisture and viscosity, it is difficult to transport and the slurry runs out if it meets water and it floats when it is dry. Slurry is the main pollution source in mining area. It is necessary to burn slurry in boiler in order to protect environment and save energy. At present, there are three ways to burn slurry in boiler: high density slurry with gangue in CFB boiler; high moisture slurry in fluid bed; making slurry into special type to burn. In this three ways, the first way is more convenient and the combustion efficiency is highest, normally, weight ratio of slurry and gangue is 7∶3.

Slurry conveying

The processing of conveying and combustion for slurry is following:

1) Slurry is conveyed to silo, the silo is the first equipment to transport slurry to boiler furnace, there is a stirring arm in the silo which has two functions, one is to agitate slurry temporarily stays in silo so that prevent slurry from depositing and silting, another is to push the slurry to the outlet of the silo bottom in order to enter next stage equipment. The stiring arm is moved uniformly by actuator with motor.

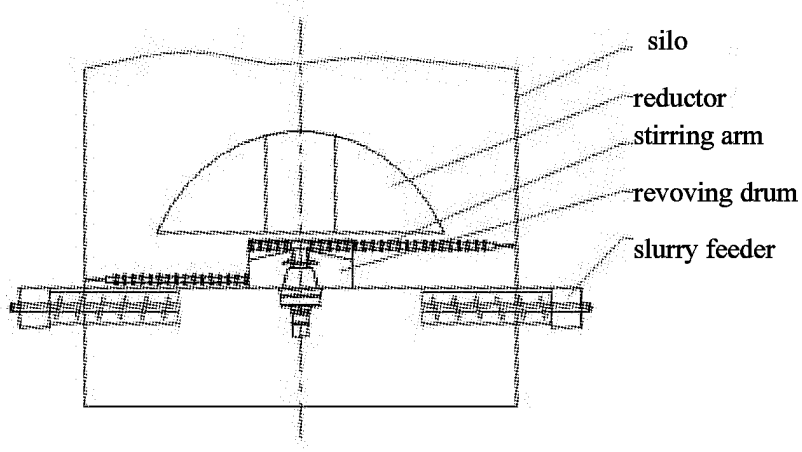

Fig. 1 Slurry silo

2) Slurry flows out of the bottom of the silo, then it passes into screw feeding machine and discharge chute to pre-compressed feeder. The squeezed slurry in the pre-compressed feeder is pushed to slurry pump. The screw feeder is moved by actuator.

3) The special designed reversing valve controls slurry to enter two cylinders of the pump alternately after the slurry comes into the inlet of the slurry pump, the slurry is pushed to conveying pipe at the next stage. For each slurry pump, there is an inlet, an inlet reversing valve, two cylinders and an outlet. The piston in the cylinder and inlet reversing valve alternately move synchronously, so the slurry can be conveyed continuously to the furnace of the boiler. Inlet reversing valve and cylinder is driven by hydraulic, there is a set of hydraulic driving equipment to control the whole system automatically.

4) Slurry is transported to slurry lance. The lance is designed for firing slurry on the big size boiler, the slurry is atomized by air to enter the furnace, and thus the combustion efficiency is improved.

There is a quick shutting off valve at the inlet of slurry lance, the slurry to the furnace is shut off to ensure safety of the boiler when boiler main fuel trip. The atomizing air is controlled by special valve, all the valves is controlled by DCS system.

5) There is a method to wash slurry gun and pipe by water to avoid obstruction when slurry system does not work. Water washing system operates according to site condition, not automatically.

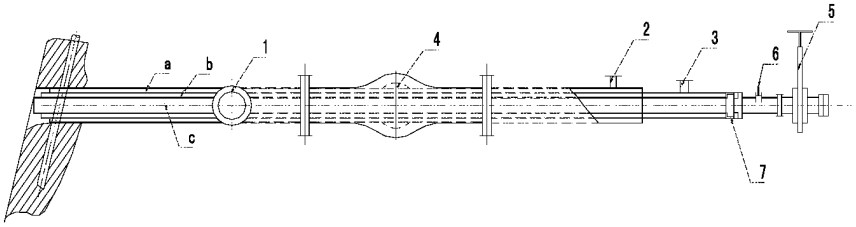

Fig. 2 Slurry lance

DESIGN AND OPERATING

Design feature and operating experience of Yanzhou powerplant 50MW CFB boiler

Boiler general arrangement

This boiler is designed and manufactured by Harbin boiler company limited (HBC), the capacity is 220t/h, it is the first big size CFB boiler in China which fire slurry, it finds a new path for utilizing slurry. The general structure of the boiler is shown in figure 3. The boiler mainly comprises furnace, hot cyclone, double return leg loopseal and backpass.

The water wall is membrane, there is a water cooled air grid with bell type nozzles at the bottom of the furnace, wing wall and panel superheater are arranged in the furnace. Combustion and desulfurization are done in furnace, then the flue gas enter to hot cyclone, the ash captured by cyclone come into the furnace to burn and desulfurize again through double loopseal. Clean flue gas after cyclone enter to backpass, SHIII, SH I, economizer and air preheater are arranged in backpass in turn.

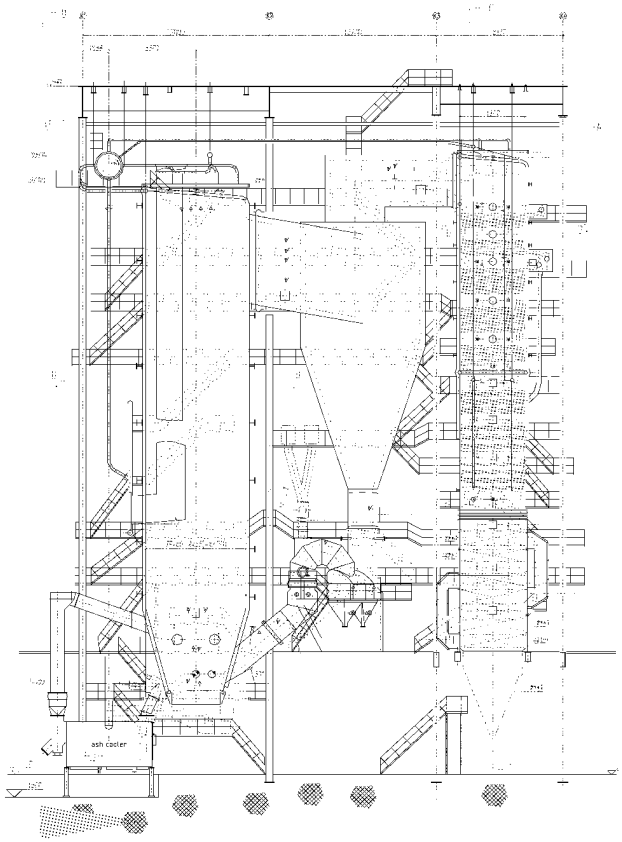

Fig. 3 50MW CFB boiler general arrangement

Performance coal

Boiler performance coal is the mixture of 70% slurry and 30% gangue, slurry ultimate analysis is in T1, gangue ultimate analysis is in Table 2, mixture fuel analysis is in Table 3.

Table 1 Slurry Ultimate Analysis

Carbon	Hydrogen	Oxygen	Nitrogen	Sulfur	Ash	Moisture	Volatile	Heat value
Car %	Har %	Oar %	Nar %	Sar %	Aar %	War %	Vdaf %	Qnet. kJ/kg
43.25	2.89	6.59	0.8	0.42	17.05	29	38.07	16309

Table 2 Gangue Ultimate Analysis

Carbon	Hydrogen	Oxygen	Nitrogen	Sulfur	Ash	Moisture	Volatile	Heat value
Car %	Har %	Oar %	Nar %	Sa r%	Aar %	War %	Vdaf %	Qnet. kJ/kg
30.46	2.07	8.2	0.52	0.62	53.83	4.3	43.32	11182

Table 3 Performance Coal Ultimate Analysis(after mixing)

Carbon	Hydrogen	Oxygen	Nitrogen	Sulfur	Ash	Moisture	Volatile	Heat value
Car %	Har %	Oar %	Nar %	Sar %	Aar %	War %	Vdaf %	Qnet. kJ/kg
39.41	2.64	7.07	0.72	0.48	28.09	21.59	39.65	14771

Design feature

(1) Membrane water wall is used for furnace, furnace section is 6.45m×6.45m.

(2) Bed temperature is 854℃， flue gas velocity in furnace is 6m/s.

(3) Fuel particle size is d_{max}=5mm,for slurry d_{50}=0.03mm， for gangue d_{50}=1.4mm， gangue is conveyed to furnace by loopseal, and four slurry pumps are arranged symmetrically, slurry is conveyed to slurry lance through pump. Four slurry lances are set about 1m above air grid. The lances are horizontal, two of them are on front wall, and there is one slurry lance on each side wall. Slurry is atomized in the lance, and then it enters to furnace to combust.

(4) Water cooled air grid is used, big diameter bell type air nozzle can distribute air homogenously and

avoid jamming and caking, it is convenient to maintain.

(5) One hot cyclone is used in the boiler, the diameter of the cyclone is 7.36m，its shell is plate, insulation material and refractory is lined inside of the plate.

(6) There are two in bed burners on each side wall, they are about 3 meters above air grid.

(7) Bottom ash is cooled by air and water ash cooler, the ash can be cooled below 150℃.

Operating experience

So far, boiler has already been operated for five years, the performance is steady, operating parameters meet design requirements, but there are still some problems as following.

(1) The ash content is high and coal particle size can not meet design requirement，so the ash cooler is difficult to operate normally. The air and water ash cooler is changed to roller ash cooler after the boiler operates for a short time.

(2) Antiwear shell is used in furnace transient area and it results in wearing seriously in this area, see Fig.4. At present, the bent tubes structure is changed, see Fig.5, wearing is avoided in transient area basically.

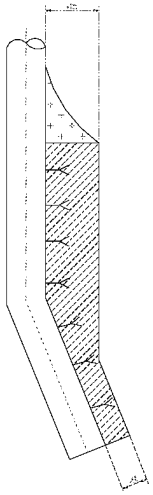

Fig. 4 Original antiwear structure

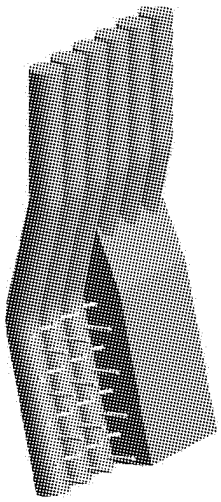

Fig. 5 Modificated antiwear structu re

Comparison of operating and design data

Table 4 Parameter Of medium Side

	Main steam flow t/h	Outlet of main steam℃	Drum pressure Bar
Design value(BMCR)	220	540	108
Operating value(50MW)	198	540	107.3

Table 5 Parameter of Flue Gas Side

	Bed temp. ℃	Furnace outlet ℃	Cyclone outlet ℃	AP inlet ℃	AP outlet ℃	Coal flow t/h
Design value(BMCR)	860	860	860	263	142	42.4
Operating value(50MW)	864	858	889	257	140	39.5

Design feature and operating experience of Yanzhou powerplant 135MW CFB boiler

Boiler general arrangement

The success of 50MW CFB boiler which fires slurry and gangue establishes a good foundation for future enlarging the boiler. In 2003，HBC manufactured two 135MW CFB boilers which fires slurry and gangue for Yanzhou power plant. See Fig.6 to find the general structure of the boiler. The boiler mainly comprises furnace, hot cyclone, double return leg loopseal and backpass. Comparing to 50MW CFB boiler, reheat system is added.

The water wall is membrane, there is a water cooled air grid with bell type nozzles at the bottom of the furnace, partition wall, panel superheater and panel reheater are arranged in the furnace. Combustion and desulfurization are finished in furnace, then the flue gas entry to hot cyclone, the ash captured by cyclone come into the furnace to burn and desulfurize again through double loopseal. Clean flue gas after cyclone enter

to backpass, SHⅢ, SH Ⅰ, RH Ⅰ, economizer and air preheater are arranged in backpass in turn.

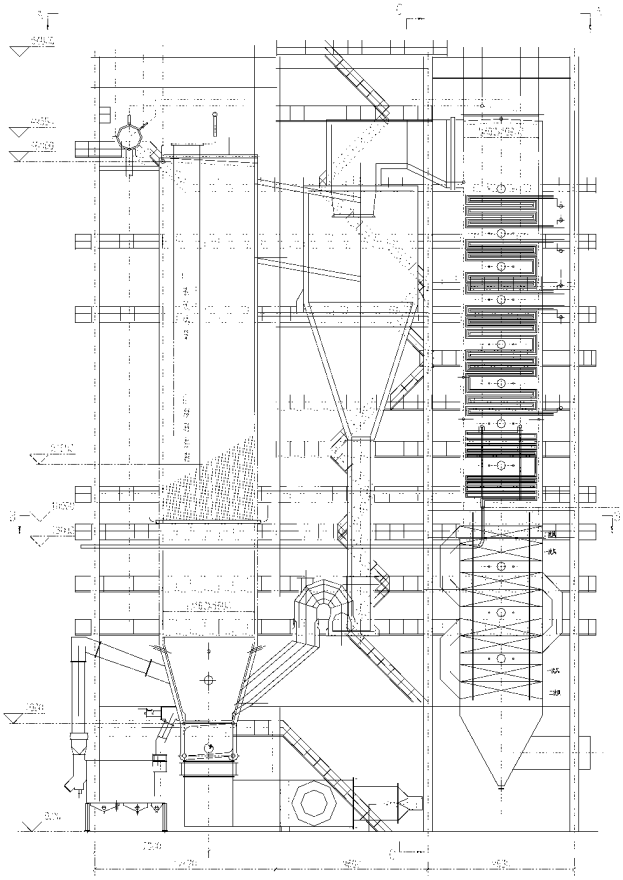

Fig. 6 135MW boiler general arrangement

Performance coal

Boiler performance coal is the mixture of 25% slurry, 65% washed coal and 10% gangue, slurry ultimate analysis is in Table 6, gangue ultimate analysis is in Table 7, washed coal ultimate analysis is in Table 8, mixture fuel analysis is in Table 9.

Table 6 Slurry Ultimate Analysis

Carbon	Hydrogen	Oxygen	Nitrogen	Sulfur	Ash	Moisture	Volatile	Heat value
Car %	Har %	Oar %	Nar %	Sar %	Aar %	War %	Vdaf %	Qnet. kJ/kg
44.8	2.87	/	/	0.33	15.66	29	21.24	16860

Table 7 Gangue Ultimate Analysis

Carbon	Hydrogen	Oxygen	Nitrogen	Sulfur	Ash	Moisture	Volatile	Heat value
Car %	Har %	Oar %	Nar %	Sar %	Aar %	War %	Vdaf %	Qnet. kJ/kg
12.15	1.21	/	/	0.29	76.45	3.8	12.67	4050

Table 8 Washed Coal Ultimate Analysis

Carbon	Hydrogen	Oxygen	Nitrogen	Sulfur	Ash	Moisture	Volatile	Heat value
Car %	Har %	Oar %	Nar %	Sar %	Aar %	War %	Vdaf %	Qnet. kJ/kg
35.5	2.48	/	/	0.31	47.17	6.22	20.51	13330

Table 9 Performance Coal Ultimate Analysis(after mixing)

Carbon	Hydrogen	Oxygen	Nitrogen	Sulfur	Ash	Moisture	Volatile	Heat value
Car %	Har %	Oar %	Nar %	Sar %	Aar %	War %	Vdaf %	Qnet. kJ/kg
41.58	2.74	7.46	0.76	0.31	35.47	11.68	41.38	16160

Design feature

(1) Membrane water wall is used for furnace, furnace section is 7.22m×13.7m.

(2) Bed temperature is 884℃， flue gas velocity in furnace is 5.4m/s.

(3) Fuel particle size is d_{max}=5mm,for slurry d_{50}=0.03mm，for gangue d_{50}=1.4mm，gangue and washed coal are conveyed to furnace by loopseal, and slurry is conveyed to furnace by slurry lance. Four slurry lances are set about 3m above air grid. The lances are horizontal, two of them are on front wall, and there is one slurry lance on each side wall. Slurry is atomized in the lance by compressed air, and then it enters to furnace to combust.

(4) Water cooled air grid is used, big diameter bell type air nozzle can distribute air homogenously and avoid jamming and caking, it is convenient to maintain.

(5) Two hot cyclones are used in the boiler, the diameter of the cyclone is 8.08m.

(6) Combine in bed burners and in duct burners to lignite to reduce start-up time and save oil. The capacity of all burners is 30.7%BMCR. There are four in bed burners and four in duct burners. The capacity of in duct burners is 11.9%BMCR.

(7) Bottom ash is cooled by air and water ash cooler, the ash can be cooled below 150℃.

(8) Reheat steam temperature is controlled by spraying water.

Operating experience

The boiler operates normally, available rate is higher than the same capacity CFB boiler, operating parameters meet design requirements, but there are still some problems as following.

(1) The air and water ash cooler is changed to roller ash cooler because of the same reason with 50MW CFB boiler.

(2) Because the post combustion is not considered during design stage, flue gas temperature at inlet of second pass is higher than design value, convection heating surface absorbs more heat, spray water quantity is higher than design data.

(3) There are reheat panels in furnace, reheat heating surface is made of austenite steel, expansion coefficient is rather large and the length of the panel is larger than 20m. The panel is soft when it is heated, expansion joint which is located at the top of the panel can not absorb the swelling increment, so the panels are bent during operating, but this doesn't impact boiler performance.

Comparison of operating and design data

Table 11 Parameter of Medium Side

	Main steam flow t/h	Outlet of main steam℃	Drum pressure Bar	Reheat inlet℃
Design value(BMCR)	440	540	150	310
Design value(BECR)	393	540	147.5	311
Operating value(135MW)	389	540	146.9	322

Table1 2 Parameter of Flue Gas Side

	Bed temp.℃	Furnace outlet ℃	Cyclone outlet ℃	AP inlet ℃	AP outlet℃	Coal flow t/h
Design value(BMCR)	884	840	868	282	141	85.2
Design value(BECR)	874	840	868	275	138	76.6
Operating value(135MW)	881	873	913	289	147	76.9

Design feature of Huaibeilinhuan powerplant 300MW CFB boiler

Boiler general arrangement

50MW、135MW CFB boiler which fire slurry and gangue operate successfully. It is a milestone in the history of Chinese CFB development. It establishes strong basic to enlarge CFB boiler fires slurry and gangue. Harbin Boiler Company designed and manufactured two 300MW CFB boilers for Huaibeilinhuan powerplant. See Fig.7 to find the boiler general arrangement. The boiler mainly comprise furnace, hot cyclone, loopseal, external heat exchanger(EHE), backpass, air and water ash cooler and Junker's air preheater.

The water wall is membrane, pantleg type double air grid, it is water cooled air grids with bell type nozzles at the bottom of the furnace, wing walls are arranged in the furnace. Four hot cyclones with 8m diameter are arranged on both side of furnace. There is a loopseal below each cyclone. One chute of loopseal connect with furnace, another chute of loopseal connect with EHE. Some circulating ash which is separated by cyclone return to the furnace directly, the others enter into EHE. SHⅢ, RHⅠ, economizer and Jounker'air preheater are arranged in backpass in turn.

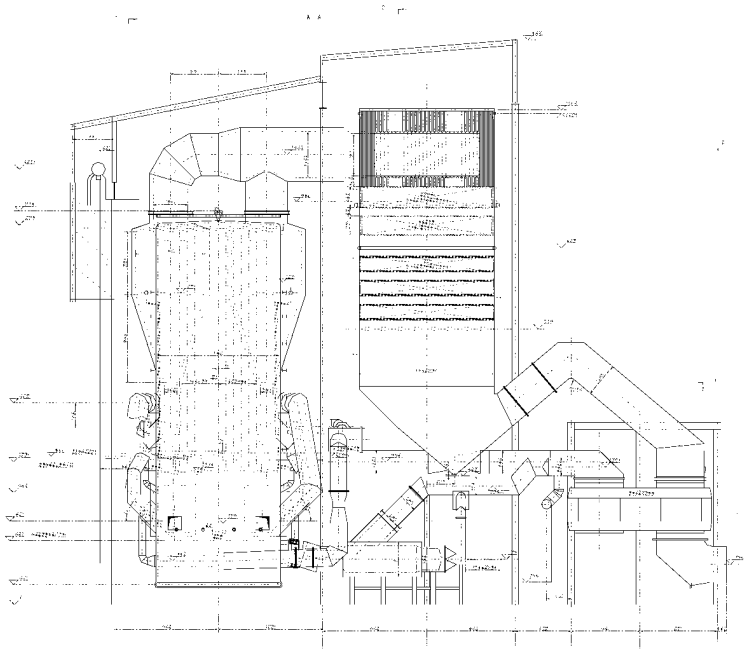

Fig. 7 300MW Boiler general arrangement

Performance coal

Boiler performance coal is the mixture of 15% slurry, 40% washed coal and 45% gangue, mixture fuel analysis is in Table 13.

Table 13 Performance Coal Ultimate Analysis(after mixing)

Carbon	Hydrogen	Oxygen	Nitrogen	Sulfur	Ash	Moisture	Volatile	Heat value
Car %	Har %	Oar %	Nar %	Sar %	Aar %	War %	Vdaf %	Qnet. kJ/kg
31.99	2.69	5.62	0.44	0.29	48.28	10.7	41.73	11960

Design feature

(1) Membrane water wall is used for furnace, furnace section is 15.051m×15.225m. The cross section is too large, it is difficult for secondary air to enter the furnace and it influences burn-off. Oxygen[0] content is low in center of the furnace section according to operating experience, so in this project, pantleg type double air grids are adopted, i.e. the upper part of the furnace is single and the lower part of the furnace is double, thus the surface of air grid is reduced, it is advantageous to distribute air and fluidize. See fig.7 to find the detail structure.

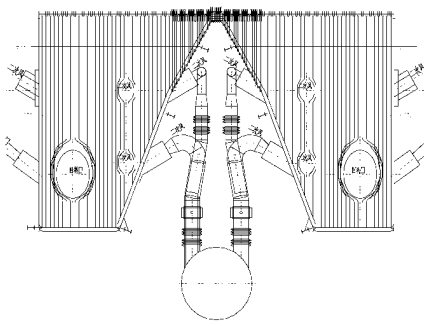

Fig. 8 Pantleg type double air grids

(2) Bed temperature is 890℃, flue gas velocity in furnace is 5.3m/s;

(3) Gangue and washed coal are conveyed to furnace by loopseal, and slurry is conveyed to furnace by slurry lance. Four slurry lances are set about 3m above air grid. The lances are horizontal, there are two slurry lances on each side wall. Slurry is atomized in the lance by compressed air, then it enters furnace to combust.

(4) Combine in bed burners and in duct burners to lignite to reduce start up time and save oil. There are two in duct burners and twelve oil lances in bed. The capacity of in duct burners is 10%BMCR and total oil lance's capacity is 20%BMCR. Oil lances are set 1.5m above air grid.

(5) Air water ash cooler is used in this project.

(6) This project has a obvious difference with the other CFB boiler in China, i.e. EHE is added in hot circulating loop to arrange heating surface and control reheat steam temperature and bed temperature, the detail structure is Fig.9.

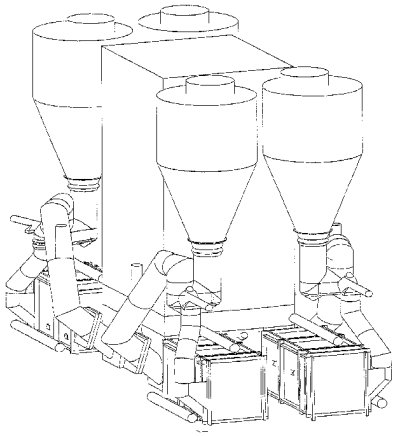

Fig.9 EHE sketch

There are four EHE for one boiler. Final reheater and low temperature is arranged in two of EHE, middle temperature superheater is set in the other two EHE. There is a cone valve at the inlet of EHE, circulating ash is separated into two parts by regulating cone valve, one part enters into furnace directly, and the other part enters into EHE to heat heating surface.

Boiler main parameter

Table 14 Boiler Main Design Parameter

SH flow t/h	SH pressure MPa	SH temp. °C	RH inlet pressure MPa	RH inlet temp. °C	RH flow t/h	RH outlet pressure MPa	RH outlet temp. °C	Feed water temp. °C
1025	17.4	540	3.93	327	846	3.75	540	282

Boiler operating

The boiler is in commissioning phase, everything is all right.

CONCLUSIONS

In big size CFB boiler, slurry can not conglomerate because of using injection lance, thus slurry can combust in CFB boiler stably. With the scale-up of the CFB boiler's capacity, the technology of CFB boiler fires slurry and gangue is developed and improved. At present, it is a mature and reliable combustion technology. It can solve difficulty of dealing with waste product in coal washery and cost of operating is lower in powerplant. This technology has widespread available prospect.

REFERENCES

[1] Cen Kefa,, Yang Jialin, Huang Guoquan. Researching of Industry Application for CFB Boiler Fired Gangue and Slurry. Chinese Journal of Power Engineering, 1999, No.1.

[2] Li Yu, Donye Guanglei, Li Congfeng. Application of slurry and gangue combustion technology in CFB boiler, Thermal Power Generation, 2003 ,Vol.32 ,No.09.

[3] Cen Kefa, Ni Mingjiang, Luo Zhongyang, CFB Boiler Theory Design and Operating. Beijing, China power publishing company, 1998.

[4] Wu Bingfu, Zhou Shanbin, Xue Yuming, Technology and economy analysis of dense slurry convey system in CFB boiler. Shanxi power, 2003 No.2.

PERFORMANCE IMPROVEMENT OF 235 MWe AND 260 MWe CIRCULATING FLUIDIZED BED BOILERS

W. Nowak[1], R. Walkowiak[2], T. Ozimowski[2], J. Jablonski[2], T. Trybala S[2]

1 Czestochowa University of Technology, Poland
2 PGE Elektrownia "Turow" S.A., Poland

Abstract: This article presents the results of studies on the operational performance of the first 235 MWe with hot cyclones and 260 MWe second-generation Compact circulating fluidised bed (CFB) boiler installed as part of the repowering of the Turow power plant in Poland with close to 1,500 MWe of new capacity based on CFB technology. The main characteristic distinguishing the second generation type of boiler is the use of an integrated solids separator rather than an external cyclone. The analysis of flue gas emissions showed that the standards relating to permissible concentrations of pollutants such as SO_2, NO_x, and CO, have been met. SO_2 levels have ranged from 157 mg/m$_n^3$ to 400 mg/m$_n^3$, levels of NO_x from 120 mg/m$_n^3$ to 342 mg/m$_n^3$, and levels of CO from 7 to 45 mg/m$_n^3$. The second-generation CFB boilers at the Turow power plant represent a major advance in CFB technology at this size. Studies on actual emissions indicated that the present standard related to permissible concentration of gas emissions and dust in flue gases have been met. The paper addresses also some performance improvements of the CFB boilers. In the boilers with external cyclones, erosion problems emerged after a time of 50 thousand hours. The problems have been quite precisely diagnosed recently and will be resolved on the occasion of the nearest shutdowns for major repairs.

Keywords: CFB boiler, Second generation Compact CFB

INTRODUCTION

In the recent years the CFB boilers have been used widely in Poland mainly as utility boilers. Users are generally interested in them as they do not need any additional equipment to fulfill the strict environmental protection restrictions. In addition to that, a wide range of fuels may be combusted in CFB boilers. To meet Poland's new environmental standards, which are now compatible with EU, Turow Power Plant decided to replace and upgrade six units (No. 1 to 6) from 200 MWe to three units each 235 MWe in capacity, three 260 MWe and remove one unit No. 7. Units No. 8, 9 and 10 were equipped with dry in-furnace sorbent desulfurization technology. Units No. 1, 2 and 3 have been already replaced with new clean coal circulating fluidized bed technology. The Turow Power Plant with six CFB units is to be the largest power station in the world based on fluidized bed technology. The contract for phase III of Turow repowering project that includes power blocks 4, 5 and 6 was signed with Consortium of Alstom Power and Foster Wheeler in December 1999. CFB Compact design has been selected for the boiler island with an incentive of having higher power generation for each unit: 261.6 MWe instead of 235 MWe within the same space restrictions that previously accommodated old, pulverized coal 200 MWe units.

The schematic of the 260 MWe CFB boiler supplied by Foster Wheeler is shown in Figure 1. The cross-section of the furnace measures 22 m×10 m, while the combustion chamber is 42 m high. The basic difference compared to the first-generation CFB boilers (with hot cyclones) is the switch to an integrated solids separator. This is made of membrane panel walls and lined on the inside with a thin layer of erosion-proof material approximately 50 mm thick. The separator is rectangular, and is integrated, with the return leg, in the side wall of the boiler. This contributes to better utilisation of the space around the combustion chamber and means that much less room is needed for installation of such a boiler. Four separators are employed, with the walls cooled with dry saturated steam from the steam drum. The introduction of the integrated separator concept has enhanced separation efficiency– the diameter of separated particles has been reduced from 150 μm to 80-100 μm after the separator. To reduce the height of the combustion chamber, wing walls have been installed inside the evaporator. Unlike CFB boilers No. 1-3, superheater I is located in the backpass of the boiler rather than in the combustion chamber, and superheater II and superheater III are Intrex™ type heat exchangers. The other steam heaters (reheaters I and II), as well as the water and air preheaters (primary and secondary air), are located in the backpass. A four-section regenerative air preheater of the Ljungstrom type is used instead of the tube preheaters employed in CFB boilers No. 1-3. The air preheater heats both primary and secondary air. The lower part of the combustion chamber covered with refractory traditionally holds inlets for all media supplied to the combustion chamber (air, fuel, inertial material, etc.). In contrast to CFB boilers No. 1-3, the sorbent is fed into the combustion chamber together with the fuel. Table 1 presents characteristic of

fuel and sorbent used in the CFB boilers. The boilers as design are capable of burning brown coal. Design high heating value of burning brown coal is 9745 kJ/kg, moisture content – 44%, ash – 22.5%, sulfur – 0.4-0.8%. Heavy oil is used as a start-up fuel and the start-up burners will be capable of 40% of MCR heat input

Table 1 Fuel and sorbent characteristic

Component	Value
Fuel	
C, %	23,9
H, %	1,9
S, %	0,4-0,8
N, %	0,2
O, %	6,8
Moisture, %	44,1
Ash, %	6,5-31,5
HHV, kJ/kg	8370-12140
Sorbent	
$CaCO_3$, %	92,0
$MgCO_3$, %	2,5
Inert, %	4,5
Moisture max., %	1,0

The Foster Wheeler CFB Compact boilers for units 4, 5 and 6 are designed for fixed pressure, natural circulation, brown coal firing units with live steam maximum continuous rating of 195.5 kg/s. Summary of basic steam-water circuit design data of CFB boilers with hot cyclones and Compact type is given in Table 2. Estimated boiler efficiency for CFB Compact is 91 % (LHV based) with flue gas temperature lowered down to 138 °C compared to 157 °C for CFB units with hot cyclones .

The total efficiency of CFB units has been improved by 4.5% due to improvement of the heat balance by introducing higher steam parameters and optimizing water-steam cycle.

When compare to CFB units in operation, the unique features of CFB Compact boilers are as follows:

- steam cooled separators instead of hot cyclones,
- different orientation of the boilers and start-up burners location (below the plenum plate),
- the use of an integrated heat exchanger (Intrex) replacing the Omega type superheater,
- stripper coolers of the bottom ash,
- rotated type air heater instead of the tubular air heater.

As a result of the Compact construction of the CFB boiler has certain distinctive features and performance characteristics:

- Intrex is located outside of the combustion chamber so that corrosive compounds of gases do not come into contact with superheater tubes (solution for high temperature chlorine corrosion),
- boiler load can be easily controlled by changing the heat transfer coefficient of surfaces located in Intrex,
- erosion of the superheater surfaces in the combustion area can be avoided by using Intrex with the low fluidizing velocity (0.1-0.5 m/s),
- about 4.5% higher efficiency of the units is expected by lowering flue gas temperature,
- by integrating the solids separator with the combustion chamber no expansion joints are needed,
- a simple gas seal is used between the separator and the combustion chamber,

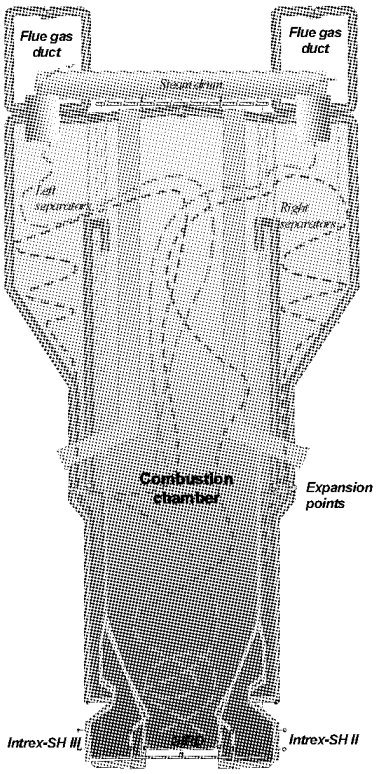

Fig. 1 Schematic diagram of the 260 MWe CFB boilers supplied to Turow: sectional view of combustion chamber

- internal and external solids circulation is applied,
- due to the use of cooled separators less refractories are needed,
- the available in the power plant space will assure installation of the boiler producing 260 MWe (the CFB boilers with hot cyclones and the same power output require more space),
- better access for the maintenance and potential repairs,
- lighter construction due to the elimination of the insulation type refractory material,
- shorter start-up time due to the thinner refractory,
- lower radiation losses.

Table 2 Comparison of design parameters of CFB units with hot cyclones and compact type

Parameter	CFB units with hot cyclones	CFB Compact
Capacity, MWe	235	262
Main steam flow, kg/s	185.4	200
Main steam pressure, MPa	13.17	16.65
Main steam temperature, °C	540	565
Hot reheat temperature, °C	540	565
Hot reheat flow, kg/s	165.5	182
Cold reheat pressure (outlet from HP turbine), MPa	2.8	4.2
Cold reheat temperature, °C	312	350
Hot reheat pressure, MPa	2.5	3.8
Feedwater temperature, °C	242.6	250
Water flow, kg/s	7470	7470
Pressure in condensator, kPa	7.2	6.5
Flue gas temperature, °C	157	138

The average power production (netto) of 260 MWe for CFB Compact boilers is considered as a very good indicator. The unit indicated consumption of the chemical energy of the fuel in the case of power production by CFB Compact boilers is lower than that for CFB units No. 1-3 with hot cyclones. Good emissions' control in CFB boiler is achieved by low combustion temperature and even temperature profile through the height of the furnace, a staged combustion, good residence times and mixing conditions. It should be noted that further lowering of the emission limits to the future EU requirements can be easily obtained with only minor adjustments. For example, for the NO_x limit of 200 mg/Nm^3 solution will be adding a simple system of weak water-solution of ammonia spraying into the separators. Lowering the sulfur dioxide emission can be achieved with more limestone injection to the furnace or with modified sorbents.

PERFORMANCE IMPROVEMENTS

Bed temperature

The optimum operating conditions for a CFB boiler is in the range of fluidized bed temperatures inside the combustion chamber between 816 °C and 899 °C, as this reflects the most favourable conditions for the simultaneous capture of sulphur oxides and reduction of NO_x. Figure 2 shows the distribution of the temperatures of the bed material in the combustion chamber and the flue gases in the boiler backpass in the second-generation design.

The temperature in the combustion chamber can vary under the influence of: fuel and sorbent particles size fuel moisture content and heating value, the height of the bed in the lower part of the combustion chamber, primary to secondary air ratio, and excess of supplied air. The parameter which has significant influence on formation of uniform temperature profile along the height of the combustion chamber is solids hold-up in the combustion chamber. The

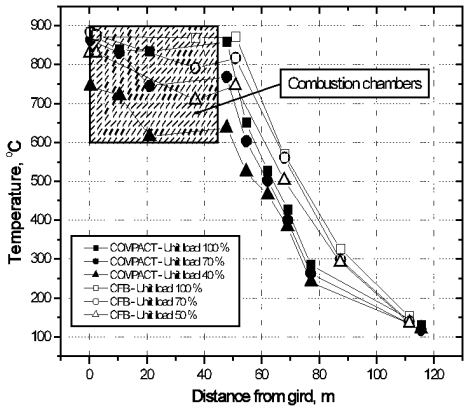

Fig.2 Temperature distribution in a second-generation 260 MWe CFB boiler compared to a conventional 235 MWe unit

stream of bed material and gas in the combustion chamber serves a number of other important functions, such as absorbing heat from the lower part of combustion chamber to keep the temperature in this zone around 850 °C, transferring heat to the heating surfaces located in the combustion chamber, (exchange of heat by convection of particles plays a fundamental role in transfer of heat in the combustion chamber), and influencing gas / particle mixing which also leads to higher residence time in the combustion chamber. As shown in Fig. 2, the second-generation boiler is characterised by lower temperatures in the furnace, as well as the backpass, compared to the design employing a conventional external cyclone employed in CFB boilers No. 1-3. This is the result of the different arrangement of heat exchange surfaces. The degree of internal circulation of the bed material, i.e. distribution of particles in the volume of the combustion chamber and the degree of external circulation of the bed material between combustion chamber and the return system, is also an important factor.

Availability

The most common measures for CFB boiler performance are Availability Factor (AF), Forced Outage Factor (FOF) and Serviced Outage Factor (SOF) defined as follows:

$$AF = \frac{\sum_{i=1}^{n} T_{pi} + T_{ri}}{\sum_{i=1}^{n} T_{ki}} 100\%, \quad (1)$$

$$FOF = \frac{\sum_{i=1}^{n} T_{ai}}{\sum_{i=1}^{n} T_{ki}} 100\%, \quad (2)$$

$$SOF = \frac{\sum_{i=1}^{n} \left(T_{kp} + T_s + T_b\right)_i}{\sum_{i=1}^{n} T_{ki}} 100\%. \quad (3)$$

The disturbances that are caused by external reasons, not under plant management, are not unavailability. The design availability of CFB units No. 1-6 was settled on the level of 85%. The problems appeared with achievement of such value from the beginning of operation of CFB units No. 1-3 (Fig. 3). This value was achieved in 2003 and 2004 . The main influence on the availability of CFB units has the maintenance time. Faults resulting from project and assembly defects were removed in first years. As can be seen in Fig. 3, it was possible to decrease the SOF in fourth year of operation, below 10%. However, this factor again began to increase from 2004 as a result of unplanned current repair, despite that the average repairs were carried out in these years. The main reason of low availability of CFB units No. 1-3 is the breakdowns of boilers (Fig.4). The erosion of refractories and heat surfaces are the most essential problems of CFB boiler performance. In addition, disturbances began to appear in turbine performance in 2003 resulting in disconnection of CFB units. The projects defect of transformers also influenced the high unavailability of these units during their exploitation. During last two years the work concentrated on planned repairs was almost the same as during the acquaintance period of CFB units No. 1-3. In spite of enlarging the expenditure of works in planned repairs, including current repairs, the Forced Outage Factor from the beginning of exploitation keeps on the high level about 5%.First years of exploitation extorted among others: improvement of the durability of compensators and air nozzles, modernisation of convective path, erosion protection of the bottom part of membrane walls, modernisation of the tubular air heaters, exchange of refractories on more durable one. Later the problems were also disclosed with the dynamic state of turbines.

Similarly as for CFB units 1-3 the initial period of exploitation of CFB Compact units No. 4-6 characterizes oneself the high FOF and lower than planned availability factor AF (Fig. 5). A high decrease of FOF below 2% already in second year of exploitation and his stabilisation on values of 1% and remaining AF on the level above 90% testifies for inevitable transition of the CFB Compact units from the acquaintance period until their normal exploitation.

Enlarged time of planned repairs in first three years of boiler operation and the high FOF in the first year was extorted because of the necessities of removal of the guarantee faults of boilers and turbines and their auxiliary devices (Fig. 6). Low times of shut downs testify that the meaning of these problems was insignificant. The lack of essential problems in the next years of CFB Compact operation proves the selection of this technology.

Certainly, such good performance of CFB units is a result of experiences acquired during the construction and operation of CFB units No. 1-3.

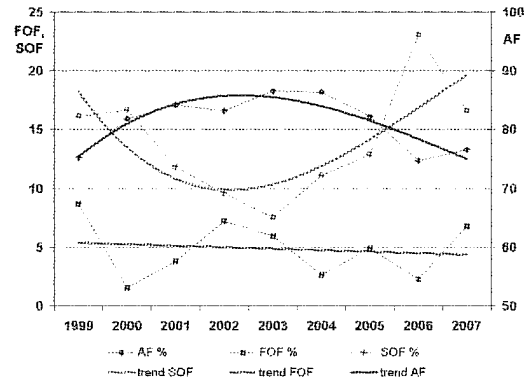

Fig. 3 Performance factors of CFB units No. 1-3 with hot cyclones

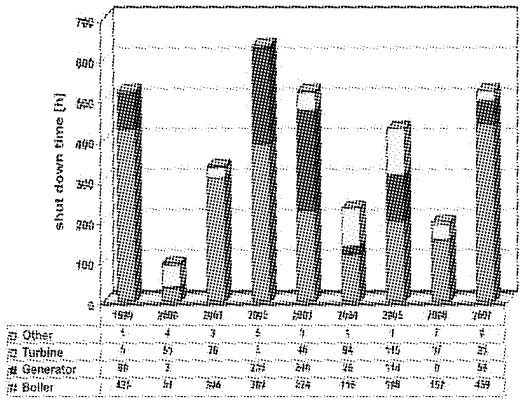

Fig. 4 Forced outages of CFB units No. 1-3 with hot cyclones

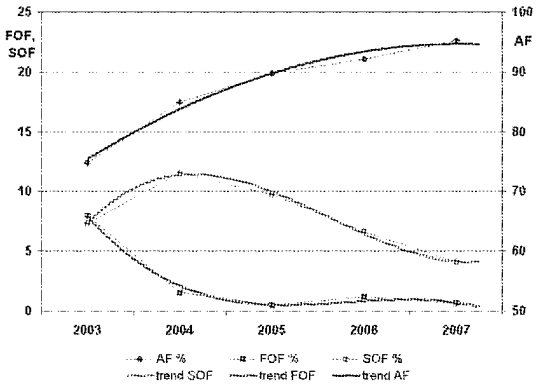

Fig. 5 Performance factors of CFB Compact units No. 1-3

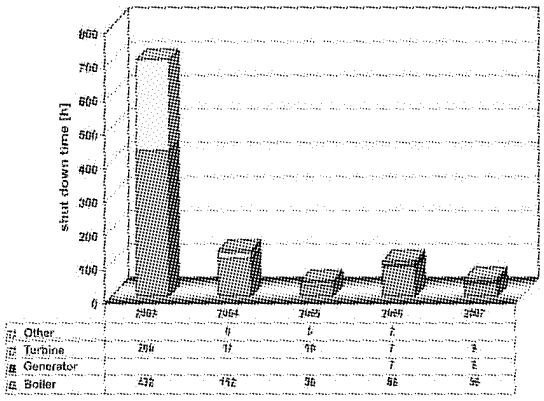

Fig. 6 Forced outages of CFB Compact

CONCLUSIONS

(1) The CFB-235 MWe and CFB-260 MWe boilers have operated from 30 to 60 thousand hours. The risk of investing in a prototype technology has paid off. The CFB boilers are attaining the parameters assumed and guaranteed by the supplier. The technical goal of modernization to restore the Power Plant's production capacity and to extend its operation by 30 years has been achieved. The same is true for the economic goal – the overall cost of modernization totalled to 1.7 billion USD which, expressed 1 MW of installed power, gives the ratio of 1.13 m. USD/MW – the total costs of Power Plant modernization (including the construction of replacement of the equipment of technological systems other than the Unit's installations) are taken into account here.

(2) The choice of CFB Compact boilers – in the mid-process of modernization - was a very good move. These boilers have better operation parameters compared to boilers with external cyclones. The advantages claimed by the boiler manufacturer have been verified in operational practice.

(3) In the boilers with external cyclones, erosion problems emerged after a time of 50 thousand hours. The problems have been quite precisely diagnosed recently and will be resolved on the occasion of the nearest shutdowns for major repairs. A very important issue is the accuracy of carrying out repair operations and the experience of the maintenance personnel, as well as the role of the Supervision in rectifying damage caused by erosion.

(4) The challenges that should be responded to in the nearest future are:
- increasing the durability of the furnace chambers and repairing (replacing) their parts that are most prone to erosion, namely: the rear chamber wall within the band of up to 7 m above the hopper lining, and the corner tubes in the front and rear corners;
- preparing the CFB units for operation complying with the emission standards that will be in force after 2012;

- implementing the co-combustion of biomass in CFB Compact boilers No. 5,6.

NOTATIONS

T_a forced outage time, h
T_b actual service outage time, h
T_k length of calculation period, h
T_p run time, h
T_r planned production limitations, h
T average service outage, h
AF Availability Factor
FOF Forced Outage Factor
SOF Serviced Outage Factor

B&W IR-CFB: OPERATING EXPERIENCE AND NEW DEVELOPMENTS

M. Maryamchik, D.L. Wietzke

Babcock & Wilcox Power Generation Group, Inc., Barberton, Ohio, USA

Abstract: The paper provides an update on B&W Internal Recirculation (IR) CFB boiler operating experience, new commercial projects, and developments in boiler design and process. Availability data for two projects in the U.S. will be presented, as well as data collected from two additional projects by a B&W licensee in India. Two new commercial projects are currently going through commissioning. Yet another unit, Great River Energy (being erected), is described in detail. To achieve the required amount of in-furnace heat absorption in higher capacity CFB boilers, a new B&W development is its patented in-bed heat exchanger (IBHX). The IBHX allows control of the bed temperature in the furnace as well as steam temperature in the superheater and reheater surfaces, thus accommodating higher capacities.

Keyword: CFB boiler, in-bed heat exchanger, heat transfer

OPERATING EXPERIENCE

Previous updates of this paper (Maryamchik and Wietzke, 2005; Maryamchik, 2008) have provided information on availability data from two Babcock & Wilcox Power Generation Group, Inc. (B&W) circulating fluidized-bed (CFB) boiler projects in the United States (U.S.). Availability data for the Ebensburg and Southern Illinois University CFB boilers are further updated in Table 1.

Table 1 Plant Availability (all data in % of total time available)

	Ebensburg CFB		SIU CFB	
	1991-2003 (reported in 2005 paper)	2004-2007	1997-2003 (reported in 2005 paper)	2004-2007
Boiler forced outages	3.3	2.2	1.6	2.0
BOP forced outages	0.5	0.3	0.1	0.4
Planned outages	5.7	3.4	5.7	1.3
Plant availability	90.5	94.2	92.6	96.3

This latest update will include availability data collected by a B&W licensee in India. B&W has a longstanding relationship with Thermax Limited, in Pune, India (via Thermax Babcock & Wilcox, or TBW, a division of Thermax Limited), through licenses of industrial boilers, CFB boilers and subcritical utility boilers. TBW has been very active in the CFB market and has successfully sold 10 CFBs in India and two in Malaysia. Five of those projects are in commercial operation. The other seven are in various stages of design, fabrication, construction and commissioning. Table 2 presents availability information on the first three CFBs by TBW.

Table 2 Plant Availability (all data in % of total time available)

	Kanoria 1 (commissioned in 1996)	Kanoria 2 (commissioned in 2005)	Indian Rayon (commissioned in 2006)
Years reported	1997-2007	2006-2007	2007
Plant availability	87.1	95.5	95.2

NEW COMMERCIAL PROJECTS

Successful operation of the existing B&W CFB units is accompanied by a substantial increase in the number of new units coming online in recent years (Table 3). Two of these units currently going through commissioning (ARPA and AGP) feature a new design of the U-beam particle separator (Fig. 1), the first stage of the two-stage solids collection system utilized on IR-CFB boilers. The design and performance characteristics of these units were described earlier (Maryamchik, 2008).

The latest IR-CFB unit is for Great River Energy (GRE) in Spiritwood, North Dakota, which is designed for firing beneficiated lignite (25.8% moisture, 13.4% ash, 0.8% sulfur). The main boiler performance characteristics specified for the project are provided in Table 4 and its arrangement is shown in Fig. 2.

Table 3 Recent B&W CFB Boiler Experience

Startup Year	Customer and Plant Location	Unit Type	Mfg by	Eng by	No. of Units	Output MWt	Steam Flow KPPH TPH	Design Pressure psig bar	Op. Pressure psig bar	Steam Temp Deg F Deg C	Fuels
2010	Great River Energy Spiritwood, ND	IR-C FB	B&W	B&W	1	275	805 365	2075 143	1780 123	1006 541	Lignite
2009	AG Processing, Inc. Hastings, Nebraska	IR-C FB	B&W	B&W	1	87	300 136	250 17	150 10	450 232	PRB coal
2009	Aluminum do Norte do Brasil, SA Alunorte	IR-C FB	B&W	B&W/ Lic.	1	270	750 340	1536 106	1325 91	909 487	Bituminous coal (high volatile); Light oil (diesel) for startup
2009	Arkansas River Power Authority Lamar, CO, USA	IR-C FB	B&W	B&W	1	125	360 163	1850 127	1586 109	990 532	Coal
2008	Grasim Cement AP, India	IR-C FB	Lic.	Lic.	1	83	254 115	1715 118	1415 97	1004 540	Coal, Lignite, Petcoke
2008	Saurashtra Cement Rajasthan, India	IR-C FB	Lic.	Lic.	1	80	242 110	1535 106	1250 86	968 520	Coal, Lignite, Petcoke
2008	UltraTech Cement, Ltd. AP, India	IR-C FB	Lic.	Lic.	2	83	254 115	1715 118	1415 97	1004 540	Coal, Petcoke
2007	Grasim Industries Kotputli, Rajasthan, India	IR-C FB	Lic.	Lic.	2	73	224 102	1690 116	1400 96	1004 540	Coal, Lignite, Petcoke
2007	Indian Rayon Aditya Birla Nuvo Veraval, Gujarat, India	IR-C FB	Lic.	Lic.	1	76	231 105	1507 104	1280 88	950 510	Lignite, Petcoke, Indonesian coal, Oil, Gas
2005	Kanoria Chemicals, Ltd. Renukoot, India	IR-C FB	JV	JV	1	89	242 110	1140 79	972 67	905 485	High ash coal
2004	Konya Sugar Corporation Cumra, Turkey	IR-C FB	Lic.	B&W/ Lic.	2	55	165 75	675 47	622 43	806 430	Lignite

Table 4 Main GRE CFB Performance Characteristics per Project Specification

Steam flow @ MCR, klb/hr (t/hr)	805 (365)
Steam pressure, psig (barg)	1795 (124)
Steam temperature, F (C)	1006 (541)
NO_x emission limit, lb/MBtu (mg/Nm^3 @ 6%O_2 dry)	0.09 (113)
SO_2 emission limit, lb/MBtu (mg/Nm^3 @ 6%O_2 dry)	0.06 (75)
CO emission limit, lb/MBtu (mg/Nm^3 @ 6%O_2 dry)	0.15 (188)

The furnace and horizontal convection pass enclosure are top-supported and made of gas-tight membrane walls. Fuel is fed to the lower furnace through the front wall using six air-assisted chutes. Limestone is injected pneumatically through multiple points uniformly across the width of the furnace near the bottom. Startup fuel (natural gas) is fired using six burners mounted on the rear wall. Separate fans supply primary and secondary

air. The bulk of the primary air is introduced through a grid of bubble caps at the furnace floor. The main portion of the secondary air is fed through nozzles at the front and rear furnace walls. Bottom ash is removed through three fluidized-bed coolers (two located at the side furnace walls and one at the rear wall).

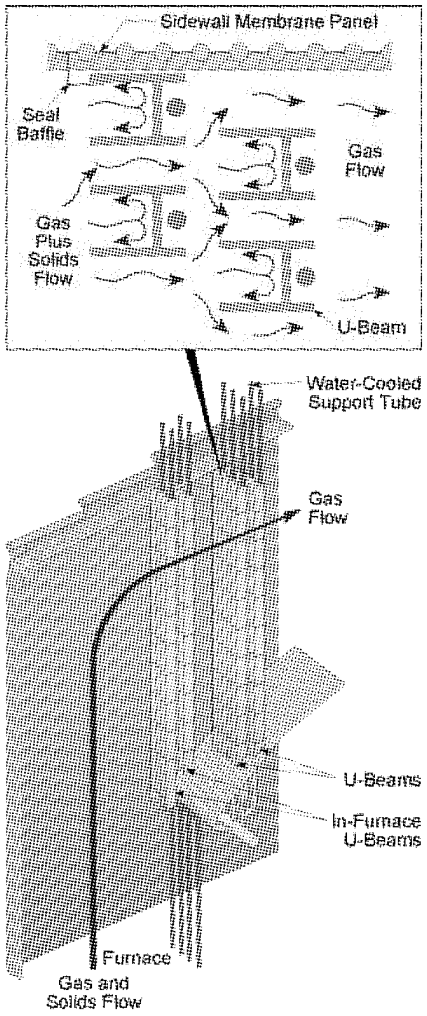

Fig. 1 Segmented U-beam particle separator

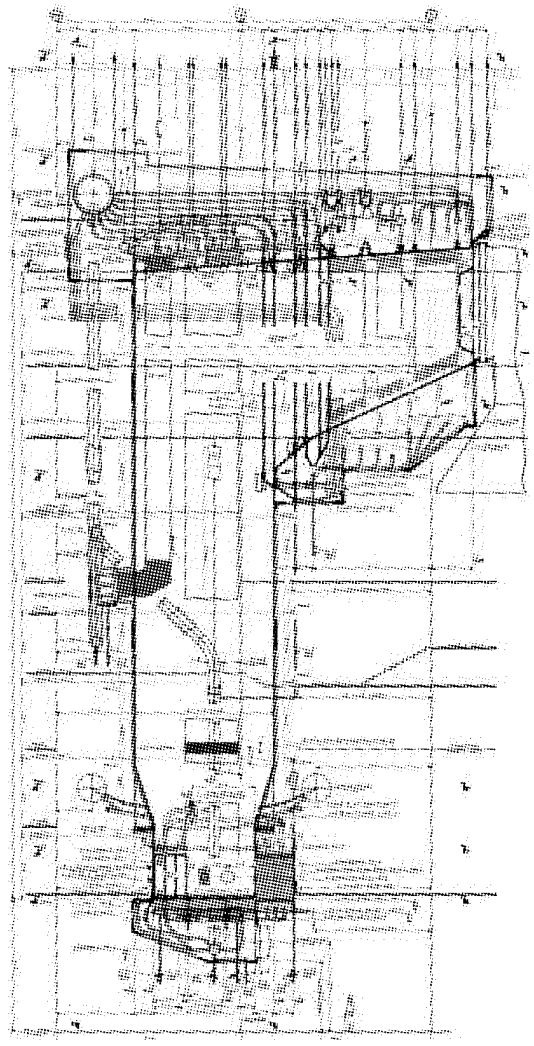

Fig. 2 B&W CFB for Great River Energy

The furnace is 48 ft (14.7 m) wide by 22 ft (6.7 m) deep and 99 ft (30.2 m) high. It contains five full furnace height water-cooled panels, or division walls, and twelve steam-cooled wing walls. The lower furnace is protected from erosion and corrosive conditions by a layer of low-cement, high-strength refractory. The membrane tubes at the upper edge of this refractory are protected from erosion by the patented Reduced Diameter Zone (RDZ) design (Fig. 3).

The U-beam particle separator (Fig. 1) system is comprised of four rows (two in-furnace and two external) of U-beams. Each beam consists of about 4-foot (1.2 m) segments supported from a water-cooled tube. Supporting the first three rows of U-beams (along the gas flow) are the furnace rear wall tubes; those for the last row are fed from a separate header. The design allows independent thermal expansion of each segment. The U-beam segments are made of SA240TP309H material, which has proved suitable for U-beam fabrication in previous B&W CFB projects. Solids collected by the U-beams fall downward along the beams and return to the furnace directly (from the first U-beam row) or by sliding along the U-beam zone floor.

Pendant superheater banks are located downstream of the U-beams in the horizontal convection pass. Steam from the drum flows through the side walls of the pendant superheater enclosure, then through the primary superheater bank followed by the wing walls and the secondary superheater bank to the main steam outlet.

The second stage of the solids collection system, a multi-cyclone dust collector (MDC), is located immediately downstream of the horizontal convection pass. Further downstream in the gas pass the MDC is followed by the economizer and tubular air heater (air inside tubes). The air heater is side-split for primary and secondary air. After the air heater, gas flows through a spray dryer absorber, a fabric filter baghouse, and an

induced draft (ID) fan to a stack.

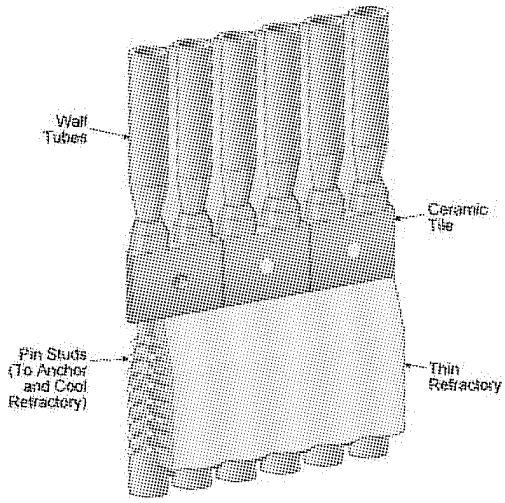

Fig. 3 Reduced Diameter Zone (RDZ) design for erosion protection at the upper refractory edge

Solids collected by the MDC are recycled back to the furnace through four recycle lines utilizing inclined screw conveyors and gravity feed. Controlling the MDC solids recycle rate allows precise and effective furnace temperature control.

Because the fuel specified for this project features relatively low ash and low sulfur content, solids input with the fuel ash and limestone may be not sufficient for maintaining furnace solids inventory required for the temperature control. Therefore, the unit is equipped with an inert bed feed system. This system allows the input of inert bed material to the furnace as directed by the boiler controls. To minimize, or eliminate, the need for external bed material, e.g., sand, the inert bed system includes recycle of the bottom ash as well as MDC and air heater hopper purge back to the inert bed silo, from where the bed material is metered to the furnace.

NEW DEVELOPMENTS IN B&W CFB DESIGN

In-Bed Heat Exchanger

As use of CFB boilers moves from industrial to utility applications, a higher fraction of the boiler heat duty goes to superheat (and reheat, where applicable). With relatively low gas temperatures leaving a CFB furnace, available gas heat capacity in the convection pass is not adequate for providing required superheater and reheater heat absorption. Therefore, more of the relevant heating surface must be placed in the furnace. Higher boiler capacities typical for the range of utility-sized units feature a reduced furnace enclosure surface-to-volume ratio compared to that of the industrial-sized units. This is another factor driving an increase of the required area of the in-furnace heating surface.

At some point, using wing walls and division walls (common design features in industrial-sized B&W IR-CFB units) becomes inefficient or inadequate for the required in-furnace heat absorption. The required amount of in-furnace heat absorption (including superheat and reheat duty) can be achieved with the B&W-patented in-bed heat exchanger (IBHX). A design version of an IR-CFB boiler with IBHX is shown in Fig. 4. Other versions in the patent include alternate locations in the furnace bottom.

Part of the lower furnace is "fenced-out" by an enclosure providing separation from the surrounding CFB on the sides while keeping the top open. In the version shown, the separating enclosure is partially comprised of the tubes forming the CFB furnace enclosure walls and partially comprised of the designated in-furnace panels. The latter also divides the IBHX into separate sections. Tube banks of a particular heating surface (such as superheater, reheater or generating surface) are placed in each of these sections, one type of surface for a given section of an IBHX. The fluidizing air flow rate to each section is controlled separately maintaining a low-velocity bubbling fluidized bed.

Bed material fills the IBHX through its open top from the CFB furnace and is discharged back to the CFB from the bottom area of the IBHX. By controlling the discharge rate, the material throughput in the IBHX is controlled. The throughput rate affects the temperature differential between the bed material and heating surface in a given section of an IBHX, thus controlling its heat absorption. Controlling heat transfer in the sections with generating surface allows control of the bed temperature in the CFB furnace. The IBHX also allows control of the corresponding steam temperature in the sectioned superheater and reheater surfaces.

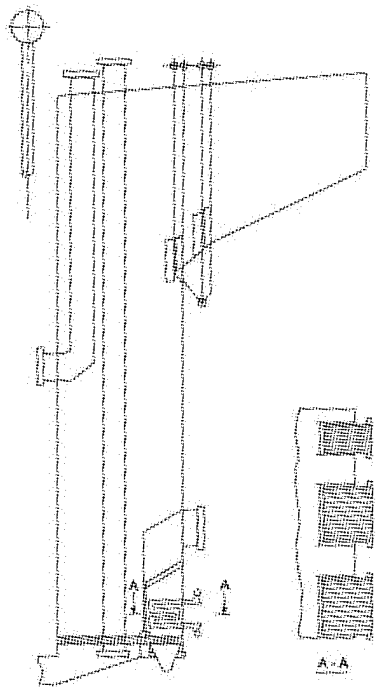

Fig. 4 Example version of the B&W-patented in-bed heat exchanger (IBHX)

CONCLUSIONS

Highlighted operational experience, commercial activity and technical developments illustrate the status and trends of B&W IR-CFB technology.

REFERENCES

M. Maryamchik and D.L. Wietzke, Proceedings of 18th International Conference on Fluidized Bed Combustion, ASME, Toronto, Ontario, Canada, May 22-25, 2005, FBC 2005-78004.

M. Maryamchik, Proceedings of the 9th International Conference on Circulating Fluidized Beds, Hamburg, Germany, May 13-16, 2008.

U.S. Patent Nos. 6,044,805; 6,491,000; 6,532,905; and 7,464,669.

DISCLAIMER

NO_x EMISSION REDUCTION BY THE OPTIMIZATION OF THE PRIMARY AIR DISTRIBUTION IN THE 235MWe CFB BOILER

P. Mirek, T. Czakiert, W. Nowak

Department of Heating, Ventilation and Air Protection,
Faculty of Environmental Protection and Engineering
Czestochowa University of Technology,
Czestochowa, Poland

Abstract: The article presents the results of experimental studies conducted on a large-scale 235 MWe CFB (Circulating Fluidized Bed) boiler, in which the primary air distribution system was modified. The modification was connected with the change of internal geometry of primary air channels as well as internal space of plenum chamber. The obtained results have shown, that the optimization of primary air flow has a great influence on the intensity of the combustion process and the temperature distribution along the height of combustion chamber. As a result, the NO_x emission has been reduced by up to ten percent and the temperature profile in the combustion chamber has been revealed to be more uniform.

Keywords: primary air, plenum chamber, NO_x

INTRODUCTION

One of the greatest advantages of the fluidized bed technology is the low-emission fuel combustion capability. With respect to the circulating fluidized bed, this results, on the one hand, from the process of combustion in the gas-fuel-ash-sorbent mixture circulating within the closed boiler contour and, on the other hand, from the possibility of carrying out simultaneous flue gas desulphurization and maintaining a low combustion temperature, which is favoured by the formation of small quantities of nitrogen oxides. In recent years, due to the stringent European Commission Directives on gas pollutant emissions, a growing interest of designers, users and researchers of the fluidized-bed fuel combustion technology in the methods of primary reduction of gaseous pollutants, and specifically nitrogen oxides, has been observed. The methods from this group, which are most frequently referred to, include: lowering of combustion temperature, staging of air, and reduction of the excess air (Basu et al., 1991). As each of the above-mentioned methods is strictly related to the boiler hydrodynamics, in order to achieve the lowest possible levels of pollutant emissions, it is postulated to make a very accurate determination of optimal hydrodynamic conditions for each unit separately. An example of such optimization could be the reduction of the emissions of NO_x and SO_2 by changing the cyclone separation efficiency, influencing thereby the concentration of particles along the combustion chamber height (Lee et al., 2003; Andrzejczyk, 2006). As indicated by operational tests (Kobylecki et al., 2008), the application of this method allows for the reduction of nitrogen oxide emissions by as much as several dozen percent. Another example can be the enrichment of the oxygen-deficient central part of the combustion chamber using the ROFA (Rotating Over Fire Air) technology developed by Mobotec company. As the experience with large boiler units shows, the application of flue gas turbulence in the upper combustion chamber part allows an NO_x emission reduction from 45 to 60% (MobotecUSA website). As the formation of nitrogen oxides is closely related with the distribution of air in the combustion chamber cross-section, the reduction of this gas will involve the optimization of air distribution in primary air channels and windboxes (Mirek et al., 2008). Moreover, as follows from operational tests, the distribution of temperature within the CFB boiler is strongly associated with the mode of air distribution, and thus with the nozzle design (Mirek et al., 2006). On this account, in the boiler design process, special consideration should be given to flow issues, which involves an optimal design of windbox geometries and the selection of an appropriate nozzle design.

The paper presents possibilities of reducing nitrogen oxides by the optimization of distribution in the primary air system. Special attention is devoted to the equalization of temperature within the boiler's combustion chamber, which has been achieved by changing the flow conditions in the primary air channels and windboxes. As a result of modifications, a nitrogen oxide reduction from 6 to 14%, depending on the boiler load, has been achieved.

EXPERIMENTAL

The experimental tests were carried out on a 670t/h circulating fluidized bed boiler presented in Fig. 1. The size of the combustion chamber at the grid level is 21.2 m wide and 5.2 m deep. The depth of the

combustion chamber is growing with increasing distance from the grid. At the height of 6.7 m, the combustion chamber depth is 9.9 m and does not change with a further increase of the distance from the grid. The total height of the combustion chamber is 44.8 m. The primary air grid of boiler was equipped with so called "pigtail" nozzles. During the tests, the boiler was running under operating conditions, parameters of which are presented in Table 1. Table 2 presents characteristics of fuel and sorbent used during the tests. For the purpose of analysis of the effect of the primary air system modification on gaseous pollutant emission, the measurements of concentrations of the normalized exhaust gas components were carried out in the boiler.

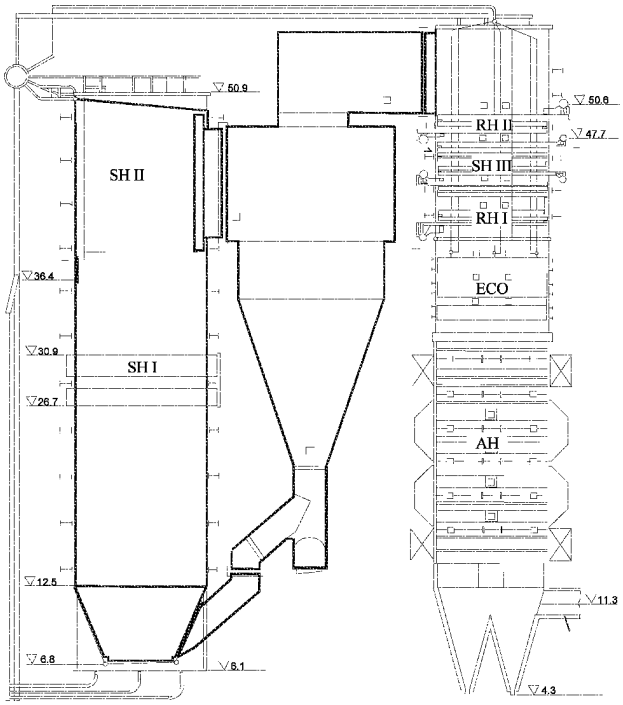

Fig. 1 CFB boiler 670MWth

Table 1 Operational parameters of CFB unit

General (100%MCR)		
Electric power	235	MW
Efficiency	91.72	%
Useful heat output	578	MW
Fuel consumption	50.03	kg/s
Live steam (100% MCR)		
Mass flow	198.72	kg/s
Pressure	13.42	MPa
Temperature	813	K
RH Steam (100%MCR)		
Mass flow	165.5	kg/s
Pressure	2.45	MPa
Temperature	813	K

Table 2 Fuel and sorbent characteristics (100% MCR)

Component	**Value**	**Component**	**Value**
Fuel		*Sorbent*	
C, %	32.3	$CaCO_3$, %	95.3
H, %	3.29	Inert, %	4.7
S, %	0.17		
N, %	0.30		
O, %	12.04		
Moisture, %	31.0		
Ash, %	20.90		
LHV, kJ/kg	12401		

PRIMARY AIR DISTRIBUTION SYSTEM

Primary air is supplied to the combustion chamber through three separate channels and windboxes, as shown in Fig. 2. As follows from Fig. 2, the mode of air supply to each of the windboxes is asymmetrical. This favours the inhomogeneous velocity profile in the grid zone and the generation of dead zones. Moreover, as has been shown by a detailed inventory of the windbox geometry, additional obstacles have been installed in their inlet spaces, which impair the air distribution uniformity.

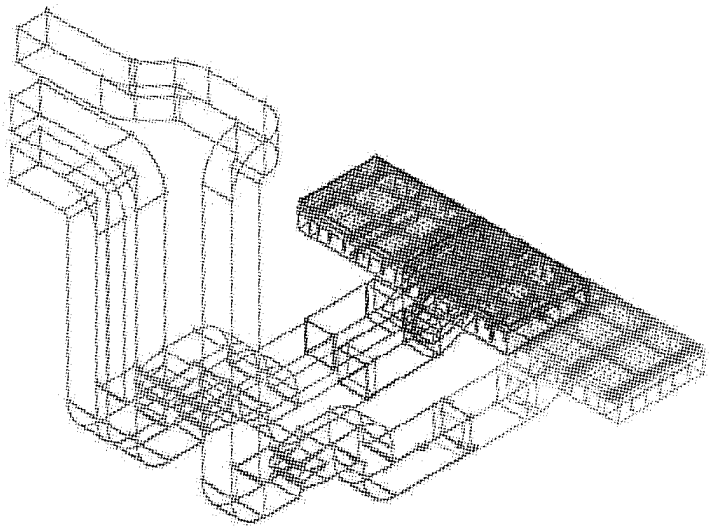

Fig.2 Primary air distribution system in 670t/h CFB boiler

As follows from numerical simulations (Mirek et al., 2008), the asymmetrical air supply system favours the generation of a vortex within the entire windbox space and the formation of a highly inhomogeneous velocity field in the vicinity of the air distributor. As a result, the adjacent air nozzles are supplied with an air stream of values differing significantly. Figure 3 shows the unmodified (Fig. 3(a)) and modified (Fig. 3(b)) geometries of the middle windbox of the 670t/h CFB boiler. Due to the non-uniformity of static pressure within the windbox inlet space, the asymmetrical construction of the inlet channel favouring the formation of an inner vortex within the entire windbox space, as well as owing to the small windbox depth, the equalization of pressure in the grid space will only be possible after a prior division of the air stream delivered to the windboxes. This function is to be performed by the baffles (Fig. 3(b)). The divided air stream should feed, in a similar proportion, three windbox zones resulting from the arrangement of the two beams mounted perpendicular to the air inlet direction. To this end, vertical partitions have been designed (Fig. 3(b)).

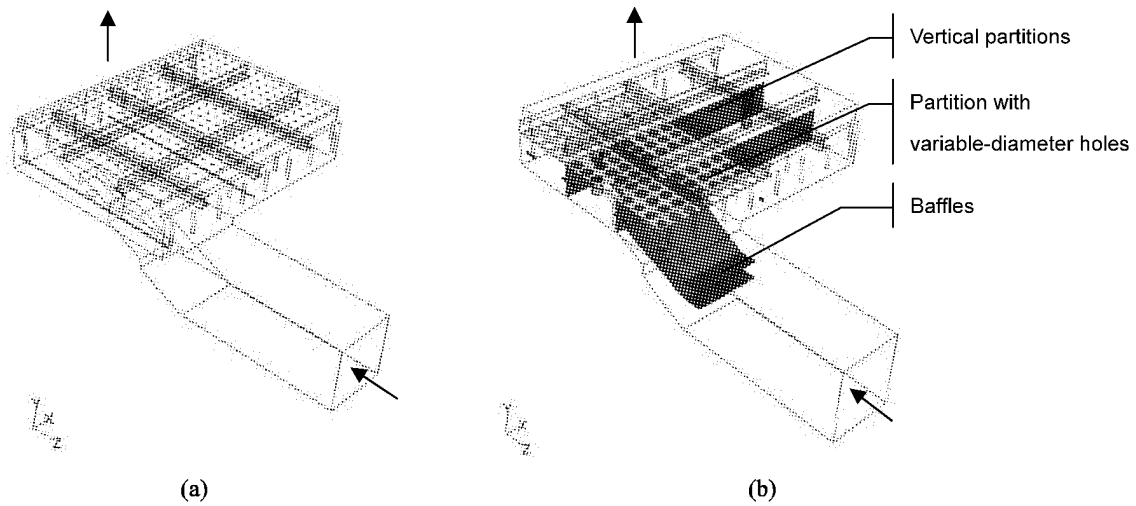

Fig. 3 The unmodified (a) and modified (b) geometry of the middle windbox

As the air stream is delivered to the windbox asymmetrically, an additional need arises to reduce the pressure in the zone immediately above the inlet channel, which should result in equalization of static pressure in the whole cross-section under the grid. This function is fulfilled by the partition with variable-diameter holes (Fig. 3(b)).

Introducing baffles into the windboxes is an elaborate way of improving the air distribution. There are opinions, that similar effects one can obtain by increasing the pressure drop across the distribution. However, this way of improvement is connected with increasing of the power station internal load, which from the economical point of view is not effective.

RESULTS AND DISCUSSION

Figure 4 summarizes the profiles of temperature along the height of the CFB 670t/h boiler's combustion chamber, as obtained with a full and a 65% load of the unit, respectively, for the condition before, and after the primary air distribution modification. The distributions have been plotted based on temperature measurements taken in parallel at a height of 0.25m, 2.5m, 37.0m and 51.0m, as measured from the combustion chamber grid bottom level. When comparing the curves obtained for the identical loads it is easy to notice that the modifications made to the geometry of the boiler primary air feeding system have not remained without effect on both the values and the distribution of temperature in the combustion chamber. Thus, on the one hand, the temperature values, as recorded after the modification, are generally lower, on average by approx. 34K at a 100% MCR, and by approx. 17K with the unit operating at a 65% MCR. The strongest effect of the implemented modifications, in terms of temperature, can, however, be observed at the lower combustion chamber part, where these differences amount to, respectively, 51K (for 100%MCR) and 39K (for 65%MCR). In general, such a temperature drop indicates a significant improvement in heat exchange occurring between the chamber and the thermodynamic medium, as separated by membrane walls. This is most likely to result from the equalized gas flow in the combustion chamber cross-section, the improvement in mixing with the resultant intensified heat exchange between bed material particles and the gas, as well as the elimination of dead zones and turbulences impairing the combustion gas – heat exchanger surface contact. On the other hand, an inversion of the temperature profile can be seen in the lower combustion chamber part, where the temperature values, as recorded 0.25 m above the grid, are higher than those measured at the level of 2.5 m. Such behaviour can result from the optimal conditions of mixing of the dense phase, where the modified distribution of air in the grid zone has changed the conditions of fuel distribution in this region. As a result, coal penetrates deeper, and the initial stage of the fuel combustion process takes place lower.

Moreover, the juxtaposition clearly indicates an equalization of the temperature profile along the combustion chamber height during boiler operation at a 65% load, which positively influences both the fuel combustion and the flue gas desulphurization processes, and the heat transfer by the thermodynamic medium.

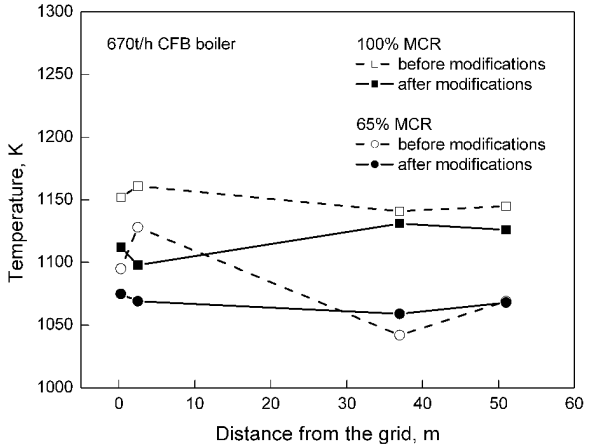

Fig. 4 Temperature distributions in 670t/h CFB boiler

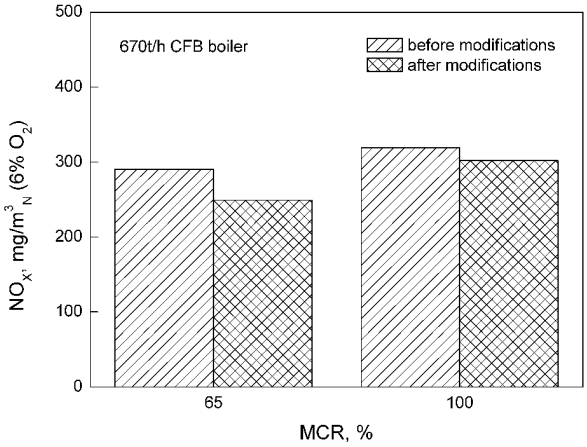

Fig. 5 NO_X emissions from 670t/h CFB boiler

The average levels of NO_X emissions, as recorded during the tests on the CFB 670t/h boiler before and after the modification, at a 65% and a 100% loads, are represented in Fig. 5. The results expressed in mg/m^3_N have been converted to standard conditions, i.e. 6 vol% of O_2 in the flue gas. In both cases, the data indicate a slight decrease in the concentration of nitrogen oxides in the exhaust gas. Thus, at 65%MCR, an NO_X emission reduction of approx. 14% is noted, where the value of C_{NOX}=290mg/m^3_N drops to 249mg/m^3_N, whereas at 100%MCR the NO_X emission has been reduced by approx. 6%, where the value of C_{NOX}=319mg/m^3_N drops to 301mg/m^3_N. The most probable cause of this behaviour seems to be the reduction of temperature in the combustion chamber (see Fig. 4), being the result of the primary air system modifications. Indeed, the temperature is one of the major factors determining the quantities of NO_X formed (Basu et al., 1991). Incidentally, it is the temperature that the main cause of the nitrogen oxide concentration differences recorded at different loads, both prior to and after the modification, is sought in, too. The relatively high value of NO_X (301mg/m^3_N) recorded after the modification, with boiler operation at the nominal power, may, however, result from the higher excess of fine limestone particles supplied to the combustion chamber to reduce the emission of SO_2. And, as is commonly known, the presence of sorbent in the fuel combustion zone has a catalytic effect on the conversion of the fuel N into NO_X (Leckner et al., 1990). During the test, the calorific value of the fuel

decreased, with the content of sulphur in the fuel remained. Therefore, to meet the live steam parameters, the fuel and thereby sulphur streams increased, which resulted directly in an increased flux of sorbent being fed.

CONCLUSIONS

The industrial-scale tests carried out on the CFB 670t/h boiler enable one to state that it is possible to reduce the emissions of NO_X by primary methods, and specifically by the optimization of the distribution of primary air in the combustion chamber. These conditions have been achieved as a result of modification to the geometry of the windboxes and the primary air inlet channels. As a result, the decreasing of the level, and the equalization of the profile of temperature within the combustion chamber contour were observed. Thus, lowering the average temperature successively by 17K and 34K resulted in a nitrogen oxide emission reduction by 14% and 6%, respectively, for 65% and 100%MCR.

REFERENCES

Andrzejczyk M., Effect of cyclone separation efficiency on emission of pollutants NO_x, SO_x during fluidized bed combustion process, Ph. D. Thesis, Czestochowa Univ. Tech., 2006, (in Polish).

Basu P., Fraser S.A., Circulation Fluidized Bed Boilers, Design and operations, Butterworth-Heinemann 1991, 152-156.

Kobylecki R, Bis Z., Emission of SO_2 and NO_x from large-scale CFBC-effect of cyclone separation efficiency, Proc. Of Circulating Fluidized Bed Technology IX, Germany 2008, 541-546.

Leckner, B., Mjornell, M., Karlsson, M., Hallstrom, C.: Int. VGB Fluidized Bed Systems Coference (1990).

Lee J.-M, Kim J.-S., Kim K.-J., Evaluation of the 200MWe Tonghae CFB boiler performance with cyclone modification, Energy 28, 2003, 575-589.

Mirek P., Jabłoński J., Nowak W., Numerical optimization of air flow in the plenum chamber of an industrial CFB boiler, TASK QUARTERLY 12 No 3, 2008, 237-244.

Mirek P., Sekret R., Nowak W., The influence of air nozzles' shape on the NOx emission in the large-scale 670 MWt CFB boiler, Fluidization XII, New Horizons in Fluidization Engineering 13-18 May 2007, Harrison Hot Springs, Canada, 969-976.

MobotecUSA website - http://www.mobotecusa.com/projects/vermilion.htm.

HEAT TRANSFER COEFFICIENT DISTRIBUTION IN THE FURNACE OF A 300MWe CFB BOILER

P. Zhang, J. F. Lu, H. R. Yang, J. S. Zhang, H. Zhang, G. X. Yue

Key Laboratory for Thermal Science and Power Engineering of Ministry of Education, Department of Thermal Engineering, Tsinghua University, Beijing, 100084, China

Abstract: Properly understanding and calculating the distributions of heat flux and heat transfer coefficient (α) in the furnace is important in designing a circulating fluidized bed (CFB) boiler, especially with supercritical parameters. Experimental study on the heat transfer in a commercial 300MWe CFB boiler was conducted. The α from the bed to the water wall was measured by the finite element method (FEM), at five different heights. The influence of suspension density and bed temperature on α was analyzed. It was found that the pressure difference between the inlet and exit of the three cyclones, and the chamber pressure of the corresponding loop seal were not equal. The results indicated the suspension solid density was non-uniform in the cross section at a certain height. Consequently, the distributions of heat flux and α in the horizontal plane in the furnace was non-uniform. The furnace can divided into three sections according to the arrangement of the platen superheaters hanging in the upper CFB furnace. In each section, the heat flux near the center showed increasing trend.

Keywords: CFB boiler, heat transfer, heat flux, heat transfer coefficient, furnace

INTRODUCTION

Properly arranging the distribution of heat flux from the bed to the water wall is important in CFB boiler design, especially for the supercritical ones. Most of the existing CFB boilers are nature circulation with drum and the steam pressure is subcritical. For such nature circulation type boilers, the heat flux deviation on water wall is not severe since the hydrodynamics in the water-steam loop possesses the so-called self-compensation capability (Xin et al., 2002). While for the supercritical boilers, the water-steam system is of once through, so the heat flux deviation on the water wall might be severe and must be carefully considered (Yu et al., 2004).

Experimental measurement of heat flux is important for the operation of the boiler. Andersson and Leckner (1992) measured the horizontal heat transfer coefficient (α) and heat flux distribution in a 1.44× 1.7m water heater, by a so-called finite element method (FEM). In the experiment, at different positions of the same tube section, on the outer surface of the tube, temperatures were measured. With the assistant of the finite element analysis, α and heat flux were calculated. However, the non-homogeneity of the pipe flow, as well as phase-change of working fluid directly affected the measurement results, making the reliability of the data questionable. Wu et al. (2004) compared the heat flux profile along the furnace between the CFB boiler and pulverized coal (PC) boiler, and found the maximum heat flux is at the bottom of the furnace where the temperature of the working fluid is low. It is easy to control the metal temperature of water-wall in a CFB boiler, but for a PC boiler, the heat flux peak occurs at where temperature of working fluid is high. Lu (2007) measured the heat flux on the water-wall through the temperature of three nodes on the membrane wall in three industrial CFB boilers with the furnace cross sections 3m×6m, 5m×10m, 7m×14m. The temperature distribution was also measured. It was found that the bed temperature was relatively uniform with a deviation of 23 ℃ or less on the normal coal-feeding condition, and the distribution of heat flux and α was similar. Similar to the previous experimental study(Zhang et al., 2005) , it was found that the α at the corner was higher than that in the center regardless of the bed cross-section size and the level of the furnace.

In the following experiments, the distribution of heat flux and the heat transfer from the bed to the water-wall will be studied further.

EXPERIMENTAL

The experiments were conducted in a 300MWe CFB boiler with single furnace, natural circulation, circulating fluidized bed combustion. The boiler mainly included three parts, a furnace of membrane water-wall, three stream-cooling cyclone separators and the HRA(heat recovery area). There were 12 platen superheaters and 6 platen reheaters near the front wall and two water cooled wing walls near the rear wall in the furnace. Eight coal-feeding ports were arranged along the width direction at the low contraction part. The air was supplied from the two sides of the wind box. Two ignition burners were located in the primary air ducts and four ignition oil guns were set up at the dense-phase area. There were four ash discharge ports below the water

wall in the bottom furnace, connecting with four water-cooled rotary ash coolers respectively. The main parameters of the boiler are shown as Table 1.

The furnace is with cross section of 8.439m × 28.275m, and height of 40m from the air distributor to the roof. The first level (L1) measurement planes located at 14.6m from the air distributor. The fluidizing velocity U_f ranges from 3.6 to 3.9m·s^{-1}. The membrane wall tube is 57mm in diameter and 87mm in pitch with 6.5mm thickness. Pressure measuring points are located symmetrically in the two side walls along the furnace height.

Table 1 Main designated parameters of the test boiler

Parameter	Units	B—MCR	B—ECR
Superheated Steam Flow Rate	t/h	1025	954.175
Superheated Steam Pressure (Gauge)	MPa	17.45	17.45
Superheated Steam Temperature	℃	540	540
Reheated Steam Flow Rate	t/h	844.867	790.294
Inlet/Outlet Reheated Steam Pressure (Gauge)	MPa	3.665/3.485	3.427/3.247
Inlet/Outlet Reheated Steam Temperature	℃	321.8/540	314.9/540
Feeding water temperature	℃	282.1	277.5

Arrangement of measuring points

The measuring points are located at 5 different heights(14.6m,17.8m,21.2m,28.1m,35.1m) along the furnace. They are located at the rear wall at the first level and only half side of the walls at other levels. The arrangement of the measuring points at the first level is shown in Fig. 1. The measuring points are not with the same interval.

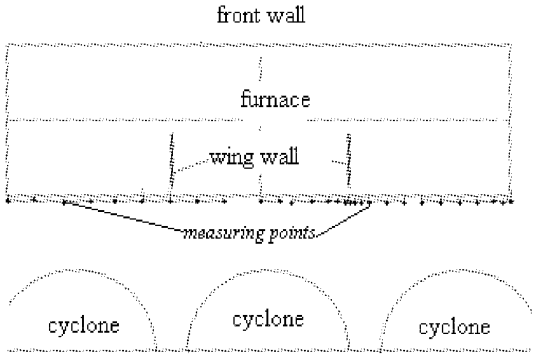

Fig.1 Arrangement of the measuring points at level 1

Measuring Method

It is difficult to directly measure the heat flux on the industrial boilers. An indirect way from the temperature measurements at different position in the same section of membrane water-wall (Bowen et al.,1991, Fang et al., 1997, Andersson and Leckner 1992, 1994). This method was also used in α measurement in a large-scale CFB (Zhang et al. 2005). In present study, the installation of the measuring points is shown in Fig. 2. The result of α was directly influenced by the accuracy of the temperature measurement. Through error analysis, as shown in the Fig. 3, temperature gradient near A and C is small, but near the B is large. If α is calculated based on the temperatures of Point A and Point C which were of distance of 5mm, the error will be within 5%.

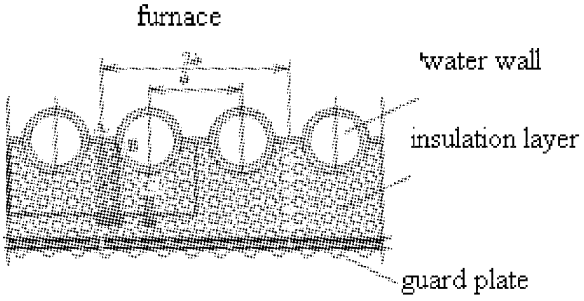

Fig .2 Installation of the thermocouples

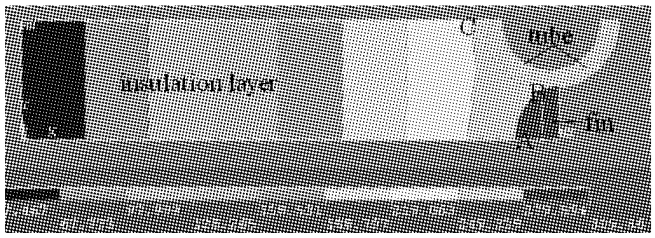

Fig. 3 The temperature distribution calculated by FEM

RESULTS AND DISCUSSION

Figure 4 shows the indirect measured results of heat flux distribution along the rear wall at level .The temperature of the water in the tube T_f ranges from 358.6 to 359.3℃, The bed temperature distribution was also measured and the results showed that the bed temperature was relatively uniform with a maximum deviation of 40°C on the normal coal-feeding condition. The distributions of heat flux and α were similar. Figure 4 shows that there exists bias among the left, middle and right sections. The middle section has higher heat flux than two side section and the left section is of little higher heat flux than the right section. The distribution at different levels has the same trend. At different load and different height, the similar distributions were observed.

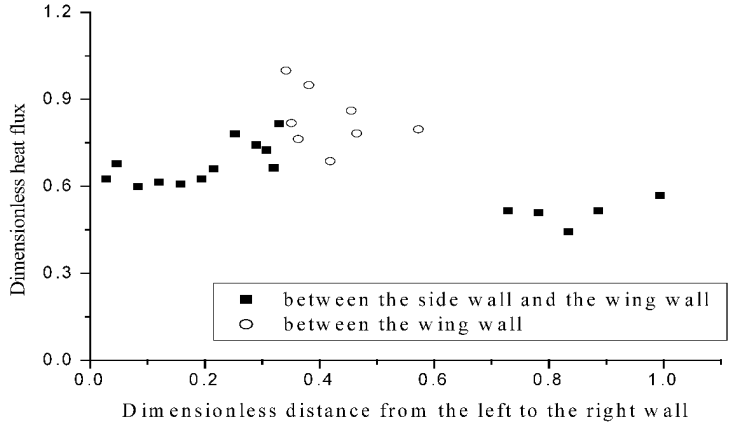

Fig. 4 Distribution of the heat flux in the whole rear wall

Figure 5 shows the pressure distribution along the height at the two side walls. The curve of the left wall is higher than that of the right wall. The average suspension solid density ρ_b at each level is proportional to the pressure gradient, and can be calculated by following expression :

$$\rho = \frac{dp}{dh} g$$

As shown in Fig. 5, in the dilute bed, the left side of the furnace has higher ρ_b than that the right side.

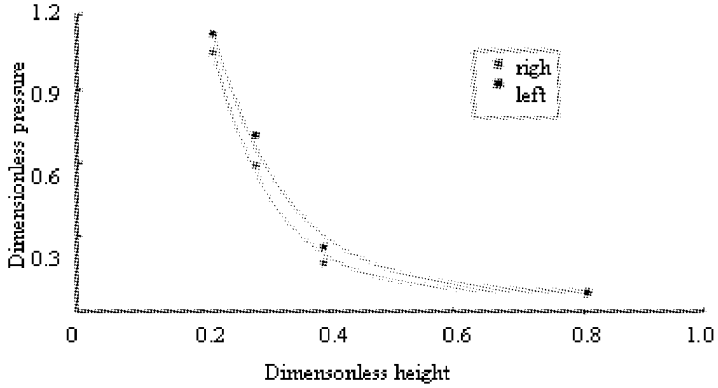

Fig. 5 Pressure drop profiles along the furnace height

The most important factors impact α is ρ_b and bed temperature, T_{bed}. In the CFB furnace, temperature is uniform. the ρ_b is difficult to be directly measured. From the axial pressure profile on both sides of the wall, pressure difference between the inlet and exit of three cyclones and the chamber pressure of the corresponding loop seal , it is suggested that two-phase flow in a CFB boiler is non-uniform in the horizontal direction. This boiler has larger width depth ratio (3.5), the horizontal flow and mixing was insufficient The middle part has less heating surface ,and the T_{bed} in the middle part is higher that in the two side parts.

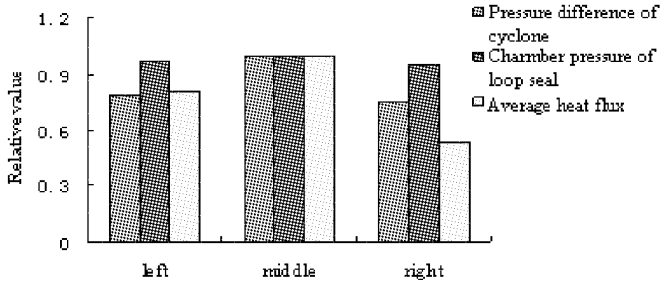

Fig. 6 Comparison of pressure drop data for the three sections

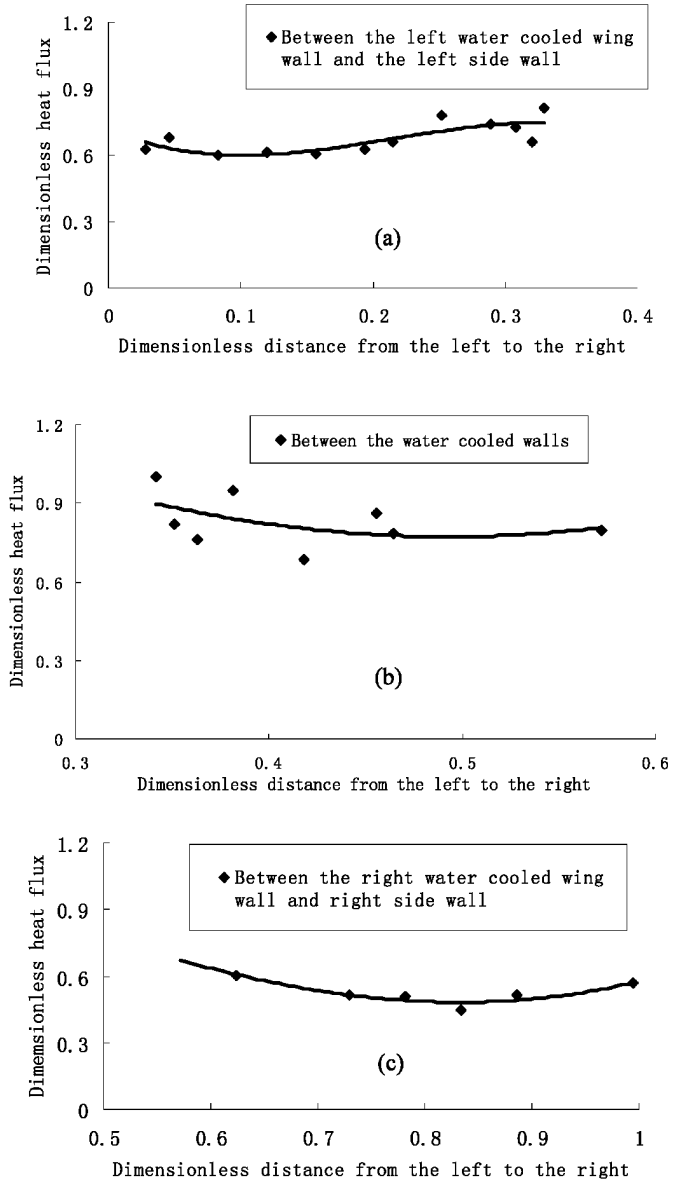

Fig. 7 Measured horizontal distribution of heat flux in the rear wall
(a) between the left water-cooled wall and the left side wall; (b) between the two water-cooled walls
(c) between the right water-cooled wall and the right side wall

There are two water-cooled wing walls near the rear wall in the furnace, shown as Fig. 1, dividing the furnace into three sections. Figure 6 compares the pressure difference between the inlet and exit of three cyclones, and the chambers pressure of the corresponding loop seal with the average heat flux of the three sections. The higher flux is associated to higher pressure difference and pressure. The relative pressure difference reflects the relative gas flow, and the relative pressure reflects the relative average solid concentration. Close the middle section of each side wall in the furnace, there are more material and larger gas flow. The uneven two-phase flow leads to the uneven distribution of the heat flux.

In the middle section, between the two wing walls, heat flux is higher. In all three sections, as shown in Fig. 7, heat flux is higher in the corner (formed by the rear wall and the wing wall). Lu (2007) found that heat flux was lower in the central section of the wall and attributed that profile the uneven horizontal ρ_b distribution. Based on his experiments, ρ_b is lower in the center and higher in the corner, consistent with what was found by Kari et al. (2003). From Fig. 7, it can be also seen that n the horizontal direction, the minimum heat flux located around the center of the wall, and heat flux increases from the center to the corner. However, the present experiments showed that minimum heat flux was not strictly at the center. This was caused by the non-uniformity of the flow in the furnace.

CONCLUSIONS

Experimental study on the distributions of heat flux and the heat transfer coefficient in a commercial 300MWe CFB boiler was conducted. The front and rear walls can be divided into three sections according to the arrangement of the platen superheaters hanging in the upper CFB furnace. In each section, the heat flux near the center showed increasing trend. The distribution heat transfer coefficient has the similar trend.

Based on the pressure drop of three cyclone separators and the pressure of their corresponding loop seal pressure, it can be concluded that the suspension solid density was non-uniform in the cross section at a certain height. The non-uniform arrangement of heating surface and non-uniform distribution of the suspension solid density could be the main cause of the non-uniform distributions of heat flux and heat transfer coefficient.

NOTATIONS

T temperature, K
T_b bed temperature, K
T_f water temperature, K
u_f fluidizing velocity, $m \cdot s^{-1}$
α heat transfer coefficient, $W \cdot m^{-2} \cdot K^{-1}$
α_b heat transfer coefficient between the bed and the wall, $W \cdot m^{-2} \cdot K^{-1}$
ρ_b solid suspension density, $kg \cdot m^{-3}$
ρ solid concentration average cross section, $kg \cdot m^{-3}$

ACKNOWLEDGEMENTS

Financial supports of this work by Key Project of the National eleventh-Five Year Research Program of China (2006BAA03B02) and National Science Fund Committee (50576041) are gratefully acknowledged.

REFERENCES

Andersson, B. A. and Leckner, B. Int. J. Heat Mass Transfer. **35** (1992), 3353-3362.
Andersson, B. A. and Leckner, B. Circulating Fluidized Bed Technology IV, (1994), pp.311-315.
Bowen, B. D, Fourier M., Grace, J. R., Int. J. Heat Mass Transfer, **34**(1991), pp.1043-1057.
Cheng, L. M, Wang, Q.H, Shi, Z.L. Journal of Power Engineering. **26**(2006), pp.305 - 310.
Fang, Z, Xie, D. Dial, N. Int. J. Heat Mass Transfer. **40**(1997),pp.3947-3953.
Harris, A. T.:AIChE Journal, **49**(2003), pp.52-64.
Kari, M.,Timo, H., Jouni, M. Proceedings of 17th International Conference on Fluidized Bed Combustion, (2003), No. 48.
Lu, J. F. Power Engineering (in Chinese), **27**(2007),pp.336-340.
Pagliuso, J.D. and Lombardi, G. Experimental Thermal and Fluid Science.**20**(2000),pp.170-179.
Wang, Y., Lu, J. F., Yang, H. R. Proceeding of the 18th International Conference on Fluidized Bed Combustion (2005), pp.327-335.
Wu, Y.X, Lu, J. F., Zhang, J.X., Liu et al., Proceedings of the 8th Circulating Fluidized Bed Technology (2005), pp.529-534.
Xin, J., Lu, J. F., Yue, G. X. Journal of Engineering for Thermal Energy and Power.**17**(2002),pp.439-441.
Yu, L., Lu, J. F., Wang, Z. W. Journal of Engineering for Thermal Energy and Power.**19**(2004),pp.336-341.
Zhang, H., Lu, J. F., Yang, H. R., Proceedings of the 8th Circulating Fluidized Bed Technology(2005),pp. 254-260.
Zhang, J.F., Yue, G. X., Fang, J. H. Boiler Technology, **12**(1998),pp.1-5.

CALCULATION AND ANALYSIS OF HEAT TRANSFER COEFFICIENTS IN A CIRCULATING FLUIDIZED BED BOILER FURNACE

Zhiwei Wang[1], Jianhua Yang[2], Qinghai Li[3]

1 Thermal Power Research Institute, Xi'an, 710032, China
2 Zhengzhou Electric Power College, Zhengzhou, 450004, China
3 Key Laboratory for Thermal Science and Power Engineering of Ministry of Education, Tsinghua University, Beijing 100084, China

Abstract: A new way for the circulating fluidized bed (CFB) boiler research is proposed by the supervisory information system (SIS) in power plant level. The heat transfer coefficient in CFB boiler furnace is calculated and analyzed by the SIS calculation analysis in a commercial CFB boiler, the way how to calculate the heat transfer coefficient in SIS is introduced, and the heat transfer coefficient is accurately received by calculating a large amount of data from database. The relation about the heat transfer coefficient to unit load, bed temperature, bed velocity, and suspension density is analyzed; the linear relation could be accepted for the commercial CFB design. A new calculating and simple way for the heat transfer coefficient of CFB boiler is proposed for CFB boiler design. Using this research result, the reheat spray water flux larger than the design value in lots of commercial CFB boilers is analyzed; the main reason is the designed heat transfer coefficient smaller than the actual value.

Keywords: circulating fluidized bed boiler, supervisory information system, heat transfer coefficient

Circulating material balance, heat balance and high combustion efficiency are the normal operation foundation of the circulating fluidized bed (CFB) boiler (Feng Junkai, 2000). In early period of China, the analysis of material balance had been the emphasis of theoretical research on CFB boiler, and how to ensure the full output of CFB boilers has been the focus on engineering application. After the CFB boiler technology from FW having been introduced by Dongfang Boiler Co. Ltd, the full output of CFB boiler is no longer a main problem due to the high cyclone separator efficient, and the engineering application mainly focuses on bout how to ensure continuous, stable and economic operation of CFB boiler, while the emphasis of theoretical research changes into the combustion characteristics, waterwall wear and furnace heat transfer in CFB boiler.

With the application of the larger CFB boiler and the development of independent development technology, the application of theoretical research results and the verification of practical engineering results will interleave with each other during the development of CFB boiler technology. Especially for the independent development technology of CFB boiler in China, many key technologies need to be developed and applied by the research institutes, and important design parameters need to be verified and summarized by engineering applications. The heat balance in material circulation loop is one of the emphasis and difficulties in the research of independent development technology for CFB boiler in China, a lot of reliable and verified data and way is needed for heat transfer coefficients used in CFB design.

The supervisory information system (SIS) in power plant level is an application with power information development in China. It can realize these basic functions of data storage, processing and analysis of unit operating parameters, and the operation optimization can be developed on this basis. The heat transfer coefficient in 135MWe CFB boiler is studied in this paper according to the first domestic application of SIS on CFB units (Wang Zhiwei, Yang Feng et al., 2007).

CALCULATING BASIS OF HEAT TRANSFER COEFFICIENT

Introduction to SIS

SIS is an information system that can analyze and process historical production information for large-capacity units. It consists of supervising network, real-time database server, interface unit, comprehensive management station, computer station and client station (He Xin et al., 2004), and can realize the functions of Running Process Supervision, Economic Indexes Analysis and Diagnosis, Operation Optimization and Guide, Performance Calculation at plant level, Economic Analysis of unit load, Statistical Analysis of process information, Operation Diagnosis of units and auxiliaries, and so on. At present SIS is developed toward two indirections: one is supervision to the power plants for power group/company or power grid (Wang Zhiwei, Yang Dong et al., 2006), another is real functional application for equipments and operations in power plant (Wang Zhiwei, Huang Yu et al., 2006).

Some real time calculating method of special parameters for CFB boilers is researched and used in SIS Performance Calculation at power plant (Wang Zhiwei, Yan An et al. 2007); the real time heat transfer analysis will be introduced below.

Introduction to unit

The Harbin Boiler Company Limited provided the CFB boilers (HG-440/13.7-L.HM29) for Chifeng thermal and power plant. The boiler mainly consists of furnace, high temperature isolation cyclone, dual loop seal and rear convection flue with the last superheater, the first reheater, the first superheater, economizer, air heater.

Waterwall

The furnace cross section A is 15320×7220 mm, the furnace center line height is 36184 mm; the waterwall tube size is Φ60×6.5 mm and pitch 80 mm. A dual division waterwall is arranged on the middle throughout the CFB furnace.

As the dense zone, the transition zone and dilute zone of the furnace can not be strictly distinguished and the stream parameters of this zone can not be measured in engineering application; so the whole furnace waterwall can be analyzed as a total heating surface for the engineering design and application, and the simplification to analyze the heat transfer coefficient is realizable.

Superheat panels

Eight superheat panels are disposed in the vertical direction of the furnace front wall, hanged on the furnace roof. The superheat panel tube size is Φ51×5.5 mm and pitch 70 mm, each panel consists of 27 tubes and the panel height is 20431 mm.

Reheat panels

Six reheat panels are disposed in the vertical direction of the furnace front wall, hanged on the furnace roof, interleaving and paralleling with superheat panels. The reheat panel tube size is Φ57×5 mm and pitch 70 mm, each panel consists of 29 tubes and the panel height is 20431 mm.

Data collection

Unit operation data can be transmitted directly from DCS, RTU, PLC, etc. to real-time historical database for storage and can be got from real-time historical database for data analysis.

Data processing

Heat transfer temperature

Temperature at water and steam working medium side t_1: taken saturated water temperature for waterwall under the average pressure of the drum pressure; taken steam average temperature at the outlet and inlet for reheat panels and superheat panels.

Temperature at flue gas side t_2: taken average temperature of the flue gas at the dense zone and the exit of furnace. A way is used to automatically eliminate the error value from several flue gas temperatures in the SIS performance calculation.

It is difficulty to calculate the wall temperature for waterwall and panels, so the temperature of average working medium is used and is easy for the commercial CFB design. Defined the heat transfer temperature difference is:

$$\Delta t = t_2 - t_1 \tag{1}$$

Heat transfer area

On considering that different boiler companies use different sized waterwalls tube and different panel pitches, so it is not universal to use the projection area for heat transfer coefficient. So the contracted area for touching the flue gas is used to calculate heat transfer coefficient. The water-cooling division panel is calculated as double sides contracted with the flue gas for the calculation of heating side of waterwall.

So the heat transfer coefficients maybe are smaller than others data from experiments since the contracted area is used instead of the projection area. The ratio of the contracted area to the projection area is:

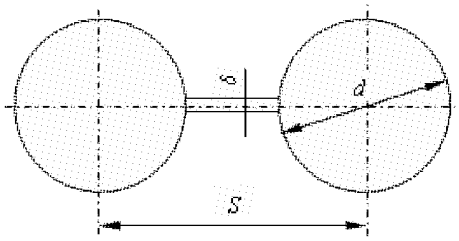

Fig. 1 membrane structure for waterwall and panel

$$\xi = 1 + [(\pi / 2 - 1)d - \delta] / S \tag{2}$$

The size data of the waterwall, reheat panels and superheat panels are listed in Table 1.

Table 1 Membrane structure for waterwall and panel

Item	symbol	unit	waterwall	division waterwall	reheat panels	superheat panels
Tube diameter	d	mm	60	60	57	51
Fin depth	δ	m	5	5	5	5.5
Tube pitch	S	mm	90	72.7	70	70
Ratio	ξ	-	1.324	1.402	1.393	1.344
Heat Transfer Area	F	m^2	1910	456	680	813

Heat transfer flux

For waterwall: working medium flow D takes the value of feed water flow. The outlet pressure P_{out} of working medium takes the value of average value of stream drum pressures; the working medium outlet enthalpy h_{out} takes the saturated value stream enthalpy under P_{out}. The inlet pressure P_{in} and temperature t_{in} takes the value located in the outlet header of economizer; thus we can get the enthalpy at the inlet of waterwall h_{in} by the P_{in} and t_{in}.

For superheat panels: working medium flow D is got by subtracting second spray water flow from the main stream flow which is calculated in the SIS performance analysis; inlet and outlet working medium enthalpy are calculated with the inlet and outlet pressure and temperature of superheat panels.

For reheat panels: working medium flow D takes the value of the reheater flow which is calculated in the SIS performance analysis; inlet and outlet working medium enthalpy are calculated with the inlet and outlet pressure and temperature of reheat panels.

Thus the heat transfer flux of the working medium side is:

$$Q = D(h_{out} - h_{in}) \tag{3}$$

Heat transfer coefficient

The calculation formula for heat transfer coefficient of waterwall, reheat panels and superheat panels can be got as below on the basis of calculation parameters from SIS:

$$\alpha = \frac{Q}{F\Delta t} \tag{4}$$

Data sieving

Calculation parameters of the furnace waterwall, reheat panels and superheat panels can be received from SIS by every second, so millions of data will be received if data for several months is extracted from real-time historical database. So it should be to decrease the data quantity. At the same time, some data is unstable and unreliable and it is necessary for data sieving.

Taking unit load, bed temperature, main stream flow, main stream pressure, and so on as stable conditions for the CFB operation, the calculation parameters can be sieved and the calculation data under stable conditions can be received.

Calculation of other parameters

Bed velocity

The actual flue gas volume V for a kg coal can be calculated on the basis of input coal quality data and gas oxygen concentration in front of the air reheater. The actual burned coal flow B can be received by the SIS calculation analysis. Thus, the bed velocity is:

$$u = \frac{(273 + t_2)BV}{273A} \tag{5}$$

Suspension density

The average suspension density in different height zones in the CFB furnace can be got on basis of pressure-measuring-points along the height of furnace, and the calculation method has been discussed in related literature (Wang Zhiwei and Li Xiaofeng, 2006). The pressure and distance between two measuring-points is p_1, p_2 and H, then the average suspension density is:

$$\rho = \frac{p_1 - p_2}{gH} \tag{6}$$

The real-time suspension balance graph in the SIS Running Process Supervision is shown in Figure 2. It

displays the distribution curves of real-time calculation of the bed velocity and the suspension density, including other important parameters, such as the cyclone efficiency, the material cycle rate, bed stag material height, plate pressure drop and so on.

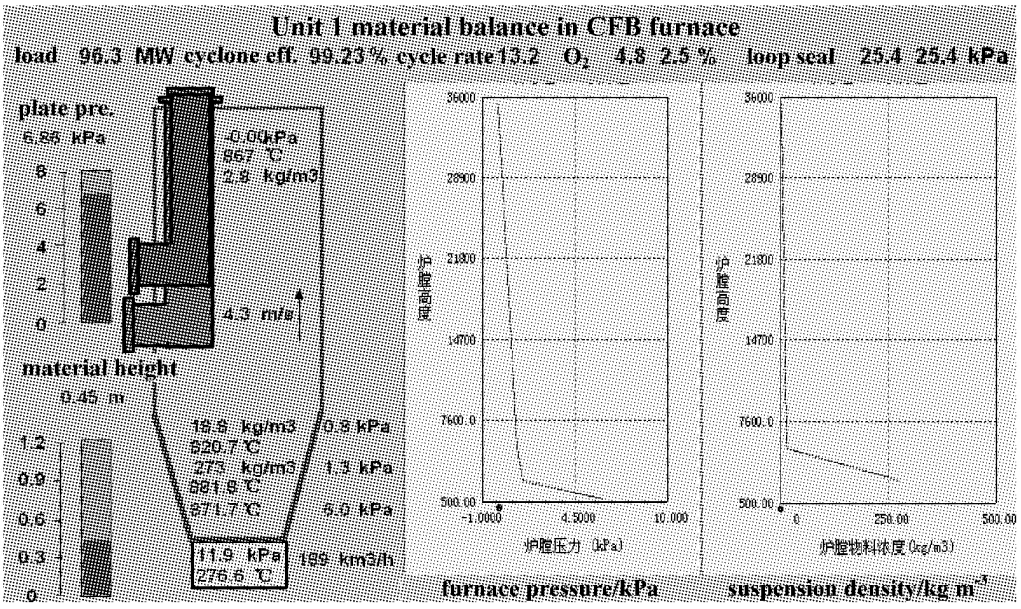

Fig. 2 Real time material balance

Balancing of the internally circulating material, especially balancing of the upper internally circulating material, is important for the operation of CFB boiler (Wang Zhiwei, 2003). It takes the value of average suspension density at the furnace's upper part in analysis of heat transfer coefficients; the upper part suspension density is easy to get for the design and operation.

RESULTS OF HEAT TRANSFER COEFFICIENTS

Heat transfer coefficient and unit load

Relation between heat transfer coefficients and unit load is shown in Figure 3. Plenty of operating data shows the relation about unit load to the waterwall, reheat panels and superheat panels can be simplified to linear relation.

The heat transfer coefficients are located between 80-125 W/(m^2℃) and load range is between 80-135 MW. The heat transfer coefficients of reheat panels are obviously higher than that of waterwall and superheat panels.

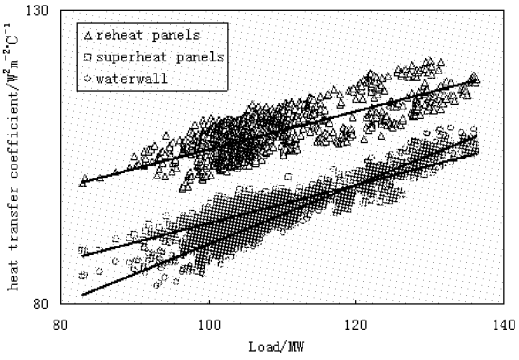

Fig. 3 Relation between heat transfer coefficients and unit load

Heat transfer coefficients and bed temperature

Relation between heat transfer coefficients and the bed temperature is shown in Fig. 4. Plenty of operating data shows the relation about bed temperature to the waterwall, reheat panels and superheat panels can be simplified to linear relation.

From Fig. 4, heat transfer coefficients increase by the bed temperature and the bed temperature is between

825-915℃.

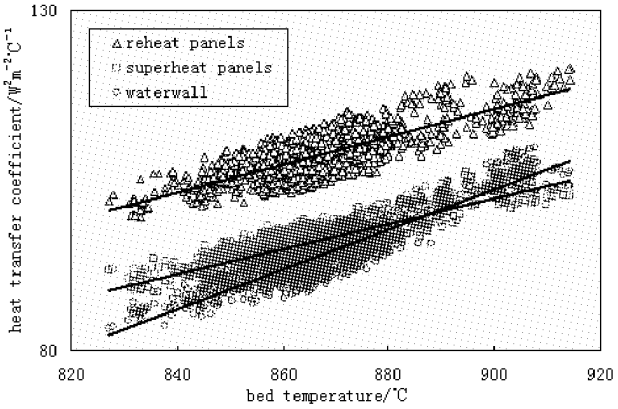

Fig. 4 Relation between heat transfer coefficients and bed temperature

Heat transfer coefficients and bed velocity

Relation between heat transfer coefficients and bed velocity is shown in Fig. 5. Plenty of operating data shows the relation about bed velocity to the waterwall, reheat panels and superheat panels can be simplified to linear relation.

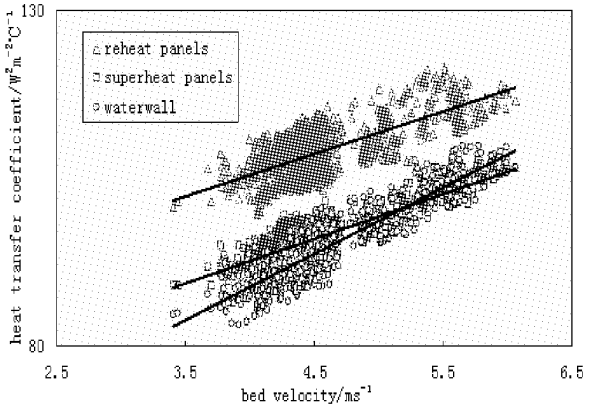

Fig. 5 Relation between heat transfer coefficients and bed velocity

Heat transfer coefficients and suspension density

Relation between heat transfer coefficients and suspension density is shown in Fig. 6. Plenty of operating data shows the relation about material density to the waterwall, reheat panels and superheat panels can be fitted to linear relation.

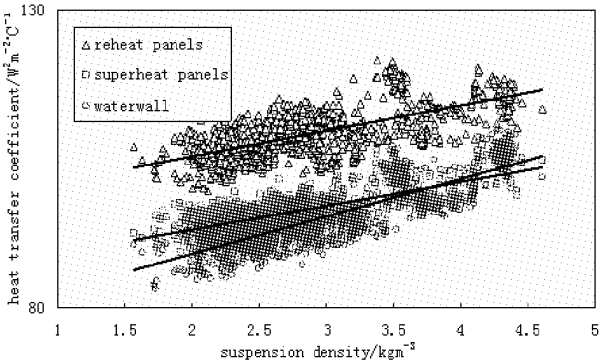

Fig. 6 Relation between heat transfer coefficients and suspension density

The average suspension density at the furnace's upper part is between 1.5-4.5 kg/m^3.

DISCUSSIONS

Calculation of furnace's heat transfer coefficients is a key point in the study on the model of CFB boiler (Wang Zhiwei, 1999; Wang Zhiwei, Li Dingkai et al. 2002). The calculation result of theoretical research model can hardly be verified in actual engineering application as well as in engineering design. In order to ensure the reliability of CFB heat balance design, it has to compare the designed heat transfer coefficient with the actual result for the CFB boiler designer. But because of the lack of necessary methods, accurate, reliable and considerable scale of actual heat transfer coefficient, results can not be received by engineers.

For example, the relation between the actual heat transfer coefficient of superheat panels and unit load of the existing 100MWe class CFB boiler, which is running in Fenyi power plant, is shown in Fig. 7 (Wang Zhiwei, 2003). These data is received mainly from the calculation of artificially noting operation parameters, the data deviation is large and the data quantity is small, it is impossible to get the real time data including in bed velocity, suspension density and so on. Fortunately SIS provides a data platform which proposes a new research method for the research of technologies for CFB boiler.

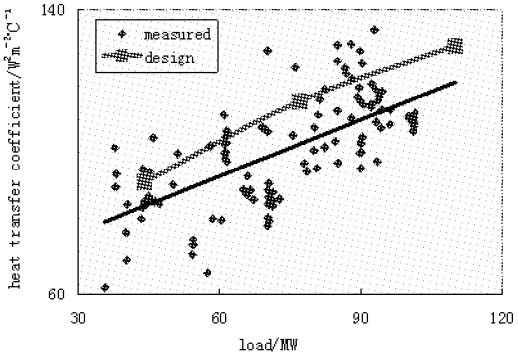

Fig. 7 Relation between heat transfer coefficients and unit load

From the above heat transfer coefficient data from Fig. 3 - Fig.6, which is received from the commercial CFB boiler, we can see that the test points are some divergent, which is related to the fluctuation of measuring parameters and running condition while measuring. As the running conditions are different, the heat transfer coefficient in CFB boiler fluctuates a lot. This fluctuation is normal, such as changes of fuel characteristics, furnace's suspension density, bed temperature, the primary air / second air ratio and so on, all of which can cause the change of furnace heat transfer coefficient.

How to solve the fluctuation in CFB design?

From view of the thermal calculation for CFB boilers, the design value of heat transfer coefficients on different loads should be a certain value and located in the fluctuation range of actual measuring data. It can adjusted the design transfer coefficient by simply adjusting operation conditions and reduce the deviation caused by design, which often happens in commercial CFB boilers, such as Fig.7 the design value locates in the upper zone of the fluctuation range which caused the higher bed temperature than designed value.

So the CFB boiler design should try to take the heat transfer coefficients located in the middle of the fluctuation range. From view of energy balance, if the selected heat transfer coefficients fit engineering practice in a suitable range, heat transfer coefficients can be adjusted by adding bed materials to increase the suspension density when the suspension density of fuel ash content accumulated in furnace is lower than the requirement of the design value of heat transfer coefficients (Wang Zhiwei, Wan Siben et al., 2007).

The above results also show that the relation about the heat transfer coefficient in CFB boilers to unit load, bed temperature, bed velocity and suspension density can be simplified to linear relation. The actual running results in CFB boiler can be verified and summarized by using this relation in engineering design. When we take a heat transfer coefficient in a CFB boiler design, the heat transfer coefficient must be fit for a bed temperature, a bed velocity and a suspension density under a load. The bed temperature and bed velocity can decide the furnace section, at the same time engineering must consider if the suspension density can be got for the design and check coal, then the total furnace area (that is the furnace height) and panel area can de decided by the heat transfer coefficients.

From the above analysis, we can get a calculating way for the heat transfer coefficient of CFB boiler, the expression is below:

$$\alpha = \alpha^0 + k_1(t^0 - t) + k_2(u^0 - u) + k_3(\rho^0 - \rho) \tag{7}$$

The parameters (α^0, t^0, u^0, ρ^0) are constants taken from the commercial CFB boiler under a load (MCR is

proposed), the heat transfer coefficient should be modified when we hope change any parameters of bed temperature t, bed velocity u or suspension density ρ.

Fig. 3 - Fig. 6 shows the relation between waterwall, reheat panels and superheat panels. The heat transfer coefficient of reheat panels is higher than that of waterwall and superheat panels, the reason maybe is that the tube wall temperature is higher than that of the waterwall and the superheat panels, which causes the higher radiation heat transfer difference between the flue gas and the tube wall. Clearly it does not fit the actual engineering project's result if the reheat panels use the same value of heat transfer coefficient as the superheat panels. Unfortunately the designed heat transfer coefficient of reheat panels often takes the value like that of superheat panels and is smaller than the actual value in commercial CFB boilers, so the reheater needs a lot of spray water flux to control the steam temperature. The phenomena often happen and deduced the reheat panels after CFB boilers commissions.

CONCLUSIONS

Large-scale data of heat transfer coefficients in CFB boiler is analyzed by using SIS at the first time. SIS provides a very powerful tool or method for theoretical research and engineering design of CFB boiler.

Conclusions can be received from calculating and analyzing results as below:

1) The relation about the heat transfer coefficient in CFB boiler to unit load, bed temperature, bed velocity and suspension density can be simplified to linear relation;
2) The heat transfer coefficient of reheat panels is higher than that of waterwall and superheat panels;
3) The heat transfer coefficient in CFB boiler has a large range of fluctuation, the design value should be in a controllable fluctuation range;
4) A simple way is proposed to calculate the heat transfer coefficient for CFB boiler design.

NOTATIONS

Symbols:

A	area	m^2
B	coal flow	kg/s
d	tube diameter	mm
D	flow	kg/s
F	area	m^2
h	enthalpy	J/kg
H	height	m
k	coefficient	
P	Pressure	kPa, Pa
Q	heat transfer flux	W
S	tube pitch	mm
t	temperature	℃
u	bed velocity	m/s
V	gas volume	m^3/kg

Greek letters:

α	heat transfer coefficient	$W/(m^2℃)$
δ	fin depth	mm
ξ	ratio of the conduct area to the projection area	-
ρ	suspension density	kg/m^3

Subscripts:

in	inlet
out	outlet

REFERENCES

Feng Junkai: Factors to Keep Circulating Fluidized-Bed Combustion Boilers in Normal Operation. Energy Information and Research. 16-1 (2000), pp. 1-6.

He Xin, Yang Dong, He Yong, et al.: Design and Study of Plant's Level Supervisory Information System of Thermal Power Plant. Electrical Equipment. 5-10(2004), pp. 4-7.

Wang Zhiwei: Modeling Approach for Design of Biomass-fuelled Circulating Fluidized Bed Boiler. Tsinghua University master thesis, Beijing, 1999.

Wang Zhiwei, Li Dingkai, Tang Songtao, et al.: Modeling approach for the biomass-fuelled circulating fluidized bed boiler. Energy Research and Information. 18-1(2002), pp. 21-29.

Wang Zhiwei: Modification Software Report on 100 MW CFB Boiler Design, In Thermal power research institute technology report (TPRI/T1-RB-081-2003).

Wang Zhiwei: Balancing Analysis of Charges of Circulating Fluidized Bed Boilers. Power Equipment. -3(2003), pp. 20-23, 35.

Wang Zhiwei, Yang Dong, Hu Honghua, et al.: Research and Development on the Corporation Information System, In 2006 high level forum of electrical information. Yangzhou, 2006, pp. 193-195.

Wang Zhiwei, Huang Yu, Chen Xiaoming, etal.: Research and Development of Operation Optimizing System for CFB Boilers. Thermal Power Generarion. 35-11(2006), pp. 1-3.

Wang Zhiwei, Li Xiaofeng: Efficiency Calculation of Cyclone of Fenyi 100 MW CFB Boiler. Boiler Manufacturing. -1(2006), pp. 1-3.

Wang Zhiwei, Yang Feng, Xin Huimin, et al.: SIS Application in Commercial CFB Unit, In 10th nation CFB technology service and intercommunion Conference. Dalian, 2007, pp. 435-442.

Wang Zhiwei, Yan An, Guo Fengbo, etal.: Slagging Analysis of CFB Boiler by SIS. Boiler Manufacturing. -4(2007), pp. 1-3, 12.

Wang Zhiwei, Wan Siben, Lin Yu: Design for Stuff Balancing in Circulating Fluidized Bed Boilers. Power Engineering. 27-2(2007), pp. 179-183.

RESEARCH ON THE HYDRAULIC CHARACTERISTICS OF A 600MW SUPERCRITICAL PRESSURE CFB BOILER

D. Yang[1], J. Pan[1], Q. C. Bi[1], Y. J. Zhang[2], X. G. Jiang[2], L. Yu[2]

1 State Key Laboratory of Multiphase Flow in Power Engineering, Xi'an Jiaotong University, Xi'an, 710049, China

2 Harbin Boiler Co. Ltd., Harbin, 150046, China

Abstract: Water wall design is a key technology of supercritical pressure CFB boiler. On account of the low heat flux and its homogeneous distribution in furnace, internally ribbed tubes with low mass flux and smooth tubes with moderate mass flux can be applied in the water wall of supercritical CFB boilers. An experimental research on the flow and heat transfer characteristics of internally ribbed tubes and smooth tubes with different inner diameters was conducted in the range of sub-critical and supercritical pressure. The departure from nucleate boiling (DNB) and dry-out boundary and the empirical correlations of heat transfer are obtained from the experiments. The mathematical model for predicting the circuit mass flux and grid pressure of a flow network system is based on the mass and momentum conservation equations and an iterative method is used to solve the nonlinear equations. Harbin Boiler Works has developed a 600MW supercritical CFB boiler with external heat exchangers and 6 separators. The mass flux and metal temperature distribution of water wall in the CFB boiler are calculated and the results show that the water wall can operate safely at BMCR and 75%BMCR load.

Keywords: supercritical pressure, CFB boiler, hydraulic characteristics, mass flux distribution, metal temperature

INTRODUCTION

In the 1980s, CFB combustion technology began to be developed in the world. On account of the good emission performance and the low pollution control cost, it has already become an important technology in coal-fired power plants at present. The first 300 MW CFB power generating unit in China, which technology was introduced from Alstom, was put into operation in 2005. More technology-imported CFB power generating units are operating or being built now. In order to further improve the boiler efficiency and reduce the pollution emission, it is a very important development trend for electrical equipment manufacturer to design large-scale and high-parameter 600MW supercritical CFB boilers with independent intellectual property in China.

At present, some electrical equipment manufacturers and research institutions including Stein, ABB-CE, Xi' an Thermal Power Research Institute, Tsinghua University and Zhejiang University, all have proposed the concept designs of supercritical CFB boiler(Sun and Li, 2005; Yang et al., 2005). In the state key laboratory of multiphase flow in power engineering, Xi'an Jiaotong University, long-term experimental and theoretical research on hydraulic characteristics of supercritical and ultra-supercritical pulverized coal fired boiler was being conducted. An in-depth experimental research on flow and heat transfer characteristics of internally ribbed and smooth tubes with different structure dimension and different arrangement mode was conducted in a wide pressure range and a large number of experimental data was obtained. The mass, momentum and energy conservation equations are obtained through the analysis on the flow network system of water wall in supercritical CFB boilers. According to the conservation equations and empirical correlations, a computation program on hydraulic characteristics and tube wall temperature is developed. The mass flux and metal temperature distribution characteristics of a design proposal at BMCR and 75% BMCR load was calculated by the computation program. The operating safety of water wall and the heat absorption deviation's impact on hydraulic characteristics are also analyzed.

WATER WALL DESIGN

Both the combustion technology of CFB boiler and the steam-water circulation technology of supercritical pulverized coal fired boiler are adopted in supercritical CFB boiler (Ragnar et al., 2003). At present vertical and spiral water wall tubes technology can be adopted in supercritical pulverized coal fired boilers. It's not spiral tubes but vertical tubes that can only be adopted in supercritical CFB boiler with the aim to avoid rubbing abrasion. The research shows that the furnace heat flux in CFB boilers is lower than that in

pulverized coal fired boilers and the heat flux distribution is also more homogeneous (Basu and Halder, 1989). The peak value of furnace heat flux in CFB boilers is much lower than that in pulverized coal fired boilers and it occurs in lower furnace. The local furnace heat flux gradually decreases with the increase of furnace height. The furnace heat flux distribution also tends to be homogeneous with the increase of furnace height. This distribution mode is safer and very beneficial for the operation of water wall in supercritical CFB boilers. Because the maximum heat flux occurs in lower furnace where the fluid temperature is low and the furnace heat flux in two-phase zone is low, DNB hardly occurs. The tube wall temperature in post-dry-out region is also in a safe temperature range. Therefore, the internally ribbed tube with low mass flux and the smooth tube with medium mass flux can be adopted in supercritical CFB boilers.

An important principle of water wall design is to ensure all water wall tubes can be cooled effectively and to keep the temperature deviation between the water wall tubes in a permissible range (Stamatelopoulds, 2005). The BENSON Vertical OUT technology (once-through utility) introduced by Foster Wheeler from Siemens is a special once-through steam-water circulation technology, which is based on the special structure and heat transfer mode of CFB boiler (Joachim and Rudof, 2001). Conventional supercritical pulverized coal fired boiler ensures the adequate cooling of tubes by high mass flux. So the frictional pressure drop is dominant in the overall pressure drop. Because the mass flux in the tubes with high heat absorption capacity is too small, restriction orifices must be adopted to regulate the mass flux. Due to the large diameter and the lower mass flux, the gravitational pressure drop is dominant in the overall pressure drop of working fluid in the internally ribbed tubes which is exploited and optimized by Siemens. The mass flux in parallel tubes has a positive response characteristic, which means the mass flux in internally ribbed tubes increases with the increase of heat absorption capacity. It is similar to that in natural circulation boiler. Φ26.9×4.09 and Φ26.9×3.64 internally ribbed tubes optimized by Siemens was adopted in the technical reconstruction of #1 boiler in Yaomeng power plant. The mass flux in this boiler is 700 kg/(m^2·s) at 100% BMCR load. Good mass flux distribution characteristic can be captured under the mass flux condition of 500~700 kg/(m^2·s) in supercritical CFB boilers.

On account of the low heat flux and the homogeneous distribution characteristic of heat flux along the furnace width and depth, the ordinary internally ribbed tubes with low mass flux can also be adopted in supercritical CFB boiler with the aim to avoid high cost of technology transfer. The ordinary internally ribbed tube technology is also mature in China.

EXPERIMENTAL RESEARCH

Experimental facility and method

It is a key precondition of hydraulic calculation to analyze the flow and heat transfer characteristics of water wall tubes. A systemic experimental study on flow and heat transfer characteristics of Φ28.6×5.8 and Φ28×6 4-thread internally ribbed tube, Φ38.1×7.5 6-thread internally ribbed tube and Φ32×3, Φ20×2 and Φ24×4 smooth tube was conducted in the two-phase flow experimental system of high-pressure steam-water. Fig. 1 is the sketch figure of the experimental system.

The deionized water from water tank is heated in heat exchanger and preheating tube, and then flows into the experimental tube section. The heat flux change in actual boiler is simulated at the experimental tube section. The flow and heat transfer characteristics of fluid in experimental tube section under different load are obtained. The flow and heat transfer characteristics under normal heat transfer condition are obtained. The critical condition of DNB and dry-out under different parameter conditions are also acquired. The detailed descriptions about the experiments can be founded in literature(Sun, 2007).

The alternative current (AC) with low-voltage and high current was adopted to directly heat the experimental tube section and the preheating tube section. The electric power was continuously regulated through regulating transformer. The total heating power of experimental system was 840 kW and the heating power of experimental tube section is 180 kW. Under the operating conditions with the pressure ranging from 11 to 30 MPa,

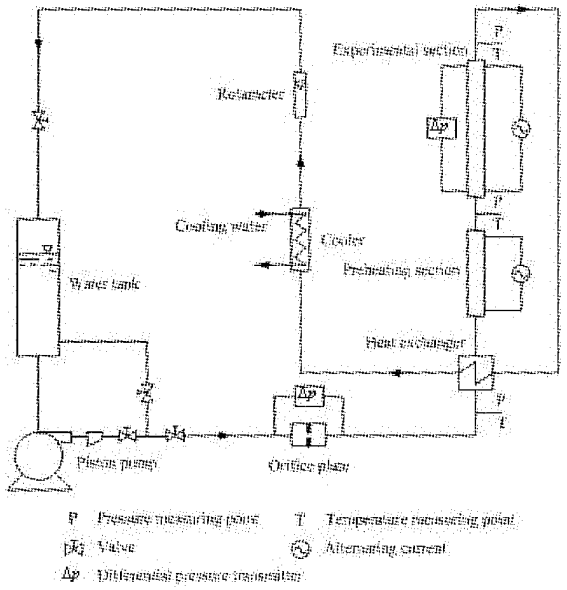

Fig. 1 Flow and heat transfer experiment system

the mass flux from 300 to 1200 kg/(m^2·s), and the inner wall heat flux from 200 to 600 kW/m^2, the experiments was conducted to study the heat transfer of working fluid in vertical rifled and smooth tubes.

Experimental result and analysis

Figure 2 shows the inner wall temperature change with the fluid enthalpy in vertical internally ribbed tube under the operating condition that the pressures are 13 MPa and 16 MPa respectively, the mass flux is 600 kg/(m^2·s) and the heat flux of inner tube wall is 650 kW/m^2. It can be seen that the fluid quality at the critical point of heat transfer deterioration has a little decrease with the increase of pressure in subcritical pressure region and the heat transfer deterioration occurs ahead. The fluid quality at the critical point of heat transfer deterioration is close to 1. It shows that it's not DNB but dry-out that can only occur in vertical internally ribbed tube.

Figure 3 shows the comparison of heat transfer characteristics between smooth and internally ribbed tubes in near critical pressure region under the operating condition that the mass flux is 400 kg/(m^2·s), the heat flux of inner tube wall is 300 kW/m^2 and the pressures is 21.5 MPa (Sun D., 2001). The critical quality of DNB in smooth tube is 0.08. The highest wall temperature is 645 ℃ under the condition of heat transfer deterioration. But under this operating condition, the heat transfer in internally ribbed tube is still kept at nucleate boiling state in a wide quality range. So the occurrence of DNB is prevented. The critical quality of the abrupt wall temperature rise at dry-out site increases to 0.98 and the wall temperature only has a little rise in post-dry-out region.

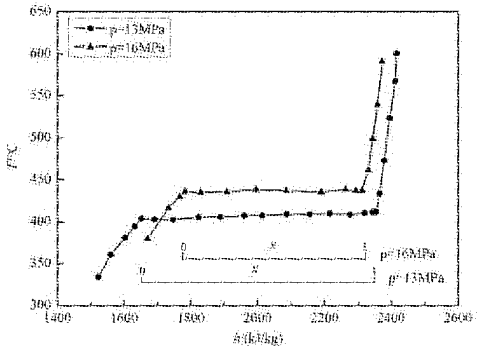

Fig. 2 Inner wall temperature in vertical rifled tube vs. fluid enthalpy

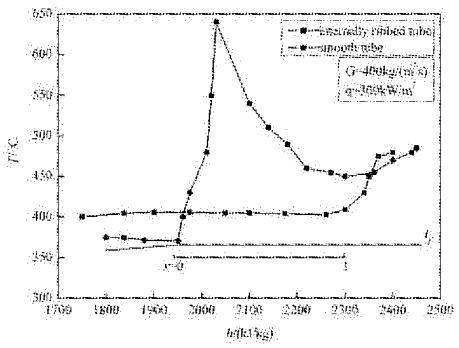

Fig. 3 Comparison of heat transfer characteristics between smooth and ribbed tubes

Figure 4 shows the comparison of heat transfer characteristics between smooth and internally ribbed tubes in supercritical pressure region. It can be seen that the inner wall temperature of vertical internally ribbed tube has a little increase under the operating condition of near-critical pressure and the increasing trend of inner wall temperature is not as prominent as that in vertical smooth tube. The maximum inner wall temperature in vertical internally ribbed tube is about 100 °C lower than that in vertical smooth tube. At the pressure condition of 24 MPa, abrupt wall temperature rise almost does not occur in vertical internally ribbed tube, the wall temperature curve is very smooth and the tube wall temperature is lower than that in vertical smooth tube.

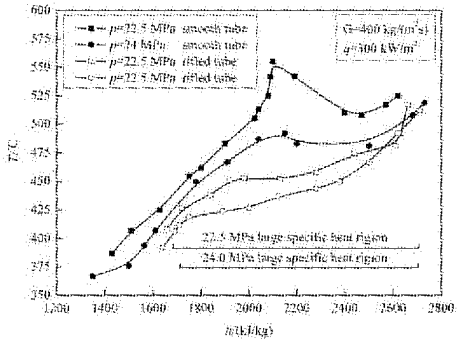

Fig. 4 Comparison of heat transfer between smooth and rifled tubes

Empirical correlations

Through the regression analysis on experimental data, the critical conditions of DNB and dry-out are obtained. The empirical correlations of normal and deteriorated heat transfer calculation are also obtained.

The critical condition of DNB in vertical internally ribbed tube in two-phase flow zone is given by

$$q_{cr} = 9.42(22.115-p)^{0.0551} G^{0.3025} (1-x)^{0.0721} \tag{1}$$

The critical condition of dry-out is given by

$$x_{cr} = 0.3664 q^{-0.1280} G^{0.1552} e^{-0.2983(p/p_{cr})} \tag{2}$$

The calculation formula of post-dry-out heat transfer coefficient is given by

$$Nu = 1.2\times10^{-2} \{\mathrm{Re}_g[x+\rho_g(1-x)/\rho_l]\}^{0.86} \mathrm{Pr}_w^{8.1} q^{0.96} (\lambda_g/\lambda_{cr})^{-1.3} (p/p_{cr})^{-0.98} \tag{3}$$

The calculation formula of frictional pressure drop in two-phase zone is given by

$$\Delta p_{tp} / \Delta p_{lo} = 1 + (\rho_l / \rho_g - 1)[C(x) + x^2] \tag{4}$$

where q is heat flux, x is mass quality, Nu is Nusselt number, Δp_{tp} is the frictional pressure drop in two-phase zone, Δp_{lo} is the frictional pressure drop in single-phase zone and $C(x)$ is the fitting coefficient (Sun, 2007).

HYDRAULIC CALCULATION

A water wall system can be treated as a flow network consisting of series-parallel circuits, pressure grids and connecting tubes. Figure 5 shows a simplified flow network system.

The mass conservation equation of grid 1 is given by

$$w = w(1) + w(2) \tag{5}$$

The momentum conservation equation of circuit n in tube panel 1 is given by

$$p_{n,i} - p_{n,o} = \Delta p_f + \Delta p_h + \Delta p_{jb} \tag{6}$$

Where $p_{n,i}$ is the inlet pressure of circuit n; $p_{n,o}$ is the outlet pressure of circuit n; Δp_f, Δp_g and Δp_{jb} are the frictional, gravitational and local pressure drops of circuit n respectively.

The energy conservation equation of circuit n in tube panel 1 is given by

$$h_{n,o} - h_{n,i} = \frac{q_n s l_n}{w(n)} \tag{7}$$

Where $h_{n,o}$ is the outlet fluid enthalpy of circuit n; $h_{n,i}$ is the inlet fluid enthalpy of circuit n; q_n is the heat flux of circuit n; s is the pitch; l_n is the length of circuit n and $w(n)$ is the mass flow rate of circuit n.

Closure non-linear equations can be obtained on the basis of the mass and momentum conservation of all circuits, pressure grids and connecting tubes in Fig. 5. Iterative method can be adopted to calculate the pressure of all grids and the mass flux of all circuits and connecting tubes.

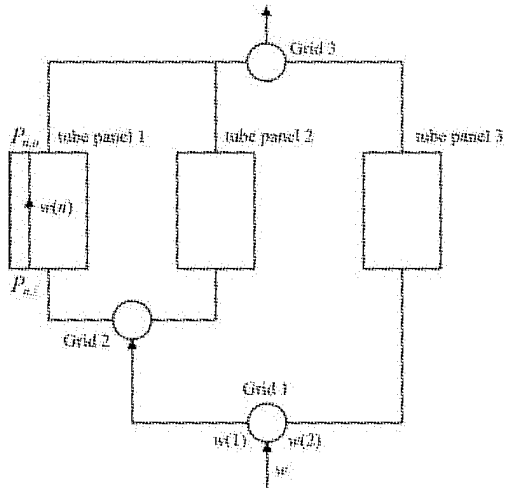

Fig. 5 A simplified flow network system

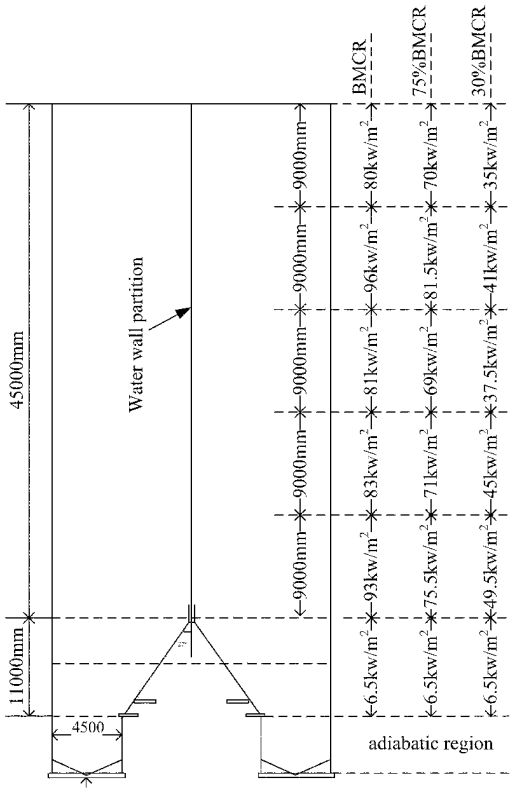

Fig. 6 Furnace heat flux distribution

Harbin Boiler Works has developed a new supercritical CFB boiler with low mass flux. Figure 6 is a sketch of the heat flux along furnace height. The heat flux distribution along the furnace width is presumed to be homogeneous. According to the furnace-sided heating characteristics, in this paper the flow network system is divided into 110 circuits. Each circuit is divided into 29 tube sections for calculation. The division principle is to ensure the heat flux change of the tube sections with the same length along the furnace height is small. According to the mass and momentum conservation equations of circuits and grids, a mathematical model for

predicting the circuit mass flux and grid pressure is built. The hydraulic characteristics are obtained through solving this model, which is made up of 167 nonlinear equations including 142 momentum conservation equations and 25 mass conservation equations.

Figure 7 shows the mass flux distribution of single tube in all circuits at BMCR and 75% BMCR load. It can be seen that the mass fluxes in circuits 1-3, 43-45, 56-58 and 98-100 are low. The mass flux in water screen (circuits 46-55 are the tubes in rear water screen and circuits 101-110 are the tubes in front water screen) is 12.5% lower than that in water wall. Because the heat flux along the furnace width is homogeneous, the mass flux deviation in 4-sided walls is low.

Figure 8 shows the temperature distribution of the outlet fluid in all circuits at BMCR and 75% BMCR load. The outlet fluid temperature in water screen is apparently higher than that in water wall. The reason is that the mass flux in water screen is lower. It also shows the importance of the mass flux balance between water wall and water screen in the water wall design.

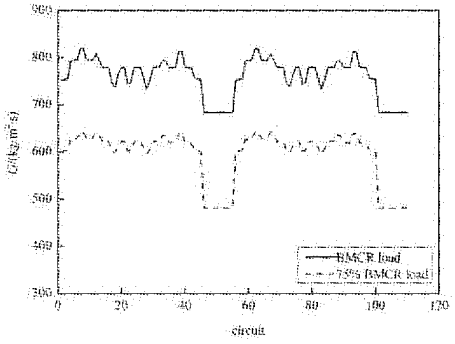

Fig. 7 Mass flux distribution at BMCR and 75% BMCR load

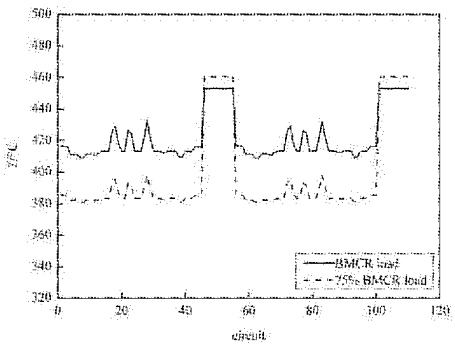

Fig. 8 Outlet fluid temperature distribution at BMCR and 75% BMCR load

Figure 9 shows the temperature distribution of the fluid and the tube wall at BMCR load in circuit 3, where the mass flux is the lowest, the outlet fluid enthalpy and temperature are the highest. The tube site with furnace height of 0 m is supposed to the inlet of the heating tube section. It can be seen from the furnace height of 0 m, the tube is heated and the temperature of the fluid and tube wall increases with the increase of furnace height. In the inlet region of heating tube section, the specific heat of supercritical water is low and the heat flux is high (100 kW/m^2), so the fluid temperature increases rapidly with the increase of furnace height. In two-phase zone, because the specific heat of fluid is obviously larger than that in single-phase zone, the fluid temperature increases slowly. In supercritical steam zone, the specific heat decreases and the fluid temperature increases rapidly.

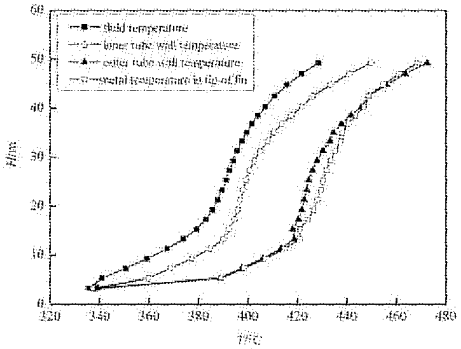

Fig. 9 Temperature distribution of fluid and tube wall in circulation 3 at BMCR load

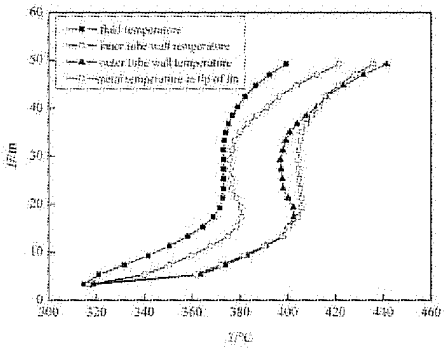

Fig. 10 Temperature distribution of fluid and tube wall in circulation 3 at 75%BMCR load

Figure 10 shows the temperature distribution of the fluid and the tube wall in circuit 3 at 75% BMCR load. It can be seen from the furnace height of 4.8 m, the tube is heated and the temperature of the fluid and the tube wall increases with the increase of furnace height. In the inlet region of heating tube section, because the specific heat of subcooled water is low and the heat flux is high (84kW/m^2), the fluid temperature increases rapidly with the increase of furnace height. In two-phase zone, the fluid temperature is 373.1 °C. Because the heat exchange coefficient of fluid is larger than that in single-phase zone, the inner tube wall temperature decreases. In supercritical steam zone, the fluid temperature increases rapidly.

CONCLUSIONS

An in-depth experimental research on flow and heat transfer characteristics of internally ribbed tubes and smooth tubes with different structure dimensions and different arrangement modes was conducted on the high pressure steam-water experiment table. The critical condition of DNB and dry-out, the heat transfer characteristics under the condition of heat transfer deterioration and the calculation formulas of flow and heat transfer under the condition of normal heat transfer are obtained.

According to the mass, momentum and energy conservation equations of water wall flow network system in supercritical CFB boiler and the experimental correlation, a computation program is developed to calculate the hydraulic characteristics and wall temperature through directly solving the nonlinear equations. On the basis of this program, a calculation on the mass flux and wall temperature distribution characteristics of a design proposal at BMCR and 75% BMCR load was performed. The result shows that the metal temperature of the water wall and fins is in a permissible range and the boiler can operate safely.

NOTATIONS

G mass flux, kg/(m^{2}s)
w mass flow rate, kg/s
h enthalpy, J/kg
$h_{n,i}$ inlet fluid enthalpy of circuit n
$h_{n,o}$ outlet fluid enthalpy of circuit n
l_n length of circuit n
Nu Nusselt number
P pressure, MPa
Δp_{tp} frictional pressure drop in two-phase flow zone, Pa
Δp_{lo} frictional pressure drop in single-phase flow zone, Pa
Δp_f frictional pressure drop, Pa
Δp_g gravitational pressure drop, Pa
q furnace heat flux, W/m^2
q_{cr} critical heat flux, W/m^2
q_n heat flux of circuit n
Re_g Reynolds number of the gas phase
s pitch
T inner tube wall temperature
x quality of working fluid, kg/kg
x_{cr} critical quality, kg/kg

ACKNOWLEDGEMENTS

Financial supports of this work by Science & Technology Support Project of the National Eleventh-Five Year Research Program of China (2006BAA03B02-03) are gratefully acknowledged.

REFERENCES

Yang, H. R., Lv, J. F. and Zhang, H., et al.: The Latest Developments of Supercritical Circulating Fluidized Bed Boiler. Boiler Technology. **36** (2005), pp.1-6 (in Chinese).

Sun, X. B., Li, G. H. and Jiang, M. H.: Study on the Frontier Projects of CFB Boiler Technology. Thermal Power Generation. **34** (2005), pp.1-6 (in Chinese).

Ragnar, L., Andre, S. and Kari, M.: A Major Step Forward–The Supercritical CFB Boiler. PowerGen International. 2003.

Basu, P. and Halder P. K.: New concept for operation of a pulverized coal fired boiler using Circulating fluidized Bed Firing. Journal of Engineering for Gas Turbines and Power. **111** (1989), pp.626-630.

Stamatelopoulds G. N. (2005). Advancement in CFB technology: A combination of excellent environmental performance and high efficiency. 18th Int. FBC Conference.

Joachim F. and Rudof K.: Benson boiler-best choice. Siemens Power Journal Online. **10** (2001), pp.1-4.

Sun D. and Chen T. K.: Water Heat Transfer Characteristics of Internally Ribbed Tube in the Near Critical Pressure Region. Journal of Xi'an Jiaotong University. **35** (2001), pp.234-238.

Sun S. W.: Experimental Research on the Flow and Heat Transfer Characteristics of Water Wall in a 1000MW Ultra Supercritical Boiler. Master Dissertation. (2007).

STUDY OF NOX EMISSION CHARACTERISTICS OF A 1025t/h COAL-FIRED CIRCULATING FLUIDIZED BED BOILER

Q.Y. Li, Z.D. Mi, Q.F. Zhang

North China Electric Power Research Institute, Beijing, 100045, China

Abstract: Measurements of emission are carried out in a 1025t/h CFB boiler. The effect of some factors including coal properties, bed temperature, unit load, excess air on the emission of NO_x are investigated. The measurement results show that the N concentration in the coal is dominant parameter to predict the NO_x emission from a large-scale CFB boiler. NO_x emission from the 1025t/h CFB boiler increases with cyclone temperature and upper pressure drop due to post combustion and external cycle.

Keywords: circulating fluidized bed, NO_x, cyclone temperature, upper pressure drop

INTRODUCTION

Coal combustion generates solid and gaseous-combustion products and is inevitably associated with the environmental pollutant, among which nitrogen oxides (NO_x) are major ones. Different from PC boilers, CFB boilers reduce much less NO_x emissions to the atmosphere. So far, literature studies including theoretical modeling and experimental ones (e.g., Liu and Gibbs, 2002; Xie et al., 2007; Leckner et al., 2004) on NO_x emission in CFB boilers were conducted on small scale CFB experimental apparatus. There are few literatures on NO_x emission from large scale CFB boilers especially a 1025t/h CFB boiler for a 300MW_e unit.

Recently, nearly 10 units of 300MW_e CFB are in operation in China, most of them are 1025t/h Alstom_type CFB boilers. The paper presents the NO_x emission from the 1025t/h Alstom_type CFB boiler burning both bituminous coal and lignite coal at different unit load.

EXPERIMENTAL

The 1025t/h Alstom_type CFB boiler is shown in Fig. 1. The process uses a water-cooled combustion chamber and refractory-lined hot cyclones to recirculate the hot-bed material. The bed material (mainly inert ash), fuel and sorbent are fluidized by the first air provided from fan systems. Combustion takes place in a hot vigorous fluidized-bed environment with second air. Reactions between the sorbent and SO_2 and other sulphur compounds in the fuel occurs in the combustor at an optimal temperature of approximately 850 - 900℃ to control the SO_2 emissions. In order to control bed temperature and the steam temperature, four groups of cone valve and Fludized Bed Heat Exchanger(FBHE) are used.

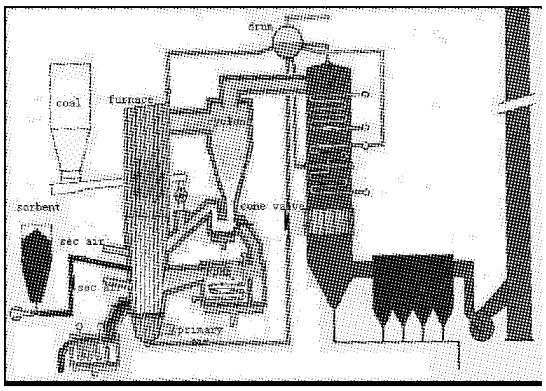

Fig. 1 1025t/h Alstom_type CFB boiler

The concentrations of O_2 and NO_x in flue gas are measured by a Testo 350 gas analyzer and a MRU 4000 gas analyzer. The gas sampling pipes from the CFB boiler flue gas tunnel between the economizer and the air preheater to the gas analyzers are made of stainless steel and Teflon. Other parameters such as bed temperature, unit load, upper pressure drop, bed temperature, cyclone temperature and so on are obtained from the Distributed Control System of the unit.

Bituminous coal from Hebei province of China is burned during the first stage of the experiment, while Lignite coal from Yunnan province of China is burned in the next stage. The proximate and ultimate analysis of bituminous coal and lignite coal are listed in Table 1.

Table 1 Chemical analysis of coal

coal	Proximate analysis(%)					ultimate analysis(%)				
	M_t	M_{ad}	A_{ar}	V_{ar}	FC_{ar}	C_{ar}	H_{ar}	N_{ar}	$S_{t,ar}$	O_{ar}
Bituminous	13.60	/	24.40	23.20	38.81	48.48	2.93	0.68	1.02	8.90
Lignite	38.90	27.84	11.85	28.55	20.70	33.92	3.40	1.05	1.53	9.35

Each experiment run is performed more than two hours under specified operating conditions when the temperature and the flue gas concentrations only fluctuate in a very narrow range. The results presented in this paper are the mean values. The operation conditions are listed in Table 2.

Table 2 Operating conditions of CFB and NO_x emission

	Unit	Burning bituminous			Burning lignite		
Unit load	MW	150	230	300	150	230	300
Bottom bed temp	℃	883.9	861.0	891.0	880.6	847.5	840.9
Middle bed temp	℃	878.5	859.4	883.0	874.8	841.6	830.8
Top bed temp	℃	876.5	842.7	877.2	840.3	834.8	836.8
Cyclone temp	℃	908.6	920.4	950.5	861.9	897.3	907.8
Bed press drop	kPa	12.0	11.8	11.3	13.2	11.8	12.7
Upper press drop	kPa	0.01	0.45	0.63	0.02	0.33	0.36
Excess air	%	15	10	10	10	10	10
Ratio of SA to PA	/	0.64	0.79	1.20	1.22	2.52	3.03
NO_x	ppm	46	55	70	65	94	157

RESULTS AND DISCUSSION

Influence of coal property

The variations of NO_x emission with unit loads burning bituminous and lignite are shown in Fig. 2. It can be seen that NO_x emission burning lignite is larger than burning bituminous at any unit load especially at full unit load. At the full unit load, the ratio of NO_x emission burning lignite to NO_x emission burning bituminous is nearly equal to or a little larger than the ratio of the N concentration in lignite to the N concentration in bituminous.

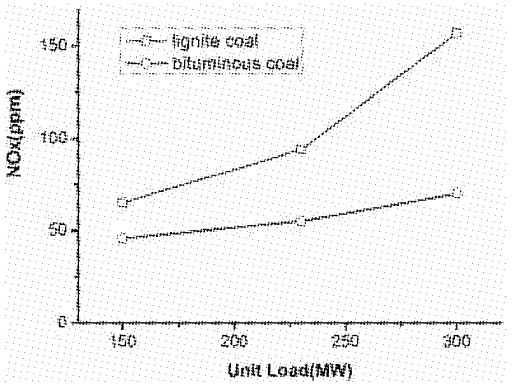

Fig. 2 Relationship of NO_x emission and unit load burning different coal

NO_x formations in combustion processes result from a combination of a thermal generation process and fuel nitrogen oxidation. At very high temperatures, thermal generation of NO_x from the air nitrogen becomes very important, while at low temperatures found in a CFB boiler, the dominant source of NO_x is fuel-nitrogen oxidation, which can be proved from Fig.2.Therefore, the N concentration in the coal is dominant parameter to predict the NO_x emission from a large-scale CFB boiler.

Influence of bed temperature and excess air

In previous study, Gungor(2008) found NO_x emission sharply increases with mean bed temperature from experiments on a 50 kW pilot scale CFBC burning lignite, especially when mean bed temperature growing from 750℃ to 900℃. Nowak(2003) found when unit load decreases 50%, bed temperature drops from 850 ℃ to 700 ℃, but the NO_x emission decreases slightly from a 235 MW_e CFB boiler burning lignite in Poland. In the 1025t/h Alstom_type CFB boiler, bed temperature can be controlled with cone valves and FBHE when unit load is above 50%(150MW). Therefore, bed temperatures at every position(bottom, middle, top) varies slightly with unit load, as it is shown in Fig.3. So, the change of bed temperature is not the dominant reason that the NO_x emission sharply increases with unit load burning lignite shown as Fig.2.

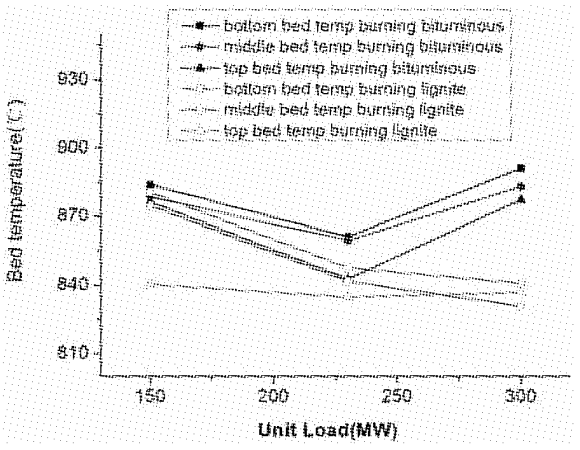

Fig. 3 Relationship of bed temperature and unit load burning different coal

Gungor(2008) found NO_x emission slightly decreases with excess air from experiments on a 50

kW pilot scale CFBC burning lignite when excess air growing from 35% to 80%. Gungor(2008) thought that the amount of oxygen increases with increasing excess air, decreasing bed temperature causes a negative effect on coal combustion efficiency which results in lower levels of NO_x formation. While for the 1025t/h Alstom_type CFB boiler, the variation of the excess air has little influence on the bed temperature because the bed temperature can be controlled by FBHE. On the other hand, the unit usually runs at the same excess air near 10% shown in table.2 burning bituminous and lignite when the unit load above 50%(150 MW_e) due to some reasons like energy saving and decreasing wearing. So, the change of excess air is not the dominant reason that the NO_x emission sharply increases with unit load burning lignite shown as Fig.2.

Influence of cyclone temperature and the upper pressure drop

For large scale CFB boiler especially 1025t/h CFB boiler, post combustion in cyclone is an important phenomenon. It is shown in Fig.4 that the cyclone temperature increases with unit load burning bituminous and lignite. In another word, the rise from bed temperature to cyclone temperature increases with unit load. The dominant source of NO_x is fuel-nitrogen oxidation in CFB boiler. Typically, significant amounts of the fuel-nitrogen remain in the char after the devolatilization. The oxidation of this char-nitrogen gives an important contribution to the total NO_x emission from the CFB boiler. Though the mechanism of char-nitrogen oxidation to the products is very complex, it is reasonable to think that the high-level cyclone temperature does great contribution to the char-nitrogen oxidation especially burning lignite with high N concentration. NO_x emission from the 1025t/h CFB boiler increases with cyclone temperature or the post combustion.

Upper pressure drop is a dominant parameter to evaluate the external cycle in the 1025t/h CFB boiler. Below 50% unit load, upper pressure drop is always zero, which means the external cycle can be neglected. While above 50% unit load, upper pressure drop increases greatly with unit load which means that external cycle plays more and more important role on combustion and heat transfer. External cycle can do especially good to the char combustion for its long cycle time. Therefore, high upper pressure drop does great good to the char-nitrogen oxidation especially burning lignite with high N concentration. NO_x emission from the 1025t/h CFB boiler increases with upper pressure drop or the external cycle.

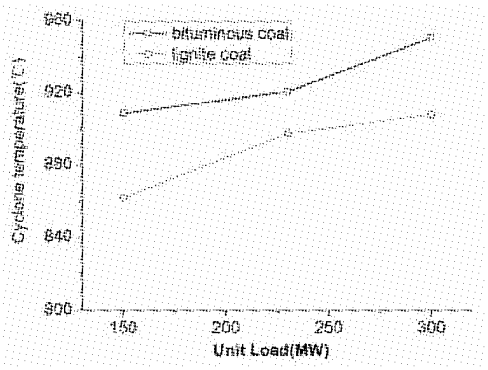

Fig. 4 Relationship of cyclone temperature and unit load burning different coal

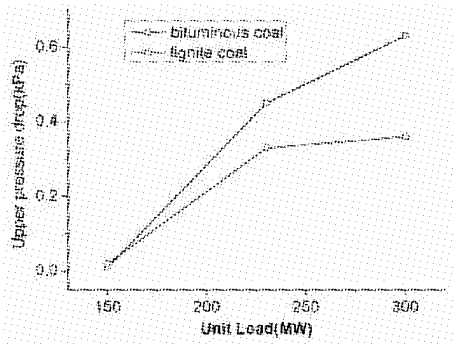

Fig. 5 Relationship of upper pressure drop and unit load burning different coal

CONCLUSIONS

NO_x emission characteristic of a 1025 t/h CFB boiler was experimentally investigated. Following main conclusions are drawn from the experiment results:

The dominant source of NO_x is fuel-nitrogen oxidation in a 1025 t/h CFB boiler. The N concentration in the coal is dominant parameter to predict the NO_x emission from a large-scale CFB boiler

NO_x emission sharply increases with unit load burning lignite in a 1025t/h CFB boiler even when the bed temperature and the excess air varies little. The tendency of NO_x emission from the 1025t/h CFB boiler is accordant with the tendency of cyclone temperature and upper pressure drop due to post combustion and external cycle.

REFERENCES

Liu, H., and Gibbs, B. M.: Fuel **81** (2002), pp.271-280.
Xie, J., Yang, X., Zhang, L., Ding, T., Song W., and Lin W.: J. Envion. Sci. **19** (2007), pp.109-117.
Leckner, B., Amand L. E. Lucke K. and Werther, J.: Fuel **83** (2004), pp.477-486.
Gungor, A.: Chem. Eng. J. submitted (2008)
Nowak, W.: Applied Energy. **74**(2003), pp.405-413.

MERCURY EMISSION AND REMOVAL OF A 135 MW CFB UTILITY BOILER

Y.F. Duan[1], Y.Q. Zhuo[2], Y.J. Wang[1], L. Zhang[2], L.G. Yang[1], C.S. Zhao[1]

1 Thermoenergy Engineering Research Institute, Southeast University, Nanjing, 210096, China
2 Department of Thermal Engineering, Tsinghua University, Beijing, 100084, China

Abstract: To evaluate characteristic of the mercury emission and removal from a circulating fluidized bed (CFB) boiler, a representative 135 MW CFB utility boiler was selected to take the onsite measurement of mercury concentrations in feeding coal, bottom ash, fly ash and flue gas using the US EPA recommended Ontario Hydro Method (OHM). The results show that particulate mercury is of majority in flue gas of the CFB boiler. Mercury removal rate of the electrostatic precipitator (ESP) reaches 98%. Mercury emission concentration in stack is only 0.062μg/Nm^3, and the mass proportion of mercury in bottom ash is less than 1%. It was found that the fly ashes were highly adsorptive to flue gas mercury because of its higher unburned carbon content. Adsorption effect is related to carbon pore structural properties of fly ash and temperature of flue gas. However mercury adsorption capacity by fly ash can not be improved any more when unburned carbon content in fly ash increases further.

Keywords: CFB boiler, mercury emission, mercury removal, mercury adsorption, fly ash, unburned carbon

INTRODUCTION

Mercury and its compounds exhausted by coal combustion are difficult to be degraded by microorganisms with a long residence time in the atmosphere. They have become another global pollution concern following greenhouse gas with serious harm to human health and ecological environment. The United Nations Environment Program (UNEP) issued a "Global Mercury Assessment Report" on 3rd February 2003 in Nairobi (US-EPA, 2003), the report pointed out that the mercury emissions into the atmosphere from various human pollution sources per year reached 1900~2200t. The largest human mercury emissions were from coal-fired industries, account for about 70% (Dang and Liu, 2005). A great deal of coal is burned in our country. The average annual growth rate of mercury emissions in the atmosphere from coal-fired power plants during 1999-2003 was 9.59% with the mercury emissions in 2003 of 86.8 t (Ren, 2005). The coal-fired mercury pollution in our country has become increasingly serious.

Many scholars at home and abroad have investigated on controlling mercury emissions from the coal-fired power plant and mercury absorbent. Yokoyama (2000), Park (2008), Chen (2007), Yang (2008), Chen (2008), etc. investigated the emission characteristics and morphological transformation of mercury from different coal under different pollution control equipments. Yang (2007), Ren (2007), Poulston (2007), etc. investigated on the absorption effect of the new adsorbent, such as modified activated carbon, natural Zeolite, bentonite, vermiculite and metals, etc. But there has not been a mature industrialized technology at present. The development of mercury absorbent of low-cost and high effect from has become the key control technology of mercury emissions from coal burning.

The circulating fluidized bed combustion, one of advanced clean coal combustion technologies, may reduce SO_2 and NO_x emissions to great extent (Cen et al., 1997). However, there are not enough research reports on mercury emissions characteristics from circulating fluidized bed boiler, especially the immediate data of mercury emissions from power plants in our country. Therefore, this paper used the Ontario Hydro Method(OHM) recommended by United States Environmental Protection Agency (EPA) to carry out mercury sampling and testing to one selected circulating fluidized bed boiler of 440 t / h from a power plant, obtaining the immediate experimental data of mercury emissions from the circulating fluidized bed boiler. Because the fly ash is a low-cost absorbent (Wang et al., 2006), the paper also investigated the absorption characteristics of ESP fly ash on mercury.

EXPERIMENTAL

Sampling and sample analysis

The boiler system of certain power plant chosen in this paper was installed with ultrahigh pressure

[1] The corresponding author: yfduan@seu.edu.cn

circulation fluidized bed steam boiler, which was adopted with solid state slag-tap and two-electrical-field cold electrostatic precipitator (Cold-ESP) and fired with mixed bituminous coal. The samples, such as coal, bottom ash, ESP ash of two electrical fields and flue gas before and after ESP, were sampled, and the solid sampling and flue gas sampling were carried out simultaneously.

Based on the Ontario Hydro Method (OHM) and the US EPA standard methods, the flue gas mercury isokinetic-sampling before and after ESP locations in the power plant was carried out on site with the self developed sampling system. The isokinetic sampling was conducted to collect sufficient particulate matters and flue gas. After the sampling was over, the sample recovery and digestion was conducted, finally it was analyzed by Hydra-AA automatic mercury analyzer. The mercury content of the solid samples was analyzed by DMA 80.

The microscopic morphological characteristics of fly ash in different electrical fields were observed and analyzed by the scanning electron microscopy (SEM) in the experiment. The pore structure of fly ash was determined by ASAP2020M automatic surface area and porosity analyzer form American Micromeritics Company, which was used to measure the samples at the state of the static isotherm absorption with the relative pressure between 0.01 and 0.995; the specific surface area of fly ash was calculated by the BET adsorption theory and the specific surface area and total volume of the pores was obtained by the BJH model.

RESULTS AND DISCUSSION

Coal-fired analysis

The experiment was carried out on a 440t/h CFB utility boiler, and the samples of flue gas and solid particles were collected at the boiler stable operation condition. The proximate analysis and ultimate analysis was shown in Table 1. From the table, it was said that the ash content of coal was about 30% and the sulfur content was very low so that it belonged to the low-sulfur coal. Also, the mercury content of the experimental coal was lower than 0.22 mg/kg of the average mercury content of Chinese coals and the chlorine content in coal was higher than 500 mg·kg^{-1}.

Table 1 Analysis of experimental coal

ultimate analysis /%						proximate analysis /%				mercury content/ (mg·kg^{-1})	calorific value $Q_{net,ad}$ /(MJ·kg^{-1})
C_{ad}	H_{ad}	N_{ad}	S_{ad}	O_{ad}	Cl_{ad}	W_{ad}	A_{ad}	V_{ad}	FC_{ad}		
60.55	3.70	2.11	0.84	0	0.077	2.10	30.71	25.82	41.37	0.155	22.70

Mercury mass balance

The mercury concentration of coal, bottom ash, flue gas before and after ESP, and ESP ash was got by the measurement analysis in this paper. The operation parameters including the given coal amount and the excessive air coefficient et al were referred, and the mercury mass balance in the process of coal combustion was calculated based on the unit time mercury entering the boiler system, as shown in Fig.1. The results indicated that the mercury mass balance of the inlet and the outlet flue gas was 98.5% and 113.7%, respectively. It was acceptable that the measurement error of mercury balance in a coal-fired utility ranged from 70% to 130%. The test results was believable allowing for the fluctuation of the operation parameters and the sampling error.

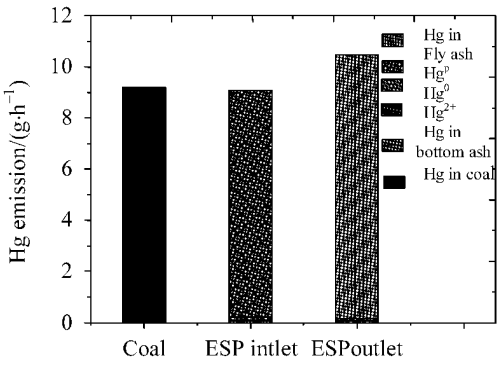

Fig. 1 Mercury mass balance in circulating fluidized bed boiler

As shown in Fig.1, the mercury amount in bottom ash was less than 1% after coal combustion, and the mercury emission into the atmosphere was only 1.9%. The mercury concentration in flue gas was 0.062μg/Nm^3, the mercury in the ESP inlet was mostly particle mercury and the particle mercury in fly ash secondly, and also fly ash could intensively absorb mercury. The combustion temperature (900 ℃) of the CFB boiler was so low that there was more unburned carbon in fly ash, whose lager specific surface area and better pore structural characteristics made fly ash become a kind of excellent mercury adsorbent.

Mercury emission characteristics

Mercury emissions factor (EF) represents the total amount of mercury emission from coal combustion.

According to the mercury concentration tests in nine coal-fired plants in 1996 by US DOE, the results showed that mercury emissions factor ranged from 1.9-22 lb/10^{12}Btu (0.82-9.46 g/10^{12}J) (Miller et al., 1996).

The practical EF in this power plant was 0.043 g/(10^{12}J) much lower than the data above. The mercury emission factor in this paper referred to University of North Dakota's report, but international units were adopted and defined as follows:

$$\text{Mercury emissions factor(g/J)}=\frac{\text{Mercury emissions to atmosphere(g/h)}}{\text{Coal in boiler(g/h)}\times\text{Coal low heat value (J/g)}}$$

Mercury, emitted from coal-fired power stations, existed in three primary forms, which were namely elemental mercury (Hg^0), gaseous oxidized mercury (Hg^{2+}) and particle-bound mercury (Hg^P). The total mercury concentration in flue gas was the sum of three primary forms. The percentage of three primary mercury forms to the total mercury was seen in Fig.2.

From the figure, there was no oxidized mercury in flue gas, and the particle-bound mercury before ESP accounted for 97.5%; the quite little Hg^0 and Hg^{2+} existed after ESP, but the total mercury concentration was very low only to 0.062μg/Nm^3. By calculation the mercury removal rate of the CFB boiler was 98% much higher than that of the pulverized coal fired boiler, because the residual time of circulated ash was longer and the carbon amount of fly ash was larger than that of the pulverized coal fired boiler.

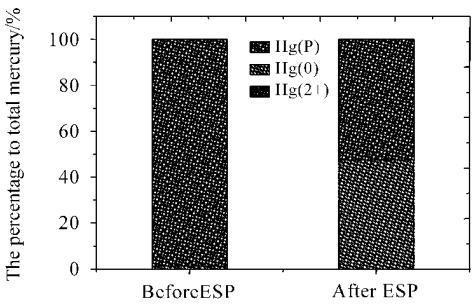

Fig. 2 Mercury Speciation in flue gas

The results represented that the mercury adsorption capacity by fly ash largely strengthened and the mercury emissions factor suddenly dropped thereupon, which was basically consistent with the results abroad. American EPA carried out the on-site measurement on five CFB-FF systems of 84 boilers, and the results found that the mercury removal rate of CFB combustion type ranged in 66%~99% (Pavlish et al., 2003). Therefore, the mercury adsorption effect on the CFB combustion type was good, and the ESP fly ash could absorb much of mercury in coal so as to decrease the mercury emission amount into the atmosphere.

The carbon amount effect on the mercury adsorption

Most of the CFB boilers in China burned low reactive active fuels such as poor coal, anthracite coal, gangue and so on, and the carbon amount of fly ash was usually higher, sometimes even high to 30%. The following factors, including the coal type, coke reaction activity, coal particle size, gas and solid mixed sufficiently in the CFB, mainly resulted in the higher carbon content of fly ash (Li et al., 2007). The CFB boiler fired with the mixed coals, and the carbon amount of two-electrical-field ESP fly ash was higher between 9.89% and 12.03%, which made fly ash be a kind of good mercury adsorbents.

The mercury enrichment factor of fly ash (E_F) was defined as follows:

$$E_F=\frac{\text{the mercury amount of fly ash (mg/Kg)}}{\text{the mercury amount of coal (mg/Kg)}}$$

Table 2 told the relation between the carbon amount of fly ash in three coal-fired power plants and the mercury enrichment factor of fly ash.

Table 2 Mercury enriched factor & carbon content

Air pollution control device[16]	Coal-fired type	Number of the samples	The carbon amount of fly ash/%	E_F
220 MW PÇESP	Shenhua#1	1	1.37	1.09
		2	1.95	1.11
		3	3.50	2.61
		4	3.02	1.97
50 MW PÇFF	Zhunger#2	5	2.87	3.58
		6	3.18	3.14
135 MW CFBESP	Mixed bituminous coal	7	9.89	7.92
		8	10.15	8.23
		9	10.34	7.46
		10	11.20	5.61
		11	12.03	3.65

The results showed that the mercury enrichment factor of CFB-ESP fly ash was apparently higher than that of PC-FF fly ash with the adsorption effect far higher than PC-ESP fly ash. The mercury adsorption by the CFB-ESP fly ash primarily depended on the unburned carbon amount, and the adsorption effect was positively relevant with the carbon amount, which was, the mercury adsorption capacity improved as the carbon amount increased (Jiang et al., 2007). However, enhancing the carbon amount largely could not widely improve the mercury adsorption capacity by fly ash, the reason for which was that the pore structure of the fly ash surface, chemical components, the existing forms of carbon, flue gas temperature et al all influenced the mercury adsorption amount by fly ash, which was similar with the research results by Skodras (2007). Carbon-oxygen radicles C=O on unburned carbon surface of porous fly ash were beneficial to oxidation and chemical adsorption of Hg, also, the oxidation extent depended on the concentration of carbon-oxygen radicles C=O (Lu et al., 2007). When the carbon amount of fly ash was very high, some chemical components of fly ash could take on the mercury desorption and the structure of carbon changed, subsequently the mercury adsorption effect could decreased.

The pore structure of fly ash

The pore structure was the major characteristic of physical-state structure of fly ash, which directly influenced the mercury adsorption degree by fly ash. The pore structure characteristic of two-electrical-field ESP fly ash was shown in Table 3. Although specific surface area and pore specific surface area of fly ash dropped, the median diameter and volume average diameter of fly ash gradually decreased and the mercury adsorption by fly ash tended to increasing. The reason was that the surface effective utilization rate of the second-field fly ash was larger than that of the first field, and the chemical reaction and chemical adsorption between the fly ash surface and mercury increased, followed by the mercury adsorption amount increasing. The results above represented that the mercury adsorption capacity by fly ash was not only relevant with particle diameter and specific surface area, but also with the surface physical property and the surface effective utilization rate of fly ash.

Table 3 Pore structure of ESP fly ashes

Fly ash type	Mercury content /(mg·kg^{-1})	Median diameter /m	Volume average diameter /m	Specific surface area / (m^2·g^{-1})	Pore specific surface area /(m^2·g^{-1})
ESP1	0.55	21.31	31.86	11.99	10.21
ESP2	1.25	8.87	23.09	10.82	8.38

Regard to the given adsorption system, when the temperature was constant, the relation graph between the adsorption amount and gas balance pressure was called the adsorption isothermal. The adsorption and desorption isothermal comprised the rich pore structure information. Figure 3 showed the adsorption and desorption isothermal of two-electrical-field ESP fly ash, wherein V_0 represented the adsorption volume of liquid nitrogen, and p and p_0 represented the measurement pressure and the saturated pressure of nitrogen, respectively. The adsorption and desorption isothermal separated and formed the hysteresis loop, wherein the hysteresis loop of fly ash from the second field was narrow, which instructed the developed micropores and more twice pores, and the porous rate became big and the mercury adsorption amount improved. Therefore, the mercury adsorption by fly ash depended on its pore distribution and pore effective utilization rate, and its wider pore distribution and lager pore effective utilization rate both contributed to mercury adsorption.

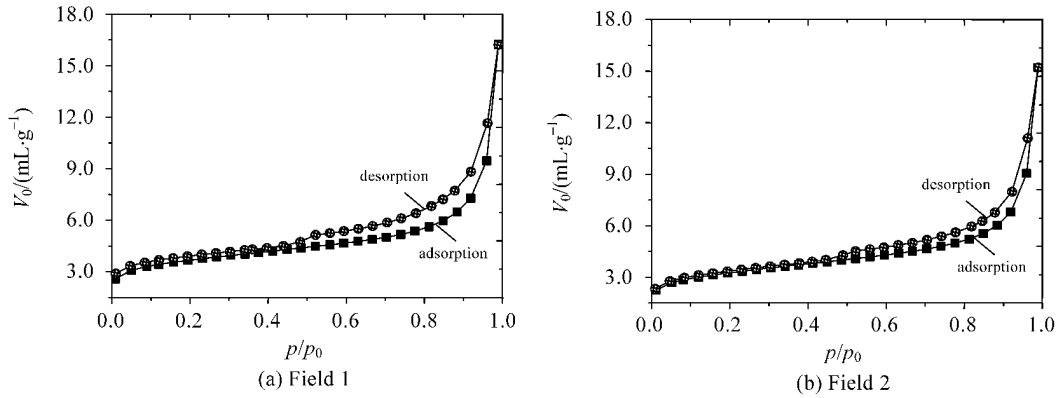

Fig. 3 Adsorption and desorption isothermal of CFB-ESP fly ashes

The apparent structure of fly ash

As shown in Fig.4, there were much porosity in different sizes on the fly ash surface, the inhomogeneous particle distribution and very loose accumulation. In the process of removing dust by ESP, the particle diameter of fly ash became smaller, and fly ash in Field 1 had more macropore, while the particles on the micro and submicro-scale increased in Field 2 and created many new micropore and the wider pore distribution. The pore structure of fly ash took on the active effective specific surface area and utilization rate, and the particle packing state adapted to mercury adsorption, also the intensive physical adsorption and chemical adsorption in the fly ash took place, which was fully accorded with the results above. From the other perspective, it testified the consistency between the macro and micro results.

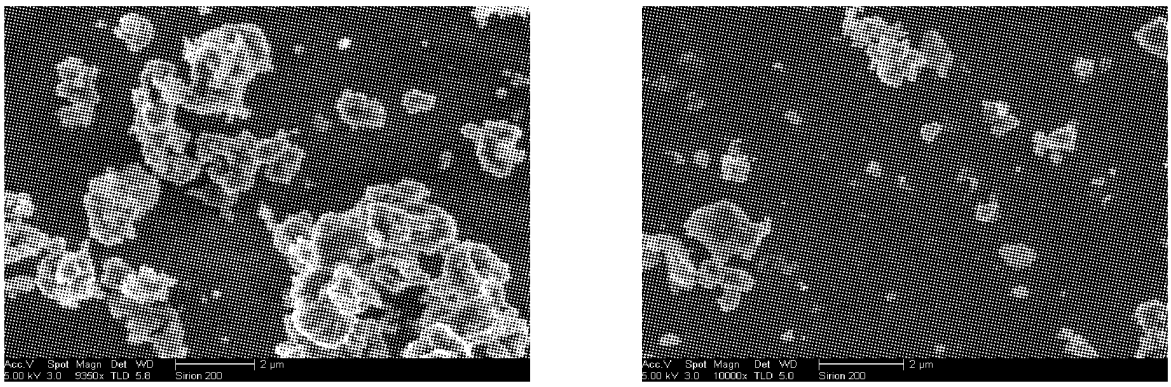

(a) Field 1 (b) Field 2

Fig. 4 SEM pictures of CFB-ESP fly ashes

CONCLUSIONS

The particulate mercury was of majority in flue gas of the CFB boiler, and the mass proportion of mercury in bottom ash was less than 1%. Mercury removal rate of ESP reached 98%. Mercury emission concentration in stack is low, only 0.062μg/Nm^3. Mercury emissions factor in the power plant was 0.043 g/10^{12}J.

The mercury adsorption by the CFB-ESP fly ash primarily depended on the unburned carbon amount, and the secondary influencing factors included the pore structure of the fly ash surface, chemical components, the existing forms of carbon, flue gas temperature et al.

The mercury adsorption capacity by fly ash was not only relevant with particle diameter and specific surface area, but also with the surface physical property and the surface effective utilization rate of fly ash.

ACKNOWLEDGEMENTS

This sub-project was joint-funded by the State Basic Research Development Program (973 Plan) of China (No. 2002CB211604 & 2006CB200300) and the Developing Plan of the Ministry of Education of China (985 - I). The authors also appreciated Professor Yuqun Zhuo, Mr. Lei Chen and Mr. Liang Zhang from the Thermal Engineering Department of Tsinghua University for their efforts to the sampling and analysis in the experiment.

REFERENCES

Cen, K. F., Ni, M. J., Luo, Z.Y., Yan, J. H., Chi, Y., Fang, M. X., Li, X. T. and Cheng, L. M. (1997). Theoretical design and operation of the circulation fluid-bed boiler.

Chen, J. S., Yuan, D. X., Li, Q. L., Zheng, J. M., Zhu, Y. Q., Hua, X. Y., He, S., and Zhou, J. S.: Proceedings of the CSEE. **28** (2008), PP. 72-76.

Chen, L., Duan, Y.F., Zhuo, Y.Q., Yang, L.G., Zhang, L., Yang, X.H., Jiang, Y.M. and Xu, X.C.: Fuel. **86** (2007), pp. 603-610.

Dang, M. T. and Liu, J.: Applied Chemical Industry. **34** (2005), pp. 394-396.

Jiang, Y. M., Duan, Y. F., Yang, X. H., Yang, L. G. and Wang, Y. J..: Journal of Southeast University (Natural Science Edition). **37** (2007), pp. 436-440.

Li, S. H., Wang, Q. M., Xiao, X. B. and Yang, H. S.: Journal of Engineering for Thermal Energy and Power. **22** (2007), pp. 52-56.

Lu, Y., Rostam-Abadi, M., Chang, R., Richardson, C. and Paradis J.: Energy & Fuels. **21**(2007), pp. 2112-2120.

Miller, S. M., Ness, S. R., Weber, G. F., Erickson, T.A., Hassett, D.J., Hawthorne, S.B., Katrinak, K.A. and Louie, P.K.K. (1996). A comprehensive assessment of toxic emissions from coal- fired power plants: Phase I Results from the U.S. Department of Energy Study.

Park, K. S, Seo, Y. C., Lee, S. J. and Lee, J.H.: Powder Technology. **180** (2008), pp. 151-156.

Pavlish, J. H., Sondreal, E. A., Man, M. D., Olson, E.S., Galbreath, K. C., Laudal, D. L. and Benson S. A.: Fuel Processing Technology. **82** (2003), pp. 89-165.

Poulston, S. J., Granite, E. W., Pennline, H., Pennline, H. W., Myers, C. R., Stanko, D. P., Hamilton, H., Rowsell, L., Smith, A.W.J., Ilkenhans, T. and Chu W.: Fuel. **86** (2007), pp. 2201-2203.

Ren, J. L., Zhou, J. S., Luo, Z. Y., Hu, C. X. and Zhong, Y. J.: Proceedings of the CSEE. **27** (2007) pp. 48-53.

Ren, J. L., Zhou J. S., Luo Z.Y., Zhong, Y. J. and Cen, K. F.: Journal of Power Engineering. **25** (2005), pp. 587-592.

Skodras, G., Diamantopoulou, I. and Sakellaropoulos, G. P.: Desalination. **210** (2007), pp. 281-286.

US-EPA (2003). Global mercury assessment [R]. US: US-EPA.

Wang, S. B. and Wu, H. W.: Journal of Hazardous Materials. **136** (2006), pp. 482-501.

Yang, H. Q., Xu, Z. H., Fan, M. H., Bland, A.E. and Judkins, R. R.: Journal of Hazardous Materials. **146** (2007). pp. 1-11.

Yang, L. G., Duan, Y. F., Wang, Y. J., Jiang, Y. M., Wu, C. J., Wang, Q. and Zhao, C.S.: Proceedings of the CSEE. **28** (2008), pp. 66-71.

Yokoyama, T., Asakura, K., Matsuda, H., Ito, S. and Noda, N.: The Science of the Total Environment. **259** (2000), pp. 97-103.

NOVEL CFB BOILER TECHNOLOGY WITH RECONSTRUCTION OF ITS FLUIDIZATION STATE

H. R. Yang[1], H. Zhang[1], J. F. Lu[1], Q. Liu[1], Y. X. Wu[1], G. X. Yue[1], J. SU[2],Z. P. Fu[3]

1Key Laboratory for Thermal Science and Power Engineering of Ministry of Education, Department of Thermal Engineering, Tsinghua University, Beijing, 100084, China
2Taiyuan Boiler Group Co. Ltd, Taiyuan, 030021, China
3Shanxi Lishi Datuhe Heat & Power Cogeneration, Lishi, 033000, China

Abstract: Compared with a conventional pulverized coal fired boiler, the combustion efficiency of a CFB boiler is lower while the self-consumed service power is 1-2% higher. The solution of these problems is the key research topic for researchers and manufacturers of CFB boilers. Based on the State Specification Design Theory of CFB boilers, Tsinghua University proposed a novel CFB technology by reconstruction of the fluidization state in the furnace by adjusting the bed inventory and bed quality. Theoretical analyses show that there is an optimal bed pressure drop, around which the boiler operation can achieve the maximal combustion efficiency and with significant reduction of the wear of the heating surface and fan power consumption. The proposed novel process was implemented in a 75t/h CFB boiler. The results of field tests on this boiler validated the theoretical analyses.

Keywords: CFB boiler, optimization, fluidization, reconstruction, State Specification

INTRODUCTION

During the past two decades, due to the outstanding advantages of wide fuel flexibility, excellent emission performance and large range of load adjustment, CFB boiler technology has been developed rapidly and has become one of the main commercially applied clean coal technologies around the world. In China, this technology dominates the market of small and medium scale industrial boilers, and becomes more and more popular in the market of large scale boilers used in power generation. So far, the total number of CFB boilers in operation is over 3,000 in China (Li et al., 2009a, b).

However, the CFB boiler technology still faces many challenges. Among them, low combustion efficiency, high self-service power consumption, and severe wear of heating surfaces are three major concerns. How to resolve these problems to make the technology more cost-effective and more reliable is among the key research topics on CFB boilers.

Obviously, the above problems are strongly related to the two-phase fluid dynamics in the CFB boiler furnace. Based on the State Specification Design Theory (SSDT) proposed by Tsinghua University (Yue, et al., 2005), the flow regime inside CFB furnace is described as the superposition of a fast bed in the upper furnace and a bubbling bed or turbulent bed in the lower furnace. Moreover, each CFB boiler is designed and operated based on a specified state, determined by fluidizing air velocity, U_g and solid circulating rate, G_s, while G_s can be adjusted by the bed inventory M and bed quality including size distribution, and ash formation properties. Therefore, a novel process was proposed to adjust the flow dynamic state in the furnace from the origin designated state (specified by U_g and G_s) to another state, such that pressure drop directly corresponding to the power consumption of the primary air fan can be significantly reduced, while combustion characteristics can be improved and heat transfer characteristics still can be satisfied. This process is also called as state reconstruction.

In this paper, the detailed theoretical analysis and the first application of the novel CFB technology with state reconstruction of fluidization are introduced. The first implementation of the state reconstruction process was done on a 75t/h CFB boiler, in January, 2006. Some results of field tests carried out on the boiler were also given.

THEORETIC ANALYSIS

The feedstock in a CFB boiler normally has a relatively wide size distribution, spanning from 0 to 8 mm, and as a result, the bed material also has a wide size distribution. Usually, the superficial gas velocity U_g in the furnace of a CFB boiler is about 4-5m/s at full load, so that the flow pattern in the furnace can be considered as a superposition of a bubbling or turbulent bed formed by large particles at the bottom and a fast fluidized bed formed by fine particles in the freeboard (Yue et al., 2005) By simplification, the bed material in a CFB boiler can be classified into two groups with respect to their contribution to fluidization and heat transfer: effective

material and ineffective material. The effective bed material consists of the fine particles that are entrained out the bottom bed, forming a fast bed in the upper furnace. The mass fraction of effective bed material is a main index of bed quality. The rest particles, with relatively large size, are the ineffective material. As their terminal velocity is larger than U_g, these particles can not be entrained into the upper furnace, but remains only in the bottom dense bed. Normally the membrane water-wall in the bottom furnace is covered with a refractory layer, so the ineffectivebed material has a minor contribution to heat transfer. From the point of combustion efficiency, the ineffective particles possess enough residence time for burning out. However, these particles also cause some negative effects including intensifying the wear of membrane water-wall near the top of the tapered part, increasing the pressure head and energy consumption of the primary air fan and increasing the penetration resistance of the secondary air in the middle of the tapered part. Thus, the mass fraction of ineffective bed material should be reduced as much as possible by controlling the size distribution of the feed coal.

Above the bottom dense bed, the flow pattern of the gas-solid flow containing fine particles is regarded as fast fluidization (Bai and Kato, 1995; Yue et al. 2005). Previous studies, mostly carried out in chemical reactors found the axial voidage in the fast fluidized bed is influenced by operating conditions such as fluidizing air velocity, U_g, solid circulating rate, G_s, and bed inventory M, and the geometric structure of the components in the circulating loop (Li et al., 1982; Weinstein et al., 1983; Li et al., 1988; Bai et al., 1992; Chang and Louge, 1992; Kim et al., 1999; Mori et al., 1992; Rhodes and Laussmann, 1992; Xu and Gao, 2003). The height of the riser affects the axial voidage profile in the riser, and the S-shaped axial voidage profile can only be observed in a high enough riser (Bai et al., 1992).

In an industrial CFB boiler, a loop seal with low gas-solid flow resistance is commonly used. The furnace height is normally higher than 20m. In order to realize fast fluidization regime at a certain U_g, the amount of bed material M should be higher than a critical values M^*, i.e., such that the particle flow rate G_s in the upper furnace can reach the saturated value G_s^* for pneumatically transport, while the bottom furnace still has a dense bed (Xu and Gao, 2003; Hu et al., 2009). The appearance of dense bed is essential for fast fluidization. However, M should be smaller than a certain amount in order to keep the freeboard length larger than TDH (Bai and Sato, 1995). The effect of bed inventory on the axial voidage profile is shown in Figure 1. It can be seen that in the fast fluidized bed, the voidages in the dense zone and upper dilute zone are held stably, while the height of dense zone ascends gradually and the voidage in the transition zone increases (Xu and Gao, 2003).

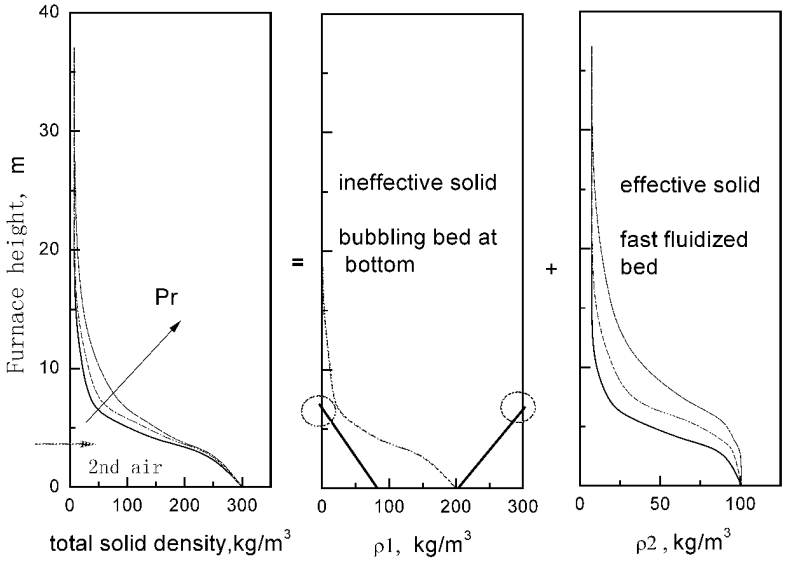

Fig.1 Effect of the bed inventory on gas-solid axial solid density profile

Based on above discussion, the further increase of M after $M>M^*$ in a CFB boiler mainly accumulates particles in the bottom furnace with a refractory layer. The extra M is not much beneficial to the heat transfer (Lu et al, 2002); instead, it introduces several disadvantages to boiler operation, such as severe wear on the membrane water-wall and extra energy consumption of the primary air fan.

Unlike to fan energy consumption and wear, the effect of bed pressure drop on the combustion efficiency is twofold. On one hand, at a certain U_g, when the flow pattern of the fine solids is in the fast fluidization regime, any increase in bed pressure drop leads larger average solid suspension density ρ in the transition zone. As a result, the dispersed solid particles intend to agglomerate into clusters above the dense bed. Since the terminal velocity of particle clusters is larger than that of dispersed particles, intensive backmixing of the clusters takes place along the vertical direction. The clusters collapse and reform periodically in the gas-solid

flow stream (Fujima et al., 1990; Bai and Jin, 1991). Such phenomenon prolongs the residence time of fine particles in the furnace, and is helpful to the burnout of the combustibles.

On the other hand, the high ρ in the transition zone has a strong impact on the gas-solid mixing. The momentum and rigidity of the upward gas-solid flow increase as ρ increases, especially in the zone where the secondary air is injected. The secondary air interacts with a more resistant main flow and its penetration depth becomes shorter (Yang et al., 2008). The oxygen in the center region can be very lean, close to zero, but near the wall the oxygen concentration may be high (Xu and Gao, 2003). This non-uniform oxygen distribution prevails at every cross section above the secondary air nozzles, inhibiting the burnout of fine carbon particles (Xiao et al., 2005).

With such twofold effect of bed pressure drop on the combustion efficiency, it can be expected that there is an optimal bed pressure drop, schematically shown in Figure 2. Under these conditions not only can the maximal combustion efficiency be obtained, but also the fan energy consumption and the wear of the heating surface can be greatly reduced.

Based on the above theoretical analyses, a novel CFB boiler combustion technology is proposed with optimal low bed pressure drop through reconstruction of the fluidization state The reconstruction means that gas-solid flow stream is maintained in fast fluidization with nearly invariant ρ in the upper dilute furnace, and the height of the dense bed and ρ near the secondary air nozzles are reduced. This leads to an enhancement of the gas-solid mixing in the furnace above the secondary air injection. The nearly invariant ρ in the upper dilute furnace and thereby G_s meets the heat transfer requirements. At same time, the power consumption of fans and heating surface wear are greatly reduced. The new technology resolves the three problems mentioned in Introduction section simultaneously.

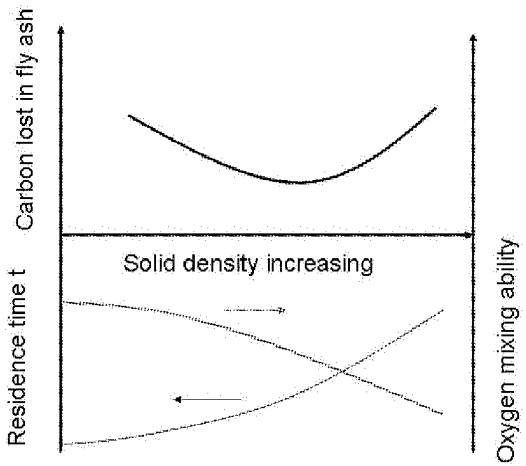

Fig. 2 Bifurcated effect of bed pressure drop on LOI

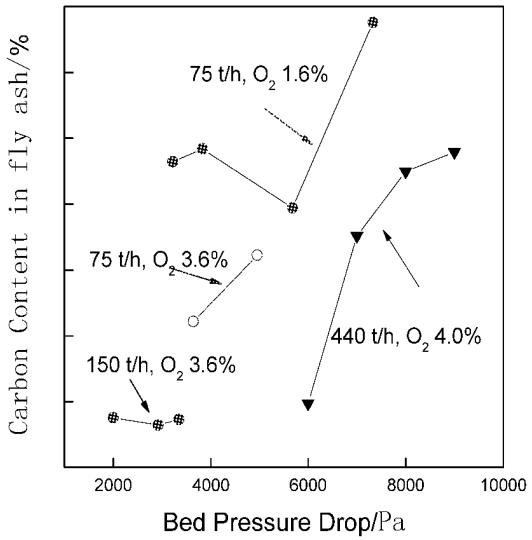

Fig.3 Carbon content in the ashes

The bed quality in a CFB boiler is the result of bed material balance, and it depends on the formation of ashes from the coal, the attrition properties of the inert materials and the cyclone efficiency (Yang et al., 2004, 2005). Generally, the fewer the ineffective coarse particles are, the better is the bed quality. Thus, the a low bed pressure operation can be obtained by reducing the mass fraction of coarse particles, i.e. ineffective solids, in the bed material in the furnace by controlling the size of feed coal (Xiao et al., 2005; Yang et al., 2005).

The objective of the novel CFB technology with reconstruction of fluidization state is to improve the bed quality and find the possible lowest bed inventory (or bed pressure drop). The state specification theory is used to optimize the bed inventory of the effective material and mass balance model and residence time model to optimize the bed inventory of the ineffective material. At same time, optimization of the mass balance system should be done in the following areas: (1) improving cyclone efficiency; (2) modifying the external loop; (3) control of the feed coal size; (4) design code of the heat transfer and combustion distribution.

FIELD TESTS IN CFB BOILERS

In order to validate the concept of reconstruction the fluidization state, a series of field tests were carried out in a few CFB boilers manufactured by Taiyuan Boiler work, Shanxi Province.. Here, the results in a 75t/h CFB boiler are given and discussed.

By utilizing the patented technology of Tsinghua University, the 75t/h CFB boiler with medium steam

temperature and pressure was re-designed by Taiyuan Boiler Works, China. The main configuration of this CFB boiler was mostly the same as that of other 75 t/h CFB boilers. Some modifications in the arrangement of the heating surface were done based on re-calculation of heat release distribution as a consequence of the reconstruction of the fluidization state. The boiler has being operated in Datuhe Power Station, Shanxi China since 2006, burning middle-rank coal from a local coal washery.

Some tests were done at full-load conditions. The bed pressure drop in the furnace was adjusted to 3.2, 3.8, 5.6 or 7.3 kPa by controlling the discharges of bottom ash and circulating ash. The circulating ash was discharged through a valve connected to the loopseal. The boiler was stable at all these pressure drops. During the tests, the flow rates of the primary and secondary air were maintained nearly constant and U_g was kept at 4.4-4.6m/s.

The field tests shown that the boiler could operate steadily with a bed pressure drop as low as 3.1 kPa, much lower than the conventional value. Shown in Figure 3, the optimal bed pressure drop was 5.0-5.8 kPa, at which the LOI was reduced from 23% to 17%, and the service power was reduced by 2.5%. Table 1 lists the performance data before and after reconstruction of the fluidization state. Operation data also show the erosion of the heating surfaces in the boiler and its auxiliaries was alleviated, and the cost of maintenance was reduced by as much as 10% per year, and the availability of unit was 95%. 5 GWh of electricity were saved every year.

Table 1 Influence of novel CFB technology on operation parameters

Parameters	With existing technology	With new technology
Windbox pressure (Pa)	11500～12000	5800～6200
Primary air flow rate (m^3/h)	47000～48000	43000～44000
Primary fan electric current (A)	19～20	11～12(fan changed)
Induce fan electric current (A)	21～22	16～17
Bottom ash discharge interval (min)	20～25	35～40
Loopseal pressure (Pa)	～12000(primary)	～11500(Roots fan7.5kW)
Q_{net}(kcal/kg)	3500～3800	3500～3800

CONCLUDING REMARKS

The concept of fluidization state construction was implemented in a 75t/h CFB boiler to optimize the operation performance. The operational results proved that the novel technology based on fluidization state construction can greatly reduce the erosion of heating surface and service power consumption, which keep the same or even improve combustion performance. The technology is a big breakthrough for increasing CFB boiler's availability and economics. By the end of 2008, Taiyuan Boiler Work has received more than 50 contracts of 75-220t/h CFB boilers with this technology, among which 2 units of 150 t/h and 2 units of 220 t/h CFB boilers with high pressure were in operation at the end of 2008. If such novel CFB technology is extended to entire Chinese market with total installed capacity of 55GWe and average annual availability of 5000h, by estimation, at least 2500 GWh of electricity can be saved every year. That means saving 7 million ton standard coal and reducing 30 million ton of CO2 emission per year. At same time, the reducing of erosion increases the availability and save the cost of maintains. More application of novel technology presented in this paper is undergoing.

ACKNOWLEDGEMENTS

Financial support of this work by Key Project of the National Eleventh-Five Year Research Program of China (2006BAD07A14) and High Technology R&D (863) (2008AA05Z3470123) are gratefully acknowledged.

REFERENCES

Bai, D. L., and Kato, K., Journal of Chemical Engineering of Japan, 28(1995) 179-185.

Bai, D. L., and Jin, Y. Journal of Chemical Industry and Engineering (Chinese). 6(1991) 697-703.

Bai, D. L., Jin, Y., Yu, Z. Q. et al. Powder Technol. 71(1992) 51-58.

Chang, H. and Louge, Powder Technol. 70(1992) 259-270.

Fujima, Y., Tagashira, K. and Takahashi, Y. et al. in: P. Basu, M. Horio and M. Hasatani (Eds.), CFB Technology III, Pergamon Press, 1990, pp.85-90.

Hu, N., Yang, H. R, Zhang, H., et al., Experimental study on gas-solids flow characteristics in a CFB riser of 54m in height, 20th International Fluidized Bed Combustion Conference, May, 2009, Xi'an China.

Kim, S., Numkung, W. and Kim S., Korean J. Eng. 16(1999) 82-88.
Li, J. F., Yang, S., Hao, J. H. et al., Operational Status of 135MWe CFB Boilers in China, 20th International Fluidized Bed Combustion Conference, May, 2009, Xi'an China.
Li, J. F., Mi, J. H., Hao, J. H. et al., Operational Status of 300MWe CFB Boilers in China, 20th International Fluidized Bed Combustion Conference, May, 2009, Xi'an China.
Li, J. Tung, Y. Kwauk, M. in: J. F. Large, P. Basu (Eds.), Criculating Fluidized Bed Technology II, Pergamon Press, Oxford, 1988, 193-203.
Li, Y., Chen, B., Wang, F. et al. M. Kwauk and D. Kunni (Eds.), Science and Technology Press, Beijing, 1982.
Lu, J. F., Zhang, J. S., Yue, G. X. et al. Heat Transfer Coefficient Calculation Method of the Heater in the Circulating Fluidized Bed Furnace. Heat Transfer – Asia Research, 31(2002) 540-550.
Mori, S., Liu, D., Kato, K., et al, Powder Technol. 70(1992), 223-227.
Rhodes, M. and Laussmann, J. P. Can. J. Chem. Eng. 70 (1992) 625-630.
Weinstein, H., Graff, R. A., Meller, M., et al. T, in: D. Kunii, R. Toei (Eds.), Fluidization, vol. IV, Engineering Foundation, New York, 1983, pp.299-306.
Xiao, X. B., Yang, H. R., Zhang, H. et al., Energy and Fuels, 19 (2005) 1520-1525.
Xu, G. and Gao, S., Powder Technol. 137(2003) 63-76.
Yang H. R., Yue, G. X., Lu, J. F., et al, CFB boiler combustion technology with low bed pressure drop. Appl. Patent No.200710176731.1; Publication No.101149146, 2007.
Yang, J. H., Yang, H. R., Yue, G.X., Journal of Power Engineering, 28(2008) 509-513.
Yang, H.R, Wirsum, M., Lu, J.F., et al., Fuel Processing Technol. 85(2004), 1403-1414.
Yang, H. R., Yue, G. X., Xiao, X. B. et al., Chemical Engineering Science, 60(2005) 5603-5611.
Yue, G. X., Lu, J. F., H. Zhang, et al. Design Theory of Circulating Fluidized Bed Boilers. in: L. Jia (Eds.),18th International Fluidized Bed Combustion Conference, May 18-21, 2005, Toronto Canada.

DEVELOPMENT OF FLEXI-BURN™ CFB POWER PLANT TO MEET THE CHALLENGE OF CLIMATE CHANGE

Horst Hack[1], Zhen Fan[1], Andrew Seltzer[1],Arto Hotta[2],Timo Eriksson[2], Ossi Sippu[2]

1Foster Wheeler North America Corp., USA
2Foster Wheeler Energia Oy, Finland
E-mail: horst_hack@fwc.com

Abstract: Carbon-dioxide capture and storage (CCS) offers the potential for major reductions in carbon- dioxide emissions of fossil fuel-based power generation in the fairly short term, and oxyfuel combustion is one of the identified CCS technology options. Foster Wheeler (FW) is working on reduction of carbon-dioxide with its integrated Flexi-Burn™ CFB technology.
The proven high efficiency circulating fluidized-bed (CFB) technology, when coupled with air separation units and carbon purification units, offers a solution for carbon dioxide reduction both in re-powering and in greenfield power plants. CFB technology has the advantages over pulverized coal technology of a more uniform furnace heat flux, increased fuel flexibility and offers the opportunity to further reduce carbon dioxide emissions by co-firing coal with bio-fuels.
Development and design of an integrated Flexi-Burn™ CFB steam generator and balance of plant system was conducted for both air mode and oxyfuel mode. Through proper configuration and design, the same steam generator can be switched from air mode to oxyfuel mode without the need for unit shutdown for modifications. The Flexi-Burn™ CFB system incorporates features to maximize plant efficiency and power output when operating in the oxy-firing mode through firing more fuel in the same boiler.
Existing boiler design tools are being modified to incorporate the features of oxy-combustion, so that various design options can be evaluated. The 460 MWe supercritical CFB power plant (recently constructed by Foster Wheeler) has been used as the basis for an integrated Flexi-Burn™ CFB study.
Keywords: CFB, CCS, oxycombustion, oxy-fuel, carbon-capture

INTRODUCTION

Coal combustion-based power generation faces continuing environmental challenges to reduce pollutant emissions, especially more recently, carbon dioxide emissions. Oxyfuel combustion is one of the methods suggested for removing carbon dioxide from the exhaust gases of a power plant, such as a PC or a CFB steam generator. Oxyfuel combustion is based on combusting carbonaceous fuel with oxygen, to produce carbon dioxide and water vapor as the main components of the exhaust gas. Thereby, the carbon dioxide can be captured relatively easily from the exhaust gas, without having to separate it from a gas stream having nitrogen as its main component, as when combusting the fuel with air. Part of the exhaust gas needs to be recycled to the furnace for temperature control, and to achieve sufficient furnace gas velocity to operate the circulating fluidized bed (CFB) with solids circulation.

Since oxyfuel combustion is still a developing technology, it is advantageous to design oxyfuel combustion boilers, where the combustion conditions are selected to be similar to those of air-fired combustion. This is done by recycling exhaust gas back to the furnace to provide an average O_2 content of 20-28%v. . Due to the similarities of air combustion and moderate O_2 level oxycombustion, oxyfuel steam generators can be built by modifying existing air-firing boilers. Due to the uncertainties related to oxyfuel combustion, capture and storage of carbon dioxide, the regulatory credit (or penalty) for CO_2 emissions and increasing need for carbon capture ready power plants, there is a need for Flexi-Burn™ boilers, i.e. boilers which can be changed from air-firing to oxyfuel combustion, preferably without any changes in the actual construction. With such a Flexi-Burn™ boiler it is also possible to have the maximum power output by using air-fired combustion mode during high load demand, such as summer, weekdays and daytime, and apply oxyfuel combustion with CO_2 removal at other times. In order to generate power more economically by an oxyfuel combusting boiler system, there is a need for an improved system design and operation for minimizing the loss of produced power, and minimizing the requirement of building new power plants to compensate the power loss due to CO_2 removal (Ref 1, 2). The Flexi-Burn™ CFB design approach addresses these needs (Ref 3, 4, 5, 6).

To enhance power generation operability and availability it may be advantageous to operate a Flexi-Burn™ boiler in air-firing mode, when, for example, the air separation unit (ASU), CO_2

purification/compression unit (CPU), or CO_2 storage system is unavailable. Due to different requirements and demands, the power generation and the steady state electrical power supply should always be readily decoupled from the upstream oxygen supply and the downstream carbon dioxide processing (Ref 4).

Combustion with oxygen differs from combustion with air mainly as a result of the different gas compositions. The fundamental change in fluegas composition affects its properties, as listed by Table 1, where both gas density and thermal capacity (specific heat) are changed. A challenge for a Flexi-Burn™ boiler is that its heat distribution varies with gas properties and operations. At a given gas velocity, due to high gas density and thermal capacity contributed from carbon dioxide and water vapor in fluegas, more heat (about 35% more in oxy-fired mode than air-fired mode as seen from Table 1) is absorbed by the flue gas and carried to the downstream heat recovery area (HRA).

Table 1 Flexi-Burn™ Flue Gas Properties

	Gas density (lb/ft3)	Specific heat(BTU/lb)	(Gas density)* (Specific heat)
Air-mode	0.2936	0.2982	0.0876
Oxy-mode	0.3637	0.3245	0.1180

To obtain suitable heat flux at the furnace waterwalls, the combination of CFB boiler operating gas velocity and temperature need to be maintained at certain levels. One can maintain the correct furnace heat flux by increasing firing temperature through reduced gas mass flow by recycling less flue gas. For a greenfield case, this can be done by designing a reduced size boiler to keep a desired gas velocity. But a reduced boiler size approach cannot be applied as a retrofit. When firing in air-mode, both air and fuel fed to such a reduced size boiler are limited and less power would be generated, which leads to a boiler which is suitable only for oxy-firing mode after conversion. Increasing firing temperature can enhance heat flux, but it also leads to an increase of waterwall temperature, which may require tube materials to be upgraded. Given the choice of upgrading tube materials to increase gas side heat flux or to produce high steam temperatures, it is generally more economical to produce higher steam temperatures due to increased steam cycle efficiency. There is a significant amount of materials research being conducted related to increasing main steam conditions, such as to 1300 F, in order to achieve greater power generation efficiency. This work will allow deployment of super-critical and ultra-super-critical Flexi-Burn™ CFB boilers (Ref 6).

Increasing power generation output is the key to minimize power derating and cost due to CO_2 removal. One can either reduce power consumption caused by (ASU+CPU) through improvements, or increase power generation output with the same boiler to reduce the power derating. It is noted that in comparison with oxy-firing, the boiler optimized for air-firing seems oversized for oxy-firing due to potentially reduced gas volume flow. The object of the present paper is to provide an oxyfuel combusting boiler system, and a methodology for using the boiler system so as to minimize the loss of produced power, and to minimize the modifications for the retrofit option.

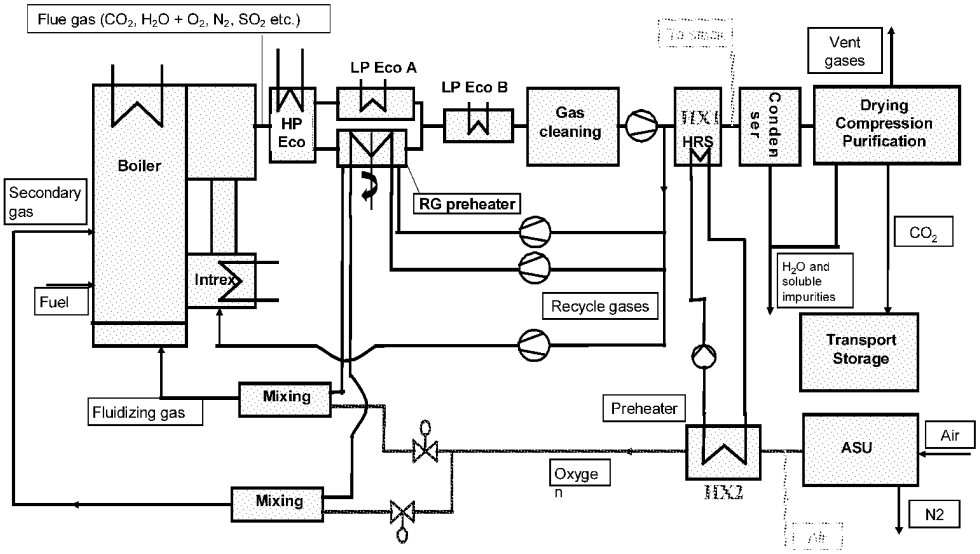

Fig.1 Process Flow Diagram of Flexi-Burn™ Steam Generator Island

FLEXI-BURN™ BOILER CONFIGURATION

Figure 1 presents a process flow diagram (PFD) of a power plant designed for both air-fired and oxy-fired operations with the capability of Flexi-Burn™ and operation switching. As shown in Figure 1, oxygen from the air separation unit (ASU) after preheating is mixed with recycled flue gas and fed to the boiler with solid fuel and sorbent for sulfur capture. The flue gas from boiler after passing through heat recovery area (HRA) is cooled down by a combination of regenerative air-air heat exchanger (AAHX) and low pressure economizers (Figure 1, LP-ECO-A, and LP-ECO-B). Most of the flue gas after the ESP and ID fan, in wet and hot condition without moisture condensation, is recycled and recuperated with hot flue gas in the AAHX. The heated recycled gas streams are then mixed with pre-heated oxygen to form the "primary air" and "secondary air" and fed to the boiler, where the mixing ratio can be adjusted for better performance. The balance of the flue gas is cooled down in the HRS (heat recovery system, a wet-end heat exchanger made of plastic material, where low-pressure circulated water recovers the low-grade heat from the flue gas and uses it to pre-heat combustion air in air-fired mode). Part of the recycled gas, without mixing with O_2, is pressurized by HP fan as "high pressure" and functions as seal and aeration gas for CFB operation.

The balance of the fluegas from the HRS is cooled by a direct water quenching (may be combined with post sulfur capture) before being forwarded to the CO_2 purification/compression units (CPU), where the remaining moisture in fluegas is removed to a ppm level by adsorption. This dry flue gas is purified by CO_2 condensation. Both liquid CO_2 and vent gases are flashed and used as cold sources to cool the inlet fluegas. The purified/flashed CO_2 streams are compressed to the final pressure and cooled down before discharged to the CO_2 pipeline.

In oxy-mode, the lack of nitrogen increases the concentration of moisture and sulfur in fluegas, which raises the acid gas dew point. To avoid acid gas condensation, the fluegas temperature to the ESP in the oxy-mode is controlled by a combination of low pressure economizers (LP-ECO-A and LP-ECO-B).

RESULTS

The development of this Flexi-Burn™ approach was based on a conceptual design of a 460 MWe supercritical CFB power plant, modified for oxyfuel combustion, as shown in Figure 2. The incorporation of the Flexi-Burn™ concept means that the boiler must be operable at, or near, full load in air-firing mode and in oxy-firing mode without modification, when it is built.

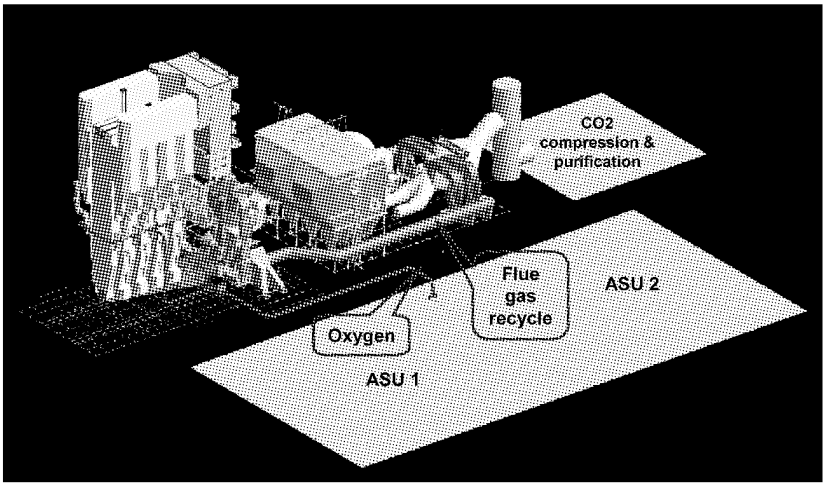

Fig.2 Retrofit applications by oxy-combustion

In both air-firing and oxy-firing modes, the Flexi-Burn™ boiler may be operated at a slightly higher furnace temperature than normally used for air-firing. Part of the reason for this increased temperature is due to the increased quantity of fuel fired, and another reason is to ensure that the limestone calcination temperature is exceeded in spite of the high CO_2 partial pressure in oxy-mode. Further pilot-scale experimental tests are required to validate sulfur capture models in oxy-mode. The gas velocity is similar regardless of firing mode. The oxygen level in the fluegas is controlled to be the same in both modes to ensure the right combustion performance.

In system level evaluation, the following assumptions were applied:

- O_2 purity as 96.5%v

- Air in-leakage as 1.5%v
- Fixed boiler and downstream sizes for Flexi-Burn™
- The same O_2%v in flue gas for both modes
- Hot gas recycled before moisture condensation
- Recycled gas recuperated by air-air heat exchanger
- Steam extraction to ASU and CPU for chilling and regeneration
- CO_2 compressor driven by extracted steam

Table 2 Results for Comparison

Performance	air	Oxy
Feed, kg/s		
Coal	42.8	52.2
Sorb	7.9	10.8
Air/oxy	427.2	102.6
Power, Mwe		
Gross	463.8	514
Aux ST	15.7	69
ASU		79
CCU		57
Aux	44	53
Net	436	393
eff, % (HHV)	42.26	31.29
eff, %(LHV)	43.49	32.20
dCO2, kg/s	0	117
derating, %		9.8

The Foster Wheeler in-house CFB design tools were utilized for this development work. After engineering design tuning and iterating for both air-firing and oxy-firing modes, a Flexi-Burn™ CFB boiler is configured, designed and integrated as shown by Figure 1. It needs to be mentioned that this Flexi-Burn™ boiler differs in arrangement of surface area from that of the original air-firing boiler. Some modifications are required such as adding or removing tubes as compared with regular air-firing boiler design. But no modifications are required after the boiler is converted for Flexi-Burn™ operation.

Figure 3 shows the resultant flue gas temperature profile for both air-firing and oxy-firing operation modes. It can be seen that the bed temperature is slightly higher in oxy-mode than that in air-mode. Fluegas exhaust temperature to the ESP is increased in oxy-mode to avoid acid gas condensation. The fluegas temperature exiting the HPECO is lower in oxy-mode due to the cold inlet feedwater temperature as result of turning-off some of feedwater heaters to allow the HPECO to pickup more heat from the fluegas. Correspondently, the steam generation rate is increased by about 10%, which means that steam flow is increased to all superheat/reheat heat exchangers.

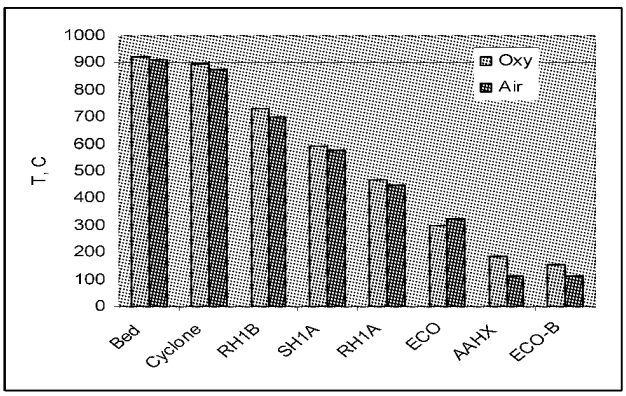

Fig. 3 Fluegas Temperature Profile

For comparison, Figure 4 shows the resultant flue gas maximum velocity at different locations from both

air-firing and oxy-firing modes. As it can be seen from the Figure 4, they are almost the same as the result from present Flexi-Burn™ approach. It is noted that gas velocities are slightly higher in oxy-mode than in air-firing mode at most of the locations due to temperature (Figure 3), except at the AAHX, where part of fluegas split to the ECO-A is increased for a better heat recovery in oxy-firing mode.

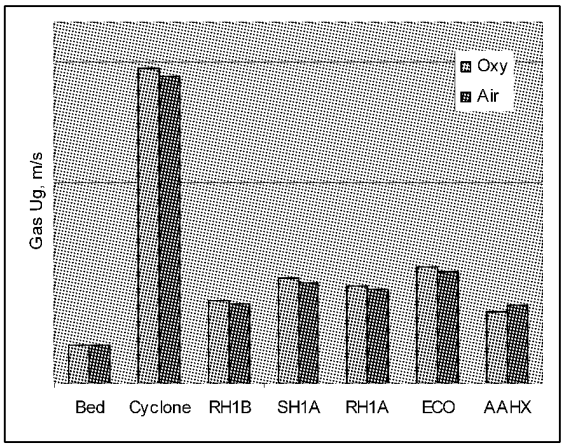

Fig. 4 Comparison of Gas velocity

Table 2 summarizes the power plant performance of the Flexi-Burn™ CFB with and without CO_2 removal. Part of the extra steam, generated from firing-more fuel and saved from less steam extraction to feedwater heaters, is extracted and used to drive the CO_2 compressor by auxiliary steam turbines, which produces about 69 MW. The plant auxiliary power is increased by about 20% due to operation for firing-more fuel, such as fuel handling.

The increase in firing is 52.2/42.8=1.22, or a 22%. The power loss for CO_2 removal from (ASU+CPU) is (79+57)/1.22=111 MW (or 111/436=26% derating), and the specific power for CO_2 removal is 332 kWh/tCO_2. By firing-more fuel, the net power loss is reduced to only 43 MW or less than 10% derating as listed in Table 2. This low power derating is important in reducing building new power plants due to CO_2 removal penalties.

The O_2%v in the gas fed to boiler in oxy-mode is about 23-24%v, which is close to the 21%v from air-mode. This ensures that the difference in operation between air-mode and oxy-mode is small. The O_2 is preheated to about 120 C and mixed with recycled fluegas after recuperation (Figure 1). The O_2 content in the "primary air" and "secondary air" can be different which will be tested in future pilot plant runs.

Regardless of the amount of fluegas recycled, the net fluegas flow to the CPU plant is almost constant. The fluegas flow to the CPU will increase with increase of fuel firing. Therefore ASU, CPU, and fuel feeding capacities have to be increased. However, fluegas recirculation and associated auxiliary power remains unchanged during firing-more fuel. Flexi-Burn™ also means less modification to the existing boiler when conversion from air-mode to Flexi-Burn™ mode.

Since part of the CO_2 is vented out with impurities, the CO_2 removal is about 116.7 kg/s out of 121.3 kg/s from fuel combustion and sorbent calcination, which leads to a CO_2 removal efficiency as 96.2%. This high efficiency partly results from less air in-leakage and increased oxygen purity (96.6%). The final CO_2 stream has purity as 95.1%v and is pressurized to 139 bar (2000 psia) as a liquid or supercritical fluid.

It is been noted that the direct penalty 332 kWh/tCO_2 (ASU+CPU) operated under a 96.5% O_2 purity and 1.5% air in-leakage is almost the same as the literature data 333 kWh/tCO_2 (Ref 1) operated under 95% O_2 purity and 3.0% air in-leakage, but the present case has a better CO_2 removal efficiency of 96.2% as compared with 90.6% from Ref 1.

The cooling tower duty increases from 500 to 800 MWth or a 60% increase because of extra cooling duty from firing-more fuel, and from flue gas cooling, compressor inter-stage and post cooling. This is substantially more than the 22% increase in coal flow rate. Part of this duty increase, about 200 MWth, comes from the cooling requirement of the ASU+CPU plants. The rest comes from a reduced steam extraction to feedwater heaters as result of heat recovery from fluegas cooling. This cooling duty change from oxy-mode requires physical modification of the cooling tower.

Gas cooling is required before, during and post compression. The low-grade heat from these cooling operations may be recoverable depending upon system integration. As heat recovery shares the gas cooling, the cooling water requirement is reduced when heat recovery is applied. The number of stages of compressor affects the heat integration, where the increased compressor discharge temperature (CDT) results from less compression stages and leads to better heat recovery and more power at the generator at a cost of increased compression power. The equivalent power gain has been calculated on the basis of steam savings for the same heating duty to water side. The degree of low-grade heat recovery may be limited by temperature difference or "pinch point". To compensate for this, less compression stages may need to be used. In the present integration, almost all of the condensate needs to be extracted for heat recovery. Less compression stages could potentially be more optimal.

Due to application of the HRS in both oxy-mode and air-mode operation, there is no relative gain in oxy-mode from flue gas cooling before CO_2 compression, which means the efficiency difference is enlarged in comparison with the case without the HRS, due to increased efficiency by use of the HRS in air-mode. For this

reason, the oxy-mode absolute efficiency may be a better measure of performance than the efficiency drop from air-mode.

It is noted that the end steam flow through steam turbine has been increased from 207 kg/s in air-fired case to 260 kg/s in oxy-fired case, which is about 26% more as compared with the 10% increase in main steam flow due to firing more fuel. More sections of low pressure steam turbine or a different size of steam turbine is required to accommodate this flow if the extra steam is not extracted to drive CO_2 compressors.

Steam driven feed water pumps have been widely applied in modern power plants, where extraction steam is taken from the IP/LP crossover or a nearby extraction point. The advantage of this approach is in that (1) it reduces the low pressure end steam flow and has a better steam turbine efficiency, and (2) it reduces all power associated with generator, transformer, motor, frequency converters, and gear loss. Based on the study for a 500 MW power plant (Ref 2), the savings from steam driven feedwater pumps could be 12% as compared with those driven by motors. About 6 MW net saving would be obtained out of 56 MW for CO_2 compression with four stages, if steam driven CO_2 compressors were applied. The corresponding end steam flow through main steam turbine would be reduced. Due to the issues of startup time requirement and upstream location of ASU, steam driven air compressors for ASU have not been included. For CO_2 compressors driven by extracted steam, this is not a problem as they are located downstream of boiler with much less startup time.

For this Flexi-Burn™ boiler, the part load condition (32-35%) with the same steam flow rate for both air-mode and oxy-mode have been evaluated and checked for the once-through operation (Benson point). The O_2 content in the fluegas was maintained as the same at full load for both modes. At the part load, the excess O_2 rises in air-mode, but stays constant in oxy-mode because oxygen fed and gas recycled can be adjusted separately. This is based on a control concept where the desired gas velocity is maintained by manipulating fluegas recycle, and the O_2 is adjusted by the demand of fuel combustion. This low excess O_2%v at part loads saves ASU power.

More oxy-mode experimental tests and large scale demonstrations measuring emissions, heat transfer, materials, and fouling are required for validation of design tools and solutions. A fully integrated CCS demonstration project, based on the Foster Wheeler Flexi-Burn™ CFB boiler design, has been proposed for the Jamestown (New York) Board of Public Utilities by a team lead by Praxair, Inc. The plant has a gross output of combined heat and power of about 50 MWe equivalent. The captured CO2 will be purified and stored in underground saline formations near the site. The Flexi-Burn™ CFB boiler design allows the plant to operate in air-mode (for low cost operation), or in oxy-mode (for CCS). Compared with a conventional air-fired unit, the major differences are the addition of ducts for flue gas circulation, mixers for O2 injection, and low pressure economizer for recovering low-grade heat for condensate.

CONCLUSIONS

System level development and CFB boiler design for the Flexi-Burn™ concept have been performed for a power plant with CO2 removal. The Flexi-Burn™ design makes a power plant capable of on-line switching between air-firing and oxy-firing modes. In addition to potential improvement in the plant availability, the Flexi-Burn™ boiler approach potentially leads to a solution for peak power by operating the plant in air-fired mode and for CO2 removal in oxy-fired mode when power demand is low. By this approach, fewer new power plants will be required to compensate for the power derating due to CO2 removal. Also, as result of adopting a "firing-more" design criterion, the plant power derating is reduced from about 25% to only about 10%, and the net power is increased from 322 to 393 MWe. This also helps to reduce the need for building additional new power plants to compensate for the power derating due to CO2 removal.

REFERENCES

1. IEA Report (IEA 2005/9), "Oxy Combustion Process for CO_2 Capture from Power Plant", July 2005.
2. Black & Veatch, "Power Plant Engineering", Chapman & Hall, 1996, p396.
3. Timo Eriksson et al, "Oxyfuel CFB Boiler as a Route to Zero CO2 Emission Coal Firing", Power-Gen Europe, Madrid, Spain, June 27, 2007.
4. Horst Hack et al, "Oxy-Fuel Coal-Fired Combustion Power Plant System Integration", The 3rd International Oxy-Combustion Network Meeting", Yokohama, Japan, March 5-8, 2008.
5. Horst Hack et al, "Ultra-Supercritical CFB Technology to Meet the Challenge of Climate Change", Power-Gen International 2008, Orlando Florida, USA, December 2-4, 2008.
6. Horst Hack et al, "Development of Integrated Dual-Firing CFB Power Plant", The 33rd International Technical Conference on Coal Utilization and Fuel Systems, Clearwater, Florida, USA, June 1-5, 2008.

DESIGN AND APPLICATION OF NOVEL HORIZONTAL CIRCULATING FLUIDIZED BED BOILER

Q. H. Li[1], Y. G. Zhang[1], A. H. Meng[2]

1Key Laboratory for Thermal Science and Power Engineering of Ministry of Education,Department of Thermal Engineering, Tsinghua University, Beijing, 100084, China

2Department of Environmental Science and Engineering, Tsinghua University, Beijing, 100084,China

Abstract: The vertical circulating fluidized bed (CFB) boiler has been found wide application in power generation and tends to be enlarged in capacity. Because CFB is one of environment friendly and high efficiency combustion technologies, the CFB boiler has also been expected to be used in the industrial area, such as textile mill, region heating, brewery, seed drying and so on. However, the necessary height of furnace is hard to be implemented for CFB with especially small capacity. Thereby, a novel horizontal circulating fluidized bed boiler has been proposed and developed. The horizontal CFB is composed of primary combustion chamber, secondary combustion chamber, burnout chamber, cyclone, loop seal, heat recovery area. The primary combustion chamber is a riser like as that in vertical CFB, and the secondary combustion chamber is a downward passage that is a natural extension of the primary riser, which can reduce the overall height of the boiler. In some extent, the burnout chamber is also the extension of primary riser. The capacity of horizontal CFB is about 4.2-24.5MWth (6-35t/h) steam output or equivalent hot water supply. The hot water boiler of 7MWth and steam boilers of 4.2MWth (6t/h) and 10.5MWth (15t/h) are all designed and working well now. The three units of hot water horizontal CFB boiler were erected in the Neimenggu Autonomous Region, Huhehaote city for region heating. The three units of steam horizontal CFB has been installed in Yunnan, Jiang Xi and Guangdong provinces, respectively. The basic principle for horizontal CFB and experiences for designing and operating are presented in this paper. Some discussions are also given to demonstrate the promising future of horizontal CFB.

Keywords: horizontal circulating fluidized bed boiler (HCFB), hot water boiler, steam boiler

INTRODUCTION

As an advanced combustion technology, CFB firing is better than bubbling bed firing in several advantages, out of which emission control and fuel flexibility are major ones. However, due to some special requirements, such as hot cyclone, bed solid classifier, high furnace height, the advantage of CFB firing is not apparent in small (<20-30MWe) capacity boiler. A CFB boiler could be a judicious choice if the following conditions are met: (1) Capactiy of the boiler is large to medium (usually more than 35t/h). (2) Sulfur retention and NOx control is important. (3) The boiler is required fire a low grade fuel or highly fluctuating fuel quality (Basu et al., 1991). For competition with coal powder fired boiler of high efficiency the CFB boiler is focused on scale-up. CFB combustors have grown in size so that the atmospheric circulating fluidized bed combustion systems for power generation can be considered in application up to 400 MWe and even more (Grace et al., 1997). Tsinghua University made contribution to this scale-up to 600MWe and a full set of design theory for vertical circulating fluidized bed (VCFB) boiler was developed (Yue et al., 2005). Due to the fuel flexibility, circulating fluidized bed combustion has proven to be effective way of converting biomass wastes into clean energy. At proper operation condition, the rice husk combustion efficiency can reach to 97%, whereas the SO_2 and NO_x emissions meet regulation standards (Fang et al., 2004). There are some important factors, such as low pollution, low building cost and maintenance cost, high efficiency which attract user select boiler. The thermal efficiency of majority of modern utility boilers is often higher than 90%. In China, it is compulsory that the thermal efficiencies of the industrial boiler that take water as the working fluid should be not less than the value listed in national standard of China, GB/T17954-2000, which required the thermal efficiency of 61%-69% for low rank bituminous, 59%-81% for bituminous, 60%-77% for lean coal, 50%-77% for anthracite, 63%-79% for lignite, 75%-89% for oil & gas at different rated heat output and operation class (Che, 2008). Because the traditional CFBB can not be applied to many of small industrial boilers, some researchers turned attention to development of horizontal circulating fluidized bed boiler (HCFB) (Zhang, 2005). The configuration of HCFB is similar to the BFBC, such as Rumania ASF type bubbling fluidized bed, which has a two-stage in series pass (Ruan et al., 1992). An overall combustion model was developed for horizontal circulating fluidized bed boiler. Characteristics of gas-solid fluid heat transfer and combustion in the HCFB which capacity is 7MW are investigated numerically with the model (Zhou,2008). The measured thermal efficiency of 7MW HCFB is

82.8% substantially higher than the general grating boiler (Zhang et al., 2008).

The basic principle for horizontal CFB and experiences for designing and operating are presented in this paper. Some discussions are also given to demonstrate the future of horizontal CFB.

DESIGN PRINCIPLE AND CONSIDERATION

The typical configuration of HCFB is shown in figure 1 and the real appearance of pass and water wall is shown in figure 2. The horizontal CFB is composed of primary combustion chamber, secondary combustion chamber, burnout chamber, cyclone, loop seal, heat recovery area. The primary combustion chamber is a riser as that in vertical CFB, and the secondary combustion chamber is a downward passage that is a natural extension of the primary riser, which can reduce the overall height of the boiler. In some extent, the burnout chamber is also the extension of primary riser. The height of general VCFB versus capacity is listed in the table 1(Lv et al. 2005). The data in table 1 are used to plot figure 3, on which the capacity less than 35t/h is extrapolated. The comparison of extrapolated VCFB furnace height and real design HCFB furnace height proves that the HCFB is significantly lower than VCFB at same capacity.

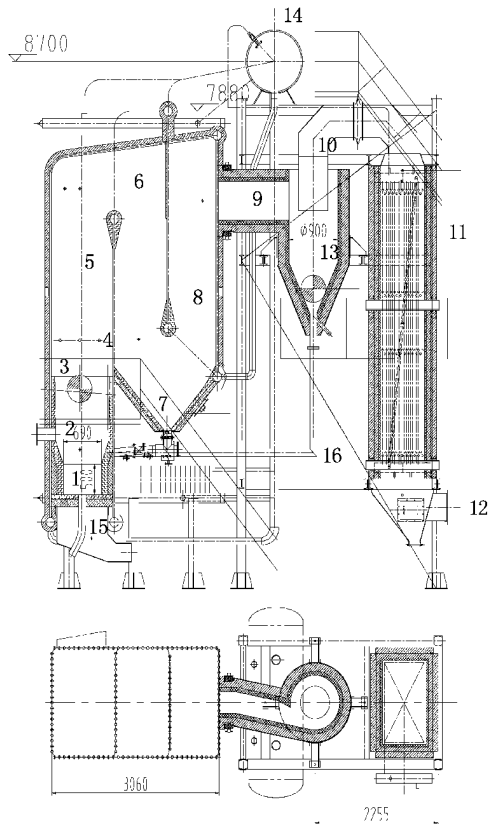

1-dense zone;2-transition zone;3-gas lance level; 4-secondary air;5-freeboard;6-secondary downward chamber;7-first stage solids recycle;8-burn out chamber;9-furnace exit;10-finder;11-backpass heating surface;12-exhaust gas;13-cyclone;14-steam drum;15-primary air chamber; 16-loop seal

Fig. 1 HCFB configuration

HCFB boiler exhibits very complex hydrodynamics, caused by multi-pass flow (one downward and tow upward) and interaction between the two-phase of gas and solid. The bottom dense zone of primary furnace shows hydrodynamic behavior similar to bubbling or turbulent fluidized bed. The dilute zone consists of the upper part of the primary furnace and all other of the secondary downward and third upward combustion chamber. The flow regime is strongly influenced by flow direction and exit geometries. The bed materials are circulating in the primary, secondary, third chamber and cyclones. The solids entrained out of primary chamber into secondary chamber are first collected by centrifugal force induced by 180° flow direction turning. The collected solids are returned back to dense zone of primary chamber. The solids that fly out of the third chamber with flue gas is separated by cyclone are circulated into primary chamber through loopseal. The height of HCFB is lower, so that the performance of loop seal is more critical than VCFB for bed material circulating. We have tried several loopseal and mechanical valve for ash circulating in the design.

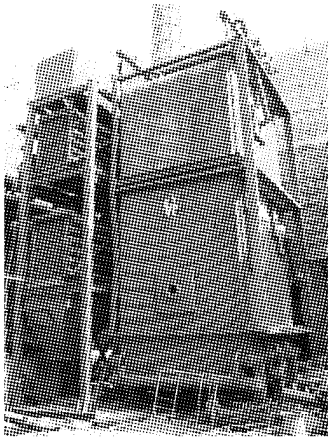

Fig. 2 Combustor and convective backpass of 10.5 MWth hot water boiler

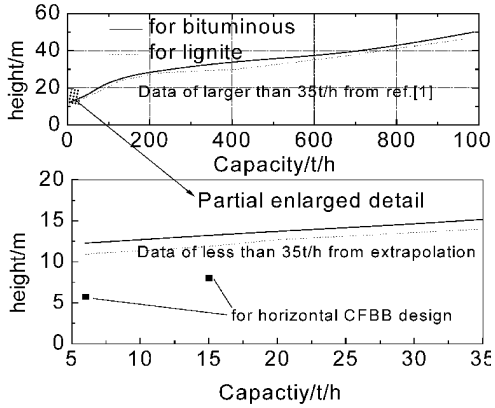

Fig. 3 Furnace heights as the function of boiler capacity

Table 1 The net height of combustion chamber in CFBB (m)

Coal	Capacity(t/h)						
	35	75	130	220	410	670	988
Bituminous	15	20	25	29	34	39	50
Lignite	14	18	24	28	30	37	47

For the requirement of fuel flexibility, the small HCFB are usually desired to burn or co-fire different fuels. For example, solid fuel and gas fuel can be co-fired in HCFB, which involves the safety and economy. In general, burner-type boilers must have a sophisticated flame supervisory system. As we know, there is no flame in CFB boiler. It has, instead, a large mass of inert hot solids. Thus even after a temporary fuel stoppage, neither the furnace temperature nor the steam temperature drop immediately. If the fuel feed is resumed within several minutes, no restart is required on the boiler(Basu et al.,2000) For oil shale and gas co-firing case, the gas supply and burner arrangement are simplified as in figure 4 according to NFPA suggestion (NFPA,2007)for tradeoff between the safety and first cost.

If the CaO or $CaCO_3$ is introduced to the furnace for sulfur removal then the Ca/S ratio can be determined by figure 5 that taken from Circofluid type CFB design consideration of Beijing Boiler Works(Beijng Boiler Works, 1991).

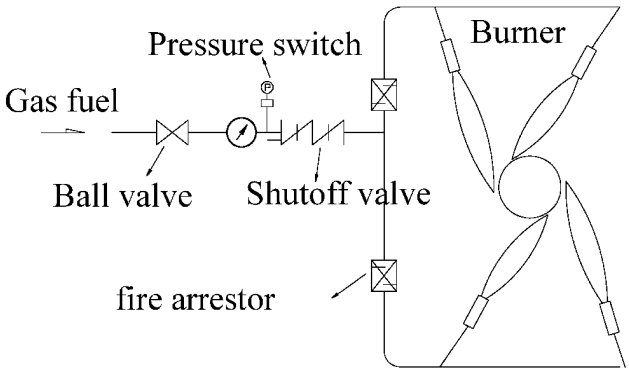

Fig. 4 Co-firing gas and solid fuel in HCFB

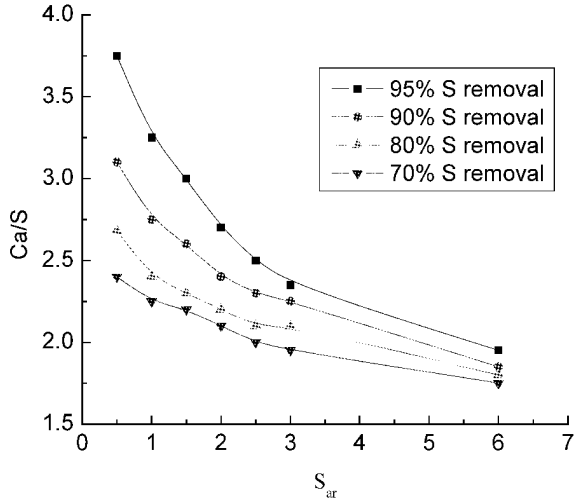

Fig. 5 Sulfur removal efficacies as the function of molar ratio of Ca/S at different S content in fuel

According to our experience and using VCFB design theory for reference, based on rules of thumb, some design parameters for HCFB are chosen and listed in Table 2. The excess air coefficients are selected from 1.2 to1.3, high value is for low grade fuel. For simplicity and low ignition fuel, the air preheater is omitted. If the air preheater is available, the hot air temperature is around 100 ℃. Feed water temperature is determined by user water treatment system, if user has thermal deaerator, the feed water is usually higher than 100 ℃, otherwise it is maintained at ambient temperature. The dense and dilute zone temperature is arbitrarily selected in the light of CircoFluid type CFB boiler design. The gas velocities in dense zone, dilute zone, secondary chamber, third chamber, and economizer are dependent on the balance between the abrasion and heat transfer.

Table 2 Parameters selection in HCFB boiler

Item	Unit	6t/h	6t/h	15t/h
Fuel		Lean coal	Oil shale & gas fuel	Anthracite
Heating value	kJ/kg	20054	9107	19855
Excess air coefficient		1.2	1.3	1.2
Hot air temp.	℃			100
Feed water temp.	℃	20	20	104
Exhaust temp.	℃	145	140	145
Efficiency	%	85	82	85

Continued

Item	Unit	6t/h	6t/h	15t/h
Dense zone temp.	℃	850	820	880
Dilute zone temp.	℃	890	860	910
Cyclone inlet temp.	℃	600	470	560
Dense zone gas velocity	m/s	3.77	3.29	4.14
dilute zone gas velocity	m/s	4.08	3.94	4.42
Gas velocity in secondary chamber	m/s	4.37	4.56	4.60
Gas velocity in third chamber	m/s	3.81	3.68	3.41
Gas velocity in economizer	m/s	6.16	7.38	7.05
Gas velocity in preheater	m/s			9.88

FIELD TEST

The three units of hot water horizontal CFB boiler were erected in Inner Mongolia Autonomous Region, Hohhot city for region heating. The three units of steam horizontal CFB has been installed in Yunnan, Jiang Xi and Fujian provinces, respectively. We performed the field test for hot water HCFB in Hohhot city. The suspension density in HCFB, thermal efficiency and pollutant emission were obtained.

Just like vertical circulating fluidized bed, the horizontal circulating fluidized bed also pose considerable challenges to our understanding. Because it is not yet possible to produce *ab initio* predictions of their complex fluid dynamics, transport and chemical behavior, experimentation remains essential. Thus, we measure the local suspension density of HCFB using sampling probe, the obtained suspension densities at primary chamber lower part(position 1), primary chamber upper part (position 2), secondary chamber medium part and third chamber medium part are shown in figure 6, four typical experimental cases are included in this figure. It is shown in Figure 6 that the suspension density decreases along the flue gas flow direction, an exceptional density rising occurs between second chamber and third chamber. This phenomenon may be induced by the geometrical effect. Other researcher's result suggested that the gas-solid flow behave as bubbling flow regime when the suspension density is larger than 0.7kg/Nm^3(Yang et al.,2006).We can see the suspension densities almost all exceed the 0.7 kg/Nm^3 from figure 6, therefore the bubbling flow regime is throughout the primary, secondary and third chamber. The bubbling flow regime is favorable to heat transfer.

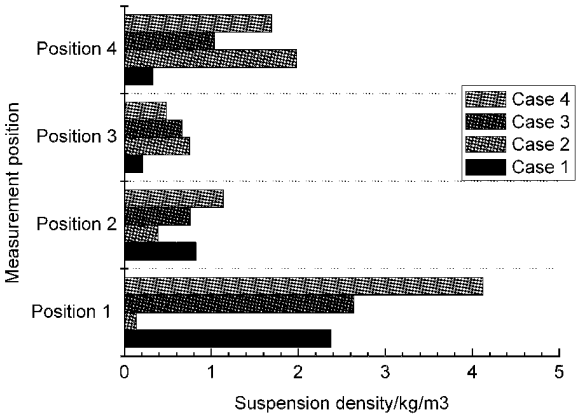

Fig. 6 Suspension densities at different locations

Table 3 Boiler efficiency (%)

	No.1	No.2	No.3	No.4	No.5	No.6
Direct procedure	88	93	85	94	90	90
Indirect procedure	88	86	86	86	87	86
Mean efficiency	88	90	86	90	89	88

Table 4 Pollutant emission (mg/m^3)

	PM	SO_2	NO_x
Measurements	40	112	120
Regulation limit	200	900	

The boiler efficiency was obtained according to Chinese test code for industrial boiler(GB 10180-88)(national standard, 1988) and shown in table 3. The measured thermal efficiencies are somewhat higher than the designed thermal efficiency in table 2. The differences between measured and designed efficiency maybe come from the measurement errors and the low operation load (off-normal design mode). We

cannot reach the normal operation mode, because the hot water HCFB is used for space heating and the weather is very warm when we performed test. The exhaust pollution emission was analyzed by flue gas analyzer and the final result is listed in table 4. The PM, SO_2 and NO_x are all satisfactory to China national standard.

Maintenance

The abrasion, corrosion and erosion is strongly influencing the availability of HCFB (Han et al., 2007; Stultz et al., 1992). The functions of the refractory in the HCFB are both providing erosion protection in the dense bed and insulating the furnace water walls and primary plenum. The steam boiler designer should pay serious attention to measures preventing abrasion wear of the tubes of heating surfaces by particles of ash and unburned fuel (Reznikov and Lipov, 1985).

The routine examination after 2 years operation shows that some leakage spots were found on the water wall due to the welding defection, bed material erosion and abrasion. The overall abrasion area amount for 3 square meter. This abnormal abrasion resulted from the blockage of return pipe of loop seal, which was full of the refractory that get off from the return pipe. The cross-section area of cavity between second and third chamber decreases so that velocity of gas increase to favor abrasion.

The maximum abrasion rate is measured to be 0.4mm/year except for the abnormal area. The problems of existence suggested that the distance and cavity between second and third chamber should be increased and the elevation of lower header of in-furnace split water wall should be lifted to maintain a trouble-free flue gas passage. The nozzles on air distributor are also found to be partially abraded. After some welding treatment these nozzles can be reused.

CONCLUSIONS

The research progress of HCFB and its some applications in China are briefly presented in this paper, and the features of HCFB are also schematically outlined here. The field test and maintenance information all showed that the HCFB combustion technology is promising and competitive due to its lower pollution and higher thermal efficiency than grating furnace of the same or similar capacity. The fuel flexibility makes it easy to burn anthracite, lean coal, lignite even gas fuel.

ACKNOLEDGEMENTS

Mr. Dang Wenda is acknowledged for performing field experiment. Mr. Wang Zhaojun, Hu Feng and Ms. Shao Suming are all acknowledged for their partial drawing preparation. The engineer, Lin Congsen is also acknowledged for providing maintenance suggestion. The senior engineer, Wang Zhiwei, working for Xi'an Thermal Power Research Institute Co., Ltd., has given valuable opinion on further modeling experiment and field test.

REFERENCES

Basu, P., Scott A. F.: Circulating fluidized bed boilers. Butterworth-Heinemann, 1991.

Basu, P., Cen, K. F., Louis, J.: Boilers and Burners. Springer-Verlag New York, Inc.,2000.

Beijing Boiler Works. Circofluid Technology Transfer Manual, 1991.

Che, D.F.: Boilers-Theory, Design and Operation. Xi'An: Xi'An Jiaotong Universtiy Press,2008.

Fang, M. X.: Experimental study on rice husk combustion in a circulating fluidized bed. Fuel processing technology 85(2004) 1273-1282.

Grace, J. R., Avidan, A. A., Knowlton, T. M.: Circulating fluidized beds. Blackie Academic & Professional, 1997.

Han, D.T., Kuang, Y.Z., Zhang, J.H.: Anti-erosion Improvement on Convective Surfaces of Circofluid Type 75 t/h CFB Boiler. Boiler technology 38(1) (2007),pp.44-48. (in Chinese).

P. R. China mechanical and electrical industrial ministry: Test code for industrial boiler(GB 10180-88),1988.(in Chinese).

Lv, J.F., Yue, G.X., Zhang, J.S., et al. :Operation and maintenance of circulating fluidized bed boilers. Beijing: China Waterpower Press,2005.(in Chinese).

NFPA.:NFPA 85 Boiler and Combustion Systems Hazards Code 2007 Edition. 1 Batterymarch Park, Quicy, MA 02169-7471,2007.

Reznikov, M. I. , Lipov. Yu. M. :Steam boilers of thermal power stations. Moscow: Mir Publishers,1985.

Stultz, S.C. , Kitto, J. B.: Steam it's generation and use, 40th edition, 1992.

Yang, H.R., Lv, J.F., Yue,G.X.: Design Theory of Circulating Fluidized Bed Boilers and Determination of the De sign Parameters. Journal of Power Engineering, 26(1)(2006),pp.42-48.(in Chinese).

Yue, G, Lv J. F., Zhang H., et al. :Design theory of circulating fluidized bed boilers. Proceedings of FBC2005 18 international conference on fluidized bed combustion, Toronto Canada, 2005:135-146.

Zhang, Y.G., Yao,Z. J., Li, Q.H., et al.: A horizontal circulating fluidized bed combustion facility and it's operation method. Chinese patent, CN200510126362.6

Ruan, Y. H.: Selected picture and drawing for bubble fluidized bed. Chengdu: Si Chuan Science and Technology Press, 1992.(in Chinese).

Zhang, Y.G., Gou, H.T.: Brief introduction and application. Boiler Manufacturing 1(2008), pp.5-7.(in Chinese).

Zhou, X. B. :Numerical investigation of the fluid flow and the combustion characteristics in a horizontal circulating fluidized bed boiler. Master thesis, Beijing Jiaotong University:2008.(in Chinese).

DESIGN AND OPERATION OF CFB BOILERS WITH LOW BED INVENTORY

Jun Su [1], Xiaoxing Zhao [1], Jianchun Zhang [1], Aicheng Liu [1], Hairui Yang [2], Guangxi Yue [2], Zhiping Fu [3]

1 Taiyuan Boiler Group Co. Ltd., Taiyuan, 030021,China
2 Department of Thermal Engineering, Tsinghua University, Beijing, 100084, China
3 Datuhe Thermal Power Plant, Lishi, 033000,China

Abstract: In this paper, the challenges and problems of the circulating fluidized bed (CFB) combustion technology are summarized and analyzed. In order to resolve the problems in CFB boiler application, design principals and method of CFB boiler with the low bed inventory is proposed by Taiyuan Boiler Group Co. Ltd., cooperated with Tsinghua University. And a full set of design code of new CFB boiler with low bed inventory has been developed, to design the product structure of new generation CFB boilers. The first CFB boiler product with the low inventory was placed and has been operated for two years in Datuhe Thermal Power Plant at Lishi, Shanxi province. The operation practice and measurement data show that the CFB boiler with the low bed inventory stands for the newest trend of the development of CFB boiler in the future. It is expected that more technical advantages will be shown when this technology is applied to the CFB boiler with larger capacity in the near future.

Keywords: low bed inventory , CFB boiler, design, application

INTODUCTION

In the past two decades, because of the three outstanding advantages such as wide fuel flexibility, excellent emission performance and large range of load adjustment, CFB boiler technology developed rapidly and becomes one of the clean coal combustion technologies commercially applied (Feng et al, 2003). In China, CFB boiler combustion technology has made an irreplaceable position in the market of small and medium scale boilers. So far, the total number of CFB boiler in commission is over 3,000 units.

As a developing technology, CFB boiler combustion technology still faces many challenges. For example, in the view of operation safety, though the availability increases greatly by solving erosion, refractory materials and auxiliary equipment, some CFB boilers with 135MWe can continuously operated over 8000h (Lu et al., 2007), which is lower than that of the pulverized coal (PC) fired boiler. In addition, the combustion efficiency of CFB boiler is lower while the service power is 1-2% higher. Even worst is that serious wear of the heating surfaces, especially caused by firing low quality coal, will reduce the boiler's availability greatly. Table 1 shows the power of auxiliary equipments in CFB boiler and PC boiler in 300MWe scale. How to solve these three problems, particularly operation economics, is the key research subject faced by the international researcher and manufacture.

As shown in Table 1, the power consumption of auxiliary in CFB boiler is one time higher than that of PC boiler. As result, the average service power is as high as 9%. The reasons lies in not only in the problem in boiler design, but also in the complexity of system layout and improper selecting of auxiliary.

By reviewing the previous design theory of CFB boiler, Tsinghua University proposed the Specific State Design Theory of CFB boilers [3], Tsinghua University provided the technical methods to solve the above mentioned problems, and developed a full set of design code and thermal calculation software. Cooperated with Tsinghua, Taiyuan Boiler Group Co. Ltd. developed the new generation CFB boiler series product with loads from 75 t/h-1000t/h.

Table 1 Auxiliary equipments in 300MW CFB boiler and PC boiler

Name	300MW CFB boiler			300MW PC boiler		
	Parameters	Power (kW)	Total power (kW)	Parameters	power(kW)	Total power(kW)
Primary air draft fan	pressure: 27800Pa flow rate: 73m³/s	3000×2units	6000	pressure: 15163Pa flow rate: 58.53m³/s	1250×2units	2500
Secondary air draft fan	pressure:15700Pa flow rate: 98m³/s	2240×2 units	4480	pressure:3277Pa flow rate: 107m³/s	560×2units	1120

Continued

Name	300MW CFB boiler			300MW PC boiler		
	Parameters	Power (kW)	Total power (kW)	Parameters	power(kW)	Total power(kW)
Induce draft fan	pressure: 7800Pa flow rate: 340m³/s	3600×2 units	7200	pressure:3737Pa flow rate: 231m³/s	1600×2units	3200
Fluidizing fan	pressure: 68000Pa flow rate: 10m³/s	800×5 units	4000			
Ball mill				58.5t/h	450×5units	2250
Total			21680			9070

The first 75t/h CFB boiler with the novel CFB technology by reconsideration of fluidization state has been operated since January, 2006 and a comprehensive field test was carried out in June, 2007. The results proved that the novel technology can greatly avoid the erosion and reduce the service power. A big breakthrough was made in boiler's availability and economics.

DESIGN PRINCIPALS OF THE LOW BED INVENTORY CFB BOILER

Theoretical fundamentals

With the researches over twenties years, Tsinghua University disclosure the essential gas solid flow regimes and mass balance in the CFB furnace and proposed the Specific State Design Theory of CFB boilers. The new theory points the flow pattern in the furnace is a superposition of a turbulent bed formed by large particles at the bottom and a fast fluidized bed formed by fine particles in the freeboard. At same time, the flow regime, i.e. the gas solid suspension density profile, may have different state, even at the same fluidizing velocity. However, in the design and operation of a real CFB boiler, the state should be constant, otherwise, it is hardly for the operator to control the boiler. It is found that the gas solid flow regime can be controlled and maintained by adjusting the bed material inventory when the state point deviates from the design points. Tsinghua University collected and shown the state points of different CFB boiler manufactures in one figure, which can direct the optimization on the CFB boiler design.

By simplification, the bed material in a CFB boiler can be classified into groups with respect to their contribution to fluidization and heat transfer: effective material and ineffetive material. The effective bed material is consists of the fine particles that are entrained out the bottom bubbling bed and forms a fast bed in the upper furnace. The mass fraction of effective bed material is often denoted as bed quality. The rest particles, with relatively large size, are the ineffetive material. As their terminal velocity is larger than Ug, these particles can not be entrained into the upper furnace, but remains only in the bubbling bed. Normally the membrane water-wall in the bottom furnace is covered with a refractory layer, so the ineffective bed material has a minor effect on heat transfer performance.

From the point of combustion efficiency, the ineffective particles possess enough residence time for burning out. However, these particles also cause some negative effects including intensifying the wear of membrane water-wall near the top of the tapered part, increasing the pressure head and energy consumption of the primary air fan and increasing the penetration resistance of the secondary air, which locates in the middle of the tapered part. In practical operation, in order to avoid the above negative effects, the mass fraction of ineffective bed material should be reduced as much as possible by controlling the size distribution of the feed coal.

Above the bubbling bed, the flow pattern of the gas-solid flow containing fine particles is regarded as fast fluidization. Based on previous studies, most of them carried out in chemical reactors, the axial voidage in the fast fluidized bed is not only influenced by operating conditions such as fluidizing air velocity, Ug, solid circulating rate, Gs, and bed inventory M.

In addition to fan energy consumption and wear, the effect of bed pressure drop, or bed inventory M, on the combustion efficiency is twofold. With such twofold effect of bed pressure drop on the combustion efficiency, it can be expected that there is an optimal bed pressure drop. Under these conditions not only can the maximal combustion efficiency be obtained, but also the fan energy consumption and the wear of the heating surface can be greatly reduced (Yang et al., 2009).

How to control the bed quality, i.e the mass fraction of the effective and ineffective materials, and to meet

the requirement of heat transfer in the upper furnace and combustion efficiency and decreasing the power and erosion, the basic task of the optimization of flow regime with low bed pressure drop or bed inventory. The engineering practices shows that, the precondition of the low bed pressure drop is high cyclone efficiency and system optimization of core parts in combustion, as result the average size of the bed material decreases and bed quality increases.

How to control the bed quality, i.e the mass fraction of the effective and ineffective materials, and to meet the requirement of heat transfer in the upper furnace and combustion efficiency and decreasing the power and erosion, the basic task of the optimization of flow regime with low bed pressure drop or bed inventory. The engineering practices shows that, the precondition of the low bed pressure drop is high cyclone efficiency and system optimization of core parts in combustion, as result the average size of the bed material decreases and bed quality increases.

Selection of flow regime and performance prediction

The flow regime in the new generation of CFB boiler with low bed inventory is selected with the design theory model proposed by Tsinghua University(Yue et al., 2005). The design theory solve the fundamentals for developing the new generation CFB boilers, i.e. the flow regime in furnace, because once the flow regime is chosen, the solid suspension density, circulating rate, the heat transfer coefficient along furnace height and the combustion fraction will be determined, and the relationship between flow regime and the above parameters should be found by accumulating the experience from engineering practice and be secured by matching the auxiliary system, which is very huge and complex system. Once the flow regime in the furnace differs from the chosen one, according the Tsinghua's design theory, it can be adjusted by changing the bed inventory in the furnace. With the design theory, the design parameters can be chosen. If the boiler products are manufactured with such parameters, the new generation of CFB boiler can operate at the optimum status, i.e. optimum economics and reliability.

The performance of the new generation CFB boiler is calculated with the Thermal Calculation Software developed by Tsinghua University(Lu et al., 2002). Based on the design theory, Tsinghua collected and evaluated the operating data and the coal analysis in over hundreds CFB boilers around the world. The Thermal Calculation Software suitable for the domestic CFB boilers was developed to calculate the optimum parameters, such as the structure of the parts in CFB boiler, by considering the environmental conditions, the parameters of fuel, desulfurization, steam parameters and so on. So far, this software as successfully applied in the design of 35t/h, 75t/h, 130t/h, 260t/h,480t/h, and 1000t/h CFB boilers of Taiyuan Boiler Group Co. Ltd.

Design code of the low bed inventory CFB boiler

Cooperated with Tsinghua University, Taiyuan Boiler Group Co. Ltd. built the full set of design code of new CFB boiler with low bed inventory is built, with which the product structure design of new generation CFB boilers are finished. This design code consists of the performance and structure calculation, the standard of boiler arrangement, standard of heating surface arrangement, the geometry calculation of the main parts, the standard of anti-erosion, seal and expansion, standard of furnace wall, method of flue gas system, standard of fuel preparation, standard of auxiliary design and selecting. Based on the above standards, Taiyuan Boiler Group Co. Ltd. applied many patents and specific technologies.

STRUCTURE FEATURES OF THE LOW BED INVENTORY CFB BOILER

The new generation of CFB boilers developed by Taiyuan Boiler Group Co. Ltd. and Tsinghua University, equip with thermal insulation cyclones. 75 t/h -480t/h CFB boilers have two cyclones at the furnace exit, while the 1000t/h CFB boiler has three cyclones. There are many patent and specific technologies used in the boiler. Under the precondition that agglomerate in cyclone and loopseal is totally solved, the reason why choosing the thermal insulation cyclone rather the water or steam cooled cyclone is that the former has better performance in the aspects such as more stable operation, more excellent combustion efficiency and separating efficiency.

The most basic guarantee of the new generation CFB boilers is to optimize the structure of the key parts, and secure the quality and quantity of the bed material in the furnace. Such hey parts should be designed into uniformity, rather than independent parts. Any function or structure design is out of coordination will influence the stable and efficient operation of the CFB boiler.

Optimization on the furnace

Following the design theory and method proposed by Tsinghua, the fluidizing velocity and circulating rate are chosen. As result, the heat transfer coefficient is determined and used to design the heating surface in the

furnace. The furnace roof uses the anti erosion structure. The coal inject tube and secondary air injection has direct seal structure and manufactured in factory. The systemic anti erosion measures and kick out tube are adopted to avoid erosion. The structure and location of measure points in the furnace are regulated. The design of the furnace exit considers the gas flow field and the design of inlet of the cyclone.

Low resistance, anti-backflow air nozzle

The patent nozzle of Taiyuan Boiler Group Co. Ltd. has similar structure as bell jar nozzle, while, in order to avoid drawback such as the heavy erosion, high resistance and difficult replacement, it has some special features, such as reasonable diameter of nozzle cap, diameter of hole and easy replacement jacket tube. Because the velocity in holes is reasonable, the erosion is reducing. After certain period, the jacket tube and nozzle cap can easily replaced. This can greatly reduce the cost of maintenance.

Optimization of the secondary air

The location of secondary air inlets around the furnace, the level and the structure of the injection, the flow rates at different location, the number of inlets and penetration velocity, the ratio of the secondary air is optimized.

Optimization on the cyclone

The thermal insulation cyclone is chosen and optimized. Base on the design code, the geometry and structure of anti erosion and insulation is selected, the inlet of the cyclone has long distance to accelerate and ratio of height to width is optimized. The vortex finder has reducing diameter and eccentric center. The diameter of the vertical part is determined with the optimized ascending velocity of the gas. The angle of conical part can match the gas low field and the standpipe.

Low resistance, high flow rate and minor fluidizing ash return system

Taiyuan Boiler Group Co. Ltd. develops the model of solid flow in the ash return system, and make the optimization on the resistance of loopseal, the descending velocity of solid in the standpipe, the diameter of the standpipe and the style and geometry of the partition wall, the style and geometry of the horizontal passage, the wind box of the loopseal and the distributor. These are the patent of Taiyuan Boiler Group Co. Ltd.

Precise control and independent adjustment on the fluidizing air rate

Based on the flow regime of negative pressure gradient moving bed in the standpipe drawn by Tsinghua, the fluidizing air rate and ash return system are chosen and designed optimally. This flow regime disclosures the operating principle of the ash return system and clarifies the dynamic relation between the solid flow and the fluidizing air, and gives the mathematical correlation.

Optimization on the second pass

The second pass is optimized to match the arrangement of heating surfaces and performance of circulating combustion system. High efficient heat transfer is secured by avoiding erosion and ash deposition on the heating surfaces in second pass.

Increasing the shop erection rate

In order to decreasing the incipient fault caused by low quality in on-site installation, Taiyuan Boiler Group Co. Ltd. keeps the design concept with maximum shop erection rate. Some key parts, such as the water cooled distributor, membrane wall, exit of furnace, kick out tubes and furnace wall supporter are manufactured integrally in factory.

Optimization on system and auxiliary

Optimization are made on the heat air system, fluidizing air system, induced air system, coal feeding system, limestone system and drainage system. The standards on air draft fan, rooster fan, coal feeder, ash cooler, ash blower and refractory are developed.

OPERATION PRACTICE OF THE LOW BED INVENTORY CFB BOILERS

In order to validate the concept of reforming the fluidization state, a series of field tests were carried out in a few CFB boilers manufactured by Taiyuan Boiler work, Shanxi Province. The first 75t/h CFB boiler with the novel CFB technology by reconsideration of fluidization state has been operated since January, 2006 and a comprehensive field test was carried out in June, 2007. The boiler has being operated in Datuhe Power Station,

Shanxi, China since 2006. The fuel is the middling coal from a local coal washery. The results proved that the novel technology can greatly avoid the erosion and reduce the service power. A big breakthrough was made in boiler's availability and economics.

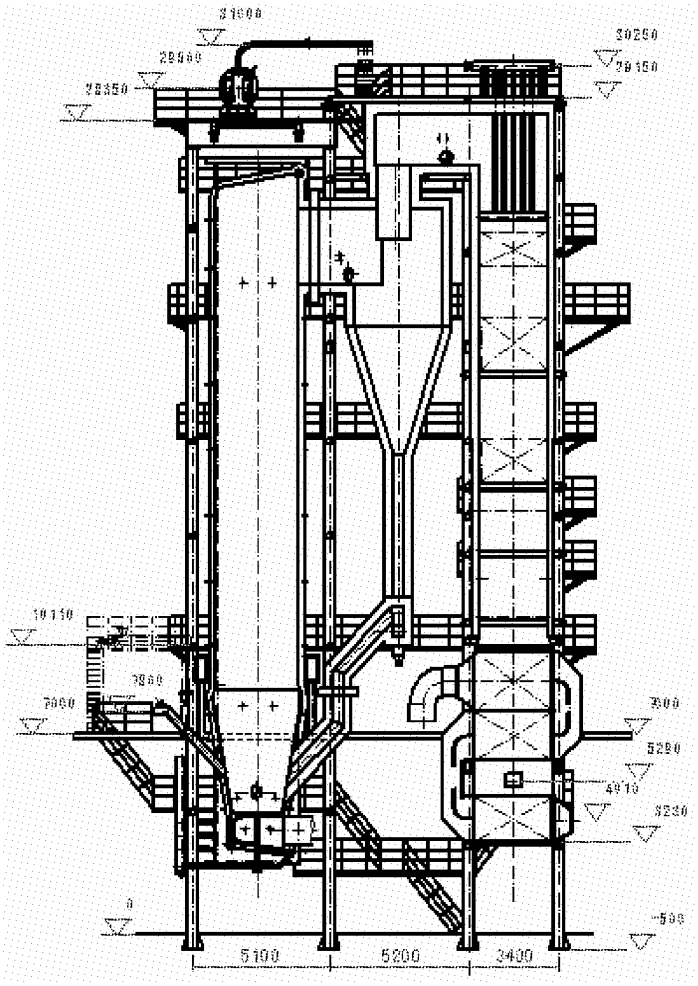

Fig.1 Boiler structure of the new CFB boiler (75t/h)

The comparison

Figure1 shows the structure of 75t/h CFB boiler with new technology. The main configuration of this CFB boiler was not obviously different from that of other 75 t/h CFB boilers. However, some modifications in the arrangement of the heating surface are done based on a new calculation of heat release distribution as a consequence of the reconsideration of the fluidization state. At same time, optimization of the mass balance system should be done in the following areas: (1) improving cyclone efficiency; (2) modifying the external loop; (3) control of the feed coal size; (4) design code of the heat transfer and combustion distribution.

The field tests shown that the boiler could operate steadily with a bed pressure drop as low as 3.1 kPa by reconsideration of the fluidization state of the solids-gas two-phase flow in the furnace.

Table 2 compares the performance with and without the new technology.

With the new technology, the viability is high as 99.9%. The combustion and boiler efficiency are increased, one unit can save coal washery 10000 tone and save 0.8 million RMB per year. The service power decreases abut 1% and save electric power 1 million KWh and 0.4 million RMB. The erosion of the heating surfaces in the boiler and its auxiliaries was alleviatedand the cost of maintenance was reduced by as much as 10% per year.

Table 2 Comparison between the new and old technologies

Parameters	With old technology	With novel technology
Wind box pressure(Pa)	11500～12000	5800～6200
Primary air(m^3/h)	47000～48000	43000～44000
Primary fan current\t (A)	19～20	11～12(fan changed)
Induce fan corrent(A)	21～22	16～17
Bottom ash discharge interval (min)	20～25	35～40
Loopseal pressure (Pa)	～12000(primary)	～11500(Roots fan7.5kW)
Qnet(kcal/kg)	3500～3800	3500～3800

Following the suggestion of Tsinghua, the client changed the primary air draft fan with lower pressure head (14.8D), the motor power decrease 100kW. The service power of unit decrease more.

Table 3 lists the fan powers in the series products with the new technologies.

Table 3 Fan power in the 75-1000t/h CFB boilers with new technolgy

Boiler load	Total power of primary air fan(kW)	Total power of the secondary air fan (kW)	Total power of rooster fan (kW)
75t/h	315	132	7.5
130t/h	560	280	22
220t/h	1000	560	30
440t/h	2000	1120	110
1025t/h	4500	3000	330

Application and outlook of the novel technology

The first 75t/h CFB boiler with the novel CFB technology by reconsideration of fluidization state has been operated since January, 2006 and a comprehensive field test was carried out in June, 2007. The results proved that the novel technology can greatly avoid the erosion and reduce the service power. A big breakthrough was made in boiler's availability and economics. So far, Taiyuan Boiler Work has received more than 50 contracts of 75-220t/h CFB boilers with novel technology, among which 2 units of 150 t/h and 2 units of 220 t/h CFB boilers with high pressure were in operation at the end of 2008. For example, the 220t/h CFB boiler in Hailaer power plant shows more excellent performance in fuel saving, service saving and low erosion comparing with other CFB boilers of same scale. The 150 t/h CFB boiler can operate at the conditions with wind box pressure 6.5Kpa, bed pressure drop 3.1Kpa. The boiler efficiency is about 90.41%.

By reconsidering the gas solid flow in the furnace, the new generation of CFB boiler can greatly avoid the erosion and reduce the service power. For the primary air draft fan, which costs most service power, the pressure head can decrease from the traditional 18-27 Kpa to 10 Kpa or even lower. 300MWe CFB boiler as example, the service power can descrease 1% at least, which means to save eclectic 10 million RMB per year.

If such novel CFB technology is extended in the whole China, at least 2500 GWh of electricity can be saved every year based on the total capacity of 64 GW of CFB units and average availability of 5000h. That means saving 7 billion ton standard coal and reducing 35 billion ton of CO2 emission per year. At same time, the reducing of erosion increase the availability and save the cost of maintains.

Achievement appraisal

The fluidization state is out of the existing patents and creative production developed independently. Patents were applied in China and abroad. (Name: CFB boiler combustion technology with low bed pressure drop. Appl. No.200710176731.1; Publication No.101149146). On 12th, October, 2008, "Novel CFB technology by reconsideration of fluidization state" passed the appraisal by Education Ministry.

CONCLUSIONS

Taiyuan Boiler Group Co. Ltd. cooperated with Tsinghua University built full set of design code of new CFB boiler with low bed inventory, with which the product structure design of new generation CFB boilers are finished. The new generation of CFB boiler breakthrough the technical bottleneck in economic and availability faced by the traditional products and has excellent performance in the fuel saving, service power service and reliability. The operation practice and measurement data show that the technology of new generation CFB

boiler with the low bed inventory stands for the newest trend of the development of CFB boiler in the future.

REFERENCES

Feng, J. K. Yue, G. X. Lu, J. F. Circulating Fluidized Bed Combustion Boiler[M]. Electric industrial Press, 2003, Beijing.

Lu, J. F., Zhang, J. S., Yue, G. X., et al. Heat Transfer Coefficient Calculation Method of the Heater in the Circulating Fluidized Bed Furnace [J]. Heat Transfer – Asia Research, 2002, 31(7):540-550.

Lu, J. F. Mao, J. X. Yue, G. X, et al. Availability of the CFB units in China. The proceeding of CBB Technology Exchange VIIII ,2007, 1-10.

Yang, H. R., Zhang, H. Lu, J. F. Novel CFB technology by Reconstruction of Fluidization State, 20th Conference on Fluidized Bed Combustion, 2009, Xi'an, China.

Yue, G. X, Lu, J. F, Zhang, H., et al. Design Theory of Circulating Fluidized Bed Boilers [A]. In: Lufei Jia ed. Proc. of the 18th Inter. Conf. on FBC. Toronto: ASME, 2005: 135-146.

OPERATIONAL STATUS OF 135MWe CFB BOILERS IN CHINA

J.F. Li[1], S. Yang[2], J. H. Hao[1], J. H. Mi[1], J. F. Lu[2], H. M. Ji[1], H. T. Huang[1], H. R. Yang[2], G. X. Yue[2]

1Scientific and Technical Service Center, China Electricity Council, Beijing 100038, China
2Key laboratory for Thermal Science and Power Engineering of Ministry of Education, Department of Thermal Engineering, Tsinghua University, Beijing, 100084, China

Abstract: CFB boiler technology has been rapidly developed in China and China has the largest installed number and capacity of CFB boiler in the world. The number of 135MWe CFB boilers is over 150. The operational performance of 135MWe CFB boilers was summarized in the article. And the reliability, economy, environmental protection index are also discussed in the article. It not only provides information of the development status of CFB industry, but also provides some experience and guidance to improve the operation and to further develop CFB combustion technology.

Keywords: 135MWe, CFB boilers, status, performance, summary

INTRODUCTION

Over the past two decades, because of its three outstanding advantages: broad fuel flexibility, excellent environmental performance, large range of load adjustment, CFB boiler technology has being under rapid development and becomes an international acceptable commercial clean coal combustion technology (Lu et al. 2006). CFB boiler has an irreplaceable position in Chinese boiler market. Up to now, the total number of CFB boiler operation is over 3,000, most of them are of small and medium capacity. The number of 410~480t/h (100~150MWe) CFB boilers is over 150 (Yue et al., 2006). CFB boilers are important for the improvement of the electric power supply structure. However, as the CFB boiler has only been adopted into coal combustion for less than 30 years and only is used power generation in recent years, many aspects are expected to be improved.

The current status of the 135MWe is introduced in this paper. The aims of this paper are not only to provide information of the development status of CFB industry, but also to provide some experience and guidance to improve the operation and to further develop CFB combustion technology.

RELIABILITY STATUS

Reliability is the fundamental of economy. Low reliability has been one of the main depute topics in CFB boiler development for years. The reliability of CFB boiler must be considered at first.

In this article, two indices are used to measure the boiler's reliability. One is unplanned outage times caused by various accidents and the other is continuous running time, namely the longest running time of the boiler.

Unplanned outage times

Figure1 shows the variation of unplanned outage times for 135MWe CFB boilers in recent years. As the improving design and operations, the unplanned outage times decreases significantly. However, the times of unplanned outage for some boilers is still over 9.

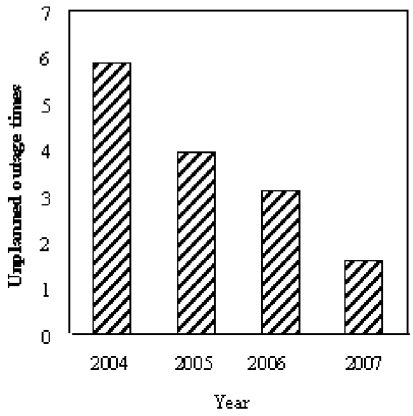

Fig.1 Average Unplanned outage times of 135MWe CFB Boiler per year

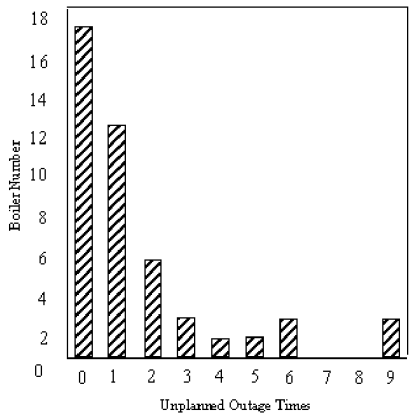

Fig.2 Unplanned outage times of 135Mwe CFB Boiler

Continuous running time

As CFB boilers were first appeared in China, they were frequently forced to shutdown by various accidents. Heating surface wear, slag discharger and crusher malfunction were the most common ones. Fortunately, with the improvement in design, manufacture operation and management, the continuous running time was prolonged gradually. As shown in Figure3, the continuous running time of 135MWe CFB boilers becomes longer and longer. To some CFB power stations, the longest running time is more than 350 days, comparable to pulverized coal fired ones (Mao, 2006).

ECONOMIC STATUS

Eonomic index includes carbon content in fly and bottom ash, loading rate, flue gas temperature, ignition and support oil, power consumption rate and supply coal consumption etc.

Carbon content in fly and bottom ash

Figure 4 shows that the carbon content in fly ash (LOI) for 135MWe boilers decreases in the year and the present average LOI is 7%.

In the initial stage of CFB boiler commissioning and operation, the high LOI is often a severe problem, decreasing the efficiency of CFB boiler. In some early CFB boilers, the LOI was as high as 40%. With better understanding CFB combustion theory and technology, LOI was decreased by optimizing the boiler design and operation (Xiao et al., 2005). Nowadays, LOI of some boilers is decreased by 2%, or even smaller (Hou et al., 2007). For most CFB units, the fuel is low rank coal or even coal stone, so LOI is relatively higher. However, for the same kind of coal, the combustion efficiency of CFB boiler is near to that of pulverized coal boiler.

Average load rate

Figure 5 shows the average load rate of CFB boilers in these years. It can be seen that the load rate of 135MWe CFB boilers is only 64.4% in the year of 2007.That is because some 135MWe units used for mere power generation were regarded as smaller units which were allowed for limited operation time under the newly promulgated energy-saving policy. However the load rate of some 135MWe CFB boilers used for self-supply power supply was more than 95%. Inevitably, the load rate variation affected the economic performance of units.

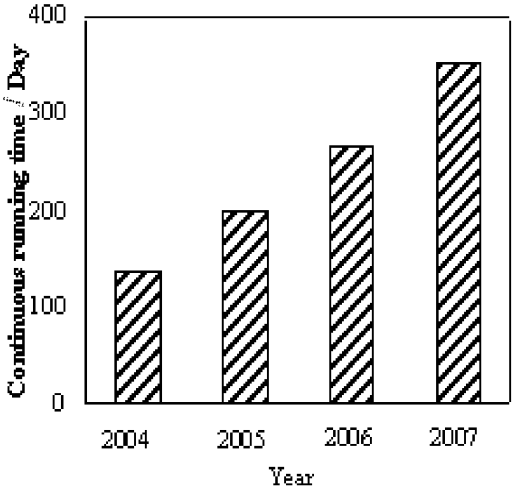

Fig. 3 Continuous running time of 135MWe CFB Boiler

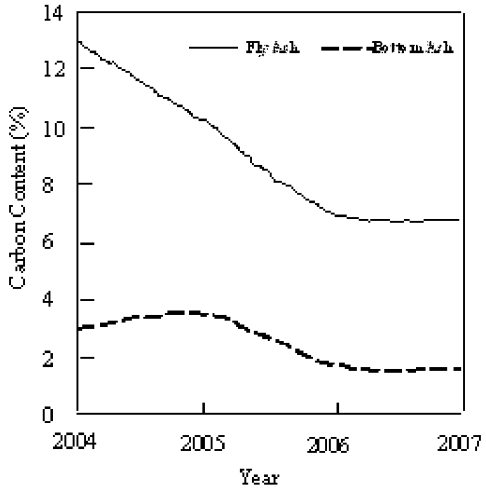

Fig. 4 Carbon content in fly and bottom ash of 135MWe CFB Boiler

Flue gas temperature

Flue gas temperature is an important factor for the boiler efficiency. Generally speaking, in CFB boilers, sulfur content in flue gas is relatively low and the low temperature corrosion is not serious, so the exhausted flue gas temperature can be set to low to reduce heat loss.

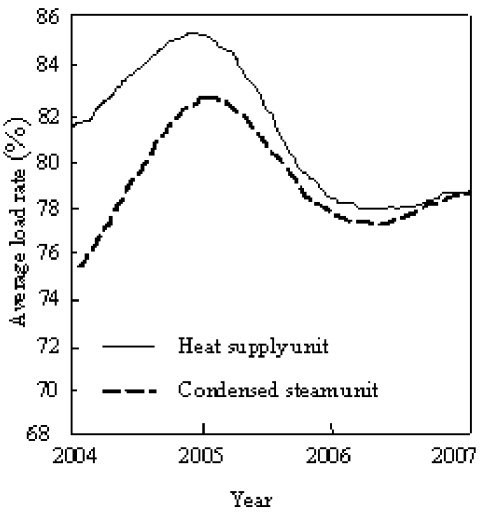

Fig. 5 Average load rate of 135MWeCFB Boiler

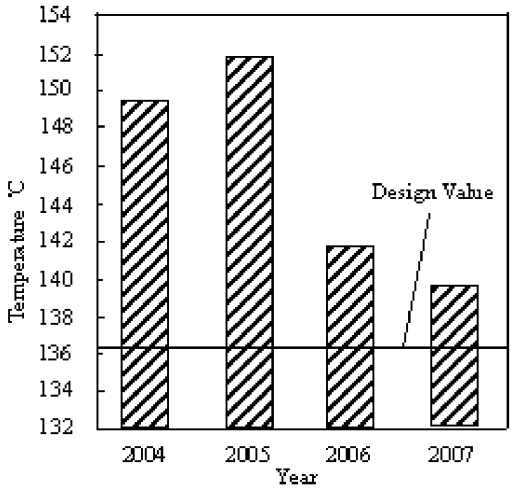

Fig. 6 Flue gas temperature of 135Mwe CFB Boiler

As Figure 6 shown, however the flue gas temperature is higher than the designate value at high loads. For example, in the year of 2005, the average flue gas temperature is almost 20℃ higher than the designate value. The first reason is ash deposition on heating surface. The second reason is high air temperature at primary fan outlet. The phenomenon is unique for CFB boilers. As calculation, air temperature at primary fan outlet is about 20°C higher than ambient temperature, certainly decreasing the temperature difference between the air and the heat transfer surfaces in the tail duct of the boiler. This phenomenon must be considered in CFB boiler design. The convection heating surfaces in the units after were enlarged and the economizers in commissioning units were modified, so that the flue gas temperature was decreased to some extent. In the same time, soot blowing was improved and excessive air ratio was controlled during operation which decreased the flue gas temperature as well.

Remarkably, because of lower SO_2 content in flue gas and higher flue gas temperature, waste heat in flue gas was attemptted to utilize by lithium bromide absorption refrigeration units in Shuangshui power plant. This attempt, which has achieved a splendid result in supplying heat cold and power in CFB power plant, is worth popularizing.

Ignition and support oil

As there are massive inert bed materials in the furnace, the performance at low load rate of CFB boilers is superior. Generally speaking, CFB boilers can be still stable burning at 35% load rate. However, the ignition oil consumption for a CFB boiler is more than that used in the same capacity PC boiler. Figure 7 shows the ignition and assist oil consumption of 135MWe CFB boiler. The amount decreased as more operational experiences were obtained (Zhang et al, 2005; Meng et al, 2007).

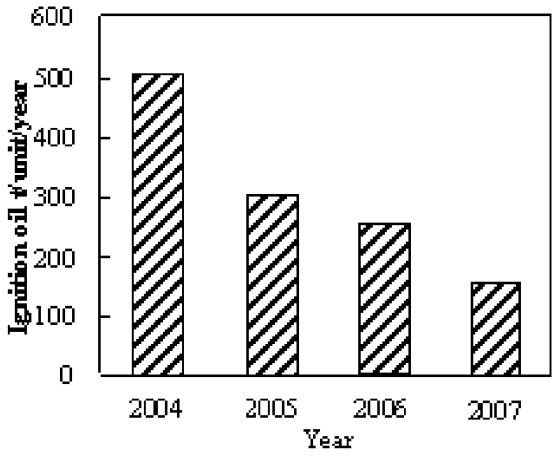

Fig. 7 Ignition and assist oil consumption for135MWe CFB boilers

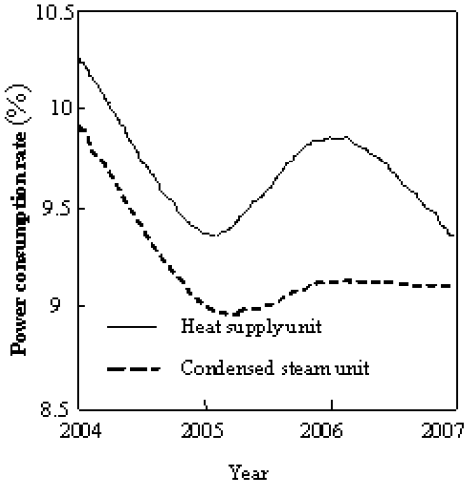

Fig. 8 Power consumption rate of 135MWe CFB Boiler

The average amount of oil consumption for cold start-up is about 30 tons each time. For hot start-up, the amount is only 13 tons each time. In addition, with the decreasing of unplanned outage times, the ignition oil consumption decreased largely.

Power consumption rate

In a CFB boiler, the distributor, bed material and cyclone cause large resistances to gas-solid flow, leading to the increasing of primary fans' pressure head and power consumption. If air-water combined slag coolers are used, the plant power consumption will further increases.

In the aspect of boiler and system design, the designate pressure head of primary fan is usually larger than the required value to keep the bed material in normal fluidization state. This design rule increases the plant power consumption.

As shown in Figure 8, the power consumption of a 135MWe CFB boiler unit is about 9%, larger than that of PC boiler unit. Between 2004 and 2005, the power consumption was greatly decreased. The reasons can be attributed to 3 aspects. Firstly, the designate pressure head of primary fan was reduced reasonably. Secondly, some improvements such as adjustment of primary and secondary air ratio was applied in practical operation.Thirdly air-water combined slag coolers was replaced by drum type cooler in some boilers.

From Fig. 8, the power consumption of heat supply units is larger than that of condensed steam generating units. It is because of the reduction of generated energy and energy loss due to heat supply.

Net coal consumption

As shown in Fig. 9, the net coal consumptionof CFB boilers is high. As the coal consumption due to heat supply, the net coal consumption of heat supply units is smaller than that of condensed steam generating units.

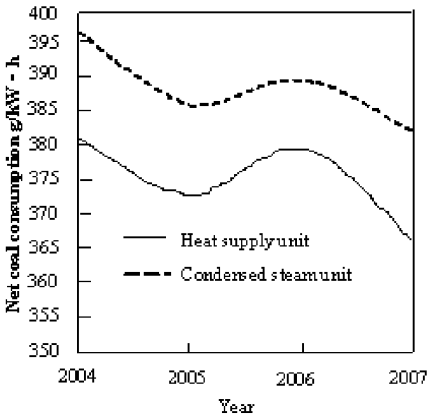

Fig. 9 Net coal consumption of 135MWe CFB Boiler

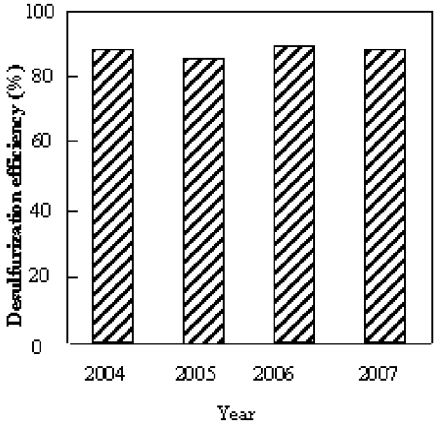

Fig. 10 Desulfurization efficiency of 135MWe CFB Boiler

From Fig. 9, it can be seen that the trend of net coal consumption variation is the same as that of boiler load rate. In 2007, net coal consumption decreased because of the increase of boiler load rate. Moreover, all the condensed steam generation units, the smallest net coal consumption one is Shenhuo power plant. Its net coal consumption is 369g/kW·h. And the heat supply power plant with smallest net coal consumption is Taishan power plantin Da Lian. Its net coal consumption,which is similar to that of PC boilers, is only 346g/kW·h.

ENVIRONMENTAL STATUS

As ESP or bag filter is used in lots of power plants, the dust emission is not considered.

SO_2 emission control status

One of the outstanding advantages of a CFB boiler is in-furnace desulfurization. As shown in Fig. 10, the desulfurization efficiency of 135MWe CFB boilers in China is higher than 85%, and many of them are even higher than 95%, at same level of advanced international unit.

From Fig. 11, it can be seen that SO_2 emission of CFB boilers meets the national emission standard. It was reported the lowest SO_2 emission for a 135MWe CFB boiler is 45.3mg/Nm^3.

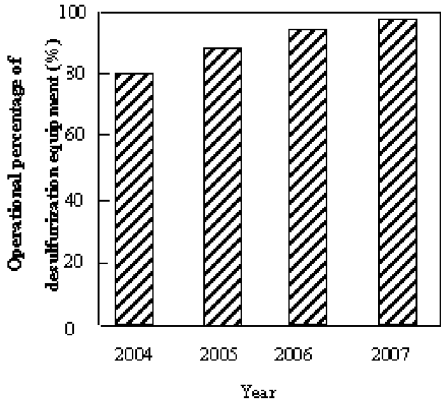

Fig.11 Desulfurization equipment operational percentage of 135MWe CFB Boiler

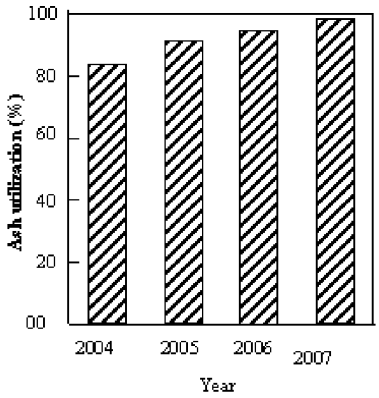

Fig.12 Ash utilization of 135MWe CFB Boiler

NO_x emission control status

As low temperature combustion and air staging combustion are used in a CFB boiler, and rather high on uncompleted burned carbon in the furnace, NO_x emission is far below the Chinese national standard (GB13223-2003). It was reported that lowest NO_x emission is 13mg/Nm^3, in Minjiang power plant,

Ash and slag utilization

It can be seen from Figure12 that ash and slag utilization of CFB boilers is improved year by year. The ash and slag from CFB boilers are generally used as raw material of building materials. Nowadays, the ash and slag deep processing is investigated by many researchers.

CONCLUSIONS

China has the largest amount of 135MWe CFB boilers. The current operational status and performance were summarized in this paper. Each unit of the 135MWe CFB boiler is in normal operation, demonstrating the great advantages of the CFB combustion technology. The boilers in this capacity are still superior in burning low rank fuels and should not be all shut down.

The power consumption rate and net coal consumption of a CFB boiler is larger than those of PC boiler. To enlarge the boiler capacity, and increase the steam parameters in supercritical state is suggested. The great achievements on design and operation of 135MWe CFB boilers are helpful for development of 300 and 600MWe CFB boiler.

REFERENCES

GB13223-2003. Emission standard of air pollution for thermal power plants. Beijing: State Environmental Protection Administration of China. 2003.12.30.

Hou X.S, Chang D.W, Zhang H, et al. (2007). CSPE8.4, Chengdu,: 27-34.

Lu Q.G, Song G.L, Sun Y.K, et al.(2006) In: Yue G, Hao J eds. Proceedings of the 1st CCCCFB & the 6th annual meeting of CFBCEC,: 56-67.

Mao J.X. (2006) Boiler Technology, , 37(3): 24-28.

Meng L.W; Xu Z.Q. (2007) Electric Power, , 40(9): 65-68.

Xiao X.B, Yang H.R, Zhang H, Lu J.F, Yue G.X. (2005). Energy and Fuels.,19 (4):1520-1525.

Yue G.X. Hao J eds. (2006) Proceedings of the 1st CCCCFB & the 6th annual meeting of CFBCEC: 2-30.

Zhang Q.S, Tian W.D, Wang B.J, et al. (2005) Electrical Equipment, 6: 77-79.

IN DEVELOPPING A BENCH-SCALE CIRCULATING FLUIDIZED BED COMBUSTOR TO BURN HIGH ASH BRAZILIAN COAL-DOLOMITE MIXTURES

Jhon Jairo Ramírez Behainne, Rogério Ishikawa Hory, Leonardo Goldstein Jr, Araí Augusta Bernárdez Pécora

Department of Thermal and Fluids Engineering, School of Mechanical Engineering, University of Campinas, POBox 6122, 13.083-970 Campinas/SP, Brazil

Abstract: This work considers some of the questions in burning high ash Brazilian coal-dolomite mixtures in a bench-scale circulating fluidized bed combustor (CFBC). Experimental tests were performed with the CE4500 coal from Santa Catarina State, in southern Brazil, with a Sauter mean diameter d_p=431μm. The coal particles were mixed with dolomite particles of d_p=111μm and this fuel mixture was fed into the circulating fluidized reactor, previously loaded with quartz sand particles of d_p=353μm.This inert material was previously heated by the combustion of liquefied petroleum gas up to the ignition temperature of the fuel mixture. The CFBC unit has a 100mm internal diameter riser, 4.0m high, as well as a 62.8mm internal diameter downcomer. The loop has a cyclone, a sampling valve to collect particles and a 62.8mm internal diameter L-valve to recirculate the particles in the loop. A screw feeder with a rotation control system was used to feed the fuel mixture to the reactor. The operational conditions were monitored by pressure taps and thermocouples installed along the loop. A data acquisition system showed the main operational conditions to control. Experimental tests performed put in evidence the problems found during bed operation, with special attention to the solids feed device, to the L-valve operation, to particle size, solids inventory, fluidized gas velocity, fuel mixture and recirculated solids feeding positions.

Keywords: circulating fluidized bed, coal combustion, operational control, L-valve, solid feed operation

INTRODUCTION

Circulating fluidized bed combustors burning mineral coal are devices used for electricity generation in large scale (Basu, 1999). Because of its recognized characteristics concerning fuel flexibility, higher operational and environmental performance in comparison with conventional combustors, the CFBC technology is currently considered interesting to be also implemented in locations where biomass sources or other alternative solid fuels, as municipal solid waste, (Ravelli et al., 2008). Therefore, the utilization of these systems around the world has received increasing attention. Although a number of CFBC configurations is possible, the basic layout is composed by the following components: riser, cyclone, standpipe or downcomer and a solid circulation valve. Concerning CFB large scale operation, there is a lot of information in the available literature (Basu, 2006). On the other hand, data from bench-scale CFB at high temperature is limited and performance characteristics obtained from experimental tests are still needed.

Stability operational conditions for CFB systems at atmospheric temperature and pressure have already been studied by many authors (Reiying, et al., 1985; Matsen, 1988; Knowlton, 1988; Rhodes and Lausmann, 1992; Srivastava et al., 1998; Basu and Cheng, 2000; Yang et al., 2009). Mass balance implies that the quantity of solid particles in the fast bed, cyclone, L-valve and downcomer must be equal to the amount fed into the system, the solids inventory. Any increase of solids in the riser must be accompanied by an equivalent decrease of solids in the return leg. The solids mass distribution is also associated to pressure equilibrium around the CFB loop. The riser pressure drop is determined by the mean concentration of the gas-solid suspension along its height, proportional to (G_s/u_f) ratio. The pressure drop through the cyclone is proportional to the square of the inlet gas velocity and is usually not dependent on the solids mass flow rate, while the L-valve pressure drop is proportional to the solids mass flux through it.

Ravelli et al. (2008) pointed out to several of the problems to be solved, by modifications in furnace design and operational parameters from the lessons learned from firing biomass, refused-derived fuel and a wide variety of other fuels.

This work analyses the problems and possible solutions for the operation of a CFBC burning a mixture of coal and dolomite, with sand particles as the inert material: the solids feed device, L-valve operation, particle diameter, solid inventory, superficial gas velocity, fuel mixture feeding position, recirculated solids return position at the riser, and stability of the operation.

CIRCULATING FLUIDIZED BED COMBUSTOR

Figure 1 shows the experimental configuration of the bench-scale CFBC system at the School of Mechanical Engineering, at the University of Campinas, for burning coal and dolomite mixtures.

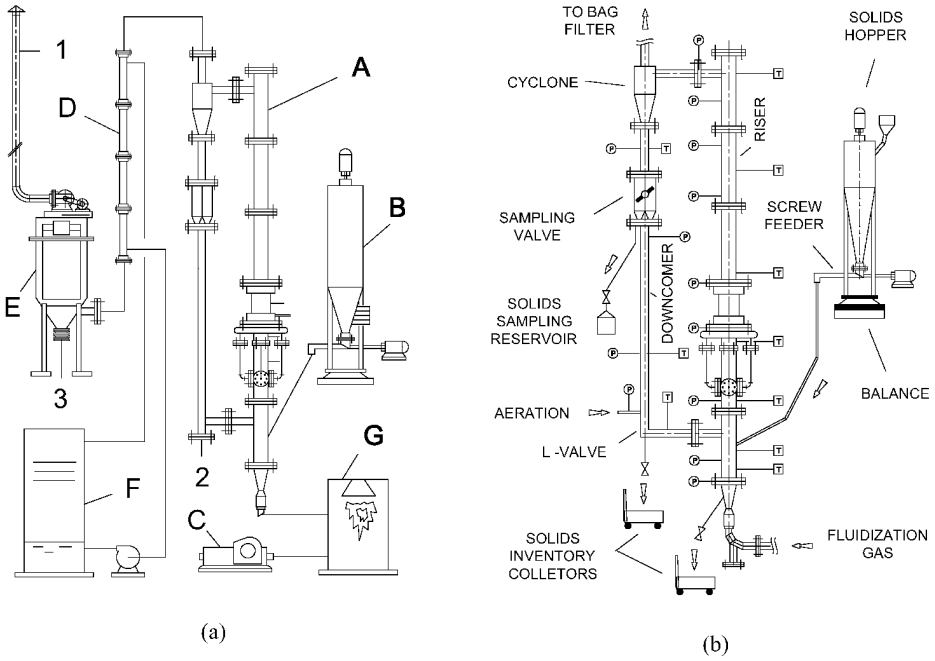

(a) (b)

Fig. 1 (a) CFBC layout; (b) Details of the CFBC combustion loop

The components of the combustion chamber (A) are made of stainless steel AISI-310 and their external surfaces are covered with thermal insulation, in order to minimize the heat lost to the surroundings. The riser is 4m high and has 0.1m of internal diameter; it doesn't have a standard gas distributor at the base. It presents lateral entrances for solids feeding, recirculating material and secondary air injection. The loop is made up of a tangential cyclone, a valve for sampling particles, and a 62.8mm internal diameter downcomer or standpipe with an L-valve positioned at the bottom to promote the recirculation of the bed particles. A compressor supplies air to the L-valve, providing the necessary aeration of the solid particles inside the return leg.

A conical piece located below the riser base accelerates the fluidization gas avoiding that the bed particles go down. An external valve is connected at the conical surface to discharge solids from the riser if necessary. Eight static pressure and seven temperature taps (K type thermocouples) are used along the riser to measure the axial pressure profile and monitor the combustion process. Additionally, five pressure taps and three thermocouples are located between the cyclone and the L-valve.

The feeding system (B) is composed of a cylindrical hopper coupled to a screw feeder, which drives the solids to the reactor. The rotation of the screw shaft is controlled by using a frequency regulator connected to an electrical motor. The solids leaving the screw are allowed to drop freely before they are finally injected into the riser by a pneumatic feeder. The fluidization gas (primary air) that is supplied at the bottom of the riser comes from a screw compressor (C,) and its mass flow rate is measured by an orifice plate, connected to U type manometers. The combustor chamber uses a data acquisition system for on-line temperatures recording, as well as, rotameters to mass flow rate measurements in gas lines, and gas analyzers to determine the composition of the flue gas. After leaving the cyclone the flue gas flows through twelve external heat exchangers placed in sequence (D) before it reaches the particulate control device (E), which is a fabric filter with nine bags for a total of 3.4 m^2 surface area. The water used in the heat exchangers is supplied by a cooling tower (F), whereas the fuel mixture in the CFBC loop reaches ignition point temperature using pre-heated air coming from an electrical heater and a GLP burner (G) placed in series.

The CFBC configuration here described was established after adapting the experimental system, which was initially built to burn oil shale. Oil shale is a low grade fuel with physical and chemical properties markedly different from those of mixtures of Brazilian coal and dolomite, and it was expected that the combustion unit would respond in a different way when the fuel was substituted for. Modifications were needed to solve operational problems related to the continuous feeding of the fuel mixture and to the pre-heater, as discussed along this manuscript.

CFBC DESIGN CONSIDERATIONS

Fuel Feeding Device

Normally, the solid mass flow rate is controlled by the rotation velocity of the screw feeder. The fuel entrance at the riser must be located in position high enough to permit a smooth and continuous operation. At positions near the bottom of the riser, the high static pressure transmitted by the gas-solid suspension causes an accumulation of solids in the lower zone of the feeding pipe device. For the system showed in Fig.1, the feed point for coal combustion was 0.69m higher than for oil-shale combustion in order to obtain stable fuel feeding. A consequence of raising the fuel feeding point is that the residence time of the particles in the riser becomes shorter. Such fact can reduce the combustion efficiency, mainly for fine particles, depending on the cyclone performance.

Another problem associated with fuel feeding device is provoked by the temperature profile along the feeding pipe, which can cause flue gas condensation inside it and subsequent agglomeration of fine particles. These difficulties were solved by designing a pneumatic feeder. The feeder, built in stainless steel AISI 304, is shown in Fig. 2. It releases pressurized air through a small tube, at the center of the pipe and close to the feed point on the riser. This tube has blades in the air exit side and they are allowed to rotate sporadically to remove particles accumulated at the inner surface of the feeding pipe. The device uses an appropriate air mass flow rate in order to accelerate the fuel particles dropping from the screw feeder. Additionally, a water jacket was placed on its external surface to maintain a uniform and low temperature along the feeding pipe, mainly near the riser.

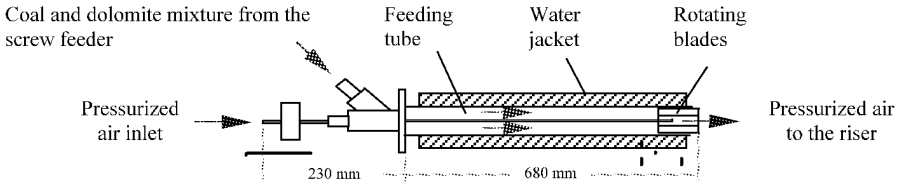

Fig. 2 The pneumatic feeder for coal and dolomite mixtures

Recirculated Solid Particles Inlet Position at the Riser

The pressure balance is established in a CFB system by the distribution of solid material along the loop. The higher the inlet position in the riser of the return particles, smaller the solid inventory inside the return leg and smaller the residence time of the particles in the riser. As a result, combustion efficiency is affected.

Air Pre-Heater System

The air pre-heater design depends on the calorific heat value of the fuel used. Operations using fuels presenting low calorific heat values require long time operation of the GLP pre-heater system. Considering operations with oil shale as fuel, it was noticed that the GLP burner was required to work continuously during the experiments. Such operation claims for resistant materials for the pre-heater walls as well as efficient cooling system for the surfaces exposed to high thermal stresses.

Influence of the Particle Size

Experimental tests at 420°C mean riser temperature were made using sand particles (2,680kg/m^3 density) as solid material. Particles with mean diameter from 210 to 595μm were fed to the CFB system. Operational stability was observed for the tests using the 353μm mean diameter particles. Particles smaller than 353μm showed irregular operation and led to excessive mass loss in the cyclone due to lower collection efficiency. On the other hand, particles larger than 353μm required a high level of air flow rate into the L-valve to get an appropriate solid circulation in the CFB system. Such operation led to reduced cyclone efficiency due to the air flow rate toward the cyclone bottom, inducing instabilities in the return leg.

Influence of the Solids Inventory

Experimental tests were carried out with solids inventories from 4.0 to 9.0kg, using the 353μm particles. It was noticed that as the solid inventory increases, the solids circulation rate (G_s) increases as well. Operational stability was reached for tests using inventories from 6 to 8kg. This behavior is associated with the quantity of solid material inside the return leg, necessary for the appropriate L-valve operation.

Influence of the Fluidization Velocity

Superficial gas velocities in the riser from 4.3 to 7.0m/s were tested, using the 353μm particle as solid material. The operational stability was obtained in all experimental tests showing that, concerning the studied

range, the L-valve operation was not significantly affected by the superficial gas velocity.

CFBC Setup for Operational Stability

Because of the lack of previous operational data on burning Brazilian coal mixed with dolomite in CFBC units, the parameters for maintaining stability under combustion conditions had to be established experimentally. Accordingly, the range of CFBC operational parameters from earlier works reported in the literature, for different coals, were adopted in the beginning of the experiments.

Operational stability under pre-heating condition - In order to establish adequate conditions for stability during the pre-heating stage of the CFBC system, tests in the fast fluidization regime were carried out using only inert material (quartz sand) heated close to the ignition temperature of the coal volatile compounds. Three key parameters were chosen for this study: the solid inventory (I_s), the superficial gas velocity (u_f), and the aeration mass flow rate into the L-valve (m_{lv}). I_s, u_f, and m_{lv} were controlled in the ranges 4.0-9.0 kg, 4.3-7.0 m/s, and 1.0-3.0 kg/h, respectively. These variables were associated to the solid circulation rate (G_s) by an experimental model based on the rotational central composite design (RCCD), described by Myers and Montgomery (2002). From it, fourteen runs for different operational conditions were obtained, and three runs at the central point were added, to determine the experimental error.

First the fluidization gas was heated up to 650°C, using both the electrical heater and the GLP burner. A superficial gas velocity close to the particle transport velocity is always verified. Next, the quartz sand inventory was introduced into the riser and the aeration of the L-valve was turned on. The solids circulation was confirmed by monitoring the pressure and temperature profiles around the system. Operational stability is verified when both the pressure and temperature profiles decrease alongside the solid flow direction. As soon as the mean riser temperature reaches 420°C and the stationary regime is verified, a solids sample is taken through the diverting sampling valve for three different periods of time: 5, 10 and 20s. The mass of solids diverted out between sample extractions is restored to the system to maintain the initial solids inventory unchanged. A maximum variation of ± 5% was allowed for the solid inventory.

Operational stability under combustion conditions - An appropriated operation of the CFBC system under combustion condition can be easily obtained whether the pre-heating setup from the procedure described earlier is implemented. For combustion tests, a fuel mixture formed by particles of the CE-4500 Brazilian coal from Santa Catarina State, and dolomite from São Paulo State were used. The properties of the fuel mixture components are shown in Table 1.

Table 1 Properties of the fuel mixture particles

Material	Composition (% mass, d.b.)	High heating value (kJ/kg)	Sauter diameter (μm)	Apparent density (kg/m^3)
Coal	C:52.0; H:3.5; N:1.1; O:7.9; S:1.9; Ash:33.6	19,580	431	1,586
Dolomite	Ca: 17.0; Mg: 8.1	-	111	1,203

With the CFBC loop previously heated to 420°C and the two heaters still in operation, around 7 kg of pure coal should be fed into the riser at a low mass rate to avoid the mean bed temperature to drop below400°C, as well as, to regain, in a few minutes, the initial temperature. The use of about 50% of air in excess was appropriate at this stage, including the fixed air mass flow rate in the pneumatic feeder. Additionally, here is noted that the bed temperature begins to increase exponentially, by which the temperature of the pre-heated air is surpassed in a short time. Because of considerable changes in the density and viscosity of the fluidization gas with temperature, the superficial velocity in the riser should be controlled permanently in order to maintain the fast fluidization regime. Flow gas rates used were only enough to guarantee the respective minimum solid transport velocity and an appropriated solid circulation rate.

Before feeding the fuel mixture, the mean bed temperature should be at least above 700°C to avoid the risk of the combustor blowing out when the fuel mixture, containing dolomite, is fed. At this time, the fluidization gas heaters are turned off and the fuel mixture mass flow rate is controlled in order to get 15 to 30% of excess air, maintaining a stationary combustion above 800°C. To finish the combustion test, the fuel mixture is interrupted and the solids of the bed discharged by opening the valves located at the bottom of both the riser and the L-valve.

Results from combustion tests in the CFBC system were obtained fixing the air excess (ξ) in 25% and the Ca/S molar ratio ($R_{Ca/S}$) in 2. The carbon conversion efficiency was determined from a material balance, taking into account the content and the mass flow rate of the element in both the fuel mixture and in the fly and residual ashes. Additionally, some components of the flue gas (CO, O_2) were measured by using the 325-M

TESTO™ digital analyzer.

Experimental Results for Operational Stability

Pre-heating condition - Figure 3 shows results for the solid circulation rate obtained in each test carried out, and the ranking of the effects of these operational parameters on the solid circulation rate. The results showed that only the solids inventory and the fluidization velocity have a significant influence on the solids circulation rate at 95% of confidence level. Such significant effects are positive, indicating that an increment in the values of I_s or u_f also produce an increase on the solids circulation rate. These results were expected and they can be explained on the basis of three main principles applied to a CFB loop operation: mass balance, pressure equilibrium, and relationships between solids circulation rate, fluidization velocity and riser height (Reiying, et al., 1985; Matsen, 1988; Knowlton, 1988; Rhodes and Lausmann, 1992; Srivastava et al., 1998; Basu and Cheng, 2000; Yang et al., 2009).

Run	Factor			
	I_s (kg)	u_f (m/s)	m_{LV} (kg/h)	G_s
1	5.0	5.0	1.4	1.08
2	5.0	5.0	2.6	2.80
3	5.0	7.0	1.4	2.69
4	5.0	7.0	2.6	4.36
5	8.0	5.0	1.4	19.64
6	8.0	5.0	2.6	21.74
7	8.0	7.0	1.4	39.23
8	8.0	7.0	2.6	40.19
9	6.5	6.0	2.0	24.11
10	6.5	6.0	2.0	21.85
11	6.5	6.0	2.0	26.47
12	6.5	6.0	3.0	26.04
13	6.5	6.0	1.0	25.40
14	4.0	6.0	2.0	0.22
15	6.5	4.3	2.0	7.69
16	6.5	7.7	2.0	27.93
17	9.0	6.0	2.0	35.67

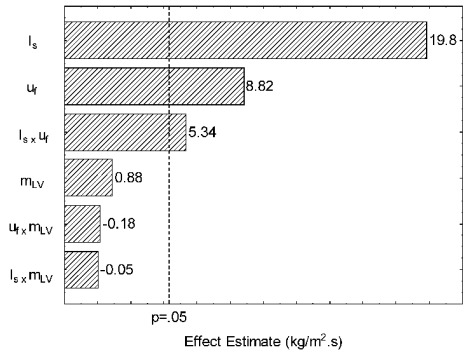

Fig. 3 Effects of I_s, u_f and m_{LV} on G_s in pre-heating conditions

Taking into account that CFB combustors normally operate with G_s in the range of 10 – 100 kg/m^2.s, results suggest that in order the bench-scale CFBC achieve stability, any combination of solids inventory in the range of 6.5 to 9.0 kg, with gas fluidization velocity in the range of 5.0 to 7.7 m/s, should be considered. Although the air mass flow rate into the L-valve didn't show a significant effect on G_s, the minimum level is recommended in order to avoid low cyclone efficiency, as described earlier.

Combustion conditions - Taking into account the results above, a combustion test was settled with I_s = 6kg of sand particles, u_f = 8.5 m/s, and m_{LV} =1.4 kg/h. A coal and dolomite mixture, with $R_{Ca/S}$ =2.0, was burned using ξ=25%. Table 2 shows the operational characteristics obtained in the test.

Table 2 Results obtained from the combustion test

T_b (°C)	G_s (kg/m^2.s)	m_{air} (kg/h)	m_{fuel} (kg/h)	η_C (%)	CO (ppmv at 6% O_2)	O_2 (%)
826	10.01	72.84	10.8	94.4	132	6.4

Performance data of the bench-scale CFBC indicate that the combustion process was carried out successfully. These results are similar to those reported by Brereton, et al. (1991), Adánez, et al. (1995), Sotudeh-Gharebaagh, et al. (1998), and Gungor (2008).

During the combustion tests the operational stability of the L-valve was verified by means of static pressure and temperature measurements, carried out in a point close to the discharge of the recirculated solids. Although short cyclical fluctuations of the pressure and of the temperature were noticeable, due to the intermittent behavior exhibited by a L-valve, stationary mean values were attained for both variables. Additionally, it was possible to adjust the external solids circulating flow by keeping up both the superficial air fluidizing velocity and the solids inventory approximately constant. The solids inventory was controlled by discharging ashes out through a mechanical valve localized on the conical section of the riser. This valve is opened when a solid accumulation in the riser is observed by means of static pressure measurements.

Figure 4 shows the axial temperature profile behavior during the combustion experiment. It can be noticed that a more uniform temperature profile was obtained only when the fuel mixture was fed into the riser. More particles increase the solid inventory, reducing the porosity of the bed. So, denser fast fluidized beds are capable to transport more heat and homogenize the temperature in the combustion loop.

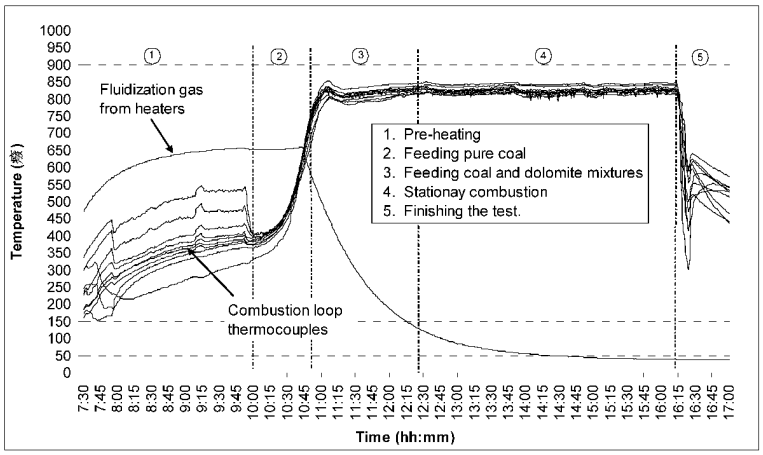

Fig. 4 Evolution of the temperature along the combustor during the test (ξ=25%; $R_{Ca/S}$ =2.0)

The temperature profile in the stationary regime also demonstrates that the operational stability of the combustion process is easily maintained for a long time. Finally, when feeding the fuel mixture was stopped, the combustor responded accordingly, by quickly cooling off, evidenced by the abrupt drop of the temperatures, a behavior expected from a bench-scale CFB combustor.

CONCLUSIONS

In this work, an experimental procedure was established to ensure a steady operation of a bench-scale CFB combustor. Experimental tests suggested that variables such as solids particle size, solids inventory, fluidization gas velocity, aeration flow rate in the L-valve, and solids circulation rate, should be previously studied at high temperatures, preferably close to the ignition temperature of the solid fuel being used by the system. For the CFBC analyzed, the appropriate operation in fast fluidization regime is obtained at high temperatures, and was determined using 6 to 9 kg of 353 μm Sauter diameter quartz sand in the combustion loop, for a superficial velocity higher than 6 m/s, and 1.4 kg/h of air into the L-valve. The combustion tests, settled on these recommended values, demonstrated that the stability of the process is adequately maintained. The results showed that a mixture of CE-4500 Brazilian coal and dolomite, with Ca/S molar ratio equal to 2.0, was efficiently burned at 25% of excess air. Experimental data obtained from the test were similar to those reported in previous works burning other kinds of coal.

ACKNOWLEDGEMENTS

The authors acknowledge the financial support from CAPES, CNPq and FAPESP (Processes 2005/56621-7 and 2007/06714-4) for the financial support.

NOTATIONS

Symbol

CO carbon monoxide concentration, ppmv
d_p particle mean diameter, m
G_s solid circulation rate, kg/m^{2}s
I_s solid inventory, kg
m_{air} air mass flow rate, kg/h
m_{fuel} fuel mixture mass flow rate, kg/h
m_{LV} aeration mass flow rate in L-valve, kg/h
O_2 oxygen concentration, %v
$R_{Ca/S}$ Ca/S molar ratio, -
T_b bed mean temperature, °C
u_f fluidization gas velocity, m/s

Greek letters

η_C combustion efficiency, %
ξ air excess, %

REFERENCES

Adánez, J., De Diego, L., Gayán, P., Armesto, L. and Cabanillas, A.: Fuel, 74 (1995), pp. 1049-1056.
Basu, P.: Chem. Eng. Sci. 54 (1999), pp.5547-5557.
Basu, P.: Combustion and Gasification in Fluidized Beds, Taylor & Francis (2006).
Basu, P. and Cheng, L.: Trans. of the Inst. of Chem. Eng. 78 (2000), pp. 991–998.
Brereton, C., Grace, J. Lim, C., Zhu, J., Legros, R., Muir, J., Zhao, J., Senior, R., Luckos, A., Inumaru, N., Zhang, J. and Hwang, I.: Final Report to EMR Canada under Contract 52SS.23440-8-9243, Dec. 1991.
Gungor, A.: Fuel 87 (2008), pp. 1083-1095.
Knowlton, T.: Proc. of the Second Int. Conf. on Circulating Fluidized Beds (1988), pp. 31–41.
Matsen, J.: Proc. of the Second Int. Conf. on Circulating Fluidized Beds (1988), pp. 3–11.
Myers, R. and Montgomery, D.: Response Surface Methodology, John Wiley & Sons. (2002).
Ravelli, S., Perdichizzi, A. and Barigozzi, G.: Prog. Energy Comb. Sci. 34 (2008), pp. 224-253.
Reiying, Z., Dabao, C. and Guilin, Y.: Fluidization '85: Sci. and Techn. (1985), pp. 148–157.
Rhodes, M. and Laussmann, P.: The Canadian Journal of Chem. Eng. 70 (1992), pp. 625–630.
Sotudeh-Gharebaagh, R. Legros, R., Chaouki, J. and Paris, J.: Fuel 77 (1998), pp. 327-337.
Srivastava, A., Agrawal, K., Sundaresan, S., Reddy Karri, S.B., Knowlton, T.M.: Powder technology 100 (1998), pp. 173-182.
Yang, S., Yang, H., Zhang, H., Li, J., Yue, G.: Chem. Eng. Process. (2009), doi:10.1016/j.cep.2008.12.004.

INDUSTRIAL APPLICATION STUDY ON NEW-TYPE MIXED-FLOW FLUIDIZED BED BOTTOM ASH COOLER

B.Zeng, X.F.Lu, H.Z.Liu

School of Power Engineering, Chongqing University, Chongqing, 400044, China

Abstract: As a key auxiliary device of CFB boiler, the bottom ash cooler (BAC) has a direct influence on secure and economic operation of the boiler. The operating situation of domestic CFB power plant is complex and changeable with a bad coal-fired condition. The principle for designing BAC suitable for the bad coal-fired condition and high parameter CFB boilers was summarized in this paper. Meanwhile, a new-type mixed-flow fluidized bed bottom ash cooler was successfully designed on the basis of the comprehensive investigation on the existing BAC's merits and drawbacks. Using coarse/fine slag separation technology and micro-bubbling fluidization are the significant characteristics of this new BAC. This paper also puts great emphasis on its industrial test in a 460t/h CFB boiler. The results indicate that it achieves significant separation of the coarse/fine slag, an obvious cooling effect, no slag block and coking phenomenon, and continuous stable operation. Figs 7, Tabs 4 and Refs 11.

Keywords: circulating fluidized bed, fluidized bed bottom ash cooler, industrial application, large-scale

INTRODUCTION

Circulating fluidized bed (CFB) boiler is one of the best clean coal-fired boiler for its special merits, such as allowing the use of a broad fuel range, meeting the considerably strict anti-pollution without additional add-on equipment, easy to load adjustment, and basically realizing commercialization and maximization (Stamatelopoulos, 2005). As a key auxiliary device of CFB boiler, whether the bottom ash cooler (BAC) operates normally or not has a direct influence on the boiler's safety and economic operation (Lv and Yue et al., 2003; Carrea et al., 1998). Investigating on the CFB boilers in domestic, many problems such as slag block, coking, abrasion on heating surface occur frequently in the BACs, which always lead the boilers to decrease load or out of work. The cooling and transportation of bottom slag becomes an important subject during the CFB boiler's large scale development (Lu, 2006). Complicated and variable coal-feeding, poor coal quality, bad preparation system and other coal-fired characteristics cause a very bad operation condition on the CFB boiler in domestic. That is the reason why the existing BAC can't operate ideally.

Kinds of BACs equipping for large-scale CFB boilers are investigated in this paper. On this basis, an idea about a new-type BAC suitable for future's high parameter (super-critical) CFB boiler has been formed and the new device has been manufactured. Based on laboratory experiment ensuring the correctness and reliable operation in theory, the authors have done industrial tests in a 460t/h CFB boiler and obtained a series of results.

STATUS ANALYSIS OF BOTTOM ASH COOLER

With a continuous development of CFB boiler, it has appeared various forms of bottom ash cooling devices at home and abroad. At present, it mainly includes two kinds of BAC using in the current electric power industry: Roller ash cooler and Fluidized bed ash cooler.

As showed in Fig.1, the roller ash cooler cools and transfers slag through the rotation of the water-cooling jacket (Sun, 2002). Simple structure, reliable operation, no need high quality of cooling water, as well as a good adaptability on particle size are the advantages. Small particles can't be recycled and returned to furnace; hence this type of BAC could not meet the high particle concentration requirement in some CFB boiler furnaces. Besides it has such shortcomings as a low ash fullness, a poor utilization rate of heating surface and heat transfer coefficient, easy to cause mechanical fault, leak water and ash, and difficult to operate and maintain. For low resistance to pressure of its heat transfer parts, it can't be suitable well to use the high-pressure water as cooling medium.

Fluidized bed ash cooler (FBAC) has a wide range of application in the overseas while the vast majority of the CFB boilers are using it, due to using the mature two-phase flow technology of fluidized bed boiler, and having a high heat transfer coefficient and high output (John et al., 2005). The uppermost problem of FBAC is the high requirement to the size of bottom slag. When the size is greater than 10mm, the traditional FBAC easily to occurs blockage and coking during operation. Because of the poor quality of feed coal, most of CFB

power plants didn't use the traditional FBAC in china. Fig.2 showed the selective fluidized bed ash cooler (Foster Wheeler, U.S.). Bottom slag flows in the "underflow" mode. A series of problems exist in the operating process, such as bad fluidization and coking in selective chamber, blockage in inlet, coking or blockage in outlet because of over-temperature, serious abrasion on blast caps, bad control on slag etc. Therefore the effect of removing and cooling slag could not achieve the anticipated aim. The overflow fluidized bed ash cooler produced by ASLTOM, France, showed in Fig.3. Because the bottom slag flows in "fluidized overflow" mode, it has merits such as high heat transfer effect, high stability of bed pressure in BAC, reducing the average particles diameter and the fluidized air flow rate by removing big bottom slag (Zhang, 2006). However, it appeared such problems while using high ash coal as no or few ash in last cooling chamber, obstruction in removing slag, coking in empty chamber, gasification in water cooling tube etc. (Liu, 2003). Furthermore, those problems can lead the boiler to a long-term high bed pressure operation state.

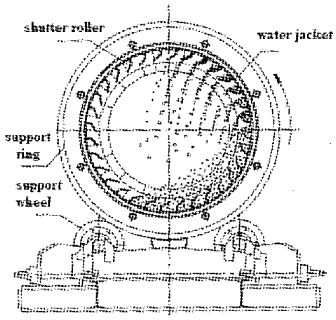

Fig. 1 The roller ash cooler

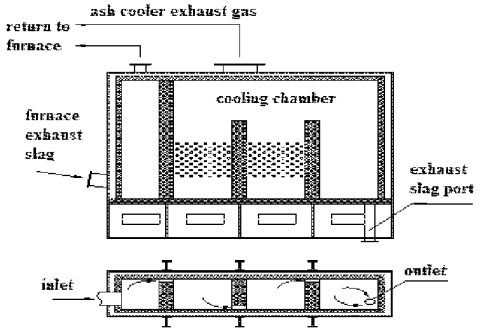

Fig. 2 F.W. selective fluidized bed ash cooler

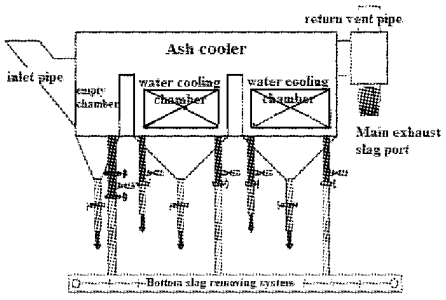

Fig.3 ASLTOM's overflow fluidized bed ash cooler

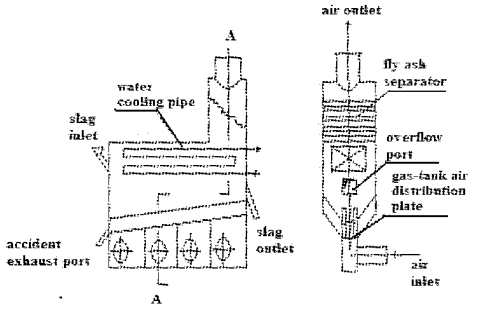

Fig.4 Gas-tank spouted bed ash cooler

Figure 4 shows the gas-tank spouted bed ash cooler (Shu, 2007; Lu, 2006). A stable axial jet formed by the gas-tank could spout and fluidize the bottom slag to prevent effectively the deposition of large slag and blockage. Because of the high fluidized air velocity, the cooling tubes usually use cast iron in gas-tank spouted bed ash cooler in order to improve the abrasion resistances, nevertheless the compression resistance capability of cast iron is so poor that the cooling tubes are easily explosive when cooling water evaporates. Moreover, the fluidizing air from ash cooler returns to furnace to participate combustion as "the secondary air", and it has a low stiffness characteristic. When one is rising, the other is falling. The secondary air decreasing due to the high fluidizing air flow rate from ash cooler results in serious lack of oxygen in the center area, hence the combustion efficiency reduces a lot.

In summary, the existing BAC can't be fully satisfied to the safety and economic operation and the development needs of large-scale CFB boiler. The main reason is the domestic coal-fired conditions. Firstly, there are many impurities such as gangue doping factitiously. The gangue always stays at the bottom of boiler causing bad fluidization. Secondly, with the continuous exploitation and consumption of coal resources, the increasing content of coal gangue, slime and other inferior coal need rational utilization for energy-saving or high economy. However the wide range of calorific value, ash content and bottom ash particle size induce the ash cooler's stability and adaptability. Thirdly, the coal preparation system is far from the particle size requirement.

The CFB combustion technology is one of the best measures to adjust to the deplorable current domestic coal-fired conditions, especially in burning coal slime and gangue. To give an example, the design coal of a power plant's CFB boiler includes gangue, slime and middling with the ratio ranges from 0% to 60%, 0% to 25%, and 32% to 75% respectively. Under such conditions, it has set a high requirement on the BAC to ensure efficient and stable combustion in furnace. Thereby, the future large-scale CFB boiler should set roller slag

cooler and fluidized bed ash cooler synchronously to exert their advantages respectively—that is, it can utilize the characteristics of good adaptability on particle size from the roller slag cooler and recycling fine particles from fluidized bed ash cooler.

NEW-TYPE MIXED-FLOW FLUIDIZED BED ASH COOLER

As the parameter of CFB boiler improving gradually, it is necessary to increase the fine particle concentration in dilute phase zone, so as to maintain a higher circulating ratio. Meanwhile, for the future super-critical CFB units, the common heating surface arrangement may do not satisfied with the load requirement. It's considerable to arrange it into BACs, and the BACs need to meet the high pressure or other parameters working demands. However, the existing BACs have many problems such as higher air-cooling ratio, poor fluidity, hard to control the particle size and fine particle recycle, which restrict its further development. According to the operating condition of domestic CFB power plant, the ideal ash cooler should have the following characteristics: removing bottom ash smoothly and controllably; realizing selective slag discharge—that is, remove big bottom slag to improve fluidization quality and recycling fine particles; using water mainly and air secondarily as cooling medium; cooling slag adequately to reduce the slag's temperature lower than the temperature restriction of ash processing mechanical equipment; effectively preventing large slag deposition to ensure a good fluidization and avoid abnormal phenomenon such as blocking, coking and so on; efficiently reducing the abrasion of heating surface.

Based on above requirements, integrating technical features of different BACs, the authors have worked out a new-type mixed-flow fluidized bed ash cooler which has two chambers. Selective chamber plays a part in coarse/fine slag separation. The fine slag is fluidized and flows into water-cooled chamber in a "fluidized overflow" mode. The water-cooled chamber has two parts both setting water-cooled tubes. The slag flows in a "Mixed-flow" mode contain "underflow" and "fluidized overflow". Finally, the ash or slag is removed into bottom slag removing system through main exhausting pipe by the rotary valve.

Compared with the existing ash cooler, the new-type mixed-flow fluidized bed ash cooler has following technical features: Firstly, it adopts the coarse/fine slag separation technology, and cooling respectively. Most of coarse slag goes through coarse slag removing pipe locating in the bottom of selectivity chamber after cooled by fluidizing air. Only a little coarse slag following with fine slag enters into cooling chamber. That benefits to avoid poor fluidity, blockage and coking due to the deposition of large slag. Secondly, the size of separated fine ash always less than 4mm insure that the water-cooling chamber can operate in bubble fluidized bed status, which reduces the abrasion of water-cooled tubes effectively. Utilizing micro-bubbling fluidization technology, the fluidization airflow of water-cooling chamber can be maintained in a lower level, and the air-cooling ratio can be controlled lower than 30%. Thirdly, a part of fine ash can return to furnace with return air for recycling, which can meet the needs of higher particle concentration. In addition, the new-type ash cooler adapts to the future high parameter and large-scale CFB boiler's development. We can also consider using membrane wall structure and high pressure water as cooling medium in the future BACs.

INDUSTRIAL APPLICATION STATUS

A power plant used DG460/13.73-Ⅱ4 CFB boiler, collocating four introduced selective fluidized bed ash coolers, which occurred such problems as former described. Some problems were solved after the BACs were replaced by the gas-tank spouted bed ash coolers. However, it brought high outlet slag temperature, thermal expansion and leakage problems synchronously, which caused a high heat loss and had a serious influence on the unit economical efficiency. According to this situation, combining with the physical parameters of the boiler bottom slag (as showed in Table 1), the authors had designed a 15t/h new-type mixed-flow fluidized bed ash cooler whose main design parameters are showed in Table 2, located in B side and close to the front wall.

Table1 Physical parameters of the boiler bottom slag

Size range (mm)	Actual density/ρ_p (kg/m^3)	Bulk density/ρ_b (kg/m^3)	Average diameter/d_p (mm)	Porpsity/ε
0~30	2492	1473	1.791	0.409

The screening results of the boiler bottom slag is showed in Fig.5. Its particle size distribution appears a serious polarization. The percentage of coarse slag (larger than 4mm) is about 30% while the fine ash (smaller than 0.85mm) is about 45%. The practical maximum particle size of coarse slag is beyond 30mm, belonging to Particle D based on Geldart's particle classification, and fluidizing difficultly; while the fine ash is easy to be

sent back to the furnace by fluidized air's elutriation and entrainment. The middle size particles, in a radio of about 25%, can be fluidized well under a low fluidized air velocity.

Table 2 Main design parameters

Items	Values
Cooling slag rate (t/h)	15
Inlet slag temperature(℃)	850
outlet slag temperature (℃)	<150
Inlet temperature of cooling water(℃)	30
Outlet temperature of cooling water(℃)	<80
Flux of cooling water(t/h)	<50
Air temperature(℃)	20

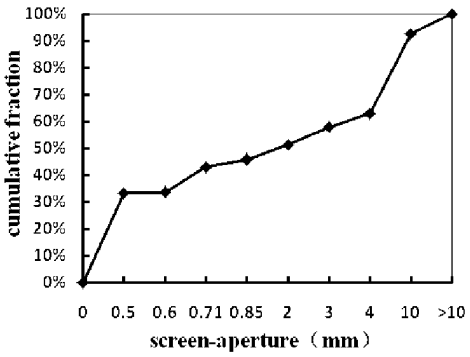

Fig.5 Boiler bottom ash sieve-analysis curve

Results and discussion of cold test

According to the air distribution plate resistance test and the cold fluidization test, some significant conclusions are as follows:

(1) The resistance of distribution plates in each chamber of the ash cooler increase with the increasing of fluidized wind velocity, and the resistance in selective chamber is smaller than in cooling chamber because of the different distributing wind ways.

(2) The cold fluidization test indicates that the fluidization quality and air distribution in chambers are all very well and homogeneous; the design and manufacture of the air distribution plate is reasonable and able to form a fine fluidization state. The fluidized velocity and the removing capability of the fine ash have been ascertained with the best separation effect in selective chamber. The greater the velocity is, the stronger the capability is. However, there is a optimum fluidized velocity existing in the particles separation. In addition, the removing capability of the fine ash is also related to the proportion of fine ash in the boiler bottom slag. The greater the proportion is, the stronger the capability is.

(3) The total amount of fluidized air is much smaller than that of Gas-tank spouted bed ash cooler in the same load.

Fig.6 shows the screening results of cold test. The proportion of the coarse slag (>4mm) in the selective chamber is above 80%, while the fine ash (<4mm) in the cooling chamber is over 90%, which implies that the selective chamber has a obvious coarse/fine slag separation effect. Thus the strong separation capacity can ensure the requirement of particle size flowing into the cooling chamber. It is beneficial to reduce the heating surface abrasion while running in a micro-bubble bed status. Meanwhile, the high content of fine particles is also favorable to fluidize the few amount of coarse slag entering into the cooling chamber.

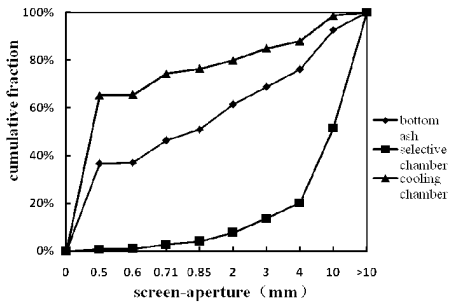

Fig.6 Cold test accumulative particle size distribution

Table 3 Test results of inlet and outlet slag amount

Tests	Furnace pressure drop (kPa)	Times (s)	Weight (kg)	Mass flux (t/h)
Inlet slag amount[I]	2.55	30	470	56.4
Selective chamber's output[II]	2.6	180	760	15.2
Outlet slag amount[III]	5.8	300	1260	15.12

Notes: I. Discharging bottom slag direct to ground; II. Cooling chamber out of operation while selective chamber fluidized and separated the coarse/fine slag; III. Ash cooler operate normally.

The slag removing capacity of ash cooler is an important evaluating standard. The inlet slag amount has a directly influence on the output. In the cold state, the ash cooler's inlet and outlet slag amount were tested. The results (showed in Table 3) indicated that the output achieved design requirement and input was more than output. When the cooler's pressure distribution kept invariant, the inlet and outlet slag amount increased

accordingly with the increase of furnace pressure.

Results and discussion of thermal test

On the basis of cold test, we carried out thermal test to verify its cooling capacity and separation ability of coarse/fine particles. Table 4 shows some results of thermal test (data from the DCS).

Table 4 Partial results of thermal tests

Items	Test Ⅰ	Test Ⅱ	Test Ⅲ	Test Ⅳ
Coal feed rate(t/h)	93	98.8	85	96.7
Unit load(MWe)	113	98	92	96.4
Furnace pressure drop: A/B(kPa)	5.7/6.1	5.7/5.8	6.2/5.9	7.3/5.0
Inlet slag temperature(℃)	851	843	826	865
Main exhaust slag temperature(℃)	78	103	95	112
Outlet temperature of coarse slag(℃)	147	150	134	154
Flux of cooling water(t/h)	44	45	45	45
Pressure of cooling water(MPa)	0.7	0.7	0.7	0.7
Inlet temperature of cooling water(℃)	40	42	42	42
Outlet temperature of cooling water(℃)	78	83	72	80
Temperature of return air(℃)	272	290	331	296

As shown in Table 4, the coarse slag removed from the selective chamber is about 150℃ in temperature after cooling, while the fine ash is about 100℃. The temperatures are much lower than the enduring maximum temperature limitation of ash treatment machinery. In addition, the water-cooled tubes have a strong cooling capability, and the cooling water is affluent, less than the design water rate. And the return air preheated to a proper temperature about 300℃ is not going to have a great impact on the furnace combustion. According to preliminary estimates by the heat balance calculation, the cooling capacity clearly exceeds the design requirement. When the furnace bed pressure is measured about 6.1kPa, the practical amount of slag (18t/h) can perfectly meet the temperature requirement of the bottom slag removing system under the rated working condition (15t/h).

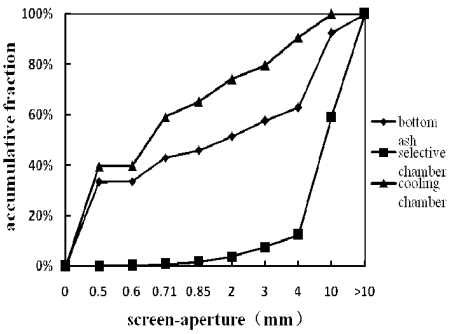

Fig.7 Thermal test accumulative particle size distribution

Figure 7 shows the screening results of the slag sampled from the new-type mixed-flow fluidized bed ash cooler. The proportion of the fine ash (<4mm) in the selective chamber is no more than 15%, and the percentage of the coarse slag in the cooling chamber is less than 10%. All of these numbers imply that the effect of coarse/fine slag separation in the thermal test is better than it in the cold test.

In the thermal operation, there are no coke buttons while opening the large slag exhaust pipe under the cooling chamber many times to remove some coarse slag, and no coking phenomenon in chambers when observing through the manhole door at the idle time. It proves that the abnormal phenomenon, such as slag blockage and coking, does not exist in the operating process. The utilization of "the coarse/fine slag separation and cooling respectively" technique makes the new-type mixed-flow fluidized bed ash cooler completely adapt to the operation using the wide-screening bed material, and solves the slag-block and coking problems in the traditional cooler.

CONCLUSIONS

The existing BACs which have a poor adaptability to the domestic coal-fired condition can't be fully satisfied to the safety and economic operation and the development needs of large-scale CFB boiler. The main reasons why the operating situation is complex and changeable are: the complex and poor coal quality, the bad coal-preparation system and low regulating ability of BACs.

It concludes the characteristics of the ideal ash cooler which adapts to high parameter CFB boiler in the future, and describes the mode of combination between roller ash cooler and fluidized bed ash cooler.

A new-type mixed-flow fluidized bed ash cooler has developed on the basis of the current CFB ash coolers. Thanks to the coarse/fine slag separation and micro-bubble technology, it can solve the common problems appearing in the traditional air-water combined ash cooler, such as slag block, coking and the heating surface abrasion etc..

The industrial test results indicate that the new-type mixed-flow fluidized bed ash cooler acquires an obvious effect in coarse/fine slag separating. Meanwhile, the running parameters meet or exceed the design requirement, and there are no slag blockage, coking, the death of the rotary slag-removing valve and the bad fluidization caused by the coarse slag aggradation.

ACKNOWLEDGEMENTS

Financial supports of this work by Jiangyin Acer Technology Ltd. and industrial application conditions supports by PanZhihua Three-dimensional Generation Company are both gratefully acknowledged.

REFERENCES

Carrea E., Scavizzi G. C., and Barsin, J. A.(1998). Dry Bottom Ash Removal-Ash Cooling vs. Boiler Efficiency Effects. Presented to the International Joint Power Generation Conference.

John, J.B., Nancy, C.M. and Jean-Claude, S. et al. (2005). CFB Technology: Can the original clean coal technology continue to compete. Power Gen International Conference.

Liu, S., Li, G.P. and Zhang, H.B.: Electric Power. **4**(2003), pp. 71-73.

Lu, X.F. (2006). The Large Scale CFB Boiler Equipment and Operation. Beijing, China Electric Power Publ, pp. 125-133.

Lu, X.F. and Ryo, S.A. (2002). Feasible Experimental Study on the Utilization of a 300MW CFB Desulfuration Bottom Ash for Construction Applications. 5th International Symposium on High Temperature Air Combustion and Gasification.

Lv, J.F. and Yue, G.X. et al. (2003). The CFB Boilers Operation and Overhaul. Beijing, China Hydropower Publ, pp. 220-229.

Nowak, W. (1999). Design and Operation Experience of 230MWe CFB Boilers at Turow Power Plant in Poland. 15th Int. FBC Conference.

Shu, M.L., Chen, J.H. and Lu, X.F. et al.: Power System Engineering. **2**(2007), pp. 29-31.

Stamatelopoulos, G.-N., Seeber, J., and Semedard, J.-C. et al. (2005). Advancement in CFB Technology: A Combination of Excellent Environmental Performance and High Efficiency. 18th Int. FBC Conference.

Sun, Z.L.: Power System Engineering. **2**(2002). pp. 26-27.

Zhang, M. and Bie, R.S.: Power System Engineering. **22**(2006), pp. 29-30.

OPERATION EXPERIENCE AND PERFORMANCE OF THE FIRST 300MWe CFB BOILER DEVELOPED BY DBC IN CHINA

Q. Guo[1] , X.S. Zheng[1] , Q. Zhou[1] , L. Nie[1] , T.S. Liu[1] , X.K. Hu[1] , J.F. Lu[2]

1 Dongfang Boiler Group Co., Ltd. Chengdu, 611731, China
2 Department of Thermal Engineering, Tsinghua University, Beijing, 100084, China

Abstract: In this paper, general layout, design, operational experience and performance of the first 300MWe circulating fluidized bed (CFB) boiler that developed by Dongfang Boiler Group Co., Ltd China, are introduced. The furnace was with large width-depth ratio. The problems occurred during in commissioning were analyzed and the corresponding modifications were presented. Cold-state experiment and operation experience showed that both fluidization quality and circulating flow rate meet the designated value in the frunace. The imbalance of circulating material flow caused by asymmetric layout of three cyclones was very limited. Heating surfaces were safe except wing wall superheater located in upper part of the furnace was overheated at low load. After commissioning, the boiler was correspondingly modified and its performance was excellent.

Key words: 300MWe CFB boiler, operation experience, performance

INTRODUCTION

The first two unit 300MWe CFB boiler in China developed by Dongfang boiler group Co. Ltd. (DBC) has been put into operation in Mei county Heshuyuan Electric Power Plant, owned by Baolihua Electric Power Ltd. of Guangdong Province. It was based on the successful experiences of 135~150MWe CFB boilers designed by DBC. The 300MWe CFB boiler had a single furnace with a single air distributor without external heat exchangers (EHE). The furnace, cyclones and secondary pass were arranged in line. Some new structure arrangements, e.g. large width-depth ratio, three cyclones with asymmetry layout, were adopted in this boiler.

One of the two units, namely No.3 boiler, successfully connected into the electricity grid on May 27, 2008. The load firstly reached 300MWe on June 1st. Then, the 168h preliminary commissioning began on June 7, and ended on June 14. Another unit, No.4 boiler successfully connected into the electricity grid for the first time on September, 3, 2008, two days after the boiler reached the rated 300MWe.

No.3 and No.4 boilers in Heshuyuan Power Plant have been put into commercial operation in May, 2008. No.3 boiler continued to operate for 75 days after 168h trial operation, and the technical parameters achieved design values, which indicate that the first 300MWe CFB boiler developed by DBC is very successful. However, some problems occurred in startup and commissioning, e.g., wing wall superheater was overheated; oil gun above bed could not work well, etc. Therefore, some solutions were adopted after comprehensive industrial test and the performance was accordingly improved.

Introduction OF THE Boiler

Design parameters

The boiler is a subcritical pressure CFB boiler, whose steam pressure is higher than that designed by Alstom. This boiler was designed to match a typical 300MWe Steam turbine. The pressure drop of reheat steam should also match the steam turbine's requirement. The temperature of feed water is determined by thermal system. The main design parameters are listed in Table 1.

Table 1 Design parameters

Main parameter	Unit	B-MCR	B-ECR
Superheat steam flow rate	t/h	1025	954.175
Superheat steam pressure	MPa.g	17.45	17.45
Superheat steam temperature	^{o}C	540	540
Reheat steam flow rate	t/h	844.867	790.294
Inlet/Outlet reheat steam pressure	MPa.g	3.665/3.485	3.427/3.247
Inlet/Outlet reheat steam temperature	^{o}C	321.8/540	314.9/540
Feed water temperature	^{o}C	282.1	277.5

Fuel properties

The design fuel is Longyan anthracite of Fujian province. This coal is famous for its low volatile content and low reaction activity. It is hard to burn even under the temperature of 1500°C in PC boiler. The properties of design coal and check coal are listed in Table 2.

Table 2 The properties of the design coal and check coal

symbol	Unit	Design coal	Check coal 1	Check coal 2
Car	%	58.60	55.44	35.51
Har	%	0.70	2.19	0.63
Oar	%	2.21	3.44	3.13
Nar	%	0.54	0.53	0.45
St,ar	%	0.76	0.84	1.04
Mar	%	8.80	9.00	6.12
Aar	%	28.39	28.56	53.12
Vdaf	%	6.83	8.33	7.66
Qnet,ar	MJ/kg	19.887	20.480	12.101

General layout

The first 300MWe CFB boiler developed by DBC (Model number: DG1025/17.45-II 16) is of natural circulation with single drum. The boiler includes three parts: membrane water wall furnace, three cyclone separators and secondary pass. In the front part of upper furnace, there are twelve pieces of wing wall superheater and six pieces of wing wall reheater. In the rear part of upper furnace, two wing wall evaporators are arranged. Eight coal feeders are laid in front wall of the furnace. The coal particles fall down towards the front water wall. The primary air box is located under air distributor, which is made of membrane water wall expanded by rear water wall of the furnace. Under bed ignition method was adopted. Primary air and the hot gas generated in duct are introduced into the air box in both sides. Secondary air is introduced into the furnace on the taper area in 2 layers from front wall and rear wall. Four oil guns above the distributor are arranged in both front and rear walls. Four bottom ash discharge openings are arranged in the rear wall above air distributor, corresponding to four roller slag ash cooler. Three cyclone separators are located between furnace and secondary pass. The auto-balance loopseal, which has one input and two outputs to improve the return of circulating material, locates under the cyclones, as shown in Fig. 1.

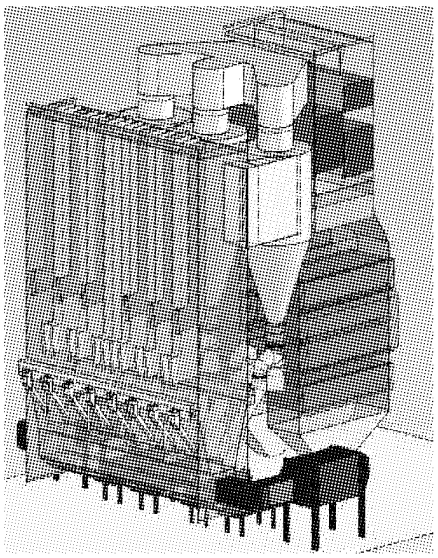

Fig. 1 Integrated layout of 300MWe CFB boiler developed by DBC

The reheat steam temperature is controlled by the flow rate of flue gas. The secondary pass includes two parallel passes. The low-temperature reheater is located in the front pass, while the final superheater and primary superheater are located in the rear pass. The economizer is arranged in the combination pass above the horizontal tube air preheater.

Two stage water spraying desuperheaters are arranged in the superheat system between two stage superheaters. There are also two stage reheater water spraying desuperheaters in reheat system. One is arranged before the inlet of the low-temperature reheater for emergency; the other is located between low-temperature reheater and high-temperature reheater to control reheat steam temperature accurately.

OPERATION AND PERFORMANCE

Fluidization quality

The 300MWe CFB boiler has a single furnace for simplicity and operation convenience. The cross section area of the boiler is very large because of its large capacity. The depth of the furnace should be less than 9m to improve the mixing of secondary air. Thus the width of the furnace is about 30 m. For such a large width-depth ratio (>3.3), the fluidization quality was paid more attention. The cold-test result is very satisfied. The bed surface was flat after shutting down the fan, no matter the air is introduce into the air box from one side or both

side, shown as in Fig. 2 and Fig. 3.

Fig. 2 Primary air introduced from one side

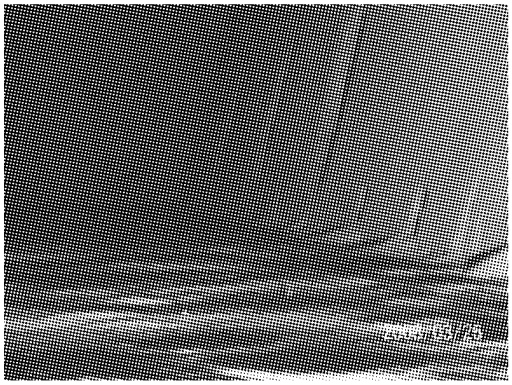

Fig. 3 Primary air introduced from both sides

Problems and corresponding solutions during commissioning

Modifications of oil guns above bed: During startup, it was found that the bed temperature could reach about 550℃ only by the duct burner below the bed. It was possible to ignite the coal under such temperature if the fuel was bituminous or lignite. However, for this boiler, it was anthracite with ignition temperature of higher than 625℃. Thus, the bed temperature should be higher than 650℃ before coal fed into the furnace. However, the oil guns above bed could only increase the bed temperature from 550℃ to 600℃. Consequently, the they were modified in three ways: 1) Placed the oil guns to the vicinity of secondary nozzles to improve the combustion of oil by rapid mixing with the air. 2) Added a stable combustion cover to make flame continuous and stable. 3) Downward-sloping layout to heat bed material better. After modification, the oil guns above the bed worked well, and the bed temperature could reach about 700℃.

Modification of wing wall superheater: It was found that most of the heating surfaces were safe. However, the metal temperatures of some wing wall superheaters were higher than the permission, especially during startup stage or at lower load (50 ~ 150MWe). Overheating problem for the wing walls located in the middle of the furnace in width direction was more obvious. DBC tried to decrease the heat absorbed by these wing walls. After modification, the maximum wall temperature decreased about 30℃ at rated load, 20℃ lower than the alarm temperature. An optimum arrangement for wing wall superheater heating surface is designed in new 300MWe CFB boilers. It will further enhance the safety of heating surface and steam temperature control ability.

Heat Distortion of the support for duct burners and damper: After steam pipe blowing, it was found that the support for duct burners as well as the air dampers near the burners were both deformed, shown in Fig. 4. To avoid heat distortion, the damper was removed because it was not necessary. The support for duct burners was coved by refractory material. After modification and a period of operation, it was found that the support was still very good, shown in Fig. 5.

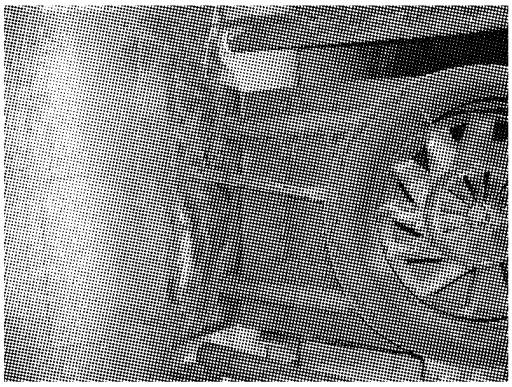

Fig. 4 The disabled support for the duct burner

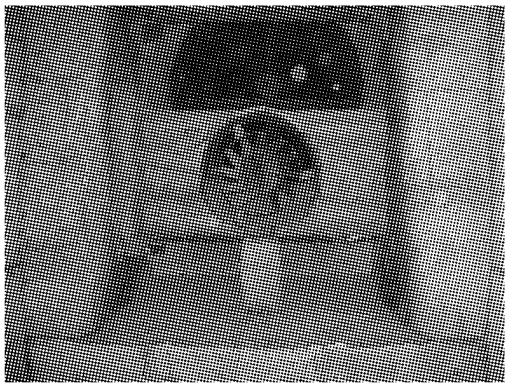

Fig. 5 The modified duct burner after operation

Bed temperature distribution

Bed temperature distribution along width direction in No.3 boiler at 300MWe load was shown in Table 3.

Table 3 Bed temperature distribution in No.3 boiler (°C)

Rear wall	Higher level	851.7	—	—	903.6	—	882.7	941.9	—	—	879
	Lower level	856	851.8	909.7	934.7	940.7	947.7	929.2	919.7	910.5	881.9
Front wall	Higher level	—	873.6	868.1	—	928.4	923.5	—	914.4	898	—
	Lower level	850.8	870.3	888.2	933.1	937.4	935.8	945.2	912.7	896.8	878

Along the width direction of the furnace, the temperature in the middle part was a little bit higher. It may be caused by less heating surface in the middle and large inner circulating material flow rate in both sides.

Characteristics of asymmetrically arranged cyclones

In the 300MWe CFB boiler developed by DBC, three cyclones are arranged asymmetrically, as shown in Fig. 6. In order to make sure the balance of gas and circulating material, a series of pilot studies were conducted by DBC and Tsinghua University (Yang et al. 2007, Yue et al. 2008). The experimental and numerical simulation results both showed that the gas-solid flow in the furnace was uniform enough. The circulating flow rate and pressure drop in three different cyclones were almost same. It was also confirmed by cold test in Heshuyuan Boilers. After shutting down the fan, the accumulative heights of material in the standpipse were measured, which were 1.29m, 1.23m, 1.30m separately.

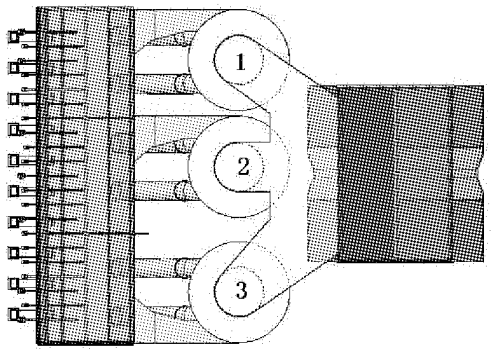

Fig. 6 Schematic diagram of cyclones

Parameters of the main loop

The circulating loop performance can be estimated by temperature profile. In Table 4, it can be seen that the bed temperature and corresponding cyclone temperature are basically the same. The temperatures in the loop are very similar and match the design values.

The pressure of the loop seal is very stable, which indicates the circulating flow rates of the three loops are almost identical. The typical pressure profile of the main loop is listed in Table 5.

Table 4 Temperature profile in main loop

Item	unit	No.3	No.4
Load	MWe	291	295
Bed temperature (left / right)	°C	869/873	885/887
Gas temperature at the furnace outlet (left / right)	°C	-/845	899/893
Gas temperature at the inlet of cyclone (left / middle / right)	°C	868/-/889	-/892/-
Gas and ash temperature at the outlet of cyclone (left)	°C	879/880	897/892
Gas and ash temperature at the outlet of cyclone (middle)	°C	888/923	960/956
Gas and ash temperature at the outlet of cyclone (right)	°C	885/885	903/880

Table 5 Pressure profile on the main loop

Item	Unit	Data	
Load	MWe	300	300
Standpipe(left /middle /right)	kPa	12.04/13.09/10.76	11.51/13.11/10.70
Return pipe(left /middle /right)	kPa	2.95/2.63/2.55	2.55/2.29/2.32
Main pipe of high pressure air for loopseal	kPa	49.28	53.75
Bed pressure drop(left/right)	kPa	9.0/8.7	8.4/7.9

The heat absorbed by the heating surface located in the main loop is close to the design values, indicating the heat transfer as well as the solid suspension density agrees well with the designate values.

The size distribution of fly ash from No.3 boiler was measured. The fly ash was finer than that of a 135MWe CFB boiler, shown in Fig. 7, indicating that the cyclones had higher collection efficiency.

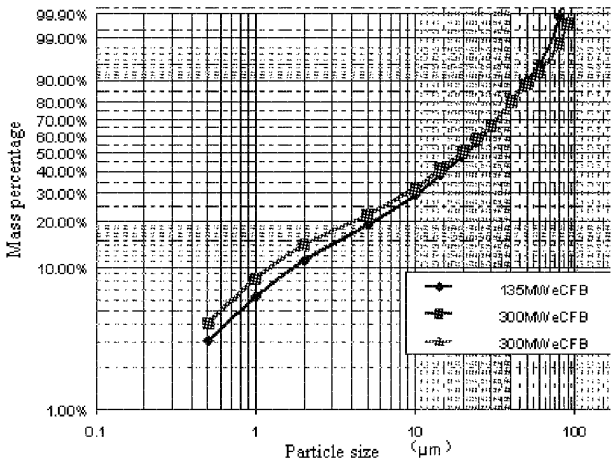

Fig. 7 Fly ash size distribution

Typical operation parameters

During the trial operation and commercial operation, the boilers were reliable and stable. The technical parameters reached the design values, which are listed in Table 6 (the data in Table 3 are all recorded from the DCS) and Table 7. The temperature profile can be found in Table 4 and Table 5.

Table 6 Operation parameters of the 300MWe CFB developed by DBC(during the trial operation)

parameter	unit	No.3	No.4
Load	MWe	291[1]	295[1]
Main steam temperature	°C	534.1	535.8
Main steam pressure	MPa	15.4[2]	15.5[2]
Reheat steam temperature	°C	534	525[3]
Reheat steam pressure	MPa	3.14	3.06
Feed water temperature	°C	276.8	276.2
Total spraying water flow rate for superheater	t/h	39.15	38.46
Total spraying water flow rate for reheater	t/h	21.9[4]	11.09[4]
Primary air pressure in the air box(left / right)	kPa	14.2/14.3	13.1/13.2
Pressure drop of the bed (left / right)	kPa	8.7/8.4	8.87/8.95
Oxygen content in gas at the furnace outlet (left / right)	%	3.38/4.22	3.32/3.3
Environmental temperature	°C	25.2	28.6
Primary air hot air temperature	°C	237	245.15
Secondary air hot air temperature	°C	207	202.4
Exhaust flue gas temperature	°C	149	154.5
Check exhaust flue gas temperature	°C	134.4[5]	139.9
Bottom ash temperature	°C	96	71.2

Note: [1] Boiler load ranged from 290 to 295MWe. [2] Main steam pressure was reduced to satisfy the requirement of steam turbine. [3] Reheat steam temperature was reduced because of steam turbine system. [4] The spraying water flow rate was influenced by damper location in the parallel pass. [5] It is corrected by local standard GB10184-88.

Table 7 Operation parameters of the 300MWe CFB developed by DBC(during the commercial operation)

parameter	unit	Data	
Load	MWe	300	303
Main steam temperature	^{o}C	536	535.8
Main steam pressure	MPa	16.8	16.7
Reheat steam temperature	^{o}C	534	533
Reheat steam pressure	MPa	3.27	3.28
Feed water temperature	^{o}C	279	279.2
Total spraying water flow rate for superheater	t/h	21.2	27.84
Total spraying water flow rate for reheater	t/h	1.59	1.53
Oxygen content in gas at the furnace outlet	%	3.49	3.50
Bed temperature (left / right)	^{o}C	896/896	902/912
Gas and ash temperature at the outlet of cyclone (left)	^{o}C	915/926	896/901
Gas and ash temperature at the outlet of cyclone (middle)	^{o}C	927/936	922/910
Gas and ash temperature at the outlet of cyclone (right)	^{o}C	895/902	903/915
Bottom ash temperature	^{o}C	67	85

CONCLUSIONS

The first 300MWe CFB boiler developed by DBC has been put into commercial operation successfully in China. After commissioning and modification, its performance reaches the guarantee value. Some optimization designs are conducted in the future boiler.

REFERENCES

Dongfang Boiler Group Co.，Ltd.(2005): BOIWA 300MWe CFB boiler manuals.

Yang S., Li W.K. and Wang Y.Z. (2007) Research on flow uniformity in main circulation loop of 300Mwe CFB boiler. 1st Conference on CFB combustion theory and technology in China.

Yue G.X., Yang H.R., Nie L., et al. (2008): Hydrodynamics of 300MWe and 600MWe CFB Boilers with Asymmetric Cyclone Layout. 9th International Conference on CFB.

OPERATIONAL STATUS OF 300MWe CFB BOILER IN CHINA

J.F. Li[1], J. H. Mi[1], J. H. Hao[1], S. Yang[2], H. T. Huang[1], H. M. Ji[1], J. F. Lu[2], G. X. Yue[2]

1Scientific and Technical Service Center, China Electricity Council, Beijing 100038, China
2Key laboratory for Thermal Science and Power Engineering of Ministry of Education, Department of Thermal Engineering, Tsinghua University, Beijing 100084, China

Abstract: China has the largest number of 300MW circulating fluidized bed (CFB) boilers in the word within, built in a short period of several years. Now, there are 13 CFB units in operating and other about 50 CFB boilers under construction or will be under construction soon. Summarization and analysis of the operational performance of the 300MWe CFB units are conducted. The reliability, economy and emission of these unite are introduced. The problems in these units are summarized. Some advices for improvement and future research are given.
Keywords: 300MWe-Class, circulating fluidized bed boiler, operation, summary

INTRODUCTION

CFB boiler technology has been rapidly developed and becomes clean coal combustion technology used in power generation in China. So far, in China the total number of 300MWe CFB boiler in commissioning or in operation is 13. Other 50 units of 300MWe CFB boilers are under construction or will be under under construction soon. The total number of 300MWe CFB boilers used in China is more than the sum of all other countries around the world. Among these CFB boilers, 18 of them are manufactured by Alstom technology and other boilers are designed with domestic independent technologies.The first 300MWe CFB of developed by domestic technology was put in operation in 2008.

During the year of 2006-2011, the installation capacity of CFB boilers burning coal waste is 2000MWe set by the government. Most of the boilers are of 300MWe-class. Based on the design and operational experience, a 600MWe supercritical CFB boiler will be built and put into commissioning at the end of 2011 (Yue et al., 2007).

The operational data of some 300MWe CFB boilers in China which have been put into operation for more than one year was collected in this article. The overall operational status of the 300MWe CFB boilers was analyzed and summarized. Some common operational problems were discussed.

300MWe CFB OPERATIONAL STATUS

Among the 13 units of 300MWe CFB boiler used in China, the first one locates at Baima Power Station, Sichuan Province as a demonstration. There are two 300MWe CFB boilers in Datang Honghe Power Station, Yunnan Province; two units in Guodian Kaiyuan Power Station, Guangdong Province; two units in Xunjiansi Power Station, Yunnan Province; two units in Qinhuangdao Power Station, Hebei Province; two units in Mengxi Power Station, Inner Mongolia; and two units in Heshuyuan Power Station, Guangdong Province. As the operational period of some boilers are too short to give sufficient data, only the performance of those with operational period over one year is summarized here. The summary includes the operational load, reliability, fuel composition, economy, and pollutant emission of the boilers.

LOAD RATE

The operational load of 300MWe CFB boilers operated in China is shown in Table 1. It can be seen that the average load rate of these units is about 77.51%, which is almost the same to the 300MWe pulverized coal-fired (PC) boilers.

Table 1 Load Rate of 300MWe CFB Boilers in China

Power Station	Unit # in the Plant	Generated Energy in 2007 [MWh]	Peak Load [MW]	Average Load [MW]	Load Rate [%]
Baima	1	1601972.5	320	234.9	78.3
Qinhuangdao	1	1814377.7	306	248.6	82.8
	2	1265622.3	306	248.6	82.8
Honghe	1	2028864	319	267	89
	2	1892082	323	265	88.3

Continued

Power Station	Unit # in the Plant	Generated Energy in 2007 [MWh]	Peak Load [MW]	Average Load [MW]	Load Rate [%]
Kaiyuan	7	948174	310	219.2	73
	8	1421622	313	222.5	74.2
Xunjiansi	6	1249898.7	325	155	51.7

RELIABILITY

The reliability of 300MWe CFB boilers is shown in Table 2. As shown in Table 2, the reliability of 300MWe CFB boilers is relatively low. For example, the average unplanned outage times is 5.625 times/year, far exceeds that of 300MWe PC boilers (which is 0.89 time/year). In addition, the continuous operational time of 300MWe CFB boilers in 2007 was only 154 days, not only far lower than that of 300MWe PC boilers, but also lower than that of 135 MWe CFB boilers. The reason for the poor reliability of 300MWe CFB boilers was due to the lack of the operational experience of large capacity CFB boiler. With the accumulation of operational experience and better understanding of large CFB boilers, the continuous operational time of 300MWe CFB boilers increases. In 2009, it becomes, for some 300MWe CFB boilers over 200 days.

Table 2 Reliability of 300MWe CFB boilers

Power Station	Unit Number	Available Hours [hour]	Unplanned Outage Time	Continuous operational time [Day]	Load Range When Firing Oil [MW]
Baima	1	7668	7	154	——
Qinhuangdao	1	7560.3	7	89	⩽80
	2	5273.7	2	——	⩽80
Honghe	1	7833.1	1	111	⩽105
	2	8150.2	1	142	⩽105
Kaiyuan	7	4490.7	6	——	⩽105
	8	6806.2	9	——	⩽105
Xunjiansi	6	6242	12	——	——

Fuel

The fuel properties for the 300 MWe CFB boilers operated in China is shown in Table 3. It can be seen that the a wide range of fuels are burnt in these CFB boilers, even the ignites with more than 40% moisture. And CFB boilers have absolute predominance in utilizing high sulfur coal.

Table 3 Proximate Analysis of the Coal Burnt in 300MWe CFB Boiler in China

Power Station	Volatile [%]	Ash [%]	Moisture [%]	Sulphur Content [%]	LHV [kJ/kg]
Baima	18.11	44.15	6.39	2.57	15235
Qinhuangdao	26	27.5	2.1	0.9	19776
Honghe	40.79	10.23	38.5	1.06	12900
Kaiyuan	41.24	18.23	33.02	1.74	12224
Xunjiansi	42.28	19.41	34.21	1.75	11147

ECONOMIC INDEX

From Table 4, it can be calculated that the net coal consumption of 300 MWe CFB boilers is 353.86g/kWh, which is far lower than that of 135 MWe CFB boilers but higher than that of 300 MWe PC boilers. In 2007, the power consumption rate of 300 MWe CFB boilers was 5.67%.

Table 4 Economic indexes of 300MWe CFB boilers

Power Station	Unit Number	LOI [%]	Carbon in Bottom Ash [%]	Net Coal Cons. [g/kWh]	Power Cons. rate [%]	Oil Cons. [t/year]	Flue Gas Temp. [℃]
Baima	1	3.99	2.43	352.79	9.18	152	126.2
Qinhuangdao	1	4.2	0	368	9.57	860	133
	2	4.2	0	368	9.57	860	133
Honghe	1	1	0.2	340.84	8.59	111.6	150
	2	1	0.3	340.84	8.52	127.9	149
Kaiyuan	7	1	0.45	347.35	9.69	218	146.9
	8	1	0.72	348.08	9.62	526.5	136.2
Xunjiansi	6	1	.0.68	363.72	10.75	925	139.7

As there are massive inert bed materials in the furnace, the ignition oil consumption in 300MWe CFB boilers is large. Thus, it is of great significance to study the low oil consumption ignition method, such as heating by neighborhood boiler, under bed ignition, etc.

Flue gas temperature is an important factor for boiler efficiency. According to the operational record, there is little difference between the practical data and designate value (Li et al, 2008). Generally speaking, decreasing the ignition oil amount is a major concern to improve the economic operation of CFB boilers. If the power consumption rate is reduced, the economic index of CFB boilers will be compatible to that of PC boilers.

Emission

Environmental protection index of 300MWe CFB boilers is shown in Table 5. The SO_2 and NO_x emission is far lower than national standards.

Table 5 Environmental protection indexes of 300MWeCFB boilers

Power Station	Unit Number	Desulfurization Efficiency [%]	Usage Rate of Desulfurization Equip., [%]	SO2 Emission [mg/Nm^3]	NOx Emission [mg/Nm^3]	Ca/S
Baima	1	94.7	100	487	87	1.7
Qinhuangdao	1	90	100	200	70	2.1
	2	90	100	200	70	2.1
Honghe	1	95	100	327	65	1.7
	2	95	100	327	65	1.7
Kaiyuan	7	95.5	100	275	147	1.9
	8	94	100	280	149	1.9

The desulfurization efficiency of all the 300MWe CFB boilers is higher than 90%, higher than 135MWe CFB boilers.

One of the outstanding advantages of CFB boilers is low NOx emission. As low temperature combustion and air staging are used in CFB boilers, and due to the unburned carbon in the furnace which can behave as a reducing agent, the NOx emission is far below national standard (GB13223-2003). Today, due to the stringent emission control policy, SCR method is popularly used in PC boilers (Wang et al., 2007; Li et al.,2007) to reduce the NOx emission. However, SCR method is rather expensive and energy cost to be applied in CFB boilers (Li et al, 2003).

ACCIDENT ANALYSIS OF 300MWe CFB BOILERS

As the operational period is short for the 300MWe CFB boilers, and little experience has been attainted, many accidents occurred during practical operation. These accidents can be classified as 3 kinds (Li et al, 2006. Liu, et al, 2007; Zhang et al, 2007; Dong et al., 2008) as discussed below.

Erosion

Similar to other CFB boilers, 300MWe CFB boilers have severe erosion phenomenon. And the severe erosion place usually locates in water wall and external bed. Sometimes, erosion happened in superheater, reheater, and economizer.

There are many reasons for erosion, such as lack of careful consideration on water wall erosion in design

phase, no positive stop between free expansion bend and adjacent tubes, difference between practical and designed coal and so on.

Tube leakage

The severe tube leakage will lead to furnace shutdown and some other accident. The main reason for the leakage is heating surface erosion. The water walls, heating exchange tubes in external bed, superheater tubes, reheater tubes are the parts apt to leak. If the cyclone efficiency is low or the coal particles are too small, the economizer tubes and air preheater tubes can leak as well. The most effective method to protect tube leakage is reducing the heating surface erosion.

Combustion

The reasons for unstable combustion of 300MWe CFB boilers are shown as below:

1. Unstable of bed material. Several 300MWe CFB boilers have ever been shut down or turned over attributed to unstable of bed material. Compared with smaller capacity CFB boilers, the 300MWe CFB boilers have much larger furnace area, decreasing the fluidization quality.

2. Slagging outside the furnace. It is found that there are large amount of slag in channels behind the feed coal point in the dipleg. It was reported that the dipleg was once almost blocked by the slag, resulting in the back flow of the high temperature ash into the coal supply pipe, and the boiler had to be shut down. Generally speaking, dense phase zone, slag cooler and dipleg are the places apt to slag.

3. Slagging in the furnace. If the cold startup time is too long, the bed material in the furnace will be too less and the bed pressure drop will become too low. When the pressure drop decreases to 3~5kPa, flow fluctuation occurs in the bed. Normal fluidization is destroyed and temperature distribution in the furnace becomes nonuniform. In some cases, slagging in the furnace happened.

4. Cyclone Overheating. When a boiler is at low load rate, the flue gas temperature at the inlet to the cyclones is often over high (950°C-990°C), largely threatening the security of boiler operation.

CONCLUSIONS

China has the largest number of 300MWe CFB boilers around the world. The operational status of these boilers was summarized and discussed in this paper.

These boilers burnt various fuel and play important role in power generation. The overall performance of these boilers is acceptable. The CFB boilers showed incomparable advantages in burning low rank fuels, in-furnace desulfurization and low NOx emission. Some problems including high net coal consumption, frequent unplanned outages, high carbon content in fly ash exist and need to be solve in the future. Advices are given to conduct researches to overcome the problems appeared in the application.

REFERENCES

Dong, Z.M., Liao P., Yuan D.Y., et al. Boiler Technology, 39 (2008), pp.38-40.
Li, J.F., Hao J.H., Lu J.F., et al. Boiler Technology, 39 (2008), pp.29-32.
Li, J.C., (2007), Energy Analysis and Process Simulation of Ammonia Plant. Master Degree Thesis, Lanzhou University.
Li, Z.Z., Feng, Z.X., Wang, Y., et al. Proceedings of the CSEE, 23(2003): pp.184-188.
Li, W.K., Zhang, P., Guangdong Electric Power, 19(2006), pp.39-42.
Liu, J., Dong, Z.Q., Zhu, J.S., (2007), Thermal Power Generation, pp.53-54.
Wang, H. Z., Chen, J.S., Boiler Technology, 38(2007), pp.62-67.
Yue, G. X., (2007), In: Yue G, Hao J eds. proceeding of 1st conference on Circulating fluidized bed combustion of China. Hainan, pp.2-30.
Zhang, Y. J., Li Z.Y., Wang, F.J., et al. Journal of Power Engineering, 27(2007), pp.507-510.

ADVANCED REFRACTORY AND ANTI-WEARING TECHNOLOGY OF CYCLONE SEPARATOR IN CFB BOILER

H. P. Chen[1], Y. Q. Shen[1] X. H. Wang[1].X. M. Dai[1] H. Y. Xue[2] D. C. Liu[1,2]

1 State Key Laboratory of Coal Combustion, Huazhong University of Science and Technology Wuhan, 430074, China

2 PUYANG REFRACTORIES GROUP CO., LTD Puyang, Henan, 457100, China

Abstract: The circulating fluidized bed is playing more and more vital role in the electric power field. Cyclone separator as the heart of the circulating fluidized bed combustion boiler, the technology of fire-resistant anti-wear layer in cyclone separator is the guarantee for the long-life and working safety of CFB unit. Based on the comparison of insulation-cyclone and water-cooled cyclone, a novel technology of Anchor bricks use in the cyclone separator was put forward. The temperature of Anchor brick surface is just 80~90℃, much lower than conventional technology. The problems caused by conventional Y-shaped hook welding were overcome, such as fire-resistant anti-wear layer burned, fire-resistant anti-wear layer rupture, the high temperature of separator's surface, a large number of heat dissipation and etc. Simultaneously, three types of Anchor brick were designed for the different parts of cyclone. It was applied successfully in Thermal Power Plant in Shaoguan Iron and Steel Company. The life time and the operation cycle of the fire-resistant anti-wear layer of the cyclone were prolonged, and the number of boiler off was reduced greatly. Hence, the continuous operation time of boiler was extended. It played a key role in improving the overall economic efficiency of power plant. It is great for the utilization and development of CFB technology.

Keywords: CFB boiler, cyclone separator, Anchor brick, refractory and anti-wearing

INTRODUCTION

CFB boiler firing is a kind of clean coal technology. In recent years, CFB boiler technology has developed fast in large-scale change and makes more and more contribution to electric power industry.

Advantages of CFB boiler

- good fuel adaptability;
- high burning efficiency;
- good performance of load adjustment;
- Ash Utilization;
- Particularly good environmental performance;

Cyclone separator as the heart of the circulating fluidized bed combustion boiler, the technology of fire-resistant anti-wear layer in cyclone separator is the guarantee for the long-life and working safety of CFB unit. This paper describes the technology of fire-resistant Anti-wear layer in insulation-cyclone separator of anchoring brick.

CYCLONE SEPARATOROF CFB BOILER

There are two kinds of cyclone separators in a CFB boiler. One is insulation-cyclone, and the other is water-cooled cyclone. The advantage of the insulation- cyclone is simple in structure and cost-effective. The disadvantage as follows: unwieldy, large, a large number of heat dissipation, high cost in fire-resistant Anti-wear layer maintenance, high demand in connectivity of thermal expansion, and long time in ignition startup. The advantage of the water-cooled cyclone is small in volume and heat dissipation, lower maintenance costs, easy to solve the problem of connectivity of thermal expansion, and short time in ignition startup. The water-cooled cyclone separator can be a part of heating surface of the boiler. The disadvantage of it is complex in structure and high production costs.

In order to overcome the large heat dissipation of fire-resistant anti-wear layer of insulation cyclone, the high cost in maintenance of the fire-resistant Anti-wear layer, a novel technology of fire-resistant anti-wear layer for anchor brick to be used in the cyclone separator was put forward in this paper. It has been used to the CFB boiler in some power plant, and has made a remarkable effect.

NEW TECHNOLOGY OF ANCHOR BRICK

Top structure of anchor brick of fire-resistant anti-wear layer

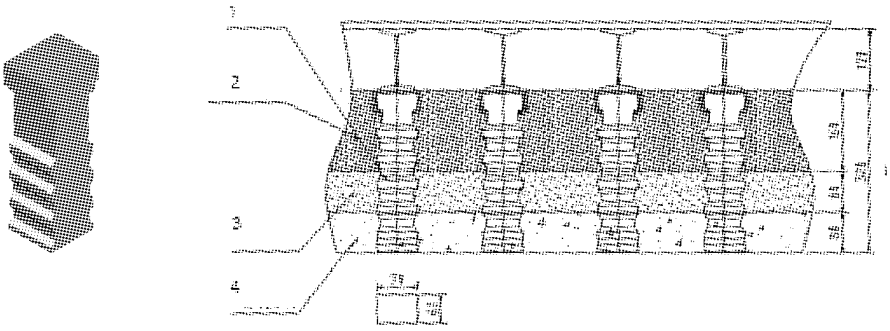

Fig. 1 Top structure of anchor brick of fire-resistant Anti-wear layer
1–anchor piece of refractory; 2-Micro porous calcium silicate without Asbestos;
3-Insulating castable; 4-Wear-resistant castable

Double layer structure of fire-resistant Anti-wear layer anchor brick on side wall

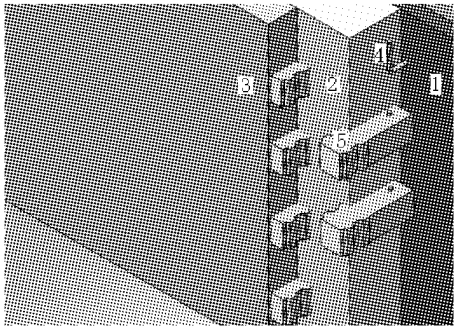

Fig. 2 Double layer structure of fire-resistant Anti-wear layer anchor brick on side wall
1-Thickness of Armor plate: 50mm; 2-Thickness of CaSiO4: 180mm;
3-Thickness of Anti-wear pouring layer:100mm; 4-U-shaped fixations; 5-anchor brick

The new technology of anchor brick is the patent of Puyangpunai high-temperature Materials (group) Co., Ltd (2006201137661). The problems caused by conventional Y-shaped hook welding were overcome by the patent, such as fire-resistant Anti-wear layer burned, fire-resistant anti-wear layer rupture, the high temperature of separator's surface, a large number of heat dissipation and etc. The exterior temperature of fire-resistant Anti-wear layer of conventional Y-shaped hook welding is 100~180℃, but the temperature of anchor brick surface is just 80~90℃. Thus, this new technology can overcome the above shortage.

The structure of fire-resistant Anti-wear layer of cyclone separators is composed of the top and the canister. And then in allusion to the two parts, we designed and fabricated 3 types of structures of anchor brick. (Show in Fig I, II, III).

Three-ply structure of fire-resistant anti-wear layer anchor brick on side wall

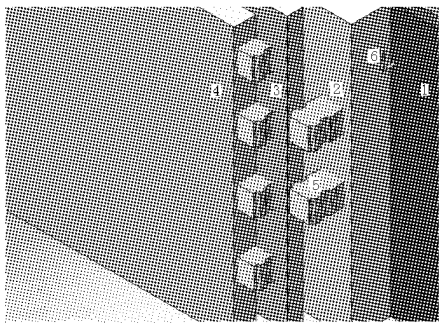

Fig. 3 Three-ply structure of fire-resistant Anti-wear layer anchor brick on Side wall
1-armor plate 50mm; 2-Fire-resistant cotton fiber layer 180mm; 3-Light poured layer 70mm;
4-Anti-wear pouring layer 100mm; 5-anchor brick; 6-U-shaped fixation

Advantage and disadvantage of fire-resistant anti-wear layer anchor brick

1) The conventional Y-shaped steel hook used in ire-resistant Anti-wear layer has been canceled, so the hook burned and fire-resistant Anti-wear layer rupture are eliminated.

2) The length is cut and fire invisible for the fixation buried in the anchor brick for the U-shaped hook is used. Besides, the quantity is less than that of Y-shaped hook. At the same time, the adiabatic ability of fire-resistant Anti-wear layer is promoted, the temperature of separator surface down to 80~90℃, far below the surface temperature that is 100~180℃ of the conventional insulation-cyclone.

3) The heat dissipation reduced significantly and the effect of coal-saving is significant because of the fall of the temperature of the cyclone separator surface.

4) The overhaul cycle and life time of the cyclone separator are prolonged, the operation and maintenance costs reduced greatly. All of the above because of the rate of disrepair and fault of the fire-resistant Anti-wear layer in the cyclone separator reduced significantly.

5) The life time and the operation cycle of the fire-resistant anti-wear layer of the cyclone were prolonged, and the number of boiler off was reduced greatly. Hence, the continuous operation time of boiler was extended. It played a key role in improving the overall economic efficiency of power plant.

6) The structure of the heterodyne anchor brick is complex, and the cost will be a little higher.

CONCLUSIONS

1) 2# 130t/h CFB boiler used in Thermal Power Plant in Shaoguan Iron and Steel Company, which used the structure of conventional Y-shaped hook welding with the fire-resistant Anti-wear layer. Hook burning, refractory layer shedding and repairing often occur during the operation of boiler. In order to prolong the operation cycle of the boiler, the patent adopted in July, 2006. The advantage of this technology has been proved by two years operation.

2) 7# 410t/h CFB boiler (made by Haerbing boiler factory) in Luoyang new power group, general contracted by Puyang overhaul company, used the patent in 2008, have put into practice. The performance will be summarized.

3) Cyclone separator as the heart of the circulating fluidized bed combustion boiler, its long-term continuous and safe operation is the key of sustained and safe operation of circulating fluidized bed combustion boilers. The application of the fire-resistant Anti-wear layer technology brings the breakthrough to the cyclone separator operating condition.

REFERENCES

He Z.F: Industrial boiler [J]. (5)2006, PP.42-46.
Du G.L,Shi M.W,Leng J.: Northeast Electric Power Technology[J].(3)2007,pp.30-34.
Liu D.C;Chen H.P, :China Electric Power Press[M].2006.
Liu X, Wang r.: Industrial boiler [J]. (4)2004, pp.56-58.

ABRASION-RESISTANT TECHNOLOGY AND ITS PROSPECT FOR CFB BOILERS

H. Zheng, Y. J. Li, L. J. Wang, S. H. Liu, Q. R. Dou

R&D Dept., Beijing Tongda Refractory Technologies Co., Ltd, Beijing, China

Abstract: In recent years, CFB boilers (CFBB) have been widely used in the commercial power plants due to its environmental benefits, high combustion efficiency, wide coal flexibility, and some other advantages. At the same time, the abrasion problem, the greatest weakness of this kind of boiler, has been gradually exposed in its application process. The abrasion, particularly on key parts such as the heating surface of water-cooled wall, furnace corners, separator entrance, seriously restricts the long-period operation ability of the CFBB. This article discusses current development status for various abrasion resistant refractory materials used in a CFBB. Some comments are provided for developing new high-performance abrasion resistant refractory materials and rapid-repaired materials according to the abrasion principle and the abrasion on different parts, as well as the economical and environmental requirements for the material. The abrasion solution and operation period of CFBB can be better improved given realization.

Keywords: CFB boiler, abrasion, abrasion resistant, refractory material

INTRODUCTION

CFBB combustion technology has become one of advanced and reliable clean coal-fired technologies nowadays with advantages of environmental friendly, high combustion efficiency and wide coal flexibility and has been widely used in boilers of power stations at home and abroad.

Different from that of some other kinds of traditional boilers, the combustion in CFBB is that solid materials are circularly burnt driven by high speed thermal current and unburnt materials are returned to furnace through separator and material-returned devices in purpose of high efficiency combustion. However, various problems still exist in practical operation of CFBB, especially abrasion which has seriously impeded the application and development of CFBB. Since the year of 1996, in China, the percentage of boiler accidents caused by abrasion has reached above 80 percent and cost more than one million RMB for maintenance every year according to incompletely statistics.

The abrasion in the furnace is inevitable for the CFB boiler. Therefore, abrasion mechanism research on heating surfaces in the furnace and effect factors, practicable abrasion resistant measures, and boiler usability has become a key issue in CFBB industry.

MAJOR ABRASION PARTS IN A CFBB

The solid materials include coal-fired, desulfurizer limestone and bed materials, whose medium grain size is 0 to 8mm, and medium grain size of circulating materials is about 100um. The density of solid materials can reach maximum 100 to 1000 kg/m^3. The hot flue gas whose average velocity is 4 to 10 m/s formed by materials combustion contains 10% to 20% fly ash which contains high melting point hard grain (SiO_2).. The abrasion degree has closed relationship with factors such as solid materials density, flue gas velocity and grain properties.

Water cooling wall tube in furnace

In the CFBB furnace, the typical two-phase flow is in shape of an annulus-core structure. In inner core zone, particles or clusters of particles flow upwards, but solid materials flow along furnace water cooling wall tubes downwards in outer ring zone. The thickness of ring zone is gradually thinner and thinner from bottom of bed to top and the main cause for water cooling wall tubes abrasion is that solid materials flow along water cooling wall surface downwards. The serious abrasion of water cooling wall tubes has usually relationship with sudden change of reflow materials direction. The parts of sudden reflow materials direction are easy to be wore include the separating surface for water cooling surface and burned band, tubes in four corners area of furnace, the spot with ash deposition and welding on membrane tube wall surface, tubes in irregular areas and common water cooling wall tubes(Song et al., 2005).

Furnace dense phase zone and lower part of water cooling expansion wall

In these area, the flue gas velocity is 4 to 6m/s, and service temperature is 800~1000℃ and density of

materials is about 100 to 1000kg/ m^3. The abrasion is mainly caused by abrasion of wearable materials and abrasion for water cooling wall tubes after wearable materials peel. Based on mechanism analysis, it is mainly because that turbulent motion of solid material has serious transverse erosion on refractory materials and water cooling wall as well as vertical erosion of much adherent materials flow, tube blasting will easily happen in shorter time.

Cyclone separator

The service temperature is about 900 to 1000℃ and flue gas velocity can reach 15 to 25m/s in this area. Because of centrifugal force, submicron particles in gas flow are separated as soon as they touch walls and produce serious abrasion (See Fig. 2-6 for details) on separator entrance and target region. (See Fig.1)

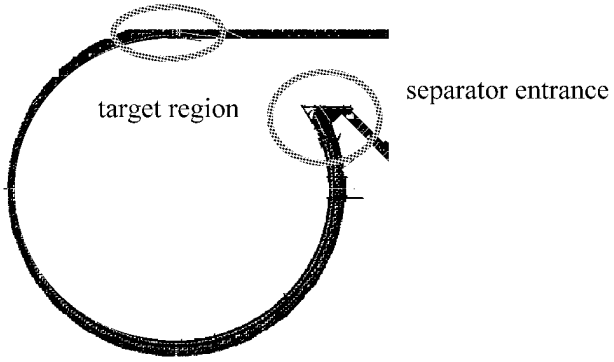

Fig.1 Serious abrasion parts of cyclone

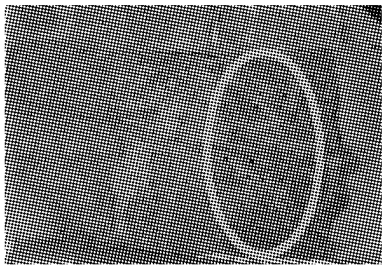

Fig.2 The abrasion of top parts for cyclone separator entrance

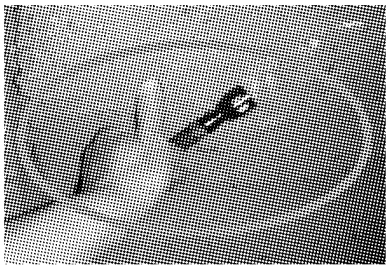

Fig.3 The abrasion of cyclone separator entrance short side wall

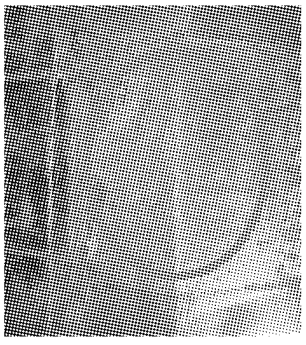

Fig.4 The abrasion of cyclone separator entrance short side wall corner

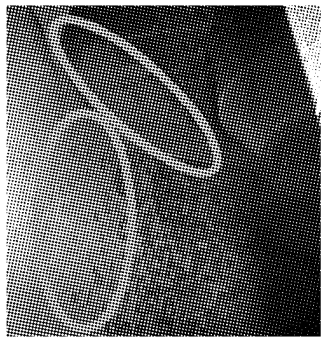

Fig.5 The abrasion of cyclone separator target region

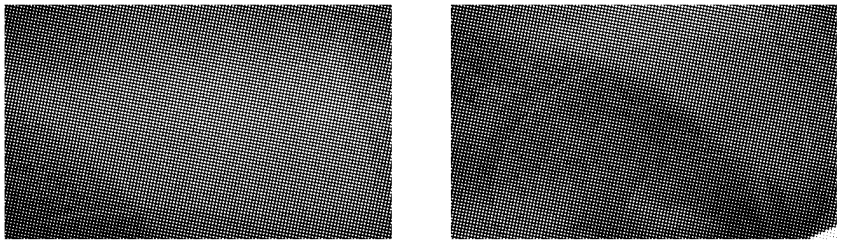

(a) (b)

Fig. 6 The abrasion zone of cyclone separator conical part

Return leg U blade part

The service temperature is about 850℃ and the flue gas velocity is less than 1m/s in this part where the bed materials are submicron and the density is high. The return channel is a fluidized and sealed ash-returning device, sending the materials separated from the cyclone separator into the furnace. The U blade of return channel (see Fig.8) is usually seriously worn under the effect of material attack and thermal stress.

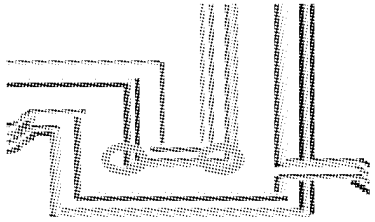

Fig. 7 Serious ahrasion parts of the return Leg U blade

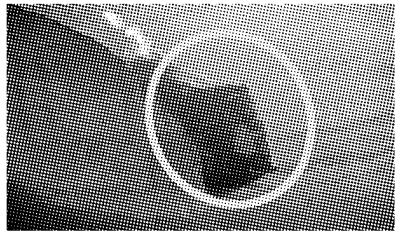

Fig. 8 The abrasion of return channel U blade (repaired)

CURRENT SITUATION OF ABRASION RESISTANT REFRACTORY MATERIALS

Nowadays, the abrasion resistant refractory material for CFBB can be divided into two categories—— metallic material and non-metallic material.

Metallic material

There are two reasons in preventing abrasion and erosion by using metallic surface coatings. Firstly, the rigidity of coatings is harder than that of based material. Secondly, in high temperature coatings can create hard, dense and chemically stable oxide layer, adhering firmly with its basal corpuscle. The second reason is more important.

Supersonic arc spraying anti-wear technique is common used for CFBB power plants now. Arc spraying has the virtue of high spraying speed, easily adjustable coating chemical components, and high deposition efficiency, especially being suitable for construction of spot large-area anti-wear parts. The heat source of this technique is a high-temperature arc and fused high-temperature wires are, atomized by high-speed air stream and sprayed into work pieces surfaces to form coating layer. This arc spray technique has been gradually developed with CFBB promotion by adding the Laval nozzle based on arc spraying and improves control system and power supply property. Anti-wear spray threads are brought out by high speed air stream while being fused in arc gun. Molten coating particles impact metal surface at a supersonic speed and become mechanical embedded. The higher speed is for particles, the denser coating is and the stronger is for embedded power, the higher is for the bond strength. Thereby a dense anti-wear coating is formed in the metal surface so that water cooling wall tubes can be prevented.

Non-metallic Material

Generally the parts which make use of non-metallic anti-wear materials in CFB boilers are as Fig.9. Because of the demands of anti-wear, erosion resistant and heat balance in dense areas of furnaces, it is necessary to lay out an anti-wear refractory layer 1, of which thickness is 50~70mm. Since the direction of air current in the furnace exit may be changed, the anti-wear layer 2 is laid out. The gas in the cyclone separator whirls at a high rate and severe abrasion happened, so anti-wear layer 3 is laid out. In the dip leg, return channel and return leg, anti-wear layers 4, 5, 6 are laid out respectively. In the flue of the separator exit, the speed of air current is fast, so anti-wear layer 7 is laid out. The speed of air current between furnace and separator is very fast, so anti-wear layer 8 is laid out.

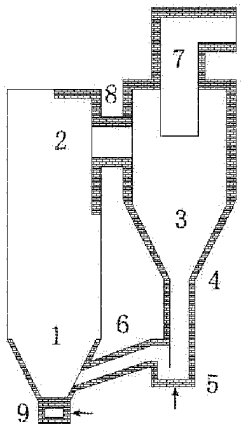

Fig. 9 Schematic diagram of CFBB abrasion resistant refractory lining
1—furnace lower part; 2—furnace exit; 3—cyclone separator; 4—dip leg; 5—return channel; 6—return leg; 7—flue gas opening; 8—connecting pipe;9--wind box

The usual non-metallic abrasion resistant refractory materials used are: phosphate-bonded brick and castable, silimanite brick and castable, carborundum brick and castable, corundum brick and castable, and the top-grade one is silicon nitride-bonded silicon carbide product. These refractory materials are not so ideal from the view of current use effect. According to the effect of these wear resistant refractory materials, we provided a detailed analysis of the performance and cost for them (Yu et al., 2000).

The phosphate-bonded brick is a type of unburned brick with heat treatment at low temperature (500°C) ,which is used in a range of 1200~1600°C. It has been used in cement kiln for years and phosphate-bonded brick and castable were used as the early design materials of CFB boiler. Because the CFB boiler operates in range of 850~900°C, the refractory materials' physical property is instability and its abrasion resistance cannot fully get developed. The phosphate-bonded castable has the same physical and chemical properties as the phosphates bricks. The difference is that its construction is more complex and restricted by environmental. The phosphate-bonded castable will be easily desquamated when contacting water unless the furnace is baked soon after castable is casted(Jiao and Zhang, 2002). Although the phosphate castable is not so ideal when used on CFB boiler, it has a certain price advantage.

The carborundum products have good abrasion resistance and better thermal shock resistance when used in a high temperature no hold on fire non-oxidative atmosphere. When sintered at a certain temperature, they will form a glaze layer for the little oxidation atmosphere during the process of combustion in the CFB boiler. Some literatures point out that it is forbidden to use carborundum refractory materials in CFB boiler in U.S.A and the price is rather high.

The varieties of corundum products are white corundum, high-alumina corundum (sub-white corundum) and brown corundum. The main property of corundum is good refractoriness, high bulk density and good abrasion resistance, but difficulties are brought in operating the CFB boiler for its bad thermal shock resistance. The corundum castable usually gets collapsed because the fire-damped and fire-developed phenomenon appears more and the temperature changed frequently in the operation of CFB boiler, which has shortened the lifespan of the refractory materials. The other reason is that the temperature is too low for the refractory to reach its sinter temperature and its abrasion resistance cannot fully get developed (Xie et al., 2005, Feng and Liu, 2001).

The above several refractory materials used in CFB boiler are representative in china. According to the using status of most users, there are many different reactions because the varieties of refractory materials chosen by the boiler manufacturers and design institutes have no unified standards. There is a little high abrasion resistance refractory material that has the same period of maintenance and operation with the furnace and brings good economy value and social benefits. The refractory materials used in the early 35t/h, 75t/h CFB boiler in China basically refer to those of related industry (such as metallurgy and petrochemical industry). The refractory materials used in CFB boiler require good abrasion resistance in high temperature and thermal shock resistance, which is different from that of high refractoriness and leaching residue of the refractory materials used in metallurgy and petrochemical industry. The abrasion resistance refractory materials and insulation sealed materials should be layered in construction with whole cementation viz. heavy and lightweight castable, shaped and unshaped refractory castable support. Refractory materials with different production process and construction mode should comply with the same technical standard (He et al., 2000). As the introduction of technology of foreign CFB boilers, according to the refractory materials requirements of foreign company, some domestic manufacturers implement the relevant technical requirements, supplement and improve the criterion system of refractory materials of domestic CFB boilers.

RESEARCH ON NEW TYPE ABRASION RESISTANT REFRACTORY MATERIALS

The abrasion problem has gradually become a key factor to restrict the rapid development as promotion of the CFBB. The abrasion problem for heating furnaces and anti-wear refractory materials is inevitable decided by CFBB characteristics and abrasion will occur as long as boiler operation and materials circulation. For eliminating this development bottleneck of the CFB boiler, several new type abrasion resistant refractory materials with excellent characteristics are required to improve the current situation and lower the abrasion degree to minimum.

ABRASION RESISTANT COATING

Abrasion resistant coating used on the metallic surfaces

The coating can be sprayed or manually brushed to the surface of metal, with the permissible thickness of 0 to 2 mm. The product would be used with the characteristics of good high-temperature abrasion resistance, better corrosion resistance as well as high absorbability, fine stability of thermal shock and seldom creation of crack and abscission when integrated with the surface of metal. It can prevent the water screen tube and overheated tube from being wore.

Repairing coating used on the surface of abrasion resistant material

The coating can be sprayed or manually brushed to the surface of castable, with the permissible thickness of 5 to 30 mm. The product can be used for the abrasion resistant liner hot-repair and prevent the vessel wall from being wore..

GUNNING MIX

The efficiency of the execution of works will be improved greatly by gunning mix, which saves 70% time compared with that of casting and ramming construction and the intensity of labour is alleviated greatly. There are two kinds of gunning ways at present.

Semi-dry gunning

The basic technological process is that put the pre-mixed dry material directly into the injecting machine, and then transport it to the ejection gun through high-pressure air and finally eject it out with water injected at the head of the ejection gun. This method often has a high rebounding probability with approximately 15%~30%, and much dust. The final effect of the liner is fairly good. This method should be used for electrical insulation gunning refractory materials.

New wet gunning

There is no application of this kind of technology at present in China because of the confine of injecting machines. The basic technological process is that stir the gunning refractory materials mixed with water evenly in the efficient mixer and transport them to the wet-injecting machine (piston pump style). Then the gunning refractory materials are transported to the ejection gun by piston pump and it is mixed with coagulant in the gun head area from which the gunning refractory materials are ejected out by high-pressure air. The molding effect of new wet gunning is similar with that of vibrating cast and the rebounding probability is relatively low and there is no dust, which is suitable for the construction of electrical abrasion resistance gunning refractory materials (Xie et al., 2006).

NEW REPAIRING REFRACTORY MATERIALS

The abrasion resistant refractory materials in the easy-abrasion area will be inspected, repaired and replaced in order to ensure a safe and economic operation of a boiler.

New abrasion resistant plastic refractory material for face-up construction

The plastic refractory material has very good performance of adhesion. It is easily constructed by facing up and has good abrasion resistance. It can be directly mixed with water and does not need to set up molders and can be rammed directly to top area.

High performance billet shape plastic refractory material

This type of plastic refractory has very good performance of adhesion and abrasion resistance. When produced, it is cut into billet shape by extruding facilities and then pack it with vacuum package. The storage life can be 4~6 months long. It can be directly used without compulsory mixing again and any steel templates and molds. It can be directly daubed or rammed in repairing area to repair any irregular easy- abrasion area. The construction period can also be shortened by lighting the fire immediately and heating the plastic refractory materials up during the operation of the boiler without firing in addition

High performance billet shape plastic refractory material is particularly applicable to the temporary or short-term maintenance of CFB boilers or other thermal kilns especially in the unexpected, temporary and partly maintenance between overhaul periods. It improves the operational economical efficiency of the boiler or other thermal equipments and reduces the loss.

The above new abrasion resistant refractory material is one of the development directions for the anti-wear technology of CFB boilers and further research and improvement are still on. If all the excellent performance of these new abrasion resistance refractory materials can be realized, the abrasion status of CFB boilers will be much improved and operational period will be extended.

CONCLUDING REMARKS

Trace the form of the boiler structure, from the initial drum polishing lathe BFBB to the current high-speed CFBB, great changes have been taken place in furnace wall structure from the heavy furnace wall to

the membrane wall (Wang, 2000). The using proportion of unshaped refractory material has been improved a lot and unshaped refractory material has replaced the firebrick lining in many parts. Although now there is a dispute in terms of the designing and using of shaped and unshaped refractory materials, it can be seen from these accidents that are brickwork deformation and collapsing soon after some boiler operation, that large-area vertical wall used masonry firebrick lining has its drawbacks, because of different heating curve and the bulk effect of drag hook and lining, leading to deformation of furnace wall, even the collapse of the entire wall surface. From view of the future, unshaped refractory material will be greatly improved in the technical and construction methods, having the capacity to compete with brick lining structure. In the material, it has achieved some results that some artificially synthesized and double firing materials also applied to the wearable castable of CFBB, such as the synthesis of homogeneous materials, mullite, etc. High-quality synthetic material and double firing material will be one of the directions of development for CFBB abrasion resistant refractory material (Li et al., 2004).

At the same time, in accordance with concepts of sustainable development and recycling economy, the wear proof refractory material of CFBB will be developed oriented to green- refractory towards direction of easy construction, low density, energy-saving, and long wear-resistant life.

REFERENCES

Feng, Y. C., Liu, Z. J.: Industrial Furnace.**23** (**1**) (2001), pp. 48-50.

He, X. L., Li, J., Tian, Q. X. et al.: Refractory Material.**34** (**4**) (2000), pp.222-223.

Li, Y. J., Feng, Y. S., Zang, L. Y.: The Proceeding of Nationwide Refractory Comprehensive Academic Annual Conference, Anshan (2004), pp.220-226.

Jiao, W. J., Zhang, L. C.: Industrial Boiler.(**4**)(2002), pp.39-40

Song, Y. P., Huang, F. Q., Li, G. B. (2005): Modern Ship Machine Maintenance Technology.

Wang, X. Y.: Henan Chemical Industry. (**12**)(2000), pp.39-40.

Xie, J. H. et al.: The Proceeding of Nationwide Electric Power Industry CFB Technology Communication Service Network. 2006, pp.390-394.

Xie, Q. Q., Wu, Z. J., Yang, F.T.: Shandong Machinery. (**1**)(2005), pp.60-62.

Yu, L., Sun, Y. L., Gong, Z. C. et al.: Generating Equipment. (**1**) (2000), pp.29-32.

COMPARION OF MERCURY EMISSIONS BETWEEN CIRCULATING FLUIDIZED BED BOILER AND PULVERIZED COAL BOILER

Y. J. Wang, Y. F. Duan*, C. S. Zhao

Thermal-energy Engineering Research Institute, Southeast University, Nanjing, 210096, China

Abstract: Mercury emissions between a circulating fluidized bed (CFB) utility boiler and two pulverized coal (PC) boilers equipped with electrostatic precipitators (ESP) were in situ measured and compared. The standard Ontario Hydro Method (OHM) was used to sample the flue gas before and after the ESP. Various mercury speciations such as Hg^0, Hg^{2+} and Hg^P in flue gas and total mercury in fly ashes were analyzed. The results showed that the mercury removal rate of the CFB boiler is nearly 100%; the mercury emission in stack is only 0.028 g/h. However, the mercury removal rates of the two PC boilers are 27.56% and 33.59% respectively, the mercury emissions in stack are 0.80 and 51.78 g/h respectively. It concluded that components of the ESP fly ashes especially their unburnt carbons have remarkable influence on mercury capture. Pore configurations of fine fly ash particles have non-ignored impacts on mercury emissions.

Keywords: circulating fluidized bed boiler, pulverized coal boiler, mercury emission, comparison

INTRODUCTION

Mercury is one of the most volatile trace elements in coal combustion. US EPA submitted a report to USA Congress in 1997, and also pointed out 33% of mercury emissions, induced by human beings, was from coal-fired power stations (Grant, 1997). The average mercury content of Chinese coals was about 0.22 mg/kg. From 1978 to 1995 the total mercury emissions in China reached 2493.8 tons with an average increasing rate of 4.8% per year during the process of coal combustion (Wang, 1999). Mercury emissions from coal combustion increased from 202 tons in 1995 to 257 tons in 2003 at an average annual rate of 3.0%. Among all of the coal consumption sectors, the mercury emissions growth of the power sectors was the largest up by 5.9% annually (Wu, 2006). Mercury emissions of coal-fired power plants, occupying 33.6% in China, were the second largest from coal combustion in China (Streets, 2005).

In order to effectively control mercury emitted from coal-fired power stations, many countries started to research the mercury emissions from various coal-fired power plants. So, the mercury content in the flue gas and solid samples were tested firstly in the power plant consisting of SCR, ESP, FF, and wet FGD. US EPA and EPRI had measured many kinds of electric coal-fired power plants such as pulverized coal power plants, circulating fluidized bed utility power plants, integrated gasification combined-cycle plants and so on. EPA's (1998) previous estimates of emission modification factors for pulverized coal (pc)-fired furnaces ranged overall from 41% to 94% and were lower for units equipped with NO_x controls. WFGD systems are installed on 151 U.S. power plants. Though testing, it was obtained that about 90% of the oxidized gaseous was removed by WFGD, and Hg^0 was not removed and appeared to increase slightly in some tests (Senior, 2000). Mercury removals by FBC with fabric filtration ranged from 66% to 99% and averaged 86% (EPRI, 2000). Extensive measurements by Meij (2006) at Dutch coal-fired power stations over a period of 25 years indicated that the average mercury percentages by cold side ESP, cold side ESP + wet FGD, and cold side ESP + wet FGD + SCR was 50%, 75% and 90% respectively. Yang et al. (2007) researched the mercury speciation and emission in a selected 220 MW pulverized-coal boiler system. Chen et al. (2007) studied that mercury could be oxidized while the flue gas passed through ESP/FF.

This paper reported that the full-scale field tests measurement results of mercury based on Ontario Hydro Method (OHM), which was carried out in two pulverized-coal boiler systems and one circulating fluidized bed utility boiler. The characteristics of mercury emission by two combustion system were investigated. Therefore some difference between two combustion system was obtained, and the reason why induced the distinctness was found out.

EXPERIMENTAL

Sampling

The Ontario Hydro Method (OHM) was used to take the flue gas samples, which was the standard method of measuring and speciating mercury in flue gas. In order to collect the representative samples, the isokinetic sampling was conducted to collect sufficient particulate matters and flue gas. Sampling gas went through a

* The corresponding author: yfduan@seu.edu.cn

probe/filter system maintained at 120 °C or the flue gas temperature. Then the sample flowed through a series of impingers, which immerged into an ice bath. Particle-bound mercury was collected in the front tip of the sampling probe. The first three impingers containing 1 N potassium chloride (KCl) solution were connected to absorb oxidized mercury (Hg^{2+}). The fourth impinger containing acidified hydrogen peroxide (H_2O_2) was used to absorb elemental mercury, and elemental mercury was mainly captured in the fifth, sixth and seventh impingers which contained the solutions of acidified potassium permanganate ($KMnO_4$). In addition, the eighth impinger containing silica gel was provided to ensure that the flue gas was thoroughly dried-up before it left the impinger train.

Testing locations

The results discussed in this paper were obtained from the tested selected power stations with pulverized coal-fired boiler systems in China. These boilers in commercial plants were operated normally during testing. Tab. 1 listed some information of the tested coal-fired power plants. The boiler loads ranged from 135 MW to 600 MW, and it could basically represent the overall structure of our current coal-fired power plants. Three coal-fired power stations were installed with dust-removing equipment (electrostatic precipitator). A diagram of the boiler was shown in Fig. 1.

The mercury concentration in the flue gas was measured at two locations, namely before and after ESP in the duct leading to the stack. OHM was used to measure the mercury concentration at both locations. In order to get the samples accurately, the coal samples were collected in the air-coal powder pneumatic conveying duct immediately before burners. The bottom ash was sampled on belt of the slag-discharging machine, and the flue gas samples used the OHM system before and after FF/ESP respectively at the same time. The fly ashes in the FF/ESP were drawn by a vacuum pump.

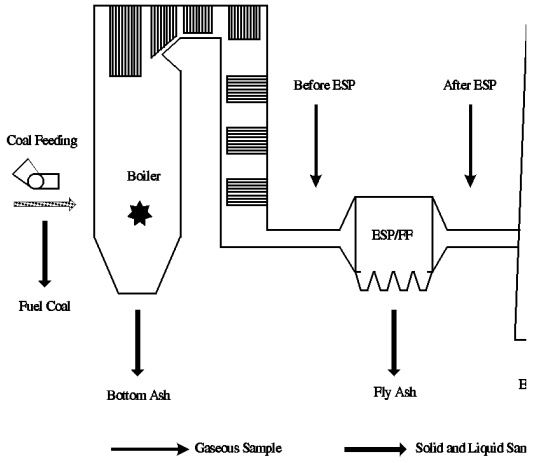

Fig.1 Sampling locations in the boiler with ESP system

Table 1 Information of three coal-fired power plants

Item	MW	The system of power plant	Fuel	Load (%)
Plant 1	220	PC+ESP	Shenhua bituminous	100
Plant 2	600	PC+ESP	Zhunger bituminous	90
Plant 3	135	CFB+ESP	Shenhua bituminous	70

RESULTS AND DISCUSSION

Coal analysis

Major components and proximate analyses in coal were showed in Tab.2. The coal burned in the plant 1 was special low sulfur coal, the content of sulfur in coal was lower than 0.50%. The coal burned in the plant 2 was low sulfur coal; the content of sulfur of coal in the plant 2 was between 0.50% and 0.90%. The coal used in the plant 3 was middle and high sulfur coal ($1.51\% \leq S_{ad} \leq 3.00\%$) (GB 15224.2/T-2004). The content of mercury for coal in power plant 2 was highest, which was 0.433 $mg \cdot kg^{-1}$, and it was over than the average mercury content of Chinese coal, but the content of mercury for coal in other two power plants was less than the average mercury content. The content of mercury for coal in power plant 1 was least, which was only 0.011$mg \cdot kg^{-1}$. The content of mercury for coal in power plant 2 was near to the average mercury content. The chlorine concentration of coal was lower than 200 $mg \cdot kg^{-1}$ in the first two power stations, but which was more than 500 $mg \cdot kg^{-1}$ in plant 3.

Table 2 Major components and proximate analyses in coal

Item	C_{ad} *wt/%*	H_{ad} *wt/%*	N_{ad} *wt/%*	O_{ad} *wt/%*	S_{ad} *wt/%*	Cl_{ad} *mg/kg*	Hg_{ad} *mg/kg*	W_{ad} *wt/%*	A_{ad} *wt/%*	V_{ad} *wt/%*	FC_{ad} *wt/%*
Plant 1	68.25	4.54	1.36	9.84	0.37	154	0.011	8.05	7.59	30.82	53.55
Plant 2	46.01	3.09	1.21	9.58	0.52	198	0.209	3.18	36.41	24.47	35.95
Plant 3	61.92	2.95	0.66	0.65	1.68	515	0.407	1.79	29.55	24.75	43.91

Mercury speciation

Mercury speciation in flue gas, which were elemental mercury (Hg^0), gaseous oxidized mercury (Hg^{2+}) and particle-bound mercury (Hg^P), were tested by using the OH method. Mercury speciation distribution before and after ESP were shown in Fig.2.

There was a great difference of mercury speciation in pulverized coal boilers and circulating fluidized bed boiler flue gas. Mercury in the coal-fired boiler flue gas was mainly in the form of gaseous, the proportion of gaseous mercury was more than 90%. However, there was little Hg^P detected before and after ESP, thanks to OHM sampling error. There was no fly ash in filter containers, and it induced error in measurement of Hg^P in flue gas. At the same time, the particulate mercury held a higher part in the circulating fluidized bed boiler flue gas. This difference was mainly due to coal combustion caused by the different ways.

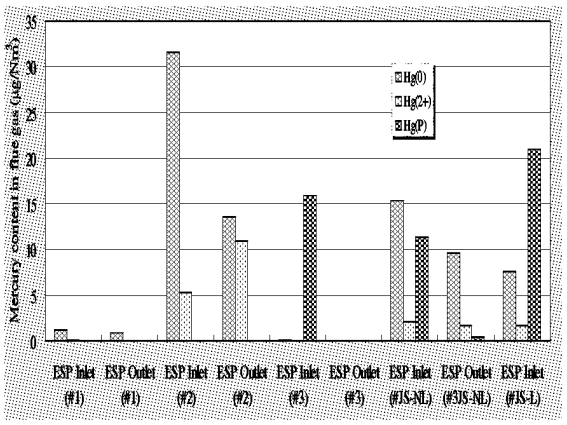

Fig.2 mercury speciation before and after ESP of the three power plants and Jiangshan (Zhou, 2004)

In the power station 1, mercury concentration, which was 1.31 μg/m^3 and 0.87 μg/m^3 before and after ESP, decreased 30% approximately when flue gas passed through ESP system. The proportion of elemental mercury in flue gas somewhat increased. The ratio of elemental mercury at the ESP inlet was 90.11%, but which added to 98.98% outlet ESP. However, the oxidized mercury was 8.17% and 2.02% in the inlet and outlet of ESP system, which reduced slightly. Mercury in flue gas was mostly in the form of Hg^0. There was a higher similitude between Plant 1 and 2, but there were a few differences in two power plants. The oxidized mercury had a higher increase, which were 5.32μg/m^3 and 10.97μg/m^3 before and after ESP. Meanwhile, the elemental mercury had higher decreases, which were 31.63 μg/m^3 and 13.57 μg/m^3 before and after ESP. The result showed that the fractional elemental mercury transformed to oxidized mercury, and the other was removed by ESP.

There was a little change of the concentration of oxidized and elemental mercury before and after ESP of plant 3. Nevertheless, higher portions of Hg^P were measured at the inlet of ESP, which was about 99%; on the other hand, at the outlet of the ESP the portion of Hg^P was none in the tested conditions at the plant 3. Fig. 2 showed the mercury speciation of Jiangsan plant synchronously. The results indicated that there was a higher comparability between Plant 3 and Jiangsan plant. There was higher portion of particulate mercury in the flue gas, no matter that there was limestone in the coal or not. Large amounts of Hg^P were removed by the use of the ESP. This effect could be explained by the fact that Hg compounds could be oxidized through the ESP because of increasing the contact time in the flue gas and fly ash or/and acidic gas components are able to enhance the mercury oxidation rate. From the Fig. 3, we could see that the unburnt carbon in the flue gas had a higher influence on the the share of Hg^P. When the unburnt carbon in the flue gas increased, the share of Hg^P increased. So, the residual carbon in fly ash on the removal of mercury was very favorable. The residual carbon content in ESP fly ash is higher, and the removal efficiency will be higher (Senior, 2005). Unburned carbon in fly ash has been shown to be an important factor in mercury capture by FF/ESP. Unburned carbon in fly ash had higher Hg adsorption capacity. The surface area of sorbents had a positive correlation with Hg adsorption capacity. Carbon-oxygen radicles C=O on unburnt carbon surface were beneficial to oxidation and chemical adsorption of Hg (Jurng, 2002). It was obtained that the porous structure and huge surface area of the unburned carbon could benefit the Hg adsorption in flue gas. Senior et al. (2004) carried out the experiments on the relationship between loss-on-ignition and mercury content in ESP fly ash and found that the removal efficiency also increased with unburned carbon increasing. Gale et al. (2008) investigated the correlation between flue-gas parameters and mercury oxidation and capture across a pilot-scale ESP in full-scale boilers. The mercury oxidation increased with the increase of UBC in the fly ash. UBC was the dominant parameter affecting the flue-gas Hg-oxidation state.

Mercury balance

During combustion, most of mercury in the coal is released, which is in the elemental mercury form. As the flue gas temperature decreases, some gaseous Hg^0 is transformed to gaseous Hg^{2+} and Hg^P. The gaseous Hg^0 is the most abundant and persistent form of mercury in the atmosphere. However, gaseous Hg^{2+} and Hg^P are more effectively captured by conventional air pollution control devices.

Based on the law of mass conservation, the mercury balance of coal-fired power plant was gained.

According to the overall balance, coal-fired power plant mercury is equal to sum of the total adsorption of mercury by various species of coal-fired power plant and the total mercury emitted to atmosphere. According to the equipment balance, mercury entering the pollution control device is equal to sum of the total mercury flowing out from it to the air and the mercury adsorbed onto the ashes discharging from it. From the Fig. 4, it could be conclude that the overall mercury mass balance was in the range of 79.4%-125.0%, which was accord with Takahisa Yokoyama's (2000) conclusions.

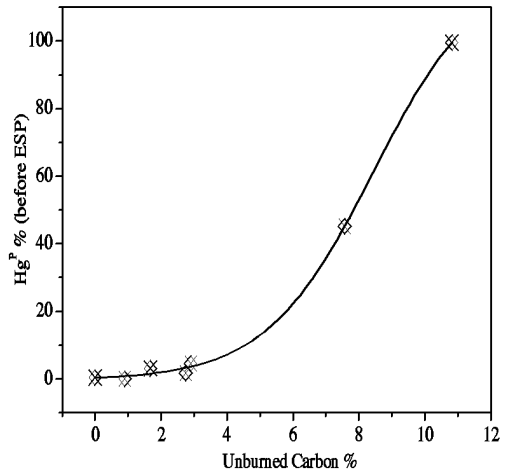

Fig. 3 The relationship between unburned carbon and the share of Hg^P in flue gas

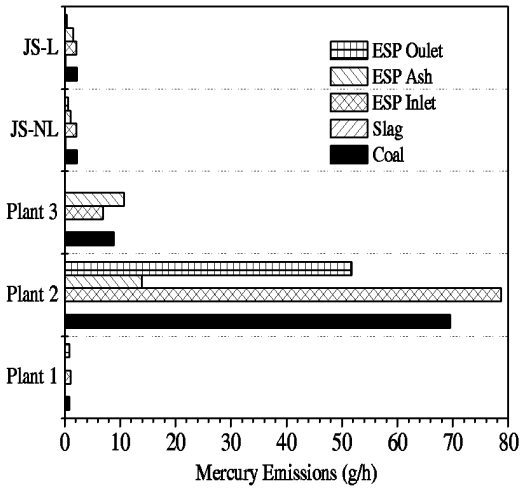

Fig. 4 Mercury mass balance of three power plants

Mercury removal

Mercury control by ESP was defined as follows:

$$\eta = \frac{Hg^T_{inlet} - Hg^T_{outlet}}{Hg^T_{inlet}} \quad (1)$$

Mercury removal rate was calculated by formula (1), and the results were shown in Fig.5. From the picture, it was clearly seen that the average mercury removal efficiencies of the PC+ESP in the test of two power plants was 33.56%, which was approach to the average mercury removal efficiency in the PC+ESP of USA's power plants, but it was lower about 17% than Japan and Netherlands's.

The average mercury removal efficiency of the CFB+ESP in the third power plant was 99.6% near by 100%. It was according to the ICR data (EPRI, 2000), but it was higher than Jiangsan plant. High mercury removals were attributed in part to mercury capture on the relatively high carbon content of the fly ash. From the Figle 3, it was clearly seen that the unburnt carbon in the fly ash of plant 3 was highest, which was advantaged to adsorb mercury in the flue gas. In general, the mercury removal efficiency of CFB+ESP was more than PC+ESP.

Mercury removal increased with the content of chlorine increasing (Fig.6). The chlorine content of the coal affected oxidation of Hg in the flue gas by homogeneous, heterogeneous and catalytic pathways. Chlorine was the most significant halogen in combustion systems as far as mercury chemistry was concerned. The primary Hg oxidation product in flue gas was believed to be $HgCl_2$, the species favored by equilibrium conditions. The gas-phase transformation pathway involved the oxidation of Hg^0 by atomic Cl. The concentration of Cl, in turn, depended on a complex series of gas-phase reactions involving O_2, water vapor, hydrocarbons, Cl compounds and S compounds. Because they could reacted with atomic Cl. Hg^0 was oxidized to HgCl by atomic Cl in flue gas firstly, and then oxidized to $HgCl_2$ (Yang, 2007). $HgCl_2$ was adsorbed by fly ash easily to form Hg^P, and it was removed by dust collector device.

Table 3 listed the average removals of gaseous mercury and mercury species for EPS. Symbol '-' represented the gaseous mercury was added, when it went across the ESP. In other word, the concentration of gaseous mercury in the outlet of ESP was higher than the inlet of ESP. From the table, it could be obtained that the gaseous elemental mercury decreased other than Lee 2003, when the flue gas got across the ESP, whereas the change of the gaseous oxidized mercury was complicated. The gaseous oxidized mercury reduced 83.6% in the Plant 1, but it added 106.1% in the Plant 2. The transformation of the gaseous oxidized mercury in Plant 2 was similar with the Lee's, although his data was lower than the Plant 2. The variety of the gaseous oxidized mercury in Plant 1 was similar with the ICR's, but the data the Plant 1 was far more than ICR's. The change of Hg^0 in two CFB+ESP was approximately quite, but the change of Hg^{2+} was not seen clearly.

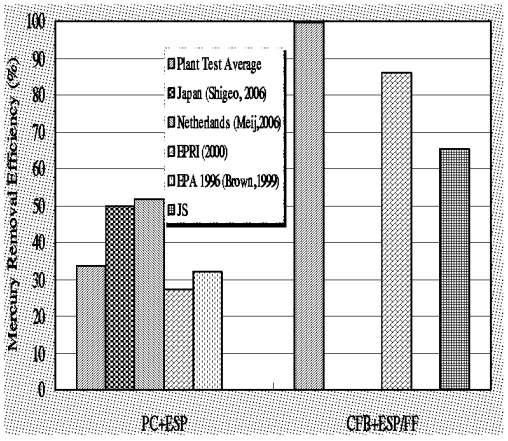

Fig. 5 Mercury removal Efficiency

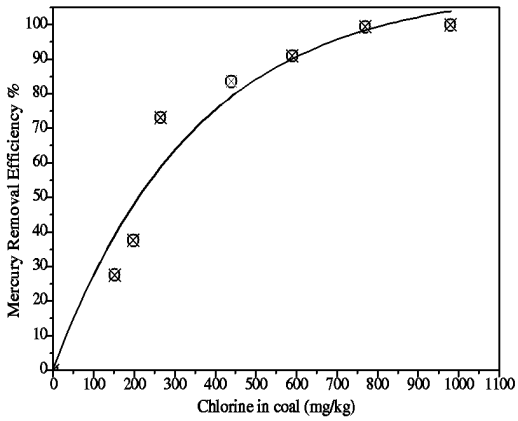

Fig. 6 The relationship between Chorine in coal and Mercury Removal Efficiency

Table 3 Average removals of gaseous mercury and mercury species for EPS

Item	System of power plant	Hg^{+2} decrease	Hg^{0} decrease
Plant 1	PC+ESP	83.6%	27.7%
Plant 2	PC+ESP	-106.1%	57.1%
US EPA(1999)	PC+ESP	9.4%	22.6%
Lee 2003(2006)	PC+ESP+WFGD	-74.2%	-0.2%
Lee 2004(2006)	PC+ESP+WFGD	-69.9%	26.0%
Plant 3	CFB+ESP	—	34.7%
JS-NL (Zhou et al., 2004)	CFB+ESP	20.1%	37.7%

CONCLUSIONS

Mercury in the flue gas mainly existed to in the form of gaseous mercury in the coal-fired power station, but which was mainly particulate mercury in CFB boiler. Generally, mercury was dissipative in bottom ash, which was enriched ESP ash.

Mercury in the flue gas of PC+ESP was mainly in the form of gaseous, the proportion of gaseous mercury was more than 90%. However, there was little Hg^{P} detected before and after ESP, thanks to no fly ash in filter containers. At the same time, the particulate mercury held a higher part in the circulating fluidized bed boiler flue gas. This difference was mainly due to coal combustion caused by the different ways.

The average mercury removal efficiencies of the PC+ESP in the test of two power plants were 33.56%. The average mercury removal efficiency of the CFB+ESP in the Plant 3 was 99.6%.

ACKNOWLEDGEMENTS

This sub-project was Joint-funded by the State Basic Research Development Program (973 Plan) of China (No. 2006CB200304).

REFERENCES

Brown, T.D., Smith, D.N., Hargis, R.A. and O'Dowd, W.J.: Journal of the Air & Waste Management Association. **7** (1999), pp 1-97.

Chen, L., Duan, Y.F., Zhuo, Y.Q., Yang, L.G., Zhang, L., Yang, X.H., Jiang, Y.M. and Xu, X.C.: Fuel. **86** (2007), pp. 603-610.

EPRI (2000), An Assessment of Mercury Emissions from U.S. Coal-Fired Power Plants.

Gale, T.K., Lani, B.W. and Offen, G.R.: Fuel Processing Technology. **89** (2008), pp. 139-151.

GB 15224.2/T-2004, Classification for quality of coal classification for sulphur content of coal.

Grant, E. (1997). Mercury Study Report to Congress Volume I: Executive Summary.

Jurng, J., Lee, T.G., Lee, G.W., Lee, S.J., Kim, B.H. and Seier, J.: Chemosphere **47** (2002), pp. 907-913.

Lee, S.J., Seo, Y.C., Jurng, J., Hong, J.H., Park, J.W., Hyun, J.E. and Lee, T.G.: Science of the Total Environment. **325** (2004), pp. 155-161.

Meij, R. and Winkel, H.: Science of the Total Environment. **368** (2006), pp. 393-396.

Shigeo Ito, Takahisa Yokoyama, Kazuo Asakura. Science of the Total Environment. **368** (2006), pp. 397-402

Senior, C., Bustard, C.J., Durham, M., Baldrey, K. and Michaud, D.: Fuel Processing Technology. **85**(2004), pp. 601-612.

Senior, C.L. and Johnson S.A.: Energy & Fuels. **19** (2005), pp. 859-863.
Senior, C.L., Helble, J.J. and Sarofim, A.F. (2000), Predicting the speciation of mercury emissions from coal-fired power plants, Proceedings of the Air Quality II: Mercury, Trace Elements, and Particulate Matter Conference.
Streets, D.G., Hao, J.M., Wu, Y., Jiang, J.K., Chan, M., H.Z. Tian, et al., Atmos. Environ. **39** (2005) 7789-7806.
Takahisa Yokoyama and Kazuo Asakura. The Science of the Total Environment. **259** (2000), pp. 97-103.
U.S. EPA (1998), A Study of Hazardous Air Pollutant Emissions from Electric Utility Steam Generating Units.
Wang, Q.C., Shen, W.G. and Ma, Z.W.: China Environmental Science. **19** (1999), pp. 318-321.
Wu, Y., Wang, S.X. and Streets, D.G.: Environ. Sci. Technol. **40** (2006), pp. 5312-5318.
Yang, X.H., Zhuo, Y.Q., Duan, Y.F., Chen, L., Yang, L.G., Zhang, L., Jiang, Y.M. and Xu, X.C.: Korean J. Chem. Eng. **24** (2007), pp. 711-715.
Zhou, J.S., Wu, X.J., Gao, H.L., Luo, Z.Y. and Cen, K.F., Thermal Power Generation. **1** (2004), pp. 72-75.

CO-COMBUSTION OF REFUSE DERIVED FUEL WITH ANTHRACITES IN A CFB BOILER

Dong-Won Kim, Jong-Min Lee, Jae-Sung Kim

Power Generation Lab., Korea Electric Power Research Institute, Daejeon 305-380, Korea

Abstract: Combustion of Refuse derived fuel (RDF) is considered as a priority solution to energy recovery from municipal solid waste (MSW). The co-combustion characteristics of anthracite coals with RDF were determined in the commercial scale Tonghae CFB Power Plant. As the feeding ratio of the RDF to the anthracites increased to 5%, temperature and pressure were not changed in comparison with firing only anthracites. The amount of the required air was reduced due to high O_2 content in RDF relative to the anthracites. The emissions of NOx, SOx, HCl and Dioxin were also measured. According to higher mixing ratio of the RDF to the anthracites, SOx, NOx emissions slightly decreased and HCl emissions increased, because RDF has relatively smaller S, N and higher Cl than the anthracites. Heavy metals of the fly ash and bottom ash and the dioxin emissions were far below Korean maximum permissible concentration level at incinerator. The results showed that it is of great use and technically possible to co-combustion of RDF with the anthracites by 5% in the form of fuel recovery and energy production in commercial scale CFB boiler.

Keywords: circulating fluidized bed (CFB), co-combustion, anthracite, refuse derived fuel (RDF), dioxin

INTRODUCTION

Recently, the interest in the effective fuel utilization has been increased since almost energy consumption in Korea is dependent on imported energy resources. Combustion of Refuse derived fuel (RDF) is considered as a priority solution to energy recovery from municipal solid waste (MSW) as well as to the environmental problem. The circulating fluidized bed combustion is known to the most efficient technology for accomplishing the combustion of alternative fuels. So, the co-combustion of coal and RDF in circulating fluidized bed has been a commercial operation for over 20 years, and the references to principles and applications are numerous and wide spread. However, few data are presented concerning the operation of large scale CFB-units and the problems encountered in industrial practice.

Korea Electric Power Corporation (KEPCO) constructed the 2×200MWe Tonghae CFB boilers in 1998 and 1999, respectively. The CFB boilers use Korean anthracite as a fuel without assistant fuel such as heavy oil although some facilities firing the anthracite use assistant oil due to the low combustion reactivity of the coal (Lee et al., 2001). However, the low reactivity of the anthracite had lower the combustion efficiency and had unstable the operating conditions of the CFB boiler. Also, the utilization of the CFB boiler has been gradually restricted because of the limitation of the production and supply of the anthracite and because of the high fuel cost of the anthracite.

A large number of researches have been accomplished to understand the effect on combustion system stability, the operational performance, the qualities of the ash and emission of pollutants etc. Hernandez et al.(2007) investigated three different RDFs combustion characteristics in two atmospheric fluidized bed combustors and found that the overall combustion efficiency of the system improved when secondary air jets were introduced into the system. Hupa(2005) reviewed the interaction of fuels in co-firing in FBC. It appeared that factors such as flue gas emission, fouling tendency or bed sintering tendency are seldom simple linear functions of the fuel mixture. Wan et al.(2008) studied the emissions during co-firing of RDF-5 with bituminous coal, paper sludge and waste tires in a commercial circulating fluidized bed co-generation boiler. The results indicated that potential problems of co-firing of RDF with coal are the corrosion of heat transfer tubes, the qualities of the ash, and the emission of pollutants. Kupka et al.(2008) investigated the ash deposit formation during co-firing of coal with RDF and found that 5% addition of RDF to the coal has substantially increased the deposition rate. There are a large number of researches about emission of HCl, organic compounds and dioxins in waste incineration using fluidized beds and influence of various inhibitors formation of dioxins in co-combustion (Ruokojarvi et al.(2004), Pandelova et al.(2006), Gulyurtlu et al.(2007) and Stnamore(2004)). These works clarified the emission mechanism of the flue gas, such as HCl, organic compounds and dioxins against various operation condition or RDF compositions. It has been also figured out that toxic emissions can be reduced by the help of various inhibitors suitable for fuels.

In this study, the co-combustion characteristics of anthracites (Korean and Vietnam coals) with RDF were

determined in the commercial scale Tonghae CFB Power Plant. Especially, we determined the special characteristics of co-combustion of based on the poor quality anthracite with rich volatile RDF, the combustion system stability and the qualities of the ash and emission of pollutants.

EXPERIMENTAL

The Tonghae thermal power plant CFB boiler was designed to fire Korean anthracite by Combustion Engineering, Inc. [ABB-CE, 1994]. The Tonghae CFB combustor is shown in Fig. 1. It consists of feeding parts of coal and limestone, PA, SA and FA supplier, main combustion part (furnace, cyclones, loopseal, FBHEs and FBAC), and convective backpass.

The furnace of the Tonghae CFB (19m(W)× 7m(L) ×32m(H)) has a rectangular footprint and is significantly wider than it is deep, incorporating as an aspect ratio of more than 2:1. As all fuel feed points are aligned on the furnace front wall, the rectangular geometry was chosen to allow for good fuel mixing. Limestone is injected with the fuel in the fuel feed chutes and it is also introduced in two injection ports along the rear wall. Flue gas and solid particles exit the furnace through three openings in the upper rear wall. Solids are returned to the furnace from the cyclones and external fluid bed heat exchangers (FBHE) via the lower front wall.

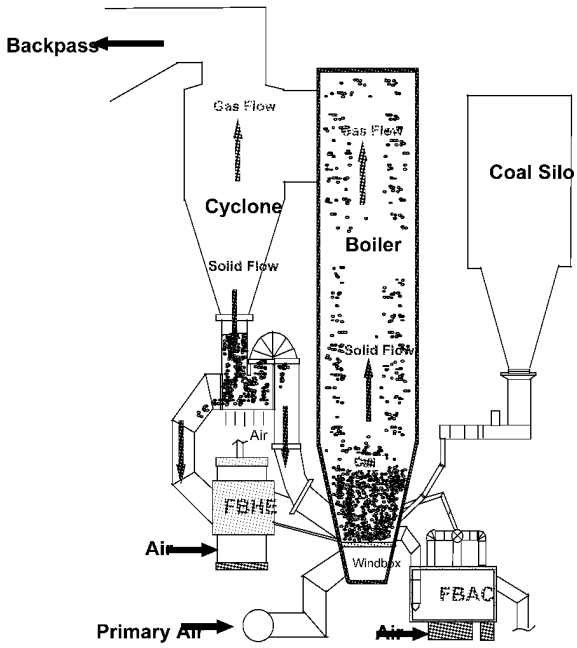

Fig. 1 Tonghae CFB Boiler Feature

Primary air is introduced to the furnace via the fluidization grate. T-style fluidizing nozzle patented by ABB-CE has relatively large openings to reduce the potential of plugging associated with many nozzle designs, while maintaining a pressure drop to preclude backsifting. Secondary air is introduced at the lower furnace along the front and rear walls. All secondary air nozzles are furnished with butterfly style dampers to maintain a steady secondary air supply-duct pressure. Secondary air is also introduced into four start-up burners.

Bottom ash is removed from the bottom of the furnace via two ash control valves (ACV). The bottom ash is introduced into a fluidized bed ash cooler (FBAC) which contains economizer and cooling water heat transfer surface. Heated fluidizing air is returned from the FBAC vents into the CFB combustor at four locations along the front wall. Most entrained particles from the flue gas are captured by three cyclone separators and are returned to the furnace, passed through the loopseals. The loopseals serve to create a pressure seal from positive pressure in the furnace to the negative pressure in the cyclone. This pressure seal prevents the flow of material back up the cyclone from the bottom of the furnace.

The Tonghae unit was designed to operate at 35% load without support fuel and at 30% load with minimal co-firing of the start up fuel oil. This stringent boiler turndown requirement, coupled with the difficulty to burn Korean anthracite, resulted in offering external fluid bed heat exchangers. At each of the loopseal, a stream of solid particles is diverged and introduced into FBHE. As the solid particles from the loopseal flow over the FBHE heat transfer surfaces, the ash is cooled. The ash is then returned to the furnace. By placing superheat and reheat heat transfer surface in separate FBHEs into which solids can be introduced in a controlled fashion, optimum turn down control is accomplished. The total unit heat duty is distributed in a fairly even fashion among the furnace, backpass, and FBHEs. The convective backpass contains the first stages of superheater and reheater heat transfer surfaces. The convective back pass is steam cooled as used on typical utility boiler designs. A typical air-through, gas-over tubular air heater is located below the convective backpass economizer.

The analyses of the anthracites (Korean and Vietnam coals) and RDF used in this study are shown in Table 1. Korean and Vietnam anthracites have comparatively rich ash and low volatile component, whereas RDF has comparatively rich volatile component and high ash. Limestone used as a sorbent for desulfurization, contains 90% of $CaCO_3$ and 4.2% of $MgCO_3$. The particle size of limestone is smaller than 1.0mm (<0.7mm-95%, <0.5mm-90%).

Table 1 Analyses of Korean and Vietnam anthracites and RDF used for co-combustion

Property	Korean Anthracite	Vietnam Anthracite	Refuse Derived Fuel
Proximate analysis (wt.%)			
Moisture	3.3	1.7	1.58
Volatiles matter	4	9.92	62.28
Fixed carbon	53.7	51.35	5.11
Ash	39	37.03	31.03
Ultimate analysis (wt.%)			
Carbon	54.7	57.47	39.15
Hydrogen	0.3	2.45	5.13
Oxygen	3.8	0.97	24.01
Nitrogen	0.2	0.79	0.11
Sulfur	0.6	0.45	0.08
Ash	40.4	37.87	31.52
Chlorine	-	-	0.79
Heating value* (kcal/kg)	4,599	4,918	4,182

* as received basis

The co-combustion test in the Tonghae CFB boiler was carried out at a constant power generation condition in which only the coal flow rate and the ratio of RDF to anthracite were varied. The experimental conditions in this study are shown in Table 2. The ratio of RDF to anthracite is based on mass.

Table 2 Operating condition for co-combustion test

RDF Co-firing ratio (%)	0	1	1	3	5
Power generation (MWe)	195.1	199.1	196.7	199.2	200.4
Korean Anthracite (ton/h)	44.8	52.7	61.7	68.8	65.6
Vietnam Anthracite (ton/h)	44.9	46.7	39.4	33.9	32.3
RDF (ton/day)	0	20	20	60	100
Total air flow (PA + SA)	143	139.2	141.7	141.4	140.6

RESULTS AND DISCUSSION

Combustion performance

The co-combustion test in the Tonghae CFB boiler was carried out at a constant power generation condition. As the feeding ratio of the RDF to the anthracites increased to 5%, operation conditions such as temperatures and pressures of the major parts in the boiler were changed insignificantly in comparison with firing only anthracite coals. Fig 2 shows the effect on total air flow rate according to the feeding ratio of the RDF to the anthracites. As the RDF co-firing ratio increased, the amount of the required air decreased slightly. Due to high O_2 content in RDF relative to the anthracite, the less amount of air may be required.

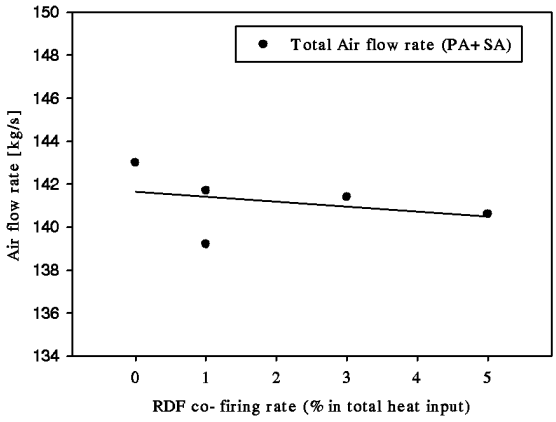

Fig. 2 Effect of RDF co-firing ratio on the amount of required air

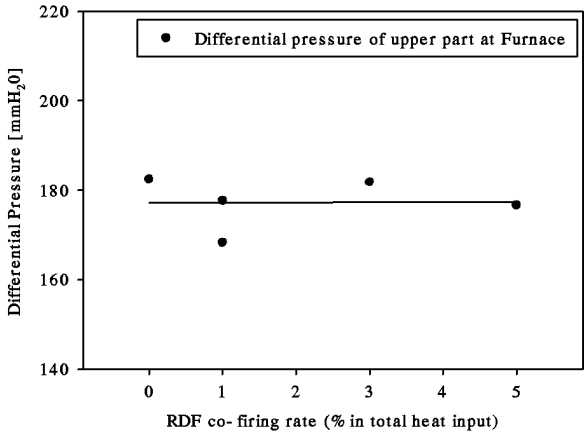

Fig. 3 Effect of RDF co-firing ratio on differential pressure of upper part at furnace

As shown Fig. 3, differential pressure of upper part at furnace did not change appreciably. Though the size of RDF (15~50mm) is bigger than that of anthracites (<6mm), decrease of the differential pressure of upper part at the furnace resulting in instability on operation condition did not happen. The reason is that RDF which has much volatile content and rapid combustion reactivity in comparison with firing only anthracites and participates in the role of fluidizing medium by being cracked.

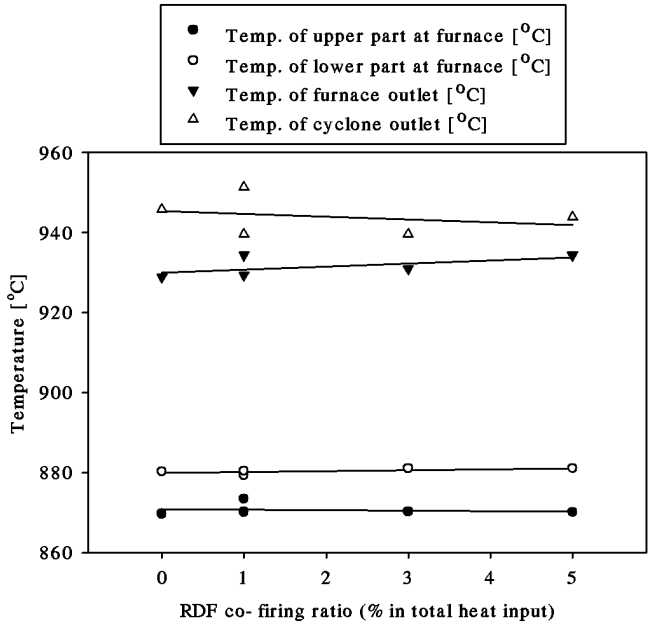

Fig. 4 Effect of RDF co-firing ratio on the temperature of parts of furnace

The change of the temperature distribution makes it possible to analyze the condition of combustibility of the co-combustion of RDF and the anthracites. Figure 4 shows the temperature distribution with the ratio of RDF during co-combustion and the all data used in the figure were obtained by averaging data for 24 hours for each co-combustion case. As shown in Fig. 4, it can be observed that temperature of furnace outlet became getting higher and temperature of lower part at the furnace increased slightly. The increase of temperature at these parts can be caused by the rapid combustion of RDF in the lower part of the furnace. When compared with anthracites, RDF used for the co-combustion has much volatile content and rapid combustion reactivity. So, most of the RDF pyrolysis and char-combustion occurred at the lower part of the combustor. The increase of temperature at furnace outlet can be explained by combustion of volatile matter at furnace outlet. As this co-combustion test was carried out at a constant supply of secondary air, the insufficient mixing with excess air for combustion of volatile matter. By changing the flow pattern at furnace outlet, combustion of the unburned volatile matter occurred. This temperature distribution is well-explained by the experience of only anthracites firing at Tonghae CFB boiler (Lee et al., 2000). The temperature of cyclone outlet at the Tonghae CFB was usually the highest due to the post-combustion of the anthracites. As the RDF co-firing ratio increased, the

temperature of cyclone outlet decreased due to the reduction of post-combustion of anthracites by substituting RDF for anthracites. This temperature reduction makes it possible to extend the capability of controlling the operation of the CFB boiler in the point of the characteristics of Tonghae CFB boiler limited by the temperatures of the cyclones outlets.

Influence of heavy metal in the fly ash and bottom ash

The heavy metal in the fly ash and bottom ash after RDF co-firing with the anthracites were measured by elution of the ash for examining the effect of RDF co-firing. As shown Table 3, the eluting amount of heavy metals of the fly ash and bottom ash was far below Korean maximum permissible concentration level. As the ratio of RDF co-firing is under 5%, the effect on the heavy metal in the RDF is insignificant.

Table 3 The eluting amount of heavy metals of the fly ash and bottom ash

Ratio of RDF co-firing	0 %		1 %		3 %		5 %		Korean permissible concentration level
	F/A	B/A	F/A	B/A	F/A	B/A	F/A	B/A	
Pb (mg/l)	ND	ND	0.01	0.02	0.01	ND	0.02	ND	3
Cu (mg/l)	ND	ND	0.028	0.036	0.022	0.023	0.021	0.021	1
As (mg/l)	ND	ND	0.017	0.004	0.008	0.005	0.01	0.012	1.5
Hg (mg/l)	ND	ND	ND	ND	ND	ND	ND	ND	0.005
Cd (mg/l)	ND	ND	ND	ND	ND	ND	ND	ND	0.3
Cr^{6+} (mg/l)	ND	ND	0.09	ND	0.11	ND	0.16	ND	1.5
CN^- (mg/l)	ND	ND	ND	ND	ND	ND	ND	ND	1.5

Influence of performance on the electrostatic precipitator

Figure 5 shows the effect of the RDF co-firing ratio on the output voltage of stages on the EP(electrostatic precipitator). As the feeding ratio of the RDF to the anthracite was increased to 5%, output voltages of 1, 2 stages of EP decreased significantly. Output voltage drops of 1, 2 stages are derived from the voltage drop between discharge electrode and collecting electrode by changing the dust resistivity, composition of flue gas. In general, EP has the best performance at the value of dust resistivity from 10^4 to 10^{11} ($\Omega \cdot$ cm). In this experiment, it is supposed that the dust resistivity increases by the composition of RDF ash and the reduction of moisture contents in the flue, because RDF has relatively lower moisture content than anthracites and RDF ash has relatively larger SiO_2, CaO and MgO to the anthracites ash.

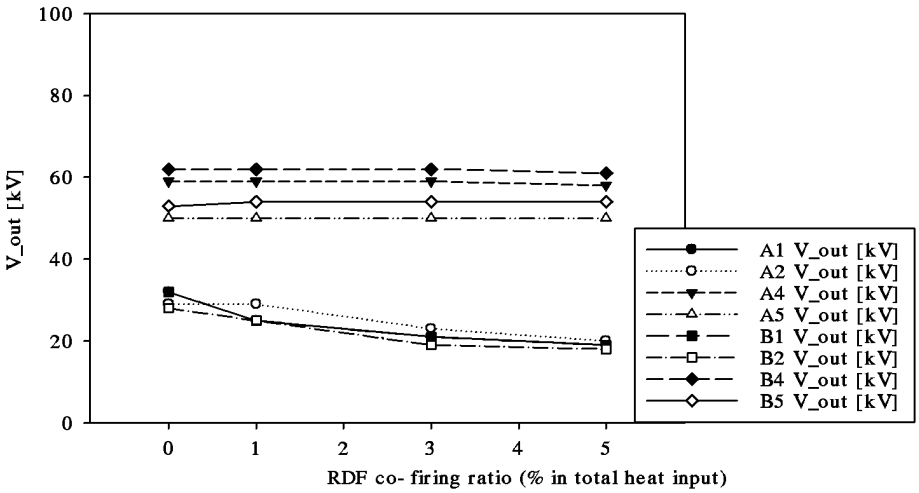

Fig. 5 Effect of RDF co-firing ratio on output voltage at the each stage of EP

But in spite of output voltage drop, as the feeding ratio of the RDF to the anthracite increased to 5%, there is no problem of the performance on the EP. As shown Fig. 6, the amount of dust which is measured in the stack increased slightly, but that is not different at the usual operation condition (3.3 ~ 4.3mg/m^3).

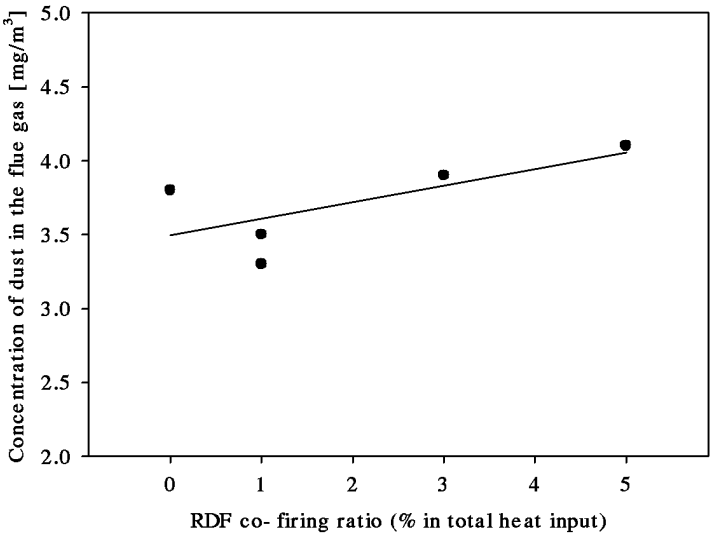

Fig. 6 Effect of RDF co-firing ratio on concentration of dust in the flue gas

Behavior of SO_x and NO_x in the Flue Gas

In general, Fig. 7 shows the effect of the RDF co-firing ration on the flue gas. Although the feeding rate of limestone decreased, the trend of SO_x emission in the flue gas was not changed as the RDF co-firing ratio increased. In the case of NO_x, its density in the flue gas slightly deceased as the RDF co-firing ratio increased. This result indicates that a portion of the anthracites was replaced by RDF which has relatively small S and N to the anthracites.

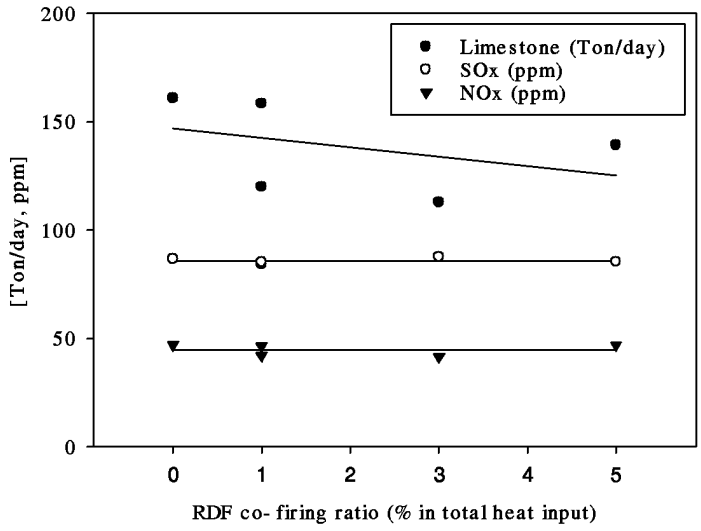

Fig. 7 Effect of RDF co-firing ratio on the flue gas

Behavior of HCl in the Flue Gas

Chlorine compounds in the RDF are very important factors for HCl generation as well as dioxin synthesis. It is known that HCl causes the air pollution and corrosion of equipments. HCl formation is a complex process, involving the availability of chlorine, a hydrogen source, and the competitive affinity of the testes metals. Generally, the reactive affinity between hydrogen and chlorine is stronger than that between the heavy metals and chlorine (Chiang. et al., 2008). Chlorinated material in the RDF such as PVC products(polyvinyl chloride) and NaCl release Cl^- at high temperature combustion, which forms HCl with hydrogen ions and chlorinated organics like CPs and CBs by incomplete combustion (Wey et al., 2007).

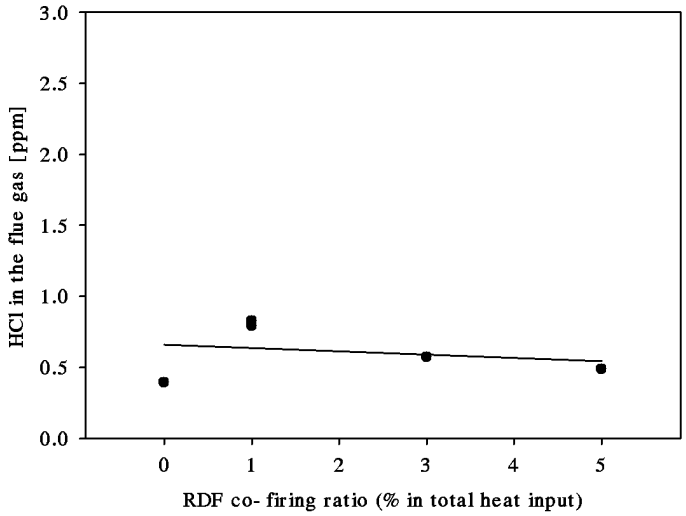

Fig. 8 The density of HCl in the flue gas against the ratio of the RDF in the fuel

As shown in Fig. 8, the amount of HCl in the flue gas was not affected by increasing the total amount of chlorine according to the ratio of the RDF to the anthracites in coal fed into the CFB boiler. The reason of no correlation between HCl in the flue gas and the total amount of chlorine compounds in the RDF is not only the different content of chlorine in the RDF at the absorption of HCl by added limestone which is used for the removal of sulfur oxide and sulfur dioxide in the conventional circulating fluidized bed boiler. The absorption of HCl with limestone can be described according to the following reactions:

$$CaCO_3(s) \rightarrow CaO + CO_2 \quad (1)$$

$$CaO + 2HCl \rightarrow CaCl_2 + H_2O \quad (2)$$

In this research, the movement of chlorine in the CFB boiler was investigated by calculating the total amount of chlorine in the fuel and measuring the density of chlorine in the fly ash and bottom ash as well as in the flue gas. Figure 9 shows that the amount of chlorine in the fuel, in the ash and in the flue gas according to the ratio of the RDF to the Korean anthracite in coal fed into the CFB reactor. This result indicated that the HCl formation potential is varied from 0.01 to 0.1 in proportion to the combustion condition. In General, the HCl removal by limestone is a complex process affected by flue gas temperature, absorbent quality, particle size and gas atmosphere on the absorption reaction (Hupa, 2005).

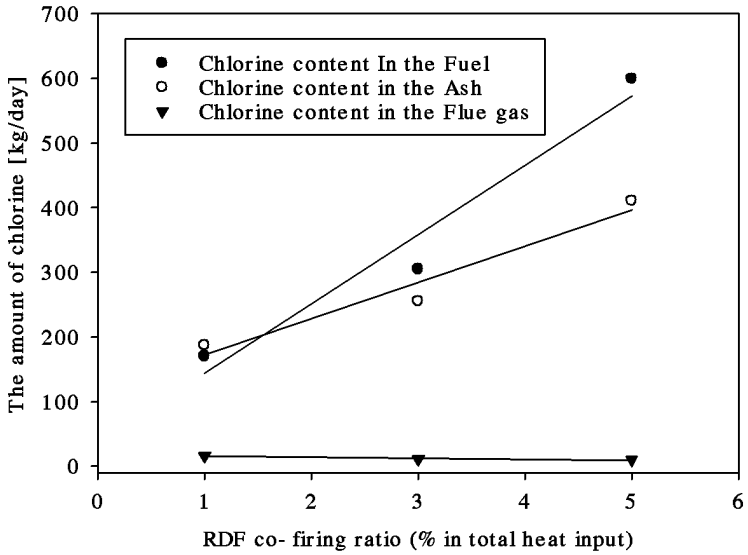

Fig. 9 The movement of chlorine in the CFB Boiler

Behavior of dioxin in the flue gas

The emissions of dioxins could be considerable when fuels with high chlorine content are used, particularly in fluidized beds due to constricts to use temperatures in the range 800~900℃ for other considerations. Dioxins generation was considered form two mechanisms. One was the de novo synthesis, which was the catalytic reaction by the metal components in the ash dust and unburned carbon. The other was precursor formation, which was the decomposition and recomposition of precursor, such as chlorophenol and chlorobenzene. Usually, both synthesis and formation proceed at a bed, boiler or bag filter at the temperature of 573K to 773K (Kobyashi et al., 2005). In this study, the level of dioxin was measured at the stack. Fig. 10 shows the level of dioxin with the ratio of the RDF. As shown Figure. 10, dioxin emissions were far below Korean maximum permissible concentration level of incinerator (0.1ng-TEQ/Sm^3). Also, there was no correlation between dioxin in the flue gas and the ratio of RDF co-firing. The reason is that chlorine was absorbed by added limestone which is used for the removal of sulfur oxide and sulfur dioxide in the conventional circulating fluidized bed boiler. This result explained -well that co-combustion of RDF with Korean and Vietnam anthracites by 5% is technically safe in the aspect of environmental standard on dioxin.

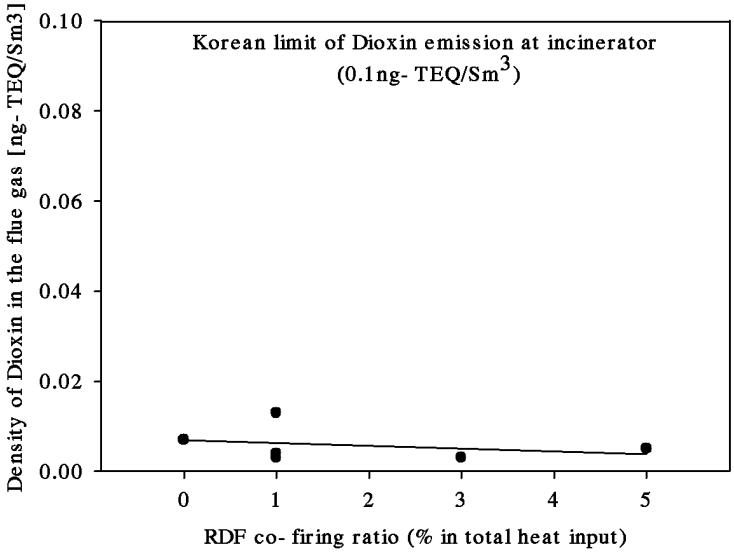

Fig. 10 The level of Dioxin in the flue gas against the ratio of the RDF in the fuel

CONCLUSIONS

Combustion tests were carried out using three different ratio of RDF co-firing in the conventional CFB boiler. Combustion performance, flue gas composition and ash contents were studied for the main conclusions obtained from this experimental test are as follows:

(1) To understand the characteristics of the RDF co-firing with anthracites, temperature and differential pressure at each parts of boiler were measured. Temperature and pressure were little variation in comparison with firing only anthracites. The temperature reduction of the furnace outlets can be caused by the rapid combustion of RDF in the lower part of the furnace. Especially, the amount of the required air was reduced due to high O_2 content in RDF relative to the anthracites.

(2) The emissions of NO_x, SO_x, HCl were studied. According to higher mixing ratio of the RDF to the anthracite, SOx, NOx emissions slightly decreased and HCl emissions increased, because part of the coal was replaced by RDF which has relatively small S, N and high Cl to the anthracites.

(3) The eluting amount of heavy metals of the fly ash and bottom ash was far below Korean maximum permissible concentration level. As the ratio of RDF co-firing is under 5%, the effect on the heavy metal in the RDF is insignificant.

(4) The level of dioxin at RDF co-firing by 5% was far below the Korean maximum permissible concentration level at incinerator (0.1ng-TEQ/Sm^3). Also there was no correlation between dioxin in the flue gas and the ratio of RDF co-firing, because chlorine compounds which are very important factors for dioxin synthesis in the RDF were absorbed by added limestone which is used for the removal of sulfur dioxide.

(5) It is of great use and technically possible to co-combustion of RDF with Korean and Vietnam anthracites by 5% in the form of fuel recovery and energy production in commercial scale CFB boiler.

ACKNOWLEDGEMENTS

The authors are grateful for the financial support from the EWP(Korea East West Power) and for the support from Tonghae thermal power plant.

REFERENCES

Chiang, K. Y., Jih, J. C., Lin, K. L.: Hazardous Materials. J. **157** (2008), pp.170-178.
Gulyurtlu, I., Crujeira, A. T., Abelha, P. and Cabrita, I.: Fuel **86** (2007), pp.2090-2100.
Hupa, M.: fuel **84** (2005), pp.1312-1319.
Hernandez, F. D., Ryu, C. K., Sharifi, V. N. and Swithenbank, J.: Chem. Eng. Sci. **62** (2007), pp.627-635.
Kobyashi, N., Itaya, Y, Piao, G., Mori, S., Kondo, M., Hamai, M. and Yamaguchi, M.: Powder Tech. **151** (2005), pp.87-95.
Kupka, T., Mancini, M., Irmer, M. and Weber, R.: Fuel **87** (2008), pp.2824-2837.
Lee, J. M.., Kim, J. S. and Kim, J. J.: 16th ASME FBC Conference (2001), pp. 889.
Lee, S. H., Lee, J. M., Kim, J. S., Choi, J. H. and Kim, S. D.: HwahakKonghak **38** (2000), pp.516-522.
Pandelova, M., Lenoir, D. and Schramm, K. W.: Chemosphere **62** (2006), pp.1196-1205.
Ruokojarvi, P. H., Asikainen, A. H., Tuppurainen, K. A. and Ruuskanen, J.: Science of the Total Environment **325** (2004), pp.83-94.
Stanmore, B. R.: Combustion and Flame **136** (2004), pp.398-427.
Wey, M. Y., Liu, K. Y., Yu, W. J., Lin, C. L. and Chang, F. Y.: Waste Management **28** (2008), pp.405-415.
Wan, H. P., Chang, Y. H., Chien, W. C., Lee, H. T. and Huang, C. C.: Fuel **87** (2008), pp.761-767.

COMBUSTION OF POULTRY-DERIVED FUEL IN A CFBC

Lufei Jia and Edward J. Anthony

Canmet ENERGY, Natural Resources Canada, Ottawa, ON, K1A 1M1, Canada

Abstract: Poultry farming generates large quantities of waste. Current disposal practice is to spread the poultry wastes onto farmland as fertilizer. However, as the factory farms for poultry grow both in numbers and size, the amount of poultry wastes generated has increased significantly in recent years. In consequence, excessive application of poultry wastes on farmland is resulting in more and more contaminants entering the surface water. One of the options being considered is the use of poultry waste as power plant fuel. Since poultry-derived fuel (PDF) is biomass, its co-firing will have the added advantage of reducing greenhouse gas emissions from power generation. To evaluate the combustion characteristics of co-firing PDF with coal, combustion tests of mixtures of coal and PDF were conducted in CanmetENERGY's pilot-scale CFBC. The goal of the tests was to verify that PDF can be co-fired with coal and, more importantly, that emissions from the combustion process are not adversely affected by the presence of PDF in the fuel feed. The test results were very promising and support the view that co-firing in an existing coal-fired CFBC is an effective method of utilizing this potential fuel, both resolving a potential waste disposal problem and reducing the amount of CO_2 released by the boiler.

Keywords: CFBC, biomass, combustion

INTRODUCTION

Poultry farming generates large quantities of waste. In Oklahoma, the current practice is to spread the poultry wastes onto farmland as fertilizer. Poultry farmers receive about US$10/ton for the waste materials. However, excessive application of this material is resulting in more and more contaminants entering the surface water and this has become a serious concern. Using poultry waste as power plant fuel could alleviate this concern. Since poultry-derived fuel (PDF) is considered biomass, its co-firing will have the added advantage of reducing greenhouse gas emissions from power generation. To date most studies on this type of fuel have been carried out using small bubbling beds (Li et al., 2008; Zhu and Lee, 2005; Sweeten et al., 2003; Annamalai et al., 2003), without dioxin and furan measurements, a critical parameter if permits are to be granted to allow firing such materials in a coal-fired boiler. Circulating fluidized bed combustion operates at higher superficial velocities than bubbling bed. The fuel particles carried out of the combustion chamber are captured by particulate separation equipment, most commonly a hot cyclone, and returned to the combustion chamber. As a result, combustion efficiency is generally higher in a CFBC compared to a BFB facility. Higher velocity results in a smaller cross-sectional area of the combustion chamber, thus reducing the need for a large number of fuel feed points. As a result of these advantages, large utility fluidized bed boilers firing coal are almost entirely CFBCs. Since the goal of this work is to examine the possibility of co-firing PDF with coal for power generation, a CFBC was chosen to carry out the tests.

Because of the size of the equipment, material handling was a major challenge for these tests. The amount of fuel mixtures used for each test was about 1500 kg including reserves. Ashes generated in each test were in hundreds of kilograms. Due to limited resources and the cost of these tests, and in particular the dioxin and furan measurements, only 5 tests were carried out. However, since there is very little or no information in the open literature dealing with co-firing of PDF and coal in CFBCs, especially in emissions of metals, PAHs and PCDD/Fs, it is believed that these results will be of significant value.

EXPERIMENTAL

AES Shady Point, LLC, and OK Industries, Inc., provided the PDF, coal and limestone used in these tests. The PDF was derived from chicken litter. Table 1 gives the analytical results for the coal and PDF. The Cl content was determined by ion chromatography. Coal was crushed to <6.4 mm. The majority of the PDF particles were -12 mm in size. The PDF was a mixture of poultry litter and materials spread on the poultry farm ground to keep the ground dry. These additional materials consisted mostly of wood wastes: saw dust and wood shavings. The PDF mixture, therefore, had lower moisture content than typical poultry litter, ~7.3%. No drying of the PDF was carried out by CanmetENERGY. Since both coal and PDF contain significant amount of sulphur, limestone crushed to <1.0 mm was used to capture SO_2 from the flue gas. The limestone used contains 96.4% $CaCO_3$.

Table 1 Coal and poultry-derived fuel (PDF) analysis (as analyzed)

	Coal	PDF
Proximate analysis (%)		
Moisture	1.12	7.34
Ash	17.32	25.07
Volatiles	17.07	54.34
Fixed Carbon	64.49	13.25
Ultimate analysis (%)		
Carbon	73.62	31.84
Hydrogen	3.21	3.98
Nitrogen	1.49	3.52
Sulphur	1.23	0.75
Oxygen (by difference)	2.01	27.50
Other analyses		
MJ/kg	29.27	12.77
Cl content, ppm	360	4000

The tests were carried out in CanmetENERGY's 0.8 MWth CFBC. The CFBC riser has an internal diameter of 0.406 m and an internal height of 6.6 m. Up to four water-cooled bayonet tubes control the temperature of the riser. Each tube can be inserted or retracted during operation by a motorized winch system. An 1800 MJ/h natural gas startup burner preheats the CFBC to the ignition temperature of the test fuel. Flue gas from the CFBC is continuously analyzed for CO_2, CO, O_2, SO_2, and NO_x. The system can operate at temperatures up to 950EC and superficial gas velocities up to 7 m/s.

Three tests were initially planned, but 5 were actually conducted. PDF/coal ratios (heating value basis) tested were 10/90, 40/60 and 0/100 (baseline). Tests lasted for ~12-15 h. Data logging was performed at 30-sec intervals. Over 1000 sets of readings for temperatures, flow rate, and feed rates were collected for each test. Stack gas sampling for semi-volatile organics, HCl and heavy metals determinations were carried out during all runs when the conditions in the CFBC stabilized. The methods used were (*Technology Transfer Network*): Dioxins/Furans (PCDD/Fs), Polyaromatic Hydrocarbons (PAHs): EPA method 23; HCl and Cl^- in fly ash: EPA method 50; Metals and particulate: EPA method 29.

The emissions and combustion characteristics of the PDF/coal mixtures were compared with the coal-only results. All runs were performed at bed temperatures of 850-900EC, superficial gas velocity of 4-5 m/s and Ca:S molar ratio of 2-2.5. Fuel was pre-mixed at the required PDF/coal ratio and the starting bed material was double-screened olivine sand with a particle size between 0.25 and 1.0 mm.

RESULTS AND DISCUSSION

Fuel Handling

Coal and PDF were mixed in a Y-shaped mixer. Mixing was rapid and the mixed fuel was easy to unload. However, the strong odor from the PDF was a problem and mixing of the fuel had to be performed when there were no other people in the work area. Subsequently, the equipment and the surrounding area required thorough cleaning. Odor control may be a problem related to firing PDF.

During combustion tests, there was no bridging in the fuel bin and no other fuel feed problems were encountered. The mixed PDF/coal fed very well through the weigh belt, two stages of screw feeders and an airlock (star feeder). The feed rate was controlled easily and we do not anticipate any fuel handling difficulties with PDF/coal mixtures in full utility/industrial-scale units at the ratios tested.

Combustion Test Results

Five runs were actually conducted. Fuel mixtures tested included:
Run 1: 10% PDF with 90% coal
Run 2: 40% PDF with 60% coal
Run 3: 10% PDF with 90% coal
Run 4: 40% PDF with 60% coal
Run 5: 100% coal
Due to blockage of the return leg, Run 1 was aborted. The cyclone temperature was low (350° -500° C)

and solid circulation was impaired. After the run, several pieces of ash agglomerates of dimensions 100 mm ×100 mm×50 mm were found in the return leg and in the main bed. The agglomerates were very weak and easily breakable by hand, and when exposed to the atmosphere, they disintegrated within days. Their chemical composition appeared to be identical to that of the bed ash. The problem appeared to be caused by low circulation rate of the bed material, due to agglomeration of stagnant material in the return leg. During subsequent runs, the amount of loop air was increase to promote circulation. No similar operational problems re-occurred. Run 1 was judged to be unsatisfactory and the data were discarded.

Table 2 gives combustion test results (averages of measurements). During Run 2, data logging failure resulted in very few readings being available. Data presented for Run 2 was mostly from handwritten notes. (No standard errors were given in Table 2 for this run). The PDF/coal mixtures burned well in the CFBC. The 40/60 PDF/coal run was later repeated (Run 4). Data for Run 2 are presented here, because other measurements (PAHs, PCDD/Fs …) are still valid.

Table 2 Combustion test results

	Run 2*	Run 3	Run 4	Run 5
Fuel (by heating value)	40% PDF and 60% coal	10% PDF and 90% coal	40% PDF and 60% coal	100% coal
Average bed temp. , °C	925.8	945.0 ± 17	930.9 ± 12	970.2 ± 17
Average riser temp., °C	861.1	862.0 ± 57	919.5 ± 45	875.0 ± 62
Average cyclone temp., °C	715.4	744.4 ± 86	919.8 ± 29	856.0 ± 27
Average baghouse inlet temperature, °C		181.3 ± 8	241.9 ± 4	190.9 ± 2
Average baghouse outlet temperature, °C	104.8	93.0 ± 4.2	116.4 ± 2	104.6 ± 1
Average fuel feed rate, kg/h	110	82.0 ± 3.0	88.8 ± 10.0	58.8 ± 3.3
Average limestone feed rate, kg/h	6.5	7.29 ± 0.64	7.51 ± 0.82	6.51 ± 0.1
Riser exit pressure, kPa	-0.082	-0.11 ± 0.27	0.45 ± 0.28	-0.12 ± 0.11
Average superficial gas velocity in the riser, m/s	4.72	4.53 ± 0.35	4.95 ± 0.31	4.89 ± 0.43
Average CO_2, %	15.35	12.01 ± 0.58	14.11 ± 0.56	6.72 ± 0.49
Average O_2, %	4.10	6.38 ± 0.63	5.16 ± 0.59	11.9 ± 0.56
Average CO, ppm	2500	894.9 ± 315	594.6 ± 294	718.8 ± 150
Average SO_2, ppm	80	116.0 ± 11.7	106.7 ± 1.7	106.6 ± 3.5
Average NO_x, ppm	-	280.8 ± 30.8	265.1 ± 30.2	233.1 ± 5.2
Fuel N to NO_x, %	-	5.73 ± 0.68	3.80 ± 0.69	9.01 ± 0.34
Estimated Ca/S molar ratio	1.91	2.38 ± 0.23	2.73 ± 0.48	2.74 ± 0.16
Sulphur capture efficiency, %	94.1	91.0 ± 10.1	90.0 ± 12.7	88.6 ± 5.9

The average bed temperature was the highest during the 100% coal run. As the amount of PDF increased, the average bed temperature decreased from 970°C to ~930°C. The average riser temperatures also changed from 860°C to 919°C. Since operation of the CFBC pilot plant was the same for all test fuel mixtures, the differences in temperature reflected the fact that a higher proportion of coal is burned in the dense bed zone.

Sulphur capture efficiency was 90.0-94.1% for the PDF/coal mixture runs, and 88.6% for the coal-only run. The Ca/S molar ratios were in the range of 1.9 to 2.7, within normal operating ranges of industrial- and utility-scale CFBC facilities (Anthony and Granatstein, 2001). NO_x emission levels were in the range of 265-280 ppm for the PDF/coal runs and 233 ppm for the 100% coal run. The conversion ratio of fuel N to NO_x was 3.8-5.73% for PDF/coal and ~9% for the 100% coal run. The NO_x concentration in the flue gas and the level of conversion of fuel nitrogen to NO_x for the coal-only run are also typical of industrial/utility-scale FBCs (Takeshita, 1994). Addition of PDF did not significantly increase NO_x emissions although PDF contains more than twice the amount of N than that of the coal used. In fact, PDF addition actually lowered fuel N-to-NO_x conversion ratio significantly as data in Table 2 show. This apparent paradox can be explained if we assume that the organic-N in the biomass fuel operates similarly to the de-NO_x effect of adding NH_3 or urea to a CFBC environment (Grace et al., 1997).

CO concentration in the flue gas was in the range of 600-900 ppm, typical of CanmetENERGY's CFBC pilot plant burning coal. While this is high compared to industrial/utility-scale FBCs, this reflects the

relatively short residence time of flue gas in the pilot-scale unit, along with the fact that the cyclone arrangement is necessarily less effective in ensuring CO burnout for pilot plants (Knöbig et al., 1998).

N_2O was not measured in this study, since it is not currently regulated and, therefore, not required in applications for permit to burn biomass wastes. However, there are many studies of N_2O emissions from biomass combustion in FBC. Leckner (2007) reviewed co-combustion technology of biomass and coal and showed that N_2O emissions decreased almost linearly as the amount of biomass in the fuel mixture increased from over 100 ppm when firing 100% coal, to below 5 ppm during combustion of 100% wood. Leckner's explanation was that, during combustion of biomass, the nitrogen is mostly transformed into NH_3, not an important precursor of N_2O at FBC combustion temperatures. Another possible explanation is that there is a high concentration of H_2 observed during FBC of wood. H_2 is an active species for reduction of N_2O. Work done by Liu et al (2002) also showed co-combustion of biomass and coal can reduce emissions of N_2O and NO_x. These emissions decrease with increase of the biomass/coal ratio. They proposed a possible mechanism for the reduction in N_2O and NO_x emissions was the rapid release of volatiles in the lower part of the fluidized bed producing a large amount of radicals, which will reduce N_2O and NO_x. In relation to the current work, as the amount of PDF increases in the fuel mixture, it is reasonable to assume that N_2O emissions will be lower than when firing 100% coal.

Stack gas sampling was conducted during every run for heavy metals, semi-volatile organics (SVOs), PAHs and HCl. Bed ash and fly ash samples were collected and analyzed for major and minor elements and char carbon content. Results for PAHs are listed in Table 3 and total TEQ for PCDD/Fs are in Table 4. There is no PAH emission data reported in the literature for PDF/coal co-firing and, therefore, current PAH values could not be compared with previous studies. However, PAH levels in all PDF/coal runs were low and comparable with the 100% coal test, except naphthalene in Run 3. Since only limited PAH emission data were available, a reasonable conclusion for the current tests is that co-firing PDF with coal does not have significant effect on PAH emissions.

It is well documented that FBCs can burn wastes more effectively at lower temperatures than can conventional technologies and EPA has acknowledged this for municipal solid waste (MSW) combustion (Nelson, 1989). Equally, those studies done on organic emissions (both PAHs and PCDD/Fs) from coal burning in FBCs have suggested extremely low emissions (Orr et al., 1993; Cianciarelli, 1989; Mortazavi, 1996). The current tests fully confirmed previous studies. All PCDD/Fs emission levels were low. Total toxic equivalents (TEQs) for Run 2 and Run 3 were 26.6 and 23.5 pg/m^3, respectively, while the 100% coal run gave a TEQ of 89.5 pg/m^3. Run 4 (40% PDF/60% coal mixture) was a repeat of Run 2 because of datalogging problems encountered during the earlier run. For reasons not completely clear, the TEQ of PCDD/Fs for Run 4 was higher than for the other runs (result for Run 1 was not reported in Table 4 but the value was in line with those of the other runs). Analytical bias, contamination of the sampling probe or extracted sample may be the most likely reason for the higher results. Nonetheless, we conclude that the addition of PDF to the fuel did not cause any increase in PCDD/Fs emissions levels.

Table 3 PAH emissions levels on dry basis, μg/m^3

Component	Run 2	Run 3	Run 4	Run 5
Tetralin	2.54	1.11	<0.123	<0.146
Quinoline	0.47	<1.20	1.22	2.7
2-Methylnaphthalene	5.18	56.30	2.37	3.4
1-Methylnaphthalene	2.83	51.69	2.28	2.2
Biphenyl	4.80	36.92	6.45	9.1
2-Chloronaphthalene	<0.142	0.72	0.25	<0.146
Benzo(a)fluorine	0.43	<0.139	<0.123	<0.146
Benzo(b)fluorine	0.32	<0.139	<0.24	<0.146
m-Terphenyl	0.48	<0.139	<0.24	<0.146
o-Terphenyl	<0.142	<0.139	<0.24	<0.146
p-Terphenyl	<0.311	<0.139	<0.24	<0.146
2-Methylanthracene	<0.216	<0.1389	<0.24	<0.146
1-Methylphenanthrene	1.88	0.28	0.24	0.2
9-Methylphenanthrene (maximun value)	1.88	0.28	0.24	0.2
9,10-Dimethylanthracene	1.41	<0.553	<0.24	<0.146

Continued

Component	Run 2	Run 3	Run 4	Run 5
Benzo(b)anthracene	1.32	0.52	0.27	<0.146
Triphenylene	8.57	0.87	1.14	0.4
Benzo(e)pyrene	1.13	0.57	0.90	<0.146
Perylene	<0.142	<0.139	<0.24	<0.146
7,12-Dimethylbenzo(a)anthracene	<0.142	<0.139	<0.24	<0.146
3-Methylcholanthrene	<2.82	<2.77	<0.24	<0.146
Dibenzo(a,c)anthracene/Picene	<0.142	<0.139	0.15	<0.146
Coronene	<0.142	0.17	0.27	<0.146
Dibenzo(a,e)pyrene	<0.282	<0.276	<0.24	<0.146
Naphthalene	69.70	3045.78	203.98	190.2
Acenaphthylene	0.73	119.99	15.50	7.1
Acenaphthene	<0.093	1.29	0.08	<0.056
Fluorene	1.32	1.48	0.38	0.1
Phenanthrene	37.67	14.77	12.24	16.2
Anthracene	0.67	0.74	0.14	0.5
Fluoranthene	16.95	3.05	5.14	4.1
Pyrene	9.04	1.57	2.69	1.5
Benzo(a)anthracene	1.32	0.52	0.27	0.1
Chrysene	8.57	0.87	1.14	0.4
Benzo(b)fluoranthene	2.54	1.11	1.31	0.2
Benzo(k)fluoranthene	0.51	0.22	0.24	<0.056
Benzo(a)pyrene	<0.076	0.26	<0.123	<0.056
Indeno(1,2,3-cd)pyrene	0.39	0.50	0.63	<0.056
Dibenzo(ah)anthracene	0.11	0.18	0.15	<0.056
Benzo(ghi)perylene	0.33	0.42	0.66	<0.056

Table 4 Total TEQ of PCDD/Fs emissions levels on dry basis, pg/m^3

	Run 2	Run 3	Run 4	Run 5
Total TEQ (pg/m^3)	26.6	23.5	483.3	89.5

Cl_2 concentrations in the gas phase were low (with a maximum of 0.145 mg/m^3). Co-firing PDF did not cause significant increase in Cl_2 concentration in the flue gas. However, HCl in the flue gas (Table 5) increased significantly when co-firing PDF compared with the levels of HCl for the coal-only run. Since PDF contained more than ten times the Cl of that in the coal, this was expected. To prevent corrosion or other problems in the back end of the boiler, proper measures should be implemented.

Stack gas sampling for metals was conducted for all runs according to EPA method 29. The metal concentrations in the flue gas were very low, even for those elements associated with high vapor pressures such as As (≤5.88μg/m^3), Pb (≤0.5μg/m^3) and Hg (≤0.35μg/m^3). Co-firing PDF did not cause heavy metal emissions to increase in the flue gas. Thus, these emissions are unlikely to cause any concerns.

A grab bag gas sample was taken during Run 5. The gas sample was analyzed using the gas chromatographic (GC) method for volatile hydrocarbons. No volatile hydrocarbons were detected above the detection limit (which was 0.01% for all compounds measured), except 1,3-butadiene, and C6+ at 0.01%. Volatile hydrocarbons are also very unlikely to cause any problems with FBC combustion.

Table 5 HCl emissions levels on dry basis, mg/m^3

	Run 2*	Run 3	Run 4	Run 5
Fuel (by calorific value)	40% PDF and 60% coal	10% PDF and 90% coal	40% PDF and 60% coal	100% coal
HCl concentration in gas phase	229.0	89.5	31.9	8.88
Cl_2 concentration in gas phase	0.145	0.061	0.042	0.040

* Some key operational data were missing. Run 4 is a repeat of Run 2.

CONCLUSIONS

Poultry-derived fuel was co-fired with coal at PDF levels of 10% and 40% in the feed (based on heating value of the fuel). The PDF was easy to handle and feed although odor was a concern. Combustion of PDF/coal mixtures was stable with no significant temperature variations, indicating that PDF/coal was properly mixed and that no segregation had occurred.

NO_x emissions levels were in the range of 265-280 ppm, about 20% higher than for the 100% coal run. However, the conversion ratio of fuel-N to NO_x was 3.8-5.73%, which is significantly lower than for the 100% coal run, which was about 9%. CO concentration in the flue gas was in the range of 600-900 ppm, typical of burning coal in CanmetENERGY's pilot-scale CFBC. The most likely explanation lies in the relatively short residence time. Stack emissions of PAHs and PCDD/Fs were comparable to coal-only firing. HCl concentration in the flue gas when co-firing PDF with coal was much higher, since PDF contained more than ten times the Cl of that of the coal used. Proper precautions should be made at the back end of the FBC system to prevent corrosion or other operating problems, but the presence of these levels of HCl appeared to have no significant influence on gas emissions. Concentrations of all metals in the flue gas were all very low. Emission of metals in the flue gas is unlikely to be a concern when co-firing PDF with coal in a CFBC.

REFERENCES

Annamalai, K., Thien, B. and Sweeten, J.: Co-firing of Coal and Cattle Feedlot Biomass (FB) Fuels. Part II. Performance Results from 30 kWt (100,000 Btu/h) Laboratory Scale Boiler Burner: Fuel 82 (2003), 1183-1193.

Anthony, E.J., Granatstein, D.L.: Sulfation phenomena in fluidized bed combustion systems: Prog. Energy Combust. Sci. 27 (2001), 215-236.

Cianciarelli, D.: Characterization of Semi-Volatile Organic Emissions from the Chatham 20 MW Circulating Fluidized Bed Demonstration Unit: Environment Canada Report, File 4030-7-15 (January 1989).

Grace, J.R., Avidan, A.A., Knowlton, T.M., (eds.): Circulating Fluidized Beds, Blackie Academic & Professional, 1997.

Knöbig, T., Werther, J., Åmand, L.-E., Leckner, B.: Comparison of Large- and Small-scale Circulating Fluidized Bed Combustors with Respect to Pollutant Formation for Different Fuels: Fuel 77 (1998), 1635-1642.

Leckner, B.: Co-Combustion – A summary of technology: Thermal Science 11(4) (2007), 5-40.

Li, S., Wu, A., Deng, S., Pan, W.: Effect of Co-combustion of Chicken Litter and Coal on Emissions in a Laboratory-Scale Fluidized Bed Combustor: Fuel Process. Technol. 89 (2008), 7-12.

Liu, D.C., Mi, T., Shen, B.X., Feng, B., Winter, F.: Reducing N_2O emissions by co-combustion of coal and biomass: Energy Fuels 16 (2002), 525-526.

Mortazavi, R.: Characterization of Semi-Volatile Organic Compounds (SVOCs) and Volatile Organic Compounds (VOCs) from the Point Aconi Coal-Fired Power Plant: Environment Canada Report PMD/96-7 (1996).

Nelson, L.P.: Municipal Waste Combustion Assessment: Fluidized Bed Combustion: U.S. EPA contract 68-03-3365, EPA-600/8-89-061 (July 1989).

Orr, D.A., Hargrove, O.W., Boyd, T., Chow, W.: Fluidized-Bed Combustion Air Toxics and the Clean Air Act: Conference Proceedings: Application of Fluidized-Bed Combustion for Power Generation, EPRI T-101816 (1993).

Sweeten, J.M., Annamalai, K., Thien, B., McDonald, L.A.: Co-firing of Coal and Cattle Feedlot Biomass (FB) Fuels. Part 1, Feedlot Biomass (Cattle Manure) Fuel Quality and Characteristics: Fuel 82 (2003), 1167-1182.

Takeshita, M.: Environmental performance of coal-fired FBC: IEACR/75, IEA Coal Research, London, 1994.

Technology Transfer Network, Emission Measurement Center, EPA, CFR Promulgated Test Methods (TM), http://www.epa.gov/ttn/emc/promgate.html

Zhu, S., Lee, S.W.: Co-combustion Performance of Poultry Waste and Natural Gas in the Advanced Swirling Fluidized Bed Combustor (SFBC): Waste Manage. 25 (2005), 511-518.

THERMAL EFFECTS BY FIRING OIL SHALE FUEL IN CFB BOILERS

D. Neshumayev, A. Ots, T. Parve, T Pihu, K. Plamus, A. Prikk

Department of Thermal Engineering, Tallinn University of Technology,
Kopli 116, EE-11712, Tallinn, Estonia

Abstract: It is well known that during firing of oil shale fuel the amount of heat released during its combustion per kg of fuel is significantly affected by the endothermic and exothermic processes taking place in mineral matter. These thermal effects are calcite and dolomite decomposing, marcasite FeS_2 oxidising, CaO sulphation and formation of the new minerals. The given paper deals with the experimental study of the influence of these thermal effects of oil shale fuel having different heating value on total amount of heat released during combustion in calorimetric bomb, circulating fluidized bed (CFB) and pulverized-firing boiler (PFB). The large-scale (250 MW_{th}) experiments were performed in the K11-1 CFB boiler of the Balti Power Plant. During experiments low heating value of a fuel varied within the range 8.5 – 11 MJ/kg. At the end some conclusions were drawn.

Keywords: oil shale, thermal effects, CFB, CO_2 emissions

INTRODUCTION

It is well known that during firing of oil shale fuel the amount of heat released during its combustion per kg of fuel is significantly affected by the endothermic and exothermic processes taking place in mineral matter (Ots, 2006). These thermal effects are calcite and dolomite decomposing:

$$\begin{aligned} &CaCO_3 \rightarrow CaO + CO_2 - 179\ \text{kJ/mole} \\ &CaMg(CO_3)_2 \rightarrow CaO + MgO + CO_2 - 315\ \text{kJ/mole} \end{aligned} \quad (1)$$

marcasite FeS_2 oxidising

$$4FeS_2 + 11O_2 \rightarrow 2Fe_2O_3 + 8SO_2 + 871\ \text{kJ/mole} \quad (2)$$

CaO sulphation

$$SO_2 + 1/2O_2 + CaO \rightarrow CaSO_4 + 502\ \text{kJ/mole} \quad (3)$$

formation of the new minerals

$$\begin{aligned} &2CaO + SiO_2 \rightarrow 2CaO \cdot SiO_2 + 139\ \text{kJ/mole} \\ &CaO + Al_2O_3 \rightarrow CaO \cdot Al_2O_3 + 70\ \text{kJ/mole} \\ &CaO + Fe_2O_3 \rightarrow CaO \cdot Fe_2O_3 + 79\ \text{kJ/mole} \end{aligned} \quad (4)$$

The extent of these reactions causing variation in the amount of heat released is determined mainly by fuel combustion technology.

In case of oil shale combustion in calorimetric bomb and pulverized-firing boilers (PFB) practically complete decomposition of carbonate minerals occurs, the extend of carbonate decomposition $k_{CO2} \approx 0.97$ (Ots, 2006), which mainly resulting from relatively high temperature in furnace (1400 - 1500 °C), low partial pressure of CO_2 which is below of equilibrium state line of reaction Eq.(1) at given temperature and small particle size of fuel. Instead, at combustion condition in CFB the incomplete decomposition of carbonates is observed ($k_{CO2} \approx 0.75$-0.85) due to low temperature in furnace and coarse fuel particle size.

Despite high molar content of Ca relatively to molar content of S in oil shale equalled Ca/S = 8 – 10 exceeding more than 2-3 times ratio of Ca/S sufficient at extensive mass transfer to completely capture of SO_2 in accordance with reaction Eq.(3), in PFB case desulfurization efficiency is equalled only 0.70 - 0.85. This could be attributed to the fact, that at relatively high temperatures 60 - 70% of CaO participating in formation of new minerals Eq.(4) combines with sandy-clay minerals in which CaO is less active toward SO_2 compared to free CaO. Whereas during CFB combustion formation of new minerals containing calcium oxide is slower due to low combustion temperature and hence most part of CaO released from carbonate minerals decomposition stays in free form resulting in practically complete capturing of SO_2.

Thus, depending on combustion technology of oil shale the extend of above stated reactions would be

different resulting in different amount of heat released during combustion of 1 kg oil shale fuel. In addition, depending on extend of these reactions amount of ash occurring during combustion would be also different. These peculiarities of oil shale combustion behavior should be taken into account in determining both heating value (HV) in calorimetric bomb and actual amount of heat released in furnace either in CFB or PFB.

The given paper deals with the experimental study of the influence of these thermal effects of oil shale fuel having different heating value on total amount of heat released as well as on CO_2 and SO_2 emissions during combustion in calorimetric bomb, CFB and PFB.

EXPERIMENTAL

The large-scale (250 MW_{th}) experiments were performed in the K11-1 CFB boiler of the Balti Power Plant (Fig. 1). Detailed description of the structure and boiler concept could be found in (Hotta et al. 2005).

The main parameters of the boiler used were as follows: steam capacity – 95/76 kg/s; primary/secondary steam pressure – 12.7/2.4 MPa; steam temperature – 535/535 °C. 17 full test runs were carried out in total.

The variation of main parameters during experiments of the studied oil shale is provided in Table 1. The tests were run at loads of 70-75 kg/s of primary steam.

During each test run regular fuel and ash sampling from separation ports was performed, followed by averaging and dividing procedures for achieving the representative average sample of the test run. In addition, the plant's own data logging system was used to register the basic data of the boiler operation and the whole power unit. To estimate the boiler thermal efficiency, the flue gas composition and parameters at the cap after the boiler and before the ESP were measured (position L in Fig. 1).

The heat balance and thermal efficiency estimations of the CFB boiler were performed on the basis of the EN 12952-15:2003 standard by the indirect method taking into account the peculiarity of the oil shale fuel (Loosaar et al. 2008).

Tabel 1 Studied oil shale characteristics as received

Parameter	Units	Value
Low Heating Value, LHV^r	MJ/kg	8.5 – 11.5
Mineral CO_2^r	%	13.3 – 19.5
Moisture, W^r	%	9.3 – 12.7
Corrected ash content, A_{co}^r	%	37.9 – 41.8
Carbon, C^r	%	20.1 – 27.4
Organic sulphur, S_o^r	%	0.39 – 0.60
Pyritic (marcasite) sulphur, S_p^r	%	0.76 – 1.16

Since the extend of the reactions Eq.(1) - Eq.(4) as it was shown above during combustion in a calorimetric bomb and in a boiler is different, a common practice of using as a heating value of oil shale so called conditional heating value (HV) as the heat released during its combustion under such circumstances when carbonates are decomposing completely (Eq.(1)) and neither sulphation nor new minerals' formation from CaO is taking place (Eqs.(3) and (4)). Knowing conditional HV the corrected HV_{COR} or actual amount of heat released during combustion per 1 kg of oil shale in boiler could be determined as the algebraic sum of the thermal effects in accordance with the aforementioned reactions:

$$HV_{COR} = HV + \Delta Q_c + \Delta Q_{S-T} + \Delta Q_{NM} \quad (5)$$

where HV – conditional heating value, ΔQ_c – thermal effect due to incomplete decomposition of carbonaceous minerals (Eq.(1)), ΔQ_{S-T} – thermal effect due to calcium sulphate formation (Eq.(3)), ΔQ_{NM} – thermal effect due to new minerals formation (Eq.(4)).

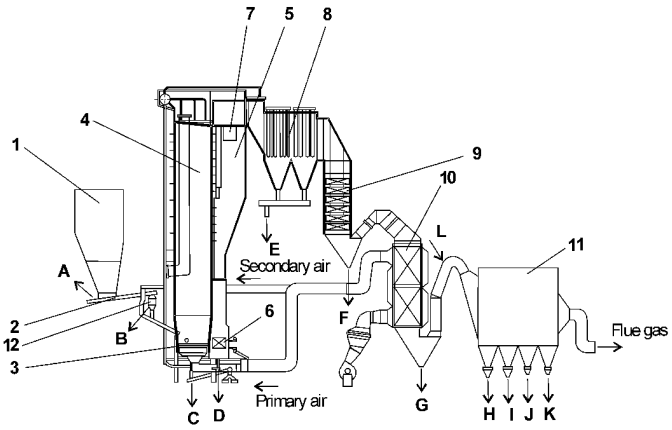

Fig. 1 Oil shale fired CFB boiler (sample ports)

1 – raw fuel silo, 2 – fuel feeder, 3 – grate, 4 – furnace chamber, 5 – separating chamber, 6 – fluidised bed internal heat exchanger (INTREX), 7 – solids separator, 8 – convective superheater and reheater, 9 – economiser, 10 – air preheater, 11 – electrostatic precipitator, 12 – fuel crusher

RESULTS AND DISCUSSION

In Fig. 2 and Fig. 3 the thermal effects corresponding to reactions Eq.(1) - Eq.(4) occurring during oil shale combustion in calorimetric bomb and CFB, respectively, in dependence of conditional LHV are depicted. In case of calorimetric bomb (Fig. 2) the thermal effect due to incomplete oxidation of marcasite additionally plotted. Instead in CFB (Fig. 3) marcasite is burning out practically entirely and therefore is not shown.

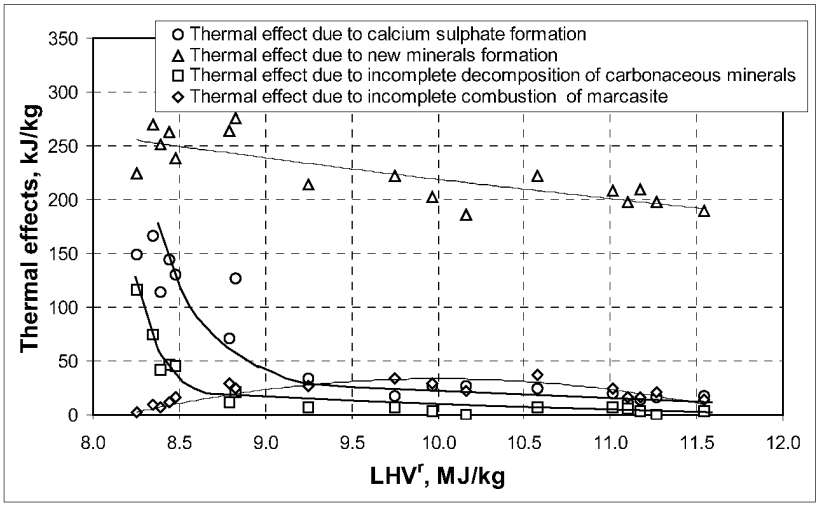

Fig. 2 Thermal effects during oil shale combustion in a calorimetric bomb

From the Fig. 2 could be seen that during combustion in calorimetric bomb the thermal effect due to incomplete decomposition of carbonaceous minerals and calcium sulphate formation sharply decreases at increasing of conditional LHV. During combustion of oil shale in CFB (Fig. 3) thermal effects had weak dependence from conditional LHV, here thermal effect due to calcium sulphate formation slightly increases and others had a tendency towards decrease.

Thus, it could be seen that actual amount of heat liberated during combustion of oil shale is differing from conditional HV. In Fig. 4 cumulative thermal effects behavior expressed in percent relative to conditional HV for various combustion technologies including PF is presented. Here, for PF case thermal effects were calculated taking into account $k_{CO2} \approx 0.97$, desulfurization efficiency ≈0.75 and CaO in free from ≈30% in accordance with (Ots, 2006). From given figure could be found that cumulative thermal effects in case of burning of oil shale in CFB depending on LHV can reach up to ~6% of conditional HV. Comparing two combustion technologies CFB and PF as appears from figure the thermal effects more substantial in CFB case, as a result mainly of greater thermal effect due to incomplete decomposition of carbonaceous minerals.

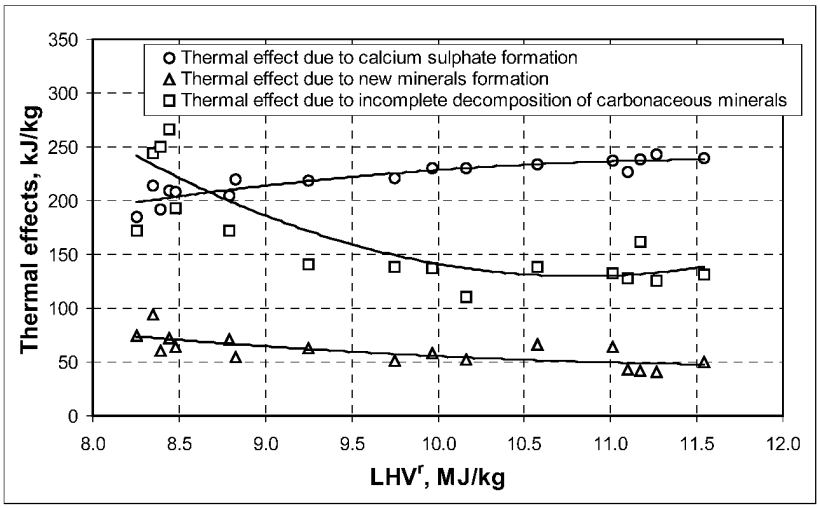

Fig. 3 Thermal effects during oil shale combustion in a CFB

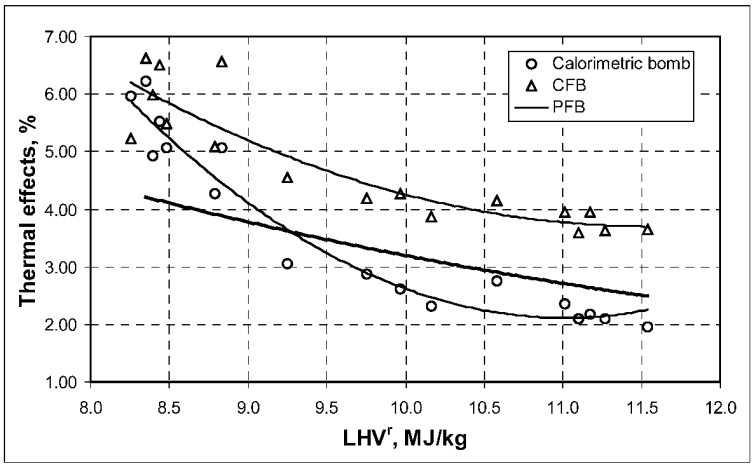

Fig. 4 Sum of the thermal effects of different combustion technologies depending on conditional LHV

Therefore, neglecting during calculation by these thermal effects could result in underestimation of actually amount of heat liberated in furnace and as a consequence of it in overestimation of fuel mass flow and related to the last others parameters like CO_2 emission, amount of ash and etc.

Specific emissions of CO_2 and SO_2 per useful heat of a boiler obtained on the base of fuel ultimate analysis taking into account actual amount of heat released in furnace for CFB and PF technologies depending on conditional LHV are depicted in Fig. 5 and Fig. 6. SO_2 emissions in case of CFB are not plotted on Fig. 6 since as it was discussed early and was also confirmed by present study there is practically complete capturing of SO_2. From these figures could be seen, that specific emissions of CO_2 and SO_2 during combustion of oil shale in CFB are much lower as compared with PFB and this effect is stronger for lower HV values of fuel.

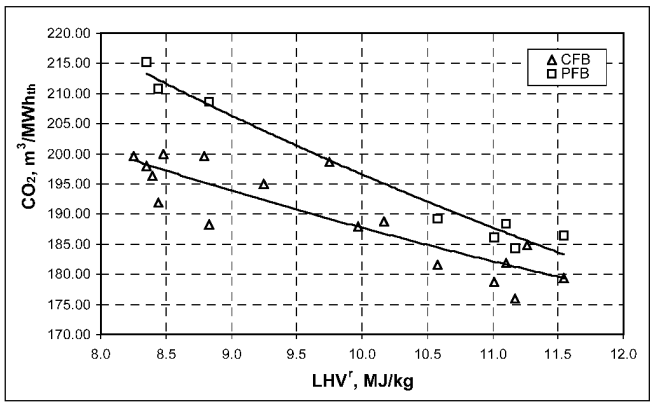

Fig. 5 Specific emissions of CO_2 per useful heat

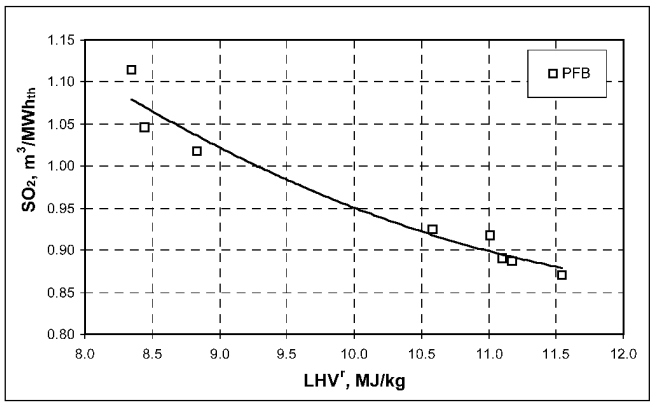

Fig. 6 Specific emissions of SO2 per useful heat

CONCLUSIONS

The influence of thermal effects occurring during oil shale fuel combustion on total amount of heat released in furnace as well as on CO_2 and SO_2 emissions in calorimetric bomb, CFB and PFB depending from heating value was experimentally investigated. During combustion in calorimetric bomb the thermal effects due to incomplete decomposition of carbonaceous minerals and calcium sulphate formation sharply decrease at increasing of conditional LHV. In case CFB thermal effects had weak dependence from conditional LHV, and thermal effect due to calcium sulphate formation slightly increases and others have a tendency towards decrease. It was found that cumulative thermal effects in case of burning of oil shale in CFB depending on LHV could reach up to ~6% of conditional HV. The thermal effects more substantial in CFB case, as a result mainly of greater thermal effect due to incomplete decomposition of carbonaceous minerals. Specific emissions of CO_2 and SO_2 per useful heat of a boiler during combustion of oil shale in CFB are much lower as compared with PF and this effect is stronger for lower HV values of fuel.

REFERENCES

EVS-EN 12952 – 15:2003, Water-tube boilers and auxiliary installations – Part 15: Acceptance tests.

Hotta A., Parkkonen R., Hiltunen M., Arro H., Loosaar J., Parve T., Pihu T., Prikk A., Tiikma T., Experience of Estonian oil shale combustion based on CFB technology at Narva Power Plants, Oil Shale, V **22**, No 4S (2005), pp. 369-381.

Loosaar, J., Arro, H., Neshumayev, D., Plamus, K., Ots, A., Parve, T., Pihu, T., Prikk, A., Rushelyuk, P. (2008). Firing Estonian oil shale fuel in CFB boilers. Werther, J.; Nowak, W.; Wirth, K-E.; Hartge, E-U. (Toim.). Circulating Fluidized Bed Technology (601 - 606). Hamburg: TUTech Innovation GmbH.

Ots Arvo, Oil shale fuel combustion, Eesti Energia AS, Tallinn 2006, 833 pp.

ECONOMICAL COMPORISON PC AND CFB BOILERS FOR RETROFIT AND NEW POWER PLANTS IN RUSSIA

G. A. Ryabov

Special boiler laboratory of All-Russian Thermal Engineering Institute (VTI), 14/23 Avtozavodskaya,Str., Moscow, Russia., Tel. (495) 675-3239, Fax (495) 234-7427, E-mail: georgy.ryabov@gmail.com, vti@vti.ru

Abstract: According to the investment programmes of Russian electricity generating companies increased attention is paid to reconstruction and building new coal TPP. The typical projects are 225, 330 and 600 MW blocks for combustion of different domestic coals. VTI had made technical and economical comparison of CFB and PC boilers for existing and perspective (European) standards of particles, NOx and SOx emissions, according to the data of the preliminary designs and investments in new power plants of 225 and 330 MW. As the basis for technical and economical evaluations was used comparison data of metal-capacity of PC and boilers, emissions-control systems and material-handling systems, with paying attention to the exact suggestions of the boiler producers. The results of the comparisons (capital costs and O&M costs) are discussed in the paper. The most perspective fuels for combustion in CFB boilers are: anthracite culm, coals of the Pechora area, lean coals of Kuznetsk, brown coals of near Moscow, brown coals of Urals and Far East, and also the wastes of coal preparations, peat, shells and biomass. A good composition could be made from Kuznetsk coals and coals of Pechora area. Brown coals are combusted very good in suitable conditions for firing biomass and peat. Also allowed co-combustion with the wastes of coal preparations for the low reactivity fuels such as anthracite culm and lean coals. The diversification of the fuel supply is an essential advantage of CFB boilers. The CFB boiler installations are rather new for the conditions of Russian Federation. For decreasing the technical risks, first installations should be supplied by engineering or license of leading foreign companies with rather big part of their participation. One of important tasks is development of the typical projects, which would allow decreasing not only capital costs, but also decrease time of project realization. The project of the new Block #9 330MW with OTU boiler of Novocherkassk TPP is the determining for the wide use of CFB technology in Russia. The block is designed for combustion of the Anthracite culm, Kuznetsk lean coals and coal slurry and should be established in 2011 year.

Keywords: economical comparison, PC and CFB boilers, fuel characteristics, capital and O&M costs

INTRODUCTION

The majority of coals for power plants in Russia are low-grade products, the coals are of various compositions and have different properties. One of the most urgent tasks for Russian coal-fired TPP is upgrading together with increasing of the amount of coal use and reducing air pollution. About 140 boilers with steam capacity near 200 t/h were started up in 1950-1960 for firing different solid fuels. The poor condition of many aged coal fired boilers makes their rehabilitation, including installation of pollution control equipment, economically unreasonable. These boilers have to be replaced. At the nearest time a retrofit or upgrading of some boilers for 200 and 300 MWe unit should also be done. The additional new coal-based generation capacity will be accomplished mainly through repowering of the existing power plants. Modern pollution control requirements are an additional impulse for implication of new ecologically friendly technologies.

The main criteria for choosing the coal firing technology is the price of electricity, determined by capital and operating costs. The cost difference between CFB and PC boilers depends on several variables, including boiler size, fuel and sorbent quality and their cost, as well as special domestic pollution control requirements, which define capital and operating cost. CFB boilers are preferable for poor coal, including difficult-to-burn fuels and high sulfur coals which would require wet flue gas desulphurization. In this case, capital cost of CFB boiler less than capital cost of PC boiler by 10% and operating cost might be equal for both boilers. Our comparison of CFB and PC Boilers for Rostovskaya TPP demonstrated that CFB boiler for anthracite culm (AC) was the preferable choice over PC boiler (Ryabov and Nadirov, 1999).

Four years ago the general design of repowering of Nesvetay thermal power plant (TPP) has been finished as near-commercial project. Some technical data of boiler and auxiliary equipment designs for Nesvetay TPP were given in Buchkov and Ryabov, (2005). Russian boiler manufacturer "Belenergomash"

(Belgorod), which has the license of Babcock&Wilcox company (USA) and Taganrog Boiler Plant could be produced most part of boiler equipment. It was planned to use it as an experimental power plant for training operators and providing operating experience for typical project. The implementation of

Standardized medium size CFB plant could be done an economical preferences. The standardization of CFB boilers has more than fulfilled the goals for price reduction and fuel flexibility and show promising results in terms of short installation time and reducing maintenance (J. Seeber and G. Scheffknecht, 1999).

But new situation in Russian energy sector after largest Russian energy produce company (RAO UES) reconstruction dictated new demands. Most preferable variants for new electricity generation companies becomes 225 MWe subcritical and 330 MWe supercritical units constructed at the territories of old TPP. At that, the main problems are the chose of combustion technology in depends of fuel characteristics and pollution demands. The standardization of utility size CFB boilers for typical Russian coals is very important also.

RESULTS AND DISCUSSION

Since 1989 VTI started experimental and analytic investigations for scientific basis of CFB technology use. Experimental base with two large aerodynamic and solid fuels firing test rigs were created; the researches were carried out at the experimental bases of other institutions. The most attention had been devoted for investigating of in-furnace hydrodynamics, heat and mass transfer, capturing and returning of particles, and also mixing of the secondary air with high-dust flow. Simplified calculation method of designing FBC boilers had bee developed. Based on this method we determined main sizes, parameters, efficiency, weight of all elements for PC and CFB boilers. Against small and medium size CFB boilers, other opportunity of refurbishment of TPP for large unit (more than 200 MWe) is world wide Foster-Wheller "compact design" technology. The multi fuels boilers, supercritical parameters and ones through boiler design would be most simply implicated in that technology. Typical fuel characteristics and layout of 330 MWe unit are done in Table 1 and Fig. 1.

Table 1 Fuels

TPP name	Fuel	Exponent				
		Wi, %	Ai, %	Si, %	V^{daf}, %	Q^{r}_{i}. Kcal/kg
Tscherepeskaya 225 MWe subcritical	Kuznetskiy	12,5	15,3	0,4	40,0	5110
	Near Moscow mixed with Kuznetskiy 10 %	31,0	32,4	1,9	55,0	1990
	Kansk-Achinsk (Irisha-Borodinskiy)	33,0	7,4	0,2	47,0	3650
	Intinskiy (Pechora region)	11,8	27,8	2,6	37,4	4080
Novo-Cherkasskaya 330 MWe supercritical	Anthracite culm	9,0	25,9	1,3	4,0	5000
	Kuznetskiy lean	7,0	18,6	0,5	12,5	6000
Verkhne-tagilskaya330 MWe supercritical	Kuznetskiy	12,5	15,3	0,4	40,0	5110
	Ekibastuzskiy	6,0	42,3	0,6	25,0	3700
	Bogoslvskiy	21,0	37,1	0,6	47,0	2200

According to the feasibility evaluation data on investment in building of 225 and 330MWe Units, VTI made a technical and economical comparison of CFB and PC boilers firing coals of different quality for existing and perspective (European) standards of particles, NOx and SOx emissions. The comparison data of CFB and PC boilers' metal capacity in terms of different fuels combustion considering certain technical and economical quotations of suppliers. The weight of the components under pressure in PC boiler is 600-700 tons less. The weight of the non-pressurized components is nearly 1000 tons less (CFB boiler has extra refractory, about 500-600 tons more, and more metal constructions of the frame due to the higher pressure in the furnace). The weight of the CFB boiler auxiliary equipment is smaller because of the absence of pulverized coal miles. As a result, the metal capacity of the CFB boiler for the 225MW unit is about 12% more, and price (regarding to the presented higher proportions of the boiler components prices) – is 14% more. This difference is decreasing by combustion of brown (slagging) coals.

The evaluations of the gas cleaning equipment capital costs were made referring to the data of suppliers and expert evaluations of VTI. Data of feasibility evaluation of investments to certain projects was used for determining other expenses for boiler island, ash handling & storage and fuel storage & handling. It is needed

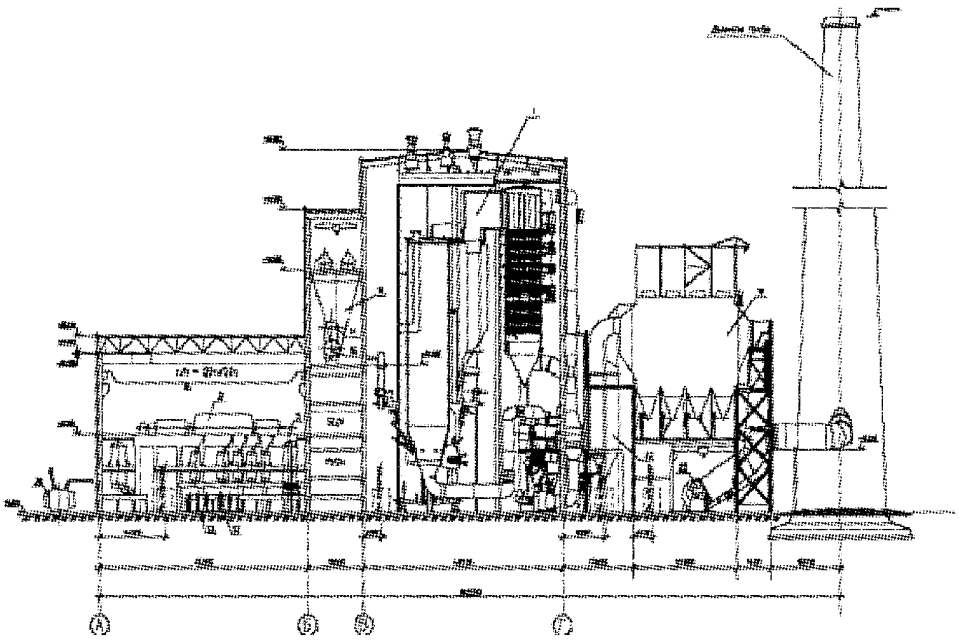

Fig. 1 Structure of the main building of 330 MW blocks of Verkhnetsgilskaya TPP

1- CFB steam boiler; 2 – K-330 steam turbine; 3 – condenser; 4-7 – LP heater; 9-11 – HP heater; 12, 13 – condensation pumps of 1&2 stages; 14 – deaeration unit; 15 – deaeration tank; 16 – feeding pump; 17 – turbine of feeding pump; 18 – raw coal silo; 19 – electric filtering unit; 20,21 – primary and secondary air fans; 22 – botton ash silo, 23 – ID fan; 24 – desalination unit; 25 – block transformer; 26 – self expenses transformer; 27 – reserve start transformer

to point out that received data could be properly used mostly for comparison of options in case of different fuels combustion at 225MWe (subcritical parameters) and 300 (supercritical parameters) MWe units. For example, two 330 MWe units boiler island specific capital costs (Figures 2 and 3) is much less (approximately to 150 USD/kWe) in comparison with two 225MWe units. This case is matching good to American TPP data in general, which are presented in B. Hoskins and G. Booras (2005).

As it is shown in Fig. 5, the least capital costs relate to the PC unit, combusting Kuznetskiy coal 9,4 % less than Ekibastuzskiy coal. The designs of PC boilers for combustion of Kuznetskiy and Irsha-Borodinskiy coals are nearly equal in capital costs. Capital costs for CFB and PC boilers, combusting Ekibastuzskiy coal, are closed. Due to the insignificant costs difference of PC boilers, combusting Kuznetskiy and Ekibastuzsky coals, the advantage of the units for Kuznetskiy coal is achieved mostly by variation of ash handling and ash storage (landfield) and flue gas cleaning costs . It is possible to expect in near futuret, that ash storage cost will decrease in case of partial ash utilization (typically, where are no ash utilization in Russia TPP), but gas purification costs can only increase.

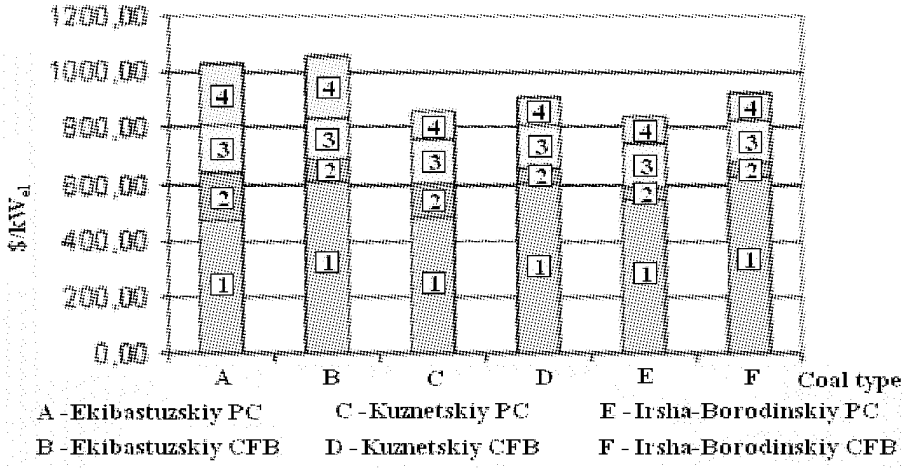

Fig. 2 Specific capital costs (boiler island: boiler, control systems, flue gas cleaning, construction works, coal handling, ash storage) for OUT supercritical 330 MWe unit (existing Russian pollution standards)

1 – boiler &control systems, 2 – flue gas cleaning, 3 – construction works, 4 – coal handling &ash handling and storage

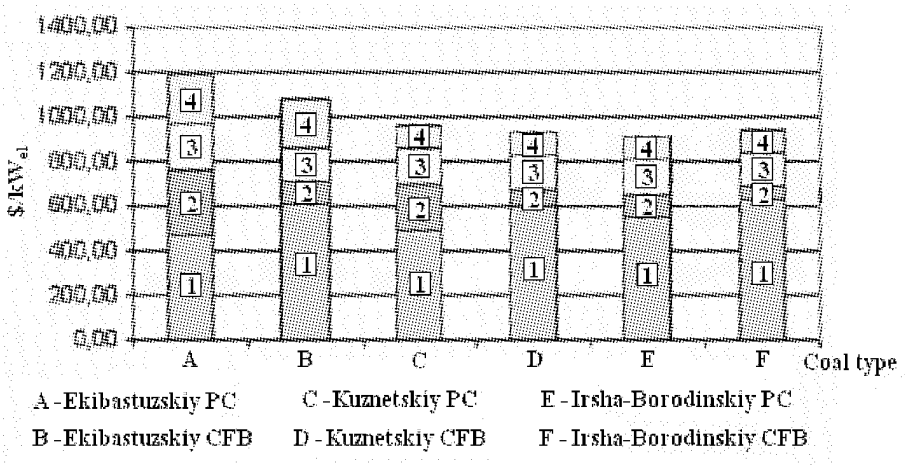

Fig. 3 Specific capital costs (boiler island) for OUT supercritical 330 MWe unit (perspective pollution standards)

1 – boiler &control systems, 2 – flue gas cleaning, 3 – construction works, 4 – coal handling &ash handling and storage

Due to the more demanding emission rates (fig. 3), the advantages of using Kuznetskiy and IrshaBorodinskiy coals, in comparison with Ekibastuzskiy coal, become more significant (13 – 15 % less expensive, including ash storage costs, and about 12% cheaper, excluding them). Units with CFB and PC boilers are comparable.

The comparison of boiler islands capital costs of two 330 MWe units of Cherepovetskaya TPP (supercritical parameters) was made also (Kuznetskiy and high sulfur, high ash Intinskiy coals). Capital costs comparison shows small advantage of using PC boilers for combusting Kuznetskiy (Khakasskiy) coal. Maximum capital costs belong to PC boilers, which combust Intinskiy coal. Capital costs for boiler island with CFB are lower than for PC boilers, combusting Intinskiy coal, higher than for PC boilers, combusting Kuznetskiy coal.

The data of B. Hoskins and G. Booras (2005) about full price of building single-unit (600 MWe) with supercritical boiler for different coal combustion are done in figure 4. The combustion of Texas lignites (TXLig) corresponds to the maximum costs, because of their low heating value (about 3330 kcal/kg) and more high ash value (about 16 %), in comparison with other fuels, represented on a diagram. It's combustion needs furnace of greater volume (and greater costs), and more sophisticated fuel and ash systems.

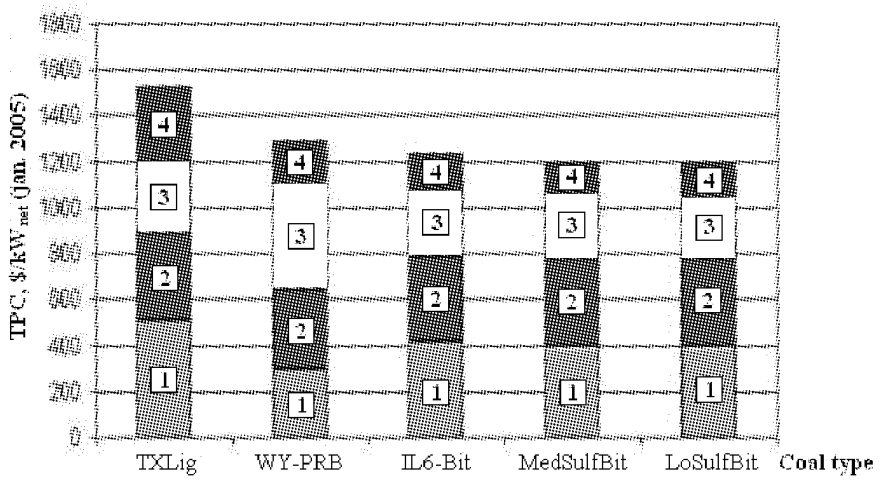

Fig. 4 Sensitivity of total plant cost (specific capital cost) to coal quality foe a 600 MWe supercritical plant by data of B. Hoskins and G. Booras (2005)

1 – boiler, 2 – turbine, 3 – coal and ash handling, 4 – flue gas cleaning and auxiliaries

Specific capital costs (TPC) for TPP designed for combustion of subbituminous Powder River Basin coal (PRB), with the heat value of 4550 kcal/kg and ash value of 5,3 %, 240$/kWe. Figure 4 presents, that TPC

plants, where Illinoice Bituminous coal № 6 (IL6-Bit) is used, will be a bit lower, than in case of PRB and TXLig combustion, because of it's higher heat value (Q^{P}_{H}≈5900 kcal/kg).

According to calculation of B. Hoskins and G. Booras (2005), total capital costs of TPP with supercritical parameters (pressure - 247 bar; temperature - 565/580℃) will be 3 % higher, than for subcritcal (pressure-170 bar, steam temperature-538/538℃). The costs of the supercritical block boiler, turbine and pipelines will be 7% higher than costs of subcritical rig. The efficiency of the supercritical installations is 2 % higher. This fact reduce expenses of fuel supply and preparation systems, ash handling systems, and also of gas purification equipment, and reduce price growth for more than twice (from 7 to 3 %). In general, supercritical TPP service and operation costs reduction level, in comparison with subcritical TPP, is higher than level of the capital costs increase. In this case, TPP with supercritical parameters during it's long operation, will be economically more profitable. Our data gives the same results. More over, TPP with height steam temperature 565/565℃(upon 585/585℃) CFB boilers are preferable that less steam temperature 545/545℃(Russian standard temperature for utility size TPP).

Figure 5 presents of the specific capital costs for two single TPP of 300MWe, equipped with CFB boilers, using fuels of different quality, and placed in a hypothetic area № 3, where more high levels of labour power costs and costs of construction hardware rent, than in area № 1 or area № 2 (Fig. 4). Figure 5 shows, that costs of CFB boiler, which use Illinoice coal № 6, will be lower, than of the boiler, combusting coals of lower quality or wastes (heat value 2930 kcal/kg). The greater part, making difference between specific capital costs of these two TPP, is taken by costs of fuel preparation and supply systems, ash handling system inside the boiler island, and limestone preparation and supply system, for the TPP, which use waste coal. According to B. Hoskins and G. Booras (2005), costs of the TPP with waste coal combustion is 17 % higher, than the same, operating with Illinoise № 6. The higher specific capital costs of TPP will be aligned by low costs of coal wastes.

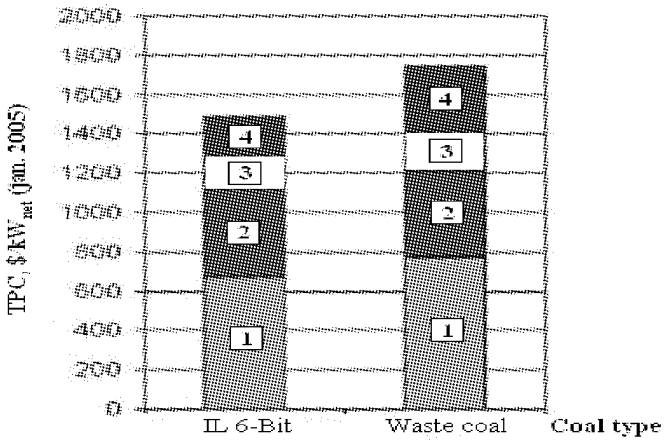

Fig. 5 Sensitivity of total plant cost (specific capital cost) to coal quality for a 300 MWe subrcritical CFB plant by data of B. Hoskins and G. Booras (2005)

1 – boiler, 2 – turbine, 3 – coal and ash handling, 4 – flue gas cleaning and auxiliaries

The capital costs comparison data for TPP and their components for combustion of different fuels, which was done in B. Hoskins and G. Booras (2005), in general matches with represented data of our developments. The take of equipment is about 70% of the TPP costs. The costs of boiler island come up to 65-70% from total costs. The influence of the fuel quality appears in boiler island costs, and data B. Hoskins and G. Booras (2005) gives significantly bigger costs increase of brown coals combustion, in comparison with hard coals, than our data. This could be caused by higher ash and sulfur content in Texas lignites, in comparison with Irsha-Borodinskiy brown coal. CFB boiler costs for 300MWe units are nearly equal for the units with PC boilers.

Additional operational costs (operation of the gas cleaning equipment, ash handling and storage and repairing costs) in application to 330 MWe units are represented in figure 6. The fuel component is evaluated at level of 2000 mln. RUR. (80 mln. $) per year. However, it is needed to consider heightened auxiliary costs for PC combustion with wet limestone desulphurization equipment

The analysis of this data shows that additional operating costs are the highest for TPP, which combust Ekibatuzskiy coal –2 times higher, than for Kuznetskiy coal. However, the most significant part of these costs referred to the operation of ash handling and storage and desulphurization. CFB boilers have less or equal

(with SCR and desulphurization) additional operation costs. These facts likely match with foreign investigations, where it is considered that CFB boilers have 3 ÷ 5 % less additional operating costs, in comparison with PC boilers, equipped with de-NOx and de-SO_2 units, at other equal conditions. Additional advantage is referred to the more deep discharge without assisting fuel, which are very hard to control at the moment.

According to the represented comparison data of CFB and PC boilers technical characteristics for 225 and 330 MWe units , it is seen that values of capital and operation costs are comparable in most cases. The diversification of the fuel supply is an essential advantage of CFB boilers in Russian conditions.

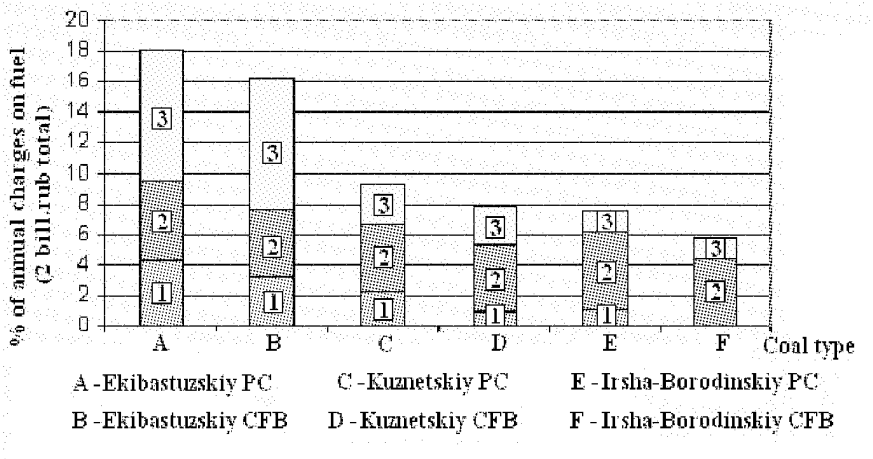

Fig. 6 Additional operating & maintaining cost (1 - operation of the gas purification equipment, 2 - repairing works, 3- ash handling and storage), % of annual fuel cost

The project of the new Unit № 9 330MW with OTU boiler of Novocherkassk TPP is the determining for the wide use of CFB technology in Russia. CFB boiler will be constructed by EM-Alliance (Russian boiler manufacture) and Foster- Wheeler. The Unit is designed for combustion of the Anthracite culm, Kuznetskiy lean coals and coal slurry and should be established in 2011 year.

CONCLUSIONS

The most perspective fuels for combustion in CFB boilers are: anthracite culm, coals of Pechora area, lean coals of Kuznetsk area, brown coals of near Moscow , brown coals of Urals and Far East, and also the wastes of coal preparations, peat, shells and biomass. Kuznetsk hard coals and coals of Pechora area combine with each other very good, and also combine with Ekibastuzskiy coals. Brown coals are combusted well with peat and biomass. Also allowed co-combustion with the wastes of coal preparations for the low reactivity fuels such as Anthracite culm and lean coals.

The important factor of the effective application of CFB technology is achievement of emission standards not only in Russian Federation, but also perspective standards without the use of de-NOx and SO_2 equipment. Diversification of the fuel supply is another significant advantage.

CFB boilers are new for Russian experience, and for decreasing technical risks, first installations should be supplied by engineering and license of the leading foreign companies and by rather large segment of their participation. The project of the new Block #9 330MW with OTU boiler of Novocherkassk TPP is the determining for the wide use of CFB technology in Russia.

It is very important to develop standard designs, which will allow to decrease not only capital costs, but also lead lines of investment projects. However, for the exact investment objects, only minimum variations could be done to such projects.

REFERENCES

G. A. Ryabov. and I. I. Nadirov , "The implication of CFB Technology for Repowering of Old Pulverized Coal Boiler in Russia", in Proc. of 15-th Int. Conf on FBC, Savannah, Georgia, USA, May 16-19, 1999. . A. M. Buchcov , G. A. Ryabov, Repowering of old pulverized coal boilers –CFB boiler on Nesvetay TPP, Proc. of the 8-th Int. Conf. on CFB, Hangzgou, China, May 10-13, 2005.

J. Seeber and G. Scheffknecht, Design concept for standardized medium size CFB plant, Proc. Of the 6-th Int. Conf. on CFB, Wurzburg. Germany, August 22÷27, 1999, pp. 933 – 942.

B. Hoskins and G. Booras, Assessing the cost of new coal-fired power plants, Power, October, 2005.

Fundamental Research on Fluidization and Fludized Combustion

CHARACTERIZATION OF FINE POWDERS

Matthew Krantz, Hui Zhang, Jesse Zhu

Department of Chemical and Biochemical Engineering, University of Western Ontario, London, Canada

Abstract: Fine powders are used in many applications and across many industries such as powdered paints and pigments, ceramics, petrochemicals, plastics, pharmaceuticals, and bulk and fine chemicals, to name a few. In addition, fine powders must often be handled as a waste by-product, such as ash generated in combustion and gasification processes. In order to correctly design a process and process equipment for application and handling of powders, especially fine powders, it is essential to understand how the powder would behave. Many characterization techniques are available for determining the flow properties of powders; however, care must be taken in selecting the most appropriate technique(s).

In this work, sample fine powders with a mean particle size between 22 and 31 μm were characterized using a variety of techniques that tested powders under different stress states, ranging from static to dynamic. In the powder coating process, for example, powders must exhibit good fluidization and resist agglomeration in order to produce a smooth paint coating. It was found that dynamic characterization techniques such as fluidized bed expansion were best suited for predicting the fluidization performance, while static characterization techniques such as cohesion were better for predicting agglomeration. It was also found that results from static and dynamic characterization techniques do not necessarily agree, where fine powders that showed good fluidization performance also displayed increased agglomeration, and vice versa. This suggests that flow properties are dependent upon the stress state and that no single technique is suitable for fully characterizing a powder. Extending this example to other industries, both static and dynamic characterization techniques must be employed to completely understand the flow properties of a powder and predict how it will behave under all process conditions.

Keywords: powder, powder characterization, flowability, flow properties, fluidization

INTRODUCTION

Powder characterization is an important area of research because it allows for a better understanding of bulk solids handling as well as fluidization and can lead to insightful improvements in many processes that depend upon powder flow. For fluidized bed combustors (FBC), a good understanding of bulk solids handling is essential for combustor design, specification of feed materials, and handling waste products. In this study, focus was placed on determining the best methodology for characterization of fine powders. Although this research is not directly tied to FBCs, the learning's are applicable for determining the flow properties of powders used in FBC processes. For example, this work can be extended to predict how different feed materials or biomass may behave in an FBC. As well, powder characterization can be used to understand differences in ash and how it may affect FBC processes, especially when it gets very fine.

To predict how a powder will perform in a given process, a diverse array of different characterization techniques have been developed, which can be used to test powders under widely varying conditions, as summarized by Schwedes (2003) and Prescott and Barnum (2000). Although access to numerous characterization techniques has made it relatively easy to characterize a powder, care must be taken to select the best characterization technique for a specific application. This is because characterization techniques are often designed to measure a specific property of a powder and may have limited utility outside of their designed scope.

Given that a large number of different characterization techniques are available, attempts have been made to generalize the flow behaviour of a powder through classification charts and indices. The most prominent powder classification system was published by Geldart (1973) and segregates powders into four groups with distinct fluidization behaviours based on the mean particle size and density of the powder. In 1965, Carr proposed a series of indices that combine the results from multiple characterization techniques into a single flowability score, which can be found in (Carr, 1965) and (ASTM D6369-99, 1999). These indices were later adopted by Hosokawa Micron Powder Systems and implemented into their powder tester (Hosokawa Micron Corporation). Similar to Carr, Taylor et al. (2000) described a composite index stemming from multiple characterization techniques and optimized for predicting the flow of powders in pharmaceutical applications. Another route was taken by Tomas and Schubert (1979) who extended the work of Jenike and used the ratio of principal stress to unconfined yield strength to categorize powders into five groups that range from hardened to

free flowing. The application of indices like these has proven to be beneficial in describing the most basic properties of a powder; however, these indices often result in over generalization. They cannot accurately identify subtle differences between powders and they cannot accurately predict how powders will perform in different processes. As summarized by Prescott and Barnum (2000), the flow behaviour of a powder is a multidimensional problem and is the result of the combination of material physical properties and the equipment used for handling, storing, and/or processing the material.

Inconsistency between different powder characterization techniques has been a long term source of confusion in industries that handle powders. Using two example powders, A and B, it is not uncommon for one characterization technique to show that powder A has superior flow properties when compared to powder B, while a different characterization technique would show powder B has better flow properties than powder A. Examples of this can be found in (Taylor et al., 2007; Ploof and Carson, 1994; Bell et al., 1994). In situations like this, it is difficult to decide which test to believe, which powder truly has the best flow properties? Furthermore, it has been found that conflicting results can be generated when using the same characterization equipment but using different operating conditions. For example, the Jenike shear cell is sensitive to how powders are conditioned before testing and can give contradictory results based upon different operating procedures, as found in (Schulze, 1996; Schulze, 1998).

The goal of this work was to investigate the relationship between different powder characterization techniques and determine the best method to characterize a powder in a holistic sense. To do so, the process of powder coating was selected as a case study because it is a process that is reliant upon good powder flow under many different conditions that are common to powder industries, including fluidized bed combustion. In powder coating manufacturing and application processes, powders are subjected to four general operations that require good flow properties: transfer from a silo or hopper, fluidization, pneumatic transportation, and mixing. Insufficient powder flow in any of these unit operations can result in poor quality of the finished product or completely disable the process.

Problems encountered due to poor powder flow can occur under a range of conditions, some being relatively static while others being quite dynamic. For instance, powder bridging in a storage hopper, powder agglomeration, and powder deposition and accumulation within equipment can be considered static because the powder is often in a settled or compacted state with little to no kinetic energy. In contrast, problems involving fluidization and pneumatic transportation can be considered dynamic because the particles are dispersed and in motion. It is known that different characterizations techniques can provide different results based upon differences in how they test powders. Therefore, multiple characterization techniques were investigated in this work, with the techniques representing a range of static and dynamic conditions. These techniques were used to analyze many powder coating samples and the results were compared to analyze the relationship between static and dynamic characterization. Finally, the results were used to address the principal question, what is the best way to judge the overall properties of a powder?

EXPERIMENTAL

Two different powder formulations, polyurethane and polyester-epoxy, were used to investigate the relationship between different characterization techniques. For each formulation, over 20 unique powder samples with particle sizes ranging between 22 and 31 μm were characterized. The two different formulations were provided by separate powder coating manufacturers and the different samples of each formulation represent different batches that were produced. The names of the manufacturers and the detailed composition of each formulation are not revealed in this paper to protect the interests and intellectual property of the manufacturers. To analyze the properties of each powder, the powders were characterized based on their particle size, bed expansion ratio (BER), angle of repose (AOR), avalanche angle, and cohesion.

The particle size of powder samples was determined using a Mastersizer 2000 laser particle size analyzer manufactured by Malvern Instruments and following standard test procedures. The BER was determined using a 2 inch column and measuring the bed height ratio between powder fluidized at a superficial velocity of 0.5 cm/s and powder allowed to settle after fluidization. The AOR was determined using a PT-N Powder Characteristic Tester manufactured by Hosokawa Micron Powder Systems and following standard test procedures. The avalanche angle was determined using a Revolution Powder Analyzer manufactured by Mercury Scientific with a 120 mL sample volume and a rotation speed of 0.6 rpm. Finally, the cohesion of powder samples was determined using a FT4 powder rheometer manufactured by Freeman Technology and applying an automated shear testing function. In this test, samples were pre-sheared under a normal force of 9.0 kPa and the yield locus was subsequently developed

by measuring the shear stress at normal forces of 7.0, 6.0, 5.0, 4.0, 3.0, 2.0, 1.5 and 1.0 kPa.

RESULTS AND DISCUSSION

Effect of Particle Size and Composition on Powder Properties

For each characterization test, the results were compared to the particle size of the powder. The powder samples were then organized by formulation (polyurethane and polyester-epoxy) and a linear trend line was drawn through the data from different powder samples using a least squares fit.

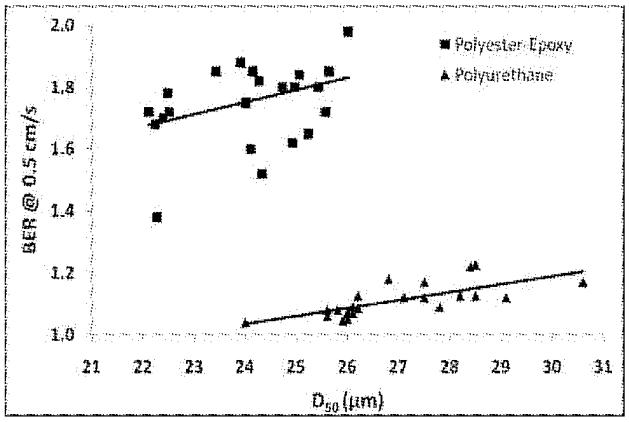

Fig. 1 Relationship between BER measured at 0.5 cm/s and particle size for polyurethane and polyester-epoxy powders

Figure 1 illustrates the relationship between the BER at 0.5 cm/s superficial gas velocity and the mean particle size, D_{50}. As expected, both polyurethane and polyester-epoxy powder formulations demonstrated a trend of reduced fluidization performance with decreasing particle size. This is indicated by a decreasing BER for powders with decreasing particle size. Although there is a considerable amount of deviation between the data and the lines of best fit, a relationship is evident between the BER and particle size as well as a clear distinction between the BER of polyurethane and polyester-epoxy powders. Deviation between individual data points of the same formulation and the line of best fit is attributed to small differences between individual powder samples. Each powder sample was obtained from a different batch of powder and it is reasonable to expect minor variations in composition and distribution of flow additives, which have been shown by Zhu and Zhang (2006) to significantly affect powder flow. Error in the BER measurement may also account for some variation seen between powder samples of the same formulation. The large difference seen between the two powder formulations is primarily a result of entirely different powder compositions, and in particular, proprietary flow additives used by the different manufacturers of these powders.

In fluidization processes, the particle size can have conflicting effects. For powders with a relatively large particle size, reducing the particle size will often increase the bed expansion ratio because the particles will have a higher specific surface area, increasing the drag force imposed by the fluidization gas. In contrast, powders with a small particle size will often show a reduced BER with decreasing particle size. This is because interparticle forces become a dominant force in fine powders and the powder no longer acts as a composition of individual particles. Instead, high interparticle forces cause fine powders to agglomerate, and the specific surface area of the resultant agglomerates is much lower than that of the individual particles, effectively reducing the drag forces that can act on the powder. As suggested by Geldart (1973), powders below 30 μm are often cohesive and experience large interparticle forces. This causes them to experience reduced fluidization with decreasing particle size, as seen in Fig. 1.

BER is a characterization technique that describes how a powder behaves when in a dynamic state, where particles are in continual motion and act like a fluid. From Fig. 1, it is seen that the polyester-epoxy powder samples demonstrated considerably higher bed expansion than the polyurethane powders at a superficial gas velocity of 0.5 cm/s. Also, when the lines of best fit for each powder formulation are compared, the polyester-epoxy powder shows superior fluidization to the polyurethane powder for all particle sizes within the scope of this study. This suggests that the polyester-epoxy powder formulation is likely to outperform the polyurethane powder formulation in dynamic applications such as fluidization.

AOR is a well established test and is commonly used for quality control because it can be used to quickly compare the flow properties of powder samples. AOR is also a technique that combines both static and dynamic elements. When the powder is dispensed during the AOR test, it flows through a funnel and falls onto

the surface of the powder heap with a defined amount of kinetic energy. On the other hand, after the powder lands, it becomes stationary and forms part of the powder heap. The AOR is measured when the powder heap builds up to a sufficient height such that further powder addition does settle onto the heap, but continues to slide down the slope of the heap and fall off the plate. Therefore, the AOR represents an equilibrium between the kinetic energy of powder falling onto the top of the heap and the static interparticle forces between powder particles that allow it build up and form a heap. When comparing powders, a higher AOR signifies higher interparticle forces which reduce the ability for the powder to flow.

The relationship between the AOR and particle size for both powder formulations are shown in Fig. 2. As with BER data, AOR data suggests a relationship of decreasing flow properties with decreasing particle size. This is illustrated in Fig. 2, with both formulations showing a trend of increasing AOR for decreasing particle size. Also agreeing with BER data, the polyester-epoxy formulation demonstrated a marked improvement in powder flow when compared to the polyurethane formulation.

Figure 3 shows the relationship between avalanche angle and particle size. The avalanche angle characterizes the powder in a similar stress state to the AOR, but instead of building the powder heap by dispersing powder on top, the heap is rotated until the powder surface avalanches. In Fig. 3, it is seen that both polyester-epoxy and polyurethane powders exhibit increasing avalanche angles with decreasing particle size and that the polyester-epoxy powder has improved flow over the polyurethane powder. This is in agreement with both BER and AOR data for these powders.

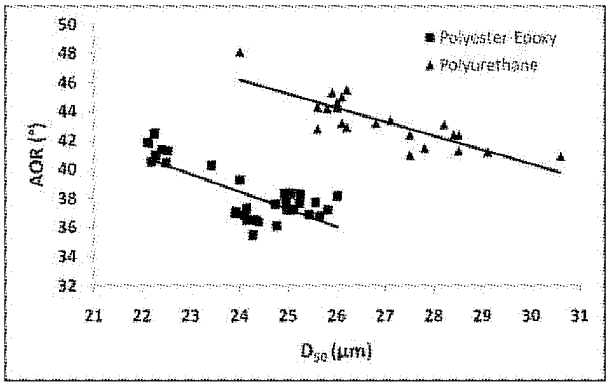

Fig. 2 Relationship between AOR and particle size for polyurethane and polyester-epoxy powders

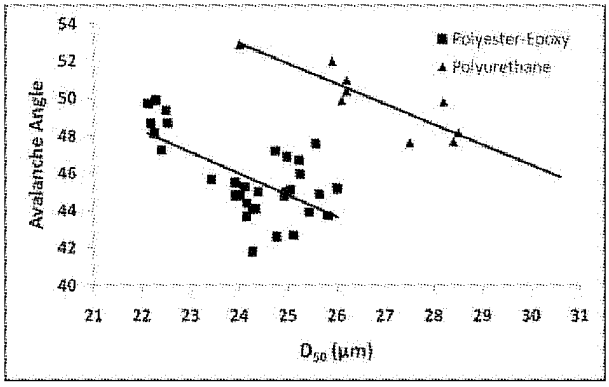

Fig. 3 Relationship between avalanche angle and particle size for polyurethane and polyester-epoxy powders

Measuring the cohesion of a powder while in a compressed state of stress is considerably more static than BER, AOR or avalanche angle. Therefore, it is expected that cohesion will be more representative of how a powder will perform in static processes. The relationship between the cohesion of a powder and particle size is shown in Fig. 4. As with BER, AOR and avalanche angle the cohesion increases with decreasing particle size for both powder formulations, indicating a trend of decreasing flow with decreasing particle size. However, it was found that the polyurethane powder exhibited lower cohesion when compared to the polyester-epoxy powder for a given particle size. This suggests that the polyurethane powder has superior flow properties to the polyester-epoxy powder when in a compressed state, and contradicts what the BER, AOR and avalanche angle predict. From the cohesion data, it is expected that polyester-epoxy powder will be more susceptible to problems such as bridging, agglomeration and deposition within equipment.

Comparing the different characterization techniques, it was found that each technique indicated that smaller particle sizes of fine powders resulted in decreasing flow properties. However, it was also found that

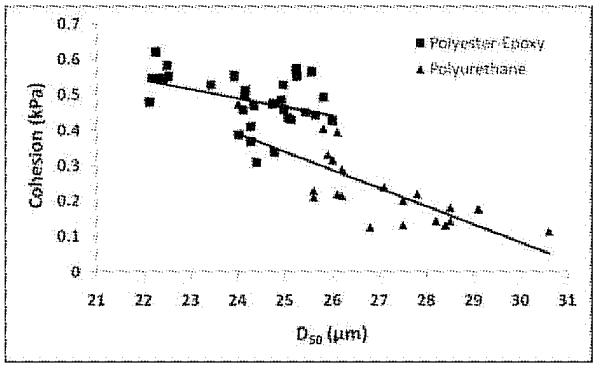

Fig. 4 Relationship between cohesion and particle size for polyurethane and polyester-epoxy powders

each characterization technique did not produce the same results for the two different powder formulations tested. The techniques that subjected the powers to dynamic or combined dynamic-static stress states predicted that polyester-epoxy powder had the best flow properties, whereas the static characterization technique predicted that the polyurethane powder had the best flow properties. Intuitively, it was expected that each characterization technique would rank the two formulations in the same order. For example, it was expected that the interparticle forces that made the polyurethane powder have a lower BER would have also made the polyurethane powder more cohesive when compressed. However, the interparticle forces that act on powder particles are complex and depend on many variables, including both the material properties of the powder and the surrounding forces which act on the powder. In this study, the two powder formulations reacted differently under different states of stress, most likely as a result of different particle properties such as flow additive interactions, particle hardness, and coefficient of friction.

The phenomenon of different characterization techniques providing conflicting results is not unique to this work and has been published in other studies (Taylor et al., 2007; Ploof and Carson, 1994; Bell et al., 1994). However, the implications of this phenomenon have not been described beyond suggesting that characterization techniques should match the application and the process equipment to be used. The results of this work support this claim while demonstrating a new concept of powder characterization: powder characterization that ranges from static to dynamic stress states should be applied to recognize a continuum of powder properties that exist over a range of stress states.

Comparison of Powder Characterization Techniques

To further investigate the relationship between different characterization techniques, the results obtained from each characterization technique were plotted against each other. Fig. 5 shows the relationship between the AOR and avalanche angle for the polyester-epoxy and polyurethane powder samples. The solid lines show the linear best fit for each powder formulation, and the dashed line shows the linear best fit for all data points, regardless of powder formulation. From Fig. 5, it is seen that the trend lines drawn for the polyester-epoxy powder and the polyurethane powder lie closely to the trend line drawn for all powder samples. Although the absolute values of AOR and avalanche angle are different, with the avalanche angle reporting slightly higher angles than AOR, there is a continuous trend between these characterization techniques without distinction between different powder formulations. This is because the AOR and avalanche angle are techniques that subject the test powder to similar stress states, making the results from these techniques transferable between each other. In other words, the AOR can be used as a good predictor of avalanche angle, or vice-versa, regardless of the powder being tested.

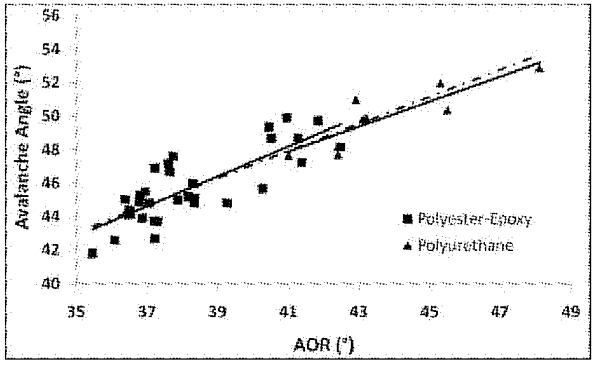

Fig. 5 AOR plotted against avalanche angle for polyester-epoxy and polyurethane powders

Figure 6 shows the relationship between cohesion and BER measurements. For individual powder types, a relationship exists between these characterization techniques as drawn by the solid trend lines. However, the trend lines for different powder formulations do not overlap and a continuous trend cannot be applied to cover all data points. This is because cohesion and BER characterization methods do not characterize the test powders under the same stress states; the BER characterizes powder samples in a dynamic state, whereas the cohesion characterizes the powder in a static state. Similar results were obtained when comparisons were drawn between the other characterization techniques. Discontinuity was observed between powder formulations when comparing AOR to cohesion and comparing AOR to BER, as shown in Fig. 7 and Fig. 8, respectively.

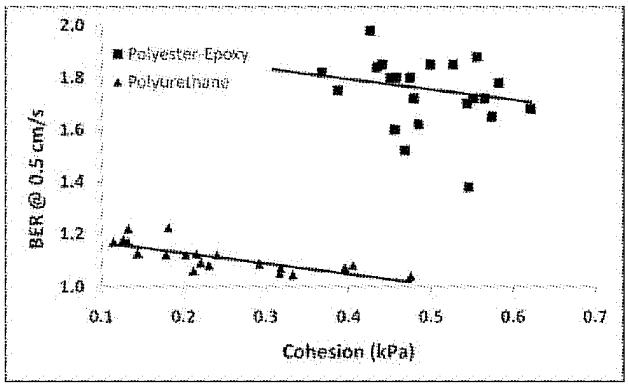

Fig. 6 Cohesion plotted against BER for polyester-epoxy and polyurethane powders

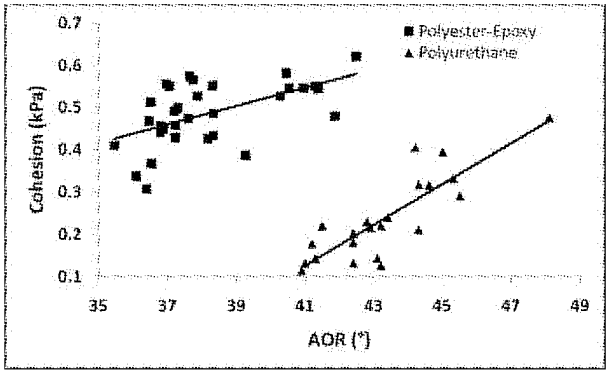

Fig. 7 AOR plotted against cohesion for polyester-epoxy and polyurethane powders

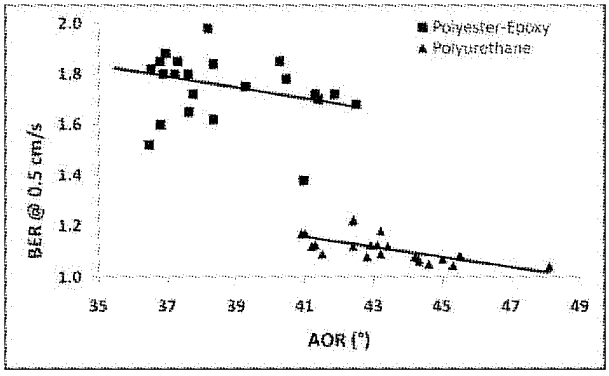

Fig. 8 AOR plotted against cohesion for polyester-epoxy and polyurethane powders

The discontinuity between the different powder formulations in Fig. 6 through 8 suggests that these powders perform differently under the different stress states and that these characterization techniques are not interchangeable. This indicates that BER, AOR, and cohesion each measure different properties of the powder being tested, and do not provide interchangeable results. Each of these characterization techniques analyze the powder under a different stress state and provides new information that is relevant only to that stress state.

In past studies where multiple characterization techniques have been used to evaluate the overall properties of a powder, the results were compiled to create a flowability score or index. In these cases, conflicting test results from different characterization techniques would be compiled into a value representing average performance (Carr, 1965; Taylor et al., 2000), or contradictory test results were completely omitted

from the index (Taylor et al., 2000). In this work, it has been shown that it is not valid to combine test results into an average score or index, as contradictory test results from different techniques can carry valuable information regarding flow properties at different stress states. Instead, it was shown that multiple characterization techniques should be performed at various stress states ranging from static to dynamic and the results should remain segregated to accurately predict the behaviour of a powder in different processes that it may be used in.

CONCLUSIONS

As suggested by Schwedes (2003) and Prescott and Barnum (2000), this work confirms that powder characterization techniques should match the powder application, and that care must be taken to select the most appropriate characterization technique. To expand on this concept, this work has investigated multiple characterization techniques that test powders under different stress states ranging from static to dynamic. It was found that different properties were measured under different stress states and that it is not appropriate to extend the results from a static characterization technique to a dynamic process and vice versa. This has multiple implications for industries that handle powders, and resolves the confusion around conflicting results from different characterization methods. First, powder characterization techniques that utilize different stress states are not interchangeable and it is important to select a technique that subjects the powder to similar conditions seen in the process at hand. Second, if a single powder is subjected to multiple processes, multiple characterization techniques will be required to fully predict the performance of that powder in all processes. In the powder coating process, for example, the BER and cohesion would be required at minimum to fully predict the performance of different paint powders, and either the AOR or avalanche angle could be used to provide additional information. For FBC processes, a similar characterization methodology should be applied to fully understand powder performance in different areas such as feed and sorbent silos, risers, return columns, ash removal, etc. Third, the results obtained from individual characterization techniques should not be simplified into a universal index or classification. This should be avoided because it risks compounding the properties of a powder under different stress states into an average value, removing the ability to predict the performance of a powder across different processes. Finally, the results of any characterization technique should be viewed as application specific. In this work, the results obtained are directly relevant to powder coatings. To extend this to fluidized bed combustors, the characterization results from different FBC powders would have to be correlated to in-plant data and experience. As well, further investigations are required to understand and correlate differences in powder behaviour that occur at high temperatures.

REFERENCES

American Society for Testing and Materials. ASTM Standard D6369-99. (1999).
Bell, T. A. et al.: Bulk Solids Handling 14 (1994), pp. 117-125.
Carr, R L.: Chem. Eng. 18 (1965), pp. 163-168.
Geldart, D.: Powder Technol. 7 (1973), pp. 285-297.
Hosokawa Micron Corporation. Operating and Maintenance Manual.
Ploof, D. A., Carson, J. W.: Bulk Solids Handling 14 (1994), pp. 127-132.
Prescott, J. J., Barnum, R. A.: Pharm. Technol. Oct. (2000), pp. 60-85.
Schulze, D.: Powder Bulk Eng. 10 (1996) Part 1: No 4, pp. 45-61. Part 2: No 6, pp. 17-28.
Schulze, D.: Silos, Fundamentals of Theory, Behaviour and Design. (Brown, C. J., Nielsen, J., (eds)) E & FN SPON. (1998), pp. 18-52.
Schwedes, J.: Granular Matter 5 (2003), pp. 1-43.
Taylor, M. K. et al.: AAPS PharmSciTech. 1 (2000).
Tomas, J., Schubert, H.: Partec 79, Nurnberg, Germany, (1979) pp. 301-319.
Zhu, J., Zhang, H. (2006), US Patent filed.

VELOCITY OF COMPLETE FLUIDIZATION OF A POLYDISPERSE MIXTURE OF VARIOUS FUELS

Yu. S. Teplitskii, V. I. Kovenskii, V. A. Borodulya

A.V. Luikov Heat and Mass Transfer Institute of NAS of Belarus, Minsk, Belarus

Abstract: Using the principle of hydrodynamic equivalence, the procedure of calculating a velocity of complete fluidization of different-density polydisperse granular materials has been developed with account for changes in their initial size distribution. It is shown that coarse particles in composition of polydisperse mixtures can be fluidized when the velocity u_{cf} is substantially smaller than their minimum fluidization velocity $(u_{mf})_{max}$.

Keywords: velocity of complete fluidization, polydisperse bed, different-density particles

INTRODUCTION

As is known (Razumov, 1972) fluidization of polydisperse beds of granular particles, which can be realized in burning of solid fuels and their compositions, differs greatly from that of monodisperse ones. If the latter are fluidized at once for the velocity u_{mf}, then a polydisperse bed of particles is fluidized progressively over a definite range of the filtration velocity: $u_{min} \div u_{cf}$. At $u = u_{min}$ the finest fractions, which form a fluidized bed in the upper part of the disperse filling, are fluidized. A motionless blown-through bed of more coarse fractions is the nearest one to the gas distributor. As the gas velocity is increased, the interface fluidized bed–motionless bed moves down and for a definite filtration velocity (u_{cf}) this interface reaches the gas distributor and all particles are fluidized. This velocity is called the velocity of complete fluidization and serves as the minimum fluidization one for a bed of monodisperse particles.

THE ANALITICAL APPROACH AND SIMULATION DETAILS

Minimum Fluidization Velocity

A procedure of calculating a minimum fluidization velocity of monodisperse particles is well tested both experimentally and theoretically. Numerous recommendations on its calculation are available at present. Todes's formula as given in (Todes and Tsitovich,1981) is most prominent

$$\mathrm{Re}_{mf} = \frac{u_{mf} d}{\nu_f} = \frac{\mathrm{Ar}}{1400 + 5.22\sqrt{\mathrm{Ar}}} \tag{1}$$

Formula (1) adequately describes the influence exerted on u_{mf} not only by the particle diameter, but also by pressure and temperature of a fluidizing gas. It is in good agreement (in a range Ar = 10–10^5) with a formula for u_{mf} proposed earlier by Leva, (1959) (see Table 1).

Table 1 Minimum Fluidization Velocity (Todes and Tsitovich, 1981)

	Size of particles, mm		
	0.164	**0.263**	**0.352**
Experimental data, cm/s	2.7	6.0	10.7
Calculated data, cm/s			
Leva, (1959)	2.9	6.8	11.5
Todes and Tsitovich, (1981)	2.5	6.1	10.2

Nevertheless for the velocities of complete fluidization of polydisperse particles Leva's and Todes's formulas give underestimated values because of incorrect evaluation of the ensemble-averaged mean diameter for polydisperse mixtures.

Velocity of Complete Fluidization

As our analysis of the above phenomenon shows, the procedure of calculating the velocity of complete fluidization should be better constructed by using formula (1). In this case, the main problem is to determine an

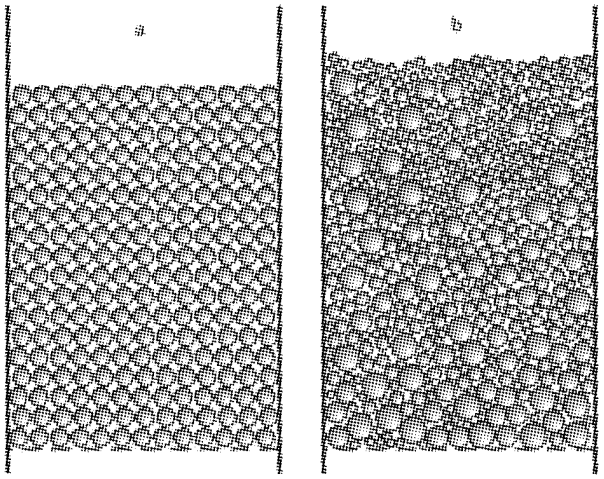

Fig. 1 Minimum fluidization of a monodisperse bed (a) and complete fluidization of a polydisperse bed (b)

effective (equivalent) diameter, d_{eq}, of a particle mixture, which allows one to use formula (1) with the change in $d \to d_{eq}$ for u_{cf} calculation.

Consider two important particular cases:

(1) ***Equal-density particles***

In (Teplitskii, 1991), based on the results of the experimental investigations into beds of aggloporite of wide fractional composition a simple formula was constructed for calculation of d_{eq}

$$d_{eq} = \langle d \rangle = \sum_{i=1}^{N} d_i \eta_i \tag{2}$$

Thus, d_{eq} is the arithmetic mean of the diameters of fractions d_i. The velocity of complete fluidization with account for (2) is found by the dependence that follows from (1):

$$\mathrm{Re}_{cf} = \frac{u_{cf} d_{eq}}{\nu_f} = \frac{\mathrm{Ar}_{eq}}{1400 + 5.22\sqrt{\mathrm{Ar}_{eq}}} \tag{3}$$

(2) ***Different-density particles***

This property of particles is important for calculation of fluidized bed furnaces with simultaneous burning of different-fuel mixtures (Baskakov et al., 1995). Because of the difference in densities of an inert material and burnt fuel species, a direct use of formula (2) is difficult, and a special technique is required for determining d_{eq} with allowance for this difference.

Discrete Distribution of Fractions

Since in fluidized bed furnaces the particles of the inert material form the major portion of the disperse material, we consider different species of fuel and the inert material separately representing them by the following density and size distributions:

$$\rho_s^{(k)}, d_i^{(k)}, \eta_i^{(k)}, \quad k = 1,..,n, \quad i = 1,2,..,N_k \tag{4}$$

$$\rho_{in}, d_{in}^{(i)}, \eta_{in}^{(i)}, \quad i = 1,2,..,N_{in} \tag{5}$$

For the concentrations $\eta_i^{(k)}$ and $\eta_{in}^{(k)}$ the following equalities are valid:

$$\sum_{i=1}^{N_k} \eta_i^{(k)} = 1, k = 1,..,n; \quad \sum_{i=1}^{N_{in}} \eta_{in}^{(i)} = 1. \tag{6}$$

In order to use formula (2) for a mixture of different materials, whose fractional composition is assigned by distributions (4) and (5), these materials should obviously have the same particle density. In doing so, it is more reasonable to take the density of the inert material, ρ_{in}, being the major portion of the bed mass. Distributions (4) were rearranged based on the principle of hydrodynamic equivalence: two spherical particles with the parameters d_1, ρ_1 and d_2, ρ_2 are hydrodynamically equivalent if their minimum fluidization

velocities are equal. Assuming $\rho_1 = \rho_{in}$ and $\rho_2 = \rho_s^{(k)}$, it is possible to rearrange distribution (4) as:

$$\rho_{in}, d_{in}^{(i,k)}, \eta_i^{(k)}, \quad k = 1,..,n, \quad i = 1,..,N_k \tag{7}$$

where $d_{in}^{(i,k)}$ is the diameter of the *i*-th fraction particles of the *k*-th type of fuel brought to that []of the inert material. Specific realization of the principle of hydrodynamic equivalence is based on using Todes's formula (1). For the above particles with the parameters d_1, ρ_1 and d_2, ρ_2 it is possible to write the condition for the equality of their minimum fluidization velocities

$$\frac{\nu_f}{d_1}\frac{\mathrm{Ar}_1}{1400+5.22\sqrt{\mathrm{Ar}_1}} = \frac{\nu_f}{d_2}\frac{\mathrm{Ar}_2}{1400+5.22\sqrt{\mathrm{Ar}_2}}. \tag{8}$$

This relation can be considered as a transcendental equation for finding the ratio d_1/d_2. To solve this equation, we consider two limiting cases:

Fine particles: $5.22\sqrt{\mathrm{Ar}} << 1400$. Solution of (8) is of the form

$$\frac{d_1}{d_2} = \sqrt{\frac{\rho_2}{\rho_1}} \tag{9}$$

Coarse particles: $5.22\sqrt{\mathrm{Ar}} >> 1400$. Equation (8) yields

$$\frac{d_1}{d_2} = \frac{\rho_2}{\rho_1} \tag{10}$$

In the general case, from (8) for the ratio d_1/d_2 we have

$$\frac{d_1}{d_2} = \sqrt{\frac{\rho_2}{\rho_1}\frac{1400+5.22\sqrt{\mathrm{Ar}_1}}{1400+5.22\sqrt{\mathrm{Ar}_2}}} \tag{11}$$

Substituting $d_1 = (\rho_2/\rho_1)d_2$ from (10) in Ar_1 gives an approximate solution of (11) in the following form

$$\frac{d_1}{d_2} = \sqrt{\frac{\rho_2}{\rho_1}\frac{1400+5.22\frac{\rho_2}{\rho_1}\sqrt{\mathrm{Ar}_2}}{1400+5.22\sqrt{\mathrm{Ar}_2}}} \tag{12}$$

A maximal error of the approximate solution of (12) does not exceed 11% and is attained for heavy (coarse) and light (fine) particles. Formula (12) as derived here permits calculating a transition from particles of a diameter d_2 with density ρ_2 to those of an equivalent diameter $d_2\sqrt{\frac{\rho_2}{\rho_1}\frac{1400+5.22\frac{\rho_2}{\rho_1}\sqrt{\mathrm{Ar}_2}}{1400+5.22\sqrt{\mathrm{Ar}_2}}}$ with density ρ_1.

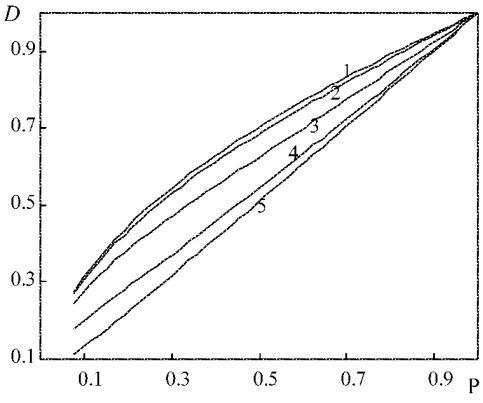

1 – $d_i^{(k)}$ = 0.1 mm, 2 – 0.32, 3 – 1, 4 – 3.16, 5 – 10

Fig. 2 $D = d_{in}^{(i,k)}/d_i^{(k)}$ as a function of $P = \rho_s^{(k)}/\rho_{in}$ at T =300 K and p = 0.1 MPa

For $\rho_1 = \rho_{in}$ and $\rho_2 = \rho_s^{(k)}$, $d_2 = d_i^{(k)}$ from (12) we can obtain a formula for calculation of the quantities $d_1 = d_{in}^{(i,k)}$ entering into the unknown distribution (7):

$$d_{in}^{(i,k)} = d_i^{(k)}\sqrt{\frac{\rho_s^{(k)}}{\rho_{in}}\frac{1400+5.22\frac{\rho_s^{(k)}}{\rho_{in}}\sqrt{\mathrm{Ar}_i^{(k)}}}{1400+5.22\sqrt{\mathrm{Ar}_i^{(k)}}}} \tag{13}$$

Figure 2 plots $d_{in}^{(i,k)}/d_i^{(k)}$ for different $d_i^{(k)}$.

An equivalent diameter of bed particles upon attaining an equal density can be calculated by formula (2) that with allowance for distributions (5) and (7) takes the form

$$d_{\text{eq}} = \langle d \rangle = \eta_{\text{in}} \sum_{i=1}^{N_{\text{in}}} d_{\text{in}}^{(i)} \eta_{\text{in}}^{(i)} + (1-\eta_{\text{in}}) \sum_{k=1}^{n} \sum_{i=1}^{N_k} d_{\text{in}}^{(i,k)} \eta_i^{(k)} \eta^{(k)} \tag{14}$$

In this case, the condition

$$\sum_{k=1}^{n} \sum_{i=1}^{N_k} \eta_i^{(k)} \eta^{(k)} = 1 \tag{15}$$

holds true.

The velocity of complete fluidization of the particle mixture as considered here is calculated by the formula

$$\text{Re}_{\text{cf}} = \frac{u_{\text{cf}} d_{\text{eq}}}{\nu_{\text{f}}} = \frac{\text{Ar}_{\text{eq}}^*}{1400 + 5.22\sqrt{\text{Ar}_{\text{eq}}^*}}. \tag{16}$$

It should be noted that in calculation of u_{cf} using d_{eq} defined by (14), it has been assumed that at $u = u_{\text{cf}}$ the particles of all fractions remain in the fluidized bed. In fact, the bed cannot contain particles, whose diameter is smaller than the floating diameter. These particles are carried away from the bed, the initial size distribution in the feeding flow varies and, as a consequence, the quantities d_{eq} and u_{cf} undergo a change. It is clear that the quantities d_{eq} and u_{cf} are found as a result of their calculation in the iteration cycle (see below).

Continuous Distribution of Fractions

It is easy to generalize the results obtained above to the case of continuous distribution of fractions. In this case, formula (14) takes the form

$$d_{\text{eq}} = \eta_{\text{in}} \langle d_{\text{in}} \rangle + (1-\eta_{\text{in}}) \sum_{k=1}^{n} \left\langle d_{\text{in}}^{(k)} \right\rangle \eta^{(k)} \tag{17}$$

where $\langle d_{\text{in}} \rangle = \int_{(d_{\text{in}})_{\min}}^{(d_{\text{in}})_{\max}} d_{\text{in}} f(d_{\text{in}}) d(d_{\text{in}})$, $\left\langle d_{\text{in}}^{(k)} \right\rangle = \int_{\left(d_{\text{in}}^{(k)}\right)_{\min}}^{\left(d_{\text{in}}^{(k)}\right)_{\max}} d_{\text{in}}^{(k)} \varphi_k\left(d_{\text{in}}^{(k)}\right) d\left(d_{\text{in}}^{(k)}\right)$

Note that the values of $(d_{\text{in}})_{\min}$ and $\left(d_{\text{in}}^{(k)}\right)_{\min}$ should be at least smaller than the floating diameter of particles with density ρ_{in}. This diameter is calculated by the formula (Kovenskii, 2006):

$$d_{\text{t}} = 0.18 \frac{u_{\text{ff}}^2}{\text{g}} \frac{\rho_{\text{f}}}{\rho_{\text{in}} - \rho_{\text{f}}} \left(1 + \sqrt{1 + 556 \frac{g \nu_{\text{f}}}{u_{\text{ff}}^3} \frac{\rho_{\text{in}} - \rho_{\text{f}}}{\rho_{\text{f}}}} \right) \tag{18}$$

Since, generally speaking, initial distributions (5), (7) can have particles with a diameter smaller than d_{t}, the quantities $(d_{\text{in}})_{\min}$, $\left(d_{\text{in}}^{(k)}\right)_{\min}$, d_{eq}, and u_{ff} can be found as a result of the iteration process similar to that given in (Teplitskii, 2008). This process is as follows:

- $(d_{\text{eq}})_0$ and $(u_{\text{cf}})_0$ are found by an assigned fractional composition of the supplied fuel and the inert material within the framework of the procedure developed;
- the floating diameter d_{t0} is determined by formula (18) for $(u_{\text{cf}})_0$;
- all particles, whose diameters are smaller than d_{t0}, are cancelled from the distributions of d_{in} and $d_{\text{in}}^{(k)}$, and then $\left((d_{\text{in}})_{\min}\right)_1$ and $\left(\left(d_{\text{in}}^{(k)}\right)_{\min}\right)_1$ are determined;
- $(d_{\text{eq}})_1$ and $(u_{\text{cf}})_1$ are found from a new fractional composition of particles;
- d_{t1} is determined by formula (18) for $(u_{\text{cf}})_1$.

ANALYSIS OF THE INFLUENCE OF FINE FRACTIONS ON THE FLUIDIZATION VELOCITY OF COARSE PARTICLES

For such an analysis to be made, define a dependence of a maximum size of polyfractional mixture particles on their mean diameter and a degree of polydispersity. Present an unknown relation as:

$$\frac{d_{\max}}{\langle d \rangle} = 1 + A\varphi^n \tag{19}$$

Formula (19) describes the influence of polyfractionality on $d_{\max}/\langle d \rangle$ and at $\varphi = 0$ yields $d_{\max} = \langle d \rangle = d$ (monofractional particles).

To determine the coefficients A and n we analyzed seven particular polydisperse mixtures (see Table 2). The data processed by (15) yielded a simple formula

$$\frac{d_{\max}}{\langle d \rangle} - 1 = 3\varphi^{0.8}, \quad 0.02 \le \varphi \le 0.39 \tag{20}$$

Table 2 Polydisperse grained mixtures used for deriving relation (20)

Material	Geldart group	d_i, mm	η_i	$\langle d \rangle$, mm	u_{cf}, m/s	φ	ρ_s, kg/m^3	d_{max}, mm
Glass beads	D	4.37	0.507	5.08	1.87	0.02	2650	5.79
		5.79	0.493					
Glass beads	D	4.37	0.2335	7.56	2.35	0.10	2650	9.85
		5.79	0.2475					
		9.85	0.5190					
Glass beads	D	4.37	0.1655	9.8	2.70	0.125	2650	12.9
		5.79	0.1515					
		9.85	0.1985					
		12.91	0.4845					
Glass beads	D	4.37	0.1280	13.63	3.20	0.128	2650	18.56
		9.85	0.1820					
		12.91	0.2700					
		18.56	0.4200					
Aggloporite	D	<1	9.69	3.43	1.1	039	1640	10
		3 - 1	43.87					
		5-3	20.5					
		7-5	16.32					
		10-7	9.58					
Anthracite	B	0.457	0.03	0.69	0.23	0.042	1970	0.914
		0.533	0.25					
		0.635	0.23					
		0.762	0.29					
		0.914	0.20					
Sand	A	0.0625	0.167	0.096	0.0092	0.1	2650	0.162
		0.0875	0.150					
		0.112	0.333					
		0.137	0.167					
		0.162	0.083					

Based on (20), we determine a ratio of a minimum fluidization velocity of particles with $d_{\max}$ to the velocity of complete fluidization of a mixture of particles with a mean diameter $\langle d \rangle$. For simplicity, consider

the case of coarse particles (Re> 1000). Then, Todes's formula (1) for them takes the form

$$\mathrm{Re}_{\mathrm{cf}} = \frac{\sqrt{\mathrm{Ar}}}{5.22} \tag{21}$$

Substitute (21) in a more convenient form

$$\mathrm{Fr}_{\mathrm{cf}} = \frac{u_{\mathrm{cf}}^2}{g\langle d\rangle} = 0.036\frac{\rho_{\mathrm{s}}}{\rho_{\mathrm{f}}}. \tag{22}$$

To determine the minimum fluidization velocity of particles with $d_{\max}$ we have

$$\mathrm{Fr}_{\max} = \frac{(u_{\mathrm{mf}})_{\max}^2}{g d_{\max}} = 0.036\frac{\rho_{\mathrm{s}}}{\rho_{\mathrm{f}}} \tag{23}$$

With account for (20), (22), we obtain a desired velocity ratio

$$\frac{(u_{\mathrm{mf}})_{\max}}{u_{\mathrm{cf}}} = \sqrt{1+3\varphi^{0.8}} \tag{24}$$

Formula (24) describes the influence of fine fractions on the fluidization of coarse ones and shows that coarse particles in the composition of polydisperse mixtures can be fluidized at the velocity u_{cf} substantially smaller than their minimum fluidization velocity $(u_{\mathrm{mf}})_{\max}$.

From formula (24) an expression for φ can be obtained:

$$\varphi = 0.25\left(\left((u_{\mathrm{mf}})_{\max}/u_{\mathrm{cf}}\right)^2 - 1\right)^{1.25} \tag{25}$$

Relation (25) makes it possible, at the given values of the filtration velocity and minimum fluidization velocity $(u_{\mathrm{mf}})_{\max}$, to choose an optimal composition of a polydisperse mixture with $u_{\mathrm{cf}} = u$ that allows fluidization of coarse particles with the diameter $d_{\max}$, whose minimum fluidization velocity $(u_{\mathrm{mf}})_{\max}$ is much larger than u.

CONCLUSIONS

Using the concept of hydrodynamic equivalence, a procedure of calculating a velocity of complete fluidization of different-density polydisperse particles and also an equivalent diameter of mixture [see (14) and (17)] has been developed. An iteration cycle of u_{cf} calculation is presented. The dependence of a maximum size of particles on their mean diameter and the polydispersity of mixture is established. Methods of selecting an optimal composition of a polydisperse mixture, which allows fluidization of coarse particles at velocities substantially smaller than their minimum fluidization velocity, have been developed as well.

NOTATIONS

Ar Archimedean number $\mathrm{Ar} = \frac{gd^3}{\nu_{\mathrm{f}}^2}\left(\frac{\rho_{\mathrm{s}}}{\rho_{\mathrm{f}}} - 1\right)$

d particle diameter, m

$f(d_{\mathrm{in}})$ distribution function of quantities d_{in}

g acceleration of gravity, m/s^2

n number of fuel species

N number of fractions

Re Reynolds number

u filtration velocity, m/s;

ε, Δ relative errors in calculation of u_{ff} and d_1/d_2, respectively

η mass fraction (concentration)

ν_{f} kinematic viscosity of gas, m^2/s

ρ density, kg/m^3

$\varphi\left(d_{\mathrm{in}}^{(k)}\right)$ distribution function of $d_{\mathrm{in}}^{(k)}$

φ degree of polydispersity, $\varphi = \sum_{i=1}^{N}\left(\eta_i\left(d_i - \langle d\rangle\right)^2/\langle d\rangle^2\right)$

Superscripts:

i number of fraction

k number of fuel species

Subscripts:

f gas

cf complete fluidization

eq equivalent

i	number of fraction	max	maximum
in	inert	s	particles
k	number of the iteration cycle	t	terminal condition for of a single particle with the density ρ_{in}
mf	minimum fluidization		
min	minimum		

REFRENCES

Baskakov, A. P., Matsnev, V. V., Raspopov, I. V.: Fluidized Bed Boilers and Furnaces, Energoizdat, Moscow, 1995.
Kovenskii, V.I. : Teor. Osnovy Khim. Tekhnol. 40, (2006), No.2, (2006), pp. 206-218.
Leva, M.: Fluidization. McGraw-Hill Book Company, Inc., New York, Toronto, London, 1959.
Razumov, I. M. : Fluidization and Pneumatic Transport of Loose Materials, Khimiya, Moscow. 1972.
Teplitskii, Yu. S. : Abstract of the Doctoral Thesis (Eng. Sci.), Novosibirsk,. 1991.
Teplitskii, Yu.S. : Inzh.-Fiz. Zh. 81, No. 2, (2008), pp. 353-357.
Todes, O. M., Tsitovich, O. B.: Fluidized Granular Bed Apparatuses, Khimiya, Leningrad, 1981.

EFFECTS OF TEMPERATURE AND PARTICLE SIZE ON MINIMUM FLUIDIZATION AND TRANSPORT VELOCITIES IN A DUAL FLUIDIZED BED

J. H. Goo[1], M. W. Seo[1], S. D. Kim[1], B. H. Song[2]

1 Department of Chemical & Biomolecular Engineering, Energy & Environment Research Center, KAIST, Daejeon, Korea
2 Department Nano-chemical Engineering, Kunsan National University, Kunsan, Korea

Abstract: Prior to operating a dual fluidized bed gasifier (DFBG) using a riser (0.078 m-I.D × 8.5 m-high) as a combustor and a bubbling bed as a gasifier (0.2 m-I.D. × 2.1 m-high), the hydrodynamic properties such as minimum fluidizing velocity and transport velocity of silica sand (270μm) as a bed material in a DFBG were determined at different temperature (25-800℃). The minimum fluidization velocity decreases from 0.065 m/s to 0.036m/s with increasing temperature. But the transport velocity, a boundary velocity between the turbulent and fast fluidization flow regimes, increases from 2.55 m/s at 25℃ to 4.47 m/s at 600℃. The effect of particle size on the minimum fluidization and transport velocities was determined and correlations are proposed to predict both velocities at different temperature. The relationship between the operating variables and solid circulation rate was also determined. The obtained data can be utilized to determine the operating conditions in the hot DFBG system.
Keywords: hydrodynamics, minimum fluidization velocity (U_{mf}), transport velocity (U_{tr})

INTRODUCTION

The dual fluidized bed gasifier consists of two fluidized bed reactors; one is a combustor and the other one is a gasifier. The energy generated by combustion of residual char in the combustor is transferred to the gasifier for endothermic steam-char gasification reaction. The circulating bed material acts as heat carrier between the two reactors. Thereby, the product gas from the gasifier contains mainly (H_2+CO) without dilution of nitrogen even air was used as an oxidant in the combustor. Since a longer reaction time is required in the gasification reactor, a bubbling fluidized bed was designed whereas; a fast fluidized bed was designed for combustion reaction. To operate the DFBG having two beds of different flow regime, hydrodynamic properties such as the minimum fluidization velocity, transport velocity and solid circulation rate at higher temperature are needed.

To predict the minimum fluidization velocity, most of previous studies proposed the empirical correlations at room temperature condition, although many commercial fluidized bed reactors are operating at high temperature. Therefore, the reported correlations at higher temperatures have shown a marked discrepancy between the predicted and the measured minimum fluidization velocities with correction of gas physical properties at the given temperature (Desai et al., 1977). Wu and Baeyens (1991) measured the minimum fluidization velocity (U_{mf}) of lime, limestone and sand at temperature up to 400℃ and reported that the values from the correlations overestimate U_{mf} at higher temperature. Previous studies on the minimum fluidization velocity at higher temperature are listed in Table 1.

Table 1 Previous studies on minimum fluidization velocity at higher temperature

Authors	Materials	d_p (㎛)	T (℃)	Correlation
Pattipati and Wen (1981)	Sand	240	20-750	-
Botterill et al.(1982)	Sand	380, 460	20-815	-
Mathur et al. (1986)	Sand	559-3788	25-1000	-
Wu and Bayens(1991)	Sand	134-939	20-400	$\mathrm{Re}_{mf} = 7.33\times10^{-5}\times10^{(8.24\log_{10}Ar-8.81)^{1/2}}$
Ryu et al. (2003)	NiO/bentonite	181	25-1000	$U_{mf} = \frac{2.997\times10^{-3} d_p^{1.636}(\rho_p-\rho_g)^{1.128} g}{\rho_g^{0.0247}\mu^{0.446}}$
Subramani et al.(2007)	Ilmenite, sand, limestone,quartz magnetite	128-200	25-700	$\mathrm{Re}_{mf} = \frac{Ar}{1502}$

The transport velocity (U_{tr}) is a transition velocity between the turbulent and fast fluidization flow regimes. To operate a constant solid circulation rate, the gas velocity should be above U_{tr}. The transport velocity can be

determined by various methods such as the emptying time, flooding point, pressure fluctuation and voidage-U_g-G_s phase diagram (Adanez et al., 1993). Many studies have also been proposed correlations of U_{tr} with variations of particle size and density, bed diameter and operating pressure. However, a limited amount of experimental data of U_{tr} as a function of temperature has been reported (Bae et al., 2001; Ryu et al., 2003). The experimental conditions and correlations of previous studies are summarized in Table 2.

Table 2 Previous studies on the transport velocity (U_{tr})

Authors	Materials	d_p (㎛)	T (℃)	Correlation
Lee and Kim (1990)	Cement, raw meal	23.6	A.C.	$Re_{tr}=2.916\,Ar^{0.354}$
Perales et al. (1990)	FCC sand	80 120-1200	A.C	$Re_{tr}=1.41\,Ar^{0.483}$
Adànez et al. (1993)	Sand coal	170-894 316-894	A.C	$Re_{tr}=2.078\,Ar^{0.463}$
Tsukada et al. (1993)	FCC	46	A.C.	$Re_{tr}=1.806\,Ar^{0.458}$
Ryu et al. (2003)	NiO/bentonite	181	25-600	$Re_{tr}=0.0428\,Ar^{0.5866}(D_t/d_p)^{0.5208}$

A.C.: ambient conditions

Prior to conduct combustion and gasification reactions, the hydrodynamic properties such as minimum fluidization velocity, transport velocity and solid circulation rate were determined in a DFBG.

EXPERIMENTAL

A new concept of dual circulating fluidized bed reactor was designed as shown in Fig. 1. It is a combined system consisting of a fast fluidized bed riser (0.078 m-I.D. × 8.5 m-high) and a bubbling fluidized bed (0.2 m-I.D. × 2.1 m-high). Two loop-seals were mounted to control the solid circulation rate and to prevent gas bypassing from the riser to the bubbling bed and vice versa. All parts of the reactor were made of SUS 304 and were wrapped by 3-kW Kanthal electric wires connected to PID controllers to regulate heating rate. To prevent heat loss, ceramic wool (0.15 m-thick) sheet enveloped all parts of the reactors. Three different sizes (210, 270, 380μm) of silica sand particles having 2500 kg/m^3 density were used as the bed material. Total amount of the inventory was 45 kg, which corresponded to the static bed height of 0.6 m in the bubbling bed. The particles were supported on a bubble-cap type distributor and compressor air was introduced into an air box. The entrained particles from the riser were collected by a cyclone and transferred to the upper loop-seal. The lower loop-seal regulated solid circulation rate from the bubbling bed to the riser by aeration.

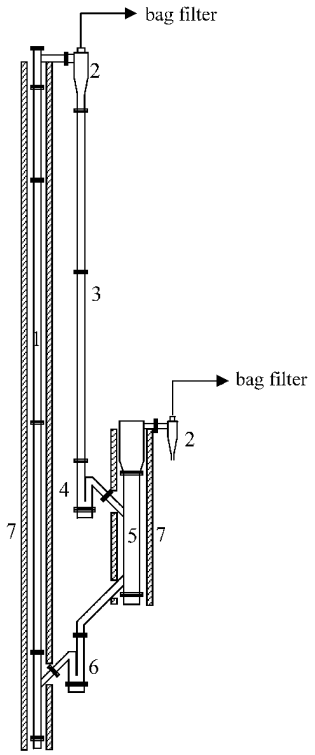

Fig. 1 Schematic diagram of DFBG:
1. riser, 2. cyclone, 3. downcomer, 4. upper loop-seal, 5. bubbling bed, 6. lower loop-seal, 7. electric heater

To measure absolute and differential pressures in the riser and the bubbling bed, online pressure transducers (DPLH series, Sensys) were connected to pressure taps at different axial heights of each column. The minimum fluidization velocities of different particles were measured at different temperature in the bubbling bed. Fluidizing gas was supplied from the compressed air and regulated by flow meters. The amount of air flow rate at different temperature was calibrated and its properties such as density and viscosity were calculated from the following relations (Svoboda and Hartman, 1981).

$$\rho_g = 1.2\frac{293}{T} \tag{1}$$

$$\mu_g = 1.46\times10^{-6}\frac{T^{1.504}}{T+120} \tag{2}$$

The transport velocity was determined by the emptying time method with the following procedure. First, the particles were circulated until DFBG reached steady state at the given riser velocity and temperature. When pressure drop in the riser became 3000 Pa, air fed into the lower loop-seal was closed and the time required to entrain all the particles from the riser was measured. In case of solid circulation rate measurement, after the system reached steady state of solid circulation, aeration into the upper loop-seal was stopped and then loss of pressure drop in a bubbling bed was measured for a given time. The amount of circulated solid at a given time can be converted into solid circulation rate.

RESULTS AND DISCUSSION

Minimum fluidization velocity

The measured minimum fluidization velocities from the pressure drop in the bubbling bed with variation of gas velocity as a function of temperature are shown in Fig. 2. As can be seen, U_{mf} decreases with increasing temperature and decreasing with increasing particle size. At higher temperatures, U_{mf} tends to become constant with all the particle size employed.

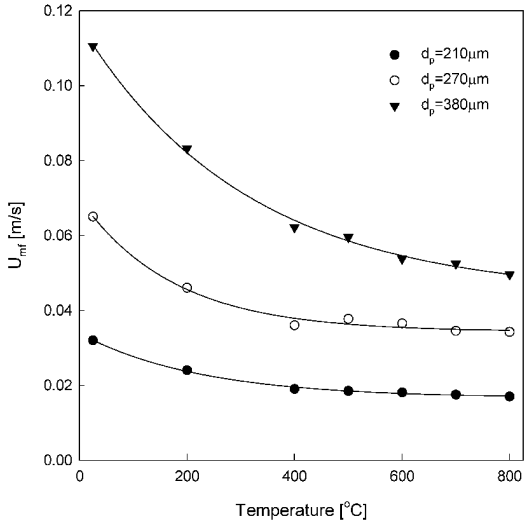

Fig. 2 Effect of temperature on U_{mf}

Most of the correlations to predict U_{mf} are based on the Ergun equation as:

$$1.75C_1 \mathrm{Re}_{mf}^2 + 150C_2 \mathrm{Re}_{mf} = Ar \tag{3}$$

where

$$C_1 = \frac{1}{\varepsilon_{mf}^3 \phi_s}; \quad C_2 = \frac{1-\varepsilon_{mf}}{\varepsilon_{mf}^3 \phi_s^2} \tag{4}$$

and Ar is the Archimedes number and Re_{mf} is the Reynolds number at the minimum fluidization condition. C_1 and C_2 are the voidage-shape factors. Wen and Yu (1966) approximated $C_1 = 14$ and $C_2 = 11$ based on the empirical data obtained with different properties of gas and solid particles. Pattipati and Wen (1981) reported that at lower Reynolds numbers ($\mathrm{Re_{mf}} < 5$), the first term of the left side (kinetic force) of Eq. (3) can be neglected so that Eq. (3) became as:

$$150C_2 \mathrm{Re}_{mf} = Ar \tag{5}$$

With the experimental data of this study, Re_{mf} vs. Ar is plotted and the resulting correlation is,

$$1667 \mathrm{Re}_{mf} = Ar \tag{6}$$

in the range of $0.02 < Re_{mf} < 2.7$ and $38 < Ar < 4700$ with a correlation coefficient of 0.996. The C_2 value in eq. (3) with the present experimental data is 11.11 which correspond well to the approximation of Wen and Yu (1966).

Then, Eq. (6) can be expressed as:

$$U_{mf} = \frac{d_p^2(\rho_s - \rho_g)g}{1667\mu} \tag{7}$$

In Eq. (7), ρ_g is very small compared with ρ_s therefore U_{mf} of the particles at different temperature is a function of gas viscosity. With increasing temperature, gas viscosity increases so that U_{mf} decreases. Relationship between Re_{mf} and Ar in the present and previous studies (Pattipati and Wen, 1981; Botterill et al., 1982; Mathur et al., 1986; Ryu et al., 2003) is shown in Fig. 3.

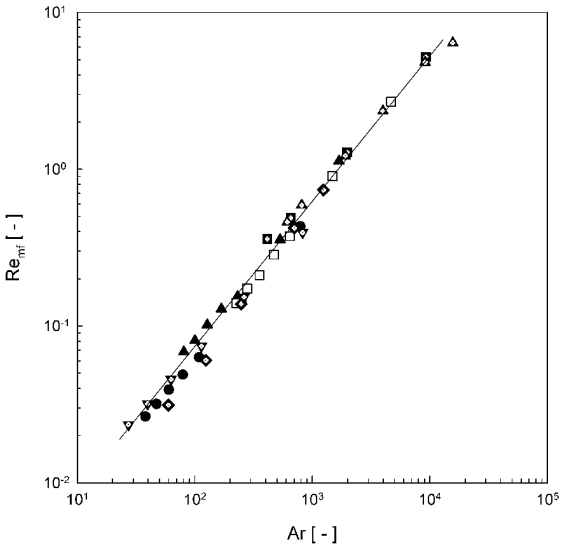

Fig. 3 Relationship between Re_{mf} and Ar in the present and previous studies (○: present study, ▲: Pattipati and Wen (1981), ▼: Botterill et al. (1982), ◆: Mathur et al. (1986), ■: Ryu et al. (2003)

Transport velocity

In this study, the transport velocity is determined by the emptying time method in which U_{tr} corresponds to a kink point between the lines at lower and higher gas velocities (Adanez et al., 1993; Bae et al., 2001). The U_{tr} values of 270 ㎛ sand particle determined by the emptying time method at different temperatures are shown in Fig. 4 in which U_{tr} increase with increasing temperature. The effect of temperature as a function of particle size on U_{tr} is shown in Fig. 5. Bae et al. (2001) reported that U_{tr} can be related to particle terminal velocity (U_t) at different temperature as:

$$U_t = [\frac{4gd_p(\rho_p - \rho_g)}{3\rho_g C_D}]^{1/2} \quad (8)$$

where C_D is drag coefficient. They explained that $C_D\rho_g$ is proportional to gas density in a fast fluidized bed in the Newton's flow region. Since gas density decreases with increasing temperature, the particle terminal velocity increases from Eq. (8). Therefore, much higher gas velocity is needed to carryover particles from the bed.

The U_{tr} values obtained in the present and previous studies of different particle size and temperatures (Bae et al., 2001; Ryu et al., 2003) have been correlated as (Fig. 6):

$$\mathrm{Re}_{tr} = 2.001 Ar^{0.405} \quad (9)$$

This equation covers the range of variables 5 <Re_{tr} < 60 and 60 < Ar < 4700 with a correlation coefficient of 0.965.

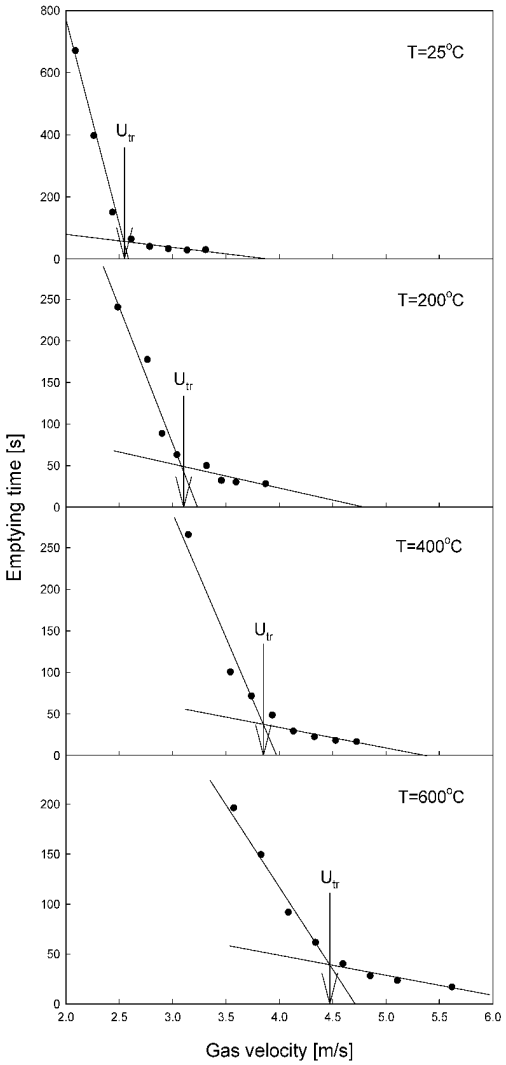

Fig. 4 Determination of U_{tr} by the emptying time method at different temperature

Solid circulation rate (G_s)

To control constant solid circulation rate is very important in the DFBG because the generated heat in the combustor should be transferred by heat carriers into the gasifier for endothermic gasification reaction. The main variables to control solid circulation rate are the amount of solids inventory and gas velocities in the riser and the loop-seal. Generally, solid circulation rate increases with increasing gas velocity and solids inventory. In our previous study in a cold model DFBG, a correlation was proposed as a function of operating variables (Goo et al., 2008). This correlation is modified with the

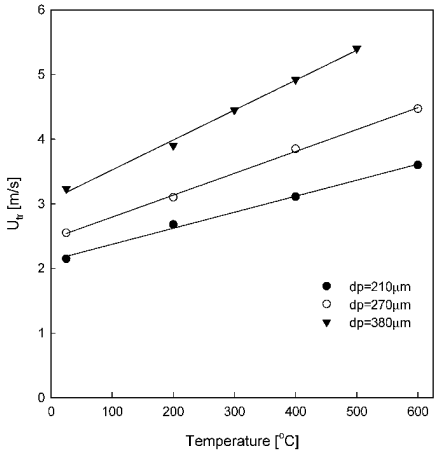

Fig. 5 Effect of temperature on U_{tr}

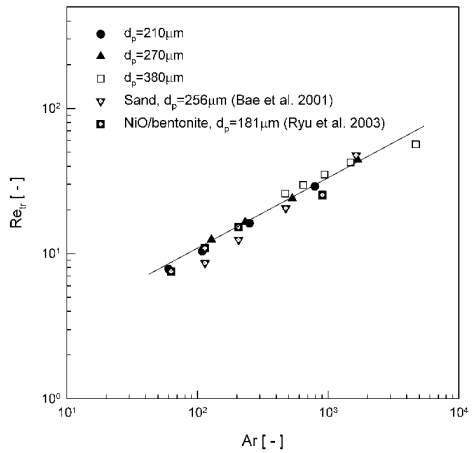

Fig. 6 Relationship between Re_{tr} and Ar in the present and previous studies

present experimental data at higher gas temperatures with correction of gas property with temperature to determine U_t and U_{mf} as:

$$\frac{G_s}{\rho_s U_g} = 3.363\times10^{-5}\left(\frac{U_g}{U_t}\right)^{0.866}\left(\frac{U_{g,l}}{U_{mf}}\right)^{3.666} \tag{10}$$

in the range of $2.1 < U_g/U_t < 4.9$ and $1.6 < U_{g,l}/U_{mf} < 2.9$ with a correlation coefficient of 0.82 as shown in Fig. 7.

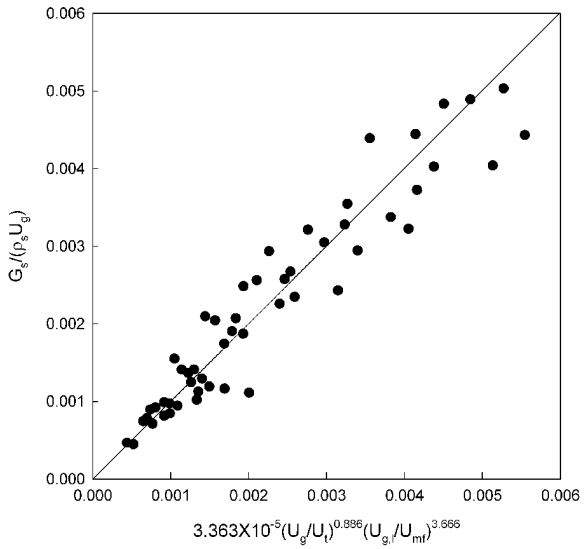

Fig. 7 Parity plot of $G_s/\rho_s U_g$ calculated from equation (10) and the experimental data

CONCLUSIONS

The fundamental data such as the minimum fluidization velocity, the transport velocity and solid circulation rate in the dual fluidized beds gasifier of different particle size at different temperature were determined. With increasing temperature, the minimum fluidization velocity decreases due to the increase of gas viscosity. The transport velocity increases with increasing temperature and the correlation in terms of Reynolds and Archimedes numbers is proposed. Solid circulation rate in the dual fluidized bed is correlated in terms of U_g/U_t and $U_{g,l}/U_{mf}$.

NOTATIONS

Ar	Archimedes number, $d_p^3\rho_g(\rho_s-\rho_g)g/\mu^2$	-	U_g	gas velocity in the riser	m/s
C_D	drag coefficient	-	$U_{g,l}$	gas velocity in the loop-seal	m/s
d_p	particle diameter	㎛	U_{mf}	minimum fluidization velocity	m/s
g	gravitational acceleration	m/s^2	U_{tr}	transport velocity	m/s
G_s	solid circulation rate	$kg/(m^2s)$	U_t	terminal velocity	m/s
Re_{mf}	Reynolds number at minimum fluidization, $d_pU_{mf}\rho_g/\mu$	-	ε_{mf}	voidage at minimum fluidization	-
Re_{tr}	Reynolds number at transport velocity, $d_pU_{tr}\rho_g/\mu$	-	μ	gas viscosity	kg/(ms)
T	temperature	℃	ρ_g	gas density	kg/m^3
			ρ_s	particle density	kg/m^3
			φ_s	sphericity	

ACKNOWLEDGEMENTS

This work has been supported by KESRI (R-2005-7-072), which is funded by MKE (Ministry of Knowledge Economy). Also, the authors would like to thank for financial support through the Brain Korea 21 project.

REFERENCES

Adànez, J., de Diego, L. F. and Gayan, P.: Powder Technol. **77** (1993), pp.61-68.

Bae, D. H., Ryu, H. J., Shun, D. W., Jin, G. T. and Lee D. K.: HWAHAK KONGHAK **39** (2001), pp.456-464.
Botterill, J. S. M., Teoman, Y. and Yuregir, K. R.: Powder Technol. **31** (1982), pp.101-110.
Desai, A., Kikukawa, H. and Pulsifer, A. H.: Powder Technol. **16** (1977), pp.143-144.
Goo, J. H., Seo, M. W., Park, D. K., Kim, S. D., Lee, S. H., Lee, J. G. and Song, B. H.: J. Chem. Eng. Japan **41** (2008), pp.686-690.
Lee, G. S. and Kim, S. D.: Powder Technol. **62** (1990), pp.207-215.
Mathur, A., Saxena, S. C. and Zhang, Z. F.: Powder Technol. **47** (1986), pp.247-256.
Pattipati, R. R. and Wen, C. Y.: Ind. Eng. Chem. Process. Des. Dev. **20** (1981), pp.705-708.
Perales, J. F., Coll, T, Llop, M. F., Puigjaner, L., Arnaldos, J. And Cassal, J. : "Circulating Fluidized Bed Technology III", edited by Basu, P., Horio, M. and Hasatani, M. Pergamon Press, New York (1990), pp.73-78.
Ryu, H. J., Lim, N. Y., Bae, D. H. and Jin, G. T.: HWAHAK KONGHAK **41** (2003), pp.624-631.
Subramani, H., Balaiyya, M. B. M. and Miranda, L. R.: Exp. Therm. Fluid. Sci. **32** (2007), pp.166-173.
Svoboda, K. and Hartman, M.: Ind. Eng. Chem. Process Des. Dev. **20** (1981), pp.319-326.
Tsukada, M., Nakanishi, D. and Horio, M.: Int. J. Multiphase Flow, **19** (1993), pp.27-34.
Wen, C. Y. and Yu, Y. H.: Chem. Eng. Prog. Symp. Ser. **62** (1966), pp.100
Wu, S. Y. and Baeyens, J.: Powder Technol. **67** (1991), pp.217-220.

FLUIDIZATION CHARACTERISTICS OF STALK-SHAPED BIOMASS IN BINARY PARTICLE SYSTEM

Y. Zhang, B. S. Jin, W. Q. Zhong

School of Energy & Environment, Southeast University, Nanjing, 210096, China

Abstract: Experimental investigation on fluidization characteristics of biomass alone and sand-biomass mixture has been carried out in a 3D fluidized bed by means of visual observation and pressure fluctuation analysis. The biomass material employed is cotton stalk, and the sands used are of three different sizes. They together make up of three kinds of mixtures, in which the percentage of biomass particle in each mixture (X_{w0}) are 1.79, 4.36, 8.36, 15.43 and 31.33 by weight. Additionally, the experiment is conducted over a wide range of gas velocity. It is found that regardless of gas velocities, the biomass alone can not archive good fluidization, whereas small additive of sand substantially improves the fluidization quality. The results also show that the fluidization regime is more sensitive to X_{w0} as compared with sand particle size. The transition velocity (U_c) from bubbling to turbulent fluidization regime decreases with X_{w0} for the same mixture, while increasing the size of sand component leads to a delay transition in different mixture.

Keywords: biomass particle, fluidized bed, turbulent, pressure fluctuation

INTRODUCTION

Biomass, fuel derived from organic matter on a renewable basis, is among the largest sources of energy in the world, third only to coal and oil (Bapat et al., 1997). There are two main reasons for their boost as an alternative energy source: one is that the use of biomass mitigates greenhouse gas emission; the other is that biomass use as an energy resource relieves municipal and agricultural waste management from the burden of voluminous waste.

Currently, conversion of biomass to energy is undertaken using two main process technologies: thermo-chemical and bio-chemical process (Mckendry, 2002). Within thermo-chemical conversion four process options are available: combustion, pyrolysis, gasification and liquefaction. In many conditions, fluidized bed reactor characterized by excellent gas-solid contacting, favourable heat transfer and uniform and controllable temperatures, is used as a process reactor. However, biomass cannot easily fluidize due to their peculiar shapes, sizes and densities. To assist fluidization of biomass, an inert material like silica sand, alumina, calcite, etc., is commonly added. Also, it acts as a heat transfer medium in the reactor. It is well known that hydrodynamic behavior of gas-solid flow in the fluidized bed depends strongly upon the particle properties. For the binary mixture of sand and biomass, each component has extreme difference in not only material density, particle size but also shape. Therefore, it may be forecasted that fluidization behavior of binary mixture including biomass is different from one of single component, which have been studied in considerable depth.

In past years, most work (Aznar et al., 1992; Abdullah et al., 2003; Rao and Ram, 2001; Reina et al., 2000; Pilar et al., 1992; Chiba et al., 1979; Patil et al., 2005; Clarke et al., 2005) has been for low-velocity fluidized beds. Aznar et al. (Aznar et al., 1992) study the fluidization behavior of sawdust by itself and find that it does not fluidize well and it exhibits channeling and Geldart C fluidization behavior. Hence, other researches shift attentions to the mixture of biomass and inert particle and investigate the fluidization characteristics, such as bed pressure drop and the minimum fluidization velocity. Patil et al. (Patil et al., 2005) also find significant segregation occurring during the fluidization process. The moisture content of biomass material, as a factor influencing fluidization behavior, has been studied by Clarke et al. (Clarke et al., 2005). The results indicate that as the moisture content of the biomass is increased, the minimum fluidization velocity of the binary mixture also increases. On the whole, the limited work that has been reported on biomass fluidization mainly dealt with the minimum fluidization velocity, ways of achieving fluidization, mixing and segregation, and residence time distributions.

For this reason, experiment studies on the fluidization characteristics of biomass alone and sand-biomass mixture have been carried out in a 3D fluidized bed over a wide range of gas velocity. Visual observation is made to examine fluidization behavior, and pressure fluctuation analysis is adopted to determine the flow regime.

EXPERIMENTAL

Figure 1 shows a schematic diagram of the experimental system used in this work. Fluidized gas is

supplied by roots blower and its flow rates are controlled by a calibrated orifice plate together with a globe valve and one U tube manometer. The fluidized vessel studied is rectangular-shaped and its dimension is: overall height of the bed, H_t=4.4 m, height of the lower part, H_l=0.76 m, height of the upper part, H_u=3.1 m, cross section area of the lower part, S_l=0.4×0.4 m and cross section area of the upper part, S_u=0.5×0.5 m. The fluidization process is recorded with high speed digital camera (Nikon Coolpix 5000) through the visual window. The dynamic pressure is monitored by means of pressure sensor. Pressure taps for measuring the pressure fluctuations are installed on the wall of the bed. One of them is installed under the distributor and others are above the distributor with heights of 50 mm, 150 mm, 680 mm and 2955 mm from the distributor.

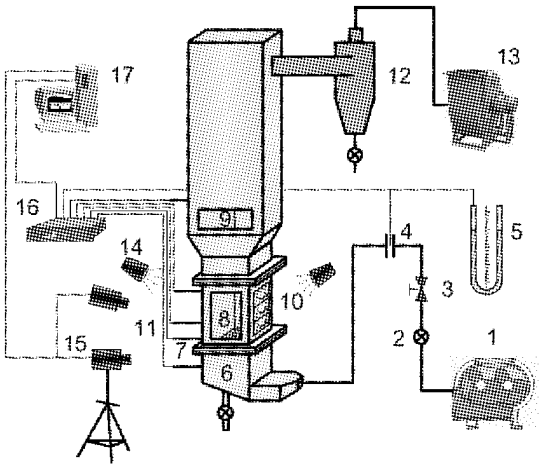

Fig.1 Experiment system

Cotton stalk is used as test biomass material, which is collected from comminution operations. This kind of biomass particle has a shape of thin long and aspect ratio (height/diameter) is 5. The other solid material used is sands of same density and different sizes, which belongs to Geldart B and D, respectively. The detailed physical properties of materials used in this study are summarized in Table 1. Biomass together with sand makes up three kinds of binary mixture. The weight percents of the biomass in each mixture are 1.72, 4.19, 8.06, 14.92 and 30.47, which correspond to the volume percents of 16.67, 33.33, 50, 66.67 and 83.33. For all the mixtures, the static bed height is kept at 300 mm.

Table 1 Properties of particle

	Sand 1	Sand 2	Sand 3	Biomass
Material	Quartz sand	Quartz sand	Quartz sand	Cotton stalk
Mean diameter, mm	0.355	0.5	0.85	5
Mean height, mm	-	-	-	25
Particle density, kg/m^3	2650	2650	2650	385.3
Bulk density, kg/m^3	1593	1530	1435	147.6
Voidage, -	0.399	0.423	0.458	0.617

At the beginning, the sand and biomass are thoroughly segregated with biomass on the top of the sand. In all experiments, such completely segregated arrangement of particles is used as the initial particle bed. Starting from the fixed-bed state, the gas velocity is slowly increased until it reached a dynamic equilibrium. During this process, the bed drop is measured on-line. Once the bed reaches complete fluidization, the airflow rate is reduced in order to study the defluidization characteristics. Using similar method, the fluidization behavior is observed and the differential pressure fluctuation is recorded.

RESULTS AND DISCUSSION

Identification of fluidization regimes

The pressure drop versus superficial gas velocity both for increasing and decreasing flow rates of air are plotted for determining the fluidization regime and minimum fluidization velocities. Fig. 2 shows the profiles of measured pressure drop for system 2 with X_{v0} =50% as a function of gas velocity. It can be observed that as the gas velocity gradually increase, the whole bed undergo different fluidization regimes, which is marked with two characteristic velocities: incipient fluidization velocity (U_{if}) and complete fluidization velocity (U_{cf}). Before U_{if}, the bed is at rest with two segregated layers. After U_{if} is reached, fluidization takes place at the bottom layer of sand and becomes a bit more vigorous with the gas velocity. The point U_{cf} marks a transition to the regime in which a state of complete (total) fluidization is attained, where practically all the solids are in movement. Then the bed pressure drop keeps nearly constant when the gas velocity is further increased. It is worth noting that U_{if} is determined during the fluidization process, whereas U_{cf} is determined in the defluidization stage.

On the other hand, with the decrease of gas velocity from the fully fluidized state, the bed pressure drop follows a different path without passing through the peak. During the defluidization process, the bed pressure drop values are lower when compared to those measured during the fluidization phase because at the beginning

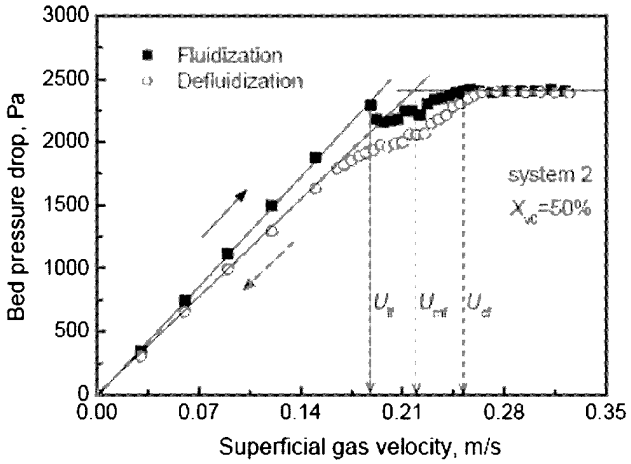

Fig. 2 Pressure drop vs. superficial gas velocity for system 2 with X_{v0}=50%

of the fluidization experiment, the fully segregated bed has less voidage and it is less permeable. By contrast, it is more permeable for the partial mixing bed due to resultant more voidage. This trend matches those observed by other researchers (Patil et al., 2005).

Visual observations are conducted in order to establish the causes for the results presented. At low gas velocity, the bed keeps silent. When gas velocity is close to U_{if}, slight bed contraction is observed. When the gas velocity is increased to U_{if}, the bottom sand commences to fluidize, followed by a rapid decrease in bed height. It is attributable that on this condition, the top biomass layer does not fluidize and immerses into the loose sand layer as a whole under the action of gravity. This also contributes to a decrease of pressure drop in Fig. 2. Subsequently, a further increase in gas velocity results in the bed expansion. Under the disturbance of sand, the biomass layer becomes loose and finally unlocks. Thus, at U_{cf}, the whole bed fluidizes and then the bed pressure drop keeps constant. After U_{cf}, the bed achieves a better fluidization state.

Figure 3 indicate the pressure drop versus velocity profiles for alone biomass. It can be seen that the pressure drop increase with the increase of gas velocity except for a transient decrease. The hydrodynamic behavior observed for alone biomass is remarkably different from that observed for binary mixture. Starting from complete-segregated packing, bed expansion is significantly observed as soon as gas is 0.245 m/s. When it is further increased to 0.383 m/s, some channels coming from the surface of the distributor to the bed surface occur, which is responsible for the trough in the pressure drop curve. Then the pressure drop continues to grow as gas velocity is further increased, while the bed keep such state all the time. Such phenomenon is different from that observed by Reina et al. (Reina et al., 2000), where slugging tend to follow the channeling. This is due to the fact that the fluidization state for these types of biomass particles depends on the nature of the system and on the physical characteristics of the particles.

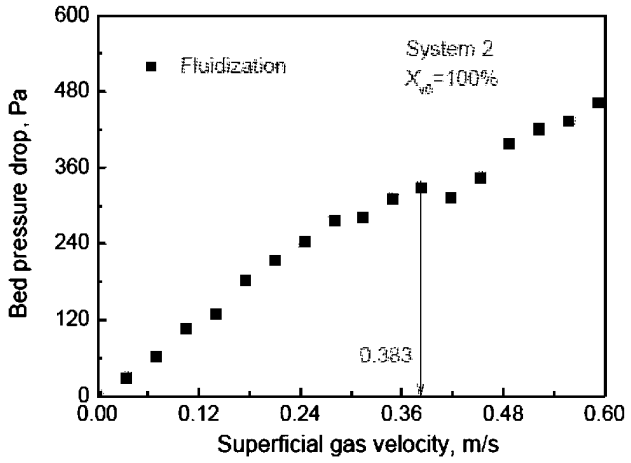

Fig. 3 Pressure drop vs. superficial gas velocity for system 2 with X_{v0}=100%

Figure 4 summarizes results obtained with above method using various systems: gas velocities corresponding to regime transitions are mapped as functions of the initial volumetric concentration of the biomass component, X_{v0}. It shows that as X_{v0} increase, the incipient fluidization velocity slightly decreases and then significantly increase while complete fluidization velocity increases greatly. This suggests that it is

difficult to achieve a complete fluidization at the case of high biomass concentration. Though all the systems exhibit similar trend, the interval between U_{if} and U_{cf} appear to slightly enlarge from system 1 to system 3. Clearly, it can be found from Fig. 4 that the velocity interval varies more significant with X_{v0} than the system. This implies that the fluidization pattern is more sensitive to biomass concentration than the sand size.

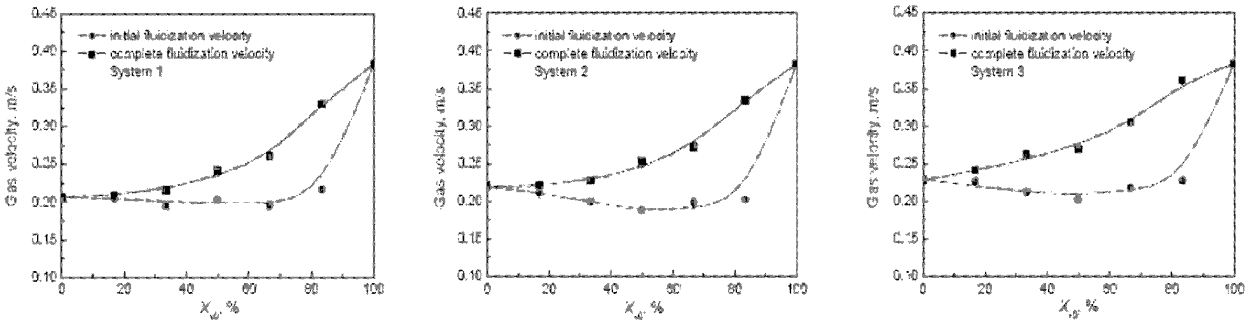

Fig. 4 Incipient and complete fluidization velocity as functions of X_{v0} for different system

Bubbling to turbulent regime transition

Typical example of differential pressure fluctuations for system 2 and at U_f=0.83 m/s is displayed in Fig. 5. It can be clearly seen that the amplitude of differential pressure fluctuations decreases with increasing X_{w0}. This means that the concentration of biomass have an great influence on bubble behavior, since the amplitude of the fluctuation signals is directly related to the behavior of bubbles. Increasing biomass concentration leads to a decrease of probability for the growth and coalescence of bubbles.

In an attempt to elucidate the bubbling phenomena in the bed more easily and quantitatively, the mean amplitude of the pressure fluctuations have been calculated based on the statistical analysis. For a given discrete pressure fluctuation signal $p(t)$, its mean amplitude is expressed as the standard deviation, which is defined mathematically as follows:

$$\sigma_p = \sqrt{\frac{1}{N-1}\sum_{t=1}^{N}(p(t)-\overline{p})^2} \quad (1)$$

where

$$\overline{p} = \sqrt{\frac{1}{N}\sum_{t=1}^{N}p(t)} \quad (2)$$

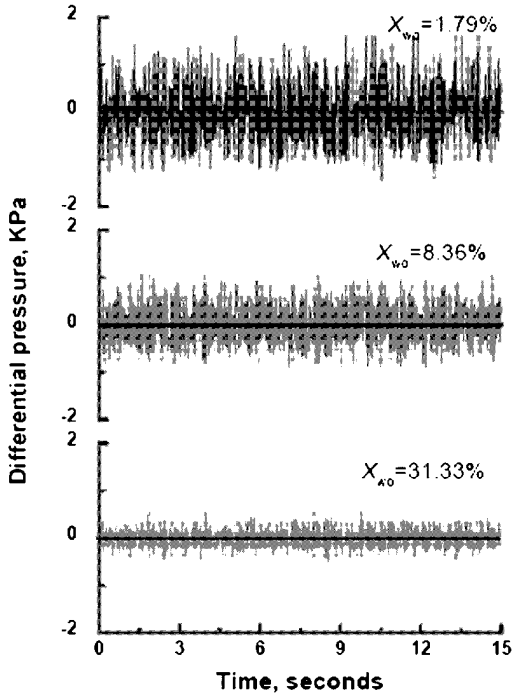

Fig. 5 Typical differential pressure fluctuation at the same gas velocity of U_f=0.83 m/s and different mixing ratio

As an example of the influence of weight fraction of biomass on the transition velocity, the standard deviation of pressure fluctuation for system 2 at varying weight fraction are presented in Fig. 6. At the beginning, the standard deviation increases with respect to the gas velocity and then decreases after passing through a peak. The increase of standard deviation in pressure fluctuations may be attributed to the increase in bubble size with gas velocity as a result of the coalescence of small bubbles into large bubbles. On the contrary, the decrease of standard deviation in pressure fluctuation is due to the eruption of large bubble into small gas voids overtaking the coalescence of small bubbles into large bubbles.

As can be seen from Fig. 6, each mixture follows the similar trend. Even that, a significant difference can be detected. The transition velocity U_c, corresponding to the gas velocity at which the standard deviation reached a maximum, has become widely accepted as the standard means of delineating the transition from bubbling to turbulent fluidization (Bi et al., 2000). This value decreases with the increase in biomass concentration. For example, at X_{w0}=1.79%, the transition velocity to the turbulent flow regime is found to be 1.38 m/s. it decreases to 1.04 m/s at X_{w0}=8.36% and 0.67 m/s at 31.33%, respectively. This suggests that the increase of biomass concentration results in a rapid transition from bubbling to turbulent flow regime.

Figure 7 shows the standard deviation of pressure fluctuation for different system with the same biomass concentration (X_{w0}=4.36%). It is interesting to note that not only the standard deviation but also the transition

velocity decrease with the variation of system from 3 to 1. This implies that the size of sand composition have an effect on the transition of flow regime. Decreasing sand size prompts the transition from bubbling to turbulent regime as a result of the presence of more small bubbles. It agrees with the general trend reported in the literature (Cai et al., 1990).

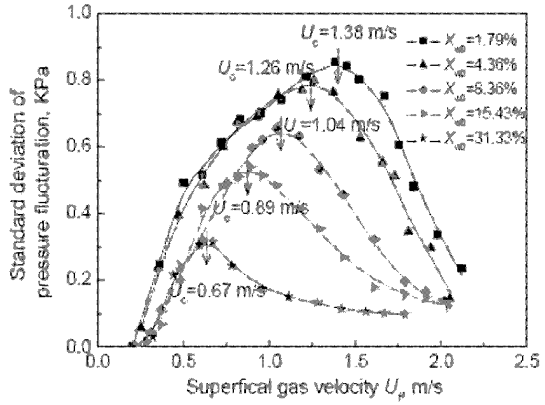

Fig. 6 Standard deviation of differential pressure for system 2 with different X_{w0}

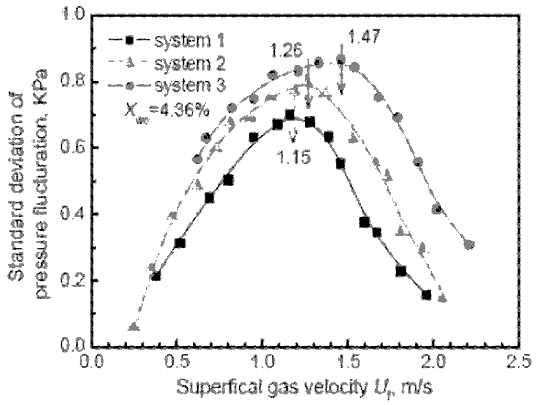

Fig. 7 Standard deviation of pressure fluctuation for different system

CONCLUSIONS

Fluidization of sand-biomass mixture has been studied experimentally in a 3D fluidized bed by means of visual observation and pressure fluctuation analysis. Three kinds of mixtures, in which the biomass material employed is cotton stalk and the sands used are of three different sizes, are examined, respectively. Additionally, the fluidization gas velocity varies over a wide range covering the bubbling and turbulent fluidization regime. The conclusions obtained from the experiment are summarized in the following points:

Over the investigated gas velocities, the thin long biomass particle alone can not archive good fluidization, whereas small additive of sand substantially improves the fluidization quality.

The interval of local fluidization regime significantly increases with the biomass concentration. Also, the fluidization regime is more sensitive to X_{w0} as compared with sand particle size.

The transition velocity, U_c, determined from differential pressure fluctuation, is found to decreasing with increasing X_{w0} and decreasing d_p within the same system.

NOTATIONS

Ar	Archimedes number, -
d	diameter of biomass particle, m
d_e	equivalent diameter, m
d_p	particle diameter, m
H_t	total height of the bed, m
H_l	lower bed height, m
H_u	upper bed height, m
h	height of biomass particle, m
h_0	static bed height, m
h_i	expansion bed height, m
$\overline{p}$	average pressure, Pa
Re	Reynolds number, -
S_l	cross section area of lower bed, m^2
S_u	cross section area of upper bed, m^2
U_c	transition velocity, m/s
U_f	fluidization velocity, m/s
U_{cf}	complete fluidization velocity, m/s
U_{if}	incipient fluidization velocity, m/s
X_{w0}	weight fraction of biomass, -
σ_p	pressure fluctuation deviation, -
ρ_b	biomass density, kg/m^3
ρ_p	particle density, kg/m^3
ρ_s	sand density, kg/m^3

ACKNOWLEDGEMENT

Financial support from the National Natural Science Foundation of China (50676021), the Foundation of Graduate Creative Program of JiangSu (CX07B-098z) and the Foundation of Outstanding Doctoral Dissertation of Southeast University are sincerely acknowledged.

REFERENCES

Abdullah, M.Z., Husain, Z., Yin Pong, S.L.: BIOMASS & BIOENERG. 24 (2003), pp. 487-494.
Aznar, M.P., Gracia-Gorria, F.A., Corella, J.: International Chemical Engineering 32 (1992), pp. 95-102.
Bai, D., Shibuya, E., Nakagawa, N., Kato, K.: Powder Technol. 87 (1996), pp. 105-111.
Bapat, D.W., Kulkarni, S.V., Bhandarkar, V.P. (1997). Proceedings of the 14th international conference on fluidized bed combustion. Vancouver, New York, NY: ASME; 1997. pp. 165-74.
Bi, H.T., Grace, J.R., Zhu, J.: Powder Technol. 82 (1995), pp. 239-253.
Bi, H.T., Ellis, N., Abba, I.A., Grace, J.R.: Chem. Eng. Sci. 55 (2000), pp. 4789-4825.
Brown, R.C., Brue, E.: Powder Technol. 119 (2001), pp. 68-80.
Cai, P., Jin, Y., Yu, Z.Q., Wang, Z.W.: AIChE Journal 36 (1990), pp. 955.
Chiba, S., Chiba, T., Nienow, A.W., Kobayashi, H.: Powder Technol. 22 (1979), pp. 255-269.
Clarke, K.L., Pugsley, T., Hill, G.A.: Chem. Eng. Sci. 60 (2005), pp. 6909-6918.
Cui, H.P., Grace, J.R.: Chem. Eng. Sci. 62 (2007), pp. 45-55.
Kashkin, V.N., Lakhmostov, V.S., Zolotarskii, I.A., Noskov, A.S., Zhou, J.J.: Chim. Eng. J. 91 (2003), pp. 215-218.
Lirag, R.C., Litman, H.: AIChE Symposium Series 166 (1971), pp. 11-22.
Mckendry, P.: Bioresource Technol. 83 (2002), pp. 47-54.
Patil, K.N., Bowser, T.J., Bellmer, D.D., Huhnke, R.L.: Agricultural Engineering International: the CIGR Ejournal 07 (2005), pp. 1-11.
Pilar, A.M., Gracia-Gorria, F.A., Corella, J.: International Chemical Engineering 32 (1992), pp. 95-102.
Rao, T.R., Ram Bheemarasetti, J.V.: ENERGY 26 (2001), pp. 633-644.
Reina, J., Velo, E., Puigjaner, L.: Powder Technol. 111 (2000), pp. 245-251.
Zijerveld, R.C., Johnsson, F., Marzocchella, A.: Powder Technol. 95 (1998), pp. 185-204.

BOTTOM ZONE FLOW PROPERTIES OF A SQUARE CIRCULATING FLUIDIZED BED WITH AIR STAGING

Zhengyang Wang, Shaozeng Sun, Xiangbin Qin, Qigang Deng, Shaohua Wu

Combustion Engineering Research Institute, School of Energy Science and Engineering, Harbin Institute of Technology, Harbin, 150001, China

Abstract: The recycled solids fed to the circulating fluidized bed (CFB) riser on one wall have a limited lateral dispersion rate, which results in an uneven solids distribution in the bottom zone of the bed. Using a reflective optical fiber solids concentration measuring system and visual observation, the flow properties in the bottom zone of a fluidized bed was investigated. The cold model CFB riser has a square cross-section of 0.25m×0.25m and a height of 6.07m with quartz sand as bed material (dp=276μm). At the condition of u_0=4m/s, Gs=21kg/m^{2}s, the back feeding particles can penetrate the gas-solid flow in the riser and get to the opposite wall. It makes a denser region near the front wall of the bed. When air-staging is adopted, solids holdup increases below the secondary air (SA) injection ports with the increase of the rate of the secondary air to the total air (SAR). The solids holdup increase also exists above the secondary air injection ports but the incremental amount decreases quickly along the riser. At SAR=0.3, a denser bottom zone limits the back feeding particles' penetration and a relatively even solids distribution is formed in the bottom bed. A W-shaped solids concentration profile is formed just above the SA injection level. At SAR=0.5, uneven solids concentration profile exists in the bottom bed and no W-shaped solids concentration profile is formed for the deeper penetration of SA jets.

Keywords: square circulating fluidized bed, solids distribution, bottom zone, air staging

INTRODUCTION

Circulating fluidized beds (CFBs) have been successfully used in fluid catalytic cracking (FCC) and fossil fuel combustion. For some CFBs, the return solids are fed to the riser only with a single inlet and have a limiting lateral dispersion rate. Using carbon ice as tracer, Schlichthaerle (2001) researched the solids dispersion in the inlet zone of the bed. Knoebig (1999) found a relatively high concentration region of char near the ash back-feeding ports by numerical simulation of a CFB boiler. Yan (2003) studied the solids concentration and velocity profile in the entrance regions of a high-flux CFB riser (Gs=550 kg/m^{2}s). Wilde (2005) gave the gas-solids mixing properties in the entrance regions of a dilute CFB riser (Gs=3kg/m^{2}s) by 3D LDA measurement and numerical simulation. The CFB risers of Yan and Wilde were circular while Schlichthaerle and Knoebig used squared risers. All above studies did not focus on the solids concentration distribution in the corner region of the squared riser which was different from other region of riser with a square cross section due to the friction effects of two walls.

In a circulating fluidized bed combustor, air staging is obtained by splitting the combustion air into primary air (PA) and secondary air (SA). Air staging changes the solids holdup profile of the riser especially in the zone below the secondary air injection ports (Cho, 1993; Marzocchella, 1996; Kang, 2000; Ersoy, 2004). However, few studies have been conducted on the bottom bed flow properties with air staging. The impact of air staging on the solids distribution near the secondary air injection ports in a square CFB riser was also less documented. In this study, a reflective optical fiber probe was used to measure the local solids holdup profile in the bottom zone of the riser. The distance between solids feeding ports and SA nozzles was 0.515m. The "bottom zone" in the paper includes the solids return region and the region influenced by SA injection.

EXPERIMENTAL SETUP

Cold circulating fluidized bed model

A circulating fluidized bed cold model (Fig. 1) has a square cross-section riser of 0.25m×0.25m and a height of 6.07m. Two stage cyclones collect most of the quartz sand particles with a mean size of 276μm (U_t=1.53m/s) and a density of 2550kg/m^3. The air from roots blower was divided into primary air, secondary air and air for U-type loop seal (30-35m^3/h, i.e. 3.4%-3.9% of total air 900 m^3/h for u_0=4m/s condition). The solids return duct was located on one wall (Rear wall, R-W) and the height of solids feeding port to the air distributor was 0.307m. Four secondary air nozzles with diameter of 25mm were arranged on the middle of four walls respectively and had a height of 0.822m above the air distributor. Ten pressure taps were located along the height of the riser to measure the axial pressure profile. The solids circulation rate (Gs) was measured through

stop-watch way by a flapper valve in the downer. And this procedure was repeated four times during an experimental run to get a mean *Gs* value.

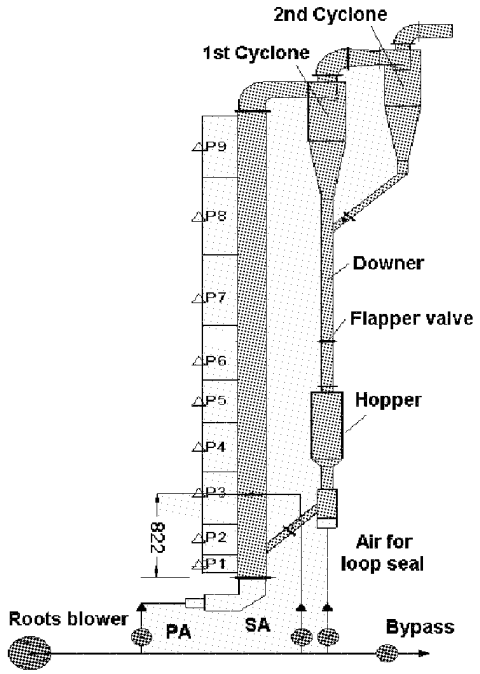

Fig.1 Experimental CFB model

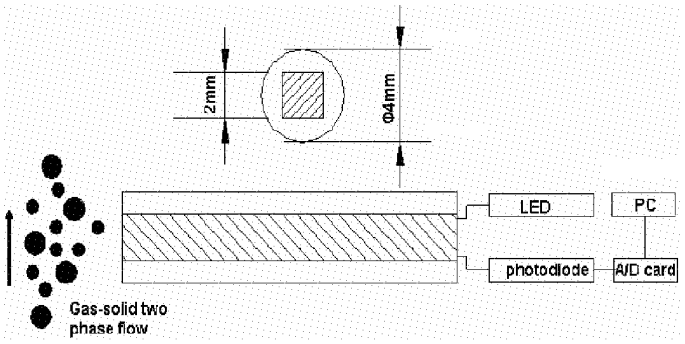

Fig. 2 Reflective optical fiber solids concentration measuring system

Reflective optical fiber solids concentration measuring system

A reflective-type fiber optic system (Fig.2) was used to measure the solids concentration. Similar to that described by Zhou(1994) and Zhang(1997), the system is composed of a light source (LED), an optic probe with a diameter of 4mm , a photodiode, a A/D converter and a computer. The active area in the probe is 2×2mm, consisting of about 5400 emitting and receiving optical fibers (each diameter is 20μm). This system was calibrated in a downer (similar to the Zhang's) to obtain the functional relationship (Fig.3) between the fiber optic system signal voltage V and the solids volume fraction ε_s, which is shown in Equation (1)

$$V = 1.4087\ln(\varepsilon_s + 0.02121) + 5.37443 \quad (1)$$

Measurements were taken at 3 levels which were 0.167m, 0.672m and 1.035m to the air distributor, noted as Level 1, Level 2 and Level 3, respectively. Because the structure is symmetrical in the x direction, only half of the cross section was measured. So at each level, measurements were performed along the centerline and diagonal section marked by *x*+, *y*+, *y*-, *D*+ and *D*- respectively (Fig.4). 11 radial positions ($l/(L/2)$=0, 0.2, 0.36, 0.52, 0.68, 0.76, 0.84,0.88, 0.92, 0.96 and 1) were chosen for each line and each position was measured for 65s at level 2 and level 3, and 130s at level 1. In this study, L stands for the center line length (0.25m) for *x*+, *y*+ and *y*-, or the diagonal length (0.354m) for *D*+ and *D*-.

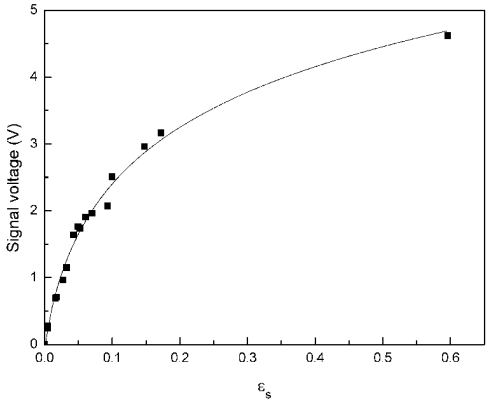

Fig. 3 Relationship between the output signal voltage and the solids concentration

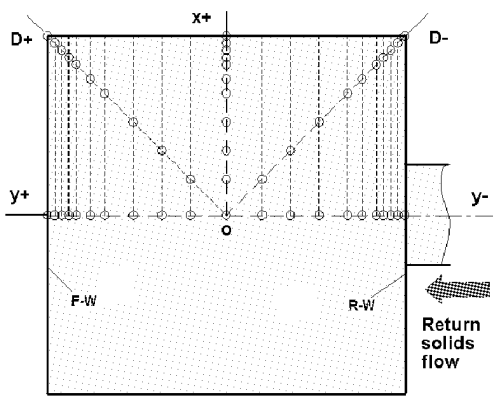

Fig. 4 The measurement positions of a cross section

RESULTS AND DISCUSSION

The bottom zone flow properties without air staging

At the condition of u_0=4m/s, pressure drop increases with increasing *Gs*, possibly due to the clustering effect and the increased back-mixing of solids. From *Gs*=8kg/m^{2}s to *Gs*=27kg/m^{2}s, the bed has similar flow properties by visual observation. In this study, local solids concentration measurement was made only with *Gs*=21kg/m^{2}s. Fig.5 shows the recycling particles moving in the inclined duct (50°). When the recycling particles are entrained by the air from the loop seal to the return duct which connects the loop seal and the riser, the duct inlet has a relatively even solids distribution. However, under the effects of the gravity, solids are separated from air and move only along the bottom section at the lower part of return duct. After acceleration through the inclined return duct by the gas entrainment and gravity, the flow of back feeding particles usually has some amount of momentum when it enters into the bottom bed. In this operating condition, solids holdup is so lean (Fig.8) that the recycling particles penetrated the gas-solid flow in front of it and get to the opposite wall (Front wall, F-W) by visually observation. In the penetration process, some solids are entrained by the upward gas-solids flow. These escaped solids from back feeding particles increase when they flows further down to the core and to the region near the front wall. The return solids which can get to the opposite wall collect the falling solids and make a denser zone near the front wall (Fig.6, Fig.7). In the bottom bed, this denser falling solids flow forced some fluidizing air turn to the rear wall. A relatively denser region is formed in all front wall regions at Level 1(Fig.9). But it is weakened at Level 2 (Fig.10) and exists only near the front wall at level 3 (Fig.11).

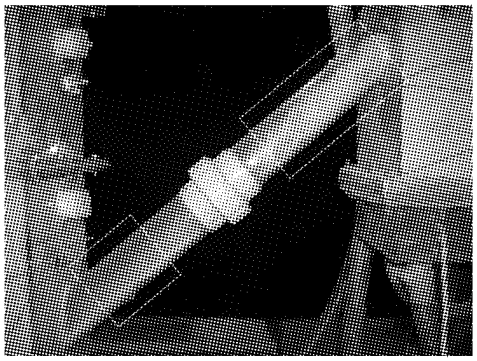

Fig. 5 The back feeding particles in the inclined duct

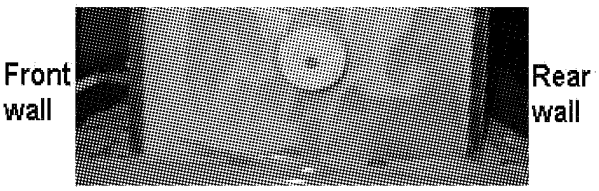

Fig. 6 The gas-solids flow in the bottom bed

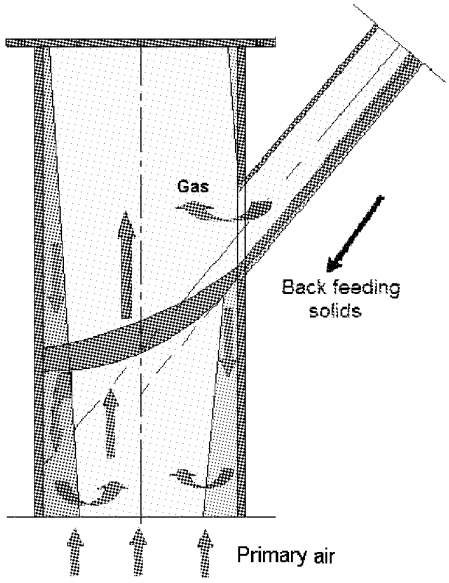

Fig. 7 The back feeding particles in the bottom zone of the riser

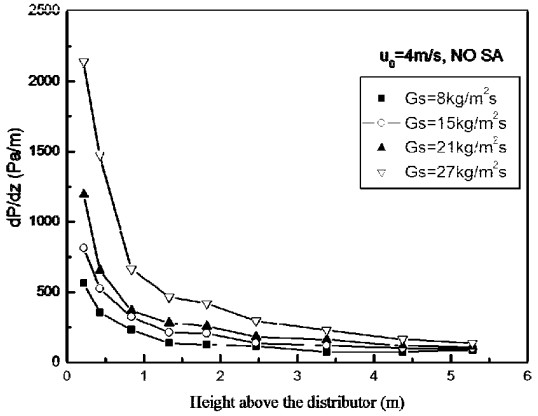

Fig. 8 Pressure drop profile along the riser in the case without SA

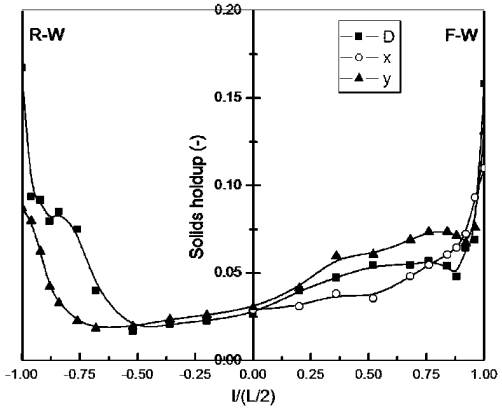

Fig. 9 The solids holdup profile at Level 1 (0.167m above the distributor) without SA

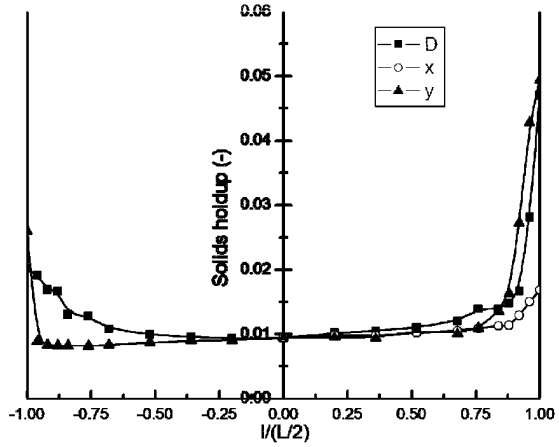

Fig. 10 The solids holdup profile at Level 2 (0.672m above the distributor) without SA

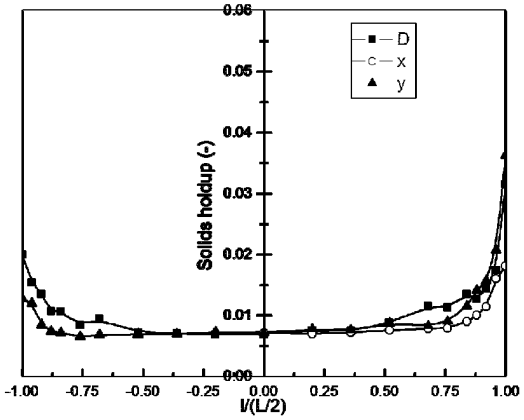

Fig. 11 The solids holdup profile at Level 3 (1.035m above the distributor) without SA

The bottom zone flow properties with air staging

In the operating condition of air staging, three rate of the secondary air to the total air (SAR, 0.15, 0.3, 0.5) was chosen but local solids concentration measurement was performed only with SAR=0.3 and SAR=0.5. The superficial gas velocity in the bottom bed below the solids inlet was 3.23m/s, 2.63m/s and 1.78m/s for SAR=0.15, 0.3, 0.5 respectively. When air staging is adopted, less air passes through the bottom bed leading to a higher solids concentration below the secondary air injection ports as well as in some region above the injection ports (Fig.12,). The secondary air jets partially block the flow of the rising gas solid suspension which also contributes to the increase of the solids concentration in the primary region.

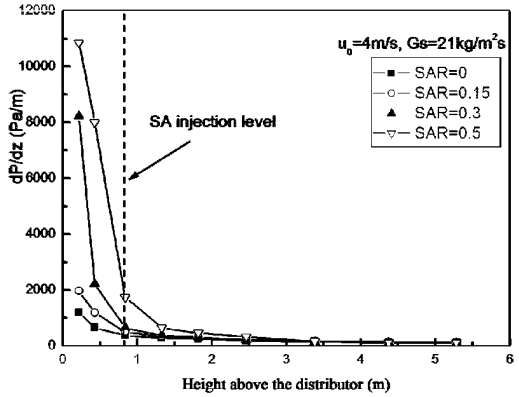

Fig. 12 Pressure drop profile along the riser with air staging

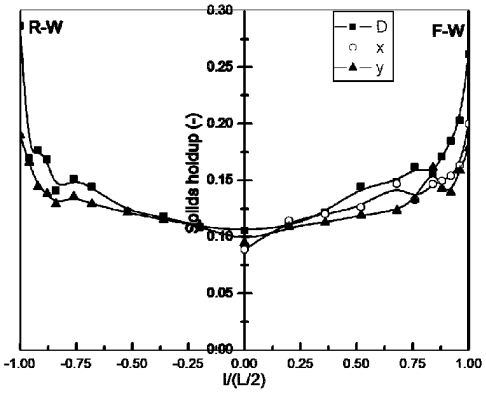

Fig. 13 The solids holdup profile at Level 1 (0.167m above the distributor) when SAR=0.3

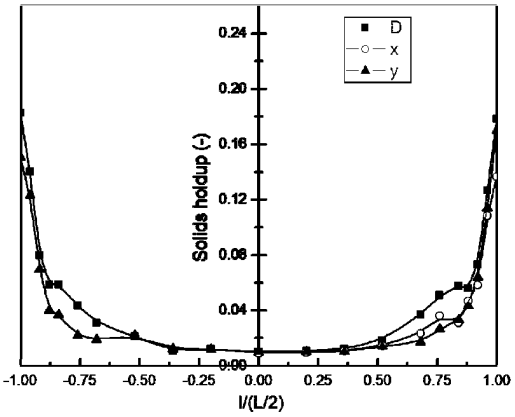

Fig. 14 The solids holdup profile at Level 2 (0.672m above the distributor) when SAR=0.3

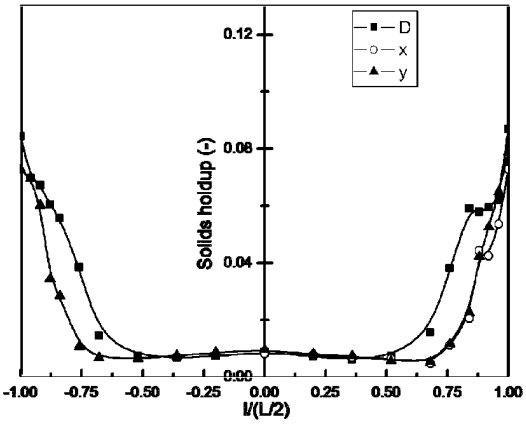

Fig. 15 The solids holdup profile at Level 3 (1.035m above the distributor) when SAR=0.3

When the air staging is utilized (SAR=0.3), a denser bottom zone limits the back feeding particles' penetration and a relatively even solids distribution is formed in the bottom bed (Level 1, Fig.13). At the second measurement level, the difference among three centerlines becomes small. At the region above the SA injection levels (Level 3, Fig.15), with the direct effects of SA jets, the solids holdup reaches a minimum at the location of about 0.52-0.68 of the half-width of the centerline and increases slightly towards the center, which forms a W-shaped solids distribution profile. That also shows that the jet (38m/s) does not penetrate enough to the riser center. The phenomena is not distinct for the diagonal line. The difference between $D+$ and $y+$ becomes larger except in the region near wall, so does the ones between $D-$ and $y-$. On the wall surface, solids concentration at the diagonal line (the corner point) is leaner than the ones at the centerline. This may be attributed to the friction effects of two walls, which makes the flow of falling solids of the corner not much continuous when the solids concentration is relatively leaner.

Higher SA fraction (SAR=0.5), of which the corresponding bottom velocity 1.78m/s is approximate to the mean terminal velocity of particle, leads to a higher solids concentration in the riser especially in the region below SA injection ports. At first measurement level, solids concentration in the core zone is similar to that of the SAR=0.3 condition while it is denser in the annulus region (Fig.17), especially in the corner region. This shows that the air flow rate in the core zone may not change much but less air pass through the annulus region when the total primary air reduces. At first measurement level, Fig.17 also shows that solids concentration at $y-$ is relatively larger than at $y+$. But solids concentration at the side walls region ($x+$) is the biggest among three centerlines. The difference between solids concentration at $D+$ and $y+$ is larger than the ones between that at $D-$ and $y-$. This may be due to the back feeding particles residence in the rear wall region which force more air flow through the front wall region and push aside solids to the corners and the side walls.

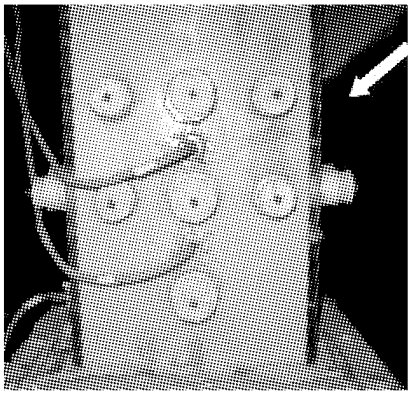

Fig. 16 The gas-solids flow in the bottom bed in the case of SAR=0.5

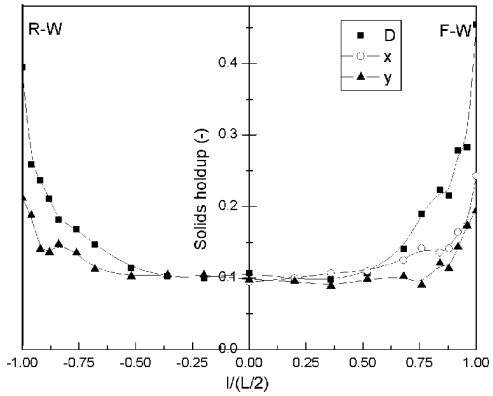

Fig. 17 The solids holdup profile at Level 1 (0.167m above the distributor) when SAR=0.5

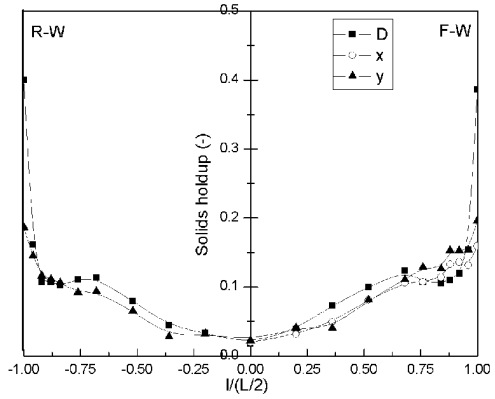

Fig. 18 The solids holdup profile at Level 2 (0.672m above the distributor) when SAR=0.5

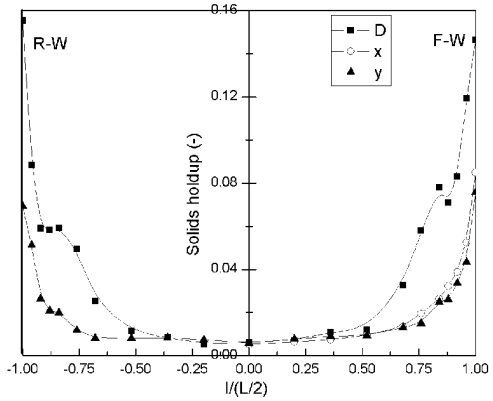

Fig. 19 The solids holdup profile at Level 3 (1.035m above the distributor) when SAR=0.5

The secondary air jets partially block the flow of the rising gas solid suspension and a denser region is

formed below the secondary air jets (Fig.18, Level 2). It decreases the solids concentration difference between the diagonal line and the center line except at the corner point. The jets entrained some falling solids to the upper bed and a leaner region is formed just above the jets (Fig.19, Level 3). Moreover, more solids turn to the corner region as a result of wider cutoff region of the secondary air jets. These two impacts increase the solids concentration difference between the diagonal and the center line and make the solids holdup profile in the cross section of Level 3 more uneven. No distinct W-shaped solids concentration profile exists at both the centerline and diagonal line above the SA injection ports. This shows that the jets with higher velocity (64m/s) can penetrate deeper into the center region of the riser and impinges with each other.

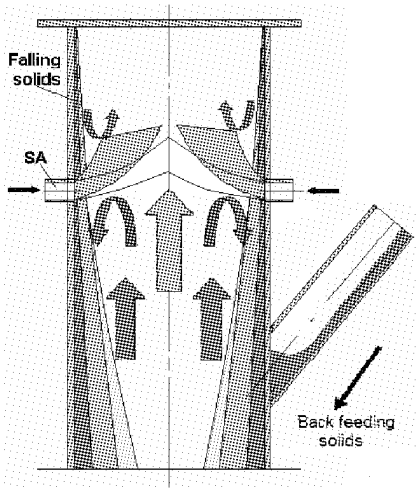

Fig. 20 The flow properties in the bottom bed with air staging

CONCLUSIONS

(1) The flow of back feeding particles usually has some momentum after acceleration through the inclined return duct by gravity and gas entrainment.

(2) In the operating condition without SA, the back feeding particles can penetrate the solids holdup near the solids inlet and get to the opposite wall, which results in a denser region near the front wall.

(3) When air staging is adopted, solids holdup increases below the secondary air injection ports. And the solids holdup increase also exists above the secondary air injection ports but the incremental amount decreases quickly along the riser.

(4) When air staging is utilized (SAR=0.3), a denser bottom zone limits the back feeding particles' penetration and a relatively even solids distribution is formed in the bottom bed. A W-shaped solids distribution profile is formed just above the SA injection level.

(5) Higher SA rate (SAR=0.5) makes the corner region become denser while other region change little. The secondary air jets reduce the flow area of main gas-solid flow from primary zone and make an uneven solids distribution profile just above the secondary air injection ports.

NOTATIONS

dP	pressure drop between two neighboring measurement ports, Pa	*Gs*	solids circulation rate, kg/m^{2}s
d*Z*	distance between two neighboring measurement ports, m	*V*	the fiber optic system signal voltage, V
		U_t	terminal velocity, m/s
		ε_s	solids volume fraction

ACKNOWLEDGEMENTS

The present study was supported financially by the Ministry of Science of China under the National Key Technology R&D Program of China through the project "Supercritical Circulating Fluidized Bed Boiler" (Contract No.: 2006BAA03B01-07)

REFERENCES

Cho, Y.J., Namkung W. and Kim S.D.: Journal of Chem. Eng. of Japan. **27** (1994), pp.158-164.
Ersoy, L.E., Gloriz, M.R., Koksal, M. and Hamdullahpur,F.: Powder Tech. **145** (2004), pp.25-33.
Kang, Y., Song, P.S., Yun S.J., Jeong,Y.Y. and Kim S.D.: Chem. Eng. Comm. **177** (2000), pp.31-47.
Knoebig, T., Luecke, K. and Werther, J.: Chem. Eng. Sci. **54** (1999), pp.2151-2160.
Marzocchella A. and Arena, U.: Powder Tech. **87** (1996), pp.185-191.
Schlichthaerle, P. and Werther, J.: Powder Tech. **120** (2001), pp.21-33.
Yan, A.J., Parssinen, J.H. and Zhu, J.X.: Powder Tech. **13** (2003), pp.256-263.
Zhou, J., Grace, J.R., Qin, S., Brereton, M.H., LIM, C.J. and Zhu, J.: Chem. Eng. Sci. **49** (1994), pp.3217-3226.
Zhang,H., Johoston, P J., Zhu, J X., H.I. de Lasa, Bergougnou,M. A.: Powder Tech. **100** (1998), pp.260-272.

EXPERIMENTAL STUDY ON PARTICLE FEEDING AND MIXING IN THE BOTTOM ZONE OF A CIRCULATING FLUIDIZED BED

X. P. Chen, D. Y. Liu, Z. D. Chen, C. S. Zhao

School of Energy and Environment, Southeast University, Nanjing, 210096, China

Abstract: The mixing behaviors of the feeding particles in the bottom zone of a circulating fluidized bed with a rectangular cross-section of 0.3 m×0.2 m and a height of 2 m were investigated by monitoring transient pressure drop and thermal tracing method. The effects of the feeding particle size, feeding port location (relative to dense bed surface), feeding gas velocity and fluidization gas velocity were examined. The bed collapse technique was also used to examine the lateral distribution of the feeding particles for four typical cases to give reference results. Results show that the mixing behaviors are greatly dependent on particle size. Under the condition that the feeding port is fully submerged in the dense bed, a hot spot occurs as the feeding gas velocity is no more than 0.24m/s. Increase in feeding gas velocity and fluidization gas velocity can both promote the mixing of the feeding particles with bed material.

Keywords: particle feeding, solids mixing, thermal tracing technique, bed collapse technique

INTRODUCTION

In circulating fluidized bed (CFB) combustors fresh fuel and recycled solids are locally fed into the lower zone of the riser at a relatively low velocity. The mixing process of the reactant solids in the bed greatly influence on the combustion performance and it is a particular concern as the unit size increases (Bellgardt et al., 1987; Glicksman et al., 2008).

A number of published works have reported valuable results on solids mixing in fluidized beds. However, the experimental conditions are very scattered. Some investigations on solids mixing have been carried out in bubbling fluidized beds, where the fluidization gas velocities are limited to low values (Kunii and Levenspiel, 1991). And some have studied residence time distribution of solids in "tall and narrow" CFB risers, which are directed towards FCC applications instead of CFB combustors (Werther et al., 1997; Du et al., 2002). For CFB combustor applications, a few groups recently have studied solids mixing in the bottom zone of CFB. Schlichthaerle and Werther (2001) examined tracer concentrations at different vertical and lateral positions with the tracer fed at three different points respectively. The mixing behavior was shown ideal in the vertical direction, while in the lateral direction it was interpreted using a convection-dispersion model. Niklasson et al. (2002) obtained a valve of the effective lateral solids dispersion coefficient (D_{sr}) from measured concentrations of H_2O above the dense bed in a fluidized bed boiler and also gave a review on the empirical equations and values of D_{sr}. Yang et al. (2002) determined D_{sr} under different operating conditions of bed height, gas velocity, and particle size of bed material in a 2-d fluidized bed. Pallares and Johnsson (2006) investigated the mixing mechanisms of fuel particles in a 2-d fluidized bed with a phosphorescent tracer particle simulating a fuel particle.

Most of the above investigations have been directed to study the mixing of bed material itself, and only a few to study fuel particles mixing with bed material (Pallares and Johnsson, 2006). However, there is a dearth in the literature concerning fine particles mixing with bed material, even though in CFB boilers large amount of fly ash is returned to the riser for carbon burning completely. The present work is devoted to study particle feeding and mixing in the bottom zone of a circulating fluidized bed, concerning both coarse and fine particle feeding.

In the present work, the effects of the feeding particle size, feeding port location (relative to dense bed surface), feeding gas velocity and fluidization gas velocity on the mixing behaviors of feeding particles were investigated by monitoring transient pressure drop and thermal tracing method, at the same time, the flow patterns were recorded to enrich understanding on solids mixing mechanisms. Still, a more accurate but laborious tracer technique, that is the bed collapse technique, was used to examine the lateral distribution of feeding particles for four typical cases to give reference results. The present study focuses on various effects on the mixing behaviors and is limited to qualitative interpretation. The quantitative analysis using a mixing model is in progress.

EXPERIMENTAL

Apparatus

The experimental apparatus is shown schematically in Fig. 1. The CFB riser has a rectangular

cross-section of 0.3 m×0.2 m and a height of 2 m. The fluidization air is provided by a roots blower and then distributed by a bubble distributor with 4.5% open fraction. The bed material consists of sand particles with density of 2600 kg/m^3 and a narrow particle size distribution of 0.45-0.6 mm, which belongs to Geldart Group B and has a minimum fluidization velocity of 0.42 m/s.

Tracer injection

A tracer container with an injection tube is located at the sidewall of the riser, seen in Fig. 1. The injection tube, 38 mm ID, connects the riser with an angle of 40 degree at a height of 0.15 m above the distributor. The tracer container is kept warm by an electrical heater in the thermal tracing tests. In each experiment, during the steady state of fluidization, the tracer particles of 1000 ml volume are charged into bed with the help of a nitrogen gas flow whose absolute pressure is 0.15MPa and flow rate can be adjusted.

Thermal tracing technique

The sand particles preheated in an oven to 100℃ are used as tracer. The PN thermistors are arranged in a 3-dimensional configuration to monitor the mixing of preheated feeding particles, as illustrated in Fig. 2. Due to the page limitation, only the lateral temperature profiles are discussed in this paper. The temperature measurements can indicate local tracer concentrations. However, the quantitative interpretation for the temperature measurements should consider the couple effects of the mixing and heat transfer of the feeding particles, bed material and fluidization gas.

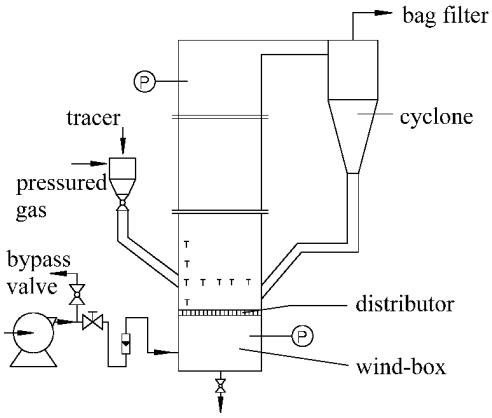

Fig. 1 Schematic of experimental system

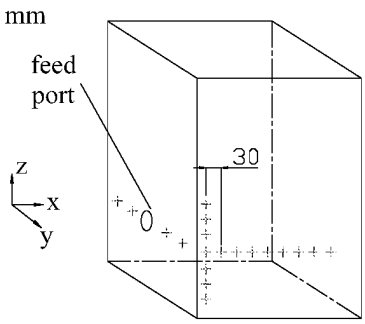

Fig. 2 Positions of PN thermistors

Thermal tracing is a convenient method to study solids mixing and permit large number of experimental cases (Glicksman et al., 2008). Experiments are designed to identify the influences of feeding particle size (d_{in}), feeding port location, feeding gas velocity (U_{in}) and fluidization gas velocity (U_0) on the mixing behaviors. The feeding port location is adjusted by changing the static bed height (H), which is located at the bed surface when H is 10cm, and fully submerged in the dense bed when H is 20cm. The feeding particles used are 0.1-0.2 mm and 0.45-0.6 mm. The feeding gas velocity is adjusted at different values of 0, 0.24, 0.48, 0.76 and 0.98 m/s. Tests are performed at three fluidization gas velocities of 1.02, 2.04, and 2.75 m/s.

Bed collapse technique

The sand particles of different size (0.1-0.2 mm and 1.0-1.2 mm) from the bed material are used as tracer. At a specified time after the tracer fed into the bed, i.e. 5 s, 10 s, 20 s, 60 s, suddenly the fluidizing gas is cut off and simultaneously the bypass valve is opened, with the bed material collapsing. Then the horizontal and vertical plates are inserted to divide the bed into several lateral and axial regions, as shown in Fig. 3. The sample in each region, consisting of the bed material and tracer particles, is then screened and weighed, yielding the tracer concentration (w) in each region. The bed collapse technique is very time-consuming, but can give accurate results. Four typical cases are examined by the bed collapse technique to give reference results.

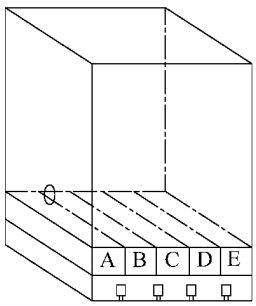

Fig. 3 Sampling cells for bed collapse method

RESULTS AND DISCUSSION

The pressure drop response, lateral temperature profiles, and results from bed collapse method are

discussed below. It is worth mentioned that, for any case in our experiment it takes less than 60 seconds that the mixing of the feeding particles with bed material to reach equilibrium state.

Effect of feeding particle size

Figure 4 shows the pressure drop response due to pulsed particle feeding at U_0=2.04m/s. As the coarse particles (0.45-0.6mm) are fed, it takes 5 seconds for pressure drop rise up and then the pressure drop remains constant, while as the fine particles (0.1-0.2mm) are fed, the pressure drop rises up within 2 seconds and then gradually falls due to particle elutriation, indicating that the residence time distributions of the particles are strongly dependent on their sizes. It is believed a particle can be carried away if its terminal velocity is smaller than the fluidization gas velocity, which should be kept in mind when analyzing the mixing behaviors of fine particles.

Figure 5 shows the lateral distribution of the tracer particle concentrations at U_0=2.04m/s by the bed collapse technique examined at 5, 10, 20 and 60 seconds after the particles fed into the bed respectively. When the coarse particles (1.0-1.2mm) are fed, the difference between local tracer concentrations can be found at 5 seconds. As time proceeds, the feeding particles are gradually dispersed from the feed port and the concentration difference gradually varies. When the fine particles (0.1-0.2mm) are fed, as indicated by pressure drop response above, the phenomena of particle elutriation are dominated. Still, a similar dispersion process to that of the coarse particles can be seen in the lateral direction. An exception is that at 5 seconds after the fine particles fed into the bed the local tracer concentration in region E is larger than in other regions. A probable explanation is that more fine particles congregate in the wall region in the upper dilute zone, and they fall down to region E when the fluidization air is cut off.

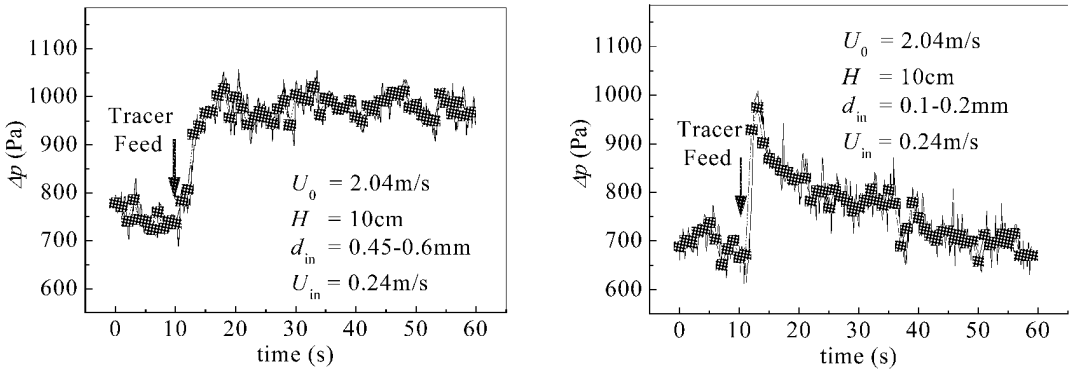

Fig. 4 Pressure drop response due to pulsed particle feeding at the conditions of U_0=2.04m/s, H=10cm, U_{in}=0.24m/s: (a) d_{in}=1.0-1.2mm; (b) d_{in}=0.1-0.2mm

From Fig. 5, when U_0 at 2.04m/s, the difference between dispersion rates of the fine and coarse particles can not be distinguished. However, the dispersion rate of the fine particles is obvious larger than that of the coarse particles when U_0 is reduced to 1.02m/s, as shown in Fig. 6. It is attributable to the fact that the movement state of a fine particle can be influenced relatively easily by drag force due to its small inertia, while under the condition of higher fluidization gas velocity, the fine particle can no longer stay in the bottom bed and will be carried up by gas, resulting limited movement in the lateral direction.

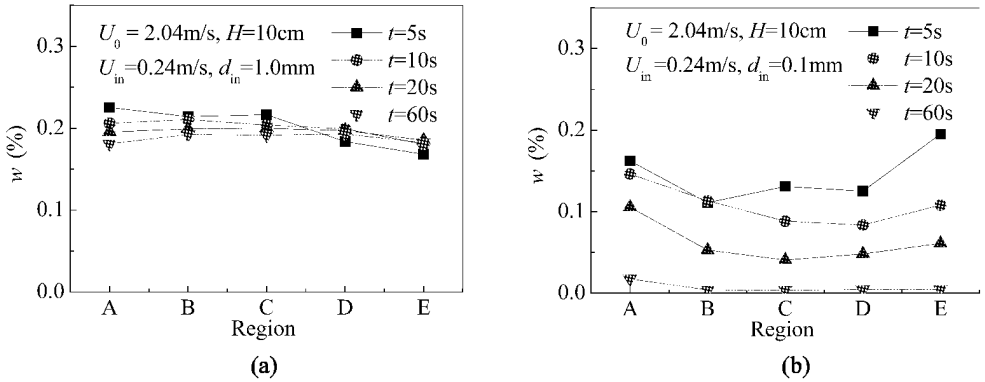

Fig. 5 Lateral distribution of pulsed fed particles at the conditions of U_0=2.04m/s, H=10cm, U_{in}=0.24m/s: (a) d_{in}=1.0-1.2mm; (b) d_{in}=0.1-0.2mm

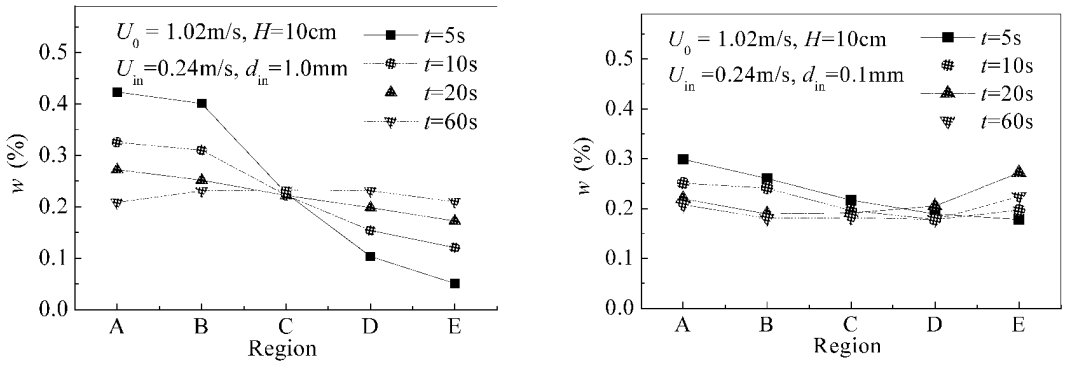

Fig. 6 Lateral distribution of pulsed fed particles at the conditions of U_0=1.02m/s, H=10cm, U_{in}=0.24m/s: (a) d_{in}=1.0-1.2mm; (b) d_{in}=0.1-0.2mm

Effect of feeding port location

Figure 7 plots the pressure drop response due to pulsed feeding of the fine particles at different superficial velocities. In order to compare the pressure drop response at different conditions, the averaged values of pressure drop before particle feeding are adjusted to 0. Given U_0=2.04m/s, a mild decrease in particle elutriation rate is observed as H increased from 10 to 20 cm. However, there is a negligible change in fine particle elutriation rate between the conditions of H at 10cm and 20cm when U_0 is increased to 2.75m/s. From these, it can be deduced that the method of laying the feed port fully submerged in the dense bed can increase the residence time of fine particles as the bed is in moderate other than high fluidization gas velocity. Still, it should be pointed out that it is not an easy task to feed particles in the dense bed as that in the bed surface, which is indicated in our repeated experiments.

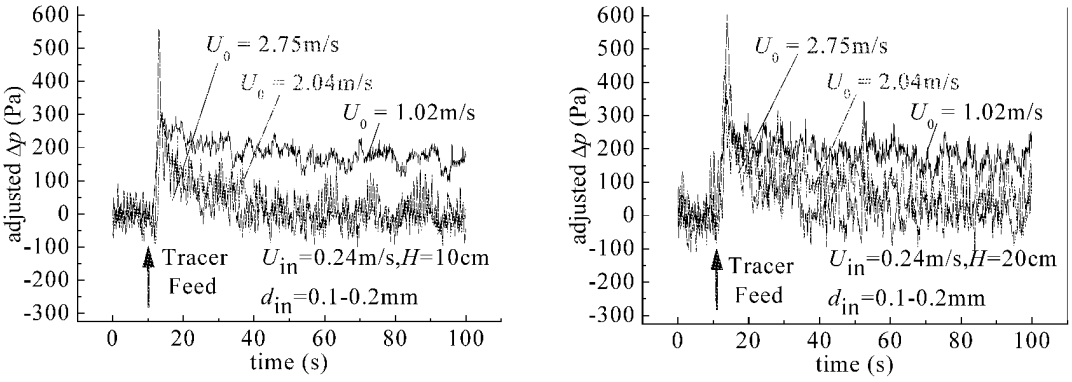

Fig. 7 The pressure drop response due to pulsed feeding of the fine particles at different superficial gas velocities: (a) H=10cm; (b) H=20cm

Figure 8 shows the lateral temperature profiles with time due to pulsed feeding of the preheated fine particles at U_0=2.04m/s. A noticeable difference between the two cases of H at 10cm and 20cm is that there is a hot spot formed near the feed port in the latter case, because high resistance is encountered for the feeding particles to disperse when the feed port is fully submerged in the dense bed. Instead, to lay the feed port in the bed surface, where the bubble bursts and solids show strong convective and back-mixing, could facilitate the feeding particles dispersion in the lateral direction.

Effect of feeding gas velocity

Because the temperature response for different lateral points in various conditions is similar that it rises with pulsed feeding of preheated particles, and reaches the maximum, and then drops gradually with time. So the maximum could partially represent the property for such a curve. In order to compare the maximum temperature rise at different conditions, the dimensionless maximum temperature rise (T_{max}/T_{t60}) is defined, where T_{t60} is the average temperature rise of the lateral thermistors at 60 seconds after the preheated particles fed into the bed. Figure 9 shows the lateral distribution of T_{max}/T_{t60} with the variation of feeding gas velocity for the conditions of both H=10cm and H=20cm. It shows that the lateral distribution of T_{max}/T_{t60} gets more uniform with increase in the feeding gas velocity. This indicates the convective transport momentum of feeding

gas can effectively facilitate the lateral distribution of particle feeding in the bottom zone of fluidized beds.

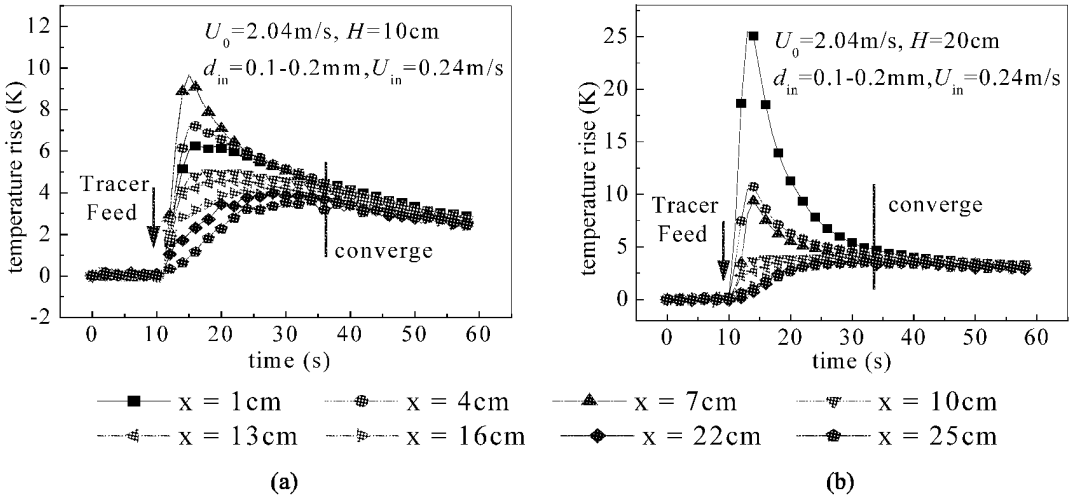

Fig. 8 The lateral temperature profiles with time due to pulsed feeding of the heated fine particles at U_0=2.04m/s : (a) H=10cm; (b) H=20cm

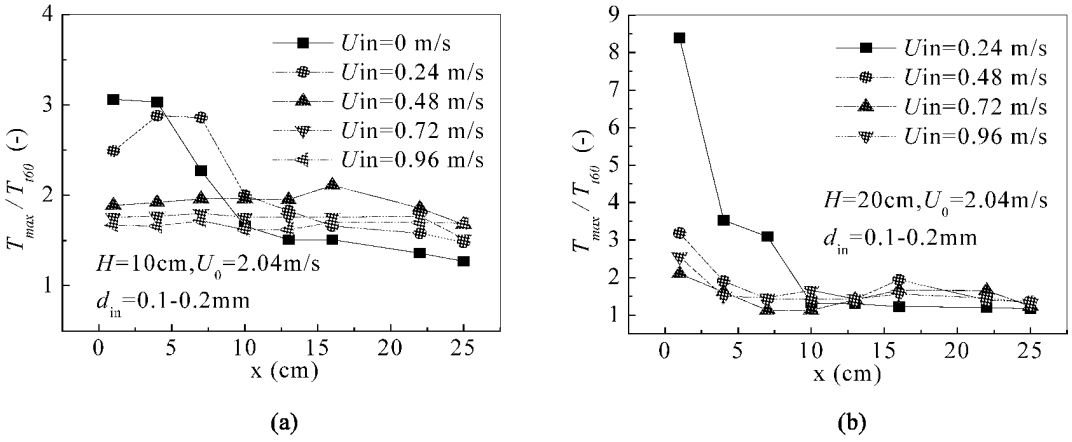

Fig. 9 The effect of the feeding gas velocity on the lateral distribution of maximum temperature rise: (a) H=10cm; (b) H=20cm

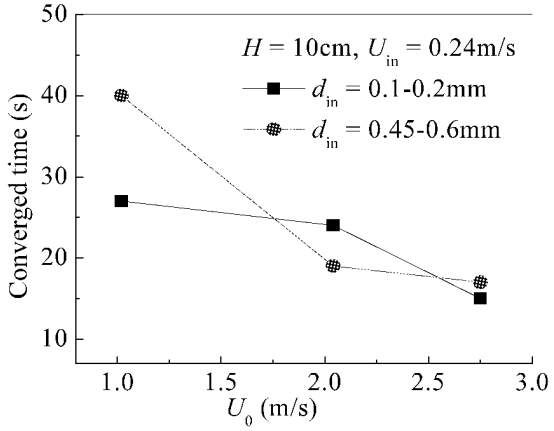

Fig. 10 The effect of the fluidization gas velocity on the converged time

Effect of fluidization gas velocity

Finally, the mixing behaviors at different fluidization gas velocities of 1.02, 2.04, 2.75 m/s are compared. The converged time, defined as the time at which the standard deviation of the lateral temperatures reaches less than 0.5 K, as sketched in Fig. 8, is employed to compare the mixing rate at different fluidization gas velocities. As shown in Fig. 10, for feeding both fine and coarse particles, the converged time decreases as U_0 increased from 1.02 to 2.75 m/s, thus increase in fluidization gas velocity promotes solids mixing, which is consistent

with the previous works.

CONCLUSIONS

The effects of the feeding particle size, feeding port location (relative to dense bed surface), feeding gas velocity and fluidization gas velocity on the mixing behaviors of the feeding particles in the bottom zone of a fluidized bed were investigated. Both the thermal tracing technique and bed collapse technique were used. The main conclusions can be drawn as follows:

(1) As the fluidization gas velocity is no more than the terminal velocity of the particles, the dispersion rate of fine particles is larger than that of coarse particles, but the fine particles can be entrained more easily, which limits their lateral dispersion at high gas velocity.

(2) To lay the feed port in the dense bed could lead to a mild decrease in elutriation rate of fine particles as the bed is under moderate other than high fluidization gas velocity.

(3) Two disadvantages are encountered when the feed port is located fully submerged in the dense bed: the one is that it is not an easy task to feed particles in the dense bed as that in the bed surface; and the other one is that a hot spot occurs as the feeding gas velocity is no more than 0.24m/s. Instead, the dispersion of feeding particles becomes better when the feeding port is located in the bed surface.

(4) The feeding gas flow can effectively facilitate the lateral distribution of the feeding particles in the bottom bed.

(5) It takes about half time that the mixing of feeding particles with bed material to reach equilibrium state when the fluidization gas velocity increased from 1.02 m/s to 2.04 m/s.

ACKNOWLEDGEMENTS

Financial supports of this work by National Key Technology R&D Program (2006BAA03B02-10) are gratefully acknowledged.

REFERENCES

Bellgardt, D., Schoessler, M. and Werther, J.: Powder Technol. **53** (1987), pp.205-216.
Du, B., Fan, L. S., Wei, F. and Warsito, W.: AICHE J. **48** (2002), pp.1896-1909.
Glicksman, L., Carr, E. and Noymer, P.: Powder Technol. **180** (2008), pp.284-288.
Knowlton T.M., eds), Blackie Academic & Professional London (1997), pp.119-148.
Kunii, D. and Levenspiel, O.: Fluidization Engineering, Chapter 9, Butterworth-Heinemann, 1991.
Niklasson, F., Thunman, H., Johnsson, F. and Leckner, B.: Ind. Eng. Chem. Res. **41**(2002), pp.4663-4673.
Pallares, D. and Johnsson, F.: Chem. Eng. Sci. **61** (2006), pp.2710-2720.
Schlichthaerle, P. and Werther, J.: Powder Technol. **120** (2001), pp.21-33.
Werther, J. and Hirschberg, B.: Chapter 4 in Circulating Fluidized Beds
Yang, H. R., Lu, J. F., Liu, Q. and Yue, G. X.: Chinese J. Chem. Eng. **10** (2002), pp.490-493.

AN EXPERIMENTAL INVESTIGATION INTO THE FRAGMENTATION OF COAL PARTICLES IN A FLUIDIZED-BED COMBUSTOR

Monika Kosowska-Galachowska[1], Adam Luckos[2]

1 Czestochowa University of Technology, Czestochowa, Poland

2 Sasol Technology, Research and Development, Sasolburg, South Africa

Abstract: The fragmentation of coal plays a significant role in combustion in fluidized-bed boilers because it accelerates combustion and influences the distribution of particle sizes in the bed. Fine char particles produced by comminution can be carried out and increase the heat loss due to incomplete carbon conversion. The thermal fragmentation depends on the initial structure of the coal and how this structure changes with an increase in temperature when the particle is dropped into the combustion chamber. Experiments with nine Polish coals were carried out to quantify the fragmentation of burning coal particles. A bench-scale bubbling fluidized bed combustor was used to determine the degree of fragmentation for spherical coal particles during devolatilization and combustion. The effects of bed temperature, particle size and coal properties on the extent of primary and secondary fragmentation have been determined. It has been found that the combination of low porosity and high volatile content is the main factor responsible for the observed extent of fragmentation.

Keywords: coal, combustion, fragmentation, fluidization, bubbling bed

INTRODUCTION

Understanding coal particle size change during fluidized-bed combustion is important for a realistic determination of combustion rate and thermal efficiency. The thermal fragmentation of coal fed into a fluidized-bed combustor is the result of many processes, both physical and chemical, taking place inside burning particles. Because coal is not a homogeneous material, fragmentation strongly depends on the initial structure of the coal and on how this structure changes during the heat-up time. The thermal fragmentation reduces the size of coal particles and, therefore, accelerates the release of voaltiles. In certain cases, however, it can also generate significant quantities of very fine char particles that are elutriated from the bed leading to a lower thermal efficiency of the combustion process (Donsi et al., 1981; Brown et al., 1992; Gajewski et al., 2004).

Thermal fragmentation is a complex process that is influenced by a number of factors including the chemical composition of the coal, its mechanical properties, the size of coal particles and the combustion environment (bed temperature and hydrodynamics, residence time, fluidizing medium) (Gajewski and Kosowska, 2003). A fresh coal particle dropped into the hot bed may undergo the following sequence of events (Basu, 1999):

- Heating and drying
- Thermal shock fragmentation (for some types of coal)
- Ignition and combustion of volatiles
- Primary fragmentation (for some types of coal)
- Char combustion
- Secondary fragmentation

Thermal shock fragmentation occurs immediately after a coal particle is dropped into the furnace that operates at 800–900°C. In this case, internal stresses caused by large temperature gradients exceed the mechanical strength of the particle which results in its disintegration. Primary fragmentation is associated with an increase in the pressure inside the network of pores within the particle during devolatilization (Chirone and Massimilla, 1991; Arena et al., 1994). Secondary fragmentation occurs during char combustion when bridges connecting different irregularly-shaped structures inside the coal particle are burned (Chirone et al., 1989; Arena et al., 1992, 1994).

Experimental and modeling works on fragmentation of different coals and waste derived fuels have been conducted by many researchers (e.g. Ragland and Weiss, 1979; Sundback et al., 1984; Chirone and Massimilla, 1988,; Ragland and Pecson, 1988; chirone and Massimilla, 1989; Dakic et al., 1989; Stubington and Linjewile, 1989; Chirone and Massimilla, 1991; Arena et al, 1992, 1994; Dacombe et al., 1994; Stanmore et al., 1996; Dacombe et al., 1999; Lee, 2001; Lee et al., 2002; Zhang et al., 2002; Lee et al., 2003). The results of earlier studies have been extensively reviewed by Chirone et al. (1991).

In this study, an investigation was undertaken to determine the fragmentation characteristics of two brown coals (lignites) and seven hard coals mined in Poland. The fragmentation behavior of these coals was tested in

an externally-heated bench-scale bubbling fluidized-bed unit. The main objective of the study was to determine the influence of the physical properties of coal on the primary and secondary fragmentation of large coal particles burning in a fluidized-bed combustor.

EXPERIMENTAL

Test apparatus

Fragmentation tests with different Polish coals were conducted in a bench-scale bubbling fluidized-bed test unit shown schematically in Fig. 1 (Kosowska, 2005). The electrically heated rectangular column, 200×120×25 mm^3, was the main component of the unit. The front of the column was made of transparent quartz through which the combustion process and particle fragmentation could be directly observed. Silica sand (particles smaller than 400 μm) to a mass of 150 g constituted the inert bed. A rotameter controlled the supply of air to the plenum chamber. A K-type thermocouple was used to measure the bed temperature with an accuracy of ±2°C. The bed temperature was held in the range 700–900°C by means of a temperature controller. Video and digital cameras were used to record combustion and fragmentation processes.

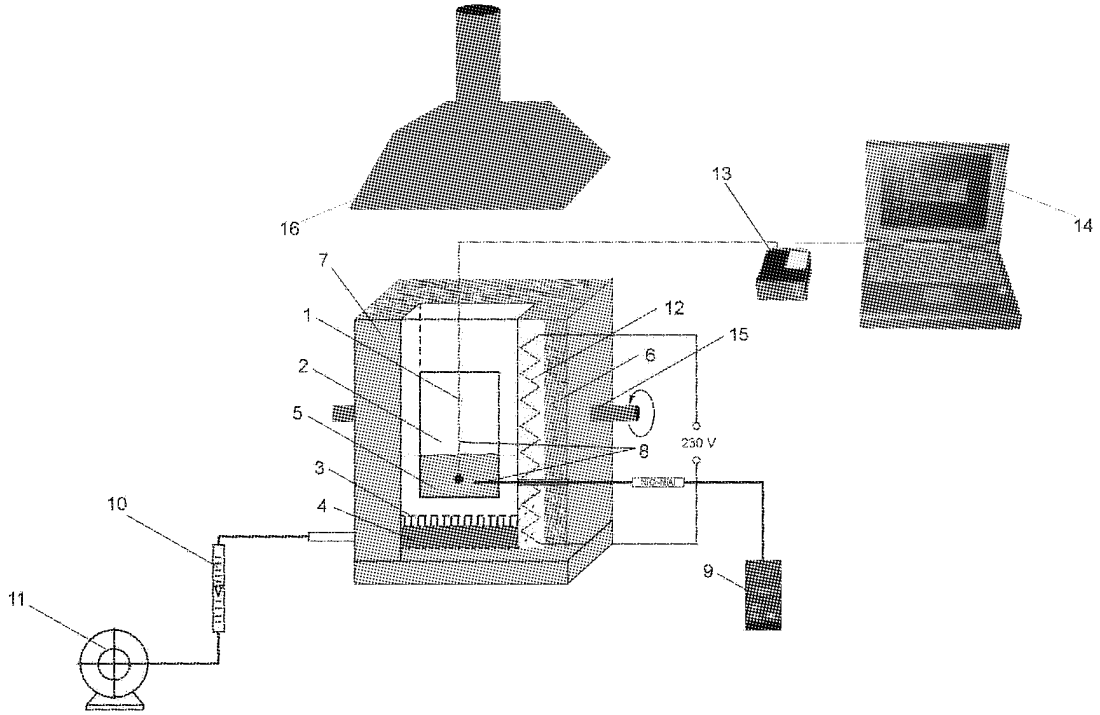

Fig. 1 A schematic diagram of the test apparatus. (1) combustion chamber, (2) quartz window, (3) distributor plate, (4) plenum chamber, (5) sand bed, (6) insulation, (7) wall, (8) thermocouple, (9) temperature controller, (10) rotameter, (11) air blower (12) heating elements

Test procedure

Once the bed had reached a required temperature a single particle was dropped into it. After certain time, the test unit was tilted and bed particles were taken out and cooled. The char particles were then separated from the sand particles and classified by a series of standard sieves. This allowed to determine the particle size distribution and to calculate the degree of fragmentation. Each coal sample was tested ten times and the average values are reported in this paper.

In this study, the degree of primary fragmentation is defined here as the ratio of the number of fragments produced as a result of primary fragmentation to the total number of particles tested. The degree of secondary fragmentation is calculated as the ratio of the number of fragments produced as a result of secondary fragmentation to the number of fragments produced during primary fragmentation.

Coals tested

Nine Polish coals, including two brown coals, were tested. Their proximate analyses, carbon content (on dry, ash-free basis) and total porosities (obtained in a mercury porosimeter) are shown in Table 1. The relationship between the carbon content and the total porosity is plotted in Fig. 2. Spherical particles 2–11 mm in diameter were produced from coal lumps through mechanical grinding.

Table 1 Proximate analyses, carbon content (daf) and total porosity of tested coals

Coal rank	Mine	VM, %	Ash, %	Moisture, %	C (daf), %	Porosity, %
brown	Belchatow	42.5	18.5	14.5	68.66	37.77
brown	Turow	39.1	22.4	16.8	49.65	52.20
hard	Julian	37.5	5.9	7.6	82.43	13.75
hard	Sobieski	25.3	23.1	3.8	78.70	18.75
hard	Czeczot	29.3	14.6	9.5	71.68	15.00
hard	Miechowice	30.2	12.0	6.7	82.41	15.34
hard	Wujek	34.0	3.6	2.7	83.78	6.68
hard	Halemba	28.5	10.3	3.6	81.07	11.80
hard	Pokoj	31.5	2.7	1.9	77.88	6.28

RESULTS AND DISCUSSION

Effect of particle diameter

The relationship between the degree of primary fragmentation and particle diameter for three hard coals is shown in Fig. 3. The number of fragments produced during devolatilization increases approximately exponentially with increasing particle diameter. The effect of primary fragmentation is much more pronounced for coals with lower porosity. As can be seen, 11-mm coal particles from Wujek mine, with porosity 6.68%, produced twice as much fragments than coal particles from Sobieski mine with porosity 18.75%. Larger coal particles contain larger total quantities of volatiles which result in a higher inner pressure therefore the primary fragmentation occurs more intensely. Similar results have been reported by Chirone and Massimilla (1988), Arena et al. (1994), Dacombe et al. (1999) and Zhang et al. (2002).

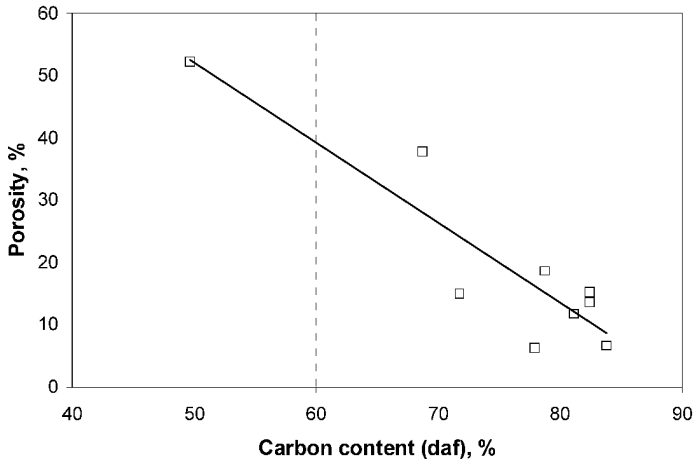

Fig. 2 Total coal porosity as a function of carbon content (daf)

The influence of bed temperature

The bed temperature is an important factor that influences coal fragmentation. At higher bed temperatures, the inner pressure of volatiles increases as the result of higher heating rates. Figure 4 shows the relationship between the degree of total fragmentation (primary + secondary) and bed temperature for two hard coals. The number of fragments produced from 10-mm particles increases proportionally with increasing bed temperature. The results shown in Fig. 4 confirm that the initial porosity of coal particles plays an important role in the fragmentation process. At 900°C, less porous particles from Wujek mine produced almost three times more fragments than particles from Julian mine.

Effect of carbon and volatile matter contents

The relationship between the degrees of primary and secondary fragmentation and carbon content for all coals tested is shown in Fig. 5. The degree of primary fragmentation increases with increasing carbon content while the degree of secondary fragmentation decreases for high-rank coals. Highly porous brow coals did not undergo primary fragmentation. A high total porosity and relatively large pore diameters resulted in low pressure gradients low resistance to volatiles transport within particles during devolatilization.

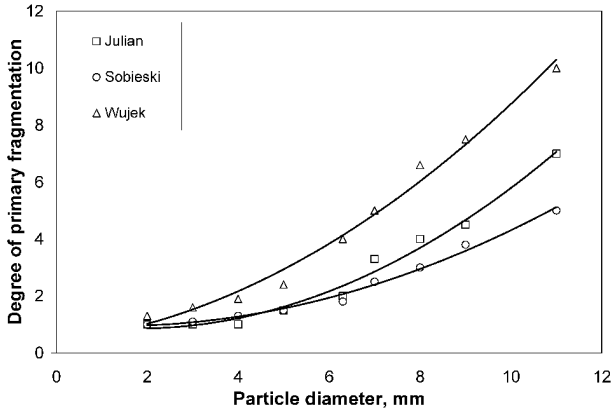

Fig. 3 The relationship between the degree of primary fragmentation and the particle diameter

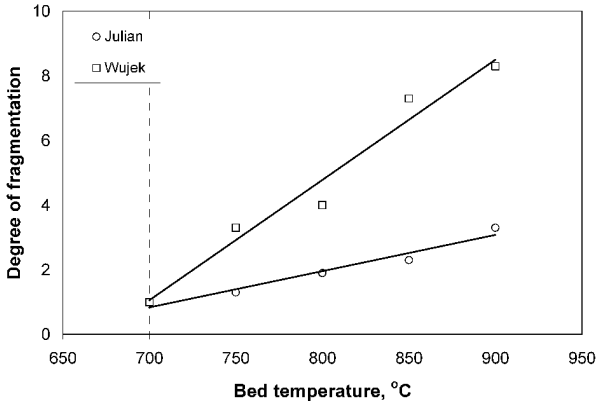

Fig. 4 The relationship between the degree of total fragmentation and bed temperature

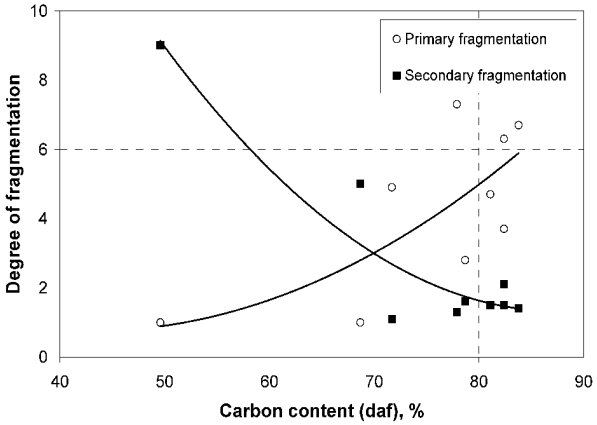

Fig. 5 The relationship between the degree of fragmentation and the carbon content

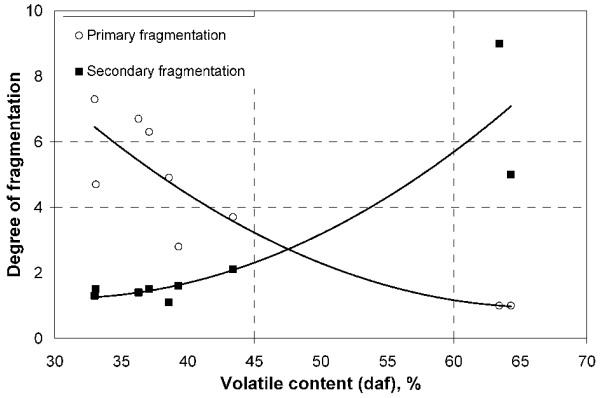

Fig. 6 The relationship between the degree of fragmentation and the volatile content

The primary fragmentation data for hard coals are scattered. The degree of primary fragmentation vary from 2.8 for Sobieski coal to 7.3 for Pokoj coal. The data on secondary fragmentation for these coals show a week dependence on carbon content with the secondary fragmentation values in the range from 1.3 (Pokoj) to 2.1 (Julian).

The relationships between the volatile content, *VM*, and degrees of fragmentation (Fig. 6) for hard coals are more consistent and show the opposite trend. The degree of primary fragmentation increases with increasing *VM* while the degree of secondary fragmentation decreases with *VM*. Generally, it can be concluded that coals with high volatile content and low porosity show the greatest tendency to fragment. The experimental data reported by Chirone and Massimilla (1988, 1989) also confirm that primary fragmentation strongly depends on the volatile content and on the strength of the coal and its char.

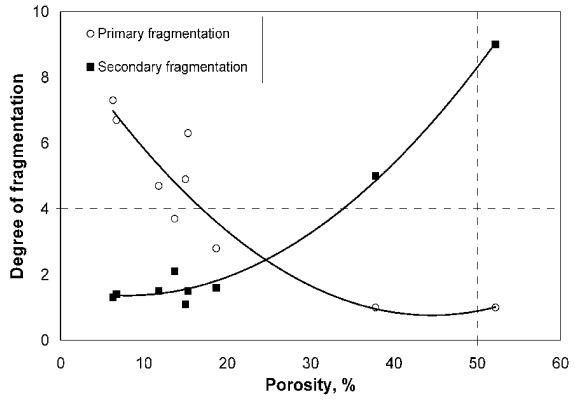

Fig. 7 The relationship between the degree of fragmentation and the total porosity

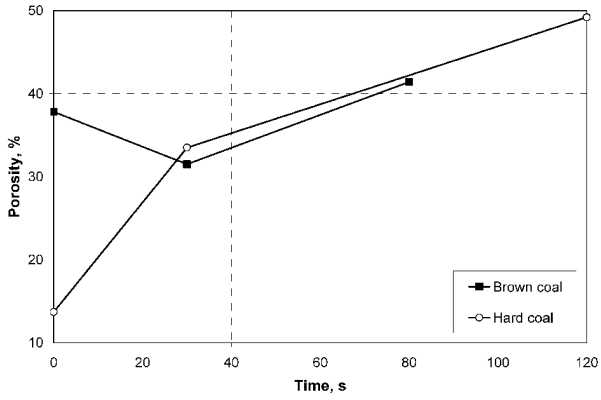

Fig. 8 Changes in the porosity of brown coal and hard coal burned at 850°C

Effect of porosity

The influence of the initial coal porosity on the fragmentation process is shown in Fig. 7. Devolatilization of coals with porosities of less than 15% can produce large number of fragments (on an average more than 6). The secondary fragmentation produces many fragments during combustion of low rank coals but its influence on combustion of high rank coals is very small.

The evolution of coal porous structure is the main reason for char weakening and particle fragmentation during combustion. As coal particles heat up, pores may be modified by such processes as devolatilization, plasticity, expansion (swelling) or contraction, the generation of thermal stresses, and the re-ordering of crystal structures. Figure 8 shows the relationship between porosity and the residence time of brown and hard coal char particles in the bed. The porosity of hard coal char increased with combustion time from the initial value of 14% to the final value of 49% after 120 s. In the case of the brown coal char the porosity decreased after 30 s and then after 80 s increased to the value higher than its initial porosity. The observed decrease in porosity was probably caused by the collapse of the macropores during the evaporation and release of moisture.

CONCLUSIONS

The fragmentation behavior of nine Polish coals during combustion in a bench-scale bubbling fluidized-bed test unit has been quantified. It was found that the fragmentation characteristics of coal particles depends on the coal rank, bed temperature, size of original coal particles, and their porosity.

Because brown coals have high total porosity, they do not undergo primary fragmentation during the devolatilization time. Mechanical stresses generated by inner pressure gradients are too low to destroy the internal structure of coal particles. On the other hand, the secondary fragmentation of these coals is very intense probably due to much weaker internal structure of their chars compared to chars produced by hard coals.

In the case of hard coals, the primary fragmentation is the main reason for the fragmentation of coal particles during fluidized-bed combustion. Coals with low porosity and high volatile contents tend to produce more fragments than porous coals with lower concentrations of volatile matter. The secondary fragmentation of char particles is not very intense and, therefore, its contribution to the total fragmentation is relatively very small.

On the basis of presented experimental data, it can be concluded that the combination of low porosity and high volatile mater content is the main factor responsible for the observed extent of fragmentation.

REFERENCES

Arena, U., Cammarota, A., Chirone, R. and Massimilla, L.: Symp. (Int.) on Combustion **24** (1992), pp. 1341-1348.
Arena, U., Cammarota, A., and Chirone, R.: Symp. (Int.) on Combustion **25** (1994), pp. 219-226.
Basu, P.: Chem. Eng. Sci. **54** (1999), pp. 5547-5557.
Brown, R.C., Ahrens, J. and Christofides, N.: Combustion and Flame **89** (1992), pp.95-102.
Chirone, R. and Massimilla, L.: Symp. (Int.) on Combustion **22** (1988), pp.267-277.
Chirone, R. and Massimilla, L.: Powder Technology **57** (1989), pp.197-212.
Chirone, R., Salatino, P. and Massimilla, L.: Combustion and Flame **77** (1989), pp. 79-90.
Chirone, R. and Massimilla, L.: Powder Technology, **64** (1991), pp.249-258.
Chirone, R., Massimilla, L. and Salatino, P.: Prog. Energy Combust. Sci. **17** (1991), pp.297-326.
Dacombe, P., Hampartsoumian, E. and Pourkashanian, M.: Fuel **73** (1994), pp.1365-1367.
Dacombe, P., Pourkashanian, M., Williams, A. and Yap, L.: Fuel **78** (1999), pp.1847-1857.
Dakic, D., Van der Honing, G. and Valk, M.: Fuel **68** (1989), pp.911-916.
Donsi, G. Massimilla, L. and Miccio, M.: Combustion and Flame **41** (1981), pp.57-69.
Gajewski, W. and Kosowska, M.: Proc. 12th ICCS&T (2003).
Gajewski, W., Kosowska, M. And Otwinowski, H.: Powder Handling & Processing **16** (2004), pp.252-257.
Kosowska, M. (2005). The thermal fragmentation of coal during combustion process. PhD Thesis. Czestochowa University of Technology.
Lee, J.: Proc. 16th Int. Conf. Fluidized Bed Combustion (2001), pp. 1513-1521.
Lee, S.H., Kim, S.D. and Lee, D.H.: Fuel **81** (2002), pp.1633-1639.
Lee, J.M, Kim, J.S. and Kim J.J.: Fuel **82** (2003), pp.1349-1357.
Ragland, K.W. and Weiss, C.A.: Energy **4** (1979), pp.341-348.
Ragland, K.W. and Pecson, F.A.: Symp. (Int.) on Combustion **22** (1988), pp.259-265.
Stubington, J.F. and Linjewile, T.M.: Fuel **68** (1989), pp.155-160.
Stanmore, B.R., Brillard, A., Gilot, P. and Delfosse, L.: Symp. (Int.) on Combustion **26** (1996), pp. 3269-3275.
Sundback, C.A., Beer, J.M. and Sarofim, A.F.: Symp. (Int.) on Combustion **20** (1984), pp.1495-1503.
Zhang, H., Cen, K., Yan, J. and Ni, M.: Fuel **81** (2002), pp. 1835-1840.

AXIAL AND RADIAL SOLIDS HOLDUP MODELING OF CIRCULATING FLUIDIZED BED RISERS

Q. Miao[1], J. Zhu[1], S. Barghi[1], C. Wang[2], X. L. Yin[2], C. Z. Wu[2]

1 Particle Technology Research Centre, University of Western Ontario, London, Canada N6A 5B9
2 CAS Key Laboratory of Renewable Energy and Gas Hydrate, Guangzhou Institute of Energy Conversion, Chinese Academy of Sciences, Guangzhou, 510640, China

Abstract: Hydrodynamics plays a crucial role in defining the performance of gas-solid circulating fluidized beds (CFB). A two dimensional model was developed considering the hydrodynamic behavior of CFB gasifiers. In the modeling, the CFB riser was divided into two regions: a dense region at the bottom and a dilute region at the top of the riser. Radial distributions of bed voidage were taken into account in the upper zone by using Zhang *et al.* (1991)'s correlation. For model validation purposes, a cold model CFB was employed, in which sawdust was transported with air as fluidizing agent. The column was 10 m in height and 280 mm in diameter, and was equipped with pressure transducers to measure axial pressure profile and with a reflective optical fiber probe to measure local solids holdup. A satisfactory agreement between the model predictions and experimental data was found.

Keywords: hydrodynamics, modeling, circulating fluidized beds, biomass, gasification

INTRODUCTION

With continuously growing energy demand for global economic development and increasing environmental issues caused by fossil fuels, considerable attention is being given to the use of biomass for energy generation, particularly for fuel gas/product gas production by gasification as the produced fuel gas can be flexibly applied in boilers, engines, gas turbines or fuel cells. CFB gasification is now undergoing rapid commercialization for biomass (Yin et al., 2002; Kersten et al., 2003).

The flow structure of gas-solid flows in a CFB is inherently very complex. Up to now, considerable work has been done on modeling of CFB reactors (Grace et al., 1997). Many modeling efforts with various assumptions and different mathematical formulations have been reported in literature. Harris and Davidson (1994) have classified these into three categories: (I) those that predict axial variation in solids suspension density, but not radial variations; (II) those that predict both axial and radial variations by assuming two or more regions, for example core-annulus flow structure or clustering annular flow models; (III) those that employ the fundamental equations of fluid dynamics to predict two-phase gas-solid flow.

Type I models are oversimplified to provide rough predictions. The radial variations are completely neglected, which seriously limited the ability of the models to represent CFB reactors. Type III models are the most rigorous, but the required simplifying assumptions combined with their mathematical complexity limit their use to studies of specific flow structures within the riser. Type II models provide more details concerning the radial distribution of solids and allow one to investigate the flow structure of CFB risers in a two-dimensional way.

Although the development of hydrodynamic modeling is prosperous, very limited work is focused on biomass particles. Whereas there has been considerable effort to develop new biomass gasification, combustion, pyrolysis and bio-conversion processes, relatively few authors have characterized the relevant flow characteristics of biomass particles in circulating fluidized beds or investigated measures that could assist in resolving flow issues. Cui and Grace (2007) reviewed recent researches on the hydrodynamics and mixing of biomass particles in fluidized beds. They pointed out since the hydrodynamics were critical to successful design and operation of fluidized bed processes, it was important to undertake research directed at improving the characterization and modeling of biomass fluidization hydrodynamics.

In this study, a detailed model on the hydrodynamics of a cold model CFB riser with sawdust is presented. Experiments are performed to be verified with the simulation. The main objective of the present study is to gain a better understanding of CFB hydrodynamics by developing a predictive model to describe both axial and radial distributions of solids in CFB risers.

EXPERIMENTAL

Experimental setup and materials

The cold model CFB is shown schematically in Fig.1. The riser is made of Plexiglas and is 10 m long and

280 mm i.d. The air distributor is made of a perforated stainless steel plate with 175 holes of 3 mm i.d. During the operation, the main air entered the riser through a distributor and the solids coming from the downcomer were fluidized at the riser bottom and then carried upwards. Solids and gas were separated in a cyclone and some fine particles were finally captured in a bag filter. The solids were eventually recycled to the riser bottom through a loopseal bubbling bed. The solids circulation rate was regulated by controlling the aeration air in the loopseal and was measured by a section of flapper valves at the top of storage tank.

The fluidization gas used in the study was air at ambient condition, supplied by a Roots-type blower. Rotameters were employed to measure the gas flowrates. The air relative humidity was maintained between 70% and 80% by introducing a stream of steam to minimize effects of electrostatics building up on the solids. According to Park et al. (2002), at a relative humidity value between 50 and 60%, the electrostatic effects and the capillary forces can be controlled in an acceptable level to avoid misleading results. The bed material used in the current studies was sawdust with mean diameter d_p = 400 μm, and particle density ρ_p = 430 kg/m^3. Its cumulative size distribution is shown in Fig.2.

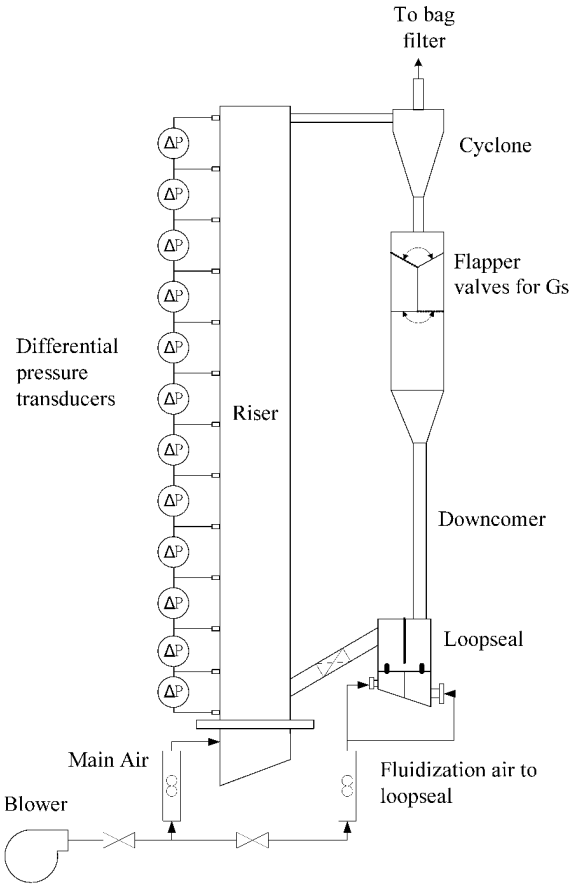

Fig.1 Schematic of cold model CFB

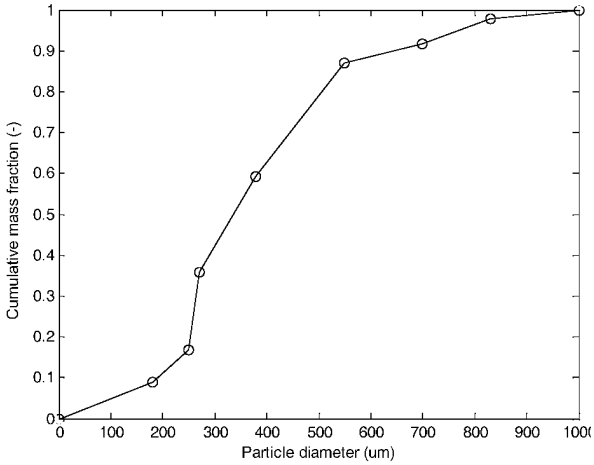

Fig. 2 Cumulative size distribution of sawdust

Experimental method

In order to estimate the axial profiles of cross-sectional average solids holdup in the riser, 12 OMEGA PX series differential pressure transducers were installed to measure pressure drops along the riser column, as shown in Fig.1. With the measured pressure drop, ΔP, and the corresponding section length, Δz, pressure gradient, $\Delta P/\Delta z$, was obtained.

A multi-fiber optical probe, PV-6, developed by the Institute of Process Engineering, Chinese Academy of Sciences, was chosen to measure local solids holdup in this study. The precise calibration procedure of the probe and other details can be found in Zhang et al. (1998). Local solids concentrations under 8 operating conditions were measured at 8 radial positions (r/R = 0.0, 0.143, 0.286, 0.429, 0.571, 0.714, 0.857, 0.929) on 8 axial levels (z = 0.85, 1.35, 2.35, 3.35, 4.35, 5.35, 6.35, 8.35 m).

MODEL DEVELOPMENT

The main assumptions of the proposed model are (1) the riser is axially divided into two regions: a dense region at the bottom and a dilute region at the top of the riser. (2) the dense region, if exists, has a constant

solids holdup. (3) in the dilute upper region solids holdup varies both axially and radially. (4) on a time averaged scale, any nonuniformity caused by clusters or packets of solids is neglected. (5) the exit effect is neglected.

Vertical profile of solids holdup

Several approaches have been proposed to investigate vertical profile of solids distribution in CFB risers (Li and Kwauk, 1980; Wen and Chen, 1982; Rhodes and Geldart, 1987). Based on the observations that the solids concentration decays exponentially from the bed surface, Kunii and Levenspiel (1990) developed a model to describe backmixing in the freeboard above the bubbling bed. The model was also suggested to be valid for circulating fluidized beds (Kunii and Levenspiel, 1991). This model is modified and applied in the present study and the vertical solids holdup distribution is expressed as:

$$\frac{\varepsilon_s-\varepsilon_s^*}{\varepsilon_{sb}-\varepsilon_s^*}=\exp\left[-a(z-H_b)\right] \tag{1}$$

where ε_{sb} is the solids holdup at the dense region, H_b is the height of the dense region and is experimentally determined. ε_s^* is the solids holdup in the fully-developed dilute region. Decay constant a is a function of particle properties and operating conditions. According to Adanez et al. (1994), the following equation was obtained to calculate the decay constant:

$$a(u_g-u_t)^2=3.5-1670d_p \tag{2}$$

Kunii and Levenspiel (1991) summarized a large amount of experimental findings and compared bottom bed solids holdup ε_{sb} in various fluidizing regimes. Then they gave a range of ε_{sb} = 0.16-0.22 for fast fluidization regime. Schlichthaerle and Werther (1999) studied solids concentration distribution in the bottom zone by performing the experiments in a cold model CFB unit with a diameter of 0.4 m and a height of 15.6 m. Operating conditions typical of CFB combustors were chosen (u_g = 3-5 m/s, G_s = 5-50 kg/m^{2}s). Quartz sand (d_p = 65-340 μm) was used in the experiments. A solids holdup of ε_{sb} = 0.2-0.3 was observed. Svensson et al. (1996) investigated fluidization regimes of the bottom bed of Chalmers 12MWth CFB boiler and a cold model CFB. They used sand as their bed material (d_p = 190-430 μm, ρ_p = 2600 kg/m^3), and operating conditions u_g = 0.4-6.5 m/s, G_s~10kg/m^{2}s. The average solid holdup of the bottom bed was obtained from pressure drop measurements and $\varepsilon_{sb} \approx$ 0.35-0.45. This value was larger than Kunii and Levenspiel's range, which may be because a fairly large square combustor (1.47×1.42×13.5 m) was employed and the superficial gas velocity was relatively low. Bai and Kato (1999) did a wide range of summarization of empirical correlations in the open literature and proposed two more generalized correlations for both ε_{sb} and ε_s^* based on experimental data from the literature and their laboratory. These correlations, however, were later experimentally verified invalid for coarse and light biomass particles (e.g. cork) by Mei et al. (2006).

Since there are very few models concerning fluid structure of biomass particles in CFB, the following correlations are proposed here for ε_{sb} and ε_s^* based on experimental data from the literature and our laboratory:

$$\varepsilon_{sb}=1.0422\left(\frac{G_s}{\rho_p(u_g-u_t)}\right)^{0.2781}\left(\frac{u_g}{\sqrt{gD}}\right)^{-0.3218}\left(\frac{d_p\rho_g u_t}{\mu}\right)^{-0.1195} \tag{3}$$

$$\varepsilon_s^*=0.0104\left(\frac{G_s}{\rho_p(u_g-u_t)}\right)^{1.2933}\left(\frac{u_g}{\sqrt{gD}}\right)^{0.0808}Ar^{0.9822} \tag{4}$$

valid for d_p >200 μm, ρ_p < 800 kg/m^3, u_g = 1.5-6 m/s, G_s = 1.12-133.8 kg/m^{2}s.

Radial distribution of voidage

Extensive researches have been conducted in recent decades to measure and to characterize the radial profiles of particle concentration (Zhang et al., 1991; Rhodes et al., 1992; Patience and Chaouki, 1995; Godfroy et al., 1999; Xu et al., 2004). The existence of a radial profile has been observed in small-scale equipment and can be represented by a core-annulus flow structure in the radial direction. The validity of this model has been confirmed by experimental observations in a large-scale CFB (Werther, 1993).

Zhang et al. (1991) reported radial void fraction profiles for four different powders in three different risers up to 0.3 m in diameter. They found that the normalized radial voidage was a unique function of radial position, r/R, based solely on the cross-sectional average voidage, $\bar{\varepsilon}$:

$$\varepsilon=\bar{\varepsilon}^{\left[0.191+(r/R)^{2.5}+3(r/R)^{12}\right]} \tag{5}$$

A correlation of voidage based only on cross-sectional average voidage is reasonable because radial voidage profiles under different operating conditions (riser radius, solids flux, and superficial gas velocity) are similar, as the measurements of Zhang et al. (1991) show. Such a correlation is convenient because a single measurement or prediction of cross-sectional average voidage can be used to map voidage at a given cross-section of the riser, rather than a three-dimensional model. Therefore, this equation is employed in the

present model.

VERIFICATION AND DISCUSSIONS

Figure 3 and Fig.4 compare the simulated and experimental axial solids holdup profiles for experiments conducted in this work and Mei et al. (2006). Both the simulation and experimental data show the same trend. The solids concentration is high at the bottom and then decreases gradually due to the acceleration of the solids until it becomes relatively constant with further increases in riser hight. According to Bai and Kato (1999), at a constant superficial gas velocity, when the solids circulation rate is increased to a value at which much of the solids begins to accumulate at the bottom of the riser, a typical S-shaped solids holdup distribution starts to form. Further increasing solids circulation rate to go beyond this critical point will have negligible effect on the solids holdup at the dense and dilute regions, although the dense region height continues to increase. This critical point is so-called saturation carrying capacity of gas, G_s^*. In Fig.4, G_s^* in Mei et al. (2006) was experimentally identified at 3.1 kg/m^{2}s. It can be seen clearly from both the experimental data and the predictions that when $G_s > G_s^*$, a dense region with a constant solids holdup appears at the bottom of the bed, and the axial solids holdup profile is a typical S-shape. The height of the bottom bed depends on particle properties and operating conditions. Generally, Fig.4 shows that the higher the solids circulation rate, the denser the solids holdup in the whole riser and the higher the bottom bed.

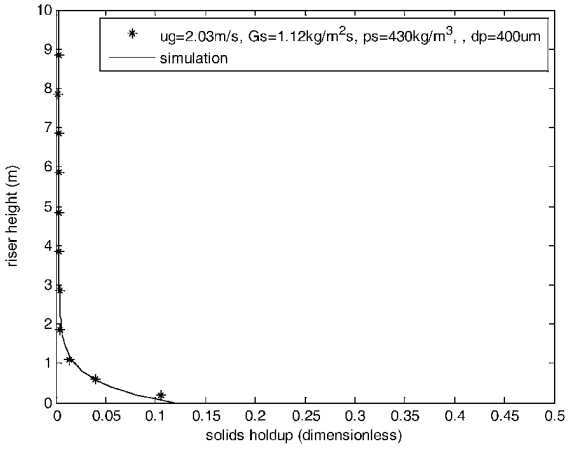

Fig. 3 Comparison of axial solids holdup (this work, sawdust as material)

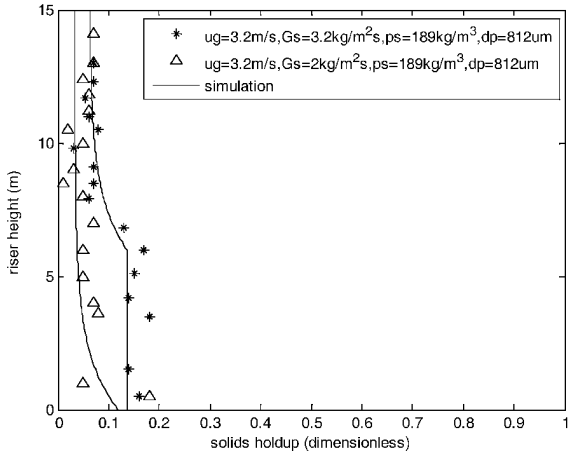

Fig. 4 Comparison of axial solids holdup (Mei et al. (2006), cork as material)

Figure 5 and Fig.6 compare experimentally determined radial voidage profiles in this work with simulation predictions. Both the model and the experimental data show that the voidage distribution is flat in the core region and steep close to the wall. The model also demonstrates that the voidage profiles under different operating conditions coincide with each others, provide they have the same average cross-sectional average bed voidage. The good agreement between the experimental data and the predictions indicates that Zhang et al. (1991)'s equation, which was derived based on Group A particles, can be applied to coarse and light biomass particles ($d_p > 200$ μm, $\rho_p < 800$ kg/m^3) as well.

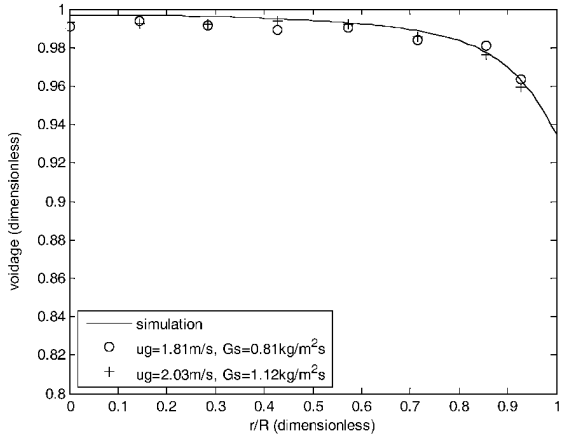

Fig. 5 Comparison of radial voidage (this work)

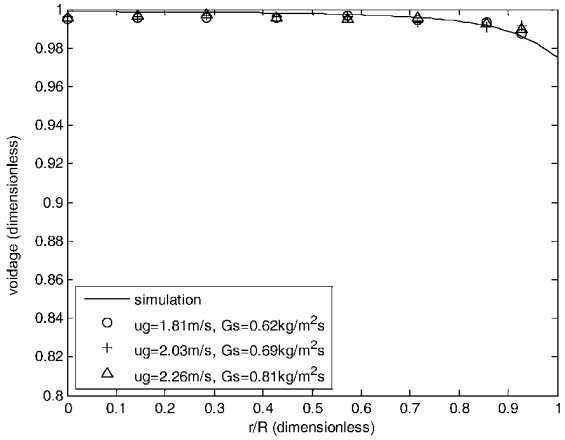

Fig. 6 Comparison of radial voidage (this work)

CONCLUSIONS

A predictive model has been developed to estimate axial and radial solids holdup profiles of CFB risers under fast fluidization conditions. Two correlations have been proposed to predict the solids holdup at dense region and dilute region, respectively. Zhang et al. (1991)'s equation was employed to describe the radial voidage profile in the present study. Through comparison with experimental data, the proposed model is shown to be able to qualitatively and quantitatively predict the effect of operating variables such as superficial gas velocity and solids circulation rate on the axial and radial solids holdup profiles.

NOTATIONS

Ar	Archimedes number ($= d_p^3 \rho_g g(\rho_p - \rho_g)/\mu_g^2$)	u_g	superficial gas velocity, m/s
a	decay constant	u_t	particle terminal velocity, m/s
D	riser internal diameter, m	z	axial position from the gas distributor, m
d_p	particle diameter, μm	ε	local bed voidage
G_s	solids circulation rate, kg/m^{2}s	ε_s	cross-sectional average solids holdup
G_s^*	saturation carrying capacity of gas, kg/m^{2}s	ε_{sb}	cross-sectional average solids holdup at dense region
g	acceleration due to gravity, m/s^2	ε_s^*	cross-sectional average solids holdup at dilute region
H_b	height of dense region, m	μ_g	gas viscosity, Pa s
R	riser radius, m	ρ_g	gas density, kg/m^3
r	horizontal distance from axis, m	ρ_p	particle density, kg/m^3

REFERENCES

Adanez, J.; Gayan, P.; Garcia-Labiano, F. and de Diego L.F, Axial voidage profiles in fast fluidized beds. *Power technology* **1994,** 81: 259-268.

Bai, D. and Kato, K., Quantitative estimation of solids holdups at dense and dilute regions of circulating fluidized beds. *Powder Technology* **1999,** 101: 183-190.

Cui, H. and Grace, J.R., Fluidization of biomass particles: A review of experimental multiphase flow aspects. *Chemical Engineering Science* **2007,** 62: 45-55.

Godfroy, L.; Patience, G.S. and Chaouki, J., Radial Hydrodynamics in Risers. *Industrial & engineering chemistry research* **1999,** 38: 81-89.

Grace, J.R.; Avidan, A.A. and Knowlton, T.M., Circulating fluidized beds, **1997**. Chapman & Hall Press.

Harris, B.J. and Davidson, J.F., 1994. Modeling options for circulating fluidized beds: A core/annulus deposition model. In: A.A. Avidan (Editor), Circulating fluidized bed technology IV. AIChE, New York, pp. 32-39.

Kersten, S.R.A.; Prins, W.; van der Drift, A. and van Swaaij, W.P.M., Experimental fact-finding in CFB biomass gasification for ECN's 500 kWth pilot plant. *Industrial & engineering chemistry research* **2003,** 42: 6755-6764.

Kunii, D. and Levenspiel, O., Entrainment of solids from fluidized beds. *Powder Technology* **1990,** 61: 193-206.

Kunii, D. and Levenspiel, O., Fluidization Engineering, (2nd ed.), **1991**. Butterworth-Heinemann, Boston.

Li, Y. and Kwauk, M., The dynamics of fast fluidization. In: J.R. Grace and J.M. Masten (Editors), Fluidization. Plenum Press, New York, **1980,** pp. 537-544.

Mei, J.S.; Monazam, E.R. and Shadle, L.J., Flow regime study of a light material in an industrial scale cold flow circulating fluidized bed. *Journal of Energy Resources Technology* **2006,** 128: 129-134.

Park, A.; Bi, H.T. and Grace, J.R., Reduction of electrostatic charges in fluidized beds. *Chemical Engineering Science* **2002,** 57: 153-162.

Patience, G.S. and Chaouki, J., 1995. Solids hydrodynamics in the fully developed region of CFB risers, Fluidization VIII (Preprints), Tours, France, pp. 33-40.

Rhodes, M.J. and Geldart, D., A model for the circulating fluidized bed. *Powder Technology* **1987,** 53: 155-162.

Rhodes, M.J.; Wang, X.S.; Cheng, H.; Hirama, T. and Gibbs, B.M., Similar profiles of solids flux in circulating fluidized-bed risers. *Chemical Engineering Science* **1992,** 47(7): 1635-1643.

Schlichthaerle, P. and Werther, J., Axial pressure profiles and solids concentration distributions in the CFB bottom zone. *Chemical Engineering Science* **1999,** 54: 5485-5493.

Svensson, A.; Johnsson, F. and Leckner, B., Bottom bed regimes in a circulating fluidized bed boiler. *International Journal of Multiphase Flow* **1996,** 22(6): 1187-1204.

Wen, C.Y. and Chen, L.H., Fluidized bed freeboard phenomena: entrainment and elutriation. *AIChE Journal* **1982,** 28(1):

117-128.

Werther, J., 1993. Fluid mechanics of large-scale CFB units. In: A.A. Avidan (Editor), Circulating Fluidized Beds Technology IV. AIChE Publications, New York.

Xu, G.; Sun, G. and Gao, S., Estimating radial voidage profiles for all fluidization regimes in circulating fluidized bed risers. *Powder Technology* **2004,** 139: 186-192.

Yin, X.L.; Wu, C.Z.; Zheng, S.P. and Chen, Y., Design and operation of a CFB gasification and power generation system for rice husk. *Biomass and Bioenergy* **2002,** 23: 181-187.

Zhang, H.; Johnston, P.M.; Zhu, J.-X.; Lasa, H.I.D.e. and Bergougnou, M.A., A novel calibration procedure for a fiber optic solids concentration probe. *Powder Technology* **1998,** 100: 260-272.

Zhang, W.; Tung, Y. and Johnsson, F., Radial voidage profiles in fast fluidized beds of different diameters. *Chemical Engineering Science* **1991,** 46(12): 3045-3052.

RESEARCH ON FLOW NON-UNIFORMITY IN MAIN CIRCULATION LOOP OF A CFB BOILER WITH MULTIPLE CYCLONES

S. Yang[1], H. R. Yang[1], Q. Liu[1], H. Zhang[1], Y. X. Wu[1], G. X. Yue[1], Y. Z. Wang[2]

1 Key Laboratory for Thermal Science and Power Engineering of Ministry of Education, Department of Thermal Engineering, Tsinghua University, Beijing, 100084, China
2 Department of Thermal Engineering, Chengde Petroleum College, Chengde, 067000, China

Abstract: Maldistribution of gas-solid tow-phase flow field in circulating fluidized bed (CFB) can cause a series of problems, such as thermal deviation, wear of water walls, etc. In this study, a cold model CFB facility, which was scaled down from a commercial 300MWe CFB boiler with three cyclones placed in an array, was built up and a series of experiments were conducted the flow non-uniformity. The results showed that in CFB boiler with multiple cyclones, the distribution of bed material in the circulation loops is different and uncertain. The gas-solid two-phase flow in the furnace is unbiased, even the circulating rates in the circulation loops are different. The circulating rate in the middle loop is larger than that in the side loops. The difference is less than 10%.

Keywords: CFB, cyclone, circulation loop, uniformity, mal-distribution

INTRODUCTION

Cyclones are popularly utilized for gas solid separation in CFB boilers. However, cyclone performance deteriorates with increasing cyclone diameter, particularly when the cyclone diameter exceeds ~8m (Lee, 1997). As a result, as CFB boilers are scaled up, multiple cyclones, rather than single cyclone are used, and often be placed in parallel near the side wall of the boiler. For example, two cyclones are placed in parallel in the 235MWe CFB boiler at Turow, Poland (Hartge et al., 2005), and three or four cyclones are placed in parallel in the 300MWe CFB boilers. Six cyclones are used and three on each side of the side walls for the 600MWe and 800MWe supercritical CFB boilers (Li et al., 2009). The former one is under manufacturing and the later one is under the conceptual design (Wu et al., 2005).

As shown in Fig. 1, a typical CFB system normally consists of a riser, one set or multiple sets of external components including a cyclone, a standpipe and a solid recycle valve. For a CFB boiler with cyclones arranged in parallel, the furnace can be virtually divided into several parallel sections hypothetically according to the number of cyclones. Each cyclone and its corresponding standpipe, recycle valve, and the furnace forms an independent circulation loop. A few studies (Smellie, 1942; Koffman, 1953; Bolthrunis et al., 2004; Boyd et al., 2005) showed that the gas-solid flow among each loop is nonuniform. The materials concentration, bed pressure drop, and solid flow rate in one circulation loop is different from the others.

The flow non-uniformity among circulation loops of CFB boilers could be a great threat to security and economy of boiler operation. As far as the sub-critical natural circulation CFB boilers concerned, due to the hydrodynamic self-compensation, the flow non-uniformity in the furnace side has little negative effect on water wall security. However, the flow non-uniformity may lead difficulties in controlling the surface temperature of tubes used in external heat exchangers (EHEs) if they are used. To supercritical CFB boilers, the water wall security largely depends on heat flux density distribution, and the hydrodynamic security might be sensitive to the flow non-uniformity.

During CFB boiler design, it was often assumed that flow dynamics in the parallel cyclone array is identical. In addition, each of the individual cyclones has an optimum inlet gas velocity at which the overall performance of cyclones will be optimized (Stern et al., 1955). The flow non-uniformity may lead differences between inlet gas velocities of parallel cyclone array and optimum inlet gas velocity. When inlet gas velocity is lower than optimum value, the gas flow can not provide sufficient centrifugal force to move particles to the outer wall. When inlet gas velocity is higher than optimum value, excessive gas flow will result in turbulence that causes particles to be re-entrained. So the research on the flow non-uniformity in circulation loop of CFB boilers is of great meaning to security and economy of boiler operation and CFB boiler design theory.

The research on the flow non-uniformity in circulation loop of CFB boilers is quite insufficient. Grace conformed that multiphase flow through parallel paths can result in significant misdistribution (Grace, 2008).Theoretical study was conducted to describe possible existence of multiple stable states for the two-phase flow in a CFB boiler with multiple parallel cyclones. According to the study, for a CFB boiler with N cyclones placed in parallel, there is N-1 degree of freedom for the flow states. This means that for a CFB boiler with single cyclone there is no degree of freedom, while for a CFB with parallel cyclones, the gas-solid flow is of

multiplicity and polymorphism. However, the theory has not been confirmed.

In this article, the overall fluid characteristics in the main loop of a CFB with multiple cyclones placed in a parallel array is studied. It focuses on the assessment of the existence of flow non-uniformity predicted in the previous study and discussion of the polymorphism of flow non-uniformity.

EXPERIMENTAL

According to a 300MWe CFB boiler designed by a Chinese boiler manufacturer, a 1:20 down-scaled cold model CFB test facility was built by using scaling law similarity criteria. The structure of the cold modeling facility is shown in Fig. 2. There are 24 pressure taps installed at different height along the riser and standpipe. The bed material was iron powder. At preset fluidizing air velocity U_g and bed inventory I_v, after flow is stabilized at a given aeration rate supplied for the return valve, the pressures and solid circulating rate G_s were measured. Table 1 lists the fluidizing air flow rate and bed inventory used the experiments.

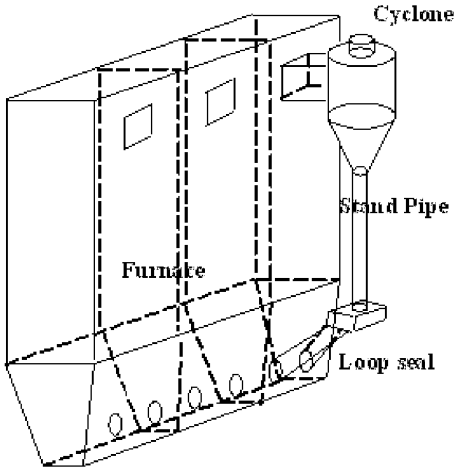

Fig. 1 schematic diagram of CFB boilers

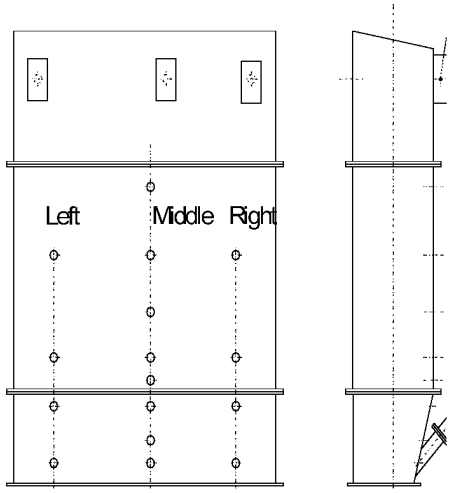

Fig. 2 Experiment system and location of pressure taps

Table 1 The test conditions of cold-model experiment

Case	Fluidizing velocity (m/s)	Bed inventory (kg)
1	0.83	35
2	1.00	50
3	0.84	50
4	1.01	24
5	1.00	30
6	0.84	50
7	1.02	50
8	1.08	50
9	1.08	50

RESULTS AND DISCUSSION

Flow uniformity in the furnace

Table 2 shows the pressure data measured in the experiments. Figures 3 and 4 further depict the pressure profile of Case 8 and 9. It can be seen that the pressure profiles of left, middle, right furnace sections are almost identical. That means that there is no remarkable preferential horizontal movement of bed material in the furnace. However, there is significant difference among the solid flow rates in left, middle, right loops. Maybe the extensive gas-solid mixing in horizontal direction makes the gas-solid two-phase flow in the furnace symmetric.

Flow non-uniformity in circulation loops

According to Table 2, the material distribution in the three circulation loops is always different from each

other. However the relative difference of G_s in the three circulation loops can be controlled within 10% by adjusting the aeration rate. For Case 8 and Case 9, G_s in the three loops are different even at the same I_v and U_g. It means that the gas-solid flow in CFB with parallel cyclones is unstable equilibrium state, any disturbance can lead the flow to another unstable equilibrium state.

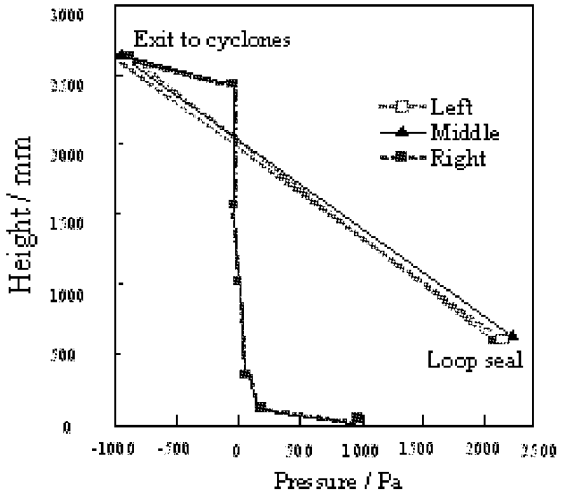

Fig.3 Pressure profile in Case 8

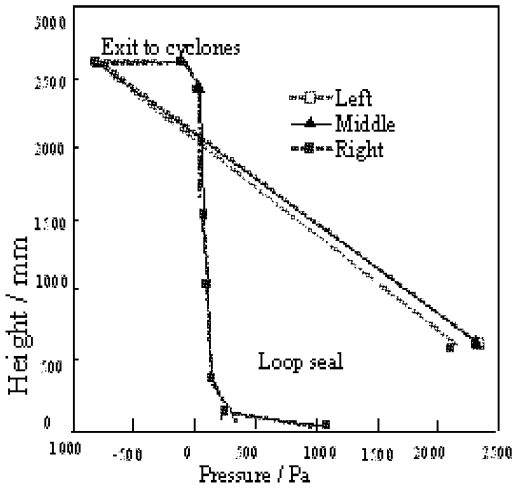

Fig. 4 Pressure profile in Case 9

Table 2 Measurement data for the experimental tests

Case	Position	Bed height (mm) 0	100	350	564	1014	1564	2014	2425	Solid circulating rate kg/s
		Pressure (Pa)								
	Left	728	103	91	78	61	48	40	47	0.115
1	Middle	740	139	98	86	69	56	48	49	0.099
	Right	733	147	91	78	62	50	43	45	0.109
	Left	1090	149	108	83	57	37	22	34	0.165
2	Middle	1095	106	102	80	53	32	19	31	0.160
	Right	1091	221	109	86	9	2	27	29	0.204
	Left	1165	151	119	103	86	78	8	82	0.106
3	Middle	1161	94	120	105	87	78	67	93	0.106
	Right	1170	117	119	105	86	77	68	89	0.112
	Left	523	83	33	22	6	-2	-9	2	0.124
4	Middle	523	80	33	22	7	-2	-10	3	0.110
	Right	523	83	33	22	6	-1	-9	2	0.165
	Left	690	126	76	62	45	34	26	23	0.125
5	Middle	690	120	75	63	46	37	17	36	0.134
	Right	690	126	76	62	44	35	26	30	0.152
	Left	1131	150	114	99	81	72	61	52	0.118
6	Middle	1136	139	118	105	7	77	68	70	0.081
	Right	1162	127	126	113	97	87	78	61	0.094
	Left	1100	145	95	66	35	13	-3	-2	0.197
7	Middle	1109	131	91	64	32	11	-5	0	0.254
	Right	1105	112	86	59	27	5	-9	-1	0.224
	Left	1004	204	68		5		-34	-41	0.245
8	Middle	1004	173	63		4		-35	-35	0.201
	Right	1004	190	64		4		-35	-52	0.195
	Left	1093	284	159		98		61	56	0.239
9	Middle	1093	260	153		97		60	41	0.219
	Right	1093	274	154		97		61	55	0.238

CONCLUSIONS

For a large CFB boiler with multiple cyclones, multiple enclosed circulation loops of the two-phase flow exist and each loop consists of the furnace and the set of external components including a cyclone, a standpipe and a solid recycle valve.

The present experimental study in a CFB with three cyclones installed in parallel confirmed the polymorphism of flow non-uniformity and thereby the fluid dynamic characteristics in each loop are not necessary to be the same. In the furnace the lateral difference of the axial pressure profiles corresponding to the cyclone location is little, indicating that the transverse material concentration distribution in the furnace is unbiased. However, the solid flow rate and the material distribution in one loop could be remarkable different from the others. Under present experimental condition, the circulating rate in the middle loop is about 10% larger than that in the side loops.

ACKNOWLEDGEMENTS

Financial supports of this work by Key Project of the National Eleventh-Five Year Research Program of China (2006BAA03B02) and National Science Fund Committee (50406002) are gratefully acknowledged.

REFERENCES

Bolthrunis, C.O., Silverman, R.W, Ferrari, D.C, (2004), Engineering Conferences International, pp. 547–554.

Boyd D. T, Grace, J. R., Lim, C. J. et al., Int. J. Chem. Reactor Eng. 3 (2005), pp.A58.

Hartge, E. U., Budinger, S., Werther, J., (2005), Circulating Fluidized Bed Technology VIII, Beijing, pp. 675–682.

Koffman, J. L., Gas and Oil Power (1953), pp: 89–94.

Lee, Y. Y., (1997), Circulating Fluidized Beds, Chapter 11, London, pp. 417–440.

Li, Y., Nie, L., Hu, X. K., et al., The structure and performance of a 600MWe Supercritical CFB boiler with water-cooled panels, 20th International Fluidized Bed Combustion Conference, Xi'an, China, (2009).

Grace, J.R., Maldistribution of flow through parallel cyclones in circulating fluidized beds, 9th International Conference on Circulating Fluidized Beds, Hamburg, German, 2008:969-974..

Smellie, J., Iron and Coal Trades Review 144 (1942), pp.3860. Stern, A., Caplan, K., Bush, P., (1955), Cyclone Dust Collectors for the API Dust-Collector Subcommittee, pp. 41–43.

Wu, Y. X., Lu, J. F., Zhang, J. S., Yue, G. X., et al., (2005), Circulating Fluidized Bed Technology VIII, Beijing, pp. 529–536.

FLOW REGIME STUDY IN A CIRCULATING FLUIDIZED BED RISER WITH AN ABRUPT EXIT: FULLY DEVELOPED FLOW IN CFB RISER

J. S. Mei[1], G. T. Lee[1], S. M. Seachman[1], J. Spenik[2]

1 National Energy Technology Laboratory, U. S. Department of Energy, 3610 Collins Ferry Road, Morgantown, West Virginia 26507-0880, USA
2 REM Engineering Services, LLC, 3566 Collins Ferry Road, Morgantown, West Virginia 26505, USA

Abstract: Flow regime study was conducted in a 0.3 m diameter, 15.5 m height circulating fluidized bed (CFB) riser with an abrupt exit at the National Energy Technology Laboratory of the U. S. Department of Energy. Solids fraction and particle velocity data for both the high and low density suspension in the riser were analyzed to investigate how the gas-solids flow could reach a fully developed condition in the riser. A fully developed condition in the riser is defined by Parssinen and Zhu (2001a) as: *The radial solids distribution in the riser no longer changes with its axial location.* Results of the data analysis are discussed in the following sections.

Radial solid fraction and particle velocity data generated from the optical fiber probe (the Vector probe) for the 200 micron glass beads during the test series were used to examine the solids flow development in the riser. The test series was a statistical designed factorial experiment included four (4) operating set points and a duplicated center point (therefore a total of 6 operating set points). The riser gas velocity for this RPB test series is to be operated above the upper transport velocity. The operating conditions for the five experiments were riser gas velocity, U_g=5.6 m/s, 6.5 m/s, and 7.7 m/s and solid mass flux, G_s=87 kg/m^2 • s, 194 kg/m^2 • s, and 303 kg/m^2 • s. The conditions for the duplicated center point were U_g=6.5 m/s, and G_s=194 kg/m^2 • s. However, only the results obtained for the higher solids flux, G_s=303 kg/m^2 • s and riser gas velocity, U_g=5.6 and 7.6 m/s are presented in this paper.

Keywords: fully develop flow, dense suspension, hydrodynamics, CFB, abrupt exit

INTRODUCTION

Circulating fluidized bed (CFB) risers have been employed commercially in many industries for gas-solid contacting processes (Reh, 1999) for examples, coal combustion, coal and biomass gasification, fluid-catalytic cracking (FCC), etc. Therefore, CFB risers have been studied extensively for the past two decades because of their practical applications to coal fired power generation. However, the majority of these studies have been conducted at low solids flux and riser gas velocity or low-density circulating fluidized bed (LDCFB) (Zhu and Bi, 1995; Grace et al., 1999) for combustion applications. CFB risers can also be operated at high riser gas velocity and high solids flux or high-density circulating fluidized bed (HDCFB) for FCC applications. Even though many fluid catalytic cracking (FCC) reactors have been operated at HDFBC conditions for several decades, the HDCFB systems have received little attention despite its prominent role in the petroleum industry. Therefore, considerable experimental and theoretical work remains to be done (Issangya et al., 1999; Issangya et al., 2000; Parssinen and Zhu, 2001a; Parssinen and Zhu, 2001b) in order to provide a better understanding of the HDCFB systems. So that it will provide a proper basis for the design, scale up, and operation of HDCFB reactors. Recently a series of studies on both low- and high-density circulating fluidized bed risers has been undertaken to provide a better understanding of the characteristics of the CFB risers (Mei, et al., 2007). In particular, the present study examines the gas-solid flow development in the riser based on the radial particle velocity and the solids fraction (Parssinen and Zhu, 2001a; Parssinen and Zhu, 2001b) along the vertical axis of the riser. However, only the results on high-density suspension in the riser are presented in this paper.

EXPERIMENTAL

Figure 1 is a schematic of NETL's cold CFB model that is described in more detail elsewhere (Mei et al., 2007, 2008). Solids enter the riser from a side port 0.23 m in diameter, its centerline 0.27 m above the gas distributor, and exit the riser through a 0.20-m 90° port about 1.2 m below the top of the riser and at a point 15.45 m above the solids entry location (centerline to centerline). Riser velocities were corrected for temperature and pressure as measured at the base of the riser. The mass circulation rate was continuously

recorded by measuring the rotational speed of a twisted spiral vane located in the packed bed region of the standpipe (Ludlow et al., 2002). This rate was converted to a mass flux using the measured packed-bed density shown in Table 1, and assuming a constant void fraction at the point of measurement. The solids circulation was varied by controlling the amount of aeration air at the non- mechanical L-Valve and the standpipe and adjusting the total system inventory to increase standpipe height. Steady-state conditions were defined as holding a constant set of flow conditions and maintaining constant pressure differentials over a 5-min period. Air velocity and density at the base of the riser was maintained at their desired set-points using both flow control and back pressure control valves. The riser superficial gas velocity was calculated from the sum of the flow at the base of the riser and the aeration air flow at the bottom of the horizontal section of the L-Valve as well as the other aeration air to the L-valve. Steam was introduced into the air supply header as needed to maintain the relative humidity at approximately 40%.

Table 1 Glass beads Characteristics

ρ_s	kg/m^3	2430	ρ_s	kg/m^3	2430
ρ_b	kg/m^3	1380	U_{mf}	m/s	0.0317
d_{sv}	μm	179	ε_{mf}	----	0.42
U_t	m/s	1.138	ϕ	----	0.86

A total of thirty incremental differential pressures were measured across the length of the riser, the standpipe, and the L-Valve using transmitters calibrated within 0.1% of full-scale or about 2 Pa/m. Twenty of the transmitters were mounted in the riser, eight in the standpipe and two in the L-Valve. The overall riser pressure drop was calibrated within 0.45 Pa/m.

Apparent solid fractions were estimated from the measured differential pressures (Louge and Chang, 1990). Particle velocities across the riser at different elevations along the riser were measured using an optical fiber probe (Mei et al., 2007, 2008). Local particle velocities were measured at different radial positions by traversing the probe horizontally. Radial particle velocity profiles were measured at different elevations and at different azimuthal angles. The orientation of azimuthal angle is defined in Fig. 2.

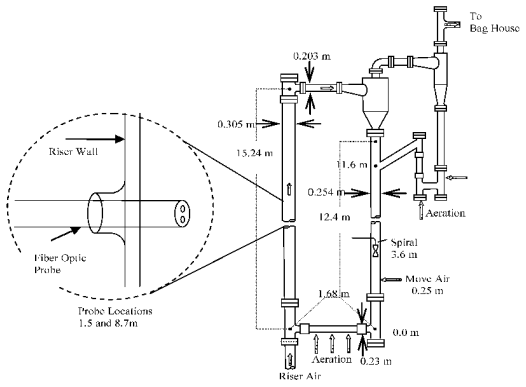

Fig. 1 Schematic diagram of the 0.3 m circulating fluidized bed cold model

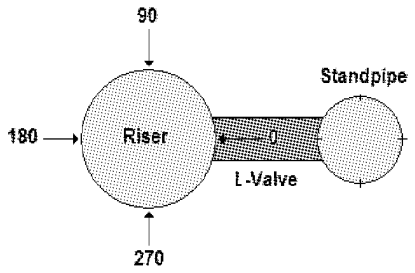

Fig. 2 Orientation of azimuthal angle

The test series conducted included four (4) operating set points and a duplicated center point (therefore a total of 6 operating set points) which were conducted in random order. The riser gas velocity for this test series was to be operated above the upper transport velocity [Monazam, et al., 2005[. Superficial gas velocities, U_g , ranged from 5.6 m/s to 7.7 m/s and solid mass fluxes, G_s , ranged from a low of G_s=87 to a high of 303 kg/m^2-s. The conditions for the center point were duplicated each time the test series was conducted at U_g=6.5 m/s, and G_s=194 kg/m^2-s. Experimental data collected from the nearly 16 repeats of this matrix included differential pressure and particle velocity measurements. However, only the experimental results obtained for the dense suspension (i.e. G_s=303 kg/m^2-s) at U_g=5.6 and 7.6 m/s are presented and discussed in this paper.

RESULTS AND DISCUSSION

Solids fraction

Data on solids fraction at six radial locations and at similar azimuthal angles were analyzed and plotted against the riser height. These plots provide an indication if the solids fraction changes along the vertical axis. Fig. 3 shows the data obtained for a high density suspension (G_s> 200 kg/m^2 • s & (1- ε)> 10%) riser, which

operated at conditions, U_g =5.6 m/s and G_s =303 kg/m^2 • s. As can be seen in Fig.3a, the solids fraction at each radial locations does not change beyond the riser height of, h=5.3 m. Furthermore, the solids fractions ranging from 10% near the center to 20% near the riser wall remained nearly unchanged all the way to the top exit region. A fully developed region, thus, was established at h=5.3 m and extended all the way to the top exit of the riser under these operating conditions. These data also suggested that the solids flow is quickly reached its fully developed flow condition near the center of the riser in comparison to the solids flow near and at the riser wall, which took approximately six (6) meters to establish it's fully developed condition. The dense suspension under these operating conditions, however, was not observed by other researchers (Parssinen, and Zhu, 2001b) with similar operating conditions but in a smaller diameter of 76-mm and 10-m tall riser. This discrepancy can be attributed to the fact that large amount of solids were reflected from the abrupt 90 degrees exit and caused the accumulation of high solids concentration in the top exit region of the riser. However, whether the high density riser could also be operated at the Dense Suspension Upflow (DSU) regime depends on the direction of the net solids flow at the riser wall. This will be discussed later when data for radial particle velocity at various axial locations is examined. Figure 4 presented the data at a higher riser gas velocity, U_g =7.6 m/s but with the same solid flux, G_s =303 kg/m^2 • s. The influence of the riser gas velocity is clearly seen from these data. Due to the higher riser gas velocity, more solids were transported out of the riser and, thus decreased the solids concentration throughout the riser. Figure 5 compares the average solids fraction at six radial locations along the vertical axis of the riser. At higher riser gas velocity, U_g =7.6 m/s fully developed condition was established at axial location, h=4 m and then extended to about 13 m. Beyond this fully develop flow region, solids fraction increases with riser height toward the top exit region. For the lower riser gas velocity, the flow development was slower, which did not establish the fully developed region until it reached axial location of h=5.5 m. However, the solids fraction remains fairly constant and continued to the top exit region of the riser. The increasing solids fraction with height beyond the fully develop region, for example, h>12 m, may be attributed to the higher solids reflection from the abrupt exit caused by higher gas velocity. The influence of riser gas velocity on the flow development is in consistent with published literature (Parssinen and Zhu, 2001b).

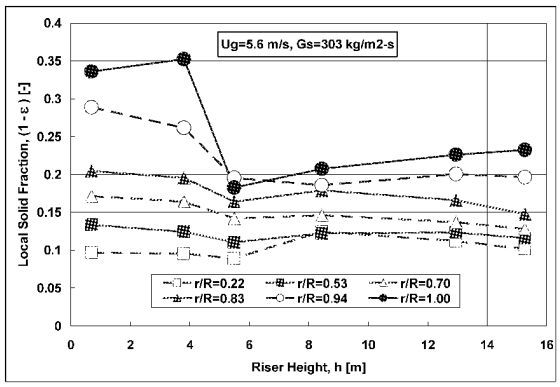

Fig. 3 Local solids fraction along the vertical Axis of riser at Ug=5.6 m/s and Gs=303 kg/m^2 • s

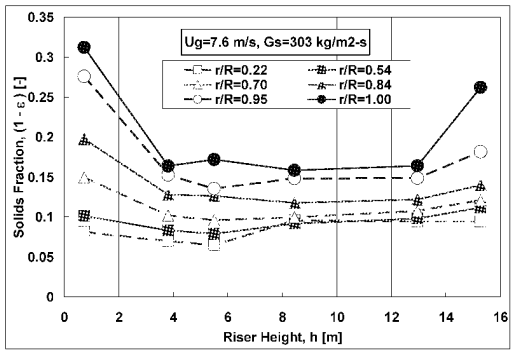

Fig. 4 Local solids fraction along the vertical axis of riser at Ug=7.6 m/s and Gs=303 kg/m^2-s

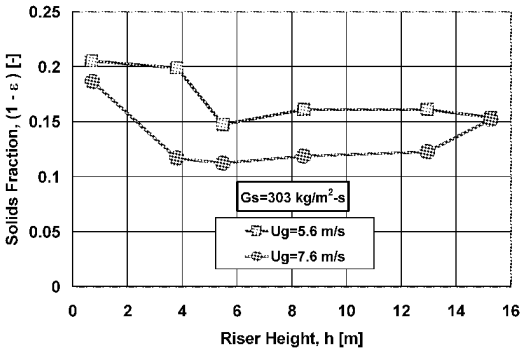

Fig. 5 Effect of riser gas velocity on flow development in riser

Particle velocity

Figue 6 shows the particle velocity in six radial locations plotted against the riser height. These data show that particles accelerated from the bottom to a height, h=5.8 m at five radial locations, which span from the central region all the way to near the riser wall r/R=0.94. At the riser wall, however, the particle started to decelerate from the bottom slowly and changed its direction to downward flow beyond 6 m. Particle at the wall region (r/R=0.95 to 1.00) accelerated beyond h=8.3 m and changed its direction again to upward flow as it reaches the upper region of the riser. In the central and middle section of the riser, r/R=0.22 to 0.83, the particle remain fairly constant without significant changes from h=5.8 m to 12.95 m. The particle, then decelerated at

the radial location r/R=0.22 to 0.70 and accelerated at r/R=0.83 to the wall region, r/R=1.00 near the top exit of the riser. These data suggested that at the bottom region, not all particles accelerated. From these data, only the layers from the center to r/R=0.95 accelerated from the bottom to h=5.83 m. Furthermore, the magnitude of the acceleration was also varied with the particle in the central layer accelerated to its highest value. The magnitude decreased with increasing radial direction r/R toward the riser wall. There is a significant particle velocity gradient in the radial direction throughout the entire riser (Grace, 2000) even the riser is operated in a dense suspension upflow regime. The influence of the wall was restricted only to the next layer, r/R=0.95. The wall effect has minimal influence to the central and the middle sections of the riser, which may be attributed to the high solids concentration in the riser. The riser gas velocity has minimal influence on this solid flow pattern as data in Figure 7 shows results obtained for a higher riser gas velocity, U_g =7.6 m/s and with the same solids flux, G_s =303 kg/m^2 • s. The minor effect caused by higher riser gas velocity is that the wall layer decelerated faster and takes shorter distance to change its direction to downward flow. The wall also exerted slightly more influence to its neighboring layer, r/R=0.95, which now decelerated even at the bottom region.

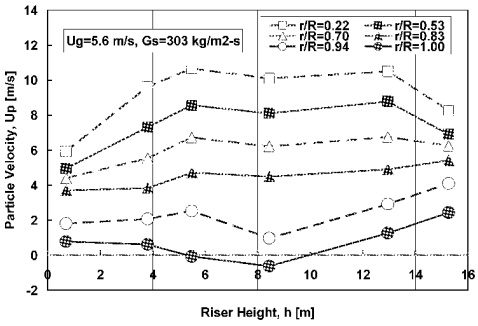

Fig. 6 Particle velocity in six radial locations along the vertical axis of the riser at U_g=5.6 m/s and G_s=303 kg/m^2 • s

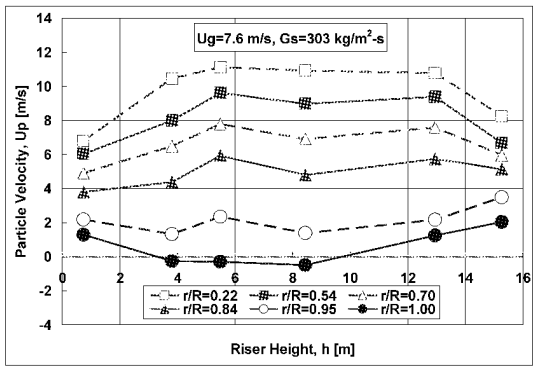

Fig. 7 Particle velocity in six radial locations along the vertical axis of the riser at U_g=7.6 m/s and G_s=303 kg/m^2 • s

As discussed previously, at high density suspension, even though the overall solids fraction was greater than 10%, under the operating conditions U_g=5.6 m/s and G_s=303 kg/m^2 •s, however, the particle velocity at the wall, as shown in Fig. 6, in the middle region shows downward flow. The riser, therefore, was not operated in the dense suspension upflow (DSU) regime in the entire riser. However, this is not surprising, as pointed out by Kim et al. (2004), that fast fluidization with a core annulus structure can co-exist with DSU in a riser. In a smooth exit configuration (Kim et al., 2004), a riser can operate in DSU regime at the bottom and fast fluidization (FF) with core annulus structure in the upper region of the riser. For the NETL's circulating fluidized bed riser, which has an abrupt exit, experimental data show that both the lower and upper region can be operated in the DSU, yet the middle region can still be in the fast fluidization regime.

EFFECT OF AZIMUTHAL ANGLE

Figure 8, presents the average particle velocity and solids fraction at six locations. These data were obtained at riser elevation of h=12.95 m and at various azimuthal angles (θ=45, 135, 245, and 340 degrees) under the same operation conditions. U_g=5.6 m/s and G_s=303 kg/m^2 • s. The azimuthal angle only affects the solids fraction slightly, which is not surprising since the riser is still in the fully developed region under these operating conditions. The average particles in the first quadrant , on the other hand, move slower than the particle in the other three quadrants. This lower particle velocity in the first quadrant may be attributed to the uneven solids distribution near the top region of the abrupt exit. However, more data in the upper (h>12.95 m) levels near the riser exit and at the lower (h<12,95 m) fully developed levels will be needed to understand the causes of this non-uniformity.

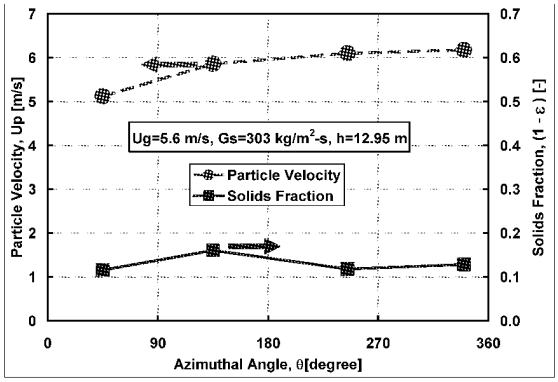

Fig. 8 Effect of azimuthal angle on average particle velocity and solids fraction at U_g=5.6 m/s and G_s=303 kg/m^2 • s

SUMMARY

Solids fraction and particle velocity along the vertical axis for high density suspension in an industrial size CFB riser were presented in this paper. As the data shown in Figs. 3、4 and 5, only three longitudinal regions were identified in the riser, which Parssinen and Zhu (2001b) shown to observe four longitudinal regions in the riser. The influence of riser gas velocity on flow development can clearly be seen in Fig. 5. The gas-solids flow can reach the fully developed region faster (i.e. a shorter distance) with increasing riser gas velocity. The riser gas velocity, however, exerts less influence on the particle velocity. By increasing the riser gas velocity, the wall layer decelerates faster and takes shorter distance to change its direction to downward flow. Furthermore, the wall also exerts slightly more influence to its neighboring layer, r/R=0.95, which now decelerated even at the bottom region. For a dense suspension riser, due to the reflection of particles from the abrupt exit, both the lower and upper region can be operated in the DSU, yet the middle region can still be in the fast fluidization regime. The influence of azimuthal angle affects the solids fraction slightly in the fully developed region. The particle velocity in the first quadrant, however, was found lower than the particle velocities in the other three quadrants.

NOTATIONS

Symbols :

d_{sv}	mean particle diameter	μm
G_s	solid flux	kg/m^2 • s
h	riser height	m
r	radial distance from riser center	m
R	radius of riser	m
U_g	riser gas velocity	m/s
U_{mf}	minimum fluidization velocity	m/s
U_p	particle velocity	m/s
U_t	particle terminal velocity	m/s

Greek letters :

ε	voidage	-----
ε_{mf}	voidage at minimum fluidization	-----
ϕ	particle sphericity	-----
θ	azimuthal angle	degree
ρ_b	bulk density	kg/m^3
ρ_s	particle density	kg/m^3

REFERENCES

Basu, P., and Fraser, S. A.: Circulating fluidized bed boilers: design and operations, Chapter 1, Butterworth-Heinemann, Stoneham, MA, 1991, pp.8-13.

Berruti, F., Chaouki, J., Godfroy, L., Pugsley, T. S., and Patience, G. S.: Can. Jour. Chem. Eng. 73 (1995), pp. 579-602.

Grace, J. R., Powder Technol, 113 (2000), pp. 242-248.

Grace, J. R., Issangya, A. S., Bai, D., Bi, H., and Zhu, J., AIChE J. 45 (1999), pp.2108-2116.

Issangya, A. S., Bai, D., Bi, H. T., Lim, K. S., Zhu, J., and Grace, J. R., Chem. Eng. Sci. 54 (1999), pp.5451-5460.

Issangya, A. S., Grace, J. R., Bai, D., and Zhu, J., (1999) Powder Technology, 111, pp. 104-113.

Zhu, J., and Bi, H. T., Can. J. Chem. Eng., 73(1995), pp. 644-649.

Kim, S. W., Kirbas, G., Bi, H., Lim, C. J., Grace, J. R.,, Chem. Eng. Sci. 59 (2004), pp. 3955-3963.

Louge, M. and Chang, H. Powder Technol., 60 (1990) 197.

Ludlow, C., Lawson, L. O. and Shadle, L. J.: 7th CFB Conf. (Grace, J.R., Zhu, J., de Lasa, H., eds.), Can. Soc. Chem. Eng, Ottawa, (2002), pp. 513-520.

Mei, J. S., Shadle, L. J., Yue, P. C., Monazam, E. R.: Prod. Fluidization XII (Bi, X., Berruti, F., Pugsley, T., eds.), Eng. Conf. Int. (2007), pp. 63-70.

Mei, J. S., Lee, G. T., Seachman, S. M., Ludlow, J. C., Shadle, L.J., 9th CFB Conf. (Werther, J., Nowalk, W., Wirth, K., Hartge, E., eds.), TuTech Innovation GmbH, Hamburg, Germany (2008), pp. 177-182.

Monazam, E. R., Shadle, L. J., Mei, J. and Spenik, J. (2005) Powder Technology, 155, 17-25.

[Parssinen, J. H. Zhu, J. X., AIChE J. 47 (2001a), pp. 2197-2205.

Parssinen, J. H. Zhu, J. X., Chem. Eng. Sci. 56 (2001b), pp.5295-5303.

Reh, L.: Chem. Eng. Sci. 54 (1999), pp. 5359-5368.

HEAT TRANSFER AT A LONG ELECTRICALLY-SIMULATED WATER WALL IN A CIRCULATING FLUIDISED BED

R. Sundaresan[1], Ajit Kumar Kolar[2]

1 School of Mechanical & Building Sciences, VIT University, Vellore, India
2 Department of Mechanical Engineering, Indian Institute of Technology Madras, Chennai, India

Abstract: In the present work, heat transfer measurements are reported in a 100mm square, 5.5 m tall, cold CFB. The test section is a 19 mm OD electrically heated heat transfer tube, 4.64 m tall (covering more than 80% of the CFB height), sandwiched between two equally tall dummy tubes of 19mm OD, thus simulating a water wall geometry, forming one wall of the CFB. Narrow cut sand particles of mean diameters 156, 256, and 362 micrometers, and a wide cut sample of mean diameter 265 micrometer were used as the bed material. The superficial gas velocity ranged from 4.2 to 8.2 m/s, and the solids recycle flux varied from 17 to 110 kg/m^{2}s. Local heat transfer coefficient at the simulated water wall varies, as expected from a low value at the top of the riser to a high value at the bottom, with an interesting increasing and decreasing trend in between. The average heat transfer coefficients were compared with those available in open literature. Correlations for average heat transfer coefficient are presented, both in terms of an average suspension density and also in terms of important nondimensional numbers, namely, Froude number, relative solids flux and velocity ratio. Comparisons are also made with predictions of relevant heat transfer models. Based on the present fifty-five experimental data points, the following correlation was presented with a correlation coefficient of 0.862 and maximum error is ± 15 %.

Keywords: CFB, average heat transfer coefficient, heat transfer correlation

INTRODUCTION

Substantial amount of open literature is available for heat transfer at the wall of a Circulating Fluidized Bed (CFB) under various design and operating conditions. Most of the laboratory-sized cold CFB, however, employed small and short heat transfer surfaces in terms of spheres, cylinders, and heated tubes. The surfaces were heated electrically or by hot water. The heat transfer measured in many of the cases (particle convective and gas convective components) was a local value while in some cases average values were measured over short length of the tubes. While these measurements are of value, two shortcomings of the method are the non-simulation of the actual water wall geometry (which affects the movement of the gas-solid motion) and the limitation of the heat transfer surface length not covering the entire wall of the riser. Experimental heat transfer results on some large commercial units and a large number of laboratory units are reported in the literature. Information available on heat transfer in CFB is reviewed by number of workers (eg. Subbarao and Basu, 1986; Basu and Nag, 1987l Furchi et al., 1988; Sekthira et al., 1988; Wu, et al., 1989; Han et al., 1996; Pagliuso et al., 2000; Xie et al., 2003). A study of the literature reveals the absence of any heat transfer correlation for furnaces of vertical orientation at the wall of a CFB riser covering more than 80% of the CFB riser. The development of a correlation for heat transfer between a long wall surface and CFB suspension will be definitely helpful in the design and operation of a CFB it incorporates the directly measurable variables such as G_s, U and d_p.

EXPERIMENTAL PROGRAMME

The experimental investigation is conducted in a CFB facility specially fabricated, installed and instrumented for the present study. Fig. 1 shows the schematic arrangement of the CFB cold facility. The major components of the facility consist of the following: (i) air supply system with control and metering (ii) CFB riser column having a bed cross section of 100 mm ×100 mm and riser height of 5.5 m (iii) solids recovery cyclone and baghouse section and (iv) solids return leg with solids measurement section and a reinjection L-valve. The description of the experimental facility is given elsewhere (e.g. Mahalingam and Kolar 1993). High pressure blower supplies the air to the CFB. Pitot static probe and a micro manometer are used to measure the air flow rate. The air is introduced into the riser column through a nozzle type distributor having 19% open area. The riser column is made up of two sections: the bottom section, 680 mm tall accommodates the particle reinjection port and the top section provides for the heat transfer measurements using a 4.64 m long heat transfer tube. The entire riser column is provided with adequate numbers of static pressure tappings for the

measurement of pressure profiles. Cyclone separator recovers most of the entrained coarse solids and is dropped through the cyclone dipleg to the solid recycle measuring section. The solids recycle flux is measured by closing the butterfly valve placed in this section and measuring the volume of solids collected in the graduated column above it over a certain time interval. The solid recycling system consists of a storage hopper, a stand-pipe and a non-mechanical L-valve. The L-valve is capable of feeding a desired solids flow rate into the CFB with pressure regulated and flow controlled aeration air supply. One wall of the riser's top section is a simulated membrane wall with the heat transfer surface in the form of 4.64 m long central cylindrical heater tube along with two adjacent dummy tubes. The bed-side of the wall is provided with three semi-circular vertical grooves of 19 mm diameter at a pitch of 38 mm. In the central groove the heater tube is fixed and dummy tubes are mounted in the two adjacent grooves. The heater tube as well as dummy tubes are 19 mm O.D. with only half of their outer surface exposed to the CFB. Along the heater tube 32 pairs of calibrated chromel-constantan thermocouples are mounted for sensing the heater tube surface temperature. Electrical energy input to the heater is controlled by a variable auto transformer and measured with a wattmeter. The heat transfer test section if the riser is fitted with eight numbers thermocouples for local bed temperature measurement and all the thermocouples are connected to a digital millivoltmeter through a selector switch. The bed materials used in the experiments are (i) narrow cut sand particles of mean diameters 156 μm, 256μm, 363μm and (ii) wide cut sand of mean diameter 265 μm. The average heat transfer coefficient is defined as the average of all the local values over the length of the heat transfer surface. The local heat transfer coefficient is determined for each of the operating conditions at steady state from the measured heat input and the local temperatures of heater wall at 32 locations and the bed at eight elevations through the following relation:

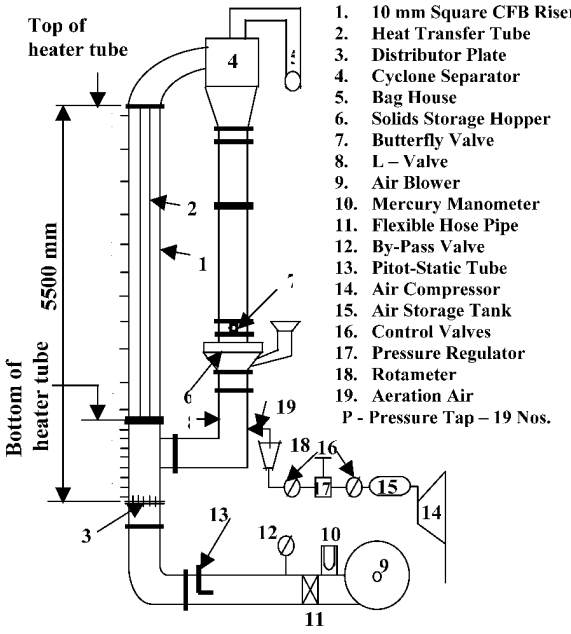

Fig. 1 Schematic diagram of CFB cold facility

$$h = \frac{(Q_I - Q_L)}{A(T_w - T_b)} = \frac{(Q_{Net}/A)}{(T_w - T_b)} \quad (1)$$

Where Q_I is the measured the heat input (W), Q_L is the estimated heat loss from the back of the tube, (W), A is the exposed surface area of tube (m^2), T_w is the local temperature of heater wall (K) and T_b is local bed temperature (K). The heat flux i.e. (Q_{Net} / A) is taken to the constant along the tube wall based on the fact that the heat flow into the CFB in the radial direction is an order of magnitude higher than that in the axial direction. The bed temperature measurements show a deviation of 1-2% in both radial and axial directions which is good agreement with the published data of both laboratory units and commercial installations. This confirms the isothermal condition of the CFB and thus the overall average of all the bed temperature probes may be used as the local bed temperature. However, the following procedure is adopted in arriving at the local bed temperature: The temperature readings obtained at six radial positions of each bed probe assembly are first averaged. Then the average of temperature of B(1) and B(2) are again averaged to obtain the local bed temperatures for use in the determination of h_I for location 1 thou'8. Similarly an average value of B(3) and B(4) is used for locations 9 thou'16; average of B(5) and B(6) for locations 17 throu'24 and average of B(7) and B(8) for location 25 throu"32. More details of heat transfer tube and installation of thermocouples are given by Mahalingam and Kolar (1993).

RESULTS AND DISCUSSION

Effect of suspension density

In the literature, the heat transfer data are generally expressed in terms of cross-sectional average suspension density measured by the pressure drop between two pressure taps on the wall. The average suspension density depends upon the solid recycle flux, the particle diameter, the superficial gas velocity, bed inventory and bed geometry. Fig. 2 shows the variation of average heat transfer coefficient as a function of suspension density for sand particle of different sizes (156 to 363μm) in the gas velocity range of 4.2 to 8.2 m/s

and a solid recycle flux range of 17 to 110 kg/m^{2}s. It is observed that the average heat transfer coefficient increases with suspension density as reported in the literature. This is obviously due to large number of solid particles in a given volume near the surface impinging upon it and transferring heat by particle convection. The influence of particle size is also seen with smaller particles giving higher heat transfer coefficient at constant suspension density values. Also with increase of particle size, the gas gap thickness which could be the order of 0.1 d_p between the surface and the particles increases resulting in the decrease of the heat transfer coefficient. Also shown are the prediction of a correlation by Breitholtz (2000) for the total convective (gas convective and particle convective) heat transfer at the wall from the data of six CFB boilers of capacity 12 MWth to 300MWth.

$$h = 25 \rho_{sus}^{0.58} \quad (2)$$

The boilers varied from about 2.5 m^2 to 95 m^2 in cross-sectional area and 12 m to 28 m in height. The bed particle size ranged from 200 μm to 400 μm and the fluidizing velocity varied from 1.8 to 6.4 m/s. The solid recycle flux was not specified. The correlation coefficient predicts the convective coefficients in the range of 95 to 212 W/m^{2}K in the suspension density range of 10 to 40 kg/m^3. Fig. 2 clearly demonstrates the dependence of 'h' on suspension density. All the present data fall within the correlation prediction which is physically realistic.

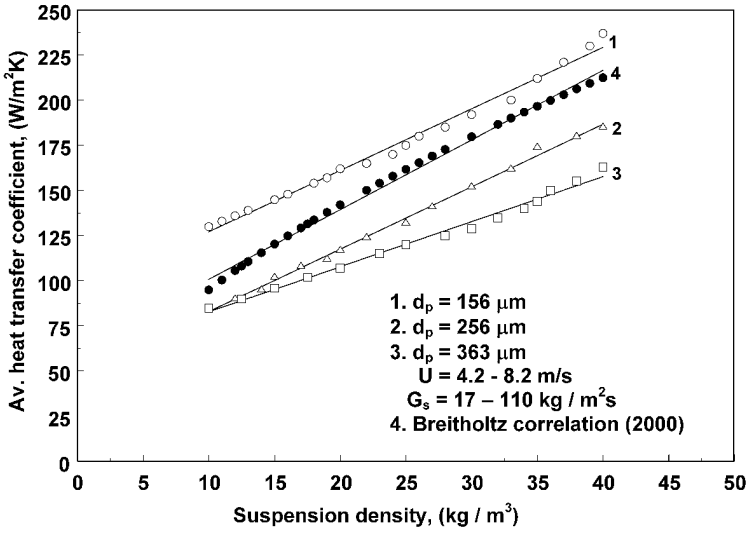

Fig. 2 Effect of suspension density on the average heat transfer coefficient

Local heat transfer coefficient variation

The local heat transfer coefficients measured over the 4.64 m long wall surface for 156μm sand material using four different values of G_s at U = 7.0 m/s is shown in Fig. 3. It can be seen that the solid recycle flux influences the heat transfer directly. Visual observations in the present experimental study indicate that at increased recycle flux levels the wall layer covers almost uniformly the entire wall layer surface when compared to the low recycle flux levels resulting in a non-uniform coverage of the wall surface. Thus one could infer that at higher solid recycle flux, the heater tube surface gets a larger inventory of moving sand particles which act as heat carriers and hence the local heat transfer coefficient has a direct dependence on solid recycle flux. It is observed that the local heat transfer coefficient shows an initial decrease upto about 0.6m starting from the top of the heat transfer surface and then increases in the next 0.6 m length reaching a peak value generally higher than the starting value. Further this trend of decreasing and increasing h herein termed as "thermal decay" and "thermal regeneration" is seen to be repeated in the remaining portion of the vertical heat transfer surface over approximately 1.2 m lengths with successive peaks having higher values than the previous value. The elevations at which these peaks occur are 55 mm, 1200 mm, 2400 mm, 1600mm and 4585mm and these points are definitely away from the elevations at which the bed temperature probe assemblies are mounted and thus the occurrence of peaks do not have any dependence on the bed temperature assembly locations. This behavoiur is observed consistently during reproducibility checks. The underlying phenomenon of layer renewal causing such a behaviour is generally reported as random. However the available information has not ruled out the possibility of a periodic behaviour. It is observed to be a periodic phenomenon for the operating conditions used in the present experimental facility. The only other available data is for a 1.6 m long tube reported in the literature (e.g. Wu et al., 1989) also showed a similar trend (not shown). This behaviour was observed in all other experiments using other particle size and superficial velocities and was repeatable thus confirming the phenomenon for our range of operating conditions. The local heat transfer coefficient was also found to

increase towards the lower sections of the bed riser, as a consequence of increasing suspension density. Another observation from the Fig. 3 is the generally increasing trend of the heat transfer coefficient from the top towards the dense bed zone which appears reasonable under the fluidizing conditions prevalent in that zone. More details on local heat transfer coefficient variation are given in Mahalingam and Kolar (1993). Also shown is the comparison of present data for local suspension-to-wall heat transfer coefficients with the experimental data of Furchi et al (1988) for various operating conditions. Fig. 4 shows the local-length average heat transfer coefficient with distance along the heat transfer surface which is defined as distances starting from the top of the surface to the bottom for a particle size of 363μm, fluidizing velocity 5.7 m/s with G_s as a parameter. For a given solid recycle flux it is observed that the local-length average heat transfer coefficient increased from top of the surface to bottom of the surface. It is also observed that the heat transfer coefficient increased with increase of solid recycle flux. Increasing the solid recycle means more particles per unit surface area near the heat transfer surface resulting enhanced heat transfer.

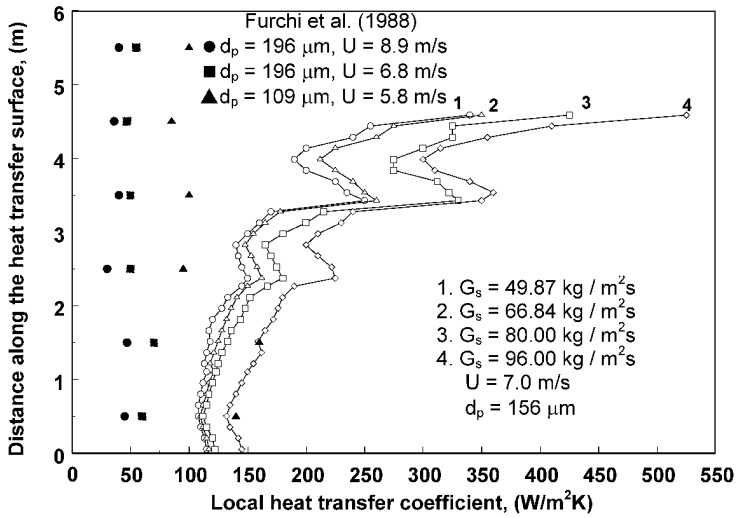

Fig. 3 Variation of local heat transfer coefficient along the surface length with G_s as a parameter

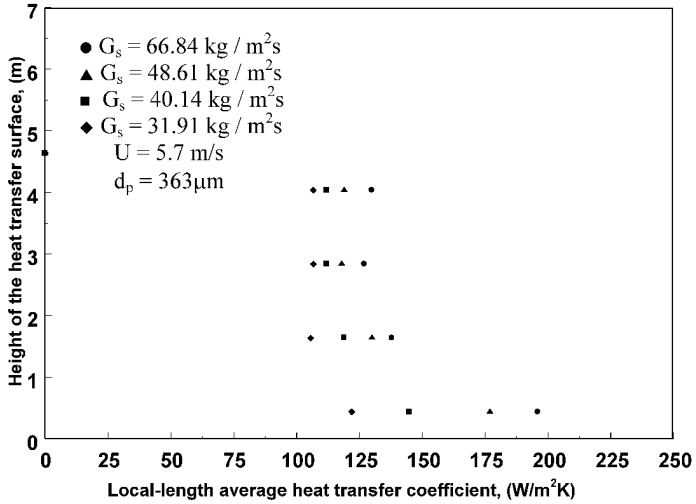

Fig. 4 Variation of local length average heat transfer coefficient along the surface length

COMPARISON

Figure 5 shows the comparison of present experimental data with the published heat transfer results under somewhat similar conditions. The experimental data of other investigators were read out from graphs in published literature and hence are prone to uncertainty. Inspite of the considerable differences in the experimental equipment, operating conditions and the measurement techniques among these studies, it is observed that the heat transfer coefficient increases with suspension density. Higher heat transfer coefficients are observed for short heat transfer surfaces and smaller particle sizes. Luan et al. (2000) presented suspension-to-membrane wall heat transfer coefficient in a 152 mm square and 7.3 m tall pilot scale CFB combustion facility using 286μm sand as the bed material. The membrane wall consisting of four identical

pipes 21.3 mm OD and 14.1 mm ID. The total length of membrane section was 1626 mm. The effect of suspension density on suspension-to-membrane wall heat transfer coefficient for two different bed temperature is also shown in the same Figure 5. It is observed that the wall data of Luan et al. (2000) are higher (i.e. total heat transfer coefficient, which includes radiative, gas and particle components) because of high temperature and short tube compared to present data. It is also observed that the present experimental results are in the same range of data of others and they do similar trends of variation with suspension density. Thus the present experimental results can now be analyzed using three directly measurable variables such as U, G_s and d_p to gain a better knowledge on CFB wall tube heat transfer.

Sl.No.	Author	d_p (μm)	Height of heat transfer tube (mm)	Bed Temp. (K)
1	Basu & Nag (1987)	227	25	311
2	Wu et al. (1989)	171	22	308
3	Subbarao & Basu (1986)	260	25	300
4	Pagliuso et al. (2000)	179	930	423
5	Pagliuso et al. (2000)	230	930	423
6	Pagliuso et al. (2000)	385	930	423
7	Ilan et al. (1996)	157	----	373-873
8	Sekthira et al. (1988)	300	700	503
9	Present work	156	4640	340
10	Present work	256	4640	340
11	Present work	363	4640	340
12	Luan et al. (2000)	286	1626	979
13	Luan et al. (2000)	286	1626	1077

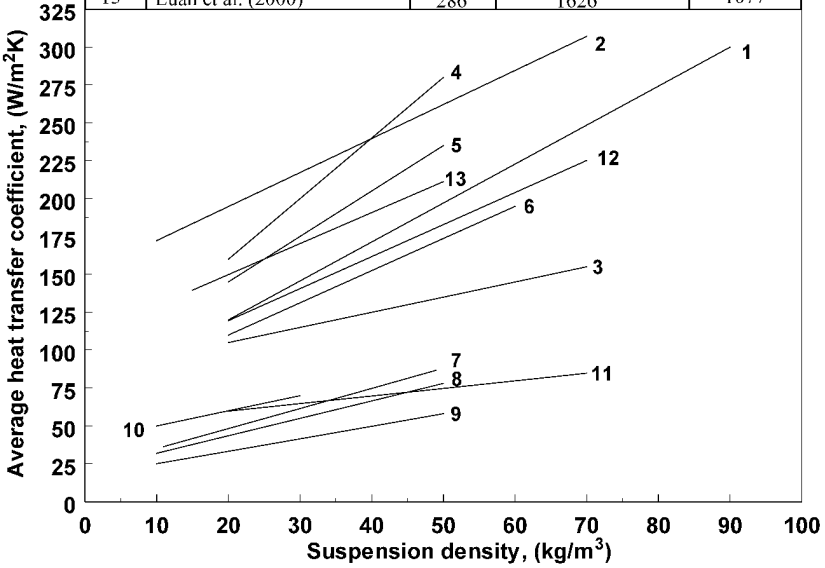

Fig. 5 Comparison of present experimental data with published heat transfer result

PROPOSED CORRELATION

A study of the literature reveals the absence of any heat transfer correlation for furnaces of vertical orientation at the wall of a CFB riser covering more than 80% of the CFB riser. The development of a correlation for heat transfer between a long wall surface and CFB suspension will be definitely helpful in the design and operation of a CFB it incorporates the directly measurable variables such as G_s, U and d_p. The heat transfer coefficient represented by the Nusselt number is a function of the above mentioned variables along with the bed temperature and the properties of both the bed material and the fluidizing medium.

$$Nu = f\ (U,\ G_s,\ d_p,\ T_b,\ \text{Gas and Solid properties}) \quad (3)$$

In the development of the correlation, the following groups are identified based on their dominant role in the heat transfer process: (i) G_s/G_o; (ii)U/U_t; (iii) Fr_p; (iv) Nu

The first group viz., the ratio of the solid recycle flux to the saturation carrying capacity of the gas is selected to represent the excess solids that migrate towards the wall which plays a major role in the heat transfer process. The second group viz., the ratio of the superficial gas velocity to the particle terminal velocity is taken as a representative of the condition that causes the special hydrodynamic condition due to which the fast fluidization regime comes into existence. The third group viz., Froude number based on the particle diameter is selected to represent the flow condition with respect to particle size. The last group involves the average heat transfer coefficient between the wall tube surface and the CFB suspension. Thus the general

correlation is written as

$$Nu_p = C_1\left[\frac{G_s}{G_o}\right]^{C_2}\left[\frac{U}{U_t}\right]^{C_3}\left[Fr_p\right]^{C_4} \quad (4)$$

Based on the present fifty five experimental data points and with the use of multiple regression analysis the values of the constant C_1 to C_4 are evaluated as $C_1 = 678.3$; $C_2 = 0.581$; $C_3 = 0.703$; $C_4 = -0.814$. Fig.6 shows the parity plot of present experimental data with the prediction of the above correlation showing the deviation of ± 15%.

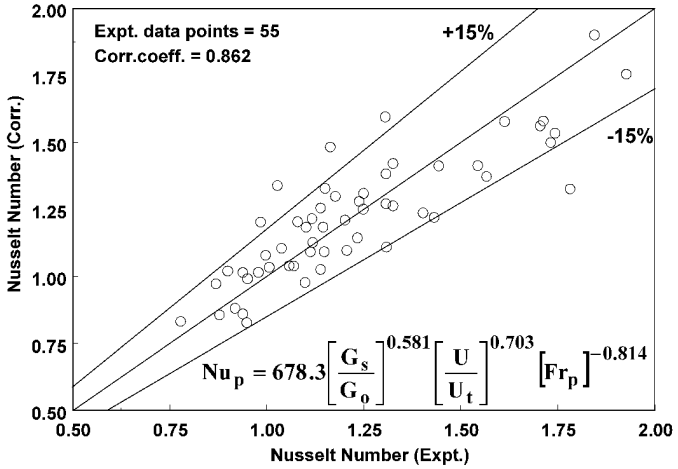

Fig. 6 Parity plot of present experimental data with the proposed correlation

A General Dimensional Correlation

While the correlation of the form of Eq. (4) is acceptable and based on the physics of the situation, it would also be useful to provide a correlation in terms of the suspension density as done by Breitholtz (2000). A correlation was attempted for the present data of wall heat transfer in the form of $h = 25\rho_s^{0.58}$ as reported by them with a correlation coefficient of 0.714 with a deviation of ± 20 %.

$$h = 35.177[\rho_{sus}]^{0.445} \quad (5)$$

It is interesting to note that Breitholtz (2000) correlation for the convective heat transfer at the wall of CFB boilers shows h varying with ρ_{sus} to the power of 0.58 while the present case h varies with ρ_{sus} to the power of 0.445. Eq. (2) however, showed the necessity of explicitly incorporating the effect of particle size and accordingly the following correlation is proposed:

$$h = 0.762\ [\rho_{sus}]^{0.488}\ [d_p]^{-0.441} \quad (6)$$

Figure 7 shows the comparison of the present experimental data with the prediction of the correlation showing a deviation of ± 10 % with a correlation coefficient of 0.979. Eq. (6) indicating the consistence of the data and correctness of the qualitative and quantitative relationship between h and the particle size variable. The available experimental data of Basu & Nag (1987) and Wu et al. (1989) are compared with the proposed correlation.

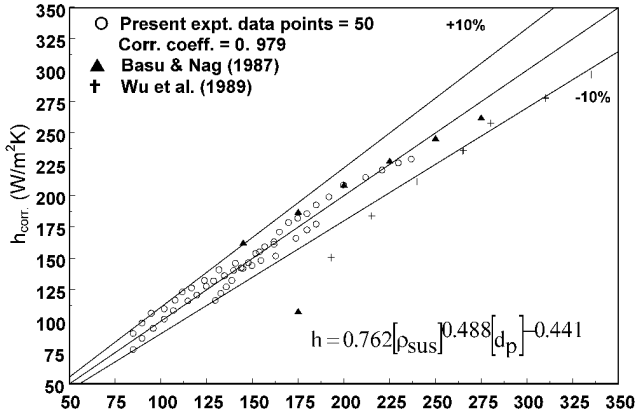

Fig. 7 Comparison of present experimental data with the proposed correlation

CONCLUSIONS

Local and length averaged heat transfer coefficients for a wall-tube surface covering more than 80% of the CFB column height are presented for the first time. Local heat transfer coefficient at the simulated water wall varies, as expected from a low value at the top of the riser to a high value at the bottom, with an interesting increasing and decreasing trend in between. The length averaged heat transfer coefficient values presented in this study are in the range of 95 to 230 W/m^2K. The average heat transfer coefficients were compared with those available in open literature. Correlations for average heat transfer coefficient are presented, both in terms of an average suspension density and also in terms of important nondimensional numbers, namely, Froude number, relative solids flux and velocity ratio. Such a correlation is to the best of author's knowledge the first of its kind in the CFB literature that will help in the design of the CFB systems after including the radiation component. Comparisons are also made with predictions of relevant heat transfer models. Based on the present fifty-five experimental data points, the following correlation was presented with a correlation coefficient of 0.862 and maximum error is ± 15 %. A dimensional correlation for average heat transfer coefficient was presented in terms of suspension density and particle size.

NOTATIONS

A_s	Surface area of the heat transfer tube (m^2)	Q_L	estimated heat loss (W)
d_p	Particle mean diameter (μm)	Re_p	Particle Reynolds number $Ud_p\rho_g/\mu_g$)
Fr_p	Froude number based on particle diameter, U^2/gd_p	T_b	Local bed temperature (K)
G_s	Solids recycle flux (kg/m^2s)	T_w	Local temperature heater wall (K)
G_o	Saturation carrying capacity of gas (kg/m^2s)	U	Fluidizing gas velocity (m/s)
g	Acceleration due to gravity (m/s^2)	U_t	particle terminal velocity (m/s)
k_g	Thermal conductivity of gas (W/mK)	ε	Cross-sectional average voidage (-)
h	Total surface-average heat transfer coeff.(W/m^2K)	ρ_g	Density of gas (kg/m^3)
Nu_p	Particle Nusselt number (hd_p/k_g)	ρ_{sus}	suspension density (kg/m^3)
Q_l	measured heat input (W)	μ_g	Viscosity of gas (kg/ms)

REFERENCES

Basu, P., and Nag, P.K.: Int. Journal of Heat and Mass Transfer, 30 (1987), pp.2399-2409.

Breitholtz, C.: Ph.D. Thesis, Chalmers University of Technology (2000).

Furchi, J.C., Goldstein, L., Lombardi, G. and Mohseni, M.: Proc. Circulating Fluidized Bed Technology II (Basu, P and large, J.F. (Eds.)), Pergamon Press, Oxford, U.K. (1988), pp.263-270.

Han, G.Y., Tuzla, K. and Chen, J.: Heat Transfer Eng., 17 (1996), pp.64-71.

Luan, W., Bowen, B. D., Lim, C. J., Brereton, C. M. H. and Grace, J. R.: Int. Journal of Heat and Mass Transfer, 43 (2000), pp.1173-1185.

Mahalingam and Kolar, A.K.: Proc. 12th Int. Conf. Fluidized Bed Combustion, (L.N. Rubow (Ed.)) ASME, San Diego, CA (1993), pp.341-348.

Pagliuso, J.D., Lombardi, G. and Goldstein, L.: Experimental Thermal and Fluid Science, 20 (2000), pp.170-179.

Sekthira, A., Lee, Y.Y., and Genetti, W.E.: Proc. 25th National Heat Transfer Conference, Houston, TX, USA (1988), pp.1-22.

Subbarao, D. and Basu, P.: Int. Journal of Heat and Mass Transfer, 29 (1986), pp.487-489.

Wu, R. L., Grace, J. R., Lim, C. J. and Brereton, C. M. H.: AIChE Journal, 35 (1989) pp.1685-1691.

Xie, D., Bowen, B.D., Grace, J.R. and Lim, C.J.: Int. Journal of Heat and Mass Transfer, 46 (2003), pp.2179-2191.

DESIGN AND OPERATION OF EXPERIMENTAL SYSTEM FOR STUDYING HEAT TRANSFER IN A SMOOTH TUBE AT NEAR AND SUPER CRITICAL PRESSURE

Li Wenkai, Wu Yuxin, Li Yan, Lu Junfu, Zhang Hai

Key laboratory for Thermal Science and Power Engineering of Ministry of Education, Tsinghua University, Beijing, 100084, China

Abstract: Boilers running at supercritical pressure with large capacity have been widely used in power generation technology. How to keep the safety of heat transfer in the riser system is an important issue. However, it is difficult to study heat transfer for the vertical smooth tubes in a boiler at sub-critical or supercritical pressure since the thermodynamic properties of water is very complex and sensitive to temperature and pressure near the critical point. Hot-state experiment of heat transfer for the tubes of diameter used in a boiler is of great value for the design of membrane wall. In order to study the heat transfer of vertical smooth tubes running at low heat flux and low mass flux for sub-critical CFB boilers, a near-supercritical pressure water test bed was built in Tsinghua University. The designed pressure is 21MPa, the mass flux of water is 550kg/m^{2}s, and the heat flux is 136kW/m^2. In this paper, the design and structure of the test bed is introduced. The experimental result is analyzed, more experimental work is needed in future research.

Keywords: near-critical pressure, two-phase flow, heat transfer crisis

INTRODUCTION

Nowadays, it is an important issue to improve the efficiency of power generation because of the high price of the fossil fuel and the more strict exhaust emission standard of pollutants for coal burning boilers[1]. As an available technology to improve the efficiency of plants, modern supercritical pressure steam generators with high capacity are applied in variable pressure operation method to make the units have higher thermal efficiency under both full load and partial load cases. This technology requires that the working fluids have to experience the transient change between supercritical pressures and sub-critical pressures. As pressure changing in this region, it is of great value to study the heat transfer between fluids and tubes at near-critical pressure point according to a large variance of fluid flow patterns.

Researches that focus on heat transfer and fluid dynamics at near supercritical pressures are started as early as the 1960s. In the next two decades, researchers in developed countries such as Soviet Union, America, Germany and Japan, did a lot of more widely and deeply studies on this topic[2]. In China, hot-state experiments of heat transfer for water in the vertical tubes at supercritical pressure were started in 1980s. However, it is difficult to do the experimental investigation due to the high temperature and pressure of the operation conditions.

As the development of computing technologies, a lot of numerical simulation studies have been carried out in recent years, such as: Kim et al. (2004)[3], Roelofs (2004)[4], Bazargan et al. (2005)[5], Cheng et al. (2007)[6]. On the other hand, many experimental investigations have been conducted at the same time. Some of researchers use water as the working fluids, such as: Swenson et al. (1965)[7], Ackerman (1970)[8], Yamagata et al. (1972)[9] and Breus and Belyakov (1990)[10] et al. The working fluids used in other experiments includes CO_2[11-14], He[15, 16], N_2[17], hydrocarbon[18], and so on. Although plenty of investigations on supercritical water have been done previously, few of them are focused on the conditions of low mass fluxes and low heat fluxes, which are usually used in the riser systems for supercritical pressure CFB Boilers.

The object of our experimental investigation is to study the characteristics of heat transfer and fluid dynamics of water at pressures near supercritical pressure in a vertical smooth tube. The inner diameter of the smooth tube is 20mm. The region of designed operating pressure is in from 18MPa to 30MPa. The mass flux of water is variable from 200 to 1000kg/m^{2}s. The heat flux changes from 30 to 200kW/m^2. In this paper, the design and operation of the Supercritical Water Test bed built in Tsinghua University is introduced. The errors of the calculation of heat transfer coefficient are analyzed. Some experimental result acquiring at a near-critical pressure point of 21MPa are presented.

SUPERCRITICAL WATER TEST RIG IN TSINGHUA UNIVERSITY

The structure test rig of Tsinghua University is shown in Fig.1. There are two parts in this test rig. One part is called supply loop, the other is called circulating loop. In order to save the electric power for the

experimental system, the fluid is pumped from the water tank to the circulating system through the high pressure piston pump at first. In the looping section, a magnetic circulating pump is used to compensate the pressure loss of the fluid and to drive water flowing in the circulating loop.

The tube used in test section is made of $1Cr_{18}Ni_9Ti$, which is the same material with that used in a boiler. The tubes of other sections are made of steel. The tubes in test section and preheating section are used as electrical heaters so that the fluid is heated up to the temperature near the critical point. The summation of the heating power of preheating section and test section is adjusted automatically so that the heat loss in the circulating system is compensated. In this case, the pressure and temperature of the water at the inlet of the test section is guaranteed to be stable.

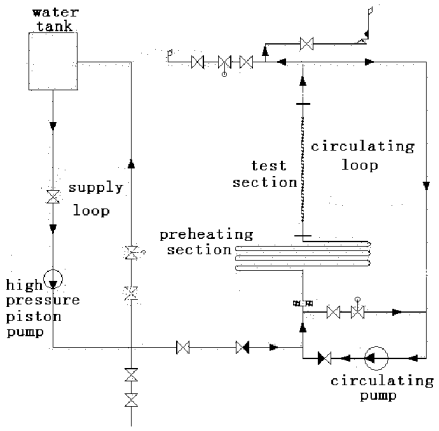

Fig. 1 Supercritical water test rig of Tsinghua University

The object of near-critical of supercritical water experiments is to study the characteristics of heat transfer and flow resistance. Therefore, several parameters should be controlled accurately, such as the system pressure, the mass flux, the heat flux, and so on. In every condition, the profiles of the fluid temperature along the tube, the profiles of the tube temperature along the tube, and the pressure drop in the test section are supposed to be obtained.

The important component parts in the experimental are introduced as follows:

1) Thermocouples: there are two sorts of thermocouples implied in the experiment. The inner tube thermocouples are used to measure the fluid temperature. The inner tube thermocouples are wrapped with a bolt in a special shape, which is shown in Fig. 2. The outside wall thermocouple is used to measure the temperatures of outside wall of the tube. The outside wall thermocouple is welded on the inner surface of a stainless steel ferrule hooping to the test section, which is shown in Fig. 3.

Fig. 2 Inner tube thermocouple

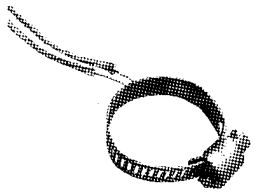

Fig. 3 Outside wall thermocouple

2) Orifice plate flowmeter: the mass flux in the test tube is measured by an orifice plate flowmeter (LGBZ-37). Based on the fluent simulation, the measurement uncertainty of the orifice plate flow meter is lower than 0.82%.

3) Magnetic circulating pump: the magnetic circulating pump is used as a circulating pump in the circulating section. This kind of pump can be used even when the fluid temperature is as high as 450℃, and the pressure head is as high as 40m.

CALCULATION OF TEMPERATURE OF INNER WALL OF THE TUBE

The tube is heated by electricity. The outside wall temperature is measured by thermocouples directly in the experiments. The temperature of inner wall can then be calculated as follows:

The energy conservation equation for the tube of test section in cylindrical coordinates is

$$\frac{1}{r}\frac{\partial}{\partial r}\left(r\lambda\frac{\partial t}{\partial r}\right)+\frac{1}{r^2}\frac{\partial}{\partial \varphi}\left(\lambda\frac{\partial t}{\partial \varphi}\right)+\frac{1}{z}\frac{\partial}{\partial r}\left(\lambda\frac{\partial t}{\partial z}\right)+\frac{KV^2}{\rho}=\rho c\frac{\partial t}{\partial \tau} \tag{1}$$

Where r is the distance from the center of the tube, m; ρ is the electrical resistance of the tube, $\Omega\cdot m$; V is the voltage of the tube per unit length, V/m; λ stands for the thermal conductivity of the tube, W/(m · ℃); K

is the coefficient as a function of tube temperature, and KV^2/ρ is the heating power per unit volume of the tube.

Assuming that the heat transfer of the whole tube is in steady state, and in one dimension, equation (1) is simplified as

$$\frac{1}{r}\frac{d}{dr}\left(r\lambda\frac{dt}{dr}\right)+\frac{KV^2}{\rho}=0 \tag{2}$$

The inner wall temperature can be obtained by series expansion solution and the final result is expressed as

$$t_{w0}-t_w=C_1\frac{q_w}{\lambda_{w0}}\left(1+\frac{C_1}{2}\frac{aq_w}{\lambda_{w0}^2}\right)$$

Where C_1 is the coefficient, which is calculated by $C_1=\frac{r_w}{r_{w0}^2-r_w^2}\left(r_{w0}^2\ln\frac{r_{w0}}{r_w}-\frac{r_{w0}^2-r_w^2}{2}\right)$, t_{w0} is the outside wall temperature, t_w is inner wall temperature, q_w is the inner wall heat flux, $\lambda_{w0}=b+at_{w0}$ is the thermal conductivity of the tube at the temperature of t_{w0} ($a=0.013398$ W/(m • ℃^{2}), $b=14.235$ W/(m • ℃) here), r_{w0} is the outside radius of the tube, and r_w is the inner radius of the tube.

EXPERIMENTAL RESULTS

The profile of temperatures of water and of outside tube at the outlet of the test section changing with enthalpy is shown in Fig.4. In this case, the operating pressure is 21.0MPa. The mass flux of water in the vertical tube is 550kg/m^2. The heat flux of the tube is 136kW/m^2. T_w is the inner wall temperature of the tube, T_s is the saturation temperature at the operation pressure, which is 369.83℃. T_b is the bulk fluid temperature measured by the thermocouple. As is shown in Fig.4, when the enthalpy is lower than 1370 kJ/kg, T_w is a little higher than T_s, the steam fraction is very low in the fluid, and the state of fluid near the tube wall is nucleate boiling. In this case, heat transfer between the tube and fluid is quite strong, and the difference between T_w and T_b is very small.

When the enthalpy of fluid is larger than 1370kJ/kg, the inner wall temperature increases quickly, while the bulk fluid temperature increases slowly. The heat transfer between the tube and the fluid becomes worse: the wall temperature increases from 370℃ to 450℃, while the bulk fluid temperature just increases from 300 ℃ to 320℃. In this region, when the steam fraction increases, DNB (Departure from Nucleate Boiling) appears in fluid near the inner wall. Steam bubbles merge into a steam membrane, which makes the thermal resistance increase and then leads to a bad condition of the heat transfer between the fluid and the tube. As a result, the tube temperature increases quickly. In engineering practice, this phenomena usually results in the broken of tubes, which is dangerous and should be avoided. In our experimental investigation, the tube temperature is lower than 500℃, the heat transfer coefficient is larger than 1kW/m^{2}s according to a lower heat flux (136kW/m^2). Besides that, the bulk fluid temperature is much lower than T_s which make the heat transfer deterioration of DNB in a gentle way.

After achieving a maximum value, the wall temperature decreases until the temperature difference drops down to a normal level. The reason can be explained as follows: due to the increase of the steam, the fluid velocity increases, the bubbles are driven to the center of the flow. Both of these two factors enhance the heat

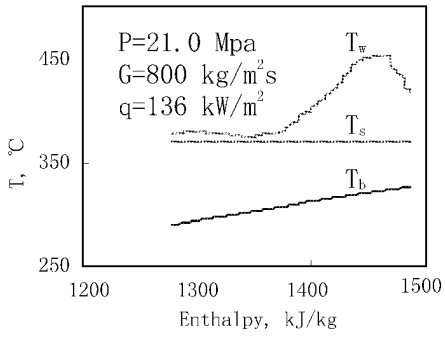

Fig. 4 Temperature vs. enthalpy at a cross section near the outlet of test section

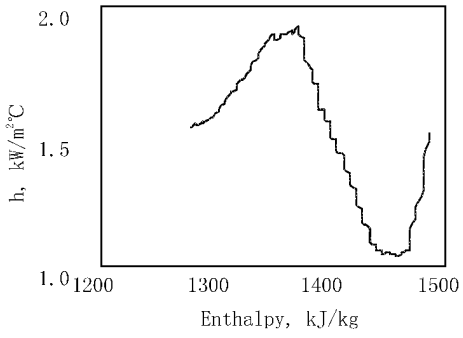

Fig. 5 Heat transfer coefficient vs. enthalpy at a cross section near the outlet of test section

transfer between the working fluid and the tube and decrease the temperature difference between the tube and fluid.

The change of temperature difference between the water and tube represents the change of heat transfer in the vertical tube, which is shown in Fig.5 in a direct way. Fig.5 shows the heat transfer coefficient changing with enthalpy of water. The heat transfer coefficient between the tube and fluid increases at first, then drops down, finally it increases again. In this process, the state of the fluid near the wall of tube plays an important role.

CONCLUSIONS

In order to study the heat transfer of vertical smooth tubes running at low heat flux and low mass flux for a CFB boiler running at sub-critical pressure, a hot-state experimental system running near-supercritical pressure is built in Tsinghua University. The design and structure of the test bed is introduced in this paper. The possible errors in the system are also analyzed.

The experimental result shows that heat transfer crsis occurs at the enthalpy of 1370kJ/kg when the system pressure is 21MPa and mass flux is 800 kg/m^{2}s respectively. Further validation and certification experimental work is needed to see if this value is correct.

More experimental investigations on heat transfer of vertical smooth tubes is needed for supercritical boilers applying variable pressure operation mode to increase the economic efficiency and to make sure the operation safety.

REFERENCES

Jiang Zemin, Reflections on energy issues in China, Journal of Shanghai Jiaotong University, 42(3), pp.345-359.

Igor L. Pioro, Romney B. Duffey, Experimental heat transfer in supercritical water flowing inside channels (survey), Nuclear Engineering and Design 235 (2005) 2407–2430.

Kim, S.H., Kim, Y.I., Bae, Y.Y., Cho, B.H., 2004. Numerical simulation of the vertical upward flow of water in a heated tube at supercritical system pressure. In: Proceedings of ICAPP04, Pittsburgh, PA, USA, June 13–17 (Paper No. 4047).

Roelofs, F., 2004. CFD analyses of heat transfer to supercritical water flowing vertically upward in a tube. NRG rapport 21353/04.60811/P, 1 December http://www.nrg-nl.com/docs/nrglib/2004/r060811.pdf.

Bazargan, M., Fraser, D., Chatoorgan, V., 2005. Effect of buoyancy on heat transfer in supercritical water flow in a horizontal round tube. Journal of Heat Transfer 127, 897–902.

Cheng, X., Kuang, B., Yang, Y.H., 2007. Numerical analysis of heat transfer in supercritical water cooled flow channels. Nuclear Engineering Design 237, 240–252.

Swenson, H.S., Carver, J.R., Karakala, C.R., 1965. Heat transfer to supercritical water in smooth-bore tubes. J. Heat Transfer, Trans. ASME, Ser. C 87 (4), 477–484.

Ackerman, J.W., 1970. Pseudoboiling heat transfer to supercritical pressure water in smooth and ribbed tubes. J. Heat Transfer, Trans.ASME92 (3), 490–498 (Paper No. 69-WA/HT-2, pp. 1–8).

Yamagata, K., Nishikawa, K., Hasegawa, S., et al., 1972. Forced convective heat transfer to supercritical water flowing in tubes. Int. J. Heat Mass Transfer 15 (12), 2575–2593.

Breus, V.I., Belyakov, I.I., 1990. Heat transfer in helical coils at supercritical pressure. Therm. Eng. 21 (1), 189–191.

R. P. Bringer, J. M. Smith, Heat transfer in the critical region, AICHE, Vol.3, No.1, 1957, pp.49-55.

R. D. Wood, J. M. Smith, Heat transfer in the critical region—temperature and velocity profiles in turbulent flow. AICHE, Vol.10, No.2, 1964, pp.180-186.

H. Tanaka, N. Nishiwaki, M. Hirata, A. Tsuge, Forced convection heat transfer to fluid near critical point flowing in circular tube, Vol.14, 1971, pp.739-750.

G. A. Adebiyi, W. B. Hall, Experimental investigation of heat transfer to supercritical pressure carbon dioxide in a horizontal pipe, Int. J. Heat Mass Transfer, Vol.19, 1976, pp.715-720.

P. J. Giaratano, M. C. Jones, Deterioration of heat transfer to supercritical Helium at 2.5 Atmospheres, Int. J. Heat Mass Transfer, Vol18, 1975, pp.649-653.

D. J. Brassingtion, D. N. Cairns, Measurements of forced convective heat transfer to supercritical Helium, Int. J. Heat Mass Transfer, Vol.20, 1977, pp.207-214.

D. Dimitrov, A. zahariev, V. Kovachev, Forced convective heat transfer to supercritical nitrogen in a vertical tube, Int. J. Heat and Fluid Flow, Vol.10, No.3, 1989, pp278-280.

G. I. Isaev, I. T. Arabova, G. K. Abdullaeva, Heat transfer in organic fluids at supercritical oressures, Heat Transfer Research, Vol.25, No.2, 1993, pp.175-178.

EXPERIMENTAL AND MODELING INVESTIGATION OF LIGNITE DRYING IN A FLUIDIZED BED DRYER

K. Zhang, C. F. You

Key Laboratory for Thermal Science and Power Engineering of Ministry of Education, Department of Thermal Engineering, Tsinghua University, Beijing, 100084, China

Abstract: The nitrogen as drying medium and the fluidized bed were used to study the drying characteristics of two kinds of lignite. The results show that the drying process of the lignite could be divided into three stages: a pre-heating period, a constant heating period, and a quick-down heating period. For the same lignite sample, the drying rate of lignite samples increases with rising drying temperature or flow rate of drying medium. For the different lignite samples, the composition structure of lignite and the modes of occurrence of moisture in the lignite influence the drying characteristics of lignite, besides drying medium temperature and flow rate influence lignite drying. According to the heat transfer rule equation of wet-ball in the forced flow, the drying rate formula of lignite particle in the fluidized bed has been got based on the heat transfer theory and mass transfer theory, and the formula can well interpret the effect of the experimental parameters on the lignite drying.

Keywords: lignite, fluidized bed; drying rate, drying model

INTRODUCTION

Lignite is a low-rank coal, characterised by its low heating values primarily due to high moisture and oxygen contents. Some lignites contain very high moisture levels, ranging between 20-70% by weight. This results in high transportation cost per thermal unit of coal. There is considerable interest in the possibility of drying prior to use, transporting or storing in the dry state for extended periods. During power generation, such high moisture levels result in reduced thermal efficiency and increased CO_2 emissions. This is because a large amount of non-recoverable energy is consumed in the evaporation of water prior to combustion or gasification and other means of thermal processing. The lignite is highly reactive towards oxygen at ambient temperatures, especially in dry state and hence is highly susceptible to low-temperature oxidation, moisture re-absorption and spontaneous combustion (Swann and Evans, 1979; Ogunsola, 1993; Dong and Stott, 1993)

Fluidized bed drying has been used widely for drying various products due to its many advantages, e.g., high rates of drying due to an excellent contact between the drying medium and the drying product, high thermal efficiency, and relatively low cost of operation (Mujumdar and Devahastin, 2003). Keeping these advantages, along with the hope of obtaining a higher-quality product, a fluidized bed dryer was proposed as an alternative for drying of lignite in the present study.

Although numerous works have been reported on the use of a fluidized bed dryer to dry various food and products (e.g., Mustafa, Ali and Ugur, 2006; Kaymak-Ertekin, 2002; Reyes, Alvarez and Marquardt, 2002; Soponronnarit, Pongtornkulpanich, and Prachayawarakorn, 1997), few data are available on its use with lignite. Therefore, batch fluidized bed drying experiments of lignite were performed. Meanwhile, a mathematical model of drying process for lignite has been established to provide theoretical basis for the industrialization design.

EXPERIMENTAL

Materials

The two kinds of lignite used in this experiment were from Australian Salmon Gums and Chinese Inner Mongolia, respectively. The lignite from Australian Salmon Gums is defined as the lignite No.1, while the lignite from Chinese Inner Mongolia is defined as the lignite No.2. As the lignite is highly susceptible to low-temperature oxidation, the nitrogen is used as the drying medium to avoid the combustion of lignite in the fluidized bed. The proximate and ultimate analyses and detail information of the raw lignite are presented in Table 1.

Table 1 Proximate and ultimate analysis and detail information of the raw lignite

serial number	proximate analyse / %					ultimate analyse / %				particle size mm	density kg/m^3
	C_d	H_d	O_d	N_d	S_d	V_d	FC_d	M_{ar}	A_d		
Lignite No.1	48.5	3.9	18.06	0.28	1.56	40.9	31.4	59.6	27.7	−4.0	1220
Lignite No.2	50.2	2.98	13.88	0.82	0.62	35	33.5	28.1	31.5	−1.0	945

The fluidized bed drying system

Figure 1 shows system diagram of the fluidized bed used to dry lignite. As can be seen from Figure 1, the system mainly comprises three subsystems: generating subsystem of dying medium, the subject subsystem of the fluidized bed, temperature control subsystem of the fluidized bed, heating subsystem of the fluidized bed and material subsystem.

The generating subsystem of dying medium consists of nitrogen gas bottle, pressure reducing valve, rotameter and gas heating and temperature control device. Through pressure reducing liquid nitrogen is transformed to nitrogen which then inpours into gas heating and temperature control device to generate hot dying medium. The subject subsystem of the fluidized bed consists of the fluidized bed and adiabatic asbestos. The material subsystem consists of the control stick and feeder which shown in the Fig. 2.

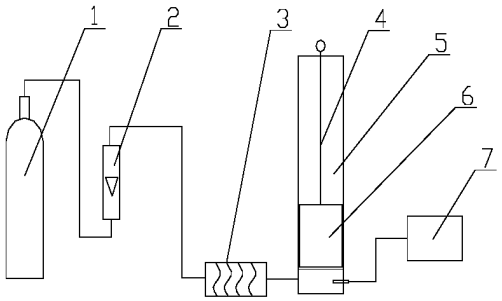

1 Nitrogen gas bottle 2 Rotameter 3 Gas heating device

4 Control stick 5 Subject system of the fluidized bed

6 Feeder 7 Temperature control device

Fig. 1 System diagram of the fluidized bed

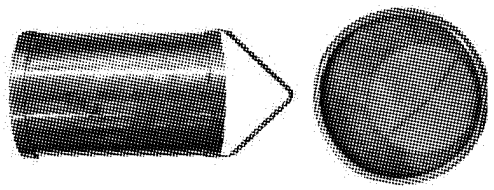

Fig. 2 Figure of the feeder

After the parameters was preset (the temperature of the drying medium, the flow rate of the drying medium), the samples (about 200g) were placed in the feeder and then heated in the fluidized bed under a nitrogen atmosphere. The sample was weighted every five minutes to obtain curves of weight loss.

RESULTS AND DISCUSSION

The effects of the temperature of the drying medium

The weight loss curves of the lignite No.1 at flow rate of 4.5m^3/h and at temperature of 120℃, 150℃, 180℃ and 210℃ were shown in figure 3(a), while the weight loss curves of the lignite No.2 at flow rate of 4.5m^3/h and at temperature of 120℃, 150℃, 180℃ and 210℃ were shown in Fig. 3(b).

Figures 3(a) and 3(b) show that the higher the temperature, the better the effect of drying of lignite. It also is showed that the weight loss rate of lignite increases with time and the average drying rate increases with rising drying temperature. At flow rate of 4.5m^3/h and at temperature of 120℃, 150℃, 180℃ and 210℃ the ultimate weight loss rate of the lignite No.1 is 26.5%, 32.6%, 39.6% and 42.2%, respectively. Because the moisture content (as-received basis) of the lignite No.1 is 59.6%, the maximum of lignite water evaporation is 56.9% and under each working condition the lignite No.1 is not in dry state at the end of experiment. At flow rate of 4.5m^3/h and at temperature of 120℃, 150℃, 180℃ and 210℃ the ultimate weight loss rate of the lignite No.2 is 5.9%, 9.4%, 10.6% and 2.2%, respectively. Because the moisture content (as-received basis) of the lignite No.2 is 28.1%, the maximum of lignite water evaporation is 43.4% and under each working condition the lignite No.2 is not in dry state at the end of experiment.

The expression of drying rate is

$$R_d = \frac{dX(t)}{dt} \tag{1}$$

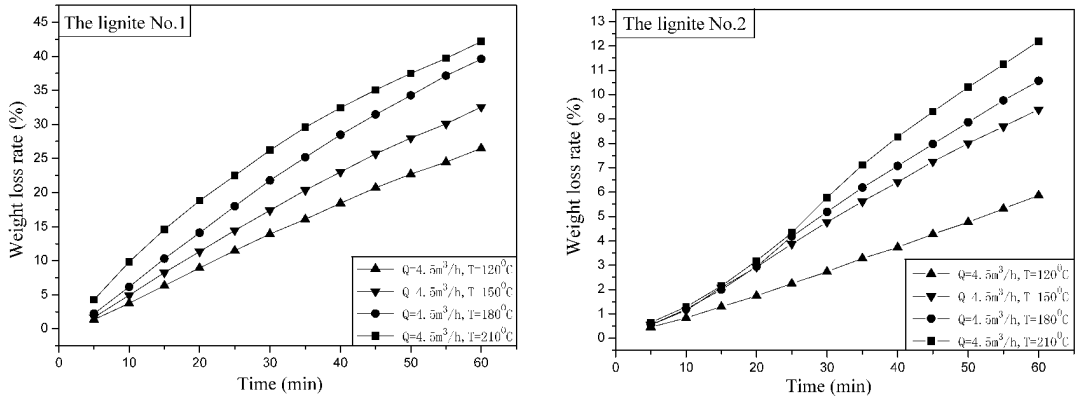

Fig. 3 (a) Weight loss curves of the lignite No.1 at different temperature and (b) Weight loss curves of the lignite No.2 at different temperature

where X(t) is the moisture content removed after drying for time t.

The drying rate curves of the lignite No.1 at flow rate of 4.5m^3/h and at temperature of 120℃, 150℃, 180℃ and 210℃ were shown in Fig. 4(a), while the drying rate curves of the lignite No.2 at flow rate of 4.5m^3/h and at temperature of 120℃, 150℃, 180℃ and 210℃ were shown in Fig. 4(b).

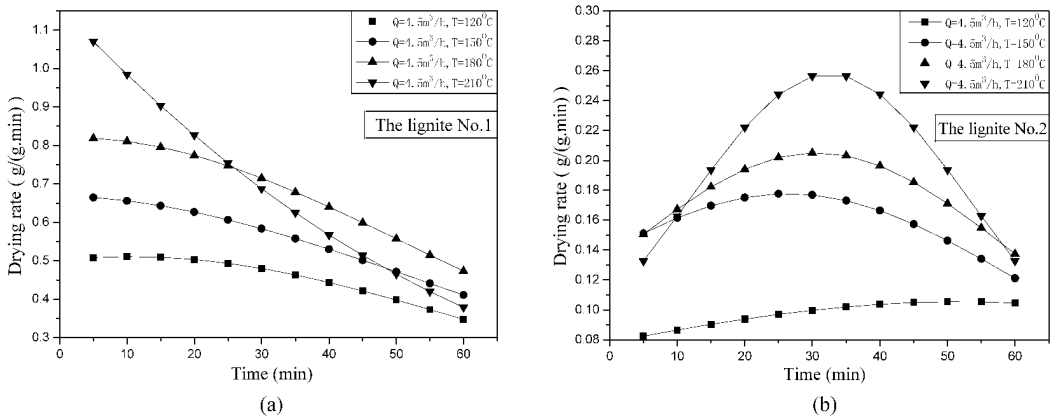

Fig. 4 (a) Drying rate curves of the lignite No.1 at different temperature and (b) Drying rate curves of the lignite No.2 at different temperature

Figures 4(a) and 4(b) show that the drying process of the lignite could be divided into three stages: a pre-heating period, a constant heating period, and a quick-down heating period. Figure 4(a) failed to show the pre-heating period of the lignite No.1, as the sampling interval of five minutes was longer than the duration of the pre-heating period. Figure 4(b) showed whole process of the drying of the lignite No.2, as the duration of the pre-heating period was significantly longer than the sampling interval of five minutes. Based on the comprehensive analysis of the drying rate curves of the lignite, it can be concluded that the duration of the pre-heating period increases with rising drying temperature, and the duration of the constant heating period decreases with rising drying temperature. The drying rate of the lignite No.1 is much higher than the drying rate of the lignite No.2 under the same working condition.

The effects of the flow rate of the drying medium

The weight loss curves of the lignite No.1 at temperature of 180℃and at flow rate of 4.5m^3/h, 9m^3/h and 13.5m^3/h were shown in Fig. 5(a), while the weight loss curves of the lignite No.2 at temperature of 180℃and at flow rate of 4.5m^3/h, 9m^3/h and 13.5m^3/h were shown in Fig. 5(b).

It is showed that the higher the flow rate of the dying medium, the better the effect of drying of lignite in Figs. 5(a) and 5(b), and it also is showed that the average drying rate increases with rising flow rate of the dying medium. At temperature of 180℃ and at flow rate of 4.5m^3/h and 9m^3/h the weight of the lignite No.1 decreases with time, and the ultimate weight loss rate of the lignite No.1 is 39.6% and 55.7%, respectively. At temperature of 180℃ and at flow rate of 13.5m^3/h the weight loss rate is nearly constant after forty minutes, and the content of the moisture in the lignite No.1 which ultimate weight loss rate is 55.6% could have apparently reached certain equilibrium. At temperature of 180℃ and at flow rate of 4.5m^3/h , 9m^3/h and

13.5m^3/h the weight of the lignite No.2 decreases with time, and the ultimate weight loss rate of the lignite No.2 is 10.6%, 19.5% and 26.5%, respectively.

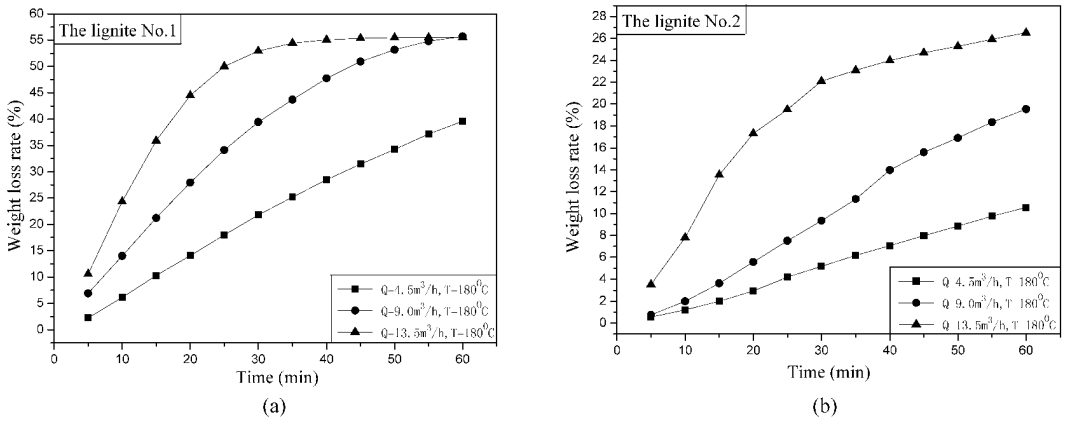

Fig. 5 (a) Weight loss curves of the lignite No.1 at different flow rate and (b) Weight loss curves of the lignite No.2 at different temperature flow rate

The drying rate curves of the lignite No.1 at temperature of 180℃and at flow rate of 4.5m^3/h, 9m^3/h and 13.5m^3/h were shown in Fig. 6(a), while the drying rate curves of the lignite No.2 at temperature of 180℃and at flow rate of 4.5m^3/h, 9m^3/h and 13.5m^3/h were shown in Fig. 6(b).

Figures 6(a) and 6(b) show also that the drying process of the lignite could be divided into three stages: a pre-heating period, a constant heating period, and a quick-down heating period, and the duration of the constant heating period decreases with rising flow rate of the drying medium. Comparing Fig. 6(a) and Fig. 6(b), it can be concluded that the drying rate of the lignite No.1 is much higher than the drying rate of the lignite No.2 under the same working condition.

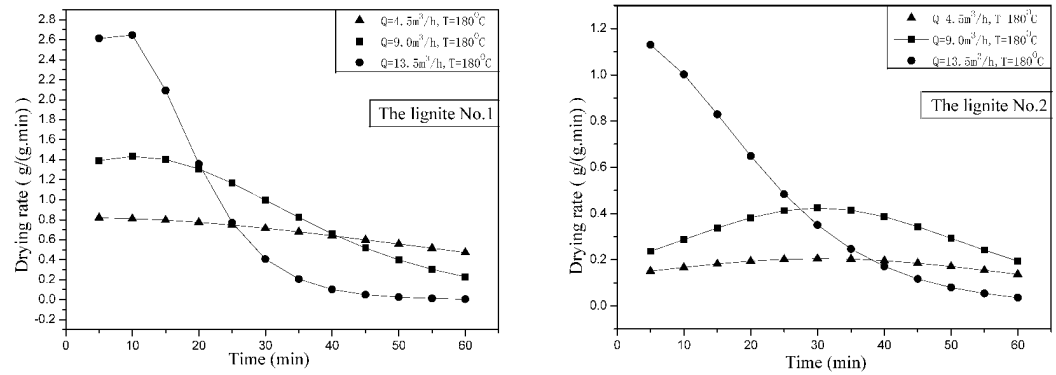

Fig. 6 (a) Drying rate curves of the lignite No.1 at different temperature and (b) Drying rate curves of the lignite No.2 at different temperature

Modeling investigation of lignite drying

The drying process of lignite particles in the fluidized bed relates to the multi-phase flow, heat transfer and mass transfer, etc, but through the drying experiment it is found that the main influence parameters of the drying are drying temperature, flow rate of the drying medium, and lignite particle size, so the main parameters were chosen to establish a mathematical model of the lignite drying. Meanwhile, the following simplifications were assumed to model the drying process(Heinrich, Ihlow, and Henneberg, 2002):

- The conditions of the experiment keep constant, neglecting the change of external environment.
- The heat of convection is only considered, neglecting heat of radiation.
- Particles of lignite are spherical and monodisperse.
- The radius of particle is invariable, neglecting the

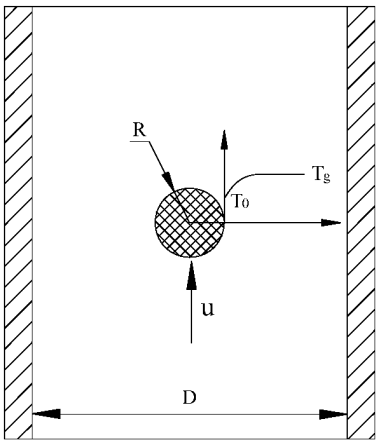

Fig. 7 Model of lignite drying

shrinkage of particle.

Based on the assumption, the heat transfer rule of wet-ball in the forced flow is shown in Eq. (2),

$$Nu = 2 + ARe^{0.5} Pr^{1/3} Gu^{0.175} \tag{2}$$

Where $Nu = \frac{hR}{\lambda}$, $Re = \frac{u \cdot R}{\nu} = \frac{Q \cdot R}{S \cdot \nu}$, $Pr = \frac{\nu}{\alpha}$ and

$Gu = \frac{t_G - t_W}{T_G}$. Pr and Gu are approximate to a constant.

Then q, M_0, $N_{H_2O}^{total}$ and υ are shown in Equation (3), (4), (5) and (6).

$$q = h\left(T_g - T_0\right) = N_{H_2O} \Delta H_V \tag{3}$$

$$M_0 = \frac{4}{3}\pi R^3 \rho \tag{4}$$

$$N_{H_2O}^{total} = 4\pi R^2 N_{H_2O} \tag{5}$$

$$\upsilon = \frac{N_{H_2O}^{total}}{M_0} \tag{6}$$

Therefore, from equations (2)-(6), we obtain

$$\upsilon = \frac{3\lambda(T_g - T_0)}{\rho \Delta H_V}\left(\frac{2}{R^2} + A\frac{1}{S^{0.5}} \cdot \frac{1}{\nu^{0.5}} \cdot Q^{0.5} \cdot \frac{1}{R^{1.5}} Pr^{1/3} Gu^{0.175}\right) \tag{7}$$

According to the drying rate formula, it can be concluded that the drying rate of the same lignite samples increases with rising drying temperature or flow rate of drying medium, and the drying rate increases with decreasing the radius of particles. For the different lignite samples, the composition structure of lignite and the modes of occurrence of moisture in the lignite influence the drying characteristics of lignite, besides drying medium temperature and flow rate influence lignite drying. Under the same working condition, although the radius of the lignite No.1 is significantly bigger than the radius of the lignite No.2, but the drying rate of the lignite No.1 is much higher than the drying rate of the lignite No.2 due to the composition structure of lignite and the modes of occurrence of moisture in the lignite.

CONCLUSIONS

Experimental and modeling investigation of lignite drying in a fluidized bed dryer was completed. Following main conclusions are drawn from the experiment results and the theoretical analysis:

The drying process of the lignite could be divided into three stages: a pre-heating period, a constant heating period, and a quick-down heating period, and the drying rate of the lignite No.1 is much higher than the drying rate of the lignite No.2 under the same working condition.

At invariable flow rate, for the same lignite the duration of the pre-heating period increases with rising drying temperature, and the duration of the constant heating period decreases with rising drying temperature. At invariable temperature, for the same lignite the duration of the constant heating period decreases with rising flow rate of the drying medium.

According to the heat transfer rule equation of wet-ball in the forced flow, the drying rate formula of lignite particle in the fluidized bed has been got based on the heat transfer theory and mass transfer theory, and the formula can well interpret the effect of the experimental parameters on the lignite drying.

The composition structure of lignite and the modes of occurrence of moisture in the lignite influence the drying characteristics of lignite, besides drying medium temperature and flow rate influence lignite drying.

NOTATIONS

A	constant coefficient
D	diameter of fluidized bed, m
h	*heat transfer coefficient*, W/(m^2.k)
M_0	weight of lignite particle, kg
N_{H_2O}	mass flux, kg/m^2
$N_{H_2O}^{total}$	mass, kg
q	heat flux, W/m^2
Q	flow rate, m^3/s
R	radius of lignite, mm
R_d	dying rate, g/(g.min)
S	cross sectional area of fluidized bed, m^2

t	dying time, min
t_G	dry bulb temperature, ℃
t_W	wet bulb temperature, ℃
T_G	absolute temperature, ℃
T_g	temperature of drying medium, ℃
T_0	temperature of particle surface, ℃
u	velocity of drying medium, m/s
X	the removed moisture content, %
ΔH_V	cyclone pressure drop, Pa
α	expansion coefficient, K^{-1}
λ	thermal conductivity, W/(m.k)
ν	kinematic viscosity, m^2/s
ρ	lignite density, kg/m^3

ACKNOWLEDGEMENTS

The authors would like to express their sincere appreciation to Zhang j and Hao y y for providing the support throughout the course of the present study.

REFERENCES

Swann, P. D. and Evans, D.G.: Fuel **58** (1979), pp.276-280.
Ogunsola, O.I.: Fuel Processing Technology **34** (1993), pp.73-81.
Dong, C X. and Stott, J.B.: Fuel **72** (1993), pp.787-792.
Mujumdar, A. S. and Devahastin, S. (2003). Applications for fluidized bed drying. New York, Marcel Dekker.
Mustafa, T., Ali, K., and Ugur, Y.: Chemical Engineering and Processing **45** (2006), pp.1019-1028.
Kaymak-Ertekin, F.: Journal of Food Science **67** (2002), pp.168-175.
Reyes, A., Alvarez, P. I., and Marquardt, F. H.: Drying Technology **20** (2002), pp.1463-1483.
Soponronnarit, S., Pongtornkulpanich, A., and Prachayawarakorn, S.: Drying Technology **15** (1997), pp.1603-1615.
Heinrich, S., Ihlow, M.and Henneberg, M.: Drying Technology **20** (2002), pp.175-194.

EXPERIMENTAL RESEARCH ON GAS-SOLID FLOW IN AN EXTERNAL HEAT EXCHANGER WITH DOUBLE OUTLETS

H. Z. Liu, X. F. Lu

College of Power Engineering of Chongqing University, Chongqing, 400044, China

Abstract: A new type scaling-up scheme of CFB boiler that takes separator as center and furnaces are laid around was put forward in this paper. In the recycle system, a new type heat exchanger device with double outlets was designed for this disposal scheme. As we know, the external heat exchanger is very important for the CFB, which be able no only to adjust the steam temperature, but also to adjust the bed temperature. In this paper, through the adjustment of air speed in different room of the heat exchanger, the adjusting performance of the new type heat exchanger was analyzed. Moreover, the test of the pressure in the whole recycle system was analyzed. The pressure balance system of the circulating circuit with this new arrangement scheme was realized. Through this test research, the main conclusions were got as follows: The external heat exchanger, which has two recycled solid outlets, could run flexibly and stably and could successfully discharge the materials from the standpipe into either of the furnaces. This test device has a good pressure and material balance system.

Keywords: CFB, external heat exchanger, heat transfer coefficient, temperature distribution, directional flow

INTRODUCTION

With the ceaseless development on CFB combustion technologies, the capacity of CFB boiler is also fast augmenting. 300MW sub-critical CFB boilers are already running in some countries and the design of 600~800MW super-critical CFB boilers had been completed. However, the large boilers with a complicated system also cause many problems. The major problem is that as the number of separators of a large CFB boiler increases, the arrangement of separators becomes more difficult. Thus, the larger furnace would result in poor penetration of the second air, as a result, it causes a non-uniformity of fluidized air. Therefore, the risks associated with the CFB boiler dimension magnification become higher. In order to resolve the technology problems of scaling-up in CFB boiler, development of a new structure and arrangement scheme is urgently needed.

As the capacity of the boiler increases, the membrane wall can't satisfy the needs of the bed temperature and the steam parameter due to the furnace particularity of the CFB boiler, such as the heat surfaces not allowed to be installed in the bottom of the furnace because the wearing by fluidized bed materials is serious to the heat surfaces. The required heat surface area to control the furnace temperature also increases necessitating increased boiler heights. However, in practice, the boiler height is limited to 35 to 40 m due to commercial considerations and hence additional heat transfer surfaces must be provided to control the furnace temperature.

The measures to increase heat surface area usually used for the units above 125 MWe are external heat exchanger or combinations of internal heat transfer and external heat exchanger（Wang et al., 2003）. The external heat exchanger is a viable way to solve the heat transfer surface arrangement and furnace temperature control with scale-up of CFB boilers. In a CFB boiler with external heat exchanger, the boiler operation including the furnace conditions and steam parameters may be adjusted for optimum performance for various fuels and boiler load conditions by controlling the flow rate of materials to the external heat exchanger. The external heat exchanger is not only a heat exchanger but also a recycle device for returning cooled ash to the furnace. Therefore, the design of external heat exchanger for a CFB boiler with external heat exchanger is very important.

Typical Lurgi CFB boilers place an external fluidized bed heat exchanger (FBHE) between the standpipe and the furnace as shown in Fig. 1.

Foster Wheeler offers an integrated recycle heat exchanger (INTREXTM) beside the furnace to contribute to the heat absorption duty(Cleve, 1999)(Voyles et al., 1995)(Werdermann and Werther, 1993) . The major characteristic of this scheme is that the high temperature square cyclone separator, heat exchanger, standpipe, and loop seal are integrated into the whole system, so the structure of the boiler is rather compact. As shown in Fig. 2, the 262MW compact CFB boiler in Poland Turow power plant uses four integrated square separators(Sekret and Mirek, 2005).

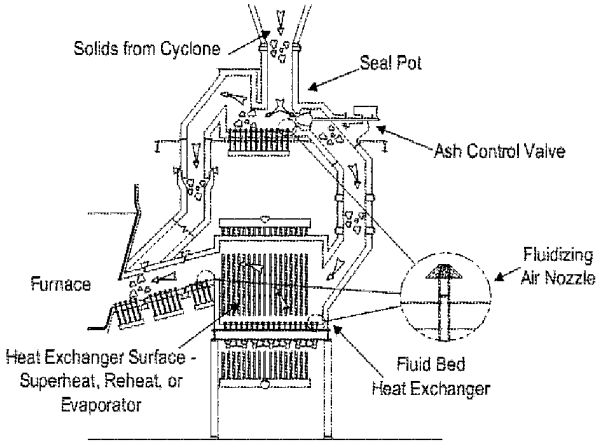

Fig. 1 The sketch map of the Lurgi/*CE* external fluidized bed heat exchanger

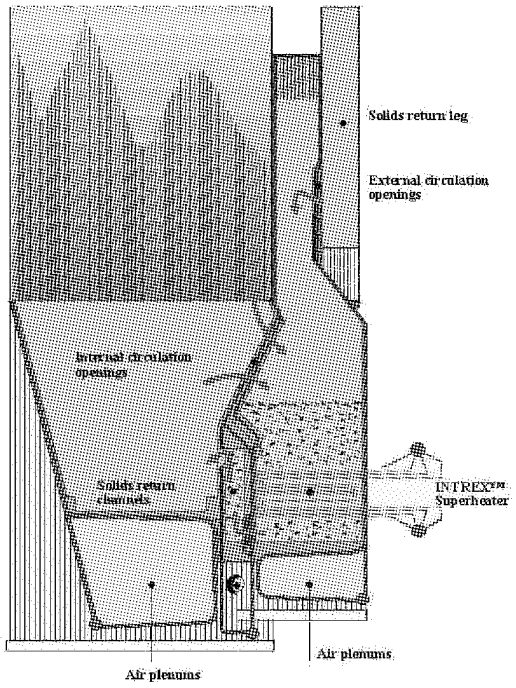

Fig. 2 The flooding INTREX fluidized bed heat exchanger

EXPERIMENTAL SYSTEM

To overcome scaling-up shortages of the CFB boilers in the word, a new type of CFB arrangement scheme was given in this paper, as shown in Fig.3. The characteristic of the boiler is using the arrangement scheme of "furnaces around separator". The major difference from other schemes is identified that a double inlet square cyclone separator is laid between two furnaces, and a new type of integrated external fluidized bed heat exchanger is installed below the separator, as shown in Fig. 3. This new-style external heat exchanger characteristic different from other congener devices(Stephen et al., 1999) is that this has two recycled materials channels. This heat exchanger is not only able to exchange heat but also is capable to recycled materials, and thus can respectively control the bed materials amount of each furnace. Therefore, it can effectively improve the flexibility and controllability of the boiler.

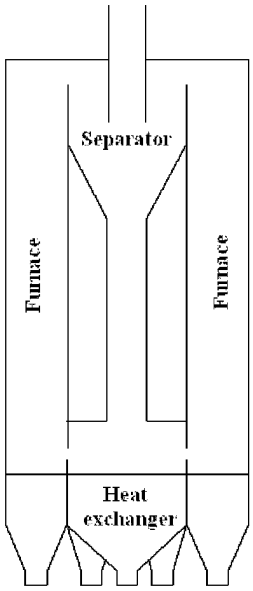

Fig. 3 The scaling-up arrangement scheme of "furnace around separator"

This scheme mentioned in the above has many advantages compared to traditional arrangement schemes as follows:

1) As shown in Fig. 4, by adopting several module-combined style, the risk of magnification could be effectually reduced.

2) The depth of furnace is small, so there is not much need for the penetration of the Second Air.

3) The furnace with separator and external heat exchanger consists of an integrated module, so there is no diversity for the expansion between each other.

4) Every module could be independently controlled; furthermore the coal supply and tapping slag can also be independently controlled, so the magnification risk could be greatly reduced.

5) According to the actual technology level, the capacity of every module could achieve 50MW.

The external heat exchanger consists of one feed room, two distribution rooms, two heat-exchanger rooms and two recycled materials channels, as shown in Fig. 5. The length of the device is 180mm, width is 170mm and height is 110mm. High-pressure air from air compressor passes though air storage tank, and then passes

through two constant pressure-cans, which is changed into two ways. One is sent to the bed of furnace as a fluidized air of furnace, another is used to fluidize "U" type valve and external heat exchanger.

The circulating materials pass through the standpipe and enter into the feed room, after fluidized, the circulating materials are transferred into distribution rooms, then, some of circulating materials enter into recycled materials channes through heat-exchanger rooms, the others directly entering into recycled materials channes. finally, all of the circulating materials return into furnaces through the external heat exchanger device.

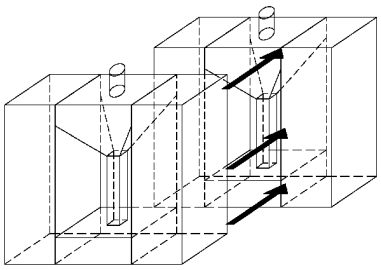

Fig. 4 Modularization integral scaling-up mode

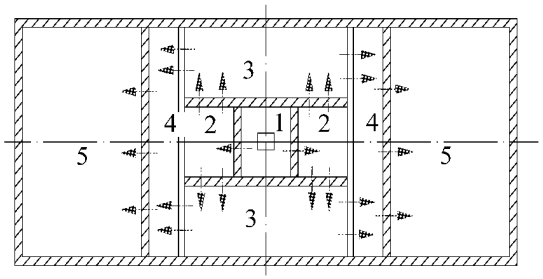

Fig. 5 The new- type External Heat Exchanger
1-feed room 2-distribution room 3- heat-exchanger room
4-recycled materials channel 5-furnace

MEASUREMENT METHOD

The main measured parameters in the test included the air volume flow, pressure and the rate of circulating materials. The airflow of the furnace was measured by vortex flowmeter (0-200m^3/h), while the airflow of the external heat exchanger was measured by the glass rotameter (0-2.5m^3/h). The pressure, after converted into electric signal by KYB-14 differential pressure gauge, was automatically collected by ADAM data acquisition system with a monitor and Control Generated System. The rate of circulating materials was measured as follows: While the test system was running normally, all the fluidized air of the external heat exchanger was abruptly cut off, and then the rate of circulating materials was measured by monitoring the height change of the solids in the standpipe in a short time.

RESULTS AND DISCUSSION

The characteristic of testing bed materials

The recycled ash of the CFB boilers in Baima Power Plant and Yibin Power Plant was selected for this test, the density is 600 kg/m^3, and the screening characteristics are shown in Fig. 6. The ash with size ranging from 0 to 0.3 mm was used as the bed materials of the new-type external heat exchanger.

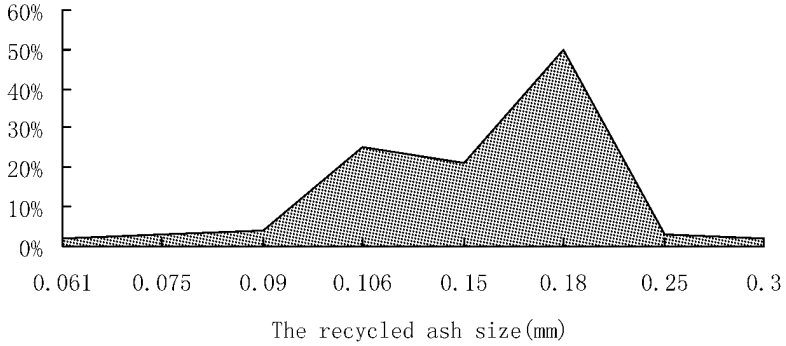

Fig. 6 The screening characteristics of the testing material

Fluidization characteristic of the materials in external heat exchanger

The characteristic curve of cold fluidization vividly describes the relation between the bed pressure drop and the fluidization velocity during the start-up process of fluidization. It also indicates the different fluidization states in the fluidization bed.

Figure 7 is a typical characteristic curve of fluidization. The curve rising region represents a fixed bed. In the fixed bed, materials are close to each other and the air distributor is used to sustain their weight. As the fluidization air velocity increases, the bed pressure drop also increases. When the velocity increases to the culmination, fluidization phenomenon begins to occur in the bed: the surface of the bed begins to become flat

and the particles near the bed begin to move slowly and rearranged. We can see that the bed pressure drop still remains unchanged while the bed height begins to grow during the experiment, which is the special expansion phenomenon of fluidized bed.

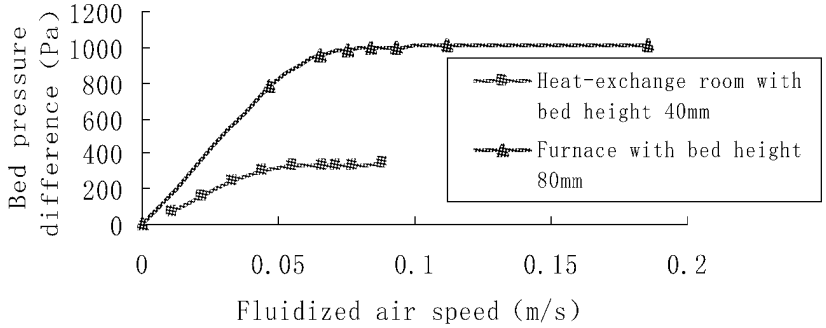

Fig. 7 The contrast of fluidized characteristic curve between external heat exchanger and furnace

In the materials circulating system, the bigger particles stay in furnace while the smaller particles enter into separator and are separated down to standpipe, and then into external heat exchanger. As shown in Fig. 7, the critical fluidizing air velocity is smaller in external heat exchanger than in furnace because the bed materials are smaller in external heat exchanger than in furnace.

Test research for adjusting the velocity of external heat exchanger

The working state of the external heat exchanger has two cases according to the different condition in the operation: (1) when heat exchange is not needed, the distribution room is in bubbling bed state and the heat-exchanger room is in fixed bed state; (2) when heat exchange is in working, the distribution room is still in bubbling bed state while the heat-exchanger room also changes into bubbling bed state. During this experiment, the materials circulating rate is determined by measuring the moving bed height in the standpipe.

The results in Fig. 8 were obtained under the condition that only left furnace was operated, and the height of static bed materials is 85mm, the airflow rate of furnace is 78 m^3/h.

As shown in Fig. 8, when no fluidized air enters into heat-exchanger room and the rate of fluidized air into distribution room maintains 0.061m/s, with the rate of fluidized air into feed room increases from 0.012 m/s to 0.122m/s, the bed height decreases from 530mm to 320mm in the standpipe. The results indicate that increasing the flowrate of fluidized air into feed room can increase the circulating velocity of the bed materials in the heat-exchanger room.

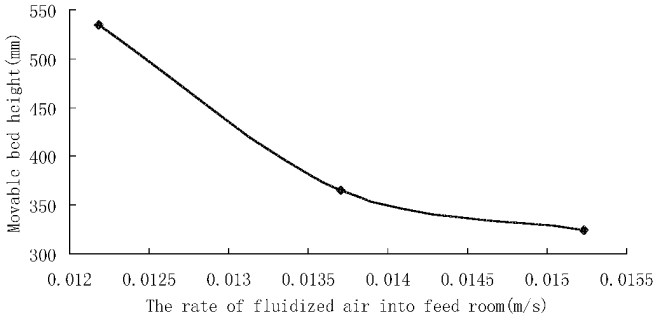

Fig. 8 The fluidized air adjusting characteristic of the feed room

The results in Fig. 9 were obtained under the condition that only left furnace was operated, and the height of static bed materials is 60mm, the airflow rate of furnace is 78m^3/h. With the flowrate of fluidized air into distribution room increases, the bed height decreases obviously, too. The test results in Fig. 8 and Fig. 9 indicate that the fluidized air of the distribution room and feed room all have a good effect to the materials circulating.

The results in Fig. 10 were obtained under the condition that only left furnace was operated, and the height of static bed materials is 50mm, the airflow rate of furnace is 78m^3/h.

As shown in Fig. 10, with the flowrate of fluidized air into heat-exchanger room increasing, the bed height decreases in the standpipe, while the circulating velocity of the bed materials increases obviously. In the case of unchanging flowrate of fluidized air into feed room and distribution room, increasing the flowrate of fluidized air into heat-exchanger room can increase the volume of the bed materials into the heat-exchanger room to increase the capacity of heat exchanging.

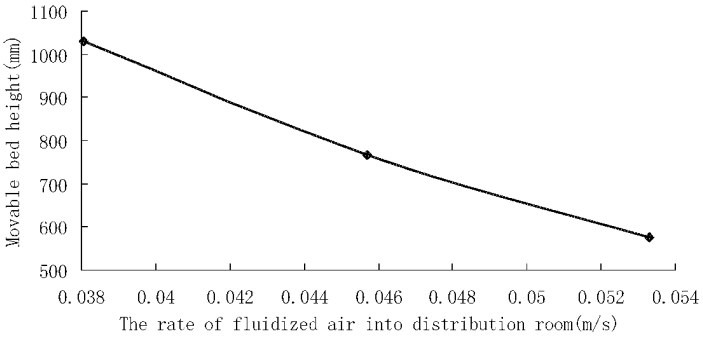

Fig. 9 The fluidized air adjusting characteristic of the distribution room

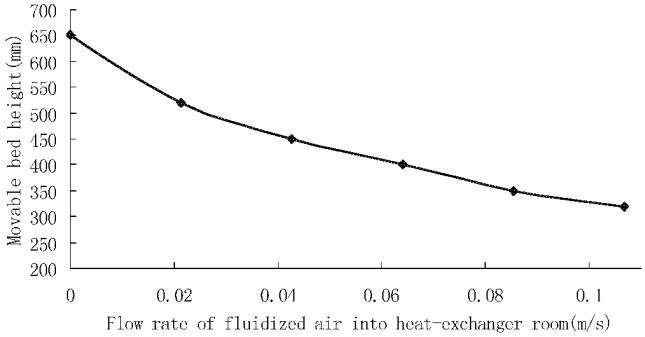

Fig. 10 The fluidized air adjusting characteristic of the heat-exchanger room

As shown in Fig. 11, Fig. 12 and Fig. 13, under the double furnaces operating, the fluidized air of all the rooms also have the same effect to the materials circulating as under the single furnace operating, increasing the flowrate of fluidized air into each room can increase the materials circulating velocity.

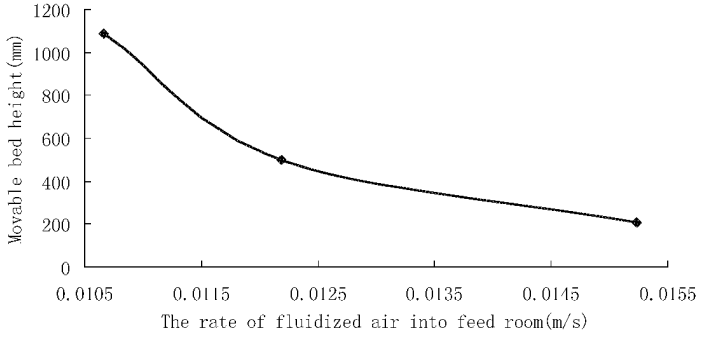

Fig. 11 The fluidized air adjusting characteristic of the feed room

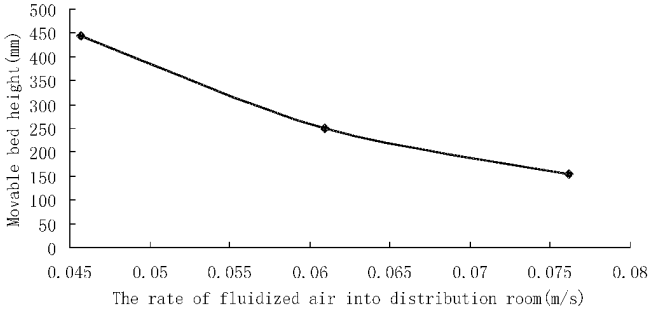

Fig. 12 The fluidized air adjusting characteristic of the distribution room

Furthermore, the recycled materials volume of the left and right furnace can be respectively controlled by the flowrate of the fluidized air into each distribution room. So only rationally adjusting the flowrate of the fluidized air into the distribution room and heat-exchanger room, the materials distribution could be flexibly adjusted by the external heat exchanger, thereby the aim of flexibly controlling the operation of the boiler will be achieved.

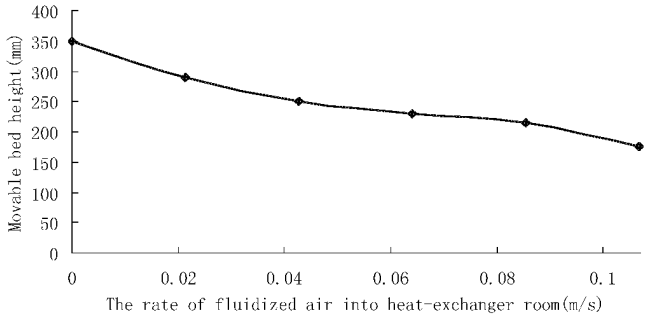

Fig. 13 The fluidized air adjusting characteristic of the heat-exchanger room

CONCLUSIONS

Considering the risks associated with the CFB boiler dimension magnification, a CFB boiler with a new-type external heat exchanger, which has two recycled solid outlets, was exploited.

The experiment improves that the new type external heat exchanger could run flexibly and stably and could successfully discharge the materials from the standpipe into either of the furnaces.

Through the experimental research, we can see that through the adjustment of air speed in different room of the heat exchanger, a good pressure and material balance can be achieved(Jüri et al, 2005).

REFERENCES

Cleve, K.: Latest development and status of long term experience in CFB-technology, in: R.B. Reuther (Ed.), Proceedings of the 15th International Conference on Fluidized Bed Combustion, ASME, Savannah, USA, 1999, p. 0006.

Jüri, L., Hendrik, A., Teet, P. : New 215 MW CFB Power Units for Estonian Oil Shale, 18th International Conference on Fluidized Bed Combustion May 22-25, 2005, Toronto, Ontario, Canada.

Sekret, R., Mirek P. : Operational Experiences of a 262 MWe Compact Circulating Fluidized Bed Boiler at TUROW Power Station, the 8th International Conference on Circulating Fluidized Beds May10-13 2005.

Stephen, J. G., Timo, H., Kari K. : CFB Boiler Design And Operation Using The INTREX™ Heat Exchanger, the 6th International Conference on Circulating Fluidized Beds August 22-27, 1999 Würzburg, Germany.

Voyles, R.C., Gagliardi, C., Wolfson,D.: Design considerations for a 250 Mwe CFB, in: K.J. Heinschel (Ed.), Proceedings of the 13th International Conference on Fluidized Bed Combustion, ASME, New York, 1995, pp. 703-712.

Wang, Q. H., Luo, Z. Y., Fang, M. X, Ni, M. J., Cen, K. F. : Development of a new external heat exchanger for a circulating fluidized bed boiler. Chemical Engineering and Processing. 42 (2003), pp. 327-335.

Werdermann, C.C., Werther, C.C.J.: Solid flow pattern and heat transfer in an industrial-scale fluidized bed heat exchanger, in: L. Rubow, G. Commonwealth (Eds.), Proceedings of the 12th International Conference on Fluidized Bed Combustion, ASME, 1993, pp. 985-990.

THE EXPERIMENTAL STUDY ON HEAT TRANSFER CHARACTERISTICS OF THE EXTERNAL HEAT EXCHANGER

X. Y. Ji, X. F. Lu, L. Yang, H. Z. Liu,

School of Power Engineering of Chongqing university, Chongqing, 400044, China

Abstract: Using the external heat exchanger in large-scale CFB boilers can control combustion and heat transfer separately, make the adjustments of bed temperature and steam temperature convenient. The state of gas-solid two phase flow in the external heat exchanger is bubbling fluidized bed, but differs from the regular one as there is a directional flow in it. Consequently, the temperature distribution changes along the flow direction. In order to study the heat transfer characteristics of the water cooled tubes in the bubbling fluidized bed and ensure the uniformity of heat transfer in the external heat exchanger, a physical model was set up according to the similarity principle and at the geometric ratio of 1:28 to an external heat exchanger of a 300MW CFB boiler. The model was connected with an electrically heated CFB test-bed which provides the circulating particles. The influencing factors and the distribution rule of the particles' heat transfer coefficient in the external heat exchanger were assessed by measuring the temperature changes of the water in the tubes and different parts of particles flow along the flow direction. At the end, an empirical correlation of particles' heat transfer coefficient in external heat exchanger was given by modifying the Veedendery empirical correlation.

Keywords: CFB, external heat exchanger, heat transfer coefficient, temperature distribution, directional flow

INTRODUCTION

Using the external heat exchanger (EHE) in large-scale CFB boilers can make the adjustments of bed temperature and steam temperature convenient, enhance the reliability of CFB boilers（Lu, 2006）. The state of gas-solid two phase flow in EHE is bubbling fluidized bed, but differs from the regular one as there is a directional flow in it. Consequently, the temperature distribution changes along the direction of the particles flow and the heat transfer characteristics of EHE are different from the regular one.

At the present, many studies have been done on the heat transfer characteristics of the bubbling fluidized bed, and some empirical correlations have been established which considered the influence of fluidizing velocity, particle size, bed temperature, tube size and so on (Tsao T. K., 1992) . However, the existent of the particle's directional flow make the EHE different from the regular one. So, the known conclusions of the bubbling fluidized bed are not enough to explain the EHE's heat transfer characteristics.

EXPERIMENTAL STUDY

Principles of the experiment and calculation

The physics model was set up according to the Glicksman's similarity principle (Glicksman L.R, Hyre M., and Wesphalen, D., 1993) and at the geometric ratio of 1:28 to an EHE of 300MW CFB boiler. The Glicksman's dimensionless numbers are:

$$\frac{u_0^{\ 2}}{gH}, \frac{u_0}{u_{mf}}, \frac{\rho_g}{\rho_p}, \frac{H}{D}, \frac{H_1}{H_2}$$

In the experiment, the model's dimensionless numbers were always kept approximating to the prototypes'. Two groups of the model's dimensionless numbers in experiment are given in Table 1 for example to compare with the prototypes'. The model 1 has the minimum differences to the prototype and the model 2 has the maximum differences.

Table 1 The dimensionless numbers values' comparison

	u^2_0/gH	u_0/u_{mf}	ρ_g/ρ_p	H/D	H1/H2
Prototype	0.020387	2.476780	0.000217	0.822089	0.603774
Model 1	0.023723	2.222222	0.000311	0.710417	0.578947
Model 2	0.057919	3.125000	0.000275	0.710417	0.578947

In the EHE, the particles' heat transfer coefficient (HTC) h_a from the particles flow to water-cooled tubes could be calculated by the follow equations (Zhao X. M., Lu J. F. and Zhang J. S. 2005):

$$\frac{1}{h_a}=\frac{1}{k}-\frac{r_0}{r_i h}-\frac{r_0 \ln(\frac{r_0}{r_i})}{\lambda} \tag{1}$$

$$k=\frac{q}{A_h(T_b-T_o)} \tag{2}$$

The thermal resistant of water $\frac{r_0}{r_i h}$ is much smaller than the thermal resistants of particles flow and tubes, so it could be ignored.

The introduction of test-bed system

The test-bed is a CFB with an EHE attached as the Fig. 1 shows, the height and width of the furnace is 300cm and 14.6cm, the EHE was designed by estimating the regular CFB test-bed's maximum particles flow rate and at the geometric ratio of 1:28 to an external heat exchanger of 300MW CFB boiler.

The EHE was divided into three chambers by walls along the width direction. Every chamber has its own wind chamber. The height and thickness of every wall is 100mm and 10mm. The widths of the chamber1, chamber2 and chamber3 are 40mm, 150mm and 150mm.The chamber1 has no heating surfaces in it, the chamber2 and chamber3 both have three groups of water cooled tube in them, and the total length, external diameter and thickness of every group of tube are 480mm, 6mm and 0.8mm. In the experiment, to avoid the influence of particles' returning to furnace, we mainly studied the chamber2. The fluidizing air was supplied by high pressure fan, and heated by electric heater. And the circulating particles were heated by the air.

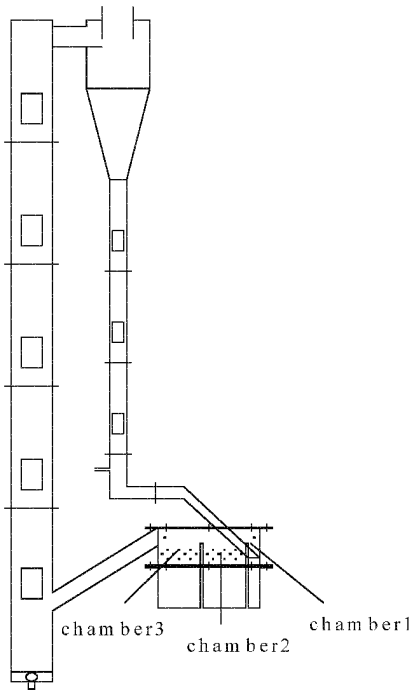

Fig. 1 The test-bed

In the experiment the follow parameters should be measured: the flux of air and water, the furnace pressure, the particle temperature distribution in EHE, the water temperature of inlet and outlet, etc. In the test-bed, thirty one temperature measuring points and fourteen pressure measuring points were set, the flux of air and water were measured by rotameters. All the parameters were inputted to the computer by date collection system and recorded.

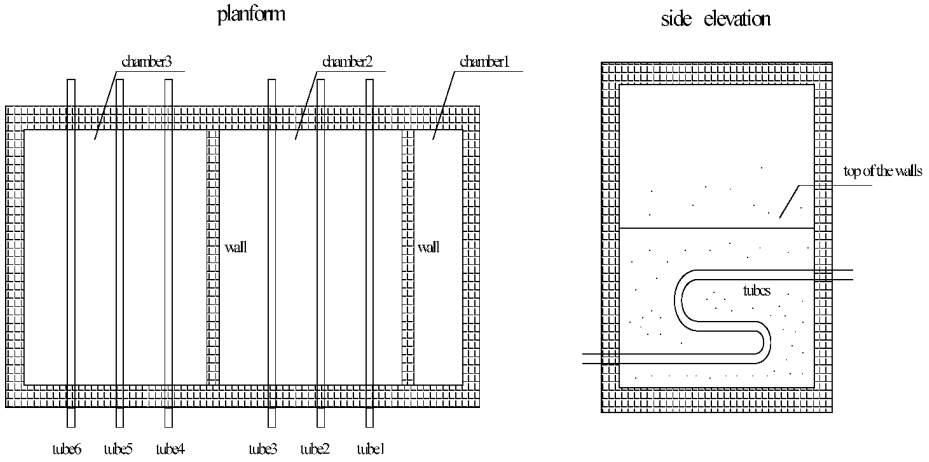

Fig. 2 The structure of the external heat exchanger (EHE)

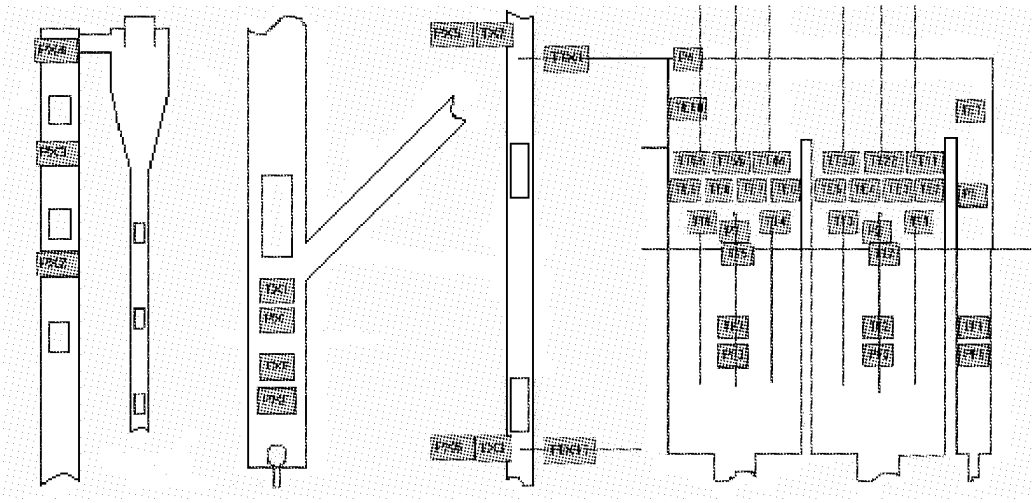

Fig. 3 The positions of pressure (P) and temperature (T) measuring points

The experimental arrangement

In the experiment, two studies should be done, one is the study of the particles flow temperature distribution, and the other is the influencing factors of the particles' HTC. We can measure the temperature distribution of particles flow directly, and the influencing factors of the particles' HTC including the particles' circulation quantity, the fluidizing velocity in EHE and the particles size should be studied in three experiments.

In the first experiment, in order to study the particles' circulation quantity affects the particles' HTC in EHE we kept the EHE working in a steady condition as the Table 2 shows, and changed the fluidized air velocity of the furnace at different particles size condition. In this experiment we also measured the temperature distribution of particles flow.

Table 2 The steady condition of EHE

	Pressure (kpa)	Air flux (m3/h)	Air flux at standard condition (m^3/h)	Air velocity at standard condition (m/s)
Chamber1	90	8	11.02724	0.478613
Chamber2	40	17.5	20.70628	0.239656
Chamber3	40	24.5	28.98879	0.335518

In the second experiment, in order to study the influence of the fluidizing velocity in EHE, we kept the furnace working in a steady condition as the Table 3 shows, and changed the fluidizing velocity in EHE. In this experiment, we also kept the mean diameter of the particles at 0.275mm.

Table 3 The steady condition of the furnace

	Pressure (kpa)	Air flux (m^3/h)	Air flux at standard condition (m^3/h)	Air velocity at standard condition (m/s)
furnace	25	100	111.8034	1.4570

In the third experiment, we changed the mean diameter of the circulating particles from 0.275mm to 0.158mm and 0.2mm, did the second experiment twice, and then compared the three groups of results to study the influence of particles size.

RESULTS AND DISCUSSION

The particles' flow temperature distribution

As Fig.4 shows, we had measured four points' temperature along the particles flow in the second chamber at three different particle size conditions, we use the software EXCEL to fit the data and conclude the following equations.

The fitting equation for 0.275mm condition is:

$$y = -0.0062x + 75.41 \tag{3}$$

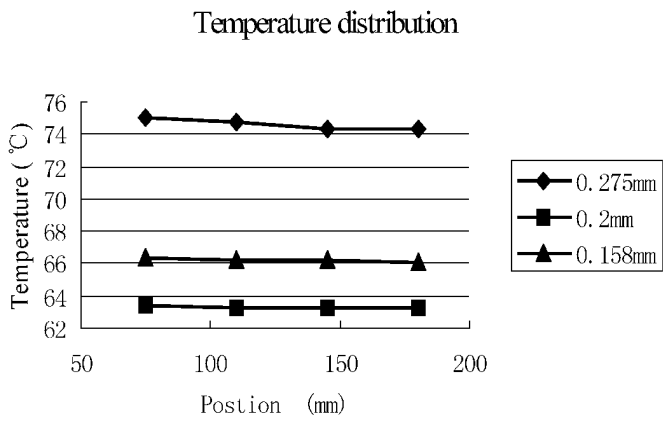

Fig. 4 The temperature distribution of particles flow

The fitting equation for 0.2mm condition is:

$$y = -0.0017x + 63.52 \tag{4}$$

The fitting equation for 0.158mm condition is:

$$y = -0.0005x + 66.31 \tag{5}$$

Because the size of test-bed is small, the temperature changed a little along the particles flow. But according to the equations, obvious temperature changes could be measured in the prototype. And we also could conclude that with the decrease of the mean diameter of particles, the temperature changes less.

The influencing factors of the particles' HTC

As the particles' circulation quantity increases with the increase of the furnace fluidized air velocity, in Fig.5, we use the influence of fluidized air velocity in furnace to reflect the relationship between particle's circulation quantity and the particles' HTC in EHE .We can get the conclusion that the HTC in EHE increases with the increase of particles' circulation quantity. For the space of EHE is limited, the changes trend is relatively slow.

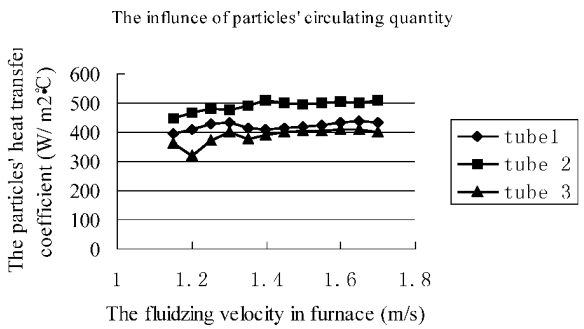

Fig. 5 The influence of particles' circulating quantity

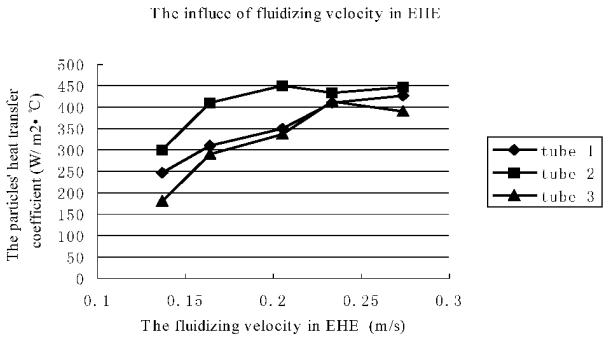

Fig.6 The influence of fluidizing velocity in EHE

According to Fig.6, the particles' HTC increases with the increase of the fluidizing velocity in EHE, but the trend become slower. The reason of this phenomena is: The increase of fluidizing velocity caused more particles joining the process of heat transfer in unit time, and made the HTC increasing, but on the other hand, it also caused the decrease of particles' density in EHE as more particles returning to the furnace. So, the existent of particles' directional flow weakened the influence of fluidizing velocity in EHE.

In Fig.7, condition1, 2 and 3 correspond to the fluidizing velocity of 0.137m/s, 0.205m/s and 0.232m/s which had been shown in the abscissa of Fig.6, the average HTC of three tubes in chamber2 were calculated out and signed on the ordinate. As the figure shows, with the decrease of the particles' mean diameter, the particles' HTC in EHE increases. This character of EHE is similar to the regular bubbling

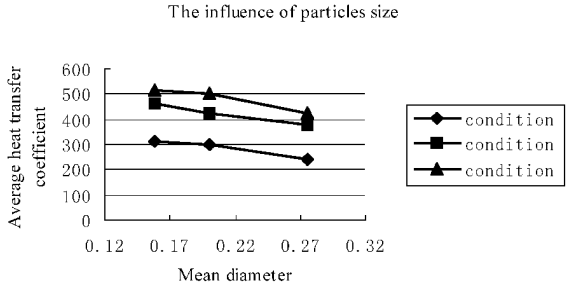

Fig. 7 The influence of particles size

fluidized beds'.

Revise the classical empirical correlation

According to the Veedendery empirical correlation (1958), two equations were list in different conditions to describe the heat transfer characters in regular bubbling fluidized bed. (Chen L. M., 1992)

$$\frac{h_{iw}\times d_t}{\lambda_g}=0.66\times(\frac{c_{pg}\times\mu}{\lambda_g})^{0.3}\times\left[R_e\times\left(\frac{\rho_p}{\rho_g}\right)\times(\frac{1-\varepsilon}{\varepsilon})\right]^{0.44}\quad \mathrm{Re}=\frac{d_t\times u_0}{u}<2500 \tag{6}$$

$$\frac{h_{iw}\times d_t}{\lambda_g}=420\times(\frac{c_{pg}\times\mu}{\lambda_g})^{0.3}\times\left[R_e\times\left(\frac{\rho_p}{\rho_g}\right)\times(\frac{\mu^2}{d_p^3\times\rho_p^2\times g})\right]^{0.3}\quad \mathrm{Re}=\frac{d_t\times u_0}{u}>2500 \tag{7}$$

Under the experiment condition, $22.4775<\mathrm{Re}<84.7403$, we chose the equation (6) to calculate the particles' HTC in EHE, and found that the results had errors more than 20% to the experiment results. So, the equation should be modified to fit for the EHE.

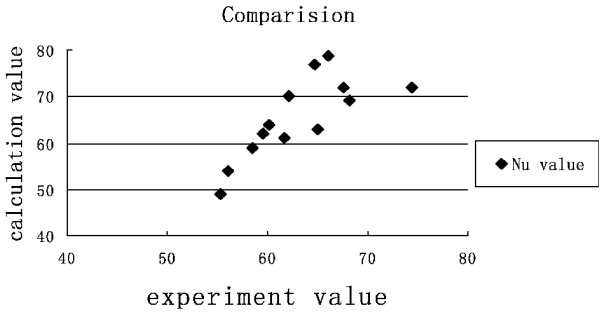

Fig.8 The comparison between experiment and calculation values

We chose the same dimensionless numbers as the equation (6), and modified the coefficient from 0.66 to 0.3568 by using minimum tolerance method, concluded the equation (8).

$$Nu=\frac{h_{iw}d_t}{\lambda_g}=0.3568(\frac{c_{p,g}\mu}{\lambda_g})^{0.3}\left[\mathrm{Re}(\frac{\rho_p}{\rho_g})(\frac{1-\varepsilon}{\varepsilon})\right]^{0.44}$$

$$\mathrm{Re}=\frac{d_t\times u_0}{u}<2500 \tag{8}$$

As Fig.8 shows, a comparison between experiment values and calculation values of Nu is given, the errors between them are always less than 20%. So the result has met the industrial requirement.

CONCLUSIONS

Because of the particles' directional flow, the temperature decline is really existent along the particles flow in EHE.

The particles' circulation quantity, fluidizing velocity in external heat exchanger and the particle size all influence the particles' heat transfer coefficient, but the influence effect differs from the regular bubbling fluidized bed.

The Veedendery empirical correlation which describes the heat transfer character in regular bubbling fluidized bed should be modified to fit for the EHE. The new empirical correlation is:

$$Nu=\frac{h_{iw}d_t}{\lambda_g}=0.3568(\frac{c_{p,g}\mu}{\lambda_g})^{0.3}\left[\mathrm{Re}(\frac{\rho_p}{\rho_g})(\frac{1-\varepsilon}{\varepsilon})\right]^{0.44}\quad \mathrm{Re}=\frac{d_t\times u_0}{u}<2500$$

NOTATIONS

ρ_g	Density of gas, kg/m^3
ρ_p	Density of particles, kg/m^3
u_0	Fluidizing velocity, kg/m^2·s
u_{mf}	Critical fluidizing velocity, kg/m^2·s
H	The height of fluidized bed, m
H_1	Height of the wall in EHE, m
D	Equivalent diameter, m
H_2	Height of EHE, m
h	Heat transfer coefficient of the working fluid in the water cooled tubes of the EHE , w/m^2·℃
T_b	Particles temperature, ℃
T_o	Average temperature of the working fluid, ℃
A_h	Heat transfer area of the water cooled tubes, m^2

h_a Particles' heat transfer coefficient, w/ $m^2 \cdot ℃$

r_0 External diameter of water cooled tubes in EHE, m

r_i Internal diameter of water cooled tubes in EHE, m

k Total heat transfer coefficient in EHE, w/ $m^2 \cdot ℃$

λ Coefficient of thermal conductivity of the water cooled tubes, w/ m·℃

q Heat absorption of the working fluid, w

d_t External diameter of water cooled tubes, m

h_{tw} Particles' heat transfer coefficient in fluidized bed, w/ $m^2 \cdot ℃$

λ_g Gas' thermal conductivity coefficient, w/ m·℃

μ Dynamic viscosity of gas, kg/m·s

ε Porocity of the fluidized bed, %

$c_{p,g}$ Specific heat at constant pressure of gas, J/kg·℃

REFERENCES

Chen, L. M. The study of heat transfer in CFB. Master degree thesis of Zhejiang University (1992).

Glicksman, L R, Hyre M, Wesphalen D. Proceedings of the 1993 Inter. Conf. on Fluidized Bed Combustion.(1993) , pp:69-79.

Lu, X. F. The equipment and operation of large-scale CFB boilers. Chinese electrical power press (2006), pp: 93-98.

Tsao, T. K., Circulating Fluidized Bed Technology: Presentation at Institute of Engineering Thermophysics. Chinese Academy of Sciences. Beijing, China. (1992).

Zhao, X. M., Lu J. F., Zhang, J. S. et al. Proceeding of the 5th International Symposium on Multiphase Flow, Heat Mass Transfer and Energy Conversion (ISMF05) (2005) , pp:121-125.

EXPERIMENTAL STUDY ON MASS AND HEAT TRANSFER CHARACTERISTICS IN A HORIZONTAL CIRCULATING DIVISIONAL FLUIDIZED BED

P. Lu[1], R. ZHang[1], J. Pu[1], C. S. Bu[1], W. P. Pan[2]

1 School of Power Engineering, Nanjing Normal University, Nanjing, 210042, China
2 ICSET, Western Kentucky University, Bowling Green, KY 42101, USA

Abstract: An innovative horizontal circulating divisional fluidized bed (HCDFB) with three fluidized-zones, one plug-zone, and a special solid material recirculating device (SMRD) located in the plug zone, was developed to generate bed materials horizontal circulating in the dense zone. The characteristics of mass transfer and heat transfer in a cold-state HCDFB model were carried out with helps of tracer technique and fast response heat transfer probes, respectively. The effects of fluidizing velocity, particle size of bed materials, initial static bed height, baffle's height, SMRD injection flowrate, and probe orientation on mass and heat transfer were analyzed. Results indicate that the amount of particle mass transfer increase with increasing of fluidizing velocity, initial static bed height, and SMRD injection flowrate. The amount of particle transfer of the low baffle fluidized-zone is higher than that of the high baffle fluidized-zone at the same fluidizing air velocity. Heat transfer coefficients increase with increasing of fluidizing velocity, and reaches their maximum value at 1.5~2.2 times of minimum fluidizing velocity. Heat transfer coefficients on the leeward side of the probe are larger than that on the windward side of the probe. Heat transfer coefficients decrease with increasing of tested bed height. It will be helpful to increase heat transfer coefficient of around 30% in a HCDFB by horizontal migration of bed materials.
Keywords: divisional fluidized bed; horizontal circulating; mass transfer; heat transfer; heat transfer coefficient

INTRODUCTION

The fluidized bed (FB) is widely used because of its high combustion efficiency, fuel flexibility, a wide range of load, and lower emission (Luo et al., 2004; Chen et al., 2005; Kim et al., 2003). Stoker retrofit by using fluidized bed can improve combustion efficiency and reduce emission. However, due to the lower cross-section heat release and larger cross-section of the stoker, fluidizing velocity of the retrofitted stocker will be lower, and mixture of gas-solid and solid-solid in dense zone will be weakened. All these will decrease mass transfer and heat transfer efficiency (Cheng et al., 2005; Liu et al., 2004). To solve these problems, an internal circulating fluidized bed (ICFB) was developed. ICFB (which makes bed material circulating by applying uneven distributor and proper baffles) is different from bubbling fluidized bed and traditional circulating fluidized bed (CFB). Bi et al. (Bi, et al. 2000), Leckner (Leckner, 1990), Basu and Nag (Basu et al., 1996), and many others have presented comprehensive reviews on CFB heat transfer. Freedman (Freedman and Davidson, 1969) and Merry (Merry and Davidson, 1973) firstly promoted that large-scale bed particles circulating can be achieved by using uneven air distributor. Tian et al. (2000) and Xu et al. (2001) studied heat transfer of an immersed tube in an ICFB, and indicated heat transfer characteristics were found to be significantly different from that in a bubbling fluidized bed. Lu et al. (2007) studied heat transfer characteristics of an immersed tube in a horizontal swirling fluidized bed (HSFB) with a rectangular baffle in the center of air distributor and three layers of horizontal secondary air nozzles located at each corner of dense zone in fluidized bed, and analyzed the effect of secondary air injection on horizontal swirling. Although many researchers have studied characteristics of mass and heat transfer of ICFBs and developed different types of ICFB (Cen, et al. 1998), it is also necessary to develop new types of ICFB and study their mass and heat transfer characteristics.

In this paper, an innovative horizontal circulating divisional fluidized bed (HCDFB) with three fluidized-zones, one plug-zone, and a special solid material recirculating device (SMRD) located in the plug zone was developed. The characteristics of mass transfer and heat transfer in a cold-state HCDFB model were carried out with helps of tracer technique and fast response heat transfer probes, respectively. The effects of fluidizing velocity, particle size of bed materials, initial static bed height, baffle's height, SMRD injection flowrate, and probe orientation on horizontal material migration and heat transfer were analyzed.

EXPERIMENTAL

The experimental apparatus consists of a HCDFB cold model, fluidizing air and injection air supplying

system, dust collecting system, and measurement system. Figure 1 shows the schematic of the experimental HCDFB. A rectangular chamber is 457 mm (width) ×584 mm (length) and 1192 mm in height. At the bottom of the chamber there is a distributor and its air caps connected to an air box. Above the distributor there are four vertical baffles with height of 355mm, 279mm, 203mm, and 165mm. Based on the distributor and baffles the HCDFB chamber is divided into three small fluidized-zones with same cross-section and a plug-zone. Each fluidized-zone has an independent air box, and resulting in three independent fluidized-zones. The solid material recirculating device (SMRD) with 7 injection nozzles is located in the plug-zone. The SMRD nozzles are corresponding with the orifices at the bottom of the high baffle. Three layers of test ports at the height (Z_h) of 30mm, 55mm, and 75mm above the air distributor are located at the each side walls. The fluidizing air flowrate of each small fluidized bed is supplied by Roots blower and measured by rotameter. The compressed air flow is measured by a mass flow meter, and then transported through SMRD nozzles to carry bed materials in plug-zone through orifices at the bottom of high baffle to the high fluidized-zone. The exhausted gas is cleaned by a bag filter before being vented. The pressure drop is measured by digital pressure meter.

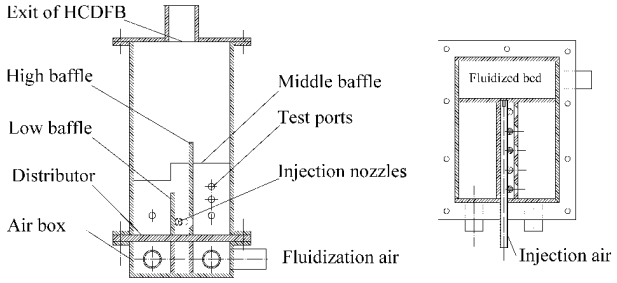

Fig. 1 Schematic of horizontal circulating divisional fluidized bed

The amount of bed materials horizontal migration between small fluidized-zones is measured by two methods: 1) Tracer technique: iron powder with diameter of less than 0.125mm is used as tracer. Mass balancing method of iron powder is used for data analysis. Correction is applied according to the loss of tracer. Test results show that the experiment errors could be controlled within 20%. 2). Method of particle migration across lower baffle: when bed materials are put into a small fluidized-zone, the amount of particle material migration across lower baffle is measured under different initial bed height and fluidizing velocity.

The schematic of heat transfer coefficient measurement system is shown in Fig. 2. It includes a Teflon tube, a mini-heater, a heat flux sensor, a thermocouple, a controller, and a computerized data acquisition system (DAS). Three miniature cylindrical Teflon probes with 25.4mm (OD) and 9.5mm (ID) are developed. A HFS-3 heat flux sensor with the dimensions of 0.18mm (thickness) × 35.0mm (length) × 28.6mm (width) is stuck to the outside surface of each probe, whose working temperature is -200~205°C. A mini heater with maximum power of 75W is placed inside each probe (Lu et al. 2007). The schematic of location and orientation of the probes is shown in Fig. 3. Heat transfer coefficients of different probes and probe orientation angles β (0°~180°) can be obtained by changing test ports and rotating the probes.

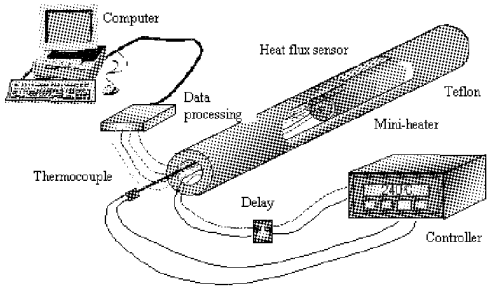

Fig. 2 Schematic of the heat transfer probe measure system

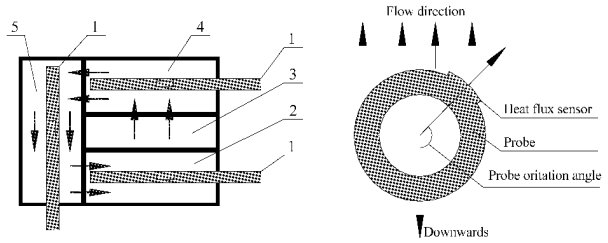

Fig. 3 Schematic of probe position and its orientation
1-Heat transfer probe; 2-Low baffle zone; 3-Plug-zone;
4-High baffle zone; 5-Medium baffle zone

Heat flux is measured by the thin film heat flux sensor stuck on the surface of the probe. All signals of bed temperature, heat flux, and temperature of the probe surface are transferred to computer. The following equation can be used to calculate the local heat transfer coefficient, h_{local} (Kim et al., 2003; Lu et al., 2007):

$$h_{local} = \frac{q}{(T_{out} - T_{bed})} \tag{1}$$

in which, T_{bed} is the bed temperature measured by a thermocouple placed inside the bed, K; T_{out} is the outside surface temperature of a probe, K; and q is heat flux, W/m^2. The average heat transfer coefficient, h, can be obtained by Equation 2, in which, h_β (including h_0, h_{45}, h_{90}, h_{135}, and h_{180}) is the average of local heat transfer coefficient, h_{local} at the different probe orientation angle.

$$h = \frac{h_0 + 2h_{45} + 2h_{90} + 2h_{135} + h_{180}}{8} \tag{2}$$

Three particle sizes of quartz sands with the particle density ρ_p of 2.65 kg/m^3 were used as bed materials. All the experiments were carried out at room temperature and atmospheric pressure. The experimental parameters are summarized in Table 1, in which d_p is average particle size, u_{mf} is minimum fluidizing velocity.

Table 1 Summary of the experimental conditions

Test samples	Particle size range, mm	d_p, mm	u_{mf}, m/s
Fine particle	0.148~0.210	0.180	0.089
Middle particle	0.297~0.420	0.359	0.177
Coarse particle	0.595~0.841	0.718	0.414

RESULTS AND DISCUSSION

The effect of injection air flowrate on mass transfer

The injection of SMRD nozzles is the main power for material migration from low baffle zone to high baffle zone. Figure 4 shows the relationship between the amount of material migration of middle particles and injection air flowrate. As can be seen, the amount of particle migration increases with increasing injection air flowrate. There is a larger increasing degree of particle migration at the range of injection air flowrate of 40~80 L/min. The main reason is: (1) when injection air flowrate is small, injection air has less penetrability; (2) when injection air flowrate is large, more injection air will penetrate particle plug layer in the plug zone, which will actually resulting in decrease of injection air flowrate. Experimental results show that there is an optimal range of injection air flowrate for a SMRD, at this optimal range the amount of SMRD particle transportation is consistent with that of particle migration between adjacent fluidized-zones. Experimental results also indicate that SMRD injection air only accounts for 5% fluidizing air for meeting the needs of particle migration. I will have bad effect on operation of fluidized bed by using this small amount of injection air. All these build a good base for horizontal circulating in a HCDFB.

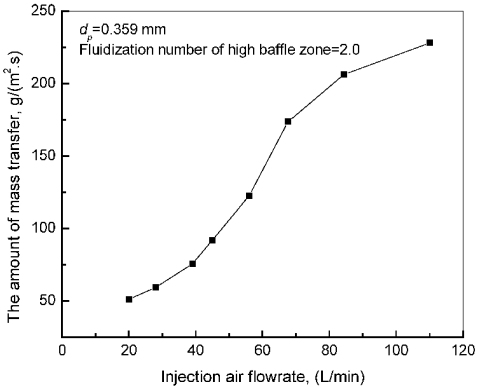

Fig. 4 The relationship between particle migration and injection air flowrate

The effect of initial bed height on mass transfer between adjacent fluidized beds

The horizontal circulation in a HCDFB is carried out by the ways of particle migration between adjacent fluidized-zones (from the high baffle zone to the low baffle zone) and particle migration from the plug-zone to the high baffle zone. So, it is significant to study the relationship between initial bed height and the amount of mass transfer characteristics from higher baffle zone to lower baffle zone for design of baffle height. The effects of three different initial bed heights on mass transfer in the high baffle zone are shown in Fig. 5, in which, d_p=0.359 mm, R_h is the ratio of initial bed height and overflow baffle height, fluidization number is the ratio of actual fluidizing velocity and minimum fluidizing velocity. The results indicate that the amount of particle migration increases with increasing fluidizing velocity in the fluidized-zone, and increase with increasing the initial bed height at the same fluidizing velocity. This is because the amount of bubbles and their sizes in the fluidized-zone increase with increasing of fluidizing velocity and the initial bed height; the bubble break is the major power for mass transfer between fluidized-zones, and results in increasing mass transfer significantly (Cang, 1991). As results indicated, change of baffle's height or initial bed height will change the amount of particle migration between fluidized-zones or particle residence time in a bed. So, it is important to

design the baffle height ratios between fluidized-zones in a HCDFB for proper horizontal mass transfer.

The effect of fluidizing velocity on particle transfer

Figure 6 shows the effect of fluidizing velocity on the amount of mass transfer in different fluidized-zones at the same initial bed height, in which d_p=0.359mm, the initial bed height is 127mm (R_h=0.455) in the high baffle zone. As can be seen, the amount of mass transfer increases with increasing of fluidizing velocity. The amount of mass transfer for low baffle zone is largest, and the amount of mass transfer is smallest for high baffle zone at the same fluidizing velocity. This can be explained by the initial bed height and the ratio of baffle height in the above section. Experimental results also indicate that fluidizing velocity of each fluidized zone is different at the same amount of mass transfer. So, in order to obtain a balance of mass transfer in a HCDFB, proper fluidizing air should be determined to guarantee a stable particle migration. On the other hand, if fluidizing velocities are the same, the difference of the amount of mass transfer between different fluidized-zones will influence residence time of bed materials in each zone. This will be helpful to create the condition of carrying out different function for each small fluidized bed.

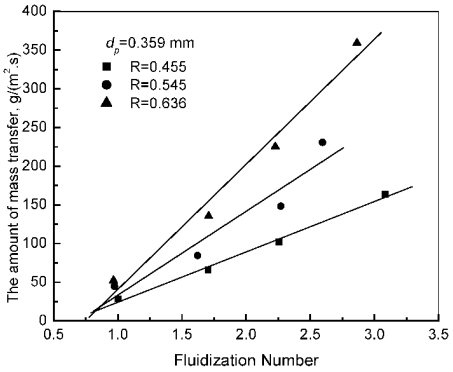

Fig. 5 Effects of initial bed height on mass transfer

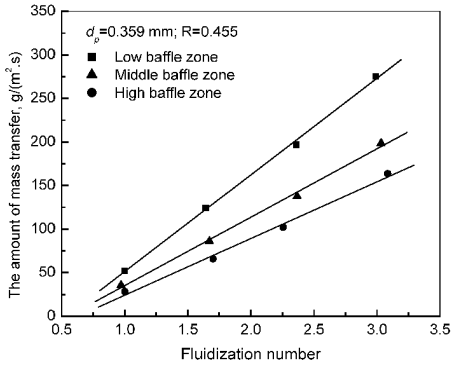

Fig. 6 Effect of fluidizing velocity on mass transfer

Figure 7 shows distribution of tracer in different fluidized zone, in which d_p=0.359mm. During the experiments, tracer (iron powder) with particle size of 0.125 mm is put in the high baffle fluidized-zone firstly, will be transferred to the other fluidized-zone, and then sampled at different fluidizing time. As can be seen, the ratios of tracer in different baffle zones tend to be the same value with increasing of fluidizing time, which indicates that bed materials are actually and continually transferred in the HCDFB.

The experiments of mass transfer characteristics show that it is necessary to properly control fluidizing velocity of each fluidized-zone for obtaining the same amount of mass transfer in a HCDFB. So, in order to obtain a stable mass transfer in the HCDFB, the fluidizing air ratio of different fluidized-zone is listed in Table 2.

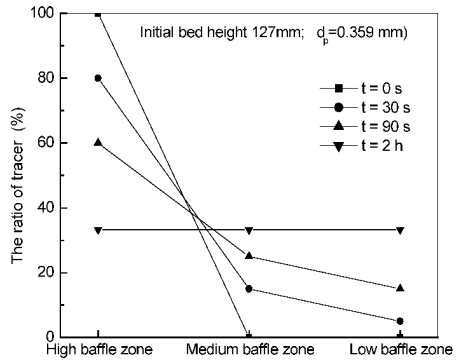

Fig. 7 Distribution of tracer in different fluidized zone

Table 2 The flowrate ratio of different fluidized zone

Baffle zone	Low	Medium	High	Plug-zone
Flowrate ratio	1.0	1.17~1.20	1.8~2.0	<5% of total

The effect of fluidizing velocity on average heat transfer

Figure 8 shows the effect of fluidizing velocity on average heat transfer of different bed materials. As can be seen that average heat transfer coefficient is very small at a minimum fluidizing velocity (n=1), and increases quickly with fluidization number. Fluidization numbers corresponding to maximum heat transfer coefficient of coarse and middle particles are around 1.5; however fluidization number of fine particles with maximum average heat transfer coefficient is about 2.2. The smaller the size of bed materials is, the higher the maximum heat transfer coefficient is. Based on Zabrodsky equation (3) (Zabrodsky et al., 1981) of calculating maximal heat transfer coefficient:

$$h_{\max} = 35.8\rho_p^{0.2} k_g^{0.6} d_p^{-0.36} \tag{3}$$

in which k_g is gas thermal conductivity, $Wm^{-1}K^{-1}$. Calculated maximum heat transfer coefficients are $266.8Wm^{-2}K^{-1}$, $342.5Wm^{-2}K^{-1}$, and $439.1\ Wm^{-2}K^{-1}$ of coarse, middle, and fine particles, respectively. The relative errors are less than 10% for coarse and middle particles, but there is a big relative error of 30% for fine particles. Although fluidization number of finer particles at maximum heat transfer coefficient is very larger than others, minimum fluidizing velocity is very small.

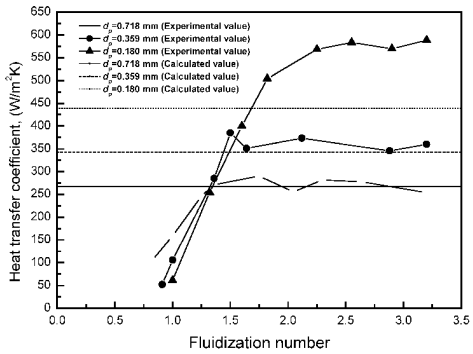

Fig. 8 Effect of particle size and fluidizing velocity on average heat transfer coefficient

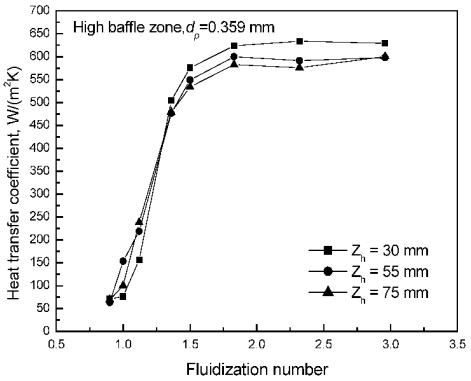

Fig. 9 Effect of bed height on heat transfer

The effect of bed height on characteristics of heat transfer

Figure 9 shows heat transfer coefficient of probes at low, middle and high locations in the high baffle zone, in which d_p=0.359mm. As can be seen, heat transfer coefficient increases with fluidizing velocity at the same location, and decreases with the tested bed height at the same fluidizing velocity. Experimental results agree with the results of heat transfer coefficient (Reddy and Nag, 1997). Reference (Kunii and Levenspiel, 1991) elucidates the effects of increasing of the bubble phase on heat transfer based on equation (4):

$$h_w = (1-f_b)(k_e \rho_e C_{ps} \frac{n_w}{1-f_b})^{1/2} \tag{4}$$

in which, f_b is contact time ratio between bubbles and the probe; n_w is bubble frequency, s^{-1}; k_e is thermal conductivity, $Wm^{-1}K^{-1}$; ρ_e is density of emulsion phase, kg/m^3; C_{pc} is specific heat capacity, $Wkg^{-1}K^{-1}$. The bubble frequency is a limited value, which is controlled by formation and growth of bubbles. Generally bubble frequency is less than 14 bubble/s, and is variational with the distance away from the wall. The closer probe to the wall is, the lower the bubble frequency is (Ozawa et al., 2002). The rapid increase of local surface heat transfer coefficient is due to the increasing of bubble frequency at that velocity when fluidizing velocity is just larger than critical fluidizing velocity. As well known, the bubbling frequency is larger and the bubble sizes are smaller at the low location. These two factors will make heat transfer coefficient decrease with increasing of tested bed height in the fluidized bed.

The effect of probe orientation on heat transfer coefficient

Figure 10 shows heat transfer coefficient of coarse, middle, and small particles at different probe orientation. As it can be seen, heat transfer coefficient increases with increasing of fluidizing velocity. Heat transfer coefficient of $\beta=0°$ is lower than that of $\beta>90°$. Generally, Heat transfer coefficients on the leeward side of the probe are larger than that on the windward side of the probe at the most of conditions. That is because the convection heat transfer is determined by contact ratio between the probes and the bubble phase or the emulsion phase. Due to smaller thermal capacity of gas phase, so heat transfer based on bubble phase at upward orientation is weaker than that based on emulsion phase at backward orientation.

Based on equation (4) we can see that the local heat transfer coefficient is direct proportional to square root of bubble frequency. That is to say, there will be a better effect on heat transfer at the beginning of bubble formation. With increasing of bubbles, the increasing of bubble frequency will be slower. So the effects of bubble frequency on heat transfer will decrease also. Otherwise, Heat transfer will decrease a little due to the increasing of contact time ratio of bubbles with probes under the condition of sufficient fluidization. At the same time, the bubble frequency and contact time ratio are almost the same in all of the probe orientation, so the change of heat transfer coefficient in different directions is very small.

As Fig. 10 shows heat transfer coefficient of small particles is larger than that of bigger ones. The cause is there are more contact points of small particles with probe surfaces than that of big ones. This makes small

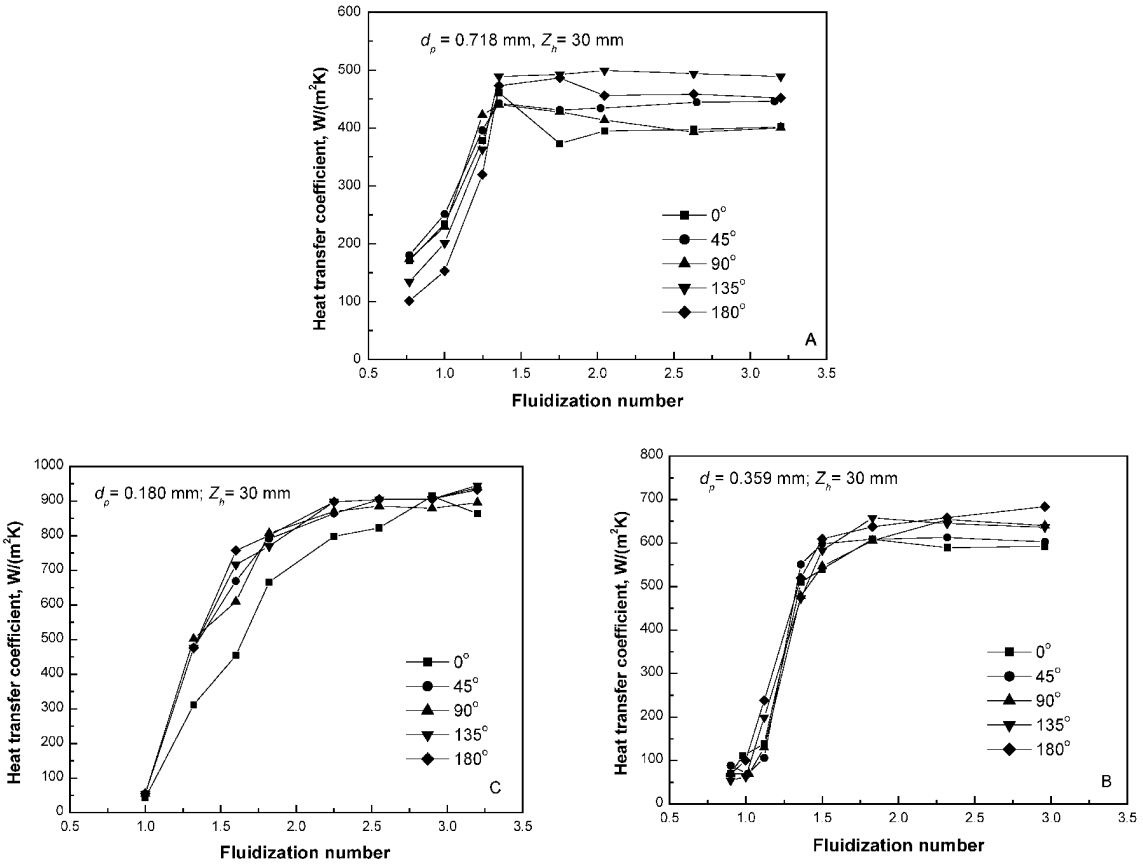

Fig. 10 Effect of probe orientation on heat transfer

particles get more contact points at the probe surface, and get more heat transfer area at the same refresh ratio of the emulsion phase, so heat transfer is enhanced. Based on the reference (Lu et al., 2007) heat transfer coefficients increase about 30% at stable horizontal circulating particle transfer (the amount of particle transfer is 200 $g/m^2 \cdot s^{-1}$). The relationship between the amount of particle transfer and heat transfer coefficient is not clear and should be further studied.

CONCLUSIONS

(1) The amount of particle mass transfer increases with increasing of injection air flowrate in a HCDFB, and increase significantly at the injection air flowrate of 40~80L/min.

(2) The amount of particle migration increase with increasing of the initial bed height, injection air flowrate and fluidizing velocity, and the amount of particle mass transfer in the low baffle zone is larger than that in high baffle zone at the same fluidizing velocity.

(3) Heat transfer coefficients increase quickly at minimum fluidizing velocity, and reach their maximum values at 1.5~2.2 times minimum fluidizing velocity.

(4) Heat transfer coefficients decrease with increasing of bed height; Heat transfer coefficients on the leeward side of the probe are larger than that on the windward side of the probe. It is helpful to increase heat transfer coefficient of about 30% at the condition of stable particle horizontal migration.

ACKNOWLEDGEMENTS

Financial supports from Natural Science Foundation of Jiangsu province of China (BK2007532), Natural Science Foundation of the Jiangsu Higher Education Institutions of China (07KJD610119), and Scientific Research Foundation for the Returned Overseas Chinese Scholars, MOP are gratefully acknowledged.

REFERENCES

Basu, P. and Nag, P. K.: Chemical Engineering Science, **51**(1996), pp.1-26.
Bi, H. T., Ellis, N., Abba, I. A., Grace, J. R.: Chemical Engineering Science, **55** (2000), pp.4789-4825.
Cang, D.: Chinese J. chemical Industry & Engineering, **1**(1991), pp.59-65.

Ceng, K.F., et al. (1998). Theory, design, & operation of CFB. Beijing, China Electric Power Press.
Chen, J. C., Grace, J. R. and Golriz M. R.: Powder Technology, **150** (2005), pp.123-132.
Cheng, L, Zhou, Q., Shi, Z. L., et al.: Thermal Power Generation, **34** (2005), pp.25-27 (in Chinese).
Freedman, W. and Davidson, J F.: Trans. Ins. Chem. Eng. **47**(1969), pp.251-262.
Kim, S. W., Ahn, J. Y., Kim, S. D., et al.: Inter. J Heat and Mass Transfer, **46** (2003), pp.399-409.
Kunii, D. and Levenspiel, O. (1991). Fluidization Engineering (2nd edn). New York, Butterworth-Heinemann.
Leckner, B. (1990). Heat transfer in circulating fluidized bed boiler. Circulating Fluidized Bed Technology III.
Liu, H., Zhou, K. Y., Xu, X. H., et al.: Proceedings of the CSEE, 24 (2004), pp.211-213 (in Chinese).
Lu, P., Cao, Y., Wu, A., et al.: Proceedings of the CSEE, **27** (2007), pp.65-70.
Luo, Z. Y., He, H. Z., Wang, Q. H., et al.: Power Engineering, **24** (2004), pp.761-767 (in Chinese).
Merry, J. M. D. and Davidson, J. F.: Trans. Ins. Chem. Eng. **51**(1973), pp.361-368.
Ozawa, M., Umekawa, H., Furui, S., et al.: Experimental Thermal and Fluid Sci, **26**(2002), pp.643-652.
Reddy, B. V., and Nag, P. K.: Intern J Energy Research, **21**(1997), pp.1109.
Tian, W. D., Hao, J. H., Wei, X., et al.: J of Comb Sci & Techn, **6**(2000), pp.296-299(in Chinese).
Xu, X., Chi, Y., Li, B., et al.: Proceedings of the CSEE, **21**(2001), pp.9-13(in Chinese).
Zabrodsky, **S. S.,** Epanov, Y. G., Galershtein, D. M., et al.: Inter J Heat & Mass Transfer, 24(1981), pp.571-579.

EXPERIMENTAL STUDY OF GAS SOLID FLOW CHARACTERISTICS IN CYCLONE INLET DUCTS OF A 300MWE CFB BOILER

J. Y. Tang[1], X. F. Lu , J. Lai[2], H. Z. Liu[1]

1 College of Power Engineering, Chongqing University, Chongqing, 400044, China
2 Dongfang Boiler Industry Group Co. Ltd., Zigong, 643001, China

Abstract: Gas solid flow characteristics in cyclone's inlet duct of a 300MW CFB boiler were studied in a cold circulating fluidized bed (CFB) experimental setup according to a 410t/h CFB boiler with a scale of 10:1. Tracer particles were adopted in the experiment and their motion trajectories in the two kinds of cyclone's inlet ducts were photographed by a high-speed camera. By analyzing the motion trajectories of tracer particles, acceleration performance of particle phases in the two inlet ducts was obtained. Results indicate that the acceleration performance of particles in the long inlet duct is better than that in the short inlet duct, but the pressure drop of the long inlet duct is higher. Meanwhile, under the same operating conditions, both the separation efficiency and the pressure drop of the cyclone are higher when the cyclone is connected with the long inlet duct. Figs 11, Tabs 4 and refs 10.
Keywords: power and mechanical engineering, cyclone's inlet ducts, gas solid flow characteristics, performance of cyclone

INTRODUCTION

As a highly-efficient clean combustion technology, the Circulating Fluidized Bed (CFB) boiler, which plays significant role in energy saving and environmental protection, has developed over 20 years, and it represents the great progress in combustion technology (Feng, 1998). The cyclone separator is the key equipment for warranting the satisfactory particle circulating ratio, combustion efficiency and desulfurization efficiency of CFB boiler, therefore, the optimization of its performance is the key technology in the development of CFB boiler (Chen et al., 2007).

To meet the demand of the scale-up of CFB boiler, many improvements of cyclone separators have been made in the world these days. The improvements generally include two aspects. The first aspect is, improving the internal geometric structure of cyclones or other hydrodynamic parameters (Peng et al., 2004), including the internal body structure and the cyclone inlet duct structure, to improve separation efficiency and meet the requirement of the large capacity of CFB boiler. The second aspect is improving the external geometric structure of cyclones (Liu et al., 2003)so that it can match the main structure of CFB boiler and solve the layout problem of cyclones during the process of the scale-up of CFB boiler.

As for the improvements of inlet ducts, Bai Yugang, Lv Junfu, et, al (Tsinghua University) obtain the following results by experimental studies (Bai et al., 1991): changing the position of the baffle to change the inlet width not only influences the inlet velocity, the pattern and the direction of gas flow, but also influences the swirling flow in the cyclone, which may exert either positive or negative influence on particle separation. A case in point is that Tonghae power station in Korea improved separation efficiency by reducing the inlet width.

By prolonging cyclone inlet duct, France's Stein Company pre-accelerated particles before they enter the cyclone, and there, the inlet duct was arranged by inclining certain angle, plus other improvements, the average particle size of recycle ash was reduced from 180μm to 80μm, at the same time, consumptions of limestone was reduced and desulfurization efficiency was improved as well (LALAK Ireneusz, et al., 2003).

France's Alstom Company holds that there are two important parameters of cyclones, one is the shape and size of the vent-pipe, the other is the shape and size of the inlet duct. Alstom 300MW CFB boiler, which was imported by Sichuan BAIMA power station, used a unique long inlet duct. In the new design, the furnace exits are on the upper water walls of the front and rear walls of furnace. and the furnace exit and the cyclones laid on the side walls are connected by the inlet duct of the cyclone; the inlet duct is a gastight flue gas duct with a declination angle and a groove, and its shape is complex, which is helpful for particles to obtain high acceleration and pre-separation and eventually improves the separation efficiency greatly and reduces the carbon content of fly ash in the flue gas (Jiang et al., 2004). This is a breakthrough compared with the previous designs of the cyclone inlet duct.

In order to compare the different gas solid flow characteristics in the traditional short inlet duct and in the improved long inlet duct, and analyze the influence on separation performance of the cyclone brought by the two different inlet ducts, in the present work, the authors have carried out the following experiments and obtained a series of results.

EXPERIMENTAL SETUP AND METHODOLOGY

Experimental setup

The test rig is comprised of the boiler proper, the air supply apparatus and pipes. The whole test rig is an open system, and it is a set of experimental apparatus with Plexiglas according to a 410t/h CFB boiler with a scale of 10:1 (Fig.1). Figure 2 is a photo of the boiler proper, and the main dimensions of the test rig are listed in Tab 1. In the experiments, the fluidized air is provided by a centrifugal fan and the high-pressure air required by L-valve is provided by an air compressor.

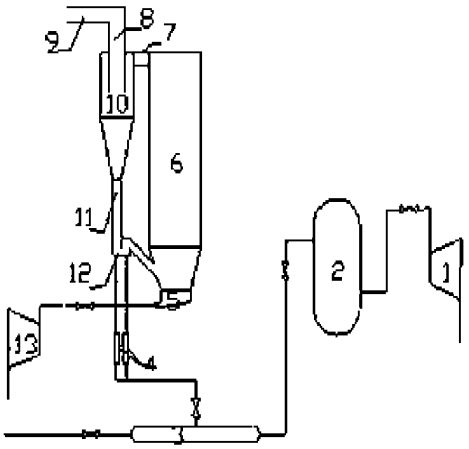

1-compressor 2-air pressure stabilizer 3-header 4-rotameter 5-fluidized air chamber 6-furnance 7-inlet duct of cyclones 8-vent pipe 9-exhaust pipe 10-cyclone 11- return leg 12-L valve 13-fan

Fig. 1 Schematics of experimental setup

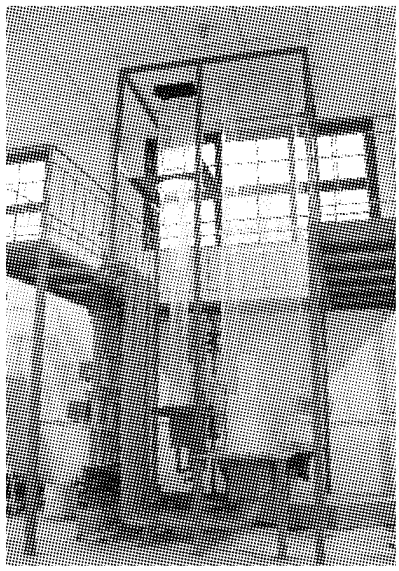

Fig. 2 A CFB boiler setup with visualized gas-solid two phase flow

Table 1 Main dimensions of the furnace and the cyclone of the experimental setup

Item	Dimension（mm）	Item	Dimension（mm）
Furnace height	3500	Cyclone cylinder height	900
Furnace width	650	Cyclone cone height	900
Furnace depth	680	Cyclone vent-pipe diameter	200
Cyclone outside diameter	450		

Experimental methodology

The experiments mainly include the following two main parts: the first part is studying gas solid flow characteristics in the long and the short inlet ducts, including studying the pressure drop of the duct, photographing particle flow in the two different inlet ducts and studying particle acceleration; the second part compares the influence of the long and the short inlet ducts on the separation efficiency and the pressure drop of the cyclone. In order to guarantee the same experimental conditions, the entrance area and the outlet area of the long and the short inlet ducts are the same, and the height-width ratio of the cyclone entrance (the outlet of the inlet duct) is the same, too, and all these may eliminate the influence of some structure sizes on the separation efficiency of the cyclone. The long and the short inlet ducts are shown in Fig. 3, and their main dimensions are listed in Table 2.

In the experiment, the cyclone inlet velocity was calculated according to the equal mass flow principle after the fluidized airflow velocity was measured by a hot-wire anemoscope. And the flux of high pressure air of L-vlave

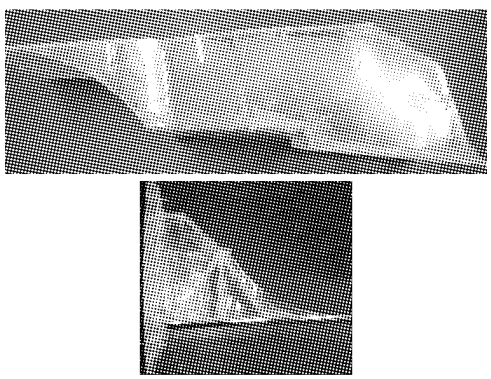

Fig. 3 the long and the short inlet ducts of the cyclone

was measured by a glass rotameter. Pressure signals in the furnace, the cyclone and the inlet ducts of the cyclone were firstly transferred to electric signals by Kangyu KYB14 type differential manometers, and then they were collected by the ADAM4000 data acquisition system. Particle flow in the two inlet ducts were photographed by a high-speed camera system, which includes a Rredlake HK100 high-speed camera, computers, data lines and some streamer laps and so on, and its layout is shown in Fig. 4. Floating beads were used as bed material in the experiment, and their density is 620 kg/m^3 and particle size is generally 0.45mm. Some of the particles were dyed white to improve their optical properties and meet the requirements of photography, and they function as tracer particles.

Table 2 Dimensions of the inlet ducts

	Height of inlet duct ,mm	Width of inlet duct ,mm	Height of outlet duct, mm	Width of outlet duct, mm	Length, mm
Long inlet duct	225	175	246.4	107.6	480
Short inlet duct	235	167.5	250	109.2	135

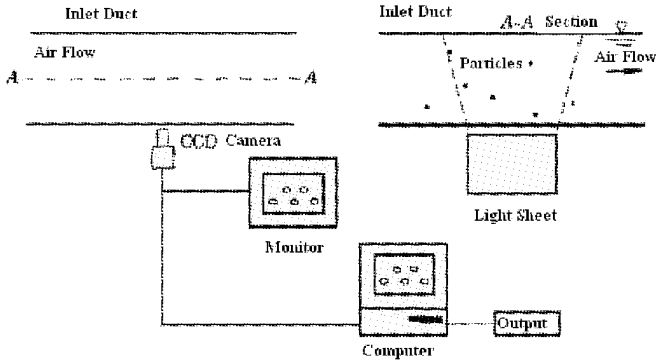

Fig. 4 Arrangement plan of the high speed video system

It is notable that, in the experiment, a high-speed camera system was used to conduct the tracking measurement of particles in the flow-field. The specific method is as follows. The camera system photographed the particle motion at regular time intervals and a series of images were obtained; the positions of the same particle in the two successive images were compared (Liu et al., 2001), and according to the definition of velocity in PTV,

$$\vec{V} = \lim_{t_2 \to t_1} \frac{r_2 - r_1}{t_2 - t_1} = \lim_{\Delta t \to 0} \frac{\Delta \vec{r}}{\Delta t}$$

the value and direction of velocity were determined (Wang et al., 2000). And the separation efficiency was indirectly calculated by measuring the change in the amount of bed material in the return leg in a given unit of time.

Table 3 Test conditions

Operating conditions	the inlet velocity of ducts, m/s	the outlet velocity of ducts, m/s
First	4.8	6.9
Second	10	14.5
Third	14.8	21.3

RESULTS AND DISCUSSION

Experimental study of gas solid flow characteristics in the long and the short inlet ducts

Under the same operating conditions (the same inlet velocity and outlet velocity of ducts), the flow behavior in the two inlet ducts was photographed, the images were analyzed, and the particle motion trajectories and particle acceleration curves were obtained. It is noteworthy that the inlet velocity of particles in the long and the short inlet ducts is almost the same under the same operation conditions.

Figures 5 and 6 represent the particle motion trajectories in the long and the short inlet ducts under different operation conditions (operating condition parameters are listed in Table 3), and the time interval of successive particles is 5ms.

Figures 5 and 6 indicate that with the increase of the inlet velocity of ducts, the distance between the

successive particles increases, therefore, the number of tracing points in each trajectory becomes less, which shows that the less time the particles use when passing the inlet ducts. Since the particles come into collision with the outer wall surface of the duct, the particle motion trajectories in the long inlet duct are divided into two parts: the first part is from the inlet to the outer wall surface; the second part is from the outer wall surface to the inlet of the cyclone. However, the particle motion trajectories in the short inlet duct are continuous.

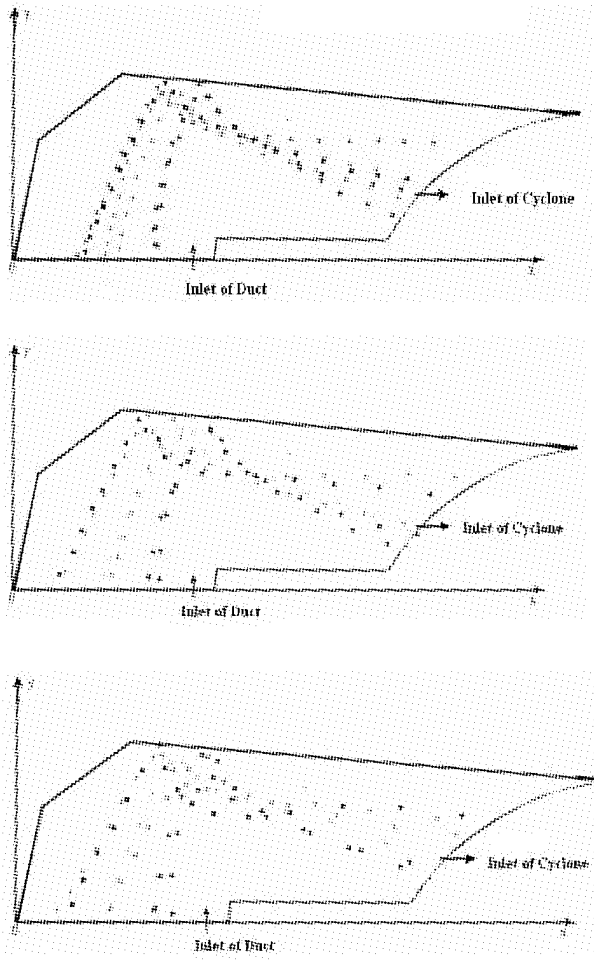

Fig. 5 Flowing track diagram of the particles in the long inlet duct

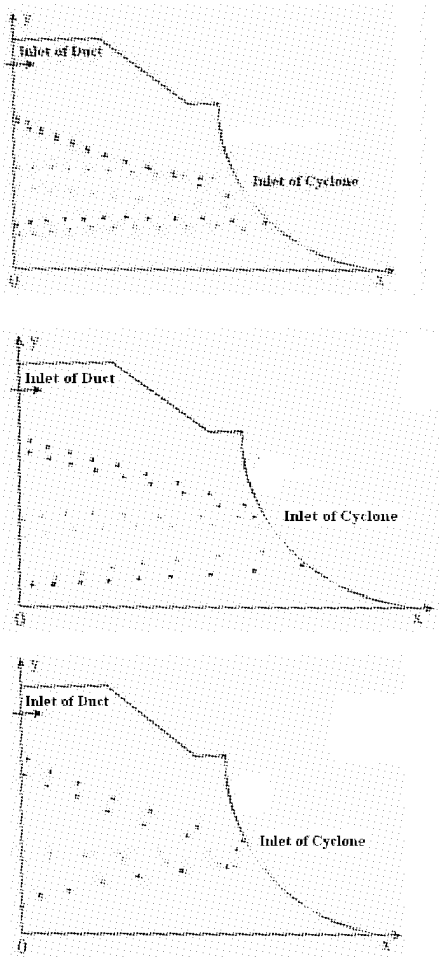

Fig. 6 Flowing track diagram of the particles in the short inlet duct

The particle acceleration curve in the inlet ducts were obtained after the treatment of the particle motion trajectories, as shown in Fig. 7 and Fig. 8.

Figures 7 and 8 show that the velocity enhancement of particles at the duct outlet section increases more than at the duct inlet section with increasing duct inlet velocity, As for the long inlet duct, under the three operation conditions, the velocity of particles increases from 2.4m/s to 5.0m/s, from 3.4m/s to 7.6m/s, from 4.2m/s to 9.5m/s respectively; while for the short inlet duct, under the same three operation conditions, the velocity of particles increases from 2.4m/s to 4.1m/s, from 3.4m/s to 5.5m/s, from 4.3m/s to 7.1m/s respectively. The velocity enhancement of particles is listed in Table 4.

Table 4 velocity enhancement of particles in ducts

	velocity change of particles （Δv）, m/s		
	First	**Second**	**Third**
The long inlet duct	2.63	4.15	5.30
The short inlet duct	1.73	2.11	2.77

Tab. 4 indicates that under the same operating conditions, the velocity enhancement of particles in the long inlet duct is higher than in the short inlet duct, namely, the particle acceleration in the long inlet duct is much better than in the short inlet duct. It is noteworthy that the particle acceleration curves in the short inlet duct

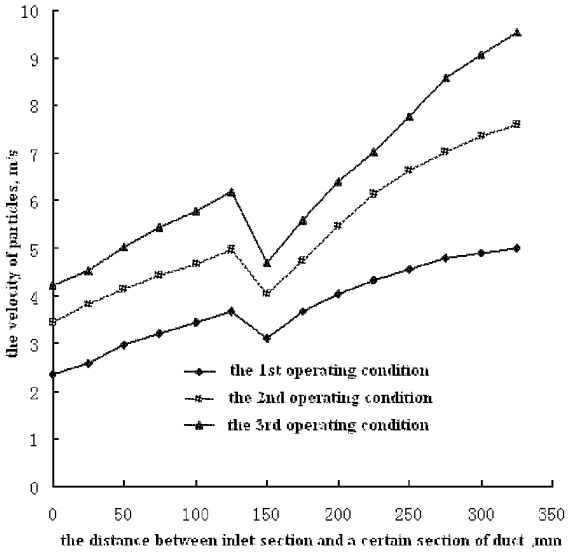

Fig. 7 The particle acceleration curve of the long inlet duct

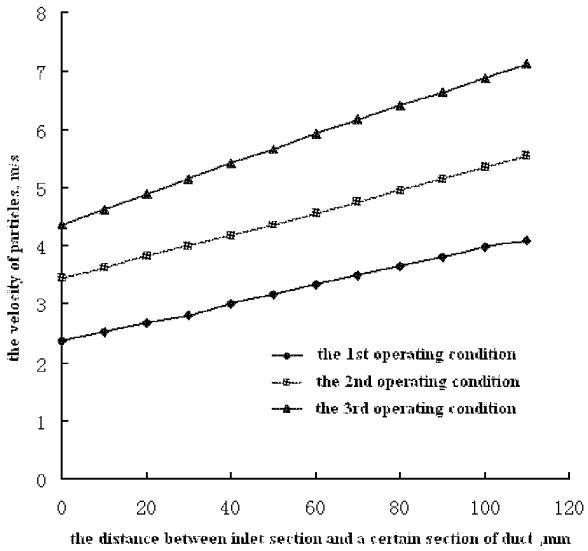

Fig. 8 The particle acceleration curve of the short inlet duct

under the three operating conditions are almost linear and the velocity of particles increases with the increasing distance, as in Fig. 8. On the other hand, there is a turning point at a distance of 125mm from the duct outlet section on all the three particle acceleration curves of the long inlet duct, which means, the velocity of particles increases until the section, after that, it decreases instantaneously, and then increases again. This phenomenon can be explained as follows: due to the 90°corner of the duct, the particles come into collision with the outer wall surface of the duct, at that moment, the velocity of particles decreases sharply, however, after collision, the particles rebound and accelerate again according to momentum conservation law.

Figure 9 shows the relationship between pressure drop and inlet velocity of ducts. From Fig 9 we can find that both the pressure drop of the long inlet duct and the pressure drop of the short inlet duct increase with increasing duct inlet velocity. This may be due to the fact that the frictional resistance of inlet duct increases with the increase of inlet velocity. What's more, the short inlet duct is very short and smooth while the long inlet duct is relatively long and has a 90°corner, which increases the route loss and local loss, Therefore, with increasing of inlet velocity of ducts, the increase amplitude of the pressure drop of the long inlet duct is much higher.

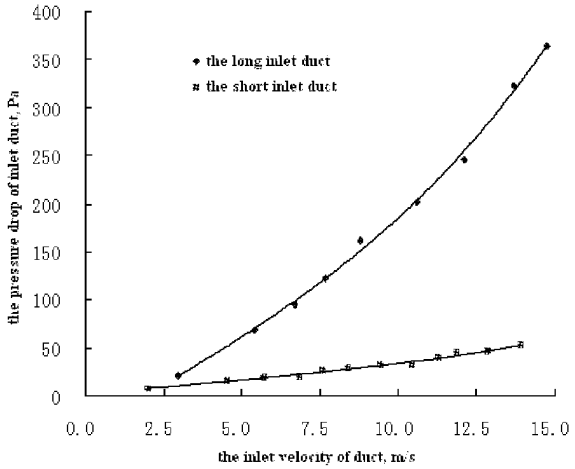

Fig. 9 Pressure drop VS inlet velocity of ducts

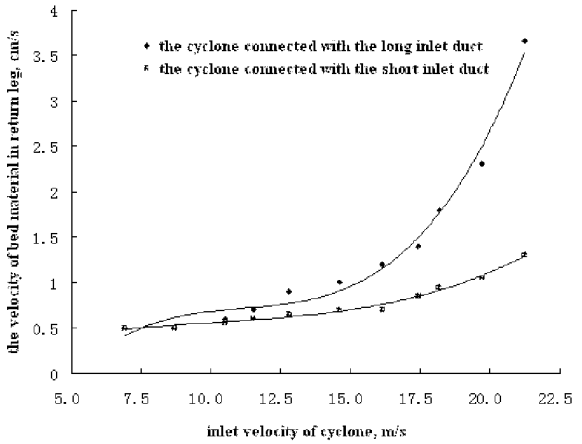

Fig. 10 Comparison of the separation efficiency

Comparative study of cyclone performance

Figure 10 compares the separation efficiency of the cyclone with the two different inlet ducts (the bed material height is 16cm). Figure 10 indicates that the deposit velocity of bed material in standpipe increases with increasing of cyclone inlet velocity under the two connection modes, namely, the separation efficiency

increases with the increase of cyclone inlet velocity. But when the cyclone inlet velocity is the same and the cyclone is connected with the long inlet duct, the deposit velocity of bed material in the standpipe is much higher, so that the separation efficiency of the cyclone with the long inlet duct is higher than that of the cyclone with the short inlet duct.

Figure 11 compares the pressure drop of the cyclone with the two different inlet ducts, the pressure drop is from the cyclone inlet to the outlet of the central duct. With the same body structure, the inlet velocity and the height-width ratio of cyclone, the pressure drop of the cyclone with the two different inlet ducts is different: the pressure drop of the cyclone with the long inlet duct is higher, and the reasons for this may be that: due to the 90°corner in the long inlet duct, the airflow in the duct becomes turbulent and the anchorage dependence of tangential wind in the cyclone becomes poorer, compared with that of the short inlet duct.

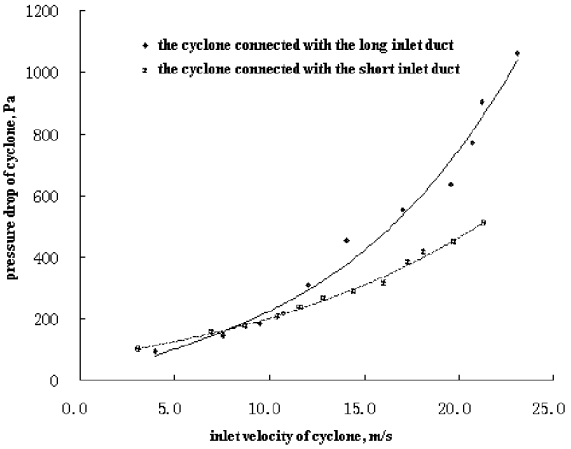

Fig. 11 Comparison of the pressure drop of cyclone

CONCLUSIONS

In the present work, the gas solid flow characteristics in cyclone's inlet duct were studied in a CFB experimental setup and the influences on separation performance of the cyclone brought by the two different inlet ducts were analyzed. Some significant conclusions of the study are as follows:

(1) Particles can be accelerated in both the long and the short inlet ducts, and the amplitude of particle acceleration increases with the increase of the inlet velocity of duct. Under the same operating conditions, the acceleration performance of the long inlet duct is better than that of the short inlet duct.

(2) The separation efficiency of the cyclone with the improved long inlet duct increases with the inlet velocity of the cyclone, which is similar to that of the cyclone with the traditional short inlet duct. However, under the same operating conditions, the separation efficiency of the cyclone with the long inlet duct is higher that of the cyclone with the short inlet duct.

(3) The pressure drop of the two inlet ducts increases with the inlet velocity of ducts. Due to the larger one-way resistance and local resistance, the pressure drop of the long inlet duct is significant higher than that of the short inlet duct. And the pressure drop of the cyclone increases with increasing the inlet velocity of the cyclone, but if the same cyclone is connected with the different inlet ducts, it has different cyclone pressure drop. Because the irregular shape of the long inlet duct has a negational effect on the airflow in the cyclone, the pressure drop of the cyclone with the long inlet duct is higher than that of the cyclone with the short inlet duct.

NOTATIONS

$\vec{V}$	particle velocity, m/s	r_2, r_1	distance to the initial position, cm
t_2, t_1	particle flowing time, ms	$\Delta\vec{r}$	displacement of the particle flowing, cm
Δt	time interval of successive particles, ms		

ACKNOWLEDGEMENTS

Financial support of this work by the Key Project of the National eleventh-Five Year Research Program of China (2006BAA03B02-06) is gratefully acknowledged.

REFERENCES

Chen, J.H., Yang, C.Y. and Lu, X.F.: Journal of Power Engineering. 27(2007), pp. 254-258.

Bai, Y.G., Lu, J.F. and Yue, G.X.: China Powder Science and Technology. 6(1991), pp. 1-4.

Feng, J.K. and Yue, G.X.(1998). New achievements of development of CFBC boilers in China. The international conference on

energy and environment.

Jiang, M.Q. and Sun, X.B.: Thermal Power Generation. 9(2004), pp. 1-3.

LALAK Ireneusz, et al. (2003). Operational experiences with high efficency cyclone: comparison between boiler A and B in the Zeran Power Plant-Warsaw, Poland. 17th International Fluidized Bed Combustion Conference.

Liu, D.C., Wu, Z.S. and Zhang, S.H.: Journal of Power Engineering. 23(2003), pp. 2377-2379.

Liu, S.K., Xu, X.C. and Deng, G.Q.: Journal of Experiments in Fluid Mechanics. 3(2001), pp. 62-66.

Peng, L., Li, J. and Wang, G.H.: Journal of Power Engineering. Journal of Engineering for Thermal Energy and Power. 27(2004), pp. 153-156.

Wang, D.C., Yu, M.Z. and Wang, X.K.: Journal of Basic Science and Engineering. 8(2000), pp. 301-309.

EXPERIMENTAL RESEARCH ON GAS-SOLID FLOW IN A SQUARE CYCLONE SEPARATOR WITH DOUBLE INLETS

B. Xiong[1], X. F. Lu[1], R. S. Amano[2], C. Shu[1]

1 School of Power Engineering, Chongqing University, Chongqing, 400044, China
2 Department of Mechanical Engineering, University of Wisconsin-Milwaukee, WI 53211, USA

Abstract: A square cyclone separator with double inlets was developed for a new type Circulating Fluidized Bed (CFB) boiler arrangement scheme including two furnaces. Experiments on the performance and gas-solid flow recorded by a high-speed photography have been conducted in a cold test rig with a separator cross section 400mm×400mm. Experimental results indicated that with the inlet velocity of 22.4m/s and the inlet solids concentration of 4.9g/m^3, the cut size is 15 μm, the critical size is 75μm, and the pressure drop coefficient is 1.7. The performance is also affected by the inlet velocity and solids concentration. The trajectory of particles shows that the particles swirl in the region near the wall and are easily separated. Especially, the instantaneous separation occurred at the corner is very significant for the improvement of the collection efficiency with the high inlet solids concentration for CFB boiler.
Keywords: circulating fluidized bed boiler, square cyclone separator, gas-solid flow, collection efficiency, pressure drop coefficient

INTRODUCTION

Aiming at the problem of circulating fluidized bed (CFB) boiler scaling-up, a new type CFB boiler arrangement scheme called "furnaces around separator" (Huang et al., 2006) was put forward. The largest difference with other schemes is identified that a cyclone separator is placed between two furnaces, and a new type integrated external heat exchanger is used under the separator. Compared with the traditional circular cross-section cyclone, a square cyclone has more advantages over the conventional cyclone, due to several reasons such as convenience in construction, easier membrane wall arrangement, shorter start-stop time, and its easy integration with the boiler. Therefore a square cyclone separator with double inlets is used in this new boiler because of employment of two furnaces.

Ahlstrom Pyropower Company developed a square water-cooled cyclone separator with upward exhaust exit for high temperature separation and applied to its compact CFB boiler design (Daring, 1995). Other authors reported the application of such a separator to commercial CFB boilers (Makkonen and Foster, 2000). A patent square separator with particle accelerating inlet was developed by Tsinghua University (Lu et al., 1998). A number of studies have focused on structure and dimensions of this square cyclone separator, with the aim of enhancing collection efficiencies and reducing pressure drops (Bai et al., 1999a; Bai et al., 1999b). Their measurement results prove that the fractional collection efficiency of square separator with particle accelerating inlet is almost unchanged during the diameter of separator scaled from 300mm to 3000mm, and the scaling up design of the square well meets the request of large circulating fluidized bed boilers (Lu et al., 2000; Lu et al., 2003). A type of square cyclone separator with downward-exhaust exit was developed and granted a Chinese patent. Its separation efficiency was shown as good as that of the traditional cyclone of circular cross-section separator and its particle cut-diameter was around 15 μm (Qiu et al., 1999). The gas-solid suspension flow in a lab-scale square cyclone separator with downward gas-exit was measured by Su and Mao (2006). All of the above mentioned research results indicate that the square cyclone separator used in CFB boiler has high collection efficiency.

According to the experimental results of Zhao et al. (2004), circular cross-section cyclone separator with direct symmetrical spiral inlet has a higher performance than that of cyclone with a conventional tangential single inlet. The square cyclone separator with symmetrically double particle accelerating inlets was developed. The performance of this square cyclone separator including the collection efficiency and the pressure drop is one of the key factors of success in the new type CFB boiler arrangement scheme. In this paper, the experimental study on the performance of this square cyclone separator with double inlets and particle trajectory recorded by high-speed photography are presented.

EXPERIMENTAL SET-UP

A cold test rig with a separator cross section 400mm×400mm was built. The geometry and dimension of the square cyclone separator with double inlets are presented in Fig. 1 and in Table 1. For the convenience of

observing and photographing purposes, the cyclone was manufactured by Perspex, as shown in Fig. 2.

Table 1 Dimensions of cyclone studied (unit: mm)

A	a	b	B	d	D	De	h	H	S	R
160	160	44	100	160	400	160	600	1400	225	180

The experimental system setup is shown in Fig. 3, which included the square cyclone, an induced fan and two particle screw feeders. The air supplied by the induced fan entered into the cyclone though two inlet pipes. The inlet velocity was measured by a hot wire anemometer at the inlet pipe. Because the construction of the inlet pipes was the same, the deviation of the inlet velocity between two inlets was less than 3%. Also the inlet velocity could be controlled by the baffle at the front of the inlet pipe. Particles were fed by two screw feeders and uniformly diffused in the inlet pipe. At last, these particles entered into the cyclone with the air flow.

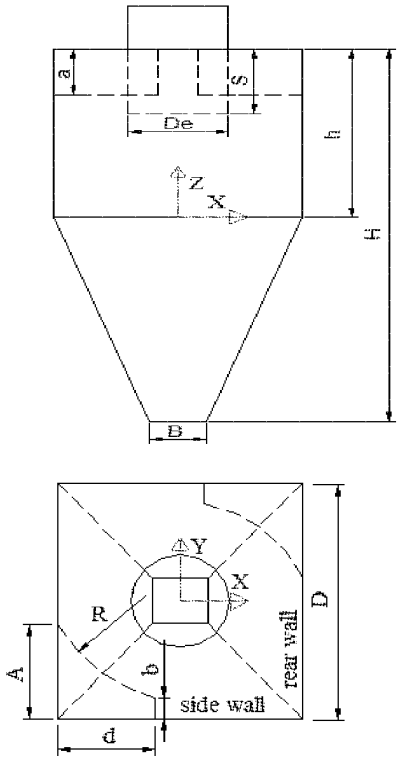

Fig. 1 Schematic diagram of the square cyclone geometry

Fig. 2 Photo of the cold test rig

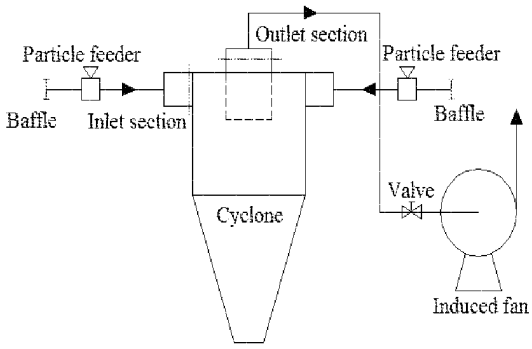

Fig. 3 Schematic diagram of the experimental system setup

The pressure was measured at the inlet and outlet sections by use of differential pressure transmitters. The electric signal from the KYB-14 transmitter was automatically collected by ADMA date collection system with a monitor and control generated system. The pressure drops were calculated from the difference of the average pressure between the inlet and outlet sections. The solid particles used in the test were talcum powder with skeletal density of 2739 kg/m^3. The particles with single size of 10, 23, 45 and 75μm were weighed and fed into the cyclone separator by screw feeder. At the dust outlet, the separated particles were collected and weighed. With these data the collection efficiency can be calculated from the following equation:

$$\eta_i = \frac{W_{t_i}}{W_{c_i}} \tag{1}$$

Where η is the collection efficiency. W_t and W_c are the weight of particles at the dust outlet and the inlet. i is the particle size.

During the experiment, high-speed photography was used to record the particle trajectory in the square cyclone. In order to make the particle trajectory clear, the polystyrene grain with bulk density of 12 kg/m^3 was used. According to the similarity theory of particle movement, the calculated size of the polystyrene grain ranges from 0.5mm to 1mm.

EXPERIMENTAL RESULTS AND DISCUSSION

Collection efficiency

Figure 4 compares the grade collection efficiency of the square cyclone with double inlets at the inlet velocities of 16.7, 22.4 and 29.0m/s, respectively, while the inlet solids concentration was kept as 4.9g/m^3. As expected, the frictional efficiencies are seen to increase with increase in particle size. From the curve in Fig. 4 with the inlet velocity of 16.7m/s, we can see that the 50% cut size is about 20μm. While the particle size increases to 75μm, the collection efficiency is close to 100%. Also the collection efficiency increases with increase in the inlet velocity. For the inlet velocities of 22.4 and 29m/s, the collection efficiencies are greater by 1-3% and 2-8% than that for the inlet velocity of 16.7m/s. the centrifugal force acting on the particle increases with increase in inlet velocity. So it is easier for particle to move to the wall and be separated. But the inlet velocity should be chose reasonably. The operation of the square cyclone separator with high inlet velocity may bring some other problems such as wear.

Figure 5 shows the collection efficiency of the cyclone at different inlet solids concentrations with the inlet velocity kept as 24.5m/s. For the 4.9, 18.4 and 73.4g/m^3 tests, a tendency of increasing collection efficiency with increase in inlet solids concentration was observed. For the inlet solids concentrations of 18.4 and 73.4g/m^3, the collection efficiencies are greater by 1-3% and 2-13% than that for the inlet concentration of 4.9g/m^3. This trend is attributed to the increase in the formation of agglomerates, which are more easily collected. Also the high inlet solids concentration made the particle pre-separated from the gas before entering the main body of cyclone (Wang et al., 1999). Generally, the inlet solids concentration of separators in CFB boilers that locates between 1kg/m^3 and 10kg/m^3 is much higher than that in the tests.

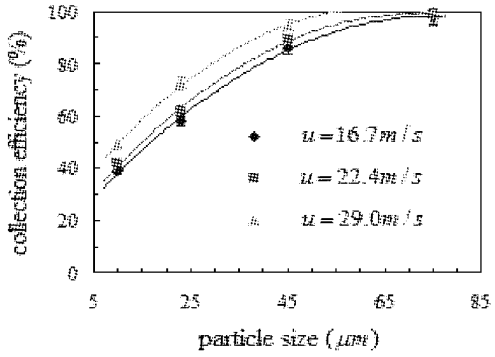

Fig. 4 Grade efficiency of the cyclone at different inlet velocities

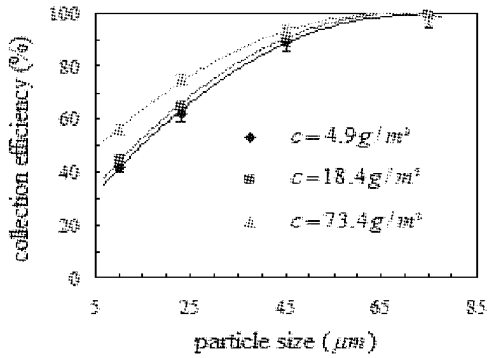

Fig. 5 Grade efficiency of the cyclone at different inlet solids concentrations

Pressure drop

The cyclone pressure drop is shown in Fig. 6 as a function of the inlet air velocity, for flow without particles, and, as expected, it increases with the inlet velocity. The pressure drop across cyclone is commonly expressed as a number named the pressure drop coefficient, which is the division of the pressure drop by the inlet kinetic pressure. The experimental data were fitted by equation:

$$\varepsilon = \frac{\Delta P}{\rho_g v_{in}^2 / 2} \tag{2}$$

Where ε is the pressure drop coefficient. ΔP is the pressure drop. ρ_g and v_{in} are the density and velocity of the inlet air. So the pressure drop coefficient for this square cyclone separator is about 1.7.

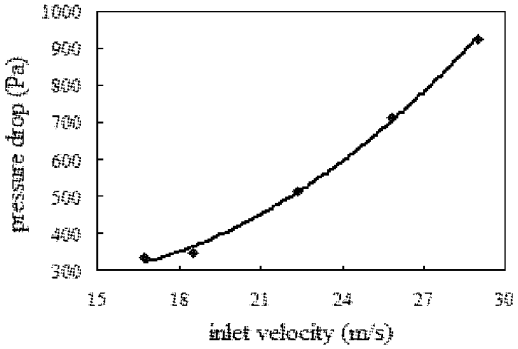

Fig. 6 Pressure drop without particles

For the particle laden flows tested, Fig. 7 shows the square cyclone pressure drop as a function of inlet solids concentration, with the inlet velocity as a parameter. As can be observed, the pressure drop increases with increasing velocity, and, for a given velocity, the pressure drop slightly decreases with the increase in the inlet solids concentration.

Gas- solid flow in cyclone

Figure 8 shows the measured pressure distribution at different sections in the square cyclone separator. The pressure distribution is very similar with that in the circular cross-section cyclone. At the section 1 (Z=80mm) near the inlet of the vortex finder, it can appear that the center low-pressure zone is surrounded by the high-pressure zone. The static pressure decreases from the wall to the center where a highly intensified forced vortex exists. The pressure gradient is large along the Y direction. But the pressure along the Y direction has almost no change at section 2 (Z=-400mm). This shows that, in the middle and lower taper, it does not form the good airflow field like the cylinder separator. Also we can see that the pressure values near the wall have litter change between the two sections. This indicates that the velocities at Y and Z directions are so small in comparison to the velocity at X direction near the wall, because the static pressure is transformed into the dynamic pressure in the cyclone.

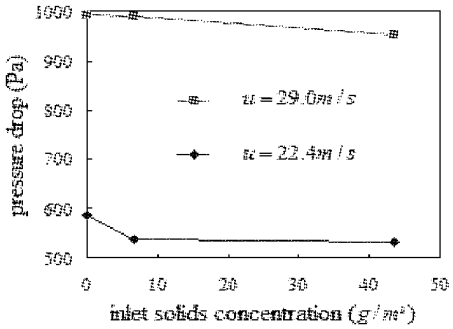

Fig. 7 Pressure drop with different inlet solids concentrations

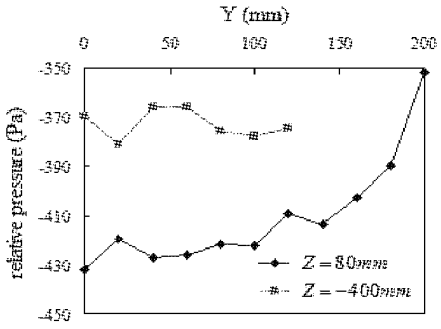

Fig. 8 Pressure distribution

There is an important phenomenon called instantaneous separation in the square cyclone with double inlets. The solid clusters rushed to the rear wall and moved along the wall to be separated from the gas at the high inlet solids concentration, as shown in Fig.9. The separation mechanism is very different from that at low inlet solids concentration. It was observed by Wang et al. (1999) in the square cyclone with single inlet and a separation model with sectional velocity was developed to predict the collection efficiency. But in the square cyclone separator with double inlets, the instantaneous separation just happened at the corner. Here the velocity of gas is much smaller than that of main air flow or the sectional velocity. So the instantaneous separation in square cyclone with double inlets is more significant than that in the square cyclone with single inlet and the circular cross-section separator. This is very helpful for the particle separation with high inlet solids concentration. Also, from the particle trajectory recorded by high-speed photography shown in Fig. 10 we can see that most part of particles into the cyclone swirl in the region near the wall, move to the corner and impact with the side and rear walls. Because the inlet width b reduces to a half compared with the cyclone separator with a single inlet, a little part of particles flow with the main air flow. Also some particles are carried by the main air flow after impacting with the wall and continue suffering rotational separation.

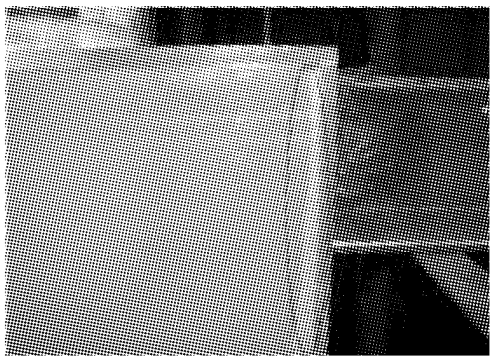

Fig. 9 Instantaneous separation

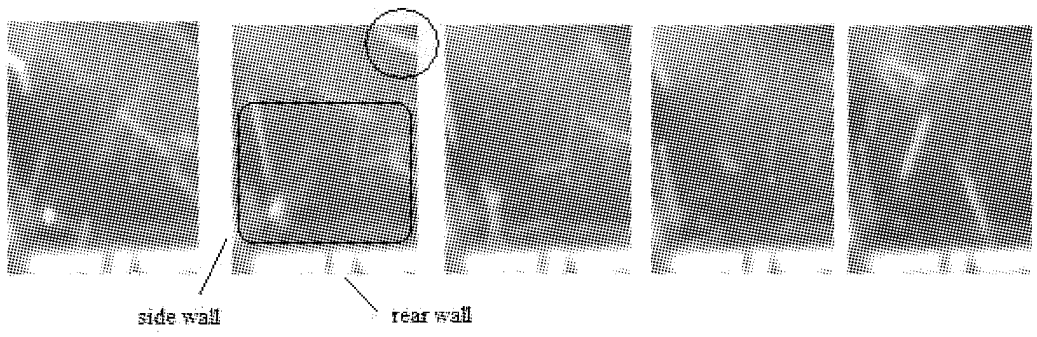

Fig. 10 Particle trajectory at the corner

CONCLUSIONS

A square cyclone separator with double inlets was developed for a new type CFB boiler arrangement scheme including two furnaces. Some experiments were completed in a cold test rig with a separator cross section 400mm×400mm. Experimental results show that:

(1) With the inlet velocity of 22.4m/s and the inlet solids concentration of 4.9g/m^3, the cut size is 15μm, the critical size is 75μm, and the pressure drop coefficient is 1.7. The cut size decreases with an increase in inlet velocity and inlet solids concentration. The pressure drop slightly decreases with increase in inlet solids concentration for a given inlet velocity.

(2) The trajectory recorded by high-speed photography illustrates that particles moving into the square cyclone swirl in the region near the wall and are easily separated on the cyclone wall because they only have to move a short distance to the wall.

(3) The instantaneous separation happened at the corner is very significant for the improvement of the collection efficiency with the high inlet solids concentration for CFB boiler.

NOTATIONS

a,A,b,B,d,D,De,h,H,S,R	dimensions of cyclone, mm
c	inlet solids concentration, g/m^3
ΔP	pressure drop, Pa
W_c	weight of particles at the inlet, kg
W_t	weight of particles at the dust outlet, kg
X,Y,Z	coordinates
v_{in}	inlet air velocity, m/s
η	collection efficiency, %
ε	pressure drop coefficient
ρ_g	air density, kg/m^3
i	particle size, μm

ACKNOWLEDGEMENTS

Financial support of this work from China Scholarship Council is gratefully acknowledged.

REFERENCES

Bai, Y. G., Lu, J. F., Liu, Q., Yue, G. X., Liu, B. S., Yang, Y. P., Yu, L. and Ma, M. H.: J. of Basic Sci. and Eng. 7 (1999a), pp.308-312.

Bai, Y. G., Lu, J. F., Yue, G. X., Liu, Q., Yang, Y. P., Ma, M. H. and Yu, L.: Ch. Powder Sci. and Technol. 5 (1999b), pp.1-3.

Darling, S. L. (1995). Pyroflow compact: the next generation CFB boiler. Int. Jnt. Pwr. Generation Conf.

Huang, Y. J., Lu, X. F. and Liu, H. Z.: J. of Pwr. Eng. 26 (2006), pp.49-53.

Lu, J. F., Jin, X. Z., Lu, X. M., Liu, Q. and Yue, G. X.: Ch. Powder Sci. and Technol. 3 (1998), pp.6-11.

Lu, J. F, Bai, Y. G, Liu, Q. and Yue, G. X.: J. of Basic Sci. and Eng. 8 (2000), pp.207-211.

Lu, J. F., Liu, Q., Zhang, J. S., Yue, G. X., Shen, J. G., Tang, G. Y., Su, X. P., Zhu, X. F. and Zhao, A. G.: Proc. of the CESS. 23 (2003), pp.178-182.

Makkonen, P. and Foster, W.:VGB Pwr. Technol. 80 (2000), pp.30-34.

Qiu, K. Z., Yan, J. H., Li, X. D., Pan, G. Q., Chi, Y., Ni, M. J. and Cen, K. F.: J. Eng. Thermal Energy Pwr. 14 (1999), pp.193-194, 199.

Su, Y. X. and Mao, Y. R.: Chem. Eng. J. 121 (2006), pp.51-58.

Wang, S. R., Fang, M. X., Luo, Z. Y., Li, X. T., Ni, M. J. and Cen, K. F.: Powder Technol. 102 (1999), pp.65-70.

Zhao, B. T., Shen, H. G. and Kang, Y. M.: Powder Technol. 145 (2004), pp.47-50.

GAS-PHASE COMBUSTION IN THE FREEBOARD OF A FLUIDIZED BED–FREEBOARD CHARACTERIZATION

Jean-Philippe Laviolette, Gregory S. Patience and Jamal Chaouki

Department of Chemical Engineering, Ecole Polytechnique, Montréal, Canada

Abstract: The prediction of propane autoignition in the freeboard of a fluidized bed is complicated by the presence of solids, intermediate products and non-homogeneities (solids, temperature and species gradients) that should be accounted for in a reaction model. However, the simultaneous characterization of these parameters during combustion is very challenging. An experimental study of propane combustion inside the freeboard (I.D. = 0.2 m) of a fluidized bed of sand (d_p = 290 μm) was performed at a low superficial gas velocity (U_g = 0.24 m/s). Propane was injected inside the fluidized bed (T_{Bed} = 650°C) through a downward-facing sparger. Also, solids flux and species volume fractions were measured using a non-isokinetic sampling probe. The results showed an exponential decrease with height of the upward solids flux (G_{SU}) – G_{SU} was zero at 0.17 m above the bed surface, which was taken as the inflection point of the G_{SU} curve. G_{SUo} measurements were significantly higher than the values given by the correlation of Wen *et al.* (1982). The bed surface (boundary condition) and freeboard were characterized by measuring pressure, solids flux, species volume fractions and temperature at several radial and axial positions. During the experiments, the fluidized bed achieved a pseudo steady-state operation that ensured that the measured temperature profile corresponded to the solids flux and species fractions. Partial propane combustion in the fluidized bed (71%) produced CO and cracking species that were transported in the freeboard. Complete combustion occurred within 0.15 m of the bed surface and the propane induction time in the freeboard (< 0.25 s) was on the same order as the values given by three induction time correlations for homogeneous systems.
Keywords: propane, freeboard, induction time, non-isokinetic sampling, combustion

INTRODUCTION

Homogeneous reactions generally result in yield lost of the desired compound, but they may also represent a significant safety hazard in the case of fast and highly exothermic reactions such as those involving oxygen and hydrocarbons. Chemical processes with oxygen and hydrocarbons are widespread in the industry and new processes are currently under development in the context of oil price fluctuations and global warming: selective oxidation of alkanes, combustion of cheaper feedstock for heating and catalyst regeneration, biomass gasification, etc. Fluidized bed reactors are currently being developed for a variety of these processes. In order to maximize productivity, they may operate within the explosion limits while feeding the oxidant and hydrocarbon separately into the bed – through spargers. This is possible due to the ability of the solids phase to suppress the homogeneous reactions (combustion) and at the same time promote selective heterogeneous reactions. However, downstream of the solids–in the freeboard, cyclones and associated piping – the effluent gas phase composition is potentially explosive–high hydrocarbon and oxygen concentrations, elevated temperature with an insufficient solids volume fraction to quench non-selective homogeneous reactions (Van der Vaart, 1988; Hesketh et al., 1991). Minimizing the risk of gas-phase combustion-deflagration in these regions remains an important design issue.

Several explosion criteria (explosion limits, autoignition temperature and induction times (Hesketh et al., 1991)) measured in homogeneous gas-phase systems as well as gas-phase kinetic models are available in the scientific literature (Marinov et al., 1998). Nevertheless, extrapolating these tendencies to a fluidized bed reactor introduces uncertainties since the entrained solid particles affect the gas-phase reactions downstream of the fluidized bed. Furthermore, fluidized beds are non-homogeneous systems - solids entrainment decreases exponentially from the bed surface to the transport disengagement height (Wen et al., 1982). Also, an axial temperature gradient may exist in the freeboard region as well as species concentration gradients depending on the hydrodynamics.

To accurately predict gas-phase combustion in the freeboard of a fluidized bed for a wide range of operational conditions, a freeboard combustion model that combines the gas/solids hydrodynamics and the reaction kinetics must be developed. This model needs to integrate through the axial gradient of solids fraction and temperature that characterize the freeboard as well as accounting for the effects of solids on the reaction kinetics. Furthermore, the model should account for the partial combustion and cracking product originating from the fluidized bed. On the other hand, the simultaneous characterization of solids fraction, species

concentration, temperature and pressure in the bed and freevoard during combustion is very challenging.

Freeboard reaction models have been previously proposed by Chen et al. (1982), Dounit et al. (2001) and Dounit et al. (2008). To estimate solids entrainment, the correlation of Wen et al. (1982) was used, which is based on the extrapolation of data measured several centimetres downstream of the bed surface (sometimes more than 0.5 m). Consequently, the existing entrainment models may yield significant errors near the bed surface and better accuracy would be obtained by directly measuring solids fraction. Also, the location of the bed surface (beginning of the freeboard region) and its corresponding boundary condition (solids fraction/flux, species fractions, temperature and pressure) need to be clearly defined.

In the present study, propane was injected inside a high temperature fluidized bed through a downward facing sparger and the freeboard region was characterized by simultaneously measuring pressure, solids flux, species volume fraction and temperature during freeboard combustion. Solids flux and species volume fractions were measured using a non-isokinetic probe. The temperature profile in the freeboard was monitored using eight thermocouples.

EXPERIMENTAL APPARATUS

The experiments were conducted in the fluidized bed reactor of Figure 1. The bed and freeboard regions had an inner diameter of 20 cm. For all experiments, sand particles (Gelda**R**t group B, ρ_s = 2650 kg/m^3 and d_p = 290 μm) were used as the bed material and air was the fluidizing media. The experimental procedure first consisted of adjusting the superficial gas velocity to 0.24 m/s (at 650°C). The fluidized bed was then heated with the natural gas burner upstream of the windbox and by injecting heavy vacuum gas oil (HVGO) through the sparger. When the bed temperature reached 680°C, the burner and HVGO injection were stopped and propane was injected through the sparger for 30 minutes to burn HVGO residues.

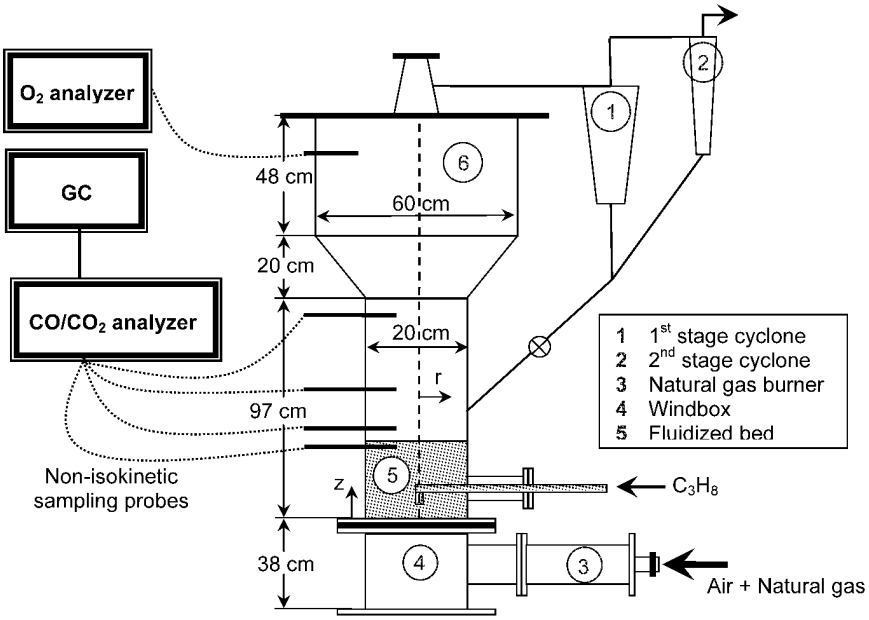

Fig. 1 Fluidized bed reactor

The propane was turned off and the fluidized bed cooled down until the bed temperature reached 645°C. Propane was then injected through the downward sparger to obtain a mixed-cup volume fraction of 2 vol% in air. A non-isokinetic probe was used to sample gas and solids simultaneous from 5 axial and 6 radial positions. The sampling system consisted of a 4.1 mm I.D. probe bent at a 90° at its tip. The sampled gas/solid stream first went through a 250 mL container that lowered the sampled gas velocity and caused the separation of the solid particles from the gas. The gas was analyzed by a Siemens Ultramat CO/CO_2 analyzer and a Varian CP-4900 micro-GC that measured the following species: O_2, H_2, CH_4, C_2H_4, C_2H_6, C_3H_6, C_3H_8, CO, CO_2 and N_2. Solids flux was calculated from the mass of the sampled solids and the sampling time.

The upward (G_{SU}) and downward (G_{SD}) solid fluxes were measured by orienting the probe tip downward and upward, respectively. The sampling flow rate was controlled using a rotameter connected to a vacuum line. Gas was also continuously sampled in the disengagement region (z = 1.47 m) and analyzed with an oxygen analyzer (Siemens Oxymat 6.1). The results from the GC, CO/CO_2 analyzer and oxygen analyzer were compared and used in a molar balance to confirm the validity of the measured species volume fractions. The

temperature along the reactor was monitored using 8 thermocouples located along the length of the reactor. The sparger consisted of a 4.1 mm I.D. tube pointing downward at the bed centreline. The sparger tip was located at a height of 0.098 m above the distributor.

RESULTS AND DISCUSSION

The reaction rate of propane combustion in the freeboard of a fluid bed depends on species volume fractions, temperature and solids fraction. They are dependent parameters and should be measured simultaneously.

Freeboard characterization

Simultaneous sampling of gas and solids

A non-isokinetic sampling probe was used to measure the species volume fractions and the solids flux simultaneously. A preliminary set of experiments showed that the measured solids flux was almost independent of sampling rate in the range of 270 - 470 mL/min. Therefore, it was not necessary to have sampling that was precisely iso-kinetic and a sampling rate of 425 mL/min was used for all experiments. Results also showed that a minimum sampling time of 60 seconds was required to reach a permanent condition. The gas sampled with the non-isokinetic sampling probes was sent to the CO/CO_2 analyzer and the GC for analysis. A sampling time of only 20 seconds was required for a representative measurement of the species volume fractions inside the reactor.

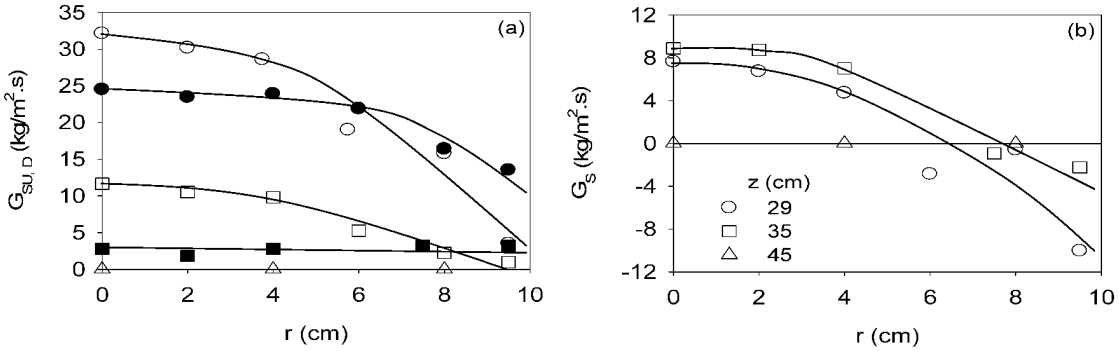

Fig. 2 Solids flux radial profile

Solids flux in the freeboard

Upward (G_{SU}) and downward (G_{SD}) solid fluxes were measured at 5 axial positions and 6 radial positions. The radial profiles of solids flux are shown in Figure 2(a) for three axial positions: 0.29, 0.35 and 0.45 m above the distributor. The upward (empty symbols) and downward (filled symbols) solids fluxes reached a maximum at the reactor centreline and decreased closer to the wall. The measurements were averaged over the fluid bed cross-section. At Z = 0.29 m, the upward and downward solids fluxes were 17.6 kg/m^{2}s and 19.0 kg/m^{2}s, respectively (difference of 1.4 kg/m^{2}s). At Z = 0.35 m, the upward solids flux was 4.7 kg/m^{2}s and the downward solids flux was 3.0 kg/m^{2}s (difference of 1.7 kg/m^{2}s). At Z = 0.45 m, the upward and downward solids flux were both zero. The radial profiles of net solids flux (G_S) are shown in Figure 2(b) for three axial positions: there was a net upward of solids at the centre of the reactor. Near the wall, there was a net downward flow of solids. This agrees well with the literature (Aguillón et al., 1995; Van Breugel et al., 1970; Rhodes et al., 1988).

At each axial position, the measurements were averaged over the fluidized bed cross-section. Figure 3(a) compares the upward solids flux of the present study with the values given by the correlation of Wen et al. (1982). The correlation of Wen et al. (1982) underestimated G_{SU} at the bed surface: the present study measured 17.6 kg/m^{2}s and the correlation estimated 8.18×10^{-4} kg/m^{2}s. Wen et al. (1982) derived the correlation by extrapolating measurements of Large et al. (1977) made at 0.50 m above the bed surface, which may explain the observed discrepancy.

Defining the bed surface

In the present study, a time-average position of the bed surface was determined by pressure and solids flux measurements. Figure 3(b) shows the time-averaged static pressure measured at 4 axial positions at the wall and the cross-sectional mean of G_{SU} measured at 5 axial positions and 6 radial positions. The pressure decreased significantly in the bed from 2.6 kPa to 0.3 kPa (Z = 0.05 to 0.25 m) and remained constant at 0.1 kPa (Z = 0.35 to 0.77 m) in the freeboard. This indicates that the bed surface was located between Z = 0.25 and 0.35 m.

The upward solids flux reached 17.6 kg/m^{2}s at a height of 0.29 m and then decreased exponentially to 4.7 kg/m^{2}s at Z = 0.35 m and zero at Z = 0.46 m. If the inflection point of the solid flux curve is taken as the bed surface as proposed by Kunii et al. (1991), the bed height (H_B) was 0.29 m. This agrees well with the pressure measurements.

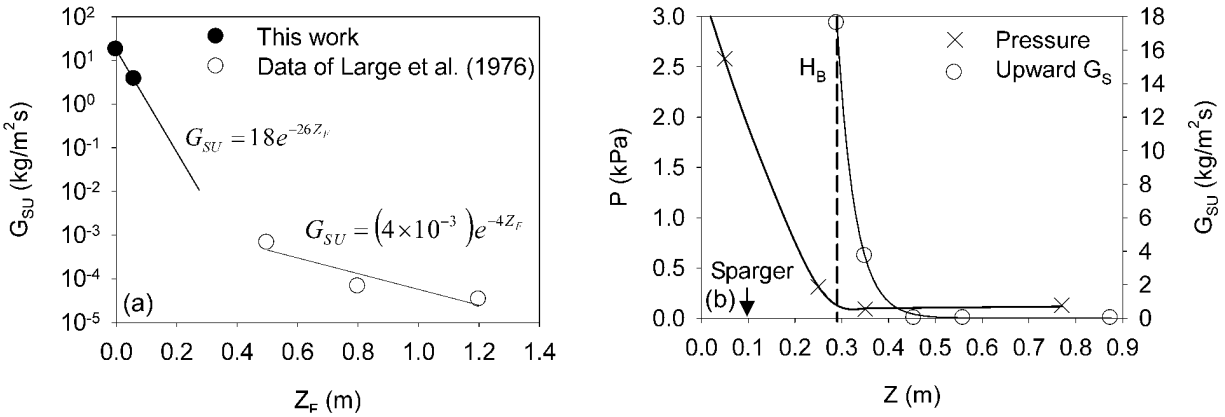

Fig. 3 Upward solids flux and pressure measurements

Temperature profile

The temperature profile inside the freeboard was monitored with eight thermocouples positioned along the length of the reactor. Two thermocouples were located inside the fluidized bed and six in the freeboard. Figure 4(a) shows the axial temperature profiles just prior to propane injection (t = 0 s) and after injection when one sample point was done (t ≈ 170 s). After injection, the temperature inside the fluidized bed and freeboard increased with time due to the exothermicity of the combustion reactions. Between each sample points, the propane was stopped to cool down the fluidized bed and freeboard. During combustion, a maximum temperature increase of 33°C was observed inside the freeboard. Using the chemical composition of the gas measured at the bed surface (z = 0.29 m) and assuming adiabatic constant pressure combustion, the theoretical temperature increase is calculated as 546°C from the CEA equilibrium code (Gordon et al., 1994). The temperature in the freeboard reached a maximum of 670°C during the experiments.

Figure 4(b) shows the temperature history of 5 thermocouples in the freeboard following the injection of propane at t = 0 s. After the sampling time of approximately 170 s, the temperature inside the reactor increased by a maximum of 2°C within 20 seconds, which was the required sampling time for a representative measurement of the species volume fractions inside the reactor. Therefore, the measured solids flux and species volume fractions corresponded to the temperature profile with an uncertainty of ±2°C.

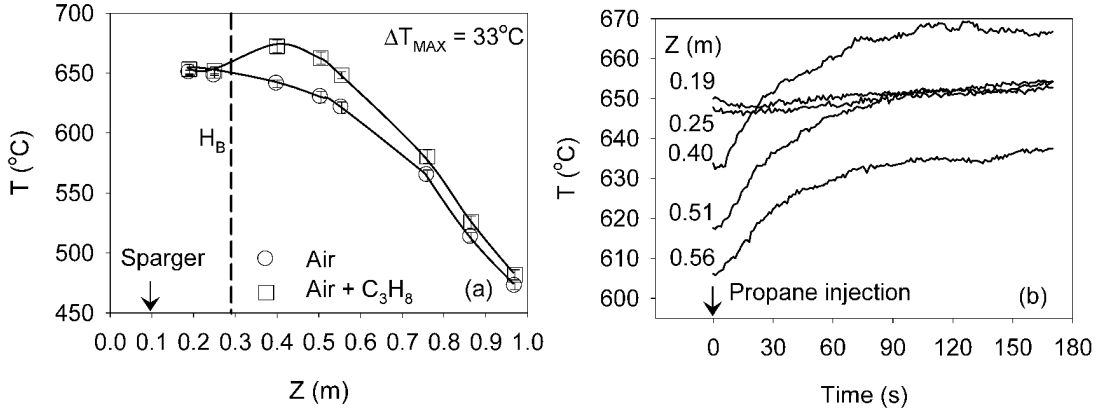

Fig. 4 Freeboard temperature profile

Species at the bed surface

Partial combustion of C_3H_8 inside the fluidized bed produced CO and CO_2. Furthermore, the high temperature resulted in C_3H_8 cracking. Figures 5(a) and 5(b) shows the volume fractions of C_3H_8, CO, H_2, CH_4, C_2H_4, C_2H_6 and C_3H_6 at the bed surface (Z = 0.29 cm). The volume fraction of C_3H_8 decreased from 0.9% at the centreline to 0.4% at 5 mm from the wall. The volume fractions of CO, H_2, CH_4, C_2H_4, C_2H_6 and C_3H_6 were approximately constant throughout the reactor radius at 0.45%, 0.07%, 0.01%, 0.06%, 0.04% and 0.04%, respectively.

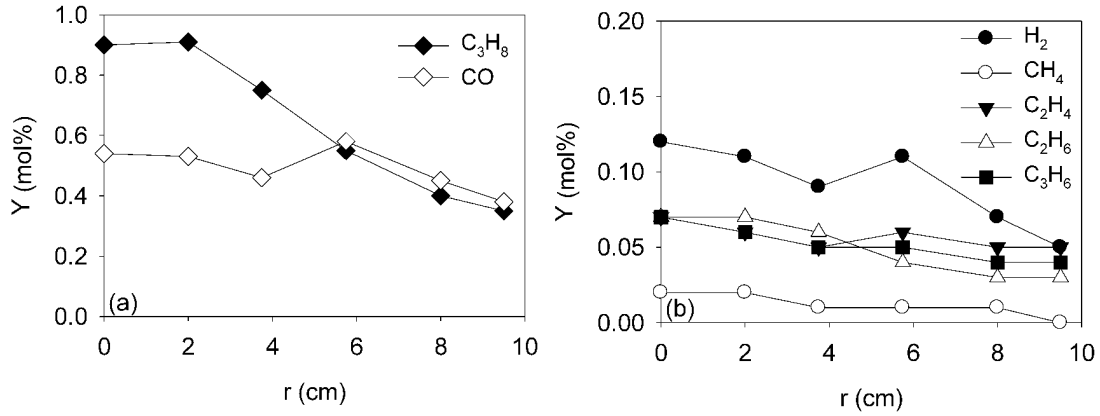

Fig. 5 Species at the bed surface

Freeboard combustion

Figures 6(a) and 6(b) show the axial profiles (cross-sectional average) of C_3H_8, CO, O_2 and CO_2 inside the fluidized bed reactor–propane conversion inside the fluid bed reached 71% as propane decreased from 1.77 vol% (mixed-cup) at the inlet to 0.51 vol% at the bed surface (Z = 0.29 m). In the freeboard, the remaining propane reacted with oxygen to form CO_2 and complete combustion was obtained at Z = 0.56 m (17 cm above the bed surface).

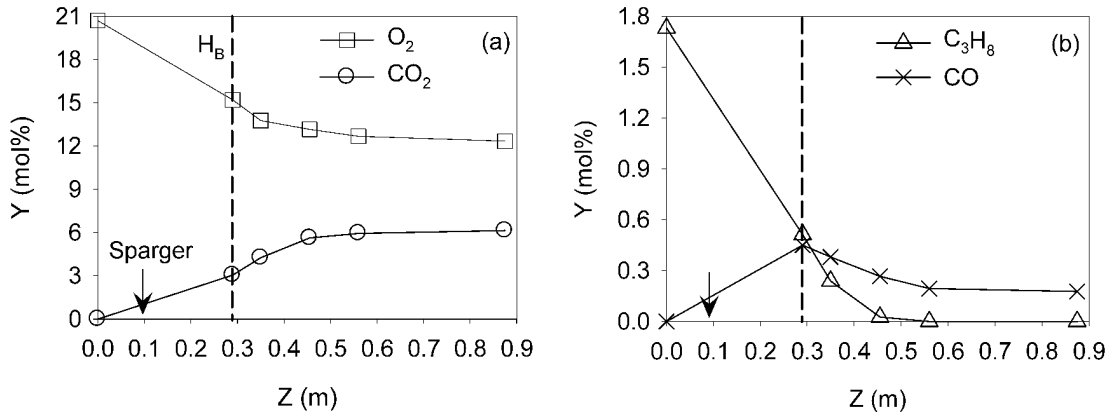

Fig. 6 Freeboard combustion

Table 1 compares the measured induction time with the values from three propane induction time correlations for homogeneous systems that are available in the scientific literature. The induction time is given for the bed temperature (650°C) and the maximum temperature observed inside the freeboard (670°C). Also, the C_3H_8 and O_2 at the bed surface were used. In the present work, the measured induction time was below 0.25 s, which was the gas residence time between the bed surface (Z = 0.29 m) and the next sampling point (Z = 0.35 m). Between these two sampling positions, a 53% decrease in propane was observed. The measured induction time was on the same order as the values given by the correlations.

Table 1 Induction time data

τ (s)		Reference
650°C	670°C	
0.28	0.18	Burcat et al., 1971
0.07	0.06	Penyazkov et al., 2005
0.68	0.33	Kim et al., 2001
< 0.25		This work

CONCLUSIONS

An experimental study of propane combustion inside the freeboard (I.D. = 0.2 m) of a fluidized bed of sand (d_p = 290 μm) was performed at low superficial gas velocity (U_g = 0.24 m/s). Propane was injected inside

the fluidized bed (T_{Bed} = 650°C) through a downward-facing sparger. Solids flux and species volume fractions were measured using a non-isokinetic sampling probe. The results showed an exponential decrease with height of the upward solids flux (G_{SU}) – G_{SU} was zero at 0.17 m above the bed surface, which was taken as the inflection point of the G_{SU} curve. G_{SUo} measurements were significantly higher than the values given by the correlation of Wen *et al.* (1982). The bed surface (boundary condition) and freeboard were characterized by measuring pressure, solids flux, species volume fractions and temperature at several radial and axial positions. During the experiments, the fluidized bed achieved a pseudo steady-state operation that ensured that the measured temperature profile corresponded to the solids flux and species fractions. Partial propane combustion in the fluidized bed (71%) produced CO and cracking species that were transported in the freeboard. Complete combustion occurred within 0.15 m of the bed surface and the propane induction time in the freeboard (< 0.25 s) was on the same order as the values given by three induction time correlations for homogeneous systems.

NOTATIONS

Symbols:			Subscripts:	
d_p	average particle size	μm	Bed	fluidized bed
G_S	solids flux	kg/m^{2}s	D	downwards
r	radial position	cm	F	freeboard
t	time	s	g	gas phase
T	temperature	°C	o	fluidized bed surface
U_g	superficial gas velocity	cm/s	s	solid phase
Z	axial position	m	U	upwards
Greek letters:				
τ	induction time	s		

REFERENCES

Aguillón, J., Shakourzadeh, K., Guigon, P.: Powder Technol. 83 (1995), pp. 79-84.

Botella, P., Lopez Nieto, J.M., Solsona, B.: J. Mol. Catal. A-Chem. 184 (2002), pp. 335-347.

Burcat, A., Lifshitz, A.: Proceedings of the 13th International Symposium on Combustion, Combustion Institute (1971), pp. 745-755.

Chen, L.H.,Wen, C.Y.: AIChE J. 28 (6) (1982), pp. 1019-1027.

Dounit, S., Hemati, M., Steinmetz, D.: Powder Technol. 120 (2001), pp. 49-54.

Dounit, S., Hemati, M., Andreux, R. Chem. Eng. J. 140 (2008), pp. 457-465.

Gordon S., McBride, B.J.: Computer program for calculation of complex chemical equilibrium compositions and applications. NASA RP-1311 (1994).

Hesketh, R.P., Davidson, J.F.: Combust. Flame 85 (1991), pp. 449-467.

Kunii, D., Levenspiel, O.: Fluidization Engineering, Butterworth-Heinemann, 1991.

Kim, K., Soo Shin, K.: Bull. Korean Chem. Soc. 22 (3) (2001), pp. 303-307.

Large J.F., Martinie, Y., Bergougnou, M.A.: J. Powders Bulk Solids Technol. 1 (1977), pp. 15-21.

Malleswara Rao, T.V., Deo, G.: Ind. Eng. Chem. Res. 46 (1) (2007), pp. 70-79.

Marinov, N.M., Pitz, W.J., Westbrook, C.K., Vincitore, A.M., Castaldi, M.J., Senkan, S.M., Melius, C.F.: Combust. Flame. 114 (1-2) (1998), pp. 192-213.

Morooka S., Kawazuishi, K., Kato, Y.: Powder Technol. 26 (1980), pp. 75-82.

Patience, G.S., Lorences, M.J.: Int. J. Chem. React. Eng. 4 (A22) (2006).

Penyazkov, O.G., Ragotner, K.A., Dean, A.J., Varatharajan, B.: Proceedings of the Combustion Institute, Elsevier Inc. (2005) pp. 1941-1947.

Reinhardt, B., Cordonnier, A., Florent, P.: Powder Technol. 101 (1999), pp. 81-90.

Rhodes, M.J., Laussmann, P., Villain, F., Geldart, D.: Circulating Fluidized Bed Technology II (Basu, P., Large, J.F. (eds)), Pergamon Press Oxford (1988), pp. 155-164.

Rhodes, M.J., Laussmann, P.: Powder Technol. 70 (1992), pp. 141-151.

Van Breugel, J.W., Stein, J.J.M., de Vries, R.J.: Proc. Instn. Mech. Engrs. 184 (1970), pp. 18-23.

Van der Vaart, D.R.: Fuel 67 (1988), pp. 1003-1007.

Van der Meer, E.H., Thorpe, R.B., Davidson, J.F.: Chem. Eng. Sci. 55 (2000), pp. 4079-4099.

Wen, C.Y., Chen, L.H.: AIChE J. 28 (1) (1982), pp. 117-128.

Werther, J.: Powder Technol. 102 (1999), pp. 15-36.

CHARACTERISTICS OF PYROLYTIC TOPPING IN FLUIDIZED BED FOR DIFFERENT VOLATILE COALS

R. Xiong, L. Dong, G. W. Xu`

State Key Laboratory of Multi-Phase Complex System, Institute of Process Engineering, Chinese Academy of Sciences, Beijing, 100080, China

Abstract: Coal is generally combusted or gasified directly to destroy completely the chemical structures, such as aromatic rings containing in volatile coals including bituminite and lignite. Coal topping refers to a process that extracts chemicals with aromatic rings from such volatile coals in advance of combustion or gasification and thereby takes advantage of the value of coal as a kind of chemical structure resource. CFB boiler is the coal utilization facility that can be easily retrofitted to implement coal topping. A critical issue for performing coal topping is the choice of the pyrolytic reactor that can be different types. The present study concerns fluidized bed reactor that has rarely been tested for use in coal topping. Two different types of coals, one being Xiaolongtan (XLT) lignite and the other Shanxi (SX) bituminous, were tested to clarify the yield and composition of pyrolysis liquid and gas under conditions simulating actual operations. The results showed that XLT lignite coals had the maximum tar yield in 823-873K and SX bituminite realized its highest tar yield in 873~923K. Overall, lignite produced lower tar yield than bituminous coal. The pyrolysis gas from lignite coals contained more CO and CO_2 and less CH_4, H_2 and C_2+C_3 (C_2H_4, C_2H_6, C_3H_6, C_3H_8) components comparing to that from bituminous coal. TG-FTIR analysis of tars demonstrated that for different coals there are different amounts of typical chemical species. Using coal ash of CFB boiler, instead of quartz sand, as the fluidized particles decreased the yields of both tar and gas for all the tested coals. Besides, pyrolysis in a reaction atmosphere simulating the pyrolysis gas (instead of N_2) resulted also in higher production of pyrolysis liquid.

Keywords: pyrolysis, topping, fluidized bed, ash

INTRODUCTION

Coal is not only the most abundant fossil fuel but also a significant potential resource for aromatic chemicals. However, presently coal is generally combusted or gasified directly, making the chemical structures containing in volatile coals completely destroyed into simple molecules like CO_2, CO, H_2 and H_2O. Coal topping refers to a process to extract the volatiles in coals into gas and liquid rich in aromatic chemicals in advance of combustion or gasification and thereby to take advantage of the value of coal as a kind of chemical structure resource. This idea can be easily realized in circulating fluidized bed (CFB) boilers, for which only a pyrolyzer is required to be mounted into the particle circulation line (i.e. the downcomer side). The pyrolyzer accepts both hot particles circulated and coal feedstock as its input streams so that coal is first pyrolyzed before it is forwarded into the riser combustor to burn off. As a consequence, the integrated system produces not only heat and electricity via the combustion inside the riser but also gas and liquid (tar) via the coal pyrolysis inside the pyrolyzer in advance of combustion.

Coal topping can be performed in downer (Wang et al. 2005), moving-bed and fluidized bed. However, in previous works, many studies generally focused on the coal topping via downer and moving-bed. Peng et al., (2007, 2008) conducted a simulation and experiments to investigate the pyrolysis characteristics of three high-volatile bituminous coals and the mixing behaviors of solid heat carrier and coal in moving-bed pyrolyzer. An essential shortcoming of the moving-bed reactor is its difficulty in mixing particles and maintaining an even temperature profile across the reactor, especially industrial-scale plants. Research about coal topping in small-size downer reactor showed that coal pyrolysis can finish in seconds, but the coal particles should be below 0.6mm in sizes for the use in downer pyrolyzer. Compared with downer, longer residence time is available for coal particles in fluidized bed, and coal particles in 0~12mm, which is also the acceptable size range for CFB boilers, can be treated. Besides, fluidized bed allows excellent mixing of particles, an issue particularly important to the pyrolysis using hot particles as heat carrier. Therefore, performing coal topping in a fluidized bed reactor integrated to the riser combustor should have some merits.

Noting that very few literature studies were done to characterize the liquid and gas productions via fluidized bed coal pyrolysis, this work is devoted to investigating the effects of various parameters simulating the possible conditions for coal topping upon the pyrolysis products in a quarz-glass fluidized bed reactor. The tested parameters include temperature, coal type, reaction atmosphere and bed material particles.

Implementing coal topping in a CFB boiler requires the use of circulated coal ash particles to supply the entailed endothermic heat of coal pyrolysis, the mental oxides containing in the ash thus may affect the pyrolysis significantly. The aspects, however, were rarely considered in literature studies.

EXPERIMENT SECTION

Fuels

Two types of high volatile coals (XLT lignite, SX bituminous coal) were used in this work. The proximate and ultimate analyses are given in Table 1. The coal was dried at 383K for three hours before experiments, and coal particle size was from 4mm to 6mm.

Table 1 Proximate and ultimate analyses for dried coals

Coal type	Proximate analysis[wt.%]				Ultimate analysis[wt.%]				
	M_{ad}	V_{ad}	A_{ad}	FC_{ad}	C_{ad}	H_{ad}	S_{ad}	N_{ad}	Q_{ad}
XLT	4.44	48.98	13.40	33.20	56.38	3.57	1.56	1.30	19.35
SX	1.71	31.21	18.20	48.88	64.58	4.08	0.62	1.1	9.71

Apparatus and method

Experiments were performed in a quartz fluidized bed reactor electrically heated. Figure 1 shows that the schematic diagram of experimental apparatus. The reactor, with an inner diameter of 60mm and a height of 700 mm, had a porous quartz plate to hold bed materials. The height of static bed material is 350mm. A K-type thermocouple located below 10mm of the bed surface was employed to measure the bed temperature. The bed materials in fluidized bed reactor were quartz sand and coal ash from CFB boiler with particle sizes from 0.212mm to 0.38mm. Table 2 lists the XRF analyses of coal ash.

In the experiments, the superficial velocity of fluidized gas was 4.05m/min. 10 g dry coal was fed quickly into the reactor by a two-stage valve. The liquid products from coal pyrolysis were collected by acetone, while the gas products were collected by gas collection bags. The gas products were analyzed by a two-channel micro gas chromatograph (Agilent 3000A, Germany, Agilent Technologies, Inc.), and the volume of gas product was measured by a wet gas-flow meter. The tar was analyzed by TG-FITR (TG, NETZSCH STC409; FTIR, NEXUS670).

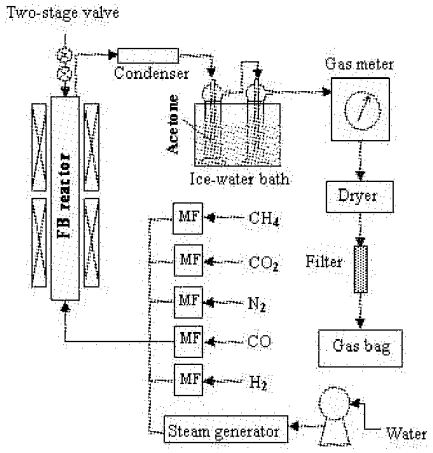

Fig. 1 Experimental system

Table 2 XRF analyses of coal ash

Compounds	SiO_2	Al_2O_3	CaO	Fe_2O_3	SO_3
Concentration (wt. %)	41.17	20.70	18.15	7.23	6.51

In order to investigate the effect of reaction atmosphere, the simulated pyrolysis gas was used in some experiments, which was composed with H_2 (22.89, vol. %), CH_4(21.12%), CO(28.79%) and CO_2(27.19%) according to the average composition of gas product from XLT coal pyrolysis at 823K and 873K in N_2 with quartz sand as bed material.

RESULTS AND DISCUSSION

Effect of residence time

A series of experiments were carried out to determine an optimal residence time for coal pyrolysis in fluidized bed reactor. The results in Figure 2 show that the tar yields of XLT coal and SX coal increase significantly from 0 to 120s, and increase slowly from 120s to 180s. Furthermore, no obvious increase was observed after 180s. According to the change of tar yield, it can be considered that coal pyrolysis would finish within 180s in the fluidized bed reactor based, which mainly results from the excellent heat-transfer performance in fluidized bed, while it needs 240-480s to finish the coal pyrolysis in moving bed. In the following study, all fuel samples were pyrolysed in the fluidized bed reactor for180s.

Effect of pyrolysis temperature

Pyrolysis temperature affects greatly the tar yield, gas yield and gas composition distribution. Figure 3 shows that the maximum tar yield appeared at 823~873K for XLT coal and at 873~923K for SX coal. It is reported (Wang et al., 2005; Cui et al., 2006) that the competition between coal pyrolysis and tar cracking contributed to this phenomenon. Besides, Fig. 3 also shows that pyrolysis gas yields monotonically increased with raising the reaction temperature.

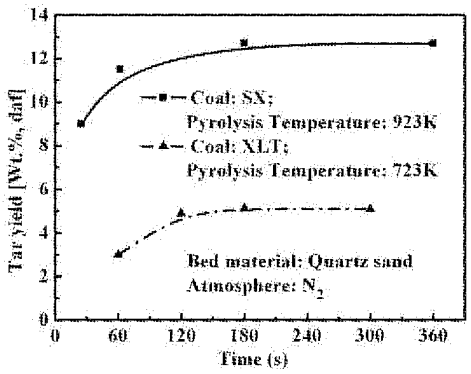

Fig. 2 Variation of tar yield with reaction time

Figure 4 presents the evolvement of major components in gas product with the increase of pyrolysis temperature. For two coal samples, the compositions of H_2, CH_4 and CO increase with the increase of pyrolysis temperature, while that of CO_2 does not change. Previous studies(kenji et al. 2002) indicated that CO_2 is mainly produced via decomposing carboxyl groups. In the pyrolysis process over 673K, there would be less carboxyl groups remained, which suggested that the increase of pyrolysis temperature from 723K to 973K cannot result in the increase of CO_2. However, because CO was produced from the decomposition of carbonyl groups (~673K), the break of oxygen heterocycle (>773K) and the reaction between CO_2 and carbon (>923K), CO can be formed at different temperatures, leading to the increase of CO with increasing pyrolysis temperature. Moreover, CH_4 was produced from the rupture and hydrogenation of methyl side chains (<873K) and cross-linking reaction of coal macromolecule (873~1073K), and H_2 was from the C-H bond and hydrogen sources in coal, which were reported to break at wide temperature. Both CH_4 and H_2 in gas product therefore increased with the increase of pyrolysis temperature, just as shown in Figure 4.

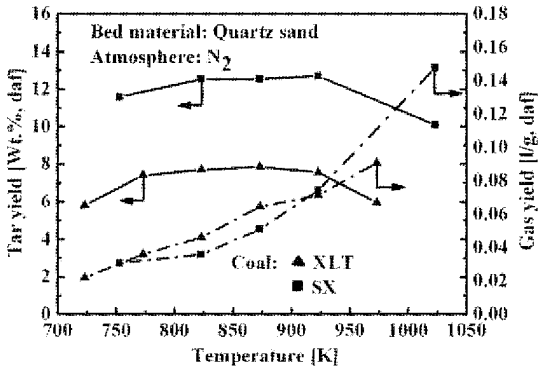

Fig. 3 Effect of temperature on tar and gas yields

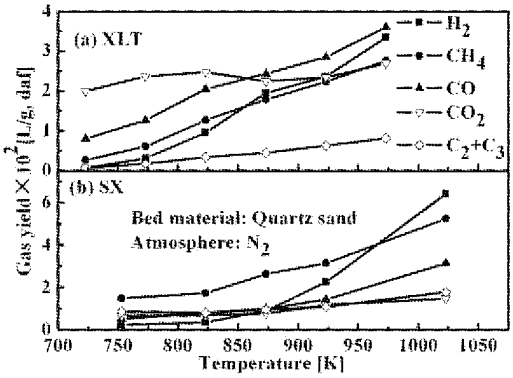

Fig. 4 Effect of temperature on gas products

Effect of coal types

Figure 3 shows that SX bituminous produced a higher tar yield than XLT lignite .Figure 4 shows that XLT lignite pyrolysis produced higher CO and CO_2 yields while lower H_2 and CH_4 than SX bituminous at the selected temperature. It has been known that the coalification factually is the process to form large molecular structure via the aromatization and polymerization. Bituminous coal has a longer coalification process than lignite, making bituminous coal less side chains (-COOH, $-C_xH_y$, -OH) left compared to lignite and making larger molecular structures be in bituminous coal. Therefore, there are less CO and CO_2 in gas products because of the lack of carboxyl groups. Besides, Because tar was produced by cracking the large molecular aromatic structure and SX bituminous coal had the longer coalification process than XLT lignite, SX bituminous coal produced more tar, and the temperature for the maximum tar yield was 873-923K, which was higher than that of 823~873K for XLT lignite, as shown in Fig. 3.

Figure 5 shows that the TG-FTIR analysis of tar. The TG results in Figure 5(e) present that tar from SX bituminous coal had less weight lost than that from XLT lignite at the same temperature, which indicated that the percentage of heavier component in tar from SX bituminous coal was higher than that from XLT lignite. Moreover, the comparative FTIR results in Figures 5(a) and (b) show that tar from SX bituminous coal would release much more CO and CO_2 than that from XLT lignite. It has been known that low rank coal, such as XLT lignite, had more oxygen content than high rank coal, such as SX bituminous coal. Oxygen in low rank coal mainly was existed in the carboxyl and hydroxyl as the side chains of aromatic rings, which favored more

oxygen to form CO_2, CO and H_2O in coal pyroysis process at low temperature, and made less oxygen be contained in tar. However, in high rank coal most of oxygen was in the oxygen heterocycles, which were hard to be destroyed at low pyrolysis temperature so that most of oxygen was left in the large molecular structure of tar or char. In the FTIR analysis of both tars, most of CO and CO_2 were detected from 1073K, and there were more CO and CO_2 released during the thermal decomposition of tar from SX bituminous. It may be concluded that the break of oxygen heterocycle was the major source of CO and CO_2 and tar from bituminous coal contained more oxygen heterocycles. According to Figure 5(c), tar from XLT lignite had more aliphatic carbon-hydrogen bond. Because lignite contained more aliphatic side chain than bituminous coal, and it was more difficult to remove the aliphatic side chains, such as methyl groups, than to break the oxygen functional groups, such as carboxyl groups, more aliphatic side chains would be distributed into tar when XLT lignite was pyrolysed. However, in Figure 5(d) less aromatics can be detected in the tar from XLT lignite compared with SX bituminous coal because of the lower coalification degree of XLT lignite.

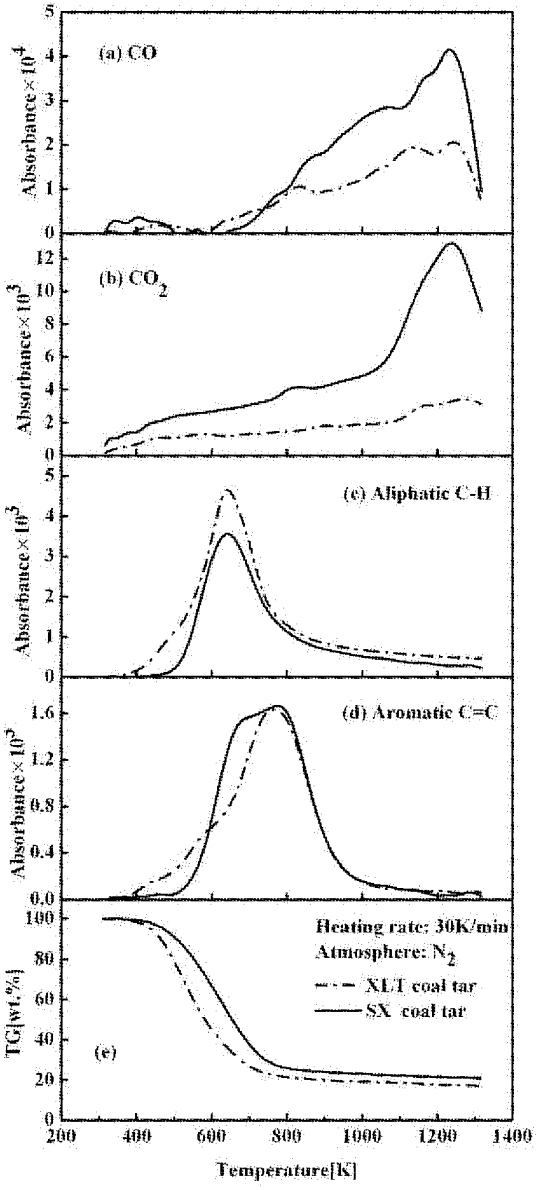

Fig. 5 TG-FTIR analysis of produced tar

Effect of coal ash as bed material

In the integrated system with coal topping technology, coal ash is used as heat carrier to heat coal particles. In this work, experiments were carried out to investigate the effect of coal ash on coal topping, in which the used coal ash was from CFB boiler, and its XRF analyses was lists in Table 2.

Figure 6 and Figure 7 shows that the effects of coal ash on the tar and gas products. It is clear that when coal ash was used as the bed materials, tar yields and gas yields of two coals decreased to some extent, and all compositions of the gas products suffered the yield drop. As shown in Table 2, coal ash contained a variety of mental oxides and CaO. The presence of CaO in coal ash would be the important reason for the decrease of tar yield because CaO can facilitate the tar decomposition(Shiying L et al. 2003). However, although it was reported that all gas product compositions except for CO_2 in coal pyrolysis can be improved by CaO, the results in Figure 6 and Figure 7 show that the yield of all gas compositions decreased when coal ash was used as the bed material in the fluidized bed reactor. This different phenomenon could result from the presence of mental oxides (MO_x), such as Fe_2O_3 in coal ash, which can react with the major components of gas products as follows:

$$M_xO_y + H_2 \longrightarrow M + H_2O, \quad M_xO_y + CO \longrightarrow M + CO_2, \quad M_xO_y + C_xH_y \longrightarrow M + H_2O + CO_2$$

Effect of atmosphere

Figure 8 shows that the tar yield from XLT lignite and SX bituminous when N_2 was replaced by simulated pyrolysis gas, which was consisted of H_2, CH_4, CO and CO_2 as shown above. It is clear that the introduction of pyrolysis gas can improve the formations of tar from both coals. Previous studies reported the presence of H_2 improved the tar yield at low heating rate(M et al., 2005, Rene et al., 1981) while decreased the tar yield at high heating rate(W. et al., 2003, H. et al., 2005, Zhang et al., 2008). In this work, because coal particles were pyrolyzed in the fluidized bed reactor, which was characterized by the high heating rate, it can be deduced that the presence of H_2 played a negative influence on the tar yield from coal pyrolysis. Compared with H_2, CH_4 and CO are favorable to the formation of tar because CH_4 can suppress the hydrodealkylation, and CO can suppress

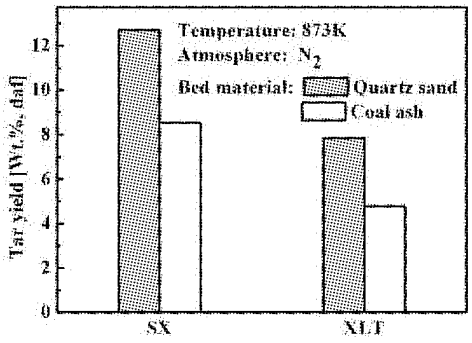

Fig. 6 Effect of coal ash on tar yield

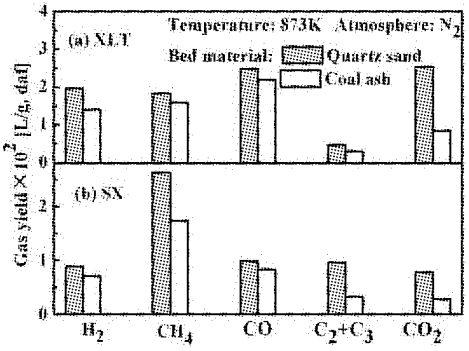

Fig. 7 Effect of coal ash on gas product

the second cracking of dimethylphenol, while CO_2 was considered as a negative composition for tar yield because it would react with volatile vapor to produce CO in coal pyrolysis. According to the above discussion, it can be concluded that the influence of pyrolysis gas on coal topping is the synergetic effect of H_2, CH_4, CO and CO_2, and in fluidized bed, the introduction of pyrolysis gas into coal topping process would increase the tar yield.

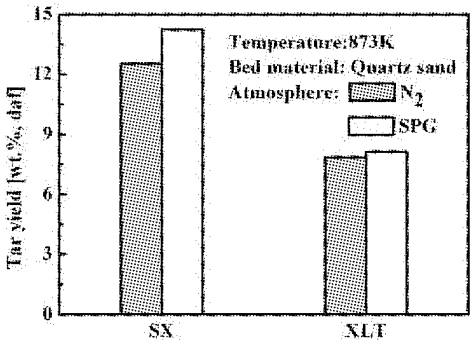

Fig. 8 Tar yields in reaction atmosphere of simulated pyrolysis gas

Furthermore, steam is present in coal pyrolysis, especially lignite. In previous studies, it has been reported that the presence of steam increased the tar yield at low heating rates, while decreased the tar yield at high temperature (1173K). However, in the coal topping process performed in fluidized bed, less influences of steam on the yields of tar and gas and the compositions of gas products can be detected, as shown in Figure 9. Two factors might contribute to this difference: First, coal in this work was pyrolyzed at high heating rates (>10^3Ks^{-1}) for only 3 minutes, while 30 minutes were used in the studies at low heating rate. The fast pyrolysis resulted in less reaction opportunities between steam and volatile vapor; second, the pyrolysis temperature in this work was 873K, which can hardly improve the reaction of gasification and reforming reaction between pyrolysis products and steam. Thus, there is little influence of steam on the coal topping in fluidized bed. However, Figure 10 shows that the presence of steam in the carrier gas increased the yield of H_2, which might be produced by the reaction between hot char and the steam. Comparatively, steam placed slight influence on other compositions in the gas product.

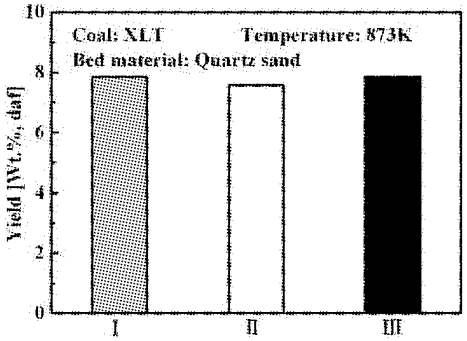

Fig. 9 Effect of steam on tar yield (Atmosphere: I N_2; II 20 vol.% N_2+80 vol.% steam; III 50 vol.% N_2+50 vol.% steam)

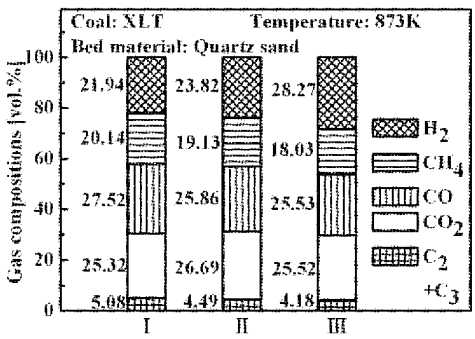

Fig. 10 Effect of steam on pyrolysis gas composition (Atmosphere: I N_2; II 20 vol.% N_2+80 vol.% steam; III 50 vol.% N_2+50 vol.% steam)

CONCLUSIONS

Coal topping is an advanced technology to convert coal not only into energy but also into chemicals through an integrated pyrolysis before its combustion for generating energy. It is easy to realize coal topping in CFB boilers, where a pyrolyzer installed in the solid circulation line can use the heat of circulated hot particles to pyrolyze coal. This pyrolysis can be in different types of reactors, and the use of a fluidized bed

reactor possesses some merits from the viewpoint of large-scale commercialization. The present article investigated experimentally the characteristics of liquid and gas production from coal pyrolysis in a quartz glass fluidized bed reactor under conditions simulating the coal topping in CFB boilers. Particular attentions were paid to reveal the effects of conditional parameters like residence time, temperature, coal types, reaction atmosphere and bed material. The obtained major conclusions include:

(1) The highest liquid yield appeared at the pyrolysis temperatures between 823 and 923K for both the tested coals, XLT lignite and SX bituminous.

(2) Lignite had lower tar yield than bituminous coal while the pyrolysis gas from lignite contained more CO and CO_2 and less CH_4, H_2 and C_2+C_3 components comparing to that from bituminous coal.

(3) Using coal ash as bed material significantly decreased the yields of tar and gas. It was shown that the reactions between the pyrolysis products (light tar gas, H_2, CO, CO_2) and the metal oxides (Fe_2O_3, CaO, etc.) in the combustion ash should be responsible for the result. .

(4) Pyrolysis in an atmosphere simulating pyrolysis gas containing H_2, CO, CO_2 and CH_4 elevated tar production, whereas the addition of steam into the atmosphere affected little the tar yield.

REFERENCES

Wang, J. G.; Lu, X. S.; Yao, J. Z.; Lin, W. G.; Cui, L. J.. Experimental Study of Coal Topping Process in a Downer Reactor. Ind. Eng. Chem. Res. 2005, 44, 463-470.

Cui, L. J. ; Lin, W. G.; Yao, J. Z.. Influences of Temperature and Coal Particle Size on the Flash Pyrolysis of Coal in a Fast-entrained Bed. CHEM. RES. CHINESE U. 2006, 22(1), 103-110.

Peng, L.; Wang, Z. F.; Bi, J. C.. Simulation of coal pyrolysis by solid heat carrier in a moving-bed pyrolyzer. Fuel. 2008, 87, 435-442.

Peng, L.; Wang, Z. F.; Bi, J. C. Process characteristics investigation of simulated circulating fluidized bed combustion combined with coal pyrolysis. Fuel Processing Technology, 2007, 88, 23-28.

Kenji M, Ryuhei K, Kiyoshi F, and Toshiaki M. Acidity distribution of carboxyl groups in Loy Yang brown coal: its analysis and the change by heat treatment. Journal of Colloid and Interface Science 260 (2003) 176-183.

Shiying L, Michiaki H, Yoshizo S, and Hiroyuki H. Comparison of Pyrolysis Products between Coal, Coal/CaO, and Coal/Ca(OH)2 Materials. Energy & Fuels 2003, 17, 602-607.

M. Canel, Z. M, A. S. Hydropyrolysis of a Turkish lignite (Tuncbilek) and effect of temperature and pressure on product distribution. Energy Conversion and Management. 2005, 46: 2185-2197.

Rene Cypres and Samuel Furfari. Fixed-bed pyrolysis of coal under hydrogen pressure at low heating rates. Fuel, 1981, 60: 768-778.

W. C. Xu, M. K, et al. High pressure hydropyrolysis of coals by using a continuous free-fall reactor. Fuel, 2003, 82: 677-685.

H. Yabe, T. Kawamura, et,al. Development of Coal Partial Hydropyrolysis Process [J]. Nippon Steel Corporation technical report, 2005,382: 8-15.

Zhang, X. F.. Study on Coal Gasification and Pyrolysis Based on Decoupling Conversion. Master Thesis (Chinese). Beijing University of Chemical Technology. 2008.

FLUIDISED BED COMBUSTION OF TWO SPECIES OF ENERGY CROPS

P. Abelha, C. Franco, H. Lopes, I. Gulyurtlu, I. Cabrita

INETI-DEECA, Est. Paço Lumiar, 22, 1649-038 Lisboa, Portugal

Abstract: The use of biomass fuels for energy production through combustion has a growing application worldwide mainly for two reasons: first, the utilization of biomass for energy contributes to mitigate emission of green house gases; second, its use decreases the dependence of imported fossil fuels in Europe. The objective of this work was to study the combustion behaviour of two endogenous biomass species: cardoon (cynara cardunculus) and arundo (arundo donax), which were specially produced in energy crops plantations. Mixtures of cardoon and a forestry biomass specie (eucalyptus) were also studied to evaluate potential benefits from synergies between both biomass fuel types. The results showed that the utilization of cardoon, in pelletized form, and loose arundo as feedstock, did not give rise to any operational problems related with the feeding system. It was verified that the mono combustion of cardoon could pose problems at industrial scale in fluidised bed systems, considering the high levels of HCl and NO_X emissions obtained and tendency to sinter the bed sand material. The addition of the forestry biomass to cardoon appeared to prevent the bed agglomeration problem. Furthermore, both the NO_X and SO_2 emissions were found to decrease at the same time suggesting potential synergy of blending different types of biomass regarding pollutant emissions and in bed agglomeration problems.

Keywords: energy crops, cynara cardunculus, arundo donax, fluidised bed combustion, gaseous pollutants, biomass

INTRODUCTION

The use of biomass fuels for energy and/or heat production through combustion processes is becoming extremely attractive worldwide and is being supported by national economic incentives for electricity production from renewable sources, mainly because of two reasons. First, the utilization of biomass contributes to decrease emissions of CO_2 due to its renewable nature, although CO_2 associated to the production/handling chain must be accounted for. Second, the dependence of imported fossil fuels in Europe could decrease, both because of economical and geo strategic reasons. Biomass has wide potential as energy source in Portugal and other European countries, since significant amounts are generated from forest management activities, from agriculture and agro-industrial activities and municipal solid wastes production. However, experience has shown that the availability of biomass could become a serious barrier for its extensive use for energy due to its seasonal availability and multiple uses. The production biofuels based on energy crop plantations may contribute to diversify the biomass resources and to assure security of supply, particularly for small decentralized installations.

The objective of this work was to study the combustion behaviour, under fluidised bed conditions, of cardoon (cynara cardunculus) and arundo (arundo donax), which were produced in dedicated energy plantations. Mixtures of cardoon and forestry biomass specie, eucalyptus, were also studied to evaluate eventual benefits from synergies of mixing different types of biomass regarding the combustion process, pollutant emissions and ash behaviour that may contribute to decrease environmental and technical impacts of utilization of these energy crops. This work was undertaken in an electrically heated cylindrical lab-scale fluidised bed with 0.08 m ID and 5 m height. The bed temperature was around 730 °C, with an excess air varying in the range of 20-50 %. Continuous measurements for O_2, CO_2, CO, NO_X and SO_2 were carried out in flue gases leaving the combustor and the HCl content was determined through bubbling combustion gases in a sampling train with impingers, using distilled water as sampling solution. In some runs dolomite was used to evaluate its effects in reducing bed agglomeration tendency and gaseous pollutant emissions. Some interesting results were obtained during the course of this work and are presented below.

EXPERIMENTAL

Experimental Installation

The combustor is a bubbling fluidised bed that operates at atmospheric pressure. It is a refractory steel tube, circular in cross-section with an inside diameter of 80 mm and has 1500 mm total height. The combustor is located inside an electrical furnace, which provides the heat for fuel ignition and constant combustion

temperature. The combustor has three independent heating zones which have PID control. Along the reactor, there are various points to measure temperature and pressure.

The fuel is supplied to the combustor above or in-bed, depending on bed height, by a continuous feeding system, composed of a set of two screw feeders. The dosing feeder which is connected to the bottom of the silo was previously calibrated for the mixture to be studied, with the help of an electronic frequency controller. The feedstock in the silo is permanently agitated to avoid blockage, by a mixer connected to the shaft of the screw through two cogwheels. The dosing feeder discharge the fuels to the screw feeder which is connected to the combustor and rotates at a fixed and fast speed in order to avoid the pyrolysis of the feedstock during feeding. In order to avoid the clogging of the tube which could be caused by pyrolysis of the feedstock prior to its entry to the combustor the feeder is externally water cooled. An auxiliary air flow is used to help the waste feeding and to avoid a back flow of the gas.

The combustion/fluidising air is introduced through a gas distributor located in the top of the windbox at the bottom end of the combustor, and secondary air is fed 0.3 m above bed. The flue gases leave the combustor, passing through a cyclone to remove particles prior to be sampled to on-line CO, CO_2, O_2, SO_2 and NO_x analysers. The bed material was composed by silica sand particles of 360 μm of average diameter. A photograph of the installation is presented in Fig. 1 and in Table 1 the operating conditions are given.

Table 1 Operating conditions

Experimental Parameter	Variation Range	Experimental Parameter	Variation Range
Bed temperature (°C)	730 - 745	Excess air - real (%)	25-50
Flow rate of biomass (g/min)	≅ 4.7	Primary/secondary air	70/30
Flow rate of air (g/min)	≅ 23.2	Pressure	Atmospheric

The biomass was supplied in bed under different forms: cardoon was fed in pelletized form (20-30 mm x 5 mm); loose arundo and eucalyptus were used milled below 5 mm. The fluidising velocity was between 0.30-0.35 m/s, depending on the level of excess air. The bed temperature was maintained below 750 °C to minimize bed agglomeration problems associated with the presence of low melting point ash compounds, containing Na or K silicates. The freeboard temperature was imposed by the electric furnace to obtain a similar temperature profile as expected when operating the INETI's pilot installation burning similar biomass materials (Gulyurtlu et al., 2007 and Gulyurtlu et al., 2005) (see Fig. 2).

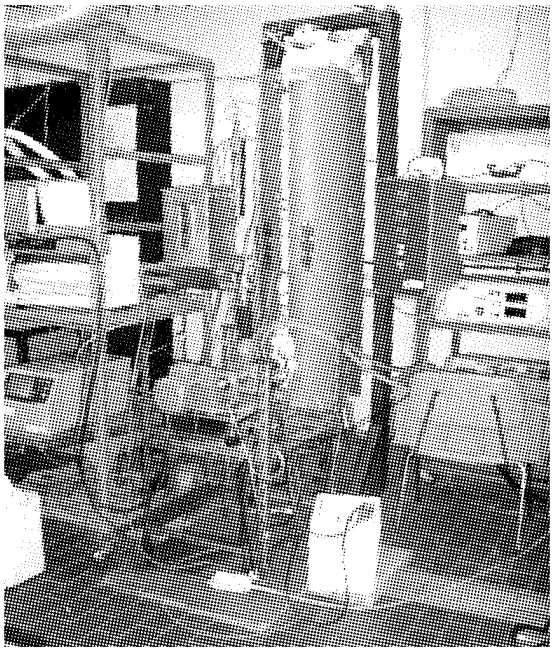

Fig. 1 Bench-scale combustion installation

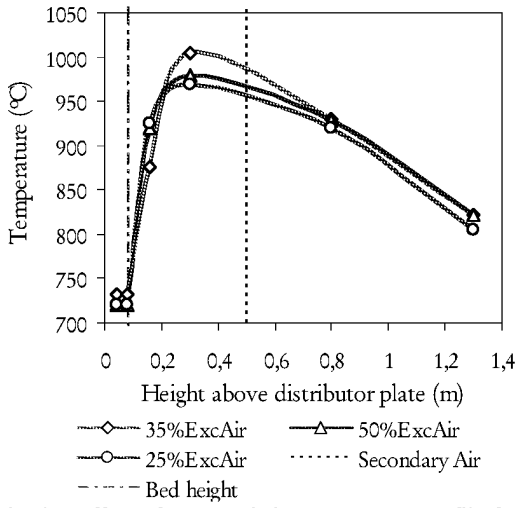

Fig. 2 Effect of excess air in temperature profile for combustion of 100% cardoon; Tbed=730°C

Fuel Characterization

Analyses of arundo, cardoon and eucalyptus are shown in Table 2. Like any other biomass fuels of similar origin (energy crops), the arundo and cardoon presented significant levels of ash, higher than that of eucalyptus,

low fixed carbon and high volatile matter and oxygen content. The nitrogen levels of arundo and eucalyptus were relatively low when compared to normal bituminous coals, usually used for energy production (1-2%). However, special attention should be paid to nitrogen oxide formation during the combustion of cardoon since its nitrogen content reached 1.7%. Sulphur was also detected, in higher amounts in the cardoon, hence the use of adsorbents during its combustion was evaluated to prevent SO_2 emissions.

Table 2 Feedstock Analysis (db - dry base)

	Arundo	Cardoon	Eucalyptus
HHV (MJ/kg db)	16.74	18.84	17.12
Moisture (%)	8.4	13.1	9.8
Ash (% db)	8.5	6.2	2.1
Vol. Matter (% db)	75.3	76.9	87.0
Fixed Carbon (% db)	16.2	16.9	10.9
Carbon (% db)	45.9	49.3	52.6
Hydrogen (% db)	5.6	6.1	5.2
Nitrogen (% db)	0.7	1.7	0.3
Sulphur (% db)	0.15	0.29	0.07
Chlorine (% db)	0.16	0.47	0.01
Oxygen & errors (% db)	39.2	36.5	39.7
Al_2O_3 (% of ash)	0.44	0.80	0.32
CaO (% of ash)	2.96	10.4	49.3
Fe_2O_3 (% of ash)	0.44	1.16	5.20
K_2O (% of ash)	21.5	13.7	14.0
MgO (% of ash)	2.21	5.39	6.30
Na_2O (% of ash)	1.01	21.5	3.78
SiO_2 (% of ash)	54.3	15.5	1.30
P_2O_5 (% of ash)	3.82	1.92	2.40
Ash Fuzibility (oxidante)			
Shrinkage Temperaure	558 ºC	549 ºC	-
Deformation Temperature	1010 ºC	624 ºC	-
Hemisphere Temperature	1114 ºC	675 ºC	-
Flow Temperature	1257 ºC	1407 ºC	-

Contents of Cl were found to be much higher in cardoon than in arundo and this may bring environmental problems because of HCl emissions and operational problems due to corrosion and fouling effects. The eucalyptus may be considered a relatively clean fuel as it presents low content of undesired elements like sulphur, chlorine and alkali metals.

DISCUSSION OF RESULTS

The arundo and cardoon species were burned individually and the influence of temperature and excess air on their combustion behaviour was studied. The addition of eucalyptus and dolomite was also investigated and correlated with the gas composition and emissions of HCl, NO_x and SO_2.

Influence of Excess Air

In Fig. 2 it is presented the temperature profile for different excess air values used during combustion of cardoon. The temperature increase just above the bed, near the feeding point, is due to a higher combustion rate of the volatile fuel fraction that have been rapidly released, increasing the temperature in that zone. On the other hand, the bed operates with less fuel. Consequently, a higher air staging ratio and a more intense mixing between fuel and the air in the freeboard are required for complete combustion.

There is a gradual increase of the maximum temperature when the excess air is raised from 25 to 35% due to a more complete combustion encouraged by the extra air supplied. However, increasing the excess air to 50% does not bring about further advantages concerning the combustion efficiency and, in fact, contributes to reducing the temperature by dilution and cooling effects.

In Fig. 3 it can be seen the effect of excess air on the SO_2 and NO_X emissions. The increase of the excess

air did not appear to influence the SO_2 emissions significantly for both arundo and cardoon; however, there was a larger effect on the NO_X production. For this reason, a compromise should be attained when optimizing the excess air level conditions for efficient combustion and NO_X formation. During the combustion of cardoon higher levels of NO_X were produced when compared with arundo combustion. This is probably related with the fact that cardoon has about 2.5 times more nitrogen content. Nevertheless, the NO_X levels obtained are excessive for both solid biofuels, when compared with typical emissions obtained in fluidised beds. The main reason for this is probably the small scale of the lab reactor, that does not allow much interaction between the N-volatile species (mainly NH_3) and the formed NO_X, severely limiting the $DeNO_X$ reduction mechanism found to be essential for NO_X abatement in biomass combustion, as reported in other works (Abelha et al., 2008).

The emission levels for SO_2 are fairly similar for the combustion of both cardoon and arundo and could easily be maintained at low values without addition of adsorbents. This is related with the presence of calcium in the biomass and the molar ratios of Ca/S, as although S is higher for cardoon, its Ca/S ratio is higher than in the case of arundo.

The concentration of HCl in the flue gases as a function of excess air is presented in Fig. 4. In the case of cardoon combustion, it seems that a less oxidant atmosphere favoured a slightly higher conversion of Cl to the gas phase and its emission as HCl. However, for arundo this effect could not be verified, as HCl was measured only in two runs.

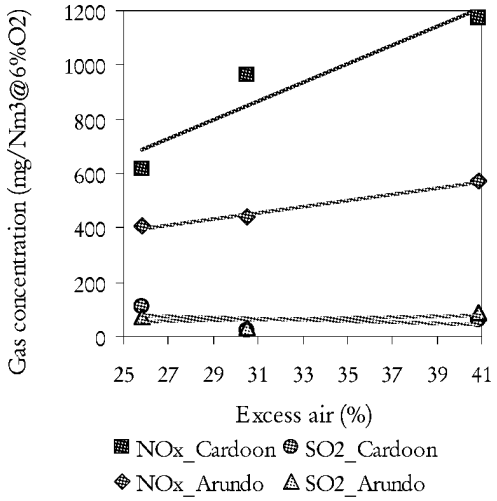

Fig. 3 Effect of excess air in NO_X and SO_2 emissions. Tbed =730ºC

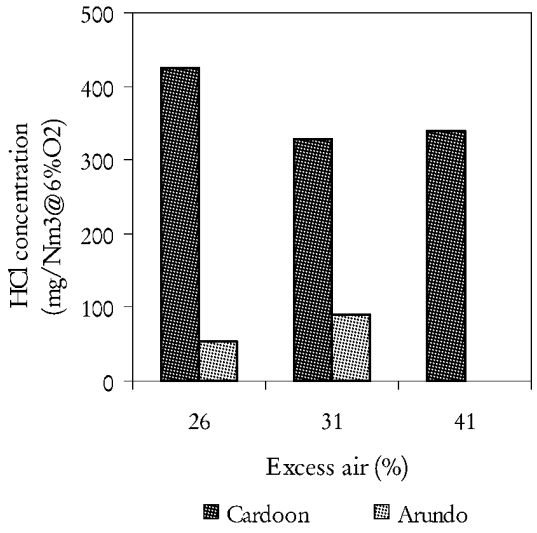

Fig. 4 Effect of excess air on HCl emissions. For 100% Cardoon and 100% Arundo; Tbed=730ºC

Cardoon has higher Cl content than arundo, almost 3 times more, and this explains the fact that more HCl was found in the combustion gases during the combustion of the former. The amount of HCl present in the combustion gases was found to be between 60 and 75% of the Cl fuel input, meaning that part of it could have been retained in the ashes due to the high concentrations of K and Na. However, alkaline-earth metals may start volatilizing at the operation temperatures utilized, releasing Cl. The HCl emission levels from the combustion of cardoon are slightly above the Portuguese emission limit values (250 $mg/Nm^3@8\%O_2$) for general industrial processes. This problem should be taken in consideration if cardoon is to be used in industrial plants (Knudsen et al., 2004, Frandsen, 2005).

Although the temperature was maintained below 750ºC to prevent bed agglomeration, during the combustion of only cardoon or arundo it was detected the formation of some agglomerates of the bed sand plus ashes, which could be related to the presence of high contents of K and Na in both biomass fuels (Zevenhoven-Onderwater et al., 2006). This means that over long periods of combustion of these biofuels it might be possible that bed defluidisation occurs because of the accumulation of agglomerates of the bed material. In fluidised bed systems, one possibility to decrease this tendency is to use additives to modify ash behaviour (Zevenhoven-Onderwater et al., 2001). One other option is to mix these problematic fuels with others less problematic to minimize this adverse effect. Hence, it was decided to use eucalyptus as a supporting fuel in several fuel fractions (0, 40, 80, 100% wt) to verify its effect in decreasing ash sintering tendency.

In Fig. 5 it is possible to observe that the addition of about 40 %wt of eucalyptus in the fuel input. Although it reduced the effect, it did not completely solve the problem of agglomerate formation. It was necessary to raise the eucalyptus fraction in fuel blend to about 80% wt to fully avoid any agglomeration (see

Fig. 6). This way, cardoon became a secondary fuel. If a woody clean biomass fuel is not available in great amounts, the use of a calcium base additive could be another route to reduce ash agglomeration tendency.

Two mixtures of 15% and 30% wt dolomite with silica sand were used as bed material, during the combustion of a mixture of 60% wt cardoon and 40% wt eucalyptus. The formation of agglomerates was totally prevented even with the lower amount of dolomite in the bed, as it can be seen in Fig. 7. The addition of dolomite also effected the pollutant emissions. In Fig. 8 it can be observed the influence of dolomite addition to the bed on the NO_x and SO_2 emissions. As expected, SO_2 decreased because dolomite acted as an adsorbent retaining the sulphur in solid phase as sulphates. However, the decrease was supposed to be more effective and the reason for this behaviour is again related to the small scale of the lab reactor, and more precisely with the small bed height (about 0.1 mm) that does not allow much interaction and sufficient residence time between the dolomite particles with SO_2. Moreover, the temperature was not adequate for the reaction process, being lower than the ideal for the calcination of the dolomite (800-900ºC) (Lyngfelt and Leckner, 1998, Anthony and Granatstein, 2001).

Fig. 5 Small agglomerates formed during combustion of 60%Cardoon+40% Eucalyptus; Tbed=730ºC

Fig. 6 No agglomerates formed during combustion of 20%Cardoon/80%Eucalyptus; Tbed=730ºC

The dolomite, as well as the limestone and other Ca based additives, are known to be active catalysts in the formation of NO_X due to the oxidation of its gaseous precursors (mainly NH_3 in the case of biomass), through both homogeneous and heterogeneous mechanism (Amand et al., 1993, Anthony and Lu, 1998, Jensen et al., 1996). This way, it is not surprising the observed increase in NOx emission levels as the share of dolomite in the bed material was greater (see Fig. 8).

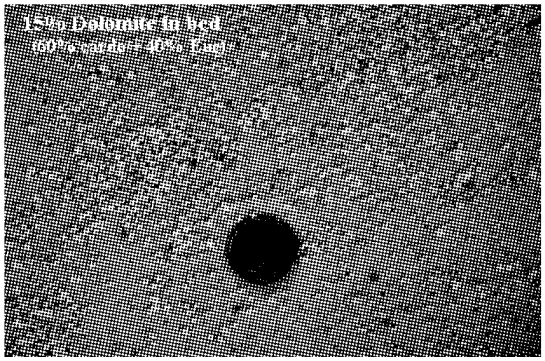

Fig. 7 No agglomerates formed during combustion of 60%Cardoon+40%Eucalyptus, with 15% wt dolomite in bed. Tbed= 730ºC

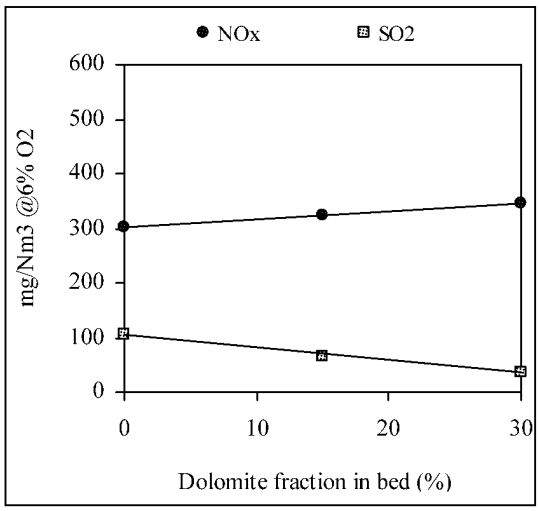

Fig. 8 Effect of dolomite on NO_X and SO_2 emissions. 60%Cardoon+40%Eucalyptus; Excess air = 30%; T = 730-745ºC

A more effective way to simultaneously decrease both NO_X and SO_2 emissions from cardoon combustion is to add some clean woody biomass like eucalyptus. In Fig. 9 it is presented the reduction in emissions obtained when supplying up to 80% wt of eucalyptus to cardoon combustion. It should be expected similar result with adding any other woody biomass instead of eucalyptus, like pinus for example, because such biomass species have very low N and S contents.

The effect of eucalyptus addition to cardoon combustion on the concentration of chlorine was also evaluated and the results are presented in Fig. 10, as a function of the eucalyptus fraction in the mixture. Since the Cl content of eucalyptus was much lower compared with cardoon, chlorine emissions were lowered when increasing the fraction of the woody biomass in the fuel. The Portuguese legal limit value for HCl emission was respected for mixtures above 20% wt of eucalyptus.

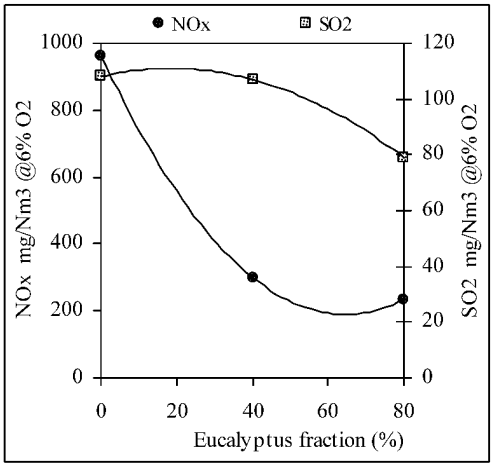

Fig. 9 Effect of eucalyptus fuel fraction increaseon NO_X and SO_2 emissions
Excess air = 30%; T = 730-745ºC

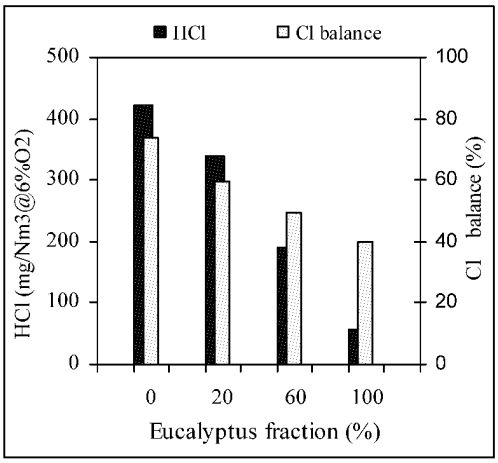

Fig. 10 Effect eucalyptus fuel fraction increase in HCl emissions
Excess air = 30%; T = 730-745ºC

CONCLUSIONS

Cardoon combustion at industrial level should take into account chlorine content in the fuel since results obtained showed high emission levels, being above the Portuguese limit emission values for general industrial process. The arundo combustion did not give rise to HCl emissions of too much concern.

High levels of NO_X were obtained during burning of cardoon and special attention should also be taken in consideration concerning this pollutant, although in industrial fluidised bed, with a more effective temperature, excess air and air staging control, maximization of $DeNO_X$ mechanism could be accomplished and lower emissions would be expected.

Addition of clean forest biomass, like eucalyptus, to cardoon or arundo during combustion, could enhance environmental benefits by decreasing SO_2, NO_X and HCl emissions. Other advantages are the improvement of bed behaviour through decreasing agglomerating tendencies by diluting the presence of alkali elements like Na and K, and minimizing other problems associated with the low ash fusibility temperatures, like slagging and fouling. Consequently, it could also reduce tendency to corrosion in steam boilers. If the mixture with woody biomass could not be possible, the use of additives like dolomite should also be considered to achieve better bed management and possible control of SO_2 and HCl.

REFERENCES

Abelha, P., Gulyurtlu. I., Cabrita, I.: Energy & Fuels 22, (2008), pp.363–371.

Åmand, L-E., Leckner, B., Dam-Johansen, K.: Fuel 72 (1993), pp. 557-564.

Anthony, E.J., Granatstein D.L.: Progress in energy and Combustion Science 27 (2001), pp. 215-236.

Anthony, E.J., Lu, Y.: Relationship between SO_2 and other pollutant emissions from fluidized-bed combustion. Proc. of the 27th Inter. Symp. on Combustion, The Comb. Institute (1998), pp. 3093-3101.

Frandsen, F. J.: Fuel 84 (2005), pp.1277–1294.

Gulyurtlu, I., Crujeira, A.T., Abelha, P., Cabrita I.: Fuel 86 (2007), pp.2090–2100.

Gulyurtlu, I., Boavida, D., Abelha, P., Lopes, M.H., Cabrita, I.: Fuel 84 (2005), pp. 2137-2148.

Jensen, A., Johnsson J.E., Dam-Johansen. K. Nitrogen chemistry in FBC with limestone addition. Proc. 26th Int. Symposium on Combustion. The Comb. Institute (1996), pp 3335-3342.

Knudsen, J. N., Jensen, P. A, Dam-Johansen, K. Quantification of the Release of Cl, K and S to the gas Phase from Combustion of Annual Biomass. Proceedings of the 2nd World Conference and Technology Exhibition on Biomass for Energy, Industry and Climate Protection, (2004), paper ref. OD4.2.

Lyngfelt, A., Leckner,. B.: Journal of the Institute of Energy 71 (1998), pp. 27-32.

Zevenhoven-Onderwater, M., Ohman, M., Skrifvars B.-J, Backman, R., Nordin, A., Hupa, M.: Energy & Fuels 20 (2006), pp. 818-824.

Zevenhoven-Onderwater, M., Backman, R., Skrifvars, B.-J. Hupa M.: Fuel 80, (2001), pp. 1489-1502.

PREDICTION OF AGGLOMERATION, FOULING, AND CORROSION TENDENCY OF FUELS IN CFB CO-COMBUSTION

Vesna Barišić[1]*, Edgardo Coda Zabetta[1], Juha Sarkki[2]*****

1 Foster Wheeler Energia Oy, Relanderinkatu 2, FI-78201 Varkaus, Finland,
** vesna.barisic@fwfin.fwc.com (corresponding author), ** edgardo.coda@fwfin.fwc.com,*
2 Foster Wheeler Energia Oy, Metsänneidonkuja 8, Fl-02130 Espoo, Finland
**** juha.sarkki@fwfin.fwc.com*

Abstract: Prediction of agglomeration, fouling, and corrosion tendency of fuels is essential to the design of any CFB boiler. During the years, tools have been successfully developed at Foster Wheeler to help with such predictions for the most commercial fuels. However, changes in fuel market and the ever-growing demand for co-combustion capabilities pose a continuous need for development. This paper presents results from recently upgraded models used at Foster Wheeler to predict agglomeration, fouling, and corrosion tendency of a variety of fuels and mixtures. The models, subject of this paper, are semi-empirical computer tools that combine the theoretical basics of agglomeration/fouling/corrosion phenomena with empirical correlations. Correlations are derived from Foster Wheeler's experience in fluidized beds, including nearly 10,000 fuel samples and over 1,000 tests in about 150 CFB units. In these models, fuels are evaluated based on their classification, their chemical and physical properties by standard analyses (proximate, ultimate, fuel ash composition, etc…) alongside with Foster Wheeler own characterization methods. Mixtures are then evaluated taking into account the component fuels. This paper presents the predictive capabilities of the agglomeration/fouling/corrosion probability models for selected fuels and mixtures fired in full-scale. The selected fuels include coals and different types of biomass. The models are capable to predict the behavior of most fuels and mixtures, but also offer possibilities for further improvements.
Keywords: agglomeration, fouling, corrosion, co-combustion, CFB

INTRODUCTION

Prediction of agglomeration, fouling, and corrosion tendency of fuels is essential to the design of any CFB boiler. During the years, tools have been successfully developed at Foster Wheeler to help with such predictions for the most commercial fuels. However, changes in fuel market and the ever-growing demand for co-combustion capabilities pose a continuous need for development. This paper presents results from recently upgraded models used at Foster Wheeler to predict agglomeration, fouling, and corrosion tendency of a variety of fuels and mixtures.

DESCRIPTION OF MODELS

Agglomeration, fouling, and corrosion probability models, which are subject of this paper, are semi-empirical computer tools that combine the theoretical basics of agglomeration/fouling/corrosion phenomena with empirical correlations. Correlations are derived from Foster Wheeler's experience in fluidized beds, including nearly 10,000 fuel samples and over 1,000 tests in about 150 CFB units. As a result, the models generate a probability index (PI), which quantifies a tendency of fuels or fuel mixtures to agglomerate (AgglPI), foul (FoulPI), and corrode (CorrPI). All PI-values range from 0 to 10, with the following meaning: $0 < \text{low} \leq 2$; $2 < \text{medium} < 4$, $4 \leq \text{high} < 5$, and $5 \leq \text{very high} < 10$. It is important to note that these models do not take into account specific boiler design and operational parameters, but they describe a fuel propensity towards agglomeration, fouling, and corrosion in the boiler design that is Foster Wheeler's standard for that type of fuel. The actual rate of agglomeration, fouling and corrosion in a given design, and a given set of operational parameters are computed with other tools (not subject of this paper) where AgglPI, FoulPI, and CorrPI are among input values.

In all three probability models, fuels are evaluated based on their classification, their chemical and physical properties by standard analyses (proximate, ultimate, fuel ash composition, etc.) alongside with Foster Wheeler own characterization methods. The input data to the probability models are listed in Table 1 for seven selected fuels among coals and biomass. Mixtures are evaluated according to their composition, and not based on the probability indexes calculated for the individual fuels.

Table 1 Fuel properties

		CASE 1			CASE 2			
		Coal A	Rice husk	Eucalypt. bark	Coal B	Straw 1	Straw 2	Rapeseed residue
LHV	MJ/kg a.r.	26.29	12.98	6.05	22.69	14.85	15.08	18.85
Moisture	wt% a.r.	7.2	11.0	54.0	16.0	14.0	12.0	7.8
Ash	wt% dry	17.5	17.3	9.7	17.5	4.9	5.4	7.5
Sulfur	mg/kg dry	5,200	4,00	600	7,500	950	1,000	7200
Chlorine	mg/kg dry	200	1,500	4,070	490	1,300	1,900	2,600
Sodium, pH 3 soluble	mg/kg dry	52	79	78	180	170	97	4,325
Potassium, pH 3 soluble	mg/kg dry	86	3,900	2,429	89	5,900	6,600	12,297
Calcium, pH 1 soluble	mg/kg dry	2,000	900	45,000	5,700	2,300	2,900	7,430
Sodium	wt% ash	0.1	0.0	0.0	0.4	1.2	1.2	6.2
Potassium	wt% ash	4.0	3.4	2.0	1.1	9.4	9.4	16.4
Calcium	wt% ash	1.2	0.9	38.4	3.4	4.8	4.8	9.4
Magnesium	wt% ash	0.5	0.3	1.1	1.0	0.7	2.5	6.0
Aluminum	wt% ash	15.7	0.0	0.6	13.0	0.8	0.8	0.1
Iron	wt% ash	3.1	0.5	1.3	4.1	0.2	2.3	0.2
Silicon	wt% ash	25.1	41.5	1.7	27.0	33.0	33.0	0.3
Titanium	wt% ash	0.5	0.0	0.1	0.8	0.0	0.0	0.0
Phosphorous	wt% ash	0.1	1.1	0.4	0.4	1.6	1.6	15.3

The agglomeration probability model is based on the hypothesis that alkali elements (sodium (Na), and potassium (K)), and phosphorous (P) from fuel, and quartz particles (SiO_2) from bed material can form low-temperature melting compounds and/or eutectics that lead to agglomeration (Barišić et al., 2008; Coda Zabetta et al., 2008). Only alkali that are soluble at pH 3 are assumed to engage in the agglomeration reactions. The probability of agglomeration, which is caused by the presence of suitable forms of alkali in the fuel, is reduced when the fuel contains aluminosilicates, especially from the kaolinite group of minerals (Davidssson et al., 2007; Davidssson et al., 2008).

The fouling probability model is based on the hypothesis that compounds of alkali (sodium (Na), and potassium (K)), and earth alkali elements (calcium (Ca), and magnesium (Mg)) from fuel can initiate fouling while compounds of aluminum (Al) and silicon (Si) can reduce the fouling tendency of a fuel. Alkali soluble at pH 3 are especially prone to deposit on convective heat exchangers. Compounds of zinc (Zn) and led (Pb) that are also known to contribute to fouling of heat exchangers are not included in the current version of the model.

The corrosion probability model is based on the hypothesis that corrosion of heat exchangers is induced by the chlorine (Cl) present in fuel. Corrosion is correlated with fouling so that if fouling is low then corrosion is also low, while if fouling is high the corrosion probability can be high or low depending on the availability of chlorine from the fuel. The availability of the chlorine to induce corrosion can be reduced by the presence of sulfur oxides (SO_2, SO_3) that form from the fuel during combustion, and if fuel contains minerals of kaolinite group (Aho et al., 2008; Davidsson et al., 2007; Davidsson et al., 2008; Hindiyarti et al., 2008; Kassman et al, 2006; Miettinen Westberg et al., 2003; Skog et al, 2008). The corrosion induced by compounds of Zn and Pb as well as by metallic aluminum (Al) is not included in the current version of the model.

The following chapter presents the predictive capabilities of the agglomeration/fouling/corrosion probability models for selected fuels and mixtures fired in full-scale. The selected fuels include coals and biomass of growing commercial interest.

CASE STUDIES

Case 1: co-combustion of coal A, rice husk, and eucalyptus bark

Figure 1 shows the predictive capability of the agglomeration, fouling and corrosion probability models for co-combustion of coal A, rice husk and eucalyptus bark – Case 1. Corresponding fuel properties are given in Table 1.

Agglomeration (Fig. 1(a)): For all three fuels and their mixtures the agglomeration probability is in the

low range. This trend has been verified in a commercial CFB boiler (370 MW_{th}, 134 kg/s, 542 °C) as highlighted by an asterisk on the figure.

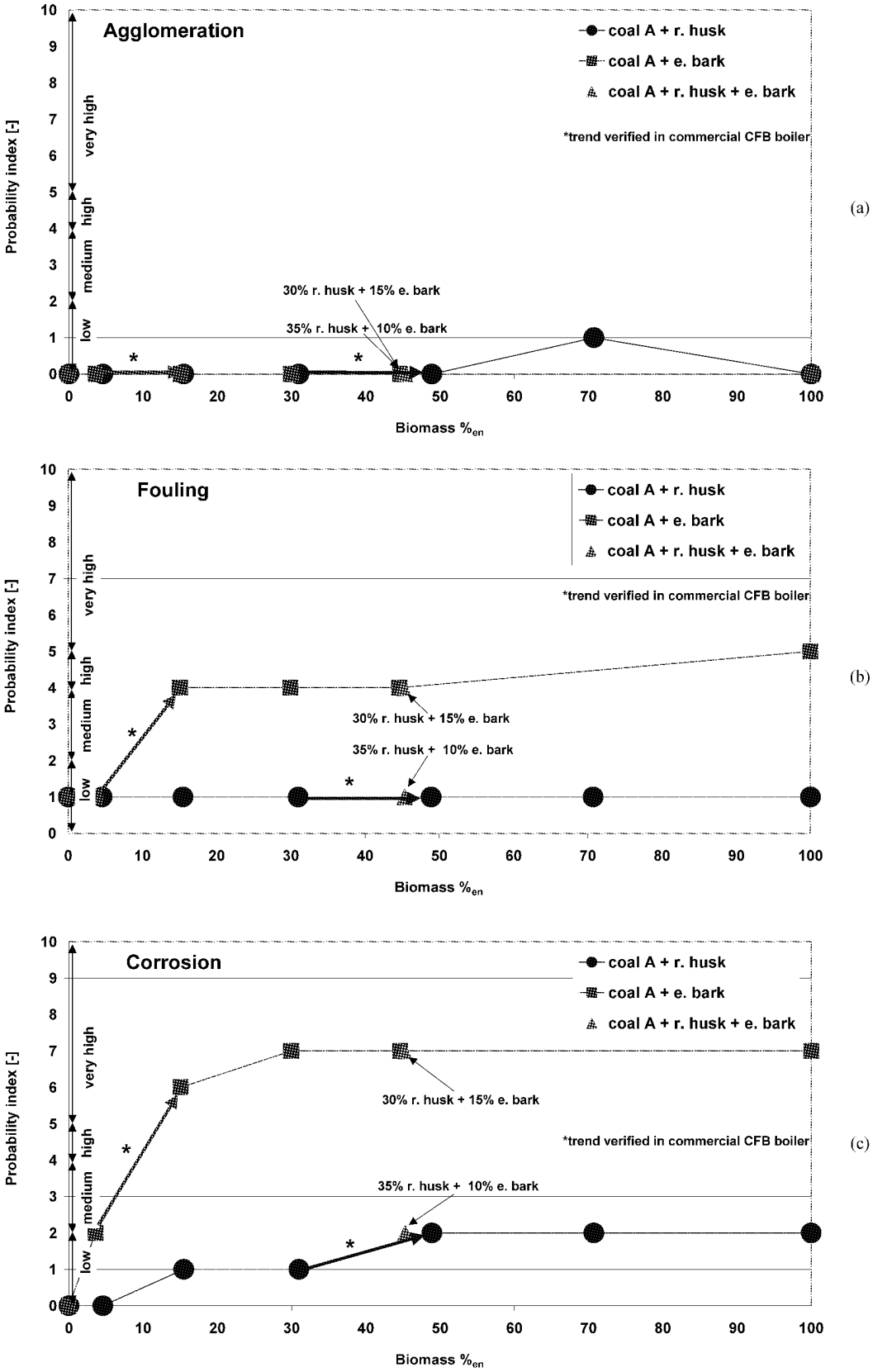

Fig. 1 (a) Agglomeration, (b) Fouling, and (c) Corrosion probability index for Case 1: mixtures of coal A, rice husk, and eucalyptus bark. The symbol "*"indicates that the trend has been verified in tests at 370 MW_{th}, 134 kg/s, 542 °C CFB boiler

Fouling (Fig. 1(b)): The model clearly predicts different fouling trends for the two types of biomass, and the corresponding co-combustion mixtures. The low fouling tendency of rice husk results from its high ash content for biomass, and silica-based composition. Since coal A is also non-fouling, all mixtures of rice husk and coal A show low fouling probability. Contrary to rice husk, eucalyptus bark is prone to increase fouling of convective heat exchanges due to its elevated contents of chlorine in connection with high potassium and calcium. The fouling probability model predicts that an addition of more than $5\%_{en}$ of eucalyptus bark to coal A can increase the fouling probability from low to high level.

Figure 1b also shows two calculations for a mixture of $55\%_{en}$ coal and $45\%_{en}$ biomass, where biomass includes both rice husk and eucalyptus bark. The fouling tendency of the fuel mixture is strongly dependent on the share of eucalyptus bark: the model predicts significantly higher fouling probability for the mixture that includes $15\%_{en}$ eucalyptus bark, compared with the mixture with $10\%_{en}$.

The behavior of rice husk has been reported previously (Skrifvars et al., 2005; Hupa, 2008; Hiltunen et al., 2008), and the calculated trend during co-combustion has been verified in test at 370 MW_{th}, 134 kg/s, 542 °C CFB boiler (see asterisk in Fig. 1(b)).

Corrosion (Fig. 1(c)): Similarly to fouling, the corrosion probability results depend strongly on the type of biomass in the fuel mixture. Rice husk shows low corrosion probability, even though not entirely insignificant for shares of more than $30\%_{en}$. Eucalyptus bark shows very high corrosion probability due to its high chlorine content, and lack of fuel components that can counteract chlorine-induced corrosion tendency. Addition of eucalyptus bark to coal A significantly increases the corrosion probability of the fuel mixture, and shares of more than $5\%_{en}$ lead to very high corrosion probability. When both rice husk and eucalyptus bark are mixed with coal A, the share of eucalyptus bark can be higher compared with the mixture without rice husk, $10\%_{en}$ and $5\%_{en}$ respectively, due to the favorable effect of silica-based ash of rice husk. The asterisk in Figure 1c indicates the trend calculated by corrosion probability model that has been verified in tests performed at commercial CFB boiler (370 MWth, 134 kg/s, 542 °C).

It is important to underline once again that the results presented here refer solely to fuel properties, and do not take into account design and operational adjustments that can by applied to favor the utilization of demanding fuel mixtures.

Case 2: co-combustion of coal B and straw, or rapeseed residue

Figure 2 shows the predictive capability of the agglomeration, fouling and corrosion probability models for co-combustion of coal B with two varieties of straw, or co-combustion of coal B with rapeseed residue. Corresponding fuel properties are given in Table 1.

Agglomeration (Fig. 2(a)): Even though the two considered straws have the same agglomeration probability when fired alone, the model predicts different behaviors during their co-combustion with coal B. Straw 1 can be fired up to $40\%_{en}$ with low agglomeration tendency, while already at $30\%_{en}$ straw 2 shows medium probability of agglomeration due to the higher content of alkali compared with straw 1. The probability of agglomeration is higher for rapeseed residue compared with straws, and that is due to high alkali and especially high phosphorous content in this type of fuel (Barišić et al., 2008).

The agglomeration tendency of straw and rapeseed residue has been reported previously (Hiltunen et al., 2008; Barišić et al., 2008), and the calculated trend during co-combustion has been verified for straw in test at 77.5 MW_{th}, 29 kg/s, 505 °C CFB boiler, and for rapeseed in tests at 12 MWth CFB boiler of Chalmers University of Technology.

Fouling (Fig. 2(b)): Higher content of soluble potassium and calcium in straw 2 increases the fouling tendency of the mixture with coal B compared with the co-combustion of the same coal with straw 1. Co-combustion with either straw, however, shows very high fouling probability for mixtures of more than $50\%_{en}$ of straw. The fouling as well as the agglomeration model (see also Fig. 2(a)) predicts that mixtures with $70\%_{en}$ of straw have higher fouling/agglomeration tendency than $100\%_{en}$ of straw. This behavior is unlikely, but it is a recognized imperfection of the models which, at the current stage of their development, tend to misestimate some of co-combustion scenarios. However, the coal mixtures with over $70\%_{en}$ of straw are currently of marginal commercial interest due to well known severe agglomeration, fouling, and especially corrosion propensity of this fuel in CFB combustion.

The fouling probability of rapeseed residues is higher compared with straws. Calculations show that firing more than $15\%_{en}$ of rapeseed residue leads to high fouling and increases with further addition of this type of fuel to the mixture with coal B. Very high fouling tendency is connected with high content of alkali, calcium, chlorine and phosphorous in rapeseed residue. The asterisks in Figure 2b indicates the trend calculated by fouling probability model that has been verified in tests performed at commercial CFB boilers.

Corrosion (Fig. 2(c)): Both straws show very high corrosion probability, and the co-combustion share of $40\%_{en}$ leads to high corrosion. Similarly to the trend observed for agglomeration and fouling, straw 1 with

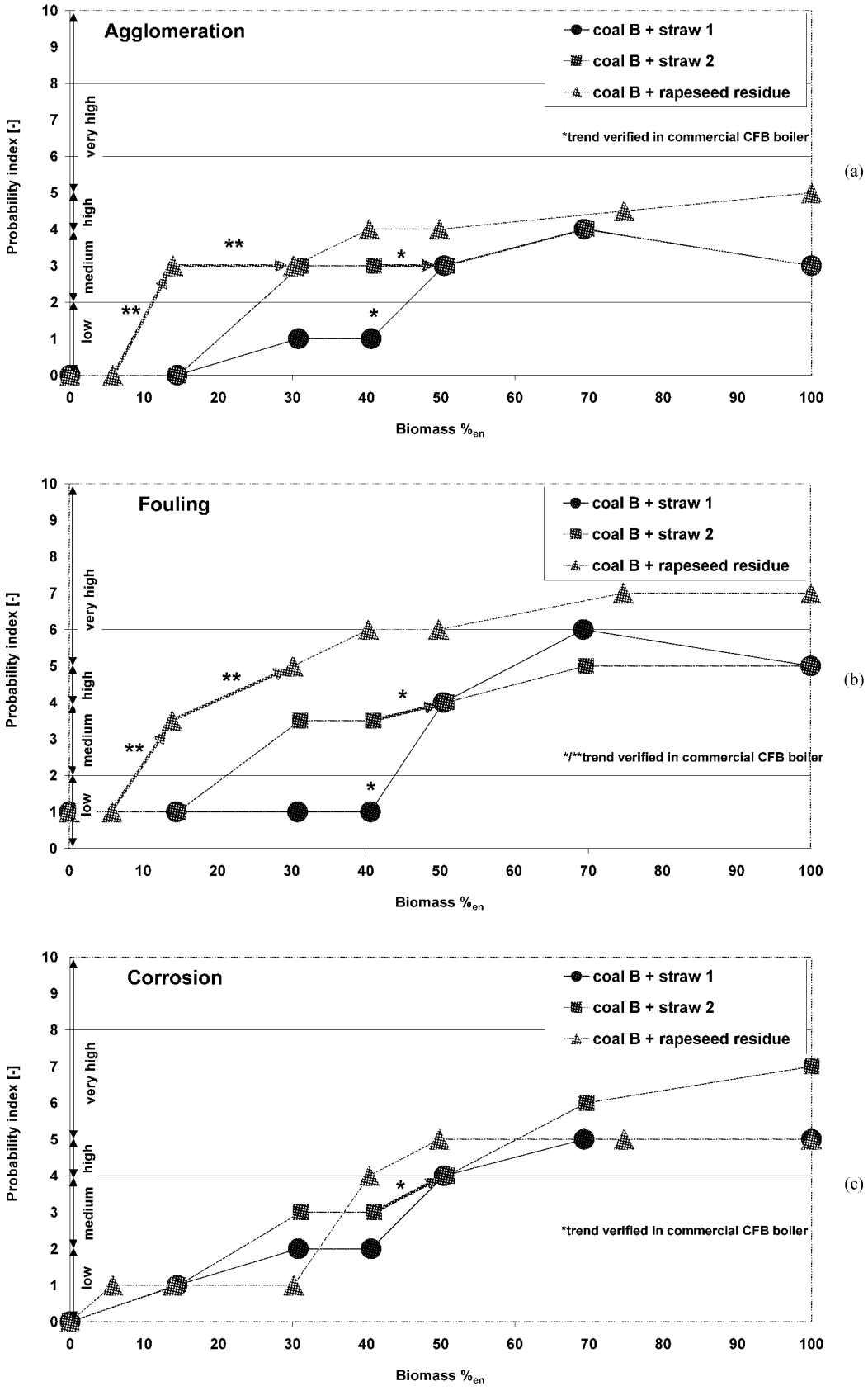

Fig. 2 Agglomeration, Fouling and Corrosion probability index for Case 2: mixtures of coal B and two straws, and coal B and rapeseed residue. The symbol "*" indicates that the trend has been verified in tests at 77.5 MWth, 29 kg/s, 505 ºC CFB boiler; the symbol "**" refers to tests at 12 MWth CFB boiler of Chalmers University of Technology

lower content of chlorine (and alkali) can be fired up to $40\%_{en}$ while maintaining low corrosion probability. The corrosion behavior of rapeseed residue is somewhat different compared with straws. The model shows that in mixtures with coal B rapeseed residue can be used up to $30\%_{en}$ with low corrosion probability, but already at $40\%_{en}$ the corrosion probability is high and increases with further increase of rapeseed share. These results appear realistic compared with observations in full-scale, though they also show a need for further developments of the corrosion probability model when used with high-phosphorous fuels such as rapeseed residue.

FURTHER DEVELOPMENTS

Agglomeration, fouling, and corrosion probability models are capable to predict trends observed during co-combustion of a variety of fuels in commercial CFB boilers, and especially to reflect diversity of combustion behaviors that exists among biomass fuels. Nevertheless, the models exhibit certain limitations, and the following items have been identified for further development:

- Extension of the probability models to fuels of growing commercial interest.
- Introduction of the effect of zinc, led, and metallic aluminum.
- Improvement in description of the effect of phosphorous.
- Improvement in description of the effect of kaolinite.

CONCLUSIONS

Changes in fuel market and ever-growing demand for co-combustion capabilities pose a continuous need for tools that can predict agglomeration, fouling, and corrosion tendency of fuels fired in CFB boilers. This paper presents results from recently upgraded models used at Foster Wheeler to predict agglomeration, fouling, and corrosion tendency of a variety of fuels and mixtures.

The probability models well predict the agglomeration, fouling, and corrosion trends observed during co-combustion in commercial CFB boilers. Results shown in this paper refer to cases co-firing coals of different carbonification degree with various types of biomass. In addition, the models have shown good agreement in combustion of other fuels, including peat, sludge, and wastes (not shown here).

Further model developments are needed to i) extend the model validity to fuels of growing commercial interest, ii) take into account the effect of zinc, led, and metallic aluminum especially in waste fuels, iii) improve the description of the effect of phosphorous especially in grain-derived fuels, and iv) improve the description of the effect of kaolinite especially in coals.

ACKNOWLEDGMENTS

This work has been carried out as a part of the SAFEC project, and the financial support of TEKES is acknowledged. The authors would like to express special gratitude to Prof. Mikko Huppa and Dr. Maria Zevenhoven from Åbo Akademi University, and Matti Hiltunen from RD Partners for fruitful discussions.

REFERENCES

Aho, M.; Gil, A.; Taipale, R.; Vainikka, P.; Vesala, H.: Fuel (2008), 87, p. 58–69.

Barišić, V., Åmand, L.-E., Coda Zabetta, E.: Proceedings of the World Bioenergy 2008, Jönköping, Sweeden (2008).

Coda Zabetta, E., Barišić, V., Peltola, K., Hotta, A.: Proceedings of 33rd International Technical Conference on Coal Utilization & Fuel Systems (Sakkestad, B.A., ed), Clearwater, Florida, USA (2008).

Daviddson, K.O.; Åmand, L.E.; Steenari, B.-M.; Elled, A.-L.; Eskilsson, D.; Leckner, B.: Chemical Engineering Science (2008), 63, p.5314–5329.

Davidsson, K.O.; Åmand, L.-E.; Elled, A.-L.; Leckner, B.: Energy Fuels (2007), 21, p.3180–3188.

Hiltunen, M., Barišić, V., Coda Zabetta, E.: Proceedings of the 16th European Biomass Conference (Schmid, J., Grimm, H.-P., Helm, P., Grassi, A., eds), Valencia, Spain (2008).

Hindiyarti, L.; Frandsen, F.; Livbjerg, H.; Glarborg, P.; Marshall, P.: Fuel (2008), 87, p.1591–1600.

Hupa, M.: Proceedings of the 9th International Conference on Circulating Fluidized Beds (Werther, J., Wojciech, N., Wirth, K.-E. and Hartge, E.-U., eds.), Hamburg, Germany (2008).

Kassman, H.; Andersson, C.; Högberg, J.; Åmand, L.-E.; Davidsson, K.: Proceedings of the 19th International Conference on Fluidized Bed Combustion (Winter, F., ed), Vienna, Austria (2006).

Miettinen Westberg, H.; Byström, M.; Leckner, B.: Energy Fuels (2003), 17, 18–28.

Skog, E.; Johansson, L.-G.; Svensson, J.-E. .: Proceedings of 33rd International Technical Conference on Coal Utilization & Fuel Systems (Sakkestad, B.A., ed), Clearwater, Florida, USA (2008).

Skrifvars, B-J., Yrjas, P., Laurén, T., Kinni, J., Tran, H., Hupa, M.: Energy Fuels (2005), 19, p. 1512–1519.

ENVIRONMENTAL IMPACT OF ESTONIAN OIL SHALE CFB FIRING

J. Loosaar, T. Parve, A. Konist

Department of Thermal Engineering, Tallinn University of Technology, Kopli 116, 11712, Tallinn, Estonia

Abstract: Oil shale based power production has been the basement of Estonia's energetical independency and economy for over 60 years. At the same time oil shale power plants emissions still give the biggest share of Estonian stationary source pollution, having significant impact to the environment. Thanks to the introduction of oil shale large scale CFB firing, reduction of the total environmental impact was achieved in last years.

Detailed information about emissions from CFB power units was collected during several research projects in last years. The paper reviews this new data and compares it with former information. Analysis and estimation of changes of charges of all main polluting components at CFB firing compared to former pulverized firing (PF) are presented. It concerns mass balance of trace metals in initial fuel and in formed ash, emissions of PCDD/F, PCB, PAH, PM 2,5/10, plus conventional air emissions as NO_x, SO_2, CO_2, CO, HCl, TSP.

Eg.it was found out, that the relative share of very small (<2,5 μm) particulates is higher in case of oil shale CFB firing, what could be explained with very efficient milling effect of relatively soft minerals of oil shale at CFB furnace.

In relation of emission studies also mass distribution of CFB boiler ash between different separation points along the flue gas duct (ash mass balance) was determined and analyses of sampled ashes were provided.

This information is important from the point of view of better understanding of thermochemical processes and emission formation in CFB boiler, wider reuse of the ashes of CFB unit.

Keywords: oil shale, CFB, emission, ash, $PM_{2.5}$

INTRODUCTION

After the start up of new CFB boilers different tests and measurements were carried out at different oil shale fired boilers during last two years. At Narva power plants two types of boilers were tested – pulverized fired (PF) TP 101 and Foster Wheeler 215 MWe CFB boilers. Technical specifications and descriptions of these boilers can be found in Ots (2006) and Hotta et al. (2005).

Most of tests were provided only at CFB boilers, since there was a lack of information about these boilers emissions. Beside the measurement of ordinary air emissions with FTIR spectrometer (SO_2, NO_x, N_2O etc.) samples for the determination PAH, PCCD/F, trace metals were collected following respective standards - CEN 1948:1999, parts 1-3; CEN 14385:2004. Quantitative determinations of PCDD/PCDF, PCB, PAH and HM were provided at laboratory of Ecochem a.s. in Prague by using ICP-MS, ICP-OES, HRGC/HRMS and AAS.

Fine particulates emissions (PM2.5/10) emissions were measured at both type of boilers, because no former data about these emissions from oil shale fired boilers exist. At the same time high health risks related to fine particulates in air are well known and more strict demands on control and reduction of this emissions are introduced nowadays. PM2.5/10 emissions were determined with Johnas II type cascade impactor system from Paul Gothe GmbH. At sampling standards CEN 13284-1 and VDI 2066 were followed. Sampling was provided to the circular 50 mm quartz fibre filters type MK 360 of Munktell (catching efficiency of 99.998 % at cutsize of 0.3 μm). The sampling was provided from one point of the flue gas cross section, which was choosed based on flue gas velocity field determination beforehand for the whole cross section.

For the verification of total solid particles (TSP) concentration measured with cascade impactor from one point, parralel measurements of TSP from the 16 points of the whole cross section were provided.

RESULTS

Ash balance

Ash content of Estonian oil shale is very high (~ 50 %). During oil shale combustion ash is removed from several (8) ports along the gas duct. For the material balance of ash and its components ash flows from these ports were measured and respective ash samples were analysed for the components under interest.

In the CFB boiler the most of ash (~50 %) is removed by the I field of ESP. The share of the bottom ash is the next in the order, forming 37.4 % and 29.3 % of the total ash amount in firing conventional (8.5 MJ/kg) and

enriched (11.5 MJ/kg) oil shale fuels respectively (Fig. 1)

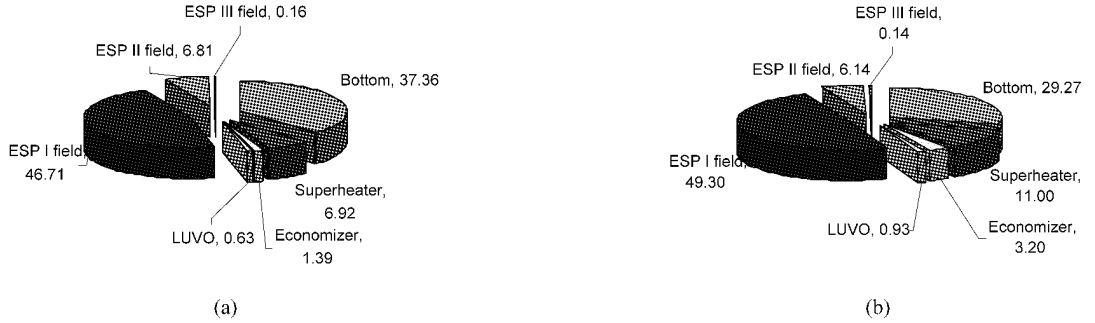

Fig.1 Relative distribution of CFB boiler ash flow, mass percents.
(a) Conventional oil shale fuel; (b) Enriched oil shale fuel

Trace metals emission and distribution

During tests and samplings, directed for the determination of specific pollutants, on-line monitoring of flue gases main components and boiler (power unit) basic operation parameters for background information was carefully provided. Results of monitoring of traditional gaseous pollutants at CFB boiler for CO, N_2O, NO, NO_x, SO_2, HCl, CO_2, TSP (total solid particles) remain in the same range as detected already during previous tests and published in (Hotta A. et al., 2005).

Determination of trace elements in the flue gases of CFB unit gave expected result. Comparing with former similar tests at PF units (Aunela L. et al., 1995, 1998;Pets L. et al., 1995), the emissions were much lower (Table 1). First of all it is explained with the effect of much more efficient ESP-s installed at CFB units, which decreased trace element release with solid particles for about two orders. Because of similar temperature distribution at the tail of the CFB boiler emission of trace elements in gaseous phase remain at the same level as in case of PF.

Much lower (over 10 times) result of Hg content in flue gases determined in case of CFB boiler was unexpected. At flue gas temperature (~160°C) most of Hg should be in gaseous phase and the results in case of CFB and PF should be comparable. Because of very low concentrations the measurement error can be the reason of this discrepancy.

Elements relative enrichment factors (by (Meij R, 1994) calculated on the basis of new data are also different from the former results (Aunela-Tapola L. et.al., 1998), which could be explained with changes in fly ash size distribution. As usual, enrichment is taking place towards finer ashes. Enrichment factor is highest for the Cd as it was also for PF ashes Oil shale power plants are firing about 13 million tons of oil shale per year. As a result 5-6 million tons of ash is formed, which is mostly (> 90 %) landfilled at ash fields.

Table 1 Trace metals emission and distribution at oil shale CFB firing

			Relative enrichment factor of TSP	
Element	**Dry flue gas, µg/m³ O_2=6 %**	**Emission factor, mg/GJ**	**versus total ash of CFB**	**versus oil shale at PF**
Al	1675	639	1.4	0.2
As	3.7	1.4	2.0	0.4
Ba	11.2	4.3	1.9	0.4
Cd	1.4	0.5	37.7	5.7
Co	1.4	0.5	0.9	0.6
Cr	5.5	2.1	1.6	1.2
Cu	11.2	4.3	2.4	1.3
Hg	0.2	0.07	n.m.	0.02
Mn	13.9	5.3	0.5	0.3
Mo	0.5	0.2	0.02	0.01
Ni	2.9	1.1	11.3	1.2
Pb	3.8	1.4	0.9	0.5
Se	<1,7	0.6	9.4	0.9

Continued

Element	Dry flue gas, µg/m³ O_2=6 %	Emission factor, mg/GJ	Relative enrichment factor of TSP versus total ash of CFB	Relative enrichment factor of TSP versus oil shale at PF
Sn	<3,5	1.3	1.3	n.m.
Sr	17.4	6.6	1.1	0.1
Ta	<1,4	0.5	15.1	n.m.
Ti	51.1	19.5	4.0	0.8
Tl	<1,3	0.5	4.3	2.1
U	1.2	0.5	0.8	0.3
V	4.1	1.5	13.7	0.6
Zn	27.6	10.5	1.7	0.3
Zr	1.9	0.7	1.8	n.m.

Fortunately trace metal concentrations in landfilled ash are in average at the same level of their content in the ground.

From that point of view oil shale ash utilization e.g. in agriculture for the acidic soil neutralization should not do any harm. On the contrary, trace metals leaching by highly alkaline water, circulating in closed ash removal system and at ash fields, is potential hazard to the surrounding environment because of unbalanced water evaporation and pre-cipitation at Estonian climate conditions.

During last years significant effort has been made to minimize the water amount in ash removal system to minimize the risk of release of ash removal system water to the nature.

Table 2 Trace metals in landfilled total ash of CFB unit

Component	Content mg/kg	Component	Content mg/kg	Component	Content mg/kg
Al	19000	Mn	460	Ta	<0,5
As	7.4	Mo	4.5	Ti	180
Ba	73	Ni	3.0	Tl	0.4
Cd	0.1	Pb	33	U	2.3
Co	4.2	Se	<1,0	V	2.9
Cr	25	Sn	1.5	Zn	31
Cu	8.0	Sr	190	Zr	7.5

The balance of nine trace metals (regularly reported components) in fired fuel and in collected from the boiler gas passes ashes, calculated to the fuel dry matter, is presented on Figure 2.

Difference of the hights of column pairs reflects the error made on ash flow measurements and the sampled fuel or ash analyses of the certain trace element. In case of Hg the difference can be explained by the share of gas phase emission.

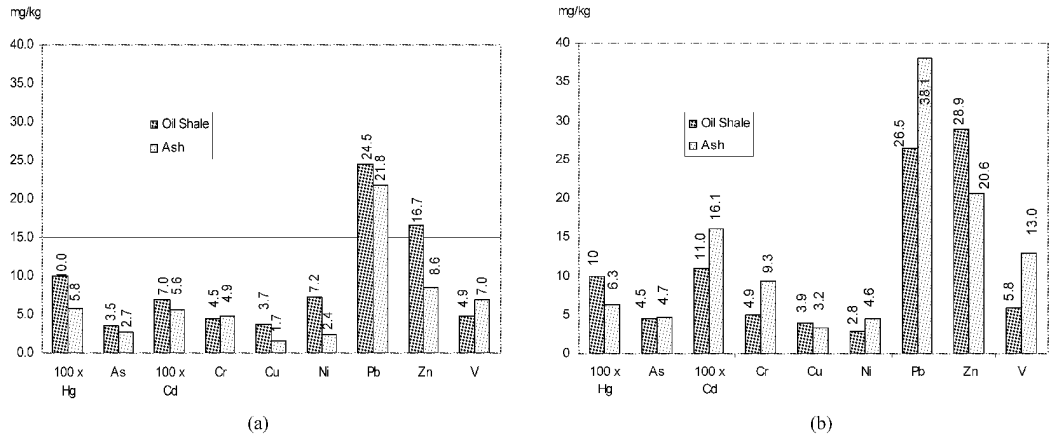

Fig.2 Trace metals balance – inserted fuel versus collected ash in mg to kg of fuel dry matter
(a) Conventional oil shale fuel; (b) Enriched oil shale fuel

Particulate matter PM 2,5/10 emissions

Impactor measurements at several PF boilers and at CFB unit (two boilers) were provided to find out emissions of fine particles to air and get more information about emitted solid particles size distribution. The information is needed for the purpose of emission inventory and for planning measures of reduction of fine particles emissions.

In all cases the main part of the collected samples (>80 %) consisted from fine particles below 10 μm (Fig.3). The relative content of PM_{10} was higher in case of CFB boiler. Also the share of very fine particles with the size below 2.5 μm ($PM_{2.5}$) was higher in CFB boiler emissions. This result can be explained at first with different construction of ESP at CFB (4 fields) and PF (3 fields) units, but can be also the result of very efficient milling effect of CFB furnace.

At this point also other factors following from oil shale firing mode (PF or CFB) and probably resulting to ESP efficiency should be mentioned (Hotta, A. et.al.,2005):

—Different ash load at the inlet of ESP – at PF about 1,5 times higher than at CFB;

—Very different shape of fly ash particles, especially fine ones (Fig. 3);

—Very different flue gas composition – in case of PF SO_2 about 1000 and NO_x about 1.5 times higher.

TSP absolute emissions from CFB and PF boilers differ several times, depending on ESP construction, condition and operating parameters. TSP concentrations at CFB unit are mainly below 50 mg/Nm^3. In case of PF units variation of TSP values is much higher, remaining in the range of 100 – 450 mg/Nm^3.

From the comparison of the results of tests with varying operating parameters and efficiency of ESP next conclusions can be made.

Higher TSP concentrations at PF boilers flue gases correspond to higher shares of particulates with size over 10 μm. E.g. at concentration 450 mg/Nm^3 the share of particulates >10 μm is about 30 % and $PM_{2.5}$ decreases to 22 %. It means, that the share of PM_{10} is remaining almost the same as it is in lower TSP concentrations. Described behaviour of changes in particle size distribution of emitted solid particles proves, that ESP is more efficient in catching particles with size over 10 μm (Table 3).

It is interesting to mention, that the relative share of particles with size between 2,5 and 10 μm remains approximately to the level of 50 % in all tests, not depending on factors mentioned before.

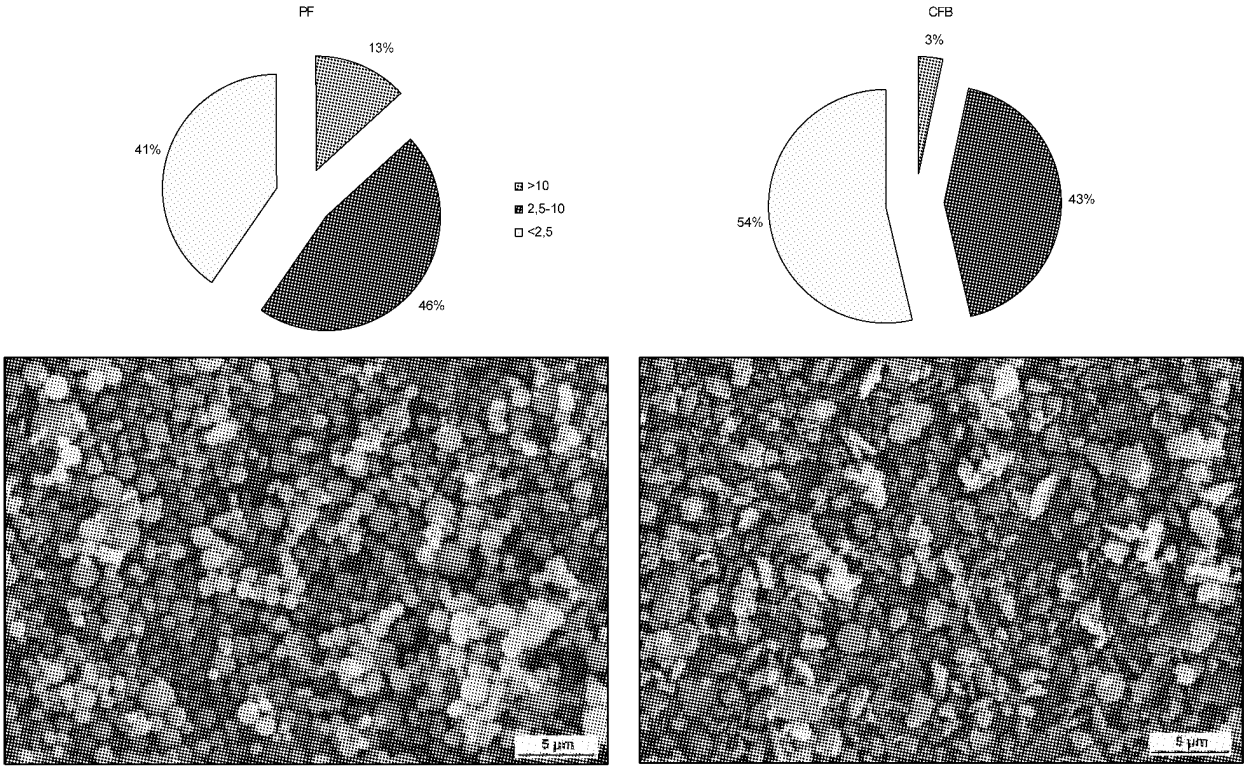

Fig.3 Size(μm) distribution(in mass per cents) and the view of emitted to air solid particles ($PM_{2.5}$) from oil shale boilers PF –pulverized firing ; CFB – circulated fluidized bed firing

Significant influence of oil shale firing mode to the shape of fine ash particles can be easily noticed from the SEM pictures of $PM_{2,5}$ fractions at oil shale PF and CFB combustion (Figure 3). The ash particles from PF (> 1400 °C) are overburnt and nicely round. Thanks to the much lower furnace temperatures of CFB boiler (<850 °C) ash particles are having irregular shape.

Table 3 Particles distribution in fly ash of oil shale fired CFB boiler before and after ESP

Sampling location	Unit	Particle size			Total
		<2.5	2,5 - 10	> 10	
ESP inlet	g/Nm^3, 6 % O_2	7.77	22.45	29.76	59.9
ESP inlet	%	13.0	37.5	49.7	100.0
ESP outlet	mg/Nm^3 6 % O_2	21.3	17.1	1.3	39.7
ESP outlet	%	53.5	43,1	3.4	100
Efficiency of ESP	%	99.9726	99.9924	99.9996	99.9934

PAH and dioxines

Priority PAH (EPA-16) contents at CFB unit flue gases (Table 4) were much lower than at oil shale PF boilers, which is probably the result of much higher residence time of fuel particles and combustion products at high temperature zone. E.g. at CFB benzo(a)pyrine content remain below 11 ng/Nm^3 (6 % O_2) comparing with concentrations 32-89 ng/Nm^3 measured at PF boilers (Loosaar et al. 1982, Aunela L. et al., 1995). Similar was the result in case of PAH concentrations at landfilled total ash (Table 4).

Table 4 PAH in flue gases and in total ash of CFB boiler

	Flue gas ng/Nm^3	Total ash mg/kg
Naphtalene	1784	0.3
Acenaphtylene	<1487	<0,25
Acenaphtene	<60	0.046
Fluorene	<23	0.084
Phenanthrene	<283	0.23
Anthracene	<23	<0,020
Fluoranthene	<11	<0,080
Pyrene	18	0.077
Benzo(a)anthracene	<11	<0,020
Chrysene	<11	<0,037
Benzo(b)fluoranthene	<11	<0,020
Benzo(k)fluoranthene	<11	<0,0070
Benzo(a)pyrene	<11	<0,010
Dibenzo(a,h)anthracene	<11	<0,010
Benzo(g,h,i)perylene	<11	<0,017
Indeno(1,2,3-cd)pyrene	<11	<0,034
PAH sum		0.74

When concentration of benzo(a)pyrine in bottom ash of PF boiler was ~230 ng/kg (Loosaar et al. 1982, Aunela L. et.al., 1995), then the same number for CFB boiler is <10 ng/kg.

The same conclusion about lower PAH concentrations at oil shale CFB firing comparing with traditional PF, only based on investigations of ESP ashes, is drawn by other researchers (Kirso U. et al., 2005).

Determination of dioxins and furans in emitted by CFB boiler flue gases gave very positive and similar to former results on PF boilers of oil shale (table 5). Measured concentrations were very low and the estimated maximum hazard equivalent of these emissions (I-TEQ 1.472 pg/Nm^3 at 6 % O_2) was almost 70 times lower than the emission limit to the waste incineration plants - 0.1 ng/Nm^3 at 6 % O_2 (DIRECTIVE 2000/76/EC). Very low concentrations of PCDD/F were also found in the landfilled summary ash.

Table 5 PCDD/F and PCB from oil shale combustion at Narva PP

Parameter	Unit	CFB boiler	PF boiler (Schleicher et al.,2005)
Total ash			
I-TEQ for PCDD/F lowerbound	µg/ton of oil shale	0.000	
I-TEQ for PCDD/F upperbound *	µg/ton of oil shale	8.381	0.0 - 0.49
Landfilled PCDD/F in 2006, max possible	g	12.0	1.6
I-TEQ for PCB lowerbound	µg/ton of oil shale	0.774	
I-TEQ for PCB upperbound	µg/ton of oil shale	6.416	
Landfilled PCB in 2006, max possible	g	9.2	
Flue gas			
I-TEQ for PCDD/F lowerbound	pg/Nm^3 (6 % O_2)	0.699	
I-TEQ for PCDD/F upperbound	pg/Nm^3 (6 % O_2)	1.472	3.144 -5.878
Air emissions of PCDD/F in 2006, max possible	g	0.015	0.139
I-TEQ for PCB lowerbound	pg/Nm^3 (6 % O_2)	0.280	
I-TEQ for PCB upperbound	pg/Nm^3 (6 % O_2)	0.360	
Air emissions of PCB in 2006, max possible	g	0.004	

Lowerbound and upperbound are levels defined in Directive 2002/69/EC and 2002/70/EC
* calculated based on detection limit values - all contents remain below detection limits (in average - 3 ng/kg)

CONCLUSIONS

With introduction of CFB firing at Estonian oil shale power plants environmental impact of oil shale power production decreased significantly, considering not only conventional air pollutants, but also trace metals, PAH and dioxins/furans.

Toxic compounds low content is not limiting possible utilization of CFB ash in agriculture and industry.

Relative enrichment of trace metals towards smaller ash fractions (flying ash versus landfilled total ash) takes place like it also was found out in former studies.

PAH concentrations in the flue gas of CFB boiler are at least several times lower than in PF boilers. Benzo(a)pyrine content remain below 11 ng/Nm^3 (6 % O_2) at CFB firing. PCDD/F and PCB air emissions of oil shale firing CFB boilers are very low and remain below 20 mg per year.

PM_{10} relative content in emissions of oil shale boilers (PF and CFB) is significant, forming over 80 % of TSP. $PM_{2.5}$ share from TSP is higher in case of CFB boiler exceeding 50 %. Absolute values are lower for the CFB boilers.

The share of solid particles with size over 10 µm tends to increase in correlation with TSP content. It proves that ESP is more efficient in catching larger particles.

ACKNOWLEDGEMENTS

The authors are grateful for financial support and co-operation of this work by Narva Power Plants Ltd. and Estonian Environmental Research Centre.

REFERENCES

Aunela, L., Häsänen, E., Kinnunen V., Larjava K., Mehtonen A., Salmikangas T., Leskela J., Loosaar J.: Emissions from Estonian oil shale power plants, Oil Shale, V 12, No 2, 1995, pp. 165-178.

Aunela-Tapola, L. et al.: Trace metal emissions from Estonian oil shale fired power plant, Fuel Processing Technology, No 57, 1998, pp. 1-24.

Loosaar, J. et al.: Release of toxic and carcinogenic compounds during the burning of Estonian oil shale in industrial boilers (in Russian), Transactions of Tallinn Polytechnic Institute, No 522, 1982, pp. 59-71.

Hotta, A., Parkkonen, R., Hiltunen, M., Arro, H., Loosaar, J., Parve, T., Pihu, T., Prikk, A., Tiikma, T.: Experience of Estonian oil shale combustion based on CFB technology at Narva Power Plants, Oil Shale, V 22, No 4S, 2005, pp. 369-381.

Kirso, U., Laja, M., Urb, G.: Polycyclic aromatic hydrocarbons (PAH) in ash fractions of oil shale combustion: fluidized bed versus pulverized firing, Oil Shale, V 22, No 4S, 2005, pp. 537-547.

Schleicher, O., Roots, O., Jensen, A. A., Hermann, A., Tordik, A.: Dioxin emission from two oil shale fired power plants in Estonia, Oil Shale, V 22, No 4S, 2005, pp. 563-571.

Pets, L., Vaganov, P., Rongsheng, Z.: A comparative study of remobilization of trace elements during combustion of oil shale and coal at power plants, Oil Shale, V 12, No 2, 1995, pp. 129-145.

Ots, A: Oil shale fuel combustion, Eesti Energia AS, Tallinn, 2006, pp. 61-64.

Meij, R.: Trace element behavior in coal-fired power plants, Fuel Processing Technology, No 39, 1994, pp. 199-217.

DIRECTIVE 2000/76/EC OF THE EUROPEAN PARLIAMENT AND OF THE COUNCIL,of 4 December 2000 on the incineration of waste

STUDY ON COMBUSTION CHARACTERISTICS OF LIGNITE IN A CFB BOILER

J. Leng, T. S. Zou, J. X. Wu, C. Jiang, J. L. Gao, J. Wu, D. Su, D. Y. Song

Northeast Electric Power Research Institute Co., Ltd, ShenYang, 110006,China

Abstract: The shortage of coal promotes the lignite utility in power plant because of the rapid economy development recently. However, lignite is high in moisture content as well as volatile content and low in calorific value. It is very difficult to burn in traditional pulverized coal fired boiler. Circulating fluidized bed (CFB) boiler is an alternative with low pollutant emission. Some CFB boilers are built and put into commercial operation in Northeast China and East Inner Mongolia where lignite is abundant. The operation experiences of these boilers are introduced in this paper. The effect of coal particle size on bottom ash ratio, combustion efficiency, thermal efficiency, pollution emission, and ash deposits in convective heating surface were investigated. It was found that for the lignite fired CFB boiler, the largest coal particle size should be 20 to 40mm to maintain bed material balance. But the bottom ash only shares less than 10% of the total ash. Due to high volatile content in the lignite, the combustion efficiency could achieve more than 99%. Meanwhile, NO_x emission was relative low and satisfied national environment protection requirement. It is suggested that flue gas velocity in convective heating surface should be ranged in a certain scope to prevent ash deposit and erosion.

Keywords: CFB boiler, lignite, coal particle size, performance

INTRODUCTION

Coal resource is abundant in China, including anthracite, lean coal, bituminous and lignite. But the coal-fired power plant mainly fire bituminous. The coal supply shortage becomes very serious because of the rapid development of power industry recent year. Since lignite reserves in Northeast China and East Inner Mongolia are abundant, there are some boilers fired bituminous mixing with lignite in these regions. However, lignite has high moisture content, high ash content, high oxygen content, high volatile content, low ash melting point, low heat value. Consequently, it is very difficult to burn lignite in pulverized coal fired boiler. Circulating fluidized bed (CFB) boiler provides an alternative way to burn lignite with low pollutant emission. Tens of CFB boilers with various capacities have been put into commercial operation or are under construction. The operation experiences of these boilers are introduced in this paper.

During the commissioning and operation, it was found that coal particle size distribution influenced boiler performance. Thus, some investigations are conducted. The effects of particle size on the combustion were focused on in the previous studies (Xiao, et al., 2005; Lu, et al., 2003). Due to the material particles size depends on the coal size distribution, it is related to gas-solid two phase flow, material mass balance(Wang, et al., 2003; Yang, et al., 2005a; Xiao, et al., 2005), and heat transfer (Zhang, et al., 2005). In this paper, in a 440t/h boiler, the effects of coal particle size on the bottom ash ratio, combustion efficiency, thermal efficiency, pollution emission, and ash deposits in the convective heating surface are investigated. And the reasons about it are also discussed.

INTRODUCTION OF THE 440T/H BOILER

The experiments were conducted in a 440t/h CFB boiler. This CFB boiler is designed and manufactured by Harbin Boiler Company Limited. The model number of boiler is HG-440/13.7-LHM28, with capacity of 440t/h. The CFB boiler is with once-reheating and connected with a 135MW steam turbine. The boiler is mainly composed of furnace, thermal insulation cyclone, "U"-shape loopseal with self-balance and back pass where the final superheater, low temperature reheater, economizer and air preheater is located in line. The rolling-cylinder type bottom ash coolers are employed in this boiler. The detail structure of the boiler was presented in the literature (Jiang et al., 2004).

The design coal of the boiler is Huolinhe lignite in Inner Mongolia. The design coal particle size is less than 10mm with d_{50} of 1.5mm. The mass ratio of particles whose size is less than 200μm should be less that 10%. Table 1 lists the main design parameters of the boiler, and Table 2 gives proximate analysis and ultimate analysis of design coal, check coal and test coal in commissioning.

Table 1 Main design parameters of boiler

Items	B-MCR
Rated evaporation /t·h^{-1}	440
Superheated steam pressure/MPa	13.7
Superheated steam temperature/℃	540
Reheated steam flow/t·h^{-1}	386
Reheated steam outlet pressure/MPa	3.627
Reheated steam outlet temperature/℃	540
Reheated steam inlet pressure /MPa	3.821
Reheated steam inlet temperature /℃	368.2
Feed water temperature/℃	249.4
Flue gas temperature/℃	142
Boiler efficiency/%	89.3
Bed temperature/℃	855
Ash and slag ratio	60:40
Inlet coal granularity /mm	0～10

Table2 Coal property

Items	design coal	check coal	coal during commissioning
Car/%	36.02	32.45	34.82
Har/%	2.36	2.37	2.34
Oar/%	9.67	10.54	9.61
Nar/%	0.58	0.50	0.42
St, ar/%	0.32	0.32	0.36
Aar/%	19.05	22.32	20.75
Mar/%	32.00	31.50	31.70
V_{daf}/%	49.46	49.03	49.63
LHV/kJ·kg^{-1}	13230	11710	12502

BOILER OPERATION EXPERIENCE

Lignite granularity

When lignite with high moisture and high moisture is heated in the furnace, the inner moisture and volatile matter are released, leading to the particle break. The interaction and attrition during fluidization and combustion process causes the particle size reducing. If raw coal particle is small, for example, following the original design requirement, it is very difficult to keep bed pressure. The decrease of bed material mass in furnace results in bed temperature increasing, and the rated load could not be achieved. Because the bed material does not maintain balance as design, heat transfer decreases (Zhang et al., 2005). While the raw particle size was controlled larger than the design value, boiler performance became better. Therefore, the coal particle size for lignite must be coarser than that for bituminous. The secondary crusher can be cancelled. It was found that the maximum lignite particle size should be 20mm~40mm from the commissioning.

Ash and slag ratio

Due to the breakout and attrition (Tang et al., 2000), the ash is relative fine, and the density is quite small because of its younger age. Therefore, the ratio of bottom ash is small although the ash content in the coal is not very low. Even the coal particle size was controlled larger than design value of 20mm~40mm in maximum, the bottom ash only shares less than 10% of the total ash. This is quit different from that fired bituminous or anthracite. Therefore, bottom ash system, and fly ash system should be carefully design as well as the boiler

performance prediction.

Combustion efficiency and thermal efficiency

Boiler thermal efficiency is measured in accordance with the Chinese local standard DL/T964-2005 (Regulation of Performance Test on CFB boiler). The boiler combustion efficiency is expressed as:

$$q_c = 100 - (q_3 + q_4)$$

The combustion efficiency and thermal efficiency of boiler under different loads were measured. Corresponding results are listed in Table 3.

Table 3 Combustion efficiency and thermal efficiency of boiler under different loads

Items	135MW	120MW	100MW	80MW
Carbon content in ash/ %	0.53	0.43	0.58	0.68
Boiler combustion efficiency/ %	99.67	99.74	99.65	99.58
Boiler thermal efficiency / %	91.74	91.89	91.37	90.34

Combustion characteristics of lignite

Combustion characteristics of coal are primarily determined by volatile, ash and moisture contents of coal and heating value. Combustion characteristics of coal with high volatile content are better. On the contrary, combustion characteristics of coal with high ash and moisture are worse.

However, the tens CFB boiler operation experience showed that the effects of ash and moisture contents in the coal are not very significant on combustion characteristics (Jiang et al., 2004). Because of the material mass balance, the ash content should be ranged in a certain scope (Liu et al., 2000).

The ignition temperature is only 250 ~350 °C, and it is easier to ignite (Yang et al., 2005b). When the bed temperature is 350°C, coal could be fed. This bed temperature is lower than that of design. And the oil gun above bed is not necessary for lignite fired CFB boiler. The oil consumption during startup is much smaller compared with those fired anthracite or bituminous.

Burnout characteristics of lignite

The factors which affect burnout characteristics of coal mainly include carbon content, volatile content, ash content, inner moisture, etc. Volatile content of lignite is as twice as bituminous, and ash content is less than bituminous, which is favor to coal burnout. At the same time, after pulverized coal particle is heated, its inner moisture evaporates. High content of inner moisture strengthen interstitial area of char particle, which leads to the better diffusion of oxygen and promotes the coal burnout.

Agglomeration characteristics of lignite

The deformation temperature of Huolinhe lignite is about 1100°C. Generally speaking, its ash melting temperature is relatively low. However, it is very seldom to agglomerate in the bed during commissioning and operation. This is the contribution of the low temperature combustion of CFB boiler of about 900°C and the good mixing of bed material.

Fouling characteristics of lignite

Fouling trend of lignite ash is relatively strong. It belongs to the middle fouling coal (Jiang et al., 2004). Because water cooled wall of furnace has the excellence ability of self-scouring by the solid circulation, fouling in water cooled wall is absolutely disappeared. But for convection heating surface located in the secondary pass, the flue gas velocity should be carefully designed because of high ash concentration. If the flue gas velocity is appropriate, there will be no ash deposited in the heating surface. The heat absorption capacity of heating surface without ash deposition will achieve the design value. However, if flue gas velocity is relatively low, it may lead to fouling and deposit problem, then the heat absorption capacity of heating surface will decrease resulting in higher exhaust temperature. Meanwhile, the flue gas velocity in the convective heating surface must be less that a critical value. If it is higher than the critical velocity, the erosion may occur. Thus a proper flue gas velocity is a key for the CFB boiler convective heating surface.

Bed material supply system

If coal particle size is appropriate, the present work shows that it is not necessary to design a bed material system for the lignite-fired CFB boiler with middle ash content. The material mass balance could be achieved by adjusting bed pressure and primary air ratio, especially the coal particle size. But it is very nervous. Thus a

bed material system is a possible solution.

Security problem for lignite

According to DL/T 5145-2002(Technology Criterion of Design and Calculation of Milling System in Thermal Power Station), the explosion grade of coal with V_{daf}>35% is Ⅳ. That means the explosion is easy to occur. Because oxygen and volatile contents of lignite are very high, lignite is easily self-ignited and exploded. Therefore, explosion prevention should be strengthened for the lignite-fired boilers.

Environment protection question for lignite fired CFB boiler

According to characteristics of CFB boiler, NO_x emission in flue gas can match relatively strict environment protection requirement (Chen et al., 2002). However, the desulfurization efficiency by limestone in CFB boilers is not as good as design of more than 90%. It depends not only on the Ca/S molecular ratio, but also on bed temperature, lime stone particle size distribution and its reactivity (Qiao, et al., 2001). For the boiler on which experiments were conducted, the NO_X and SO_2 emissions were low, shown in Table 4, where the Oxygen content in the flue gas was converted to 6%. During the commissioning, there are a lot of troubles in the limestone system and it could not work. Thus, SO_2 concentration was the original emission. Therefore, the further research on desulfurization characteristic of limestone in CFB boiler must be carried on to meet much strict environment protection criteria.

Table 4 Practical emission concentrations of SO_2 and NO_x (6%O_2)

Items	135MW	120MW	100MW	80MW
SO_2/mgNm^{-1}	926.9	823.7	843.2	864.9
NO_x /mgNm^{-1}	288.2	289.9	296.4	296.5

EXISTING PROBLEM

The main problem of boiler is the higher flue gas exhaust temperature. It is caused by two reasons. One is the low flue gas velocity; the other is the fine and high fly ash particle concentration in the gas.

Table 5 lists the designated flue gas velocities in different convective heating surfaces of the boiler. Low flue gas velocity causes relatively severe ash deposit on heating surfaces in the convective pass, which deteriorates heat transfer and leads to the exhaust temperature increasing.

Table5 Flue gas designated velocities in each heating surface section in the boiler

Items	B-MCR	THA	75%THA	50%THA	higher pressure heater pass by
flue gas speed in furnace/m·s^{-1}	5.4	5.1	3.8	2.53	5.2
Final superheater/m·s^{-1}	8.6	8.1	5.9	3.9	8.3
low temperature reheater/m·s^{-1}	8.4	7.8	5.7	3.8	8.0
primary superheater/m·s^{-1}	8.5	7.9	5.8	3.9	8.2
economizer/m·s^{-1}	7.6	7.04	5.14	3.51	7.02
air preheater/m·s^{-1}	9.1	8.5	6.2	4.2	8.1

Moreover, the ratio of bottom ash to fly ash is 60:40 in the design. However, in practical operation, fly ash and bottom ash ratio is more than 90:10. It causes fly ash content in the flue gas is much higher than design value. The flue gas velocity mentioned above causes ash deposit on the heating surface. But according to component analysis, the ash fouling characteristic is a little bit above the average level. The ash is relatively fine and it is easy fouling. Unfortunately, the soot blower in the boiler did not work and a new one is necessary.

CONCLUSIONS

For the Inner Mongolia lignite fired CFB boiler, the largest coal particle could be 20 to 40mm to balance the bed material. But the bottom ash only occupied less than 10% of the total ash. Due to the high volatile content in the lignite, the combustion efficiency can achieve more than 99% while NO_x emission was relative low, which could satisfy the national environment protection requirement. The oil gun above bed is not necessary for lignite fired CFB boiler. When the bed temperature is 350°C, coal could be fed because of its lower ignition temperature. It is suggested that the gas velocity in convective heating surface should be in a certain range to prevent ash deposit and erosion.

NOTATIONS

d particle diameter, μm;

V_{daf} dry and ash-free base volatilized content, %;

q_3 heat loss due to incomplete gas combustion, %;

q_4 heat loss due to unburntout carbon, %

q_c combustion efficiency, %

REFERENCES

Chen K.Y., Zhao X.M., Lu J.F., et al.: Emission in an Industrial Scale Circulating Fluidized Bed Boiler. Proceeding of the 4th China-Korea Clear Energy Workshop, Seogwipo, 2002: pp.339-343.

Jiang Y. D.: Operation performance of lignite-fired CFB with big capability [J]. Boiler manufacture, 2004(4): pp.4-8.

Liu B.S., Lu J.F., Li Z.Y., et al.: Fuel Flexibility of Circulating Fluidized Bed Boiler and the Relation of Fuel with Material Balance. Power System Engineering, 2000, 16(2): pp.71-74.

Lu J.F., Feng J.K.: On Design of CFBC Boilers. In: Xuchang Xu ed. Proceeding of the 5th International Symposium on Coal Combustion, Nanjing China, 2003: pp.309-313.

Qiao R., Lu J.F., Yue G.X., et al.: Modeling of Sulfur Retention in Circulating Fluidized Bed Coal Combustors. Tsinghua Science and Technology, 2001, 6(4): pp.314-318.

Tang Z., Lu J.F., Cao Y., Wang X., et al.: A Simple Method to Investigate the Ash Size Distribution and Its Attrition for Use in Circulating Fluidized Bed. The 5th International Conference on Measurement and Control of Granular Materials, Xi'an, 2000: pp.118-122.

Wang Z.W.: Materiel balance analysis of CFB [J]. Power Engineering, 2007, 27(2): pp.179-183.

Xiao P., Lu H.S, Jiang J.Z, et al.: Study on enhancing integral performance of CFB by emitting circulation ash [J].Thermal Generate Electricity, 2007(4): pp.5-10.

Xiao X.B., Yang H.R., Zhang H., et al. : Research on carbon content in fly ash from circulating fluidized bed boilers. Energy and Fuels, 2005, 19(4): pp.1520-1525.

Yang H.R., Yue G.X., Xiao X.B., et al.: 1D modeling on the material balance in CFB boiler. Chemical Engineering Science, 2005a, 60(20): pp.5603-5611.

Yang H.R., Lu J.F., Zhang H., et al.: Coal Ignition Characteristics in CFB Boiler. Fuel, 2005b, 84(14-15): pp.1849-1853.

Zhang H., Lu J.F., Yang H.R., et al.: Heat Transfer Measurements inside the Furnace of a 135MWe CFB Boiler. In: Cen Kefa ed. Proceeding of the 8th Circulating Fluidized Bed Technology. International Academic Publishers World Publishing Corpration. Hangzhou, 2005: pp.254–260.

STUDY OF HEAVY METALS CONDENSATION BY CONSIDERING VARIANT CONDITIONS OF INCINERATOR COOLING ZONE

Yi Cheng, Atsushi Sato, Yoshihiko Ninomiya

Department of Applied Chemistry, Chubu University, Kasugai, Aichi 487-8501,Japan

Abstract: The adhesion of heavy metals as they flow to the cooling surface of FBC (fluidized bed combustor) has been investigated under laboratory conditions. Model wastes spiked with mixture of Pb, Zn and Cu were used. The vaporizing ratio of these metals was kept as constant by fixing the reaction gas composition under 1223 K. Then the condensation behavior of these heavy metals was investigated by varying the tail gas composition and operational parameters such as Cl/S ratio and quenching rate. The results indicate that Cl/S ratio remarkably influence the partition and chemistry of the heavy metals. Increasing H_2O concentration in the tail gas makes heavy metals condense in the form of sulfate instead of chloride at relatively low temperature section (573 K). In addition, quenching rate of tail gas also plays an important role on the redistribution of heavy metals between sulfate and chloride. The unavailability of equilibrium calculation for the quenching mode and some differences between the experimental and calculation results imply the complexity of the adhesion process of heavy metals.

Keywords: heavy metals, fluidized bed combustor, chlorine, incineration, quenching rate

INTRODUCTION

With increasing amount of waste being produced in the world, more efficient treatment of solid waste and materials recycling are needed (Lind et al., 2007). As a successful treatment method of waste, the incineration is increasingly applied due to its significant advantages. Most solid waste materials can be incinerated in one or both of these facilities. Yet one of the major environmental concerns is the emission of toxic heavy metals during this thermal treatment and their possible leaching from the different residues produced by municipal solid waste incinerators: bottom ash, boiler ash, filter ash, and dusts collected by the flue gas cleaning processes (Abanades et al., 2002). Due to the relatively high content of chlorine characterized by MSW, heavy metals are known to be easily vaporized by chlorination. Then, these heavy metal species condensing on very small particles or aerosols, which typically are formed late in the cooling process of the flue gas, have a larger potential to escape through the stack as larger particles will be captured by the flue gas cleaning system. Hence, there are several reasons why knowledge on the portioning and chemistry of heavy metal species in MSW combustion plants are needed (Obernberger 1998; Sorum et al., 2004). Up to now, several studies using equilibrium calculation systems on the behavior of heavy metals in incineration systems has been undertaken (Verhulst et al., 1996). However, some influencing factors, including residence time of flue gas in cooling process and quenching rate, on the partition of heavy metals is unavailable to be considered by equilibrium calculation. Additionally, the competition between HCl and SO_2 for combining with heavy metals will directly influence the partition and the condensation due to the different dew point (Miller et al., 2003).

The objectives of this research program are to experimentally investigate the influencing factors, including temperature, tail gas composition and tail gas quenching rate, on the deposition and redistribution of heavy metal (Pb, Zn, Cu) in $HCl//Cl_2/H_2O/O_2/CO_2/N_2$ atmosphere. Focus is on the influence of Cl/S ratio in tail gas and the quenching rate.

EXPERIMENTAL SECTION

Experimental setup and conditions

The experimental setup is shown in Figure 1. This instrument is mainly composed by two parts: vaporizing zone with constant temperature (1223 K) and cooling zone. The decreasing temperature profile is evaluated by temperature versus length (Fig. 2), which is measured by six thermocouples placed in equidistance alone the cooling tube. As can be seen from Fig 2, the approximate linear characteristics of the decreasing temperature line makes the cooling rate can be approximately evaluated as 100 K/s by Eq (1), in which *T(i)* and *T(o)* represent the temperature of inlet and outlet of the cooling zone, and t represents the residence time of the flue gas passing through the cooling zone.

$$\overline{Q} = \frac{T(i) - T(o)}{t} \tag{1}$$

Three filters are put at different position of the cooling zone where temperature was separately controlled as 973 K, 773 K and 573 K along the tube. The reacting tube, which is made of quartz, also consists of two parts, inner tube and outer tube. By fixing the composition of reacting gas passing through the inner tube, we can get the constant vaporization rate of the heavy metals located in the inner tube. Meanwhile, the rotary of inner tube attained by the motor makes the sample contact with the reacting gas completely. The flue gas from inner tube mixes with the gas injected from outer tube flow into the cooling zone, and the heavy metals condense at the filters. By means of adjusting the composition of gas from outer tube, only the tail gas composition can be changed. The related experimental conditions parameters are shown in Table 1. Then, the compounds sticked on filters are analyzed by scanning electron microscopy-energy dispersive X-ray (SEM-EDX) and X-ray diffraction (XRD) to identify the composition and the potential compounds. The depositing amount of metals is measured by atomic absorption spectrophotometer (AAS) assisted acid digestion. In addition, ion chromatography (IC) is used to measure the concentration of Cl^- and SO_4^{2-}, which is used to calculate the proximate amount of metal chloride and metal sulfate.

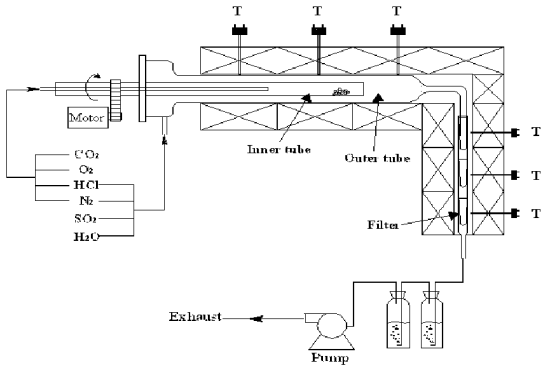

Fig.1 Schematic diagram of apparatus

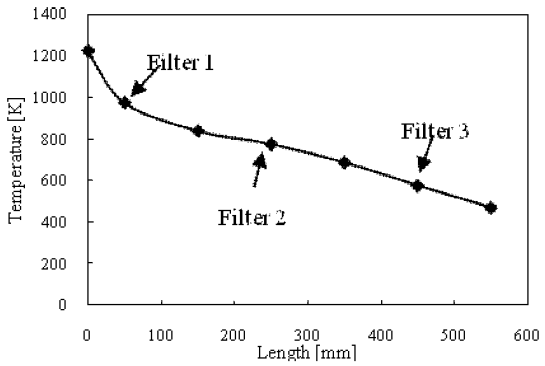

Fig. 2 Temperature profile of cooling zone

Table 1 Experimental settings and conditions

Parameter		Setting	Gas species		Composition
Reactor temperature		1223 K	Flue gas	HCl	2017, 4034 ppm
Reaction time		45 min		SO_2	1008, 2017 ppm
Total gas flow rate		1432 ml/min		H_2O	8.5 %
Residence time in cooling zone		8 s		CO_2	4.5 %
Pressure		1 atm		Zn	43 ppm
Temperature of cooling zone	Filter 1	973 K		Cu	131 ppm
	Filter 2	773 K		Pb	329 ppm
	Filter 3	573 K		N_2	Balance

Model waste sample

Zn, Cu and Pb, behaving differently during incineration according to the classification of heavy metals (Ratafia, 1994), were considered simultaneously. The porous TiO_2 was selected as the carrier of the heavy metals, and was calcined for 2 hours under 1223 K to burn out the volatile impurities. The heavy metals were spiked into the porous TiO_2 by impregnating solutions of the acetate of heavy metals and evaporating the water by vaporizer. Then the porous carriers were calcined again under 773 K for 4 hours to eliminate the organic substances.

EQUILIBRIUM CALCULATION CONDITIONS

Factsage 5.2 soft package was used to take equilibrium calculation of Pb/Zn/Cu/Cl/O/H/N reaction system. The equilibrium gas composition of each temperature subtracted the amount of the deposit was considered as the input for next lower temperature to simulate the condensing process, as shown in Fig 3. A rough comparison of trends observed from experimental investigation on condensation in the flue gas by performing a comprehensive parametric study is performed.

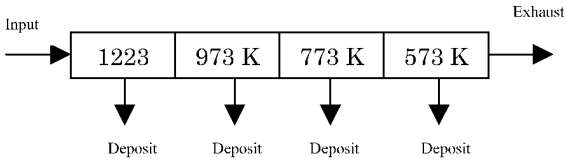

Fig. 3 Schematic of calculation procedure

RESULTS AND DISCUSSION

Condensation of heavy metals in $HCl/O_2/N_2$

Considering the relatively high content of chlorine in the MSW, the concentration of HCl produced during the incineration of MSW has the important effect on the vaporization as well as the condensation of the heavy metals. So, in the first experiment, the condensation of the heavy metals in the $HCl/O_2/N_2$ with 2017 ppm HCl was investigated. As shown in the Fig.4, both of experimental result and equilibrium calculation indicate that the heavy metals mostly deposit at the filter 2 and filter 3 (773 K and 573 K), and the main condensation form of these metals is characterized as chloride by SEM-EDX analysis (Fig.5). In addition, according to the morphological specificity, two type of particle can be identified from SEM-EDX picture. One type, marked 1, is characterized with smooth surface and approximate 2 to 1 atom ratio of chlorine to metal. The morphological specificity of particle 2 is obviously different with particle 1, and the composition is not MCl_2 due to the atom ratio of Cl to metal. So, this particle probably is an amorphous formed by nucleation. To further understand the condensation process of these heavy metals, an equilibrium prediction for the distribution of Heavy metals was carried out. As can be seen from Fig.6, all of heavy metals present in form of gaseous chloride at 973 K. With temperature decreasing, Zn and Pb condense from gas $ZnCl_2$ and $PbCl_2$ to solid $ZnCl_2$ and $PbCl_2$. However, about 82% Cu condense in form of CuO at 773 K, and the left 18% Cu condense in form of $CuCl_2$ at 573 K. As can be speculated, the two kinds of condensing form, CuO and $CuCl_2$, imply that the condensation of Cu in $HCl/O_2/N_2$ potentially has two routes: (1) CuCl and $(CuCl)_3$ are oxidized by O_2 and condense at higher temperature in form of CuO; (2) combining with Cl radical to condense at lower temperature in form of $CuCl_2$.

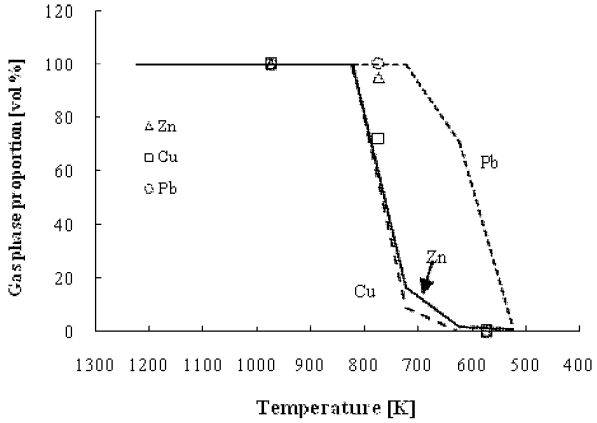

Fig. 4 Condensation of Zn, Cu, Pb at different temperature in $HCl/O_2/N_2$
(lines represent equilibrium results; symbols represent experimental results)

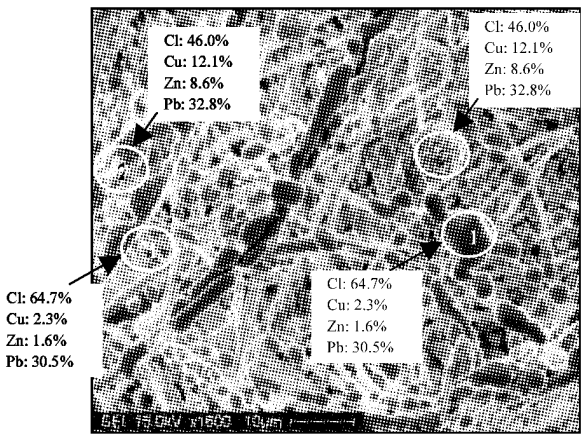

Fig. 5 SEM-EDX for the filter 3 in case $HCl/O_2/N_2$

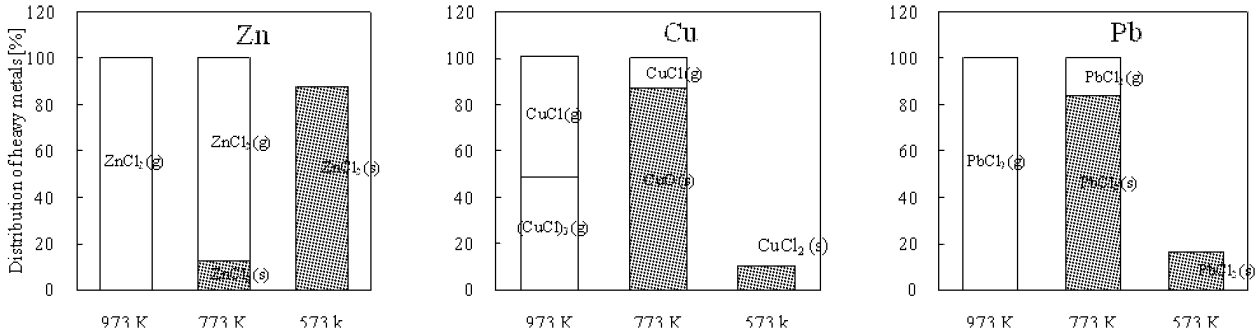

Fig. 6 Equilibrium prediction for the distribution of heavy metals

Influence of Cl/S ratio on the condensation

The ratio of Cl/S is controlled by adjusting the flow rate of HCl and SO_2 in the outer tube. Firstly, the influence of SO_2 on the condensation of heavy metals was investigated with 1:1 Cl/S ratio. As shown in Fig.7, when the Cl/S ratio is 1:1, about 60% Zn, 25% Cu and 75% Pb deposit at filter 1 (973 K), and except for a little amount of Cu almost no Zn and Pb deposit at filter 3. Comparing with no SO_2 condition, the presence of SO_2 in flue gas is seen to make Zn, Cu and Pb deposit at higher temperature. To confirm the condensation form of these heavy metals on the filters, XRD qualitative analysis was carried out. The diffraction spectra showed in Fig.9 indicates that most of heavy metals condense at filter 1 and 2 in form of sulfate. Also, no spectra from filter 3 correspond to the little depositing amount of heavy metals showed in Fig.7. By keeping the SO_2 concentration, the Cl/S ratio was adjusted to 1:0.5 through increasing the HCl concentration in flue gas. As can be seen from the experimental results, except Pb still deposits at filter 1 with a remarkable amount, Zn and Cu keep the gas phase at this temperature. As another result, the condensing mass of Zn, Cu and Pb at filter 3 was increased. The equilibrium calculation was carried out to analyze the distribution of heavy metals during the cooling process with 1: 0.5 Cl/S ratio. As shown in Fig.8, all of the heavy metals present in gaseous chloride at high temperature, and completely condense in form of sulfate when temperature decreasing. However, a little amount of metal chloride was observed in the filter 3 (573 K) by SEM-EDX (Fig.10). The morphological specificity of this particle is similar to the particle 2 showed in Fig.5 as well as the irregular atom ratio. The formation of this amorphous chloride which cannot be predicted by equilibrium calculation indicates that the quenching rate potentially can affect the redistribution of the heavy metals, because equilibrium calculation cannot take residence time into account.

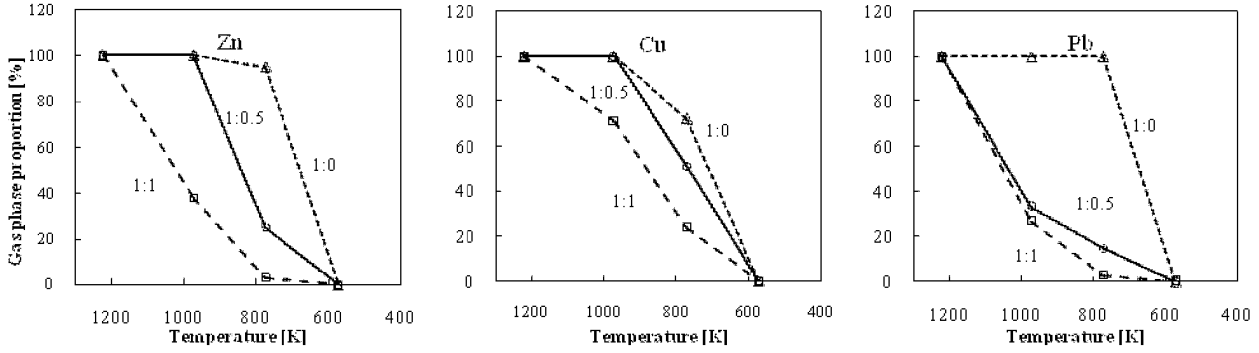

Fig.7 The effect of Cl/S ratio on the condensation of heavy metals

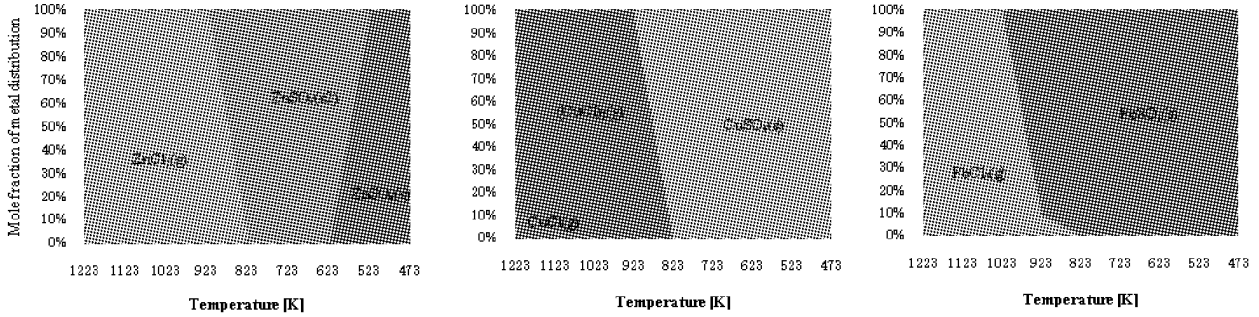

Fig. 8 Equilibrium calculation of the distribution of heavy metals during the cooling process ($HCl:SO_2$=1:0.5)

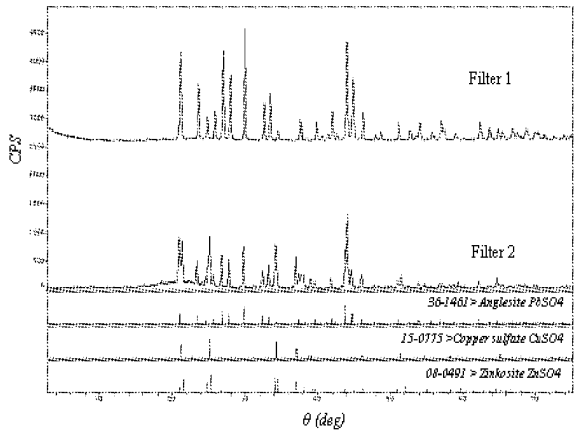

Fig. 9 XRD spectra of filters in case HCl:SO_2=1:1

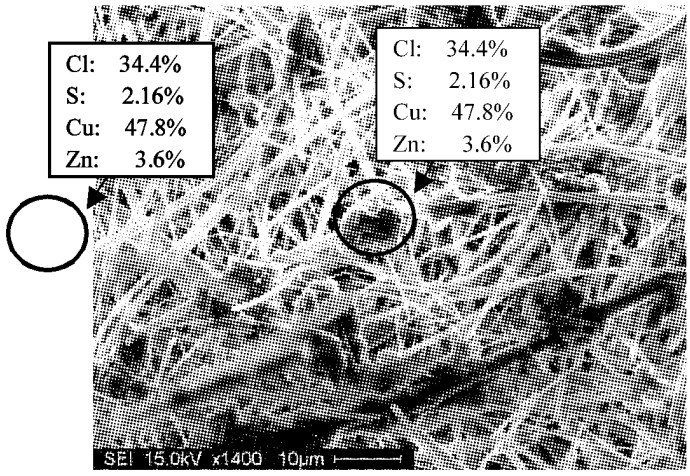

Fig. 10 SEM-EDX for the filter 3 in case HCl:SO_2=1:0.5

Influence of quenching rate on the condensation

As speculated previously, the fast quenching rate of flue gas is potentially able to increase the production amount of metal chloride. In this section, the naturally quenching mode was introduced to observe the influence of quenching rate, in which the temperatures of three filters were controlled as 1223 K, 503 K, and room temperature respectively. The cooling rate of this mode was roughly evaluated four times higher than previous quenching mode. It can be seen from figure 11 more than 90 % of vaporized metals condensed at filter 2 (503 K). Furthermore, the mole ratio of chloride to sulfate in the filter 2 was measured as 7.6:1 by IC. Comparing with another quenching mode, only 0.8:1 mole ratio of chloride to sulfate got in filter 3, this significant change indicates that the quenching rate has an obvious effect on the condensation of heavy metals. Because the main gas phase of Cu at the high temperature is CuCl and $(CuCl)_3$, the formation of $CuCl_2$ is caused by CuCl+Cl=$CuCl_2$. As to Zn and Pb, their main gas phases are $ZnCl_2$ and $PbCl_2$, so the condensation of $ZnCl_2$ and

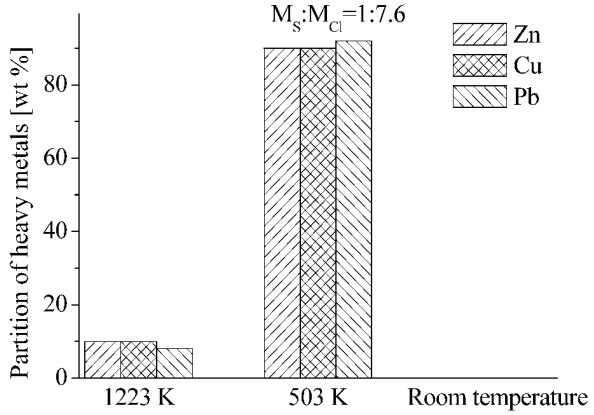

Fig. 11 Distribution of Zn, Cu, Pb with natural quenching mode (Cl/S ratio 1:1/2)

$PbCl_2$ at low temperature is maybe caused by the lack of residence time to react with SO_2. The transformation from MCl_2 to MSO_4 can be looked as a dechlorination process, so the equilibrium concentration of Cl radical in the flue gas can influence the distribution of Zn and Pb among chloride and sulfate. As a result, the reaction route happening during the cooling process, can be speculated as follows:

$$MCl_n \xrightarrow{SO_2} MSO_4$$

$$MCl_n \xrightarrow{Cl} MCl_2$$

Influence of H_2O on the condensation

H_2O has a significant effect on the chlorine behavior, which can decrease the concentration of Cl radical (Cheng, 2009). So, according to the reaction routes assumed in previous section, H_2O is able to increase the proportion of sulfate during the condensing process due to the lower concentration of Cl radical. If it is true, more heavy metals will condense at higher temperature in form of sulfate. To investigate the effect of H_2O on the condensation of heavy metals, 8.5 % water steam was injected into the flue gas. As can be seen from figure 12, the equilibrium calculation indicates that the assumed influence trend of H_2O on the heavy metals condensation is true. However, the experimental results shows that the condensing mass of heavy metals at filter 3 (573 K) is increased, which seems unreasonable because of the lower dew point of chloride than that of sulfate. Yet for all that, no condensation of Cu and the gentle reduction of Zn gas phase showed from 1100 K to 800 K make more mass of condensation metals at lower temperature is possible. At same time, the ratio of chloride to sulfate measured by IC analysis (table 2) indicates that the proportion of sulfate in filter 3 is increasing in case injection of H_2O. This result further confirms that the concentration of Cl radical has an important role on the heavy metals condensation due to the radical reaction.

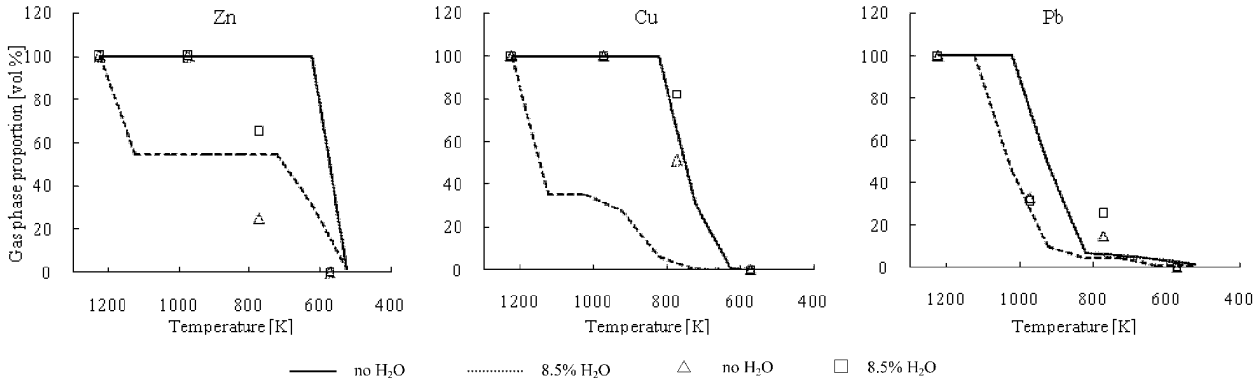

Fig.12 The effect of H_2O the condensation of heavy metals with Cl/S ratio 1:1/2
(lines represent equilibrium results; symbols represent experimental results)

Table 2 The ratio of chloride to sulfate for the deposition of heavy metals

	Filter 1	Filter 2	Filter 3
No H_2O	1:0	0.8:1	2.5:1
8.5% H_2O	1:0	0.4:1	1.8:1

CONCLUSIONS

As the first step of this study, the condensation behavior of these heavy metals was experimentally and thermodynamically investigated. Some conclusions were summarized as follows:

(1) Comparing with HCl, SO_2 presenting in the flue gas is easier to make heavy metals form sulfate and deposit at relatively high temperature section.

(2) The formation of chloride found in the experiment with 1 to 1/2 Cl/S ratio, being unavailable in the equilibrium calculation, implies that residence time or the quenching rate of flue gas in the cooling zone is able to influence the condensation of heavy metals. This speculation was verified by the quenching experiment, and the results indicate that rapid quenching rate tends to condense the heavy metals in form of chloride.

(3) The role of concentration of Cl radical in the flue gas was evaluated by the experiment with injecting H_2O. The reduction of Cl radical concentration caused by the H_2O increased the condensation amount of sulfate.

So the main condensing routes of heavy metals in the $O_2/HCl/SO_2/N_2$ can be roughly speculated as $MCl_n+SO_2 \rightarrow MSO_4$ and $MCl_n+Cl \rightarrow MCl_2$.

The experimental results got in this work are significant to control the behavior of heavy metals according what we want. If the formation of metal chloride needs to be inhibited due to the corrosivity, toxity and small particle size of the metal chloride, it can be implemented through improving the concentration of SO_2 or decrease the quenching rate of flue gas to deposit the heavy metals at suitable position in form of sulfate. As to the rough condensing model speculated here will be studied in more detail in future work.

NOTATIONS

$\overline{Q}$ average quenching rate, K/s
T(i) inlet temperature of cooling zone, K
T(o) outlet temperature of cooling zone, K
t residence time of flue gas in cooling zone, s

ACKNOWLEDGEMENTS

The financial support from Grant-in-aid for Scientific Research on Priority Areas (B), 20310048, Ministry of Education, Science, Sports and Technology, Japan was gratefully acknowledged.

REFERENCES

Abanades S., Flamant G., Gauthier D.: Environ. Sci. Technol, 36 (2002), pp.3879-3884.
Cheng Y. et al., Proc. Combust. Inst. (2009), doi:10.1016/j.proci.2008.07.021.
Lind T., Hokkinen J., Jokiniemi J. K.: Fuel Processing Technology, 88 (2007), pp.737-746.
Miller B., Dugwell D. R., Kandiyoti R.: Energy & Fuel, 17 (2003), pp.1382-1391.
Obernberger I. 1998. Austria, TU Graz, ISBN 3-7041-0254-7.
Ratafia B. J.; Fuel Process Tech, 39 (1994), pp.139-157.
Sorum L. Frandsen F. J., Hustad J. E.: Fuel, 83 (2004), pp.1703-1710.
Verhulst D., Buekens A. Spencer P. J., Eriksson G.: Environ. Sci. Technol., 30 (1996), pp.50-56.

DUAL-FUEL FLUIDIZED BED COMBUSTOR PROTOTYPE FOR RESIDENTIAL HEATING: STEADY-STATE AND DYNAMIC BEHAVIOR

Antonio Cammarota[1], Riccardo Chirone, Michele Miccio[2], Roberto Solimene[1], Massimo Urciuolo[3]

1Istituto di Ricerche sulla Combustione, Consiglio Nazionale delle Ricerche, Napoli, Italy
2Dipartimento di Ingegneria Chimica ed Alimentare, Università di Salerno, Fisciano (SA), Italy
3Dipartimento di Ingegneria Chimica, Università di Napoli Federico II, Napoli, Italy

Abstract: Fluidized bed combustion of biogenic fuels can be recognized as an attractive option for an ecologically sustainable use of biofuels in residential applications. Nevertheless, biomass combustion in fluidized bed reactors presents some drawbacks that are mainly related to mixing/segregation of fuel particles/volatile matter during devolatilization inside the bed and in the freeboard or to bed agglomeration. A prototype of a 30-50 kWth fluidized bed boiler for residential heating has been designed to burn either a gaseous combustible or a solid biomass fuel or both fuels at the same time. The prototype has been equipped with a gas burner located in the wind-box to optimize the start-up stage of the boiler and with a fluidized bed characterized by a conical geometry ("Gulf Stream" circulation) to improve the mixing of the fuel particles during both devolatilization and char burn-out. The operation of the combustor adopting wood pellets as fuel has been investigated to evaluate their use in residential combustion applications. Steady-state thermally stable regimes of operation have been recognized analyzing both boiler temperatures and gaseous emissions. The optimization of the steady-state operation of the boiler in terms of gaseous emissions has been achieved by varying the nominal thermal power and air excess. An *ad-hoc* experimental campaign has been carried out to analyze the dynamic performance of the prototype as a response to changes of the demanded thermal power. On the basis of the experimental data, an interpretation of the dynamic behavior of the fluidized bed boiler has been proposed.

Keywords: biomass, residential heating, dual-fuel boiler, gaseous emissions, dynamic model

INTRODUCTION

Fluidized bed combustion (FBC) has been indicated as one of the most promising and feasible technologies to burn biomass fuels (Saxena and Jotshi, 1994; Anthony, 1995), because of its fuel flexibility, high combustion efficiency and low environmental impact. Nevertheless, large scale applications of biomass fluidized bed combustion highlighted some drawbacks mostly related to the segregation/combustion of volatile matter (Leckner et al., 1984; Scala and Salatino, 1995) and to the fate of the ash components (Ohman et al., 2000). Biogenic fuels are typically characterized by a high volatile matter content which determines a large contribution of gas phase homogeneous combustion to overall heat release. This feature emphasizes the relevance of the localization of volatile matter release and of the mixing/segregation phenomena of volatiles with oxygen-rich streams inside the fluidized bed and in the upper regions of the reactor (freeboard). It is widely documented that devolatilization of high-volatile solid fuel particles occurs predominantly at or nearby the bed surface, as a consequence of the extensive particle segregation phenomenon (Nienow and Rowe, 1976; Fiorentino et al., 1997; Bruni et al., 2002; Rees et al., 2005). Accordingly, fuel burn-out takes place in a "stratified" manner with the establishment of diffusive or partly-premixed flames of volatile matter above the bed surface. This combustion pattern underlines the key role of the splash zone of the combustor as the prime location of volatile matter burn-out, often limited as a reaction controlling step, by gas-mixing phenomena occurring between oxygen-rich gas pockets issuing from the fluidizing gas bubbles and fuel-rich gas mainstream (Scala and Salatino, 2002; Niklasson and Johnsson, 2003; Solimene et al., 2004). The efficiency of the volatile matter combustion is intrinsically and strongly dependent on the efficient contact between volatiles and bed material as well as on the lateral spreading of fuel particles on the bed surface (Niklasson et al., 2002). As matter of fact, the entire bed section is scarcely interested by fuel particle devolatilization determining lower reactor performances. A reliable strategy to reduce the axial fuel particle segregation during devolatilization in the bed is to "force" the circulation of bed material. The circulation of bed material has to be enhanced in order to involve the devolatilizing fuel particles, too. This concept was firstly proposed by Merry and Davidson (1973) who suggested inducing gross circulation of bed particles by means of an uneven distribution of fluidizing gas flow through the distributor plate. These authors individuated a pair of cells of circulation in shallow fluidized bed evocating the "Gulf Stream" circulation. The "Gulf Stream" circulation has been adopted to the design of

the internally circulating fluidized bed combustors and gasifiers made by EBARA company. They use this kind of reactor to avoid floating of light fuel particles (biomass, waste) during devolatization and char burn-out (Steiner and Selinger, 2008). An alternative option is the use of a tapered fluidized bed configuration. In this case, the "Gulf stream" circulation in the dense phase can be established since the uneven fluidizing gas distribution in the bed is determined by bed geometry. The bed particle motion - upwards in the middle of the fluidization column and downwards along the walls - can determine an efficient solid mixing inside the bed (Schaafsma et al., 2006). Based on this concept, the performance of fluidized bed combustors characterized by a conical geometry and fuelled with different biogenic solid fuels has been tested verifying encouraging results in terms of gaseous emissions and combustion efficiency (Kuprianov et al., 2005; Toniato et al., 2007).

The aim of this work is the study of the steady state and dynamic behavior of a fluidized bed combustor prototype designed for the combustion of biogenic solid fuels for small-scale applications. The boiler prototype has been equipped with: i) a gas burner located into the wind-box to enable rapid the heating-up of the fluidized bed; ii) a fluidized bed characterized by a conical geometry. The prototype design has been suggested by previous experiments carried out with a tapered two-dimensional fluidized bed column. An experimental campaign has been carried out in order to characterize the boiler in terms of gaseous emissions by varying the nominal thermal power and air excess during the combustion of wood pellets. An *ad-hoc* experimental campaign has been carried out to analyze the dynamic performance of the prototype as a response to changes of the demanded thermal power. On the basis of the experimental data, a discussion of the dynamic behavior of the fluidized bed boiler prototype is carried out and a semi-quantitative description is developed.

EXPERIMENTAL

The combustor prototype used to assess the combustion behavior of a conical fluidized bed is sketched in Fig.1 together with the ancillary equipments. The experimental apparatus, basically, consists of a cylindrical wind-box, a fluidized bed characterized by conical geometry, an upper cylindrical section, a heat recovery system, a fuel particle feeding device, a particulate collection system, a set of gas analyzers and a data acquisition system. The steel cylindrical wind-box (ID 0.314m) is 0.2m high and is equipped with a premixed-gas burner (type Riello RX 70). The burner is located at the center of the wind-box perpendicularly to the axis of the column. The flame of the burner extends just below the distributor plate in order to quickly heat up the fluidized bed. The fan of the burner is also used to supply the necessary air to fluidize the bed and to burn the solid fuel. The internal lateral wall of the wind-box is insulated with ceramic material to minimize heat losses. The fluidizing gas flows thorough the wind-box and then through a low-pressure drop gas distributor plate having 37 *ad-hoc* diffusers. The plate of the distributor is made of stainless steel (AISI 310) and the diffusers are made of Inconel 600 in order to have a good thermal resistance. The bottom of the bed is cylindrical (stainless steel AISI 310 ID 0.2m) and 0.05m high. It is equipped with a tap to measure bed temperature and gas pressure at the bottom of the bed. The upper section of the bed is conical (stainless steel AISI 310) and 0.1m high. The angle of the walls of this section with respect to the vertical axis was chosen equal to 26°. The external lateral wall of the fluidization column is insulated by means of ceramic material. The fluidized bed column is also equipped with one pipe located just above the gas distributor to drain the bed inert material and with another one positioned just above the bed to keep the bed inventory constant. The steel upper cylindrical section (ID 0.314) is 0.8m high and acts as freeboard. It is equipped with: i) three probes to measure temperature and gas pressure along the column axis at heights above the top of the fluidized bed of 0.115 (TC1), 0.23 (TC2) and 0.64 m (TC3), respectively; ii) a smooth elbow duct to easily feed fuel particles into the boiler. The initial part of the freeboard to the level of TC2 is insulated by means of ceramic material. The flue gases leaving the freeboard are conveyed, first, into a water-cooled shell-tube heat exchanger for the heat recovery and, then, into the chimney. A cylindrical vessel coaxial to all the sections of the fluidization column is fitted externally to the column. A water stream flows from the bottom to the top of the gap between the external vessel and the fluidization column to reduce the operating temperature of column wall. This water stream is fed to the shell-tube exchanger for the heat recovery from the flue gases. The same water stream is cooled in a water-water plate heat exchanger and, then, it comes back into the boiler at the bottom forming a close circuit for the heat recovery. The cooling water of the plate heat exchanger is coming from the civil pipeline present in the laboratory and is discharged outside in suitable ducts. The inlet and outlet temperatures into the boiler of the water of the close circuit for the heat recovery are in the order of 50-60 and 70-90°C, respectively. The water temperature in the circuit after the wind-box and bed section is measured in order to estimate the heat losses. The continuous over-bed feeding system of the fuel particles consists of a belt conveyer used as metering device, a charge hopper, a measurement hopper and a set of flexible tubes interconnected and fixed to the smooth elbow duct present in the freeboard section of the fluidization column. The fuel mass rate is varied increasing the rotation velocity of the belt. The emptying time of the fuel measurement hopper enables one to

estimate the fuel mass feed rate.

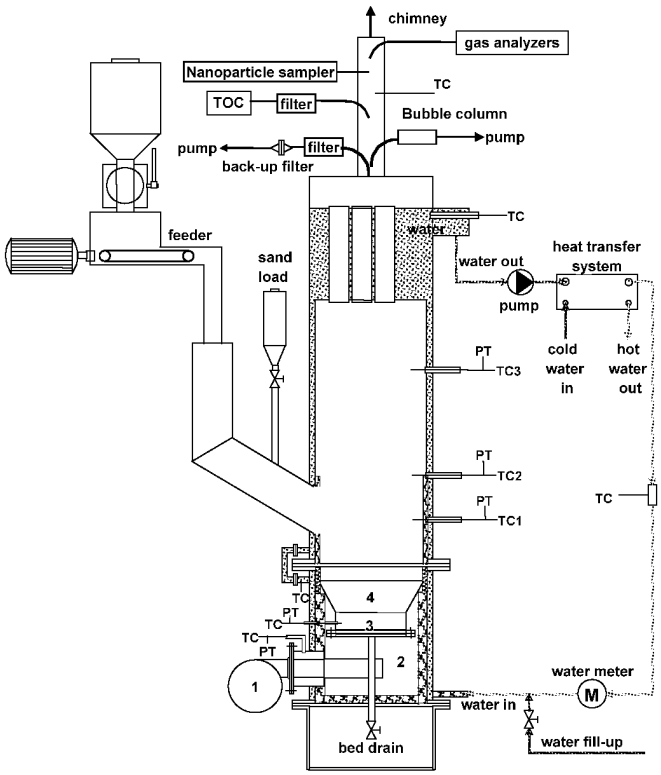

Fig. 1 Sketch of the experimental apparatus

Composition of the exhaust gas is measured by on-line sampling carried out with a heated probe connected to a set of continuous gas analyzers. The gas analyzers (ABB AO2020) are able to measure O_2 (Magnos 106), CO (Uras 14), CO_2 (Uras 14), NO_x (Limas 11), SO_2 (Limas 11) and Total Organic Carbon (TOC, Multi-Fid 14). Thermocouples, typically K-type, and high-precision piezo-resistive gas pressure transducers have been adopted to measure the temperature and the gas pressure along the fluidization column and for the different water streams. The data acquisition system consists of a PC equipped with an A/D converter (National Instruments cDAQ 9172). The system is able to acquire the electrical signals coming from pressure transducers, thermocouples and gas analyzers.

Quartzite sand sieved in size range 600-850 μm (U_{mf}=0.455m/s @ 293 K and 101 kPa) has been used in the experiments with a bed inventory kept constant at a value of 4 kg.

The fuel consists of wood pellets (cylindrical shape, 6 mm OD) whose proprieties are reported in Table 1 in terms of proximate and ultimate analysis and of lower heating value. Natural gas coming from the city pipeline available in the laboratory has been used as gaseous combustible for the gas burner. Technical air has been used as fluidizing gas in all the experiments.

The experimental campaign consisted of the combustion tests carried out both under steady state conditions with the continuous feeding of the wood pellets and under dynamic conditions generated by step variations of fuel feeding. In particular, the steady state operation of the fluidized boiler prototype was explored in a large variety of conditions, with different fuel mass flow rate and gas superficial velocity at the bottom of the bed, and, hence, variable nominal inlet thermal power, P.

Table 1 Properties of the tested wood pellets

Proximate Analysis, $\%_w$ (as received)	
Moisture	8.0
Volatile Matter	74.2
Ash	0.4
Fixed Carbon	17.4
Ultimate Analysis, $\%_w$ (dry basis)	
Carbon	50.4
Hydrogen	6.1
Nitrogen	0.1
Sulfur	0.1
Ash	0.4
Oxygen (by difference)	42.7
Lower Heating Value (MJ/kg)	18.24

RESULTS AND DISCUSSION

Steady State Behavior

The steady state operation of the boiler has been achieved for different operating conditions mainly varying fluidization velocity, air excess and fuel feeding rate (Toniato et al., 2007). As an example of the performances of the boiler during steady state operation, Figure 1 reports the CO emissions normalized with respect to the 11%v O_2 concentration as a function of P in the range 20÷60 kWth. CO is by far the largest unburned species and, hence, the main responsible for combustion efficiency loss. The experimental data highlight that in the range of air excess 50-100%, the normalized CO concentration does not depend on the air excess and presents a minimum value at about 35 kW. This nominal inlet thermal power corresponds to the best operating condition for the boiler from the point of view of CO emissions.

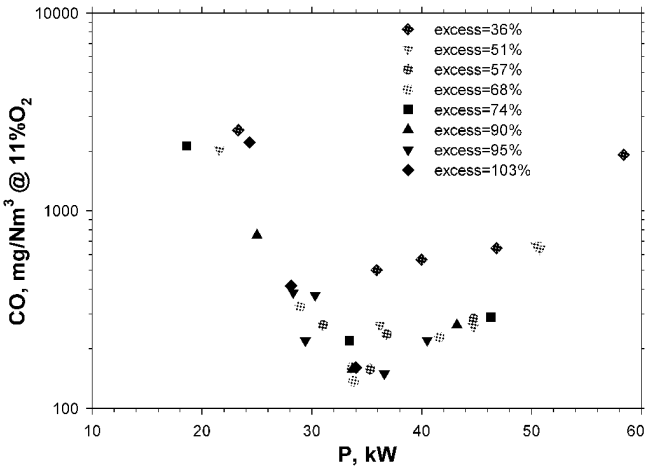

Fig.2 CO emissions at the exhaust as a function of the nominal inlet thermal power for different operating conditions

DYNAMIC BEHAVIOR

Approximation of dynamics with the FOPDT model

As a first approach for the description of the domestic boiler dynamics, a simplified linear model, i.e., the First Order Plus Dead Time (FOPDT) model, has been adopted (Stephanopoulos, 1984; Cooper, 2008). It is constituted by a first order dynamic model in series to a pure delay; its transfer function in the Laplace domain is:

$$\frac{K_p \cdot e^{-t_d s}}{\tau_p s + 1} \tag{1}$$

where K_P is the process gain, τ_P the process time constant and t_d the process dead time.

These parameters have been determined from experimental data according to the method of the "Process Reaction Curve" (Stephanopoulos, 1984). Some purposely planned dynamic tests were carried out by stepping down and up the fuel feed rate as an "input" process variable and by observing (with contemporary acquisition) the behavior of some selected "output" variables. A steady-state operation of the domestic boiler was both ensured before the step change and allowed to be reached again after it.

Temperatures of the combustion system and emissions of macro-pollutants have been considered as variables able to give a characterization of the domestic boiler dynamics. They are the temperature of the bed, T_b, the freeboard, T_{fb}, the stack gases, T_{fg}, and of water, T_{H2O}, taken at half-way along the cooling circuit; moreover, the stack emissions of the main macro-pollutants, i.e., the carbon monoxide [CO] and nitrogen oxides [NO_x] volume fractions in the flue gases, were also taken. All in all, they are the most relevant variables for process monitoring and performance evaluation; in addition, some of them are the most likely candidates to take the role of controlled variables in the development of regulation and automatic control of the domestic fluidized bed boiler.

The Loop-Pro® software (Cooper, 2008) has been used as a tool for elaboration, calculation and graphical representation. Basically, for each output variable, it determines the curve that better fits the observed dynamic response, minimizes the correlation coefficient, R^2, and, therefore, supplies the optimal FOPDT parameters.

The results are reported in Table 2 and in Fig.3.

Main Features of the Observed Dynamics

The process gain, K_p, which is the ratio between the variation of the observed process variable and the variation of the fuel feed rate, turns out positive in all cases; this means that the boiler dynamics is characterized by a "direct acting" response for all the observed variables. Values of K_p for the combustion temperatures, i.e., T_b, T_{fb} and T_{fg}, have the same units and fall within the same order of magnitude. Vice versa, the cooling circuit temperature displays a much smaller K_p, this latter finding being clearly related to the large thermal inertia of water contained in it. Values of K_p for the macro-pollutant emissions, which have different units, are consistently dissimilar for [CO] and [NO_x]. In particular, [CO] displays a much greater sensitivity than [NO_x] to the change in fuel feed rate, as demonstrated by a drop of 3 orders of magnitude for K_p.

Table 2 Values of the FOPDT parameters for the main process variables

Process Variable	Test code[0]	Step mode	K_p, °C/(kg/h)	τ_p, s	t_d, s	R^2
	08.10.08-IV	40% down	44.9	97.5	53.6	0.9834
T_b	08.10.08-V	40% up	51.8	197	31.0	0.9834
	25.06.08-III	20% down	39.7	154	19.7	0.9267
	08.10.08-IV	40% down	49.0	132	7.01	0.9796
T_{fb}	08.10.08-V	40% up	48.1	168	3.14	0.9811
	25.06.08-III	20% down	38.0	142	5.52	0.9126
	08.10.08-IV	40% down	14.7	301	0	0.9863
T_{fg}	08.10.08-V	40% up	13.7	225	14.3	0.9888
	25.06.08-III	20% down	11.2	244	2.19	0.9555
	08.10.08-IV	40% down	5.44	716	281	0.9896
T_{H_2O}	08.10.08-V	40% up	4.44	318	235	0.9917
	25.06.08-III	20% down	4.62	420	103	0.9877
			K_p, ppm/(kg/h)			
	08.10.08-IV	40% down	1.17E+03	17.5	34.7	0.7347
[CO]	08.10.08-V	40% up	1.24E+03	88.0	56.0	0.5372
	25.06.08-I	20% down	256.4	13.8	35.5	0.5464
	08.10.08-IV	40% down	5.24	32.5	97.5	0.7783
[NO_x]	08.10.08-V	40% up	3.80	9.01	68.3	0.7544
	25.06.08-I	20% down	7.10	3.55	72.9	0.6522

The process time constant, τ_P, which is a measure of the system ability to adjust itself after a dynamic change in an input variable, spans over 3 orders of magnitude. The macro-pollutant emissions exhibit the smallest τ_P values and, therefore, are the observed process variables that are more prone to achieve the new steady condition following the step change in fuel feed rate. Vice versa, the cooling circuit temperature displays the longest τ_P values: in this case both the overall resistance to heat transfer and the thermal inertia of water play together and determine the same dynamic effect. The combustion temperatures, i.e., T_b, T_{fb} and T_{fg}, are characterized by τ_P values in between: it is the thermal inertia of the bed that plays the role of a capacitance and determines a dynamic delay to an extent, however, that is less relevant compared to the water circuit.

The process dead time t_d, which is an indication of a measurement transportation lag in the system, spans over 2 orders of magnitude. Values of t_d are generally large for the macro-pollutant emissions: this is easily explained because the combustion gases have to spend a travel time from the bed to the stack once a step change is given in fuel feed rate. The longest t_d values are again found for the cooling circuit temperature, this finding being due to the same aforementioned reasons. The t_d values are generally low for combustion temperatures, i.e., T_b, T_{fb} and T_{fg}, but exhibit a certain spread; in particular, the zero value for T_{fg} in the case of the 40% step down appears unreasonable, although the authors checked that it was correctly calculated by the software.

It is well known that a linear system exhibits the same values of the FOPDT parameters independently of the size of the variation to which the input variable is subjected during a step test (Cooper, 2008); on the other side, a shift in values of the FOPDT parameters is an indication of non-linearity in the dynamic system. To this end Table 2 reports also the values of the FOPDT parameters as determined following a 20% step down of the fuel feed rate rather than 40%. It is difficult to draw a sharp conclusion from the above comparison because the

parameter values present some spread; however, [CO] seems to be the process variable whose dynamic response clearly departs from linearity, K_p decreasing by 1 order of magnitude when changing the step down size from 40% to 20%.

Finally, Table 2 reports the linear correlation coefficient, R^2, as an index of the statistical quality of FOPDT model fitting. There is a sharp distinction between temperatures on one side and macro-pollutant emissions on the other side, with $R^2<0.80$ for the latter ones. The explanation is clearly to be related to the fluctuating pattern that the macro-pollutant emissions generally exhibit around an average value representative of the steady-state, as it is confirmed without any doubt by the experimental time profiles of [CO] and [NOx] shown in Fig. 3.

CONCLUSIONS

A prototype of a 30-50 kWth fluidized bed boiler for residential heating has been successfully designed and effectively put into operation to burn either a solid biomass fuel or a gaseous combustible. The combustion of both fuels at the same time or an appropriate sequencing of their supply will be a future objective of the research work for optimization of the boiler management and of the heat end use.

The steady-state operation of the boiler carried out varying fluidization velocity, air excess and feed rate of wood pellets demonstrated that a nominal inlet thermal power of about 35 kW determines the best operating conditions from the view point of CO emissions, with the air excess in the range of 50-100%.

The dynamics of the domestic boiler prototype has been simply described in terms of First Order Plus Dead Time (FOPDT) model, which is the first step required to develop automatic regulation in terms of single-loop PID feedback control. All in all, it can be simply stated that the dynamics of the macro-pollutant emissions is the fastest one, whereas the dynamics of the cooling water circuit is the slowest one. Therefore, an appropriate decoupling of the control systems will be required in the future development work to ensure smooth and, at the same time, non-polluting performance of the domestic boiler during the expected load change operations.

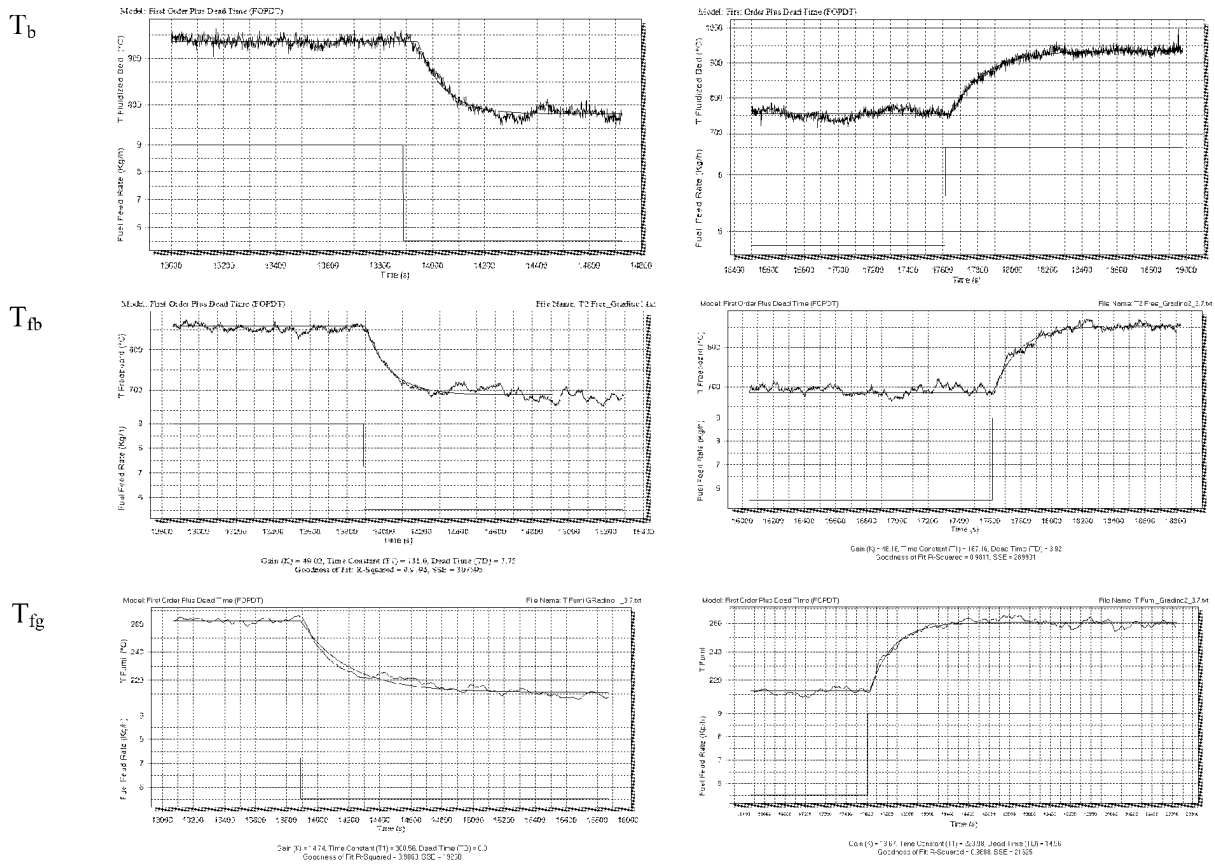

Fig.3 Dynamic response of the main process variables to a step change of the fuel feed rate: comparison of the FOPDT model to the actual time profile

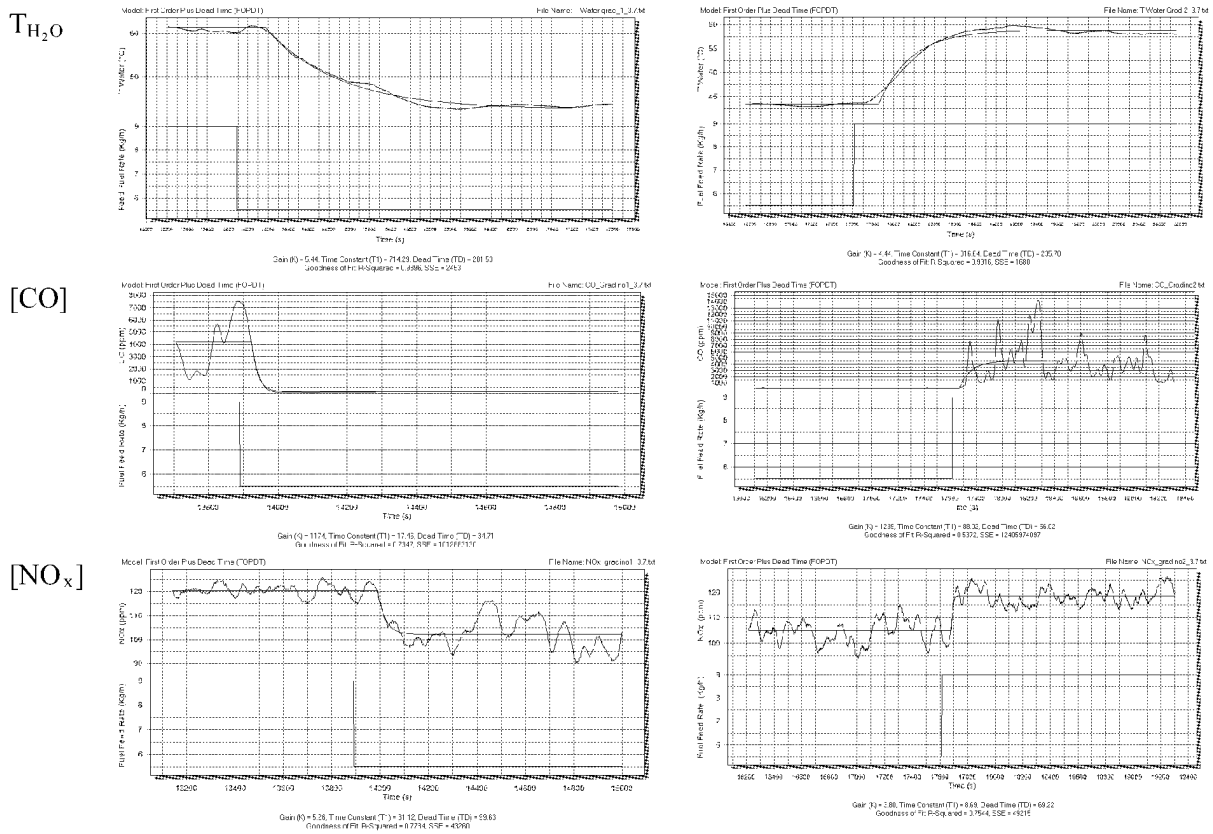

Fig.3 (Continued)

REFERENCES

Anthony, E. J.: Prog. Energy Combust. Sci. **21** (1995), pp.239-268.

Bruni, G., Solimene, R., Marzocchella, A., Salatino, P., Yates, J. G., Lettieri, P. and Fiorentino, M.: Powder Technol. **128** (2002), p.11.

Cooper D.J.: Practical Process Control, Control Station Inc., 2008.

Fiorentino, M., Marzocchella, A. and Salatino, P.: Chem. Eng. Sci. **52** (1997) p.1909.

Kuprianov, V. I., Permchart, T. W. and Janvijitsakul, K.: Fuel Process. Technol. **86** (2005), p.849.

Leckner, B., Andersson, B. A. and Vijil, J. (1984). Fluidized bed combustion of coal and biomass. In Proceedings of the conference: Combustion of Tomorrow's Fuels-II.

Merry, J. M. D. and Davidson, J. F.: Trans. Instn Chem. Engrs., **51** (1973), p.361.

Nienow, A. W. and Rowe, P. N. (1976). Fluidised bed mixing segregation and incineration in solid refuse treatment. In *Proceeding of the 1st International Symposium on Materials and Energy from Refuse*.

Niklasson, F., Thunman, H., Johnsson, F. and Leckner, B.: Ind. Eng. Chem. Res. 2002, 41, 4663.

Niklasson, F. and Johnsson, F. (2003). The local heat balance in a stationary fluidized-bed furnace burning biomass fuels. In Proceedings of 17th International Conference on Fluidized Bed Combustion.

Ohman, M., Nordin, A., Skrifvars, B., Backman, R. and Hupa, M.: Energy Fuels **14** (2000), p.169.

Saxena, S. C., and Jotshi, C. K.: Prog. Energy Combust. Sci. **20** (1994), pp.281-324.

Solimene, R., Marzocchella, A., Ragucci, R. and Salatino, P.: Ind. Eng. Chem. Res. **43** (2004), p.5738.

Scala, F. and Salatino, P.: Chem. Eng. Sci. **57** (2002), p.1175.

Schaafsma, S. H., Marx, T., and Hoffmann, A. C.: Chem. Eng. Sci. **61** (2006), p.4467.

Steiner, Ch. and Selinger A. (2008). Internally circulating fluidized bed boilers for biomass and waste: experience from large capacity plants (40-100 MWTH) in Asia and Europe. In Proceedings of the 9th International Conference on Circulating Fluidized Beds.

Rees, A. C., Davidson, J. F., Dennis, J. S. and Hayhurst, A. N. (2005). The rise and combustion of particles of sewage sludge and petroleum coke in a slugging fluidized bed. In Proceedings of 18th International Conference on Fluidized Bed Combustion.

Stephanopoulos G.: Chemical process control: an Introduction to theory and practice, Prentice Hall, 1984.

Toniato, G., Accordini, C., Cammarota, A., Chirone, R., Solimenę, R., and Urciuolo, M. (2007). Design and set-up of a bi-fuel fluidized bed combustor prototype for residential applications. In Proceedings of the 3rd European Combustion Meeting ECM 2007.

EXPERIMENTAL STUDY ON GAS-SOLID FLOW CHARCTERISTICS IN A CFB RISER OF 54m IN HEIGHT

N. Hu, H. R. Yang, H. Zhang, R. Q. Zhang, J.N.Cao, Q. Liu,J.F.Lu, G.X.Yue

Key Laboratory for Thermal Science and Power Engineering of Ministry of Education, Department of Thermal Engineering, Tsinghua University, Beijing, 100084, China

Abstract: Understanding the height effect on the gas-solid flow characteristics in a CFB riser is important as more and more large capacity CFB boilers are used and to be developed. In this study, a cold CFB test rig with a riser of 240mm in I.D. and 38m and 54m in height was built. The influences of operating conditions, such as solid inventory and fluidizing gas velocity, on the axial voidage profile along the riser were assessed. When the gas velocity exceeds the transport velocity, the S-shaped profile of voidage in the riser was established. At the same time, the voidage in top-dilute section reached the saturation carrying capacity, and the solids circulation rate did not vary with the height of the riser nor the solids inventory. It was also found the critical solids inventory for the saturation carrying capacity increases as the riser height increases. When the height was changed from 38m to 54m, the critical solids inventory increased about 25% from about 40kg to about 50kg, and pressure drop in the furnace also increased about 25%.
Keywords: CFB, gas-solid flow, riser height, bed inventory

INTRODUCTION

Circulating fluidized bed (CFB) boiler combustion technology is a clean coal combustion technology featured with excellent fuel flexibility and cost-effective emission control. More than 3000 CFB boilers are in operation in China (Yue, 2006). More and more CFB boilers are used in power generation. It is estimated more than 150 units of 135MWe CFB boiler (Li et al., 2009a) are in operation and more 60 units 300 MWe CFB boiler are in operation or construction (Li et al., 2009b). A 600MWe supercritical CFB boiler has been designed and is planned to be put into commissioning by the end of 2011 in Baima (Wu et al., 2005).

For those CFB boilers used in power generation, the furnace is tall. For a 300MWe CFB boiler, the furnace height, H_r is about 35-38m; and the 600MWe CFB boiler, H_r can be as large as 54m. Obviously, the height of these boilers is much larger than that of the CFB apparatus used in laboratory experiments. In laboratory, the CFB riser usually is a few meter high and seldom heriger than 20m. Thus, when H_r >30 m, the furnace is often called very tall or ultra-tall. Obviously, to properly design and operate large capacity CFB boilers, it is necessary to understand the gas-solid two-phase flow characteristics in the so-called ultra-tall furnace.

In the furnace of a CFB boiler, the flow pattern in the furnace can be considered as a superposition of a bubbling or turbulent bed formed by large particles at the bottom and a fast fluidized bed formed by fine particles in the freeboard (Yue et al., 2005). The axial profile of the solid suspension density, ρ_b or voidage ε_b along the furnace height strongly couples with that of heat transfer coefficient and thereby the arrangement of heating surfaces. It also affects the penetration depth and diffusion rate of the secondary air, as well as the residence time, thereby the combustion efficiency (Xiao et al., 2005). In addition, the ρ_b profile directly couples with the solid inventory I_v, the axial profile of pressure drop in the furnace, and thus the selection of the primary air fan. Therefore, the axial ρ_b profile is one of the most important flow characteristics to be studied in a CFB boiler.

According to the previous studies, the total solid inventory I_v in a CFB is normally a controllable variable. The axial profile of ρ_b or ε_b in both the dense bed and fast fluidized bed are influenced not only by operating conditions such as fluidizing gas velocity U_g, solid circulation rate G_s and the geometric structure of the components in the circulating loop, but also by I_v (Weinstein et al., 1983; Li et al., 1988; Mori et al., 1992). However, so far, the impact of I_v on gas-solid flow characteristics in the riser is in controversy. Based on the experiment results obtained in a cold CFB rig with a riser of 10m height and 90mm in diameter, Li et al. (1988) reported that the height of the bottom dense bed H_{bd} increases with increasing I_v but the ε_b in top dilute section remains unchanged when U_g and G_s are constant. They also found that to realize fast fluidization regime at a certain U_g, the I_v should be maintained above a critical values I_v^*, so G_s in the upper riser can reach the saturated value G_s^* for pneumatically transport and a dense zone can appear in the bottom of the riser. Similar results were found by Xu et al. (2003) based on the experiments in a cold CFB rig with a riser of 3m in height and 97mm in diameter. On the contrary, some researchers argued that the ε_b distribution in the riser does not change with I_v, and instead it is only the function of U_g and G_s (Rhodes et al., 1992; Chang and Louge, 1992). It

is suspected that the controversy of the I_v effect on the flow characteristics was at least partially attributed to the height of experimental rig.

In design and operation of the ultra tall CFB boilers, it is important to know existing experimental data and model for the ρ_b axial profiles are valid, and how much extend is the effect of the riser height, and is there any unique feature as the height of the riser is out of conventional range. Consequently, a cold CFB experimental rig with a ultra-tall riser (38 and 54 m respectively) was built. The influence of operating conditions, such as H_r, I_v and U_g, on the axial voidage profile along the riser was assessed.

EXPERIMENTAL

The experimental rig was installed next to a 300MWe CFB boiler in Baima, China, and the schematic is shown in Fig. 1. The main body consists of a riser, a cyclone, a return leg and a loop seal. The riser has inner diameter of 240 mm. The cyclone was installed close to the riser roof, at the height of 38 m and 54 m above the distributor respectively. The fluidizing air was induced from the secondary air fan of the boiler, with pressure head of 40 kPa. The air distributor was composed of an orifice plate and stainless sieve. The flow rate of the fluidizing air was controlled by an adjustable valve and online measured by a vortex flow meter. Solid particles were carried by the fluidizing air upward in the riser and then into the cyclone. After separation, nearly all of them were collected and returned to the riser through the return leg and the loop seal. The return leg is 75mm I.D., made of transparent plexiglass for observation. A butterfly valve and three-way valve were installed on the return leg.

All the experiments were carried out at ambient temperature and pressure. Solid material used was quartz sand with the diameter ranged from 150 μm to 250 μm. It has the real density of 2630 kg/m^3 and bulk density of 1550kg/m^3.

The axial voidage along the riser was derived by pressure drop measured along the riser height. The lowest measurement point P_0 was installed right below the air distributor and the next one P_1 was installed 5cm above the distributor. The rest pressure taps were installed with 2 m interval along the riser. At same time, the voidage (or solid concentration) at 27m height (from the air distributor) was measured by a fiber optic probe. The methods measuring the solid circulation rate, G_s, was based on the time accounting for the returning particles to reach a certain height in the return leg after a sudden close of the butterfly valve.

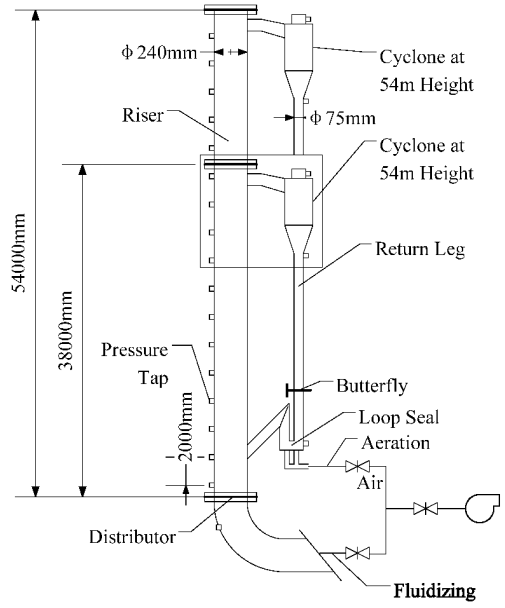

Fig. 1 Schematic diagram of experimental apparatus

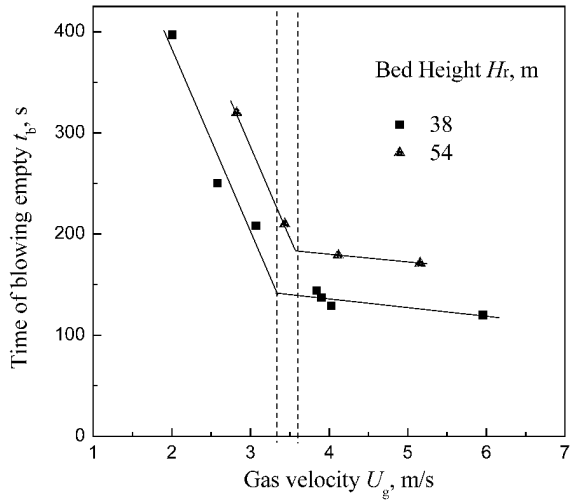

Fig. 2 Time required for all solids inventory to leave the riser at different fluidizing gas velocity

Table 1 U_{tr}'s calculated from different empirical formula (m/s)

Matsen (1982)	Li (1982)	Adanz (1993)	Bai (1993)	Subbarao (1988)
7.0	5.3	2.87	2.24	36.1

To ensure the gas-solid flow in the riser in fast fluidization, U_g was kept above the transport velocity, U_{tr} (*Yerushalmi* et al., *1979*). In this study, the empty time (blow-off) method developed by *Perales* et al. (*1991*) was adopted to determine the U_{tr}. On the curve of blow-off time verse U_g, as shown in Fig. 2, the bending point is corresponding to the U_{tr}.

Based on above blow-off method, the U_{tr} was measured in 38m and 54m riser respectively under the same I_v of 40kg, and the results are shown in Fig. 2. It can be seen that at the same U_g, the blow-off time is about 20% longer for higher riser in the pneumatic transport regime, and 30%-40% longer in the fast bed regime. However, the difference of U_{tr} is much less sensitive to the riser height. It is about 3.5m/s for both risers, and for 54m riser the value is less than 10% higher. In the experiments, the U_{tr} was chosen higher than 3.5m/s. Table 1 gives U_{tr}'s calculated from different empirical formula. For the different of experiment method and solid particles, the discrepancy among the values is wide. The results are similar to the values calculated by the empirical correlation obtained from the experiments with the solids of sands and coal.

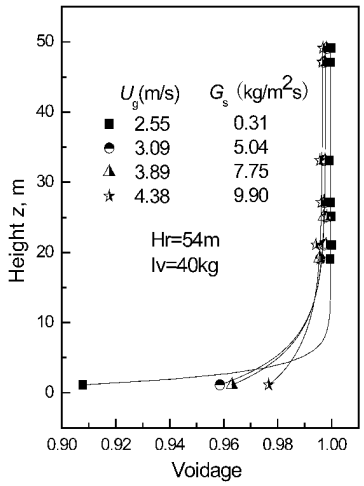

Fig.3 Variations of axial voidage profile with U_g

RESULTS

The influence of gas velocity U_g

The axial voidage profiles at different gas velocity in the 54m riser are shown in Fig. 3 When I_v keeps 40kg and U_g increases, the voidage increases at bottom region but decreases at top region. The solids circulating, G_s is increasing at the same time. It indicates that more solid particles were carried by gas with the increasing of U_g. The results are consistent with what found by Bai et al. (1992).

The influence of solids inventory I_v

Figure 4(a) and 4(b) shows the axial voidage profiles at different solid inventories, I_v's, in the 38m riser and 54m riser respectively. The voidage at bottom dense bed and transition zone dramatically decreases when I_v increases. However, in the top zone, the voidage obviously decreases when I_v is small and it becomes nearly constant when I_v is greater than a certain value.

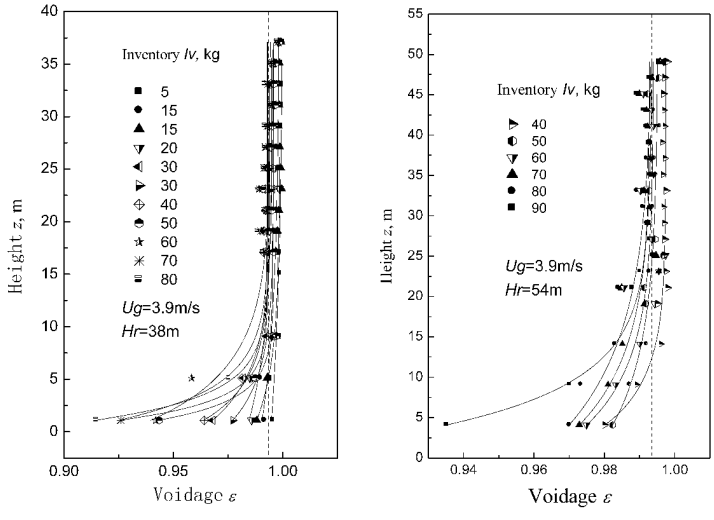

Fig. 4 Variations of axial voidage profile with solids inventory and riser height

The results of solid fraction measured by fiber optic probe at height 27m (shown in Fig. 5b) shows for both risers, the solid fraction linearly increases with I_v, and then turns in to a nearly constant as I_v exceeds a certain value. Combined with the results shown in Fig. 4, it can be concluded that the voidage above 25m does not appreciably change with height increasing.

At a given U_g, the variations of G_s versus I_v in different riser heights are plotted in Fig. 5c. Clearly, two stages can be found for the variation of G_s with I_v. In the first stage, G_s increases rapidly with I_v; and in the second stage, G_s is nearly constant as Iv exceeds a critical value, I_v^*. This G_s between the two stages is named as the saturated G_s^*. In the second stage, the further increase of I_v mainly accumulates particles in the bottom riser. Figure 5a shows the variation of total pressure drop along the riser with I_v. As the I_v increasing, the pressure drop along the whole riser increased linearly.

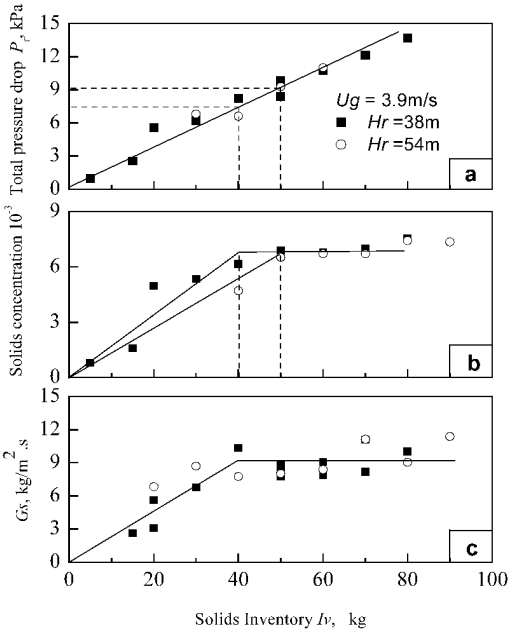

Fig. 5 Variations of pressure drop across the riser, solid fraction at 27m high, and G_s with solids inventory

The influence of riser height H_r

As mentioned above, the voidage in the top zone and G_s are maintaining constant when I_v exceed a critical value. From Fig. 5b and 5c, it can be seen that with different riser height, the values of G_s^* keeps nearly the same, and so does the corresponding voidage. However, the critical value of I_v is larger for the taller riser. When H_r=38m, I_v^*= 40kg and when H_r=54m, I_v^*=50kg. The total pressure drops of the riser are 7.4kPa and 9.1kPa, respectively, seen in Fig. 5a. Moreover, when the solids inventories are equivalent, the total pressure drop along the riser doesn't change with different riser height.

DISCUSSION

By analyzing the results of our experiments and the structure of the experimental rigs in the published literature, it is believed that the controversy in the I_v effect on gas-solid flow characteristics in the riser lies in the restriction of return valve. When the return valve is with weak restriction, the height of dense bed in a S-shaped voidage profile is affected significantly by I_v while the voidage in the bottom dense section and in the upper dilute section remain nearly constant. On the contrary, when a strong constraint return valve is used, at given U_g and G_s, the increment of I_v accumulates in the standpipe compensates the resistance of the return valve. Consequently, the variation of I_v plays minimal effect on the axial voidage profile (Rhodes et al., 1992; Chang and Louge, 1992).

At same time, the height of the riser also affects the axial voidage profile in the riser, and the S-shaped axial voidage profile can only be observed in a high enough riser (*Li* et al., *1988*). For a short riser, the gas-solid flow in the upper dilute region could not reach the saturation carrying capacity at certain U_g because the freeboard length was lower than TDH (*Bai* et al., *1995*). For a tall riser that could keep the freeboard length larger than TDH at certain U_g, when a return valve of weak resistance was equipped, S-shaped voidage profile is formed and the variation of Iv would have no influence on the voidage on top dilute region or G_s.

In the CFB boilers, a loop seal with low gas solid flow resistance is commonly used. The furnace height is normally higher than 20 m. At typical U_g of 4-5m/s, when $I_v < I_v^*$, fast fluidization regime can be realized, i.e., gas-solids flow in the upper dilute furnace reaches the saturation state (*Xu* et al., *2003*).

CONCLUSIONS

To properly design the large capacity CFB boilers used in power generation, it is of significance to conduct experimental study on the flow characteristics in the riser with ultra-tall heights (>30m). In this study, a cold CFB test rig with a riser 38 m and 54 m in height respectively was built to investigate the influence of operating conditions, including total solids inventory I_v, and fluidizing gas velocity U_g, on the axial voidage profile along the riser and solids circulation rate G_s in these risers. Experimental results showed that at an U_g greater than the transport velocity, when I_v is above a critical value, the S-shaped voidage profile for fast fluidization appears in the riser. The voidage in top dilute section and Gs does not change with Hr nor I_v. The critical I_v for saturation carrying capacity increases from 40 kg to 50 kg when the height of riser increases from 38 m and 54 m. The pressure drops in the riser are about 7000Pa and 9000Pa, respectively. For the 600MWe supercritical CFB boiler with 54m furnace in height, only a modest increment in I_v and power of forced draft fans is needed to obtain high enough G_s to meet the requirements of heating surfaces arrangement in furnace and the circulation loop. The distribution of gas-solid concentration in the riser is affected not only by the U_g and G_s, but also by I_v. When the riser is high enough and the return valve is of weak restriction, the fast fluidization with S-shaped voidage profile is easier to be formed in the riser.

NOTATIONS

G_s	solid circulating rate, kg/m^{2}s	H_{bd}	height bottom-dense, m
G_s^*	saturation carrying capacity, kg/m^{2}s	H_r	height of riser, m
I_v	solid inventory, kg	P_{dr}	pressure drop, Pa
I_v^*	saturation carrying I_v, kg	ε_b	voidage
U_g	fluidizing gas velocity, m/s	ρ_b	solid suspension density

ACKNOWLEDGEMENTS

Financial supports of this work by Key Project of the National Eleventh-Five Year Research Program of China (2006BAA03B01) and National Science Fund Committee (50406002) are gratefully acknowledged.

REFERENCES

Adanez J, LF de Diego, P Gayan, Powder Technology, 77 (1993) 61-68.
Bai D., Jin Y., Yu Z., Chem. Eng. Technol. 16(1993) 307-313.
Bai D., Jin Y., Yu Z., et al., Powder Technol. 71(1992) 51-58.
Bai D., Kato K, Journal of Chemical Engineering of Japan, 1995, 28(2), 179-185.
Hirama T. And Takeuchi H., Powder Technol. 70(1992) 215-222.
Chang H. and Louge M., Powder Technol. 70(1992) 259-270.
Li S.H., Zhang H., Yang H.R., Chem. Eng. Technol. 30 (2007) 1-7.
Li J.F., Yang S., Hao J. H. et al., Status of 135MWe CFB Boilers in China, 20th International Fluidized Bed Combustion Conference, (2009a), Xia'an China.
Li J.F., Hao J. H.Yang D., et al., Status of 300MWe CFB Boiler Operation in China, 20th International Fluidized Bed Combustion Conference, (2009b), Xia'an China.
Li J., Tung Y., Kwauk M., in: J. F. Large, P. Basu (Eds.), Circulating Fluidized Bed Technology II, Pergamon Press, Oxford, 1988, 193-203.
Li Y., Chen B., Wang F. et al. M. Kwauk and D. Kunni (Eds.), Science and Technology Press, 1982, 124-134.
Matsen J.M., Powder Technology, 32(1), 1982, 21-33.
Mori S., Liu D., Kato K., et al, Powder Technol. 70(1992), 223-227.
Perales J.F., Coll T., Liop M.F. et al, in: P. Basu, M. Horio, M. Hasatami (eds.), Circulating fluidized Bed Technology III, Pergamon, Oxford, 1991, 73-78.
Rhodes M. J., Laussmann P., Can. J. Chem. Eng. 70 (1992) 625-630.
Subbarao D., Reprints for the 2nd int. conf. on CFB, Compiegne, France, 1988, 14-18.
Weinstein H., Graff R. A., Meller M., et al., in: D. Kunii, R. Toei (Eds.), Fluidization, vol. IV, Engineering Foundation, New York, 1983, pp.299-306.
Wu Y., Lu J., Zhang J., et al., in: K.F. Cen (Eds.), Circulating Fluidized Bed Technology VIII, International Academic Publisher, Hang Zhou, 2005, 529-544.
Xiao X., Yang H., Zhang H. et al., Energy & fuels, 2005,19 (4): 1520-1525.
Xu G., Gao S., Powder Technol. 137(2003) 63-76.
Yerushalmi J. and Cankurt N.T., Powder Technol., 1979, 24(2): 187-205.
Yue G, Lu J, Zhang H, et al. Design Theory of Circulating Fluidized Bed Boilers. 18th International Fluidized Bed Combustion Conference, May 18-21, 2005, Toronto Canada.
Yue G., in: Yue G. (eds.), 1st Fluidization combustion and technology in China, 2006, 1-30.

STUDY OF AIR JET PENETRATION IN A FLUIDIZED BED

X. L. Zhou, L. M. Cheng, Q. H. Wang, M. X. Fang, Z. Y. Luo, K. F. Cen

Institute for Thermal Power Engineering, State Key Laboratory of Clean Energy Utilization, Zhejiang University, Hangzhou, 310027, China

Abstract: This work presents experimental and numerical simulation results on secondary air jet penetration into a dense phase of a 2-D fluidized bed. Velocity measuring method and non-intrusive methods based on images were used in the experiments. Effects of secondary air nozzle size and angles, secondary air jet flow velocity and suspension density of the fluidized bed material on the air jet penetration were tested. The results show that with increasing of secondary air jet velocity, the jet range increases exponentially. Secondary air jet range decreases exponentially with increasing of average bed suspension density. The size of secondary air nozzle does not have significant impact on jet range. However, larger nozzle size may result in a lower velocity decay coefficient. It was also found the secondary air nozzle angle is not an independent parameter affecting jet range. The jet range may penetrate the most depth point into the fluidized bed with the angle of -30°. As a comparison, the numerical simulation was done with same parameters in the experiments. Comparison of experimental and numerical results shows good agreements.

Keywords: fluidized bed,secondary air,jet range,penetration

INTRODUCTION

Circulating fluidized bed (CFB) boilers have excellences of extensive fuel flexibility, low NO_x emission, high desulfurizing efficiency and flexibility in load capability (Koornneef et al., 2007). The capacity of CFB boiler is fast augmenting these years. In China about more than ten CFB boilers of 300MWe with sub-critical steam parameters have been put into operation. The development of 600 MW super-critical CFB boiler is on the agenda (Cheng et al., 2008). With the scaling up of capacity, the cross section of a CFB boiler furnace is increased. One important question raised is the secondary air jet penetration into the fluidized bed furnace.

Secondary air plays an important role in a CFB boiler. Its injection supplied oxygen to the combustion and enhanced the turbulence intensity of furnace. It is also an effective way to control the thermal nitrogen oxide (NO_x) formation. Further more, it is used for load control in operating CFB boilers (Brereton, 1997).

Available studies in the literatures have been mostly carried out on chemical industrial CFB risers. Zheng et al. (1992) reported an increase in radial dispersion coefficients with a secondary air injection. Marzochella and Arena (1996) studied the mixing phenomena of secondary air using two different types of injectors: four-point radial injection and circumferential injection. They observed completely different patterns of gas mixing. Namkung and Kim (2000) investigated the effects of the secondary air injection on radial gas mixing using one-point tangential and radial injectors. They also reported an increase in radial gas dispersion coefficient with secondary air. Koksal and Hamdullahpur (2004) used three different types of injectors (tangential, radial and mixed) to study the gas mixing in CFB riser. They found that the most effective injector in improving gas mixing was the radial injector.

A CFB used in power plants has different with a chemical industrial CFB riser. Usually CFB boilers have rectangular furnaces with large cross sections. There is not much information on hydrodynamics of secondary air injection, specially the secondary air jet penetration into a gas-solids suspension phase in a fluidized bed furnace. Researches on effects of secondary air injection can not only enhance the understanding of gas–solid flow patterns in CFB units with secondary but can also be applied in large-scale CFB boilers' design. This paper presents the results of experimental and numerical simulation studies on secondary air injection in a fluidized bed.

EXPERIMENTAL

Experimental setup

The experiments were carried out in a two-dimensional cold fluidized bed set up shown in Fig.1. It has a height of 1000 mm with 400 mm × 50 mm cross-section. It was mainly made of plexiglass. There are 81 small openings at secondary air injection region on the rear wall used for gas velocity measuring. The air distributor was formed by 260 holes (5 mm diameter) and covered by a filtration fabric. At the top of fluidized bed, a wire netting was set to prevent particles escaping. The fluidized bed front wall was made of toughened glass through

which longitudinal section of the bed could be photographed. During the non-intrusive tests a black cloth covered the rear wall to generate more contrast on the images. The secondary air nozzle was located at a height of 300 mm above the distributor plate and its injecting angle may be varied from 0° to 45°. Different size nozzles were used with diameters of 10 mm–30 mm.

The Geldart-B glass particles (Geldart, 1973) were used as the bed materials for the experiments. It has a density of 2460 kg/m^3 and 605 μm in average sieve diameter. The properties of the bed material were given in Table 1.

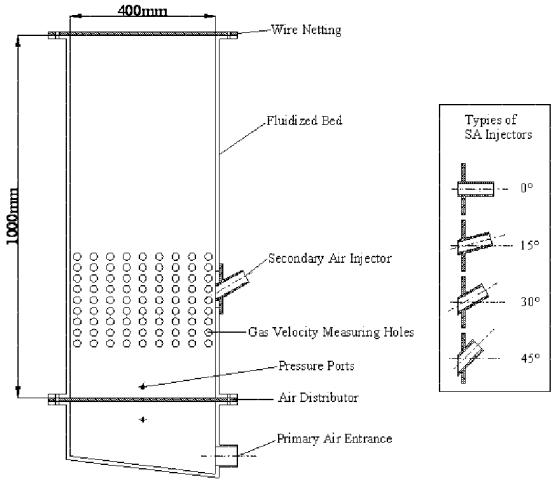

Fig. 1 2-D cold fluidized bed used in the experiments

Table 1 Properties of the particles used in the experiments

Parameters	Glass particle
Geldart's classification	B
Mean sieve diameter, mm	605
Density, kgm^{-3}	2460
Bulk density, kgm^{-3}	1460
Terminal velocity, ms^{-1}	4.81
Minimum fluidization velocity, ms^{-1}	0.31

Experimental procedure

The experiments included two parts. First a 2-D air velocity profiles in secondary air region were measured while the bed was operated without bed material. A S-shaped pitot tube was put into the 81 points (9 rows × 9 lines) to measure the horizontal and vertical gas velocities separately in the tests.

Second the bed was operated at fluidization conditions with the bed material. A digital camera was used to take pictures of the moving particles in the bed. A spotlight of 1000 watts was used for bed illumination. The image resolution factor was set to 1200×1600. Since the bed material is white and background is black, the contrast may give the message of solid concentration for each pixel. The pictures were dealt with visualization analysis as following steps: (1) The images were converted to grayscale pictures, which contained a gray level for each pixel; (2) Then grayscale pictures were converted to pseudo-color pictures to enhance the displayed contrast; (3) Finally a concentration map of the gas-solids phase was obtained and then the secondary air jet flow could be identified from the map for each test conditions. Similar methods were performed by Sánchez-Delgado et al. (2008) and Lim et al. (2006). The variation of the operational parameters in the experiments is given in Table 2.

Table 2 Operational parameters

Parameter	Values	
	Empty bed	Fluidized bed
Height of static bed, mm	/	150, 200, 250, 300
Velocity of primary air, m s^{-1}	1.67, 1.94, 2.22, 2.50	1.30, 1.52, 1.74, 1.95, 2.17
Velocity of secondary air, m s^{-1}	10, 15, 20, 25	10~40
Angles of secondary injector, °	0, 15, 30, 45	0, 15, 30, 45
Diameters of secondary injector, mm	10, 15, 20, 25, 30	10, 15, 20, 25, 30

RESULTS AND DISCUSSION

Description of secondary air jet range

Different conceptions of jet flow range were used to describe the jet flow penetration through different experimental methods, such as temperature method, velocity method and image method（Wang and Shen，1987）. When a secondary air jet is injected into a gas-solid mixed flow at an angle to horizontal in a fluidized

bed, it spreads on both axial and radial directions. The surrounding gas-solid flow plays a role of resistance through collision and entrainment. This results in velocity of jet core decreases on both horizontal and vertical directions while moving forward. Figure 2 shows a typical contour map of the jet horizontal velocity. For an oblique downward jet flow, it has an inflexion point when the vertical velocity decays to zero, and then it begins to move upward. The horizontal velocity also decays during the whole process.

In order to describe this phenomenon clearly, 3 different concepts of secondary air jet range are defined. Shown in Fig.2, the jet flow enters the gas-solids phase. Its moves upward at a inflexion point and then its axial line meets the horizontal line from the nozzle level. The distance from this meeting point to the secondary nozzle is defined as **core range** (x_{core}). At same level, the distance between the intersection point of jet edge with horizontal line and the secondary air nozzle is defined as **edge range** (x_{edge}). When the horizontal velocity was decayed to zero, the jet flow reached its **maximum range** (x_{max}).

These three ranges of secondary air jet flow may be measured with measuring local gas velocities by pitot tube in a pure air running bed. In case the bed is run with bed material, symbol x_f is taken as the maximum range. It may be obtained with analysis of the images taken (Figure 3).

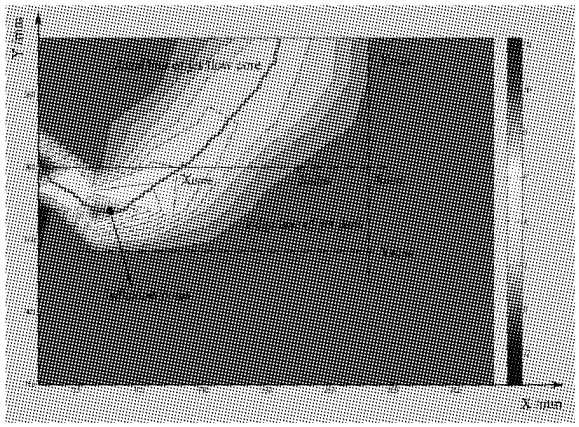

Fig. 2 Jet flow ranges in horizontal velocity contour map

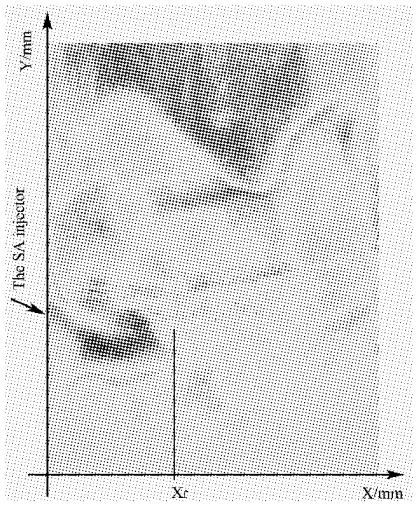

Fig. 3 A typical image taken in the fluidized bed tests

A parameter k, defined as velocity decay coefficient of jet flow core, is introduced to describe the velocity decay of jet flow core by equation (1):

$$k = \left(1 - \frac{u_{xcore}}{u_{SA}}\right) \Big/ X_{core} \tag{1}$$

where u_{xcore} is the horizontal velocity of jet flow core at X_{core} and u_{SA} is the initial horizontal velocity at secondary air jet outlet. X_i is a non-dimensional jet range. It is calculated by the following equation:

$$X_i = x_i / d \tag{2}$$

where x_i is an absolute jet range and d is the nozzle diameter of secondary air.

Effect of nozzle diameter on secondary air jet range

Five different size nozzles of secondary air were tested while the other parameters remained same. In the tests the nozzles' angle was kept as -30°.

Figure 4 shows the variation of secondary jet ranges X_{core}, X_{edge}, X_{max} and X_f with different size of nozzles. The tests were done while the primary air velocity was 2.89 m/s and the secondary air velocity was 15 m/s.

Numerical simulations using FLUENT were done with the same parameters. The computed jet ranges X^s_{core} and X^s_{edge} are also shown in Figure 4.

Both experimental data and simulation results show week relationship between the jet range and nozzle size. However, it can be clear see that the velocity decay coefficient k measured decreases as the nozzle size

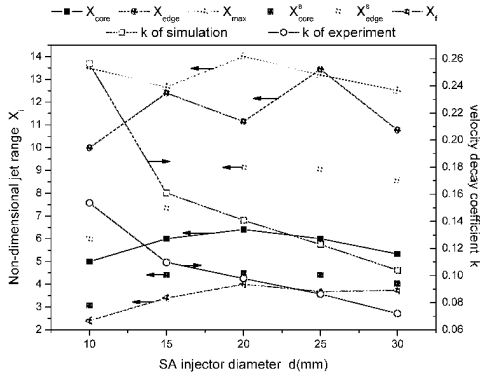

Fig.4 Effect of nozzle diameter on secondary air jet range and velocity decay coefficient k

increases. Simulation results got similar shape curve but with higher values.

Effect of injector angle on jet range

Figure 5 shows the variation of secondary air jet ranges at different nozzle injecting angles in the fluidized bed experiments. The tests were done while the primary air velocity is 1.74m/s and the bed suspension density is 680 kg/m^3. It may be found the jet range reaches the longest distance while the nozzle injecting angle is -30° among the three tests. However the results from the only air running tests gave a different phenomenon (Figure 6): the jet ranges increase and the velocity decay coefficient decreases with the injector angle increment. This may be caused by much higher resistance in a fluidized bed to secondary air jet as the higher density of the gas-solids phase, comparing to the only air running bed. In case the jet angle inclines too much, e.g. -45°, much more momentum may be consumed on the vertical direction. This will result in a decrease of jet range.

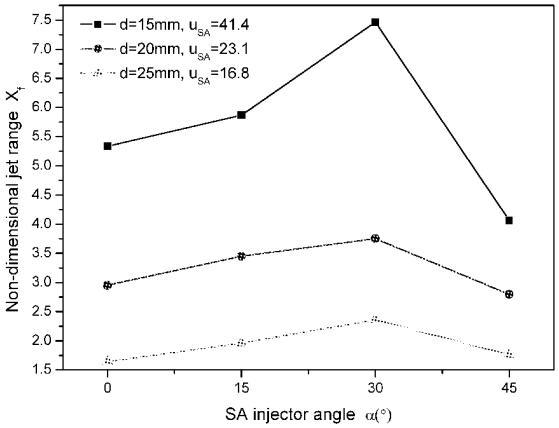

Fig. 5 Effect of injector angle on SA jet range in fluidized bed

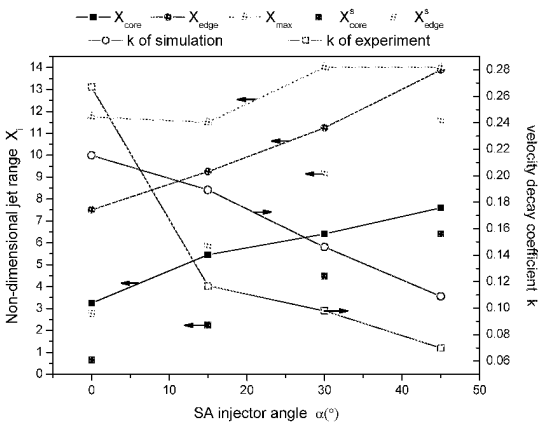

Fig. 6 Effect of injector angle on SA jet ranges in only air running bed

Effect of secondary air velocity on jet range

The secondary air velocity is a significant parameter influencing jet flow range. The experimental and computing results for the only air running bed are shown in Fig.7. The left vertical axis represents non-dimensional jet range and the right axis represents the velocity decay coefficient *k*. The jet ranges increase with increasing of secondary air jet velocity. However the velocity decay coefficient *k* decreases exponentially with increasing of secondary air jet velocity. The reason is that higher secondary air velocity means larger momentum, so the effect of primary air flow is relatively small. As a result, the horizontal velocity of jet flow core decays slower for a jet with high secondary air velocity.

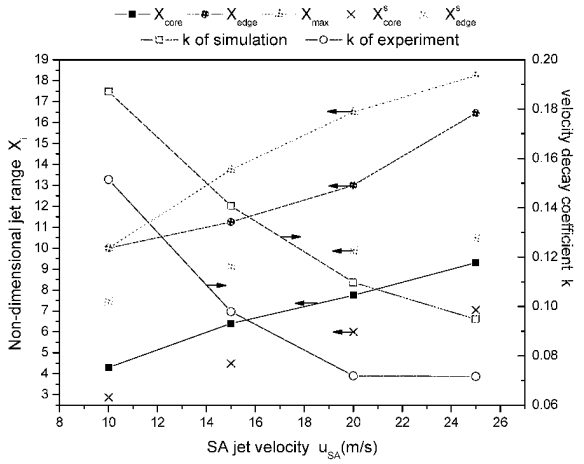

Fig.7 Effect of SA jet velocity on jet ranges and velocity decay coefficient in only air running bed

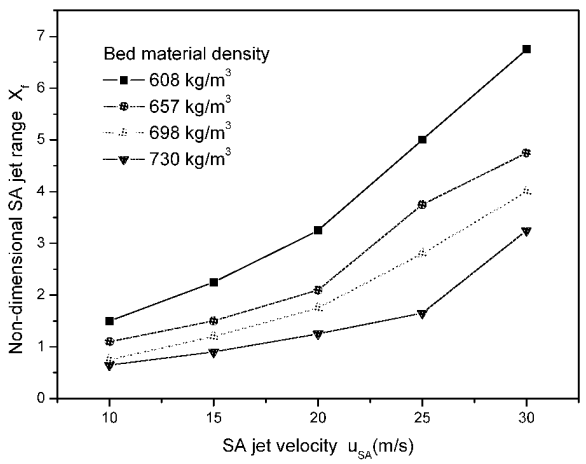

Fig.8 Effect of SA jet velocity on jet ranges in fluidized bed

Figure 8 shows the variation of secondary air jet range with different secondary air jet velocity in the fluidized bed experiment, while a 20 mm nozzle with -30° was used at a primary air velocity of 1.74m/s . There

are four curves given at different suspension bed density among 600-730 kg/m^3. The maximum jet range in fluidized bed (X_f) increases as the secondary air jet velocity increases. The jet may moves farther in thinner suspension density bed. These curves from different suspension density all show an increase of exponential form, so raising the secondary air velocity is a significant way to raise the secondary air penetration.

Effect of bed suspension density on jet range

To form different bed suspension density in the tests, the fluidized bed was run under different inventory at same primary air flow velocity. By measuring the static material height of fixed bed and the dense phase height of the fluidized bed, the suspension density is calculated from their ratio multiplied by the bed material bulk density. Figure 9 shows the variation of secondary air jet ranges at different bed suspension density. The maximum range X_f decreases when the bed suspension density increases at same secondary air jet velocity. It is reasonable since higher resistance occurs to the air jet as the bed suspension density increases. Besides it may be noticed more jet range can be reached with same increment of the secondary air velocity from the curves.

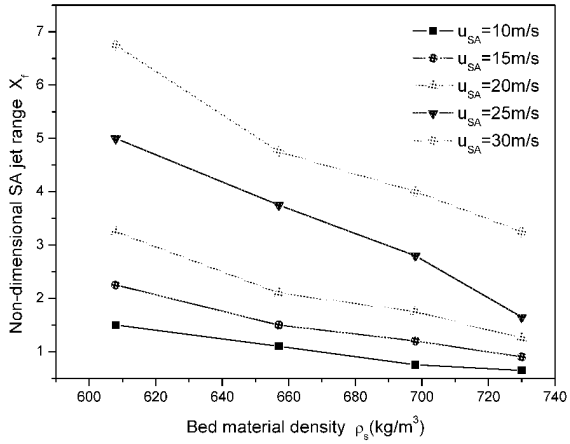

Fig. 9 Effect of average bed material density on jet ranges in fluidized bed

CONCLUSIONS

From this work it can be concluded that the size of secondary air nozzle, secondary air jet velocity and the bed suspension density influenced the secondary air jet range in a fluidized bed. The secondary air velocity and bed suspension density play important roles on the jet ranges. With increasing of secondary air jet velocity, the maximum jet range increases and velocity decay coefficient decreases. The secondary air jet range decreases exponentially with the increasing of bed suspension density. Although the size of secondary air nozzle does not show direct relationship with the non-dimensional jet range, a larger size nozzle may result in a lower velocity decay coefficient. In the conditions of this work, the jet range may reach the deepest distance in the fluidized bed with a nozzle angle of -30°.

ACKNOWLEDGMENTS

Financial support from the National Key Technologies R & D Program of China (No. 2006BAA03B02-08) is greatly acknowledged.

NOTATIONS

d	diameter of SA injector, mm	X_{core}	non-dimensional core range of SA jet
α	angle of SA injector, °	X_{max}	non-dimensional maximum range of SA jet
u_{xcore}	horizontal velocity of jet core at X_{core}, m/s	X_{edge}	non-dimensional edge range of SA jet
u_{SA}	secondary air jet flow velocity, m/s	ρ_p	bed material density, kg/m^3
u_{PA}	primary air flow velocity, m/s	k	velocity decay coefficient

REFERENCES

Brereton, C.: Combustion performance in Circulating Fluidized Beds, (Grace, J.R., Avidan, A.A. and Knowlton, T.M. eds), Chapman & Hall, London, UK, (1997). pp. 369-416.

Cheng, L.M., Zhou, X.L., Zheng, C.H., Wang, Q.H., Fang, M.X., Shi, Z.L., Luo, Z.Y. and Cen, K.F.: Journal of Power

Engineering, 6 (2008), pp. 817-826.
Geldart, D.: Powder Technol, 7 (1973), pp. 285-292.
Koksal, M., and Hamdullahpur, F.: Chem Eng Research and Design, 82 (2004), pp. 979-992.
Koornneef, J., Junginger, M. and Faaij, A.: Progress in Energy and Combustion Sci, 33 (2007), pp. 19-55.
Lim, C.N., Gilberston, M.A. and Harrison, A.J.L.: Chem Eng Sci, 62 (2006), pp. 56-59.
Marzocchella, A. and Arena, U.: Powder Technol, 87 (1996), pp. 185-191.
Namkung, W. and Kim, S.D.: Powder Technol, 113 (2000), pp. 23-29.
Sánchez-Delgado, S., Almendros-Ibáñez, J.A., Soria-Verdugo, A., Santana, D., and Ruiz-Rivaset, U. (2008). Coherent structures and bubble-particle velocity in 2-d fluidized beds. 9th Int. CFB Conference, Hamburg, Germany, , pp. 1007-1012.
Wang, Z.J. and Shen, J.Q. (1987). Boiler Combustion Process. Chongqing, Chongqing University Press.
Zheng, Q., Wei, X. and Fei, L.: Fluidisation VII (Potter, O.E., Nicklin, D.J., eds)), Engineering Foundation New York (1992), pp. 285-293.

SOLIDS MIXING IN THE BOTTOM ZONE OF FLUIDIZED BEDS

D. Y. Liu, X. P. Chen, C. Liang, C. S. Zhao

School of Energy and Environment, Southeast University, Nanjing, 210096, China

Abstract: In the literature, the values of lateral solids dispersion coefficient (D_{sr}) in dense fluidized beds determined by different authors are scattered, ranging from 0.0001 to 0.1m^2/s. The present work is aimed to investigate the reasons for the divergence through CFD-DEM simulations. Results indicate that the particle trajectory shows multi-scale characteristics: macro-scale movement following the gross circulation of emulsion phase, and local-scale movement induced by bubbles closing to it. The effects of fluidizing velocity and bed width on D_{sr} are examined. It is deduced that D_{sr} embodies multi-scale mixing mechanisms, which makes D_{sr} difficult to predict or scale up.

Keywords: solids mixing,lateral dispersion coefficient,multi-scale analysis,scale up

INTRODUCTION

For design and scale up of fluidized bed boilers, it is significant to predict solids mixing rate, especially in the lateral direction of the bottom zone (Schlichthaerle and Werther, 2001). A number of researchers have already investigated the lateral solids mixing in fluidized beds and usually modeled the mixing process using a simple diffusion equation, where an effective lateral solids dispersion coefficient (D_{sr}) is to determine. Niklasson et al. (2002) has made a thorough survey on empirical equations and values of D_{sr} from the literature. Additional works are, Yang et al. (2002), Chirone et al. (2004), Pallares and Johnsson (2006), Pallares et al. (2007) and Winaya (2007). However, the results are very scattered, and much still remains to explore when they are used to predict D_{sr} for a large-scale fluidized boiler.

It is generally known the divergence of D_{sr} determined by different authors is due to different particle properties, bed geometries, experimental conditions, etc. The present work is aimed to investigate the reasons further, which would be very helpful to generalize or scale up the empirical formulates/values of D_{sr}. The investigation is based on CFD-DEM simulations, and the flow pattern, overall solids mixing, particle trajectory and lateral solids dispersion coefficient are examined.

THEORY

The solid mixing in dense fluidized beds is caused by bubbles (Kunii and Levenspiel, 1991). In the literature, it is common to simplify the lateral solids dispersion process by a dispersion model

$$\frac{\partial C}{\partial t} = D_{sr}\nabla^2 C \tag{1}$$

where C is the concentration of tracer particles and D_{sr} is the effective lateral solids dispersion coefficient. The mixing mechanisms, which include local bubble movement, bubble collapse and burst, gross emulsion circulation, and others, are all embedded in D_{sr}.

MODEL

Different from the above semi-empirical models, multiphase CFD simulation from the first principles can give detail information about gas and particle flow. The mostly used CFD models for dense gas solids flow are Eulerian-Granular model (Gidaspow et al., 1994) and DEM-CFD model (Tsuji et al., 1993). They both have been successfully applied and validated in lots of flow phenomena in dense gas solid flow, since first proposed in early 1990s. In the present work, the DEM-CFD model is employed, in order to capture the trajectories of particles as well as the overall solids mixing in fluidized beds.

The DEM-CFD model is more fundamental, which employs a continuum description for gas phase while accounts for the motion of each particle individually. The trajectories of particles are determined by integrating Newtonian equations of motion. The DEM-CFD model requires fewer postulations than the Eulerian-Granular model, but it is more computational expensive. A more detail description of DEM-CFD model is referred to Deen et al. (2007).

RESULTS AND DISCUSSION

Simulation condition

The simulation conditions are listed in Table 1. The superficial gas velocities (U) are selected to be 1.82, 3.0 and 4.5 m/s. In order to study the scale-up effect, the fluidized beds with different bed widths are also simulated. The parameters used in the CFD-DEM model are listed in Table 2.

Table 1 Simulation conditions of fluidized beds

	$W \times H$ (cm^2)	U_g(m/s)	Particle Number
Case 1	30 × 100	1.82	15000
Case 2	30 × 100	3.0	15000
Case 3	30 × 100	4.5	15000
Case 4	10 × 100	3.0	5000
Case 5	20 × 100	3.0	10000
Case 6	40 × 100	3.0	20000

Table 2 Parameters used in DEM-CFD simulations

Parameters	Valve	Parameters	Value
Particle diameter	1.5 mm	Bed depth	1.5 mm
Particle density	2600 kg/m^3	Fluid density	1.2 kg/m^3
Static bed height	~10 cm	Fluid viscosity	1.8e-5 kg/ms
Initial solids volume fraction	~0.58		
Spring constant	800 N/m	Time step	5×10^{-5} s
Restitution coefficient	0.85	Simulation time	10 s
Friction coefficient	0.1	Computational cell	1cm×2cm

Overall solids mixing process and trajectory of a single particle

Given the bed width, the overall solids mixing process for about 2.5 s at the conditions of U=1.82 m/s and U=3.0 m/s are presented in Fig. 1 and Fig. 2 respectively. The trajectory of a typical particle selected from the simulation results of U=1.82 m/s and U=3.0 m/s is shown in Fig. 3 and Fig. 4, respectively. As presented, when U is increased from 1.82 to 3.0 m/s, the bubble size increases, and the mixing of particles in the left and right part of the bed becomes more quickly (Figs. 1-2), on the other hand, both the step displacement and overall moving range of the selected particle become larger (Figs. 3-4). This finding indicates that the solids mixing of a whole bed can be reflected by the trajectory of a single particle, or in other words that the solids mixing expressed by the trajectory of a single particle is consistent with that by the solids mixing of a whole bed.

At the first look, the trajectory of a single particle seems stochastic, but it is cognitive. Its complexity is due to the strong interaction between the single particle and bubbles or emulsion solids. For example, from the trajectory of the selected particle shown in Fig. 4, it can be said that the particle falls down with emulsion phase initially, and then rises and drifts under the force of bubbles, and then is injected into the upper dilute region by bursting bubbles. Subsequently it falls down under the gravitational force and enters into the bed again, and so on. The macro-scale movement of the particle, that is following the gross circulation of emulsion solids, can be distinguished from its local-scale movement, which is induced by bubbles closing to it. This demonstrates that the particle movement shows multi-scale characteristic.

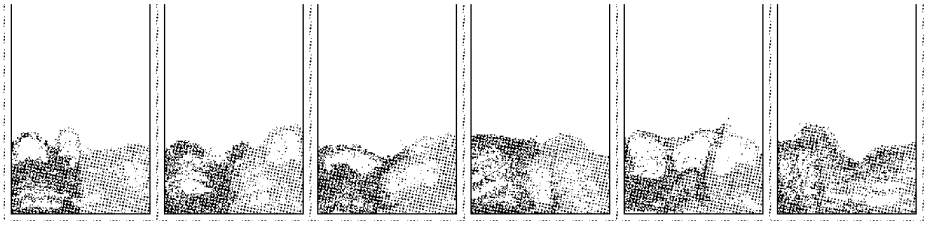

(a) t=4.7 s (b) t= 4.8 s (c) t=4.9 s (d) t=5.3 s (e) t= 6.0 s (f) t=7.2 s

Fig. 1 Snapshots of solids mixing process with time at U=1.82 m/s

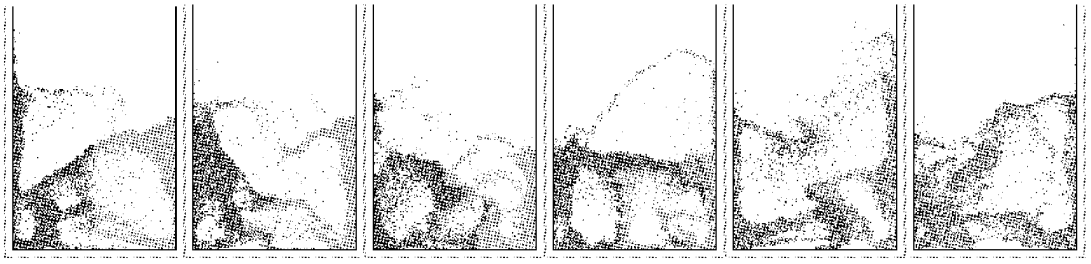

(a) t=4.7 s (b) t= 4.8 s (c) t=4.9 s (d) t=5.3 s (e) t= 6.0 s (f) t=7.2 s

Fig. 2 Snapshots of solids mixing process with time at U=3.0 m/s

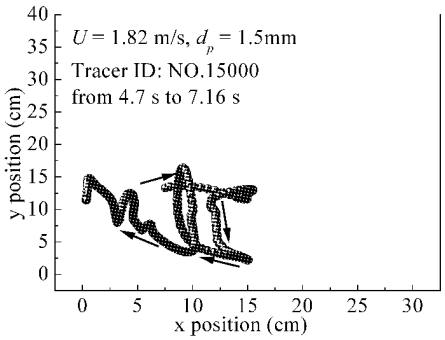

Fig. 3 The trajectory of a selected particle for about 2.5 seconds at U=1.82m/s

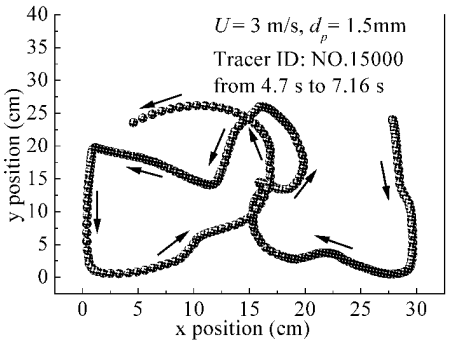

Fig. 4 The trajectory of a selected particle for about 2.5 seconds at U=3.0m/s

The lateral solids dispersion coefficient

The lateral solids dispersion coefficient is calculated based on the trajectories of the particles (Mostoufi and Chaouki, 2001; Pallares and Johnsson, 2006). If at time $t = t_0$, the particle is at (x_0, y_0); at time t, its position is (x_t, y_t). $(\Delta x)^2$ is defined as the average of squared x-displacement of all the particles.

$$(\Delta x)^2 = \frac{1}{N}\sum_{n=1}^{N}(x_t - x_0)_n^2 \quad \text{for } n = 1,2,\ldots,N \tag{2}$$

where N is the number of particles. Then the effective lateral solids dispersion coefficient can be calculated as

$$D_{sr} = \frac{1}{2}\frac{(\Delta x)^2}{\Delta t} \tag{3}$$

where Δt is the time interval. Considering the stochastic of the particle movement, for each simulation case different initial time t_0 is selected to compute D_{sr}. And the averaged value gives the final D_{sr}.

Attention should be paid when choosing Δt. As indicated by Pallares and Johnsson (2006), by setting too small or too large value of Δt, D_{sr} could be misestimated. Here, by trail and error, we tried different values for Δt. Fig. 5 shows the computed values of D_{sr} corresponding to different values of Δt. It is shown that both too small and too large Δt lead to underestimate for D_{sr}. Similar to the way by Mostoufi and Chaouki (2001), for the first estimate for D_{sr} at the present work, Δt is chosen to be a constant value of 0.3 s.

Effect of superficial gas velocity and bed width

Figure 6 shows the computed values of D_{sr} for the 6 cases. Given the bed width at 30 cm, by increasing U from 1.82 to 4.5 m/s, D_{sr} increases almost linearly. This is consistent with common sense, as shown in Fig. 1 and Fig. 2, with increase in the fluidizing velocity, the bubbles become larger and more vigorous, which leads to more intense solids mixing. Given the fluidizing velocity at 3.0 m/s, by increasing bed width from 10 cm to 40 cm, D_{sr} also increases markedly. Fig. 7 gives the instant flow patterns for the fluidized beds with different bed width accordingly. It can be seen that, by increasing bed width from 10 to 40 cm, the bubble size gradually gets no longer restricted by the bed walls and the emulsion solids circulation develops more intense, thus D_{sr} increases continuously.

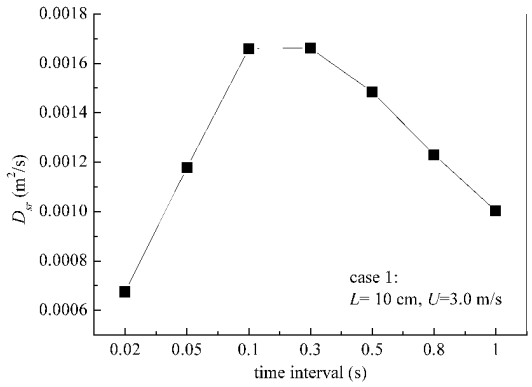

Fig.5 The effect of time interval on the computed value of lateral solids dispersion coefficient

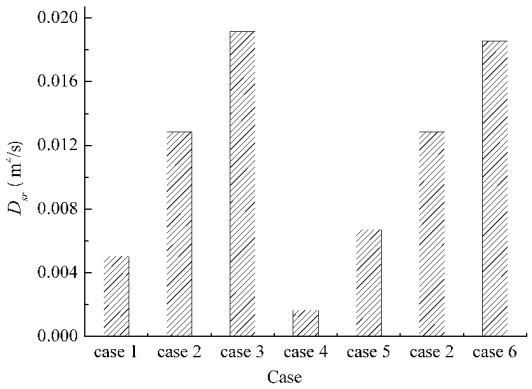

Fig.6 Computed values of lateral solids dispersion coefficient

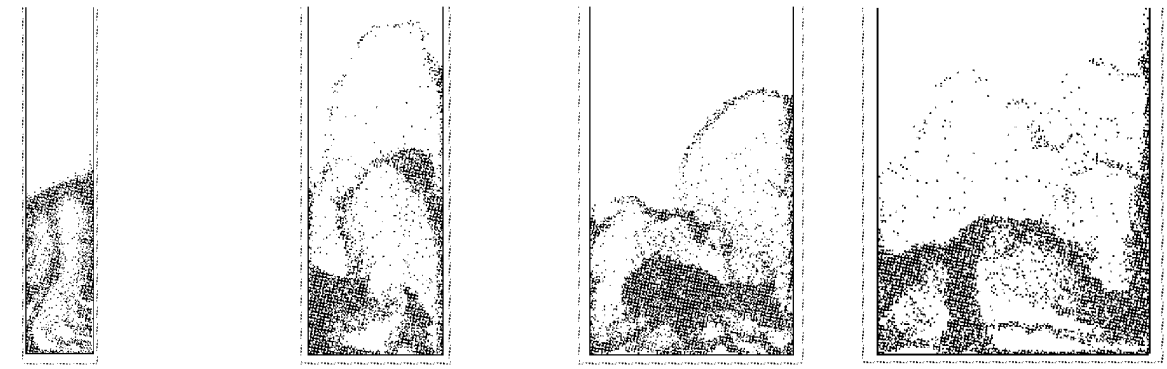

(a) case 4 (b) case 5 (c) case 2 (d) case 6

Fig. 7 Instant flow patterns for the fluidized beds with different bed width

DISCUSSION OF D_{SR}

The values of D_{sr} reported by different authors are shown in Fig. 8. Niklasson et al. (2002) has makes a thorough survey on empirical equations and values of D_{sr} from the literature. Additional works shown in Fig. 8 are, Yang et al. (2002), Pallares and Johnsson (2006) and Winaya (2007). Generally, these values differ by up to 4 orders of magnitude, and increases in fluidizing velocity and bed width can both improve D_{sr}. For example, the works by Shi and Fan (1984), Berruti et al.(1986), Bellgardt and Werther(1986), Mostoufi et al. (2001) and Winaya et al. (2007) report that the values of D_{sr} are around 0.001 m^2/s. The common of these investigations is that they are carried out either in small beds or at low fluidizing velocity. While the works by Xiao et al.(1998), Schlichthaerle and Werther(2001), Niklasson et al.(2002), and Yang et al.(2002), which are carried out in relative large beds and at high fluidizing velocity, report that the values of D_{sr} are around 0.1 m^2/s.

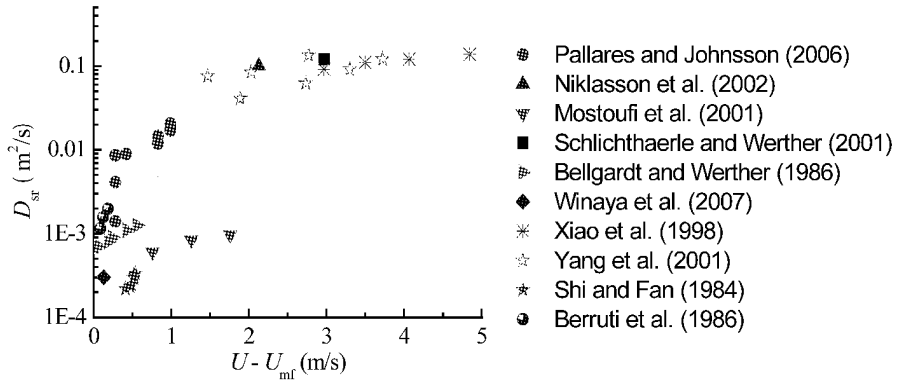

Fig. 8 Relation of solids lateral dispersion coefficient and gas velocity

Our simulation results show that both the fluidizing velocity and bed width have significant positive effects on D_{sr}, which is consistent with the collective results of the experimental studies. Furthermore, the

simulation results reveal that the overall D_{sr} is a superposition of local-scale fluctuation and macro-scale circulation. The particle local-scale movement is related with closing bubbles, while the macro-scale movement is following gross emulsion circulation. Therefore, D_{sr} embodies multi-scale mixing mechanisms. All the operating parameters, which affect the bubble dynamics and emulsion circulation, can affect the solids mixing rate. Therefore, D_{sr} is very sensitive to operating parameters. It is the reason that makes D_{sr} difficult to predict or scale up.

CONCLUSIONS

In the literature, the values of lateral solids dispersion coefficient (D_{sr}) in dense fluidized beds determined by different authors are scattered, ranging from 0.0001 to 0.1m^2/s. The reasons for the divergence are investigated in the present work. The main conclusions are:

（1）The solids mixing of a whole bed can be reflected by the trajectory of a single particle. The particle trajectory shows multi-scale characteristics: macro-scale movement following the gross circulation of emulsion phase, and local-scale movement induced by bubbles closing to it, indicating D_{sr} is a multi-scale variable.

（2）Provided the dense bed exists, D_{sr} increases markedly with both increase in fluidizing velocity and bed width.

（3）D_{sr} embodies multi-scale mixing mechanisms, which makes D_{sr} difficult to predict or scale up.

ACKNOWLEDGEMENTS

Financial supports of this work by National Key Technology R&D Program (2006BAA03B02-10) are gratefully acknowledged.

REFERENCES

Berruti, F., Scott, D. S. and Rhodes, E.: Can. J. Chem. Eng. **64** (1986), pp.48-56.
Bellgardt, D. and Werther, J.: Powder Technol. **48** (1986), pp.173-180.
Chirone, R., Miccio F. and Scala F.: Enger. Fuel **18** (2004), pp.1108-1117.
Deen, N. G, Van Sint Annaland, M., Van der Hoef, M. A. and Kuipers, J. A. M: Chem. Eng. Sci. **62** (2007), pp.28-44.
Gidaspow D.: Multiphase Flow and Fluidization: Continuum and Kinetic Theory Descriptions, Academic Press, 1994.
Kunii, D. and Levenspiel, O.: Fluidization Engineering, Chapter 9, Butterworth-Heinemann, 1991.
Mostoufi, N. and Chaouki, J.: Powder Technol. **114** (2001), pp.23-31.
Niklasson, F., Thunman, H., Johnsson, F. and Leckner, B.: Ind. Eng. Chem. Res. **41**(2002), pp.4663-4673.
Pallares, D., Diez P. and Johnsson F.: Experimental analysis of fuel mixing patterns in a fluidized bed. Proc. of the 12th Int. Conf. on Fluidization, Harrison, 2007.
Pallares, D. and Johnsson, F.: Chem. Eng. Sci. **61** (2006), pp.2710-2720.
Shi Y. F. and Fan, L. T.: Ind. Eng. Chem. Process Des. Dev. **23** (1984), pp.337-341.
Schlichthaerle, P. and Werther, J.: Powder Technol. **120** (2001), pp.21-33.
Tsuji Y., Kawaguchi T., Tanaka T.: Powder Technol. **77** (1993), pp.79-87.
Winaya, I. N. S., Shimizu T. and Yamada D.: Powder Technol. **178** (2007), pp.173-178.
Xiao, P., Yan, G. and Wang, D.: J. Therm. Sci. **7** (1998), pp.78-84.
Yang, H. R., Lu, J. F., Liu, Q. and Yue, G. X.: Chinese J. Chem. Eng. **10** (2002), pp.490-493.

EFFECT OF RISER GEOMETRY STRUCTURE ON LOCAL FLOW PATTERN IN A RECTANGULAR CIRCULATING FLUIDIZED BED

Chen Tian, Qinhui Wang, Zhongyang Luo, Ximei Zhang, Leming Cheng, Mingjiang Ni, Kefa Cen

State Key Laboratory of Clean Energy Utilization, Zhejiang University Hangzhou,310027, China

Abstract: By using a high-speed video camera and particle image velocimetry (PIV) technique, the local flow properties of the solid-gas two phases flow were studied in a plexiglass rectangular CFB cold model with the a riser of $1.5\times0.864\times4.9m^3$. Measurements were carried out with transparent spherical glass bead between 0.1-0.425mm as bed materials and cold air as flow medium. The experimental results showed that the secondary air has an important influence on the particle velocity distribution. Because of the secondary air penetrating effect, the particle lateral movement was acute. In the dilute region, the outlet and the corner effect induced the defluxion of the particles movement and the core-annular distribution was broken. The closer to the outlet, the stronger the lateral velocity is. The obstruct of hanging screen reduced the furnace outlet effects between the hanging screen and the front wall, where the particle movement in the area was controlled by the gas flow and the constrain of the wall. High particle concentration areas were formed in the junction between the screen and the front wall and in the corner between the left wall and the front wall.

Keywords: PIV, rectangular CFB, gas-solid two-phase flow, secondary air, Hanging screen

INTRODUCTION

Due to the efficient mass and heat transfer characteristics, the circulating fluidized Beds (CFB) have been widely employed in industrial applications, covering chemical, petrochemical, pharmaceutical, metallurgical, as well as environmental and energy industries. A lot of research work has been carried out on the dynamics characteristic of CFB and the main feature of the gas-solid two phase flow in the CFB boilers can be described as flowing words: Structural heterogeneity, Irregular, Randomness and Chaos. Generally, the flow pattern in CFB is typically core-annulus flow and the whole riser can be defined as three regions: the bottom dense region, the transition region and the upper dilute region. Besides, with the rapid development of large-scale circulating fluidized bed boiler，the furnace structure was also in the form of diversification, such as different furnace heating face location ,different outlet position e.g. A few experimental studies have been conducted about the effect of the furnace structure on the gas-solid flow pattern in the CFB. Huang et.al (1995) wrote there was a re-distribution of particle flow in the rectangular CFB corner and the aspect ratio of rectangular cross-section had important influence on the thickness of the solid down flow: the longer the side wall is, the thinner the solid flow is and the opposite is also established. Wang and Li (2003) wrote that mounting the separating component, choosing smaller gas superficial velocity and suitable particle circulating flow rate are significant for reducing the thickness or density of the wall particle layer. It would be useful for improving the gas-solid flow structure in the circulating suspension bed with internals addition. Yang et al. (2002) wrote the axial solids mixing behavior in the riser changes insignificantly with the addition of internals, but the lateral solids mixing can be intensified remarkably, especially at a high gas velocity and high solids fraction. Besides, Zhou (1994, 1995) wrote that the low gas velocity in the corner induced the high concentration solid down flow distribution. Harris A T (2003) conducted measurements of particle residence time distribution in the riser of a square cross section, cold model, circulating fluidized bed and reported that the riser exit geometry had significantly influence on the particle residence time distribution and the flow properties in the CFB cold model. However, there were still limitations and shortcoming on the gas-solid two phase flow research in CFB, especially lack of focus on the effect of geometry structure and the local flow properties, the related literature is sparse. To investigate the effect of the furnace geometry structure on the local flow pattern in a square cross-section CFB cold model, this paper utilizing PIV (particle image velocimetry) conducted experiment study on the gas-solid flow properties in the riser.

EXPERIMENTAL APPARATUS AND METHODS

The main apparatus used in this experiment include a rectangular cold CFB model made of Plexiglas and glass and a high-speed digital imaging system. The cold CFB experiment system is shown in Fig. 1. The riser is

4m in height and with a 0.348 m ×0.479m cross section. In the dense region, the furnace cross section expands to the back wall. The top of the furnace inclines slightly from the front wall to the back wall and the riser exit is arranged in the back wall deflecting to the left wall. Two boards are installed in the dilute region to simulate the actual boiler structure with screen superheater. To investigate the local flow pattern near the secondary air inlet, 8 secondary air pipes with size of Φ38×2mm are arranged in the front wall and the back wall.

When the experiment started, the bed material (glass bead) is fluidized by air that is introduced through a distributor plate, and then carried into the cyclone separator where coarse particles are separated. Solid-phase circulation is built up when the particles are fed back to the riser through the loop seal and the fine particles escaping from the cyclone are collected by the bag filter.

The secondary air inlet and the riser exit section in the upper dilute region were chosen as the measurement areas. The measurement section in dilute region is respectively from the left wall 0.02m and from the front wall 0.04m. Fig. 2 shows the coordinate of the dilute region test cross-section. The dotted line section is the test region where is 0.3m distances in axial from the exit. Considering the fact of too much particle mass loading in dense and transition zones, the laser sheet light is not powerful enough to penetrate and the particles on images are overlapping, the test section near the secondary air inlet was chosen the area chose to the back wall where the laser sheet is injected into the furnace. Spherical glass beads were chosen as the bed material with the mean size of 0.278mm and the real density is 2400~2600kg/m^3.

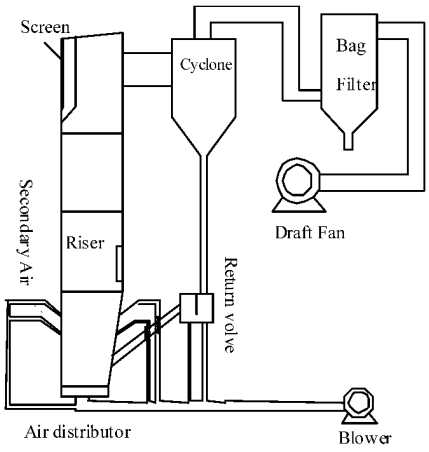

Fig. 1 Schematic of cold CFB system

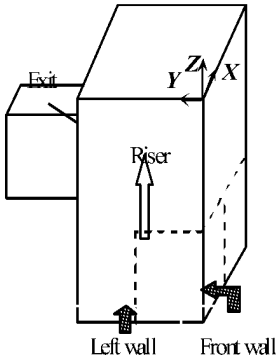

Fig. 2 Arrangement of test cross-sections

The local flow pattern of different sections of the riser under a stable operation condition was investigated. The CFB cold model was working at a fixed bed height H=300 mm, a superficial gas velocity Ug=2m/s, the secondary air volume flow rate Q_{SA}= 480 m^3/h. A PIV system was specially constructed to measure the gas solid flow characteristics in the CFB riser, the typical PIV system arrangement is shown in Fig. 3. A high-speed CMOS digital imaging system was selected, its maximum speed is up to 1× 10^4 frames per second and 1024×768 spatial resolution under 1000 frames per second was selected in this experiment. An Nd: YAG laser with a wave length of 532 nm and a power of 8 W is used as illuminant. A column lens is installed to form the laser light as a fan-shaped light sheet with a depth no more thick than 4 mm and an angle of flare about 30°.FFT cross-correlation algorithm which is the most commonly used algorithm on present digital image velocimetry, was applied to analyze the recorded images and obtained the velocity vector fields.

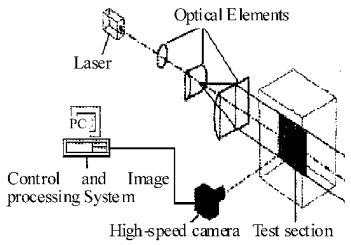

Fig. 3 Arrangement of PIV system

RESULTS AND DISCUSSION

Local flow pattern near the secondary air inlet

Figure 4 shows the local particle flow pattern near the secondary air inlet which is arranged on the back wall. We can see that the local gas-solid flow in this area was complex, the mixing and the collision of the particles was significantly acute. This is because on the one hand, the expanding structure of the furnace dense region and the secondary air jet flow distinctly affected the movement of the particles which were transported from the bottom dense zone, and made apparent deflection of the particles to the back wall; on the other hand,

the solid down flow along the back wall from the upper dilute region was obstructed by the secondary air inject, the down flow was almost cut off. So the acute mixing and collisions between the up and down particle flow near the secondary air inlet region were formed. Meanwhile the addition of the secondary air affected the particles velocity distribution significantly. Fig. 5 shows the particles velocity vector distribution at different time in this area. From Fig. 5 (a), it can be found that solid down flow was still clearly observed above the secondary air inlet, but below the inlet the particles movement was dominated by the entrainment of the primary air and the influence of the expanding arrangement of the dense region, the particles raised incline to the back wall which is more clearly in Fig. 5 (b). In Fig. 5, we can also see that the particles lateral movement was not acute near the inlet where the secondary air velocity maximum was. This is because near the wall the particles volume density was high and the accelerate effect of the secondary air also needed an action distance. Apart from the inlet, the particles were injected into the centre of the furnace at an angle to the horizontal and vertical position and the effect of the secondary air on the motion trace of the particles became apparently. Close to the centre of the furnace the gas-solid two phase flow pattern became more complex. In this area, the particles were under the resultant force of the primary and secondary air. Acute mixing and collisions occurred between the particles which were entrained from the dense region and secondary air inlet. Some intensity vortices formed at the same time.

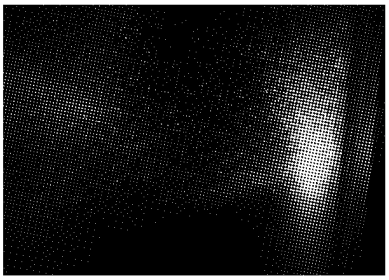

Fig. 4 The particle distribution near the SA inlet

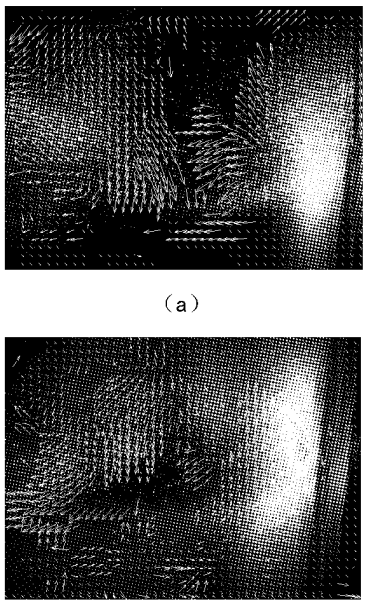

(a)

(b)

Fig. 5 The particle velocity vector profile at different times near the SA inlet

Figure 6 shows the particles average axial and lateral velocity distribution along the width of the furnace. It can be found that near the wall, under the force of the gravity and wall friction, the particles axial velocity direction was vertical-down. But the downward velocity was small because of the interference of the secondary air inject. Otherwise, due to the high density particle down flow layer near the wall, the lateral motion of the particles was not distinct. With a certain distance from the back wall, the particles entrained by the secondary air were injected into the furnace central area and the particles local mean axial velocity direction turned to vertical-up. At the same time, under the acceleration of the secondary air injection, the particles lateral motion became more acute and the lateral velocity directed to the centre of the boiler. The closer to the axis of the furnace, the stronger the primary air effect was. As discussed above, the most complex flow pattern appeared in the region between the centre and the back wall. Under the resultant force of the primary air and the secondary air, the particles mixed and collided significantly which decreased the solids average axial and lateral velocity. As we know, the secondary air jetting into the primary flow belongs to transverse jet flow, the interaction between the primary flow and the secondary air jet flow will result in the formation of a wake eddy at the back side of the secondary air jet flow, thus, the intensity of the secondary air inject is gradually reduced due to the entrainment. So, at the centre of the boiler, the particles flow pattern was dominated by the primary air and the influence of the secondary air declined distinctly. Meanwhile the particles axial velocity direction became vertical-up again, on the other hand the lateral movement of the particles almost disappeared. In the whole test region at the secondary air inlet height,

the particles lateral average velocity was significantly larger than the average axial velocity and the lateral velocity was the main component of the particles motion. This result confirms that the secondary air had evident influence on the local gas-solid flow pattern in the riser.

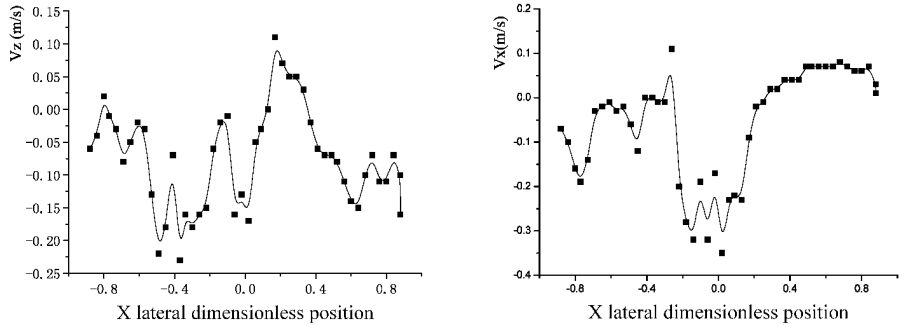

(a) X lateral profile of particle axial velocity (b) X lateral profile of particle lateral velocity

Fig. 6 X lateral profile of particle axial and lateral velocity near the SA inlet

The effect of exit deflecting arrangement on local flow pattern

To investigate the gas-solid flow properties in the upper dilute region, the section with a 0.3m distance from the exit has been selected as the capture area. Fig. 7 shows the particles velocity distribution in this area where is close to the left wall and deflecting to the front wall. From the velocity vector profile we can see that in the corner close to the front wall, with low gas phase velocity and constrains of the walls, the particles motion directed downward under the gravity force and wall effect. In this region the particles lateral movement was not distinctly and the accumulation was easy to form. Thus, a typical annulus particle down flow with a high solid density formed close to the wall. As we know the gas phase flow in the vertical riser is a typical shear flow, high gas velocity appears in the centre. Close to the axis of the riser, the gas drag force impact on the particles enhanced and the particles axial velocity gradually turned to upward. Otherwise, the particles lateral motion directing to the exit increased obviously and the particles volume density decreased.

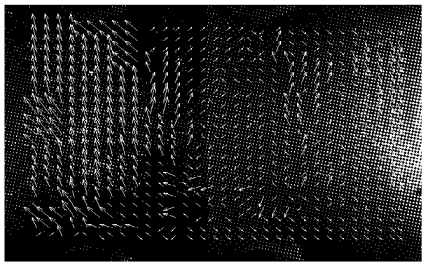

Fig. 7 Local velocity vector profile near the left wall in the dilute region

Figure 8 shows the particles mean axial velocity and lateral velocity distribution in the test region. We can see that although the capture plane was on the opposite side to the exit, the effect of the exit on the particles flow properties was still evident. The particles lateral velocity inclined to the exit apparently and the impact of the exit arrangement on the lateral velocity of particles was more remarkable than that on the particles axial velocity. According the particles lateral velocity V_y distribution, it can be found that in the region close to the front wall, because of the corner effect, the particles moved to the front wall corner.

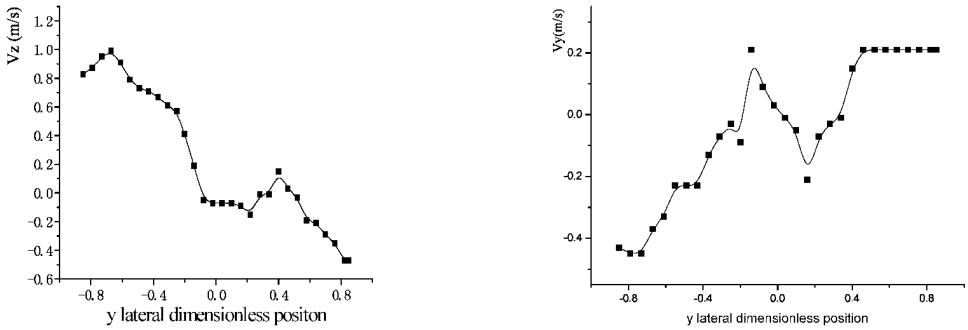

(a) Y lateral profile of the particles axial velocity (b)Y lateral profile of the particles lateral velocity

Fig. 8 y lateral profile of particle axis and lateral velocity near the left wall in the dilute region

However, the closer to the exit, the stronger the exit effect was. With constant gas motion to the exit, the drag force of the gas phase made the particles lateral velocity turn to the exit direction and enhanced the solid lateral motion gradually. Based on the above analysis, we can conclude that the deflected exit arrangement has

a distinct impact on the gas-solid flow pattern through the whole dilute region including the area near the front wall far away from the exit,. The particles lateral movement was acute during the rising motion. The complexity and heterogeneity of the gas-solid two phase flow were enhanced and the attrition of the corner and wall was aggravated at the same time.

Local flow pattern near the screen superheater

Figure 9 and Fig. 10 show the particles flow pattern between the left wall and the hanging screen. We can see that the gas-solid flow in this area is complex. The particles movement in this area was affected by the furnace corner effect, the hanging screen arrangement and the effect of the defected exit. Because of the corner effect, the gas phase velocity was reduced, thus, the interactions between the gas phase and the solid phase decreased. So under the gravity force and the wall friction, the particles formed a solid down flow with high volume density in the corner. Otherwise, because the riser exit was arranged deflected to the left wall, the resistance to the particles motion was small in the corner. Thus the particles more likely moved from the right side of the test region to the left wall and this impact had expanded to the center of the front wall. However, due to the obstruct of the screen and the screen wall friction, both the particles axial and lateral motion were reduced distinctly which weaken the impact of the corner and exit effect on the local flow properties in some degree.

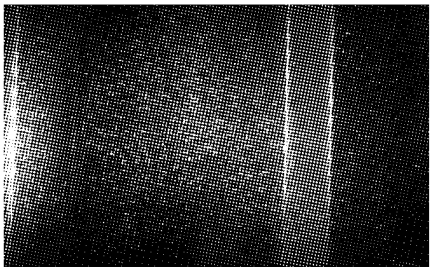

Fig. 9 The particle distribution between the left wall and the hanging screen

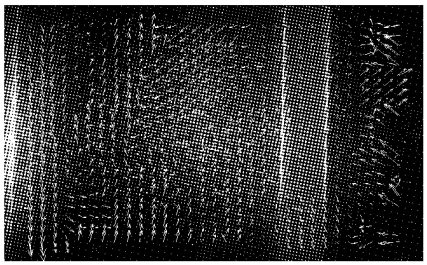

Fig. 10 The particle velocity vector profile between the left wall and the hanging screen

Figure 11 is the x lateral profile of particle axis and lateral velocity between the left wall and the hanging screen. As a whole, the local flow pattern in the corner is more complex, the core effect affected both the particles axial motion and lateral motion and the exit effect only had impact on the particles lateral movement. On the other hand, the arrangement of the screen superheater decreased the flow area in the dilute region but added wall constrains. This geometry structure change induced a re-distribution of the particles axial and lateral movement. The screen arrangement decreased the impact of the corner and exit effect but aggravated the complexity of the particles local flow properties. According to the Fig. 11, we can see that under the gravity force and the wall friction, the particles axial velocity V_z directed vertical-down. However, the maxim of the down flow velocity didn't appear adherent the wall but it was at a distance from the wall. The reason is that adherent the wall the particle volume density was high and the furnace wall gave an intensity friction resistance to the particles motion, which decreased the particles down flow velocity. With the left from the left wall, the gas drag force on the particles became stronger, while the particles axial velocity increased and the velocity direction gradually turned to upward. When the particles moved close to the screen, due to the obstruct and the friction of the screen plate, the particles axial velocity V_z decreased in some degree. Part of the particles collided to the screen and then splashed down to the transition region. The closer to the center of the furnace, the stronger the impact of the gas drag force on the particles movement is. The particles axial velocity reached the maxim and the velocity direction turned to upward again at the centre of the riser. From the Fig. 11 (b) we can see that the corner and exit effect had a remarkable influence on the particles lateral velocity Vx distribution. Adherent the wall, under the wall constraint, the particles collided to the wall and splashed back to the furnace, so the lateral velocity Vx direction pointed to the right wall. With the left away from the wall plate, the impact of the wall on the particles lateral movement decreased while the particles motion was affected by the exit and corner effect. From Fig. 11 (b) we can clearly see that with a distance from the corner, the particles lateral velocity was positive which means the particles moved incline to the left wall and dashed the corner. Close to the screen, due to the obstruct of the screen plate, the particles lateral movement decreased.

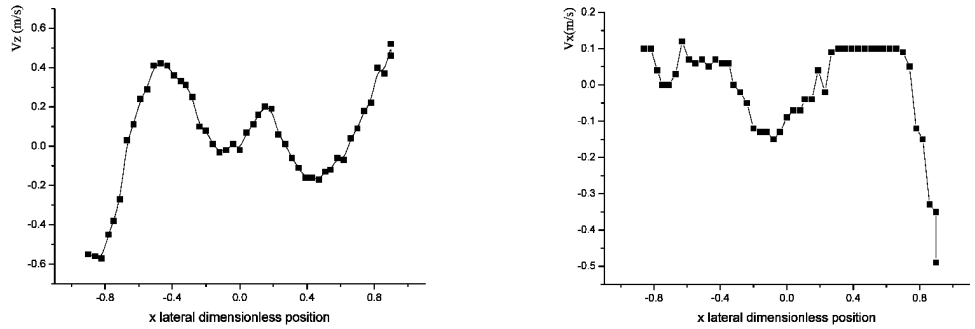

(a) X lateral profile of particle axial velocity (b)X lateral profile of the particle lateral velocity

Fig. 11 X lateral profile of particle axis and lateral velocity between the left wall and the Hanging screen

Figure12 and Fig. 13 give us the particles velocity distribution between the right wall and the screen superheater. It can be found that in this area, the corner effect and the constraint of screen plate were the main factors affecting the particles motion while the exit effect had disappeared. Close to the right wall, due to the corner effect and the wall plate constraint, the particles flow pattern was typical down flow layer. With a distance from the right wall, the particles tended to move from the furnace centre to the right wall corner. From Fig. 13 we can see that the arrangement of the screen had significant influences on the particles velocity distribution. Adherent the screen plate, because the plate obstruct and friction gave resistance to the particles movement, the particles average velocity was reduced. However, in the area close to the right wall, due to the flow area decrease caused by the screen arrangement, the particles velocity increased apparently and a similar parabola velocity distribution was observed. Adherent the right wall, the wall friction and the collision between particles increased, so that the particles average velocity was reduced.

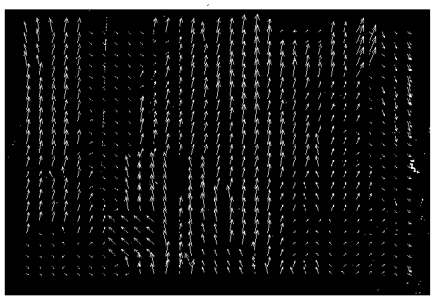

Fig. 12 The particle velocity vector profile between the right wall and the hanging screen

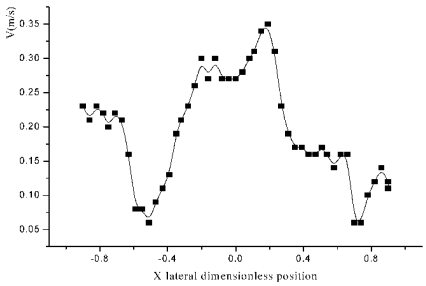

Fig. 13 *x* lateral profile of particle average velocity between the right wall and the hanging screen

Figures 14 and 15 show the particles flow properties in the junction between the front wall and the hanging screen. From the figures we can see that lots of particles aggregated in this region. The gathered particles mainly came from the solid down flow layer along the furnace wall. Because the gas drag force affected the particles movement insignificantly while the wall and screen constraint effect were in dominant. In this narrow region, the collision and friction between particles were acute which induced constant scour and wear on the front wall and the screen. The local flow pattern in this area was irregularity and complexity.

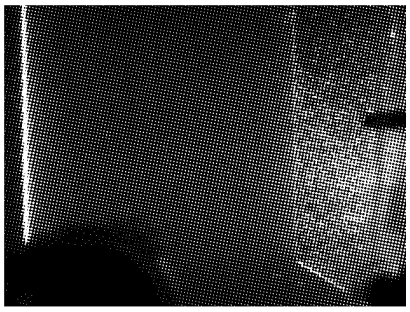

Fig. 14 The particle distribution between the front wall and the hanging screen

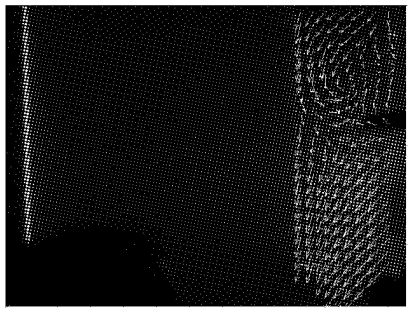

Fig. 15 The particle velocity vector profile between the front wall and the hanging screen

CONCLUSIONS

An experimental investigation about the effect of the riser geometry structure on the local flow pattern in a rectangular CFB based on PIV technique has been carried out in this paper. According to experiment results, we can get conclusions as below:

（1）In macroscopic view, the particles velocity distribution in a rectangular CFB is still typical core-annulus flow pattern. But the local particle flow pattern is more complex and stochastic compared with the flow properties in a cylinder CFB riser. The complexity and heterogeneity are much acute in the exit region and the riser corners.

（2）The secondary air penetration aggravates the complexity and chaos of the local flow pattern. The particles lateral movement is enhanced by the secondary air inject.

（3）In the dilute region, the exit effect is aggravated by the deflected arranged outlet. As a result, the particles lateral motion, which has broken the core-annulus flow pattern in some degree, is distinctly enhanced. Meanwhile, the arrangement of the screen superheater increases the wall plate constraints on the particle movement and decreases the flow area which induces a re-distribution of particles. In the junction between the front wall and the screen, many particles aggregate and induce the furnace wear.

NOTATIONS

H	fixed bed height	mm	Q_{SA}	the secondary air volume flow rate	m^3/h
U_g	superficial gas velocity	m/s	V	the particles velocity	m/s

REFERENCES

Huang S H., Lu J D., Qian S Z. et al. A study on the cold-state flow characteristics of a rectangular flat wall circulating fluidized bed [J] . Journal of Engineering for Thermal Energy & Power, 1995 10(3) : 144-148.

Harris A T., Davidson J F., Thorpe R B. Particle residence time distributions in circulating fluidized beds[J]. Chemical Engineering Science, 2003, 58 (11): 2181-2202.

Harris A T, Davidson J F, Thorpe R B., The influence of the riser exit on the particle residence time distribution in a circulating fluidized bed riser [J]. Chemical Engineering Science, 2003, 58(16): 3669-3680.

Liu H E., Yang Y H., Wei F., Jin Y. et al Solids Mixing Behavior in Riser with Internals[J] . Chemical Reaction Engineering and Technology, 2002,18(2): 109-114.

Qian S Z., Lu J D., Huang S H. et al. Effects of geometric structure of circulating fluidized bed walls on gas-solid flow characteristics[J]. Journal of Chemical Industry and Engineering, 1996, 47(6): 706-711(in Chinese) .

Wang C P, Li D K, Lu Z A, et al. Analyses of Wall and Corner Effects in Square-cross section Circulating Suspension Beds[J] . Chemical Reaction Engineering and Technology, 2003,19(1): 57-62.

Zhou J., Grace J R., Qin S. et al. Voidage profiles in a circulating fluidized bed of square cross-section [J] . Chemical Engineering Science, 1994, 49 (19) : 3217-3226.

Zhou J., Grace J R., Lim C J. et al . Particle velocity profiles in a circulating fluidized bed riser of square cross-section[J]. Chemical Engineering Science, 1995, 50(2): 237-244.

EXPERIMENTAL STUDY ON COAL FEEDING PROPERTY OF 600MW CFB BOILER

H. P. Chen, L. N. Tian, Q. Du, H. P. Yang, X. H. Wang, K. Zhou, S. H. Zhang

State Key Laboratory of Coal Combustion (SKLCC),
Huazhong University of Science and Technology, Wuhan 430074, China

Abstract: In the CFB boiler technology, improving the steam parameters can lead to the improvement of power plant efficiency. However, during the process of large scale, there exist some key problems, such as uniformity of coal feeding, it is a major factor which showed great influence on the boiler efficiency, temperature distribution, etc. In the paper, based on the structure of commercial 600MW CFB boiler unit and similarity principle, the experiment-rig was set-up; using hot trace particle injection and thermocouple temperature collection system, the three-dimensional diffusing property of hot trace particle was analyzed by measuring the temperature distribution at different positions under different operating conditions of variant bed material height and fluidized air velocity.

Keywords: CFB, three-dimensional experiment, temperature distribution, diffusion

INTRODUCTION

As one of the most promising clean coal technologies, the technology of CFB boiler developed quickly with high combustion efficiency, good coal adoptability and low pollutant emission. However, during the process of large scale, there exist many problems. The uniformity of coal feeding of the CFB is a major factor which showed great influence on the boiler efficiency, temperature distribution, etc. During the process of devolatilization, if coal particles cannot fully diffuse, regional severe hypoxia may happen in the coal feeding area, which can lead to a bad combustion in the furnace, increase the incomplete combustion loss of combustible gas and cause the slagging and accumulated ash into afterburning on the heated surface at the end. It is critical to the design and operating of CFB boiler (Yang et al.,2001).

So far, some achievements in the gas-solid diffusion have been obtained at home and abroad, mainly manifested in the following aspects: Rhodes et al.(1991) used salt as tracing particles, Ambler et al.(1980) used radioactive particles as tracing particles, Avidan (1980) used magnetic particles and Kojima et al. (1989) used FCC fluorescence staining and optical fiber technology to study particle diffusing property; Yang et al.(2001) and Li et al.(2006) used contrast method between experiments and empirical model; Wei et al.(1999) built mechanism model and motion model by theory analysis; Zhou et al.(2007) used software simulation to describe the flow characteristics in bubbling fluidized-bed. Many researches have made significant progress in the aspect of coal feeding diffusion. However, due to the faultiness in theory model and the limitation of experimental conditions, it is still difficult to reveal the laws of the complicated three-dimensional feeding diffusion in the dense phase of the fluidized bed.

In the paper, based on the urgent requirement of development of large scale CFB boiler, and the support of "National Key Technology R&D Program" for the development of 600MW supercritical CFB boiler unit, the feeding behavior of 600MW CFB boiler was investigated in depth. At first, according to the structure of commercial 600MW CFB boiler unit and similarity principle, the experiment-rig was set-up. Simultaneously, the temperature distribution was measured by thermocouple temperature collection system under different operating conditions of variant bed material height and fluidized air velocity, and then the three dimensional diffusing property of hot trace particle was analyzed by those temperature distribution.

EXPERIMENTAL

In order to build an experiment device, similarity criterions was deduced under the background of similarity principle and the real size of commercial 600MW CFB unit. Those criterions were deduced based on mass conservation equation, momentum conservation equation, Ergun equation and terminal conditions (Glicksman, 1984; Glicksman and Yule, 1987; Horio and Nonaka, 1986). Then, according to the criterion, the parameters of similarity principles were selected. Ultimately, the parameters of experiment device were decided and built. The experiment-rig is refereed to Fig. 1.

The main-bed height is 3.8m, with square cross-section of 900mm×470mm, in order to observe solids mixing in the dense phase, the furnace wall was made of organic glass, a perforated plate distribution with 4% open fraction was equipped. There have three feeding points in the upper of air distribution plate. To catch the

influence feeding height on coal distribution property, the distance from feeding point to air distribution plate was set 400mm, 600mm and 800mm separately. Simultaneity, the injection position of the secondary air was arranged on both sides of feeding point, the distance between them is 140mm, and the distance between the injection position of the secondary air and the air distribution plate is 200mm, 400mm, 600mm, 800mm and 1000mm separately. The sullage pipe is 100mm diameter. The experimental material is screening river sand with average particle size of 1.1mm, packing density of 1600kg/m^3, and the critical fluidization wind speed at 0.59m/s.

In the experiment, the tracer particles is the same as bed material, because there is no need to separate used tracer, it were heated outside the bed. In order to measure the temperature distribution of the tracer particle, 24 thermocouple was install in furnace by 6 lines and 4 rows, the distance of two lines is 200mm, the layout diagram and numbering was shown in Fig. 2, every thermocouple has four thermocouplepoints. The experimental data was measured and recorded at real time by Monitor and Control Generated System (MCGS).

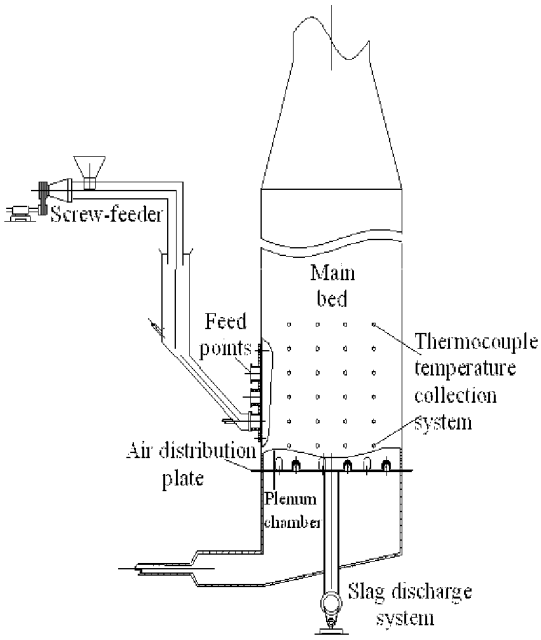

Fig. 1 Experiment system

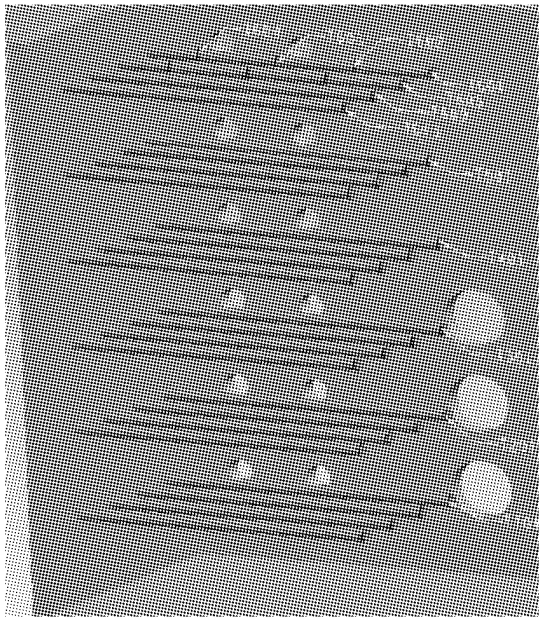

Fig. 2 Thermocouple Temperature Collection System

RESULTS AND DISCUSSION

The temperature responsing curves of the six layers are showed in Fig. 3. It can be observerd that the longer distance between feeding point and measuring point, the longer the times at which the curves reached the peaks, and the smaller of the peak value. The reducing extent of temperature rising range was getting smaller with the distance getting longer. Finally, the heat trace and the original bed materials reached heat balance.

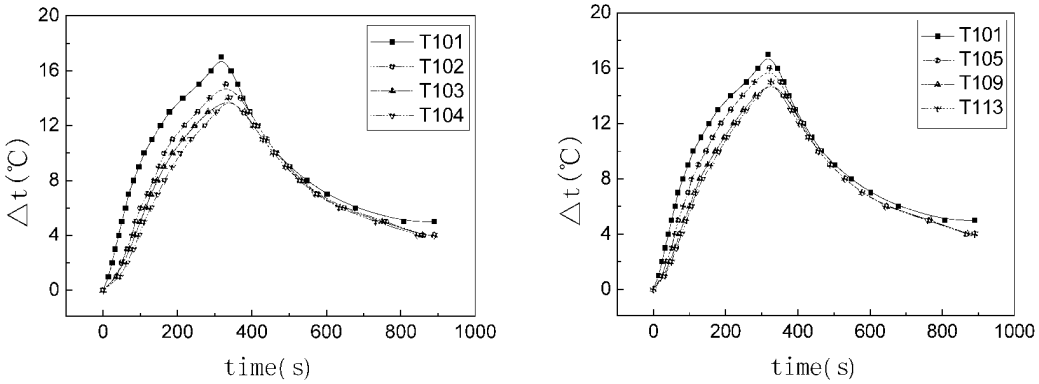

Fig. 3 Temperature increasing with time (Material bed height: 150mm; fluidized air velocity: 1.05m/s)

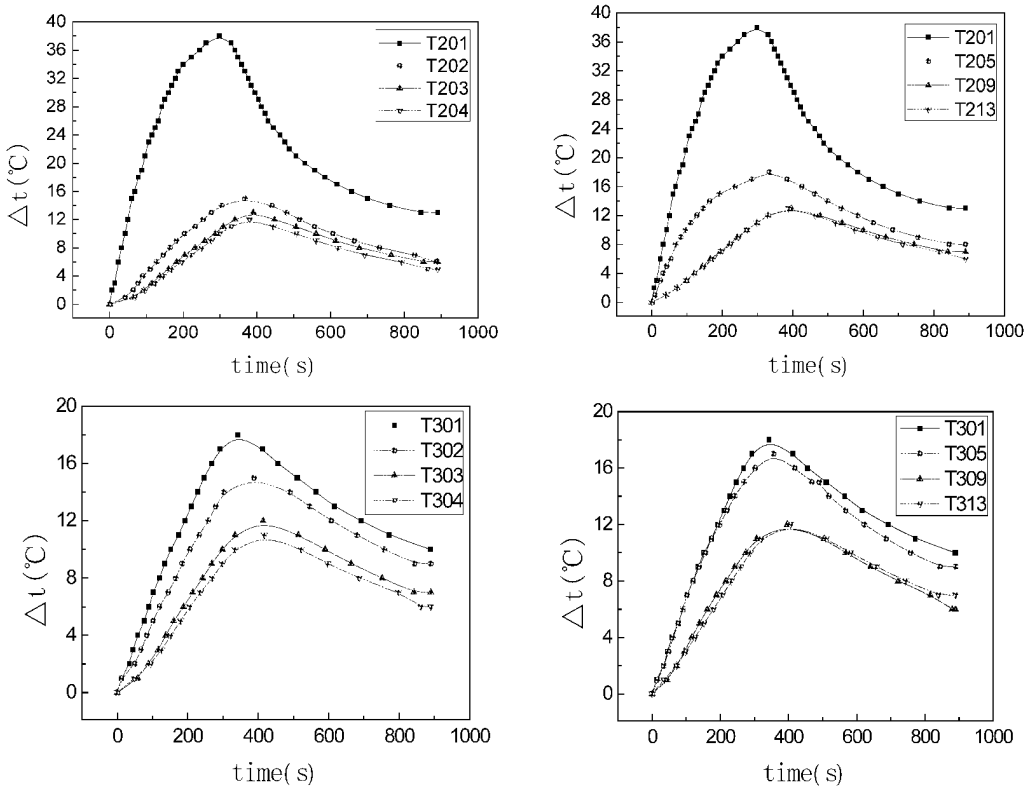

Fig. 3 (Continued)

In the same layer, the peak value of the 5 measuring point is larger than that of the 2 measuring point; but the 2 measuring point has short distance from feeding point, as shown in Fig. 3. It might be attributed to that the initial velocity of the tracer particles is much faster. Thus the tracer particles diffuse quicky in outlet angle.

Compared the first layer and the third layer which has the same distance from the second layer, some differences can be found. In the first layer, the diffusing velocity of the heat tracer was quickly, the time at which the curves reached the peaks is shorter than that for third layer, and the difference of the peak value is smaller among the measuring points. In the third layers, with the distance from the feeding point increasing, the temperature rising extent decreased obviously. The downward diffusion rate of the tracer particles is higher than the upward diffusion rate.

Effect of the fluidized air velocity

Figs. 4, 5 show the temperature distribution at variant fluidized air velocities, it can be seen that the peak value decreased with fluidized air velocity increasing, and the fluidized air take out more heat. As the fluidized air velocity increasing, the diffusing velocity of the heat tracer got quickly, hence the lag time of temperature response in the further measuring points is getting short, and the solid mixing was intensified.

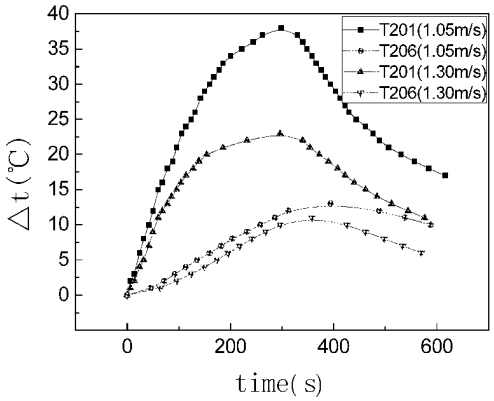

Fig.4 Temperature increasing with the time(Material bed height: 150mm)

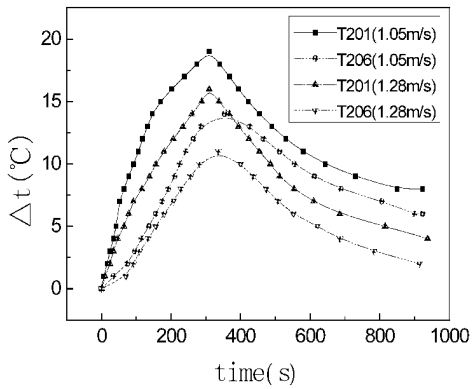

Fig.5 Temperature increasing with the time(Material bed height: 200mm)

Effect of the material bed height

Figure. 6 shows the temperature distribution at several material bed heights. When the fluidized air velocity is fixed, with increasing of the material bed height, the temperature rising appeared dramatic decrease, the lag time of temperature response in the further measuring points is getting shorter, and the difference of temperature rising is getting smaller. The reason for this behavior is that the more particles absorb more heat and intensify the solids mixing.

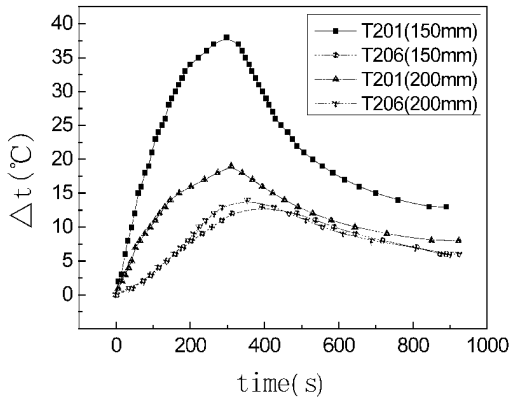

Fig. 6 Temperature increasing with the time(Fluidized air velocity: 1.05m/s)

CONCLUSIONS

The temperature distribution and the feeding property in 600MW CFB boiler were investigated with the three-dimensional experiment using hot trace particles in this study. The main conclusions can be drawn as follows:

Under the same operating conditions, the temperature rising decrease obviously with the distance from the feeding point increasing, while the downward diffusion rate of the tracer particles is higher than the upward diffusion rate.

With fluidized air velocity increasing, the particles diffuse quickly, and intensifying the solid mixing.

With the increase of the material bed height, the more particles absorb more heat and intensify the solids mixing, thus increasing the effective diffusion.

In the paper, many factors were studied, the basic data was supplied for the set-up of coal diffusing mathematic mode. It is significant for the design and operating of 600MW CFB boiler unit.

ACKNOWLEDGEMENTS

A financial support of this work by "National Key Technology R&D Program" (2006BAA03B02) and the National Nature Science Foundation of China (50721005) are gratefully acknowledged.

REFERENCES

Ambler, P., Milne, B. J., Berruti, F., Scott, D. S.: Chem. Eng. Sci. 45(1990), PP.2179-2186.

Avidan, A. A. (1980). Bed Expansion and Solid Mixing in High Velocity Fluidized Beds. New York: City College of New York.

Glicksman, L. R.: Chem. Eng. Sci. 39(1984), PP.1373-1379.

Glicksman, L. R., Yule, T., Dyrness, A., Carson, R. (1987). Scaling the Hydrodynamics of Fluidized Bed Combustors with Cold Models in Experimental. Proceedings of the 1987 Inter. Conf. on Fluidized Bed Combustion.

Horio, M., Nonaka, A., Sawa, Y., Muchi, I.: A. I. Ch. E. 32(1986), PP.1462-1482.

Kojima, T., Ishihara, K., Guilin, Y., Furusawa, L. T.: J. Chem. Eng. Japan. 22(1989), PP.341-346.

Li, B. S. (2006). Coal Diffusion and Combustion Fraction in Circulating Fluidized Bed Furnace. Beijing: Institute of Engineering Thermophysics; Chinese Academy of Sciences.

Rhodes, M. J., Zhou, S., Hirama, T., Cheng, H.: A. I. Ch. E. 37(1991), PP.1450-1458.

Wei, X. L., Tian, W. D., Sheng, Z. H.: J. Eng. Thermophysics. 20(1999), PP.462-466.

Yang, H. R., Lu, J. F., Liu, Q., Yue, G. X.: J. Eng. for Therm. Energy & Power. 16(2001), PP.395-398.

Zhou, J. L., Zou, Z. S., Yu, A. B.: J. Mater. Metall. 6(2007), PP.126-129.

THE HEAT RELEASE RATIO AND PERFORMANCE TEST AT A SMALL-SCALE RDF-5 BUBBLING FLUIDIZED BED BOILER

Hou-Peng Wan[1], Chien-Song Chyang[2], Chyh-Sen Yang[1],

Ching-I Juch[1], Kuo-Chao Lo[2], Hom-Ti Lee[1]

1 Energy & Environment Labs, Industrial Technology Research Institute (ITRI), Bldg. 64, 195, Sec. 4, Chung Hsing Rd., Chutung, Hsinchu, Taiwan 310,China
2 Department of Chemical Engineering, Chung Yuan Christian University 200, Chung Pei Rd., Chung Li, Taiwan 320,China

Abstract: Design and operation of boilers using biomass or waste present a number of challenges. It is also well known that the flue gas emissions are strongly dependent on the fuel. Consequently, it is a major challenge to be able to control and maintain all emissions and combustion behavior under their designated limits for all fuel combinations required. Lately, the constant substantial rise in the price of fossil fuels has resulted with RDF (refuse derived fuel) technology becoming more valuable for generating heat in various types of boilers. A small-scale bubbling fluidized bed (BFB) RDF-fired boiler with a steam capacity of 4 ton/hr was developed by ITRI. In this paper, heat release in the fluidized bed region was calculated and the performance testing for this demonstration boiler including the items of bed temperature distribution, flue gas emissions, and the ash characteristics is analyzed and discussed. Finally, a series fuel flexibility tests were conducted in the RDF-5 BFBB.

Keywords: refuse derived fuel (RDF), bubbling fluidized bed boiler (BFBB), heat-release ratio, ash, pollution emission, biomass

INTRODUCTION

Design and operation of boilers using biomass or waste present a number of challenges. The overall capacity and efficiency of the boiler are always strongly dependent on the fuel, and the supplier has to be able to guarantee the capacity and efficiency within the whole range of the fuel mixture being burned. It is also well known that the flue gas emissions are strongly dependent on the fuel. Consequently, it is a major challenge to be able to control and maintain all emissions under their designated limits for all fuel combinations required.

Fuel ashes easily cause various types of problems, and especially as the interaction between ashes from complex components of fuels is poorly understood, a number of surprises have been reported when fuel mixtures have been used in FBC boilers(Hupa, 2005).

The pellet fuel, RDF-5, is made of waste products such as municipal solid waste (MSW), industrial waste (IDW), and agricultural waste (ACW). The specifications of the RDF-5 include: higher heating value (HHV) higher than 4,000 kcal/kg, moisture content lower than 10%, and ash content lower than 20%, etc.

RDF-5 manufacturing process consists of shredding, magnetic / air separating, drying, conditioning, and pelletizing. The characteristics of RDF-5 pellet fuel include: homogeneous composition, uniform shape and size, low moisture content, high heating value, easy to store and transport, low CO_2 emission, efficient energy recovery, and renewable biomass energy. The RDF-5 can be used in RDF-5 power plants, coal-fired power plants, cement kilns, co-generation plants, and industrial steam/heat boilers.

RDF technology has been developed and disseminated by Industrial Technology Research Institute (ITRI) for almost a decade in Taiwan. After RDF manufacturing technology took root, several tests of co-firing RDF with coal in commercial fluidized boilers were conducted. To meet the market demand for middle-to-small scale steam boiler, a small-scale BFB demonstration RDF-fired boiler with a steam capacity of 4 ton/hr at 10 kgf/cm^2 was developed.

DESIGN OF THE RDF-5 BUBBLING FLUIDIZED BED BOILER

Because of the higher volatile content of RDF-5, the time of burnout of RDF-5 is very short compared to that of coal. This makes the combustion temperature distribution uneven in the furnace. Besides that, some of the PVC or alkaline metal contents in the RDF-5 cause the potential dioxin emissions, fouling or corrosion in the heat exchange surface. Therefore, the temperature distribution of the furnace (the control between the amount of primary air and secondary air), the soot blower of heat transfer surface, and the air pollutant control device are very important in the design of BFBB.

The RDF-5 analytical data for the BFBB design is listed in Table 1. The RDF-5 was made from the paper rejects from the paper mill. From Table 1, we find the lower heating value of the RDF-5 was 5,198 kcal/kg, the volatile content was 69.6%, and the content of sulfur and chlorine was 0.23%, 0.72%, respectively. The fuel feeder system, the layout of secondary air injector (Fig. 1), the layout of heat transfer tube, and the air pollutant control devices of the BFBB were designed for the RDF-5. The design specifications of the RDF-5 BFBB are listed in Table 2.

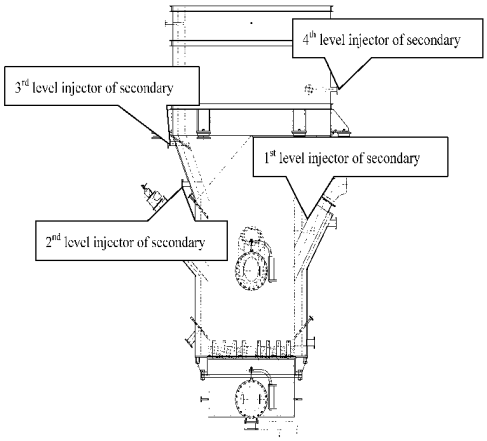

Fig.1 The layout of the secondary air injector of the RDF-5 BFBB

Table 1 The fuel properties of RDF-5

Item		Magnitude
Proximate Analysis (%)	Moisture	6.17
	Ash	13.99
	Volatile	69.61
	Fixed Carbon	10.23
Ultimate Analysis (%)	C	42.93
	H	6.56
	O	29.12
	N	0.28
	S	0.23
	Cl	0.72
Heating Value (kcal/kg)	HHV	5589.8
	LHV	5198.6

Table 2 The design specification of the RDF-5 bubbling fluidized bed boiler

Item	Unit	Magnitude	Item	Unit	Magnitude
Steam Capacity @ 10 kgf/cm^2	kg/hr	4,000	Bubbling fluidized bed		
Fuel (RDF-5 from paper reject)	kg/hr	620~700	Gas distributor type	-	Tuyere
Boiler efficiency	%	> 82	Gas distributor open ratio	%	0.7
Bed temperature	°C	< 800	Fluidized bed diameter	m	1.87
Bed material-slica sand			Total height of BFBB	m	10.2
Mean diameter	μm	437	The emissions are within the limits of the air pollution act (stationary pollutant) (Taiwan)		
Particle density	kg/m^3	2,600			

Bubbling fluidized bed combustor characterized by its recognized combustion regions: fluidized bed region and freeboard region. Because of the great differences of solid / gas distribution between these two regions, the combustion behavior is portioned out in these two regions. After a series of preliminary operation tests and heat release analysis, we knew that great amount parts of heat must be removed from fluidized bed to maintain bed temperature lower than 850°C.

In the BFBB, an immersed area of heat transfer tube (IAHTT) was considered to remove and use the heat released in fluidized bed region. The overall heat transfer coefficient (U_{bed}:1,333,393W) was obtained from Eq.(1):

$$U_{bed} = \frac{1}{\frac{1}{h_{tube}} + \frac{1}{h_{bed}}} \tag{1}$$

The heat transfer coefficient in IAHTT h_{tube} (W/m^{2}K) was evaluated by graphic Kern's correlation(Kern, 1959). The value of heat transfer coefficient in fluidized bed was obtained by Vreedenberg's correlation(Yang, 2003). The total heat transfer area in the IAHTT was calculated from Eq.(2):

$$A = \frac{Q_{rev}}{U_{bed} \times \Delta T} \tag{2}$$

The Q_{rev} (the total heat should be removed from the fluidized bed region to keep the temperature in 850°C) was calculated by the energy balance in the fluidized bed region as shown in Eq.(3):

$$Q_{rev} = \overbrace{\dot{m}_{fg,bed} \times \int_{T_R}^{T_{bed}} Cp_{AIR} dT}^{ENERGY-OUTPUT} - \overbrace{\dot{m}_{air,1} \times \int_{T_R}^{T_{pre}} Cp_{AIR} dT}^{ENERGY-INPUT} \quad (3)$$

From Eq.(1)-(3), we can obtained the total immersed surface area of heat transfer tube around 3.77 m^2. The parameters in heat transfer tube design are listed in Table 3.

Table 3 The parameter in immersed heat transfer area design in the fluidized bed region

Parameter	Unit	Magnitude	Parameter	Unit	Magnitude
Q_{Rev}	W	1,333,393	U_{bed}	W/m^2K	517
h_{bed}	W/m^2K	568	ΔT	K	685
h_{tube}	W/m^2K	5,776	A	m^2	3.77

The flowchart of the RDF-5 BFBB is shown in Fig. 2. The BFBB consists of a furnace (with a windbox, fluidized bed, and freeboard), water tube boiler, air preheater, fuel feeding system, air supply system, control system (Human-Machine Interface Technology), and flue gas treatment system (semi-dry scrubber, bag-filter, active carbon injector). The total height of the BFBB is 10.2m with a diameter 1.8m of fluidized bed section, expended section, and rectangular cross-section of 2.7m×2.7m. The fuel feeding system employs over-bed feeding of fuels with two stage gate valve. Main air supplied for combustion includes preheated primary air, which is used as the fluidization gas through the gas distributor above the windbox, and preheated secondary air, which is injected at four levels above the distributor as shown in Fig.1.

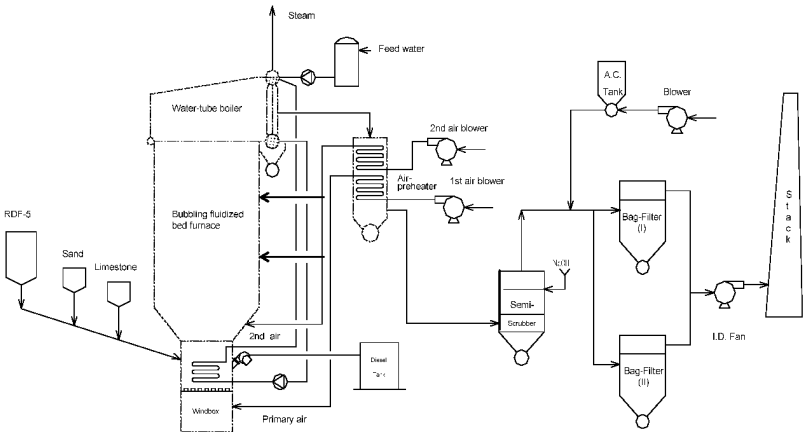

Fig. 2 The flowchart of the small-scale RDF-5 bubbling fluidized bed boiler

RESULTS AND DISCUSSION

Heat release ratio in fluidized bed region

The energy balance of fluidized bed region was analyzed to obtain the quantity of the removal energy. A parameter, heat release ratio (φ), was defined as the ratio of heat released from fuel combustion in a specific region to total potential heat energy contained in fuel. Heat release ratio figures out the distribution of usable energy in combustor. Heat release ratio in fluidized bed was defined as:

$$\varphi_{bed} = \frac{Q_{bed}}{F_{RDF} \times LHV_{wb}} \quad (4)$$

The value of Q_{bed} was obtained from the energy balance of the fluidized bed.

$$Q_{bed} = \overbrace{\dot{m}_{fg,bed} \times \int_{T_R}^{T_{bed}} Cp_{AIR} dT + \dot{m}_{H_2O} \times \left(\Delta H_{T_R}^{V} + \int_{T_R}^{T_{bed}} Cp_{H_2O} dT \right)}^{ENERGY-OUTPUT} - \overbrace{\dot{m}_{air,1} \times \int_{T_R}^{T_{pre}} Cp_{AIR} dT}^{ENERGY-INPUT} \quad (5)$$

The heat release ratio of fluidized bed region (φ_{bed}) was about 0.55 under the operating condition of design based from Eq.(5). It should be noticed that heat release ratio does not reflect the combustion proportion in the corresponding region. Over half of energy of fuel released in fluidized bed region is due to the internal heat transfer in whole combustor. RDF-5 is a high volatile matter fuel, therefore lots of volatile matter combusted and meanwhile plenty of heat energy released in the freeboard. However, there is no effective temperature difference to drive the heat transfer in freeboard region. Great parts of energy amount transfer to

fluidized bed by radiation and to the boiler above freeboard by bulk flue gas flow and radiation. In addition the huge heat capacity of bed material played an important rule to absorb heat from freeboard. This result also demonstrated that fluidized bed combustor have good fuel flexibility.

Performance testing of the BFBB

The performance testing was held on June 16-19, 2008. The total testing duration was more than 70 hours. After the testing, the BFBB was still in operation. The total operation time was more than 3,300 hrs till the end of Dec. 2008. In the performance testing, the system stabilization, temperature distribution of the BFBB, the emissions of the flue gas, and the ash quality were examined. The boiler efficiency was also calculated after this testing. The operation conditions were listed in Table 4.

Table 4 The operation conditions of the performance testing

Item	Magnitude	Item	Magnitude
RDF-5 Feeding rate	520 kg/hr	Bed temp. / bed Pres. (sand)	750℃ / 350mmAq
Steam Capacity	4.0 tonner/hr	Bed surface temp.	< 1,050 ℃
Steam Pres.	6.5 kg_F/cm^2	Freeboard temp.	900℃
1st air flow rate / temp	2,400Nm^3/hr, 180℃	Boiler outlet temp.	310～335℃
2nd air flow rate / temp	1,600Nm^3/hr, 190℃	Stack flue gas temp.	120 ℃

The emissions of flue gas of the BFBB were: O_2 4~6%; SO_x 50~65ppm; CO 150~300ppm; NO_x 80~100 ppm From the emission data, All of the emission data of air pollutants were lower than the limitation of the air pollution act (stationary pollutant) Taiwan.

The temperature distribution of the BFBB during the performance testing is shown in Fig.3. We can find the temperature of the bed was lower than 800°C. Owing to the high volatile content of RDF-5, the highest temperature was found in the surface of the bed. Biomass fuels are known to have reactive ashes, which may cause various difficulties in the FBC. Several recent studies have been focused on innovative fuel characterization methods or prediction techniques to establish the behavior of these ashes in co-firing(Wan et al., 2008; Skrifvars et al., 1999; Zevenhoven et al., 2000).

Figure 4 shows the LOI (loss on ignition) of ash in various sampling locations. Based on the analysis results of ash, we found the LOI in the bottom ash, the boiler convention section, and the air preheater ashes were lower than 1.5%. It means most of the combustion materials had burnt out in these sections. Besides that, the LOI of the bag-filter ash was 4.89%, which was higher than other places, but lower than the traditional coal-fired boiler (6%). We can infer that the characteristic of high volatile contents in RDF-5 will enhance the combustion behavior.

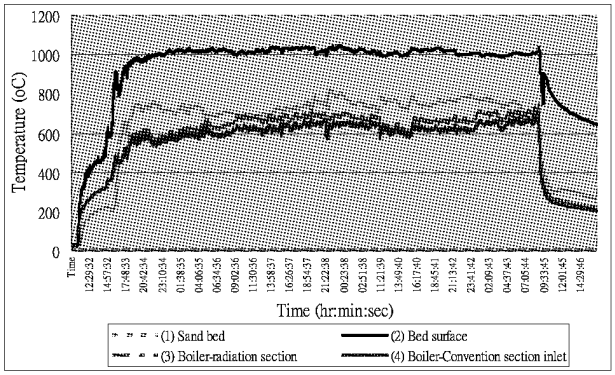

Fig.3 The temperature distribution of the BFBB

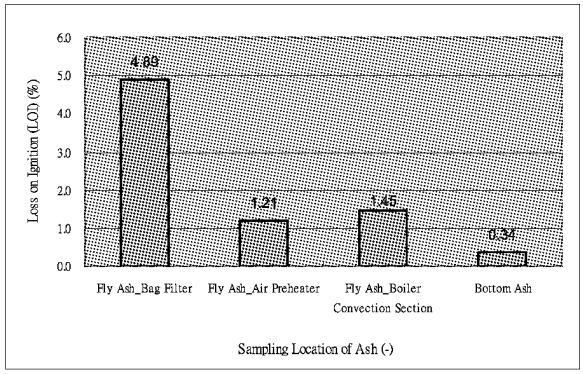

Fig. 4 The LOI of ash in the BFBB

The fly ash of burning biomass has a typical particle size of several hundreds to thousands of micrometers. The particle size distribution (PSD) of fly ash from the bag-filter is shown in Fig. 5. In the PSD analysis, we found the mean diameter of fly ash from the boiler convention section, the air preheater section, and the

bag-filter was 153μm, 98μm, and 17μm, respectively. The SEM analysis is shown in Figs.6(a)-7(c). We can find the structure of the fly ash from burning RDF-5 was coral-like, different from that of the coal-fired fly ash shown in Fig.6(c). Finally, we calculated the boiler efficiency based on the heat loss method of the CNS 2141 B1025. The efficiency of the RDF-5 BFBB was 87.4%.

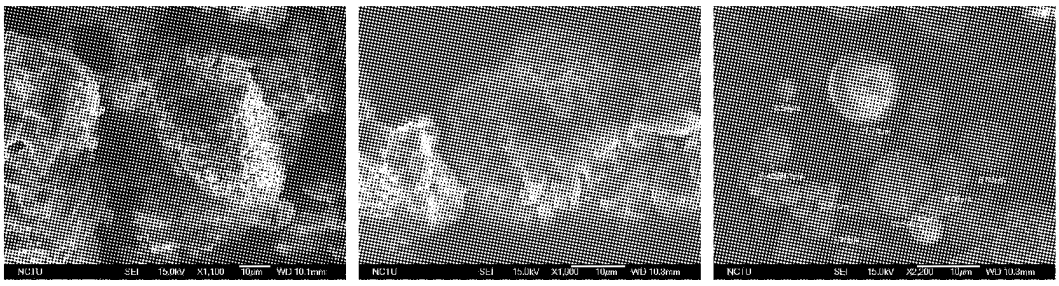

(a) Fly ash - RDF-5 (b) Fly ash - RDF-5 (c) Fly ash-Coal

Fig.5 The SEM of fly ash from the RDF-5 and coal burn in boilers

The fuel flexibility tests of the BFBB

The performance testing was conducted on June 16-19, 2008. After the performance testing, the BFBB was still kept in operation. The total operation time was more than 3,300 hrs till the end of Dec. 2008. In order to understand the fuels flexibility of the BFBB, two different bio-fuels (mushroom cultivate soil and woody construction waste) were tested during the long-term operation. The descriptions and characteristics of the two bio-fules were listed in Table 5. The testing conditions of fuel flexibility tests were listed in Table 6.

Table 5 The characteristics of the testing fuels

Biomass Type	Proximate analysis (*wt.*%)			Ultimate analysis (*wt.*%)						HHV(W)
	moisture	Ash	Combustible	C	H	O	N	S	Cl	(kcal/kg)
Mushroom cultivate soil	53.29	3.23	43.49	22.56	2.17	17.84	0.6	0.22	0.1	2,120
Woody construction waste	20.01	4.87	75.12	35.04	5.50	33.76	0.5	0.07	0.24	3,768

Table 6 Testing conditions of fuel flexibility tests

Item / Unit	Test No	Testing duration	Co-firing ratio (vol.%) (Biomass/RDF-5)	Boiler loading (tonner/hr)
Mushroom cultivate soil	A	2008/08/28 - 2008/08/29	100; 50	3.2 (normal)~4.0 (maximum)
Woody construction waste	B	2008/10/22 - 2008/10/24	67	3.2 (normal)~4.0 (maximum)

During the fuel flexibility tests period, the following items were observed or recorded: temperature (fluidized bed region, bed surface, freeboard, boiler outlet), pressure (furnace, exhaust), system stability, boiler loading (steam pressure, steam flowrate), oxygen concentration in boiler outlet, and appearance of bottom ash and fly ash.

The temperature distribution of the BFBB during the fuel flexibility tests were shown in Figs.6 & 7. From the figures, the temperatures were around: 230-300°C (at boiler outlet), 500-800°C (at fluidized bed region), 800-1,000°C (at bed surface), 500-600°C (at freeboard), respectively. We can find the test A temperature distribution was more stable than test B, it attributed the unstable temperature distribution to feeding unstable. The rough pretreatment of woody construction waste cause wide fuel size, large fuel piece blocked up the feed system frequently.

Furthermore, the combustion behavior, the steam pressure, the oxygen concentration (3~8%), and whole boiler systems were also stable during the test duration. The results of fuel flexibility tests shown that mushroom cultivate soil or woody construction waste can be used in the demonstration RDF-5 BFBB via 100% combustion or co-firing with the RDF-5. However, it needs further evaluation of pollutant emissions when combustion or co-firing the agriculture or other biomass wastes.

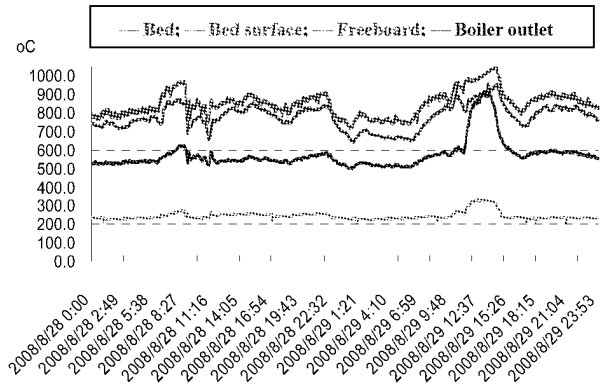

Fig.7 The temperature distribution in BFBB (Test A)

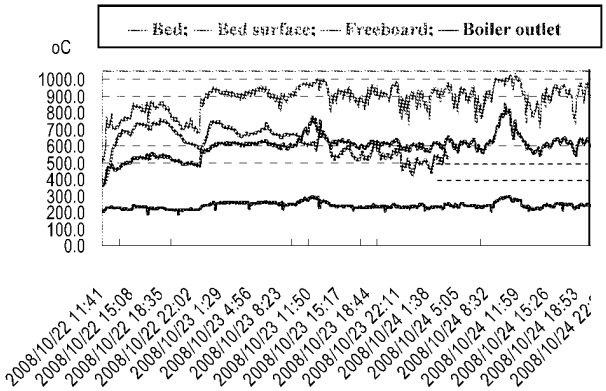

Fig.8 The temperature distribution in BFBB (Test B)

CONCLUSIONS

RDF technology has been developed and disseminated by Industrial Technology Research Institute (ITRI) for almost a decade in Taiwan. To meet the market demand for middle-to-small scale steam boiler, a small-scale BFB demonstration RDF-fired boiler with a steam capacity of 4 ton/hr at 10 kgf/cm^2 was developed. In this paper, the biomass-fired BFB demonstration boiler was introduced. Based on the calculations of heat transfer and heat balance, the heat release ratio was 0.55 in the fluidized bed region. Besides, the BFBB performance test was conducted. All the testing data were met with the origin design. Finally, the fuel flexibility tests showed the RDF-5 BFBB had good fuel adaptability.

NOTATIONS

A	total heat transfer tube area in fluidized bed region, m^2
Cp_{AIR}	heat capacity of air, J/kg • K
Cp_{H2O}	heat capacity of water, J/kg • K
F_{RDF}	RDF feeding rate, kg/hr
h_{bed}	heat coefficient in bed, W/m^2 • K
h_{tube}	heat coefficient in heat transfer tube, W/m^2 • K
$\Delta H^V_{T_R}$	enthalpy of vaporization, J/kg
LHV_{wb}	wet based low heating value of RDF, J/kg
U_{bed}	overall heat transfer coefficient, W/m^2 • K
φ_{bed}	heat release ratio, %
$\dot{m}_{fg,bed}$	mass flow rate of flue gas leaved from fluidized bed region, kg/hr
$\dot{m}_{H_2O}$	mass flow rate of cooling water injection, kg/hr
$m_{air,1}$	mass flow rate of primary air, kg/hr
Q_{bed}	rate of heat release of fuel in fluidized bed, J/hr
Q_{rev}	The total heat should be removed from the fluidized bed region
T	temperature, K (subscript, *bed*=fluidized bed, *pre*=preheat, *R* = reference state of 298K.)

ACKNOWLEDGEMENTS

The authors would like to acknowledge financial support provided by the Bureau of Energy, MOEA, Taiwan,China.

REFERENCES

1. Kern, (1959), Process heat transfer, McGraw-Hill, INC. p.474.
2. Mikko Hupa, Fuel, **84** (2005), pp.1312–1319.
3. Skrifvars BJ, et al., Energy Fuels **2** (1999), pp.359–363.
4. Wan, H. P., Y. H. Chang, W. C. Chien, H. T. Lee, and C. C. Huang, Fuel **87** (2008), pp.761–767.
5. Yang, W. C., (2003), Handbook of fluidization and fluid-particle system, Marcel Dekker, INC.
6. Zevenhoven-Onderwater M, et al., Fuel **79** (2000), pp.1353–1361.

INTEGRATED USE OF FLUIDIZED BED TECHNOLOGY FOR OIL PRODUCTION FROM OIL SHALE

Andres Siirde, Ants Martins

Tallinn University of Technology, Ehitajate tee 5, 19086 Tallinn, Estonia

Abstract: The plant unit which consists of a fluidized bed retort and CFB furnace for burning the by-products of retorting (semicoke and semicoke gas) is presented in this paper. The oil shale retort consists of a fast fluidized bed shaft, coarse semicoke bit, semicoke separation chamber and cyclone for the separation of fine semicoke particles. The crashed oil shale and hot ash from the CFB ash separator are fed concurrently into the fast fluidized bed shaft. For fluidizing the mixture of oil shale and hot ash particles, the recycle semicoke gas is used. The pyrolysis of oil shale begins in fluidized bed and is completed in the semicoke separation chamber. The coarse semicoke particles are separated from fluidized bed directly while the medium size particles are separated from the gases in the semicoke separation chamber and the finest semicoke particles in the cyclone. All the fractions of semicoke from the fluidized bed retort and semicoke gas from the oil fractionator are burnt in the CFB furnace. The semicoke ash is separated from flue gases in the CFB ash separator. A part of separated hot ash is fed into the fluidized bed retort as a solid heat carrier material and the rest into the furnace through the ash cooler or separated from the process. The retention of sulphur dioxide formed during the semicoke and semicoke gas combustion, is guaranteed for about 99 % due to the high CaO content in the semicoke ash and convenient temperature (about 850 °C) in the CFB furnace. The described plant unit is useful for retorting oil shale and other solid hydrocarbon-containing fuels. The advantages of the present retorting process and system are: improved oil yield, greater throughput, lower retorting time, avoidance of moving parts in the retorting zones, reduced downtime, etc. A new plant unit for oil shale oil production has been elaborated and defended by the Estonian Utility Model EE 2007 00671 U1.
Keywords: fluidized bed retort, CFB, shale oil, semicoke, semicoke gas combustion

INTODUCTION

Due to the decrease of world oil resources, because of the intensive use of oil and oil products, the demand for additional alternative hydrocarbon sources will be increasing in the future. One promising source is oil shale, whereof the world resources are sufficiently large. Compared to coal, the organic matter of oil shale (kerogen) contains mere hydrogen and therefore can be subjected to its thermal conversion into oil and gas. There is already a lot of experience in oil production from oil shale (Yefimov,2000; Golubev,2003; Kann et al;2004; Quin et al.,2006). Two main industrial retort technologies for oil shale processing can be named: the first using retort gas as a gaseous heat carrier or second applying semicoke for a solid heat carrier. The first one is implemented in Estonia and known as the Kiviter process which is also implemented in China, Russia and Brazil; the second is the Galoter process. The Alberta Taciuk Process (ATP) used in Canada and Queensland, belongs to the solid heat carrier category. The Kiviter process is suitable for retorting high-calorific lumpy oil shale. The equipment for the Kiviter process is notable by its compactness, but a harmful residue - semicoke is formed in the process. The Galoter process is suitable for fine-grained and lower quality oil shale. It has higher production efficiency (85 – 90%) and yields the semicoke gas of higher calorific value. But the Galoter process is associated with a more complicated multistage technological scheme and apparatuses. One of the hindrances to oil shale becoming a widely exploited resource is the complexity of its extracting and processing. The new retorting methods are a key to the future viability of oil shale, both in terms of lower production cost and less aggressive environmental impact. The retorting process and system presented in this work should contribute to the improvement of oil shale retorting process and oil production.

Description of the plant unit for oil production from oil shale

Figure 1 gives the layout of the plant unit for oil production from oil shale. The plant unit consists of two parts: 1 - fluidized bed retort and 15 - circulating fluidized bed boiler for burning semicoke and semicoke gas (Siirde et.al (2007)).

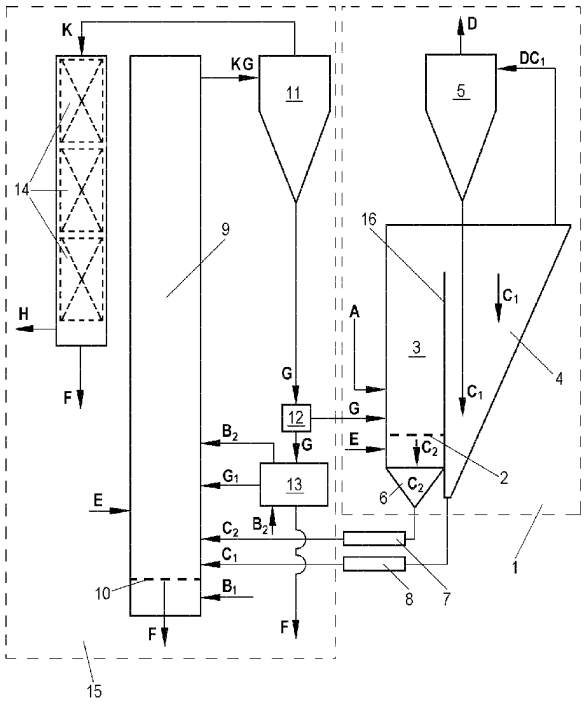

Fig. 1 The layout of the plant unit for oil production from oil shale

A – oil shale, B_1 – primary air, B_2 – secondary air, C_1 – fine semicoke, C_2 – coarse semicoke, D – mixture of liberated hydrocarbons and gas-steam, DC_1- mixture of liberated hydrocarbons and gas-steam with fine coke, E –semicoke gas, F – ash, G - hot fly ash, G_1 – cooled fly ash, H – flue gases, KG – ash-laden furnace gases, K – cleaned furnace gases, 1 – fluidized bed retort, 2 –grate under fluidized bed shaft, 3 – fluidized bed shaft, 4 – semicoke separation chamber, 5 – cyclone of fine semicoke, 6 – bunker of coarse semicoke, 7 – conveyor of coarse semicoke, 8 – conveyor of fine semicoke, 9 – furnace of the boiler with circulating fluidized bed, 10 – grate under furnace, 11 – fly ash separator, 12 – hot fly ash distributor, 13 – fly ash cooler, 14 – convective heating surfaces, 15 – circulating fluidized bed boiler, 16 – partition between fluidized bed shaft and semicoke separation chamber

The crushed dry oil shale A is fed into the fluidized bed shaft 3 together with the hot semicoke ash G (a solid heat carrier) from the hot fly ash distributor 12. For fluidizing the mixture of oil shale and hot ash the semicoke gas E is used. The semicoke gas E is directed into the fluidized bed shaft through the grate under the shaft 3. In the fluidized bed shaft the oil shale particles are roughly divided into two fractions: fine particles leave the fluidized bed and coarse particles keep moving in the fluidized bed. The suitable gas velocity in the fluidized bed shaft depends on the grain composition of oil shale particles. The retorting of coarse oil shale particles takes place within fluidized bed. The formed coarse semicoke C_2 is disposed from fluidized bed into the bunker of coarse semicoke 6. The retorting of fine oil shale particles begins in the fluidized bed shaft 3 and is completed in the semicoke separation chamber 4. The most of medium and fine size semicoke particles are separated from gases in the separation chamber, because of the steep decrease of gas velocity and its reversal flow direction. The mixture of liberated hydrocarbons and gas-steam with the finest semicoke particles leave the semicoke separation chamber 4. The fine semicoke is separated from gases in the cyclone 5. Clean gases leave the fluidized bed retort 1 and move into the condensation department where the shale oil is condensed from the gases and semicoke gas E is separated. The finest semicoke particles from the cyclone 5 are directed into the under part of the semicoke separation chamber 4.

The fine C_1 and coarse C_2 semicoke particles and semicoke gas E are burnt in the boiler 9 of circulating fluidized bed furnace 15. The fine C_1 and coarse C_2 semicoke particles are conveyed by the screw conveyors 8 and 7 into the furnace 9. The semicoke gas is fed into the furnace 9 from the opposite side of semicoke injection. The primary air B_1 is injected into the furnace through the grating 10. The secondary air B_2 is used to cool the hot fly ash G in the cooler of fly ash 13 before its injection into the furnace space. The combustion temperature in the furnace 9 ranges from 800 °C to 850 °C. In this temperature range the maximum SO_2 retention with CaO in the ash is provided. The fly ash is separated from the ash-laden furnace gases KG in the fly ash separator 11. The separated hot ash is discharged by the gravity flow into the hot fly ash distributor 12. From the fly ash distributor a part of hot ash is fed into the shaft 3 of fluidized bed retort 1 as a solid heat carrier. The rest of hot fly ash is discharged from the hot fly ash distributor into the fly ash cooler. The cooled fly ash is used for controlling the furnace temperature. The ash F is separated from the furnace 9 (bottom ash), ash cooler 13 and convective heating surfaces 14 of circulating fluidized bed boiler. The flue gases H are dedusted in an

electrostatic precipitator and discharged into the atmosphere.

Fluidized bed retort process

In the fluidized retort the crashed oil shale particles are divided roughly into two fractions: coarse particles which stay in fluidized bed and fine particles which move with gases in the freeboard. The distribution of crashed oil shale particles between the bed and freeboard depends mainly on the physical properties of particles (the size, density) and gas velocity.

The time for the retorting process of oil shale particles depends on the particle size, ambient temperature and gas speed. The data on the retorting time of oil shale particles with different size are practically lacking. The dimensions of a fluidized bed retort depend substantially on the retorting time of oil shale particles with different size.

The retorting time of oil shale consists of two parts:

$$\tau = \tau_1 + \tau_2, \qquad (1)$$

where

τ_1 - heating time of oil shale particles to attain $T_s = T_f$ depend on T_a

τ_2 - retorting time of oil shale particles to attain $T^* = T_f$ depends on T_a.

In this work on oil shale particles with different particle size the calculation method of volatiles separation time from oil shale particles in fluidized bed is used for estimating the retorting time (Kartau (1975)). The heating time of oil shale particles τ_1 was determined experimentally and volatiles separation time τ_2 experimentally and theoretically.

For the estimation of the retorting time for oil shale particles with different size the next formula is used:

$$\tau_2 = r^2_x/2a_2 + (k + \xi r)\, r/a_2 + \ln[(1 - r/(mnr - k)^{\eta})(k/(r + k)^{k}2/a_1)], \qquad (2)$$

where

$\xi = q_{pk}/c\Delta T^* + mn(1 - a_2/2a_1) - k/r - 1$;

$\eta = n\xi r^2/a_2 + k^2/2a_1$;

$\Delta T = T_s - T_f$; $\Delta T^* = T_f - T^*$; $n = \Delta T/\Delta T^*$;

$k = \lambda_1/\alpha_\Sigma$, $m = \lambda_1/\lambda_2$.

Figure 2 shows the heating time τ_1 of oil shale particles depend on r and Ta to attain $T_s = T_f$ (experimental data).

Figure 3 shows the retorting time τ_2 of oil shale particles depend on r and T_a to attain $T^* = T_f$ (formula (2) and experimental data).

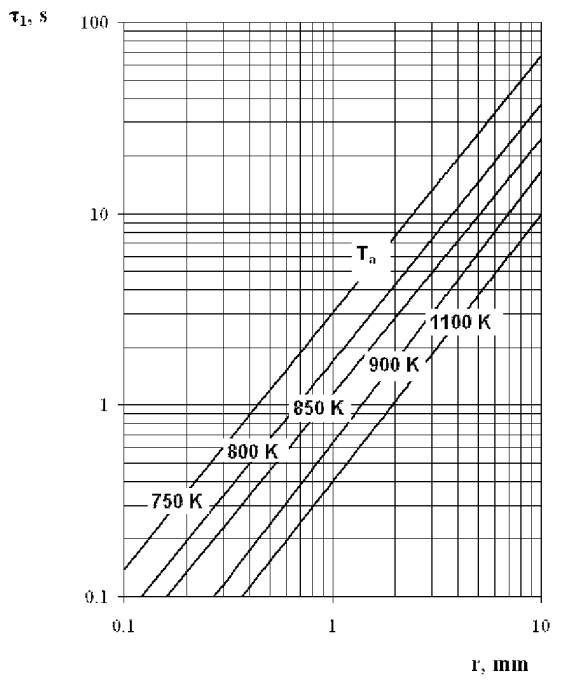

Fig. 2 The heating time τ_1 of oil shale particles to attain $T_s = T_f$ depends on T_a

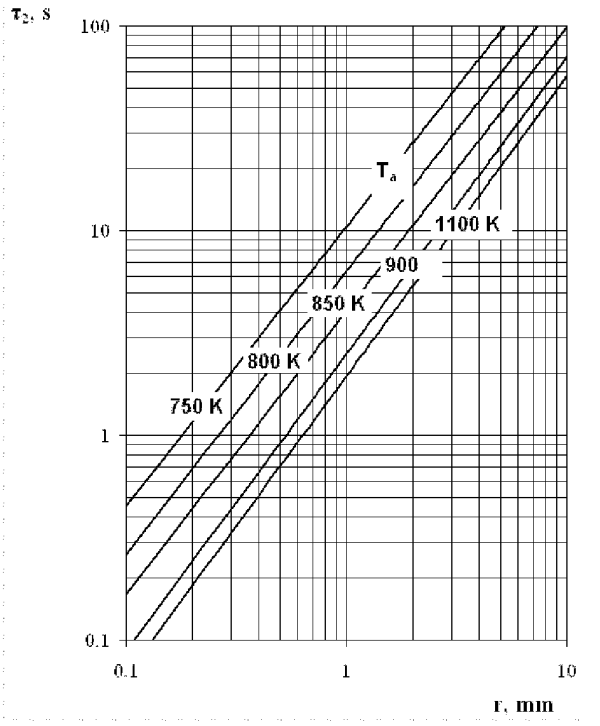

Fig. 3 The retorting time τ_2 of oil shale particles to attain $T^* = T_f$ depends on T_a

To get an idea about the operation load and size of fluidized bed retort, its parameters are analysed taking in consideration the heating and retorting time of Estonian oil shale particles, fraction composition of crashed oil shale and other parameters.

Analysed Estonian oil shale fraction composition, prepared for retorting is given in Table 1, based on shale fraction composition in Galoter retort TSK-140.

Table 1 Estonian oil shale fraction composition

d_p, mm	10-6.3	6.3-1	1-0.5	<0.5
version 1	2	11	15	72
version 2	3	15	18	64
version 3	3	23	13	61

From Table 1 follow, that the best fraction composition of crashed oil shale is version 3, because the content of coarse particles (1-10 mm) is substantially bigger than that of the others. For further estimations of oil shale retorting process in fluidized bed reactor, the fraction composition of crashed oil shale of version 3 is chosen. On the basis of available experimental data about 25% - 30% of oil shale particles with the same fraction composition stay in fluidized bed (a_r = 0.25 – 0.3) (Martins (1997)). It means that the retorting process of course particles takes place in fluidized bed and the remainder in the freeboard and semicoke separation chamber.

The retorting time of coarse oil shale particles in fluidized bed depends on several factors: the depth and cross-section of bed, medium temperature of the mixture of oil shale particles and heat carrier, retorting gas velocity etc. The retorting time is the longest for the particles with the maximum size, in the present case d_p = 10 mm (r = 5 mm).

For estimating the retorting load of fluidized bed grating the next parameters have been chosen: the area of fluidized bed grating F_b = 1.0 m^2; depth of a fluidized bed h_b = 0.8 m; medium temperature of the mixture oil shale particles and heat carrier T_a = 800 K, apparent density of oil shale γ_s = 1.5 t/m^3. It is presumed in the calculations that the fine hot ash particles (the solid heat carrier) are carried out of the bed.

The heating and retorting time of particles with the radius r = 5 mm at the temperature T_a = 800 K were assessed from Fig 2 and 3: τ_1= 14 s, τ_2 = 60 s and τ = 74 s, respectively. In Galoter retort TSK-140 the retorting time of oil shale particles is 15 – 20 min (Kaidalov et. al (2007)).

The retorting load of 1.0 m^2 fluidized bed grating can be expressed as:

$$M_b = F_b \times h_b \times \gamma_s \times 3600/\tau = 1.0 \times 0.8 \times 1.5 \times 3600/74 = 58.4 \text{ t/h.}$$

The entire load of the fluidized bed retort with 1 m^2 grating can be expressed as:

$$M_r = M_b/a_r,$$

where a_r = 0.25, then M_r = 58.4 : 0.25 = 233.6 t/h and

where a_r = 0.30, then M_r = 58.4 : 0.30 = 194.7 t/h.

Retorting of fine oil shale particles with maximum particle size 0.7 – 1.0 mm takes place in freeboard of the fluidised bed shaft. The heating and retorting time of particles with radius r = 0.5 mm at medium temperature T_a = 780 K was assessed from Fig. 3: τ_1= 0.7 s, τ_2 = 2.4 s and τ = 3.1 s. The circulating semicoke gas speed in the cross-section of the grating is 0.6 m/s and amount G_{cg} = 2160 m^3/h. The total volume of retorting products of oil shale is G_s = 73.2 nm^3/t (Blohin (2005)). The volume of retorting products from fluidized bed is $G_b = a_r \times G_s$ = 0.25 × 73.2 =18.3 nm^3/t, at the end of the fluidized bed shaft G_{sh} = 0.95 × G_s = 0.95 × 73.2 = 69.54 nm^3/t and medium volume of retorting products in the fluidised bed shaft $G_M = (G_b + G_{sh})/2$ = (18.3 + 69.54)/2 = 43.97 nm^3/t. The medium total volume of retorting products at oil shale feed M_r = 233.6 t/h and temperature 780 K: $G_r = G_M \times M_r \times 780/273$ = 43.97 × 233.6 × 780/273 = 29346.8 m^3/h. The amount of retorting products with circulating semicoke gas $G_\Sigma = G_r + G_{cg}$ = 29346.8 + 2160 = 31526.8 m^3/h. The medium velocity of gases v_g in cross-section of the fluidised bed shaft F_s = 2.2 m × 2.2 m = 4.84 m^2 is:

$$v_g = G_\Sigma/F_s \times 3600 = 31526.8/4.84 \times 3600 = 1.81 \text{ m/s.}$$

The entire depth of fluidised bed shaft can be expressed as

$$h_\Sigma = h_g + h_b = v_g \times \tau + h_b = 1.81 \times 3.1 + 0.8 = 6.4 \text{ m.}$$

SUMMARY

An analysis of the operation of oil shale plant unit which consists of a fluidized bed retort and circulating fluidized bed boiler is presented here.

The retorting process in the fluidized bed retort depends substantially on the fraction composition of oil shale: on the one hand, the large amount of course particles in the prepared shale enables to remove coarse

semicoke particles directly from fluidized bed (during processing and combustion the oil shale particles preserve the permanent volume), but on the other hand, the overall load of the retort will decrease while the increase of bed depth is not desirable. Practically, the fraction composition of prepared oil shale depends on the crushing technology. The present analyses were carried out with the fraction composition of oil shale prepared for the Galoter retort (Table 1). Approximate calculations show that the throughput of the fluidized bed retort is 6.5 –7.8 tons of oil shale per one m^3 of retort per hour, but the same value of Galoter retort is about 0.6 tons of oil shale per one m^3 of retort per hour. The avoidance of moving parts in the retorting zones is a presumption for the reduced downtime that increases additionally the total productivity of the fluidized bed retort.

The semicoke and semicoke gas are completely burnt in the furnace of circulated fluidized bed boiler in the temperature range from 800 °C to 850 °C. In this temperature range the retention of sulphur dioxide formed during the semicoke and semicoke gas combustion is provided for about 99% due to the high CaO content in the semicoke ash. Hot fly ash is separated from the ash-laden furnace gases and partly fed into the fluidized bed retort as a solid heat carrier. The remainder of hot fly ash is cooled and fed back into the furnace for the control of combustion temperature or separated from the process. The steam generated by combustion of semicoke and semicoke gas could be used for electricity or/and heat production.

The described plant unit is useful for retorting oil shale and other solid hydrocarbon-containing fuels.

NOTATIONS

τ_1	heating time of oil shale particles, s;
τ_2	retorting time of oil shale particles, s;
T_s	particle surface temperature, K;
T_f	temperature of decomposition front in particle, K;
T^*	temperature in the centre of particle at the beginning of heating process, K;
T_a	medium temperature of oil shale particles and heat carrier mixture, K;
r	conventional radius of oil shale particle, mm;
q_{pk}	heat of decomposition of oil shale organic matter, kJ/kg;
a_1 and a_2	temperature conductivity coefficient, m^2/s;
λ_1 and λ_2	heat conductivity coefficient, W/mK;
c_1 and c_2	specific heat capacity, kJ/m^3K;
α_Σ	summary heat transfer coefficient, W/m^2K;
index 1	zone of the particles of spent shale;
index 2	zone of the particles of oil shale.

REFERENCES

Yefimov V.: Oil Shale Processing in Estonia and Russia. Oil Shale.2000, Vol.17, No. 4, pp. 367-385.

Golubev N.: Solid Oil Shale Heat Carrier Technology for Oil Shale Retorting. Oil Shale. 2003, Vol. 20, No. 3 SPECIAL, pp.324-332.

Kann J., Elenurm A., Rohtla I., Golubev N., Kaidalov A., Kindorkin B.: About Thermal Low-temperature Protssing of Oil Shale by Solid Heat Carrier Metod. Oil Shale. 2004,Vol. 21, No. 3, pp. 195-203.

Qian J., Wang J.: Word Oil Shale retorting Technologies. International Conference on Oil Shale: "Recent Trends in Oil Shale", 7-9 November 2006, Amman, Jordan.

Siirde A., Martins A.: Plant unit for oil production from oil shale, Utility Model EE 00671 U1. 2007, The Patent Office of the Estonian Republic, Tallinn.

Kartau J.: The Investigation of Volatiles Separation Process from Oil Shale Particles. The theses paper of technical sciences candidate (Ph.D). Tallinn,1975, 21 pages (in Russian).

Martins A.: The First Industrial combustion of Oil Shale with Gasification in Fluidized Bed. Energia Teatja, Eesti Energia, 1997,1/2 (16), pp. 14-17 (in Estonian, Summary in English).

Kaidalov K., Kaidalov A., Elenurm A., Kindorkin B., Vereshcaka S.: Method for Improving the Quality of Middle-heavy Shale oil and for Increasing Commodity Output at Thermal processing of Fuels in the Solid Heat Carrier Unit. Oil Shle.2007, Vol. 24, No. 4, pp. 499-508.

Blohin A., Zaretski M., Stelmah G., Fraiman G.: Energy Technological Processing of Fuels in the Solid Heat Carrier Unit. Moskva, Stalnõi Stan, 2005 p 331 (in Russian).

THE INFLUENCE OF SORBENT PROPERTIES AND REACTION CONDITIONS ON ATTRITION OF LIMESTONE BY IMPACT LOADING IN FLUIDIZED BEDS

Fabrizio Scala, Piero Salatino

Istituto di Ricerche sulla Combustione, Consiglio Nazionale delle Ricerche, Napoli, Italy
Dipartimento di Ingegneria Chimica, Università degli Studi di Napoli Federico II, Napoli, Italy

Abstract: The extent of attrition associated with impact loading was studied for five different limestones pre-processed in fluidized bed under different reaction conditions. The experimental procedure was based on the measurement of the amount and the particle size distribution of the debris generated upon impact of sorbent samples against a target at velocities between 10 and 45 m/s. The effect of calcination, sulfation and calcination/re-carbonation on impact damage was assessed. Fragmentation by impact loading of the limestones was significant and increased with the impact velocity. Lime samples displayed the largest propensity to undergo impact damage, followed by sulfated, re-carbonated and raw limestones. Fragmentation of the sulfated samples followed a pattern typical of the failure of brittle materials. On the other hand, the behavior of lime samples better conformed to a disintegration failure mode, with extensive generation of very fine fragments. Raw limestone and re-carbonated lime samples followed either of the two patterns depending on the sorbent nature. The extent of particle fragmentation increased after multiple impacts, but the incremental amount of fragments generated upon one impact decreased with the number of successive impacts.
Keywords: limestone, attrition, fragmentation, fluidized bed, impact

INTRODUCTION

Attrition brings about substantial changes in the particle size distribution of sorbents in fluidized bed (FB) combustors (Chandran and Duqum, 1989; Couturier et al., 1993; Scala et al., 1997; Di Benedetto and Salatino, 1998; Scala et al., 2000; Saastamoinen and Shimizu, 2007). Scala et al. (1997, 2000 and 2007) classified sorbent attrition phenomena in fluidized beds on the basis of the relevant breakage mechanism and the size of generated fragments. Primary fragmentation occurs immediately after the injection of the particles in the bed, as a consequence of thermal stresses and of internal overpressure due to CO_2 emission. Primary fragmentation occurs in the dense bed or in the splashing zone of either bubbling or circulating FB combustors, resulting in the generation of either coarse or fine fragments. Further breakage of particles occurs as a consequence of mechanical stresses experienced by the particles during their lifetime in the reactor. Attrition by abrasion generates fine particles that are quickly elutriated. This breakage process is related to the occurrence of surface wear as the emulsion phase of the fluidized bed is sheared by the passage of bubbles. Secondary fragmentation generates coarser fragments that are typically retained within the reactor for relatively long residence times. Secondary fragmentation may onset as a result of high-velocity collisions against targets, which can be either bed material or reactor walls and internals. High-velocity impact conditions are experienced by the particles in the grid (jetting) region of FB combustors and are closely related to the design of the gas distributor. The exit region of the riser and the cyclone are other potential locations of impact damage of sorbent particles.

The influence of the progress of calcination and sulfation on attrition of limestone in FB combustors has long been recognized (Chandran and Duqum, 1989; Scala et al., 1997). These reactions cause significant modifications of the mechanical and morphological properties of the sorbent particles, influencing the extent and mechanisms of particle breakage. In particular, the progress of sulfation significantly decreases the attrition rate of porous CaO, due to the formation of a tougher sulfate shell at the periphery of the particle. Neglecting particle strengthening as sulfation progresses in the particle outer shell leads to significant overprediction of attrited fines generation. Most of the published investigations on sorbent attrition during sulfur capture in fluidized beds refer to moderate bubbling test conditions, which emphasize the contribution due to surface wear. Only recently did attrition by impact damage receive consideration (Scala et al., 2000; Chen et al., 2007; Scala et al., 2007 and 2008). Calcination and sulfation were shown to significantly affect the extent and pattern of sorbent fragmentation due to impact.

The present study was focused on the characterization of the propensity of Ca-based sorbents to undergo impact damage. The test procedure consisted of entraining limestone particles in a gas stream at controlled flow rate and impacting them against a target in a purposely designed impactor. The particle size distribution of the debris remaining after the impact was worked out to define a fragmentation index. The impact testing technique

was applied to five different limestones. Either raw or pre-processed sorbent samples were characterized from the standpoint of impact damage. Pre-processed samples included: a) calcined limestone; b) limestone calcined and sulfated to exhaustion; c) limestone calcined and then re-carbonated. The pronounced influence of particle pre-processing on attrition extent and pattern was highlighted. Multiple impact cycles were also tested on selected limestone samples.

EXPERIMENTAL

Apparatus

Calcination, sulfation and re-carbonation of limestone were carried out in a stainless steel atmospheric bubbling FB reactor. The reactor, 40 mm ID and 1 m high, was electrically heated. The gas distributor was a perforated plate with 55 holes of 0.5 mm diameter in a triangular pitch. Flue gases were continuously sampled for CO_2 and SO_2 concentration measurement by means of two on-line NDIR analyzers, in order to monitor the progress of reactions. The bed material consisted of mixtures of 20 g of limestone and 150 g of silica sand. Silica sand was sieved in the particle size range 0.85-1.0 mm. Further details on the FB apparatus can be found elsewhere (Scala et al., 2001).

Impact testing of either raw or pre-processed sorbent samples was carried out in an apparatus based on the well established concept of entraining particles in a gas stream at controlled velocity and impacting them against a target (Yuregir et al., 1986; Scala et al., 2000; Salman et al., 2002; Samimi et al., 2004; Chen et al., 2007). The test rig consisted of a vertical stainless steel eductor tube equipped with a particle feeding device. The eductor tube was 10 mm ID and 1 m high. The particle feeding device was fitted at the top of the eductor tube and consisted of a stainless steel hopper with a 10 mm ID at the top section and 4 mm ID at the bottom section. The bottom end of the hopper was connected through a valve to a steel tube (4 mm ID) running coaxially for 0.2 m inside the eductor tube. The air also entered the top section of the eductor tube and flowed downward between the inner and outer tubes. When the valve was opened, the limestone particles contained in the hopper flowed through the inner tube driven by gravity and by the acceleration effect caused by the air flowing in the eductor tube. The hopper could be isolated from the environment by means of a top valve, to avoid air bypass when the bottom valve was open. After feeding, the particles were accelerated by the air flow in the eductor tube. The particle velocity was controlled by regulating the air flow in the eductor tube, by means of a flowmeter. When the particles exited the eductor tube, they impacted on a rigid target plate placed in a collection chamber 50 mm below the bottom end of the tube. The target was made of stainless steel and was inclined by 30° with respect to the horizontal. This inclination was chosen as a trade-off between the need of avoiding interference between the impacting and reflected particles and the need of minimizing the departure of results from those obtained with a target perpendicular to the particle trajectory (Salman et al., 2002; Samimi et al., 2004).

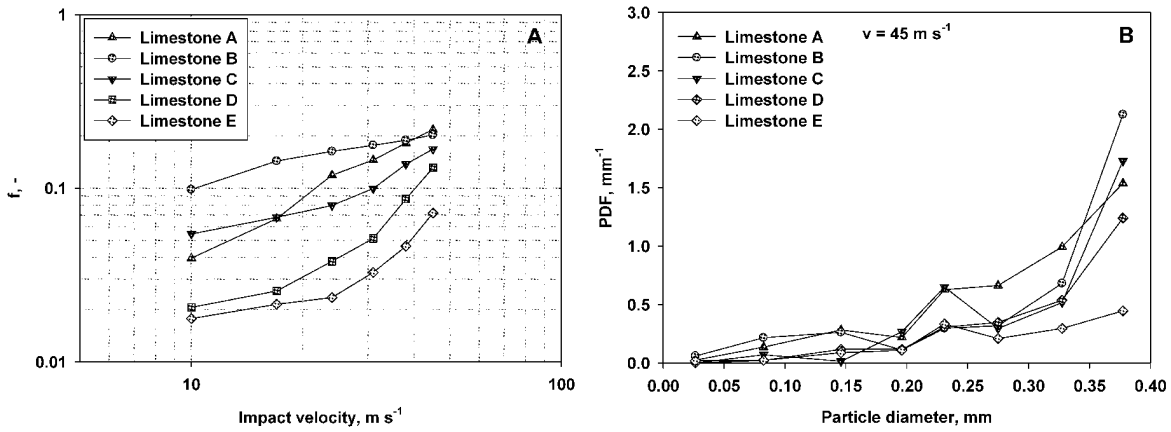

Fig. 1 Raw limestone impact tests: A) weight fraction of fragmented material (f) as a function of the impact velocity; B) probability density function of particle size of fragments (d < 0.4 mm) collected after impact at v = 45m s^{-1}

The collection chamber was made of glass, 80 mm ID and 0.55 m high. The air flow left the collection chamber from the top section where it passed through a porous cellulose filter (for the capture of finer particulate). The impacted limestone particles settled at the bottom, where they were collected for further analysis. Further details on the impact test apparatus can be found elsewhere (Scala et al., 2007).

Procedures

Five different high-calcium limestones were used for the experiments. Fresh limestone particles were first sieved in the particle size range 0.4-0.6 mm, falling well within the range of particle sizes that are customarily

employed in practical circulating FB combustion. Limestone particles were then either calcined (in air) or simultaneously calcined and sulfated (1800 ppmv SO_2) for 120 min in the FB reactor operated batchwise at 850°C with a gas superficial velocity of 0.8 m/s, following the procedure reported by Scala et al. (2001). Some calcined limestone samples were also re-carbonated (10%v/v CO2) for 15 min in the same FB reactor operated at 700°C at a gas superficial velocity of 0.7 m/s. At the end of each test the sorbent was discharged from the bed and easily sieved out of the bed material (sand) because of its smaller particle size. Calcined, sulfated or re-carbonated limestone particles were again sieved in the particle size range of 0.4-0.6 mm and stored in a desiccator to prevent hydration and/or re-carbonation of the material.

Samples (approximately 2.0 g) of raw (R), calcined (C), sulfated (S) or re-carbonated (RC) limestone were weighed and used for fragmentation tests in the impact testing apparatus. The tests were carried out in air with the following particle impact velocities v: 10, 17, 24, 31, 38, 45 m/s. These velocities were selected so as to reproduce impact conditions that are likely to establish near the gas distributor of industrial-scale FB combustors. The tests were carried out at room temperature. This should only moderately affect the possibility to extend the present results to the actual operating FB temperatures: the influence of temperature on attrition propensity has been shown to be moderate as far as no chemical modifications of the sorbent are brought about by temperature changes (Lee et al., 1993; Cook et al., 1996). After each test the sample was retrieved from the collection chamber and weighed. Closure of the mass balance was checked to estimate the loss of material during testing. The closure was always within 3% of the initial sample weight. The collected particles were then sieve-analyzed to obtain their particle size distribution. Few tests were repeated to check the reproducibility of the particle size distributions. Multiple impact cycles were also tested on selected limestone samples, by repeating several times the impact testing at the same velocity on already impacted samples. Sieve-analysis was performed after each impact.

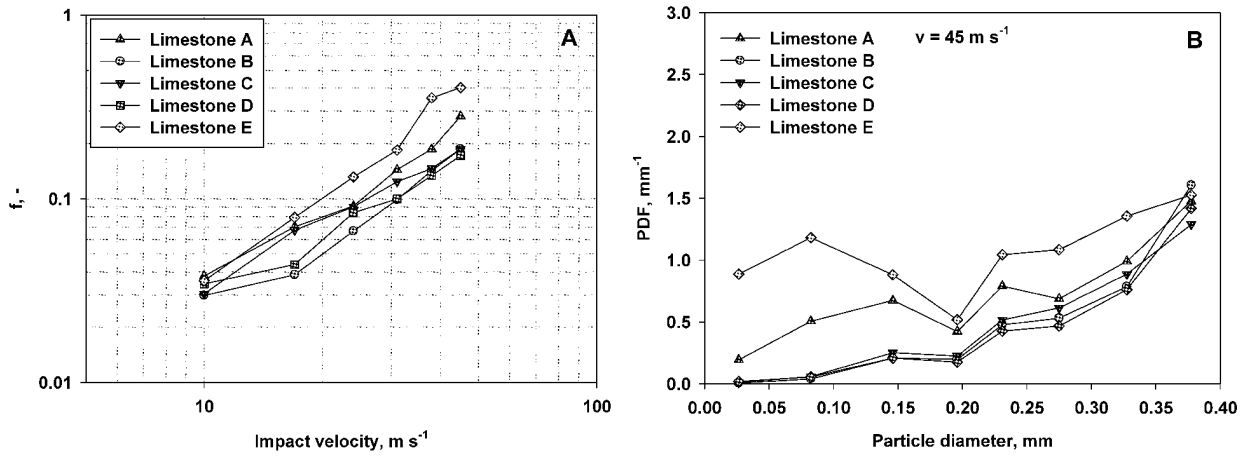

Fig. 2 Calcined limestone impact tests: A) weight fraction of fragmented material (f) as a function of the impact velocity; B) probability density function of particle size of fragments (d < 0.4 mm) collected after impact at v = 45m s^{-1}

RESULTS AND DISCUSSION

Impact fragmentation of raw limestones (R)

Figure 1A reports the fractional mass *f* of fragments versus impact velocity for R samples. By "fragments" we mean all the particles collected after the impact tests whose size falls below the lower limit of the feed size interval (< 0.4 mm). The log-log plot was chosen so as to better highlight the establishment of power-law *f* versus *v* relationships ($f \propto v^k$) that are often used to correlate these data. For the raw limestones, results in Figure 1A show that the extent of impact fragmentation is variable in a relatively broad interval, limestones A and B being more prone to breakage, while limestone E appears to be the most resistant. For all the limestones *f* increases moderately as *v* increases from 10 to 45 m/s. Some of the R samples (limestones C, D and E) display impact attrition patterns typical of brittle or semi-brittle materials (Scala et al., 2007). The plots display a transition at impact velocities around 25 m/s, witnessed by a change of the slope. For the other two limestones (A and B) no change of slope is evident in the plots.

Figure 1B reports the probability density function (PDF) of the sizes of fragments collected after impact of R samples at 45 m/s. The PDF was obtained by dividing the fractional mass of particles in a given size bin by the width (in mm) of the size bin. Figure 1B better highlights how the size of fragments is distributed. At any impact velocity and for all the limestones a dominance of relatively coarse fragments, of size just slightly

smaller than 0.4 mm, is observed. R samples mostly undergo particle splitting (breakage of a particle into a relatively small number of fragments of size comparable with the parent particle size), possibly combined with moderate chipping (generation of a limited number of fragments of size much smaller than the parent particle size), with prevailing generation of relatively coarse fragments. This is suggested by the non-uniform, monotonically increasing PDF of particle sizes with pronounced maxima close to the lower limit of the feed particle size (0.4 mm).

Impact fragmentation of calcined limestones (C)

Figure 2A reports the fractional mass f of fragments versus impact velocity for C samples. The extent of impact fragmentation in this case is generally larger than that observed for the raw limestones (Figure 1A). Moreover, the effect of increasing v on the extent of particle fragmentation is more pronounced. The plots in Fig. 2A do not exhibit singularities. Large values of f obeying a power-law relationship ($f \propto v^k$) establish throughout the range of impact velocities investigated for all the limestones. Noteworthy, in this case limestone E is the most susceptible one to breakage.

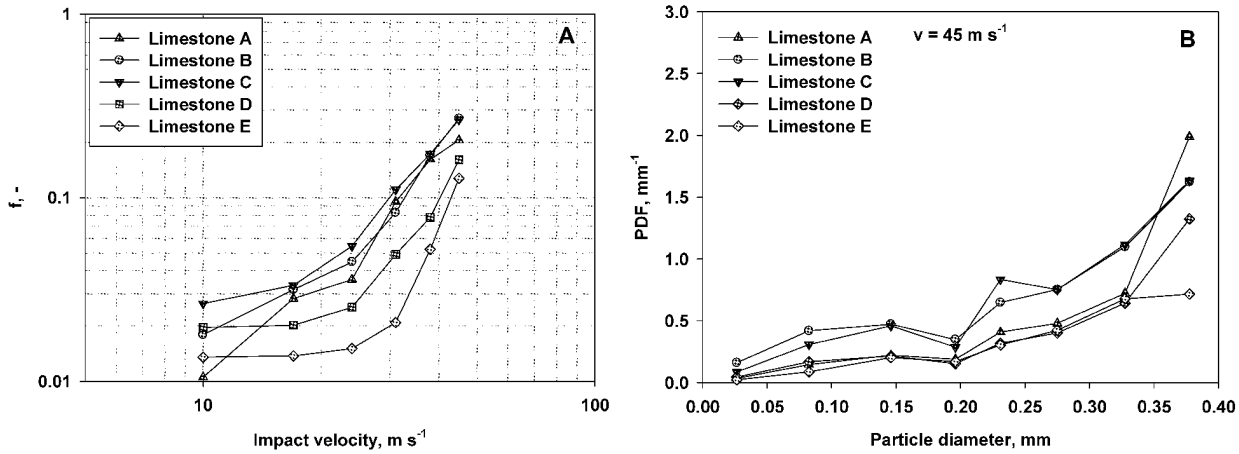

Fig. 3 Sulfated limestone impact tests: A) weight fraction of fragmented material (f) as a function of the impact velocity; B) probability density function of particle size of fragments (d < 0.4 mm) collected after impact at v = 45m s^{-1}

Data points expressing the fractional mass of fragments curves in Fig. 2A for the different calcined limestones are far less scattered than data points referring to the raw limestones (Fig. 1A). It can be speculated that calcination plays an equalizing role on the apparent mechanical properties of the limestones.

Figure 2B reports the probability density function of the fragments size collected after impact of C samples at 45 m/s. Compared with results obtained with the R samples, the sizes of fragments are more evenly distributed over the 0-0.4 mm size range, especially for limestones A and E. The breakage of C particles takes place most likely according to the disintegration failure pattern typical of soft materials (extensive loss of particle connectivity which results into the generation of a large number of small fragments). The large porosity of calcined samples is possibly a key for this behaviour.

Impact fragmentation of sulfated limestones (S)

S particles were obtained by sulfation of R particles to exhaustion, as revealed by inspection of SO_2 profiles at the reactor outlet during sulfation. The final degrees of calcium conversion of the limestones were: 30, 19, 14, 23 and 28% for limestones A, B, C, D and E, respectively. Figure 3A reports the fractional mass f of fragments versus impact velocity for S samples. When comparing these results with those obtained with R and C samples, it can be observed that S samples display an intermediate propensity to undergo impact damage. The composite nature of S particles is responsible for a more complex breakage phenomenology. The fractional mass f for the S samples is very low at low impact velocity, whereas it approaches that of the calcined (C) samples at large impact velocity. It is likely that the hard sulfated shell acts as a shelter for the particle at small impact velocities, though the boundary between the sulfated shell and the unconverted core might be the location where stress concentration and crack generation/propagation might occur. At high impact velocity, the region of the particle exposed to failure extends to the more porous unreacted core which undergoes fragmentation according to the disintegration mode. The transition between these regimes is reflected by the change of the slope of the f vs v plots. Interestingly, in this case limestone E is the least susceptible one to breakage. Again, the f curves lie much closer one to the other than for the raw limestones.

Figure 3B shows the PDF of the fragments size for S samples subjected to impact fragmentation tests at 45

m/s. There is some resemblance of the fragments size PDF for the S and R samples: fragments are mostly coarse (just below 0.4 mm) with a limited contribution of fragments of size smaller than 300 μm.

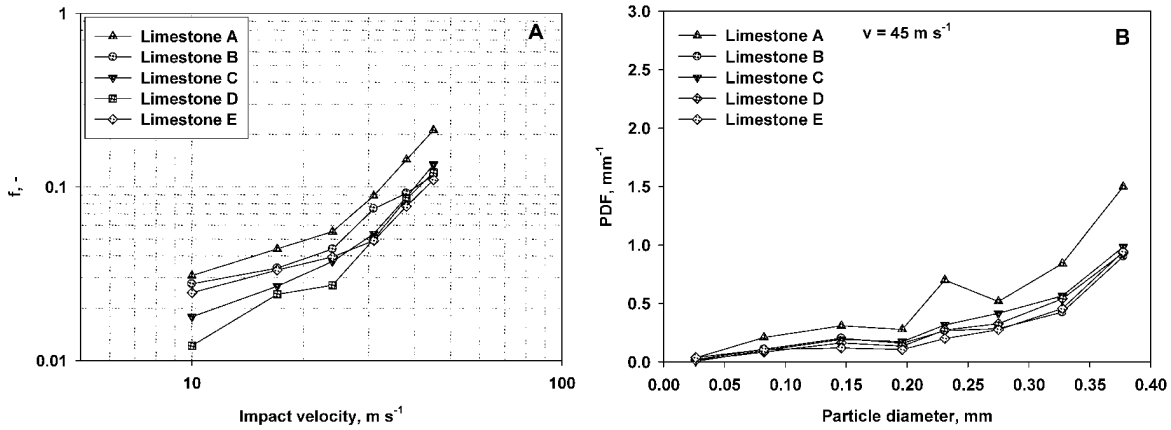

Fig. 4 Re-carbonated limestone impact tests: A) weight fraction of fragmented material (f) as a function of the impact velocity; B) probability density function of particle size of fragments (d < 0.4 mm) collected after impact at v = 45m s^{-1}

Impact fragmentation of re-carbonated limestones (RC)

RC particles were obtained from re-carbonation of C particles to exhaustion, monitored by inspection of CO_2 profiles at the reactor outlet during carbonation. The final degrees of calcium conversion of the limestones were: 61, 63, 52, 70 and 69% for limestones A, B, C, D and E, respectively. Figure 4A reports the fractional mass *f* of fragments versus impact velocity for RC samples. Comparison of these results with those obtained with the R, C and S samples, shows that re-carbonation is effective in reducing the impact damage propensity of the sorbent, to the point of restoring or even exceeding the mechanical resistance of the raw (R) samples. A composite nature of the particles might be expected for the RC sample as well. However, because of the much larger conversion of CaO (nearly 70%), the degree of heterogeneity of RC particles is far less pronounced than that of the S sample. A change of slope is evident for the plots in Fig. 4A, for all the limestones. Also in this case, pre-treatment of the limestones clearly generates samples with more uniform mechanical properties, as witnessed by the closeness of the *f* curves reported in Fig. 4A. Figure 4B shows the PDF of the fragments size for RC samples subjected to impact fragmentation tests at 45 m/s. The results are similar to those obtained with the R and S samples.

Multiple impact fragmentation tests

Multiple impact tests were carried out on selected limestone samples, by impacting the same sample consecutively 10 times at the same velocity. Sieve-analysis was performed after each impact. Figures 5A and 5B report the cumulative particle size distribution and the cumulative fractional mass of fragments collected after multiple impacts. Data refer to raw (R) limestone E impacted at the velocity of 31 m/s. As expected, the cumulative fractional mass of fragments increases after multiple impacts. The incremental attrition is maximum after the first two/three impacts, eventually approaching a nearly linear attrition rate of about 0.8% incremental fractional mass of fragments per impact.

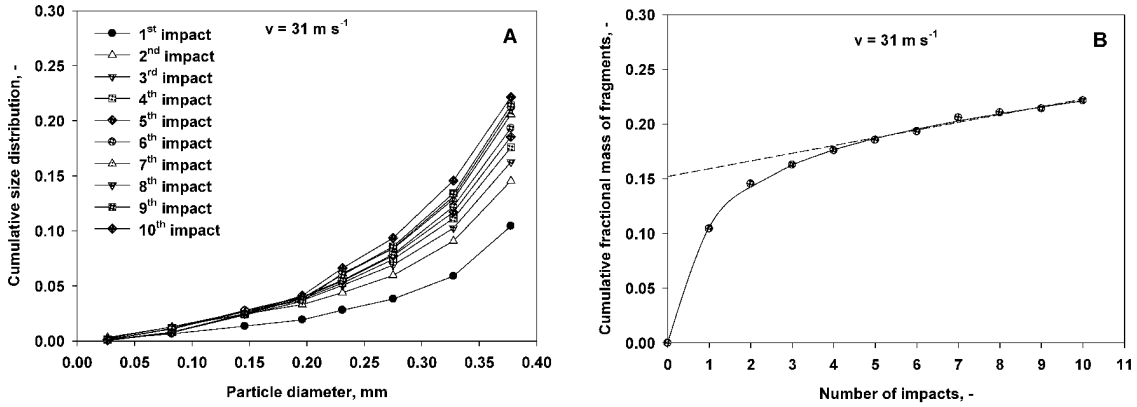

Fig. 5 Multiple impact tests on raw limestone E at v = 31m s^{-1}: A) cumulative size distribution and, B) cumulative fractional mass of fragments (d < 0.4 mm) collected after multiple impacts as a function of the number of impacts

CONCLUSIONS

Five limestones were characterized as regards their propensity to undergo fragmentation by impact loading. The test protocol was applied to both raw and pre-processed (calcined, sulfated, re-carbonated) limestone samples. The following conclusions could be drawn:

- Calcination, sulfation and re-carbonation significantly affect the fragmentation extent and pattern of the sorbent. The raw and re-carbonated materials are the most resistant to impact loading.
- The fully sulfated limestones exhibit a fragmentation pattern which is affected by the composite nature of the particles. A transition between chipping and splitting is observed at impact velocities beyond 25 m/s.
- Lime samples undergo impact fragmentation according to a particle disintegration pattern into a population of polydisperse fragments. No change of regime is observed as impact velocity is increased.
- Raw and re-carbonated limestones exhibit either of the two patterns depending on the sorbent nature.
- The cumulative fractional mass of fragments increases after multiple impacts, to a larger extent after the first two/three impacts, to a smaller and nearly constant extent after the successive impacts.

ACKNOWLEDGEMENTS

The experimental support of Mr. Antonio Lombardo is gratefully acknowledged.

REFERENCES

Chandran, R. R., Duqum, J. N.: Fluidization VI (Grace, J. R., Shemilt, L. W., Bergougnou, M. A., eds.), Engineering Foundation, New York (1989), pp. 571-580.
Chen, Z., Lim, J., Grace, J. R.: Chem. Eng. Sci. 62 (2007), pp. 867-877.
Cook, J. L., Khang, S. J., Lee, S. K., Keener, T. C.: Powder Technol. 89 (1996), pp. 1-8.
Couturier, M. F., Karidio, I., Steward, F. R.: Circulating Fluidized Bed Technology IV (Avidan, A. A., ed.), Amer. Inst. Chem. Eng., New York (1993), pp. 672-678.
Di Benedetto, A., Salatino, P.: Powder Technol. 95 (1998), pp. 119-128.
Lee, S. K., Jiang, X., Keener, T. C., Khang, S. J.: Ind. Eng. Chem. Res. 32 (1993), pp. 2758-2766.
Saastamoinen, J. J., Shimizu, T.: Ind. Eng. Chem. Res. 46 (2007), pp. 1079-1090.
Salman, A. D., Biggs, C. A., Fua, J., Angyal, I., Szabó M., Hounslow, M. J.: Powder Technol. 128 (2002), pp. 36-46.
Samimi, A., Moreno, R., Ghadiri, M.: Powder Technol. 143 (2004), pp. 97-109.
Scala, F., Cammarota, A., Chirone, R., Salatino, P.: AIChE J. 43 (1997), pp. 363-373.
Scala, F., Salatino, P., Boerefijn, R., Ghadiri, M.: Powder Technol. 107 (2000), pp. 153-167.
Scala, F., Montagnaro, F., Salatino, P.: Ind. Eng. Chem. Res. 40 (2001), pp. 2495-2501.
Scala, F., Montagnaro, F., Salatino, P.: Energy Fuels 21 (2007), pp. 2566-2572.
Scala, F., Montagnaro, F., Salatino, P.: Cand. J. Chem. Eng. 86 (2008), pp. 347-355.
Yuregir, K. R., Ghadiri, M., Clift, R.: Powder Technol. 49 (1986), pp. 53-57.

CHARACTERISTICS OF A MODIFIED BELL JAR NOZZLE DESIGNED FOR CFB BOILERS

Z. M. Huang, H.R. Yang, Q.Liu, Y.Wang, J. F. Lu, G. X. Yue

Key Laboratory for Thermal Science and Power Engineering of Ministry of Education, Department of Thermal Engineering, Tsinghua University, Beijing, 100084, China

Abstract: One of the most important factors for trouble free operation of CFB boilers is the pressure drop of the gas distributor. The pressure drop characteristic of the gas distributor depends on the nozzles used. A modified bell jar nozzle was designed and developed for use with large-scale industrial circulating fluidized bed (CFB) boilers. The nozzle consists of a vertically tapered tube with a larger end at the top, a float which is free to move within the tube and a cover with holes. The pressure drop characteristics of the nozzle were measured experimentally by using different floats and moving out the float respectively. The gas distributor equipped with the modified bell jar nozzle has a unique pressure drop characteristic. It has a higher resistance than other nozzles which results in the formation of an effective barrier against backflow at low boiler loads, which results from the pressure fluctuation caused by bubble burst and solids coming from the recycle system. In addition, it has a relatively low pressure drop at high or full boiler loads, which can greatly reduce the energy cost of the primary air fan.

Keywords: CFB boiler, air distributor, float, bell nozzle, pressure drop

INTRODUCTION

The gas distributor is a crucial component in a circulating fluidized bed (CFB) boiler. It has three important functions. The first one is to support the bed material in the furnace, and the second one is to provide sufficient resistance for distributing air uniformly, and the last one is to prevent bed material back flow from the furnace to the wind box (Yang et al., 2007). Hartge and Evard (2004) categorized operational problems associated with the gas distributor in CFB boilers into three kinds as material backflow through the nozzles into the wind box, the maldistribution of air and nozzle erosion.

Several factors could influence the operation of the distributor, e.g., the type of wind box, the shape of the distributor, the nozzle shape and arrangement and the position of the recirculation point. However, the most important factor for trouble free operation of CFB boilers is the pressure drop of the gas distributor. The material backflow is also related to the pressure fluctuation in the furnace, caused by bubble burst or solid recycling, especially at low boiler loads.

It was found that a CFB boiler can be generally described as the superposition of a fast bed in the upper part with a bubbling bed or turbulent bed in the bottom furnace (Yue et al., 2005). The bubbles in the dense bed have high rising velocity and they grow in size due to coalescence. The pressure fluctuation occurs when the bubbles burst at the bed surfaces (Chirgui et al.,1997; Mirek and Nowak.,2006). The bubble then moves both upwards and downwards in the form of a plane wave. The amplitude of the pressure fluctuation in the furnace changes with the height of the dense bed (Chirgui et al., 1997). At low boiler loads, the pressure drop at the distributor decreases with decreasing fluidizing air velocity U_g. When the amplitude is higher than that of the distributor itself, the instantaneous wind-box pressure becomes lower than the pressure in the furnace and a reversed pressure gradient appears. In this condition, the distributor cannot provide enough resistance to form a barrier against the back flow of material (Hartge and Werther,1998; Mirek and Nowakl,2006).

Theoretically, the higher the pressure drop, the smaller the possibility of the back flow is. For the nozzles widely used in CFB boilers, such as bubble cap, arrowhead, pigtail tube and bell jar nozzles, their resistances is approximately proportional to the square of U_g (Hartge and Werther,1998). In order to prevent the back flow at a low boiler load, the resistance has to be increased by changing the structure of the nozzle. It can be done by reducing the flow section area or extending the length of the flow passage (Mirek and Nowakl,2006). However, high resistance will cause too high pressure drop when the boiler is operated at a high load. As a result, the energy cost of the primary air fan increases and the system efficiency reduces.

In view of the CFB boiler operation, the optimized resistance of the distributor should meet two major requirements. One is to provide enough resistance to prevent material from back flowing and distribute air uniformly at low boiler load, and the other is have relatively a low pressure drop to reduce the energy cost of

the primary air fan at high boiler load. Based on the operating principle of a float meter, a float nozzle was designed and developed for large-scale industrial CFB boilers (Yang et al.,2007), meeting the requirements mentioned. Such a float nozzle ameliorated the pressure drop characteristics of the distributor apparently. However, because the float is exposed directly to the bed material, it can not remain a stable position when it moved by the bed material. The swing of the float would badly influence the stability and uniformity of distributing air. Bell jar nozzles that are widely used in current commercial CFB boilers can avoid this problem. A modified bell jar nozzle combining the advantages of the float nozzle and bell jar nozzle was designed and developed for large-scale CFB boilers.

TRADITIONAL BELL JAR NOZZLE

Figure 1 is a schematic diagram of a bell jar nozzle which is widely used in the 135 MWe CFB boilers in China. It consists of an inner tube and outer cover (Schoenborn and Colburn,1939; Zhang,2004). There are large holes in the cover and small holes at the top of the inner tube. This structure helps to prevent the back flow at low boiler load, while the pressure drop is fairly high at full load, and is even higher than the pressure drop of the total bed inventory in the chamber. Although the solids cannot flow back into the wind box, the pressure fluctuation drives the solid into and out from the cover, in a periodic manner, which causes serious wearing down of the holes in the covers.

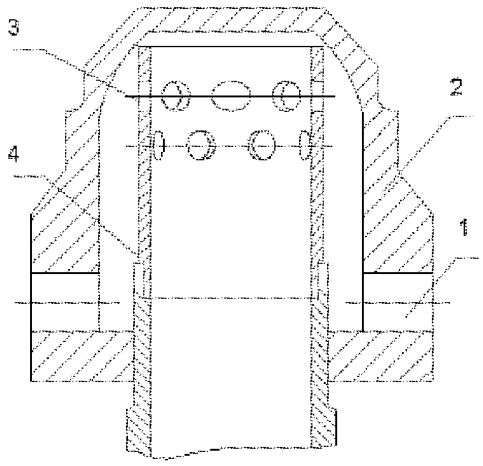

Fig.1 Schematic of the bell jar nozzle

(1) Large holes;(2) Cover; (3) Small holes; (4) Inner tube

MODIFIED BELL JAR NOZZLE AND THE EXPERIMENTAL TEST RIG

The traditional bell jar nozzle prevents back flow through its specific bushing structure, while its pressure drop characteristic still is not satisfied. Figure 2 shows a schematic drawing of the modified bell jar nozzle, which not only keeps the advantages of the traditional bell jar nozzle but also has a unique pressure drop characteristic similar with the float nozzle. The nozzle consists of a cover, an inner tuber with a tapered channel and a float. The main difference between the traditional bell jar nozzle and the modified one is that there is a float in the modified one and a tapered channel replaces the inner tube with small holes at the top.

The pressure characteristic of the float nozzle was measured in the laboratory scale fluidized bed rig, shown in Fig. 3. The fluidized bed has a rectangle riser of 150 mm in length, 30 mm in width and 1.5 m in height. Five modified nozzles were installed in the distributor with a fractional open area of 3.8%. The fractional open area is chosen to be similarly with that of the bell jar nozzle used in industrial CFB boilers in order to compare the pressure drop of these two nozzles (Zhang,2004).

The differential pressures between points located at 0.1 m above and under the distributor were measured using pressure transducers (Setra C264). The air flow rate was measured with a flow meter with full ranges of 0–200 Nm^3/h. The experimental procedure followed two steps. Firstly, the pressure drop of the tapered channel and the holes, ΔP_c, versus U_g was measured, and then the total pressure drop across the distributor, ΔP_t, was measured. The differential pressure caused by the float, ΔP_f, can be calculated by subtracting ΔP_c from ΔP_t. The ambient temperature was 25°C during all of the experiments.

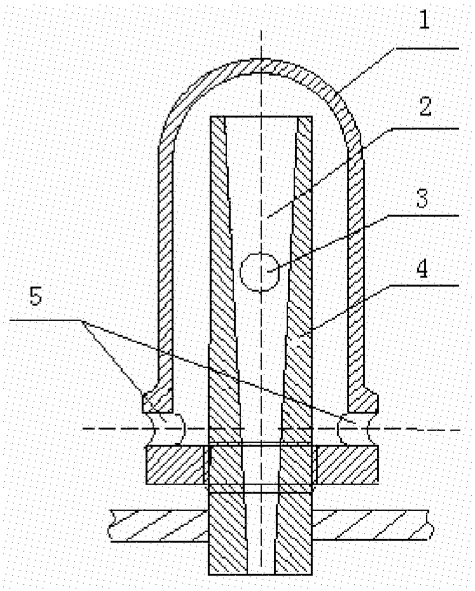

Fig.2 Schematic of the Modified bell jar nozzle: (1) Cover;(2) Tapered Channel; (3) Float; (4) Inner tube; (5) Large holes

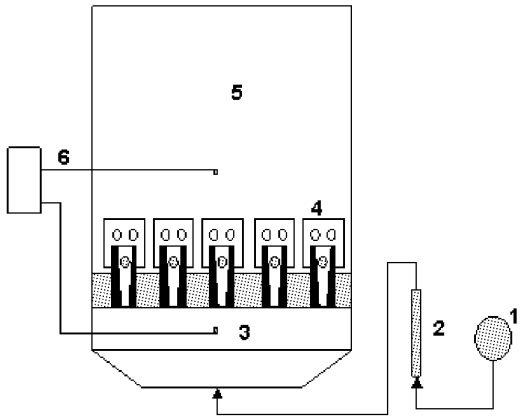

Fig.3 Schematic of the fluidized bed rig apparatus: (1) Primary air fan; (2) Rotameter; (3) Wind box; (4) Float nozzle; (5) Riser; (6) Pressure sensor

THE PRESSURE CHARACTERISTICS OF THE MODIFIED BELL JAR NOZZLE

Two kinds of float were used. One is steel ball with 8mm diameter, the other is T-type float. Figure 4 shows that the pressure drop of the channel, ΔP_c, versus the inlet velocity of the channel is an approximate square curve. The differential pressure caused by the float, ΔP_f, is almost constant with an average value of 380 Pa for the steel ball float nozzle and 1700 Pa for the T-type float respectively. The product of the differential pressure and the section area of the dome equals the weight of the float. These are in agreement with the principles of the float meter outlined earlier.

The total pressure drop consists of two parts, the pressure drop for the float and the pressure drop resulted from channels, including the tapered channel in the inner tube and the holes on the cover. The former part which determines the pressure drop of the distributor at low boiler loads, lies on the weight of the float. The later part which is the main portion of the pressure drop at high boiler loads, depends on the fractional open area of the distributor and the size of the holes. Thus, it is flexible to adjust the weight of the float and fractional open area to obtain appropriate resistance characteristic.

Figure 4 also compares the pressure drops for the modified bell jar nozzle and the traditional one used in

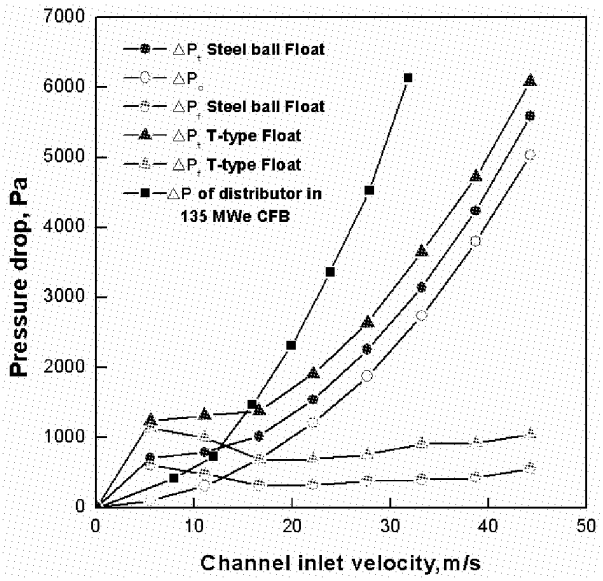

Fig.4 The pressure drop of the modified nozzle versus the velocity

135 WMe CFB boiler (Yang et al. 2004). It can be seen that the modified nozzle has a relatively flat pressure drop curve. Such a resistance characteristic can prevent material backflow and distribute air uniformly at low boiler loads, while it reduces the energy cost of the primary air fan at high boiler loads.

CONCLUSIONS

A modified bell jar nozzle was designed and developed for large-scale industrial CFB boilers. The nozzle coupled the advantages of float nozzle and traditional bell jar nozzle. The gas distributor equipped with the float nozzle has a flat pressure drop versus velocity curve. Such a characteristic helps to prevent solid backflow at low boiler loads and reduces the energy cost of the primary air fan at high loads.

ACKNOWLEDGEMENTS

Financial supports of this work by Key Project of the National eleventh-Five Year Research Program of China (2006BAA03B02) and National Science Fund Committee (50406002) are gratefully acknowledged.

NOTATIONS

ΔP_c pressure drop of channel, Pa
ΔP_f pressure drop of float, Pa
ΔP_t pressure of distributor, Pa
U_g fluidizing air velocity, m/s

REFERENCES

Chirgui, A. M., Tadrist, H., Tadrist, L.: Phys. Fluids 1997, 9 (3),500.
Hartge, E.U., Evard, M.: VGB Workshop, HKW Moabit, Vortrag 10, Berlin 2004.
Hartge, E.U., Werther, J.: in Fluidization IX (Eds: L. S.Fan, T. M. Knowlton), Engineering Foundation, New York 1998.
Mirek, P., Nowak, W.: Proc. of the 19th Int. Conf. on Fluidized Bed Combustion (Ed: F. Winter), Vienna, Austria 2006.
Schoenborn, E. M., Colburn, A. P.: AIChE J. 1939, 35 (3), 359.
Yang, H.R., Huang, Z.M., Yue, G.X., Lu, J.F.: Chem. Eng. Technol. 2007, 30, No. 10, 1398 - 1400.
Yang, J. H., Qu, W. D., Yang, Y.: Boiler Technol. 2004, 35 (1), 12.
G. Yue, J. Lu, H. Zhang, et al. Design Theory of Circulating Fluidized Bed Boilers. in: L. Jia (Eds.),18th International Fluidized Bed Combustion Conference, May, 2005, Toronto Canada.
Zhang, Q. G.: M.Sc. Thesis, Tsinghua University 2004.

HEAT BALANCE ANALYSIS OF BAIMA'S 300 MWe CFB BOILER IN CHINA

J. Y. Lu[1], X. F. Lu[1], G. Yin[2],H. Z. Liu[1]

1 College of Power Engineering, Chongqing University, Chongqing,400044, China
2 Dongfang Turbine Co., Ltd., Deyang,618000, China

Abstract: By analyzing the 336-hour performance testing period operation parameters and the actual measurement data at the scene, this paper took a study of the heat balance on Baima's 300MWe CFB boiler. Through calculating and by the use of DL/T964-2005 standard in China, the efficiency of this boiler under the full load was 91.9089%. The result was very close to the manufacture's assurance efficiency. In all the heat loss, the value of dissipated heat loss calculated in this paper was about 0.63%, which was higher than the manufacture's provided value 0.25%. Besides analyzed the reason, it was discussed about the influence factors of CFB boiler's dissipated heat loss in this paper, including the radiation areas and the out-surface temperature. Additionally, when calculated the heat loss due to the physical heat of bottom ash, the selection of output ash temperature was important. It was discussed in paper about how to choose different output temperatures for different types of ash coolers.

Keywords: circulating Fluidized Bed (CFB) boiler, heat balance, dissipated heat loss, heat loss of bottom ash

INTRODUCTION

The atmospheric circulating fluidized bed (CFB), which is applied in the field of electric power generation just for a few decades, is internationally recognized as one of the best commercialized clean combustion technology for its low emissions of nitrogen oxides, realization of direct desulphurization in the combustion process, wide range of fuel adaptability and load regulation etc(Yue, 2007). Therefore, a series of large–scale CFB boilers had been imported from abroad. In order to test the performance of a boiler, it is necessary to analyze the boiler's heat balance. Heat balance is an important performance parameter for a boiler. It reflects the balance relation between the heat input and output and expatiate the efficiency with all the heat losses of the boiler in a visual way (Joris et al., 2007).

There are mainly two methods to calculate heat balance: Input-output method and heat loss method. For the first method, the efficiency is defined as the ratio of heat absorbed by the working fluid(water and steam)to the heat input(chemical heat plus heat credits added to the steam generator).the heat loss method requires the determination of all accountable heat losses, heat credits and the heat in the fuel. The efficiency is then equal to 100 minus the ratio of the sum of all heat losses to the sum of heat in the fuel plus heat credits. It is extremely difficult to accurately measure the solid fuels mass flow in a CFB boiler, so the heat-loss method maybe the better choice.

At the present stage, the test code of a large-scale CFB boiler's heat balance mostly includes ASME PTC 4-1998 standard from America, DIN1942 standard from Germany and GB/T10184-1988 with DL/T964-2005 standard from China. ASME PTC4-1998 standard is suitable for fired steam generators include both sub-critical and supercritical units. In this code, the heat input is based on the higher heating value and the heat losses are shown in a very detailed way. (ASME PTC4-1998). Din1942 standard is intended as the thermal performance testing of direct-fired steam and hot-water generators. The heat input is based on the lower heating value. The latest edition of this standard was issued in 1994, and the particularity of CFB boiler such as the limestone desulphurization is considered in this code. (DIN1942-1994)

Drafted out by Xi'an Thermal Power Research Institute, DL/T964-2005 standard, which is a supplement to the GB/T10184- 1988 standard, is specially aiming at the CFB boiler. In this standard, high pressure fans, primary air fan and secondary air fan are involved in the heat balance system, while the induced fan is out of consideration. The effect of limestone desulphurization on CFB boiler's efficiency is also considered. In this testing code, q_2 is stand for heat loss in flue gas, q_3 , q_4 are heat loss due to chemical incomplete combustion and mechanically incomplete combustion respectively, q_5 is heat loss due to surface radiation and convection, q_6 is physical heat loss of bottom ash, and q_7 is heat loss due to desulphurization. The basic formula is:

$$\eta_{gl} = 100 - (q_2 + q_3 + q_4 + q_5 + q_6 + q_7) \quad \text{(DL/T964-2005} \qquad (1)$$

Since the different condition of basic unit in each country and the massive differences among the measurements of those test codes above, there might be some distinguishes in calculating the boiler efficiency with different standards. Referring to the boiler's 336-hour performance testing data, this paper made a study on the heat balance of Baima's 300MWe CFB boiler.

This boiler was the largest CFB boiler under operation in China. It is a sub-critical natural circulation boiler with single furnace, once intermediate reheat and "H" type arrangement. (Jiang and Sun, 2004). Figure 1 shows the general schematic diagram of BaiMa's 300MW CFB. One of this boiler's biggest characteristics is the external heat exchanger (EHE) were disposed in the circulation loop. Inside the external heat exchanger, there is superheater and final reheater, by use of the heat transfer characteristics of these EHEs, the reheat steam temperature can be adjusted under different loads (Lu, 2006). Additionally, the manufacturer optimized this boiler by using a series of new methods, such as trousers type furnace, high running pressure, and the novel cyclone separator technology etc(Yin et al., 2007) .

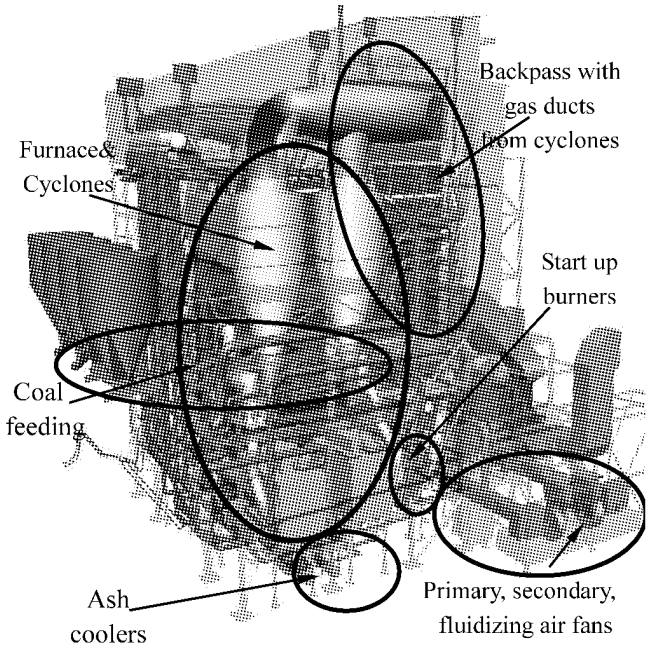

Fig. 1 General Schematic diagram of BaiMa's 300MW CFB boiler

CALCULATION PROCESS

The calculation of this paper was based on DL/T964-2005 standard, using heat loss method to calculate the efficiency and every heat loss. All the data were from the 336-hour performance testing period (The Main performance parameters of BaiMa's 300MW CFB is shown as Table 1). Choose 290MWe, 300MWe and 320MWe as working condition. Before programming, several parameters should be confirmed.

Table 1 Main performance parameters of BaiMa's 300MW CFB

Item	unit	value	Item	unit	value
Boiler drum pressure	MPa	17.10	Reheater outlet temperature	℃	532
Superheater outlet pressure	MPa	15.80	Feed water temperature	℃	264
Reheater inlet pressure	MPa	3.30	Superheater spraywater temperature	℃	263
Reheater outlet pressure	MPa	3.11	Feed water pressure	MPa	17.42
Superheater spraywater pressure	MPa	17.42	Feed water flow rate	t/h	881
Superheater outlet temperature	℃	527	Superheater outlet flow rate	t/h	971
Reheater inlet temperature	℃	325	Total ash flow rate	t/h	45.33

Calculation of the reheat steam flow

There are two stages of extraction steam of high pressure cylinder of steam turbine. The schematic diagram is presented in Figure 2.

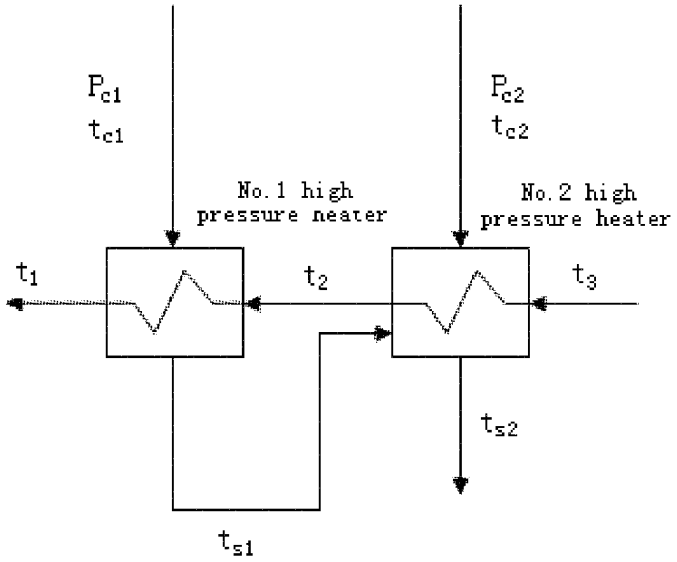

Fig. 2 The extraction steam schematic diagram of high pressure cylinder

Take the 300MWe working condition for example, from the DCS diagram: the pressure and temperature of the primary and secondary extraction steam (Pc1, Pc2, tc1, tc2) were 4.56MPa, 3.26MPa, 382℃, 321℃ respectively. The input and output water temperature of No.1 high-pressure heater (t2 , t1) were 239℃ and 262℃. The input water temperature of No.2 high-pressure heater (t3) was 202℃. The hydrophobic temperature of No.1 and No.2 high-pressure heater (ts1, ts2) were 250℃ and 232℃ respectively. By use of enthalpy entropy diagram, the enthalpy of the primary and secondary extraction steam (hc1 , hc2) were 3162.42 kJ/kg and 3040.91kJ/kg, And the hydrophobic enthalpy of No.1 and No.2 high-pressure heater (h_{s1}, h_{s2}) were 1085.78kJ/kg and 999.67kJ/kg. In addition, according to the pressure of feed water was 17.42MPa, we could determine h_1, h_2, h_3, which were 1143.54kJ/kg, 1035.09kJ/kg and 868.07kJ/kg by use of enthalpy entropy diagram.

Suppose the flow of the primary and secondary steam extractions were mc1 and mc2, from the heat balance of each high-pressure heater:

Heat balance of No.1 high-pressure heater:

$$m_1 (h_1 - h_2) = m_{c1} (h_{c1} - h_{s1}) \tag{2}$$

Heat balance of No.2 high-pressure heater:

$$m_1 (h_2 - h_3) = m_{c2} (h_{c2} - h_{s2}) + m_{c1} (h_{s1} - h_{s2}) \tag{3}$$

Put the data into the formula above, the solutions were : mc1 = 46.01t/h，mc2 = 70.16t/h. So the flow of reheat steam was 854.83 t/h, due to the flow of the main steam was 971t/h.

From the DCS diagram, there was no desuperheating water injecting into the reheat system under the working condition chose in this paper. All the desuperheating water was only injecting into the superheat steam system.

Calculation of the ratio of fly ash and bottom ash

Without desulphurization, the ratio of bottom ash a_d is:

$$a_d = \frac{G_d(1 - C_d/100)}{A_{ar}/100} \tag{4}$$

So the portion of fly ash a_f is: $a_f = 1 - a_d$. In a CFB boiler, as limestone is fed into the furnace to desulphurization, the condition is much complex. In this case, a parameter A_{ar}^D was defined as equivalent ash:

$$A_{ar}^D = \frac{A_{ar} + A_{zz} + A_{wfj} + A_{CaO} + A_{CaSO_4}}{1 + B_d} \tag{5}$$

In the equation, ash from fuel Aar and impurities from limestone Azz could be obtained by proximate analysis. The non-decomposed calcium carbonate Awfj、non-reacted calcium oxide ACaO and generated calcium sulfate A_{CaSO_4} could be calculated following the DL/T964-2005 standard regulations. So the ratio of bottom ash under desulphurization working condition a_d^D could be expressed as:

$$a_d^D = \frac{G_d \times (1 - C_d / 100) \times 100}{(1 + B_d) \times A_{ar}^D} \tag{6}$$

And $a_f^D = 1 - a_d^D$ .The mass of bottom ash G_d could be attained by measuring the weight of ash in an appointed period.

The output ash temperature

There were four fluidized bed ash coolers with this boiler. During the 336-testing period, the behavior of the ash coolers was not as good as expected: Most of the ashes were detained in No.1 chamber, and there was little ash in No.2 and No.3 chamber.

The ashes could only be expelled by accident ash removal ports, and the output ash temperature was usually about 600℃.

And in this paper, 600℃ was used as the output ash temperature.

Calculation of the dissipated heat loss

The dissipated heat loss of furnace and back pass was obtained from the test code's diagram, while the heat loss of the cyclones and EHEs could be calculated as follows: firstly, calculate the radiation areas of all the four cyclones and EHEs, then suppose the out-surface temperature of cyclone was 80℃, and that of EHE was 60℃. In this case, the boiler's dissipated heat loss could be confirmed from empirical formula. (Yan, 2004)

Programming

As these parameters above could be determined, the heat balance was calculated by programming. Figure 3 was the programming process.

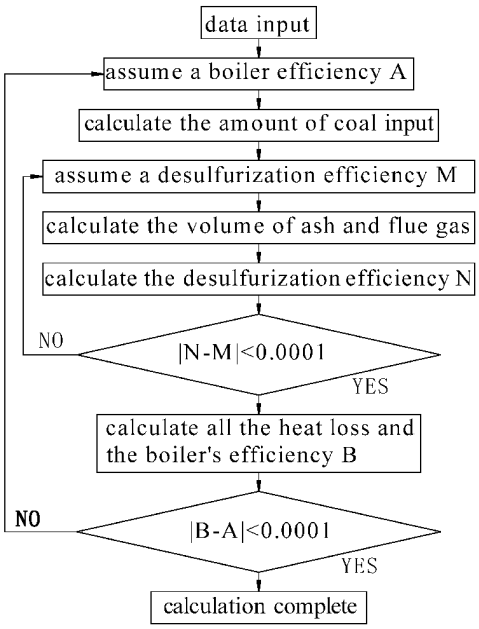

Fig. 3 The program process of calculation

RESULTS DISCUSSION

Input the data in the calculation process, and results are shown in Table 2. As shown in Table 2, this boiler's efficiency was respectively 91.9429%, 91.9089% and 91.4701% under the chosen working condition, very close to the assurance efficiency 91.9%.

Although the total efficiency of the boiler was close to the assurance one, there were some differences in the heat losses. In this paper, it was mainly discussed about the dissipated heat loss and the heat loss due to physical heat of bottom ash.

Table 2 Calculation result of the boiler efficiency

Item	Symbol	Unit	Result		
			290MW	300MW	320MW
flue gas loss	q_2	%	5.1258	5.1531	5.2336
heat loss chemical incomplete combustion	q_3	%	0.0467	0.0461	0.0472
heat loss mechanically incomplete combustion	q_4	%	2.6594	2.621	2.7518
dissipated heat loss	q_5	%	0.6198	0.6207	0.6358
physical heat loss of bottom ash	q_6	%	0.5526	0.5493	0.6014
desulphurization heat loss	q_7	%	-0.9472	-0.8991	-0.7399
Efficiency of boiler	η	%	91.9429	91.9089	91.4701
mole ratio of calcium to sulfur	*Ca/S*	——	1.54	1.57	1.69
Efficiency of desulphurization	η_s	%	91.5088	91.5096	93.3689

Discussion of dissipated heat loss

According to the calculation, the result of dissipated heat loss was about 0.63%, higher than the manufacture's provided value 0.25%. Compared with ASME test code which the manufacture used, the calculation in this paper was based on GB/T10184-1988 and DL/T964-2005 standard. The selection of different standards may cause some differences.

In a CFB boiler, there are many particularities. These particularities can influence the calculation result of this kind of heat loss.

Firstly, compared to pulverized coal boiler, there are cyclones and EHEs in CFB boiler. Thus lead to an increase of the radiation area.

Secondly, there are arrangement differences between the same-capacity CFB boilers. Take the 300MWe boiler for example: some boilers had 4 cyclones with EHEs (like BaiMa's CFB), while some deposited 3 cyclones without any EHE (A domestic 300MWe CFB boiler with 3 cyclones and no EHE is shown in Fig 4). Thus lead to a difference in the radiation area.

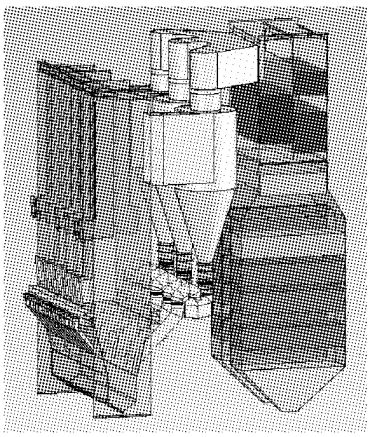

Fig. 4 Domestic 300MWe CFB boiler with 3 cyclones and no EHE

At last, there are mainly two kinds of cyclones: steam cooling cyclone and insulated cyclone. The out-surface temperature of steam cooling cyclone is always lower than the insulated one.

So, the calculation of dissipated heat loss of a CFB boiler should be calculated concretely, including measuring the out-surface temperature and calculating the radiation area etc.

Discussion of physical heat loss of bottom ash

During the 336-testing period, the physical heat loss of bottom ash of the boiler was about 0.56% by computing. It was a little higher than the manufacture's design value.

It can be inferred that the main reason was the difference between the design coal and the coal in use. From Table 3, the ash of coal under operation was much higher than the design one while the heat value was lower than the design one, so the amount of bottom ash was larger.

From the calculation view, the output ash temperature was very important. When the cooling water was condensed water from the condenser, the unit's efficiency decreased although it seemed that the heat of the bottom ash had been recovered.

So, different types of ash coolers should be selected different output ash temperatures.

For air-water combined ash cooler, the temperature rise of cooling water should be back-calculated into the output ash temperature.

For full-water cooling ash cooler, the output ash temperature should be the ash cooler's inlet ash temperature.

For full-air cooling ash cooler, the output ash temperature should be the ash cooler's outlet ash temperature.

Table 3 Comparison of design coal and operation coal

Item	Symbol	Unit	Design data	Practical data
Carbon	C	% wt	49.20	44.68
Hydrogen	H	% wt	2.09	1.98
Oxygen	O	% wt	1.65	2.64
Nitrogen	N	% wt	0.56	0.10
Sulfur	S	% wt	3.54	2.96
Ash	A	% wt	35.27	42.84
Moisture	Mf	% wt	7.69	4.8
Low heating value	LHV	KJ/Kg	18495	16640

CONCLUSIONS

Through calculation by means of programming, the boiler efficiency was respectively 91.9429%, 91.9089% and 91.4701% at the working condition of 290MW, 300MW and 320MW during the 336-testing period. These results did not consider the environment condition. All the results were very close to the assurance efficiency provided by the manufacture.

Compared to the manufacture's provided value 0.25%, this boiler's dissipated heat loss calculated in this paper was about 0.63%.

From calculating, the physical heat loss of bottom ash of this boiler is 0.56%. The main reason due to the coal in use was different from the designed one.

ACKNOWLEDGEMENTS

Financial support of this work by the Key Project of the National eleventh-Five Year Research Program of China (2006BAA03B02-06) is gratefully acknowledged.

REFERENCES

ASME PTC4-1998, Performance test code for fired steam generators

DIN1942-1994, Acceptance testing of steam generators

D/T964-2005, Performance test code for circulating fluidized bed boiler

GB 10184-88, Performance test code of utility boiler

Joris, K., Martin, J. and Andre'Faaij: Progress in Energy and Combustion Science .**33** (2007), pp.19–55.

Jiang, M.Q and Sun X.B.: Thermal Power Generation. **33** (2004), pp.1-3.

Lu, X.F. (2006). Large-scale Circulating Fluidized Bed Boiler Equipment Movement. Beijing, China Electric Power Publ.

Lv, J.F., Yu. L., Zhang, Y.J., Yue, G.X., Li, Z.Y.and Wu, Y.X.: Journal of Power Engineering.**27** (2007), pp.497-501

Yan, W.P.: Performance test code for fired steam generators. Beijing, China Electric Power Publ.

Yin, G., Chen, J.H., Lu, X.F.and Liu, H.Z.: Boiler Technology.**38**(2007), pp.29-33.

Yue, G.X. (2007).Development and future of the circulating fluidized bed combustion technology. Proceedings of 1st circulating fluidized bed combustion conference of China. Hainan.

CO_2 Capture and Chemical Looping

DIFFERENT METHODS OF MANUFACTURING FE-BASED OXYGEN CARRIER PARTICLES FOR REFORMING VIA CHEMICAL LOOPING, AND THEIR EFFECT ON PERFORMANCE

J.P.E. Cleeton[1], C.D. Bohn[2], C.R. Müller, J.S. Dennis[2], S.A. Scott[1]

1Department of Engineering, University of Cambridge, Trumpington Street, Cambridge, CB2 1PZ, United Kingdom

2Department of Chemical Engineering, University of Cambridge, Pembroke Street, Cambridge, CB2 3RA, United Kingdom

Abstract: Chemical looping combustion (CLC) is a means of combusting carbonaceous fuels, which inherently separates the greenhouse gas carbon dioxide from the remaining combustion products, and has the potential to be used for the production of high-purity hydrogen. Iron-based oxygen carriers for CLC have been subject to considerable work; however, there are issues regarding the lifespan of iron-based oxygen carriers over repeated cycles. In this work, haematite (Fe_2O_3) was reduced in an N_2+CO+CO_2 mixture within a fluidised bed at 850°C, and oxidised back to magnetite (Fe_3O_4) in a H_2O+N_2 mixture, with the subsequent yield of hydrogen during oxidation being of interest. Subsequent cycles started from Fe_3O_4 and two transition regimes were studied; Fe_3O_4↔$Fe_{0.947}O$ and Fe_3O_4↔Fe. Particles were produced by mechanical mixing and co-precipitation. In the case of co-precipitated particles, Al was added such that the ratio of Fe:Al by weight was 9:1, and the final pH of the particles during precipitation was investigated for its subsequent effect on reactivity. This paper shows that co-precipitated particles containing additives such as Al may be able to achieve consistently high H_2 yields when cycling between Fe_3O_4 and Fe, and that these yields are a function of the ratio of [CO_2] to [CO] during reduction, where thermodynamic arguments suggest that the yield should be independent of this ratio. A striking feature with our materials was that particles made by mechanical mixing performed much better than those made by co-precipitation when cycling between Fe_3O_4 and $Fe_{0.947}O$, but much worse than co-precipitated particles when cycling between Fe_3O_4 and Fe.

Keywords: chemical looping, hydrogen production, co-precipitation, iron

INTRODUCTION

The ever-growing demand for energy, and the concomitant release of the greenhouse gas CO_2 into the atmosphere by its generation from fossil fuels, imposes an absolute requirement to produce energy in a sustainable manner. Of the fossil fuel reserves, those for coal remain the most abundant; known reserves might last for almost another 150 years at current rates of consumption (World Coal Institute, 2008). However, it is also by far the most polluting fossil fuel, in terms of CO_2 produced per kWh. Therefore, extensive work is being undertaken on the combustion of coal with the subsequent capture and sequestration of the carbon dioxide produced.

Chemical looping combustion (CLC) provides one means of achieving this. The simplest version of the process would work by initially gasifying coal and then combusting the syngas *via* a redox process with a metal oxide. First, the syngas would reduce the metal oxide, and produce a stream of CO_2 and H_2O, from which the CO_2 could be captured by condensing out the water vapour. The metal oxide would subsequently be re-oxidised to be used again; if the oxidation were carried out with air, the overall heat output would be identical to that of a conventional combustion process. In a modified version of CLC (Cleeton *et al.*, 2008), three oxides of iron could be employed, together with steam as one oxidising agent, to produce high-purity hydrogen, suitable for fuel cell applications.

An iron-based oxygen carrier presents numerous benefits; it is relatively cheap and is safe. Also, its numerous stable oxide phases, *viz.* haematite (Fe_2O_3), magnetite (Fe_3O_4) and wuestite ($Fe_{0.947}O$), together with elemental ferrite (Fe), are highly suitable for hydrogen production, because the equilibria of the transitions between these phases when oxidising with steam shows that both the Fe_3O_4↔$Fe_{0.947}O$ and $Fe_{0.947}O$↔Fe transitions are feasible at reasonable partial pressures of steam. However, the final Fe_2O_3↔Fe_3O_4 transition is not suitable, because the ratio of partial pressures of H_2O to H_2 would need to exceed 10^5. Furthermore, satisfactory rates of reaction are achievable for both reduction and oxidation (Mattison et al., 2001). However, there are also drawbacks, most notably the deposition of carbon upon the surface of the particles during the reduction process due to the Boudouard reaction:

$$2CO \rightleftharpoons CO_2 + C_{(S)} \quad (1)$$

The subsequent oxidation of the particles converts the carbon to CO and CO_2, thus diminishing the purity of the hydrogen product stream. The Boudouard reaction is most prominent at temperatures < 750 °C; however, the work of Bohn *et al.* (2008) suggests that ferrite is a catalyst for the Boudouard reaction. Subsequently, the cycling of particles between Fe_3O_4 and Fe results in a much quicker loss in reactivity than cycling between Fe_3O_4 and $Fe_{0.947}O$. This is in agreement with the work of Galvita and Sundmacher (2005), who suppressed carbon deposition by simply limiting the amount of oxide converted during the reduction process.

However, even at higher temperatures, Bohn et al. (2008) found that reducing as far as Fe resulted in a rapid loss in reactivity, which was attributed to the effects of thermal sintering. This problem can be mitigated by a careful choice of one or more metal additives. Takenaka et al. (2004) discovered that alloying an Fe-oxide with Cr reduced sintering, but also inhibited the reduction process at lower temperatures. The further addition of Ni, however, was found to mitigate this problem. Urasaki et al. (2005) found that both Zr and Pd suppressed sintering and improved reaction rates, and considerably enhanced particle performance when used together. However, the choice of additives must be made with great care. Galvita et al. (2008) found that the additions of La_2O_3 and CeO_2 resulted in the undesirable formations of $LaFeO_3$ and $CeFeO_3$ respectively, both of which reduce the oxygen carrying capacity of the particles. However, in the latter case, the inclusion of Zr resulted in the stable formation of $Ce_{0.4}Zr_{0.5}O_2$. The subsequent impregnation of Mo upon the surface of these particles was found to reduce sintering. The benefits of Mo amongst a wide range of other additives have also been demonstrated by Wang et al. (2008) and Takenaka (2003, 2004).

Besides the choice of additive, the way in which these particles are manufactured is also important. In the above work, additives were included using either impregnation or co-precipitation methods. However, within these manufacturing methods there are many variables. Notably for co-precipitated particles, the final pH value has a marked effect on particle performance: e.g. as found by Chuang et al. (2008) for copper-based particles.

In this paper, haematite (Fe_2O_3) was used as the base oxygen carrier. Two different methods of manufacturing oxygen carrier particles were considered: (i) mechanical mixing and (ii) co-precipitation, as described below. The subsequent use of the carrier particles to produce hydrogen, and their performance over several cycles of oxidation and reduction is investigated.

EXPERIMENTAL

Methods of particle manufacture

Mechanically-mixed particles were made from iron(III) oxide powder (Sigma-Aldrich,< 5 μm, purity > 99 wt. %) which was sprayed with distilled water and then mixed so that the powder agglomerated to form larger particles. These particles were sieved to the required size of 425-600 μm and then placed in an oven and sintered for 3 hours at 900°C.

The co-precipitated particles included Al (in the form of an oxide) as an additive. A 1M solution of iron nitrate ($Fe(NO_3)_3{\cdot}9H_2O$, Acros Organics, purity > 98 wt. %) was mixed with a 1M solution of aluminium nitrate ($Al(NO_3)_3{\cdot}9H_2O$, Fisher Scientific, purity > 98 wt. %) in quantities such that the mass ratio of Fe:Al = 9:1. This solution was then mixed with 1M sodium carbonate (Na_2CO_3, Acros Organics, purity 99.5 wt. %) solution, from which the particles were precipitated. The quantity of Na_2CO_3 added determined the overall pH of the mixture: three different specimens of co-precipitated particle were formed by adding increasing quantities of the solution, with pH values of 7.80, 8.96 and 10.59 respectively. The particles were then repeatedly washed with distilled water to remove any unreacted ions, until the conductivity of each sample had fallen below 40 μSv. The particles were then filtered to form a cake, which was subsequently dried in an oven for 24 hours at 150°C. The particles were then calcined for 3 hours at 900°C before being ground and sieved to particle sizes of 425-600 μm.

Experimental method

Fig. 1 shows the experimental set-up of the fluidised bed reactor used to cycle each specimen. The reactor consists of a 20 mm i.d. tube made from recrystallised Al_2O_3, with a porous distributor plate made from 1.4 mm alumina sand (Boud Mineral, purity > 99.9 wt. %) cemented into the tube. The fluidised material consisted of 8 cm^3 (settled, tapped volume) alumina sand (Boud Mineral, purity > 99.9 wt. %), sieved to 300-425 μm. The reactor was heated electrically by a furnace, such that the temperature of the bed, as measured by a K-type thermocouple, was maintained at 850 °C in all experiments. In an experiment described below, ~0.3 g of carrier particles, sieved to 425-600 μm, was added to the reactor. Gases were obtained from three cylinders containing, respectively (i) pure N_2, (ii) pure CO_2 and (iii) a mixture of 10 vol. % CO in N_2. Steam was supplied by metering 20 ml/h of water, using a syringe pump, to a length of copper tube wrapped in trace heating. The bed

was fluidised by various gas mixtures, obtained by blending from these cylinders, such that the superficial velocity of the flow divided by the minimum fluidisation velocity (U/U_{mf}) was always between 4 and 5 at the temperature in the bed. The volumetric flow rates were controlled using manually adjustable valves in conjunction with calibrated mass flow sensors (AWM5101VN, Honeywell), and the overall process was automated using solenoid valves.

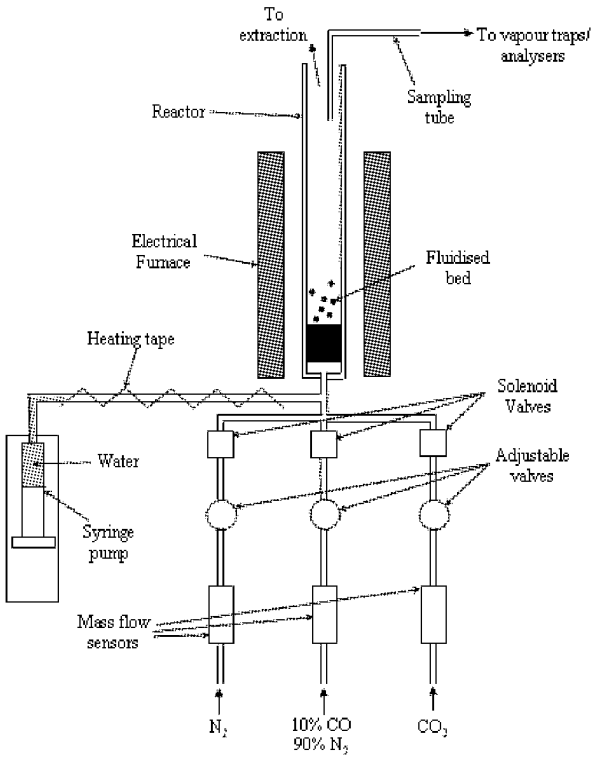

Fig. 1 Experimental set-up for cycling of iron oxide

An experiment for cycling between Fe_3O_4 and $Fe_{0.947}O$ was carried out in the following manner. First, the particles were reduced in ~ 9 vol. % CO, 11 vol. % CO_2, balance N_2 for 5 minutes. The molar ratio of CO_2 to CO, $[CO_2]/[CO]$ was chosen to ensure that each specimen could, on a thermodynamic basis, be reduced as far as $Fe_{0.947}O$, but not to Fe. Afterwards, the bed was purged with pure N_2 for 90 seconds, before the particles were re-oxidised to Fe_3O_4 with steam mixed with N_2 for 4 minutes, so as to produce H_2. After this, the bed was purged with N_2 for 2 minutes before the cycling process was repeated by admitting the reducing gas. For cycling between Fe_3O_4 and Fe, the process was identical, except that the reduction of the particles was carried out with 10 vol. % CO, balance N_2, to ensure that $[CO_2]/[CO]$ was sufficiently small to allow reduction to Fe. The reduction and oxidation times were increased to 7 and 5 minutes respectively, owing to the slower kinetics of the $Fe_{0.947}O \leftrightarrow Fe$ transition, and the larger expected H_2 yields. It should be noted that in all cases, the first cycle began with Fe_2O_3, but all subsequent cycles began with Fe_3O_4; whilst the $Fe_3O_4 \leftrightarrow Fe_2O_3$ transition is useful in the complete combustion of syngas, it is not considered here. Each specimen of carrier completed six cycles. Before each experiment, a complete cycle was carried out with the bed containing just the alumina particles to verify that there was no reaction between the reactant gases and either the bed or the reactor vessel.

RESULTS

Cycling between Fe_3O_4 and $Fe_{0.947}O$

Table 1 shows a theoretical calculation of the expected yields of H_2 in m^3 (at 298 K and atmospheric pressure) based on a 0.3 g mass of the sample, and the subsequent mass of reactive iron within that sample. For the co-precipitated particles, it was assumed that all of the aluminium forms $FeAl_2O_4$ with the iron, and that this fraction of the iron (calculated to be 22%) does not take part in the redox process. In order to provide a fair comparison between the mechanically-mixed and co-precipitated particles, all of the results shown henceforth are given as a ratio of the measured H_2 yield ($H_{2,meas}$) to the expected H_2 yield ($H_{2,exp}$), and not as their absolute values. Fig. 2 shows an example of an experiment, in this case the first two cycles with the mechanically-mixed particles; note that the reduction step for Cycle 1 begins at Fe_2O_3, but from Cycle 2 onwards begins at Fe_3O_4.

Table 1 Expected H_2 yields for various particle samples and transitions (sample mass = 0.3 g)

Type of particle	% of Fe that is active	Expected H_2 yield $\times 10^5$ (m^3)	
		$Fe_3O_4 \leftrightarrow Fe_{0.947}O$	$Fe_3O_4 \leftrightarrow Fe$
Mechanically-mixed	100	2.55	12.25
Co-precipitated with mass ratio Fe:Al = 9:1	78.0	1.99	9.55

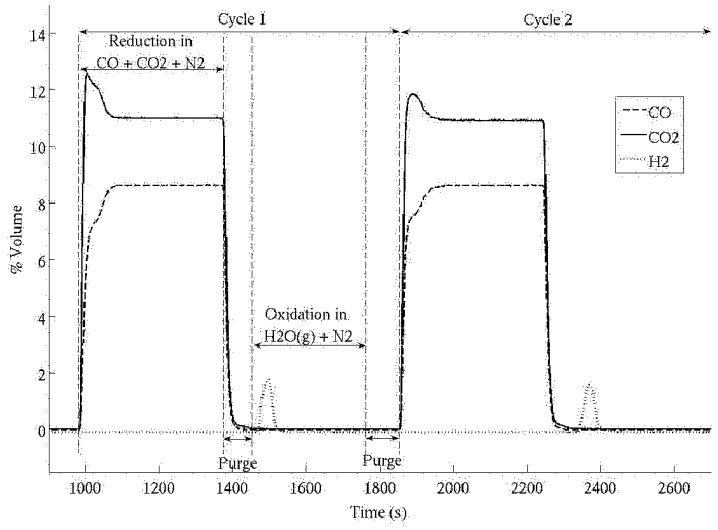

Fig. 2 Gas analyser reading for first two cycles with mechanically-mixed particles between Fe_3O_4 and $Fe_{0.947}O$

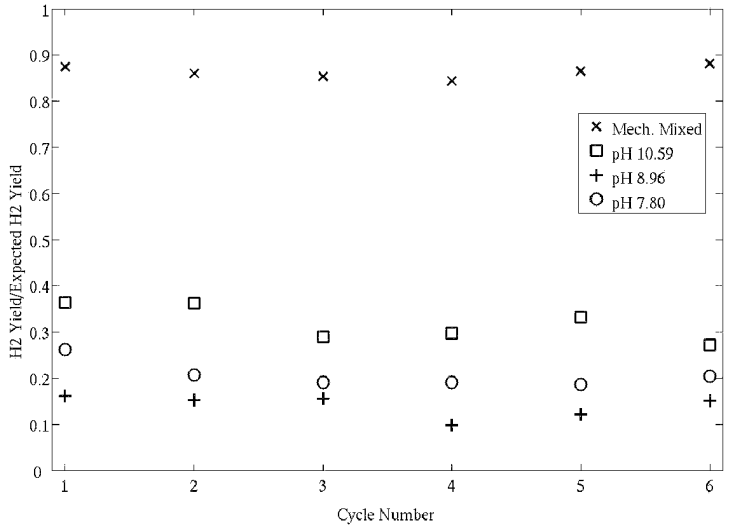

Fig. 3 Performance of various particle samples over 6 cycles between Fe_3O_4 and $Fe_{0.947}O$

Fig. 3 shows a plot of $H_{2,meas}/H_{2,exp}$ over 6 cycles of each sample. It can be seen that the mechanically mixed sample produced over 87% of the expected yield on its first cycle, and continued to perform well over the next 5 cycles, with no evident decline in performance.

The co-precipitated particles did not perform nearly so well, with $H_{2,meas}/H_{2,exp}$ always below 40%. The best performance came from the particles produced at the highest value of pH (10.59), although the pH 7.80 particles performed better than the pH 8.96 particles.

Cycling between Fe_3O_4 and Fe

Fig. 4 shows how each set of particles performed over 6 cycles. It should be noted that the additional transition from $Fe_{0.947}O$ to Fe accounts for almost 80% of the maximum achievable hydrogen yield; thus particles which can perform well over several cycles between this transition promise much higher yields of hydrogen overall.

It can be seen that in contrast to Fig. 3, the mechanically-mixed particles performed extremely poorly, with almost no H_2 produced after the first cycle. The considerable and rapid decline in the performance of these

particles is consistent with Bohn *et al.* (2008). During the oxidation process, no CO or CO_2 was detected, thus ruling out the possibility of the Boudouard reaction, and the decline in performance is instead likely to be a result of thermal sintering.

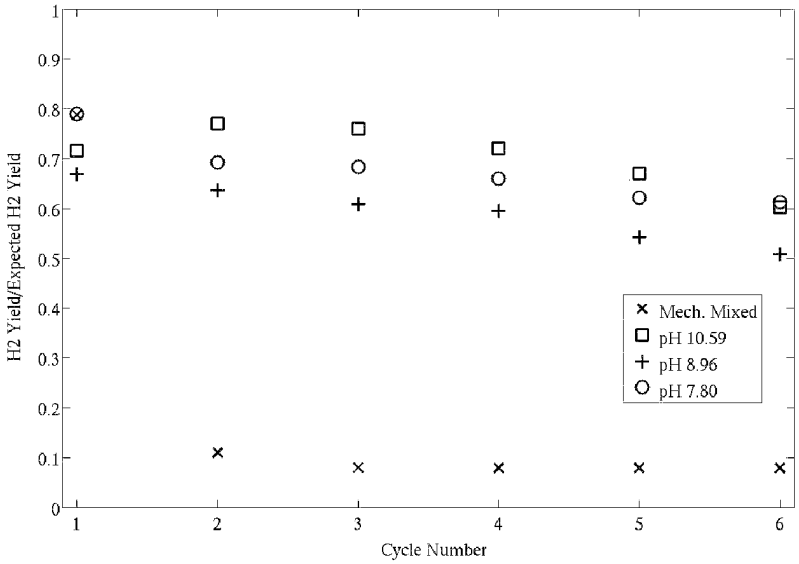

Fig. 4 Performance of various particle samples over 6 cycles between Fe_3O_4 and Fe

In contrast, significant improvements were seen in all of the co-precipitated samples, relative to the yields seen previously between Fe_3O_4 and $Fe_{0.947}O$. All of the co-precipitated particles out-performed the mechanically-mixed particles, and whilst performance was seen to deteriorate over six cycles, the ratio of the H_2 yields on the 6th and 1st cycles was always observed to be 75% or better. The improvement in performance is likely due to the inclusion of the Al species, which effectively acts as a spacer between the Fe particles, thus reducing the effects of thermal sintering.

The effects of pH during co-precipitation on the ultimate performance as oxygen carriers were not entirely clear. Once more, particles made at pH 7.80 performed slightly better than those made at pH 8.96, and even those made at pH 10.59 during cycles 1 and 6. Further work is, however, required to verify that the results from particles co-precipitated at different pH values are indeed different: numerous sources (Torbacke *et al.*, 2004; Zauner and Jones, 2000, 2002; Kim et al., 2004) have highlighted the complexities of scaling up the co-precipitation method.

DISCUSSION

The effect of the ratio of CO_2 to CO in the reducing gas on performance

To explore the reason for the significant improvement in the performance of the co-precipitated particles for the $Fe_3O_4 \leftrightarrow Fe$ transition, compared to that for $Fe_3O_4 \leftrightarrow Fe_{0.947}O$, a 0.3 g sample of the pH 7.80 co-precipitated particles was tested over seven cycles, with the value of $[CO_2]/[CO]$ at inlet randomly varied for each cycle (to remove any systematic effect of cycle number). In each cycle the value of $[CO_2]/[CO]$ was such that Fe_3O_4 should reduce only to $Fe_{0.947}O$; the equilibrium values of $[CO_2]/[CO]$ for the $Fe_3O_4 \leftrightarrow Fe_{0.947}O$ and $Fe_3O_4 \leftrightarrow Fe$ transitions are 1.847 and 0.500 respectively (McBride et al., 2002). After each reduction, the bed was oxidised in 10 vol. % CO_2, N_2 balance, with the yield of CO produced being analogous with that of H_2 when oxidising with steam. Figure 5 shows how the yield of CO (shown in the form $CO_{,meas}/CO_{,exp}$) varies with the inlet $[CO_2]/[CO]$, and the cycle number (shown above each data point). Although cycles 3 and 5 are slightly above the threshold of 1.847, some reactivity was nevertheless seen. Evidently there is a clear dependence of the performance of the particles with the value of $[CO_2]/[CO]$. Even for cycles 6 and 7 (by which time the loss in particle reactivity had become a factor), the product yield was much greater than that achieved for much higher values of $[CO_2]/[CO]$, say for cycles 2 and 4.

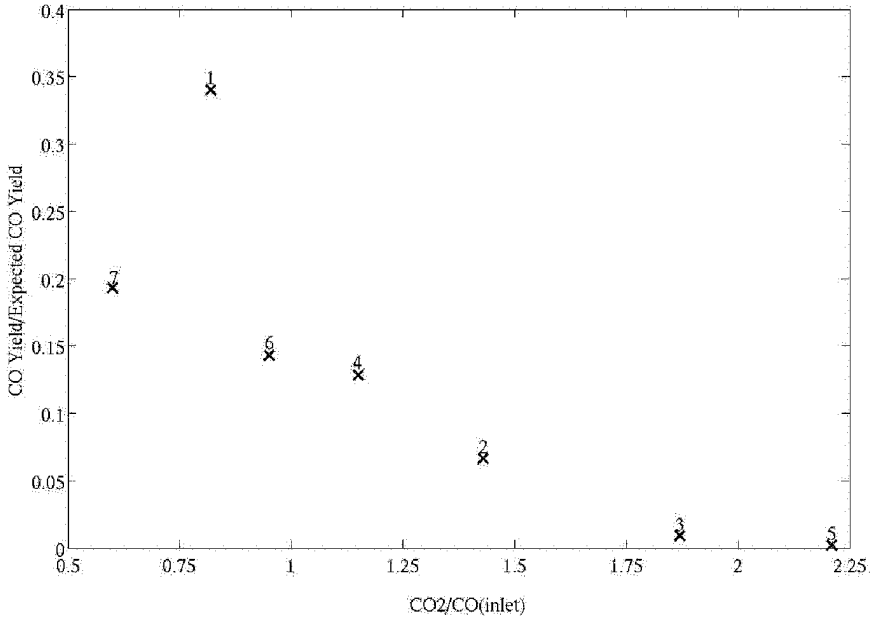

Fig. 5 The performance of a co-precipitated particle sample (pH 7.80) with varying volumetric inlet ratios of $[CO_2]/[CO]$ (numbers above data points denote cycle number)

Thus, it would appear as if the final yield is a strong function of the ratio $[CO_2]/[CO]$, which would not be expected from thermodynamic arguments. In deriving the equilibrium constant K_p for the Fe_3O_4 to $Fe_{0.947}O$ reaction, it is normally assumed that the solid species have a constant activity of 1. Thus, the equilibrium value of $[CO_2]/[CO]$ is not a function of the amount of solid present. The consequence of this is that the final yield in Fig. 5 should be unity for $1.847 > [CO_2]/[CO] > 0.500$ (at 850°C) and zero for $[CO_2]/[CO] > 1.847$. Also, crucially, the yield should otherwise be independent of the value of $[CO_2]/[CO]$.

One possible explanation for this dependence of the amount of reduction on $[CO_2]/[CO]$, is that the activity of the solid species differs from that of bulk Fe_3O_4 or $Fe_{0.947}O$. For the ultimate yield to be a continuous function of $[CO_2]/[CO]$, there would have to be a distribution of solid phase activities. The assumption that the solid Fe_3O_4 or $Fe_{0.947}O$ have a free energy equal to that for bulk material (here the values of K_p were calculated using the Gibbs Free Energies from McBride *et al.* (2002)), may not be valid. For example, if during the precipitation process, very small crystals are formed to give a solid composed of nanocrystals, the free energy of the solid species will also include a contribution from the surface free energy (Sanfeld and Steinchen, 2000). More work is to be carried out on co-precipitated particles of similar composition to verify this hypothesis and whether or not this dependency on the final degree of reduction on $[CO_2]/[CO]$ continues to much lower values (i.e. in the regime previously assumed to be occupied only by Fe).

CONCLUSIONS

In this work, two different methods of manufacturing haematite (Fe_2O_3) particles (mechanical mixing and co-precipitation) have been tested in their ability to produce hydrogen over repeated redox cycles. The particles were tested between the $Fe_3O_4 \leftrightarrow Fe_{0.947}O$ and $Fe_3O_4 \leftrightarrow Fe$ transitions. The co-precipitated particles included the addition of Al, such that the ratio by weight of Fe to Al was 9:1. Additionally, an attempt was made to understand the effect of pH on the performance of co-precipitated particles.

It was found that over 6 cycles for the $Fe_3O_4 \leftrightarrow Fe_{0.947}O$ transition, the mechanically-mixed particles performed much better than the co-precipitated particles, with little evidence of any decline in performance. However, for the $Fe_3O_4 \leftrightarrow Fe$ transition, the performance of the mechanically-mixed particles was extremely poor from the second cycle onwards, most likely owing to the effects of thermal sintering, whilst all of the co-precipitated samples produced consistently high hydrogen yields over 6 cycles, probably due to the addition of Al forming the inert $FeAl_2O_4$, which acts as a spacer between Fe molecules. Given that the significant proportion of the theoretical maximum yield of hydrogen arises from the transition between $Fe_{0.947}O$ and Fe, the importance of being able to reduce particles consistently as far as Fe is apparent. A test on the performance of the co-precipitated particles with varying ratios of CO_2 to CO during reduction showed very strong correlation, and suggested that the equilibrium of the reaction is affected by the Gibbs surface energy of the crystals within the co-precipitated particles. Such behaviour strongly suggests that the co-precipitation method

forms particles comprising nanocrystals, although further work is required to confirm that this is not due to any kinetic limitations. There was no clear correlation between particle pH value and performance, and more work is required to ensure that co-precipitated particles can be manufactured with a high degree of reproducibility.

ACKNOWLEDGEMENTS

The authors would like to thank the Engineering and Physical Sciences Research Council for funding this work through Grant No. EP/F027435/1.

REFERENCES

Bohn C.D., Müller C.R., Cleeton J.P., Scott S.A., Dennis J.S., Davidson J.F., Hayhurst A.N.: Ind. Eng. Chem. Res. 47 (2008), pp. 7623-7630
Chuang S.Y., Dennis J.S., Hayhurst A.N., Scott S.A.: Combust. Flame 152 (2008), pp. 109-121
Cleeton J.P.E., Bohn C.D., Müller C.R., Dennis J.S., Scott S.A.: Int. J. Hydrogen Energy (2008), in press
Galvita V., Hempel T., Lorenz H., Rihko-Struckmann L.K., Sundmacher K.: Ind. Eng. Chem. Res. 47 (2008) pp. 303-310
Galvita V., Sundmacher K.: Applied Catalysis A: General 289 (2005), pp.121-127
Kim W.S., Kim W.S., Kim K.S., Kim J.S., Ward M.D.: Materials Research Bulletin 39 (2004), pp. 283-296
Mattison T., Lyngfelt A., Cho P.: Fuel 80 (2001), pp. 1953-1962
McBride B.J., Zehe M.J., Gordon S. (2002). NASA report TP-2002-21155
Otsuka K., Kaburagi T., Yamada C., Takenaka S.: J. Power Sources 122 (2003), pp. 111-121
Sanfeld A., Steinchen A.: Surface Science 463 (2000), pp. 157-173
Takenaka S., Hanaizumi N., Son V., Tho D., Otsuka K.: J. Cat. 228 (2004), pp. 405-416
Takenaka S., Tomohiro K., Chisa Y., Kiyoshi N., Kiyoshi O.: J. Cat 228 (2004), pp. 66-74
Torbake M., Rasmusen A.C.: AIChE Journal 50 (2004), pp. 3107-3119
Urasaki K., Tanimoto N., Hayashi T., Sekine Y., Kikuchi E., Matsukata M.: Applied Catalysis A: General 288 (2005), pp. 143-148
Wang H., Wang G., Wang X., Bai J.: J. Phys. Chem. C (2008), pp. 5679-5688
World Coal Institute. Information available at http://www.worldcoal.org/pages/content/ index.asp?PageID=188; [accessed April 2008]
Zauner R., Jones AG.: Ind. Eng. Chem. Res. 39 (2000), pp. 2392-2403
Zauner R., Jones AG.: Chem Eng Science 57 (2002), pp. 821-831

KINETICS OF OXIDATION OF A REDUCED FORM OF THE Cu-BASED OXYGEN-CARRIER FOR USE IN CHEMICAL-LOOPING COMBUSTION

S.Y. Chuang[1], J.S. Dennis[1], A.N. Hayhurst[1], S.A. Scott[2]

1Department of Chemical Engineering and Biotechnology, University of Cambridge Pembroke Street, Cambridge, CB2 3RA, UK

2University of Cambridge, Department of Engineering, Trumpington Street, Cambridge, CB2 1PZ, UK

Abstract: A co-precipitated mixture of CuO and Al_2O_3 is a good oxygen-carrier for chemical-looping combustion. The kinetics of regeneration of this reduced oxygen-carrier (355 – 500 μm) were measured from 300 to 750°C when reacting it with O_2. Care was taken to ensure these measurements were not affected by interphase mass transfer. Efforts were also made to minimise sampling problems by using a rapid-response mass spectrometer for reactions lasting for 45 s or less; otherwise, a paramagnetic analyser for O_2 was used, since the mass spectrometer drifted with time. The order of reaction with respect to O_2 was found to be ~ unity at 300 to 750°C. Below 600°C, the reduced oxygen-carrier was incompletely oxidised to a mixture of Cu_2O and Al_2O_3. Above 600°C, regeneration was completely to CuO and Al_2O_3 and was controlled to a considerable extent by external mass transfer. At these higher temperatures, regeneration involved a shrinking core mechanism and the two consecutive steps:

$$2Cu + 1/2O_2 \rightarrow Cu_2O, \quad (1)$$

$$Cu_2O + 1/2O_2 \rightarrow 2CuO. \quad (2)$$

The activation energies and pre-exponential factors for both reactions were measured from initial rates. The kinetics in the first cycle of operations were found to be similar to those in the subsequent cycles.

Keywords: chemical-looping combustion, oxygen-carrier, kinetics, fluidised bed

INTRODUCTION

Chemical-looping combustion (CLC) is a technique for burning a fossil fuel, with the inherent property of separating CO_2 from the products. Conventionally, CLC involves two interconnected fluidised beds and an oxygen-carrier, in the form of a solid metal oxide. Gaseous fuel enters the first reactor and reacts with the oxygen-carrier, Me_xO_y, where Me represents metal:

$$(2n + m)Me_xO_y + C_nH_{2m} \rightarrow (2n + m)\ Me_xO_{y-1} + mH_2O + nCO_2. \quad (3)$$

The reduced carrier is transported to the second reactor, where it is oxidised back to its original state for re-use by the incoming air:

$$Me_xO_{y-1} + 1/2O_2 \rightarrow Me_xO_y \quad (4)$$

The regenerated carrier is then recycled back to the first reactor for more cycles of operation. Such a scheme has the disadvantage that it is unsuitable for the combustion of solid fuels, owing to the difficulty of separating particles of the oxygen-carrier from the solid fuel. To circumvent this, Scott *et al.* (2006) proposed a modified version of CLC, in which oxidation and reduction occur successively in one fluidised bed. In this scheme, a solid fuel such as coal, is fed continuously to the reactor and is gasified by the fluidising agent, *i.e.* steam or a combination of steam and CO_2, to form synthesis gas. The synthesis gas is then oxidised in the bed of CuO to produce H_2O and CO_2. When the inventory of CuO becomes depleted, the feed of solid fuel is stopped and the remaining carbon in the bed is allowed to gasify and combust further until all of it has been used up. The fluidising agent is then switched to atmospheric air, which regenerates the depleted CuO. It turns out that CuO is a suitable carrier because reactions (3) and (4) are both exothermic and CLC depends on the reduction of oxygen-carrier being sufficiently exothermic to provide heat to gasify the solid fuel into synthesis gas for subsequent combustion.

There is little literature on the kinetics of the regeneration reaction:

$$Cu + 1/2O_2 \rightarrow CuO. \quad (5)$$

Garcia-Labiano *et al.* (2004) found that for a wet-impregnated oxygen-carrier with 10 wt% CuO, the oxidation of the reduced carrier was controlled by chemical kinetics; the order of reaction with respect to O_2 was unity and the activation energy was 15 kJ mol^{-1}. Chuang *et al.* (2008a) have previously prepared particles of a co-precipitated mixture of CuO and Al_2O_3. These particles maintained 100% conversion for up to 18 consecutive cycles of operation inside a fluidised bed, without any sign of attrition or agglomeration, when

used to oxidise CO. Chuang *et al.* (2008b) have also measured the kinetics of the reduction of such a carrier by CO: they found that the reduction took place indirectly *via* the intermediate, Cu_2O, at high temperatures (~ 800°C) and directly to Cu at low temperatures (~ 300°C). The aim of this study was to measure the kinetics of the oxidation of the reduced carrier by O_2. This is important, because the rate at which the particles oxidise influences the design of reactor.

EXPERIMENTAL

The experimental set-up used in this work is shown in Fig. 1. The laboratory-scale fluidised bed is a vertical quartz tube (i.d. 29.5 mm; length 460 mm), with a sintered quartz plate as distributor (110 mm from the base of the tube) and a plenum chamber below the distributor. Silica sand (20 ml, sieved to 355 – 425 μm, unfluidised bed depth 30 mm) was the material fluidised. The tube was housed in an electric furnace and the temperature of the bed was measured with a K-type thermocouple. The bed was fluidised with 10.4 vol.% O_2 in N_2; experiments were conducted from 300 to 900°C, corresponding to U/U_{mf} being 2.5 to 7.9. When measuring the order of reaction, the concentration of oxygen was varied by diluting with pure N_2, while keeping the total volumetric flow rate constant at ~ 73.5 cm^3/s, at room temperature and pressure. In an experiment, a batch of ~ 0.01g of the reduced carrier (details of its production will be discussed below) was tipped into the bed *via* a metal funnel. The off-gas was sampled continuously *via* a quartz probe to a quadrupole mass spectrometer (Hiden Analytical) and a paramagnetic gas analyser (ABB EL3020), both of which measured $[O_2]$ in the off-gases. The sampling system, consisting of sampling tubing and an analyser, was modelled as a plug flow reactor in series with a continuously stirred tank. The sudden addition or removal of O_2 from the fluidising gas confirmed that the sampling system followed a first-order response, *i.e.* the true concentration of oxygen, $[O_2]_t$, can be approximated with $[O_2]_t = [O_2]_m + \tau d[O_2]_m/dt$, where $[O_2]_m$ is the measured concentration of oxygen and τ is a time constant for the sampling system. The value of τ was found to be 0.6 s with the mass spectrometer and 3.0 s for the paramagnetic analyser. The measured $[O_2]_m$ were corrected using this equation to derive $[O_2]_t$. The rate of consumption of O_2 was measured as the product of the flow rate through the bed and the drop in $[O_2]$, after the reduced oxygen-carrier had been added to the bed. Measurements from the mass spectrometer were calibrated in such a way that the total amounts of O_2 consumed, as measured by the mass spectrometer and the paramagnetic analyser, were identical. Measurements from the mass spectrometer were used whenever possible, because it has a lower value of τ, *i.e.* the measurements of $[O_2]$ required a smaller correction. However, mass spectrometric measurements have the problems of a baseline drifting with time and its noise-to-signal ratio being high. Therefore, the paramagnetic analyser was used when the reaction lasted a long time (> 45 s), *i.e.* when the rate of reaction was low.

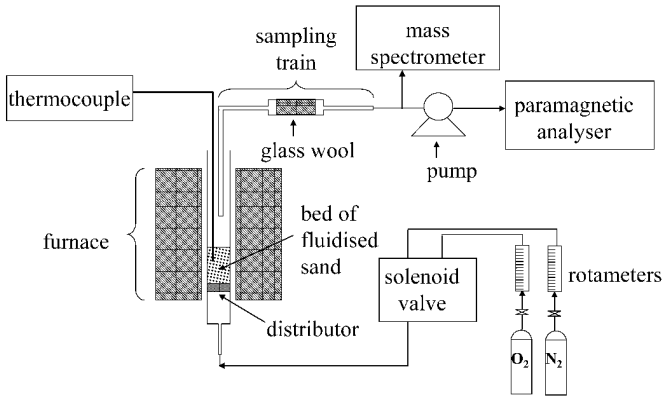

Fig. 1 Experimental set-up (not to scale)

The reduced oxygen-carrier was prepared by reducing the co-precipitated mixture of CuO and Al_2O_3 mentioned earlier with 2.5 vol.% CO in N_2 at 800°C. Upon completion of the reaction, the furnace was turned off and the bed was allowed to cool down to room temperature with N_2 flowing through it, before recovering the particles. The resulting particles were sieved to 355 – 500 μm and 850 – 1000 μm. The density, ρ_d, and porosity of the reduced carrier, ε, were determined from Hg porosimetry to be respectively ~ 4.5×10^6 g/cm^3 and ~ 0.77. From N_2 adsorption analysis, its BET surface area, S_{BET}, was ~ 6.3 m^2/g. The mean radius of the pores, $\overline{r_p} = 2\varepsilon/S_{BET}$, was 102 nm. A co-precipitated mixture of Cu_2O and Al_2O_3 was also used at some stage in this work. It was made by heating the co-precipitated mixture of CuO and Al_2O_3 in the fluidised bed at 950°C in pure N_2, so that the CuO decomposed to Cu_2O and O_2, as previously reported by Chuang *et al.* (2008a).

When the evolution of O_2 had become negligible, the furnace was turned off and the bed was cooled down to room temperature with N_2 flowing through it. The resulting particles had a density of ~ 4.2 $\times 10^6$ g/m^3, with S_{BET} ~ 11 m^2/g, ε ~ 0.66 and $\overline{r_p}$ ~ 59 nm.

The particles were also characterised using an X-ray diffractometer (Philips PW1830) and an optical microscope (Digital Blue QX5), to gain a better understanding of the mechanism of reaction. The diffractometer operates at 40 kV and 40 mA, using Ni-filtered Cu-K α radiation. A database containing the X-Ray Diffraction (XRD) patterns of most known crystalline compounds was used to identify the species present in the oxygen-carriers. The particles were also mounted on epoxy (Agar Scientific) and polished with silicon carbide paper (RS; P1200) until the cross-sections were exposed, which were then viewed under the microscope.

RESULTS

Variation of conversion with temperature

Figure 2 shows measurements of [O_2] in the off-gases from a bed to which a batch of reduced carrier was suddenly added. The measurements were deconvoluted as described above; the derived rates of reaction are shown in Fig. 2(b). It is possible to measure the fraction of carrier converted back to CuO from the area under Fig. 2(b). The fractional oxidation of the reduced carrier, X, is defined as the ratio of the measured number of moles of O_2 consumed to the theoretical number required to fully oxidise the Cu to CuO. Preliminary experiments were performed at 1.3 vol.% O_2 in N_2, using carrier sieved to 355 – 500 μm, at 300 – 900°C, to obtain the relationship between X and temperature. At least 4 experiments were performed at each temperature and the results are shown in Fig. 3. This shows that $X < 1$ below 600°C; XRD analysis of the oxidised particles at these lower temperatures showed that this was because they were incompletely oxidised to Cu_2O and CuO; the latter only became apparent above 500°C. Above 900°C, X drops, probably due to the decomposition of the CuO to Cu_2O and O_2, as previously noted by Chuang *et al.* (2008a). To ensure the oxidation was not affected by such decomposition, experiments were performed at 750°C and below.

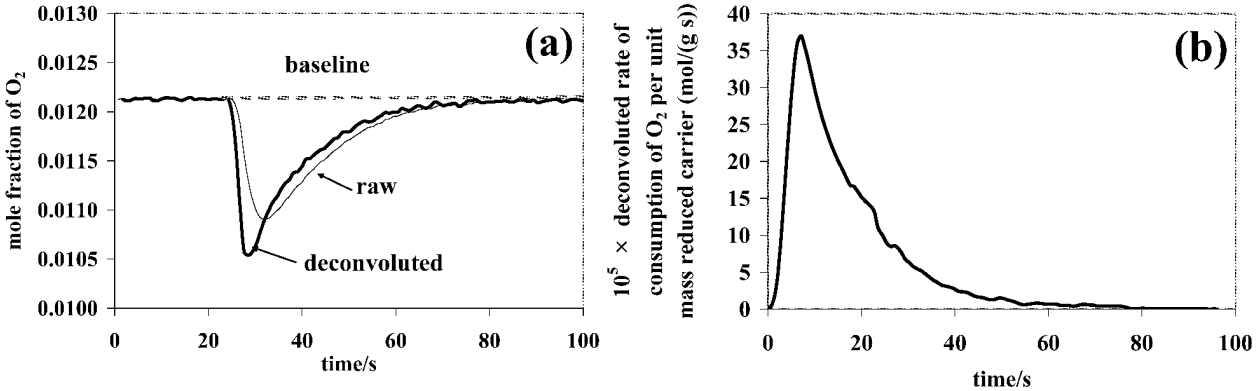

Fig. 2 Measurements of[O_2] after 0.0122 g of reduced carrier containing Cu (sized to355– 500μm) was added at 700°C to the bed fluidised with 1.22 vol.%O_2 in N_2 and U/U_{mf}= 5.9: (a) the change in mole fraction of O_2 against time, measured by the paramagnetic analyser and shown in the raw and deconvoluted forms, (b) the corresponding plot of deconvoluted rate of consumption of O_2 per unit mass of reduced carrier against time

Interphase Mass Transfer

Interphase mass transfer, *i.e.* the transfer of O_2 from the bubble to the particulate phase in the fluidised bed, can be rate-limiting if the intrinsic kinetics are comparatively fast. To check this, batches with different masses were oxidised with 1.23 vol.% O_2 at 750°C; the resulting rates of reaction are shown in Fig. 4. There is no appreciable change in the specific rate when the mass was increased from 0.0121 g to 0.219 g; however, the maximum rate dropped by ~ 50 % and the time of reaction increased by ~ 50%, when the mass was increased to 0.087 g. This indicates the onset of interphase mass transfer. Since the average mass of carrier used in this study was ~ 0.01 g, the effect of interphase mass transfer was negligible.

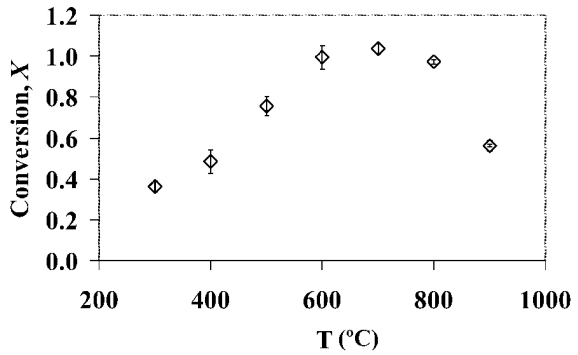

Fig. 3 Variation of final conversion with temperature for the oxidation of carrier containing Cu to CuO

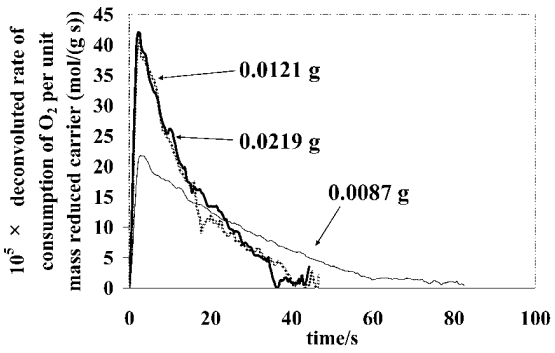

Fig. 4 The specific rates of oxidation of reduced carrier (355 –500 μm) by 1.23 vol.% O_2 in N_2 at 750°C for 3 different masses of carrier.Measurements made with the mass spectrometer

The order of reaction

In Fig. 2(b), the deconvoluted curve has a well-defined maximum, which was taken as the initial rate of reaction. The reaction was assumed to follow the rate equation: $r = k[O_2]^n$. To derive the order of reaction, n, and rate constant, k, $[O_2]$ was varied. The variation of initial rate with $[O_2]$ is shown in Fig. 5, for both carriers, *i.e.* containing either Cu or Cu_2O, at selected temperatures. It is important to note that there is always a proportional relationship between the initial rate and $[O_2]$ at low $[O_2]$, but this rate levels off at higher $[O_2]$. This might suggest that the reaction was following the Langmuir-Hinshelwood mechanism, in which case n changes from 1 to 0, when $[O_2]$ is increased. However, reaction at high $[O_2]$ was too fast for reliable measurements to be made. This is illustrated in Fig. 6, which gives plots of the rate against time and rate against conversion for the oxidation of carrier at 7.3 vol.% O_2 in N_2 at 400 and 650°C.

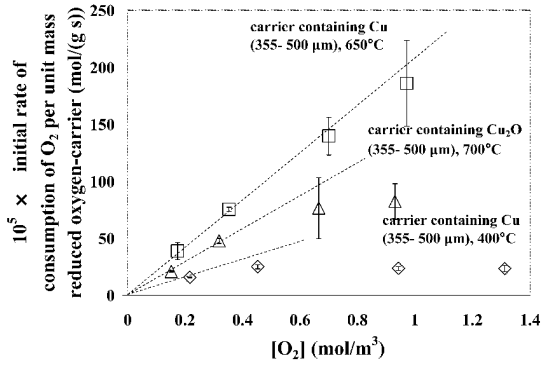

Fig. 5 Plots of rate of consumption of O_2 (by unit mass of carrier) against $[O_2]$ for carriers containing Cu or Cu_2O (355 –500 μm)at selected temperatures

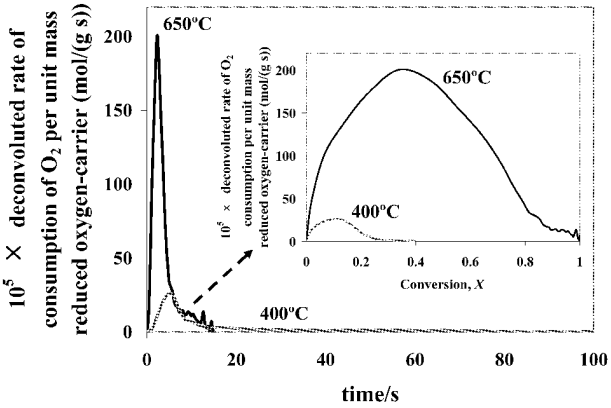

Fig. 6 Plots of specific rate of consumption of O_2 by Cu (355 –500 μm) against $[O_2]$ at 7.3 vol.% O_2 in N_2 at 400 and 650°C. The corresponding plots of rate against conversion are also shown

The measurements at 650°C were made with the mass spectrometer and those at 400°C were made with the paramagnetic analyser, because the mass spectrometric measurements at 400°C were noisy and the baseline drifted. As seen in Fig. 6, at 650°C, the reaction took ~ 15 s to complete and the resulting plot of rate against conversion shows a maximum at X ~ 0.4, which made it a poor estimate of the initial rate. The reaction at 400°C took ~ 100 s to finish, but most of the O_2 was consumed in the first 15 s, when X ~ 0.25. The maximum rate was reached at X ~ 0.1. However, the value of X after 15 s, when the reaction is mostly finished, is ~ 0.25. Because the reaction by and large stops after 15 s, it is likely that the maximum rate is a poor estimate of the initial rate, because at these high $[O_2]$, reaction is too fast for the analysers to measure an accurate initial rate. Nevertheless, measurements at lower $[O_2]$ were used here to study intrinsic kinetics; in these cases the maximum rates occur at lower X. The proportionality between rate and $[O_2]$ suggests that the order of reaction is unity; alternatively, it might imply that reaction is controlled by external mass transfer, for which $n = 1$.

Effect of external mass transfer

The plots of the rate of oxidation of the reduced carriers, when reacted in 1.3 vol.% O_2 in N_2 are plotted in Fig. 7 against 1/T, for carriers in both size-ranges. The measured rates are also compared in Fig. 7 with the

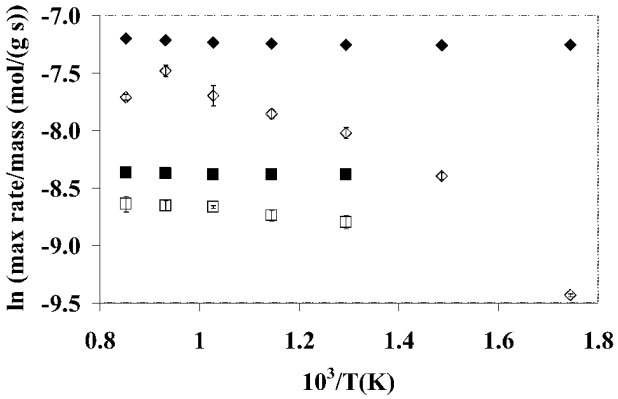

Fig. 7 Plots of the rate of oxidation of reduced oxygen-carrier (containing Cu and Al_2O_3) by 1.3 vol.% O_2 in N_2. ◇refers to carrier sized to 355-500 μm; □refers to carrier sized to 850 – 1000 μm. The filled symbols are to theoretical external mass transfer rates; the open symbols refer to measured rates

theoretical external mass transfer rates, calculated using:

$$r_{ext} = k_g S_m (C_B - C_S), \tag{6}$$

with C_S = 0. The rate of oxidation of the larger carrier particles exhibits a weak dependence on temperature, suggesting that the reaction was controlled mainly by external mass transfer. The rate of reaction of the smaller particles, on the other hand, depends more strongly on temperature and is therefore less likely to be controlled by external mass transfer. The drop in rate at 900°C for the small particles can be attributed to the decomposition of CuO, as discussed above. This is not seen for the larger particles. This can be explained by the fact that the rate of transfer of O_2 to the external surface of the larger particles was slower than that to the smaller particles. Therefore, the corresponding oxidation of Cu and decomposition of CuO at 900°C of the large particles were less likely to be detected. This provides additional evidence that the measurements from the smaller particles are more representative of the intrinsic kinetics. Hence, kinetic information was only obtained from experiments on the smaller particles (355 – 500 μm).

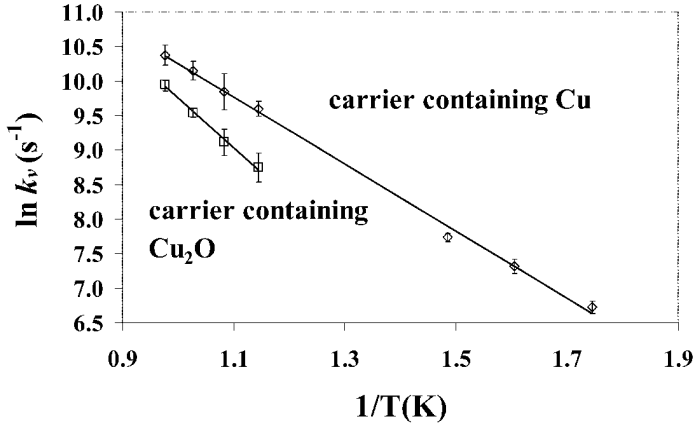

Fig. 8 Plots of k_v against 1/T for carriers containing Cu and Cu_2O (355 –500 μm)

Determining the intrinsic kinetics

Having established that n = 1 and the reaction is controlled to a considerable extent by external mass transfer, the rate expression: $r = k_{overall}[O_2]$ can be written, where the overall rate constant, $k_{overall}$, can be approximated as

$$1/k_{overall} = 1/k_g S_m + 1/k_s \eta. \tag{7}$$

The effectiveness factor, η, for a first-order reaction is:

$$\eta = (1/3\Phi^2)(3\Phi \coth 3\Phi - 1), \tag{8}$$

where the Thiele modulus, Φ, for a spherical particle is calculated according to

$$\Phi = (d_p/6)\sqrt{k_v/D_{eff}}. \tag{9}$$

All symbols are defined below. To determine k_v, ηk_s was obtained from Eq. (7), with k_g obtained from a correlation deduced by LaNauze *et al.* (1982) for the Sherwood number, *Sh* (see nomenclature). Then, an initial guess of η yielded an estimate of k_s, which was multiplied by ρ_d to obtain k_v, which was then substituted into

Eqs. (9) and (8) to obtain η iteratively. The values of η decrease from 0.9 at 300°C to 0.4 at 750°C, suggesting a transition from control by intrinsic kinetics at lower temperatures to diffusion and reaction inside pores, when the temperature was increased. Arrhenius plots of k_v for carriers containing Cu and Cu_2O (sized to 355 – 500 μm) are shown in Fig. 8. These good linear plots imply that one reaction is involved in each case. Also, the rate constant for Cu exceeds that for Cu_2O.

Discussion

Figure 3 shows that oxidation of the carrier containing Cu reaction proceeds incompletely and, most probably, indirectly *via* the intermediate Cu_2O below 600°C when $X < 1$. Although full oxidation is thermodynamically possible (McBride *et al.* (2002)), a likely explanation for the incomplete oxidation is the slow oxidation of Cu_2O at these low temperatures. It is not known if the same mechanism applies above 600°C, where $X \sim 1$. There is the possibility that at these higher temperatures, oxidation proceeds both directly to CuO and indirectly *via* Cu_2O, when the rate of the former step becomes relatively fast. To investigate this, a batch of carrier previously reduced to Cu (850 – 1000 μm) was partially oxidised by 2.4 vol.% O_2 in N_2 for 4 s at 800°C. Cross-sections of some resulting particles, with $X \sim 0.25$, are shown in Fig. 9. A shrinking core pattern is observed, as expected from the low η for such large particles. XRD analysis failed to detect CuO, but confirmed the presence of Cu and Cu_2O, which probably correspond, respectively, to the dark red inner core and the outer reddish orange layer. The outermost dark brown layer of the particle on the right is probably the external surface of the particle just below the sectioned surface. The failure to detect CuO by XRD suggests that the direct oxidation of Cu to CuO did not occur, *i.e.* the oxidation of the carrier reduced to Cu takes place entirely *via* the intermediate, Cu_2O, at both low and high temperatures. This is supported by the linearity of the Arrhenius plots in Fig. 8. With this information, Fig. 8 can be analysed with more certainty. It indicates that the rate constant for reaction (2), $k_{v2} = 3.6 \times 10^6 \exp(-40 \pm 15 \text{ kJ mol}^{-1}/RT) \text{ s}^{-1}$, whereas for reaction (1), $k_{v1} = 2.3 \times 10^7 \exp(-60 \pm 15 \text{ kJ mol}^{-1}/RT) \text{ s}^{-1}$.

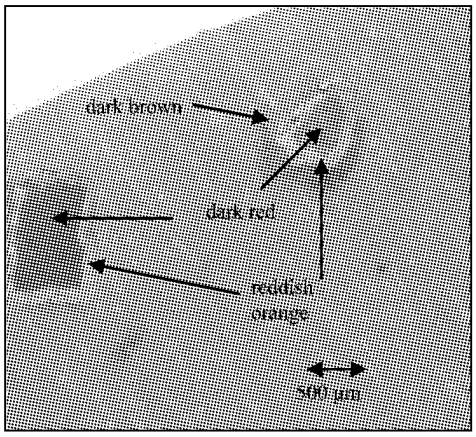

Fig. 9 Cross-sectional view of the partially oxidised carrier containing Cu

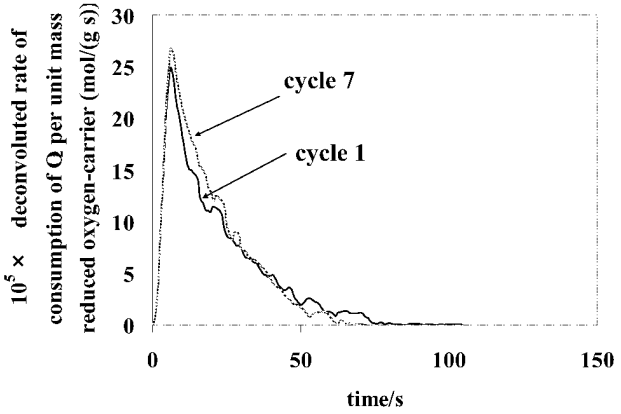

Fig. 10 Rates of oxidation of fully reduced carrier (850 –1000 μm) by 2.5 vol.% O_2 in N_2 at 800°C

Of course, CLC is a cyclic process, so it is necessary to measure the kinetics in later cycles of operation. To do so, the rates of oxidation in the 1st and 7th cycles of operation are compared in Fig. 10. It must be noted that reaction was studied with the largest particles (850 – 1000 μm), because some carrier particles from previous experiments were stuck on the wall of the reactor and so would consume O_2 during the cyclic operation. Therefore, it was necessary to perform cyclic operations for the desired number of cycles of before recovering the carrier in its reduced state. The reduced carrier was then added to a new bed at identical oxidising conditions since the size of the sand used (355 – 425 μm) was similar to that of the smaller particles, the bigger particles were used instead. Fig. 10 shows that rates of reaction in the 1st and the 7th cycles of operation were identical within experimental error, *i.e.* the kinetics in later cycles of oxidation can be approximated by those in the first.

CONCLUSIONS

The initial rates of oxidation of a co-precipitated mixture of Cu and Al_2O_3 are fast enough to be controlled largely by external mass transfer, but, in this work, not by interphase mass transfer. Reliable measurements of the initial rates of reaction could not be obtained above 600°C and high concentrations of O_2 (5 vol.% O_2 in N_2),

due to the reaction being too fast to follow. Nevertheless, measurements at low [O_2] were used to derive initial kinetics, after accounting for external mass transfer. The oxidation of carrier fully reduced to Cu apparently proceeds *via* the intermediate, Cu_2O, from 300 to 750°C and *via* a shrinking core mechanism at 800°C. The rate constants for both steps of oxidation were measured. The kinetics in later cycles of CLC can be approximated by those in the first.

NOTATIONS

D_{eff} effective diffusivity of O_2 in N_2, m^2/s, $D_{eff} = \varepsilon^2/(1/D_G + 1/D_K)$

D_G molecular diffusivity, m^2/s

D_K Knudsen diffusivity, m^2/s

d_p diameter of a particle of carrier, m

k global rate constant

k_g external mass transfer coefficient, m/s

$k_{overall}$ overall rate constant, $m^3/(g\ s)$

k_s intrinsic rate constant, $m^3/(g\ s)$

k_v volumetric intrinsic rate constant, s^{-1}

n order of reaction, dimensionless

r rate of oxidation, mol/(g s)

r_{ext} external mass transfer rate, mol/(g s)

$\overline{r_p}$ mean radius of a pore, nm

Re_p Reynolds number in the particulate phase, dimensionless, $Re_p = U_{mf}d_p/v$

Sc Schmidt number, dimensionless, $Sc = v/D_G$

Sh Sherwood number, $Sh = 2\varepsilon_s + 0.69(Re_p/\varepsilon_s)^{1/2}Sc^{1/3}$

S_{BET} BET surface area, m^2/g

S_m external surface area per unit mass of reduced carrier, m^2/g

U superficial velocity, m/s

U_{mf} minimum fluidising velocity, m/s

ε porosity of particle, dimensionless

ε_s voidage of fluidised sand, dimensionless

ρ_d density of particle, g/m^3

η effectiveness factor, dimensionless

Φ Thiele modulus, dimensionless

τ time constant of sampling system, s

v kinematic viscosity of the gas, m^2/s

REFERENCES

Chuang S.Y., Dennis J.S., Hayhurst A.N., Scott S.A.: Combust. Flame **154** (2008a), pp.109-121.

Chuang S.Y., Dennis J.S., Hayhurst A.N., Scott S.A.: Proc. Combust. Inst., (2008b), doi:10.1016/j.proci.2008.06.112 (in press).

García-Labiano F, de Diego LF, Adánes J, Abad A, Gayán P.: Ind. Eng. Chem. Res. **43** (2004), pp.8168-8177.

LaNauze RD, Jung K.: 19th Symposium (Int) on Combustion, 1982, pp 1087-1092, The Combustion Institute, Pittsburgh.

McBride B.J., Zehe M.J., Gordon S.: NASA Glenn Coefficients for Calculating Thermodynamic Properties of Individual Species. NASA. (2002) report TP-2002-21155.

Scott S.A., Dennis J.S., Hayhurst A.N., Brown T.A.: AIChE J. **52** (2006), pp.3325-3328.

REDUCTION KINETICS OF A $CaSO_4$ BASED OXYGEN CARRIER FOR CHEMICAL-LOOPING COMBUSTION

R. Xiao, Q. L. Song, W. G. Zheng, Z. Y. Deng, L. H. Shen, M. Y. Zhang

Department of Thermal Engineering, Southeast University, Nanjing, 210096,China

Abstract: The $CaSO_4$ based oxygen carrier has been proposed as an alternative low cost oxygen carrier for Chemical-looping combustion (CLC) of coal. The reduction of $CaSO_4$ to CaS is an important step for the cyclic process of reduction/oxidation in CLC of coal with $CaSO_4$ based oxygen carrier. Thermodynamic analysis of $CaSO_4$ oxygen carrier with CO based on the principle of Gibbs free energy minimization show that the essentially high purity of CO_2 can be obtained, while the solid product is CaS instead of CaO. The intrinsic reduction kinetics of a $CaSO_4$ based oxygen carrier with CO was investigated in a differential fixed bed reactor. The effects of gas partial pressure (20%-70%) and temperature (880-950 °C) on the reduction were investigated. The reduction was described with shrinking unreacted core model. Experimental results of CO partial pressure on the solid conversion show that the reduction of fresh oxygen carriers is of first order with respect to the CO partial pressure. Both chemical reaction control and product layer diffusion control determine the reduction rate. The dependences of reaction rate constant and effective diffusivity with temperature were both obtained. The kinetic equation well predicted the experimental data.

Keywords: CO_2 capture, chemical-looping combustion, oxygen carrier, kinetics, $CaSO_4$

INTRODUCTION

Chemical-looping combustion (CLC) was proposed to improve the combustion efficiency and later identified to be a novel method for inherent CO_2 capture at lower cost (Lyngfelt et al., 2001). Many investigations have been performed on gaseous fuels focusing on the reactivity of oxygen carrier. Few studies have been published on CLC of solid fuels (Leion et al., 2008b). Most of the previous literature reported intensive research on metal oxides based oxygen carriers (Chuang et al., 2008; Leion et al., 2008a). Recently a calcium-based oxygen carrier, natural anhydrite ($CaSO_4$) has been intensively studied in our research group (Shen et al., 2008; Song et al., 2008a; Song et al., 2008b). Thermodynamics and reactivity studies demonstrated that the $CaSO_4$-based oxygen carrier may be suitable for CLC of solid fuels with higher oxygen capacity and lower cost which is in agreement with the literature (Wang et al., 2008). The concept of CLC of solid fuels with $CaSO_4$ oxygen carrier is as follows. The coal is gasified in the fuel reactor using H_2O or CO_2 to produce gasification gas. $CaSO_4$ oxygen carrier is reduced by the intermediate gasification syngas to CaS simultaneously which results a high purity stream of CO_2 after condensation:

$$CaSO_4+4CO \rightarrow CaS+4CO_2 \quad \Delta H_{298K}=170.96 \text{ kJ/mol} \tag{1}$$

$$CaSO_4+4H_2 \rightarrow CaS+4H_2O \quad \Delta H_{298K}=6.41 \text{ kJ/mol} \tag{2}$$

Then CaS is transported to the air reactor to be oxidized back to $CaSO_4$:

$$CaS+2O_2 \rightarrow CaSO_4 \quad \Delta H_{298K}=960.90 \text{ kJ/mol} \tag{3}$$

Therefore, the clean combustion of coal can be achieved via the $CaSO_4$ oxygen carrier.

Reaction kinetics of oxygen carrier is quite important for design, modeling and scale-up of the CLC reactor (Abad et al. 2007a; Jung et al., 2008). Many investigations have successfully applied the shrinking core model to represent the reduction and oxidation kinetics of oxygen carriers in CLC. (Abad et al., 2007b; Ryu et al. 2001) Most of these studies were obtained from the mass conversion recorded in Thermogravimetric Analyzers (TGA). Compared to TGA, the advantage of a differential fixed bed is that the reaction rate and composition of gas can be both clearly obtained while the overall conversion rate can also be obtained on the basis of mass balance (Adánez et al., 2004).

The purpose of this study focus on the reduction kinetics of $CaSO_4$ with CO in a differential fixed bed. The effects of temperature (800-950 °C), gas partial pressures (20% -70%) on the reduction were investigated and the kinetic regime for the reduction was determined. The experimental data was analyzed and the limiting mechanism that controlled the reduction process was determined. The reaction order with respect to CO partial pressure for the fresh oxygen carriers was determined. The kinetic parameters for reduction of $CaSO_4$ oxygen carrier were finally obtained using the shrinking unreacted core model.

THERMODYNAMIC ANALYSIS

Chemical reaction thermodynamics is important to understand the reaction mechanism, the product composition as well as the design criteria of CLC system. In this work the equilibrium compositions of reduction were studied based on the principle of the Gibbs free energy minimization by means of Aspen Plus® software.

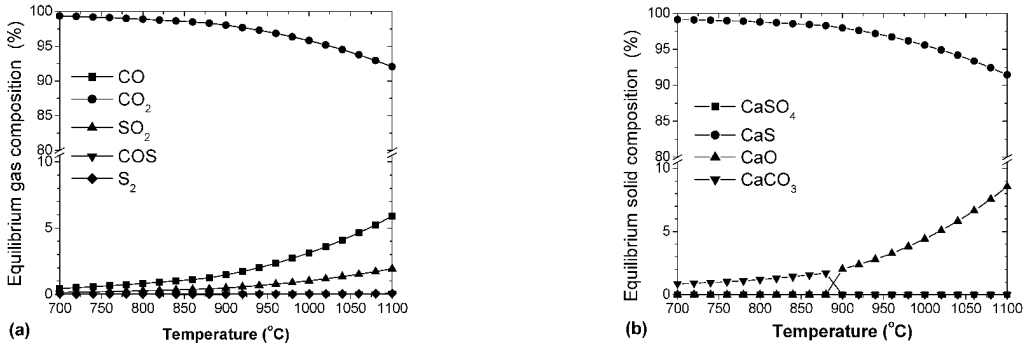

Fig. 1 Equilibrium composition as a function of temperature of reduction of $CaSO_4$ with CO. The molar ratio of $CaSO_4$/CO is 0.25. (a) gas phase and (b) solid phase.

Figures. 1(a) and 1(b) show the equilibrium composition of major gas and solid phase species present as a function of the temperature. The calculation was conducted with 100% CO over a stoichiometry molar ratio ($CaSO_4$/CO =0.25). The gaseous phases are assumed as CO, CO_2, SO_2, COS, S_2. The solid phases are $CaSO_4$, CaS, and CaO ($CaCO_3$). As shown in Fig. 1a, a high purity of CO_2 (>97%) can be obtained within the suitable temperature (900-950 °C). Also, it is evidently that there is thermodynamic limitation for $CaSO_4$/CaS that caused the incomplete conversion of CO which is lower than 2% at 950 °C. Some other gases are also generated and SO_2 is the major sulfur release component. CaS is the dominant product in solid species at equilibrium condition which is in agreement with that of gas phase.

Figures. 2(a) and 2(b) demonstrate the equilibrium composition of gas phase and solid phase as a function of the CaSO4/CO molar ratio, respectively. The $CaSO_4$/CO ratio means ratio of the oxygen provided by the oxygen carrier to the fuel gas, which is defined as recirculation ratio in the literature (Abad et al., 2007c). The stoichiometric ratio (*b*) defined as mol of $CaSO_4$ per mole of fuel gas, is 0.25 for CO. As presented in Fig. 2, a high conversion of CO and high purity of CO_2 could be attained when the $CaSO_4$/CO molar ratio is higher than the stoichiometric ratio while a certain amount of SO_2 and COS would also be generated. The sulfur release accounts a small fraction of the total amount of oxygen carrier and would be recycled to $CaSO_4$ by adding CaO sorbent (Song et al. 2008b; Wang et al. 2008). If the $CaSO_4$/CO molar ratio is lower than 0.25, the sulfur release is less than 0.01% and can be neglected with reduction product mainly CaS.

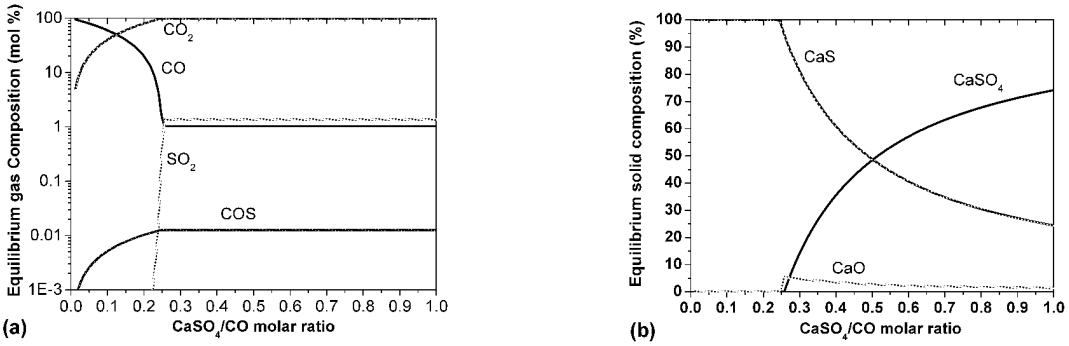

Fig. 2 Equilibrium composition as a function of $CaSO_4$/CO molar ratio at 900 °C. (a) gas phase and (b) solid phase

Thermodynamics analysis provides important reference to determine the suitable reaction conditions for kinetics study and product compositions. In the experiments the temperature was within 880-950 °C.

EXPERIMENTAL

The oxygen carrier particle was natural anhydrite ore produced in Nanjing. The natural anhydrite ore was crushed to particles with a size range of 150-200 μm. $CaSO_4$ is the main content in natural anhydrite ore (94.38%). The other components primarily consisted of MgO, SiO_2 and Al_2O_3.

The experiment was conducted under atmospheric pressure in a laboratory fixed bed shown in Fig. 3. The stainless steel tube reactor (i.d. = 25 mm, length = 950 mm) was electric furnace. The reaction gases, CO (99.99%), O_2 (99.99%) and N_2 (99.99%) were introduced by three mass flow controllers with the detecting limit at 1.0 mL/min. The pressure of the fixed bed was measured by a U-type pressure gauge. More information can be found in our recent articles (Song et al., 2008a; Song et al., 2008b).

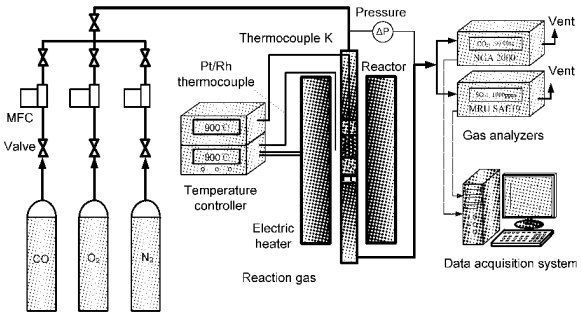

Fig. 3 Experimental setup

In this work the gas measurement was semi-continuous instead of real-time. To decrease the gas dispersion form the reactor to the gas analyzers, the product gas was collected by sample bag. Then the sample gas was measured by an Emerson multi-component gas analyzer including a Rosemount NGA 2000 gas analyzer used to measure the concentrations of CO_2, CH_4, CO, and O_2 with a detecting limit at 0.01%, and a Hydros 100 analyzer to detect the concentration of H_2 with a detecting limit at 0.1%. The gas analyzer was calibrated with standard gas and provided high measurement accuracy. In some experiments the sample gas was diluted with certain amount of N_2 and measured by an MRU SAE19 flue gas analyzer to detect the concentration of SO_2. The gas composition in the sample bag was the average value during the sample time, and the delay time from the reactor to gas analyzers was avoided. However, this method may not be applicable when the reaction rate was too fast. In that case, the gas concentration should be measured online and recorded and corrected in order to obtain the gas concentration at the reactor exit by a deconvolution method as presented in the literature.(Abad et al., 2007c; Chuang et al., 2008)

Typically, a sample of 1.000 g $CaSO_4$ oxygen carrier particles with a size range of 150-200 μm was placed in the center of quartz bed which increased the bed heat capacity and preheated the fuel gas. The height of oxygen carrier bed around 1.3 mm, which is a thin layer and could act as a differential reactor. Therefore, the solid conversion of oxygen carrier samples would be roughly the same for all particles in the reactor. The particles were heated to the reaction temperature (880-950 °C) under a N_2 flow of 1000 mL/min. Then the inlet gas was switched to the reducing gas of 20-70% CO balanced with N_2. The flow rate was controlled at 1000 mL/min. The reduction period was generally within 60 min to 120 min which was determined by the operation conditions. Yet in some experiments the particles was not completely reduced because reduction rate was quite low at late period, therefore side reactions such as carbon deposition was avoided. At the end of the run, the reactant gas was switched to N_2 and cooled down to room temperature.

The oxygen carrier conversion rate during reduction can be calculated based on the mass balance of oxygen which transferred from the oxygen carrier to the fuel gas:

$$\frac{dX}{dt} = \frac{\dot{n}_{out} M_O}{m_{ox} R_O} (y_{CO_2,out} + 2y_{SO_2,out}) \quad (4)$$

Therefore the solid conversion (X) can be obtained with accumulation of reduction rate (dX/dt) with time (t). This method has been successfully applied in our previous study and in the literature (Song et al. 2008a; Song et al. 2008b). In this study the SO_2 concentration was quite low as measured (less than 200 ppmv) under the strong reducing condition. Compared to CO_2 and CO, it was neglected in the calculation.

RESULTS AND DISCUSSION

Proof and assumptions of kinetic model

Previously it was found that shrinking unreacted core model may fit the reduction of $CaSO_4$ based oxygen carrier with simulated coal gas well (Song et al. 2008a). The experimental data obtained and characterization analysis verified the assumptions of shrinking core model. The oxygen carrier particles are assumed spherical. During the reduction of $CaSO_4$, CO and H_2 diffuse to the $CaSO_4$ core through the film surrounding the particle, react with the $CaSO_4$ on the surface to form CaS, and CO_2. The particle size

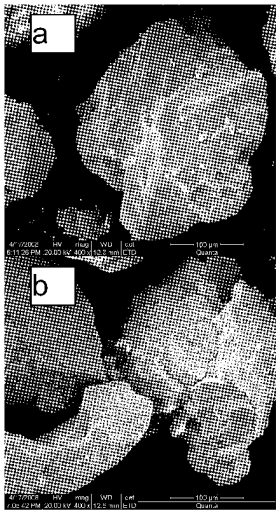

Fig. 4 SEM micrographs of (a) fresh and (b) reduced particles at 950 °C with simulated coal gas in a fluidized bed (Song et al., 2008a)

was approximate the same as before reduction as demonstrated in ESEM study shown in Fig. 4. The inner core is $CaSO_4$ and the out layer is mainly CaS as demonstrated by EDX. The completely reduced product is dominantly CaS from XRD analysis. CaS is much more porous than $CaSO_4$. The porous product layer provides less resistance for the gas diffusion and the reaction can proceed further to the core. The gaseous products, mainly H_2O and CO_2 diffuse from the solid reaction surface into the surrounding gas stream. The external diffusion resistance is largely eliminated. Also temperature within the bed is stable and the particles can be considered isothermal and the reaction is considered at pseudo-steady state condition. With the proof of characterization analysis, the reduction of $CaSO_4$ oxygen carrier with fuel gas may be accounted by shrinking unreacted core model and is further studied in this work.

Effect of mass-transfer

During the preliminary experiments, the effect of external mass transfer on reaction rate was studied. Some experiments were performed under different sample masses (1.000, 5.000, 8.000 g) at 900 °C under a gas flow of 1000 mL/min and the results are shown in Fig. 5. The initial reaction rate was significantly influenced. A high temperature increase of around 10 °C was observed during the initial 300 s for 8 g, which promoted the reduction rate. The overall reaction rate

seemed to be independent of sample bed mass below 1.000 g which is a thin layer of 1.3 mm height. Thus in the following experiments, a sample mass of 1.000 g was used. To compare the kinetics in previous fluidized bed tests, the size range of particles in this work was kept within the range of 150-200 μm, which may be a little larger for kinetics study due to internal mass transfer resistance. However, chemical reaction control is the major concern in CLC and the product layer diffusion control would be determined as well.

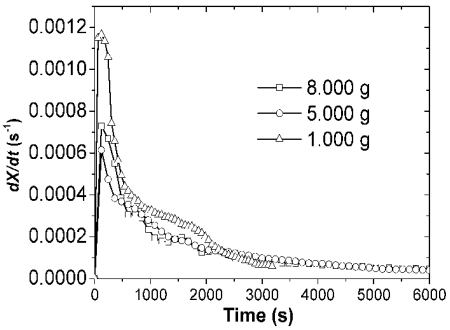

Fig. 5 Plot of dX/dt as a function of time at different sample mass

Effect of CO partial pressure

To investigate the effect of CO partial pressure on the reduction of $CaSO_4$ based oxygen carrier, experiments were performed with the CO concentration varied at 20%, 40%, and 70% in N_2 balance. The typical CO and CO_2 concentrations in the product gas at 900 °C are displayed in Fig. 6, respectively. The CO concentration was in excess and generally varied within 10% in the reactor which satisfied the requirement of differential reactor. The CO_2 concentration was as high as 6% at the initial period due to chemical reaction control but soon decreased which suggested the product layer diffusion control occurred at the late period. Fig. 7 shows the variation of solid conversion at different CO partial pressures.

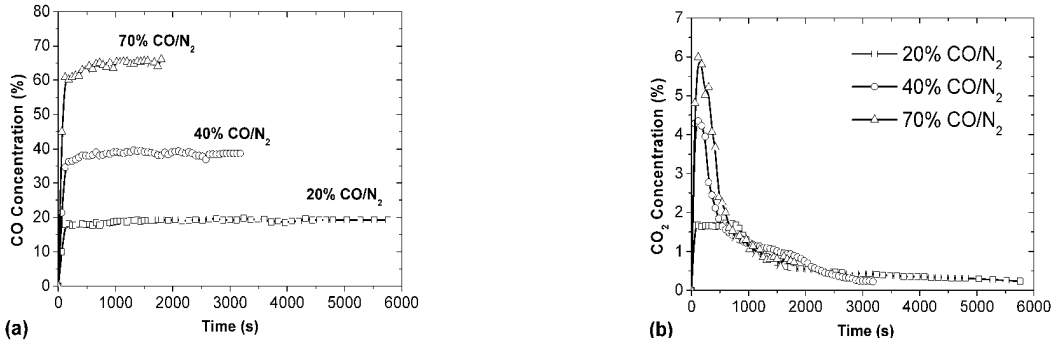

Fig. 6 Variation of (a) CO and (b) CO_2 concentration in product gas with time at different CO partial pressures

The typical relationship between the conversion of oxygen carrier (X) and time (t) at the kinetic regime of chemical reaction control for spherical particles is described as follows:

$$[1-(1-X)^{1/3}]=\frac{bkC_{CO}^{n}}{\rho_m R_p}t=k_{app}t \tag{5}$$

$$Ln\,(k_{app})=Ln\,(\frac{bk}{\rho_m R_p})+nLn\,(C_{CO}) \tag{6}$$

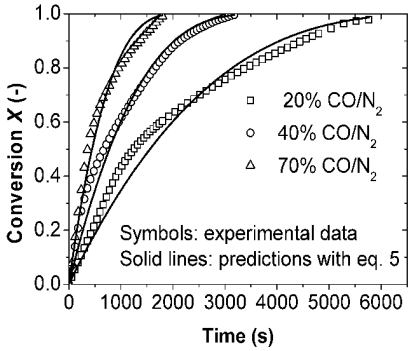

Fig. 7 Effect of CO partial pressure on solid conversion

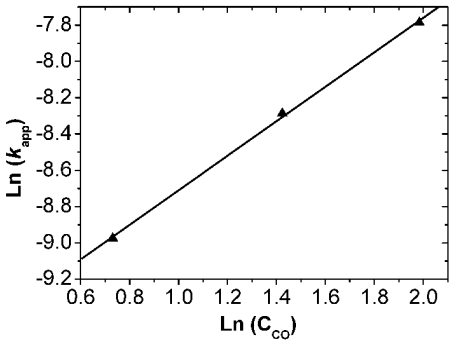

Fig. 8 Plot of Ln (k_{app}) as a fuction of Ln (C_{CO})

The reaction order n was obtained from the linearization of the logarithmic plots of k_{app} with molar concentration C_{CO} as shown in Fig. 8. The best fitted value of reaction order at different CO partial pressures was 0.95126, which verified that the reduction order of $CaSO_4$ with CO could be considered as 1.0 (Song et al. 2008a). The chemical reaction constant k at 900 °C is 9.1566×10^{-4} m/s. The model predictions are shown as solid lines in Fig. 7. It can be seen that the predicted conversion seems to be a little lower than the experimental data initially and higher at late period, which is due to the underestimation of chemical reaction constant and the internal transfer is not considered.

Effect of reaction temperature

The effect of reaction temperature on the reduction of $CaSO_4$ oxygen carrier was investigated by varying the temperature in the range of 880-950 °C. Figure. 9 shows the variation of CO_2 concentration with time at typical temperatures at 40% CO/N_2. With the temperature increases the CO_2 concentration increased rapidly from 880 °C to 900 °C and gradually increased above 900 °C. Figure. 10 presents the solid conversion with time. Accordingly the oxygen carrier conversion is strongly influenced by temperature. At higher temperatures, the reaction rate is very fast and particles are completely reduced within 30 min.

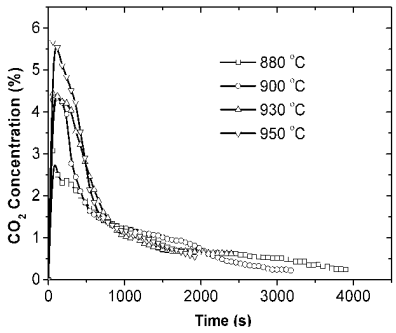

Fig. 9 Variation of CO_2 concentration with time at different temperatures at 40% CO/N_2

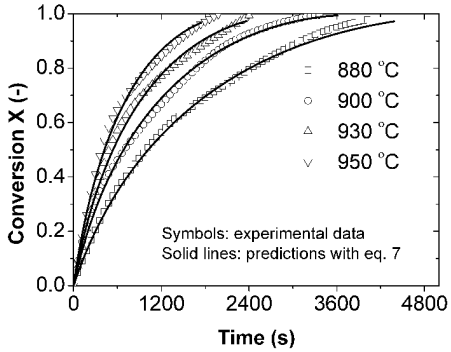

Fig. 10 Effect of temperature on solid conversion at 40% CO/N_2

The variation of reduction rate with time suggested that chemical reaction control may be the limiting step for reduction during the early period and product layer diffusion control may also play certain role when the solid conversion X was high.

Kinetic determination and analysis

The equations that describe the shrinking unreacted core model under both chemical reaction control and product layer diffusion control are presented as follows:

$$t=\frac{\rho_m R_p}{bkC_{CO}}[1-(1-X)^{1/3}]+\frac{\rho_m R_p^2}{6bD_eC_{CO}}[1-3(1-X)^{2/3}+2(1-X)] \tag{7}$$

The coefficient and mechanism function of chemical reaction control:

$$k_1=\frac{\rho_m R_p}{bkC_{CO}^n} \tag{8}$$

$$g(X)=[1-(1-X)^{1/3}] \tag{9}$$

The coefficient and mechanism function of product layer diffusion control:

$$k_2 = \frac{\rho_m R_P^2}{6bD_e C_{CO}^n} \tag{10}$$

$$p(X) = [1-3(1-X)^{2/3} + 2(1-X)] \tag{11}$$

Therefore the relationship of reaction time with conversion is described as:

$$t = k_1 g(X) + k_2 p(X) \tag{12}$$

Therefore, the coefficient k_1 and k_2 can be obtained from the relations between reaction time t and mechanism functions $g(X)$ and $p(X)$) with nonlinear least square fitting method. Consequently, kinetic parameters including chemical reaction constant k, effective diffusivity *De, and* dimensionless modulus σ_s^2 can be obtained from Eqs. (8) and (10) and listed in Table 1.

Table 1 Kinetic parameters

T, °C	C_{CO}, mol/m^3	k, m/s	D_e, m^2/s	$\sigma_s^2 = kR_p/6D_e$
880	4.2278	9.1424×10^{-4}	4.2915×10^{-8}	0.6214
900	4.1557	1.4513×10^{-3}	5.7579×10^{-8}	0.7352
930	4.0521	1.8362×10^{-3}	8.0391×10^{-8}	0.6661
950	3.9858	2.3016×10^{-3}	1.1681×10^{-7}	0.5747

As judged from the value of σ_s^2, for the sample particles in this study, the reduction of oxygen carrier was controlled by both chemical reaction and product layer diffusion where the latter dominates.

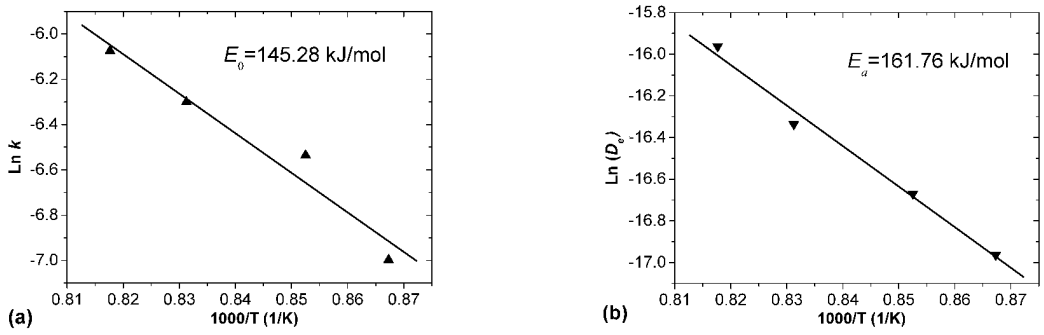

Fig. 11 Arrhenius plot of (a) Ln k and (b)Ln (D_e) against 1000/T

The chemical reaction constant k and effective diffusivity D_e follow Arrhenius type of expression:

$$k = 3.7896\times10^{3} \exp\left(-\frac{17474.5}{RT}\right) \text{ (m/s)} \tag{13}$$

$$D_e = 9.0704\times10^{-1} \exp\left(-\frac{19456.3}{RT}\right) \text{ (m/s)} \tag{14}$$

The activation energy (E_0) of chemical reaction is 145.28 kJ/mol while the apparent activation energy (E_a) of the product layer diffusion is 161.76 kJ/mol. Compared to the activation energies of metal oxides based oxygen carrier, the activation energy in this work is much higher which also suggested that the relative low reactivity of natural anhydrite. The model prediction results are shown in Fig. 10 and were in good agreement with the experimental results.

Limitations of present work and kinetic model

The effect of SO_2 on the reduction reaction was not studied. In practice SO_2 is an important component in the reaction gas such as coal gasification gas. Yet previous study demonstrated that CaS is the direct product of reduction at strong CO and H_2 partial pressures even without presence of SO_2. Therefore this model is still applicable to the target reaction to CaS and CO_2. As for the reduction of $CaSO_4$ with low CO concentration (less than 10%), the side reactions may be intensified. So the current model obtained is applicable only to the strong reducing conditions in CLC in which case the release of SO_2 could be neglected and may not applied to low CO concentrations. Previous studies show that the oxygen capacity would decrease because of sulfur release in the cyclic reduction and oxidation. Therefore fresh oxygen carriers are necessary to make up if $CaSO_4$ oxygen carrier is to be used in CLC. Thus all the tests in this work applied the fresh unreacted anhydrite particles. It may not be applicable to represent kinetics in redox cycle. Besides, the particles are assumed to be

spherical which may be not the case in practice. The particle change due to attrition and fragmentation in fluidized bed was neglected in this model. Further study would adopt smaller particles to obtain the kinetic regime under mainly chemical reaction control.

CONCLUSIONS

Thermodynamic analysis of $CaSO_4$ oxygen carrier with CO based on Gibbs free energy minimization was performed. The main gas product of reduction is CO_2, while the solid product is CaS. The reduction kinetics of a $CaSO_4$ based oxygen carrier with CO was investigated in a differential bed. The effects of CO partial pressure (20%-70%) and temperature (880-950 °C) on the reduction were investigated. The shrinking unreacted core model was used to describe the reaction. The reduction was found to be first order with respect to the CO partial pressure for fresh oxygen carriers. The reduction reaction was controlled by both chemical reaction and product layer diffusion and the latter dominated. The dependences of reaction rate constant and effective diffusivity with temperature were both obtained. The kinetic model well predicted experimental results. The kinetic study provides important information for future use of $CaSO_4$ oxygen carrier in CLC of solid fuels and design criteria of a CLC system.

NOTATIONS

b stoichiometric factor, b=1/4 for CO

C_i molar concentration of gas species i in the inlet gas, mol/m^3

dX/dt the reduction rate of oxygen carrier, 1/s

E_0 activation energy of chemical reaction, kJ/mol

E_a apparent activation energy of product layer diffusion, kJ/mol

$g(X)$ mechanism function of chemical reaction control

k kinetic rate constant, m/s

k_1 coefficient of chemical reaction control

k_2 coefficient of product layer diffusion control

k_{app} apparent rate constant, 1/s

m_{ox} mass of the sample when fully oxidized, kg

Mo atomic mass of oxygen, 16 g/mol

n reaction order

$\dot{n}_{out}$ molar flow of the gas exiting the reactor, mol/s

$p(X)$ mechanism function of product layer diffusion control

R Constant of the ideal gases, 8.314 J/mol·K

R_o oxygen transport capacity, or oxygen ratio of the oxygen carrier

R_P particle radius, m

t time, s

T absolute temperature, K

X Oxygen carrier conversion

$y_{i,out}$ outlet moloar fraction of the gas species i exiting the reactor, dry basis.

ρ_m molar density of $CaSO_4$ in the anhydrite, mol/m^3

σ_s^2 dimensionless modulus, defined as $\sigma_s^2=kR_p/6D_e$

ACKNOWLEDGEMENTS

Financial supports from National Natural Science Foundation of China (Grant Nos. 50606006, 90610016) for this study are gratefully acknowledged. The authors sincerely appreciate Dr. Alberto Abad in CSIC in Spain for valuable advice on kinetic study on Chemical-looping combustion.

REFERENCES

Abad, A., Adánez, J., García-Labiano, F., de Diego, L. F., Gayán, P. and Celaya, J.: Chem. Eng. Sci. **62** (2007a), pp.533-549.

Abad, A., García-Labiano, F., de Diego, L. F., Gayán, P. and Adánez, J.: Energy Fuels **21** (2007b), pp.1843-1853.

Abad, A., Mattisson, T., Lyngfelt, A. and Johansson, M.: Fuel **86** (2007c), pp.1021-1035.

Adánez, J., Abad, A., de Diego, L. F., García-Labiano, F. and Gayán, P.: Ind. Eng. Chem. Res. **43** (2004), pp.4132-4139.

Chuang, S. Y., Dennis, J. S., Hayhurst, A. N. and Scott, S. A.: Combust. Flame **154** (2008), pp.109-121.

Jung, J. and Gamwo, I. K.: Powder Technol. **183** (2008), pp.401-409.

Leion, H., Lyngfelt, A., Johansson, M., Jerndal, E. and Mattisson, T.: Chem. Eng. Res. Des. **86** (2008a), pp.1017-1026.

Leion, H., Mattisson, T. and Lyngfelt, A.: International Journal of Greenhouse Gas Control **2** (2008b), pp.180-193.

Lyngfelt, A., Leckner, B. and Mattisson, T.: Chem. Eng. Sci. **56** (2001), pp.3101-3113.

Ryu, H. J., Bae, D. H., Han, K. H., Lee, S. Y., Jin, G. T. and Choi, J. H.: Korean J. Chem. Eng. **18** (2001), pp.831-837.

Shen, L. H., Zheng, M., Xiao, J. and Xiao, R.: Combust. Flame **154** (2008), pp.489-506.
Song, Q. L., Xiao, R., Deng, Z. Y., Shen, L. H., Xiao, J. and Zhang, M. Y.: Ind. Eng. Chem. Res. **47** (2008a), pp.8148-8159.
Song, Q. L., Xiao, R., Deng, Z. Y., Zheng, W. G., Shen, L. H. and Xiao, J.: Energy Fuels **22** (2008b), pp.3661-3672.
Wang, J. S. and Anthony, E. J.: Applied Energy **85** (2008), pp.73-79.

INVESTIGATION OF COAL FUELED CHEMICAL LOOPING COMBUSTION USING Fe_3O_4 AS OXYGEN CARRIER

Wenguo Xiang[1], Xiaoyan Sun[1], Sha Wang[1], Wendong Tian[2], Xiang Xu[2], Yanji Xu[2], Yunhan Xiao[2]

[1]*School of Energy and Environment, Southeast University, Nanjing, 210096, China*
[2]*Institute of Engineering Thermophysics, Chinese Academy of Sciences, Beijing, 100080, China*

Abstract: Chemical-looping combustion (CLC) is a novel combustion technique with CO_2 separation. Magnetite (Fe_3O_4) was selected as the oxygen carrier and Shenhua coal (Inner Mongolia, China) as the fuel for this study. The influences of operation temperatures, and coal to Fe_3O_4 mass ratios on the reduction characteristics of the oxygen carrier were investigated using an atmosphere TGA. The sample, comprised of 2.25mg coal and 12.75mg Fe3O4, was heated to 1000 °C. Experimental results show that the reaction between the coal volatile and Fe_3O_4 began at 700 °C while the reaction between the coal char and Fe_3O_4 occurred at 800°C and reached a peak at 900 °C. Fe_3O_4 was fully reduced into FeO, while some FeO was further reduced to Fe. As the operation temperature rises, the reduction conversion rate increases. At the temperatures of 850°C, 900°C, and 950°C, the reduction conversion rates were 37.1%, 46.5%, and 54.1% respectively. When the mass ratios of coal to Fe_3O_4 were 5/95, 10/90, 15/85, and 20/80, the reduction conversion rates were 29.5%, 40.8%, 46.5%, and 46.6% respectively. With the increase of coal to Fe_3O_4 mass ratio, the conversion rate increases first and then changes no more. There exists an optimal coal to Fe_3O_4 mass ratio.

Key words: chemical-looping combustion, CO_2 separation, magnetite, coal

INTRODUCTION

Concerns about rising concentrations of greenhouse gases in the atmosphere, together with pollution problems in congested urban areas, are the main drivers towards a widespread utilization of hydrogen as energy carrier to satisfy the needs in amid to long term future. Since fossil fuels are likely to remain the main source of primary energy for a long time, a significant reduction on climate change could be accomplished by systems including CO_2 capture and storage to fully exploit the benefit of the Hydrogen Economy (DOE, Hydrogen Program Plan). Damen et al. (2006) described that present technologies producing hydrogen from natural gas can be adapted to produce CO_2 as a separated, liquefied flow at the plant exit, but substantial additional hardware is required. The technologies increase the investment costs and lower the conversion efficiency, sometimes with a rather poor CO_2 capture efficiency as reported by Consonni and Viganò (2005). An alternative solution may come from a completely different technology, based on the chemical looping concept.

Chemical-looping combustion (CLC) is a new alternative to conventional combustion that prevents the CO_2 from being mixed in the combustion gases. This is accomplished by preventing the air–N_2 to be present in the part of the reactor system where the oxidation of the fuel takes place. A circulating metal oxide is submitted to numerous cycles in which it is oxidized in an air reactor and reduced in a fuel reactor, meanwhile providing the oxygen required for the combustion. If the air reactor is replaced by a steam reactor, where the steam is used as the oxidant reagent, chemical looping can be used for hydrogen generation (CLHG).

There have been a number of publications investigating different aspects of the CLC process. Xiang and Chen (2007) showed a potential efficiency of 58.33% for generating hydrogen and electricity when gasification combined cycle is integrated with iron oxide CLC technology. Chiesa et al. (2008) assessed the potential of natural gas fired power cycles based on a three iron oxide CLC reactor arrangement. Ishida et al.(2002) and Jin et al.(2002) investigated iron oxides CLC. Piotrowski et al. (2007), Piotrowski et al. (2005) and Mondal et al. (2004) studied the kinetics of hematite to wüstite on TGA with CO+ H_2 or CO. From the thermodynamic and chemical equilibrium point of view, Svoboda et al. (2007) studied the reduction of Fe_2O_3 by H_2, CO, CH_4 and a model syngas and the oxidation of iron by steam. Since coal is considerably more abundant, it would be highly advantageous if the CLHG process could be adapted for solid fuels. Leion et al.(2007,2008) and Berguerand et al.(2008a,2008b) studied the feasibility of using solid fuel in the CLC based on $Fe_2O_3/MgAl_2O_4$ or ilmenite in a laboratory fluidized bed reactor. Dennis et al. (2006), Fan et al.(2008), Gupta et al.(2007) and Velazquez-Vargas et al.(2006) investigated the possibility of utilization of chemical looping in coal gasification processes for hydrogen generation.

For CLHG, the iron oxides recycled between the fuel reactor and the steam reactor are mainly Fe_3O_4 and Fe or FeO. However, few studies used Fe_3O_4 as the oxygen carrier. This paper focused on the feasibility of

solid fueled CLC using Fe_3O_4 as the oxygen carrier. Shenhua coal from Inner Mongolia, China, is selected as the fuel. Tests on the reduction of Fe_3O_4 by the selected solid fuel were conducted using atmosphere TGA under nitrogen (N_2) atmosphere. The influences of operation temperatures and coal to Fe_3O_4 mass ratios on the CLC characteristics were discussed.

EXPERIMENTAL

Sample Preparation

The proximate and ultimate analyses of tested coal are shown in Table 1. The oxygen carrier Fe_3O_4 was 97.0% pure (and 3% inert materials). The particle sizes of the coal and Fe_3O_4 were both greater than 200 mesh (less than 75μm).

Table 1 Proximate and ultimate analysis of three samples

Sample	Proximate analysis/%(mass, ad)				Ultimate analysis/%(mass, d)					$Q_{net,\ ad}$/MJ/kg
	A	M	VM	FC	C	H	O	N	S	
Shenhua coal	5.58	6.98	33.59	53.85	69.94	4.66	17.18	0.93	1.29	24

Experimental Principle

Assuming the oxygen in the coal is oxidized by its hydrogen forming steam vapor, the reaction between Fe_3O_4 and the coal could be thought as the reaction between Fe_3O_4 and combustible compound C_mH_{2n}. According to the calculated C_mH_{2n}, the ratio of solid fuel to Fe_3O_4 could be confirmed.

According to the coal proximate and ultimate analysis data, free hydrogen is 3.89% and free oxygen is 10.98%. Assuming partial free hydrogen oxidized by free oxygen in coal to form H_2O, carbon moles m=54.2 and hydrogen moles $2n$=23.4 in 1kg coal. Actual reactions between the coal and Fe_3O_4 are regarded as the reactions between $C_{54.2}H_{23.4}$ and Fe_3O_4 as follows:

$$C_{54.2}H_{23.4}+120.1Fe_3O_4 \rightarrow 360.3FeO+54.2CO_2+11.7H_2O \quad (1)$$

$$C_{54.2}H_{23.4}+120.1FeO \rightarrow 360.3Fe+54.2CO_2+11.7H_2O \quad (2)$$

If the reaction goes fully, it is described as reaction (3):

$$4C_{54.2}H_{23.4}+120.1Fe3O4 \rightarrow 360.3Fe+216.8CO_2+46.8H_2O \quad (3)$$

According to reaction (3), the weight ratio of Shenhua coal to Fe_3O_4 is 1 / 7.2. In this research, the ratio is set to 1/5.7, i.e. coal to Fe_3O_4 mass ratio of 15/85.

Experimental Instrumentation

The atmosphere TGA was a STA-PT1600 TG-DSC. The pyrolysis products were analyzed on-line with FT-IR VECTOR22. A RIGAKU D/max-TTR III was used to analyze the residues of the samples.

Experimental schedule

In order to determine the possible reaction temperature and the optimum reaction temperature, two samples (coal 2.25mg and the mixture of coal 2.25mg and Fe_3O_4 12.75mg) were heated from the ambient temperature to 1000 °C with a heating rate of 5 k/min on atmosphere TGA. Three terminal temperatures (850 °C, 900 °C, and 950 °C) at a heating rate of 20 k/min were selected for this work. Mixtures with coal to Fe_3O_4 mass ratios of 5/95, 10/90, 15/85, and 20/80 were also conducted at 900 °C. Tests were performed under the N_2 atmosphere (99.999%) at a flow rate of 30 mL/min.

Experimental Data Processing

The reduction conversion rate of Fe_3O_4 was defined as Equation (4):

$$X = \frac{\Delta W_{mix,t}}{\Delta W_{Fe} + \Delta W_C} \times 100\% \quad (4)$$

Where X is the conversion rate, %; $\Delta W_{mix,t}$ is the weight loss of time t, mg; ΔW_C is the possible maximum weight loss of coal in the mixture, mg; ΔW_{Fe} is the weight loss of Fe_3O_4 converted completely to Fe, mg. More attentions were paid to the reduction conversion of the oxygen carrier in order to study the hydrogen generation of the reduced oxygen in the steam reactor, so the carbon conversion of the coal is not included in this research.

RESULTS AND DISCUSSION

Determination of the reaction temperature

The programmed temperature experiments of the coal and the mixture were carried out in TGA to determine the reaction temperature between coal and Fe_3O_4. FT-IR was used to observe the characteristics of the product gases. Experiments were performed under the condition of 0.1 MPa, a N_2 flow rate of 30 mL/min, a heating rate of 5°C/min, and the final temperature of 1000°C. The TG weight loss and DTG curve of the coal and the mixture are shown in Fig.1. As to the pyrolysis of coal, a peak occurred at the temperature of 420 °C, which is attributed by the pyrolysis of the volatile material in the coal. For the mixture, the tendency of the weight loss is similar to that of coal pyrolysis before 700 °C. The first peak occurred at the temperature of 420°C and its weight loss was almost the same as that of coal, so the weight loss of the mixture must be caused mainly by the coal pyrolysis. As the temperature increases, DTG curve of the mixture shows two peaks at 770 °C and 900 °C, which indicates that the weight loss of the mixture is great at the temperature of 770-900 °C. The reduction of Fe_3O_4 by coal volatile begins at 700 °C and reaches a peak at 770 °C. The reduction of Fe_3O_4 by coal char occurs at 800 °C and becomes strongest at 900 °C. The weight loss peak of the mixture comes at 900 °C, which shows the strong reaction occurring at 900 °C.

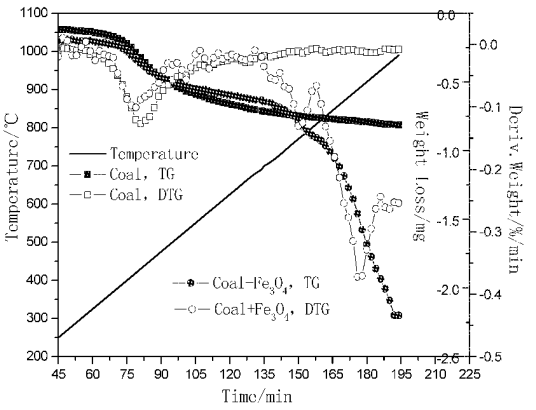

Fig.1 TG and DTG curves of two samples

FT–IR three-dimensional spectra of the coal and the mixture are given in Fig.2(a) and Fig.2(b). The data survey the range 4000–500 cm^{-1} at the sample rate of 16s. As can be seen in Fig. 2(a) and Fig. 2(b), the prolysis products of coal are the same as that of the mixture in species, but are different in mount. The basic components of the coal and the mixture are circular aromatic hydrocarbon, heterocyclic compound, nitrogenous heterocyclic compound or sulfurous cyclic-compound as shown in Fig.2(c) and Fig.2(d). The pyrolysis of coal is divided into three stages (Pang et al., 2007). The first phase is drying stage (about to 350°C). The basic decomposition products are water, CO, CO_2, alkyl-benzene and a few of oxygenic function groups. The second stage (350–550°C) is semi coke forming stage. It can be seen from Fig.2 that DTG curve of the coal has a peak value as the TG curve changes deeply. The decomposition products are quite complexity, including CO_2, satisfied hydrocarbon, unsaturated hydrocarbon, aromatic compound and so on. According to the reference (Ibarra et al., 1996; Richard et al., 1999), a correspondence between the absorption bands and functional groups can be established. It can be seen from Fig.2(c) that at DTG peak value (about 420°C) 3020 cm^{-1} is the characteristic absorption peak to aroma ring matter, 2958 cm^{-1} to CH_3, CH_2 and CH, 2920, 2310 cm^{-1} to CO, 2340 cm^{-1} to CO_2, 2180 and 2100 cm^{-1} to triple-bond and amass double-bond, and at the same time it is typical C=C weak absorption peak at 1510 cm^{-1}.

The pyrolysis decomposition products are mostly the tar, light oil and hydrocarbon gas, and the oxygenic function groups are increased. The third stage (550–1000°C) is the secondary degas stage. It is mainly fasciculation reaction, forming a great deal of syngas. Fig.2 (d) shows that the pyrolysis products are mainly CO, CO_2, unsaturated hydrocarbon and oxygenic aromatic compound at 770°C. On the first and the second stage (lower than 700 °C), the products of the mixture have the same components as those of the coal and the weight loss is almost the same, so the weight loss of the mixture is caused by the pyrolysis of the coal in the mixture. But the absorbance occurring at 2330 - 2360 cm^{-1} is 4.5 times that of the coal as shown in Fig.2(c). The observation indicates that very little Fe_3O_4 must react with the volatile from the coal forming CO_2. When the temperature is above 700 °C, DTG curve of the mixture has two peak values (at 770 and 900 °C) and the TG curve changes deeply especially when the peak occurs at 900 °C. Fe_3O_4 was reduced by the coal volatile above 700 °C. As the temperature rises, more volatile is released and the reaction between Fe_3O_4 and coal volatile becomes stronger and reaches a peak at 770 °C forming more CO_2, which accords well with the absorbance peak (as shown in Fig.2(d)). At 800 °C, the volatile released decreases (as shown in Fig.1) but the weight losses of the mixture increased. The weight losses were caused by the reaction between Fe_3O_4 and the coal char. The reaction between Fe_3O_4 and coal char reaches its peak at 900 °C.

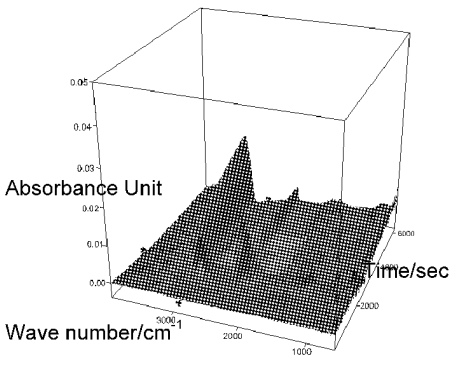

(a) FT-IR three-dimensional spectra of the coal

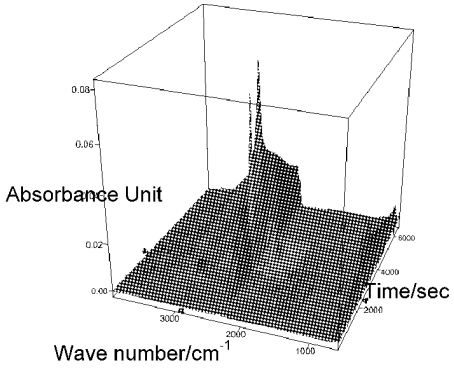

(b) FT-IR three-dimensional spectra of the mixture

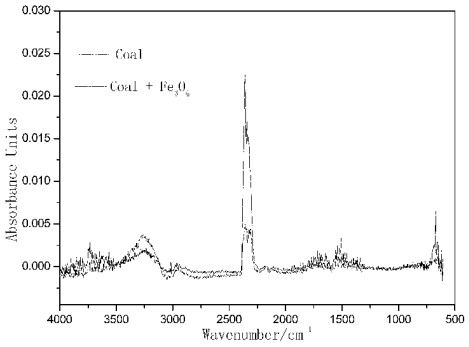

(c) 420 ℃

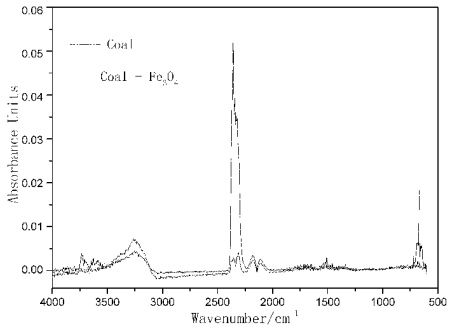

(d) 770 ℃

Fig. 2 FT-IR spectrograms for the coal sample and the mixture sample

Because of the reduction of Fe_3O_4 by coal char, the weight loss rate increases significantly above 800 °C. Fe_3O_4 is reduced prominently by coal char above 800 °C and a high reactivity is reached at 900 °C. As the temperature increases from 800 °C to about 1000 °C, the weight loss rate on Fe_3O_4 bases is about 12.5%. According to the approximate reaction model of $C_{54.2}H_{23.4}$ and Fe_3O_4, the weight loss rate is theoretically 6.9 % or 27.6% when Fe_3O_4 is reduced into FeO or Fe. It could be concluded that Fe_3O_4 is fully reduced into FeO, while some FeO is further reduced to Fe, which is in agreement with the XRD analysis results of the mixture residues, shown in Fig. 3. No Fe_3O_4 was detected and Fe_3O_4 was converted into FeO or Fe. The main peak of FeO appears in 42°, while the secondary peaks appear in 36°, 62°, 73°, 77°, and the main peak of Fe appears in 45°, while the secondary peak appears in 65°.

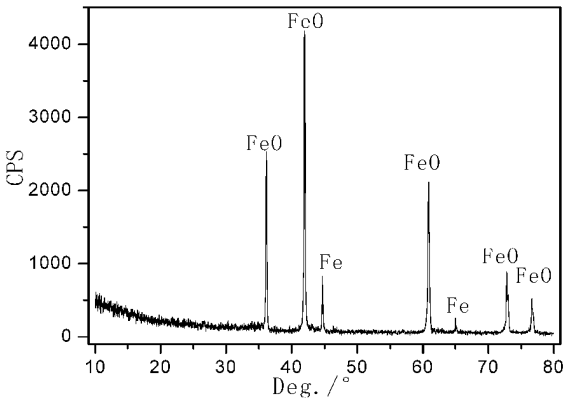

Fig. 3 XRD characterization of the mixture

Effects of the final temperature

The mixtures of coal and Fe_3O_4 were heated to three temperatures (850, 900, and 950°C) with a heating rate of 20 k/min under N_2 atmosphere, and the total reaction time was kept for 100 min. The TG curves are shown in Fig.4. As we can see from TG curves in Fig.4, the weight losses at the temperatures of 850, 900, and 950°C are 2.09mg, 2.62mg and 3.05mg and the weight loss rates are 13.9%, 17.5%, and 20.3% respectively. After a total reaction time of 100 minutes, the conversion rates are 37.1%, 46.5%, and 54.1% correspondingly. As the final temperature rises, more volatile is released from coal (Alonso et al., 1999) and more Fe_3O_4 is reduced by its volatile and coal char. Furthermore the reactivity of the coal char is increased as the temperature rises. The reaction between Fe_3O_4 and the coal char becomes stronger. As shown in Fig.1, the maximum DTG is reached at 900 °C, which indicates Fe_3O_4 is reduced by the coal char. Operation temperature is a key parameter to affect the reaction conversion. But melting or sintering of Fe_3O_4 may be caused at a high temperature and destroys the cyclic physical performance of the oxygen carriers. Therefore the temperature

should be kept at an appropriated value to reach a higher conversion rate and to avoid the sintering or the melting of the oxygen carrier.

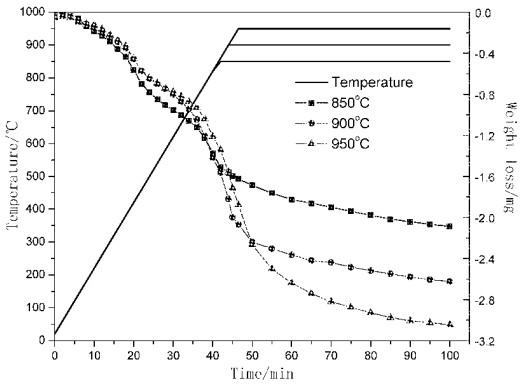

Fig.4 TG curves at different temperatures

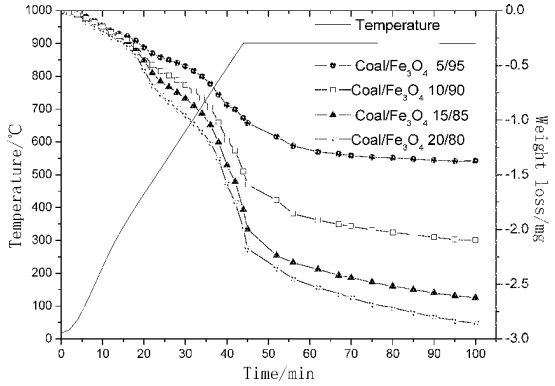

Fig. 5 TG curves with different coal to Fe_3O_4 mass ratios

Effects of different mass ratios

The mixtures with different coal to Fe_3O_4 mass ratios (5/95, 10/90, 15/85, and 20/80) were heated to 900°C with a heating rate of 20 k/min under N_2 atmosphere, and the total reaction time was kept for 100 minutes. The TG curves are shown in Fig.5. As we can see from Fig.5, the weight losses in the ratios of 5/95, 10/90, 15/85, and 20/80 are 1.37mg, 2.09mg, 2.62mg and 2.86mg and the weight loss rates are 9.1%, 14.0%, 17.5%, and 19.1% respectively. After a total reaction time of 100 minutes, the conversion rates are 29.5%, 40.8%, 46.5%, and 46.6% correspondingly. According to Reactions (1) and (3), the coal to oxygen carrier mass ratio is theoretically 3.4/96.6 if Fe_3O_4 is reduced to FeO by coal, while the ratio is 12/88 if it is reduced to Fe. The ratios were selected in the range of 5/95 and 20/80 to observe the effects of oxygen in the oxygen carrier on the conversion rate. With the increase of coal in the mixture, the conversion rate increases. The conversion rate at the coal to Fe_3O_4 mass ratio of 15/85 is 1.58 times that of 5/95, while the conversion rate of 20/80 is almost the same as that of 15/85. The increase of coal in the mixture leads to the increase of the volatile released from the coal and the increase of the reduction of Fe_3O_4 by the pyrolysis gas products. However, there exists an optimal mass ratio, which is near to the theoretical ratio of 12/88. When the mass ratio reaches the value, the conversion changes no more. In this research the mass ratio of coal to oxygen carrier is selected as 15/85.

CONCLUSIONS

The main conclusions from this work are:

(1) Fe_3O_4 was first reduced by coal volatile above 700 °C and then reduced by coal char at a temperature above 800 °C. Fe_3O_4 was fully reduced into FeO, while some FeO was further reduced to Fe, which was in agreement with the XRD analysis results of the mixture residues

(2) Temperature was a key parameter affecting the reduction conversion rate of Fe_3O_4 by coal. As the operation temperature rises, the conversion rate gets increased.

(3) There exists an optimal coal to Fe_3O_4 mass ratio. When the ratios were 5/95, 10/90, 15/85, and 20/80, conversion rates were 29.5%, 40.8%, 46.5% and 46.6% respectively. With the increase of coal, the conversion rate goes up. But it tends to keep unchanged when the mass radio of the coal to the oxygen carrier is about the theoretical ratio.

ACKNOWLEDGEMENTS

The authors thank the National Natural Science Foundation of China (50776018) and the Special Fund of the National Priority Basic Research of China (2007CB210101) for the financial support of this project.

REFERENCES

Alonso, M. J. G.; Borrego, A. G.; Alvarez, D.; Menendez, R. Fuel, 1999, 78(5): 1501-1513.
Berguerand, N.; Lyngfelt, A. Int. J. Greenhouse Gas Control, 2008(2): 169-179.
Berguerand, N.; Lyngfelt, A. Fuel, 2008, 87 (12): 2713–2726.
Chiesa, P.; Lozza, G.; Malandrino, A.. Int. J. Hydrogen Energy, 2008, 33(9): 2233 – 2245.
Consonni, S; Viganò, F.; Int. J. Hydrogen Energy 2005; 30(7): 701–718.

Damen, K.; Troost, M. V.; Faaij, A. Prog. Energy Comb. Sci. 2006, 32(2): 215-246.
Dennis, J.S.; Scott, S.A.; Hayhurst, A.N. Journal of the Energy Institute. 2006, 79 (3):187–190.
Fan, L.-S.; Li, F.-X.; Ramkumar, S. Particuology 2008, 6 (1): 131–142.
Gupta, P.; Velazquez-Vargas, L. G.; Fan, L-S. Energy Fuels,2007, 21(5): 2900-2908.
Hydrogen Program Plan - Hydrogen from Natural Gas and Coal: The Road to a Sustainable Energy Future. US Department of Energy, Office of Fossil Energy.
Ibarra, J.; Munoz, E.; Moliner, R. Org. Geo. 1996, 24(6-7): 725-735.
Ishida M, Yamamoto M, Ohba T. Energy Convers. Manage. 2002, 43(9-12):1469-1478.
Jin, H., Ishida, M. Ind. Eng. Chem. Res. 2002; 41(16): 4004–4007.
Leion, H.; Mattisson T.; Lyngfelt, A. Fuel, 2007, 86 (12-13):1947–1958.
Leion, H.; Mattisson, T.; Lyngfelt, A. Int. J. Greenhouse Gas Control, 2008, 2(2):180-193.
Mondal, K.; Lorethova, H.; Hippo, E. Fuel Processing Technol. 2004, 86 (1):33–47.
Pang, K.-L.; Xiang, W.-G.; Zhao, C.-S. J. Anal. Appl. Pyrolysis 2007, 80 (1):77–84.
Piotrowski, K.; Mondal, K.; Wiltowski, T. J. Chem. Eng., 2007,131 (1-3): 73–82.
Piotrowski, K.; Mondal, K.; Lorethova, H. Int. J. Hydrogen Energy, 2005, 30 (15):1543 – 1554.
Richard, L.; Shobha, P.; Yang, X.-D.; John; H. Fuel Process Technol. 1999, 59 (1): 35-50.
Svoboda, K.; Slowinski, G.; Rogut, J. Energy Convers. Manage. 2007, 48 (12): 3063–3073.
The Hydrogen from Coal Research, Development, and Demonstration Plan. US Department of Energy, Office of Fossil Energy.
Velazquez-Vargas, L. G.; Gupta, P. 23rd Annual International Pittsburgh Coal Conference, PCC - Coal- Energy, Environment and Sustainable Development. Sep 25-28 2006 Pittsburgh, PA, United States International Pittsburgh Coal Conference, Pittsburgh, PA 15261, United States.
Xiang, W.-G.; Chen, Y.-Y. Energy Fuels .2007, 21(4): 2272-2277.

DESIGN AND COLD MODE EXPERIMENT OF DUAL BUBBLING FLUIDIZED BED REACTORS FOR MULTIPLE CCR CYCLES

F. Fang, Z. S Li, N. S. Cai

Key Laboratory for Thermal Science and Power Engineering of Ministry of Education, Department of Thermal Engineering, Tsinghua University, Beijing, 100084,China

Abstract: The dual fluidized bed reactors are the key technology to fulfill the multiple CCR (calcination/carbonation reactions) cycles for CO_2 capture from the flue gases. Firstly, the dual bubbling fluidized bed reactors were selected in this work based on analyzing different types of dual fluidized bed reactors. Secondly, the design method of dual fluidized bed reactors for CO_2 capture with CCR concept was proposed. Thirdly, with the designed results, a cold mode of the dual bubbling fluidized bed reactors was built. The long-term stable operation and the continuous solid circulation between two reactors could be achieved successfully. The experimental results indicated that the solid circulation rate was increased with an increase of bed height, diameter of solid injection nozzle, and diameter of holes on the solid injection nozzle.

Keywords: dual fluidized bed reactors, solid circulation rate, CO_2 separation

INTRODUCTION

The environmental impact of anthropogenic CO_2 emissions is now recognized to be the major risk to mankind, because the CO_2 emissions into the atmosphere have been reported to account for half of the greenhouse effect which causes the global warming. Therefore, reducing the CO_2 emissions will be the greatest industrial challenge of the 21st century. CO_2 (or carbon) capture and storage (CCS) has the potential to make a significant contribution to reduce CO_2 released from large point sources. CCS aims to reduce CO_2 emissions by capturing CO_2 from industrial (power, cement, steel) processes that burn fossil fuels, and storing the CO_2 in deep saline aquifers, depleted oil/gas fields, deep coal seams, or deep ocean reservoirs to allow the continued use of coal, oil and gas whilst avoiding the CO_2 emissions currently associated with fossil fuel use. The estimated costs for CO_2 transport (U.S. \$1-3 per ton per 100 km (Freund, 2003)) and sequestration (U.S. \$4-8 per ton of CO_2 (Lyngfelt et al., 2001)) are small compared to the cost for CO_2 capture, estimated at U.S. \$35-55 per ton of CO_2 captured (Singh et al., 2003). Therefore, appropriate CO_2 capture approaches are the absolute focuses of CCS.

There are various approaches to separate CO_2 from flue gas streams. This paper focuses on the use of the multiple carbonation/calcination reaction (CCR) cycles with Ca-based sorbents as shown in Fig. 1. The overall system consists of two fluidized bed reactors; one is the carbonator and the other the regenerator. In the carbonator, CaO is carbonated to $CaCO_3$ at a relatively low temperature in the flue gas (about 600-700°C) at atmospheric pressure:

$$CaO(s)+CO_2(g)\rightarrow CaCO_3(s) \quad (1)$$

$$CaCO_3(s)\rightarrow CaO(s)+CO_2(g) \quad (2)$$

For continuous processes, the CO_2 sorbents must be regenerated after the carbonation reaction to be used repeatedly. Accordingly, the $CaCO_3$ is then removed from the carbonator and delivered to the regenerator. The calcination of $CaCO_3$ regenerates the sorbent to CaO and produces a concentrated stream of CO_2 at higher temperatures (>900 °C).

In the CCR cycles, CO_2 sorbent circulates between the carbonator and the regenerator, and the dual fluidized bed reactors being connected with solid transportation lines are considered to be a suitable system. Therefore, the dual fluidized bed reactors are the key technology to fulfill the multiple cyclic CCR process for CO_2 capture. In this paper, the dual bubbling fluidized bed reactors were selected based on analyzing different forms of dual fluidized bed reactors, then a detailed design of this type of dual fluidized bed reactors was presented and the cold mode of the dual bubbling fluidized bed reactors were built. Finally, based on the cold model of dual bubbling fluidized bed reactors, the effects of structure and operation conditions on the solids circulation rate and gas leakage were investigated, for giving useful information for the design of the hot state dual fluidized-bed CO_2 capture system.

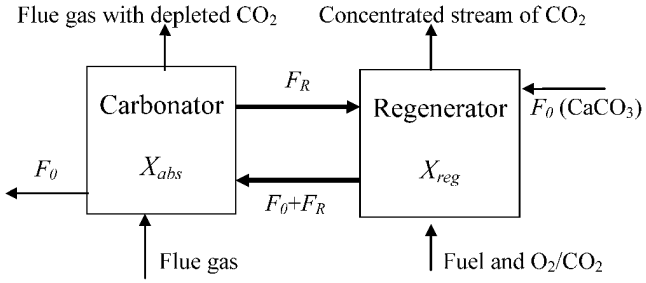

Fig. 1 Schematic of carbonation/calcination cycles using Ca-based sorbents

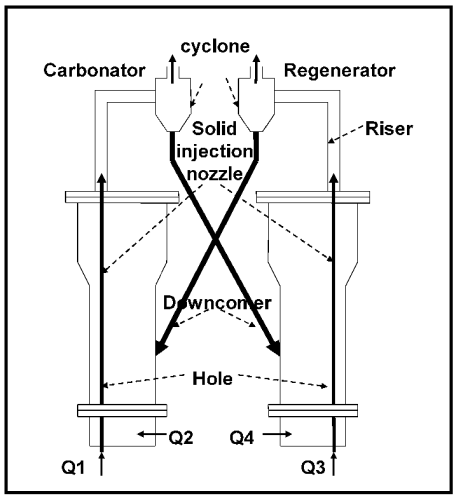

Fig. 2 Schematic of the dual bubbling fluidized bed reactors

TYPE OF DUAL FLUIDIZED BED REACTOR

The CCR process consists of the dual fluidized bed reactors, which are carbonator and regenerator, both operating at atmospheric pressure and being connected with solid transportation lines. There are four types of dual fluidized bed reactors, which are (1) dual bubbling fluidized bed reactors, (2) dual high velocity fluidized bed reactors, (3) a bubbling fluidized bed reactor as the regenerator and a high velocity fluidized bed reactor as the carbonator, and (4) a bubbling fluidized bed reactor as the carbonator and a high velocity fluidized-bed reactor as the regenerator. For the CCR process, the main role of the regenerator is to regenerate the sorbents, and it needs not to deal with large amount of gas in multiple calcination processes, so the bubbling fluidized bed reactor is considered to be appropriate as the regenerator, in which the $CaCO_3$ can be calcined more completely. Therefore, there are two types of dual fluidized bed reactors which are suitable for CCR process respectively: (1) the dual bubbling fluidized bed reactors and (2) a bubbling fluidized bed reactor as the regenerator and a high velocity fluidized bed reactor as the carbonator. The advantage of using the high velocity fluidized bed reactor as the carbonator is to dispose more flue gases, but the CO_2 in flue gases may not be absorbed efficiently if the height of carbonator is not enough and the attrition will be increased because of high gas velocity. If we use the bubbling fluidized bed reactor as the carbonator, the gas-solid contact is sufficient, and the CO_2 in flue gases is expected to be absorbed efficiently.

In this paper, the dual bubbling fluidized bed reactors were selected as a lab scale system to capture CO_2, and the schematic of the dual bubbling fluidized bed reactors can be seen in Fig. 2. This type of dual bubbling fluidized bed reactors, which is based on Ryu's dual fluidized beds (Ryu et al. 2007), consists of two bubbling fluidized bed reactors, solid injection nozzles, risers, cyclones and downcomers. In practical applications, the flue gas can be injected to the carbonator by Q2 and is reacted with the sorbents in the carbonator. For any process using carbonation/calcination cycles, the gas at the outlet of the regenerator must be in a rich CO_2 atmosphere and the decomposition of $CaCO_3$ is endothermic, so the O_2/CO_2 mixture is injected by Q4. There are holes on the solid injection nozzle, and the sorbents in the reactors go into the solid injection nozzles from the holes and are carried to the risers by the gases from Q1 or Q3. Then, the sorbents go to the other reactor through the risers, the cyclones and the downcomers.

DESIGN OF THE DUAL BUBBLING FLUIDIZED BED REACTORS

There are two critical parameters when we design the dual fluidized bed reactors: (1) reactors size, which must be adequate to carry enough bed material for a sufficient conversion of reacting gas, and (2) the solid circulation rate between the carbonator and the regenerator, which must be high enough to transfer the regenerated sorbents necessary for the CO_2 capture.

Eq. (3) represents the amount of absorbed CO_2 in the carbonator $F_{CO_2} = F_{CO_2,\ in} - F_{CO_2,\ out}$ (kmol/s) (3)

The mass of absorbed CO_2 is therefore $\dot{m}_{CO_2} = 44 \cdot F_{CO_2}$ (kg/s) (4)

The conversion of CaO, X, is the actual mass of CO_2 absorbed divided by the mass of CO_2 that would be absorbed if the sorbent was fully carbonated, as

$$X = \frac{M_{\text{actual}} - M_{\text{f,reg}}}{M_{\text{f,abs}} - M_{\text{f,reg}}} \tag{5}$$

The solids in the two reactors are assumed to be well mixed, and the conversion of the sorbents is equal to the conversion of the solid flows living these reactors. Since CO_2 is transferred from the carbonator to the regenerator, the average conversion in the carbonator, X_{abs}, is higher than that in the regenerator, X_{reg}. The difference in conversion is shown by Eq. (6). It should be noticed that in practical applications, because the calcination is much faster than carbonation, it is assumed that $CaCO_3$ is decomposed completely in the regenerator; therefore, X_{reg} equals to zero in the following (Li et al., 2008). It is assumed that the size of the regenerator is equal to that of the carbonator in this work.

$$\Delta X = X_{\text{abs}} - X_{\text{reg}} \tag{6}$$

The solid material balance is

$$(F_{\text{R}} + F_0)\Delta X = F_{\text{CO}_2} \quad \text{(kmol/s)} \tag{7}$$

Eq. (8) was adopted to describe the activity decay of sorbents (Fang et al., 2009)

$$X_{\text{abs}} = \frac{afF_0}{F_0 + F_{\text{R}}(1-f)} + b \tag{8}$$

Then the first critical parameter, the solid circulation rate, can be calculated by Eqs. (9) and (10):

The solid circulation rate from the carbonator to the regenerator

$$m_{sol} = F_R M_{CaO}(1 - X_{abs}) + F_R M_{CaCO_3} X_{abs} \tag{9}$$

The solid circulation rate from the regenerator to the carbonator

$$m_{sol,reg} = (F_R + F_0) M_{CaCO_3} \tag{10}$$

The capacity of the sorbent, C, defined as the ratio of a fractional mass increase to an increase in conversion as (Lyngfelt et al. 2001)

$$C = \frac{1}{m}\frac{\mathrm{d}m}{\mathrm{d}X} \tag{11}$$

After some manipulation, the capacity can be expressed as a function of the conversion for the carbonator

$$C_{\text{abs}} = \frac{R_0}{1 - (1 - X_{\text{abs}})R_0} \tag{12}$$

Eq. (13) presents the capacity for CO_2 carrying of the sorbents

$$R_0 = (M_{\text{f,abs}} - M_{\text{f,reg}}) / M_{\text{f,abs}} \tag{13}$$

Therefore, the bed mass can be given by

$$m_{\text{bed,abs}} = \dot{m}_{\text{CO}_2} \Bigg/ \left(C_{\text{abs}} \cdot \overline{\frac{dX_{abs}}{dt}} \right) \quad \text{(kg)} \tag{14}$$

$\overline{\frac{dX_{\text{abs}}}{dt}}$ is the average carbonation rate. From Fig. 3, there must be sorbent undergoing 1~N cycles in the carbonator. Their carbonation rates are different. The estimation of the average carbonation rate of sorbents in the system, $\overline{\frac{dX_{\text{abs}}}{dt}}$, requires the knowledge of the population of sorbents in the carbonator in terms of the carbonation/calcination cycle numbers that they have experienced. The mass fraction of sorbents, r_{N}, entering the carbonator in the solid stream F_0+F_{R}, which have circulated N times is calculated from a succession of mass balances (Abanades, 2002)

$$r_{\text{N}} = \frac{F_0 F_{\text{R}}^{N-1}}{(F_0 + F_R)^{\text{N}}} \tag{15}$$

Therefore, the average carbonation rate is

$$\overline{\frac{\mathrm{d}X_{\text{abs}}}{\mathrm{d}t}} = \sum_{N=1}^{N=\infty} \frac{F_0 F_{\text{R}}^{N-1}}{(F_0 + F_R)^{\text{N}}} \cdot \overline{\frac{\mathrm{d}X_{\text{N}}}{\mathrm{d}t}} \tag{16}$$

where $\overline{\frac{dX_N}{dt}}$ is the average carbonation reaction rate of sorbent undergoing the N cycle in the carbonation processes.

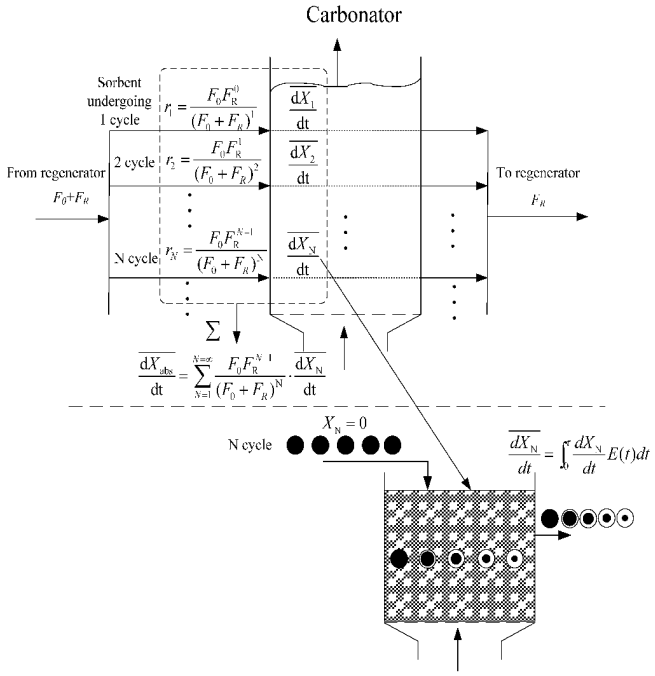

Fig. 3 Average carbonation reaction rate

The sorbent undergoing the same cycle must have different residence time in the carbonator. Consider the reactor of Fig. 3 here, with a constant feed rate of both solid and gas, the solids being of uniform size in the carbonator. The carbonation reaction rate of an individual particle of solid depends on its length of stay in the bed. For this reason, the reaction rate level varies from particle to particle which all have circulated N times in the carbonation/calcination cycles. So on accounting for this, the average carbonation reaction rate of the exit stream of solids undergoing the N cycle is

$$\begin{pmatrix}\text{average carbonation}\\ \text{reaction rate of sorbents}\\ \text{in the leaving solids}\end{pmatrix} = \sum_{\substack{\text{particles}\\ \text{of all ages}}} \begin{pmatrix}\text{carbonation reaction}\\ \text{rate of sorbents staying in}\\ \text{the carbonator for the time}\\ \text{between } t \text{ and } t+dt\end{pmatrix}\begin{pmatrix}\text{fraction of exit}\\ \text{stream that stays this}\\ \text{length of time in the}\\ \text{carbonator}\end{pmatrix}$$

In symbols,

$$\overline{\frac{dX_N}{dt}} = \int_0^\tau \frac{dX_N}{dt} E(t)dt \tag{17}$$

where the exit age distribution for the solids in the carbonator is

$$E(t) = \frac{1}{\tau_{abs}} \exp\left(-\frac{\tau}{\tau_{abs}}\right) \tag{18}$$

$\frac{dX_N}{dt}$ is presented as (Fang et al. 2009)

$$\frac{dX_N}{dt} = k_c \left(1 - \frac{X_N}{X_{u,N}}\right)^{2/3} (\overline{C} - C_{eq,CO_2}) \tag{19}$$

After mathematic manipulation

$$\overline{\frac{dX_{abs}}{dt}} = \sum_{N=1}^{N=\infty} \frac{F_0 F_R^{N-1}}{(F_0 + F_R)^N} \lambda_{abs} (\overline{C} - C_{eq,CO_2}) \tag{20}$$

where

$$\lambda_{abs}=k_c X_{u,N}^{-\frac{2}{3}}\{X_{u,N}^{\frac{2}{3}}-(X_{u,N}^{\frac{1}{3}}-a_{abs}\tau)^2 e^{-\frac{\tau}{\tau_{abs}}}-2a_{abs}\tau_{abs}[X_{u,N}^{\frac{1}{3}}-(X_{u,N}^{\frac{1}{3}}-a_{abs}\tau)e^{-\frac{\tau}{\tau_{abs}}}]+2(a_{abs}\tau_{abs})^2(1-e^{-\frac{\tau}{\tau_{abs}}})\} \quad (21)$$

$$a_{abs}=\frac{1}{3}k_c X_{u,N}^{-\frac{2}{3}}(\overline{C}-C_{eq,CO_2}) \quad (22)$$

τ_{abs} is the average solid residence time in the carbonator, as

$$\tau_{abs}=\frac{m_{bed,abs}}{(F_0+F_R)(1-X_{abs})M_{CaO}+(F_0+F_R)(1-X_{abs})M_{CaO}} \text{ (s)} \quad (23)$$

The bed mass, $m_{bed,abs}$, was iteratively calculated by Eqs. (12)~(23), then the height of the carbonator is:

$$h_{abs}=m_{bed,abs}/[\rho_{abs}(1-\varepsilon_{abs})(0.25\pi d^2)] \text{ (m)} \quad (24)$$

The chosen or assumed parameters value a lab-scale carbonation reactor used here were presented in Table 1.

Table 1 Chosen or Assumed Parameters Values

Inlet flue gases	CO_2 bulk fraction in the flue gases	Carbonation temperature T_{abs}	Diameter of reactor d	Constant a (fang et al. 2009)
5.0 Nm^3/h	15%	650 °C	0.14 m	1.75
Constant b (fang et al. 2009)	Constant f (fang et al. 2009)	X_{abs}	void fraction in the carbonator ε_{abs}	carbonation rate k_c
0.063	0.56	0.13	0.5	0.0021 $m^3/(mol\cdot s)$

RESULTS AND DISCUSSION

Eqs. (3)-(23) together with the values of Table 1 gave the results of the reactor design: the lowest height of the reactor was 0.25 m and the lowest circulation rate was 4 g/s. Based on the design results, the cold mode of dual bubbling fluidized bed reactors was built. The air was used as the fluidized gas. The particles used here were glass microspheres with a bulk density of 1526 kg/m^3 which were similar to the bulk density of CaO particles. All the particles were between 200 and 300μm in size. When the dual fluidized bed reactors works steadily, we diverted solid flow from downcomer to measure the solid circulation rate based on the weight of solids and time (Rye et al., 2007).

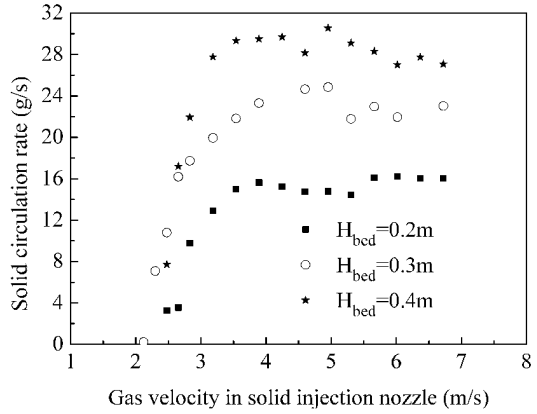

Fig. 4 Solid circulation rate with the different solid mass in the fluidized bed

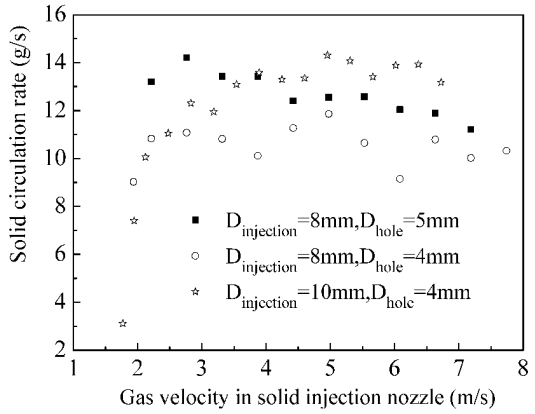

Fig. 5 Solid circulation rate with the different size of the injection nozzle

The long-term stable operation and the continuous solid circulation between two reactors could be achieved and the amount of circulation rate was met the need of designing. Rye (Rye et al., 2007) found that the structure of the injection nozzle and the operation condition may affect the amount of circulation rate between the two reactors. Therefore, the operation condition and injection nozzle structures were changed to test solid circulation rate between the two fluidized bed reactors.

Figure. 4 shows the solid circulation rate with the different solid mass in the fluidized bed reactors (U_{bed}=0.108 m/s, $D_{injection}$=10 mm, D_{hole}= 6 mm). From Fig. 4, the solid circulation rate increased with an increasing of the gas velocity in the solid injection nozzle firstly and was stable when the gas velocity was high enough. The solid circulation rate also increased as the amount of sorbents in the reactors increasing. Fig. 5 shows the solid circulation rate with the different size of the solid injection nozzle (U_{bed}=0.108 m/s, H_{bed}=0.3 m). As can be seen from Fig. 5, when we increased the diameters of the injection nozzle and the diameters of

the holes on the injection nozzle, the solid circulation rate was increased. Therefore, we could control the amount of solid circulation rate by changing the gas velocity in the solid injection nozzles, the amount of sorbents in the reactors, and the structure of the nozzles. The gas leakage was also an important parameter for the design of a dual fluidized bed system (Lyngfelt et al. 2001), besides the size of the reactor and the solid circulation rate. Rye found that there was no gas mixing between the two bubbling fluidized beds and nearly no gas leakage from the solid injection nozzle to the bubbling fluidized bed (Rye et al., 2007). However, as can be seen in Fig. 6, there were ~7.5% gas leaked from the reactors to the injection nozzles by the holes on the injection nozzles, when CO_2 gas was added as the tracer gas to solid injection nozzle for investigating the gas leakage (U_{bed}=0.108 m/s, $D_{injection}$=8 mm, D_{hole}= 4 mm, H_{bed}=35 cm).

From Fig. 7 (U_{bed}=0.108 m/s, D_{hole}= 4mm, $D_{injection}$=8 mm), the solid circulation rates had negligible difference when the solid heights above the hole on the solid injection nozzle were same. Therefore, we could increase the height of the hole on the solid injection nozzle with the CO_2 in the flue gas efficiently absorbed before leakage.

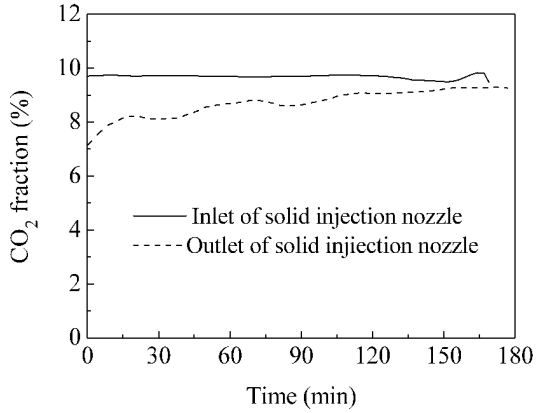

Fig. 6 CO_2 fraction at the outlet and inlet of the injection nozzle

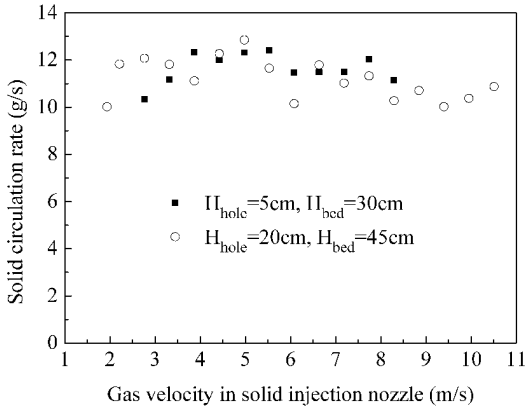

Fig. 7 Solid circulation rate with different height of holeon the injection nozzle

CONCLUSIONS

The dual bubbling fluidized bed reactors were selected in this work to be the lab scale dual fluidized bed system to capture CO_2 based on analyzing different forms of dual fluidized bed reactors. When designing this type of reactors system, the effect of many parameters, such as mass balance, sorbent circulation rate, sorbent activity loss, and average carbonation kinetic rate etc, on the structures of the reactors is required to be clarified. With the proposed design method and calculated results, a cold mode of dual bubbling fluidized bed reactors was built and the long-term stable operation and the continuous solid circulation between two reactors were achieved successfully.

The experimental results indicated that the solid circulation rate was increased with an increase of amount of bed material, diameter of solid injection nozzle and diameter of holes on solid injection nozzles. The gas leakage between the solid injection nozzle and the reactors was measured by adding CO_2 as the tracer gas into the injection nozzles. The results indicated that there was gas leakage from the reactors to the solid injection nozzles and it needed to increase the height of the hole on the solid injection nozzle to prevent gas leakage.

NOTATIONS

a,b constants (Fang et al. 2009)
$C_{eq,CO2}$ equilibrium concentration of CO_2 over CaO, mol/m^3
$\overline{C}$ average CO_2 concentration in carbonation process, mol/m^3
$D_{injection}$ diameter of the injection nozzle, mm
D_{hole} diameter of the hole on the injection nozzle, mm
f constants (Fang et al. 2009)
$F_{CO2,in}$ molar flow rate of the inlet CO_2 in the flue gas, kmol/s
$F_{CO2,out}$ molar flow rate of the inlet CO_2 in the flue gas, kmol/s
F_0 molar flow rate of fresh sorbent added, kmol/s
F_R molar flow rate of circulation sorbent from carbonator to regenerator, kmol/s
H_{bed} height of sorbents in the reactor, m

H_{hole} height of hole above distributor plate, cm
k_c carbonation rate constant, $m^3/(mol \cdot s)$
M_{actual} actual molar mass of the sorbent in carbonated state, kg/kmol
$M_{f,abs}$ molar mass of the fully carbonated sorbent, kg/kmol
$M_{f,reg}$ molar mass of the fully calcined sorbent, kg/kmol
M_{CaO} CaO molecular weight, kg/kmol
M_{CaCO3} $CaCO_3$ molecular weight, kg/kmol
t time, s
U_{bed} fluidized velocity, m/s
$X_{u,N}$ final carbonation conversion in the bed at Nth cycle
τ_{abs} average solid residence time in carbonation, $\tau_{abs} = \frac{m_{bed,abs}}{m_{sol,abs}}$, s

REFERENCES

Abanades, J. C.: Chem. Eng. J. **90** (2002), pp. 303-308.
Alberto, A., Juan, A., and Francisco G. L.: Chem. Eng. Sci. **62** (2007), pp. 533-549.
Li, Z. S., Cai, N. S. and Croiset, E.: AIChE Journal, **54** (2008), pp. 1912-1925.
Fang, F., Li, Z. S., Cai, N. S.: Energy & Fuels, in press
Freund, P.: Proc. Inst. Mech. Eng. **217** (2003), pp. 1-7.
Lyngfelt, A., Leckner, B. and Mattisson, T.: Chem. Eng. Sci. **56** (2001), pp. 3101-3113.
Ryu, H. J., Lee S. Y., Park, Y. C. and Park, M. H.: Proceedings of World Academy of Science, Engineering and Technology, **22** (2007), pp. 169-174.
Singh, D., Croiset, E., Douglas, P. L. and Douglas, M. A.: Energy Convers. and Manag. **44** (2003), pp. 3073-3091.

ACKNOWLEDGEMENT

This work was supported by the National Basic Research Program of China (2006CB705807) and the National Natural Science Funds of China (No. 50806038).

ROLE OF THE WATER-GAS SHIFT REACTION IN CO_2 CAPTURE FROM GASIFICATION SYNGAS USING LIMESTONES

D.Y. Lu, R.T. Symonds, R.W. Hughes and E. J. Anthony

CANMET Energy Technology Centre-Ottawa,Natural Resources Canada, Ottawa, Canada

Abstract: The work in this paper aims at determining the effect of gasification syngas on the carbonation reaction and conversion for several naturally occurring calcium-based sorbents. Experiments were performed *via* the use of a thermogravimetric analyzer (TGA) and it was observed that the presence of CO and H_2 caused an increase in initial rate of approximately 70.6%. The increase in reaction rate was attributed to the CaO surface sites catalyzing the water-gas shift reaction; as well, the shift reaction was assumed to be responsible for the increase in activation energy for limestone based on the formation of intermediate complexes.

A pilot-scale dual fluidized bed reactor system was applied to further investigate the effect of the shift reaction on CO_2 capture and sorbent conversion for two limestones (Polish and Cadomin limestone). During carbonation with steam present in the feed gas, it was observed that the high CO_2 capture period was significantly extended as compared to carbonation with only CO_2 present. This resulted in an increase in CaO conversion from approximately 16.1 to 29.7% for the initial carbonation cycle and reinforced the conclusions drawn *via* TGA experimentation. Based on the outlet gas analysis, it was confirmed that the CaO particles were in fact catalyzing the water-gas shift reaction, increasing the overall sorbent conversion to approximately 46.9% for the first cycle. In terms of sorbent regeneration, the oxy-fuel combustion conditions employed (high CO_2 and O_2 atmosphere), resulted in enhanced sorbent sintering, thus producing the negative effect on carbonation conversion.

Keywords: CO_2 capture, CaO-sorbent looping, shift reaction, gasification.

INTRODUCTION

Integrated gasification combined cycle (IGCC) systems have the potential to achieve near-zero or zero emissions of CO_2 if the CO in the syngas from the gasifier is converted to CO_2 through a water-gas shift process (Rx 1) and the CO_2 is separated from hydrogen. Henderson (2005) summarized that the removal of CO_2 would be carried out in an acid gas removal plant that would also remove the sulphur gases through absorption by amine solutions, chilled methanol (Rectisol process), or mixtures of dimethylethers of polyethyleneglycol (Selexol process). The amine process requires high thermal energy for regeneration of the solvent. The Rectisol process is complex and very expensive because of its need of refrigeration. The Selexol process can be more expensive than the amine process, and the chilling option could further increase the process costs (Pennline et al., 2007). Moreover, sulphur present in the syngas is poisonous to shift catalysts and is normally removed before the shift reaction; therefore, two absorption steps would be required. The high cost associated with current CO_2 separation technologies has necessitated development of economical alternatives. Dry absorption processes for CO_2 separation employing physical and chemical sorbents such as limestone and dolomite, *via* the reaction between CaO and CO_2 (Rx 2), are thought to be technically feasible and economically advantageous in a high-temperature process to control CO_2 emissions (Abanades et al., 2004; MacKenzie et al., 2007).

$$CO + H_2O = CO_2 + H_2 \quad (1)$$

$$CO_2 + CaO = CaCO_3 \quad (2)$$

Since the shift reaction is limited by reaction equilibrium, the sorption process of Rx 2, which lowers the partial pressure of CO_2, would move the equilibrium toward the product side. The overall reaction is

$$CO + H_2O + CaO = CaCO_3 + H_2 \quad (3)$$

As a result more hydrogen is produced, and the solid product, $CaCO_3$, would be easily separated from the gas. Regeneration of the sorbent and recovery of the sorbed CO_2 can be achieved in a calciner which operates at higher temperatures to decompose $CaCO_3$ *via* the reversible reaction, Rx 2 (Shimizu *et al.*, 1999; Lu *et al.*, 2008).

This would result in nearly pure CO_2, which merges with the CO_2 from $CaCO_3$ for use or sequestration. The CaO is sent back to the shift reactor for subsequent sorption of CO_2. A simplified schematic for this process is given in Fig. 1. Experimental analysis has shown that reaction equilibrium can be closely approached.

As temperature increases, the reaction rate increases and the partial pressure of CO_2 also increases. But even at 600°C, where the carbonation reaction (Rx 2) is reasonably fast, the equilibrium partial pressure of CO_2 is only 0.3%, or in other words, high CO_2 removal is possible (Anthony, 2008). The thermal efficiency of systems using dual fluidized beds (FB) for carbonation and sorbent regeneration have been shown to be comparable to conventional combustion systems without CO_2 segregation (Hughes *et al.*, 2005; MacKenzie *et al.*, 2007). Both the internal and external solids transport and gas-solid reactions, such as absorption and desorption, are greatly enhanced by the FB's material circulation, which results in excellent mixing of the reactants. This in turn maximizes both heat and mass transfer, resulting in higher rates of reaction.

To date there has been significant research on the effect of CO_2 feed gas partial pressures on the reaction kinetics of the CaO-CO_2 reaction (Bhatia and Perlmutter, 1983; Kyaw et al., 1996; Sun et al., 2008). The reaction kinetics have been applied to both methane steam reforming (Lee et al., 2004) and water-gas shift processes (Han and Harrison, 1994) utilizing CaO for in-situ CO_2 removal to enhance the production of H_2. Unfortunately, little or no work has been performed on determining if the presence of methane steam reforming feed/product gases (CH_4, H_2O/CO, H_2) or water-gas shift feed/product gases (CO, H_2O/H_2) have an effect on the carbonation reaction kinetics or sorbent deactivation. Thus, the main object of this work is to investigate the effect of gasification syngas on the gas-solid carbonation reactions in a lab-scale pressurized thermogravimetric analyzer (TGA) unit and in a pilot-scale dual-fluidized bed system.

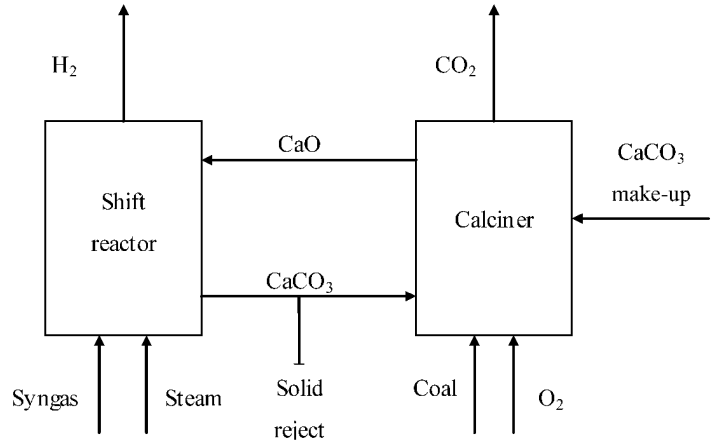

Fig. 1 Schematic for H_2 production with CO_2 capture using sorbent looping process in gasification

EXPERIMENTAL

Sorbents

Initially, three limestone sorbents were selected for testing but due to an excessive loss of material through attrition after the initial calcination, one sorbent was removed from experimentation. Thus, based on the criterion that the material must have a minimal loss due to attrition, only two limestones were chosen for further testing. These two naturally occurring limestones were Piasek Wapienny limestone (which will be referred to as Polish limestone) and Cadomin limestone from Canada, and the chemical analysis determined *via* X-ray diffraction (XRD) of each is provided in Table 1.

Table 1 XRD chemical analysis of Polish and Cadomin limestone (in %wt)

Sorbent	SiO_2	Al_2O_3	Fe_2O_3	TiO_2	P_2O_5	CaO	MgO	SO_3	Na_2O	K_2O	LOF
Polish Limestone	0.85	0.24	0.09	<0.03	<0.03	54.10	0.89	<0.100	<0.200	0.06	43.64
Cadomin Limestone	1.30	0.40	0.11	0.04	<0.03	50.64	3.28	<0.100	<0.200	0.14	43.99

From Table 1, the purity of each sorbent is 95.6 and 90.0% CaO for Polish and Cadomin limestone, respectively, where the lower CaO purity for Cadomin is offset with an increased MgO content. Since the sorbents were to be calcined and carbonated under bubbling fluidized bed conditions, the particle size range was of great importance. From sieve analyses, the surface-to-volume mean diameters are approximately 512 and 612 μm for the raw Polish and Cadomin limestones, respectively. To lower the minimum bubbling fluidization velocity (*i.e.*, to minimize the amount of feed gas), the upper limit on the particle size was set at approximately 1.4 mm.

Thermogravimetric analyzer system

Figure 2 is a schematic drawing of a high-pressure TGA system, comprised of a hang-down tube reactor column made of Inconel 600 alloy with an inner diameter of 0.025 m. Housed within the reactor column is a sample tray (which holds the limestone samples) suspended from a Cahn 1000 Electrobalance with 1 μg sensitivity. Gas cylinders containing N_2, CO_2, and a mixed gas (10% CO_2, 25% CO, 50% H_2 and 15% N_2) allow gas mixing at the inlet of the reactor column. Dwyer mass flow controllers (0-100 mL/min) are used to accurately control the gas flow rates to obtain desired feed gas concentrations. Steam is fed to the reactor inlet *via* a Harvard PHD 440 syringe pump and steam generator. Feed lines containing both steam and the mixed gas are insulated and electrically heat traced to ensure no steam condensation. System temperatures are monitored using K-type thermocouples located at the steam generator, reactor inlet, sample tray, electric heater, and reactor outlet. A purge gas (typically N_2) is top-fed through the balance into the reactor column to ensure the sensitive balance electronic components do not overheat and that reaction gases do not enter the balance housing. Outlet gases are subsequently cooled, by passing through a double-tube heat exchanger, and vented to the atmosphere. The detailed information about the experimental setup, operation and control can be found in the reference by Sun *et al.* (2007).

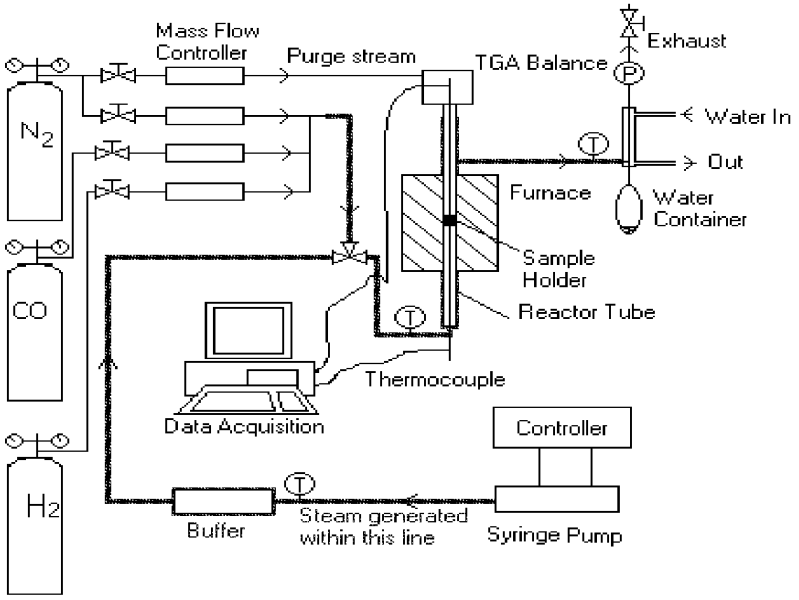

Fig. 2 Schematic drawing of ressurized thermogravimetric analyzer (TGA) system

The run conditions include the carbonation of a limestone and dolomite over the temperature range of 580 to 700°C under both syngas and non-syngas conditions. Calcination is performed both under N_2 and N_2/CO_2 conditions with an associated calcination temperature of 850 and 915°C, respectively. In each case, the system was run under atmospheric pressure for 10 cycles using particles in the size range of 250-425 μm.

Pilot-scale dual fluidized bed system

The pilot-scale dual fluidized bed system for the calcium looping process to simultaneously capture CO_2 and promote the water-gas shift reaction is illustrated in Fig. 3. The system is comprised of two separate fluidized bed reactors: a sorbent calciner, which is a circulating fluidized bed combustor (CFBC) that can run under either air- or oxy-fuel-firing mode using recycled flue gas; and a carbonator that is capable of operating under synthesized combustor flue gas or gasification syngas conditions. Each reactor is comprised of one 100 mm ID pipe surrounded with three 4.5 kW electric heaters that provide supplemental heating during start-up operation. In the case of the calciner, an additional insulated pipe riser section with an identical internal diameter is placed above the bottom section resulting in a total reactor length of approximately 4.5 m. Similar to the calciner, the carbonator has an additional 1 m refractory/insulated-lined section added above the heated section (100 mm ID), giving a total reactor length of 2 m. For both reactors instrumentation ports are distributed at approximately 0.3 m intervals over the total length of the risers. For more information concerning the experimental setup/operation of the calcination reactor system including, primary/secondary reactor entrance flows, fuel/sorbent feeding, gas recycle, and solids transfer please refer to the work of Lu *et al.*, (2008).

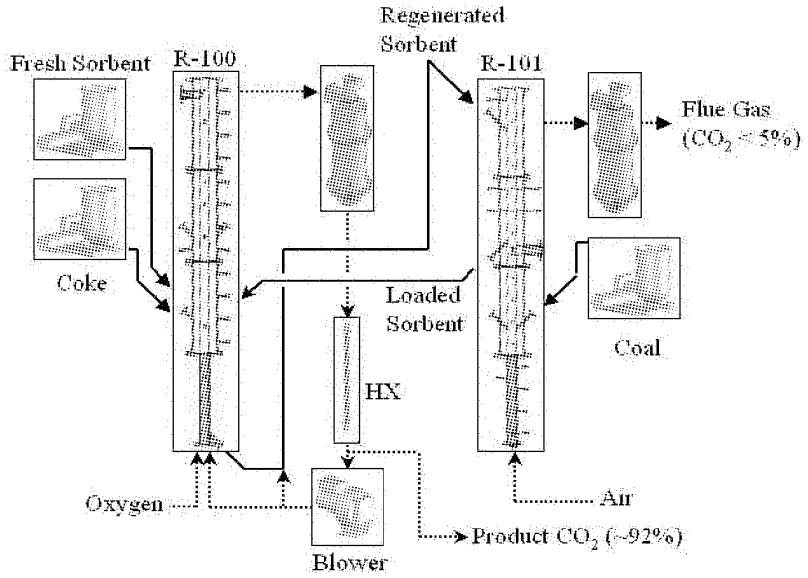

Fig.3 Schematic of the pilot-scale dual fluidized sorbent looping facility

It was of particular interest to observe the effect of calcination conditions on the overall performance of the limestone sorbents; thus, the sorbents were calcined under two conditions. The first condition was calcination in air and the second was with oxy-fuel. The approximate gas compositions in the bed are listed in Table 2. Under oxy-fuel conditions the CO_2 concentration in the bed is significantly higher than under air conditions, as the flue gas leaving the calciner is recycled (the main objective is to produce high-concentration CO_2 suitable for sequestration directly).

Biomass (wood pellets) was burned to bring the calciner up to reaction temperature. Based on Rx 1, under oxy-fuel calcination, the temperature required for complete calcination of the limestone sorbents is significantly higher, and calcination temperatures used during the operations for both limestones are higher than the theoretical equilibrium temperatures required to achieve full calcinations in a satisfactory timeframe (860°C for O_2-enhanced air combustion and 910°C for oxy-fuel combustion, respectively).

Table 2 Gas compositions, fuel feed rate, and oxygen flow rate for Polish and Cadomin limestone under air and oxy-fuel calcination conditions

Sorbent	Calcination Condition	Composition (vol%)				Fuel Feed Rate (kg/h)	Oxygen Flow Rate (SLPM)
		N_2	O_2	CO_2	CO		
Polish Limestone	Air	48.97	6.3	43.7	1.030	1.5	40
	Oxy-Fuel	8.33	7.0	84.2	0.474	1.7	70
Cadomin Limestone	Air	50.44	4.9	43.6	1.061	1.5	45
	Oxy-Fuel	4.27	2.4	91.8	1.533	1.7	65

Similar to the TGA experiments, it was of particular interest to observe the effect of carbonation conditions on the overall performance of the limestone. Thus, the sorbent was carbonated under three conditions: air/CO_2, air/CO_2/steam, and N_2/syngas, where the approximate feed gas compositions can be found in Table 3. It should be noted that during the initial stage of carbonation, where the CO_2 capture is kinetically limited, the temperature remained relatively constant. Once the CO_2 concentration at the carbonator outlet began to increase significantly (diffusion limited), the temperature was raised to increase the driving force. The procedure was repeated when necessary and, after roughly a 70-min carbonation period, the CO_2 flow was shut off and the material was discharged.

Table 3 Feed gas composition and initial carbonation temperature for three carbonation conditions

Sorbent	Carbonation Condition	Feed Gas Composition (vol%)						Initial Carbonation Temperature (°C)
		N_2	O_2	CO_2	CO	H_2	H_2O	
Polish Limestone	CO_2	72.7	19.3	8	0	0	0	600
	CO_2 / Steam	59.3	15.7	8	0	0	17	550
	Syngas	12	0	8	42	21	17	500

RESULTS AND DISCUSSION

Effect of shift reaction in carbonation

TGA results indicated that the rate of carbonation was roughly 70% greater when the sorbent particles were carbonated with CO and H_2 in the feed gas. As indicated by Kyaw *et al.* (1996) and Sun *et al.* (2008), for CO_2 partial pressures less than 10 kPa, the carbonation reaction rate is solely a function of the particle surface area, carbonation temperature, and CO_2 partial pressure. Since the experiments were performed using "nominally" identical limestone samples and reaction temperatures, this might indicate that differences in the reaction rate are related to the CO_2 partial pressure.

A number of metals and metal oxides are known as water-gas shift catalysts (Rofer-DePoorter, 1984), although CaO is not mentioned in particular as catalyzing the reaction. Experiments performed by Han and Harrison (1994) on the simultaneous shift reaction and carbon dioxide separation for the direct production of hydrogen have shown that the water-gas shift reaction proceeds in the absence of a heterogeneous shift catalyst at temperatures in the vicinity of 550°C. Although not measured during the TGA experiments, it is plausible that the water-gas shift reaction indeed takes place and is catalyzed on the surface of the sorbent limestone particles.

Figure 4 shows a plot of the sample (Cadomin limestone) weight gain *vs.* time, where the slope at any given time is equal to the rate of carbonation. Here the slow-down stage can be observed for both carbonation feed gas conditions, but it should be pointed out that this stage occurs approximately 100 seconds earlier, which is considered to be significant, in the case where CO and H_2 are present in the feed gas. This would indicate that the rate of carbonation is greater a these conditions even as the reaction proceeds partially limited by product-layer diffusion. This could be explained *via* the water-gas shift argument, since, in the case where CO and H_2 are not present, the rate of carbonation is partially limited by the diffusion of CO_2 through the $CaCO_3$ product layer, resulting in a CO_2 surface concentration lower than that of the bulk gas. Conversely, when CO and H_2 are present in the gas, they may diffuse through the $CaCO_3$ product layer and react on the CaO surface, producing CO_2 and consequently increasing the CO_2 surface concentration to a level higher than that without CO and H_2 present in the feed gas.

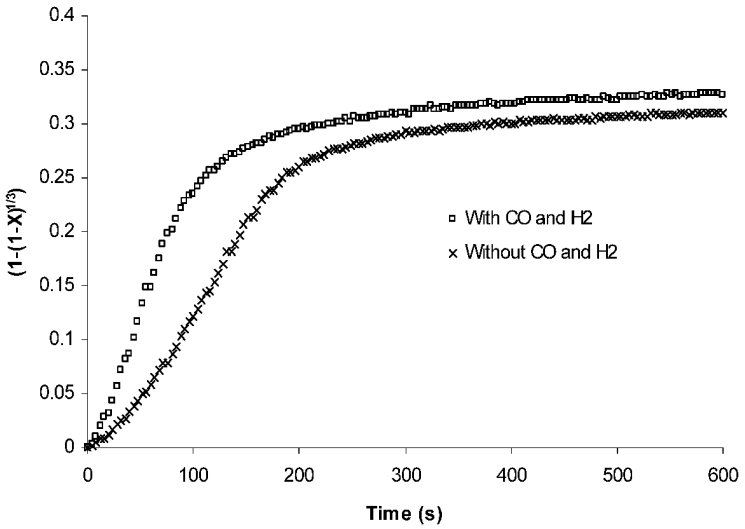

Fig. 4 Cadomin limestone partic les calcined at 850°C with N_2 and carbonated at 620°C with and without CO and H_2

Based on the TGA results, it is of particular interest to investigate the effect of steam and steam/syngas present during carbonation on the sorbent conversion, using the CO_2 (balance air) experiments as a baseline.

Figure 5 depicts the CO_2 concentration and average bed temperature as a function of carbonation time for the initial carbonation under 8% CO_2 and 17% steam (balance air). Comparing the capture efficiency during carbonation with steam to that without steam, it can be clearly observed that the capture efficiency is much better and the duration for this capture is also a great deal longer. In this case the average CO_2 capture over the first 2800 s of carbonation was approximately 97.1%. As well, the carbonation appeared to be less sensitive to changes in temperature, as the temperature fluctuated between 600 and 625°C over this period. Thus, it can be inferred that steam is promoting the CaO carbonation reaction and limiting the diffusion resistance into the inner pores of the particles, which was the reason for the poor CO_2 capture under the 8% CO_2 carbonation conditions. This result can be further illustrated by examining the CO_2 concentration after the steam flow had been cut to the carbonator. At approximately 4000 s into the carbonation period, the steam was cut; consequently there was a dramatic decrease in CO_2 capture and the exit CO_2 concentration jumped from 2.7 to 6.8%. It should be noted that after 2800 s there was an increase in CO_2 concentration, indicating that the reaction was becoming diffusion limited, similar to that without steam, and the carbonation could be enhanced by increasing the temperature.

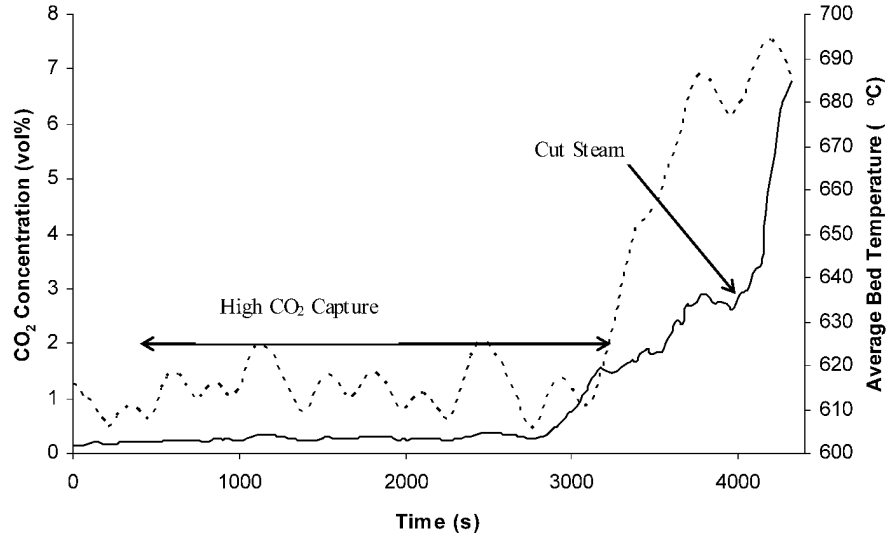

Fig.5 CO_2 concentration and average bed temperature vs. time-Air calcination-8% CO_2,17% steam, balance air carbonation feed as-1stcycle-Polish limestone

The results from the dual-FB facility also confirm that the water-gas shift reaction is indeed taking place, because the CO/H_2 ratio is less than what was fed to the carbonator, which for all syngas runs was a 2/1 ratio. Another indication that the water-gas shift reaction is producing CO_2 is that, when the syngas flow is cut to the carbonator, there is a significant drop in the exit CO_2 concentration. This drop in CO_2 concentration clearly shows the production of CO_2 *via* the water-gas shift reaction, as now the CaO particles can no longer increase the capture efficiency because they are not subject to high CO_2 flow rates. It should be noted that, after the syngas had been cut to the carbonator, the steam continued to allow the CaO particles to capture CO_2 at a similar level as the carbonation performed with just CO_2 and steam. Once again, as was the case discussed above, after the steam flow was cut, the outlet CO_2 concentration increased significantly.

Effect of carbonation temperature

Figure 6 shows the decay in CaO conversion over 10 calcination/carbonation cycles for 4 temperatures ranging from 580 to 700°C in the presence of CO and H_2 during carbonation. It indicates that the carbonation temperature has little or no effect on the maximum carbonation conversion over repeated cycles although the intrinsic rate constants increased with increasing temperature and the calculated activation energy was approximately double that of carbonation in the absence of CO and H_2. This result is not in agreement with experiments performed by Bhatia and Perlmutter (1983), and Gupta and Fan (2002), whose work showed an increase in maximum conversion with increased temperature. It should be mentioned that, although the partial pressure of CO_2 in the carbonation feed gas varies in the various studies discussed here, it has been confirmed by the work of Sun *et al.* (2007) that carbonation is insensitive to the CO_2 partial pressure in terms of the final conversion.

It is unclear at the moment why some authors observe an increase in CaO conversion with increasing temperature. Based on identical calcination conditions, which dictate the level of particle sintering and change in particle porosity, it seems reasonable that, provided with a sufficient duration for carbonation, the maximum

carbonation conversions should be nearly identical for all carbonation temperatures. Some variability in maximum conversion, as seen in Fig. 6, is expected as the limestone samples are relatively small, which can lead to slight variance in CaO content and average particle size from sample to sample.

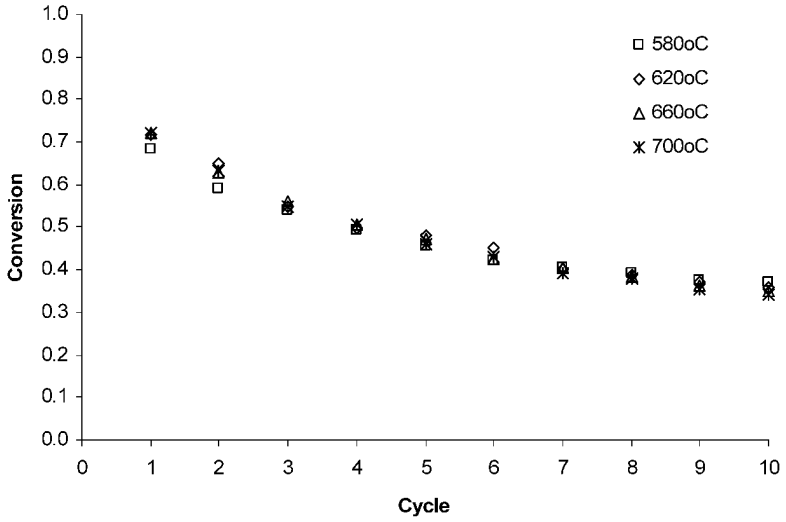

Fig. 6 Decay in carbonation conversion with cycles calcined at 850°C with N_2 and carbonated at 4 temperatures with 8% CO_2,21% H_2, 42% CO, 17% H_2O, and 12% N_2

Effect of oxy-fuel calcination

The oxy-fuel combustion for sorbent regeneration creates a high concentration of CO_2 and H_2O during calcination and may have adverse effects on CaO conversion due to accelerated particle sintering and pore closure. However, there is little information on the effect of CO_2 during calcination on the initial rate of carbonation. Therefore, it is of particular interest to compare carbonation and CaO conversion under varying calcination feed gas conditions.

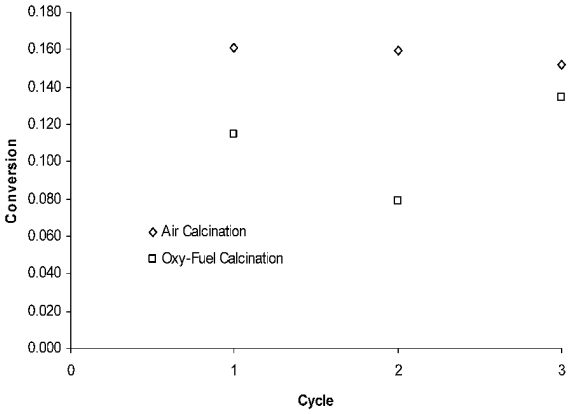

Fig. 7 Polish limestone carbonation conversion over 3 cycles under air and oxy-fuel calcination conditions – 8% CO_2, balance air carbonation feed gas

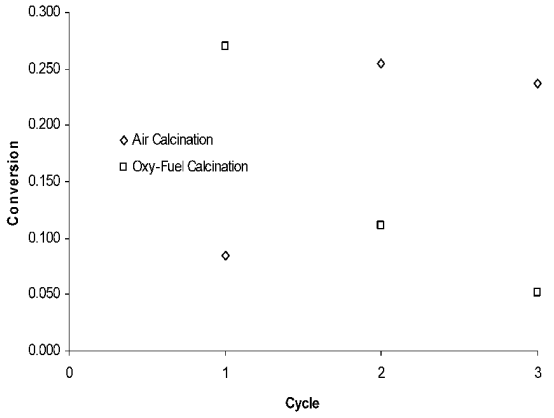

Fig. 8 Cadomin limestone carbonation conversion over 3 cycles under air and oxy-fuel calcination conditions – 8% CO_2, balance air carbonation feed gas

Figures 7 and 8 show the carbonation conversions in the pilot-scale dual fluidized bed units over three cycles for the Polish (Fig. 7) and Cadomin limestone (Fig. 8) calcined under air and oxy-fuel conditions, where in each case, the feed contains 8% CO_2 (by volume), balance air or recycled flue gas. As expected, the carbonation conversions were higher over three cycles when the calcinations were performed under air. This result is in agreement with the TGA experiments that showed a lower carbonation conversion under high CO_2 concentrationsThis cannot be said for the carbonation conversions achieved under oxy-fuel calcination as there is a decrease in carbonation conversion of approximately 31.3% from cycle 1 to 2 (Polish limestone). As well, the initial carbonation is about 40% higher under air calcination. Oddly, the third carbonation conversion determined under oxy-fuel calcination conditions was found to be higher than for both the previous cycles. The most likely explanation for this increase in conversion is that, either the calcination for the third cycle was more complete, or that the carbonation period was longer, resulting in an increased carbonation conversion.

A similar trend can be observed when comparing the Cadomin limestone (Fig. 8), specifically that the carbonation conversions achieved under air calcination are greater than under oxy-fuel calcination. One main difference is that the initial carbonation conversion under oxy-fuel calcination is similar to the conversion achieved under air calcination, followed by a significant decrease to similar levels determined for the Polish limestone. As well, comparing sorbent conversions for the air calcination runs, the Cadomin limestone performed far better than the Polish limestone. Excluding the first carbonation, the second and third carbonation conversions are approximately 59.3% and 55.9% higher for the Cadomin limestone, respectively. Interestingly, the first carbonation conversion is only 8.4%, which is significantly lower than what is expected based on the second and third cycle. This oddity can be explained by looking at the calcination conversion. For the second and third cycles the calcination was complete (*i.e.*, the material contained no $CaCO_3$ after calcination) but the initial calcination was only 87.8% complete. Thus, the remaining $CaCO_3$ might have limited the surface area for CO_2 absorption causing the reaction to be diffusion limited as the CO_2 must now penetrate through the $CaCO_3$ surface.

BET analysis was performed on the material carbonated under both CO_2 and syngas conditions, which can be seen in Fig. 9. Based on the results shown above, the carbonation conversions were 16.1 and 46.9% for the first carbonation under CO_2 and syngas conditions, respectively. Thus, it was expected that there would be a decrease in both pore volume and surface area with a higher conversion of CaO to $CaCO_3$. It should be noted that there is a proportionally larger decrease in pore volume associated with the macropores than micropores, indicating that the majority of the carbonation conversion takes place in the larger pores (10-100 nm). This result has also been confirmed by examining the particle surface area, which indicates that almost all of the surface area in the larger pores has been consumed due to carbonation.

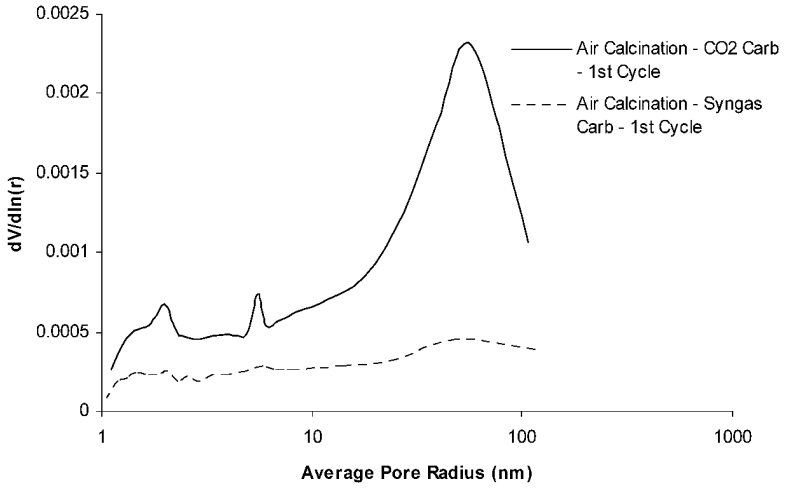

Fig. 9 Differential pore volume vs. average pore radius for polish limestone calcined under air and carbonated under CO2 and syngas-1st cycle

CONCLUSIONS

This paper presents the effect of gasification syngas on the carbonation reaction and conversion for two naturally occurring calcium oxide-based sorbents. The TGA results indicated that the presence of CO and H_2 caused an increase in initial rate of approximately 70.6% for the limestone. The increase in rate was attributed to the CaO surface sites catalyzing the water-gas shift reaction, increasing the local CO_2 concentration. As well, the water-gas shift reaction was assumed to be responsible for the increase in activation energy. Several experiments were performed using a pilot-scale dual fluidized bed reactor system to further investigate the effect of steam and gasification syngas on CO_2 capture and sorbent conversion under air or oxy-fuel conditions. Calcination under oxy-fuel conditions did result in a decreased carbonation conversion, due primarily to particle sintering and pore pluggage. On average there is a decrease in carbonation conversion of approximately 36.5 and 33.4% for steam and steam/syngas, respectively. It should be noted that, although the carbonation conversion decreased, the presence of steam and syngas did result in an increased conversion as compared to carbonation under only CO_2.

ACKNOWLEDGMENTS

Financial supports of this project by Environment Canada's and Natural Resources Canada's PERD

program are gratefully acknowledged.

REFERENCES

Anthony, E.J. (2008). *Ind. Eng. Chem.* 47, 1747-1754.
Abanades, J.C., Alvarez, D. (2003). *Energy Fuel* 17, 308.
Abanades J.C., Anthony E.J., Alvarez D., Lu D., Salvador, C. (2004). *A.I.Ch.E. Journal* 50, 1614–22 .
Bhatia, S.K., Perlmutter, D.D. (1983). *A.I.Ch.E. Journal* 29 (1), 79–86.
Gupta, H., Fan, L.S. (2002). *Ind. Eng. Chem. Res.* 41, 4035-42.
Han, C., Harrison, D.P. (1994). *Chem. Eng. Sci.* 49, 5875-83.
Henderson, C. (2005). *Towards zero emission coal-fired power plants.* IEA Clean Coal Centre, London, UK.
Hughes, R., Lu, D., Anthony, E.J., Macchi, A. (2005). *Fuel Process. Technol.* 86, 1523-31.
Kyaw, K., Kanamori, M., Matsuda, H., Hansatani, M. (1996). *J. Chem. Eng. Japan* 29 (1), 112-118.
Lee, D.K., Baek, I.H., Yoon, W.L. (2004). *Chem. Eng. Sci.* 59, 931-942.
Lu, D.Y., Hughes, R.W., Anthony, E.J. (2008). *Fuel Process. Technol.* doi:10.1016/j.fuproc.2008.06.011.
MacKenzie, A., Granatstein, D.L., Anthony, E.J., Abanades, J.C. (2007). *Energy Fuels* 21(2), 920-926.
Pennline, H.W., Luebke, D.R., Jones, K.L., Morsi, B.I., Heintz, Y.J., Ilconich, J.B. (2007). Proceedings of 100th AWMA Annual Conference and Exhibition, Pittsburgh, PA, June 26-29.
Rofer-DePoorter, C. (1984). *Catalytic Conversions of Synthesis Gas and Alcohols to Chemicals.* Plenum Press, NY, 97-128.
Sun, P., Grace, J.R., Jim Lim, C., Anthony, E.J. (2007). *Environ. Sci. Technol.* 41, 2943–49.
Sun, P., Grace, J.R., Jim Lim, C., Anthony, E.J. (2008). *Chem. Eng. Sci.* 63, 47-56.

POSTCOMBUSTION CAPTURE OF CO_2 WITH CAO IN A CIRCULATING FLUIDIZED BED CARBONATOR

M Alonso[1], N Rodriguez[1], B González[1], G Grasa[2], R Murillo[2], J C Abanades[1]

1CSIC-INCAR Spanish Research Council (Oviedo-Spain)
2CSIC-ICB Spanish Research Council (Zaragoza-Spain)

Abstract: There is an emerging postcombustion capture technology that uses CaO to capture CO_2 from combustion flue gases in a circulating fluidized bed reactor. This paper summarizes recent work conducted at CSIC to understand and develop this technology. The paper includes experimental results at conditions close to those expected in the real system, carried out in continuous mode in a 30kW test facility made up of two interconnected circulating fluidized bed reactors. In one of the reactors, CO_2 is captured from the gas phase by the CaO continuously circulating from a calciner. In the second reactor, the $CaCO_3$ formed in the carbonator is regenerated to CaO and CO_2 by calcination. Modeling of the system at process level, at reactor level (in particular the CFB carbonator), and at particle level (decay in capture capability of CaO) is also outlined. The work carried out so far confirms that the carbonator reactors can be designed to attain capture efficiencies between 70-90%, operating at fluid dynamic conditions close to those present in circulating fluidized bed combustors.

Keywords: CO_2 capture, carbonation, calcination, reactor modeling, pilot testing

INTRODUCTION

The UN Intergovernmental Panel for Climate Change (IPCC), Nobel Prize laureate for Peace in 2007, has already established that CO_2 capture and storage *"would be an option in the portfolio of actions for stabilization of greenhouse gas concentrations while allowing for the continued use of fossil fuels"* (Metz et al. 2005). Despite the maturity of several of the existing capture systems in the gas and oil industries, it is widely recognized that there is need for large reductions in the CO_2 capture costs and energy efficiency penalties. One promising means of CO_2 capture for coal based power plants is to use a lime carbonation-calcination cycle illustrated in Fig. 1. This process was originally proposed by Shimizu et al. 1999, and uses CaO as a regenerable sorbent to capture CO_2 from combustion flue gases. Other processes that use CaO for combustion systems have been proposed (Wang et al. 2004; Abanades et al. 2005) while others have also been considered for H2 production routes (see recent reviews by Anthony, 2008 and Harrison, 2008).

In the basic system of Fig. 1 CO_2 is captured from the combustion flue gas of a power plant in a circulating fluidized bed carbonator operating between 600-700ºC. When the solids leave the carbonator (with some of the CaO being converted to $CaCO_3$) they are directed to a second fluidized bed where calcination/regeneration takes place. Coal burns in the calciner in an atmosphere of O_2/CO_2 at temperatures over 900ºC, thus producing the heat necessary to calcine the $CaCO_3$ back to CaO and CO_2. It is assumed that this second fluidized bed calciner operates with oxygen supplied by an air separation unit, but other more efficient sources of heat for calcination may be used in the future (Abanades et al. 2005). The CO_2 captured from the flue gases as $CaCO_3$, and the CO_2 produced by the oxy-fired combustion of coal in the calciner, are recovered in concentrated form from the calciner gas, which is now suitable for final purification and compression, and subsequently for transport and safe storage in a deep geological formation. The calciner employs a considerable fraction (35-50%) of the total energy entering the system to provide the heat necessary for the endothermic calcination of $CaCO_3$ and heat up the incoming gas and solid streams up to the calciner temperatures (Rodriguez et al. 2008). However this energy leaves the system in mass streams at high temperature (at T>900ºC) or is recovered as carbonation heat in the carbonator (at around 650ºC). Thus the large energy input into the calciner comes out of the system as high quality heat that can be recycled in a highly efficient steam cycle (Shimizu et al., 1999; Abanades et al., 2005; Romeo et al. 2008). The calciner functions in fact like a new oxyfired fluidized bed power plant. But in this new power plant it may be possible to almost double the amount of CO_2 output thanks to the CO_2 captured in the carbonator as $CaCO_3$ and regenerated back to CaO and CO_2 in the oxyfired calciner.

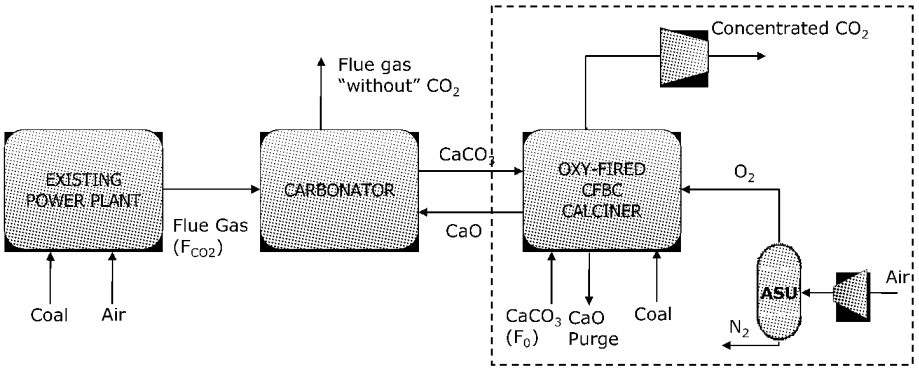

Fig. 1. Schematic of a carbonate looping system to capture CO_2 from an existing power plant, that generates more power when the oxyfired circulating fluidized bed combustor acts as calciner (area inside dotted line)

The carbonator reactor depicted on the left hand side of Fig. 1 must be designed and operated in such a way as to achieve high capture efficiencies of CO_2 from the flue gas. The flow rates of flue gases from a typical 1000 MWth power plant are about 300 Nm^3/s. Bringing this huge flow of gas into contact with CaO particles is only possible with reactors of a very high gas throughput per unit area such as circulating fluidized bed reactors. In addition, we may take advantage of the mechanical similarities between the carbonator and the currently employed large scale CFBCs that operate at similar fluid-dynamic conditions to those required to implement the carbonation-calcination loop.

Despite the increasing number of published works that deal with different aspects of such systems (sorbent performance and reactivation studies, batch experiments and modeling, process simulation work, etc., as reviewed in Anthony, 2008) there is a lack of information about the role of the circulating fluidized bed carbonator reactor in systems such as that depicted in Fig. 1. The purpose of this study was to start to fill this knowledge gap by conducting continuous experiments in a small test facility made up of two interconnected CFB reactors. A simple reactor model based, that integrates existing knowledge about sorbent capture capacity and reactivity to the residence time distribution functions of the particles cycling between the carbonator and calciner reactors has also been recently developed (Alonso et al., 2008) and is briefly discussed here for a first interpretation of experimental results.

EXPERIMENTAL

The 30kW test facility built at INCAR-CSIC is made up of two interconnected circulating fluidized bed reactors as shown in Fig. 2. Both reactors have a 0.1 m internal diameter; the calciner is 6 m in height and the carbonator 6.5 m in height. Each riser is connected to a high efficiency primary cyclone. The solids fall from the cyclone through a vertical standpipe to bubbling fluidized bed loop sealsand then to the opposite reactor. There is a bypass just below the loop seals to extract solid samples and to measure solid circulation rates (Gs, in kg/m^2s) by diverting solids to a dead volume for a certain period of time. Other solid samples can also be extracted directly from several riser ports. A mixture of gas containing CO_2 is fed into the carbonator. No air distributor is used for these small diameter risers, allowing the easy feed of solids when needed (screw feeders for solid fuels, in particular for the air-fired calciner, are not shown in the Figure for simplicity). The loop seals are aerated with air. Electric ovens cover the first 2.5 m of the risers and also the loop seals. After start up, the ovens are switched off in the carbonator and then opened up slightly in order to release the heat generated in the carbonation reaction.

In the second circulating fluidized bed reactor, the $CaCO_3$ formed in the carbonator is regenerated under typical combustion conditions in a CFBC (800-900ºC with 2-6% air excess). The calciner is air-fired in these particular experiments. Continuous analyses of CO_2, O_2 and CO are carried out from different points in the installation. There are a number of ports for installing differential pressure transducers and thermocouples. CaO content and Ca conversion to $CaCO_3$ are analysed in solid samples. Selected samples from the carbonator are taken to measure the carbonation reaction rate in a thermobalance specially designed for multi-cycle experiments (see Gonzalez et al., 2008). A typical high purity limestone (>98% $CaCO_3$) was used in all the experiments, with a particle size range below 350 microns and with activity curves that have been reported elsewhere (Gonzalez et al., 2008). Once the limestone had been calcined, solids in the circulation loop had a typical average particle size distribution below 100 due to attrition. From this point, attrition was no longer a serious problem. Solids collected in the secondary cyclones were fed back to the main circulation loop. The bed inventory in each riser was calculated assuming that the ΔP measured in the riser is due to the bed inventory (W) as in minimum fluidization conditions ($\Delta P = W/A$).

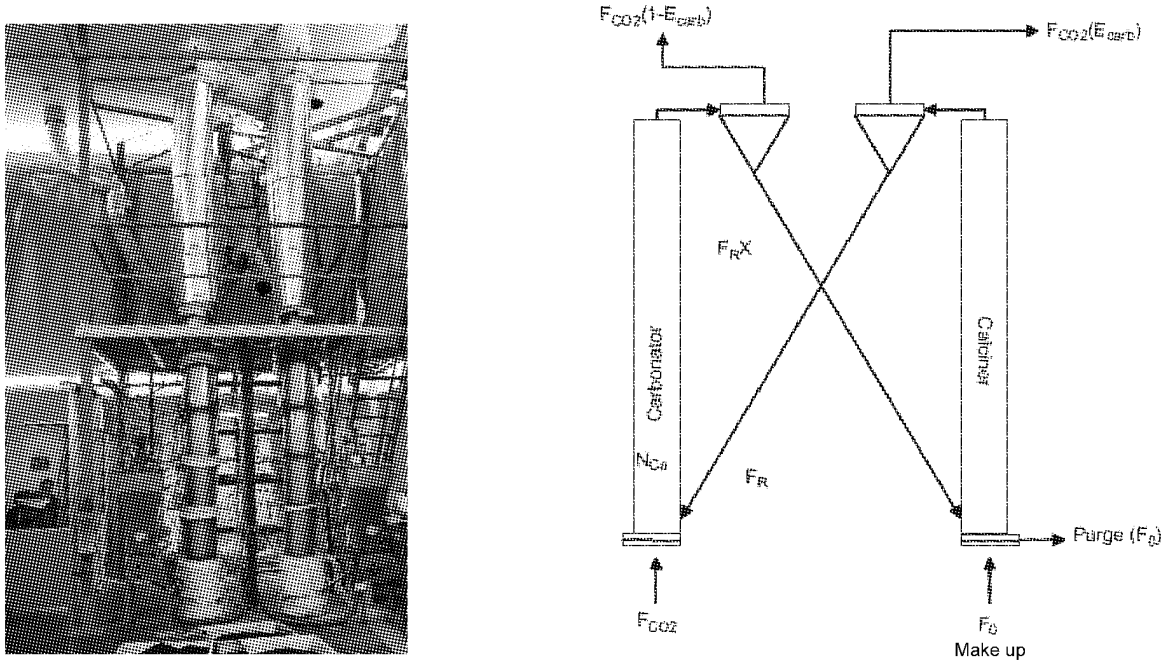

Fig. 2. Schematic and overview of the interconnected circulating fluidized beds to test carbonate looping at INCAR-CSIC

RESULTS AND DISCUSSION

Examples of experimental results

Figure 3 presents some examples of results, plotting experimental information on gas compositions as instant capture efficiency (red dotted lines) and comparing this value with the maximum amount of CO_2 capture allowed by the equilibrium at the average temperature in the carbonator reactor. As can be seen in the Figure on the left hand side, CO_2 capture efficiencies are consistent and stable to over 70% and close to 90% (superficial gas velocities between 2.0-2.1 m/s; solids circulation rates of 0.8-2.3 kgCaO/m^{2}s; maximum activity of the material 0.2-0.3; average temperature= 650ºC). However, there are two events in this figure that show a much lower capture efficiency, illustrating the importance of a good solid circulation and sufficient solids inventory in the riser. The first event (at around 22:15) corresponds to the deliberate switching off of the aeration of the loop seal, which interrupted the solids circulation to the carbonator. As a result, efficiency dropped to zero as due to the lack of solids reacting in the carbonator. The second low efficiency peak in the same figure at around 22:40 corresponds to a measurement of the solids circulation rate (when solids were diverted to a container for a certain period of time) that translates into a rapid reduction of the solids inventory in the carbonator and an associated reduction in capture efficiency.

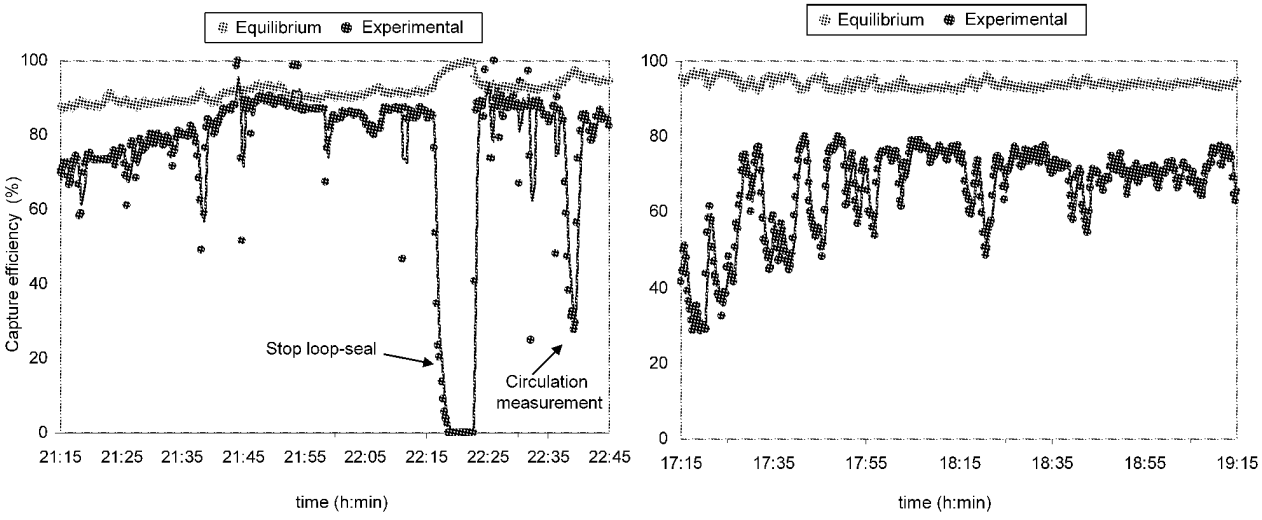

Fig. 3. Example of experimental results for the rig of Fig. 2 which operates with continuous carbonations and calcinations

The Figure on the right of Fig. 3 corresponds to an experimental period conducted under similar conditions but with CaO particles highly deactivated and close to the residual activity expected for most limestones (0.07-0.12) after hundreds of carbonation calcination cycles (Grasa and Abanades, 2006). This particular experiment ran for more than eight hours under stable conditions, with relatively modest circulation rates (1-1.8 kg/m^{2}s) and solids inventories (20 cm H_2O or 200 kg/m^2). Higher efficiencies would be feasible in taller risers or conditions sustaining higher circulation rates and higher solids inventories in the carbonator. The low efficiencies measured on the left hand side of the Figure 3 correspond to a period when the ovens of the calciner were switched off. This caused the temperatures in the calciner to drop below 750ºC and calcination intensity to fall. In these conditions, the progressive carbonation of the material in the system took place and this led to low (eventually zero) capture efficiencies. When the ovens were switched on at 17:15, calcination intensity was restored and capture efficiencies recovered in less than one hour to a stable value of between 70-75%.

Basic modelling of the carbonator reactor

The main objective of a reactor model for the carbonator is to estimate CO_2 capture efficiency, E_{carb}, as a function of operating conditions and fundamental sorbent performance properties (capture capacity along cycling and carbonation rates). A simple mathematical model has been recently completed (Alonso et al., 2008) based on the closure of the balance:

$$\begin{pmatrix} CO_2 \textit{ reacting with} \\ CaO \textit{ in the bed} \end{pmatrix} = \begin{pmatrix} CO_2 \textit{ removed from} \\ \textit{the gas phase} \end{pmatrix} = \begin{pmatrix} CaCO_3 \textit{ formed in the} \\ \textit{circulating stream of } CaO \end{pmatrix} \quad (1)$$

The model is solved when all the terms in the previous equation have been calculated for a given set of input operating and design conditions. It can be seen from the notation in Fig. 2 that the flue gas entering the carbonator reactor contains a feed of CO_2 (F_{CO2} in mol CO_2/s), which will disappear through the carbonation reaction of the CaO active particles present in the bed. The bed contains N_{Ca} mol of Ca but only a fraction of the CaO, f_a, reacts in the bed at a rate r_{ave} (average reaction rate of the active material, s^{-1}). The remaining fraction of bed particles (1-f_a) are considered inactive. At the same time, there is a continuous arrival of new calcined particles (F_R) that are converted in the perfectly mixed carbonator reactor to a carbonation conversion X:

$$\begin{pmatrix} CO_2 \textit{ removed from} \\ \textit{the gas phase} \end{pmatrix} = F_{CO_2} \times E_{carb} \quad (2)$$

$$\begin{pmatrix} CaCO_3 \textit{ formed in the} \\ \textit{circulating stream of } CaO \end{pmatrix} = F_R \times X \quad (3)$$

$$\begin{pmatrix} CO_2 \textit{ reacting with} \\ \textit{the } CaO \textit{ bed} \end{pmatrix} = N_{Ca} \times f_a \times r_{ave} \quad (4)$$

The concept of f_a was already introduced in a previous work modelling batch carbonation experiments (Abanades et al. 2004). To explain the meaning of f_a in this work we must first review what is known about the reaction mechanism and reaction rates of the carbonation reaction. It is well known that the carbonation reaction has a fast reaction regime followed by a slow reaction regime controlled by CO_2 diffusion through the product layer of $CaCO_3$ formed on the free CaO surfaces (Dedman and Owens, 1962; Bhatia and Perlmutter, 1983; Mess et al., 1999). Furthermore, it is also well established that the maximum conversion of CaO (that marks the end of the fast carbonation period) decreases rapidly as the number of carbonation calcinations cycles increases (Curran et al., 1967; Barker, 1973; Abanades and Alvarez, 2003; Grasa and Abanades, 2006). In order to model these key sorbent features, and to facilitate the integration of the rate and the residence time distributions it is assumed that the CaO particles attain the maximum conversion, X_N, at a constant rate, in a characteristic time t^*, and after that the reaction rate becomes zero.

The maximum conversion, X_N in Eq. (5) is the conversion that the particles reach at the end of the fast carbonation period, which depends on the number of calcination-carbonation cycles in accordance with the following equation:

$$X_N = \frac{1}{\frac{1}{(1-X_r)} + Nk} + X_r \tag{5}$$

where typical values of $k = 0.52$ and $X_r = 0.075$ (Grasa and Abanades, 2006). With the continuous feed of fresh particles and the purging of solids from the perfectly mixed beds of Figures 1 and 2, there will be a large population of particles in the system with different cycle numbers, different capacities for CO_2 capture (depending on N) and different reactivities (also depending on N). The mass balance to estimate the fraction of particles that have been cycling in the system N times was solved in a previous work (Abanades, 2002) for a carbonation-calcination loop with full maximum carbonation conversion (represented by Eq. (5)) and total calcination. As shown in Fig. 2, the fraction of active particles, f_a, corresponds to the particles that have not yet fully reached their maximum possible conversion or, in other words, f_a is the fraction of particles with a residence time in the carbonator below t^*. Therefore, for a perfect mixed model, f_a is defined as:

$$f_a = \left(1 - e^{-t^*/\tau}\right) \tag{6}$$

where τ is the average particle residence time in the carbonator. Thus, it can be seen that the $CaCO_3$ leaving the carbonator reactor is the sum of two contributions: carbonate in particles converted to their maximum level of conversion (with a residence time higher than t*) depending on their individual cycle number, and particles with a residence time lower than t*, which abandon the carbonator when they are still reacting at the rate characteristic of the fast reaction regime. It can therefore be shown (Alonso et al., 2008) the flow of carbonate being formed in the carbonator reactor as:

$$\begin{pmatrix} \mathrm{CaCO_3}\ \textit{formed in the} \\ \textit{circulating stream of}\ \mathrm{CaO} \end{pmatrix} = F_R X = F_R X_{ave} \frac{f_a}{\ln(1/(1-f_a))} \tag{7}$$

As stated in Eq. (1), the carbon balance in the reactor demands identical carbonation efficiency to account for the disappearance of CO_2 from the gas phase and to account for the reaction of CO_2 with the active CaO in the bed (also depending of f_a according to Eq. (4)). For a given set of input data F_R, F_0, F_{CO_2}, W_{CaO} (or N_{Ca}), and for a given sorbent defined by its deactivation and reactivity constants, there is only one value of f_a that provides the solution to the Eq. (1) (see Alonso et al., 2008, for details). Once that the model is solved, it can be run for conditions similar to those present in the experiments, in order to obtain predictions such as Fig. 4. As can be seen, the solid inventory in the carbonator during is a key variable to understand the limited capture efficiencies obtained in these first experiments and show the potential for much higher capture efficiencies in other conditions where higher inventories of material in the carbonator can be achieved.

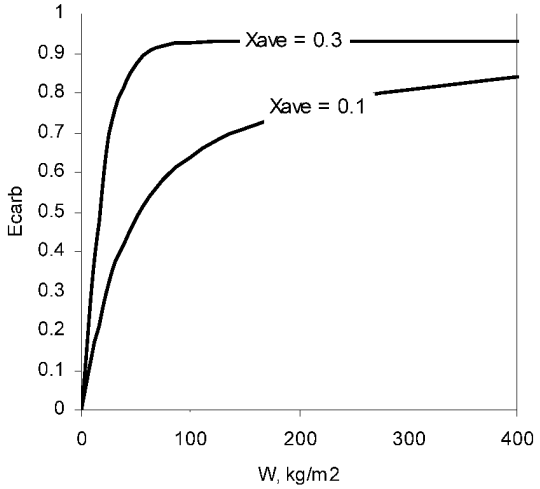

Fig. 4 Example of model predictions at conditions close to the experiments reported in Fig. 3 (F_R/F_{CO_2}=10 mol CaO/mol CO_2,F_{CO2}=3.5mol CO_2/m^2s,F_0=0 mol $CaCO_3/m^2s$)

Work is in progress to adapt more precisely the model predicitions to the experimental results obtained from the operation of the reactors of Fig. 2, tuning (reducing) the reaction rate constants in the model to account for other resistances to the progress of reaction in the CFB reactor. Once this model validation exercise is completed, the model should be a valuable tool to move to the next phase, which involves the testing of the process at a scale around 1MWt. An agreement has been recently signed between CSIC, Hunosa (owner of a CFBC power plant in "La Pereda", Spain) and Endesa to have operational such a rig in 2010.

CONCLUSIONS

Carbonate looping cycles are very promising concepts for post-combustion CO_2 capture applications. The carbonator reactor functions as an effective absorber of CO_2 as long as there is a sufficient bed inventory and solids circulation rate, even with highly deactivated CaO . Temperatures, solid circulation rates and bed

inventories associated to the operation of the carbonator are relatively mild, compared to the established operating conditions for large scale CFBC boilers. Experimental results from a 30kW test facility designed, constructed and operated by CSIC (Spain) have demostrated the essential viability of the process and these results are confirmed indirectly by a simple model of the carbonation reactor that integrates our knowledge of sorbent performance and basic fluid dynamics in the CFB reactor. Plans have already been made to extend the experimental database and gain experience and design data for the next 1MW scale pilot in Spain.

ACKNOWLEDGEMENTS

Financial supports of this work by Endesa and Hunosa is gratefully acknowledged as well as individual fellowships to N.R. and B.G from FICYT.

REFERENCES

Abanades, J. C., Alvarez, D., Energy Fuels, **17**(2) (2003), 308-315.
Abanades, J. C., Anthony, E. J., Alvarez, D., Lu, Y., Salvador, C., AIChE J., **50**(7) (2004), 1614-1622.
Abanades, J. C., Anthony, E. J., Wang, J. S., Oakey, J. E. Env. Sci. & Tech. **39**(8), (2005), 2861-2866.
Abanades, J. C., Chem. Eng. J., **90**(3) (2002), 303-306.
Alonso, M., Rodríguez, N., Grasa, G., Abanades, J.C., Chem. Eng. Sci., In press. ie-2008-10.044
Anthony, E. J., Ind. Eng. Chem. Res. **47** (2008), 1747-1754.
Barker, R., J. Appl. Chem. Biotechnol. **23**(10) (1973), 733-742.
Bhatia, S. K. and D. D. Perlmutter, AIChe J. **29** (1983) 79-86.
Curran, G. P., Fink, C. E., Gorin, E., Adv. Chem. Ser. **69** (1967), 141-161.
Dedman, A. J., Owens, A. J., Trans. Faraday Soc., **58**(1962) 2027-2035.
González, B., Grasa, G. S., Alonso, M., Abanades, J. C., Ind. Eng. Chem Res. In press. ie-2008-009318.
Grasa G. and Abanades J.C., Ind. Eng. Chem. Res. **45**(26) (2006), 8846-8851.
Harrison P., Ind. Eng. Chem. Res., **47**(17) (2008), 6486–6501.
Metz, B., Davidson, O., Coninck, H. de, Loos, M., Meyer, L. (Eds.) (2005) Special Report on Carbon Dioxide Capture and Storage. IPCC, Cambridge Univ. Press.
Mess, D., Sarofim, A. F. Longwell, J. P. Energy & Fuels **13** (1999), 999-1005.
Rodríguez, N., Alonso, M., Grasa, G., Abanades, J. C., Chem. Eng. J., **138**(1-3) (2008), 148-154.
Shimizu, T., Hirama, T., Hosoda, H., Kitani, K., Inagaki, M., Tejima, K., Trans. Inst. Chem. Eng., **77**(Part A) (1999), 62-68.
Romeo, L. M., Abanades, J. C., Escosa, J. M., Paño, J., Giménez, A., Sánchez-Biezma, A., Ballesteros, J. C. Energy Conversion and Management, **49**(10) (2008), 2809-2814.
Wang, J. S., Anthony, E. J., Abanades, J. C., Fuel, **83**(10) (2004), 1341-1348.

MEASURING THE KINETICS OF THE REDUCTION OF IRON OXIDE WITH CARBON MONOXIDE IN A FLUIDIZED BED

C.D. Bohn[1], J.P. Cleeton[2], C.M. Müller[2], S.A. Scott[2], J.S. Dennis[1]

1Department of Chemical Engineering and Biotechnology, University of Cambridge, Cambridge CB2 3RA, U K

2Department of Engineering, University of Cambridge, Cambridge CB1 1PZ, U K

Abstract: Combusting a solid fuel in the presence of a metal oxide rather than air, chemical looping combustion, generates CO_2 suitable for sequestration and the reduced metal. For the case of iron, the reduced oxide can be re-oxidized with steam to produce high-purity hydrogen. The reduction reactions of iron oxide in carbon monoxide and carbon dioxide mixtures were investigated in a fluidized bed. Activation energies and pre-exponential factors for the reactions (i) 3 Fe_2O_3 + CO⇌2 Fe_3O_4 + CO_2 and⇌(ii)0.947 Fe_3O_4 + 0.788 CO⇌3 $Fe_{0.947}O$ + 0.788 CO_2⇌were determined. The reaction order was verified to be unity, and the change in rate with conversion was examined.

Keywords: reduction kinetics, iron oxide, fluidized bed, chemical looping combustion

INTRODUCTION

The reduction of iron oxides with CO and H_2 and their re-oxidation with H_2O and air provides one means of generating H_2 from the gasification of coal or biomass, whilst producing CO_2 suitable for sequestration (Bohn *et al.*, 2008). The iron species involved are Fe_2O_3, Fe_3O_4, $Fe_{(1-x)}O$ and Fe, where $0.05 < x < 0.17$ arises from vacancies in the lattice (v. Bogdandy and Engell, 1971). The reduction of Fe_2O_3 by CO or H_2 occurs *via* the following reactions, given for CO:

$$3\ Fe_2O_3 + CO \rightleftharpoons 2\ Fe_3O_4 + CO_2; \qquad \Delta H^\circ_{1023\ K} = -44.3\ kJ/mol \qquad (R1)$$

$$0.947\ Fe_3O_4 + 0.788\ CO \rightleftharpoons 3\ Fe_{0.947}O + 0.788\ CO_2; \quad \Delta H^\circ_{1023\ K} = +21.1\ kJ/mol \qquad (R2)$$

The reduced metal oxide, $Fe_{0.947}O$, can then be re-oxidized with steam to produce hydrogen:

$$3\ Fe_{0.947}O + 0.788\ H_2O_{(g)} \rightleftharpoons 0.947\ Fe_3O_4 + 0.788\ H_2; \Delta H^\circ_{1023\ K} = -48.0\ kJ/mol \qquad (R3)$$

To return the Fe_3O_4 to its original form, Fe_2O_3, thermodynamics dictates that oxidation in air or O_2 is required:

$$2\ Fe_3O_4 + 0.5\ O_2 \rightleftharpoons 3\ Fe_2O_3; \qquad \Delta H^\circ_{1023\ K} = -238.4\ kJ/mol \qquad (R4)$$

The equilibrium constant for R1, $K_p = p_{CO_2}/p_{CO}$, is larger than 10^4 between 298 K and 1400 K so that the presence of Fe_2O_3 will permit nearly complete conversion of the CO (and, or, H_2) to CO_2 (and, or, H_2O) in the thermodynamic limit. Hence, iron oxide is a good oxygen carrier for carbon capture by chemical looping. The objective of this study is to determine pre-exponential factors and activation energies for the reduction of iron oxides with mixtures containing CO and CO_2 in a temperature range where an industrial process using these reactions might operate and where chemical reaction limitations constitute the principal kinetic resistance. This is distinct from previous work (*e.g.* Tsay et al., 1976; Trushenski et al., 1974) in that it (i) measures the rates in a fluidized bed as opposed to a thermogravimetric device, (ii) presents rates over repeated cycles of reduction and oxidation instead of just for an initial cycle, and (iii) verifies the kinetic parameters by, *e.g.* showing that the activation energy approximately halves for large particles.

EXPERIMENTAL

Particles were prepared from powdered Fe_2O_3 (Sigma-Aldrich, 5 μm, purity >99.9 wt. %). Agglomerates were formed by spraying reverse osmosis water on to the powder and mechanically mixing. The resulting particles were heated at 1173 K for 3 h, then sieved to the desired size fraction. The BET surface area of the sintered Fe_2O_3 particles, $d_p \approx$ 300-425 μm, was 1 m^2/g; the porosity measured by Hg porosimetry was 0.6.

The fluidized bed reactor, shown in Fig. 1, consisted of a tube of recrystallized alumina, fitted with perforated plate distributor also made from alumina; both had purities >99.7 wt. % Al_2O_3. The plate had 5 holes, each 1 mm in dia., aligned in a square array, side 8mm, with one central hole. The plate and tube were cemented together (ALCS, Multilab). For each experiment, the material fluidized was 15 g of Al_2O_3 particles with a sieve size fraction of $d_p \approx$ 300-425 μm and purity >99.9 wt. % Al_2O_3 (Boud Mineral). At minimum fluidization, H_{mf} = 30 mm and H_{mf}/D_{bed} = 1.5. The reactor was placed in a tubular furnace and the temperature was measured with a stainless steel type K thermocouple 5 mm above the distributor, inside the bed.

Gas was supplied to the reactor variously from cylinders containing (i) 10 vol. % or 30 vol. % CO, balance

N_2, (ii) pure N_2, (iii) laboratory air and (iv) pure CO_2. Using a syringe pump and hypodermic tubing (0.8 mm i.d.), steam was supplied by injecting water into a chamber packed with stainless steel mesh and heated electrically to 433 K. The flowrates of the gas streams (i)-(iii) were measured using mass flow meters (AWM5101VN, Honeywell); that for stream (iv) was measured with a rotameter; the liquid H_2O flowrate was 30 mL/h for all experiments. The total rate of gas flow was adjusted in all experiments such that for the bed material, $U/U_{mf} \sim 7$ at the given gas composition and temperature as determined by the correlation of Wen and Yu (1966). Solenoid valves located just after the flowmeters and rotameter for streams (i)-(iv) permitted automatic gas switching.

A sample of the off-gas was removed from the fluidized bed *via* a quartz probe (5 mm i.d.) followed by three impinger tubes immersed in an ice bath at 273 K and a tube filled with $CaCl_2$. For the reduction and oxidation reactions between Fe_2O_3 and Fe_3O_4, no steam was required and the tubes were removed from the sampling line. The composition of the gas was monitored by (i) a non-dispersive infrared analyzer (NDIR) measuring [CO] and [CO_2] in the range 0-20 vol. % (ABB Easyline), (ii) a NDIR analyzer measuring [CO] in the range 0-2000 vol. ppm (ABB Easyline) and (iii) a thermal conductivity analyzer measuring [H_2] in the range 0-30 vol. % (ABB Caldos27). Deconvolution of the analyzer signals for [CO] and [CO_2] was performed by assuming that the sampling line could be modelled as a plug flow reactor in series with a well-mixed reactor. The mixing time constants for the case without the drying tubes and with the drying tubes were, respectively, $\tau_{CO} = 1.0$ s, $\tau_{CO_2} = 2.5$ s and $\tau_{CO} = 2.0$ s, $\tau_{CO_2} = 3.5$ s. Deconvolution did not significantly alter the results since the time for reduction was typically one order of magnitude greater than the mixing times.

Cycles of reduction with mixtures of N_2+CO+CO_2 (respectively, 82, 3 and 15 vol. %) and oxidation with N_2+air (respectively, 82 and 18 vol. %) were performed for the transition from Fe_2O_3 to Fe_3O_4 at temperatures between 723 and 973 K. For these conditions at 1 bar, thermodynamics dictates that cycling between Fe_3O_4 and Fe_2O_3 will occur. Mixtures of N_2+CO+CO_2 (respectively, 82, 9 and 9 vol. %) for reduction and N_2+steam (respectively, 70-85 and 15-30 vol. %) for oxidation were used for the transition from Fe_3O_4 to $Fe_{0.947}O$ at temperatures between 923 and 1173 K. For these conditions at 1 bar, cycling is between $Fe_{0.947}O$ and Fe_3O_4. Overall solids conversions were used to confirm that a specified transition had occurred and typically returned values of $0.75 < X < 0.85$. A stream of N_2 was used to purge the system for 60 to 120 s between the reducing and oxidizing phases. A complete reduction and oxidation cycle was first performed without any iron oxide present prior to each experiment to ensure inertness of the bed material, thermocouple and reactor. The designated particles were then poured into the reactor during a phase of N_2 flow. Pouring the particles into the bed prior to the reducing gas being switched on allowed the temperature of the particles to equilibrate and permitted the displacement of any air within the particle matrix prior to reaction. The reduction and oxidation cycles were then performed and the rate was determined as the difference between the inlet and the outlet mole fraction of the reactant multiplied by the total molar flowrate of fluidizing gas. To obtain the initial rate, a linear fit of rate (r″) *versus* conversion, X, was performed over the range $0.1 < X < 0.7$ and the intercept at $X = 0$ was used.

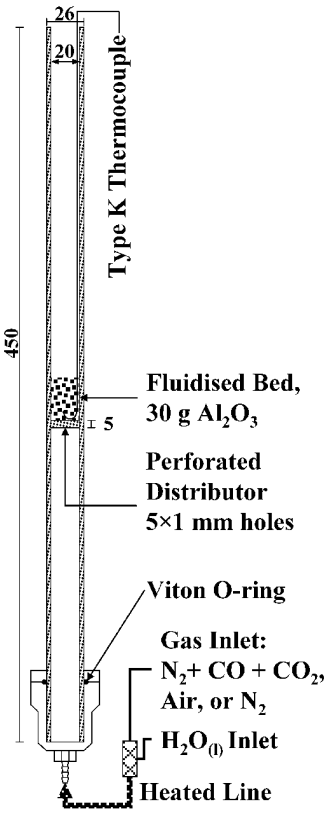

Fig. 1 Schematic diagram of the fluidized bed. All lengths are in mm

THEORY

For each particle, the reactions proceed *via* a series of steps, a combination of which could be rate limiting: (i) mass transport of gaseous reactant to the particle surface, (ii) diffusion of the reactant through the product layer, (iii) chemical reaction between reactant gas and solid species, (iv) diffusion of the gaseous product through the product layer, and (v) mass transport of product gas from the surface into the bulk gas. Because the investigation pertains to a kinetic rather than a hydrodynamic study, the size of the fluidized bed is irrelevant so long as it provides sufficient mass and heat transfer, i.e. it can be assumed to have uniform temperature and gas composition throughout. Mass transfer resistances between the particulate phase and the bubble phase within the fluidized bed were determined to be negligible: by measuring the rate as increasingly large samples were added, a crossflow factor > 2.6 was determined for all experiments (Davidson and Harrison, 1963). This implies that the difference between a perfectly mixed CSTR and the reactor was less than 7 %, confirming satisfactory mass transfer.

The rate of reduction for reaction R1 or R2 in a single particle can be expressed as,

$$r' = \frac{k_j}{W_p}\int_0^R \left(c_A(r) - \frac{c_B(r)}{K_p} \right) 4\pi r^2 dr \quad \frac{\text{mol}}{\text{s g}} \tag{1}$$

where k_j is the forward rate constant for reaction j based on a unit volume of solid, K_p is the equilibrium constant, W_p is the mass of the particle, $c_A(r)$ and $c_B(r)$ are, respectively, the concentration of reactant species A and product species B, r is the radial position, and R is the external radius of the particle. In an individual particle, the rate of reaction could depend on both intraparticle diffusion and intrinsic reaction. Assuming, (i) equimolar counterdiffusion, (ii) the pseudo-steady state hypothesis and (iii) first order reactions, the spatially-dependent concentration terms $c_A(r)$ and $c_B(r)$ can be calculated. Incorporating the resistance to mass transfer through the gas film external to the particle and assuming the reactor behaves as a well-mixed CSTR due to large crossflow then gives:

$$r'' = k_{j,ov}\frac{N}{W}\left(c_{A,out} - \frac{c_{B,out}}{K_p} \right) \quad \frac{\text{mol}}{\text{s g}} \tag{2a}$$

where,

$$k_{j,ov} = \frac{1}{\underbrace{\frac{1}{4\pi R^2 k_{A,g}}}_{\text{external mass transfer A}} + \underbrace{\frac{3}{4\pi R^3 \eta k_j}}_{\text{reaction}} + \underbrace{\frac{1}{4\pi R^2 k_{B,g} K_p}}_{\text{external mass transfer B}}} \tag{2b}$$

$$\eta = \frac{3}{\phi^2}(\phi\coth(\phi) - 1) \quad \text{and} \quad \phi = R\sqrt{\frac{k_j}{D_A} + \frac{k_{-j}}{D_B}} \tag{3}$$

Here, $c_{A,out}$ and $c_{B,out}$ are the outlet concentrations of A and B in the gas, η is the effectiveness factor, N the number of reacting particles, W the total mass of the particles, ϕ the Thiele modulus, and D_i the effective diffusivity of species i. This definition of η and ϕ is similar to that of Levenspiel (1999), but includes the reverse reaction. D_i was calculated with $D_i = D_{i,mix}\varepsilon/\tau$ with the diffusivities, $D_{i,mix}$, taken from Hirschfelder *et al.* (1954) and τ being a fitted tortuosity discussed later. The value of $k_{i,g}$ in Eq. (2) was determined using: $Sh = 2\varepsilon_{mf} + 0.69Re^{1/2}Sc^{1/3}$ (La Nauze, 1985). The product $k_j\eta$ can be interpreted as an observed rate constant and is denoted here as $k_{j,obs}$.

RESULTS AND DISCUSSION

Transition from Fe_2O_3 to Fe_3O_4

Figure. 2 shows a plot of k_1 and $k_{1,obs}$ *versus* particle radius, R, for the second reduction cycle from Fe_2O_3 to Fe_3O_4 at 823 K. The first cycle is omitted from the graph because it was found to be markedly different from the subsequent nine cycles. For R < 300 μm, the observed rate constant is approximately independent of particle size with $k_1 \approx 480$ s^{-1}. As the radii of the particles increase, however, $k_{1,obs}$ begins to decrease. The transition point, $R \approx 300$ μm, therefore corresponds to the radius where intraparticle mass transfer begins to appreciably influence the observed reaction rate. The value of k_1 is also shown in Fig. 2 and was calculated iteratively by (i) choosing a value of η, (ii) solving for k_1 using Eq. (2), (iii) checking the value of η from ϕ using Eq. (3), and (iv) returning to step (i) with a new estimate of η until convergence was achieved. Here, the value for the tortuosity, τ, was taken as a fitting parameter. By applying this method, Fig. 2

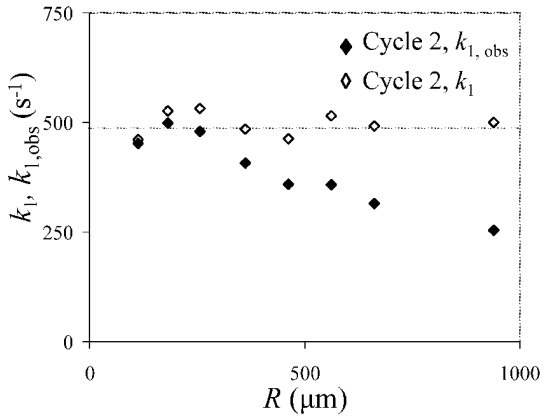

Fig. 2 Rate constants, k_j and $k_{j,obs}$, *versus* particle radius for the transition from Fe_2O_3 to Fe_3O_4 at 823 K

demonstrates that the constant value of $k_1 \approx 480$ s^{-1} can be successfully calculated from $k_{j,obs}$ for particles with 100 μm < R < 940 μm using $\tau = 3$. For smaller particles, $\eta \approx 1$, and Fig. 2 shows that the effectiveness factor correction has little influence on the value of k_1. Rate constants for particles with R < 115 μm could not be obtained due to elutriation.

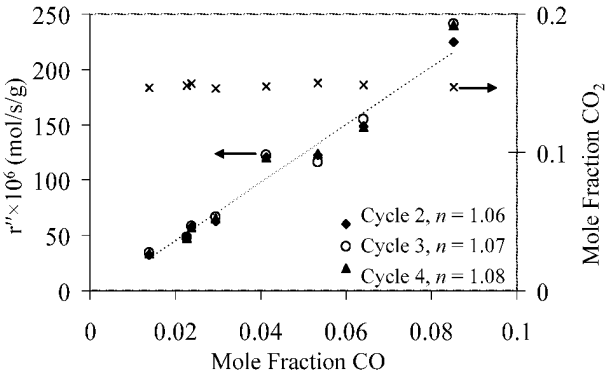

Fig. 3 Rate *versus* mole fraction of CO supplied to the reactor for the transition from Fe_2O_3 to Fe_3O_4 at 823 K

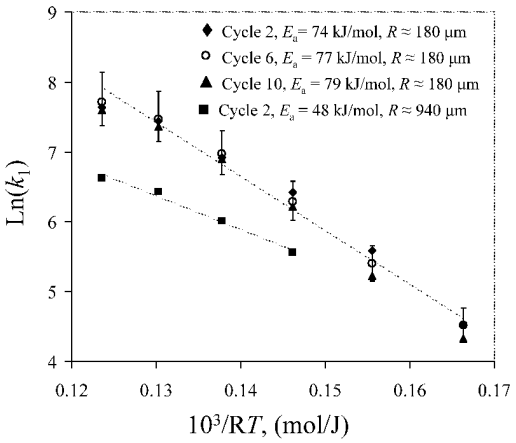

Fig. 4 Activation energy plot for the transition from Fe_2O_3 to Fe_3O_4 from 723 to 923 K

The analysis in the previous section was based on the reduction of Fe_2O_3 to Fe_3O_4 being first order with respect to [CO] and [CO_2]. At constant T, flowrate of the inlet gas, and particle size, Eq. (2) gives $r'' \propto c_{CO,out} - c_{CO_2,out}/K_p$. Considering the bed to be a well-mixed CSTR, the rate can be rewritten in terms of the inlet concentrations such that $r'' \propto c_{CO,in} - c_{CO_2,in}/K_p$ for a first order reaction. This has the form $y = mx^n + b$ with n = 1. Here, $b = c_{CO_2,in}/K_p$ is the equilibrium offset which was held constant by maintaining a fixed mole fraction of CO_2 in the inlet gas of 15 vol. %, as shown by the right hand ordinate in Fig. 3. A fit of r'' versus inlet [CO], see Fig. 3, demonstrates that the power on the [CO] term is near unity. The rate as a function of [CO] supplied can therefore be approximated by a straight line passing through the origin, confirming the first order assumption. The influence of [CO_2] on the reduction from Fe_2O_3 to Fe_3O_4 (R1) is overwhelmed by the large equilibrium constant, $K_p = 1.47\times10^5$, at 823 K. As a result, the effect of the back reaction was negligible.

The activation energies for the transition from Fe_2O_3 to Fe_3O_4, were found by assuming that k_1, in Eq. (2), is of an Arrhenius form, *i.e.* $k_1 = k_0\exp(-E_a/RT)$. From Fig. 4, it is clear that the rates are reproducible over several cycles of reduction. The E_a for particles with $R \approx 180$ μm is 75 ± 12 kJ/mol; the pre-exponential factor is $k_0 = \exp(17.1)$. The error in the rate constant is listed as an error in the activation energy only and was determined *via* a t-statistic such that ± *Error* = (t*)(standard error in slope of line). t* is the critical t-statistic for a two-tailed test with a 90 % confidence interval and $m - 2$ degrees of freedom, where m is the number of points used to fit the line. The combination of $E_a = 75$ kJ/mol and $k_0 = \exp(17.1)$ s^{-1} predicts all rate constants to within 50 % for particles with $R \approx 180$ μm. The error bars in Fig. 5 were calculated by considering the combination of experimental errors that gave the largest and smallest values of k_j; they therefore represent maximum experimental error, not the error from the t-statistic analysis.

Fig. 4 also shows the activation energy obtained from $k_{1,obs}$ to be 48 ± 13 kJ/mol for particles with $R \approx 940$ μm in cycle 2. This value is slightly greater than half the E_a for the particles with $R \approx 180$ μm, which would be expected if these larger particles were reacting with a significant intraparticle concentration gradient and an effectiveness factor of ~3/ϕ. Fig. 2 already confirmed that intraparticle diffusion markedly influenced the rate for these larger particles. This analysis serves as a check of the reported E_a and suggests that the measurements of the reduction of particles from Fe_2O_3 to Fe_3O_4 with $R \approx$ 180 μm capture the correct kinetics.

One consideration when incorporating a rate expression into a kinetic model is how k_j varies with conversion. A convenient form of incorporating the conversion dependence is to define $k_j(X) = k_j f(X)$, where

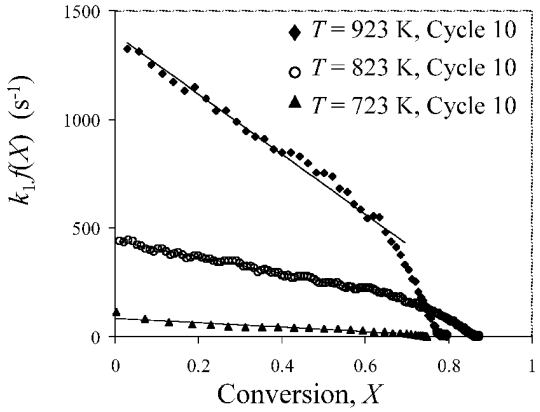

Fig. 5 Rate constant, k_j, *versus* conversion for the transition from Fe_2O_3 to Fe_3O_4

the function $f(X)$ is unity at $X = 0$ and k_j is, as before, the initial rate constant. Fig. 5 shows $k_1 f(X)$, as a function of X, which, as expected, approaches zero at $X = 1$. For $0.1 < X < 0.7$, k_1 can be fitted to a linear function of X (as seen by the solid black lines in Fig. 5). At $T = 923$ K, the linear fit is unsatisfactory at higher conversions; but still approximately passes through the point $(k_1 f(X), X) = (0,1)$.

Transition from Fe_3O_4 to $Fe_{0.947}O$

To investigate the reduction of Fe_3O_4 to $Fe_{0.947}O$, the temperature was raised to 923 – 1173 K. Fig. 6 shows the rate constant, $k_{2,obs}$, as a function of particle radius at 1023 K. Because the initial transition in cycle 1 corresponds to the reduction of Fe_2O_3 to $Fe_{0.947}O$, cycle 2 is shown. The observed rate constant, $k_{j,obs}$, for the reduction reaction (R2) is independent of particle size for $R < 300$ μm. As the radius increases, this rate constant decreases. Applying the iterative procedure with the effectiveness factor correction, the original value of $k_2 \approx 650$ s^{-1} can be recovered from $k_{2,obs}$ for all particles tested with 100 μm $R < 1200$ μm and using a fitted tortuosity of $\tau = 3.5$. From Fig. 6, in order to conduct experiments where the intrinsic kinetics present the most significant resistance, particles with $R < 300$ μm should be used.

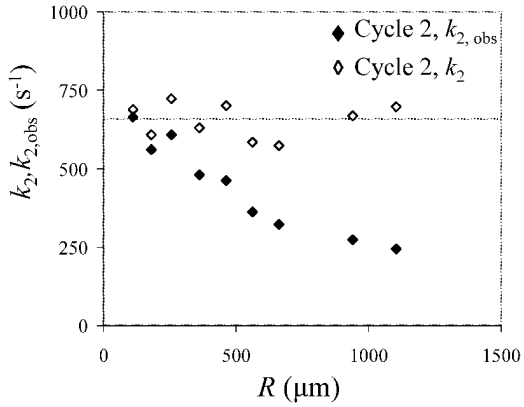

Fig. 6 Rate constants, k_j and $k_{j,obs}$, *versus* particle radius for the transition from Fe_3O_4 to $Fe_{0.947}O$ at 1023 K

The dependence of the rate on [CO] and [CO_2] was investigated using particles with $R \approx 180$ μm at 1023 K. Again, assuming a first order reaction, r″ can be written in terms of the inlet concentrations such that $r'' \propto c_{CO,in} - c_{CO_2,in}/K_p$. Fig. 7 shows that a power law fit of the form $y = mx^n + b$ gives a linear dependence upon inlet [CO]. Here, temperature, flowrate of the inlet gas and inlet [CO_2] were held approximately constant and inlet [CO] was varied between 7 vol. % and 13 vol. %. The equilibrium offset is indicated by the vertical dashed line (left) representing the equilibrium mole fraction of CO for the transition from $Fe_{0.947}O$ to Fe_3O_4; the dashed line (right) corresponds to the transition from $Fe_{0.947}O$ to Fe. The narrow window of operation is evident. A power law fit offset by the equilibrium mole fraction of CO indicates that the reaction from Fe_3O_4 to $Fe_{0.947}O$ is, to a good approximation, 1st order in [CO]. The linear fit is reproducible over multiple cycles of reduction. Fig. 8 shows the dependence of the rate on the inlet mole fraction of CO_2 at 1023 K for the transition from Fe_3O_4 to $Fe_{0.947}O$. Here, the mole fraction of CO has been maintained at ~9 vol. %. The left dashed line is the equilibrium mole fraction of CO_2 for the transition from $Fe_{0.947}O$ to Fe, while the right dashed line represents that for the transition from Fe_3O_4 to $Fe_{0.947}O$. A power law fit demonstrates that a reaction order of 1 is a good approximation for the exponent on the [CO_2] term. Thus, both forward and reverse reactions for (R2) are first order.

The activation energy for the reduction from Fe_3O_4 to $Fe_{0.947}O$ was determined using the values of k_2 obtained from Eq. (2). Fig. 9 shows E_a *vs.* cycle number for particles with $R \approx 180$ μm. Here, the activation energy drops progressively with cycle number: $E_a = 184 \pm 53$ kJ/mol in cycle 2, $E_a = 129 \pm 29$ kJ/mol in cycle 6 and $E_a = 89 \pm 17$ kJ/mol in cycle 10. The overall rate constant decreases. The error bars, shown only for particles with $R \approx 180$ μm and cycle 2, represent the experimental error and increase with temperature. The

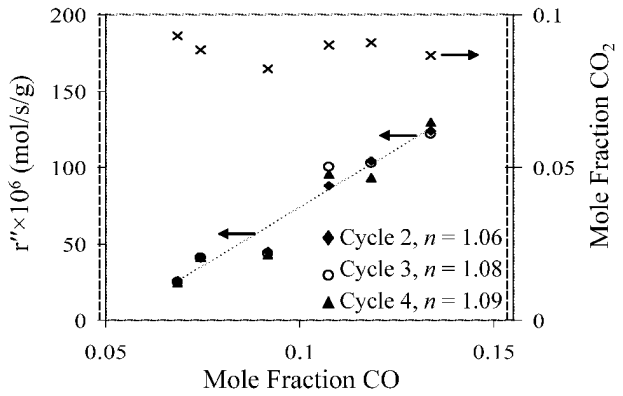

Fig. 7 Rate versus mole fraction of CO in the inlet gas for the transition from Fe_3O_4 to $Fe_{0.947}O$ at 1023 K

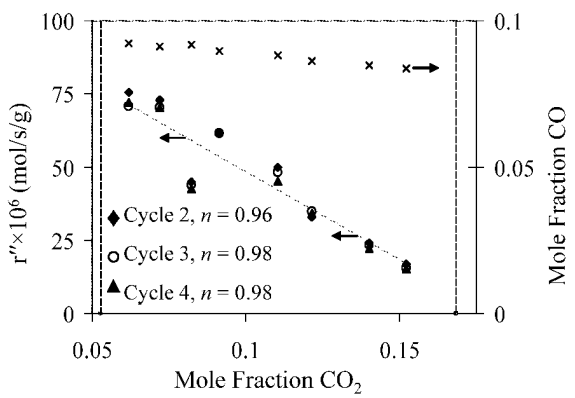

Fig. 8: Rate versus mole fraction of CO_2 in the inlet gas for the transition from Fe_3O_4 to $Fe_{0.947}O$ at 1023 K

higher error at higher temperatures is a result of dividing the rate by the term, $c_{CO,out} - c_{CO2,out}/K_p$, which approaches the equilibrium value, *i.e.* 0, more readily when the rate is faster. At T = 1173 K the lower flowrates used to obtain U/U_{mf} ~ 7 mean that uncertainty in the mass transfer coefficients, $k_{i,g}$, which was estimated to be 20 %, also affects the error. The error in $k_{i,g}$ was not important at temperatures below 1173 K. If only the four points for cycle 2 between 923 K and 1023 K are taken, a revised analysis gives E_a = 121 kJ/mol. Fig. 9 also shows $\mathrm{Ln}(k_{j,obs})$ for particles with $R \approx 940$ μm at cycle 2. Here, E_a = 51 ± 14 kJ/mol, significantly less than that observed for cycle 2, but approximately one half that observed for cycle 10. Considering the rate analyses above, a reasonable approximation for rate of reduction from Fe_3O_4 to $Fe_{0.947}O$ was determined to have E_a = 90 ± 29 kJ/mol and $k_0 = \exp(16.6)$ s^{-1} for particles with $R \approx 180$ μm. This combination, with E_a fixed at 90 kJ/mol, predicts rate constants for cycles 6 through 10 to within a factor of 2.

Fig. 10 shows a plot of $k_2 f(X)$ as a function of conversion, X. Similar to the case for the Fe_2O_3 to Fe_3O_4 transition, the rate constant decreases monotonically with X. Unlike the prior transition however, the curvature is positive. A linear fit is shown by the solid lines in Fig. 10 and is reasonable for T = 923 K. At the higher temperatures, the linear fit of the rate is unsatisfactory, particularly for $X < 0.2$.

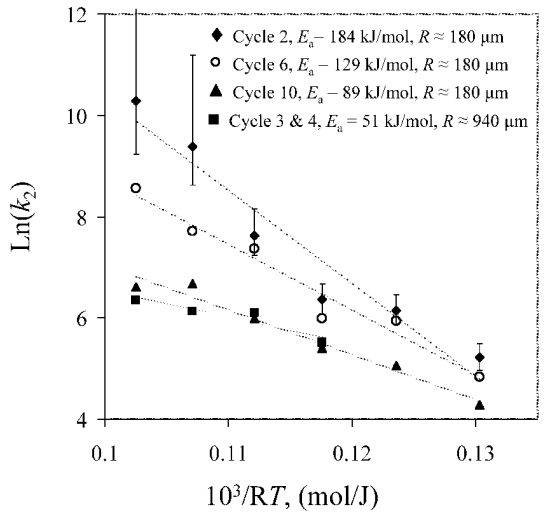

Fig. 9 Activation energy plot for the transition from Fe_3O_4 to $Fe_{0.947}O$ from 923 to 1173 K

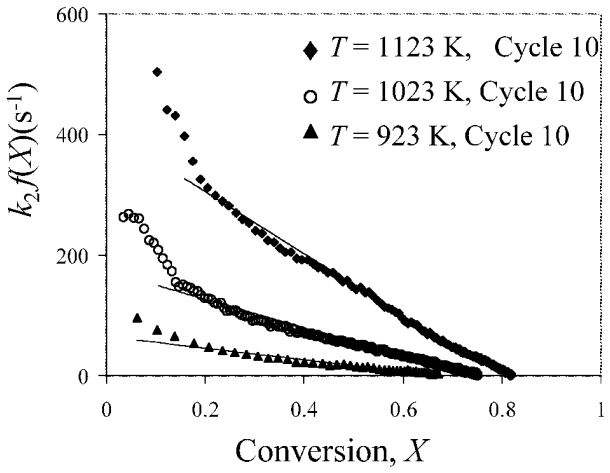

Fig. 10 Rate versus conversion for the transition from Fe_3O_4 to $Fe_{0.947}O$

CONCLUSIONS

The kinetics for the reduction of Fe_2O_3 to Fe_3O_4 and Fe_3O_4 to $Fe_{0.947}O$ in mixtures of CO and CO_2 were studied in a fluidized bed reactor. It was determined that both reactions are first order with respect to concentration of CO and CO_2. The rate constants can be expressed in Arrhenius form, $k_j = k_0 \exp(-E_a/RT)$ with:

$k_0 = \exp(17.1)$ s^{-1}	E_a = 75 ± 12 kJ/mol	Fe_2O_3 to Fe_3O_4	(R1)
$k_0 = \exp(16.6)$ s^{-1}	E_a = 90 ± 29 kJ/mol	Fe_3O_4 to $Fe_{0.947}O$	(R2).

The activation energy for the transition from Fe_2O_3 to Fe_3O_4 remained approximately constant with cycle number, while that for the transition from Fe_3O_4 to $Fe_{0.947}O$ decreased. Both values of activation energy were verified by showing that for particles where diffusion is influencing, the observed activation energies decrease by a factor of ~2.

NOTATIONS

A,B species of CO and CO_2, no units
$c_{i,out}$ concentration of species i at outlet, mole/m^3
$c_{i,in}$ concentration of species i at outlet, mole/m^3
D_{bed} diameter of fluidized bed, m
D_i effective diffusivity of species i, m^2/s
$D_{i,mix}$ diffusivity of species i in the mixture, m^2/s
d_p particle diameter, m
E_a activation energy, J/mol
H_{mf} bed height at minimum fluidization, m

k_j rate constant of reaction j, s^{-1}
$k_{i,g}$ mass transfer coefficient for species i, m/s
k_0 pre-exponential factor, s^{-1}
K_p equilibrium constant, no units
$k_{j,ov}$ overall rate constant, m^3/s
N number of particles, no units
r′ rate constant for a single particle, mol/(s g)
r″ rate constant for N particles, mol/(s g)
R ideal gas constant, J/(mol K)
R initial particle radius, m
r particle radius, m
Re Reynolds number
Sc Schmidt number
Sh Sherwood number, $k_{i,g}d_p/D_{i,mix}$
T temperature, K
U superficial fluidizing velocity, m/s
U_{mf} minimum fluidizing velocity, m/s
W weight of particles, kg
W_p weight of single particle, kg
X conversion, no units
ε porosity of particle, no units
η effectiveness factor, no units
τ tortuosity of particle (=2), no units
τ_i mixing time constant for species i, s
ϕ Thiele modulus, no units

ACKNOWLEDGEMENTS

Financial support from the following organizations is gratefully acknowledged: Engineering and Physical Sciences Research Council (EP/F027435/1); Gates Cambridge Trust.

REFERENCES

Bohn, C.D., Mueller, C.M., Cleeton, J.P., Hayhurst, A.N, Davidson, J.F., Scott, S.A., Dennis, J.S.: Production of very pure hydrogen with simultaneous capture of carbon dioxide using the redox reactions of iron oxides in packed beds. Ind. Eng. Chem. Res. 47 (2008), pp. 7623-7630.

v. Bogdandy, L.; Engell, H.J.: The Reduction of Iron Ores. Springer-Verlag. (1971), pp. 19-30.

Hirschfelder, J.O., Curtiss, C.F., Bird, R.B.: Molecular theory of gases and liquids. John Wiley. (1954).

La Nauze, R. D.: Chem. Eng. Res. Des. 63 (1985), pp. 3-33.

Levenspiel, O.: Chemical Reactor Engineering, 3rd Edition. John Wiley. (1999), pp. 385-391.

Trushenski, S.P., Li, K., Philbrook, W.O.: Non-topochemical reduction of iron oxides. Metall. Trans. 5 (1974), pp. 1149-1158.

Tsay, Q.T., Ray, W.H., Szekely, J.: The modelling of hematite reduction with hydrogen plus carbon monoxide mixtures. AIChE J. 22 (1976), pp. 1064-1071.

Wen, C.J., Yu, Y.H.: A generalized method for predicting the minimum fluidization velocity. AIChE J. 12 (1966), pp. 610-612.

CO_2 CAPTURE USING DRY POTASSIUM-BASED SORBENTS IN A BUBBLING FLUIDIZED-BED REACTOR

C.W. Zhao, X.P. Chen, C.S. Zhao

School of Energy & Environment, Southeast University, Nanjing, 210096, China

Abstract: A bubbling fluidized-bed reactor was used to study the CO_2 capture characteristics of dry potassium-based sorbents. Potassium-based sorbents were prepared by impregnation with potassium carbonate on supports such as cocoanut activated charcoal (AC#1), coal active carbon (AC#2), activated alumina (Al_2O_3), silica gel (SG) and diatomite. Sorbents such as K_2CO_3/AC#1, K_2CO_3/AC#2, and K_2CO_3/Al_2O_3 showed excellent carbonation capacity, the conversion rates of those sorbents were 92.5%, 85.1%, and 88.2%, respectively. The regeneration rates of those sorbents were 87.1%, 83.9% and 86.7%, respectively. SEM and N_2 adsorption tests showed that the surface area and pore volume of those sorbents were 669 m^2 g^{-1}, 390 m^2 g^{-1}, 139 m^2/g, and 0.08 cm^3/g, 0.17 cm^3/g, 0.34 cm^3/g, respectively. The particle morphologies of those sorbents are propitious to the carbonation reaction. However, K_2CO_3/diatomite and K_2CO_3/SG showed poor carbonation capacity, the conversion conversions were only 2.0% and 1.9%, respectively. The surface area and pore volume of two sorbents were 1.1 m^2/g, 39 m^2/g and 0.004 cm^3/g, 0.33 cm^3/g, respectively. The carbonation capacity is affected by the particle morphology of those sorbents. The present work has provided data base for designing and operating a large scale CO_2 capture process with two fluidized-bed reactors.

Keywords: CO_2 capture, potassium-based sorbent, carbonation, fluidized-bed reactor

INTRODUCTION

Global warming is emerging as the important environmental issue of the 21st century. Since CO_2 is the principal greenhouse gas of interest, and fossil-fuel fired power plants are the largest stationary sources of CO_2 emissions (Berger, 2002), capturing CO_2 from these sources is of critical importance.Although various CO_2 capture options are available, such as precombustion decarbonization (Freund and Haines, 2002), O_2 combustion with CO_2 recycle (Jordal et al., 2004), chemical looping combustion (Hossain and Lasa, 2008), and post-combustion capture (Oexmann et al., 2008). However, a process which is inexpensive, low energy demand, and has high activity with CO_2, is still under development.

Recently, dry alkali metal-based sorbents for capturing CO_2 from flue gas is investigated as an innovative concept for CO_2 recovery (Hoffman and Pennline, 2001; Liang et al., 2004; Yi et al., 2005; Cho et al., 2006; Seo et al., 2007; Lee et al., 2008 (a, b, c)). CO_2 capture using dry sodium-based sorbent were reported (Liang et al., 2004; Seo et al., 2007; Lee et al., 2008a). However, when CO_2 reacted with Na_2CO_3, the global carbonation reaction rate was rather slow. The CO_2 absorption and regeneration of potassium-based sorbents such as K_2CO_3/AC, K_2CO_3/TiO_2, K_2CO_3/MgO, K_2CO_3/ZrO_2 and K_2CO_3/Al_2O_3 were studied in a fixed-bed reactor using multiple tests (Lee et al., 2006, 2007, 2008b, 2008c). The mechanism was mainly investigated from the changes in chemical constituents of sorbents before/after carbonation reaction. However, the effect of the microscopic structure of sorbents for carbonation was not mentioned. The kinetics of CO_2 sorption by K_2CO_3 in porous matrix were even studied in fixed-bed reactor (Okunev et al., 2000; Sharonov et al., 2004). However, Cho et al. (2006) suggested that the proper reactor for this process to treat flue gases from fossil-fuel fired power plants is fluidized-bed or transport reactor. Yi et al. (2005, 2006, 2007) presented some results from a fluidized-bed reactor or two fluidized-bed reactors. Their main sorbent was sodium-based sorbent. The CO_2 capture characteristics of dry potassium-based sorbents in fluidized-bed reactor have not been reported.

Zhao et al. (2008) reported that K_2CO_3 with microstructure of hexagonal crystal has excellent carbonation capacity. This paper studies CO_2 capture characteristics of dry potassium-based sorbents which are prepared by impregnating K_2CO_3 with microstructure of hexagonal crystal on several porous matrix in a bubbling fluidized-bed reactor. In addition, the mechanism is analyzed from the differences in microscopic structure, particle morphology and chemical constituents of those sorbents.

EXPERIMENTAL

Sorbents Preparation

The potassium-based sorbents used in this study were prepared by impregnating K_2CO_3 with microstructure of hexagonal crystal on supports such as cocoanut activated charcoal (AC#1), coal active carbon

(AC#2), activated alumina (Al_2O_3), silica gel (SG) and diatomite. 100 g supports were added to an aqueous solution containing 50 g of K_2CO_3 in 500 ml of de-ionized water. Then, it was mixed with a magnetic stirrer at room temperature for 10 h. After stirring, the mixture was dried in a oven at 105 °C. The dried samples were calcined in a muffle furnace for 2 h at 300 °C. The samples were prepared with the same particle sizes of 450-600 μm.

Apparatus and procedure

Figure. 1 shows the schematic diagram of the experimental apparatus for the carbonation and regeneration of these potassium-based sorbents.

The apparatus consists of a gas injection part (CO_2 and N_2 were obtained from high purity cylinders with mass flow controllers to control flow. H_2O was fed using a high-precision piston pump, then heated to ensure water complete vaporization), a bubbling fluidized-bed reactor (with an inner diameter of 0.05 m and a height of 1.0 m, was made of stainless steel, and placed inside of electric heating. temperature was controlled by a temperature controller, and measured by a precision digital thermometric instrument), gas post-treatment part (a filter to remove dust, and a condenser to remove H_2O), and gas analyzer (analyzes CO_2 every 2 s).

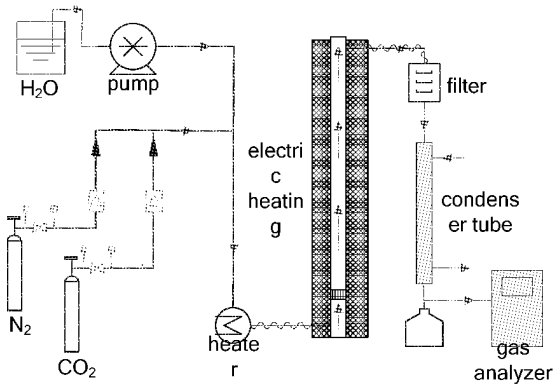

Fig. 1 The schematic diagram of experimental apparatus for potassium-based sorbents capturing CO_2

As the critical fluidization velocity of those sorbents is in the range of 0.08-0.1 m/s, 0.2 kg of the sorbent was placed into the reactor, to simulate real flue gas composition, a gas mixture of 15% CO_2, 70% N_2 and 15% H_2O at 2 m^3 h^{-1} was used for carbonation reactions. The carbonation temperature was maintained at 60 °C. After carbonation reaction completed, the gas composition was changed to 100% N_2 at 2 m^3 h^{-1}. When CO_2 concentration decreased to zero, the temperature was risen to 200 °C. Calcination was carried out.

An Accelerated Surface Area and Porosimetry 2020 Micropore Physisorption Analyzer was used for BET surface area and porosity determinations. The amount of alkali metal impregnated was determined by a Hitachi 180-80 atomic absorption spectrometer, the shape of sorbents from the view of microscopic was observed with a JSM-5610LV-VANTAGE SEM, and the structural change of sorbents before and after the carbonation reactions was examined with a D/max2500 VL/PC X-ray diffractometry (XRD).

RESULTS AND DISCUSSION

Test result of a single carbonation–regeneration cycle

A typical test result during carbonation–regeneration cycle using those potassium-based sorbents in a bubbling fluidized-bed reactor is shown in Fig. 2 where CO_2 concentration is plotted versus time. The left part of the figure represents the carbonation reaction and the right part represents the regeneration reaction.

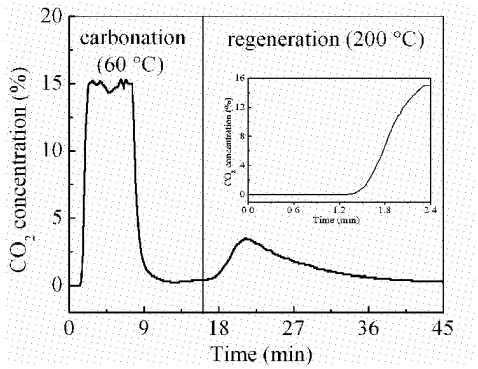

Fig. 2 Typical test result of a single carbonation–regeneration cycle. The box shows the carbonation section within 2.4 minutes

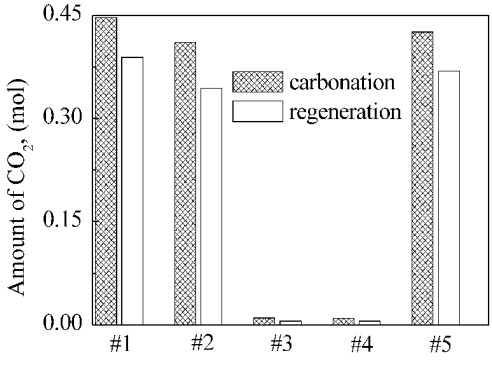

Fig. 3 The amount of CO_2 removed by carbonation and released by regeneration #1: K_2CO_3/AC#1; #2: K_2CO_3/AC#2; #3: K_2CO_3/ diatomite; #4: K_2CO_3/SG; #5: K_2CO_3/ Al_2O_3

CO_2 was not detected at beginning. After 1.3 minutes, CO_2 concentration was rapidly increased to 15%

within 1 minute. 15 minutes letter, calcination was carried out. CO_2 was initially detected at about 120 °C, reached a maximum of 3.5% after just over 6 minutes, and then decreased to zero by 25 minutes, indicating that calcination was complete. Good material balance closure was obtained with numerical integration of the area upon/under the curve. The amount of CO_2 removed by carbonation and released by regeneration for those sorbents was shown in Fig. 3.

Based on the conversion of K_2CO_3 to $KHCO_3$, the carbonation conversion η_C and the regeneration conversion η_R are calculated from:

$$\eta_C = \frac{n_{CO_2\ removel} \times M_{K_2CO_3}}{200 \times \frac{1}{3}} \times 100\% \quad (1)$$

$$\eta_R = \frac{n_{CO_2\ release}}{n_{CO_2\ removel}} \times 100\% \quad (2)$$

where, $n_{CO_2\ removel}$ (mol) is the amount of CO_2 removed by carbonation, $n_{CO_2\ release}$ (mol) is the amount of CO_2 released by regeneration, 200 (g) is the total weight of sorbents, $\frac{1}{3}$ is the content of K_2CO_3 in sorbent, and $M_{K_2CO_3}$ (g/mol) is the molecular weight of K_2CO_3. The result is shown in Table 1

Table 1 The carbonation conversion and the regeneration conversion of those sorbents

	K_2CO_3/AC#1	K_2CO_3/AC#2	K_2CO_3/ diatomite	K_2CO_3/SG	K_2CO_3/ Al_2O_3
η_C	92.5%	85.1%	2.0%	1.9%	88.2%
η_R	87.1%	83.9%	53.3%	55.6%	86.7%

Table 1 shows that both the carbonation conversions and the regeneration conversions of K_2CO_3/AC#1, K_2CO_3/AC#2 and K_2CO_3/Al_2O_3 are about 83.9%-92.5% at single cycle test. The CO_2 capture capacity is very higher. Lee et al. (2006, 2007, 2008b, 2008c) reported that K_2CO_3/AC and K_2CO_3/Al_2O_3 showed high CO_2 capture capacity in fixed-bed reactor test. This result is similar. However, the carbonation conversions of K_2CO_3/diatomite and K_2CO_3/SG are only 1.9%-2.0%. In order to find out the reason behind this result, the characteristics of these sorbents were investigated.

XRD tests results of those sorbents

The structural change of those sorbents before/after carbonation reaction was examined by XRD, and the XRD patterns are shown in Fig. 4. As the XRD patterns of K_2CO_3/AC#1 and K_2CO_3/AC#2 are similar, they are shown in Fig. 4 (a) using the same symbol of K_2CO_3/AC.

The XRD result shows that the main constituents of K_2CO_3/AC and K_2CO_3/Al_2O_3 are K_2CO_3 besides SiO_2 or Al_2O_3 in Fig. 4(a: I) and Fig. 4(d: I). After carbonation reaction, K_2CO_3 is completely converted to $KHCO_3$ (Fig. 4(a: II) and Fig. 4(d: II)). So the CO_2 capture capacities of K_2CO_3/AC#1, K_2CO_3/AC#2 and K_2CO_3/Al_2O_3 are very higher. Lee et al. (2006, 2007) showed that SiO_2 was not observed in the case of K_2CO_3/AC, and a new phase of $KAl(CO_3)_2(OH)_2$ was observed in the case of K_2CO_3/Al_2O_3. We attribute this to the difference of support materials and sorbents prepared process.

The XRD of K_2CO_3/SG shows that it is of amorphous state (Fig. 4(b: I)), which is assigned to silica gel. It is an amorphous substance, and its molecular formula is $mSiO_2 \cdot nH_2O$. The XRD patterns of K_2CO_3/SG have not changed after carbonation reactions in Fig. 4(b: II). The patterns of K_2CO_3 or $KHCO_3$ were not observed through the carbonation reaction. Okunev et al. (2000) reported that a new phase of K_2SiO_3 was formed by reaction between silica gel and K_2CO_3. It is not observed in this paper.

The main constituents of K_2CO_3/diatomite are $K_2CO_3 \cdot 1.5H_2O$ and SiO_2(Fig. 4(c: I)). After carbonation reaction, $K_2CO_3 \cdot 1.5H_2O$ is not converted to $KHCO_3$ (Fig. 4(c: II)). Zhao et al. (2008) reported that the carbonation reactivity of $K_2CO_3 \cdot 1.5H_2O$ was weak. This result can obtain the similar conclusion.

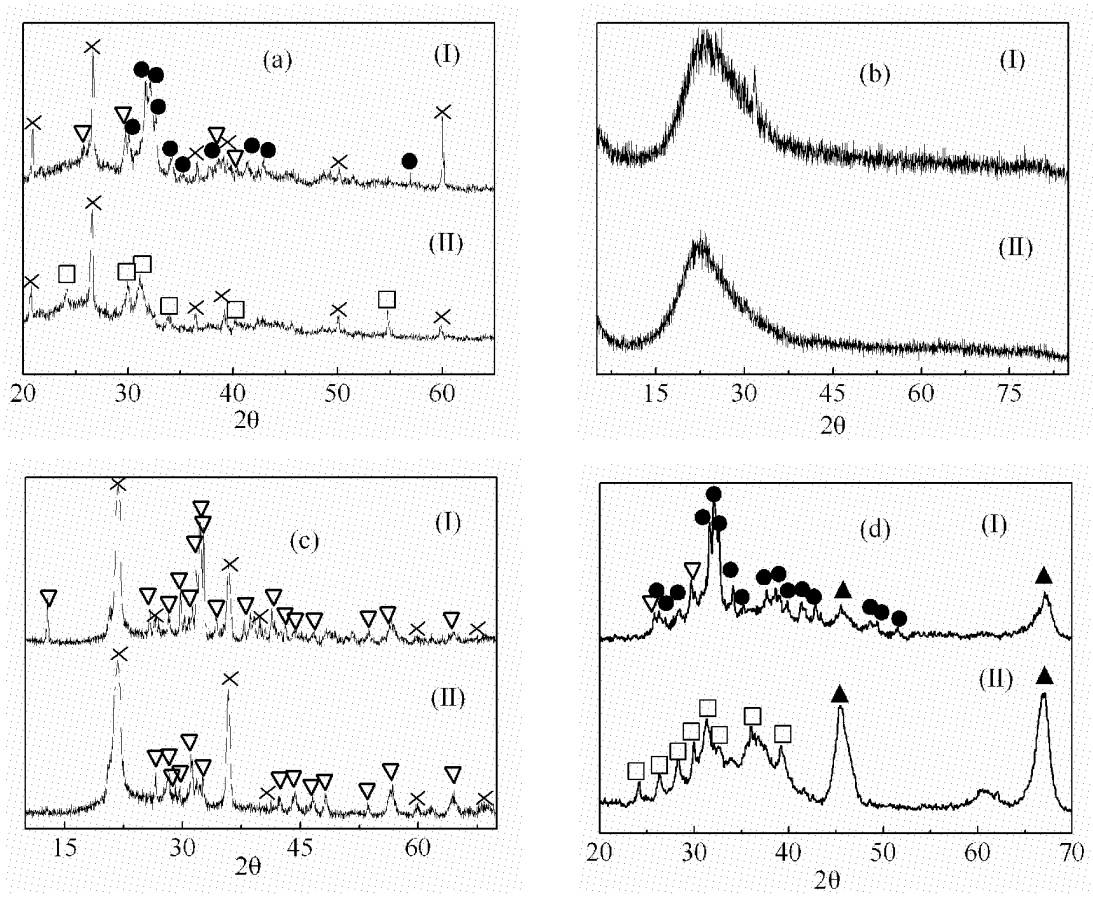

Fig. 4 The XRD patterns of those sorbents before/after carbonation reactions
(a) K_2CO_3/AC; (b) K_2CO_3/SG; (c) K_2CO_3/diatomite; (d) K_2CO_3/Al_2O_3;
(I) fresh; (II) after carbonation reaction; (×-SiO_2; ▽-$K_2CO_3 \cdot 1.5H_2O$; •-K_2CO_3; ■- $KHCO_3$; ▲- Al_2O_3)

N_2 adsorption tests results of those sorbents

In order to understand the reason that CO_2 capture capacities of various sorbents were different in detail, the surface area, pore volume and pore size distribution of these samples were obtained from N_2 adsorption tests, and the isotherm linear plots of those sorbents were shown in Fig. 5.

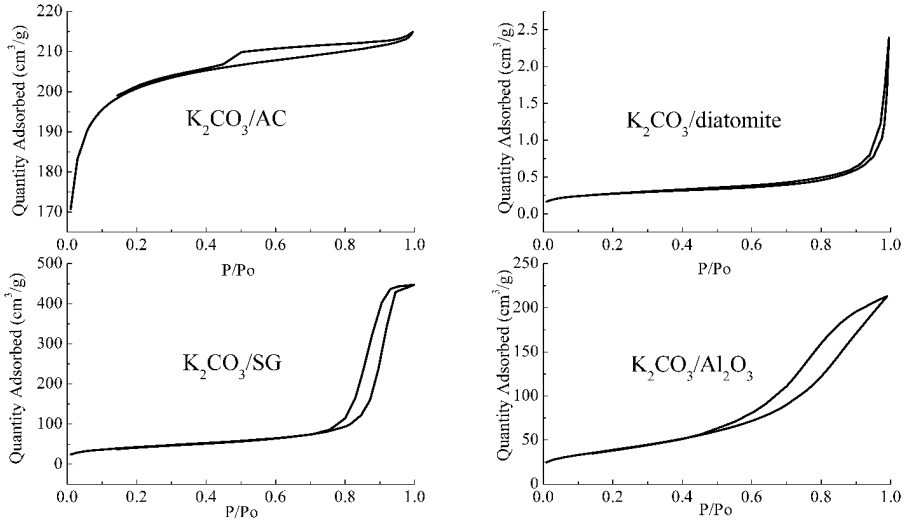

Fig. 5 The N_2 adsorption–desorption isotherm linear plots of those sorbents

The isotherm linear of K_2CO_3/AC belongs to Type II isotherms, K_2CO_3/diatomite is Type III adsorption, K_2CO_3/SG and K_2CO_3/Al_2O_3 are Type IV adsorption. Analyzed from Fig. 5, the pores of K_2CO_3/AC are mainly microporous, and the pore shapes are capillary space between parallel plates or open slit-shaped capillaries. K_2CO_3/diatomite is nearly non-porous, there are few conical or biconical capillaries, and the

adsorbate-adsorbent interactions are weak. K_2CO_3/SG and K_2CO_3/Al_2O_3 possess the characteristics of mesopores, and the pore shapes are mainly open-ended cylindrical pores lying in narrow range of radius. (Gregg and Sing, 1982)

According to the BET method, and Dubinin–Radushkevich (DR) method, the surface areas and pore volumes of those sorbents were obtained in Fig. 6.

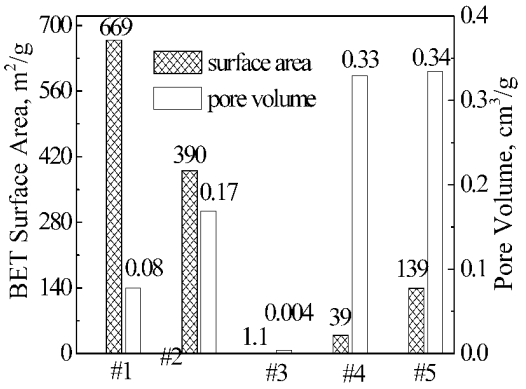

Fig. 6 The surface area and pore volume of those sorbents

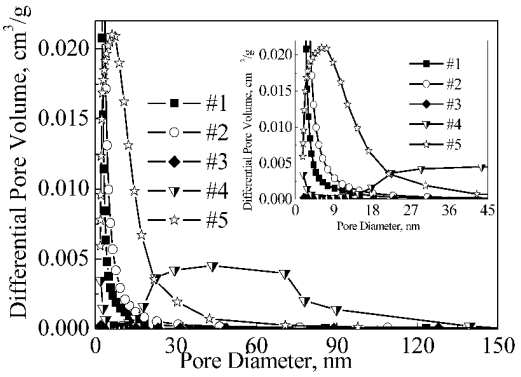

Fig. 7 The pore size distribution of those sorbents #1: K_2CO_3/AC#1; #2: K_2CO_3/AC#2; #3: K_2CO_3/diatomite; #4: K_2CO_3/SG; #5: K_2CO_3/Al_2O_3

As shown in Fig. 6, the surface areas of K_2CO_3/AC#1, K_2CO_3/AC#2, K_2CO_3/diatomite, K_2CO_3/SG and K_2CO_3/Al_2O_3 are 669 m^2/g, 390 m^2/g, 1.1 m^2/g, 39 m^2/g and 139 m^2/g, respectively. Their pore volumes are 0.08 cm^3/g, 0.17 cm^3/g, 0.004 cm^3/g, 0.33 cm^3/g and 0.34 cm^3/g. The surface areas of K_2CO_3/AC#1 and K_2CO_3/AC#2 are higher, and 90% pores of these sorbents are distributed from 0 nm to 4 nm which is shown in Fig. 6. The excellent CO_2 capture capacities of K_2CO_3/AC#1 and K_2CO_3/AC#2 are attributed to the extensively micropore structures of AC.

90% pores of K_2CO_3/Al_2O_3 are distributed from 2nm to 15nm (Fig. 6). As its pore volumes is the highest one among those sorbents. It can be deduced that K_2CO_3/Al_2O_3 has the extensively mesopores structures, and this character can improve the CO_2 adsorption.

There are two pore distribution ranges for K_2CO_3/SG, one is 0 nm to 5 nm, and another is 10nm to 100 nm. The average pore size of K_2CO_3/SG is 36.35 nm. Amine-modified ordered mesoporous silica with the similar pore size distribution of our K_2CO_3/SG has excellent CO_2 capture capacity (Zeleňák et al., 2008). However, Okunev et al. (2000) reported that CO_2 capture capacity of K_2CO_3/SG was low. This is an interesting result.

Both the surface area and pore volume of K_2CO_3/diatomite are very low, and the pore size distribution plot is a horizontal line near the zero. This character of microscopic structure is one reason for its bad CO_2 capture capacity.

SEM results for those sorbents

The particle morphologies of those sorbents were examined by scanning electron microscopy (SEM), and the results were shown in Fig. 8.

The differences of those sorbents in particle morphologies are clearly visible. The surfaces of K_2CO_3/AC#1, K_2CO_3/AC#2 and K_2CO_3/Al_2O_3 are uneven, and a lot of small pores and cracks distribute on the surface. By contraries, the surface of K_2CO_3/SG is smooth, pores are hardly seen on magnification of 1000.

Combined with the N_2 adsorption tests results, we can deduce that the pores of K_2CO_3/SG are mainly deep pores lying in narrow range of 10 nm-100 nm. This character of microscopic structure decreases CO_2 capture capacity. Then, combined with XRD result, we deduce that the solution of K_2CO_3 can hardly infiltrate into silica gel. So K_2CO_3 have not been loaded on the support.

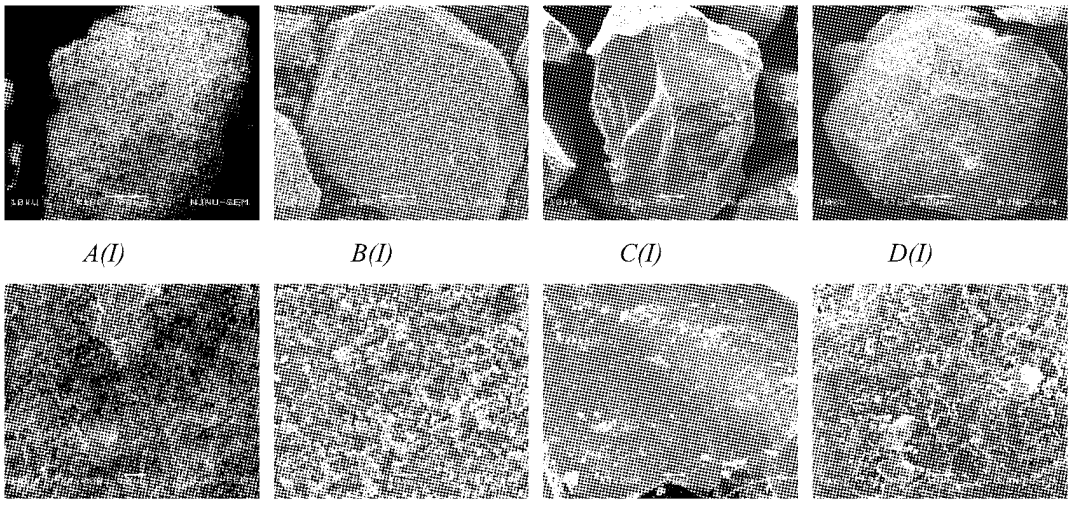

A(I) B(I) C(I) D(I)

A(II) B(II) C(II) D(II)

Fig. 8 The SEM images of different sorbents
(a) K_2CO_3/AC#1; (b) K_2CO_3/AC#2; (c) K_2CO_3/SG; (d) K_2CO_3/Al_2O_3
I: the whole particle morphology; II: Instrumental magnification ×1000

CONCLUSIONS

The CO_2 capture characteristics of dry potassium-based sorbents such as K_2CO_3/AC#1, K_2CO_3/AC#2, K_2CO_3/diatomite, K_2CO_3/SG and K_2CO_3/Al_2O_3 were studied in a bubbling fluidized-bed reactor. K_2CO_3/AC#1, K_2CO_3/AC#2, and K_2CO_3/Al_2O_3 showed excellent carbonation capacity. However, K_2CO_3/diatomite and K_2CO_3/SG showed poor carbonation capacity. The reason was analyzed from the microscopic structures, the crystal structures and the structural changes before/after carbonation reaction for those sorbents.

As the microscopic structure of K_2CO_3/diatomite is nearly non-porous structure, and the main constituent formed on diatomite is $K_2CO_3 \cdot 1.5H_2O$. The CO_2 capture capacity of K_2CO_3/diatomite is low. As K_2CO_3 could hardly be loaded on the support of silica gel. Silica gel is not a proper choice as the sorbent support either. K_2CO_3/AC shows excellent CO_2 capture capacity. However, its anti-attrition character is poor. So K_2CO_3/AC could not be used in fluidized bed. Maybe it can be used in fixed-bed reactor in future.

K_2CO_3/Al_2O_3 could be used as the sorbent that has the potential for a large scale CO_2 capture process with two fluidized-bed reactors. In order to investigate the sorbent durability, CO_2 capture capacity of K_2CO_3/Al_2O_3 as a function of cycle number in fluidized bed reactor should be reported later.

ACKNOWLEDGEMENTS

Financial support from National Natural Science Foundation (No. 50876021), the National Key Program of Basic research of China (No. 2006CB705806), the Foundation of Graduate Creative Program of Jiangsu Province (No. CX08B_141Z) and the Foundation for Excellent Doctoral Dissertation of Southeast University were sincerely acknowledged.

REFERENCES

Berger, A. (2002). The effect of greenhouse gases on climate. Proceedings of the Conference on Future Energy Systems and Technology for Abatement.

Cho, K.C., Lee, E.Y., Yoo, J.S., Choung, Y.H., Park, S.W., Oh, K.J. : Stud. Surf. Sci. Catal. **159** (2006), pp.549-552.

Freund, P. and Haines, M.R. (2002). Precombustion decarbonisation for power generation. Proceedings of the 6th International Conference on Greenhouse Gas Control Technologies.

Gregg, S.J. and Sing, K.S.W. (1982). Adsorption, surface area and porosity, 2ed, Academic Press, London

Hoffman, J.S. and Pennline, H.W. : J. Energy Environ. Res. **1** (2001), pp.90-100.

Hossain, M.M. and Lasa, H.I. : Chem. Eng. Sci. **63** (2008), pp.4433-4451.

Jordal, K., Anheden, M., Yan, J., Strömberg, L. (2004). Oxyfuel combustion for coal-fired power generation with CO_2 capture-Opportunities and challenges. Proceedings of the 7th International Conference on Greenhouse Gas Control Technologies.

Lee, J.B., Ryu, C.K., Baek, J., Lee, J. H., Eom, T. H., Kim, S. H. : Ind. Eng. Chem. Res. **47** (2008a), pp.4465-4472.

Lee, S.C. and Kim, J.C. : Catal. Surv. Asia. **11** (2007), pp.171-185.

Lee, S.C., Chae, H.J., Lee, S.J., Choi, B.Y., Yi, C.K., Lee, J.B., Ryu, C.K., Kim, J.C. : Environ. Sci. Technol. **42** (2008b), pp.2736-3741.

Lee, S.C., Chae, H.J., Lee, S.J., Park, Y.H., Ryu, C.K., Yi, C.K., Kim, J.C. : Journal of Molecular Catalysis B: Enzymatic. 2008c, **In Press**

Lee, S.C., Choi, B.Y., Lee, T.J., Ryu, C.K., Ahn, Y.S., Kim, J.C. : Catal. Today. **111** (2006), pp.385-390.

Liang, Y., Harrison, D.P., Gupta, R.P., Green, D.A., McMichael, W.J. : Energ. Fuel. **18** (2004), pp. 569-575.

Oexmann, J., Hensel, C., Kather, A. : Int. J. Greenhouse Gas Control. **2** (2008), pp.539-552.

Okunev, A.G., Sharonov, V.E., Aristov, Y.I., Parmon, V.N. : React. Kinet. Catal. L. **71** (2000), pp.355-362.

Seo, Y.W., Jo, S.H., Ryu, C.K., Yi, C.K. : Chemosphere. **69** (2007), pp.712-718.

Sharonov, V.E., Okunev, A.G., Aristov, Y.I. : React. Kinet. Catal. L. **82** (2004), pp.363-369.

Yi, C.K., Jo, S.H., Ryu, H.J., Yoo, Y.W., Lee, J.B., Ryu, C.K. : Greenhouse Gas Control Technologies. **7** (2005), pp.1765-1769.

Yi, C.K., Jo, S.H., Seo, Y., Park, S.D., Moon, K.H., Yoo, J.S., Lee, J.B., Ryu, C.K. : Stud. Surf. Sci. Catal. **159** (2006), pp.501-504.

Yi, C.K., Jo, S.H., Seo, Y.W., Lee, J.B., Ryu, C.K. : Int. J. Greenhouse Gas Control. **1** (2007), pp.31-36.

Zeleňák, V., Badaničová, M., Halamová, D., Čejka, J., Zukal, A., Murafa, N., Goerigk, G. : Chemical Engineering Journal. **144** (2008), pp.336-342.

Zhao, C.W., Chen, X.P., Zhao, C.S. (2008). Characteristics of Dry Potassium-Based Sorbents for CO_2 Capture. The 7th China-Korea Workshop on Clean Energy Technology.

HYDRATION AND PELLETIZATION OF $CaCO_3$-DERIVED SORBENTS FOR *IN-SITU* CO_2 CAPTURE

Dennis Y. Lu, Robin W. Hughes, Tiffany Reid and Edward J. Anthony

CanmetENERGY, Natural Resources Canada, Ottawa, Canada

Abstract: Steam hydration and pelletization of limestone were investigated using a thermogravimetric analyzer (TGA) to improve the sorbent utilization for *in-situ* CO_2 capture under typical fluidized bed combustion (FBC) operating conditions. Steam hydration of CaO improves carbonation capacity but the hydrated sorbent is very fragile, which will be a problem for FBC applications. Similar sorbent improvements in terms of maintaining/enhancing reactivity were observed by sorbent fine grinding and pelletization, which appears to be a method of using hydrated sorbent in fluidized bed applications.

Keywords: CO_2 capture, hydration, pelletization, calcination, carbonation

INTRODUCTION

Adsorption processes for CO_2 separation employing physical and chemical sorbents such as limestone are thought to be technically feasible and economically competitive with amine scrubbing (Abanades et al., 2007; MacKenzie et al., 2007). The reversible reaction between CaO and CO_2 may find application in a high-temperature process to capture CO_2 emissions from advanced power generation processes. For sorbents derived from limestone:

$$CaO\,(s) + CO_2\,(g) \leftrightarrow CaCO_3\,(s) \quad (1)$$

At appropriate temperature and pressure, CO_2 from a flue gas stream can be captured by CaO to form $CaCO_3$. At higher temperature and/or lower pressure, calcination occurs to produce a high-CO_2-concentration gas stream suitable for use or sequestration (the reverse reaction of Rx. (1)).

Unfortunately, the carrying capacity of natural sorbents falls off rapidly with increasing reaction cycles, achieving levels of less than 10% by ≤100 cycles, because of decay in sorbent microporosity due to sintering (Anthony, 2008). Superior CO_2 capture capacity can be achieved by using highly porous or finely divided sorbent particles, but these cannot be used in FBC systems. Early work by Barker (1974) suggests particles around 10 nm displayed almost total reversibility in the carbonation reaction (for extended carbonation times and mild calcination conditions).

If sorbent utilization can be improved, not only will less fresh limestone be needed, but solids handling and disposal will be minimized, thereby reducing overall CO_2 emissions and total costs. Work by Hughes et al. (2004) on crushed limestone regarding CO_2 adsorption, has shown that conversion to calcium carbonate as high as 52% could be obtained consistently, if pore surface area and volume of the crushed rock were increased by steam hydration. Gupta et al. (2004) showed that by using a pressure pelletization technique, the compaction of lime powder derived from calcination of mesoporous $CaCO_3$ preserved the porosity of limestone powder, allowing for 50-80% conversion to carbonate, but carbonation decreased with increasing pellet thickness. In this work, the sorbent modification technique used is steam hydration followed by pulverization and pelletization.

METHODOLOGY

CaO Hydration with Steam

Hydrated lime can be produced by adding water or steam to quicklime:

$$CaO + H_2O \leftrightarrow Ca(OH)_2 \quad (2)$$

Hydration of FBC bed ash usually results in sorbent reactivation and improved sorbent utilization (Anthony et al., 2007) and a very similar phenomenon is seen for Ca looping cycles (Hughes et al., 2004). During hydration of the spent sorbent, liquid water or steam reacts with CaO. The product, $Ca(OH)_2$, has a larger molar volume (33 cm^3/mol) than the CaO (17 cm^3/mol) and so the particle swells, leading to cracking and regeneration of porosity lost due to sintering and/or carbonation, although it is more effective to hydrate sorbents from the calcination step (Manovic et al., 2007a, b) . Unfortunately, such small particles have a reduced residence time in FB systems, limiting their conversion as demonstrated in recent pilot-scale tests of a Ca-based looping cycle (Lu et al., 2008).

Pelletization

Agglomeration of small particles into pellets can alleviate the effect of elutriation from a FB reactor and offers a method of using additives. Here, we used a disc pelletizer, together with a binder to enhance the strength of the pellet (Pietsch, 1991) to agglomerate and form semi-spherical pellets.

Binders

Water is a common liquid binder (Baykal and Doven, 2000), but produces highly variable results if the water addition is not precisely controlled. Hamer (1986) used Na_2CO_3 solution as a binder in FBC applications and found that a 5% Na_2CO_3 solution made pellets strong enough for use in a FBC for sulphur capture, with sorbent sulphation capacity increasing ~30% for pellets made with Na_2CO_3, compared to untreated, crushed limestone. Parameters affecting the sulphation also affect carbonation; therefore, much of what has been learned from sulphation ought to be applicable to carbonation studies. Na_2CO_3, when heated with limestone above 700°C, can form eutectic melts in trace quantities, increasing the strength of the pellets, but reducing the particle pore surface area.

Bentonite is a hydrated aluminosilicate clay primarily composed of montmorillonite, $(Na,Ca)_{0.33}(Al_{1.67},Mg_{0.33})Si_4O_{10}(OH)_2 \bullet nH_2O$. Bentonite binders can also result in eutectic melts forming very strong pellets. Pellets in the iron ore industry use a bentonite binder and must have compressive strengths > 22 N after firing at temperatures of ~1300°C (Ripke and Kawatra, 2000). Pellet strength and porosity are also critical for use in the dual FB process proposed by Hughes et al. (2005). They must be strong enough to withstand repeated transportation (pneumatic) from carbonator to calciner, and abrasion from other particles and bed internals, and must be porous enough to allow high carbonation conversion rates. Hence a balance must be made between strength and porosity.

EXPERIMENTAL

Hydration of Limestone

The raw limestone samples were calcined for 2 h in an oven at 820°C at atmospheric pressure in air. Each sample was weighed before and after to verify complete calcination. Hydration was then performed within a Parr 4522M pressure reactor with saturated steam and the procedure has been described in detail elsewhere (Manovic et al., 2007a, b). The hydration temperatures were controlled at 150, 200 and 250°C and the equivalent steam pressure employed was 4.8, 15.6 and 39.9 bar for hydration times of 0.5, 1 and 2 h at each temperature. At the end of the desired hydration time, the bomb was taken out of the heater and an exhaust valve was opened to release the pressure and decrease temperature in the reactor. This reduced sample time in the bomb to less than 5 min after the desired hydration duration. The solids were then rinsed with de-ionized water and filtered under suction for 1.5-2 min and then transferred to a vacuum oven at 45°C to dry for 3-4 h. The dried samples were analyzed to obtain free lime and $Ca(OH)_2$ content, or used in the CO_2 capture tests.

Pelletization

A disc pelletizer was used here and the pellet size was partially controlled by disc angle. Pellets were made of binder and sorbents (<75 μm), including original limestone, commercial hydrated lime and hydrated lime prepared in our laboratory. Binders used in combination with the sorbent were: water, 5% Na_2CO_3 solution, sodium bentonite, and calcium bentonite. Bentonite was premixed with sorbents in a ratio of 50:1 (limestone:bentonite). Here, the pelletizing disc was set to a 53.4° angle to the horizontal. For a batch, about 50 g of sorbent was placed on the pelletizing disc, which was then turned on and water or 5 wt% Na_2CO_3 solution was sprayed onto the disc surface at the four o'clock position. After a spray of water, the sorbent was allowed to roll in the disc. Any material not scraped off the disc by the pelletizer scraper was finally removed manually with a scoopula at the six o'clock position. Water was sprayed again in the same position, and the scoopula was used to scrape the disc. The process of spraying 1-2 sprays of water onto the disc and scraping was repeated every 1-2 minute as needed to form pellets (requiring about 20 min to produce correctly sized pellets). On achieving, the desired pellet size with no sorbent powder remaining on the disc, the pellets were rolled in the disc for 10 min. The total pelletization time was approximately 30 min.

The pelletizing disc used here had a fixed speed (35 rpm), depth (90 mm) and diameter (400 mm). Freshly made pellets were placed in a vibrating wire mesh sieve for 1 min. Pellets 0.725-1.4 mm were considered acceptable and placed in a drying oven at 105°C overnight, but not fired at an elevated temperature. Pellets were stored in a vacuum oven at 55°C for the duration of the experiment. Pellet strength was tested in an Optimal Control friabilator. This has two 254 mm ID rotating cylinders with the circular axis in the horizontal plane. Inner baffles extend inwards from the outer perimeter of the cylinders and as the cylinder rotates

pellets are repeatedly carried upwards until they slide off the baffle and impact the wall of the cylinder. Samples were first weighed, sized and then rotated in the friabilator for 20 min at 26 rpm. Percent weight loss from the pellets was calculated in these tests by resizing and reweighing pellets in the 0.725-1.4 mm size range.

Thermogravimetric Tests

Calcination/carbonation cycling of the limestone sorbents was conducted in a thermogravimetric analyzer (TGA). The system and its operating procedures have been described in detail elsewhere (Manovic and Anthony, 2007). In this experiment of calcination/carbonation cycles, the TGA furnace temperature was set to 750°C for both carbonation and calcination. N_2 was used for the calcination steps and a digital mass flow controller (Matheson Gas Products) regulated the flow rate at 100 mL/min for the reactant stream and 60 mL/min for the balance housing purge stream. When the sample mass stopped decreasing, the process was switched from calcination to carbonation with 15% CO_2 and 3% O_2 (N_2 balance) for 20 min. Some tests were performed with a carbonation gas composed of 0.5% SO_2, 15% CO_2 and 3% O_2 (N_2 balance). When the carbonation was complete, the gas stream in the reactor was switched back to the calcining gas, for 4-6 cycles of calcination/carbonation.

Limestone powder, crushed limestone, and pellets with each binder were tested in the TGA. Each sample was run through 4 to 6 cycles (calcination/carbonation), in the presence or absence of SO_2 in the carbonation step. Pellets run in the absence of SO_2 were carbonated for 20 min. Table 1 gives the composition of the limestone, and bentonite binders, using X-ray fluorescence spectroscopy (XRF). Limestone was pulverized to <75 μm prior to pelletization. Crushed stone was in the size range 0.425-1.4 mm. Binder compositions are typical for material as supplied by the vendor (American Colloid Company). The sodium and calcium bentonites contain small proportions of feldspar, calcite, and quartz. The sodium bentonite (SPV-200) size was specified as minimum 65% passing 200 mesh (74 μm). The calcium bentonite (Panther Creek 200) size was specified as 70% passing 200 mesh.

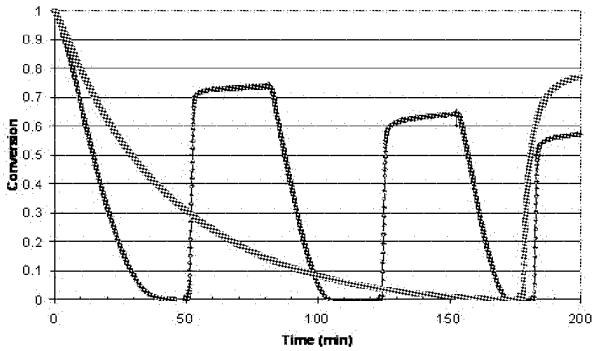

Fig. 1 Calcination/carbonation cycles, Na bentonite-bound pellets (diamond), crushed limestone (square) at 750°C calcined in N_2 and carbonated in 15% CO_2, 3% O_2 in N_2 at 750°C

Table 1 Limestone and binder composition

Component	Cadomin	Sodium Bentonite	Calcium Bentonite
CaO	55.12	0.65	3.14
SiO_2	1.50	63.02	60.50
Al_2O_3	<0.10	21.08	18.20
Fe_2O_3	<0.01	3.25	5.52
FeO	<0.01	0.35	<0.01
Na_2O	<0.20	2.57	0.20
K_2O	0.21	<0.02	0.14
SO_3	0.32	<0.10	<0.10
Trace	n.d.	0.72	n.d.
Loss on ignition (LOI)	n.d.	5.64	4.85
Loss on fusion (LOF)	42.77	n.d.	n.d.

RESULTS AND DISCUSSION

Pelletization

Table 2 gives results of the friability testing for four batches of pellets made with the Cadomin limestone. The lower mass loss from the desired size range indicates that Na_2CO_3-bound pellets are stronger and more durable than pellets made with the other binder combinations.

Table 2 Percent of material lost from 0.425-1.4 mm size range during friability testing with various binders

Binder	% weight loss
5 wt% Na_2CO_3 solution	31.3
Water	100.0
Na bentonite/H_2O	86.5
Ca bentonite/H_2O	78.2

Sodium and calcium bentonite increased resistance to attrition (Table 2), compared to water-bound pellets. Na bentonite-bound pellets had higher mass loss than Ca-bound ones and tended to swell more than Ca bentonite upon hydration. This may create a more open pore structure upon dehydration, but this could reduce strength compared to pellets made with Ca bentonite.

For comparison, crushed limestone was also run through the friabilator. Crushed limestone sprayed with water had a weight loss of 8.6%, and crushed limestone sprayed with sodium carbonate solution had a weight loss of 6.7%. The data in Table 2 show that the pellets are significantly weaker than the original material. This material has not been heat treated, which would result in much stronger pellets.

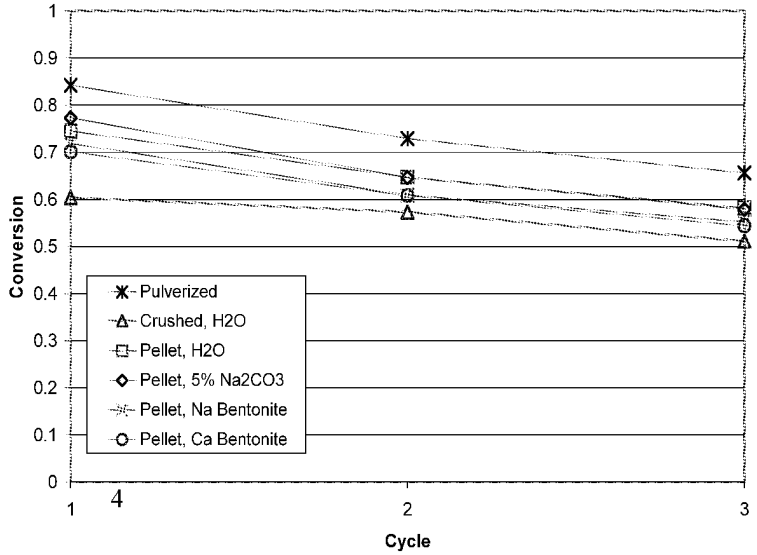

Fig. 2 Carbonation conversion of sorbents after 5 min of reaction; carbonation at 750°C with 15% CO_2, 3% O_2 in N_2

Thermogravimetric Tests

Figure 1 shows conversion for pellets using crushed limestone and Na bentonite. The reaction proceeds more quickly in the pelletized material for both calcination and carbonation. The calcination time for the crushed stone was 3.5 times as long as for the pellet, even though the stone and the pellet were of similar size. If this is typical for pellets, it would be advantageous in a real system.

Figure 2 shows carbonation conversion after 5 min for samples without SO_2 present in the carbonation step. As expected (Oates, 1998) finely divided lime carbonates more fully than larger and the pelletized material conversions fall between the pulverized and crushed limestone. Conversions of pellets formed with bentonite are nearly identical, as are the pellets formed with water and Na_2CO_3.

Carbonation conversions in the presence of 0.5% SO_2 are shown in Fig. 3 and the sulphation conversions for the same tests are shown in Fig. 4.SO_2 reduces the ability of limestone sorbents to capture CO_2, since $CaSO_4$ prevents CO_2 reacting with free CaO (Sun et al., 2007). As expected, pulverized limestone captures more CO_2 and SO_2 than does crushed limestone. In general, the pelletized material that has high capacity for SO_2 has a reduced capacity for CO_2, and vice versa. Pellets were prepared using Na bentonite as binder and the results are presented in Figs. 3 and 4 for both batches (SO_2, Pellet, Na Bentonite; and SO_2, Pellet, Na Bentonite REP 1). The two batches significantly differ for capture of CO_2 and SO_2 for the limited number of samples examined here. Repeat testing from each of the batches indicates that the variation results from differences in pellet formation in each batch and not variability of pellets within a batch. One of the Na bentonite pellet batches shows a CO_2 capture capacity equivalent to that of pulverized limestone and higher capacity for SO_2, which could be important since, otherwise, one must separate the processes of sulphation and carbonation (Sun et al., 2007; Manovic and Anthony, 2007).

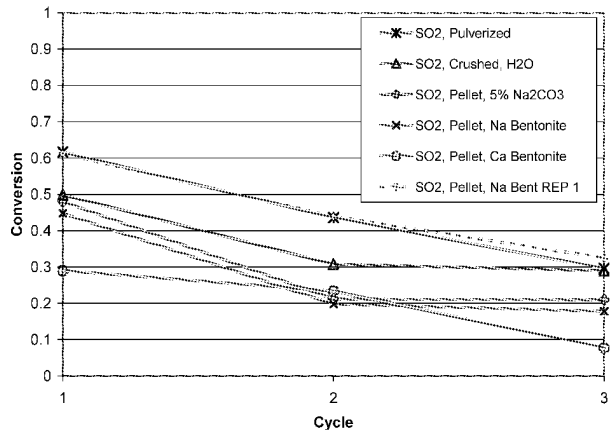

Fig. 3 Carbonation conversion of sorbents after 5 min of reaction at 750°C with 0.5% SO_2, 15% CO_2, 3% O_2 in N_2

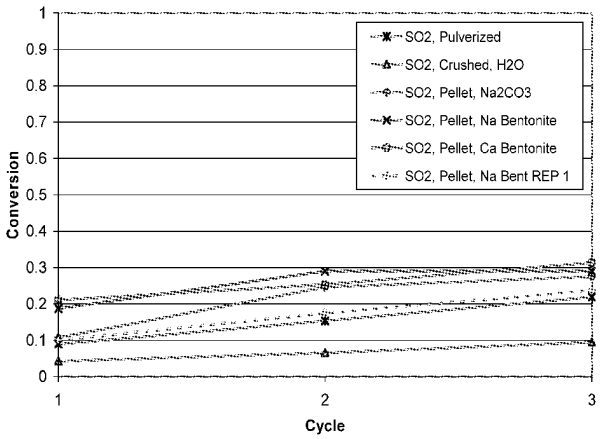

Fig. 4 Sulphation conversion of sorbents after 5 min of reaction at 750°C with 0.5% SO_2, 15% CO_2, 3% O_2 in N_2

As expected from the work of Hamer (1986), all the pelletized sorbents showed improved SO_2 capacity.

Figure 5 shows carbonation conversion for finely divided $CaCO_3$-derived materials including commercial quick lime (denoted c-q-lime), pulverized limestone, commercial hydrated lime (denoted c-h-lime), and hydrated lime prepared in our laboratory from pulverized limestone. Commercial quick lime is prepared at high temperature and is heavily sintered, so it has a low capacity for CO_2 capture. The capacity of the quick lime increased slightly as cycles progressed and achieved a maximum value of about 20%, which is similar to the results of Manovic and Anthony (2008), in which heavily sintered materials recover carbon capture capability after multiple carbonation/calcination cycles. The pulverized limestone follows a typical reduction in CO_2 capture capacity, as seen previously (Abanades and Alvarez, 2003). The two hydrated limes show a much greater capacity for CO_2 capture than the other materials. Unfortunately the hydrated material is also quite soft and would undergo excessive attrition from impact, thermal shock and reaction in dual fluidized bed systems. Carbonation conversions for hydrated materials in pellet form are shown in Fig. 6. Pelletized commercial hydrated limes performed more poorly than the parent material, in fact, nearly as poorly as the sorbent derived from pulverized limestone. The hydrated and pelletized material performed much better. If this material deactivates in the same manner as limestone-derived sorbents do, and follows the deactivation model suggested by Abanades and Alvarez (2003):

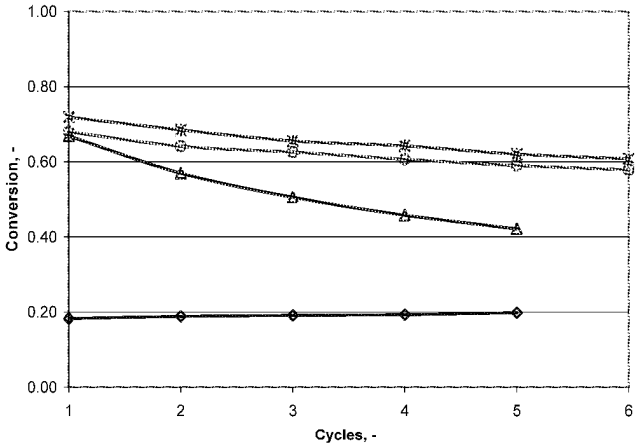

Fig. 5 Carbonation conversion for pulverized limestone (triangle), c-q-lime, <30 μm (diamond), c-h-lime, <50 μm (circle), Lab-h-lime (asterisk); 750°C, 3% O_2, 15% CO_2 in N_2

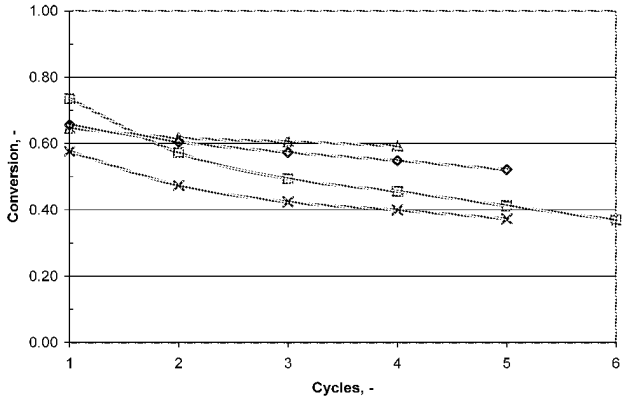

Fig.6 Carbonation conversion for hydrated and pelletized sorbents; Lab-h-lime pellet with water binder 1-2 mm (diamond), Lab-h-lime pellet with 5% Na_2CO_3 binder 1-2 mm (triangle), c-h-pellet 0.6-1.4 mm (square), c-h-pellet 3.0-4.0 mm (X); 750°C, 3% O_2, 15% CO_2 in N_2

$$X_{b,N} = f_m^N (1 - f_w) + f_w \tag{3}$$

after 50 cycles the pellets formed with water as binder would have a carbonation conversion of 42% while the pellets made with 5% Na_2CO_3 would have 57% conversion, although such predictions should be treated with caution for modified materials. Previous economic analysis (Abanades et al., 2004) indicates that CO_2

looping is attractive if the conversion of the sorbent is in excess of 40% for at least 20 cycles. These results are promising as material that was previously considered too fragile for use in fluidized beds (Hughes et al., 2004) has maintained excellent activity (albeit for a limited number of cycles) after having been physically strengthened using pelletization. Also, surprisingly, whereas Na_2CO_3 has an unfavorable effect on lime-based materials in both TGA and FB units, they did not do so here (Manovic et al., 2008; Salvador et al., 2003).

CONCLUSIONS

Pelletized particles in general showed good performance, comparable to or better than steam-hydrated samples. Such pellets should allow the use of fine materials in a FBC, either by using the fines from a real FB looping cycle or by using pulverized limestones and making pellets with sufficient strength to survive multiple cycles. Further work needs to be done, using more realistic calcination conditions (*i.e.*, higher temperatures in the presence of pure CO_2), and over a greater number of cycles, to confirm these results. Surprisingly, the presence of Na_2CO_3 in the binders, which has deleterious effects in a real FBC system, did not do so here, with a pulverized limestone sample.

ACKNOWLEDGMENTS

We would like to thank Dr. Yinghai Wu for preparing the hydrated samples.

REFERENCES

Abanades, J.C., Alvarez, D.: Conversion Limits in the Reaction of CO_2 with Lime. Energy Fuels 17 (2003), 308-315.

Abanades, J.C., Rubin, E.S., Anthony, E.J.: Sorbent Cost and Performance in CO_2 Capture Systems. Ind. Eng. Chem. Res. 43 (2004), 3462-3466.

Abanades, J.C., Grasa, G., Alonso, M., Rodrigues, N., Anthony, E.J., Romeo, L.M.: Cost Structure of a Postcombustion CO_2 Capture System using CaO. Environ. Sci. Technol. 41 (2007), 5523-5527.

Anthony, E.J., Bulewicz, E.M., Jia, L.: Reactivation of Limestone Sorbents in FBC for SO_2 Capture. Prog. Energy Combust. Sci. 33 (2007), 171-210.

Anthony, E.J.: Solid Looping Cycles: A New Technology for Coal Conversion. Special anniversary edition of Ind. Eng. Chem. Res. 47 (2008), 1747-1754.

Barker, R.: The Reactivity of Calcium Oxide towards Carbon Dioxide and Its Use for Energy Storage. Appl. Chem. Biotechnol. 24 (1974), 221-227.

Baykal, G., Doven, A.: Utilization of fly ash by pelletization process; theory, application areas and research results. Resources, Conservation and Recycling 30 (2000), 59-77.

Gupta, H., Iyer, M., Sakadjian, B.B., Fan, L.: Reactive separation of CO_2 using pressure pelletised limestone. Int. J. Environ. Technol. Manage. 4 (2004), 3-19.

Hamer, C.A.: Evaluation of SO_2 Sorbent Utilization in Fluidized Beds. CANMET Report No. 86-9E (1986), Energy, Mines and Resources Canada.

Hughes, R.W., Lu, D.Y., Wang, J., Anthony E.J.: Design, Process Simulation and Construction of an Atmospheric Dual Fluidized Bed Combustion System for In Situ CO_2 Capture using High-Temperature Sorbents. Fuel Process. Technol. 86 (2005), 1521-1531.

Hughes, R., Lu, D., Anthony, E.J., Wu, Y.: Improved Long-Term Conversion of Limestone-Derived Sorbents for In Situ Capture of CO_2 in a Fluidized Bed Combustor. Ind. Eng. Chem. Res. 43 (2004), 5529-5539.

Lu, D., Hughes, R.W., Anthony, E.J.: Ca-based Sorbent Looping Combustion for CO_2 Capture in Pilot-Scale Dual Fluidized Beds. Fuel Process. Technol. 89 (2008), 1386-1395/

MacKenzie, A., Granatstein, D.L., Anthony, E.J., Abanades, J.C.: Economics of CO_2 Capture using the Calcium Cycle with a Pressurized Fluidized Bed Combustor. Energy Fuels 21 (2007), 920-926.

Manovic, V., Anthony, E.J.: SO_2 Retention by Reactivated CaO-based Sorbent from Multiple CO_2 Capture Cycles. Environ. Sci. Technol. 41 (2007), 4435-4440.

Manovic, V., Anthony, E.J.: Steam Reactivation of Spent CaO-based Sorbent for Multiple CO_2 Capture Cycles. Environ. Sci. Technol. 41 (2007a), 1420-1425.

Manovic, V., Anthony, E.J.: Sequential SO_2/CO_2 capture enhanced by steam reactivation of a CaO-based sorbent. Fuel 87 (2007b), 1564-1573.

Manovic, V., Anthony, E.J.: Thermal Activation of CaO-based Sorbent and Self-Reactivation during CO_2 Capture Looping Cycles. Environ. Sci. Technol. 42 (2008), 4170-4174.

Manovic, V., Anthony, E.J., Abanades, J.C., Grasa, G.: CO_2 Looping Cycle Performance of a High-Purity Limestone after Thermal Activation/Doping.Energy Fuels 22 (2008), 3258-3264.

Oates, J.A.H.: Lime and Limestone: Chemistry Technology, Production and Uses, Wiley-VCH, New York 1998.

Pietsch, W.: Size Enlargement by Agglomeration, John Wiley & Sons Ltd., Chichester, UK, 1991.

Ripke, S.J., Kawatra, S.K.: Can fly-ash extend bentonite binder for iron ore agglomeration? Int. J. Miner. Process. 60 (2000),

181-198.

Salvador, C., Lu, D., Anthony, E.J., Abanades, J.C.: Enhancement of CaO for CO_2 Capture in a FBC Environment. Chem. Eng. J. 96 (2003), 187-195.

Sun, P., Grace, J.R., Lim, C.J., Anthony, E.J.: Removal of CO_2 by Ca-Based Sorbents in the Presence of SO_2. Energy Fuels 21 (2007), 163-170.

Ni/γ-Al_2O_3 CATALYST FOR CO_2 REFORMING OF BENZENE AS A MODEL COMPOUND OF BIOMASS GASIFICATION TAR: PROMOTIONAL EFFECT OF ULTRASONIC TREATMENT ON CATALYTIC PERFORMANCE

B. Li, H. P. Chen, H. P. Yang, G. L. Yang, X. H. Wang, S. H. Zhang

State Key Laboratory of Coal Combustion, Huazhong University of Science & Technology, Wuhan, 430074, China

Abstract: This paper aims to understand the promotional effect of ultrasonic treatment on catalytic performance of Ni/γ-Al_2O_3 catalyst for CO_2 reforming of benzene as a model compound of tar derived from biomass gasification, and the catalytic cracking mechanism was also discussed. Firstly, three Ni/γ-Al_2O_3 catalysts were prepared by ultrasonic impregnation as the ultrasonic power variant at 0, 120 and 500W, and the physicochemical property of catalysts were characterized using N_2-adsorption, SEM and XRD, etc. Then the catalytic performance of three catalysts for CO_2 reforming of benzene was tested in a micro-reactor. The outlet gas was measured using a Micro-GC. Finally, the coking amount on the catalyst surface was measured by thermogravimetry (TG). The results showed that ultrasonic treatment significantly modified the pore size distribution of the catalysts especially in the pore size range of 10-50nm and also improved the capability of the coke resistance. It's beneficial to increase the lifetime of the catalyst. Meanwhile, lower ultrasonic power (120W) was more favorable to improve the coke resistance of the catalyst in the power range tested (120 and 500W). The main surface reactions over Ni/γ-Al_2O_3 catalysts included two steps: Firstly, benzene adsorbed on the catalyst surface, the metal active sites dehydrogenation took place, and the residual molecule fragments (coke precursor) would condense further which led to coke formation. Then, CO_2 reacted with coke precursor and coke for coke elimination. The first step carried out very quickly, and the second step was the rate-determining step. To reduce the coke deposition on the catalyst surface, the performance of CO_2 adsorption and activation and surface oxygen transmission capacity should be improved further.

Keywords: Ni/γ-Al_2O_3, tar; ultrasonic treatment, CO_2 reforming of benzene, coking

INTRODUCTION

R&D of biomass gasification technology especially large-scale fluidized bed gasification technology has displayed a wide application prospect. It's a key technology for biomass gasification power generation, liquid fuel synthesis and chemical production. The quality of the gas products would directly affect the operation and technical economy of the downstream process. Besides gas products, biomass gasification also produces large amount of tar. Due to the different raw materials and gasification processes, the tar content in gas products differs greatly. For the most process, the tar content is 2-50 g/m^3 (Devi et al., 2003), which is much higher than the maximum level allowed for the downstream process. Tar is an undesirable component in the gasification process, it not only reduce the gasification efficiency, but also seriously affect the stable operation of the gasification system due to the low-temperature condensation, thus the tar should be removed before application (Wang et al., 2000).

Catalytic cracking has been proved as an effective way for tar removal in the gas products (Delgado et al., 1996; Kuhn et al., 2008; Nishikawa et al., 2008). Considering the tar is a very complex mixture ranging from single ring to multi-ring condensable aromatic compounds, various model compounds of tar are usually chosen to facilitate the study of catalytic cracking mechanism, including benzene (Coll et al., 2001; Zhang et al., 2007), toluene (Zhang et al., 2007; Bona et al., 2008), naphthalene (Furusawa and Tsutsumi 2005; Furusawa and Tsutsumi 2005), phenol (Polychronopoulou et al., 2004; Polychronopoulou et al., 2004) and so on. In the present work, benzene was chosen as a model compound of tar due to the highest content in tar (Coll et al., 2001). Among many different catalysts, nickel is one of the most promising catalysts for tar removal due to the high activity of tar decomposition and also capable of methane reforming (Horiuchi et al., 1996) and ammonia decomposition (Zhang et al., 2005; Zhang et al., 2005). However, nickel-based catalyst would be easy to deactivate due to the coke formation on the catalyst surface. Numerous literatures (Zhang et al., 2007; Ma and Baron 2008; Nishikawa et al., 2008) have reported that by adding different additives or changing preparation conditions could modify the catalyst performance, and some good results also have been achieved.

Sonochemical technology is considered to be a useful way to prepare novel material with different

properties. Ultrasonic technique has displayed a wide industrial application potential due to the physical, mechanical, thermal, chemical and biological effects caused by ultrasonic cavitation (Suslick et al., 1991). Especially in recent years, ultrasonic technique has obtained rapid development in the catalytic chemistry area (Bianchi et al., 1997; Wang and Zheng 2006; Yang et al., 2006), including catalytic nanomaterials preparation, active components dispersion on the catalyst carrier and heterogeneous catalytic reactions. However, the study of ultrasonic treatment in tar cracking catalyst modification is still rarely reported.

Therefore, in this study, ultrasonic treatment was introduced to promote the performance of the nickel-based catalyst. Three Ni/γ-Al_2O_3 catalysts were prepared by ultrasonic impregnation, an experiment of CO_2 reforming of benzene as a model compound of tar was carried out to investigate the influence of ultrasonic treatment on catalytic performance, and the catalytic cracking mechanism was also discussed.

EXPERIMENTAL

Catalyst preparation

Three catalysts marked as 1, 2 and 3 were prepared where the catalyst carrier was γ-Al_2O_3 with particle size of 0.25-0.35mm, the content of active component Ni was 14%, and 2% La_2O_3 (Garcia et al., 2000) was added as promoter. The details were described as follows.

Firstly, γ-Al_2O_3 was dried in an oven at 140℃ for 3h, and kept in a drying cabinet. Subsequently, corresponding quality ratio of $Ni(NO_3)_2{\cdot}6H_2O$ and $La(NO_3)_3{\cdot}3H_2O$ were dissolved in de-ionized water, and then a certain amount of γ-Al_2O_3 was mixed with the solution for impregnation. In the impregnation process, the ultrasonic power was varied at 0, 120 and 500W for 40 min, respectively. After 24h, the mixture was put into a rotatory evaporator to dry water out, and then dried in an oven at 80℃ for 3h. Finally, the solid particle was calcined at 450℃ in a muffle furnace for 3h so that $Ni(NO_3)_2$ and $La(NO_3)_3$ would be decomposed into NiO and La_2O_3, and the catalyst precursor (NiO/γ-Al_2O_3) was obtained, it could be used after H_2 reduction.

Experimental setup and procedure

The catalytic performance of Ni/γ-Al_2O_3 for CO_2 reforming of tar with benzene as model compound was tested in a micro-reactor (WFS-3010) produced by Xianquan Science and Technology Ltd, Tianjin, China. The schematic diagram of the micro-reactor is shown in Fig. 1. Benzene was injected into the evaporator by a liquid pump mixed with CO_2, then the mixed gas entered into a fixed-bed catalytic reactor (ID. 8mm, length 280mm). The catalyst was placed in the center of the reactor, and the temperature of the catalyst bed was measured by a k-type thermocouple. A typical reforming test is shown as follows.

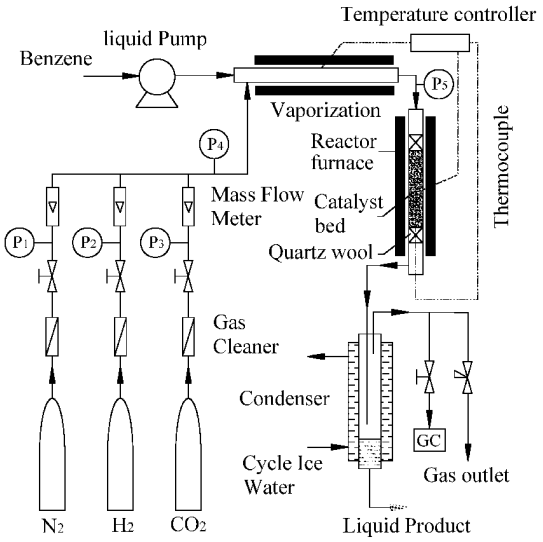

Fig.1 Schematic diagram of the micro-reaction system

1.5g catalyst precursor was placed in the reactor previously, and the reactor was heated to 550℃ in N_2 flow (40ml/min). Then, a H_2 flow of 10ml/min was introduced into the reactor to reduce the catalyst. After 3h, the catalyst bed was purged with N_2 for 10min. Finally, the N_2 flow was switched into the mixed gas of CO_2 (40ml/min) and benzene (1.5ml/h) from the evaporator (Weight hourly space velocity of benzene of 60ml/g·h). The outlet gas was measured using a quad-channel Micro-gas chromatograph (Micro-GC, Agilent 3000, Agilent Technologies Inc., Germany) with thermal conductive detector. After the test, the reactor was shut down, the feeding of benzene and CO_2 was cut off, the gas was switched to N_2 until the reactor cooled down to room temperature, and the catalyst was taken out for analysis.

Catalyst characterization

The specific surface area (BET method) and pore size distribution (BJH method) of the fresh and used catalysts and γ-Al_2O_3 carrier were analyzed with liquid N_2-adsorption at 77K by Automated Surface Area and Pore Size Analyzer (ASAP2020, Micromeritics, USA). The surface morphology and pore characteristics were measured by Environmental Scanning Electron Microscope (ESEM, FEI Quanta 200, Holland). The elemental mapping over the desired region of the catalyst was detected by an Energy-Dispersive X-ray Spectrometer

(EDS) attached to the ESEM. The phase structures were characterized by X-Ray Diffraction (XRD, Panalytical B.V., χ'Pert PRO, Holland) with CuKα radiation (k = 0.15406nm). The coking amount deposited on the catalyst surface was measured by ThermoGravimetry Analyzer (TGA, STA 409, NETZSCH Instruments) in air atmosphere.

RESULTS AND DISCUSSION

Effect of ultrasonic treatment on physicochemical structure of catalysts

Table 1 shows the results of specific surface area and pore size distribution of three fresh and used catalysts (reaction time of 3h, marked as 1', 2' and 3') and γ-Al_2O_3 carrier. The results indicate that the specific surface area of the γ-Al_2O_3 carrier decreased rapidly from 233.34 to 159.21-172.08m^2/g after active component impregnation. Meanwhile, the pore volume decreased significantly from 0.533 to ~0.4cm^3/g, while the average pore width increased slightly. The reason may be that after impregnation, the active component was loaded on the surface of the pores in the carrier, thus the pore volume decreased. The active component impregnation caused the original pore size decreasing, part of the micropore blockage and the macropore and mesopore moving to a range of smaller pore, but these might lead the percentage of the macropore and mesopore increasing and the micropore decreasing, thus the average pore width increased. From the table, it can be also observed that after ultrasonic treatment, the specific surface area, pore volume and average pore width of the three catalysts did not show obvious regularity. After reforming test, the pore volume and average pore width of the three used catalysts decreased significantly due to the coke formation, which indicated that coke was formed in the pore of the catalysts. However, an interesting thing was found that the specific area of the three used catalysts were similar to that of the fresh ones, which indicated that the specific area did not change significantly during coking although the pores shrank. Further study should be taken to explain the phenomenon.

Table 1 Results of specific surface area and pore size distribution of three fresh and used catalysts and γ-Al_2O_3 carrier

	Specific surface area (m^2/g)	Pore volume at p/p_0=0.975 (cm^3/g)	Average pore width (nm)
γ-Al_2O_3	233.34	0.533	9.14
1	160.28	0.396	9.87
2	159.21	0.397	9.98
3	172.08	0.413	9.61
1'	167.66	0.264	6.31
2'	160.08	0.296	7.39
3'	170.37	0.304	7.13

Figure. 2 shows the BJH pore volume distribution of the fresh and used catalysts and γ-Al_2O_3 carrier. It can be observed that the pore size distribution of the catalysts and carrier were both mainly ranged between 2 and 100nm, and about 10nm was an important dividing point. The pore volume of different pore ranges could be calculated by integral. For catalyst 1, the percentage of the pore volume less than 10nm was 54.4%, and between 10 and 50nm was 29.6%. While for catalysts 2 and 3, the percentage of the pore volume between 10 and 50nm was 51.2% and 50.4%, respectively. This suggested that ultrasonic treatment could promote the formation of larger pores, particularly in the size range of 10-50nm. It indicated that ultrasonic treatment was beneficial to active component diffusion, could abate the active component conglobation to block the pore structure of the carrier, and simultaneously could expand the pores of the carrier. It is in agreement with the results of Tonanon et al. (2005) and Yu et al. (2006). Previous studies have shown that the average size of the NiO grain was mainly distributing between 10 and 30nm (Roh et al., 2003; Richardson et al., 2004). Therefore, catalysts 2 and 3 had a better pore size distribution comparison to catalyst 1 due to ultrasonic treatment. After reforming test, it can be seen that the pore volume of the three catalysts in the mesopore range (2-50nm) were all reduced significantly due to coke formation in the pores, especially the pore volume in the pore size range of 10-50nm reduced sharply, thus caused the activity of the catalyst decrease

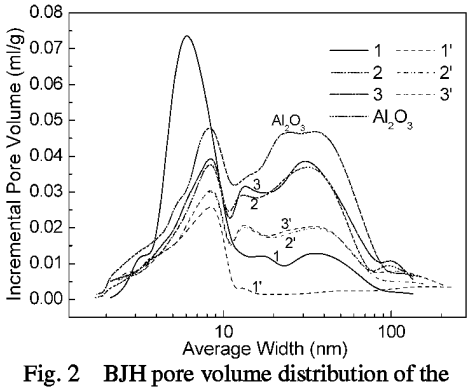

Fig. 2 BJH pore volume distribution of the fresh and used catalysts and γ-Al_2O_3 carrier

rapidly. It can be also observed that the pore size distribution of the catalysts 2 and 3 did not show obvious difference, it indicated that the change in pore size distribution was not sensitive to the power output of the ultrasonic device in the power range tested (120 and 500W).

Good catalyst performance requires uniform distribution of the active component throughout the carrier and well developed microstructure. Fig. 3 shows the SEM/EDS images of the three fresh and used catalysts. The speckled patterns demonstrated the uniform distribution of the Ni component over the full carrier. For the three fresh catalysts, it can be seen that there were plenty pores on the surface of the catalysts, and the pore size of the catalysts 2 and 3 was bigger than catalyst 1. Besides, few cracks of 1-4μm occurred on the surface of catalyst 3, and it was also found in other non-photo area. It might be attributed to that the ultrasonic treatment led to the pores transfixion. And it also proved that ultrasonic treatment could expand the pores of the carrier. After reforming test, due to coke formation, it can be seen that the pore structure of the catalyst was blocked by carbon deposition on the surface, and catalyst 1 was the most serious one. It indicated that ultrasonic treatment could abate the coke formation on the catalyst surface. From the coked images, it can be observed that there were three coke morphologies on the catalyst surface, including particulate coke, filamentary coke and membranous coke, and it will be studied further in the near future.

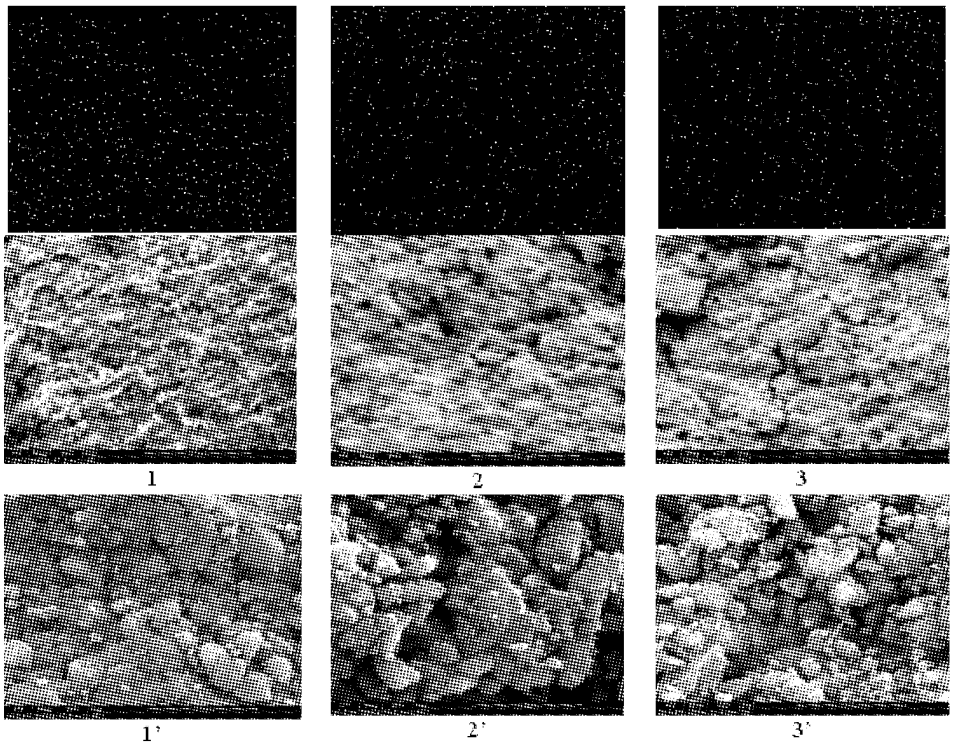

Fig.3 SEM/EDS images of the fresh and used catalysts

The XRD patterns of three fresh catalysts are shown in Fig. 4. The La_2O_3 phase was not detected due to the low content. And the $NiAl_2O_4$ spinel was also found in the catalysts. The XRD patterns did not show significant difference among the three catalysts. It indicated that the phase composition of the catalysts was similar to each other, and ultrasonic treatment did not affect the phase composition of the catalysts.

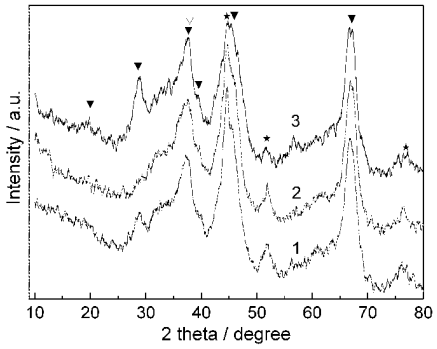

Fig. 4 XRD patterns of three fresh catalysts:
▼—Al_2O_3, ★—Ni, ▽—$NiAl_2O_4$

Analysis of catalytic cracking process and mechanism

The pathway of CO_2 reforming of benzene can be descried as reaction (1). And the reaction process over Ni/γ-Al_2O_3 catalyst belongs to the category of heterogeneous catalysis which the conversion of reactants into products is through the cycle of elementary steps. Firstly, benzene vapor diffused to the surface of the catalyst and dissociatively adsorbed onto a Ni active site where the metal-catalyzed dehydrogenation occurred to form coke precursor. If the coke precursor could not be eliminated in time, it would be condensed further to form coke. Meanwhile, the

coke precursor and coke would also react with CO_2 and H_2 for coke elimination, as shown in reaction (2) and (3).

$$C_6H_6 + 6CO_2 \rightarrow 12CO + 3H_2 \quad (1)$$

$$C + 2H_2 \rightarrow CH_4 \quad (2)$$

$$C + CO_2 \rightarrow 2CO \quad (3)$$

The profiles of gas products evolving from CO_2 reforming of benzene are shown in Fig. 5. It can be seen that the H_2 content in the micro-reactor outlet firstly increased slightly and then decreased gradually with reaction time prolonging, and reduced to near zero after 50min, while the CH_4 content also reduced to near zero after ~60min. This is similar to the results of Almeida et al. (2006). It should be noted that the higher content of CH_4 was mainly due to the lower reaction temperature which was favorable for methanation reaction, and this was different from the previous study (Coll et al. 2001; Zhang et al. 2007; Bona et al. 2008; Nishikawa et al. 2008). The CO content increased gradually with the CH4 content decreasing, and got a maximum value at ~60min. It indicated that there were two competitive reactions between CO_2 and H_2 with coke. Thereafter, the CO content decreased gradually, but it can be still detected a higher content of CO after 200min. It indicated that the coke elimination (reaction (3)) rate was relatively lower which caused the surface active sites of the catalyst to be deposited by the coke and rapid deactivation of the catalyst. Therefore, reaction (3) was the rate-determining step, and the CO_2 reforming of benzene over Ni/γ-Al_2O_3 catalyst could be descried as Fig. 6. From the above discussion, it can be obtained that the whole process has obvious stepwise reaction characteristics, and to upgrade the coking resistance of the catalyst, the performance of CO_2 adsorption and activation and surface oxygen transmission capacity should be improved further. After ~60min, it can be found that the CO content of the catalysts with ultrasonic treatment was higher than that untreated one. It might indicate that ultrasonic treatment could improve the coke resistance of the catalyst, and it is beneficial to increase the lifetime of the catalyst. This might be due to the pore structure modification of the catalyst by ultrasonic treatment. Meanwhile, lower ultrasonic power (120W) was more favorable to improve the coke resistance of the catalyst in the power range tested (120 and 500W).

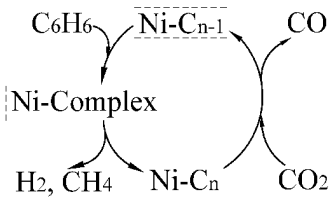

Fig. 6 Schematic diagram of mechanism of CO_2 reforming of benzene over Ni/γ-Al_2O_3 catalyst

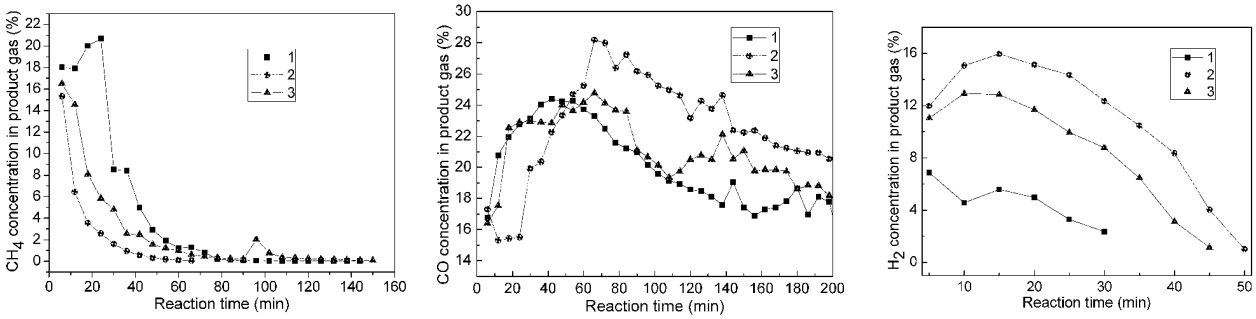

Fig. 5 Gas products evolving from CO_2 reforming of benzene

Effect of ultrasonic treatment on coking tendency of catalysts

Coke formation is the main factor to impact the activity of the Ni-based catalyst. The coke deposited on the catalyst surface would cover the surface active sites, leading to not only rapid deactivation of the catalyst but also sharp rise of the bed resistance which seriously affected the stable and safe operation of the cracking bed. Hence, the capability of the coke resistance of the catalyst is an important target for catalytic performance evaluation. Meanwhile, the coke burning test of the catalyst is also an important step for determination of the catalyst regeneration conditions.

Figure. 7 shows the results of the TG-DTG curves of the three catalysts after 3h reforming test. The TG condition was chosen as air atmosphere with flow rate of 75ml/min and heating up from room temperature to 700℃ with the heating rate of 10℃/min. It can be observed that after ~400℃, the three catalysts all occurred obvious weight loss due to coke burning, and the maximum weight loss peaks appeared at 561, 533 and 564℃, respectively. The different peak position might be related to the different composition and structure of the coke deposited on the catalyst surface, further characterization test will be taken in the near future. From the TG curves, it can be also found that the coke deposition of the catalyst 1 was the most serious (with weight loss of 25.59%), the next was catalyst 3 (21.32%), and the least was catalyst 2 (19.15%). It indicated that a suitable ultrasonic treatment is beneficial to reduce the coke deposition on the catalyst surface, and catalyst 2 with

ultrasonic power of 120W has stronger coke resistance capability than catalyst 3 with ultrasonic power of 500W.

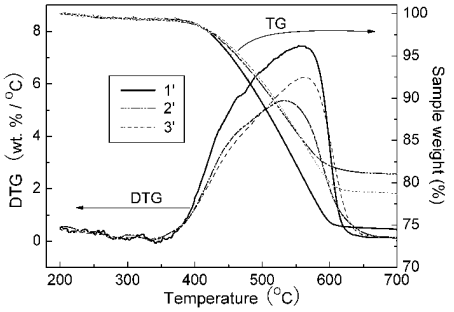

Fig.7 TG-DTG curves of three used catalysts

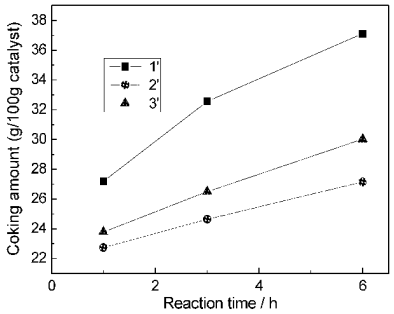

Fig.8 Effect of ultrasonic treatment on the average coking amount of three catalysts

To further investigate the effect of the ultrasound treatment on the coke resistance of the catalyst, three repeat tests of the three catalysts at different reaction time have been carried out, and the average coking amount of the three catalysts at different reaction time was obtained as shown in Fig. 8. The results were coincident with Fig. 7, and the advantage of coke resistance capability of the catalyst with ultrasonic treatment was more obvious when reaction time was longer. Meanwhile, lower ultrasonic power (120W) was more favorable in the power range tested (120 and 500W).

CONCLUSIONS

In this work, the promotional effect of ultrasonic treatment on catalytic performance of Ni/γ-Al_2O_3 catalyst for CO_2 reforming of benzene as a model compound of tar derived from biomass gasification was investigated, and the catalytic cracking mechanism was also discussed simultaneously. The main conclusions can be derived as follows.

Ultrasonic treatment could significantly modify the pore size distribution of the catalysts especially in the pore size range of 10-50nm, but not affect the phase structure of the catalysts. It could improve the capability of the coke resistance which was beneficial to increase the lifetime of the catalyst. Meanwhile, lower ultrasonic power (120W) was more favorable to improve the coke resistance of the catalyst in the power range tested (120 and 500W).

The pathway of CO_2 reforming of benzene over Ni/γ-Al_2O_3 catalyst can be descried as several elementary steps: Firstly, benzene vapor diffused to the surface of the catalyst and dissociatively adsorbed onto a Ni active site where the metal-catalyzed dehydrogenation occurred, and the residual molecule fragments (coke precursor) would condense further which led to coke formation. Then, CO_2 reacted with coke precursor and coke for coke elimination. The first step carried out very quickly, and the second step was the rate-limiting step. To reduce the coke deposition on the catalyst surface, the performance of CO_2 adsorption and activation and surface oxygen transmission capacity should be improved further.

ACKNOWLEDGMENTS

The authors wish to express the great appreciation of the financial support from Key Projects of National Fundamental Research Planning (National 973 project: 2007CB210202) and National Nature Science Foundation of China (No. 50676037 and No. 50721005).

REFERENCES

Bianchi, C. L., Gotti, E., Toscano, L. and Ragaini, V. Ultrason. Sonochem. **4** (1997), pp. 317-320.
Bona, S., Guillen, P., Alcalde, J. G., Garcia, L. and Bilbao, R. Chem. Eng. J. **137** (2008), pp. 587-597.
Coll, R., Salvad, J., Farriol, X. and Montan, D. Fuel Process. Technol. **74** (2001), pp. 19-31.
de Almeida, R. M., Fajardo, H. V., Mezalira, D. Z., Nuernberg, G. B., Noda, L. K., Probst, L. F. D. and Carreno, N. L. V. J. Mol. Catal. A: Chem. **259** (2006), pp. 328-335.
Delgado, J., Aznar, M. P. and Corella, J. Ind. Eng. Chem. Res. **35** (1996), pp. 3637-3643.
Devi, L., Ptasinski, K. J. and Janssen, F. J. J. G. Biomass Bioenerg. **24** (2003), pp. 125-140.
Furusawa, T. and Tsutsumi, A. Appl. Catal. A: Gen. **278** (2005), pp. 207-212.
Furusawa, T. and Tsutsumi, A. Appl. Catal. A: Gen. **278** (2005), pp. 195-205.
Garcia, L., French, R., Czernik, S. and Chornet, E. Appl. Catal. A: Gen. **201** (2000), pp. 225-239.
Horiuchi, T., Sakuma, K., Fukui, T., Kubo, Y., Osaki, T. and Mori, T. Appl. Catal. A: Gen. **144** (1996), pp. 111-120.

Kuhn, J. N., Zhao, Z., Felix, L. G., Slimane, R. B., Choi, C. W. and Ozkan, U. S. Appl. Catal. B: Environ. **81** (2008), pp. 14-26.
Ma, L. and Baron, G. V. Powder Technol. **180** (2008), pp. 21-29.
Nishikawa, J., Miyazawa, T., Nakamura, K., Asadullah, M., Kunimori, K. and Tomishige, K. Catal. Commun. **9** (2008), pp. 195-201.
Nishikawa, J., Nakamura, K., Asadullah, M., Miyazawa, T., Kunimori, K. and Tomishige, K. Catal. Today **131** (2008), pp. 146-155.
Polychronopoulou, K., Costa, C. N. and Efstathiou, A. M. Appl. Catal. A: Gen. **272** (2004), pp. 37-52.
Polychronopoulou, K., Fierro, J. L. G. and Efstathiou, A. M. J. Catal. **228** (2004), pp. 417-432.
Richardson, J. T., Scates, R. M. and Twigg, M. V. Appl. Catal. A: Gen. **267** (2004), pp. 35-46.
Roh, H.-S., Jun, K.-W. and Park, S.-E. Appl. Catal. A: Gen. **251** (2003), pp. 275-283.
Suslick, K. S., Choe, S. B., Cichowlas, A. A. and Grinstaff, M. W. Nature **353** (1991), pp. 414-416.
Tonanon, N., Siyasukh, A., Tanthapanichakoon, W., Nishihara, H., Mukai, S. R. and Tamon, H. Carbon **43** (2005), pp. 525-531.
Wang, L. and Zheng, J. Ultrason. Sonochem. **13** (2006), pp. 215-219.
Wang, W., Padban, N., Ye, Z., Olofsson, G., Andersson, A. and Bjerle, I. Ind. Eng. Chem. Res. **39** (2000), pp. 4075-4081.
Yang, C., Hu, X., Wang, D., Dai, C., Zhang, L., Jin, H. and Agathopoulos, S. J. Power Sources **160** (2006), pp. 187-193.
Yu, F., Ji, J., Xu, Z. and Liu, H. Ultrasonics **44** (2006), pp. e389-e392.
Zhang, J., Xu, H., Jin, X., Ge, Q. and Li, W. Appl. Catal. A: Gen. 290 (2005), pp. 87-96.
Zhang, J., Xu, H. and Li, W. Appl. Catal. A: Gen. 296 (2005), pp. 257-267.
Zhang, R., Wang, Y. and Brown, R. C. Energ. Convers. Manage. 48 (2007), pp. 68-77.

PARAMETRIC STUDY ON THE CO_2 CAPTURE EFFICIENCY OF THE CARBONATE LOOPING PROCESS IN A 10 kW DUAL FLUIDIZED BED

Charitos, C. Hawthorne, A.R. Bidwe, H. Holz, T. Pfeifer, A. Schulze, D. Schlegel, A. Schuster, G. Scheffknecht

Institute of Process Engineering and Power Plant Technology (IVD), University of Stuttgart

Abstract: Carbonate Looping is a promising option for the capture of CO_2 from power plant flue gases. The Carbonate Looping process is carried out in a Dual Fluidized Bed (DFB) system with continuous looping of CaO, which is the CO_2 carrier, between the two beds. The system consists of a carbonator, where CO_2 is absorbed by CaO, operating at 600- 700 °C and a regenerator operating at temperatures above 900 °C. Experiments was carried out in a 10 kW DFB facility so as to investigate critical parameters affecting the CO_2 capture efficiency of the process which are the CaO looping rate, the carbonator space time and the carbonator temperature. The rate of sorbent attrition was found to be 2% wt./h and is below the required sorbent make-up rate. Steady state CO_2 capture efficiencies of 90% are demonstrated under realistic process conditions.

Keywords: CO_2 capture, CaO, dual fluidized bed(DFB), carbonate looping

INTRODUCTION

Carbonate Looping is a post combustion route for power generation with CO_2 capture. It is economically feasible when compared to alternatives, as shown in (Abanades et al., 2004) and (Abanades et al., 2007). The concept utilizes a Dual Fluidized Bed (DFB) system with continuous looping of CaO that was initially demonstrated by Shimizu et al. (1999). The process concept is shown in Fig.1. The carbonator operates at a temperature of 600- 700 °C and is fed with a molar flow of CO_2 (F_{CO_2}) contained in the flue gas. The CO_2 is absorbed from CaO, as shown by Eq.(1):

$$CaO_{(s)} + CO_{2(g)} \leftrightarrow CaCO_{3(s)} \quad (1)$$

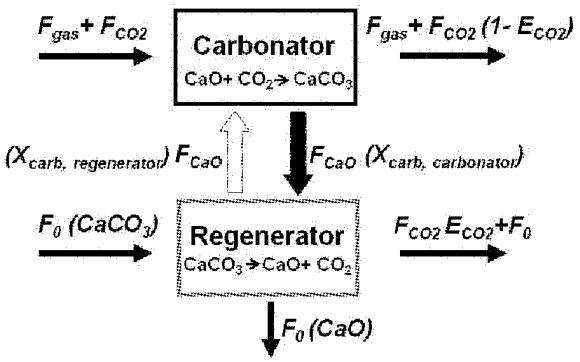

Fig. 1 Scheme of the carbonate looping process

Therefore, a CO_2 lean flue gas is produced. A portion ($X_{carb,\ carbonator}$) of the CaO looping rate (F_{CaO}) exiting the bed is carbonated. The CO_2 captured, expressed as $F_{CaO}X_{carb,\ carbonator}$ is transferred to the regenerator with the solid flow. The sorbent is regenerated to a great extent in the regenerator utilizing the reverse reaction of Eq.1 at temperatures above 900°C. The CaO looping rate exiting the regenerator is carbonated only to a limited portion ($X_{carb,\ regenerator}$). A make-up flow of $CaCO_3$ is necessary (F_0) to compensate for the decay of the carrying capacity of the sorbent, as shown in (Alvarez et al., 2005). Eventually, a CO_2 rich stream can be produced from the regenerator. The process has been proved at DFB systems in the range of 10-50 kW, as shown in (Lu et al., 2008) and (Abanades et al., 2008), achieving high CO_2 capture efficiencies.

THEORETICAL BACKGROUND

The CO_2 capture efficiency of a carbonator is dependant naturally on the space time (τ), which is defined as the ratio of moles of CaO (n_{CaO}) present in the carbonator and the moles of CO_2 per h in the flue gas feed. The space time is given from Eq. (2):

$$\tau = \frac{n_{CaO}}{F_{CO_2}} \tag{2}$$

Moreover, the CO_2 capture efficiency depends on factors influencing the particle reaction rate of carbonation. A reaction rate equation is first found in (Bhatia and Perlmutter, 1983), while Grassa et al. (2006) produced a similar equation considering particles having undergone a great number of carbonation- calcination cycles. Recently, Hawthorne et al. (2008) modified this equation, as shown in Eq. (3):

$$\frac{dX_{carb,carbonator}}{dt} = \frac{k_s S_o}{1-e_o}(X_{max} - X_{carb,carbonator})^{2/3}(C_{CO_2} - C_{CO_2,eq.}) \tag{3}$$

Where (3) k_s is the rate constant for surface carbonation, S_o is the initial CaO surface area and e_o is the particle porosity which are all constants and are dependant slightly on the type of limestone used. Furthermore, the C_{CO2} is the concentration of CO_2 in the flue gas while the $C_{CO2,eq.}$ is the equilibrium CO_2 concentration. In addition, $X_{carb,\ carbonator}$ is the actual conversion of CaO particles to $CaCO_3$ in the carbonator while the X_{max} represents the maximum possible conversion. The CO_2 concentration in the flue gas is given by the combustion of a given fuel. The equilibrium CO_2 concentration is a function of temperature and is given by Eq. (4), as found in (Baker,1962).

$$C_{CO_2,eq.} = \frac{1.462*10^{11}}{T_{carb}} \exp\left(\frac{-19130}{T_{carb}}\right) \tag{4}$$

The $X_{carb,\ carbonator}$ is a function of the CaO looping rate ratio which is defined as the ratio of F_{CaO}/F_{CO_2}.This is derived by the CO_2 mass balance over the carbonator from Fig. 1 , as shown in Eq. 5.

$$\frac{F_{CaO}}{F_{CO_2}} = \frac{E_{CO_2}}{X_{carb,carbonator} - X_{carb,regenerator}} \tag{5}$$

Eqwation (5) pinpoints that the solid stream amount entering and exiting the carbonator is linked to the carbonation conversion in the carbonator and of the exit stream. X_{max} depends on the carbonation-calcination cycle number of the average particle. The X_{max} has been linked to the ratio F_0/F_{CaO}, as found in (Abanades et al., 2002) and (Abanades et al., 2003). Hawthorne et al. (2008) has linked the X_{max} to the F_0/F_{CaO} and to the $X_{carb,\ carbonator}$.

EXPERIMENTAL

For this study a synthetic flue gas of 15% vol. CO_2 has been used. Based on the analysis above the CaO looping rate ratio, the space time and the carbonator temperature have been varied. The CaO looping rate ratio (F_{CaO}/F_{CO2}) has been varied between 4 and 18 by means of controlling the solid flow between the two beds with use of a cone valve. The carbonator space time has been varied between 0.32- 0.78 h by varying the superficial velocity and thereby the moles of CO_2 per h entering the carbonator. The carbonator temperature was varied between 630 - 700 °C. Simplifications have been met in this study with regard to the real process. There was no SO_2 in the flue gas fluidizing the carbonator and no SO_2 was generated in the regenerator. The effects of SO_2 on the process are found in (Grassa et al., 2008) and (Ryu et al., 2006). In addition, the regenerator was fluidized with air and the energy required was supplied by electrical heaters and sometimes by natural gas combustion. Thus, calcination temperatures of 850° C were possible avoiding higher temperatures and potential sorbent sintering problems. The suitability of an oxy-fired regenerator is shown in (Lu et al., 2008). Moreover, since the sorbent inventory used was "fresh" enough during the experimentation, no make-up flow was required in maintaining high sorbent activity. Therefore, the X_{max} in this case is a function of the CO_2 captured by the system inventory during the experimentation.

A DFB carbonate looping facility has been built utilizing a 12.4 m high, 7 cm diameter riser and a 11.4 cm diameter BFB, as shown in Fig. 2. To assure the suitability of the facility previous scaled cold model testing has been performed, as presented in (Charitos et al., 2008). The BFB is used as the carbonator (1) and the riser as a regenerator (2). Using the BFB as the carbonator allows great space time variation through velocity variation. Novelty of this rig in comparison to other DFB systems is the control of the solid looping rate between the beds by a cone valve. Synthetic flue gas consisting of CO_2 and N_2 enters the BFB carbonator, while regenerated CaO flows from the double exit loop seal (3) through the cone valve (4) and enters the BFB carbonator where CO_2 is absorbed from CaO. The CaO looping rate is controlled by varying the cone valve opening and the BFB absolute pressure through a pressure control valve (5) in the range of 0-100 mbar. An equal molar flow of partially carbonated CaO to the incoming exits the carbonator through the overflow (6), enters the lower standpipe (7) and subsequently the lower loop seal (8) through which the sorbent flow proceeds to the regenerator. The regenerator off gas proceeds to the stack while the riser entrainment is separated with a

cyclone (9), proceeds to the upper standpipe (10) and reaches the double exit loop seal. The CaO looping rate proceeds to the BFB and the rest of the flow returns to the riser through the loop seal weir (11).

For control of the facility and data acquisition LabView software is used. Limestone from the region of Schwabian Alb in Germany was used, which was pre-calcined partially prior to experimentation. During operation temperature and pressure drop are measured through type N thermocouples, differential and absolute pressure transducers, which are placed so that the respective profiles of the facility can be obtained. All flows are controlled with Mass Flow Controllers (MFCs) except loop seal aeration which is controlled by rotameters. Carbonator off-gas was analyzed by an ABB Advance Optima 2020 cabinet measuring CO_2 (0-30% range) and O_2 (0- 29% range) while the regenerator off gas was analyzed by an ABB EasyLine 3020 cabinet measuring CO_2 (0-100% range) and O_2 (0-100% range). The air flow stream coming from the loop seals to the BFB freeboard is calculated from O_2 measurements in the carbonator off-gas allowing for estimation of the CO_2 capture efficiency. Results stem from steady state operation of the DFB system defined as the situation where all input and output parameters remain constant for a period bigger than 15 min. Solid probes were taken so as to determine the $X_{carb,\ carbonator}$ and $X_{carb,\ regenerator}$. The CaO looping rate is measured with use of a quartz glass standpipe segment (12), located immediately above the lower loop seal, by stopping its aeration and measuring the height of accumulation of solids in the quartz standpipe segment over a given period of time. In addition, the CaO looping rate is determined through the CO_2 mass balance over the carbonator of Eq. (5), since the CO_2 capture efficiency is measured continuously and $X_{carb,\ carbonator}$ and $X_{carb,\ regenerator}$ are known from TGA analysis.

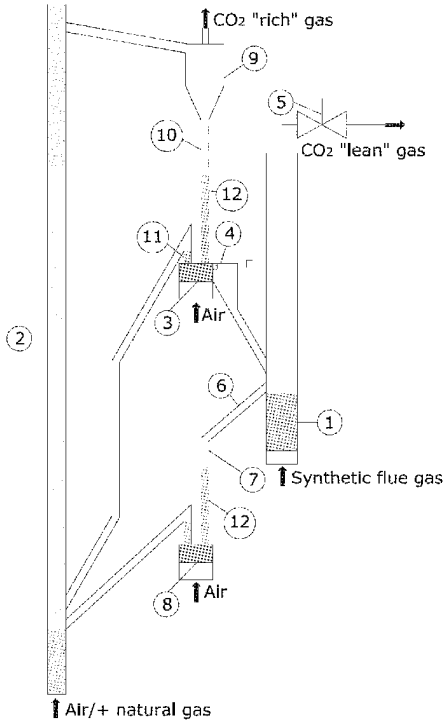

Fig. 2 Scheme of IVD carbonate looping DFB facility: (1) BFB carbonator, (2) riser regenerator, (3) double exit loop seal, (4) cone valve, (5) pressure control valve, (6) BFB overflow, (7) lower standpipe, (8) lower loop seal, (9) cyclone, (10) upper standpipe, (11) loop seal weir, (12) quartz standpipe segments

RESULTS AND DISCUSSION

The operation of the DFB system of Fig. 2 is generally very straight forward. Achieving a steady state is met with relative ease and the only intervention after some hours of operation is the adding of minor amounts of mass so as to replace the loss of inventory due to attrition. During a day of experiments various steady states were achieved through parameter variation. An example of a 2 h steady state is shown in Fig. 3 where a CO_2 capture efficiency of above 90 % is presented at the given process parameters.

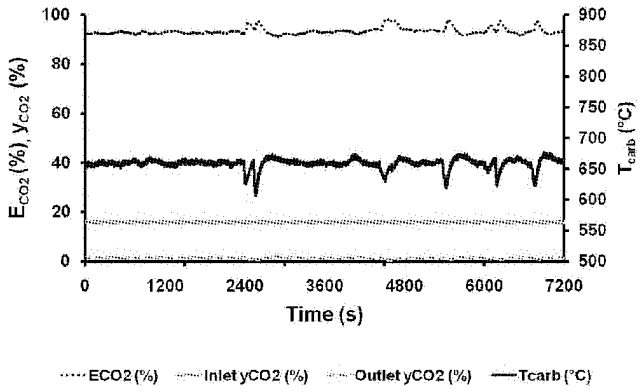

Fig. 3 Example of a high E_{CO_2} steady state: Inlet y_{CO_2}, T_{carb}, outlet y_{CO_2} and E_{CO_2} are plotted vs. time at τ of 1.41 h and F_{CaO}/F_{CO_2} of 16.8

Effect of the CaO looping rate ratio (F_{CaO}/F_{CO_2}) and space time (τ)

Figure 4 plots the $E_{CO_2}/E_{eq.}$, $X_{carb,\ carbonator}$ of the carbonator bed against the CaO looping rate ratio for three steady states, which where conducted consecutively, at constant process conditions and only the CaO looping rate ratio was varied by increasing the sorbent flow to the carbonator. The equilibrium-normalized CO_2 capture efficiency ($E_{CO_2}/E_{eq.}$) quantifies the reactor performance in comparison to the optimum allowed by thermodynamics. An increase of the CaO looping rate ratio results in a lower CaO conversion ($X_{carb\ ,carbonator}$) and to an increase in CO_2 capture efficiency. For a F_{CaO}/F_{CO_2} value around 4 the $E_{CO_2}/E_{eq.}$ is around 55% while the $X_{carb,\ carbonator}$ is 12%. When increasing the F_{CaO}/F_{CO_2} to above 16 the $E_{CO_2}/E_{eq.}$ almost reaches 100% while the carbonation conversion of the bed ($X_{carb,\ carbonator}$) drops below 6%. Since the data in Fig. 4 are from consecutive steady states it can be assumed that the maximum CaO carrying capacity, X_{max}, remains constant. Therefore, the decrease of $X_{carb,\ carbonator}$ with increasing the CaO looping rate ratio results in increasing the particle reaction rate in the carbonator, as expected from Eq. (3) and thereby higher CO_2 capture efficiencies are attained.

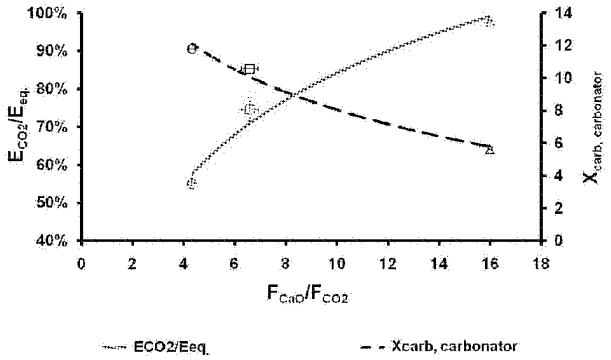

Fig. 4 $E_{CO_2}/E_{eq.}$ and $X_{carb,\ carbonator}$ vs. F_{CaO}/F_{CO_2} for steady states with inlet y_{CO_2} of 15%, T_{carb} of 660 °C and τ of 0.47 h

Figure 5 plots the equilibrium-normalized CO_2 capture efficiency against the CaO looping rate ratio for three series of steady states conducted under different values of space time in the carbonator, namely 0.32 h, 0.47 h and 0.78 h. Space time variation has been achieved by varying the BFB carbonator velocity from 0.5 m/s to 1.2 m/s. For experiments conducted under constant space time the conclusion made above that the increase of CaO looping rate ratio results in an increase of carbonator CO_2 capture efficiency holds true. However, for the same CaO looping rate ratio, the space time has a significant influence on the CO_2 capture efficiency. For modest F_{CaO}/F_{CO_2} values of 5 to 8, as shown in Fig. 5, the CO_2 capture efficiency obtained when operating with a τ value of 0.78 h, is 1.5 to 2 times higher than when operating with a τ value of 0.32 h. This is because modest F_{CaO}/F_{CO_2} values of 5 to 8 lead to lower carbonation reaction rates in the carbonator in comparison to the higher F_{CaO}/F_{CO_2} values. Therefore, at F_{CaO}/F_{CO_2} values of 5 to 8, it is critical to have enough moles of CaO per moles of CO_2 per h entering the carbonator and hence adequate values of space time so as to achieve substantial CO_2 capture efficiency. For higher values of F_{CaO}/F_{CO_2} the difference noted for the CO_2 capture efficiency between runs conducted at different space times becomes less significant since the carbonator bed becomes more active. Hence, when operating at large F_{CaO}/F_{CO_2} values of above 15, CO_2 capture efficiency values are reached that are close to equilibrium values regardless of space time. Since the carbonator would be a CFB for industrial applications it is has to be noted that the conditions of Fig. 5 can also be realized in a CFB.

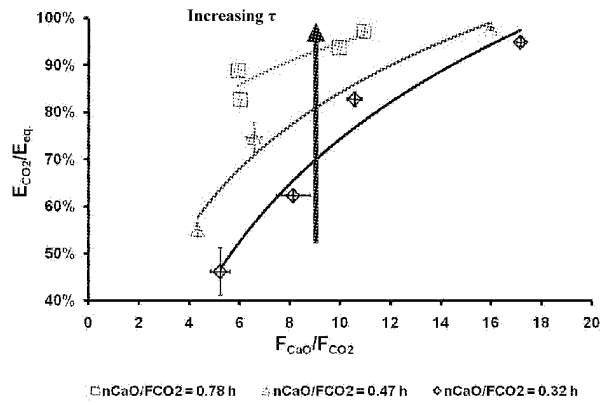

Fig. 5 $E_{CO_2}/E_{eq.}$ vs. F_{CaO}/F_{CO_2} for steady states with inlet y_{CO_2} of 15%, T_{carb} of 660 °C and varying n_{CaO}/F_{CO_2}

Effect of carbonator temperature (T_{carb})

The carbonation reaction rate and equilibrium CO_2 capture efficiency decrease with increasing carbonator temperature as is derived by Eq.(3) and Eq.(4). In Fig. 6 the carbonator temperature is increased between four consecutive steady states. The equilibrium CO_2 capture efficiency is plotted for every steady state and decreases with increasing carbonator temperature. In all 4 steady states the F_{CaO}/F_{CO_2} was kept higher than 14 so as to achieve maximum possible CO_2 capture efficiency. The CO_2 capture efficiency, as shown in Fig. 6, follows the decrease of the equilibrium CO_2 capture efficiency. A temperature of 630 °C gives the best CO_2 capture efficiency. The CO_2 capture efficiency at a given temperature can reach the equilibrium value provided that the CaO looping rate ratio is sufficient.

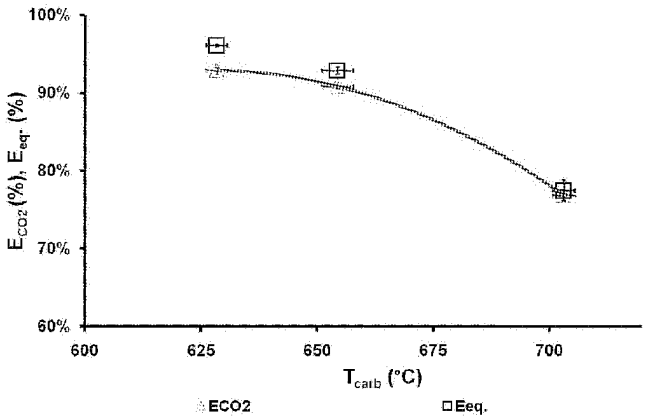

Fig. 6 E_{CO2}, $E_{eq.}$ vs. T_{carb} for steady states with inlet y_{CO_2} of 15%, τ of 0.55 h and F_{CaO}/F_{CO_2}>14

Sorbent attrition

Attrition is linked to the first calcination of limestone, as shown in (Jia et al., 2007), while Lu et al. (2008) shows that it also evolves with operation. In Fig. 7 the Particle Size Distribution (PSD) of the raw $CaCO_3$, of the CaO after the first pre- calcination and of the bed material after 8 h operation is shown. After the first pre-calcination the median particle size (dp_{50}) reduced from 340 μm to 325 μm. More significant attrition was observed after 8 h of operation with 20% of the total material collected from the DFB loop, secondary cyclones and candle filters being below 125 μm. The dp_{50} further reduced to 300 μm, while 16% of the material was collected outside the DFB loop. The rate of attrition is found to be 2% wt./h and is below the rate of make- up $CaCO_3$ required to maintain the desired sorbent activity.

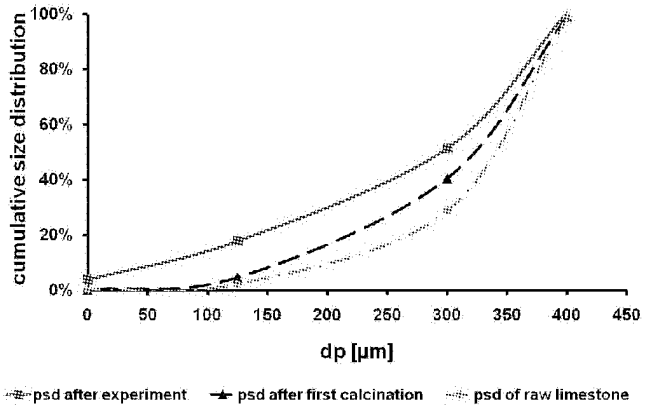

Fig. 7 PSD of initial $CaCO_3$, of CaO after first pre-calcination and of bed material after 8 h of operation

Comparison of methods for determining F_{CaO}/F_{CO_2}

The CaO looping rate ratio values were measured visually with use of the quartz standpipe segment and were calculated with the CO_2 mass balance over the carbonator of Eq.(5). The calculated values of F_{CaO}/F_{CO_2} from Eq.(5) are plotted against the values measured visually in Fig. 8. For lower F_{CaO}/F_{CO_2} both methods produce similar results because visual measurement is easy. Deviation exists for higher F_{CaO}/F_{CO_2} values resulting from the difficulty of visual measurements. Since CaO looping rate ratio values derived match for low

F_{CaO}/F_{CO_2} values the use of Eq.(5) is considered accurate and is used for data analysis while visual measurement is considered to be a good indicator during experimentation.

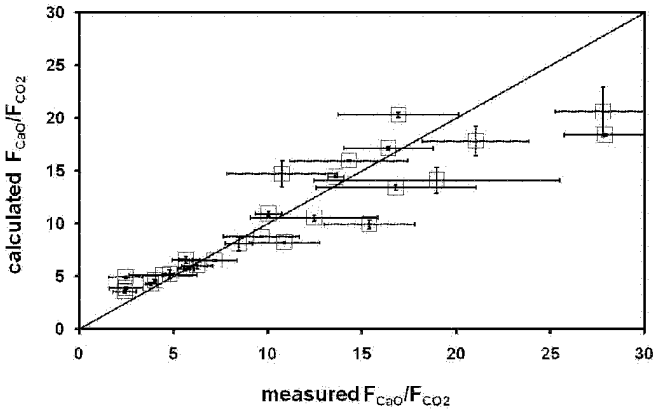

Fig. 8 Measured F_{CaO}/F_{CO_2} vs. calculated F_{CaO}/F_{CO_2}

CONCLUSIONS

The Carbonate Looping process has been demonstrated on a 10kW DFB facility achieving CO_2 capture efficiency above 90%. Stable steady states were achieved and attrition was found not to be an obstacle. The CO_2 capture efficiency is an increasing function of the CaO looping rate ratio and the carbonator space time. A CaO looping rate ratio higher than 15 provides equilibrium CO_2 capture efficiency even at low space time values. High CO_2 capture efficiency (i.e. $E_{CO_2}/E_{eq.}$> 80%), can be obtained also at modest solid looping rate ratios of 5 to 8 if the space time is sufficiently high. Increasing temperature leads to a decrease in the CO_2 capture efficiency and carbonation reaction rate. The highest value of CO_2 capture efficiency was attained at 630 °C. Calculation of the CaO looping rate ratio through a mass balance over the carbonator provides trustworthy results while visual measurement is a good operational indicator.

NOTATIONS

C_{CO_2} CO_2 concentration in flue gas, moles/m^3
$C_{CO_2,eq.}$ Equilibrium CO_2 concentration, moles/m^3
dp Particle size, μm
dp_{50} Median particle size, μm
E_{CO_2} CO_2 capture efficiency of the carbonator, %
$E_{eq.}$ Equilibrium CO_2 capture efficiency, %
e_0 Sorbent particle porosity
F_0 $CaCO_3$ make up flow and purge, moles/ h
F_{CaO} CaO looping rate between beds, moles/h
$\frac{F_{CaO}}{F_{CO_2}}$ CaO looping rate ratio
F_{CO_2} CO_2 flow to the carbonator, moles/ h
F_{gas} Flue gas flow other than CO_2, moles/ h
k_s Surface carbonation rate constant, m^{4}mol/s
n_{CaO} Amount of CaO in carbonator, moles
S_0 Initial CaO surface area, m^2/cm^3
T_{carb} Carbonator temperature, °C
X_{max} Average CO_2 carrying capacity of CaO, %
X_{carb} Actual conversion of CaO to $CaCO_3$, %
y_{CO_2} Vol. (%) of CO_2 in gas
τ Carbonator space time, h

ACKNOWLEDGEMENTS

The research activities are funded by the European Union within the 6th framework program under contract number 019914.

REFERENCES

Abanades, J. C.: Chem. Eng. J. 90 (2002), pp. 303-306.
Abanades, J. C., Alvarez, D., Anthony, E. J., Lu, D.: 17th Int. FBC Conference. (Pisupati, S.V., eds), ASME New York, Jacksonville (2003), pp. 133-140
Abanades, J. C., Rubin, E. S., Anthony, E. J.: Ind. Eng. Chem. Res. 43 (2004), pp. 3462-3466
Abanades, J. C., Grasa, G., Alonso, M., Rodriguez, N., Anthony, E. J., Romeo, L. M.: Environ. Sci. Technol. 41 (2007), pp. 5523-5527

Abanades, J. C., Alonso, M., Rodriguez, N., Gonzàlez, B., Grasa, G., Murillo, R.: 9th Int. GHGT Conference, Washington DC (2008)
Alvarez, D., Abanades, J.C.: Energy & Fuels 19 (2005), pp. 270-278.
Baker, E. H.: J. Chem. Soc. 70 (1962), pp. 464- 470
Bhatia, S. K., Perlmutter, D. D.: AIChE J. 29 (1983), pp. 79-86.
Charitos, A., Hawthorne, C., Bidwe, A., He, L., Scheffknecht, G.: 9th Int. CFB Conference (Werther, J., Nowak, W., Wirth, K. E., Hartge, E. U. eds), TuTech Innovation, Hamburg (2008), pp. 753-758
Jia, L., Hughes, R., Lu, D., Anthony, E.J., Lau, I.: Ind. Eng. Chem. Res. 46 (2007), pp. 5199- 5209
Grasa, G., Abanades, J.C., Alonso, M., Gonzàlez, B.: Chem. Eng. J. 137 (2006), pp 561- 567
Grasa, G., Alonso, M., Abanades, J.C.: Ind. Eng. Chem. Res. 47 (2008), pp. 1630- 1635
Hawthorne, C., Charitos, A., Perez-Pulido, C. A., Bing, Z., Scheffknecht, G.: 9th Int. CFB Conference (Werther, J., Nowak, W., Wirth, K. E., Hartge, E. U. eds), TuTech Innovation, Hamburg (2008), pp. 759- 764
Lu, D., Hughes, R., Anthony, E.J.: Fuel Process Technol. 89 (2008), pp. 1386- 1395
Ryu, H. J., Grace, J. R., Jim Lim, C.: Energy & Fuels 20 (2006), pp. 1621-1628.
Shimizu, T., Hirama, T., Hosoda, H., Kitano, K., Inagaki, M., Tejima, K.: TransIChemE, 77- A (1999), pp. 62- 68

EXPERIMENTAL INVESTIGATION OF TWO MODIFIED CHEMICALLOOPING COMPUSTION CYCLES USING SYNGAS FROM CYLINDERSAND THE GASIFICATION OF SOLID FUELS

C.R. Müller, T.A. Brown, C.D. Bohn, S.Y. Chuang, J.P.E. Cleeton, S.A. Scott and J.S. Dennis

Department of Chemical Engineering and Biotechnology, University of Cambridge, Pembroke Street, Cambridge CB2 3RA, U K

Department of Engineering, University of Cambridge, Trumpington Street, Cambridge CB2 1PZ, U K

Abstract: Two modified Chemical Looping Combustion (CLC) schemes were investigated: (a) CLC with in situ gasification of a solid carbonaceous fuel in the fuel reactor, and (b) CLC for the production of high purity hydrogen from low grade syngas. A comparison between the performance of the two modified cycles using (i) syngas from cylinders and (ii) syngas derived from the gasification of various solid fuels was made. Preliminary results indicate that both processes can be operated with sufficient conversions using low and high-rank coals. However, agglomeration of the oxygen carrier was observed if wood was used in process (a), probably owing to the formation of low-melting eutectics between the oxygen carrier and metals from the wood ash.

Keywords: chemical looping combustion, gasification, hydrogen, oxygen carrier, solid fuel

INTRODUCTION

World reserves of coal far exceed those of oil and gas, and its use is projected to increase by ~ 80% by 2030 (IPCC, 2001). However, coal is the most polluting fossil fuel, in terms of CO_2 produced per unit of power generated and so it is imperative to find ways of using it whilst avoiding the release of CO_2 into the atmosphere. Chemical looping combustion (CLC) provides one means of combusting such a fuel, whilst capturing the CO_2 as a pure stream, suitable for subsequent sequestration into the earth. In conventional CLC, a gaseous fuel, e.g. natural gas, or syngas, is oxidised in one reactor (the fuel reactor):

$$(2n + m)\ MeO + C_nH_{2m} \rightarrow (2n+m)\ Me + m\ H_2O + n\ CO_2$$

Subsequent condensation of the steam yields a stream of pure CO_2. The reduced metal oxide, Me, is conveyed to an oxidation reactor where it is regenerated with air:

$$Me + \frac{1}{2} O_2 \rightarrow MeO$$

In effect, the fuel has been combusted in air, but the CO_2 is produced in a pure form, avoiding the major cost of CO_2 separation from N_2 in the flue gases from conventional combustion in air. So far, research has predominantly focused on the CLC of gaseous fuels, e.g. Ishida and Jin (1994), De Diego et al., (2007) and Cho et al., (2004), but its extension to solid fuels is desirable. One option would be a pre-gasification step, in which coal or biomass is first gasified using CO_2 and, or, steam (Anthony, 2008). Another option (Dennis et al. 2006, Scott et al., 2006) proposes the gasification and the reduction of the oxygen carrier in a single reactor. Potentially, the advantages would be: (i) avoiding the complexity of separate gasification, which would need to receive heat at high temperature from the oxidation (or fuel) reactor, (ii) the rapid removal of H_2 and CO by the metal oxide could enhance the gasification kinetics, inhibited by high concentrations of H_2 and CO and (iii) the level of solids conveyed and handled, with concomitant attrition, is considerably reduced. However, there are potential problems: (a) the carrier is in direct contact with ash and carbon fines with possibly deleterious effects, (b) the ash from some biomass contains elements, which may form low melting eutectics with the oxygen carrier, causing bed agglomeration, and (c) the influence of sulphur on the oxygen carrier.

In a separate modification, CLC can produce ultra-pure H_2 with inherent CO_2 separation (Bohn et al. 2008). Here, iron oxide is used as an oxygen carrier and is first reduced by crude syngas from a gasifier according to (for CO):

$3\ Fe_2O_3 + CO \leftrightarrow 2\ Fe_3O_4 + CO_2$

$0.947\ Fe_3O_4 + 0.788\ CO \leftrightarrow 3\ Fe_{0.947}O + 0.788\ CO_2$

$Fe_{0.947}O + CO \leftrightarrow 0.947\ Fe + CO_2$

The hydrogen in the crude syngas also reacts to produce Fe. Subsequently, it has been found that ultra-pure hydrogen can be generated from either Fe or $Fe_{0.947}O$ by oxidising it with steam:

$0.947\ Fe + H_2O \leftrightarrow Fe_{0.947}O + H_2$

$3\ Fe_{0.947}O + 0.788\ H_2O \leftrightarrow 0.947\ Fe_3O_4 + 0.788\ H_2$

To return the Fe_3O_4 to its original form, Fe_2O_3, thermodynamics dictates that oxidation in air is required:

$$2\ Fe_3O_4 + \frac{1}{2}\ O_2 \leftrightarrow 3\ Fe_2O_3$$

Generally, research on CLC has mainly focused on the use of fairly pure gaseous fuels, e.g. natural gas or cylinder gas mixtures to "simulate" the syngas leaving a typical gasifier. However, to make these novel cycles attractive for industry, experiments with gases derived from a real gasifier, e.g. containing sulphurous species, ash and tars, are essential. This paper describes some current research at Cambridge aimed at comparing the performance of oxygen carriers, either in simulated gases of high purity or as generated from the actual gasification of carbonaceous fuels, such as coals and biomass.

EXPERIMENTAL

Two different experimental setups were used to study the two schemes for CLC, described above, namely (i) for the production of high purity hydrogen and (ii) for the combustion of solid fuels. CLC for the production of high-purity hydrogen

(i) Experiments with syngas generated by a fluidized bed gasifier. The experimental set-up is shown in Fig. 1. The fluidized bed gasifier was constructed from a 20.5 mm i.d. stainless steel tube. A perforated plate distributor containing 8 holes, each 1.0 mm in diameter was fitted 180 mm above the bottom of the bed. The inert material fluidized was 15 ml of Al_2O_3 (> 99.9 wt. % purity, Boud Mineral) sieved to size fraction 300 - 425 Fm. Gasification was by air; the flow-rate was controlled via a mass flow controller. Owing to limitations in the feed-rate of the screw-feeder, the bed was operated at only $U/U_{mf} = 1.3$. The low U/U_{mf} ratio had no implications for the experiment, as the only purpose of the gasifier was to produce a realistic syngas. The gasifier was contained within an electrically-heated tubular furnace, temperature was monitored via a Ntype thermocouple inserted into the fluidized bed and maintained at 923 K. The syngas leaving the gasifier was directed through a packed bed, containing iron oxide, constructed from a 20.5 mm i.d. stainless steel tube, arranged with downflow of gas, as seen in Fig. 1. The packed bed was contained in a second electrically-heated tubular furnace with a N-type thermocouple inserted into the packed bed, maintained at 1083 K. A perforated plate distributor containing 8 holes, each 1.0 mm dia. was fitted 250 mm above the bottom of the packed bed. The active part of the bed consisted of 20 g iron oxide particles (425 - 600 Fm), sandwiched between 2.5 and 7.5 g of Al_2O_3 (1400 Fm, > 99.9 wt. %, Boud Mineral). The iron oxide particles were prepared via a mechanical mixing technique (Bohn et al., 2008) from Fe_2O_3 powder (< 5 Fm, Sigma-Aldrich, > 99 wt%). A typical experiment was performed by allowing the gasifier to reach a steady state outlet concentration of [CO] and [CO_2], while purging the packed bed with nitrogen (SV1 open, SV2 closed). Next, the off-gas from the gasifier was diverted though the packed bed until steady-state gasifier composition had been detected at the outlet for 200 s.

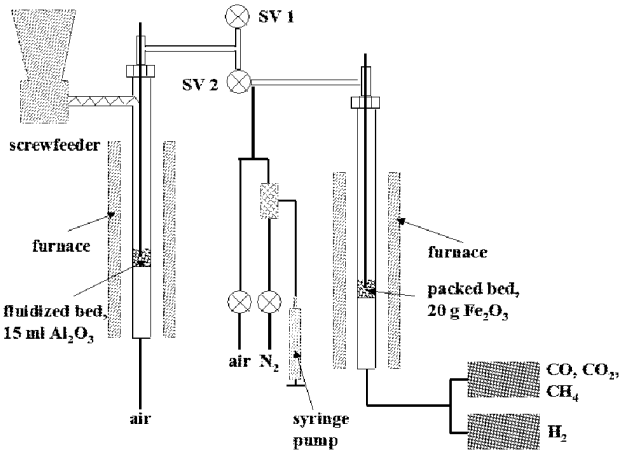

Fig. 1 Experimental setup for the production of high purity hydrogen using a bed of iron and a fluidized bed gasifier to produce a 'realistic' syngas

The packed bed was subsequently purged with N_2 for 500 s. The reduced iron was then re-oxidized to Fe_3O_4 by a steam-N_2 mixture ([H_2O]:[N_2] = 20:80 mol %) for 1700 s. The composition of the gas was determined by (i) an infrared analyzer (ABB EL3020) measuring CO_2 (0-30 mol %), CO (0-30 mol %) and CH_4 (0-30 mol %) and (ii) a thermal conductivity meter, measuring H_2 (ABB Caldos27, 0-30 mol %).

(ii) Experiments with syngas made from high-purity cylinder gases. A very similar experimental setup was

used to study the reduction of iron oxide via cylinder syngas and subsequent re-oxidation with steam (Bohn et al., 2008). To study the potential of the process to produce a pure stream of CO_2 without any CO slip, gases contained in two cylinders, i.e. one with a gas mixture with molar [N2]:[CO] = 9:1, the other with pure CO_2, were mixed so that the final ratio of mole fractions of $CO:CO_2:N_2 = 9:9:82$ mol %. A flow-rate of 2 L/min at STP was passed through a packed bed (20 g of 425 - 600Fm Fe_2O_3) of i.d. 10.2 mm, reducing the Fe_2O_3 to $Fe_{0.947}O$. After the breakthrough of CO, the bed was purged with N_2 and re-oxidized to Fe_3O_4 via a mixture of N_2 and steam (ratio of mole fractions of $N_2:H_2O$ = 75:25). The temperature was 1023 K, which is only 50 K lower than the gasifier experiments. Therefore, the cyclic stability of the particles should be identical in the ideal case. To study the stability of the oxide particles over repeated cycles, the mass of Fe_2O_3 particles in the bed was decreased to 1 g. Using a reducing gas with a ratio of mole fractions of $CO_2:CO:N_2 = 9:9:82$ and a re-oxidizing composition of $N_2:H_2O$ = 75:25 mol %, the particles were cycled between Fe_3O_4 and $Fe_{0.947}O$.

CLC with direct gasification of the solid fuel in the fuel reactor

(i) Gasification of solid fuels. The fluidized bed, shown in Fig. 2, consisted of a quartz tube (i.d. 30 mm; length 460 mm), which was held vertically in an electrically heated furnace. A porous frit was situated 110 mm from the base of the reactor. The pressure drop across the frit was larger than the pressure drop across the bed at $U = U_{mf}$,. The temperature of the bed was controlled via a K-type thermocouple and maintained at 1123 K. The bed material consisted of 20 ml sand (355 – 500 Fm) and ~ 1.0 g of a co-precipitated oxygen carrier, containing CuO and Al_2O_3 ($CuO:Al_2O_3$ = 82.5 : 17.5 wt. %, sieved to 355 – 500 Fm). Full details of the method of preparation of this material are given by Chuang et al. (2008). Copper oxide particles were chosen for this work since its exothermic reduction and oxidation reactions can provide heat for the endothermic gasification of a solid fuel to form synthesis gas, subsequently burned when in contact with CuO. The value of U/U_{mf} at the operating temperature was 5.7. The off gases leaving the reactor were sampled through a quartz probe via a pump at a rate of 13 ml/s at STP. The water in the sample gas was condensed out by first passing it through impinger tubes, placed in an ice-cooled water bath, and then through a tube of $CaCl_2$. The sampled gases were analyzed using an ABB EL3020 continuous infrared analyzer measuring CO (0-20 mol%), CO_2 (1-100 mol%) and SO_2 (1-10000 ppmv). Four different fuels were investigated: (i) lignite, (ii) bituminous coal, (iii) petcoke and (iv) wood chips, summarised in Table 1. A cycle is shown in Fig. 3.

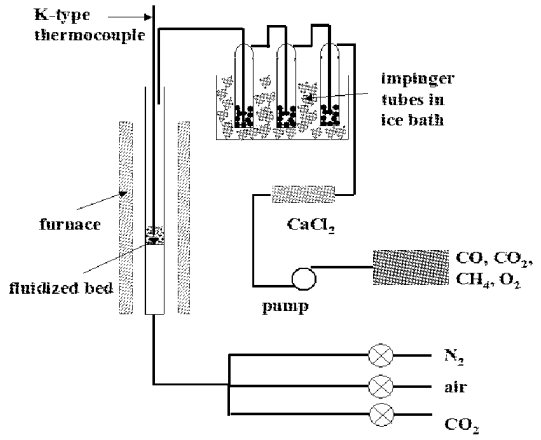

Fig. 2 Experimental setup to test the cyclic stability of co-precipitated Cu-Al oxygen carriers using batches of different solid fuels

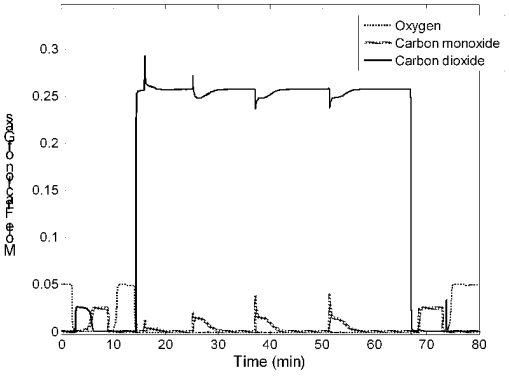

Fig. 3 Typical profiles of CO, CO_2 and O_2 for a batch experiment

Table 1 Composition of the solid fuels used (ultimate analysis)

Fuel	C[wt%]	H[wt%]	S[wt%]	O[wt%]	N[wt%]
Wood	46.5	6.05	N/A	N/A	0
Lignite(Hambach)	69.9	5.5	0.31	23.5	0.94
Taldinsky bituminous	66.6	5.18	0.3	27	0.9
Petroleum Coke	89.9	3.37	1.08	4.23	1.4
Lignite Char (Sigma- Aldrich)	75.9	1	N/A	6.0	0.73

At the start of each cycle, prior to the addition of solid fuels, the conversion of the CuO to Cu was tested by reacting it with cylinder syngas with ratio of mol fractions $CO:N_2$=2:98 (mixed from two cylinders containing 100 % N_2 and $CO:N_2$ = 10:90 mol %, respectively). This procedure is referred to as a 'titration' in the following. The CuO was then regenerated in 5 mol % O_2 in N_2 after which the bed was fluidized with

CO_2:N_2 = 23:73 mol % and batches of solid fuel (0.05 g for lignite and wood and 0.2 g for the bituminuous coal and petcoke) were added to the bed until the carrier appeared to be fully depleted, i.e. CuO was reduced to metallic Cu. This was assumed to occur when the addition of a batch of fuel gave the same CO concentration profile for two consecutive batches, viz. only gasification was occurring in the reactor. This was confirmed by a second titration prior to regeneration to check if there was any remaining active CuO in the bed. The oxygen carrier was then re-oxidised. Here, batches of solid fuel were used to avoid the build-up of a large inventory of char.

(ii) Oxygen carrier analysis using a syngas mixture from cylinder. For these experiments the set-up was very similar to that shown in Fig. 2. The bed typically consisted of 25 ml of silica sand (355-425 Fm, U_{mf} = 0.08 m/s) and ~ 0.5 g of the oxygen carrier (500 – 710 Fm) contained in the same quartz fluidized bed reactor as described above. The temperature of the bed was controlled via a K-type thermocouple to 1073 K. Values for U/U_{mf} (at 1073 K) between 4.6 and 6.2 were used. Gases from two cylinders, containing 100 % N_2 and CO:N_2 = 10:90 mol %, were mixed in such a way to yield a gas blend of CO:N_2 = 2.5:97.5 mol % and used to reduce the oxygen carrier for 480 s. After a N_2 purge for 90 s, the re-oxidation was performed for 400 s using air, followed by a N_2 purge for 90 s; further details of experiments are given by Chuang et al. (2008).

RESULTS AND DISCUSSION

Chemical looping cycle for the production of high-purity hydrogen from coal or biomass

(i) Experiments with bottled cylinder gas. Fig. 4 shows the composition of the effluent gas as a function of time for a bed containing 20 g Fe_2O_3 and reduction via a cylinder syngas blend at 1023 K. It can be seen that initially all the CO entering the bed was converted into CO_2, the [CO] being less than 5 ppmv at the outlet. Once the Fe_2O_3 was exhausted, i.e. converted to $Fe_{0.947}O$ or Fe_3O_4, CO broke through between t = 810 s and t = 850 s. The reducing gas was then turned off and the bed was purged with N_2 for 650 s. During this time, [CO] decreased to < 5 ppmv. Next, the bed was re-oxidised using steam, yielding a high purity stream of hydrogen with [CO] never exceeding 5 ppmv. Figure. 4 therefore confirms that the proposed CLC process can convert a cylinder syngas mixture of CO and CO_2 into a pure stream of CO_2 suitable for sequestration, and can also produce a stream of high-purity hydrogen suitable for, e.g., PEM fuel cells. However, for operating the newly proposed CLC process economically, it is imperative that the iron oxide particles maintain both their reactivity and yield over a large number of cycles, ideally of the order of a few hundred. Fig. 5 presents the results of experiments investigating the cyclic stability of the iron oxide particles over 10 cycles. Using a cylinder syngas mixture of CO:CO_2:N_2 = 9:9:82 mol %, the Fe_2O_3 particles were cycled between the Fe_3O_4 - $Fe_{0.947}O$ transitions at 1023 K. Fig. 5 shows that when using a cylinder syngas for the reduction, the iron particles possess a very good cyclic stability at 1023 K. The theoretical limit of H_2 production is marked by a dashed line in Fig. 5. (ii) Experiments with a syngas produced by a gasifier continuously fed with lignite char. Figure. 6 shows the composition of the effluent gas as a function of time for a bed containing 20 g of Fe_2O_3, operated at 1083 K. The reduction of Fe_2O_3 via syngas can be divided into 4 time periods as indicated. Initially, all of the syngas (flow-rate 2.1 L/min at STP) entering the bed was converted into CO_2. This period is labelled (I) and lasted for ~ 300 s. A simple mass balance on the CO_2 produced during the time of zero CO slip (grey shaded area) shows that all the Fe_2O_3 is converted to Fe_3O_4. In addition only a minimal amount of the Fe_3O_4 is further reduced to $Fe_{0.947}O$ during this time (~ 3 mol%). Thus, the kinetics for the Fe_2O_3-Fe_3O_4 transition are fast enough to reach equilibrium within the residence time of the gas in the bed, which for the given conditions was ~ 0.19 s. After the breakthrough of CO (point A in Fig. 6), i.e. the point at which all the Fe_2O_3 has been converted to Fe_3O_4 or $Fe_{0.947}O$ in the reactor (based on a mass-balance on the exit CO_2 stream), the Fe_3O_4 – $Fe_{0.947}O$ equilibrium transition is reached. For the transition from Fe_3O_4 to $Fe_{0.947}O$ thermodynamics gives $K_p = p_{CO2}/p_{CO}$ = 2.27 at 1083 K. This equilibrium value corresponds to the kink in Fig. 5, at point B. The experimentally-calculated K_p = 2.37, and is thus very close to the theoretical value. After the kink, a region of flat [CO_2] and [CO] profiles can be observed, labelled II. This period lasted for ~ 240 s, during which the kinetics of the Fe_3O_4 – $Fe_{0.947}O$ transition are fast enough to reach equilibrium within the residence time of the reactor. However, as the reaction rates decrease with conversion, starting from t = 3130 s the kinetics were not sufficiently rapid to reach equilibrium within the residence time of the gas in the bed. This yielded a period, labelled III, of continuously-decreasing [CO_2] and increasing [CO] in the effluent gas. Given that after that point a constant ratio of mole fraction of CO to that of CO_2 can be observed, it is assumed that all the Fe_3O_4 which can be converted has been converted to $Fe_{0.947}O$, and the syngas at the gasifier concentration breaks through. This period is labelled IV. It can be seen from Fig. 6 that the composition of the syngas leaving the gasifier is [CO_2]:[CO] H 15:10 (on a N_2-free, molar basis). After the breakthrough of the syngas, the gasifier valves SV1 and SV2 in Fig. 1, were switched in such a way that the gasifier gas by-passed the iron oxide bed. The bed of Fe_2O_3 was subsequently purged for 500 s with N_2 (flow-rate 2 L/min at STP). Starting from t = 4850 s, the reduced iron oxide was re-oxidised by a stream of gas containing [H_2O]:[N_2] = 20:80 mol % (flowrate of N_2 = 2

L/min at STP) stream to Fe_3O_4. A mass balance reveals, that, assuming all Fe_2O_3 is converted to Fe_3O_4, 70 mol % of the Fe_3O_4 was further reduced to $Fe_{0.947}O$ during the reduction period. Bohn et al. (2008) reported conversion rates of ~ 80 - 85% for the Fe_2O_3-$Fe_{0.947}O$ transition if a syngas mixture from cylinders is used. This would imply that using the syngas of an actual gasifier, slightly smaller conversion rates can be expected, at least in the case of lignite char. Further studies will investigate the cyclic stability and different fuels, e.g. high-rank coals, biomass etc.

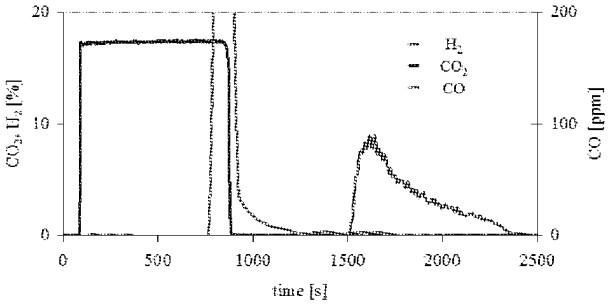

Fig. 4 Reduction using a cylinder gas mixture of $CO:CO_2:N_2$=9:9:82 mol% and subsequent oxidation in steam for the transition from Fe_2O_3 to $Fe_{0.947}O$ at 1023 K using a bed of 20 g Fe_2O_3.

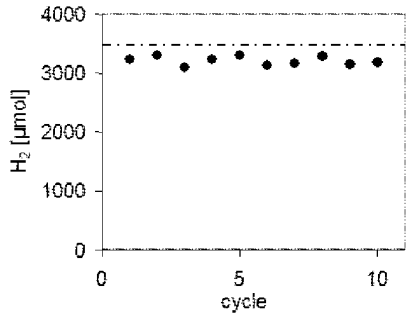

Fig. 5 Cyclic stability of Fe_2O_3 particles cycled between the Fe_3O_4 – $Fe_{0.947}O$ transition using a cylinder syngas for reduction

A modified Chemical Looping Cycle for the combustion of solid fuels

(i) Experiments with bottled cylinder gas. Chuang et al. (2008) reported the development of a co-precipitated Cu-Al (mass ratio $CuO:Al_2O_3$ = 82.5 : 17.5) oxygen carrier for chemical looping combustion. Figure. 7 shows the cyclic stability of the oxygen carrier over 18 cycles at 1073 K using a gas mixture of $CO:N_2$ = 2.5:97.5 mol % and air for reduction and re-oxidation of the oxygen carrier, respectively. Here, the ratio of the measured total number of moles of CO_2, to the theoretical amount, assuming full conversion of the known mass of CuO in the oxygen carrier to metallic Cu is defined as the yield of CO_2. It can be seen from Fig. 7 that the oxygen

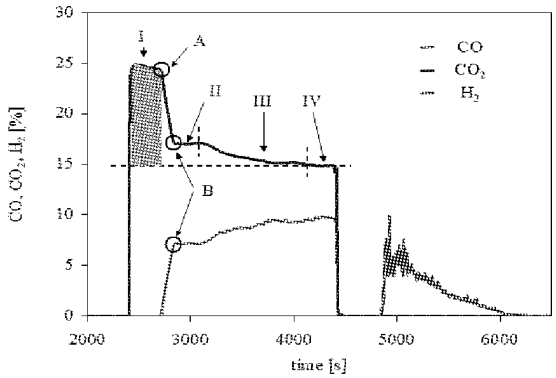

Fig. 6 Reduction and subsequent oxidation in steam for the transition from Fe_2O_3 to $Fe_{0.947}O$ at 1083 K using a bed of 20 g Fe_2O_3

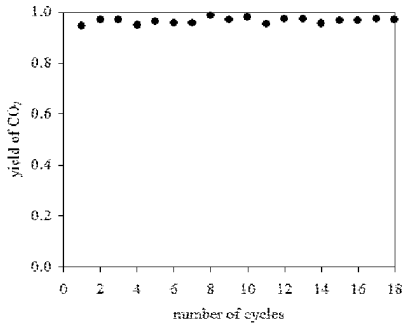

Fig. 7 Yield of CO_2 at 1073 K using a Cu-Al oxygen carrier and cylinder gas for reduction ($CuO:Al_2O_3$ = 82.5:17.5 wt.%)

carrier maintained a constant yield of CO_2, close to unity over 18 cycles, demonstrating its potential, at least as far as "pure"cylinder gases are concerned. Similar results were obtained using mixtures of H_2 and CO, balance N_2.

(ii) Batch experiments using various solid carbonaceous fuels. Fig. 8 shows the stability of the co-precipitated Cu-Al oxygen carrier, studied over 5 cycles; for lignite, bituminous coal and petcoke the cyclic stability is good. However, with wood, agglomeration of the bed material occurred from cycle 3, onwards, eventually giving deactivation of the carrier. Figure. 8 indicates that merging the gasification and reduction step of the oxygen carrier into one single reactor is feasible with most fuels, as the presence of ash and fines of carbon does not significantly decrease the CO_2 yield of the co-precipitated CuO-Al_2O_3. However, great care has to be taken with

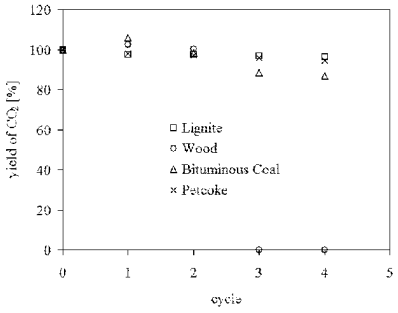

Fig. 8 Yield of CO_2 at 1123 K using a Cu-Al ($CuO:Al_2O_3$= 82.5:17.5 wt.%) oxygen carrier. Batched of solid fuel were added to the bed containing the oxygen carrier

wood owing to the fusibility of its ash when in contact with the oxygen carrier particles. Furthermore, the influence of sulphurous species on the reactivity of the particles requires a detailed study, but was beyond the scope of this paper.

CONCLUSIONS

Two modified CLC cycles: (i) to produce ultra-pure hydrogen using iron oxide particles as the oxygen carrier and (ii) direct gasification of solids fuels and reduction of a Cu-Al oxygen carrier by the produced syngas in a single reactor were studied using (i) syngas mixtures from cylinders and (ii) syngas produced by the gasification of solid fuels, such as coal, petcoke and wood. The kinetics of the Fe_2O_3-Fe_3O_4 transition of the iron oxide particles were sufficiently high to oxidise both the syngas from cylinders and a gasifier entirely to CO_2, which would be suitable for sequestration. However, the use of gasifier syngas revealed slightly smaller total conversions compared with the cylinder syngas, viz. 70 mol % vs. 85 mol % total conversion in the Fe_2O_3-$Fe_{0.947}O$ transition. It was confirmed that the Cu-Al oxygen carrier is suitable for use with bituminous coals and petcoke, but wood can result in severe agglomeration in the bed.

ACKNOWLEDGEMENTS

The authors are grateful to the UK's EPSRC (EP/F027435/1) for financial support.

REFERENCES

Bohn, C.D., Muller, C.R., Cleeton, J.P.E., Dennis, J.S., Scott, S.A.: Ind. Eng. Res. Chem 47 (2008), pp. 7623-7630.
IPCC (2001). Climate Change 2001. Third Assessment Report, Intergovernmental Panel on Climate Change (IPCC), U.N. (available on http://www.grida.no/climate/ipcc_tar/index.htm).
Leion, H., Mattison, T. and Lyngfeld A.: Fuel 86 (2007), pp. 1947-1958
De Diego, L.F., Garcia-Labiano, F., Gayan, P., Celaya, J., Palacios , J.M., Adanez, J.: Fuel 86 (2007) pp.1036
Cho, P., Mattisson, T., Lyngfelt A.: Fuel 83 (2004), pp. 1215-1225.
Anthony, E.J.: Ind. Eng. Chem. Res. 47 (2008), pp. 1747-1754.
Dennis, J.S., Scott, S.A., Hayhurst, A.N.: J. Energy Inst. 79 (2006) pp. 187-190
Scott, S.A., Dennis, J.S., Hayhurst N.A., Brown T.A.: AICHE J 52 (2006) pp. 3325-3328.
Chuang, S.Y., Dennis J.S., Hayhurst, A.N., Scott, S.A.: Combustion and Flame 154 (2008) pp. 109-121.

DEVELOPMENT OF FLY ASH-BASED SORBENT TO CAPTURE CO_2 FROM FLUE GAS

I. Majchrzak-Kucęba, W. Nowak

Czestochowa University of Technology, Department of Heating, Ventilation and Air Protection, Poland

Abstract: In the present work the thermogravimetric characterization of the sorption of carbon dioxide on polymer-modified mesoporous materials (MCM-41) from fly ashes is described. In order to obtain MCM-41 materials from three different types fly ashes,(including CFB fly ash) hydrothermal processes using the supernatants of coal fly ashes and surfactants as the structure-directing agents, have been carried out. The obtained mesoporous materials were subjected to polyethylenimine (PEI) modification by their impregnation to obtain samples with PEI contents of 30, 50 and 70%, respectively. CO_2 sorption/desorption tests on loaded PEI samples were carried out in a flow of a mixture of gasses (CO_2-10%, O_2-10%, N_2-80%) at different temperatures: 25 and 75°C. The highest CO_2 sorption value was obtained for the sample that contained the best-quality MCM-41 and was impregnated with PEI in the amount of 50%. This sample at a temperature of 75°C can take CO_2 in an amount equivalent to 111.7 mgCO_2/g sample weight. Under the same conditions, but without PEI impregnation, this sample can take CO_2 in an amount equivalent to 3.2 mgCO_2/g sample weight, thus 35 times less. The research of CO_2 adsorption on polymer-modified mesoporous materials from fly ashes carried out within this work has shown that these materials are characterized by high CO_2 adsorption capacity under conditions typical of coal combustion boiler flue gas and have the chance of becoming an efficient adsorbent for application to post-combustion CO_2 separation. For PEI impregnated samples, a different behaviour of adsorption/desorption profiles has also been observed (both sorption and desorption progresses very rapidly).

Keywords: CO_2, mesoporous materials, MCM-41, CFB fly ash

INTRODUCTION

The proposed techniques of boiler (including CFB boiler) flue gas CO_2 removal are: chemical and physical absorption, cryogenic methods, membrane methods, and adsorption methods. Developing the latter (PSA, TSA) requires numerous studies aimed at the simplification of the operational mechanism and the reduction of energy demand. The key factor for the improvement of this process is to develop solid regenerable sorbents that have high selectivity, high regenerability and high adsorption capacity for post-combustion CO_2 capture in suitable conditions, long term regeneration capacity in power plant flue gas environment, and low energy requirement for regeneration (Metz and Davidson, 2005).

Currently available adsorbents include activated carbon, zeolites (molecular sieves), metal oxides, hydrotalcites, microporous metal organic frameworks (MOFs) and amine-enriched sorbents. The CO_2 adsorbents have recently included those derived from fly ashes, such as amine-treated fly ash-derived carbons. Also amine-treated fly-ash derived mesoporous materials (MCM-41) can be categorized into this group, whose synthesis and sorption properties in respect to CO_2 are presented in the present study.

The aim of the present work was to synthesize the MCM-41 mesoporous material on the basis of different fly ashes and preparation of the polyethylenimine (PEI) modified MCM-41 by uniformly dispersing PEI into the pores of mesoporous molecular sieve. In the present work the thermogravimetric characterization of the sorption of CO_2 on MCM-41 modified PEI was presented.

EXPERIMENTAL

Preparation of the MCM-41 from fly ashes

The starting material for the synthesis of the mesoporous material MCM-41 were three different coal fly ashes (including CFB fly ash) (designated as 1F, 2F, 3F) which were obtained from an utility power stations in Poland. The fly ashes were chemically analyzed and used to prepare the mesoporous materials MCM-41. The preparation procedure of the MCM-41 from fly ash comprised two stages: the extraction of Si from the fly ash and the proper synthesis of MCM-41 on the basis of the obtained silicon extract. In order to extract silicon from fly ashes, a method consisting in the fusion of fly ash with NaOH was used, followed by dissolving of the formed solid substance in water. The obtained solutions containing sodium silicate were subjected to ICP analysis for the following elements: Si, Al, Na, Ca, Mg, Fe. The obtained sodium silicates was stirred using a mechanized stirrer. After a while, a surfactant (cetyl trimethylammonium chloride - CTMACl - Aldrich) was

started to be slowly added by drops in such an amount that the Si : CTMACl weigh ratio was 20.5. After the surfactant had been added, the pH of the solutions was adjusted so as to its value was 11. Sulphuric acid (VI) was used for this purpose. Next, the mixtures were put in an oven for 24 hours at a temperature of 100 °C. After this time, the pH value was corrected again to 11, and then the mixtures were placed in the oven for another 24 hours at 100 °C. Subsequently, the obtained solid substances were separated from the solutions and flushed with distilled water. The obtained materials was first dried and then calcined at 550 °C (at a temperature increase rate of 5 °C /min), with dried helium being passed through the oven at a rate of 60 ml/min during the whole period of temperature increase and during the first hour of calcination. Thus obtained fly ash-derived materials were designated as 1FM (no mesoporous material presence has been found in the sample), 2F-MCM-41,3F-MCM-41.

Preparation of the adsorbents

Three different fly ash-derived materials were, at the subsequent stage, subjected to PEI modification with the aim of achieving an efficient CO_2 sorbent. For the modification of the three samples of fly ash-derived materials polyethylenimine (PEI) and the wet impregnation method was used, according to the procedure described by Xu et al. (Xu et al. 2003). Following this procedure, the appropriate amount of PEI was dissolved in methanol under stirring, and finally fly ash-derived material was added to the PEI/methanol solution. The obtained mixtures were stirred and then dried at 70°C for 16 hrs under 700 mm Hg. Thus obtained adsorbents were designated as F-MCM-41-PEI-x, where x denotes the percentage share of PEI in the test sample. By varying the percentage content of PEI in particular samples (i.e. 30 wt%, 50 wt%, 70 wt%), the following modifications were obtained: for material derived from fly ash 1 (1FM-PEI-30, 1FM-PEI-50, 1FM-PEI-70), for material derived from fly ash 2 (2F-MCM-41-PEI-30, 2F-MCM-41-PEI-50, 2F-MCM-41-PEI-70), for material derived from fly ash 3 (3F-MCM-41-PEI-30, 3F-MCM-41-PEI-50, 3F-MCM-41-PEI-70).

Characteristics of adsorbents investigated

The mesoporous materials from fly ashes (before and after modification), were characterized by X-ray diffraction, N_2 adsorption/desorption and TGA. X-ray diffraction (XRD) patterns were recorded on a Bruker AXS D8 Advance (with monochromatic CuKα radiation $\lambda = 0.154$ nm). Diffraction data were recorded: between 1.4° and 8° 2 theta at an interval of 0.02° 2 theta and between 6° and 60° at an interval of 0.05° 2 theta.

The porous properties were investigated by determing their N_2 gas adsorption and desorption isotherms at 77 K, using an ASAP 2010 Instrument (Micromeritics Instrument Corporation, Norcross, GA, USA). For this procedure, the sample was outgassed under 1MPa for 24h at 573K prior to the nitrogen adsorption measurements. The specific surface area was calculated by the BET method from the linear part of BET plot according to IUPAC recommendations using the adsorption isotherm (relative pressure (p/p_o)=0.05-0.23). The pore size distribution was calculated by the BJH method and the pore volume was obtained from the maximum amount of adsorption at p/p_o of 0.99. The thermal properties were characterized using a Mettler TGA/SDTA 851e thermobalance. About 10 mg of the sample was heated at 20 ℃/min to 1000 ℃ in N_2 flow (50 ml/min).

CO_2 adsorption measurements

Carbon dioxide sorption/desorption on the fly ash-synthesized and modified F-MCM-41 materials was studied using a Mettler TGA/SDTA 851e thermobalance. The change in weight during the carrying out of a temperature programme applied enabled the determination of the sorption/desorption capacities of the adsorbents examined. About 10 mg of adsorbent was heated up to a temperature of 100℃ under N_2 atmosphere (50ml/min), and then heated isothermally at that temperature for about 15 minutes until a constant sample mass had been reached. Next, the temperature was changed to 25℃ (as well as to 75℃ and 100℃) and sorption of CO_2 was carried out isothermally at atmospheric pressure in a flow (50 $cm^3 \cdot min^{-1}$) of a mixture of gasses (O_2 (10% vol.), CO_2 (10% vol.), N_2 (80% vol.) during 150 min. After completion of the adsorption process the gas flow was switched from CO_2 to N_2 at a flow rate of 50ml/min to measure the CO_2 desorption performance. The process of desorption was researched in order to determine the possibility of zeolites' regeneration. The adsorption capacity for the adsorbents tested was expressed in mg CO_2/g adsorbent.

RESULTS AND DISCUSSION

Characterization of the mesoporous materials F-MCM-41

As the starting material (silicon source) for the synthesis of the MCM-41 sieve, three different types of fly ash were used, which originated from the combustion of hard coal and brown coal in pulverized-fuel and CFB boilers. The ashes were not subjected to pretreatment. The composition of starting fly ashes, as determined by

the XRF method (on a WD-XRF analyzer) is given in Table 1. As can be seen from the table, the contents of the main ash constituents, i.e. SiO_2 and Al_2O_3, vary, depending on the fly ash type. The highest Si/Al ratio is found for fly ash 3, and the lowest for fly ash 1.

Table 1 Chemical composition of fly ashes as determined by XRF analysis (wt.%)

Element as oxide	Fly ash No.1 (1F)	Fly ash No.2 (2F)	Fly ash no. 3 (3F)
SiO_2	36,89	51,68	50,21
Al_2O_3	26,59	27,56	26,31
CaO	14,44	2,94	3,11
Fe_2O_3	2,5	5,4	4,9
MgO	2,28	2,21	2,12
TiO_2	2,23	1,14	1,14
Na_2O	0,29	0,3	0,3
K_2O	0,86	2,75	2,88
Si/Al	1,38	1,87	1,9
Loss on ignition	1,45	6,06	2,97

The performed X-ray diffraction (XRD) analysis of samples obtained in this work showed that the MCM-41 mesoporous material was obtained from fly ashes No.2 & No.3, whereas it was not obtained from fly ash No.1. This is confirmed by the diffraction patterns shown in Fig. 1, on which well developed XRD reflections can be observed in the low-angle range (Fig. 1(e)) for the fly ash-derived materials obtained from fly ash No.3 (which suggests that this material is a good-quality MCM-41), poorly developed peaks on the diffractions patterns for material No.2 (which suggests that this material does not represent a good hexagonal ordering of mesopores, typical of good-quality MCM-41 materials) (Fig. 1(c)) and no reflections in the low-angle range for materials obtained from fly ash No.1 (Fig. 1(a)) (which confirms the absence of mesoporous structure in this sample).

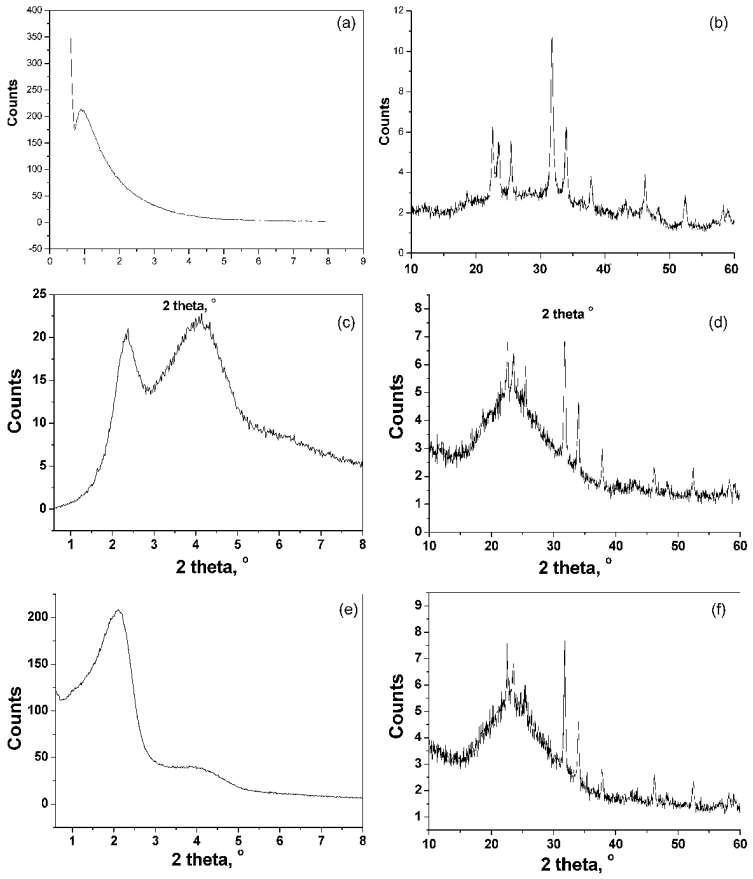

Fig. 1 X-ray diffraction patterns: (a),(b) materials obtained from fly ash No.1,(1FM), (c),(d) materials obtained from fly ash No.2(2F-MCM-41), (e),(f) materials obtained from fly ash No.3(3F-MCM-41)

The diffraction patterns indicate also that fly ash-derived materials 2 & 3, in which the formation of the MCM-41 material was found, are not "pure" mesoporous materials. The diffraction patterns in the high-angle range (Fig. 1(b),(d)) show reflections that can be ascribed to zeolite structures.

All samples were subjected to PEI impregnation, even though in one of them (materials obtained from fly ash No.1) no MCM-41 presence was found (the XRD analysis and the obtained BET values indicated only a certain amount of zeolite structures).

Characterization of the adsorbents (modified F-MCM-41 mesoporous materials)

The BET specific surface of the fly ash-derived materials obtained from fly ash No.2 (was 470 m^2/g, and that obtained from fly ash No.3 - 610 m^2/g. Thus, the achieved specific surface values confirmed that a good-quality mesoporous material was only obtained from fly ash No.3. The low specific surface value achieved for the materials obtained from fly ash No.1 additionally confirmed the lack of mesoporous structure in that sample. In turn, the pore volume and diameter, calculated for the mesoporous material obtained from fly ash No.3, amounted to, respectively: 1.03 cm^3g^{-1} and 6.29 nm. The pore volume and diameter, calculated for the mesoporous material obtained from fly ash No.2, amounted to, respectively: 0.6 cm^3g^{-1} and 4.75 nm. The chemical impregnation process results in a decrease of BET surface areas and pore volume of all the samples, indicating a blocking of some of the micro- and meso-pore volume. The reduction in the surface areas and the pore volume was the greater, the greater the PEI load was (Figs. 2(a) and (b)). For example, the BET surface area for 3F-MCM-41 (610 m^2/g) has decreased to 109.2 m^2/g (30wt.%PEI), 26,5m^2/g (50wt. %PEI) and 10.9 m^2/g (70 wt.%PEI). For example, the pore volume for 3F-MCM-41 (1.03 cm^3g^{-1}) has decreased to 0.42 cm^3/g (30 wt.%PEI), 0.13 cm^3/g (50 wt. %PEI) and 0.03 cm^3/g (70 wt.%PEI). A reduction in the surface area and the pore volume occurred also for 1FM, where no presence of mesoporous material, but only the presence of a certain quantity of zeolite structures, was found. In contrast to 3F-MCM-41 & 2F-MCM-41, however, the surface areas and the pore volume decreased most at a PEI content of 30% , and least at a PEI load of 70 wt.% (thus, differently to 3F-MCM-41 & 2F-MCM-41). This is confirmed by the fact that PEI filled the channel of the synthesized MCM-41 during impregnation. A similar reduction in surface areas and pore volume after impregnation, though for pure (not fly ash-derived) MCM-41, was found by Xu et al in their studies (Xu et al. ,2003).

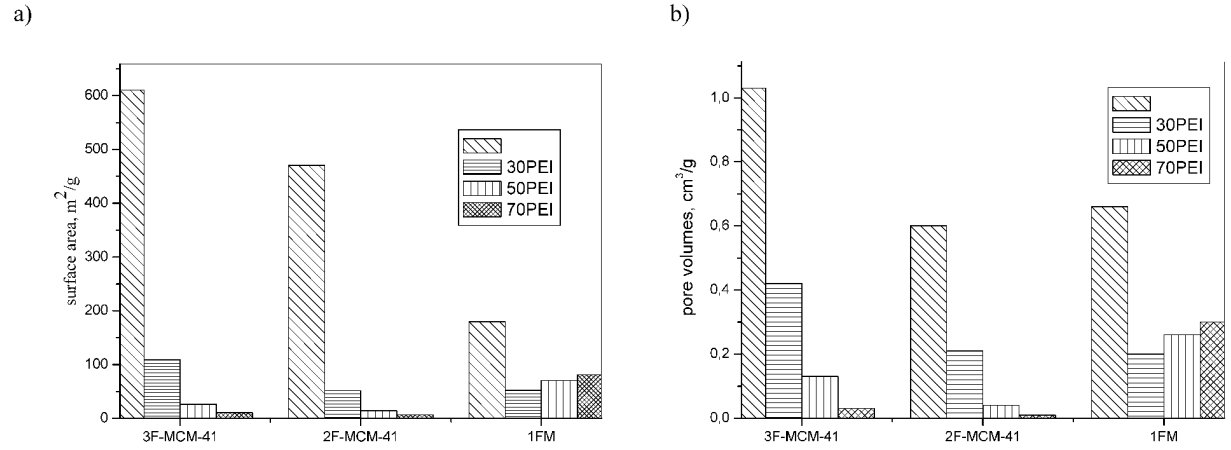

Fig.2 (a) BET surface areas for the fly ash-derived mesoporous materials and its chemical modification (30,, 50, 70 wt.% PEI), (b) Pore volume for the fly ash-derived mesoporous materials and its chemical modification (30, 50, 70 wt. % PEI)

Carbon dioxide sorption on modified mesoporous materials from fly ash

The investigation of CO_2 sorption was carried out for the fly ash-derived mesoporous materials and the adsorbent obtained as a result of its chemical modification PEI. All samples were subjected to CO_2 sorption/desorption tests before and after PEI impregnation.

The CO_2 adsorption profiles of the fly ash-derived mesoporous materials and the adsorbent obtained as a result of its chemical modification are presented in Figs. 3-6 and the adsorption capacity results of the CO_2 uptake are also listed in Table 2.

Table 2 Adsorption capacity of the fly ash-derived mesoporous materials and the adsorbent obtained as a result of its chemical modification PEI ($mgCO_2/g$ adsorbent) at 25and75°C

Modified samples	Adsorption capacity, $mgCO_2/g$ adsorbent	
	25℃	75℃
1FM	***2.3***	***1.5***
1F-PEI-30	23.9	29.3
1F-PEI-50	32.7	38.3
1F-PEI-70	3.8	5.9
2F-MCM-41	***5.1***	***2.8***
2F-MCM-41-PEI-30	37.9	28.0
2F-MCM-41-PEI-50	37.3	102.8
2F-MCM-41-PEI-70	40.8	111.6
3F-MCM-41	***5.9***	***3.2***
3F-MCM-41-PEI-30	38.5	85.0
3F-MCM-41-PEI-50	59.3	111.7
3F-MCM-41-PEI-70	32.7	17.9

As can be seen, the fly ash-derived materials (1FM, 2F-MCM-41, 3F-MCM-41) exhibits a low sorption capacity toward CO_2. For example, the sorption capacity for 3F-MCM-41material was 5.9 mg CO_2/g adsorbent at 25°C and 3.2 mg CO_2/g adsorbent at 75°C. The CO_2 uptake on the fly ash-derived mesoporous materials decreased with increasing adsorption temperature. This is probably because the CO_2 adsorption on mesoporous materials from fly ash is a physical process (CO_2 is physically adsorbed on the mesoporous materials). The low sorption capacity of the MCM-41, either synthesized classically or fly ash-derived, results from weak interaction with CO_2, particularly at higher temperatures. The pure silica surfaces do not interact very strongly with CO_2 because the residual hydroxyl groups are not able to induce enough strong interactions and further specific adsorption sites are missing (Macario et al., 2005).

Figures 3-6 show the CO_2 adsorption profiles of the fly ash-derived mesoporous materials (2F-MCM-41 and 3F-MCM-41) loaded with PEI.

The impregnation of fly ash-derived 3F-MCM-41 with the PEI (30, 50, 70 wt.%) has resulted in a significant increase in its CO_2 sorption capacity (at 25℃) as shown in Fig. 3. 3F-MCM-41 before PEI impregnation adsorbed 5.9 mg CO_2/g adsorbent (at 25℃) (Fig.3), while after impregnation 38.5 mg CO_2/g adsorbent (at a PEI load of 30 wt.%), 59.3 mg CO_2/g adsorbent (at a PEI load of 50 wt.%), and 32.7 mg CO_2/g adsorbent (at a PEI load of 70 wt.%).

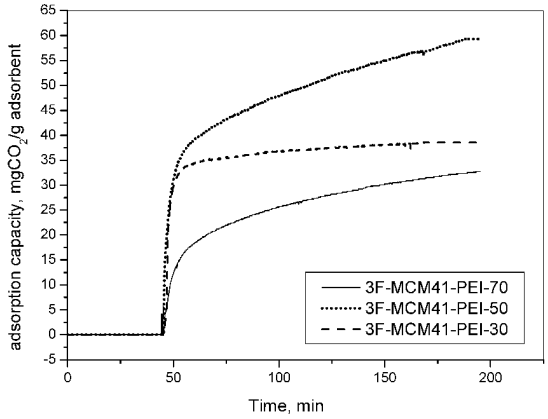

Fig.3 CO_2 adsorption profiles of the modified mesoporous materials 3F-MCM-41 from fly ash (loaded with PEI -30, 50 i 70 wt.%) at 25℃

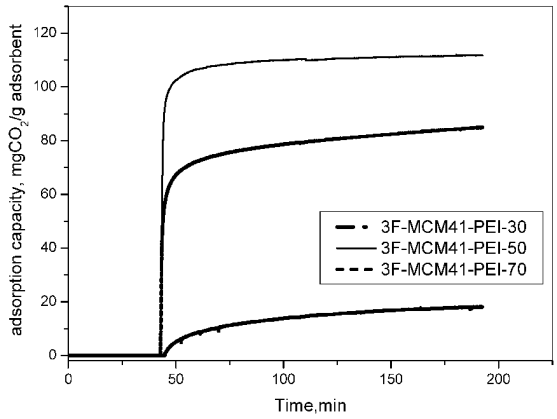

Fig.4 CO_2 adsorption profiles of the modified mesoporous materials 3F-MCM-41 from fly ash (loaded with PEI in 30, 50 and 70 wt.%) at 75℃

The curves of CO_2 adsorption on three 3F-MCM-41 modifications differing in PEI content, as represented in Fig. 3, indicate that the sorption process proceeds in a similar manner for each of the modifications examined, with the highest CO_2 sorption capacity at 25°C being shown by the 3F-MCM-41-PEI- 50. That sample showed also the highest sorption capacity at the temperature of 75°C (Fig. 4). This sorption capacity amounted to 111.7

mg CO_2/g adsorbent, while for samples 3F-MCM-41-PEI- 70 and 3F-MCM-41-PEI- 30 -17.9 and 85 mg CO_2/g adsorbent, respectively.

Also for sample 2FMCM-41, whose CO_2 adsorption profiles are shown in Fig. 5, a considerable increase in sorption capacity was obtained as a result of PEI impregnation, with the highest sorption capacity at 75°C being obtained for the sample impregnated with PEI in 70 wt.% (111.6 mg CO_2/g adsorbent) being almost the same as for sample 3FMCM-41 loaded with PEI in 50 wt.%. The adsorption capacity for 2FMCM-41 loaded with PEI in 50 wt.% amounted to 102.8 mg CO_2/g adsorbent. The curves of CO_2 adsorption on three 2F-MCM-41 modifications differing in PEI content, as represented in Fig. 5, indicate that the sorption process proceeds in a similar manner for each of the modifications examined.

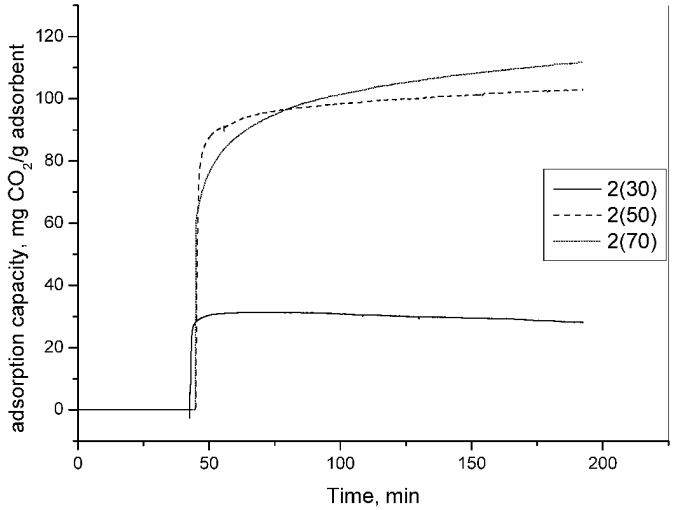

Fig. 5 CO_2 adsorption profiles of the modified mesoporous materials 2FMCM-41 from fly ash (loaded with PEI -30, 50 i 70 wt.%) at 75℃

The highest sorption capacity under boiler flue gas conditions was achieved for the 3F-MCM-41 sample loaded with PEI (50 wt.%) at a temperature of 75°C. As could have been expected, the lowest sorption capacity under boiler flue-gas conditions was exhibited by the 1FM sample, in which no presence of mesoporous material was found, and which could be defined as an unordered macroporous amorphous material, probably doped with zeolite.

Figure 6 shows an example of the sorption/desorption profile for 3F-MCM-41, as impregnated with PEI (30 wt.%) at a temperature of 75°C. As indicated by the figure, the desorption process is complete and progresses equally rapidly as the adsorption process.

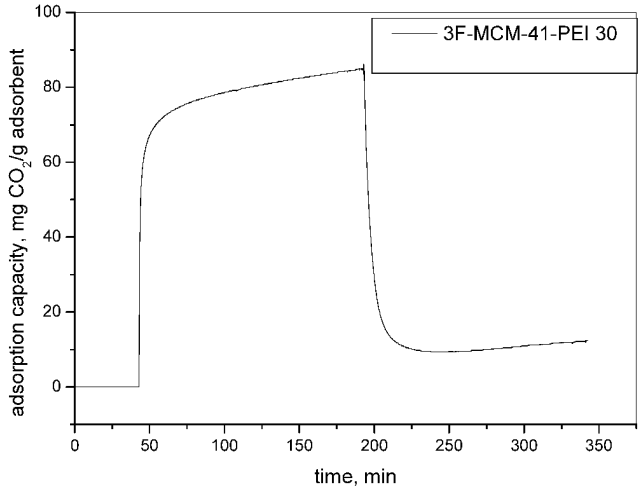

Fig.6 Isothermal (75℃) adsorption -desorption profile for modified 3F-MCM-41-PEI-30

The desorption tests carried out showed that the process was complete, both for the starting materials F-MCM-41 (without PEI), and for the PEI impregnated samples, which confirms that the process is reversible and the samples can be recovered and used in cyclic operations. According to Xu *et al.* (*2003*), the quick desorption can be explained by the high dispersion of PEI in the channels of MCM-41.

CONCLUSIONS

The investigation carried out has shown that the proposed sorbents (amine-treated fly-ash derived mesoporous materials, MCM-41) exhibit high sorption capacity at temperatures typical of power plant flue gases (i.e. 50-120°C) and at CO_2 concentration typical of boiler flue gas. Achieving the high sorption capacity was possible owing to the impregnation of the fly-ash derived mesoporous materials (MCM-41) with polyethylenimine (PEI). The obtained adsorption/desorption profiles for the samples tested showed a very rapid progress of both the sorption and desorption processes. The possibility of recovery of the adsorbents tested, as demonstrated in the investigation, has shown that the sorbent is recoverable and can be used in cyclic (sorption-desorption) operations.

ACKNOWLEDGEMENTS

This work was carried out with support from the Polish Project PBZ-MEiN-4/2/2006 (Report Cz.U.T) and Project supported by a grant from Iceland, Liechtenstein and Norway through the EEA Financial Mechanism and the Norwegian Financial Mechanism (E031/T02/2008/02/85).

REFERENCES

METZ B., DAVIDSON O. Carbon Dioxide Capture and Storage. IPCC Special Report, Cambridge University Press, New York, USA, 2005.

MACARIO A., KATOVIC A., GIORDANO A., IUCOLANO F. Synthesis of mesoporous materials for carbon dioxide sequestration. Microporous and Mesoporous Materials 81,139,2005.

XU X., SONG CH, ANDRESEN J.M., MILLER B.G., SCARONI A. W. Prepared and characterization of novel "molecular basket" adsorbent based on polymer-modified mesoporous molecular sieve MCM-41. Microporous and Mesoporous Materials. 62,29, 2003.

XU X., SONG CH, ANDRESEN J.M., MILLER B.G., SCARONI A. W. Adsorption of carbon dioxide from flue gas of natural-fired boiler by a novel nanoporous "molecular basket" adsorbent. Fuel Processing Technology. 86, 1457, 2005.

CHEMICAL LOOPING AUTOTHERMAL REFORMING AT A 120 kW PILOT RIG

Johannes Bolhàr-Nordenkampf, Tobias Pröll, Philipp Kolbitsch and Hermann Hofbauer

Vienna University of Technology, Getreidemarkt 9/166, 1060 Vienna, Austria

Abstract: Chemical looping with selective oxygen transport allows two step combustion or autothermal reforming without mixing of fuel and air. The reactor system consists of two reactors, an air reactor and a fuel reactor with a suitable oxygen carrier that transports the necessary oxygen for operation. In the present study, a highly active nickel based oxygen carrier is tested in a novel dual circulating fluidized bed (DCFB) system at a scale of 120 kW fuel power. The mean particle size of the oxygen carrier is 120 µm and the pilot rig is fueled with natural gas. For the investigated oxygen carrier high CH_4 conversion is achieved. Air/fuel ratio is varied at three different fuel reactor temperatures. For chemical looping reforming one can observe synthesis gas composition close to thermodynamic equilibrium. In spite of the fact that no additional steam has been added to the fuel besides the one present through steam fluidization of the loop seals, coke formation does not occur at global stoichiometric air/fuel ratios above 0.46.

Keywords: chemical looping autothermal reforming, oxygen carrier, gas-solid reactor, fluidized bed system, nickel oxide

INTRODUCTION

The chemical looping (CL) system based on metal oxides is a novel fuel conversion technology allowing inherent CO_2 separation. The technology was invented by Lewis and Gilliland (1954) then proposed by Richter and Knoche, (1983) and Ishida et al. (1987) to increase the reversibility of combustion processes. More recently, CL systems have been identified as a promising technology for carbon capture from power plants (Ishida and Jin, 1994; Lyngfelt et al., 2001; Ryu et al., 2002). The chemical looping system for carbon capture needs no gas separation step to gain a concentrated CO_2 stream. This systematical advantage of such a system lowers the energy penalty paid for carbon capture compared to pre-, post combustion capture or oxyfuel combustion. Chemical looping systems consist of two reaction zones in which different gas streams are in contact with circulating solids. The circulating solids transport oxygen and heat from one reaction zone to the other. Several metal oxides allow such a selective oxygen transport. In the fuel converting zone, fuel is oxidized by the metal oxide. This reaction zone is called fuel reactor (FR). In the second zone, called air reactor (AR), the metal oxide is reoxidized with air. Figure 1 shows a basic setup of chemical looping system.

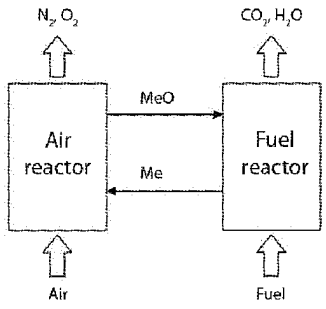

Fig. 1 Basic chemical looping system (e.g. chemical looping combustion)

A chemical looping system operated at a global air to fuel ratio above 1 is referred to as chemical looping combustion (CLC) and operation at a global air to fuel ratio below 1 is called chemical looping reforming (CLR). In the case of CLC, the fuel conversion in the fuel reactor is most likely limited by reactivity (gas-solids contact, chemical kinetics) and by the thermodynamics of the oxygen carrier system. In the case of CLR, the fuel reactor exhaust gas contains significant amounts of H_2 and CO due to insufficient oxygen supply. The novel design of the 120 kW chemical looping pilot rig at Vienna University of Technology allows stable operation of both CLC and CLR without any adaptations.

THE DCFB SYSTEM

The chemical looping pilot rig is a dual circulating fluidized bed (DCFB) system for gaseous fuels. The pilot rig is designed with a direct focus on scalability to larger size. The nominal power of the pilot rig is 120 kW with natural gas as the fuel. Loop seals between the reactors avoid mixing of AR and FR gases. These loop seals are fluidized with superheated steam. The flow regime in the AR is fast fluidization and in the FR turbulent fluidization. Downstream of each reactor, gas and solids are separated in cyclone separators. A principal setup is shown in Figure 2.

A variable cooling system, consisting of three double jackets, is attached to the AR. It allows controlled heat extraction for varying operating conditions. The properties of the pilot rig, the design and the variable cooling, enable operation points from combustion to reforming (global stoichiometric air/fuel ratio range 0.4 – 1.5). A detailed description of the cooling system and the other auxiliary units can be found elsewhere (Kolbitsch et al., 2009).

The 120kW chemical looping pilot rig has been successfully operated since January 2008. For hot commissioning of the pilot rig a natural ore (ilmenite, $FeTiO_3$) was used. (Pröll et al., 2008). The present study focuses on the Ni-based particles which the pilot rig has actually been designed for.

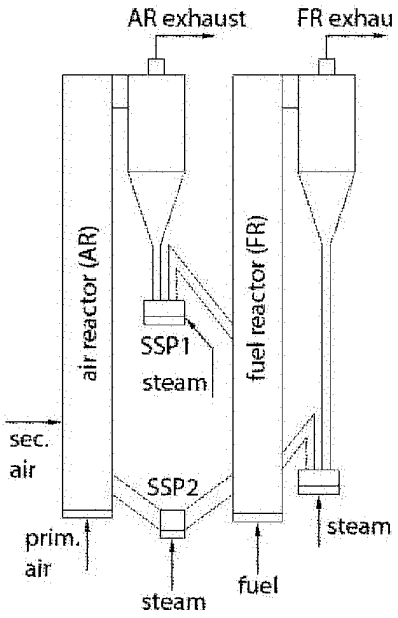

Fig. 2 Principal setup of the DCFB reactor system

OXYGEN CARRIER CHARACTERIZATION

The basic requirements for oxygen carriers (OCs) are mechanical stability, lowest possible costs and high oxygen transport capacity. Depending on the used fuel the OC has to fulfill other requirements too. For hydrocarbon fuels a high catalytic activity is beneficial (especially for methane conversion). Ni-based carriers have a good catalytic activity and are suitable for methane combustion and reforming. Other possible metals besides Ni are: Cu, Fe, Co, Mn and Cd (Abad et al., 2007b; Garcia-Labiano et al., 2006; Johansson et al., 2006; Mattisson et al., 2006; Son & Kim, 2006; Abad et al., 2007a; Corbella & Palacios, 2007). Most oxides have to be supported by other inert materials to gain the necessary mechanical strength and attrition stability to be operated in a CFB. Such support materials can be Al_2O_3, TiO_2 or yttria-stabilized zirconium (YSZ) (Lyngfelt et al., 2001).

In the present study, highly active carriers manufactured by VITO, Belgium under the guidance of Chalmers University of Technology, Sweden are used. The OC is based on NiO, α-Al_2O_3 and MgO. After sintering the particles consist of NiO and inert $NiAl_2O_3$ and $MgAl_2O_3$. More information on the OCs used can be found in the article by Jerndal et al. (2008). The mean particle size of the OC is approximately 120 µm.

CHEMICAL LOOPING AUTOTHERMAL REFORMING

Different technologies for steam reforming of natural gas exist in industrial applications. Most of the technologies described by Dybkjaer (1995) are fixed bed reformers at elevated pressure. The most important process steps for synthesis gas production are tubular reforming and autothermal reforming or secondary reforming.

Chemical looping autothermal reforming belongs to the atmospheric pressure reforming processes. A similar process idea was first published in 1950 but chemical looping reforming as described in this paper was first proposed by Mattisson and Lyngfelt (2001).

In the air reactor, as in chemical looping combustion, the metal oxide will be oxidized by air via reaction (1).

$$Me + \tfrac{1}{2}O_2 \leftrightarrow MeO \quad (1)$$

This reaction is always strongly exothermic. The main heat in the system is produced in the air reactor, whereas the fuel reactor overall reaction can be either endothermic or exothermic depending on the operating parameters (global air/fuel ratio, OC and fuel).

Different exothermic and endothermic reactions take place in the fuel reactor at the same time:

- Partial oxidation of the fuel with the OC,
- Steam reforming with present steam,
- CO_2 reforming and
- oxidation of H_2 and CO with the OC.

For CLR operation, the overall fuel reactor reaction is endothermic and heat is transported from the air reactor to the fuel reactor by the circulating solids.

The principle of chemical looping autothermal reforming is illustrated in Fig. 3.

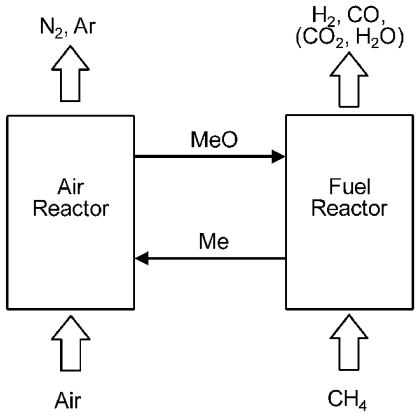

Fig. 3 Schematic description of chemical looping autothermal reforming

A 120 kW chemical looping pilot rig has been designed, built and operated in both CLC and CLR mode. It has been operated from 750°C to 900°C in the FR and down to an air/fuel ratio of 0.45 - 0.52. The pilot rig is fueled for all experiments presented here at approximately 140 kW of natural gas.

The natural gas from Vienna's gas grid consists mainly of methane (over 98 vol% CH_4). The detailed fuel composition can be found in Table 1.

Table 1 natural gas composition

species	conc.[vol%]
C_2H_6	0.54
C_3H_8	0.16
CH_4	98.66
CO_2	0.10
N_2	0.54

The main reactions in the fuel reactor are steam reforming and water gas shift reaction:

$$CH_4 + H_2O \leftrightarrow CO + 3H_2 \quad (2)$$

$$CO + H_2O \leftrightarrow CO_2 + H_2 \quad (3)$$

partial oxidation with NiO:

$$CH_4 + NiO \leftrightarrow CO + 2H_2 \quad (4)$$

internal combustion:

$$CO + NiO \leftrightarrow CO_2 \quad (5)$$

$$H_2 + NiO \leftrightarrow H_2O \quad (6)$$

$$CH_4 + 4NiO \leftrightarrow CO_2 + 2H_2O \quad (7)$$

The steam to (organic) carbon (S/C) ratio entering the reformer has a major impact on coke formation and on the synthesis gas composition (H_2/CO ratio). For classical steam reforming the value of the S/C ratio varies from 2 up to 5 as described in (Dybkjaer, 1995). Equation (8) defines this ratio.

$$\frac{\text{steam}}{\text{carbon}} = \frac{H_2O}{CH_4 + 2C_2H_4 + 2C_2H_6 + 3C_3H_8 + CO}\Bigg|_{feed} \quad [\text{mol\%}] \quad (8)$$

RESULTS AND DISCUSSION

The presented results show graphs for the four gas species H_2, CO, CO_2 and CH_4 versus the air/fuel ratio. During variation of the global air/fuel ratio the fuel power, FR temperature and the steam to carbon ratio are kept constant with only small fluctuations. Additionally, the FR is operated at three temperatures, approximately 900°C, 800°C and 750°C. In all diagrams the solid lines represent the values as measured at the pilot unit whereas the dashed lines represent the thermodynamic equilibrium calculated by minimization of Gibbs free enthalpy (JANAF data, formal reactions (2) and (3)). All measured values represent reconciled solutions that fulfill mass and energy balances. A more detailed description of the data reconciliation method applied can be found elsewhere (Bolhar-Nordenkampf et al., 2009).

Figure 4 shows the synthesis gas composition at a FR temperature of approximately 903°C. One can observe a decreasing CH_4 concentration with decreasing air/fuel ratio. The thermodynamic equilibrium

concentration of CH_4 is close to zero for all temperatures. The graphs of the other gas species run along the equilibrium concentrations with small deviations mainly due to incomplete CH_4 conversion at air/fuel ratios > 0.8. The air/fuel ratio is varied down to approximately 0.52, at which stable operation can be guaranteed. This ratio is determined by the heat loss of the pilot rig at that operation temperature. At this air/fuel ratio and a S/C ratio of approximately 0.4 (considering all loop seal steam from the lower loop seal to enter the FR), the H_2/CO ratio in the synthesis gas reaches 2.0.

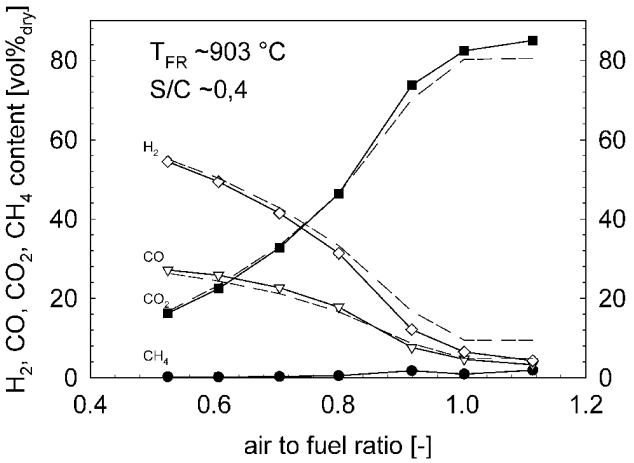

Fig. 4 Dry-gas concentration in the FR exhaust gas at 903°C 140 kW natural gas and S/C =0.4

To maximize the ratio of H_2/CO temperature can be reduced. The energy balance of the reactor system has at any time to be fulfilled which determines some limiting constraints, such as air/fuel ratio, reaction velocity and coke formation. The next figures show the gas species H_2, CO, CO_2, CH_4 in the synthesis gas (i.e. fuel reactor exhaust gas) at two lower temperatures of 798°C and 747°C, respectively. Again, methane conversion is incomplete at higher values of the air/fuel ratio. The other graphs run along the equilibrium lines. In some operating points the thermodynamic equilibrium is reached. At the lowest air/fuel ratio of 0.5 at a temperature of 798°C and a steam/carbon ratio of approximately 0.4, the ratio of H_2/CO is increased to 2.4. A further increase in the H_2/CO ratio can be seen by lowering the temperature further to approximately 747°C. At an air/fuel ratio of 0.51 and a steam/carbon ratio of 0.4 another 10% increase to 2.6 can be observed. At the lowest temperature energy balance and heat loss respectively allow to lower the air to fuel ratio down to 0.46. No significant increase in H_2/CO ratio can be seen.

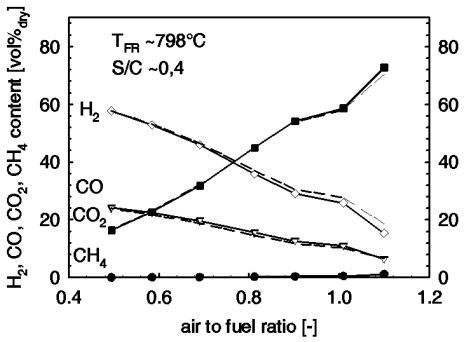

Fig. 5 Dry-gas concentration in the FR exhaust gas at 798°C 140 kW natural gas and S/C =0.4

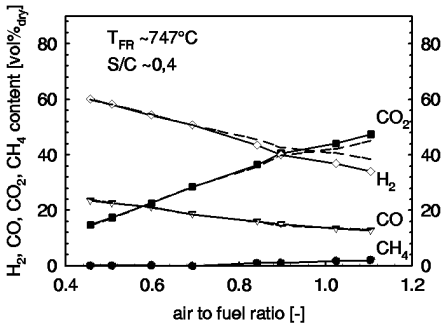

Fig. 6 Dry-gas concentration in the FR exhaust gas at 747°C 140 kW natural gas and S/C =0.4

It is important to notice that no coke formation has been observed at any of the operating points shown in the graphs. From measurement of CO_2 in the air reactor exhaust gas, exact detection of carbon loss to the air reactor is possible. These measurements reveal the following:

(1) No gas leakage occurs at any time from the fuel reactor to the air reactor (even though system pressure in the bottom region of the fuel reactor is higher than in the bottom region of the air reactor)

(2) The onset of coke formation has been found at global air/fuel ratios as low as 0.4 for practically all the temperatures investigated.

The second point represents an unexpected result with respect to the fact that no additional steam is added to the fuel at all. Only the steam from fluidization of the loop seals is present in the fuel reactor.

CONCLUSIONS

The 120 kW chemical looping system at Vienna University of Technology has successfully demonstrated chemical looping autothermal reforming at atmospheric pressure. The dual circulating fluidized bed system (DCFB) design allows variation of air/fuel ratio over a wide range without adaptations. For all experimental results high methane conversion is observed. Methane conversion reaches thermodynamic equilibrium for all FR temperatures at an air/fuel ratio below 0.7. All other species run along the equilibrium curves with significant deviations only where methane conversion is incomplete. The maximum H_2/CO ratio in the synthesis gas of 2.6 can be seen at a FR temperature 747°C. Even though no steam has been added to the fuel apart from the loop seal fluidization (which would result in an S/C ratio of 0.4), no coke formation has been observed for global air/fuel ratios above 0.46.

NOTATIONS

AR	air reactor
CFB	circulating fluidized bed
CL	chemical looping
DCFB	dual circulating fluidized bed
FR	fuel reactor
OC	oxygen carrier
S/C	steam to (organic)

ACKNOWLEDGMENTS

This work was part of the EU financed project CACHET (FP6 Contract No. 019972), coordinated by BP. The project is also part of Phase II of the CO_2 Capture Project (CCP). The oxygen carrier has been produced by the Flamish Institute for Research and Technology (VITO), Belgium under the guidance of Chalmers University of Technology, Sweden in the context of the EU financed project CLC GAS POWER (FP6 Contract No. 019800).

REFERENCES

Abad, A., Mattisson, T., Lyngfelt, A., & Johansson, M.: *Fuel* **86**(7-8) (2007a). pp.1021–1035.

Abad, Alberto, Adanez, Juan, Garcia-Labiano, Francisco, de Diego, Luis F., Gayan, Pilar, & Celaya, Javier: *Chem. Eng. Sci.* **62**(1-2) (2007b) pp.533–549.

Bolhar-Nordenkampf, Johannes, Pröll, Tobias, Kolbitsch, Philipp, & Hofbauer, Hermann: *accepted for publication in Chemical Engineering Technology* (2009).

Corbella, Beatriz M., & Palacios, Jose Maria: *Fuel* **86**(1-2) (2007) pp.113–122.

Dybkjaer, Ib.: *Fuel Process. Technol.* **42**(2-3) (1995) pp.85–107.

Garcia-Labiano, Francisco, Adanez, Juan, de Diego, Luis F., Gayan, Pilar, & Abad, Alberto: *Energy Fuels*, **20**(1) (2006) pp.26–33.

Ishida, M., Zheng, D., & Akehata, T.: *Energy*, **12**(2) (1987) pp.147–154.

Ishida, Masaru, & Jin, Hongguang: *Energy*, **19**(4) (1994) pp.415–422.

Jerndal, Erik, Thijs, Ivo, Snijkers, Frans, Mattisson, Tobias, & Lyngfelt, Anders: *accepted for publication in Energy Procedia* (2008)

Johansson, Marcus, Mattisson, Tobias, & Lyngfelt, Anders: *Ind. Eng. Chem. Res.* **45**(17) (2006) pp.5911–5919.

Kolbitsch, Philipp, Bolhar-Nordenkampf, Johannes, Pröll, Tobias, & Hofbauer, Hermann.: *accepted for publication in Chemical Engineering Technology* (2009)

Lewis, Warren K., & Gilliland, Edwin R.: *Production of pure carbon dioxide*. U.S. Patent Office, Number 2,665,972. (1954)

Lyngfelt, A., Leckner, B., & Mattisson, T.: *Chem. Eng. Sci.*, **56**(10) (2001) pp.3101–3113.

Mattisson, T., & Lyngfelt, A.: *Second nordic minisymposium on carbon dioxide capture and storage* Applications of chemical-looping combustion with capture of CO2 (2001).

Mattisson, Tobias, Johansson, Marcus, & Lyngfelt, Anders: *Fuel*, **85**(5-6) (2006) pp.736–747.

Pröll, Tobias, Mayer, Karl, Bolhar-Nordenkampf, Johannes, Kolbitsch, Philipp, Mattisson, Tobias, Lyngfelt, Anders, & Hofbauer, Hermann: *accepted for publication in Energy Procedia* (2008).

Richter, Horst J., & Knoche, Karl F.: *ACS Symposium Series* **235** (1983) pp. 71–85.

Ryu, H.J., Bae, D.H., & Jin, G.T.: (2002). Chemical-looping combustion process with inherent CO2 separation; reaction kinetics of oxygen carrier particles and 50kwth reactor design. *The world congress of Korean and Korean ethnic scientists and engineers, Seoul, Korea.*

Son, Sung Real, & Kim, Sang Done.: *Ind. Eng. Chem. Res.*, **45**(8) (2006) pp.2689–2696.

EFFECTS OF STEAM AND CO_2 IN THE FLUIDIZING GAS WHEN USING BITUMINOUS COAL IN CHEMICAL-LOOPING COMBUSTION

H. Leion[1], A. Lyngfelt[2], T. Mattisson[2]

[1]*Department of Environmental Inorganic Chemistry*
[2]*Department of Energy and Environment, Chalmers University of Technology, S-412 96 Göteborg, Sweden*

Abstract: Chemical-looping combustion (CLC) is a combustion technology where an oxygen carrier is used to transfer oxygen from the combustion air to the fuel in order to avoid direct contact between air and fuel. Thus, the CO_2 is inherently separated from the flue gases with a potential for considerably lower energy penalty and cost compared to other techniques for CO_2 separation. The oxygen carrier is circulated between two reactors, a fuel and an air reactor, where the flue gas from the air reactor contains oxygen depleted air and the flue gas from the fuel reactor contains mainly CO_2 and H_2O. The water can easily be condensed and the remaining CO_2 can be transported for underground storage. Most of the prior work with CLC has focused on using natural gas and syngas as fuel and oxygen carrying material normally produced from pure chemicals. However, recent work on adapting the CLC process for solid fuels with ores and natural minerals as oxygen carrier shows promising results. This paper will present results from reactivity investigations in a laboratory fluidized-bed reactor system using previously investigated natural mineral ilmenite as oxygen carrier and a bituminous Colombian coal as fuel. Experiments were conducted at a temperature of 970°C with N_2, steam, and/or CO_2 in the fluidizing gas. Synergy effects between steam and CO_2 on fuel conversion was noted. The results show that the fuel conversion was a roughly a factor 5 faster with steam as compared to CO_2 in the fluidizing gas.
Keywords: CO_2-capture, chemical-looping combustion, ilmenite, oxygen carrier

INTRODUCTION

It is today believed that the increase in greenhouse gas concentrations has caused changes in today's climate (Rosenzweig, et al., 2008). Chemical-looping combustion (CLC) has emerged as an attractive option for carbon dioxide capture. Here CO_2 is inherently separated from the other flue gas components, i.e. N_2 and unused O_2, and thus no energy is expended for the separation. The concept of CLC was proposed already in 1954 (Lewis and Gilliland, 1954) and the CLC-system consists of two reactors, a fuel and an air reactor. An oxygen carrier, usually a metal oxide, transports oxygen from the air reactor to the fuel reactor. The oxygen carrier is circulating between the reactors and is oxidized in the air reactor, according to the overall reaction (1), and reduced by the fuel in the fuel reactor to its initial state according to the overall reaction (2). The total amount of heat evolved from reaction (1) and (2) is equal to the heat released from conventional combustion, where the oxygen is in direct contact with the fuel.

$$O_2(g)+2M_yO_{x-1} \leftrightarrow 2M_yO_x \quad (1)$$

$$C_nH_{2m}+(2n+m)Me_xO_y \leftrightarrow nCO_2+mH_2O+(2n+m)Me_xO_{y-1} \quad (2)$$

A majority of the publications concerning CLC have used gaseous fuel such as natural gas or methane (Hossain and de Lasa, 2008). When using solid fuel in CLC the fuel is fed directly into the fuel reactor. Here the gasification of the fuel and subsequent reactions of the gasification products, mainly CO and H_2, with the metal oxide particles will occur simultaneously in the same reactor. Successful attempts have been made to use solid fuels in CLC (Berguerand and Lyngfelt, 2008a).

Since the solid-solid reaction between coal and an iron based metal oxide is not very likely to occur at any appreciable rate the fuel conversion will proceed via gas phase reactions, involving slow gasification of the fuel. As a result of this a large solids inventory of oxygen carrying material will be needed in such a system (Leion, et al., 2007). An important advantage compared to normal gasification is that it will take place in a high concentration of H_2O and/or CO_2 which is beneficial for the reaction rates (Leion, et al., 2008a, Leion, et al., 2007). The main overall gasification reactions are:

$$C+H_2O \Rightarrow CO+H_2 \quad (3)$$

$$C+CO_2 \Rightarrow 2CO \quad (4)$$

The formed CO and H_2 can react with the oxygen carrier particles to CO_2 and H_2O. The composition of the gas phase in also affected through the CO-shift reaction:

$$CO+H_2O \Rightarrow CO_2+H_2 \quad (5)$$

This paper presents batch laboratory fluidized bed CLC experiments where a bituminous Colombian coal is used with the natural mineral ilmenite as oxygen carrier. Experiments were conducted at a temperature of 970°C with steam, CO_2 and N_2 in the fluidizing gas.

EXPERIMENTAL

The experiments were conducted in a fluidized-bed reactor of quartz. In order to achieve good solids mixing in the bed, the reactor was conically shaped just above the distributor plate. The reactor had a total length of 870 mm with a porous quartz plate placed 370 mm from the bottom of the reactor. The porous plate and the reactor below the plate had an inner diameter of 10 mm. Above the distributor plate the inner diameter of the reactor increased to reach 30 mm at a height of 20 mm above the porous plate. The diameter was then constant for 250 mm. The reactor diameter was then increased further to 45 mm for a length of 100 mm. This disengaging section was constructed to avoid that smaller coal and metal oxide particles leave the reactor.

A sample of 40 g of ilmenite particles of size 125-180 μm was placed on the porous plate and was then initially heated in 5% O_2 in N_2 to the reaction temperature of 970°C. When the bed was not fluidized the bed height was approximately 30 mm. The particles were then alternatingly exposed to 5% O_2 and the fuel in a steam/N_2/CO_2 mixture, thus simulating the cyclic conditions of a CLC system burning solid fuel. Pure nitrogen gas was introduced for 180 s between each reducing and oxidizing period. During the reducing period the following four cases of fluidizing gas were used: (I) 50% steam in nitrogen, (II) 50% CO_2 in nitrogen, (III) 50% steam in CO_2, and (IV) pure nitrogen.

The fluidizing gases were introduced from the bottom of the reactor. At the start of the reducing period, i.e. at the same time as the fluidizing gas of the reducing cycle started to come into the bottom of the reactor, the fuel was inserted in the top of the reactor, falling down into the fluidized bed. Also a small flow of nitrogen was added at the top of the reactor to sweep the fuel down into the reactor. The experiments were performed in this manner for 4-5 cycles for each test case investigated.

The gas from the reactor was led to an electric cooler, where the water was removed, and then to a gas analyzer (Rosemount NGA-2000) where the concentrations of CO_2, CO, CH_4 and O_2 were measured in addition to the gas flow. H_2 could unfortunately not be measured in the present setup. The temperature was measured 5 mm under and 10 mm above the porous quartz plate, using thermocouples "Pentronic CrAl/NiAl inconel-600" in quartz shells. The upper temperature in the bed was kept at 970°C in all experiments. The temperature measured by thermocouple below the bed was generally 20°C lower.

All experiments were conducted with a gas flow of 600 mL/min (at 1 bar, 0°C), both for the reducing and oxidizing periods. This flow rate was chosen so fuel particles and oxygen carriers should be well mixed. However, reference experiments indicate that small fuel particles still elutriated from the reactor. Also some fuel was lost in the feeding device. These losses are excluded from the calculations, which are based on the amount of CO_2 and CO leaving the reactor. From high frequency measurements of the pressure drop it was possible to see whether the bed was fluidized or not (Cho, et al., 2006).

The oxygen carrier used was the natural mineral, ilmenite ($FeTiO_3$), which was obtained from Titania A/S. The molar ratio of iron and titanium is close to 1:1 in this material. XRD measurements on fresh samples show ilmenite and small fractions of hematite. Fresh ilmenite had a BET area of 0.11 m^2/g as determined by a Micromeritics Gemini 2362. This ilmenite has recently been investigated by Berguerand et al. (Berguerand and Lyngfelt, 2008a, Berguerand and Lyngfelt, 2008b) and Leion et al. (Leion, et al., 2008b, Leion, et al., 2008a). The analysis of the coal used is presented in Table 1. The fuels were crushed and sieved to obtain particles in the size range 0.125-0.180 mm i.e. the same size as the oxygen carrier particles, see Table 1 for the fuel analysis. 0.2 g of coal was used for every reducing cycle.

Table 1 Analysis of Colombian bituminous coal

Fuel analysis									
H_i [MJ/kg]	Proximate [wt %, as received]			[%d.a.f]	Ultimate [wt %, d.a.f.]				
(as received)	M	A	Combustibles	VM	C	H	N	S	O
29.1	3.3	5.2	91.5	44.7	80.8	5.4	1.5	0.7	11.6

RESULTS AND DISCUSSION

Fig. 1 shows the outlet gas concentrations after condensation of water as a function of time for a reducing period with a temperature of 970°C and with 50% steam in N_2 in the fluidizing gas. The fuel is inserted at time equal to zero. The initial peak of CH_4 is due to some initial pyrolysis of the fuel. The initial peaks of CO and

CO_2 are then due to reaction of volatiles, with the ilmenite. These peaks are quickly followed by release of CO and CO_2 due to reaction of the char with the fuel with the oxygen carrier. The pulse-like peaks in the CO_2, and to some extent the CO, concentration are due to uneven steam feed which is caused by the water pump upstream of the steam generator.

First a number of reference experiments were conducted with 50% H_2O in N_2, Fig. 1. The amount of CO_2 and CO produced during these experiments integrated and the average amount of CO_2 and CO over 5 such cycles were set to 100%. Several experiments were then conducted using one of the four cases: (I) 50% steam in nitrogen, (II) 50% CO_2 in nitrogen, (III) 50% steam in CO_2, and (IV) pure nitrogen as a fluidizing/reactant gas. Since it is impossible to separate the CO_2 produced during the reduction from the CO_2 added with the inlet flow the reduction period was in these experiments terminated before all of the fuel had been converted and the amount of CO_2 and CO produced during the following oxidation was integrated to assess the amount of fuel converted during that cycle. This was compared to the integrated amount of CO and CO_2 during the reference experiments without any premature termination. The concentrations presented in Fig. 2 are from one such experiment with premature termination using 50% H_2O in N_2. Again, the peaks in the CO_2 concentration are due to uneven steam feed. In both Fig. 1 and 2 the concentrations are presented as detected in the analyser, after condensation of steam but with the dilution from the sweep gas added on in the top of the reactor. Since the flow of the sweep gas is about the same as the flow of steam the presented concentration is, during reduction, more or less the conditions in the reactor.

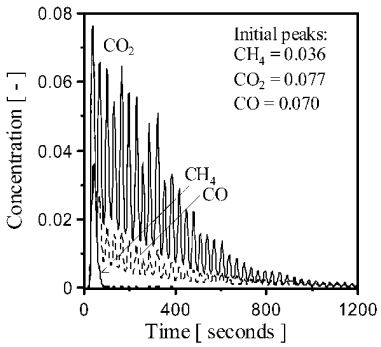

Fig. 1 Concentration profile during reduction. The inlet H_2O content is 50% in N_2 and the temperature in the bed is 970°C

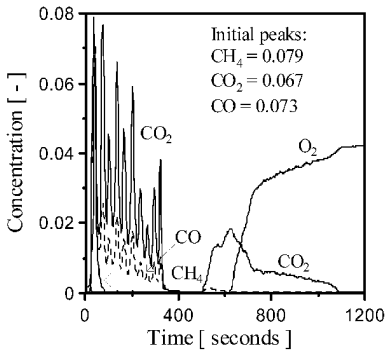

Fig. 2 Concentration profile during reduction and oxidation. The inlet H_2O content is 50% in N_2 during reduction and 5% O_2 in N_2 during oxidation. The temperature in the bed is 970°C

Figure 3 presents the average amount of fuel converted to CO_2 and CO at different termination times for the four experimental cases. The amount of CO was directly measured during all experiments. Fig. 4 presents the integrated amount of CO up until the termination as a fraction of the total amount of CO and CO_2 during the unterminated reference experiments.

With pure N_2 in the fluidizing gas there is basically no fuel conversion apart from the initial period of volatiles release. It is clear that the fuel conversion in H_2O is much faster than in CO_2. If the initial period with volatiles is excluded, the fuel conversion with H_2O is roughly a factor 5 faster with 50% H_2O in N_2 as compared to 50% CO_2 in N_2. With the 50% H_2O/50% CO_2 mixture the conversion is somewhat faster than with 50% CO_2 in N_2, but the small difference compared to 50% H_2O in N_2 is within the uncertainty of the experiment.

The amount of fuel converted to CO is as expected larger for the experiments were CO_2 was present. The increased CO_2 concentration affects the equilibrium of the shift reaction (Reaction 5) towards more CO and H_2O.

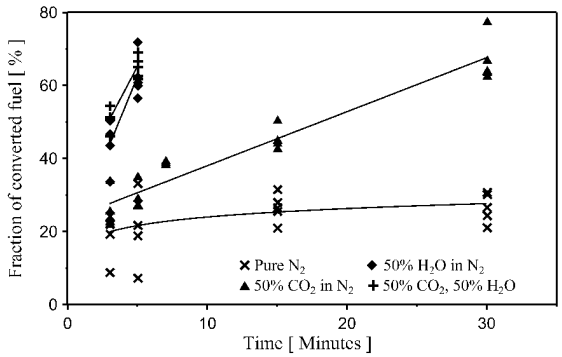

Fig. 3 Fraction of the fuel converted as a function of time for different gas composition in the fluidizing gas

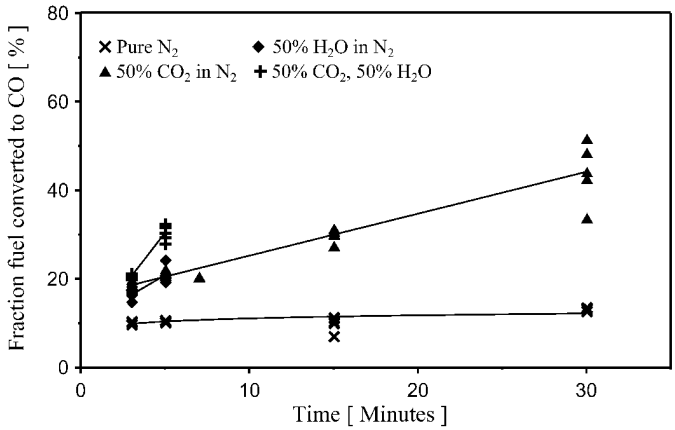

Fig. 4 Fraction of the fuel converted to CO as a function of time for different gas composition in the fluidizing gas

CONCLUSIONS

When constructing a large scale CLC-unit it would be an advantage if recycled CO_2 could be used as fluidizing medium. The results in this paper show that the conversion of the Colombian coal was roughly a factor five faster when using H_2O instead of CO_2 in the fluidizing gas at a temperature of 970°C. The results can be used to assess how a substitution of part of the steam by CO_2 would affect the fuel conversion rate and hence the needed solids inventory of the fuel reactor.

ACKNOWLEDGEMENTS

The work was partially funded by Statens Energimyndighet (STEM) Dnr 2006-04665 Projektnr 21670-2 and partly funded by Ångpanneföreningens forskningsstiftelse. Titania A/S provided the ilmenite and Alstom provided the coal. A part of the experiments was performed by Mikael Israelsson.

REFERENCES

Rosenzweig, C., Karoly, D., Vicarelli, M., Neofotis, P., Wu, Q., Casassa, G., Menzel, A., Root, T. L., Estrella, N., Seguin, B., Tryjanowski, P., Liu, C., Rawlins, S. and Imeson, A., Nature **453**, (2008). pp. 353-357.
Lewis, W. K. and Gilliland, E. R., US patent no. 2665972. (1954)
Hossain, M. M. and de Lasa, H. I., Chem. Eng. Sci. **63**, (2008). pp. 4433-4451.
Berguerand, N. and Lyngfelt, A., Fuel **87**, (2008a). pp. 2713–2726.
Leion, H., Mattisson, T. and Lyngfelt, A., Fuel **86**, (2007). pp. 1947-1958.
Leion, H., Mattisson, T. and Lyngfelt, A., Int. J. Greenhouse Gas Control **2**, (2008a). pp. 180-193.
Cho, P., Mattisson, T. and Lyngfelt, A., Ind. Eng. Chem. Res. **45**, (2006). pp. 968-977.
Berguerand, N. and Lyngfelt, A., Int. J. Greenhouse Gas Control **2**, (2008b). pp. 169-179.
Leion, H., Lyngfelt, A., Johansson, M., Jerndal, E. and Mattisson, T., Chem. Eng. Res. Des.**86**, (2008b). pp. 1017-1026.

EXPERIMENTAL RESEARCH OF THE OXYGEN-ENRICHED COMBUSTION OF SEWAGE SLUDGE AND COAL IN CFB

S. W. Xin, X. F. Lu, H. Z. Liu

Clean Coal Combustion Laboratory, School of Power Engineering, Chongqing University, Chongqing, 400044, China

Abstract: Sewage sludge is the by-products of sewage treatment, and it is a fuel of high moisture, high ash and low caloric. Oxygen-enriched combustion technology is one of the new and clean coal combustion technologies that can control pollutant emission, which makes CO_2 separation, SO_2 treatment become easier, and NO_X emission reduced. In this paper, we carried out the experimental research on the advantages of oxygen-enriched combustion and the characteristics of sewage sludge in a CFB incinerator that the diameter of the furnace is 100 mm. It is an important foundation for the industrialized application of the oxygen-enriched combustion of sewage sludge and coal in CFB. Experimental analyzed on the combustion characteristics of three conditions in the oxygen concentration of 21%~35%, which were the weight ratio of coal and sludge were 1:1, 1:2 and also the coal was given. Furthermore, the change of gas composition along with the change of oxygen content and the temperature of dense phase region was analyzed. The results showed that the combustion characteristics differ from the different mixing rate between coal and sludge in different oxygen atmosphere, when the fluidized air velocity was 1.56 m/s~1.88 m/s, the combustion stability; When the amount of the fuel was constant, as the increase of the oxygen contents in the experimental atmosphere, the total air volume decreased, the furnace temperature increased gradually, the concentration of SO_2 and NO_X showed increasing trend, which is beneficial to the removal of SO_2; The concentration of NO_X was increased gradually as temperature of the fluidized bed increased.

Keywords: co-combustion, sludge and coal, CFB, oxygen-enriched combustion

INTRODUCTION

Sewage sludge is the by-products of sewage treatment, and it is a fuel of high moisture, high ash and low caloric. At present, the treatments of sewage sludge are landfill, composting and incinerate (Chi Y. et al., 2006). The method of incineration obtains increasing recognition because of its large reduction of capacity, and also its abilities of eliminating large harmful substances. The combustion in CFB have the advantages of higher efficiency, lower environmental pollution, wider range fuels and wider scope adjusting loader, which is being widely popularization and application (Lu, 2006).

Oxygen-enriched combustion technology is one of the new and clean coal combustion technologies that can control pollutant emission, which makes CO_2 separation and SO_2 treatment become easier, and also reduces the NO_X emission (Glen et al., 2005). At present, several countries and institutions had been studied the technology of oxygen-enriched combustion in CFB, such as Hokkaido National Industrial Research Institute in Japan (Hirma et al., 1998), Delft University of Technology in Netherlands (Andries et al., 1997), Czestochowa University of Technology in Poland (Czakiert et al. 1996), Ottawa energy and technique center in Canada (LAMBERT et al., 1996), ALSTOM in USA (Nsakala et al., 2004), InfraServ Hochst and Messer Greisheim in Deutschland (Dipl et al., 2001) and Zhejiang University(Mao et al., 2005), The focus of those researches were the combustion mechanism of oxygen-enriched combustion, pollutant emissions and the influence of O_2 concentration on CFB design. But they had not grasped the characteristic of oxygen-enriched co-combustion about sewage sludge and coal. In order to generalize the CFB oxygen-enriched combustion technology, based on the former researches, this paper combined the CFB incinerate of sewage sludge with the advantages of oxygen-enriched combustion, studied the combustion characteristics of fuel with different mass ratio in different oxygen concentration and the factor that affects the pollutant emissions, which was an important preparation for industrialized application of oxygen-enriched combustion technology of sewage sludge in CFB.

EXPERIMENTAL

The experiment was carried out on the CFB incinerator of Clean Coal Combustion Laboratory of Chongqing University. The test-bed consisted of CFB incinerator, feeding system, air and O_2 supplying system, electric heating and ignition system, fluidizing air heating system, measuring system for temperature and pressure, and the measurement system about flue composition. Whose system diagram is as follows.

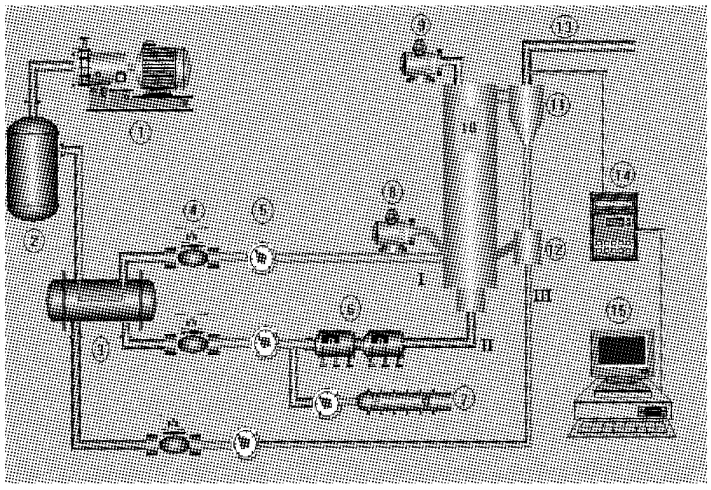

Fig.1 The system diagram of CFB incinerator
1. Air compressor 2. Steady pressure jar 3. Heater 4. Valves 5. Rotameters 6. Fluidizing air heaters 7. Oxygen unit 8. Screw feeder (for coal)9. Screw feeder (for sludge) 10. CFB incinerator 11. Separator12. Return valve 13. Gas flue 14. Gas analyzer 15. Industrial computer
I. Fuel spreading air II. Fluidizing air III. Flexible air

The CFB incinerator is consisted of furnace, separator, and return valve and gas flue. The air distribution plate used nozzle distributor, the height of furnace is 2200 mm. the diameter of inner section is 100 mm and with the fouling hole in the center.

The straight pipe of separator adopted seamless steel tube whose diameter is 150 mm. The riser used carborundum tube of the diameter of 40 mm. The return system used "U" return valve, whose enclosure is also seamless steel tube. Above the air distribution plate of return valve, installed a temperature measuring point to test the temperature of returned materials. In order to observe the return products in the riser, a quartz glass tube resisting high temperature with the length of 40 cm was substituted for seamless steel tube. We adopted dense drilling structure in the air distribution plate of return valve, with a piece of stainless steel mesh of 80 meshes to keep off circulating ash into the air compartment of return valve.

The air supplying system consisted of QG55F single screw compressor, steady pressure jar, rotameters and fluidizing air heaters. After being compressed by compressor, the cold air went through rotameters, mixed with O_2 and then went to the fluidizing air heaters. After being pre-heated, they went to the air compartment.

The O_2 supplying system was employed on the compressed cylinder, with the volume of 40 L. The O_2 went through the rotameter to the heater, mixed with the air from compressor.

The test-bed consisted of two units of screw feeder, one for coal, and the other for sludge. The coal feeding system included screw feeder and fuel spreading air, the feed point was 50 mm above the air distribution plate. The sludge feeding system also included screw feeder, which was on the top of furnace.

The system of electric heating and ignition system consisted of two groups of resistance wire on the bottom of furnace, with the total power of 4kW. The fluidizing air heating system composed of 8kW and 12kW electric heater in series of the fluidizing air.

The testing system of temperature and pressure consisted of thermocouple, differential pressure transmitter (KYB14A), ADAM4000 data acquisition module and industrial computer. The monitoring system of flue gas adopted Testo350EPA gas analyzer to monitor the gas components on-line.

Characteristics of coal, sludge and bed materials

In the experiment, the coal was from Chongqing industrial coal, with the diameter less than 2 mm being smashed. The sludge was the black powder materials from the by-product of Chongqing sewage treatment plant. The element analysis, proximate analysis and the low heat value of coal and sludge as Table 1.

Table1 The element analysis, proximate analysis and low heat value of coal and sludge

Item	Element Analysis				Proximate Analysis				Low Heat Value
Symbol	C_d	H_d	N_d	O_d+S_t	M_{ad}	A_d	V_{daf}	FC_d	Q_{net}
Unit	%	%	%	%	%	%	%	%	MJ/kg
Coal	49.23	4.14	1.05	16.27	4.25	29.31	51.96	33.96	13.22
Sludge	16.72	2.20	8.93	2.03	4.60	70.12	26.33	3.55	7.435

The bed materials in the experiment were used of circulating ash of CFB being sieved, with the entity density of 2600 kg/m^3, the bulk density was 1560 kg/m^3, and the average particle size was 0.26 mm, the bed materials belonged to group B particles (Lu, 2006), who had good fluidization characteristic.

Experimental method

This paper studied the combustion of three kinds of fuel (coal, coal/sludge=1:1, coal/sludge=1:2) in the O_2 concentration of 21%, 25%, 30%, 35%, and adopted Testo350EPA gas analyzer to monitor the gas components on-line. In the experiment, the rotating speed of the feeders was kept constant and the O_2 concentration in the gas outlet was 6%. This paper studied the combustion characteristics of mixed fuel, and analyzed the change of gas composition as the change of oxygen content and the temperature of dense phase region.

RESULTS AND DISCUSSION

Experimental ignition

The ignition was difficult in the experiment, so the ratio of air and coal must be controlled, otherwise it would be coking and flameout. After many experiments, we concluded the air-coal ratio of practical operation was 1×10^4~2×10^4(m^3/kg). In the beginning of initiating phase, the coal was feed when the temperature of bed materials was around 600℃. We adopted the MCGS measuring system for temperature to measure the temperature of dense phase region and the gas analyzer to monitor the amount of O_2 on-line.

Figure 2 shows at the ignition starting, the change of the O_2 concentration and the temperature of dense phase region as time changed. As can be seen, at the initial stage of coal feeding, the temperature of dense phase region in the furnace decreased slightly, because the coal would be endothermic at ignition starting. As the combustion of coal, the temperature of dense phase region was increased gradually, when the temperature of dense phase region reached 850℃ and increased slowly, it could be normal for coal and adjust air flow flexibly, controlled the temperature gradually increasing so that the bed temperature maintained at 850℃-950℃. When the combustion stability, feed the mixed fuel, adopted the MCGS temperature measurement system to monitor the temperature of dense phase region and the gas analyzer to monitor the gas composition on-line.

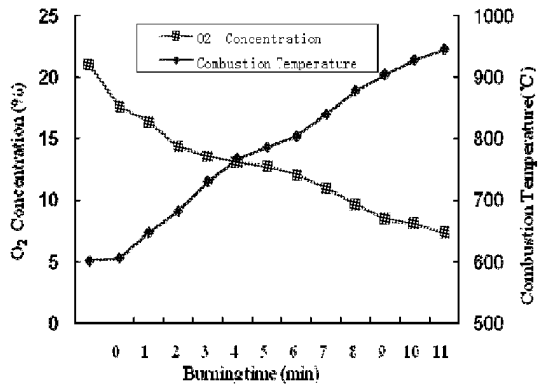

Fig.2 the changes of the O_2 concentration and the temperature of dense phase region as time changed

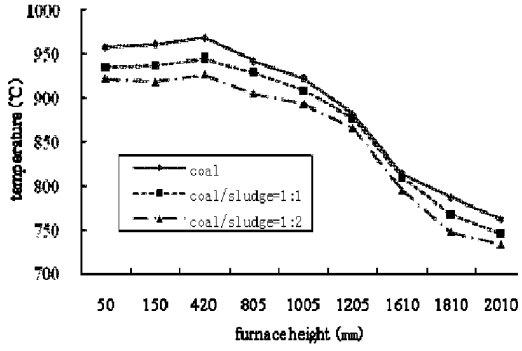

Fig.3 The change of combustion temperature along the furnace height with different ratio of coal and sludge

Combustion characteristics

When the fluidized air velocity was 1.88m/s, the oxygen concentration was 25%, the temperature changed along the height of furnace with different mass rate of fuels as Fig.3 shows. As known in Fig.3, when the amount of the fuel was stable, the combustion temperature was reducing as the sludge's ratio in the fuel increased, because the heat value of coal is higher than sludge, the more mixture ratio of sludge, the lower temperature of furnace.

Fig.4 shows the temperature change along the height of furnace when the fluidized air velocity was 1.88m/s、the mass ratio of coal and sludge was 1:1. From Fig.4, we concluded that when the amount of the fuel was stable, the combustion temperature was ascending as the increasing of O_2 content. This is because the more the O_2 content, the greater of burning-up degree of fuel and the higher of accumulating heat of furnace. From Fig.3 and Fig.4, it was known that at the same combustion conditions, the temperature increased firstly and then reduced, and the temperature of dense phase region was 200℃ higher than the top of furnace.

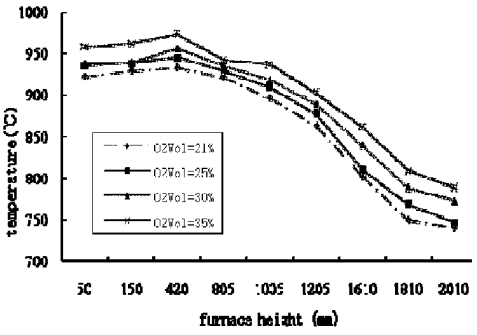

Fig.4 The changes of combustion temperature along the furnace height with different O_2 concentration (coal/sludge=1:1)

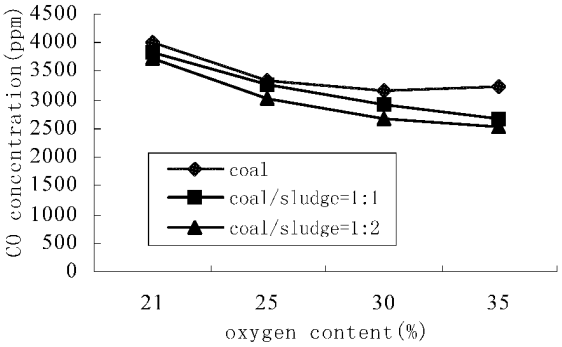

Fig.5 The changes of CO as the oxygen content of air-supplyt=850℃~900℃

Flue gas emission

A great amount of gas discharged in the process of combustion. With the gas analyzer, we tested the composition of O_2, CO, NO_X, SO_2, and analyzed the change of gas composition as the changes of oxygen content and the temperature of dense phase region.

CO emission characteristic

The experiment measured the impact of oxygen content to the CO emissions. Fig.5 shows the change of CO concentration as the oxygen content. When the fluidized air velocity was 1.88m/s, and the temperature was 850℃～900℃, the average concentration of CO reduced with the increase of he oxygen content. This because when the amount of the fuel was stable, the more of oxygen content, the greater of burning-up degree of fuels.

SO_2 emission characteristic

The experiment got the effect of different oxygen content on the characteristic of SO_2 emission, as Fig.6 shows. When the amount of the fuel was stable, with the oxygen content increased in the fluidizing air, the concentration of SO_2 increased gradually, because the total air quantity reduced to maintain the concentration of oxygen was 6% in outlet flue gas. It's beneficial to increase the contacting time of SO_2 and desulfurizer and improve desulfurization efficiency in furnace. The concentration of SO_2 reduced gradually with the sludge content increased in fuel under the same condition, just because of the sulfur content in sludge is lower than in coal. And the proportion of sludge in fuel could increase properly under good condition to meet the requirement of environmental protection.

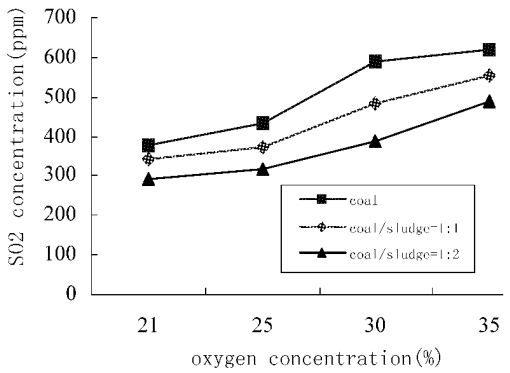

Fig.6 The changes of SO_2 as the oxygen content of air-supply

NO_X emission characteristic

There are three mechanisms of NO_X formation: thermal NO_X, fuel NO_X and prompt NO_X, under the condition of bed temperature of CFB (800 ~ 950℃), the total emission of thermal NO_X and prompt NO_X is very small, mainly is fuel NO_X, therefore, we can assume that all of NO_X are generated from the nitrogen of fuel component(Cen et al. 1998).

The experiment affected by different oxygen content and the temperature of dense phase region on the characteristic of NO_2 emission, as the Fig.7 and Fig.8 shows. We concluded that when the amount of the fuel was stable, with the oxygen content increased in the fluidizing air, the concentration of NO_X increased gradually, because the total air quantity reduced to maintain the concentration of oxygen was 6% in outlet flue gas. It also shows that NO_X emission concentration increased gradually when the temperature of dense phase region raised, and due to that the releaf of nitrogen in the fuel increased itself with temperature raising. Because nitrogen content in sludge is higher than in coal, the NO_X emission increased gradually as sludge content in mixed fuel increasing. Considering SO_2 emission decreased with the sludge content in mixed fuel increasing, we suggested that the mixture ratio of coal and sludge was 1:1, which could raise the fuel utilization, at the same time can reduce the removing cost of pollutants.

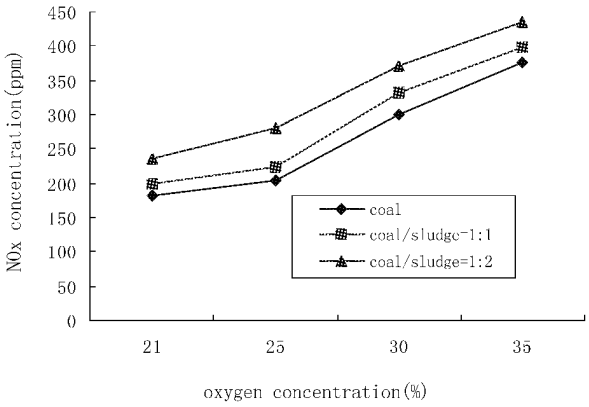

Fig.7 The changes of NO_X as the content oxygen of air-supply(t=850℃~900℃)

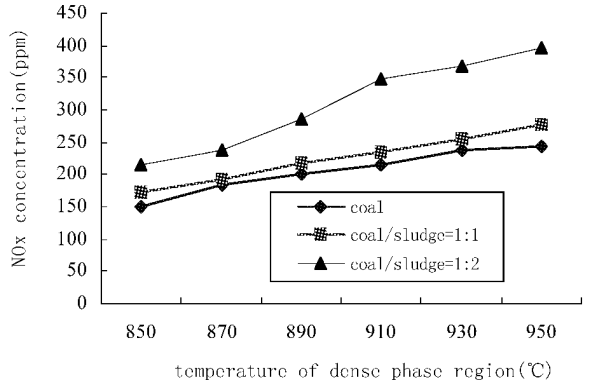

Fig.8 The changes of NO_X as the temperature of dense phase region

CONCLUSIONS

The characteristic varies in different mixing ratio of coal and sludge. Under the same combustion situations, when the proportion of sludge in the fuel mixture increased, the combustion temperature reduced gradually, because of the coal's calorific capacity is higher than the sludge.

When the amount of the fuel was stable, the temperature of furnace increased as the oxygen content in the fluidized air increased.

When the amount of the fuel was stable, with the oxygen proportion in the fluidized air increased, which caused the total amount of fluidized air to reduce, the concentration of CO reduces gradually, while the concentration of SO_2 and the NO_X increased. Under the same combustion situations, when the temperature of dense phrase region increased, the NO_X emissions density increased also.

The sulfur component in sludge is lower than in coal, while the nitrogen component in sludge is higher than in coal. Therefore under the same combustion situation, when the sludge proportion increased in the mixed fuel, the emission concentration of SO_2 reduced gradually while the emission concentration of NO_X increased gradually. So we suggested that the mixture ratio of coal and sludge was 1:1, which could raise the fuel utilization, at the same time can reduce the removing cost of pollutants.

ACKNOWLEDGEMENTS

Financial supports of this work by Natural Science Foundation Project of CQ CSTC of China (2006BB6224) are gratefully acknowledged.

REFERENCES

Andries, J., Becht, J.G.M., Hoppesteyn, P.D.J.: Energy Convers Mgmt Vol. **38** (1997), pp.117~122.

Cen, K.F. Ni, M.J. Luo, Z.Y. et al. (1998). Theoretical Design and Operation of Circulating Fluidized Bed Boiler. Beijng, China electric power publi.

Chi, Y., Li X. D., Yan, J. H., Ni, M. J., Cen, K.F. (2006). Incineration technology and engineering practice of coal washery sludge and sludge. Beijing, Chemi Indu Publ.

Czakiert, T., Bis, Z., Muskala, W., Nowak, W.: Fuel Pro Technol **87** (2006), pp. 531~538.

Dipl, I., Paul, L. (2001). Debottlenecking of Fluidized Bed Furnace for Sewage Sludge Incineration by Oxygen. 16th Int. CFB

Conference.Lu, X.F. (2006). Large-scale Circulating Fluidized Bed Boiler Equipment Movement. Beijng, China Electric Power Publ.

Glen, J., Greg, L., Nsakalaya, N., et al (2005). An ALSTOM vision of future CFB technology based power plant concepts, 18th Int. CFB Conference.

Hirma, T.H., Hosoda, N., Azuma, N. et al. (1998). Int. Sym Eng Foun FLUIDIZATION IX. USA

Lambert, J., Sorin, M., Paris, J.: Analysis Of Oxygen-Enriched Combustion For Steam Methane Reforming. (1996), pp. 158~161.

Mao, Y. R., Luo, Z.Y. Cen, K. F. : Journal of Comb Sci Technol **4** (2005), pp. 188~191.

Nsakala ya Nsakala.: Greenhouse Gas Emissions Control by Oxygen Firing in CFBB. **7** (2004). pp. 4～7.

KINETICS OF COAL CHAR COMBUSTION IN OXYGEN-ENRICHED ENVIRONMENT

T. Czakiert, W. Nowak

Department of Heating, Ventilation and Air Protection,
Faculty of Environmental Protection and Engineering,
Czestochowa University of Technology, Czestochowa, Poland

Abstract: The influence of oxygen-enriched gaseous atmosphere on coal char combustion was studied. Two different coals, i.e. lignite and bituminous coal, were used as a basic fuel and the reacting gases of oxygen & CO_2 were used to simulate flue gas recirculation. Moreover, a broad range of in-furnace conditions, i.e. five temperatures of 873, 973, 1073, 1173, 1273K and five oxygen concentrations of 20, 40, 60, 80, 100%vol., was investigated. Thermogravimetric method of measurement was employed to obtain the processing data on fuel conversion rate under foregoing investigated conditions. For further calculations, simplified Shrinking-Core Model was introduced. Finally, fundamental kinetic parameters, i.e. pre-exponential factor, activation energy and reaction order, were established and then on the basis of their values reaction-controlling regime for coal char combustion in oxygen-enriched environment was predicted. The investigations, financially supported by Polish Government, are a part of Framework Project "Supercritical Coal-fired Power Units".

Keywords: oxy-combustion, coal-char, kinetics

INTRODUCTION

Recently, combustion of solid fuels in gaseous atmosphere with increased oxygen concentration has attracted more and more attention. Moreover, two different technologies of oxy-fuel combustion, i.e. PC's (Pulverized Coal) and CFB's (Circulating Fluidized Bed), have been developed in parallel (Stromberg, 2007; Eriksson et al., 2008; Saastamoinen et al. 2006). However, there is still the lack of fundamental knowledge on solid fuel behavior in oxygen-enriched environment. Therefore, a broad range of investigations for comprehension of the process and to facilitate the further development of oxy-combustion technology is really necessary.

Regardless of the combustion environment, five following and often overlapping stages of solid fuel burn-out can be distinguished (Basu, 1999): a) heating-up of fuel particles, aa) drying of fuel particles, aaa) volatile matter release and their combustion, aaaa) fragmentation of fuel particles, aaaaa) char burn-out. Devolatilization is rather fast compared to char conversion and the combustion of volatiles runs generally in a gas film in some distance from fuel particle. Therefore, presented work has been focused on char combustion, since the rate of char conversion closely depends on in-furnace conditions. Obtained data seem to be also crucial for process engineers and constructors of new generation oxy-fuel boilers, especially CFB's operated with coarse fuels where char particles are returned to combustion chamber in a circulating loop.

The combustion of char particles may run under four different reaction-controlling regimes, i.e. a) internal-kinetic, aa) internal-diffusion, aaa) external-kinetic, aaaa) external-diffusion. The regime depends mainly on in-furnace conditions, particularly temperature and partial pressure of oxygen, as well as the size of fuel particles. At low temperature, diffusion rate in pores is much higher than reaction rate and combustion takes place in the whole volume of fuel particle. The reaction runs under "internal-kinetic controlling regime" and Progressive-Conversion Model of combustion is usually employed to describe the process (Sorensen et al., 1996a). Then, with increasing temperature, reaction rate is going to be higher than the internal diffusion rate. Oxygen concentrations at external surface of fuel particle and in surrounding gas are still equal but it decreases in opposite direction, towards the core of the particle. It means that reaction falls into "internal-diffusion controlling regime". If the temperature still increases, the reaction rate is much higher than the internal diffusion rate and the combustion in pores disappears, however, external diffusion rate still exceeds the reaction rate. It is said that reaction runs under "external-kinetic controlling regime" and then Shrinking-Core Model is a suitable tool to study the progress in fuel conversion (Sorensen et al., 1996b). Finally, at very high temperatures, the reaction rate is so rapid that diffusion takes over the control of the combustion taking place only on an external surface of unreacted core of fuel particle, and hence, the conditions are called "external-diffusion controlling regime". Moreover, for increased partial pressure of oxygen and for coarser particles, combustion nature changes from "internal-kinetic" towards the "external-diffusion". All the above information were taken

into consideration when the regime of investigated oxygen-enriched combustion was initially assumed.

EXPERIMENTAL

Apparatus

Thermogravimetric analyzer (TGA/SDTA 851^e, Mettler-Toledo) was employed to obtain the processing data on fuel conversion rate and sample temperatures under the following investigated conditions. Two different Polish coals, i.e. lignite and bituminous coal, were used as a basic fuel and they were devolatilized in advance to obtain chars for further analyses. The samples were 30mg±1% in weight and particles size was in a range of 0.8-1.0mm. The properties of coals and chars are shown in Table 1. Five oxygen concentrations of 20, 40, 60, 80, 100%vol. in the gas mixtures of oxygen & CO_2 were set and CO_2 component simulated environment of flue gas recirculation. Moreover, five temperatures of 873, 973, 1073, 1173, 1273K were investigated. Standard open 150µl alumina pans were used and a gas flow of 50ml/min (STP) was set. The experimental settings are shown in Fig. 1, where can be seen that nitrogen was supplied to the reaction cell in the heating-up stage. It prevents char samples from oxidizing of combustible matter before the steady temperature is achieved.

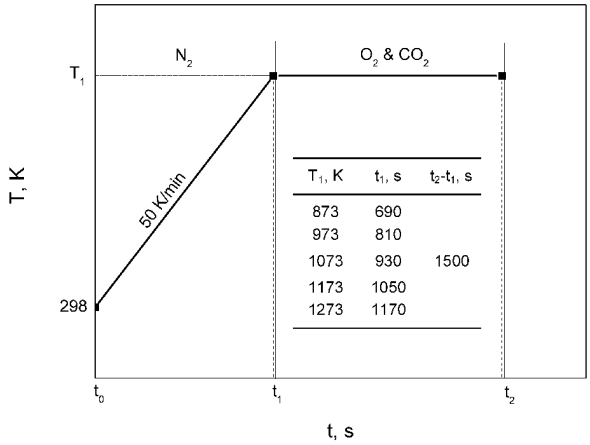

Fig. 1 Experimental settings

Table 1 Properties of coals and chars

		Lignite	Bitumin. coal	Char (Lign.)	Char (Bitum.)
LHV (kJ/kg)		23183	24708	22690	21117
Proximate analysis (%)	Moisture	4.2	3.5	2.2	1.8
	VM	48.3	31.7	-	-
	FC $^{(diff.)}$	33.0	41.4	68.0	62.8
	Ash	14.5	23.4	29.8	35.4
Ultimate analysis (%)	C	55.7	58.1	66.0	60.3
	S	0.47	1.08	0.43	0.95
	H	5.80	3.92	0.68	0.44
	N	0.62	1.36	0.76	0.92
	O $^{(diff.)}$	18.71	8.64	0.13	0.19

Calculations

Because of the experimental conditions, i.e. the temperature from a range of 873-1273K and the oxygen concentration increased up to 100% as well as the use of rather coarse fuel particles of 0.8-1.0mm in size, it was assumed that combustion occurs only in a thin skin of unreacted core of fuel particles. Therefore, Shrinking-Core Model of combustion was employed to describe the progress in fuel conversion. The simplification of the introduced model lies mainly in the fact that diffusion of oxygen through the forming ash layer as well as the diffusion of oxygen to the particle surface through a gas film were not considered.

Many investigators claim that the calculations of combustion rate (Eq. 1) can be based on Arrhenius expression, since the nature of carbon & oxygen reaction remains still unclear (Murphy et al., 2006).

$$r = -\frac{1}{A_e}\frac{dm}{dt} = kP_{O2}^n = k_0 \exp\left(-\frac{E_a}{(MR)T}\right)P_{O2}^n \quad (1)$$

The apparent reaction rate (r) expressed in g/m^{2}s can be determined directly from thermogravimetric data, as TG curves show mass loss in time unit (dm/dt), only when it is known what is the progress of shrinkage of the surface area (A_e) where combustion takes place. The values of A_e, however, can be estimated using following equations (Eqs. (2)-(4)):

$$A_{e\,i} = \pi\, D_i^2 n_s \quad (2)$$

where, n_s means the number of fuel particles, and:

$$D_i = \left(\frac{m_i - m_{ash}}{\rho_{cm}\,\frac{1}{6}\pi\, n_s}\right)^{1/3} \quad (3)$$

where density of combustible matter (ρ_{cm}) can be calculated as follows:

$$\rho_{cm} = \frac{m_1 - m_{ash}}{\frac{1}{6}\pi\, D_1^3 n_s} \quad (4)$$

The logarithmic form of power-low expression (Eq. (5)) points at straight relation between reaction rate and partial pressure of oxygen. Thus, apparent reaction order (n) can be easily found directly from a plot (Fig. 2) based on the Eq. (5).

On the other hand, a plot (Fig. 3) of logarithmic form of Arrhenius equation (Eq. 6), which shows the influence of temperature on reaction rate constant (k), allows to establish both: pre-exponential factor (k_0) and apparent activation energy (E_a).

$$\ln r = n \ln P_{O2} + \ln k \quad (5)$$

$$\ln k = -\frac{E_a}{MR}\frac{1}{T} + \ln k_0 \quad (6)$$

where, according to Eq. 1:

$$k = \frac{r}{P_{O2}^n} \quad (7)$$

Hence, a broad range of in-furnace conditions (temperatures, oxygen concentrations in reacting gas) was investigated to obtain a number of processing data.

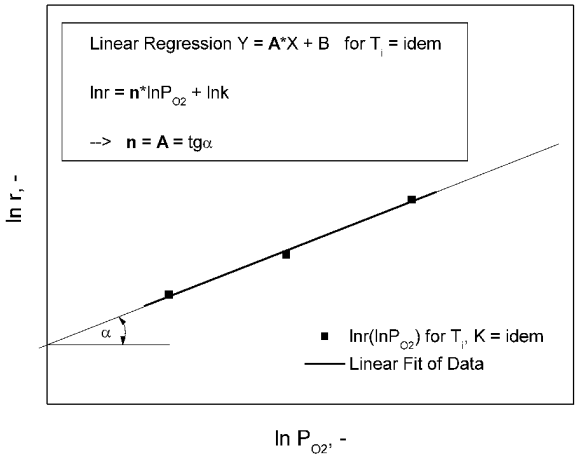

Fig. 2 Logarithmic plot of power-low expression

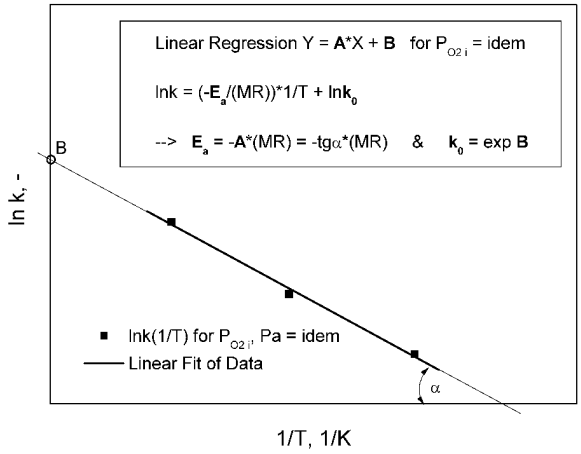

Fig. 3 Logarithmic plot of Arrhenius equation

RESULTS AND DISCUSSION

An example curves (Fig. 4) describe the changes in the apparent reaction rate with conversion ratio (CR) of the combustible matter in the fuel. It can be seen that the reaction rate is higher and higher when the partial pressure of oxygen is raised up to 100%. It results in an increasing temperature of fuel samples, what is shown in Fig. 5, where ΔT means an excess of sample temperature over gas temperature. The above mentioned relations are rather obvious, however, the exact values of these parameters, for different temperatures in

combustion zone and different oxygen concentrations in reacting gas, are necessary for further calculations of n, k_0 and E_a. The values of the reaction rate for the beginning and for the end of combustion process were omitted. It is because of the fluctuations coming from the substitution of N_2 for O_2&CO_2-mixture in the initial stage and because of the very high values of r for CR close to 100% that make the plot illegible. Moreover, for the calculations of kinetic parameters, the average values of both: r and T were taken only from a range of fuel conversion of 40-60%, since they are not constant during the whole combustion process.

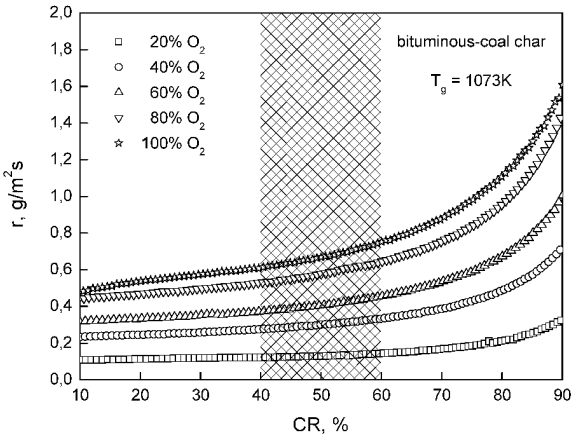

Fig. 4 Apparent reaction rate in a function of conversion ratio

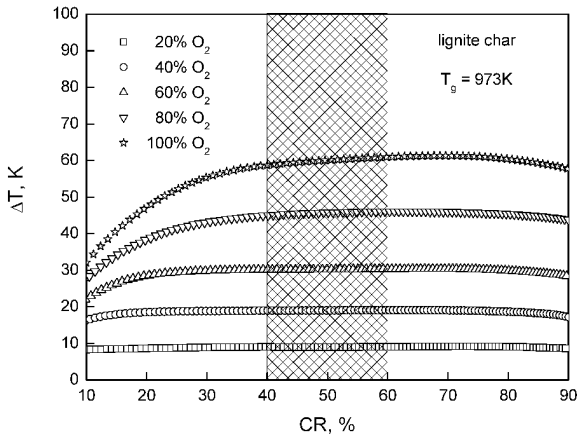

Fig. 5 Excess of sample temperature in a function of conversion ratio

Following the directions given in the Fig. 2, apparent reaction orders were determined directly from Figs. 6 and 7, for lignite char and bituminous-coal char, respectively. The inlet partial pressure of oxygen was taken as oxygen partial pressure in combustion zone, since pressure drop of oxygen calculated for the highest reaction rate was below 2.5%. The data initially obtained for the oxygen concentrations of 80% and 100% were not considered here, since the excess of sample temperature over gas temperature seems to be too high (see Fig. 5). The increase in temperature under lower partial pressures of oxygen remains below 5% for all investigated conditions, thus it should not cause significant errors in the results obtained.

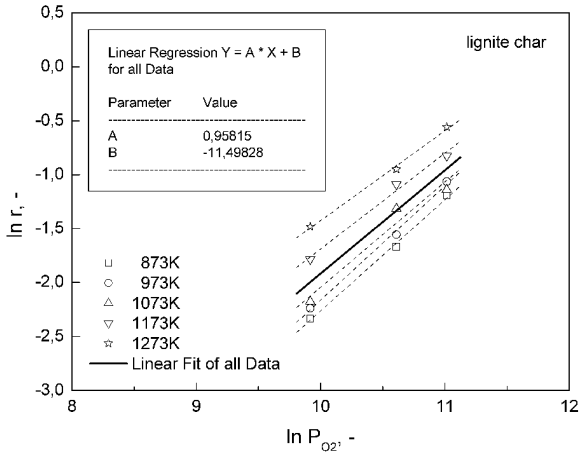

Fig. 6 Determination of reaction order for lignite char

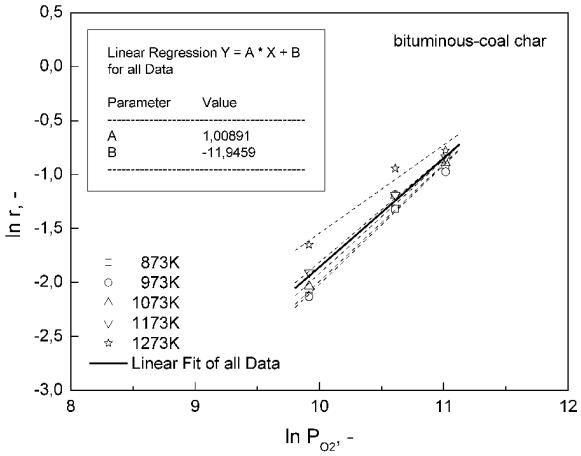

Fig. 7 Determination of reaction orderfor bituminous-coal char

Reaction orders from a broad range of 0.25-1.0 are reported for reaction of carbon & oxygen (*Hu* et al., *2001*). The differences in the values come mainly from the fuel type and the experimental conditions as well as the employed equipments and the introduced model of combustion (*Sorensen* et al., *1996*b). Apparent reaction orders determined for both investigated fuels, i.e. lignite char and bituminous-coal char, are close to unity. It confirms the results of other investigations, as the content of C in combustible matter of both chars exceeds 95% wt. (see Table 1).

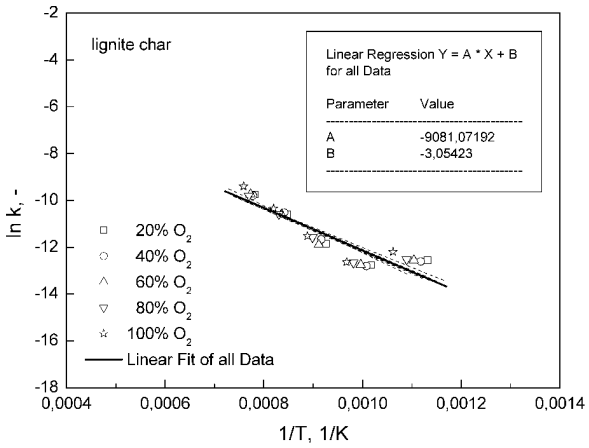

Fig. 8 Determination of activation energy and pre-exponential factor for lignite char

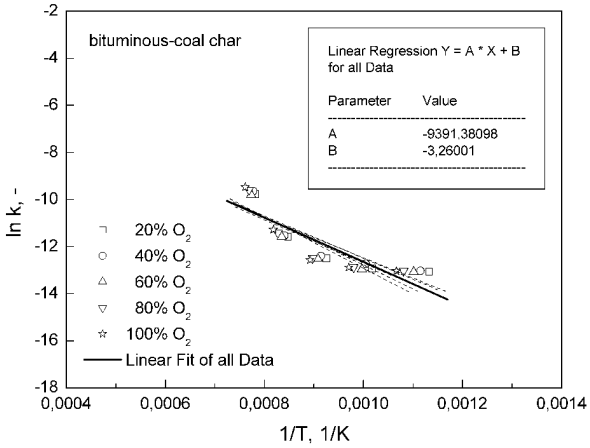

Fig. 9 Determination of activation energy and pre-exponential factor for bituminous-coal char

The values of pre-exponential factor and apparent activation energy were found using Figs. 8 and 9, in the way explained in Fig. 3, for lignite char and bituminous-coal char, respectively. An increase in sample temperature can be considered in this case and changes in oxygen concentration under the following investigated partial pressures of oxygen were negligible, as was mentioned above. Therefore, all initial data were introduced into Arrhenius plots to estimate k_0 and E_a.

The values of 0.047 and 0.038g/m^{2}sPa for k_0 and 75.5 and 78.1kJ/mol (18.0, 18.7kcal/mol) for E_a were established, for lignite char and bituminous-coal char, respectively. Some investigators claim that activation energy depends on the reaction-controlling regime, where E_a from a range of 17-23kcal/mol fulfills the regime of pore-diffusion control, whereas, E_a from a range of 35-45kcal/mol relates to the kinetic controlling regime (*Hu* et al., *2001*). Therefore, it can be expected that the combustion of coal char in oxygen-enriched environment of O_2&CO_2 and temperature range of 873-1273K runs under pore-diffusion controlling regime, since the obtained values of E_a are slightly higher than 17kcal/mol for both investigated fuels. It means that reaction takes place only in a thin skin of unreacted core of fuel particles, and hence, the Shrinking-Core Model used in this study is a suitable tool to describe the progress in char conversion.

CONCLUSIONS

The combustion of lignite char and bituminous-coal char in O_2&CO_2 environment with oxygen concentration increased up to 100% and in temperature range of 873-1273K has been investigated. A simplified Shrinking-Core Model of fuel conversion was employed for processing of initially obtained thermogravimetric data. Previously, an increase in apparent reaction rate and sample temperature was found when partial pressure of oxygen was raised. Finally, the fundamental kinetic parameters, i.e. reaction order, activation energy and pre-exponential factor, were established. The values of reaction order are close to unity for both investigated fuels where carbon content in combustible matter exceeds 95% wt. Activation energies of ca. 18kcal/mol point to pore-diffusion controlling regime of coal char combustion under conditions mentioned above.

NOTATIONS

A_e external surface area, m^2
CR conversion ratio, %
D diameter, m
D_1 initial diameter, m
E_a apparent activation energy, J/mol
k reaction rate constant, g/m^{2}sPa
k_0 pre-exponential factor, g/m^{2}sPa
m mass, g
m_1 initial mass, g
(MR) universal gas constant, 8.31434J/molK
n apparent reaction order, -
n_s number of fuel particles, -
P_{O2} partial pressure of oxygen, Pa

r apparent reaction rate, g/m^2s
STP standard reference conditions, 273.15K & 101325Pa
t time, s
T temperature, K
ρ_{cm} density of combustible matter, g/m^3

ACKNOWLEDGEMENTS

Financial support of this work by Polish Government, as a part of Framework Project: Supercritical Coal-fired Power Units, is gratefully acknowledged.

REFERENCES

Basu, P.: Chem. Eng. Sci. 54 (1999), pp. 5547-5557
Eriksson, T., Nuortimo, K., Hotta, A., Myohanen, K., Hyppanen, T.: 9th Int. CFB Conference (2008), pp. 819-824
Hu, Y.Q., Nikzat, H., Nawata, M., Kobayashi, N., Hasatani, M.: Fuel 80 (2001), pp. 2111-2116
Murphy, J.J., Shaddix, C.R.: Combust. and Flame 144 (2006), pp. 710-729
Saastamoinen, J., Tourunen, A., Pikkarainen, T., Hasa, H., Miettinen, J., Hyppanen, T., Myohanen, K.: 19th Int. FBC Conference (2006)
Sorensen, L.H., Gjernes, E., Jessen, T., Fjellerup, J.: Fuel 75 (1996a), pp. 31-38
Sorensen, L.H., Saastamoinen, J., Hustad, J.E.: Fuel 75 (1996b), pp. 1294-1300
Stromberg, L.: 2nd Int. IEA-GHG Oxy-Combustion Workshop (2007)

COMBUSTION OF COAL CHAR PARTICLES UNDER FLUIDIZED BED OXYFIRING CONDITIONS

Fabrizio Scala, Riccardo Chirone

Istituto di Ricerche sulla Combustione, Consiglio Nazionale delle Ricerche, Napoli, Italy

Abstract: In this work combustion of single coal char particles was studied at 850°C in a lab-scale fluidized bed under simulated oxyfiring conditions. The burning rate of the particles was followed as a function of time by continuously measuring the outlet CO and O_2 concentrations. Some preliminary evaluations on the significance of homogeneous CO oxidation in the reactor and of carbon gasification by CO_2 in the char were also carried out. Results showed that the carbon burning rate increases with oxygen concentration and char particle size. The particle temperature is approximately equal to the bed one up to an oxygen concentration of 2%, but it is considerably higher for larger oxygen concentrations. Both CO_2 gasification of char and homogeneous CO oxidation are not negligible. The gasification reaction rate is slow and it is likely to be controlled by intrinsic kinetics. During purely gasification conditions the extent of carbon loss due to particle attrition by abrasion (estimated from the carbon mass balance) appears to be more important than under combustion conditions.

Keywords: coal, char, combustion, fluidized bed, oxyfiring

INTRODUCTION

Production of energy from fossil fuel combustion results in the emission of greenhouse gas species, with the most significant fraction being CO_2. The constant increase in greenhouse gas emissions has resulted in the development of new technologies with lower emissions and technologies that can accommodate capture and sequestration of carbon dioxide. Oxyfiring (or oxyfuel) technology can produce an almost pure CO_2 outlet stream, by using pure oxygen instead of air for fuel combustion (Buhre et al., 2005). Flue gas is partly recycled back into the furnace to control the combustion temperature. In this way the costs of CO_2 separation from the flue gas can be substantially reduced. Although most of the research activity in oxyfiring has concentrated on pulverized coal boilers, recently the application of this technology to circulating fluidized bed (CFB) coal boilers has been examined (Jukkola et al., 2005; Czakiert et al., 2006; Saastamoinen et al., 2006; Jia et al., 2007; Eriksson et al., 2008). CFBs appear to be particularly suited for oxyfiring conditions because of the fuel flexibility and better temperature control (which allows to reduce the amount of recycled flue gas). The feasibility of CFB coal oxyfiring has been successfully demonstrated in pilot-plant tests, and no particular technological barrier appears to exist for implementing this technology in the near-term.

However, a number of issues still need to be addressed in more detail to obtain a more fundamental understanding of the changes between oxyfiring and conventional air-fired combustion (Buhre et al., 2005). One of these issues regards the combustion characteristics of coal in an O_2/CO_2 atmosphere. In fact, it has been suggested that under these conditions (and especially at the high temperatures experienced in pulverized fuel combustion) carbon gasification by CO_2 might contribute significantly to the char mass loss (Buhre et al., 2005). In this work, combustion of single coal char particles in a lab-scale fluidized bed under simulated oxyfiring conditions was studied. The burning rate of the particles was followed as a function of time by continuously measuring the outlet CO and O_2 concentrations. Some preliminary evaluations on the significance of homogeneous CO oxidation in the reactor and of carbon gasification by CO_2 in the char particle at the relevant operating conditions are also reported.

EXPERIMENTAL

Apparatus

A circular stainless steel atmospheric bubbling fluidized bed reactor 40mm ID and 1m high was used for the experiments (Fig. 1). The gas distributor was a 2mm thick perforated plate with 55 holes 0.5mm in diameter disposed in a triangular pitch. A 0.6m high stainless steel column, containing a number of steel nets for gas preheating and mixing, was placed under the distributor. The fluidization column and the preheating section were heated by two semicylindrical electric furnaces. The temperature of the bed, measured by means of a thermocouple placed 40mm above the distributor, was kept constant by a PID controller. Temperature variations during the runs were always within ±1°C of the set point. A stainless steel circular basket could be inserted from the top to retrieve char particles from the bed.

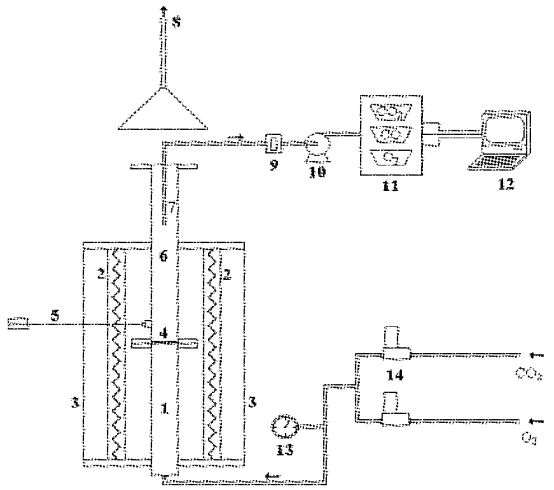

Fig.1 Experimental apparatus
1) gas preheating section; 2) electrical furnaces; 3) ceramic insulator; 4) gas distributor; 5) thermocouple; 6) fluidization column; 7) gas suction probe; 8) stack; 9) cellulose filter; 10) membrane pump; 11) gas analyzers; 12) personal computer; 13) manometer; 14) digital mass flowmeters

Gases were fed to the column via two high-precision digital mass flowmeters/controllers (accuracy ±1% full scale). Each flowmeter/controller was calibrated with a bubble flowmeter. Gases were supplied from two cylinders containing carbon dioxide and oxygen.

The top section of the fluidization column was left open to the atmosphere and the exit gas was sucked by a hood. A stainless steel probe was inserted from the top of the column to convey a known fraction ($0.06m^3/h$) of the exit gas directly to the gas analyzers. A high efficiency cellulose filter was inserted in the line to avoid dust entrainment into the analyzers. The probe, 2mm ID, was positioned 0.6m above the distributor, approximately at the axis of the column. The absence of any gas leakage and/or suction to/from the surrounding environment in the sampling probe and line was carefully checked.

A NDIR analyzer (accuracy ±1% full scale) was used for on-line measurement of CO and a paramagnetic analyzer (accuracy ±2% full scale) for O_2 concentration in the exhaust gases. The measuring range of the O_2 analyzer was 0 – 10% (v/v) and for CO 0-1000ppmV. Data from the analyzers were logged and further processed on a PC.

Table 1 Properties of Snibston coal

Proximate analysis, %	(as received)		
		Moisture	14.6
		Ash	4.0
		Volatile Matter	35.2
		Fixed Carbon	46.2
Ultimate analysis, %	(dry and ash free basis)		
		Carbon	81.3
		Hydrogen	5.3
		Nitrogen	1.6
		Oxygen	10.8
		Sulphur	1.0
Char density, kg/m^3			1040

Materials

A Snibston bituminous coal was selected as the test fuel. Table 1 reports the fuel properties. The fuel particles were first devolatilized by dropping them in the fluidized bed with N_2 at 850°C. After 5min, char particles were retrieved from the bed and machined into almost spherical particles with an average size of ~6-7mm (Fig. 2(a)). The particles were pre-processed in air for 8h in the fluidized bed at ambient temperature and 0.3m/s to smoothen the particle surface. Some combustion tests were performed with a thin (250μm OD) thermocouple inserted inside the particle to measure its temperature during the oxy-combustion test (Figs.

2(b),(c)). The thermocouple tip was placed approximately at the center of the particle.

The bed material consisted of 180g of quartz sand, corresponding to an unexpanded bed height of 0.1m. Sand was double sieved in the 500 – 600μm particle size range. The minimum fluidization velocity was 0.13m/s. The particle density of the quartz sand was 2560kg/m^3, and the bed voidage at minimum fluidization was 0.44.

Procedures

In all the tests performed in this experimental campaign the inlet oxygen concentration was lower than 10% (v/v), because these are the relevant local O_2 concentrations near a burning particle in a fluidized bed under oxyfiring conditions. If low oxygen concentrations are used (< 2% v/v), it is known that the particle temperature can be assumed approximately equal to the bed one (Scala, 2009). Since some tests were performed with a higher O_2 concentration, in these tests a thermocouple was inserted inside the particle to measure its temperature.

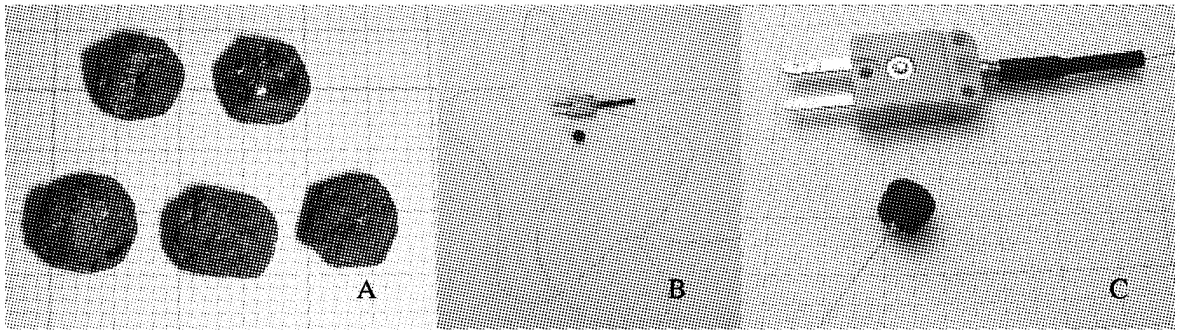

(a) (b) (c)

Fig. 2 (a) Coal char particles used for the experiments; (b) and (c) char particle with thermocouple inside

The experiments were performed in a fluidized bed at 850°C, atmospheric pressure, with a fluidization velocity of 0.3m/s, which corresponds to bubbling/slugging conditions. An inlet gas mixture was introduced in the bed made of CO_2 and O_2 in the combustion tests and only CO_2 in the gasification tests; O_2 concentration assumed the values 1, 2, 4.5 and 8 % (v/v). Each test consisted in the injection of one char particle, of known mass and diameter, in the fluidized bed and in the continuous measurement of CO and O_2 concentrations at the outlet. In order to obtain the char burning rate during the tests, a balance on oxygen and carbon in the reactor was carried out:

$$\dot{m}_{O_2}^{in} + \dot{m}_{CO_2}^{in}\frac{32}{44} = \dot{m}_{O_2}^{out}(t) + \dot{m}_{CO}^{out}(t)\frac{16}{28} + \dot{m}_{CO_2}^{out}(t)\frac{32}{44} \quad (1)$$

$$\dot{m}_{CO_2}^{in}\frac{12}{44} + \dot{m}_{C}^{consumed}(t) = \dot{m}_{CO_2}^{out}(t)\frac{12}{44} + \dot{m}_{CO}^{out}(t)\frac{12}{28} \quad (2)$$

where $\dot{m}_i^{in}$ or $\dot{m}_i^{out}$ is the mass flow rate of species *i* that enters or exits the reactor and $\dot{m}_C^{consumed}$ is the carbon consumption rate, all in g/s. Combining these two equations gives:

$$\dot{m}_C^{consumed}(t) = \frac{12}{32}\left[\dot{m}_{O_2}^{in} - \dot{m}_{O_2}^{out}(t)\right] + \frac{3}{14}\dot{m}_{CO}^{out}(t) \quad (3)$$

By integrating the curve obtained with Eq. (3) between time zero and the end of the test it is possible to calculate the total mass of carbon consumed during the test:

$$m_C^{consumed} = \int_0^{t_f} \dot{m}_C^{consumed}(t)dt \quad (4)$$

Assuming that the spherical particle burns according to a constant density shrinking particle model, the char particle diameter as a function of time is given by:

$$d(t_1) = \left(6\left(m_C^{initial} - \int_0^{t_1} \dot{m}_C^{consumed}(t)dt \right) \Big/ \pi \cdot \rho_{char} \right)^{1/3} \quad (5)$$

The reactions that can occur during the oxy-combustion process are:

$$C(s) + O_2 \rightarrow CO_2 \quad (A)$$

$$C(s) + \frac{1}{2}O_2 \rightarrow CO \quad (B)$$

$$C(s) + CO_2 \rightarrow 2CO \quad (C)$$

$$CO + \frac{1}{2}O_2 \rightarrow CO_2 \quad (D)$$

where (A) and (B) represent carbon combustion reactions, (C) carbon gasification by CO_2 and (D) homogeneous CO oxidation reaction. In order to check if reaction (D) occurred, a test was done in which a mixture of CO, CO_2 and O_2 was introduced in the fluidized bed (without the presence of a char particle) first at ambient temperature and then at 850°C, and the concentration of CO at the exit was measured in both cases. It was observed that at 850°C the concentration of CO at the exit significantly decreased when compared to ambient temperature, meaning that in the conditions of the tests reaction (D) is not negligible.

RESULTS AND DISCUSSION

In Fig. 3A the typical concentration curves of CO and O_2 at the exit of the bed are shown, for a combustion test with 2% O_2 at the inlet. The absence of peaks or sudden changes in the slope of the CO curve reveal that no particle fragmentation occurred during the test.

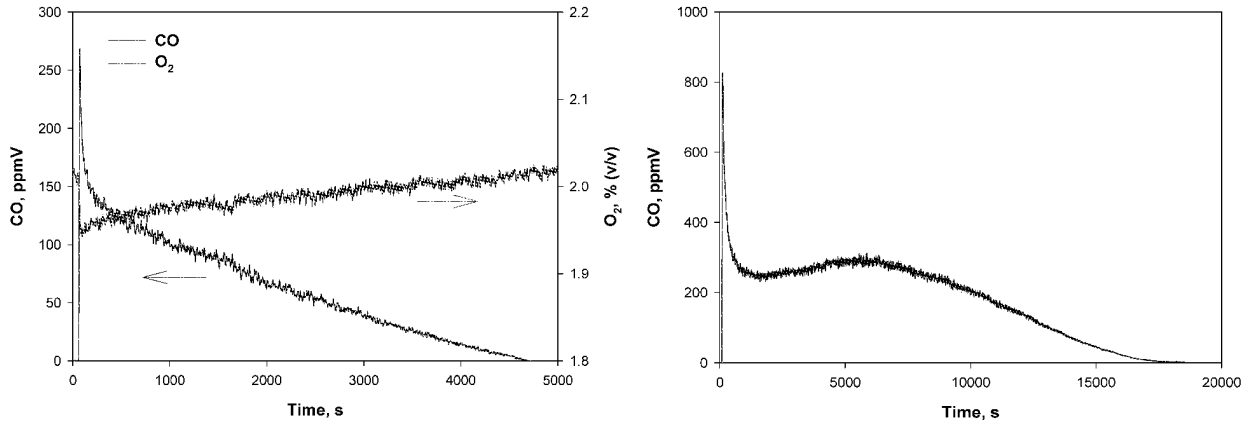

Fig. 3 (a) CO and O_2 concentration profiles during a typical oxyfiring char combustion test, T = 850°C, O_2 = 2% (v/v); (b) CO concentration profile during a typical char gasification test, T = 850°C, CO_2 = 100% (v/v)

Using the data from these curves together with Eqs. (3) and (5) it was possible to determine the variation of the particle diameter with time. As stated previously, some of the combustion tests were performed with a thermocouple inserted in the char particle to measure its temperature during the test. Table 2 reports the results in terms of the peak temperature difference between the particle and the bed. For oxygen concentrations larger than 2% the error done by considering that the char particle has the same temperature as the bed can be larger than 10°C.

Another series of tests was performed at 850°C to quantify how important is reaction (C) during the tests. A typical outlet CO concentration profile obtained during a gasification test (100% CO_2) is shown in Fig. 3B. The gasification test clearly shows a much longer reaction time with respect to the combustion ones.

Figure 4A reports the carbon burning rate (calculated with Eq. (3)) as a function of the particle diameter for the oxyfiring combustion tests at different O_2 inlet concentrations. Results show that the combustion rate increases as the concentration of O_2 in the bed increases. This result can be expected both in the case of kinetically controlled and diffusion controlled combustion. Fig. 4(a) also shows that the combustion rate increases almost linearly with the particle diameter, indicating that diffusion of oxygen through the particle boundary layer is likely to control (at least partially) the burning process, as it is the case during air combustion (Scala, 2009).

Figure 4(b) shows the carbon consumption rate as a function of time for the same gasification test shown in Fig. 3(b). For this test the curve was not plotted as a function of diameter, since in these conditions the constant density shrinking particle model (and in turn Eq. (5)) is likely not to apply anymore.

Table. 2 Peak temperature difference between the char particle and the bed for different inlet oxygen concentrations

Inlet O_2 concentration (% v/v)	Peak temperature difference (°C)
2	10
4.5	25
8	60

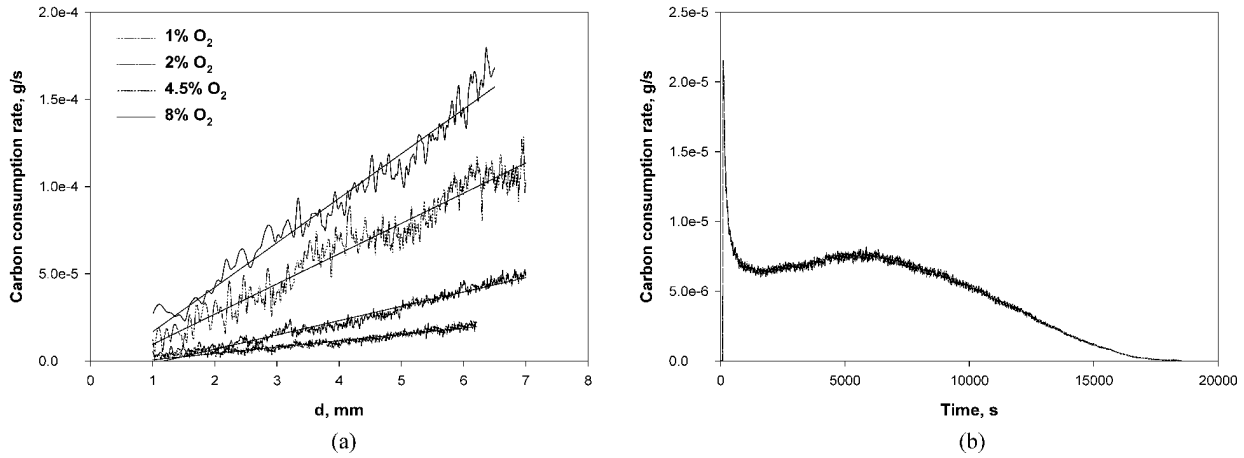

Fig. 4 Carbon consumption rates
(a) as a function of particle diameter during oxyfiring char combustion tests at different O_2 concentrations, T = 850°C; (b) as a function of time during a typical char gasification test, T = 850°C, CO_2 = 100% (v/v)

By comparing Figs. 4(a) and 4(b) it can be clearly noted that the gasification reaction rate at 850°C is always slower than the combustion rate and that it is less dependent on the actual char particle mass (especially in the first half of the run, see Fig. 4(b), denoting a significant contribution of the intrinsic kinetics on the reaction rate. Nevertheless, the gasification rate under high CO_2 bulk concentrations at 850°C is not negligible, contrary to what happens under typical air combustion conditions (Scala, 2009).

The carbon mass balance for the char particle was calculated by comparing the initial carbon mass in the particle and the total amount of carbon consumed during the test. For the tests under simulated oxyfiring combustion conditions this balance had an absolute error which was always less than 5%. On the other hand, for the gasification tests the error was in the order of 20% (the calculated consumed mass was smaller than the initial mass of carbon). This suggests that abrasion by attrition is important during the gasification tests and that part of the char probably exited the reactor as elutriated material without reacting.

CONCLUSIONS

Results from the preliminary experimental tests showed that during oxy-combustion of coal char in a bubbling fluidized bed at 850°C, besides the heterogeneous combustion reactions, the CO_2 gasification reaction and the homogeneous CO oxidation reaction are not negligible.

During coal char oxyfiring the temperature of the particle is approximately equal to the bed temperature up to an oxygen concentration of 2%, for higher concentrations the temperature of the particle is considerably higher than the bed one.

The gasification reaction is always slower than the combustion reaction, and intrinsic kinetics is likely to control the gasification rate. During gasification conditions particle attrition phenomena appear to be more important than under combustion conditions.

ACKNOWLEDGEMENTS

This work has been carried out under the EC 6th Framework Program – INECSE training project – Marie Curie Actions. The support of C. F. N. Cavalheiro in the experimental tests and of S. Russo for making the photographs of the char particles is gratefully acknowledged.

REFERENCES

Buhre, B.J.P., Elliott, L.K., Sheng, C.D., Gupta, R.P., Wall, T.F.: Prog. Energy Combust. Sci. 31 (2005), pp. 283-307.
Czakiert, T., Bis, Z., Muskala, W., Nowak, W.: Fuel Process. Technol. 87 (2006), pp. 531-538.

Eriksson, T., Nuortimo, K., Hotta, A., Myohanen, K., Hyppanen, T., Pikkarainen, T.: Proc. 9th Int. Conf. Circulating Fluidized Beds, Hamburg, Germany (2008), pp.819-824.

Jia, L., Tan, Y., Wang, C., Anthony, E.J.: Energy Fuels 21 (2007), pp. 3160-3164.

Jukkola, G., Liljedahl, G., Nsakala, N., Morin, J., Andrus, H.: Proc. 18th Int. Conf. Fluidized Bed Combustion, Toronto, Canada (2005), paper #78104.

Saastamoinen, J., Tourunen, A., Pikkarainen, T., Hasa, H., Miettinen, J., Hyppanen, T., Myohanen, K.: Proc. 19th Int. Conf. Fluidized Bed Combustion, Vienna, Austria (2006), paper #49.

Scala, F.: A new technique for the measurement of the product CO/CO_2 ratio at the surface of char particles in a fluidized bed. Proc. Combust. Inst. 32 (2009), in press.

Gasification

OPTIMIZATION OF BIOMASS GASIFICATION PROCESS FOR F-T BIO-DIESEL SYNTHESYS

Jae Hun Song, Yeon Kyung Sung, Tae U Yu, Young Tae Choi, Uen Do Lee

Korea Institute of Industrial Technology, Cheonan, Korea

Abstract: The characteristics of biomass steam gasification were investigated to make an optimum syngas for Fischer Tropsch (F-T) synthesis of bio-diesel. Korean pine wood chip was used as a fuel and the experiment was conducted in a lab scale bubbling fluidized bed (0.1m I.D. x 3.0m height). Gas composition was evaluated by changing operating parameters such as gasifier temperature, and steam to fuel ratio. Major syngas was monitored by on-line gas analyzer (ND-IR spectroscopy) and gas chromatography (GC). As the temperature of gasifier increases hydrogen in the syngas increases while CO in the product gas decreases. The low concentration of sulfur compound and nitrogen in the product gas shows the potential advantages in the purification process of the syngas for F-T process. Optimum operating condition of the gasifier was found concerning the following gas cleaning and F-T process; H_2-CO ratio and total gas yield increase while decreasing methane and CO_2 concentrations in the syngas.

Keywords: steam gasification, biomass, syngas, bubbling fluidized bed, F-T synthesis

INTRODUCTION

With the depletion of fossil fuel as well as the global warming issues, people have a renewed interest in biomass as an alternative for fossil fuel. Regarding the economic feasibility and application area, making bio-syngas from biomass is the most competitive technology. The bio-syngas mainly composed of H_2, CO, CH_4 and CO_2 can be used as a gas fuel, ingredient for chemical synthesis or bio-diesel. Due to the recent sky-rocketing oil price, synthesis of liquid fuel with bio-syngas becomes very promising technology of biomass to energy. With the help of gas to liquid (GTL) technologies, better known as Fisher-Tropsh (F-T) process we can synthesis alcohol, dimethylether (DME), and bio-diesel. Liquid fuel, obtained from F-T process, offers important emission benefits compared with conventional diesel, reducing nitrogen oxide, carbon monoxide, and particulate matter. In general, F-T process synthesis reacts one mole of CO with two moles of H_2 to form hydrocarbons over catalysts (Boerrigeter and Den Uil, 2002). Hence, proper composition of syngas is essential to optimize the F-T synthesis and highly purified syngas is necessary for avoiding any contamination of catalyst. Some recent studies indicated that possibility for production of F-T liquid via biomass gasification (Tijmensen et al., 2002) and F-T technology application for biomass conversion to synthetic hydrocarbons (Srinivas et al., 2007). Tristantini et al. (2007) studied the effect of syngas composition on F-T synthesis over catalysts. The proper condition of gasification is important in attempts to provide a desirable gas for the effective synthesis of liquid fuel from F-T technology. In this paper, we investigated the optimum condition of biomass gasification using steam which increases hydrogen content in the syngas to meet the necessary condition for F-T bio-diesel synthesis.

EXPERIMENTAL

Korean pine wood chips were used as fuel for the gasification. The properties of wood chip used in this work is given in Table 1. The experiment was carried out at atmospheric, on a lab scale bubbling fluidized bed (0.1m I.D.×3.0m height) gasifier. A schematic diagram of the experimental set-up is shown in Fig. 1. The gasifier was placed inside an electric furnace, which provided necessary heat to maintain the gasifier temperature for each case. Steam was used as fluidizing/gasifying agent and introduced into the reactor through the distributor and the flow rate of the steam was measured by a voltex flowmeter. Gas composition was evaluated by changing various operating parameters such as gasifier temperature, and steam to fuel ratio. The gasification conditions of this work were as follows: reaction temperature 700 ~ 900℃, steam flow rate 2.7 ~ 8.0kg/hr (steam to biomass ratio 0.5 ~ 1.6), fuel size ≤ 10 mm. The gas produced from gasification was cooled through a quenching system to remove condensable compounds. The composition of major syngas was monitored by gas analyzer(ABB CO. Ltd., Germany, Model: AO2020).

Table 1 Properties of wood chip used in the experiments

Proximate analysis(wt.%, wet basis)		Ultimate analysis (Dry basis)	
Moisture	6.4	C (wt %)	50.8
Volatile matter	75.9	H (wt %)	5.37
Fixed carbon	17.4	O (wt %)	43.6
Ash	0.3	N (wt %)	0
LHV(J/g)	19700	S (mg/kg)	61.8

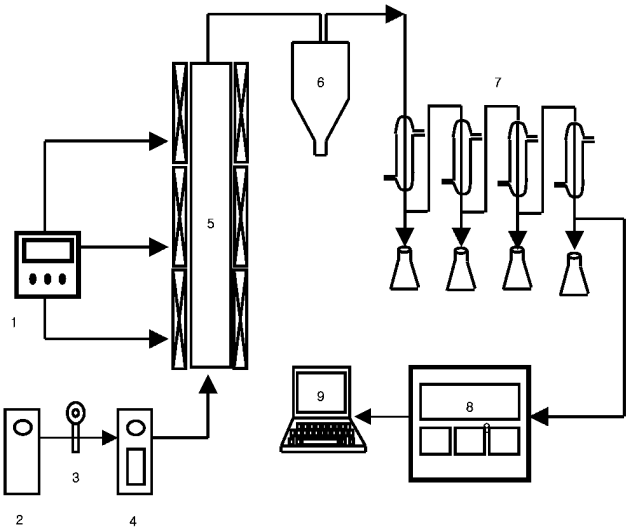

Fig. 1 Schematic diagram of the experimental set-up for the gasification

1—Temperature Controller; 2—Steam Generator; 3—Voltex Flowmeter; 4—Superheated Heater; 5—Gasifier; 6—Cyclone; 7—Tar & Water Trap; 8—Gas Analyzer; 9—DAQ system

RESULTS AND DISCUSSION

Effect of temperature

Figure 2 illustrates effect of temperature, ranging from 700 to 860℃ on the syngas composition while keeping the amount of steam and biomass (S/B: 0.5). As shown in Fig. 2, H_2 increases with increasing the temperature while CO decreases on the contrary. As temperature increases, CH_4 slightly decreases and there is no significant changes in CO_2 content which was around 15%. This result can be explained by the influence of water-gas shift reaction above 700℃, as suggested by Walawender et al.(1985), Brink and Massoudi(1978), and Franco et al.(2003) also reported that the presence of steam favoured that reaction leading to an increase in H_2 and a decrease in CO content with the rise of temperature. H_2/CO ratio of the syngas varies from 0.87 to 1.15 as the temperature changes from 770 and 860℃.

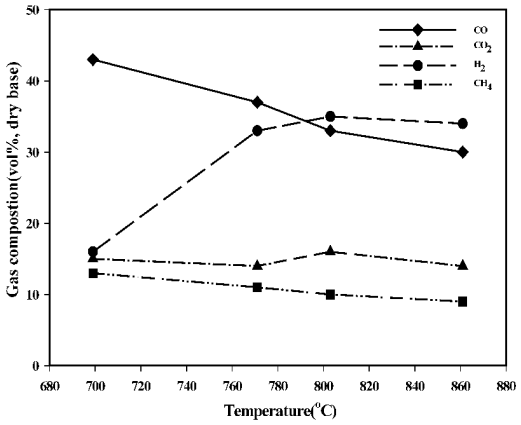

Fig. 2 Effect of temperature on syngas composition (steam/biomass ratio = 0.5)

Effect of steam/fuel ratio

The effects of steam/fuel ratio on the gasification process were investigated. The steam/biomass ratio (0.5~1.6) was varied by changing the steam flow rate while keeping biomass feeding rate (5 kg/hr) as constant. Gasifier temperature was maintained at 770℃ for all cases. Fig. 3 shows the effect of steam/fuel ratio on syngas composition. As shown in Fig. 3, when S/B is less then 0.75 H_2/CO increases as the amount of steam increases, but H_2/CO decreases as the amount of steam increases when S/B is more than 0.75. In this study, gas composition with steam/biomass ratio on the gasification showed that H_2 formation was maximum 38%, for a ratio of about 0.75, while CO revealed minimum value (28%).

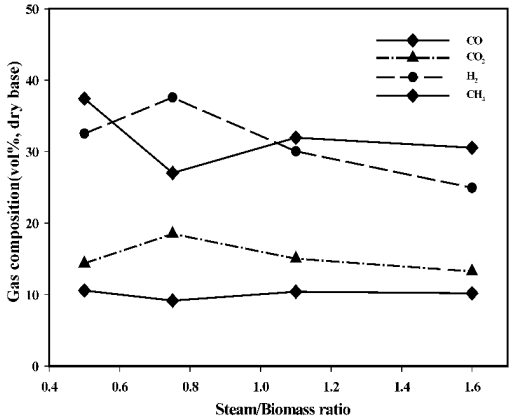

Fig. 3 Variation of gas composition with steam/fuel ratio ($T_{reactor}$ = 770℃)

CONCLUSIONS

Parametric study of biomass gasification was conducted by varying the reactor temperature and steam to biomass ratio for application of the syngas to the F-T process. The result shows that the reactor temperature is very important factor on gas composition and H_2 content increases with increasing reactor temperature while CO content decreases gradually in the range of 700℃ to 860℃. The effect of steam to biomass ratio was also found for a fixed reactor temperature; the highest hydrogen content was achieved at steam to biomass ratio 0.75. Further investigations will be carried out to assess other process option including optimized gas cleaning process to provide appropriate syngas composition for F-T synthesis.

ACKNOWLEDGEMENTS

This research was supported by MKE via "Development of bio-syngas production process using biomass gasification project"

REFERENCES

Boerrigter, H. and Den Uil, H. Pyrolysis and Gasification of Biomass and Waste, Expert meeting, Strasbourg, 30 September-1 October, (2002)

Brink DL and Massoudi MS, J FIRE Flammab 9 (1978), pp.176-188

C. Franco, F. Pinto, I. Gulyurtlu, I. Cabrita, Fuel 82 (2003), pp.835-842

S. Srinivas, R.K. Malik, Sanjay and M. Mahajani, Energy for Sustainable Development 11 (2007), pp.66-71

Tijmensen A, Hamelinck C and Hardeveld M., Biomass and Bioenergy 23 (2002), pp.129-152

Tristantini D., Logdberg S., Gevert B., Borg O. and Holmen A. Fuel processing technology 88 (2007), pp.643-649

Walawender WP, Hoveland DA, Fan LT., Elsevier (1985), pp.813-817

CHEMICAL LOOPING GASIFICATION OF BIOMASS FOR HYDROGEN ENRICHED GAS PRODUCTION WITH IN-PROCESS CARBON-DIOXIDE CAPTURE

Animesh Dutta[1], Bishnu Acharya[2], Prabir Basu[2]

1 Engineering Department, Nova Scotia Agricultural College, PO Box 550, Truro, NS, Canada
2 Mechanical Engineering Department, Dalhousie University, Halifax, NS, Canada

Abstract: The research presents an innovative idea of developing a continuous H_2 production process employing fluidized bed technology from agricultural biomass with in-situ CO_2 capture and catalyst regeneration. Novelty of the process lies in the generation of relatively pure H_2 from biomass with CO_2 as a by-product using steam as the gasifying agent. Another unique feature of the process is internal regeneration of the catalyst, fouled in the gasifier. Thus, the technology will serve the twin purpose of regenerating the catalyst, and generation of N_2 free H_2 and CO_2. The work also reports the experimental results conducted in a batch type fluidized bed steam gasifier using CaO as the catalyst. A 71% concentration of H_2 and nearly 0 concentration of CO_2 were achieved in the product gas when sawdust was used as the feedstock. In a separate test using a circulating fluidized bed reactor as the regenerator, a 40 % regeneration of CaO was also achieved at a calcination temperature of 800℃.

Keywords: chemical looping gasification, hydrogen, biomass, regeneration, catalyst

INTRODUCTION

"Decarbonizing" energy supply is a technological solution to address global CO_2 emissions and in this context the idea of "hydrogen energy economy" has significant merit. The major challenge in moving towards a H_2 economy is to produce sufficient H_2 economically, sustainably, and environment-friendly to meet future demand. Currently, 96% of the total H_2 production is sourced from fossil fuels. Thus, clean and renewable resources and sustainable pathways are necessary if H_2 is to become a fundamental energy resource for the future. In this context biomass represents an immense and renewable source (carbon neutral) for the production of H_2.

A variety of reaction processes are suggested by the researchers for the conversion of biomass to H_2. The merits of these pathways have been cited in literature [Nath and Das, 2003; Ni et al., 2006]; however, the most suitable conversion pathway is reported to be thermochemical conversion via gasification [McKendry, 2006]. The value and interest for further uses of this raw gas can still be improved if the H_2 content is increased and the CO_2 is eliminated. This can be achieved by eliminating the CO_2 in situ in the same bed of the gasifier. Past studies demonstrate the suitability of fluidized bed reactors (FBR) for biomass gasification (Franco et al., 2003; Abanades et al., 2004), and the superior solid–gas contacting, which occurs in a fluidized bed (Corella et al., 2006; Corella et al., 2008; Acharya, 2008), is expected to enhance CO_2 capture if suitable sorbent is used.

However, the very few studies that are available on the production of H_2 from biomass with CO_2 separation possess a number of limitations. Ni et al. (2006) investigated the production of H_2 with post capture of CO_2 in a conventional gasifier. This type of system requires additional investment on water gas shift reactor and in separation/cleaning. Mahishi and Goswami (2007) carried out their experiment in batch type fluidized bed steam gasifier and so as Hanaoka et al. (2005) in an Autoclave. The major disadvantage of their processes is that a continuous H_2 production cannot be achieved and after every batch experiment, the absorbent bed used in the process had to be replaced by a fresh one, therefore, no provision for regeneration of absorbent within the process. Guan et al. (2007) and Pfeifer et al. (2007) proposed improved processes based on a duel FBR. However, in the process, air was supplied during the combustion results in a production of flue gas, which contains mainly N_2 and CO_2. Therefore, an expensive post combustion separation system is required if one wishes to capture CO_2. Supplying O_2 alone is energy intensive and expensive as it has to be separated from air. Therefore, there is a dire need of developing a continuous process that can produce H_2 enriched gas from biomass with in-process CO_2 capture and catalyst regeneration.

PROCESS DETAILS

In this research, an innovative concept of continuous H_2 enriched gas production from biomass using fluidized bed technology with in-process CO_2 capture is proposed. A custom designed circulating fluidized bed (CFB) reactor would be the centre piece of this research. The coupled gasification/CO_2 capture proposed in this

research is illustrated in following schematic diagram (Fig. 1). It would be in a loop with end-to-end configuration composed of a bubbling fluidized bed (BFB) as a gasifier (1), a CFB as a regenerator (2), and a cyclone (3). The regenerator would be connected to the gasifier through the cyclone. The riser section of the proposed CFB would act as a regenerator where the catalyst, $CaCO_3$, would be converted into CaO and CO_2 by the application of external heat typically at about 900℃. The product CaO and CO_2 would be separated in the cyclone and CaO would be fed to the loop seal (gasifier) through the standpipe and CO_2 would be collected and supplied to the riser (regenerator) after filtration for continuous fluidization. The loop seal would act as a BFB gasification system where biomass and steam would be supplied and CaO would be fed from the cyclone. The loop seal is expected to be operated at 650℃ where gasification with in process CO_2 capture is expected. After completion of the reaction, mostly H_2 enriched gas would be produced and collected from the BFB gasifier (loop seal) and the CaO once converted to $CaCO_3$ by absorbing CO_2 produced during gasification process would be fed back to the regenerator to continue the cycle.

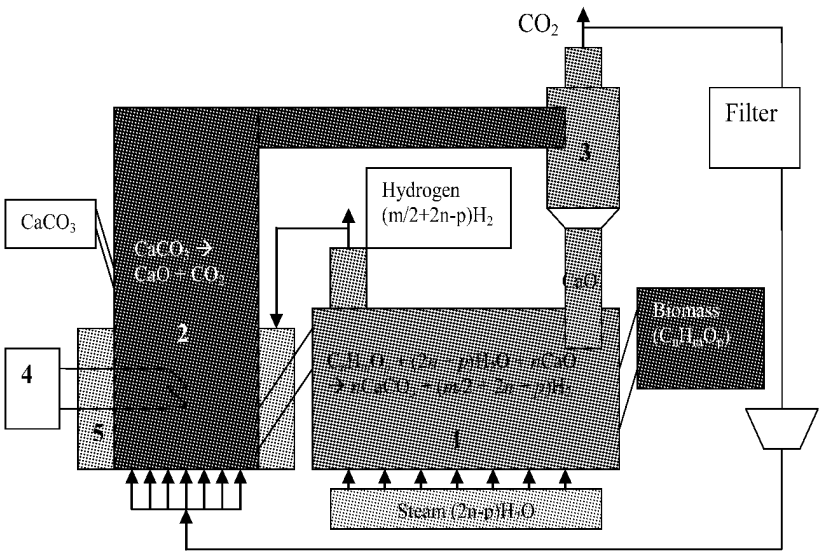

Fig. 1 Schematic diagram of the proposed process

The regenerator would be heated either by an external heat source (4) or using a part of H_2 produced (5). External heating of the fluidized bed could be accomplished by the insertion of heat transfer tubes into the bed. Direct burning of fuel inside the regenerator would be a more efficient way of supplying the heat, but would require downstream separation of CO_2 unless H_2 is burned with pure O_2. To avoid separation processes downstream, captured CO_2 (as shown in the figure) and/or H_2O can be used as the fluidizing gas in the regenerator, thus, eliminates the need for an expensive oxygen plant.

Biomass fuel would be continuously fed to the gasifier (1) and sorbent material would continually circulate from the gasifier in the form of $CaCO_3$ to the regenerator (2) and from the regenerator in the form of CaO back to the gasifier. The delivery of the hot CaO to the gasifier/carbonator would provide additional heat for the gasifier/carbonator vessel. In addition, heat release by the exothermic carbonization reactions would supply most of the heat required by the endothermic gasification reactions.

Furthermore, controlling the rate of solids circulation allows for the regulation of heat delivered to the gasifier. A make-up stream of fresh sorbent ($CaCO_3$) would be supplied to maintain capture capacity.

The reactions associated with this process could be summarized as follows:

Gasifier (1) $C_nH_mO_p + (2n - p)H_2O + nCaO \rightarrow nCaCO_3 + (m/2 + 2n - p)H_2$ (a)

Regenerator (2) $CaCO_3 \rightarrow CaO + CO_2$ (b)

ENERGY BALANCE

The energy balance of the above process was performed based on the lowing assumptions:

a) In gasifier the following reaction takes place;

$$C_nH_mO_p + (n - p)H_2O \rightarrow nCO + (m/2 + n - p)H_2 + 112\ kJ \quad (1)$$

$$CO + H_2O \rightarrow CO_2 + H_2 - 41.2\ kJ \quad (2)$$

$$CaO + CO_2 \rightarrow CaCO_3 - 178.3\ kJ \quad (3)$$

Thus the overall reaction in gasifier can be written in form:

$$C_nH_mO_p + (2n - p)H_2O + nCaO \rightarrow nCaCO_3 + (m/2 + 2n - p)H_2 - 107.5\ kJ \quad (4)$$

b) In regenerator, following reaction takes place:

$$CaCO_3 \rightarrow CaO + CO_2 + 178.3\ kJ \quad (5)$$

Based on the equation 4 and 5, the flow rate of reactants and products from gasifier and regenerator are calculated for 1 kg/s of biomass supply. The Gasifier and regenerator are assumed to be maintained at 800°C and 950℃; respectively. Calculation shows that an amount of 0.18 kg/s H_2 could be produced and 0.074kg/s of H_2 would be required to maintain the regenerator temperature at 950℃. No external heating would require for gasifier to maintain the defined temperature. The product gas leaving the gasifier and carbon dioxide leaving the regenerator are at high temperature and the energy with these two hot streams would be used to produce steam supplied to the gasifier. Under all the assumption mentioned, a net amount of 0.1063 kg/s of H_2 could be produced from 1 kg/s of biomass.

EXPERIMENTAL SETUP

The proposed concept is tested at batch mode. Two experimental units were built for studying Eq. (a) and Eq. (b). Figure 2 shows the schematic diagram of the experimental system to study the hydrogen enriched gas production from biomass gasification with in process carbon dioxide capture. The reactor was a bubbling fluidized bed. Steam was used as the fluidizing medium. The reactor was 10 cm×10cm in cross-section and 15 cm in height. The proximate and ultimate analysis of sawdust used for the test is shown in Table 1. Sawdust and CaO were mixed in known proportion and was fed into the reactor by a screw feeder. Biomass was supplied at rate of 0.5 kg/hr. Sand (0.15-0.3mm) was used as an inert bed material.

Table 1 Proximate and ultimate analysis of sawdust

	Proximate analysis				Ultimate analysis				
	FC	VM	Ash	Moisture	Carbon	Hydrogen	Oxygen	Ash	N_2
Sawdust	16.69	75.45	0.75	7.09	49.2	6.0	43	0.8	1

The bed temperature was measured by a thermocouple and data were recorded in a data logger. For gas sampling, the on-line gas analyzer, Fisher-Rosemount NGA 2000 MLT, was fitted to measure the gas composition, and show the percentages by volume of CO, CO_2, H_2, and CH_4. The gas analyzer was calibrated by using standard gases, in which the concentration of each species is known. Nitrogen gas, 99.99% pure, was used to set zero condition. Before moving to the gas analyzer, the producer gas was made to pass a condenser coil to remove the water vapor and tar. After this, it was cleaned again with fiber filter.

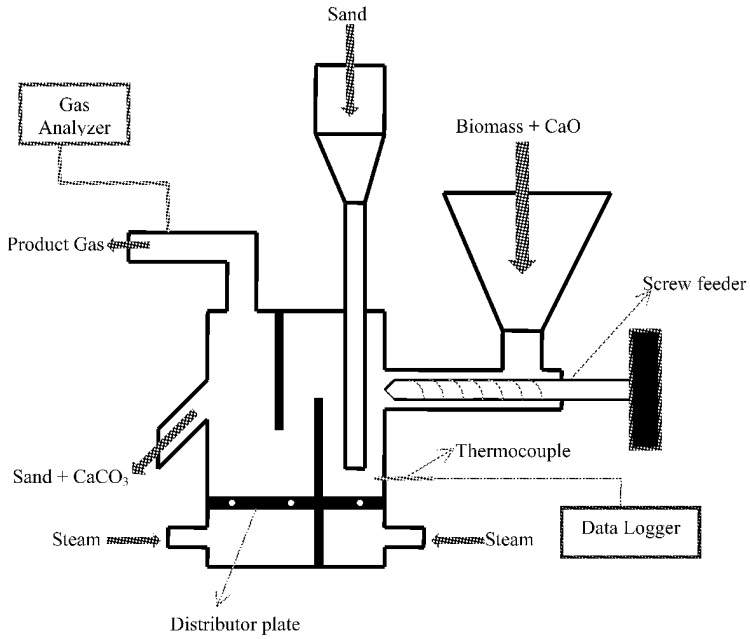

Fig. 2 Experimental Setup of fluidized bed steam gasifier

In order to start, the reactor was heated externally until the bed temperature reaches the desired temperature. Once it reaches the desired temperature, the external heating was cut off and mixture of biomass

and CaO was supplied to start the reaction (a) which was a combination of gasification and carbonization reactions.

The schematic of the experimental set up to study the regeneration of CaO from Calcium Carbonate is shown in Fig 3. This is a CFB reactor was expected to act as the regenerator of the process proposed in the process details section. The reactor was a cylindrical pipe of 7.5cm diameter. The calcium carbonate ($CaCO_3$) was fed into the reactor from top. In this case, air was supplied as the fluidizing medium. In the proposed process either CO_2 or H_2O would be supplied. As the reaction is highly endothermic, a significant amount of energy was required for maintaining a temperature of 850℃ and higher. However, in this case we could achieve on 800℃ by supplying external heat using charcoal. Temperature inside the reactor was measured by using a thermocouple and data was recorded in a data logger. The concentration of Carbon dioxide at outlet is measured by the same Gas Analyzer.

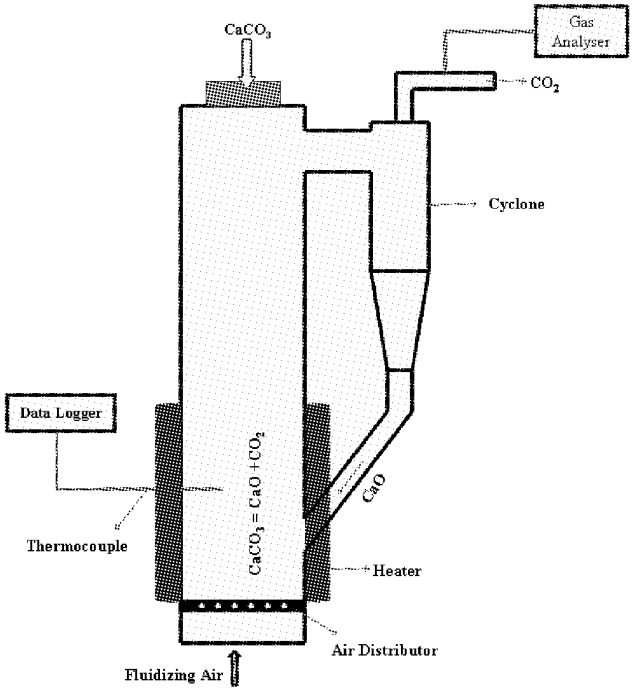

Fig. 3 Experimental setup to study the regeneration of CaO

RESULTS AND DISCUSSION

The experiments was conducted at steam/biomass [S/B] = 1.5 and [Ca/C] =1. Figure 4 shows the composition of the product gas with the time at a temperature of 580℃. The hydrogen concentration up to a maximum of 71% was obtained. The carbon dioxide was nearly zero at that condition. The methane concentration remains more or less constant while carbon monoxide reduces with time.

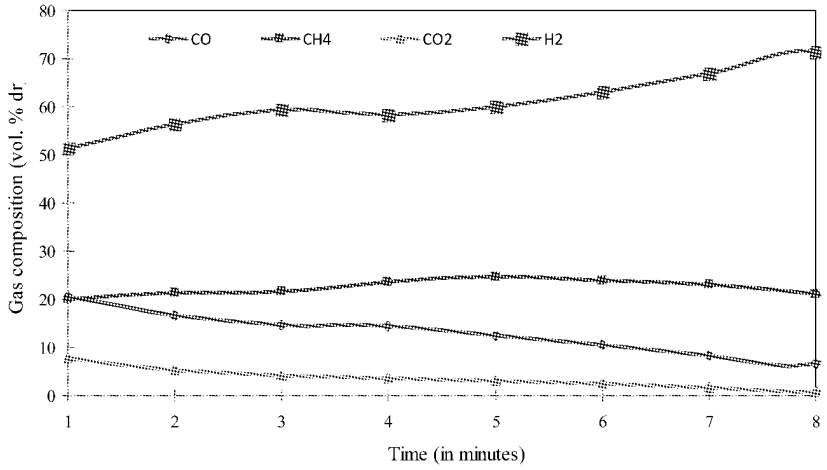

Fig. 4 Composition of product gas

Fig 5 shows the effect of temperature on the concentration of hydrogen and carbon dioxide obtained experimentally. The hydrogen concentration was found to be 55.87 % at 500℃. It was increased to 71% at 580 ℃. Without calcium oxide, the concentrations of hydrogen at 500℃ and 550℃ were found to be 20% and 35.83%; respectively. Thus, the use of calcium oxide has found to increase the hydrogen concentration by 2.8 times more than that of without calcium oxide when tests were conducted at 500℃. The concentration of carbon dioxide was found to reduce to nearly zero at 580℃ by using CaO. At 500℃, the concentration of carbon dioxide has found to reduce by half by using CaO as the sorbent. Thus, the presence of CaO not only lowers the carbon dioxide but at the same time increases the concentration of hydrogen in product gas.

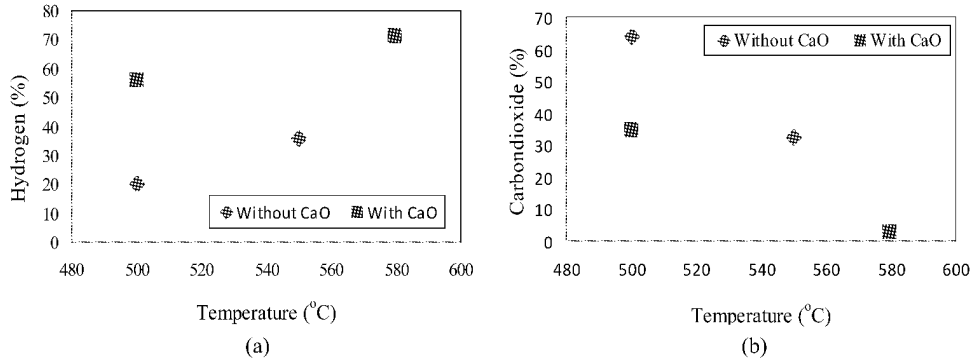

Fig. 5 Effect of temperature and use of CaO on (a) Hydrogen and (b) carbon dioxide concentration

Figure 6 shows the temperature inside the gasifier with time for the cases of gasification with and without using CaO. Gasification with CaO maintains the temperature more or less constant. This is because the carbon dioxide capture (carbonization) reaction is an exothermic one, thus generated heat supplements the heat required for gasification. Therefore, no external heating was required in that case. Where as, in case of gasification without CaO, the temperature rapidly drops, required external heating for the gasification reaction.

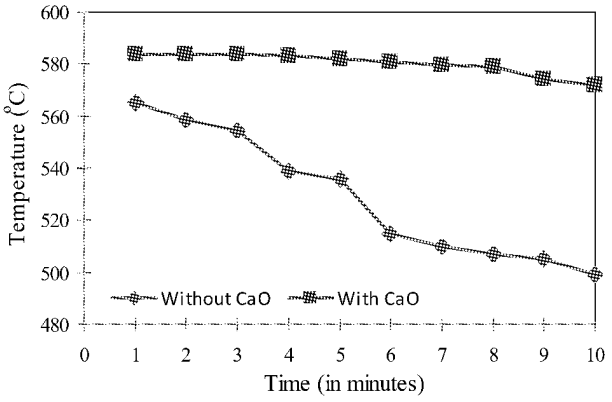

Fig. 6 Effect CaO on gasifier system temperature

The results of regeneration of CaO from $CaCO_3$ [reaction (b)] in the CFB regenerator is shown in Fig 7.

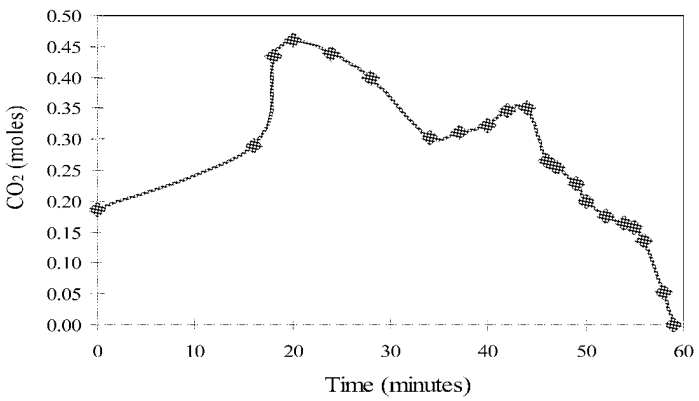

Fig. 7 Moles of CO_2 generated with time

From the result, it can be seen that about 40% of calcium carbonate was converted to CaO within the period of one hour when the reactor is heated at a temperature of 800℃. Further tests are under in process with a temperature at 850℃ and higher. It is expected that the calcination rate would be much higher at a higher temperature.

CONCLUSIONS

The research proposes an innovative idea of developing a continuous H_2 production process employing fluidized bed technology from agricultural biomass with in-situ CO_2 capture and catalyst regeneration. Novelty of the process lies in the generation of relatively pure H_2 from biomass with CO_2 as a by-product using steam as the gasifying agent. Another unique feature of the process is internal regeneration of the catalyst, fouled in the gasifier. Thus, the technology will serve the twin purpose of regenerating the catalyst, and generation of N_2 free H_2 and CO_2. Theoretical calculation shows that a net amount of 0.1063 kg/s of H_2 could be produced from 1 kg/s of biomass.

Experimental results show that the use of calcium oxide not only helps to reduce the concentration of carbon dioxide to nearly zero but also increases the hydrogen concentration and also helps to maintain the gasifier temperature constant thus avoiding the additional heat required for endothermic gasification reaction to take place. At 580℃ gasification temperature, the hydrogen concentration was found to be 71 % for [Ca/C] ratio 1 and S/B ratio of 1.5 and carbon dioxide concentration was nearly zero. Experimental results on regeneration show that a 40% regeneration of CaO is possible within one hour of time period when the temperature is maintained at 800℃. However, this reaction is expected to be much faster at a higher temperature (above 850℃). Further research on this concept is underway.

REFERENCES

Abanades, J.C., Anthony, J.E., Lu, D.Y., Salvador, C., Alvarez, D. Env and Energy Eng 2004; 50: 1614–1622.
Acharaya, B. Masters Thesis 2008; AIT.
Corella, J., Toledo, J.M., Molina, G. J. Ind Eng Chem Res 2008.
Corella, J., Toledo, J.M., Molina, G., (2006). Ind Eng Chem Res 45, 6137–6146.
Franco, C., Pinto, F., Gulyurtlu, I., Cabrita, I. Fuel 2003; 82: 835–842.
Guan. J, Wang. Q, Li. X, Luo. Z, & Cen. K (2007). Renewable Energy 32, 2502-2515.
Hanaoka, T., Yoshida, T., Fujimoto, S., Kamei, K., Harada, M., Suzuki, Y., Hatano, H., Yokoyama, S.-Y., Minowa, T., (2005). Biomass and Bioenergy 28, 63–68.
Mahishia M. R. & Goswami, D.Y. (2007). Int J Hydrogen Energy 32, 2803-2808.
McKendry, P. Biosource Technology 2002; 83: 37–46.
Nath, D., Das, D. Current Science 2003; 85 : 265–271.
Ni, M., Leung, Y.C., Leung, M.K.H., Sumathy, K. Fuel Proce Techno 2006; 87,:461–472.
Ni. M., Leung D.Y.C., Leung M.K.H., & Sumathy K, (2006). Fuel Processing Technology 87, 461 – 472.
Pfeifer, C., Puchner, B., Hofbauer, H., (2007). Int J of Chem Reactor Eng 5, A9.

THE THERMAL CRACKING EXPERIMENT RESEARCH OF TAR FROM RICE HULL GASIFICATION FOR POWER GENERATION

Z. S. Wu[1], T. Mi[2], Q. X. Wu[1], Y. F. Chen[1], X. H. Li[1]

1 The chemistry college in Huazhong Normal University, Wuhan, 430079, China
2 Jianghan University, Wuhan, 430079, China

Abstract: the tar from rice hull gasification for power generation which is cracked in high temperature is studied in this paper, the results reveal the part of compositions which have smaller RT in tar is first cracked into H_2, CO_2 and carbon, and then carbon react with H_2 and CO_2, and CH_4, CO are formed; the cracked efficiency of tar can reach 28.66%, the carbon deposit among cracked tar can reach 12.76%, the results of the GC-MS analysis showed the aromatic extent of tar and carbon content of un-cracked tar increase. The pressure drop of cracking reactor increases with tar cracking reaction carrying out in high temperature.
Keywords: tar, thermal cracking

INTRODUCTION

Tar formed in the thermo-chemical processing of biomass was a complex mixture of organic compounds, producer gas from biomass gasifier entrained with tar, which forms a serious problem for its use in e.g. engines and turbines. Tar would impose serious limitations in the use of producer gas due to fouling of downstream process equipment, engine wear and high maintenance costs. By far, tar removal was the most problematic(Hesp et al., 1970). Thus the successful implementation of gasification technology for gas engine/turbine based power projects depended much on the effective and efficient removal/conversion of tar from the producer gas. Tar removal methods were classified as primary or secondary (Corella et al., 1999; Narva´ez et al;1999; Sutton et al; 2001;Wu et al, 2006). Primary methods included all the measures taken in the gasification step itself to prevent tar from being formed in the gasifier or to convert it. Secondary methods can be chemical or physical treatments downstream the gasifier. Both primary and secondary methods included either the thermal cracking of tar or the catalytically cracking of tar(Orı´o et al., 1987; Aznar et al., 1998; Narva´ez et al., 1998; Marquevich et al., 1999; Rapagna et al., 2000; Moersch et al., 2000)

The objective of the present paper was to investigate the composition variation of tar with the thermal cracking temperature; this result could be of importance for the finding of the racking mechanism of the tar and developing the cracking catalyst of tar, because the catalytically racking of tar was along with the thermally cracking of tar. Meanwhile, The gas composition from tar being thermally cracked was analyzed by the gas chromatograph, the thermal cracking efficiency and the deposit carbon efficiency were calculated in this paper.

EXPERIMENTALS

The thermally cracking reaction of tar was carried out in small-type evaluation experiment equipment which was consisted of vaporization, quartz tube reactor for tar cracking, condenser, temperature controller and analysis system for gas and liquid tar, the flow diagram of system was shown in Fig. 1, the carrying gas was argon at 40ml/min. Tar, which was controlled by metric pump at 2ml/min, was first gasified by vaporization, and then entered quartz tube reactor with carrying gas, the quartz tube reactor was filled with the 5g crystal ball of 2mm diameter in order to increase the residence time of gas, the gas product from exit of reactor was analyzed by gas chromatography (GC) on-line through sextuple sampling valve, the carrying gas in GC was same as argon at 35ml/min, the filling column of thermal conduction detector (TCD) was 2m×3mm，and the gas-adsorbent compound in the filling column was AE.TEX-01； the gas product entrained un-cracked tar was separated by condenser, the tar sample separated by condenser was analyzed by GC-MS (Type: Finnigan Trace Ms, USA). The column was a 50m×0.25mm, 0.25μm packed with HP-5 5% diphenyl-95% polysiloxane. Column temperature was 60℃-10℃/min-290℃(23min), Helium was used as carrier gas at 35ml/s. the chloromethane was used as a diluent for tar, the injection(1μL) was carried out in the splitless mode (1 min, injector temperature 250℃). Transfer line temperature was 280℃. Mass spectra were recorded at 70eV(1 scan s-1, source temperature 180℃).

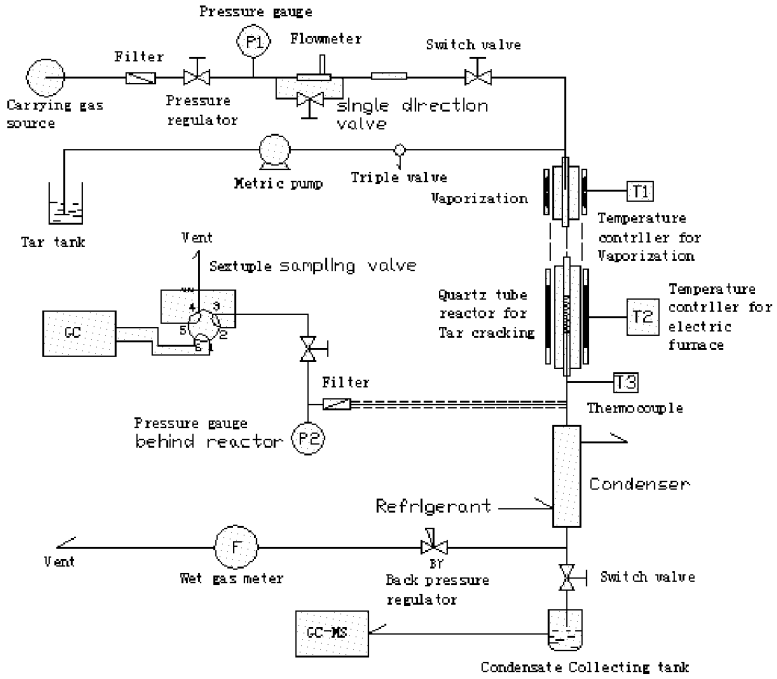

Fig. 1 Flow diagram of thermal cracking of tar

RESULTS AND DISCUSSION

The Composition Analysis of Tar Before and After Being Thermally Cracked

The tar was provided by MW-scale rice hull gasification for electric power generation, The operation parameters included that gasification temperature was (700 °C), equivalence ratio (ER) 0.26, gasification efficiency (70%), conversion efficiency of carbon (80%). The purifying system consisted of a Venturi tube and three-stage water scrubbers for gas cleaning in order to eliminate the tar content and fly ash in the fuel gas. However, the tar in the form of aerosols was very difficult to remove by scrubbing systems and gathered by horizontal cyclone separator for the thermal cracking experiment of tar.

The GC-MS analysis of tar before and after being thermally cracked was illustrated in Fig. 2 and 3; the different RT composition of tar was shown in Tables 1 and 2. Compared Fig. 2 with Fig. 3, it could be seen that the composition whose RT was 7.28, 9.02, 9.24 clearly decreased, namely, the composition of tar could change after being thermally cracked at 800℃, the composition of lower RT decreased, and higher RT increased. Table 3 revealed that the composition of tar after being thermally cracked was the hydrocarbon compounds of oxygen free, and the aromatic compound of these compounds was in the majority, this was because of the aromatic extent of tar and carbon content of un-cracked tar increasing.

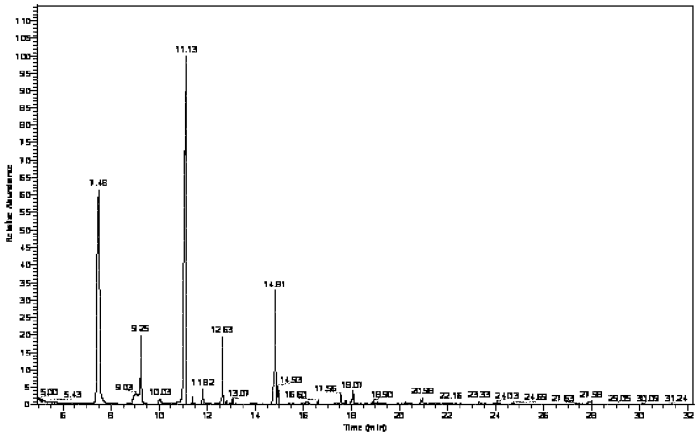

Fig. 2 GC-MS analysis of tar before being thermally cracked

Table 1 Tar composition and content before being thermally cracked

RT	Composition	Content (%)
7.48	$C_{12}H_{15}O$	30.39
9.02	$C_{11}H_{10}$	2.11
9.24	$C_{11}H_{10}$	5.39
11.10	$C_{17}H_{30}O$	48.43
12.62	$C_{13}H_{10}$	2.81
14.82	$C_{14}H_{10}$	8.39

Table 2 Tar composition and content after being thermally cracked at 800℃

RT	Composition	Content (%)
12.54	$C_{13}H_{10}$	2.11
13.50	$C_{12}H_8$	65.33
15.11	$C_{13}H_{10}$	7.38
17.29	$C_{14}H_{10}$	20.23

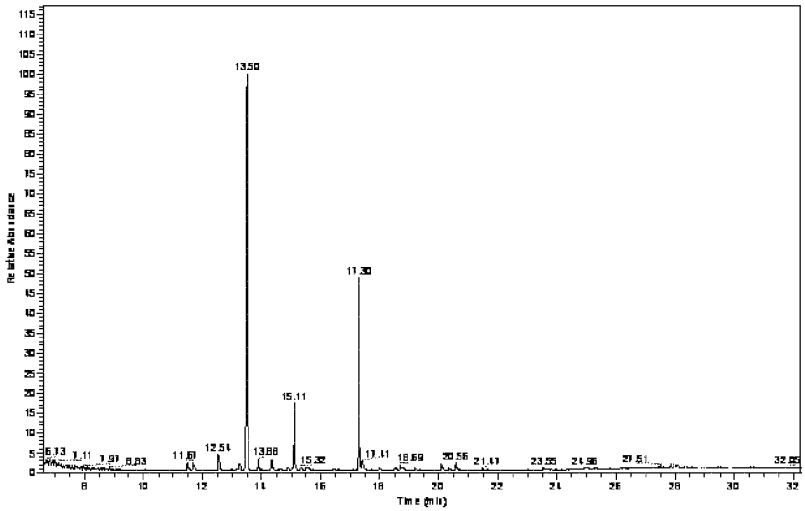

Fig. 3 GC-MS analysis of tar after being thermally cracked

The Determination of the Cracking Efficiency and the Deposit Carbon of Tar

During the thermally cracking experiment of tar, the quantitative tar entered the tar cracking reactor, the gas produced from the tar cracking reactor was cooled, and the un-cracked reaction tar was condensed and collected by condenser, the cracking efficiency of tar could be calculated according to the tar reacted, The cracking efficiency of tar could be calculated according to the following formulation, the thermally cracking efficiency of tar was determined by the experiment results to be 28.66%.

$$\text{the cracking efficiency of tar} = \frac{\text{the weight of tar reacted by thermal cracking in reactor}}{\text{the total weight of tar of entrance reactor}}$$

The deposit carbon efficiency could be calculated according to the following formulation,

$$\text{the deposit carbon efficiency of tar} = \frac{\text{the weight of the deposit carbon}}{\text{the weight of tar reacted by thermal cracking in reactor}}$$

The deposit carbon efficiency was determined by the experiment results to be 12.76%.

The element analysis of tar before and after being thermally cracked was shown in Table 3, it could be seen from Table 3 that the carbon content of tar after being thermally cracked increased, and hydrogen content decreased, this was because of the aromatic extent of un-cracked tar increasing.

Table 3 the elements analysis of tar before and after cracked

Sample	Element content (%)	
	C	H
Tar before being cracked	85.65	5.89
Tar after being cracked	86.78	5.81

The Gas Composition Analysis from Tar Being Cracked

The gas composition from tar being thermally cracked was analyzed the gas chromatograph (GC) using unitary method in Fig. 4, it could be seen that the earliest gas composition mainly consisted of H_2, 96.59%, CO_2, 2.37%, the CH_4, CO were produced by H_2, CO_2 reacting with the deposit carbon, the typical gas composition was analyzed by GC in Fig. 5, which consisted of H_2, 73.94%, CH_4, 4.94%, CO, 18.6%, this was because of the following reaction being taken place.

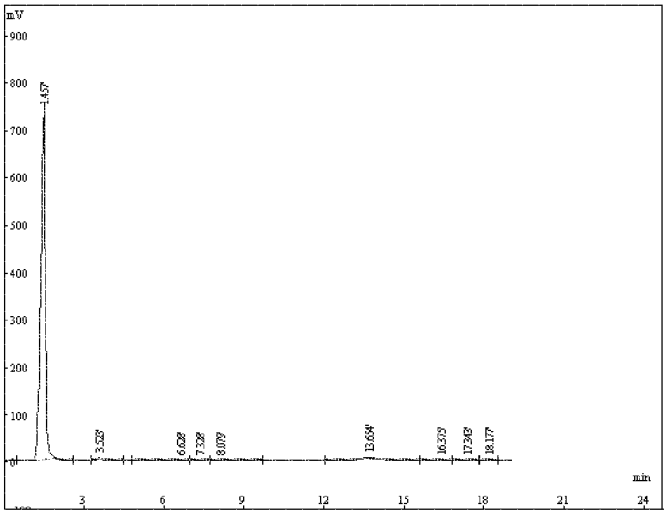

Fig. 4 The gas composition analysis for tar primary cracked

starting at: $TAR \xrightarrow{\text{thermally cracked}} C + H_2 + CO_2$

then:

$C + 2H_2 \rightarrow CH_4$

$C + CO_2 \rightarrow 2CO$

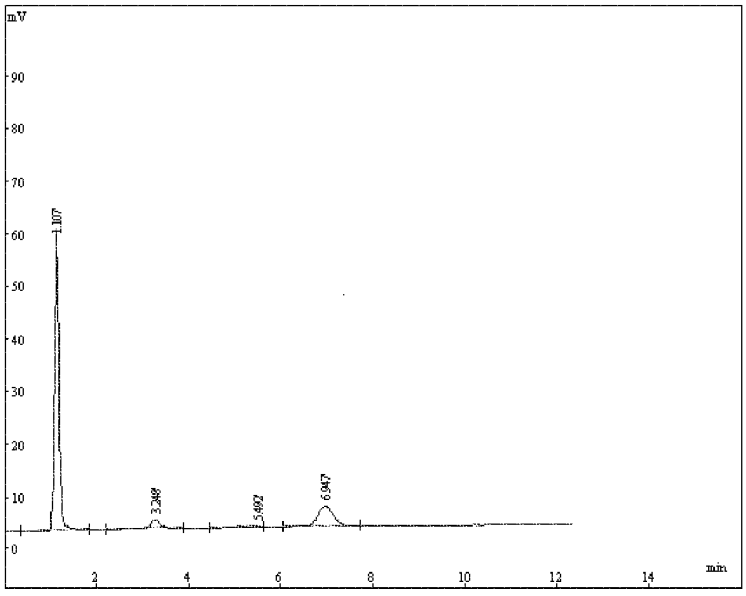

Fig. 5 The gas composition analysis for tar cracked

The XRD and DSC Analysis for the Deposit Carbon

The deposit carbon from tar being thermally cracked was determined by weighting the crystal ball before and after being adsorbed carbon after thermally cracking experiment of tar finishing, and separated by sieving. The XRD of the deposit carbon was shown in Fig. 6, it could be seen from Fig. 6 that the X diffraction peak was found at 25.5℃, and were identical with the standard library of 75-444 carbon. The DTA and TG diagram of the deposit carbon in air condition was seen in Fig. 7, the loss weight peak of the deposit carbon oxidation at

549℃ was found in Fig. 7.The SEM photograph of the deposit carbon in Figure 8 revealed that the deposit carbon was shape of slice.

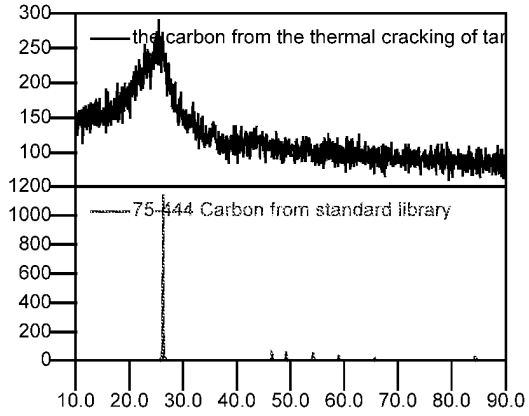

Fig. 6 The XRD diagram of carbon from tar cracked

(The top X diffraction peaks was the deposit carbon and the bottom X diffraction peaks was the standard library of 75-444 carbon)

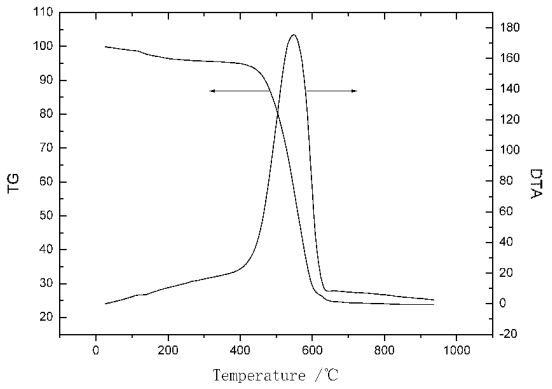

Fig. 7 The DTA and TG diagram of carbon from tar cracked

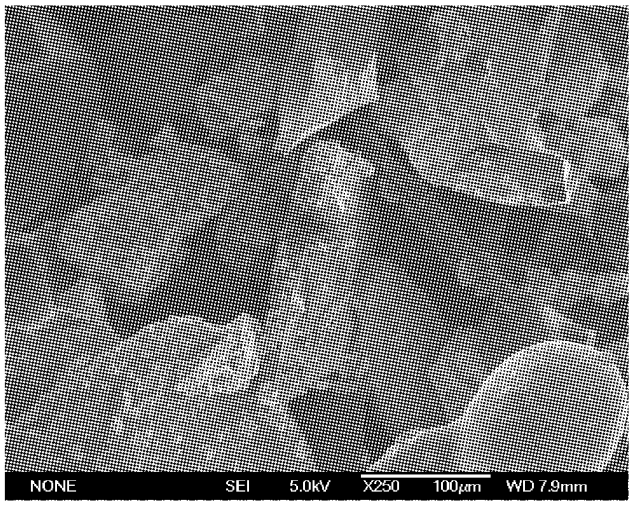

Fig. 8 SEM images of a deposited carbon from the thermal cracking of tar at 800℃

The Pressure Variation of Experimental System

The pressure variation of experimental system was shown in Fig. 9 during experiment, it could be seen that the pressure of experimental system increased with the experiment carrying out for tar being cracked, this is because of the hole of the crystal ball bed being blocked up by the deposit carbon from tar being cracked.

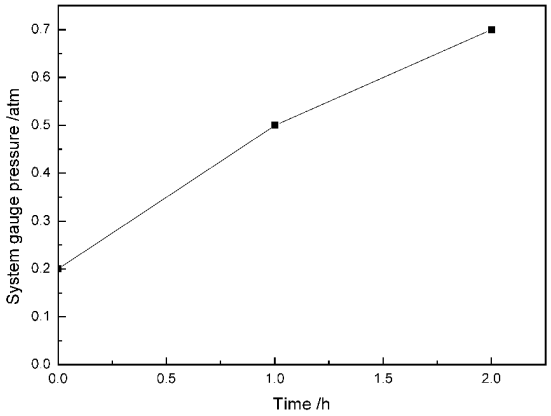

Fig. 9 The variation of experimental system gauge pressure

CONCLUSIONS

The thermally cracking of Tar from the tar from rice hull gasification for power generation was studied in small-type evaluation experiment equipment at 800℃. The following conclusions could be drawn according to above experimental results.

(1) The gas composition of H_2, CO_2 and carbon was produced by the thermal cracking of the lower RT composition of tar, and carbon could react with H_2 and CO_2 to produce CH_4 and CO with tar being thermally cracking.

(2) The cracking efficiency of tar from rice hull gasification for power generation could reach 28.66% at 800℃, and the deposit carbon was 12.76% for tar being thermally cracked.

(3) The GC-MS analysis illustrated the aromatic extent of tar and carbon content of un-cracked tar increase.

(4) The pressure drop of gas passing through catalyst bed increased because of the hole of filling bed being blocked up by the deposit carbon, it was different for us to operate the cracking reactor of tar.

ACKNOWLEDGEMENTS

The authors acknowledge the financial support of the Natural 973 project of China (Project: 2007CB210202-03) and the key project of Wuhan city(20066002064). The authors are grateful the referees for their comments and recommendations.

REFERENCES

Aznar, M. P.; Caballero, M. A.; Gil, J.; Martı´n, J. A.; Corella, J.Ind. Eng. Chem. Res. 37(1998), 2668-2680.
Corella, J.; Aznar, M. P.; Gil, J.; Caballero, M. A. Energy Fuels. 13 (1999), 122-1127.
Hesp. W. R, Waters, R L. Ind. Eng. Chem. Prod Res. Dev. 9(1970)(2): 194-202.
Marquevich, M.; Czernik, S.; Chornet, E.; Montane´, D. Energy Fuels. **13**（1999）, 1160-1166.
Moersch, O.; Spliethoff, H.; Hein, K. R. G. Biomass Bioenergy. **18**（2000）, 79-86.
Narva´ez, I.; Orı´o, A.; Aznar, M. P.; Corella, J. Ind. Eng. Chem. Res. 35(1996), 2110-2120.
Narva´ez, I.; Corella, J.; Orı´o, A. Ind. Eng. Chem. Res. 36(1999), 3317-327.
Orı´o, A.; Corella, J.; Narva´ez, I. In Developments in Thermo- chemical Biomass Conversion; Bridgwater, A. Rapagna`, S.; Jand, N.; Kiennemann, A.; Foscolo, P. U. Biomass Bioenergy, 19（2000）, 187-197.
Sutton, D.; Kelleher, B.; Ross, J. R. H. Fuel Process. Techno. 73(2001), 155-173.
Boocock V.,, D. G. B., Eds.; Blackie Academic & Professional: London, U.K., (1987); pp 1144-1157.
Wu, Z. S., Li, W., Wu, C. Z., Chem. Eng (China). 34(2006), No.10: p67-70.

CATALYTIC PYROLYSIS OF COTTON STRAW BY ZEOLITES AND METAL OXIDES

X.X.Cao, B.X.Shen,F.Lu,Y.Yao

College of Environmental Science & Engineering, Nankai University, Tianjin, 300071, China

Abstract: The influences of zeolites and metal oxides on the pyrolysis of cotton straw have been studied by thermogravimetric analysis (*TGA*). And performance of different catalysts to volatile and yield of ash was compared. The results showed that the catalytic pyrolysis experienced three stages: water losing stage, activated pyrolysis stage(APS), passive pyrolysis stage(PPS). The passive pyrolysis stage for pure cotton straw was small. The addition of the catalysts decreased the percent of volatile conversion for activated pyrolysis stage, but with the decreasing temperature for passive pyrolysis stage and increasing the percent of volatile conversion for passive pyrolysis stage. These catalysts promoted the pyrolysis of lignin, but showed less performance to the pyrolysis of cellulose and hemicellulose. The yield of ash increased in the presence of catalysts,and the yield was higher when catalyzed by metal oxide than by zeolite.

Keywords: cotton straw, catalytic pyrolysis, TGA, catalysts

INTRODUCTION

In the past 20 years biomass has become more attractive to industry since it is a low CO_2, alternative energy source. Due to its easy availability biomass is still the most traditional fuel used in the rural sector all over the world, where it is utilized in a highly inefficient manner with a low overall efficiency, contributing significantly to environmental pollution and health hazards. Pyrolysis is considered as a promising alternative method that converts biomass to clean energy and valuable chemicals. Catalytic pyrolysis involves degradation of biomass by the application of catalyst in absence of air where a relatively low temperature (400～600℃) is employed in order to obtain biomass oil (Zhang.Q,2006), which can be utilized more efficiently in an environmentally accepted manner. Comparing with the traditional pyrolysis way, the catalytic pyrolysis may get more aim industrial stuff at lower temperature. In recent years many studies have been performed on the basis of thermogravimetric analysis (TGA) to understand the pyrolysis process and mechanism of catalytic or uncatalytic pyrolysis of biomass.

In this study, the influences of zeolites（ZSM-5,USY,MCM-41）and metal oxides（MgO, AL_2O_3,CuO, Na_2CO_3）on the pyrolysis of cotton straw have been studied by thermogravimetric analysis (*TGA*).

EXPERIMENTAL

Biomass

The experimental materials of cotton straw came from farmland in Tianjin , which was dried at 383K for 5 hour after being primarily broken, ground and sieved to obtain the size of less than 100mesh. The ultimate, proximate and component analysis of cotton straw is shown in Table 1.

Table 1 Ultimate, proximate and component analysis of cotton straw

Biomass	Ultimate analysis w_{daf}/%			Proximate analysis w/%			Analysis of component wt/%		
	C	H	O	V_{daf}	A_d	M_{ad}	hemicellulose	cellulose	lignin
Cotton straw	48.22	7.12	44.00	68.12	2.12	4.40	18.1	42.3	19.0

Catalysts

Al_2O_3,MgO,Na_2CO_3,CuO,ZSM-5,USY and MCM-41 were used as catalysts in this experiment .Al_2O_3、MgO、Na_2CO_3、CuO were bought from Tianjin Jiangtian chemical company. USY (offered by Qilu Petrochemical Huaxing Company Ltd.) was used as the catalyst with a pore size of 9.0 A °, and silica/alumina (Si/Al) ratio of 5 representing a high acidity. The BET surface area, concentration of Na_2O are 800 m^2/g and 1.5 wt%, respectively. For ZSM-5, the pore size and Si/Al ratio are 5.6 A ° and 38, respectively, which was offered by the Catalytic Industry of Nankai university. MCM-41 were bought from Tianjin Kaimeite company with the pore size being 3.5nm, and the water content is 7%. The concentration of Na_2O is less than 0.2%. All the catalysts were respectively dried, broken and screened with the particles less than 100 mesh.

Experimental instrument and conditions

TGA was carried out using a NETZSCH TG 209 thermal analyzer in the experiments, the mass of sample used was about 10 mg with catalyst ratio of 10%. The temperature was increased at a rate of 10K/min from room temperature (about 20℃) to 873K linearly. The flow rate of air was fixed at 20 ml/min.

RESULTS AND DISCUSSION

The data recorded by *TG* thermal analyzer are temperatures, time , "*W*"(remaining /initial sample weight) and *DTG*.

$$DTG = dW/dT$$

The pyrolysis process of cotton straw without catalyst

Fig. 1 is the *TG* and *DTG* curves of pure cotton straw. As it can see from the TG and DTG curves, the pyrolysis process consists of several continuous reaction intervals. The first tiny peak at 380~475K is due to the removal of the moisture and defined as water losing stage. The adsorbed water is lost at about 383K and bound water at 383k~473K (Moghtaderi, B,2004). The second interval at 431.4~679.9K corresponds the biggest peak on the DTG curve with the weight loss of 59.1% . The third interval is a slow process with the weight loss of 14.4%, of which corresponding peak on *DTG* is not obviously. And the weight loss of third interval doesn't end until the highest temperature of 873.2K. R.Fahmia(R.Fahmia,2007) defines the latter two intervals as activated pyrolysis stage (APS) and passive pyrolysis stage(PPS) ,respectively. And the weight loss of APS is due to the pyrolysis of cellulose and semi-cellulose, whereas the loss in PPS is attributing to lignin decomposed.

The pyrolysis process of APS begins with the pyrolysis of semi-cellulose and then reaches the peak when cellulose was decomposed(MANSARAYKG,1998).Cellulose is a kind of polysaccharide making up of β-1,4 anomer and D-glucose, it begins to decompose at the temperature range between 480~490K, by contrast, lignin decomposes between the more highly range of 623~1073K(Chen.Y,2007) because of the higher thermal stability for its composition of polysaccharide with phenylpropane units .

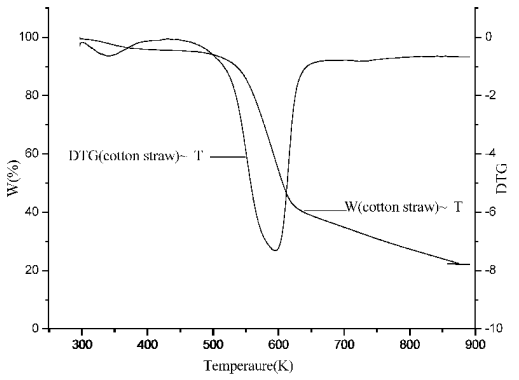

Fig. 1 uncatalytic pyrolysis of cotton straw

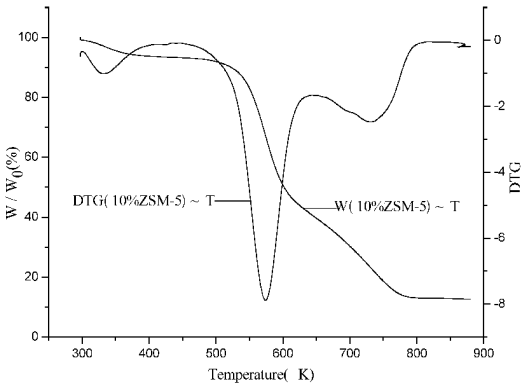

Fig. 2 catalytic pyrolysis of cotton straw by 10%ZSM-5

Pyrolysis process of cotton straw with catalyst

The influence of catalysts on pyrolysis process of cotton straw are investigated, Fig. 2 shows the *TG* and *DTG* curves on catalytic pyrolysis of cotton straw by 10%ZSM-5.The 10%ZSM-5 catalytic pyrolysis process is consisted of water losing stage, APS and PPS as well. Comparing with the pyrolysis process without catalyst, PPS is more significant when catalyzed by ZSM-5. The peak on *DTG* curve is broader in PPS without catalyst, while it turns sharp and recorded the maximum peak value at 730.6K under catalyzing by ZSM-5. So it is indicated that ZSM-5 promoted pyrolysis of lignin. Another difference is that ZSM-5 decreased the ending temperature of the process. The weight loss is over before 800K when catalyzed by ZSM-5, but for pyrolysis under no catalyst, the weight loss doesn't end until the highest temperature of 873.2K. The pyrolysis process catalyzed by MgO(Fig.3),Al_2O_3,CuO,USY, MCM-41,Na_2CO_3 are similar to ZSM-5 catalytic pyrolysis process. Secondary reaction may lead to the fourth weight loss interval when catalyzed by Na_2CO_3(Fig.4).

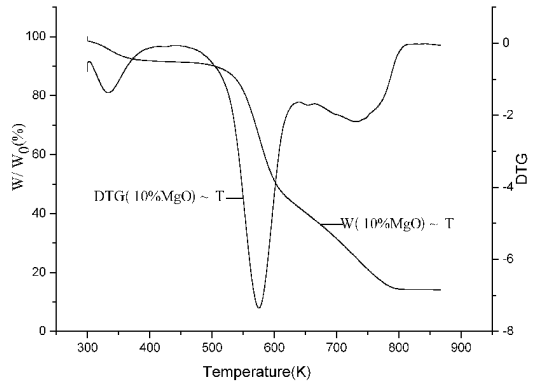

Fig. 3 catalytic pyrolysis of cotton straw

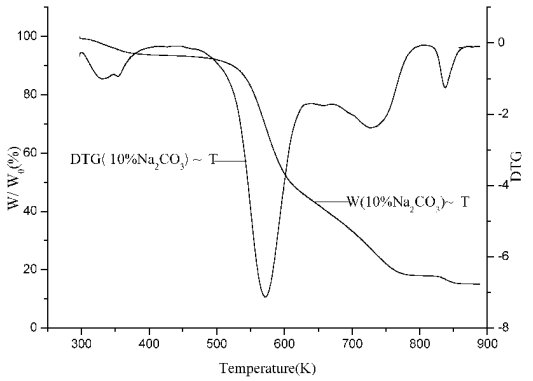

Fig. 4 catalytic pyrolysis of cotton straw by 10%MgO by 10%Na_2CO_3

The pyrolysis characteristic of cotton straw volatile

The Precipitation and pyrolysis of volatile are the main body of biomass pyrolytic reaction. In order to compare the different influences of catalysts on cotton straw volatile, the conversion rate of volatile(α) is introduced, and defined as precipitated volatile divided by total volatile. The formula of α is as followed:

$$\alpha = \frac{M_s(W^1_{onset} - W_{Ti})}{M_c(1 - A_d - W_{water})} = \frac{M_s(W^1_{onset} - W_{Ti})}{0.9334M_c}$$

Where M_S is the total mass of sample, W^1_{onset} is the residual mass ratio of the sample when temperature reaches starting point of APS, and W_{Ti} is the residual mass ratio of the sample at temperature T_i which ranges from T^1_{onset} to T^2_{end}, T^1_{onset} is temperature starting point of APS, whereas T^2_{end} is temperature ending point of PPS .M_C is the mass of cotton straw, A_d is ash ratio of proximate analysis on cotton straw with value being 2.12%, W_{water} is water losing ratio of pyrolysis on pure cotton straw ,and its value is 4.44%.

The effect of catalysts to precipitated characteristic of cotton straw volatile

Table 2 shows the precipitated characteristic parameters of cotton straw volatile. Where "$\Delta\alpha$" is the cumulative ratio of volatile conversion, superscript "*1*" represents the APS, "*2*" represents the passive pyrolysis stage. And T^1_{end} is equal to T^2_{onset}.

Table 2 Precipitated characteristic parameters of cotton straw volatile

Sample	Activated pyrolysis stage			Passive pyrolysis stage		
	T^1_{onset}/k	T^1_{end}/k	$\Delta\alpha^1$/%	T^2_{onset}/k	T^2_{end}/k	$\Delta\alpha^2$/%
cotton straw	431.4	679.9	63.20	679.9	>873.2	15.34
with 10%ZSM-5	446.0	643.5	62.44	643.5	817.4	33.07
with10%MCM-41	445.4	643.1	60.54	643.1	856.2	33.43
with 10%USY	446.1	648.0	62.52	648.0	814.2	31.90
with 10%MgO	445.8	640.2	58.87	640.2	826.7	33.05
with 10%CuO	445.2	643.5	62.16	643.5	825.7	31.70
with 10%AL_2O_3	446.7	642.2	62.71	642.2	833.1	31.20
with10%Na_2CO_3	436.1	640.2	59.05	640.2	806.1	30.91

The temperature starting point of APS under catalysts is increased than that of non-catalytic proylysis. The corresponding temperature increases from 431.4K for no catalyst to a range form 436.1K to 446.7K for catalytic pyrolysis. However, the temperature ending point of APS is significantly decreased. The corresponding temperature decreases from 679.9K to a range from 640.2K to 648.0K, and the performance of each catalyst is similar. The temperature ending point of PPS is also decreased obviously, but the catalysts show remarkable difference in the performance. The corresponding temperature decreases from more than 873.2K to a range from 806.1K to 856.2K. The sequence of catalyst performance to decreasing temperature ending point of PPS is described as: Na_2CO_3> USY > ZSM-5 >CuO > MgO >Al_2O_3 > MCM-41. So it is demonstrated that these catalysts narrowed the temperature range of APS, whereas in PPS, the temperature range is turned to the Low Temperature region.

The adding of catalysts decreases the cumulative ratio of volatile conversion in APS. The corresponding

ratio decreases from 63.20% for no catalyst to a range from 58.87% to 62.71% for catalytic pyrolysis, and there is the minimum cumulative ratio of volatile conversion in APS when catalyzed by MgO. However, The adding of catalysts increases the cumulative ratio of volatile conversion in PPS which was reverse with that of in APS. The corresponding ratio is 15.34% under no catalyst, while the ratio was increased significantly to a range from 30.91% to 33.43% after adding catalysts, and the sequence of catalyst performance is described as :MCM-41> ZSM-5> MgO > USY >CuO > AL_2O_3 >Na_2CO_3.

The catalytic effect to the volatile average pyrolytic velocity

Table3 shows average pyrolytic velocity parameters of cotton straw volatile. Where DTG_{ma}, T_{max} represent the peak value and peak temperatures on DTG curve, respectively. "$\Delta\alpha/\Delta t$" is volatile average pyrolytic velocity.

Table 3 Average pyrolytic velocity parameters of cotton straw volatile

Sample	Activated pyrolysis stage			Passive pyrolysis stage		
	DTG^1_{max}	T^1_{max}/k	$\Delta\alpha^1/\Delta t^1$ /min^{-1}	DTG^2_{max}	T^2_{max}/k	$\Delta\alpha^2/\Delta t^2$ /min^{-1}
cotton straw	-7.316	595.6	2.562	-0.820	723.0	0.770
with 10%ZSM-5	-7.889	574.2	3.182	-2.471	730.6	1.913
with10%MCM-41	-7.882	574.2	3.079	-2.705	723.0	1.579
with 10%USY	-8.064	579.8	3.122	-2.404	726.2	1.925
with 10%MgO	-7.349	575.4	3.046	-2.172	732.4	1.785
with 10%CuO	-7.790	572.7	3.155	-2.409	727.8	1.747
with 10%AL_2O_3	-8.274	571.3	3.223	-2.988	716.4	1.645
with10%Na_2CO_3	-7.128	571.8	2.912	-2.379	727.6	1.874

Compared with pure cotton straw, the maximum peak value of *DTG* under catalyzing is bigger and the peak temperature turns to the lower region. At the same time, the average pyrolytic velocity of the volatile is increased both in APS and PPS. However, the catalytic performance is different from each other, and the performance of one catalyst in different pyrolysis stages are distinguished, too. According to the average pyrolytic velocity of the volatile in the APS, the sequence of catalytic performance is described as: Al_2O_3>ZSM-5> CuO>USY>MCM-41>MgO>Na_2CO_3, while in the PPS it was: USY >ZSM-5> Na_2CO_3 >MgO>CuO> Al_2O_3> MCM-41. Whatever, the catalytic performance is limited in APS. Al_2O_3 with the best performance in APS increases the average pyrolytic velocity of the volatile from 2.562 to 3.223, increased 125.8%; while in the PPS , MCM-41 with the worst performance increases the average pyrolytic velocity of the volatile from 0.770 to 1.579, increased 205.1%. It indicates that the catalyst accelerated the pyrolysis of lignin obviously, but to cellulose and hemicellulose, the performance was lower.

The influences of catalysts on ash yield

Table 4 shows the ash yield of the corresponding sample. Where M_C is the mass of cotton straw, $M_{catalyst}$ is the mass of catalyst, and M_R is the residual mass of sample, M_A is ash yield per unit mass of cotton straw, and the was calculated by the formula followed:

$$M_A=(M_R - M_{catalyst})/ M_C$$

Table 4 The yield of ash to the corresponding sample

Sample	M_C /mg	$M_{catalyst}$/mg	M_R /mg	M_A /mg.mg^{-1}
cotton straw	9.948	—	0.211	0.021
with 10%ZSM-5	9.175	1.020	1.286	0.029
with10%MCM-41	9.408	1.082	1.486	0.043
with 10%USY	9.131	1.023	1.273	0.027
with 10%MgO	9.095	1.026	1.445	0.047
with 10%CuO	9.063	1.025	1.522	0.055
with 10%AL_2O_3	9.030	1.018	1.368	0.039
with10%Na_2CO_3	9.110	1.020	1.434	0.045

The amount of ash is increased from 0.021(wt,mg/mg)to 0.027~0.045(wt,mg/mg)after adding catalysts. The increments varied significantly to different catalysts and the results is as follows:Na_2CO_3> MgO > AL_2O_3 > MCM-41 >CuO> ZSM-5> USY. Then it could be summarized that zeolite produced the smaller yield of ash

than metal oxides.

In correlation of hygroscopicity(R.Fahmia,2007), the pyrolysis catalyzed by Na_2CO_3 produced the most amounts of ash. There would be complicated compounds which were hard-Decomposed even in the high temperature if sodium carbonate could react with water and carbon dioxide produced in the process of pyrolysis .It was reported that calcium oxide, as the biomass pyrolysis catalyst, would absorb carbon dioxide to make the yield of the ash increased significantly(Chantal et al.,1984; Chen et al., 2007). It would explain the react mechanism of magnesium oxide.

When zeolite used as pyrolysis catalyst, there would be coking which led to the increments of ash. It was reported that the pyrolysis of lignin could introduce a lot of phenols which were the main reason for coking of zeolite(Sharma et al,1991). The zeolite with larger pore structure has bigger space for coking, so mesoporous MCM-41 products much more ash comparing with microporous ZSM-5 (Aho,2008) USY. And it was reported that high acidity could decrease coking, so microporous USY with high acidity produced least ash.

CONCLUSIONS

It could not distinguish the activated pyrolysis stage and passive pyrolysis stage obviously when cotton straw pyrolyzed without catalyst. The process of catalytic pyrolysis is made of dehydration stage、activated pyrolysis stage and passive pyrolysis stage after adding catalyst, and passive pyrolysis stage is more significantly observed. The catalysis do well to the pyrolysis of lignin, but did not promote the pyrolysis of cellulose and hemi-cellulose significantly. The adding of catalyst increases the yield of ash, and zeolite produced the smaller yield of ash than metal oxides.

ACKNOWLEDGEMENTS

The authors would like to acknowledge the financial support by The National Basic Research Program (No.2007CB210202).

REFERENCES

A.Aho, Fuell 9(2008),pp.2493-2501.
Chantal P., Kaliaguine S,Grandmaison J, et al.: Applied Catalysis10(1984),pp.317-332.
Chen,Y., Luo Y.H., Lu Fang., Duan J.: Journal of Fuel Chemistry and Technology, 35(2007), pp.370-374.
Fahmia, R., Bridgwatera A.V Fuel86(2007),pp.1560-1569.
Mansara Y K G., Ghal Y A E. : Bioresource Technol , 65(1998), pp.132.
Moghtaderi, B., C. Meesri, T. F. Wall.: Fuel 83 (2004),pp. 745-749.
Sharma R K., Bakhshi N N.: Bioresource Technology35(1991),pp.57-66.
Zhang, Q: Petrochemical Technology 35 (2006), pp.493-498.

EXPERIMENTAL STUDY ON ASH-RETURNED REACTOR OF CFB ATMOSPHERIC AIR GASIFIER

Zhang Shihong, Tian Luning, Zhou Xianrong, Chen Hanping, Yang Haiping, Wang Xianhua

State Key Laboratory of Coal Combustion (SKLCC),
Huazhong University of Science and Technology, Wuhan, 430074, China

Abstract: In an attempt to improve the gasification efficiency and decrease the carbon content in fly ash of atmospheric air CFB gasifiers, an innovatory equipment by name ash-returned reactor is put forward by SKLCC. Ash-returned reactor is an ash-returned apparatus on line of ash circulation, typically like "U" type valve in CFB boilers, with additional function of some extent combustion of residual carbon and increase the furnace inlet temperature of returning ash, and hence the coal conversion of gasifiers is enhanced. As to its configuration compared to conventional "U" type valve, ash-returned rector has two distinguished features of several times of height scale of fluidizing transportation region to meet the combustion reaction time need and appropriate heat transfer tube bundles arranged in the region to moderate the local temperature so as to avoid slagging. And hence, corresponding to the structure renovation, the material transportation and regulation performance of ash-returned reactor is primarily investigated through a series of experiments in a cold lab-scale facility in this paper. The heat transfer characteristic of the tube bundles is then researched and its influential factors are further discussed. These works lay a foundation on the following study of hot state experiments and industrial applications.

Keywords: CFB gasifier, ash-returned reactor, fly ash

INTRODUCTION

The technology of atmospheric air CFB gasification has widely applied in industrial processes and utilities services to produce low to medium heat-value coal gas with simple system and high gas production and low cost. However, it unfortunately has several inherent shortages, such as low coal conversion ratio, high carbon content in fly ash and in coarse ash discharged from bed bottom, and etc., leading to unpleasant more coal consumption (Chen, 1998). To make the technology in a greater vitality, the carbon content of fly ash and coarse ash must be reduced (Wu and Yan, 2002; Yan et al., 2001).

As the residual carbon in fly ash has low gasification reactivity, if it directly sends back to gasifier by ash return device just like in CFB boilers, there has no obvious effect on enhancement of carbon conversion. So, an innovatory equipment by name ash-returned reactor is put forward by State Key Laboratory of Coal Combustion (SKLCC). Comparing with the conventional "U" type valve, it is differently designed to make the fly ash retain more than 3 seconds and some extent burnout of carbon in fly ash, which would basically not participate in the gasification reaction. So more sensible heat is brought into gasifier and coal gasification reaction is predictably promoted. To moderate the temperature of the reactor at a desired level, appropriate heat transfer tube bundles are arranged in the upward fluidizing transportation region, preventing the materials from slagging and ensuring transportation smooth operation.

In this paper, the material transportation and regulation performance of ash-returned reactor is primarily investigated through a series of experiments in a cold lab-scale facility in this paper. The heat transfer characteristic of the tube bundles is then researched and its influential factors are further discussed. These works lay a foundation on the following study of hot state experiments and industrial applications.

EXPERIMENTAL

The cold experimental system of ash-returned reactor is shown in Fig. 1; its main composition contains the main fast bed, the gas-solid separator and the ash-returned reactor. The main-bed height is 3.6m, with square cross-section of 240mm by 240mm; the gas-solid separator is a cyclone separator with downward exhaust gas; the ash-returned reactor is a small slow FB, the height is 1.48m, cross-section is 300mm by 300mm; the standpipe of the ash-returned reactor is a PMMA tube, with the diameter of φ89×2mm, the ash-returned chamber and ash-transported chamber connect with a baffle which height is adjustable, so as to research the effects of horizontal orifice height on the speed of returning fly ash. Under the ash-returned chamber and the ash-transported chamber are fluidizing plenum and loosing plenum. In order to measure the distribution of heat

transfer coefficient, 15 test holes opened by 5 lines and 3 rows in the lateral wall of the ash-returned reactor. The experimental material is screening river sand with weighted average size of 0.44mm, packing density of 1500kg/m^3, actual density of 2380kg/m^3 and the critical fluidization velocity at 0.275m/s.

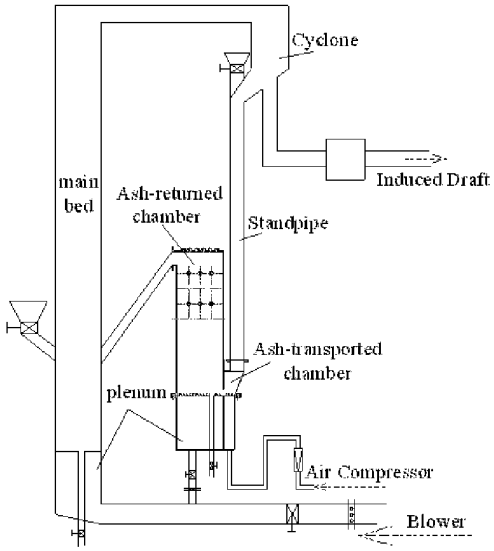

Fig. 1 Experiment system

COAL RETURNED MATERIAL PROPERTY

Start-up characteristics

The startup characteristic of ash-returned reactor is similar to conventional non-mechanical valves in CFB boilers. It has a minimum airflow in start-up process, and when there is fluidizing air only, the minimum start-up airflow decreased with the increasing of the height of horizontal orifice and the bed depth, as shown in Figs. 2 and 3.

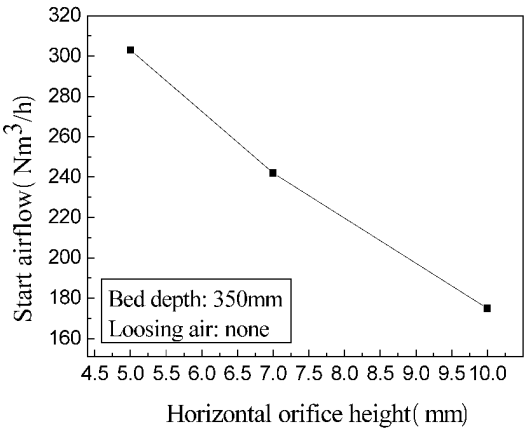

Fig. 2 The relationship of the horizontal orifice height and the start airflow

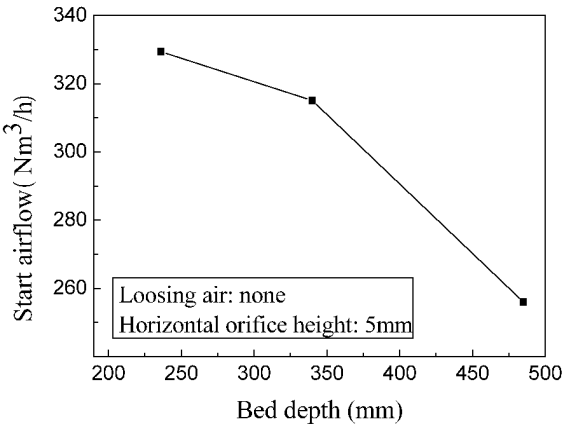

Fig. 3 The relationship of the bed depth and the start airflow

Regulating performance of amount of fly ash[0] returning

Researching the effects of fluidizing air only, fluidizing air and loosing air together, the horizontal orifice height on the amount of returning of fly ash is helpful to master the range of the operational parameters and the best controlled manner of the ash-returned reactor.

Regulating performance of one kind of air

Regulating performance of one kind of air refers to the effects of only fluidizing air on the amount of returning fly ash in the paper, that's because the loosing airflow is small, and the bed depth is too high, the loosing air couldn't start the ash-returned reactor alone. Comparing the three curves in Fig. 4, when the bed depth less than 350mm, the amount of returning fly ash increased significantly with the increasing of the bed depth, but not steady. With the bed depth gradual increasing, the amount of returning fly ash increased even

more steadily with the increasing of fluidizing airflow. This is because when the bed depth is low, the resistance is weak; the pressure inside the bed has a larger fluctuation with the changing of fluidizing airflow, so the fly ash returning is unstable. In order to make the fly ash returning be steady during the ash-returned reactor running, the bed depth should not be less than 350mm, as well as the ratio with the bed height is 0.24.

When the fluidizing airflow is small, it will present a solid particles stagnation region which is mainly close to the horizontal orifice between ash-transported chamber and ash-returned chamber (Wang et al. 2006). With the fluidizing airflow increasing gradual, the region will be small gradually. In order to prevent the solid particles from being stagnant even slagging at the transport part, the fluidizing airflow should be larger than the requirement, and it would be best of 2 to 3 times of the critical fluidization airflow.

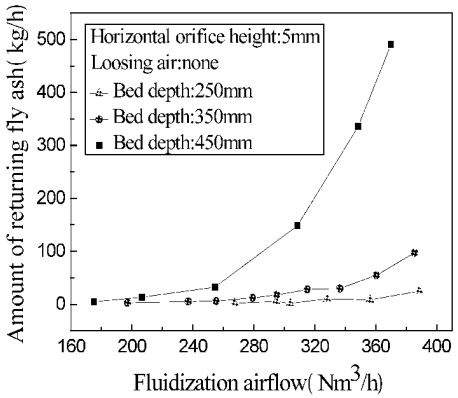

Fig. 4 The effect of fluidizing airflow on amount of returning fly ash

Regulating performance of both two kinds of air

Regulating of both two kinds of air means achieving material returned by fluidizing air and loosing air together. Comparing Figs. 5 and 6, it can be seen that when the fluidizing air is fixed, with the increasing of the loosing airflow, the amount of returning fly ash appeared linear increasing and can be regulated easily, thus this is the most adequate way of regulating the amount of returning fly ash. With the aid of the loosing air, the speed of fly ash returning doesn't suddenly increase from zero; it realizes stably returning of material. According to the experiments, when the loosing airflow less than the critical fluidization airflow, there will appear a flow dead region nearby the horizontal orifice, in order to prevent solid particles from depositing and slagging in actual running, the loosing airflow should be 1.2~1.5 times of the critical fluidization airflow (Basu and Fraser, 1991).

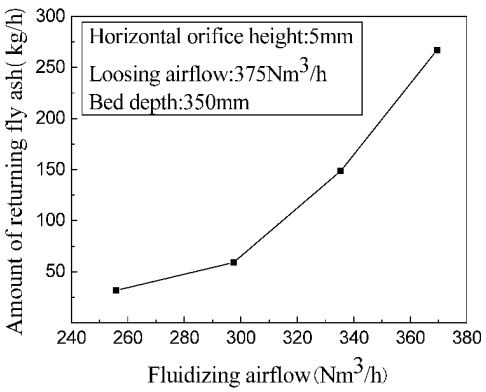

Fig. 5 The influence of fluidizing airflow on amount of returning fly ash

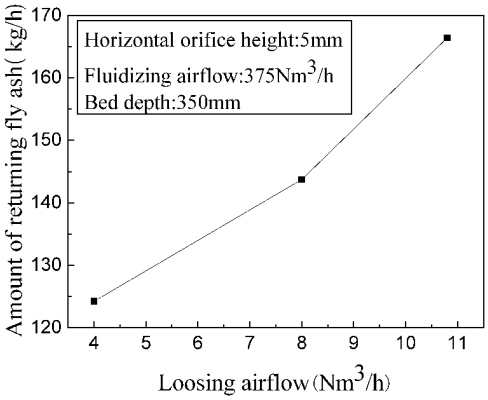

Fig. 6 The influence of loosing airflow on amount of returning fly ash

The influence of the horizontal orifice height

When fluidizing airflow and loosing airflow certain, the amount of returning fly ash increased with the horizontal orifice height increasing, and became flat gradually. There should opt a appropriate horizontal orifice height to a certain airflow (Zhou et al. 2003), when it is large enough to let fly ash returning flow through under a certain airflow, continuing amplify the horizontal orifice height will form a solid particles stagnation layer at the bottom of the horizontal orifice, and the thickness of the layer will increase with the horizontal orifice height increasing. The following is the relationship of the material flow state and the horizontal orifice height in the ash-returned reactor observed in the experiment. (A_1, the area of the horizontal orifice; A_0, the sectional area of the standpipe)

(1) When the horizontal orifice height is 5mm, A_1/A_0 is 0.264. There exists layered phenomenon between flowing particles and stagnant particles in the ash-transported chamber; this will lead to slagging and clogging in ash-returned reactor actual running.

(2) When the height of the horizontal orifice is 7.5, 10mm, A_1/A_0 is 0.397, 0.529. The material fluidization state is well. The flow of material is steady.

(3) When the horizontal orifice height is 13mm, A_1/A_0 is 0.69. The material in the standpipe will easily reach to critical fluidization sate with the airflow increasing, the running is not steady. When A_1/A_0 is 1.06, the material in the standpipe will be fluidizing totally, there is no ash returned at this time.

When the area of orifice is 0.3~0.5 times of the area of standpipe, the reactor can work well, the regulating and controlling performance is good, so the flow dead region in ash-returned reactor could be eliminated, and the transport of the material could be controlled steadily.

HEAT TRANSFER PROPERTY

In the paper, a group of orthogonal experiment is designed before the experiment, a significant scheduling of the factors impact on heat transfer coefficient distribution was found through significance analysis by using the experimental result: bed depth > fluidizing airflow > horizontal orifice height > loosing airflow. The factors of influence were studied by the sequence of significant scheduling as below.

The influence of bed depth on the distribution of heat transfer coefficient

According to the significance analysis, the bed depth is the most influential factors affecting the distribution of the heat transfer coefficient (h). It can be seen from Fig. 7 that when the axial height of measuring hole is 600mm, the bed depth is 300mm, h is 256.634 W/ (m^2·K) ; when the bed depth is 440mm, h is 403.78W/ (m^2·K), the changing is significant. When the axial height of measuring hole is 1400mm, h differs little in the three bed depths. Fig. 8 shows that the heat transfer coefficient decreased and the decreasing extent was getting smaller with the height rising. The gap of the heat transfer coefficient is less than 10% at the axial height of the measuring hole in 1000mm, 1200mm and 1400mm.

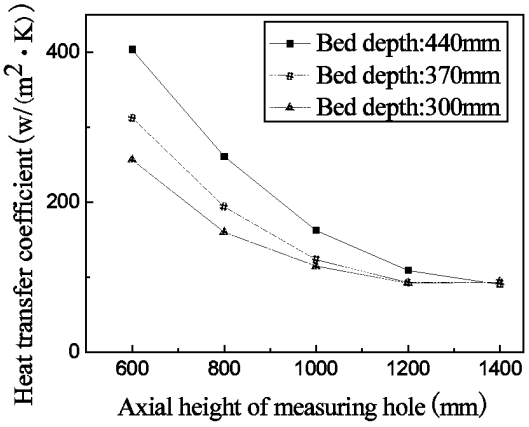

Fig. 7 The heat transfer coefficient in various axial heights of measuring hole

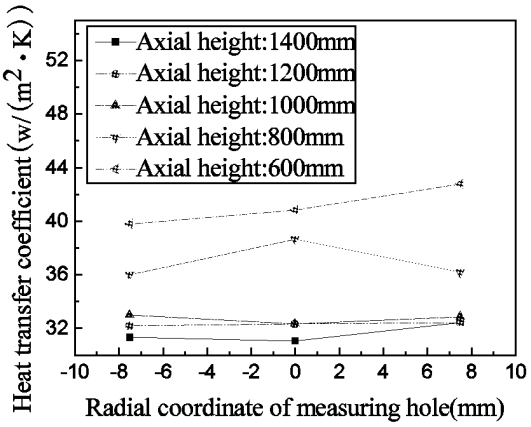

Fig. 8 The heat transfer coefficient in various radial coordinates of measuring hole

In fact, the bed depth indirectly reflects the particle volume fraction in the ash-returned chamber; the material bed height has a great influence on the particle concentration in the lower of the ash-returned chamber, and has little influence in the top of the ash-returned chamber. According to the analysis, the increasing of the bed depth has two roles: on the one hand, the number of particles increased; on another hand, the bed layer height also increased. By the theory of the FB, the increasing of particles has less influence on the particles concentration in the top of FB, the increasing of bed layer height clearly make the low dense phase upward migration. Therefore, the experimental result is consistent with the theory of FB very well.

The influence of the fluidizing airflow on the distribution of heat transfer coefficient

Fluidizing airflow is the second influential factors on the distribution of the heat transfer coefficient, because the fluidizing air can change turbulence intensity and particle motion behavior clearly in CFB, thus change the distribution of particle concentration in the ash-returned chamber, and then impact the distribution of heat transfer coefficient (Wang et al., 1996). When the fluidizing airflow is very low, the particle concentration in the lower part of the ash-returned chamber is also very low, the bed layer porosity basically unchanged in axial direction, the whole bed layer form dilute phase pneumatic conveying, as shown in Fig. 9. When the fluidizing airflow increased to a certain value, the particle concentration increased rapidly in the lower part of the bed layer, the porosity reduced sharply, but it increased in index along the axial direction from bottom to top, therefore, the particle concentration decreased in anti-index, reached a certain value and

suspended. Fig. 10 shows the rule that the heat transfer coefficient in different axial height gradually stabilized with the fluidizing airflow increasing; while the fluidizing airflow further increasing, the particle concentration changed from the anti-index curve to the s-shaped distribution (Lucat and Jaud, 1993), the particle concentration remained constant in the upper and reached saturation value at the bottom. Since then, the fluidizing airflow increased continuously, and the particle concentration remained in a saturation value at the bottom and kept a fixed constant at the top, but the inflection point of s-shaped continued to upper shift.

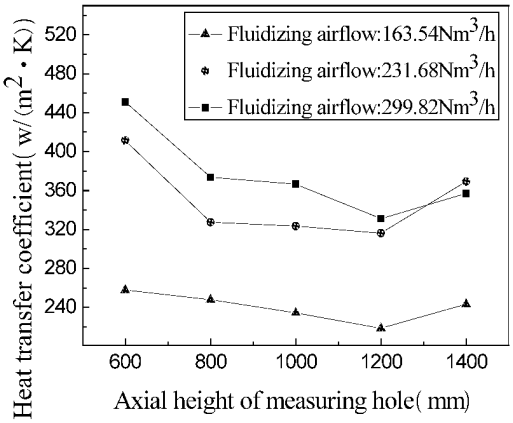

Fig. 9 The heat transfer coefficient in various axial heights of measuring hole

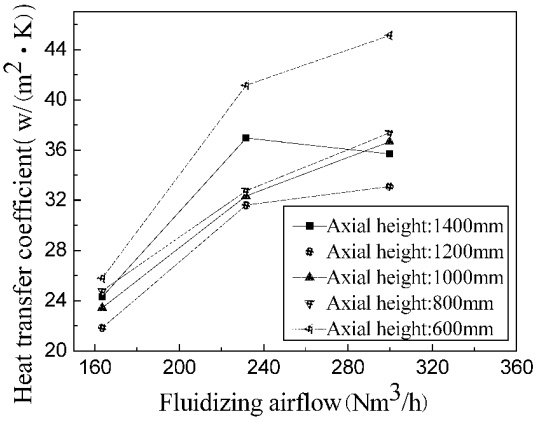

Fig. 10 The relationship between fluidizing airflow and the heat transfer coefficient

The influence of the horizontal orifice height and the loosening airflow on the distribution of heat transfer coefficient

According to the significant analysis, the influence of the horizontal orifice height and the loosening airflow on the distribution of heat transfer coefficient is not very significant, but also cannot be ignored. Fig. 11 shows that the heat transfer coefficient in different axial height show the similar trends with the variation of loosening airflow, that is, the less loosening air has a little influence on the distribution of the heat transfer coefficient, when the loosening airflow become larger, the heat transfer coefficient increased in different axial heights, has obviously changing in the lower part and has little changing in the upper part of the ash-returning chamber.

Fig. 12 shows the relationship of the horizontal orifice height and the heat transfer coefficient, the horizontal orifice height has promotion effect on the heat transfer coefficient; especially the axial height is 600mm. This is because the horizontal orifice height has obvious effect on the amount of returning fly ash, thereby, indirectly affects the bed depth, and obviously intensifies the heat transfer in the lower of ash-returned chamber.

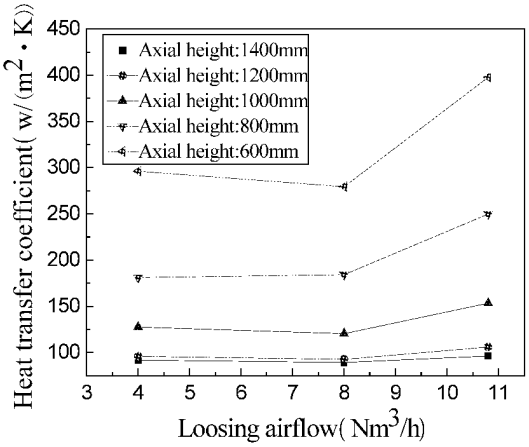

Fig. 11 The relationship of loosing airflow and the heat transfer coefficient

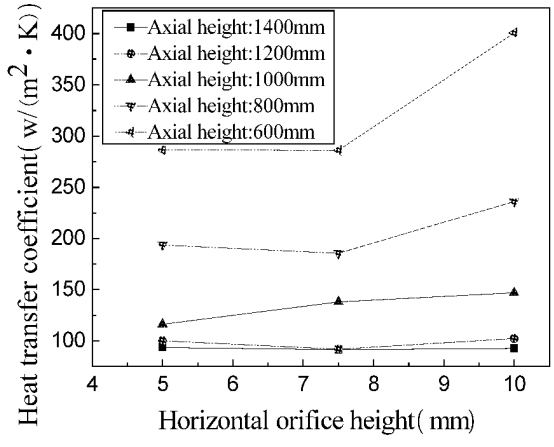

Fig. 12 The relationship of horizontal orifice height and the heat transfer coefficient

CONCLUSIONS

The performance of ash-returned reactor was experimentally investigated. Following main conclusions are drawn from the experiment results:

Ash-returned reactor with tall fluidizing transportation bed can get an even transporting state by accommodating air supply. Ash-returned reactor exists a critical start-up airflow for material beginning to transport, and when there is only fluidizing wind, the critical start-up airflow decreased with the increasing of the bed depth and the height of horizontal orifice.

Fixed the fluidizing airflow, the loosing air can easily control the amount of fly ash returning, which is recommended as the most suitable regulation method.

The influence of the height of horizontal orifice on fly ash returning is relatively obvious, and when the passing area of orifice is 0.3~0.5 times of the cross-area of standpipe, the ash-returned reactor can fully exert its returning potential.

The bed depth indirectly reflects the particle volume fraction. The influencing factors affect the distribution of the heat transfer coefficient through impacting the distribution of the particle concentration. The heat transfer coefficient incresed with the fluidizing airflow increasing, but the increasing extent of the heat transfer coefficient rising range was getting smaller. When the loosening airflow is larger, the heat transfer coefficient increased in different axial heights. The horizontal orifice height has promotion effect on the heat transfer coefficient.

ACKNOWLEDGEMENTS

The author wishes to express the great appreciation of financial support from "Key Projects of National Fundamental Research Planning" (National 973 project: 2007CB210202) and National Nature Science Foundation of China (No. 50676037 and No. 50721005).

REFERENCES

Basu, P., Fraser, S. A. (1991). Circulating Fluidized Bed Boilers: Design and Operation. Stoneham, Butterworth-Heinemann Publ.
Chen, J. R.: Clean Coal Technol. (4)1998, PP.8-15.
Lucat, P., Jaud, P. (1993). Utility-Type CBF Boilers: 250MWe And Beyond. Proceeding of the 12th Int. Conf. On CFB.
Wu, F., Yan, C. X.: Coal Chem. Indus. (3)2002, PP.76-79.
Wang, Q., Luo Z. Y., Li, X. T., Cen, K. F., Ni, M. J., Sun, J.: Power Eng. (19)1999, PP.24-28.
Wang, Z. F., L, P., Dong, Z. B., Bi, J. C.: J. North Univ. China (Natural Science Edition). (27)2006, PP.324-327.
Wang, Q., Luo Z. Y., Li, X. T., Cheng, F., Ni, M. J., Cen, K. F., Sun, J.: Power System Eng. (12)1996, PP.28-32.
Yan, C. X., Wu, F., Sun, Y. H.: J. the Chem. Fert. Indus. (28)2001, PP.18-20.
Zhou, Z. Q., Lv, T., Zhao W. G.: Boiler Technol. (34)2003, PP.38-41.

FIRST EXPERIENCES WITH THE NEW CHALMERS GASIFIER

H. Thunman, M. C. Seemann

Department of Energy conversion, Chalmers University of Technology, Göteborg, Sweden

Abstract: During summer 2007 a 2-6 MWth indirect gasification section was integrated into the loop of the existing 8-12 MWth circulating fluidized bed boiler at Chalmers University. With help of a particle distributor the gasification unit is connected to the loop after the cyclone. Hot bed material entrained from the boiler is so transferred to the gasifier providing the heat for the production of a nearly nitrogen free product gas. Non-gasified char is returned together with the bed material into the boiler and converted. Biomass can be fed into both sections; the boiler and the gasifier. The gasification is separated from the boiler via two loop seals and a particle distributer, directing particles either back to the boiler or into the gasification section. For that reason the CFB boiler can be operated even after the retrofit independently, just like before, or in combined combustion/gasification mode. This possibility keeps the risk for a retrofit low. As, furthermore, the investment costs for the integration are considerably lower than standalone gasification units of that size, the retrofit is an easy way to extend the potential of a CFB Boiler towards bi- and tri-generation (heat, power, fuel) and enter new markets.

The first experimental season with the installation proved stable operation of both the boiler and the gasification. Furthermore, the full functionality in combustion only mode was shown. The gasifier was operated for 60 h with wood pellets and wood chips. First analysis of the producer gas composition shows high contents of methane, making the installation a good match for SNG production. The heating value of the gas is about 14.4 MJ/Nm^3.

Keywords: gasification, biomass, CFB, retrofit

INTRODUCTION

An efficient use of biomass resources is an important part of the global strategy to reduce the emission of greenhouse gases to the atmosphere. In what way this restricted resource should be used for energy conversion can be discussed, but with the urgent need for action all technical options need to be exploited. From a pure efficiency evaluation the best use of biomass is to just burn it for heat and power production. However, to integrated technologies using renewable sources are generally most efficiently done in the stationary energy sector and the challenge is to find the solutions that could replace fossil fuels for all kinds of energy use. In this context gasification of biomass is attractive as the solid biomass is converted to a gas of suitable quality, which can be used directly, or after further process steps, as a substitute for the fossil fuels in various sectors. Gasification is, however, not a new technology, nor is the concept of poly-generation, where several energy carriers are produced in a flexible production unit.

Even though gasification has been identified as having a great potential to become cost-competitive, thermally efficient and environmentally friendly, the market penetration of the technology is slow, especially for biomass. For biomass there have been a large number of pilot and demo projects commissioned during the last twenty to thirty years, but the status of most of them can be summarized: worked fine, now closed down. There are, nevertheless, some exceptions where the gasifier in Güssing (Hofbauer, 2006) perhaps being the best example. The challenges to overcome in order to introduce the gasification technology at large scale are to increase the reliability and decrease the investment costs. The target of the concept proposed in this work is to provide a solution for the gasifier itself, with the aim to maximize the reliability and the overall efficiency at the same time as the investment cost is minimized.

THE CONCEPT

The rationale behind the concept is that poly-generation of various energy carriers from biomass is a cost effective option to initiate production of biofuels. This paper presents the concept for which the available infrastructure of existing boilers can be used as the basis for introducing the gasification technology, which in itself should lower the cost and minimizes risks. The concept is based on retrofitting existing fluidized bed boilers (FB-boiler) by using the thermal flywheel of the fluidized bed as means of devolatilising the biomass. The principle is similar to the indirect gasification process which for example is applied in the Güssing gasifier (Hofbauer, 2006). But, instead of building a single gasification reactor, a fluidized bed boiler, Fig. 1, is combined with a gasification reactor. A principle figure of the process is shown in Fig. 2, where the circulating fluidized bed (CFB) boiler in Fig. 1 is retrofitted with a gasification reactor and one additional particle seal.

The second particle seal secures the flow direction of the heat carrier and prevents gas leakage between the combustor and the gasifier. In the process, the heat carrier is transported up through the combustion reactor with the combustion gas, separated from the gas in the cyclone and falls down to the first particle seal. The heat carrier falls, thereafter, down to the gasification reactor, where it releases its heat before it is transported back to the combustion reactor.

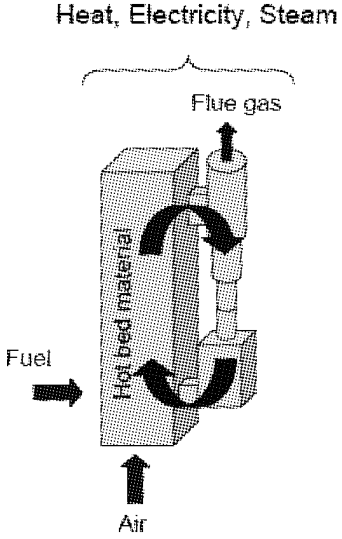

Fig. 1 Principle scheme of a FCB-boiler

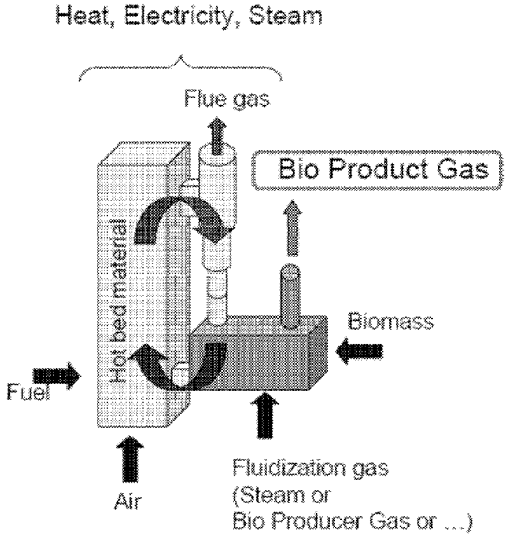

Fig. 2 Retrofitted FCB-boiler with integrated gasifer (brown)for the production of bio product gas

There are several technical motivations why one should integrate a gasifier onto a FB-boiler instead of building a pure gasification reactor, for example:

Heat balance always fulfilled

In a pure gasification reactor the heat produced for gasification always has to be balanced to the heat requirement for the gasification process. All heat produced on top of this is a loss to the system. In a direct gasifier, where part of the fuel is burned within the gasification reactor, one often has to provide the process with at least 20 % more oxygen than that is required for the process to assure a stable process and compensate for variations in input fuel feed rate. In an indirect gasifier the process tends to become unstable, and as the evenness of the char transport to the combustor varies over time, this often requires that additional fuel is fed into the combustor to stabilize the process. For the proposed process, the heat production in the combustor is always much larger than the heat needed for the gasification, i.e. this assures a stable operation.

Minimization of char losses

The rates of gasification reactions with carbon dioxide and water vapour are low at the temperatures present in a fluidized bed gasifier. This means that in a direct gasifier most of the char converted in the gasifier is converted by the oxygen provided to the process. It is difficult to design the process so that the oxygen selects the char instead of the more reactive volatile gases. The result is instead that the char remaining in the gasifier undergo attrition, resulting in that a large part of the char leaves the gasifier with the fly ash. An estimate based on data from existing gasifiers indicates that around 50 % of the char leaves the gasifier unconverted. In many cases a lower figure is presented, but then this is often accomplished in combination with high oxygen to fuel ratio. The conversion efficiency of the fuel is one of the great advantages of the indirect gasifier, where the unreacted char is recirculated to the combustor for final combustion. All attempts to increase the gasification of the char in the gasifier results in an increase in the attrition of the char, and consequently, in a loss of char. In the concept proposed here, the fuel conversion can be optimized to minimize the attrition. The variable amount of char transported from the gasifier to the combustor is compensated by the fuel fed to the combustor.

Optional fluidization medium

In a pure gasification reactor the reactor design is adjusted for a specific fluidization medium. In the indirect gasifier, and especially in the concept presented here the fluidization medium can be optimized with respect to the gas quality that is going to be produced. This can be done without any significantly negative impact on the heating value of the product gas. The first obvious option is steam that could be removed by

condensation during the subsequent gas treatment, producing a medium heating-value gas. The drawback of the use of steam is the energy needed for its production. From an energy-efficiency point of view a more attractive medium is recirculation of hot product gas, which would remove the heat needed for the steam production at the same time as the gas contact time with the bed material is increased and beneficial catalytic effects could be improved. The third choice is recirculation of flue gas. This option will, of course, dilute the gas with nitrogen, but, yet, the gas will have a sufficiently high heating value for many applications. In some special operations the gasifier could also be fluidized by air or oxygen/steam. In these latter cases the heat needed for the gasification process is produced within the gasifier, but the circulation of the heat carrier makes the process more stable and provides a possibility to reduce the oxygen to fuel ratio, in order to increase the efficiency of the process.

Operation at "any" temperature

In the proposed process the conversion temperature in the gasifier could be controlled in a wide temperature range. The ratio of the rate of biomass fed to the gasifier and the circulation rate of the bed material between the two reactors allows control of the bed temperature. As the char produced in the gasifier always is efficiently converted in the combustor, the temperature in the gasifier can be anything between 500 °C, suitable for production of liquids, and 900 °C, suitable for gasification of non-problematic biomass.

Secondary oxygen injection

Secondary combustion with air or oxygen could be used to raise the temperature further, in order to reduce the amount of tar, without a significant reduction of the heating value. For a direct gasifier, especially air-blown, the heating value is low from the beginning and a further reduction of the heating value restricts the possible use of the gas.

Possibility to gasify wet fuel with a high efficiency

If there is an over production of heat in the system the system could be adjusted so there is a net heat flow to the gasifier and the gasification processes could be operated even for wet biomass, without any significant negative effects on the efficiency of the process. The advantages are that there is no need for a separate dryer, which decrease the complexity and the cost of the plant. This is especially a great advantage for a plant that receives fuels with a wide variation in moist content.

Possibility to burn fuel with higher moisture content in combustor

Many fluidized bed boilers especially, bubbling beds, burns wet and problematic fuels. These boilers often use a support fuel that releases its heat in the lower part of the boiler where the moisture is released. By connecting a gasifier to the bubbling fluidized bed the char produced in the gasifier will be transported to the boiler to act as a premium fuel, as it is already heated and consists of more or less pure carbon.

Fluidized bed boilers are common and available all over the world.

The major producers outside China and India are Alstom, Foster Wheeler and Metso Power, which have delivered more than 700 plants world wide (Johnsson 2007). These installations provide the basis for a low risk step into gasification technology for plant owners and boiler producers. It can be concluded that the market potential for the gasification concept presented here is large and even larger if one considers the extensive number of fluidized bed installations in India and China.

THE DEMONSTRATION

At Chalmers power central, a well functioning and well exploited 12 MWth research CFB-boiler of industrial scale exists (Leckner, 1991). The flexibility of the boiler is unique and it can handle up to three different solid fuels, if desired simultaneously, one wet fuel like sludge and one oil or gaseous fuel. The boiler itself is equipped with a great number of sensors and measurements ports that allow in-situ measurements in the entire furnace volume at the same time as the global conditions can be monitored. In order to perform measurements in the boiler a unique measurement infrastructure for advanced combustion and gasification investigations has been built up. It has continuously provided high quality data for research projects for more than twenty years. During these years the operators and research staff have improved their skill in performing advanced measurement campaigns at industrial scale.

This 12 MWth CFB-boiler was retrofitted during summer 2007 and a gasifier was integrated into the loop as described above. The basic design started in October 2006, the reconstruction and integration of the gasifier was be accomplished in November 2007 and the gasifier was handed over for research in spring 2008.

The integration has been a great challenge as the available space was limited and the condition that the reconstruction should not negatively affect any part of the unique, flexible, research CFB-boiler. During the basic design, one parameter that needed to be optimized was the fuel input to the gasifier. In the actual state, the raw gas outlet of the new reactor is connected to the CFB boiler according to figure 3 and the produced gas is transported back to the boiler and is burned. To keep the temperatures in the boiler within certain limits the fuel input to the gasifier was restricted to 2 MWfuel.

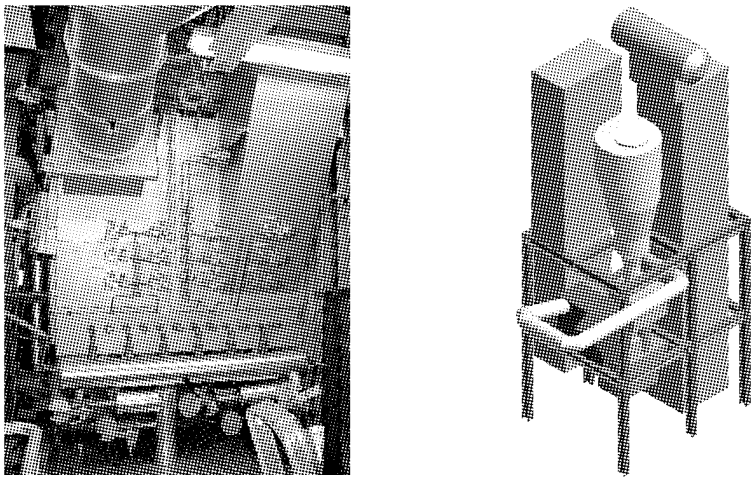

(a) (b)

Fig. 3 Picture of gasification reactor at Chalmers power central and scheme of the coupling of the gasification reactor (red) with the boiler (blue) via the particle distributer (brown) and two loop seals (brown)

The budget for this first step was 1.4 million euro. Future plans are to complement the reactor with autothermal reformer, product gas recirculation. The final aim is to include the entire chain required to produce synthetic fuel.

FIRST RESULTS

The most important result is probably that the function and operation of the CFB-boiler was not affected by the integration of a gasifier. During 120 hours of circulation through the gasifier no negative effects were reported. Furthermore, by changing the fluidization in the two loop seals, the flow through the gasification reactor can be stopped so that the boiler can be operated as usual. Is the extra loop opened, works the gasifier as an external heat exchanger by cooling down the bedmaterial. The heat is consumed by the endothermic drying, devolatilization and gasification processes. However, the heat available in form of hot bed material is sufficient to gasify up to 6 MW fuel. This is much more than the 2MW the gasifier is restricted to due to its coupling to the boiler. By minor changes in the design (Berguerand 2008) it is possible to increase the residence time of the fuel and increase the fuel input up to 10 MW.

In the actual state the raw gas is transported back and burned in the boiler. From that pipeline gas was sampled cooled down to 2°C. The gaseous fraction was than analyzed by means of a micro-gas-chromatograph (Varian GC4900) (Table 1). The gas composition showed high amounts of methane resulting also in a high heating value of 14,4 MJ/nm^3. During the measurement was the temperature in the gasifier at about 780°C.

Table 1 Dry raw gas composition spring 2008

	mol %
H_2	24.2
CH_4	13.3
CO	42.5
CO_2	16.6
C_2H_4	2.9
C_2H_6	0.5

In spring 2008 totally 60 hours of gasification were achieved before the warm weather ended the experimental season mid of April. The installation was set into operation again in autumn of this year (2008)

without any problems.

CONCLUSIONS

A concept using the existing infrastructure of boilers forms the basis for introducing a gasification technology that lowers cost and minimizes risks is presented. The concept is based on retrofitting existing fluidized bed boilers. The process uses the thermal flywheel of the fluidized bed as means of devolatilising the biomass. The potential of the concept is extensive and could give a significant push to the introduction of biomass gasification in the world. Moreover, several advantages with integrating a gasifier onto a combustor are identified.

A demonstration a 2 MW fuel project was realized, integrated into a 12 MWth CFB-boiler and is in operation since December 2007.

- The gasifier does not have any negative effects on the functionality of the CFB boiler
- Combustion only mode is still possible
- The produced gas has a high heating value and is very suitable for synthesis of SNG

ACKNOWLEDGEMENTS

This project is cooperation of Chalmers, Göteborg Energi AB, Metso and Akademiska hus. A great engagement from S.E.P was also a key to the successful realisation of the project. Finally the Swedish Energy Agency is recognised in providing resources for the research at Chalmers' power station.

REFERENCES

H. Hofbauer, Scale Up of Fluidized Bed Gasifiers from Laboratory Scale to Commercial Plants: Steam Gasification of Solid Biomass in a Dual Fluidized Bed System , In F. Winter editor, 19th Int. Conf. on Fluidized Bed Combustion, Vienna (2006).

F. Johnsson, Fluidized Bed Combustion for Clean Energy, In Proceeding of the 12th Int.Conf. on Fluidization, (2007).

B. Leckner, M. Golriz, W. Zhang, B.-Å. Andersson and F. Johnsson, Boundary layer-first measurements in the 12 MW CFB research plant at Chalmers University. In: E.J. Anthony, Editor, 11th Int. Conf. on Fluidized Bed Combustion, ASME, New York (1991), p. 771.

N. Berguerand and A. Lyngfelt, Design and Operation of a 10 kWth Chemical-Looping Combustor for Solid Fuels – Testing with South African Coal, Fuel 87 (2008), pp. 2713–2726.

A HYDRODYNAMIC CHARACTERISTIC OF A DUAL FLUIDIZED BED GASIFICATION

Yeon Kyung Sung, Jae Hun Song, Byung Ryeul Bang, Tae U Yu, Uen Do Lee

Korea Institute of Industrial Technology, Cheonan, Korea

Abstract: A cold model dual fluidized bed (DFB) reactor, consisting of two parallel interconnected bubbling and fast fluidized beds, was designed for developing an auto-thermal biomass gasifier. The combustor of this system burns the rest char of the gasification process and provides heat to the gasifier by circulating solids inventory. To find an optimal mixing and circulation of heavy solid inventory and light biomass and char materials, we investigate two types of DFB reactors which have different configuration of distributor and way-out location of the solid inventory and char materials in the gasifier. To determine appropriate operating conditions, we measured minimum fluidization velocity, solid circulation rate, axial solid holdup and gas bypassing between the lower loop seal and the gasifier.

Keywords: Hydrodynamics, dual fluidized bed, Biomass gasification, cold model

INTRODUCTION

Recently, clean utilization of low-rank fuel is a key issue in energy and thermal power system due to unstable prices of fossil fuels and environmental problems. Biomass utilization is a very promising technology because it is carbon neutral and one of the most abundant resources in the world. Among various ways of using biomass as energy, gasification technology is known to be very effective process because syngas from the gasification process can be applied to poly-generation: combustion, power generation, synthetic fuel and chemical production. Korea Institute of Industrial Technology (KITEHC) has been focused on the clean use of low-quality fuels such as coal, waste, and biomass and we launched an extensive research project on biomass gasification including gas cleaning and biomass-to-liquid (BTL) with F-T process. For biomass gasification, we are developing dual bed gasification system consist of a bubbling fluidized bed gasifier and a circulating fluidized bed combustor. Our goal is to develop a gasification process which satisfies the requirement of F-T process which needs high contents of hydrogen with less impurity such as sulfuric compounds, tar and particular matters.

There have been extensive researches on biomass gasification with fluidized bed gasifier and various gasifying medium. Generally, high temperature gasification with steam or oxygen has been used for getting hydrogen-rich syngas. To maximize gasification and tar removing efficiency, combined system which has low velocity fluidized bed & high velocity pneumatic riser (Xu et al., 2006) is known to have an excellent performance (Hofbauer et al., 1995; Fang et al., 1998; Murakami and Xu, 2006). A dual fluidized bed (DFB) reactor has two fluidized beds: gasifier (bubble fluidized beds) and combustor (circulating fluidized beds) which produces syngas and combustion gas respectively. This combined system has many advantages, such as cold gas efficiency, tar removing performance, and gas composition. By separating gasification and combustion processes, we can produce middle-caloric-value syngas without nitrogen dilution and less carbon dioxide. By adding steam or oxygen to the gasifier, we can control the caloric value of syngas. In this study, we investigated hydrodynamics of DFB reactor for developing an auto-thermal biomass gasifier.

Table 1 Properties of solid inventory

Properties	
Mean diameter (μm)	376.1
Bulk density (kg/m^3)	1220
Minimum fluidization velocity (m/s)	Type 1=0.12 , Type 2=0.1
Terminal velocity (m/s)	1.3

Two types of gasifier with different way-out location of the circulating solids and the shape of distributor were tested. For each type, we examined solid circulation rate, axial solid holdup distribution and stable operating conditions.

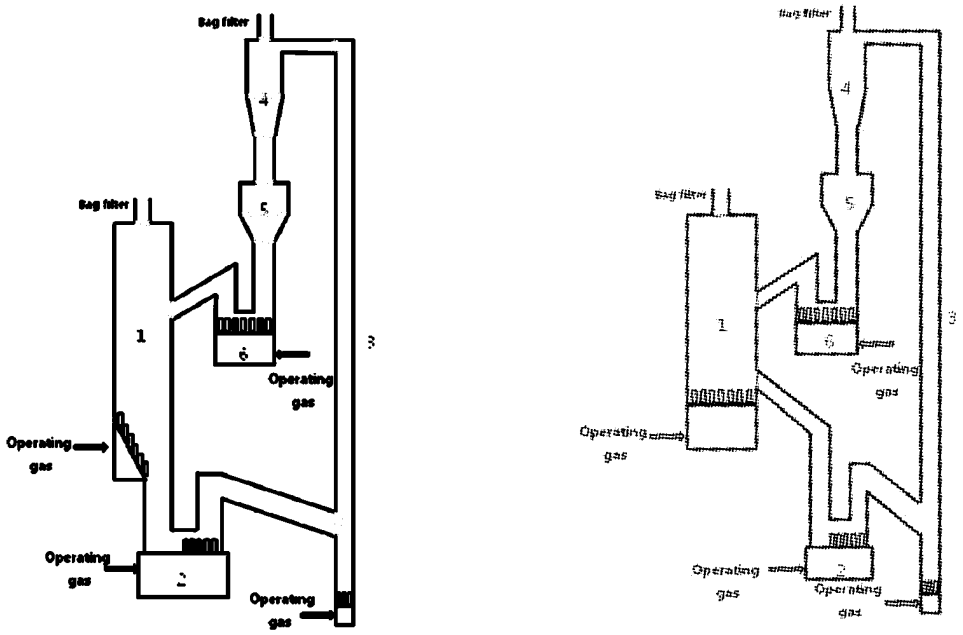

(a) Type 1 (B) Type 2

Fig. 1 Schematics of dual fluidized bed gasification systems
1—Bubbling fluidized bed; 2—Lowe loop seal; 3—Riser; 4—cyclone; 5—hopper; 6—Upper loop seal

EXPERIMENTAL

Figure 1(a) and 1(b) shows the schematics of DFB reactor consisting of a fast fluidized bed riser and a bubbling fluidized bed reactor. As shown in the figure, there are differences in the location of the solid way-out and distributor of the gasifier. The way-out of the gasifier is connected to lower loop seal which controls solid circulation rate and prevents back flowing gas from the riser. In case of Type 1, the way-out of the gasifier is located just below the bottom of the gasifier and the distributor is installed on a slat wall. In this type, the way-out is located lower than the distributor. On the other hand, the way-out of the Type 2 is located on the side of the gasifier which is upper than the distributor and the distributor is installed on a flat wall. Other than the solid way-out location and the shape of distributor, all the other parts such as upper loop seals, riser, cyclone, and down comer are the same for the two types. The gasifier has 0.2 m wide × 0.2 m depth × 2.95 m high and the riser has 0.07 m I.D×5.18 m high. The solid from lower loop seal accelerates in the bottom riser and enters through abrupt exit into the cyclone, down comer, hopper by turns. Then it returns to gasifier. The silica sand belonged to geldart group B(Geldart, 1973) was used as a bed material and its physical properties listed in Table 1. Dried air was used as an operating gas and the flow rate was controlled by float flowmeters. To examine the leakage from lower loop seal to the gasifier, we monitored CO_2 concentration of the gasifier with gas analyser(ABB CO. Ltd., Germany, Model: AO2020) while introducing CO_2 in the lower loop seal and dried

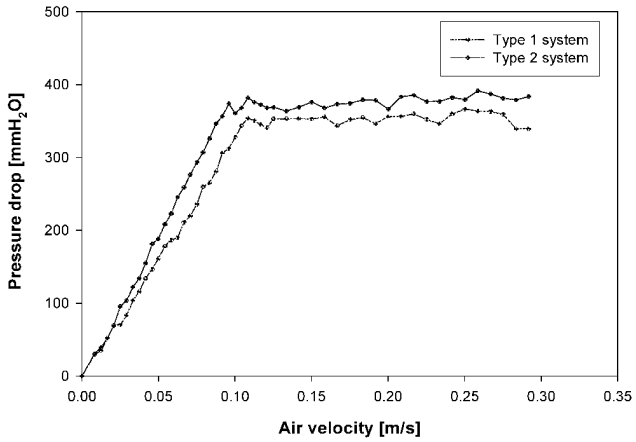

Fig. 2 The minimum fluidization velocity of the two different systems with same silica sand

air in the gasifier respectively. The solid circulation rate was measured by monitoring the accumulated height of solid in the down comer. Minimum fluidization velocity of the gasifier and axial solid hold up distributions of the riser were measured with differential pressure transmitter (DPLH series, Sensys). The pressure signal was recorded with DAQ system (Daqbook 2000, IO tech.)

RESULTS AND DISCUSSION

We measured the minimum fluidization velocity of the gasifier by monitoring the differential pressure of the bubbling fluidized bed reactor. With the same silica sand, the minimum fluidization velocity of Type 1 is $u_{mf,1}$ = 0.12 m/s and that of Type 2 is $u_{mf,2}$ = 0.1 m/s. Pressure drop has steadily increased with increasing air velocity until it reached maximum point(ΔP_{max}), then with further increase in air velocity it came up to the static pressure which is lower than ΔP_{max}. In fact, minimum fluidization velocity is determined by particle size(d_p), particle density(ρ_s), gas density(ρ_g), viscosity(μ), and voidge(ε_{mf}) according to the Wen & Yu et al. (1966). Despite of using the same silica sand, u_{mf} is different between the two as seen in Fig. 2. This implies that minimum fluidization velocity can be influenced by the shape of the reactor and the distributor. The minimum fluidization velocity of Type 2 is closer to the calculated value: $u_{mf,cal}$ = 0.09 m/s. When the pressure drop across the bed equals the weight of the bed, the fluid drag (F_D) is directly proportional to differential pressure and cross-sectional area. If distributor is on the flat wall (Type 2), the drag force is divided uniformly over the cross-sectional area which helps the fixed-bed transform into fluidized bed more easily.

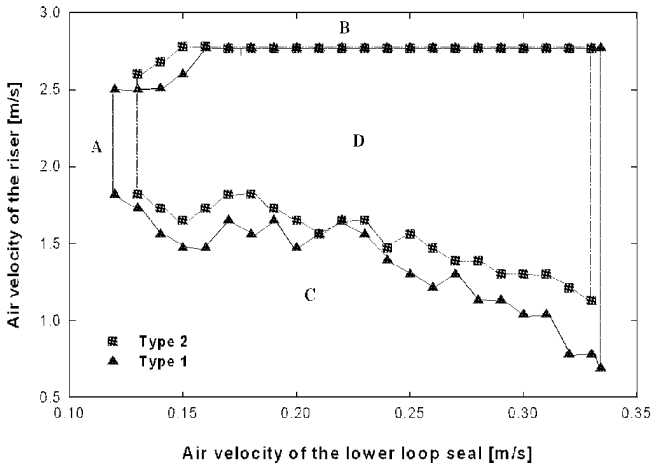

Fig. 3 The map of the possible operation condition

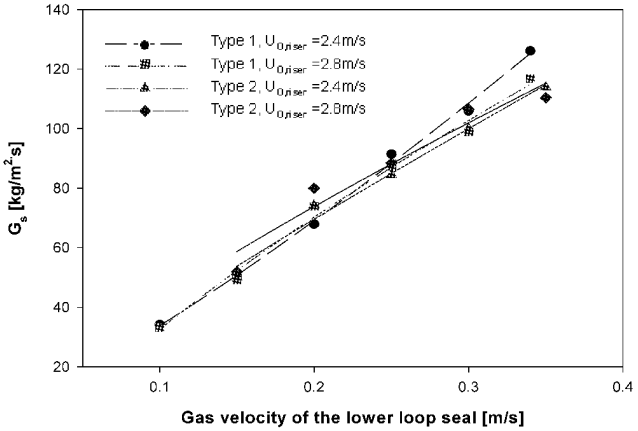

Fig. 4 Solid circulation rate as a function of gas velocity of the riser and lower loop seal

To find a stable operation region, we investigated characteristics of solid moving as a function of riser and lower loop seal velocity. It is important to provide a continuous solid circulation into the gasifier as a heat carrier to maintain auto-thermal system. Figure 3 shows the map of possible operating conditions of lower loop seal and riser. As shown in the map, DFB reactor can be operated in a stable manner inside the boundary (region **D**). In region **A**, the solid circulation from the lower loop seal to the riser is not smooth because the velocity of lower loop seal is too low and sluggish motion occurs in the gasifier. In region **B**, the riser velocity is too high so that the solid holdup of the riser is too low for combustion. In region **C**, the riser velocity is not

enough to transfer the solid in the riser to the cyclone. We can operate the DFB reactor in a stable manner inside the boundary of region **D** for each case. There are difference in the stable operation map between Type 1 and Type 2 and the stable operating region of Type 1 is larger than Type 2 for all conditions except for the low velocity condition of the lower loop seal and high velocity of the riser. In addition, the effect of the gas velocity in the lower loop seal and gasifier on the G_s is investigated. Figure 4 shows the change of the solid circulation rate as a function of the gas velocity of the lower loop seal and riser. The result shows that solid circulation rate is mainly affected by the gas velocity of the lower loop seal while the riser velocity slightly affects the solid circulation rate.

Figure 5 shows the effect of the gas velocity of bubbling fluidized bed on the solid circulation rate. In the experiment, the gas velocity of the lower loop seal and the riser are fixed as 0.13 m/s and 2.2 m/s respectively. The gas velocity of the BFB was changed from u_{mf} to $2.5u_{mf}$. When the gas velocity is smaller than $2.0u_{mf}$ the solid circulation of the two types are almost same. However when the gas velocity is above $2.0u_{mf}$, the solid circulation rate of Type 1 decreases as gasifier velocity increases while the solid circulation rate of Type 2 slightly increases as the gasifier velocity increases. This difference can be explained by the different configuration of the gasifier way-out. In addition, to access gas bypassing fractions between gasifier and lower loop seal, CO_2 is used as a tracer gas and introduced to the lower loop seal while the gasifier is fluidized with dry air (Li and Weinstein, 1989). In this case, gas bypassing fraction of Type 1 is less than Type 2.

Figure 6 shows axial solid holdup distribution of the riser as a function of riser velocity for two different solid circulation rate: 38.5 and 75.3 kg/m^{2}sec. Axial solid holdup distribution has decreased as increasing riser velocity due to the increase of particle entrainment with gaining drag force on the particle surface. At lower gas velocity, the 3 regions, dense region, dilute region, and transition region are clearly observed (Li and kwauk, 1980). As increasing gas velocity and G_s, the top of riser has an additional solid holdup distribution under a given condition owing to considerable increase of internal reflux with a descending solid. Near the top of the riser, ε_s is increased due to the end effect caused by abrupt exit of the riser (Namgung et al., 1994). At higher G_s, the end effect is occurs even in the lower gas velocity. In case of G_s = 38.5 kg/m^{2}s, the solid holdup sharply decreases as the riser velocity increases while the change of the solid holdup is rather gentle at higher G_s.

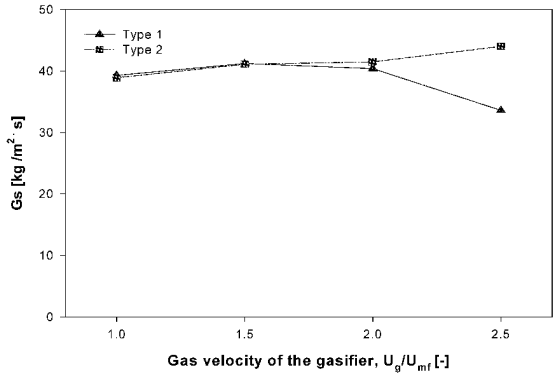

Fig. 5 The solid circulation rate according to the BFB velocity

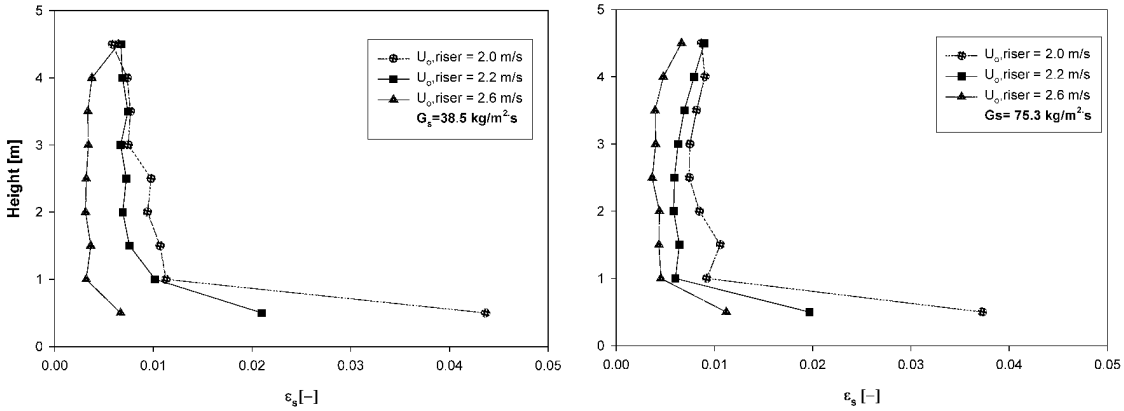

Fig. 6 Axial solid holdup distribution (Type 1)

CONCLUSIONS

In this study, we investigated hydrodynamic characteristics of DFB reactor with different configurations

of the solid way-out and distributor. We measured a minimum fluidization velocity, stable operating conditions, solid circulation rate, solid holdup in the riser and gas bypassing fractions between gasifier and lower loop seal. There is meaningful difference between Type 1 and Type 2. Type 1 has larger stable operation conditions and less gas bypassing from the lower loop seal to the gasifier. On the other hand, Type 2 has lower minimum fluidization velocity for the gasifier. For both cases, the solid circulation rate G_s is mainly affected by the gas velocity of lower loop seal. In addition, G_s of Type 1 is also affected by the gas velocity of the gasifier if its velocity is larger than $2.0u_{mf}$.

NOTATIONS

G_s	solid circulation rate	kg/m^2s
$u_{o,\,riser}$	gas velocity of the riser	m/s
$u_{o,\,loop\ seal}$	gas velocity of the lower loop seal	m/s
u_{mf}	minimum fluidization velocity	m/s
ε_s	solid holdup	-

REFERENCES

Bai, D.R., Jin, Yu, Z.Q. and Zhu, J. -X, The Axial Distribution of the Cross-Sectionally arranged Voidge in Fast Fuidiation Beds, Powder Technology, 1992

C. Riehle, Measuring and circulating solid carry over in a CFB cold flow model for different materials, Powder technology, 2000

D. Bai, K. Kato, Quantitative estimation of solid holdups at dense and dilute regions of circulation fluidized beds, powder technology, 1999

Guanwen Xu., T. Murakami, T. Suda., H. Tani., Y Mito., Efficient gasification of wet residue to produce middle caloric gas, Particuology, 2008

H. Zhu., J. Zhu., Characterization of fluidization behavior in the bottom region of CFB risers, Chemical Engineering Journal, 2008

J. H. Goo, M.W. Seo, D. K. Park, S. D. Kim, S. H. Lee, J. K. Lee, B. H. Song, Hydrodynamic Properties in a Cold-Model Dual Fluidized-Bed Gasifier, Journal of Chemical Engineering of Japan, 2008

Kunii, D., Levenspiel, O.: Fluidization Engineering, Chapter 3, Butterworth-Heinemann, 1991.

Ph. Boukis., P. Grammelis., S. Bezergianni., A.V. Bridgwater., CFB air-blown flash pyrolysis.Part 1: Engineering design and cold model performance, Fuel, 2007

THE CRACKING EXPERIMENT RESEARCH OF TAR BY CAO CATALYST

X. H Li[1], T. Mi[2], Z. S. Wu[1], Y. F. Chen[1], Q. X. Wu[1]

1 The chemistry college in Huazhong Normal University, Wuhan, 430079, China
2 Jianghan University, Wuhan, 430079, China

Abstract: The tar from rice husk gasification for power generation was taken as an example to be catalytically cracked by CaO catalyst. The experimental results showed the cracking efficiency of tar greatly increased from 28.66% by thermal cracking to 65.6% by catalytic cracking, the gas compositions from tar being cracked were H_2, CO, CH_4, and CO2, and the H_2 was a majority of them. The DSC and XRT analysis revealed that the deposit carbon could be found after tar was catalytically cracked and the deposit carbon efficiency could reach 30.51%. The SEM photographs of CaO catalyst used as catalyst showed that the CaO catalyst was enwrapped by the deposit carbon and decreased its catalytic activity, at the same time, the pressure drop of gas passing through catalyst bed increased because of the deposit carbon, it was different for us to operate the cracking reactor of tar and CaO catalyst in the cracking reactor must be regenerated for its stable operation.

Keywords: calcium oxide，catalyst，tar cracked

INTRODUCTION

Gasification of biomass is a promising technology for power generation or chemical production. One of the main inconveniences for commercializing biomass gasification is the product gas quality. Among the impurities present in product gas, tar represents a serious impediment that has received significant attention in literatures (Devi et al., 2003; Zhang et al., 2004; Huber et al., 2006).

Tar is a complex mixture of condensable hydrocarbons; producer gas from biomass gasifiers entrains with tar, which forms a serious problem for its use in e.g. engines and turbines. Tar will impose serious limitations in the use of producer gas due to fouling of downstream process equipment, engine wear and high maintenance costs. By far, tar removal is the most problematic. Thus the successful implementation of gasification technology for gas engine/turbine based power projects depends much on the effective and efficient removal/conversion of tar from the producer gas.

Tar removal methods can be classified as primary or secondary (Baker et al., 1987). Primary methods include all the measures taken in the gasification step itself to prevent tar from being formed in the gasifier or to convert it. Secondary methods can be chemical or physical treatments downstream the gasifier. Both primary and secondary methods include the use of bed additives. These can be metallic catalysts, mainly Ni-based catalysts (Gil et al., 1999; Corella et al., 1999; Rapagn`a et al., 2000; Garc´ıa et al., 2001; Corella et al., 2004; Bain et al., 2005), dolomites(Wang et al., 2005; Srinakruang et al., 2005; Swierczy´nski et al., 2006; Zhang et al.,, 2007), olivines(Swierczy´nski et al., 2006; Z. Abu El-Rub et al., 2004) or a combination of metals on dolomite or olivine(Coll et al., 2001;Polychronopoulou, 2004; Furusawa et al., 2005;Polychronopoulou et al., 2006;). Metallic catalysts have the advantage of being more active at low temperatures but they can suffer the inconvenience of deactivation caused mainly by the carbon deposits, The CaO is effective and relatively cheap catalyst for tar cracked compared with nickel-based catalysts are deactivated by coke formation and are more expensive, which helped decrease the cost of the gas cleaning process, and increase the gasification efficiency of biomass.

Some reviews in the literature have presented catalysts for biomass tar destruction and a more detailed description of these catalysts can be found elsewhere (Juutilainen et al., 2006), but most of them aimed at a kind of model compound such as benzene, toluene and naphthalene etc, it was a no clear significance for removing industry tar.

In this context, the tar from rice husk gasification for power generation was taken as an example to be catalytically cracked by CaO catalyst. The catalytically cracking performance of tar by CaO was studied. The experiments were performed in small-type catalyst evaluation equipment, all the experiments were carried out at 800℃, during experiment, it was considered for the effect of thermal cracking of tar on catalytically cracking of tar, the catalytically cracking efficiency and the deposit carbon efficiency was calculated in the present work, the influence of the deposit carbon to CaO catalyst activity was investigated, producer gas content and system pressure drop were also analyzed.

EXPERIMENTALS

The cracking reaction of tar was carried out in small-type catalyst evaluation equipment which was consisted of vaporization, quartz tube reactor for tar cracking, condenser, temperature controller and analysis system for gas and liquid tar, the flow diagram of system illustrated Fig. 1, the carrying gas was argon at 40ml/min. Tar, which was controlled by metric pump at 2ml/min, was first gasified by vaporization, and then entered quartz tube reactor with carrying gas, the quartz tube reactor was filled with 5g CaO catalyst, the gas product from exit of reactor was analyzed by gas chromatography (GC) on-line through sextuple sampling valve, the carrying gas in GC was same as argon at 35ml/min, the filling column of thermal conduction detector (TCD) was 2m×3mm，and the gas-adsorbent compound in the filling column was AE.TEX-01；the gas product entrained un-cracked tar was separated by condenser, the tar sample separated by condenser was analyzed by GC-MS with a Model HP-5971A detector (Hewlett-Packard, Palo Alto, CA, USA). The column was a 50m×0.25mm, 0.25μm packed with HP-5 5% diphenyl-95% polysiloxane. Column temperature was 60℃-10℃/min-290℃(23min), Helium was used as carrier gas at 35ml/s. Injection(1μl) was carried out in the splitless mode (1 min, injector temperature 250℃). Transfer line temperature was 280℃. Mass spectra were recorded at 70eV(1 scan s-1, source temperature 180℃).

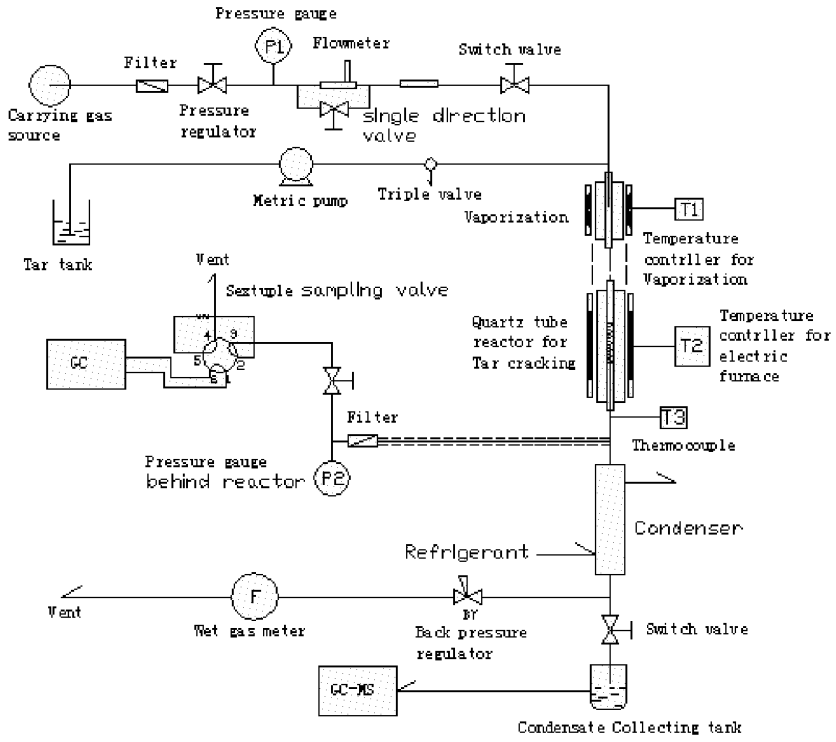

Fig. 1 The flow diagram for tar being catalytically cracked

RESULTS AND DISCUSSION

The Composition Analysis of Tar Before and After Being Thermally Cracked

The tar was provided by MW-scale rice hull gasification for electric power generation, the operation parameters included that gasification temperature was (700 °C), equivalence ratio (ER) 0.26, gasification efficiency (70%), conversion efficiency of carbon (80%). The purifying system consisted of a Venturi tube and three-stage water scrubbers for gas cleaning in order to eliminate the tar content and fly ash in the fuel gas. However, the tar in the form of aerosols was very difficult to remove by scrubbing systems and gathered by horizontal cyclone separator for the catalytic cracking experiment of tar.

The GC-MS analysis of tar before being catalytically cracked was illustrated in Figure 2; the different RT composition of tar was shown in Table 1. It could be seen from Table 1 that the tar was made of the hydrocarbon with one oxygen atom, which mainly consisted of aromatic ketone, ether and others heterocyclic compound with oxygen.

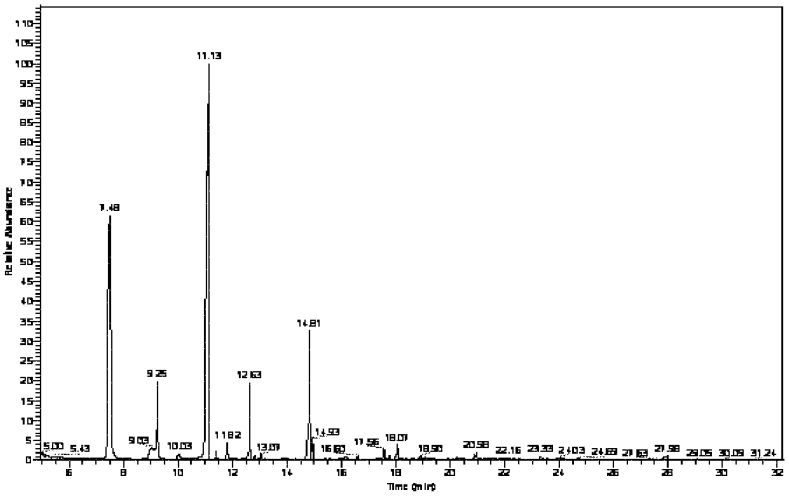

Fig. 2 The GC-MS analysis of tar from rice hull gasification at 700℃

Table 1 The composition of tar from rice hull gasification at 700℃

RT	Composition	Content (%)
7.48	$C_{12}H_{15}O$	30.39
9.02	$C_{11}H_{10}$	2.11
9.24	$C_{11}H_{10}$	5.39
11.10	$C_{17}H_{30}O$	48.43
12.62	$C_{13}H_{10}$	2.81
14.82	$C_{14}H_{10}$	8.39

The XRD Analysis of Cao Before and After Being Used As Catalyst for Tar Being Cracked

The CaO used as catalyst for tar being cracked was analysis pure stage, the XRD analysis of CaO before and after being used as catalyst for tar being cracked could be shown in Fig. 3 (before CaO being used as catalyst) and 4 (after CaO being used as catalyst) in order to understand the variation of CaO, it could be seen from Fig. 3 that the X `diffraction peaks could be clearly found at 18.3℃,28.94℃,29.65℃,34.4℃, 47.63℃ and 51.05℃, and were identical with the standard library of CaO containing water, this was because of CaO adsorbed water bebore being used as catalyst; it could be seen from Fig. 4 that the X diffraction peaks could be clearly found at 32.38℃,37.56℃,54.07℃,64.38℃, 67.57℃, and were identical with the standard library of CaO, this was because of CaO dehydration at high temperature after being used as catalyst.

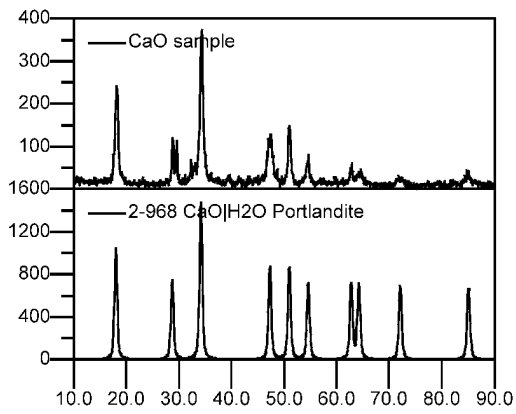

Fig. 3 The XRD diagram of calcium oxide before used as catalyst for tar being cracked
(The top X diffraction peaks was CaO sample before being used as catalyst and the bottom X diffraction peaks was the standard library of CaO containing water)

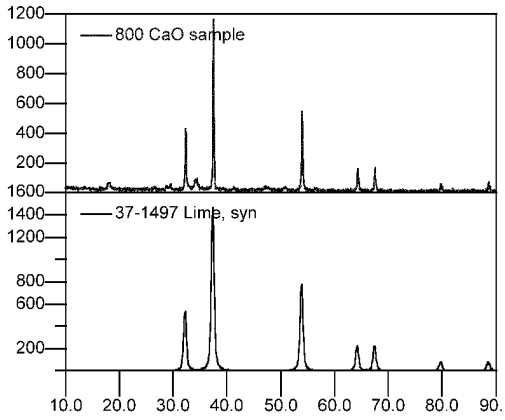

Fig. 4 The XRD diagram of calcium oxide after used as catalyst for tar being cracked
(The top X diffraction peaks was CaO sample after being used as catalyst and the bottom X diffraction peaks was the standard library of CaO no containing water)

The DSC Analysis of CaO After Being Used As Catalyst for Tar Being Cracked

It had been found from the experiment that the color of CaO catalyst changed from white to black after being used as catalyst for tar being cracked. The DSC analysis in the air was as follows Figure 5, It could be seen from Figure 6 that there were two peaks at 500℃ and 715℃ for CaO catalyst for tar being cracked, among them, the peak at 500℃ was gas absorbed peak, the deposit carbon from tar being cracked reacted with air belonged to chemical control below 500℃, and the other peak at 715℃ was loss weight peak of the deposit carbon oxidation.

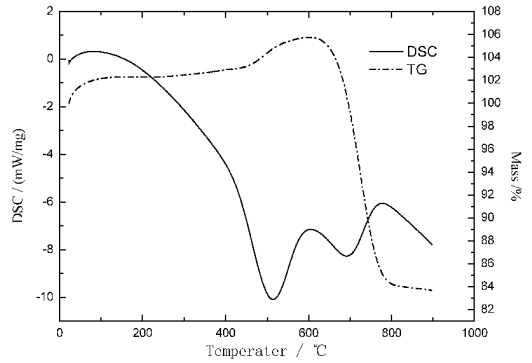

Fig. 5 The DSC and TG diagram of calcium oxide after used as catalyst for tar being cracked

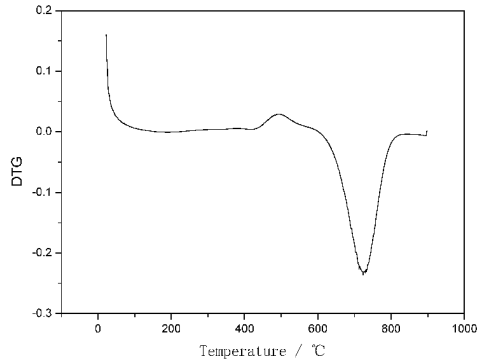

Fig. 6 The DTG diagram of calcium oxide after used as catalyst for tar being cracked

The Determination of the catalytically Cracking Efficiency and the Deposit Carbon of Tar

the carbon and hydrogen elements analysis for calcium oxide after being used as catalyst for tar being cracked were as follows in Table 2, it could be seen from table that the deposit carbon content of calcium oxide catalyst used as catalyst for tar being cracked could reach 12.38%.

Table 2 the elements analysis of calcium oxide used as catalyst for tar being cracked

Sample	Element (%)	
	C	H
CaO after being used as catalyst for tar being cracked	12.38	0

the temperature of reactor in catalyst evaluation equipment was controlled at 800℃ in order to understand the performance of CaO catalyst for tar being cracked, the quantitative tar entered the tar cracking reactor, the gas produced from the tar cracking reactor was cooled, and the un-reaction tar was condensed and collected by condenser, the cracking efficiency of tar could be calculated according to the tar reacted, the tar reacted in reactor equaled to the un-reaction tar condensed and collected by condenser being subtracted from the total mass of tar of entrance reactor the calculation formulation of the cracking efficiency of tar was as follows:

$$\text{the cracking efficiency of tar} = \frac{\text{the tar reacted in reactor}}{\text{the total mass of tar of entrance reactor}}$$

The calculation results were shown in following table 3 in different experimental period, it could be seen that the cracking efficiency of tar could increase from 28.66% by the thermally cracking to 65.6% by CaO catalytically cracking.

Table 3 The cracking efficiency of tar in different experimental period

Sample	The cracking efficiency of tar
The thermal cracking efficiency of tar（no CaO catalyst, the crystal ball of 5g, diameter 2mm was used as the filling bed）	28.66%
The CaO catalytical cracking efficiency of tar (the CaO catalyst of 5g, diameter 1mm was used as the filling bed）	65.6%

The deposit carbon could be found in thermal and catalytic experiments of tar cracked, The SEM photograph of the deposit carbon from thermal cracking of tar revealed that the deposit carbon was the shape of slice in Fig. 7. Compared the SEM photographs in Fig. 8 with Fig. 9 for CaO before and after being used as catalyst for tar being cracked, it was found that the CaO catalyst in Figure 9 was enwrapped by the deposit carbon and decreased its catalytic activity. The deposit carbon efficiency could be calculated according the

weight of the deposit carbon on CaO catalyst; the calculation formulation of the deposit carbon efficiency of tar was as follows:

$$\text{the deposit carbon efficiency of tar} = \frac{\text{the weight of the deposit carbon on CaO catalyst}}{\text{the tar reacted in reactor}}$$

The deposit carbon efficiency was 30.51% for tar being catalytically cracked.

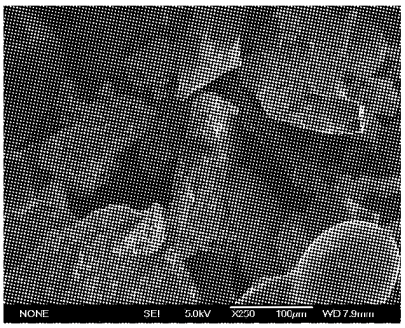

Fig. 7 The SEM images of a deposited carbon from the thermal cracking of tar at 800℃

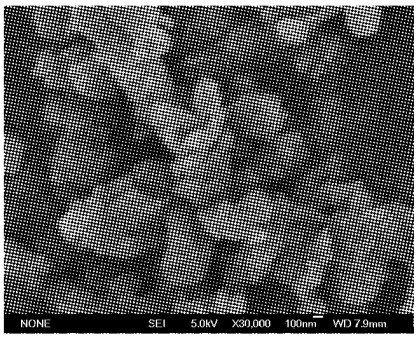

Fig. 8 The SEM photograph of the CaO before used as a catalyst to crack tar at 800℃

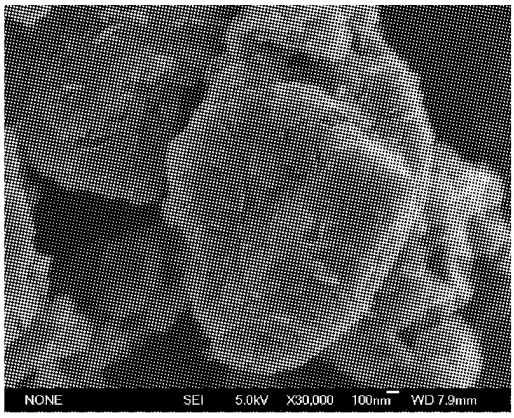

Fig. 9 The SEM photograph of the CaO after used as a catalyst to crack tar at 800℃

The Gas Composition Analysis from Tar Being Cracked

The gas production from tar cracked was analyzed by gas chromatograph (GC) using unitary method in Figure 10, it could be seen from Figure 10 that the volumetric composition of gas consisted of H_2: 90.68%; CH_4:0. 27%; CO: 4.52%; CO_2: 2.76%, the gas composition would change with the carbon deposited on CaO catalyst, because the CaO catalyst was enwrapped by the deposit carbon, its catalytic activity decreased, the typical gas composition consisted of H_2: 88.02%, CH_4:0. 17%, CO: 5.76%, CO_2: 2.37%, compared with the earliest gas composition, the H_2 content decreased, and CO content increased, this was because the following

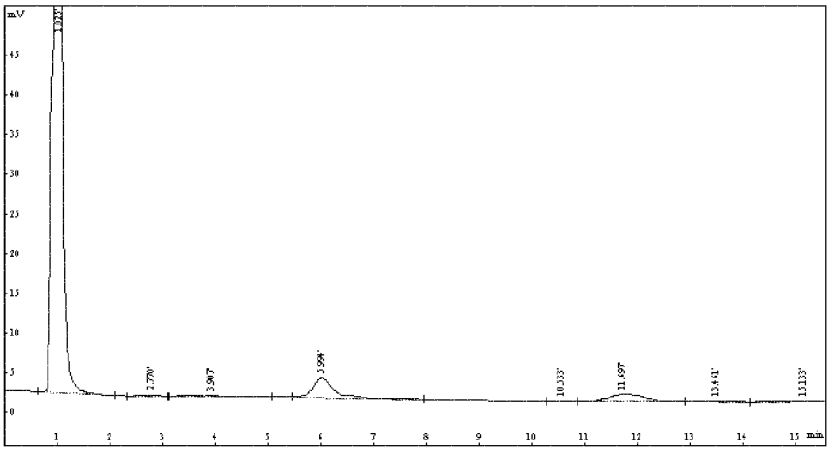

Fig. 10 The gas chromatogram analysis of gas produced by tar being catalytically cracked

reaction took place as follows:

$$TAR \xrightarrow{\text{catalytically cracking}} C + H_2 + CO_2$$

$$C + CO_2 \rightarrow 2CO$$

$$C + 2H_2 \rightarrow CH_4$$

With the deposit carbon increasing, the CaO catalyst was completely enwrapped and lost its catalytic activity, the hole of catalyst bed was blocked up by the deposit carbon from tar being cracked, the pressure drop of gas passing through catalyst bed increased, the CaO catalyst in the cracking reactor should be regenerated for its stable operation.

CONCLUSIONS

Experimental results indicated that the cracking efficiency for tar from rice hull gasification could reach from 28.66% by thermal cracking to 65.6% by catalytically cracking of CaO at 800℃, the gas compositions from tar being cracked were H_2, CO, CH_4, and CO2, and the H_2 was a majority of them, the gas composition would change with CaO catalyst activity. The DSC and XRD analysis revealed that the deposit carbon could be found in both thermal cracking and catalytically cracking of tar, the deposit carbon efficiency could reach 30.51% for catalytically cracking of tar. The SEM photographs of CaO catalyst used as catalyst for tar being cracked showed that the deposit carbon was the shape of slice, and the CaO catalyst was enwrapped by the deposit carbon and decreased its catalytic activity, at the same time, the pressure drop of gas passing through catalyst bed increased because of the hole of catalyst bed being blocked up by the deposit carbon, it was different for us to operate the cracking reactor of tar and CaO catalyst in the cracking reactor should be regenerated for its stable operation.

ACKNOWLEDGMENT

The authors acknowledge the financial support of the Natural 973 project of China (Project: 2007CB210202-03) and the key project of Wuhan city（20066002064）. The authors are grateful the referees for their comments and recommendations.

REFERENCES

Abu El-Rub Z., Bramer, E.A. Brem G., Ind. Eng. Chem. Res. 43 (2004) 6911–6919.
Bain, R .L. Dayton D.C., Carpenter D.L.,et al., Ind. Eng. Chem. Res. 44 (2005) 7945–7956.
Baker, E.G. Mudge, L.K. Brown,M.D. Ind. Eng. Chem. Res. 26 (1987) 1335–1339.
Coll R., Salvad´o J., Farriol X., et al., Fuel Process. Technol. 74 (2001) 19–31.
Corella, J. Aznar,M.P. Gil, J. Caballero, M.A. Energy Fuels 13 (1999) 1122–1127.
Corella, J. Toledo J.M., Padilla R., Energy Fuels 18 (2004) 713–720.
Devi L., Ptasinski K.J., Janssen F.J.G., Biomass Bioenergy 24 (2003) 125–140.
Furusawa T., Tsutsumi A., Appl. Catal. A 278 (2005) 195–205.
Garc´ıa, L., Salvador M.L., Arauzo J., Bilbao R., J. Anal. Appl. Pyrolysis58–59 (2001) 491–501.
Gil J., Caballero M.A., Mart´ın J.A., et al., Ind. Eng. Chem. Res. 38 (1999) 4226–4235.
Huber, G.W., Iborra,S., Corma, A. Chem. Rev. 106 (2006) 4044–4098.
Juutilainen S.J., Simell P.A., A. Krause O.I., Appl. Catal. B 62 (2006) 86–92.
Polychronopoulou K., Bakandritsos A., Tzitzios V., et al. J. Catal. 241 (2006) 132–148.
Polychronopoulou K., Fierro J.L., Efstathiou A.M., J. Catal. 228 (2004) 417–432.
Srinakruang J., Sato K., Vitidsant Fujimoto T., K., Catal. Commun. 6 (2005) 437–440.
Swierczy´nski D., Courson C. Bedel , L., et al.,, Chem. Mater. 18 (2006) 4025–4032.
Rapagn`a S., Jand N., Kiennemann A., et al., Biomass Bioenergy19 (2000) 187–197.
Wang T., Chang J., Lu P., et al., Energy Fuels 19 (2005) 22–27.
Zhang, R. Brown R.C., Suby A., K. Cummer, Energy Convers. Manage. 45 (2004) 95–1014.
Zhang, R., Wang Y., Brown R.C., Energy Convers. Manage. 48 (2007) 68–77.

EXPERIMENT INVESTIGATION OF THE INFLUENCING FACTORS ON BED AGGLOMERATION DURING FLUIDIZED-BED GASIFICATION OF BIOMASS FUELS

Y. Q. Chen, H. P. Chen, H. P. Yang, X. H. Wang, S. H. Zhang

State Key Laboratory of Coal Combustion, Huazhong University of Science and Technology, Wuhan, 430074, China

Abstract: With the depleting of fossil fuel and environmental polluting increasing, the utilization of biomass resources caught increasing concern. Biomass gasification in fluidized bed, as one promising technology, developed quickly. However, serious agglomeration was displayed as biomass ash reacted with bed material （silica sand） at higher temperature. It hindered the wide utilization of CFB gasifier. The objective of this work is to investigate the agglomeration behavior between biomass ash and silica sand, and catch the inherent mechanism. Firstly, the influence of ash compounds on the agglomeration behavior was analyzed with biomass ash and synthesis ash compounds addition in fixed bed as ash sample mixed with bed material evenly before every trial. The reaction temperature was set 850℃ that is the operated temperature for many fluidized bed gasificated biomass fuels. Then the influence of reaction time was analyzed. The characteristics of the agglomerated silica sand particles were analyzed by the XRD. Finally, it was simulated with HSC computer mode based on thermodynamic equilibrium. It was observed that when the ratio of the biomass ash to the silica sand was above 0.2, the agglomeration was observed. With the increase of the reaction time, more silica sand particles agglomerated with the biomass ash. There are two kinds of silicate eutecticum investigated by the XRD. It is of great significance for the running of CFB biomass gasifier and the development of biomass utilization technology.

Keywords: agglomeration, biomass fuel, roasting time, gasification

INTRODUCTION

The need for non-polluting and renewable sources of energy is demonstrated by the increasing energy demand and the polluting nature of existing fossil fuel energy sources. The biomass, found as by products in various industries such as agricultural and wood processing, is used increasing for heat and power production since it is renewable and does not contribute significantly to the greenhouse effect. However, most of biomass has high ash contents whose behavior determines the use of particular conversion technology and its efficiency. The significant operational problem caused by the ash contents of biomass is the formation of deposits in the furnace (slagging) and in the heat exchange sections (fouling).

The fluidized bed technology has been found to be the most suitable approach to convert a wide range of biomass fuels into energy since the inherent advantages of low process temperatures, isothermal operating condition, and fuel flexibility(Zevenhoven-Onderwater, et al.,2006). Besides the advantages, like high electrical and total efficiency and limited slag/deposit formation, the agglomeration of bed particles during combustion/gasification of biomass in fluidized-bed boilers is becoming a well-identified problem, which in the most severe cases can results in total defluidization of the bed materials.(Skrifvars et al., 1999)

The agglomeration mechanisms when using biomass in normal silica bed is studied by many researchers. And there are three documented dominating initial stages mechanisms for agglomeration(Lundholm, et al.,2005, De Geyter et al.,2007): (1) for alkali-rich fuels, direct attack by potassium in gas or aerosol phase and forming low-melting which induce viscous-flow sintering and agglomeration, (2) for woody fuels, agglomeration induced by ash-coating formation on silica bed particles with attack and diffusion of calcium, forming low-melting silicates also including minor amounts of potassium, with subsequent viscous-flow sintering and agglomeration, (3) for fuels containing both potassium and high amounts of reactive silica, direct adhesion by partly melted ash-derived potassium silicate particles/droplets.

The potential of biomass in China has been estimated to be equivalent to an annual energy of 500 million ton standard coal. It is anticipated that the installed capacity of the biomass electricity generation in China will up to 5,500 MWp(Zhijun,2008). The properties of the biomass in China are different to that in European where the technology of biomass converting equipment come from, then there may be more different ash-related problem encountered because the difference between the Chinese biomass fuel and the European one. So it is important to investigate the ash-related properties of the biomass.

The main objective of present work was therefore, to experimentally determine the agglomeration tendencies of one typical biomass (rape straw from Hubei Province, China) in the gasification of the fluidized

bed by a simple roasting of the mixture of the ash and the silica sand and the equilibrium calculations are combined with an attempt to explain the formation mechanism of agglomeration.

EXPERIMENTAL

Materials

The biomass fuels chosen for the study were rape straw from Hubei Province, as a typical Chinese biomass. Proximate analyses of rape straw were conducted using ASTM standards to obtain moisture content, volatiles, fixed carbon, and ash content. Ultimate analyses of the dried samples for carbon, hydrogen, nitrogen, and sulfur were carried out with a CHNS/O elementary analyzer (Vario Micro cube, Germany). The calorimetric values of the dried rice husks samples were measured by bomb calorimeter (Parr 6300, USA) (listed in Table 1).

Table 1 The proximate and ultimate analysis result of rape straw[a]

Proximate analysis (wt. %)				Ultimate analysis (wt.%, ar)					LHVar (MJ/kg)
M_{ar}	V_{ar}	A_{ar}	FC_{ar}	C	H	N	S	O*	
11.19	67.62	7.47	13.73	41.61	2.21	0.93	0.09	36.51	16.339

[a]M, moisture content; V, volatile matters; A, ash; FC, fixed carbon; ar, on as received basis; LHV, lower heating value. The O content was determined by difference.

The main components of the ash and the silica sand are list in Table 2 analyzed by the XRF.

Table 2 The properties of the rape straw ash and the silica sand（unit, %）

	Na	K	Ca	Mg	Al	Fe	Si	S	Cl	P
Rape straw	0.12	35.92	28.24	2.36	0.56	0.43	2.16	7.85	20.65	1.62
Silica sand		0.04	0.05	0.12	1.23	0.23	56			0.01

Roasting of the mixture

It was demonstrated that the actual bed or process temperature is the most important individual parameter influencing the bed agglomeration (Ohman and Nordin,1998). The agglomeration tendency would be increasing with the accumulation of the biomass ash in the bed, so it is necessary to investigate the influence of the ratio of the biomass ash to silica sand. Different ratios (0~1) of the mixture were prepared. The mixture were roasted in fixed bed reactor，and the condition is the same with typical biomass fluidized bed gasification unit and the process temperature was 850℃.The retention time when a significant agglomeration commenced was investigated from 2h.

To examine the generation of the agglomeration between ash and silica sand, the X-ray diffraction pattern was measured using X-ray diffraction equipment (X'Pert PRO).

HSC chemistry equilibrium calculations

Chemical equilibrium model calculations were performed using the software program HSC Chemistry 4.0. which uses the method of minimization of the total Gibbs free energy of the system. Fuel used was rape straw ash, and the compositions shown in Table 2 were. The calculations were performed using a global approach for atmospheric pressure, and air-to-fuel ratio set at 0.35, corresponding to the gasification bench-scale experiments. The calculations were conducted at furnace temperature of 850℃.

The elements and solution model used in the chemical equilibrium model calculations were based on the Ohman's research(Ohman, et al.,2005), which are listed in the Table 3.

Table 3 Elements and solution models used in the chemical equilibrium model calculations

elements	C, H, O, N, S, Cl, P, K, Na, Ca, Mg, Fe, Mn, Si, Al
solution models	
slag	slag-liquid (MgO, FeO, MnO, Na2O, SiO2, CaO, K2O)
salt	A salt-liquid (NaCl, KCl, NaOH, Na2SO4, K2SO4, Na2CO3, K2CO3)
(Ca, Mg)	liquid-K,Ca/CO3,SO4 (-LCSO)
	solid-K,Ca/CO3,SO4 (-SCSO)
	solid-Ca(SO4),Mg(SO4) (-SCMO)
	liquid-Ca,Mg,Na/(SO4) (-LSUL)
	solid-Ca,Mg,Na/(SO4) (-SSUL)

RESULT AND DISCUSSION

The result of roasting of the mixture

The influences of the ratio of ash to sand and the roasting time were investigated (lists in Table 4). There was no agglomeration generated when the roasting time were 2h for all. Increasing the roasting time, the agglomeration began be investigated and increasing the ratio of the ash the agglomeration generated earlier in the range of 0.4-0.8, while there was no agglomeration generated for the ratio of 0.2. It is suggested that maintaining the ratio of biomass ash to bed particle lower 0.2 would reduce the agglomeration tendency. The photos of the agglomeration investigated in different ratio (0.4-0.8) are shown in Fig 1.

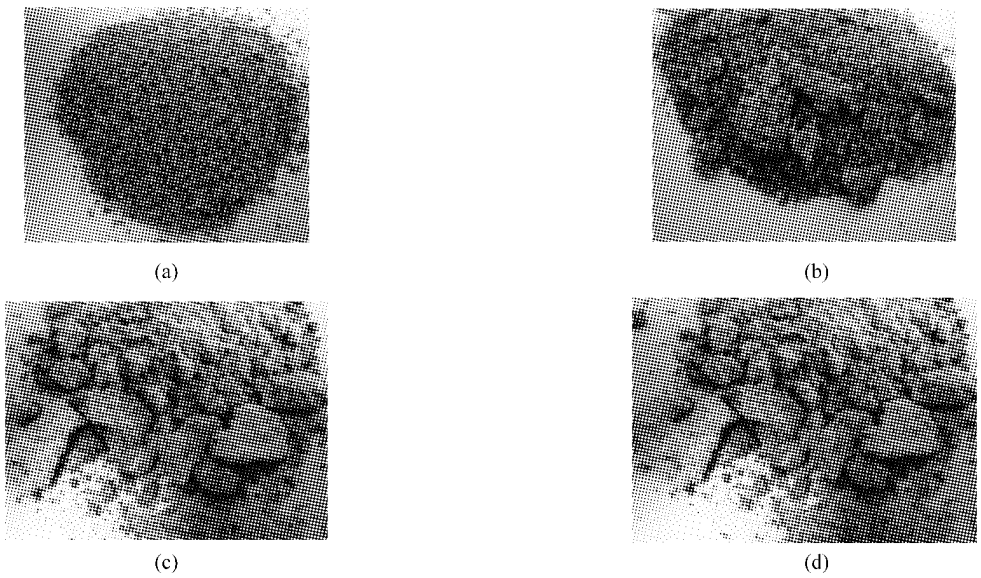

Fig. 1 The photo of the agglomeration investigated for three ratio
(a) 0.2, (b) 0.4, (c) 0.6, (d) 0.8

Table 4 The influences of the ratio of ash to sand and roasting time on ash agglomeration

Roasting Time (h)	Ratio (ash/sand)			
	0.2	0.4	0.6	0.8
2	no	no	no	no
4	no	no	no	*
6	no	no	*	**
8	no	no	**	***
10	no	no	***	***
12	no	*	***	***

Note: no) no agglomeration generated; *) agglomeration began; **) visual agglomeration; ***) large agglomeration

The XRD analysis

The X-ray diffraction patterns of four agglomerations in different ratio of ash are shown in Fig.2. The structure of the mixture after roasted is very complicated, the sample consists many kinds of chemical compound such as silicate and aluminosilicate whose melting point temperature are higher than 850℃. The principal characteristics peaks of the silicate eutecticum are concentrated in the range of 15° -45° 2θ. The eutecicum of potassium calcium silicate ($K_4CaSi_3O_9$) was investigated since there are high content of potassium and calcium in the rape straw ash (see Table 2). It is consistent with the Ohman's conclusion (Ohman, Pommer and Nordin, 2005). Little amount another eutecium Na_2MgSiO_4 also was investigated for three samples, which has also a low melting point temperature. The result analyzed from XRD is different from the chemical equilibrium calculations that may be the experiment error induced by chemical dynamics.

The result of chemical equilibrium calculations

The result from equilibrium calculations (see Table 5) showed the same result with previous literature(Ohman, Pommer and Nordin, 2005). An oxide/silicate (slag) melt is predicted to form for the rape straw ash containing high calcium, potassium, sulfur and chlorine.

Table 5 Phase/solutions predicted to form during gasification in 850℃, according to equilibrium

The ratio of the condensed phase	The chemical compound
Dominant(>50mol%)	$Ca_3Fe_2Si_3O_{12}$, $Ca_3(PO_4)_2$, $Ca_3MgSi_2O_8$
Subdominant(20-50mol%)	$CaAl_2Si_2O_8$, $Ca_2MgSi_2O_7$, $3CaO \cdot 2SiO_2$, $KAlSi_2O_6$,
Minor(5-20mol%)	$CaSiO_3$, K_2SO_4, $CaMgSi_2O_6$, $K_2O \cdot 2SiO_2$
Trace(<5mol%)	K_2SiO_3, $MgSiO_3$

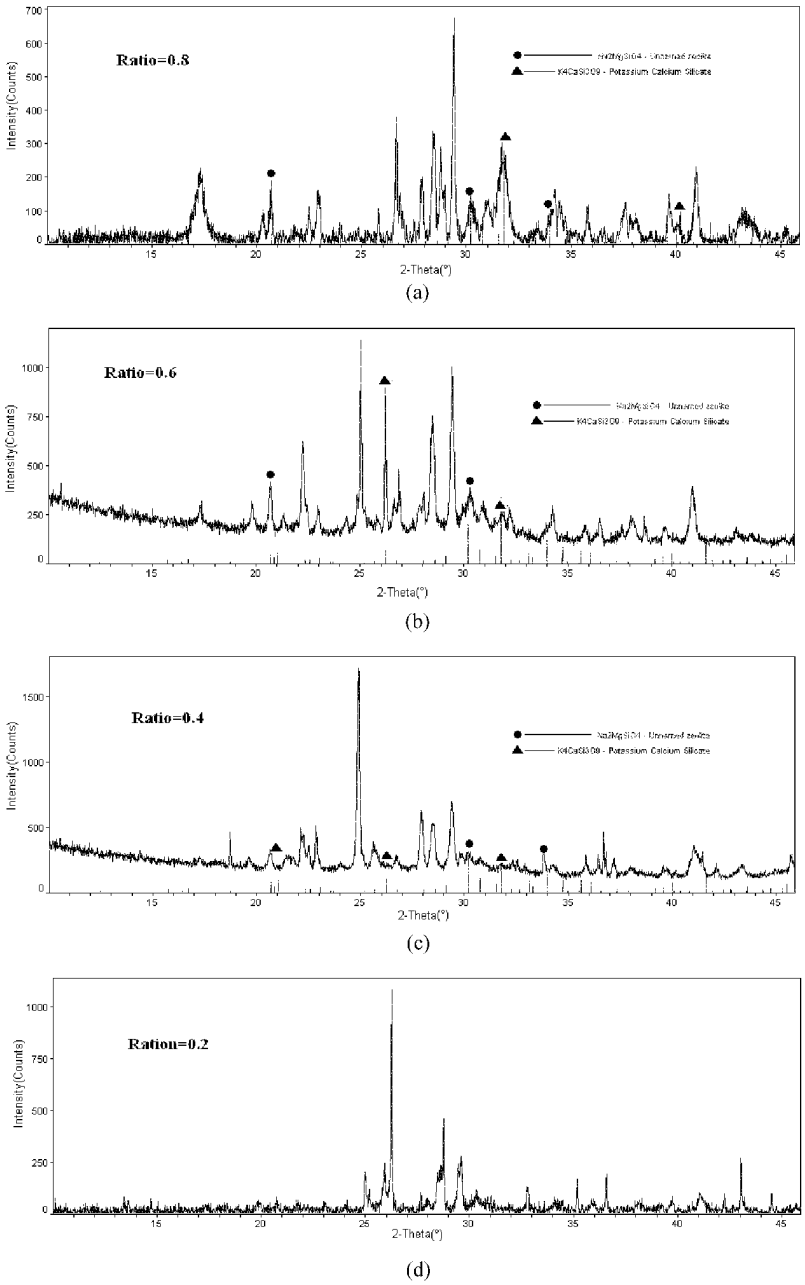

Fig. 2 The X-ray diffraction patterns of four agglomerations

CONCLUSIONS

In this work, the roasting experiment at gasification atmosphere for several mixture contained different ratio of biomass ash has been carried out. It was observed that when the ratio of the biomass ash and the silica sand was above 0.2, the agglomeration was showed. Increasing the roasting time, the agglomeration began be investigated and increasing the ratio of the ash the agglomeration generated earlier in the range of 0.4-0.8. It is suggested that maintaining the ratio of biomass ash and bed particle lower 0.2 would reduce the agglomeration tendency. From the XRD analysis, two silicate eutecium such as $K_4CaSi_3O_9$ and Na_2MgSiO_4 melted at low

temperature caused the agglomeration for rape straw gasificated in the fluidized bed.

ACKNOWLEDGMENTS

The authors express great appreciation of financial support from "Key Projects of National Fundamental Research Planning" (National 973 project 2007CB210202) and the National Nature Science Foundation of China (50806027 and 50676037).

REFERENCES

De Geyter, S., Ohman, M., Bostrom, D., Eriksson, M. and Nordin, A. Energy Fuels 21(2007), pp 2663-2668
Lundholm, K., Nordin, A., Ohman, M. and Bostrom, D. Energy Fuels 19(2005), pp 2273-2278
Skrifvars, B. J., Ohman, M., Nordin, A. and Hupa, M. Energy Fuels 13(1999), pp 359-363
Ohman, M. and Nordin, A. Energy Fuels 12(1998), pp 90-94
Ohman, M., Pommer, L. and Nordin, A. Energy Fuels 19(2005), pp 1742-1748
Zevenhoven-Onderwater, M., Ohman, M., Skrifvars, B. J., Backman, R., Nordin, A. and Hupa, M. Energy Fuels 20(2006), pp 818-824
Zhijun, L. Technology Economics 27(2008), pp 34-38

FLOW REGIME DISTINGUISH IN A CIRCULATING FLUIDIZED BED GASIFIER BASED ON WAVELET MODULUS MAXIMA

F. Duan[1,2], Y.J. Huang[1], B.S. Jin[1], B. Li[1], M.Y. Zhang[2]

1 Key Lab of Clean Coal Power Generation & Combustion Technology of Ministry of Education, Southeast University, Nanjing, 210096, China

2 School of Metallurgy and Resource, Anhui University of Technology, Ma'anshan, 243002, China

Abstract: Pressure fluctuation is often used to analyze the dynamic changes of the gas-solid fluidized beds. In this paper, cold tests were carried out to study the gasification system of circulating fluidized beds gasifier, to find out the change law of the solid circulation rate *Gs* and the holdup by altering such parameters as air velocity, particle size and integrated particle, and recognize the flow regime in the boiler through analysis of the differential pressure fluctuation signals with wavelet transform modulus maximum method. Results indicate that *Gs* increases with the increase of the superficial gas velocity. When the superficial gas velocity is higher than 2m/s, the three kinds of particles with higher distribution concentration of particle size exhibit characteristics of fast fluidization at the bottom of the riser, and the number of modulus maxima lines is almost the same as that in the top area. Change the distribution range of particle sizes of bed materials, and the larger particles in the riser after particle separation exhibit characteristics of both the turbulence region at the bottom and the fast region on the top, prolonging their residence time in the bed. There are more modulus maxima lines for the differential pressure fluctuation signals at the bottom than on the top. The regime recognition method based on modulus maximum and its experimental results will help us learn more about the design, enlargement and operation of circulating fluidized beds.

Keywords: CFB, two-phase flow, turbulence, pressure fluctuations, modulus maxima

INTRODUCTION

Circulating fluidized bed (CFB) technology has been developed for years and now widely applied in many gas-solid reacting processes such as combustion, catalytic cracking and synthesis. It has been used in the coal gasification processes to overcome the deficiency that a great deal of coal is converted into thermal energy, but not chemical energy. Coal, as a mixed organic mineral containing many impurities, exhibits different chemical reactivity for different compositions. The reaction characters of low-activity coal components call for high temperature, high pressure and long residence time in the gasification process. The residence time required for the overall gasification during the coal gasification process calculated approximately by shrinking core model controlled by chemical reaction is two times of that required for 90% of carbon conversion. It can be found in (Levinspiel, 1974). The ways to prolong the residence time of coal particles in the CFB Gasifier are to increase the back mixing in the tube by the core-annulus flow in the upper part of the riser, to increase the solid circulation rate, or to produce turbulent flow at the lower part of the riser.

In recent years, many valuable achievements have been obtained in the research of CFBs. These researches are mainly concentrated in the fields of the overall structural diagram of particle flow in beds (Bai et al., 1995a, b),and the signal analysis (Sharma et al., 2000; Lu et al.,2005; Fuchs et al., 2007; Ludlow et al., 2008), etc. Bai et al. (1995a, b, c) investigated into the changes of the transient kinetic energy in the upper dilute phase zone and the lower dense phase zone of the bed and validated the results successfully with experiments and available data. Few researches has been reported to study the flow pattern that not only has large solid circulation rate but also keeps "fast in the upper region and turbulent in the lower region" in the bed. Therefore, before carrying out the hot tests in the gasification system of the pressurized CFB, it is necessary to study the solid circulation rate and the holdup distribution of particles of different sizes under various operation conditions in the circulating beds, to find out the flow patterns and prolong the residence time of particles in the boiler, laying foundations for the initialization of hot test parameters.

The analysis of the pressure fluctuation signals has always been an important part in the fundamental theoretical research of fluidized beds. One of its main research purposes is to identify the two-phase flow pattern, such as analyzing the flowing characteristics and estimating the flow pattern transition with such statistical parameters as pressure fluctuation amplitude, standard deviation, flatness, skewness, probability distribution and main frequency, etc. In the past decade, with the development of nonlinear science, the deterministic chaos theory has been widely used in the analysis of pressure fluctuation signals of CFBs, the study of complex intrinsic flow patterns of CFBs, and the investigation into the enlargement of CFBs by characterizing different flow patterns and flow regions with such parameters as dimension and entropy. But

because of the complexity, the strong nonlinearity and the high randomness of the gas-solid two phase flow, the researches on CFBs up to now are not profound enough to provide a good and overall understanding of many critical issues and a uniform knowledge about the transition and classification of the flow pattern in the CFBs.

Kim and Han (1999) used pressure fluctuations and chaos theory to describe the flow behavior. Guenther and Breault (2004) used discrete wavelets to analyze the common hydrodynamic feature in heavily loaded CFB. While the complex dynamic system often engenders irregular signals, whose singularity points and irregular jumps always carry important dynamic information. This is one significant property of signals. Wavelet transform, derived from the evolution and expansion of Fourier transform, is a time-frequency localization method using windows with fixed size and flexible shape, and variable time window and frequency window. It has the multi-resolution capability and can describe the local characteristics of the signals both in the time domain and in the frequency domain. These make wavelets especially powerful in the analysis of non-stationary signals (Chen et al., 2004). The wavelet modulus maximum method is applied in this paper to study the singular characteristics of the differential pressure fluctuation signals in the boiler, in order to establish a relation between the differential pressure and the flow pattern in the gasification boiler of the CFB through experiment, and accordingly provide a characterizing method for the normal running of gasification boiler.

EXPERIMENTAL

Experiments were carried out in a circulating fluidized bed made of transparent acrylic resin column, as shown in Fig. 1. The apparatus was mainly composed of the experimental system (consisting of a riser, a downer, a cyclone dust extractor, a bag dust extractor and a sealed return feeder), the feeding and discharging system and the differential pressure measurement system. The riser was 5m long, with the inside diameter of 0.06m. And the downer was 3.5m long, with the inside diameter of 0.038m. The quartz sands were brought into the high-efficiency cyclone dust extractor by the fluidized air and the air was exhausted through the bag dust extractor. The separated particles got into the sealed return feeder through the downer, and got back into the riser after a second fluidization. The part between the riser exit and the inlet of the cyclone dust extractor is a T shape configuration. The return feeder exit is located 0.65m above the air distribution plate. The fluidized air was supplied by the Roots blower and the air rate was controlled by a flowmeter. There are 4 measuring points in the riser, each of which leads to a differential pressure by comparing with the wind chamber pressure. The output signals of the differential pressures collected by data acquisition card (ADVANTECH, PCI1713) were transmitted to the computer with differential pressure transmitter (Central Asia, PT201B). The pressure data were collected with computer program designed by ourselves. The measurement range of the differential pressure transmitter is 0～10KPa, with the precision of 0.1FS. Table 1 gives the size distributions of the above four groups of particles.

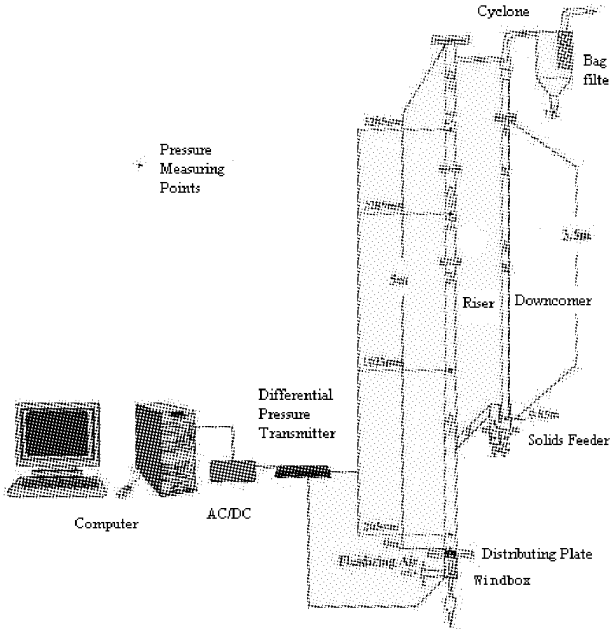

Fig. 1 Experiment system

A scale was installed on the downer. Under each operation condition, the butterfly valve on the downer

was shut off quickly, and the dropping distance of bed materials in the down pipe within a fixed time t was measured three times and the mean value H was used. Based on the principle of material balance, the solid circulation rate in the riser can be obtained by formula transformation. The bulk density of the quartz sands is taken as 1300kg/m^3.

Table 1 Size distributions of the quartz sand particles

Particle size distribution (mm)	Particle A Mass percent (%)	Particle B mass percent (%)	Particle C mass percent (%)	Mixed particle mass percent (%)
>0.90	0	0	0.09	0.4
0.50~0.90	0.1	0.13	0.36	2
0.22~0.50	0.6	0.85	83.8	30.2
0.17~0.22	35.2	38.61	9.28	20.8
0.01~0.17	49.1	55.66	4.94	43
<0.01	15.0	4.75	1.53	3.6
Average dp(mm)	0.10	0.15	0.30	0.24

The fluidized air velocity was gradually increased, leading to the increase of superficial gas velocity in the riser from 1.95m/s to 4.9m/s. After running steadily for 20 min under each operation condition, the differential pressure fluctuation signals and the solid circulation rates were recorded. Record the pressure drop fluctuation signals for 3 min, with the 50 ms intervals. The flow patterns in the bed were analyzed with wavelet transform modulus maximum method. The modulus maxima of wavelet transform correspond to the singularity points of the signals. And the number of the local maximum modulus lines indicates the number of the singularity points of signal. To minimize the effect of noise, the pressure fluctuation signals were denoised with wavelet denoising method. Still the noise may lead to the appearance of some very short local maximum modulus lines, which were neglected in this study.

RESULTS AND DISCUSSION

Effect of particle size on solid circulation rate

Wang et al. (2002) wrote that when the flow velocity of the CFB is low, i.e. ug=1.33~2.38m/s, the particle distribution tend to be dilute on the top and dense at the bottom. But at such low velocity, the solid circulation rate is relatively small (Gs=0.50 ~ 13.37kg/m^{2}s). The experiments in our work were carried out under relatively high fluidized air velocities for bed materials with different sizes. Fig.2 gives the solid circulation rates under various operation conditions.

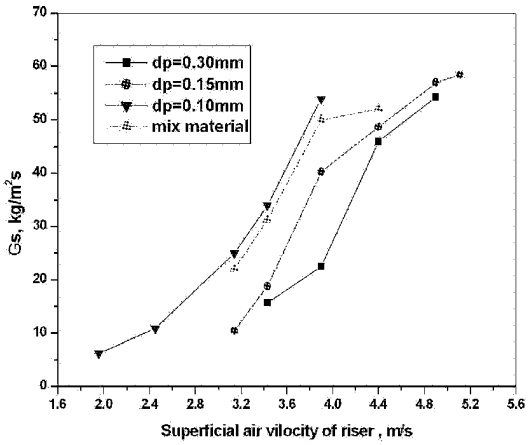

Fig. 2 Solid circulation rates of particles with different sizes

For each particle size, with the increase of the air velocity of the main bed, the particle circulation rate increases gradually, but the increase of Gs will slow down when the air velocity reaches a certain point. And under each air velocity of the main bed, Gs for the smaller bed materials is larger than that for the bigger ones. But it is found in the previous discussion of holdup that turbulent flow is not easy to form at the bottom of the riser with bed materials of small sizes. Therefore, to add a certain proportion of big bed materials into the ones of the smallest size can create the flow pattern of "turbulent flow in the lower region and fast flow in the upper region" on the premise of guaranteeing relatively high ***Gs***.

Effect of particle size on axial holdup in the riser

Fig. 3 shows the change of the axial holdup at the four measuring points in the riser for different sizes and different flow rates obtained with the above data processing method. The holdup can reflect the mass transfer between different heights in the riser. It can be found that, in the lower part (Z=205mm) of the riser, the holdup is smaller than that in the mid and upper part, the particle concentration is higher and the gas-solid slip velocity is faster. Moreover, with the increase of the particle diameter and fluidized air rate, the holdup in the dense

phase zone in the lower region gradually decreases and the particle concentration gradually increases. Because the fluidized air rate is high in the riser, the bottom of the riser shows the characteristic of fast zone under most conditions. Evident "core-annulus flow" were observed in the middle region of the bed (Z=1023mm, Z=2280mm) in the experiment. The particles changed little at the upper bed layer (Z=3280mm).

As shown in Fig. 3(d), the bed layer is composed of a dense phase zone at the bottom (with big and fine particles) and a dilute phase zone on the top (only with fine particles), because the big particles stay at the bottom of the bed layer. After the CFB reaches the pressure equilibrium, with the increase of the flow rate, the solid circulation rate increases, the holdup of the dense phase zone at the bottom also increases a little, and the height of the dense phase zone moves upward. The presence of big particles intensifies the collision between particles and increases the back mixing, and reduces the particle movement velocity, consequently enhancing the particle holdup in the dense phase zone. On the other hand, the existence of big particles results in the reduction of air flow area, leading to the increase of motion velocity of the fine particles, consequently increases the solid circulation rate. Thus the three requirements to prolong the residence time of particles in the CFB are all satisfied.

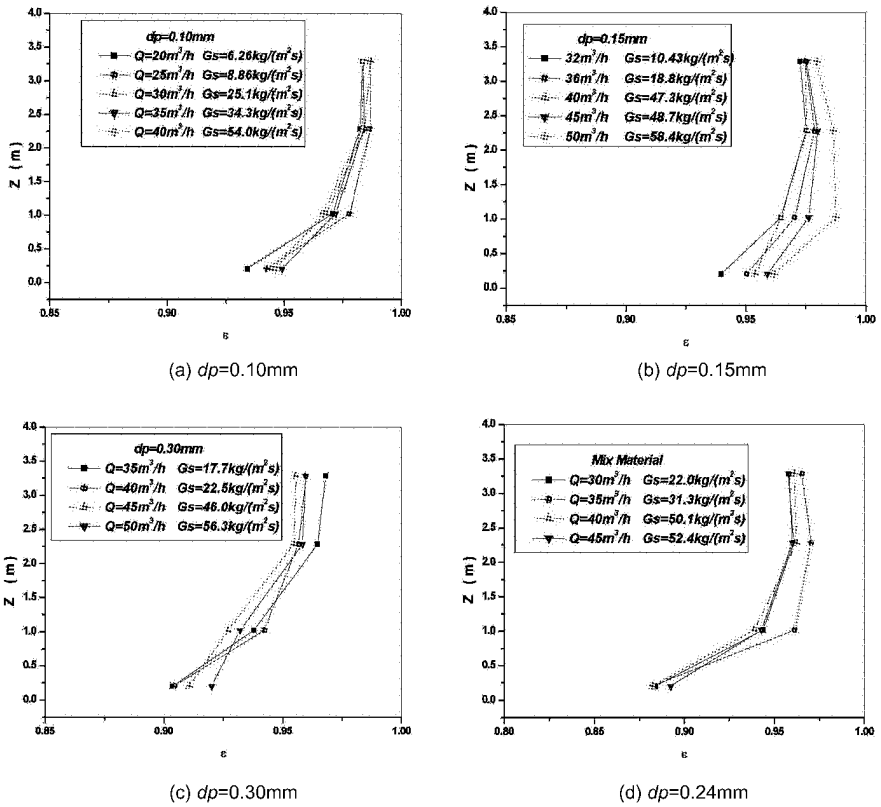

(a) dp=0.10mm (b) dp=0.15mm

(c) dp=0.30mm (d) dp=0.24mm

Fig. 3 Change of the axial holdup for different sizes and different flow rates

Modulus maxima of pressure fluctuation signals for different particle sizes

The modulus maxima of pressure fluctuation signals are similar under different superficial gas velocities for each size group. The modulus maxima at two randomly selected points (Z=205mm and Z=3280mm) in the experimental system at the same superficial gas velocity for the four size groups were analyzed by comparison. Fig.4 gives the modulus maxima of pressure fluctuation signals at superficial velocity of 3m/s in the bottom zone (a, c, e, g) and in the top zone (b, d, f, h). Here, a and b are for particles of ***dp***=0.30mm, c and d are for ***dp***=0.15mm, e and f are for ***dp***=0.10mm, and g and h for mixed materials. All the modulus maxima lines are characterized by paroxysm. It can be found that among the four graphs for the bottom zone, there are 2-3 long modulus maxima lines in a, c and e, whereas there are 5 long modulus maxima lines in g. This indicates that the flow pattern of the mixed materials at the bottom is different from those of the other three size groups. Because the gas-solid contact is not even in the dense phase zone, there are more long modulus maxima lines at the singularities, and the flow pattern of the mixed material is turbulent at the bottom.

As to the comparison of the same size (Fig. 4 (a) and (b), Fig. 4 (c) and (d), Fig. 4 (e) and (f)), the number of long modulus maxima lines of the bottom zone are almost the same as that on the top. The reason is that the gas velocity is high in the riser, the bed layer expands, and the gas-solid contact is relatively even, so that the long modulus maxima lines at the bottom zone, similar to those on the top, exhibit the characteristics of fast

fluidization under most conditions.

Different for mixed materials, the modulus maxima lines in the bottom zone are not similar to that in the top zone. The long modulus maxima line on the top (Fig.4(h)) is far less than that at the bottom (Fig. 4 (g)). This demonstrates that the flow pattern in the bed can be changed effectively by changing the particle size distribution, presenting a flow pattern of "fast on the top and turbulent at the bottom" under relatively high superficial velocities.

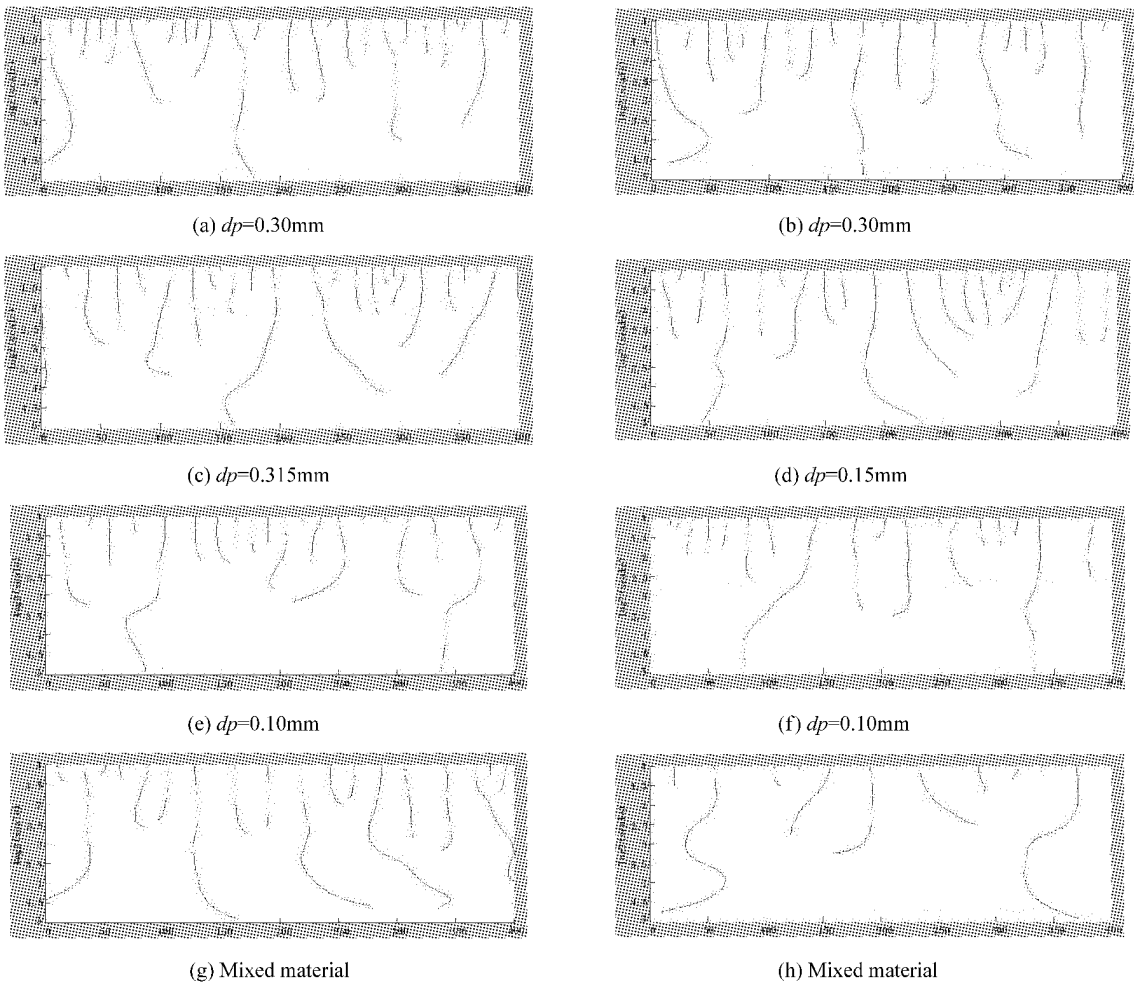

(a) dp=0.30mm (b) dp=0.30mm

(c) dp=0.315mm (d) dp=0.15mm

(e) dp=0.10mm (f) dp=0.10mm

(g) Mixed material (h) Mixed material

Fig. 4 Modulus maxima lines of pressure fluctuation signals for different particles

CONCLUSIONS

In this paper, the differential pressure signal fluctuation of the CFB is studied with the wavelet transform modulus maximum method. The changes of the solid circulation rate ***Gs*** and the holdup with the gas velocity indicate that Gs increases with the increase of the air velocity, and the increase of Gs will slow down after the air velocity reaches a certain value. And under each air velocity, Gs for bed materials with smaller size is larger than that with bigger size. The three groups of bed materials with more concentrated size distribution exhibit the characteristics of fast zone under most conditions at air velocities of 1.95~4.9m/s, due to the high fluidized air velocity. There is almost the same number of modulus maxima lines of differential pressure fluctuation signals at the bottom and on the top. If changing the size distribution range of bed materials, particles with different sizes will separate from each other. A great proportion of big particles present a flow pattern of "turbulent at the bottom and fast on the top" in the riser. The modulus maxima line of the differential pressure fluctuation signals is more at the bottom than on the top.

Wavelet transform modulus maximum method is a simple, easy and efficient method for the identification of flow patterns. It helps to find the relation between differential pressure fluctuation singularity and the change of the flow patterns, providing a new research tool for the development of new gasification technologies of CFBs.

NOTATIONS

d_p particle diameter, m
Gs solid circulating rate, kg/s
U_g fluidized gas velocity, m/s
u_t terminal velocity, m/s
ε voidage
μ Dynamic viscosity, Pa·s
υ Kinematic viscosity, m^2/s
ρ_s Gas density, kg/m^3
ρ_g Particle density, kg/m^3

ACKNOWLEDGEMENTS

Financial supports of this work by scientific and technological innovation platform of 985 project of southeast and excellent youth talented fund (2009SQRZ073) are gratefully acknowledged.

REFERENCES

Bai D. R., Zhu J.X., Jin Y. et al.: Powder Technol.85(1995a), pp179-188.
Bai D.R., Shibuya E., Nakagawa N. et al.: Powder Technol.87(1995b),pp105-111.
Bai D.R., Shibuya E., Masuda Y. et al.: Powder Technol.84(1995c),pp75-81.
Chen Y.G., Tian Z.P., Miao Z.Q.: Chem. Eng. Sci. 59(2004),pp3569-3575.
Fuchs A., Zang H., Wypych P.: Powder Technol. 173 (2007),pp126-139.
Guenther C., Breault R.: Powder Technol.173(2007), pp163-173.
Kim S.H., Han G.Y.: Korean J. Chem.Eng. 16(1999),pp677-683.
Levinspiel O. (1974).Chemical Reaction Engineering. New York.John Wiley&Sons,Inc.
Lu X.S., Li S.G., Yao J.Z. et al.:Chem. Eng. J. 112(2005), pp23-31.
Ludlow J.C., Monazam E.R., Shadle L.J.: Powder Technol. 182(2008), pp379-387.
Sharma A. K., Tuzla K., Matsen J. et al.: Powder Technol. 111(2000),pp114-122.
Wang L.N., Zhong L., Jin D.J. et al.: Chinese J. Chem. Eng.,10(2002), pp70-76.

WOOD GASIFICATION IN A LAB-SCALE BUBBLING FLUIDIZED BED: EXPERIMENT AND SIMULATION

L. He[1], E. Schotte[1], S. Thomas[1], A. Schlinkert[1], A. Herrmann[1], V. Mosch[1], V. Rajendran[1], S. Heinrich[2]

1 Process and Plant Engineering Business Unit (PAT), Fraunhofer Institute for Factory Operation and Automation IFF, 39106 Magdeburg, Germany

2 Institute of Solids Process Engineering and Particle Technology, Hamburg University of Technology, 21073 Hamburg, Germany

Abstract: In theory, an integrated biomass gasification and fuel cell system has a higher overall plant efficiency when compared to the efficiency of biomass gasification combined with simple combustion systems and gas engines. In order to develop a prototype of this new concept of power plant operating in the range of 150kW to 5MW, several institutes of the Max Planck Society and the Fraunhofer-Gesellschaft in Germany have been working on the ProBio project with focus on the theoretical and experimental investigation of an integrated 1-2kW$_e$ system. The paper will firstly describe the gasification unit of the system: a lab-scale atmospheric bubbling fluidized bed gasifier. Wood gasification experiments were conducted and the influence of operation parameters, i.e. gasification agents, equivalence ratio ER and steam to biomass ratio S/B on gas yield and gas composition was analyzed. In parallel with the experimental work, chemical kinetics of wood gasification was studied and simulated. Furthermore, simulation of bubbling fluidized bed hydrodynamics at high temperature, using commercial computational fluid dynamics (CFD) software FLUENT, was also conducted to better understand the phenomenon of fluidization inside the bed.

Keywords: biomass, gasification, fluidized-bed, experiments, simulation

INTRODUCTION

Given the growing shortage of fossil fuels and the signatories to the Kyoto Protocol to reduce the collective greenhouse gas emissions by 5.2% by 2012 compared to the year 1990, renewable energies hold great potential for the future. Among renewable energy sources (solar, wind, biomass, geothermal and hydro), biomass makes the largest contribution (65%) in Europe. To further increase their consumption, technologies for electricity, heat and biofuels production from biomass are being intensively developed and demonstrated. The gasification process, firstly applied in 1800s and today a well established technology, is most commonly used for biomass conversion, which converts the solid biomass feedstock into gas products with high heating value, e.g. carbon monoxide, methane and hydrogen. After appropriate gas cleaning, the product gas can be burned directly to produce heat or used in gas turbines or engines to generate electricity. A current research topic of interest is the coupling of fuel cell and biomass gasification to produce electricity and heat simultaneously. Theoretically, an integrated biomass gasification and fuel cell system has a higher overall plant efficiency when compared to the efficiency of biomass gasification combined with simple combustion systems or gas turbines. The estimated efficiency by Lobachyov and Richter (1998) of a biomass gasification-MCFC combined cycle is around 53%, about 10% higher than the traditional system. In order to develop a prototype of this new concept of power plant operating in the range of 150kW to 5MW, several institutes of the Max Planck Society and the Fraunhofer-Gesellschaft in Germany have been working on the ProBio project with focus on the theoretical and experimental investigation of an integrated 1-2kWe system. The system consists of a gasification unit, gas cleaning stages and fuel cells (solid oxide fuel cell- SOFC and polymer electrolyte membrane fuel cell- PEMFC). Both experimental studies to test the process steps integrated in the planned overall system and theoretical studies of the optimal interconnection of the individual processes are planned for the initial three-year phase of the project. As the gasification process unit of this system, a bubbling fluidized bed reactor was built up. The reactor has advantages of good solid-gas mixing, uniform temperature distribution, high heat transfer and having the ability to handle wide variety of fuels. Though an extensive literature on biomass gasification process in bubbling fluidized bed is available regarding different operating conditions (e.g. gasification agents, reactor temperature, fuel characteristics, bed material and additives), for the application of product gas in fuel cells special emphasis must be given to the gas components, namely hydrogen and carbon monoxide, and the gas quality. The objective of the present study is to determine the hydrogen-rich gas production from wood gasification. In parallel with experimental work, wood gasification process is simulated, using Matlab/Simulink, by employing the kinetic model from Tepper (2005).

Experimental results are used to compare with simulation ones and help further improving the process simulation. With the help of commercial computational fluid dynamics (CFD) software FLUENT, hydrodynamics simulation of the bubbling bed is conducted to better understand the phenomenon of fluidization inside the bed.

EXPERIMENTAL

The experimental set-up, shown in Fig.1, consists of solid feeding unit, bubbling fluidized bed gasifier, gas cleaning stages, gas analysis system and post-combustion unit.

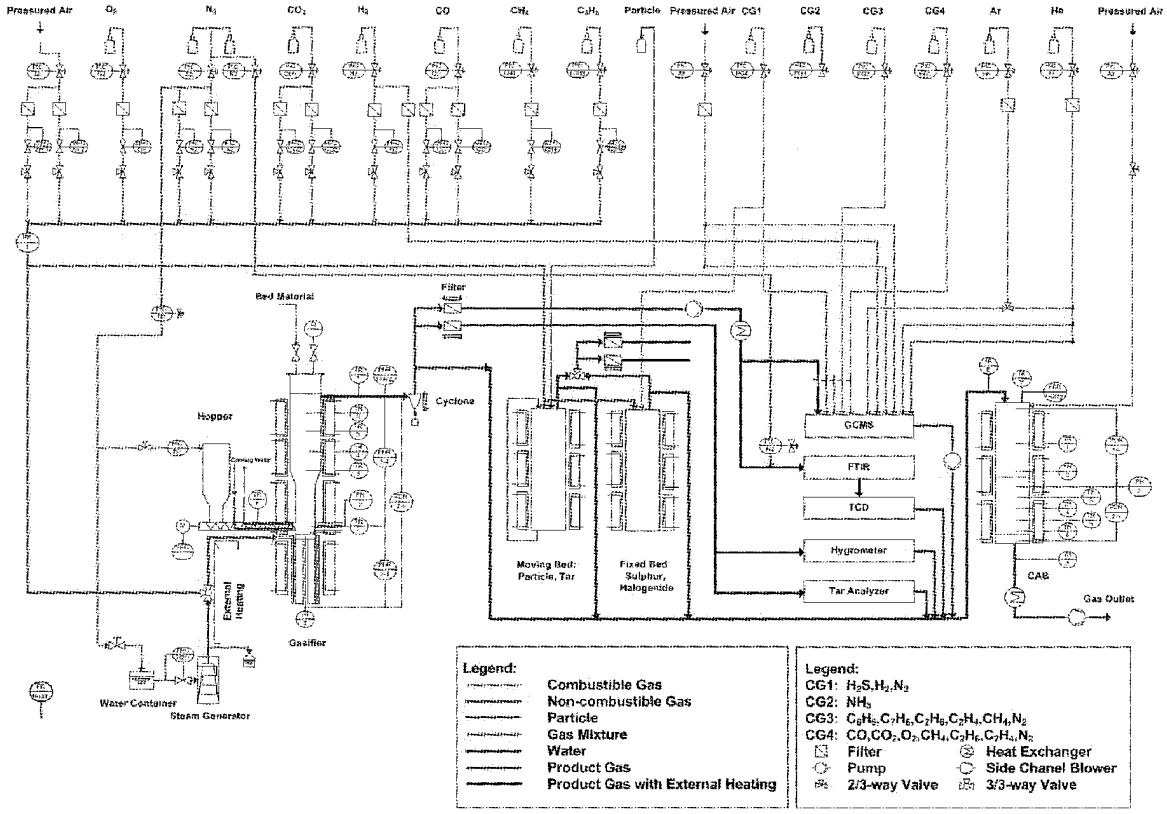

Fig. 1 Flowchart of a lab-scale bubbling fluidized bed gasifier system

The solid feeding unit is a twin-screw volumetric feeder with a hopper pressurized with N_2 to avoid the hot gas returning from the gasifier. The screw type was chosen based on the physical properties of biomass, i.e. particle size and bulk density. Cooling water channel was installed in the stainless-steel screw pipe to prevent biomass pyrolysis inside the pipe. Before experiment, the feeder was calibrated for the selected biomass to determine the output as a function of screw rpm to ensure the accurate mass flow rate. The gasifier has three sections: gas preheating zone, bed and freeboard. Before entering the bed, the gas was heated up to 500°C in the preheating zone. A porous plate was used as the gas distributor and pressure drop of the plate was determined beforehand. The bed section has 5cm inner diameter and 28cm height, with the biomass feeding point at 7cm above the distributor. The freeboard is widened to 8cm inner diameter and with 58cm height. A 9cm conical reduction zone connects the bed and freeboard section. The whole reactor is constructed of stainless steel and heated through external electric oven with an operating temperature up to 1200°C. The temperatures inside the reactor are measured by seven K-type thermocouples located at different heights. Four pressure drop transducers were installed to monitor the pressure drop fluctuation at different locations inside the reactor. A cyclone is positioned at the gas outlet and can separate particles with diameter larger than 5μm. Glass fiber thimbles were used to further remove particles bigger than diameter 0.8μm before the product gases are fed into the gas analysis system. Gas cleaning system, including a moving bed for dust/ tar removal and a fixed bed for sulphur/ halogenide removal, is at the stage of development and not yet connected to the gasifier. The gas analysis system includes gas chromatography (GC), Fourier transform infrared spectroscopy (FTIR), thermal conductivity gas analyzer (TCD), tar analyzer and hygrometer. A catalytic afterburner (CAB), employing Pt/Al_2O_3 as catalyst, is used to burn out the gases before they will be emitted to atmosphere. Before each experiment the hopper was filled with the selected wood particles. Wood particle characteristics are listed

in Table 1.

Table 1 Wood Particle Characteristics

Proximate Analysis [wt%]		Ultimate Analysis [wt%, daf]	
Fixed Carbon	15	Carbon	50.15
Volatile Matter	76.26	Hydrogen	5.99
Ash	0.18	Sulphur	1.11
Moisture	8.56	Oxygen	42.75
Lower Heating Value [MJ/kg]	16.81	Particle Diameter [mm]	1-2

Silica sand with diameter of 300 to 700 μm was chosen as the bed material. The bed aspect ratio *H/D* was kept as 2 for all experiments. Sand minimum fluidization velocity u_{mf} at operating temperature was previously determined in the reactor. Under operating condition, the minimum fluidization velocity u_{mf} of sand and char mixture was calculated according to Aznar et al. (1991):

$$(u_{mf})_{\text{mixture of sand and char}} = 1.3(u_{mf})_{\text{sand}}$$

The fluidization number $u_0/u_{mf\_mixture}$ was selected between 4 and 6 to have a stable condition in the bed even for long operating hours (without ash removal and bed material refill). Biomass input was kept 0.48kg/h in most of experiments. Equivalence ratio ER varied from 0.20 to 1 and steam to biomass ratio from 0.4 to 2.2. As the temperature inside the reactor reached operating temperature, biomass was fed into the gasifier and gasification agent flow (air or steam) was adjusted according to the previously selected ER and/or S/B. Additional N_2 flow was necessary in most of the experiments to ensure good fluidization condition. After about thirty minutes the process reached a steady state, indicated by constant temperature, pressure drop and gas profile. With known input N_2 flow and measured concentration in product gas by GC, the gas yield coul be calculated. Cyclone ash container and filters were weighed before and after to measure the dust concentration in the product gas. Some typical experimental results of the product gas composition and the corresponding operating conditions are listed in Table 2.

Table 2 Operating Parameters and Gas Analysis for Some Gasification Experiments.

Operating Parameters						
Gasification Agent	Air			Steam		
ER [-]	0.19	0.29	0.39	-	-	-
S/B [kg/kg daf]	0.09	0.09	0.09	0.80	1.60	2.20
Bed Temperature T_b [°C]	794	794	797	763	743	749
Freeboard Temperature T_{fb} [°C]	800	800	800	835	820	820
Gas Analysis						
H_2 [Vol.%, dry]	10.8	7.1	4.5	37.9	39.8	41.5
CO [Vol.%, dry]	25.5	20.7	16.7	32.5	28.7	24.8
CO_2 [Vol.%, dry]	14.8	15.8	16.9	16.9	19.7	20.9
CH_4 [Vol.%, dry]	7.1	5.8	3.6	8.3	7.7	8.5
C_2H_6 [Vol.%, dry]	3.1	2.5	1.8	3.6	3.4	3.6
C_2H_4 [Vol.%, dry]	0.24	0.18	0.12	0.22	0.21	0.22
C_6H_6 [Vol.%, dry]	0.32	0.28	0.21	0.41	0.36	0.39
C_7H_8 [Vol.%, dry]	0.09	0.11	0.06	0.12	0.10	0.11
H_2O [Vol.%]	10.9	12.9	15.1	20.2	34.6	44.2
Gas yield [Nm^3/kg of daf fuel]	1.8	2.2	2.4	1.1	1.3	1.1

SIMULATION

Reaction kinetics

Besides thermodynamics equilibrium model, for predicting the composition of product gas, kinetics study has been carried out to incorporate the real application with limited fuel reactivity and residence time. Biomass gasification is a complex thermochemical process including a number of steps like drying, pyrolysis, partial oxidation, char gasification and further tar cracking. Given a high heating rate in fluidized beds, drying is assumed to commence at the time as the fuel particles enter the reactor (Nemtsov and Zabaniotou, 2008). Char and gas production from pyrolysis is estimated based on experimental results from Wiest (1998), and tar yields

from Rath and Staudinger (2001). The tar yield is classified into reactive components (Tar 1) and less reactive ones (Tar 2):

- Char: $m_{char} = 0.256m_{biomass}$
- CO: $m_{CO} = 0.029m_{biomass}$
- CO_2: $m_{CO_2} = 0.073m_{biomass}$
- Tar 1: $m_{Tar\ 1} = 0.529m_{biomass}$
- Tar 2: $m_{Tar\ 2} = 0.113m_{biomass}$

The main reactions considered in the simulation study performed are listed in Table 3. Hypothetical empirical formulas are given as $C_1H_{2.43}O_1$ for tar and $C_1H_{0.62}O_{0.12}$ for char by Tepper (2005).

Table 3 Chemical reactions considered in the simulation study

Chemical Reactions	Description
$C_1H_{0.62}O_{0.12} + 1.095\ O_2 \Rightarrow CO_2 + 0.31\ H_2O$	Char combustion
$C_1H_{2.43}O_1 + 0.5\ O_2 \Rightarrow CO + H_2O + 0.215\ H_2$	Tar oxidation
$C_1H_{0.62}O_{0.12} + 0.88\ H_2O \Rightarrow CO + 1.19\ H_2$	Water gas reaction
$C_1H_{2.43}O_1 \Rightarrow 0.66CO + 0.33CH_4 + 0.33H_2O + 0.215H_2$	Tar decomposition
$CH_4 + 2\ O_2 \Leftrightarrow CO_2 + 2\ H_2O$	Methane oxidation
$CH_4 + H_2O \Leftrightarrow CO + 3\ H_2$	Methane reforming
$CO + H_2O \Leftrightarrow CO_2 + H_2$	Water-gas shift reaction
$C + CO_2 \Leftrightarrow 2\ CO$	Boudouard reaction

Hydrodynamics

The performance of a bubbling fluidized bed gasifier is significantly influenced by the flow behaviour inside the reactor. The classical two-phase model, introduced by Toomey and Johnstone (1952), assumes that all gas in excess of u_{mf} flows through the bed as bubbles. And the rising bubbles are the main reason for solid mixing in reactor bed. Furthermore, since bubbles contain very less or no fuel particles, they can hardly take

Table 4 Operating and boundary conditions for hydrodynamics simulation using FLUENT

System Definition			
Reactor Geometry (Bed Section)		**Solids**	
Diameter	0.05m	Type	Sand
Height	0.28m	Size	464μm
Gas		Density	2600kg/m3
Type	Air and Nitrogen	Coefficient of restitution	0.9
Pressure	101325Pa	Temperature	700°C
		Fixed bed height	0.1m
Initial Conditions		**Boundary conditions**	
Air velocity	0.454	Inlet	Velocity
Min. fluidization velocity	0.110m/s	Outlet	Pressure
Volume fraction of solids	0.45	Walls	no slip
Model Description			
Governing equations (Discretization Technique)			
Flow equation	Second order upwind		
Energy equation	First order upwind		
Granular temperature	Second order upwind		
Volume fraction	Quick		
Closing equations	Model I	Model II	
Granular viscosity	Gidaspow	Syamlal-O'Brien	
Granular conductivity	Syamlal-O'Brien	Syamlal-O'Brien	
Solid pressure	Lun-et-al	Lun-et-al	
Radial distribution	Lun-et-al	Lun-et-al	
Drag correlation	Gidaspow	Syamlal-O'Brien	

part in any gas-solid reactions. Thus, understanding of bubble formation and solid distribution is essential for process control and optimization. Two-dimensional simulation of the fluidized bed has been conducted using commercial CFD software FLUENT, to obtain hydrodynamics information. Considering large volume fraction of solids in the bubbling bed, Eulerian-Eulerian modeling approach was used, which assumes that gas and solid phase are fully interpenetrating. Mass, momentum and energy continuum equations are defined for each phase. Additionally, the kinetic theory of granular flow, taking into account the energy dissipation, is also applied due to the non-ideal particle-particle collisions. Various operating and boundary conditions are studied. Table 4 lists the parameters used in one of the simulation work.

RESULTS AND DISCUSSION

The effect of ER and S/B on gas composition is shown in Figures 2-5, in which the simulation results obtained from the kinetic model are also presented.

Due to the dilution effect from nitrogen and the combustion reactions, production of gases with heating value (H_2, CO and CH_4) from air gasification is low while having a high CO_2 percentage. An increasing ER decreases H_2, CO and CH_4 yields but increases CO_2 amount and dry gas yield. The same trends of gas production can be seen for both experimental and simulation results.

In steam gasification, because of the use of low temperature steam and the dominant endothermic reactions, reactor temperature seldom reaches 800°C even with constant external heating. With increasing S/B ratio, concentration of H_2 and CO_2 increases while that of CO decreases, indicating an enhanced water-gas shift reaction. The decrease of gas yield was observed when S/B exceeded 1.6. This is mainly due to the fact that the high amount of heat necessary for steam evaporation lowers the reaction temperature. The simulation results show a good agreement in H_2 and CH_4 production but discrepancy of predicting the CO and CO_2 trends compared with the experimental results.

The effect of ER and S/B on the yield of each gas is shown in Figures 6-7. Hydrogen yield is more than double in steam gasification with S/B=0.8 (0.42Nm^3/kg daf) in comparison with air gasification with ER=0.19 (0.19Nm^3/kg daf).

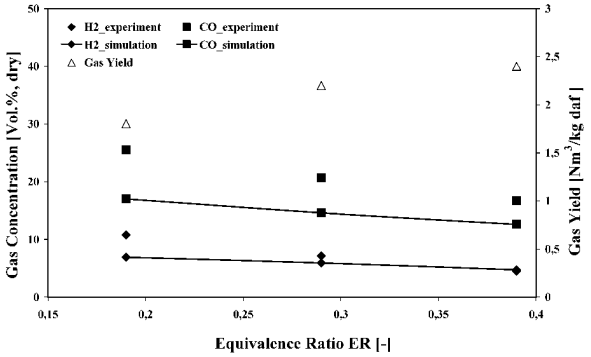

Fig. 2 Effect of ER on H_2 / CO and gas yield

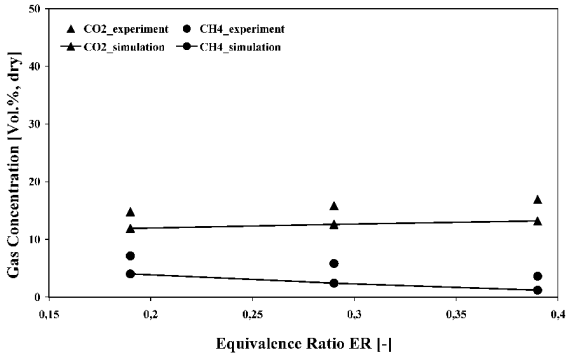

Fig. 3 Effect of ER on CO_2 and CH_4

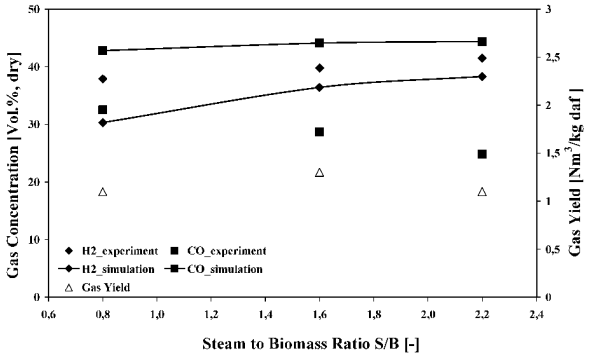

Fig. 4 Effect of S/B on H_2/ CO and gas yield

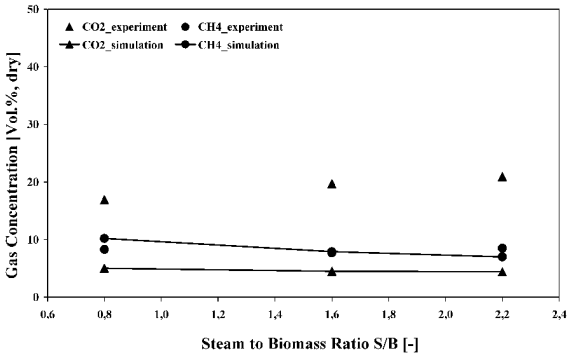

Fig. 5 Effect of S/B on CO_2 and CH_4

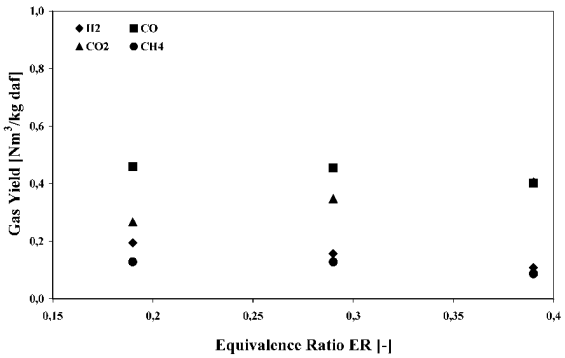

Fig. 6 Effect of ER on single gas yield

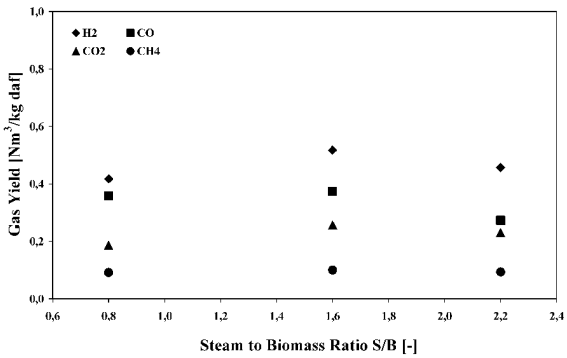

Fig. 7 Effect of S/B on single gas yield

CFD study, using FLUENT, gives a useful insight into the flow characteristics and hydrodynamic behavior of the bubbling fluidized bed. Figure 8 shows the solid distribution inside the fluidized bed under conditions given in Table 4. Bed expansion, bed mixing condition and bubble information can be obtained from the simulation. Results from model II present more bubbles with smaller size and a better mixing condition than model I. This is mainly due to the fact that model I employs the granular viscosity and drag correlation from Gidaspow, which is normally suitable for studies of large scale reactors.

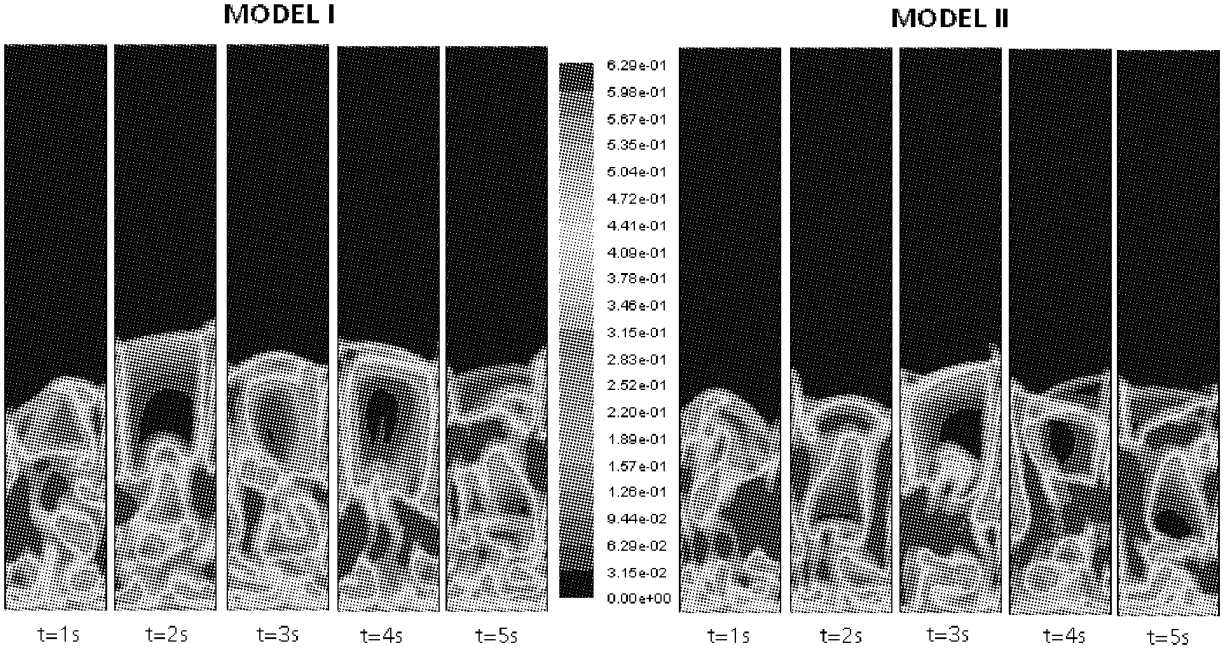

Fig. 8 Sand distribution at t=1-5s (air/ nitrogen mixture, u_o=0.454m/s, T=700°C)

CONCLUSIONS AND OUTLOOK

Wood gasification experiments were conducted in a lab-scale atmospheric bubbling fluidized bed system to study the effect of different operating parameters, i.e. gasification agents, equivalence ratio ER and steam to biomass ratio S/B, on the gas composition and gas yield. Experimental results are plausible and comparable with literature values (e.g. Gil et al., 1999). Reaction kinetic simulation model can well predict trends of major gas species (H_2, CO, CO_2 and CH_4) produced from air gasification, as well as the gas species H_2 and CH_4 for steam gasification. Hydrodynamics information obtained from CFD simulation helps better understand the fluidization phenomena inside the bed.

Within the project, further research activities are planned:

(1) Experimental study about the influence of additives (dolomite and olivine) on the tar load of raw fuel gas.

(2) Investigation of the effect of both CO_2 capture, using CaO in the fluidized bed, and steam spraying into the freeboard on product gas composition, aiming at H_2-rich fuel gas.

(3) Improvement of kinetic model for steam gasification.

(4) Development of a process model combining chemical kinetic (gasification) and hydrodynamics (bubbling fluidized bed). Scale up of the hydrodynamics information from a 2D model to a 3D model.

ACKNOWLEDGEMENTS

Financial support of this project by the Germany's Federal Ministry of Education and Research (BMBF) is gratefully acknowledged.

REFERENCES

Aznar, M.P., Corella. J., Herguido, J.: La Fluidization 5 (1991), pp. 377-383.
Gil, J., Corella, J., Aznar, M.P., Caballero, M.A.: Biomass and Bioenergy 17 (1999), pp.389-403.
Lobachyov, K.V., Richter , H.J.: Energy Convers. Mgmt 39 (1998), pp. 1931-1943.
Nemtsov, D.A., Zabaniotou, A.: Chem. Eng. J. (2008), doi; 10.1016/j.cej.2008.01.023.
Rath, J., Staudinger, G.: Fuel 80 (2001), pp. 1379-1389.
Tepper, H.: Dissertation, Otto-von-Guericke-Universität Magdeburg, 2005.
Toomey, R.D., Johnstone, H.F.: Chem.Eng.Prog. 48 (1952).
Wiest, W.: Dissertation, Universität Gesamthochschule Kassel, 1998.

A COMPARATIVE STUDY OF EULER-EULER AND EULER-LAGRANGE MODELLING OF WOOD GASIFICATION IN A DENSE FLUIDIZED BED

S. Gerber, F. Behrendt, M. Oevermann*

Berlin Institute of Technology, Department of Energy Engineering
Chair for Energy Process Engineering and Conversion Technologies for Renewable Energies
Fasanenstr. 89, 10623 Berlin, Germany
**Corresponding author. E-mail: michael.oevermann@tu-berlin.de*

Abstract: In this work we compare two different modelling strategies for the simulation of wood gasification in a dense fluidized bed. In the first method we adopt an Euler-Lagrange approach where the fluid phase is modelled as a continuum and the particulate phase is modelled on the individual particle level using the Discrete Element Method (DEM). In the second method we use an Euler-Euler or continuum approach where the multiple solid phases for wood and char particles are treated as a continuum. Both models allow the time-dependent prediction of velocity, temperature, and composition fields. Both models have been run to a statistically stationary state. We compare the numerical results of both methods against each other and with experimental data obtained at a laboratory scale bubbling fluidized bed reactor.
Keywords: Euler-Lagrange, DEM, Euler-Euler, fluidized bed, biomass gasification

INTRODUCTION

The recent discussions on climate change, CO2 emissions, and the limited availability of fossil fuels have renewed the interest in gas from biomass and wood. Despite the long tradition of utilising the combustible fuel gas from wood gasification there still is a lack of detailed scientific knowledge about the complex interactions between the gasifications reactions and the fluid mechanics of fluidized beds. Numerical methods like Euler-Euler or Euler-Lagrange methods can complement experiments for a better understanding of the physical and chemical processes in fluidized bed reactors.

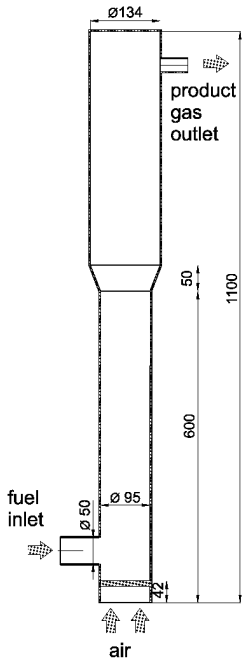

Fig. 1 Bubbling fluidized bed reactor

In order to improve and optimise the thermal efficiency and to predict product gas composition and emission rates, numerous mathematical models for coal - and more recently biomass - gasification in fluidized beds have been developed. Whereas the simpler models such as zone/cell models and equilibrium models are suitable for design optimisation of industrial size gasifiers, the more comprehensive models such as Euler-Euler (Lathouwers and Bellan, 2001; Agrawal et al., 2001; O'Brien et al., 2003) and Euler-Lagrange (Rong and Horio, 1999; Kaneko et al., 1999; Zhou et al., 2004; Limtrakul et al., 2004) models are more targeted towards fundamental investigations of the chemical and fluid mechanical aspects of fluidized beds.

Euler-Euler and Euler-Lagrange models are both comprehensive models suitable for fundamental investigations of the chemical and fluid mechanical aspects of fluidized beds. Especially Euler-Lagrange allow a detailed modelling of mass, momentum, and energy transfer on the individual particle level. However, the detailed modelling capabilities of Euler-Lagrange models come at the price of high computational costs. With current and foreseeable computer resources it does not seem feasible to perform Euler-Lagrange simulations of large scale fluidized bed reactors using a relatively detailed gasification model for each individual particle. In a recent study Zhou et al. (2004) used only 20 reactive coal, 2000 inert sand particles and simulation times of 2 s in their Euler-Lagrange simulation of a bubbling fluidized bed.

Euler-Euler or continuum models allow a realistic description of the time dependent processes in nonreacting and reacting fluidized beds. Sofisticated closure models based on the kinetic theory of granular flow allow realistic predictions of unsteady fluid mechanical phenomena of particulate flows Agrawal et al. (2001). Compared to Euler-Lagrange models continuum models are computationally less demanding and allow the calculation of larger reactors. Therefore they are very useful tools for simulating fluidized beds. One of most severe difficulties associated with Euler-Euler models are the complicated closure models describing the momentum and energy transfer between multiple continuous phases. Although they are limited to smaller

systems, the more physical modelling approach of Euler-Lagrange methods are useful to improve closure models for continuum models.

In this work we present an Euler-Lagrange model coupled with a Discrete Element Method (DEM) and an Euler-Euler model for the simulation of reactive gas-solid flow in dense fluidized beds. Both models take into account detailed gas phase chemistry, pyrolysis models, and heterogeneous gasification reactions. Different models for pyrolysis and gasification reactions from the literature have been implemented. We apply the methods for the numerical simulation of wood gasification and compare the results against results obtained with an Euler-Euler model and against experimental data of a laboratory scale bubbling fluidized bed reactor. Reasonable agreement between the numerical results and measurements have been found for the exhaust gas compositions and temperature.

MATHEMATICAL MODELLING

Gas phase

The gas phase in the Euler-Euler and the Euler-Lagrange model is treated as a continuum, which can be described by a set of volume averaged Navier-Stokes equation. For the global mass balance we have in conservative form

$$\frac{\partial \varepsilon_g \rho_g}{\partial t} + \nabla \cdot (\varepsilon_g \rho_g \boldsymbol{u}_g) = 0, \tag{1}$$

where ε_g, ρ_g, and u_g are the void fraction, the gas density, and the gas phase velocity, respectively. The balance equations for the individual species _ in the gas phase can we written as

$$\frac{\partial \varepsilon_g \rho_g Y_\alpha}{\partial t} + \nabla \cdot (\varepsilon_g \rho_g Y_\alpha \boldsymbol{u}_g) = \varepsilon_g \dot{w}_{\alpha,g} + \varepsilon_g \dot{w}_{\alpha,s}. \tag{2}$$

Here Y_α denotes the massfraction of species α in the gasphase, $w_{\alpha,g}$ is the net production rate of species α due to gas phase chemical reactions, and $w_{\alpha,,s}$ is the mass transfer term between the solid phase and the gas phase.

The gas phase momentum equation is

$$\frac{\partial \varepsilon_g \rho_g \boldsymbol{u}_g}{\partial t} + \nabla \cdot (\varepsilon_g \rho_g \boldsymbol{u}_g \boldsymbol{u}_g) + \varepsilon_g \nabla p + \varepsilon_g (\nabla \cdot \boldsymbol{\tau}_g) + \varepsilon_g \rho_g \boldsymbol{g} = \boldsymbol{I}_{gs}. \tag{3}$$

Here, p, τ_g, g, and I_{gs} are the pressure, the stress tensor (modelled as a Newtonian fluid), the gravitational force, and the momentum exchange term between the gas phase and the particulate phase, respectively.

In the Euler-Lagrange model we follow a conservative discretisation scheme with an energy budget equation written in the mass-specific energy e:

$$\frac{\partial \varepsilon_g \rho_g e}{\partial t} + \nabla \cdot \left(\varepsilon_g \boldsymbol{u}_g (\rho_g e + p)\right) + \varepsilon_g (\nabla \cdot \boldsymbol{q}) = \dot{Q}_{gs}, \tag{4}$$

where q is the heat flux vector and Q_{gs} denotes the heat transfer term between the solid phase and the gas phase. Here e is the sum of the internal energy plus the chemical energy. In the limit of a small Mach-number Ma the kinetic energy and the contribution of the viscous stresses can be neglected in the total energy budget. The gas phase temperature T_g is implicitly given by the caloric equation of state $e(T_g) = \Sigma_\alpha Y_\alpha e_\alpha(T_g)$; where $e_\alpha(T_g)$ is the mass-specific energy of species _ which depends on temperature only for an ideal gas. The pressure is given by the equation of state for an ideal gas as

$$p = \rho_g T_g \sum_\alpha Y_\alpha R_\alpha, \tag{5}$$

where R_α is the individual gasconstant of species α.

For the Euler-Euler model we use the MFIX software where the energy equation is solved in form of a temperature equation:

$$\epsilon_g \rho_g c_{pg} \left(\frac{\partial T_g}{\partial t} + \boldsymbol{v}_g \cdot \nabla T_g \right) = -\nabla \cdot \boldsymbol{q}_g + \sum_{m=1}^{N_m} \gamma_{gm} (T_{sm} - T_g) - \Delta H_g. \tag{6}$$

with the heat flux vector q, the heat transfer coefficient between gas phase and solid phase m γ_{gm}, the temperature of the solid phase T_{sm}, and the heat of reaction Δ_{Hg}.

Particulate phase

Euler-Euler model: In the Euler-Euler model the particulate phase is modelled as a set of multiple continuous solid phases each representing a characteristic diameter. For each solid phase m we solve a mass balance equation

$$\frac{\partial \varepsilon_{sm} \rho_{sm}}{\partial t} + \nabla \cdot (\varepsilon_{sm} \rho_{sm} \boldsymbol{v}_{sm}) = \varepsilon_{sm} \sum_l \dot{w}_{sml} + \varepsilon_{sm} \sum_\alpha \dot{w}_{smg\alpha}, \tag{7}$$

where ε_{sm}, ρ_{sm}, and v_{sm} are the void fraction, the density, and the velocity of the solid phasem, respectively. Here, $\dot{W}_{sml}$ denotes the mass transfer term between solid phases m and l (e.g. the conversion of fresh wood into charcoal) and $\dot{W}_{smg\alpha}$ is the mass transfer term between solid phase m and the gas phase component α. With (2) we have $\dot{W}_{\alpha s} = -\sum_m \dot{W}_{smg\alpha}$ _Pm _ wsmg_. The momentum balance for solid phase m can be written as

$$\frac{\partial}{\partial t}(\varepsilon_{sm}\rho_{sm}\boldsymbol{v}_{sm}) + \nabla\cdot(\varepsilon_{sm}\rho_{sm}\boldsymbol{v}_{sm}\boldsymbol{v}_{sm}) = -\varepsilon_{sm}\nabla p_{sm} + \nabla\cdot\boldsymbol{\tau}_{sm} - \sum_{\substack{l=1\\ l\neq m}}^{N_m} \boldsymbol{I}_{ml} + \boldsymbol{I}_{mg} + \epsilon_m\rho_m\boldsymbol{g}. \tag{8}$$

where p_{sm} and τ_{sm} are the pressure and the stress tensor of the solid phase m and I_{mg}, I_{ml} denote momentum exchange terms between solid phase m and the gas phase and the solid phase l. In addition to mass and momentum balance equations we solve a temperature equation for each solid phase m:

$$\varepsilon_{sm}\rho_m c_{pm}\left(\frac{\partial T_{sm}}{\partial t} + \boldsymbol{v}_{sm}\cdot\nabla T_{sm}\right) = -\nabla\cdot\boldsymbol{q}_{sm} - \gamma_{gm}(T_m - T_g) - \Delta H_{sm}. \tag{9}$$

For the details of modelling the different terms in the governing equations we refer to the MFIX documentation.

Euler-Lagrange model. The motion of each particle in the system is calculated by integrating Newton's equation of motion:

$$\dot{\boldsymbol{x}} = \boldsymbol{v}, \qquad \boldsymbol{v} = \frac{1}{m_p}\sum_i \boldsymbol{F}_i, \qquad \dot{\boldsymbol{\omega}} = \frac{1}{I_p}\sum_i \boldsymbol{T}_i, \tag{10}$$

where x, v, w are the position, the velocity and the angular velocity of the particle. I_p is the moment of inertia for the spherical particle with $I_p = \frac{1}{10} m p d_P^2$. Under the various forces acting on a single particle in a gas flow (drag, weight, buoyancy, Saffmann, Magnus, etc.) we consider only the drag force F_D and and the weight force F_g. According to an analysis of Sommerfeld [2000], these are the dominat forces under the conditions in this work. Therefore, the sums of the forces and torques acting on a particle can be written as:

$$\sum_i \boldsymbol{F}_i = \boldsymbol{F}_D + \boldsymbol{F}_g + \boldsymbol{F}_C, \qquad \sum_i \boldsymbol{T}_i = \boldsymbol{T}_F + \boldsymbol{T}_C, \tag{11}$$

where F_C is the force from collisions with other particles and the walls of the reactor, and T_F and T_C; denote the torques due to viscous friction and particle-particle contacts. The drag force is modelled using the usual correlation $F_D = \frac{1}{8}\pi C_d f(\varepsilon)\varepsilon^2\rho_g |\boldsymbol{u}_g - \boldsymbol{v}|(\boldsymbol{u}_g - \boldsymbol{v})$. The drag coefficient C_d distinguishes between the Stokes and the transient regime on the one hand and the Newton regime on the other hand. For the Newton regime we use the relation from Wen and Yu (1966) for $f(\varepsilon)$. The weight force in (11) is simply $\boldsymbol{F}_g = m_P\boldsymbol{g}$.

The sum of the torques acting on the particles in (11) is modelled as the sum of a fluid dynamic part and the torque from particle-particle and particle-wall collision. For the fluid dynamic part of the torque due to viscous stresses we have $\boldsymbol{T}_F = \frac{\rho_g}{2}\frac{d_p}{2}^5 C_R |\boldsymbol{\Omega}|\boldsymbol{\Omega}$; where $\boldsymbol{\Omega}$ is a relative angular velocity between the particle and the fluid: $\boldsymbol{\Omega} = \frac{1}{2}(\nabla\times\boldsymbol{u}_g) - \boldsymbol{\omega}$. The torque coefficient C_R has been taken from the usual literature. The void fraction ε_g in each computational cell of the Euler-Lagrange model is calculated based on the actual number n of particles within that cell.

For each particle in the system we solve a set of three ordinary differential equations to model pyrolysis, gasification, and shrinkage of the particle. The zero-dimensional model consists of equations for the wood mass m_w, the particle temperature T, and the charcoal mass mcc:

$$\begin{aligned}
\frac{dm_w}{dt} &= -(\dot{r}_{wg} + \dot{r}_{\mathrm{tar(g)}} + \dot{r}_{cc})\, m_w, \\
c_p m_p\frac{dT}{dt} &= \sum_i(\Delta h_i w_i) + \alpha A(T - T_g) + \epsilon\sigma A(T^4 - T_g^4), \\
\frac{dm_{cc}}{dt} &= -(\dot{r}_{\mathrm{H_2O}} + \dot{r}_{\mathrm{CO}})\, m_{cc}, -V_p\, M_p\, \dot{r}_{\mathrm{CO_2}},
\end{aligned} \tag{12}$$

where c_p is the mass-specific heat capacity of the particle, $m_p = m_w + m_{cc}$ is the total mass of the particle, Δhi is the heat of reaction of the heterogeneous reaction i with reaction rate w_i, α is the heat transfer coefficient,

A is the surface area of the particle, σ is the Stefan-Boltzmann constant, ε is the emissivity with an assumed value of 0.7, V_p is the volume of the particle, and M_p is the mean molar mass of the particle. The reaction rates for the conversion of wood (index *w*) into wood gas (index *wg*), tar (index *t*), and charcoal (index *cc*) in the first equation of (12) are taken from Grönli and Melaaen (2000). The reaction rates for the charcoal conversion are given in the following section. Shrinkage of the particles is simply assumed to be mass proportional, i.e. $r = (3/4m_p/(\pi\rho_p))^{1/3}$.

Chemistry modelling

Homogeneous gas phase reactions. In the present work the following simple kinetic mechanism for syngas has been used:

$CO + H_2O \rightleftharpoons H_2 + CO2$	De Souza-Santoz [1989]
$2\ CO + O_2 \rightarrow 2\ CO_2$	Dryer [1972]
$2\ H_2 + O_2 \rightarrow 2\ H2O$	Mitani and Williams [1980]
$CH_4 + 2\ O_2 \rightarrow CO_2 + 2\ H_2O$	Dryer and Glassman [1972]
$CH_4 + 1{:}5\ O_2 \rightarrow CO + 2\ H_2O$	Dryer [1972]

The kinetic parameters for all reactions are from the cited literature.

Pyrolysis. Primary pyrolysis denotes the decomposition of solid biomass into gases, tar, and char:

wood → H_2O(g); CO(g); CO_2(g); H_2(g); CH_4(g); tar(g); char(s):

The rate constants for the primary pyrolysis reactions as well as the fixed mass-fractions of the products are taken from Grönli and Melaaen [2000]. Primary pyrolysis is followed by secondary cracking of tar. In this study we consider two different models for the secondary pyrolysis. In the first model of Boroson et al. [1989] for beech wood, tar reacts to gas phase components and inert tar:

tar → CO(g); CO_2(g); H_2(g); CH_4(g); tar_{inert}.

The second pyrolysis model of Rath and Staudinger [2003] has been developed for spruce wood. Primary and secondary pyrolysis in this model can be summarised as follows:

wood → char, tar_1, tar_2, tar_{inert},

tar_1 → H_2O(g), CO(g), CO_2(g), H_2(g), CH_4(g), C_2H_4(g), C_2H_6(g), C_3H_6(g),

tar_2 → H_2O(g), CO(g), CO_2(g), H_2(g), CH_4(g), C_2H_4(g), C_2H_6(g), C_3H_6(g).

Heterogeneous reactions. Heterogeneous reactions of solid char with species in the gas phase are modelled using the following overall reactions:

$C + O_2 \rightarrow CO_2$	Ross and Davidson (1982)
$C + CO_2 \rightarrow 2\ CO$	Biggs and Agarwal (1997), Klose et al. (2004)
$C + H_2O \rightarrow CO + H_2$	Hobbs et al. (1992), Klose et al. (2004)
$C + 2\ H_2 \rightarrow CH_4$	Hobbs et al. (1992)

Rate expressions and kinetic parameters are taken from the cited literature. The model of Klose et al. (2004) was used alternatively to the models of Biggs and Agarwal (1997) and Hobbs et al. (1992) only for the Euler-Euler simulations.

RESULTS AND DISCUSSION

Experimental setup

The experimental data in this study were taken from a laboratory scale bubbling fluidized bed reactor at the Institute of Energy Engineering at Berlin University of Technology. Figure 1 shows the reactor and its dimensions. The freeboard area and the bubbling bed zone have inner diameters of 134 mm and 95 mm, respectively. The reactor is operated at atmospheric pressure. The bed material consists of pure wood and is fed in the lower part of the reactor with a feeding rate of 2 kg/h. Preheated air with a velocity of 0.25 m/s at a temperature of 400_C enters the reactor from the bottom over the whole diameter of the reactor. Six thermocouples inside the reactor at heights 5, 150, 325, 500, 700, and 900 mm above the air intake are monitoring the temperature inside the reactor. Product gases concentrations at the exit of the reactor are analysed with a combination of gas chromatography and laser mass spectroscopy, see Neubauer and Behrendt (2007) for details.

Figure 2 shows experimental temperature data over time at different heights above the inlet in the reactor for a complete experiment. The reactor was started with a bed of pure charcoal and a pure heated nitrogen mass flow below the fluidization velocity to heat up the system. After the heating period of approximately 60 min the reactor has been operated with heated air entering the reactor with a velocity of 0.25 m/s and a temperature of 400℃. The temperature peaks seen in Figure 2 at about 88 min operating time are due to an interrupted fuel supply. Between t=100 min and t=120 min the reactor runs at almost steady state conditions. We use the data

from this time window to compare with numerical simulations. After 120 min of operating time several tests were performed leading to the unsteady temperature data seen in Figure 2.

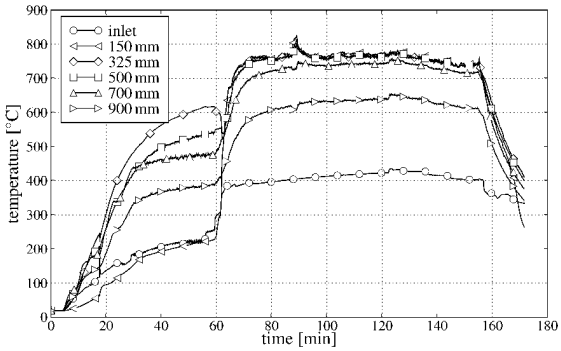

Fig. 2 Experimental temperature data over time for a complete run of the reactor at different heights above the air inlet

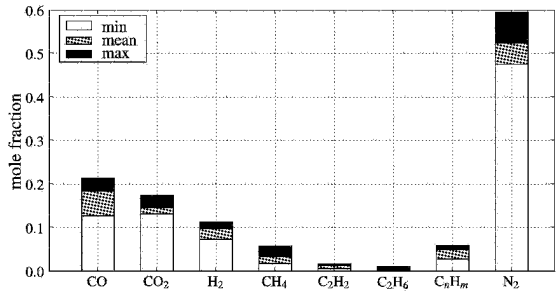

Fig. 3 Experimental data of the exhaust gas composition sampled from 19 different experiments with different wood charges

Figure 3 shows minimum, mean, and maximal measured exhaust gas concentrations. The concentrations are sampled values of time-averaged data from 18 different experiments with different charges and types of wood. Usually, the exhaust gas concentrations of CO are higher then those of CO_2 as can be seen from Figure 3. However, among the 18 different experiments their were also two case with higher CO_2 than CO concentrations. The huge variance of wood properties (density, water content, structure, etc.) leads to big uncertainties in the modelling of wood gasification and should be kept in mind when comparing numerical results against experimental data.

Computational Setup

The reactor shown in Figure 1 has been discretised in the two-dimensional Euler-Euler model with a grid spacing of 1 cm in radial and axial direction. Due to the residence time of the wood particles in the fuel supply the temperature of the wood entering the reactor has been assumed to be 150℃. The gas composition entering the reactor through the fuel supply with a velocity of 4:5 cm/s has been set to be 100% H_2O at T = 150℃. This massflow corresponds to complete drying of wood in the fuel supply. Inflow conditions for the air are taken from the experiments. Three solid phases have been used in the continuum model: spherical wood particles (diameter 3 mm, density 6.5 g/cm^3, water content 10%, volume fraction 0.35, molar mass 128 g/mol), and two classes of spherical char particles (diameter 1 and 2 mm, density 0.35 g/cm^3, volume fraction 0.35, and molar mass 12 g/mol) with carbon being the only constituent. The walls of the reactor are modeled isothermal with a temperature of Tw = 600 K.

In the Euler-Lagrange simulation the reactor has been discretized with a uniform grid spacing of 1 cm and a depth of 4mm corresponding to the largest wood particles. The wood feeding rate from the experimet is transformed into a particle injection rate per second. The reactor is filled at the beginning of the calculation with 4000 charcoal particles with diameter of 3mm and a temperature of 1050 K.

Results

Fig. 4 and 6 show temperature results at the reactor outlet of the Euler-Lagrange and the Euler-Euler model versus time. Although we were able to run the Euler-Euler model for much longer realtimes than the Euler-Lagrange model (500 S compared to 80 s), both computations have reached an almost statistically stationary state in temperature and volume fractions (Figs. 5 and 7). Mean values of the temperature for the Euler-Euler and the Euler-Lagrange model are in excellent agreement. However, the Euler-Lagrange model shows strong peaks with a frequency of approx. 3.4 Hz negative to the mean. This feature of the solution is

even more pronounced in the concentration results for the main species CO, CO_2, and H2 in Fig. 5. These peaks are due to larger gas bubbles of fresh gas rising fast through the fluidized bed reaching the outlet of the reactor in a state of much less reaction progress than the mean. Compared to the experimental data at 900 mm between 100 - 120 min in Fig. 2 the agreement between the experiments and the simulations is quite reasonable.

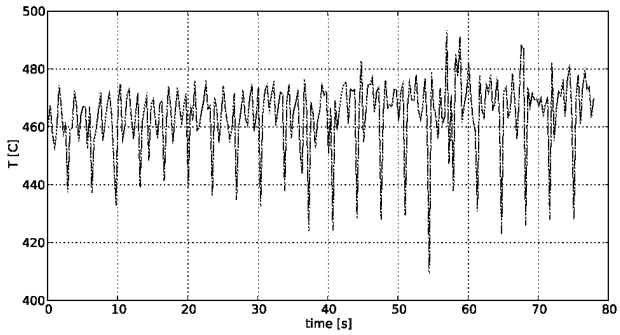

Fig. 4 Temperature vs. time for the Euler- Lagrange simulations

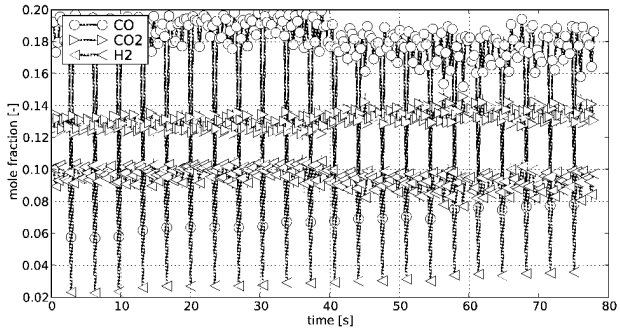

Fig. 5 Molefractions vs. time for the Euler- Lagrange simulations

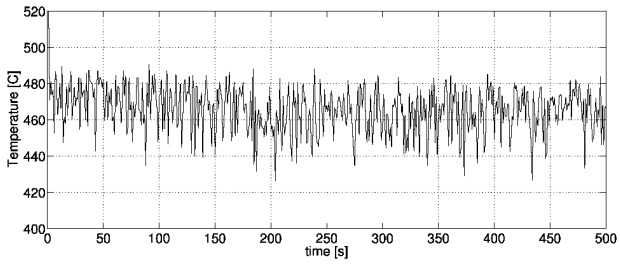

Fig. 6 Temperature vs. time for the Euler-Euler simulations

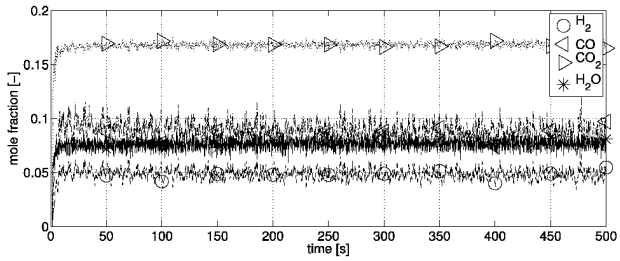

Fig. 7 Molefractions vs. time for the Euler-Euler simulations

Figs. 5 and 7 show some molefractions of the Euler-Lagrange and the Euler-Euler model, respectively. Although both models feature a comparable chemical model, the molefractions in both models differ qualitatively as well as quantitatively. Whereas we see higher CO than CO_2 concentrations in the Euler-Lagrange case, the situation is reversed for the Euler-Euler model. The absolute values for all shown molefractions in both models are quite different. Compared to the experimental results in Fig. 3 the molefraction results of the Euler-Lagrange modelare in better agreement than the Euler-Euler model for the experimental data available. However, it has to be pointed out that the picture might change in favor to th Euler-Euler model with differnt kinetic models or different types of wood. E.g., using kinetic data from Klose et al. (2004) for the heterogeneous ractions we get molefraction values for CO=0.26, CO_2=0.07, and H_2=0.09

for the Euler-Euler model.

The differences in the molefraction results between the two models can be related to, e.g., i) neglected particle-particle heat transfer in the Euler-Lagrange model, ii) different amounts of wood within the reactor, iii) missing tar component in the Euler-Lagrange model, and iv) different 2D/3D mapping to.

CONCLUSIONS

We have presented two different models for the simulation of wood gasification in bubbling fluidized beds. Good quantitative agreement between measurements and calculations has been achieved with both models for the temperature at the reactor outlet. Quite reasonable agreement to experimental date for reactor outlet compositions has been obtained with the Euler-Lagrange model.

Although we have presented 2D results only, both codes are fully 3D. Further research will be conducted towards the investigation of different models for pyrolysis and gasification reactions and performance tuning of the Euler-Lagrange model.

ACKNOWLEDGEMENTS

The financial support of this work by the Deutsche Bundesstiftung Umwelt (DBU) is gratefully acknowledged.

The experimental data was provided by York Neubauer, who is gratefully acknowledged, too.

REFERENCES

K. Agrawal, P. N. Loezos, M. Syamlal, and S. Sundaresan. J. Fluid Mech., 445:151-185, 2001.
M. J. Biggs and P. K. Agarwal. Chem. Eng. Sci., 52(6):941-952, 1997.
M. L. Boroson, J. Howard, J. P. Longwell, and W. A. Peters. AIChE J., 35:120-128, 1989.
M. L. De Souza-Santoz. Fuel, 68(12):1507-1521, 1989.
F. L. Dryer. PhD thesis, Princeton Univ., Aerosp. a. Mech. Sci. Dep., Princeton, NJ, USA, 1972.
F. L. Dryer and I. Glassman. Proceedings of the 14th International Symposium on Combustion, 14:987-1003, 1972.
M. Gr ¨ onli and M. Melaaen. Energy Fuels, 14:791-800, 2000.
M. L. Hobbs, P. T. Radulovic, and L. D. Smoot. AIChE J., 38(5):681-702, 1992.
Y. Kaneko, T. Shiojima, and M. Horio. Chem. Eng. Sci., 54:5809, 1999.
M. Klose, T. W ¨ olki. Fuel, 84:885, 2005.
D. Lathouwers and J. Bellan. Int. J. of Multiphase Flow, 27:2155-2187, 2001.
S. Limtrakul, A. Boonsrirat, and T. Vatanatham. Chem. Eng. Sci., 59:5225-5231, 2004.
T. Mitani and F. A. Williams. Combust. Flame, 39:169-190, 1980.
Y. Neubauer and F. Behrendt. In 15th Eur. Biomass Conf. Ex., Berlin, May 2007.
T. J. O'Brien, M. Syamlal, and C. Guenther. In 3rd Int. Conf. CFD Min. Proc. Ind., 469-474. CSIRO, 2003.
J. Rath and G. Staudinger. Fuel, 80:1379-1389, 2003.
D. Rong and M. Horio. In 3rd Int. Conf. on CFD in the Min. a. Proc. Ind., 469-474. CSIRO, 1999.
I. B. Ross and J. F. Davidson. Chem. Eng. Res. Des., 60a:108-114, 1982.
M. Sommerfeld. Lecture Series 2000-06, von Karman Institute for Fluid Dynamics, April 2000.
C. Y. Wen and Y. H. Yu. Chem. Eng. Prog., 62:100-111, 1966.
H. Zhou, G. Flamant, and D. Gauthier. Chem. Eng. Sci., 59:4205-4215, 2004.

BED MATERIAL AND PARAMETER VARIATION FOR A PRESSURIZED BIOMASS FLUIDIZED BED PROCESS

Bernhard Puchner, Christoph Pfeifer, Hermann Hofbauer

Institute for Chemical Engineering, Vienna University of Technology, A-1060 Vienna, Austria

Abstract: A pressurized gas at high temperatures with low impurities often is a basic requirement for applications for biomass gasification. Therefore, the Vienna University of Technology, in cooperation with the Austrian Bioenergy Centre, operates a pressurized gasification pilot plant in order to investigate the pressurized gasification process and estimate its potential. Within the scope of this paper this test facility as well as its operation behavior is described. Furthermore the parameters pressure, gasification temperature, lambda value and gasification agent have been investigated regarding to their influence on the producer gas composition and are presented and discussed in the following.

Keywords: pressurized gasification, biomass, fluidized bed

INTRODUCTION

In times of increased awareness of climate change more and more attention is drawn to renewable energy and its potentials. Biomass is supposed to have the potential to be used as one main substitute for fossil fuels. Especially pressurized gas produced from biomass is a renewable resource that attracts a great deal of attention due to its wide range of industrial applications (Marquard-Möllenstedt et al., 2004). The high contents of CO and H_2 as well as the pressure of the producer gas predestine this technology for the use as synthesis gas for chemical synthesis and offer the possibility to produce high grade fuels, such as Methanol or Fischer-Tropsch fuels. The producer gas can also be directly used in a gas turbine or in a fuel cell. Currently industrial scale applications of pressurized gasification processes mostly deal with the gasification of coal for the production of mainly Fischer Tropsch fuels. Some data are also available for the co-gasification of biomass and coal, as well as for the gasification of pure biomass. The industrial scale pressurized gasification of biomass has been realized through the Värnamo, IGCC plant (Lundqvist et al., 1993) and the Renugas Project (Lau et al., 1994). The research activity of these institutions as well as others has been focused on the gasification agents air, oxygen, and steam. The most promising technology to produce a high calorific value gas is biomass gasification using steam as fluidization agent. Another approach to produce a widely nitrogen free gas is the gasification with oxygen.

In order to be able to investigate the pressurized gasification process, to compare its specifications with the atmospheric gasification process and to test different fuels, bed materials, gasification agents and applications a pressurized fluidized bed gasification research unit has been built at the Institute of Chemical Engineering at the Vienna University of Technology.

DESCRIPTION OF THE PILOT PLANT

The pressurized bubbling fluidized bed reactor (shown in Fig. 1) realized at the Vienna University of Technology provides producer gas from biomass gasification with temperatures up to 500°C. The pilot plant is able to operate at temperatures between 600°C to 950°C and pressures up to 10 bars, with a thermal fuel power production of up to 70 kW at full load. The test facility is able to perform gasification of wood chips, pellets, coal, and other fuels with the gasification agents steam, air, and oxygen (or mixtures of these) as well as other fluids like nitrogen or CO_2. Table I gives an overview of the characteristic data of the test facility. The gasification agent enters the preheating fluidized bed at a temperature of about 180 to 200°C. There the fluidization agent can be heated up to 600°C before it enters the main reactor fluidized bed. At this stage biomass, in form of wood pellets, is fed through screw conveyors from a pressurized hopper to the main reactor and the gasification supported by additional tracing takes place in a bubbling fluidized bed of a defined turbulence state at temperatures between 600°C and 950°C.

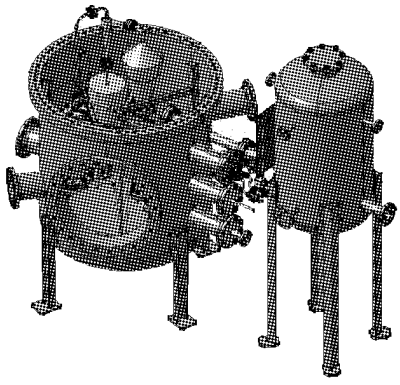

Fig. 1 Overview of the test facility

The gasification agent enters the preheating fluidized bed at a temperature of about 180 to 200°C. There the fluidization agent can be heated up to 600°C before it enters the main reactor fluidized bed. At this stage biomass, in form of wood pellets, is fed through screw conveyors from a pressurized hopper to the main reactor and the gasification supported by additional tracing takes place in a bubbling fluidized bed of a defined turbulence state at temperatures between 600°C and 950°C. To ensure adequate resistance times a freeboard is attached to the reactor fluidized bed. Following that the generated producer gas flow streams through a gas cleaning unit, in which, after a cyclone, the particles are separated in a auto-dedusting battery of metallic high temperature membrane filters. Both, particles separated by the cyclone and by the filter are collected in severed intercepting tanks to be on the one hand able to offer the possibility to investigate and evaluate the performance of these parts of the test facility and on the other hand be able to provide important data for simulation models as well as mass balances.

PLANT OPERATION

Within this section the main operation sequences during an experiment is shown on the basis of experiment V071220 which corresponds to the predefined standard conditions of the parameter variation within the scope of this work (T = 825°C, p = 3 bar, λ = 0.3). Gasification agent was mixture of air/nitrogen (10:1). The fuel was wood pellets.

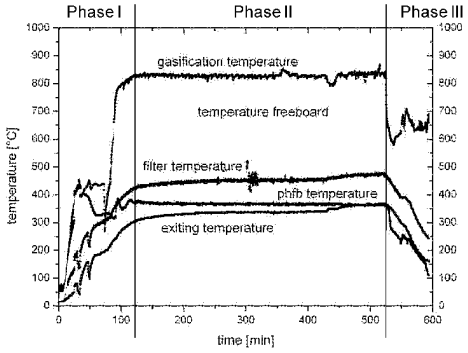

Fig. 2 Temperature pattern during an experiment (Puchner, 2008)

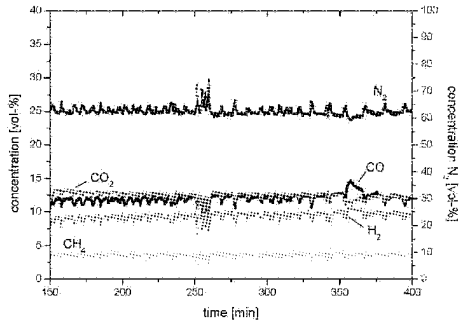

Fig. 3 Producer gas composition during steady operations of experiment V20122007 (Puchner, 2008)

Experiments carried out at the test facility described in this work can be divided into three main phases. Figure 2 shows the start-up phase (phase I), the phase of steady operation (phase II) and the cool-down phase (phase III). All measurements take place during the phase of steady operation in order to ensure representative data. In the course of this experiment series H_2, CO, CO_2 and CH_4, which are considered to be the main producer gas components, as well as the contingent of NH_3, H_2S and the gravimetric tars have been determined online during each experiment. In addition, the composition of the tars occurring in the producer gas has been identified via GC-MS (according to Hüttler, 2008). Figure 3 displays the pattern of the main producer gas components during steady operation of the test facility.

Table 1 gives an overview of the average producer gas composition, including tar, ammonium and H_2S content for the experiment displayed in this chapter. Due to the use of air as gasification agent the LHV is no more than 4.8 MJ/Nm³.

Table 1 Producer gas composition

H_2	9.5	[vol-% $PG_{dr.}$]
CO	12.1	[vol-% $PG_{dr.}$]
CO_2	12.4	[vol-% $PG_{dr.}$]
CH_4	3.6	[vol-% $PG_{dr.}$]
N_2	62.4	[vol-% $PG_{dr.}$]
Tars	0.57	[g/Nm³ $PG_{dr.}$]
NH_3	600	[ppm]
H_2S	11	[ppm]
LHV	4.8	[MJ/Nm³ $PG_{dr.}$]

RESULTS OF THE PARAMETER VARIATION

Variation of Gasification Temperature

In order to investigate the influence of the temperature on the gasification process under pressure, the gasification temperature has been varied between 810°C and 920°C. In order to point out only the influence of the changing temperature, changes in the producer gas composition due to other parameters such as lambda have been eliminated as far as possible. This series of experiments has been carried out at a constant pressure level of 3 bars and a lambda value of 0.3.

Figure 4 shows that within this series of experiments the CO and H_2 content of the producer gas increase with raising gasification temperature, whereas the CO_2 content decreases and the CH_4 level stays constant. Due to the higher temperatures the endothermal reactions within the gasification process, such as the Boudouard-Reaction, are enhanced and the products of the reactions are therefore shifted towards H_2 and CO. As shown in Figure 5 the overall tar content in the producer gas decreases with increasing gasification temperature, which results from the fact that the tar cracking reactions are endothermal.

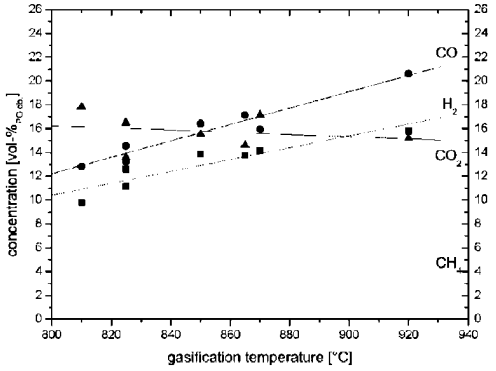

Fig. 4 Influence of the gasification temperature on the main producer gas composition obtained during pressurized operation of the test facility

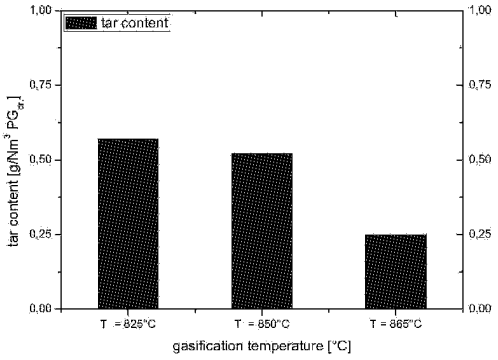

Fig. 5 Influence of the gasification temperature on the tar content of the producer gas

Variation of the Lambda Value

Another parameter of great influence on the gasification process investigated within the scope of this work is the lambda value. In order to determine its influence, the lambda value has been varied between 0.2 and 0.4 in two series of experiments at a constant pressure level of either 3 or 5 bars, a gasification temperature of 830°C and constant fluidization conditions (fluidization number between 3 and 7). Figure 6 shows the results of the experiment series at 3 bars, whereas the fraction of non-combustibles in the producer gas increases with rising lambda value independent from the present gasification pressure of either 3 or 5 bars. In order to be able to point out the influence of the lambda value on the producer gas composition in detail, the main components resulting from the gasification process are displayed in Figure 6 relating to a nitrogen-free producer gas. The CO_2 content increases, whereas the CO, H_2 and CH_4 content of the producer gas decreases with raising lambda value. A higher lambda value corresponds to a higher amount of O_2 and therefore favors the combustion reactions

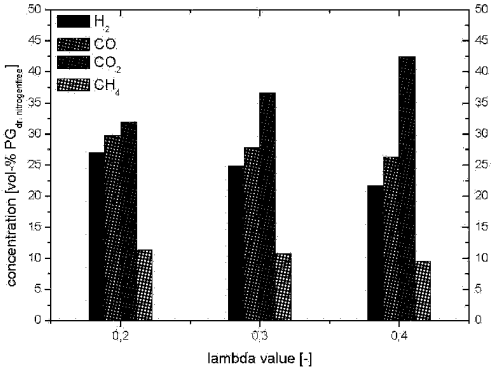

Fig. 6 Influence of the lambda value on the main producer gas composition obtained during pressurized operation of the test facility

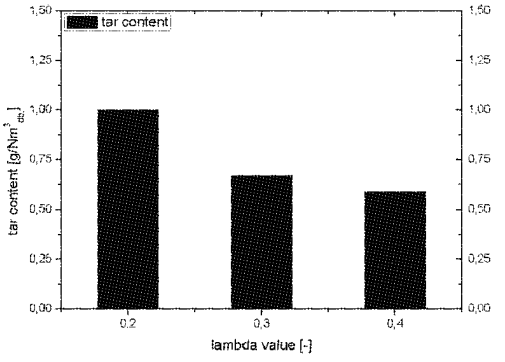

Fig. 7 Influence of the lambda value on the tar content of the producer gas

and the production of CO_2 during the gasification process.

Figure 7 shows that the tar content in the producer gas decreases with increasing lambda value, or in other words, the higher the amount of oxygen available for the gasification process, the lower the tar content in the producer gas.

Variation of the Gasification Agent

For most experiments and their results presented in this work the gasification agent "air" has been used mainly. In order to be also able to investigate the influence of the gasification agent on the producer gas composition and the operation performance of the test facility mixtures of air and steam as well as mixtures of oxygen and steam have been used within the scope of this work too. Instead of using not only air but a combination of air and steam as a gasification agent the gasification reactions are influenced by the steam added, as shown in Figure 8. If the air is replaced by oxygen in a gasification agent mixture with steam, the nitrogen content within the producer gas is reduced severely and the content of valuable components in the gas increased (Figure 8). In order to ensure constant fluidization conditions for all experiments, the steam content of the gasification agent in the oxygen/steam mixture is higher than for the air/steam mixture.

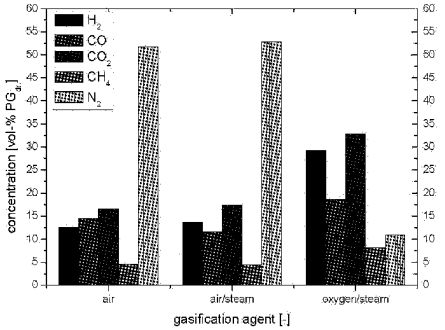

Fig. 8 Influence of the gasification agent on the main producer gas composition obtained during pressurized operation of the test facility

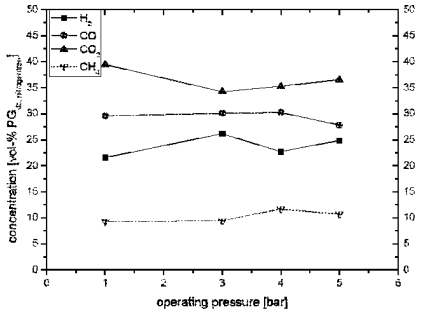

Fig. 9 Influence of the operating pressure on the main producer gas composition obtained during pressurized operation of the test facility

Variation of Operating Pressure

Based on the standard conditions (λ = 0.3, gasification temperature = 830°C and fluidization number = 3-7) the gasification pressure has been varied between 1 bar, which is equivalent to atmospheric conditions, and 5 bars in order to investigate the influence of the pressure on the main producer gas composition.

Figure 9 illustrates the correlation between the operating pressure and the producer gas composition, relating to a nitrogen-free basis, within the scope of experiments concerning pressure variation carried out in the course of this work. As expected, the CH_4 content slightly increases with increasing operating pressure. Since the amount of CH_4 in the producer gas is mainly generated from volatiles at lower pressures (Huang et al., 2003), this trend can be traced back on the higher conversion rates of volatiles with increasing operating pressures. The development of the H_2 - increasing from atmospheric conditions to an operating pressure of 3 bars and leveling off at higher pressures has also been observed by (Xiao et al., 2006), which may be explained by the gasification kinetics being directly enhanced by pressure.

Nevertheless, there is only little influence of the operating pressure on the main producer gas composition in the pressure range observed within the scope of this work. Within the scope of this work the operating pressure during gasification has been varied between 1 bar (atmospheric conditions) and 8 bars.

During, in other respects, constant gasification conditions, the influence of this changing operating pressure on the tar content in the producer gas has been investigated. Contrary to the main producer gas components an effect of the gasification pressure on the tar content in the producer gas has been detected. Figure 10 illustrates that an increase of the gasification pressure causes a decrease of the tar content and therefore has a positive effect on the quality of the producer gas.

Variation of Bed Material

Within the scope of this work besides olivine, which has been used as standard bed material, also calcite and silica sand have been tested as bed material for the pressurized gasification process. In the following the results achieved during the experiments carried out at standard conditions using the three different bed materials are compared in order to point out the influence of the bed material on the gasification process and in particular on the producer gas composition.

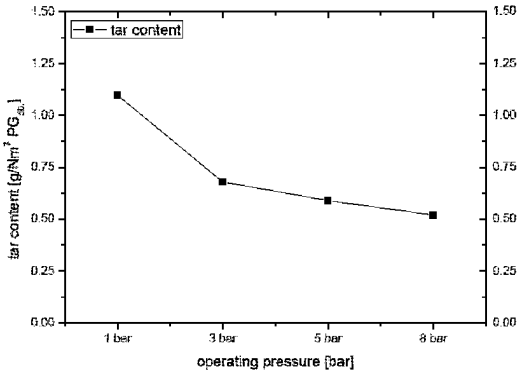

Fig. 10 Influence of the gasification pressure on the tar content of the producer gas

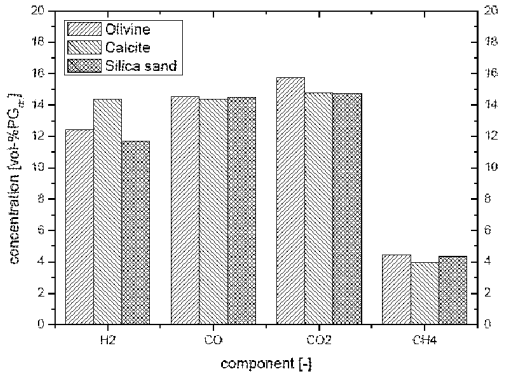

Fig. 11 Influence of the type of bed material on the main producer gas composition obtained during pressurized operation of the test facility

Figure 11 shows, that replacing the bed material olivine by calcite or silica sand has influence on the mean producer gas composition. If calcite is used as bed material, on the one hand the hydrogen content in the producer gas increases in comparison to the experiments carried out under similar conditions but using olivine as bed material, and consequently on the other hand the methane content decreases. Furthermore a shifting of the CO/CO_2 ratio has been detected. Using calcite as bed material shifts the ratio in favor of the CO content in the producer gas, which could result from the shifting of the CH_4 combustion reaction and the dry reforming reaction. Though, a larger effect of the bed material on the overall tar content in the producer gas has been expected on the basis of past experiences in other projects. The use of calcite instead of olivine as bed material had a much higher positive effect on the amount of tars found in the producer gas in previous experiments under atmospheric conditions. However, Figure 12 illustrates that also under pressure a certain amount of tar reduction can be expected in the producer gas if calcite is used as bed material instead of olivine.

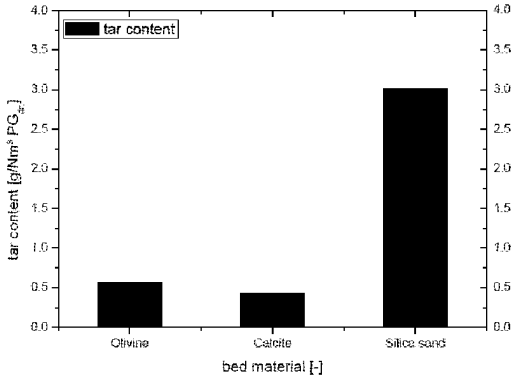

Fig. 12 Influence of the type of bed material on the tar content of the producer gas

Using silica sand as bed material instead of olivine does not have as much effect on the mean producer gas composition as if calcite is used instead of olivine, but the tar content in the producer gas shows that, contrary to olivine and calcite, silica sand is not catalytically active relating to tar cracking reactions.

CONCLUSIONS

The pressurized bubbling fluidized bed reactor (PRU) realized at the Vienna University of Technology is able to perform, due to the electrical heating of the reactor, allothermic as well as autothermic. Therefore it opens the possibility to investigate the gasification process at different pressures using several different gasification agents, such as steam and steam/O_2 mixtures, which are so far sparely published. At this stage of the project the influence of the gasification temperature, the chosen gasification agent, the operating pressure and the equivalent ratio on the producer gas as well as tar content and its composition have been investigated.

Due to the integration of a new filter regeneration system long-term experiments are made possible and results presented in this work show that continuous operation of the bubbling fluidized bed reactor under different operating conditions is feasible. At pressures up to 8 bar, the contingent of main producer gas components resulting from the gasification process are comparable to results of atmospheric bubbling fluidized bed gasifiers. An average tar content of only 0.25 to 1.15 g/Nm³ PG, depending on the operating conditions, affirms the good performance of the test facility. Especially the decrease of the overall tar content due to increasing operating pressures of the test facility seems to be a promising benefit of the pressurized gasification. Within this test series it has been shown that an increase of the gasification temperature up to a certain degree causes an increase of CO and H_2 at a concurrent decrease of CO_2 and CH_4 as well as a decrease of tars in the producer gas. Higher equivalent ratios have a positive effect on the tar content in the producer gas, but also implicate less combustible components. If instead of using only air as gasification agent also steam is added to

the gasification process, the heterogenic water gas reaction and in succession the homogenic water gas reaction are shifted which causes an increase of the H_2 and CO_2 and a decrease of the CO and CH_4 contents in the producer gas. The substitution of air by oxygen, hence the use of a mixture of oxygen and steam as gasification agent, lowers the nitrogen content in the producer gas and therefore leads to a higher calorific value producer gas. Variation of bed material shows that calcite seems to be a possible alternative to olivine due to its positive effects relating to H_2 and tar content in the producer gas.

Within the scope of this project further experimental research with a focus on the use of steam and mixtures on the basis of steam as gasification agent will be carried out. Especially the influence of the operating pressure on the producer gas composition, including tar composition, ammonium content as well as H_2S content will be investigated. The installation of a continuous dedusting system for the gas cleaning rig of the plant has been realized and opens the possibility of long term experiments (Puchner et al, 2008). The flexible construction of the pilot plant also allows the integration of a two-zone fluidized bed using the DFB-process, which could be the next step of an upgrade of the test facility.

Resulting from the constructed test facility exact data have been achieved and validated and a simulation model is about to be generated. Therefore existing gasification models have already been extended with the parameter of pressure. The cognitions of the pressurized gasification unit should give fundamentals for the development of bigger pilot plants and provide a basis for scale up to demonstration plants.

NOTATIONS

Symbols:

DFB	dual fluidized bed	-	Greek letters		
IGCC	integrated gasification combined cycle	-	λ	lambda value	-
p	operating pressure	bar	Subscripts		
PG	producer gas	-	*dr.*	dry basis	
PRU	pressure research unit	-			
T	temperature	°C			

ACKNOWLEDGEMENTS

The Authors are highly indebted to the Austrian Bioenergy Centre (ABC) for their financial support. ABC is a Competence Centre which corporate objective is pre-competitive research and development in the area of "energetic biomass use". The work also received scientific support from RENET-Austria, which has been a competence network in the framework-programme of K_{ind}/K_{net}. This support is gratefully acknowledged.

REFERENCES

Huang J., Fang Y., Chen H., and Wang Y.: Coal Gasification Characteristic in a Pressurized Fluidized Bed. Energy and Fuels, 17 (6):1474-1479, (2003).

Hüttler H., Quantifizierung von Teerkomponenten in Biomassevergasern. PhD-Thesis, Institute of Chemical Engineering, Vienna University of Technology (2008).

Lau, Francis S. and Carty, Ronald H., Development of the IGT RENUGAS process, Proceedings of the Intersociety Energy Conversion Engineering Conference, (1994), 1549-1554.

Lundqvist, Ragnar G. ., The IGCC demonstration plant at Varnamo. Bioresource. Technol., (1993), 49-53.

Marquard-Möllenstedt, T., Sichler P., Specht M., Michel M., Berger R., Hein K.R.G., Höftberger E., Rauch R., Hofbauer H.: New Approach for Biomass Gasification to Hydrogen, 2nd World Conference and Technology Exhibition on Biomass for Energy, Industry and Climate Protection, (10-14th May 2004), Rome, Italy.

Puchner B. Experimental Investigations on a Pressurized Bubbling Fluidized Bed Biomass Gasification Research Unit, PhD Thesis, Vienna University of Technology (2008).

Puchner B., Pfeifer C., Schoeneborn A., Hofbauer H., High temperature metal membrane filter as particle seperator downstream of a pressurized bubbling fluidized bed biomass Gasifier, 7th International Symposium on Gas Cleaning at High Temperatures (GCHT-7), Shoal Bay Resort, Newcastle, Australia (2008).

Xiao R., Zhang M., Jin B., Huang Y., and Zhou H.: High-Temperature Air/Steam- Blown Gasification of Coal in a Pressurized Spout-Fluid Bed. Energy and Fuels, 20 (2):715-720, (2006).

PROCESS ANALYSIS OF LIGNITE CIRCULATING FLUIDIZED BED BOILER COUPLED WITH PYROLYSIS TOPPING

Baoqun Wang[1], Li Dong[1], Yin Wang[1], Y. Matsuzawa[2], Guangwen Xu[1]

1 State Key Laboratory of Multiphase Complex System, Institute of Process Engineering, Chinese Academy of Sciences, Beijing, China
2 Research Laboratory, IHI Corporation, Ltd., Yokohama, Japan

Abstract: We developed a comprehensive process model in ASPEN Plus to simulate the energy and mass balances of a lignite-fueled atmospheric circulating fluidized bed (CFB) boiler integrated with coal predrying and pyrolysis topping. In this model, it is assumed that the heat from exhausted flue gas was employed for coal predrying, and the sensible heat derived from circulated bed material was used for the pyrolysis topping (endothermic process). The simulation was conducted with respect to the Yunnan Kaiyuan CFB boiler, and two representative lignite coals from Xiao Long Tan (XLT) and Xin Shao (XS) were considered. The result shows that the predrying of coal with the sensible heat of above 363 K from flue gas, the amount of coal consumed in the boiler can be reduced by 3.5% and 5.3% for XLT lignite and XS lignite, respectively. It was also found that integration of pyrolysis topping with the boiler increased the coal consumption of the boiler, and the extent of consumption-increase varies with the yields of tar and gas in the pyrolysis topping process. For a gas yield of 5.2% and a tar yield of 5-6%, the consumption of XS lignite increased by about 20% comparing to that in the case without topping.
Keywords: Pyrolysis topping, Coal drying, Process modeling, CFB boiler

INTRODUCTION

It is well-kwon that the chemicals are almost produced from petroleum, especially ring-based chemicals. Recent years, due to the global depletion and supply instability of the petroleum (Energy Information Administration, 2008), the abundant coal natural recourse as the substitute for petroleum to produce chemicals is being widely considered. This is because the volatiles in around 80% of coal of the world contain a large number of organic compounds with various ring-based chemical structures (Nolan et al., 2004), which could be employed to produce diverse chemicals. However, directly burning or gasifying the coal with high volatiles at high temperatures normally cause these chemical structures to be decomposed and creating many small molecules, such as CO, CO_2, H_2 and H_2O. Moreover, it is very difficult to directly reform these structures again via general synthetic processes. Therefore, it is remarkably significant to produce these aromatic chemicals from coal.

Coal topping, as one of potentially chemical processes which may fulfill the production of ring-based chemicals from coal, was developed recently. Some chemicals with hydrogen-rich structures in the form of liquid can be extracted from coal before combustion or gasification (Yao et al., 1995) as shown in Fig. 1. The liquid produced in topping process can offer an effective resource for high value ring-based chemicals, including phenol, BTX and poly-ring aromatics, and meanwhile other products from coal topping can be combusted to generate heat/steam/power or gasified to produce syngas. Therefore, development and integration of topping process with traditional combustion and gasification in coal chemical process become more important, particularly in China, where more than 80% of coal resource contains large amount of compounds with middle or high volatiles (Wang et al., 2005).

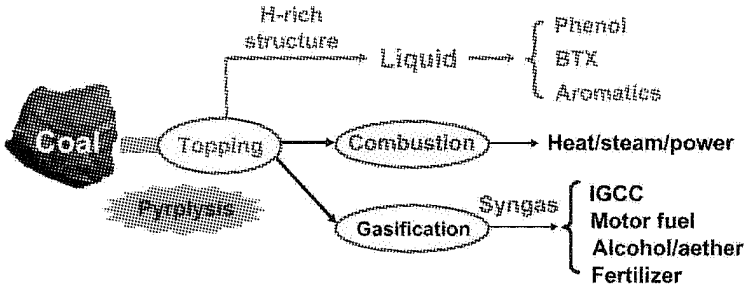

Fig.1 Conception of the coal topping

Coal topping includes catalytic liquefaction and pyrolysis. Pyrolysis is more feasible and easily to be integrated with the existing combustion or gasification processes (Kwauk et al., 1998). Figure 2 presents a

convenient system integrated with circulating fluidized bed (CFB) boiler and pyrolyzer to perform coal toping. Coal is introduced into the pyrolyzer and devolatilized with the heat of circulated hot coal ash to produce liquid and pyrolysis gas. The liquid oil is collected and the pyrolysis gas is recycled to the pyrolyzer and combustor as for the atmospheric gas and fuel gas, respectively. Then, the produced char is transferred into the combustor and is burned, and the heat is recovered. In China, around 14% of total coal reserves is lignite that is one of prevalent fuels used in power plant of Inner Mongolia and Yunnan province (China Coal Industral Net), possessing high content of water and volatile. Integration coal predrying with pyrolysis topping in power plant would be one of attractive approaches considering the comprehensive utilization of lignite and economy.

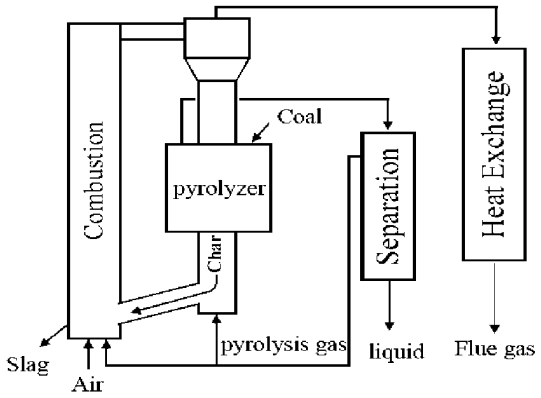

Fig. 2 Schematic of CFB boiler coupled with pyrolysis topping

In this paper, an ASPEN plus model was developed to demonstrate the feasibility and economic level of coupling coal drying and pyrolysis topping in a 300MW lignite-fueled CFB power plant based on simulating the mass and energy balance. The performance of integrated system using sensible heat of flue gas to dewater coal and the effect of introducing pyrolysis topping on coal consumption were investigated.

MODELING APPROACH

Figure 3 shows the schematic of ASPEN Plus model for CFB boiler integrated with coal predrying and pyrolysis topping. The model consists of six units, e.g. dryer, pyrolyzer, combustor, cyclone, heat exchanger and external heat exchanger (EHE). Coal is first dewatered in dryer by the exhausted flue gas, and then heated in pyrolyzer via the circulated solid bed material collected by cyclone. The gas produced from pyrolysis is separated and introduced into tar and pyrolysis gas containing H_2, CO, CH_4, CO_2 and C2~C3 hydrocarbons. The pyrolysis gas can be used as city gas or sent back to boiler, while char is transferred to combustor. In cyclone unit, circulated bed material is separated from flue gas. The heat exchange between flue gas and water/steam occurs in the heat exchanger unit, and the EXE unit is used to heat one part of bed material.

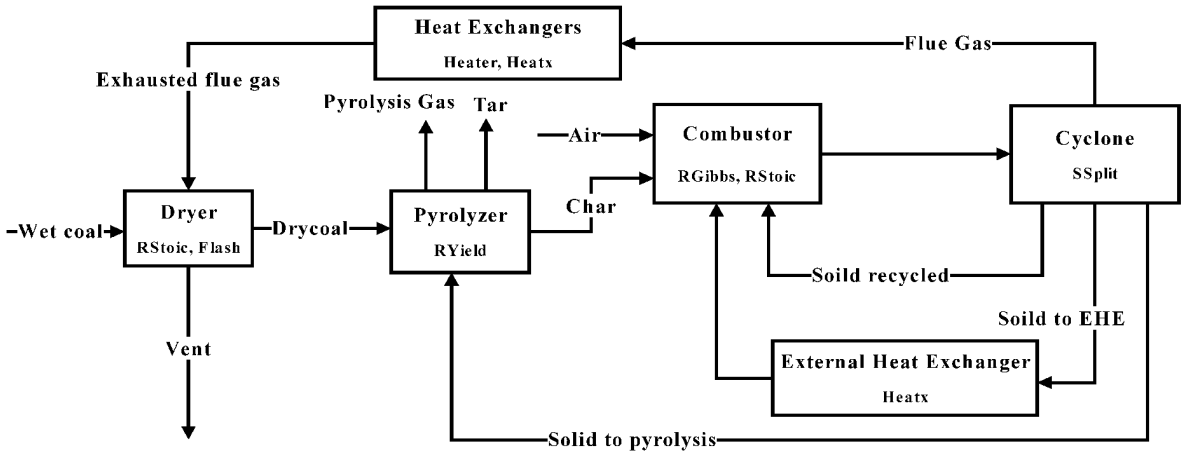

Fig. 3 Schematic of ASPEN Plus model for CFB boiler coupled with predrying and coal topping

The dewatering of raw coal is proceeded by using the sensible heat of flue gas with the temperature of 422K. In this model, a predry block was made particularly for specifying the water content of dry coal and calculating the corresponding removal of water from coal with the drying ratio against the original water content of coal.

The Yield reactor module (RYield) in ASPEN Plus is commonly used to model the pyrolysis/ devolatilization process via converting the feed into the equivalent elemental components at the same enthalpy level. However, ASPEN Plus has no general model for predicting tar and pyrolysis gas compositions from coal pyrolysis. Here we input experimental results of pyrolysis products into the model. This is one of the most feasible ways to process. Additionally, since the composition of coal tar is very complex, coal tar was supposed as a kind of hydrocarbon CmHn, such as C6H6 or C14H10 according to the ASPEN Plus model reported (Carlo et al., 2004). The ultimate analysis of tar was used as tar constituent in this work. The composition of pyrolysis gas was analyzed by GC and the composition of char was determined by element balance of pyrolysis process.

Three modules were employed for simulation, e.g. RYield reactor, RGibbs reactor, and RStoic reactor. Coal is first decomposed in RYield reactor into the components composed of carbon, hydrogen, nitrogen, sulfur, oxygen, steam, and ash according to the ultimate and proximate analyses. Then, the RGibbs reactor module was used to calculate the compositions of flue gas via the phase and chemical equilibriums at a given pressure and temperature. Considering the fact that carbon in coal can not completely burn in the boiler furnace, it was supposed that in RGibbs model that carbon conversion in combustion process was 99%. RStoic reactor module was used to simulate desulphurization in the CFB boiler based on the reactions of $CaCO_3 \rightarrow CaO+CO_2$ and $CaO+SO_2 \rightarrow CaSO_3$ to typify the desulphurization reactions involved. Furthermore, in this combustion model, the hydrodynamic complexity of fluidized-bed reactor was neglected, and the carbon conversion was specified according to the actual data provided by power plant, instead of considering the combustion kinetics.

In the process simulation, the performance of two lignites from Xiao Long Tan (XLT) lignite and Xin Shao (XS) lignite, were investigated in the integrated system. Table 1 presents the analyses of lignite and coal tar, which was produced from decomposing XS lignite at 873K. The composition of pyrolysis gas from decomposing XS lignite at 873K was shown in Table 2.

Table 1 Properties of lignite and coal tar

	XLT lignite	XS lignite	Coal tar
Water (wt%)	34.7	35.2	-
	Proximate analysis (wt%, dry basis)		
Volatile matter	43.46	64.94	-
Fixed carbon	39.01	9.3	-
Ash	17.53	25.76	-
LHV (kJ/kg)	12435	11560	-
	Ultimate analysis (wt%, dry basis)		
C	56.23	46.95	75.92
H	2.86	4.18	9.61
N	1.56	0.77	0.74
S	2.54	0.96	0.88
O	19.28	21.38	12.85

Table 2 Component analysis for pyrolysis gas

Components	H_2	CO	CO_2	CH_4	C_2H_4	C_2H_6	C_3H_6	C_3H_8
Vol. %	18.63	31.7	26.65	18.71	2.1	2.15	0.02	0.04

RESULTS AND DISCUSSION

Model validation

A process model was first established reproduce the performance data of the 300MW CFB boiler fueled with XLT lignite under the maximum continuous rating (BMCR) condition. The coal feeding rate was varied to maintain the temperature of boiler furnace at 1113K. Based on the design data of power plant, a ratio of Ca/S=2 was adopted to calculate the flow rate of $CaCO_3$. Table 3 presents the comparisons of major performance parameters between the simulated results and the boiler design data. It can be seen that the simulated results are in good consistence with the design data, which demonstrated that the model using ASPEN Plus established in this work is very effective and has sufficient accuracy for estimating the performance of a CFB boiler. Nonetheless, the RGibbs reactor module used in combustion model is unable to predict the NO_X concentration in the flue gas. The prediction of NO_X formation has to be conducted based on some other kinetic methods.

Table 3 Comparison of major boiler parameters between simulation results and design data

100% BMCR, design coal	Design data	Simulated data
Coal consumption rate, t/h	226.3	228.7
$CaCO_3$ consumption rate, t/h	27.5	23.5
Bottom slag flow rate, t/h	21.0	20.6
Fly ash flow rate, t/h	31.6	30.5
Combustion air flow rate, Nm^3/h	917900	946567
Flue gas flow rate, Nm^3/h	1061700	1091426
SO_2 emission rate, mg/Nm^3	400	463
NO_X emission rate, mg/Nm^3	350	62.5
Boiler efficiency, %	93.4	93.76

Coal predrying using flue gas

Lignite used in this CFB boiler has high water content, as shown in Table 1. In order to prevent the steam condensation from flue gas, the relatively high temperature of exhausted flue gas, about 422K, was chosen, leading to low efficiency of power plant. However, the high temperature of gas made it possible to dewater lignite with the sensitive heat of flue gas.

Water in coal includes free water and crystal water. The former may present in the forms of both surface water and inherent water. The evaporation of inherent water occurs at temperature above 373K, whereas the temperature for vaporizing crystal water can be above 473K. When the flue gas below 473K was used to dewater coal, only free water can be removed. Figure 4 shows the simulated results of coal consumption and water in coal after dewatering at varied ratios of wet coal being dewatered. XLT lignite was investigated, in which water content was shown in Table 1. All flue gas was forwarded into the drier. The temperature of flue gas vented from the drier was set at 383K.

By varying the amount of coal consumed for drying, it can be found that the coal consumption rate for coal drying in this case decrease about 3.5% compared with that of prototype case, but the drying ratio has little effect on coal consumption rate of the four drying cases (30%, 50%, 80% and 100% drying ratio). As expected, the water in dry coal decreases with drying ratio. For example, 13% of water in wet coal can be removed for the case of 100% drying ratio, whereas 55% of water in wet coal can be removed in the case of 30% drying ratio. The boiler efficiency can thus increase by about 3.5-4 % due to the contribution of coal drying.

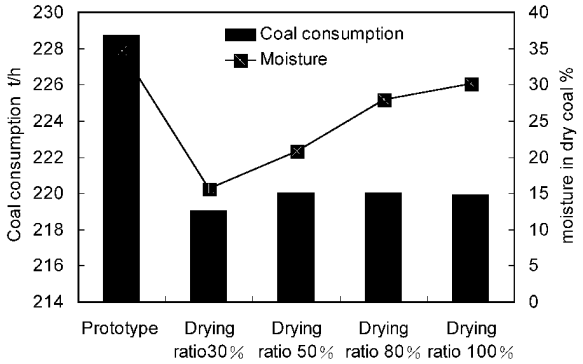

Fig. 4 Coal consumption and water in cases without and with coal predrying using sensible heat of flue gas

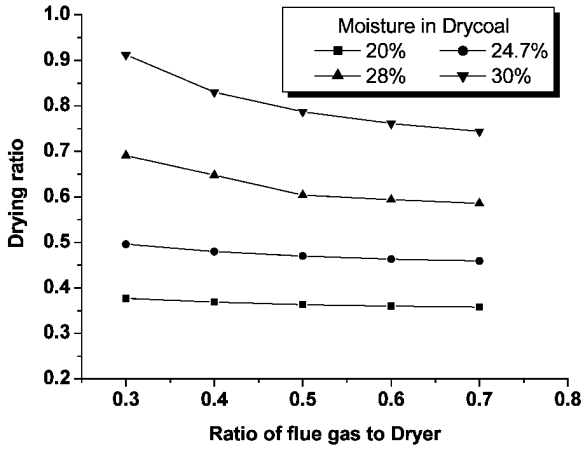

Fig. 5 Variation of drying ratio with the ratio of flue gas to Dryer at different water in Drycoal

As known, it is difficult to use total flue gas for drying in power plant because the velocity of flue gas from boiler was too fast to be controlled easily. Accordingly, we simulated the case of partial flue gas recycled, in which the ratio of flue gas to the Dryer varied from 0.3 to 0.7, and the water in Drycoal was fixed to 20%, 24.7%, 28% and 30%, respectively. The temperature of flue gas vented was set at 393K. Figure 5 shows the variation of drying ratio with the ratio of flue gas to Dryer at different water in Drycoal. With the ratio increase of flue gas that was delivered into dryer, the ratio of dewatered coal with the same water content decreases with the increase of flue gas, while it increases with the increase of water content in Drycoal at the same ratio of flue gas. When the ratio of flue gas to Dryer is more than 0.5, the variation of the drying ratio becomes constant. Thus, we can easily calculate how much wet coal can be dried to the water required in Drycoal at a given ratio

of flue gas to Dryer. For example, if we use only 30% of flue gas to dry wet coal, we can remove 29% of water from one half of wet coal feed.

Integrated with pyrolysis topping

In order to investigate the effect of predrying and pyrolysis topping on CFB boiler performance, four cases, including prototype CFB boiler, CFB boiler with predrying, CFB boiler with predrying and pyrolysis toping, and CFB boiler with pyrolysis topping, were simulated and compared. XS lignite was employed as a representative, and its pyrolysis temperature was set at 873K. The yields of tar and pyrolysis gas based on dry coal are 9% and 5.2%, respectively. We assumed that the boiler evaporation rate was constant, and the outlet temperatures of steam from each heat exchanger are the same as that in the prototype CFB boiler.

Figure 6 presents the comparative results among four cases mentioned above. For XS lignite, coal consumption in the boiler with predrying is 278.8 t/h, which is lower than that in prototype boiler about 5.3%. On the contrary, the coal consumptions in the CFB boiler with pyrolysis topping and the CFB boiler with predrying and pyrolysis topping are 51.8% and 42.4%, respectively, higher than that in prototype boiler about. These results indicate that the presence of predrying unit could reduce coal consumption of CFB boiler, whereas the introduction of pyrolysis topping led to the increase of coal consumption so as to maintain the constant steam evaporation rate for CFB boiler.

Furthermore, the sensitive analysis of coal consumption toward tar and gas production rate in the CFB with predrying and pyrolysis topping was performed. Figure 7 presents the sensitive result without recycling pyrolysis gas into combustor, and Figure 8 shows that of pyrolysis gas being recycled to combustor. These results show that with the decrease of tar yield, coal consumption rate decreases significantly, especially in the former case. Our laboratory experimental data revealed that tar yield obtained is about 9%. However, tar yield in the industrial facility is usually lower than that obtained in the laboratory experiment, reasonably in a range of 5-6%. For obtaining 5-6% of tar yield, the increase of coal consumption by intergrading predrying and pyrolysis topping into CFB boiler is about 20%.

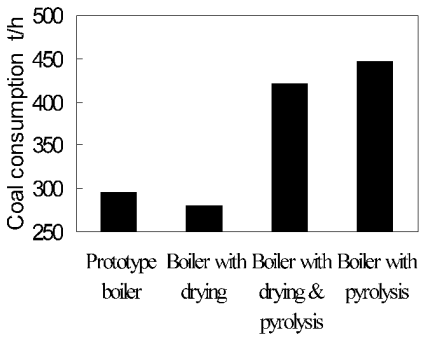

Fig. 6 Comparison of coal consumption for prototype boiler, boiler with drying, boiler with drying & pyrolysis and boiler with pyrolysis

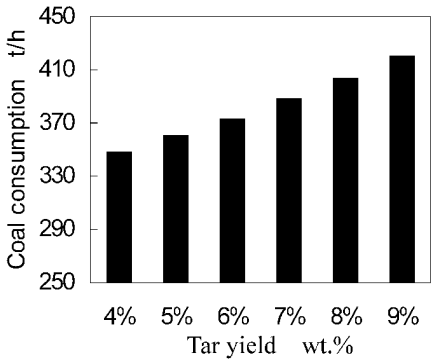

Fig. 7 Sensitive analysis to tar yield for CFB boiler with predrying and pyrolysis topping (pyrolysis gas is not recycled to combustor, gas yield is 5.2%)

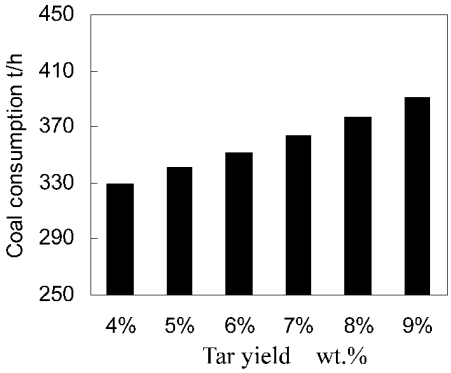

Fig. 8 Sensitive analysis to tar yield for CFB boiler with predrying and pyrolysis topping (pyrolysis gas is recycled to combustor, gas yield is 5.2%)

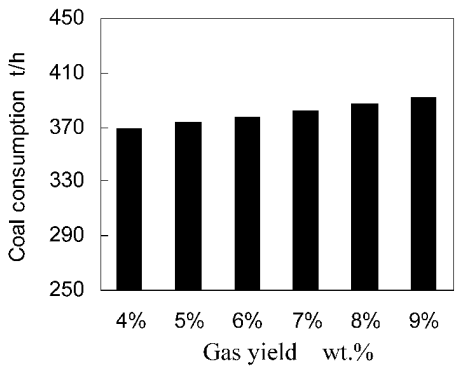

Fig. 9 Sensitive analysis to gas production rate for boiler with drying & pyrolysis (pyrolysis gas is not recycled to combustor, tar production rate is 6%)

Figure 9 shows the sensitive analysis of coal consumption to gas yield in the CFB boiler that was integrated with predrying and pyrolysis topping under the condition of 6% of tar yield and without pyrolysis gas recycle. It can be seen that coal consumption is proportional to the gas yield. However, the increment of

coal consumption is much less than that in Figure 7 and Figure 8, implying that the variety of coal consumption in CFB boiler integrated with predrying and pyrolysis topping depends on the tar yield from pyrolysis topping instead of the gas yield.

CONCLUSIONS

In this paper, an ASPEN Plus model was developed to simulate the mass and energy balance and the performance in CFB boiler. Three modules (RYield reactor, RGibbs and RStoic reactors) were built in simulation for evaluating the potential influences of predrying coal and pyrolysis topping on the performance of a 300MW CFB boiler fueled lignite. The results show that about 4% of water content from wet coal can be extracted by using the sensible heat of flue gas from 423K to 383K and coal consumption was decreased by about 3.0%. Integration of the pyrolysis topping process with the CFB boiler would increase coal consumption due to the co-production of tar and pyrolysis gas. When tar yield is 5-6% and pyrolysis gas yield is 5.2% of dry base coal, the increase of coal consumption may be 20% for the CFB boiler fueled with XS lignite. Coal consumption in CFB boiler with predrying and pyrolysis topping is more sensitive to the tar yield from pyrolysis topping than the gas yield. The simulation results demonstrated that Aspen plus can be used to effectively analyze the performance of CFB boiler.

ACKNOWLEDGEMENTS

The authors express their gratitude to Kaiyuan power plant, Yunnan Datang International Honghe Power Generation Co., Ltd. for providing basic data for this study (No. 2008110031002741) and IHI Corporation, Japan for providing computational resources.

REFERENCES

Carlo, N. H., Andre, P. C. F., Herman, den U. and Harold, B.: Energy. 29 (2004), 1743-1771.
China Coal Industral Net. China coal resources, www.chinacoal.org.cn/mtzy/254/390.aspx.
Energy Information Administration (EIA), International Energy Outlook 2008, US Department of Energy (DOE), Washington, www.eia.doe.gov/oiaf/ieo/index.html.
Kwauk, M. S. (1998). Coal Topping Process. 9th member forum of Academia Sinica.
Nolan, P., Shipman, A. and Rui, H.: European management. J. 22 (2004), 150-164.
Wang, J. G., Lv, X. S., Yao, J. Z., Lin, W. G. and Cui, L. J.: Ind. Eng. Chem. Res. 44 (2005), 463-470.
Yao, J. Z. and Kwauk, M.: Process in chemistry 7 (1995), :205-208.

APPLICATION OF CAO-BASED BED MATERIAL FOR DUAL FLUIDIZED BED STEAM BIOMASS GASIFICATION

S. Koppatz, C. Pfeifer, A. Kreuzeder, G. Soukup, H. Hofbauer

Institute of Chemical Engineering, Vienna University of Technology, A-1060 Vienna, Austria

Abstract: Gasification of biomass is a suitable option for decentralized energy supply based on renewable sources in the range of up to 50 MW fuel input. The paper presents the dual fluidized bed (DFB) steam gasification process, which is applied to generate high quality and nitrogen-free product gas. Essential part of the DFB process is the bed material used in the fluidized reactors, which has significant impact on the product gas quality. By the use of catalytically active bed materials the performance of the overall process is increased, since the bed material favors reactions of the steam gasification. In particular, tar reforming reactions are favored. Within the paper, the pilot plant based on the DFB process with 100 kW fuel input at Vienna University of Technology, Austria is presented. Actual investigations with focus on CaO-based bed materials (limestone) as well as with natural olivine as bed material were carried out at the pilot plant. The application of CaO-based bed material shows mainly decreased tar content in the product gas in contrast to experiments with olivine as bed material. The paper presents the results of steam gasification experiments with limestone and olivine, whereby the product gas composition as well as the tar content and the tar composition are outlined.

Keywords: fluidized bed gasification, bed material, limestone, steam gasification, biomass

INTRODUCTION

Energy from renewable sources is considered to become an important part of the energy economy. Climate change, increasing energy demand, progressive energy costs or limited fossil fuels are a few decisive reasons to enforce the integration of renewables and are currently in intensive discussion. However, the utilization and the technical processes for energy conversion require developments and optimization to ensure technical efficiency and profitability. Biomass or ligneous feedstock is a carbon containing source, which is discussed with special interest for energy supply. Beside conventional heat and power production the conversion into liquid fuels, the generation of synthetic natural gas or hydrogen for fuel cell operation is possible and enables a broad range of application, the so called polygeneration.

The steam gasification of biomass is a suitable option of thermo-chemical conversion, since a nitrogen-free product gas characterized by heating values of 12 – 15 MJ/Nm³ is provided, which offers product flexibility based on its high quality. Undesirable constituents of the product gas are tars, whose formation occurs over the entire progress of gasification. The tar containing product gas can cause severe problems in downstream process units (e. g. clogging of heat exchanger), since certain tar compounds condense at relatively high temperatures (e.g. boiling point of naphthalene 218 °C). Furthermore, the heating value of the product gas is decreased because an essential fraction of the chemical energy is bounded in the tar and do not contribute in terms of the favoured product gas components H_2, CO.

CATALYTIC TAR CONVERSION IN FLUIDIZED BEDS

Beside tar removal technologies, which operates at low temperature level (e.g. gas scrubber, filter), the so called hot gas cleaning is an issue of current investigations, above all regarding to product gas treatment originating from biomass gasification.

The hot gas cleaning comprehends catalytic conversion of tar and can be distinguished between primary and secondary measures. Primary tar reduction is achieved by catalytic tar conversion, which proceeds in the reactor while the gasification takes place. By means of secondary measures the product gas treatment is executed in a second reactor downstream of the gasification reactor. Primary tar reduction is the most attractive, since advantages can be achieved in many respects. Conversion efficiency is increased, hence the need for downstream product gas treatment is reduced or in ideal case it becomes redundant.

The primary tar reduction is in investigation by several authors, whereas different catalytic materials are in discussion. The range of materials usable for catalytic tar reduction includes natural minerals (e.g. dolomite, limestone, olivine, iron ores) as well as synthetic materials (e.g. Ni-supported olivine, Fe-supported olivine, alkali metal based material, char). Comprehensive reviews on catalysts for biomass gasification and tar reduction, respectively are given by Abu El-Rub et al. (2004), Sutton et al. (2001), and Dayton (2002). The

present paper concentrates on limestone (CaO-based materials), since limestone is a promising candidate for high tar conversion, which is widely available at low costs and non-toxic. Various materials for catalytic tar conversion have been considered and have been investigated, e.g. by Simell et al. (1999) or Devi et al. (2005).

DUAL-FLUIDIZED-BED (DFB) STEAM GASIFICATION

The DFB-concept for steam gasification has been developed at Vienna University of Technology and is continuously under investigation regarding different aspects (e.g. hot gas cleaning, hydrogen production). The process contains two fluidized bed reactors whose connections enable an interchange of solid matter (bed material), see Fig. 1. By means of bed material circulation heat transfer is effected which is required for the heat demand of the steam gasification (allotherm), whose overall reaction is endothermic, since no partially oxidation takes places. The steam gasification proceeds in the gasification reactor (gasifier), which is continuously fed with hot bed material coming from the riser. Combustion of residual char oncoming altogether with the bed material from the gasifier takes places in the riser. Hence the bed material is heated to be subsequently separated from the flue gas stream for recycling into the gasifier.

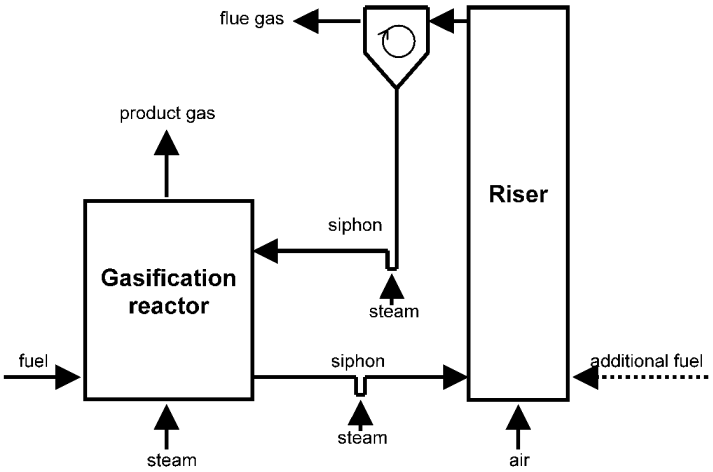

Fig. 1 Principle of Dual-Fluidized-Bed concept for steam gasification

The gasification reactor is fluidized with steam and the fluidisation regime is a bubbling fluidized bed. The air fluidized riser is operated in a fast fluidized or turbulent regime. The reactors are connected through siphons, which are fluidized with steam to avoid oxygen containing gas flow towards the gasifier. The DFB-process is further detailed by Hofbauer et al. (1997) and Hofbauer et al. (2002).

The bed material serves primarily as heat carrier for heat supply of the gasification reactor. Furthermore, the bed material can fulfil the function as tar conversion catalyst, since the bubbling bed effect an adequate gas-solid contact in the gasifier.

The steam gasification results in the product gas components H_2, CO, CO_2, CH_4, and C_2/C_3-hydrocarbons as wells as in a certain amount of higher hydrocarbons with high boiling point (tars). Eq. (1) represents the idealised overall reaction of the steam gasification of ligneous feedstock.

$$CH_xO_y + (1-y)H_2O \rightarrow CO + (0.5x+1-y)H_2 \quad (1)$$

According to tar compound and tar quantity, the overall formation depends on various conditions, e.g. temperature, heating rate of fuel particle, residence time, water content of biomass. Tar formation will occur unavoidably as well as a present tar reforming with steam. However, the tar reforming is limited due to temperature or residence times. To achieve significant tar conversion and low tar content, respectively the tar reforming has to be supported by a suitable catalyst. General tar reforming reaction can be expressed by Eq. (2).

$$C_nH_m + nH_2O \rightarrow nCO + \left(n + \frac{m}{2}\right)H_2 \quad (2)$$

EXPERIMENTAL

A pilot plant based on the dual-fluidized-bed system for steam gasification of biomass has been designed and erected at Vienna University of Technology. Fig. 2 displays the scheme of the pilot rig which has maximum fuel input of 100 kW.

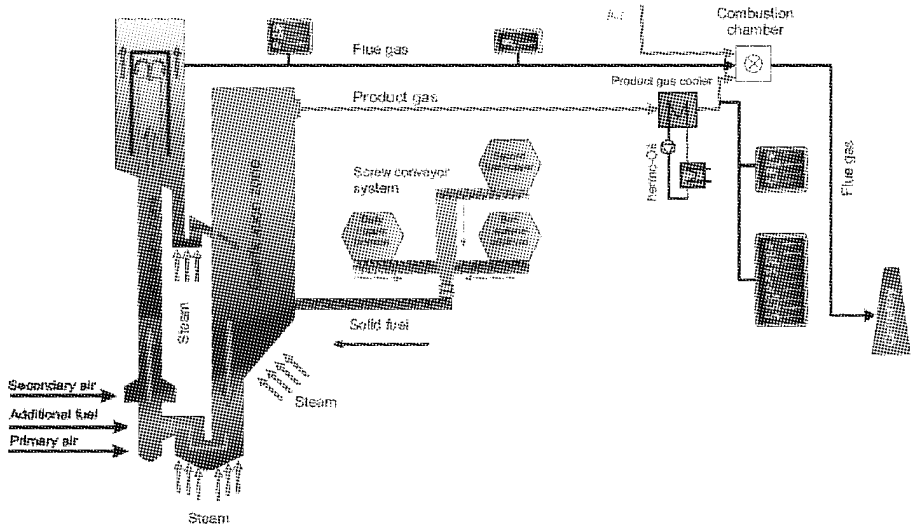

Fig. 2 Flow sheet of the dual fluidized bed steam gasification pilot plant at Vienna University of Technology

Instead of solid separation by means of a cyclone (as indicated in Fig. 1), the separation of solids from the flue gas is realized by a separation plate arranged over the riser, see Fig. 2. Fuel supply is realized by a screw conveyor, which feeds directly into the bubbling bed of the gasifier. Three hoppers are available, so that fuel mixtures as well as continuously feeding with bed material is possible. The fluidization of the riser is realized by feed of primary and secondary air. Supply with additional fuel (oil) is possible to control and keep temperatures. The product gas passes through a heat exchanger to attain moderate temperatures (~200 °C), essential for the measurement of product gas composition. Characterization of the flue gas is done by measuring of CO, CO_2 and O_2. The gas stream (flue gas and product gas) are combusted in the combustion chamber. Further details on the pilot rig are given by Pfeifer et al. (2007).

In order to research and investigation purposes, the reactor system is designed to allow large operation flexibility. Table 1 summarizes main operation parameters to be varied for a flexible pilot plant operation.

Table 1 operation data of the DFB-pilot plant

Fuel input (full load)	(kW)	100	
Particle size of fuel		up to 40 mm	
		Gasification reactor/gasifier	**Combustion reactor/riser**
Temperature range	(°C)	650-850	850-900
Fluidization agent		Steam/air	Air
Fluidization regime		Bubbling bed	Fast fluidized
Steam/fuel ratio	(-)	0.6-1.2	-

Experimental series were carried out at the pilot rig, whereas natural olivine and limestone have been investigated as bed materials concerning to steam gasification of biomass. The properties of the natural olivine and the limestone are indicated in Tables 2 and Table 3. Furthermore, mechanical properties of the materials are summarized in Table 4.

Table 2 chemical composition of the limestone

(wt-%)	$CaCO_3$	CaO	$MgCO_3$	SiO_2	Al_2O_3	Fe_2O_3	MgO	Trace elements
Limestone	94.00	-	-	2.77	1.40	0.60	0.70	0.53

Table 3 chemical composition of the olivine

(wt-%)	MgO	SiO_2	Fe_2O_3	Al_2O_3+Cr_2O_3+Mg_3O_4	CaO	NiO
Olivine	48.0-50.0	39.0-42.0	8.0-10.5	0.8	<0.4	<0.1

Table 4 mechanical properties of the bed materials

		Olivine	Limestone
Particle size	(mm)	0.4-0.6	0.7-1.2
Density	(kg/m³)	~2900	~2600

Concerning experimental procedure, specific attention has to be paid to the application of limestone in contrast to olivine. Calcium oxide (CaO) is the catalytically active part of the material, but not existent to a great extent in the raw material, which consists mainly of calcium carbonate ($CaCO_3$), Table 2. Hence, CaO has to be formed by calcination, which occurs sufficiently at a temperature range of 800 – 900 °C, under release of CO_2 (Eq. (3)). Calcination as well as the reverse reaction, the carbonation of limestone is item of numerous studies and investigations. For further details it is referred to specific publications, e.g. Stanmore et al. (2005), *Florin* et al. (2008).

$$CaCO_3 \leftrightarrow CaO + CO_2 \tag{3}$$

Within the experiment a certain period of time is required, which is characterized by energy consumption necessary for calcination of the bed material, since the calcination is an exothermic reaction. The biomass used within the experimental series was wood with a mean water content of about 10 wt-%. The fuel was fed to the system in the form of chips and pellets, respectively. The mean composition of the biomass used within the experimental series is indicated in Table 5.

Table 5 ultimate analysis of the biomass in wt-%$_{daf}$

C	H	O	N	S	Cl
48.40	6.09	45.30	0.20	0.01	-

RESULTS AND DISCUSSION

Within the following section results of the experimental series with natural olivine and limestone at the pilot plant are described and discussed. The process monitoring and control is realized by continuously recording of significant measurements (temperature, pressure, mass and volume flow, gas composition). The measurement for the determination of tar content and composition of tars originated from biomass gasification was developed at the Institute of Chemical Engineering (Vienna University of Technology) and is based on the tar protocol given by Neeft et al. (1999). The measurement of the tar content comprises a determination by gravimetric methods (i.e. tar components with molecular weight higher than toluene). Furthermore a gas-phase chromatograph coupled with a mass spectrometer (GC-MS) was used to determine the tar content as well as the tar composition. The tar measurement is detailed by Pfeifer (2004).

The duration of a single experiment last 12 to 14 hours, whereas this period includes the start up, steady state and shut down procedure of the experimental device. Steady state period is kept for 4 to 6 hours meanwhile the necessary measurements are taken. The experimental series is detail by means of a selected example for both bed materials. Figs. 3 and 4 display the progress of significant measurements (temperature in gasifier and riser, pressure drop over the fluidized bed in the gasifier and product gas composition) during steady state for a selected experiment with limestone and olivine, respectively as bed material. Steady state period is characterized by stable conditions (temperatures, gas composition).

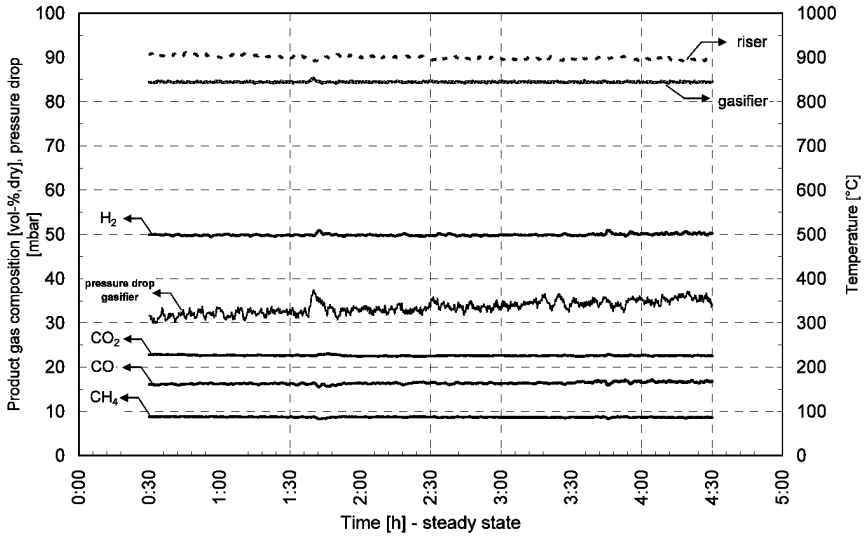

Fig. 3 Product gas composition (H_2, CO, CO_2, CH_4), gasification and riser temperature, pressure drop in gasifier for selected experiment with limestone

Comparing the pressure drop over the bubbling bed in the gasifier it appears that the pressure drop is

lower during experiments with limestone. The calcination of the limestone and consequently the release of CO_2 results in a certain mass loss of the inventory of bed material into the gasifier.

The temperature in the gasifier was kept at 840 to 850 °C and in the riser at 890 to 900 °C. Product gas composition given by H_2, CO, CO_2 and CH_4 and progress respectively are shown in Figs. 3 and 4. Furthermore Table 6 indicates mean product gas composition for the selected experiments.

Despite similar temperature in the gasifier it appears, that the application of limestone as bed material results in different product gas composition compared to the application of olivine.

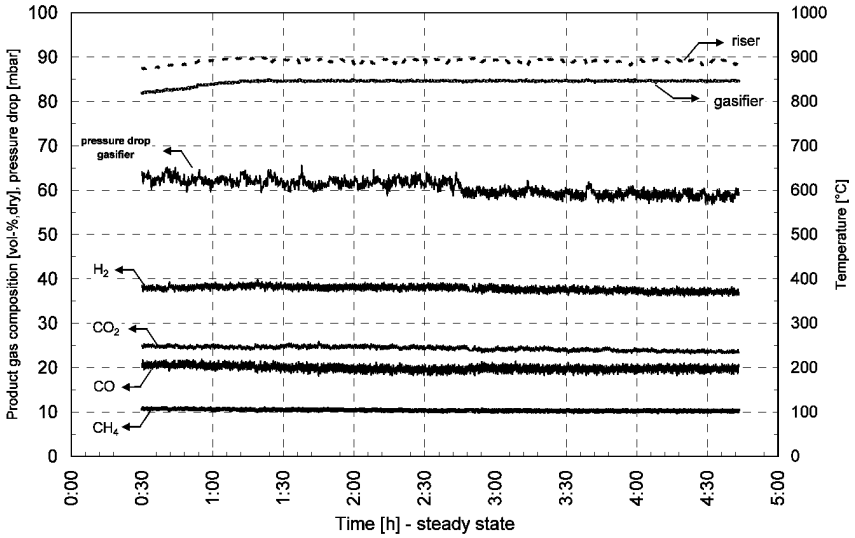

Fig. 4 Product gas composition (H_2, CO, CO_2, CH_4), gasification and riser temperature, pressure drop in gasifier for selected experiment with olivine

It appears that significant higher hydrogen content of 50 vol-%,$_{dry}$ was achieved using limestone in comparison to olivine with 38 vol-%$_{dry}$. The amount of CO_2 is almost the same, but slightly lower for limestone. Furthermore the contents of CO and CH_4 are somewhat lower for limestone.

Table 6 Mean product gas composition for selected experiment with limestone and olivine as indicated in Figs. 3 and 4

product gas composition*) [vol-%,$_{dry}$]	**H_2**	**CO_2**	**CO**	**CH_4**
limestone	49.9	22.6	16.4	8.7
olivine	37.8	24.3	19.9	10.4

*) low amounts of N_2 and C_2-C_3 hydrocarbons (C_2H_4, C_2H_6 and C_3H_8) complete to 100 vol-%,dry

Summarizing the experimental series, Fig. 5 display the range of values regarding to main product gas components obtained for limestone and olivine. Furthermore, the tar contents are depicted. The product gas composition differs between limestone and olivine, mainly indicated by the H_2 content, which is significantly higher for limestone. Moreover, the application of limestone shows lower contents in CO and CH_4 at almost the same CO_2 content. This suggests favoured impact regarding to the homogeneous reactions of the gaseous compounds with the fluidization agent steam. Steam reforming e. g. the reforming of CH_4 (Eq. (4)) results in the formation of CO and H_2 (see also Eq. (1)) and suggest to be enhanced by limestone.

$$CH_4 + H_2O \leftrightarrow CO + 3H_2 \quad (4)$$

Furthermore, significant contribution regarding to H_2 content is caused by the water gas shift reaction (Eq. 4), which forms CO_2 and H_2.

$$CO + H_2O \leftrightarrow CO_2 + H_2 \quad (5)$$

Tar measurements were carried out, whereas the tar determination comprise gravimetric and GC-MS method. Hence, two values for the tar content are given, characterized as gravimetric tars and GC-MS tars, respectively. The gravimetric tars comprise low boiling components (<200°C), whereas the GC-MS tars comprise high boiling components. It appears within Fig. 5 that the amount of gravimetric tars as well as GC-MS tars is lower for limestone. This suggests a favorable effect of limestone according to tar reforming reactions.

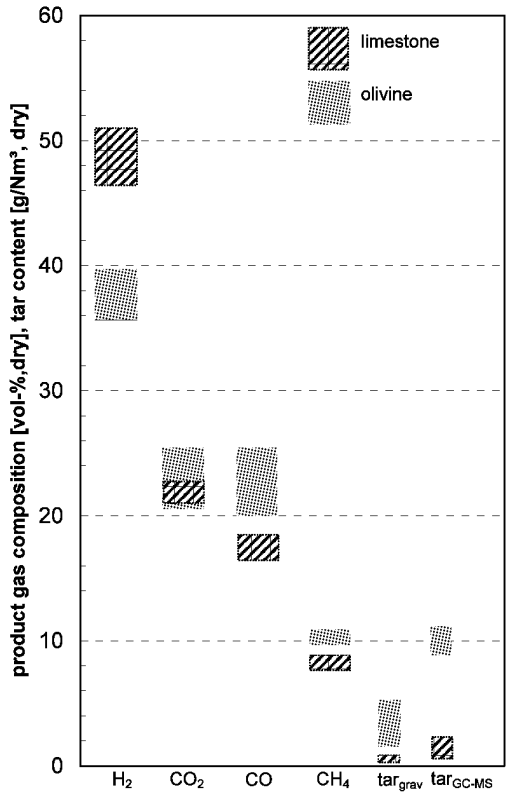

Fig. 5 Product gas composition: typical range within the experimental series for limestone and natural olivine

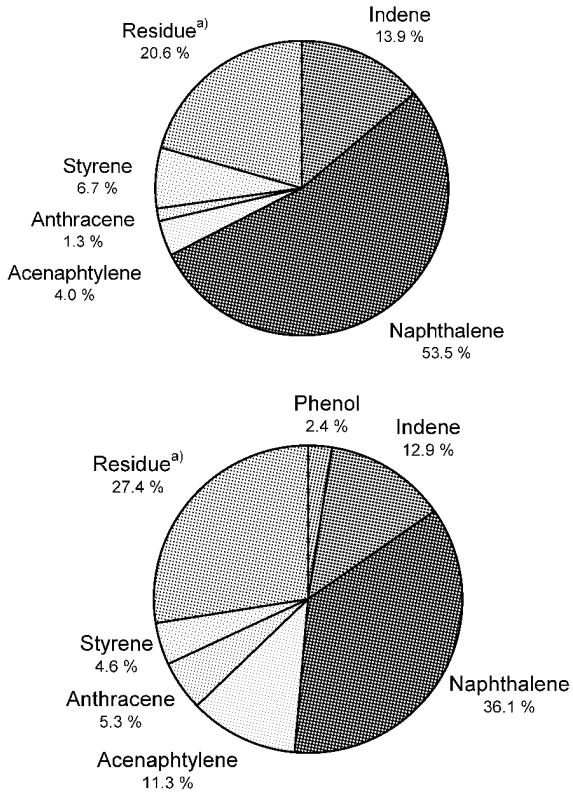

Fig. 6 Example for tar composition (measured by GC-MS method) for selected experiment with limestone (above) and natural olivine (below)

Fig. 6 displays the tar composition for a selected experiment with limestone and olivine. Indicated in Fig. 6 the residue tars are e.g. mesitylene, fluoranthene, phenanthrene or biphenyl. It appears that naphthalene is the main component and typical for a tar resulting from gasification of biomass. However, the naphthalene content is lower for experiment with olivine compared to experiment with limestone. Milne et al. (1998) classifies tars originating from biomass gasification into primary, secondary and tertiary tars. Naphthalene is a typical representative for polycyclic aromatic hydrocarbons (PAH) and is classified as tertiary tar compound by Milne et al. (1998). Further tertiary tar compounds are acenaphthylene, anthracene, fluoranthene or phenanthrene. Indene is classified as secondary tar, but is a compound that appears in the other classes as well. According to the classification phenol is a representative for secondary tar compounds.

Evan and Milne (1987) specify that primary tars are generated in the temperature range of 400-700 °C, secondary tars between 700-850 °C and tertiary tars at a temperature range of 850-1000 °C. This corresponds well to determined tar components, since the gasification temperature was at 840 to 850 °C for the experimental series and mainly tertiary (e.g. naphthalene) as well as secondary (e.g. indene, phenol) tars occur.

CONCLUSIONS

Within the present work, experimental series were carried out at a dual fluidized bed biomass steam gasifier of 100 kW fuel input. In order to investigate the application of CaO-based bed material, experiments using limestone as bed material were accomplished. Furthermore experiments were carried out with natural olivine as bed material.

It has been found that limestone increases the product gas quality, since higher H_2 content is achieved. The product gas shows lower contents of CO, CH_4 and above all significant lower tar contents. This suggest, that the CaO-based bed material favours the gasification, since limestone acts catalytically concerning tar reforming and water gas shift reaction. Hence, limestone is a potential candidate for fluidized bed steam gasification of biomass using a catalytic active bed material.

Deactivation of the limestone, due to the formation of $CaCO_3$ which is considered to be the inactive part, instead of CaO, is excluded. Despite high CO_2 partial pressure which dominates in the gasification reactor, the temperatures of over 800 °C do not favour the carbonation reaction, Eq. (3). According to temperatures the CO_2 equilibrium partial pressure of the carbonation is above the CO_2 partial pressure in the gasifier as well as in the

riser, Florin et al. (2008).

Further investigations will focus on the tar reduction potential of limestone regarding to long term activity, since a promising contribution to hot gas cleaning could be achieved, due to the primary tar reduction. Another main item to be investigated in the future is the mechanical stability of the material, since it has been found that the limestone is less mechanical stable than the natural olivine.

REFERENCES

Abu El-Rub, Z., Bramer, E.A., Brem, G.: Ind. Eng. Chem. Res. 43 (2004), pp. 6911-6919.

Dayton, D.: Milestone Completion Report, USA: National Renewable Energy Laboratory, (2002).

Hofbauer, H., Veronik, G., Fleck, T., Rauch, R.: In Developments in thermochemical biomass conversion, Vol. 2 (1997), pp. 1016-1025.

Hofbauer, H., Rauch, R., Loeffler, G., Kaiser, S., Fercher, E., Tremmel, H.: In 12th European Biomass Conference (2002), Florence, Italy, pp. 982-985.

Pfeifer, C., Puchner, B., Hofbauer, H.: International Journal of Chemical Engineering 5 (2007).

Sutton, D., Kelleher, B., Ross, J. R. H.: Fuel Processing Technology 73 (2001), pp. 155-173.

Stanmore, B.R., Gilot P.: Fuel Processing Technology 86 (2005), pp. 1707-1743.

Florin, N.H., Harris, A.T.: Chem. Eng. Sci. 63 (2008), pp. 287-316.

Simell, P.A., Hirvensalo, E.K., Smolander, V.T.: Ind. Eng. Chem. Res. 38 (1999), pp. 1250-1257.

Devi, L., Ptasinski, K.J., Janssen, F.J.J.G.: Fuel Processing Technology 86 (2005), pp. 707-730.

Neeft,J.P.A.;Knoef,H.A.M.;Zielke,U.;Sjöström,K.;Hasler, P.;Simell,P.A.;Dorrington,M.A.;Abatzoglou, N.;Deutch, S.;Greil, C.; Buffinga, G.J.;Brage, C.;Soumalainen.

M.: Guideline for Sampling an Analysis of Tar and Particles in Biomass Producer Gas, Version 3.1; Energy project EEN5-1999-00507 (Tar protocol), 1999.

Pfeifer, C.: PhD-Thesis, Institue of Chemical Engineering, Vienna University of Technology 2004.

Milne, T.A., Abatzoglou, N., Evans, R.J.: Report NREL/TP-570-25357, National Renewable Energy Laboratory, US Department of Energy (1998).

Evans, R.J., Milne, T.A.: Energy and Fuels 1 (1987), pp. 123-137.

FAST PYROLYSIS OF AGRICULTURAL WASTES IN A FLUIDIZED BED REACTOR

X. H. Wang, H. P. Chen, H. P. Yang, X. M. Dai, S. H. Zhang

State Key Laboratory of Coal Combustion, Huazhong University of Science and Technology, Wuhan, 430074, China

Abstract: Solid biomass can be converted into liquid fuel through fast pyrolysis, which is convenient to be stored and transported with potential to be used as a fossil oil substitute. In China, agricultural wastes are the main biomass materials, whose pyrolysis process has not been researched adequately compared to forestry wastes. As the representative agricultural wastes in China, peanut shell and maize stalk were involved in this paper and pine wood sawdust was considered for comparing the different pyrolysis behaviors of agricultural wastes and forestry wastes. Fast pyrolysis experiments were carried out in a bench-scale fluidized-bed reactor. The bio-oil yields of peanut shell and maize stalk were obviously lower than that of pine sawdust. Compared with pine sawdust, the char yields of peanut shell and maize stalk were higher but the heating value of uncondensable gas was lower. This means that the bio-oil cost will be higher for agricultural wastes if taking the conventional pyrolysis technique. And the characteristic and component analysis results of bio-oil revealed that the quality of bio-oil from agricultural wastes, especially maize stalk, was worse than that from pine wood. Therefore, it is important to take some methods to improve the quality of bio-oil from agricultural wastes, which should promote the exploitation of Chinese biomass resources through fast pyrolysis in a fluidized bed reactor.
Keywords: fast pyrolysis, agricultural wastes, fluidized bed reactor

INTRODUCTION

China is a developing country with a huge population, but with a relative shortage of resources. After several decades of rapid development of the national economy, the contradiction between the energy supply and environmental protection has become gradually apparent. In order to achieve sustainable development, raising energy utilization efficiency and exploiting renewable energy resources are both very important and necessary measures.

Biomass is a unique renewable energy resource with the potential to substitute fossil fuels completely. As the biggest agricultural country in the world, the most available biomass resources are agricultural wastes in China, and over 800 million tons of agricultural residues are produced per annum (Cai et al., 2007).

Besides using for fodder and fertilizer, the majority of agricultural residues can be converted into energy by thermochemical or biochemical methods. Among the thermochemical processes, pyrolysis is a promising technology for the production of bio-oil, gas, and char, which can be used as fuel or chemical feedstock (Yaman, 2004). Biomass pyrolysis processes have been reviewed by Bridgwater and Peacocke (2000), and Yaman (2004) summarized the biomass species (nearly 100 types) subjected to pyrolysis conditions.

The researches on biomass pyrolysis have been carried out mainly in the developed countries of Europe and North America for a long time, where forestry residues are a major source of biomass, as a result, most work has been performed on wood (Mohan et al., 2006). In the literatures on the pyrolysis of agricultural wastes, as far as we know, there were few references focusing on both the pyrolytic products distribution and the characteristics of every product, but either bio-char (Demirbas, 2004) or bio-oil (Ates et al., 2004). Furthermore, most studies were performed in a packed bed reactor (Di Blasi et al., 1999; Manya, 2007) instead of a fluidized bed reactor, which has been proved more appropriate for commercial application with advantages of simple structure, easy operation, and convenient scale-up. In addition, agricultural residues are lack of consistency and comparability in general, comparing with forestry residues, thereby the crop species and growing region have strong effects on the pyrolysis behavior of agricultural residues.

Therefore, in China, the practical application of pyrolysis technology taking agricultural wastes as raw materials is absent of sufficient knowledge on pyrolysis process and products properties. In this paper, the pyrolysis of two representative agricultural wastes (peanut shell and maize stalk) in China was carried out in a bench-scale fluidized-bed reactor, and in order to understand the pyrolysis process of agricultural wastes veritably, the distribution and properties of pyrolytic products from pine wood (a representative forestry waste) was also involved in this study for comparison.

EXPERIMENTAL

Materials

The ultimate and proximate analysis results of three biomass samples are listed in Table 1. It can be observed that pine wood sawdust had higher volatile content, while peanut shell and maize stalk contained more ash. The particle sizes of all samples studied were in the range of 0.5~1.0mm.

Table 1 Properties of biomass

Samples	Pine wood sawdust	Peanut shell	Maize stalk
Ultimate analysis (daf, wt %)			
C	49.21	46.15	42.47
H	5.22	3.07	3.27
N	0.04	1.27	1.18
S	0.17	0.08	0.26
O*	45.36	49.43	52.82
Proximate analysis (ad, wt %)			
Moisture	8.14	8.84	8.52
Volatile matter	77.28	68.48	68.09
Ash	0.30	4.69	7.09
Fixed carbon	14.28	17.99	16.30
LHV (MJ/kg)	17.2	16.1	15.5

* Calculated by difference

Experimental method

The pyrolysis experiments were performed in a bench-scale fluidized-bed reactor (ID 35mm, height 1500mm) shown in Fig. 1. Details about the setup can be found in the literature (Wang et al., 2008). The bed material was silica sand, with the particle size of 0.3~0.45mm and a static bed depth of 300mm, and the carrier gas was pure nitrogen. The apparent vapor residence time in the free volume of the reactor was controlled within 1s. In each experiment, after the system reached steady state at 500°C, the screw motor was put on and biomass stored in a hopper was fed to the reactor combined with pneumatic conveying at 2kg/h feeding rate. The pyrolysis vapors and chars releasing from the reactor passed through a cyclone to separate the most chars and an added hot filter coated with aluminum silicate fibre was used to capture the fine char particles escaping from the cyclone. The clean gases condensed in an ice-water condenser operating at about 0°C. The uncondensable gases were collected for further analysis.

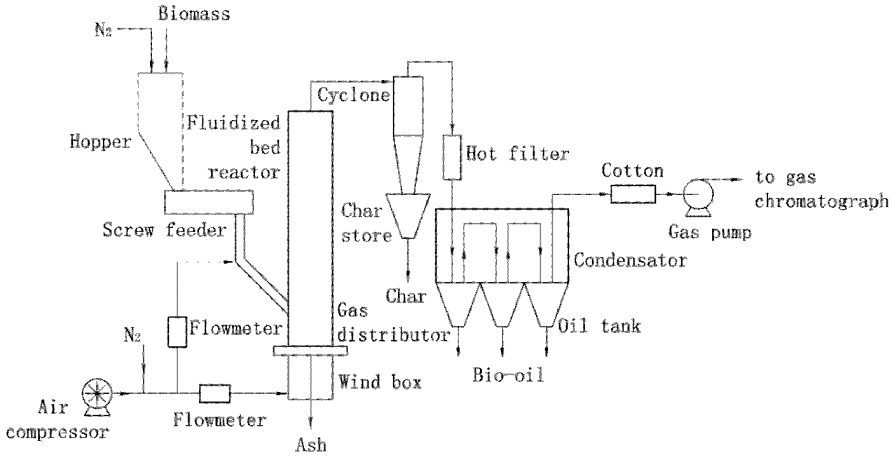

Fig. 1 Experiment system

After each experiment, the residues collected from the reactor and the separators were combined and recorded as solid char yield after subtracted the weight of bed material. The weight of the liquid oil exhausted from the condenser and the increased weight of connection tubes and cotton filter were recorded as the liquid yield. The total gas yield (wt. %) could thus be calculated by difference based on the mass balance of the fed biomass in a specific time period at a constant feeding rate.

The stable operation time of every trial was not under 1h to ensure the representative products. At the

same time, the pyrolysis experiment of pine wood sawdust had been carried out twice and repetitive results were obtained. This indicated the repeatability of experiments was good in this study.

Analysis method

The gas product from the fast pyrolysis of biomass materials was analyzed using a quadchannels GC (Micro GC 3000, Agilent) with a thermal conductivity detector (TCD), with helium as the carrier gas. During the stable operation period, the uncondensable gas was sampled every 10 min and each gas sample was measured 3 times to get the average.

Water content, pH value, viscosity, and heat value are the main properties affecting the oil quality. To catch the physical characteristics of bio-oil in detail, water content was measured with Karl-Fischer titration (TitroLine KF-10, SCHOTT, Germany), and the pH value was detected by a pH meter (Delta 320, Mettler-Toledo, Columbus, OH). Viscosity was analyzed with a rotary viscosimeter (NDJ-5S, Shanghai, China) at 40 °C, and a low heating value (LHV) was detected using a bomb calorimeter (6300, Parr, Moline, IL). Element analysis of liquid oil was preformed using a CNHS/O analyzer (EL-2, Vario).

The main components of bio-oil in detail were specified using gas chromatography-mass spectroscopy (GC-MS) (FINNIGAN TRACE MS). The column used in GC-MS was a capillary column DB-1301 (30 m × 0.25 mm i.d., 0.25 μm film thickness). Helium was the carrier gas, with a constant flow of 0.5 mL/min. The GC initial oven temperature was held at 50°C for 5 min and then programmed to increase to 250°C at 10 °C/min. The oven temperature was held at 250°C for 20 min. The mass spectrometer ion source was at 200°C. MS was operated in electron ionization mode with a 70 eV ionization potential, and a m/z range from 30 to 500 was scanned. The identification of the peaks was based on computer matching of the mass spectra with the National Institute of Standards and Technology (NIST) library.

Before all tests, bio-oil was sufficiently stirred and then sampled. Double tests were carried out, and the average values were provided at last.

RESULTS AND DISCUSSION

Product distribution

The product yields from the fast pyrolysis of three biomass wastes at 500°C are given in Fig. 2. It can be seen that the bio-oil yields of peanut shell and maize stalk were similar, about 50%, but markedly lower than that of pine wood, nearly 70%. It is well known that biomass species has significant effect on the pyrolysis behavior. As shown in Table 1, pine wood has the highest volatile content (77.28%) making for high bio-oil yield, whereas agricultural wastes contain higher ash content enhancing secondary reactions of volatile products and leading to less bio-oil obtained (Das et al., 2004). The pyrolytic gas yields from three biomass ranged from ~18% (pine wood and peanut shell) to 22.3% (maize stalk), which indicated that the gas yield wasn't influenced by biomass type obviously during the fast pyrolysis process in this study. On the other hand, the char yields of peanut shell and maize stalk were about twice as high as that from pine wood fast pyrolysis. The reason may be linked in part to the different decomposition degrees of three biomass wastes in a short time heating reactor, which meant that more volatile fraction of pine wood was released during pyrolysis, compared with peanut shell and maize stalk. In addition almost all ashes were retained in the chars after biomass pyrolysis, hence more ash meant more char for biomass. Owing to the higher char yield, how to utilize solid product should be taken into account when taking agricultural wastes as raw materials for the fast pyrolysis plant, according to the characteristics of chars.

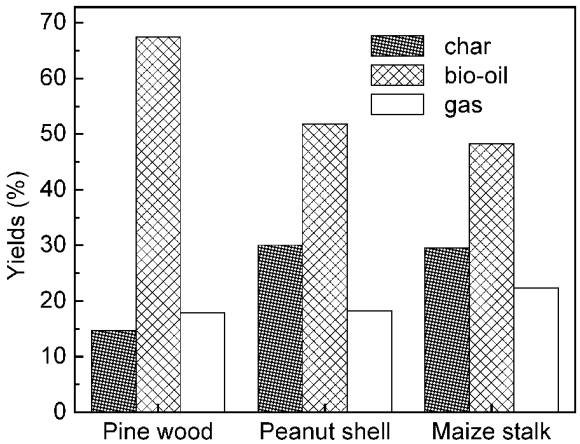

Fig. 2 Product distributions

Char properties

The routine analysis results of the chars from the pyrolysis of three biomass residues are listed in Table 2. Peanut shell and maize stalk have higher ash contents and almost all ashes are retained in the chars after pyrolysis, therefore the ash contents of the chars from agricultural wastes pyrolysis are far higher than that from pine wood, as a result, the heating values and the volatile matter contents of the chars are both lower. Although

the heating value of the char from biomass pyrolysis is comparable to coal, and with low N and S contents, whereas using bio-char as a fuel fired in the boiler/furnace isn't worthy of recommendation on account of the higher operating cost compared with the direct combustion of biomass. For agricultural residues, with higher char yields during pyrolysis, the pyrolytic chars should be made into high-value products, such as activated carbon (Ioannidou and Zabaniotou, 2007), which will significantly improve the economic feasibility of pyrolysis technique. The residence time of the chars in pyrolysis reactor was very short, so the thermal decomposition was incomplete and a small quantity of volatile compounds were still reserved in the chars, as shown in Table 2, the chars had a substantial amount of volatile matter. Based on the volatile contents of raw biomass samples and the pyrolytic chars and the char yields, the relative variation in weight and percent of the volatiles could be obtained by calculation, which were 92.7% (pine wood), 86.4% (peanut shell), and 85.7% (maize stalk), respectively. This proved that the ratio of volatilization of organic components in the agricultural wastes was low in comparison with pine wood under the pyrolysis condition of less than 1s residence time and 500°C pyrolysis temperature.

Table 2 Properties of chars

Char from	Pine wood sawdust	Peanut shell	Maize stalk
Ultimate analysis (daf, wt %)			
C	74.19	77.31	80.97
H	4.05	3.23	3.28
N	0.10	1.00	1.47
S	0.29	0.40	1.51
O *	21.37	18.06	12.77
Proximate analysis (d, wt %)			
Volatile matter	42.70	32.96	33.75
Ash	2.28	16.54	24.53
Fixed carbon	55.02	50.50	41.72
LHV (MJ/kg)	26.9	23.4	20.5

* Calculated by difference

Gas properties

The uncondensable gas from the pyrolysis of biomass was mainly comprised of H_2, CH_4, CO, CO_2, C_2H_4, C_2H_6, C_2H_2, C_3H_6, and C_3H_8. The gas components measured by GC are provided in Table 3. The volume concentration was determined according to the normalization method since the amount of other gases was negligible. The heating value of gas product was obtained by calculation based on the volume concentration of flammable gas and its calorific value. It could be seen that the main gas components in the uncondensable gas were CH_4, CO, and CO_2 for the three biomass residues pyrolysis at 500°C. While the H_2 contents were similar, about 1 vol. %, and the C2 and C3 hydrocarbons were all small. Among them, pine wood had highest CH_4 and CO concentrations in the pyrolytic gas, peanut shell the second, maize stalk the lowest. But the CO_2 concentration was just the opposite. As a result, the heating value of the uncondensable gas from pine wood was highest, peanut shell the second, maize stalk the lowest, and the maize stalk's was half of pine wood's. In the biomass fast pyrolysis technology, partial heat required for the pyrolysis reactor is provided by the uncondensable gas combustion. Thus, considering the gas yields from different biomass are equivalent (see Fig

Table 3 Properties of gases (vol. %)

Gas from	Pine wood sawdust	Peanut shell	Maize stalk
H_2	0.91	1.05	1.06
CH_4	10.62	7.38	2.66
CO	56.42	39.60	36.52
CO_2	26.93	49.20	57.31
C_2H_4	2.54	1.31	1.58
C_2H_6	0.61	0.50	0.33
C_2H_2	0.13	0.03	0.00
C_3H_6	0.01	0.06	0.02
C_3H_8	1.83	0.87	0.52
Heating value (MJ/m^3)	13.9	9.2	6.9

2), more energy from outside is needed when taking agricultural wastes as raw materials, which would increase the operating cost of biomass pyrolysis.

Oil properties

The physical and chemical characteristics of bio-oil from biomass pyrolysis were summarized in Table 4. It could be seen that C and O were the two main elements in bio-oils (dry basis), and the O content in excess of 40% indicated that large amounts of oxygen-containing organic compounds were involved in bio-oil, leading to a low heating value. Bio-oil derived from raw biomass samples was low with S and N contents. It was interesting that the H content of bio-oil (dry basis) was higher than that of raw biomass, especially peanut shell and maize stalk. This would facilitate the high-value utilization of bio-oil. Bio-oil had a high water content, about 30% in this study, which came from raw materials' moisture and the pyrolysis process, such as some secondary cracking reactions. Water content is a key parameter of bio-oil: the density, viscosity, acidity and calorific value decrease with increasing water content. Therefore the quality of bio-oil from agricultural wastes is worse for a liquid fuel because of high water content and low heating value, compared with pine wood's.

Table 4 Properties of bio-oils

Bio-oil from	Pine wood sawdust	Peanut shell	Maize stalk
Ultimate analysis(wt %) [a]			
C	49.67	50.60	50.59
H	7.37	7.01	7.37
N	0.56	1.75	1.60
S	0.14	0.18	0.01
O [b]	42.26	40.46	40.43
Water (wt %)	26.8	33.3	35.2
Density (kg/m^3)	1165	1111	1066
pH	2.46	2.88	2.85
Viscosity (mPa·s, 40 °C)	15.1	13.3	<9.0
LHV (MJ/kg)	14.7	14.0	12.6

[a] Dehydrate base, [b] Calculated by difference.

The compounds in bio oil were very complex and the typical compounds were mainly alcohols, ketones, furfural, phenol, alkylated phenols, furan derivatives, and guaiacols, etc. (listed in Table 5). The percentage values of the peak area were calculated by dividing the area of individual peaks by the total area. These values just give rough estimates of the major compounds. Standard curves should be obtained to determine the actual quantity of those compounds (Branca et al., 2003). However, it still provided sufficient information to compare the same species of liquid oil obtained from different biomass, with other measure parameters consistent.

The identifying compounds usually have a boiling point over 100°C because of the disturbance from acetone and water contained in analysis samples, but including most high-value chemicals in bio-oil, such as furfural, phenol, guaiacol, eugenol, vanillin, and so on. It could be found from Table 5 that the relative concentrations of above-mentioned compounds of bio-oil from agricultural wastes pyrolysis were lower than those from pine wood. Therefore the quality of bio-oil from agricultural wastes is worse for a chemical feedstock in comparison with pine wood's.

Table 5 Compounds detected by GC/MS

ID	Compound	Formula	Peak area (%)		
			Pine wood	Peanut shell	Maize stalk
1	acetol	$C_3H_6O_2$	278066	133902	141166
2	isobutyl alcohol	$C_4H_{10}O$	36411	38454	9373
3	propanal	C_3H_6O	13136	11844	2890
4	methyl pyruvate	$C_4H_6O_3$	12784	999	0
5	furfural	$C_5H_4O_2$	36235	48138	32703
6	2-cyclopenten-1-one	C_5H_6O	0	0	1383
7	2-butanone	C_4H_8O	4673	3288	3179
8	acetol acetate	$C_5H_8O_3$	8993	10794	7455
9	2-methyl-2-cyclopentenone	C_6H_8O	3879	6639	1707

Continued

ID	Compound	Formula	Peak area (%)		
			Pine wood	Peanut shell	Maize stalk
10	2-furyl methyl ketone	$C_6H_6O_2$	1940	4890	1752
11	2-hydroxy-2-cyclopentenone	$C_5H_6O_2$	19484	0	559
12	butyrolactone	$C_4H_6O_2$	5819	4971	2119
13	2(3H)-furanone	$C_4H_4O_2$	17280	2076	9387
14	3-methyl-2-cyclopentenone	C_6H_8O	2821	1986	2829
15	3-methyl-2(5H)-furanone	$C_5H_6O_2$	9433	2094	2366
16	2,3-dimethyl-2-cyclopenten-1-one	$C_7H_{10}O$	2998	624	893
17	2-hydroxy-3-methyl-2-cyclopenten-1-one	$C_6H_8O_2$	24068	14400	11194
18	phenol	C_6H_60	10668	8601	10130
19	2-methoxy-phenol	$C_7H_8O_2$	71853	137064	12799
20	2-methyl-phenol	C_7H_8O	19308	3828	1510
21	2,3-dimethyl-phenol	$C_8H_{10}O$	2557	0	0
22	3-ethyl-2-hydroxy-2-cyclopenten-1-one	$C_7H_{10}O_2$	0	0	1329
23	4-methyl-phenol	C_7H_8O	8640	5769	2172
24	2-methoxy-4-methyl-phenol	$C_8H_{10}O_2$	106148	76674	2824
25	4-ethyl-phenol	$C_8H_{10}O$	1851	7551	2927
26	4-ethyl-2-methoxy-phenol	$C_9H_{12}O_2$	17456	21537	1297
27	2-methoxy-4-vinylphenol	$C_9H_{10}O_2$	23451	25263	2697
28	eugenol	$C_{10}H_{12}O_2$	18691	16104	926
29	2,6-dimethoxy-phenol	$C_8H_{10}O_3$	0	0	10307
30	isoeugenol (cis+trans)	$C_{10}H_{12}O_2$	73175	108093	3006
31	vanillin	$C_8H_8O_3$	16222	9057	2238
32	1-(4-hydroxy-3-methoxyphenyl)-ethanone	$C_9H_{10}O_3$	14811	8502	663
33	1-(4-hydroxy-3-methoxyphenyl)-2-propanone	$C_{10}H_{12}O_3$	4496	11823	929
34	4-(3-hydroxy-1-propenyl)-2-methoxy-phenol	$C_{10}H_{12}O_3$	4849	0	0
35	2,6-dimethoxy-4-(2-propenyl)-phenol	$C_{11}H_{14}O_3$	0	0	490

CONCLUSIONS

The fast pyrolysis of two agricultural wastes (peanut shell and maize stalk) was carried out in a fluidized-bed reactor at 500°C and <1s residence time. Normally a maximum bio-oil yield could be obtained in this condition on the basis of other researchers' conclusions. But compared with forestry waste (pine wood sawdust), the agricultural wastes had lower bio-oil and higher char yields, and the heating values of three pyrolytic products were all lower. This is directly related to the biomass characteristics, e.g. agricultural waste with lower volatile organic compound content and higher inorganic mineral content, and pyrolysis behavior, e.g. agricultural waste with incomplete devolatilization process and significant secondary reaction.

In order to improve the quality of pyrolytic products and the economical feasibility of agricultural wastes fast pyrolysis, a maximum bio-oil yield shouldn't be excessively highlighted. Next research should be devoted to the high-efficiency conversion of biomass and high-value utilization of products, including bio-oil and char, through optimizing process parameters of fast pyrolysis.

ACKNOWLEDGEMENTS

The authors are grateful for the support of the National Basic Research Program of China (973 Program, Grant No. 2007CB210202) and the National Natural Science Foundation of China (Grant No. 50721005 and 50676037).

REFERENCES

Ates, F., Putun, E. and Putun, A. E.: J. Anal. Appl. Pyrolysis **71** (2004), pp.779-790.
Branca, C., Giudicianni, P. and Di Blasi, C.: Ind. Eng. Chem. Res. **42** (2003), pp.3190-3202.
Bridgwater, A. V. and Peacocke, G. V. C.: Sustain. Renew. Energy. Rev. **4** (2000), pp.1-73.

Cai, J. M., Liu, R. H., Deng, C. J. and Shen, F.: J. Energy Inst. **80** (2007), pp.243-246.
Das, P., Ganesh, A. and Wangikar, P.: Biomass Bioenerg. **27** (2004), pp.445-457.
Demirbas, A.: J. Anal. Appl. Pyrolysis **72** (2004), pp.243-248.
Di Blasi, C., Signorelli, G., Di Russo, C. and Rea, G.: Ind. Eng. Chem. Res. **38** (1999), pp.2216-2224.
Ioannidou, O. and Zabaniotou, A.: Renew. Sust. Energ. Rev. **11** (2007), pp.1966-2005.
Manya, J. J., Ruiz, J. and Arauzo, J.: Ind. Eng. Chem. Res. **46** (2007), pp.9061-9070.
Mohan, D., Pittman, C. U. and Steele, P. H.: Energy Fuels **20** (2006), pp.848-889.
Wang, X. H., Chen, H. P., Luo, K., Shao, J. A. and Yang, H. P.: Energy Fuels **22** (2008), pp.67-74.
Yaman, S.: Energy Conv. Manag. **45** (2004), pp.651-671.

HYDRATION REACTIVATION OF CaO-BASED SORBENT FOR CYCLIC CALCINATION-CARBONATION REACTIONS

Long Han, Qinhui Wang*, Qiang Ma, Jian Guan, Zhongyang Luo, Kefa Cen

State Key Laboratory of Clean Energy Utilization, Zhejiang University, Hangzhou, 310027, China

Abstract: Cyclic calcination-carbonation (CC) reactions have important applications, such as carbon dioxide (CO_2) capture from power plant flue gases and zero emission systems for hydrogen production. A critical challenge is the severe activity loss of CaO-based sorbent with increasing cycle numbers. In present study, A Thermax 500 high pressure thermogravimetric analyzer (PTGA) and the Scanning Electron Microscopy (SEM) technology were used to examine hydration reactivation on CaO-based sorbents. Two hydration methods, liquid hydration and steam hydration, were both investigated. It was found that CaO sorbents calcined under lower CO_2 partial pressure lose activity more slowly with cycle number. Both the two hydration methods efficiently improved sorbent activity during cyclic CC reactions. The mean values of activity increase for liquid hydration and steam hydration after 6 cycles were ~22% and ~27% respectively. SEM images showed that the hydrated CaO particles both exhibited surface area and porosity more favorable for CO_2 diffusion through the $CaCO_3$ product layer. It seemed that hydration frequency could affect sorbent cyclic performance and a relatively high frequency should be beneficial. Moreover, comparison with previous study confirmed that hydration reactivation could be efficient at a wide range of condition. Results of the present study demonstrate that hydration is a promising method to improve long performance of CaO sorbents in cyclic CC reactions, which provide consultations for process designing in flue gases CO_2 capture and zero emissions systems.

Keywords: CO_2 capture, Hydration, CaO, Sorbent reactivation, Calcination-carbonation

INTRODUCTION

Utilization of fossil fuel increases the atmospheric carbon dioxide content, which is a major contributor to the greenhouse effect. China is the one of largest CO_2 emission countries in the world due to great amount of fossil fuel consumption especially in coal. Consequently, reducing CO_2 emissions is becoming a rather important goal for China. CO_2 capture from power plant flue gases, and storage in geological formations, is a viable option to cut CO_2 emissions in the near future (Shimizu et al., 1999; Abanades et al., 2003; Abanades et al., 2004; Salvador et al., 2003). In the longer term, a novel low- or zero- CO_2 emissions system adopting CO_2 sorbent gasification methodology, which can produce both high concentration hydrogen (H_2) and sequestration-ready CO_2 stream, is considered promising for generating clean H_2 energy and cut CO_2 emissions (Ziock et al., 2001; Rizeq et al., 2001; Lin et al., 2001; Wang et al., 2006; Guan et al., 2007). The basic schemes of the processes, in which fludized bed reactors (FBR) are generally adopted, are depicted in Fig. 1 (Salvador et al., 2003; Guan et al., 2007).

In both cases, the CO_2 capture process is based on the reversible reactions (1):

$$CaO(s) + CO_2(g) \underset{Calcination(endothermic)}{\overset{Carbonation(exothermic)}{\rightleftharpoons}} CaCO_3(s) \quad (1)$$

However, there are several limitations using CaO carbonation reaction and the reverse reaction, calcination, to capture CO_2. First, CaO typically reaches conversions of only ~0.7-0.8 at low or moderate temperatures (550 ℃-750℃). It is well known that carbonation reaction could be characterized as two distinct stages. A rapid initial reaction, likely kinetically controlled, then followed by a much slower reaction, which is mostly likely diffusion controlled (Abanades et al., 2003; Abanades., 2002; Lee., 2004). For effective CO_2 capture, both high sorbent conversion and rapid reaction rate are required. Second, carbonation and calcination (CC) reactions are limited by the thermodynamic equilibrium Eq. (2), given by Baker (Hughes et al. 2004), where $P_{co_2,eq}$ is the equilibrium CO_2 partial pressure at temperature T:

$$\log_{10} P_{CO_2,eq}[atm] = 7.079 - \frac{8308}{T} \quad (2)$$

Equation (2) indicates that there exists a maximum temperature that allows CO_2 capture at a certain CO_2 concentration in the carbonator and a minimum temperature necessary to obtain sufficient CO_2 concentration in the calciner. Moreover, a critical issue for applications of the CO_2 capture processes is the activity durability of CaO sorbent. It is estimated that the CO_2 capture process would not be economical unless the value of CaO conversion after 20 cycles increased to a value of at least 0.45 (Hughes et al., 2004).

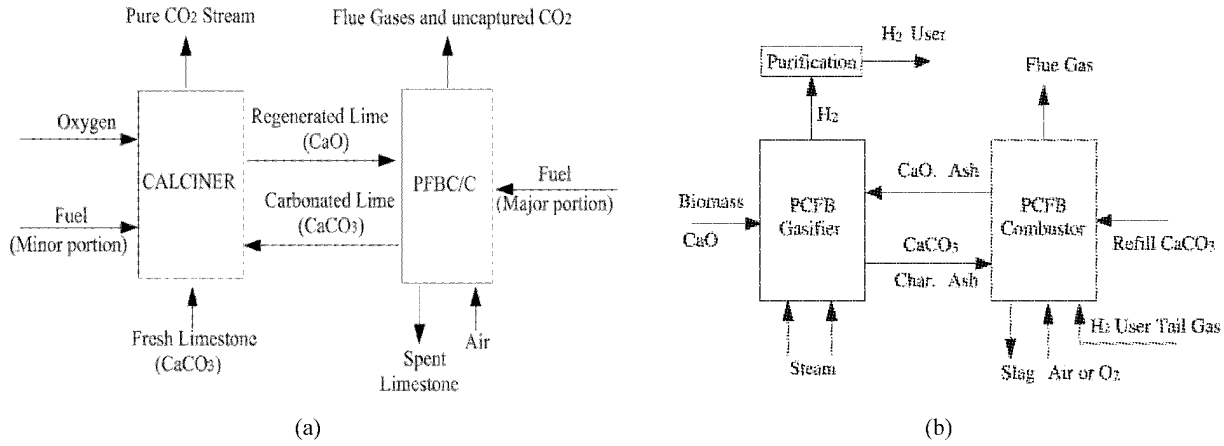

Fig. 1 Schematic diagrams of CO_2 capture from flue gases (a) and zero emissions system for H_2 production (b)

However, previous studies show that CaO sorbents lose activity dramatically during cyclic CC reactions (Abanades et al., 2003; Salvador et al., 2003; Hughes et al., 2004), which would increase both comsumption of fresh sorbents and storage of spent sorbent, consequently, reduce process economic and result in environment problem. Abanades proposed a simple Equation 3 to estimate the CaO conversion, X_N, after the N_{th} CC cycles, claiming that values of f_m=0.77 and f_w=0.17 fit most experimental data of both previous researchers and themselves well (Abanades et al. 2003).

$$X_N = f_m^N (1 - f_w) + f_w \tag{3}$$

According to Equation (3), X_N equals 0.174 after 20 CC cycles, which is greatly lower than the value 0.45, as mentioned above. On the basis of a qualitative SEM study, Abanades et al (2003) concluded that the decay in activity throughout CC cycles was due to a decrease in micro-porosity and an increase in meso-porosity. To improve sorbent cyclic performance, some papers identified sorbent hydration as a probably efficient means for enhancing CC cycles (Manovic et al. 2008). However, experiment data are indeed few and more research work regarding the hydration mechanism is needed. This paper aims to demonstrate the enhancement effect of hydration on the CaO sorbent activity during CC reactions. Two hydration methods, liquid hydration and steam hydration are investigated to compare with sorbent activity data without hydration treatment. Microscopy evidences of textural changes in the sorbent were given to elucidate the observed results.

EXPERIMENTAL

Materials and apparatus

Calcined sorbents of reagent grade $CaCO_3$ were used in this study. A simple diagram of the modified Thermax 500 high pressure thermogravimetric analyzer (PTGA) system is shown in Fig. 2. The PTGA is capable of working at temperatures of up to 1100℃ and pressures 1000psi with weight sensibility of 1 μ g. Temperature and sample weight signals were continuously recorded on computer and the reaction pressure was controlled by a pressure control valve automatically. The samples were suspended in a ceramic tube (i.d. 20mm) on a quartz pan (i.d. 15mm). The reacting gas flow rates were controlled by mass flowmeters.

In order to hydrate CaO sorbents in the PTGA, a steam generator (electrically heated) and a steam vent bypass were specially added to the system. The steam generator produced saturated steam of up to 2.5MPa at a maximum flow rate of 5g/s and excess steam after hydration was discharged from the vent bypass. A JSM-35CF scanning electron microscopy (SEM) equipment was used to obtain textural images of CaO sorbents.

CC tests

Two sets of CC reactions were performed under different calcination conditions. Calcination was conducted at 950℃, 15%CO_2 (N_2 balanced), for 30min, during which $CaCO_3$ would decompose completely. Two calcination total pressures were adopted: one 0.1MPa and the other 2MPa. Carbonation was conducted at 750℃, 25%CO_2 (N_2 balanced) at total pressure of 2MPa for 20min. The gas flow rates were 1L/min. To start the experiments, ~30mg $CaCO_3$ was heated at a typical rate of 25℃/min to 950℃ in N_2 atmosphere. The gas flow was then switched to the calcination gas (15%CO_2 +N_2). After calcination, the sample was cooled down to the desired carbonation temperature, 750℃, in N_2 atmosphere. Then the gas flow was switched to the

carbonation gas (25%CO_2 +N_2) and carbonation initiated. CaO conversion, X, was calculated according to the mass loss of calcination and mass increase of carbonation in each cycle. Cyclic CC reactions were performed 8 (calcination at total pressure of 0.1MPa) or 6 (calcination at total pressure of 2MPa) times respectively. Calcined sorbents after the first calcination were sampled and used for SEM observations.

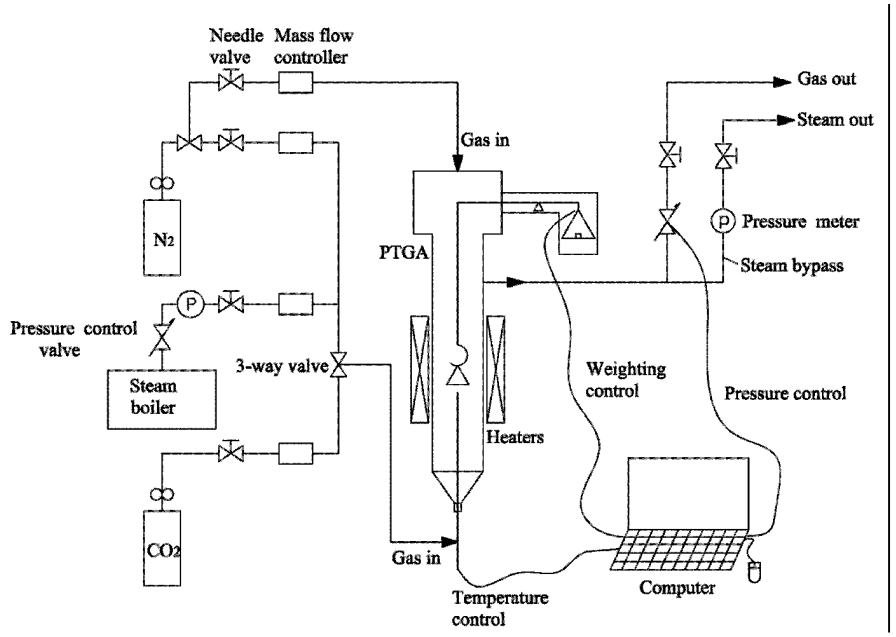

Fig. 2 Schematic diagram of the modified PTGA system

CHC (calcination-hydration-carbonation) Tests

To examine effect of hydration on sorbent activity, CHC tests, in which an intermediate hydration process was added, were performed under the same pressurized CC conditions as the above CC tests (at 2.0MPa calcination total pressure). Two types of CHC tests, namely, CLHC (Calcination-Liquid hydration-Carbonation) and CSHC (Calcination-Steam hydration-Carbonation), were performed respectively. In the CLHC case, the calcined sorbent was loaded into a small, capped glass jar (i.d. 15mm, h.t. 20mm), which was then filled with sufficient distilled water and vibrated in a orbital shaker for 30min at atmospheric condition. In this way, the sorbent was hydrated uniformly into a slurry-phase. Liquid hydration was performed only once after the first calcination reaction. In the CSHC case, the calcined sorbent was firstly cooled down from calcination temperature (950℃) to a desired temperature (300℃) in N_2 at total pressure of 2MPa. When the temperature was stable, the steam needle valve was opened and saturated steam mixed with N_2 gas flow was kept loading into the PTGA furnace, for 10min. Differently from the CLHC test, steam hydration was performed after each calcination reaction. After hydration in both cases, the hydrated sorbents were transferred to a electronic oven and dried at 500℃ for 1h. This completely converted the sorbents (containing calcium hydroxide) to CaO, as confirmed by later TGA analyses. The reactivated sorbents were smashed into particles of ~75 μm and subsequently used for activity examinations in next carbonation reactions. A small part of the sorbents was sampled for SEM observations.

RESULTS AND DISCUSSION

Effect of calcination pressure

Sorbent reactions during CC tests are presented in Fig 3. It can be seen that the activity dramatically decreases with increased cycle numbers. With calcination at total pressure of 0.1MPa, it decreases from 0.72 to 0.36 after 8 cycles. However, with calcination at total pressure of 2.0MPa, it decreases from 0.69 to 0.32 only after 6 cycles. Both results are basically consistent with calculated values of Equation 3 (solid line). It should be noted that the activity decay at calcination total pressure of 0.1MPa is less noticeable than that at 2MPa. We believe that this could be attributed to the mild sorbent sintering (Borgwardt 1989) in the case of 0.1MPa, which had a relatively lower CO_2 partial pressure as a result of the same CO_2 concentration in comparision with the case of 2MPa. This is also confirmed by SEM results in this study (Fig.4). CaO particles calcined at 0.1MPa (Fig.4(a)) possess relatively high porosity on the morphology surface, which is favorable for CO_2 diffusion

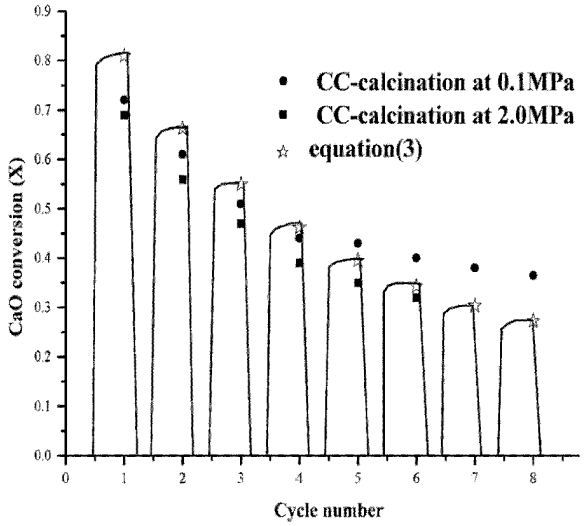

Fig. 3 Sorbent activity during CC tests

through the $CaCO_3$ product layer. However, for those calcined at 2MPa, severe sintering of sorbent particles characterized by compact surface without cracks, occurs (Fig.4(b)), resulting in acute decrease of sorbent activity.

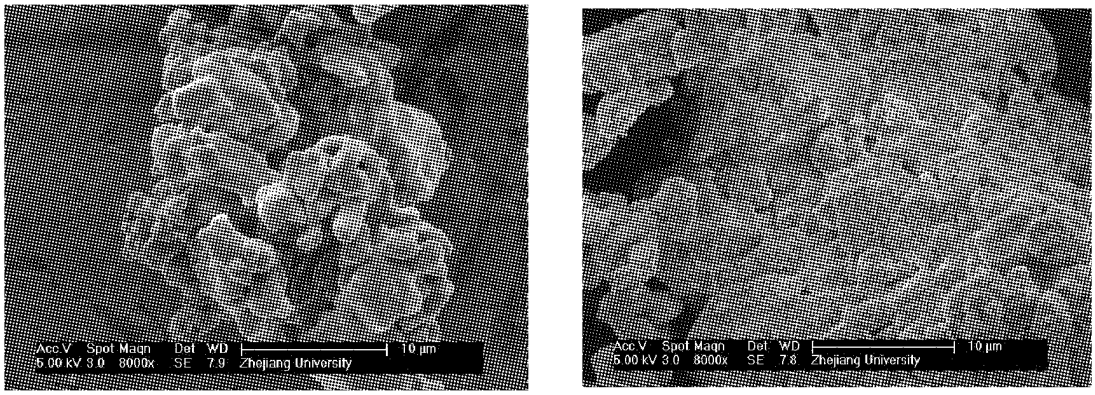

(a) (b)

Fig. 4 Images of the first calcined sorbents at 0.1MPa (a) and 2MPa (b)

Effect of hydration treatment

Sorbent reactions during CHC tests are presented in Fig. 5. Results of previous study by Manovic (2008, using calcined sample of Havelock limestone, steam hydration at 200℃ for 30min in a pressurized tube furnace) and CC test at total calcination pressure of 2MPa (solid line) discussed above in this study are also represented for comparison. The most important result of this study is that both two hydration methods, i.e., liquid hydration and steam hydration, have efficiently improved sorbent activity during cyclic CC reactions. The mean increment of activity after 6 cycles are ~22% (in CLHC test) and ~27% (in CSHC test). It is interesting that CaO sorbent hydrated with saturated steam seems to lose activity much slower than those hydrated with distilled water. This indicates that hydration times or frequency might affect sorbent cyclic performance, since liquid hydration was performed only after the first calcination while steam hydration after each calcination in present study. It should be also noted that the sorbent cyclic performance obtained after steam hydration closely agreed with that obtained by Manovic (2008), who had conducted experiments at quite different conditions, such as hydration pressure, temperature, reactor type, etc. This reveals that steam hydration can efficiently improve sorbent activity at a wide range of condition. Moreover, SEM images of hydrated sorbent morphology (Fig.6, Fig. 7) show different particle evolutions using different hydration methods. In the case of liquid hydration, sorbent particles are of "coral reef" shape with abundant small pores (Fig.6(a), (b)). In the case of steam hydration, particles are of "filmy squama" shape with lots of gaps and a large quantity of cracks are observed not only after the first hydration (Fig.7(a)), but also the fifth hydration(Fig.7(b)). Summarizing, both hydration methods have been favorable to increase the particle surface area and porosity, resulting in improved CO_2 capture activity.

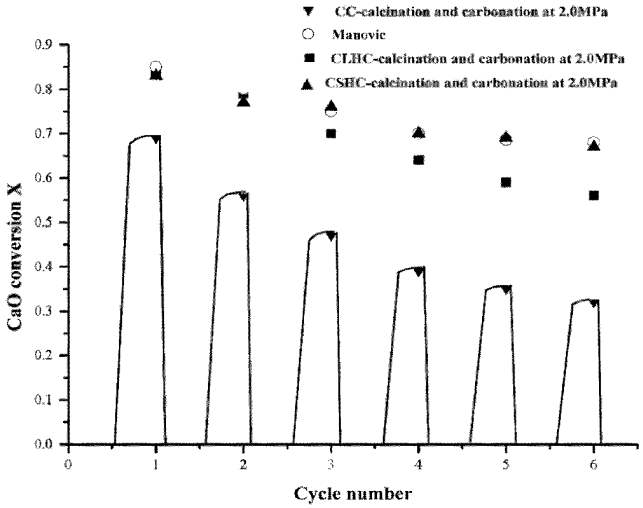

Fig. 5 Hydrated sorbent activity during CHC tests

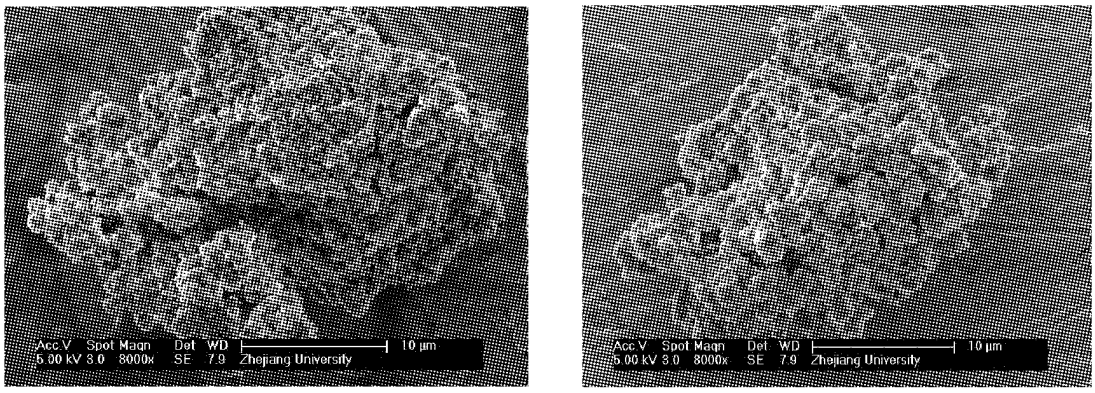

(a) (b)

Fig. 6 Images of two liquid-hydrated sorbent particles

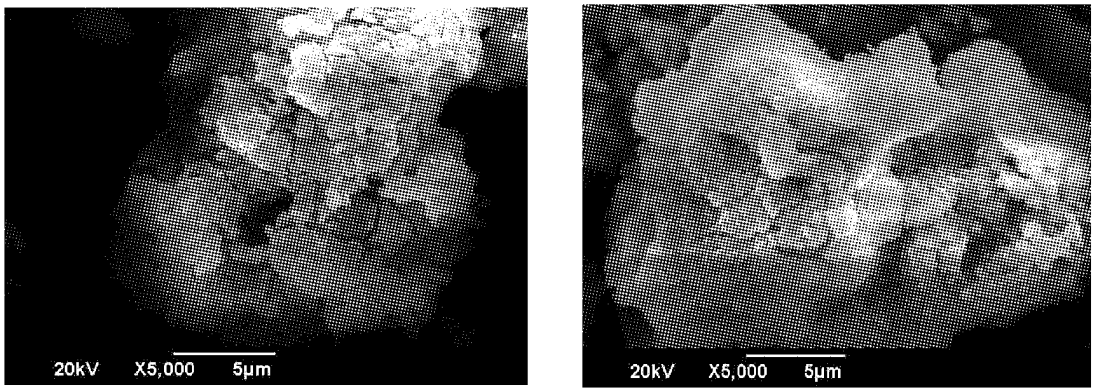

(a) (b)

Fig. 7 Images of the first (a) and fifth (b) steam-hydrated sorbents

Further discussion

The results above reveal the large potential to improve CaO sorbent cyclic performance using hydration methods. However, from a practical point of view, several issues are also important and needed to pay attention. First, it is somewhat conflicting between increasing CO_2 partial pressure in the calciner for convenient subsequent CO_2 disposal and decreasing CO_2 partial pressure to produce a highly reactive sorbent during cyclic CC reactions. A dilute gas that is easily separable from the CO_2 gas is critical. In this regard, steam is a potential choice because it can be easily condensed out from the CO_2 stream. In addition, there is merit in designing an optimal hydration procedure to maintain or enhance sorbents activity. In this study, calcined samples have been hydrated once or six times, for liquid hydration and steam hydration respectively. We argue

that it is viable to hydrate sorbents using distilled water before being loaded into the reactor and frequently inject steam into the reactor after sorbents loading. Further research with regard to hydration frequency is necessary. Moreover, it is also critical to survey effects of fluidized bed conditions, such as sorbent attrition, ash, tar etc., on the sorbent activity. However, that is beyond the scope of the present study. Experiment studies in actual fluidized bed system are also needed in future.

CONCLUSIONS

Investigations on reactivation of CaO-based sorbents from cyclic CC reactions were performed to examine the influence of hydration conditions on CaO conversion. CaO sorbents calcined under lower CO_2 partial pressure were found to lose activity more slowly with cycle number. This indicated large potential to dilute CO_2 stream and hydrate CaO sorbents in the calciner by steam injection. Liquid hydration and steam hydration were performed under atmospheric and pressurized conditions respectively. The most important result of this paper was that both two hydration methods had efficiently improved sorbent activity during cyclic CC reactions. The mean values of activity increase for liquid hydration and steam hydration after 6 cycles were ~22% and ~27% respectively. The hydration reactivation was confirmed by SEM images. Increased surface area and porosity favorable for CO_2 diffusion through the $CaCO_3$ product layer were observed in both cases. CaO particles exhibited Coral Reef shape after liquid hydration and Filmy Squama shape after steam hydration. Moreover, it seemed that hydration frequency would affect sorbent cyclic performance and a relatively high frequency should be beneficial. Comparison work with previous study showed that hydration reactivation could be efficient at a wide range of condition. Results of the present work show that hydration is a promising method to improve long time performance of CaO sorbents in cyclic CC reactions, providing consultations for process design in flue gas CO_2 capture or zero emissions systems.

ACKNOWLEDGEMENTS

This work was supported by the National High Technology Research & Development Program of China (No. 2006AA05Z114).

REFERENCES

Abanades, J.C.: Chem. Eng. J., v 90 (3), 2002, pp.303-306.
Abanades, J.C., Alvarez, D.: Energy Fuels, v 17 (2), 2003, pp.308-315.
Abanades, J.C., Anthony, E.J., Lu, D.Y., Savador, C.: AIChE J, v 50 (7), 2004, pp.1614-1621.
Borgwardt, R.H.: Ind. Eng. Chem. Res., v 28 (4), 1989, pp.493-500.
Guan, J., Wang, Q.H., Li, X.M., Luo, Z.Y., Cen, K.F.: Renew. Energy, v 32 (15), 2007, pp.2502-2515.
Hughes, R.W., Lu, D., Anthony, E.J., Wu, Y.H.: Ind. Eng. Chem. Res., v 43 (18), 2004, pp.5529-5539.
Lee D.K.: Chem. Eng. J., v 100 (1-3), 2004, pp.71-77.
Lin, S.Y., Suzuki, Y., Hatano, H., Harada, M.: Energy Fuels, v 15 (2), 2001, pp.339-343.
Manovic, V., Anthony, E.J.: Fuel, v 87 (8-9), 2008, pp.1564-1573.
Rizeq, R.G., Lyon, R.K., Zamansky, V.M.: In: Proceedings of the 26th international technical conference on coal utilization and fuel systems. Clearwater, Florida, USA, 2001.
Salvador, C., Lu D., Anthony, E.J., Abanades J.C.: Chem. Eng. J., v 96 (1-3), 2003, pp.187-195.
Shimizu, T., Hirama, T., Hosoda, H., Kitano, K., Inagaki, M. and Tejima, K.: Transactions of the Institute of Chemical Engineers, v 77 (A), 1999, pp.62-68.
Wang, Z.H., Zhou, J.H., Wang, Q.H., Fan, J.R., Cen, K.F.: Int. J. Hydrog. Energy, v 31 (7), 2006, pp.945-952.
Ziock, H.J., Lackner, K.S., Harrison, D.P.: In: Proceedings of the first national conference on carbon sequestration. Washington, DC, USA, 2001.

CHARACTERISTICS OF CATALYTIC GASIFICATION OF NATURAL COKE WITH H_2O IN A FLUIDIZED BED

L.S. Lin, C.S. Zhao, S. Wang, G. Zhu, W.G. Xiang

School of Energy & Environment, Southeast University, Nanjing,210096, China

Abstract: The experimental investigation on gasification characteristics of natural coke from Peicheng, Jiangsu with steam were conducted in a fluidized bed gasifier setup. The effects of several parameters, in terms of the catalyst type, the catalyst mixed manner and the dosage of catalyst over coke on the yield, the components, the heating value of fuel gas and the carbon conversion rate were examined. Results indicate that the fluidized bed gasification technology could overcome the shortcomings of natural coke. Ca-, Fe- and Cu-based nitrates could improve the gasification reaction effectively with a little difference, they could be listed in a descending sequence as follows: Cu-based>Fe-based>Ca-based according to their catalytic effect. The influences of Fe/Ca ratio and Cu/Ca ratio on gasification are similar, gas yield, carbon conversion rate and gas heating value per hour increase as Fe/Ca ratio or Cu/Ca ratio increases, but all of them go up first and then drop with decrease in Fe/Cu ratio. When the dosage of Ca-, Fe- and Cu-based nitrates mixed with the ratio of Ca/Fe/Cu= 10/35/55 is 3%, the best catalytic effect is achieved.

Keywords: natural coke,gasification,fluidized bed,catalyst

INTRODUCTION

Natural coke, high metamorphic grade coal as a by-product of the coal mining process, is a combustible solid fossil fuel formed from coal bed which is invaded, pyrolyzed and carbonized by high temperature magma with a heating value of 18~30MJ/kg(Pang et al.,2007; Kwiecinska and Petersenb, 2004; Sanyal, 1994). Reserves of natural coke are rich in China, the detected reserves are more than 4 billion tons in eastern part of China according to the recent investigation (Jiang, 1995; Wang et al.,2006). At present, natural coke is discarded or left in the mine without scheduled exploitation, which would cause tremendous energy waste and harm to the environment. Therefore, considering the challenge of energy crisis sources, it is necessary to utilize it for power generation etc.

However, the current technical challenges for natural coke are its hot burst factor and ignition difficulty. To overcome these problems, the fluidized bed gasification technology is proposed. Fluidized bed gasification technology has many advantages(Hiroyuki et al.,2004; McLendon et al.,2004; Domazetis et al.,2005), such as its good coal flexibility and strong gasification intensity. Material in the fluidized bed is in a vigorous fluidization and could be quickly heated to the gasification temperature by the bed inventory with high temperature, which could prevent the shortcomings of natural coke.

Natural coke is a high metamorphic grade coal with very complex chemical composition. In order to obtain better gasification results, the appropriate conditions for gasification and effective catalyst added to natural coke are necessary. Lots of work on the catalytic activity has been done so far. For example, Khan and Seshadri (1991) found that the addition of calcium oxide was in favor of the tar cracking and approved the coal gasification. Xu et al.(1996) showed that Ca element led to higher gasification reactivity of chars loaded with iron or nickel. Chen et al.(2001) discovered that the carbon formation during CO_2 reforming of methane by a $Ni/CaO\text{-}Al_2O_3$ catalyst deactivated faster than the dry reforming.

The influences of the catalyst type, the catalyst mixed manner and the dosage of catalyst over coke on natural coke-steam gasification reaction are presented in the paper.

EXPERIMENTAL

Experimental setup and procedure

The gasification tests were performed on a fluidized bed gasification system, shown in Fig.1. The system consists of a high-temperature steam generation system, a coke feeding and ash removal system, a gasifier, a fuel gas clean-up system, an analysis and combustion system, and a temperature measuring and control system. During the experiments, natural coke fed via a rotary valve reacted with high-temperature steam in the gasifier. After removing ash in the cyclone, the product gas was introduced into the cooler where the superheated steam was condensed and removed. Then the cooled gas was dehydrated in the dryer before passing through a flow

meter, at last the dry and cool gas was analyzed in the multicomponent gas analyzer (NGA2000MLT1).

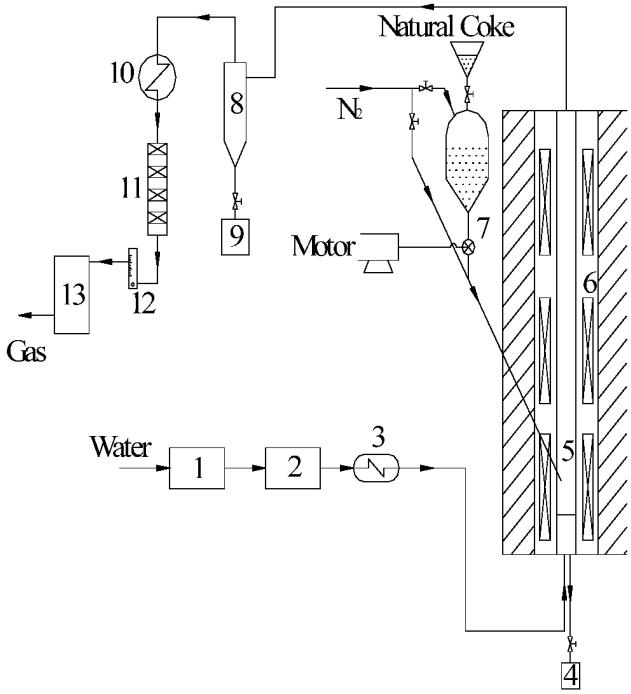

Fig. 1 Natural coke-steam fluidized bed gasification system
1—Water Tank; 2—Steam Generator; 3—Steam Superheater; 4—Bottom Ash Discharge Tank;
5—Gasifier; 6—Electric Heater; 7—Rotary Valve; 8—Cyclone; 9—Fly Ash Tank;
10—Gas Cooler;11—Drier; 12—Flowmeter; 13—Gas Analyzer

Experimental samples and conditions

Natural coke with an average size of 1 mm from Peicheng, Jiangsu, China was used as the sample in the study. Its proximate and ultimate analysis results are shown in Table1. The bed material was quartz sand with the average size of 0.23mm and density of 2400kg/m^3, which belong to Class B based on Geldart's particle classification(Timpe et al. 1997).

Calcium acetate, iron nitrate and copper nitrate were selected as the catalyst in the experiments, and recorded as Ca-, Fe- and Cu-based catalyst, respectively. During the experiments, three kinds of catalysts were mechanically mixed with natural coke with mass ratio of 3% (metal atom over the natural coke) except runs in the 3.3 section below.

Basic experimental conditions were set as follows:

- Sample mass flow rate: 0.1kg/h
- Steam mass flow rate: 0.45kg/h
- Bed material mass per time: 0.27kg
- Gasification pressure:0.1MPa
- Gasification temperature: 900℃
- Duration for each test: 60min

Table 1 The proximate and ultimate analysis of Peicheng natural coke

Proximate Analysis/%(mass, ad)				Ultimate Analysis/%(mass, daf)					Qnet,ad /MJ·kg^{-1}
M	A	V	FC	C	H	O	N	S	
0.81	16.15	9.05	73.99	93.12	1.99	3.21	1.10	0.58	26.59

Data processing

The heating value of syngas from natural coke-H_2O gasification is the sum of heating value of every effective component gas, defined as:

Table 2 Influence of catalyst type on the fuel gas components

Catalyst	H_2/%	CO/%	CO_2/%	CH_4/%	Effective gas/%
none	60.64	18.61	19.31	1.44	80.69
Ca	61.19	18.90	18.43	1.48	81.57
Fe	61.80	18.62	18.15	1.43	81.85
Cu	61.98	18.65	17.92	1.45	82.08

$$Q_{vm}=126[CO]+108[H_2]+359[CH_4] \quad (1)$$

The carbon conversion rate(X) is defined as:

$$X=\frac{12V([CO_2]+[CO]+[CH_4])}{22.4WC_{ad}}\times\frac{273}{273+t_0}\times 100\% \quad (2)$$

Where, [CO], [CO_2], [H_2] and [CH_4] denotes its volume share in the whole product gas(%), respectively. Q_{vm} means the low heating value per volume of the syngas(kJ/m^3). V is the whole gas yield(m^3/h), W is the mass flow rate of natural coke(kg/h), C_{ad} is the air dry based carbon content in the natural coke(%), t_0 is the room temperature(℃).

The gas heating value per hour in the paper is the product value of gas heating value and gas yield(kJ/h).The effective gas is the sum of CO, CH_4 and H_2.

RESULTS AND DISCUSSION

Influence of catalyst type on gasification reaction

The catalytic gasification experiments were conducted with Ca-, Fe- and Cu-based catalyst individually mixed with natural coke. The analysis of fuel gas components under the conditions without catalyst and with three kinds of metal salt catalysts were shown in Table 2. With the addition of catalyst, the content of H_2 or effective gas increases, CO_2 content decreases, and the content of CO or CH_4 varies very little. The gasification gas product of natural coke with Cu-based catalyst has the greatest gain among them.

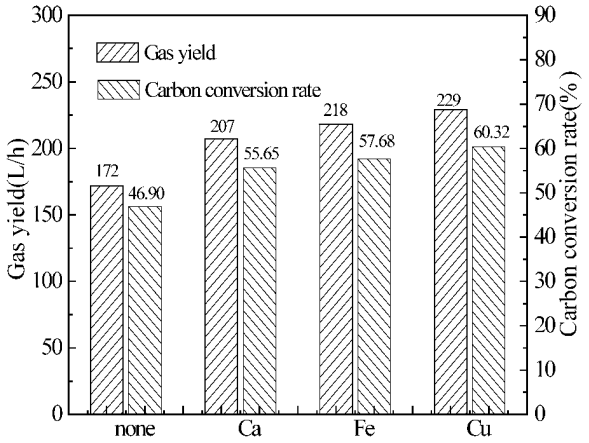

Fig. 2 Influence of catalyst type on gas yield and carbon conversion rate

The gas yield and carbon conversion rate under the conditions without catalyst and with three kinds of metal salt catalysts are shown in Fig.2. The addition of catalyst significantly increases the gas yield and the carbon conversion rate. Compared with the sample without catalyst, the gas yield and the carbon conversion rate of the sample with catalyst increase by more than 20% and 10% respectively. Because the addition of catalyst accelerates the gasification reaction rate, the gasification of natural coke tends to more complete. It can be seen from the Fig. 2, the catalytic effect of three kinds of metal salt catalysts has certain difference, they could be listed in a descending sequence as follows: Cu-based>Fe-based >Ca-based.

The gas heating value from natural coke gasification with catalysts addition is shown in Fig.3. For natural coke gasification with catalysts, the gas heating value increases slightly. Gas heating value per hour is subject to the combined effect of the gas heating value and the gas yield. Since the gas heating value varies slightly, gas heating value per hour is mainly influenced by the gas yield. The accelerated gasification reaction rate makes the obvious increase in gas yield, so the gas heating value per hour increases considerably and its amplitude for adding Cu-based catalyst is the largest, by 35%.

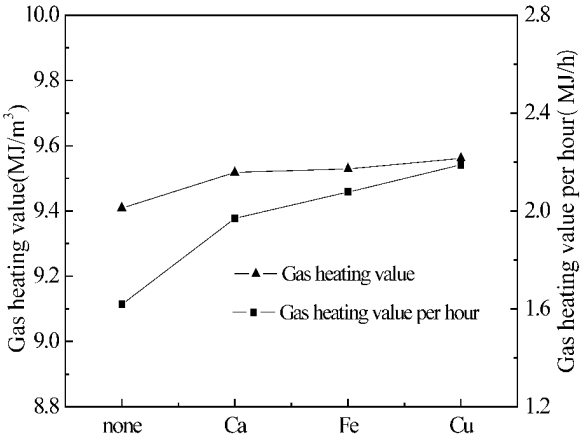

Fig.3 Influence of catalyst type on gas heating value

Influence of catalyst mixed manner on gasification reaction

Either of Ca-, Fe- and Cu-based nitrate could improve the gasification of natural coke with steam, but the catalytic effect with single catalytic was not good enough. In order to obtain better catalytic effect, the different preparing manners to mix the three catalysts with coke were adopted during the experiments.

Fe/Ca ratio

Keeping the Cu-based catalyst content in the mixed catalyst was 10%, the ratio of Fe- over Ca-based catalyst (Fe/Ca ratio) was adjusted at the following levels: 25/65, 35/55, 45/45, 55/35 and 65/25, recorded as Run A1, Run A2, Run A3, Run A4 and Run A5, respectively. The influence of Fe/Ca ratio on the gasification reaction of natural coke was shown in Fig.4. With the increase of Fe/Ca ratio from Run A1 to Run A5, the gas yield and the carbon conversion rate increase continuously by 33L/h and 8.11%, respectively. However, when Fe/Ca ratio is bigger than 55/35, the growth rates of gas yield and carbon conversion rate slow down, and their increment is just 1L/h and 0.33%, respectively.

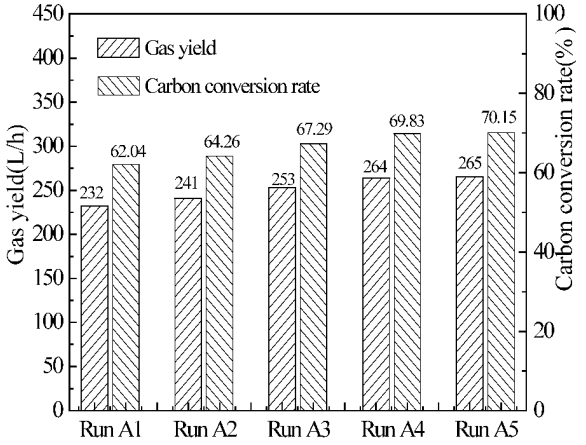

Fig.4 Influence of Fe/Ca ratio on gas yield and carbon conversion rate

With the increase in Fe/Ca ratio, the gasification reaction accelerates, the gas yield increases, CO and CH_4 yields slightly increase and CO_2 yield has a little decrease, but the overall variation in gas component is small, so the gas heating value just has an increment of 0.08 MJ/m^3, shown in Fig.5. In this case, the gas heating value per hour is proportional to gas yield, so the gas heating value per hour increases continuously. The gas heating value per hour under Run A5 is bigger than that under Run A1 by 0.33MJ/h, but the gas heating value and gas heating value per hour under Run A4 and Run A5 have small differences. Therefore, When Fe- and Ca-based catalyst are mixed as the ratio of 55/35(Run A4), the gasification reaction of natural coke with steam could reach ideal catalytic effect.

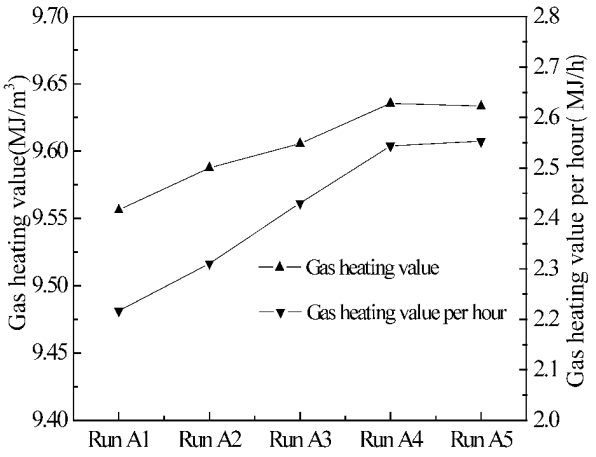

Fig.5 Influence of Fe/Ca ratio on gas heating value

Cu/Ca ratio

Keeping the Fe-based catalyst content in the mixed catalyst was 10%, the ratio of Cu- over Ca-based catalyst (Cu/Ca ratio) was adjusted at the following levels: 25/65, 35/55, 45/45, 55/35 and 65/25, recorded as Run B1, Run B2, Run B3, Run B4 and Run B5, respectively. The influence of Cu/Ca ratio on the gasification reaction of natural coke was shown in Fig.6. With the increase in Cu/Ca ratio from Run B1 to B5, the gas yield increases continuously by 35L/h, but the increase amplitude gets small after Cu/Ca ratio reaches 55/35. The carbon conversion rate increases from 64.61% under Run B1 to 73.20% under Run B5.

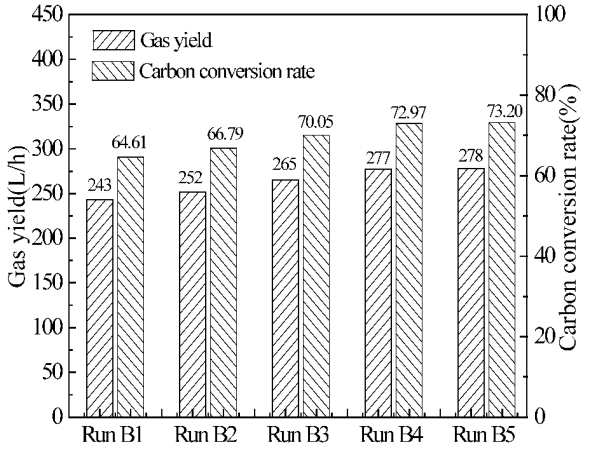

Fig.6 Influence of Cu/Ca ratio on gas yield and carbon conversion rate

Figure 7 shows the gas heating value change curve under different Cu/Ca ratio. With the increase in Cu/Ca ratio, the gas heating value just increases by 0.07MJ/m^3, because the gasification reaction accelerates with the increase in Cu/Ca ratio, the gas yield increases, the effective gas yield increases a little. The gas heating value per hour also increases with the Cu/Ca ratio, from 2.33MJ/h under Run B1 to 2.69MJ/h under Run B5, by an increment of 0.36MJ/h, but the gas heating value per hour between Run B4 and Run B5 only has a difference of 0.01MJ/h. Therefore, when Cu- and Ca-based catalyst are mixed as the ratio of 55/35(Run B4), the gasification reaction of natural coke with steam could reach ideal catalytic effect.

Fe/Cu ratio

Keeping the Ca-based catalyst content in the mixed catalyst was 10%, the ratio of Fe- over Cu-based catalyst (Fe/Cu ratio) was adjusted at the following levels: 25/65, 35/55, 45/45, 55/35 and 65/25, recorded as Run C1, Run C2, Run C3, Run C4 and Run C5, respectively. The influence of Fe/Cu ratio on the gasification reaction of natural coke is shown in Fig.8. With the increase in Fe/Cu ratio, both the gas yield and the carbon conversion rate increase first and then decrease, both of peaks appear at the Fe/Cu ratio of 35/55. Under above conditions, the gas yields are not less than 271L/h and the carbon conversion rates are more than 71.61%, which have great enhancements compared with the results under Run A and Run B. So it proves again that the catalytic effect of Fe- and Cu- based catalyst is better than that of Ca-based catalyst.

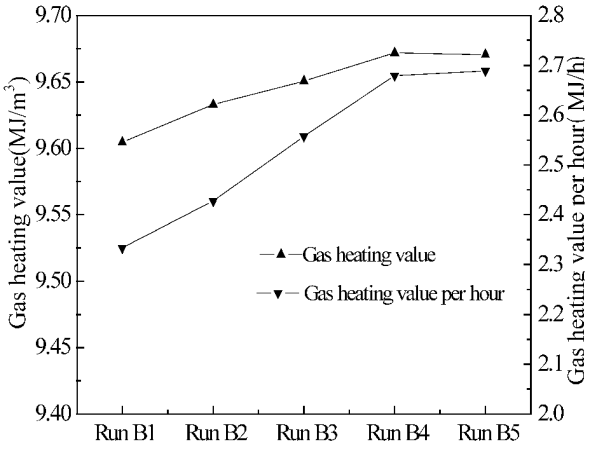

Fig. 7 Influence of Cu/Ca ratio on gas heating

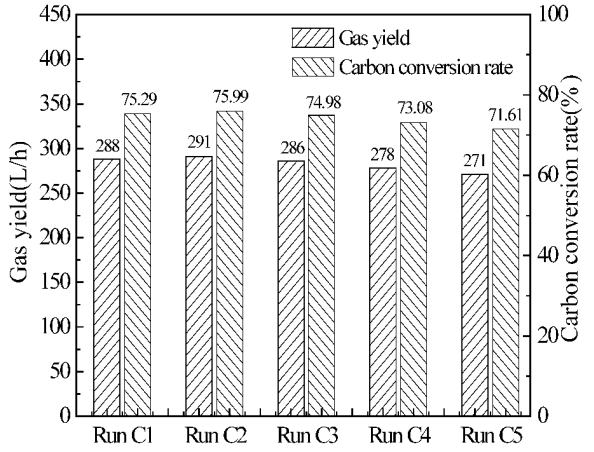

Fig. 8 Influence of Fe/Cu ratio on gas yield and carbon conversion rate

Gas heating value only has the relationship with effective gas content. With the increase in Fe/Cu ratio, H_2 and CO yield reach the maximum value and CO_2 reaches the minimum value under the condition of Run C2, but CH_4 yield is almost unchanged. So the gas heating value achieves the maximum value of 9.71MJ/m^3, higher than its minimum value by only 0.07MJ/m^3, shown in Fig.9. For the gas heating value per hour is proportional to gas heating value and gas yield, the gas heating value presents the same change trend of them. So the gas heating value per hour also increases first and then decreases, its turning point appears at Run C2 with the peak value of 2.83MJ/h. Therefore, when Fe- and Cu-based catalyst are mixed at the ratio of 35/55(Run C2), the gasification reaction of natural coke with steam could reach ideal catalytic effect.

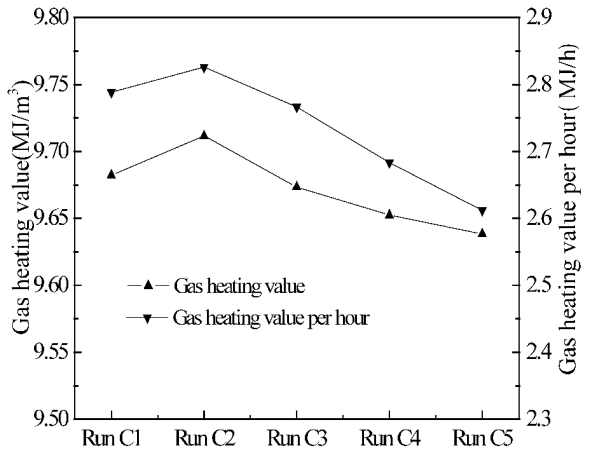

Fig. 9 Influence of Fe/Cu ratio on gas heating value

Table 3 Comparison of catalytic effect under the three mixed manners

Condition	Gas yield (L/h)	Carbon conversion rate (%)	Gas heating value (MJ/m^3)	Gas heating value per hour (MJ/h)
Run A4	264	69.83	9.64	2.54
Run B4	277	72.97	9.67	2.68
Run C2	291	75.99	9.71	2.83

The catalyst mixed manner optimization

Above all, the gasification reaction of natural coke with steam achieves the best catalytic effect when Fe/Ca ratio, Cu/Ca ratio and Fe/Cu ratio are under the condition of Run A4, Run B4 and Run C2. Table 3 shows the comparison of catalytic effect under this three mixed manner. From Table 3, not only carbon conversion rate but also gas yield and gas heating value under Run C2 are greater than that under Run A4 or Run B4. Therefore, Ca-, Fe- and Cu-based nitrates could achieve the best mixed manner when they are mixed as the ratio of 10/35/55.

Influence of dosage of mixed catalyst on gasification reaction

During the experiments, Ca-, Fe- and Cu-based nitrates were mixed at the ratio of 10/35/55. In order to verify effect of dosage of mixed catalyst on gasification reaction, the experiments with mixed catalyst dosage of 1%, 2%, 3%, 4% and 5% were conducted. Table 4 reflects the influence of mixed catalyst dosage on gas component. Overall, the influence of mixed catalyst dosage on gas component is very small, the fluctuation of each component's content is less than 0.5%, only the effective gas' content changes bigger relatively, which reaches the maximum value between 3% and 4%.

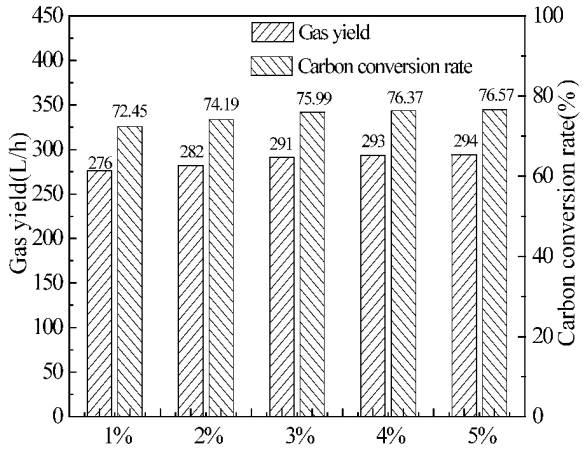

Fig. 10 Influence of mixed catalyst dosage on gas yield and carbon conversion rate

The results of gas yield and carbon conversion rate with the increase in mixed catalyst dosage are shown in Fig.10. It can be seen from the figure, with the increase in mixed catalyst dosage, both of gas yield and carbon conversion rate increase, but their amplitudes are very small after the mixed catalyst dosage is over 3%. When the mixed catalyst dosage increases from 1% to 3%, the gas yield and carbon conversion rate have the increment of 15L/h and 3.54%, respectively, which just increase by 3L/h and 0.58% when the mixed catalyst dosage increases from 3% to 5%.

The relationship between gas heating value and mixed catalyst dosage is shown in Fig.11. Seen from the figure, the change curve of the gas heating value presents the shape of parabola, and the peak value appears when the mixed catalyst dosage is between 3% and 4%. And the change curve of gas heating value per hour appears a turning point at the mixed catalyst dosage of 3%. Before the point, the gas heating value increases continuously. But after the point, the amplitude of gas heating value per hour is very small, there is a less than 0.03MJ/h increment when the mixed catalyst dosage is adjusted from 3% to 5%.

The results indicate that when the mixed catalyst dosage is 3%, content of each of all gas components, total gas yield, gas heating value are close to the maximum value. The increase in catalytic effect is not obvious with further increase in catalyst dosage. From the point of view of economy in the industrial applications, the increase in mixed catalyst dosage would undoubtedly increase operation cost. From comprehensive consideration, the best catalyst dosage should be in the vicinity of 3%.

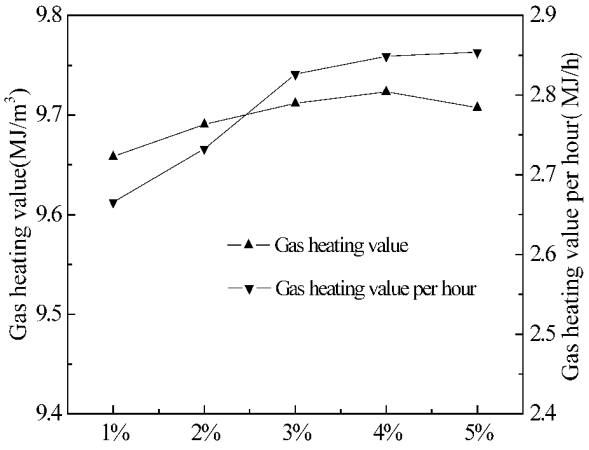

Fig.11 Influence of mixed catalyst dosage on gas heating value

Table 4 Influence of mixed catalyst dosage on gas components

Dosage/%	H_2/%	CO/%	CO_2/%	CH_4/%	Effective gas/%
1	62.11	19.27	17.16	1.46	82.84
2	62.03	19.61	16.91	1.46	83.09
3	62.31	19.68	16.61	1.41	83.39
4	62.38	19.58	16.59	1.45	83.41
5	62.41	19.48	16.68	1.44	83.32

CONCLUSIONS

The experimental results indicate that the fluidized bed gasification technology can overcome the shortcomings of natural coke. The findings provide a valuable basis for large-scale development and utilization of natural coke resources. Main conclusions are as follows:

(1) Either of Ca-, Fe- and Cu-based catalysts could promote gasification reaction rate of the natural coke samples effectively. But the effect of Fe- and Cu-based catalyst is better than Ca-based catalyst.

(2) The influences of Fe/Ca ratio and Cu/Ca ratio on gasification are similar, the gas yield, the carbon conversion rate and the gas heating value per hour increase as Fe/Ca ratio or Cu/Ca ratio increases, but all of them go up first and then drop with decrease in Fe/Cu ratio. They reach optimal values with the fraction of Ca/Fe/Cu of 10/35/55.

(3) For the catalyst ratio of Ca/Fe/Cu=10/35/55, the gasification characteristic presents a turning point when the catalyst dosage is 3%, where best results could be obtained.

ACKNOWLEDGEMENTS

Financial supports from the National Natural Science Foundation of China (90410009, 50776018) and the Special Funds for Major State Basic Research Projects of China (2007CB210101) were sincerely acknowledged.

REFERENCES

Chen, D., Lodeng, R., Anundsks, A.: Chem.l Eng. Sci. **56**(2001), pp.1371-1379.
Domazetis, G., Liesegang, J., James, B.D.: Fuel Process. Technol. **86**(2005), pp. 463-486.
Hiroyuki, N., Akio, N., Marc, B., Kouichi, M.: Fuel, **83** (2004), pp.719-725.
Jiang, M.: Coal Process. Comprehen. Utilization. **6**(1995), pp.46-48. (in Chinese)
Khan, M.R., Seshadri, K.: Fuel Process. Techno. **27**(1991), pp.83-94.
Kwiecinska, B., Petersenb, H. I.: Int.J. Coal Geology. **57**(2004), pp. 99-116.
McLendon, T. R., Lui, A. P., Pineault, R. L., Beer, S. K., Richardson, S.W.: Biomass Bioenerg. **26**(2004), pp.377-388.
Pang, K.L., Xiang, W.G., Zhao, C.S.: J. Anal. Appl. Pyrol. **80**(2007), pp.77-84.
Sanyal, S.P.: Memoirs of the Geological Survey of India, **117**(1984), pp.111-124.
Timpe, R. C., Kulas, R.W., Hauserman, W.B., Sharma, R.K., Olson, E.S., Willson, W.G.: Int. J. Hydrogen Energ. **22**(1997), pp.487-492.
Wang, B.Y., Wang, Y.H, Ning, Y.H.: Land and Resources in Shandong Province, **22**(2006), pp.53-55. (in Chinese)
Xu, X.F., Cui, H., Gu Y.D.: Clean Coal Technol. **4**(1996), pp.28-31.

NOVEL APPROACH TO TAR REMOVAL FROM BIOMASS PRODUCER GAS BY MEANS OF A NICKEL-BASED CATALYST

M. Vosecký, P. Kameníková, M. Pohořelý, S. Skoblja, M. Punčochář

Institute of Chemical Process Fundamentals, Academy of Sciences of the Czech Republic, Rozvojová 135, 165 02 Prague 6-Suchdol, Czech Republic

Abstract: The nickel-based catalyst was exposed to the raw gas from gasification of woody biomass with air in a fluidized-bed. After dust removal on a barrier filter and sulphur compounds capture, namely H_2S, on an active sorbent made of CuO and ZnO, higher hydrocarbons as tar components were decomposed/reformed on a Ni-catalyst. Steam reforming reactions led to decomposition of tar and all hydrocarbons higher than CH_4 into mainly H_2 and CO which further underwent reaction with steam via the water gas shift reaction to CO_2. The reforming reactions caused approximately 10–20 % decrease in the lower heating values of the producer gas from the inlet values 5.0–6.5 MJ m^{-3}. The gas yield increased from values 2.4–2.6 m^3 kg^{-1} to values 2.8–3.0 m^3 kg^{-1} on dry biomass basis. The chosen tar removal concept based on combination of dolomite in the fluidized-bed with the secondary catalytic reactor was proved by 20 hours long experiment in which the final tar content below 30 mg m^{-3} was attained corresponding to more than 97 % tar conversion. H_2S content in producer gas was expected to be below 100 vol. ppm, bulk of which was captured on the sorbent. Only limited deactivation of the catalyst by sulphur compounds was found in the front of the catalyst bed where sulphur content was determined as high as 173 wt. ppm compared to 22 wt. ppm in the fresh sample.

Keywords: catalytic tar removal, nickel catalyst, steam reforming, fluidized-bed, biomass gasification.

INTRODUCTION

Producer gas cleaning is the key issue in successful industrial implementation of gasification technology. The design of the gas cleaning system reflects demands of the end user of producer gas. In the field of biomass gasification the tar removal represents the strong challenge because tar, besides the other gas contaminants, can cause severe operational problems.

There are several strategies how to remove tar as it was reviewed e.g. by Stevens (2001) and Torres (2007). The one of particular interest, specified in our study, is catalytic destruction of tar by means of a steam reforming nickel-based catalyst. Principal reaction of endothermic steam reforming process is the steam reforming reaction (Eq.1), which is followed by the water gas shift reaction (Eq.2) and the methanation reaction (Eq.3).

$$C_nH_m + n\,H_2O = n\,CO + \left(n + \frac{m}{2}\right) H_2 \quad \Delta H_{298} > 0\ \text{kJ.mol}^{-1} \tag{1}$$

$$CO + H_2O = CO_2 + H_2 \qquad \Delta H_{298} = -41\ \text{kJ.mol}^{-1} \tag{2}$$

$$CO + 3\,H_2 = CH_4 + H_2O \qquad \Delta H_{298} = -206\ \text{kJ.mol}^{-1} \tag{3}$$

The steam reforming of tar in producer gas has been broadly studied. These studies can be divided into two principal groups. The first group includes studies where model tar compounds in well-defined pre-mixed gas have been used. As the model tar compounds toluene (Simell et al. (1997)), naphthalene (Bangala et al.,1998, Nacken et al.,2007) or different mixtures (Gebhard et al.,1994, Coll et al.,2001; Sato and Fujimoto,2007) have been chosen.

The second group consists of experiments performed with real producer gas from biomass gasification. Catalyst was mainly placed in a secondary reactor, either in the fixed-bed (Simell and Bredenberg,1990; Wang et al.,2000; Pfeifer and Hofbauer,2008 and others) or in the fluidized-bed (Baker et al.,1987; Arauzo et al.,1994; Bain et al.,2005 and others). Experiments within the above discussed research work were conducted mainly in the temperature range 700–900 °C which has been often associated with further catalyst reheating downstream to gasifier; heating to balance heat losses is excluded.

Therefore, the aim of the present work has been experimental proving of feasibility and effectiveness of tar removal on selected Ni-based catalyst in the optimized temperature window from 450 to 550 °C. To fulfill the objectives of the work, raw gas from biomass fluidized-bed gasification was cleaned at high temperatures according to the proposed cleaning concept, which is shown in Fig. 1. The concept was designed with an emphasis on decreasing temperature profile over the whole process, which could contribute to its technological

simplicity.

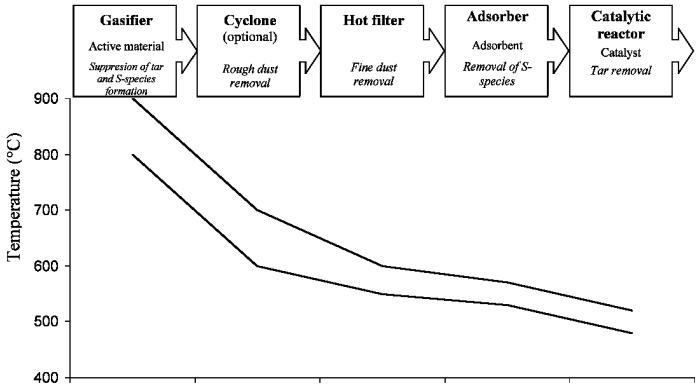

Fig.1 Proposed gas cleaning concept

EXPERIMENTAL

Characterization of materials

Woody biomass of properties indicated in Table.1 was used as the fuel for gasification experiments in a fluidized-bed gasifier. Two materials such as silica sand (> 99 wt. % SiO_2) and dolomite (67 wt.% CaO, 30 wt.% MgO and 1 wt. % SiO_2) were used as materials of the fluidized-bed. Moreover, identical silica sand was used in the barrier filter for dust removal.

According to the given experimental set-up specified in the next section two commercial active materials were tested. One played role as the sulphur adsorbent and the second was nickel-based catalyst for tar removal via reforming reactions. However, their detailed properties and composition are considered as confidential and therefore only basic description is provided. Active components of the sulphur adsorbent are zinc and copper oxides in equal ratio on an alumina carrier. The nickel-based catalyst is composed of bulk of nickel oxide with addition of silica oxide, magnesium oxide, alumina and other oxides. The both materials were in a form of cylindrical pellets of size 3 mm both in diameter and height.

Table 1 Proximate and ultimate analysis

Components, wt.% (raw state)	Biomass
Moisture	7.32
Ash	0.82
Combustibles*	91.86
Volatiles	77.77
Fixed carbon	14.09
Higher heating value (MJ/kg)	17.61
Lower heating value (MJ/kg)	16.15
Carbon	45.99
Hydrogen	5.66
Oxygen	39.78
Sulphur	<0.01
Nitrogen	0.55

*in wt.%: Combustibles = 100 - Moisture - Ash

Experimental facility and conditions

Experiments have been conducted on the atmospheric fluidized-bed gasifier coupled with the unit for high-temperature producer gas cleaning as it is depicted in Fig. 2.

The gasifier is made of heat resistant stainless steel with the maximum operating temperature of 1000 °C and the maximum input of 10 kW. Sampling points for gas and tar analyses are placed on the top part of the gasifier. Values gained from this sampling point refer to the catalyst inlet values. The bulk of hot raw producer gas is dedusted in a cyclone and sampled for on-line analysis of major components.

A side stream of the raw gas is fed to the unit for high-temperature gas cleaning. The gas flows through the horizontal and vertical section of heated sampling line to the first reactor (R1). During experimental run water was injected to the gas stream through injection point placed in between sampling line and R1 in order to increase H_2O/C ratio of producer gas. R1 (outer diameter (∅) 60 mm and length 278 mm) with maximum operation temperature 600 °C served as dust removal section with filtration on dense metal barrier of cylindrical shape. Gas came to the outer side of the cylinder with area of 202 cm^2 filled with silica sand. R1 as well as other reactors in the unit were electrically heated. Dedusted producer gas entered the fixed-bed reactor R2 (outer ∅ 44 mm and length 380 mm) with effective volume of about 450 ml filled with the sulphur sorbent. R2 has an operation temperature 500–600 °C. The last but crucial part of the unit was reactor R3 with the fixed-bed of nickel-based catalyst. Effective volume of R3 is about 590 ml with outer ∅ 60 mm and length 200 mm. Downstream to R3 there is gas water-cooler and pump which together with valve ensures desired gas flow through the unit.

Tar samples referring to catalyst outlet values were taken upstream to the cooler while gas samples were taken downstream to the cooler. Moreover, nitrogen for purging of the unit was optionally fed with the reverse flow in between R3 and the cooler. Before the experimental run nitrogen was enriched by hydrogen for activation (reduction) of inactive nickel oxide to active form of metallic nickel. Concentrations of the major components (CO, CO_2, CH_4 and H_2) have been measured by ABB Advance optima analyzers. The presented data are based on the off-line analysis of the major and minor components of the producer gas by means of gas chromatography on HP 6890 equipped with flame-ionization detector and thermal conductivity detector. Tar was sampled by absorbtion in acetone and determined on gas chromatograph HP 6890 coupled with MS detector.

Experimental conditions are specified in Table 2.

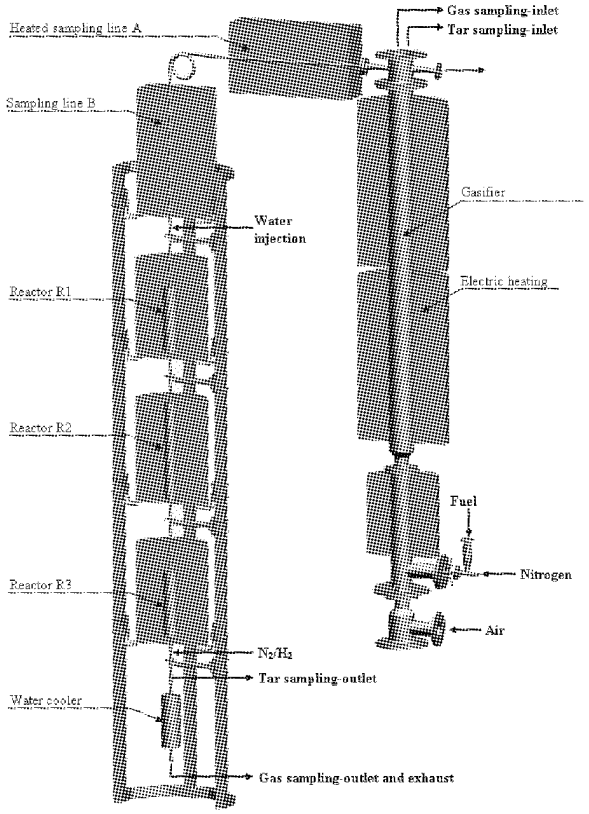

Fig. 2 Gasifier and high-temperature gas cleaning un

Table 2 Experimental conditions

Time on stream (hh:mm) **Fludized-bed material**	**0:00-6:47 sand**	**6:48-22:12 sand+dolomite**
Fuel flow (g h^{-1})	1246	1371
Gas flow (m^3 h^{-1}) *		
Gasification air	2.5	2.5
Pneumotransport - N_2	1.6	1.6
Gas flow cleaning unit	0.375–0.667	0.574–0.648
Gas hourly space vel. (h^{-1})	3750–6670	5740–6480
Gasification ratio	0.45	0.41
H_2O/C (mol mol^{-1})	1.8–2.5	1.3–1.8
Measured temperatures (°C)		
Fluidized-bed	890±10	896±5
Freeboard	900±3	900±4
R1	570±10	570±10
R2	535±15	535±15
R3	500±10	510±10
Inlet of materials (g)		
Fluidized-bed - sand	2727	2727
Fluidized-bed - dolomite	---	590
R1 - sand	210	210
R2 - sulphur adsorbent	190	190
R3 - Ni catalyst	100	100

RESULTS AND DISCUSSION

Major gas components

Content of major producer gas components, i.e. CO, CO_2, CH_4 and H_2 both in the inlet and outlet of the nickel-based catalyst is shown in Fig. 3.

As it can be seen from Fig. 3, producer gas composition was considerably changed over the catalyst as a result of steam reforming reactions. The steam reforming reaction (Eq.(1)) of higher hydrocarbons led to significant increase in H_2 content. The second main product should be one of the carbon oxides. It has been reported, e.g. by Rostrup-Nielsen (1984), that both CO and CO_2 are present at roughly the same content under typical conditions for steam reforming in range of 700–950 °C. However, CO reacts under the given experimental conditions (temperatures around 500 °C) with steam via the water gas shift reaction (Eq.(2)) to CO_2. Thus, the CO content decreased over the catalyst bed while the CO_2 content has shown strong rise. Significant prevalence of CO_2 over CO has been reported in steam reforming of *n*-hexane at 450 °C by Arena et al. (2004) and Arena (2006) or in steam reforming of C_3–C_7 hydrocarbons at 460–480 °C by Chen et al. (2006). Both groups have found selectivity to CO lower than 3 % at comparable H_2O/C molar ratios 2.5–2.8 mol mol^{-1}.

Changes for all components with exception of CH_4 are generally the same both when single sand and sand with dolomite were in fluidized-bed. Addition of dolomite to the bed led to limited promotion of steam reforming

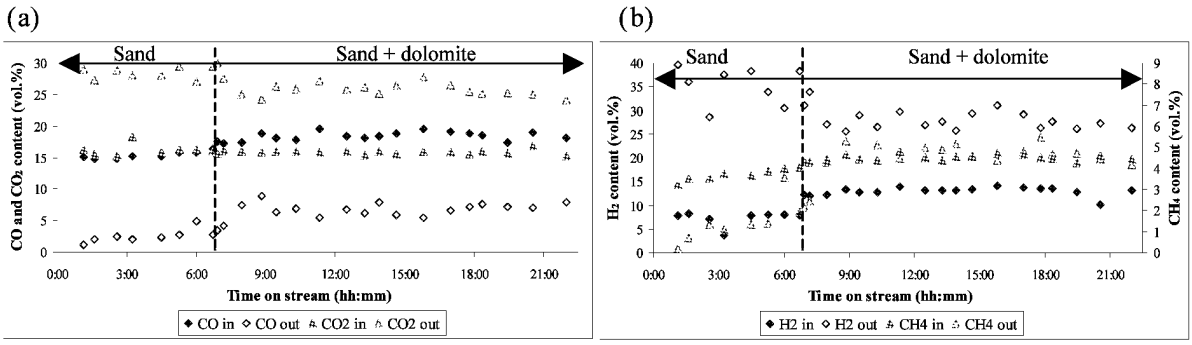

Fig. 3 Dependence of (a) CO and CO_2 content or (b) H_2 and CH_4 content on time on stream in dry gas

reactions taking place directly in the fluidized-bed with resulting increase in the H_2 content of about 5 % and the CO content of about 3 %. Increase in the CO inlet content caused increase in its outlet content whilst the CO_2 outlet content simultaneously slightly decreased with inlet content being roughly constant. The CH_4 content showed different tendencies. While there was single sand in the bed, CH_4 was partially decomposed via steam reforming reaction (Eq.(1)). However, when mixture of silica sand and dolomite was in the bed, the CH_4 content remained almost unchanged across the catalytic bed. It follows that under the given conditions, CH_4 was not important product of decomposition reactions on the catalyst, or alternatively, CH_4 was formed and decomposed at fairly similar rate.

It should be pointed out that nitrogen as one of major gas components is not shown having 44–57 % in the inlet and 27–39 % in the outlet dependently on the conditions and process fluctuations.

Minor gas components

Minor producer gas components are meant as gaseous hydrocarbons higher than CH_4 detectable by GC. From this group, only few components have been found in raw gas at considerable amounts, i.e. ethane, ethylene, acetylene, benzene and toluene, with sum of their content over 99 % of all determined minor gas components. Content of selected components such as ethylene, acetylene and benzene together with sum of all detected minor components both in the inlet and outlet is depicted in Fig.4.

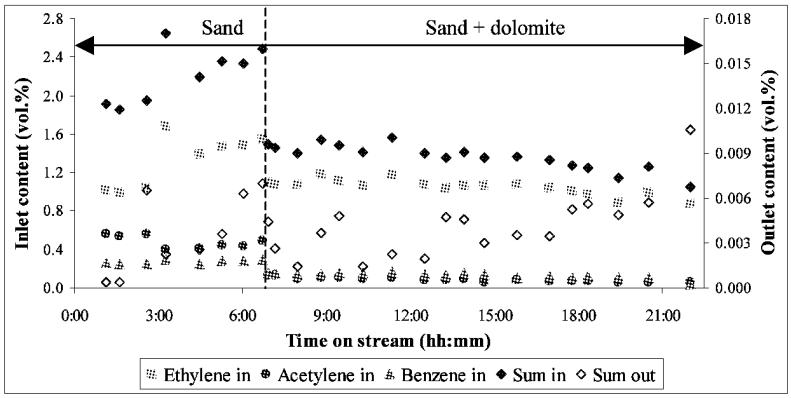

Fig. 4 Dependence of minor producer gas components on time on stream (dry gas)

Fig. 4 shows how content of minor components of producer gas was affected by presence of dolomite in the fluidized-bed. Addition of dolomite caused decrease in their sum from 1.8–2.4 % to 1.0–1.5 % with appropriate decrease in each component content.

When sum of minor gas components is compared in the inlet and outlet from the catalyst, it is obvious that more than 99 % of these components underwent decomposition reactions on catalyst with outlet values in most samples less than 0,006 %. Thus, minor gas components are almost completely removed from gas.

Lower heating value and gas yield

Energy content of the gas, so called lower heating value (LHV) and gas yield of the dry gas are shown in Fig.5. LHV was counted from detailed producer gas composition as determined by means of GC analysis.

Lower heating value reflects above shown changes in gas composition. Its decrease of about 10–20 % over bed of catalyst was given by nearly complete decomposition of minor gas components, which would otherwise significantly contribute to the LHV. Even though the LHV was supported by increase in gas yield which was accompanied with decrease in nitrogen content in the gas, this contribution was not sufficient enough. Changes

on the LHV are in general dependent on experimental conditions, because both its decrease over the catalytic bed (Wang et al.,(2000) or its increase (Corella et al.,1998) have been reported.

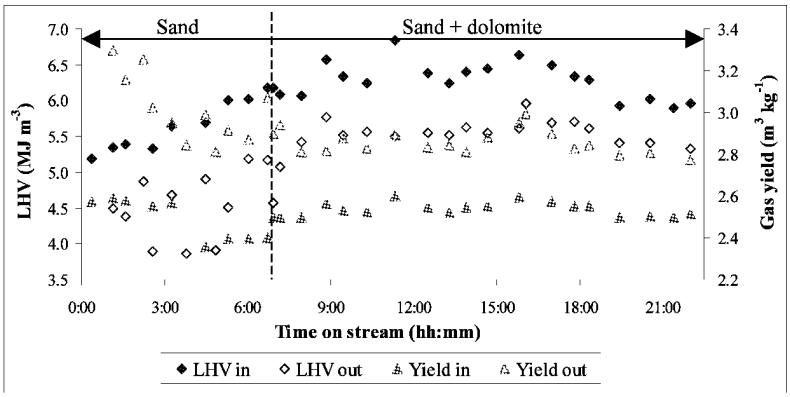

Fig. 5 Lower heating value and gas yield

Gas yield was found to clearly increase which could be interpreted as the consequence of steam reforming reactions and it has been always observed as far as catalyst was active for the steam reforming.

Tar content

Tar content in the inlet and the outlet from the catalyst was sampled and determined as indicated in Table 3.

Table 3 Tar content in the producer gas.

Sample number	1 in	1 out	2 in	2 out	3 in	3 out	4 in	4 out	5 in	5 out	6 in	6 out
Sampling time (hh:mm)	1:42-2:31	1:38-2:36	5:15-5:45	5:20-6:10	8:42-9:37	8:46-9:34	13:14-14:01	13:11-14:04	17:40-18:37	17:44-18:35	21:14-22:08	21:17-22:05
Fluidized bed	sand		sand		sand+dolomite		sand+dolomite		sand+dolomite		sand+dolomite	
Gasifier temperature (°C)	900±10	900±10	900±10	900±10	900±10	900±10	900±10	900±10	900±10	900±10	900±10	900±10
Catalyst temperature (°C)	500±25	500±25	500±25	500±25	510±10	510±10	510±10	510±10	510±10	510±10	510±10	510±10
H_2O/C (mol mol^{-1})	2.5	---	1.8	---	1.3	---	1.4	---	1.4	---	1.8	---
Content (mg m^{-3})												
Benzene	7661.8	0.0	6833.3	142.7	3952.5	19.9	4636.3	27.6	3493.0	24.6	3357.4	41.0
Toluene	647.1	1.8	1130.2	23.4	833.4	13.5	959.9	15.7	780.7	13.9	745.1	20.0
o+m+p-xylene+ethylbenzene	150.2	0.0	157.7	0.0	36.4	0.0	31.2	0.0	30.8	0.3	27.5	0.0
Styrene	278.3	0.0	534.5	1.8	178.3	0.0	175.0	0.0	120.1	0.0	163.3	0.0
Sum of BTX	8737.8	1.8	8680.3	168.0	5016.4	33.5	5823.8	43.3	4435.7	38.9	4304.7	61.0
Oxygenated hydrocarbons	78.4	0.0	150.5	0.7	19.0	0.0	8.3	0.0	11.9	0.0	4.8	0.0
Indene+indan	203.5	0.4	285.9	1.8	46.8	0.2	37.7	0.0	20.6	0.0	14.9	0.0
Naphthalene	1879.1	8.2	1682.9	35.9	377.8	10.5	404.2	10.1	281.2	6.6	248.7	8.1
Methylnaphthalenes	67.3	0.7	141.7	2.8	29.6	0.5	26.5	0.5	19.9	0.0	16.3	0.0
Alkylnaphthalenes (alkyl ≥ C_2)	17.9	0.0	35.2	0.3	7.2	0.0	7.3	0.0	5.2	0.0	2.9	0.0
Biphenyl	93.1	0.6	120.3	1.6	21.1	0.2	16.7	0.2	16.5	0.0	12.0	0.0
Acenaphthylene	604.6	0.9	526.1	3.8	65.2	0.2	45.5	0.1	30.3	0.0	19.0	0.0
Fluorene	71.5	0.6	95.8	1.6	8.7	0.2	4.3	0.2	3.4	0.0	0.9	0.0
PAH; M/Z=165,166	13.7	0.0	29.7	0.0	3.8	0.0	3.4	0.0	1.6	0.0	1.8	0.0
Phenanthrene	420.5	2.4	439.7	9.0	43.8	0.8	24.6	1.1	20.0	0.0	6.1	0.0
Anthracene	139.7	0.6	118.1	4.1	13.8	0.3	10.4	0.3	6.4	0.0	3.9	0.0
Fluoranthene	188.4	1.0	150.1	1.9	15.3	0.4	5.3	0.1	2.8	0.0	0.4	0.0
Pyrene	155.3	2.1	132.9	3.1	12.7	0.6	4.6	0.2	2.0	0.0	0.4	0.0
4 ring PAH [a] (m/z=226,228)	156.5	0.9	140.6	1.5	9.9	0.0	1.6	0.0	0.0	0.0	0.0	0.0
5 ring PAH [b] (m/z=252)	94.4	0.5	77.0	0.4	3.6	0.0	0.0	0.0	0.0	0.0	0.0	0.0
6 ring PAH [c] (m/z=276)	27.0	0.3	23.0	0.0	0.0	0.0	0.0	0.0	0.0	0.0	0.0	0.0
Other	132.2	0.8	209.6	2.4	14.8	0.2	10.6	0.1	7.6	0.0	5.1	0.0
Total tar (excluding BTX)	4343.2	20.0	4359.3	70.9	693.2	14.0	611.0	13.0	429.4	6.6	337.2	8.1
Total tar (toluene and higher)	**5418.8**	**21.8**	**6181.6**	**96.2**	**1741.3**	**27.5**	**1777.0**	**28.8**	**1361.1**	**20.9**	**1273.1**	**28.1**
Conversion (%)												
Benzene	---	≈100	---	97.9	---	99.5	---	99.4	---	99.3	---	98.8
Toluene	---	99.7	---	97.9	---	98.4	---	98.4	---	98.2	---	97.3
BTX	---	≈100	---	98.1	---	99.3	---	99.3	---	99.1	---	98.6
Naphthalene	---	99.6	---	97.9	---	97.2	---	97.5	---	97.6	---	96.7
Total tar (excluding BTX)	---	99.5	---	98.4	---	98	---	97.9	---	98.5	---	97.6
Total tar (toluene and higher)	**---**	**99.6**	**---**	**98.4**	**---**	**98.4**	**---**	**98.4**	**---**	**98.5**	**---**	**97.8**

[a] benz[e]phenanthrene, benzo[ghi]fluoranthene, 3,4-dihydrocyclopenta[cd]pyrene (acepyrene), cyclopenta[cd]pyrene, benz[a]anthracene, chrysene, naphtacene.

[b] benzo[j]fluoranthene, benzo[k]fluoranthene, benzo[e]pyrene, benzo[a]pyrene, perylene.

[c] indeno[1,2,3-cd]pyrene, dibenzo[a,h]anthracene, benzo[ghi]perylene, dibenzo[def,mno]chrysene.

From Table 3 it follows, that catalyst exhibited high activity towards reforming of tar hydrocarbons. Tar residual concentrations were well below 30 mg m^{-3} even after more than 20 hours of experimental run. Correspondingly, tar conversions were kept above 97 %. Moreover, these result were obtained in unfavorable conditions for the catalyst, namely at very low H_2O/C ratios. From the table it can be seen that H_2O/C ratios were for most of samples below 1.8 mol mol^{-1}. These values are significantly below recommended levels in literature, e.g. Twigg (1996) advises H_2O/C ratio for naphtha steam reforming at minimum 2.2 and preferably in the range from 3.5–4.5 mol mol^{-1}. Therefore, it is believed that outlet tar concentrations below 10 mg m^{-3} under the optimized experimental conditions would be attainable.

Catalyst deactivation

The nickel-based catalyst from R3 was after the experiment along its height sampled into samples Ni1-Ni7, as it is indicated in the following Tab. 4. Besides, comparison is given with the fresh sample. Catalysts are in such processes deactivated by either carbon formation or sulphur poisoning (Rostrup-Nielsen (1984)). Thus, carbon and sulphur content was determined to observe the extent of deactivation.

Table 4 Carbon and sulphur content in catalyst

Catalyst sample	Weight (g)	C (wt.%)	S (wt.ppm)
fresh catalyst		3.17	22 0
Ni1 - inlet	7.5	4.52	173
Ni2	9.4	---	114
Ni3	13.7	4.00	111
Ni4	21.9	---	---
Ni5	20.7	3.59	59
Ni6	12.6	---	---
Ni7 - outlet	14.3	3.76	83

When catalyst was displaced from the reactor, the front part of it was clearly covered by carbon, which was proved by analysis. In addition, considerable amount of sulphur was captured on this sample.

From the table it can be seen that trend in carbon content corresponds to that of sulphur content. It has been reported by Rostrup-Nielsen (1984) that active sites deactivated by sulphur are more susceptible to carbon formation. To minimize the both phenomena would be of primary importance in further research.

CONCLUSIONS

Main conclusions from performed experiments could be drawn as follows:

(1) The selected nickel-based catalyst has shown high activity towards higher hydrocarbons including tar species.

(2) Very low tar content below 30 mg m^{-3} was attained with outlook to reach less than 10 mg m^{-3} at temperatures about 500 °C in the catalyst bed.

(3) The catalyst converts higher hydrocarbons mainly into H_2 and CO_2 resulting in increase in gas yield.

(4) Only limited signs of catalyst deactivation under the given conditions, which could be further optimized, proved strength of selected catalyst and promissing viability of the proposed cleaning concept.

ACKNOWLEDGEMENTS

The financial support within the project MSMT No. 2B08048 granted by Ministry of Education, Youth and Sports of the Czech Republic and the project No. 104/07/0977 granted by the Czech Science Foundation are gratefully acknowledged.

REFERENCES

Arauzo, J., Radlein, D., Piskorz, J., Scott, D.S.: Energy Fuels **8** (1994), pp. 1192–1196.
Arena, F., Trunfio, G., Alongi, E., Branca, D. and Parmaliana, A.: Appl. Catal. A-Gen. **266** (2004), pp. 155–162.
Arena F.: AIChE J **52(8)** (2006), pp. 2823–2831.
Bain, R.L., Dayton, D.C, Carpenter, D.L. Czernik, S.R. et al: Ind. Eng. Chem. Res. **44** (2005), pp.7945–7956.
Baker, E.G., Mudge, L.K., Brown, M.D.: Ind. Eng. Chem. Res. **26** (1987), pp. 1335–1339.
Bangala, D.N., Abatzoglou, N., Chornet, E.: AIChE J, **44(4)** (1998), pp. 927–936.
Chen, Y., Xu, H., Jin, X., Xiong, G.: Catal. Tod., **116** (2006), pp. 334–340.
Coll, R., Salvado, J., Farriol, X., Montane, D.: Fuel Process. Technol. **74** (2001), pp. 19–31.
Corella, J., Orio, A., Aznar, P.: Ind. Eng. Chem. Res. **37** (1998), pp. 4617–4624.
Gebhard, S.C., Wang, D., Overend, R.P., Paisley, M.A.: Biomass Bioenerg. **7** (1994), pp. 307–313.
Nacken, M., Ma, L., Engelen, K., Heidenreich, S., Baron, G.V.: Ind. Eng. Chem. Res. **46** (2007), pp. 1945–1951.
Pfeifer, C., Hofbauer, H.: Powder Technol. **180** (2008), pp. 9–16.
Rostrup-Nielsen, J.R.R.: Catalytic Steam Reforming. Berlin : Springer, 130 pp. ISBN 3–540–12665–1.
Sato, K., Fujimoto, K.: Catal. Commun. **8** (2007), pp. 1697–1701.

Simell, P.A., Bredenberg, J.B.: Fuel, **69** (1990), pp. 1219–1225.
Simell, P.A., Hepola, J.O., Krause, A.O.I.: Fuel, **76** (1997), pp. 1117–1127.
Stevens, D.J.: National Energy Laboratory Report No. NREL/SR-510-29952, USA, 2001, 103
Torres, W., Pansare, S.S., Goodwin, J.G: Catal. Rev.-Sci. Eng. **49** (2007), pp.407–456.
Twigg, M.V. Catalyst Handbook. 2nd ed. London:Manson Publishing. 1996, 608 pp. ISBN 1–874545–36–7.
Wang, W., Padban, N., Ye, Z., Olofsson, G..; Andersson, A.: Bjerle, I.: Ind. Eng.Chem. Res. **39** (2000), pp. 4075–4081.

DEVELOPMENT OF CATALYTIC TAR DECOMPOSITION IN AN INTERNALLY CIRCULATING FLUIDIZED-BED GASIFIER

Xianbin Xiao[1,2], Duc Dung LE[2], Kayoko Morishita[2], Liuyun LI[1],Takayuki Takarada[2]

1 Gunma Industry Support Organization, Maebashi 371-0854, Japan

2 Department of Chemical and Environmental Engineering, Gunma University, Kiryu 376-8515, Japan

Abstract: Biomass gasification in an Internally Circulating Fluidized-bed Gasifier (ICFG) using Ni/Al_2O_3 as tar cracking catalyst is studied at low temperature. Reaction conditions of the catalyst bed are discussed, including catalytic temperature and steam ratio. High energy efficiency and hydrogen-rich, low-tar product gas can be achieved in a properly designed multi-stage gasification process, together with high-performance catalyst. In addition, considering the economical feasibility, a newly-developed Ni-loaded brown coal char is developed and evaluated as catalyst in a lab-scale fluidized bed gasifier with catalyst fixed bed. The new catalyst shows a good ability and a hopeful prospect of tar decomposition, gas quality improvement and catalytic stability.

Keywords: Biomass gasification, Internally Circulating Fluidized-bed Gasifier, Catalyst, Tar decomposition, Ni-loaded brown coal char

INTRODUCTION

With respect to global issues of sustainable energy and reduction in greenhouse gases, biomass is getting increased attention as a potential source of renewable energy. Among all technologies of biomass utilization, gasification is an efficient and environmentally friendly method for the thermochemical conversion of biomass to energy or synthesis gas, and it is expected to play a key role in expanding the use of biomass as a major renewable source. The conversion of the solid feedstock to a gaseous fuel significantly increases its potential. The combination of steam gasification and heat or power generation, or chemical production from the syngas gives a lower energy loss than the direct combustion of the fuel. Therefore, steam gasifier is an excellent thermal-chemical energy transformer (Hayashi and Mae, 2004).

However, in that highly endothermic process, energy efficiency needs to be paid more attention to and how the necessary heat is input should be well considered. On the one hand, biomass gasification with pure steam in a fluidized bed can be connected in several ways to a fluidized bed combustor, to burn the char that is generated in the gasifier (generally called dual fluidized bed (DFB) biomass gasifier) (Corella et al., 2007). And the bed material, such as silica sand, circulates through the two reactors as a heat carrier that absorbs the heat of char combustion in the combustor and then releases it in the gasifier. The key features are the separation of pyrolysis and subsequent steam reforming/gasification of nascent pyrolysis products from the O_2 oxidation of the residual char, and the absorption as much of oxidation heat by the endothermic pyrolysis and steam reforming/gasification as possible. It avoids the dilution of the product gas by the flue gas instead of partial combustion of the biomass, and is catching an increasingly greater interest in recent years because it is an important candidate for gasification with high cold gas efficiency (Hayashi et al., 2006). On the other hand, low-temperature gasification is becoming an interesting alternative, both from the energy point of view (García et al., 1999), and to avoid the ash-related problem at high temperature, such as sintering, agglomeration, deposition, erosion and corrosion (Garíca-Ibañez et al., 2004). When the process is carried out at lower temperature to get higher efficiency and easier operation, more tar is produced, which can cause plugging in the colder parts of the plant (Asadullah et al., 2002). Among the possible gas cleaning methods, catalytic tar decomposition is considered to the solution to this problem, because of the complete destruction of the tars instead of creating a waste stream which is difficult to dispose (Pferfer and Hofbauer, 2008).

In this paper, an Internally Circulating Fluidized-bed Gasifier (ICFG), which shares the same concept of DFB gasifier, and the development of tar catalytic decomposition are introduced.

INTERNALLY CIRCULATING FLUIDIZED-BED GASIFIER

Test facility

An Internally Circulating Fluidized-bed Gasifier for steam gasification is currently operated in Gunma University, Japan at a scale of about 30 kW (fuel power) (Xiao et al., 2008). The flowchart of the plant is given in Fig. 1. The core reactor consists of a gasification chamber (fluidized with steam) and a combustion chamber (fluidized with air). A circulation loop of the bed material is created between those two chambers to deliver the

heat for the gasification process. It has a height of 1,250 mm, with a 212×212 mm square cross-section in the bed zone and 412×412 mm in the freeboard.

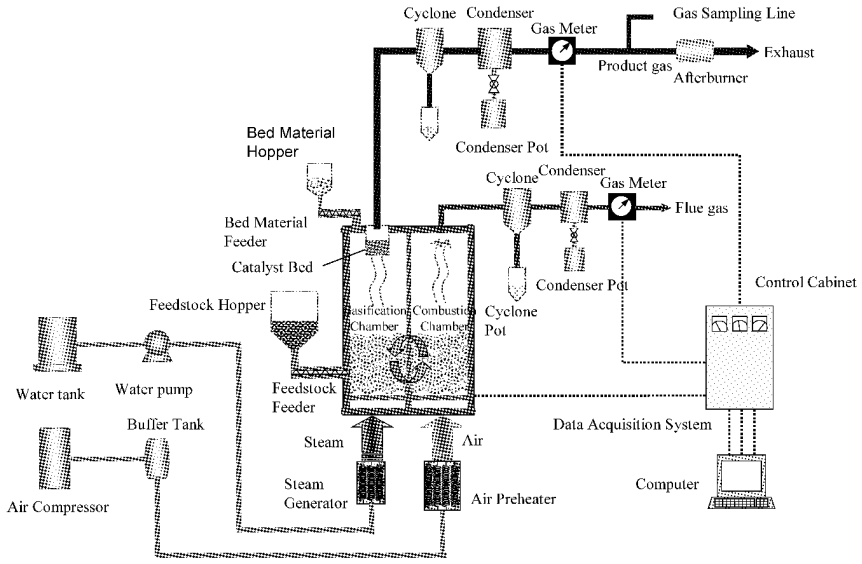

Fig. 1 Flow sheet of ICFG

Corella et al. (2007) gave a thorough review of DFB gasifiers which existed in the history and are operated today all over the world. After an in-depth and detailed evaluation and analysis of all the available data, the authors presented their doubt about the economical feasibility. For example, external heat energy supply is necessary to keep the operating temperature of >800 ℃ because of the highly endothermic gasification with pure steam, and the heat required to generate steam to such temperature. Therefore, relatively lower temperature range (600-700 ℃) is especially investigated in this study. Secondly, the flue gas from the combustion chamber still carries off a portion of the thermal energy from the char combustion without supplying it to the gasification chamber directly (Hayashi, et al. 2006). Consequently, the catalyst bed is settled in the freeboard of the gasification chamber, surrounded by hot flue gas for enhanced heat transfer. That arrangement is both to utilize the heat in the reactor for the endothermic reforming reactions and to eliminate the downstream cleanup economically. It is a column container with the inner diameter of 93.6 mm and the height of 320 mm. Catalyst is put inside the catalyst bed, which is operated as fixed bed.

Table 1 Feedstock characteristics

Feedstock		PC	RP
Proximate analysis			
Moisture	wt. %, a.r.	18.4	5.8
Volatile matter	wt. %, d.b.	67.4	85.2
Fixed carbon	wt. %, d.b.	12.8	14.0
Ash	wt. %, d.b.	19.8	0.8
Ultimate analysis			
Carbon	wt. %, d.b.	40.8	53.8
Hydrogen	wt. %, d.b.	5.4	7.1
Nitrogen	wt. %, d.b.	4.1	0.05
Sulfur	wt. %, d.b.	0.6	0.3
Oxygen (differential)	wt. %, d.b.	29.3	38.8

Effects of catalytic reaction conditions

Although the gasifier performance is influenced by many different operating parameters, this work mainly focused on the catalyst and the catalytic reaction conditions. From a literature review (Dayton, 2002) it is evident that currently best available tar reforming process is based on a fixed bed nickel catalyst downstream of the gasifier. Thus, one selected commercial catalyst Ni/Al_2O_3 (C13-4, Süd-Chemie Catalysts Japan Inc., Ni

loading 20±2%) was tested at different temperatures and with different steam ratios according to the review (Devi et al., 2003). Other parameters, such as feedstock feed rate, pyrolysis temperature, combustion temperature, fluidization velocity of steam and air, bed material amount, pressure drop and circulation ratio, were tried to be kept in the same level. An animal-waste-derived biomass (named PC) with both water content and ash content of about 20 %, was used as fuel, whose characteristics are given in Table 1. Silica sand is used as inert bed material in the fluidized beds.

After the pyrolysis stage, the produced gas and tar pass through the catalyst bed, where the tar is converted to gas, together with some steam reforming and water shift reactions. The product gas composition is shown in Fig. 2 at different catalytic temperature. The increase of the H_2 content at higher catalytic temperature is due to the promotion of thermal cracking and steam reforming, and such cracking and reforming reactions produce hydrogen (Lv et al., 2004). Correspondingly, CH_4 and CO show the opposite trend because higher temperature promotes the endothermic reforming reaction of CH_4 and water gas shift reaction of CO.

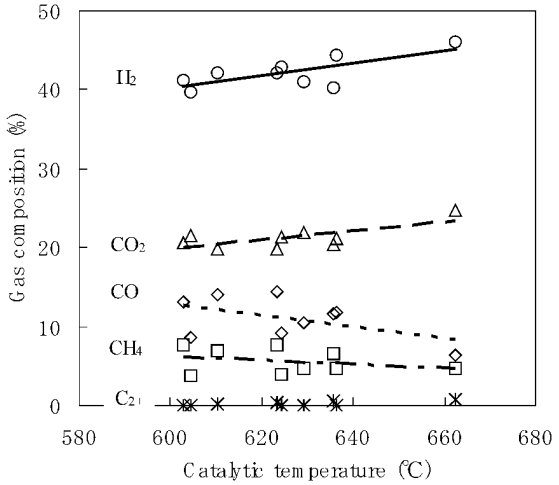

Fig. 2 Effect of catalytic temperature on product gas composition (Pyrolysis temperature: 666-691 ℃; Steam/ Carbon ratio: 0.9-1.2 mol/mol; Space velocity: 2154-2553 h^{-1})

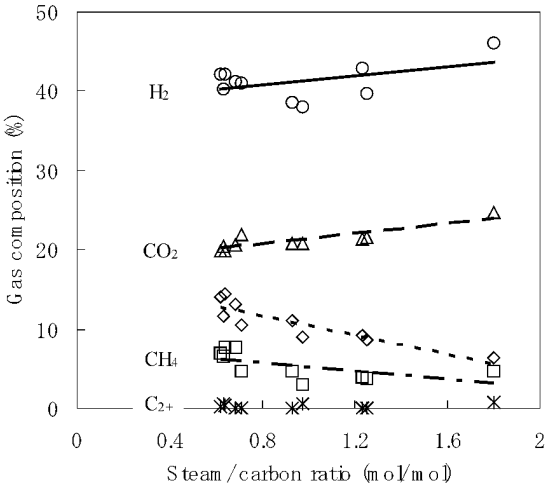

Fig. 3 Effect of steam/carbon ratio on product gas composition (Pyrolysis temperature: 666-691 ℃ ; Catalytic temperature: 610-636 ℃)

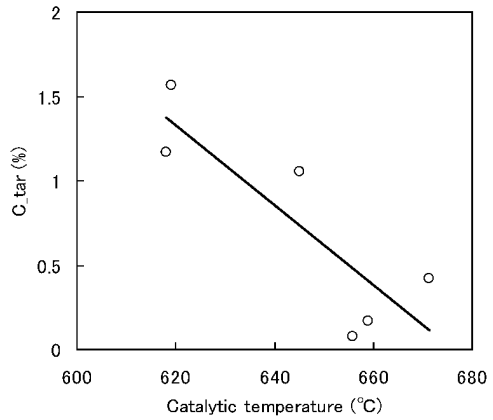

Fig. 4 Effect of catalytic temperature on C_tar (Pyrolysis temperature: 662-691 ℃ ; Steam/Carbon ratio: 0.5-0.7 mol/mol; Space velocity: 2390-2567 h^{-1})

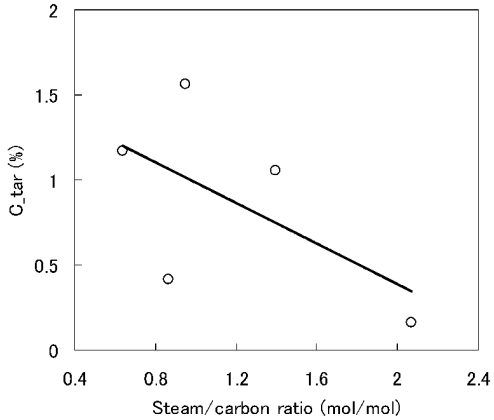

Fig. 5 Effect of steam/feedstock ratio on C_tar (Pyrolysis t emperature: 678-691 ℃; Catalytic temperature: 610-645 ℃)

The steam content in the raw gas is an important variable. For instance, when the tar present in such a gas is going to be destroyed with a catalyst bed, the effectiveness of such tar destruction depends on the steam content in the gas phase because it is an important reactant for tar removal reactions (Gil et al., 1997). Moreover, the steam also takes part in the steam reforming reaction of methane and the water gas shift reaction of carbon monoxide (Asadullah et al., 2002). That is why lower methane and carbon monoxide concentration, higher hydrogen and carbon dioxide are obtained at a larger steam ratio, shown in Fig. 3.

The tar content in the product gas is a very important data which indicates the gas quality and usefulness. The product condensates (water and tars, collected as liquids but in the gas phase in the gasifier) were analyzed by Total Organic Carbon Analyzer, as a preliminary estimation of the tar level. In this study, tar level is

evaluated by defining C_tar (carbon conversion from biomass to tar) as the index. Effects of catalytic temperature and steam ratio were investigated, shown in Fig. 4 and Fig. 5. The tar content is heavily dependent on the temperature. The reason for this effect is that the catalyst shows an increased activity at higher temperature (Aznar, et al., 1998). It can also be clearly observed that the C_tar is decreased from more than 1.5 % to 0.2 % with the steam ratio increasing because the steam directly takes part in the conversion of tar.

On an average, the tar content in the product gas was about 0.3 g/Nm^3. Above all, under good conditions, a time-averaged product gas of about 1.0-1.2 Nm^3/kg feedstock was obtained, with about 39-47 vol. % H_2, about 7-15 vol. % CO, 4-8 vol. % CH_4, 20-25 vol. % CO_2, and 8-10 MJ/Nm^3 LHV. The carbon conversion to product gas and the cold gas efficiency could reached above 65 % and 70 % respectively, revealing a hopeful prospect.

NI-LOADED BROWN COAL CHAR CATALYST

Catalyst improvement for biomass gasification

Although it can be concluded that gasification gas derived from biomass can be purified efficiently from tar with Ni/Al_2O_3 catalyst, there are still some problems that have not been completely solved so far, especially the economical feasibility. It is relatively expensive which increase the investment cost of the process. Thus, long lifetime is required for economical operation (Pferfer and Hofbauer, 2008). Unfortunately, Ni catalysts are gradually deactivated by the deposition of coke on the catalysts.

Several methods to enhance the catalyst lifetime have already been tried by many researchers (Sutton et al., 2001; Dayton, 2002; Devi et al., 2003). First, active materials are used as in-bed additive. These bed additives should be economically available, attrition resistant, and of course active and selective in terms of tar reduction. Among all additives used so far dolomite, olivine and char are important and there is need for further research to develop other cheap additives (Seshadri, 1998; Corella, et al., 1999; Rapagná, et al., 2000). Secondly, the use of a guard bed of inexpensive catalytic material upstream of a metallic catalyst bed has been demonstrated to improve the life of the metallic catalysts (Aznar et al., 1998). The inexpensive mineral catalyst converts many of the heavy tars, while the metallic catalysts serve to reduce tar concentrations to very low levels (Narváez et al., 1997). Calcined dolomites are the most widely used non-metallic catalysts for tar conversion (Caballero, et al., 2000). Thirdly, modifications of nickel catalysts by addition of promoters and supports have also been investigated (Promoter: K, Na, Li, Mg, Fe, Cu, Cr, La, Co, Mo, etc.; Support: Al_2O_3, ZrO_2, TiO_2, SiO_2, MgO, La_2O_3, CeO_2, CaO, olivine, dolomite, etc.) (Sutton et al., 2001; Dayton, 2002). There is one important point we need to pay attention to. Coke formation on nickel results from a balance between coke formation and gasification. In industrial operations, coke gasification is accelerated by the use of alkali or alkali containing supports. Magnesium and potassium based materials are mainly used. Zhang et al., (2004) focused on nickel based catalysts treated with alkali in an effort to promote steam gasification of the coke that deposits on catalyst surfaces.

Thus, this work is a part of the third method, which uses brown coal as the supported material. It is supposed to combine several advantages: (1) Lower catalyst cost (Le et al., 2009); (2) Catalyst activity of inherent alkali and alkaline earth metal (AAEM) species in brown coal in the steam reforming of tar (Hayashi et al., 2002); (3) Acceleration of coke gasification by AAEM species (Zhang et al., 2004). (4) Tar decomposition by the coal-derived char (Brandt, et al. 2000).

Catalyst preparation

The Ni-loaded brown coal char catalyst was prepared by ion exchange, whose procedure was introduced in detail by Le et al., (2009). Yallourn coal (Austrian brown coal, shorted as YL) was crushed, sieved to the desired particle size, and dried at 380 K for 12 h. The nickel addition to the coal matrix was achieved by ion exchange with a solution of basic hexa ammine nickel carbonate $(NH_3)_6NiCO_3$. The coal was mixed with the solution and distilled water for 24 h, and recovered by filtration. The recovered solid was washed and filtered again with distilled water. Then the washed solid was dried under N_2 flow at 380 K for 24 h, finally to Ni-loaded Yallourn coal (YL-Ni). Ni loading amount was 9 ± 1% and the specific surface area was 350 m^2/g.

Catalyst evaluation

A lab-scale fluidized bed gasifier was used to test the new catalyst, which included a sand fluidized bed (i.d. 53.5 mm) and a fixed catalyst bed. Detailed descriptions of the apparatus can be found in (Le et al., 2009). Woody biomass (Red pine, shorted as RP) was fed continuously at about 1.5 g/min for about 2 h, whose characteristics are given in Table 1. Steam and N_2 acted as gasification and fluidization agents. The nearly same

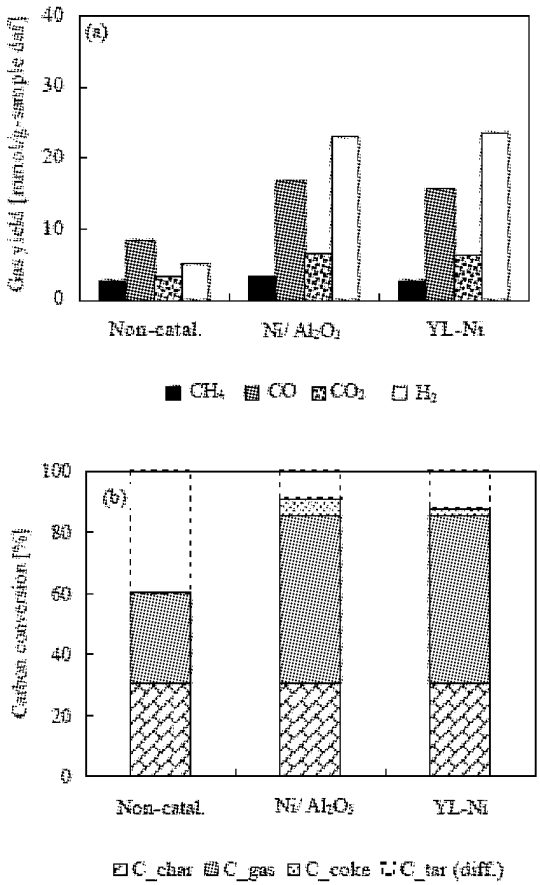

Fig. 6 Pyrolysis experimental results (Temperature: 650 ℃): (a) Gas yield; (b) Biomass carbon balance

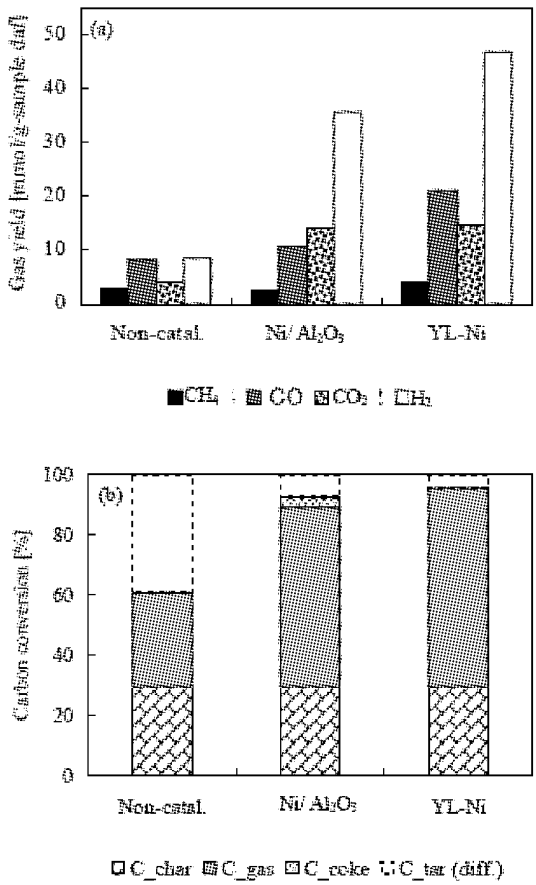

Fig. 7 Steam gasification experimental results (Temperature: 650 ℃; Steam/Carbon ratio: 0.9 mol/mol): (a) Gas yield; (b) Biomass carbon balance

reaction temperature, steam ratio and space velocity were chosen in comparison with Ni/Al_2O_3 catalyst which was used in section 2.2, as the reference catalyst.

Pyroysis experimental results (without steam feeding) are presented in Fig. 6. Both YL-Ni and Ni/Al_2O_3 have effective catalytic activity, with the similar gas yield, about 5 times H_2, about twice CO and CO_2 compared to those of non-catalyst. The carbon conversion to gas (C_gas) is calculated by "A/B×100%", where A represents the forming rate of carbon (CO, CO_2, CH_4, C_{2+}) in the product gas, and B represents the total carbon supplying rate of biomass. The carbon conversion to char (C_char) and coke (C_coke) are determined by the amount of gas (mainly CO_2) formed when combusting the char sample and catalyst sample after the gasification experiment. The carbon conversion to tar (C_tar) is defined as (100-C_gas-C_char-C_coke)× 100% (Asadullah et al., 2003). Coke formation is observed on the surface of both YL-Ni and Ni/Al_2O_3 (C_coke in Fig. 6 (b)), resulting in the loss of some active surface and gradual deactivation. That makes C_tar a littler higher in Fig. 6 (b). The trend can also be found in the gas yield variations over reaction time, shown in Fig. 8 (pyrolysis results). Then, steam was fed to test the catalyst activity of tar reforming, with the results shown in Fig. 7. Great improvement of gas yield and much lower C_tar are obtained in the case of YL-Ni, compared to Ni/Al_2O_3. The deposited carbon on the surface of LY-Ni could be gasified with steam, probably by the catalytic effect of AAEM species. And the steam reforming of tar is also promoted by nickel, char and AAEM species at the same time. The satisfactory results indicate the evidence of realizing the advantages of Ni-loaded brown coal char catalyst mentioned in section 3.1. There is still some contribution by the coal char gasification itself. Therefore, the carbon content in the fresh LY-Ni catalyst and the used LY-Ni were analyzed to calculate its own contribution to gas. Fig. 7 (b) is the carbon balance of only biomass, already distinguishing the carbon conversion to gas from the coal char. Highest C_gas and lowest C_tar are achieved using LY-Ni, indicating better performance than Ni/Al_2O_3.

Finally, Fig. 8 illustrates the variations of gas yield for YL-Ni in a 2-hour operation. All gas yields in steam gasification are much higher and more stable than those of pyrolysis. Steam acts a reactant not only for tar reforming reactions, but also for coke gasification, which is especially important to protect the catalyst from deactivation.

According to the lab-scale tests, LY-Ni seems to have a better ability and a hopeful prospect for stability

with coking resistance. Of course, further extended assessment of its lifetime is necessary.

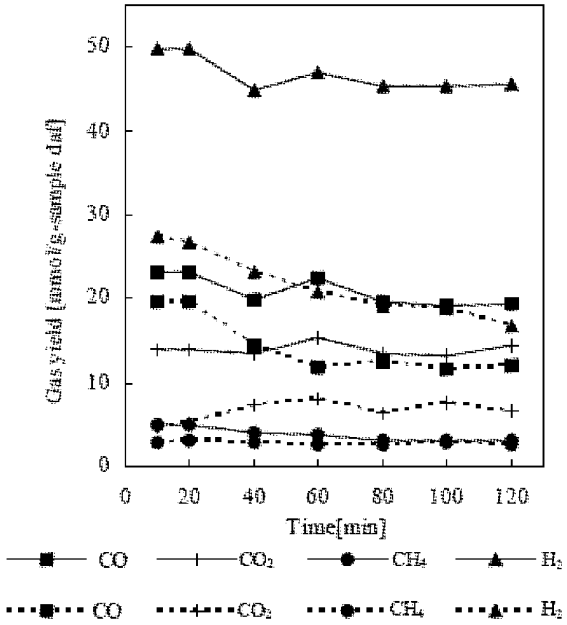

Fig. 8 Gas yield variations over reaction time (Catalyst: YL-Ni, Temperature: 650 ℃, Steam/ Carbon ratio: 0.9 mol/mol, Solid line: Pyrolysis, Dash line: Steam gasification)

CONCLUSIONS AND OUTLOOK

Although biomass gasification technologies are still under development they are expected to play a major role in future energy systems. ICFG design affords a multi-stage process for biomass and waste treatment, with high potential and several advantages. Bed material acts as the medium for char combustion and heat exchange by its internal circulation.

Improving gas cleaning technology is definitely important for the technical and economical feasibility of these processes. The combination of high-performance catalyst with fluidized bed reactor can provide a feasible system for hydrogen and syngas production from biomass at low temperature with high energy efficiency. Temperature and steam ratio have important roles on tar destruction.

The newly-developed Ni-loaded brown coal char catalyst has indicated a good activity of tar decomposition, gas quality improvement and catalytic stability. But there are still some uncertainties on the catalyst assessment. More and deeper research is needed to explore the optimum conditions of tar reforming, and to test the catalyst lifetime in long-term runs.

ACKNOWLEDGEMENTS

This work is supported by Prefecture Collaboration of Regional Entities for the Advancement of Technological Excellence, Japan Science and Technology Agency.

REFERENCES

Asadullah, M., Ito, S., Kunimori, K., Yamada, M., Tomishige, K.: J. Catal. 208 (2002), pp. 255-259.
Asadullah, M., Miyazawa, T., Ito, S., Kunimori, K., Tomishige, K.: Appl. Catal. A-Gen. 246 (2003), pp. 103-116.
Aznar, M.P., Caballero, M.A., Gil, J., Martín, J.A., Corella, J.: Ind. Eng. Chem. Res. 37 (1998), pp. 2668-2680.
Brandt, P., Larsen, E., Henriksen, U.: Energ. Fuel. 14 (2000), pp.816-819.
Caballero, M.A., Corella, J. Aznar, M.P., Gil, J.: Ind. Eng. Chem. Res. 39 (2000), pp. 1143-1154.
Corella, J., Aznar, M.P., Gil, J., Caballero, M.A.: Energ. Fuel. 13 (1999), pp.1122-1127.
Corella, J., Toledo, J.M., Molina, G.: Ind. Eng. Chem. Res. 46 (2007), pp. 6831-6839.
Dayton, D.: Report NREL/TP-510-32815, National Renewable Energy Laboratory, Golden (2002).
Devi, L., Ptasinski, K. J., Janssen F. J. J. G.: Biomass Bioenerg. 24 (2003), pp. 125-140.
García, L., Salvador, M. L,. Arauzo, J., Bilbao, R.: Energ. Fuel. 13 (1999), pp. 851-859.
Garíca-Ibañez, P., Cabanillas, A., Sánchez, J. M.: Biomass Bioenerg. 27 (2004), pp. 183-194.
Gil, J., Aznar, M. P., Caballero, M. A., Francés, E., Corella, J.: Energ. Fuel. 11 (1997), pp. 1109-1118.
Hayashi, J.-I., Iwatsuki, M., Morishita, K., Tsutsumi, A., Li, C., Chiba T.: Fuel 81 (2002), pp. 1977-1987.
Hayashi, J.-I. and Mae, K.: Proc. 17th Annual Int. Pittsburgh Coal Conf., Osaka (2004).

Hayashi, J.-I., Hosokai, S., Sonoyama, N.: Process Saf. Environ. Prot. 84 (B6) (2006), pp. 409-419.
Le, D.D., Xiao, X., Morishita, K, Takarada, T.: J. Chem. Eng. Jpn. (2009), at press.
Lv, P.M., Xiong, Z.H., Chang, J., Wu, C.Z., Chen, Y., Zhu, J.X.: Bioresource Technol. 95 (2004), pp. 95-101.
Narváez, I., Corella, J., Orío, A.: Ind. Eng. Chem. Res. 36 (1997), pp.317-327.
Pferfer, C., Hofbauer, H.: Powder Technol. 180 (2008), pp.9-16.
Rapagná, S., Jand, N. Kiennemann, A., Foscolo, P.U.: Biomass Bioenerg. 19 (2000), pp.187-197.
Seshadri, K.S.: Ind. Eng. Chem. Res. 37 (1998), pp.3830-3837.
Sutton, D., Kelleher, B., Ross J. R. H.: Fuel Process. Technol. 73 (2001), pp. 155-173.
Xiao, X., Morishita, K., Li, L., Le, D. D., Zhang, S., Takarada, T.: Circulating Fluidized Bed Technology IX (Werther, J., Nowak, W., Wirth, K-E., Hatge E-U., eds.), TuTech Innovation GmbH, Hamburg (2008), pp. 655-660.
Zhang, R., Brown, R. C., Suby, A., Cummer, K.: Energ. Convers. Manage. 45 (2004), pp. 995-1014.

Modling and Simulation

DEVELOPMENT AND VALIDATION OF A 3-DIMENSIONAL CFB FURNACE MODEL

Ari Vepsäläinen[1], Kari Myöhänen[2], Timo Hyppänen[2], Timo Leino[3], Antti Tourunen[3]

1 Research and Development Department, Foster Wheeler, Finland
2 Lappeenranta University of Technology, Finland
3 VTT Technical Research Centre of Finland

Abstract: At Foster Wheeler, a three-dimensional CFB furnace model is essential part of knowledge development of CFB furnace process regarding solid mixing, combustion, emission formation and heat transfer. Results of laboratory and pilot scale phenomenon research are utilized in development of sub-models. Analyses of field-test results in industrial-scale CFB boilers including furnace profile measurements are simultaneously carried out with development of 3-dimensional process modeling, which provides a chain of knowledge that is utilized as feedback for phenomenon research. Knowledge gathered by model validation studies and up-to-date parameter databases are utilized in performance prediction and design development of CFB boiler furnaces. This paper reports recent development steps related to modeling of combustion and formation of char and volatiles of various fuel types in CFB conditions. Also a new model for predicting the formation of nitrogen oxides is presented. Validation of mixing and combustion parameters for solids and gases are based on test balances at several large-scale CFB boilers combusting coal, peat and bio-fuels. Field-tests including lateral and vertical furnace profile measurements and characterization of solid materials provides a window for characterization of fuel specific mixing and combustion behavior in CFB furnace at different loads and operation conditions. Measured horizontal gas profiles are projection of balance between fuel mixing and reactions at lower part of furnace and are used together with both lateral temperature profiles at bed and upper parts of furnace for determination of solid mixing and combustion model parameters. Modeling of char and volatile based formation of NO profiles is followed by analysis of oxidizing and reducing regions formed due lower furnace design and mixing characteristics of fuel and combustion airs effecting to formation of NO furnace profile by reduction and volatile-nitrogen reactions. This paper presents CFB process analysis focused on combustion and NO profiles in pilot and industrial scale bituminous coal combustion.
Keywords: 3-dimensional CFB model, furnace profiles, combustion, NO_x model

INTRODUCTION

The complexity of the CFB furnace process and the large dimensions of commercial CFB units set challenges for the 3-dimensional CFB furnace process modeling. Generally agreement exists that development of microscopic CFD modeling approaches suffers from both lack and difficulty of having relevant measured validation data from industrial-scale CFB furnace operation and long calculation times. Another approach is macroscopic modeling with empirical or semi-empirical expressions to solve the furnace process with a coarser mesh and longer time step or in steady-state conditions. The model used for the present work solves the three-dimensional CFB furnace process in steady state condition using semi-empirical approach and it is based on original code developed in 1989 (Hyppänen et al., 1991).

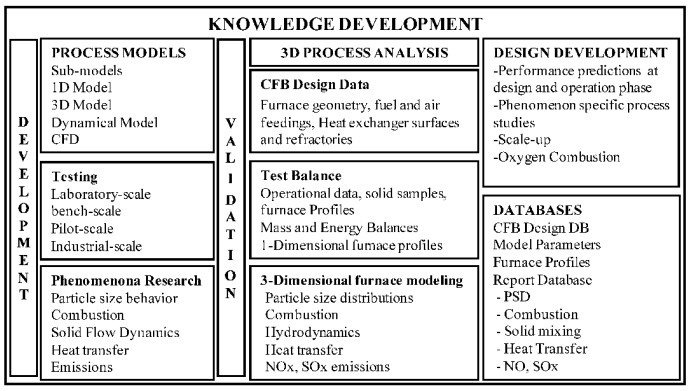

Fig. 1 CFB process knowledge development

The 3-dimensional CFB furnace model is a CFB process expert tool providing framework for testing and validating developed sub-models and theories, e.g. considering combustion and NO formation, against pilot and industrial scale test data with systematic approach. Knowledge gathered with CFB process analyses including 3D furnace modeling supports both CFB design development and operation phase optimization aspects (Fig. 1).

MODEL DESCRIPTION

The model solves the three-dimensional CFB furnace process in steady-state conditions using semi-empirical approach. Fig. 2 presents the general structure of the model. The different boundary conditions are defined directly from a boiler design tool. Furnace volume is discretized by hexahedral control volumes with typical cell dimensions 0.2...0.5 m and first-order upwind scheme is used as a solution method. Typical calculation time for grid sizes of 200 000 cells is 10-20 minutes for first calculation and less than 5 minutes for consequent calculations with minor modifications. The geometry and the location of the inlets and outlets are modeled as true as possible, given the limited density of the calculation mesh. Balance equations are defined for mass, momentum, species and energy for gas and solid phases. Empirical correlations govern various phenomena: solid concentration of different solids (char, ash, sand, limestone – all divided to six particle size fractions), mixing of solid and gaseous species by diffusion/dispersion, reaction rates, comminution and heat transfer. The validation of empirical correlations is based mostly on field tests at commercial units. The model principle and previous validation studies have been presented in earlier articles (Myöhänen et al.).

Combustion and NO_x models

Fig. 3 presents the principle of the fuel combustion model. Fuel particle is divided to char, volatiles, ash and moisture according to standard proximate analysis and to six particle size fractions in order to enable simulation of comminution and effects of particle size on reactions and flow dynamics. The elemental composition of char and volatiles are determined based on ultimate analyses of char and fuel of different fuel types. Volatile release rate is defined by correlation counting particle diameter and by coefficient depending on fuel type and temperature.

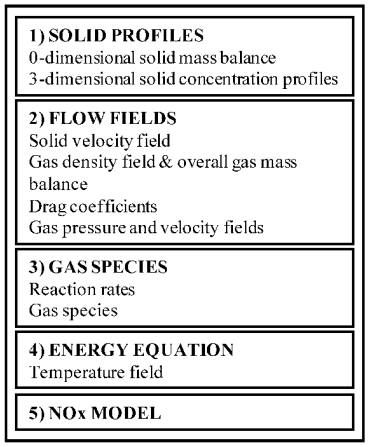

Fig. 2 General model structure

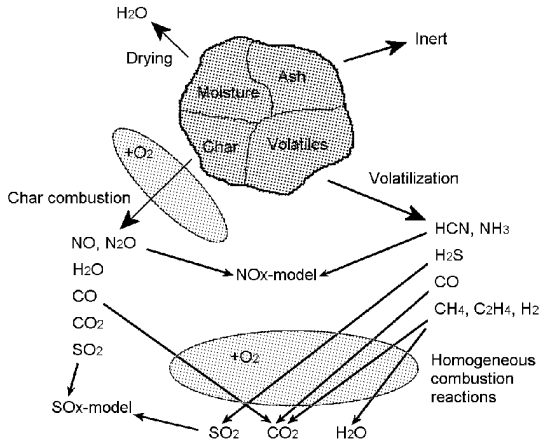

Fig. 3 Solid fuel combustion model

The formation of different gaseous species from devolatilization is modeled according to following principles: 1) nitrogen forms hydrogen cyanide (HCN) and ammonia (NH_3), 2) sulfur forms hydrogen sulfide (H_2S), 3) Oxygen forms carbon monoxide (CO) limited by the amount of carbon left, 4) excess oxygen forms molecular oxygen (O_2) and 5) remaining carbon and hydrogen form methane (CH_4), ethylene (C_2H_4), hydrogen (H_2) and free carbon (free-C) based on the molar ratio of H/C.

The split between the HCN and NH_3 is fuel specific and a correlation based on fuel O/C-ratio is used. The NO precursors (HCN and NH_3) are handled according to NO_x model reactions and the other formed gas species are combusted in the presence of oxygen according to combustion reactions (Table 1).

The local reaction rate is depending on the local concentrations of combusting gas, oxygen, water vapor, excess pressure and temperature. The reaction rate is calculated with a generic expression having empirical parameters. Reaction rate for carbon monoxide is

$$R'''_{CO} = k_{CO}\,[CO]^{aCO}\,[O_2]^{bCO}\,[H_2O]^{cCO}\left(\frac{p}{p_0}\right)^{pCO} e^{-E_{CO}/RT} \quad . \tag{1}$$

Table 1 Combustion and NOx reactions

No.	REACTION	No.	REACTION
	Volatiles	R4	$HCN + O_2 + NO \rightarrow N_2O$
1	$H_2S + 1.5\ O_2 \rightarrow SO_2 + H_2O$	R5	$2\ HCN + O_2 \rightarrow N_2O$
2	$CO + 0.5\ O_2 \rightarrow CO_2$	R10	$NH_3 + O_2 \rightarrow NO$
3	$CH_4 + 0.5\ O_2 \rightarrow CO + 2\ H_2$	R11	$NH_3 + O_2 + CaO \rightarrow NO$
4	$C_2H_4 + 0.5\ O_2 \rightarrow CH_4 + CO$	R12	$NH_3 + O_2 + Char \rightarrow NO$
5	$H_2 + 0.5\ O_2 \rightarrow H_2O$	R13	$NH_3 + NO \rightarrow N_2$
6	$C_{free} + 0.5\ O_2 \rightarrow CO$	R16	$N_{char} + O_2 \rightarrow NO$
	Char	R17	$2\ N_{char} + O_2 \rightarrow N_2O$
7	$C_{char} + (1-0.5\gamma)O_2 \rightarrow \gamma CO + (1-\gamma)CO_2$	R18	$N_{char} + O_2 + NO \rightarrow N_2O$
8	$S_{char} + O_2 \rightarrow SO_2$	R19	$NO + Char \rightarrow N_2$
9	$H_{char} + 0.25\ O_2 \rightarrow 0.5\ H_2O$	R20	$NO + CO + CaO \rightarrow N_2$
	NOx Reaction (incl. catalysts)	R22	$N_2O \rightarrow N_2$
R1	$HCN + O_2 \rightarrow NH_3$	R23	$N_2O + CaO \rightarrow N_2$

The char consists of C, H, S and N. The parameter γ in Table 1 (7) controls the CO/CO_2-ratio of carbon combustion. During combustion of char, the nitrogen forms NO and N_2O according to NO_x model. The other elements burn according to reactions in Table 1.

The NO_x reactions are solved after solution of the main furnace process. Fig. 4 presents the reactions paths of the current 3D CFB furnace NO_x model. The development of the new NO_x model for 3D-model is based on Foster Wheeler's 1D NO_x model. In the 1D model, NO_x reaction rate parameters have been empirically set by utilizing data and knowledge from test balances carried out at Foster Wheeler's commercial CFB units. The new NO_x model replaces the earlier model presented by Tsuo et al. (1995).

VALIDATION

Scope and principles

Foundation of current 3D model validation concept is based on horizontal CFB furnace gas and temperature profile measurements together with mass and energy balance back-calculations with 1D CFB furnace model - validated with hundreds of test balances - providing for example fractional semi-empiric solid and char density profiles and solid comminuting characteristics.

The validation scope of the 3-dimensional CFB furnace model considering specifically lateral mixing based on horizontal furnace profile measurements consists of eight large-scale coal combusting CFB boilers and several peat, wood, biomass and waste fired CFB boilers. Bituminous coal combustion characteristics have been most extensively researched and range of validations cover capacities up to $370MW_{th}$ and furnace depths of over 10m. Validations cover different operation conditions with full and lower load operation - unbalancing tests, air staging tests and co-combustion tests. Char and volatile release profiles with consequent combustion gas profiles are mainly determined by balance between fuel reactivity and mixing within constrains given by furnace design: anthracite tend to form even horizontal gas and temperature profile, lignite forms reductive zones above fuel feedings and combustion behavior of bituminous coal is between of those.

Horizontal shape and concentration level of oxygen, carbon monoxide and carbon dioxide is adjusted in 3D model validation calculations to correspond results of furnace profile measurements with combustion and solid mixing related validation parameters. Main validation parameters regarding combustion are char reaction rate, volatile release rate and CO reaction rate coefficient, which also consists micro-scale mixing limitation to reaction kinetics. Fractional char and volatile release profiles are formed according to relation of fuel mixing rate and reaction rate. Dispersion of fuel is defined with fractional char density related dispersion coefficients. Shape and level of vertical and horizontal temperature profiles are adjusted

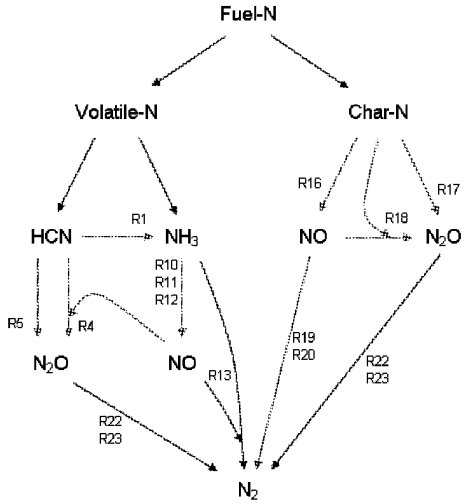

Fig. 4 NO_x reaction paths

with model parameters affecting to solid mixing by fractional solid dispersion coefficients and by estimating heat flux profile with internal circulation model parameters and heat transfer coefficients.

Fig. 5 presents validation parameters effecting to char mixing and reactivity for bituminous coals. Recently also several combustion test periods executed at pilot-scale CFB test rig have been analyzed. 3D furnace model analysis of bituminous coal combustion pilot and industrial scale test balances aiming both to model validation and detailed process characterization are here presented.

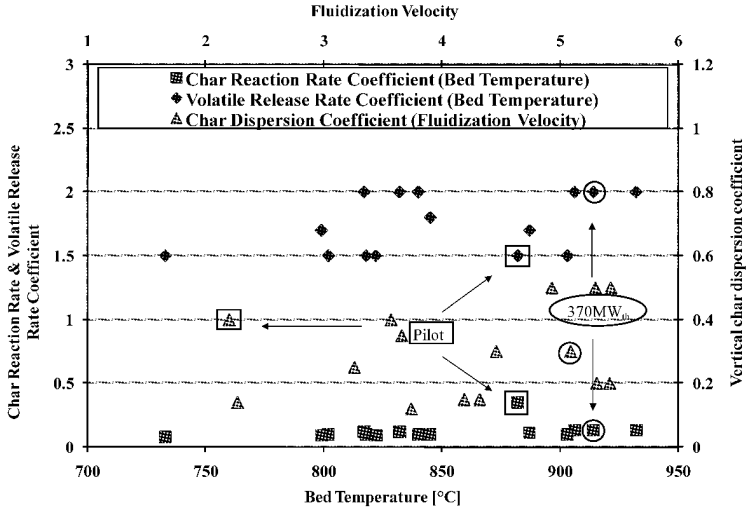

Fig. 5 Validated fuel dispersion (fluidization) and reactivity (temperature) parameters for bituminous coals

Pilot-scale CFB process analysis

VTT CFB pilot reactor (50 kW) described in detail in (Tourunen et al., 2008) is equipped with several separately controlled electrically heated and water/air cooled zones and three secondary air levels providing operation flexibility for controlling load and vertical oxygen and temperature levels independently.

Operational conditions of analyzed bituminous coal test balance are shown in Table 2. CFB Pilot reactor having 8 m riser height and 167 mm inner diameter was operated with 60% primary air ratio, 882°C bed temperature and 2.3m/s fluidization velocity. 3D-modeling approach for solid behavior characterization includes determination of both fractional solid and char density profiles. Total solid density profile is adjusted according to measured vertical pressure profile similarly to large-scale CFB boilers. Total solid loading was 4.3kg with solid density of 2.1kg/m^3 at dilute zone of reactor and 470kg/m^3 at dense bed area. Char density of 0.2kg/m^3 was measured from dense bed area and 0.003kg/m^3 from upper dilute zone of reactor. As a part of char mixing and combustion analysis modeled fractional char density profiles are compared and fitted with measurements as shown in Fig. 6b. Char and volatile combustion profile, solid mixing behavior and heating/cooling profile of furnace define the temperature profile (Fig. 6(a)) of reactor.

Table 2 Operational Conditions

	VTT Pilot	370MW$_{th}$ CFB	Operational Conditions	VTT Pilot	370MW$_{th}$ CFB
Fuel	Bit. Coal	Bit. Coal			
Proximate analysis			Furnace		
Moisture, w-%	9.5	20	Fluidization velocity, m/s	2.3	5.2
Ash (815C), w-%	13.8	5.5	Grid air ratio, %	60	62
Volatile content, w-%	30.9	42.8	Temperature: bed, °C	882	932
Ultimate analysis			Solid density exit,kg/m^3	2.1	2.4
C, w-%	72.9	69.7	Bed pressure, kPa	2.07	5.3
H, w-%	4.29	5.0	Stack		
N, w-%	1.27	1.33	NO, ppm-dry	135	49
S, w-%	0.78	0.92	CO, ppm-dry	806	79
O, w-%	6.94	17.55	O_2, %-dry	4.8	2.7
LHV-dry, MJ/kg	28.6	26.9			
Fuel size, D50	<0.5mm	1.6			

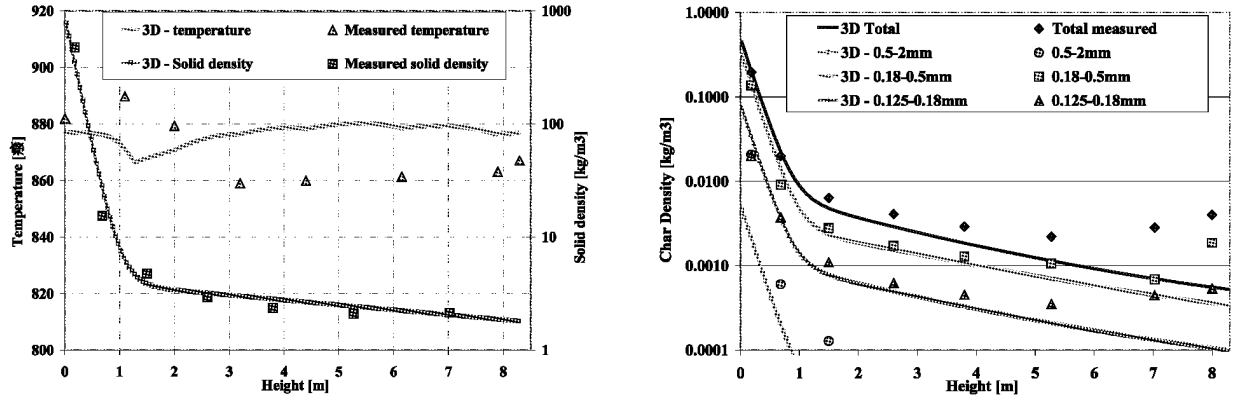

Fig. 6 (a) Temperature and solid density profiles (b) Fractional char profiles

Fig. 7 shows comparison of measured and modeled vertical combustion gas profiles and followed NO formation analysis with profile measurements of nitrogen compounds and NO model. Preliminary fit for NOx model parameters used earlier in NOx modelling of large-scale CFB furnace was here done based on experiments focused on effect of temperature and oxygen level to NO formation (Tourunen et al., 2008). In future empirical NOx model parameter study combined to bench and pilot scale testing is required for further development of NOx prediction capability.

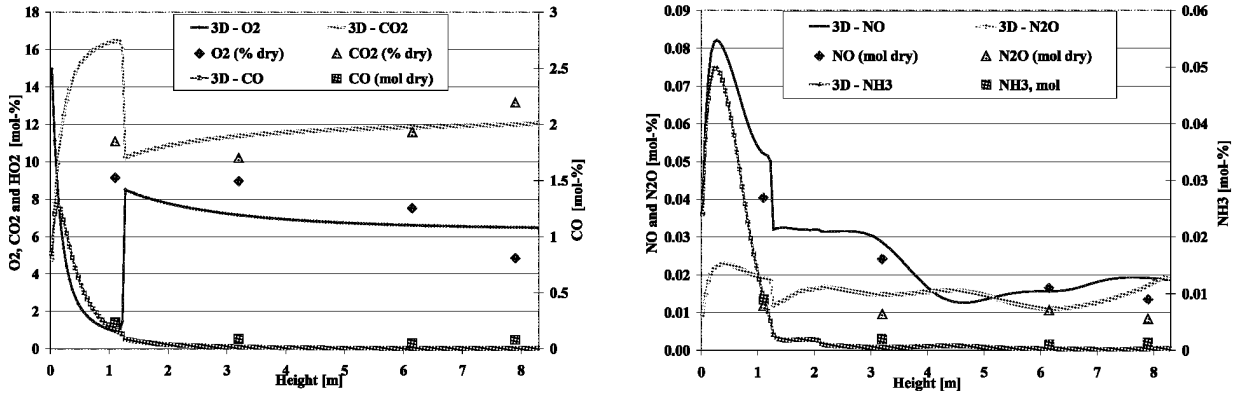

Fig. 7 Combustion (a) and NO (b) modeling of bituminous coal combustion at CFB Pilot

Stabilization of N-compound concentrations as well as combustion gas concentrations is both measured and modeled at upper parts of reactor, while conditions in dense bed area and in influence of secondary air mixing and reaction zone are mainly determining combustion and nitrogen chemistry related reaction rates, thus determining the levels of gas compound concentrations at upper part of reactor. Behavior is analogous for larger scale CFB furnaces and in future profiles are measured also at dense bed area.

Bituminous Coal Combustion in a Large-scale CFB Boiler

Results of 3D furnace model validation analysis of one bituminous coal test balance in 370MW$_{th}$ CFB boiler are presented. Investigated CFB furnace has 40.5m height and 15.9m x 7.8m cross-section with six fuel feedings located at two opposite walls and 24 secondary air nozzles at 2.5m above grid. CFB boiler is operated with 100% load, 62% grid-to-total air-ratio, 5.2m/s fluidization velocity and 932°C bed temperature. Combusted coal has relatively high volatile, 43% on dry basis, and low ash content, 5.5% on dry basis. Main operation parameters and fuel analysis are summarized in table 2.

Furnace profile measurements show increased CO and low O_2 concentrations above fuel feedings at horizontal cross-section 10m above grid, while adjacent measurements above related secondary air nozzles shows low CO and respectively high O_2 concentrations. Similar combustion gas profile shapes and concentration levels were achieved by 3D furnace model process and validation analysis including predicting fractional char mixing and reactivity, volatile release profiles and both mixing and reactivity of gases species. High CO concentrations are modeled in front of fuel feedings from dense bed area to SA nozzle level. Secondary air fed to this region of intensive volatile release combusts CO at SA jet influence area and further CO reactions controlled by macro and micro scale gas mixing taking place in upper parts of furnace reduce CO concentration with much lower gradient.

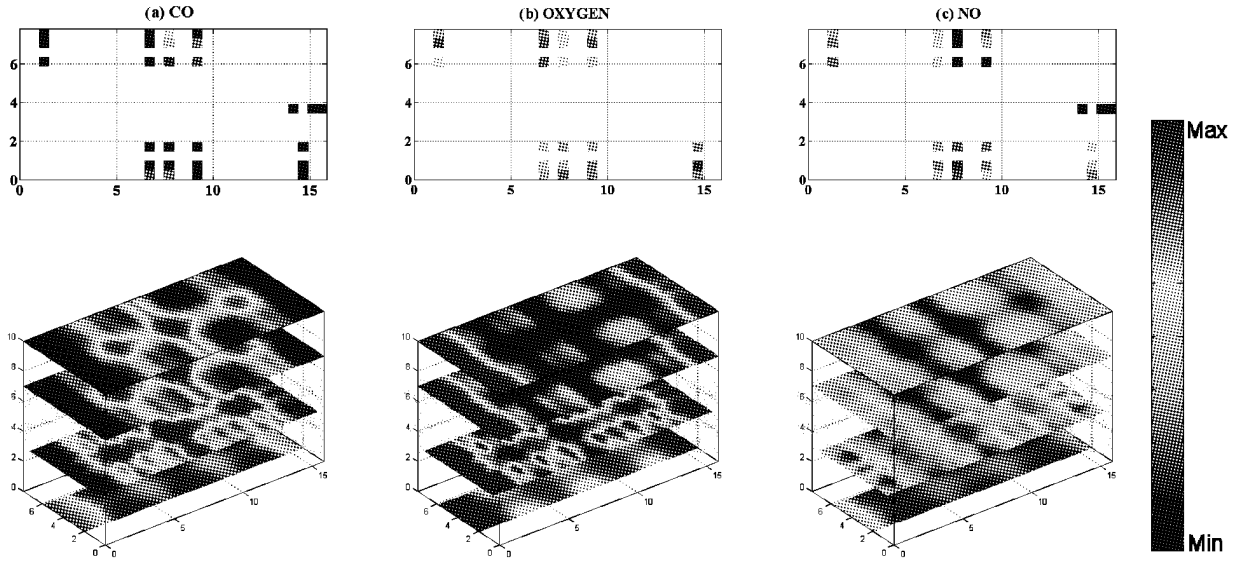

Fig. 8 Measured (10m) and modeled (a) CO, (b) oxygen and (c) NO concentration profiles

Basis for NO_x model post-calculation is provided by predicted char density, oxygen, carbon monoxide and temperature profiles. Fig.6 presents comparison of measured horizontal profiles and modeled formation of NO concentration profile in lower furnace. Similar NO profile shape is achieved with NO_x model as measured in horizontal cross-section 10m above grid. High NO concentrations are both modeled and measured above SA nozzles next to fuel feedings, while reductive char and CO rich conditions above fuel feedings resulted lower modeled NO concentrations shown also by the measurements.

CONCLUSIONS

3-dimensional furnace model is part of overall CFB process know-how development carried out by testing, modeling and analyzing in different scales: from laboratory-scale analyses to field tests at large-scale industrial CFB boilers. Sub-models are continuously further developed, and here principle of combustion model and updated NOx model was presented. Reactions and parameters of implemented NOx model are based on 1-dimensional NOx model that has been validated against hundreds of test balances carried out in CFB boilers firing different types of fuels.

3D CFB furnace model is validated against several steady-state test balances carried out in industrial-scale CFB boilers combusting different types of coals and biomass regarding combustion and solid mixing characteristics. Horizontal furnace profile measurements being part of the process analysis have provided information on lateral mixing, which is one of the key factors concerning scale-up of CFB boilers. Additionally presented NOx model has been utilized for NO profile formation analyses of several coal-fired CFB boiler furnaces. Recently results of pilot-scale experiments are utilized in 3D furnace model validation and pilot characterization. Focus has been on formation of combustion and NO profiles due fuel and operating condition specific char and volatile profiles.

Vertical and lateral combustion gas profiles and temperature profiles can be predicted also for design phase CFB boiler furnaces. Prediction of NO formation requires pre-modeled 3-dimensional char density, volatile release and temperature profiles and combustion gas profile with its reductive and oxidizing regions to be comparable with real process conditions. With current NOx model formation of volatile and char based nitrogen compounds can be simulated and comparison with horizontal gas profile measurements in case of bituminous coal combustion in large-scale CFB boiler showed that similar NO profile shape can be achieved by NOx model implemented to 3D CFB furnace model.

ACKNOWLEDGEMENTS

This paper includes results from work carried out with a financial grant from the Research Fund for Coal and Steel of the European Community (Contract No. RFCR-CT-2005-00009).

REFERENCES

Hyppänen, T., Lee, Y.Y. and Rainio, A.: Proceedings of the 11th Int. Conf. on FBC (Anthony, E.J., ed.). ASME, New York

(1991), pp. 439-448.
Tsuo, Y.Y.P., Lee, Y.Y., Rainio, A. and Hyppänen, T.: Three-dimensional modeling of N2O and NOx emissions from circulating fluidized bed boilers. Proc. of the 13th Int. Conf. on Fluidized Bed Combustion, ASME (1995), pp. 1059-1069.
Myöhänen K., Hyppänen T., Miettinen J. and Parkkonen R.: Three-Dimensional Modeling and Model Validation of Circulating Fluidized Bed Combustion, Proceedings of the 17th Int. Conf. on FBC (Pisupati, S.V., ed.), ASME Jacksonville (2003).
Myöhänen K., Hyppänen T. and Loschkin M.: Circulating Fluidized Bed Technology VIII (Kefa Cen, ed.). International Academic Publishers, Beijing (2005), pp. 306-312.
Myöhänen, K., Hyppänen, T. and Vepsäläinen, A.: SIMS 2006 Proceedings of The 47th Conference on Simulation and Modelling (Juuso, E., ed.), Finnish Society of Automation, Helsinki (2006), pp. 194-199.
Tourunen, A., Saastamoinen, J., Nevalainen, H.: Experimental trends of NO in circulating fluidized bed combustion. Submitted to Fuel, 2008.

A SIMPLIFIED MODEL FOR THE BEHAVIOR OF LARGE BIOMASS PARTICLES IN THE SPLASHING ZONE OF A BUBBLING BED

Anders Brink, Oskar Karlström, Mikko Hupa

Faculty of Inorganic Chemistry, Åbo Akademi University, Turku, Finland

Abstract: A model for the behavior of biomass particles in the splashing zone of a bubbling bed has been developed. The model is intended for use in CFD studies of bubbling beds, where it provides a way of modeling particle dispersion in the splashing zone. In the model, particles landing on the bed surface are assumed to reenter the splashing zone. Two initial velocities are used for the reentering particles: one represents particles landing on bursting bubbles and one for the emulsion phase. The fraction of the bed consisting of bubbles is calculated using standard expressions from the literature. The re-entering velocity of fuel particles from the bubbles is set such that the flight trajectory reaches the typical height of the splashing zone. The velocity from the emulsion phase is assumed to be of the order of the fluidization velocity. In both cases the initial direction of the trajectory is allowed to take random values. Using these simple assumptions an approximation of the logarithmic material distribution in the splashing zone is achieved.

Keywords: CFD, bubbling bed, splashing zone

INTRODUCTION

Fluidized bed combustion – FBC - of biomass is becoming a more and more important alternative for energy production. Today, the two main FBC technologies are circulating fluidized beds – CFBC - and bubbling fluidized beds – BFBC - (Hupa, M., 2007). A significant amount of research has been done on FBC of biomass. Frequently, modeling of FBC is pointed out to be extremely important as a tool for designing, understanding and optimizing FBC-processes (e.g. Ravelli, S. et al., 2008). Models for FBC can roughly be divided into one-dimensional models and multi-dimensional models.

In literature, numerous studies have been presented on one-dimensional FBC-models. Scala et al. (2002) have presented a comprehensive one-dimensional model of a bubbling fluidized bed for high-volatile fuels. In the study, the combustor is divided into a bed region, a splashing region and a freeboard region. Output variables are, among other, fraction of volatile matter burned in the three regions, oxygen concentration of the emulsion phase of the bed, total combustion efficiencies of the bed and the splashing zone temperature. In spite of the successful modeling results, the authors argue for a need for lateral, in addition to axial, non-uniformities, such as uneven fuel spreading across the combustor. Thus, there is need for three-dimensional FBC-models, which also other authors point out (e.g. Ravelli, S. et al., 2008).

Computational fluid dynamic-based modeling of bubbling beds is usually restricted to the freeboard region of the combustor. The complicated fluid dynamics in the bed and in the splashing zone is usually transformed into a simple boundary condition. Using such an approach, the release of volatiles and the char burn out has to be included in the boundary condition. The simplest approach is to assume the fuel is converted equally throughout the whole bed. Then, an equilibrium approach can provide the product gas composition from the bed. This approach is not very sophisticated, since it does not take into account the design of fuel feeding to the boiler. A slightly modified approach is to presume the landing areas of the fuel (Lundmark, D, 2002, Saario, A, 2008). It is then usually assumed that the volatile part of the fuel is released from the landing areas, whereas the products from the char conversion are released in the rest of the bed. Also this approach relies heavily on the assumptions used by the modeler; no clear guidelines for how to determine the landing areas have been presented. A slightly more sophisticated approach presented by Mueller at al. (2005) is to model the trajectories of the fuel particles from the fuel chutes until they reach the bed. In this way, entrainment of small particles can also be accounted for, and the landing is no longer determined in an arbitrary way. The problem with this approach is that most large fuel particles will land in almost exactly the same spot. Assuming instantaneous drying on the bed surface then easily results in unrealistically cold spots on the bed surface.

In this work, a modification of the last approach is proposed. Here, the trajectories are not terminated when the fuel particle reach the bed surface. Instead, a model is put forth that describes the behavior of the fuel particle in the splashing zone. Although this model too is a simplification, it offers a way to obtain a more realistic description of the fate of the particle after reaching the bed. The model is based on a simplification that the bed can be divided into a part consisting of bubbles and an emulsion phase. It is assumed that the particles hitting a bubble will be ejected into the splashing zone with a certain characteristic velocity. If the particles

reach the emulsion phase, it will reenter the splashing zone with a velocity characteristic of this part of the bed. In this way the particle trajectories can be continued, resulting in a dispersion of particles on the bed surface. This model does not longer rely on the modeler defining the release region, and the cold spots connected with the assumption that the trajectories are terminated when the particle hit the bed are avoided.

SPLASHING ZONE FUEL PARTICLE MODEL

Modeling fuel particle trajectories in the splashing zone is necessary for understanding the fuel particle dispersion in the region. Understanding the dispersion is important in order to model the devolatilization and the drying correctly. It has been found that large parts of the devolatilization take place in the proximity of the bed surface in BFBC (e.g. Scala et al. (2002)). Therefore, a reasonable assumption is that also the drying takes place close to the bed surface. A rigorous description of the fate of a fuel particle in a bubbling bed cannot be incorporated into a present-day CFD study of an industrial scale FBC. The alternative is to describe the bed, and the processes inside it, using boundary conditions. The boundary conditions can, e.g., describe the flow from the bed surface, including, velocity profile, temperature profile, and species profiles. The problem with such an approach is that it is difficult to take the fuel injection system into account. Modeling particle trajectories starting from the fuel chutes and terminating them when reaching the bed surface does not significantly improve the situation since most of the large fuel particles will land in approximately the same region.

One alternative is to develop a model describing the dispersion of fuel particles on the bed. Since the fluid dynamics is complicated, simplifications are required. In this study, it is assumed that the fuel particles have a much lower fluidization velocity than the bed material. It is then argued that this results in that the fuel particles mainly can be found in the splashing zone. To further simplify the situation, the same model that is used to describe the particle conversion in the free board is also used in the splashing zone. This is probably a rather rough description, since in the presently used model fragmentation of particles and attrition are not taken into account. Neither is the enhanced heat transfer due to the interaction with bed particles. To describe the movements in the splashing zone it is assumed that the fuel particles reenter the splashing zone, from the top of the bed surface. Two distinct initial velocities are given in the bed, one assigned if the fuel particle originates from a part of the bed characterized as bubbles, and one if the particle originates from the fraction of the bed characterized as the emulsion phase. This approach was presented by Mann, I. (2006) in a model for calculating the entrainment of bed material in a bubbling bed.

The necessary model parameters can be viewed as purely empirical. If the dispersion rate can be determined experimentally, it would be possible to use the results tuning the model. Until then, these parameters need to be based on some simple assumptions. The first parameter needed is the probability that the particle land on a bubble. This parameter, taken as the fraction of the bed consisting of bubbles, can be estimated using the simple two-phase model of Toomey and Johnstone (1952):

$$\delta = \frac{u_0 - u_{mf}}{u_B - u_{mf}}$$

where u is velocity, indexes B is bubble, 0 is superficial and mf is minimum fluidization velocity. This equation is identical that for the fraction of the bed in fast bubbles in the K-L model (Kunii and Levenspiel 1991).

The initial velocity of the particles re-ejected into the splashing zone from a bubble can be estimated to be of the same order as the velocity of the bed material thrown into the splashing zone as the bubble burst. This velocity can vary depending on from which part of the bubble this material originates. E.g., George and Grace (1978) provide a way to estimate this velocity. Here it is assumed that this velocity is approximately three times the fluidization velocity. This value was chosen because it provides a realistic height of the splashing zone. The initial direction of the fuel particle can also be estimated assuming that the bursting bubble is the cause for the fuel particle being thrown into the splashing zone. Here, it is assumed that the bubble burst when is can be viewed as a hemisphere. In this way, the initial direction can be in any positive angle away from the bed surface. A similar assumption is made for the particles reentering the splashing zone from the emulsion fraction of the bed. Here the particles are assumed to have an initial velocity similar to the minimum fluidization velocity of the bed material following the simple two-phase model of Toomey and Johnstone (1952).

RESULTS AND DISCUSSION

To test the model two types of simulations are carried out. The first type is calculations with inert particles. In these calculations the drag force is neglected. Figure 1 shows the distribution of particles on the bed 30

seconds after being released from the center of the computational domain. The figure shows that the particles have moved away from the release point. Plotting the number of particle as a function of distance from the release point and normalizing the area under the curve to unity results in distributions such as that presented in Figure 2. The fraction of particles between x and $x+dx$ is now given by $E dx$. In a similar way, Figure 2 shows the distribution of particles 1, 5, 10 and 30 seconds after being released on the bed. Figure 3 shows the vertical distribution of particles in the splashing zone according to the model. In the figure the particles being released from the bubble phase and the emulsion phase can be separated. Nevertheless, the vertical distribution can approximately be described with a logarithmic function. From the figure the height of the splashing zone can also be read. Since this model is based on a highly simplified view of the phenomena in the bed, the initial velocity of the particles originating from the bursting bubble phase could alternatively be determined such that a correct height of the splashing zone is obtained.

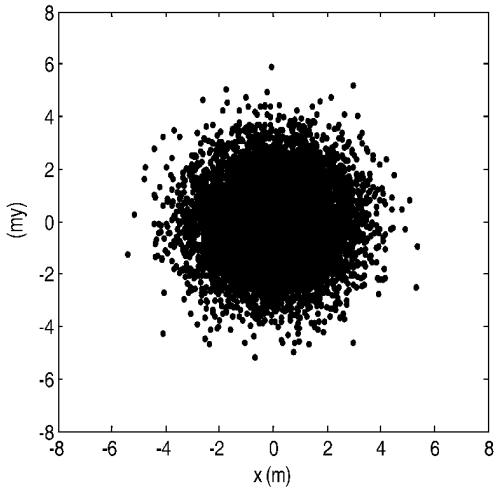

Fig.1 Horizontal distribution of particles 30 seconds after a simultaneous injection, starting point: x=0, y=0

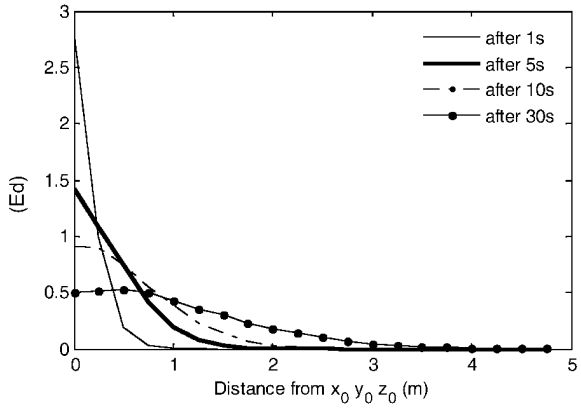

Fig. 2 Distribution of particles as function of the distance from the starting point. 30 % of the bed surface consists of bursting bubbles

Figure 4 shows the influence of changing the probability of the bubble phase from 0.3 to 0.5. In this case, the fuel particle dispersion rate is approximately 10 percent higher. The height of the splashing zone is still the same, but the vertical distribution of fuel particles in the splashing zone has changed. Now, the probability of finding a particle in the upper part of the splashing zone has increased. Nevertheless, these calculations demonstrate how to calibrate the model if experimental data are available.

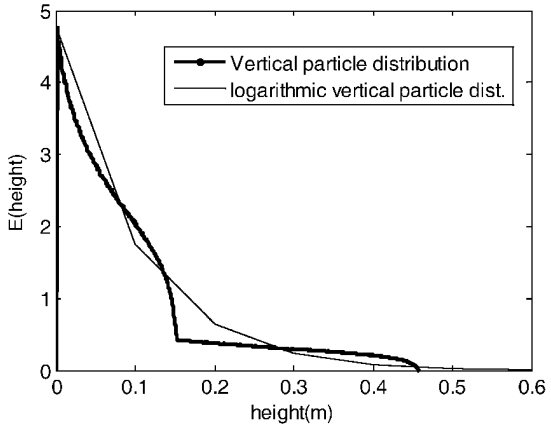

Fig. 3 Vertical particle distribution as function of height above the bed surface

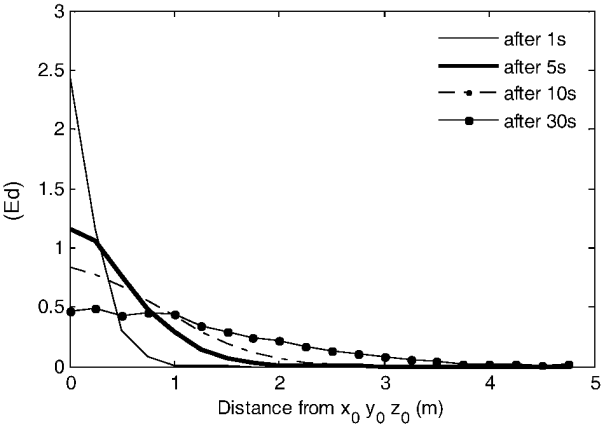

Fig. 4 Distribution of particles as function of the distance from the starting point. 50 % of the bed surface consists of bursting bubbles

Figure 5 shows a CFD calculation of the surface temperature of a 5 mm wood particle injected from a fuel chute and moving in the splashing zone. The fuel particle trajectory has been terminated after 60 seconds. The figure shows that the particle moves a significant distance before drying is completed. When drying is completed the particle surface temperature is heated up during the devolatilization stage. When the devolatilization stage is ended, the char combustion stage starts. During this stage the particle temperature

reaches approximately 1400 K.

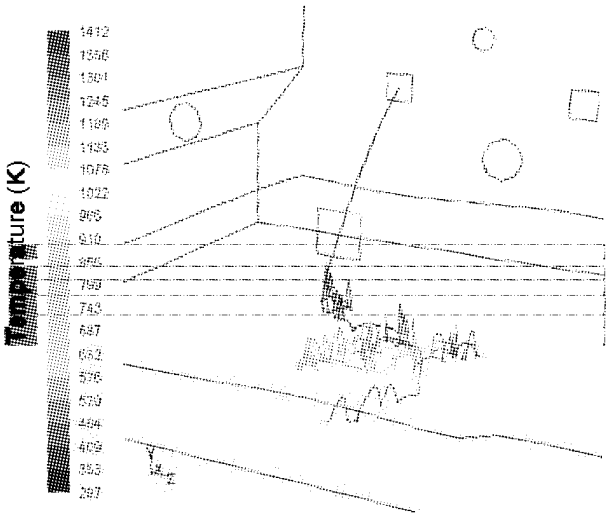

Fig. 5 Trajectory of a 5 mm wooden particle in the splashing zone

CONCLUSIONS

A model that can be used to model the fuel particle dispersion in the splashing zone has been presented. The model is based on a highly simplified view of the fluid dynamics in the bed. The model has three parameters that can be calculated from simple bubbling bed theory. The model can easily be incorporated in CFD models, since it acts as boundary condition for fuel particles on the bed. Compared to other simple models, the model has the advantage that the users do not need to define landing regions. Also cold spots on the bed due to most particles drying in the same spot can be avoided. The tradeoff using the model is an increased computational cost associated with modeling fuel particles.

ACKNOWLEDGEMENTS

This work has been carried out within the frame of the Nordic Graduate School in Biofuel Science and Technology-2 and the project ChemCom 2.0 as part of the activities of the Åbo Akademi Process Chemistry Centre. Funding by the Nordic Energy Research, the Academy of Finland in their Centres of Excellence Program, National Technology Agency of Finland and industrial partners Andritz Oy, Metso Power Oy, Oy Metsä-Botnia Ab, Foster Wheeler Energia Oy, UPM-Kymmene Oyj, Clyde Bergemann GmbH, International Paper Inc is gratefully acknowledged.

REFERENCES

George, S.E., Grace, J.R.: A.I.C.H.E Symposium Series 176, (1978).

Hupa, M.: Advanced Combustion and Aerothermal Technologies (Syred, N., Khalatov, A., eds), pp. 87-101, 2007.

Kunii D., Levenspiel, O., Fluidization Engineering, 2nd edition. Butterworh-Heineman.

Lundmark, D.: Fly ash behaviour in a fluidized bed boiler co-firing peat and biomass – a CFD study, M.Sc. thesis, Åbo Akademi Univerity, Finland, 2002.

Mann, I.: Model describing mixing of solids and gases in the near-bed region of a bubbling fluidized bed, M.Sc. thesis, Åbo Akademi Univerity, Finland, 2006.

Mueller, C., Brink, A., Hupa, M.: Numerical Simulation of the Combustion Behavior of Different Biomasses in a Bubbling Fluidized Bed Boiler, 18th International Conference on Fluidized Bed Combustion, 2005.

Ravelli, S., Perdichizzi, A., Barigozzi, G.: Energy and Comb. Sci. 34 (2008), pp. 224-253.

Saario, A.: PhD-thesis, Tampere University of Technology, http://webhotel.tut.fi/library/tutdiss/pdf/saario.pdf, 2008.

Scala, F., Salatino, P.: Chem. Eng. Sci. 57 (2002), pp. 1175-1196.

Toomey, R.D., Johnstone, H.F.: Chem.Eng.Prog. 48 (1952), pp. 220-226.

HYDRODYNAMIC MODEL WITH BINARY PARTICLE DIAMETERS TO PREDICT AXIAL VOIDAGE PROFILE IN A CFB COMBUSTOR

J. J. Li, H. Zhang, H. R. Yang, Y. X. Wu, J. F. Lu, G. X. Yue

Key Laboratory for Thermal Science and Power Engineering of Ministry of Education, Department of Thermal Engineering, Tsinghua University, Beijing, 100084, China

Abstract: A hydrodynamic model with binary particle diameters was developed to better predict axial voidage profile in a CFB combustor. In the model, the CFB is regarded as a superposition of two sub-beds, a fast fluidized bed in the upper riser with a characteristic particle diameter of 0.2mm and a bubbling fluidized bed or turbulent bed in the bottom riser with a characteristic particle diameter of 2mm. Furthermore, a variable critical particle diameter whose terminal velocity equals to the superficial gas velocity was employed to determine which flow regime the particle belongs to. The results show that binary particle diameter model has the advantages in describing wide particle diameter distribution while reducing the complexity of computation. The model was verified by the field data of voidage profile in a 300MW CFB boiler.

Keywords: CFB boiler, hydrodynamics, binary particle diameters, voidage profile

INTRODUCTION

Voidage profile is one of the most important flow behaviors in CFB (circulating fluidized bed) boiler simulation. In development of the CFB power plant simulators, modeling method of the pulverized coal fired system are inherited, and thereby CFB combustor is regards as a cell with even operating parameters, ignoring the pressure and temperature distribution. In these models, bed materials are mostly with a single particle diameter. This kind of assumption facilitates the computational speed but loses the function of describing distributed parameters, which correspond to data in practical operation. A more elaborated model with high computational speed needs to be developed.

In conventional hydrodynamic models (Hannes et al., 1995), the bed materials with wide particle size distribution are graded into several internals, each of which takes a certain value of particle diameter as its characteristic particle diameter. In numerical calculation, the whole CFB is regarded as a combination of several sub-beds marked by their characteristic particle diameters. Iteration is required to calculate the voidage profile in each sub-bed. The corresponding models are often called elaborated models. Although these models are in favor of detailed description of hydrodynamic behavior, more than 10 sub-beds usually need to be considered because of the wide particle diameter distribution in CFB furnace. This may cost much time in iteration. The computational complexity limits the availability of elaborated hydrodynamic model. Especially, in real-time simulation of CFB boiler system, the hydrodynamic model should be simplified in order to speed up the numerical computation.

According to the State Specification Design Theory of a CFB boilers (Yue et al., 2005), the flow pattern in a CFB combustor is the superposition of a fast fluidized bed consisting of fine particles and a bubbling or turbulent fluidized bed consisting of coarse particles. Based on the hydrodynamic characteristics, the bed materials in CFB combustor can be divided into to two types of solid particle - coarse particles at the bottom and fine circulating particles. Figure 1 shows the typical particle size distribution in a CFB combustor. Using the grading method of elaborated models, the bed materials are categorized into two internals with different diameter - 2mm and 0.2mm respectively (Yu, 1989). Consequently, two sub-beds, a fast bed of fine particles and a bubbling or turbulent bed of coarse particles, are considered in this simulation. Based on this idea, hydrodynamic model of binary particle is developed.

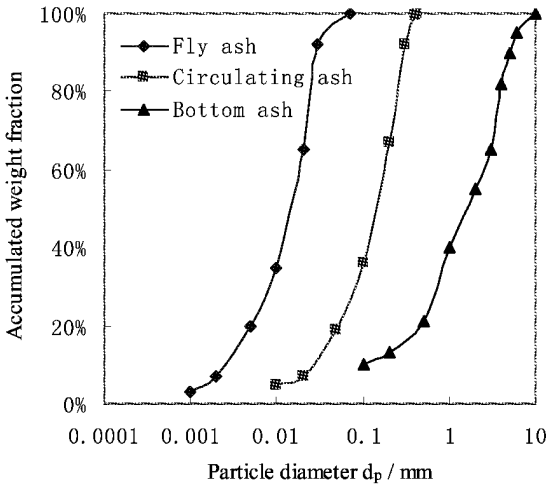

Fig. 1 Typical particle size distribution of bed materials in circulating fluidized bed

MODELING

S-type voidage profile

The primary difference between a CFB and a bubbling bed with fly ash recirculation is that flow regime in the upper CFB combustor is not freeboard elutriation but a fast fluidized bed (Yue et al., 2005). Li et al. (1979) studied on axial voidage profile in a fast fluidized bed using 5 kinds of solid particles and found that the axial voidage profiles were in S-shape And there are 3 kinds of S-type curves, according to different the height of curve inflexion, z_i. Shown in Fig. 2, normally, a complete S-shaped, i.e., Type 2 profile exists. When z_i is too high or too low, the profile is in Type 1 and 3 respectively.

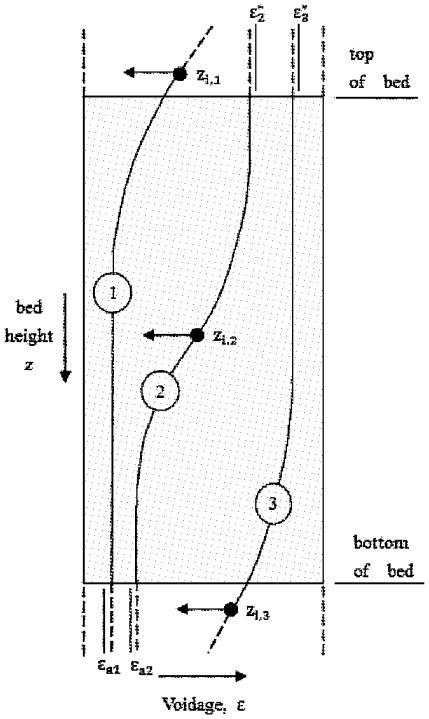

Fig. 2 S-type voidage profile (Li et al., 1980)

In a stable state, the mathematical expression of S-type voidage profile can be written as (Li et al., 1980)

$$\ln\left(\frac{\varepsilon-\varepsilon_a}{\varepsilon^*-\varepsilon}\right)=-\frac{z-z_i}{Z_0} \tag{1}$$

Where, ε^* and ε_a are the asymptotic values of voidage at the top and bottom of combustor respectively. Z_0, called the characteristic length, is in the unit of length.

$$Z_0=\frac{\xi\rho_s}{\omega\left(\rho_p-\rho_g\right)}\cdot\frac{\varepsilon-\varepsilon_a}{\varepsilon^*-\varepsilon} \tag{2}$$

Where, ξ and ω are the fraction constant of upgoing and downgoing particles, ρ_p are ρ_g the densities of particle and fluid.

The key parameters, ε^*, ε_a, Z_0 and z_i are functions of geometric properties and operating conditions. Kwauk et al. (1980) correlated their experimental data and gave the empirical formula for these four parameters as follows.

$$1-\varepsilon_a=0.2513\left(\frac{18\,\mathrm{Re}_a+2.7\left(\mathrm{Re}_a\right)^{1.687}}{Ar}\right)^{-0.4037} \tag{3}$$

$$\mathrm{Re}_a=\frac{d_p\rho_g}{\mu}\left[u_0-u_s\left(\frac{\varepsilon_a}{1-\varepsilon_a}\right)\right] \tag{4}$$

$$\mathrm{Ar}=\frac{\rho_g\left(\rho_p-\rho_g\right)gd_p^3}{\mu_g^2} \tag{5}$$

$$1-\varepsilon^*=0.05547\left(\frac{18\mathrm{Re}^*+2.7\left(\mathrm{Re}^*\right)^{1.687}}{Ar}\right)^{-0.6222} \tag{6}$$

$$\mathrm{Re}^*=\frac{d_p\rho_g}{\mu}\left[u_0-u_s\left(\frac{\varepsilon^*}{1-\varepsilon^*}\right)\right] \tag{7}$$

$$Z_0=500\exp\left[-69\left(\varepsilon^*-\varepsilon_a\right)\right] \tag{8}$$

Previous experimental studies (e.g. Pham, 1996) showed that the axial voidage in a bubbling fluidized bed is also in the S- shape profile (Fig. 3). Similarly, the axial voidage profile also can be written in Equation 1, but the values of ε^* and ε_a are much different from each other. The value of ε^* is near unity for most operating conditions. The value of Z_0 is extremely low because the bed surface is much clearer.

As the profile of voidage in fast bed $\varepsilon_f(z)$ and in dense bed $\varepsilon_c(z)$ can be calculated individually, the overall axial voidage profile in the bed is approximately calculated using the following equation

$$\varepsilon(z)=1-\left[\left(1-\varepsilon_f(z)\right)+\left(1-\varepsilon_c(z)\right)\right] \tag{9}$$

The continuity of the voidage profile guarantees the computational stability of power plant simulator, when the operating condition alters rapidly.

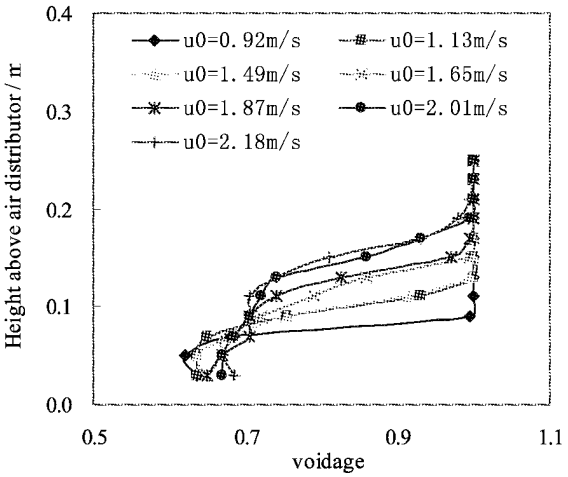

Fig.3 S-type voidage profile in bubbling bed (Pham, 1996)

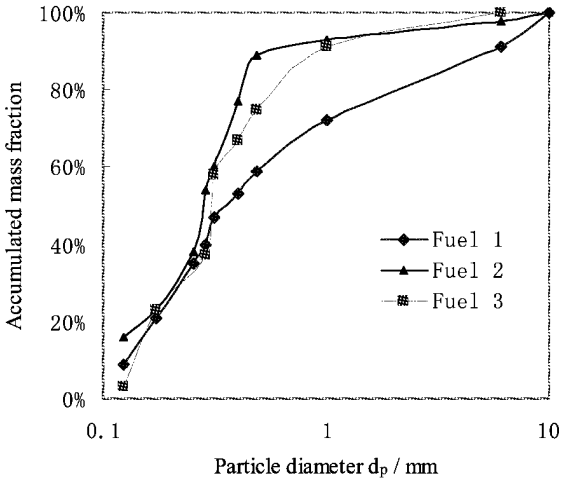

Fig. 4 Particle size distributions in CFB combustor

Ration of bed inventory

Shown in above equations, for given a bed material and fluid, the height of voidage profile inflexion z_i only depends on the bed inventory, if the fluidizing air velocity is given. Moreover, the voidage profile varies with the particle size distribution, even though the total bed inventory in combustor is constant. Consequently, it is necessary to determine the ration of bed inventory – the mass fraction of coarse particles in low dense bed and that of fine particles in upper fast bed. Obviously, the rational bed inventory depends on the operational conditions and the particle size distribution. The later one depends on mass balance resulted from the ash formation of coal, the fragmentation and attrition of limestone, the separation efficiency of cyclone, and so on. The size distributions of the bed material in the combustor of 300MW CFB boilers burning different types of fuels are shown in Fig. 4.

Normally, the combustor of a 300MW CFB boiler is over 30m in height (above the air distributors), so that there is a full developed zone with a quite long axial distance in the upper combustor. In that zone, the time average voidage ε is usually greater than 0.99, thus the superficial gas velocity u_0 is approximate to the real gas velocity u_0/ε. Because the particles in fast bed are all fine and can be carried out of the combustor by flue gas, their terminal velocities are absolutely less than u_0. Thus, a critical particle diameter d_{pt} is defined as the diameter of particle whose terminal velocity is equal to u_0. Particles with diameter smaller than d_{pt} belong to the fast bed inventory, while particles with diameter larger than d_{pt} belong to the bubbling or turbulent bed inventory. If particle size distribution is given (such as in Fig.4), the ration of bed inventory can be determined easily.

There are many empirical expressions proposed to calculate the terminal velocity of single particle (Khan and Richardson, 1987). In real-time simulation, iterations should be minimized. In this study, the method proposed by Haider and Levenspiel (1989) is employed, because of its high accuracy and explicit expression

$$U_t^*=\left[\frac{18}{d_p^{*2}}+\frac{2.3348-1.7439\phi}{d_p^{*1/2}}\right]^{-1} \tag{10}$$

Where, ϕ is the average sphericity of ash particle, regarded as a constant 0.7 according to the study of Liu et al (2007). U_t^* and d_p^* are the dimensionless terminal velocity and particle diameter, defined as following equations. Equation 10 works in the range of $0.5\le\phi\le1$ and $1\le d_p^*\le3000$, covering most operational

conditions in the combustor of a CFB boiler.

$$U_t^* = u_t \left[\frac{\rho_g^2}{g\mu(\rho_p - \rho_g)} \right]^{1/3} \tag{11}$$

$$d_p^* = d_p \left[\frac{g\rho_g(\rho_p - \rho_g)}{\mu^2} \right]^{1/3} \tag{12}$$

RESULTS AND DISCUSSION

The voidage profile is an important factor for determining the temperature profile. In this model, the combustor of CFB boiler is divided into 4 cells along the height in energy balance calculation. The 4 temperatures characterize the axial temperature profile. In a power plant simulator, these characteristic temperatures should agree well with to the operational data at 3 different loads at least. Consequently, the average voidage in these 4 cells must agree well with the operational data firstly. Unfortunately, the simplified model with single particle diameter (0.2mm), which was widely used in simulators in the past, can not satisfy the axial voidage profile (Fig.5) under the conditions mentioned above. Both voidage at the bottom and the length of transition zone are overestimated, especially when the fluidizing velocity is high. The discrepancy in axial voidage profile may induce greater discrepancy in temperature profile, so that a better model is needed.

The errors of voidage value at different dimensionless height (h/h_f=0.009, 0.046, 0.091, 0.163, 0.283, 0.476 and 0.776) calculated by single particle diameter model are shown in Fig. 6, where h is the height above air distributor and h_f is the total height of CFB combustor above air distributor. The gross errors (points outside the 5% error lines) occur in the dense zone and the transition zone, where voidage is small. This result means that single particle diameter model can not well describe hydrodynamics at the bottom of combustor. As mentioned above, the flow pattern in CFB combustor is a superposition of a fast fluidized bed in the upper zone and a bubbling or turbulent bed at the bottom zone. The single particle diameter model is suitable for the fast bed (voidage values near 1.0), but not for the bubbling or turbulent bed. Different characteristic particle diameter should be adopted for the bubbling bed from that used in the fast bed. Thus, binary particle diameter model is developed by adding another sub-bed with coarse particles in the model to enhance the description of bubbling or turbulent bed.

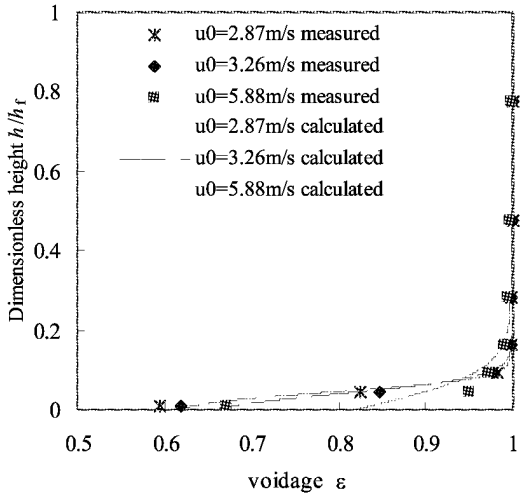

Fig. 5 Voidage profile calculated by model with single particle diameter

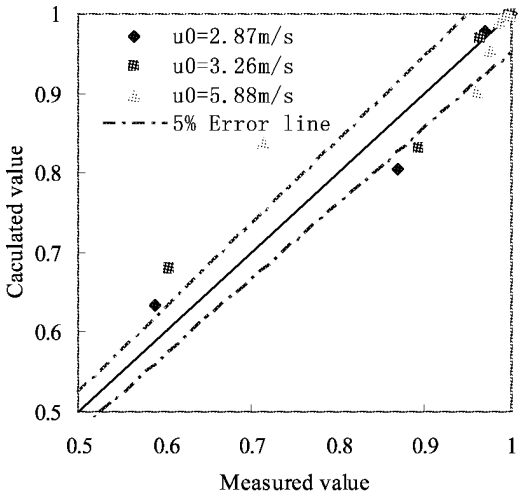

Fig. 6 Error analysis of voidage profile calculated by single particle diameter model

Under same conditions (the average voidages in 4 cells equal to the measured value), axial voidage profile in CFB combustor was recalculated and results are shown in Fig. 7. the error analysis of binary particle diameter model is shown in Fig.8. It can be seen that almost all the points are within the 5% error lines. The results prove that binary particle diameter model is more appropriate to predict the axial voidage profile in the combustor, especially in the dense bed (voidage value near 0.6). When the critical particle diameter d_{pt} is employed, nested loops in computation are avoided successfully. The main additional time cost is the iteration to determine the bed surface of dense bed. This time cost is compatible to that for fast bed calculation. Thus

overall time cost of binary particle diameter model is nearly 2 times of that of single particle diameter model. This is acceptable for the simulator.

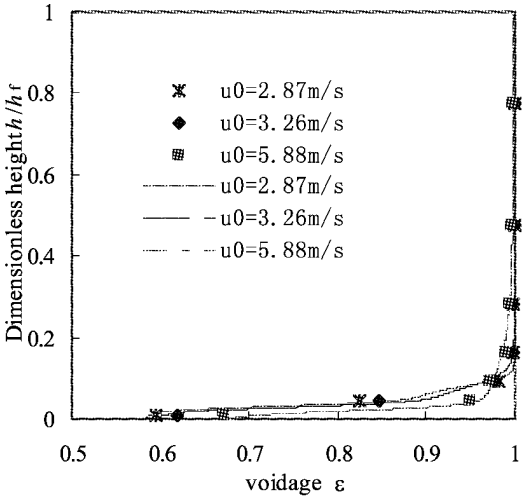

Fig. 7 Voidage profile calculated by binary particle diameter model

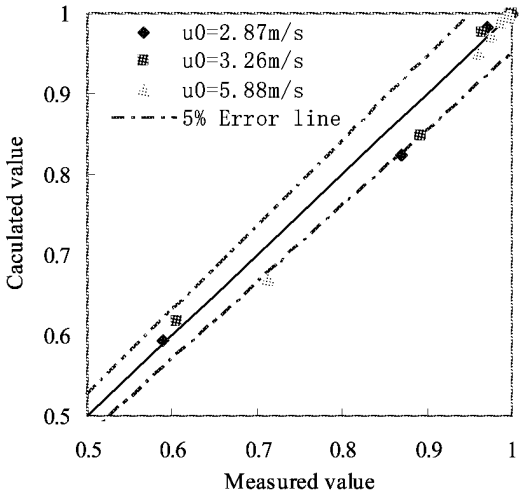

Fig. 8 Error analysis of voidage profile calculated by binary particle diameter model

CONCLUSIONS

Using the hydrodynamic model with single particle diameter, the length of transition zone and the calculated values of voidage at the bottom of combustor are overestimated. The results indicate that single particle diameter model is not suitable to the overall axial profile in a CFB boiler, especially in the bubbling or turbulent bed in the lower combustor. A binary particle diameter model is proposed to better predict the axial voidage profile in the CFB boiler. An internal of coarse particle is added in the binary particle diameter model to enhance the description of dense bed.

A critical particle diameter is defined to determine the ration of bed inventory without nested loops in computation. The binary particle diameter model improves the prediction with limited extra time cost. It is available for real-time simulators.

NOTATIONS

Ar The Archimedes number, in Equation 5
d_p^* Dimensionless particle diameter, m, in Equation 12
d_p Particle diameter, m
d_{pt} Critical particle diameter to determine the ration of bed inventory, m
g Acceleration of gravity, 9.806 m/s^2
h Height, m
h_f Height of combustor above air distributor, m
Re Reynolds number, in Equation 4 and 7
U_t^* Dimensionless terminal velocity, m/s, in Equation 11
u_s Solid phase velocity, m/s
u_t Terminal velocity, m/s
u_0 Superficial gas velocity, m/s
Z Height above air distributor, m
Z_0 Characteristic length, standing for the length of transition zone, m
z_i Height of voidage profile inflexion, m
ε Voidage at certain height
ε_a Asymptotic value of downside voidage
ε^* Asymptotic value of upside voidage
ε_f Voidage in fast bed
ε_c Voidage in bubbling bed
ϕ Sphericity of ash particle, ϕ=0.7
μ_g Gas viscosity, Pa • s
ρ_g Gas density, kg/m^3
ρ_p Solid particle density, kg/m^3

ACKNOWLEDGEMENTS

Financial supports of this work by Key Project of the National eleventh-Five Year Research Program of China (2006BAA03B02) and National Science Fund Committee (50406002) are gratefully acknowledged.

REFERENCES

Haider, A. and Levenspiel, O.: Powder Technology. **58**(1989),pp.63-70.

Hannes, J., Renz, U., and Van den B.: American Society of Mechanical Engineers, Advanced Energy Systems Division. **1**(1995),pp.287-296.

Liu, B., Su, W. and Hong, H.: Journal of Engineering for Thermal energy and power. **22**(2007), pp.46-51.

Li, Y., Chen, B., and Wang, F.: Chinese Journal of Chemical Engineering. **2**(1979), pp.143-152.

Khan, A. R. and Richardson, J. F.: Chemical Engineering Communications. **62**(1987),pp.135-150.

Kwauk, M.: The hydrodynamics of fast fluidization. New York: Plemum Press(1980).

Pham, H. L., Mora, J-C and Kita J-C: International Journal of Energy Research **20**(1996), pp.989-998.

Yu, L.: Experimental Study on hydrodynamics of circulating fluidized beds with wide coarse particle size distributions. Beijing: Tsinghua University(1989).

Yue, G., Lu, J., and Zhang, H.: Design Theory of Circulating Fluidized Bed Boilers. 18th International Conference on Fluidized Bed Combustion (2005), pp.1-12.

3D-SIMULATION OF CONCENTRATION DISTRIBUTIONS INSIDE LARGE-SCALE CIRCULATING FLUIDIZED BED COMBUSTORS

R. Wischnewski[1], L. Ratschow[2], E. U. Hartge[3], J. Werther[3]

1 now with Hydro Aluminium AS, Oslo, Norway
2 now with Pöyry Energy GmbH, Hamburg, Germany
3 Institute of Solids Process Engineering and Particle Technology, Hamburg University of Technology, D21071Hamburg, Germany

Abstract: With increasing size of modern CFB combustors the lateral mixing of fuels and secondary air gains more and more importance. Strong concentration gradients, which result from improper lateral mixing, can lead to operational problems, high flue gas emissions and lower boiler efficiencies. A 3D-model for the simulation of local gas and solids concentrations inside industrial-sized CFB boilers has been developed. The model is based on a macroscopic approach and considers all major mechanisms during fuel spreading and subsequent combustion of char and volatiles. Typical characteristics of modern boilers like staged combustion, a smaller cross-sectional area in the lower section of the combustion chamber and the co-combustion of additional fuels with coal can be considered. The 252 MWth combustor of Stadtwerke Duisburg AG is used for the validation of the model. A comprehensive picture of the local conditions inside the combustion chamber is achieved by the combination of local gas measurements and the three-dimensional simulation of concentration distributions.
Keywords: simulation, local concentrations, CFB combustor, industrial-scale

INTRODUCTION

The mixing behavior of gas and solids in circulating fluidized bed combustors must be well studied for the design and scale-up of industrial CFB boilers. The combustion chambers of modern plants have reached heights of over 40 m and cross-sectional areas of more than 200 m². Fuels and limestone are fed at discrete points. The lateral mixing in CFBs is small so that concentration gradients of gas and solids are present. Near the feeding points low oxygen concentrations are present which result from the high concentrations of reactive char and volatiles. Distant from the feeding point oxygen is present in excess. The type of fuel and its particle size distribution affect its devolatiliziation time and thus the locations and strengths of volatile and char sources. With increasing volatiles contents of the fuels the potential problems of maldistributions increase. The secondary air injection is another design criterion which affects local gas concentrations. The gas jets have a limited penetration length only, so that additional maldistributions of oxygen may arise.

At present large-scale CFB combustors can comprehensively only be modeled by a macroscopic approach. CFD approaches are not applicable due to their extensive computational demand and time requirement. Only few comprehensive 3D models are reported. Foster Wheeler developed a model which is largely based on empirical expressions. This model is only briefly described in public literature (e.g. Myöhänen et al. (2005)). The model by Lücke et al. (2004) describes all major mechanisms in a CFB combustor and proved to be applicable to large-scale CFB combustors. However, the model is limited to simple geometries and cannot consider co-combustion. Recently Pallarès et al. (2008) presented a 3D-model for CFB combustors which needs, however, to be further tested and applied to different large-scale CFB combustors.

3D-MODEL FOR LARGE-SCALE CFB COMBUSTORS

The present model can consider all characteristics of typical large-scale CFB combustors. Arbitrary shapes of the combustion chamber with circular or rectangular cross-sections can be modeled as well as smaller cross-sectional areas in the lower part of the combustion chamber for boilers with staged combustion. The location of ports can freely be defined and heterogeneous, homogeneous and heterogeneous catalytic reactions can be considered for an arbitrary number of gas and solids components. Co-combustion of several fuels can be considered. The model extends the modeling concept by Lücke et al. (2004). Several submodels needed to be modified and new submodels had to be added. Furthermore, the data-structure needed to be extended and re-designed in order to account for the flexibility in combustion chamber shapes.

The four fluid dynamical zones bottom zone, splash zone, upper dilute zone and exit zone are considered. In the bottom zone the two-phase model by Werther and Wein (1994) is used. It distinguishes a solids-free bubble phase and a suspension phase which contains gas and solids. Ideal mixing of solids in vertical direction

is assumed and horizontal solids dispersion is considered. The splash and upper dilute zones are described by the core-annulus model of Pugsley and Berruti (1996). The model was fitted to the conditions in combustion chamber of large diameters based on measurements in the Duisburg CFB combustor which were part of this work. Horizontal gas and solids dispersion coefficients are considered. The core-annulus structure of the upper dilute zone is used in the exit zone. Horizontal gas and solids velocities are calculated by a 2D potential flow field approach for each height element.

The combustion submodel considers the drying and devolatilization of fuel particles including primary fragmentation and the subsequent combustion of char and volatiles according to the approach by Lücke et al. (2004). The model was extended so that co-combustion can be considered. The devolatilization step and the char combustion are calculated individually for each fuel. Solids separation in the cyclones is considered as well as post-combustion of reactive gas components in the cyclone. The combustion in the external heat exchangers is modeled in a simplified way by defining the reaction extent for the reactions there.

All submodels are connected by a mass balance which is solved in all volume elements of the mesh. A mesh consists of non-orthogonal hexahedrons so that typical geometries of industrial plants can be modeled.

MEASUREMENTS IN THE COMBUSTION CHAMBER

Co-combustion tests have been performed at the 252 MWth CFB combustor of Stadtwerke Duisburg AG. The tests had a total duration of 12 days and were accompanied by local measurements in the combustion chamber. Gas concentrations, fluid dynamics and solids fluxes have been measured. Details of the campaign can be found in Wischnewski et al. (2006). For the present work the results from local gas measurements for pure coal combustion have been used (test periods I, IV).

The combustion chamber of the Duisburg combustor has a height of about 30 m and a circular cross-section with a diameter of 5 m at the nozzle floor and 8 m at its upper section. In Fig. 1 the combustion chamber and one of its two primary cyclones are shown. Coal is fed pneumatically from the front side through two parallel ports at a height of 3.5 m above the nozzle floor. Secondary air is injected through four downwards inclined ports which are located around the circumference of the combustion chamber at height of 9.5 m.

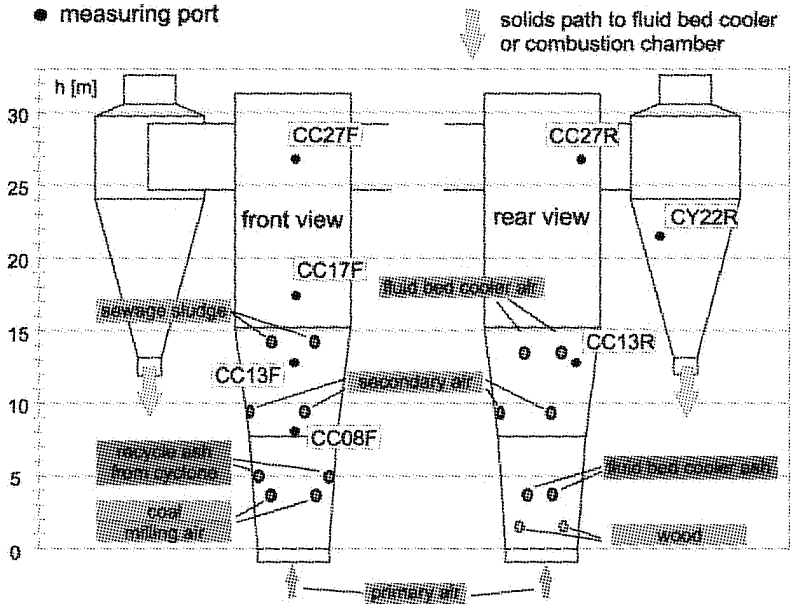

Fig. 1 Front and rear view of combustion chamber and one primary cyclone of the 252 MWth CFB combustor of Stadtwerke Duisburg AG

Six measurement ports were available at the combustion chamber, four on the front side at 8 m (CC08F), 13 m (CC13F), 17 m (CC17F) and 27 m (CC27F) above the nozzle floor and two on the rear side at 13 m (CC13R) and 27 m (CCC27R). In addition, one port was available in the conical part of one of the primary cyclones (CY22R).

MODEL VALIDATION

Most of the semi-empirical submodels of the present model are developed on small- or pilot-scale CFBs. To apply these models to large-scale CFBs means often to use them far outside the range they are intended for.

Therefore it was necessary to investigate systematically the different mechanisms inside the combustion chamber of a large-scale boiler. Based on a physical understanding of the phenomena model parameters had to be adapted where necessary.

The mesh

Initial simulations were performed with different meshes that represent the combustion chamber by simple geometries. It resulted that only a refined mesh which considers the circular cross-section and the conical lower part leads to good results. The mesh used in this work consists of 10,830 cells.

Gas exchange in the bottom zone

In the bottom zone the two-phase model by Werther and Wein (1994) is used. It distinguishes a solids-free bubble phase and a suspension phase which contains both gas and solids. A dispersive exchange of gas between the two phases is described based on the model of Sit and Grace (1981):

$$k_{g,i} \cdot a = \beta \cdot \left(\frac{u_{mf}}{3} + \sqrt{\frac{4\, D_i\, \varepsilon_{mf}\, u_{br}}{\pi\, d_b}} \right) \cdot \frac{6}{d_b} \cdot f_b \qquad (1)$$

where $k_{g,i}$ is the mass transfer coefficient, a the surface area of the bubbles per unit bed volume, u_{mf} the minimum fluidization velocity, D_i the diffusion coefficient of species i, ε_{mf} the bed voidage at u_{mf}, u_{br} the bubble rise velocity and d_b the local mean bubble diameter.

The correlation was developed in a laboratory-scale fluidized bed at fluidization velocities slightly above the minimum fluidization velocity (u_{mf} = 0.112 m/s). In the Duisburg plant superficial gas velocities of 4.5 - 5 m/s are present. The highly turbulent flow leads to increased gas mixing in the bottom zone compared to the original model. A fitting parameter β was therefore introduced.

In Fig. 2 the cross-sectional average oxygen concentrations in the lower third of the combustion chamber are shown. With β=1 the concentration profile of the original model is obtained. Concentrations of about 8 mol-% are resulting at the top of the bottom zone. With an increased gas mixing much lower concentrations are found here, namely 6 mol-% for β=3 and 5 mol-% for β=5. The decrease of the average oxygen concentration results from an increased reaction rate. The reactive char is present only in the suspension phase. Devolatilization takes place also in this phase so that the combustion occurs mainly here. The reactions are inhibited if the oxygen concentrations in the suspension phase decreases to zero. Through the dispersive inter-phase gas exchange oxygen is transported from the bubble into the suspension phase. Enough oxygen is present for the reactions and higher combustion rates are found locally in the bottom zone.

In Fig. 3 the local oxygen concentration profiles at port CC08F resulting from the sensitivity study are shown. The port is located about 5.5 m above the top of the bottom zone. Unfortunately no port was available closer to the bottom zone. Despite the vertical distance the effect of increased gas mixing can clearly be seen. The comparison of simulation results with the measured profiles indicates that gas mixing is increased compared to the original model and can be well described by using a value of β=3. This result illustrates the strong interaction between the different submodels, in this case the fluid dynamics and the combustion submodel.

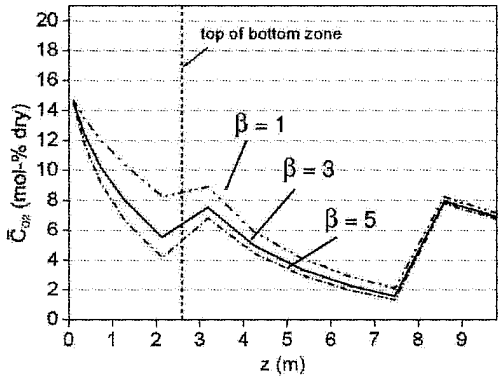

Fig. 2 Influence of dispersive gas exchange between bubble and supension phase in the bottom zone on horizontal average oxygen concentrations

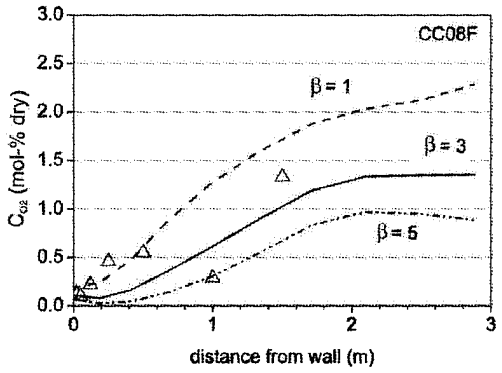

Fig. 3 Influence of dispersive gas exchange between bubble and supension phase in the bottom zone on local oxygen concentrations at port CC08F, i.e. in the upper dilute region of the combustion chamber

Secondary air injection

The secondary air injection forms gas jets which penetrate the fluidized bed to a certain length. Correlations for the estimation of jet penetration lengths have been developed on small-scale CFBs but are not applicable to ports of half a meter in diameter or more which are found in industrial plants. The investigations on laboratory CFBs have shown that gas jets form as shown in Fig. 4 for a downwards inclined port.

The gas enters the fluidized bed to a penetration length L_j. At the tip of the jet the gas is released. For large-scale CFBs such a penetration pattern is likely but it has to be considered that the jet may be disturbed by the massive solids downflow near the wall. Therefore a sensitivity study was performed to investigate the jet penetration characteristics in large-scale plants. Three options have been investigated. In case A it is assumed that no jet is formed and all gas is released at the port opening. In case B it is assumed that a jet forms but that in contrast to the findings from the lab investigations the gas is released along the whole length of the jet. In case C the release of gas is assumed to occur at the tip of the jet only.

Fig. 5 shows the resulting oxygen profiles at port CC13F at a position slightly oblique 3.5 m above the secondary air injection. For cases B and C a jet penetration length of L_j = 1.4 m and a radius of the tip of the jet of r_j = 0.4 m were assumed. The comparison of the calculated oxygen profiles with the measured ones indicates that a similar penetration pattern is present as found in small CFBs (case C). Furthermore, it can be seen that not only the oxygen concentrations near the port and at the location of the jet is affected by the penetration pattern, but also the concentrations of oxygen towards the center of the combustion chamber is affected.

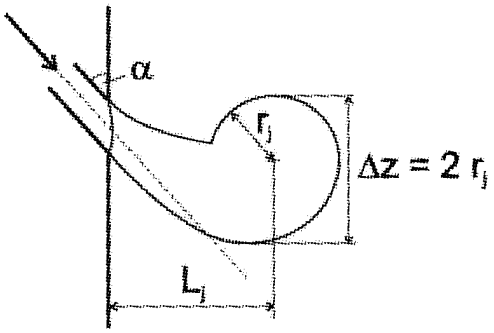

Fig. 4 Jet region geometry from nozzles of small diameters

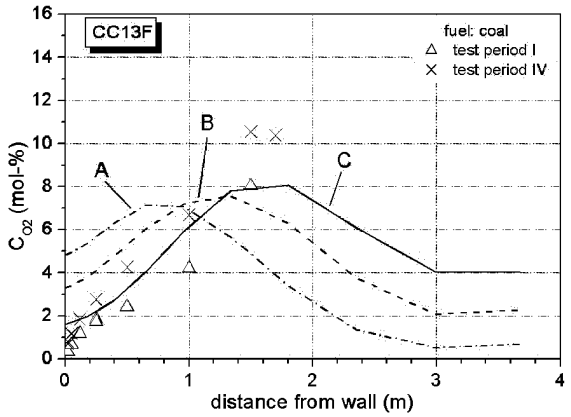

Fig. 5 Influence of mechanism of O_2-release from gas jets of secondary air on local O_2-profiles: (A) release at port, no jet, (B) jet release along whole jet length, (C) jet with release around tip only

After the jet penetration pattern has been determined the jet penetration length L_j was determined by an additional sensivity study. A penetration length of L_j of 1.4 m was found for the secondary air jets.

Injection of off-gas from external heat exchangers (EHE)

Similar investigations were made for the injection of off-gas from the external heat exchangers ("fluid bed cooler air" in Fig. 1). The gas is injected on the rear side of the combustion chamber at a height of 13.2 m

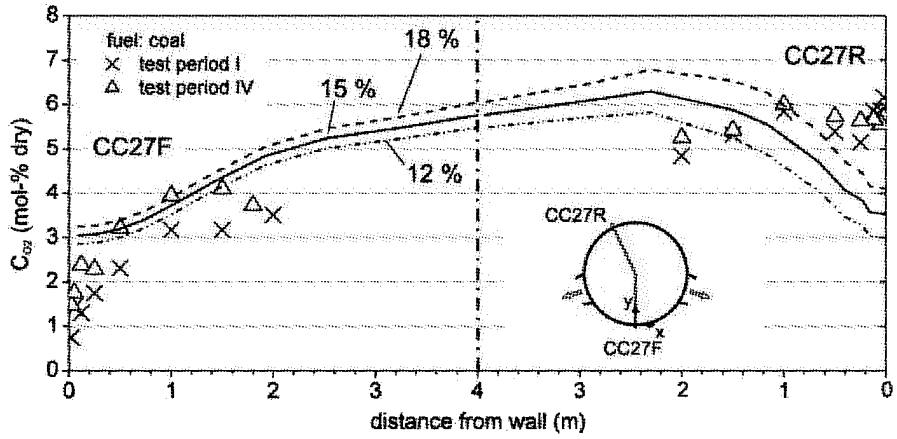

Fig. 6 Influence of the oxygen concentration in the off-gas from the external heat exchangers on the local O_2 profile measured at ports CC27F and CC27R, respectively

above the nozzle floor. The velocity of the gas jet at the opening of the port is $u_{o,EHE}$ = 46 m/s, while the velocity of the secondary air jet is $u_{o,sa}$ = 118 m/s. The much smaller gas velocity reflects in a smaller penetration length of the gas jet for the off-gas from the external heat exchangers. It was determined to be $L_{j,EHE}$ = 0.1 m.

The composition of the EHE-off-gas could not be measured so that it had to be determined by simulations. In Fig. 6 the oxygen concentration profiles at the ports CC27F and CC27R are shown for different oxygen concentrations in the EHE off-gas. The measured profile at the front side can be modeled with good accuracy but at CC27Ron the rear side (which is near the cyclone entrance) some differences between the simulated and the measured concentrations are present.

RESULTS AND DISCUSSION

After the validation of the model has been finished and additional model parameters like the reaction kinetics of char and CO combustion, horizontal dispersion coefficients and the fuel injection pattern had been investigated the measured gas concentrations in the combustion chamber could be modeled with good accuracy. In Fig. 7 the simulated concentrations of oxygen and carbon monoxide are compared with measurements. A good agreement could be obtained for oxygen. For carbon monoxide some discrepancies are present with regard to the shape of the local profiles. However, the level of concentrations is well met and the reduction of carbon monoxide along the vertical axis is fully met.

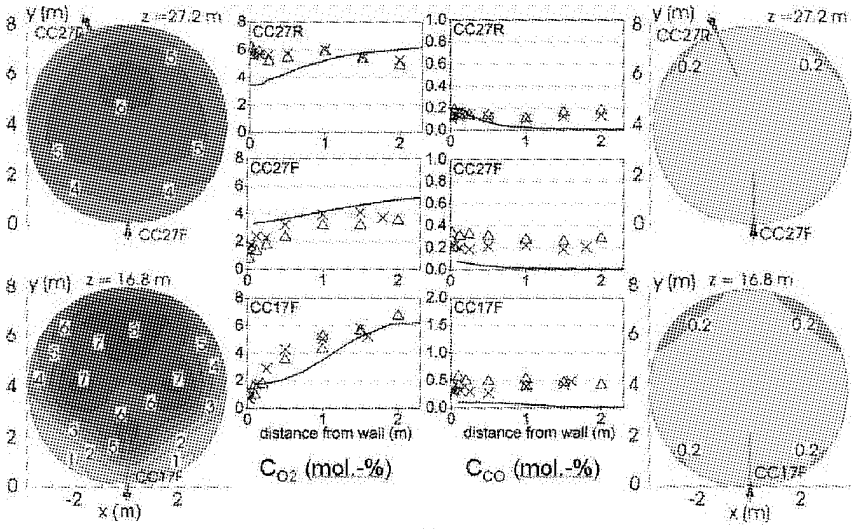

(a)

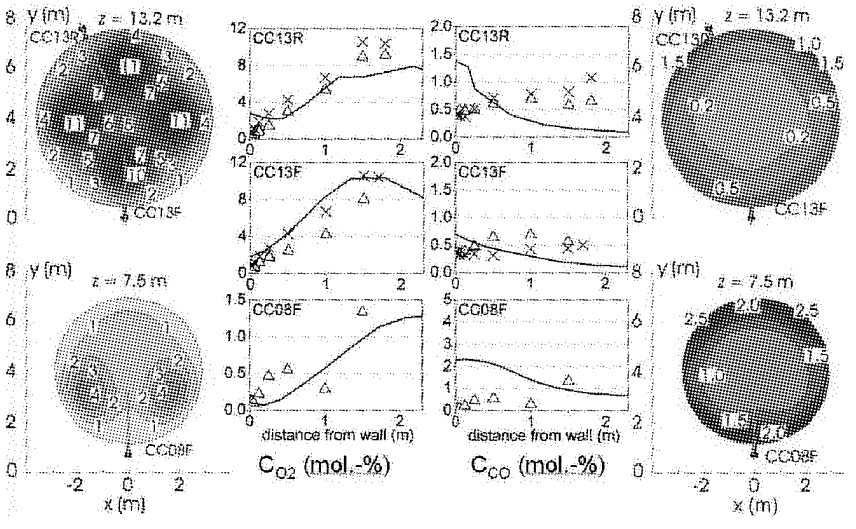

(b)

Fig. 7 (a) Comparison of simulation and measurements for local oxygen and carbon monoxide concentrations for 27.2 and 16.8 m, respectively, above the distributor and (b) comparison of simulation and measurements for local oxygen and carbon monoxide concentrations for 13.7 and 7.5 m, respectively, above the distributor

From the simulation results it becomes obvious that a mal-distribution of oxygen between front and rear side is present. The reason is the feeding of coal through two ports from the front side. Near the feeding points enlarged concentrations of char and reactive volatiles are present. This results in locally higher reaction rates and small oxygen concentrations.

CONCLUSIONS

A comprehensive 3D model for the simulation of local gas and solids concentrations in large-scale CFB combustors was developed. Measurements in the combustion chamber of an industrial plant have been used for the validation of the model. After different model parameters have been adapted based on a physical understanding of the preceding phenomena a good agreement between measurements and simulation was achieved.

REFERENCES

Lücke, K., Hartge, E.-U. and Werther, J., Int. J. Chem. Reactor Engng. **2** (2004).
Myöhänen, K., Hyppänen, T. and Loschkin, M. (2005), Circulating Fluidized Bed Technology VIII.
Pallarès, D., Johnsson, P. and Palonen, M. (2008), Circulating Fluidized Bed Technology IX.
Pugsley, T.S. and Berruti, F. Powder Technol. **89** (1996), pp. 57-69.
Sit, S.P. and Grace, J.R.. Chem. Eng. Sci. **36** (1985), pp. 327-335.
Werther, J. and Wein, J. AIChE Symp. Ser. **90** (1994), 301, pp. 31-44.
Wischnewski, R.; Ratschow, L.; Redemann, K., Hartge, E.-U. and Werther, J. (2006), FBC 19.

THREE-DIMENSIONAL SIMULATION OF TEMPERATURE DISTRIBUTIONS IN LARGE-SCALE CIRCULATING FLUIDIZED BED COMBUSTORS

L. Ratschow[1], R. Wischnewski[2], E. U. Hartge[3], J. Werther[3]

1 Institute of Solids Process Engineering and Particle Technology, Hamburg University of Technology, D21071Hamburg, Germany
2 now with Pöyry Energy GmbH, Hamburg, Germany
3 now with Hydro Aluminium AS, Oslo, Norway

Abstract: Circulating fluidized bed combustors (CFBC) of industrial scale have sometimes diameters of more than 10 m and heights exceeding 40 m. Depending on the intensity of the reactions and the location of the insertion of reactants into the bed, temperature effects can not be neglected. A simulation tool for the investigation of these large-scale systems including sub-models for fluid dynamics, dispersion, reactions, mass balances and an enthalpy balance has been implemented. The simulation results provide three-dimensional distributions of temperatures inside the combustion chamber. The simulation results have been validated with results of local measurements in a 235 MWe CFBC of Elektrownia Turow in Poland.
Keywords: simulation, temperature distribution, enthalpy balance, circulating fluidized bed combustion, industrial scale

INTRODUCTION

It is commonly agreed that the advantages of circulating fluidized beds (CFB) lie in their good mixing properties and a good heat transfer between solids, fluid and eventual heat exchangers in the reactor thanks to the internal and external solids recirculation. As a consequence a homogeneous temperature distribution is often assumed to prevail in the reactor. Actually, temperature profiles can hardly be detected in circulating fluidized bed combustors of laboratory scale.

However, reactors of industrial scale have diameters and heights of more than 10 m and 40 m respectively. Here it becomes evident that depending on the intensity of the reactions and depending on the location of the feeding of reactants into the bed, temperature effects can not be neglected. For CFB combustors of industrial scale it is likely that hot regions will occur near the feed points of gaseous or liquid combustibles. Hot regions are also conceivable at the location of feed ports for combustibles with a high volatile content or at feed ports of very fine, fast burning particles. Even if these temperature inhomogeneities are considerably lower in circulating fluidized beds, they still exist and were measured in several plants of industrial scale (Leuschke et al., 2008; Wischnewski et al., 2006; Hartge et al., 2002).

The aim of this work is to describe temperature effects in large-scale circulating fluidized bed combustors. A three-dimensional simulation tool was developed for this purpose. The simulation tool is based on classical semi-empirical sub-models which permit the calculation of large-scale combustion processes in reasonable time.

THE MODEL

If spatial effects within a combustion chamber shall be evaluated by help of a simulation tool, a suitable grid is required. In the present work the grids for the combustion chambers were generated by help of the software Ansys Icem CFD (2008) and exported in the Star-CD (2008) format. In order to allow for complex combustion chamber geometries, non-orthogonal grids were chosen. It was assumed that the grid consists of hexagonal cells forming horizontal layers.

The simulation tool is written in C++. It consists of several sub-models, including fluid dynamics and gas and solids mixing submodels as well as a reaction kinetics submodel as shown in Fig. 1. The fluid dynamic submodel of the combustion chamber alone considers the mass balance of the solids mixture and the gas mixture. The other submodels of the combustion chamber are merged to the fluid dynamics via the mass balances of the different gas and char species. Temperature fields can be calculated via an enthalpy balance. The temperature field influences directly the reaction kinetics. Due to this coupling effect, the enthalpy balance occupies the same central position as the mass balances.

A gas cyclone sub-model was incorporated into the simulation tool that enables the calculation of the char concentration and particle size distribution in the return legs. For the simulation, the combustion chamber

model and the cyclone model are solved iteratively in order to find the stationary values.

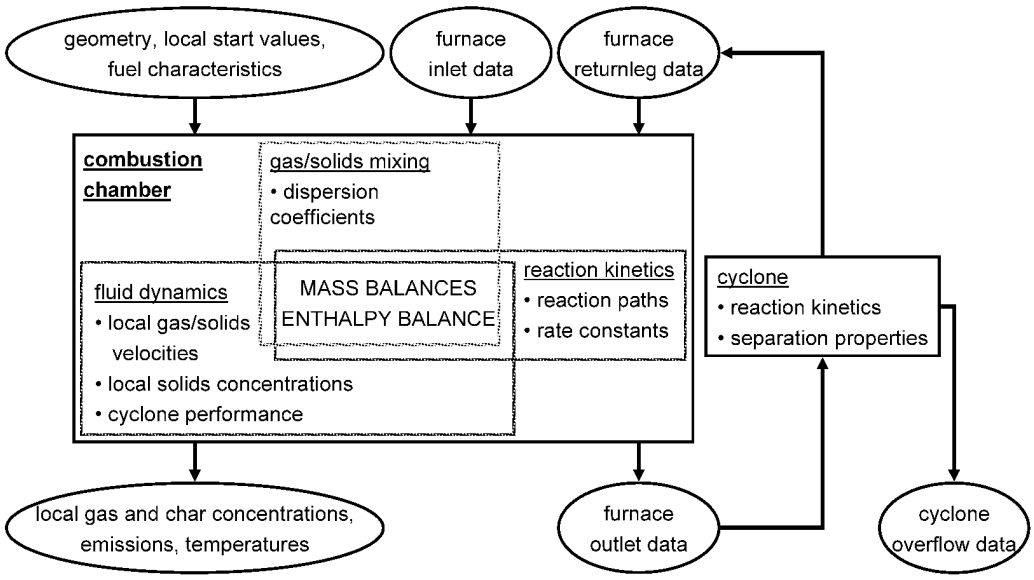

Fig. 1 General layout of the simulation tool

The simulation tool requires a set of input data containing the cell geometries, inlet parameters of the fuel including ash characteristics and the entering gas, operating conditions like the pressure drop in the combustion chamber, reaction paths, reaction kinetic constants etc. The program stores output files for local char species and gas species concentrations, mean average values as well as temperature fields in the form of ASCII files. The post-processing for the visualization of the simulation results has mainly been realized by help of the commercial software Matlab.

THE ENTHALPY BALANCE

The general structure of the enthalpy balance has been expressed as follows:

$$\underbrace{\frac{\partial(\rho \cdot c_p \cdot T)}{\partial t}}_{accumulation} = \underbrace{-div(u \cdot \rho \cdot c_p \cdot T)}_{forced\ convection} \underbrace{- div(-\Lambda_{eff} grad \quad T)}_{effective\ conduction} + \underbrace{\sum_j r_j(\Delta H_{R_j}) + S}_{reaction} \tag{1}$$

In this equation, c_p, u and ρ are general placeholders for a specific heat capacity, velocity and density, respectively. T and t denote the time and temperature. r_j is the reaction rate based on unit reactor volume with regard to the reaction *"j"* and ΔH_{Rj} is the corresponding reaction enthalpy. The term S is a local sink term including the heat for devolatilization and evaporation and heat sinks due to heat exchangers. The dispersive properties in the reactor are accounted for by the introduction of the effective conduction, which contains the intrinsic effective heat conduction coefficients Λ_{eff}. They can be decomposed as a function of horizontal or vertical dispersion coefficients for the solid and fluid phase, respectively. The heat conduction coefficient for the solids in horizontal direction holds for example for the core zone

$$\lambda_{s,h,c} = c_v \cdot \rho_s \cdot c_{p,s} \cdot D_{s,h,c} \tag{2}$$

Here, $D_{s,h,c}$ denotes the dispersion coefficient for the solids in horizontal direction. Other dispersion coefficients describe mixing in the wall zone of the CFB and in the bottom zone, respectivel. Consequently, the effective heat conduction term in the enthalpy balance is set up proportional to the solids concentration gradient in the direction of the decreasing concentration. This set up is similar to Fick's first law of diffusion for the modeling of molecular transport phenomena due to diffusion. In contrast to that application, the dispersion coefficients of the effective conduction are no physically intrinsic properties of the material, but depend on the flow conditions and the orientation between the concentration gradients and the direction of the convective flow. The dispersion coefficients in the mass and for the enthalpy balances are assumed to be the same.

An approach according to a Taylor's series ending after its linear term is applied for discretization of the enthalpy balance. The enthalpy balance is set up for the mixture of all solids components and all particle size classes. To be exact, different temperatures for every kind of solid as well as the flue gas could be distinguished. In that case, accordingly several heat balances would be required, which would increase the calculation time for the simulation tool dramatically. The solids species and the gas matter can only be assembled into one overall

enthalpy balance under the assumption that in one cell, the solids and flue gas have the same average temperature. Keeping in mind that typical particles introduced into a circulating fluidized bed combustor heat up at a rate of more than 100 K/s as shown by La Nauze (1985), this assumption is reasonable for the flue gas and the suspended inert particles forming together circa 99% of the mass flow through the cell volume. The differing surface temperatures of the colder raw fuel particles are compensated for by the higher surface temperature of reacting char particles. Therefore, their influence was neglected.

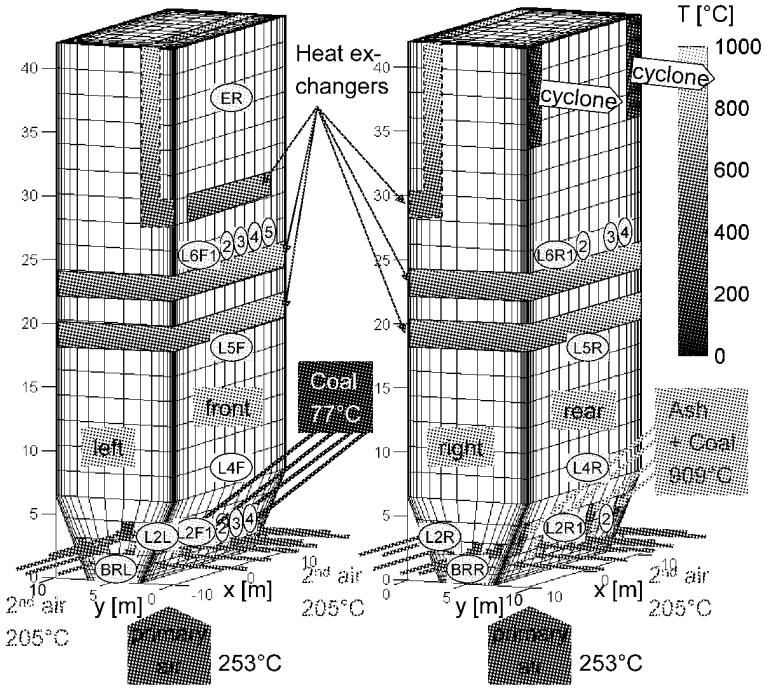

Fig. 2 Sketch of the geometry of the Turów combustion chamber with inlets, outlets and return legs. The heat exchangers in the combustion chamber are indicated in gray. The location of ports where measurements in the real combustion chamber were carried out are indicated by the corresponding port numbers

RESULTS AND DISCUSSION

Two CFB combustion chambers of industrial scale were so far investigated by help of the simulation tool; namely the 235 MW_e CFB combustor of the Elektrownia Turów S.A. power plant and the 105 MW_e CFB combustor of Stadtwerke Duisburg. For this manuscript, the simulation results will be compared exemplarily to measurement results for the case of the Turów CFBC. The plant is well described and extensive experimental data are available from preceding measurement campaigns (Hartge et al. 2005, Johnsson et al. 2002). These data are used here in order to investigate the quality of the simulations.

A sketch of the grid for simulation of the Turów CFB combustor is shown in Fig. 2. It consists of 10,166 volume elements in total. Close to the walls, the elements have a thickness of 0.1 m. This thickness increases up to max. 1.82 m in x-direction or max. 1.66 m in y-direction. The horizontal layers have a height of 0.2 m at the bottom, which increases up to max. 1.97 m at the top of the combustion chamber. The locations of the coal inlets at the front side and the coal-with-ash inlets on the rear side are indicated as well as the locations of the primary and secondary air inlets and the outlets to the two cyclones. Membrane walls cover nearly the whole

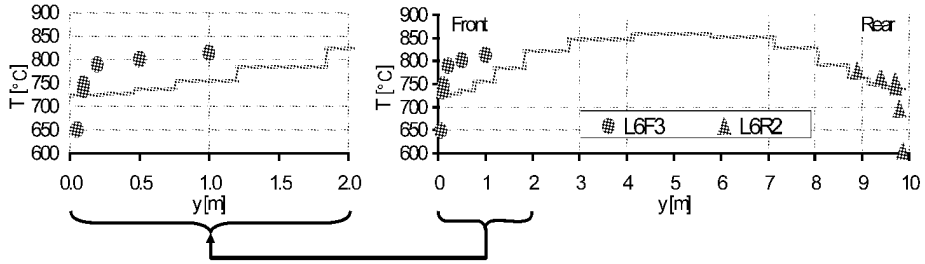

Fig. 3 Measured temperatures (dots) and simulated temperatures (lines) at level 6 of the Turów combustion chamber. Equal values of the dispersion coefficients in core and annulus, respectively

surface of the sides of the combustion chamber. The locations of the measurement ports where measurements were carried out by means of capacitance probes (equipped with additional thermocouples) and gas concentration measurement probes are indicated by their corresponding port numbers (L6F1 etc.)

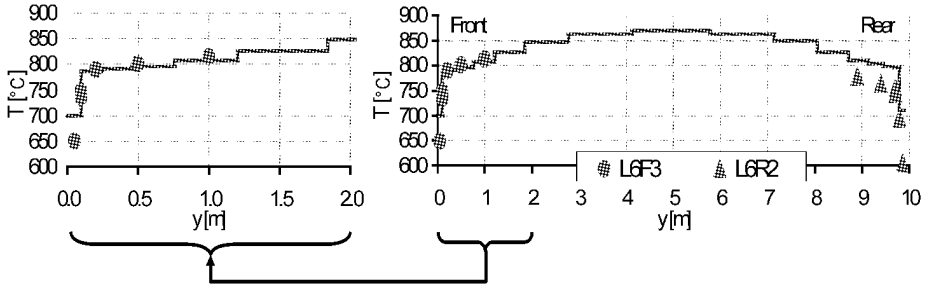

Fig. 4 Simulation run for the same operating conditions as Fig. 3, but the dispersion coefficient in the annulus region has been reduced by a factor of 100

Horizontal dispersion coefficients

For CFBC's equipped with membrane walls, it is well known, that a horizontal temperature profile exists such that inside a thermal boundary layer the temperatures are decreasing from a high level in the core to lower values near the wall (Hartge et al. 2005). As an example, the measured radial temperature profiles of ports L6F3 and L6R3 are shown in Fig. 3.

First simulation results where the dispersion coefficients in the wall zone and in the core zone, respectively, were assumed to be equal revealed that the core temperatures could well be reflected by the simulation tool. In the annulus region, however, the temperature decrease in the proximity of the wall could not be reproduced.

The physical reason is that the conditions for horizontal mixing are different in the core and wall zones, respectively. The dense down falling curtain of particles in the wall zone provides much less freedom to the particles for lateral mixing than the up flowing lean suspension in the core. In order to consider these differences a new simulation was started for the operating conditions of Fig. 3, however, with horizontal dispersion coefficients in the annulus for solids $D_{s,h,a}$ and gas $D_{f,h,a}$ being decreased by a factor of 100 in comparison to the core zone. As is seen from the results in Fig. 4 this gives a good description of the steep temperature decrease in the wall zone. Since another test with the dispersion coefficient in the wall zone being decreased by a factor of 500 gave no better results all following simulations were calculated with

$$D_{s,h,a} = D_{f,h,a} = D_{s,h,c}/100 \qquad (4)$$

with $D_{s,h,c}$ calculated from a Peclet number Pe of 150 (Lücke et al., 2004).

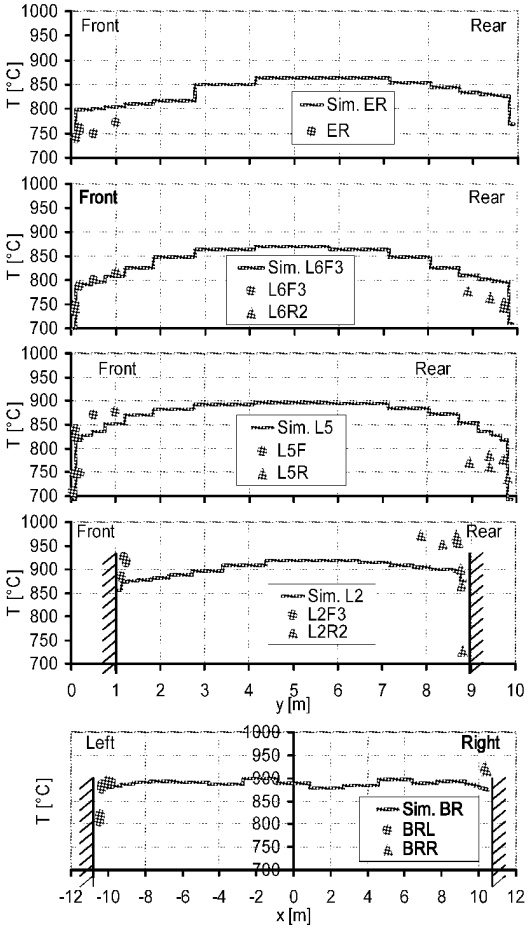

Fig. 5 Measured and simulated temperatures in the Turów combustion chamber at different measurement ports at the front side and at the rear side

Comparison of model calculations with measurements

A simulation run with input parameters adopted from the operating data obtained during one of the measurement campaigns (Hartge et al., 2005) was carried out for comparison of model calculations with measurements. In Fig. 5, measured and simulated temperature profiles are shown for the measurement ports in the middle of the combustion chamber at levels 2, 5, 6 and in the exit region respectively. Level five is in the

proximity of the lowermost internal heat exchanger bundles.

Although the simulation is not always in full agreement with the local temperature measurements it can be stated that the general temperature pattern is well met. We see that the temperatures in the wall zone are decreasing towards the membrane wall which is in agreement with the measurements. We also see that the temperature level is increasing with increasing height above the distributor until the first layer of horizontal heat exchanger tubes at level 5 is reached (cf. Fig. 2). In evaluating the measurements we have to consider the fact that the temperature measurements were taken over a time span of roughly one week and it may well be that the boiler load was not always constant during this long period. In view of the inevitable inaccuracies the general agreement between simulation and measurement is quite good.

Fig. 6 shows vertical cuts of the spatial temperature distribution. The cooling effect of the internal heat exchanger bundles is clearly seen.

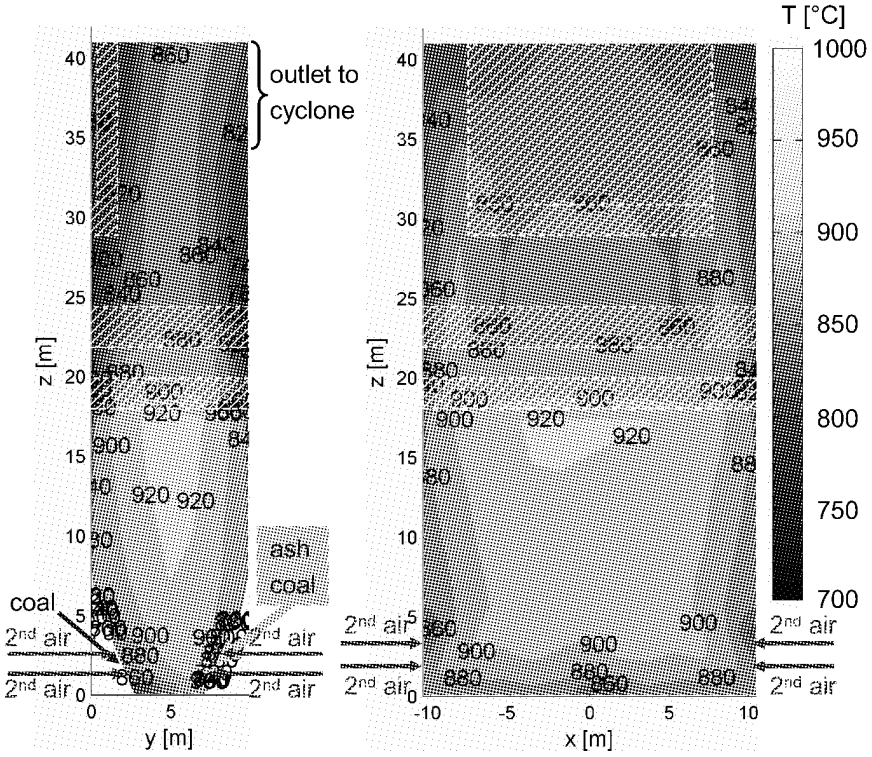

Fig. 6 Simulated temperature distribution in the Turów boiler's combustion chamber (left: section at x=0 m, right: section at y=5 m)

CONCLUSIONS

A three-dimensional simulation tool was developed for the three-dimensional simulation of temperature effects in large-scale circulating fluidized bed combustors. The simulation tool was validated with available measurements from the 235 MWe CFBC in Turów, Poland.

The simulation tool permits the calculation of temperature distributions in circulating fluidized bed combustors and the estimation of the risk of local overheating (hot spots).

NOTATIONS

c_p	specific heat capacity, kJ/(kg K)
$D_{f,h,}$	fluid horizontal dispersion coefficient, m^2/s
$D_{s,h,}$	solids horizontal dispersion coefficient, m^2/s
$\Delta H_{R,j}$	reaction enthalpy of reaction "j", kJ/mol
r_j	reaction rate, mol/(m^3 s)
S	local heat sink due to devolatilization, evaporation and heat transfer to heat exchanger surfaces, kJ/s
t	time, s
T	temperature, K
u	velocity, m/s
$\lambda_{s,h}$	heat conduction coefficient for the solids in horizontal direction, kW/(m K)
Λ_{eff}	effective heat conduction coefficient, kW/(m K)
ρ	density, kg/m^3

REFERENCES

ANSYS ICEM CFD: Homepage: http://www.ansys.com/products/icemcfd.asp, 2008.

CD-Adapco Star-CD: Homepage: http://www.cd-adapco.com/products/STAR-CD/index.html, 2008.

Hartge, E.-U.; Werther, J.; Wiesendorf, V.: Circulating Bed Technology VII (Grace, J.R., Zhu, J.X., deLasa, H, eds.) Can. Soc. Chem. Engng. , Ottawa (2002), pp. 325-332.

Hartge, E.-U.; Budinger, S.; Werther, J.: Proc. 8th Int. Conf. Circulating Fluidized Beds (Cen, K. ed.) Hangzhou/China (2005), pp. 675-682.

Johnsson, F. et al.: Circulating Bed Technology VII (Grace, J.R., Zhu, J.X., deLasa, H, eds.) Can. Soc. Chem. Engng. , Ottawa (2002), pp. 607-614.

La Nauze, R. D.: Chem. Eng. Res. Des. 63 (1985), pp. 3-33.

Leuschke, F.; Bleckwehl, S.; Ratschow, L.; Werther, J.: Circulating Fluidized Bed Technology IX (Werther, J., Nowak, W., Wirth, K.-E., Hartge, E.-U., eds.), TuTech Innovation Hamburg (2008), pp. 943-948.

Lücke, K. ; Hartge, E.-U.; Werther; J.. Int. J. Chem. Reactor Engng. (2004) A11.

Wischnewski, R.; Ratschow, L.; Redemann, K.; Hartge, E.-U.; Werther, J., Heidenhof N.: Proc. 19th Conf. Fluidized Bed Combustion (Winter, F., ed.) Wien (2006).

NUMERICAL CALCULATION OF HEAT TRANSFER DISTRIBUTION IN A 600MWe SUPERCRITICAL CIRCULATING FLUIDIZED BED BOILER

Y. Li[1], W. K. Li[1], Y. X. Wu[1], H. R. Yang[1], L. Nie[2], S. S. Huo[2]

1 Key Laboratory for Thermal Science and Power Engineering of Ministry of Education, Department of Thermal Engineering, Tsinghua University, Beijing, China
2 Dongfang Boiler Group Co. Ltd., Zigong, China

Abstract: The water wall heat transfer and heat flux distribution in a 600MWe supercritical CFB boiler with water-cooled panel in the furnace was numerically studied. The water wall was made of smooth tube membrane. The solid suspension density ρ, heat flux q and heat transfer coefficient K distribution in the furnace were predicted at rated boiler load (100%BMCR), 75% of turbine heat acceptance load (75% THA) and 50% THA. The results show that for a large-scale CFB boiler, the convection is the main part of heat transfer in the lower furnace, and radiation is the main in the upper lower. The ρ, q and K have the similar axial and radial distributions. Their radial distributions depend on the position of the water wall and boiler load, and show a peak value in the corner. The ρ is a sensitive to K. With increasing of the height in furnace, ρ decreases, thereby the q and K decrease. The radial distributions of q and K are similar at different height. The study shows that the three-dimensional model is valid to predict the heat transfer in the furnace of the 600MWe supercritical CFB boiler.
Keywords: wing wall, supercritical CFB boiler, 600MWe, heat transfer, distribution

INTRODUCTION

In recent years, supercritical CFB (circulating fluidized bed) technology has attracted much attention, because of the high power generation efficiency in addition to the merits of a conventional CFB boiler such as cost-effect emission controls and excellent fuel flexibility. For this technology, the water wall arrangement and hydrodynamic stability in the furnace must be considered to ensure the operation safety. In order to increase the penetration depth of the secondary air for better gas-solid mixing, the 600MWe supercritical CFB boiler was designed in pant-leg structure (Nowak and Laskawiec, 1999; Semedard and Gauville et al., 2001; Liu et al., 2003; Wu, 2005). Some water walls, e.g., water-cooled panel, were arranged in the furnace to add the heating surfaces. It is important to predict the distribution of solid suspension density and heat transfer coefficient in furnace with such structure by using available heat transfer models (Robert and Thomas, 1993; Li et al., 2007). Aimed at a 600MWe supercritical CFB boiler with water cooled panel, the solid suspension density, heat flux and heat transfer coefficient will be predicted at the boiler loads of 100% BMCR, 75% THA and 50% THA based on a three-dimensional model of heat transfer. It is expected that the results can be useful to improve the design the supercritical CFB boilers in the future.

DISCRIPTION OF THE FURNACE OF THE 600MWE CFB BOILER

Several types of CFB boilers with different structure features have been developed by different manufacturers and research institutes (Nowak and Laskawiec, 1999; Halder, 2001; Semedard, 2001; Stephen, 2001). The pant-leg structure furnace and the external heat exchangers (EHEs), are often used in the large scale CFB boilers, including the 600MWe supercritical one.

The schematic of the furnace and the panel wall is shown in Fig.1. The furnace is bilaterally symmetric. Besides the front wall, rear wall, two sidewalls, there is public panel wall in the middle of the furnace, and it is heated on both sides. The panel wall is used to decrease the furnace height and increase the heating surfaces. The height, width and depth of the furnace are 55m, 17.64m and 25.11m respectively. The water walls on the both inner side of the leg are bent upwards to form the panel wall. For pressure balance, there are holes opened on the panel wall. On the bottom of the water walls, thin refractory linings are laid to alleviate the abrasion. Above 78% THA, the boiler operates in the supercritical condition.

This paper studies on the water wall system in furnace from the water-cooled air chamber to the top of the furnace. To decrease the system complexity, the structure differences of the water wall tubes caused by the holes on the walls are neglected. The heat transfer between the air and water walls in the air chamber is neglected too, since the amount of the heat is very small compared with that in the furnace. A quarter of the furnace is studied because of the symmetric structure. The origin of the coordinate is set on the central bottom

of the furnace.

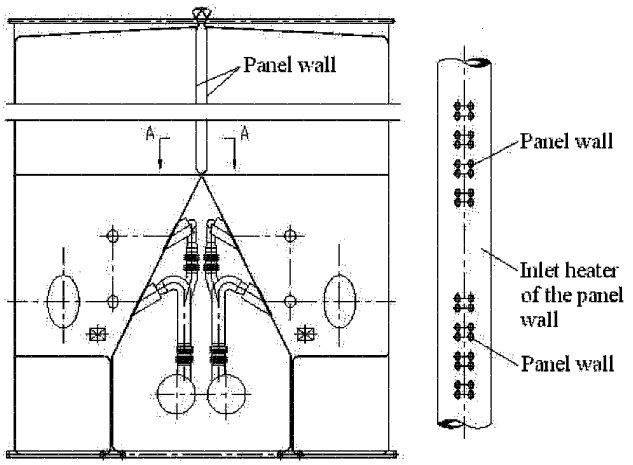

Fig.1 Simplified structure of the furnace and the water cooled panels in the furnace

Table 1 Boiler design parameters at the different loads

Load	Steam flow rate (t/h)	Steam pressure (MPa)	Steam temperature (℃)	Bed temperature (℃)
100%BMCR	1900	25.4	571	875
75%THA	1212	19.7	571	820
50%THA	809	13.1	571	790

NUMERICAL CALCULATION METHOD

Heat transfer model on the furnace side

The solid suspension density ρ, the bed temperature T_b and the fluidizing air velocity U_g, as well as the heating surface arrangement, the geometry of the furnace and the physical properties of solid particles, are the important factors for the heat transfer characteristics in a CFB boiler (Lints and Glicksman, 1993; Robert and Thomas, 1993; Lu et al., 2002; Li et al., 2007).

In the CFB furnace, shown in Eq. (1) and Eq. (2), the heat transfer coefficient on the furnace side α_b can be calculated as the linear superposition of the radiation heat transfer coefficient α_r and the convection heat transfer coefficient α_c, while α_c t can be divided as the gas part and the particle part (Lu et al., 2005; Wu, 2005).

$$\alpha_b = \alpha_r + \alpha_c \tag{1}$$

$$\alpha_c = \alpha_c^g + \alpha_c^p \tag{2}$$

And α_b can be calculated by Eq. (3), as

$$\alpha_b(x,y,z) = f\left[\rho(x,y,z), u_f, t_b(x,y,z), t_f(x,y,z)\right] \tag{3}$$

Where, $\rho(x,y,z)$、$t_b(x,y,z)$、$t_f(x,y,z)$ are respectively ρ, T_b and working fluid temperature at a position (x, y, z).

Field measurement results showed that the ρ distributions are similar on the different heights of different boilers, and thus the empirical formula was proposed for ρ calculation as Eq. (4) (Wu, 2005):

$$\rho = D_X(X) D_Y(Y) D_z(z, u_f, G_S) \tag{4}$$

By ignoring the furnace exit end effect, it can be known that ρ distribution in the depth direction is similar with that in the width direction, and it was also proposed that the distribution patterns of the relative ρ in the horizontal direction is quadratic equations (Zhang et al., 1998):

$$D_X(X) = a_0 + a_2 \left(\frac{u_f}{u_c}\right)^c X^2 \tag{5}$$

$$D_Y(Y) = a_0 + a_2 \left(\frac{u_f}{u_c}\right)^c Y^2 \tag{6}$$

Where, $\left(\frac{u_f}{u_c}\right)^c$ is a correctional parameter at certain fluidization condition.

Based on experimental results of some CFB boilers, it is regarded that the ρ profile along the furnace height has "two stages" which is separated by a outlet of the dense phase region as the inflection point (Lu et al. 1998). If G_s represents the solid circulating flow rate (kg/(m^2·s)) and ρ_s represents solid particle's true density(kg/m^3), the ρ distribution above the dense phase region can be calculated as follow Eq. (7):

$$D_z(z,u_f,G_s,\Delta P)=f(\Delta P)\left\{n_0\left(\frac{G_s}{\rho_s u_f}\right)+n_1\left(\frac{G_s}{\rho_s u_f}\right)\left(\frac{u_f}{u_c}\right)^d \exp[-n_2 z]\right\} \quad (7)$$

Where, the first term in the bracket refers to the influence of the solid circulating flow, and the second term refers to the influence of the solid backmixing and flow conditions. $f(\Delta P)$ refers to the influence of the bed inventory:

$$f(\Delta P)=p_0+p_1\exp(p_2\Delta P) \quad (8)$$

All the coefficients in the model are determined by the experiments (Wu, 2005), and showed in Table.2.

Table 2 The coefficients in the formula (1) to (8)

a_0	a_2	c	u_c	p_0	p_1	p_2	n_0	n_1	n_2	d
1	2.1	0.96	6.01	39.662	-0.01	41.17	15000	400000	0.18	-0.18

Heat transfer model on the working fluid side

The heat transfer coefficient on the working fluid side α_2 can be calculated by the hydrodynamic calculating methods. Supercritical fluid has some special properties. On the working fluid side, the heat transfer coefficient α_2 can be calculated by Eq. (9) when the enthalpy is out of the range of 1050 to 2720 kJ/kg.

$$\alpha_2=0.023\cdot\frac{\lambda}{d}\cdot \mathrm{Re}^{0.8}\cdot \mathrm{Pr}^{0.4} \quad (9)$$

Based on the heat transfer models of the furnace and the working fluid inside the tube, the furnace of the 600MWe supercritical CFB boiler with water cooled panels is studied. In this study, ρ, as well as α_b and hydrodynamic parameters, is divided into many sections along the height of furnace (Wu, 2005). In each section, the heat flux is assumed as the same, and the working fluid can use the average parameter. By this way, the ρ distribution, q and α_b can be calculated.

RESULTS AND DISCUSSION

Overall heat transfer characteristics in furnace

The local average ρ affects α_r and α_c which caused by the particle flow in the thermal boundary layer (Lu, 2002). Based on the experimental measurement, it was found that, with decreasing of ρ, the percentage of the particle convection heat transfer decreases, while the percentage of the radiation heat transfer increases. The calculation results obtained by the three-dimension model for the furnace of the 600MWe CFB boiler (Fig.2) show the similar trends. The heat release of the solid particles in the furnace is controlled by both the radiation

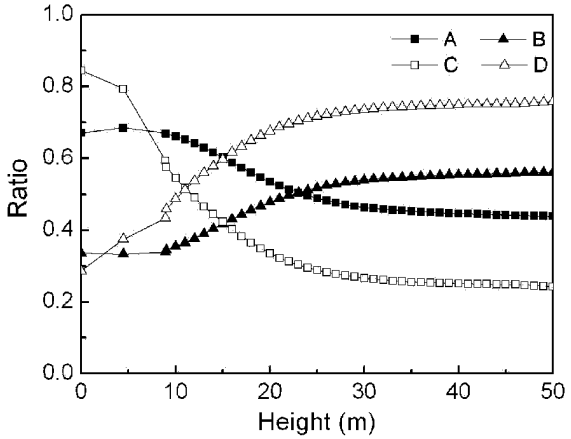

Fig. 2 The percentage of radiation and convection heat transfer distribution along the furnace height at the load of 100%BMCR and 50%THA, when the gas velocity in furnace is 5.5 m/s and 2.31 m/s respectively. (A is ratio of the convection heat transfer at 100% BMCR, B is ratio of the radiation heat transfer at 100% BMCR, C is ratio of the convection heat transfer at 50% THA and D is ratio of the radiation heat transfer at 50% THA)

and convection at the higher load; however, if ρ is small, the radiation heat transfer is dominant. While at the lower load, the heat transfer is controlled by the radiation in the fast fluidization region at the upper part and the particle convection in the dense phase region at the lower part. This is generally applicable for a large-scale CFB boiler. The region governed by the radiation is larger at a lower load.

Distribution of solid suspension density in furnace

The distribution of the local ρ in furnace (Fig. 3) shows that there is a maximum value above the air distribution plate, and the ρ monotonically decreases with the increasing of height. At the load of 100% BMCR, the ρ is nearly constant above 20 m height. When the load decreases, the ρ becomes smaller, and transient point for the constant ρ is lower. At the load of 50%THA, the difference of axial ρ profiles is not obvious. That is mainly because that, with the decreasing of the load, the fluidizing velocity u_f and the circulating flow rate G_s decrease, leading to the decrease of ρ near the water walls. On the side water wall or the water cooled panel, ρ at the corner is the highest while at the center is the lowest. However for the front-wall and the rear-wall, the highest ρ is near the side wall and the water cooled panel. Compared with other water walls, ρ on the front-wall and the rear-wall is the highest. With the decreasing of the load, the circumferential distribution is more uniform, it means that the deviation is less.

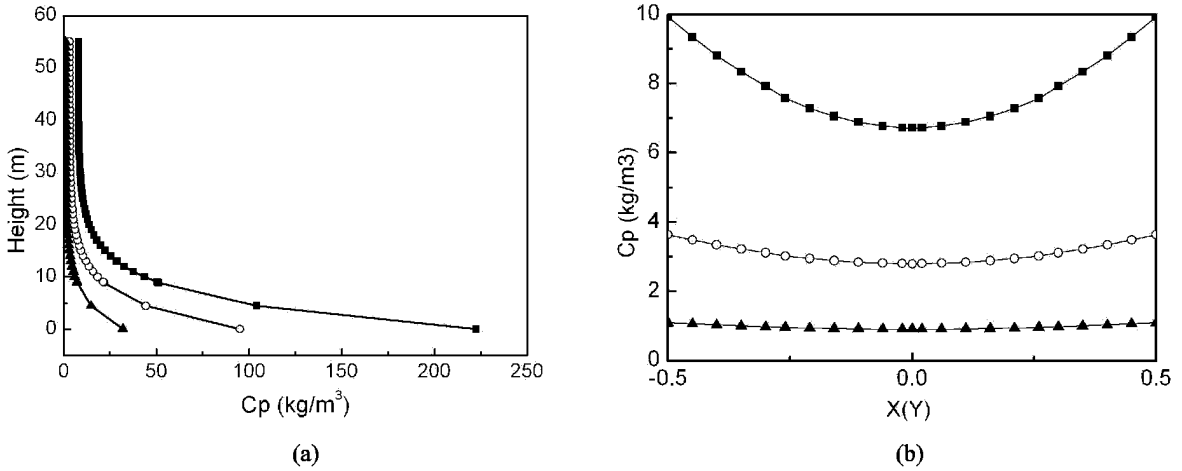

Fig. 3 The axial distribution(a) and the radial distribution (b) of average local solid particle suspension density at different loads

100% BMCR 75% THA 50% THA

Distribution of the heat flux

The distribution of heat flux q in furnace along the altitude direction is shown in Fig. 4. It shows that q is decreasing with increasing of the height. Q above the air distribution is the maximum along the height, where ρ is the highest in the furnace. At the load of 100% BMCR, the violent change of the q is occurred on about 20 m above the air distribution palate, while the change of q is smaller above this position. And it also shows that the average q in furnace is decreasing while the load is decreasing. In Fig.5, the q distribution along the height is similar with the distribution of total heat transfer coefficient K (K is the total heat transfer coefficient from the

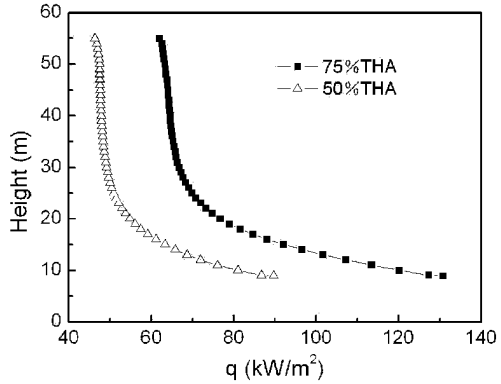

Fig. 4 The axial distribution of average heat flux at the loads of 75%THA and 50%THA

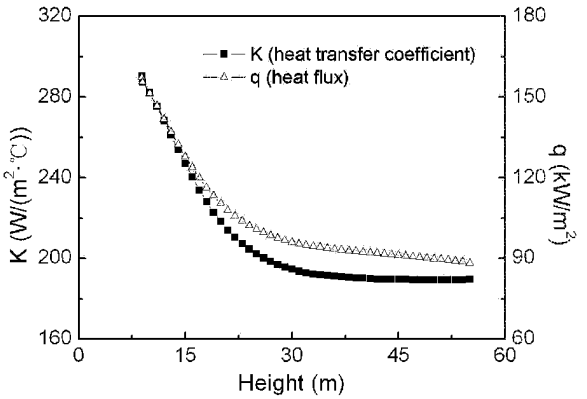

Fig. 5 The axial distribution of heat transfer coefficient and heat flux

particle to the working fluid in the water wall tubes, which consider the interaction of α_b and α_2), and the distribution of ρ has the similar trends, too.

The raidal distribution of the q is not uniform, as shown in Fig.6. (The distribution on the side wall is similar with the water cooled panel). At the corner of the side wall and panel wall, q is higher than that in the center on the same level. For the water cooled panel divides the furnace into two parts, q near the panel is as higher as that near the side wall.

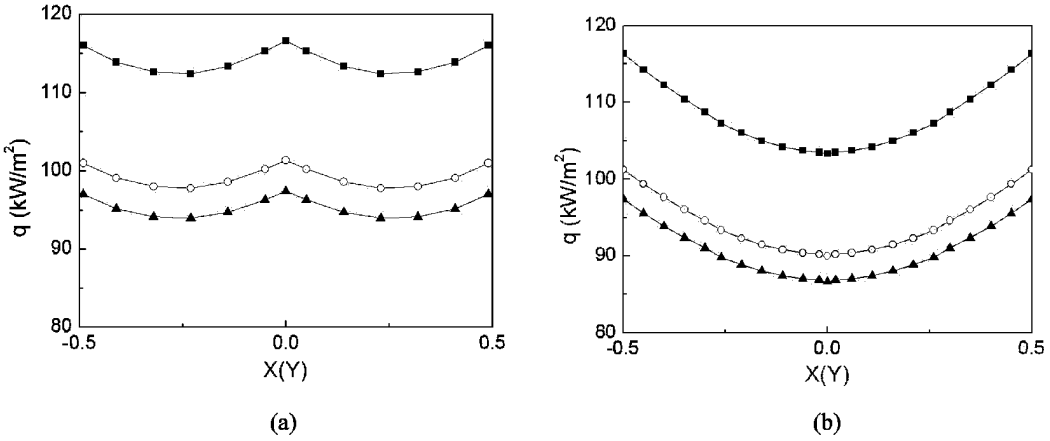

Fig. 6 The radial heat flux distribution on the front-wall(a) and the side-wall(b)
20 m 30 m 40 m

The solid particle suspension density ρ changes greatly in the lower part of the furnace, while the heat transfer coefficient on the working fluid side α_2 is almost the same in the area, so, the q is uniform in this area; in the upper part of the furnace, ρ is decreasing, which affects the heat transfer greatly, so it causes the significant changes of the heat transfer coefficient circumferential distribution, while in this area, the heat transfer on the working fluid side is different in the tube, so the circumference bias distribution of the q is great. And it is found that the distributions of q are similar on the different height of the boiler.

Distribution of the heat transfer coefficient

The upward and circumferential distributions of total heat transfer coefficient K are similar with that of ρ and the q. K is decreasing with the increase of height, and decreasing from the corner to the central of the furnace. K is lower when the load is decreasing, and the position which becomes uniform is lower.

The ρ has great influence on the heat transfer characteristic in furnace. The ρ increases with the decrease of the load, which directly affects the radiation and convection heat transfer, and leads to the reduction of K.

In Fig.7, at the load of 100% BMCR, the heat transfer coefficient on the working fluid side α_2 in the supercritical region shows the trend of firstly increasing then decreasing. When the load is at 75% THA, the α_2 in the tube is higher because the working fluid is in the sub-critical state, and the mechanism is two-phases nucleate boiling. When the load is 50% THA, the highest α_2 reduces and the position of the highest α_2 moves to the inlet of the water wall tubes.

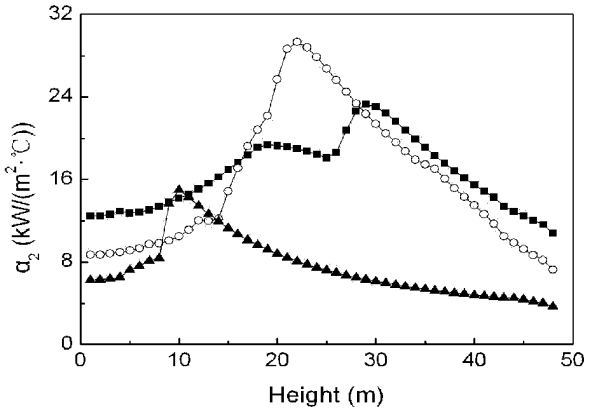

Fig. 7 The heat transfer distribution on the working fluid side on the loads of 100% BMCR, 75% THA and 50% THA
100%B-MCR 75%THA 50HA

CONCLUSIONS

The solid suspension density ρ, heat flux q and K decrease with the increase of the height in the furnace, and is nearly constant when the height is more than about 20 m in the 600MWe supercritical CFB boiler.

The radial heat flux on the side walls and water cooled panel are high at corner, and low in the centre of the furnace. On the front-wall and rear-wall, the higher heat flux positions are near the side-walls and the water cooled panel. And the radial distribution of the q or ρ is similar at the different height of the boiler.

The total ρ decreases with the decrease of the load, and so does the radial distribution. It is a sensitive factor on α_b in the furnace of the 600MWe supercritical CFB boiler.

NOTATIONS

Symbols

d	inner diameter of the water wall tube	m
G_s	solid circulating rate	kg/s
K	The total heat transfer coefficient	kW/(m^2·℃)
Re	Reynolds number	-
P_r	Prandtl number	-
t	Temperature	℃
u	Fluidizing velocity	m/s
u_c	The model parameter, experimental data	m/s
x_0	The width of the furnace	m
y_0	The height of the furnace	m
x	The x coordinate	m
y	The y coordinate	m
z	The z coordinate	m
X	The relative depth of the furnace, $X = \frac{x}{x_o}$	
Y	The relative width of the furnace, $Y = \frac{y}{y_o}$	

Greek Letters

A	Heat transfer coefficient	kW/(m^2·℃)
α_b	Furnace side α	kW/(m^2·℃)
α_c^g	Gas convection α_b	kW/(m^2·℃)
α_c^p	Solid particle convection α_b	kW/(m^2·℃)
α_2	Working fluid side α	kW/(m^2·℃)
ρ	solid suspension density	kg/m^3
ρ_s	True density of the solid particle	kg/m^3
λ	thermal conductivity	kW/(m·℃)

ACKNOWLEDGEMENTS

Financial support of this work by Key Project of the National eleventh-Five Year Research Program of China (2006BAA03B02) is gratefully acknowledged.

REFERENCES

Halder, P.: Proceeding of 16th International Conference on Fluidized Bed Combustion. 2001. Nevada: ASME.(2001)

Li, J J., Li, Y., Lu, J F.: Journal of Tsinghua University (Science and Technology), 47(2007), pp.2026-2030.

Lints, M C., Glicksman, L R.: AIChE Symposium Series 296, Fluid-particle Process: Fundamentals and Applications, 89(1993), pp.297-304.

Liu, J., Wang, Q H., Luo, Z Y.: Power Engineering, 23(2003), pp.2179-2204.

Lu, J. F., Jin, X Z., Yue, G X.: Journal of Tsinghua University (Science and Technology) , 38(1998), pp. 7-10.

Lu, J. F., Zhang, J S., Yue, G X.: Heat Transfer – Asia Research, 31(2002), pp.540- 550.

Nowak, W B Z., Laskawiec, J.: Proceedings of the 15th International Conference on FBC. Savannah: ASME. (1999), No.0122.

Robert, J D., Thomas, J B.: Proceedings of the 4th International Conference on CFB. New Jersey, 1993: pp.334-339.

Semedard, J C., Gauville, P., Morin, J X.: Proceeding of 16th International Conference on FBC. Nevada: ASME, (2001), No.171.

Stephen, J., Goidich, T. H.: Proceeding of 16th International Conference on Fluidized Bed Combustion. Nevada, (2001)

Wu, Y X.: Proceeding of the 5th International Symposium on MFHT. (2005), No.149.

Zhang, J S., Lu J F., Jin, X Z.: Journal of Tsinghua University (Science and Technology), 38(1998), pp.11-14.

IMPROVEMENT OF CFD METHODS FOR MODELING FULL SCALE CIRCULATING FLUIDIZED BED COMBUSTION SYSTEMS

Srujal Shah[1], Marcin Klajny[2], Kari Myöhänen[1], Timo Hyppänen[1]

1 Lappeenranta University of Technology, Lappeenranta, Finland
2 Foster Wheeler Energia Oy, Varkaus, Finland

Abstract: With the currently available methods of computational fluid dynamics (CFD), the task of simulating full scale circulating fluidized bed combustors is very challenging. In order to simulate the complex fluidization process, the size of calculation cells should be small and the calculation should be transient with small time step size. For full scale systems, these requirements lead to very large meshes and very long calculation times, so that the simulation in practice is difficult. This study investigates the requirements of cell size and the time step size for accurate simulations, and the filtering effects caused by coarser mesh and longer time step. A modeling study of a full scale CFB furnace is presented and the model results are compared with experimental data.

Keywords: modeling, multiphase, computational fluid dynamics, filtering, averaging

INTRODUCTION

The current development trends of circulating fluidized bed (CFB) combustion technology include ever increasing unit sizes, improvement of plant efficiency and reduction of emissions including possibility of carbon capture with oxyfuel combustion when using fossil fuels. The technological development requires valid and efficient modeling tools so that the future plants can be optimally designed and operated.

The complexity of the furnace process and the large dimensions of commercial CFB units set challenges for the modeling. Just the simulation of the fluid dynamics of a full scale circulating bed is extremely difficult – yet the fluid dynamics have a large effect on all the other process phenomena in a CFB. With fundamental, microscopic CFD models, such as Eulerian multiphase models based on kinetic theory of granular flow, the required mesh spacing is very fine (typically 10 – 100 particle diameters), and consequently, the required time step for a stable calculation is small (typically 0.1 – 1.0 ms). Various researchers are addressing the problem of increasing the spatial and temporal spacing for simulation of larger scales, but it is very unlikely that a commercial scale fluidized bed process can be simulated with full set of equations for chemistry, energy and particle comminution in any near future (Agrawal et al., 2001; Reh, 2003; Ibsen et al., 2004; Andrews et al., 2005; Kallio, 2005; Igci et al., 2008).

The first section of this paper presents a two-dimensional laboratory scale case of gas-solid flow simulation for bubbling fluidized bed. The purpose of this small scale study is to analyze the effect of grid and time step size. Microscale and mesoscale flow structures and fluctuations are observed when using very fine mesh and small time step. If the mesh cell size and the time step size are increased, these phenomena are filtered and information is lost. This has an effect on the drag force between the fluidization gas and solids, which influences the macroscopic behaviour of the gas-solid flow.

The second section presents an example of CFD modeling of industrial scale CFB furnace. At full scale, the size of the calculation cells must be relatively large to enable reasonable calculation speed, thus filtering of the data is expected. The model results are compared with the measurements and different options for improving the calculation with a coarse mesh are presented and discussed.

Finally, a semi-empirical, steady-state, three-dimensional CFB furnace model is applied for simulation of the full furnace process. In the original 3D process model, the solid concentration fields are based on empirical correlations. In this work, the simulation of the solids flow field in the semi-empirical model is modified by applying the CFD modeling results, and the effect on the results is presented.

TWO-DIMENSIONAL BUBBLING FLUIDIZED BED STUDY

A small scale study of 2D bubbling fluidized bed was performed. A schematic of the geometry is shown in Fig. 1. The lowermost left corner has the co-ordinates (0, 0). The fluidization gas is introduced through four inlets at the bottom of the domain. The width of each inlet is 0.03m.

The domain was discretized by a structural, orthogonal mesh created in Gambit. Gas-solid flow simulations were performed by a commercial CFD package, Fluent 6.3.26. Eulerian-Eulerian approach applying the kinetic theory of granular flow was used in the transient simulations of gas and solid phases.

Discretization scheme for time was 1st order implicit and for space was 1st order upwind. Turbulence model for the simulation was standard kappa-epsilon dispersed multiphase model. Boundary condition at the outlet was pressure outlet and no-slip condition for both gas and solid phase was used at all walls. Initially the solids were patched with 0.6 volume fraction in the bottom region (0.2m X 0.2m). The inlet gas phase velocity was kept to be 1 m/s and no solid enters the bed through inlets. The value of restitution coefficient was kept as 0.9 and no other forces were considered except gravity.

A complete set of governing equations for two-fluid model (gas phase and one granular phase) which have been used in this study can be found from Fluent 6.3.26 manual (2006). Several researchers (e.g. Boemer et al. 1997; Van Wachem et al. 2001) have done comparative analysis of closure models for Eulerian simulations for gas-solid flow. The model parameters and closing equations used in these simulations are given in Table 1. It should be noted that the purpose of this study was to see the effect of grid and time step size and for that reason, the models chosen were according to either default settings in Fluent or from literature. Comparison of different closure model studies is not considered here and all simulation cases were done with single set of closure models as given in Table 1.

In each of the different grid cases, the calculation was performed for 5 seconds in the beginning to reach the stable solution. Then the calculations were allowed to continue for 180 seconds for different time step size cases to achieve statistically valid results. In each of these 180 seconds calculation, scaled residuals convergence limit for all the variables except continuity was set to 1E-03. The continuity error was evaluated by determining a relative mass imbalance in calculation cells, and it was found out to be small, less than 0.1% in all cases.

Time averaged (Reynolds averaged) values of pressure and volume fractions and Favre averaged velocities were determined for each case c Figure 2 presents the time averaged volume fractions of solid phase.

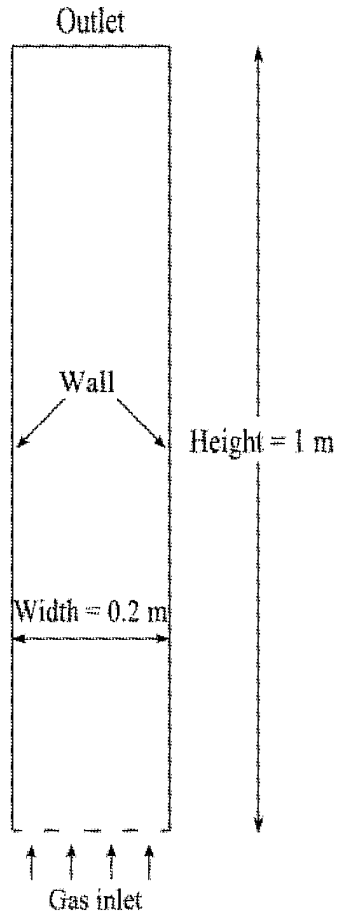

Fig. 1 Geometry of 2D BFB

Table 1 Model Parameters and Closure Models

Material Properties		Closure models	
Gas phase:	Density: 1.225 kg/m^3	Drag correlation:	Gidaspow
	Viscosity:1.789E-05 kg/ms	Granular viscosity:	Gidaspow
Solid phase	Density: 2500 kg/m^3	Granular bulk viscosity:	Lun-et-al
	Diameter: 500E-06 m	Frictional viscosity:	Schaeffer
Grid and Time Steps		Solids pressure:	Lun-et-al
Cell size (cm):	0.25, 0.5, 1.0	Radial distribution:	Lun-et-al
Time step size (ms):	0.5, 1.0, 5.0	Granular temperature:	Algebraic

The different model names are given as selected in Fluent. In Fluent, the radial distribution Lun-et-al is actually the radial distribution used by Ogawa et al. (1980).

When the mesh cell size is increased to 1 cm, the averaged solid volume fraction fields show clearly more uniform distribution, indicating filtering of information. A clear exception in the results is the case with 5 ms time step and 0.25 cm cell size. This case shows unsymmetric average values, although the boundary conditions are symmetrical. This is due to unstable transient calculation caused by a too high Courant number. According to Hulme et al. (2005), the Courant number should be maintained below 0.3. The maximum Courant number can be obtained as

$$C_{\max} = v_{\max} \frac{\Delta t}{\Delta x} \tag{1}$$

in which the Δt and Δx are the time step size and the cell size. The maximum instant velocities in all cases were around v_{max} = 1.0 m/s. In the case of 5 ms and 0.25 cm, this gives C_{max} = 2.0, which is clearly higher than the limit determined by Hulme. However, in this study, reasonable values could be achieved with Courant number as high as 1.0 (Δt = 5 ms, Δx = 0.5 cm).

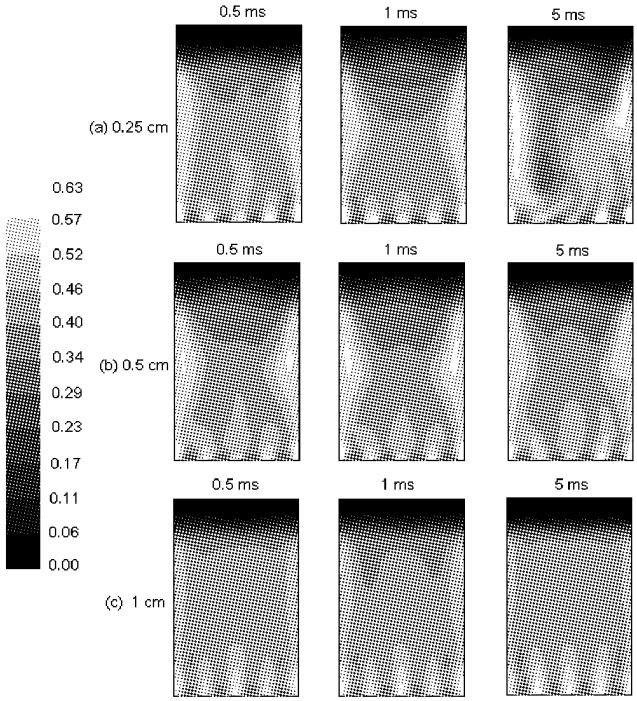

Fig. 2 Contours of time averaged solid volume fraction with different time step size (0.5, 1.0, 5.0 ms) and cell size (0.25, 0.5, 1.0 cm)

More detailed analysis of the results was performed by monitoring the instantaneous process values at different locations of the domain. Figure 3 presents examples of time averaged vertical drag force, calculated from the monitored values for a point with co-ordinates (0.04 m, 0.25 m). The drag coefficient in these simulations was based on model by Gidaspow et al. (1992), which is a combination of Wen-Yu model for dilute phase and Ergun equation for dense phase. From this model, the averaged drag force F_D is determined:

$$\alpha_f \le 0.8 : < F_D > = \left(\frac{150\langle \alpha_s \rangle^2 \mu_f}{\langle \alpha_f \rangle d_s^2} + 1.75 \frac{\rho_f \langle \alpha_s \rangle \langle |v_{s,y} - v_{f,y}| \rangle}{d_s} \right) \langle v_{f,y} - v_{s,y} \rangle$$

$$\alpha_f > 0.8 : < F_D > = \frac{18\mu_f \langle \alpha_s \rangle}{d_s^2} \left[1 + 0.15 \left(\langle \alpha_f \rangle \langle \mathrm{Re}_s \rangle \right)^{0.687} \right] \langle \alpha_f \rangle^{-2.65} \langle v_{f,y} - v_{s,y} \rangle, \quad \mathrm{Re}_s = \frac{\rho_f d_s |v_{s,y} - v_{f,y}|}{\mu_f} \tag{2}$$

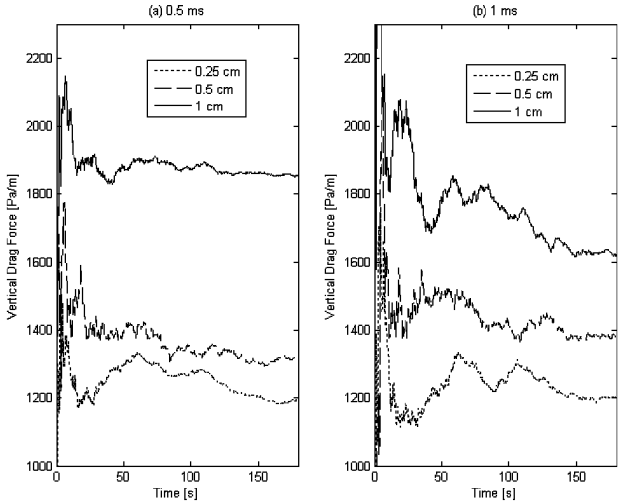

Fig. 3 Time-averaged vertical drag force for different cell size at a point for: (a) 0.5 ms and (b) 1 ms

The drag force value in the figure is the averaged drag force up to time t at the x-axis, thus they should convergence to a constant value during the simulation. The vertical drag force is clearly increased when the cell size is increased to 1 cm as seen from (a). When compared with 1 ms case (b), the value of drag force is similar for finer grids of 0.25 cm and 0.5 cm, and 1 cm is still showing higher value. Based on these results, the drag

force should be corrected already at cell size 1 cm in order to achieve similar results as with finer mesh. Similar results have been found with other drag coefficient models and by other researchers as well (Kallio, 2005; Igci et al., 2008).

LARGE SCALE CFD STUDY

The object of the large scale CFD study was a 274 MWt CFB unit burning bituminous coal. The height of the furnace is 43.3 m and the cross-section 14.3 m × 6.7 m. The model boundaries included primary air through grate, secondary air through multiple SA nozzles and other ports, and solid feed rates from the solid circulation ports. The inlet values were based on measured test balance values and on design data. The model did not include any reactions. The furnace temperature and the expansion of colder inlet gases were simulated by setting the solid phases to a fixed temperature (1150 K), specifying the gas inlet temperatures (490 K) and modeling the heat transfer between the gas and solids. The heat transfer to walls was neglected. The bed material was modeled as a mixture of two solid phases with different particle diameters: 128 and 1500 μm. At first, the model was calculated until stable operating conditions were reached. After this, the calculation was continued for 21.7 seconds and the different process variables (pressure, velocities, volume fractions) were averaged. Table 2 presents the main model parameters and used closure models. The maximum cell dimension was about 0.3 m and the number of calculation cells was about 400 000, using hexahedral cells for most of the domain and tetrahedral cells for tapered lower furnace section. Based on small scale studies, the used cell size is coarse and will cause filtering of the results. Figure 4 presents the modeled instantaneous and average solid concentration and vertical solid velocity.

Table 2 Model Parameters and Closure Models

Material Properties		Closure models	
Gas phase: Incompressible ideal gas		Drag correlation	
M = 28.966 kg/kmol, μ = 6E-05 kg/ms		gas-solid:	Syamlal-Obrien
Solid phases: ρ = 2500 kg/m^3		solid-solid:	Syamlal-Obrien-symmetric
Solid phase 1 (Solid 128)	d_s = 128E-06 m	Heat transfer coefficient:	Gunn
Solid phase 2 (Solid 1500)	d_s = 1500E-06 m	Granular viscosity:	Syamlal – Obrien
Grid and Time Steps		Granular bulk viscosity:	Lun-et-al
Cell size (m):	0.1 – 0.3	Frictional viscosity:	none
Time step size(ms):	2.5	Solids pressure:	Lun-et-al
Averaging time (s):	21.7	Radial distribution:	Lun-et-al
		Granular temperature:	Algebraic

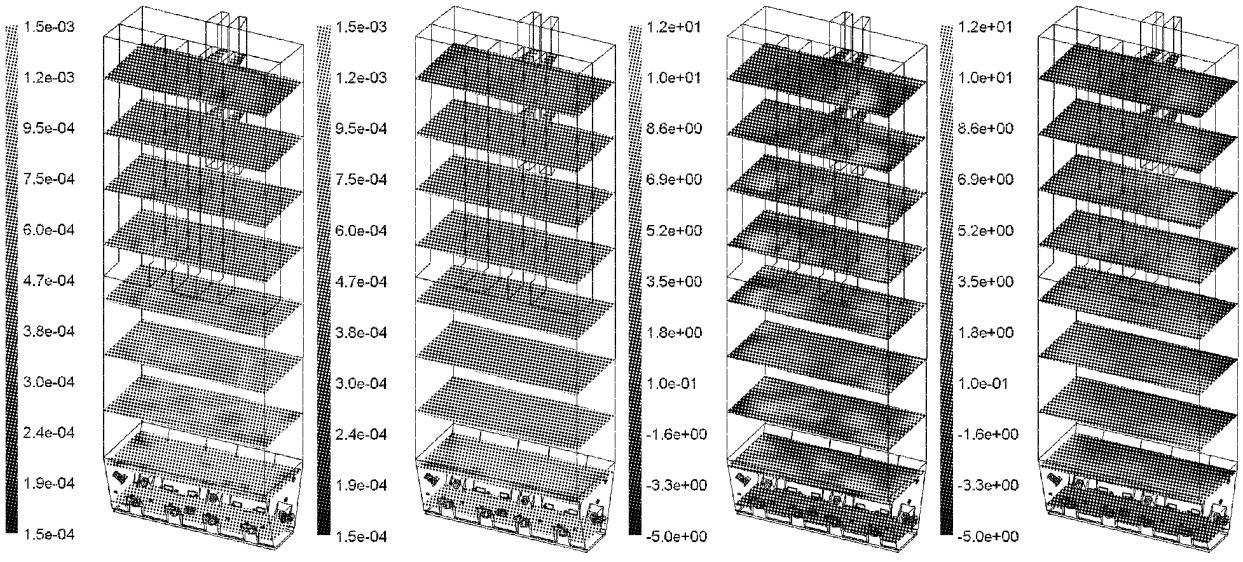

Fig. 4 Instant (a) and time-averaged (b) volume fraction of solid phase. Instant (c) and Favre-averaged (d) vertical solid velocity, m/s

The following figure compares the calculated solid concentration and pressure profiles with the measured profiles.

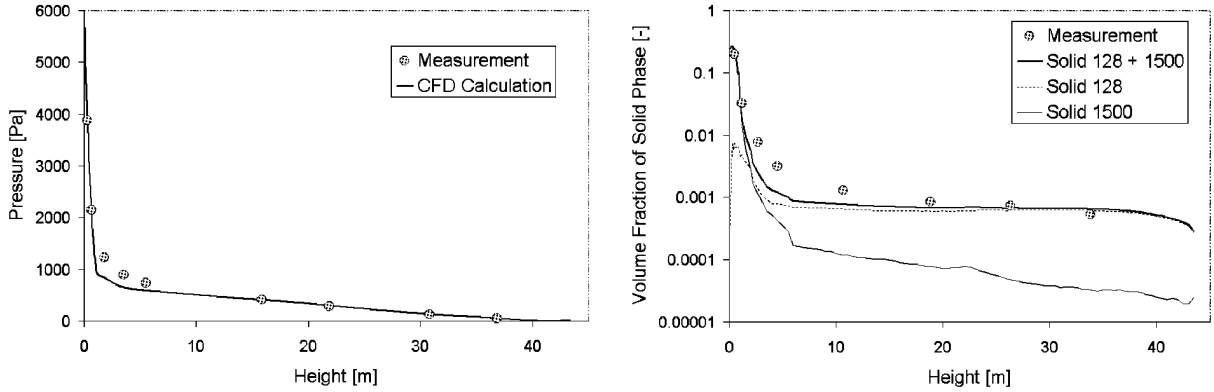

Fig. 5 Profiles of pressure and volume fraction of solid phases: measured and calculated in Fluent

Often in a CFD calculation, the solids concentration at the lower part of the furnace is too low and at the upper part of the furnace too high compared with the measurements. This is due to overestimated gas-solid drag force when using too coarse mesh, as was demonstrated in the small scale BFB study. In this study, when simulating the solids with two particle phases, one coarse and one fine, the measured pressure and solid concentration profiles could be simulated with reasonable accuracy. Apparently in large scale, the macroscopic solid concentration profile can be achieved, if the number of cells is large enough to allow bypassing of gas through solid phase, even if the microscale flow features have not been accurately simulated.

Downflowing solids were modeled near the walls, but not in all regions. Usually, a downflowing wall layer has been observed in cold model studies and in large scale pilot tests and in commercial units. The cell dimensions were up to 30 cm, which is likely to cause filtering of the results and for example poor simulation of the solids flow near the walls.

One interesting result to notice is that the averaged process data fields are not symmetrical, although all the boundary conditions and the model geometry are symmetrical. The used averaging time was probably too short for producing actual "steady-state"-values, which is a probable reason for this phenomenon. In real conditions, the duration to reach stable operating conditions can be several hours.

The calculation results could be improved by different methods: a) decreasing the cell size, b) increasing the number of particle phases (e.g. Ibsen et al., 2004), and c) modifying the drag function (e.g. Kallio, 2005). The first two alternatives have a negative effect on calculation speed. The calculation speed is inversely proportional to the number of cells. With a very small cell size, the time step must be reduced as well in order to maintain stable calculation. This reduces the computation speed further. The above calculation case was tested with four solid phases, but the required calculation time would have been in the order of several months, so this was not proceeded – at least for the time being. Modifying the drag function would be a feasible option, if valid measurement data is available for validating the modified models.

PROCESS MODEL STUDIES

The above described CFB boiler was analyzed by a three-dimensional, steady-state, semi-empirical furnace model, which is described by Myöhänen et al. (2003). In this macroscopic model, the different solid materials (char, ash, limestone, inert bed) are divided to six particle size fractions with average diameters 32, 94, 153, 340, 1250 and 4000 μm. In the original model code, the solid concentration fields of different materials except char are set by empirical correlations, which are following the format given by Johnson and Leckner (1995).

$$\rho_s(h)=(\rho_{sb}-\rho_{st}e^{C_{di}H})e^{-C_{tr}h}+\rho_{st}e^{C_{di}(H-h)} \quad (3)$$

The coefficients are determined from measured vertical pressure profile or by empirical correlations. The parameters for each material and size fraction are adjusted so that the total integrated mass over furnace height is equal to mass solved by the process model. In horizontal direction, the solid concentration is assumed to be constant except for a denser wall layer, which is used for simulating the internal circulation.

In this study, the horizontally uniform solid concentration fields were replaced by the solid concentration fields determined from the above CFD study. First, the CFD calculation was averaged to produce steady-state results. Due to the time constraints, the averaging time was relatively short, only 9 seconds. Consequently, the results are only approximating the actual steady state values.

For the process model, the concentration fields of the two finest particle size fractions were set according to 128 μm solid phase and the remaining size fractions according to 1500 μm solid phase modeled by CFD. For a better simulation, the number of particle size fractions in the CFD calculation would need to be larger, but this would mean more time-consuming calculations.

As this was a first trial of the applicability of this method, all other process submodels were left unchanged: e.g. the solid velocities were determined by a potential flow approach, the internal circulation was modeled by empirical wall layer model and the different mixing phenomena were modeled by dispersion.

The calculation mesh of the process model was different from the CFD-model, so the transported solid concentration values were interpolated to match the mesh. The following figure illustrates the solid concentration of the CFD calculation, the original process model and the modified process model.

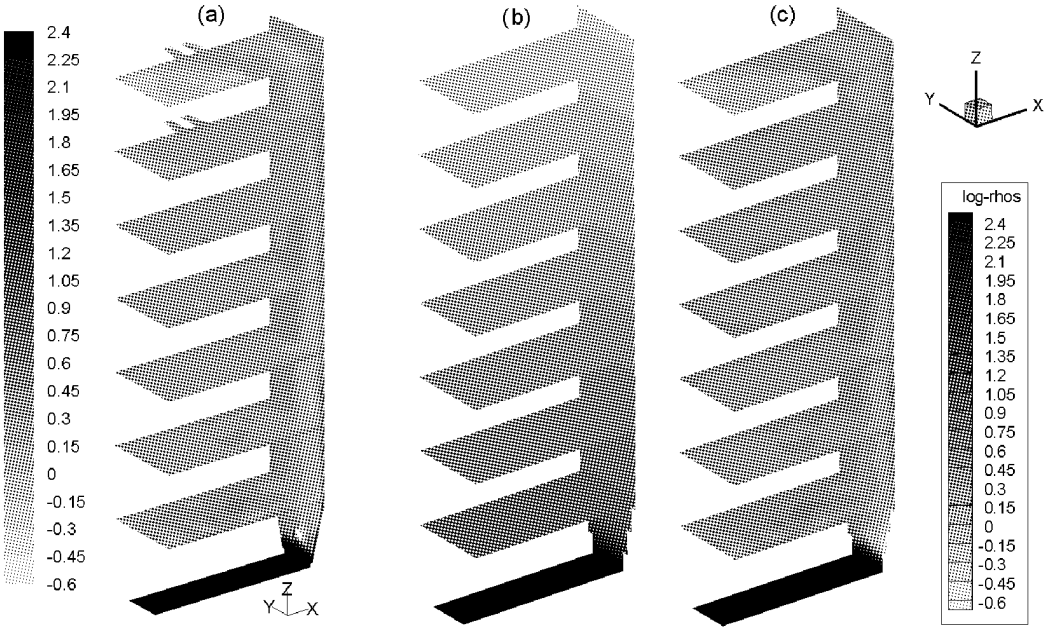

Fig. 6 Solid concentration fields, $\log_{10}(\rho_s)$: (a) Fluent-CFD, (b) original process model, (c) modified process model

Figure 7 shows the average vertical solid concentration profiles of different models compared with the measured solid concentration profiles. With the CFD-based profiles, the solid concentration was smaller at the lower part and higher at the upper part of the furnace than with the original model and measurements. Due to higher concentration at furnace exit, the solid concentration was higher as well: 133→192 kg/s. The differences in the solid concentration field have a direct effect on the energy transfer inside the CFB. Figure 8 compares the temperature fields of the two calculations.

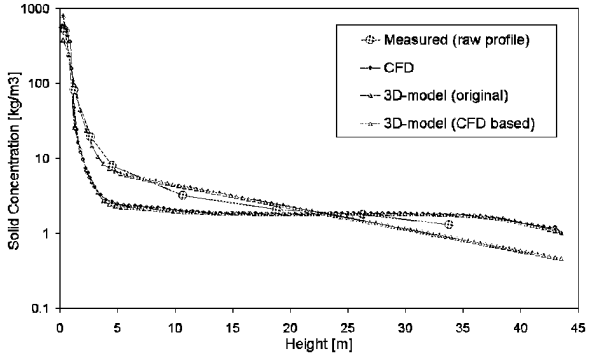

Fig. 7 Average vertical solid

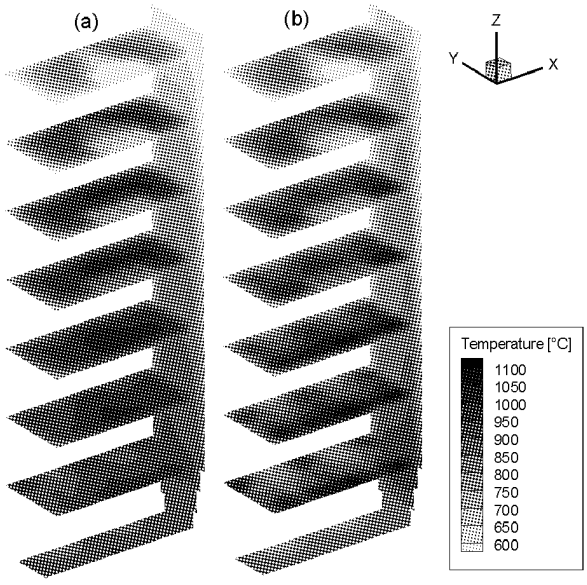

Fig. 8 Temperature profiles: (a) original, (b) modified

Especially at the lower furnace, the temperature gradients are clearly larger in the modified calculation. The cross-sectional average temperatures are smaller in the modified case and the temperature at the furnace exit decreases 854→835°C.

In this simple study, the mixing phenomena in the process model were not yet altered. Clearly, the transient solid mixing has a large effect on different phenomena and this would need to be accounted for when transferring the data from CFD calculations to the process model. The transient mixing can be evaluated by monitoring the fluctuations of the solid volume fraction and the velocities. This data would need to be applied in the steady state process model. This will be the subject of future studies. The largest challenge is how to produce valid CFD results. In this study, the vertical solid concentration profiles modeled by CFD did not quite match the measured profiles. Moreover, the modeled gas and solid velocity fields were not exactly fitting with the current understanding.

CONCLUSIONS

The 2D bubbling fluidized bed study showed that the time step size and the mesh size play important roles in CFD simulations. Very fine mesh and small time steps are very computationally expensive and thus practically not possible for large scale studies. Comparison of modeled drag forces show that 1 cm grid is already coarse for the simulations of gas-solid flow and thus when using 1 cm or even more coarser grid, the drag force must be properly modeled in order to get valid results for gas-solid flow simulations.

The example CFD modeling of a large scale CFB furnace showed that the measured pressure and solid concentration profiles can be approximately simulated if multiple solid phases representing different particle sizes are used. In this study, only two particle size phases were used and the results were already quite promising. However, the modeled velocity fields showed suspicious results. The calculation speed with multiple solid phases remains to be a problem.

If the solid flow field can be accurately modeled, then the acquired data can be directly utilized with the existing macroscopic process models. The presented study showed how just the solid concentration field can have a large effect on the modeled process values. For better model results, the flow fields of different phases and the data of the transient mixing processes would need to be utilized as well.

NOTATIONS

C	Courant number	t	time, s
C_{di}	decay constant of dilute region	v	velocity, m/s
C_{tr}	decay constant of transient region	x	dimension, m
d_s	particle size, m	α_f, α_s	volume fraction of fluid, solids, -
F_D	drag force, Pa/m	ρ, ρ_f	density, density of fluid, kg/m^3
h	height dimension, m	ρ_s	solid concentration, kg/m^3
H	total height, m	ρ_{sb}, ρ_{st}	solid concentration at bottom, top, kg/m^3
M	molar weight, kg/kmol	μ, μ_f	viscosity, viscosity of fluid, kg/ms
Re	Reynolds number		

REFERENCES

Agrawal, K., Loezos, P.N., Syamlal, M. and Sundaresan, S.: J. Fluid. Mech. 445 (2001), pp. 151-185.

Andrews, A.T., Loezos, P.N. and Sundaresan, S.: Ind. Eng. Chem. Res. 44 (2005), pp. 6022-6037.

Boemer, A., Qi, H. and Renz, U.: Int. J. Multiphase Flow 23 (1997), pp. 927-944.

Fluent 6.3.26, User's guide, Fluent Inc. (2006)

Gidaspow, D., Bezburuah, R., and Ding, J.(1992): Hydrodynamics of circulating fluidized beds, kinetic theory approach. 7th Engineering Foundation Conference on Fluidization.

Hulme, I., Clavelle, E., Van Der Lee, L., Kantzas, A.: Ind. Eng. Chem. Res. 44 (2005), pp. 4254-4266.

Ibsen, C.H., Helland, E., Hjertager, B.H., Solberg, T., Tadrist, L. and Occelli, R.: Powder Technology 149 (2004), pp. 29-41.

Igci, Y., Andrews, A.T., Sundaresan, S., Pannala, S., O'Brien, T.: AIChe J. 54 (6) (2008), pp.1431-1448.

Johnsson, F. and Leckner, B. Proc. of the 13th Int. Conf. on FBC (Heinschel, K.J. Ed.), ASME, New York (1995), pp. 671–679.

Kallio, S.: Circulating Fluidized Bed Technology VIII (Kefa Cen, ed.). International Academic Publishers, Beijing (2005), pp. 105-112.

Myöhänen K., Hyppänen T., Miettinen J. and Parkkonen R. Proc. of the 17th Int. Conf. on FBC (Pisupati, S.V., ed.) , ASME, New York (2003), Paper FBC 2003-048.

Ogawa, S., Umemura, A. and Oshima, N. Journal of Applied Mathematics and Physics 31 (1980), pp. 483-493.

Reh, L.: China Particuology 1 (2003), pp. 185-200.

Van Wachem, B. G. M., Schouten, J. C., Van Den Bleek, C. M., Krishna, R. and Sinclair, J. L.: AIChE J. 47 (2001), pp. 1035-1051.

EXPERIMENTAL STUDY AND CFD SIMULATION OF A 2D CIRCULATING FLUIDIZED BED

S. Kallio[1], M. Guldén[2,3], A. Hermanson[2]

1 VTT Tecnical Research Centre of Finland, P.O.Box 1000, FI-02044 VTT, Finland
2 Åbo Akademi University, Heat engineering Lab., Piispank. 8, FI-20500, Turku, Finland
3 Present affiliation: Wärtsilä Finland Oy, P.O.Box 252, FI-65101 Vaasa, Finland

Abstract: Computational fluid dynamics (CFD) gains popularity in fluidized bed modeling. For model validation, there is a need of detailed measurements under well-defined conditions. In the present study, experiments were carried out in a 40 cm wide and 3 m high 2D circulating fluidized bed. Two experiments were simulated by means of the Eulerian multiphase models of the Fluent CFD software. The vertical pressure and solids volume fraction profiles and the solids circulation rate obtained from the simulation were compared to the experimental results. In addition, lateral volume fraction profiles could be compared. The simulated CFB flow patterns and the profiles obtained from simulations were in general in a good agreement with the experimental results.
Keywords: hydrodynamics, CFB, two-phase flow, measurement, CFD modeling

INTRODUCTION

Good understanding of mixing of gas and solids is required for successful design of fluidized bed combustors. To assist in the development, computational fluid dynamics (CFD) has gained popularity as a tool for fluidized bed modeling. The results of CFD simulations are not always as expected and, therefore, further testing of the models and comparisons with experimental results are necessary to improve the reliability of the models. There is also a lack of detailed measurements under well-defined conditions that could be used for model validation. In the present study, experiments were carried out to facilitate validation of CFD models and modeling techniques. For this purpose, a new 2D CFB unit was built. The experimental facility is a 40 cm wide and 3 m high 2D circulating fluidized bed. In the present paper, the apparatus and two experiments are described. The experiments were simulated by means of the Eulerian multiphase models of the Fluent CFD software. Comparisons between measurements and simulations are done in the present paper.

THE 2D CIRCULATING FLUIDIZED BED

A 2D CFB unit was designed at VTT Technical Research Centre of Finland and constructed at Åbo Akademi University (Guldén, 2008). The height of the riser is 3 m and width 0.4 m. The distance between the riser walls is 0.015 m which makes the bed fairly two-dimensional. The 0.4 m wide riser walls, the side walls of the solids separator and the walls of the stand pipe are made of polycarbonate plates. Plywood is used for the wind box and for the narrow side walls. The rest of the walls in the solids separator and in the duct between the separator and the stand pipe are made of metal plates. The total height of the CFB unit is about 3.7 m. The CFB was designed for fluidization velocities up to 4 m/s. Pressurized air to fluidize the bed is supplied from a 30 kW vane compressor. Air distributor consists of 8 equally spaced air nozzles with 0.013×0.013 m^2 cross-sections at the outlets. To provide the required air distributor pressure drop, tubes with inner diameter of 4 mm were placed at the bottom end of the nozzles. The CFB pilot is shown in Figure 1.

Solids separation is done in a simple separation box to which particles move straight from the riser through a smooth exit. The separated particles fall through the stand pipe into the loop seal and from there they are blown back to the bed. The loop seal consists of two fluidized 10 cm wide sections. Below each section there is an air box from which air is led to the loop seal through three orifices that are identical to the ones located at the bottom of the riser. If the air flow to the loop seal is suddenly switched off, solids will start to collect in the return leg. The amount of solids in the loop seal and the solids circulation rate can then be determined from videos taken of the loop seal region.

In laboratory scale fluidized beds made of plastics, static electricity often becomes a serious problem. The fact that the return leg and parts of the solids separator are made of metal plates that are earthed reduces the risk for serious problems. A further measure taken to prevent electrical charges was to humidify the air with an air moisturizer in which water is sprayed though a nozzle to the gas stream coming from the compressor.

The fluidization air flow rates supplied to the wind boxes are measured and controlled by Bronkhorst High-Tech B.V. Thermal Mass Flow Controllers. Pressure is measured at several locations round the CFB with a custom made manometer.

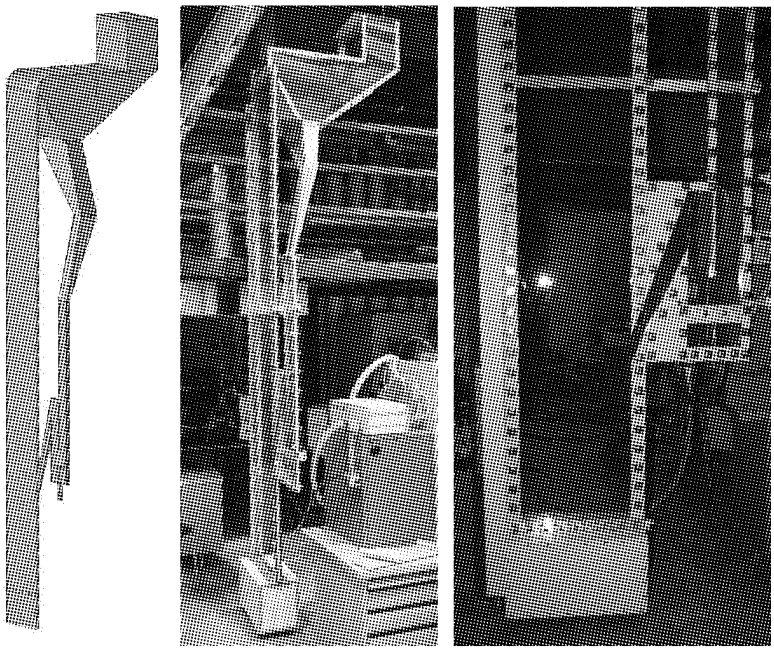

Fig. 1 The 2D CFB system: a rough sketch, the 2D CFB, and its lower part with the wind box and the loop seal

EXPERIMENTAL

The bed material consisted of spherical glass particles with material density 2480 kg/m^3. The bed material was sieved and had Sauter mean diameter of 0.385 mm. In the ambient conditions of the experiments, the terminal velocity of an average size particle is 2.9 m/s. The total amount of bed material was 3.5 kg. Two experiments with superficial gas velocities 3.1 m/s and 3.5 m/s were conducted. The amount of solids in the riser was determined by deducting from the total mass the amount measured in the loop seal. The mass in the riser was in the two experiments 2.76 kg and 2.50 kg, respectively.

In the experiments, a dense vigorously fluctuating bottom region was observed with highest particle concentration in the wall regions. Above the bottom zone, the suspension was in fluctuating motion and traveled mainly upwards in form of clusters and more dilute suspension between the clusters. At the narrow sides walls clusters were seen to fall down. Some 3D flow patterns were also observed. Especially in the upper part of the riser close to the exit clusters fell also along the front and back walls. Also elsewhere in the riser it was occasionally observed that the flow direction at the front and back walls and in riser centre differed.

Fig. 2 illustrates the flow structure at the bed bottom and at 114-145 cm height. A denser wall region with falling clusters is seen at both heights. The figures show long narrow clusters and strands everywhere in the bed. The widths of the narrowest strands observed on the videos were about 2 mm. At the higher elevation, solids concentration inside the clusters was significantly lower than in the clusters in the bottom region.

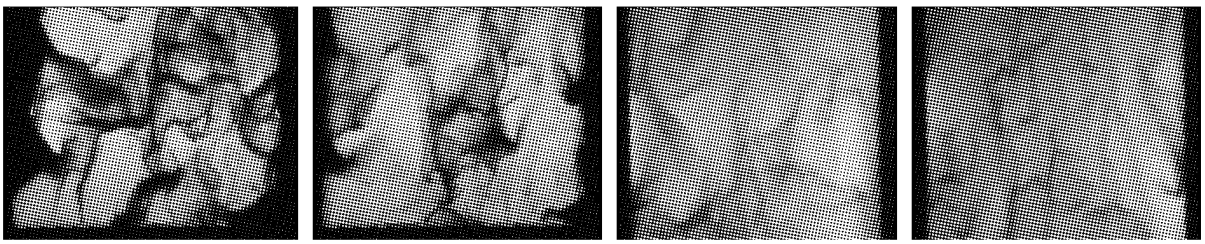

Fig. 2 Images from the experiments, from the left: at the bottom at U_0=3.1 m/s, at the bottom at U_0=3.5 m/s, at 1.14-1.45 m height at U_0=3.1 m/s, at 1.14-1.45 m height at U_0=3.5 m/s

The behavior of the CFB at bed bottom and at 114-145 cm height was video recorded in both experiments. From each case a 30 s section of the video was analyzed to estimate the average volume fractions in the studied locations. The estimate was based on a comparison between the local instantaneous grey scale values of the video image with the reference values corresponding to an empty bed and to a packed bed. In the interpretation of the concentration Beer-Lambert law of absorbance of light was utilized. The reference image corresponding to an empty bed at bed bottom and the reference corresponding to a packed bed higher up were not available. Thus the reference values had to be extrapolated from other regions. Since the lighting conditions were not

fully uniform, the poor reference values reduced the accuracy of the method. A more uniform lighting arrangement would significantly improve the results.

MODELING

The two experiments were simulated with the models based on the kinetic theory of granular flow available in Fluent 6.3.26 CFD software (Fluent, 2006). The granular temperature was obtained from a partial differential equation using the Syamlal et al. (1993) model for granular conductivity. The solid phase kinetic viscosity was calculated from the model by Syamlal et al. (1993). The k-ε turbulence model used in the simulations was the version modified for multiphase flows ("dispersed turbulence model", Fluent (2006)). At the walls, the partial slip model of Johnson and Jackson (1987) was used for the solids with specularity coefficient equal to 0.001 and the free slip boundary condition was used for the gas. For gas-particle interaction, a combination of Wen & Yu (1966) (at voidage above 0.8) and Ergun (1952) equations was used. Frictional stresses in the solid phase were taken into account by the model of Schaeffer (1987).

The simulation was limited to the riser section of the 2D CFB and to the solids return channel. In the simulation, the solids leaving the computation domain through the riser top were fed back to the process at the inlet of the solids return channel.

First order discretization for time stepping and second order interpolation for spatial discretization were employed. The 2D grid of the simulation consisted of 31648 elements. The time step in the simulation was 0.2 ms. The simulations were first run till steady state and then for an extra 10 s time period to obtain averages of the velocities and void fractions.

SIMULATION RESULTS AND COMPARISONS TO MEASUREMENTS

The time averaged volume fractions of particles were calculated for the 10 s calculation period in the studied cases. Fig. 3 illustrates the typical flow patterns obtained in the simulation and the corresponding time averages at the two fluidization velocities. The entire simulated region is shown in this figure. The flow patterns are similar to the ones observed in the experiments. Due to the coarseness of the computational mesh, however, the simulated clusters are wider. The 2 mm wide clusters seen on the videos would require a much finer mesh than the one with 6.25 mm mesh spacings used in the simulations. The thinnest clusters in the simulations were about 1.5 cm wide. Otherwise the flow structure is the same with a dense bottom bed and dense wall regions with downflow of solids.

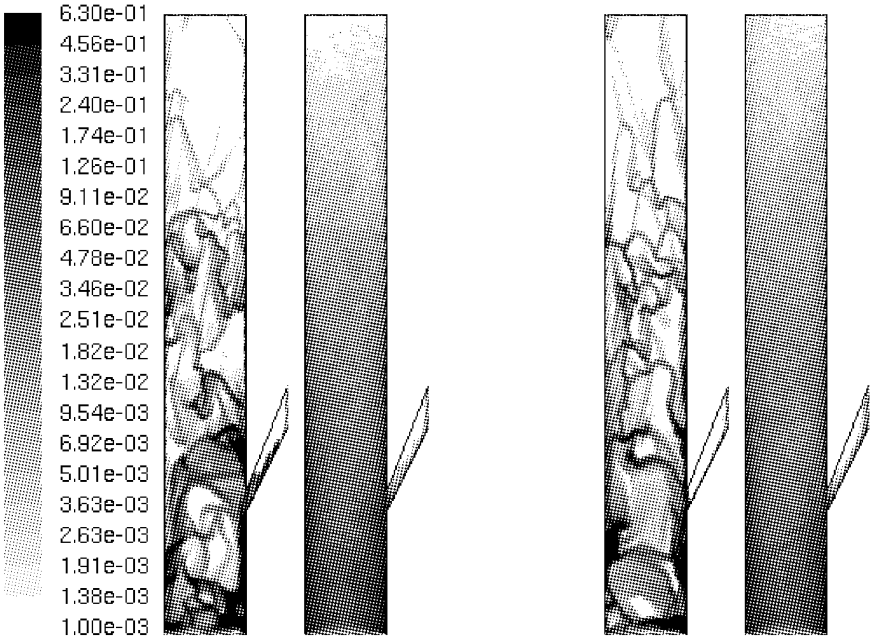

Fig. 3 Instantaneous and average solids volume fractions at U_0=3.1 m/s (left) and at U_0=3.5 m/s (right)

A comparison between measured and simulated solids circulation rates is given in Fig. 4. The circulation rate of solids determined from the simulations is given in Fig. 4 at 0.2 s intervals. The time resolution in the measurements was poorer, 1 s, and thus the frequency of the fluctuations in the solids circulation rates shown in Fig. 4 differ. Both in the experiments and in the simulations, an increase in the fluidization velocity increases

the circulation rate. Moreover, solids circulation rates obtained in the simulation are of the same order as measured in the laboratory unit.

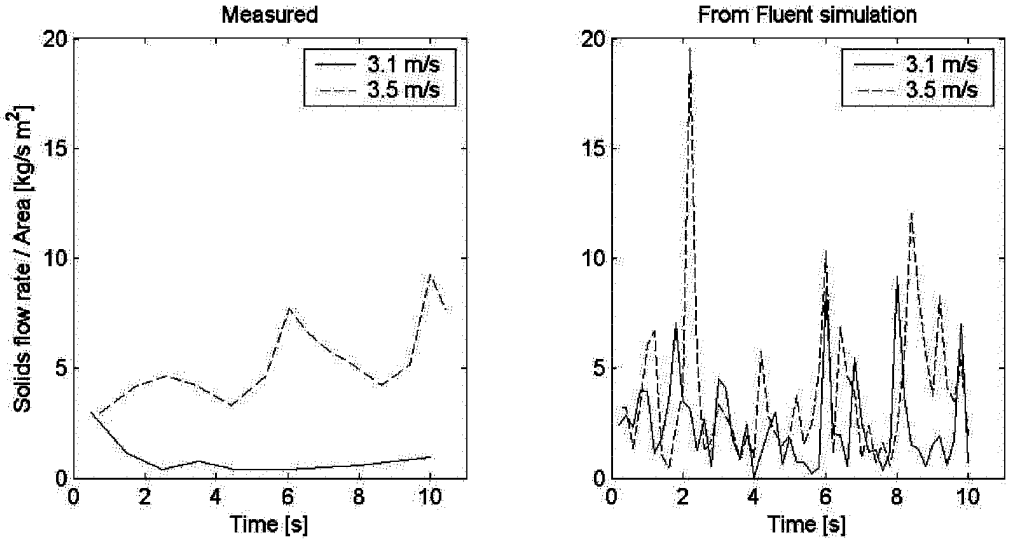

Fig. 4 Measured and simulated solids circulation rates per area at fluidization velocities 3.1m/s and 3.5 m/s, respectively

Gas phase static pressure was measured at several locations at the left wall (the wall opposite to the solids return). Figure 5a shows a comparison between the measured and simulated average pressure profiles at the wall. The simulated pressure profile is close to measured one at the lower fluidization velocity but a clear discrepancy is seen at the higher velocity. In addition, the area-average of the simulated pressure, taken over the riser cross-section at different elevations, is depicted in the figure. In the simulation, there is a difference between the pressure at the wall and the cross-sectional average in the bottom bed but not higher up. In the bottom bed area the pressure is clearly higher at the wall. No similar difference could be measured in the experiments.

From the measured pressure profile, the vertical voidage profile could be estimated. The results are depicted in Fig. 5b together with the average solids volume fraction profile obtained from the simulations. In addition, the average values obtained from the analysis of the videos, taken at two elevations during the experiments, are marked in the same figure.

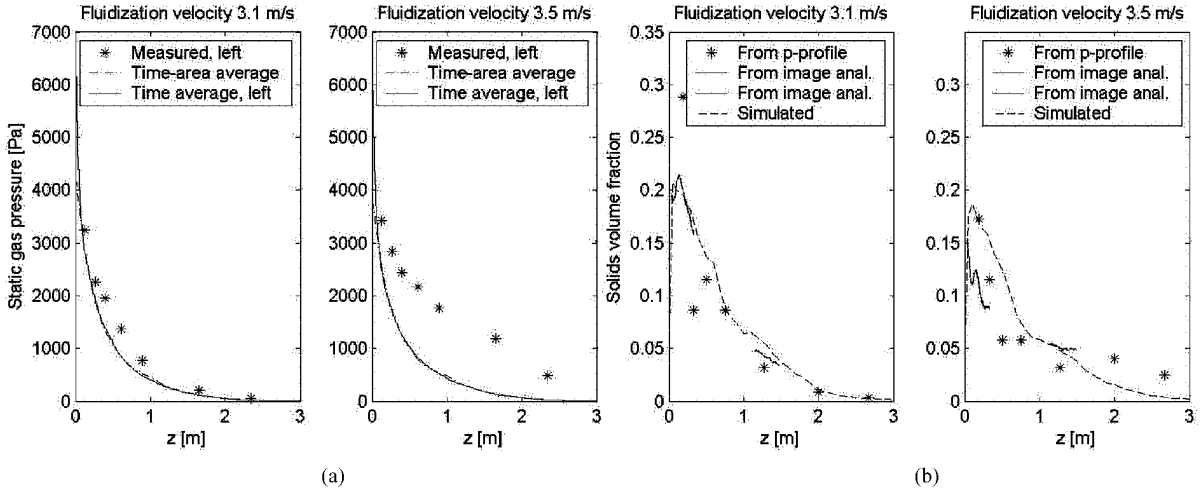

Fig. 5 Comparison of measured and simulated vertical pressure (a) and solids volume fraction (b) profiles in the experiments with fluidization velocities 3.1m/s and 3.5 m/s

In general, the match is reasonably good considering the inaccuracies in both of the measurement methods. The biggest discrepancy between the measured and simulated pressure profiles occurs at the higher fluidization velocity. On basis of Fig. 5 alone, we cannot determine which of the two curves is more erroneous. In the experiments, static electricity incurs problems and can reduce the repeatability of the measurements. One obvious source of errors in the simulations is the mesh, which is too coarse to describe the finest clusters. A mesh-dependent gas-solids drag law would be required to remedy this problem, but unfortunately such models

are not yet available.

From the videos, the average lateral solids volume fraction profiles were determined at 20 cm and 130 cm heights. Figure 6 shows a comparison between the measured and simulated lateral solids volume fraction profiles. In the profiles determined from the videos there is clear asymmetry. This is probably caused by the uneven lighting in the experiments combined with the lack of good reference images for fixing the concentration scale. Otherwise the measured and simulated profiles are in good agreement., which indicates that simulations predict the solids concentration levels correctly. The thin dense wall region observed in the simulations could also be detected from the videos.

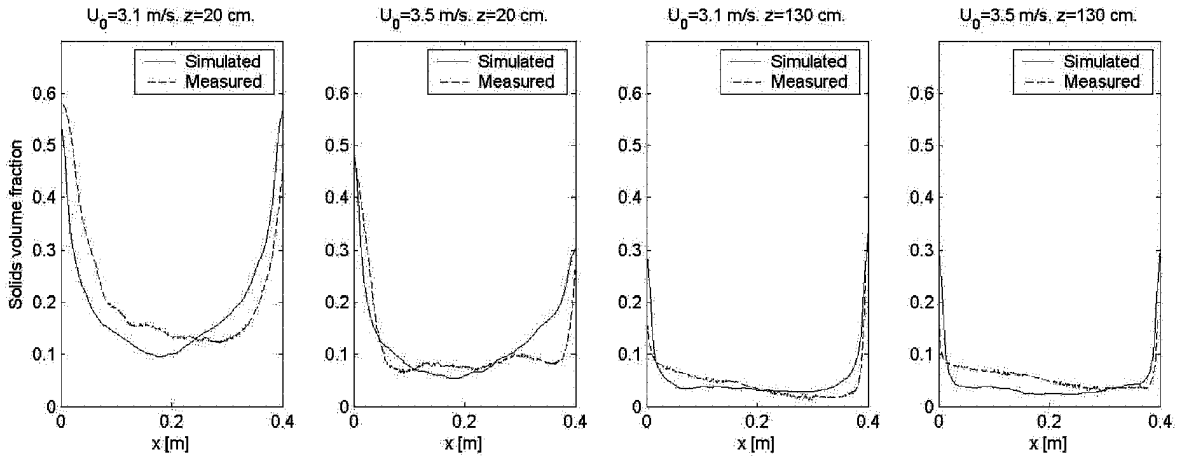

Fig. 6 Comparison of simulated and measured lateral solids volume fraction profiles at 20 cm and 130 cm heights at fluidization velocities 3.1 m/s and 3.5 m/s

No velocity profiles could be measured but from the simulations average lateral velocity profiles could be calculated. Figure 7 shows the profiles obtained in the two simulations at 20 cm and 130 cm heights. A downflow region is seen at the walls. This corresponds to the visual observations. In the bottom region, solids velocity has increased as the fluidization velocity increased whereas at 1.2 m height solids velocity has remained unchanged which is somewhat unexpected. At the higher elevation the bed is denser at the higher fluidization velocity, which increases clustering and could have a reducing effect on the average solids velocity.

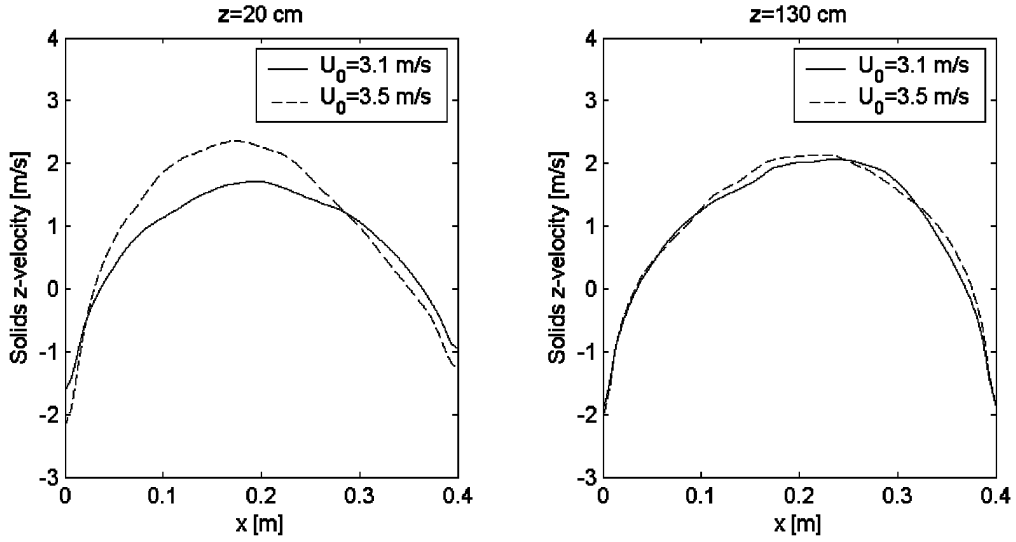

Fig. 7 Lateral profiles of the solids vertical velocity component at fluidization velocities 3.1 m/s and 3.5 m/s determined from the simulations at 20 cm and 130 cm heights

CONCLUSIONS

For validation of CFD models for simulation of fluidized beds, there is a lack of detailed measurements under well-defined conditions. For this purpose, a new 2D CFB unit has been built. The experimental facility was a 40 cm wide and 3 m high 2D circulating fluidized bed. In the present study, experiments were carried out to facilitate validation of CFD models and modeling techniques. In the experiments, a dense vigorously

fluctuating bottom region was observed with highest particle concentration in the wall regions. The behavior of the process was video recorded and the videos were analyzed to characterize the average behavior of the gas-solid suspension in the CFB. Two experiments were simulated by means of the Eulerian multiphase models of the Fluent CFD software. The vertical pressure profiles and the solids circulation rates obtained from the simulation were compared to the experimental results. The simulated CFB flow patterns were generally in a good agreement with the experimental results.

ACKNOWLEDGEMENTS

The financial support of Tekes, VTT Technical Research Centre of Finland, Fortum Oyj, Foster Wheeler Energia Oy, Neste Oil Oyj and Metso Power Oy is gratefully acknowledged. The authors wish to thank prof. Henrik Saxén for his input to the work.

REFERENCES

Ergun, S.: Fluid flow through packed columns, Chem. Eng. Progress (1952), **48**, pp. 89-94.

Fluent Inc., Fluent 6.3 Users manual (2006).

Guldén, M., Masters thesis (in Swedish), Åbo Akademi Univ., Heat Engineering Lab., (2008).

Johnson, P.C., Jackson, R. J. Fluid Mech. (1987), **176**, pp. 67-93.

Schaeffer, D. G., J. Diff. Eq. (1987), **66**, pp. 19-50.

Syamlal, M., Rogers, W., and O'Brien T. J., MFIX Documentation: Volume 1, Theory Guide. National Technical Information Service, Springfield, VA, DOE/METC-9411004, NTIS/DE9400087 (1993).

Wen, C.Y., Yu, Y.H., Chemical Engineering Progress Symposium Series (1966), **66**, pp.100-111.

3D NUMERICAL PREDICTION OF GAS-SOLID FLOW BEHAVIOR IN CFB RISERS FOR GELDART A AND B PARTICLES

A. Özel[1,2], P. Fede[1,2], O. Simonin[1,2]

1 Université de Toulouse ; INPT, UPS ; IMFT Allée Camille Soula, F-31400 Toulouse, France
2 CNRS ; IMFT ; F-31400 Toulouse, France

Abstract: In this study, mono-disperse flows in squared risers conducted with A and B-type particles were simulated by Eulerian n-fluid 3D unsteady code. Two transport equations developed in the frame of kinetic theory of granular media supplemented by the interstitial fluid effect and the interaction with the turbulence (Balzer et al., 1996) are resolved to model the effect of velocity fluctuations and inter-particle collisions on the dispersed phase hydrodynamic. The studied flow geometries are three-dimensional vertical cold channels excluding cyclone, tampon and returning pipe of a typical circulating fluidized bed. For both type of particles, parametric studies were carried out to determine influences of boundary conditions, physical parameters and turbulence modeling. The grid dependency was analyzed with mesh refinement in horizontal and axial directions. For B-type particles, the results are in good qualitative agreement with the experiments and numerical predictions are slightly improved by the mesh refinement. On the contrary, the simulations with A-type particles show a less satisfactory agreement with available measurements and are highly sensitive to mesh refinement. Further studies are carried out to improve the A-type particles by modeling subgrid-scale effects in the frame of large-eddy simulation approach.
Keywords: circulating fluidized beds, mono-disperse flow, A and B-type particles

INTRODUCTION

Numerical analysis of fluidized beds by Eulerian multi-fluid approach appears to be a powerful tool to improve design and performance of industrial facilities. To have better understanding of complex physical mechanisms in fluidized beds, 3D numerical simulations of pilot and industrial flow configurations are needed and have been performed since few years. However, modelling of coupling term between phases, boundary conditions and mesh refinement have crucial influences of 3D numerical simulations and are still being improved.

In this paper, simulations with A and B type particles have been carried out using an Eulerian n-fluid modelling approach for fluid-particle turbulent polydispersed flows developed and implemented by IMFT (Institut de Mécanique des Fluide de Toulouse) in the *NEPTUNE_CFD v1.07@Tlse* version. *NEPTUNE_CFD* is a multiphase flow software developed in the framework of the NEPTUNE project, financially supported by CEA (Commissariat à l'Energie Atomique), EDF (Electricité De France), IRSN (Institut de Radioprotection et de Sûreté Nucléaire) and AREVA-NP. Mesh sensitivity has been investigated for both of particle types and parametric studies have been performed in order to determine influences of physical and numerical parameters. Numerical results are compared with existing experimental data and discussed. Numerical results conducted with B-type particles are acceptable. However, to resolve flow characteristics more accurately for A-type particles, very fine mesh has to be used. For industrial applications, numerical simulations obtained by finer mesh are not feasible and the model that takes into account subgrid-scale effects in the frame of large-eddy simulation approach is stated for the perspective of this study.

MODELLING APPROACH

The modelling approach is based on the multi-fluid model formalism that involves mean separate transport equations of mass, momentum and energy for each phases. Interactions between phases are coupled through interphase transfers. The modified two-equation turbulence model (turbulent kinetic and dissipation energy) that takes into account effects of dispersed phase is used to solve gas-phase turbulence. Two transport equations, developed in the frame of kinetic theory of granular media supplemented by the interstitial fluid effect and the interaction with the turbulence (Balzer et al., 1996), are resolved to model the effect of velocity fluctuations and inter-particle collisions on the dispersed phase hydrodynamic. Concerning the transfers between the phases with non-reactive isothermal flow, drag force was only taken into account for the transfer of momentum. Neither terms of added mass nor lift force were considered. Gravity was imposed along opposite direction of the mean flow.

Transport Equations

The multi-fluid mass balance equation for the phase k is written:

$$\frac{\partial}{\partial t}(\alpha_k \rho_k)+\frac{\partial}{\partial x_i}(\alpha_k \rho_k U_{k,i})=0 \tag{1}$$

with α_k, ρ_k, U_k the volume fraction, the density and the mean velocity of phase k (when subscript k=g, we refer to the gas and k=p to the particulate phase). The multi-fluid momentum balance equation for the phase k is defined as follows:

$$\frac{\partial}{\partial t}(\alpha_k \rho_k U_{k,i})+\frac{\partial}{\partial x_j}(\alpha_k \rho_k U_{k,j} U_{k,i})=-\alpha_k \frac{\partial P}{\partial x_i}+I_{k,i}+\alpha_k \rho_k g_i+\frac{\partial}{\partial x_j}\Sigma_{k,ij} \tag{2}$$

with P the mean pressure, g_i acceleration due to gravity, $\Sigma_{k,ij}$ is the effective stress tensor, $I_{k,i}$ the average interfacial momentum transfer.

Interfacial momentum transfer

The term $I_{g,i}$ accounts for momentum transfer rate from the gas phase (carrier or continuous phase) to solid phase. This term can be modeled by taking into account only the drag force between phases:

$$I_{g,i}=-I_{p,i}=\frac{\alpha_p \rho_p}{\tau_{gp}^F} V_{r,i} \quad \text{with} \quad \frac{1}{\tau_{gp}^F}=\frac{3}{4}\frac{\rho_g}{\rho_p}\frac{\langle C_D \rangle_p}{d_p}\langle |\mathbf{v}_r| \rangle_p \tag{3}$$

τ_{gp}^F is the particle relaxation time scale, $\langle . \rangle_p$ the ensemble average operator over the particle (Simonin, 1996). The mean drag coefficient of a single particle, $\langle C_D \rangle_p$, can be written as function of a particle Reynolds number and defined by Wen and Yu (1965) and Ergun correlation. The combination of two correlations was given by Gobin et al. (2003):

$$\langle C_D \rangle_p=\begin{cases} Min\left[\langle C_D^{Wen\&Yu} \rangle_p, \langle C_D^{Ergun} \rangle_p\right] & \text{if } \alpha_p > 0.3 \\ \langle C_D^{Wen\&Yu} \rangle_p & \text{if not} \end{cases} \tag{4}$$

where $\langle C_D^{Wen\&Yu} \rangle_p=\frac{24}{\langle \mathrm{Re}_p \rangle}\left[1+0.15\langle \mathrm{Re}_p \rangle^{0.687}\right]\alpha_g^{-1.7}$ and $\langle C_D^{Ergun} \rangle_p=1.75+\frac{150}{\langle \mathrm{Re}_p \rangle}$ with the definition of the mean particle Reynolds number $\langle \mathrm{Re}_p \rangle=\alpha_g d_p \langle |\mathbf{v}_r| \rangle_p / \upsilon_g$ where d_p is the particle diameter and υ_g is the viscosity of gas, respectively. The term $\mathrm{v}_{r,i}^{gp}$ in Eq.(4) represents the local instantaneous relative velocity and is equal to difference between the local particle velocity, $u_{p,i}$, and the instantaneous gas velocity, $u'_{g,i}$ undisturbed by presence of the particle at the particle position. $V_{r,i}$ is the averaged of the local relative velocity, $V_{r,i}=\langle u_{p,i}-u_{g,i} \rangle_p$. It can be expressed in terms of the averaged velocity between phases and drift velocity, $V_{d,i}$, due to the correlation between the instantaneous distribution of dispersed particles and the turbulence structure of gas phase: $V_{r,i}=U_{p,i}-U_{g,i}-V_{d,i}$. The drift velocity, $V_{d,i}$, in the special case of particles suspended in homogeneous turbulence can be modeled (Deutsch and Simonin, 1991).

Turbulence Modelling

The effective stress tensor, $\Sigma_{k,ij}$, in Eq.(2) consists of two parts for gas phase; molecular viscosity, $\theta_{g,ij}$, and Reynolds stress tensor $\langle \rho_g u'_{g,i} u'_{g,i} \rangle_g$. The Reynolds stress tensor is modelled by using Boussinesq-like approximation with introducing μ_g^t and q_g^2 the turbulent viscosity and the turbulent kinetic energy or fluid velocity correlations of the gas.

$$\langle \rho_g u'_{g,i} u'_{g,i} \rangle_g=-\mu_g^t\left[\frac{\partial U_{g,i}}{\partial x_j}+\frac{\partial U_{g,j}}{\partial x_j}\right]+\frac{2}{3}\left[\rho_g q_g^2+\mu_g^t \frac{\partial U_{g,m}}{\partial x_m}\right]\delta_{ij} \tag{5}$$

The turbulent kinetic energy is defined as $q_g^2=\frac{1}{2}\langle u'_{g,i} u'_{g,i} \rangle_g$ and the turbulent viscosity is determined by

Balzer and Simonin (1996) as:

$$\mu_g^t = \frac{2}{3}\rho_g q_g^2 \tau_g^t \left[1 + C_{12}\frac{\alpha_p \rho_p}{\alpha_g \rho_g}\frac{\tau_{gp}^t}{\tau_{gp}^F}\left(1 - \frac{q_{gp}}{2q_g^2}\right)\right] \tag{6}$$

The effective stress tensor for solid phase has two contributions as of the gas phase. The first contribution, $\left\langle \rho_p u'_{p,i} u'_{p,i} \right\rangle_p$, is the kinetic stress tensor which represents the transport of the momentum by the particle velocity fluctuations. The second one, $\theta_{p,ij}$, is the collisional stress tensor which accounts for destruction and exchange of the momentum during inter-particle collisions. The constitutive relations for viscosity and diffusivity are derived in frame of the extension of kinetic theory of dry granular flow and given by Balzer et al. (1995). The constitutive equation of the effective stress tensor is:

$$\sum_{p,ij} = \left[P_p - \lambda_p \frac{\partial U_{p,m}}{\partial x_m}\right]\delta_{ij} - \mu_p\left[\frac{\partial U_{p,i}}{\partial x_i} + \frac{\partial U_{p,j}}{\partial x_i} - \frac{2}{3}\frac{\partial U_{p,m}}{\partial x_m}\delta_{ij}\right] \tag{7}$$

The collisional pressure and the bulk viscosity are written according to Balzer et al. (1995) as follow:

$$P_p = \frac{2}{3}\alpha_p \rho_p q_p^2 \left[1 + 2\alpha_p g_0 (1 + e_c)\right] \qquad \lambda_p = \frac{4}{3}\alpha_p^2 \rho_p d_p g_0 (1 + e_c)\sqrt{\frac{2}{3}\frac{q_p^2}{\pi}} \tag{8}$$

with e_c the restitution coefficient that determines energy loss during inter-particle collisions. The shear viscosity is the linear combination of the collisional and the kinetic stress with the effect of interstitial gas: $\mu_p = \alpha_p \rho_p \left[v_p^{kin} + v_p^{coll}\right]$ where

$$v_k^{kin} = \left[\frac{1}{3}q_{gp}\tau_{gp}^t + \frac{2}{3}q_p^2\frac{1}{2}\tau_{gp}^F(1 + \alpha_p g_0 \Phi_c)\right] / \left[1 + \frac{\tau_{gp}^F}{2}\frac{\sigma_c}{\tau_p^c}\right] \tag{9}$$

$$v_p^{coll} = \frac{4}{5}\alpha_p g_0 (1 + e_c)\left[v_p^{kin} + d_p\sqrt{2q_p^2/3\pi}\right] \tag{10}$$

with $\sigma_c = \frac{1}{5}(1 + e_c)(3 - e_c)$ and $\Phi_c = \frac{2}{5}(1 + e_c)(3e_c - 1)$ Modeling fluid, particle and fluid-particle correlations are beyond of this study, for further information, see Simonin (1996).

Characteristic Times Scales

In the formulation of the transport equations several characteristic time scales are defined. The time of interaction between particle motion and gas phase fluctuations or the eddy-particle interaction time is defined by $\tau_{gp}^t = \tau_g^t (1 + C_\beta)^{-1/2}$ where $\xi_p^2 = 3\left|V_{r,i}\right|^2 / 2q_g^2$, τ_g^t is the characteristic time scale of the large eddies of the gas phase and C_β is a constant and equal to 1.8. The particle-particle collision time is $\tau_p^c = \left[(24\alpha_p g_0 / d_p)\sqrt{2q_g^2/3\pi}\right]^{-1}$ where g_0 is a distribution function that accounts for the increase of the probability of collisions as the suspension becomes denser. Lun and Savage (1986) proposed the correlation function for the distribution function as $g_0 = (1 - \alpha_p / \alpha_p^{\max})^{-2.5\alpha_p^{\max}}$ with $\alpha_p^{\max} = 0.64$ maximum random packing of an identical sphere particle suspension. These characteristic times scales are useful to determine the dominant mechanism in a suspension.

RESULTS AND DISCUSSION

Simulations of Dilute Gas-particle Flow in a CFB riser (CERCHAR)

In this case, B-type particles are conducted and the results are compared with experimental data of Fabre (1995) and numerical results of Batrak et al.(2005). The experimental setup of CERCHAR done by Fabre (1995) is a representative cold model of typical CFB. For three-dimensional simulations, the experimental setup was simplified by removing cyclone, tampon and return pipe. The riser cross-section is rectangular area with 0.8 m in length and 1.2 m in depth. The height of riser is equal to 9.4 m and the cross-section of riser at 10.0 m is resized with homethety equal to 0.5 . The injector area is 0.032 m^2 and is located at z=0.1 m. The length of the particle inlet is equal to 0.25m and the configuration is shown in Fig. 1-a.

The grid is defined in Cartesian coordinate and has approximately 150 000 cells. The number of nodes is

41 in direction x, 31 in the direction y and 131 in the direction z. The grid is uniform in direction x, y (Δx=0.02m,Δy=0.04m). In the direction z, it is uniform up to z=0.4 m with Δz=0.02m, and then it is extended with successive ratio equal to 1.02.

Flow Structure

Flow structures in dense and dilute zones are shown in Fig.1-b. The formation of dense zone can be seen close to particle inlet and clusters are formed. In the upper dilute part of CFB riser, clusters are disappeared in the gas suspension. These clusters move downwards along the riser and create a negative net-flux close to the wall. The velocity profiles in Fig. 2(d) show the core-annulus flow.

The "steady-state" condition was assumed as the total mass of particles in the riser oscillated around a constant value. It was considered that the flow regime was reached "stabilized-state" and the time-averaged values of volume fractions, velocities and pressure were then calculated for approximately *50 s* in physical time. Time averaged pressure profiles by Batrak et al. (2005) and Fabre (1995) are compared with numerical results with a reference value at z_{ref}=9 m. The single phase air hydrostatic pressure was subtracted from numerical results $P^*(z)=P(z)-\rho_g g(z_{ref}-z)$. Time averaged pressure profile shows a good agreement with experimental results in the dilute region, but there is significant difference close to velocity inlet. Time averaged pressure profile is presented in Fig. 2(a).

Averaged solid mass flux captures the general trend in flux profile of experimental data. However, mass flux is underestimated in the center of riser and close to the wall. Gas and particle velocities obtained by Batrak(2005) are identical to the results obtained in this study.

Influence of Wall Boundary Condition

The particle behavior may be considerably affected by particle bouncing with rough wall. In order to account for this effect, the model proposed by Konan et al. (2006) was tested on the CERCHAR configuration. In this case, the wall roughness standard deviation was set to 6.5° corresponding to high roughness. The accumulations of particles in riser and pressure distribution along z-direction are compared in Fig. 3(a) and 3(b), showing that the wall roughness leads to an increase of the solid mass accumulated in the riser.

Gas Phase:
ρ_g = 1.123 kg/m^3
T_g = 313.14 K
μ_g = 1.6x10^{-5} kg/m.s
W_{inlet}= 4 m/s
Solid Phase:
ρ_p = 2650 kg/m^3
d_p = 260μm
e_c = 0.9
V_{inlet} = 0.64 m/s

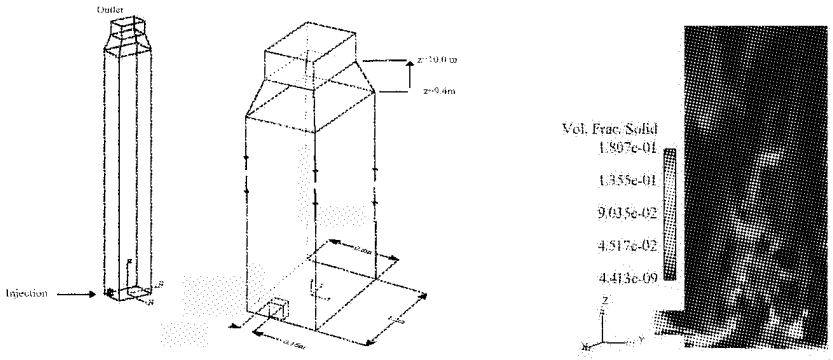

(a) (b)

Fig. 1 (a) The computational domain and (b) The volume fraction of solid in the dense regime (y-z surface, x=0).

Influence of Turbulence Modeling

Unsteady RANS is a questionable approach for these kinds of fluidized bed applications and in this part, the sensitivity analysis of the turbulence modeling is discussed. In this approach, the turbulence modulation by particles is taken into account by source term in the turbulence kinetic energy equation. To investigate influence of the turbulence modeling, the case with laminar flow has been done. There is not any significant difference between results obtained without and with turbulence model. Another remarkable point is that the same turbulent scale may be predicted by the laminar case because of too coarse mesh. To investigate this effect, the turbulent case has been computed with a finer mesh. In order to reduce the computational cost, the mesh was refined in x,y and z direction only close to mixing area. After mesh refinement, number of cell is approximately 720 000. It is stated that he refinement mesh has weakly effect on results.

Simulations of a Cold Circulating Fluidized Bed with A-type Particle

B-type particles have been attaining good simulations in 2-D or 3-D domain for ten years. In contrast, simulations of A-type particles have problems and, at least, 3D fine mesh is needed (Andreux et al., 2007). In this case, A-type particles are used and the results are compared with experimental and numerical data of

Andreux et al. (2007). For 3D simulations, the computational domain geometry is similar to the CERCHAR case and the experimental setup except for the particle inlet. Indeed, the circular cross section of particle inlet was transformed to rectangular section with the same hydraulic diameter in order to avoid non-conformal mesh configuration. The height of riser is equal to 10.5 m and the cross-section of riser at 10.75 m is resized with homethety equal to 0.5. The injector area is $3.6\times10^{-3}m^2$ and is located at z=0.075 m. The riser cross-section is square with 0.011 m edge. The computational domain was constructed by approximately 30000 cells and the grid is uniform in direction x, y, z ($\Delta x=\Delta y=0.011$m,$\Delta z=0.038$m). Flow parameters are shown in Table 1.

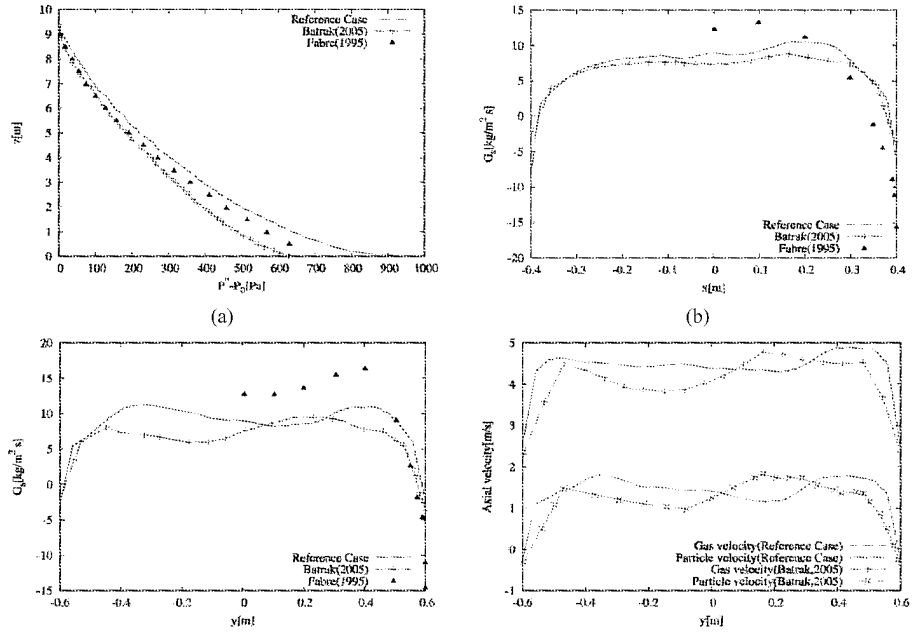

Fig. 2 (a) Averaged pressure distribution along the positive z direction; (b) Averaged mass flux of solid along the x-direction at z=6.66m, y=0; (c) Averaged mass flux of solid along the y-direction at z=6.66m, x=0; (d) Averaged particle and gas velocities along the y-direction at z=6.66m, x=0

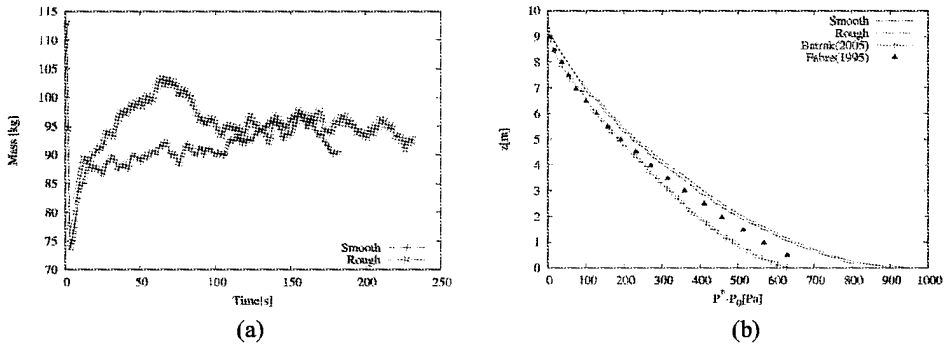

Fig. 3 (a) Solid accumulation in the riser by smooth and rough wall cases; (b) Time averaged pressure distribution along the z-direction

Table 1 Flow parameters of simulations of A-type particles

Gas phase		Solid Phase	
ρ_g	=1.123 kg/m^3	ρ_p	=1400 kg/m^3
T_g	=313.14 K	d_p	=70 μm
μ_g	=1.6$\times10^{-5}$ kg/m.s	e_c	=0.9
W_{inlet}	=4 m/s	V_{inlet}	=0.64 m/s

Flow Structure

In the mixing part, particles are immediately transported by gas. Dense zone does not form and the mixing of gas/solid is poor. The core-annulus flow does not occur and a negative net-flux cannot be observed. The formation of clusters is not observed, but accumulation of particles in the quarter part of riser deviates gas and increases the gas velocity close to wall. To avoid these kind unphysical results, the computational grid was refined two times in all directions. However, the results obtained with finer mesh have the same behavior. The

mass time-evolution in the riser of fine and coarse mesh configuration is plotted in Fig. 4(a). The accumulation of particles in the quarter part of the riser can be seen in Fig. 4(b).

It is obvious that computational grid has to be too fine to resolve flow characteristics accurately. Due to the computational cost, it is not feasible. The coarse-grid simulation of gas-particle flows must be included subgrid models, to account for the effects of the unresolved scales (Andrews, 2005).At this point, we proposed the following model but it should be stated that this model is under-development. However, the preliminary results obtained by this model are promising and it seems an alternative way to simulate gas-solid flows of A-type particles. The filtered interfacial momentum transfer is defined (the "overline" defines the filtered quantity) as the following and can be decomposed into two parts by introducing the subgrid drift velocity:

$$\overline{I}_{g,i} = -\overline{I}_{p,i} = \frac{\alpha_p \rho_p}{\tau_{gp}^F} V_{r,i} = \frac{\overline{\alpha}_p \rho_p}{\overline{\tau}_{gp}^F} (\overline{V}_{r,i} + \overline{V}_{d,i}) \tag{11}$$

The subgrid drift velocity can be modeled as function of resolved quantities:

$$\overline{V}_{d,i} = \left(-\frac{\Delta^{1/3} / (\overline{\tau}_{gp}^F \overline{V}_{r,i})}{1 + \Delta^{1/3} / (\overline{\tau}_{gp}^F \overline{V}_{r,i})} \right) \frac{\overline{\alpha}_p \rho_p}{\overline{\tau}_{gp}^F} \overline{V}_{r,i} \tag{12}$$

with the mesh volume equal to $\Delta = \Delta x \Delta y \Delta z$. Averaged volume fractions of solid and particle velocities obtained by with and without subgrid model are compared in Fig. 4. The accumulation in the quarter of riser vanishes and the particle velocity profile, obtained by fine mesh, is in a good agreement with the one obtained by subgrid model. However, solid volume fraction close to outlet is overestimated and this model will be improved by information obtained from very fine mesh simulations.

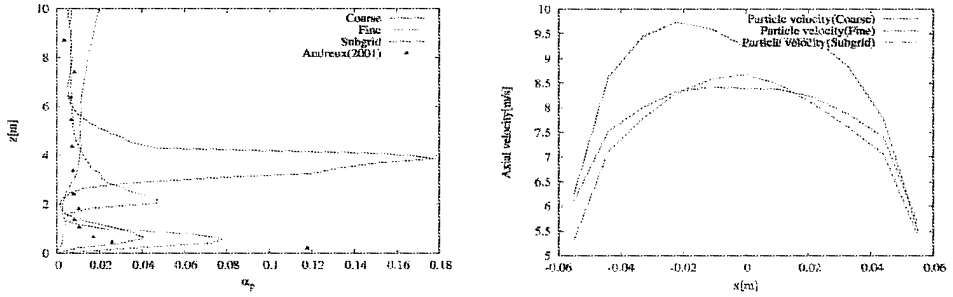

(a) (b)

Fig. 4 (a) Averaged volume fraction of solid distribution along z-direction; (b) Averaged particle along the x-direction at z=8.50m, y=0

CONCLUSIONS

3D unsteady simulations of mono-disperse gas-solid flows with A and B type particles by Euler-Euler multi-fluid approach in typical fluidized beds risers have been presented in this study. Results of B-type particles simulations have been investigated. A good agreement with experimental results has been obtained. The effect of roughness slightly increases mass of solid in the riser, but there is no crucial effect on averaged pressure distribution along mean flow direction. Turbulence of gas phase is suppressed by the existence of particle in the flow simulated by fine and coarse mesh. On contrary, simulations of A-types particles give unphysical results. Indeed, the refine mesh needed to represent accurately the small structure of the flow is much too expensive in terms of computational cost. To overcome this problem, subgrid scale model is proposed to model interfacial momentum transfer between phases in the frame of large eddy simulation. This model allows to use coarse mesh by accounting for subgrid scale effects on resolved flow.

First results are compared with previous results and it is concluded that this approach is promising. However, this approach has to be developed for particle properties such as viscosity and diffusivity to achieve the entire goal.

REFERENCES

Andrews, A.T., Loezos, P.N., Sunderasan, S. : Ind. Eng. Chem. Res 44(2005), pp 6022-6037.

Andreux, R., Petit, G., Hemati: Chemical Engineering Process 47 (2007), pp 463-473.

Balzer, G., Simonin, O., Boelle, A., Laviéville, J.: Proc. of the 5th Int. Conf. on Circulating Fluidized Beds, M. Kwauk, J. Li (Editors), Science Press(1996), pp 432-439.

Balzer, G., Boelle, A., Simonin O., : Fluidization VIII (1995), pp 409-418.

Batrak, O., Patino, G, Simonin, O., Flour, I., Le Guevel, T., Perez, E.: Proc. of the 5th Int. Conf. On Circulating Fluidized Beds, Int. Academic Publishers(2005), pp 370-378.

Deutsch, E., Simonin, O.: ASME FED 110 (1991), pp. 35-42.

Fabre, A.: Thèse de Doctorat (1995), Université de Compiégne, France.

Gobin, A., Neau, H., Simonin, O., Llinas, J.R., Reiling, V., Selo, J.L. : Int. Journal of Numerical Methods in Fluids 43 (2003), pp 1199-1220.

Lun, C., Savage, S.: Acta Mechanics 63 (1986), pp 15-44.

Konan, N.A., Simonin, O., Squires, K.D.: Proc. Symposium Fluid-Particle Interactions in Turbulence, 2006 ASME Joint U.S. European Fluids Eng. Summer Meeting.(2006), FEDSM2006.

Simonin, O.: Von Karman Lecture Series 1996-02.

NUMERICAL SIMULATION OF SLUDGE DRYNESS UNDER FLUE GAS ATMOSPHERE IN THE RISER OF A FLUIDIZED BED

H. M. Xiao, X. Q. Ma, K. Liu, Z. S. Yu

School of Electric Power, South China University of Technology, 381 Wushan Road, Guangzhou, 510641, China

Abstract: A numerical algorithm is developed for a detailed 3D simulation of the gas/particle flow behavior used for drying of sludge under flue gas atmosphere in the riser section of a circulating fluidized bed. The gas phase is described with standard $\kappa - \varepsilon$ turbulence model, whereas a Lagrangian formulation with a stochastic particle dispersion model is adopted for the particulate phase. Conservation equations of mass and momentum for each phase were solved using the volume numerical technique. Fluid-particle interaction is taken into account to calculate the mass, momentum, and heat transfer between phases. The numerical algorithm is used to predict the circulating fluidized bed performance under various inlet profiles of the flue gas velocity. Gas and particle flow profiles were obtained for velocity and temperature parameters for each phase. The influence of the flue gas inlet velocity and the sludge mass flow rate on drying is discussed.

Keywords: sludge, flue gas, drying, numerical simulation

INTRODUCTION

Sewage sludge is formed during wastewater treatment, it is harmful for human and environment if not be dealt with. Sludge has a high amount of moisture, which should be removed before their utilization. A wide reduction of these waste volumes is necessary. The mechanical dewatering by pressure filters or centrifuges is not always sufficient to satisfy new environmental regulations and a thermal drying step is often needed(Vaxelaire et al., 2000). The versatility of fluidized bed technology, with its excellent heat and mass transfer characteristics, operational flexibility, and easy scale-up and maintenance, is finding increased industrial applications in recent years(Balasubramanian et al., 2007).

Mathematical modeling of fluidized bed drying is crucial for optimizing the performance of existing systems and designing new dryers(Assari et al., 2007).

(Roustapour et al., 2009) used computational fluid dynamics method to simulate the drying of lime juice in a spray dryer. Base on experimental results of moisture contend variation along the length of chamber and numerically estimated residence time of droplets. Drying kinetic of lime juice in spray dryer was determined. A parametric study carried out to investigate the effects of some important parameters.

(Xu and Yu, 1997) modeled the gas-solid flow in a fluidized bed by a combined approach of discrete particle method and computational fluid dynamics. The coupling between DPM and CFD is achieved directly by applying the principle of Newton's third law of motion to the discrete particle and continuum gas. They demonstrated that the proposed model is able to capture the gas-solid flow features in a fluidized bed from the largest length and time scales relevant to the processing equipment down to the smallest ones relevant to the individual particles.

The analysis of the sludge drying and the numerical simulation of fluidized bed have already been investigated by numerous of studies, However, there are fewer literatures to study the numerical simulation of sludge dryness under flue gas atmosphere in the riser of a fluidized bed with a spray nozzle.

The aim of this paper is to present a model of drying of sludge in a fluidized bed. The gas phase is described with standard $\kappa - \varepsilon$ turbulence model, whereas a Lagrangian formulation with a stochastic particle dispersion model is adopted for the particulate phase. The drying of sludge particles in a 4m riser height is performed experimentally for comparison with the numerical results.

MATERIALS AND METHODS

Experimental setup

Fig. 1 is a laboratory fluidized bed dryer with a cylindrical chamber which 0.3m in diameter and 4.0 high. Drying was carried out in this equipment. A distributor with a 30% free surface area (3mm holes in a triangular arrangement) was mounted at the bottom of the chamber. Spray nozzle has three channels, the first and the third channel are gas inlet, the middle channel is sludge inlet channel. Eleven temperature taps were located along the height of the riser to measure the axial temperature profile. Fig.2 shows the location of the taps.

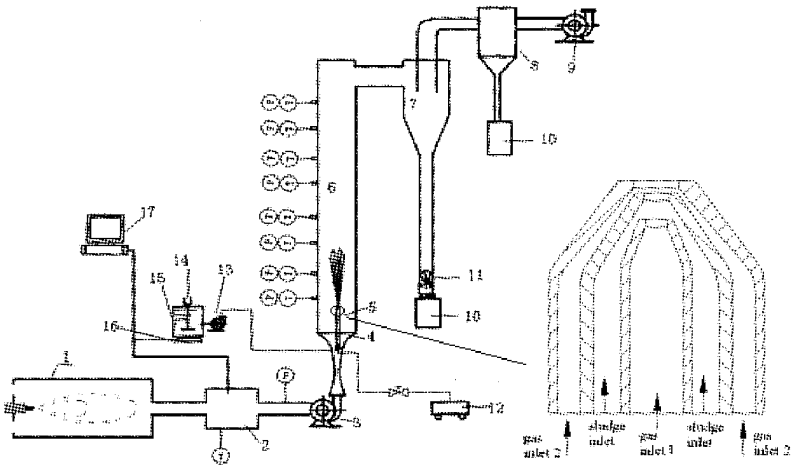

Fig. 1 schematic diagram of the drying system

1-combustion box; 2-mixture box; 3-blower; 4- distributor; 5-spray nozzle; 6-riser; 7-cyclone; 8-bag filter; 9- blower; 10- dry product containers; 11-rotary valve; 12-air compressor; 13-sludge pump; 14-blender; 15-tank; 16-electronic balance; 17-computer.T-temperature probe; P-pressure probe; F-flow rate indicator

The sludge was obtained from the treatment of waste waters from Guangzhou city Guangdong Province in China. The materials' ultimate and proximate analyses are shown in Table 1. The moisture content of sludge is 80%.

Table 1 Ultimate (wt%, daf.) and proximate analyses (wt%, dB.) of sewage sludge

Samples	Ultimate analyses (wt%, daf.)					Q_{net} (kJ/kg)	Proximate analyses (wt%, dB)			
	C	H	O	N	S		M_{ar}	V_{ar}	A_{ar}	FC
Sewage sludge	19.11	3.64	19.93	0.60	1.86	5320	80	10.52	9.01	0.47

In order to study the effects of temperature variation on sludge drying, three temperature levels (413K, 423K and 433K) were considered.

Simulation model and conditions

The flow inside the riser of the fluidized was mainly considered. Fig.2 shows the initially generated mesh using GAMBIT. An Eulerian-Lagrangian approach was used for two phase flow modeling. This model uses Eulerian approach to calculate the fluids motion, Lagrangian approach to calculate the particle motion. Standard κ-ε model is used for turbulence and P0 model for radiation.

The mass flow rate of gas was measured by the flow rate probe. The Navier-stokes momentum equation was used to simulate the flow field inside the riser. The equations are used for Newtonian fluids in which stress versus rate of strain curve is linear. Sludge particle conditions in modeling and properties show in Table 2 and 3, respectively.

Table 2 Sludge particle conditions in modeling

Initial velocity coordination (m/s)	5		
Initial particle temperature(K)	300		
Initial particle diameter(mm)	Min. diameter	Max. diameter	Mean diameter
	0.1	1	0.5
Injection location(m)	Z=0.3		
Spread parameter(n)	3.5		
Feed flow rate (kg/s)	0.0083		

Table 3 Sludge particle properties

Item	Value
Density (kg/m3)	1250
Vaporization temperature(K)	400
Cp(j/kg-k)	3472.8
Thermal conductivity(w/m-k)	1.5521

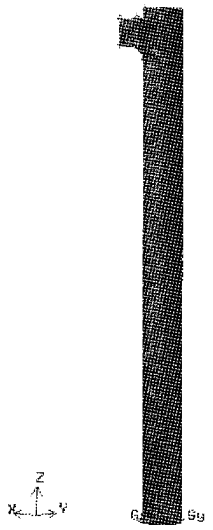

Fig. 2 The produced meshes

RESULTS AND DISCUSSION

Experimental procedure

For the purpose of validating the numerical calculations, an experimental apparatus was designed and built to investigate the process of drying of particles in fluidized bed. Hot air was generated by combusting natural gas. The hot air passes through a distributor in order to have more uniform flow. The air flow rate and temperature at the entrance to the bed range up to 740m3/h and 433K, respectively. Table 4 shows the results of the experimental.

Table 4 The temperature along with the drying bed height

Distance from distributor (mm)	-100	788	1088	1388	1688	2212	2512	2812	3112	3412	3712
Temperature (K)	432	324	325	325	342	374	376	384	391	357	391

Influence of the inlet drying temperature

When sludge is spouted into the drying bed, a intensively heat transfer from the heat convection of flue gas and the radiation from the drying bed wall, at the same time, the flue gas was cooled by the sludge particle, so the temperature of flue gas is decrease immediately, around 390K (as shown in Fig 3). As it flows upward, the temperature drops as heat is lost to heat up the sludge and evaporate the water in sludge particle; the value is about 20K less than the temperature of gas inlet. The temperature rises again due to the mixing of sludge particle and flue gas, the particles' temperature increase too, about 10K less the flue gas inlet temperature, at this moment, a certain number of water was evaporated from the sludge particle.

Fig. 4 shows the velocity profile of dry bed crosses plane under various inlet temperatures, it shows that the bulk of the flow out of the drying bed keeps close to the bed bottom, around 3m/s. The main flow slowly because the drying bed passage section area is large than through hole of air distributor and the flue gas was cooled by the sludge particles, the value is about 2.6m/s. The velocity arise along with the height of drying bed due to the water was evaporated into moisture from sludge particles. However, there is a distinct difference in the gas outlet, because the area of gas outlet is small than of gas inlet, the velocity is about 17m/s.

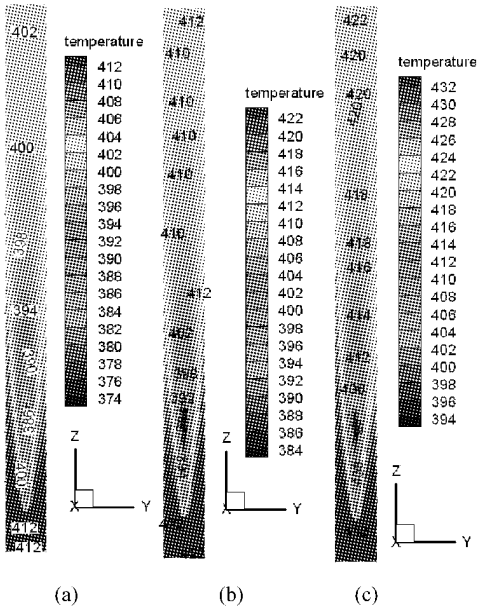

(a) (b) (c)

Fig. 3 The temperature profile of drying bed crosses plane under various inlet temperatures
(a) 413K; (b) 423K; (c) 433K

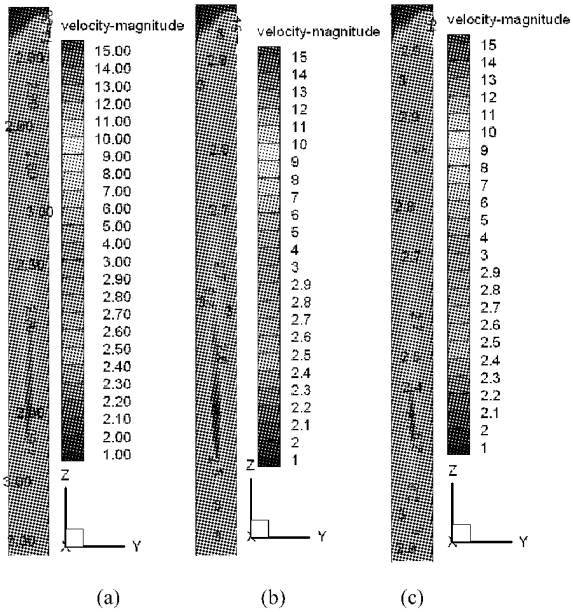

(a) (b) (c)

Fig. 4 The velocity profile of drying bed crosses plane under various inlet temperatures
(a) 413K; (b) 423K; (c) 433K

Fig.5 indicates that the mole fraction of H_2O profile of drying bed crosses plane under various inlet temperatures, when the fresh sludge was spouted into the drying bed, the H_2O was drive out along the track of particle movement, so its shape look likes a solid-cone, and go with the flue gas arise up, the enough mixing of sludge and flue gas, much more water was evaporated from the wet sludge particle. At the top section of drying bed, the mole fraction of H_2O reaches the maximum; from 0.03 to 0.04, but it reduce at the gas out.

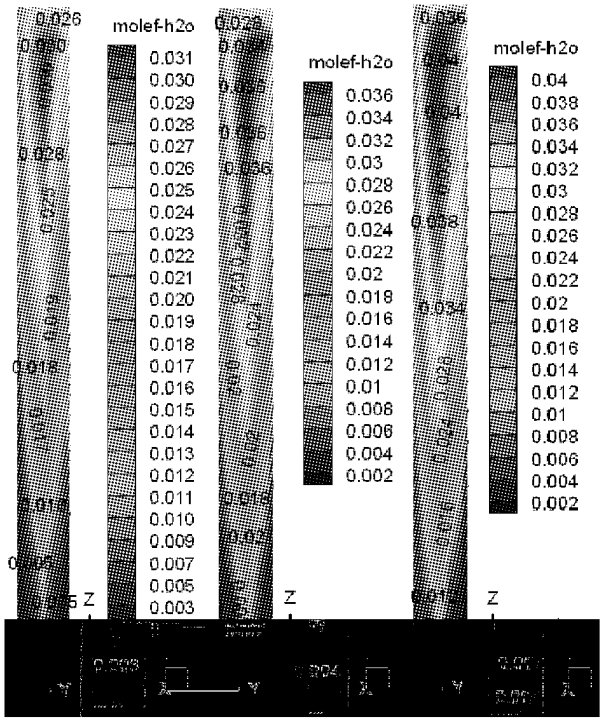

Fig. 5 The mole fraction of H2O profile of drying bed crosses plane under various inlet temperatures
(a) 413K; (b) 423K; (c) 433K.

The influence of various temperature of inlet gas on the dry process of sludge is shown as Table 5; it indicates that the flue gas out temperature is about 10K lower than the temperature of inlet. There is no distinct change between velocities of gas outlet; the value is about 17.6m/s. But the H_2O mass percent of flue gas outlet is remarkable, it rise from 1.66% to 2.35% along with the temperature increasing of flue gas inlet, so that the temperature of gas inlet can influence the drying of sludge particle, but the temperature of flue gas is restrict because of it is waste heat from boiler combustion, therefore, the temperature of 433K can satisfy the drying requirements.

Table 5 The influence of various temperature of inlet gas on the dry process of sludge.

Area-Weighted Average					
Temperature (K)		**Velocity (m/s)**		**Mass Concentration of H_2O (wt. %)**	
Gas inlet	**Gas outlet**	**Gas inlet**	**Gas outlet**	**Gas inlet**	**Gas outlet**
413.15	401.25	2.76	17.46	2.65E-03	1.66
423.15	411.32		17.60	2.28E-03	2.02
433.15	420.94		17.69	2.58E-03	2.35

CONCLUSIONS

The following conclusions have been drawn as results of this study:

(1) The flue gas temperatures were measured along the height of drying bed, the temperatures' range from 432K to 391K;

(2) Numerical study of the proposed Euler-Lagrangian model carried out to investigate the effects of particle and gas behavior for fluidized bed dryer;

(3) When the flue gas inlet temperature is 433.15 K, the predicted gas outlet temperature is about 420.94, the temperature various trend is good agree with experimental data;

(4) Three kinds of operational conditions was modeled by CFD, the temperature is 413.15, 423.15 and 433.15 respectively, the predictions indicate that the effect of drying was influenced by the flue gas inlet temperature, the high inlet temperature is, the more water was evaporated, the mass percent of H_2O is 1.66%, 2.02% and 2.35%.

ACKNOWLEDGEMENTS

This work was supported by Natural Science Foundation of Guangdong Province (China) Research Team (No. 003045) and Project Foundation of Guangdong Key Laboratory of Clean Energy Technology (No.2008A060301002)

REFERENCES

Assari, M. R., H. B. Tabrizi and M. Saffar-Avval. Appl Therm Eng **27** (2007), pp. 422-429.
Balasubramanian, N., C. Srinivasakannan and C. A. Basha. Dry Technol **25** (2007), pp. 1595-1599.
Kudra, T., Z. Gawrzynski, R. Glaser, J. Stanislawski and M. Poirier. Dry Technol **20** (2002), pp. 917-933.
Roustapour, O. R., M. Hosseinalipour, B. Ghobadian, F. Mohaghegh and N. M. Azad. J Food Eng **90** (2009), pp. 20-26.
Vaxelaire, J., J. M. Bongiovanni, P. Mousques and J. R. Puiggali. Water Res **34** (2000), pp. 4318-4323.
Xu, B. H. and A. B. Yu. Chem Eng Sci 52 (1997), pp. 2785-2809.

APPLICATION OF MULTIVARIABLE MODEL PREDICTIVE ADVANCED CONTROL FOR A 2×310T/H CFB BOILER UNIT

Zhao Weijie[1], Dai Zongliao[1] Gou Rong[2], Gong Wengang[2],

Sinopec Shanghai Petrochemical Company Limited Thermoelectricity Division, Shanghai,200540, China
1 Honeywell Process Control System (China), Shanghai, 200051, China
2 Shanghai Power Equipment Research Institute, shanghai, 200240, China

Abstract: When a CFB boiler is in automatic control, there are strong interactions between various process variables and inverse response characteristics of bed temperature control target. Conventional PID control strategy cannot deliver satisfactory control demand. Kalman wave filter technology is used to establish a non-linear combustion model, based on the CFB combustion characteristics of bed fuel inventory, heating values, bed lime inventory and consumption. CFB advanced combustion control utilizes multivariable model predictive control technology to optimize primary and secondary air flow, bed temperature, air flow, fuel flow and heat flux. In addition to providing advanced combustion control to 2×310t/h CFB + 1×100MW extraction condensing turbine generator unit, the control also provides load allocation optimization and advanced control for main steam pressure, combustion and temperature. After the successful implementation, under 10% load change, main steam pressure varied less than ±0.07MPa, temperature less than ±1℃, bed temperature less than ±4℃, and air flow (O_2) less than ±0.4%.

Keywords: circulating Fluidized bed boiler system, multivariable predictive model, advanced control

INTRODUCTION

CFB is used as a clean combustion technology developed within the past 30 years. Advantages of this technology consist of broad range of fuel type, desulfurization, low NO_x emission, high combustion efficiency, wide load operating range, ease of ash disposal, etc. This clean combustion technology has been widely accepted and used in the power, district heating as well as chemical processing industries.

Strictly on control point of view, CFB has distributed parameters and non-linearity, and is a tightly coupled multivariable control target. Due to its complex and peculiar operating characteristics, research and development of CFB boiler control characteristics and system has become today's new area of research.

The Sinopec's 2×310t/h CFB station utilizes a mixture of coal and petroleum coke as main fuel supply and is operated like typical CFB. The 2×310t/h CFB and 1×100MW extraction steam turbine supplies process steam to a steam header supply system . Superheated steam is extracted from turbine and stepped down to medium and low pressure steam supplies which are then directed to the appropriate steam supply system, Two desuperheaters and decompressors were also installed to insure the reliability and safety of steam supply system.

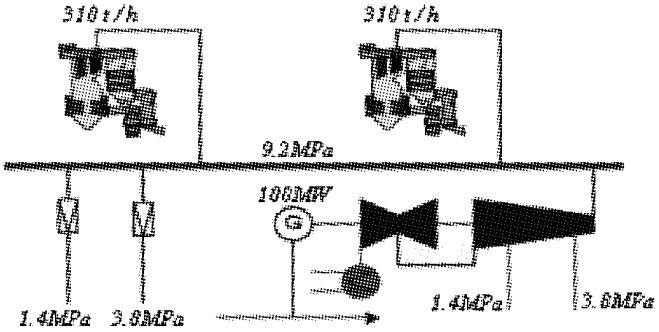

Fig. 1 Sinopec Power Plant CFB Units Architecture

This unit utilizes a Honeywell Distributed Control System (DCS) with an Advance Energy Solutions (AES), a Honeywell's integrated multivariable model predictive advanced control and optimization solution . AES is specifically designed for power generation and captive thermal power plant. AES optimizes the operations while adhering to the strictest operating conditions and emissions of SO_2, CO, and NOx.

Section 2 presents the CFB control characteristics, section 3 on CFB advanced control, section 4 on advanced control operations, and section 5 on actual operating results.

CHARACTERISTICS OF CFB BOILER CONTROL

Long lag time, strongly coupled, multi-in/multi-out non-linear system

Due to the special internal fluidization characteristics, CFB is a system of long lag time, strongly-coupled, multi-input/multi-output, non-linear. Table 1 displays the interaction of CFB main control targets and its related control parameters.

Table 1 the interaction of CFB boiler main control targets and its related control parameters

Variable		CV1	CV2	CV3	CV4	CV5	CV6	CV7	CV8
		Steam pressure	*Bed temperature*	*Oxygen in fuel gas*	*SO_2 in fuel gas*	*Bed pressure*	*Chamber pressure*	*Drum level*	*Steam temp.*
MV1	*Fuel feed*	C	S	S	S	M	M	S/M	S/M
MV2	*Primary air*	S	C	S			S	S/M	S
MV3	*Second. air*	S		C					S
MV4	*Limestone*		M		C	M			
MV5	*Ash removal*		M			C			
MV6	*Flue gas*						C		
MV7	*Feed water*	M						C	
MV8	*Spray water*	M							C
DV1	*Steam flow*	S							S/M

C: —single input/single output variable relationship.
S: —strongly interaction.
M: —Minor interaction

Bed temperature control target has inverse response characteristic

Primary air flow V_1 steps down can cause a non-linear bed temperature θ response (see Fig. 2). Its transfer function is:

$$G_{\theta V_1}(s) = \frac{K_1}{1+T_1 s} \cdot e^{-\tau_1 s} - \frac{K_2}{1+T_2 s} \cdot e^{-\tau_2 s} \qquad (1)$$

When there is a drop in primary air flow, the bed temperature responds first by dropping inversely, then rising past its original value, and finally stabilizing at a new value. This is caused by open-loop zeros of the system on right half of complex plane.

Equation (1) indicates a delayed circular inverse response system. The inverse response characteristic with delay described in Equation (1) has been proven to be very unstable.

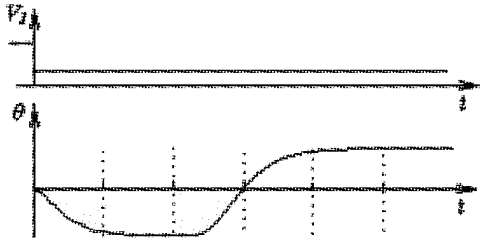

Fig. 2 Bed temperature θ response by Primary air flow V_1 steps down

Effects on control process from fuel and limestone inventory on bed

The dynamic characteristic of the heat flux in the furnace is based on the amount of bed fuel inventory. The inverse response characteristic of bed temperature due to the drop of primary air is also caused by the bed fuel inventory. Limestone, as a desulfurization agent, has direct impact on the combustion efficiency and desulfurization effectiveness. Especially when high sulfur petroleum coke requires higher bed lime inventory which further heightens the impact on combustion efficiency and desulfurization effectiveness. Thus, predicting the fuel and limestone inventory on bed will greatly improve the efficiency of CFB boiler control.

Load Response characteristics

Figure 3 shows the combined effect of fuel flow and primary air flow on main steam pressure p.

Figure 3 indicates how primary air flow V_1 influences the combustion system load response speed. Control system is able to satisfy load change demand. However, due to longer lag and inertia of combustion characteristics in CFB boiler it will require longer response time. Despite the required longer lag time, the load change response characteristic is better than regular coal fired boilers.

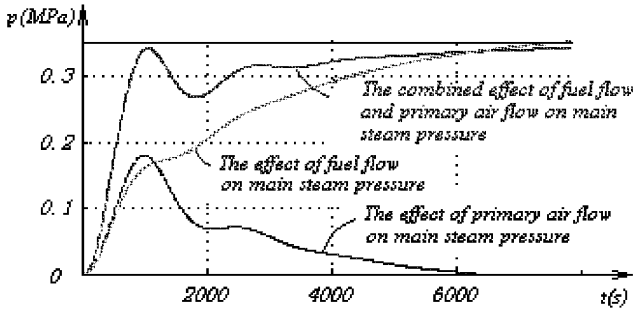

Fig. 3 Load Response characteristics of main steam pressure p

CFB ADVANCED CONTROL SYSTEM CONFIGURATION

Figure 4 is the AES configuration diagram. AES modules consist of Master Pressure Control (MPC), Economic Load Allocation – Boiler (ELA_B), Advanced Combustion Control (ACC) and Advanced Temperature Control (ATC). These modules are installed on Honeywell's APP node or APC server.

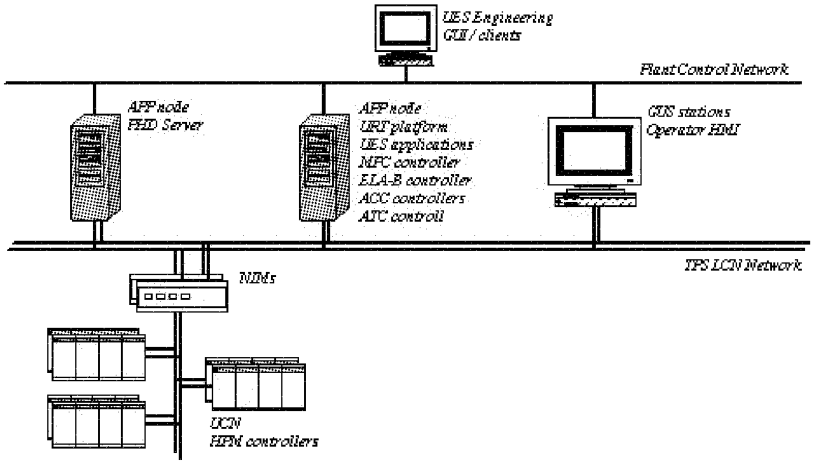

Fig. 4 Sinopec Power Plant AES System Architecture

Master pressure control

Master Pressure Control (MPC) is the overall steam production control. It maintains the steam supply pressure operating range based on steam flow demand. The output of all boilers on the same steam supply header is controlled via load allocation control through ELA_B module.

The main steam pressure controller uses steam header pressure as controlled variable (CV1). The actual steam consumption fluctuation is the disturbance variable (DV1). The manipulated variable (MV1) is the total boiler heat output demand, which is also used in the economic load allocation calculations. Figure 5 shows input/output relationship of the main steam pressure controller.

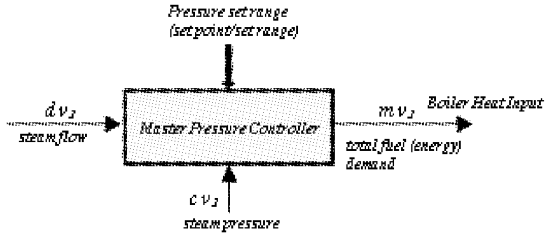

Fig. 5 Input/output relationship of the main steam pressure controller

Economic load allocation for boiler (ELA_B)

Economic Load Allocation module optimizes the load allocation of the boilers and provides steam pressure control for each boiler on the same steam header. ELA_B performs economic load allocation while strictly adheres to boiler operational requirements and maintains steam header demand stability.

Under the optimized load allocation of corresponding overall steam load demand, the incremental cost of each boiler is the same and unrelated to the absolute cost. The final incremental cost of optimized boiler operation is equal. Therefore:

$$\frac{dC_1}{dD_1} = \frac{dC_2}{dD_2} \tag{2}$$

Under the optimized load allocation, boiler load allocation is restricted by the total load demand limit. Other limiting factors are individual boiler permissible operational limit, load differential limit, re-allocation limit, and boiler load cross limiting, etc.

Advanced combustion control

Advanced Combustion Control (ACC) is one of the most effective methods for reducing operational cost. Optimizing combustion process results in reduction of fuel consumption and extension of operational life of the equipment.

Master Pressure Controller determines the total heat load demand, which is used by the ELA_B module to allocate load demand to individual boiler. The ACC optimizes the individual boiler operation to match the load demand from ELA_B. ACC manipulated variables are fuel flow, primary and secondary air flow, and limestone flow. The results are used as the set point to DCS control loops.

Advanced combustion controller

ACC, by adjusting fuel flow, primary and secondary air flow, and limestone flow, minimizes the difference between steam pressure, determined by MPC, and load demand, determined by ELA_B. Similarly, the output from ACC is used as the set point to the cascading control loops.

Based on high level combustion control of the Multivariable Advanced Control Engine, boiler combustion control and optimization can be executed concurrently. ACC can control combustion while maintaining steam pressure, bed temperature and other factors, and communicating predictive trend of these variables to the subsequent control system.

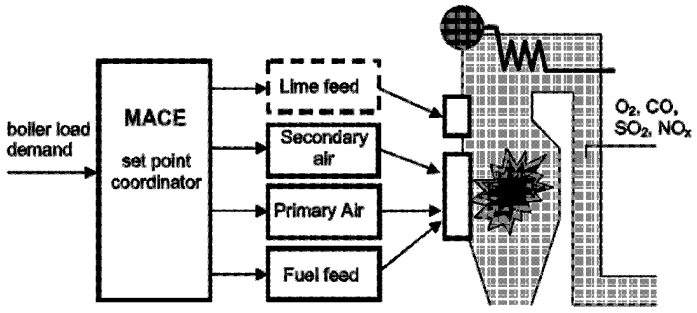

Fig. 6 The output from ACC is used in the cascading control loops

Soft measurement sensor

Soft Measurement Sensor is used for estimating combined inferred values which are needed in the boiler response calculation but cannot be measured directly. Kalman wave filter is used for this purpose.

Soft Measurement Sensor can supply the following signals:

1. Bed fuel inventory CV4 – the quantity of total unburned fuel in the bed.
2. Bed limestone inventory – the quantity of total limestone has not reacted with sulfur dioxide.

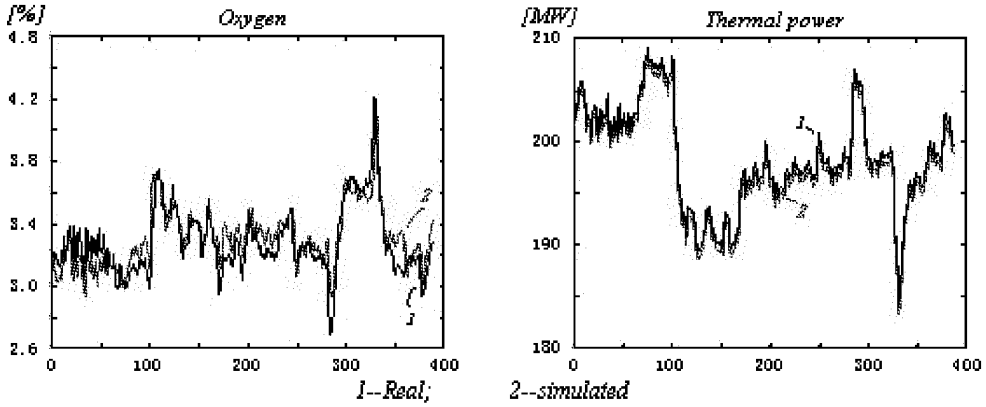

Fig. 7 A high degree of similarity when comparing air flow and heat flux models with actual measured data

3. Instantaneous limestone consumption rate – required feed rate of limestone to maintain bed limestone inventory constant.

4. The instantaneous heat released within bed. The heat release calculator uses the following process variables: drum pressure, main steam flow and temperature, feed water flow and temperature.

Heat flux in the CFB boiler is directly proportional to the bed fuel inventory. After further understanding of the CFB boiler control characteristics, a new control strategy is proposed: Use primary air flow to control heat flux and fuel feed rate to control bed fuel inventory stability. These are non-linear mathematical modeling. Therefore, Fig. 7 shows a high degree of similarity when comparing excess oxygen and heat flux models with actual measured data.

These effects are also apparent in the mathematical modeling of CFB boiler: internal bed temperature is directly proportional to heat flux; the heat flux is closely related to the availability of bed fuel inventory; complex relationship between primary air flow and fuel flow. Thus, simple PID control can never achieve necessary operational requirement. Fig. 8 demonstrates the internal bed temperature trend line of mathematical modeling and actual measurement.

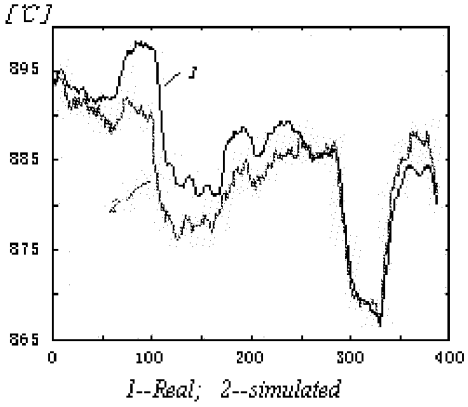

Fig. 8 Bed temperature

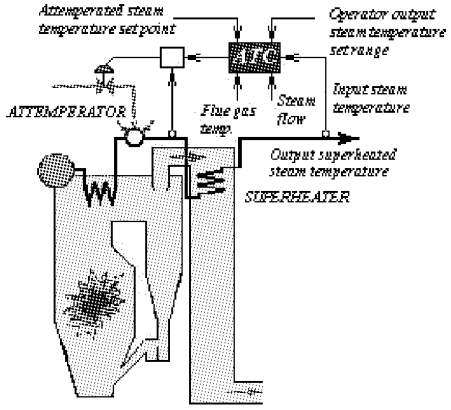

Fig. 9 Demonstrates the principle of ATC

CFB boiler combustion control strategy

Non-linear modeling helps the understanding of bed fuel inventory and bed limestone inventory. However, it appears too complicated for control system design based on this non-linear modeling. Control strategy can be greatly simplified by using linear modeling which is indicated in equation 3, based on heat flux, bed fuel inventory, starting fuel flow, fuel oil flow, and primary air flow.

$$\begin{cases} \dfrac{d}{dt}Q(t) = -\dfrac{1}{\tau}Q(t) + \dfrac{Q_0}{\tau \times BFI_0}BFI(t) + \dfrac{k \times BFI_0}{\tau}PA(t) + d_1 \\ \dfrac{d}{dt}BFI(t) = -\dfrac{Q_0}{H \times BFI_0}BFI(t) - \dfrac{k \times BFI_0}{\tau}PA(t) + F(t) + d_2 \end{cases} \tag{3}$$

Embedding linearized real-time model in the ACC, fuel flow, heat flux, bed fuel inventory, bed temperature and excess oxygen can be controlled. Primary and secondary air flows are used as control variables; coal and petroleum coke ratio and fuel oil flow as disturbance variables. The intangible state variables can be estimated using soft measurement sensor. The time constant of various model parameters can be verified on-line and updated real-time.

Advanced temperature control

Advanced Temperature Control can minimize variability of superheat temperature and increase boiler exit steam temperature stability. Furthermore, it allows superheater to operate at a higher temperature, thereby higher thermal efficiency.

Figure 9 demonstrates the principle of ATC. To achieve a desired exit steam temperature, the ATC controls the set point of inlet steam temperature of the superheater to DCS control loop.

Based on boiler test result, the combustion chamber heat flux is derived from the interaction between fuel flow, primary air flow and bed fuel inventory. Primary superheat spray water is the CV, and steam flow and secondary air flow are the DVs. Combustion chamber heat flux and convection thermal disturbance are immeasurable state variables estimated by soft measurement sensor.

OPERATION OF ADVANCED CONTROL SYSTEM

The collection of operational data

Prior to the implementation of Advance Energy Solutions（AES）, 12-month operational history of CFB boiler unit was collected by the station's real-time historian. Detailed analysis of the data provided understanding of CFB boiler operation characteristics. Analysis of the data also confirmed and resolved static relationship of various CFB boiler operational parameters. Collecting and analyzing the operational history enabled convenient and accurate validation of AES implementation and effectiveness.

Construction of dynamic and static models

To implement boiler combustion optimization, a series of tests were performed to assist construction of dynamic and static models:

1. Equation Carbon monoxide (CO) vs air/fuel ratio static model
2. Equation Oxygen (O_2) vs air/fuel ratio static model
3. Air flow, fuel flow, vs CO/ SO_2, bed temperature dynamic model
4. Equation (3) SO_2 vs limestone/fuel ratio static model
5. bed lime inventory SO_2, Equation (3) dynamic model

Production operation tests

The purpose of production operation test:

(1) Evaluate boiler efficiency based on boiler load, excess air and effect on limestone flow change

(2) Evaluate the economic benefit and dynamic relationship, of the 2 boilers on the same steam header, between various parameters during load allocation optimization. The test was performed under 4 different load conditions. 4 different bed temperature setpoints were tested under each load condition. 4 different excess oxygen setpoints were tested under each bed temperature setpoint.

Control target characteristic test

Control target characteristic test was performed at 3 load levels (60%, 80%, 100%) and with 2 different coal/petroleum coke ratio. PRBS sequential signal was used to obtain different transfer functions. For process variables and disturbance variables, Kalman wave filter was used to minimize noise disruption sensitivity and other variables disturbance fluctuation.

Through testing, latent differences of each boiler were identified and optimal point of operation with lowest cost and maximum benefit were found. Diagram 10 demonstrates the effects of steam flow and limestone flow on the efficiencies of boilers 5A and B. Steam flow was also parameterized in the excess oxygen. Though the two boilers were identical, the efficiency curve surfaces are different due to latent differences.

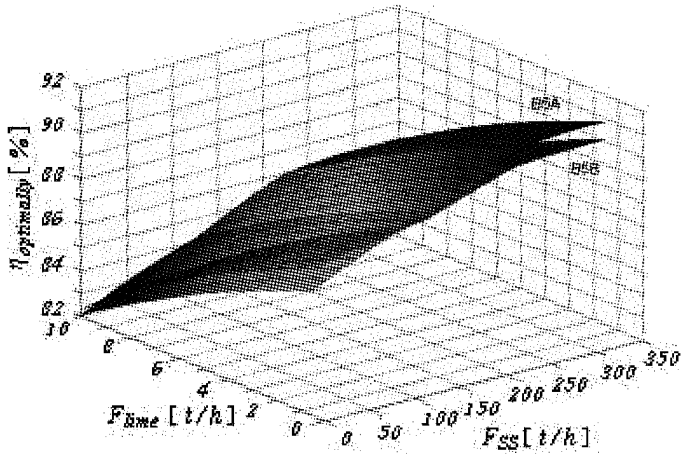

Fig. 10 Demonstrates the effects of steam flow and limestone flow on the efficiencies of boilers 5A and 5B

EFFECTIVE OF OPERATION

After the implementation of MPC, ACC and ATC, the standard deviation for:

Bed temperature deviation $StdDev < 1°C$ .Steam temperature deviation $StdDev < 0.5°C$ .Excess oxygen deviation $StdDev < 0.1\%$ .Carbon dioxide deviation $StdDev < 25 mg/m^3$

After the previous modules were put in operation, with 10% load change, Fig. 11 shows the operation process trend lines of steam header pressure, steam flow, steam temperature, and excess oxygen. The steam header pressure varied less than ±0.07MPa, steam temperature less than ±1℃, bed temperature less than ±4℃, and excess oxygen less than ±0.4%.

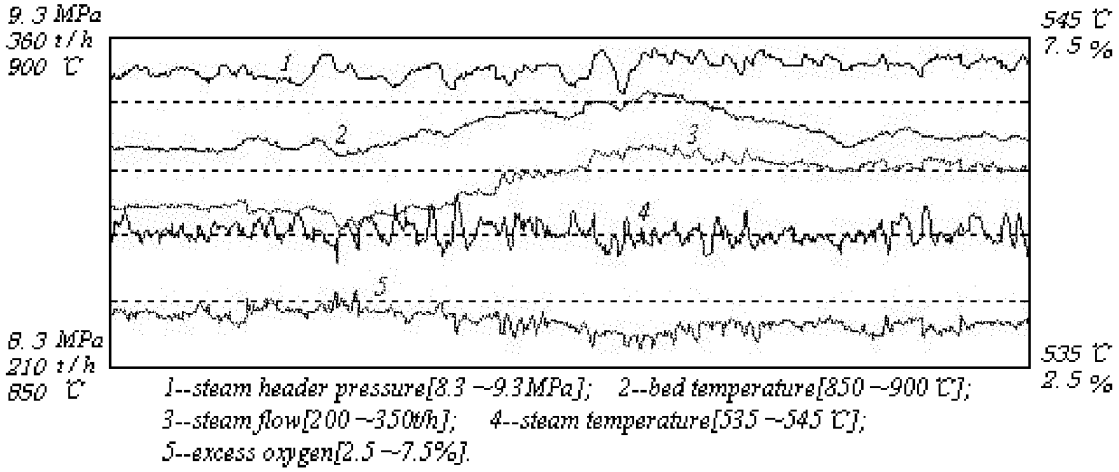

Fig 11 The operation process trend lines of steam header pressure, steam flow, steam temperature, and excess oxygen

REFERENCES

Skogestad, S. & Rostlethwaite, I. Multivariable Feedback Control: Analysis and Design[D], John Wiley & Sonsco, Ltd. England. (1996).

Yang Jingqi, Zhao Weijie, Guo Rong, etc. Analysis and Design of Control System of Circulating Fluidized Bed Boilers, [J], Journal of Power Engineering, 2005/25(4), pp. 517-522.

Zhao Weijie, Zhang Wenzhen, Feng Xiaolu Analysis of the Control Properties for CFBB's Bed Temperature, [J], Journal of Power Engineering, 2007/37(4), pp.545 –550.

COMBUSTION MODEL FOR A CFB BOILER WITH CONSIDERATION OF POST-COMBUSTION IN THE CYCLONE

S. H. Li, H. R. Yang, H. Zhang, Y. X. Wu, J. F. Lu, G. X. Yue

Key Laboratory for Thermal Science and Power Engineering of Ministry of Education
Department of Thermal Engineering, Tsinghua University, Beijing, 100084, China

Abstract: Severe post combustion in the cyclone of CFB boilers could destroy heat absorbing balance among the heating surfaces and cause overheating problem for reheaters and superheaters. However, post combustion in the cyclone is rarely considered in the design phase of a CFB boiler. Based on our previous experiment results, group combustion model is used in this study to estimate the combustion of particles in the cyclone. It is found that the combustion of particles in the cyclone did not contribute as much as we anticipated to the temperature augment in the cyclone because of great oxygen diffusion resistance in near-wall particle layer. Post combustion model in the cyclone is then added into a one-dimensional combustion model of CFB boiler, in which the gas-solid flow, reaction, and heat absorption at different vertical locations in a CFB boiler can be well predicted with the knowledge of operation parameters. The new model was used to estimate the influence of some operation parameters on the post combustion in the cyclone and heat releasing fraction in the cyclone. The prediction results are very good.
Keywords: CFB boiler, post combustion, cyclone, combustion model

INTRODUCTION

Cyclones are widely used as gas-solid separators in circulating fluidized bed (CFB) boilers because of their high separation efficiency, simple structure, good adaptability and low cost. Many studies focused on separation efficiency and pressure drop. The performance of the cyclone is important for material balance in the boiler (Yue et al., 2005). The cyclone can be water cooled, steam cooled, or thermal insulated.

In some CFB boilers with thermal insulated cyclones, post combustion of combustible was often found. The post combustion could result in a temperature augment of flue gas in the cyclone in the range of 30-50℃(Yue et al., 2006). This phenomenon does not occur in CFB boilers with water or steam cooled cyclones, since the heat released in the cyclone is absorbed.

If post combustion is remarkable, it destroys the heat absorption balance, causing overheating problem for reheaters and superheaters. In the same time, flue gas exhaust temperature could be higher than designated value, causing extra heat loss and thus lower boiler efficiency. It was reported that the over high temperature of flue gas even damaged electric static precipitator (ESP) (Yue et al., 2006). Well predicting post combustion in a CFB boiler is helpful to the designers to adjust the arrangement of back-end heating surfaces and to the operators to adjust operation conditions to prevent corresponding problems.

In this paper, a mathematical model to describe post combustion in the cyclone is developed. Then this model is integrated into a 1D model to describe the overall combustion of a CFB boiler. Some influencing factors on post combustion and the influence of post combustion on the overall combustion performance are discussed.

POST COMBUSTION MODEL AND 1D COMBUSTION MODEL OF A CFB BOILER

Combustible matters in the cyclone include carbon monoxide (CO) and residual carbon. The combustion mechanism of CO is rather simple. However, the combustion mechanism of residual carbon is complex.

In a CFB boiler, cyclones are usually operated at high solid loadings above 5kg-solid/kg-gas (Muschelknautz and Greif, 1997). In these cases, only a small part of solids is continuously carried by the turbulence air stream, and the rest forms strands or a continuous solid layer near the wall. Namely, only a small amount of the particles remain in the gas flow and undergo centrifugal separation in the vortex of the cyclone.

According to our previous experimental results (Li et al., 2008b), in the center of the cyclone the particles are nearly free, i.e. the particle number density is very small. Consequently, the combustion of carbon particles in the center region can be treated as *isolated particle combustion* (ISOC) (Annamalai et al., 1994).

Group Combustion theory (Annamalai et al., 1994) can be further applied to describe the combustion of the carbon particles near the wall where the solid concentration is higher. According to the theory , with the increasing number density, the particle cloud undergoes the stages of *interactive combustion* and then *partial group combustion*. When the number density is very large, the oxygen mass fraction at the cloud surface

approaches zero and the entire cloud can be treated as a single large particle with the density the same as the cloud mass density. This stage is called *sheath combustion*. To estimate combustion of the near-wall particles in the cyclone, following simplifications and assumptions were made:

(1) Near-wall particles cloud can be simplified as a slab, whose characteristic length is the thickness of the near-wall particle layer, δ.

(2) The near-wall particles cloud is uniform, e.g. the volumetric solid concentration at different locations there equals to the average one, 1-$\overline{\varepsilon}$.

(3) Near-wall particles cloud is isothermal.

(4) Temperatures of gas at cyclone outlet and solid at dust exit are the same.

$$G' = G \Big/ \left(1 + \frac{Sh_p D}{fkd_p}\right) \tag{1}$$

$$G = S_{V,C}\delta^2 Sh_p / (fd_p) \tag{2}$$

$$\eta_{eff} = \frac{\tanh[(G')^{\frac{1}{2}}]}{(G')^{\frac{1}{2}}} \tag{3}$$

Group combustion number G' of near-wall particles in the layer, seen in Eq. (1), is defined as the ratio of oxygen transport rate among the particles in the cloud to that between the cloud and ambience. In Eq. (1) and (2), $S_{V,C}$ is the surface area of particles per unit volume. Sh_p is Sherwood number of single particle. f is carbon content in bed material. δ is thickness of particle layer at the wall. The detail information about Eq. (1) and (2) can be found in previous study (Li et al., 2008a).

The combustion effectiveness factor, η_{eff}, defined as the average ratio of reaction rate of particles inside the cloud to that of particle on cloud surface. η_{eff}, is expressed in Eq. (3). The equation is deduced from species conservation equation of oxygen (Li et al., 2008a). To calculate the average residence time, experimental previous results (Li et al., 2007 and Li et al., 2008c) are adopted. Volumetric solid concentration and velocity distribution in the near-wall region of the cyclone was described by previous study (Li et al., 2008b).

Combined with the combustion model of solid particle with the one for combustible gas, post combustion model in the cyclone of a CFB boiler was established.

The post combustion is then integrated into a 1-D combustion model originating from a material mass balance model purposed by Yang et al (2005a). The material balance model consisted of several sub-models such as attrition and size reduction model, residence time model, segregation model and hydrodynamic model. More recently, the model was further developed into a 1-D combustion model, including several sub-model in combustion as char combustion model, volatile combustion model, lime mass balance model, gas component mass balance model, energy balance model, heat transfer model and desulfurization model (Yang and Yue, 2006). The 1-D combustion model was used to predict the temperatures, content of gas components, particle size distribution, fraction of heat releasing profile, heat absorbing profile and carbon content profile of different size particles along the furnace height. Through this study, the novel 1D CFB combustion model with the consideration of post combustion was established.

PREDICTION OF POST COMBUSTION IN A 135MWE CFB BOILER

The proposed 1D CFB combustion model was used to predict post combustion of a 135MWe CFB boiler and the influences of various operation parameters on post combustion were also investigated.

This 135MWe CFB boiler, of which designated parameters can be seen in Tab. 1, has two insulated cyclones. As found in the application, the temperature augment caused by post combustion in the cyclone was about 20~50K. The feeding coal was a lean coal.

With the operation parameters, post combustion in the cyclone was estimated. Combustion of near-wall carbon particles in the cyclone was estimated by using Eq. (1) ~ Eq. (3). The calculation results show that G'>>100 and η_{eff} <5%. According to Group Combustion theory (Annamalai et al., 1994), combustion of near-wall carbon particles are *sheath combustion*. The high concentration of particles at the near-wall region prevents oxygen diffusion into the particle cloud, greatly hindering carbon combustion in the near-wall particles. However, combustion of CO and carbon particles relative far away from the wall is still intensive. The calculation results show that temperature augment caused by post combustion is about 25K, which is consistent with measured values (Yue et al., 2006).

Table 1 Performance parameters of a 135MWe CFB boiler at full load

Designated parameters	Unit	Value	Performance parameters	Unit	Value
Main steam flow rate	t/h	465	Feed water temperature	℃	244
Main steam pressure	MPa	13.7	Bed Temperature	℃	885
Main steam temperature	℃	540	Exhaust gas temperature	℃	138
Reheat steam flow rate	t/h	411	Primary air temperature	℃	243
Reheat steam pressure at inlet	MPa	4.06	Secondary air temperature	℃	243
Reheat steam temperature at inlet	℃	374	NO_X emission ($6\%O_2$)	mg/m^3	250
Reheat steam pressure at outlet	MPa	3.93	SO_2 emission($6\%O_2$)	mg/m^3	300
Reheat steam temperature at outlet	℃	540			

In order to study the effect of coal type on post combustion in the boiler, calculations with the proposed model were also conducted for three CFB boilers with the same thermal output but burning different fuel, lignite, bituminous and anthracite respectively. The geometry of the furnace, operational parameters, and layout of heating surfaces were only with minor difference and corresponding modification was done in the modeling. The effect of the geometric was regarded negligible.

Table 2 shows the coal properties and calculated results of post combustion when different type of coal is fired at the same load. In the table, R_c and R_{co} are reaction rates of carbon and CO in the cyclone respectively. ΔT_c is temperature augment in the cyclone. $Q\%$ is heat releasing fraction in the cyclone. C% is carbon content in the material in the cyclone.

Table 2 Post combustion estimation in 135MWe CFB boilers burning different coals

Items	lignite	bituminous coal	anthracite
V_{ar}	0.21875	0.167293	0.04332
C_{ar}	0.295	0.518523	0.679
H_{ar}	0.0242	0.02904	0.017
N_{ar}	0.0086	0.01042	0.004
O_{ar}	0.1061	0.05837	0.02
S_{ar}	0.0036	0.00492	0.002
Ash_{ar}	0.0862	0.334368	0.228
H_2O_{ar}	0.4763	0.044358	0.05
$Q_{ar,net,p}$ (kJ/kg)	10920	21000	23040
R_c (kmol/s)	8.90E-03	4.64E-02	8.86E-02
R_{co} (kmol/s)	1.25E-02	4.49E-02	8.31E-02
ΔT_c (K)	6.2	25.1	44.4
$Q\%$	1.40%	5.70%	10.27%

Since the pyrolysis rate and combustion rate of char particles for lignite were fast, most of the combustible matters including carbon and CO burned in the furnace and the combustible matters entrained into cyclone were less. For lignite-firing CFB boiler, R_c and R_{co} were the smallest and the corresponding temperature augment in cyclone was only 6.2K. On the contrary, reactions of anthracite were slow and the combustible matters enter cyclone were much more, and thus R_c and R_{co} for anthracite firing CFB boiler were the highest and corresponding temperature augment in cyclone was as high as 44.4K.

The influence of excess air ratio was also investigated with the purposed 1D combustion model. The calculated results show that temperature augment in the cyclone slightly increases with increment of excess air ratio. This tendency is consistent with measurement results obtained on the same boiler (Yue et al., 2006). Corresponding heat releasing ratio also increases with increment of excess air ratio. The calculated results of ΔT_c and $Q\%$ for different excess air ratios can be seen in Fig.1. With the increasing total air flow rate, oxygen concentration in the cyclone become higher, which result in more intensive combustion. Consequently, more heat was released in the cyclone. At the same time, gas and solid flow rate also increased with of total air flow rate. However, the increase tendency of heat release is stronger than that of gas and solid flow rate, leading to a gradual increase of temperature augment in the cyclone.

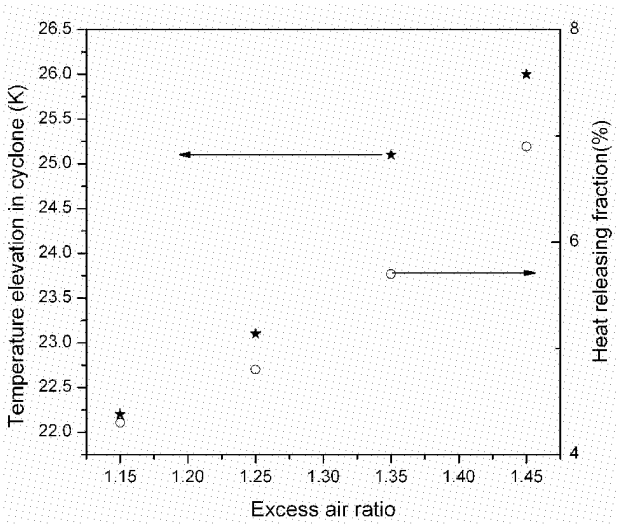

Fig. 1 Calculated results of ΔT_c and Q% for different coals

CONCLUSIONS

In this study, post combustion in cyclone was modeled and a novel 1D combustion model of CFB boiler with consideration of post combustion in cyclone was developed. This model was used to predict post combustion in CFB boilers with the capacity of 135MWe, and the predictions were consistent with measured data. The influences of coal rank and excess air ratio on post combustion were also studied by this model. It was found the influence of coal rank on post combustion is significant and post combustion is more intensive when anthracite is fired than that when bituminous and lignite is fired. With the increment of excess air ratio, temperature augment and heat release ratio in the cyclone also increase.

In the future, the 1D CFB combustion model with consideration of post combustion in the cyclone will be further improved. For example, to take the non-uniform distribution of volumetric solid concentration in the cycle as found by our recent experiments (Li et al., 2008b). Some other influencing factors on post combustion and the more detailed influence of post combustion on the overall combustion performance will be studied.

ACKNOWLEDGEMENTS

Financial supports of this work by Key Project of the National Eleventh-Five Year Research Program of China (2006BAA03B02) and National Science Fund Committee (50406002) are gratefully acknowledged.

NOTATIONS

D	diffusion coefficient	[m^2/s]	$S_{V,C}$	surface area of particles per unit volume	[m^2/m^3]
d_p	mean diameter of particles	[μm]	ΔT_c	temperature augment in cyclone	[℃]
f_c'	carbon content in bed material	[%]	W	width of the particle layer	[m]
G'	group combustion number	[-]	δ	thickness of the continuous particle layer at the wall	[mm]
k	chemical reaction rate constant	[m/s]	η_{eff}	combustion effectiveness factor	[-]
M	number density	[-]	Sh_p	particle Sherwood number	[-]
$Q\%$	heat releasing fraction in cyclone	[-]			
R_c	reaction rate of carbon	[kmol/s]			
R_{co}	reaction rate of CO	[kmol/s]			

REFERENCES

Annamalai, K., Ryan, W. and Dhanapalan, S. "Interactive processes in gasification and combustion-part III: coal/char particle arrays, streams and clouds" Prog. Energ. Combust., 20(6), (1994) pp.487-618.

Li, S. H., Zhang, H., Yang, H. R., Yang, S., Lu, J. F. and Yue, G. X. "Determining Cyclone Particle Hold-up by the Pressure Drop for a CFB Boiler" Chem. Eng. Technol., 30(12), (2007) pp.1726-1731.

Li, S. H., Li, Y., Li, J. J., Yang, S., Yang, H. R., Zhang, H., Lu, J. F. and Yue, G. X. "Measurement of characteristics of solid flow in the cyclone separators with fiber optical probe". The 6th International Symposium on Measurement Techniques for Multiphase Flows, Naha, Okinawa, JAPAN, (2008a).

Li, S. H., Yang, H. R., Zhang, H., Lu, J. F. and Yue, G. X. "Hydrodynamics of two-phase flow and particle motion in the cyclone

of a CFB boiler". 9th International Conference on Circulating Fluidized Beds Hamburg, Germany, (2008b) pp.975-980.

Li, S. H., Yang, S., Yang, H. R., Zhang, H., Liu, Q., Lu, J. F. and Yue, G. X. "Particle holdup and average residence time in the cyclone of a circulating fluidized bed boiler" Chem. Eng. Technol.(2), (2008c).

Muschelknautz, E. and Greif, V. (1997). "Cyclone and other gas-solid separators" in "Circulating Fluidized Beds". Grace, J. R., Avidan, A. A. and Knowlton, T. M., Blackie Academic & Professional, pp.181-213. 1997.

Yang, H. R., Yue, G. X., Xiao, X. B., Lu, J. F. and Liu, Q. "1D modeling on the material balance in CFB boiler" Chemical Engineering Science, 60(20), (2005a) pp.5603-5611.

Yang, H. R., Zhao, X. M., Wang, Y., Xiao, X. B., Lu, J. F. and Yue, G. X. "Research on Post Combustion in CFB Boiler" Power System Engineering, 21(1), (2005b) pp.23-24.

Yang, H. R. and Yue, G. X.. Development and validation of a 1D CFB boiler combustion model. Beijing, Project report to EDF, (2006).

Yue, G. Lu, J.F., Zhang, H. et al. Design Theory of Circulating Fluidized Bed Boilers. in: L. Jia (Eds.),18th International Fluidized Bed Combustion Conference, May 18-21, 2005, Toronto Canada.

Yue, G. X., Yang, H. R. and Zhang, H. "Post Combustion in Circulating Fluidized Bed Boilers". 19th International Fluidized Bed Combustion Conference, Vienna, Austria, (2006).

NUMERICAL SIMULATION IN A SUPERCIRTICAL CFB BOILER

Yanjun Zhang[1], Xiang Gao[1], Zhongyang Luo[1], Xiaoguo Jiang [2]

1 Zhejiang University, Hangzhou, 310027 China
2 Harbin Boiler Co., Ltd, Harbin, 150040 China

Abstract: The dimension of the hot circulation loop of the supercritical CFB boiler is large, and there are many unknowns and challenges that should be identified and resolved during the development. In order to realize a reasonable and reliable design of the hot circulation loop, numerical simulation of gas-solid flow in a supercritical CFB boiler was conducted by using FLUENT software. The working condition of hot circulation loop flow field, gas-solid flow affected by three unsymmetrical cyclones, air distribution and pressure drop in furnace were analyzed. The simulation results showed that the general arrangement of the 600MWe supercritical CFB boiler is reasonable.

Keywords: supercritical, CFB boiler, numerical simulation, 600MWe, design

INTRODUCTION

Supercritical CFB boiler is regarded as one of the most promising new generation clean coal technology (Lu et al, 2002). All major CFB boiler manufacturers around the world, including Foster Wheeler USA and ALSTOM Finland have developed the supercritical CFB boiler, and Foster Wheeler has also signed the world unique 460MW CFB boiler contract, which is now in commissioning and will put into operation in 2009.

China is the country operating largest number of CFB boilers in the world. The successful operation of Kaiyuan and Baima 300MW CFB boiler represents that China possesses the international level technology on large CFB boiler manufacture and operation, and matured condition to develop its own proprietary CFB technology. Therefore, at the beginning of the Eleventh Five-Year Plan (2006-2010), China formally started the technical development project.

Because the dimension of hot circulation loop of the supercritical CFB boiler is large, for example, with height over 50 meters, many unknowns and challenges should be identified and resolved during the development. Doing field test on such a large boiler is difficult and costing. Therefore, in order to guarantee a reasonable and reliable design of hot circulation loop, numerical simulation and theoretical analysies on supercritical CFB gas-solid flow is necessary.

GENERAL LAYOUT OF HOT CIRCULATION LOOP

The hot circulation loop scheme is showed in Figure 1. In the loop, there is single furnace, two air distributors, and three cyclones, which are arranged at each of furnace two sides. Below each cyclone, a loop seal is equipped. Cone valves are also used to separate dust circulation into two ways, one returns to the furnace directly and the other enters the furnace through external bed.

The furnace size is 16.952m×25.736m×54m, and the air distributor size is 4.5×25.736m. Six cyclones with 9.3m diameter are adopted. The main items to be test are: analysis on evenness of hot circulation loop gas-solid flow, analysis on distribution of secondary air flow, etc.

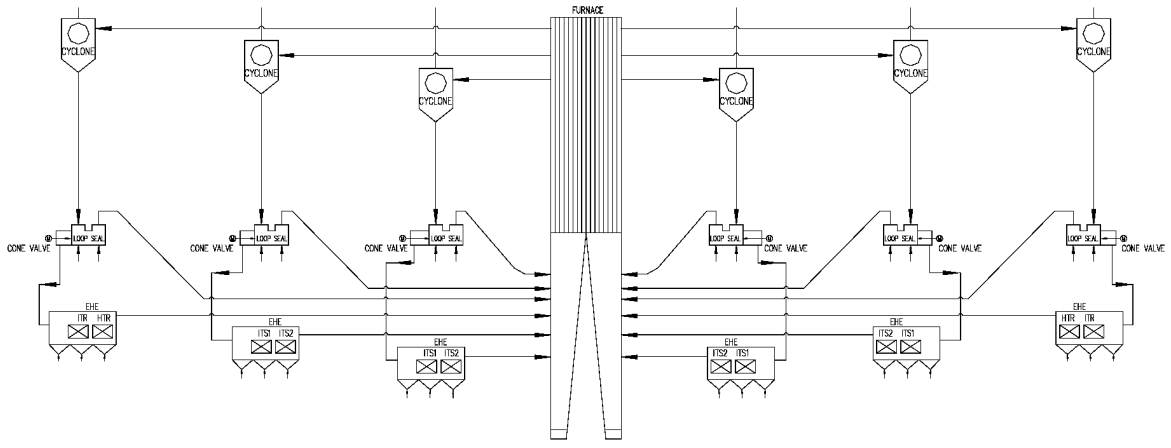

Fig. 1 Schematic Hot circulation loop system

NUMERICAL SIMULATION

Mature FLUENT software is adopted to take simulation analysis. To the physical characteristic, adapt k-s & three-dimensional model is selected to take the calculation. Three-dimensional model is the most complicated polyphase flow model, which contains a set of N momentum equation and continuous formula for solving one item. This model mainly used in the research on bubble column, float, particle suspension and CFB.

Simulation model built up

The simulation model is built up by GAMBIT software with 1:1 proportion. The whole model includes 1 furnace, 6 cyclones, 6 double-path loop seals, 28 air openings and 12 coal feeding openings. In order to guarantee the precise simulation, this model is separated into 2 million grids, and local encryption treatment has also been done to the grids at key part. The Fig. 2 is physical model.

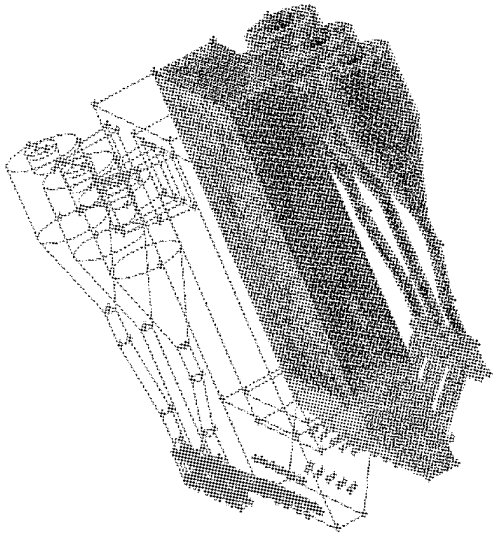

Fig. 2 Physical model

Boundary condition

As per the characteristic of gas-solid flow, 4 phases are arranged, in which gas phase is the basic and three ash solid phase whose grain size is 0.3mm, 0.6mm and 1mm separately. Based on the experiences of conventional 300MW CFB boiler, D_{50}= 0.6~0.7mm is selected to ease calculation. It is assumed all grains are round.

Sixty six boundary conditions of this model adopted detailed are listed Table 1.

Table 1 Numerical simulation boundary condition

name	quantity	medium	data
furnace air distributor	2	Primary air	4.5m/s
secondary air opening	28	Secondary air	60m/s
Moving packed bed air distributor of loop seal	6	HP fluidized air	0.5m/s
loop seal air distributor	12	HP fluidized air	1.8m/s
coal feeding opening	12	Gas flow with ash	Inputting speed：10m/s Ash flow of each opening：25t/h
cyclone outlet	6	Gas flow with ash	Pressure balance point

Analysis on the hot circulation loop flow field

First of all, we simulate the concentration field and vector field of the hot circulation loop. Figure 3 is the cyclone flow field and Figure 4 is vector distribution drawing of solid grain in cyclone. The two Figures present that:

(1) The whole loop flow field is even, no irregular flow field such as vortex and distortion happened. The whole gas-solid flow field is reasonable and return system operates normally.

(2) The cyclone efficiency is good and large amount of solid grain can be trapped. Through analysis, 100% grains with 1mm and 0.6mm diameter have been trapped and about 2% 0.3mm grain leaves the cyclone with gas phase.

(3) The Figure 5 is a pressure curve along the furnace height.The nozzle grid level is -8m at Figure 5. It is similar with the one actually measured in 300MW class CFB boiler site. The pressure curve can reflect indirectly mass concentration distribution in furnace. From the curve, we can see that the pressure drop is very sharp within 2 meters zone above air distributor because the mass concentration is high at this zone, and pressure drop will become mild after passing secondary air opening. At zone 35 meters above air distributor, pressure will become weaker, which means the mass concentration is low at the furnace top.

(4) Cyclone flow deviation. Since 6 cyclones and asymmetric distribution are adopted by supercritical CFB boiler, it is inevitable that 3 cyclones will have flow deviation. Therefore, this simulation compares the flow evenness of 3 cyclones. From the result we can know that at rated load the difference between three cyclones is not significant (about 2~3%), and detailed is seen Figure 6. This valve is about 7% lower than the test valves reported by other researchers (Semebard et al., 2003).

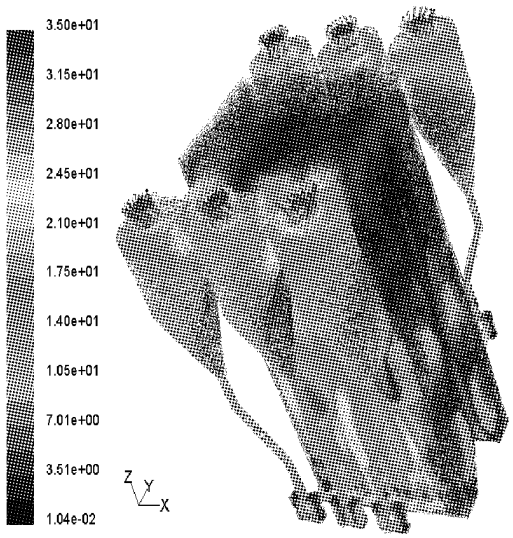

Fig. 3 Numerical simulation result of the whole loop

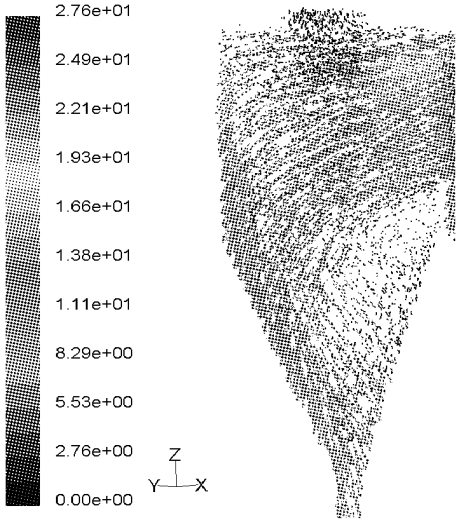

Fig. 4 Vector graph of solid phase in cyclone

(5) Top effect simulation at furnace outlet. Figure 7 presents that obvious top effect exists, which is similar to 300MW unit, because large amount of gas enter furnace outlet port after shocking the roof. Conclusion gotten by the simulation is that sufficient distance should be kept between furnace outlet port and roof.

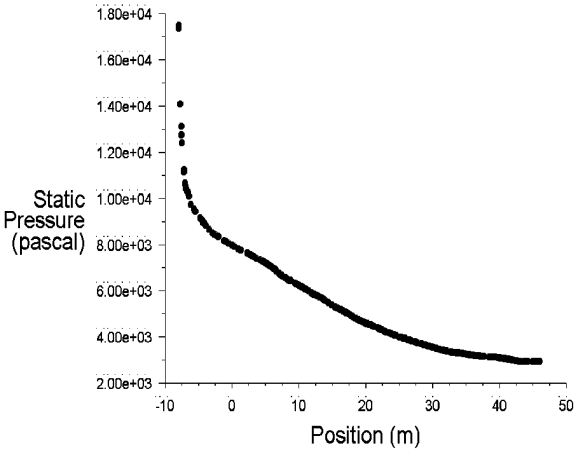

Fig. 5 Furnace pressure curve

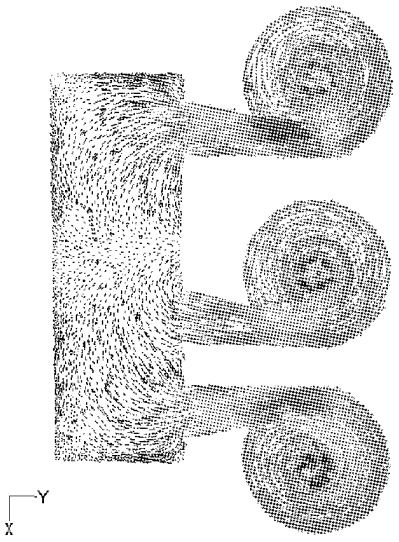

Fig. 6 Evenness comparison of flow distribution in cyclone

(6) Secondary air penetration simulation. Figure 8 presents the secondary air field simulation result of gas-solid flow. The result of calculation is that secondary air can reach furnace central zone basically and the effect is ideal at 60m/s air speed.

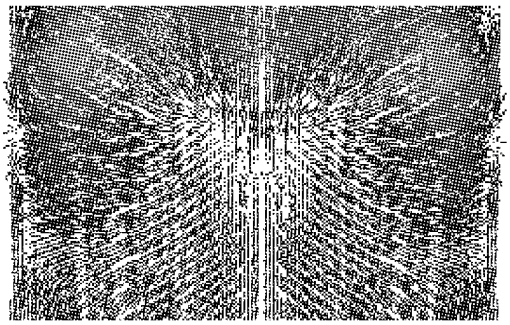

Fig. 7 furnace top effect

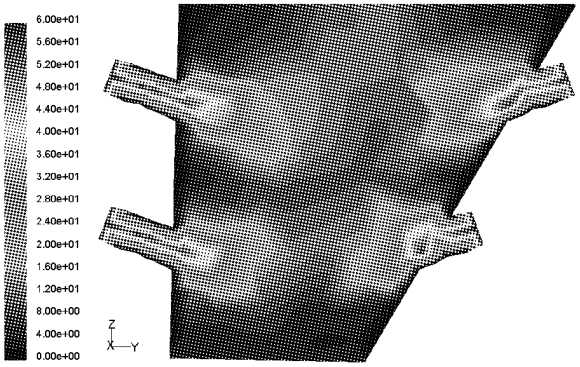

Fig. 8 simulation result of secondary air flow field

CONCLUSIONS

In general, numerical simulation result is mostly consistent with the theory analysis. However, limited by the computational force, grids are still separated too rough, so no ideal boundary is obtained. The efficiency of cyclone to 0.3mm grain is low which may be the problem of grid itself.

Moreover, although some data show the correct trend, yet a certain difference still exists if compared to actual working condition of 300MWe CFB boiler. For example, the below-bed pressure is slightly higher in simulation which might be caused by simplification of boundary condition, so suitable revision should be taken to calculation result as per actual engineering.

Because the flow distribution between three cyclones is not fully even, suitable revision is necessary to be taken to cyclone inlet gas pass.

REFERENCES

Lu, J. F., Yue, G. X., Zhang, J. S. Feasibility of the Supercritical Pressure CFB Boiler, Boiler manufacture, (2002) 4: 1~5.

Semedard J. C, Gauville P, Morin J. X., Development Of Ultra Large CFB Boilers, 16th FBC Conference, (2003) 171.

Su H., Zeng X. M. Hou, S. S. Numerical Simulation and Analysis of the Flowing Characteristics of Gas-solid Two-phase Flow in Cyclone of CFB Boilers, Dongfang Electric Remark, (2004) 18(4):179~184.

STUDY OF CFB SIMULATION MODEL WITH COINCIDENCE AT MULTI-WORKING CONDITION

Z. Wang, F. He, Z. W. Yang, Z. Li, W. D. Ni

State Key Lab of Power Systems, Department of Thermal Engineering, Tsinghua-BP Clean Energy Center, Tsinghua University, Beijing, 100084, China

Abstract: A circulating fluidized bed (CFB) two-stage simulation model was developed. To realize the model results coincident with the design value or real operation value at specified multi-working conditions and with capability of real-time calculation, only the main key processes were taken into account and the dominant factors were further abstracted out of these key processes. The simulation results showed a sound accordance at multi-working conditions, and confirmed the advantage of the two-stage model over the original single-stage simulation model. The combustion-support effect of secondary air was investigated using the two-stage model. This model provides a solid platform for investigating the pant-leg structured CFB furnace, which is now under design for a supercritical power plant.
Keywords: CFB, boiler, simulation, model

INTRODUCTION

Circulating fluidized bed (CFB) boiler has been widely used due to its intrinsic advantages in high efficiency, low pollution and excellent fuel flexibility. A recent trend is to employ CFB boiler for large-scale units, which leads to new CFB boiler structure such as pant-leg or even four-leg layout. As a result, new requirement arises with respect to the operators training as well as the CFB boiler performance simulation.

The internal flow, combustion, and heat transfer processes are very complex in the CFB boiler. Solid particles in the combustor are carried by air, rising up and down in the furnace, forming such a distribution in the axis direction that the lower part of the furnace has a greater local density than the upper part. Meanwhile, due to the elutriation and the boundary effect, the internal gas-solid flow is characterized by the core-annulus flow, with solids carried upward in the core and traveling downward near the outer wall (Brereton, 1993; Yue, 2007). Accompanying this flow pattern, there are processes involving the burst of particles, friction, combustion process and heat transfer with the surroundings. Consequently, great computational effort is required for a detailed mathematical model depicting all these complex processes regarding combustion, fluid flow and heat transfer. However, since the capability of real-time calculation is highly preferred for a dynamic simulation model, it is necessary to simplify the description of the physical and chemical processes in the CFB. And moderate adjustment may be required for a specified CFB model, depending on the structure of the simulation object, accuracy requirement and the scope of interest.

Despite the long history of CFB research and application, there are not much studies reported on CFB dynamic simulation models. Most of the models are based on material and energy balances, and the operating behavior of CFB is described by the dominant processes. Zhang et al. (2000a, 2000b, 2000c) divided the CFB into a series of compartments along the height of the furnace, and combustion model and flow model were built for the combustion process and the flow respectively. With many operating details involved regarding the particle distribution, the generation and deoxidization of hazardous substances, it was difficult to for the CFB model to reach a multi-working condition coincidence. Gao et al. (2004) built a CFB dynamic simulation model using governing equations of the dynamic mass conservation (including char, limestone and feedstock) and dynamic energy conservation. This simulation model, however, did not abstract key factors of the dominant processes, and thus could not reach coincidence at multi-working conditions. Li et al., (1997a, 1997b) developed a methodology to develop a dynamic simulation model with the model results agreeing remarkably well with measured data of the CFB at multi-working conditions. However, this model considered the CFB as a node, and lumped parameter approach was used to simulate the combustion system. Thus it was unable to reflect the temperature difference between the lower and upper parts of the furnace. To solve this problem, Liu et al. (2003) based on the work of Li et al.(1997a, 1997b, 1999a, 1999b), introduced the concept of virtual heat exchanger (VHE), and successfully simulated the temperature difference of the furnace at low load conditions. The VHE was defined as a fictitious heat exchanger on top of the CFB furnace, which took up no space, contained no solid quality, and involved no combustion process. The only function of the VHE was to cool the high-temperature gas and solid at the outlet of the furnace.

Though successfully in predicting the temperature difference between the upper and lower parts of the CFB furnace, the VHE approach was problematic regarding its obscure and confusing physical meaning due to

the virtual heat exchanger contains no physical space. Another drawback was its inapplicability for the pant-leg structured CFB (Lu et al., 2007). Because of the intrinsic characteristics of the pant-leg structure, there is considerable material exchange between the left and right chambers in the upper part of the furnace, mainly due to the imbalanced air introduced at the bottom of the CFB furnace. Essentially, the VHE approach considered the furnace as a node in a whole, so it was unable to accurately depict this material exchange and was not able to reflect the possible combustion auxiliary effect of the secondary air supply. A possible solution is to divide the CFB furnace into two sections of the top part and the bottom part. This approach can describe the material exchange at the top part of the CFB furnace, but it is constrained by the great effort required in obtaining the model results coincident with design values at multi-working conditions, which was also a main obstacle in the previous studies (Li et al. 2000; Liu et al. 2003).

DEVELOPMENT OF TWO-STAGE CFB DYNAMIC SIMULATION MODEL

The two-stage CFB dynamic simulation model was developed based on overall energy conservation and mass balance equations, adopting the methodology of dominant factors analysis. The particle movement in the furnace was described by simplified momentum equations and was de-coupled from mass balance and energy conservation calculations. As shown in Fig. 1, the overall mathematical model consists of different sub-models for different section of the CFB such as the top and bottom sections of the furnace, cyclone, and return leg. The solid black arrows represent the flow of solid materials; and hollow arrows represent the gas flow. The cyclone model and return leg model are basically the same with the ones described by Li et al. (2000) and Liu et al. (2003), so they were not addressed in detail here. Different from the VHE approach, calculations were conducted on the material and energy exchange depicting the entrainment and elutriation process between the top and bottom sections, as well as on the combustion of residual carbon in the top section.

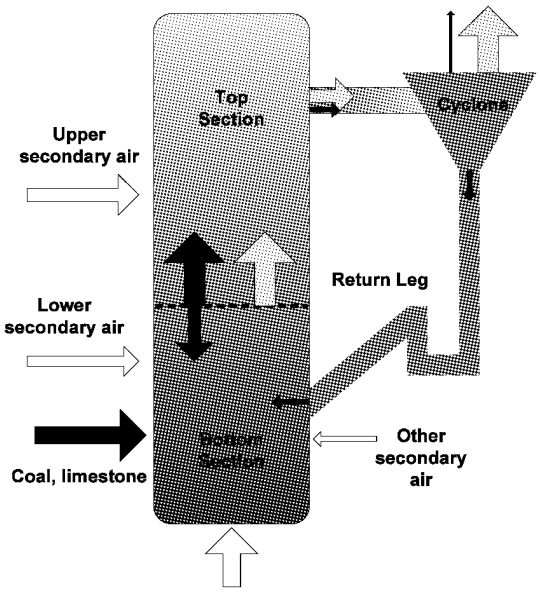

Fig. 1 Schematic representation of the two-stage CFB boiler model

It was found out that, among the various complex processes in the CFB, the following could be identified as the dominant ones, which determined the key dynamic characteristics of the CFB (Li et al. 1999b): 1) Dynamic conservation of unburned carbon: the main heat source of the CFB is closely related to the combustion rate of the unburned carbon inside the whole furnace, rather than the instant coal-feed rate which was the case for conventional boilers. 2) Dynamic conservation of materials: the process reveals the dynamic relationship among the total amount of the bed materials in the CFB, coal ash flow and slag. 3) Dynamic conservation of energy: the thermal inertia of CFB is influenced not only by the high-temperature-resistant lining and by metal wall of the furnace, but also by the large amount of bed material in the CFB, which affected the intensity of internal heat transfer and dynamic response speed. 4) Compounded pressure drop: the dynamic behavior of the CFB furnace was associated with the whole flue gas loop; in return, the CFB furnace also had a considerable impact on the pressure profile of the entire flue gas loop

By analyzing the internal flow condition, heat transfer and combustion process inside the CFB, the calculation for different processes were de-coupled by comparing the relative speed of the real physical processes, which would greatly reduce the calculation time and simplify the model solving process: the change of the internal flow in the furnace is a relatively fast process compared with combustion and heat transfer process, therefore, once the operating condition (such as the air supply, bed material, etc.) changes, the flow status (including the solid materials distribution along the height of the furnace, materials exchange between the top and bottom sections of the furnace, the amount of fly ash, etc.) would change immediately and be calculated alone; by this assumption, an overall calculation was carried out for the total mass conservation of the solid material inside the CFB furnace, rather than modeling the top and bottom sections respectively; Due to the metal wall and large amount of bed material in the furnace, the change of the furnace temperature is relatively slow; Meanwhile, the accumulation of bed material and char in the furnace is also a relatively slow process.

CFB furnaces normally contain a relatively dense region near the bottom and a dilute zone toward the top

(Yue et al. 2005). With the increase of the height, the solid entrainment declines in an exponential form as well as intensive material exchange of entrainment and elutriation away from the bottom of the CFB. If boundary of the two sections was specified in the dense-phase zone, the heat and material exchange would be too intense to reflect the temperature difference between the two sections. Therefore, the boundary of top and bottom sections had to be carefully chosen in the model.

Furthermore, the following assumptions were also made in the present model: 1) an averaging particle size model is simply used to boost the computing speed. To compensate for such a simplification, difference particle sizes were specified for the top and bottom sections. 2) In this simulation model, in order to spare computing effort, the char concentration in the bottom and top sections were assumed to be the same because of the intensive mass transfer. 3) The pyrolysis of volatile, limestone decomposition and the desulfurization process are relatively fast compared with the full combustion process. 4) The gas and solid material in the furnace were assumed to be perfectly mixed, so in normal flow conditions, gas and solid material in the same region were considered to have an identical temperature. Based on the above analyses and assumptions, the main governing equations of the dynamic model are listed as follows:

(1) Overall dynamic conservation equation of solid mass conservation

$$\frac{dM}{dt} = B(C_{FC} + A_{ar} + 0.4S_{ar}\eta_{SO_2}) + L(0.56Ca + 0.4Mg + In) - (R_{CD} + R_{CU}) - D_{out} - W_{FL} \quad (1)$$

where M is the total bed material, B is the coal-feed rate, C_{FC} is the percentage of fixed carbon in the coal, Mg is the percentage of ash (as-received basis), S is the percentage of sulfur in the coal (as received basis), η_{SO_2} is the desulferization efficiency, L is the feed rate of limestone, Ca is the mass percentage of $CaCO_3$ in the limestone, Mg is the mass percentage of $MgCO_3$ in the limestone, In is the percentage of solid inert in the limestone, R_{CD} is the carbon conversion rate in the bottom section of the furnace, R_{CU} is the carbon conversion rate in the top section of the furnace, D_{out} is the flow rate of slag, W_{FL} is the flow rate of the fly ash. Compared with the VHE approach, the two-stage model introduced a new variable: the carbon conversion rate in the top section of the furnace.

(2) Dynamic conservation equation of carbon conservation

$$\frac{dM_C}{dt} = B \cdot C_{FC} - R_{CD} - R_{CU} - D_{out}\chi + W_{FL}\chi_{FL} \quad (2)$$

where M_C is the total carbon in the CFB,, χ is the carbon content in the bed materials, χ_{FL} is the carbon content in the fly ash. Similarly, the burning of fixed carbon was considered for both the top and bottom sections.

(3) Dynamic conservation equation of mass conservation for the bottom section

$$(M_D + M_{yx-D})c_p \frac{dT_D}{dt} = B \cdot Q_v + H_{air} + H_{gt} + R_{C\_D}Q_C - H_{D_{out}} - H_{W_{ml}} + H_{W_{mb}} - Q_D \quad (3)$$

where M_D is the total bed material in the bottom section, M_{yx_D} is the equivalent mass regarding the liner and metal wall of heat exchangers, T_D is the temperature of the bottom section, c_p is the specific heat capacity, Q_V is the lower heating rate of the volatilizer (including the carbon in the volatilizer), H_{air} is the enthalpy of all the air introduced from the bottom section, H_{gt} is the physical enthalpy of all the solid, Q_C is the lower heating value of the carbon, $H_{D_{OUT}}$ is the physical enthalpy of the slag, $H_{W_{ml}}$ and $H_{W_{mb}}$ are the physical enthalpy of the entrainment and elutriation between the top and bottom sections of the furnace. Q_D is the total heat exchange in the bottom section. Compared with the VHE approach, the material exchange between the up and bottom sections were added into the model.

(4) Dynamic equilibrium equation of carbon conservation for the bottom section

$$(M_U + M_{yx\_U})c_p \frac{dT_U}{dt} = H_{air\_U} + R_{C\_U}Q_C + H_{W_{ml}} - H_{W_{mb}} - H_{W_{ENTR}} - Q_U \quad (4)$$

where: M_U is the carbon in the top section, M_{yx_U} is the equivalent mass regarding the liner and metal wall of heat exchangers in the top section, T_U is the temperature of the top section, $H_{air\text{-}U}$ is the physical enthalpy

of the air introduced from the top section of the furnace, $H_{W_{ENTR}}$ is the physical enthalpy of the entrainment traveling from top section to the cyclone, Q_U is the heat exchange in the top section of the furnace.

It is noted that, concerning the distinction between fast and slow processes, the flow model can be solved by de-coupling from the main body of the CFB model. The fast process and slow process can be solved by implicit and explicit Euler algorithm respectively, thus retaining the computing stability and accuracy while significantly reducing the effort required for the solution of the governing equations.

RESULTS AND DISCUSSION

Calibrating the two-stage CFB model at multi-working conditions

Different from the model with overall node approach or the VHE approach, the two-stage model requires additional parameters to describe dominant processes with respect to the material distribution and mass exchange rate between the top and bottom sections. These parameters have to be carefully chosen or specified, for instance, one of the key parameters required is the height of the interface between the top and bottom sections, which greatly affected the temperature difference between the two sections. Fig. 2 schematically visualizes that the temperature difference between top and bottom sections is affected greatly by specifying different heights of the interface at the same model input. If the height was chosen too low (e.g. below 1.45m in Fig. 2), the material exchange between the two sections would become so intensive that the temperature difference would be too small (around 1°C in Fig. 2). With the increase of the height, the temperature difference firstly experienced a significantly increase, and then roughly stabilized at a peak value, which is believed to be primarily dependent of the density distribution of the bed material. It is noted that to address the temperature discrepancy between the top and bottom sections at low CFB working conditions, it is necessary to select the height of the boundary high enough to reach relative small mass exchange between the bottom and top sections. The height of the joint point for the two legs of the pant-leg CFB would be a good selection since at this point, the mass density would be very small.

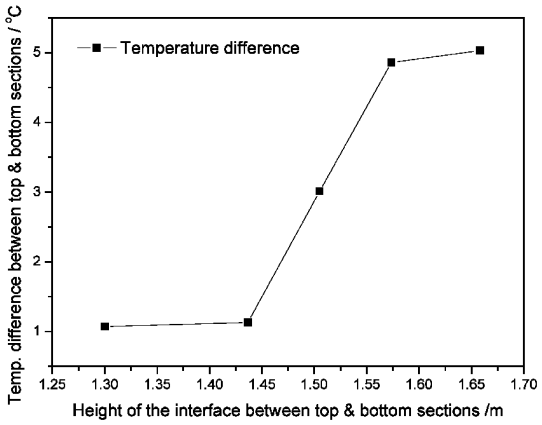

Fig. 2 Schematic representation of temperature difference vs. the height of the interface

Beside the height of the interface, other factors are also considered to be critical for the model calibration, including the different equivalent diameters of the char particles, the heat transfer coefficient in the two sections, etc. All these factors are not completely independent, which makes it a demanding procedure to match the model with real measured data of the CFB boiler. In the present two-stage model, dominant parameter was abstracted for these processes using the same methodology as Li et al. (2000) to calibrate the model by propriety specifying the distribution of materials in the furnace, the material exchange between the two sections and other parameters such as heat transfer coefficients.

Dynamic performance of the CFB boiler

The two-stage model also provides a closer insight into the CFB boiler responses to step disturbances than single-stage model. As an example, Fig. 3 illustrates the different behaviors of the top and bottom sections following a step decrease in coal input. The initial status is set at 70% load, in precise accordance with the design point of the CFB boiler, and then a step disturbance of 10% reduction in coal input is given while the air supply and limestone-feed rate are kept constant. The temperature drops towards a new equilibrium in both sections, and the top section suffers a slightly greater offset, which leads to a larger temperature difference between two sections. Fig. 3 also depicts the contribution of the two sections to the carbon combustion rate, which experiences a small decline due to the disturbance imposed on the coal-feed rate, but the effect is small compared to that in furnace temperature. Comparison of the carbon combustion rates in the two sections suggests that the combustion process mainly takes place in the bottom section, which agrees well with the results reported in literature (Lu et al. 2007).

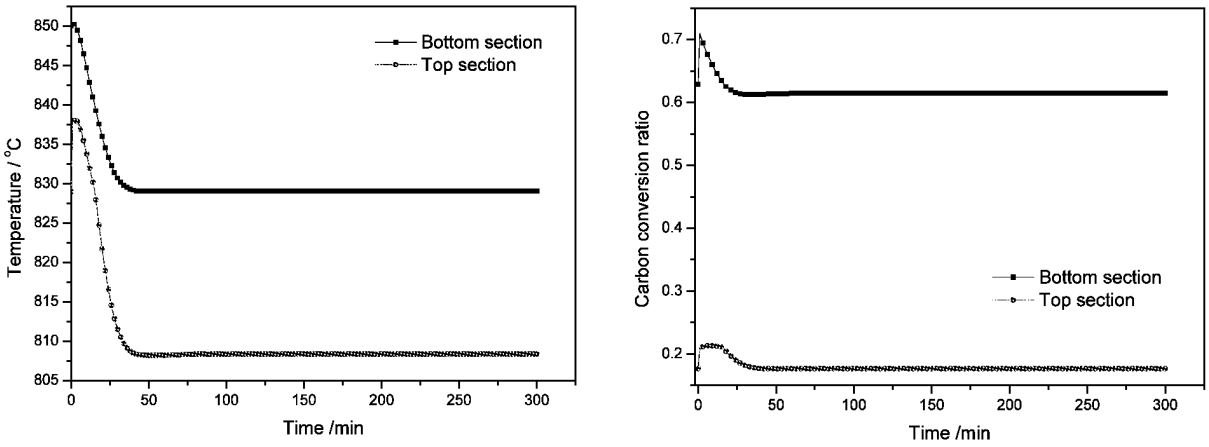

Fig. 3 Dynamic response to a 10% decrease in coal feed rate @70% load

Impact analysis of secondary air distribution

As previously introduced, one advantage of the two-stage model over the single-stage model is that the former one has the capability to predict the temperature difference between the upper and lower part of the CFB boiler in a wide load range. Another potential advantage is that the impact of secondary air distribution upon the overall CFB combustion can be obtained with less effort.

Fig. 4 shows the response to a step increase in the distribution ratio of upper secondary air in total air supply predicted by single-stage model and two-stage model respectively. The distribution ratio increases from 17.3% to 22.3% while all the other operating conditions such as coal-feed rate, limestone-feed rate, secondary air supply and total air supply etc. are kept constant. In the single-stage model, neither furnace temperature nor the carbon conversion rate changes with the step disturbance in the distribution of secondary air, which is probably due to the inherent drawback posed by the lumped parameter assumption in the VHE approach. In contrast, the two-stage model was found to give reasonable predictions. It is observed that the temperature in both sections is increased and stabilized at a higher value. The increase in furnace temperature coincides with an increased carbon conversion ratio, which is in accordance with actual physical expectations and further confirms the combustion-supporting effect of the upper secondary air.

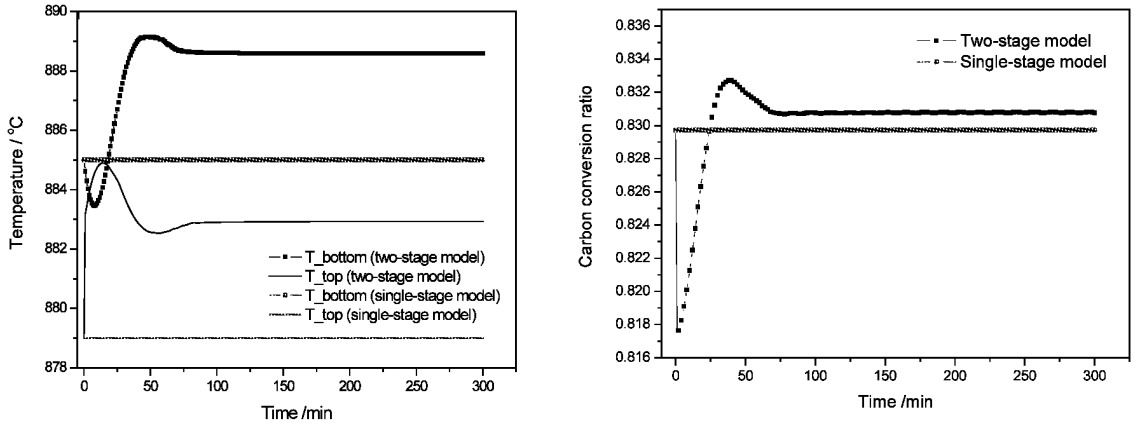

Fig 4 Dynamic responses to a decrease in the distribution ratio of upper secondary air in total air supply (distribution ratio changed from 17.3% to 12.3% with constant flow rates of secondary air and total air @ 100% load)

Calculations were conducted with the two-stage model to obtain an overview of the impact of upper secondary air distribution ratio in total air supply on the furnace temperature and carbon conversion ratio. The results are illustrated in Fig. 5. Provided that all the other working conditions are kept constant, the carbon conversion ratio is seen to reach a peak and then gradually decline with the increase of the distribution ratio of upper secondary air. The similar trend can be observed on the behavior of the temperature in the bottom section, which is resulted from the combined effect of the variation in carbon conversation ratio and in the heat transfer in the bottom section. The observation is in accordance with the actual physical expectation, and confirms the validity of the two-stage model. Furthermore, it suggests that there is an optimum distribution ratio of upper secondary air with respect to the CFB combustion.

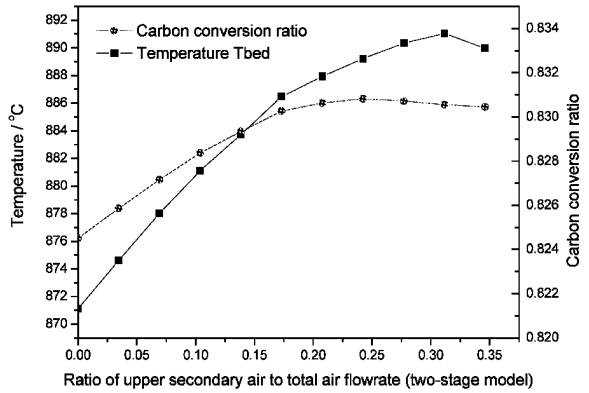

Fig. 5 Impact of the distribution ratio of upper secondary air

CONCLUSIONS

A CFB dynamic model was developed, where the furnace was divided into two sections and the combustion and heat transfer were considered respectively. This model was closer to the physical basics of the actual CFB process, and thus facilitated the simulation of the material exchange in the upper chamber of the pant-leg structured CFB boiler. This investigation contributed a solid foundation to develop the simulation training tool for large-scaled pant-leg CFB boilers.

The main obstacle in calibrating the two-stage model is to properly specify key parameters with respect to the material exchange between the top and bottom sections. In the present paper an attempt was made to tune the model by specifying the distribution of materials in the furnace and the material exchange between the two sections using the methodology developed by Li et al.(2000), which proved to be a feasible and satisfactory approach. The impact of the distribution ratio of secondary air was examined by the two-stage model, and the response to step disturbance of the CFB boiler was also investigated. The predicted results agreed reasonable with physical expectation, which confirms the advantage of two-stage model over the single-stage model.

ACKNOWLEDGEMENTS

Financial support of this work by the 863 national key scientific and technological projects 600MWe Supercritical Simulation Project (2006BAA03B04) is gratefully acknowledged.

REFERENCES

Brereton, C.M.H., Grace, J.R.: Chemical Engineering Science, 1993, 48(14), 307-314.
Gao Jianqiang, Ma Liangyu, Wang Bingshu, Song Zhiping, Du Chaobo: Proceedings of the CSEE, 2004, 24(11), 241-245.
Li Zheng, Ni Weidou, Yue Guang xi, Sun Xin, Zhang Wei: Power Engineering, 1997a, 17(3), 13-16.
Li Zheng, Ni Weidou, Zhang Wei, Sun Xin: Journal of Tsinghua University, 1997b, 37(2), 24-27.
Li Zheng, Zhang Wei, Gou Jianbin: Journal of Tsinghua University, 1999a, 39(3), 100-102.
Li Zheng, Ni Weidou, Wang Zhe, Zhang Wei, Yue Guang xi: Power Engineering, 1999b, 19(2), 33-36.
Li Zheng, Wang Zhe, Ni Weidou: Power Engineering, 2000, 20(2), 511-514.
Liu Binggang, Li Zheng, Sun Xin, Jiang Ning, Ni Weidou: Power Engineering, 2003, 23(1), 2173-2178.
Lu J., Yu L., Zhang Y. Yue G. et.al: Power Engineering, 2007, 27(4), 497-502.
Yue, G., Lu, J., Zhang, H.: Proceeding of The 18th International Conference on Fluidized Bed Combustion. ASME, Torento, Canada, 2005, 135-146.
Yue, G. The first Chinese CFB combustion principle and technology conference, 2007, 2-30.
Zhang Yongzhe, Xu Xiangdong: Coal Conversion, 2000a, 23(1), 51-55.
Zhang Yongzhe, Xu Xiangdong: Journal of Tsinghua University, 2000b, 40(6), 76-79.
Zhang Yongzhe, Xu Xiangdong: Proceedings of the CSEE, 2000c, 20(12), 84-87.

NUMERICAL INVESTIGATION OF 3-D TRANSIENT COMBUSTING FLOW IN A 1.2MWTH PILOT POWER PLANT

A. Nikolopoulos[1], I. Rampidis[2], N. Nikolopoulos[2], P. Grammelis[2], and E. Kakaras[1]

1 Laboratory of Steam Boilers and Thermal Plants, Mechanical Engineering Department, National Technical University of Athens, Heroon Polytechniou Ave., 157 80 Zografou Athens, Greece
2 Centre for Research and Technology Hellas, Institute for Solid Fuels Technology and Applications, Athens, Gr-15310, Greece

Abstract: As industrial Circulating Fluidized bed Combustors (CFBCs) tend to be scaled up, numerous design and operating problems emerge. At the same time uncertainties which concern hydrodynamics, combustion and pollutants formation mechanisms, come in to sight. Along with experience, CFD analysis can play crucial role providing further insight on the complex multiphase combusting flow occurring in CFBCs. This work aims to present a methodology for CFBCs comprehensive modeling, taking into consideration the coupling of hydrodynamics – heat transfer – chemical phenomena that take place in the bed. A combination of acceptable accuracy with high computational efficiency was also an objective. For this purpose, a simple combustion mechanism was integrated in an isothermal model and applied on a 1.2 MWth pilot plant. In this comprehensive model gas, inert-material and fuel are taken into consideration, as three discrete, pure eulerian phases. Solids inventory in the riser as well as temperature of the bed were predicted with satisfactory accuracy. Moreover, major chemical components as O_2 and CO_2 concentrations were predicted along the bed with acceptable accuracy. Concluding, the developed CFD model is capable of efficiently modeling a CFBC. However in order to further increase total accuracy, the need for improved closure equations for the set of Partial Differential Equations solved was made obvious. Finally, the computational cost for such modeling was found extremely high but not prohibitive for large scale CFBC simulations.
Keywords: CFBC, combustion mechanisms, CFD, Euler approach

INTRODUCTION

Technology applications of Circulating Fluidized Bed Combustors have been developed rapidly in the power generating industry as they combine fuel flexibility and high efficiency especially for biomass co-combustion. At the same time as the applications of CFB technology scale up, an 800 MWe CFBC unit is already under design process as reported by Wu et al. (2004), new challenges arise in the field of the numerical prediction of their hydrodynamic behavior and their combustion and emissions performance. Reliable 3-D models are essential for the optimization of large scale units design, as they can predict inert material concentration in bed, fuel mixing efficiency and temperature profiles of the phases. Simulation with the aid of CFD may be regarded as one of the most appropriate approaches for the prediction of critical parameters controlling the efficient operation of such installations. Furthermore these CFD techniques are expected to merely substitute empirical or semi-empirical models in large scale CFBC design process.

Nevertheless the majority of the relevant CFD studies on CFBs has been focused on isothermal modeling of CFBCs (Kallio, 2006; Rampidis et al., 2007; Wang et al., 2008). Such numerical approaches constituted the basis onto which combustion and pollutants formation models can be incorporated, in order to have a validated and reliable tool for the description of the operation of the CFBCs. However, even for the CFD cold flow simulation, the uncertainty behind a substantial number of utilized parameters is significant. The most important parameter as reported by Wang et al. (2008) is the momentum exchange coefficient between gas and inert material (Ge et al., 2008).

Regarding the numerical simulation of CFB risers, limited literature is available, especially concerning combustion mechanisms (Gungor and Eskin, 2008). Moreover the majority of these studies, approach the complicated physics, which dominate the operation of CFB combustor, in a two-dimensional way (Gungor and Eskin, 2008), overlooking this way their three dimensional character (Myöhänen, 2006). The present work focuses on the development of a three-dimensional model, taking into account full fuel particle combustion mechanisms, as drying, devolatilization and char combustion, in the CFBC riser. The basis for the incorporation of chemistry and heat transfer models is an already developed and validated isothermal model (Rampidis et al., 2007).

As concerns proper modeling of momentum and heat exchange coefficients between solids (inert-material and fuel), little information is reported in the literature. Even in the simpler case of cold flow modeling, it is

worth noticing that models which are based on the assumption of homogeneous conditions for each computational cell, fail to predict the governing physics of such processes, under certain conditions (Wei Ge et al., 2008). Thus recent studies have been mainly focused on more sophisticated drag models, which take into account the flow heterogeneity in each computing cell (EMMS, Ge et al., 2008, Wang et al., 2008). However, it has been stated by Ge et al., (2008) that for industrial purposes simplified equations may be utilized under proper grid density (Ge et al., 2008, Zhang and VanderHeyden 2001).

In the present work, full 3-D combusting approach is adopted, in order to be able to successfully describe in a more precise and detailed way the patterns of the induced flow and heat transfer effects in a CFB riser, highlighting the necessity for the three dimensional numerical approaches.

METHODOLOGY FOR BED HYDRODYNAMICS MODELING

In the present work a $1.2MW_{th}$ pilot plant is simulated. Geometry is illustrated in Figure (1) and boundary conditions are described by Leithner et al. (1993). The installation has 9.5m height and 0.4 m^2 mean cross section (Fig. 1). The combustion chamber of the rig consists of two sections. The lower part (the furnace hopper) has a height of 3.15m. It is totally refractory lined and the cross section increases linear from $0.39\times0.45m^2$ at the distributor plate to $0.54\times0.81m^2$ at the top of the hopper. The upper part (the rectangular freeboard) has a constant cross section of $0.54\times0.81m^2$ and a height of about 6.35m. Combustion air is fed as primary air through the distributor plate, while additional primary air is fed into the bottom region of the furnace hopper with the fuel and the recirculated bed material. Secondary air is fed through five inlets along the height of the combustion chamber. The ratio of primary to secondary aeration is 86 to 14. The computational grid consists of 5,724 hexahedral, structured and uniform cells, with a mesh resolution of 9cm distance per computational cell (Fig. 2). The returning system has been excluded from the simulation for simplicity.

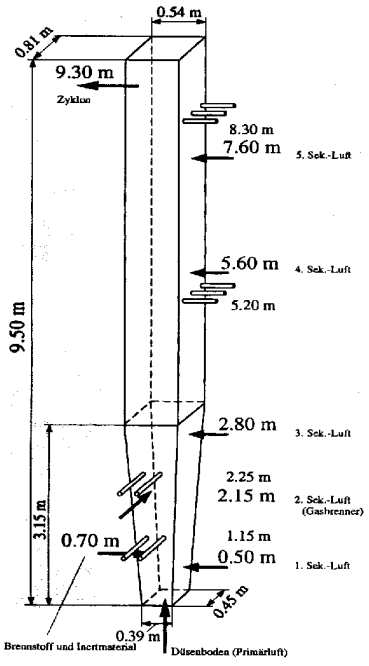

Fig. 1 Combustion Chamber Of The Test Rig.

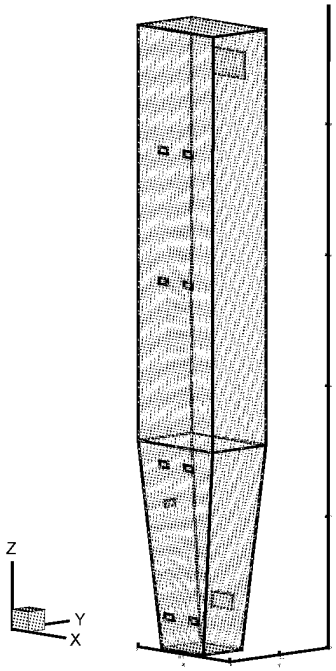

Fig. 2 Structured Hexahedral Numerical Grid.

In order to simulate the transient, purely 3-D (Myöhänen, 2006) bed hydrodynamics, the multi-fluids theory was applied (Euler approach). Gas, inert-material and fuel were modeled as three discrete interacting Euler phases. The Eulerian description is essential for the simulation of inert-material phase due to its high volume and mass loading in the surrounding primary, gas phase.

For the fuel-phase Eulerian approach has been preferred over the Lagrangian, since it presents inherently good coupling between phases, as well as efficient code parallelization. On the other hand Particle Size Distribution introduction for fuel phase in the Eulerian approach is not easily feasible in terms of computational cost. Therefore fuel particles were considered and modeled as monosized, simplification which is expected to have an impact on the most precise description of the induced flow field. Fuel composition derived from approximate analysis, which yielded 0.023 ash, 0.1907 char, 0.57 moisture and 0.2163 volatiles content (Leithner et al., 1993).

Numerical Equations

The description of multiphase flow as interpenetrating continua incorporated the concept of phases volume fractions, denoted by α. The continuity equation for phase q is:

$$\frac{\partial}{\partial t}(a_q\rho_q)+\nabla\bullet(a_q\rho_q\vec{u}_q)=S_q, \tag{1}$$

where $\vec{u}_q$ is the velocity of phase q, whilst S_q represents mass source terms for q phase. The momentum equation for q phase is:

$$\frac{\partial}{\partial t}(a_q\rho_q\vec{u}_q)+\nabla\bullet(a_q\rho_q\vec{u}_q\vec{u}_q)=-a_q\nabla p+\nabla\bullet\bar{\bar{\tau}}_q+a_q\rho_q\vec{g}+\sum_{p=1}^{n}(\vec{R}_{pq}+\dot{m}_{pq}\vec{u}_{pq}-\dot{m}_{qp}\vec{u}_{qp})+(\vec{F}_q+\vec{F}_{lift,q}+\vec{F}_{vm,q}) \tag{2}$$

The enthalpy equation for each phase is:

$$\frac{\partial}{\partial t}(a_q\rho_q h_q)+\nabla\bullet(a_q\rho_q\vec{u}_q h_q)=-a_q\frac{\partial p_q}{\partial t}+\bar{\bar{\tau}}_q+\nabla\vec{u}_q-\nabla\vec{q}_q+S_q+\sum_{p=1}^{n}(\vec{Q}_{pq}),\ Q_{pq}=h_{pq}\cdot(T_p-T_q) \tag{3}$$

In the fuel phase ash, moisture, volatile matter and char are taken into consideration, while accordingly in the gas phase CH_4, H_2, CO_2, CO, H_2O, O_2 and N_2. The combustion mechanism comprise of three heterogeneous reactions (moisture evaporation, devolatilization, char combustion (Basu et al., 1999)), and three homogeneous reactions referring to combustion of CH_4 (Gungor and Eskin, 2008), H_2 and CO (Zhao et al., 2007). The moisture evaporation rate is calculated as:

$$m_{ws}=\left(\frac{6\cdot\dot{m}_p}{\pi\cdot\rho\cdot d_p^{\,3}}\right)\left(-\pi\cdot d_s\cdot Nu_p\cdot\frac{k_s}{Cp_s}\cdot\ln\left(1+\frac{Cp_s\cdot(T_q-T_s)}{1-L_w}\right)\right) \tag{4}$$

where the subscript '*s*' denotes the properties of liquid water at the particle's surface, k_s and Cp_s are the thermal conductivity and heat capacity of water respectively and L_w the latent heat of water at temperature T_s. The change in mass of the solid phase in each computational cell, due to devolatilization, was calculated by a simple one step reaction model according to:

$$\dot{m}_{devol}=\frac{6\cdot\dot{m}_p}{\pi\cdot\rho\cdot d_p^{\,3}}\cdot A_{vol}\cdot e^{-E_{vol}/(RT_p)}\cdot Y_{vol} \tag{5}$$

where A (492000 s^{-1}) is the pre-exponential factor, E (7.4×10^7 J/kmol) is the corresponding activation energy of the equation describing devolatilization and Y_{vol} the mass of volatiles in fuel phase. In the same way the reaction of the solid fuel phase due to char combustion ($C_{(s)}$ + (1/φ) O_2→ (2-2/φ)CO_2+(2/φ-1)CO) is accounted through the following expression:

$$\dot{m}_{char}=(\pi\cdot d_c^{\,2})\cdot\frac{P_{O_2(g)}}{1/h_m+1/k_c},\ where\ h_m=12\phi ShD_{O_2(g)}/(d_cRT),\ k_c=0.0117\exp(-2859/T_p) \tag{6}$$

$$\text{and}\ \ Sh=2\alpha_g+0.69\left[\frac{|\vec{u}_g-\vec{u}_p|d_c}{\alpha_g\gamma_g}\right]^{0.5}Sc^{0.33},\ \text{with}\ S_c=\frac{\nu}{D_{O_2(g)}} \tag{7}$$

where Sh, Sc are the Sherwood and Schmidt numbers respectively. h_m and k_c are the diffusion and kinetics rates coefficients and $P_{O_2(g)}$ and $D_{O_2(g)}$ are the partial pressure and diffusivity of oxygen respectively. The shrinking diameter of char d_c is given by Equation 8 (shrinking core approximation):

$$\frac{d_c}{d_o}=(1\text{-}U)^{1/3} \tag{8}$$

where U is the time instant fractional burn-off of carbon (Smith, 1971).

As far as the effect of turbulence is concerned, it was found to be an important parameter albeit in bed hydrodynamics seemed to have a small influence (Rampidis et al., 2007; Wang et al., 2008). In order to simulate in a realistic way the homogeneous reactions rates, values of k and ε are needed as inputs for the Finite Rate/Eddy dissipation reaction concept. Heat and momentum exchange coefficients between solids phases and gas were modeled using Gunn's (1978) and Syamlal – O'Brien (customized with minimum fluidization velocity) models respectively. Although Gunn's model generally refers to gas – solid interaction, in this work is also used for the thermal interaction between the two solid phases since the information for their thermal interaction which is reported in the literature is very limited. Though this approximation does not seem to be

the most accurate, the numerical results agree quite well with the corresponding experimental data. Additionally Syamlal's (1987) symmetric model was used for momentum exchange coefficient between solid phases (fuel and inert-material).

RESULTS AND DISCUSSION

The initialization for the case of the integrated model was obtained from the solution of the corresponding isothermal case, in order to reduce the computational time for reaching solids inventory and temperature stabilization. To be more detailed, it was observed, that the quantity of inert material in the riser, after the initialization, started to decrease rapidly, away from the equilibrium state. In order to reach the equilibrium again, an additional, large amount of seconds was necessary to be solved.

A set of 25 partial differential equations governing the phenomenon, is solved. The prescribed set of equations, presented a very stiff numerical behaviour. Therefore an efficient coupling among phases was found crucial in terms of numerical stability. In general, the comprehensive combusting model was found much more computational expensive than the isothermal flow model, but certainly not prohibitive for application in pilot scale CFBC units.

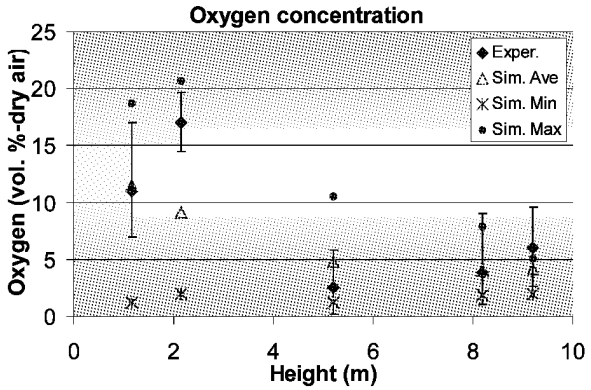

Fig. 3 Time averaged volumetric (% dry) O_2 concentration along the bed (simulated and experimental values)

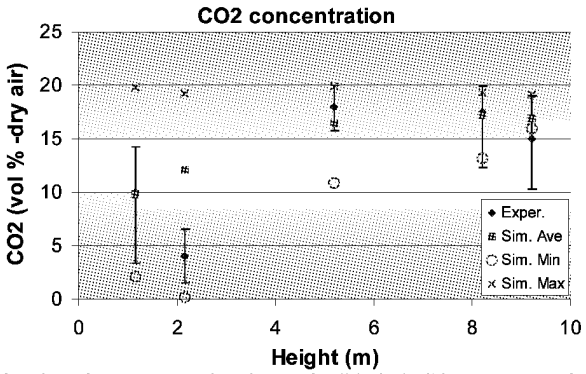

Fig. 4 Time averaged volumetric (% dry) CO_2 concentration along the bed (simulated and experimental values)

For the validation of the numerical methodology, mean CO_2 and O_2 concentration profiles in the bed in the axial direction (along the height of the combustor), averaged at each height, are illustrated in Fig. 3 and 4 against the corresponding experimental data (Leithner et al., 1993). The minimum, maximum and mean experimental values are presented. The mean value is calculated based on the area weighted averaging method. In each height there were 9 available experimental measurements in different locations, across each slice. Exception is the measurements conducted at the height of 2.15 meters where only two measurements are available. Unfortunately it is not clear by the report at which exact point of each slice (X, Y coordinates of the corresponding numerical grid) these measurements are taken. Fig. 3 and 4 illustrate that the agreement with the experimental data is very good, except for the respective profiles at the 2.15 meters height. Concerning this cross-section (Fig. 5), the numerical approach presented in this study predicts O_2 and CO_2 concentrations with values close to the experimental data at certain regions of this area.

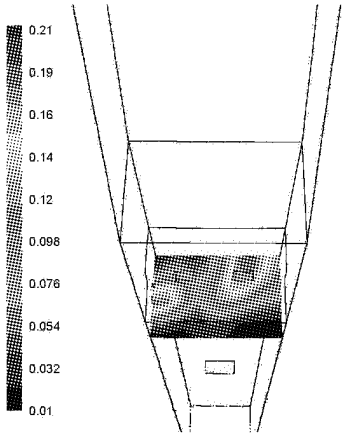

Fig. 5 Time Averaged dry volumetric (%) concentration of O_2 for height 2.15m

Nevertheless, it should be noted that for this height if these quantities are calculated as area weighted based, there is a difference between their mean values and the corresponding experimental data.

Nonetheless, the experimental measurements that were used for deriving the mean value of the abovementioned height are only two. The experimentally observed increase of mean oxygen concentration from Z=1.1m to Z=2.15m, should be further investigated, since there is not a secondary air opening placed between these two cross-sections. In general the developed model predicts that O_2 is consumed faster close to walls where fuel concentration is higher (in the annulus region), than in the core region of the bed (Fig. 6). Additionally in the core region O_2 values are generally higher, which is consistent to the literature (Zhao et al., 1997).

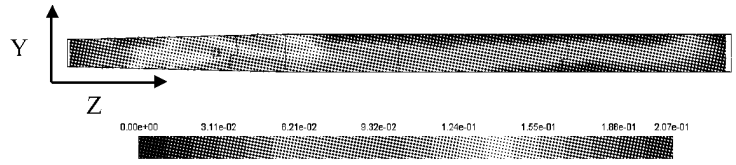

Fig. 6 Time Averaged dry volumetric (%) concentration of O_2 for X=0.405m

The mean temperature distribution inside the riser was accurately predicted when compared with the corresponding experimental data. A mean value 1095 K is predicted, while the experimental data give 1100K (Leithner et al. 1993). The predicted temperature field clearly shows domination of uniformity. Gas, inert-material and fuel phase temperature values are very close to each other, indicating the extremely efficient heat transfer in the bed. Figure 7 illustrates temperature profiles along the height of the bed for inert and fuel phases. Fuel phase generally is found to have a slightly higher temperature than the other phases at maximum 5K. Nonetheless, at height Z=1m where the fuel enters the bed, there is a temperature difference between fuel and inert phase which takes a maximum value of 350K. This is expected, since the fuel has not yet been heated at that point and has high moisture content (57%). Additionally near the riser exit a temperature difference of 80K is predicted, which is attributed to further local char combustion and results in fuel temperature increase. At the same time, inert material at this height of the riser has very low volume fraction which leads to decreased heat transfer coefficient and high temperature difference with the fuel phase. The considerable reaction rate of char combustion at the exit pipe is also verified experimentally (Leithner et al. 1993).

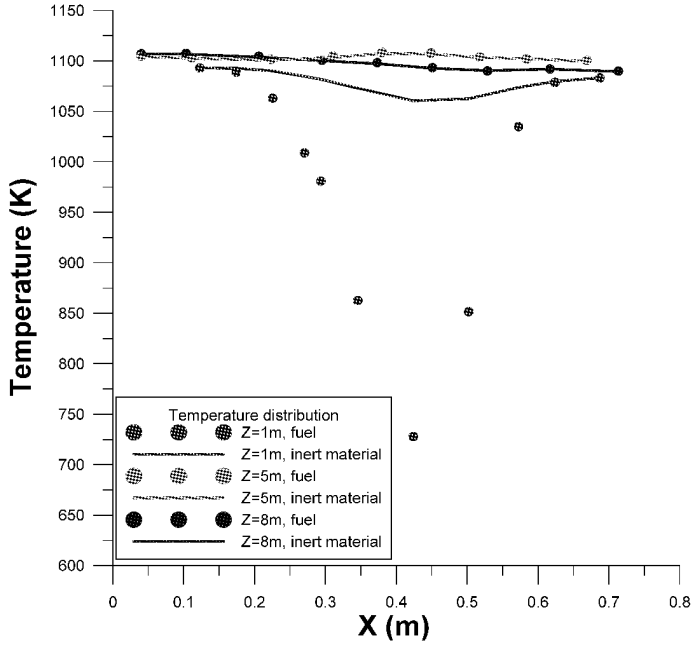

Fig. 7 Temperature profiles along X (Y=0.27) axis, for inertmaterial and fuel for different heights

CONCLUSIONS

A three dimensional comprehensive numerical investigation (incorporating combustion mechanisms) of a CFBC is presented. Despite the numerous assumptions of the model and the uncertainties which come out of these, good agreement between experimental data and numerical results is achieved. Oxygen and CO_2 profiles are well predicted except for the height of Z=2.15m. At this height the deviations with the experimental data are attributed to the incomplete set of experimental data in combination with the non uniform distribution of the oxygen concentration field at this height. Moreover the mean temperature field in the bed, as well as the increased difference between the fuel and inert material temperature at the exit of the combustion chamber are well predicted. As the proper modeling of heat exchange between fuel and inert-material is concerned, Gunn's equation gives qualitatively correct results. Nevertheless, more sophisticated models should be developed, taking into consideration flow heterogeneity in each computational cell, in order to have more accurate numerical results for the operation of CFBC power plants.

ACKNOWLEDGEMENTS

The authors would like to thank Pr. Leithner R. for his precious support and his help with the experimental data. This paper includes results from work carried out with a financial grant from the Research Fund for Coal and Steel of the European Community (Contract No. RFCR-CT-2005-00009).

REFERENCES

Basu P.: Chemical Engineering Science, **54**, Issue 22 (1999), pp. 5547-5557.

Fluent Inc., Fluent 6.3 User guide, (2006).

Gungor A., Eskin N: International Journal of Thermal Sciences **47** (2008), pp 157-174.

Gungor A., Eskin N: Journal of the Chinese Institute of Chemical Engineers **39** (2008) 541–556.

Gunn D. J.: Int. J. Heat Mass Transfer, **21**(1978), pp. 467-476.

Kallio S. (May 2006). Characteristics of gas and solids mixing in a CFB determined from 3D CFD simulations. 19th International conference on Fluidized bed Combustion, Austria.

Leithner R., Müller H., Müller J., Schlutz A., Vorckrodt S., Wang J., Papageorgiou N., Kakaras E., Ntouros Z., Carvalho M., Azevedo J. and Saraiva P., Minimization of the Formation of Air Pollutants in the CAFBC by Using European Fuels and Additives,1993

Myöhänen K. (Finland 2006). Modeling of circulating fluidized bed combustion with a semi-empirical three-dimensional model. 47th Conference on Simulation and Modelling.

Rampidis I., Nikolopoulos A., Koukouzas N., Grammelis P. and Kakaras E. (2007). Optimization of Computational Performance and Accuracy in 3-D Transient CFD Model for CFB Hydrodynamics Predictions. 5th International conference on Numerical Analysis and Applied Mathematics, Greece.

Smith I.W.: Combustion and Flame **17**, (1971), pp.303-314.

Syamlal M. and O'Brien T. J.: National Technical Information, Springfield, VA 1987.

Wang J., Wei Ge, Jinghia Li.: Chemical Engineering Science **63** (2008), pp 1553-1571.

Wei Ge, Wei Wang, Weigang Dong, Junwu Wang, Bona Lu, Qingang Xiong and Jinhai Li (2008). Meso-scale structure-A challenge of computational fluid dynamics for circulating fluidized bed risers. 9th International Conference on Circulating Fluidized Beds.

Wu Y., Lu J.and Zhang J. et al: *Boiler Technology* **35**, Issue 3 (2004), pp 12-16.

Zhang D.Z., VanderHeyden W.B: High Powder Technology **116** (2001), pp.133–141.

Zhao Jinsheng, Brereton Clive, Grace John R., Lim C. Jim and Legros Robert,: Fuel **79**, NO. 9 (1997), pp.853-860.

Zhao Yunhua, Kim Ho Young, Yoon Sam S.: Fuel, **86**, Issues 7-8 (2007), pp.1102-1111.

DYNAMICAL MODELING OF THE GAS PHASE IN FLUIDIZED BED COMBUSTION-ACCOUNTING FOR FLUCTUATIONS

D. Pallarès, F. Johnsson

Department of Energy and Environment
Chalmers University of Technology, SE-41296, Göteborg, Sweden

Abstract: A model for gas phase mixing in fluidized bed boiler furnaces is presented. The model takes its basis in a description of the dynamics of the dense bottom bed which strongly govern the gas mixing up through the furnace. Thus, a time-resolved approach is used to link the modeling to the physics of the underlying processes determining the gas mixing. As output, the model gives the fluctuating flux of gas species, in contrast to the classical modeling approach which is limited to time-averaged gas fluxes. Such a dynamical approach allows assumption of the volatile combustion system as transport-controlled which avoids complete consumption of either oxygen or combustible gases in each modeled cell. Thus, the time-resolved analysis employed enables application of a realistic criterion for the mixing such as that reactants can coincide in both space and time in order to react. While fitting of kinetics is strongly dependent on the system and operational conditions, the present model integrates key system variables such as the bottom bed height and the characteristic pressure-drop constant over the primary air distributor, allowing application of transport-controlled (*i.e.* infinitely fast kinetics) volatile combustion.

The model of the bottom bed divides the gas flow into two phases, a throughflow and an emulsion gas, and calculates their respective fluctuations in velocity and composition. Having these, in-furnace gas probe measurements can be simulated and compared with in-situ gas suction probe measurements, *i.e.* the probe signal is modeled. Such an approach is crucial in fluidized bed-boilers furnaces since in-situ gas probe measurements in regions with high fluctuations in gas velocity lead to results which are biased towards reducing conditions.

Model results, including simulation of the gas suction probe, are analyzed and compared with experimental data from the Chalmers 12 MW_{th} CFB boiler and a good agreement is obtained.
Keywords: modeling, gas mixing, fluctuations

INTRODUCTION

A thorough understanding of combustion applications requires knowledge on the behavior of the gas phase, which brings oxygen in contact with the fuel to be oxidized. In solid fuel combustion, including fluidized bed (FB) combustion, the combustion process is characterized by the release of volatile gas species (part of which are combustible) and by char burn out. Oxygen is mainly supplied to an FB furnace through gas injection in the lower part, often divided into primary and secondary air. Typically, a relatively dense bed exists directly above the primary air distributor. Due to the limited pressure drop across this distributor, the primary gas flow is highly intermittent, with strong fluctuations, as shown by Svensson *et al.* (1996). These highly fluctuating dense bed dynamics strongly influence how oxygen is brought into contact with combustibles, both with respect to the char and volatiles.

Figure 1 shows measured time-averaged vertical profiles of oxygen and methane from the Chalmers 12 MW_{th} CFB boiler. As can be seen, in several positions both gas species seem to coexist, in spite of the high furnace temperature which should ensure rapid methane oxidation as both gas species meet. The explanation to this apparent contradiction is found in the time-resolved measurements with a zirconia cell probe which is given in Fig. 2. As seen, there are rapid fluctuations between oxidizing and reducing conditions (low and high signal values, respectively) at the sampling point. Thus, the pattern observed in Fig. 2 indicates that there is no coexistence of oxygen and combustible gases on a real, time-resolved basis, but only due to limitations in the time-averaged measurements as will be explained later.

The classical approach used in macroscopic modeling of the gas phase in FB units models time-averaged gas concentration values, without accounting for the existing fluctuations which govern the contact between oxygen and combustibles. Yet, such modeling does obviously still need some artifact to allow coexistence of combustion reactants with fast reaction kinetics at any location, which is usually solved by applying combustion kinetics fitted to experimental data, *i.e.* reduced kinetics. This fitting (which indeed is an indirect way to account for gas fluctuations) is strongly dependent on operational conditions and nozzle characteristics. This classical approach is illustrated in Fig. 3.a, where r and k represent empirically-fitted combustion kinetics and inter-cell gas mixing rate, respectively.

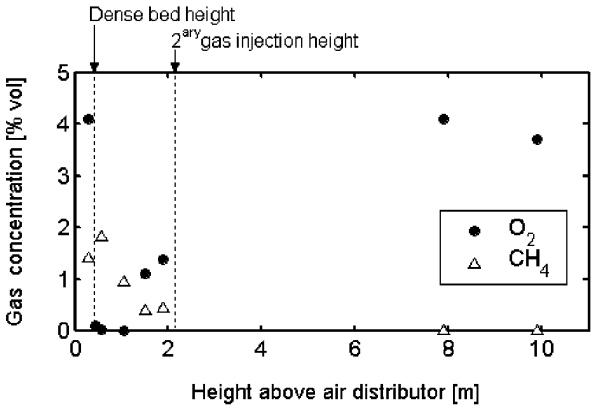

Fig. 1 Time-averaged gas concentration profiles in the Chalmers 12 MW_{th} CFBC. From Åmand (1994)

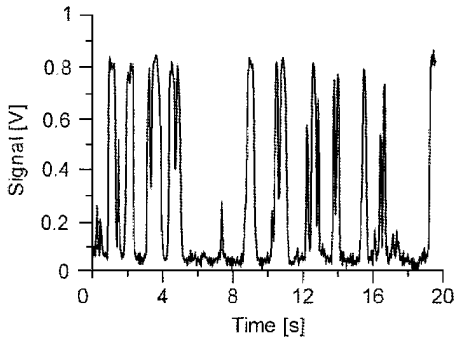

Fig. 2 Time-resolved voltage signal from a zirconia cell probe. From Niklasson et al. (2003)

The present model (schematized in Fig. 3(b)) is time-resolved and assumes volatile combustion to be transport-controlled, thus not allowing coexistence of combustion reactants at a given location and time step. The model describes fluctuations in flow of the gas species and comparison with time-averaged experimental data therefore requires time-averaging of the modeled data.

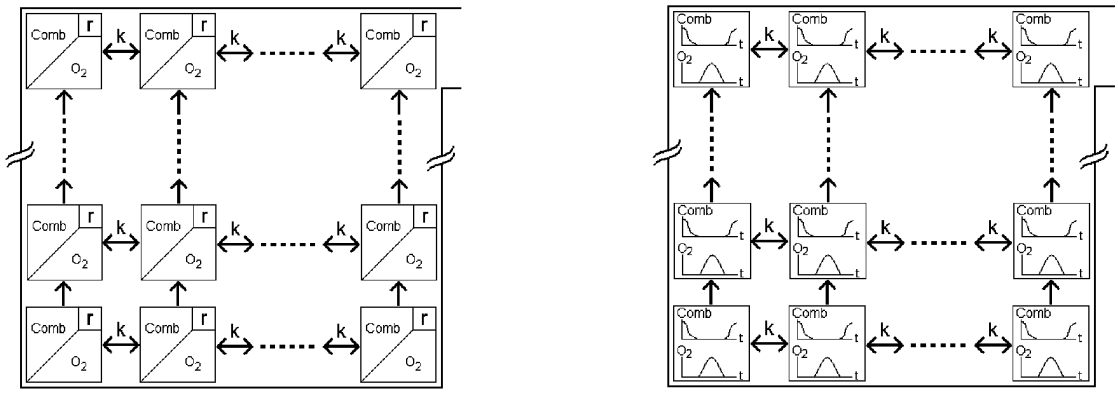

(a) Classical model (time-averaged) (b) Present model (time-resolved)

Fig. 3 Schemes for macroscopic modeling of the gas phase in fluidized beds. Inter-cell gas mixing mechanisms are represented by *k* and experimentally-fitted combustion kinetics are represented by *r*

From Fig. 1 can also be seen that oxygen concentration increases with height in the region between the dense bed surface and the secondary air injection height. This effect (studied by Lyngfelt *et al* 1996) is a consequence of that, in the bottom bed region, oxygen-rich gas flowing through the bubbles (*aka throughflow*) has a higher velocity than oxygen-poor gas flowing through the dense bed emulsion (called *emulsion* gas in this work), a phenomenon experimentally studied by Olowson and Almstedt (1990). This means that gas suction probe measurements in the bottom region will be biased according to this gas velocity difference, with the fast-flowing oxygen being underrepresented. In the splash zone, these differences in velocity due to the bubbles are reduced with height and then disappear and consequently, there is an increase in measured oxygen concentration (Fig. 1) up to a certain height (although in Fig. 1 measurement points not dense enough to resolve this position). The model presented in this paper describes both the throughflow and the emulsion phase, allowing for simulation of local gas concentration values as seen by a gas sampling probe. Thus, the modeled values can then be compared with in-situ gas probe measurements, provided that also the measurement probe is modeled.

THEORY

The dense bed in the bottom region of an FB furnace is characterized by the presence of gas bubbles which grow as they rise. Semiempirical correlations for the bubble size and velocity (Eqs. 1 and 2 respectively) are given by Darton et al. (1977) and Clift and Grace (1985) which, once coupled and solved, provide a time-resolved description of the size and location of the bubble as it rises through the bed.

For simplicity, the present model is formulated over a portion of the bed containing one single bubble. For

this portion to be representative for the entire bed, its width, L^*, is adjusted so that the bubble fraction equals the bubble fraction, δ, in the bed (which can be estimated by any of the submodels available in literature, here applying the one by Pallarès and Johnsson, 2006). Thus, having the dimensions of the bubble and the analyzed bed portion, the relative cross sections, σ, of the throughflow and emulsion gas phase can be calculated (Eqs. (3) and (4)).

$$D_{bub} = 0.54 \cdot \left(u_0 - u_{mf}\right)^{0.4} \cdot \left(h + 4\sqrt{A_0}\right)^{0.8} \cdot g^{-0.2} \tag{1}$$

$$v_{bub} = 0.71 \cdot \sqrt{g \cdot D_{bub}} \tag{2}$$

$$\sigma_{tf} = \frac{D_{bub}}{L^*} \tag{3}$$

$$\sigma_{em} = 1 - \sigma_{tf} \tag{4}$$

The basis of the present modeling is the dynamic pressure balance which accounts for the division between the two gas phases (throughflow and emulsion) expressed by Eq. 5 and illustrated in Fig. 4. Two pressure drop terms are considered for both gas phases: the pressure drop across the distributor (Eq. (6)) and that across solid emulsion (Eq. (7), Ergun equation). Thus, with an initial value for the total pressure loss, $\Delta P_{bot}=P_{plenum}-P_{freeb}$, the pressure balance can be solved at each time step, providing the evolution of the velocities of each gas phase during the bubble rise. Integration over time of the gas flows corresponding to these velocities gives the time-averaged gas velocity, $\overline{u}$, a result from the ΔP_{bot} chosen. With this, a value for ΔP_{bot} can be found which provides a value of $\overline{u}$ equal to the fluidization velocity given as input.

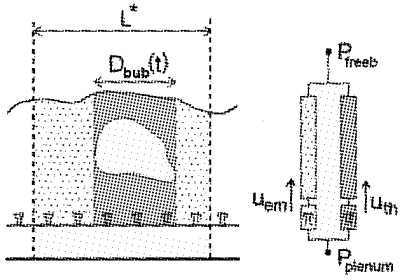

Fig. 4 Pressure balance for the two gas phases considered

$$\Delta P_{bot} = \Delta P_{dist}(u_{em,t}) + \frac{dP_{emul}(u_{em,t})}{dh} \cdot H_b = \ldots$$

$$\ldots = \Delta P_{dist}(u_{tf,t}) + \frac{dP_{emul}(u_{tf,t})}{dh} \cdot H_{emul\,tf,t} \tag{5}$$

$$\Delta P_{dist}(u) = a \cdot u^2 \tag{6}$$

$$\frac{dP_{emul}(u)}{dh} = 150\frac{\mu \cdot (1-\varepsilon)^2}{d_p^2 \cdot \phi^2 \cdot \varepsilon^3} \cdot u + 1.75\frac{\rho_g \cdot (1-\varepsilon)}{d_p \cdot \phi \cdot \varepsilon^3} \cdot u^2 \tag{7}$$

Figure 5 shows gas flow profiles exemplifying the outcome from the dynamic pressure balance expressed by Eqs. (5) to (7), for a 0.42 m-high dense-bed at 850 °C at a superficial gas velocity of 3.1 m/s for two different gas distributors (a equal to 120 and 800 Pa·s^2/m^2, respectively). It can be seen that with the low-pressure gas distributor (representative for large-scale CFB boilers) a large part of the fluidization gas crosses the dense bed as throughflow (solid line without bullets) whereas this fraction becomes substantially lower with a high pressure drop distributor (lines with bullets). The throughflow gas flow reaches a maximum as the gas bubble reaches the dense bed surface. The high pressure drop gas distributor leads to a more even distribution of the gas between the throughflow and emulsion phases than with the low pressure drop gas distributor, reducing the magnitude of the total gas flow fluctuations with as much as a factor five in the example given. Thus, the air-distributor pressure drop has a large influence on the gas flow division into a throughflow and emulsion phases. Having this, gas phase divisions obtained from the dynamic pressure balance (as exemplified in Fig. 5) can be used as boundary condition for the primary air at the bottom cells in the riser mesh. This is seen in the oxygen flow profile in the emulsion gas phase for a mesh cell located at h=0 m, shown in Fig. 6.

The present model requires as input the spatial distribution of fuel release rates (*i.e.* moisture and volatiles) and char size and concentration (providing char surface), which in the present simulations are provided by another model (Pallarès and Johnsson, 2008). The char combustion rate in a specific cell can be calculated according to Field et al. (1967). Thus, combustion of volatile species and char can be combined with the fluid dynamical inlet boundary conditions for both gas phases calculated above, yielding a model for the transport-controlled oxygen consumption in the dense bed. Figure 6 shows modeled data of the evolution of the oxygen consumption with height during a bubble cycle. From Figure 7 it can be seen that along the furnace

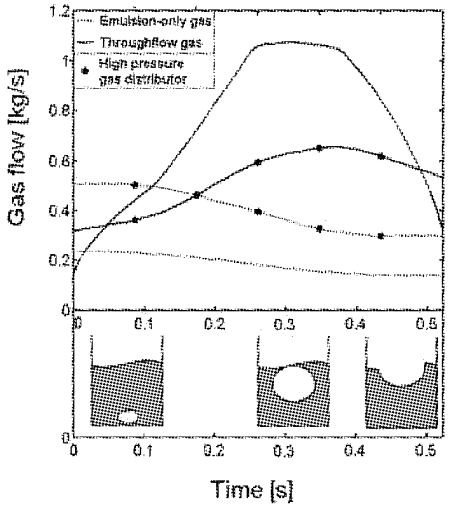

Fig. 5 Modeled emulsion- and through-flow in a single-bubble bed. Lines with bullets (•) are for the high pressure-drop gas distributor

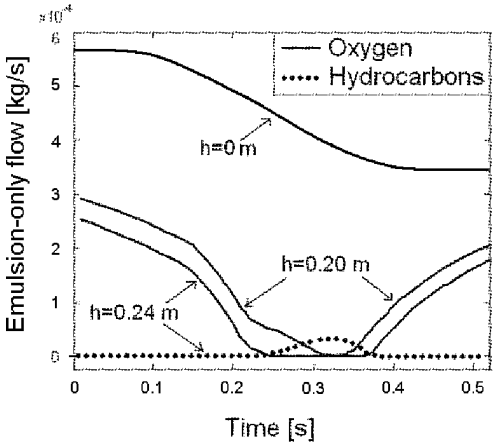

Fig. 6 Modeled gas species flows in the emulsion phase at different heights in the furnace centerline

centerline, 0.2 m is the lowest height for which oxygen concentration reaches zero in the emulsion gas flow during a bubble cycle. Above this height, the duration of emulsion gas flow with a zero oxygen concentration lasts for longer periods. In absence of oxygen, released volatile hydrocarbons will remain unburned and add to the gas flow, as observed in the curve corresponding to h=0.24 m.

In the splash zone cells, flow fluctuations in both gas phases are assumed to vanish gradually according to:

$$u_{cell,\,top} = u_{cell,\,bot} - f \cdot u'_{cell,\,bot}, \qquad \text{where } f = \frac{h_{cell,\,top} - h_{cell,\,bot}}{h_{splash,\,top} - h_{cell,\,bot}} \tag{8}$$

where u' is the fluctuating component of the gas velocity, u. Damping of the gas velocity fluctuations implies a rearrangement of the gas flow with mass transfer between time steps. However, if reduction of the gas velocity fluctuations is considered independently for each gas phase, there would obviously be two different time-independent gas velocities at the top of the splash zone, *i.e.* one for each gas phase. Thus, the reduction in velocity difference between the fast-throughflow and the low velocity emulsion gas must also be modeled. This is done by gradually adjusting the relative gas phase cross sections, *i.e.* for the emulsion gas cross section:

$$\sigma_{em,\,top} = \sigma_{em,\,bot} + f \cdot \left(\sigma_{em,\,aim} - \sigma_{em,\,bot}\right), \qquad \text{where } \sigma_{em,\,aim} = \sigma_{em} \frac{u_{em}}{u_{phase-avg}} \tag{9}$$

With these two damping mechanisms for the gas velocity fluctuations within each gas phase (Eq. 8) and for the difference in gas velocity between the two gas phases (Eq. 9), a constant gas velocity value common to both gas phases is reached at each cell at the top of the splash zone (*i.e.* in the top of the splash zone, the gas velocity varies over the cross section but not over time).

In the transport zone (*i.e.* from the top of the splash zone to the riser exit) the gas mixing between cells is modeled by means of lateral diffusion of the mass flux G of each gas species i considered, with Peclet number-based value of the gas lateral dispersion coefficient, α_g, as proposed by Kruse *et al.* (1995), *i.e.*

$$\frac{\partial G_i}{\partial t} = \alpha_g \cdot \nabla^2 G_i, \qquad \text{where } \alpha_g = \frac{u \cdot D_{eq}}{387} \tag{10}$$

As explained above in relation to Fig. 1, the velocity differences between the throughflow and emulsion gas phases results in a bias of gas probe measurements in the bottom region (*i.e.* dense bed and splash zone) of a FB boiler. The present model accounts for this gas phase division and provides the data required to simulate the values measured by a gas probe. The time-averaged mass concentration of a certain gas species, i, is defined as the ratio between the mass flow of gas species i to the total gas mass flow, namely:

$$\overline{C_i} = \frac{F_i}{F_{TOT}} = \frac{\sum_t \left(u^t_{em} C^t_{em,i} \sigma^t_{em,i} + u^t_{tf} C^t_{tf,i} \sigma^t_{tf,i}\right)}{\sum_i \sum_t \left(u^t_{em} C^t_{em,i} \sigma^t_{em,i} + u^t_{tf} C^t_{tf,i} \sigma^t_{tf,i}\right)} \tag{12}$$

Then, what is measured by a gas probe is given by the following expression:

$$\overline{C}_{i,probe} = \frac{\sum_t \left(C^t_{em,i} \sigma^t_{em,i} + C^t_{tf,i} \sigma^t_{tf,i} \right)}{\sum_i \sum_t \left(C^t_{em,i} \sigma^t_{em,i} + C^t_{tf,i} \sigma^t_{tf,i} \right)} \tag{13}$$

RESULTS AND DISCUSSION

The modeled data are compared with measurements from the Chalmers 12 MW_{th} CFB boiler (riser outlined in Fig. 7, see Åmand, 1994 for details).

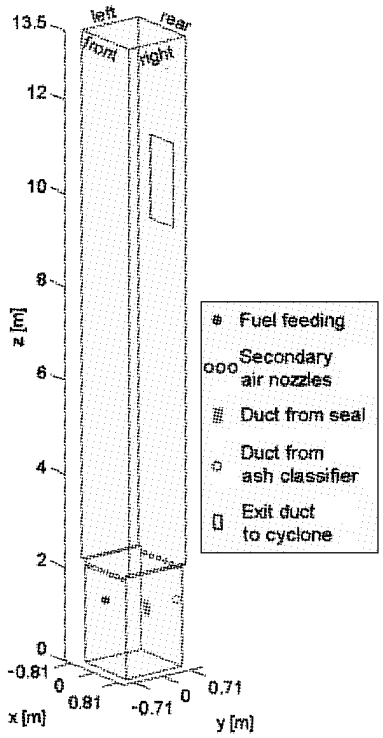

Fig. 7 Computational domain of the Chalmers 12 MW_{th} CFB riser

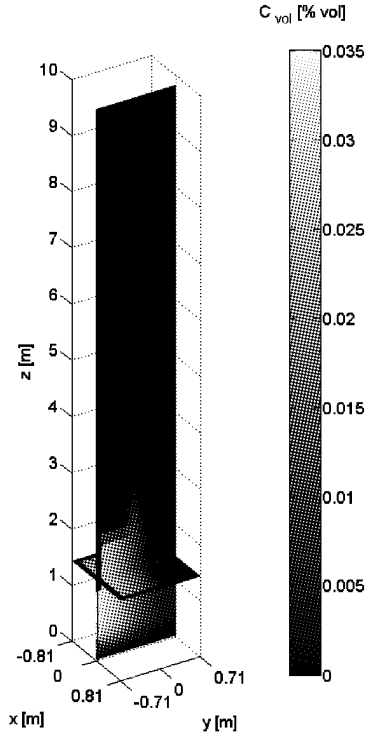

Fig. 8 Modeled concentration of combustible volatiles (sum of hydrocarbons, H_2 and CO)

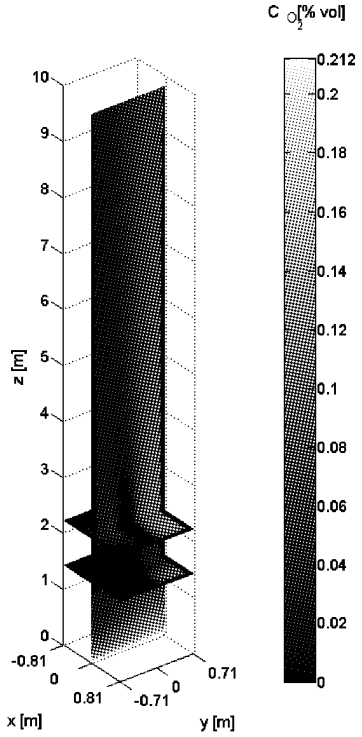

Fig. 9 Modeled concentration of O_2

Figure 8 shows the modeled concentration of volatile matter for a run burning coal at a rate of 0.43 kg/s with a fluidization velocity of 2.9 m/s and a secondary air rate of 1.24 kg/s. As seen, all combustible volatiles released immediately above the air distributor are fully consumed and it is not until a few centimeters above the distributor that there is some unburnt volatile matter which is due to the lack of oxygen in some periods of the gas fluctuations, as explained above (*cf.* Fig. 6). This effect takes place mainly close to the fuel feeding point, where volatile release is high due to that the kinetic rate of volatile release is fast compared to the horizontal fuel mixing rate. Thus, the model predicts a buildup of combustible volatiles close to the fuel feeding point. These volatiles are then combusted by the relatively high secondary air flow injected from the front wall at a height of 2.1 m (the secondary air penetration is assumed to 0.35 m for the present calculations). Figure 9 gives the modeled oxygen concentration, which decrease slightly faster with height closer to the front wall than in the rest of the furnace, due to the higher release of both volatile matter and moisture close to the fuel feeding point. The lower horizontal

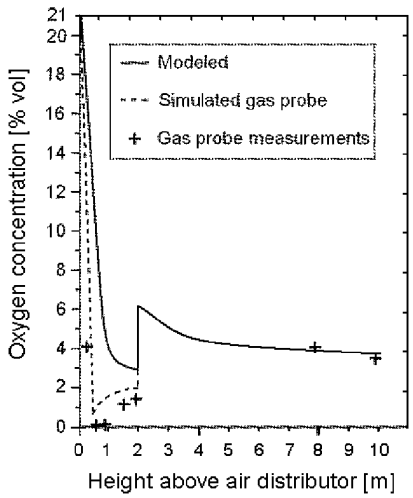

Fig. 10 Measured and modeled vertical oxygen profiles at 0.37 m from the rear wall center

slice in Fig. 9 shows the injection of gas coming from the ash classifier (located at the rear wall, 0.2 m from the right wall). An increase in oxygen concentration is predicted close to the corner between the rear wall and the left wall (dead angle in plot) due to injection of gas from the particle seal.

Figure 10 compares modeled and measured axial O_2 profiles. As seen, measured O_2 concentration increases along the splash zone (between h=0.5 and 2 m). The modeled O_2 concentration decreases along the bottom region, due to combustion. A sudden increase in O_2 concentration is observed at a height of 2.1 m due to secondary air injection. The modeled data which simulates the gas probe (dashed curve) yields lower O_2 concentration values than the modeled concentration in the bottom region of the furnace and agrees much better with measurements in the bottom region, where experiments and modeled data without the probe disagree, *i.e.* as explained in the above-given discussion.

CONCLUSIONS

A new modeling approach for the gas phase mixing in FB units is presented and validated with experimental data from the Chalmers 12 MW_{th} CFB boiler. The model accounts for both the fluctuating nature of the gas flow and the existence of two different gas phases with different dynamics and composition, features which are necessary if modeling should have a realistic coupling to the underlying physics of the gas mixing. The present approach allows a formulation of the gas combustion reactions as transport-controlled and, thus, there is no need for an empirical fit of the kinetics. Good agreement between modeled data and experiments is observed. In addition, the gas phase division employed by the model allows the simulation of gas probe measurements in the bottom region of the furnace. Inclusion of probe modeling is required in order to make a valid comparison with measurements.

ACKNOWLEDGEMENTS

Financial support by the Swedish Energy Agency and METSO POWER Oy within the project "An overall CFB model" is acknowledged.

REFERENCES

Clift, R., Grace, J.-R.. Fluidization (1985). Davidson, Harrison and Clift Eds, Academic Press Inc, London. Darton, R., LaNauze, R., Davidson, J., Harrison, D. *Trans of the Inst of Chem Eng*, 55 (1977) pp. 274-80.

Field, M.A., Gill, D.W. Combustion of pulverized coal (1967). British Coal Research Assoc, Surrey (UK).

Kruse, M., Werther, J. *Chem Eng and Proc*, 34 (1995), pp. 185-203.

Lyngfelt, A., Åmand, L.-E., Leckner, B. *Proc. 26th Int. Symp. on Combustion* (1996), pp. 3253-3259.

Niklasson, F., Johnsson, F., Leckner, B. *Chem Eng Journal*, 96 (2003), pp. 145-155.

Olowson, P.A., Almstedt, A.-E. *Chem Eng Sci* (1990) 45 (7), pp. 1733-1743.

Pallarès, D. PhD thesis (2008) Chalmers Univ of Tech (Sweden).

Svensson, A., Johnsson, F., Leckner, B. *Int Journal of Multiphase Flow*, (1996) 22 (6), pp. 1187-1204.

Åmand, L-E. PhD thesis (1994), Chalmers Univ of Tech (Sweden).

CFD MODELLING OF PARTICLE MIXTURES IN A 2D CFB

M. Seppälä, S. Kallio

VTT - Technical Research Centre of Finland,Espoo,Finland

Abstract: The capability of Fluent 6.2.16 to simulate particle mixtures in a laboratory scale 2D circulating fluidized bed (CFB) unit has been tested. In the simulations, the solids were described as one or two particle phases. The loading ratio of small to large particles, particle diameters and the gas inflow velocity were varied. The 40 cm wide and 3 m high 2D CFB was modeled using a grid with 31080 cells. The outflow of particles at the top of the CFB was monitored and emanated particles were fed back to the riser through a return duct. The paper presents the segregation patterns of the particle phases obtained from the simulations. When the fraction of large particles was 50% or larger, large particles segregated, as expected, to the wall regions and to the bottom part of the riser. However, when the fraction of large particles was 10%, an excess of large particles was found in the upper half of the riser. The explanation for this unexpected phenomenon was found in the distribution of the large particles between the slow clusters and the faster moving lean suspension.

Keywords: particle mixtures, CFD, 2D, hydrodynamics, CFB

INTRODUCTION

In CFB combustors, the suspension contains a wide variety of particles with different sizes, densities and chemical compositions. These particle properties affect the hydrodynamic behavior of the gas-solid suspension in the CFB riser. Particle mixtures and segregation phenomena in fluidized beds have been studied by many groups in the past. CFD studies of segregation in bubbling beds have been conducted e.g. by Van Wachem et al. (2001), Huilin et al. (2003, 2006), Owoyemi and Lettieri (2007), and Leboreiro et al. (2008) using in-house codes and the commercial program CFX. Gao et al. (2008) simulated with the Fluent code segregation of a binary mixture in a turbulent bed. Strumendo et al. (2008) took the particle size distribution function into account with a method of moments in their simulation of a CFB riser with the MFIX code. Batrak et al. (2005) implemented a description of particle-particle interaction forces in EDF's 3D code and simulated a mixture of three solid phases in a CFB. Mathiesen et al. (1999) studied both numerically and experimentally lateral segregation of particle mixtures in a CFB. A number of experimental studies on segregation have also been published, e.g. in Das et al. (2008) both lateral and vertical segregation of particles was measured in suspensions of particles with different densities and size distributions.

This paper concentrates on the behavior of mixtures of particles with the same density but with different diameters. The commercial CFD code Fluent is used for the simulations. First, the reliability of the numerical treatment of particle mixtures in Fluent is verified by simulating a test case with two identical particle phases. The results are compared to simulations conducted with a single solid phase. One aim of this study of binary mixtures in a 2D CFB was to assist in the design of the corresponding experimental unit. Hence, several particle mixtures with different particle diameters and mixing ratios were studied at different fluidization velocities. The simulation results were used for the design of the loop seal of the CFB, and they will also be used to plan experiments and measurement locations such that the key features of binary mixture fluidization can be observed and CFD models validated.

CFD MODEL

Transient CFD simulations were carried out by using the Eulerian multiphase model of Fluent 6.2.16. (Fluent, 2006). Due to the large amount of particles in a CFB the particle-particle interactions have to be taken into account. The viscous forces and the solids pressures of particle phases are described by the kinetic theory of granular flow. They are given as functions of the granular temperature which is a measure of the kinetic energy of the random motion of particles. The solid phase kinetic viscosity was calculated from the model by Syamlal et al. (1993). The k-ε turbulence model used in the simulations was the version modified for multiphase flows ("dispersed turbulence model", Fluent (2006)).

For gas-particle interaction, the combination of Wen & Yu (1966) and Ergun (1952) equations is used. The particle-particle drag force is expressed by the particle-particle exchange coefficient of the symmetric model of Syamlal and O'Brien (Syamlal et al., 1993). For two solid phases, the drag term is

$$K = \frac{3(1+e)\left(\frac{\pi}{2}+C_{fr}\frac{\pi^2}{8}\right)\alpha_1\rho_1\alpha_2\rho_2\left(d_1+d_2\right)^2 g_0}{2\pi\left(\rho_1 d_1^3+\rho_2 d_2^3\right)}\left|\vec{v}_1-\vec{v}_2\right| \quad (1)$$

where e is the restitution coefficient set to 0.9, C_{fr} is the friction coefficient between the two solid phases, d is the particle diameter and g_0 is the radial distribution coefficient. Alternatives for this model have been suggested e.g. by Leboreiro et al. (2008), but those were not tried in this work, which mainly was aimed at testing the models available in Fluent.

The computational grid used in the simulations was based on a preliminary sketch of the experimental unit, see Fig. 1. The height of the CFB unit is 3 m and the width 0.4 m. The walls are located 1.5 cm apart. Thus the equipment can be considered two-dimensional. The 2D grid of the CFD simulation consists of 31080 elements. At the top of the riser, gas and solids flow through a smooth outlet into a separation box from which particles fall to the loop seal and return back to the bed through a return duct. In the simulation, the upper edge of the riser constitutes the outlet and a return duct is placed at 0.6 m height. The outflow of particles was monitored and the particles were fed back to the simulation at the inlet of the return duct. The maximum circulation rate of particles observed in the simulations was used to design the loop seal of the experimental CFB unit. Spherical glass particles of different sizes will be used as bed material in the experiments. Material density of the glass is 2480 kg/m^3. Terminal velocities of the particles are 2.0 m/s, 2.9 m/s and 4.7 m/s for the 0.270 mm, 0.385 mm and 0.650 mm diameter particles, respectively.

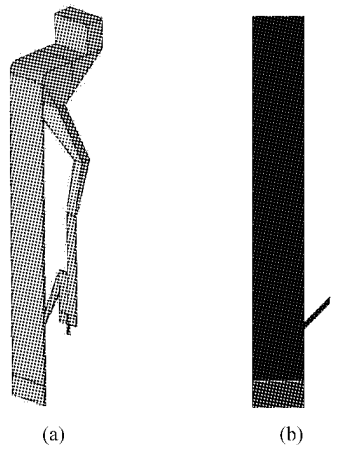

Fig.1 (a) Sketch of the experimental unit and (b) The 2D CFD geometry, in which the initial bed height is denoted.

First order discretization for time stepping and second order interpolation for spatial discretization were employed. The time step in the mixture simulations was 0.5 ms. In the simulations with one particle phase, conducted for reference, it was 1 ms. The simulation was initially ran until the outgoing flow of particles evened out after which a further simulation of 10 seconds was conducted for data sampling for time statistics. The results from the transient simulations were averaged to obtain averaged velocities, voidage, and pressure.

RESULTS AND DISCUSSION

Total of 9 cases, listed in Table 1, were simulated at fluidization velocity 4 m/s. Simulations of particle mixtures were conducted to identify conditions under which significant size segregation could easily be detected. The simulation times were longer than in two-phase simulations, but not unreasonably long. A halved time step and heavier under-relaxation were necessary to stabilize the convergence. The typical core-annulus flow structure of a CFB was produced in all simulations.

Table 1 The simulated suspensions at U_0=4m/s

Case	Particle diameter, μm		Fraction of phase	
	phase 1	phase 2	phase 1	phase 2
A	385	-	1.0	-
B	270	-	1.0	-
C	385	385	0.5	0.5
D	385	270	0.5	0.5
E	385	650	0.5	0.5
F	385	270	0.1	0.9
G	270	385	0.1	0.9
H	650	270	0.1	0.9
I	270	650	0.1	0.9

First, Fluent's capability to simulate two identical solid phases was evaluated by comparing results from cases A (a single solid phase) and C (two identical solid phases). Fig. 2(a) shows that the behaviour of the sum of the two phases in case C is nearly identical to that of the single solid phase in case A. The small discrepancy

in the bottom bed is probably due to a too short time integration period. The average vertical volume fraction profiles of the solid phases in Fig. 2(a) and the instantaneous volume fractions in Fig. 2(b) show a good agreement between the identical phases.

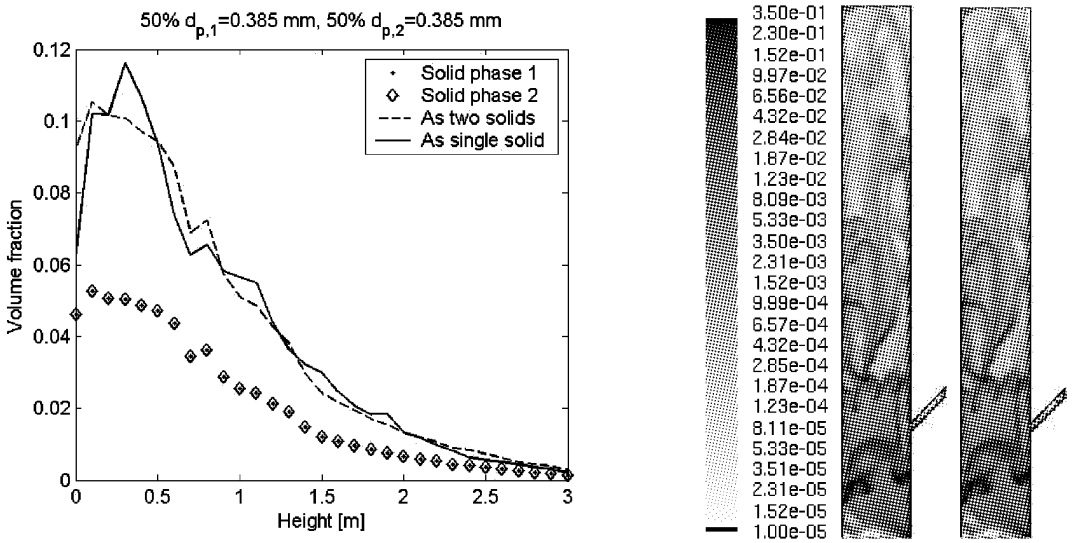

(a) (b)

Fig. 2 (a) Vertical solids volume fraction profiles of the two identical particle phases of case C and the total solids volume fraction in cases A (a single solid phase) and C (two identical solid phases). (b) Instantaneous volume fractions of the identical solid phases 1 (left) and 2 (right) in Case C

In cases D and E, the ratio of solid phases was kept at 50% / 50% but one of the diameters was varied. In Case D the diameter of the second solid phase was reduced to 270 μm and in Case E increased to 650 μm. The two solid phases in Case D, with diameters 270 mm and 385 mm, follow each other well, as can be seen from Fig. 3. The vertical profile of the total solids volume fraction of case D is given in Fig. 3(b) together with the profiles obtained from the single solid phase simulations A (385 μm) and B (270 μm). In case D the highest bottom bed density is found to be close to the highest bed density obtained in case A (d_p = 385 μm) whereas the height of the bed agrees with the bed height of case B (d_p = 270 μm). It can also be noted, that the solids concentration higher up in the riser falls in between the concentrations of cases A and B. Similar results were obtained in case E with particle diameters of 385 μm and 650 μm. The phases were found to remain well mixed, as in case D. Compared to case D, the bottom bed, however, was shallower and denser and the top region leaner in case E.

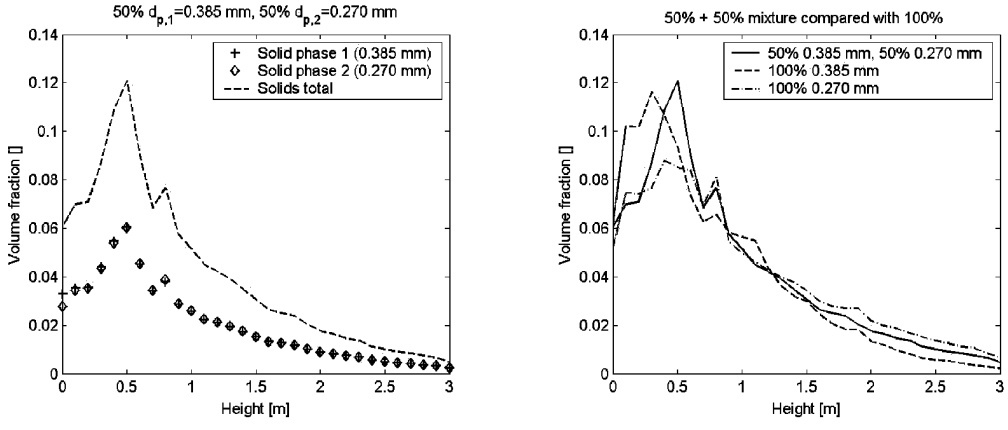

(a) (b)

Fig. 3 Vertical solids volume fraction profiles: (a) the two solid phases with d_p = 385 μm and d_p = 270 μm in case D, where the loading ratio of the solid phases was 50%/50% and (b) a comparison of the total solids volume fraction of case D with results of cases A (d_p = 385 μm) and B (d_p = 270 μm)

Fig. 4 shows that, in case D, small particles are in excess in the central regions and large particles in wall regions. Fig. 4 also shows a thin film of solids rich in smaller particles adjacent to the walls. Formation of this kind of a wall layer is common to all the studied mixture cases in which the mass fraction of small particles was

50% or above. Our analysis of the simulations showed that this thin wall layer, rich in small particles, is formed when clusters with high loading ratio of small particles move from riser centre to the walls. There this small-particle-rich suspension forms the outermost layer of the solids downflow region, while in the rest of the downflow region large particles are overrepresented.

Cases F-I considered binary particle mixtures of two different particle sizes in ratios of 10 % to 90 %. When the fraction of small particles was 90%, the smaller particles were found to concentrate in the central regions and large particles in the wall regions. When the large particles constituted 90% of the solids, large particles where in excess in the bottom part of the riser. Even local segregation was observed: the content of larger particles was in general somewhat higher in the lean suspension regions while small particles were typically in excess in the clusters. This can best be observed by comparing the areas of high content of large particles, see Fig. 5(d), with the locations of clusters in Fig. 5(c). In Fig. 5(d), the highest concentration of large particles is always found in the dilute regions between clusters. There the large particles can even be significantly more abundant than the small particles. These figures are from case H. The same local segregation pattern was observed to some extent also in cases F, G and I.

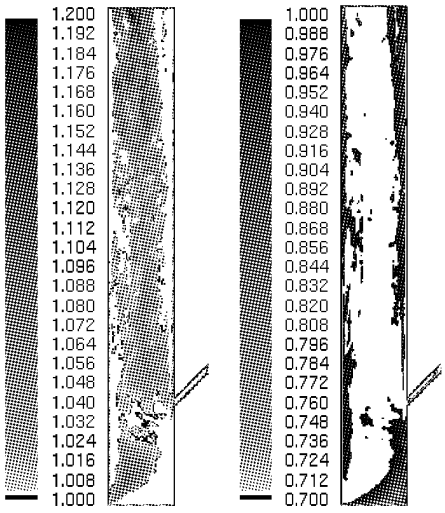

Fig. 4 Case D: Regions with (a) high content and (b) low content of small particles, given by the ratio of the volume fraction of small particles to the fraction of large particles

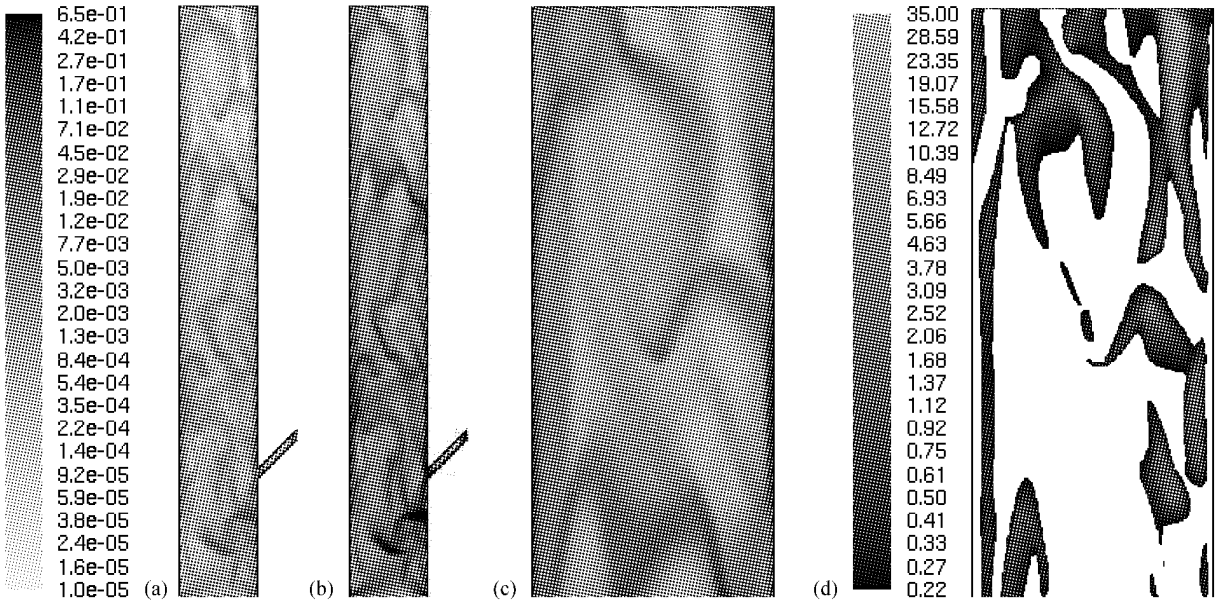

Fig. 5 Case H with 10% of particles with d_p =650 μm and 90% with d_p =270 μm. (a) Instantaneous volume fraction of solid phase 1 (650 μm). (b) The total volume fraction of solids. (c) The total volume fraction of solids at the top. (d) Volume fraction of solid phase 1 (650 μm) divided by the volume fraction of solid phase 2 (270 μm). White background represents the area where the ratio between the solid phases is below 0.222 (twice the average loading ratio 10%/90%)

During the simulations the outflow of the particles was monitored. Fig. 6(a) gives the volumetric flow rates of small and large particles and Fig. 6(b) the ratio of the two flows in case H. As the ratio of perfectly mixed small and large particles would be 9, it can be seen in Fig. 6(a) that the solids outflow contains larger particles in excess which is contrary to our expectations. To evaluate the reasons behind this unexpected result, the time-averaged and Favre-averaged (mass-weighted average) velocities of the two solid phases were computed. Everywhere in the riser, the time-averaged velocity of the small particles exceeded the corresponding average velocity of the large particles, as expected. However, the Favre averaged velocity of large particles was higher than the Favre averaged velocity of the small particles in the upper half of the riser, showing that a strong correlation must exist between the void fraction of a solid phase and its velocity and that,

in addition, local segregation has taken place. Clusters rich in small particles travel slower upwards than the dilute interstitial suspension which, according to Fig. 5, contains a disproportionally large fraction of large particles.

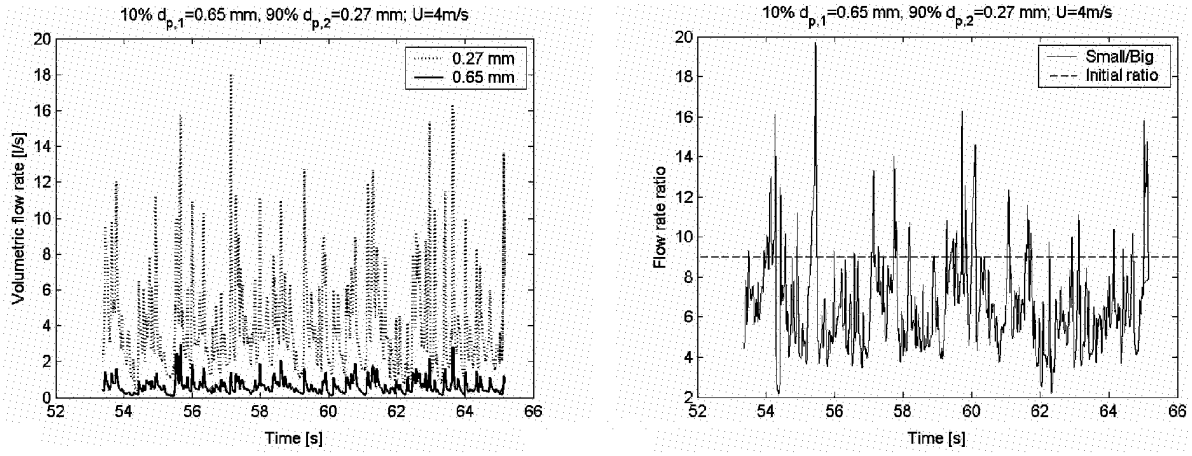

Fig. 6 Case H: Volumetric flow rates at the riser exit of (a) small and large particles, (b) ratio of the flow rates

The results of this local segregation seen in Fig. 5 and the strong correlation between the volume fraction and the velocity of a particle phase is seen in Fig. 6(b) and also in Fig. 7, which shows the vertical profiles of the ratios of the volume fractions of the two solid phases in cases F-I. In all cases, the solid phase having mass fraction of 10 % is overrepresented in the upper part of the riser, whereas the phase with mass fraction of 90 % is in excess in the lower part of the riser. The slowly moving clusters always contain an excess of the particle size that constitutes the bulk of the solids. Thus the mass-weighted velocity of these particles is lower than that of the particles constituting the remaining 10% of the bed mass. This leads to the concentration profiles seen in Fig. 7.

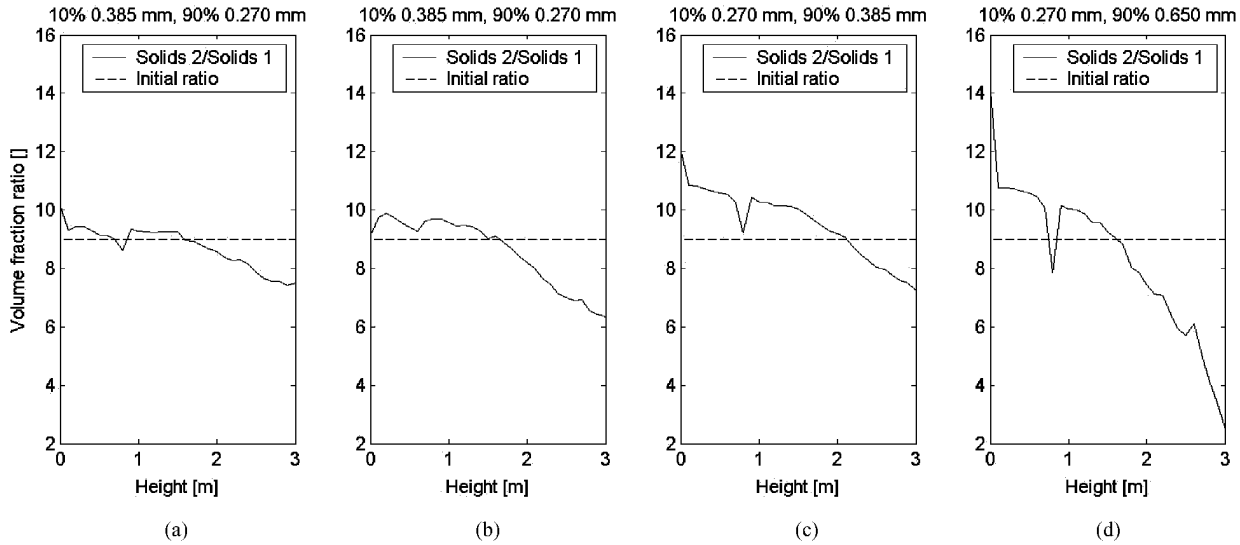

Fig. 7 The volume fraction of particles constituting 90% of the solids volume (solid phase 2) divided by the volume fraction of particles constituting the remaining 10 % (solid phase 1), plotted as a function of height in (a) case F, (b) case G (c) case H and (d) case I

CONCLUSIONS

The performance of the commercial CFD code Fluent version 6.2.16 was evaluated in simulations of particle mixtures. The purpose of the simulations was also to assist in the design of a laboratory scale CFB unit and in the planning of experiments. When a suspension of a single particle size was divided into two identical interacting solid phases, the results were practically unchanged, which indicates that Fluent treats correctly the division into phases.

In the simulations of binary mixtures of particles, small particles were found to concentrate in the central

regions and large particles concentrate in wall regions when the fraction of small particles was 50% of the solids mass or larger. The phases remained fairly well mixed and no remarkable separation was apparent when the mass ratio of small and large particles was 50% to 50%. However, with mass ratio of 90% to 10%, an abundance of particles with the smaller mass fraction could be detected in the upper part of the riser and in the outflow. The explanation to this phenomenon was found in the local segregation of the phases. The particles constituting the bulk of the solids are in excess in the slower moving clusters while the other size fraction prefers the leaner suspension that travels up at a high velocity. The preferential distribution of large particles that are in minority in the solids mixture could in a CFB combustor lead to an increase in the concentration of fuel particles in the upper parts of the riser. Since this study was entirely based on numerical modeling, this finding should be confirmed by experiments.

NOTATIONS

Symbols:

C_{fr} friction coefficient between solid particles
d_p particle diameter, m
e restitution coefficient
g_0 radial distribution coefficient
K drag coefficient
v phase velocity, m/s

Greek letters:

α voidage
ρ density, kg/m^3

ACKNOWLEDGEMENTS

The authors gratefully acknowledge the financial support of Tekes, VTT Technical Research Centre of Finland, Fortum Oyj, Foster Wheeler Energia Oy, Neste Oil Oyj and Metso Power Oy.

REFERENCES

Batrak, O., Patino, G., Simonin, O., Flour, I., Le Guevel, T., Perez, E.: (2005). 8th Int. CFB Conference.
Das, M., Meikap, B. C., Saha, R. K.: Chem. Eng. J. 145 (2008), pp. 32-43.
Ergun, S., Chem. Eng. Progress 48 (1952), pp. 89-94.
Fluent Inc., Fluent 6.3 Users manual (2006).
Gao, J., Chang, J., Lu, C., Xu, C.: Particuology 6 (2008), pp. 59-71.
Huilin, L., Yurong, H., Gidaspow, D., Lidan, Y., Yukun, Q.: Powder Technol. 134 (2003), pp. 86-97.
Huilin, L., Yunhua, Z., Ding, J., Gidaspow, D., Wei, L.: Chem. Eng. Sci. 62 (2007), pp. 301-317.
Leboreiro, J., Joseph, G.G., Hrenya, C.M., Snider, D.M., Banerjee, S.S., Galvin, J.E.: Powder Technol. 184 (2008), pp. 275-290.
Mathiesen, V., Solberg, T., Arastoopour, H., Hjertager, B.H.: AIChE J. 45 (1999), pp. 2503–2518.
Owoyemi, O., Lettieri, P.: (2007). A CFD study into the influence of the particle particle drag force on the dynamics of binary gas solid fluidized beds. ECI 12th Int. Conf. on Fluidization.
Strumendo, M., Arastoopour, H., Ahmadzadeh, A.: (2008). Numerical simulation of poly-dispersed systems. 9th Int. CFB Conference.
Syamlal, M., Rogers, W., O'Brien T. J.: MFIX Documentation: Volume 1, Theory Guide. National Technical Information Service, Springfield, VA, DOE/METC-9411004, NTIS/DE9400087 (1993).
Van Wachem, B.G.M., Schouten, J.C., Van den Bleek, C.M., Krishna, R., Sinclair, J.L.: AIChE J. 47 (2001), pp. 1292-1302.
Wen, C.Y., Yu, Y.H.: Chemical Engineering Progress Symposium Series Vol. 66 (1966), pp.100-111.

CFD ANALYSIS OF BUBBLING FLUIDIZED BED USING RICE HUSK

Ravi Inder Singh[1], S.K.Mohapatra[2], D.Gangacharyulu[3]

1 Lecturer, Department of Mechanical Engineering, Guru Nanak Dev Engineering College, Ludhiana, Punjab, India

2 Professor and Head, Department of Mechanical Engineering, Thapar University, Patiala, Punjab, India

3 Associate Professor and Head, Department of Chemical Engineering, Thapar University, Patiala, Punjab, India

Abstract: Rice is Cultivated in all the main regions of world. The worldwide annual rice production could be 666million tons (www.monstersandcritics.com,2008) for year 2008. The annual production of rice husk is 133.2 million tons considering rice husk being 20% of total paddy production. The average annual energy potential is 1.998 $*10^{12}$ MJ of rice husk considering 15MJ/kg of rice husk. India has vast resource of rice husk; a renewable source of fuel, which if used effectively would reduce the rate of depletion of fossil energy resources .As a result a new thrust on research and development in boilers bases on rice husk is given to commercialize the concept. CFD is the analysis of systems involving fluid flow, heat transfer and associated phenomena such as chemical reactions by means of computer-based simulation. High quality Computational Fluid dynamics (CFD) is an effective engineering tool for Power Engineering Industry. It can determine detailed flow distributions, temperatures, and pollutant concentrations with excellent accuracy, and without excessive effort by the software user. In the other words it is the science of predicting fluid flow, heat and mass transfer, chemical reactions and related phenomena; and an innovate strategy to conform to regulations and yet stay ahead in today's competitive power market. This paper is divided into two parts; in first part review of CFD applied to the various types of boilers based on biomass fuels/alternative fuels is presented. In second part CFD analysis of fluidized bed boilers based on rice husk considering the rice husk based furnace has been discussed. The eulerian multiphase model has used for fluidized bed. Fluidized bed has been modeled using Fluent 6.2 commercial code. The effect of numerical influence of bed superheater tubes has also been discussed.

Keywords: CFD, combustion, eulerian multiphase model

INTRODUCTION

With declining reserves and fluctuating prices of fossil fuels, the search for an alternative renewable raw material to replace petroleum has intensified all over the world. The new concept of collected solar energy, converted into new forms and stored in plant, has bought about the introduction of new notions, such as energetical cultures, agro-energetical and oil bearing plantations, photo-biofuels, green energy etc. The worldwide annual rice production could be 666million tons (www.monstersandcritics.com,2008) for year 2008. The annual production of rice husk is 133.2 million tons considering rice husk being 20% of total paddy production. The average annual energy potential is 1.998 $*10^{12}$ MJ of rice husk considering 15MJ/kg of rice husk. India alone produces (Jain et al. 1995) about 22 million tones of rice husk per year as by product from rice milling. Ravi Inder singh et al. (2008) did the detailed study of an Atmospheric Bubbling Fluidized bed Combustor 10MW power plant based on rice husk. He explained an experience, an environmental assessment, a model for exit gas composition, agglomeration problem and a model for solid population balance of 10 MW power plant at Jalkheri, Distt. Fatehgarh Sahib,Punjab, India based on rice husk has been discussed. Fluidized bed combustion (FBC) is one of the most promising energy conversion options available today. FBC combines high efficiency combustion of low-grade fuels viz. high ash coal, coal washery rejects and middling, wood and other biomass of agri-waste and municipality waste. Computational fluid dynamics (CFD) is the science of predicting fluid flow, heat & mass transfer, chemical reactions and related phenomenon by solving the full Navier-Strokes equations on a discrete grid. The solution in cell could include, three velocity components, pressure, temperature, turbulent kinetic energy and dissipation and various species concentrations as primary data. Fluidized bed is the important part in the boiler. Bubble formation is very important part of fluidized bed reactors. So in this paper CFD analysis of fluidized bed based on rice husk has done to look solid volume fraction contours and velocity profiles considering the bed body with and without bed super heater tubes.

REVIEW OF CFD IN BOILERS BASED ON ALTERNATIVE FUELS

The most important component in a power plant is the boiler. Biomass is the major fuel after coal used in boiler operation and is the major source of energy. Major efforts are being invested in making the use of biomass more efficient and environmentally acceptable. A significant portion of these efforts for the past quarter century has focused on the development of multidimensional, mathematical models of boilers, reactors, gasifiers and pyrolyzers that can be used to design and analyze coal combustion processes. These models serve as tools when characterizing reactive flow processes that complement and in, some cases, replace physical experiments with equivalent 'numerical experiments'. Generally biomass combustion was modeled in a similar approach as coal combustion, the reason being that biomass fuels followed the same sequence of pyrolysis, devolatilisation and combustion as seen in low-rank coal combustion mechanisms. Biomass burning was assumed to have happened in two global steps; first, a homogeneous combustion and second, a heterogeneous combustion. In homogeneous combustion, devolatilization of biomass particles occurred and combustion in gaseous phase took place whereas in heterogeneous combustion, burning of solid char happened. The devolatilization of biomass was based on a single kinetic rate model in which the rate of production of volatiles followed a first order reaction. The rate constant for this reaction was expressed in the Arrhenius form, in which rates of weight loss was correlated to temperature. For the gaseous phase volatiles combustion, the mixture fraction/PDF approach was used, in which transport equation for individual species were not solved. However, the predicted mixture fraction distribution could be used to derive the individual component concentrations for a species of interest. For char combustion, a kinetic/diffusion-limited rate surface reaction model was chosen, implying that the reaction was determined by either the kinetics or by a diffusion rate. Combustions in furnaces occurred at high temperature and thus, radiative heat transfer was a predominant mechanism for heat transfer. Radiative heat transfer was in fact not only the major energy transport mechanism but also one of the most complicated problems in combustion process. Information available from model predictions can include the Temperature distributions, gas composition, velocity, particle trajectories, extent of particle burnout, NO_x formation and reduction, SO_x formation and capture, pressure distribution, particle size distribution, ash/slag accumulations and so forth. Comprehensive combustion models offer many advantages in characterizing combustion processes that can effectively complement experimental programs. The gas phase and temperature fields are strongly influenced by combustion reaction pattern through the heat release rates and resulting expansion of gas. The velocity field is also governed by locations of air injection nozzles which represent an important means of controlling the combustion process. The gas phase properties all show a complex three dimensional variation which is difficult in detail in graphically. Stastny et al. (2002) had performed a 3-D combustion modeling for a 200 MW dedicated biomass-fired boiler in a power plant in Fyris, Sweden, in which the pulverised fuel was made up of wood residuals and peat. The software used to model the combustion process in the boiler was FLUENT. In this work, the turbulence model chosen was RNG k-ε and the mixture fraction/Probability Density Function (PDF) approach was applied in modeling the reaction between the fuel and oxidizer. However, the standard k-ε model was used for the preliminary solution before proceeding with RNG k- ε model for the final calculations. In this study, biomass combustion was modeled in a similar approach as coal combustion. Walsh (2006) had modeled the combustion of volatiles released from burning biomass particles via the species transport model in FLUENT. In this method, the combustion reactions rates were defined by the stoichiometry, kinetics and turbulent reaction rates. The turbulence model chosen was the standard k-ε model whereas the rates of reactions in the model were controlled by the kinetic finite rate/eddy dissipation mechanism. The eddy dissipation mechanism stated that the reaction rate was defined by turbulence and concentrations of both reactants and products. The radiation model used was the P1radiation model. Sorain K Kaer (2001) presented numerical modeling of a Straw-fired grate boiler. The CFD prediction was carried out using CFX. In this steady state governing equations were solved using the SIMPLE algorithm and the effect of turbulence on the mean flow field was accounted for using the RNG k-ε model. Radiative heat transfer was modeled using the discrete transfer model. La. Ma et al. (2007) formulated CFD model that simulates combustion of biomass in existing pf coal fired furnaces and model results for the combustion of a typical wood in a 1 MW industrial test facility have been presented. The model is primarily based on coal combustion submodels using an Eulerian–Lagrangian frame of reference.

CFD ANALYSIS OF FLUIDIZED BED FURNACE BASED ON RICE HUSK

Here CFD analysis of fluidized bed has been done using eulerain-multiphase model approach. Here combustion has not been considered due to limited computational approach as it results increase in size of sand particles due to inorganic content in ash of rice husk.

Assumptions of above work

(1) The CFD model used in this work is based on the extended two-fluid model (TFM), which employs granular kinetic theory for the particulate phase.

(2) Particles are considered smooth, spherical, inelastic and undergoing binary collisions. The fundamental equations of mass, momentum, and energy conservation are solved for each phase.

(3) Due to combustion of rice husk particles the size of sand particles is going to increase.

(4) Density of sand particles and rice husk after combustion in fluidized bed rice husk combustor combined is assumed to be 1200kg/m^3.

(5) Size of sand particles is assumed to be 80μm.

(6) Due to limited computational space the bed is assumed to be two dimensional.

(7) The dimensions of the bed are assumed to be 1× 0.28m.

(8) Appropriate constitutive equations are specified in order to describe the physical and rheological properties of each phase and to close the conservation equations.

(9) The granular temperature is estimated by solving a fluctuating kinetic energy equation for the particles. The solid viscosity and the pressure can then be computed as a function of the granular temperature at any time and position.

(10) Three phase mathematical modeling is assumed to be present.

(11) Bed is assumed to be in isothermal conditions.

GOVERNING EQUATIONS

$$\frac{\partial}{\partial t}\left(\varepsilon_g \rho_g\right)+\nabla.\left(\varepsilon_g \rho_g \vec{v_g}\right)=0 \tag{1}$$

$$\frac{\partial}{\partial t}\left(\varepsilon_s \rho_s\right)+\nabla.\left(\varepsilon_s \rho_s \vec{v_s}\right)=0 \tag{2}$$

$$\varepsilon_g+\varepsilon_s=1 \tag{3}$$

MOMENTUM EQUATIONS

$$\frac{\partial}{\partial t}\left(\varepsilon_g \rho_g \vec{v_g}\right)+\nabla.\left(\varepsilon_g \rho_g \vec{v_g}\vec{v_g}\right)=-\varepsilon_g \nabla P_g+\nabla T_g+\varepsilon_g \rho_g g+\beta(\vec{v_s}-\vec{v_g}) \tag{4}$$

$$\frac{\partial}{\partial t}\left(\varepsilon_s \rho_s \vec{v_s}\right)+\nabla.\left(\varepsilon_s \rho_s \vec{v_s}\vec{v_s}\right)=-\varepsilon_s \nabla P_s+\nabla T_s+\varepsilon_s \rho_s g-\beta(\vec{v_s}-\vec{v_g}) \tag{5}$$

FLUCTUATING ENERGY EQUATION FOR SOLID

Equivalent to the thermodynamic temperature for gases, the granular temperature can be introduced as a measure for the fluctuating kinetic energy of the particles. The granular temperature is defined as

$$\Theta=\frac{1}{3}\vec{v'_s}^2 \tag{6}$$

Where $\vec{v'}_s$ is the solids fluctuating velocity. The equation of conservation of the solids fluctuating energy is given as

$$\frac{3}{2}\left[\frac{\partial}{\partial t}\left(\varepsilon_s \rho_s \Theta\right)+\nabla.\left(\varepsilon_s \rho_s \vec{v_s}.\Theta\right)\right]=T_s:\nabla\vec{v_s}+\nabla.\kappa\nabla\Theta-\gamma \tag{7}$$

Where $T_s:\nabla\vec{v_s}$ the generation of the fluctuating energy due is work done by shear stress in the particle phase and $\nabla.\kappa\nabla\Theta$ is the conduction of the fluctuating energy

CONSTITUTIVE EQUATIONS

The solid phase and the gas phase were considered incompressible. The gas phase was modeled as an incompressible Newtonian fluid. The gas phase tensor can thus be represented as

$$T_g=2\varepsilon_g \mu_g \tau_g \tag{8}$$

$$\tau_g=\frac{1}{2}\left[\nabla\vec{v_g}+(\nabla\vec{v_g})^T\right]-\frac{1}{3}(\nabla\vec{v_g})I \tag{9}$$

The solid stress tensor, T_s can be expressed in terms of the solid pressure, P_s, bulk viscosity ξ_s, and shear viscosities, μ_s, as

$$T_s = (-P_s + \xi_s \nabla.\vec{v}_s)I + 2\mu_s \tau_s \tag{10}$$

$$\tau_s = \frac{1}{2}\left[\nabla.\vec{v}_s + \left(\nabla.\vec{v}_s\right)^T\right] - \frac{1}{3}(\nabla.\vec{v}_s)I \tag{11}$$

These solid properties can be determined as a function of granular temperature according to the following relations:

$$P_s = \varepsilon_s \rho_s \Theta\left[1 + 2(1+e)g_o \varepsilon_s\right] \tag{12}$$

$$\xi_s = \frac{4}{3}\varepsilon_s^2 \rho_s d_s (1+e) g_o \left(\frac{\Theta}{\pi}\right)^{1/2} \tag{13}$$

$$\mu_s = \frac{\mu_s, dil}{(1+e)g_o}\left[1 + \frac{4}{5}(1+e)g_o \varepsilon_s\right]^2 + \frac{4}{5}\varepsilon_s^2 \rho_s d_s (1+e) g_o \left(\frac{\Theta}{\pi}\right)^{1/2} \tag{14}$$

$$\mu_s, dil = \frac{5\sqrt{\pi}}{96}\rho_s d_s \Theta^{1/2} \tag{15}$$

where $\mu_{s,\,dil}$ is the dilute viscosity and g_o is the radial distribution function expressing the statistics of the spatial arrangement of particles. In this study the following expressing were used:

$$g_o = \left[1 - \left(\frac{\varepsilon_s}{\varepsilon_{s,\max}}\right)^{1/3}\right]^{-1} \tag{16}$$

The granular conductivity, κ and the collisional rate of energy dissipation per unit volume, γ, is adopted as:

$$\kappa = \frac{2\kappa_{dil}}{(1+e)g_o}\left[1 + \frac{6}{5}(1+e)g_o \varepsilon_s\right]^2 + 2\varepsilon_s^2 \rho_s d_s \left(\frac{\Theta}{\pi}\right)^{1/2} \tag{17}$$

$$\kappa_{dil} = \frac{75\sqrt{\pi}}{384}\rho_s d_s \Theta^{1/2} \tag{18}$$

$$\gamma = 3(1-e^2)\varepsilon_s \rho_s g_o \Theta\left[\frac{4}{d_s}\left(\frac{\Theta}{\pi}\right)^{1/2} - \nabla.\vec{v}_s\right] \tag{19}$$

FRICTIONAL STRESS

Zhang and Rauenzahn (1997) concluded that at very high solid volume fraction particle collisions are no longer instantaneous, as is assumed in kinetic theory. Several approaches have been presented in the literature to model the frictional stress. The models are however very empirical. The frictional stress is written in a Newtonian form:

$$\sigma = P_f I + \mu_f\left[\nabla\vec{v} + (\nabla\vec{v})^T\right] \tag{20}$$

The frictional stress is added to the stress predicted by kinetic theory for $\varepsilon_s > \varepsilon_{s,\min}$:

$$P_s^* = P_s + P_f \tag{21}$$

$$\mu^*_s = \mu_s + \mu_f \tag{22}$$

In the present work, the frictional viscosity model proposed by schaeffer (1987) is used to describe the frictional stress:

$$P_f = A(\varepsilon_s - \varepsilon_{s,\min})^n \tag{23}$$

$$\mu_f = \frac{P_f.\sin\varphi}{\varepsilon_s\sqrt{\frac{1}{6}\left(\frac{\partial u_s}{\partial x} - \frac{\partial v_s}{\partial y}\right)^2 + \left(\frac{\partial v_s}{\partial y}\right)^2 + \left(\frac{\partial u_s}{\partial x}\right)^2 + \frac{1}{4}\left(\frac{\partial u_s}{\partial y} + \frac{\partial v_s}{\partial x}\right)^2}} \tag{24}$$

Values of $A=10^{25}$, $n=10$, $\varepsilon_{s,\min}=0.59$, and $\varphi=25^o$ are typically employed.

Instead of solving the complete balance of the solids fluctuating energy, equation 7 an algebraic expression was proposed was by syamlal et al. (1993).It results in

$$(-P_s^* I + \tau_s) : \nabla\vec{v}_s - \gamma = 0 \tag{25}$$

INTER-PHASE MOMENTUM EXCHANGE

We need to specify the gas-solid drag coefficient for different solid concentrations. In this work the drag model suggested by gidaspow (1994) was used For $\varepsilon \geq 0.8$

$$\beta = \frac{3}{4} C_d \frac{\varepsilon_s \rho_s \left|\vec{v_g} - \vec{v_s}\right|}{d_s} \varepsilon_g^{-2.65} \tag{26}$$

Where the drag coefficient C_d is given by

$$C_d = \frac{24}{\mathrm{Re}_s}(1 + 0.15\mathrm{Re}_s^{0.687}) \quad \text{for} \quad \mathrm{Re}_s \leq 1000 \tag{27}$$

$$C_d = 0.44; \text{ for } \mathrm{Re}_s \geq 1000 \tag{28}$$

$$\mathrm{Re}_s = \frac{\varepsilon_g \rho_g d_s \left|\vec{v_g} - \vec{v_s}\right|}{\mu_g} \tag{29}$$

for $\varepsilon < 0.8$

$$\beta = 150\frac{\varepsilon_s^2 \mu_g}{\varepsilon_g^2 d_s^2} + 1.75\frac{\rho_g \varepsilon_s \left|\vec{v_g} - \vec{v_s}\right|}{d_s \varepsilon_g} \tag{30}$$

The governing conservation equations to be solved and their solution for the unknown scalars $\varepsilon_g, \varepsilon_s, u_g, v_g, u_s$ and v_s by CFD essentially gives the full flow details in the flow domain. The basic CFD methodology consists of declining a suitable grid, discretizing the above differential equations on the grid to yield a set of algebraic equations whose solution gives the flow –field variables and then post-processing to make the large amount of solution data intelligible. This methodology is described in somewhat more detail in the following. The actual implementation, however, was done using the well known commercial code Fluent 6.2 and not by writing fresh one.

GRID GENERATION

The entire modeling of the geometry is done in GAMBIT pre processor for Fluent 6.2. Meshed geometry for fluidized bed combustor with bed super tubes is shown in fig. 1 and without super heater tubes is shown in fig. 6. The boundary zones are specified as VELOCITY_INLET, PRESSURE_OUTLET, WALLS and PRESSURE OUTLET. The grid is then checked after which the entire geometry is exported to the solver, which is the FLUENT 6.2 itself.

RESULTS AND DISCUSSION

Results of CFD simulations in terms of solid volume fraction contours are shown in figure 3 to figure 5 for the fluidized bed combustor with super heater tubes at gas velocity of 0.4m/s. When air is passed through a bed of solid particles above the minimum fluidization velocity, small bubbles form at the bottom of the fluidized bed. They rise, coalesce, and erupt as large bubbles at the fluidized bed top surface. Red color indicates the solid phase in the bed, white circles represent the tubes and their arrangement and blue-green patches within the bed indicate the bubbles. For a qualitative description, near the inlet the bubbles are small in size and they increase with height until they encounter the first row of tubes. When bubbles encounter a series of tubes, there are two possibilities: (i) smooth splitting of bubbles to form smaller bubbles of roughly equal size (ii) the bubbles bridging the gaps between the tubes. Figure

2 shows the velocity contours in fluidized bed combustor at real time 0.02s. Velocity of air near the wall is

Table 1 Geometry of Bed

Geometry	Two Dimensional	Geometry	Two Dimensional
Height of Fluidized Bed	1 m	Maximum solid packing	0.63
Width of Riser	0.28m	Main Inlet gas velocity	0.4m/s
Flow Type	Laminar	Initial Condition	Bed at minimum fluidization
Gas-Solid model	Eulerian-Eulerian , with Kinetic Theory	Bed porosity at minimum fluidization	0.41
Garnular Viscosity model	Gidaspow(1994)	Bed Height at minimum fluidization	0.4m
Drag Model	Gidawpow(1994)	Outlet condition	Atmospheric pressure

Continued

Geometry	Two Dimensional	Geometry	Two Dimensional
Frictional Viscosity model	Schaeffer(1987)	Particle-Particle restitution coefficient	0.9
Wall boundary condition for the solid phase	Full slip	Particle-wall restitution coefficient	0.95
Wall boundary condition for gas phase	No slip	Particle Density	1200
Time	0.1sec	Sand Particle Diameter	80 microns
Maximum number of iterations per time step	20 sec	Gas Density	1.21 Kg/m^3
Convergence criteria	0.001	Gas Viscosity	1.81*10^{-5}
Pressure velocity coupling	Phase coupled SIMPLE	Diameter of bed super heater tubes	1.5cm

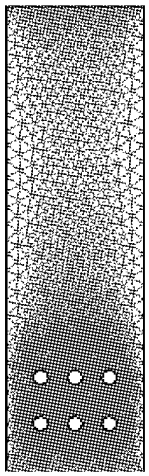

Fig. 1 Grid

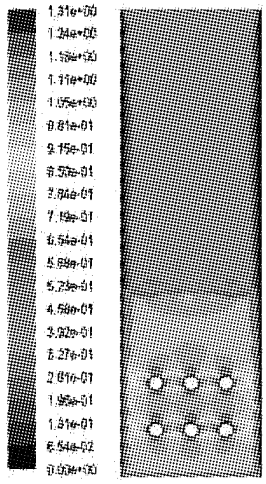

Fig. 2 Velocity contour at 0.02s

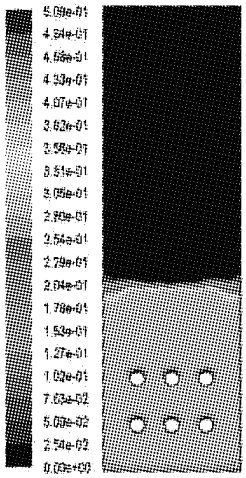

Fig. 3 Solid volume Fraction at 0.02s

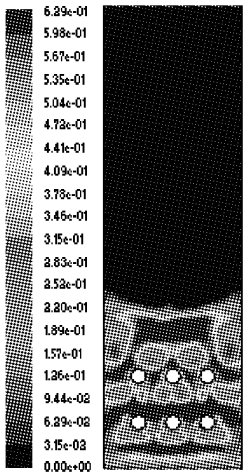

Fig.4 0.36s

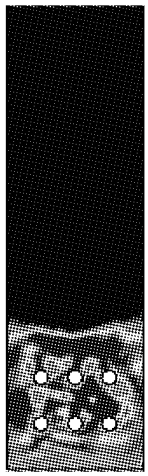

Fig.5 2 s

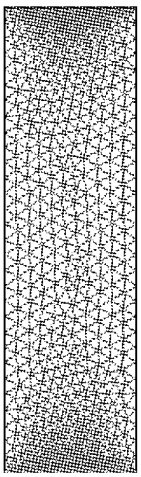

Fig. 6 Grid

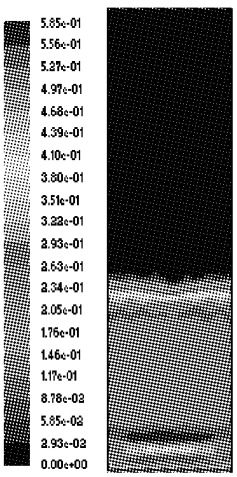

Fig. 7 Solid volume fraction at 0.3s

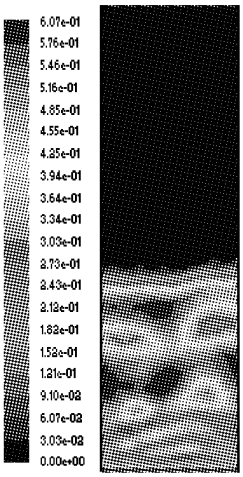

Fig.8 At 0.3s

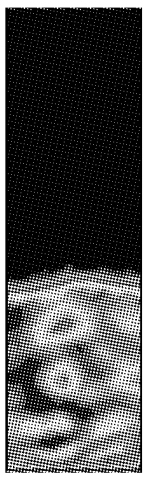

Fig. 9 At 1.2s

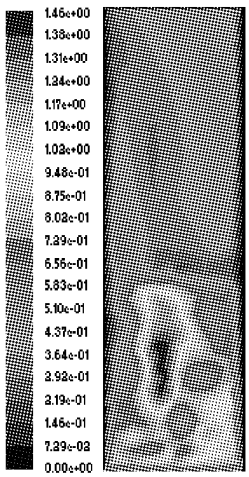

Fig. 10 Velocity contours at 3.9s

less and at the top of bed super heater tubes at the start of process is zero. For bubbling bed without tubebank solid volume contours is shown in fig 7 to fig 9. Green patches within the bed indicate bubbles. Velocity contour for fluidized bed without bed super heater tubes is shown in fig 10. Velocity of air is less near the walls. Three phase model is clearly present in both fluidized bed combustors. In fluidized bed combustor bubbles represent the in which the oxygen consumption is less. Where as in emulsion phase oxygen consumed is higher and in cloud wake phase oxygen consumption lies in between these two.

CONCLUSIONS

1. Simulations of the hydrodynamics of a dense, gas-solid bubbling fluidized bed considering rice husk with and with out bed super heater tubes were carried out using CFD.
2. Three phase mathematical modeling has been predicted by CFD analysis based on rice husk.
3. Bubbles vary in size along with bed height in fluidized bed combustor based on rice husk.
4. With the bed super heater tubes bubbles formed and erupted at the tubes.
5. Velocity of air along the walls in the fluidized bed combustor is nil.
6. Velocity of air at the top of tube in FBC is zero or minimum as compare to bed.
7. The bubble flow structure is affected due to the presence of tubes. This is due to bubble breakage either by direct interaction with tubes or due to bridging of tubes.

NOTATIONS

C_d: drag coefficient
d_s : particle diameter
d_t : bed diameter
e : coefficient of restitution
g_o : radial distribution function
G: solid stress modulus
G_s: solid mass flux, kg/m^2/s
H_{mf} : bed height at minimum fluidization, m
K_{sg} : gas-solid momentum exchange term
P_g,P_s : gas, solid phase pressure, N/m^2
P_f: frictional contribution to solid pressure, N/m^2
Re_s: Reynolds number, based on slip velocity
U_b: bubble rise velocity/s
v_g , v_s : gas, solid phase velocity vector, m/s
U_g: gas velocity/s
U_{mf} : minimum fluidization gas velocity, m/s

Greek Letters:

ε_g , ε_s gas, solid phase volume fraction
ε_{mf} : gas volume fraction at minimum fluidization
$\varepsilon_{s,min}$: minimum solid fraction
$\varepsilon_{s,max}$: maximum solid volume fraction
β : inter-phase drag coefficient
η: specularity co-efficient
φ: internal angle of friction
ρ_g,ρ_s : gas, solid phase density, kg m^{-3}
ξ_s : solid phase frictional stress, Nm^{-2}
σ: Solid phase shear stress, Nm^{-2}
τ_s : gas, solid phase shear stress, N/m^2
γ : dissipation of granular energy, kgm^{-3}s^{-1}
κ : solid thermal conductivity, kg m^{-1}s^{-1}
μ_g, μ_s : gas, solid phase shear viscosity, Pa s
μ_f : frictional contribution to solid viscosity, Pa s
Θ : granular temperature, m^{2}s^{-2}

Subscript

b : bubble
g : gas phase
s : solid phase
m_f : minimum fluidization
w : wall

REFERENCES

Demirbas, A., 2003, Progress in Energy and Combustion Science, Vol. 30, pp. 219-230.

http://www.monstersandcritics.com/news/business/news/article_1404829.

Jain, A., Rajeshwar, Rao T., Sambi, S.S. and Grover, P.D.,1995, ,7,pp.285-289.

Jenkins BM, Baxter LL, Miles Jr TR, Miles TR.,1998, Fuel Process Technol ;54:pp.17.

Herna´ndez JR, Kilpinen P., 2005, Proc. of the 4th med. combustion symposium, Lisbon, Portugal.

Singh Ravi Inder, Mohapatra S.K. ,Gangacharyulu D., Energy Conservation and Management, Elsevier, Vol 49 No.11, pp 3086-3103.

Stastny, M., Ahnert, F., Spliethoff, H., 2002. Advanced Computational Methods in Heat Transfer VII, edited by B. Sundén, C.A. Brebbia, WIT Press, Boston,pp.439-448.

Soren K. Kaer,2004, *Fuel,*Vol.83,pp.1183-1190.

L.Ma,J.M.Jones,M.Pourkashinian and A.Williams,2007, Fuel, Vol. 86,pp.1959-1965.

Sanjib K. Das Sharma and Ratan Mohan,2003 ,Int. j.chem. react. Engg., Vol 1, article 26.

Schaeffer,D.G., 1987, J.Diff. Eq., 66,pp19.

Syamlal, M., Rogers, W., and O'Brien, T.J., 1993, MFIX Documentation: Theory Guide, U.S. Dept of energy, Office of fossil energy, DOE/METC-94/1004(DE94000087) Technical note.

Walsh, A.R. ,2006, In: 7th European Conference on Industrial Furnaces and Boilers, Porto, Portugal, April 18-21, pp. 1-11.

Zhang, D.Z., and Rauenzahn, R. M., 1997, J.Rheo., 41,pp.1275.

HYDRODYNAMIC SIMULATION OF GAS-SOLID BUBBLING FLUIDIZED BED CONTAINING HORIZONTAL TUBES

Teklay Weldeabzgi Asegehegn, Hans Joachim Krautz

E-mail: teklay.asegehegn@tu-cottbus.de
Chair of Power Plant Technology, Brandenburg University of Technology Cottbus, Cottbus, Germany

Abstract: Hydrodynamic simulation of 2-D gas-solid bubbling fluidized bed containing staggered horizontal tubes was performed. The bubble hydrodynamics, bubble diameter and bubble rise velocity, were investigated and compared with experimental results elsewhere in the literature (Hull et al., 1999, Influence of Horizontal tube Banks on the Bubbling and Solids Mixing Behavior of Fluidized Beds. 15th Int. FBC Conference). The Eulerian-Eulerian Two Fluid Model (TFM) implemented in Fluent, version 6.3, was used for the governing equations with closure equations based on the Kinetic Theory of Granular Flow (KTGF). The numerical simulation showed that the horizontal tubes were the main source of bubble break up where bubbles break when they interact with the tubes and grew by coalescence until they reach the next row of tubes. Quantitative investigation of the bubble hydrodynamics also revealed that the predicted average bubble diameter and bubble rise velocity were in good agreement with the experimental results reported in the literature. It was observed that there were small bubbles formed on the lower-half part of the tubes which were usually interacted with an incoming bubble from below and left the tube after coalescence. As a result, the numerical simulation predicted a lower average bubble diameter and bubble rise velocity at the bottom of the tube banks than that reported in the literature.

Keywords: numerical simulation, bubble hydrodynamics, fluidized bed, horizontal tubes

INTRODUCTION

Fluidized beds containing immersed tubes have many industrial applications such as fluidized bed combustors (FBC), fluidized bed dryers and fluidized bed heat exchangers. The presence of immersed tubes was seen to have a significant influence on the bubble hydrodynamics. However, it was not satisfactorily investigated. In recent years, as a result of rapid growth of computer capacity, numerical simulation is becoming a powerful tool in determining the macro-and microscopic phenomenon of gas-solid fluidized beds. Two types of computer models are widely applied today, the Two Fluid Model (TFM) based on the Eulerian-Eulerian approach (Anderson and Jackson, 1967) and the Discrete Element Method (DEM) based on the Eulerian-Lagrangian approach (Tsuji et al., 1993; Hoomans et al., 1996). The DEM is a more fundamental approach for fluidized bed applications; however, the need of very high computational efforts has made it more prohibitive and limited to only few particles and very small fluidized beds. On the other hand the TFM requires less computational time and hence is the realistic approach for parametric investigation of gas-solid fluidized bed of engineering scales (van Wachem et al., 2001; van der Hoef et al., 2008).

The modeling task of fluidized beds is however very challenging due to the complex behavior of gas-solid flow. Furthermore, the presence of horizontal tubes complicates the modeling process. Bouillard et al. (1989) investigated the porosity distribution around an immersed rectangular tube using the TFM. They observed that the porosity was higher at the bottom of the tube and lower at the top. Gamwo et al. (1999) performed computer simulation to investigate solid flow patterns for a bed with staggered horizontal tubes. Gustavsson and Almstedt (2000) used a general curvilinear coordinate system and investigate bubble properties at different pressure levels. Yurong et al. (2004) used a body fitted coordinate system in order to match the boundaries of the immersed tubes. Pain et al. (2001) used the finite element method formulation and perform numerical simulation of fluidized bed with a single cylindrical obstruction. On the other hand, Rong et al. (1999) and Rong and Horio (2001) used the Discrete Element Method (DEM) and analyzed the behavior of bubbles and particles around horizontal tubes immersed in a fluidized bed. In this work the TFM CFD model was used to investigate the influence of immersed horizontal tubes on the bubble hydrodynamics. The bubble diameter and bubble rise velocity across the bed height was estimated and compared with experimental results reported by Hull et al. (1999b).

NUMERICAL MODEL

The TFM implemented in Fluent, version 6.3, with closure equations based on the KTGF were used, see

Table 2 for the complete set of equations used in this work. The bed was 2-D, 0.2 m wide and 1 m high, with simulated staggered horizontal tubes of diameter 26 mm and horizontal and vertical pitch of 50 mm, Fig. 1. A triangular mesh of size 8 mm was used for the bed with slight refinement of up to 5 mm near the tube surfaces to capture the higher velocity gradients there. This gave a total of 7316 computational cells. The QUICK and second order upwind were used for discretizing the continuity and momentum equations respectively while time was discretized with first order implicit. The Phase-Coupled SIMPLE algorithm was used for the pressure-velocity coupling. Table 1 shows additional parameters used in this work.

Boundary and Initial Conditions

At the inlet the velocity inlet boundary condition with uniform superficial velocity of the gas phase was set. At the outlet the pressure outlet boundary condition was set for the mixture phase, in addition, the height of the free board was made long enough such that a fully developed flow was achieved (Neumann boundary condition) for the gas phase. At the wall the gas phase was assumed to have a no slip boundary condition while the particulate phase was assumed to have a partial slip boundary condition (Johnson and Jackson, 1987), Table 2. The initial conditions of the bed were set to minimum fluidization condition with all parameters at minimum fluidization as given in Table 1.

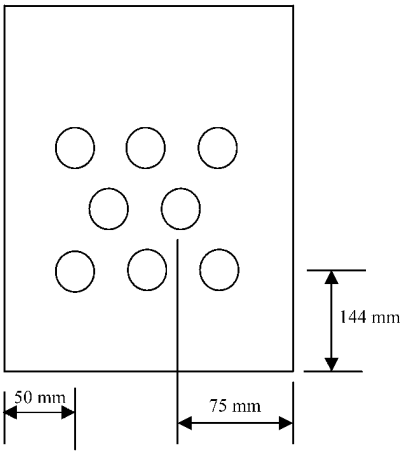

Fig. 1 Geometry of the simulated 2-D bed, from Hull et al. (1999a). Drawing not to scale.

Table 1 Physical properties and simulation parameters

	Values	Comment
Gas density	1.2 kg/m^3	
Gas viscosity	1.7894 x 10^{-5} Pa·s	
Particle density	2700 kg/m^3	Estimated
Particle diameter	0.518 mm	Hull et al. (1999b)
Minimum fluidization velocity	0.27 m/s	>>
Minimum fluidization void fraction	0.42	Estimated
Bed height at minimum fluidization	0.3 m	Hull et al. (1999a)
Restitution coefficient	0.9	Taghipour et al. (2005)
Superficial velocity	0.379 m/s	
Maximum particle packing limit	0.63	
Specularity coefficient	0.25	Johnson et al. (1990)
Time step size	5x10^{-5} s	

Method of Analysis

The simulation was run for 8 s of real flow time which took about 14 days of simulation time (this was seen to decrease significantly if no parameter was monitored during the simulation) with a single processor of a 32 GB RAM and double Quad-Core Intel® Xeon® processor X5355 work station and 2.66 GHz each. The first 3 s were neglected to reduce the start-up effect. Hence, all the results reported in this paper are averages of the last 5 s of real flow time. The bubble properties, diameter and rise velocity, were calculated from the volume fraction contour produced by Fluent, Fig. 2. There is no clear definition of bubble boundaries, however, many previous investigators defined the boundary to be 0.8 for the gas volume fraction (Hulme et al., 2005) and this definition was adopted in this investigation. The bed was divided into equal vertical segments of 0.01 m. Taking into account the bubble breakup and coalescence, the bubble properties like area and centroid were determined for each bubble in the time interval of 0.02 s. The diameter was then determined from the area assuming it is circular and the area equivalent diameter given in Eq. (1) was used if the centroid of more than one bubbles lie in one segment. The rise velocity was then calculated from the difference in the vertical coordinate of the centriod between consecutive time frames and dividing by the time interval. The diameter and velocity in each frame were finally averaged over the 5 s real flow time considered.

$$d_B = \sqrt{\frac{4A_b}{\pi}} \quad where \quad A_b = \frac{\sum A_i}{N} \tag{1}$$

Table 2 Governing and closure equations (KTGF)

Mass conservation (q=g for gas, and q=s for solid)

$$\frac{\partial(\varepsilon_q\rho_q)}{\partial t}+\nabla\cdot(\varepsilon_q\rho_q\mathbf{u}_q)=0$$

Momentum conservation

$$\frac{\partial(\varepsilon_g\rho_g\mathbf{u}_g)}{\partial t}+\nabla\cdot(\varepsilon_g\rho_g\mathbf{u}_g\mathbf{u}_g)=\nabla\cdot(\boldsymbol{\tau}_g)-\varepsilon_g\nabla P-\beta(\mathbf{u}_g-\mathbf{u}_s)+\varepsilon_g\rho_g\mathbf{g}$$

$$\frac{\partial(\varepsilon_s\rho_s\mathbf{u}_s)}{\partial t}+\nabla\cdot(\varepsilon_s\rho_s\mathbf{u}_s\mathbf{u}_s)=\nabla\cdot(\boldsymbol{\tau}_s)-\varepsilon_s\nabla P-\nabla P_s+\beta(\mathbf{u}_g-\mathbf{u}_s)+\varepsilon_s\rho_s\mathbf{g}$$

Conservation of solid fluctuating kinetic energy*

$$\frac{3}{2}\left(\frac{\partial(\varepsilon_s\rho_s\Theta)}{\partial t}+\nabla\cdot(\varepsilon_s\rho_s\mathbf{u}_s\Theta)\right)=(-P_s\mathbf{I}+\boldsymbol{\tau}_s):\nabla\mathbf{u}_s-\nabla\cdot\mathbf{q}-\gamma-J$$

*In this work the algebraic form of this equation was used (Syamlal et al., 1993).

Inter-phase momentum transfer coefficient

$$\beta=150\frac{(1-\varepsilon_g)^2}{\varepsilon_g}\frac{\mu_g}{(d_p)^2}+1.75(1-\varepsilon_g)\frac{\rho_g}{(d_p)}|\mathbf{u}_g-\mathbf{u}_s| \quad \text{for } \varepsilon_g>0.8$$

and $$\beta=\frac{3}{4}C_d\frac{\varepsilon_g(1-\varepsilon_g)}{(d_p)}\rho_g|\mathbf{u}_g-\mathbf{u}_s|\varepsilon_g^{-2.65} \quad \text{for } \varepsilon_g<0.8$$

where

$$C_d=\begin{cases}\frac{24}{\mathrm{Re}_p}\left[1+0.15(\mathrm{Re}_p)^{0.687}\right], & \mathrm{Re}_p<1000\\ 0.44, & \mathrm{Re}_p>1000\end{cases}$$

and $$\mathrm{Re}_p=\frac{\varepsilon_g\rho_g|\mathbf{u}_g-\mathbf{u}_s|d_p}{\mu_g}$$

Gas phase stress tensor

$$\tau_g=-\varepsilon_g\left[\left(\xi_g-\frac{2}{3}\mu_g\right)(\nabla\cdot\mathbf{u}_g)\mathbf{I}+\mu_g\left((\nabla\mathbf{u}_g)+(\nabla\mathbf{u}_g)^T\right)\right]$$

Solid phase shear stress tensor

$$\tau_s=-\varepsilon_s\left[\left(\xi_s-\frac{2}{3}\mu_s\right)(\nabla\cdot\mathbf{u}_s)\mathbf{I}+\mu_s\left((\nabla\mathbf{u}_s)+(\nabla\mathbf{u}_s)^T\right)\right]$$

Solid shear viscosity

$$\mu_s=\frac{4}{5}\varepsilon_s\rho_s d_p g_o(1+e)\sqrt{\frac{\Theta}{\pi}}+\frac{10}{96}\sqrt{\Theta\pi}\frac{\rho_s d_p}{(1+e)\varepsilon_s g_o}\left[1+\frac{4}{5}g_o\varepsilon_s(1+e)\right]^2$$

Radial distribution function

$$g_o=\left[1-\left(\frac{\varepsilon_s}{\varepsilon_{s,\max}}\right)^{1/3}\right]^{-1}$$

Solid pressure

$$P_s=[1+2(1+e)\varepsilon_s g_o]\varepsilon_s\rho_s\Theta$$

Solid bulk viscosity

$$\xi_s=\frac{4}{3}\varepsilon_s\rho_s d_p g_o(1+e)\sqrt{\frac{\Theta}{\pi}}$$

Frictional viscosity

$$\mu_f=\frac{p_s\sin\phi}{2\sqrt{I_{2D}}}$$

Frictional pressure

$$P_f=Fr\frac{(\varepsilon_s-\varepsilon_{s,\min})^p}{(\varepsilon_{s,\max}-\varepsilon_s)^p}$$

Wall boundary condition (Johnson and Jackson, 1987)

$$\tau_w=-\frac{\pi}{6}\sqrt{3}\phi'\frac{\varepsilon_s}{\varepsilon_{s,\max}}\rho_s g_o\sqrt{\Theta}\mathbf{u}_{slip}$$

RESULTS AND DISCUSSION

Figure 2 shows the instantaneous solid volume fraction contours. It was observed that the tubes were the main cause for bubble splitting. Small bubbles which were usually formed at the bottom of the bed rise and grew by coalescence until they reach the first row of tubes. The bubbles then spilt and further grew by coalescence until they reach the second row of tubes. This will continue until the last row of tubes which above this the bubble coalescence and form very few but large bubbles up to the top of the bed where they finally erupted. Details of the simulation results are presented in the following sections.

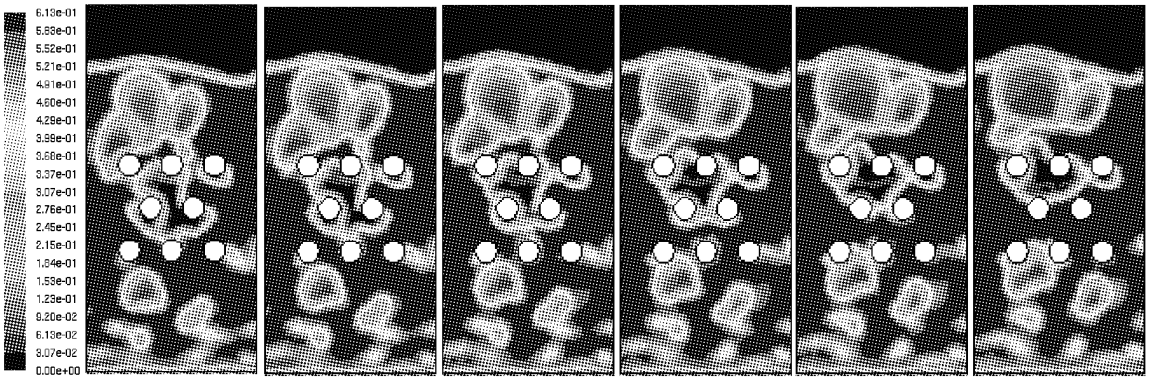

Fig. 2 Instantaneous volume fraction contours

Bed Expansion and Pressure Drop

The bed expansion height and pressure drop across the bed are two parameters examined and compared with available correlations. The time-averaged expanded bed height from the simulation was determined from the pressured drop as the pressure drop of the bed was linearly interpolated to zero at the free board pressure (Löfstrand et al., 1995). The result from this method was found to be 0.325 m which is slightly higher than the calculated value of 0.3225 m from the correlation of Löfstrand et al. (1995). The pressure drop across the bed can be estimated from Eq. (2) which gives approximately 4610 Pa while the predicted value from the simulation was 4500 Pa.

$$\frac{\Delta P}{H} = (1-\varepsilon_{mf})(\rho_s - \rho_g)g \tag{2}$$

Bubble Diameter

Figure 3 shows the time averaged bubble diameter as predicted by the simulation and the results of Hull et al. (1999b). The results agreed well. However, the simulation under predicted slightly on the lower side of the tube banks. This was seen due to the fact that, small bubbles were observed to form at the bottom of the tubes which resulted in significant change of the bubble hydrodynamics around the tube bank region. Such phenomenon was not reported in the experimental results. In Fig. 3 the instantaneous gas void fluctuations monitored at two different horizontal locations of the bed, at the bottom of a tube (a) and away from the tube (b), are plotted. It is clearly seen that a high bubbling frequency (defined to be the number of peaks per second above void fraction of 0.8) of about 5-6 Hz at the bottom of the tube were observed as compared to the 2-3 Hz away from the tube.

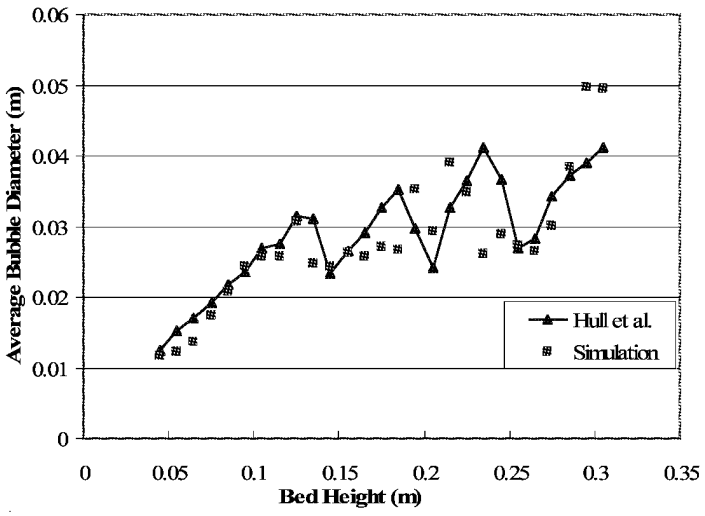

Fig. 3 Time averaged bubble diameter

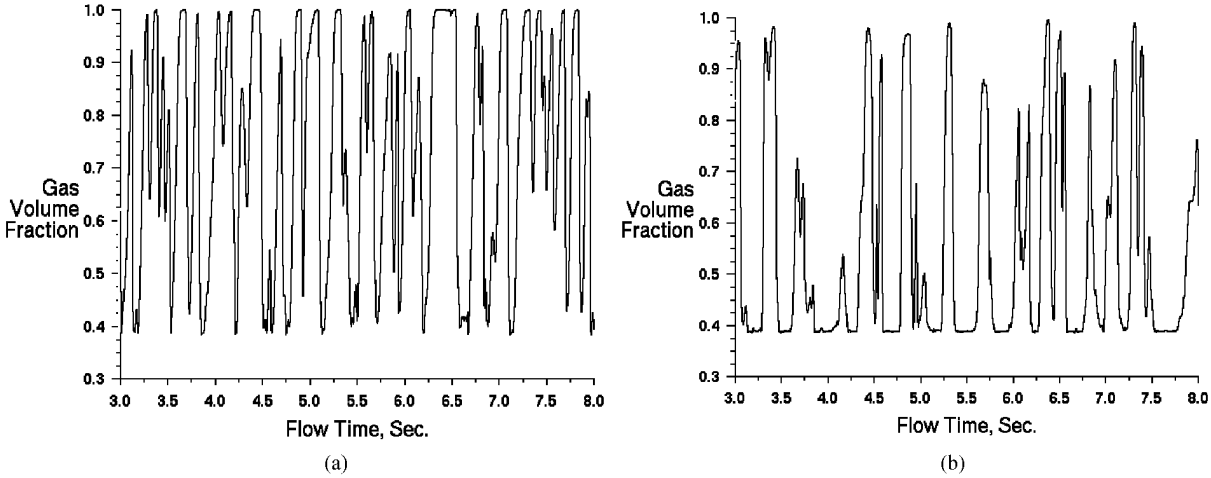

Fig. 4 Instantaneous void fluctuations at two different horizontal positions, (a) at the bottom of a tube, x=0.1 m and y=0.13 m and (b) away from a tube, x=0.125 m and y=0.13 m

The presence of gas voids or bubbles at the bottom of horizontal tubes immersed in fluidized beds have been reported by other investigators earlier: Sintai and Whitehead (1985), Bouillard et al. (1989), Pain et al. (2001), Kim et al. (2003), Schmidt and Renz (2005) to mention some. However the mechanism or source of these gas voids or bubbles is not agreeable reported. Sintai and Whitehead (1985) associated the phenomenon as a result of an increase in the vertical component of the gas velocity around the obstacles which eventually leads to local fluidization around the obstacles while Rafailidis et al. (1992) reported this to be due to a decrease in vertical component of the gas velocity. In this work the gas velocity was found to be lower at the bottom of the tubes. However, it is not clear how this leads to local bubble formation.

Bubble Rise Velocity

Figure 5 shows the time average bubble rise velocities as compared with the experimental results of Hull et al. (1999b). The results show good agreement. Similar to the bubble diameter, the rise velocities are lower at the bottom of the tubes. It was observed that the small bubbles that was formed at this surface and those resulted from the splitting were semi-stagnant. They adhere to the tube usually until they encounter and coalescence with the incoming bubble from below. Sometimes these bubbles were seen to slide along the tube and detached when they reach the tube horizontal axis (Pain et al., 2001). In their experimental work, Hull et al. (1999a and b) didn't observe such phenomenon and they explained the result of lower rise velocity above the tubes is due to the reduction in bubble size as a result of splitting. However, in this work the tubes were observed to reduce the average rise velocity by a significant amount on the lower part than on the upper part of the tubes.

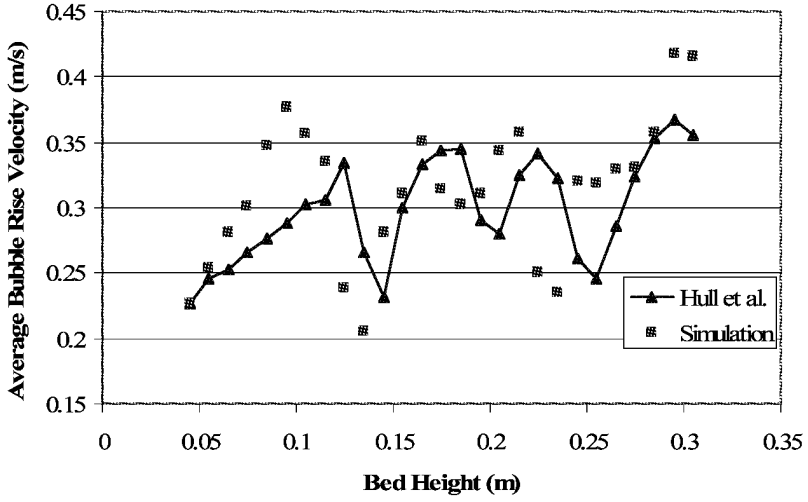

Fig. 5 Time averaged bubble rise velocity

CONCLUSIONS

Hydrodynamic simulation of dense gas-solid fluidized bed containing staggered horizontal tubes was performed. The Eulerian-Eulerian Two Fluid Model was successfully predicted the bubble characteristics, bubble average diameter and rise velocity. It was observed that the presence of horizontal tubes was the main cause of bubble break up hence reduces the average bubble diameter and rise velocity in the vicinity of the tube banks. Particularly, the numerical simulation was able to predict the bubble behavior around the tube surfaces where bubble formation was observed at the lower part of the tubes. But the mechanism that leads to the formation of bubbles at this particular position of tubes are not clearly understood. The simulation predicted lower vertical velocity of the gas phase and slightly higher pressure at this position which to some extent resembles the formation of stagnation point. However, further studies are required to verify this situation and how this leads to a local bubble formation. Moreover, the tubes were observed to slow down the bubble rise velocity where semi-stagnant bubbles were observed again at the lower part of the tubes. Further numerical simulations and comparison with experiment are required to validate the CFD TFM model for bubble characteristics of fluidized beds containing immersed tubes.

NOTATIONS

Symbols:

A_i Area of a bubble, m^2

C_d Drag coefficient

d_B Bubble diameter, m

d_p Particle diameter, m
e Coefficient of restitution
Fr Empirical material constant in frictional stress, N/m^2
g Gravitational acceleration, m/s^2
g_o Radial distribution function
H Bed height, m
$\boldsymbol{I}$ Unit tensor
N Number of bubbles in a section or segment
n Empirical constant in frictional stress
p Empirical constant in frictional stress
P Pressure, Pa
Re_p Particle Reynolds number
t Time, s
u_{mf} Minimum fluidization velocity, m/s
u Velocity, m/s
u_{sl} Particle-wall slip velocity, m/s
ΔP Bed pressure drop, Pa

Greek letters:

β Inter-phase drag coefficient, kg/m^3 • s
ε Volume fraction
ε_{mf} Voidage at minimum fluidization
ϕ Angle of internal friction
ϕ' Specularity coefficient
γ Dissipation of fluctuating energy, Pa/s
μ Shear viscosity, Pa·s
Θ Granular temperature, m^2/s^2
ρ_s Solid particle density, kg/m^3
ρ_g Gas density, kg/m^3
τ Shear stress tensor, N/m^2
τ_w Shear stress at wall, N/m^2
ξ Bulk viscosity, Pa·s

Subscripts:

B Bubble
f Frictional
g Gas phase
max Maximum
mf Minimum fluidization
min Minimum
p Particle
s Solid phase
sl Slip

ACKNOWLEDGEMENTS

The authors would like to gratefully acknowledge to Brandenburg Ministry of Higher Education, Research and Culture and Brandenburg University of Technology Cottbus for their financial support of this work.

REFERENCES

Anderson, T. B., and Jackson, R.: I & EC Fundamentals **6** (1967), pp. 527-539
Bouillard, J. X., Lyczkowski, and Gidaspow, D.: AIChE Journal **35** (1989), pp. 908-922
Gamwo, I. K., Soong, Y., and Lyczkowski, R. W.: Powder Technol. **103** (1999), pp. 117-129
Gustavsson, M., and Almstedt, A. E.: Chem. Eng. Sci. **55** (2000), pp. 857-866
Hoomans, B. P. B., Kuipers, J. A. M., Briels, W. J., and Van Swaaij, W. P. M.: Chem. Eng. Sci. **51** (1996), pp. 99-118
Hull, A. S., Chen, Z., Fritz, J. W., and Agarwal, P. K.: Powder Technol. **103** (1999a), pp. 230-242
Hull, A. S., Chen, Z., Fritz, J. W., and Agarwal, P. K.: (1999b), Influence of Horizontal tube Banks on the Bubbling and Solids Mixing Behavior of Fluidized Beds. 15th Int. FBC Conference
Hulme, I., Clavelle, E., van der Lee, L., and Kantzas, A.: Ind. Eng. Chem. Res. **44** (2005), pp. 4254-4266
Johnson, P. C. and Jackson, R.: J. Fluid Mech. **176** (1987), pp. 67-93
Johnson, P. C., Nott, P., Jackson, R.: J. Fluid Mech. **210** (1990), pp. 501-535
Kim, S. W., Ahn, J. Y., Kim, S. D., and Lee, D. H.: Int. J. Heat and Mass Transfer **46** (2003), pp. 399-409
Löfstrand, H., Almstedt, A. E., and Andersson, S.: Chem. Eng. Sci. **50** (1995), pp. 245-253
Pain, C.C., Mansoorzadeh, S., and de Oliveira, C. R. E.: Int. J. Multiphase Flow **27** (2001), pp. 527-551
Rafailidis, S. V., Clift, R., Addis, E. J., Bagshaw, W., Cheesman, D. J., and Yates, J. G.: Fluidization VII (Potter, O. E., Nicklin, D. J., eds), Engineering Foundation New York (1992), pp. 875-883
Rong, D., Mikami, T., and Horio, M.: Chem. Eng. Sci. **54** (1999), pp. 5737-5754
Rong, D., and Horio, M.: Int. J. Multiphase Flow **27** (2001), pp. 89-105
Schmidt, A. and Renz, U.: Heat Mass Transfer **41** (2005), pp. 257-270
Sitnai, O. and Whitehead, A. B.: in Fluidization edited by Davidson, J. F., Clift, R., and Harrison, D., (1986), Academic Press Inc. London
Syamlal, M., Rogers, W., O'Brien, T. J.: MFIX Documentation: Theory Guide, National Technical Informaion Service, (1993), Springfield, VA
Taghipour, F., Ellis, N., and Wong, C.: Chem. Eng. Sci., **60** (2005), pp. 6857-6867
Tsuji, Y., Kawaguchi, T., and Tanaka, T.: Powder Technol. **77** (1993), pp. 79-87
Van der Hoef, M. A., van Sint Annaland, M., Deen, N. G., and Kuipers, J. A. M.: Annu. Rev. Fluid Mech. **40** (2008), pp. 47-70
Van Wachem, B.G.M., Schouten, J. C., van den Bleek, C. M., Krishna, R., and Sinclair, J. L.: AIChE Journal **47** (2001), pp. 1035-1051
Yurong, H., Huilin, L., Qiaoqun, S., Lidan, Y., Yunhua, Z., Gidaspow, D., and Bouillard, J.: Powder Technol. **145** (2004), pp 88-105

MATHEMATICAL DESCRIPTION OF THE HYDRODYNAMIC REGIMES OF AN ASYMPTOTIC MODEL FOR TWO-PHASE FLOW ARISING IN PFBC BOILERS

S. de Vicente[1], G. Galiano[2], J. Velasco[2], J.M. Aróstegui[3]

1 Dept. of Applied Mathematics and Computational Methods, Universidad Politécnica de Madrid, Spain
2 Department of Mathematics, Universidad de Oviedo, Spain
3 Energy Department, CIEMAT, Madrid, Spain

Abstract: Two-phase systems where a dense phase of small particles is fluidized with a gas flow appear in many industrial applications, among which the fluidized bed combustors are probably the most important. A homogenization technique allows us to formulate the mathematical model in form of the compressible Navier-Stokes system type with some particularities: 1) the volumetric fraction of the dense phase (analogous to the density in the Navier-Stokes equations) may vanish, 2) the constitutive viscosity law may depend in a nonlinear form on this density, 3) the source term is nonlinear and coupled with state equations involving drag forces and hydrodynamic pressure, and 4) the state equation for the collision pressure of dense phase blows up for finite values of the density. We develop a rigorous theory for a special kind of solutions we call *stationary clouds*. Such solutions exist only under restrictions on the geometry of combustor and on the boundary conditions that usually meet in engineering applications. In return, these solutions have a stationary one-dimensional structure very simple and, from them, it is possible to reconstruct much of the dynamics of the whole system, responding to most of the practical issues of interest. Finally, we study the linear stability for the trivial solutions corresponding to uniform fluidized states injecting plane wave perturbations in our equations. Depending on the parameters of the equations of state describing the collisions between solid particles, hydrodynamic pressure, and the values of blowing boundary condition, we can draw detailed abacus separating stable regions of unstable regions where bubbles appear. Then, we use the dispersion relations of this multidimensional linearized model, combined with the stationary phase theorem, to approach the profiles and the evolution of the bubbles appearing in unstable regimes, and verify that the obtained results adjust to the observations.

Keywords: mathematical modeling, PFBC, two-phase flow, stability, bubbles

INTRODUCTION

The complete asymptotic mathematical model for a two-phase system where a dense phase of small particles is fluidized with a gas flow, can be written as a non-dimensional Navier-Stokes system (see [2], [3] and [4]):

Conservation Equations (1)

$$\left.\begin{array}{c} \partial_t \rho + div\ \mathbf{m} = 0 \\ \partial_t \mathbf{m} + \operatorname{div}\left(\frac{\mathbf{m}}{\rho} \otimes \mathbf{m}\right) + \nabla p = \frac{1}{Re} \operatorname{div}\ \bar{\tau} - \nabla p_h - \frac{1}{Fr}\,\rho\,\mathbf{e}_d \\ \rho = 0, \quad \mathbf{m} = \mathbf{0} \\ div\ \mathbf{M} = 0 \end{array}\right\} \begin{array}{l} \text{in } \Omega_+(t) \\ \\ \text{in } \Omega_0(t) \\ \text{in } \Omega \end{array} \Bigg\} \quad \forall t \in (0,T)$$

where ρ and **m** are the volume fraction, and momentum of the solid phase, p and p_h are the collision and hydrodynamic pressures, $Re>0$ and $Fr>0$ the usual non-dimensional Reynolds and Froude numbers, $\mathbf{e}_d$ the unit vector in the direction of gravity, and **M** the total momentum of both phases. The mass and momentum conservation equations (1) must be completed with the state equations for collision pressure p (describing interaction between solid particles) and hydrodynamic pressure p_h (in order to model interaction between phases), and also adequate constitutive laws for stresses τ due to the viscosity of the solid phase, and a function Φ modeling the friction between phases:

Equations of State (2)

$$\left.\begin{array}{c} \nabla p_h = -\frac{1}{Fr}\frac{\rho}{\Phi}\left(\mathbf{M} - \frac{\mathbf{m}}{\rho}\right) \\ p = p(\rho) \end{array}\right\} \quad \text{in } \Omega_+(t)$$

Constitutive Laws (3)

$$\left.\begin{array}{c} \bar{\tau} = \bar{\tau}\left(\rho, \frac{\mathbf{m}}{\rho}\right) \\ \Phi = \Phi(\rho) \end{array}\right\} \quad \text{in } \Omega_+(t)$$

It is also necessary to complete the system with initial conditions for the momentum of dense phase and for the amount of solid mass and its initial distribution:

Initial Conditions (4)

$$\left.\begin{array}{l} \rho(\mathbf{x},0)=\rho^0(\mathbf{x}) \in [0,1] \quad \text{such that} \int_\Omega \rho^0(\mathbf{x})\, d\mathbf{x} = 1 \\ \mathbf{m}(\mathbf{x},0)=\mathbf{m}^0(\mathbf{x}) \quad \text{such that } \mathbf{m}^0=\mathbf{0} \text{ in } \Omega_0(0) \end{array}\right\} \text{ in } \overline{\Omega}$$

and with adequate boundary conditions on all the boundary $\delta\Omega$ and on the "input" boundary Γ_{+0} and "exit" boundary Γ_-:

Boundary Conditions (5)

$$\left.\begin{array}{l} \mathbf{m}\cdot\nu=0 \text{ if } \mathrm{Re}=+\infty \\ \mathbf{m}=\mathbf{0} \text{ if } \mathrm{Re}\in\Re_+ \\ \text{on } \partial\Omega\times(0,T) \end{array}\right\} \qquad \begin{array}{l} \mathbf{M}\cdot\nu=-M_0 \quad \text{on } \Gamma_{+0} \\ p_h=0 \quad \text{on } \Gamma_- \end{array}$$

being ν the outer unit normal on the boundary. Finally, we must add a condition on the free boundary Γ that separates the zone where we have solid particles from the area in which there is only gas phase:

Free Boundary Condition (6)

$$\mathbf{m}\cdot\nu=0 \text{ and } \bar{\sigma}\,\nu=\mathbf{0} \quad \text{on} \quad \Gamma(t), \quad \forall t\in(0,T)$$

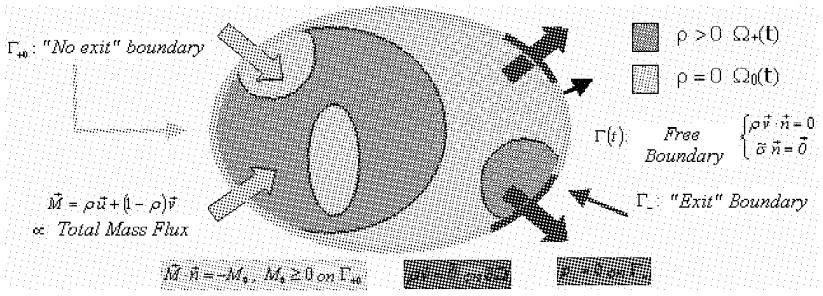

Fig. 1 Boundary Conditions

STATIONARY CLOUDS AND STATES OF UNIFORM FLUIDIZATION

Our aim is the rigorous (mathematical) study of two key aspects of the model (1) to (6). First, what we might call the *Rigorous Engineering Theory of Fluid Beds*. This engineering theory is based on the study of a particular class of simple solutions to the whole system (1) to (6), which we have called *solutions of stationary cloud kind.* From this type of particular simple solutions, anyone can rebuild the qualitative dynamics of the whole system, responding to the majority, or at least many of the practical issues of interest in engineering applications. We say that this theory is rigorous, because it gives a precise answer, obtained only from the equations of the model, to the key issue of under what conditions it is justified to consider such simple solutions, and what are its essential properties. For a summary of this theory, see [5] and [6]. We define the ***stationary clouds*** as solutions of (1) to (6) such that $\rho\geq 0$ and $\mathbf{m}=\mathbf{0}$. Such solutions do not always exist. We can prove that these engineering solutions are justified only by assuming important geometric constraints for the domain and its boundary, which meet or do much about, in most industrial designs.

The precise conditions assuring *existence of stationary clouds* are the following:

- The size of the domain (combustion chamber of PFBC boilers) is large enough: $|\Omega|>1$ .Compatibility between the domain geometry and the *blowing boundary condition* (see Fig. 2):

  $\Gamma_{+0}=\{\vec{x}\in\partial\Omega:\vec{g}\cdot\vec{n}\geq 0\}$ *There is a constant* $M\geq 0$ *such that :*

  $\Gamma_-=\{\vec{x}\in\partial\Omega:\vec{g}\cdot\vec{n}<0\}$ $\quad M_0=M_0(\vec{x})=-M\left(\vec{e}_d\cdot n(\vec{x})\right)\ \forall\vec{x}\in\Gamma_{+0}$

- An additional geometrical restriction (see Fig. 3): Ω *is connected and bounded in the directions* x_i *i=1,...,d-1, and simply connected in these directions.*

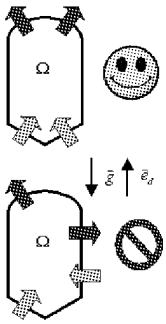

Fig.2 Necessary compatibility between the domain geometry and the blowing boundary condition

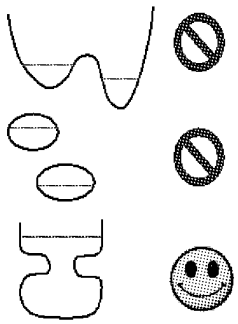

Fig. 3 Necessary properties about domain connection

In these conditions, we can proof the **existence of such stationary clouds** characterized by having one-dimensional structure in which $x=x_d$, and verifying: $\vec{M} = M\,\vec{e}_d \ \left(M \geq 0 \text{ constant}\right)$ and $\rho = \rho(x) \geq 0$ such that:

$$\frac{dp}{dx} = -\frac{\rho}{Fr}\left(1 - \frac{M}{\phi}\right) \quad when\ \rho > 0 \tag{7}$$

with the state equation p=p(ρ) increasing, the constitutive law ϕ=ϕ(ρ) decreasing, both C^1 functions, and the normalization condition: $\int_\Omega \rho\, dx = 1$ (total mass fixed).

The solutions to the non-linear problem (7) may or may not have free boundary (which separates the area with dense phase particles, or *bed*, from the area free of them, or *freeboard*), depending on the nature of the domain (combustion chamber) (bounded or unbounded) and of his size. The existence of a free boundary (and his position) depends also on the total mass of particles and on the magnitude of the boundary condition (blowing gas). In addition, we proof that the regularity of the solution depends essentially on the properties of the equation of state for the pressure of collision between solid particles. *The main result states that (7) has a unique weak solution* $\rho \in C^0(\Omega) \cap C^1(\rho > 0)$. *This solution is a classical solution* $\rho \in C^1(\Omega)$, *if and only if: (a) Or* Ω *is bounded and there is not free boundary, (b) Or* Ω *is unbounded and*

$$\lim_{\rho \to 0_+} \rho / p'(\rho) = 0 \tag{8}$$

In particular, in the very important case of a equation of state for the dense phase of the form:

$$p(\rho) = \alpha^2 \rho^{\gamma_0} L(\rho/\rho_*),\ \gamma_0 > 1,\ \text{with } \lim_{\varepsilon \to 0_+} L_\varepsilon(z) = 1,\ \lim_{\varepsilon \to 0_+} \frac{L'_\varepsilon(z)}{L_\varepsilon(z)} = 1 \ \textit{uniformly}\ \forall z \in [0,1) \tag{9}$$

The condition (8) corresponds to $1 < \gamma_0 < 2$. For $\gamma_0 \geq 2$ the global solution is only a weak solution.

Behavior of the stationary clouds: Profiles of the solutions

Especially, we have focused our attention on studying the *dependence of the position of the free boundary in function of the magnitude of the blowing boundary condition.* This allows us, for example, to design practical policies to minimize erosion problems in the reactor.

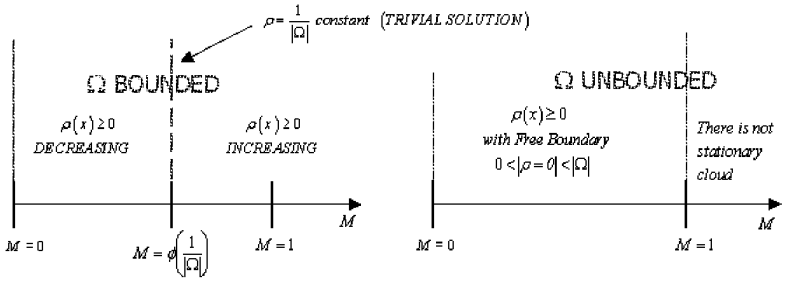

Fig. 4 Qualitative behavior in function of the boundary condition (blowing Mach M)

We can proof theorems (see [6]) about the global behavior of the profiles of solutions to the stationary clouds problem (7) (see Fig,3). More precisely, calling *h=h(M)* for the position of the free boundary which

corresponds to the *bed height* in engineering language, we can consider the following cases:

1. *Unbounded domain case (open or very large unrealistic reactor)*: In this case, there is always a free boundary so that its height *h(M)* verifies:

$$h:[0,1)\to\mathbb{R}_+ \ \textit{increasing and s.t.}\ \lim_{M\to 1_-} h(M)=+\infty$$

and *M=1* appears as the blowing boundary condition for which the fluid bed disappears (ρ=0). For this reason, *M=1* is called *flying Mach*. See Fig.5.

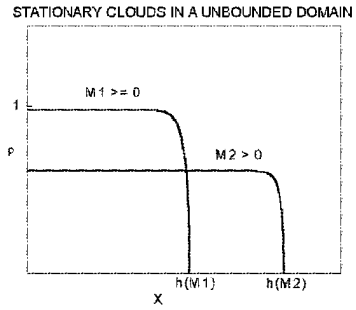

Fig.5 Stationary clouds in a unbounded domain

2. *Bounded domain. Case 1: short reactors.* In this case there is not a free boundary for the blowing boundary condition less than a *critical Mach M** verifying: $M^*>\phi\left(1/|\Omega|\right)>0$ .For *M>M**, it appears a free boundary whose position *h(M)* is bounded by the size of the reactor:

$$h:(M^*,+\infty)\to\mathbb{R}_+ \ \textit{strictly increasing s.t.}\ \lim_{M\to M^*} h(M)=0_+ \ \textit{and}\ h(M)<|\Omega|-1.$$

This case only appears if the reactor is sufficiently short, i.e. if his height *L<L**, where the *critical height* *L** is given by: $L^*=1/\phi(M^*)$.

3. *Bounded domain. Case 2: long reactors (the most usual case for PFBC boilers).* In this case there is always an initial free boundary, leaving a *free board* in the reactor. Its height grows with the blowing boundary condition up to a first critical Mach M_0 such that:

$$0<M_0<\phi\left(1/|\Omega|\right) \ \textit{and}\ h_0:[0,M_0)\to\mathbb{R}_+ \ \textit{strictly increasing and s.t.}\ \lim_{M\to M_0} h_0(M)=|\Omega|$$

For $M_0<M<M_1$, being M_1 a second critical Mach verifying $M_1>\phi\left(1/|\Omega|\right)$, the bed completely fills the reactor without free boundary. For $M>M_1$, a free boundary appears again, whose position is such that: $h_1:(M_1,+\infty)\to\mathbb{R}_+ \ \textit{strictly increasing s.t.}\ \lim_{M\to M_{1+}} h_1(M)=0_+ \ \textit{and}\ h_1(M)<|\Omega|-1$, leaving a particles free area in the bottom of the reactor.

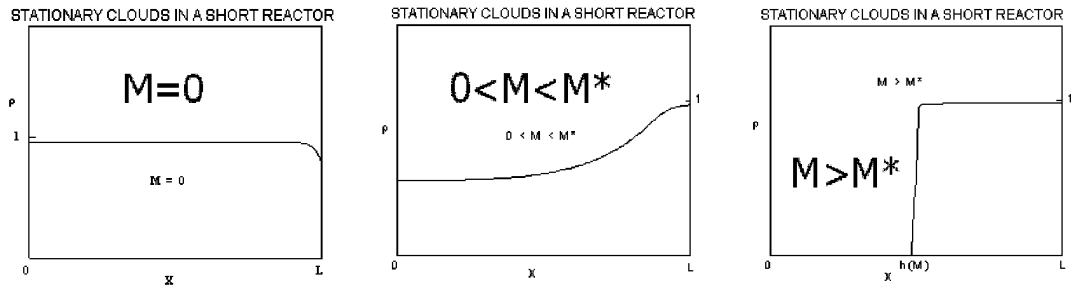

Fig. 6 Stationary clouds in a bounded and short reactor

Engineering theory of uniform fluidization states

Another key issue addressed in our study was which we have called *Engineering theory of fluidized beds*, based on *trivial solutions* of (7), which are nothing other than the uniform distributions of volume fraction of dense phase, widely used in Engineering because its simplicity. These simple distributions, are really a solution to the problem (7) only in the case of a bounded domain and for certain privileged values of the blowing boundary condition. In fact, the *states of uniform fluidization* can also be defined as a limit of the *stationary solutions* (7) when $Fr\to+\infty$. These states are only determined by the properties of the law of friction between the solid and gas phases Φ, but they not depend, however, of the equation of state for the pressure of collision between particles. Then, we can easily proof that, *in the case of an unbounded, or very large reactor*, the *states of uniform fluidization* satisfy:

$$\rho(M)=\left\{\begin{array}{ll} 1 & \textit{if } M\in[0,\phi(1)] \\ \bar{\rho}\in(0,1),\ \textit{unique solution of}\ \phi(\rho)=M & \textit{if } M\in(\phi(1),1] \\ 0 & \textit{if } M>1 \end{array}\right\};\ h(M)=\frac{1}{\rho(M)}$$

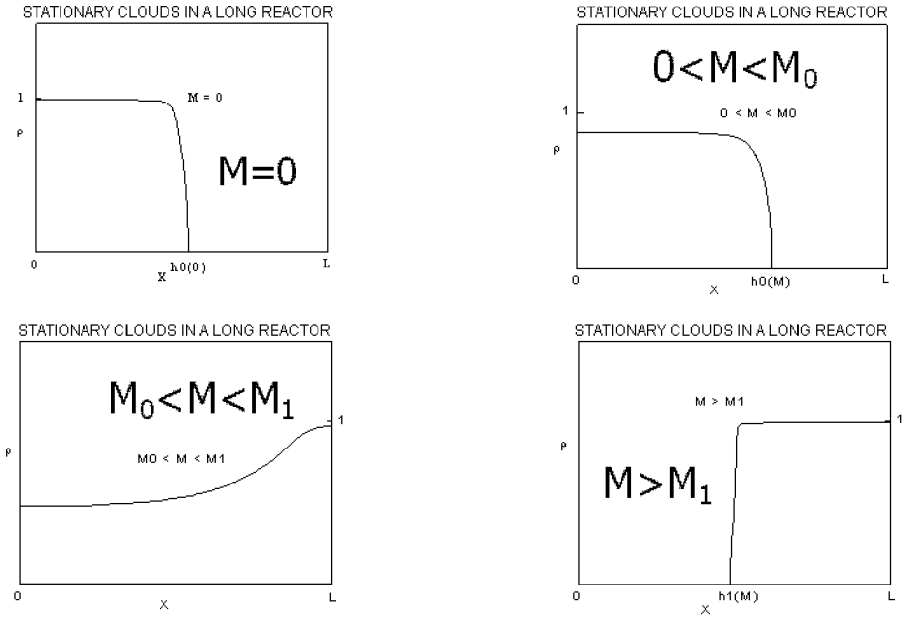

Fig. 7 Stationary clouds in a bounded and long reactor

where $M_{\_} = \phi(1)$ is known as the *Mach of minimum fluidization*. In the case of bounded domains, the theory becomes much more complex (see Fig. 8(b)).

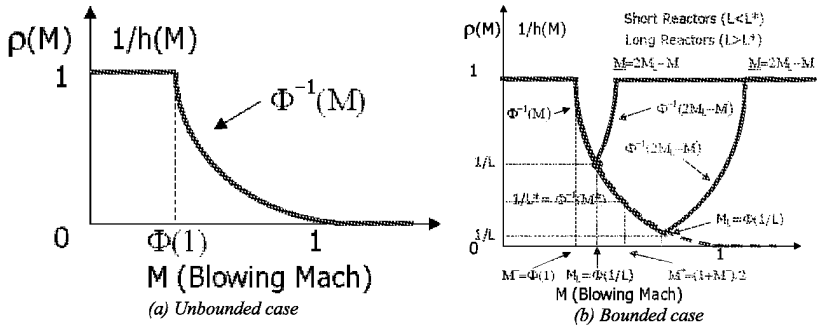

Fig. 8 Engineering theory of fluidized beds

STABILITY OF TRIVIAL SOLUTIONS AND BUBBLES

The interest of the study conducted here is to highlight that, depending mainly on the properties of the equation of state for the pressure and thus on the regularity of the *stationary clouds*, may appear regimes in which such simple solutions are linearly unstable. This question is not merely formal, since the existence of unstable regimes lies the interest of the industrial use of fluid bed systems, thus contributing to the intimate mixing of particles in the dense phase, and promoting chemical reactions to be seized. To study the *linear stability* of the *trivial solution*, we introduce small perturbations. Then, the following linear equations for small perturbations holds:

$$\left.\begin{array}{c} \partial_t(\delta\rho) + div\ (\delta \mathbf{m}) = 0 \\ \partial_t(\delta \mathbf{m}) + p'(\bar{\rho})\,\nabla(\delta\rho) = \frac{1}{\mathrm{Re}}\ \mathbf{div}\ (\delta\bar{\tau}) - \nabla(\delta p_h) - \frac{1}{Fr}\ (\delta\rho)\ \mathbf{e}_d \\ div\ (\delta \mathbf{M}) = 0 \end{array}\right\}$$

$$\nabla(\delta p_h) = -\frac{1}{Fr\ \Phi(\bar{\rho})}\left(\bar{\rho}\ (\delta \mathbf{M}) - (\delta \mathbf{m}) + \left(1 - \bar{\rho}\ \frac{\Phi'(\bar{\rho})}{\Phi(\bar{\rho})}\right)\Phi(\bar{\rho})\ (\delta\rho)\ \mathbf{e}_d\right)$$

Then, looking for solutions of plane wave kind:

$$\delta\varphi = \delta\varphi_0\ exp\, i\left(\vec{k}\cdot\vec{x} - \omega t\right)\ exp(\Omega t)\quad with\quad \left|\vec{k}\right| = 2\pi/\lambda$$

we can proof that the plane wave are linearly stable if and only if:

$$\Omega \geq 0 \Leftrightarrow M_g = -\frac{\bar{\rho}\,\phi'(\bar{\rho})}{\sqrt{p'(\bar{\rho})}} \leq 1 \Leftrightarrow M_p^2 = \left(\frac{\omega}{|\vec{k}|}\right)^2 \frac{1}{p'(\bar{\rho})} \leq 1 \tag{10}$$

being M_g and M_p the Mach number for the perturbations of the gaseous phase and of particle phase, respectively. For the particular, but important case in practice, of a state equation for collision pressure as (9) and a law of friction between both phases of the form:

$$\phi(\rho) = (1-\rho_*\,\rho)^{m+1} \quad with \quad \rho_* \in (0,1) \quad and \quad m \geq 0$$

we obtain the picture of the region where the trivial solutions are linearly stable in the plane Mach of blowing (M) versus pressure coefficient (α in (9)). As it is shown in Fig. 8, for a particular value $\gamma_0 = 3$ of the exponent of the equation of state for collision pressure between particles, we obtain a region of absolute stability when a high pressure happens. If $\gamma_0 > 3$ the absolute stability for high pressure is asymptotic. For $\gamma_0 < 3$ we also obtain a region of marginal stability for high blowing Mach (not shown in Fig. 9). Finally, we have formally proved that the mechanism by showing the instability is manifested in the formation of bubbles within the dense phase. These bubbles, or areas with very few particles, are increasing in size, and they travel through the dense phase at a constant speed given by M_p in (10). This can be shown by calculating the asymptotic form of disturbances for small values of the wavelength λ:

$$\delta\rho(\mathbf{x},t;\lambda) = \frac{1}{2\,\pi\,|\mathbf{x}|}\left(sen\ \varphi_+\ e^{\Omega_+\,t} + sen\ \varphi_-\ e^{\Omega_-\,t}\right) + O\left(\left(\frac{\lambda}{|\mathbf{x}|}\right)^2\right)$$

$$\Omega_\pm = \Omega\left(\pm\frac{2\,\pi}{\lambda}\,\frac{\mathbf{x}}{|\mathbf{x}|}\right), \quad \omega_\pm = \omega\left(\pm\frac{2\,\pi}{\lambda}\,\frac{\mathbf{x}}{|\mathbf{x}|}\right), \quad \varphi_\pm = \frac{2\,\pi}{\lambda}\,|\mathbf{x}| \mp \omega_\pm\,t$$

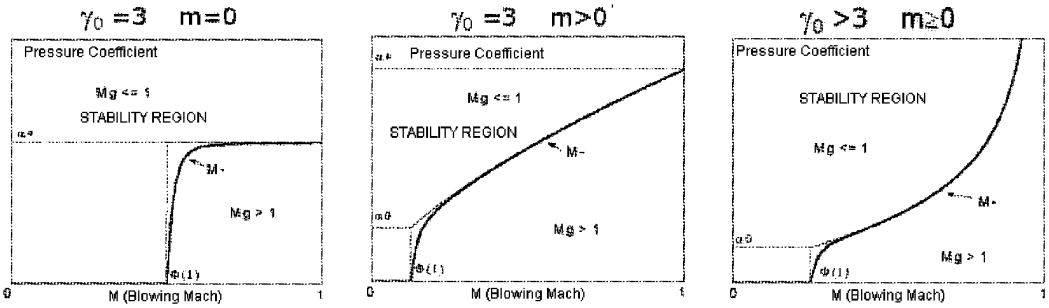

Fig. 9 Linear stability regions for trivial solutions

Then, the bubbles appears from the interaction of damping backward waves and amplified forward waves. The results obtained are substantially consistent with experimental observations described in the literature.

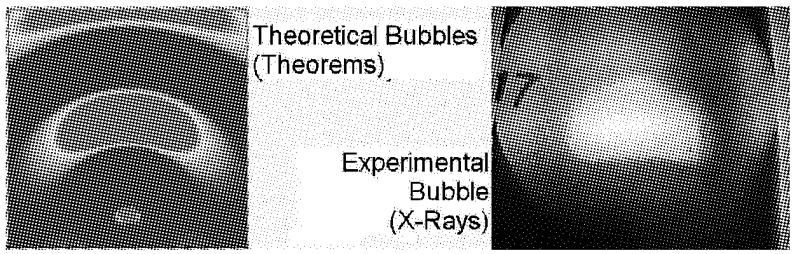

Fig. 10 Comparison between theoretical mechanism for bubbles and a experimental bubble (this last from [1])

CONCLUSIONS

From an asymptotic model of two-phase flow we have been identified and studied the stationary solutions that recover the behavior of clouds of particles in gas flows. We have derived, as a limit of these solutions, when the Froude number tends to infinity, a rigorous engineering theory about uniform fluidization states arising in both short and long reactors. Finally, we have studied the linear stability of these uniform fluidization states, showing the conditions under which bubbles are produced in the fluidized bed. These conditions depend on the equation of state of the solid phase and also on the law of friction between the two phases, but they are

viscosity independent. The analysis shows that the bubbles are generated by small perturbations whose propagation speed is higher than the speed of the collision waves between particles.

REFERENCES

[1] J. F. Davidson, D. Harrison: Fluidized particles. *Cambridge University Press.* (1963).
[2] G. Galiano, J. Velasco and S. de Vicente: A vanishing viscosity fluidized bed model. *Differential and Integral Equations,* Vol. 16, No. 4, pp. 473-498. (2003).
[3] J.A. Hernández: Estudio numérico y analítico de inestabilidades de flujos bifásicos. *Tesis Doctoral, Universidad Politécnica de Madrid* (1990).
[4] T. Luo, Z. Xin, Thong Yang: Interface behavior of compressible Navier-Stokes equations with vacuum. *SIAM J. Math. Anal.*, Vol. 31, No. 6, pp 1175-1191, (2000).
[5] A. Márquez y S. de Vicente: Contribución al Estudio de Inestabilidades Hidrodinámicas en Flujos Bifásicos. *XIV CEDYA, IV Congreso de Matemática Aplicada.* Vic, Spain. (1995).
[6] J. Velasco: Análisis de un problema de frontera libre que aparece en el modelado de flujos bifásicos. *Tesis Doctoral, Universidad de Oviedo* (2001).

COMBUSTION CHARACTERISTICS OF SEWAGE SLUDGE USING A PRESSURIZED FLUIDIZED BED INCINERATOR WITH TURBOCHARGER

T. Murakami[1], A. Kitajima[1], Y. Suzuki[1], H. Nagasawa[2], T. Yamamoto[2], T. Koseki[3], H, Hirose[3] , S. Okamoto[4]

1 Energy Technology Research Institute, National Institute of Advanced Industrial Science and Technology (AIST), 16-1, Onogawa, Tsukuba, Ibaraki 305-8569, Japan, takahiro-murakami@aist.go.jp
2 Tsukishima Kikai Co., Ltd., Tokyo, Japan
3 Sanki Engineering Co., Ltd., Kanagawa, Japan
4 Public Works Research Institute (PWRI), Tsukuba, Japan

Abstract: A new type of sewage sludge incinerator that combines a pressurized fluidized bed combustor and a turbocharger driven by flue gas was proposed. This plant has four main advantages. (1) The combustion rate can be improved since the oxygen partial pressure in the combustor is increased by the pressurization. The incinerator volume can be substantially smaller than that of an atmospheric incinerator with the same incineration capacity. Thus, the amount of supplementary fuel can be reduced because the heat loss from the incinerator can be decreased. (2) Because the maximum operating pressure is 0.3 MPa (absolute pressure), which matches the pressure required for the turbocharger, a pressure vessel is unnecessary. (3) An energy savings of more than 40% can be achieved compared with a conventional plant since the FDF and the IDF are unnecessary. (4) Because steam in the flue gas becomes the working fluid of the turbocharger, the turbocharger can generate surplus air in addition to the combustion air. The surplus air can be used in other processes, such as aeration, in sewage works. We constructed a demonstration plant (4.32 t/d scale) at a sewage works in Japan. The operation and combustion characteristics of the plant were clarified, and the design data of a commercial plant was obtained.
As a result, the steady operation exceeded 600 hours in total. Consequently, about 40 % of CO_2 emissions originating from electric power consumption and supplementary fuel is expected to be reduced annually compared with emissions from a conventional plant at an incineration capacity of 100 tons/d. CO, NO_x and N_2O emissions in the flue gas were less than half those of a conventional plant due to the effect of the pressurization. Therefore, this proposed incinerator can realize energy recovery and saving as well as a low environmental impact.
Keywords: sewage sludge, pressurized fluidized bed, turbocharger, combustion characteristics, energy recovery and saving

INTRODUCTION

Annual production of sewage sludge in Japan increased to 2.17 million tons (d.b.) in 2004. About 70% of sewage sludge is incinerated (Japan Sewage Works Association, 2007). In a typical conventional incineration plant (Fig. 1), de-watered sludge containing 80 wt% moisture is supplied to a bubbling fluidized bed combustor fueled by a supplementary fuel such as crude oil. Drying, devolatilization, and combustion take place in the combustor. Flue gas is exhausted from a stack into the atmosphere after first passing through an air preheater, a smoke-prevention preheater, a gas cooler which includes a feed water pump, a bag filter, and a scrubber. Sludge incineration consumes electric power because the process utilizes many auxiliaries. A typical incinerator with a capacity of 100 t/d, which is the average capacity in Japan, consumes 350 kW during steady operation (Sanki Engineering Co., Ltd. et al., 2008). In particular, the forced draft fan (FDF) that generates the combustion air and the induced draft fan (IDF), which exhausts the flue gas into the atmosphere, together consume at least 40 % of the total power. The higher heating value of the dry sludge is 16-21 MJ/kg. However, because the de-watered sludge contains 80 wt% moisture, the high temperature flue gas is used only for heat exchange. Additionally, the nitrogen content of the sludge is considerably higher than that of other fuels, such as coal and wood. Thus the emissions of NO_x and N_2O are anticipated to be high. The global warming potential of N_2O is 310 times that of CO_2, so the emission of N_2O is a big problem.

To reduce power consumption and to recover energy from sludge, we have proposed a new design of a fluidized bed incinerator equipped with a turbocharger (Fig. 2). The major differences between our proposed incinerator and the conventional one shown in Fig. 1 are that ours uses a pressurized combustor and that a turbocharger is used in the subsequent stage. Our plant has four main advantages (Suzuki, et al., 2006). (1) The

combustion rate can be improved because the oxygen partial pressure in the combustor is increased by the pressurization. The incinerator volume can be substantially smaller than that of an atmospheric incinerator with the same incineration capacity. Thus, the amount of supplementary fuel can be reduced because the heat loss from the incinerator can be reduced. (2) Because the maximum operating pressure is 0.3 MPa (absolute pressure), which matches the pressure required for the turbocharger, a pressure vessel is unnecessary. Therefore, the material cost of plant construction can be reduced. (3) An energy savings of more than 40% can be achieved compared with a conventional plant, and consequently CO_2 emissions originating from power generation can be reduced because the FDF and the IDF are unnecessary. (4) Because steam in the flue gas becomes the working fluid of the turbocharger, the turbocharger can generate surplus air in addition to the combustion air. The surplus air can be used in other processes, such as aeration, in sewage works. This new design positively utilizes the sludge moisture, which until now has been considered negatively. Therefore, our proposed design will not only save energy but also generate energy.

A demonstration plant (4.32 t/d scale) at a sewage works in Oshamanbe Cho in Hokkaido. The objectives of this work were to obtain the design data for a commercial plant and to compare our proposed plant and a conventional one using the experimental results. In this report, we describe the operation and emission characteristics of this plant.

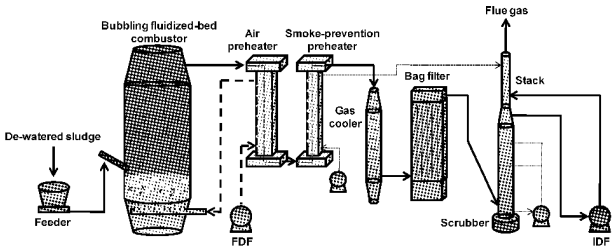

Fig. 1 Schematic diagram of a conventional incineration plant, which is equipped with an atmospheric bubbling fluidized bed combustor

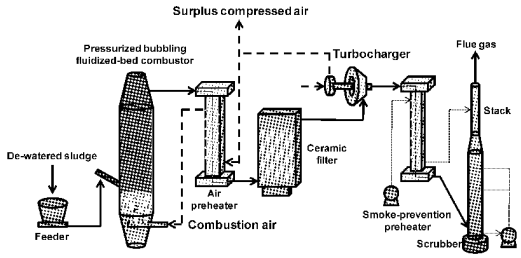

Fig. 2 Schematic diagram of the proposed plant, which is equipped with a pressurized bubbling fluidized bed combustor coupled with a turbocharger

EXPERIMENTAL

The constructed demonstration plant (Fig. 3) consisted of a fuel feeder, a pressurized bubbling fluidized bed combustor, an air preheater, a ceramic filter, a turbocharger, and a stack. The combustor was 700 mm in internal diameter and 9200 mm in height. Silica sand was used as the bed material, and the mean diameter was about 550 μm. The fluidized bed height during operation was about 950 mm. The turbocharger had been designed and manufactured for the use with a diesel engine on a motor truck. The fuel properties are listed in Table 1. The as-received sludge moisture content was 87.0 wt%, and the nitrogen content on dry basis was 7.50 wt%; these values are considerably higher than those of the other solid fuels.

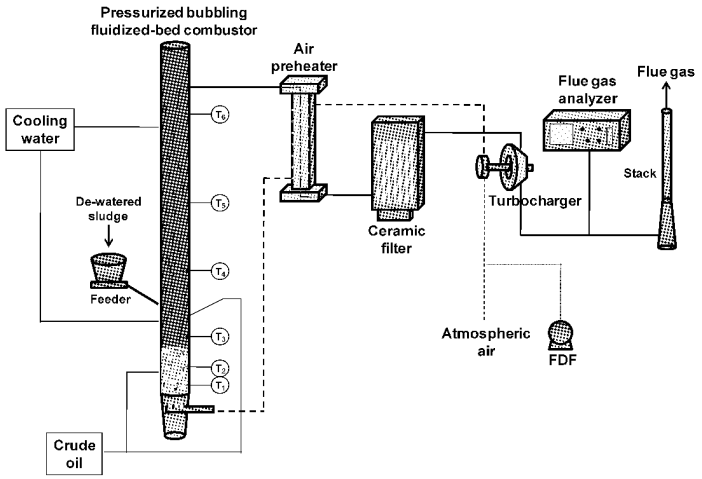

Fig. 3 Schematic diagram of the demonstration plant, T in this figure shows a thermocouple

During the start-up, the combustor temperature was increased by supplying the combustor with crude oil. During the start-up period, the turbocharger was driven by air from FDF. When the inlet gas temperature of the turbocharger exceeded 623 K, the FDF was stopped, and the system simultaneously became self-sustaining;

that is, all the combustion air was generated by the turbocharger driven only by the flue gas. De-watered sludge was continuously supplied through the fuel feeder at 2100 mm when the bed temperature exceeded 1073 K (Nagasawa, et al., 2008).

Table 1 Sewage sludge properties

Moisture [wt%]		87.0
Ignition loss [dry, wt%]		85.0
Ultimate analysis [dry, wt%]	C	43.7
	H	6.84
	N	7.50
	S	0.96
	O	26.1
Higher heating value [MJ/kg (d.b.)]		20.1

The sludge feeding rate was 180-190 kg/h. The mean combustor temperature was 1019-1075 K in the bed and 1138-1205 K in the freeboard. The absolute combustor pressure was about 0.2 MPa. The air ratio was about 1.60 based on the oxygen concentration in the flue gas. The U_o/U_{mf} ratio was about 6.0. The O_2, CO, CO_2, and NO_x concentrations in the flue gas were analyzed with continuous gas analyzers (IR400 Yokogawa Elec. Corp., Tokyo, Japan; VA-3000 HORIBA, Ltd., Kyoto, Japan), and N_2O concentration was measured with a gas chromatograph (CP-4900 Varian Inc., California, U.S.A.). Gas samples were extracted at the stage subsequent to the turbocharger. Most data were recorded at 1-min intervals by a logger, but data for N_2O were taken only every 10 min.

RESULTS AND DISCUSSION

Operation characteristics

The fuel feeding rate, combustor temperature (in the freeboard and in the bed), pressure, inlet air flow rate, and flue gas flow rate were steady throughout 5 hours of continuous operation (Fig. 4). The steady operation exceeded 600 hours in total. However, only about 70% of the inlet air flow rate for the combustor could be supplied by the turbocharger driven by flue gas; the other 30% was supplied by the

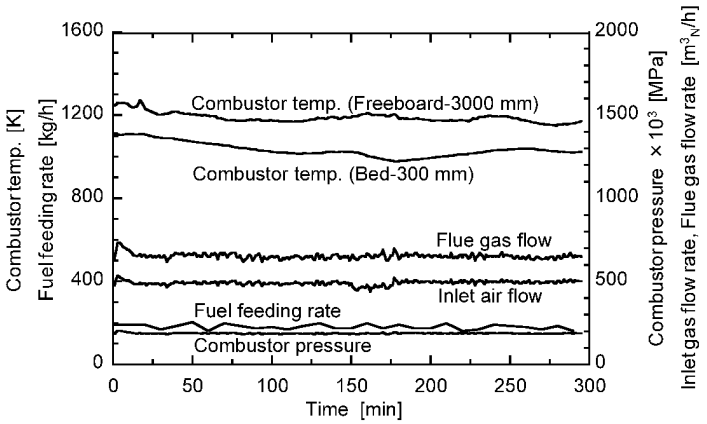

Fig. 4 Typical change of operation parameters with time during a continuous combustion test in the demonstration plant

FDF. The flow rate of compressed air from the turbocharger was less than that of specification because of low flue gas temperature at the inlet of turbocharger. The inlet gas temperature of the turbocharger was only 651 K because the heat loss from each auxiliary was much greater than 10%.

The efficiency of turbocharger is expected to be improved by scale-up because inlet temperature is expected to be higher than that of small-scale unit. The heat loss from each auxiliary at a commercial plant (100 t/d scale) is less than 5.0% (Sanki Engineering Co., Ltd. et al., 2008). According to the design specifications of the turbocharger, if the inlet gas temperature can be maintained at 873 K, the turbocharger can generate not only enough air for sludge combustion but also surplus compressed air.

Flue gas characteristics

Because N_2O emission in conventional incinerators is a big problem, the flue gas characteristics of our plant were elucidated. Figure 5 shows the relationship between the CO, NO_x, and N_2O emissions and the O_2 concentration in the flue gas. CO emission increased slightly with decreasing O_2 concentration, and low CO emission was maintained under all experimental conditions. The combustion rate was improved by the increase in the combustor oxygen partial pressure due to the pressurization. NO_x emissions tended to increase with decreasing O_2 concentration. This tendency, which was also reported for atmospheric bubbling fluidized bed combustor of wet sludge (Sanger et al., 2001), is opposite to the trend of other fuels such as coal, wood, and dry sludge (Pels et al., 1995, Leckner, 1998, and Sanger at al., 2001). In addition, these emissions were lower than that observed for coal combustion (Leckner et al., 2004 Svobada et al., 2004 and Atimtay et al., 2008). The moisture content in the sludge was so high that the steam partial pressure was also high. In addition, pressurization facilitates the generation of O and OH radicals in the reactive area of the combustor, and these radicals inhibit NO formation reaction (Shoji et al., 2005). N_2O emission changed little even when the O_2 concentration changed substantially. The dependence of N_2O emission on freeboard temperature in an atmospheric combustor has been reported (Sanger et al., 2001). In our study, N_2O emission decreased with increasing freeboard temperature (Fig. 6). Therefore, N_2O emission can be arranged by the temperature when de-watered sludge is burned under elevated pressure conditions.

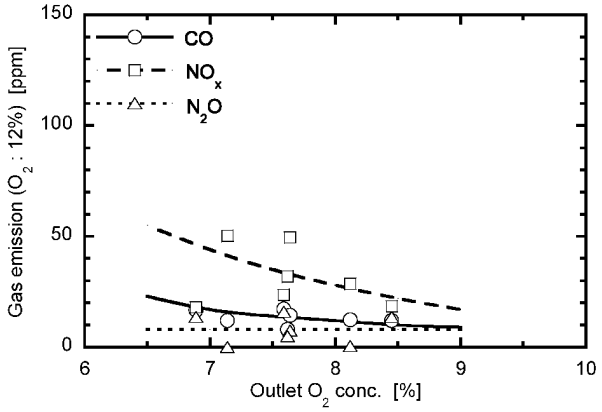

Fig. 5 Relationship between CO, NO_x, and N_2O emissions and O_2 concentration in the flue gas

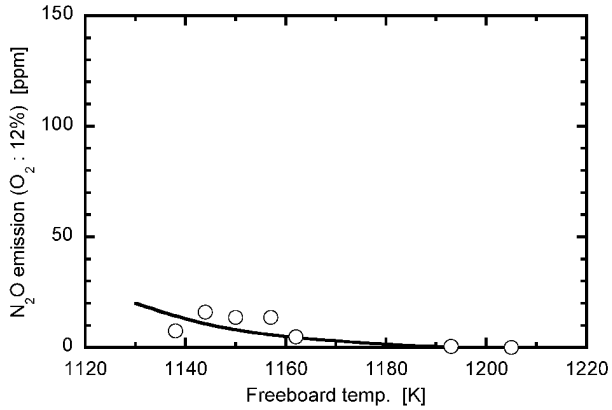

Fig. 6 Dependence of N_2O emission on freeboard temperature

Comparison of the proposed plant and a conventional plant

CO_2 emissions and the cost of the proposed plant and a conventional plant were compared at an incineration capacity of 100 t/d. Because two fans and a feed water pump can be omitted in the pressurized plant, electric power consumption is reduced by about 50% (from 350 to 180 kW) (Table 2). Operation at 0.3 MPa can permit reduction of the combustor volume by 1/3 in comparison with a conventional combustor, which operates at 0.1 MPa. This volume reduction led to a reduction in the combustor air requirements for the same incineration capacity. Thus, heat loss is greatly reduced, and the amount of supplementary fuel is reduced by about 25% (from 54 to 40 L/h). CO_2 emissions originating from electric power consumption and supplementary fuel were calculated using CO_2 emission indexes of 0.555 t-CO_2/MWh for electric power and 2.71 kg-CO_2/L for crude oil (Ministry of the Environment, 2007) (Table 2). The calculation indicated that CO_2 emissions can be reduced by about 1000 tons per year per commercial plant over 300 days of operation, which

corresponds to an approximately 40% reduction over a conventional plant. In addition, the cost of fuel and electricity for our plant would be 23 million yen less than that of the conventional plant (Table 2) (We used values of 12 yen/kWh for electric power and 80 yen/L for crude oil to do these calculations (Sanki Engineering Co., Ltd. et al., 2008).).

The N_2O emission factor, which is the amount of N_2O emitted from 1 ton of de-watered sludge and used the emission factor at 1123 K (mean freeboard temperature) (Japan Institute of Wastewater Engineering Technology, 2007), of the proposed plant was less than half of that of the conventional plant (Table 2).

Table 2 Comparison of parameters for the proposed and conventional plants

	Conventional	**Proposed**
Electric power consumption by the auxiliaries [kW]	350	180
CO_2 emissions [ton-CO_2/year]		
Electric power consumption	1399	714
Supplementary fuel	1054	780
Fuel and electric costs [million yen/year]		
Electric power consumption	30.2	15.6
Supplementary fuel	31.1	23.0
N_2O emission factor [g-N_2O/t-de-watered sludge]	645	280

This difference in N_2O emission factor was elucidated by considering the temperature distributions in the conventional combustor and the proposed combustor. Figure 7 compares the temperature profiles in the two combustors with same scale (Sanki Engineering Co., Ltd. et al., 2008). The temperature in the sand bed where drying and pyrolysis of the fuel occurred, was the lowest in both the combustors. However, in the freeboard region temperature profiles were significantly different. In the conventional combustor, temperature rises slowly with combustor height and the highest temperature was reached at about 4500 mm from the distributor suggesting that the pyrolysis gases burned in the whole freeboard. On the other hand, in the proposed combustor, temperature rose sharply and the highest temperature was reached at around 3000 mm and then decreasing to nearly same level as that in the conventional plant at 4500 mm. This suggests that pyrolysis gases in the proposed plant were burned in a much shorter region generating much higher localized temperatures than that in the conventional plant. N_2O thus was decomposed in this localized high temperature zone leading to decrease in emission factor. This phenomenon was verified qualitatively by simulating the effect of pressure on the temperature profiles using a simulation package (CHEMKIN Ver. 3.7). The combustion reaction equations available from GRI-Mech site (http://www.me.berkeley.edu/gri_mech/) were used for calculation. The scale of the combustor was the same as that of the demonstration plant. It was assumed that heat loss was zero in the combustor. Figure 8 shows the simulated temperature profiles in the combustor at different pressures. With increasing pressure, the temperature rises sharply in narrow zone. The height at which highest temperature was reached decreased with increasing pressure. In a future study, we plan to make a quantitative simulation by considering the heat loss in the combustor.

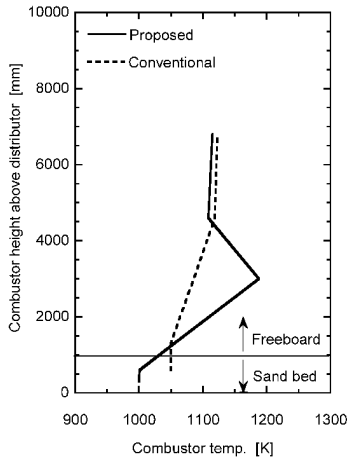

Fig. 7 Comparison of temperature distribution in the combustor between the proposed and conventional plants

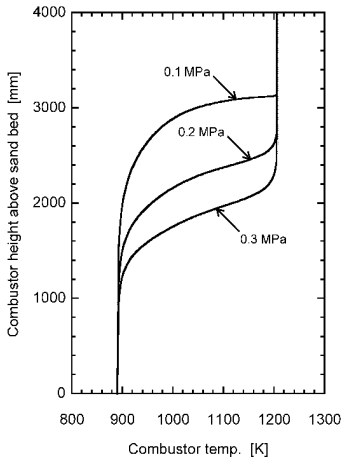

Fig. 8 Effect of pressure on pyrolysis gas combustion in the freeboard calculated by using simulation package

CONCLUSIONS

The operation and combustion characteristics of sludge were clarified for a new type of incineration plant consisting of a pressurized fluidized bed combustor coupled with a turbocharger. Following main conclusions were drawn from the experimental results:

The steady operation exceeded 600 hours in total. Because the FDF, the IDF, and the feed water pump can be eliminated in the proposed plant at an incineration capacity of 100 t/d, an energy savings of approximately 50 % can be achieved compared with a conventional plant.

In our plant, drying and pyrolysis of the fuel occurred mainly in the bed, and the pyrolysis gas burned in bottom zone of the freeboard.

N_2O emission could be controlled by the freeboard temperature in spite of the high nitrogen content of the fuel.

The N_2O emission of the proposed plant was less than half of that of the conventional plant. It is thought that N_2O was decomposed at a local high temperature zone in the freeboard. This phenomenon was verified qualitatively by investigating the chemical reaction rates.

The proposed fluidized bed incinerator with the turbocharger can achieve not only energy recovery but also a low environmental impact.

NOTATIONS

U_o superficial gas velocity, m/s

U_{mf} minimized fluidized velocity, m/s

ACKNOWLEDGEMENTS

This work was conducted during a research program financed by The New Energy and Industrial Technology Development Organization (NEDO), Japan, on developing a technology of high efficiency conversion of biomass energy.

REFERENCES

Atimtay, A. T. and Kaynak, B.: Fuel Proc. Tech. **89** (2008), pp.183-197.
Japan Institute of Wastewater Engineering Technology, Global Warming and Inventory, 2007 [in Japanese].
Japan Sewage Works Association, Investigation report for the current status of the sludge treatment in 2004, (2007) [in Japanese].
Leckner, B.: Prog. Energy Combust. Sci. **24** (1998), pp.31-61.
Leckner, B., Amand, L. E., Lucke, K. and Werther, J.: Fuel **83** (2004), pp.477-486.
Nagasawa, H., Kihara, H., Ochi, S. and Suzuki, Y.: Circulating Fluidized Bed Tech. 9, Germany, (2008), paper number 09_05.
Ministry of the Environment, Guide Line for Calculation Method of Total Emissions of Greenhouse Gas, (2007), pp.1-71 [in Japanese].
Pels, J. R., Wojtowicz, M. A., Kapteijn, F. and Moulijn, J. A.: Energy & Fuels **9** (1995), pp.743-752.
Sanger, M., Werther, J. and Ogada, T.: Fuel **80** (2001), pp.167-177.
Sanki Engineering Co., Ltd., Tsukishima Kikai Co., Ltd., PWRI, 2005-2007 NEDO report for developing a technology of high efficiency conversion of biomass energy, (2008) [in Japanese].
Shoji, M., Yamamoto, T., Tanno, S, Aoki, H. and Miura, T: Energy **30** (2005), pp.337-345.
Suzuki, Y., Ochi, S., Terakoshi, K. and Iwai, Y.: 19th Int. Conf. on FBC, Austria, (2006), paper number 48.
Svoboda, K. and Pohorely, M.: Fuel **83** (2004), pp.1095-1103.

NUMERICAL SIMULATION ON HYDRODYNAMICS AND COMBUSTION IN A CIRCULATING FLUIDIZED BED UNDER O_2/CO_2 AND AIR ATMOSPHERES

W. Zhou, C. S. Zhao, L. B. Duan, C. R. Qu, J. Y. Lu, X. P. Chen

School of Energy and Environment, Southeast University, Nanjing, 210096, China

Abstract: Oxy-fuel circulating fluidized bed (CFB) combustion technology is in the stage of initial development for carbon capture and storage (CCS). Numerical simulation is helpful to better understanding the combustion process and will be significant for CFB scale-up. In this paper, a computational fluid dynamics (CFD) model was employed to simulate the hydrodynamics of gas-solid flow in a CFB riser based on the Eulerian-Granular multiphase model. The cold model predicted the main features of the complex gas-solid flow, including the cluster formation of the solid phase along the walls, the flow structure of up-flow in the core and downward flow in the annular region. Furthermore, coal devolatilization, char combustion and heat transfer were considered by coupling semi-empirical sub-models with CFD model to establish a comprehensive model. The gas compositions and temperature profiles were predicted and the outflow gas fractions are validated with the experimental data in air combustion. With the experimentally validated model being applied, the concentration and temperature distributions in O_2/CO_2 combustion were predicted. The model is useful for the further development of a comprehensive model including more sub-models, such as pollutant emissions, and better understanding the combustion process in furnace.

Key words: CFD comprehensive model; multiphase flow; combustion; heat transfer; O_2/CO_2 combustion

INTRODUCTION

CFB combustion technology is the most commercial clean coal combustion technology, and becomes one of the most important developing directions for coal-fired boiler (Basu, 1999). Oxy-fuel combustion of fossil fuel is one of the most promising methods to produce a stream of concentrated CO_2 ready for sequestration or enhanced oil recovery (Buhre et al., 2005). Combining the two will extend both their advantages (Czakiert et al., 2006). The evolution of oxy-fuel CFB combustion is in the initial stage.

Numerical simulation is helpful to better understanding the combustion process and will be significant for CFB scale-up. The Two-Fluid continuum model (TFM) using the kinetic theory of granular flow (KTGF) shows its advantages in simulating hydrodynamics of gas-solid flow in CFB riser, due to less CPU and memory resource requirements than trajectory model (Benyahia et al. 2007; Schmidt et al. 2000; Mathiesen et al. 2000). This model has been successfully used to predict and validate lots of flow phenomena in the gas-solid systems, e.g. Almuttahar et al. (2008) simulated the hydrodynamics of gas-solid flow in a circulating fluidized bed (CFB) riser at various fluidization conditions with this model and predicted the main features. Yu et al. (2007) and Wang et al. (2008) used KTGF to simulate coal gasification in a bubbling fluidized bed gasifier, in the two-dimensional and three-dimensional numerical model, respectively. But numerical simulations about CFB combustion using KTGF are rarely reported, especially in O_2/CO_2 mixture.

In this study, a CFD model was employed to simulate the hydrodynamics of gas-solid flow in a CFB riser by using KTGF, coupled with heat transfer and chemical reaction sub-models. Gas-solid flow patterns, gas velocities, particle velocities, composition profiles of gas product and other important characteristics in a circulating fluidized bed coal combustor were simulated. Experimental data in air combustion were achieved to validate the model, and O_2/CO_2 combustion phenomena were predicted.

EXPERIMENTAL

The multifunctional circulating fluidized bed combustor (MFCBFC) experiment system was designed and built for studying the O_2/CO_2 combustion characteristics, as shown in Fig. 1. The ultimate and proximate analysis of experimental coal is shown in Tab. 1. The whole facility consists of the CFB combustor, gas supply system, coal feeding system, primary-air preheating system, back end ductwork, and sampling and measurement system. The combustor includes the riser, the high temperature insulated vortex cyclone, the down comer and the non-mechanical loop seal. The combustor is made of refractory stainless steel 2520. Concentrations of flue gas components were monitored on line with VARIO plus flue gas analyzer.

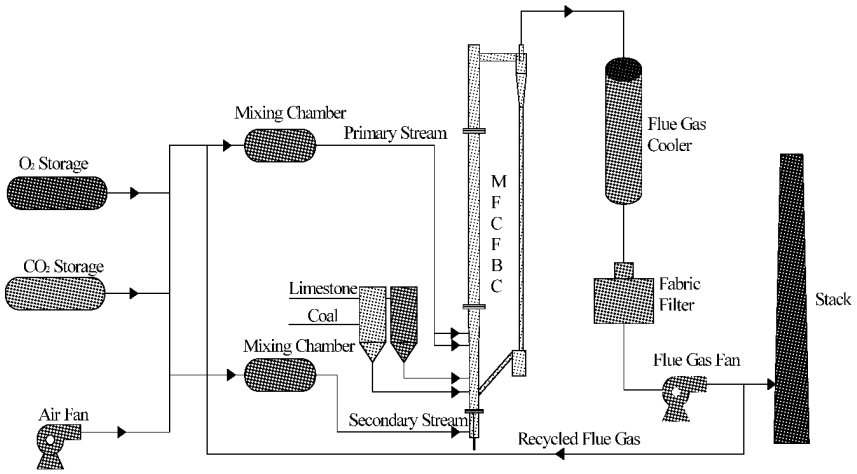

Fig. 1 Multifunction CFBC Experiment system

Table 1 Ultimate and proximate analysis of Xuzhou bituminous coal

Sample	Ultimate analysis/ wt %					Proximate analysis/ wt %			
	Cad	Had	Oad	Nad	Sad	Mad	Aad	Vad	Cfix
Xuzhou coal	58.97	3.65	7.30	0.67	1.76	2.10	25.55	25.02	47.33

MATHEMATICAL MODEL

Main assumptions on coal CFB combustion

In order to decrease the impact of the strong nonlinear characteristic of the model and ensure the good convergence and acceptable computational time, the gas-solid hydrodynamic and coal combustion models are simplified as follows: (1) Only the riser section of the CFB combustor is taken into consideration. It is assumed as two-dimensional. (2) Particle is isothermal and the mean diameter is assumed as 0.5mm. Particles are assumed inelastic, smooth and monodispersed spheres (Yu et al. 2007). (3) Small interaction forces such as lift force, thermophoretic force, Brownian force and virtual mass force are neglected. Energy transfer due to pressure stress work and viscous dissipation are not considered.

Governing equations

A set of the mass, momentum and energy conservation equations is solved for each phase, and species conservation equations are solved for every species. These equations can be found in the commercial CFD code Fluent 6.3 help documents in detail.

Chemical reactions

As part of the comprehensive model, the complicated processes of chemical reactions are simulated and set as the source term of species transport equations when the reactants are consumed and the products are created. The heat exchanged between phases and released from chemical reactions is taken into account by energy equations. The solid phase consists of raw coal, char and ash, and gas phase consists of O_2, CO_2, CH_4, H_2O and N_2 (no N_2 in O_2/CO_2). The following chemical processes are introduced in coal combustion:

(a) Raw coal devolatilization is modeled by the reaction:

$$1\,\text{kg rawcoal} \rightarrow Y_C\,\text{kg char} + Y_V\,\text{kg volatile} + (1 - Y_C - Y_V)\,\text{kg ash} \quad (1)$$

where volatile matter consists of CO_2, H_2O and CH_4 for the sake of simplification and the fraction compositions are determined on the basis of proximate and elemental analysis of experimental coal (shown in Table 1). In the present model, reactions related with sulfur or nitrogen are not taken into account for their little amount, and they are considered passing directly to ash, but they are expected to be considered in the future work. The reaction rate of (1) is:

$$r_d = A_d \exp(-E_d / RT_p) C_{rawc} \quad (2)$$

where R is the universal gas constant; A_d and E_d are obtained from literature such as Eaton et al. (1999), Wang et al. (2008) and William et al. (2003).

(b) For homogeneous volatile combustion:

$$CH_4 + 2O_2 \rightarrow CO_2 + 2H_2O \quad (3)$$

both chemical reactions and turbulent flow effect are considered and the finite-rate/Eddy-dissipation model is taken which calculates both the Arrhenius and Eddy-dissipation (Spalding 1970) reaction rates. The minimum of these two rates is taken as the net reaction rate.

(c) The char is consumed by heterogeneous combustion reaction. It can be simplified by

$$C+O_2 \rightarrow CO_2 \quad (4)$$

And the combustion rate is expressed as

$$r_c = 6 \bullet V_c k_c / d_p \cdot C_{O_2} \quad (5)$$

where k_c is rate constant computed by Arrhenius reaction rate (Smith, 1982; Jeffery, 2006).

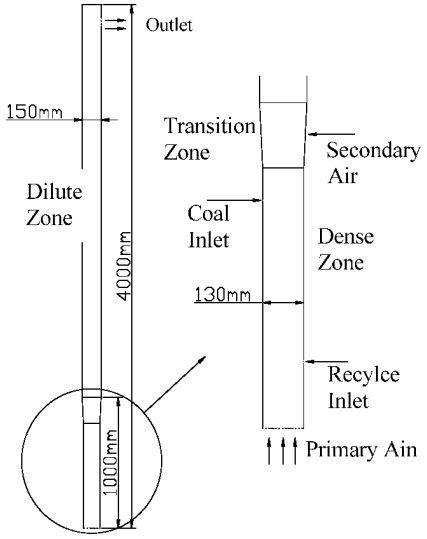

Fig. 2 Sketch of simulated CFB riser

Numerical considerations

As shown in Fig.2, the calculation domain is divided into three zones (dense, transition and dilute zones). The primary air or O_2/CO_2 mixture flows into the bottom of the CFB riser at uniform velocity. The secondary air injection is located at 0.9m above the inlet of the primary air on the right side of the riser. Solids are fluidized and both gas and solid phases are allowed to outflow the riser through the top outlet on the right side of the riser. At the same side, a recycle inlet is adopted to simulate the circulating of gas and solid. These boundaries are set to be velocity inlets and pressure outlet and the parameters of these boundary conditions are listed in Table 2.

Table 2 Parameters used in simulations

Parameters	Value	Parameters	Value
Particle density	2000 kg/m^3	Outside heat transfer coefficient	30W/m^{2}K
Particle diameter	0.5 mm	Coal feed rate	80kg/h
P-P restitution coefficient	0.9	Excess air coefficient	1.2
W-P restitution coefficient	0.95	Primary air ratio	0.6
Specularity coefficient	0	Secondary air ratio	0.3
Outlet pressure	-50Pa	Coal injecting air ratio	0.05
Ambient temperature	298K	Solid recycle air ratio	0.05
Inlet gas temperature	298K	O_2/N_2 volume fraction	21/79
Recycled gas and solid temperature	700K	O_2/CO_2 volume fraction	21/79

The bed was initially filled with particles with static height of 0.4m, where the volume fraction of solids was patched as 0.55. The maximum particle packing was limited to 0.63. The no-slip wall condition was used for the gas phase and free slip boundary condition for solid phase. 5mm×5mm grid (30×800 control volumes in all) was applied. When the grid increased to 50,000 (50×1000), the modeling results did not change significantly, indicating mesh independent results was reasonably achieved with mesh equal or greater than 30 ×800. The time step was set as 1×10^{-4}. The simulation was conducted for 35s and the time-averaged distributions of flow variables were computed for the period of 15s-35s.

RESULTS AND DISCUSSION

Flow characteristics under cold condition

Fig.3 displays the simulated axial profile of time-averaged pressure under cold circulating fluidized condition with only the primary air. It presents a typical exponential decay distribution proposed by Kunii & Levenspiel (2000). Radial profiles of time-averaged solid volume fraction, solid velocity and gas velocity at three different height levels are shown in Fig.4-6, respectively. H=400mm, H=2000mm and H=3850mm are located at the middle of dense zone, the middle of dilute zone and the outlet height, respectively. In this

operating condition, the clusters of particles accumulate near the wall until they become sufficiently heavy that they could not be carried by the gas, forming a core-annular flow structure with a dilute rising core and a dense descending annular region. The maximum axial velocity is detected in the core for both solid and gas in the most region of the riser. While at the outlet level, higher gas and solid velocities on the right side are displayed, which reveals the impact of outlet geometry. In general, those figures show that the model is capable of predicting the nearly axisymmetrical flow patterns for the case, despite the unsymmetrical configuration of the outlet geometry (Almuttahar et al. 2008).

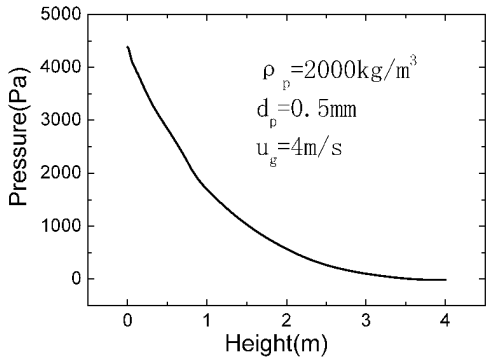

Fig. 3 Axial profile of time-averaged pressure

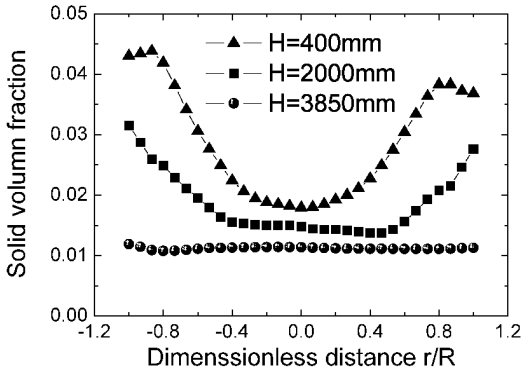

Fig. 4 Radial profiles of time-averaged solid volume fraction

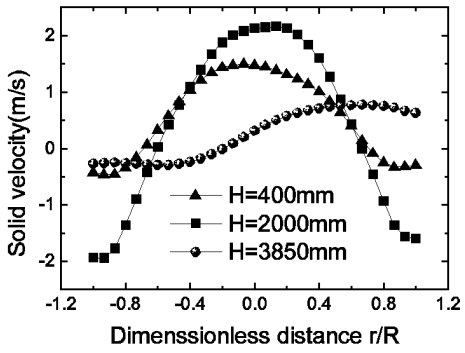

Fig. 5 Radial profiles time-averaged solid velocity

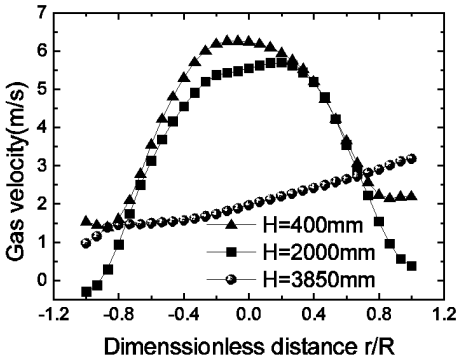

Fig. 6 Radial profiles of time-averaged gas velocity

Profiles under air combustion condition

To verify the validity of the present developed model on combustion, comparisons of the predicted flue gas compositions with the experimental data are shown in Fig. 7, where the form of area-averaged molar fraction is adopted. The results show a good agreement of these main gas phase components with experiments. Underestimated O_2 concentration and overestimated CO_2 concentration are predicted due to ignoring incomplete combustion loss of chars in ash. The maximum error is less than 16%.

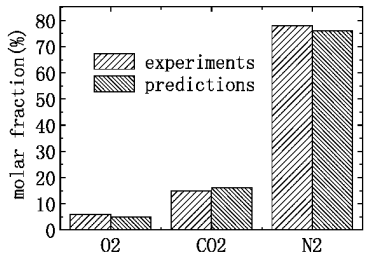

Fig. 7 Comparisons between predictions and experimental data

Contours of simulated distributions for gas compositions in the form of molar fraction at a typical moment of steady state are shown in Fig. 8. As observed from Fig. 8, the concentration of O_2 decreases along the height of the combustor with a sudden increase near the secondary air inlet, while CO_2 shows the opposite tendency. The very high CH_4 concentration appears near the coal feeding point due to the devolatilization and then CH_4 drops down immediately because of combustion reaction. The right figure of contours reveals a relatively uniform gas temperature in this CFB combustor, with the maximum difference of 200K. It implies that the present 2D numerical simulations are reasonable and the validity of the present model is verified.

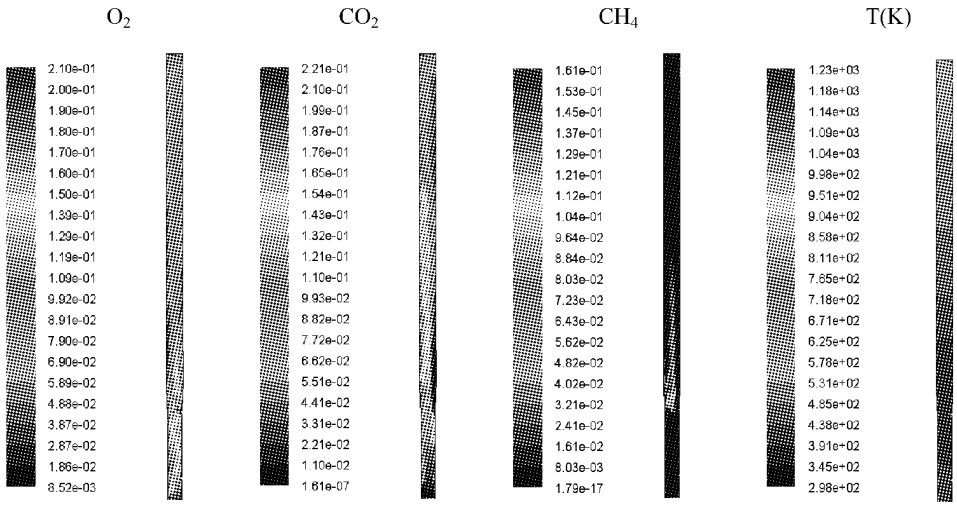

Fig. 8 Contours of transient molar fraction of O_2, CO_2, and CH_4 and temperature profile in air

Profiles under O_2/CO_2 combustion condition

Computational modelling of O_2/CO_2 combustion has been carried out with the same O_2 volume fraction in the inlet gas as the air, substituting CO_2 for N_2. That is 21/79 volume ratio for O_2/CO_2. As shown in Fig.9, the same trends with O_2 and CO_2 concentration evident in air combustion also appear in O_2/CO_2 combustion, with CO_2 concentration more than 90% in flue gas.

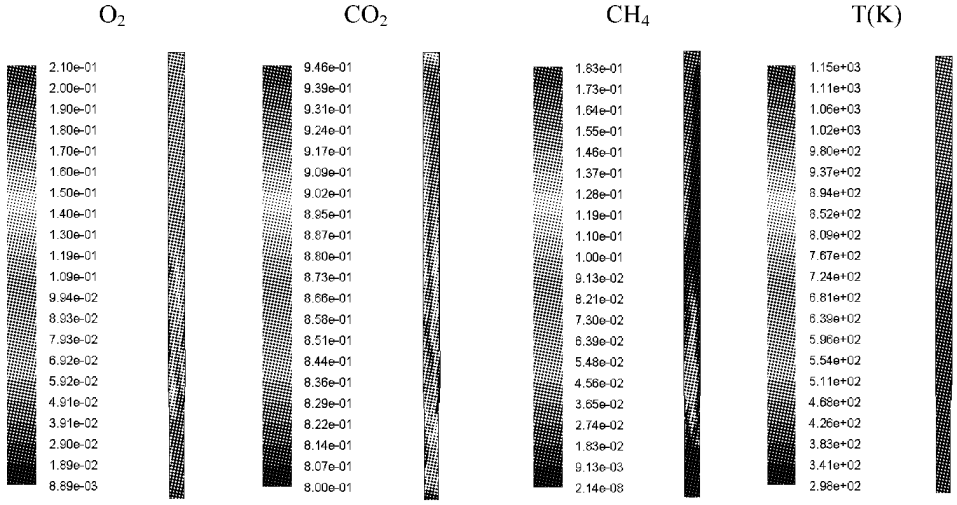

Fig. 9 Contours of transient molar fraction of O_2, CO_2, and CH_4 and temperature profile in O_2/CO_2

Compared with air combustion, the O_2 and CH_4 concentrations in the riser are higher and the gas temperature is lightly lower in O_2/CO_2 combustion, indicating lower carbon conversion rate. But the temperature distribution is more uniform in riser with the maximum difference of 100K, which can be explained by the larger specific heat of carbon dioxide. These phenomena suggest the necessity of increasing the O_2 concentration in O_2/CO_2 mixture to obtain similar flame temperature and carbon conversion rate as air combustion. These attempts are in our plans for future work.

CONCLUSIONS

A comprehensive model based on TFM including KTGF and simplified reactions was developed to simulate the MFCFBC numerically which can be used to predict and analyze the impacts of flow behavior and atmosphere on chemical reaction. From the results, a reasonable interpretation of gas composition profile, the distributions of temperature, gas/solid velocity and gas/solid volume fraction in the combustor can be obtained. The calculated exit gas compositions are in good agreement with the experimental data. The predicted results in O_2/CO_2 combustion reveal the differences with air combustion and can provide practical guidance for the ongoing work. This model is expected to be coupled with pollution emission sub-models and validation for both hydrodynamic and hot experimental data in air and O_2/CO_2 combustion will be executed subsequently.

NOTATIONS

A_a, A_d	pre-exponential factor	H	riser height, m
Cfix	fixed carbon % by weight on air dried basis	H_0	initial static bed height, m
		T_g	gas mean temperature, K
C_{O2}	O_2 mole concentration, kmol/m^3	U_g	fluidizing gas velocity, m/s
dp	particle diameter, m	w_i	molecular weight for species i
E_a, E_d	activation energy, kJ/kmol	Y_i	mass fraction for species i
g	gravity, m/s^2	ρ_g	gas density, kg/m^3
G_s	solid circulating rate, kg/ s	ρ_s	Particle density, kg/m^3

ACKNOWLEDGEMENTS

Financial supports of this work by the National Key Program of Basic research of China (2006CB705806) and National Key Technology R&D Program (2006BAA03B02) are gratefully acknowledged.

REFERENCES

Buhre, B.J.P., Elliott L.K., Sheng, C.D., Gupts, R.P. and Wall, T.F.: Prog. Energ. Combust. Sci. 31 (2005), pp.283-307.
Basu P., Chem Eng Sci 54 (1999), pp. 5547-5557.
Czakiert, T., Bis Z., Muskala, W. and Nowak, W.: Fuel. Process. Technol. 87 (2006), pp: 531-538.
Benyahia. S., Syamlal, M., O'Brien, T.J.: AIChE Journal 53 (2007) pp:2549-2568.
Schmidt, A., Renz, U.: Int. J. Therm. Sci. 39 (2000), pp:871-885.
Mathiesen, V., Solberg, T., Hjertager, B.H.: Int. J. Multiphas. Flow. 26 (2000) pp. 387-419.
Almuttahar, A. and Taghipour, F.: Chem. Eng. Sci. 63(2008), pp. 1696-1709.
Yu, L. Lu, J. Zhang, X. Zhang, S.: Fuel 86 (2007), pp. 722-734.
Wang, X. et al.: Chem. Eng. Process. (2008).
Syamlal, M. O'Brien, T.: Int. J. Multiphas. Flow. 14(1988) pp: 473-481.
Gunn. D. J.: Int. J. Heat Mass Transfer, 21(1978), pp: 467-476.
Launder, B.E. and Spalding, D.B.: Comput. Method. Appl. M. 3 (1974), pp: 269-289.
Eaton. A. M., Smoot. L. D., Hill. S. C., Eatough. C. N. Prog. Energ. Combust. 25 (1999), pp: 387-436.
William V., Salvador O., Javier A., Esteban B. Appl. Therm. Eng. 23 (2003), pp: 1993-2008.
Smith. I.W. Symposium (International) on Combustion. 19 (1982), pp: 1045-1065.
Spalding. D.B. Mixing and chemical reaction in steady confined turbulent flames. Proceedings of the 13th Symposium on Combustion, The Combustion Institute, 1970.
Kunii D, Levenspiel O.: Chem. Eng. Sci. 55 (2000): 4563-4570.

MODELLING OF CO_2 ADSORPTION FROM EXHAUST GASES

Marcin Panowski, Roman Klainy, Karol Sztekler

Faculty of Engineering and Environmental Protection, Czestochowa University of Technology ul. Dabrowskiego 73, 42-200 Czestochowa, Poland

Abstract: World tendencies in environmental protection points out necessity of reduction of CO_2 emission to atmosphere. The one of the main sources of CO_2 emission is placed in energy sector where electric energy and heat are produced based on fossil fuels combustion. Therefore, it seems to be necessary to perform research on CO_2 emission reduction in this sector. The main aim of work presented in this paper was focused on the analysis and assessment of CO_2 separation from flue gases on the total efficiency of conventional power station. The paper shows the numerical calculations performed with IPSEpro simulation software by SimTech.For the CO_2 separation the PTSA (**P**ressure-**T**emperature **S**wing **A**dsorption) process was chosen and the numerical as well as simulation model of such process was formulated. The calculations were made for few different adsorbents taking into account varying values of such thermodynamic parameters of separation process like temperature or pressure. Results obtained from calculations point out that mixed PTSA technology is not very energy consuming process. Owing to utilisation of waste heat for sorbent regeneration, it does not decrease the total efficiency for more than 0.6%. However, that is caused by separation only, while after that CO_2 must be compressed for further treatment.
Keywords: CO_2 capture, process modelling, simulation

INTRODUCTION

Recent studies in the field of CO_2 separation are concentrated on two distinct areas, which are the pre- and post-combustion separation. Any pre-combustion separation process requires proper fuel pre-processing, whereas a separation process conducted after the combustion stage does not need a special fuel treatment and can be done (among the others like cryogenic or membrane separation) by implementation of ab- or adsorption process. These two techniques are well known [1], widely used especially in the chemical industry and is expected they could be also implemented in the energy sector.

The main problem appearing in chemical separation of CO_2 by absorption concerns sorbent regeneration. Since sorption properties of absorbents decrease with time and number of cycles (sorption-desorption), the main cost of CO_2 separation by absorption is connected with sorbent cost. Unlike the absorption, separation by adsorption is only the surface process, therefore, adsorption-desorption processes do not much influence adsorbent properties and its lifetime.

Adsorption process depends heavily on sorbent efficiency, which is a function of both: pressure and temperature. Commercially available adsorption systems are rather small scale units used for much lower polluted gas flow rate than flue gases flow rates generated by the boilers of the power stations. Therefore, the possibility of using currently available adsorbents for large scale separation was analysed in this work, and is presented further in the paper.

Existing adsorption techniques have developed, among the others, into three distinct methods[2, 3]:

- pressure swing adsorption (PSA)
- temperature swing adsorption (TSA)
- pressure-temperature swing adsorption (PTSA)

Since the work presented in the paper concentrates on application of adsorption unit to CO_2 separation from exhaust gases in the conventional power station, the mixed PTSA technology was chosen and studied. The numerical and simulation model of CO_2 PTSA separation process was developed and combined with model of an existing 380MW power station.

The calculation were made for 6 different, commercially available adsorbents such as zeolites: Na-A, 13X, 5A, 4A, klinoptilolit and sodalit, taking into account various thermodynamic parameters of separation process.

SIMULATION MODEL OF CO_2 SEPARATION UNIT

Separation of carbon dioxide from exhaust gases by adsorption is realised in two stages. First, flue gases flow into adsorption column where in the low temperature and high pressure carbon dioxide is adsorbed on sorbent. Free from CO_2 gases are pull out from column while sorbent with CO_2 is than "virtually transported"

to desorption column where in high temperature and low pressure sorbent is cleaned from CO_2. Heat for sorbent regeneration is derived from steam taken out from steam bleeding of the power station turbine and after condensation it is returned to power station cycle. Pure carbon dioxide from desorption column is then compressed, while clean sorbent "virtually goes" back to adsorption column. However, because of high temperature of desorption, heated sorbent must be cooled before it is put back into adsorption column. Sorbent cooling is realised by main condensate from power station cycle. The scheme of separation process described above is placed on Fig. 1.

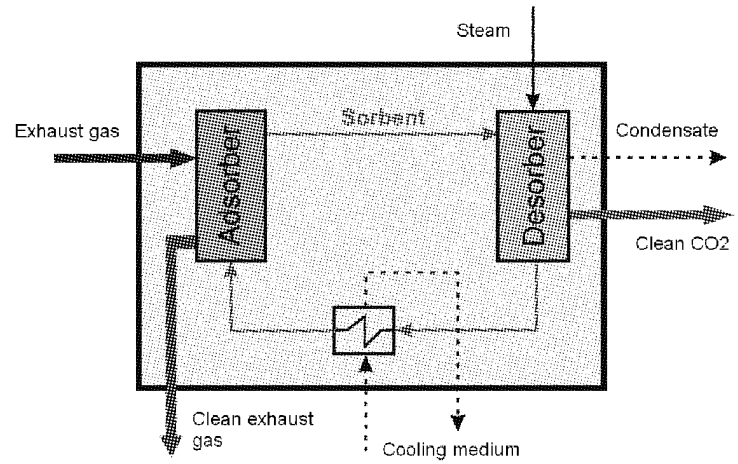

Fig.1 Scheme of PTSA separation

To properly formulate a set of model equations for such process, some assumptions had to be needed, especially for energy fluxes exchanged between media participated in the process of separation. The following assumptions were made:

1) heat of CO_2 adsorption is transferred directly to cleaned exhaust gases,

2) heat from steam in desorption process (sorbent regeneration) is used to heating sorbent and pure CO_2 as well as to cover demand for heat of desorption necessary for releasing carbon dioxide from sorbent

3) part of CO_2 remains in sorbent after regeneration,

4) the product of sorbent regeneration is pure carbon dioxide,

5) characteristics of sorbent such us adsorption isotherms are known.

The scheme of a process of CO_2 separation presented on Fig. 1. supplemented with above assumptions allowed to formulate mathematical model of the CO_2 separation unit. For simulation model development and further calculations the IPSEpro software by SimTech[4] was used. This software allows modelling and simulation of almost any kind of thermal processes by graphical connecting different components, which are prescribed by set of parameters and equations, mainly representing governing equations of mass and energy flow balances. All the model equations for PTSA process were combined together, and as a single simulation model were rewritten in the IPSEpro software.

SIMULATION MODEL OF POWER PLANT WITH CO_2 SEPRATION UNIT

Elaborated simulation model of CO_2 PTSA separation unit was combined with model of conventional 380MWe power station. The scheme of power plant with CO_2 separation unit and carbon dioxide compression system is shown on Fig. 2. The boiler of power station is supplied with coal and produces fresh steam which temperature and pressure are 535 °C and 169 bar respectively. At nominal parameters, exhaust gases flux generated in the boiler is about 464 kg/s with 0.1886 kg/kg CO_2, which gives about 87.6 kg/s CO_2 under partial pressure of about 23 kPa. The source of energy for desorption process is steam from turbine steam bleeding, while its condensed stream is directed back to the main cycle as a recycled stream to third low pressure heat exchanger. The sorbent after regeneration is cooled by condensate from main cycle which allows at least part of energy consumed by separation process to be recuperated.

Pure CO_2 leaving desorption column is compressed to 35 bar by intercooled 2 stage compressor propelled by turbine which is fed with fresh steam. At the outlet of the compression system, carbon dioxide is cooled to temperature in which the CO_2 under 35 bar pressure is condensed. Energy recovered by carbon dioxide cooling in the compression process could be then recuperated for total efficiency increase, however, in the presented work this heat is not utilised at all.

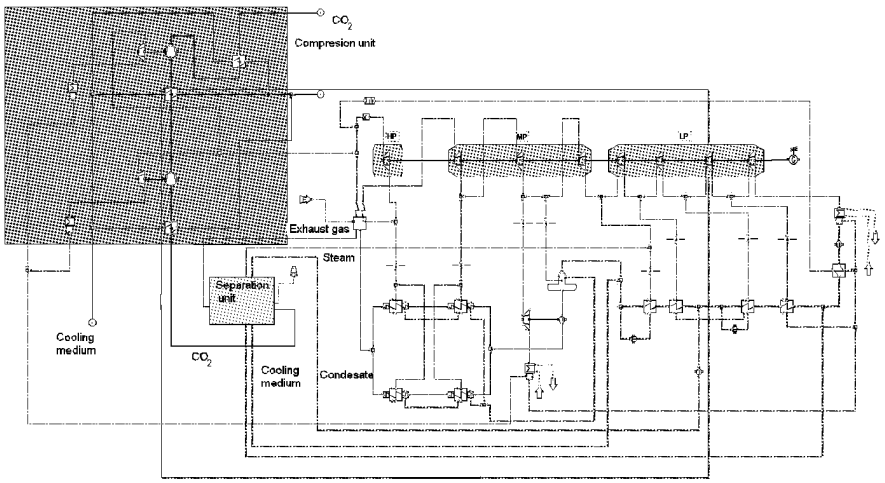

Fig. 2 Simulation model of power station with CO_2 separation and compression units

SIMULATION RESULTS

As a result of determined separation unit placement in the thermal cycle of a power station, thermodynamic parameters (temperature and pressure) of media used for sorbent heating in the desorption column, at the inlet to the separation unit and at the outlet as well, are fixed. Therefore, the temperature of sorbent regeneration process is also fixed which has a significant impact on the sorbent purification ratio. Moreover, it must be mentioned that the CO_2 separation unit placement in the exhaust gases duct is also fixed, which means determined thermodynamic parameters of exhaust gases and as a consequence also of adsorption process parameters. Since temperature and pressure of adsorption and sorbent regeneration are the most important parameters influencing separation process the proper choice of extraction seam parameters for sorbent regeneration and placement in the exhaust gases duct are of primary importance.

Optimal localization of the separation unit in the exhaust duct enforces certain limits for thermodynamic parameters of the exhaust gas and parameters of CO_2 adsorption. Following up adjustments are still possible only with the installation of additional equipment controlling the temperature and pressure of exhaust gas.

Influence of CO_2 separation coefficient

The amount of heat necessary for releasing CO_2 from sorbent depends directly on mass flux of desorbed carbon dioxide only. Therefore, as a consequence of increasing separated CO_2 mass flux the demand for sorbent grows up which causes heat demand for sorbent regeneration also to increase. Assuming constant fresh steam stream, that is why the output power and total energetic efficiency of a power station should decrease.

These observations are acknowledged by results presented on Figs. 3. to Fig. 5. where characteristics of CO_2 separation ratio influence on sorbent demand, electric power and total energetic efficiency are shown respectively. Significant differences in the sorbents properties can be observed on the Fig. 3, where the sorbent demand against CO_2 separation coefficient (which is in per cent value of CO_2 separated from exhaust gases) for different adsorbents is presented. The figure shows that as a consequence of sorbents characteristics the most efficient adsorbents are zeolites 4A, 5A and 13x, while the worst one is zeolite Na-A.

On the Fig. 4 and Fig. 5, the dash lines show values for referenced power station without carbon dioxide separation. Presented results show that separation process itself (without CO_2 compression) leads to about 0.6 % decrease of total efficiency while meaningful decrease is caused by compression process. However, it must be mentioned that such small decrease is achieved owing to utilisation of exhaust heat and the the total efficiency decrease (with CO_2 compression) is not greater than 6 % for 100 % of CO_2 separated from exhaust gases. The Figs. 4 and Fig. 5 also show that sorbent properties have meaningless influence on electric power and total efficiency as well.

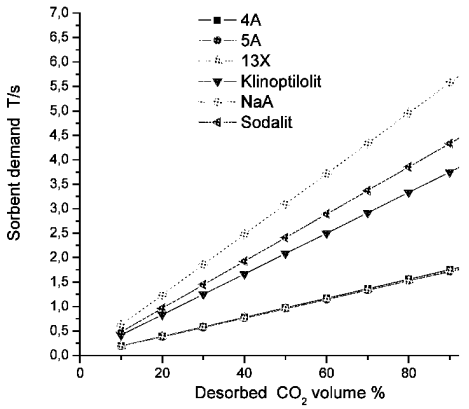

Fig. 3 Sorbent demand vs. CO_2 separation coefficient

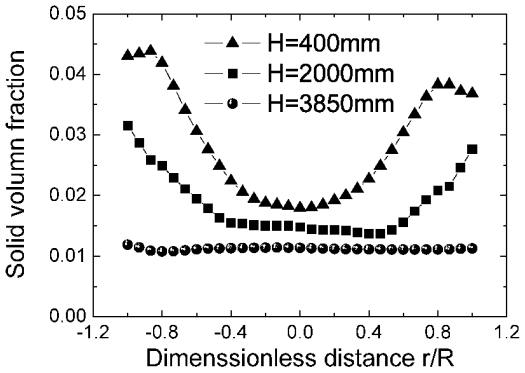

Fig. 4 Total power vs. CO_2 separation coefficient

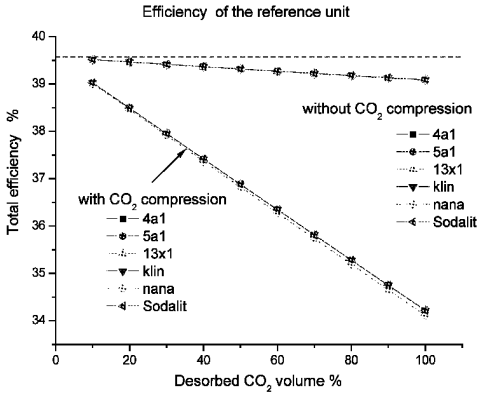

Fig. 5 Total efficiency vs. CO_2 separation coefficient

Influence of flue gases parameters

The temperature and pressure of exhaust gases are meaningful parameters influencing separation process, therefore, their impact on total efficiency of power station was studied. The simulation experiments where done assuming constant fresh steam stream and separation of all CO_2 from exhaust gases (CO_2 separation coefficient equal 100%).

Increase of pressure of exhaust gases entering separation unit causes partial pressure of CO_2 in flue gases to grow up. For fixed flue gases temperature, the characteristic of sorbent demand is directly linked to sorbent isotherms, so was expected it should be nonlinear and inversely proportional. The calculated of sorbent demand versus flue gases pressure was depicted on Fig. 6.

The data on Fig. 6. shows strong impact of flue gases pressure on sorbent demand which is mostly observed for lover pressure less than 2.0 bar. The pressure impact is weaker in the range of 2.0 to 3.5 bar and for higher pressure values almost decays. It must be mentioned that almost quadruple exhaust gases pressure increase from 1.2 to 4 bar leads to significant sorbent demand decrease of about 60% for all sorbents except zeolite Na-A, for which the decrease is almost 10 times lower.

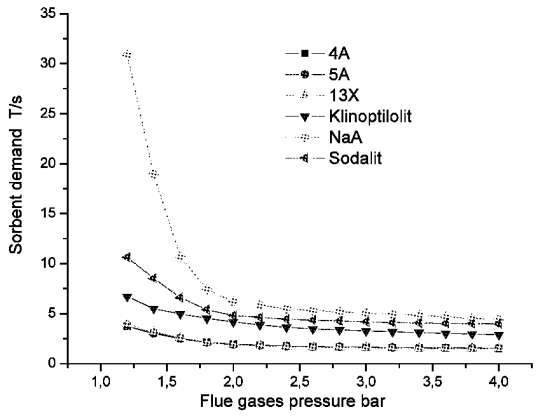

Fig. 6 Sorbent demand vs. flue gases pressure

As a consequence of lower sorbent consumption caused by higher flue gases pressure, the energy demand for sorbent regeneration decreases. Therefore, the decrease of negative impact of desorption process on electric power and total energetic efficiency should be expected. However, having in mind that amount of separated CO_2 is fixed (100% of it is separated) the energy loss in the desorption process is constant. It is because for changing sorbent demand, the amount of heat for its regeneration and that recuperated after desorption also change adequately. Therefore, the separation process as a whole shouldn't influence electric power and total efficiency of power station neither at all. The effect of pressure change influence on these power station parameters are shown on Figs. 7. and Fig. 8. respectively.

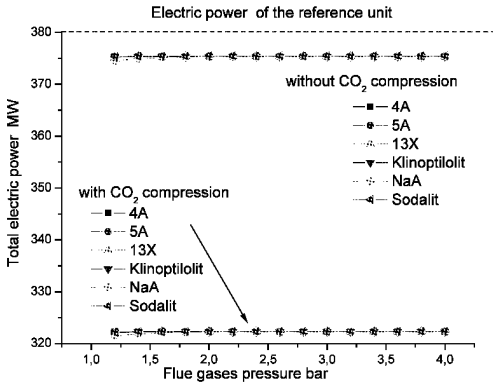

Fig. 7 Total electric power vs. flue gases pressure

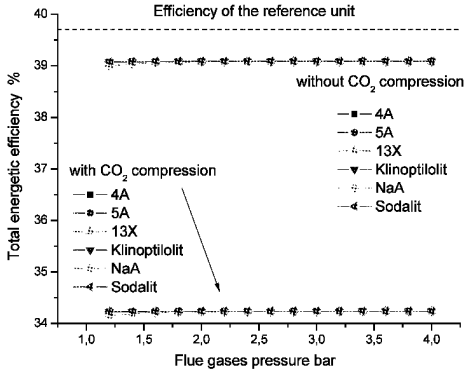

Fig. 8 Total energetic efficiency vs. flue gases pressure

Presented data acknowledge above assumptions. However, there were no energetic costs of flue gases compression taken into account. Since the amount of flue gases is huge and the energetic costs of their compression is also significant, the results shown on Figs. 7. and Fig. 8. should be treated as qualitative ones rather than quantitative.

As a result of compression, besides pressure increase, the temperature of medias grows up. The temperature of exhaust gases entering separation unit is important from separation process point of view. Its growth negatively affects sorption properties of sorbent which leads to increase of sorbent demand. Therefore, the temperature of exhaust gases should be as low as possible. How strong is the impact of flue gases temperature on sorbent demand, total electric power and energetic efficiency of power station is shown on Figs. 9. - Fig. 11. respectively.

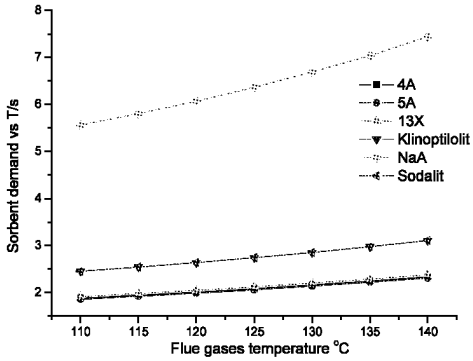

Fig. 9 Sorbent demand vs. flue gases temperature

The flue gases temperature strongly affects the demand for sorbent. The relationship is almost linear and shows that about 30% increase in temperature causes similar increase in sorbent demand for all types of sorbent analysed. The Fig. 9 acknowledges once again that the most efficient sorbents are zeolites 4A, 5A and 13X.

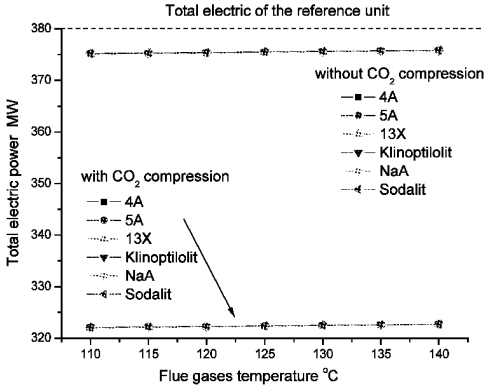

Fig. 10 Electric power vs. flue gases temperature

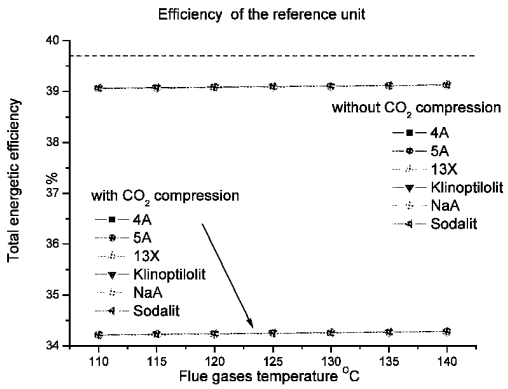

Fig. 11 Total energetic efficiency vs. flue gases temperature

There may be seen on the Figs. 10 and Fig. 11 slightly increasing values of electric power and total efficiency of power station with flue gases temperature. However, the relative growth of total efficiency observed on Fig. 11. is less than 1% which seems to be meaningless. Therefore, as for flue gases pressure it may be concluded that there is no impact of flue gases temperature on electric power and total energetic efficiency of a power station at all. Moreover, Figs. 10 and Fig. 11 show once again that there is no impact of sorbent properties on electric power and total energetic efficiency of a power station and these parameters are only important from separation process point of view (they influence sorbent demand only).

CONCLUSIONS

The paper presents results of numerical simulations of a power station with carbon dioxide separation unit. The mathematical and simulation model of CO_2 separation by adsorption process was elaborated and combined with simulation model o a power station. Calculations were made with use of IPSEpro software and concentrated on analysis of influence of CO_2 separation process on total energetic efficiency of a power station, taking into account different, commercially available adsorbents.

The results show that adsorption process itself is not very energy consuming and, owing to recuperation of exhaust heat for sorbent regeneration and from sorbent cooling, leads to decrease of power station efficiency less than 0.6% (without CO_2 compression). Meaningful decrease of the efficiency is caused by CO_2 compression process which is needed for its transportation, and makes total efficiency lower of about 6% (for 100 % of CO_2 separated and compressed to 35 bar). Moreover, presented results show that sorbent properties do not influence the electric power neither total energetic efficiency of a power station and the sorbent used for carbon dioxide separation affects only its demand in the separation unit.

Calculation results also show that currently available sorbents are not efficient enough for their application in energy sector, due to their low sorption capacity. Therefore, since the energetic cost of CO_2 separation by

adsorption is acceptable and such process may be considered for further application in energy sector, the research should concentrate on finding new more efficient sorbents that could be used for huge flue gases stream which is generated by power station boiler.

REFERENCES

[1] G. Gottlicher, R. Pruschek, *Comparison of* CO_2 *removal systems for fossil-fueled power plant processes*, Energy Convers. Mgm, Vol. 38, pp. S173-S178, Elsevier Science Ltd., 1997.
[2] D. M. Ruthven, *Principles of Adsorption and Adsorption Processes*, John Wiley & Sons: New York, 1984.
[3] R.T. Yang, *Gas separation by adsorption processes*, Butterworths, Boston, 1987.
[4] IPSEpro User Documentation Program Modules Model Libraries.

Environmentals and Pollution Control

NO_x REDUCTION IN A FLUIDIZED BED REACTOR WITH Fe/ZSM-5 CATALYST AND PROPYLENE AS REDUCTANT

Terris Yang and Xiaotao Bi

Department of Chemical and Biological Engineering
University of British Columbia, Vancouver, BC, V6T 1Z3, Canada

Abstract: The performance of a fluidized bed catalytic reactor was investigated for NO_x reduction using a Fe/ZSM-5 catalyst and propylene as the reducing agent. The effects of inlet NO_x concentration, propylene to NO_x molar ratio, flue gas oxygen concentration and fluidizing gas velocity on NO_x conversion were studied using simulated flue gases. The results showed that the NO_x conversion decreased with decreasing the inlet NO_x concentration, and propylene to NO_x molar ratio. The increase in flue gas oxygen concentration also imposed a significant negative impact. As the flue gas oxygen concentration increased, NO_x reduction decreased while propylene conversion increased at a given propylene to NO_x molar ratio, due to the oxidation of propylene in the presence of high oxygen concentration. The increase in fluidization gas velocity reduced the contact time between reactant and the catalyst particles due to the increased bubble size and bubble rise velocity. As a result, the NO_x reduction decreased as the gas velocity increased.
Key words: NO_x, SCR, propylene, Fe/ZSM-5, fluidized bed

INTRODUCTION

Selective catalytic reduction, so called SCR, selectively reduces NO_x to N_2 and H_2O by the use of a catalyst and a reducing agent. Due to its high efficiency and selectivity, SCR is considered to be the only method applicable for the control of NO_x in the combustion flue gases requiring high control efficiencies. Despite extensive research reported on SCR of NO_x with various catalyst/reductant combinations since 1975, only SCR with NH_3 or urea as the reducing agent has been commercially practised to date (Forzatti, 2001).

Hydrocarbons instead of NH_3 are considered as the most promising reducing agents for the SCR process. The first study on SCR of NO_x with hydrocarbons was reported by Iwamoto et al. (1988). Thereafter, SCR of NO_x by hydrocarbons (HC-SCR) has attracted considerable attention as an alternative of ammonia or urea process for the treatment of NO_x-laden flue gases, and numerous studies on various types of catalysts and reducing agents have been widely investigated (Parvulescu et al., 1998; Traa et al., 1999; Wichtelova et al., 2003; Liu and Woo, 2006). Although many studies have been carried out on the development of catalysts, the selection of reducing agents and the understanding of the reaction mechanisms of the process, there have been few studies on the design and performance of SCR reactors using hydrocarbons as the reducing agent. For a technology to be of practical applications, so called "engineering" approach, where the focus is on the reactor design and application to address technical challenges of the HC-SCR process, needs to be considered.

The NO_x SCR performance of Fe/ZSM-5 catalyst with propylene had been investigated in a fixed bed reactor and Fe/ZSM-5 catalyst exhibited promising results for the treatment of simulated flue gases (Yang et al., 2008). To further evaluate the performance of the NO_x SCR process in a fluidized bed catalytic reactor, the SCR of NO_x in simulated flue gases using a Fe/ZSM-5 catalyst and propylene as the reducing agent was performed in this work to investigate the effects of inlet NO_x concentration, propylene to NO_x molar ratio, flue gas oxygen concentration and fluidizing gas velocity on NO_x and HC conversions.

EXPERIMENTAL

The fluidized bed catalytic reaction system is schematically shown in Fig. 1. The parent catalyst was Na/ZSM-5 purchased from China University of Petroleum, and the method for the preparation of Fe/ZSM-5 and its characterization has been described elsewhere (Delahay et al., 2005; Yang et al., 2008). The particles are spherical of quite uniform size, with a mean diameter of 1.04 mm, and a bulk density of 926 kg/m^3. The minimum fluidization velocity was measured to be 0.18 m/s under ambient condition and 0.39 m/s when converted to 350 ℃. The model flue gas used in the experiment was a mixture prepared from a gas cylinder containing 20% NO balanced with N_2 and a liquid N_2 Dewar, with both supplied from Praxair Products Inc. Building air was used as the source of O_2. The reducing agent used in the experiment was propylene from a gas cylinder containing 40% propylene balanced with N_2 from Praxair Products Inc.

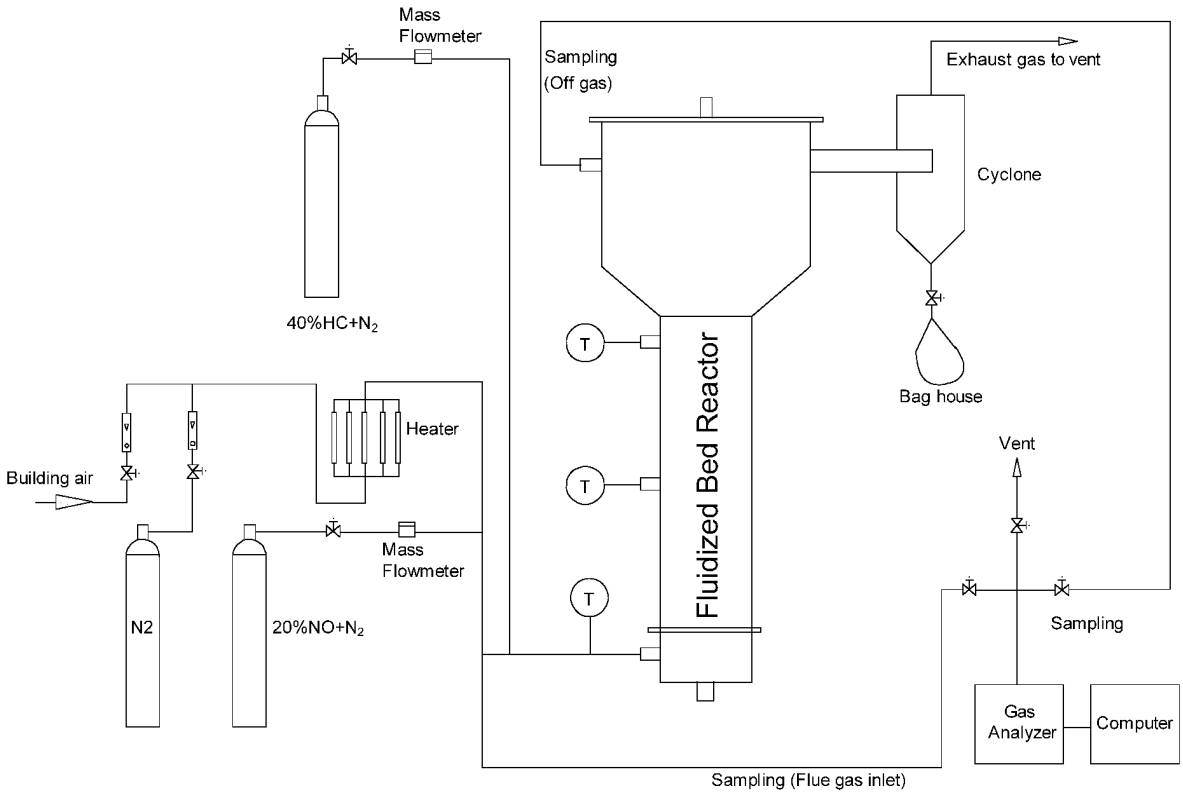

Fig. 1 Schematic of fluidized bed reaction system

In the experiment, 20% NO + N_2 gas mixture was mixed with preheated building air flow and pure N_2 to prepare the model flue gas with various NO and O_2 concentrations. Based on the propylene to NO molar ratio required in the experiment, a given amount of 40% propylene + N_2 was mixed with the model flue gas right after the sampling point of the model flue gas. The fluidized bed was first preheated by the preheated building air. After the desired reaction temperature was reached in the reactor, the mixture of the model flue gas and reductant was injected into the fluidized bed reactor of 108 mm I.D. and 1092 mm high, and NO_x was reduced by propylene in the reactor on the pre-loaded Fe/ZSM-5. The reduction performance of the reactor was evaluated by measuring the gas composition at the inlet and outlet of the reactor using a Horiba PG-250 flue gas analyzer.

RESULTS AND DISCUSSION

Effect of inlet NO concentration on NO_x conversion

Figs. 2 to 4 show that the inlet NO concentration in the model flue gas had some influence on NO_x conversion. At O_2 concentrations of 4% (Fig. 2) and 2.5% (Fig. 3), NO_x conversion increased monotonically with increasing NO concentration from 300 ppm to 900 ppm at a given fluidizing gas velocity. This may be explained by the fact that the increase in NO_x concentration enhanced the NO_x adsorption capacity of the catalyst and also the reaction rate. For the flue gas with 1% O_2 (Fig. 4), a 10~15% increase in NO_x conversion was observed when the inlet NO concentration increased from 300 to 600 ppm. The NO_x conversion slightly decreased as the flue gas NO concentration increased from 600 to 900 ppm. As discussed earlier (Yang et al., 2008), NO must be oxidized to NO_2 before it is

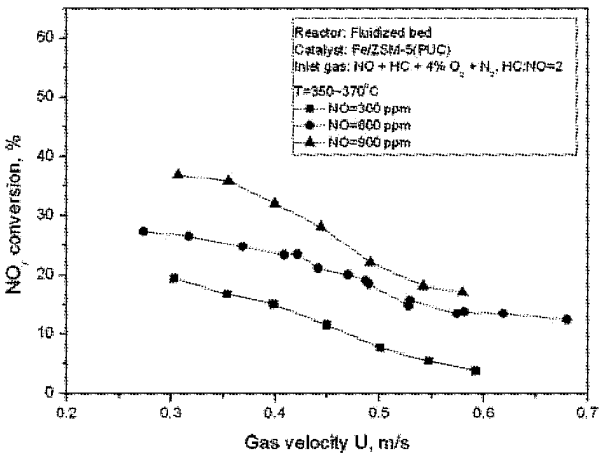

Fig.2 Effect of inlet NO concentration on NO_x conversion

reduced by the HC. At an O_2 concentration of 1% and a NO concentration of 900 ppm, the HC concentration in the gas flow was 1800 ppm at a HC:NO ratio of 2. If all HC was completely converted to CO_2 and H_2O, it could have reduced the flue gas O_2 level from 1% to 0.44%. Therefore, there may not be enough O_2 for the oxidization of NO to NO_2, resulting in a NO_x conversion slightly lower than the case with 600 ppm of NO in the flue gas.

It is also observed from Figs. 2 to 4 that, with the increase in gas velocity, NO_x conversion decreased significantly. The increase in gas velocity decreased the gas residence time and thus decreased the amount of NO_x adsorbed by the catalyst particles, which led to the decrease in NO_x conversion. At the same time, the

contact time between reactant and the catalyst particles decreased due to the increased bubble size and bubble rise velocity incurred by the increasing fluidization gas velocity, which could further decrease the NO_x conversion.

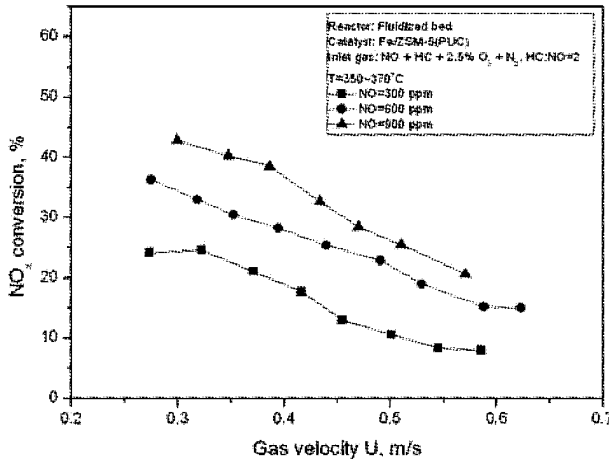

Fig.3 Effect of inlet NO concentration on NO_x conversion ($[O_2]$=2.5%)

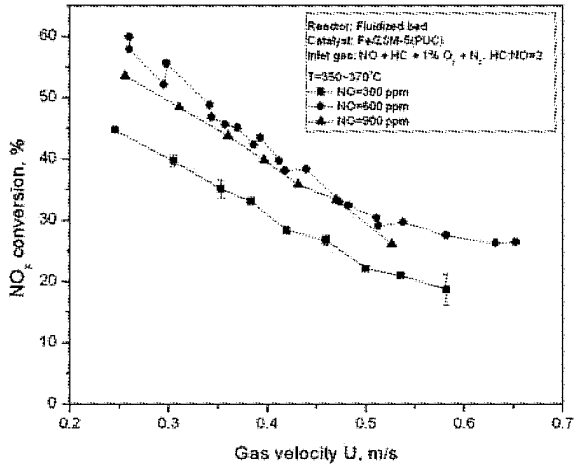

Fig. 4 Effect of inlet NO concentration on NO_x conversion ($[O_2]$=1%)

Effect of HC : NO molar ratio on NO_x and HC conversions

It is anticipated that an increase in HC:NO will enhance the NO_x conversion at given O_2 and NO concentrations in the fluidized bed.

For the flue gas with 300 and 600 ppm NO, as shown in Figs. 5 and 6, at 1% flue gas O_2, the increase of HC : NO ratio from 1 to 2 increased NO_x conversion significantly. At O_2 concentrations of 2.5% and 4%, NO_x conversion also increased by increasing HC : NO ratio, although the effect was not as significant as at 1% O_2. The amount of free O_2 towards the oxidation of propylene is relatively low at lower flue gas O_2 concentration, leading to more propylene available for the reduction of adsorbed NO_x when the HC : NO molar ratio is increased from 1 to 2, and thus increasing NO_x conversion significantly. At higher O_2 concentrations, most of the increased propylene is consumed by the relatively abundant free O_2, and could not contribute more to the reduction of adsorbed NO_x. As a result, the NO_x conversion increased more significantly with the increase of

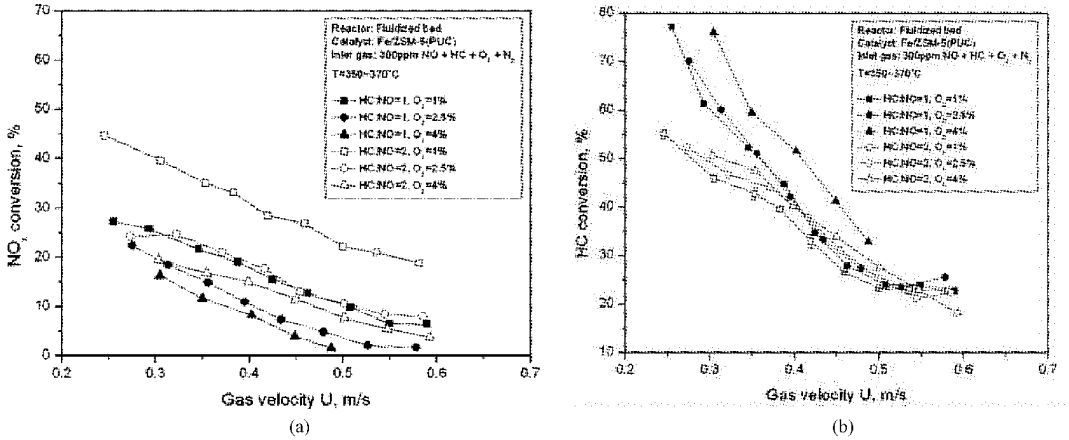

(a) (b)

Fig.5 (a) Effect of HC : NO molar ratio on NO_x conversion ([NO]=300 ppm) and (b) Effect of HC:NO molar ratio on HC conversion ([NO]=300 ppm)

HC:NO molar ratio at low O_2 concentration. At low gas velocities, HC conversion decreased notably with the increase in HC:NO ratio at all tested O_2 concentrations. When a high gas velocity was used, the effect of HC:NO ratio on HC conversion was insignificant.

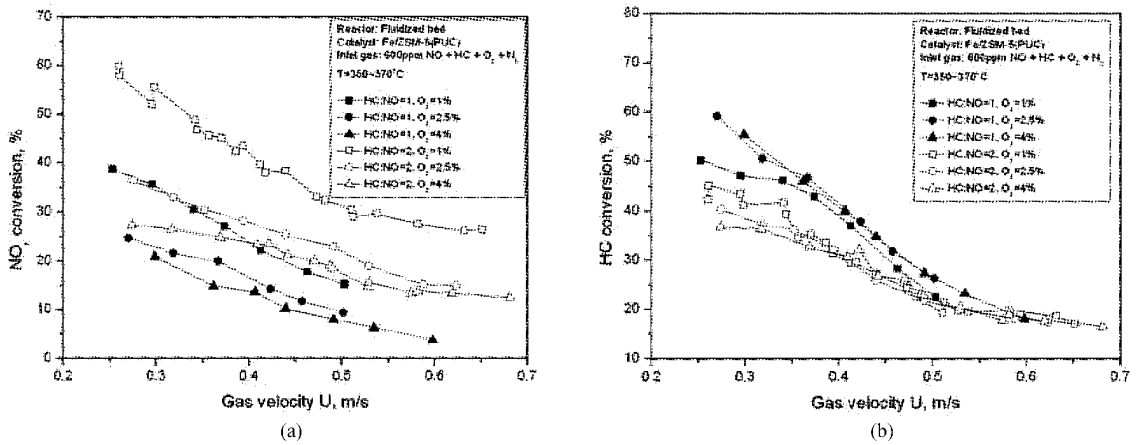

(a) (b)

Fig.6 (a) Effect of HC:NO molar ratio on NO_x conversion ([NO]=600 ppm) and (b) Effect of HC:NO molar ratio on HC conversion ([NO]=600 ppm)

For an inlet NO concentration of 900 ppm, as shown in Figs. 7(a) and 7(b), the increase of HC:NO led to significant increase in NO_x conversion and a slight decrease in HC conversion at both 2.5% and 4% O_2. For the flue gas with 1% O_2, the effect of HC:NO on NO_x conversion was insignificant at 300 and 600 ppm NO, and the HC conversion dropped to a relatively low level at HC : NO=2. Again, this is likely due to the insufficient supply of O_2. In fact, as observed in the experiment, the outlet O_2 concentration approached zero when the flue gas of 900 ppm NO + 1% O_2 was used with a HC:NO ratio of 2.

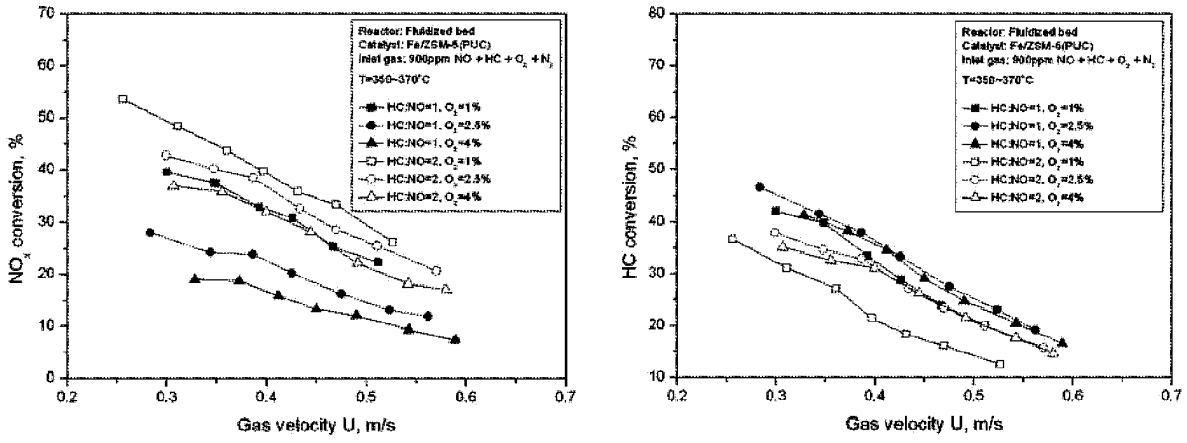

(a) (b)

Fig.7 (a) Effect of HC:NO molar ratio on NO_x conversion ([NO]=900 ppm) and (b) Effect of HC : NO molar ratio on HC conversion ([NO]=900 ppm)

Effect of flue gas O_2 concentration on NO_x and HC conversions

Fe/ZSM-5 showed high reactivity on NO_x reduction in the fluidized bed for flue gas with low O_2 concentration, as shown in Figs. 8(a) and 8(b).

NO_x conversion reached 60% at O_2=1% and U=0.27 m/s. Increase of O_2 concentration led to the decrease of NO_x conversion at a given gas velocity. As a key component of the flue gas under lean-burn conditions, the influence of excess oxygen has been widely investigated. One of the main NO reduction mechanisms states that NO is first oxidized to NO_2, followed by the reduction by the reducing agent (Yokoyama et al., 1994; Adelman et al., 1996; Yan et al., 1998; Kikuchi et al., 1996). The presence of O_2 is thus essential for the HC-SCR process. This mechanism appears to agree with many experimental findings that the presence of small amount O_2 (e.g., <2%) is essential for HC-SCR (Captain et al., 1998; Shi et al., 2002; Lee, et al., 1997). However, it has been proven in the fixed bed experiments that the excess O_2 in the flue gas (>2%) inhibited the activity/selectivity of most HC-SCR catalysts (Corma et al., 1997; Chen et al., 1998a; Yang et al., 2008), which agrees well with our experimental findings in this study.

It is worthwhile to point out that the performance of Fe/ZSM-5 was negatively influenced by the gas velocity due to the shortened residence time of gas reactants. The catalytic activity was more sensitive to the gas velocity at lower O_2 concentrations than at higher O_2 concentrations. The change in O_2 concentration showed less influence on HC conversion than on NO_x conversion, with the highest HC conversion consistently lower than 50%. However, the increase of the gas velocity decreased HC conversion significantly under current experimental conditions, likely due to the reduced gas residence time, which appears to be consistent with the result from the fixed bed reactor.

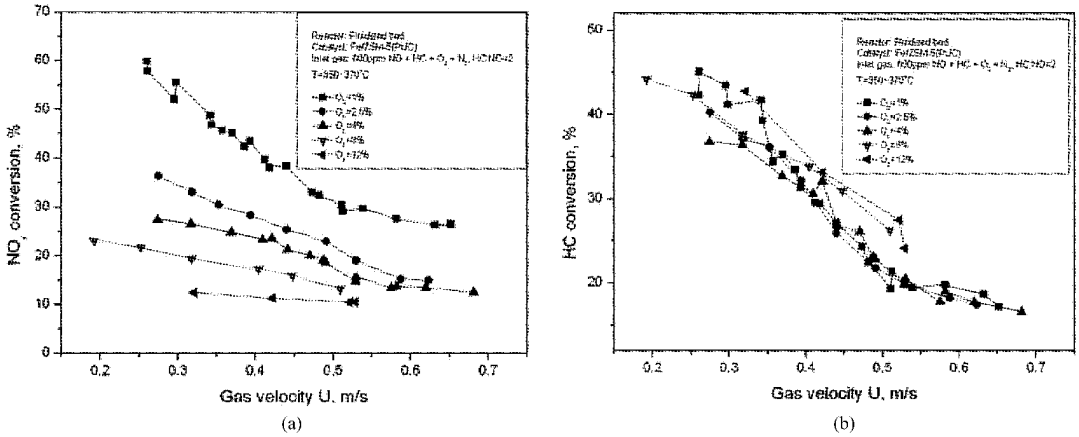

Fig.8 (a) Effect of flue gas concentration on NO_x conversion and (b) Effect of flue gas concentration on HC conversion

CONCLUSIONS

Experiments on the catalytic reduction of NO_x with propylene in the presence of excessive O_2 were carried out over Fe/ZSM-5 catalyst in a fluidized bed catalytic reactor. Various reaction conditions were investigated to evaluate the catalytic performance of Fe/ZSM-5 in HC-SCR of NO_x in the fluidized bed. NO_x conversion increased with the increase in the flue gas NO concentration and propylene to NO molar ratio, but decreased with the increase of the flue gas O_2 concentration at a given gas velocity. Fe/ZSM-5 showed some SCR performance at give reaction conditions, but not as good as that exhibited in the fixed bed experiment (Yang et al., 2008). The increase of gas velocity also imposed significant negative impact on the reduction performance of Fe/ZSM-5, demonstrating that it is critical to further improve the catalytic performance of Fe/ZSM-5 for the application of the fluidized bed reactor in the HC-SCR process.

ACKNOWLEDGEMENTS

Financial support from Canada Foundation for Innovation (CFI) and the Natural Sciences and Engineering Research Council of Canada (NSERC) is gratefully acknowledged. Terris Yang is also grateful to a NSERC postgraduate scholarship.

REFERENCES

Adelman, B.J.; Beutel, T.; Lei, G.-D. and Sachtler, W.M.H.: J. Catal. **158**(1996), pp.327-335.
Captain, D. K.; Roberts, K.L. and Amiridis, M.D.: Catal. Today. **42**(1998), pp.93-100.
Chen, H.Y. and Sachtler, W.M.H.: Catal. Today. **42(1-2)** (1998), pp.73-83.
Corma, A.; Fornes V. and Palomares E.: Appl. Catal., B: Environ. **11**(1997), pp.233-242.
Delahay, G.; Valade, D.; Guzman-Vargas, A. and Coq, B.: Appl. Catal., B: Environ. **55**(2005), pp.149-155.
Forzatti, P.: Appl. Catal., A: General. **222**(2001), pp.221-236.
Iwamoto, M.; Yahiro, H. and Tanda, K.: Successful Design of Catalysts. (1988) (Inui, T., ed., Elsevier, Amsterdam), p. 219.
Kikuchi, E.; Ogura, M.; Terasaki, I. and Goto, Y.: J. Catal. **161**(1996), pp.465-470.
Lee, C.W.; Chong, P.J.; Lee, Y.C.; Chin, C.S. and Kevan, L.: Catal. Lett. **48**(1997), pp.129-133.
Liu, Z. and Woo, S.: Catal. Rev. **48(1)** (2006), pp.43-89.
Parvulescu, V.I.; Grange, P. and Delmon, B.: Catal. Today. **46**(1998), pp.233-316.
Shi, C.; Cheng, M.; Qu, Z.; Yang X. and Bao, X.: Appl.Catal., B: Environ., **36**(2002), pp.173-182.
Traa, Y.; Burger, B. and Weitkamp, J.: Micro. Meso. Mater. **30**(1999), pp.3-41.
Wichtelova, B., Sobalik, Z. and Dedecek, J.: Appl. Catal., B: Environ. **41**(2003), pp.97-114.
Yan, J.Y.; Kung, H.H.; Sachtler, W.M.H. and Kung, M.C.: J. Catal. **175**(1998), pp.294-301.
Yang, T.; Zhang, T. and Bi, H.T.: Can. J. Chem. Eng. **86(3)**(2008), pp.395-402.
Yokoyama, C. and Misono, M.J.: Catal. **150**(1994), pp.9-17.

THE IMPACT OF ZEOLITES DURING CO-COMBUSTION OF MUNICIPAL SEWAGE SLUDGE WITH ALKALI AND CHLORINE RICH FUELS

A Pettersson[1], A-L Elled[1], A Möller[3], B-M Steenari[2], L-E Åmand[3]

1University of Borås, SE-501 90 Borås, Sweden
2Department of Chemical and Biological Engineering, Chalmers University of Technology SE-412 96 Göteborg, Sweden
3Department of Energy and Environment, Chalmers University of Technology,Sweden

Abstract: Municipal sewage sludge has proven to eliminate alkali metals and chlorine related problems during combustion of straw and refuse derived fuels (RDF). However, the mechanisms involved have not been clarified. The aim of this work was to gain more knowledge about the behaviour of sewage sludge and detergent zeolites in combustion and about their effects on alkali metal chemistry.

Co-combustion tests with combinations of municipal sewage sludge, wood and straw were carried out in a 12 MW fluidised bed (FB) boiler. In addition, a detergent zeolite, Doucil A24, was used as additive during co-combustion of wood and straw. The chemical characteristics of fuels and fly ashes were studied using several methods, such as chemical fractionation and scanning electron microscopy with element analysis by energy dispersive fluorescence detection (SEM-EDX) and X-ray diffraction (XRD).

In the co-combustion tests involving sewage sludge no KCl was found in the flue gas prior to the convection pass. The zeolite addition was less effective but the KCl concentration was reduced to some degree in favour of HCl compared to the reference case. Both SEM-EDX and XRD confirmed the presence of potassium-aluminium-silicates in the fly ash fraction in all cases. In addition, the laboratory study showed that Doucil A24 had the ability to capture potassium and KCl at temperatures in the range of 700-900°C.

Keywords: zeolites, alkali, chlorine, capture, fly ash

INTRODUCTION

At the same time as the energy consumption in the world is increasing, the reports on global warming becomes more serious, ICCP (2007). In the efforts to reduce the net emissions of green house gases new fuels and fuel mixes for heat and power production are considered. Some of these fuels contain high concentrations of alkali metals and chlorine making the utilisation of these fuels rather difficult. Fluidised bed (FB) boilers are known to be very fuel flexible, but as the combustion takes place in a sand bed, chemical interactions between bed particles and fuel ash compounds may occur. This can lead to formation of eutectic melts causing bed agglomeration and in the worst case expensive operating shut downs. Additional combustion problems as deposit formation and corrosion are also caused by alkali and chlorine.

Municipal sewage sludge has proven to have an ability to capture available alkali metal species (k and/or Na) when used as additive in combustion of straw and RDF (Davidsson et al., 2007; Pettersson et al., 2008; Elled et al., 2008). In general municipal sewage sludge contains high concentrations of Si, Al, K, S, P, Fe and Ca (Eriksson, 2001). In addition the contents of ash and moisture are high. The zeolite Doucil A24 is a common component in phosphate free household detergents and thus it occurs in sewage water. The zeolites are mainly collected in the sewage sludge in the wastewater treatment plant. Zeolites are aluminium silicates and their structure are characterised by the presence of systems of interconnected cavities, tunnels, in 3D structures. This anionic sieve has a resulting charge and a mesh size in the molecular range making them excellent cat-ion exchangers, water softener and molecular sieves. Both Doucil A24 and its forerunner zeolite A (or NaA) are manufactured as Na zeolites, meaning that the zeolite cavities are filled with Na-ions. These zeolites have an affinity for K^+, Ca^{2+} and Mg^{2+} and exchange their Na^+ for these ions in the washing water.

The aim of this work was to investigate more closely the zeolites ability to capture alkali and chlorine in the combustion since this mechanism is suspected to be important for the effects of sewage sludge addition in combustion.

EXPERIMENTAL SECTION

Boiler, sampling and analyses

The 12 MWth circulating fluidised bed (CFB) boiler located at Chalmers University of Technology was used for the combustion tests, Fig. 1. The boiler is described by Pettersson et al. (2008). The boiler system consists of a combustion chamber (1), fuel feed chute (2), air plenum (3), secondary air inlet at 2.1m (4), hot primary cyclone (5), loop seal (6), cyclone exit duct (7), cold secondary cyclone (8), bag house filter (9), flue gas recirculation fan (10), fuel bunkers (11), sludge pump (12), sand bin (13), kaolin and zeolite bin (14), sampling hole for bed material (15), measurement spot (before convection pass) IACM instrument, deposit probe and FTIR (16), measurement spot (after convection pass) FTIR (17), measurement spot (stack) FTIR (18). Fuel samples were taken at the input to the boiler. Bed samples were taken at point 15 in the bottom of the combustion chamber and from the return leg after the loop seal (6) at a temperature of 850°C. Fly ashes were sampled from the secondary cyclone and the bag filter both at 150°C. An air-cooled deposit probe was inserted at location 16. The probe was held at a constant temperature of 500°C to simulate a superheater tube. During the combustion tests the boiler was held at stable conditions with a bottom bed temperature of 850°C and a load of 6 MWth. The content of ash, moisture and combustibles were analysed by LECO MAC 400 proximate analyzer 785-700 system. The main elements were analysed by means of X-Ray Florescence (XRF) and the trace elements by Inductive Coupled Plasma-Mass Spectrometry (ICP-MS). Mercury was analysed by cold vaporisation. To investigate the type of binding between the elements chemical fractionation was used (Pettersson et al., 2008, Zevenhoven-Onderwater, 2001). The mineralogy of the fly ash samples were studied by X-Ray powder Diffraction (XRD) for the crystalline compounds. In addition Scanning Electron Microscopy-Energy Dispersive X-ray (SEM-EDX) was used for analyses of element distribution in fly ash samples.

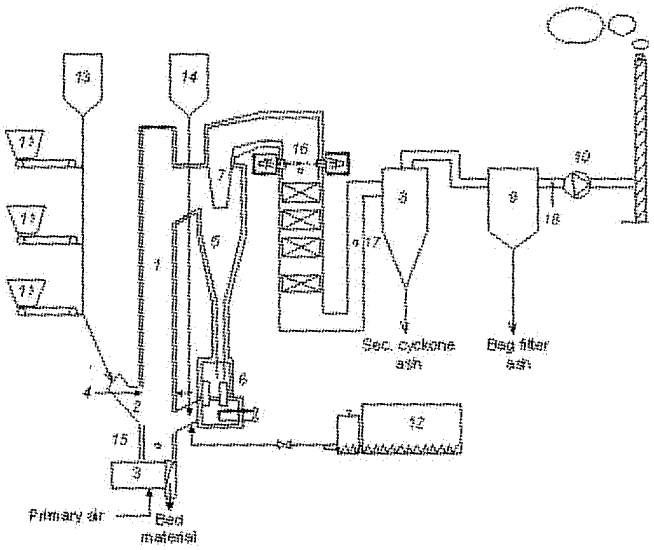

Fig. 1 The 12-MWth FBC boiler at Chalmers University of Technology

Table 1 Test series

Test	
Ref	Reference test. Combustion of wood and straw pellets.
	21 wt-% dry straw pellets.
MSS	Combustion of wood and straw pellets with sewage sludge.
	21 wt-% dry straw pellets and 12 wt-% dry sewage sludge.
Zeolite	Addition of zeolite Doucil A24 to the reference test.

Fuels and additives

Wood pellets, a well defined bio fuel with low ash content, was used as base fuel in the combustion tests. Different fuel mixes were combusted as shown in Table 1. To increase the alkali and chlorine concentration in the fuel mix straw was used as co-fuel. In the combustion test municipal sewage sludge was added to the reference fuel mix (MSS). The fuel properties are given in Table 2. In the third combustion test the reference

fuel mix was combusted with zeolite Doucil A24 as an additive (Zeolite). The molar ratio of Doucil A24 to K in with fuel was 1.1 reflecting the zeolite concentration in the sewage sludge used in the combustion test MSS.

Table 2 Average fuel properties

Fuel:	Wood pellets(*)	Sewage sludge (*)	Straw(*)
Proximate analysis			
Water [wt-%. raw]	7.9	73	8.8
Ash [wt-%. dry]	0.4	48	5.6
Volatiles [wt-%. daf]	90.7	94.8	81.1
Ultimate analysis [wt-%. daf]			
C	51	52	49.4
H	6.1	7.5	6.3
O	43	32	43.4
S	<0.01	1.9	0.1
N	0.06	6.1	0.59
Cl	<0.01	0.11	0.3
Heating value [MJ kg^{-1}]			
HHV. daf	18.9	20.4	18.4
LHV. raw	17.4	1.9	15.6
Ash analysis [g kg^{-1} dry ash]			
K	99	14	110
Na	10.6	8.3	9
Al	5.9	76	6.5
Si	142	142	300
Fe	8.4	162	2.1
Ca	219	44	52
Mg	33	11	10
P	11	59	14
Ti	2.1	4.7	0.4

daf= dry and ash free, raw= as received
(*)= average

Laboratory experiments

To get a better understanding of the thermal behaviour of the zeolite Doucil A24 a laboratory study was made. Doucil A24 belongs to the same structure group as the natural zeolite Gismondite, GIS and the NaA and CaA zeolites belongs to the LTA structure group. The thermal stability of such zeolites increases as a function of the Si/Al ratio in the lattice (Schwuger, 1996). Gismondite starts to decompose and form Ca-feldspars at temperatures above 375°C whereas zeolites NaA and CaA start to transform to feldspathoid lattices at temperatures above approximately 700°C and 800°C respectively.

The study made here focussed on the ion-exchange and thermal behaviour of the zeolite in the temperature range of 700-900°C (Möller, 2008). The Doucil A24 samples were pre-treated to simulate zeolites collected in the sewage sludge in a waste water treatment plant. Three Doucil A24 samples were investigated: the original Na zeolite and the zeolite ion-exchanged with Ca^{2+} and with K^{+} respectively, Table 3. Due to the high moisture content in sewage sludge two specimen of each sample material were heated simultaneously, one dry and one with addition of water to simulate the increased amount of water vapour. To investigate the ability of the zeolites to take up potassium during combustion, samples of the original and the Ca exchanged Doucil A24 were heated in the presence of KCl at 700, 800 and 900°C. Analysis of the samples were made by AAS (Atomic Absorption Spectroscopy), XRD and SEM-EDX.

Table 3 Sample matrix of the laboratory tests on zeolites

	Ion exchange	AAS	KCl added	Water added	
Samples of the original zeolite Doucil A24	-		x	x	700°C
	CaCl	x	x	x	800°C
	KCl	x			900°C
	-		x		
	CaCl	x	x		
	KCl	x			
	Pretreatment		Heat treatment		

RESULTS AND DISCUSSION

Element balance

The element balance over the boiler is shown in Table 4. Especially in the MSS case a good element balance could be achieved. The high outflow of aluminium in the Ref case most likely depends on uncertainty in the results since the molar flow of Al in this case is low. However, it can not be excluded that a memory effect from previous combustion tests having a high Al concentration causes these results. In the Ref case 50% of the chlorine and sulphur entering the boiler were found in the flue gases, Table 4. In the Zeolite case it was observed that a large fraction of the added zeolites were elutriated by the gas flow through the combustion chamber and predominantly collected in the bag filter fraction.

Table 4 Element balance over the boiler and element distribution in the ashes of the combustion tests

Case wt-%	Ref	Sludge	Zeolite	Case Total molar flow in with fuel	Ref	Sludge	Zeolite
$K_{out}\ K_{in}^{-1}$	76.4	102.4	40.7	K	65.5	82.0	105
$Na_{out}\ Na_{in}^{-1}$	191.0	114.2	26.0	Na	3.7	19.9	237
$Ca_{out}\ Ca_{in}^{-1}$	143.0	109.6	35.6	Ca	46.1	119	60.2
$Al_{out}\ Al_{in}^{-1}$	1015	102.7	30.6	Al	1.7	199	235
$S_{out}\ S_{in}^{-1}$	88.9	104.7	90.2	S	10.1	59.2	12
$Cl_{out}\ Cl_{in}^{-1}$	71.3	108.2	70.9	Cl	20.0	24.0	32.7
Sec. cyclone (wt-% of tot out)				**Sec. cyclone (mole h^{-1})**			
K	28.3	72.4	22.7	K	14.2	61	9.7
Na	34.6	71.9	9.7	Na	2.5	16	5.9
Ca	31.1	57.8	43.5	Ca	20.5	75	9.3
Al	46.8	78.4	14.6	Al	8.1	160	10.5
S	23.0	3.5	15.4	S	2.1	2.2	1.7
Cl	8.2	0.7	1.5	Cl	1.2	0.2	0.4
Bag filter (wt-% of tot out)				**Bag filter (mole h^{-1})**			
K	9.0	14.8	71.3	K	4.5	12	30.4
Na	7.4	7.5	84.1	Na	0.5	1.7	51.2
Ca	11.6	18.3	47.2	Ca	7.6	24	10.1
Al	4.5	9.1	80.9	Al	0.8	19	58.1
S	0.3	10.9	32.2	S	0.0	6.8	3.6
Cl	26.1	0.4	38.4	Cl	3.7	0.1	8.9
Bottom bed (wt-% of tot out)				**Bottom bed (mole h^{-1})**			
K	62.7	12.8	6.0	K	31.4	11	2.6
Na	58.0	20.6	6.2	Na	4.1	4.7	3.8
Ca	57.3	23.9	9.3	Ca	37.7	31	2.0
Al	48.7	12.5	4.5	Al	8.4	25	3.2
S	13.1	2.1	0.4	S	1.2	1.3	0.05
Cl	1.9	0.9	0.1	Cl	0.3	0.2	0.02
Flue gas (wt-% of tot out)				**Flue gas (mole h^{-1})**			
S	63.5	83.5	51.9	S	5.7	52	5.8
Cl	63.8	98.0	60.1	Cl	9.1	26	13.9

Deposit formation

Large differences in deposit formation at the entrance of the convection section (No. 16 in Fig. 1) were found as shown in Fig. 2. The deposit formation rate was reduced by sewage sludge addition and strongly increased by zeolite addition. The deposits in the Ref case consisted of fine particles evenly distributed on the windward side of the probe. The colour of the deposits was white with elements of grey. In the MSS case the deposits consisted of a thin dust layer with a reddish brown colour not completely covering the steel surface of the deposit rings. The thickest deposit layers were formed in the Zeolite case. These deposits consisted of white and grey particles and covered the windward side completely.

The results from analyses of the element composition of the deposits are given in Table 5. The Ref case gave deposits mainly consisting of K and Cl, whereas, the addition of sewage sludge resulted in significant reduction of Cl and K in the deposits. Instead the dominating elements in these deposits were Al, Ca, K, S and Si. The composition of the deposits from the Zeolite case very much reflected the composition of the zeolite powder with the exception that 50% of the sodium was exchanged for potassium and that some Ca was found as well.

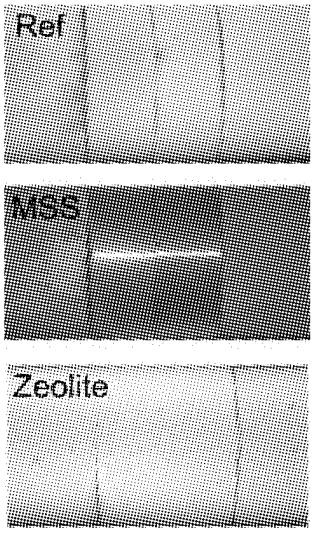

Fig. 2 Deposit probes with rings, windward side

Fly ash composition

The results of the chemical fractionation analysis are presented in Fig. 3. The analysis of the reference fuel mix and fly ashes showed that Ca, Mg, K and Na were less soluble after combustion, thus transformed into more stable compounds. In contrast, sulphur and chlorine were more soluble in the ash than in the fuel mix. However, the element balances for K, Cl and S were not closed, see Table 4. Part of the reason is that these elements were accumulated as deposits in the convection section of the boiler (see deposit ring in Fig. 2 and composition in Table 5). In the MSS case the difference between the solubility of K and Na in the fuel mix and that in the fly ashes was much larger than in the Ref case, increasing from 8 to 90% and 35 to 95% respectively.

Chlorine was equally soluble in the fly ashes as in the fuel mix. Sulphur was the only element showing an increased solubility after combustion and no changes in the solubility of aluminium and silicon were found. The fly ash from the zeolite case had the highest Al and Na concentrations derived from the original zeolites and most alkali were hard bound in the ash.

Table 5 Element composition of deposits recalculated as oxides (except for chlorine)

	Wet chemistry			SEM-EDX		
	Ref	MSS	Zeolite	Ref	MSS	Zeolite
Al_2O_3	1	12	23	1	10	26
CaO	9	11	6	6	13	3
Cl	19	4	3	27	0	4
K_2O	43	8	14	42	22	13
MgO	4	3	1	2	4	0
Na_2O	3	1	12	2	2	13
P_2O_5	0	5	1	1	6	1
SO_3	12	29	2	13	24	3
SiO_2	9	27	38	8	19	38

The results from the SEM-EDX mapping of fly ash samples from the three combustion cases are shown in Figs. 4 to 6. In the secondary cyclone ash from the Ref case clear correlations between K, S and Ca were seen, Fig. 4 (Pettersson, 2008). This was also confirmed by the spot analysis (spot 1,4-6). There was also a more diffuse correlation of K, Na and Cl due to the presence of NaCl and KCl in small crystals as confirmed by XRD. In addition K_2SO_4 and $KAlSi_3O_8$ were found by the XRD analysis (Pettersson, 2008). In the bag filter ash correlations of K, Na and Cl were found and the spot analysis confirmed the higher Cl and Ca concentrations in this ash. Potassium was more evenly distributed in the bag filter ash and more KCl was found by the XRD in this ash compared to the secondary cyclone ash. The EDX maps of the fly ash samples from the MSS case are shown in Fig. 5. In this case clear correlations between Si, Al and K were found and also to P, Ca and Fe (Pettersson, 2008). Furthermore, no correlations with K to S or Cl were found. These findings are consistent with results from a study on particle formation in combustion using a low-pressure impactor (Bäfver, 2008). Bäfver and co-workers found Al and K only in coarse particles when sewage sludge was added to the fuel mix. In addition, the number of fine particles (<1μm) was significantly reduced compared to combustion of the Ref fuel (the same fuel as in this work). The secondary cyclone ash contained particles only containing Si, Al and K (as spot 6 in Fig. 5) probably zeolites from the sewage. In addition Fe and P correlated well in both these fly ashes. In the XRD analysis potassium and sodium aluminium silicates, sodium silicates, haematite, and phosphates containing Fe, Mg, Ca and K were found. The EDX results from the zeolite case had the same correlations between Si, Al and K as found in the MSS case, Fig. 6. In addition, particles with the same composition were found both in the secondary cyclone and bag filter ash. Furthermore, different K and Na aluminium silicates were found by XRD together with K and Ca aluminium silicates and calcium sulphates (Elled, 2008; Pettersson, 2008).

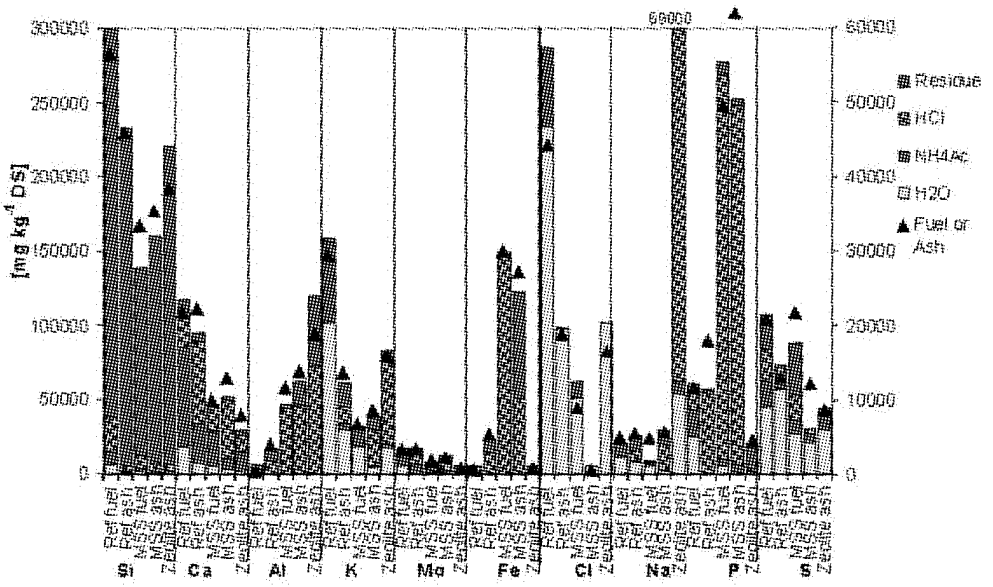

Fig. 3 Fractionation results of fuel mixes and fly ashes (mixture of sec. cyclone and bag filter ashe) from the reference, MSS and zeolite case

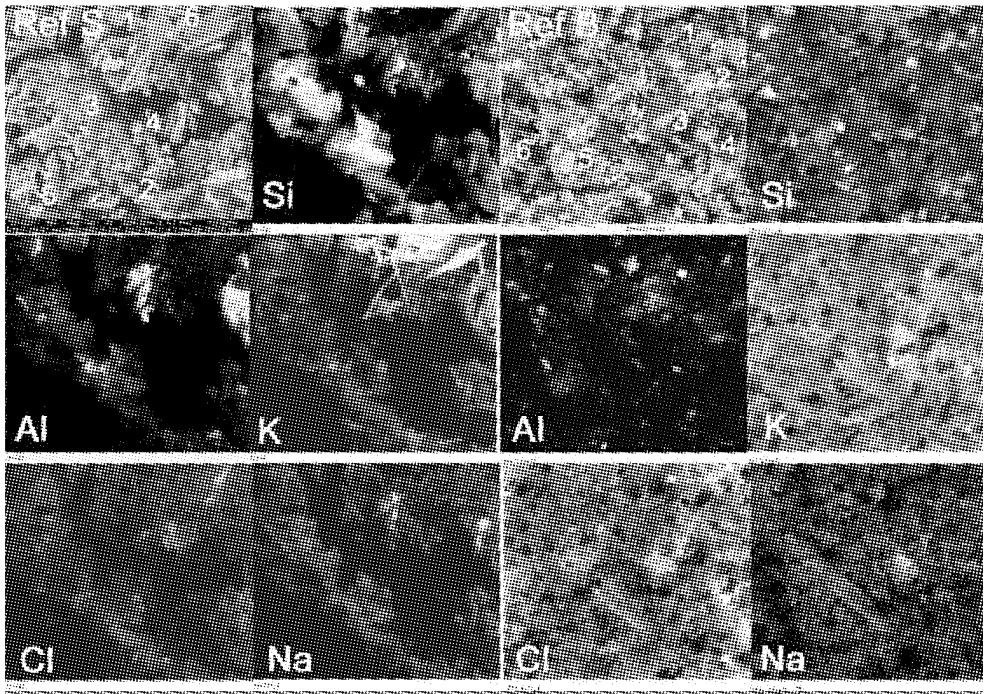

wt-%	Na_2O	MgO	Al_2O_3	SiO_2	P_2O_5	SO_3	Cl	K_2O	CaO	Fe_2O_3	Na_2O	MgO	Al_2O_3	SiO_2	P_2O_5	SO_3	Cl	K_2O	CaO	Fe_2O_3
Ref Sec. cyc											Ref Bag									
Spot 1	0	1	1	26	1	34	0	18	17	2	Spot 1	1	2	1	48	5	5	1	5	28	1
Spot 2	5	0	9	76	0	0	1	6	1	0	Spot 2	0	15	1	27	16	4	1	3	37	2
Spot 3	1	4	0	86	2	0	0	2	4	1	Spot 3	1	28	1	14	11	7	3	9	26	1
Spot 4	0	0	0	44	0	47	0	7	0	0	Spot 4	1	6	0	31	16	5	1	5	32	1
Spot 5	0	0	0	49	10	0	0	16	25	0	Spot 5	0	4	0	6	2	23	2	3	58	1
Spot 6	0	1	0	15	1	48	1	21	10	3	Spot 6	0	9	1	28	6	11	3	8	32	2

Fig. 4 SEM-EDX mapping and spot analysis recalculated as oxides (except for chlorine) in wt-% on fly ashes of the ref. case. S for secondary cyclone ash and B for bag filter ash

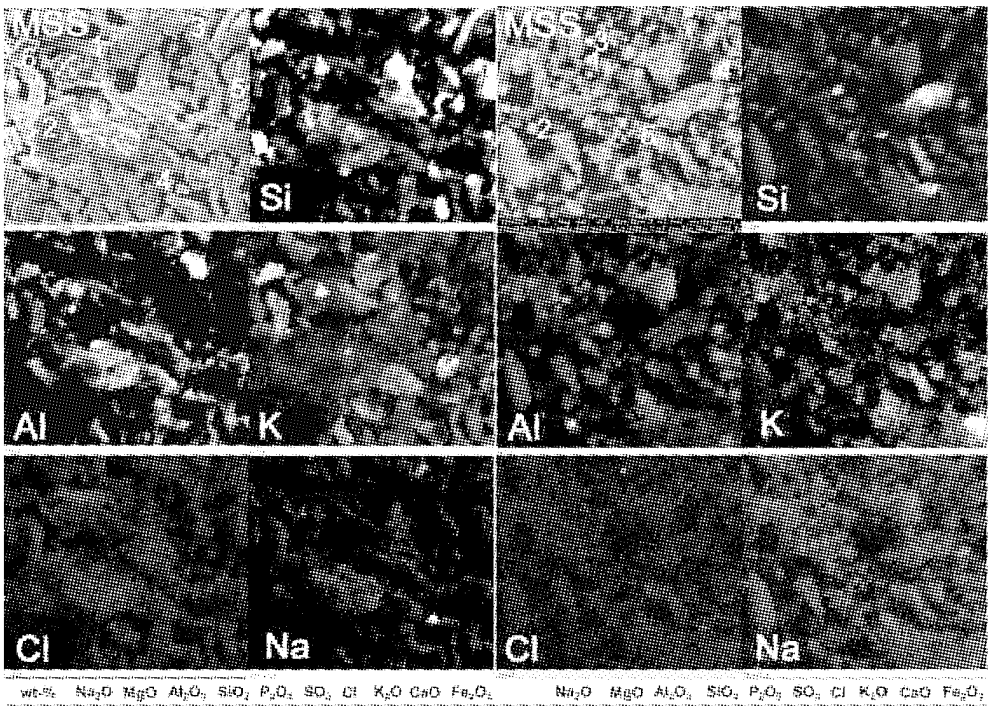

wt-%	Na_2O	MgO	Al_2O_3	SiO_2	P_2O_5	SO_3	Cl	K_2O	CaO	Fe_2O_3	Na_2O	MgO	Al_2O_3	SiO_2	P_2O_5	SO_3	Cl	K_2O	CaO	Fe_2O_3
MSS Sec. cyc											MSS Bag									
Spot 1	2	3	18	28	18	6	5	9	10	14	Spot 1	0	12	22	46	6	2	0	6	4	2
Spot 2	6	2	18	29	17	0	0	2	6	24	Spot 2	0	11	28	50	4	2	0	7	7	2
Spot 3	1	1	26	31	14	1	0	3	7	15	Spot 3	2	3	16	21	48	4	0	3	7	1
Spot 4	1	2	19	33	20	0	0	4	7	14	Spot 4	0	4	15	31	21	5	0	2	17	1
Spot 5	0	1	11	22	10	0	0	8	9	31	Spot 5	1	3	12	56	14	3	0	4	6	0
Spot 6	0	0	17	65	2	0	0	14	1	1										

Fig. 5 SEM-EDX mapping and spot analysis recalculated as oxides (except for chlorine) in wt-% on fly ashes of the MSS case. S for secondary cyclone ash and B for bag filter ash

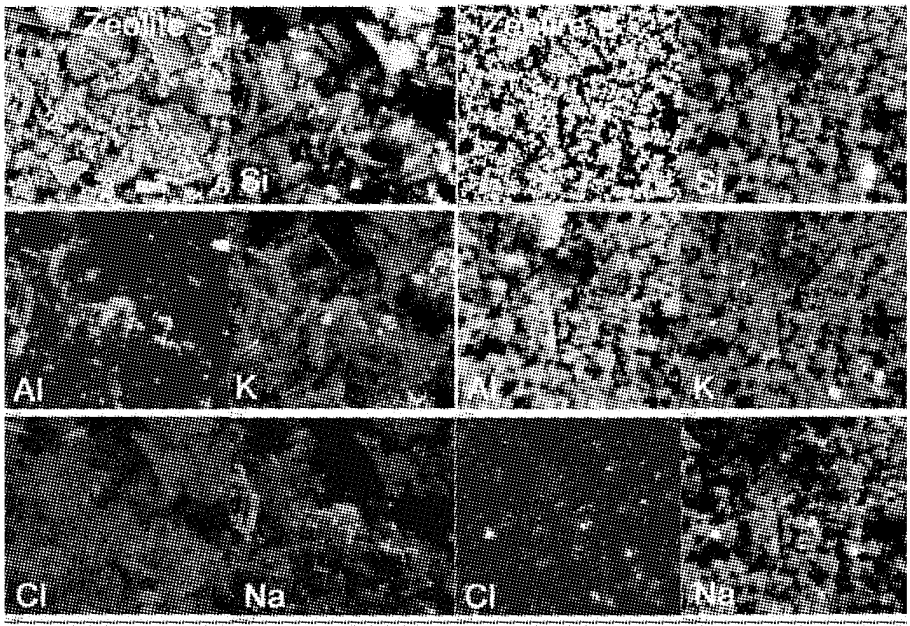

wt-%	Na_2O	MgO	Al_2O_3	SiO_2	P_2O_5	SO_3	Cl	K_2O	CaO	Fe_2O_3
Zeolite Sec. cyc										
Spot 1	13	3	4	39	1	11	6	15	6	2
Spot 2	1	1	2	17	0	65	1	22	18	0
Spot 3	1	8	5	58	13	1	0	6	22	6
Spot 4	3	5	0	13	1	4	2	4	69	0
Spot 5	3	2	4	43	1	23	1	12	15	0
Spot 6	1	0	25	71	0	0	0	2	0	0

	Na_2O	MgO	Al_2O_3	SiO_2	P_2O_5	SO_3	Cl	K_2O	CaO	Fe_2O_3
Zeolite Bag										
Spot 1	1	1	1	88	1	1	1	2	4	0
Spot 2	4	0	21	66	1	1	1	4	3	0
Spot 3	5	1	5	16	0	7	11	7	48	0
Spot 4	6	0	20	58	1	1	1	9	3	0
Spot 5	3	0	5	75	1	2	1	6	6	1

Fig. 6 SEM-EDX mapping and spot analysis recalculated as oxides (except for chlorine) in wt-% on fly ashes of the zeolite case. S for secondary cyclone ash and B for bag filter ash

Laboratory experiments

The ion-exchange of the Doucil A24 to Ca and K was established by mixing with a $CaCl_2$ or KCl solution. Both solutions had a surplus of Ca or K ions of approximately ten times the theoretical amount of ion sites in the zeolite sample. The result of the ion exchange and the thermal treatment are presented in Table 6. The concentration for Doucil A24 is the theoretical concentration of the pure zeolite and the concentrations for the ion exchanged zeolites are SEM-EDX results from spot and area analysis. The concentrations given in brackets are calculated based on the AAS analysis of the Na concentration in the eluate after the ion exchange. All results in Table 6, except Doucil A24, are mean values of several area or spot analyses of each sample. It was observed that the ion exchanged zeolites had a very uneven distribution of ions over the sample. The reason for this is that MAP zeolites (the group including Doucil A24) have a very flexible structure and the ion exchange rate is increased by increased conversion (Allen et al. 2002), thus isles of high concentrations of Ca^{2+}or K^+ ions are formed. This means that an EDX analysis over a larger area of the sample (marked by * in Table 6) gives a more accurate mean value than a spot analysis. In the thermal treatment of the original zeolite and the ion exchanged zeolite 0.5g of KCl was added. This corresponds to 6.7 mmol of K and Cl. The results in Table 6 show

Table 6 Element composition of the different samples. Results from the SEM-EDX analysis in addition to results from AAS (in brackets)

[mmol/2g]	O	Na	Al	Si	K	Ca	Cl
Doucil A24	56.3	14.1	14.1	14.1	-	-	-
$Ca_{exchanged}$	68.6	0.5 [4.1]	11.7	12.3	-	5.8 [5.0]	-
$K_{exchanged}$	61.3	1.1 [2.1]	11.8	12.8	8.9 [12.0]	-	-
CaKCl 700	46.1	0.9	14.4	16.1	3.7	8.0	2.4
CaKCl 800	56.6	0.4	11.2	12.3	2.4	6.4	2.4
CaKCl 900*	55.9	0.4	7.2	6.5	5.2	9.5	3.8
CaKCl 800 steam	56.6	0.4	11.3	11.7	2.8	6.0	2.9
NaKCl 800*	48.8	7.2	10.6	11.2	6.4	-	5.7
NaKCl 800 steam*	52.7	4.1	12.0	12.7	5.6	-	4.7
K 900*	59.3	0.8	12.6	13.2	8.3	-	-
K 700 steam*	66.1	0.5	13.3	14.2	4.4	-	-
K 800 steam	43.8	0.2	21.9	18.4	4.7	-	-
K 900 steam*	72.2	0.5	11.4	11.9	4.9	-	-

that the zeolites could capture both K and Cl during the heating of the sample. In addition, the original Doucil A24 (NaKCl) captured more KCl than the Ca exchanged zeolite (CaKCl). These results were confirmed by the XRD analysis of the samples which showed that both K and KCl were incorporated in the zeolite structure. No losses of Ca were detected during the thermal treatment in contrast to Na where especially the original zeolite lost much of its Na-ions. This could explain the higher capacity of KCl capture by the original zeolite. The thermal experiments of the potassium exchanged zeolites were performed to investigate the ability of the zeolite to keep the potassium ions even at an increased temperature. The results showed that the zeolite (K in Table 6) encapsulated most of the potassium. Also these results from the EDX varied a lot because of the uneven ion exchange over the sample.

CONCLUSIONS

Addition of sewage sludge in the combustion of biomass rich in alkali and chlorine gives a significant reduction of the gas phase KCl level. Addition of zeolites to the boiler gave some smaller reduction of KCl as well. This indicates similar KCl absorption mechanisms. The laboratory study shows that KCl can be captured as a whole in the zeolite structure at high temperatures, probably by encapsulation when the structure is starting to change due to the heating.

The chemical fractionation showed that potassium and sodium are less soluble in the fly ash after combustion of the MSS fuel mix than in the reference case. This can be explained by the formation of aluminium silicates containing alkali metal ions, like feldspars.

REFERENCES

Allen, S., Carr, S., Chapple, A., Dyer, A. and Heywood, B.: PCCP **4** (2002), pp. 2409-2415.

Bäfver, L. (2008). PhD thesis, Chalmers University of Technology, Sweden, ISBN 978-91-7385-177-0.

Davidsson, K. O., Åmand, L.-E., Elled, A.-L. and Leckner, B.: Energy and Fuels **21** (2007), pp 3180-3188.

Elled, A-L. (2008) PhD thesis. Department of Energy and Environment, Chalmers university of Technology, ISSN 0346-718X, ISBN 978-91-7385-139-8.

Elled, A.-L., Åmand, L.-E. and Davidsson, K. (2008) Effects from co-firing municipal sewage sludge with biomass on deposit formation. Submitted to Biomass and Bioenergy.

Eriksson, J. (2001). Report 5159, Swedish Environmental Protection Agency, Stockholm, ISBN 91-620-5159-8, ISSN 0282-7298.

ICCP (2007). Climate change 2007: Mitigation. Contribution of Working group III to the Fourth Assessment Report of the Intergovernmental Panel on Climate Change [B. Metz, O. R. Davidson, P .R. Bosch, R. Dave, L. A. Meyer (eds)], Cambridge University Press, Cambridge, United Kingdom and New York, NY, USA.

Möller, A. (2008). Chalmers University of Technology, Göteborg, Sweden, Report nr. T2008-310.

Pettersson, A. (2008) PhD thesis. Department of Energy and Environment, Chalmers university of Technology, ISSN 0346-718X, ISBN 978-91-7385-174-9.

Pettersson, A., Zevenhoven, M., Steenari, B.-M., Åmand, L.-E.: Fuel **87** (2008), pp 3183-3193.

Schwuger, M. J. Detergents in the environment. 1996, ISBN 0-8247-9396-X.

Zevenhoven-Onderwater, M. (2001). PhD thesis. Department of Chemical Engineering, Åbo Akademi University, Finland, ISSN 1457-7895, ISBN 952-12-0813-9.

EMISSIONS DURING CO-FIRING OF RDF-5 WITH COAL IN A 22 t/h STEAM BUBBLING FLUIDIZED BED BOILER

Hou-Peng Wan, Jia-Yuan Chen, Ching-I Juch, Ying-Hsi Chang, and Hom-Ti Lee

New Energy Technology Division, Energy & Environmental Laboratories (EEL), Industrial and Technology Research Institute (ITRI), Taiwan, China

Abstract: The co-firing of biomass and fossil fuel in the same power plant is one of the most important issues when promoting the utilization of renewable energy in the world. Recently, the co-firing of coal together with biomass fuel, such as "densified refuse derived fuel" (d-RDF or RDF-5) or RPF (refuse paper & plastic fuel) from waste, has been considered as an environmentally sound and economical approach to both waste remediation and energy production in the world. Because of its complex characteristics when compared to fossil fuel, potential problems, such as combustion system stability, the corrosion of heat transfer tubes, the qualities of the ash, and the emission of pollutants, are major concerns when co-firing the biomass fuel with fossil fuel in a traditional boiler. In this study, co-firing of coal with RDF-5 was conducted in a 22t/h bubbling fluidized bed (BFB) steam boiler to investigate the feasibility of utilizing RDF-5 as a sustainable fuels in a commercial coal-fired steam BFB boiler. The properties of the fly ash, bottom ash, and the emission of pollutants are analyzed and discussed in this study.

Keywords: bubbling fluidized bed (BFB), densified refuse-derived fuel (d-RDF or RDF-5), co-firing, pollution emission, biomass

INTRODUCTION

There had been remarkably rapid progress over the past decade in the development of the utilization of renewable energy for many countries in the world to decrease the dependency on imported energy. Furthermore, the price of fossil fuel is steadily rising recently and the issue of reduction of greenhouse gases is highlighted globally, which also compel the boiler users to search for cheap and sustainable substitute fuels.

Under these circumstances, the energy recycling from waste has been attracting attention. RDF is one of the waste-to-energy technologies to transform MSW or ISW into a uniform fuel, following process of crushing, screening, drying, and pelletizing. It has potential for promising substitute fuel with significant benefits of economic, environment, and reduction in effective CO_2 emissions (Baxter, 2005).

RDF properties, including varied chemical compositions and physical characteristics (e.g. particle size, heating value, moisture content, ash content, volatile matters, fixed carbon, and bulk densities) are affected by waste stocks stream and differ from those of conventional coal fuel. These different properties between RDF and coal result in causing differences in the combustion characteristics of fuels which, in turn, affect the type of combustion equipment required and the combustion and environmental concerns that must be deal with (Wan et al., 2007). In general, the dedicated RDF boiler or incinerator should be specifically designed. Otherwise, it will be more expensive in capital cost than conventional coal-fired boiler.

The biomass co-firing options can be categorized as follows (Loo and Koppejan, 2002): direct co-firing (the pre-processed biomass is directly fed to the boiler furnace), indirect co-firing (after gasification of the biomass, the product fuel gas is fed to the boiler furnace), and parallel combustion (the combustion of the biomass in a separate boiler and the utilization of the steam produced within the power plant).

Direct co-firing is the most straightforward applied, most commonly applied and low-cost of all (Baxter, 2005; Dai et al., 2008). For direct co-firing of biomass, two methods have been developed: (a) blending the biomass and coal in the fuel handling system, with the blended fuel then being fed; and (b) separate fuel handling and separate burners for the biomass, thereby avoiding impact on the conventional coal delivery system (Brem, 2005). However, Dai et.al. reviewed the research findings and found that an apposite modifying of coal-fired facilities and proper adjustments of combustion operation are needed for biomass co-firing with coal except low co-firing ratios(less than 10% thermal) (Dai et al., 2008).

In this study, RDF-5 pellets were employed to co-firing with coal in existing industrial BFB coal-fired boilers without modifying original facilities of boiler system. The blend flow/handling characteristics, the boiler operation stability, and the emissions of pollutant were observed and compared with the behaviors of coal-fired operations for individual boiler to investigate the feasibility of co-firing RDF-5 in existing coal-fired boiler.

EXPERIMENT AND APPARATUS

The bubbling fluidized bed steam boiler

The RDF co-firing trials were conducted in an existing industrial coal-fired 22t/h BFB boiler. The BFB boiler with capacity of 22 t/h (203°C with 20kgf/cm^2) is two-drum water tube type steam producing system. The fuel feeding system of BFB boiler is including: daily bunker, chutes, screw feeder etc. Flue gas treatment consists of bag-house and FGD. The flue gas sampling location is set in stack outlet. A schematic diagram of the BFB boiler is shown in Fig.1.

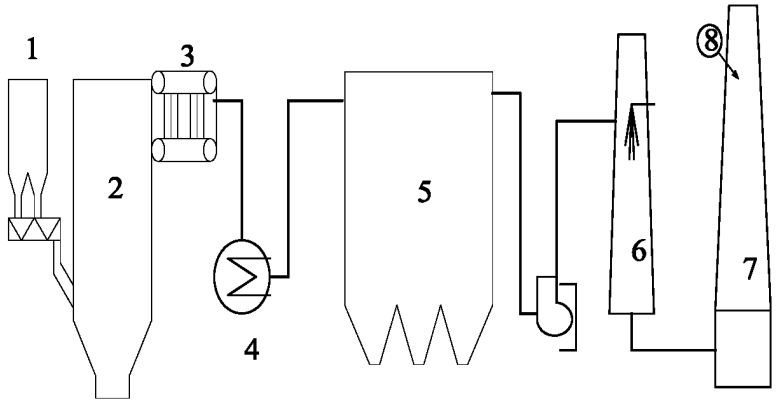

Fig. 1 Schematic diagram of 22t/h BFB boiler (1: fuel bin; 2: BFB; 3: boiler; 4: economizer; 5: bag-house; 6: FGD; 7: stack; 8: flue gas sampling location)

The fuel property

RDF-5 has been a commercial product in Taiwan. The RDF-5 pellets employed for BFB boiler co-firing tests were prepared from industrial waste stream which contained mainly paper and plastics. Bituminous coal was imported from Indonesia for BFB as primary fuel. The characteristics of fuels used in the experiments are listed in Table 1.

Table 1 Characteristics of fuels used in the experiments

Fuel Type	Proximate analysis (*wt.%*)				Ultimate analysis (*wt.%*)						LHV /(kcal/kg)	Bulk density/ (g/cm^3)	Ave. particle size /mm
	moisture	Ash	Volatiles	Fixed carbon	C	H	O	N	S	Cl			
Bituminous coal	9.5	16.4	35.8	38.2	51.0	6.2	15.3	0.4	1.0	0.02	5,068	0.76	1-30
RDF-5	7.3	13.3	74.3	5.0	42.8	5.3	29.1	0.3	0.4	1.22	5,497	0.60	20

The moisture content of RDF-5 is lower than that of coal but chlorine content of RDF-5 is evidently higher compared with those of coals. Low heating value of fuels are above 5,000 kcal/kg. Coal particles within a certain size range are more irregular than RDF-5 pellets with 20mm diameter.

Test conditions and procedure

A series testing was conducted for the BFB boiler on Normal Continuous (or Capacity) Rating (NCR; 17t/h in the BFBB). The first step (Test Run #1) to evaluate the feasible co-firing RDF-5 ratio was changing the RDF-5 ratio from 10%, 20%, 30%, to 40% (by heat content as shown in Table 2, the 40% was set the max. value). For each test run, a two-hour monitoring of the emission of flue gas was conducted continuously. RDF-5 and coal blends were pre-mixed in intake pit then fed to the furnace using the existing fuel handling equipments. The procedure of finding feasible co-firing ratio was listed in Fig.2.

Table 2 The amount of coal and RDF-5 under various co-firing ratio

Co-firing ratio (at 77.2 % operation ratio)	0 %	10 %	20 %	30 %	40 %
Coal (kg/h)	2281	2053	1825	1597	1369
RDF-5(kg/h)	0	275	551	827	1103

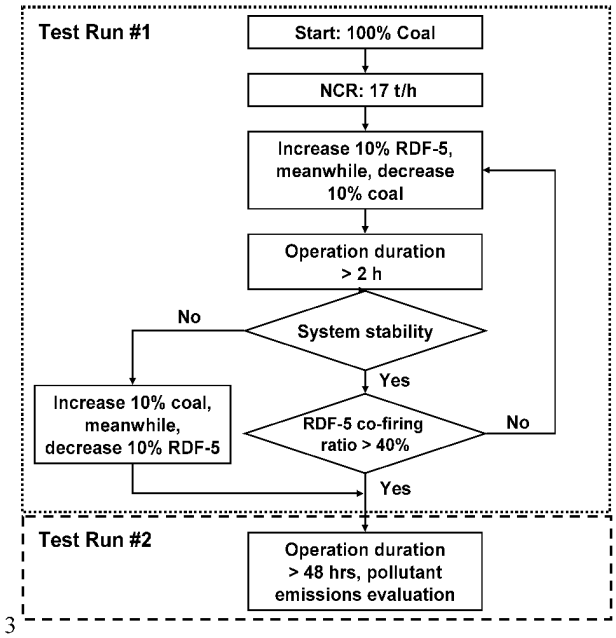

Fig. 2 Flowchart of the test procedure

To complete feasibility assessment (Test Run #1), the following parameters would be monitored during the tests: the blend flow/handling characteristics (e.g. fuel bridging, fuel segregation, and flow stoppage in the fuel transport or storage systems), the boiler operation stability (e.g. furnace temperature distribution, steam production, bag-house differential pressure, burn-back, and any significant operational change), and the emissions of pollutant (e.g. sulfur dioxide (SO_2), nitrogen oxide (NO_x), O_2, CO, and HCl. Finally, Test Run #2 was conducted with 40% co-firing ratio of RDF-5.

Flue gas emission analysis

The concentrations of the flue gases, such as SO_2, NO_x, O_2, and CO, measured on-site via the flue gas exhaust channel, were monitored continuously by employing a HORIBA PG-250 portable non-dispersive infrared (NDIR) multi-gas analyzer during the experiments. The sampling process and the analysis approach for the HCl in the flue gas were based on NIEA A412.70A method issued by Environmental Protection Administration.

RESULTS AND DISCUSSION

The blend flow/handling characteristics

Low bulk density (0.6 g/cm^3) and larger particle size (20 mm) of RDF-5 compared with those of coal caused fuel segregation in conveying system and in daily bunker for the BFB boiler. But there were noparticle bridge and arch happening during tests. The additional fuel crusher equipped before BFB feeding system could decrease coal particle size near as that of RDF-5 leading to mitigate coal/RDF blend segregation.

Combustion performance (Test Run #2)

Base on the BFB boilers operational experiences, there isn't any significant operational change or burn-back trouble during co-firing test. To meet the plant actual steam demand, turn-down operation was adapted during night time. However, it provided a stable steam production with average outlet pressure at 15.57kg$_f$/cm^2 for co-firing RDF-5 with coal, which was fairly similar to that of coal fired alone.

For BFB boiler system, steam produced stably on NCR with average outlet pressure at 16.8kgf/cm^2. When co-firing RDF with coal, the bed temperature was slightly higher than burning 100% coal, on the contrary, the freeboard temperature was slightly lower than coal fired alone. The steam flow property and furnace temperature of BFB boiler are shown in Fig. 3.

The differential pressure between inlet and outlet of bag-house was easily satisfying normal operation limit for both boilers during test. The bag-house differential pressure under different operation conditions is listed in Table 3.

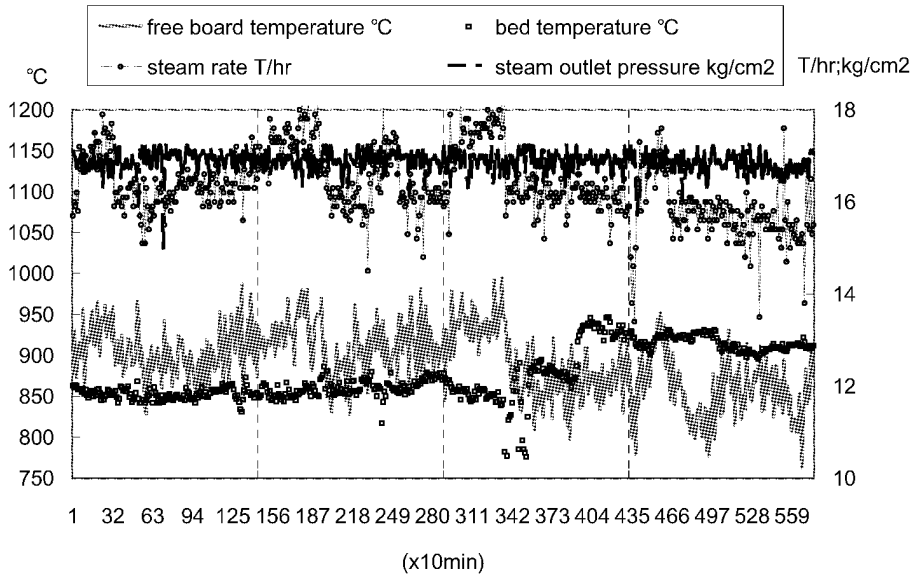

Fig. 3 The temperature distribution and steam property of BFB boiler (100% coal and 60% coal / 40% RDF-5)

Table 3 Bag-house operational parameter during Test Run #2.

Operation Conditions	Differential pressure (mmAq)
100% coal-firing (0% RDF-5)	64.3
40% RDF-5 co-firing (60% coal)	65.8 (47-71)
Normal operation limit	170

Emissions of RDF co-firing with coal

Based on the stationary air pollution regulations in Taiwan, the concentration of flue gas emission had been corrected to 6% O_2. The continuous flue gas measured is shown in Fig.4. Form Fig.4, we can find the emissions of pollution were stable during the testing period in the BFB boiler.

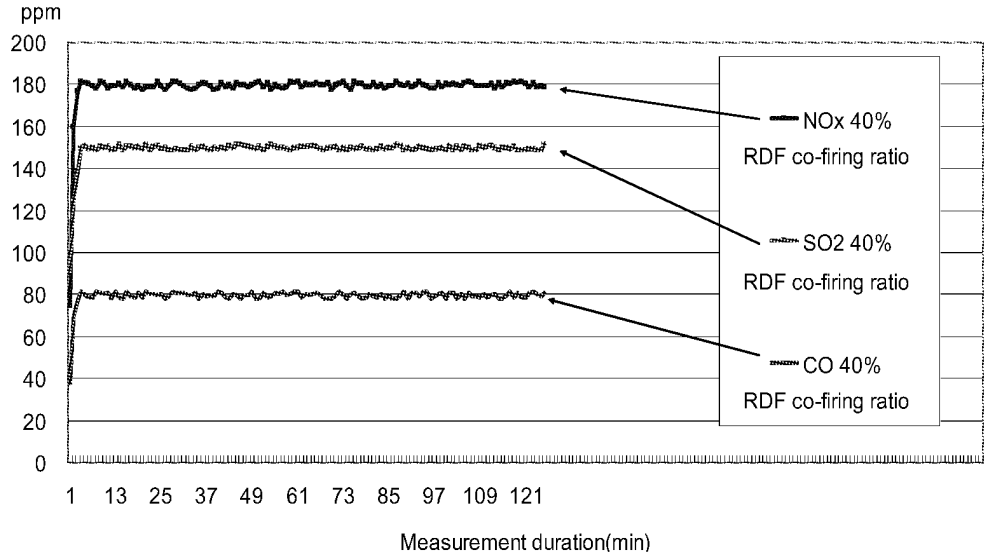

Fig. 4 The continuous flue gas measurement of concentrations of NO_x, SO_2, and CO during 40% RDF-5 co-firing test in the BFB boiler

The Flue gas emission results of BFB boiler were shown in Fig.5. The concentrations of SO_2, NO_x, and CO emission during 100% coal-firing are relatively higher and fluctuated sharply compared with co-firing RDF-5 with coals.

These results indicate that co-firing RDF-5 with coal in coal-fired boiler could help combustion and decrease the flue gas emissions except that HCl are consistent with previous study findings (Baxter, 2005; Wan

et al., 2007; Aittola and Seppo, 1989; Demirbas, 2004; Sami and Wooldridge, 2001, Wan et al., 2008). The high chlorine content of RDF-5 might lead to the formation of HCl which significantly increased in flue gas emission of RDF co-firing with coal compared with the concentration of combustion of 100% coal. The average concentration of HCl emission reached 12ppm during co-firing test run.

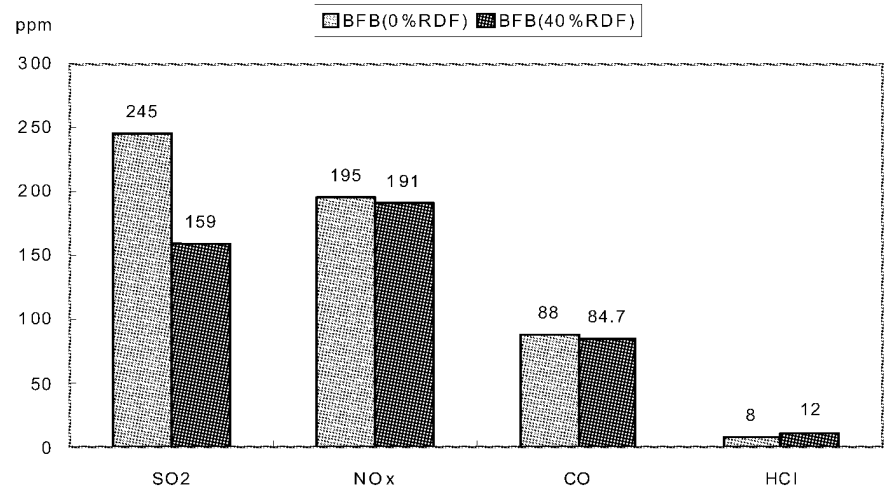

Fig. 5 Flue gas emission of BFB boiler (100% coal feeding and 40% RDF-5/60% coal feeding)

The qualities of fly ash and bottom ash

Fuel combustion ashes cause various types of problems, especially when the interaction between ashes from different fuels is poorly understood. The RDF-5 was derived from paper rejects consisting of waste paper, waste plastics, rubber, rope, staples, and steel wire, etc. However, all the TCLP measurement data were lower than the regulation limitation as listed in Table 4.

Table 4 The qualities of fly ash and bottom ash via TCLP test (40% co-firing RDF-5)

Item / Extract solution	Unit	Ash qualities		Regulation
		Fly ash	Bottom ash	
Total Pb	mg/L	ND < 0.20	ND < 0.2	5.0
Total Cd	mg/L	ND < 0.02	ND < 0.01	1.0
Total Cr	mg/L	ND < 0.02	ND < 0.02	5.0
Total Se	mg/L	ND < 0.1	ND < 0.1	1.0
Total Cu	mg/L	0.04	0.15	15.0
Total Ba	mg/L	0.42	0.21	100.0
Cr^{6+}	mg/L	ND < 0.01	ND < 0.01	2.5
Total As	mg/L	ND < 0.03	ND < 0.03	5.0
Total Hg	mg/L	ND < 0.0001	ND < 0.0001	0.2
Loss on ignition (LOI)	%	16.8	ND < 0.1	-
Dioxin	ngI-TEQ/g	0.003	0.0001	1.0

CONCLUSIONS

Commercial RDF co-fired with coal in existing industrial steam coal-fired BFB boilers without modifying original facilities of boiler system was available with moderate co-firing ratio. The RDF co-firing test results indicated that fuel blend ratio 40% RDF-5 for BFB was capable. The difference of bulk density and particle size between RDF-5 and coal could lead to blend segregation but did not affect stable steam production. Co-firing of RDF-5 with coal could decrease SO_2 and NO_x emission compared to coal-firing alone, in spite of increasing HCl levels due to the RDF-5.

RDF-5 is seen as one of the potential options to mitigate greenhouse gas emissions and substitute fossil

fuels. This is certainly evident in Taiwan, where is not rich in land-based energy resources and the ratio of imported energy is over 95% at present. Overall, the co-firing of RDF-5 in existing coal-fired boilers provides an attractive approach to nearly every aspect of the complement fuels for boiler users.

ACKNOWLEDGEMENTS

The authors acknowledge financial support provided by the Bureau of Energy, MOEA, Taiwan, China.

REFERENCES

1. Aittola, J.P. and Seppo, V., Chemosphere **19** (1-6), (1989), pp. 353-359.
2. Baxter, L., Fuel **84**, (2005), pp.1295-1302.
3. Brem, G., (2005).GCEP. Advanced Coal Workshop, Provo (UT), USA.
4. Dai J, S. Sokhansanj, Grace, J. R. X. Bi, C. J. Lim, S. Melin, (2008). The Canadian journal of chemical engineering **86**, pp.367-386.Wan, H.P. Chang, Y.H. and Chen, J.Y. (2007). The Combustion Institute, 17th combustion seminar, Taipei.
5. Demirbas A., Progress in Energy and Combustion Science **30**, (2004), pp.219-230.Loo, Sjaak Van and Koppejan, Jaap (2002). Handbook of Biomass Combustion and Co-firing, The Netherlands, Twente University Press, Enschede.
6. Loo, Sjaak Van and Koppejan, Jaap (2002). Handbook of Biomass Combustion and Co-firing, The Netherlands, Twente University Press, Enschede.
7. Sami, M., Annamalai, K. and Wooldridge, M.Prog. Energy Combust. Sci. **27**, (2001) pp.171-214.
8. Wan, H.P. Chang, Y.H. and Chen, J.Y. (2007). The Combustion Institute, 17th combustion seminar, Taipei.
9. Wan, H.P., Chang, Y.H., Chien, W.C. Lee, H. T. and Huang, C.C., Fuel **87**, (2008), pp.761-767.

MERCURY EMISSION FROM CO-COMBUSTION OF SLUDGE AND COAL IN A CFB INCINERATOR

Y.F. Duan*, C.S. Zhao, C.J. Wu, Y.J. Wang

Thermal-energy Engineering Research Institute, Southeast University, Nanjing, 210096, China

Abstract: An experimental study on co-combustion of sludge and coal were conducted in a circulating fluidized bed incinerator with the dense bed cross section area of 0.23m×0.23m and the height of 7m. The mercury mass balance was measured and the distribution of mercury speciation in flue gas was discussed. Effects of major operational parameters such as Ca/S molar ratio, desulfurization sorbents, excess air coefficient, co-combustion temperature, and SO_2 and NO_x concentrations on the distribution of mercury speciation in flue gas, mercury in fly ash and slag were investigated during the co-combustion process. The results show that majority of mercury goes into the flue gas in which the elemental mercury is the major speciation. Ca-based sorbent can remove Hg^{2+} in flue gas effectively, in which CaO has better mercury removal effect than $CaCO_3$. The content of Hg^{2+} in flue gas increases with increasing of the concentration of SO_2 and NO_x in flue gas. It can also be concluded that the excess air coefficient exerts dominant influences on mercury speciation among the flue gas, fly ash and bottom ash.

Keywords: CFB incinerator, sludge, coal, co-combustion, mercury emission

INTRODUCTION

Sewage sludge is a kind of heterogeneous body composed of organic fragments, microorganisms, inorganic particles and colloids (Zhou et al., 2000), containing pathogenic microorganisms, toxic organic compounds, as well as heavy metals Hg. It will cause water, soil and air pollutions, and at last bring health problem to human being when being stacking without any treatment. Therefore, the sludge must be made treatments such as reduction, stabilization and harmless process.

The final treatments of sludge including agricultural fertilizer, landfill, incineration, drying, heat treatment and composting (Li et al., 2003), in which incineration is considered to be the most effective way. Incineration can not only greatly reduce the volume of sludge, effectively kill microorganisms such as bacteria, as well as effectively use the heat of the sludge. CFB having a good adaptability to many fuels can be used to burn those fuels with high-moisture but low heat value, so it is very suitable for sludge incineration.

The mercury contained in sludge can not be ignored. Mercury emitted from the sludge incineration will cause serious harm to the ecosystem, and will bring direct or indirect harm to people's health (Belen et al., 2003; Helena et al., 2003).

Extensive research has been carried out in the world on the mercury emission during sludge and coal co-combustion. Mercury emission from incinerators is not only related to the character of sludge, but also to the factors such as type of auxiliary fuel, operating parameters, the state of combustion, flue gas composition and dust removal equipment (Dirk, 1996; Thomas, 2004; Ren, 2002; Zhou, 2004). However, the reports about mercury emission and speciation during the co-combustion of sludge and coal in the circulating fluidized bed combustor are very few.

The experiment was conducted on a 0.1MWth circulating fluidized bed in Thermal Engineering Institute of Southeast University. Coal is used as auxiliary fuel. In this paper, we investigated the mercury emission characteristic and speciation in flue gas, fly ash and button ash under different operating parameters and conditions, analyzed and discussed the main factors and variation of mercury emission during the co-combustion of sludge and coal.

EXPERIMENTAL

The circulating fluidized bed incinerator used in the experiment was shown in Fig.1. The whole system is composed of fluidized bed combustor, set-up burner, air supply system, sludge-feeding system, coal-feeding system, high temperature cyclone, fly ash recirculation, instrumentation system, sampling system and operating control system.

* The corresponding author: yfduan@seu.edu.cn

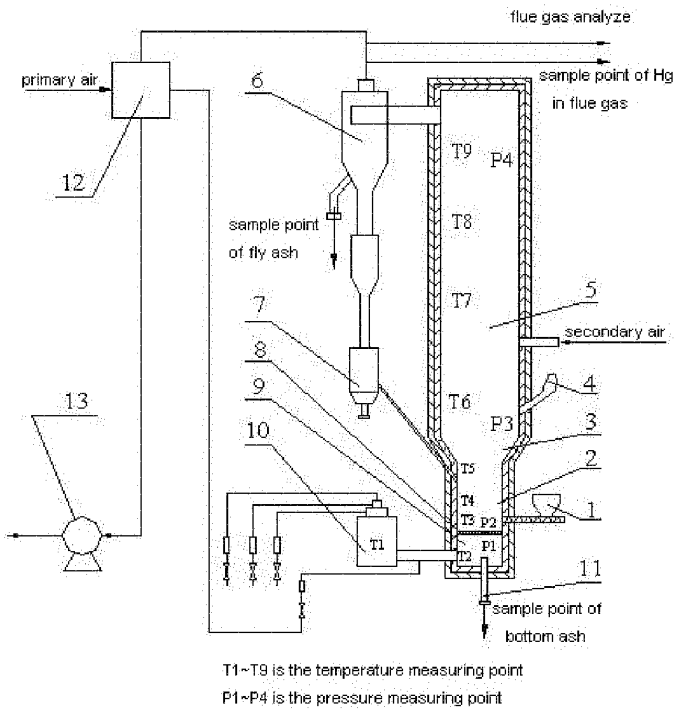

1 coal-feeding system
2 dense phase region
3 transition section
4 sludge-feeding
5 dilute phase region
6 high temperature cyclone
7 fly ash recirculation loop seal
8 air distribution plate
9 air box
10 set-up burner
11 bottom ash discharge pipe
12 heat exchanger
13 induced draft fan

Fig.1 Schematic diagram of the CFB incinerator

The fluidized bed incinerator is a total height of 7m with a dense bed cross section area of 0.23m×0.23m and height of 1.16m, a freeboard cross section area of 0.46m×0.395m and height of 4.56m. Primary air was sent to air box after preheating. Secondary air was sent to the lower region of the freeboard without preheating. Coal and desulfurization sorbents were premixed and then sent to the furnace by screw feeding system. Sludge was fed through an inclined tube by a special impeller feeder. There existed some sampling points for flue gas, fly ash and bottom ash. The ultimate and approximate analyses of the sludge and coal were shown in Table 1.

Table 1 Ultimate and approximate analyses of coal and sludge samples

Items	C_{ar}	H_{ar}	O_{ar}	S_{ar}	N_{ar}	M_{tol}	A_{ar}	V_{ar}	FC_{ar}	heat value /(MJ • kg^{-1})	Cl	Hg
											/mg • kg^{-1}	
Coal /%	50.67	3.44	4.90	0.46	0.77	6.50	33.26	26.73	33.51	18.86	26	0.24
Sludge /%	18.10	2.79	7.04	1.63	1.41	55.27	13.69	24.99	6.05	7.58	21	4.54

Flue gas mercury was sampled and analyzed by using the Ontario-Hydra method shown in Fig.2. Sampling system is composed of quartz sampling tube, heating device, fiber-glass filter, absorption flask (placed in ice bath), flow meter and vacuum pump. Flue gas adsorption system includes eight absorption bottles. The first, second and third bottles containing 1N potassium Chloride (KCl) solution were connected to absorb oxidized mercury (Hg^{2+}). The fourth bottle was filled with acidified hydrogen peroxide (H_2O_2), which was used to absorb elemental mercury, but elemental mercury was mainly captured in the fifth, sixth and seventh bottles which contained solutions of acidified potassium permanganate ($KMnO_4$). In addition, the eighth bottle containing silica gel was provided to ensure the flue gas was thoroughly dried-up before it left the bottle train. The bottom ash and fly ash from cyclone were collected every 30min, which is synchronize with the flue gas sampling.

Aqua regia digestion method was used to determine mercury in solid samples such as coal,, sludge, fly ash and bottom ash by use of a atomic fluorescence spectrometer (AF-630). Hg^0 and Hg^{2+} in the flue gas were determined by Leeman Labs Hydra AA automatic mercury analyzer.

RESULTS AND DISCUSSION

Mercury speciation of co-combustion of sludge and coal

Distribution of mercury concentration in flue gas, fly ash and bottom ash was listed in Table 2 while the

mass ratio of sludge to coal was 10:90. It can be seen that Hg^0 concentration, which is much higher than that of Hg^{2+} in flue gas, accounts for 87.4% of total mercury in the process of sludge and coal co-combustion in circulating fluidized bed. This is because the lower content of Cl in both sludge and coal used in this experiment. Despina et al. (1998) pointed that a higher content of Cl in coal is beneficial to the oxidation of Hg^0 in flue gas. Thus the proportion of Hg^0 is much higher than that of Hg^{2+} in flue gas.

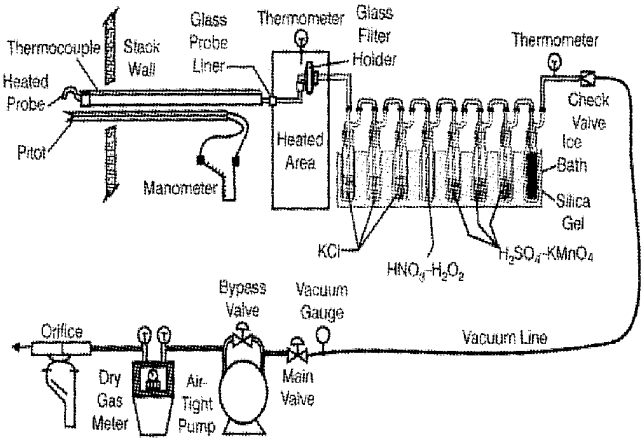

Fig. 2 Mercury sampling system in flue gas

The data also showed that the mercury enrichment in fly ash is significantly higher than in bottom ash. The reason is that mercury leaves high temperature furnace in the form of Hg^0, with decreasing of flue gas temperature, some are oxidized, and some elemental Hg and oxidized Hg condensed and are adsorbed to the surface of fly ash particles (David et al., 1999).

Table 2 The mercury concentration

Items	Unit	Concentration
Hg^0 in flue gas	$mg \cdot Nm^{-3}$	27.326
Hg^{2+} in flue gas	$mg \cdot Nm^{-3}$	3.931
Hg in fly ash	$mg \cdot kg^{-1}$	0.06
Hg in bottom ash	$mg \cdot kg^{-1}$	0.0066

Table 3 shows the results of mercury mass balance in sludge and coal incinerator with a less error. The mercury distribution proportion in bottom ash, fly ash and flue gas, which is obtained from above mercury mass balance results in sludge and coal co-combustion in Circulating Fluidized Bed, is illustrated in Fig.3.

Table 3 Mass balance of Hg

Items	Sample	Flowrate /($g \cdot h^{-1}$)
Inlet	Fuel	0.0074
Outlet	Flue gas	0.007059
	Fly ash	0.000619
	Bottom ash	7.56E-06
Balance/%	(Inlet/Outlet) ×100	103.27

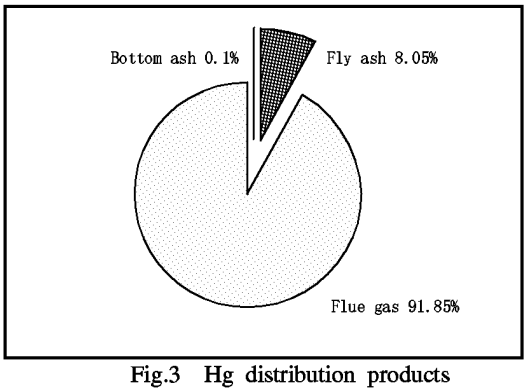

Fig.3 Hg distribution products

From Fig.3, most mercury exists in flue gas, with its proportion reaching 92%. However, mercury content in bottom ash is very little, and can be neglected. There is about 8% mercury was condensed onto the surface of fly ash particles when flue gas was exiting and cooling.

Influence of Ca/S molar ratio to mercury speciation

The influence of Ca/S molar ratio to mercury speciation in flue gas and mercury content in ashes, during the ratio of sludge to coal being 10:90, secondary air ratio 20% and excess air coefficient 1.3, was shown in

Fig.4 (a) and (b).

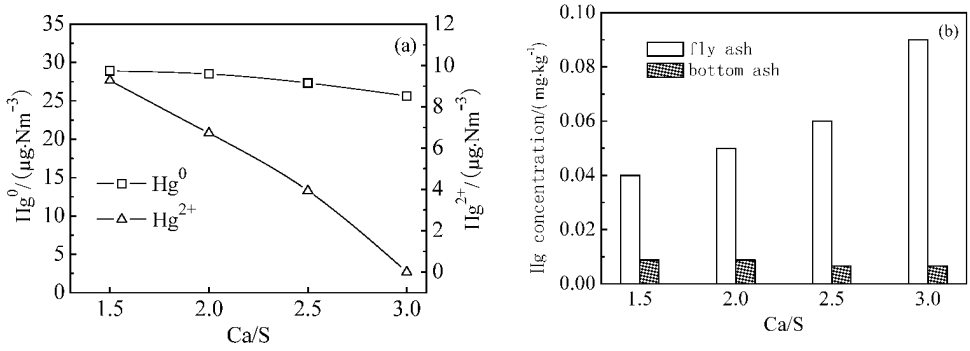

Fig. 4 Mercury in flue gas (a) and ashes (b) at different Ca/S molar ratio

It can be seen that Hg^0 concentration in flue gas decreases slightly from 28.91μg • Nm^{-3} to 25.65μg • Nm^{-3}. That shows the removal efficiency of Hg^0 by calcium-based desulfurization is poor, while the removal efficiency of Hg^{2+} is well. Hg^{2+} concentration is 9.27 μg •Nm^{-3} while Ca/S molar ratio being 1.5. When the Ca/S molar ratio increases to 3, Hg^{2+} in flue gas was all removed by adsorption. With the raise of Ca/S molar ratio, mercury content slightly increases in fly ash but remained almost no changes in bottom ash. This is caused by the increasing of the amount of solid bed material and the particle concentration of calcium-based desulfurization in fly ash. Therefore it can adsorb more Hg^{2+}.

The influence of Ca/S molar ratio to the proportion of oxidized Hg is illustrated in Fig.5. The proportion of oxidized Hg decrease from 24.27% to 0% while Ca/S molar ratio increase from 1.5 to 3.0. The reason is that calcium-based desulfurization can adsorb Hg^{2+} and making it decreased. Conclusively, the proportion of Hg^{2+} is much lower than that of Hg^0.

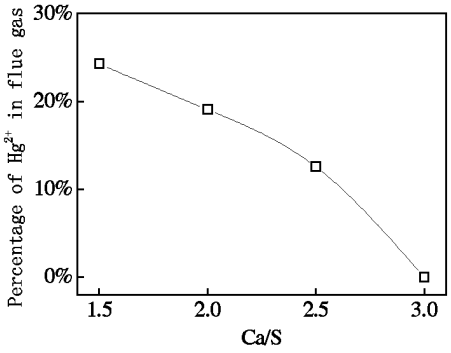

Fig.5 Effect of Ca/S to Hg^{2+} in flue gas

Table 4 Mercury concentration affected by sorbents

Desulfurization	Ca/S	Hg^{FG}/(μg • Nm^{-3})		Hg^{FA}
		Hg^0	Hg^{2+}	/(mg • kg^{-1})
$CaCO_3$	2	28.51	6.72	0.05
	3	25.65	0	0.09
CaO	2	26.58	2.51	0.06
	3	23.30	0	0.12

(Remarks: Hg^{FG}-Hg in flue gas; Hg^{FA}- Hg in fly ash)

Influence of sorbents to mercury emission

Above analysis shows that calcium-based desulfurization can adsorb and remove oxidized Hg highly and efficiently. The adsorption effect of mercury in flue gas by different desulfurization (quick lime and limestone) is also studied in this experiment. The change of mercury concentration in flue gas and fly ash by adding these two kinds of desulfurization is shows in Table 4.

It can be seen that the concentration of mercury in flue gas is higher using $CaCO_3$ than using CaO in the same Ca/S molar ratio. And mercury concentration in fly ash was lower. This shows that the mercury adsorption effect by CaO is better than that of $CaCO_3$. These results are consistent with the conclusions of Li (2003).

Influence of excess air coefficient to mercury emission

Under conditions of the same mass mixing ratio of sludge and coal (10:90), secondary air ratio (20%) and Ca/S molar ratio, mercury speciation in flue gas and bottom ash versus the excess air coefficient was shown in Fig.6. With the excess air coefficient increased, the concentration of Hg^0 in flue gas increased at first then decreased, and that of Hg^{2+} increased slightly; meanwhile the content of mercury decreased firstly then increased in fly ash, and remained relatively constant in bottom ash.

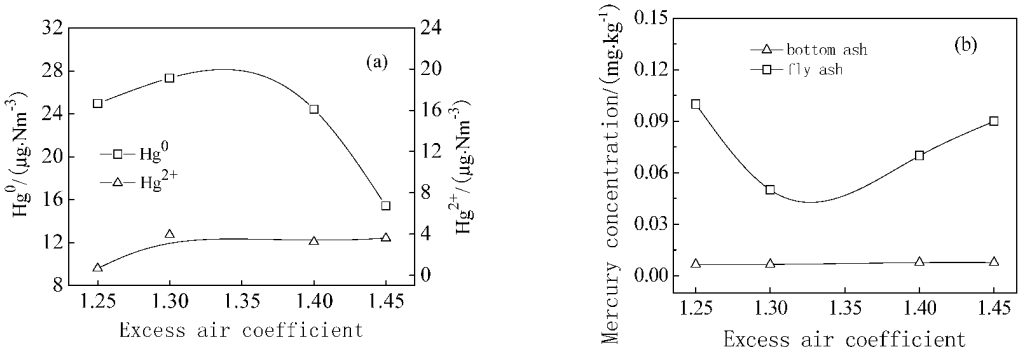

Fig. 6 Mercury concentration in flue gas (a) and fly ash and slag (b) vs. excess air coefficient

With the excess air coefficient increased from 1.25 to 1.3, the concentration of Hg^0 increased from 24.96μg/Nm^3 to 27.33μg/Nm^3 in flue gas, and there is distinct decrease of mercury in fly ash. While with excess air coefficient further increased from 1.3 to 1.45, the content of Hg^0 decreased from 27.33μg/Nm^3 to15.42μg/Nm^3 in flue gas and mercury concentration in fly ash raised obviously. The reason is that as the excess air coefficient increases, the situation of fluidization and mixing is improved for the increasing of oxygen concentration and fluidized air velocity, and then the heat and mass transfer reinforces, at the same time the strong disturbance of secondary air makes the combustion condition ameliorative in suspension space. All of these cause the decreasing of carbon content in fly ash and the reduction of mercury adsorption in fly ash, eventually mercury concentration in flue gas increased. However, when the excess air coefficient further increases, fluidized air velocity goes up accordingly, which leads to the drop of residence time of flue gas and fly ash through the furnace and the reduction of co-combustion efficiency, therefore the carbon content in fly ash rises correspondingly, then hasten mercury adsorption conversely in flue gas. In addition, higher excess air coefficient caused the bed layer temperature decrease, as a result, the incompletely volatized mercury in fuel transfer into bottom ash, eventually the content of mercury in flue gas is reduced.

Figure 7 showed the effect of the excess air coefficient on mercury oxidation in flue gas. From the analysis of Fig.6, at first the percentage of Hg^{2+} in flue gas increasing with the excess air coefficient increased. This is because of that the increasing of oxygen concentration in the furnace created a preferable reaction conditions for mercury oxidization, namely enhanced the conversion rate of Hg^0. Nevertheless, as the excess air coefficient goes on rising, the ratio of Hg^{2+} began to increase by reason of the elemental mercury decrease.

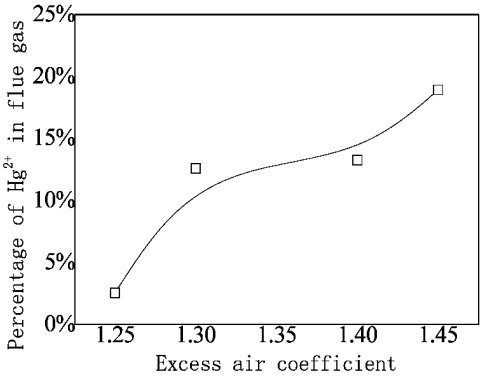

Fig.7 Effect of excess air coefficient on the percentage of Hg^{2+} in flue gas

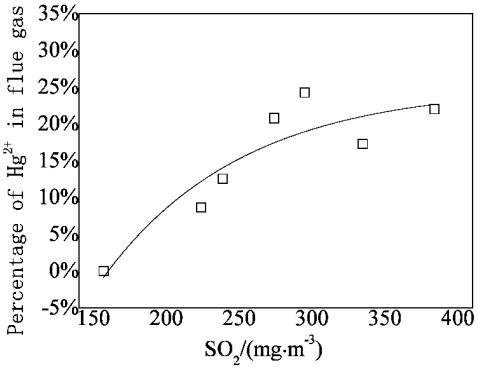

Fig.8 Effect of SO_2 content on the percentage of Hg^{2+} in flue gas

Effect of SO_2 content on the percentage of Hg^{2+} in flue gas

Figure 8 showed that the percentage of Hg^{2+} in the flue gas change along with the SO_2 concentration. Obviously, with the SO_2 concentration increased, the percentage of Hg^{2+} in the flue gas increased simultaneously. This shows that SO_2 can promote the oxidation of Hg^0. SO_2 may react with the mercury in the flue gas as following (Pavlish et al.,2003):

$$Hg(g)+\tfrac{1}{2}O_2(g)\xrightarrow{\text{catalyst}}HgO(s,g)$$

$$2SO_2(g)+2HgO(s,g)+O_2(g)\rightarrow 2HgSO_4(s,g)$$

Thermodynamic calculations show that the stability of $HgSO_4$ is higher than that of HgO. $HgSO_4$ is very hard to decompose after generate, and this causes the increasing of Hg^{2+} in the flue gas, eventually leads to the

percentage of Hg^{2+} in the flue gas increased.

Effect of NO_x on the percentage of Hg^{2+} in flue gas

Figure 9 showed the effect of NO_x concentration on the percentage of Hg^{2+} in flue gas. We can see that the percentage of Hg^{2+} in the flue gas increasing along with the SO_2 concentration. This shows that NO_x can promote the oxidation of Hg^0 also. Redox reaction between Hg^0 and flue gas contents will occur with the temperature decreasing. The reaction NO_x may involve is showed as follows (Dunham et al., 2000; Olson et al., 1999):

$$NO(g) + O_2(g) \rightarrow NO_2(g) + O$$

$$Hg^0(g) + O \rightarrow HgO(g)$$

$$Hg^0(g) + NO_2(g) \rightarrow HgO(g,s) + NO(g)$$

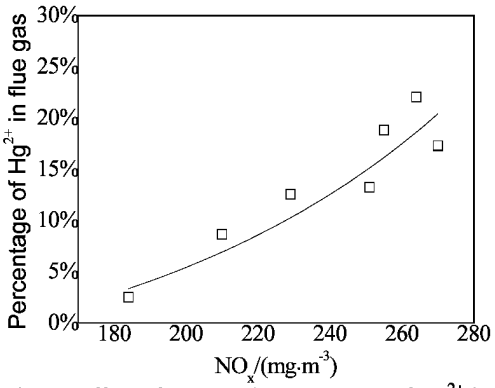

Fig.9 Effect of NO_x on the percentage of Hg^{2+} in flue gas

In the high temperature flue gas, NO reacts with O_2, generate free O and NO_2. Free O has very high activity, can oxide Hg^0 to Hg^{2+}. At the same time, NO_2 generated in the reaction can also oxide Hg^0 in the flue gas. The series of reactions mentioned above cycle happened, and this caused the concentration of Hg^{2+} increasing. Therefore, in the condition of our experiment, the percentage of Hg^{2+} in the flue gas increased along with the concentration of NO_x.

CONCLUSIONS

1) In the process of sludge and coal co-combustion, most of mercury in fuel was emited into the flue gas, only a little part was adsorbed on the surface of fly ash, and mercury in the bottom can be neglected; Hg^0 is the main occurrence form of mercury in the flue gas.

2) With the raise of Ca/S molar ratio, mercury content increases in fly ash and concentration of Hg^{2+} in flue gas drops greatly. It is suggested that Ca-based sorbent has a stronger adsorption of Hg^{2+}, but can not adsorbs Hg^0 effectively. CaO has better mercury removal effect than $CaCO_3$.

4) Excess air coefficient can affect furnace temperature and the amount of residual carbon in fly ash, and then affect the mercury speciation in flue gas and bottom ash. Generally speaking, higher temperature will cause the mercury concentration increased in the flue gas and decreased in the fly ash.

5) SO_2 and NO_x in flue gas have a greater influence on mercury speciation. The content of Hg^{2+} in flue gas increases with increasing of concentrations of SO_2 and NO_x in flue gas.

REFERENCES

[1] Zhou L X, Shen Q R, *et al.* : ACTA Scientiae circumstantiae, 20(2000), pp.269-274.
[2] Li A M, Qu Y L, *et al.* Journal of combustion science and technology, 9(2003), pp.404-408.
[3] Belen M F, Ramoma M D, *et al.* Fuel. 82(2003), pp.1939-1948.
[4] Helena M L, Abelha P and Lapa N. Waste Management, 23(2003), pp.859-870.
[5] Dirk V. and Alfons B. Environ.Sci.Technol., 30(1996), pp.50-56.
[6] Thomas W.M., Brendan P.M., William R.S., *et al.* Waste Management, 24(2004), pp. 193-198.
[7] Ren J L, Zhou J S, Luo ZH Y, *et al.* Acta scientiae circumstantiae, 22(2002), pp.289-293.
[8] Zhou J S, Wu X J, Gao H L, *et al.* Thermal power generation, 2004, pp.72-75.
[9] Despina K, Amedeo L and Dino M. Environ.Sci. Technol, 32(1998), pp. 3999-4000.
[10] David J H and Kurt E E. Fuel, 78(1999), pp. 243-248.
[11] Li J X, Yan J H, *et al.* Proceedings of the CSEE, 12(2003), pp.179-183.
[12] Pavlish J H, Sondreal E A, Mann M D, *et al.* 2003. A. Status Review of Mercury Control Options for Coal-Fired Power Plants [J]. Fuel Process Technol, 82: 89—165
[13] Dunham G. E., Olson E. S, Miller S. J. Proceedings of the Air Quality II: Mercury, Trace Elements, and Particulate Matter Conference, McLean, VA, Sept. 19-21, 2000, Paper A4-3
[14] Olson E S, Sharma R K, et al. Proceedings of the Specialty Conference on Mercury in the Environment, Minneapolis, MN, Sept. 15–17, 1999, pp.121-126.

CO-FIRING OF SEWAGE SLUDGE WITH BARK IN A BENCH-SCALE BUBBLING FLUIDIZED BED —A STUDY OF DEPOSITS AND EMISSIONS

Patrik Yrjas[1], Martti Aho[2], Maria Zevenhoven[1], Raili Taipale[2], Jaani Silvennoinen[3], and Mikko Hupa[1]

1Process Chemistry Centre, Åbo Akademi University, Turku, Finland
2VTT Processes, Jyväskylä, Finland
3Metso Power Oy, Tampere, Finland

Abstract: It has been shown that addition of either sulfur and/or aluminosilicates such as kaolinite may reduce alkali induced deposit formation when firing biomass fuels. Sewage sludge is a fuel containing substantial amounts of sulfur and aluminosilicates, such as zeolites. In this work different amounts of sewage sludge (0, 2, 4, 6 and 8%$_{en}$) were co-fired with bark in a bench-scale BFB. SO_2 and HCl emissions were measured and deposits were sampled during 3 hrs with an air-cooled probe with a surface temperature of 500°C at two different locations with flue gas temperatures of 850°C and 650°C, respectively. The test results showed that an increase of the share of sewage sludge to the fuel mixture increased the formation of HCl and simultaneously decreased the Cl-content in the deposits. Usually this is considered to be a sign of sulfation of alkali chlorides. However, the increase of HCl can also be caused by Al-silicates capturing alkali, thus releasing Cl as HCl to the gas phase. Although, sulfur increased in the fuel input with an increased share of sewage sludge, this was not reflected in the gaseous emissions as may be expected. Up to 4%$_{en}$ sewage sludge was fired together with bark without increasing the sulfur content in the emissions. At higher shares of sewage sludge the sulfur emissions increased linearly with an increase of sewage sludge. The amount of water soluble potassium fed into the boiler remained relatively constant in the different tests. This potassium is usually released as volatile salts. Nevertheless, the amount found in deposits decreased with an increase in sludge feeding. In this paper it was shown that interaction of potassium with Al-silicates in the bed is a probable cause for the decrease of potassium in the deposits, while both the sulfation of potassium chlorides and possibly also, the alkali capture by Al-silicates can weaken the deposition of Cl.
Key words: waste co-firing, deposits, emissions

INTRODUCTION

Mono-firing of waste derived and biomass fuels has been found to be sometimes problematic in fluidized bed combustion (FBC). Ash agglomeration, deposit formation and corrosion may cause un-planned boiler shut-downs. However, during co-firing of fuels, sometimes positive synergetic effects have been shown to take place according to e.g. reactions 1 and 2.

$$Al_2O_3{\cdot}2SiO_2(s) + 2KCl(g) + H_2O(g) \longrightarrow K_2O{\cdot}Al_2O_3{\cdot}2SiO_2(s) + 2HCl(g) \quad (1)^*$$

$$2KCl(g) + SO_2(g) + \tfrac{1}{2}\,O_2(g) + H_2O(g) \longrightarrow K_2SO_4(s) + HCl(g) \quad (2)$$

Öhman et al. (2000) and Steenari and Lindqvist (1998) have shown that kaolinite may hinder bed agglomeration and may also scavenge alkali from the gas phase, thereby reducing the formation of low melting alkali chlorides. Zheng et al. (2008) showed that significantly higher potassium capture was reached with kaolinite and bituminous coal ash, due to higher amounts of Si and Al compared to mullite, silica, alumina and lignite coal ash at 900°C. They explained this by the fact that both kaolinite and the bituminous coal ash contained significant amounts of both Si and Al, compared to the other tested materials. Aho and Silvennoinen (2004) showed that the addition of kaolinite also has an effect on the deposit formation, Reaction 1, while Kassman et al. (2009) and Aho et al. (2008) also showed that different sulfur-containing additives play an important role in decreasing the existence of alkali chlorides in the upper parts of the boiler (Reaction 2). Åmand et al. (2006) studied the combustion of biomass with sewage sludge in a 12MWth CFB. They showed that both the chlorine in the deposits and the total deposit formation rate decreased with the introduction of

---

* It should be noticed that Reaction 1 is only one example of how aluminosilicates, in this case kaolin, may react with potassium. There are several different aluminosilicates and alkali(alumino)silicates that can react or be formed.

sewage sludge. They concluded this to be an effect of four different phenomena 1) sulfation of alkali chlorides (Reaction 2), 2) condensation of aerosols on particles, 3) reaction of alkalis with aluminosilicates (Reaction 1), and 4) abrasion of the deposits due to the high ash content in sewage sludge. They also considered that the first and the third phenomena were the most important, however, they were not able to differentiate the effects.

Sewage sludges often contain high contents of either iron or aluminium originating from the water cleaning treatment. Either $Al_2(SO_4)_3$ or $Fe_2(SO_4)_3$ is added to waste water to precipitate phosphates. Besides these compounds, sewage sludge often contains a high amount of aluminosilicates in the form of zeolites, which may originate from e.g. washing powder. Petterson et al. (2008) showed that sewage sludge in a share of some 12 wt-% may be co-fired successfully with wood and waste derived fuels in a 12 MW_{th} CFB. It is claimed that the zeolites in the sewage sludge act as kaolinite.

This study describes co-firing experiments carried out in a bench-scale FBC. In an attempt to explain the interaction between volatile alkali compounds with sewage sludge's ash forming matter more thoroughly, shares of up to 16 wt-% sewage sludge (8% on energy base) were co-fired with bark.

EXPERIMENTAL

The Combustion Tests

Bark and mixtures of bark with sewage sludge were burned in a bench-scale BFB reactor at VTT. The compositions of the fuels are listed in Table 1, while the reactor is shown in Fig. 1.

Table 1 Standard fuel analyses

	wt-%						MJ/kg d.s.		Elements in ash calculated as oxides, wt-%									
	Ash, 550°C	C	H	N	S	Cl	HHV	LHV	SiO_2	Al_2O_3	Fe_2O_3	TiO_2	MnO	CaO	MgO	P_2O_5	Na_2O	K_2O	SUM
Bark	3.30	51.4	5.90	0.40	0.036	0.021	20.6	19.3	7.71	1.75	1.03	0.07	2.08	40.1	4.09	3.58	1.00	6.83	68.3
Sewage sludge	55.60	23.0	3.40	2.60	1.19	0.076	9.86	9.14	25.7	7.20	32.4	0.70	0.07	6.72	1.64	15.4	1.08	1.45	92.4

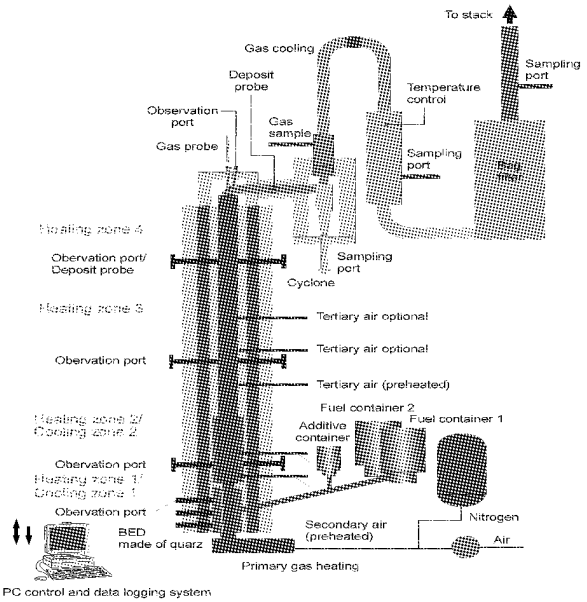

Fig. 1 A schematic diagram of the 20 kW BFB used in this study

In Table 1 the oxide sums do not equal 100% because of the low ashing temperature (550°C), resulting in $CaCO_3$ remaining in the ash. By calculating the CaO in bark to $CaCO_3$ the sum would equal 99.8%.

The reactor is an electrically stabilized 20 kW bubbling fluidized bed with a bed diameter and height of 0.16 m and 0.55 m, respectively. The height of the freeboard zone is 3.5 m with a diameter of 0.23 m. The bed material was sand with a mean particle diameter of 0.33 mm (0.1-0.6 mm). The mean gas velocity in the reactor was about 0.5 m/s corresponding to a total residence time of 7 – 8 s. Air staging was kept constant (prim./sec./tert. 50:30:20). The bed temperature was kept between 850-870°C. Sulfur dioxide, SO_2 (+ O_2, CO_2, CO, NO) was analyzed from a dried flue gas stream with standard on-line analysers while HCl (+ CO_2, CO, NO, NO_2, CH_4, SO_2, H_2O) was analyzed directly from a non-dried and non-cooled (180°C) flue gas stream by means of FTIR. Two air-cooled deposit sampling probes were placed in the test rig. In both cases the surface temperatures were adjusted to 500°C. One of the probes was placed in the upper part of the freeboard, where the gas temperature was roughly 850°C and the other was placed in the flue gas channel where the gas

temperature was about 650°C. The deposit collection time was three hours. After the tests, the collected deposits were analyzed with a SEM/EDX on three locations of the deposit ring: wind side, 50° from wind side, and lee side.

The test matrix is shown in Table 2 together with some calculated elemental values based on the standard analyses.

Table 2 The fuel mixtures in the test runs. The mixtures are goal values.

Test	Energy based / %		$mmol_{in}$/MJ (LHV d.s.)								Ash / wt-%	Molar ratio	
number	Bark	Sewage sludge	Al	P	S	Cl	K	Na	Ca	Fe	550°C	S/Cl	Ca/S
1	100	0	0.59	0.86	0.58	0.30	2.48	0.56	12.3	0.22	3.3	1.9	21.3
2	98	2	2.30	3.49	1.38	0.34	2.81	0.97	13.5	5.17	5.5	4.0	9.8
3	96	4	4.01	6.11	2.18	0.38	3.13	1.38	14.7	10.1	7.5	5.7	6.7
4	94	6	5.73	8.74	2.99	0.42	3.46	1.80	15.9	15.1	9.5	7.0	5.3
5	92	8	7.40	11.4	3.79	0.47	3.78	2,21	17.1	20.0	11.4	8.1	4.5

The Advanced Fuel Analysis Method

The advanced fuel analysis method is based on selective leaching by water, ammonium acetate, and hydrochloric acid (Fig. 2). The method was originally developed by Benson et al. (1985) for the characterization of coal and further modified by Baxter (1994) for the characterization of biomass fuels. The method has also been presented earlier in the 16th, 17th, and 18th FBC-conferences (Zevenhoven et al., 2001, Zevenhoven et al., 2003, Yrjas et al., 2005).

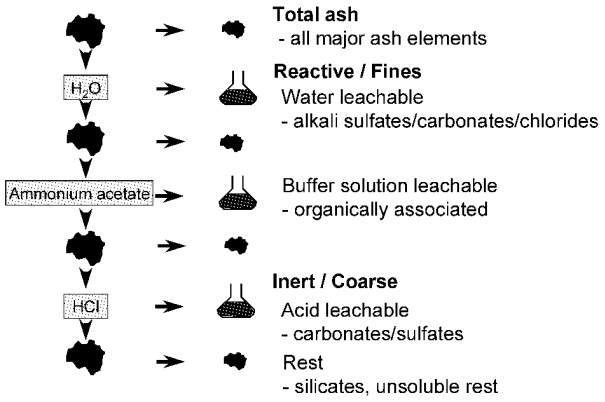

Fig. 2 The advanced fuel analysis method (based on Zevenhoven et al., 2001)

Increasingly aggressive solvents, i.e., water (H_2O), 1M ammonium acetate (NH_4Ac), and 1M hydrochloric acid (HCl) leach samples into a series of four fractions (including the residue) for analysis. Typical ash-forming components, which are leached out by water include alkali sulfates, carbonates, and chlorides. Elements leached out by NH_4Ac are believed to be organically associated, such as magnesium, calcium as well as potassium and sodium. HCl leaches the carbonates and -sulfates of alkaline earth and other metals. Silicates and other minerals remain in the insoluble residue.

Usually in wood based biomasses the HCl-leached calcium corresponds to the calcium oxalate amount, which during combustion decomposes to small calcium oxide particles which in turn are active sulfur absorbents. However, when different kinds of wastes are leached the situation may differ and it is not clear how much of the HCl-leached calcium originates from oxalate and not e.g. from sulfate. Accordingly, in this work it was necessary to specifically determine the concentration of the oxalate ion ($C_2O_4^{2-}$) and this was done with an ion chromatograph for both the bark and the sludge.

RESULTS AND DISCUSSION

Ash deposits were sampled at two locations during the test runs. In this paper we focus on the deposits sampled in the flue gas channel, since in these deposits higher chlorine concentrations were found. This was probably due to the lower gas temperatures, enhancing the amount of condensed alkali chlorine in the gas. The deposit compositions from the wind, 50° from the wind and the lee sides are shown in Table 3, and in Fig. 3a-3b (lee and 50 deg.) of some chosen elements that will be further discussed.

Table 3 SEM/EDX analyses of deposits sampled from the flue gas channel when burning different fuel mixtures (T_{probe} = 500°C, $T_{flue\ gas}$ = 650°C, *w* = windward, *l* = leeward, and *s* = 50 deg. from windward)

	Na2O	Al2O3	SiO2	P2O5	SO3	Cl	K2O	CaO	TiO2	Cr2O5	Fe2O3	MgO	MnO	SUM
100% Bark, w	0.91	1.46	5.07	3.82	5.73	0.15	2.27	68.78	0.19	0.00	1.84	5.78	4.01	100.0
2% Sewage sludge, w	0.84	3.96	12.74	7.43	6.49	0.04	1.95	49.24	0.40	0.00	9.32	4.79	2.80	100.0
4% Sewage sludge, w	1.11	2.90	8.91	8.65	18.24	0.14	3.37	30.94	0.11	0.16	18.39	3.73	3.34	100.0
6% Sewage sludge, w	2.61	3.38	7.27	18.65	7.85	0.00	1.76	23.73	0.80	0.00	28.65	3.92	1.38	100.0
8% Sewage sludge, w	1.32	3.38	11.48	11.50	16.03	0.10	1.71	25.00	0.22	0.03	24.47	3.07	1.69	100.0
100% Bark, s	2.63	1.30	2.79	4.52	22.94	7.26	21.71	28.39	0.27	0.24	1.82	3.36	2.77	100.0
2% Sewage sludge, s	3.08	1.09	2.32	4.06	37.50	0.42	21.82	19.29	0.10	0.00	4.37	3.62	2.34	100.0
4% Sewage sludge, s	1.60	2.25	9.34	9.94	19.62	0.18	7.77	29.32	0.81	0.02	11.50	4.73	2.92	100.0
6% Sewage sludge, s	1.46	3.16	5.84	13.34	18.26	0.08	5.23	30.30	0.37	0.14	14.30	5.12	2.39	100.0
8% Sewage sludge, s	1.05	1.67	6.49	14.80	17.45	0.24	0.67	34.69	0.44	0.59	12.46	6.85	2.62	100.0
100% Bark, l	1.43	1.80	4.36	4.54	10.88	1.21	5.69	58.14	0.29	0.00	2.44	5.74	3.47	100.0
2% Sewage sludge, l	1.38	2.28	6.95	7.33	16.59	0.16	5.39	39.69	0.72	0.13	12.24	4.04	3.12	100.0
4% Sewage sludge, l	1.34	3.11	8.52	9.42	12.13	0.01	3.92	26.09	0.75	0.00	29.77	3.24	1.69	100.0
6% Sewage sludge, l	0.82	3.29	9.73	5.73	22.32	0.10	2.00	36.27	0.32	0.33	16.18	1.50	1.42	100.0
8% Sewage sludge, l	0.79	3.94	15.74	10.30	11.28	0.02	2.54	25.04	0.92	0.00	25.59	2.57	1.27	100.0

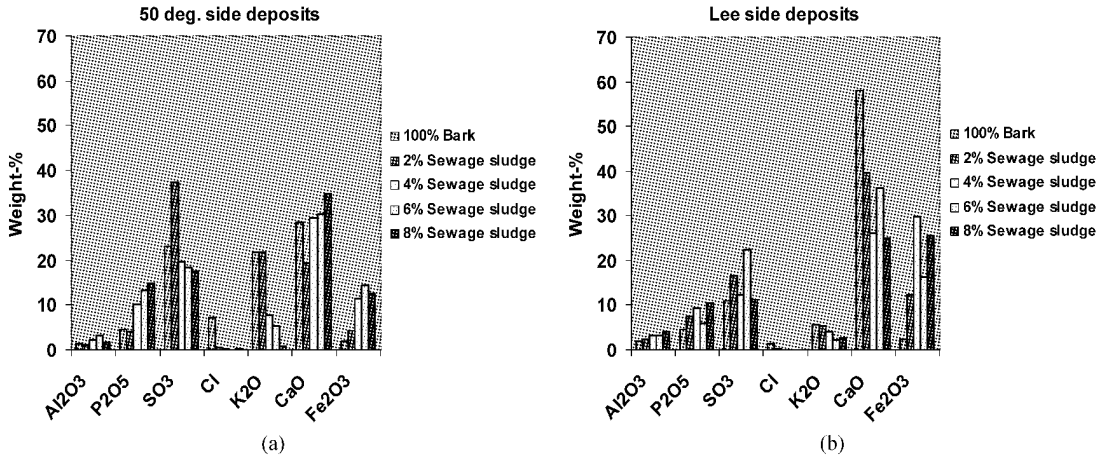

Fig. 3 (a) Composition of 50 deg. side deposits.and (b) Composition of leeward side deposits

From Figs. 3(a) and 3(b) we can see that the chlorine amounts were above 1 wt-% only in the case with 100% bark, and already when co-firing with only 2% (enb) sewage sludge most of the chlorine disappeared from the deposits. This can be explained firstly by the increase in sulfur, that reacts with potassium according to Reaction 1 releasing HCl, and secondly by an increase of the amount of kaolinite- type minerals e.g. zeolites that can accommodate alkalis and earth alkalis, e.g. Reaction 2. The increase in HCl-emissions can be observed from Fig. 4, where also the SO_2 emissions are plotted, as well as average values of the amounts of chlorine in the deposits from the different runs.

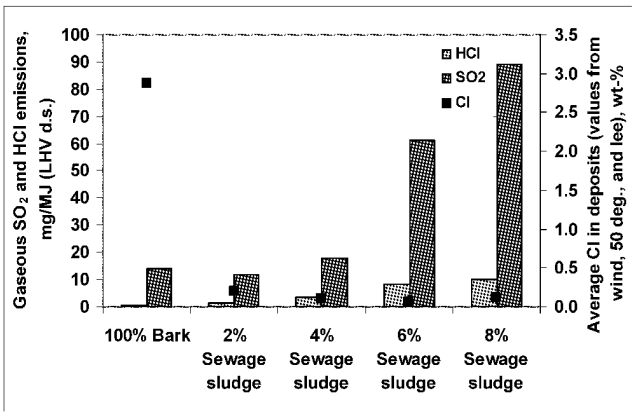

Fig. 4 SO_2 and HCl gaseous emission during the tests. The average values of Cl in the deposits are plotted against the secondary y-axis

It is quite clear that sulfur weakens or inhibits Cl deposition (Yrjas et al., 2005; Kassman et al., 2008; Aho et al., 2008). Chlorine present in deposits from biomass firing will be present mainly as potassium chloride (KCl), while the rest of the potassium consists of potassium sulfate (K_2SO_4) and possibly potassium carbonate (K_2CO_3). Since there is no or very small amounts of chlorine in the deposits when burning 2% sewage sludge

in the mixture it could be assumed that most of the potassium in the deposits is present as K_2SO_4.

The deposit composition with increasing amount of sewage sludge is expected to show a quite stable or slightly increasing amount of potassium, since the input flow of easily soluble alkalis remained fairly constant and the total input of potassium even increased (Fig. 5). This expectation is supported by the fact that the input of sulfur also increased (Fig. 5), ensuring increasing amounts of sulfur for potassium to react with.

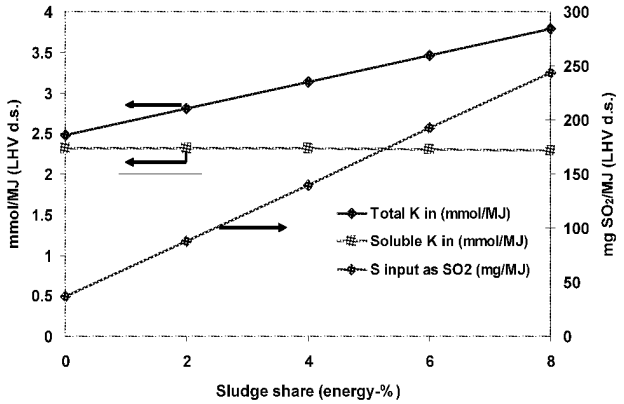

Fig. 5 The amounts of total and easily soluble potassium and of total sulfur as SO_2 in the different fuel mixtures

However, on the contrary the amount of potassium in the deposits showed a clear decreasing trend with increasing share of sludge (Fig. 3). This decrease was also verified by calculating the absolute amount of potassium in the deposits based on the SEM/EDX analyses and the deposit amounts sampled.

The decrease in potassium can be explained with reactions where aluminosilicates react with potassium to a product less prone to form deposits or, alternatively, stay in the bed. However, to differentiate between the "positive" effects of sulfur and aluminosilicates is challenging – one possibility would be to plot the $S/(Ca+Na_2+K_2)_{soluble}$ as a function of chlorine in deposits according to Yrjas et al. (2005), and study the displacement of the curves. The original idea with calculating this ratio was to evaluate the risk for chlorine deposits, and estimate the protection effect of sulfur (the higher the ratio the smaller the risk). However, if also aluminosilicates influence on the amount of chlorine in the deposits it could be expected that chlorine-free deposits are achieved at even lower ratios with fuel mixtures containing significant amounts of these minerals. For the calculation of the ratio, results from the chemical fractionation, as described in the Experimental section, were used (Fig. 6).

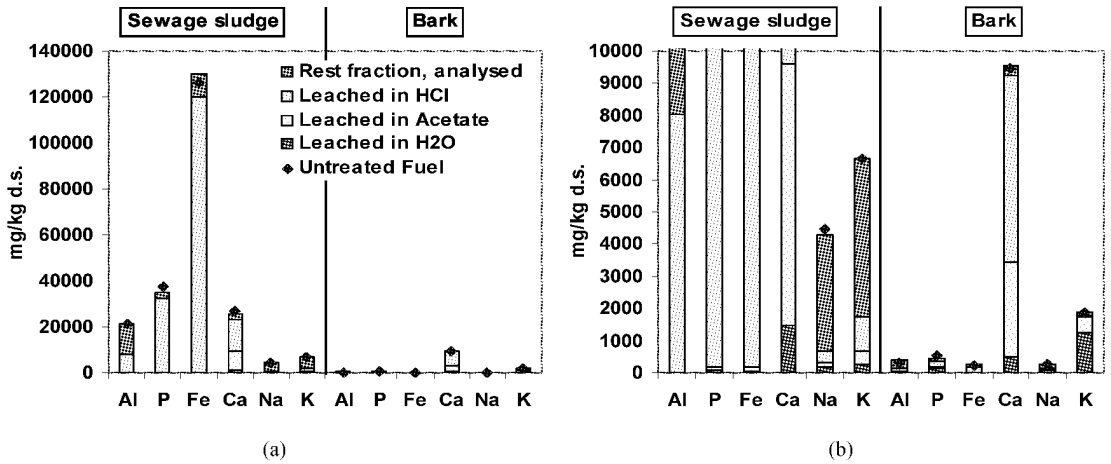

Fig. 6. Fractionation results of sewage sludge and bark (same results but different scales)

From Fig. 6(b) it is worth noticing that practically all potassium in bark is easily soluble, while in the sewage sludge only about 10% of the potassium is easily soluble. Also, it may be of interest to note that part of the aluminium is HCl soluble and thus this aluminium fraction is not present as silicates but as e.g. sulfate.

To calculate the ratio $S/(Ca+Na_2+K_2)_{soluble}$ H_2O- and Ac-soluble potassium and sodium are summed up, while for calcium the HCl-soluble oxalate is accounted for as well. For bark nearly 100% of the HCl-soluble calcium corresponded to the oxalate ion determined by ion chromatograph, while for the sewage sludge it was only about 15%. Figure 7 shows the ratio results from the test runs and for comparison also recalculated results

from earlier tests in the same facility, when burning REF (recovered fuel) mixed with bark (Aho et al., 2008), while Fig. 8 shows the corresponding plot when burning mixtures of forest residue, wood chips, bark, peat, and coal in a full scale CFBC (Yrjas et al., 2005).

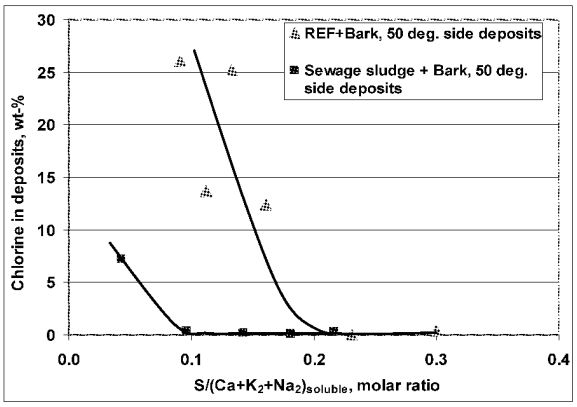

Fig. 7 $S/(Ca+Na_2+K_2)_{soluble}$ as a function of Cl in deposits for different fuel mixtures burned in the 20 kW bench-scale BFB. The results with REF and bark are based on the work by Aho et al., 2008

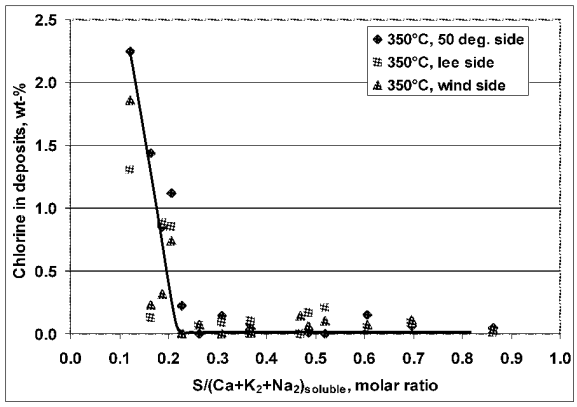

Fig. 8 $S/(Ca+Na_2+K_2)_{soluble}$ as a function of Cl in deposits when burning mixtures of forest residue, wood chips, bark, peat, and coal in a full scale CFBC (Yrjas et al., 2005)*

From Figs. 7 and 8 it can be observed that when the $S/(Ca+Na_2+K_2)_{soluble}$ ratio exceeded 0.2 no or only very small amounts of chlorine were found in the deposits. However, in the case with sewage sludge, the corresponding value was as low as 0.1. This difference may be attributed to the aluminosilicates in the sludge and if we, as a first approximation, assume that the amount of these silicates correspond to the amount of non-soluble aluminium, we can estimate the efficiency of these aluminium compounds as potassium absorbers.

Since, the inflow values of soluble calcium, potassium, and sodium remained fairly constant, the only significant variation, which influenced on the $S/(Ca+Na_2+K_2)_{soluble}$ ratio was the input value of total sulfur in the different sewage sludge mixtures (Table 4). Accordingly, based on Figs. 7 and 8 and Table 4 it could be expected that to, a fuel mixture with an $S/(Ca+Na_2+K_2)_{soluble}$ ratio of 0.1, we would need to add 1.6 mmol sulfur/MJ (3.0-1.4 = 1.6) to prevent chlorine to deposit. However, in the case with sludge the need for additional sulfur is unnecessary, since the addition of the aluminosilicates seemed to be enough, to prevent chlorine to deposit. The amount of added aluminosilicates, here expressed as non-soluble aluminium, was sufficient already with 2% sludge, corresponding to an addition of 1.7 mmol $Al_{non\text{-}soluble}$/MJ. Consequently, the sulfur and the aluminosilicates (expressed as $Al_{non\text{-}soluble}$) were nearly equally efficient, on a molar basis (1.6 vs. 1.7 mmol/MJ), in preventing chlorine to deposit.

Table 4 Input values and ratios of key numbers for three of the fuel mixtures

Input values, mmol/MJ	0 % sludge	2 % sludge	6 % sludge
S_{total}	0.6	1.4	3.0
$Al_{non\text{-}soluble}$	0.0	1.7	3.8
$(Ca+Na_2+K_2)_{soluble}$	13.3	13.7	14.5
$(Na_2+K_2)_{soluble}$	1.31	1.32	1.34
$S/(Ca+Na_2+K_2)_{soluble}$	0.04	0.10	0.21

Furthermore, it should be noticed that the sewage sludge itself contained non-soluble aluminosilicate-potassium compounds. If the amount of this bonded potassium is assumed to be the potassium remaining in the solid rest after fractionation, and assuming that this bonded potassium would deactivate some of the non-soluble aluminium, it would mean that the "free" aluminosilicate would be even more efficient alkali binders than discussed above.

It should be noticed that such a high activity of these aluminosilicates, as discussed above, is valid for this specific municipal sewage sludge. The compositions between different sludges may vary significantly, and in this sludge, being municipal sewage sludge, the aluminosilicates are to a large extent present as highly reactive zeolites (originating from among others detergents).

* The trendlines in Figs. 7 and 8 were drawn on free-hand (not calculated).

CONCLUSIONS

In this work we have presented results from bench-scale BFB combustion tests with a biomass (bark) mixed with different amounts of sewage sludge. Both gaseous emissions and probe deposits have been discussed in combination with detailed fuel analyses. The conclusions can be divided into two groups; Firstly, practical observations that influence on the direct operation and secondly, more theoretical conclusions that increase the understanding, and give tools for predicting the risk for the formation of Cl-deposits.

- Bark alone may cause deposits with high amounts of chlorine. This may both lead to high corrosion and decrease the heat transfer (increase of rate of deposit build-up).
- Already a relatively small addition of sewage sludge decreased the chlorine in the deposits significantly. On energy base 2% (corresponding to about 4 wt-% dry) was, in this experimental setup, sufficient to suppress chlorine deposits.
- HCl emissions increased with increasing share of sewage sludge. However, with low addition the increase was marginal.
- SO_2 emissions remained low until larger amounts of sewage sludge (> 4% enb) were co-fired.
- The ash flow increased significantly with an increase of sewage sludge in the fuel mixture, already an amount of 4% sewage sludge on energy base more than doubled the ash flow.
- The $S/(Ca+Na_2+K_2)_{soluble}$ molar ratio can be used in biomass firing for evaluating the risk for chlorine containing deposits. However, the ratio does not account for possible positive effects of aluminosilicates in preventing chlorine to deposit. Accordingly, the ratio may at certain conditions be too "pessimistic".
- About 60% of the aluminium in the sewage sludge was concluded to be as active aluminosilicates, when assuming that this amount corresponded to the amount of non-soluble aluminium, and, simultaneously assuming that non-soluble potassium did not influence on the reactivity.
- On a molar basis, the aluminosilicates (expressed as non-soluble aluminium) in the sewage sludge were nearly as efficient as sulfur in preventing chlorine to deposit. This was shown by using the $S/(Ca+Na_2+K_2)_{soluble}$ molar ratio for the different cases, both with and without sewage sludge, thus pinpointing the effect of the sludge.
- It is known that municipal sewage sludges contain zeolitic-type aluminosilicates. These have a very large surface areas and may be very active, thus, cautiousness should be exercised when comparing results with other sludges and/or types of aluminosilicates.

ACKNOWLEDGEMENTS

This work has been done within the mainly Tekes funded project "Biosafe". Other funders are Metso Power, Lassila & Tikanoja, Kemira, and Helsinki Water. Other research partners are VTT, Jyväskylä, Finland and University of Kuopio, Department of Environmental Sciences, Kuopio, Finland. The project is coordinated by VTT.

REFERENCES

Aho M. and Silvennoinen J., Preventing chlorine deposition on heat transfer surfaces with aluminium-silicon rich biomass. Fuel 83, pp. 1299-1305, 2004

Aho M., Vainikka P., Taipale R., and Yrjas P., Effective new chemicals to prevent corrosion due to chlorine in power plant superheaters. Fuel 87, pp. 647-654, 2008

Baxter, L. L; Task 2. Pollutant emission and deposit formation during combustion of biomass fuels, Quarterly report to National Renewable Energy Laboratory, Sandia National Laboratories, Livermore, California, USA, 1994.

Benson, S., Holm, P.L.; Comparison of inorganic constituents in three low-rank coals, Ind. Eng. Chem. Prod. Res. Dev. Vol. 24, pp 145-149, 1985.

Kassman H., Holmgren M., Edvardsson E., Åmand L-E., and Öhlin J., Nitrogen containing additives for simultaneous reduction of KCl and NO_x during biomass combustion in a CFB boiler, 9th International Conferene on Circulating Fluidized Beds, Hamburg, May 2008.

Petterson A., Zevenhoven M., Steenari B-M., Åmand L-E., Application of chemical fractionation methods for characterisation of biofuels, waste derived fuels and CFB co-combustion fly ashes, Fuel 87, pp. 3183-3193, 2008.

Steenari B. and Lindqvist O., High temperature reactions of straw ash and the anti-sintering additives kaolin and dolomite. Biomass and Bioenergy 14(1), pp. 67-76, 1998.

Yrjas P., Skrifvars B-J, Hupa M, Roppo J., Nylund M., and Vainikka P., Chlorine in deposits during co-firing of biomass, peat, and coal in a full-scale CFBC boiler, 18th International Conference on Fluidized Bed Combustion, Toronto, Canada, May 2005.

Zheng Y., Jensen P. A., and Jensen A. D., A kinetic study of gaseous potassium capture by coal minerals in a high temperature fixed-bed reactor. Fuel 87, pp. 3304-3312, 2008.

Zevenhoven M., Ash forming matter in biomass fuels, Åbo Akademi Report 01-03, Ph.D-thesis, ISSN 1457-7895, ISBN 952-12-0813-9, Åbo, Finland 2001.

Zevenhoven, M., Skrifvars, B-J., Yrjas, P., Backman, R., Mueller, C., Hupa, M., Co-firing in FBC – A Challenge for Fuel Characterization and Modeling, 17th International Conference on Fluidized Bed Combustion, Jacksonville, Florida, USA, May 2003.

Zevenhoven, M., Skrifvars, B-J., Yrjas, P., Hupa, M., Nuutinen, L., Laitinen, R., Searching for improved characterization of ash forming matter in biomass, 16th FBC Conference, May 2001, Reno, Nevada, USA.

Åmand, L-E., Leckner B., Eskilsson D., and Tullin C., Deposits on heat transfer tubes during co-combustion of biofuels and sewage sludge, Fuel, 85 (10-11) pp. 1313-1322, 2006

Öhman M., Nordin A., Skrifvars B-J., Backman R., and Hupa M., Bed agglomeration characteristics during fluidized bed combustion of biomass fuels, Energy and Fuels 14(1), pp. 169-178, 2000.

NH_3 ABATEMENT IN FLUIDIZED BED CO-GASIFICATION OF RDF AND COAL

I. Gulyurtlu, Filomena Pinto, Mário Dias, Helena Lopes, Rui Neto André, I. Cabrita

INETI- DEECA, Est. Paço do Lumiar, 22, 1649-038 Lisboa, Portugal

Abstract: Gasification of wastes may come out as an alternative technology to produce a gas with many potential applications, from direct burning in a boiler or motor to the production of synthetic chemicals and hydrogen. High tar production and high operational costs are preventing gasification wider dissemination. Besides these problems, the presence of NH_3 in the syngas may have a negative impact as it can be converted into nitrogen oxides if the gas is further burnt. To reduce NH_3 formation it is required a full understanding of how operational parameters contribute to the formation/reduction of this pollutant. A full study on the effect of fuel composition, temperature and equivalence ratio on the formation of NH_3 is given. Experimental results are compared to theoretical ones obtained with FactSage software. It is also analyzed the effect of feedstock mineral matter in NH_3 release during gasification. To accomplish a significant decrease in the release of NH_3, different catalysts and sorbents were tested with the aim of achieving high energy conversions and low environmental impact.

Keywords: NH_3 abatement, co-gasification, RDF, coal

INTRODUCTION

Incineration has been the most disseminated technology for energetic valorisation of wastes, however due to low energetic efficiencies (13-24%) and the increasing environmental restrictions related to the emission of pollutants more efficient and less pollutant alternatives have to be found. Gasification comes out as an alternative, as it produces gas to be used in different applications ranging from boilers to H_2 production. However, gasification failed to reach its maturity due to technical difficulties and pollutants precursors compounds. The formation of NH_3, which is a precursor of NO, may bring adverse effects on the gasifier and on proper functioning of downstream equipments.

According to Van der Drift et al. (2001) NH_3 is the main nitrogen species formed during gasification, although HCN, HNCO and N_2 can also be found in the syngas. A strong relation between the formation of NH_3 and the levels of nitrogen in the solid fuels was suggested by Zhou et al. (2000). The chemical form in which nitrogen is present in the fuels and even the presence of inorganic matter; that can act as a catalyst in the formation of ammonia, are also important factors.

Other parameters have an important influence in the formation of NH_3, like ER (equivalence ratio) and temperature. Liu et al. (2003) observed that the ER increase leads to a decrease in the concentration of NH_3 and HCN and an increase in NO concentration, due to higher amounts of oxygen in the system. Zhou et al. (2000) also observed a decrease in NH_3 levels with the rise of ER (from 0.17 to 0.25). However, for ER>0.25 they only found out a slight increase trend. The use of steam may also influence the formation of NH_3. According to Tian et al. (2005) steam leads to an increase of NH_3 levels, due to the formation of H radicals that will further react with N-char, forming NH_3.

According to Gangwal et al. (1999) higher temperatures tend to favour the decomposition of NH_3 into N_2 and H_2. Zhou et al. (2000) concluded that the increase of temperature until 900ºC provoked a reduction in NH_3, NO and HCN and an increase in N_2 concentration. However, for higher temperature an increase of NH_3 and a reduction of N_2 was observed. At lower temperatures, nitrogen is mainly retained in the solid fraction and in the liquids, while at higher temperatures (>900ºC) the proportion of nitrogen in gases increases sharply. Some authors believe that the formation of NH_3 starts at 500ºC, reaches a maximum at 700ºC and starts to decrease as the temperature is increased (Amure et al., 2003). The decomposition of NH_3 is thermodynamically limited. In the range of temperatures between 500-600ºC the formation of methane is favoured reducing the concentration of H_2, thus favouring the decomposition of NH_3. For temperatures ranging 600-900ºC, the thermodynamic decomposition of NH_3 is favoured as it is an endothermic reaction (Gangwal et al., 1999).

Tian et al. (2005) and Zu et al. (2007) observed that when coal is used, the conversion of N-fuel into NH_3 ranges from 20 to 50%, and may reach 90% when the fuel is biomass. In coals, the dominant forms of nitrogen are heteroaromatic structures, predominantly of the pyrrolic and pyridinic types, and therefore, the volatile decomposition will originate, basically, HCN. In biomass, nitrogen is present essentially as biopolymers, in structures such as DNA and chlorophyll. Aho et al. (1993) suggested that the O/N ratio in the fuel may act as an indicator of the ratio of nitrogen bound in side-chains of the aromatic structures in the fuel (much of the

nitrogen in side-chains may exist in the amino form). As the amino compounds may be easily converted into NH_3, the O/N ration may be used to predict the formation of NH_3.

The role of mineral matter in the early stages of devolatilization is still uncertain according to Friebel et al. (1999). However, iron seems to participate in the selective removal of N-char and calcium and potassium seem to favour the formation of NH_3 and N_2 at the expenses of HCN (Tsubouchi et al., 2004). Friebel et al. (1999) observed that some ash components give rise to a preferential release of nitrogen, suggesting that Si, Fe, Ca, Mg, Al, and even S, have some impact in the formation and release of NH_3.

EXPERIMENTAL

A bubbling fluidized bed gasifier working at atmospheric pressure was used. The gasifier height is 1500 mm and it is circular in cross section with an internal diameter of 80 mm. The gas exiting the reactor is passed through an insulated cyclone and a quenching system. NH_3 was measured in the condensates collected in the gas quenching system and in gas samples, according to method CTM-027 US EPA. Different blends of RDF and coal were used. Coal was from Puertollano mines in Spain. RDF was a mixture of 50% wood, 15% plastics (no PVC), 35% paper and cardboard. RDF composition in coal blends varied between 0 and 100% (w/w). Temperature was varied between 750ºC and 900ºC, for a fuel blend containing 70% RDF and 30% coal, while ER varied from 0 to 0.4. The fuel and steam flows were kept constant at 5 g daf/min. For the tests with catalysts, the blend with 70% of RDF and 30% of coal was used, at 850ºC and for an ER of 0.2. Different catalysts were introduced in the bed, including calcined dolomite (CD), commercial ZnO in a pellet form (ZP) and a commercial ZnO crushed (ZC).

Table 1 Feedstock Characterization

	RDF	Puertollano Coal
HHV (MJ/kg daf)	23.90	29.83
Fixed Carbon (% w/w)	14.2	29.9
Volatiles (% w/w)	74.6	20.8
Ash (% w/w)	4.5	43.6
Moisture (%w/w)	6.7	5.7
Carbon Content (% daf)	53.4	73.1
Hydrogen Content (% daf)	7.8	6.5
Sulphur Content (% daf)	0.07	1.92
Nitrogen Content (% daf)	0.43	1.71
Chlorine Content (% daf)	0.06	0.07
Oxygen Content (% daf)	38.3	16.7
Iron Content (% w/w)	0.10	1.62
Aluminium Content (% w/w)	0.29	6.72
Calcium Content (% w/w)	1.32	0.34
Potassium Content (% w/w)	0.09	0.82
Sodium Content (% w/w)	0.07	0.06
Magnesium content (%w/w)	0.06	0.29

The simulation work was carried out using FactSage 5.4 and the Fact5.3 database. The results were obtained for a blend of 70% of RDF and 30% of coal.

RESULTS AND DISCUSSION

Fuel mixture effect

Ammonia was found to be mostly captured in the quenching system independently of the operational conditions used. The results shown in the figures contemplate the concentration of NH_3 in the gas phase, NH_3(g), as well as the concentration of ammonia in the gas phase plus its concentration in the condensates NH_3(g+c).

The effect of coal addition on the formation of NH_3 is shown if Fig. 1. The increase of coal in the fuel blend seems to increase the amount of NH_3 released, which may partially explained by the higher N content of coal than in RDF. However, the observed NH_3 balance, N(g+c)%, decrease as greater amounts of coal were used, suggests that the formation of NH_3 is more complex than expected. It appears than in coal most of N-fuel may remain in the carbonaceous residues whilst in the case of RDF, N-fuel may be mostly released with the volatiles. Tian et al. (2005) and Zu et al. (2007) suggested that the chemical forms in which nitrogen is present in different fuels may play an important role in the release of nitrogen and in the conversion of N-fuel. The dominant nitrogen structures in biomass are biopolymers, while in coal they are heteroaromatic compounds, giving rise to HCN through thermal cracking, while biopolymers generally results in the formation of NH_3. Considering that the RDF used was mostly biomass, the results obtained may be in accordance with the explanation given above.

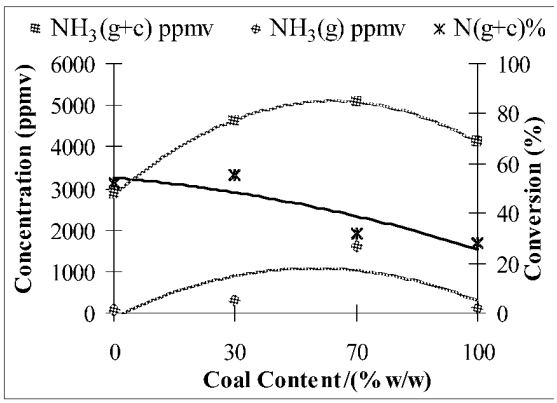

Fig. 1 Effect of coal on NH_3 formation (850°C, ER:0.2)

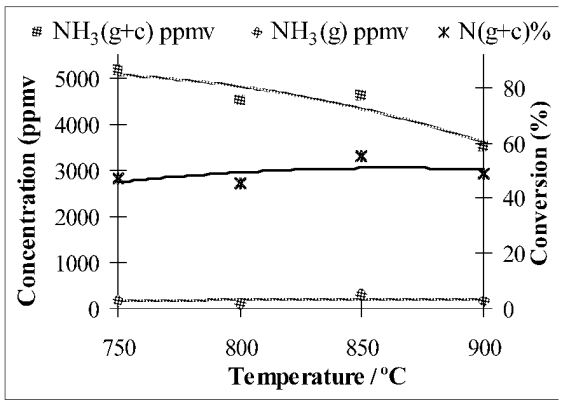

Fig. 2 Temperature effect on NH_3 formation (ER 0.2)

Considering Table 1, the O/N ratio for RDF is 89 and the O/N ratio for coal is 9.8, which suggests that nitrogen in RDF may be mostly present in side-chains in amino forms with higher tendency to release NH_3.

Temperature effect

The effect of temperature on the formation of NH_3 for a blend of 70% of RDF and 30% of coal is shown in Fig. 2. It can be observed that higher temperatures seem to lead to lower NH_3 concentration is the gas (g+c).

Increase of temperature shall lead to higher devolatilization, and therefore, it could be expected higher amounts of NH_3 in the syngas (in fact it was observed a decrease of 58% in nitrogen retention in the char). However, the results show an opposite trend, explainable by the fact that NH_3 decomposition is an endothermic reaction, meaning that even if more NH_3 is formed more is decomposed into N_2 and H_2.

ER effect

The effect of equivalence ratio on the formation of NH_3 is shown in Fig. 3. The increase of ER until 0.2 led to an increase of NH_3 concentration in the gas phase. However, higher ER led to a reduction on NH_3 concentration as well as on the conversion of N-fuel into NH_3.

As all experiments were carried out with a fixed amount of steam (5 g/min), it is expected that for lower ER (from 0.0 to 0.2) the steam has played an important role as a donor of free H radicals that would have reacted with nitrogen originating NH_3. As the amount of oxygen was increased, oxidizing reactions became more important leading to the formation of oxidized nitrogen species such as NO, that were not quantified in this work. The formation of these species is somehow supported by the fact, shown in Fig. 3, that as ER was increased the conversion of N-fuel was decreased (specially for ER>0.2).

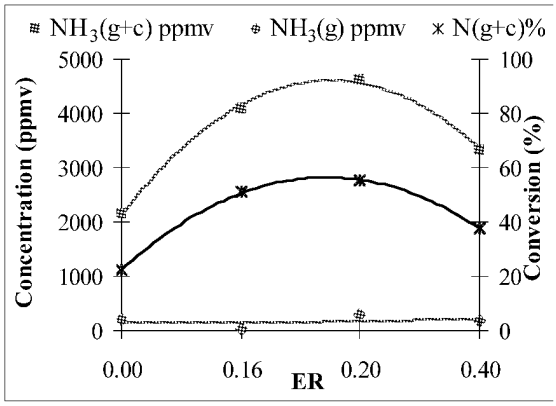

Fig. 3 Effect of ER on NH_3 formation (850°C)

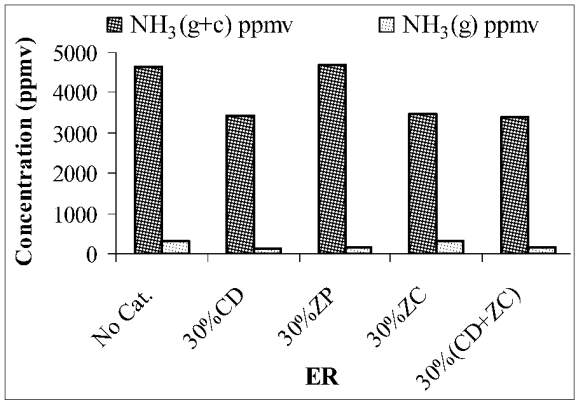

Fig. 4 Effect of catalyst on NH_3 formation (850°C, ER 0.2)

Catalysts effect

The effect of some catalysts on the formation of NH_3 is shown in Fig. 4. The results do not evidence a great effect on the formation of NH_3.

The use of catalysts such as calcined dolomite (CD), crushed ZnO (ZC) and mixtures of CD with ZC have led to a reduction of 25 to 27% on the concentration of NH_3. The use of ZnO in the form of pellets (ZP) did not prove to be efficient, probably because the available surface area of the pellets is too small, and therefore it is

easily deactivated by coke deposition. Despite a slight reduction on the concentration of NH_3, the results seem to show that NH_3 it is not very affected by the use of catalysts added to the bed of the gasifier.

Predictions using FactSage

In the present simulation the possible interactions between gas and solid phases (heterogeneous reactions) were not considered, and therefore the results will only represent an estimation of the influence of certain parameters in the formation of NH_3.

The results presented in Fig. 5, indicate that in all range of temperatures studied the dominant nitrogen species in the gas phase is $N_2(g)$. $NH_3(g)$ is the second most important nitrogen species; however, its concentration in the gas phase seems to decrease 93% with the rise of temperature. These results agree with those from Zhou et al. (2000) that found out a decrease in NH_3 with the temperature rise. The results from the simulation also agree with the experimental results obtained, once in both cases the raise of temperature reduced the release of NH_3 into the gas phase.

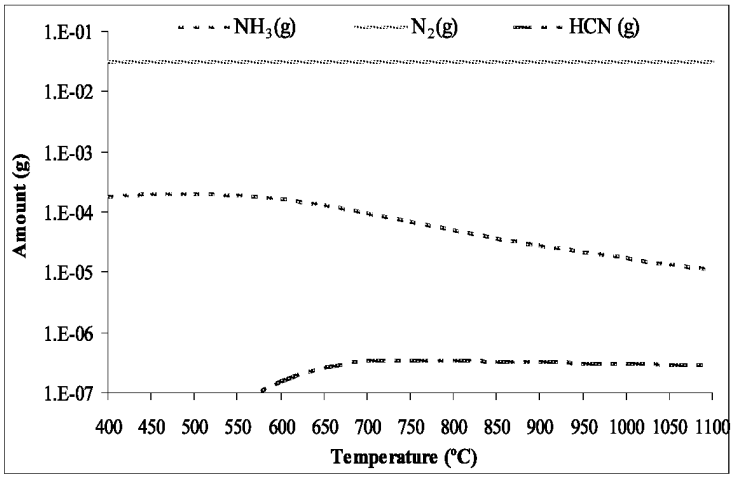

Fig. 5 Prediction of temperature effect on NH_3 formation

The third most important species is HCN(g), however, its concentration is much lower than that of NH_3. Formation of HCN begins at 600°C, and the amount released into the gas phase suffers an increase of 90%. An important aspect is that the formation of HCN begins at the same time that the reduction of NH_3 gains importance, suggesting a relation between the reduction of NH_3 and the formation of HCN.

In Fig. 6 it is presented the prediction of the effect of oxygen amount (in the absence of steam) in the formation of NH_3, for a temperature of 850°C and for a blend of 70% of RDF and 30% of coal.

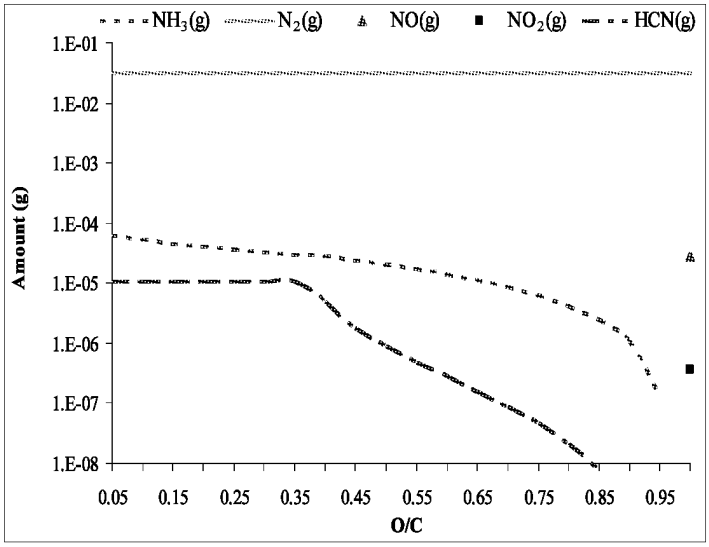

Fig. 6 Prediction of O/C ratio effect on NH_3 formation

The increase of oxygen does not seem to influence the amount of N_2 produced, which is the dominant form of nitrogen in the gas phase. The second most important nitrogen species is NH_3. However, its amount in

the gas is reduced as the amount of oxygen increases, and for a O/C of 1, NH_3 is no longer produced. Instead, oxidized forms of nitrogen such as NO(g) and NO_2(g) are predicted to become the dominant forms of nitrogen in the gas phase (beside N_2(g)), because of the predominance of oxidising reactions.

As it would be expected, these results show that the more oxidizing the atmosphere the most probable is the production of oxidized nitrogen species in the gas phase, although this is true only for high O/C ratios, very close to combustion conditions. These results agree with the ones obtained experimentally, as the increase of oxygen led to a decrease of NH_3(g).

Another important observation is that HCN(g) amount in the syngas is expected to increase with the increase of oxygen in the system, until a ratio of 0.4, showing some evidence that the NH_3(g) is originating HCN(g), but for higher O/C ratios the amount of HCN(g) starts, likewise, to decrease. These results agree with the ones obtained experimentally once in both cases the increase of oxygen led to a decrease of NH_3(g). However, the reduction observed experimentally is, probably, not related to an increase of oxidized nitrogen species but to the formation of HCN (g), according to the simulation results.

In Fig. 7 it is shown the effect of calcium, as Ca/C ratio, on the formation of nitrogen species, for a blend of 70% of RDF and 30% of coal, a temperature of 850ºC and an equivalence ratio of 0.2.

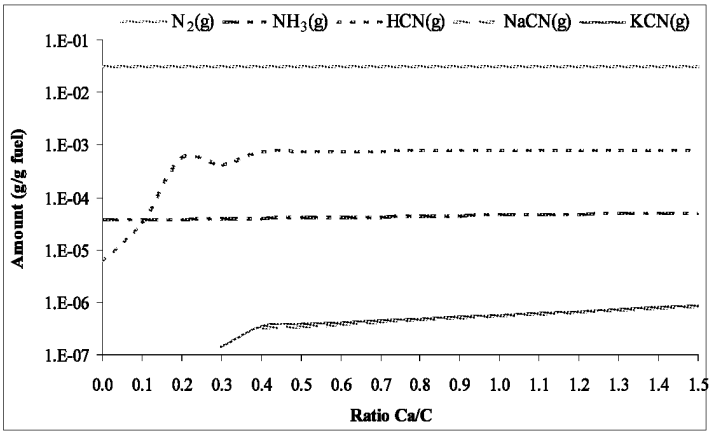

Fig. 7 Prediction of Ca/C ratio effect on NH_3 formation

The dominant nitrogen species is N_2 which does not seem to be influenced by the amount of calcium. On the other hand, NH_3 suffers an increase of 36% (not visible in Fig. 7 due to the logarithmic scale used). NH_3 is the second most important form of nitrogen in the gas phase till the Ca/C ratio of 0.1, but for higher ratios HCN is predicted to increase. Calcium seems to play an indirect role in the formation of nitrogen species by promoting an increase of HCN(g), as well as an increase of NaCN(g) and KCN(g).

As the production of N_2(g) remained constant, two conclusions could be withdrawn from the results shown in Fig. 7. The first is that the amounts of nitrogen species other than N_2(g) are so low that any change in their levels does not have any impact in N_2(g) concentration in the syngas. The other, is that calcium may play an important role in the release of nitrogen from the solid matrix (char), probably acting as a catalyst for the reaction of nitrogen with H_2, K and Na, promoting the formation of NH_3, HCN, KCN and NaCN and reducing the amounts of nitrogen retained in the char.

Experimentally, the use of calcined dolomite led to a reduction of about 25% on the concentration of NH_3(g), which is in opposition to the results presented in Fig. 7, that suggest that the presence of calcium would led to an increase of NH_3(g). The predictions for the effect of potassium in the formation of NH_3(g) is similar to the effect of calcium, the major difference is that the increase of potassium seems to lead to an increase in the formation of KCN(g).

In Fig. 8 it is shown the prediction of the effect of the ratio Zn/C in the formation of NH_3, for a blend of 70% of RDF and 30% of coal, at a temperature of 850ºC and an equivalence ratio of 0.2. As observed, in the previous cases analysed, the main nitrogen species is N_2(g) which seems to be insensitive to the variations of Zn in the system. NH_3 is the second most important nitrogen form in the gas phase until a Zn/C ratio of 0.5 is reached. For higher ratios, HCN(g) becomes more important than NH_3(g). As no nitrogen-zinc species are predicted to be formed, it seems that zinc has an indirect effect in the formation of nitrogen species, acting, possibly, as a catalyst in the formation of NH_3(g) and mainly of HCN(g). However, this prediction does not seem to be in agreement with the results obtained experimentally for the effect of the addition of ZnO in the concentration of NH_3(g).

The simulation results (for all the cases studied) have shown that, independently of the effect or metal studied the dominant nitrogen species is N_2(g), and that NH_3(g) and HCN(g) are probably less important than it

would be expectable. These results agree fairly well with those from Friebel et al. (2007), that showed that, at least for fixed bed gasification, there is an almost complete conversion of N-fuel into N_2, mainly due to the existence of sufficient supply of reactants, and that NH_3(g) plus HCN(g) only represent 20% of the converted N-fuel.

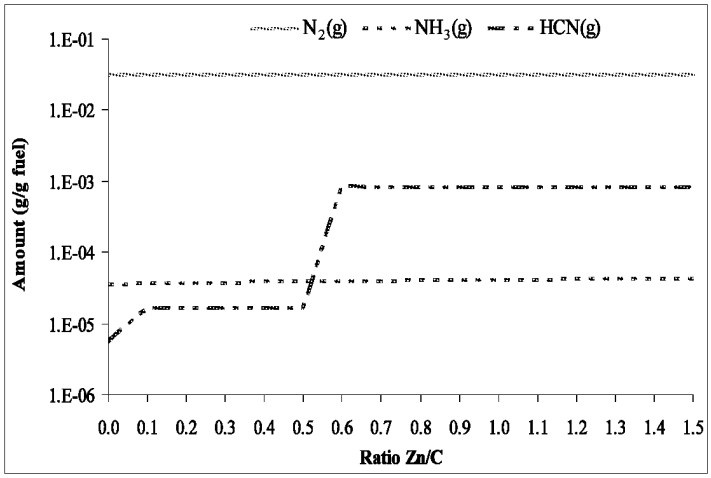

Fig. 8 Prediction of Zn/C ratio effect on NH_3 formation

CONCLUSIONS

The formation of NH_3(g) seems to be not only dependent on the amounts of N-Fuel but also on the form in which nitrogen is present in the solid fuels. Biomass seemed to promote the formation of ammonia in comparison to coal. Temperature increase seems to lead to a decrease in the formation of NH_3(g) once the decomposition of NH_3(g) is an endothermic reaction leading, probably, to the formation of N_2 and H_2. The increase in equivalence ratio led to a decrease of NH_3(g) due to the formation of oxidised nitrogen species or HCN according to the simulation results.

The use of dolomite and ZnO did not appear to have a great impact in the reduction of NH_3(g) in the syngas. However, if ZnO is chosen, it would be preferable to use small sized particles instead of pellets in order to increase the efficiency in the removal of NH_3(g).

The results of the simulation showed that, independently of the effect studied, the main nitrogen species in the syngas is N_2(g). Similar trends were found when comparing the experimental results with the predictions for the effect of temperature and ER on the formation of NH_3(g). Increase of inorganic matter seems to favour the release of nitrogen gaseous species, probably at the expenses of N-fuel. Calcium and Zinc appeared to have an indirect effect, increasing the formation of HCN(g).

REFERENCES

Aho, M. J., Hämäläinen, Jouni P., Tummavuori, Jouni L.: Combustion and Flame 15 (1993), pp. 22-28.
Amure, O., Hanson, S., Cloke, M., and Patrick, J. W.: Fuel 82 (2003), pp. 2139-43.
Friebel, J., Köpsel, R.: Fuel 78 (1999), pp. 923-932.
Gangwal, S., K., Gupta, R., P., Portzer, J., W., Turk, B., S (1999), "Catalytic ammonia decomposition for coal-derived fuel gases", U.S. Department of Energy's Morgantown Energy Technology Center: http://www.netl.doe.gov/publications/proceedings/96/96ps/ps_pdf/96ps4a7.pdf.
Leppälahti, J., Koljonen, T.: Fuel Processing Technology 43 (1995), pp. 1-45.
Liu, H., Gibbs, B. M.: Fuel 82 (2003), pp. 1591-1604.
Tian, F. J., Yu, J. L., McKenzie L. J., Hayashi, J., Chiba, T. and Li, C. Z.: Fuel 84 (2005), pp. 371-376.
Tsubouchi, N., Ohtsuka, S., Hashimoto, H. and Ohtsuka, Y.: Energy Fuels 18 (2004), pp. 1605 -1606.
Van der Drift, A., van Doorn, J., Vermeulen, J.W.: Bioenergy 20 (2001), pp. 45-56.
Zhou, J., Masutani, S. M., Ishimura, D. M., Turn, S. Q., Kinoshita, C. M.: Industrial & Engineering Chemistry Research 39 (2000), pp. 626-634.
Zu, Q., Brage, C., Chen, G., Sjöström, K.: Fuel 86 (2007), pp. 611-618.

EFFECT OF OPERATING CONDITIONS ON SO_2 AND NO_x EMISSIONS IN OXY-FUEL MINI-CFB COMBUSTION TESTS

L. Jia, Y. Tan and E.J. Anthony

CanmetEnergy, Natural Resources Canada,
1 Haanel Drive, Ottawa, K1A 1M1, Canada

Abstract: Anthropogenic CO_2 production is caused primarily by fossil fuel combustion. In consequence, it is increasingly necessary to find ways to reduce these emissions when fossil fuel is used. CO_2 capture and storage (CCS) appears to be among the most promising. All of the CCS technologies involve producing a pure stream of CO_2 either by concentrating it from the flue gases, or by using pure oxygen as the combustion gas. The latter option, oxy-fuel combustion, has now been well studied for pulverized coal combustion, but has received relatively little attention to date in the case of oxy-fuel circulating fluidized bed combustion. Recently, oxy-fuel CFBC has been examined in a 100 kW pilot plant operating with flue gas recycle at CanmetEnergy. The results strongly support the view that this technology offers all of the advantages of air-fired FBC, with one possible exception. Emissions such as CO or NO_x are lower or comparable to air firing. It is possible to switch from air-firing to oxy-firing mode easily, with oxygen concentrations as high as 60-70%, and flue gas recycle levels of 50-60%. Only sulphur capture is poorer. However, this result is not in good agreement with other studies, and the reasons for this discrepancy need further exploration. Here, longer tests have confirmed previous findings from CanmetEnergy with two coals and a petroleum coke. It also appears that changing from direct to indirect sulphation with the petroleum coke improves sulphur capture efficiency, although a similar effect could not be confirmed with coal from these results.
Keywords: oxy-fuel, CFBC, emissions

INTRODUCTION

CO_2 capture and storage (CCS) appears to be the most promising method for reducing CO_2 emissions from power generation (Buhre et al., 2005). Oxy-fuel combustion generates a nearly pure stream of CO_2 ready for capture and storage. However, oxy-fuel CFB combustion has received relatively little attention to date. The oxy-fuel concept was examined over 30 years ago for bubbling FBC, but rejected on the basis of cost (Yaverbaum, 1977). More recently, the boiler companies Alstom and Foster Wheeler have explored the concept using pilot-scale equipment. Alstom's work included testing in a unit of up to 3 MWth in size, but did not involve recycle of flue gas (Liljedahl, 2006). Foster Wheeler's work (Eriksson et al., 2007) also involved pilot-scale testing, using a small (30-100 kW) CFBC owned and operated by VTT (Technical Research Centre of Finland), and this work along with CanmetEnergy's own work with its 100 kW CFBC appear to be the first such units operated with oxy-fuel combustion using full flue gas recycle.

The advantages of FBC are already well known in terms of its ability to burn a wide range of fuels, both singly and co-fired, to achieve relatively low NO_x emissions, and to remove SO_2 with limestone (Grace et al., 1997). Another advantage of CFBC technology in the context of oxy-fuel firing is that external solid heat exchanger(s) can be used to extract heat from the combustion process, therefore, allowing a significant reduction in the amount of recycled flue gas required for combustion temperature control. Alternatively, it is possible to use a much higher oxygen concentration in the combustor. This allows the economics of oxy-fired CFBC to be significantly improved over oxy-fired PC. It appears possible to achieve a reduction in area of the CFBC boiler island by as much as 50% (Liljedahl et al., 2006; Stamatelopoulos and Darling, 2008; Hotta et al., 2008).

CanmetEnergy started studying oxy-fuel CFB combustion in 2006 with initial results published in early 2007 (Jia et al., 2007). Subsequent tests have focused on the effects of operating conditions. This paper discusses the results generated in CanmetEnergy's mini-CFBC unit, particularly SO_2 and NO_x emissions over a wider range of oxy-fuel CFB combustion conditions.

EXPERIMENTAL

The test facility has been described in detail elsewhere (Jia et al., 2007). The mini-CFBC contains a 0.1 m ID stainless steel riser covered with 100 mm of insulation. Independent feed augers can supply multiple fuel types and sorbents. Oxygen and recycled flue gas flow rates are controlled by a combination of mass flow

controllers and rotameters.

Eastern bituminous (EB) coal and Kentucky coal (a bituminous coal) were used in this series of tests. Table 1 gives the analysis of the two coals. Both coals were crushed to -6 mm. Petroleum coke was also used (analyses in Table 1). The particle size of petroleum coke was smaller, about -4 mm. For sulphur capture, Havelock limestone and Czatkowice limestone were used. Table 2 gives the analysis of the two limestones. Havelock is a Canadian limestone and Czatkowice limestone is from Poland. The particle size of the limestones was in the range of 0-0.8 mm. In all cases, 5 kg of olivine sand of size 0.15-0.35 mm was used as the initial bed material.

Table 1 Analysis of fuels

	Eastern bituminous (EB)	Kentucky Coal	Petroleum Coke
Proximate Analysis, wt% (dry)			
Moisture, wt% (as analyzed)	1.08	2.01	0.66
Ash	8.86	11.31	1.00
Volatile Matter	35.78	37.35	11.46
Fixed Carbon	55.56	51.34	86.97
Ultimate Analysis, wt% (dry)			
Carbon	77.81	74.05	86.91
Hydrogen	5.05	5.06	3.22
Nitrogen	1.49	1.62	1.83
Sulphur	0.95	1.56	5.88
Ash	8.86	11.31	1.00
Oxygen (by difference)	6.04	6.40	1.16
Heating Value (MJ/kg)	32.51	30.93	34.71

Table 2 Analysis of limestones

	Havelock	Czatkowice		Havelock	Czatkowice
CaO	53.99	54.32	Cr_2O_3	<0.01	
MgO	0.59	0.48	P_2O_5	<0.02	
SiO_2	1.23		SO_3	0.20	0.08
Al_2O_3	<0.38	0.04-0.09	V_2O_5	<0.02	
Fe_2O_3	<0.55	0.08-0.11	SrO	0.02	
Na_2O	<0.17	0.01-0.03	BaO	0.02	
K_2O	<0.08	0.02-0.04	NiO	0.01	
MnO	0.08		LOF	43.34	42.70
TiO_2	<0.04		SUM	99.48	

The mini-CFBC was operated at a nominal bed temperature of 850°C and 950EC. Superficial gas velocity was about 3-4 m/s. During oxy-fuel combustion, oxygen concentrations in the primary gas were in the range of 44% to 66% and 32% to 75% in the secondary gas. Global oxygen concentration was from 34% to 45% (volume per cent). Primary gas fractions were from 0.6 to 0.7 and secondary gas fractions were from 0 to 0.07, respectively. The remainder of the gas was supplied through the return leg and the coal feed port. Errors associated with these estimates were about 5-10%.

RESULTS AND DISSCUSSION

General Comments

Experimental results for Eastern bituminous coal and pet coke during stable operation under air firing and oxy-fuel firing conditions are given in Table 3. Table 3 shows that, during oxy-fuel firing, temperatures across the mini-CFBC were very similar to those seen during air firing. Gas velocities in the dense bed zone and in the riser were also similar but highly dependent on bed and riser temperature.

The flue gas recirculation ratios were estimated to be between 49.1-62.5%. The recycle ratio was significantly lower than that for pulverized fuel oxy-fuel firing. One of the reasons for the low recycle ratio was that, in the mini-CFBC, the solid particles were cooled in the return leg (all insulation material was removed from the return leg for these runs). The temperature of the solids entering the combustor from the return leg was

several hundred degrees lower than the cyclone temperature. If an external solid heat exchanger were available to cool the solids to a lower temperature, the flue gas recirculation ratio could be further reduced.

Table 3 Experimental results for Eastern bituminous coal and pet coke

	Eastern bituminous coal			Petroleum coke		
	Air firing Czatkowice (Nov. 7)	Oxy-fuel Czatkowice (Nov. 7)	Oxy-fuel Havelock (Nov. 14)	Oxy-fuel Czatkowice (Oct. 1)	Oxy-fuel Czatkowice (Oct. 1)	Oxy-fuel Havelock (Jun. 25)
O_2, %	3.04±0.23	3.72±0.8	3.47±0.53	4.74±1.90	3.64±0.56	3.28±1.06
CO_2, %	14.7±0.20	91.1±0.8	92.9±0.48	4.40±1.7	86.3±1.0	92.3±1.3
CO, ppm	47.1±11	186±40	83.0±9	94.7±12.8	25.1±2.8	30.5±32
SO_2, ppm	281±9	1165±40	704±80	5866±827	2142±390	2386±630
NO_x, ppm	245±4	210±6	170±6	394±121	443±38	387±60
Fuel mix feed rate, kg/h	3.5±0.35	4.5±0.45	4.5±0.45	6.25±0.62	6.5±0.65	6.0±0.6
Gas velocity in bed, m/s	1.70±0.08	2.25±0.1	2.59±0.1	2.25±0.11	3.25±0.2	2.73±0.12
Gas velocity in riser, m/s	3.23±0.16	3.28±0.16	3.64±0.18	3.17±0.15	4.20±0.3	3.73±0.25
Avg. bed temp., °C	836±5	838±4	828±6	842±5	930±12	961±15
Avg. riser temp., °C	902±30	860±23	853±19	843±4	946±32	950±10
Avg. cyclone temp., °C	854 ±11	808±2	842±7	813±2	884±8	896±7
Avg. return leg temp., °C	280±13	268±1	320±8	612±10	471±13	612±29
Avg. baghouse inlet temp., °C	374±4	330±18	449±4	256±2	314±10	288±7
Ca/S molar ratio	3	3	3	3	3	2
S capture efficiency, %	74.4±8	65.0±7	77.1±8	64.5±8	87.3±10	85.6±10
Fuel N to NO_x, %	6.22±6.3	1.76±0.19	1.54±0.16	3.35±3.5	3.69±0.4	3.28±0.4
Recycle ratio, %	-	59.7±2.5	61.0±2.7	54.6±2.5	62.5±3.2	54.2±2.8
O_2 in primary gas, %	20.9	50.8±2.5	44.0±2.1	58.3±2.8	44.1±2.5	60.5±3.5
O_2 in 2nd gas, %	20.9	3.72±0.8	60.9±3.0	69.1±5.6	75.0±7	-
Global O_2, %	20.9	34.9±1.8	34.2±1.8	44.2±3.0	36.2±3.5	43.7±4

NO_x Emissions

For Eastern bituminous coal in this series of tests, NO_x concentrations in the flue gas during the oxy-fuel-firing period were lower than levels under the air-firing mode at comparable temperatures (~850°C, Table 3). The fuel nitrogen-to-NO_x ratio decreases very significantly from 6.22% to 1.54-1.76%. The same phenomenon was observed with Kentucky coal with both Czatkowice and Havelock limestone for tests conducted at ~850°C. These NO_x results were better than those from the initial oxy-fuel tests published earlier by the current authors, which showed comparable or lower nitrogen conversion ratios. Better control of the mini-CFBC combustion conditions and extended test durations were the most likely cause. Change of limestone apparently had no effect on NO_x concentration.

NO_x concentration under oxy-fuel CFBC was sensitive to temperature, similar to the situation for CFBC air-firing mode for coal and petroleum coke, Fig. 1 and Table 3. Nonetheless, it should be pointed out that NO_x levels observed here were still much lower than for pulverized fuel oxy-fuel combustion (*Tan* et al., 2004). Tan et al. (2004) reported oxy-fuel pulverized fuel combustion with flue gas recirculation in a 0.3 MW_{th} test facility. Using Highvale coal, results indicated that NO_x concentration increased to 1183 ppm from 707 ppm in the air-firing mode. Since there are no data on oxy-fuel CFB combustion with flue gas recirculation in the open literature, the current results cannot be evaluated with comparable test data reported elsewhere, but there are some studies without flue gas recycle. Thus, Nsakala et al. (2004) conducted CFB combustion tests with O_2 and CO_2 mixtures in a 0.533 m dia. CFBC firing medium volatile bituminous coal. They noted that, at about 30% O_2 in the combustion gas, NO_x concentrations in the flue gas were 55 to 72 ppm, which was significantly lower than for air firing of the same coal in their tests (220 ppm). Czakiert et al. (2006) suggested that oxy-fuel CFB combustion results in a significant reduction in fuel nitrogen conversion to NO_x.

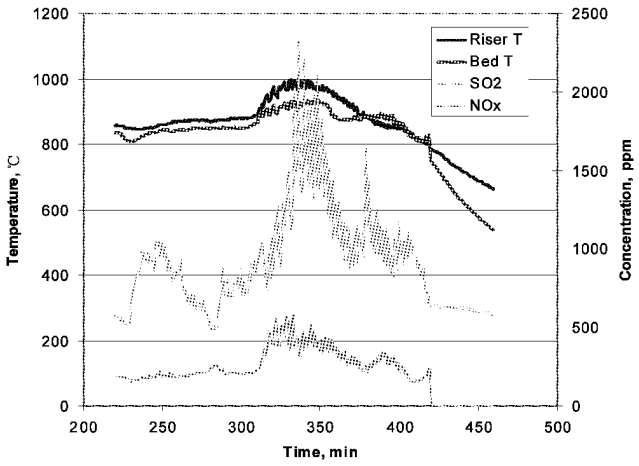

Fig. 1 Temperature effect on NO_x for coal combustion under oxy-fuel CFBC conditions. Eastern bituminous coal and Czatkowice (Polish) limestone

Sulphur Capture

At temperature around 850°C during air-firing periods, sulphur capture efficiency for both coals was in the range of 74.4-86.6%. These values were lower than that of full-scale CFBC units as up to 90% sulphur capture is typically achievable in utility/industrial CFBC units with Ca/S ratios of 2 to 2.5 (Anthony and Granatstein, 2001). However, the current tests were short runs (7-8 h), and steady state of ash composition in the mini-CFBC may not have been achieved. Performance of the two limestones was similar in air-firing mode. During oxy-fuel firing, sulphur capture efficiency decreased slightly to levels of 65% to 78.2%, with Havelock limestone performing somewhat better. No apparent explanation can be offered at this time, but to note the differences in performance. These results are potentially problematic since VTT and Foster Wheeler workers found that very high Ca utilizations could be achieved in their FBC with full flue gas recycle (Eriksson et al., 2007) and even the Alstom workers, who ran their equipment with bottled gases, found that with a reactive limestone, capture ranged from 72 to 96% (36 to 48% Ca utilization).

At ~850EC sulphur capture was via direct sulphation of $CaCO_3$. However, it is not clear whether direct sulphation of $CaCO_3$ under oxy-fuel-firing conditions was the cause of the lower sulphur capture efficiency. Snow et al. (1988) and Hajaligol et al. (1988) found that, in TGA studies, direct sulphation of $CaCO_3$ produced a higher conversion than the sulphation of precalcined limestone, and that the diffusion resistance through the $CaSO_4$ product layer was significantly smaller than that encountered in the usual sulphation of CaO, since a more porous $CaSO_4$ layer was formed during direct sulphation. However, there is work in the literature that suggests the high partial pressures of CO_2 can impede direct sulphation, possibly by slowing the diffusion of CO_2 away from the limestone particles, which would be in accordance with our findings (Hu et al., 2006).

It was noted in earlier tests that at ~850°C in oxy-fuel CFB firing mode, sulphur capture efficiency was low for petroleum coke combustion. However, it was noted in one of those tests that, when temperature was over ~920EC, significant improvement in sulphur capture occurred. The duration of the higher temperature period was not long enough for firm conclusions to be drawn at that time. In this series of tests, it was decided to run for longer periods at nominal temperatures of ~850°C and ~950°C for petroleum coke oxy-fuel CFB combustion to verify previous observations. This test (including preheating, not shown on the graph) lasted for ~12 h. It started with combustion in air and then changed to oxy-fuel firing without having to stop the fuel feed. The bed temperature was kept at 850°C during air firing and the first part of the oxy-fuel test, and was then increased to 950°C for the second period of oxy-fuel testing. The concentration of SO_2 decreased significantly when the bed temperature increased from 850°C to 950°C, from about 6000 ppm at 850°C to about 2000 ppm at 950°C, a reduction of more than 65%.

Data in Table 3 indicate that, at ~850EC during oxy-fuel CFB combustion, sulphur capture was in the 60-70% range. When temperature was increased to ~950°C, the sulphur capture efficiency increased to 85.6-87.3%. Performance of both limestones tested was very similar.

The temperature change from 850°C to 950°C corresponds to a change from direct to indirect sulphation. Most likely for petroleum coke oxy-fuel CFB combustion, indirect sulphation resulted in higher sulphur capture efficiency.

The finding that higher temperatures result in higher sulphur capture efficiency was confirmed with petroleum coke, and tests were also conducted with coals at higher temperature to see if similar sulphur capture

improvement could be realized. Figure 1 also shows SO_2 results for one of the coals tested. It can be seen that when the temperature was increased from ~850°C, SO_2 started to increase and variations were very significant. When temperature was lowered, SO_2 concentration followed. Unfortunately, given these large fluctuations in both the bed temperature and SO_2 concentration, some caution has to be exercised in coming to firm conclusions based on the current results; however, at the moment there appears to be no firm evidence that higher temperature (indirect sulphation) causes significant improvements in sulphur capture for coal. During the coal tests, it was observed that these fluctuations seemed to be closely correlated to the limestone calcination temperature. As bed temperature approached 930°C, we observed a sudden drop in the lower bed pressure accompanied by poor solid recirculation, which led to a rapid rise in bed temperature. In the case of petcoke, this effect was not as obvious. Further tests are being planned to elucidate this observation.

CONCLUSIONS

Oxy-fuel CFBC tests were successfully conducted with flue gas recirculation for both coals and petroleum coke. CO_2 concentration in the flue gas was very stable, in the range of 84.4-92.3%. Global oxygen concentrations in the combustion gas were 34.1-45%. Flue gas recycle ratio was in the range of 49.1-62.5%. The recycle ratio is significantly lower than that required for oxy-fuel pulverized fuel combustion. NO_x emissions were lower than for air-firing mode even at temperatures as high as 950°C in the fluidized bed. CO concentration was basically the same for air firing and oxy-fuel firing with flue gas recirculation. Better sulphur capture efficiencies were obtained compared to earlier tests; better control of operating parameters and longer duration of tests appeared to be the reason. At ~850°C, sulphur capture was lower in oxy-fuel CFB combustion, ranging from 65% to 78.2%. For petroleum coke, a higher operating temperature of ~950°C resulted in 20% improvement in sulphur capture. Apparently, indirect sulphation performed better in coke combustion. However, the same cannot be confirmed for the two coals studied. The two limestones performed basically the same with Havelock slightly better in oxy-fuel CFB coal combustions at ~850°C.

REFERENCES

Anthony, E.J., Granatstein, D.L.: Sulfation phenomena in fluidized bed combustion systems: Prog. Energy Combust. Sci. 27 (2001), 215-236.

Buhre, B.J.P., Elliot, L.K., Sheng, C.D, Gupta, R.P., Wall T.F.: Oxy-fuel Combustion Technology for Coal-Fired Power Generation: Prog. Energy Combust. Sci. 31 (2001), 283-307.

Czakiert, T., Bis, Z., Muskala, W., Nowak, W.: Fuel conversion from oxy-fuel combustion in a circulating fluidized bed: Fuel Process. Technol. 87 (2006), 531-538.

Eriksson, T., Sippu, O., Hotta, A., Myohanen, K., Hyppanen, T., Pikkarainend, T.: Oxy-fuel CFB Boiler as a Route to Near Zero CO_2 Emission Coal Firing: Power Generation Europe, Madrid, Spain, June 26-28, 2007.

Grace, J.R., Avidan, A.A., Knowlton, T.M. (eds.): Circulating Fluidized Beds, Blackie Academic and Professional, London, 1997.

Hajaligol, M.R., Longwell, J.P., Sarofim, A.F.: Analysis and modeling of the direct sulfation of $CaCO_3$: Ind. Eng. Chem. Res. 27(12) (1988), 2203-2210.

Hotta, A., Nuorimo, K., Eriksson, T., Palonen, J., Kokki, S.: CFB Technology Provides Solutions to Combat Climate Change: Proceedings of the 9th International Conference on Circulating Fluidized Beds, in conjunction with the 45th International VGB Workshop, "Operating Experience with Fluidized Bed Systems" (J. Werther, W. Nowak, K-E. Wirth, E-U. Hartge, eds.), Hamburg, Germany (May 13-16, 2008), pp. 11-17.

Hu, G., Dam-Johansen, K., Wedel, S., Hansen, J.P.: Review of the Direct Sulfation of Limestone: Prog. Energy Combust. Sci. 32 (2006), 386-407.

Jia, L., Tan, Y., Wang, C., Anthony, E.J.: Experimental Study of Oxy-Fuel Combustion and Sulphur Capture in a Mini CFBC: Energy Fuels 21 (2007), 3160-3164.

Liljedahl, G.N., Turek, D.G., Nsakala, N.Y., Mohn, N.C, Fout, T.E.: Alstom's Oxygen-Fired CFB Technology Development Status for CO_2 Mitigation: 31st International Technical Conference on Coal Utilization and Fuel Systems, Clearwater, Florida (May 21-25, 2006).

Nsakala, N., Liljedahl, G., Turek, D.: Greenhouse gas emissions control by oxygen firing in circulating fluidized bed boilers, Phase II: pilot scale testing and updated performance and economics for oxygen fired CFB: PPL Report No. PPL-04-CT-25 under cooperative agreement No. DE-FC26-01NT41146 (2004).

Snow, M.J.H., Longwell, J.P., Sarofim, A.F.: Direct sulfation of calcium carbonate: Ind. Eng. Chem. Res. 27 (1988), 268-273.

Stamatelopoulos, G.N., Darling, S.: Alstom's CFBC Technology: Proceedings of the 9th International Conference on Circulating Fluidized Beds, in conjunction with the 45th International VGB Workshop, "Operating Experience with Fluidized Bed Systems" (J. Werther, W. Nowak, K-E. Wirth, E-U. Hartge, eds.), Hamburg, Germany (May 13-16, 2008), pp. 3-9.

Tan, Y., Croiset, E., Douglas, M., Thambimuthu, K.: Combustion characteristics of coal in a mixture of oxygen and recycled flue gas: Fuel 85 (2006), 507-512.

Yaverbaum, L.: Fluidized Bed Combustion of Coal and Waste Materials, Noyes Data Corp., Park Ridge, New Jersey, 1977.

DESULFURIZATION CHARACTERISTICS OF FLY ASH RECIRCULATION AND COMBUSTION IN THE CIRCULATING FLUIDIZED BED BOILER

S. F. Li, M. X. Fang, B. Yu, Q. H. Wang, Z. Y. Luo

State Key Laboratory of Clean Energy Utilization, Zhejiang University, Hangzhou, 310027, China

Abstract: The experiments of the fly ash recycle combustion using Guizhou anthracite were carried out in a bench scale circulating fluidized bed (CFB) combustor. Effects of some key operating parameters such as recycle ash to coal mass ratio (Ca to S molar ratio), temperature, reactivation mode of fly ash, circulation rate and fluidization velocity on the desulfurization efficiency were intensively investigated. It is shown that the limestone utilization efficiency could be improved about 30% with the following operating conditions: the mass ratio of fly ash (reactivated by water and dried at 90℃) to coal was 0.45, the furnace temperature was 880℃, the water to ash mass ratio was 4.5% (the water-to-calcium molar ratio was 0.55) and circulation rate was 18.

Keywords: fly ash recycle combustion, reactivation, CFB, desulfurization

INTRODUCTION

Circulating fluidized bed (CFB) boiler as a clean combustion technology, has been extensively developed (Basu, 1999; Chen Jihui and Lu Xiaofeng, 2007), due to the friendly environmental characteristic and the adjustable capability. Calcium sorbents (e.g. limestone) are widely used for the removal of SO_2 from the combustion of fuels containing sulfur in CFB combustors (Anthony et al., 2007; Saastamoinen and Shimizu, 2007). Under oxidizing conditions and atmospheric pressure, limestone-based sorbents are initially calcined to yield the porous CaO, as presented by the reaction (1).

$$CaCO_3(s) \longrightarrow CaO(s) + CO_2(g) \qquad \Delta H=178.2\ kJ/mol \tag{1}$$

Then, CaO reacts with SO_2 through the chemical pathway (2).

$$CaO(s) + SO_2(g) + 1/2O_2(g) \longrightarrow CaSO_4(s) \qquad \Delta H=-481.4\ kJ/mol \tag{2}$$

It is theoretically deduced that one mole of S was removed by one mole of Ca. Desulfurization is established to proceed in the core-shell pattern. The inner cores of the unreacted porous CaO might be packed by $CaSO_4$-rich shell to prevent the following desulfurization. The degree of limestone utilization is very low, as claimed about 25-45%. Carbon content in the fly ashes from the CFB combustors is estimated to be up to 20% in China. The issues, how to improve the utilization degree of limestone in fly ash and how to reduce the carbon content in fly ash, become more and more important.

The fly ash with the partially reacted sorbent and unburn-off carbon could be further utilized by various ash recycling processes, such as dry ash recirculation or reactivated ash recycle (Gora et al., 2006; Montagnaro et al., 2003; Montagnaro et al., 2008; Y. Tsuo, 1999). The ash recycling process not only prolongs the residence time for ash burning, but also exposes the unreacted cores of sorbents, improving the limestone utilization and burn-off rate of carbon. Zhong et al. (Zhong Zhaoping et al., 1997) reports that the desulfurization under the reductive atmosphere had higher efficiency with the application of fly ash recirculation. Wu et al. (Wu Xin et al., 1999) demonstrated that under-feeding was safer and more reliable than above-feeding for ash reinjection. Recently, some investigators address the reactivation of the sulfur capture ability of the fly ash by both water and steam hydration (Montagnaro et al., 2008).

The research in this paper extends the knowledge of dry ash and hydrated ash recirculation in a bench-scale CFB combustor. The influence of the factors (e.g. ash to coal mass ratio, temperature, reactivation mode, circulation rate, fluidization velocity) on desulfurization efficiency is estimated, in order to obtain the optimal operation parameters for ash reactivation and recycle. The mechanisms for the reactivation and the increased degree of calcium utilization are investigated by means of the visual scanning electron microscope analysis. The pore surface area and volume distribution of the original and reactivated fly ashes were determined by a PoreMaster 60 porosimeter.

EXPERIMENTAL

Materials

Coal and limestone used in this study were provided by a power plant at Guizhou in China. The analysis data of fuel are shown in Table 1. The fuel is a high-sulfur blind coal. The original fly ash used in our experiments was collected from the plant of a 135 MW CFB boiler. Table 2 gives the chemical composition analysis of the limestone and original fly ash analyzed by X-ray fluorescence. The particle size distribution of the original fly ash (Fig. 1) was analyzed by the particle size analyzer (Mastersizer, 2000E).

Table 1 Proximate analysis and Ultimate analysis of coal

Sample	Proximate analysis (%)				$Q_{b,ad}$ (J/g)	Ultimate analysis (%)				
	M_{ad}	A_{ad}	V_{ad}	FC_{ad}		C_{ad}	H_{ad}	N_{ad}	$S_{t,ad}$	O_{ad}
Coal	4.24	30.28	7.61	57.87	23107	57.92	2.38	1.11	2.68	1.39

Table 2 Chemical composition analysis of the limestone and the original FBC fly ash

Sample	Combustion loss (%)	Chemical composition (%)					∑(%)
		MgO	Al_2O_3	SiO_2	CaO	Fe_2O_3	
Limestone	42.18	0.43	1.06	4.09	51.27	0.06	99.09
Original fly ash	20.64	1.58	13.74	19.71	25.34	17.97	98.98

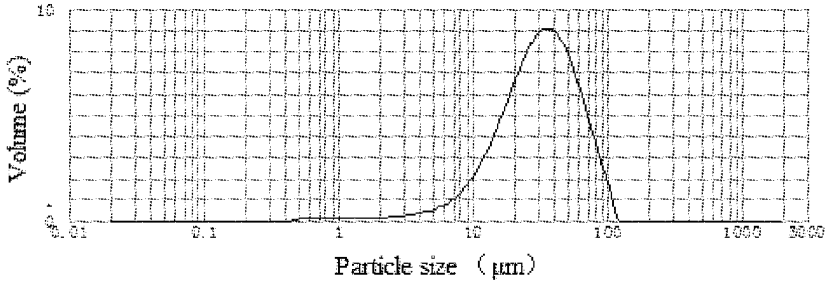

Fig. 1 Particle size distribution of the original fly ash

The apparatus

The experiments for combustion and desulfurization were carried out in the CFB combustor, which is depicted schematically in Fig. 2. The bed of the reactor is 80 mm in diameter and 2.6 m in height. A refractory steel plate is used as the distributor. Two connected cyclones are employed to collect the fine fly ash. The reactor furnace is electrically heated. The temperature distribution of the reactor is determined by ten thermocouples. A screw feeder is used to feed the mixture of fuel and sorbent. The gas concentration in the outlet flow is continuously analyzed using a gas analyzer (TESTO 350XL).

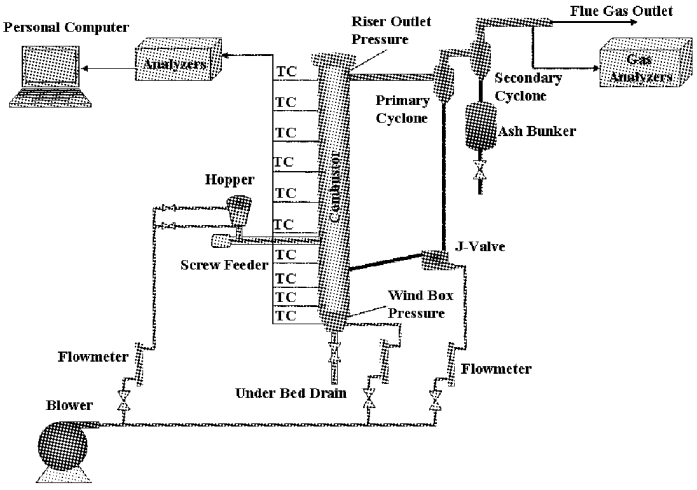

Fig. 2 Schematic of the experimental equipment

The operating conditions during the hydration, combustion and desulfurization are given in the Table 3.

Table 3 Operating conditions of experiments

Operating conditions	Hydration	Combustion and Desulfurization
Coal size range		0-4mm
Bed material		Silica sand (2kg)
Limestone size range		0-1mm
Operating temperature	Room temperature, 90℃	800℃, 850℃, 880℃, 900℃, 920℃, 940℃
Limestone to coal mass ratio		0.1, 0.2, 0.25
Ash to coal mass ratio		0.15, 0.2, 0.3, 0.45
Water to ash mass ratio	1%, 3%, 4.5%	
Test duration	24 h	60 min.
Fluidization velocity		1.88 m/s, 2.31 m/s

The concentration of oxygen in flue gas is changed for the different experiments. For comparison, all of the determined results need to be converted, according to the excess air coefficient λ=1.4. Then the desulfurization efficiency can be defined as follows:

$$\eta_S = \frac{E_{WSO_2} - E_{TSO_2}}{E_{WSO_2}} \times 100\% \tag{3}$$

Where E_{WSO_2} and E_{TSO_2} are the SO_2 concentration at outlet in the baseline test without any desulfurization measure and the tests with fly ash recycle, respectively.

RESULTS AND DISCUSSION

Microstructural characterization of the ashes

The original and hydrated ashes were analyzed by scanning electron microscope (SEM) and mercury porosimetry. The hydration process breaks the sulfate shell through blocking off unreacted lime. This permits a sequential dehydration of $Ca(OH)_2$ to yield CaO with the larger specific surface area in the combustor (Fig. 3). It is favourable for the sulfur capture. The pore size ranges before and after hydration were 10-20 nm and 50-8000nm, respectively (Fig. 4).

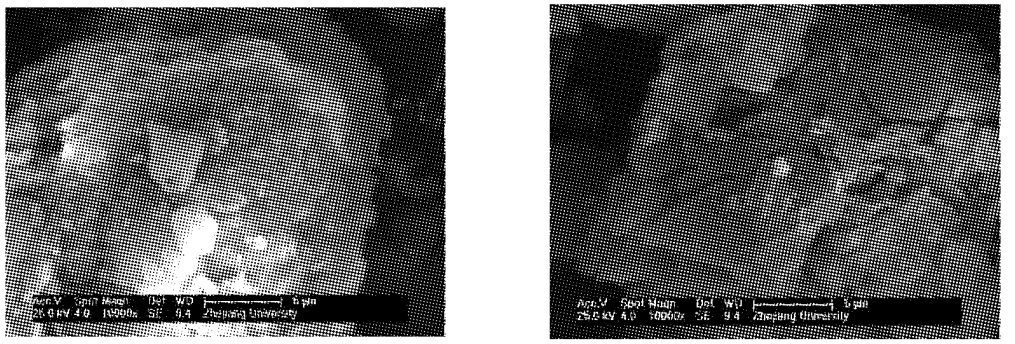

(a) Unhydrated (b) Room temperature, water to ash mass ratio 3%

Fig. 3 Hydration effect on microstructure of the ash

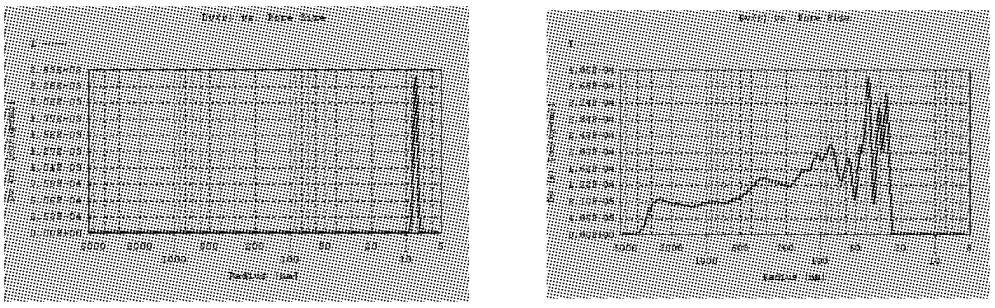

(a) Unhydrated (b) 90℃, water to ash mass ratio is 3%

Fig. 4 Pore size distribution of ashes

Effects of ash to coal mass ratio on the desulfurization efficiency

The ash to coal mass ratio has a great influence on desulfurization efficiency, indicating that the Ca to S molar ratio has a significant effect on desulfurization efficiency. The desulfurization efficiency increases with the increased ash to coal mass ratio, but this trend becomes lower and lower. It is shown that as the ash to coal mass ratio increases from 0.15 to 0.45 (Fig. 5), the desulfurization efficiency is improved from 36.91% to 50.14%. It is worthily noted that the desulfurization efficiency is slightly improved as the ash to coal mass ratio is too high. In addition, if the ash to coal mass ratio is too high, heat loss of the system will be augmented, boiler efficiency will be decreased, and even the operation stabilization of the boiler will be influenced.

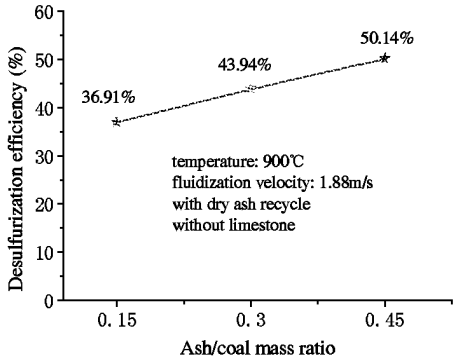

Fig. 5 Effect of ash to coal mass ratio on sulfur capture efficiency (without limestone)

Effects of temperature on the desulfurization efficiency

The experiments, investigating the influence of temperature on desulfurization efficiency, are divided into two parts: one is the ash recirculation experiments with limestone sorbent for sulfur capture, while the other one without limestone. The operating temperature is changed from 800 to 950 ℃.

It is shown that the desulfurization efficiency reaches the maxima at about 880 ℃ for the experiments without limestone (Fig. 6). The desulfurization efficiency increases smoothly from 800 ℃ to 880 ℃, but decreases promptly from 880 ℃ to 950 ℃. The ash used in the experiments contains some of limestone which could be converted to CaO by calcination at high temperature. Furthermore, the optimal calcination temperature is about 880 ℃ where the CaO is highly active. Hence, the highest desulfurization efficiency could be obtained within the selected temperature interval.

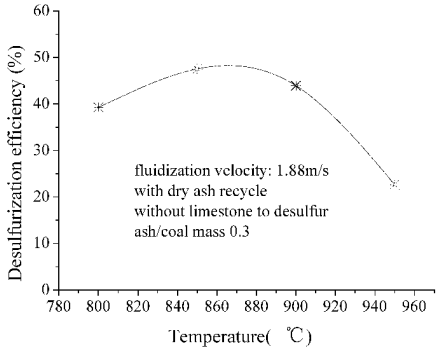

Fig. 6 Effect of temperature on sulfur capture efficiency (without limestone)

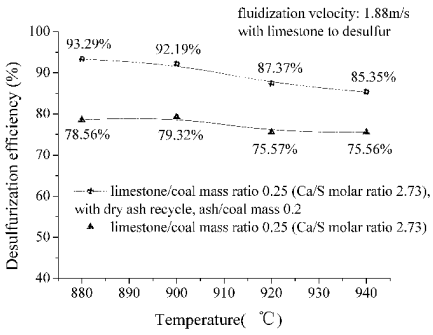

Fig. 7 Effect of temperature on sulfur capture efficiency (with limestone)

The influence of temperature on the desulfurization in the experiments with limestone is shown in Fig. 7. As the limestone to coal mass ratio was 0.25 (correspondingly, the Ca to S molar ratio is 2.73), the desulfurization efficiency is changed from 85.35% to 93.39% and from 75.56% to 79.32% for the experiments with and without ash recirculation, respectively. It could be concluded that the desulfurization efficiency is slowly improved with the increased limestone to coal mass ratio.

Effects of the ash reactivation mode on the desulfurization efficiency

Hydration is currently taken as a feasible technique for the sorbent reactivation, and the influence of the water to ash mass ratio on the sulfur capture ability is also extensively discussed in the literature (Laursen et al., 2001; Laursen et al., 2000; Laursen K, 2003; Manovic and Anthony, 2008). The value of the SO_2 uptake rate, as a function of the water to ash mass ratio in the ash recycle experiments with and without limestone, is shown in Fig. 8 and Fig. 9. The desulfurization efficiency is enhanced from 43.94% to 57.78% with the increased water to ash mass ratio from 0 to 4.5% (Fig. 8). The improvement of SO_2 capture of the hydrated ash might be ascribed to the enhancement of the hydration reaction $CaO \longrightarrow Ca(OH)_2$. This leads to the swelling of the particle core, accounting for the break-up of the $CaSO_4$-rich external layer. Since the hydrated ash is reinjected into the combustor, the bound water would be removed, resulting in the further shell cracking, enhancement of

surface area and better accessibility to gaseous reactants, which are available for further desulfurization.

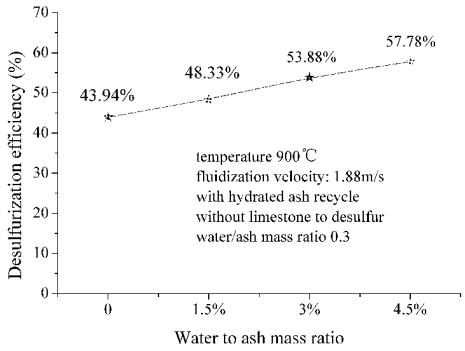

Fig. 8 Effect of water to ash mass ratio on sulfur capture efficiency (without limestone)

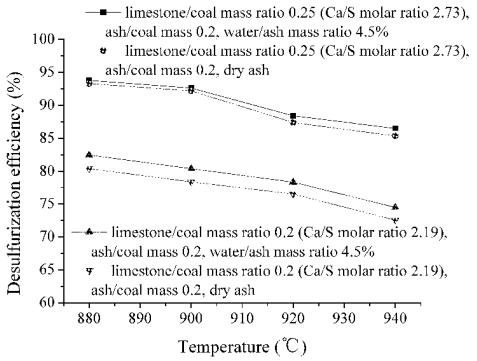

Fig. 9 Effect of water to ash mass ratio on sulfur capture efficiency (with limestone)

The influence of the limestone amount on the desulfurization efficiency in ash recycling experiments was investigated as shown in Fig. 9. The reactivated ash was hydrated under the room temperature, and the water to ash mass ratio was 4.5%. The desulfurization efficiency in the experiments with hydrated ash recycle is 2% higher than that with dry ash recycle, as the limestone to coal mass ratio is 0.2. Comparatively, the desulfurization efficiency is just 0.8% higher since the limestone to coal mass ratio is 0.25. It could be concluded that, hydration could improve the sulfur capture ability of ash with the low limestone to coal mass ratio.

Effects of the circulation rate on the desulfurization efficiency

The process, referring to the mass and heat transfers, combustion efficiency, sulfur capture, temperature distribution and attrition, is highly affected by the circulation of the particles in the CFB combustor. Most of the issues, such as the recycle passes of particles, the residence time and the SO_2 removal rate, would be improved with the increased circulation rate for the low circulation-rate CFB boilers. It is found that the desulfurization efficiency is improved with the increased circulation rate, but the effect becomes small gradually. The desulfurization efficiency is increased from 17.96% to 43.94% with the increased circulation rate from 6 to 12 (Fig. 10). In contrast, the desulfurization efficiency presents a raise of 9.5% while the circulation rate increases from 12 to 18.

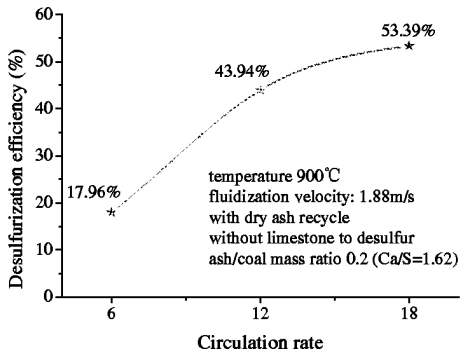

Fig. 10 Effect of circulation rate on sulfur capture efficiency (without limestone)

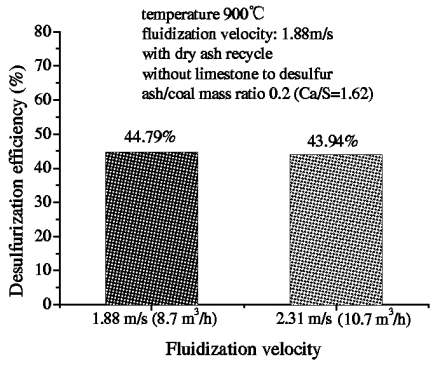

Fig. 11 Effect of fluidization velocity on sulfur capture efficiency (without limestone)

Effects of the fluidization velocity on the desulfurization efficiency

The boiler load and primary to secondary air ratio in the boiler is considerably related to the fluidization velocity. Only under the conditions that when fluidization velocity causes a great impact on the fluidizing behavior, elutriation and attrition of fine particles as well as the contacting of phases, it could play an important role in the sulfur capture process. The fluidization velocity is not too much related to the desulfurization process (Fig. 11). The circulation amount is estimated to be improved with a proper increased fluidizing velocity for the CFB boiler, through prolonging the residence time of sorbent. It could be approved that the extent that the fluidizing velocity affects on desulfurization efficiency is greatly influenced by the magnitude of

circulation rate.

CONCLUSIONS

The desulfurization efficiency and utilization efficiency of limestone could be improved by the fly ash hydration and recycling technology in CFB boiler. The microstructural characteristics of the original ash and the hydrated ashes were determined by the SEM and mercury porosimetry. It is concluded that the specific surface area and formation of fractures of the sorbent in ash are highly modified by the hydration process, accounting for the increased calcium utilization.

The effect of temperature on the desulfurization process is intensively investigated. Noticeably, the desulfurization efficiency is increased with the increased amount of ash. The desulfurization efficiency in the ash recycling experiments, as the limestone to coal mass ratio was 0.25 (Ca to S molar ratio 2.73), is 9.8%-14.7% higher than that of the baseline test which leads to about 14 to 22% reduction in limestone consumption.

The desulfurization efficiency is increased with the increased water to ash mass ratio, since the water to ash mass ratio ranges from 0 to 4.5% (the water to calcium molar rate 0-0.55). The desulfurization efficiency in the hydrated ash recycling experiments was about 14% higher than that in dry ash recycling experiments.

NOTATIONS

η_s	Desulfurization efficiency, %
E_{WSO_2}	SO_2 concentration at outlet in the baseline test, ppm
E_{TSO_2}	SO_2 concentration at outlet in the tests with fly ash recycle, ppm

ACKNOWLEDGEMENT

This work was supported by a grant from the National High Technology Research and Development Program of China (863 Program) (No. 2007AA05Z334).

REFERENCES

Anthony, E. J., Bulewicz, E. M., and Jia, L.: Progress in Energy and Combustion Science. 33(2007), pp. 171-210.
Basu, P.: Chemical Engineering Science. 54(1999), pp. 5547-5557.
Chen Jihui, and Lu Xiaofeng: Resources, Conservation and Recycling. 49(2007), pp. 203-216.
Gora, D., Anthony, E. J., Bulewicz, E. M., and Jia, L.: Fuel. 85(2006), pp. 94-106.
Laursen, K., Duo, W., Grace, J. R., and Jim Lim, C.: Fuel. 80(2001), pp. 1293-1306.
Laursen, K., Duo, W., Grace, J. R., and Lim, J.: Fuel. 79(2000), pp. 153-163.
Laursen K, M. P., Lim.C.J, Grace JR: Environ Eng Sci. 20(2003), pp. 11-20.
Manovic, V., and Anthony, E. J.: Fuel. 87(2008), pp. 1564-1573.
Montagnaro, F., Salatino, P., Scala, F., Bernardo, G., and Valenti, G. L.: Fuel. 82(2003), pp. 2299-2307.
Montagnaro, F., Salatino, P., Scala, F., and Chirone, R.: Powder Technology. 180(2008), pp. 129-134.
Saastamoinen, J., and Shimizu, T.: Chemical Engineering Science. 62(2007), pp. 574-583.
Wu Xin, Duan Yufeng, Zhao Changsui, Cheng Xiaoping, Wu Shuzhi, and Wenzhi, W.: Boiler Technology. 30(1999), pp. 29-32.
Y. Tsuo, J. M., K. Sellakumar. (1999). Improving Limestone Utilization in a Commercial-Scale Circulating fluidized Bed Boiler Through Ash Reactiviation and Recycle. Proceedings of the 15th International Conference on Fluidized Bed Combustion, Savannah, Georgia.
Zhong Zhaoping, Lan Jixiang, Han Yongsheng, Wu Xin, and Haiyun, Z.: Journal of Thermal Science. 6(1997), pp. 75-79.

NITRIC OXIDE REDUCTION OVER SEWAGE SLUDGE AND COAL CHARS AT CONDITIONS RELEVANT TO STAGED FLUIDIZED BED COMBUSTION

P. Salatino, R. Solimene, R. Chirone

Istituto di Ricerche sulla Combustione, Consiglio Nazionale delle Ricerche,
Dipartimento di Ingegneria Chimica, Università degli studi di Napoli Federico II, Napoli, Italy

Abstract: The de-NO_x potential of coal and of dried and pelletized sewage sludge, a waste-derived fuel candidate for cofiring with coal, is assessed. The experimental procedure is based on operation of a bench scale fluidized bed reactor where NO-doped nitrogen is contacted with batches of the fuel. A second type of experiment has been purposely designed to assess the loss of reactivity of chars toward gasification by NO_x as char is heat-treated for pre-set times at temperatures typical of fluidized bed combustion. A simple phenomenological model is developed to shed light on the basic features of the interaction between heterogeneous char-NO_x reaction and thermal annealing of the char.

Keywords: co-combustion, nitric oxide reduction, thermal annealing, synergistic effects

INTRODUCTION

Cofiring of biogenic fuels with coal in fluidized bed reactors is attractive as it combines reduction of CO_2 emissions from fossil fuels with exploitation of biomass- and waste-derived fuels in high-efficiency large-scale power plants. Co-combustion of substitute fuels up to 20-30%w of the thermal throughput of the plant is generally feasible with minimal impact on the efficiency and reliability/availability of the plant. Cofiring of coal and biogenic fuels is also attractive as it enables the exploitation of synergistic effects between the co-fuels as regards prevention and control of pollutant emissions. Synergy is favoured by the widely different behaviour of coal and biogenic fuels as to: i) volatile matter emission; ii) fuel particle segregation/mixing during devolatilization; iii) char reactivity and combustion pattern; iv) fuel/char fragmentation and attrition. Due to these differences, coal and biogenic fuels give rise to distinctively different axial burning profiles along the combustor which correspond to inherently fuel-staged combustion conditions. The combined use of a biogenic fuel with coal can, under specified conditions, positively impact pollutant emissions as compared with combustion of the base-fuel only. One such example is represented by positive impact that cofiring can exert on nitrogen chemistry and NO_x emissions (Liu et al., 2002; Leckner et al., 2004). The inherent fuel-staged conditions typical of cofiring give rise to reducing atmospheres in the splash zone which, together with the large intrinsic reactivity of biomass char toward nitric oxide, may promote effective exploitation of the de-NO_x potential of the substitute fuel. The reactivity of chars from coal and biogenous fuels with respect to the reduction of NO has received much attention in the literature (Chan et al., 1983; Illan-Gomez et al., 1996; Aarna and Suuberg, 1997; Chambrion et al., 1998; Guo and Hecker, 1998; Zevenhoven and Hupa, 1998; Sørensen et al., 2001; Molina et al. 2002; Garcia-Garijo et al., 2003; Glarborg et al., 2003). The present study aims at characterizing the de-NO_x potential of in-situ prepared chars from a pelletized sewage sludge and a bituminous coal, under conditions relevant to staged fluidized bed combustion. The specific focus is represented by the characterization of the change of char reactivity along gasification associated with the parallel course of thermal annealing of the char. The extent and rate of thermal annealing are assessed by a combination of purposely designed experiments and of a descriptive model.

EXPERIMENTAL

The experimental apparatus (Fig. 1) consists of a fluidized bed reactor made of a stainless steel tube 0.5 m long, 0.017 m ID. The top flange bears two probes. The first movable probe is used to measure the pressure along the axis of the column. The second probe, 0.49 m long, bears a thermocouple to measure the temperature in the fluidized

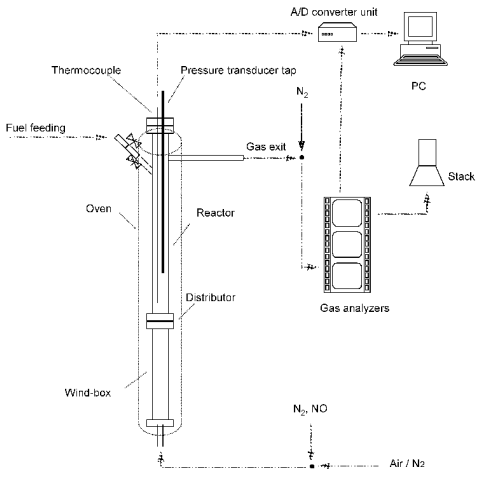

Fig. 1 xperimental apparatus

bed at the level of about 0.01 m above the distributor plate. The exhaust duct (0.006 m OD) is welded perpendicular to the column axis 0.026 m below the top flange and is connected to a vent. Fuel feeding is accomplished via a feeding duct (0.0095 m ID, 0.014 m OD and 0.13 m long) welded to the column with an inclination of about 45° with respect to the column axis, 0.08 m below the top flange. The feeding duct was equipped with a double valve system in order to inject batches of fuel particles over-bed with minimal perturbation of bed hydrodynamics. The fluidizing gas was metered through a windbox filled with a packing of copper wires and a porous low-pressure-drop gas distributor made of steel mesh. The fluidizing gas flow rate was measured by high-precision rotameters. The column was maintained at the desired temperature by means of a cylindrical oven (Carbolite) 0.75 m high.

A piezo-resistive electronic pressure transducer with small time response and 70 mbar full scale was connected to the pressure probe to monitor gas pressure in the reactor. A K-type thermocouple was used to monitor bed temperature. Gas analysers are used to continuously monitor the concentration of the exhausted gases in terms of CO_2 (H&B Uras 10E), CO (H&B Advance Optima Uras 14), O_2 (H&B Magnos 6G), NO (ABB AO2020 Limas 11 UV), NO_2 (ABB AO2020 Limas 11 UV), N_2O (H&B Advance Optima Uras 14), SO_2 (H&B Uras 10E), H_2 (H&B Caldos 5G)and CH_4 (H&B Uras 10P).The electrical signals coming from the analyzers, the pressure transducer and the thermocouple were acquired and A/D-converted by means of a data acquisition unit (National Instruments PCI 6023E) and a personal computer.

Fluidizing gas was pure nitrogen or a mixture of nitrogen and nitric oxide (520 ppm_v) obtained by mixing gases from cylinders. Bed material was quartzite with a size range of 300-400 μm. Bed inventory was 13 g corresponding to a static bed height of about 0.04 m. Correspondingly, the bed aspect ratio was about 2.4. The fluidization regime corresponded to incipient slugging. The minimum fluidization velocity measured at 850°C was about 0.065 m/s.

Fuel samples consisted of batches of Polish coal and of a pelletized sludge whose properties are reported in Table 1. A single particle of either Polish coal (about 3mm size and 23mg) or pelletized sludge (about 5mm size and 50mg) was charged into the bed in each test. The values of the fuel sample size and mass were chosen so as to keep the same total heating value of the fuel feeding. Based on previous experience, the occurrence of primary fragmentation was unlikely for the fuel types and particle sizes adopted.

Table 1 Fuel properties

	SLUDGE	COAL
LHV, MJ/kg (as received)	12.7	25.2
Proximate analysis, $\%_w$ (as received)		
Volatile matter	42.9	27.7
Fixed carbon	12.7	63.4
Ash	32.9	5.9
Moisture	11.5	3.0
Ultimate analysis, %w (on dry basis)		
Carbon	30.8	77.8
Hydrogen	4.5	4.5
Nitrogen	4.3	1.2
Sulphur	1.2	0.5
Ash	37.1	6.1
Oxygen	22.1	9.9

Experiments aimed at characterizing the extent to which NO contained in the fluidization gas could be reduced by batches of the different types of fuels. Experiments consisted of the following stages: i) heating-up of the reactor in air until bed temperature approaches 850°C; ii) establishment of a constant gas superficial velocity of 0.14 m/s at bed temperature with an inlet feeding of either nitrogen or a mixture of NO (520 ppm_v) in nitrogen; iii) charging of a fuel batch, of pre-set mass, to the reactor; iv) monitoring of the progress of the char-NO reaction by continuous recording of the concentrations of the gaseous species in the flue gas; v) switching of the inlet gas feeding to air so as to burn all the char remaining in the reactor. Two types of experiments were carried out: A) the fluidizing gas was a mixture of NO and nitrogen all along the duration of the test; B) the fluidization gas was initially pure nitrogen, then at a pre-set time t* was switched over to a NO/nitrogen mixture.

RESULTS AND DISCUSSION

Figures 2 and 3 report typical results obtained in type-A experiments carried out with the two fuels tested. Each figure reports the time-resolved concentrations of NO recorded along the test. A baseline corresponding to NO concentration at the reactor inlet has also been drawn in the figures to better appreciate the extent of NO reduction. The concentrations of the main reducing compounds, namely H_2 and CO, have also been reported in the figures. A shaded area, immediately following injection of the fuel batch in the reactor, marks the time interval during which extensive release of volatile matter took place.

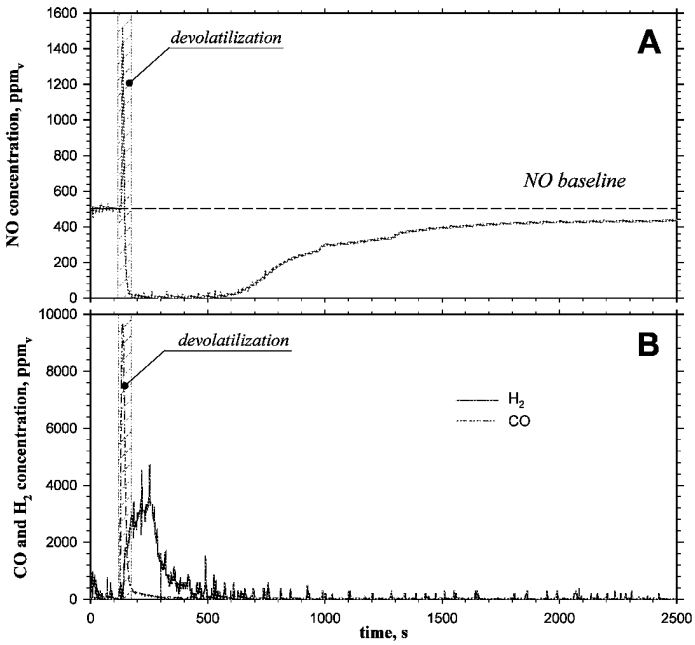

Fig. 2 Results of a type-A experiment: pelletized sludge

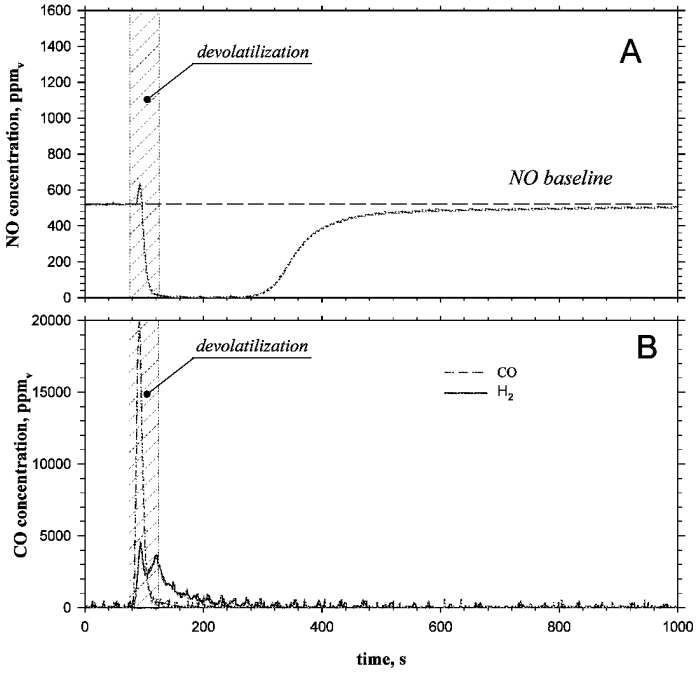

Fig. 3 Results of a type-A experiment: coal

The following general features can be recognized by inspection of these figures:

- A sharp peak of NO release, well above the baseline, is recorded during early devolatilization of the two nitrogen-bearing fuels (sludge, coal);
- Emission of CO is pronounced during devolatilization, to vanish thereafter;
- Emission of H_2 occurs in multiple stages. A significant extent of H_2 emission is associated with secondary pyrolysis which extends far beyond devolatilization;
- Once devolatilization is complete, NO concentration drops to values that are within the detectable limits of the analyzers. Eventually, the NO vs time profile displays a "breakthrough" pattern: NO concentration rises steadily from nearly zero to a finite value. A nearly steady offset of NO concentration at the exhaust with respect to the baseline NO is established in the long term. Only over very long times (much longer than time intervals reported in the Figures) would the offset vanish as a consequence of full gasification of the char.

The NO vs t profiles in Figs. 2 and 3 have been worked out to determine the amount of carbon gasified by NO all over the tests. To this end the assumption was made that NO reduction was only related to the char-NO reaction according to the stoichiometry $C+2NO \longrightarrow CO_2+N_2$. The ultimate carbon conversion degrees were 34 and 6% for the sludge and the coal samples, respectively. Though appreciable, the ultimate carbon conversion degrees were too small to justify the extensive loss of char gasification reactivity observed during the tests. Moreover, the pronounced breakthrough pattern of the NO vs time profiles was poorly correlated with the parallel decay of H_2 concentration, suggesting that the key process responsible for NO reduction is heterogeneous reduction of NO over the fuel char rather than homogeneous reduction.

Type-B experiments were purposely carried out to shed additional light on the mechanisms responsible for the loss of char gasification reactivity observed during type-A tests. Typical results of type-B experiments are reported in Figs. 4 and 5 for the two fuels tested. Time series of NO concentration recorded after the fluidizing gas was switched over from nitrogen to NO-nitrogen mixtures - i.e. after the char had been subjected to heat treatment at T=850°C for a time t^* - are reported in these figures, compared with NO concentration vs time profiles measured during type-A experiments.

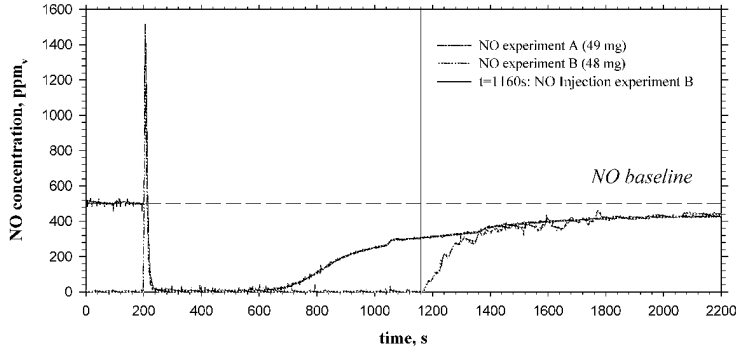

Fig.4 Comparison of results obtained in type-A and -B experiments: pelletized sludge

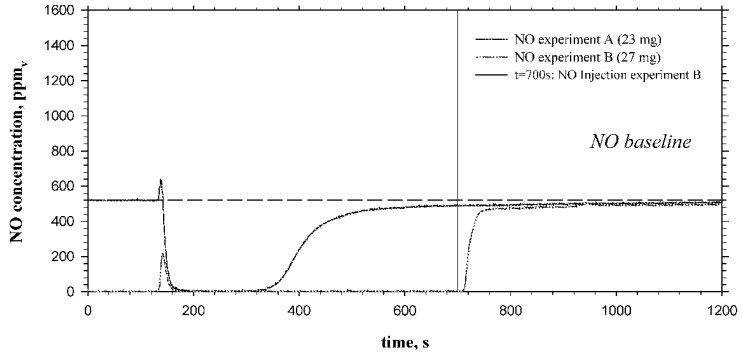

Fig.5 Comparison of results obtained in type-A and -B experiments

A first feature emerging from the comparison is that the early peak of NO emission during devolatilization is much more pronounced in type-B experiments than in type-A experiments, when the absolute values of NO concentration are referred to the respective baselines. A plausible explanation for this finding might be that the nitric oxide present in the fluidizing gas during type-A experiments could easily interact with volatile compounds as they are emitted after particle feeding and be reduced. The same process could not occur during type-B experiments.

The second and most remarkable feature is that the level of NO at the exhaust after the switch-over from nitrogen to nitrogen/NO mixture (i.e. at $t>t^*$) rises very quickly, approaching the corresponding value of NO concentration measured during type-A experiments. The close overlap of NO vs time profiles at $t>t^*$ rules out possible arguments related to the dynamics of adsorption and NO uptake as the key for the interpretation of the increased level of NO at the exhaust during the late stage of both type-A and type-B experiments. A more likely explanation for this effect, which is consistent with the comparison of results from the two types of experiments, is that the rate at which NO is reduced by the char decreases along the test as the char is increasingly annealed, hence deactivated. The extent to which a char is deactivated is, to a first approximation, uniquely related to its time-temperature history, as this is consistent with the close overlapping of NO concentration vs time profiles at $t>t^*$.

The relevance of time-temperature history to the NO-gasification rate has already been highlighted in the past (Aarna and Suuberg, 1997; Guo and Hecker, 1998; Molina et al., 2002; Garcia-Garijo et al., 2003). Garcia-Garijo et al. (2003) explained the broad discrepancies that characterize the kinetic parameters for the char-NO reaction reported by various researchers in the literature as a consequence of the variability of the char preparation conditions.

A descriptive model of char-NO reaction with consideration of thermal annealing of char

The experimental results have been interpreted in the light of a descriptive model which embodies carbon gasification by NO and loss of gasification activity of carbon induced by thermal annealing. By "thermal annealing" it is meant here the whole bundle of solid state transformations brought about by heat treatment. These may involve changes of the "turbostratic" carbon structure and modifications (e.g. sintering) of the inorganic constituents, some of which (e.g. Mg, Ca, K, Fe) exert appreciable catalytic activity toward the char-NO reaction (Zevenhoven and Hupa, 1998; Hayhurst and Ninomiya, 1998). Senneca et al. (1997) and Salatino et al. (1999) modeled annealing during gasification of chars/cokes with carbon dioxide using a triangular reaction network. Their model proved to be able to correctly represent thermodeactivation data from a variety of sources referred to the char-O_2 and char-CO_2 reactions (Senneca and Salatino, 2002). This simple approach has been borrowed here to model the interaction of the char-NO reaction with thermal annealing. Accordingly the following reaction scheme:

$$C_Y + NO \xrightarrow{1} \text{gasification products}$$

$$C_A + NO \xrightarrow{2} \text{gasification products}$$

$$C_Y \xrightarrow{3} C_A$$

has been chosen to follow the fate of char and NO. C_Y and C_A are, respectively, "young" and "annealed" chars, reactions 1 and 2 represent carbon gasification by NO and reaction 3 represents annealing of the young char C_Y yielding C_A. The kinetics of heterogeneous gasification steps 1 and 2 has been assumed linearly dependent on NO concentration and mass of either the C_Y or the C_A components: $r_1=k_1[NO]m_Y$; $r_2=k_2[NO]m_A$, where $r_i\,[=]\frac{\text{kmol NO}}{\text{s}}$ and m_Y and m_A are the values of the carbon mass in the young/annealed chars. The actual concentration of NO in the emulsion phase of the fluidized bed has been calculated assuming well-stirred behaviour. Diffusional resistances either in the boundary layer around the particle or within the particle itself were neglected, based on order of magnitude assessment of Biot number and particle Thiele modulus. In the absence of fuel-specific data, a simple first-order equation has been used to express the rate of reaction 3: $r_3 = k_3 m_Y \quad [=]\frac{\text{kg C}}{\text{s}}$. The annealing rate constant k_3 has been treated as an adjustable parameter.

Figure 6 reports typical results of computations. This figure reports the computed profiles of the (fractional) NO concentration at the exhaust of the converter during gasification of a batch of char in a fluidized bed reactor continuously fed with a stream of NO ($520ppm_v$) in N_2. Figure 6 reports results for both type-A and type-B simulated conditions, considering batches of coal and sludge. The values of the rate parameters which gave the best fit with experimental data are reported in Table 2.

Table 2 Model parameters

	SLUDGE	COAL
k_1, $m^3/(kgC\ s)$	1400	500
k_2, $m^3/(kgC\ s)$	1.2	0.05
k_3, s^{-1}	0.004	0.015

Analysis of Fig. 6 suggests that the model is able to reproduce fairly well the basic features of the phenomenology (see Figs. 4 and 5). This finding supports the validity of the theoretical framework underlying the model. The model displays a limited sensitivity to the value of k_1, consistently with the finding that conversion is essentially stoichiometrically controlled in the very early stage. It turned out that k_1 values reported in Table 2 were the minimum value of the gasification rate constant of the "young" char that could be consistent with the nearly vanishing concentration of NO observed during the early stage of type-A tests. Values of k_2 and of the annealing constant k_3 could easily be related to the value of the long-term offset of NO concentration and to the time t^* at which the breakthrough was observed, respectively. The extent of thermodeactivation inferred from computation results is huge, the gasification reactivities of the young and of the "fully" annealed chars differing by five and more than three orders of magnitude for the coal and sludge samples respectively. The effect of char heat treatment in the NO-free atmosphere held during the first stage of type-B experiments was also well reproduced: a very small gasification rate was displayed as soon as NO was

admitted in the reactor at $t=t^*$, very close to the value found at the same time during type-A experiments. The results obtained in simulations referred to samples of coal and sludge pellets. The main differences between the two tested fuels can be highlighted from the values of the kinetic constant reported in Table 2. The kinetics of the gasification reactions are more rapid in the case of the biogenic fuel both for the "young" and the annealed char. In particular, the kinetic constant of the gasification of the annealed char is sufficiently high to convert a significant part of NO in the inlet gas. At the same time, smaller values of k_3 were inferred for sludge samples, consistent with longer deactivation times.

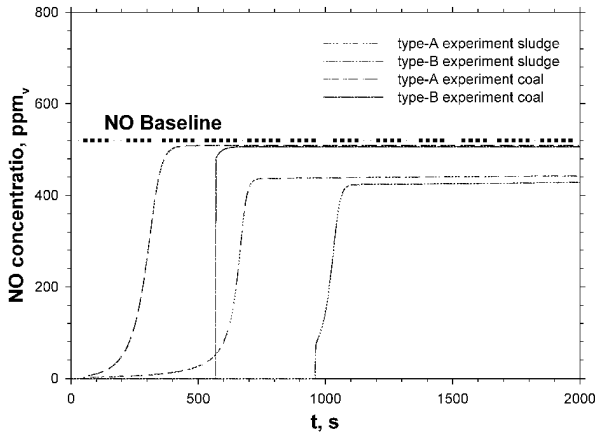

Fig.6 Results of model computations: comparison between fractional NO concentration at the exhaust for type-A and type-B experiments with coal and sludge samples

CONCLUSIONS

The rate of NO reduction over chars from a coal and a waste-derived fuel has been characterized by means of experiments carried out in a bench scale fluidized bed reactor operated at 850°C. Chars were prepared in-situ by charging batches of fuel samples to the reactor while it was fluidized with a NO/nitrogen mixture.

The rate of char-NO gasification, very large at first, decreases during the experiments, to an extent than cannot be justified by the parallel decrease of char carbon content nor by the vanishing emissions of reducing volatile compounds, like CO and H_2. A mechanism based on the hypothesis that char undergoes thermal annealing during gasification, with associated loss of gasification reactivity, is invoked to explain the phenomenology. A simple phenomenological model based on the consideration of the series-parallel course of heterogeneous NO-gasification reactions and of thermal annealing proves to be effective in reproducing the key features of the phenomenology.

ACKNOWLEDGEMENTS

The support of Mr Antonio Cammarota in the set up of the experimental apparatus and of Miss Anna Di Somma in the experimental campaign is gratefully acknowledged.

REFERENCES

Aarna, I. and Suuberg, E.M.: Fuel **76** (1997), pp.475-491.
Chambrion, P., Kyotani, T. and Tomita, A.: Energy & Fuels **12** (1998), pp.416-421.
Chan, L.K., Sarofim, A.F. and Beer, J.M.: Combust. Flame **52** (1983), pp.37-45.
Garcia-Garijo E., Jensen, A. D. and Glarborg, P.: Energy & Fuels **17** (2003), pp.1429-1436.
Glarborg, P., Jensen, A.D. and Johnsson, J.E.: Prog. Energy Combustion Sci. **29** (2003), pp.89-113.
Guo, F. and Hecker, W.C.: Proc. Comb. Inst., **27** (1998), pp.3085-3092.
Hayhurst, A. N. and Ninomiya, Y.: Chemical Engineering Science, **53** (1998), pp. 1481-1489.
Illan-Gomez, M.J., Linares-Solano, A., Radovic, L. and Salinas-Martina de Lecea, C.: Energy & Fuels, **10** (1996), pp.158-168.
Leckner, B., Amand, L.-E., Luecke, K. and Werther, J.: Fuel **83** (2004), pp.477-486.
Liu, D.C., Zhang, C.L., Mi, T., Shen, B.X.and Feng, B.: J. Inst. Energy **75** (2002), pp.81-84.
Molina, A., Eddings, E.G., Pershing, D.W. and Sarofim, A.F.: Proc. Comb. Inst. **29** (2002), pp.2275-2281.
Salatino P., Senneca, O. and Masi, S.: Energy & Fuels **13** (1999), pp.1154-1159.
Senneca O., Russo P., Salatino P. and Masi M.: Carbon **35** (1997), pp. 141-151.
Senneca O. and Salatino P., Proc. Comb. Inst. **29** (2002), 485-492.
Sørensen, C.O., Johnsson, J.E. and Jensen, A.D.: Energy & Fuels, **15** (2001), pp.1359-1368.
Zevenhoven, R and Hupa, M.: Fuel, **77** (1998), pp. 1169-1176.

DESTRUCTION OF N_2O OVER DIFFERENT BED MATERIALS

M. Pilawska[1,2], H. Zhang[1], X. S. Hou[1], Q. Liu[1], J. F. Lu[1], G. X. Yue[1]

1Key Laboratory for Thermal Science and Power Engineering of the Ministry of Education, Tsinghua University, Beijing, China

2Department of Environmental Engineering, Institute of Thermal Engineering and Air Protection, Cracow University of Technology, ul. Warszawska 24, 31-155 Kraków, Poland

Abstract: Since under fluidized bed conditions N_2O is produced as a by product of the De-NO_x process, the thermal decomposition of N_2O was investigated under conditions relevant to those in FBC installations. Laboratory experiments were made in a current of nitrogen using a fixed bed of pure quartz sand or sand with 10% (wt.) of the solids tested, CaO and Fe_2O_3. With a sand bed the decomposition was slightly faster than in the empty reactor and the reaction was first order with respect to [N_2O]. Both fresh CaO and Fe_2O_3 strongly catalysed N_2O decomposition. Their effectiveness diminished after they were heated to temperatures typical for FBC, but they still retained appreciable activity. This activity went down with increasing particle size. The flue gas components investigated were O_2, water vapour and CO_2. Their presence appeared to interfere with N_2O decomposition and increased with the concentration of the additive. The observations indicated that this could only be due to heterogeneous effects. Thus the effects of the bed solids and of the gas phase components are opposed. The effects associated with N_2O decomposition have proved to be surprisingly complex and instead of supplying simple answers, this work uncovered more problems.

Keywords: N_2O decomposition, bed material activity

INTRODUCTION

NO_x emissions from fluidized bed combustors, FBC, can be brought down using the thermal De-NO_x process, usually involving the addition of ammonia. The gas phase reaction between NO and NH_3 has been extensively studied in the laboratory and it is known that some N_2O is formed as a by-product(Braun et al., 1991; Moritomi et al., 1999). It is a potent greenhouse gas, long-lived in the atmosphere and also affecting the ozone layer, Wayne (1991), so its emissions should be kept down.

In FBC installations with no de-NO_x some N_2O is always formed (de-Diego et al., 1996), and our earlier results, when the behaviour of N_2O was studied in a laboratory reactor with a fixed bed of quartz sand demonstrated that the appearance of some N_2O during the "Thermal De-NO_x" process, in the temperature range typical of FBC installations, was unavoidable and strongly affected by the presence of the sand (Hou et al., 2008). Without the sand, the concentration of N_2O remained low. The N_2O concentrations observed resulted from the opposed processes of N_2O formation and its destruction, with the equilibrium concentration under the given conditions as the ultimate reference level.

The present work was aimed at assessing the role of the bed material and of selected flue gas constituents on the decomposition of N_2O. The solid material tested in earlier work was pure quartz sand. From the practical point of view all typical components of FBC bed material should be investigated, as it has already been shown that in FBC units the bed ashes display catalytic activity(Barišic et al., 2005; Yue, 2006). The substances selected were, in addition to quartz sand, CaO and Fe_2O_3, both common constituents of FBC coal ash. Some tests were also carried out with Fe_3O_4. The flue gas constituents used were O_2, water vapour and CO_2, added to the N_2 carrier gas, separately and together. The experiments were made in the laboratory, using a small, heated plug flow reactor with a stationary bed of solids. Fourier Transform Infrared Spectroscopy methods, FTIR, were used for analysing the post-reaction gases.

The results obtained can be expected to be relevant to what can happen in real installations, e.g. those used for the combustion or co-combustion of wastes with conventional fuels.

THE APPARATUS AND TEST PROCEDURE

The apparatus used was made available at the Department of Thermal Engineering at Tsinghua University, Beijing and it is shown schematically in Fig.1. The central element of the system is a plug flow reactor, with a fixed bed of solids. The body of the reactor is a 720 mm length of quartz tube, of internal diameter 45 mm, standing upright. The gases flow downwards and a layer of the solids tested rests on a platform of sintered ceramic (to avoid catalytic effects with a metal platform), fixed approximately half way down the tube. The reactor is heated from the outside by heating spirals, fitted inside insulated reactor casing. The reactor

temperature can be varied within the range 600 – 1000°C and is monitored by a K-type thermocouple. The vertical temperature profile is illustrated in Fig.2. The original measurements were made under steady state conditions, using a set of thermocouples placed inside the reactor and the points represent direct measurements. The horizontal temperature distribution is practically flat, the vertical one trapezoidal. In the central region of the reactor there is a section, ca 150 mm long, most of it above the ceramic support, where the temperature is uniform. The thickness of the fixed bed and the support is small compared with the height of the constant temperature region. Outside this region the temperature decreases rapidly.

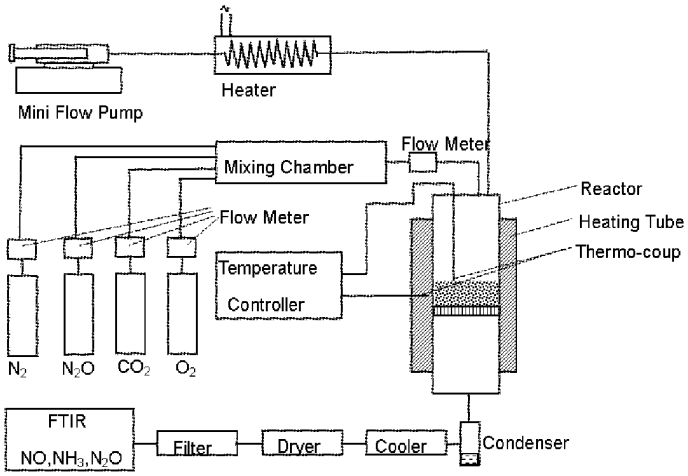

Fig.1 Schematic of the stationary bed plug flow reactor at TU, Beijing, China

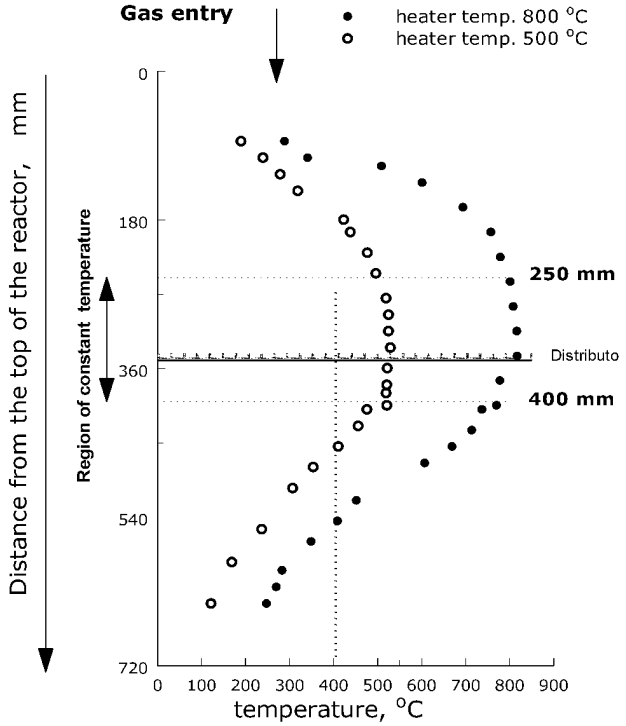

Fig.2 Vertical temperature distribution on the axis of the reactor

In the present tests, the reference bed material bed was pure quartz sand, to which the other solids were added: 10% of CaO, Fe_2O_3 powder (Sigma-Aldrich, <5 μm, ⩾99%) or Fe_3O_4. The particle size distribution for the sand, determined by a laser analyzer, Mastersizer 2000, is given in Table 1. The usual height of the fixed bed was 6.3 mm and the voidage fraction was taken as $\varepsilon = 0.47$.

Table 1 Particle size distribution for the quartz sand used for the fixed bed

Particle size/μm	<50	50-100	100-200	200-300	300-400	400-500	>500
Mass/%	2.93	4.14	37.97	33.33	15.86	5.66	0.11

For SiO_2 and Fe_2O_3 the pore surface area was determined using a Mercury Porosimiter, Autopore II 9220 and was 0.049 and 5 m^2/g respectively. The composition of the sand was determined by X-Ray Fluorescence Analysis, XRF-1700 XRD. In oxide form, SiO_2 accounted for 98.9% of the mass, with 0.8% Al_2O_3 and less than 0.3% of other components.

The carrier gas was pure N_2 and the gases tested were N_2O, O_2, water vapour and CO_2. Initial concentration of N_2O was usually kept at 300 ppm; the concentrations of the added gases were varied, while the total gas stream was constant at 2.5 l/min, at NTP. The flow rates of AR grade gases were measured by mass flowmeters, type MFM. The gas stream entering the reactor via a mixing chamber was controlled by a rotameter. The mole fractions of gases added to the N_2 stream were: O_2 - 0, 0.5, 1 or 2 %; CO_2 – 0, 5, 10% and H_2O vapour – 0, 2.5 and 5%. The gas residence time in the stationary bed lay between 0.059 and 0.04s, depending on the temperature. The concentration of N_2O in the gases leaving the reactor was determined using FTIR analyzer #A10720 VEN, equipped with a detection chamber 0.2l/4m.

The aim of the measurements was to verify the temperature dependence of the thermal decomposition of the N_2O, assess the effect of the composition of the bed solids and test the influence of the main components of FBC flue gases.

RESULTS AND DISCUSSION

The effects of reactor temperature and initial N_2O concentration

Empty reactor and a fixed bed of sand

Decomposition of N_2O fed in with the gas stream was first studied with the reactor empty and with a bed of pure quartz sand. In both cases the [N_2O] v. temperature curve has the characteristic "S" shape (see below), with strongest temperature dependence in the 800 – 950 °C range. The results shown in Figs.3 and 4 illustrate, respectively, the effect of the height of the sand bed and of the initial concentration of N_2O. (Note that the sand and the ceramic support are where the temperature is uniform, but the gases experience temperature gradients

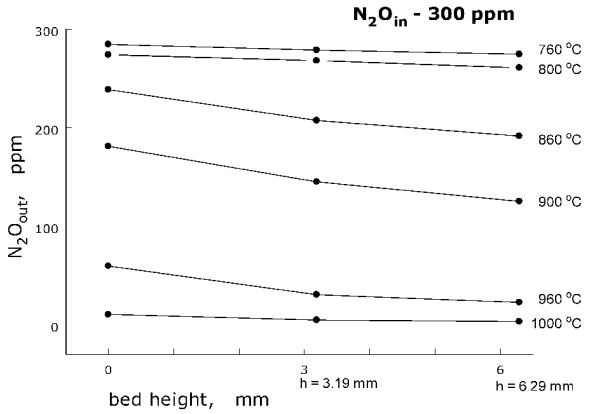

Fig.3 Decomposition of N_2O in a stream of N_2, at different temperatures, with the reactor empty and with two heights of the sand bed. [N_2O] as a function of bed height, initial [N_2O] – 300 ppm

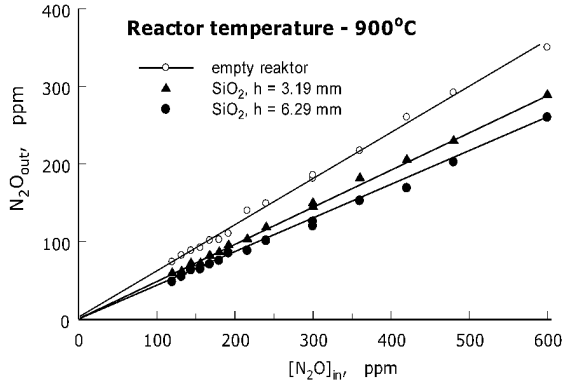

Fig.4 Decomposition of N_2O at 900 °C in a stream of N_2, as a function of initial [N_2O], with the reactor empty and for two heights of the fixed bed of quartz sand

both at the top and bottom of the reactor. But since temperature gradients are large and the decomposition of N_2O strongly temperature dependent, the effect of the hottest part of the reactor must always dominate.) The effect of the sand increases with the bed height and appears to be strongest around 900 °C, but even then the effect is not dramatic. In Fig.4 final [N_2O] is plotted against its initial level, different heights of the sand bed. As expected, the plots pass through the origin, i.e. with no O_2 no N_2O is formed. The decomposition of N_2O is apparently first order with respect to [N_2O] and its rate increases with the bed height, i.e. in the empty reactor the process is, overall (1) and with the sand bed, additionally (2),

$$N_2O + N_2 \longrightarrow 2N_2 + \tfrac{1}{2}O_2 \quad (1)$$

$$N_2O + SiO_2(s) \longrightarrow 2N_2 + \tfrac{1}{2}O_2 + SiO_2(s) \quad (2)$$

The sand is a weak catalyst for the process, its effect increasing with the height of the bed, but does not appear to be a linear function of it. At each temperature the final [N_2O] must tend to the equilibrium level. This can be calculated from the equilibrium constant for

$$N_2O \longleftrightarrow N_2 + \tfrac{1}{2} O_2 \quad (3)$$

In this experiment only traces of O_2 can come from N_2O decomposition.

The effect of the addition of CaO to a bed of quartz sand

CaO is an important constituent of FBC ashes from coal burned with SO_2 capture. Figure 5 shows $[N_2O]$ as a function of temperature after the gas stream was passed through a bed of sand and sand with 10% (mass) of AR grade CaO, mean particle size 0.01 mm, with results for the empty reactor also given for comparison. While the characteristic "S"– shaped curves for the reactor empty and with a bed of pure sand lay fairly close together, addition of CaO to the sand brought about a dramatic change, with the reaction moving to much lower temperatures. In the empty reactor, with pure sand and sand + 10% CaO, 50% decomposition was observed at ~920, 890 and 665 °C respectively. Thus CaO appears to be an effective catalyst for N_2O decomposition.

Figure 6 illustrates the relationship between measured $[N_2O]$ and initial $[N_2O]$ at 700°C, with 10% of CaO in the sand. The plot resembles those in Fig.4, and if it is taken as linear, indicates that the CaO catalysed reaction is still first order in $[N_2O]$.

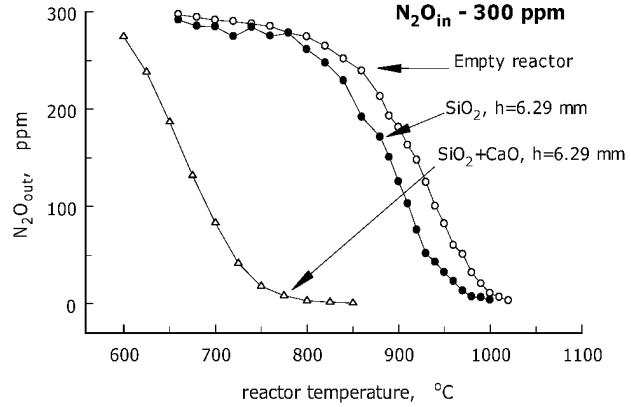

Fig.5 $[N_2O]$ as a function of temperature, with the reactor empty and with a bed of quartz sand and sand + 10% CaO. Initial $[N_2O]$ – 300 ppm, bed height 6.29 mm, mean CaO particle size 0.01 mm

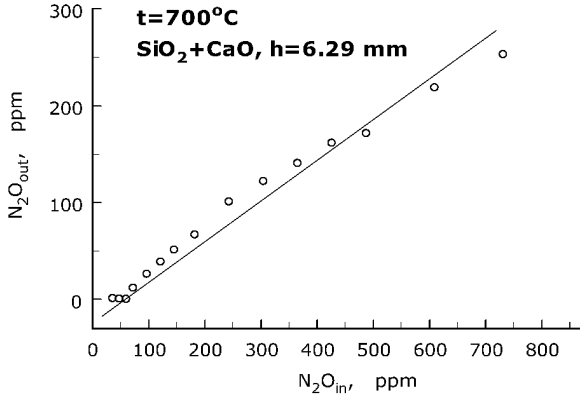

Fig.6 The effect of CaO on N_2O decomposition at 700°C in a stream of N_2. $[N_2O]$ as a function of initial $[N_2O]$. Initial $[N_2O]$ – 300 ppm, fixed bed of quartz sand + 10% CaO, mean CaO particle size 0.01 mm, bed height 6.29 mm

The catalytic activity of CaO for N_2O decomposition is affected by the temperature to which the CaO had been heated. The effect is illustrated in Fig.7, where measured $[N_2O]$ is plotted as a function of temperature using CaO heated to 950, 850 and 800°C. Increasing the temperature of the heat treatment reduces the catalytic activity of the CaO, which could be due to sintering of the fine CaO particles(Sun et al.,2007); Lu et al., 2008).

The CaO used could be separated into several size fractions and the effect of the particle size was investigated. The results are given in Fig.8. The points are scattered, particularly at lower temperatures, possibly because small CaO particles were sticking together and/or agglomerates were breaking up, but indications are that the effectiveness of the CaO as a catalyst for N_2O decomposition falls with increasing particle size.

The effect of oxygen added to the gas stream was also tested, as a function of the reactor temperature, with three O_2 concentrations, at temperatures between 650 and 900 °C. The results are shown in Fig.9 - increasing O_2 concentrations depress N_2O decomposition, but it can be shown that this was not because of a shift in the position of equilibrium (1).

The effect of the addition of Fe_2O_3 to the bed of quartz sand

$[N_2O]$ in the exit gases was measured for temperatures 230 – 1025°C with sand bed and sand + 10% Fe_2O_3. The conditions for experiments with Fe_2O_3 are given in Table 2. The results from runs 1 and 11 are shown in Fig.10, with those from run "0" for pure sand and with the curve for the empty reactor. It can be seen that Fe_2O_3, like CaO catalyses N_2O decomposition (compare Fig.5). However, the curve from test 11, at the end of the series, lies about half way between those for test 1 and for "0". This was unexpected and raised the question of the reproducibility of the results. Test 1 was therefore repeated with fresh Fe_2O_3 (plot 1a). At the end of the run the temperature was raised to over 800 °C and maintained for 1 hour and measurements were repeated with the

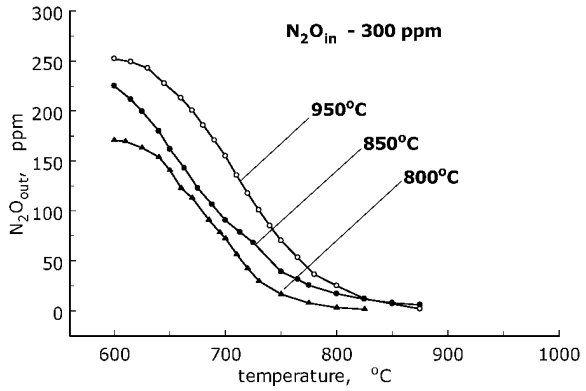

Fig.7 The temperature dependence of [N_2O]. Fixed bed of quartz sand + 10% CaO, heated at 950, 850 and 800°C. Initial [N_2O] 300 ppm, mean CaO particle size before heat treatment 0.01 mm

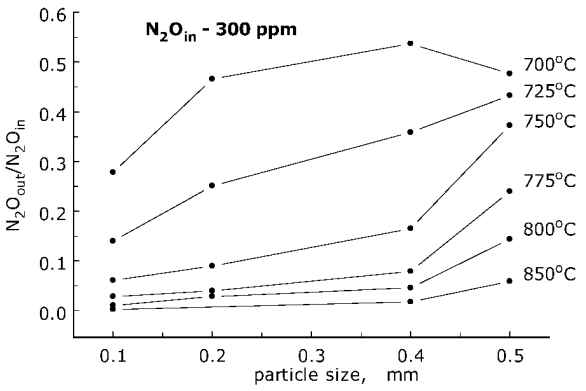

Fig.8 Fraction of N_2O left at several reactor temperatures as a function of the CaO particle size. Fixed bed of quartz sand +10% CaO. Initial [N_2O] – 300 ppm, bed height 6.29 mm

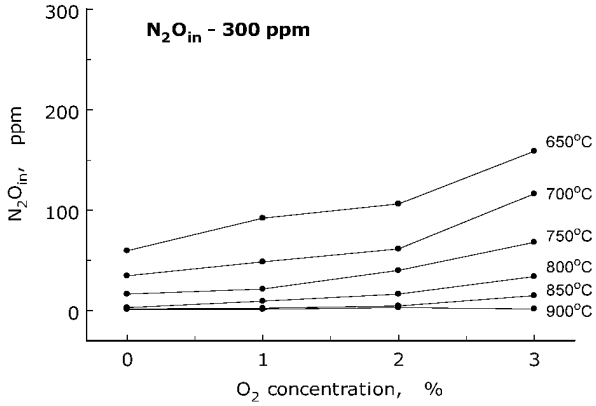

Fig.9 The fraction of initial [N_2O] left, as a function of [O_2] in the gas, at different reactor temperatures. Fixed bed of quartz sand + 10% CaO (heated to 850 °C), bed height 6.29 mm

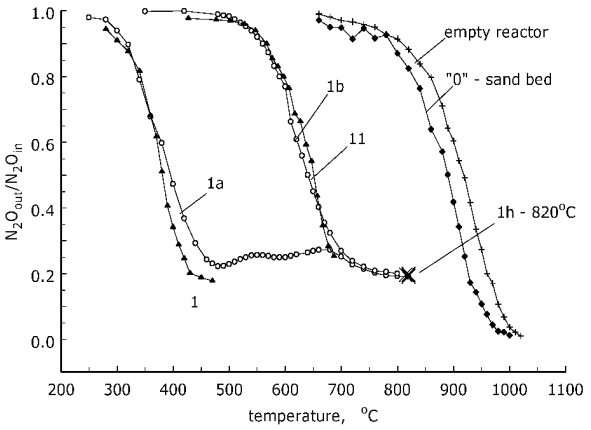

Fig. 10 Fraction of initial N_2O left as a function of temperature. Fixed bed of quartz sand + 10% Fe_2O_3, bed height 6.29 mm. Results from tests 1 and 11, with those for test "0" and the empty reactor included for comparison. Results from a temperature cycle with fresh bed material, 1a and 1b have been added. X – const. temperature 1 hour

temperature falling (test 1b) and the results have been added to Fig.10. Curves 1 and 1a lie close together, so measurements with fresh Fe_2O_3 are reproducible. Those from test 11, at the end of the whole series and from 1b are also very similar. Thus heating the bed material reduces its catalytic activity drastically, but reproducibly. Later some old bed material with Fe_2O_3 was put through a temperature cycle. This time the hysteresis was quite small, but these results have not been used since a full record of the temperature history of the material was not available.

The hysteresis, very pronounced with fresh material, is probably due to changes associated with the Fe_2O_3. After the bed is heated to temperatures typical of FBC, the catalyst becomes less active but still promotes N_2O decomposition. This is similar to the effect seen with CaO, Fig.7 and could be due to sintering (Sun et al.,2007; Lu et al.,2008), but without detailed examination of the microstructure of the solids this explanation can only be tentative.

In Fig.10 another observation can be made. While with CaO in the bed at about 800 – 900 °C little N_2O was left, as at with sand only, with Fe_2O_3 the [N_2O] appeared to level off. This cannot be due to a shift in the position of equilibrium and has no ready explanation.

Table 2 The composition of the gas mixture used in tests with a bed of SiO_2 with 10% of Fe_2O_3.Test "0" – bed of SiO_2 alone. Carrier gas N_2, initial N_2O concentration – 300 ppm

Test No	"0"	1	2	3	4	5	6	7	8	9	10	11
O_2(%)	0	0	**0.5**	**1**	**2**	0	0	0	0	**1**	**2**	0
H_2O (%)	0	0	0	0	0	**2.5**	**5**	0	0	**2.5**	**5**	0
CO_2(%)	0	0	0	0	0	0	0	**5**	**10**	**5**	**10**	0

The effects observed on with other gases added to the N_2 stream are shown in Fig.11(a), b, c and d, for the addition of O_2 (tests 3,4,5), of H_2O (tests 5,6) of CO_2 (tests 7,8) and all these together (tests 9,10) respectively. For comparison, results from test 11 and "0" are included. In all cases the influence of the additives on N_2O decomposition is unfavorable. The effect increases with the additive concentration and temperature for 50% decomposition shifts to higher values. In run 9 all three gases were used together and in 10 their concentrations were doubled. Clearly, the effect of the mixture is greater than of its components added singly, suggesting that the effects are probably additive.

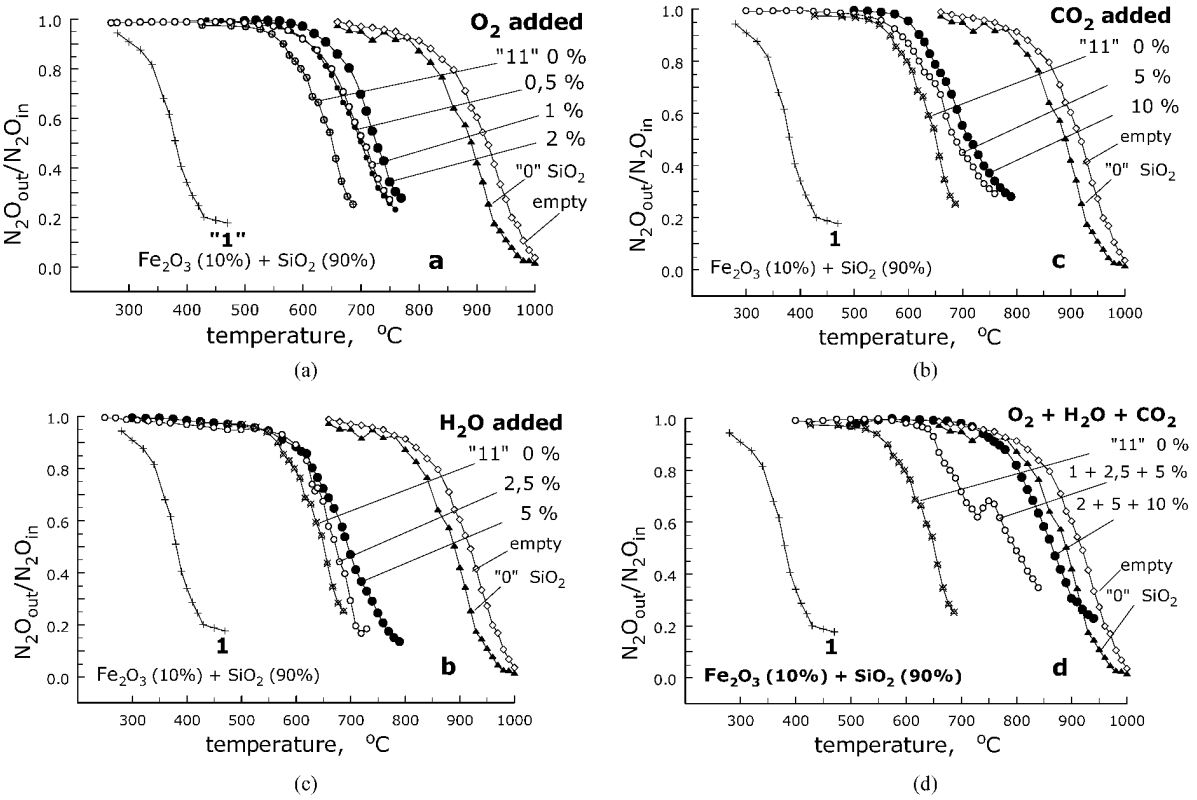

Fig.11 Measured [N_2O] as a function of temperature after adding other gases to the N_2 stream, (a) – O_2 (tests 3,4,5); (b) – H_2O (tests 5,6); (c) – CO_2 (tests 7,8); (d) – three additives together (tests 9,10). Initial [N_2O] – 300 ppm, fixed bed of sand + 10% Fe_2O_3, bed height 6.29 mm. Results from tests "0", 1 and 11 included for comparison

These results clearly suggest that the effect cannot be due to homogeneous processes, with the molecules of the added gases, M, taking part in the reaction,

$$N_2O + M \rightarrow N_2 + O + M \qquad (4)$$

M supplies the activation energy required and the relative efficiencies of N_2, O_2, H_2O and CO_2 are known and fall in the order $N_2 \sim O_2 < CO_2 < H_2O$ (Gradoń, 2003). Hence the replacement of N_2 by O_2 should make little difference and the introduction of H_2O or CO_2 should facilitate N_2O decomposition. This is certainly not the case, thus the added gases probably influence the process via heterogeneous effects. This may be interesting from the scientific point of view and deserves further study. For applications in CFBC it is relevant that the catalytic effect of the solids on the decomposition of any N_2O formed earlier will be opposed by that of the flue gases. Although this has not been tested, it is reasonable to suppose that the positive catalytic effects of the solids are additive and it might be possible that under practical conditions and with the help of suitable technical measures they could dominate over those of the components of the flue gases.

In addition to experiments with Fe_2O_3 an exploratory test was made with 10% of Fe_3O_4 in the bed. The

effectiveness of Fe_3O_4 as a catalyst appeared to be below that of fresh Fe_2O_3, but a proper comparison would have to be made for the same particle size and after taking the bed through the same temperature cycles.

SUMMARY AND CONCLUSIONS

The SiO_2 (quartz sand), CaO and Fe_2O_3 tested were representative of the main components of CFBC ashes. Sand is uniquitous in coal, most CaO is from calcined, unreacted limestone sorbent used for SO_2 capture in 2-3 fold excess (Anthony, Granatstein, 2001). Fe_2O_3 is formed during the oxidation of iron pirites, FeS_2, containing most of the sulphur in coal. The Fe_2O_3 usually contains some Fe_3O_4. The oxides of Ca and Fe, added to quartz sand catalysed the decomposition of N_2O, so that it could occur at temperatures much lower than in a stream of N_2 or in the presence of quartz sand only. The effect decreased with increasing particle size of the additive. The composition of the gas phase was also important. The presence of the main components of the flue gases other than N_2, i.e. O_2, water vapour and CO_2 hindered N_2O decomposition. This was ascribed not to a gas phase effect but an interaction with the catalyst surfaces. Under practical conditions all the effects would be observed together and it is possible that the combined catalytic effect of the bed solids would outweigh that of the flue gases.

ACKNOWLEDGEMENTS

Financial support of this work by National Key fundamental research program of China (2004CB217705) and High Technology R&D (863) (2007AA05Z303) are gratefully acknowledged.

REFERENCES

Anthony E.J., Granatstein D.: Progr. Energy Comb. Science, 2001, 27, 215-236.
Barišic, V.; Klingstedt, F.; Naydenov, A., et al.: Catalysis Today 2005, 100, 337-342.
Braun, A.; Bu, C.; Renz, U.; Drischel, J.; Koser, H. J.: Proceedings of the 11th International Conference on FBC, Montreal, Canada, 1991.
de-Diego, L. F.; Londono, C. A.; Wang, X. S.; Gibbs, B. M.: Fuel 1996, 75, (8), 971-978.
Gradoń, B., In polish, Hutnictwo, z.67 2003.
Hou, X.; Zhang, H.; Pilawska, M.; Lu, J.; Yue, G.: Fuel 2008, Volume 87, (Issue 15-16), Pages 3271-3277.
Lu D., Hughes R., Anthony E.J., Manovic V.: J. Env. Eng., 2008, submitted for publication.
Moritomi, H.; Shimizu, T.; Suzuki, Y.; Ninomiya, Y.: Proceedings of the 15th International Conference on FBC, by ASME: Savannah, Georgia, 1999.
Sun P., Grace J.R. Kim C.J., Anthony E.J.: AIChE J., 2007, 21, 2432-2442.
Wayne, R. P.: Chemistry of Atmospheres. 2nd Edition ed.; Oxford University Press: New York, 1991; p 450.
Yue, G. X., H. R. Yang, H. Zhang, in Proc. of the 19th Int. Conf. on FBC (Ed: F. Winter), , May 21-24, 2006, Vienna, Austria.

SIMULTANEOUS REDUCTION OF SO_X AND FINE ASH PARTICLES DURING COMBUSTION OF COALS ADDED WITH ADDITIVES

Yoshihiko Ninomiya[1], Shuyin Xu[1], Qunying Wang[1], Yi Cheng[1], Isao Awaya[2]

1 Department of Applied Chemistry, Chubu University1200 Matsumoto-cho, Kasugai, Aichi 487-8501, Japan

2Research Laboratory, Taihokohzai Co.,Ltd.9 Kirihara-cho, Fujisawa, Kanagawa, 252-0811, Japan

Abstract: SO_2 emission from coal combustion is the important problem in many countries. This paper aims to evaluate the possibility of simultaneous reduction of SO_x and fine ash particles during combustion of coal added with inorganic Ca-containing sorbent and organic Mg-containing sorbent in the fluidized bed conditions. Compared to addition of limestone particles to coal, the use of these sorbents produces the ultra-fine active oxides in the coal/char at higher temperature. The formed ultra-fine active oxides provide larger reaction surface area for the S and chemical sorbents, and, therefore, the high desulfurization efficiency will be expected in the fluidized bed coal combustion. In addition, the addition of chemical additives can affect the mineral transformation process during combustion. The results indicate that at certain temperature, higher sulfur removal efficiency can be obtained for selected Ca- and Mg-rich sorbents than those of natural limestone under fluidized bed combustion conditions. It is mainly due to the fine dispersion of Ca and Mg in impregnated coal so that a good is obtained between calcium and sulfur-containing coal particles. The addition of additives has a visible impact on the particle size distribution and chemical composition of the PM, wherein, it improves the degree of coalescence of sub-micron and fine mineral particles, which reduces $PM_{2.5}$ emissions. For the selected coal, the effect on the reduction of $PM_{2.5}$ emissions strongly depends on the addition and the type of sorbent being used.

Keywords: chemical additives, FBC, reduction of $PM_{2.5}$, De-SO_x

INTRODUCTION

Coal is the most abundant fossil fuel in China and accounts for over 75 percent of the energy consumption. The primary environmental issues relating to the consumption of coal are PM emissions, trace elements, oxide of sulfurs (SO_x) and nitrogen (NO_x). Minimizing the negative impacts of energy consumption on the natural environment is a key global priority (Sloss, 2004; Pope et al., 2004; Nelson, 2007; Lighty et al., 2000).

In CFBC and BFBC, the SO_2 formed is captured by the sorbent added as bed material, which most commonly is limestone or dolomite. The sulfur retention can be greater than 95% but sorbent utilization levels are relatively low. Particulate matter (PM) coming from the coal combustion is generally considered to contribute to air pollution and hence constitutes a significant threat to human health. Minimizing the negative impacts from global coal consumption on air pollution has become a key priority.

Stringent regulations on PM have forced coal-fired power plants to become equipped with air pollution control devices, such as ESPs and baghouse filter, in order to control their PM emissions. Unfortunately, these devices are not capable of efficiently capturing from particle diameters of < 2μm, which results in massive PM_1 and $PM_{2.5}$ emissions, especially in developing countries like China and India (Nalbanian, 2004; Soud et al., 1997; Smith, 2002). In order to keep decreasing the $PM_{2.5}$ emissions from coal combustion, a good understanding of the transformation of minerals in the combustion process is required. Our previous experimental results suggests that the combustion of coal with high concentrations of Ca and/or Fe-species produces lower emissions than coal using lower concentrations(Wang et al., 2007). By studying selected coal blends with different Ca contents, it was found that PM_{10} emissions during combustion are not linearly proportional to the weight percentage of the original raw coal. Increasing the coal blend Ca concentration promotes the formation of a liquid phase, and hence, affects the emissions of PM_{10} (Wang et al., 2008; Bryant et al., 2000). Therefore, by modifying the coal ash components, the fouling and slagging properties can be improved (Huggins et al. 1981; Huffman et al. 1981; Gupta et al., 1998). Based on these conclusions, the combustion of coal with additives is expected to lower the coal ash fusion point and viscosity, as well as decrease PM emissions. Furthermore, it has been shown that coal additives can modify ash composition by generating more desirable chemical compounds, which can then be used as ash residuals for construction purposes (Yazici, 2007).

This paper aims to evaluate the possibility of simultaneous reduction of SO_x and fine ash particles during combustion of coal added with inorganic Ca-containing sorbent and organic Mg-containing sorbent in the

fluidized bed conditions. Compared to addition of limestone particles to coal, the use of these sorbents produces the ultra-fine active oxides in the coal/char at higher temperature. The formed ultra-fine active oxides provide larger reaction surface area for the S and chemical sorbents, and, therefore, the high desulfurization efficiency will be expected in the fluidized bed coal combustion. In addition, the addition of chemical additives can affect the mineral transformation process during combustion.

EXPERIMENTAL CONDITIONS

Properties of coal and chemical sorbents used

Coal A was used in this study. It was pulverized to less than 150 μm, and dried prior to use. Proximate and ultimate analyses of coal A and the components of its ash were summarized in Table 1. Apparently, the sulfur content in ash is 1.25 wt%. SiO_2 and Al_2O_3 are the most abundant in the ash of coal A. The additives used are inorganic Ca-containing and organic Mg-containing pure chemicals with provided by Taihokohzai Lt. Co.(Japan). Either Ca-based or Mg-based chemical additive was expected as sulfur capture sorbent. The molar ratio of added Ca and Mg to sulfur was 1.0 and 2.0. Coal A was firstly mixed with the aqueous solution of either Ca-based or Mg-based chemical additives; and was then stirred and evaporated at 30°C under vacuum. The mixture of coal with additive was finally dried at 90°C for two hours.

Table 1 Properties of coal A

Analysis	Coal A
Proximate, wt.%, air-dry basis	
Moisture	2.7
Ash	13.8
Volatile Matter	42.4
Fixed Carbon	41.9
Ultimate, wt.%, air-dry basis	
C	78.27
H	6.32
N	1.02
S	0.42
O	14.06
Ash components, wt.%, dry basis	
SiO_2	66.59
Al_2O_3	25.15
CaO	2.44
Fe_2O_3	1.94
MgO	0.9
Na_2O	0.74
K_2O	0.17
SO_3	1.25
P_2O_5	0.04
TiO_2	1.74

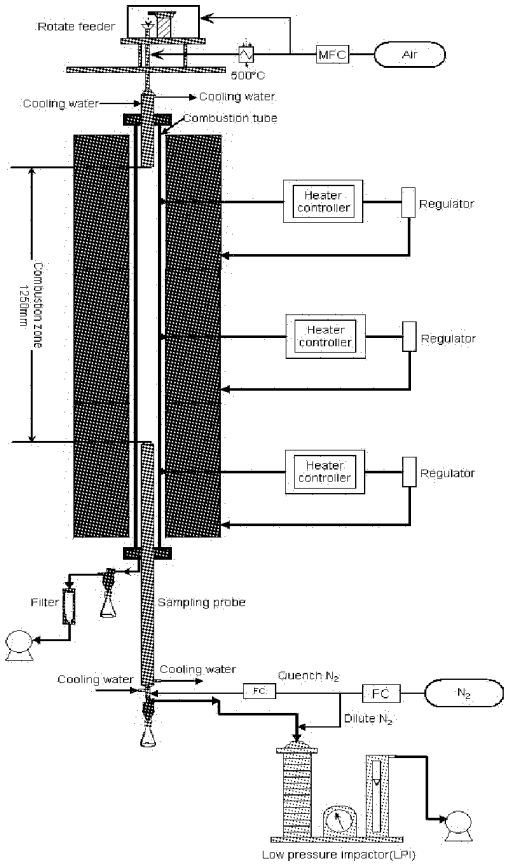

Fig. 1 Schematic diagram of DTF

Combustion conditions

Coal combustion tests were carried out in drop tube furnace (DTF), shown as Fig. 1. The main part of the DTF is a quartz tube with a length of 2000mm and an inner diameter of 50mm. The top and the middle zone of the furnace were heated to 1300°C, higher than the coal ignition temperature, while the bottom zone was controlled at 1100°C for desulfuration, which has been well described in elsewhere (Zhang et al., 2002). In each run, both furnace and burner were cooled continuously with water. The raw material, at a feeding rate of about 0.2g/min, was entrained by air into the furnace; the air flow rate was selected as 11.5 L/min. Mass flow rate of the primary gas was kept at 1.5L/min to carry the samples entering the drop tube furnace. The secondary gas was kept at 10L/min and preheated to 500°C. The entire system is sealed except the exhaust.

A probe is installed within DTF; it is connected with a suction pump to capture the falling char or fly ash

entrained by the flue gas. The exit gas was analyzed by gas flow meter for outlet SO_2 concentration. Fly ash was collected by vacuum suction system connected to the cyclone and the low-pressure impactor (LPI). The coarse PM is mainly collected by cyclone, and the flue gas carrying the fine PM is further diluted by particle free nitrogen and pulled into LPI to capture the fine PM ranging from 0.03 to 12.1 μm. The collected PM was analyzed for the physical and chemical properties (Wang et al., 2007; Zhang et al., 2006).

CHARACTERIZATION OF ASH SAMPLES

Fly ash taken from coal combustion was analyzed by laser particle analyzer (LPA), X-ray florescence (XRF), scanning electron microscopy energy dispersive spectroscopy (SEM-EDS), computer controlled scanning electron microscopy (CCSEM) (Zhang et al., 2002; Wang et al., 2008).

RESULTS AND DISCUSSION

Mineralogical properties in raw coal

The mineral composition, size and their association with organic materials in the raw coals were analyzed by CCSEM, and plotted in Fig. 2(a). The results show that the selected coal A is rich in kaolinite and quartz. Sulfur mainly exists as inorganic pyrite. The particle size distributions of included and excluded minerals are shown in Fig.2(b), which indicate that almost all the size of included minerals in coal A are smaller than 10 μm and the size of excluded minerals are close to 10μm.

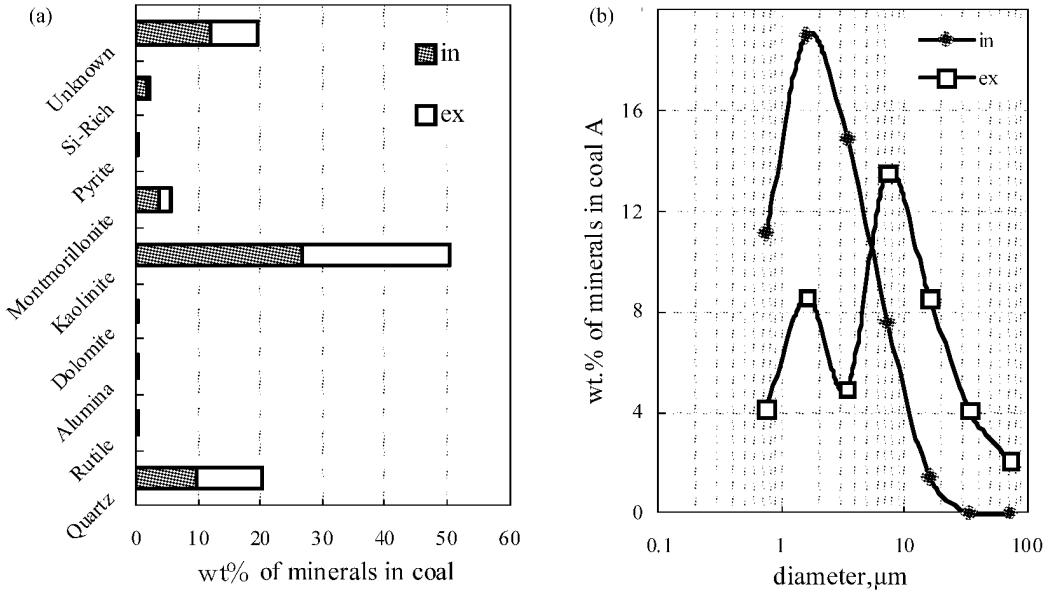

Fig.2 Chemical properties of minerals in coal A: (a) morphology; (b) particle size distribution (in: included minerals; ex: excluded minerals)

Chemical additives effects on the reduction of SO_2

Coal A mixed with Mg- or Ca-based additives were combusted, respectively. The upside of DTF was heated to 1573K whilst the downside was controlled at 1373K. The effects of additives on desulphurization in combustion are show in Fig. 3.

The results show that the addition of additive in coal during combustion decreases sulphur emissions. It is also noted that both the type and the addition of additives affect sulphur emissions. For the cases of Ca/S=1 and Mg/S=1, about half amounts of S are reduced.

Effects of chemical additives on the reduction of $PM_{2.5}$

The effects of added Ca- and Mg- additives on the emissions of $PM_{2.5}$ during combustion are investigated and introduced here. For their relative high desulphurization, the cases of Ca/S=1 and Mg/S=1 are analyzed and plotted in Fig. 4. The results show that both the reduction of PM_1 and $PM_{2.5}$ are realized through the combustion of coal A with the selected additives.

With respect to the reduction of PM_1, about 30wt% emissions are decreased when coal A with Ca-containing additive are combusted. On the other hand, the addition of Mg-containing additive are not contribute to reduction the PM_1 emissions.

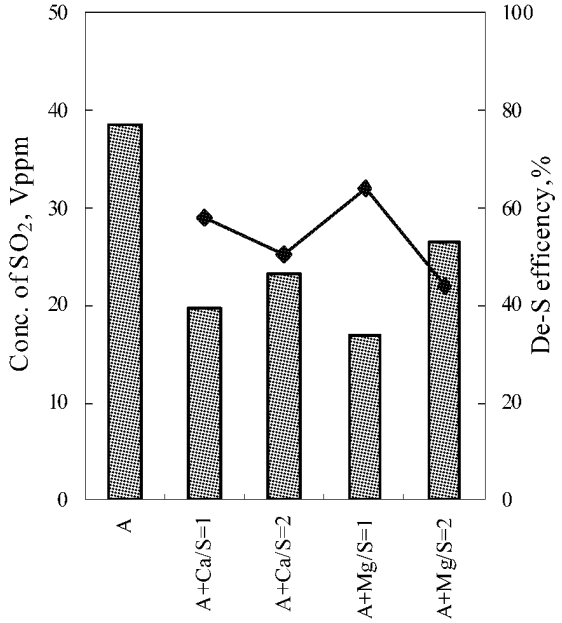

Fig. 3 Desulfurization of coal A impregnated with Mg- and Ca-containing additives

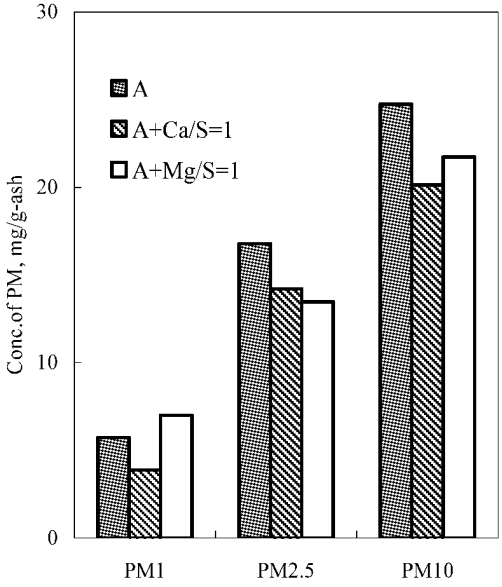

Fig.4 Comparison of $PM_{2.5}$ emissions generated by the combustion of coal and coal with additives

With respect to the reduction of $PM_{2.5}$, both Ca-containing and Mg-containing additives show a certain efficiency. The effect of Mg-containing additive is better than that of Ca-containing additive. SEM images, shown as Fig.5, indicate that the addition of Ca and Mg-containing additives change particle surface property and then improve the coalescence between particles, especially for the coalescence of sub-micron particle with coarse particles, shown as Fig. 5(b) and Fig. 5(c).

CONCLUSIONS

The addition of additives has a visible impact on the emission of the PM and SO_2 during coal combustion at controlled conditions. The degree of coalescence of sub-micron and fine mineral particles are the main reason for reducing $PM_{2.5}$ emissions, and desulfurization. It can be concluded that for the selected coal, the effect on the reduction of $PM_{2.5}$ emissions and desulfurization simultaneously strongly depends on the addition and the type of sorbent being used.

ACKNOWLEDGEMENTS

The financial support from Grant-in-aid for Scientific Research on Priority Areas (B), 20310048, Ministry of Education, Science, Sports and Technology, Japan was gratefully acknowledged.

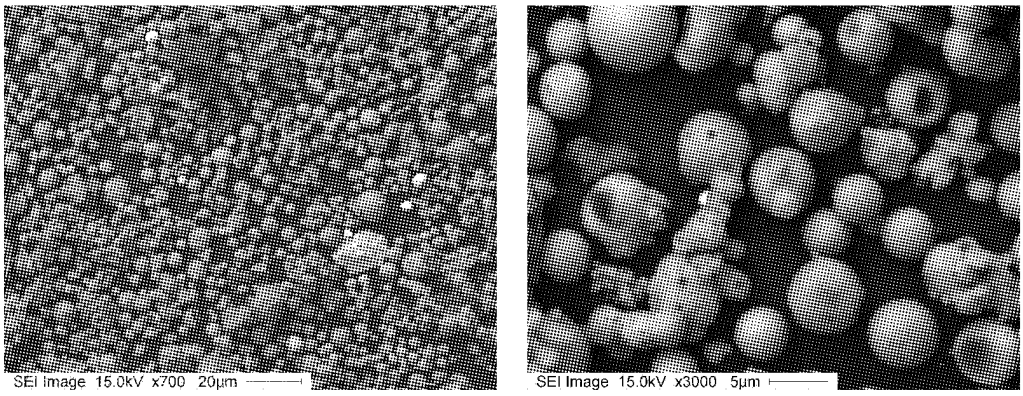

(a) coal A

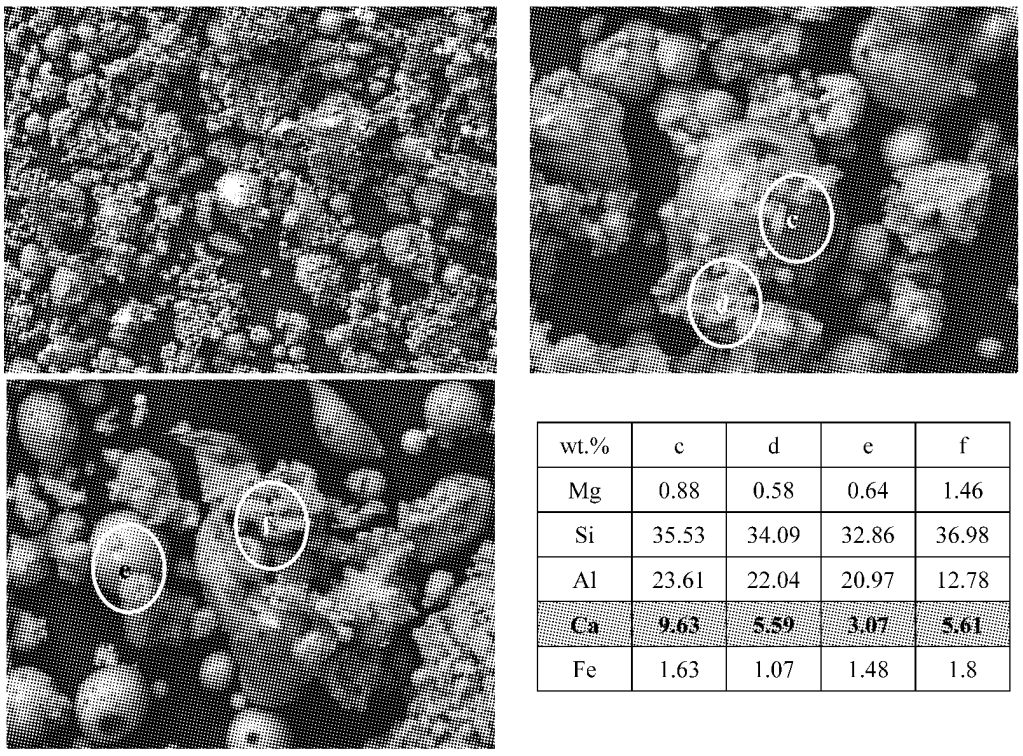

wt.%	c	d	e	f
Mg	0.88	0.58	0.64	1.46
Si	35.53	34.09	32.86	36.98
Al	23.61	22.04	20.97	12.78
Ca	9.63	5.59	3.07	5.61
Fe	1.63	1.07	1.48	1.8

(b) Coal A+Ca/S=1

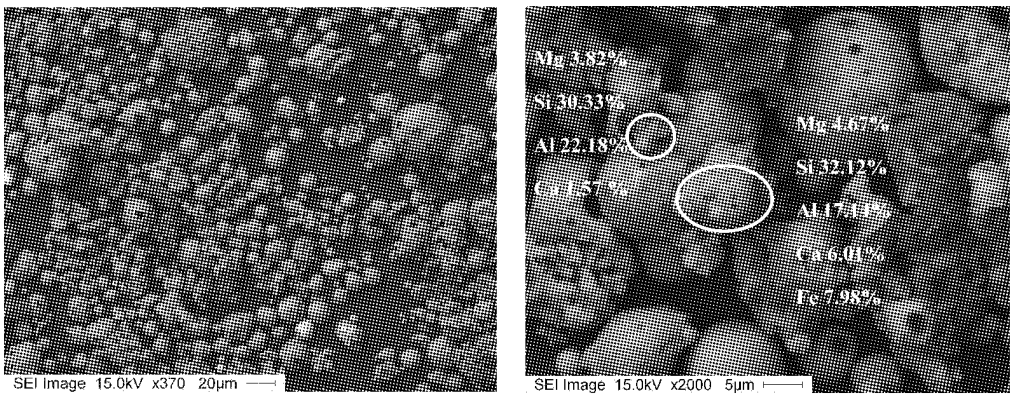

(c) Coal A+Mg/S=1

Fig. 5 SEM images of ash particles

REFERENCES

Bryant, G. W.; Browning, G. J.; Emanuel, H.; Gupta, S. K.; et al. The fusibility of blended coal ash. Energy Fuels **14** (2000), pp316-325.

Gupta, S. K.; Wall, T. F.; Creelman, R. A.; Gupta, R. P. Ash fusion temperatures and the transformations of coal ash particles to slag. Fuel Processing Technology **56**(1998), pp33-43.

Huffman, G. P.; Huggins, F. E.; Dunmyre, G. R. Investigation of the high-temperature behaviour of coal ash in reducing and oxidizing atmospheres. Fuel **60** (1981), pp585-597.

Huggins, F. E.; Kosmak, D. A.; Huffman G. P. Correlation between ash-fusion temperatures and ternary equilibrium phase diagrams. Fuel **60** (1981), pp577-584.

Lighty, J. S.; Veranth, J. M.; Sarofim, A. F. Combustion aerosols: Factors governing their size and composition and implications to human health. J. Air & Waste Manage. Assoc. **50** (2000), pp1565-1618.

Nalbanian, H. Air pollution control technologies and their interactions; IEA Coal Research: London, United Kingdom, Nov 2004.

Nelson, P. F. Trace metal emissions in fine particles from coal combustion. Energy Fuels **21** (2007), pp477-484.

Pope, C. A. III; Burnett, R. T.; Thurston G. D.; Thun, M. J.; Calle E. E.; et al. Cardiovascular mortality and long-term exposure to particulate air pollution: epidemiological evidence of general pathophysiological pathways of disease. Circulation **109** (2004), pp71-77.

Sloss, L. L. The importance of $PM_{10/2.5}$ emissions; IEA Clean Coal Centre: London, October 2004.

Smith, D. J., New technologies aim to control multiple pollutants. Power Engineering **106** (2002), pp53-57.

Soud, H. N., Mitchell S. C. Particulate control handbook for coal-fired plants; IEA Coal Research: London, United Kingdom, July 1997.

Wang, Q.; Zhang, L.; Sato, A.; Ninomiya, Y.; Yamashita, T. Interactions among inherent minerals during coal combustion and their impacts on the emission of PM_{10}. 1. Emission of micrometer-sized particles. Energy Fuels **21** (2007), pp756-765.

Wang, Q.; Zhang, L.; Sato, A.; Ninomiya, Y.; Yamashita, T. Effects of coal blending on the reduction of PM_{10} during high-temperature combustion. 1. Mineral transformations. Fuel **87** (2008), pp2997-3005.

Wang, Q.; Qiu, J.; Liu, Y.; Zheng, C. Effect of atmosphere and temperature on the speciation of mineral in coal combustion. Fuel Processing Technology **85** (2004), pp1431-1441.

Yazici, H. Utilization of coal combustion byproducts in building blocks. Fuel **86** (2007), pp929-937.

Zhang, L.; Sato, A.; Ninomiya, Y. CCSEM analysis of ash from combustion of coal added with limestone. Fuel **80** (2002) , pp1499-1508.

Zhang, L.; Ninomiya, Y.; Yamashita T. Emission of particulate matter from coal combustion and its correlation with coal mineral properties. Fuel **85** (2006), pp194-203.

SORBENT INVENTORY AND PARTICLE SIZE DISTRIBUTION IN AIR-BLOWN CIRCULATING FLUIDIZED BED COMBUSTORS: THE INFLUENCE OF PARTICLE ATTRITION AND FRAGMENTATION

Fabio Montagnaro[1], Piero Salatino[2,3], Fabrizio Scala[3], Massimo Urciuolo[2]

1Dipartimento di Chimica, Università degli Studi di Napoli Federico II, Complesso Universitario del Monte di Sant'Angelo, 80126 Napoli, Italy
2Dipartimento di Ingegneria Chimica, Università degli Studi di Napoli Federico II, Piazzale Vincenzo Tecchio 80, 80125 Napoli, Italy
3Istituto di Ricerche sulla Combustione, Consiglio Nazionale delle Ricerche (CNR), Piazzale Vincenzo Tecchio 80, 80125 Napoli, Italy

Abstract: Attrition and fragmentation of limestone during FB combustion of sulphur-bearing fuels have a profound influence on sorbent inventory and particle size distribution establishing at steady state in the bed. A population balance model is presented aiming at the prediction of the inventory and of the particle size distribution of sorbent particles establishing at steady state in the bed of an air-blown CFBC. The core of the model is represented by a population balance equation on sorbent particles which embodies terms expressing the extent/rate of each attrition/fragmentation process. The effect of the progress of sulphation on attrition/fragmentation is also taken into account. Constitutive equations needed to quantify attrition/fragmentation are developed on the basis of published data. Model results are presented and discussed with the aim of clarifying the influence of particle attrition/fragmentation on sorbent inventory and particle size distribution in a CFBC and on the closely related variables. Research needs and priorities within the specific field of investigation are also discussed.
Keywords: SO_2 capture, sorbent inventory, attrition, fragmentation, population balance

INTRODUCTION

Substantial changes in the particle size distribution of limestone-based SO_2 sorbents can be brought about by particle attrition/fragmentation in FBC, and the mutual interference between chemical reactions (calcination/dehydration, sulphation) and attrition/fragmentation of limestone has been largely disclosed (Chandran and Duqum, 1989; Couturier et al., 1993; Scala et al., 1997, 2000, 2007, 2008; Di Benedetto and Salatino, 1998; Werther and Reppenhagen, 2003; Chen et al., 2007; Saastamoinen and Shimizu, 2007; Montagnaro et al., 2008). It has been shown that primary fragmentation occurs immediately after the injection of sorbent particles in the hot bed, as a consequence of thermal stresses and internal overpressures due to release of gas (CO_2 following calcination of raw sorbent, steam following dehydration of spent/reactivated sorbent). Primary fragmentation takes place in the dense bed/splashing region of FBC reactors, resulting in the generation of coarse and fine fragments. Further breakage occurs as a consequence of mechanical stresses experienced by the particles during their lifetime in the reactor. Attrition by abrasion is related to the occurrence of surface wear as the emulsion phase of the FB is sheared by the passage of bubbles, and generates fine fragments that are quickly elutriated. Secondary fragmentation gives rise to coarse and fine fragments, and may onset as a result of high-velocity impacts against targets (bed material, reactor walls/internals), conditions likely experienced by the particles in the jetting region of FBC. The exit region of the riser and the cyclone are other potential locations of impact damage of sorbent particles.

The main features of these three attrition/fragmentation mechanisms are summarized in Table 1, and a conceptual framework for analyzing the effects of particle attrition/fragmentation on the fate of sorbents is represented in Fig. 1(a), where the simplifications of lumping sorbent particles into coarse and fine and the whole population of sorbent particles (of different age and sulphation degree) into lime and sulphated limestone components have been adopted.

In this work, a population balance model is presented, which aims at predicting the particle size distribution of sorbent particles establishing at steady state in the bed of an air-blown CFBC and the fractional mass of sorbent reporting to the bottom vs fly ash. The influence of attrition and fragmentation on mass fluxes, particle size distributions and related variables is assessed.

Table 1 Main features of attrition/fragmentation mechanisms

mechanism	caused by...	location	generation of...
Primary fragmentation (decrepitation)	thermal/mechanical stresses	dense bed/splashing zone	coarse/fine fragments
Attrition by abrasion (surface wear)	rubbing of bed solids	dense bed	fine fragments
Secondary fragmentation (impact fragmentation)	collisions against targets	jetting region + riser exit/cyclone	coarse/fine fragments

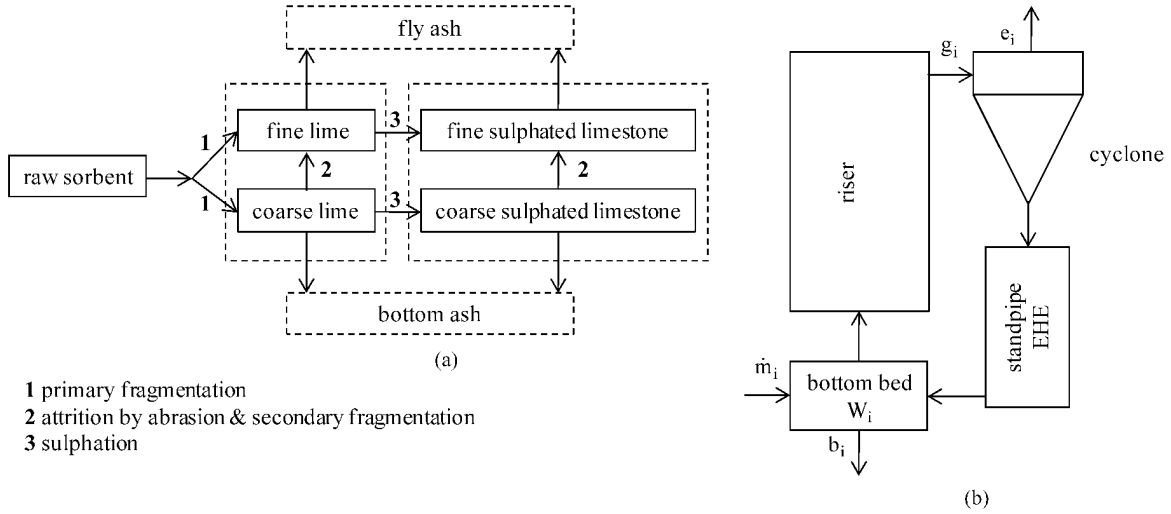

Fig. 1 (a) Particle sulphation/attrition/fragmentation network for the assessment of the fate of sorbents; (b) schematic representation of the CFBC loop with the Indication of relevant sorbent fluxes

MODEL

A schematic representation of the CFBC loop with the indication of relevant sorbent fluxes is reported in Fig. 1(b). A population balance equation can be written on the sorbent present at steady state in the combustor. Calcination and primary fragmentation are assumed to occur almost instantaneously so that the inventory of the raw limestone can be neglected. Each particle in the population is characterized by two variables: the particle size d, the sulphation degree X_S. A simplified version of the population balance is hereby developed based on the assumption that the sorbent can be lumped into two classes as far as the sulphation degree X_S is concerned: the unconverted lime, L, and the sulphated limestone, SL. Accordingly, the population balance in the d-X_S domain simplifies yielding two 1-D equations in the domain of the sorbent particle size d. Upon discretization of the domain and referring to the i-th particle size bin, equations referring to the lime (L) and sulphated limestone (SL) components read:

$$\dot{m}_{i,L} + \frac{R_{i+1,L}W_{i+1,L}}{\Delta d} + \sum_{j=i+1}^{n} k_{a,L} U \frac{W_{j,L}}{d_{j,L}} P_a(d_{i,L})\Delta d = \frac{R_{i,L}W_{i,L}}{\Delta d} + e_{i,L} + a_{i,L} + b_{i,L} + kW_{i,L} \quad (1)$$

$$kW_{i,L} + \frac{R_{i+1,SL}W_{i+1,SL}}{\Delta d} + \sum_{j=i+1}^{n} k_{a,SL} U \frac{W_{j,SL}}{d_{j,SL}} P_a(d_{i,SL})\Delta d = \frac{R_{i,SL}W_{i,SL}}{\Delta d} + e_{i,SL} + a_{i,SL} + b_{i,SL} \quad (2)$$

where each term is expressed in kg/(m^{2}s). In the first equation, the inlet term $\dot{m}_{i,L}$ represents the mass rate of lime particles having size d_i fed to the bed (all mass and mass rates in this work were expressed per unit riser cross-sectional area):

$$\dot{m}_{i,L} = \dot{m} \cdot P_0(d_{i,L})\Delta d \quad (3)$$

where $\dot{m}$ is the overall mass feed rate of lime particles and $P_0(d_{i,L})$ is the particle size distribution of the lime particles taking into account the effect of primary fragmentation. The terms $R_{i+1}W_{i+1}/\Delta d$ and $R_iW_i/\Delta d$ represent inlet and outlet contributions to the balance on the i-th size bin due to shrinkage of particles. R [m/s], the rate of particle shrinkage, is expressed as:

$$R = \frac{k_a U}{3} \tag{4}$$

where U is the gas superficial velocity in the primary region of the riser and k_a is a dimensionless attrition/fragmentation constant. The inlet term under summation takes into account particles formerly belonging to coarser particle size bins that fall into the i-th size bin due to attrition/fragmentation.
The outlet term e_i is the mass rate of material having size d_i lost by elutriation at the cyclone:

$$e_i = (1 - \eta(d_i))g_i \tag{5}$$

where g_i is the net solids mass flux along the riser of bed material having size d_i (computed according to Wirth, 1991), and $\eta(d_i)$ is the cyclone collection efficiency:

$$\eta(d_i) = \frac{1}{1 + \left(\frac{d_{cut}}{d_i}\right)^n} \tag{6}$$

The other outlet terms in Eqs. (1) and (2) are a_i, the attrition rate sorbent in the size bin:

$$a_i = k_a U \frac{W_i}{d_i} \tag{7}$$

and b_i, the mass flow rate at which sorbent bed material is drained as bottom ash. According to the hypothesis of perfect mixing of bed material in the bottom bed, b_i reads:

$$\frac{b_i}{b} = \frac{W_i}{W} \tag{8}$$

where b is the overall mass rate of sorbent bed drain and W is the overall mass of sorbent in the bottom bed.

The transfer from the lime phase to the sulphated limestone phase, driven by the sulphation kinetics, is expressed by the term $kW_{i,L}$, k being a sulphation kinetic constant. It has been discussed (Shimizu et al., 2001; Scala and Salatino, 2009a) that sorbent sulphation in FBC takes place in two subsequent stages: stage I, associated with the initial build-up of a sulphate-rich particle shell, stage II, associated with attrition-enhanced sulphation promoted by continuous removal of sulphated material by attrition. The sulphation process relevant to transfer from the L to the SL classes is that related to stage I, and the kinetic constant k has been evaluated accordingly. For the same reason, the influence of attrition on sulphation, dominant in stage II, is neglected with reference to stage I, hence k is assumed independent of attrition. For the sake of simplicity, the sulphation constant has been assumed independent of the lime particle size and embodies the influence of the average concentration of sulphur oxides in the combustor.

RESULTS AND DISCUSSION

Evaluation of Model Parameters

The model was solved in MATLAB™ environment, assuming the following input parameters: $\dot{m}$ =0.013 kg/(m^{2}s); $k_{a,L}=5\times10^{-9}$; $k_{a,SL}=10^{-9}$; U=2.5 m/s; $k=2\times10^{-4}$ s^{-1}. The total bed inventory in the riser per unit cross-sectional area has been set at 800 kg/m^2, a typical figure based on admissible pressure drops across the riser in practical operation of CFB combustors. Based on realistic sorbent feeding rates and fuel ash content, it is further assumed that the total bed inventory consists of W=250 kg/m^2 of sorbent (either L or SL) and 550 kg/m^2 of fuel ash.

The initial lime particle size distribution P_0 (embodying the effect of primary fragmentation) was expressed as a Gaussian distribution, having mean=475 μm and standard deviation=108 μm. Cyclone parameters were set at n=3 and d_{cut}=20 μm. The particle size distribution of attrited fragments has been expressed by an exponential-decay function:

$$P_a(d_{i,J}) = \frac{1}{\overline{d_J}} \exp\left(-\frac{d_{i,J}}{\overline{d_J}}\right); \quad J=L,SL \tag{9}$$

with average fragment sizes $\overline{d_L} = \overline{d_{SL}} = 35$ μm. It is here recalled that attrition/fragmentation was considered

to be active for particles greater than 35 μm, while for smaller particles its contribution was supposed to be negligible ($k_{a,L}=k_{a,SL}=0$). Moreover, the values of $k_{a,L}$ and $k_{a,SL}$ take into account both attrition by surface wear (Scala et al., 1997) and impact fragmentation (Scala et al., 2007; Scala and Salatino, 2009b). This latter contribution was calculated by estimating the fractional mass of fragments formed upon multiple particle impacts in the jetting region of a typical full scale CFBC. The entrainment rate of sorbent particles into the jets, required to calculate the frequency and kinetic energy of impacts, has been estimated according to Massimilla (1985).

MODEL RESULTS

Results of base case computations are reported in Fig. 2 and Table 2. The influence of attrition on model results has been assessed by comparison with results obtained in computations performed by neglecting attrition. This is obtained by setting the attrition rate constants for both lime (L) and sulphated limestone (SL) to 0. Results of computations for the no-attrition case are reported in Table 2 and Fig. 3. Figs. 2 and 3 report the following variables:

upper-left: the cumulative oversize Particle Size Distributions (PSD) of the lime in the feeding, P_0, and of the sorbent in the bottom bed (referred to both lime and sulphated limestone);

upper-right: the cumulative oversize PSD of sorbent leaving the riser as fly ash;

lower-left: the cumulative oversize PSD of the whole sorbent inventory in the riser (referred to both lime and sulphated limestone);

lower-right: the fractional mass of sorbent reporting to the bottom ash.

The main features emerging from analysis of data in Table 2 and Figs. 2 and 3 are hereby discussed.

The particle size distribution of both the lime and the sulphated limestone components in the bed closely reproduce those of the feeding in the no-attrition case. Departures are instead observed when attrition is at work, the distribution of both L and SL components being shifted toward smaller values.

A direct consequence of this feature is that a much larger fractional mass of sorbent reports to fly ash as a consequence of attrition: a remarkable 32% in the base-case vs 12% in the no-attrition case. This is consistent with the plot of the fractional mass reporting to bottom ash reported in Figs. 2 and 3: nearly all the particles coarser than 400 μm report to the bottom ash in the no-attrition case (Fig. 3) whereas they extensively report to fly ash (as a consequence of attrition) in the base case. Conversely, extensive generation - by attrition/fragmentation - of particles falling in the 35-200 μm size range is responsible for the pronounced maximum of the curve expressing the fractional mass reporting to bottom ash for the base case, peaking at about 90 μm (Fig. 2). Altogether, the combined effect of the original feeding of particles in the 100-1000 μm particle size range and of their re-distribution by attrition into the 35-200 μm size range is responsible for the pronounced bi-modal character of the curve expressing the fractional mass of sorbent reporting to the bottom ash.

The relative contributions of lime and sulphated limestone to the total sorbent inventory is relatively unchanged when comparing the base case and the no-attrition case: about 20% of the total sorbent inventory consists of lime. The slight increase of the lime inventory (at the expense of the sulphated limestone inventory) in the no-attrition case is consistent with the larger propensity of lime to undergo attrition/fragmentation.

Table 2 Selected output parameters of the Model

	f (-)[a]	G_S (kg/(m^{2}s))[b]	W_L (kg/m^2)[c]	W_{SL} (kg/m^2)[d]	d_{Sauter} of sorbent in the carryover (μm)
With attrition	0.32	12.9	48	202	54
Without attrition	0.12	11.1	51	199	330

[a]Fractional mass of sorbent reporting to fly ash; [b]overall net mass flux of sorbent along the riser; [c]overall lime mass in the bottom bed; [d]overall sulphated limestone mass in the bottom bed.

A remarkable feature is represented by the significant decrease of the average Sauter diameter of the circulating sorbent material, i.e. the sorbent bed material leaving the bottom bed in the carry over, when attrition is active: 54 μm vs 330 μm of the no-attrition case (Table 2). This feature is consistent with the larger axial sorbent mass flux G_s found in the base case: 12.9 kg/(m^{2}s) vs 11.1 kg/(m^{2}s) of the no-attrition case. This feature is bound to significantly affect important aspects like the extent and effectiveness of heat transfer in the upper riser, the loading of the cyclones, the axial uniformity of bed temperature.

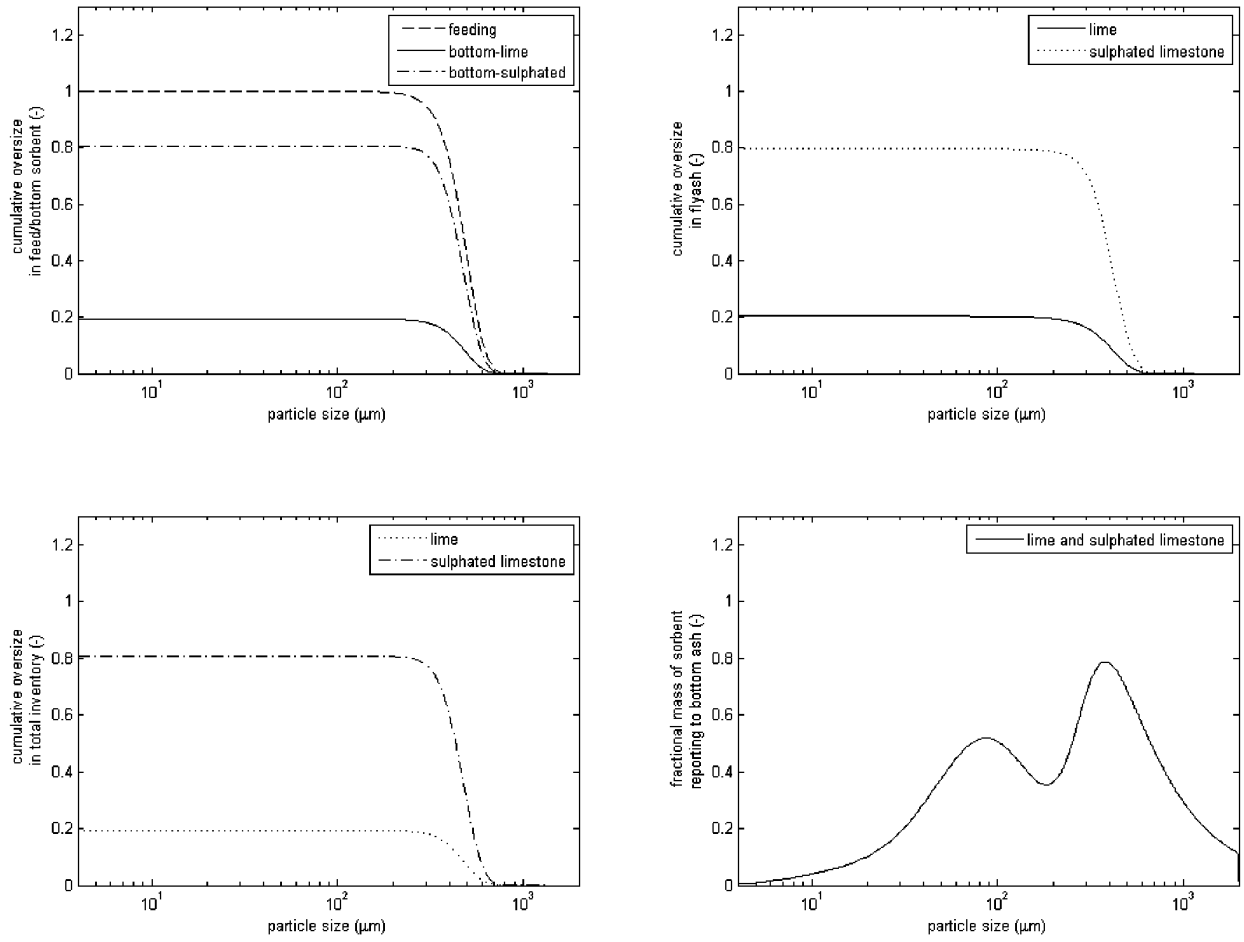

Fig. 2 Results of the model in the base case (with attrition)

CONCLUSIONS

A population balance model has been set up to predict the particle size distribution of sorbent particles establishing at steady state in a CFBC. The model is based on the simplification consisting of lumping the sorbent into two classes: lime and sulphated limestone, each characterized by its own attrition propensity. Primary fragmentation of sorbent is taken into account by proper modification of the particle size distribution of the sorbent feeding to yield the PSD of the incoming lime. Attrition by surface wear and secondary fragmentation are taken into account in the population balance equation.

Model computations have been carried out with reference to two cases: a base case, where constitutive parameters and equations expressing attrition and fragmentation of sorbent particles have been implemented, based on data and submodels desumed by the relevant literature with a choice of realistic values of the attrition parameters; a no-attrition case, where attrition and fragmentation have been deliberately neglected. The comparison of the two computations has been directed to assess the relevance of attrition/fragmentation to the population balance on sorbent particles in a CFBC.

The following conclusions can be drawn, based on model results:

- Attrition/fragmentation appreciably change the particle size distribution of sorbent establishing at steady state in the bed when compared with that of the incoming lime;
- Attrition/fragmentation dramatically affect the balance between sorbent reporting to the bottom ash vs fly ash;
- The influence of attrition on the relative contribution of lime and sulphated limestone to the overall sorbent inventory is moderate;
- Attrition/fragmentation significantly affect the Sauter average diameter of the circulating bed material, which is reduced by almost one order of magnitude. This feature is directly reflected by the increase of the axial net bed solids mass flux along the riser.

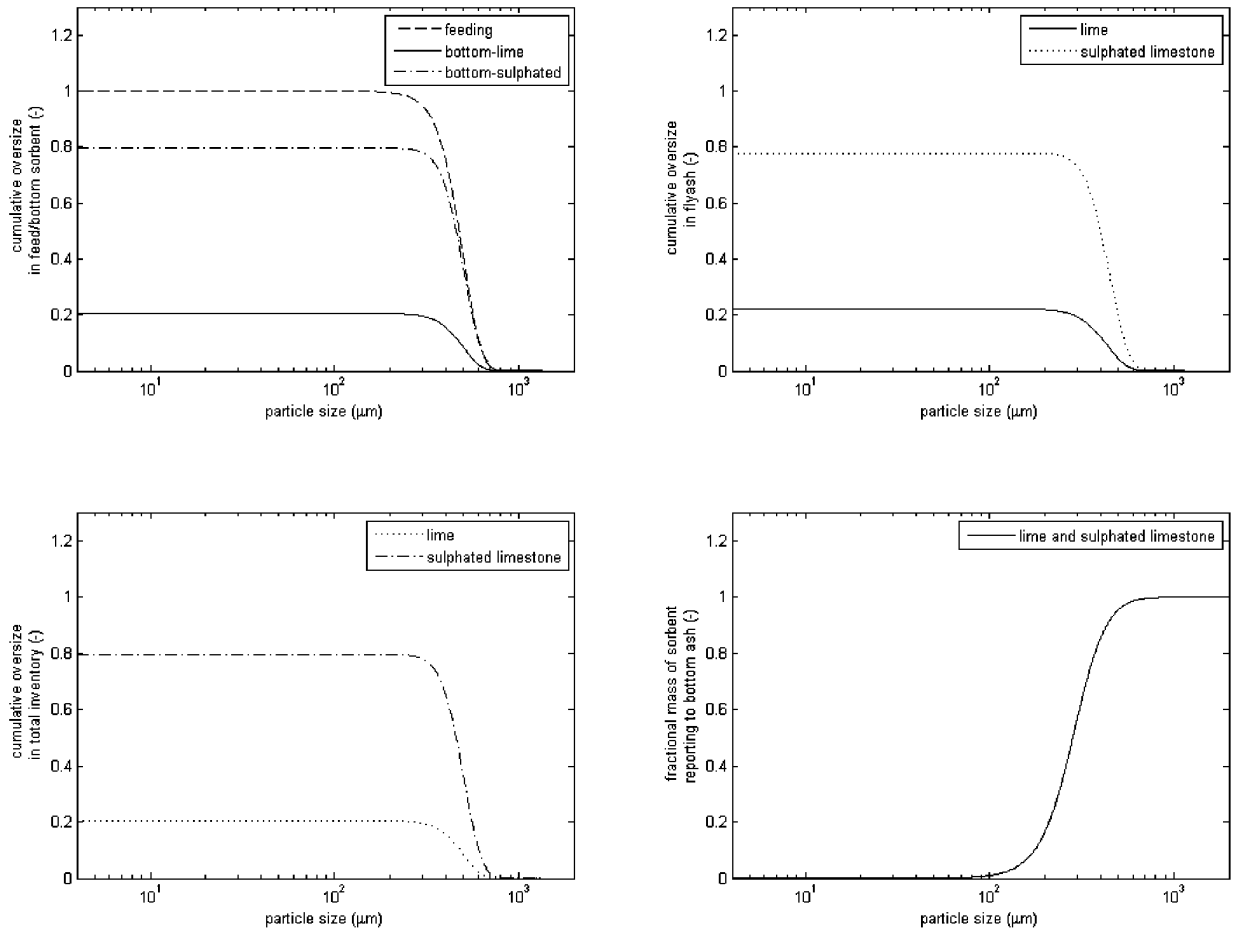

Fig. 3 Results of the model in the no-attrition case

Altogether, model computations confirm the relevance of attrition and fragmentation to the performance of circulating fluidized bed combustors.

REFERENCES

Chandran, R.R., Duqum, J.N.: Fluidization VI (Grace, J.R., Shemilt, L.W., Bergougnou, M.A., eds), Engineering Foundation New York (1989), pp. 571-580.

Chen, Z., Lim, J., Grace, J.R.: Chem. Eng. Sci. 62 (2007), pp. 867-877.

Couturier, M.F., Karidio, I., Steward, F.R.: Circulating Fluidized Bed Technology IV (Avidan, A.A., ed), American Institution of Chemical Engineers New York (1993), pp. 672-678.

Di Benedetto, A., Salatino, P.: Powder Technol. 95 (1998), pp. 119-128.

Massimilla, L.: Fluidization II (Davidson, J.F., Clift, R., Harrison, D., eds), Academic Press London (1985), pp. 133-172.

Montagnaro, F., Salatino, P., Scala, F., Chirone, R.: Powder Technol. 180 (2008), pp. 129-134.

Saastamoinen, J.J., Shimizu, T.: Ind. Eng. Chem. Res. 46 (2007), pp. 1079-1090.

Scala, F., Cammarota, A., Chirone, R., Salatino, P.: AIChE J. 43 (1997), pp. 363-373.

Scala, F., Salatino, P., Boerefijn, R., Ghadiri, M.: Powder Technol. 107 (2000), pp. 153-167.

Scala, F., Montagnaro, F., Salatino, P.: Energy Fuels 21 (2007), pp. 2566-2572.

Scala, F., Montagnaro, F., Salatino, P.: Can. J. Chem. Eng. 86 (2008), pp. 347-355.

Scala, F., Salatino, P.: Chem. Eng. Technol. 32 (2009a), pp. 380-385.

Scala, F., Salatino, P.: 20th Int. FBC Conference, Xian City, China, May 18-20 (2009b).

Shimizu, T., Peglow, M., Sakuno, S., Misawa, N., Suzuki, N., Ueda, H., Sasatsu, H., Gotou, H.: Chem. Eng. Sci. 56 (2001), pp. 6719-6728.

Werther, J., Reppenhagen, J.: Handbook of Fluidization and Fluid-Particle Systems (Yang, W.C., ed), Dekker New York (2003), pp. 201-237.

Wirth, K.E.: Chem. Eng. Technol. 14 (1991), pp. 29-38.

THE PERFORMANCE OF A NOVEL SYNTHETIC CA-BASED SOLID SORBENT SUITABLE FOR THE REMOVAL OF CO_2 AND SO_2 FROM FLUE GASES IN A FLUIDISED BED

R. Pacciani, C.R. Müller, J.F. Davidson, J.S. Dennis, A.N. Hayhurst

Department of Chemical Engineering and Biotechnology, University of Cambridge, Pembroke Street, Cambridge, CB2 3RA, UK

Abstract: The extent and mechanism of the sulphation and carbonation of a limestone, dolomite and chalk, have been compared with a novel, synthetic sorbent (85 wt% CaO and 15 wt% $Ca_{12}Al_{14}O_{33}$), from experiments in a small, electrically-heated fluidised bed. The sorbent particles were either (i) untreated, but then sieved into two particle sizes and reacted with SO_2 of two different concentrations, or (ii) cycled 20 times between (a) carbonation in 14 vol.% CO_2 in N_2, and (b) calcination, in pure N_2, at 750°C. The uptake of SO_2 by untreated limestone and dolomite was generally low (< 0.2 $g_{SO2}/g_{sorbent}$) and dependent on particle size, confirming previous results. In comparison with limestone and dolomite, the untreated chalk and the synthetic sorbent were found to be substantially more reactive with SO_2; their final uptake was significantly higher (> 0.5 $g_{SO2}/g_{sorbent}$) and essentially independent of the particle size. Hg-intrusion porosimetry, performed on calcined sorbents, revealed that the volume inside the pores of limestone and dolomite was entirely in small pores (< 200 nm dia.), confirmed by EDAX analysis. The small pores were easily plugged, hindering the diffusion of SO_2 through the particle. On the other hand, calcined chalk and fresh synthetic sorbent possessed large volumes in wide pores (> 200 nm dia.); these bigger pores were not blocked by newly formed $CaSO_4$. This allowed sulphation to proceed uniformly throughout the particle. It was also found that the uptake of SO_2 by limestone, dolomite and chalk was substantially lower when the particles had been subjected to cycles of calcination and carbonation in CO_2 prior to sulphation; this was attributed to a loss of volume inside the small pores during carbonation and calcination, confirmed by Hg-intrusion porosimetry. The uptake of SO_2 by the synthetic sorbent, on the other hand, was much closer to that achieved when it was used untreated, because large pores remained accessible after cycling.

Keywords: sulphation, ca-based sorbents, fluidised bed, particle technology, FBC

INTRODUCTION

Ca-based sorbents, such as limestone, are commonly used to remove SO_2 from flue-gases derived from fluidised-bed combustors (Dennis & Hayhurst, 1990; Anthony & Granatstein, 2006; Anthony et at., 2007). At the typical operating temperatures for combustion, 800–900°C, $CaCO_3$ decomposes to CaO and CO_2; the CaO then reacts with the SO_2 and O_2, or with SO_3, to form $CaSO_4$. The two-step overall process can therefore be described in:

$$CaCO_3(s) \longrightarrow CaO(s) + CO_2(g) \qquad \Delta H^\circ_{1123} = +169 \text{ kJ/mol} \qquad (1)$$

$$CaO(s) + 1/2O_2(g) + SO_2(g) \longrightarrow CaSO_4(s) \qquad \Delta H^\circ_{1123} = -481 \text{ kJ/mol} \qquad (2)$$

Sulphation thus requires 1 mole of Ca for each mole of S released during combustion. However, previous work with limestone and dolomite (e.g. Hartman & Coughlin, 1978; Dennis & Hayhurst, 1990; Yrjas et al., 1995; Anthony et al., 2007) has shown that the overall conversion of the calcined limestone to calcium sulphate is low, typically 20-30% on a molar basis; this low conversion is sensitive to the pore size distribution developed during calcination (Dennis & Hayhurst, 1989). The molar volume of the product $CaSO_4$ (~52.2 cm^3/mol) is about three times that of the parent CaO (~16.9 cm^3/mol); consequently, owing to the diffusional limitations to mass transfer within a particle of calcined limestone, its pores plug at their entrances with product, the reaction ceases prematurely, and the resulting conversions are low. Because of this, a large proportion of the sorbent leaves a fluidised combustor unreacted. Increasing the conversion of sorbent would therefore decrease the amount of raw materials required, and the costs of operation and disposal. Several methods have been proposed to achieve better conversion, e.g. (i) hydration of spent sorbent, i.e. reaction with water (Laursen et al., 2000; Wu et al., 2006; Manovic & Anthony, 2007; Montagnaro et al., 2007), (ii) mixing with additives (Jozewicz et al., 1989; Wang et al., 2002) and (iii) investigating alternative, synthetic sorbents (Wolff et al., 1993; Wei et al., 1997; Gavaskar and Abbasian, 2006; Chen et al., 2007). This paper describes a study into ways of enhancing the capture of SO_2 in a fluidised coal combustor by means of a novel synthetic sorbent (Pacciani et al., 2008a,b). Its conversion and SO_2 uptake were compared to those of natural sorbents, such as

limestone, dolomite and chalk, both in their fresh state and after being subjected to 20 cycles of carbonation and calcination. The factors affecting the performance of these sorbents were investigated.

EXPERIMENTAL

The synthetic sorbent (called HA-85-850) consisted of 85 wt% CaO and 15 wt% $Ca_{12}Al_{14}O_{33}$ (mayenite); details of its preparation can be found in Pacciani et al. (2008a). Naturally-occurring limestone (Purbeck Quarry, Swanworth, UK, 95 wt% purity), dolomite (91% purity, obtained from Steetley Ltd, UK) and chalk (95 wt% purity, Wilbraham, UK) were used in the comparative experiments. The selected sorbents, pre-sieved to either 355-500 μm or 500-710 μm, were sulphated in a bench–scale fluidised bed, depicted in Fig. 1.

It consisted of a quartz tube with an internal diameter of 29.5 mm and length 460 mm, equipped with a sintered quartz plate as distributor located 110 mm from the base of the tube. The bed temperature was measured by a K–type thermocouple, 1.5 mm dia., suspended above the distributor and controlled by setting the desired temperature on the furnace. The feed gas to the reactor was supplied by three gas cylinders, one for pure N_2, one for pure O_2 (or air) and one for a mixture of 0.8 vol. % SO_2 in N_2. The sand in the bed, sieved to 355-425 μm, was first heated to the desired temperature of 850°C by an electric furnace surrounding the bed, while fluidised with a mixture of 0.8 vol.% SO_2 in N_2. When this temperature was reached, the gas feed was diluted to the desired composition using mixtures of pure N_2 and air, or pure N_2 and pure O_2, from cylinders (all gases were supplied by BOC). At the beginning of each experiment, the gas flow-rate from each cylinder was measured using rotameters at a pressure of 100 kPa gauge. The composition of the fluidising gas was set to either 0.18 vol.% SO_2 and 5.2 vol.% O_2 in N_2, or 0.6 vol.% SO_2 and 5.2 vol.% O_2 in N_2. The total flow-rates (at STP) were 63.5 $cm^3\ s^{-1}$ and 64.3 $cm^3\ s^{-1}$, respectively. At 850°C the ratio of the superficial velocity of the fluidising gas, U, to its value at minimum fluidisation, U_{mf}, was ~ 6.8, with U_{mf} = 5.2 $cm\ s^{-1}$ at 850°C. An experiment began when a batch of particles, pre-weighed to 0.030 ± 0.001 g, was tipped into the hot sand bed *via* the open top of the reactor using a quartz funnel. The mass of sorbent was chosen so that the drop in temperature of the bed, upon adding cold sorbent particles, was less than 5°C. Each experiment was repeated at least 3 times. The molar concentrations of SO_2 and O_2 in the gas leaving the bed were measured continuously using a non-dispersive infrared SO_2 analyser (ABB EL3020), coupled with a paramagnetic analyser for O_2. During an experiment, a sample of the off–gas was continuously transferred to the analyser at 1 dm^3/min at room temperature and pressure by means of a quartz probe positioned such that the probe tip was located at the upper end of the furnace; the excess gas was vented to air. The probe was connected to a glass wool filter in order to prevent fine particles from reaching the analyser; the volume of the whole sampling system was kept as small as possible. Prior to a set of experiments, the IR analyser was calibrated for SO_2 using a mixture of 0.8 vol.% SO_2 in N_2 initially employed to fluidise the bed of sand.

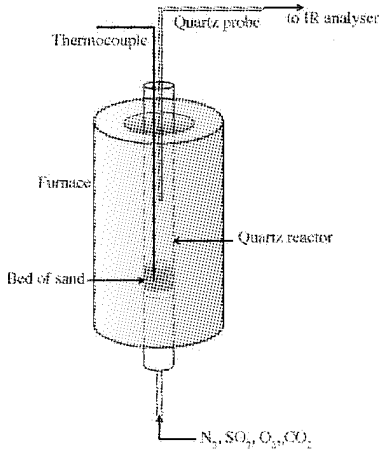

Fig. 1 Schematic diagram of the fluidised bed.

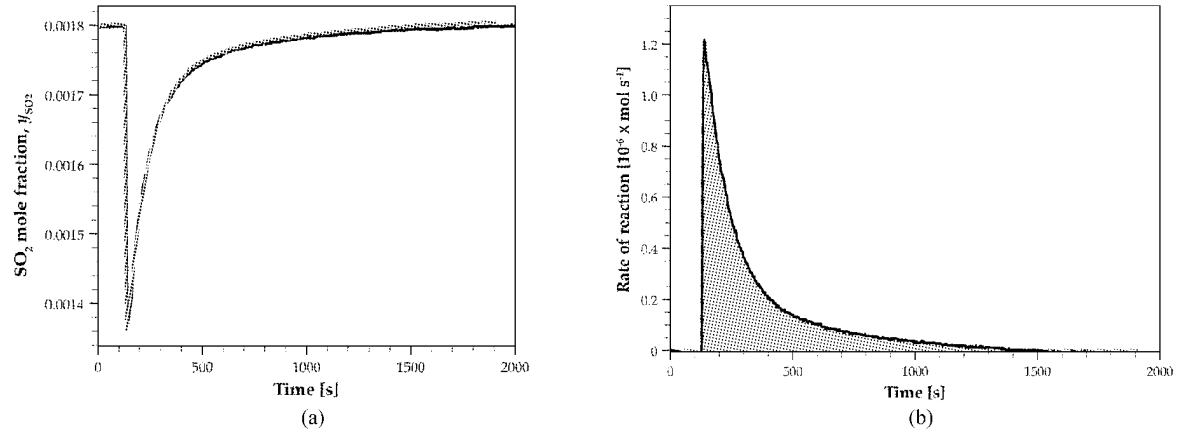

Fig. 2 A typical plot showing the mole fraction of SO_2 in the off-gas during sulphation (from two separate experiments, Fig. 2(a)) and the corresponding rate of reaction (Fig. 2(b)) for 0.030 ± 0.001 g of HA-85-850; T = 850°C, d_p =500-710 μm, Q_{N2} = 33.3 $cm^3\ s^{-1}$, Q_{air} = 15.7 $cm^3\ s^{-1}$, $Q_{SO2/N2}$ = 14.5 $cm^3\ s^{-1}$, y^o_{SO2} = 0.0018, y_{O2} = 0.052. Bed of sand d_p = +355-425 μm, U/U_{mf} = 6.8

The CO_2-cycling experiments (i.e. calcination in pure N_2, followed by carbonation in 14 vol.% CO_2 in N_2, followed by calcination, etc.) were performed at 750°C in the same fluidised bed. The detailed procedure for these experiments is described by Pacciani et al. (2008a). The particles were retrieved calcined after the 20th calcination. In this experiment U/U_{mf} = 6.4 and 7.1, respectively, at 750°C.

A typical plot of the mole fraction of SO_2, y_{SO2}, against time, t, for 0.030 ± 0.001 g of fresh HA-85-850, sulphated at 850°C in 0.18 vol.% SO_2 and 5.2 vol.% O_2 in N_2, is shown in Fig. 2(a). The corresponding molar rate of sulphation against time was obtained by multiplying the molar flow-rate of gas through the bed by the drop (y^o_{SO2}-y_{SO2}) in the off-gases. A typical result is shown in Fig. 2(b); the number of moles of SO_2 absorbed during sulphation, n_{SO2}, was measured as the product of the shaded area in Fig. 2(b) and the molar flowrate of the fluidising gas. The error of a measurement was less than 10%. Sometimes, particles 500-710 μm in size, sulphated at 850°C in 0.18 vol.% SO_2 and 5.2 vol.% O_2 in N_2, were sieved from the bed of sand and recovered for further analysis.

The volume inside the pores of calcined and sulphated sorbent particles was measured by Hg-intrusion (Micromeretics Autopore IV) and N_2 adsorption (Micromeritics ASAP 2000). SEM (Scanning Electron Microscopy) and EDS (Energy Dispersive Spectrometry) analyses of the cross section of sulphated sorbent particles were performed using a JEOL 580 Scanning Electron Microscope. The cross-section of the particles was exposed by embedding them in black conductive phenolic resin (Conducto Mount, Metprep), and grinding them using silicon carbide paper until the cores were exposed.

RESULTS

SO_2 uptake and conversion by a sorbent

The conversion of CaO in a sorbent is defined as $X = n_{SO2}/n^o_{CaO}$, i.e. the ratio of the moles of SO_2 taken up to the initial number of moles of CaO. However, the uptake X', defined as the mass of SO_2 absorbed divided by the mass (m_o) of uncalcined sorbent, is a better parameter than X for comparing the performance of a sorbent for SO_2, because it takes into account the actual amount of sorbent, including its inerts and any unreacted CaO. The uptake, X', can be easily calculated as $X' = 64\ n_{SO2}/\ m_o$.

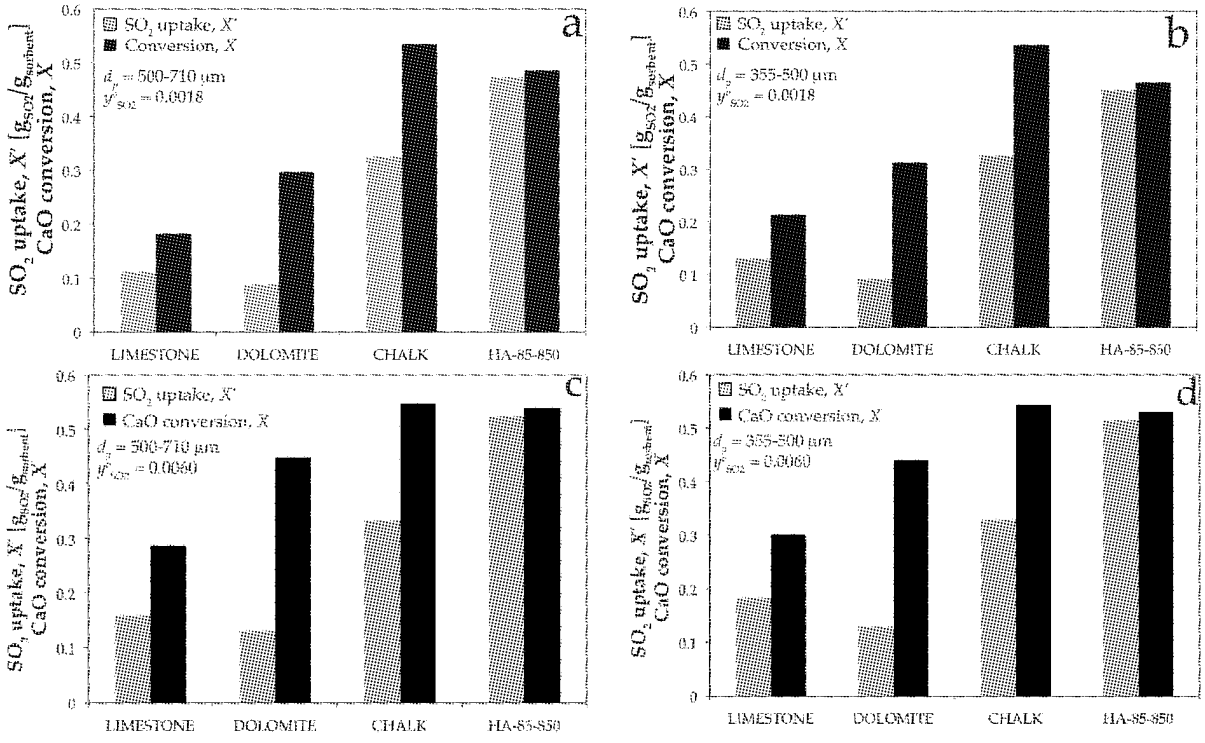

Fig. 3 Final SO_2 uptake, X', (grey bars) and CaO conversion, X, (black bars) by limestone, dolomite, chalk and HA-85-850. T = 850°C, m_o = 0.03 g, d_p = 355-500 μm (Figs 3b,d) or 500-710 μm (Figs 3a,c), Q_{N2} = 33.3 cm^3 s^{-1}, $Q_{SO2/N2}$ = 14.5 cm^3 s^{-1}, Q_{air} = 15.7 cm^3 s^{-1}, y_{SO2} = 0.0018, y_{O2} = 0.052 (Figs 3a,b), $Q_{SO2/N2}$ = 48.3 cm^3 s^{-1}, Q_{O2} = 16.0 cm^3 s^{-1}, y^o_{SO2} = 0.0060, y_{O2} = 0.052 (Figs 3c,d). Bed of sand d_p = + 355-425 μm, U/U_{mf} = 6.8

Figure 3 show the final uptake of SO_2, X', (grey bars) and conversion, X, (black bars) for all four sorbents, sieved to 500-710 μm (Figs 3a,c) or 355-500 μm (Figs. 3(b),(d)), when sulphated at 850°C in 0.18 vol.% SO_2

and 5.2 vol.% O_2 (Figs. 3(a),(b)), or in 0.60 vol.% SO_2 and 5.2 vol.% O_2 (Figs. 3(c),(d)). Fig. 2(a) shows that limestone attained $X' \sim 0.1$ $g_{SO2}/g_{sorbent}$, corresponding to a conversion $X \sim 0.18$, after ~ 2000 s of sulphation, in agreement with previous findings (e.g. Dennis & Hayhurst, 1989, 1990; Laursen et al., 2000). The conversion of the dolomite, $X = 0.3$, was higher than that of limestone, as previously found e.g. by Yiras et al., (1995). However, its SO_2 uptake was lower than that of limestone, i.e. ~ 0.08 $g_{SO2}/g_{sorbent}$, owing to the presence of the inert MgO. In comparison, both chalk and HA-85-850 achieved much higher conversions, i.e. 0.55 and 0.5, respectively; in fact, HA-85-850 achieved the highest SO_2 uptake, i.e. 0.53 $g_{SO2}/g_{sorbent}$. Chen et al. (2007) showed that mayenite can react with SO_2. However, its uptake of SO_2 was considerably lower than that of limestone. Thus, since the amount of mayenite present in a particle of HA-85-850 is small (i.e. 15 wt%), the contribution of mayenite to the overall uptake of SO_2 by the synthetic sorbent was assumed negligible.

By comparing Figs. 3(a) and 3(b), it can be seen that the size of the sorbent particles affected the performance of limestone and dolomite, i.e. both X and X' were higher for particles 355-500 μm in diameter (Fig. 3(b)). This is in agreement with previous findings (Dennis & Hayhurst, 1989). However, no such effect could be seen with the chalk and HA-85-850. Increasing y^o_{SO2} from 0.0018 to 0.0060 slightly increased the uptake of limestone and dolomite, as previously observed by, e.g., Adanez et al. (1996), but no effect is seen with chalk and HA-85-850; c.f. Fig. 3(a) with Fig. 3(c) and Fig. 3(b) with Fig. 3(d). The uptakes of SO_2 for all of the sorbents, sulphated at the conditions used in Figs. 3(a) and 3(b), are plotted against time in Fig. 4. The curves for limestone and dolomite represent a typical change from fast to slow reaction, marking the onset of diffusion through the product layer of newly formed $CaSO_4$ as the rate-limiting step. The dependences of the final uptake and of the rate of reaction on particle size for limestone and dolomite are clearly visible: the smaller particles (355-500 μm) reacted faster during the first stage of reaction than larger particles (500-710 μm). Also, they attained a higher final uptake after ~ 1500 s. Conversely, the final uptakes of chalk and HA-85-850 were essentially independent of the particle size. The rate of reaction for chalk was initially faster for smaller particles; for HA-85-850 was almost independent of particle size.

Figure 5 shows the conversion of each sorbent, both fresh and previously subjected to 20 cycles of calcination and carbonation, and sulphated at 850°C in 0.18 vol.% SO_2 and 5.2 vol.% O_2 in N_2. In all cases, the conversions are lower than those of the fresh sorbent. Limestone, dolomite and chalk lost more than 50% of their conversion, whereas for HA-85-850 the conversion after cycling only fell from ~ 0.5 to ~ 0.4, so that cycled HA-85-850 retained the highest conversion. Quite remarkably, this was 4 times higher than for cycled limestone.

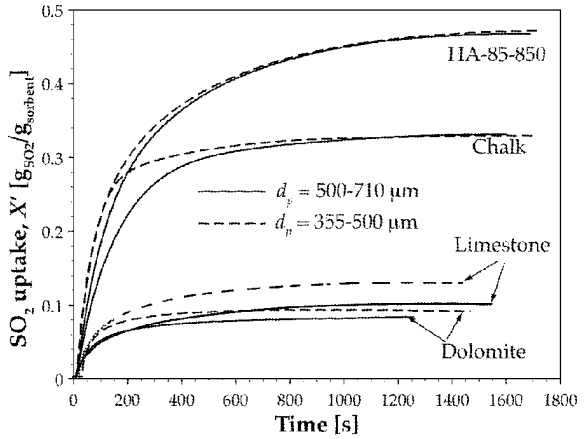

Fig. 4 SO_2 uptake by 0.03 g of limestone, dolomite, chalk and HA-85-850, sulphated at T = 850°C, d_p = 355-500 μm (grey lines) or 500-710 μm (black lines), Q_{N2} = 33.3 cm^3s^{-1}, $Q_{SO2/N2}$ = 14.5 cm^3 s^{-1}, Q_{air} = 15.7 cm^3 s^{-1}, y^o_{SO2} = 0.0018, y_{O2} = 0.052. Bed of sand d_p = + 355-425 μm, U/U_{mf} = 6.8

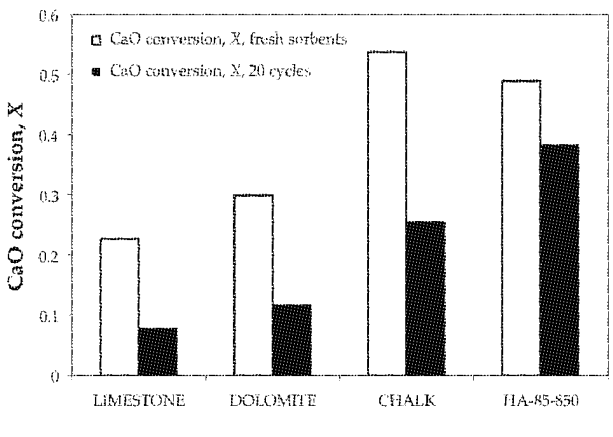

Fig. 5 Final CaO conversion for 0.03 g of fresh sorbents (white bars) and pre-cycled sorbents (black bars), sulphated at T = 850°C, m_o = 0.03 g, d_p = 500-710 μm, Q_{N2} = 33.3 cm^3 s^{-1}, $Q_{SO2/N2}$ = 14. cm^3s^{-1}, Q_{air} = 15.7 cm^3s^{-1}, y^o_{SO2} = 0.0018. Bed of sand d_p = +355-425 μm, U/U_{mf} = 6.8

Characterisation of sorbents

The porosities of fresh HA-85-850 and also of limestone, dolomite and chalk, after calcining at 750°C in pure N_2, were measured using Hg porosimetry (Fig. 6). For limestone and dolomite, most of the pores were narrower than 200 nm in diameter; almost no volume was measured in pores wider than 200 nm. Chalk, on the other hand, presented two very distinct peaks, one at d_{pore} ~ 30 nm, and another one at d_{pore} ~ 500 nm, as previously found by Dennis & Hayhurst (1989). By contrast, fresh HA-85-850 showed very little porosity in pores < 200 nm, whereas it appeared to be highly porous inside pores wider than 200 nm, with a peak at d_{pore} ~

600 nm. The pore size distributions of HA-85-850 cycled 20 times and uncycled after sulphation at 850oC in 0.18 vol.% SO2 and 5.2 vol.% O2 in N2 are also shown in Fig. 6. It is apparent that HA-85-850 lost part of its pore volume in the big pores after 20 cycles of carbonation and calcination. Finally, the pore size distribution of sulphated HA-85-850 shows that no pore volume is present in pores narrower than 200 nm; conversely, residual pore volume is present in the sulphated particles of HA-85-850.

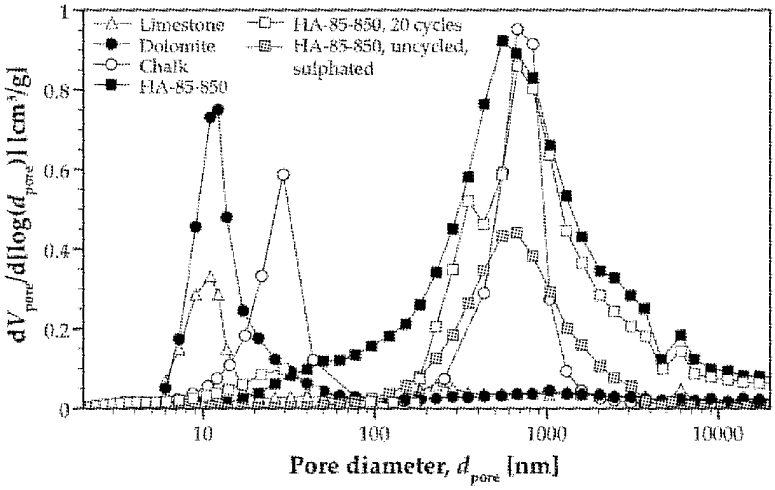

Fig. 6 Hg porosimetry for limestone, dolomite, chalk, calcined at 750oC in pure N2, and for HA-85-850, calcined at 750oC in pure N2, pre-cycled and sulphated, uncycled, at 850 oC in 0.18 vol.% SO2 and 5.2 vol.% O2 in N2, dp = 500-710 μ m

Images of the cross-section of sorbent particles, together with their corresponding chemical mapping for sulphur, are shown in Figs. 7(a)-(h). Figs. 7(a) and 7(e) clearly show that the sulphation of limestone resulted in the sulphur almost entirely present along the edge of the particle. In the case of dolomite (Figs. 7(b), 7(f)) the sulphur was distributed along the edges of macro-grains; Laursen et al. (2000) observed a similar pattern, which they called "network-like", in one of their sulphated limestones. Such a distribution of sulphur is attributed to macro- and microfractures developing during sulphation, along which the SO_2 is able to react with the exposed CaO. The cross-section of dolomite, Fig. 7(b), revealed various cracks, formed during reaction. Chalk (Figs. 7(c), 7(g)) appears uniformly sulphated, essentially confirming previous findings (Dennis & Hayhurst, 1989). Finally, the mapping of HA-85-850 shows an even distribution of sulphur within a particle.

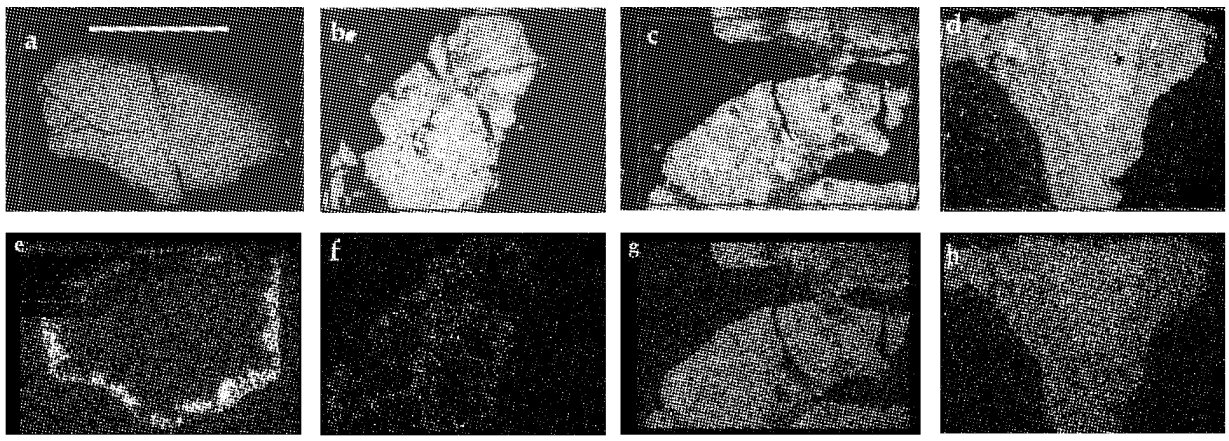

LIMESTONE DOLOMITE CHALK HA-85-850

Fig. 7 SEM images ((a)-(d)) and X-ray mapping ((e)-(h)) of sulphated particles, uncycled, of limestone ((a),(e)), dolomite ((b),(f)), chalk ((c),(g)) and HA-85-850 ((d),(h)). All images were taken using the same magnification. The scale bar in Fig. 7(a) corresponds to 500 μm

DISCUSSION

The pore structure (and also its surface area and pore volume) of a sorbent for SO_2 plays a crucial role in determining the overall conversion and rate of reaction. If its pores were to be filled with $CaSO_4$, limestone can achieve a maximum conversion of 57%. However, such a value is hardly ever achieved in limestone, because

its pores have widths between 20 and 50 nm, which plug with $CaSO_4$. The pore volume in the dolomite is higher, giving a higher conversion than limestone. However, owing to the presence of inert MgO in the dolomite, its overall uptake was lower. Chalk, on the other hand, has a large proportion of its volume in wide pores, so its ultimate conversion is higher than that for limestone, as confirmed by Fig. 4. Finally, HA-85-850 has a very small portion of its total pore volume, ~ 0.93 cm^3/g, in narrow pores; it contains mostly big ones, not susceptible to early plugging, so HA-85-850 reacts more completely than limestone and dolomite. In fact, the pore size distribution of uncycled HA-85-850 after sulphation shows that part of its pore volume was still available after it had been fully sulphated. However, the maximum theoretical uptake for HA-85-850, assuming all of the volume available is filled with $CaSO_4$, is ~ 0.83 $g_{SO2}/g_{sorbent}$, much higher than that achieved under the experimental conditions used here. Thus, sulphation of HA-85-850 seems to stop before all the pores are plugged with product. This matter requires further investigation.

One issue arising from this work is why the conversion of every sorbent decreased after being subjected to 20 cycles of carbonation and calcination. In the case of limestone, this contrasts with results reported by Grasa et al. (2008). They found that the uptake of SO_2 by a limestone increased after being subjected to a large number of cycles. This was attributed to a shift in pore volume from smaller pores to bigger ones (as measured by Hg intrusion) caused by sintering during cycling. Table 1 summarises the BET areas and pore volumes for all sorbents when (i) calcined, or fresh in the case of HA-85-850, and (ii) after being calcined and carbonated 20 times, in their calcined state. In all cases the total pore volume decreases with cycling; perhaps some of the pores closed off during cycles and therefore became unavailable for sulphation. Alternatively, the particles may shrink during cycling, resulting in lower extents of sulphation for cycled particles than untreated ones. Furthermore, the conversion to sulphate of cycled particles of HA-85-850 is lower than that of fresh particles (Fig. 5). As shown in Table 1, this sorbent developed more volume in small pores, during repeated carbonation and calcination, as previously reported (Pacciani et al., 2008a,b). However, Table 1 also reveals that this increase in volume inside small pores was accompanied by a loss in porosity in the large pores. The net loss of total porosity could explain why the conversion of cycled particles of HA-85-850 was somewhat lower than that of fresh particles, although to a lesser extent than for the other sorbents.

Table 1 BET area (measured by N_2 adsorption), total pore volume (from Hg intrusion) and BJH pore volume (obtained by applying the BJH model to the isotherm obtained from N_2 adsorption, valid for pores narrower than 200 nm) contained in sorbents, both subjected to one calcination and to 20 cycles of carbonation and calcination

Sorbent	BET area [m^2/g]	Total V_{pore} [cm^3/g]	BJH V_{pore} [cm^3/g]
Limestone (calcined/20 cycles)	23.7/12.2	0.37/0.20	0.19/0.07
Dolomite (calcined/20 cycles)	72.7/21.0	0.39/0.29	0.27/0.18
Chalk (calcined/20 cycles)	29.1/10.3	0.64/0.48	0.22/0.04
HA-85-850 (fresh/20 cycles)	5.7/15.5	0.93/0.67	0.07/0.13

CONCLUSIONS

The extent and mechanism of sulphation of a novel synthetic sorbent, HA-85-850, made of 85 wt% CaO and 15 wt% $Ca_{12}Al_{14}O_{33}$, was compared with those of limestone, dolomite and chalk. The measure of the extent of sulphation of limestone and dolomite, together with the analysis of their pore volumes and sulphur distribution, confirmed that sulphation of these sorbents was prematurely stopped by formation of a layer of $CaSO_4$, which hindered diffusion of SO_2 through the particle, as further confirmed by EDAX analysis. Conversely, the pore size distribution in calcined chalk and fresh HA-85-850 revealed the presence of pores with diameters up to 10 μm. Consequently, chalk and HA-85-850 reacted uniformly, owing to these large pores, not susceptible to premature blocking. It was also found that the uptakes of SO_2 by limestone, dolomite and chalk were substantially lower, after the particles had been subjected to cycles of calcination and carbonation in CO_2 prior to sulphation; this was attributed to a loss of pore volume both in small and big pores owing to cycling. The uptake of the synthetic sorbent, on the other hand, was much closer to that achieved with untreated sorbent. The unusual features of our synthetic sorbent make it very attractive for desulphurisation in FBC.

NOTATIONS

d_p	diameter of a sorbent particle, mm	t	time, s
d_{pore}	pore diameter, nm	U	superficial velocity of the fluidising gas at 850°C, cm/s
ΔH^o_{1123}	specific enthalpy of reaction at 850°C, kJ/mol	U_{mf}	value of U at minimum fluidisation at 850°C, cm/s
m_o	initial mass of uncalcined sorbent	V_{pore}	pore volume, cm^3/g
n_{SO_2}	moles of SO_2	X	conversion
n^o_{CaO}	moles of CaO in a sorbent particle	X'	SO_2 uptake, $g_{SO_2}/g_{sorbent}$
Q_i	volumetric flowrate of species i at STP, cm^3/s	y_i	mole fraction of species i
T	temperature, °C	y^o_i	inlet mole fraction of species i

ACKNOWLEDGEMENTS

The authors are grateful to the Engineering & Physical Sciences and Research Council (EPSRC, Grant N. GR/T22032/01) for financial support. The authors also thank Simon Griggs (Department of Material Science and Metallurgy, University of Cambridge) for his help characterising particles.

REFERENCES

Adanez, J., Fierro V., de Diego, J.A., de Diego, L.F. and Garcia-Labiano, F. Thermochimica Acta **277** (1996), pp. 151-164.
Anthony, E.J., Bulewicz, E.M. and Jia, L. Progr. Energy Comb. Sci. **33** (2007), pp.171–210.
Anthony, E.J. and Granatstein, D.L. Progr. Energy Comb. Sci. 27 (2001), pp.215–236.
Borgwardt, R. H. and Bruce, K. R. AIChE J. **32** (1986), 239.
Chen, Q., Yoshida, K., Yamamoto, H., Uchida, M. and Sadakata, M. Energy Fuel, 21 (2007), pp.3264–3269.
Dennis, J.S. and Hayhurst, A.N. Chem. Eng. Sci. **45** (1986), pp.1175–1187.
Dennis, J.S. and Hayhurst, A.N. J. Energy Inst. **62** (1989), pp.202–207.
Fennell, P.S., Pacciani, R., Dennis, J.S., Davidson, J.F. and Hayhurst, A.N. Energy Fuel, **21** (2007), pp. 2072–2081.
Gavaskar, V.S. and Abbasian, J., Ind. Eng. Chem. Res. **45** (2006), pp. 5859-5869.
Grasa, G., Alonso, M. and Abanades, J.C., Ind. Eng. Chem. Res. **47** (2008), pp. 1630-1635.
Hartman, M., Pata, J. and Coughlin, R.W. Ind. Eng. Chem. Proc. Des. Dev. **17** (1978), pp. 411–419.
Jozewicz, W. and Kirchgessner, D.A. Powder Technology 58 (1989), pp. 221–229.
Laursen, K., Duo, W., Grace, J.R. and Lim, C.J. Fuel, 79 (2000), pp.153–163.
Manovic V. and Anthony, E.J. Environ. Sci. Technol. **41** (2007), pp. 4435-4440.
Montagnaro F., Salatino P., Scala F. and Chirone R. Powder Technology **180** (2008), pp. 129 – 134.
Pacciani, R., Müller, C.R., Davidson, J.F., Dennis, J.S. and Hayhurst, A.N. Can. J. Chem. Eng. **86** (2008a), pp.356–366.
Pacciani, R., Müller, C.R., Davidson, J.F., Dennis, J.S. and Hayhurst, A.N. AIChE J. **54** (2008b), pp. 3308-3311.
Wang C., Shen X., Xu Y. Fuel Process. Technol. **79** (2002), pp.121 – 133.
Wei, S., Mahuli, S., Agnihotri, R. and Fan, L.S. Ind. Eng. Chem. Res. **36** (1997), pp. 2141–2148.
Wolff, E.H.P., Gerritsen A.W. and van den Bleek, C.M. Can. J. Chem. Eng. **71** (1993), 83.
Wu, Sun, Anthony, Jia, Grace. Fuel **85** (2006), pp. 2213–2219.
Yrjas, P., Iisa, K. and Hupa, M. Fuel, **74** (1995), pp.395–400.

FATE OF PHOSPHORUS DURING CO-COMBUSTION OF RAPESEED CAKE WITH WOOD

P. Piotrowska*[1], M. Zevenhoven[1], M. Hupa[1], K. Davidsson[2], L.E. Åmand[2], E. C. Zabetta[3], V. Barišić[3]

1 Process Chemistry Centre, Åbo Akademi University, Turku, Finland
2 Department of Energy and Environment, Division of Energy Technology, Chalmers University of Technology, Gothenburg, Sweden
3 R&D Department, Foster Wheeler Energia Oy, Varkaus, Finland

Abstract: Recent studies show that deposit formation and agglomeration in fluidized bed boilers may be aggravated by a high phosphorus content besides alkali metals, chlorine and sulphur in a fuel. This paper presents the fate of phosphorus during co-combustion of wood chips and wood pellets with rapeseed cake pellets, a high phosphorus fuel in a 12MW CFB boiler. 12 hour tests with 12% and 18% (energy basis) of rapeseed cake with wood were performed with and without limestone addition. All fuels were characterised by means of standard fuel analyses combined with chemical fractionation. Retrieved ash samples were analysed using wet chemical analysis complemented with SEM/EDXA. Gaseous alkali metal chlorides as well as HCl and SO_2 were measured upstream of the convective pass at a flue gas temperature of 800°C where also the deposit samples were collected with a deposit probe. The composition of deposits was studied with SEM/EDXA. Analyses of bed material particle cross-sections showed phosphorus compounds present within a K-silicates matrix between the agglomerated sand particles, indicating direct attack of gaseous potassium compounds on the bed surface followed by adhesion of rich in phosphorus ash particles. Build-up of the deposits took place mainly on the windward side of the probe; where up to 9 wt-% of phosphorus was present. SEM/EDXA shows that rapeseed cake addition caused an increase of K, Na besides P indicating presence of low melting phosphate salts in the deposits. During limestone addition in the deposit samples the increase of Cl could be noticed however no significant change in P content was observed. This paper shows that agglomeration and fouling when co-firing rapeseed cake may be linked to its high content of organically bonded phosphorus - phytic acid salts; together with high content of water soluble fraction of alkali metals chlorides and sulphates in the fuel mixture.
Keywords: rapeseed cake, co-combustion, phosphorus, agglomeration, fouling

INTRODUCTION

In order to save fossil fuels and prevent global warming, biomass, the main one among renewable sources of energy, have been given increased attention. Challenges connected with biomass combustion in fluidized bed boilers, are caused by ash chemistry which may induce agglomeration, fouling and corrosion. It is commonly known that alkali metals, chlorine and sulphur are the main factors lowering the first melting temperature of ash (Hupa M., 2008; Jenkins B.M. et al., 1998). However, recent studies showed that these problems may be aggravated by a high phosphorus content in the fuel (Barišić V. et al., 2008; Coda Zabetta E. et al., 2008; Lindström E. et al., 2007; Nevalainen H. et al., 2008). An interesting example of a fuel rich in phosphorus, alkali metals and chlorine is Rapeseed Cake, a residue from the production of Rapeseed Methyl Ester (RME). Interactions of phosphorus with other ash forming elements during combustion are not fully understood and are subject of this paper.

The work is a continuation of a study on the role of limestone in preventing agglomeration and slagging during CFB combustion of high-phosphorus fuels (Barišić V. et al., 2008). Here the investigation covers both agglomeration and deposit formation during co-combustion of a mixture of wood chips and wood pellets with rapeseed cake pellets. Results are supplemented with gaseous chlorides, sulfates, and alkali metal chlorides present in the beginning of the convective pass.

* corresponding author: ppiotrow@abo.fi

EXPERIMENTAL

Boiler

The 12 MWth CFB boiler located at Chalmers University of Technology, shown in Fig. 1, was used for the tests. The boiler is large enough to be representative for a semi-industrial CFB boiler and is described in detail elsewhere (Åmand L.-E., 2004)

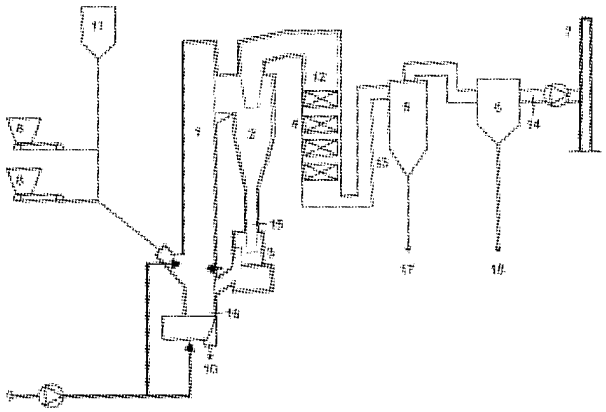

Fig. 1 Schematic of the boiler.
1: furnace, 2: primary cyclone, 3: particle seal, 4: convection pass, 5: secondary cyclone, 6: bag-house filter, 7: stack, 8: fuel bunkers, 9: air, 10: bottom material removal, 11: bed sand, 12: measurement position before convection pass, 13: measurement position after convection pass, 14: measurement position after bag-house filter, 15: cyclone leg material sampling spot, 16: bed material sampling spot, 17: secondary cyclone ash sampling, 18: bag-house filter ash sampling

Combustion experiments

The experimental plan consisted of 4h preliminary tests and 12h tests listed in Table 1. The varied parameters were the rapeseed cake (RC) ratio and the addition of limestone ($CaCO_3$) to the bed consisting of silica sand. During the tests wood chips (WC) and wood pellets (WP) were used as a base fuel. The highest share of RC was co-combusted during a 4h test here named as WNL45_preliminary. This test was preceded with two other 4h preliminary tests during which 12 and 21% (energy basis) of RC was co-fired respectively. During tests WNL12 and WL18 a RC ratio of 12 and 18% (energy basis) was used, respectively. In the latter test limestone was added. Both tests lasted approximately 12h and were preceded with the reference tests, reference_WNL and reference_WL, when no RC was co-combusted however limestone was used in the latter one. The limestone was taken from Ignaberga in south Sweden. The operational conditions were chosen to represent a typical case of an industrial CFB boiler with a bottom bed temperature of 850°C and an excess air ratio of 1.2. The flue gas temperature was maintained at the level of 800°C before the convective pass and around 150°C in the secondary cyclone and bag house filter in all tests. The load was kept at about 6 MW in all tests corresponding to a fluidizing velocity of about 5 m/s in top of the furnace. 12 MW is an overload used for special research activities. Samples from all outgoing solid material streams - namely bed material, secondary

Table 1 Rapeseed cake and wood co-combustion tests

test name	test duration [h]	RC ratio [$\%_{en}$]	Fuel load [kg ds/h]		Ash with fuel[1] [kg ash/h]		Lime addition [kg/h]	Bed regen. [kg sand/h]	ash balance[2]
			RC	WP+WC	RC	WP+WC			
WNL12_preliminary	4	12	136	1175	9,4	5,1	0,0	0,0	47,2
WNL21_preliminary	4	21	229	1048	15,9	4,5	0,0	0,0	37,2
WNL45_preliminary	4	45	524	771	36,3	3,3	0,0	4,4	37,5
Reference_WNL	16	0	0	1309	0,0	6,4	0,0	0,0	160,1
WNL12	13	12	135	1190	9,6	4,9	0,0	0,0	66,7
Reference_WL	14	0	0	1328	0,0	7,0	54,5	0,0	52,9
WL18	12	18	196	1101	14,0	7,6	54,9	0,6	38,1

RC – rapeseed cake; WP – wood pellets; WC– wood chips; $\%_{en}$ – percentage on energy basis;

[1] – ash content in the fuel measured at ChUT; [2] – $(ash_{out}/ ash_{in})*100\%$

cyclone and bag filter, were collected at the end of each test. Deposit samples were collected on steel rings which were fitted on an air-cooling probe situated in the middle of the flue-gas stream before the convective pass. The surface temperature of the steel rings was set to 500°C during all three preliminary tests and 480°C in case of other 12h tests to simulate a superheater tube.

Analyses of gases

In the convective pass gaseous HCl and SO_2 were measured with Fourier Transform Infrared (FT-IR) spectroscopy. In addition gaseous alkali chlorides were continuously measured at this position using the In-situ Alkali Chlorides Monitor (IACM) developed by Vattenfall. The instrument uses a sampling time of 5-10 seconds. The detection limit at a 5 meter measuring length (width of the flue gas channel) is 1 ppm for KCl and NaCl (Kassman H. et al., 2006). HCl emissions were measured by means of FT-IR and SO_2 with non dispersive ultra-violet (NDUV) analyzer; the results were used for the mass balances calculation over the boiler.

Analyses of fuels and ash samples

Fuel samples (WP, WC and RC) were analyzed using standard fuel analysis and chemical fractionation. Chemical fractionation is a method based on selective consecutive leaching by water (H_2O), 1M ammonium acetate (NH_4Ac) and 1M hydrochloric acid (HCl) (Baxter L.L., 1994; Benson S.A., 1985; Skrifvars B.-J. et al., 1998; Zevenhoven M. 2001, Zevenhoven M. et al., 2001, 2004). The increasingly aggressive solvents leach samples into a series of four fractions (including the unleached residue). The untreated samples, the liquid fractions and the remaining solids were analyzed by an external laboratory according to Swedish standards. Ash samples from all outgoing solid material streams were collected and analyzed quantitatively according to ASTM D3683 and ASTM D3682 by the same external laboratory. Additionally semi quantitative analyses of bottom ash and deposit samples (from the windward (0°) side of the deposit ring) were performed by means of SEM/EDX. Hereto, ash samples were mounted on carbon tape and covered with a thin carbon layer. Also the bed material particle cross-sections were studied by means of SEM/EDX spot analyses. Hereto investigated samples of bed material particles were embedded in epoxy and polished with ethanol to obtain cross-sections and smooth surface that was consecutively covered with carbon for SEM/EDXA.

Table 2 Properties of fuels

Fuel		RC	WP	WC
Ash[1]	[% db]	7,5	0,4	0,6
HHV	[MJ/kg db]	22,157	20,193	19,980
LHV	[MJ/kg db]	20,672	18,873	18,665
C	[% db]	49,900	50,600	49,900
H	[% db]	6,900	6,100	6,000
N	[% db]	5,100	0,100	0,200
O (calculated)	[% db]	29,62	42,800	43,300
S	[% db]	0,720	0,006	0,007
Cl	[% db]	0,26	na	na
Si	[mg/kg db]	261,0	165,0	346,0
Al	[mg/kg db]	43,4	36,5	207,0
Fe	[mg/kg db]	152,0	43,9	204,0
Ti	[mg/kg db]	3,6	1,8	8,4
Mn	[mg/kg db]	59,7	112,0	166,0
Ca	[mg/kg db]	7040,0	783,0	1100,0
Mg	[mg/kg db]	4500,0	160,0	224,0
P	[mg/kg db]	11500,0	55,9	120,0
Na	[mg/kg db]	4660,0	28,9	49,7
K	[mg/kg db]	12300,0	432,0	594,0

[1]-ashed at 550°C; [2]-calculated; RC-rapeseed cake, WP-wood pellets, WC-wood chips; ar-as received, db-on dry basis; na-not available (below detection limit of 500 ppm)

RESULTS AND DISCUSSION

Fuel analyses

Standard fuel analysis, shown in Table 2, indicates clearly the main ash forming matter constituents of

rapeseed cake (RC) pellets are potassium and phosphorous, an additional feature is the high content of chlorine. High ash content of RC results in up to 11 times higher RC ash inflow compared to WP and WC ash inflow during test WNL45-preliminary (Table 1).

Results from the chemical fractionation are presented in Fig. 2. This figure shows the elemental composition of the fuel divided into four obtained fractions, facilitating the comparison between the chemical compositions of the co-combusted fuels. Leaching with water releases simple soluble salts, usually volatile alkali compounds, with ammonium acetate the ion exchangeable part of the fuel ash forming matter is released; in the final step the acid soluble inorganic salts are leached while in the rest (insoluble) fraction mainly silicates are present but also sulphur and chlorine when covalently bonded into the organic structure of the fuel. The chemical fractionation results show that the difference between woody biomass and rapeseed cake is not only the ash content. Woody biomass ash forming matter consists mainly of potassium leached in water and calcium leached by ammonium acetate indicating its association with carboxylic groups of hemicelluloses and calcium oxalate (Werkelin J., 2008; Zevenhoven M., 2001). Only a small amount of phosphorus is found present in the fraction leached by water and hydrochloric acid.

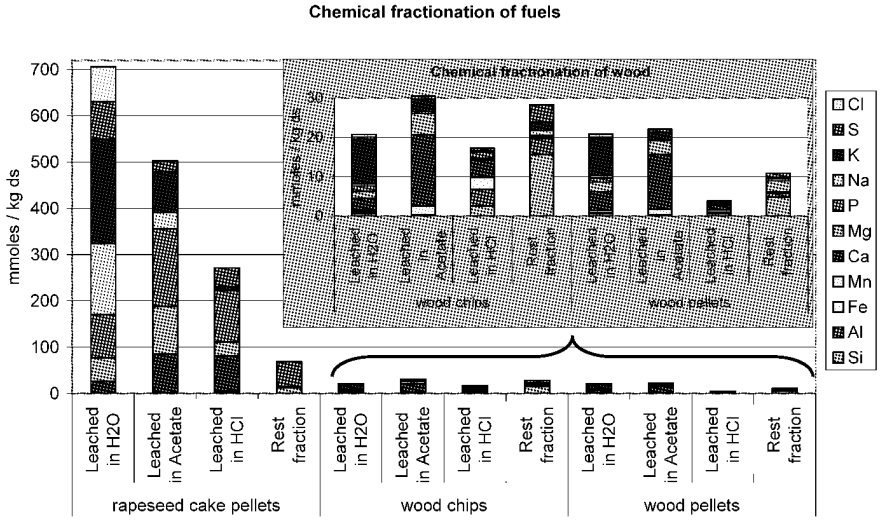

Fig. 2 Chemical fractionation results of co-combusted fuels

In rapeseed cake high shares of phosphorus are present. This phosphorus is leached in all three procedure steps, indicating different associations. A large part of the rapeseed cake ash forming matter is leached by water indicating simple salts like alkali chlorides, sulphates and phosphates (Werkelin J., 2008; Zevenhoven M., 2001). As shown in previous studies (Pontoppidan K. et al., 2007) around 70% of total phosphorus present in rapeseed cake can be associated with phytic acid (myo-inositol hexaphosphate) and its degradation products (mainly inositol pentaphosphate). These phosphorus compounds are probably found in the ammonium acetate and hydrochloric acid fractions. The solubility depends strongly on the type of complexes the phytic acid is forming with cations and proteins (Cheryan M., 1980; Shahidi F., 1990). In the hydrochloric acid fraction mainly calcium, magnesium, but also iron, zinc and manganese were found next to phosphorus.

Mass balance and distribution of ash in the CFB boiler

The ash balance has been calculated for each test and results are presented in Table 1. For the calculation all the incoming and outgoing inert flows were used. Ash forming matter entering the boiler with the fuels but also silica entering as substitute for removed bed material and ash produced by limestone addition were considered to constitute the incoming streams. In order to determine the limestone ash flow, the assumption that it fully converts to CaO to form $CaSO_4$ was made. The closure of the ash balances is shown in Table 1 as the ratio between the total ash outgoing flows to the total ash incoming flows in the percentage form. The closure for RC co-combustion tests was poor indicating ash accumulation in the system. This was proven after the 4 hour tests that resulted in heavy build up of agglomerates in the particle seal of the boiler. A total shut down of the boiler happened, and the restart was not possible until the particle seal and tube from the cyclone was cleaned from large agglomerates. The boiler was started with fresh bed material after which reference test, reference_WNL, was performed. The mass balance closure for reference_WNL of 160% suggests that ash still present elsewhere in the boiler was removed during the reference case.

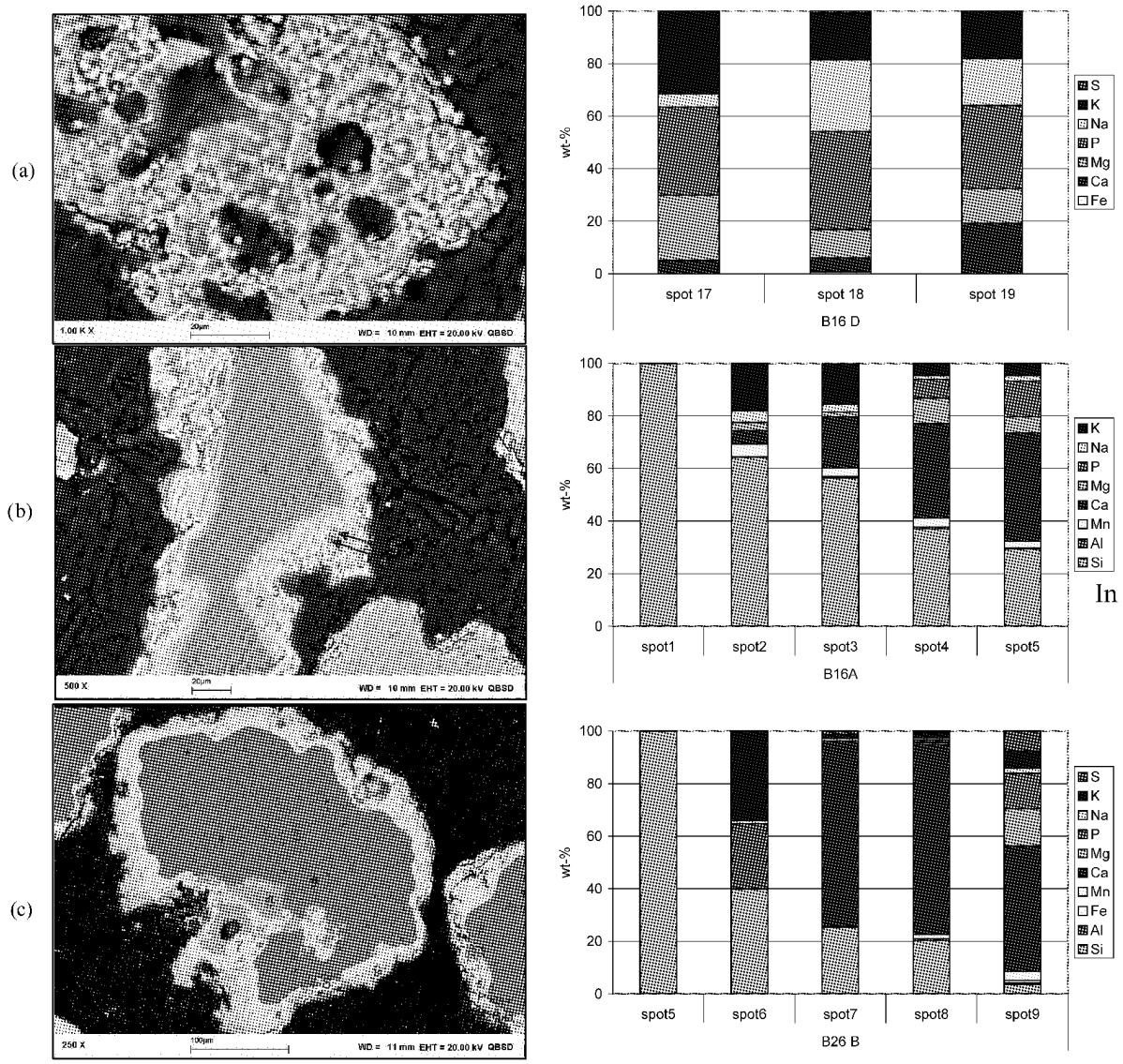

Fig. 3 Bed material cross-sections (a) RC ash particle - Test WNL45_preliminary; (b) bed material particle - WNL45_preliminary; (c) bed material particle - Test WL18

Elemental flows were calculated using the quantitative analyses of the incoming and outgoing inert streams. The inflow of the particular element was defined as 100%, and thus the elemental distribution over outgoing streams could be calculated. Results are shown in Table 3. During test WNL12, a forced agglomeration test was performed by shutting off bed regeneration and bottom ash removal (indicated with a "-" in Table 3). The concentration of chlorine in bottom ash samples could not be analyzed due to method detection limit (500 ppm). Na and K show a similar behaviour in the boiler and are considered here as a combined fraction of alkali metals. The values presented in Table 3 give an indication of the pathway that ash forming matter is taking through the boiler. It can be seen that high phosphorus and alkali metals accumulation in the boiler and/or convective pass took place. The rest was found in the secondary cyclone ash. In contrast, sulfur and chlorine form small particles that were captured in the bag filter or were emitted in the form of sulfur dioxide or hydrogen chloride. During test with lime addition (WL18), next to obvious sulfur and chlorine retention, a small increase of K+Na in the bag filter fraction occurred, most probably caused by increased formation of alkali metal chlorides as shown in Table 4.

Table 3 Elemental distribution over outgoing ash fractions – inflow of the element is defined to be 100%

Test name		Ash fractions [%]				
		BA	SC	BF	E	Δ
P	WNL12	-	21	4	-	75
	WL18	1	23	4	-	72
K+Na	WNL12	-	22	8	-	70
	WL18	2	22	12	-	64
Mg	WNL12	-	30	13	-	57
	WL18	2	26	8	-	64
S	WNL12	-	9	12	40	40
	WL18	2	5	7	1	85
Cl	WNL12	-	4	17	60	18
	WL18	-	7	28	5	60

BA – bottom ash; SC – secondary cyclone; BF – bag filter; E- emissions;

$\Delta = \left(100\% - \frac{Out_i}{In_i}\% \right)$ = accumulation + error

Table 4 Measurements at the beginning of convective pass

test name	RBU	KCl+NaCl	HCl	SO_2
	[g/m²*h]	[ppm_v dry flue gas, 6% O_2]		
WNL45_preliminary	16,9	114	171	140
WNL_reference	1,2	1	0	0
WNL12	2,6	14	44	52
WL18	6,3	49	44	3

The role of P in agglomeration

Figure 3(a) a rapeseed cake ash particle found in the bottom ash sample during test WNL45_preliminary is shown. Within the ash particle the high concentration of phosphorus next to alkali metals can be noticed (about 35 wt-%) indicating that formation of low melting RC ash particles could take place (Lindström et al., 2007). The analyses of bed material cross-sections as shown in Figure 3(b) indicate a reaction of potassium compounds with bed material forming low melting alkali silicates (Öhman M., 1999) followed by adhesion of RC ash particles rich in phosphorus. Probably among others potassium phosphates reacted with silica initiating agglomerates formation Barišić V. et al. (2008). The formation of low melting potassium-calcium-silicates during biomass combustion was discussed by Öhman M. (1999) and seems to be valid also in the present co-combustion tests. Addition of limestone changed the combustion behavior by decreasing agglomeration tendency (Fig. 3(c)). The sand particles were coated with a calcium rich layer preventing low melting potassium-silicates formation. This is in agreement with studies done by Barišić et al. (2008) regarding the same experiments.

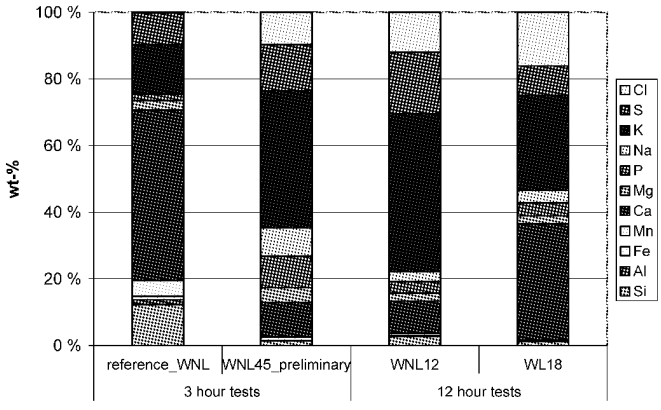

Fig. 4 Windward side deposits composition

The role of P in deposit formation

Rates of deposit build-up (RBU) presented in Table 4 indicate that co-firing of wood with RC showed high fouling rates; rapeseed cake addition from 0-45% on energy basis caused an increased RBU most probably due to alkali chloride condensation. However, the deposit formation was also aggravated by fine phosphates particles as shown in Fig. 4 where the elemental analysis done with the use of SEM/EDX is presented. Figure 4 shows not only an increase of K, Na in the deposit samples but also of P (9 wt-%). Increased concentration of (KCl+NaCl) in the dry flue gas entering the convective pass can be noticed during test WL18 (Table 4). This could be a result of limestone addition which by binding S didn't allow sulfation of (KCl+NaCl) (Kassman H. et al., 2006) and as a consequence higher RBU were observed. No influence of limestone addition can be noticed on HCl entering the convective pass (Table 4) most probably due to measurement uncertainties. Limestone addition seemed to have no impact on the amount of phosphorus (Fig. 4) present in the windward side deposits.

CONCLUSIONS

The fate of phosphorus was investigated during co-combustion tests of rapeseed cake with mixture of wood chips and wood pellets. Chemical fractionation shows that P in rapeseed cake has different chemical forms: easily soluble (K+Na) phosphates or organically associated phytic acid salts. Rapeseed cake, rich in P and (K+Na), forms ash particles of probably partially molten phases that are aggravating agglomeration, slagging and fouling upon combustion. The elemental distribution over outgoing ash fractions shows that P is mainly found in the secondary cyclone if not accumulated in the system. Formation of low melting K-silicates followed by adhesion of ash particles, which are rich in P, results in bed agglomeration. Limestone addition causes coating of sand particles preventing low melting silicates formation. Rapeseed cake addition causes an increased rate of deposit build-up (RBU). Windward side of 3-hour exposed ring deposit consists mainly of alkali metal chlorides and sulfates with up to 9 wt-% of P. Limestone addition does not have significant influence on P content in the deposit. Combustion of the studied rapeseed cake results in high concentrations of (KCl+NaCl) but also causes increase in HCl (g) and SO_2 (g) in the beginning of the convection pass. Co-firing of rapeseed cake with wood turned out to be a problematic case however some 18% of rapeseed cake on energy basis could be co-fired with wood when limestone is added to the bed.

ACKNOWLEDGEMENTS

This study was carried out as part of the SAFEC project. The financial support of Academy of Finland the Graduate School of Chemical Engineering is gratefully acknowledged. Results of IACM could be used with a permission of Vattenfall AB, which is highly appreciated. Special thankfulness goes to Matti Hiltunen for his key contribution in the early phases of this work. Linus Silvander, Tor Laurén and Piia Leppäsalo are kindly acknowledged for help with the experimental work. Akademiska Hus and the measurement team at the ChUT are kindly acknowledged for their continuous efforts to operate the boiler.

REFERENCES

Åmand L.-E., Leckner B. "Metal emissions from co-combustion of sewage sludge and coal/wood in fluidized bed" Fuel, 83 (2004) 1803-1821

Barišić V., Åmand L.-E., Coda Zabetta E. "The role of limestone in preventing agglomeration and slagging during CFB combustion of high phosphorus fuels" World Bioenergy, Jönköping (Sweden), May 2008

Baxter L.L. "Pollutant emission and deposit formation during combustion of biomass fuels", Livermore (CA, USA), 1994

Benson S.A., Holm P.L. "Comparison of inorganic constituents in three low-rank coals" Ind. Chem. Eng. Prod. Res. Dev., 24 (1985) 145-149

Cheryan M. "Phytic acid interactions in food systems" Critical reviews in food science and nutrition, 13: 4 (1980)

Coda Zabetta E., Barišić V., Peltola K., Hotta A. "Foster Wheeler Experience with biomass and waste in CFBs" Proceedings of the 33rd Clearwater Conference, Clearwater (Florida, U.S.A.), June 2008

Hupa M. "Ash behavior in fluidized bed combustion-recent research highlights" Proceedings of the 9th International Conference on Circulating Fluidized Beds, Hamburg (Germany), May 2008

Jenkins B.M., Baxter L.L., Miles Jr. T.R., Miles T.R. "Combustion properties of biomass" Fuel processing Technology, 54 (1998) 17-46

Kassman H., Andersson C., Högberg J., Åmand L.-E., Davidsson K., "Gas Phase Alkali Chlorides and Deposits during Co-Combustion of Coal and Biomass", FBC2006-99, Proceedings of 19th International Conference on Fluidized Bed Combustion, Vienna (Austria), May 21-24 2006

Lindström E., Sandström M., Boström D., Öhman M. "Slagging characteristics during combustion of cereal grains rich in phosphorus" Energy&Fuels, 21 (2007) 710-717

Nevalainen H., Leino T., Tourunen A., Hiltunen M., Coda Zabetta E. "Deposits and emissions during the co-combustion of

biodiesel residue with coal and biomass in a CFB pilot" Proceedings of the 9th International Conference on Circulating Fluidized Beds, Hamburg (Germany), 2008 May 2008

Öhman M. Experimental studies on bed agglomeration during fluidized bed combustion of biomass fuels. PhD thesis, Department of Chemistry, Umeå University; 1999, ISBN91-7191-646-6

Pontoppidan K., Pettersson D., Sandberg Ann-Sofie "The type of thermal feed treatment influences the inositol phosphate composition" Animal feed Science and Technology 132 (2007)

Shahidi F. "Canola and rapeseed: production, chemistry, nutrition and processing technology", Van Nostrand Reinhold Company Inc. (AVI Book); 1990, ISBN 0-442-00295-5

Skrifvars B.-J., Blomquist J.-P., Hupa M., Backman R. "Predicting the ash behavior during biomass combustion in FBC conditions by combining advanced fuel analysis with thermodynamic multicomponent equilibrium calculations" Proceedings of the 15th Annual International Pittsburgh Coal Conference, Pittsburgh, (PA, USA), 1998

Werkelin J. "Ash forming elements and their chemical forms in woody biomass fuels" PhD thesis, PCC, Åbo Akademi University; 2008, ISBN 978-952-12-2125-5

Zevenhoven-Onderwater M., "Ash-Forming Matter in Biomass Fuels" PhD thesis, Department of Chemical Engineering, Åbo Akademi University; 2001, ISBN 952-12-0813-9

Zevenhoven M., Skrifvars B.-J., Yrjas P., Hupa M., Nuutinen L., Laitinen R. "Searching for improved characterisation of ash forming matter in biomass", Proceedings of the 16th International Conference on Fluidized Bed Combustion, Reno (NV, USA) 2001

Zevenhoven M., Yrjas P., Backman R., Skrifvars B.-J., Hupa M. "The Åbo Akademi database-fuel characterization", FBC2005-78093, Proceedings of the 18th International Conference on Fluidized Bed Combustion, Toronto (Ontario, Canada), May 18-23 2005

SULPHATION OF CaO-BASED SORBENT MODIFIED IN CO_2 LOOPING CYCLES

Vasilije Manovic[1], Edward J. Anthony[1], Davor Loncarevic[2]

1CANMET Energy Technology Centre-Ottawa, Natural Resources Canada, 1 Haanel Drive, Ottawa, Ontario, Canada K1A 1M1

2Department of Catalysis and Chemical Engineering, Institute of Chemistry, Technology and Metallurgy, Njegoseva 12, 11000 Belgrade, Serbia

Abstract: CaO-based looping cycles for CO_2 capture at high temperatures are based on cyclical carbonation of CaO and regeneration of $CaCO_3$. The main limitation of natural sorbents is the loss of carrying capacity with increasing numbers of reaction cycles, resulting in spent sorbent ballast. Use of spent sorbent from CO_2 looping cycles for SO_2 capture is a possible solution investigated in this study. Three limestones were investigated: Kelly Rock (Canada), La Blanca (Spain) and Katowice (Poland). Carbonation/calcination cycles were performed in a tube furnace with original limestones and samples thermally pretreated for different times (i.e., sintered). The spent sorbent samples were sulphated in a thermogravimetric analyzer. Changes in the resulting pore structure were then investigated using mercury porosimetry. Final conversions of both spent and pretreated sorbents after longer sulphation times were comparable or higher than those observed for the original sorbents. Maximum sulphation levels strongly depend on sorbent porosity and pore surface area. The shrinkage of sorbent particles during calcination/cycling resulted in a loss of sorbent porosity ($\leqslant$48%), which corresponds to maximum sulphation levels ~55% for spent Kelly Rock and Katowice. However, this is ~10% higher than for the original samples. By contrast, La Blanca limestone had more pronounced particle shrinkage during pretreatment and cycling, leading to lower porosity, <35%, resulting in sulphation conversion of spent samples <30%, significantly lower than for the original sample (45%). These results showed that spent sorbent samples from CO_2 looping cycles can be used as sorbents for SO_2 retention if significant porosity loss does not occur during CO_2 reaction cycles. For spent Kelly Rock and Katowice samples final conversions are determined by the total pore volume available for the bulky $CaSO_4$ product.

Keywords: CaO-based sorbent, CO_2 capture, sulphation, SO_2 retention

INTRODUCTION

Sulphation is the reaction between SO_2 and CaO widely used for SO_2 retention from flue gas produced during combustion of fossil fuels. This reaction has been investigated with reference to fluidized bed (FBC) conversion technologies for utilization of fossil fuels, such as coal and petroleum coke (Anthony and Granatstein, 2001). The advantage of the approach is in situ SO_2 retention by sorbent that calcines at high temperature. Sulphation is a typical heterogeneous gas-solid reaction during which deactivation occurs because of solid product formation at the reacting surface. The product of sulphation, $CaSO_4$, covers the available surface area of CaO and diffusion through the product layer becomes the limiting step for the process. Gas diffusion control in the pores of partially sulphated sorbent can continue until the product layer thickness reaches the point where diffusion in that layer becomes the limiting step. Reaction rate at the start of sulphation, as well as the shift to the diffusion controlled step, depends on available surface area for reaction. The maximum surface area of CaO, 110 m^2/g (Borgwardt, 1989), was obtained for very fine limestone particles (2-10 μm) under mild calcination (700°C). This surface area for nascent CaO is available only immediately after calcination, decreasing asymptotically with sintering, reaching a much lower final value. The final surface area depends on the precursor type, calcination conditions, CO_2, and H_2O concentrations.

CaO-based sorbents were recently intensively investigated for CO_2 capture in carbonation/calcination cycles (Anthony, 2008; Lysikov et al., 2007; Fennell et al., 2007; Abanades et al., 2005). During looping cycles, sorbents change their morphology as a result of sintering (Sun et al., 2007; Abanades and Alvarez, 2003; Manovic et al., 2009c). Consequently, sorbent activity decreases with increasing numbers of reaction cycles (Alvarez and Abanades, 2005; Grasa and Abanades, 2006) causing economic penalties for CaO-based CO_2 looping cycle technology (Abanades et al., 2007; MacKenzie et al., 2007). Thus, different possibilities to improve sorbent utilization in CO_2 cycles were investigated (Manovic and Anthony, 2009). It was found that spent sorbent after hydration had excellent sulphation performance, with conversions after a few hours that were typically >70% and sometimes almost quantitative (Manovic and Anthony, 2007; 2008; Manovic et al.,

2008a). Moreover, investigation of the pore structure of spent sorbent (Manovic and Anthony, 2007; 2008) or sorbent pretreated at high temperatures (Manovic et al., 2009a) showed that small pores disappeared, resulting in low ratios of pore surface area vs. porosity. The sulphation tests (Manovic and Anthony, 2008) showed that reaction rate was slower at the beginning, but its shift to slow reaction stage was less pronounced and occurred later, resulting in higher sorbent activity during longer sulphation periods. For prolonged sulphation times, comparable with residence times in FBC, conversions that are higher than those observed for the original sorbents may be expected for sorbents with modified pore structure. This concept led to the investigation of spent/modified sorbents, the results of which are presented here.

EXPERIMENTAL

Three limestone samples were used in this study: Kelly Rock (KR-Canada), particle size 0.300-0.425 mm, La Blanca (LB-Spain), particle size 0.400-0.600 mm, and Katowice (KT-Poland), particle size 0.400-0.800 mm. The X-ray fluorescence (XRF) elemental analyses of these samples are given elsewhere (Manovic et al., 2009a). It should be noted that LB and KT are very pure limestones, while KR contains 6% impurities with the highest concentration of impurities being provided by SiO_2 and Al_2O_3, indicating the presence of silicates and aluminosilicates in the sorbent. On the other hand, the content of Na_2O in LB (1.07%) is unusually high for limestones.

Four different types of samples from each limestone were examined with regard to their sulphation performance: (i) original sample, (ii) sample after 30 CO_2 cycles in a tube furnace (TF), (iii) sample pretreated at high temperatures, and (iv) sample pretreated in CO_2 (in a TF) at 1000°C for 24 h, followed by 30 CO_2 cycles. Calcination was performed in 100% N_2 and carbonation in 100% CO_2, both for 15 min, isothermally at 800°C. The 30 calcination/carbonation cycles were done with 3.0 g limestone samples and gas flow rate of 500 cm^3/min. The pretreated samples (iii) were obtained in the TF at high temperatures (1000 and 1100°C) in an atmosphere of 100% CO_2 for 24 h (also 6 and 64 h at 1000°C). The flow rate of CO_2 was 200 cm^3/min and samples used were 3.0 g. At the end of the experiments, during cooling, the TF atmosphere was replaced by 100% N_2 to prevent reaction of hot samples with atmospheric CO_2 and moisture. The obtained calcines were characterized by nitrogen adsorption/desorption tests (Manovic et al., 2009a), and by mercury porosimetry.

A Mettler Toledo TGA/SDTA851e/LF/1100°C instrument was used for TGA sulphation runs. Sulphation tests were done at 850°C, typically for 15 h. Synthetic flue gas mixture (15% CO_2, 3% O_2, 0.5% SO_2 and N_2 balance) was used. Sample masses in the TGA experiments were equivalent to ~15 mg CaO. Sulphation conversion was calculated on the basis of the mass change during TGA runs, assuming that mass increase occurred only due to formation of $CaSO_4$. Pore size and volume distribution were determined by mercury intrusion porosimetry (Carlo Erba 2000 porosimeter with Macropores unit 120, software Milestone 200).

RESULTS AND DISCUSSION

The pore surface area and porosity of the original limestones, corresponding calcines, thermally pretreated samples, and samples spent in cycles are given in Table 1. Porosity of limestones was 3.00-4.63%, increasing after calcination to 47.45-48.80% due to the lower molar volume of CaO *vs.* $CaCO_3$. Carbonation/calcination cycles led to loss of porosity of ~2% for KR and KT, and 11% for LB. Interestingly, KR and KT samples pretreated at high temperature showed slightly increased porosity, while LB lost further porosity. Changes in pore volume during pretreatment/cycles can be attributed to particle size changes (shrinkage/growth-see Table 1), as confirmed by helium pyncnometry (Manovic et al., 2009b). Drastic shrinkage of LB is seen during pretreatment/cycles (38.23% for the pretreated sample). This is unfavorable, reducing the theoretical sulphation maximum, which is 30-35% for LB, significantly lower than for the original sample after calcination (55.9%). On the other hand, maximum calculated sulphation values for pretreated KR and KT samples were higher (67.77 and 65.51%, respectively) in comparison with values for the original samples (64.98 and 57.52%).

Pore size distribution is another parameter determining sorbent performance during sulphation (Fig. 1). General tendencies are seen, the most pronounced being the shift of pore size distribution to larger pores in samples pretreated for 24 h. The peak of pore size distribution after pretreatment was at ~1000 nm for KR and KT and at ~300 nm for LB. The similar behavior of KR and KT can be seen for samples that experienced carbonation/calcination cycles, where cycling led to bimodal pore size distribution. The distribution shift to larger pores was especially pronounced for the original KT sample after CO_2 cycles, while pretreated KR and KT after cycles showed the reappearance of smaller pores (peak at ~50 nm), confirming the self-recovery of sorbent surface morphology of pretreated samples during CO_2 cycles. The original LB samples after CO_2 cycles did not show a shift of pore size distribution to larger pores nor bimodal distribution. However, pretreated LB recovered small pores, which were even smaller than for the original samples. The SEM investigation of sample morphologies is presented elsewhere (Manovic et al., 2009a), and is in agreement with mercury

porosimetry measurements.

Table 1 Results of mercury porosimetry analyses

Sample[a]	S_{Hg} [m^2/g]	$(S_{BET})^b$ [m^2/g]	Porosity [%]	Shrink[c] [%]	Max. sulphation[d] [%]
KR-limestone	1.22	(n.d.)	4.63	n.a.	n.a.
KR	7.18	(4.7)	48.80	4.12	63.01
KR-30cyc	4.00	(2.5)	46.13	9.37	56.61
KR-24h	1.90	(0.8)	49.85	2.06	65.72
KR-24h-30cyc	10.78	(8.4)	44.66	12.25	53.35
LB-limestone	0.23	(n.d.)	3.00	n.a.	n.a.
LB	22.45	(23.5)	47.45	10.80	54.21
LB-30cyc	13.35	(10.1)	36.43	31.52	34.40
LB-24h	1.54	(1.8)	32.86	38.23	29.38
LB-24h-30cyc	12.50	(3.9)	34.85	34.49	32.11
KT-limestone	0.39	(n.d.)	3.45	n.a.	n.a.
KT	15.19	(13.5)	47.78	7.90	55.78
KT-30cyc	8.98	(6.3)	45.62	12.06	51.14
KT-24h	1.92	(1.0)	51.03	1.63	63.53
KT-24h-30cyc	9.63	(7.5)	48.53	6.45	57.48

[a]Sample designations: KR, LB, KT=calcined limestone, 30cyc=30 carbonation/calcination cycles, 24h= pretreatment in CO_2 for 24 h, 24h-30cyc=pretreatment in CO_2 for 24 h followed by 30 carb./calc. cycles.
[b]Manovic at al., 2009a.
[c]Shrink - relative loss of pore volume = (theoretical porosity - measured porosity)/(theoretical porosity); theoretical porosity is calculated with assumption that particle dimensions are constant and that pore volume change occurs solely as a result of difference in molar volumes of $CaCO_3$ (37 cm^3/mol) and CaO (17 cm^3/mol).
[d]Maximum sulphation - calculated assuming that particle dimensions are constant and that the product, $CaSO_4$, fills all available space in the sorbent particle.

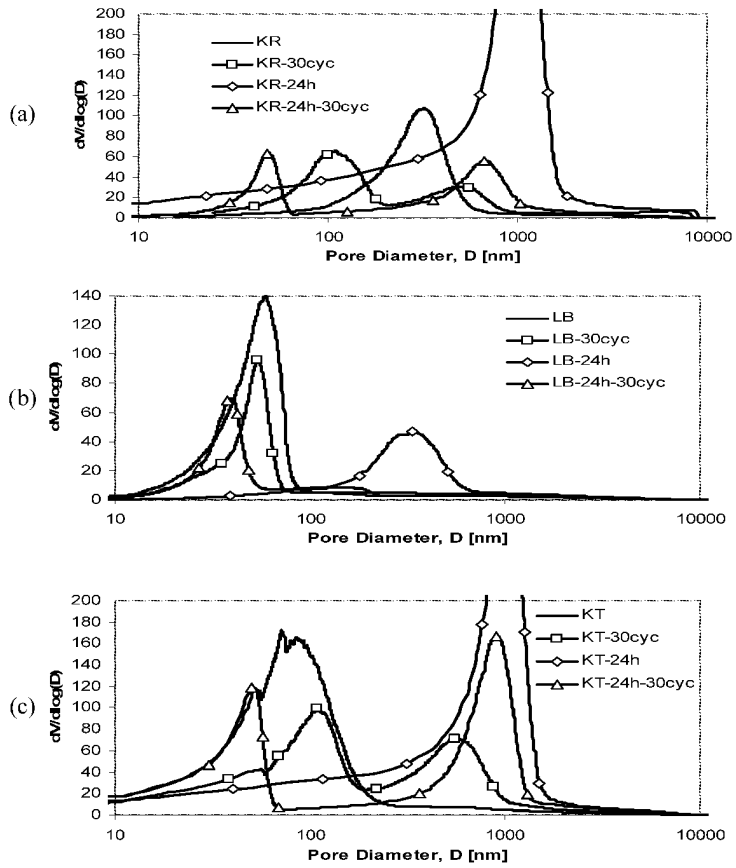

Fig. 1 Pore size distribution (Hg porosimetry) of original, pretreated and/or cycled samples: (a) Kelly Rock, (b) La Blanca, and (c) Katowice. Sample designation can be seen from Table 1

The conversions for original and pretreated/spent samples during TGA sulphation runs are shown in Fig. 2. There is a clear difference in the behavior of LB *vs.* that of KR and KT. Conversions of pretreated/spent LB are one half those for the original samples, as a result of porosity loss (Table 1). The conversions are close to the calculated maximum, 30-35%. This shows that LB spent in CO_2 cycles is not suitable for SO_2 retention. Similar differences in LB performance *vs.* other limestones were noted earlier when CO_2 capture was investigated (Manovic et al., 2008b).

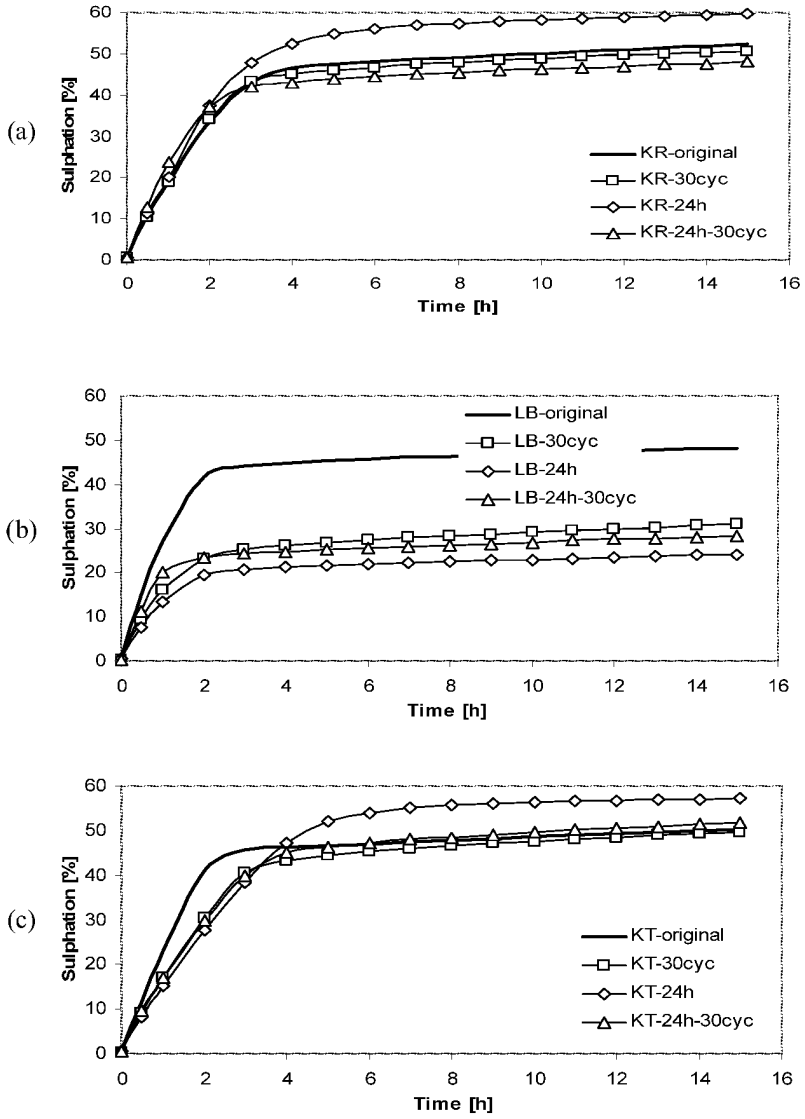

Fig. 2 Sulphation conversions in TGA at 850°C, 0.5% SO_2, 15% CO_2, 3% O_2, and N_2 balance: (a) Kelly Rock, (b) La Blanca, and (c) Katowice. Sample designations can be seen from Table 1

Spent KR and KT experienced significantly lower shrinkage, resulting in sulphation conversions that were ~50%, similar to the original samples. Moreover, samples pretreated for 24 h showed ~10% higher conversions. The conversions were also close to the calculated maximum (Table 1), with a somewhat higher discrepancy in the original KR sample, suggesting the formation of unreacted core/sulphate shell pattern. These results showed that these limestones, after use for CO_2 capture, are suitable for SO_2 retention. The main criterion is that they do not lose porosity as a result of carbonation/calcination cycles. Moreover, the cycles may be favorable in the case of sorbents with predisposition to formation of an unreacted core pattern. The sorbent morphology with larger pores, typical for spent sorbents, reduces the tendency to form a sulphate shell, which prevents higher conversions.

The clear influence of sorbent porosity, *via* maximum calculated conversions, on measured conversions can be seen in Fig. 3. There is excellent correlation (R^2 = 0.97) between calculated and measured values. The maximum conversion is never reached and this may be a result of additional sorbent particle shrinkage during sulphation, local unreacted areas, inactive CaO in the form of other calcium compounds, or other influences,

but this issue cannot be resolved or confirmed by results obtained here. However, the large difference between calculated maximum and measured conversions for the original KR sample are most likely to result from the formation of a sulphate shell.

Figure 3 shows that sorbent porosity is the main determinant of conversion after long sulphation periods, which is especially noticeable in the case of spent/pretreated samples with larger pores and lower surface areas. The sorbent surface area determines conversion in the first stage of reaction (Fig. 4). The correlations are not strong, and cannot be attributed to all points (samples) considered together, suggesting that reaction rate depends also on limestone type. But, for each group of samples originating from the same limestone, correlations are noticeable.

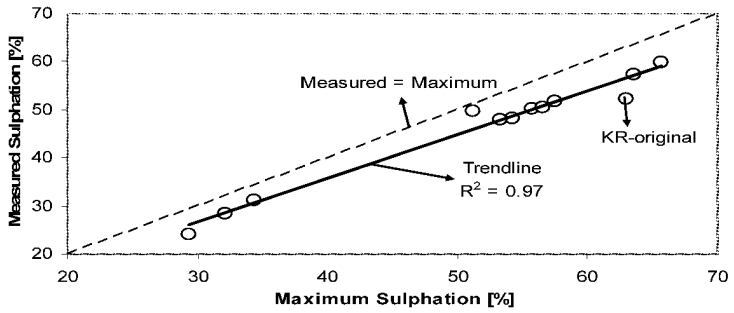

Fig. 3 Maximum calculated sulphation conversions *vs.* measured conversions (Fig. 2)

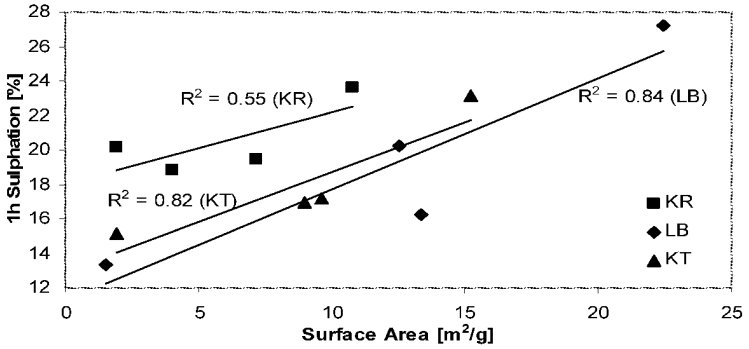

Fig. 4 Sulphation conversions after 1 h (Fig. 2) *vs.* surface area (Table 1)

An interesting result from Fig. 2, significantly higher sulphation of samples pretreated for 24 h, led us to investigate performance of samples pretreated for different times/temperatures. The results (KR shown, Fig. 5) show that changes in conditions during pretreatment do not improve sulphation conversion for pretreated LB samples, but the influence is obvious for KR and KT. The best results are obtained with these samples pretreated for 6 h. The conversions are >60%, and ~12% higher than those for the original samples. Increased duration/temperature of pretreatment reduces sulphation conversion; i.e., during pretreatment at high temperature, more pronounced shrinkage takes place. These results show that suitable thermal treatment of CaO-based sorbent can cause morphology changes that enhance sulphation performance. It is important to find a balance between sorbent particle shrinkage, which reduces available space for $CaSO_4$ and is an undesirable effect, and pore size modification, *i.e.*, formation of large pores that are not prone to plugging and provide space for $CaSO_4$, which is a desirable phenomenon.

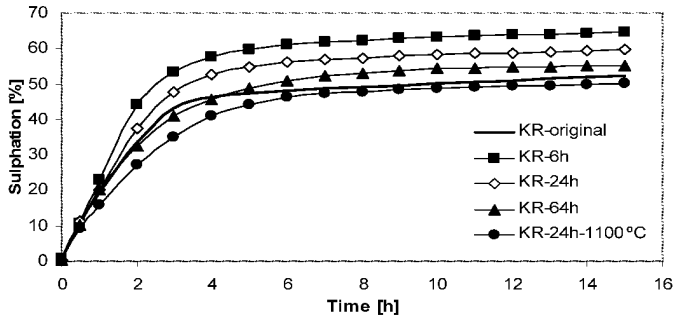

Fig. 5 Sulphation conversions in TGA at 850°C, 0.5% SO_2, 15% CO_2, 3% O_2, and N_2 balance, of Kelly Rock samples pretreated for different time (6, 24, and 64 h) at 1000°C and for 24 h at 1100°C

CONCLUSIONS

The sulphation performance of CaO-based sorbents modified during thermal pretreatment and/or CO_2 capture carbonation/calcination cycles was investigated. It has been shown that the final conversions of both spent and pretreated sorbents after longer sulphation times were comparable or higher than those observed for the original sorbents under comparable conditions. These results showed that spent sorbent samples from CO_2 looping cycles can be used as sorbents for SO_2 retention in cases where significant porosity loss does not occur during CO_2 reaction cycles. In the case of spent KR and KT samples final conversions are determined by the total pore volume available for the bulky $CaSO_4$ product. The combination of CO_2 capture and SO_2 retention with spent sorbent is one potentially important route that can improve the economics of CaO-based CO_2 capture. This option provides us with an opportunity to use spent sorbent, while reducing disposal problems, make-up of fresh sorbent, and the amount of sorbent needed for SO_2 retention as a result of the higher sulphation capacity of spent sorbent.

REFERENCES

Abanades, J.C., Grasa, G., Alonso, M., Rodriguez, N., Anthony, E.J., Romeo, L.M.: Cost structure of a postcombustion CO_2 capture system using CaO. Environ. Sci. Techn. 41 (2007), 5523-5527.

Abanades, J.C., Alvarez, D.: Conversion limits in the reaction of CO_2 with lime. Energy Fuels 17 (2003), 308-315.

Abanades, J.C., Anthony, E.J., Wang, J., Oakey, A.: Fluidized bed combustion systems integrating CO_2 capture with CaO. Environ. Sci. Techn. 39 (2005), 2861-2866.

Alvarez, D., Abanades, J.C.: Pore-size and shape effects on the recarbonation performance of calcium oxide submitted to repeated calcination/recarbonation cycles. Energy Fuels 19 (2005), 270-278.

Anthony, E.J.: Solid looping cycles: A new technology for coal conversion. Ind. Eng. Chem. Res. 47 (2008), 1747-1754.

Anthony, E.J., Granatstein, D.L.: Sulfation phenomena in fluidized bed combustion systems. Prog. Energy Comb. Sci. 27 (2001), 215-236.

Borgwardt, R.H.: Sintering of nascent calcium oxide. Chem. Eng. Sci. 44 (1989), 53-60.

Fennell, P.S., Pacciani, R., Dennis, J.S., Davidson, J.F., Hayhurst, A.N.: The effects of repeated cycles of calcination and carbonation on a variety of different limestones, as measured in a hot fluidized bed of sand. Energy Fuels 21 (2007), 2072-2081.

Grasa, G.S., Abanades, J.C.: CO_2 capture capacity of CaO in long series of carbonation/calcination cycles. Ind. Eng. Chem. Res. 45 (2006), 8846-8851.

Lysikov, A.I., Salanov, A.N., Okunev, A.G.: Change of CO_2 carrying capacity of CaO in isothermal recarbonation-decomposition cycles. Ind. Eng. Chem. Res. 46 (2007), 4633-4638.

MacKenzie, A., Granatstein, D.L., Anthony, E.J., Abanades, J.C.: Economics of CO_2 capture using the calcium cycle with a pressurized fluidized bed combustor. Energy Fuels 21 (2007), 920-926.

Manovic, V., Anthony, E.J.: SO_2 retention by reactivated CaO-based sorbent from multiple CO_2 capture cycles. Environ. Sci. Techn. 41 (2007), 4435-4440.

Manovic, V., Anthony, E.J.: Sequential SO_2/CO_2 capture enhanced by steam reactivation of a CaO-based sorbent. Fuel 87 (2008), 1564-1573.

Manovic, V., Anthony, E.J.: Improvement of CaO-based sorbent performance for CO_2 looping cycles. Thermal Science (2009), accepted.

Manovic, V., Lu, D., Anthony, E.J.: Sulphation and carbonation properties of hydrated sorbents from a fluidized bed CO_2 looping cycle reactor. Fuel 87 (2008a), 2923-2931.

Manovic, V., Anthony, E. J., Loncarevic, D.: CO_2 looping cycles with CaO-based sorbent pretreated in CO_2 at high temperature, Chem. Eng. Sci. (2009a), submitted.

Manovic, V., Charland, J.-P., Blamey, J., Fennell, P.S., Lu, D., Anthony, E.J.: Influence of calcination conditions on carrying capacity of CaO-based sorbent in CO_2 looping cycles. Fuel (2009b), submitted.

Manovic, V., Anthony, E.J., Grasa, G., Abanades, J.C.: CO_2 looping cycle performance of a high-purity limestone after thermal activation/doping. Energy Fuels 22 (2008b), 3258-3264.

Sun, P., Grace, J.R., Lim, C.J., Anthony, E.J.: The effect of CaO sintering on cyclic CO_2 capture in energy systems. AIChE. J. 53 (2007), 2432-2442.

MODELING OF NITROGEN OXIDES EMISSIONS FROM CFB COMBUSTION

S. Kallio, M. Keinonen

VTT Technical Research Centre of Finland, P.O.Box 1000, FI-02044 VTT, Finland

Abstract: In this work, a simplified description of combustion and nitrogen oxides chemistry was implemented in a 1.5D model framework with the aim to compare the results with ones earlier obtained with a detailed reaction scheme. The simplified chemistry was written using 12 chemical components. Heterogeneous chemistry is given by the same models as in the earlier work but the homogeneous and catalytic reactions have been altered. The models have been taken from the literature. The paper describes the numerical model with emphasis on the chemistry submodels. A simulation of combustion of bituminous coal in the Chalmers 12 MW boiler is conducted and the results are compared with the results obtained earlier with the detailed chemistry description. The results are also compared with measured O_2, CO, NO and N_2O profiles. The simplified reaction scheme produces equally good results as earlier obtained with the more elaborate chemistry description.

Keywords: CFB, 1D modeling, nitrogen oxides, emission

INTRODUCTION

Fluidized bed technology plays an important role in finding solutions for energy production. At the same time, our capabilities to numerically predict emission formation from CFB combustion are still far from complete. Both mixing and chemical reactions play an important role in the process and need to be taken into account in the models. Mixing can best be described by a transient CFD simulation of the complicated gas-solids flow patterns. The best chemistry models should be based on detailed reaction mechanisms including, in addition to homogeneous and heterogeneous reactions, also catalytic reactions. Unfortunately, the combination of CFD with detailed chemistry is computationally too heavy and thus simplified approaches have been developed. In Kallio et al. (1999) and Kilpinen et al. (1999), mixing was described by a 1.5D description while the chemistry was a detailed one, including the oxidation reactions of methane, ethane, HCN, and NH_3, as well as the interactions between hydrocarbon species (CH_i, HCCO) and nitrogen components (NO, NH_i, N_2), and N_2 fixation. The mechanism consisted of about 300 elementary steps between around 50 chemicals.

In this work, a simplified chemistry was implemented in the same 1.5D model framework with the aim to compare the results with the ones earlier obtained with the detailed mechanisms. If the simplified mechanism would perform well, it could later be moved to CFD environment. The simplified description of combustion and nitrogen oxides chemistry of the present study is written using 12 chemical components. Heterogeneous chemistry is given by the same models as in the earlier work but the homogeneous reactions have been altered and catalytic reactions added. The models have been taken from the literature.

MODELING

Model structure and hydrodynamics

In the 1.5D model the riser is divided into three regions: a dense bottom bed, a vigorously mixed splash zone and a transport zone (Fig.1(a)). The two upper zones are horizontally split into a core region and a wall layer. In the vertical direction, the three regions are further divided into computational cells. Solids recirculation is taken into account only by returning the solids from the cyclone back to the bottom of the riser. The description of fluid dynamics, including the axial voidage profile and the external solids circulation rate, are related to measured conditions in existing furnaces (Kallio et al.,2002).

Experiences from furnaces show that gases are not fully mixed over the cross-section in the splash zone. In order to take this into account, alternative descriptions of gas mixing were introduced in Kallio et al. (2001). The model used here divides the core into particle-laden high-velocity regions (jet centers) and a denser, slower suspension region (Fig.1(b)). The oxygen-rich gas from the jets is assumed here to mix gradually into the surrounding suspension over 5 m height.

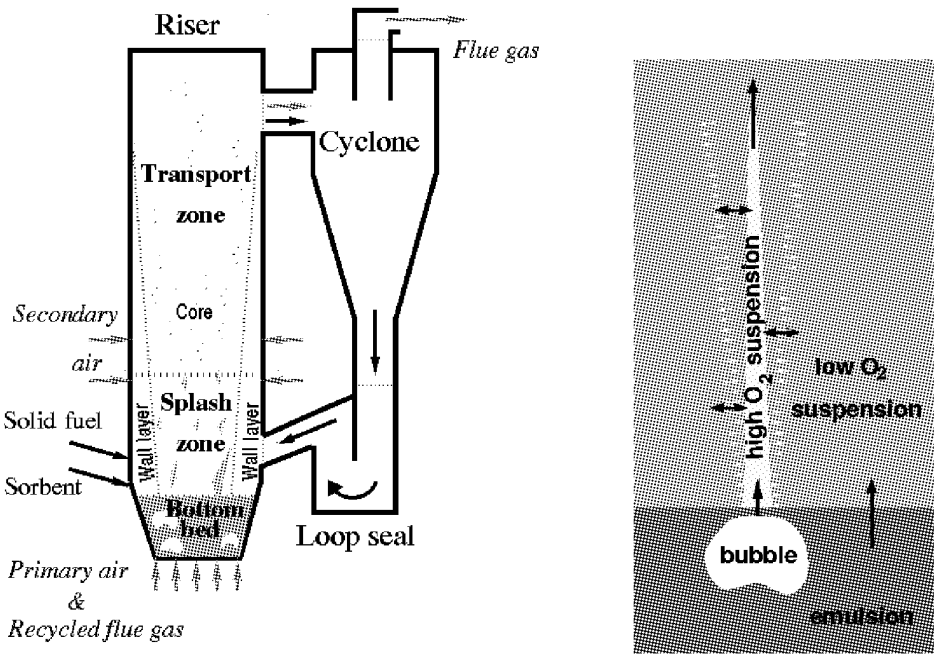

Fig. 1 (a) Different regions and flows of gas and solids in the 1.5D model and (b) regions in the gas mixing model used in this study. Adapted from Kallio et al. (2002)

Heterogeneous chemistry

The description of char particle oxidation is the same as applied in Kallio & Konttinen (2006). It is based on the shrinking particle model developed by Goel (1996) and Goel et al. (1994) on the basis of detailed Char-C oxidation and Char-N oxidation and reduction mechanisms. The model includes external and internal mass transfer, and chemical kinetics inside the char particle. The model yields concentration profiles inside the particle and the transfer rates to/from the surrounding gas atmosphere. Two alternative sets of kinetic constants were used in the present work. The kinetic parameters KKK2 were determined by Konttinen et al. (2001) from data from laboratory experiments and CFBC conditions. The set KKK3 was determined from laboratory data by Konttinen et al. (2004). In addition to the reactions in KKK2, KKK3 includes the reduction reaction of N_2O with CO to N_2, catalyzed by carbon. The full mechanism is illustrated in Fig.2. KKK3 was meant to be used together with models for catalytic reduction of NO by CO, catalyzed by the bed material. The bulk reaction parameters KKK2 should be used without separate catalytic CO-NO reaction since the reaction between CO and NO inside the char particle was enhanced by this parameter set to compensate for the missing reduction reaction on surfaces of the bed material. The parameter set KKK2 was thus determined assuming that the spatial distribution of char and bed material is similar enough to allow lumping together the catalytic reactions on bed material and on char.

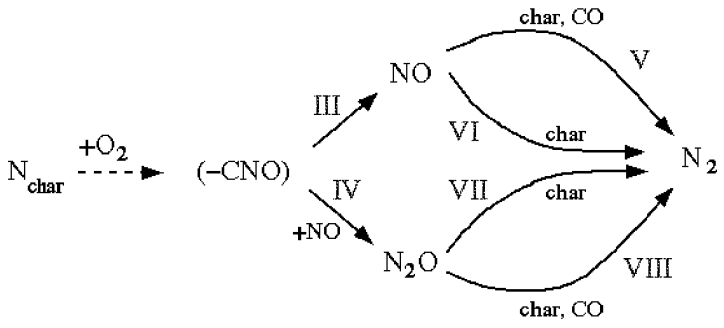

Fig. 2 The quasi-global kinetic mechanism consists of eight net reactions and includes 6 chemical species. Adapted from Konttinen et al. (2004)

Homogeneous chemistry

The homogeneous reactions and the corresponding reaction rates were taken from literature sources. The reactions are as follows:

I: $CH_4 + 3/2\ O_2 \longrightarrow CO + 2H_2O$
II: $CO + ½\ O_2 \longrightarrow CO_2$
III: $2H_2 + O_2 \longrightarrow 2H_2O$
IV: $C_2H_6 + 5/2\ O_2 \longrightarrow 2CO + 3H_2O$
V: $NH_3 + NO + ¼\ O_2 \longrightarrow N2 + 3/2\ H_2O$
VI: $NH_3 + 5/4\ O_2 \longrightarrow NO + 3/2\ H_2O$
VII: $N_2O \longrightarrow N_2 + ½\ O_2$
VIII: $HCN + ½\ O_2 \longrightarrow CNO$
IX: $CNO + ½\ O_2 \longrightarrow NO + CO$
X: $CNO + NO \longrightarrow N_2O + CO$
XI: $NO + CH_4 \longrightarrow HCN + H_2O + ½\ H_2$

Major part of the set of reactions was taken from Liu & Gibbs (2002) to which reactions I and III were taken from Jensen et al. (1995), IV from Zimont & Trushin (1969), V and VI from Zijlma et al. (1999), VII from Johnsson et al. (1996), VIII, IX and X from Desroches-Ducarne (1998) and XI from Chen et al. (1996). Reaction rate for reaction II was taken from Dryer & Glassman (1973), where it was recommended to be used in dilute conditions only since in a dense bed CO does not significantly burn. This is due to the fact that combustion of CO involves reactions between radicals, which are prevented in dense conditions where radicals get destroyed on particle surfaces. In the detailed reaction mechanism quenching of radicals was taken into account as a separate step in the reaction mechanism. In the simplified chemistry approach of our model, the effect of radical quenching is accounted for by altering the reaction rate of CO with oxygen as a function of the local solids concentration.

Catalytical reactions

A large number of catalytic reactions can take place on surfaces of the different types of solid particles in a CFB boiler. Catalytic reactions on bed materials and especially the reaction rates are strongly dependent on the fuel burned and on the bed particles. Ashes of different fuels show totally different catalytic activities. Likewise, in a bed of sand and in a bed of sorbent material the catalytic reactions differ. Thus the reaction rates taken from the literature are not necessarily appropriate for the studied case and measurements should be done using the actual bed material from the combustion process that is to be simulated. That, however, was not done in the present work where the reaction rates were taken from literature taking into account that the bed material in the case simulated in the present work was sand.

Catalytic reduction reactions of NO and N_2O on char were taken into account in the heterogeneous reaction mechanism. Oxidation of NH_3 catalyzed by char has to be modeled separately. The reaction rate parameters were taken from Johnsson (1990). Catalytic oxidation of NH_3 is modeled by two reactions taken from Jensen (1996). In many cases bed material catalyzes also the reduction of NO. In the present study, the reaction rate for the reaction between NO and CO on bed particles was taken from Johnsson & Dam-Johansen (1991). The reactions used are thus:

XII: $NH_3 + 3/4\ O_2 \xrightarrow{char} ½\ N_2 + 3/2\ H_2O$
XIII: $NH_3 + 3/4\ O_2 \xrightarrow{bed} ½\ N_2 + 3/2\ H_2O$
XIV: $NH_3 + 5/4\ O_2 \xrightarrow{bed} NO + 3/2\ H_2O$
XV: $NO + CO \xrightarrow{bed} ½\ N_2 + CO_2$

SIMULATIONS

Input data for simulation of a 12 MW boiler

The case presented here is a simulation of combustion of bituminous in Chalmers' CFBC (Åmand et al., 1997). The riser height is 13.5 m and the cross-sectional area 2.073 m^2 up to 2.2 m height, and 2.374 m^2 higher up. Axial voidage distribution is obtained from Åmand et al. (1997). Coal is divided into four species according to the particle size (diameters 0.02 mm, 0.1 mm, 0.2 mm and 0.8 mm). Density of coal char is assumed to be 1400 kg/m^3. The properties of the fuel are shown in Table 1. They and the description of fuel behavior during devolatilization are taken from the earlier simulations (Kallio et al., 1999). The same C/N ratio as in fuel was assumed to remain in char. The split of volatile-nitrogen to $HCN/NH_3/N_2$ was assumed equal to 35/35/30 (Kallio et al., 1999). The ratio of primary air to total air was 0.53, and the excess air ratio 1.21.

The core region is divided into dense and lean regions between the bottom bed and 5 m elevation. Fresh char and half of volatiles and water vapor are mixed in the bottom bed. Half of the volatiles and H_2O are mixed

between bottom bed surface and 2.5 m height in linearly decreasing proportion. Above the bottom bed, volatiles and H_2O are mixed in both lean and dense zones relative to the solids flow rate in each region.

Table 1 Fuel data (daf = dry and ash free, a.r. = as received).

Volatiles, wt% daf	39.9	**Ultimate analysis (wt% daf)**	
Proximate analysis (wt% a.r.)		C	79.8
Combustibles	78.6	N	1.56
Ash	6.6	S	0.72
Moisture	14.8	H	5.30
		O	12.6

The two sets of reaction rate constants, KKK2 and KKK3, were used. With KKK3, particle temperature was calculated from an energy balance while with KKK2 particle temperature was assumed to exceed the gas temperature by constant 50 K. Gas temperature was set to 850 °C in the core region and 800 °C in the wall layer. Secondary air was divided into 21 separate air steams between 2.1 m and 2.6 m heights and it is assumed to be mixed in the lean and dense sections of core region in proportion to the air flow rates in the zones. No primary fragmentation, secondary fragmentation or attrition is assumed to take place.

The measured concentration profiles used for comparisons were obtained from Chalmers University of Technology, and they are the same as in Kallio et al. (1999). For comparison, simulated concentration profiles were taken from Kallio & Konttinen (2006), where the same case was simulated with the detailed reaction mechanism for homogeneous gas phase chemistry using exactly the same input data and parameter values.

Simulation results

In the simulation of Kallio & Konttinen (2006), the parameter set KKK2 was used for the heterogeneous chemistry. Thus the first simulations here were conducted using the same parameters to allow evaluation of the effect of the change in the homogeneous reaction mechanism. The catalytic reactions XII-XV were not used in Kallio & Konttinen (2006) and thus they were omitted also here in the first simulation. In a second simulation, the catalytic reactions XII-XIV were included. Since reaction XV is indirectly taken into account in the parameter set KKK2, it was omitted. In Fig.3 the obtained simulation results are compared with measurements and with results from the earlier simulation with the detailed homogeneous chemistry description.

Burning of CO is clearly slower in the simplified model, which is seen in the higher concentrations of CO and O_2 in the lower part of the furnace. Compared to the measured profiles, the simpler mechanism would seem to produce a more correct amount of CO. However, especially in the lower part of the furnace, the measured CO, NO and N_2O values are likely to be too high since the measurement represents a time-averaged concentration in which the faster moving oxygen-rich regions have too small a weight in comparison to the weight of the slowly moving dense suspension regions with higher CO content. This same problem in the measurements is seen in the measured too low concentration of oxygen at furnace bottom. This effect is significant in the bottom bed and in the splash zone while the measured values at riser top are more reliable.

Higher CO concentration obtained with the simpler mechanism has increased reduction of NO which is seen in the lower NO concentration in Fig.3. Compared to the measurements, both the old simulation with detailed homogeneous chemistry and the new simulation with the simpler mechanism have produced reasonable amounts of NO. The simpler mechanism produced a higher amount of N_2O. With both mechanisms N_2O content at the top of the furnace is significantly lower than what was measured. The failure to predict N_2O correctly can be attributed to the heterogeneous combustion model. Both KKK2 and KKK3 parameter sets produce too small amounts of N_2O (Konttinen et al., 2001; 2004). Inclusion of the catalytic reactions XII-XIV increased the amount of NO but, as expected, had only a minor effect on N_2O.

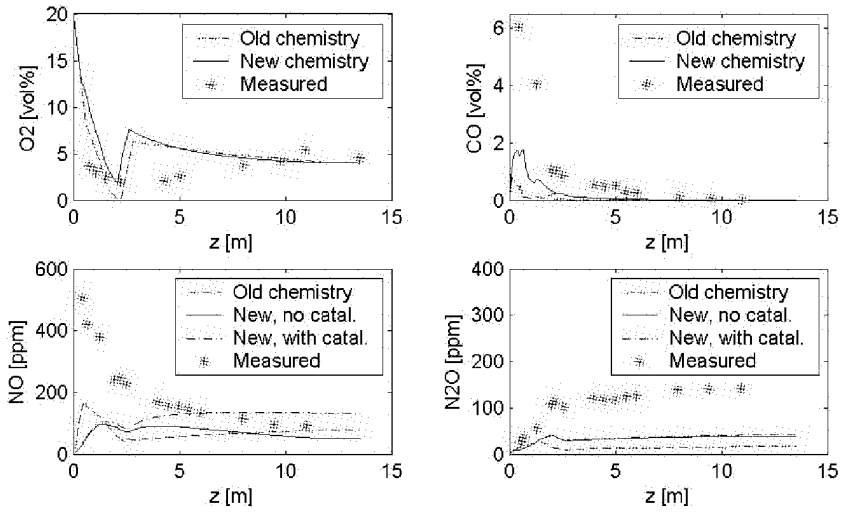

Fig. 3 Simulation results obtained with the KKK2 parameter set for heterogeneous chemistry and the simplified mechanism for homogeneous chemistry, compared with measurements and with results from the earlier simulation with the detailed homogeneous chemistry description (denoted by "Old chemistry"). Simulations with the simpler homogeneous chemistry model were conducted both with and without the catalytic reactions XII-XIV

Further simulations were done using parameters KKK3 for heterogeneous chemistry and the catalytic reactions XII-XIV, the results of which are shown in Fig.4. First the case was simulated without reaction XV for reduction of NO by CO on bed material. The effect of the rate of the reduction reaction was studied by first simulating the case with the reaction rate given by Johnsson & Dam-Johansen (1991) after which the reaction rate was multiplied by 5 and 10, respectively, in the consecutive simulations. Figure 4 shows the results from these four simulations in comparison to the measurement data. Compared to simulations with KKK2, CO concentration is now higher and N_2O lower which both changes can be attributed to the differences in the heterogeneous reaction mechanism and the reaction rates.

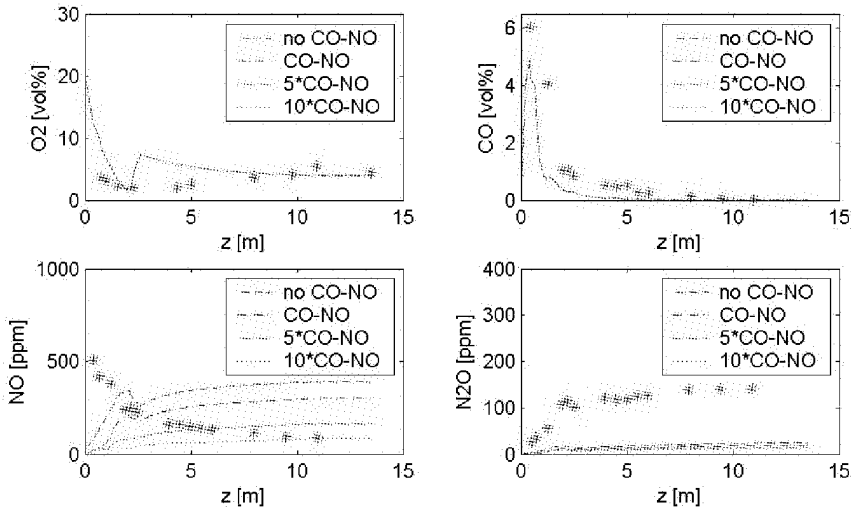

Fig. 4 Simulation results obtained with the KKK3 parameter set for heterogeneous chemistry and the simplified mechanism for homogeneous chemistry, compared with measurements. Simulations were conducted both with and without the reaction step XV for catalytic reduction of NO by CO on bed material. The reaction rate for reaction XV was either the one obtained from Johnsson & Dam-Johansen (1991) or the rate multiplied with 5 or 10, respectively

When catalytic reduction of NO by CO on bed material was excluded, the obtained concentration of NO was unreasonably high. Inclusion of reaction XV brought NO concentration down but not to the required degree. By changing the rate of NO reduction to 5~10 times higher level the simulated outlet NO concentration came closer to the measured value. The necessity to change the reaction rate can partly be related to the differences between the bed material used while determining the reaction rate parameters and the bed material in the combustion experiment. Another reason for the discrepancy could be the inhomogeneous distribution of the reactants in a CFB boiler. In the laboratory, reaction rates are determined in as homogeneous conditions as possible whereas in a furnace the highest concentrations of NO and CO could be found in the denser

suspension regions while in the fast moving oxygen rich regions the suspension is lean and the concentration of these reactants low. In addition, the fuel is distributed unevenly over the furnace cross-section which leads to uneven gas composition over the bed width. Thus, due to the strong correlation between the relevant variables on both local and macroscopic scales, the average suspension density and average concentrations used in the models predict poorly the average reaction rate in the furnace. Part of this effect is taken into account in the division of the riser cross-section into oxygen rich and oxygen lean sectors but the uneven distribution of the fuel and local distributions of concentrations and voidage cannot be fully accounted for in a simple 1D/1.5D model.

CONCLUSIONS

In the present work, a simplified description of combustion and nitrogen oxides chemistry was implemented in a 1.5D model framework with the aim to compare the simulation results with ones earlier obtained with a detailed reaction scheme. The simplified chemistry was written using 12 chemical components while the previously used detailed mechanism involved about 50 components. Heterogeneous chemistry was described by the same models as in the earlier work but the catalytic reactions were altered. The chemistry models were taken from the literature. A simulation of the Chalmers 12 MW boiler was conducted and the results were compared with the ones earlier obtained with the detailed chemistry description. The results were also compared with measured O_2, CO, NO and N_2O profiles. Simulations with both old and new chemistry models produced too low concentrations of N_2O which can be attributed to the defects in the heterogeneous submodel. Both models produced reasonable profiles for NO. Thus the simpler mechanism could be used equally well and especially in CFD simulations it would be the preferred alternative due to its shorter computation time.

ACKNOWLEDGEMENTS

The financial support from VTT Technical Research Centre of Finland is gratefully acknowledged. The authors warmly thank prof. B. Leckner and Dr. L.-E. Åmand for discussions and for the data.

REFERENCES

Åmand L.-E., Lyngfelt A., Karlsson M. and Leckner B., Report A 97-221, CTH, Göteborg (1997)
Chen, W.. Smoot, L.D., Hill, S.C, Fletcher, T.H., Energy & Fuels 10, pp. 1046-1052 (1996)
Desroches-Ducarne, E., Dolignier, J.C., Marty E., Martin, G., Delfosse, L., Fuel 77, pp. 1399-1410 (1998)
Dryer F L, Glassman I, The Combustion Institute, pp. 987 – 1003 (1973)
Goel, S.K., Ph.D. Dissertation. MIT, USA (1996)
Goel, S. K.; Morihara, A.; Tullin, C. J., Sarofim, A. F.:, In: Twenty-fifth Symposium (International) on Combustion, pp. 1051-1059 (1994)
Jensen, A., Johnsson, J.E., Andries, J., Laughlin, K., Read, G., Mayer, M., Baumann, H., Bonn, B., Fuel 74, pp. 1555-1569 (1995)
Jensen, A., Department of Chemical Engineering, Technical University of Denmark, Ph.D. Thesis (1996)
Johnson, J.E., A new module for the IEA-model, 21st IEA-AFBC Meeting, Beograd (1990)
Johnsson, J.E., Dam-Johansen, K., FBC11, New York, pp. 1389-1396 (1991)
Johnsson, J.E., Åmand, L., Dam-Johansen, K., Leckner, B., Energy & Fuels 10, pp. 970-979 (1996)
Desroches-Ducarne, E., Dolignier, J.C., Marty, E., Martin G., Delfosse L., Fuel 77, pp. 1399-1410 (1998)
Kallio, S., Kilpinen, P., Hupa, M., Proceedings of the Int. Conf. on Circulating Fluidized Bed Technology VI, Würzburg, Germany (1999)
Kallio, S., Kilpinen, P., Konttinen, J., 10th Int. Conf. on fluidisation, Beijing, China (2001)
Kallio., S.; Kilpinen, P.; Konttinen, J.; Leckner, B.; Åmand, L-E., 7th Int. Conf. on Circulating Fluidised Beds, Niagara Falls (2002)
Kallio, S., Konttinen. J., Åbo Akademi University, Heat Engineering Laboratory, Report 2006-2 (2006)
Kilpinen, P., Kallio, S., Hupa, M., Proceedings of the 15th International FBC Conference, Savannah (1999)
Konttinen, J.; Kilpinen, P.; Kallio, S., 16th Int. Conf. on Fluidised Bed Combustion, CD-ROM, Paper No. FBC01-215, Reno, May 13-16 (2001)
Konttinen, J., Kallio, S., Kilpinen P., Report 02-4, Åbo Akademi University, Process Chemistry Group (2004)
Liu, H., Gibbs, B.M., Fuel 81, pp. 271-280 (2002)
Zimont, V.L., Trushin, Y.M., Combust. Explosion Shockwaves 5, pp. 567-573 (1969)
Zijlma, G.J., Gerritsen A.W., van den Bleek, C.M., CBC 15, Paper No. FBC99-0168 (1999)

STUDY OF NO EMISSION FROM A PILOT SCALE VORTEXING FLUDIZED BED COMBUSTOR USING RESPONSE SURFACE METHODOLOGY

F. P. Qian,[1] C. S. Chyang,[2] W. S. Yen[2]

1School of Civil Engineering and Architecture, Anhui University of Technology, Ma'anshan, China
2Department of Chemical Engineering, Chung Yuan Christian University, Chung-Li 320, Taiwan,China

Abstract: All the experiments were conducted in a pilot scale vortexing fluidized bed combustor (VFBC), an integration of circular freeboard and rectangular combustion chamber. The dimension of the freeboard is 0.75 m I.D. and 4.6 m in height. The cross section of the combustion chamber is 0.8×0.4 m^2 and the height of the combustion chamber is 1.35 m. The secondary air injected nozzles were installed tangentially at the bottom of the freeboard. Coal was used as the fuel. Silica sand was employed as the bed material. Acetic acid was used as the reductant to reduce NO emissions. The operating conditions, such as the stoichiometric oxygen in the combustion chamber, the bed temperature and the injecting location of acetic acid, were determined by means of response surface methodology (RSM), which enables the examination of parameters with a moderate number of experiments. In RSM, the NO emission concentration at the exit of the VFBC is used as the objection function. A mathematical model for the NO emission as a function of the operating conditions was empirically proposed. The results show that NO emission increases with the stoichiometric oxygen in the combustion chamber and the bed temperature. NO emission can be decreased by injecting the acetic acid into the combustion chamber. The NO emission decreases with the height of the acetic acid injecting location above the distributor. Meanwhile, the bed temperature has more important effect on the NO emission than the other two factors.

Keywords: VFBC, NO emission, operating conditions, RSM

INTRODUCTION

As well know to all, NO is a harmful pollutant causing direct injuries of the respiratory organs and is the precursor for acid rain and ground-level ozone. Meanwhile, NO is also an intermediate in the formation of N_2O in combustion systems (Armesto et al., 2003). Moreover, NO_x is known to play a role in the formation of photochemical smog, too. Compared with other combustors, lower NO emissions can be achieved by employing the fluidized bed combustor (FBC). It can be attributed to the lower operating temperature (700~900℃) to prevent the formation of the thermal NO and prompt NO during the combustion process. The paths of formation and reduction of NO in fluidized bed combustors were complex and it was difficult to explain the variation in NO emission for different operation conditions. When coal was burnt in the FBC, the heterogeneous reduction of NO at the char surface has been considered to be one of the most important reactions of NO destruction. Generally speaking, NO emissions increase with bed temperature and excess air (Glarborg et al., 2003). It is generally thought that the conversion of fuel-N to nitric oxides is through the intermediates, hydrogen cyanide (HCN) and ammonia (NH_3), formed during fuel combustion. The mechanistic pathways among fuel-N, HCN, NH_3 and nitric oxides are strongly dependent on chemical structures of the fuel. It is reported that most nitrogen functional groups in fuels are present as pyrrolic and pyridinic type structures (Nelson et al., 1991). Some research work has demonstrated that pyrrolic and pyridinic function groups are related to emission of nitric oxides. It was investigated the formation of NO from 14 nitrogen-containing model compounds, and found the N_2O/NO ratio is a function of the HCN/NH_3 ratio (Hamalained et al., 1994). However, the concentration and location of functional groups, such as- OH groups, of the compound may cause much more complicated effects on the emissions of nitric oxides. Most studies, including recent reports (Armesto et al., 2003; Svoboda and Pohořely, 2004; Permchart and Kouprianov, 2004; Li et al., 2004; Tarelho et al., 2005; Shimizu et al., 2007; Zhao et al., 2008) have studied NO emission firing coals and biomass in detail. In order to improve the performance of FBC, a vortexing fluidized bed combustor (VFBC), an integration of bubbling fluidized bed and cyclone, was developed early in the 70's (Iwasaki et al., 1979). The first pilot scale VFBC was constructed and operated by Korenberg (1983). It was modified and renamed by Nieh and Yang (1986) later. The concept of the VFBC is to establish a vortex-generating system by injecting

the 2nd air tangentially into the freeboard to increase the combustion intensify, the calcium utilization, and the turndown capability. The advantages of low pollutant emissions and high combustion efficiencies by operating a VFBC have been demonstrated for combustion of waste tires in the previous study. Chyang et al. (2007, 2008a, 2008b) have been studied the NO and N_2O emission characteristics from the pilot scale vortexing fluidized bed combustor when firing different fuels, for example, rice husk, soybean and high sulfur subbituminous. They found that NO emission could be reduced by adding soybean to the fuels. Furthermore, NO emission is decreased with increasing the amount of the soybean. They think that the possible reason could be that the carboxyl (-COOH) group in the soybean has the ability for reducing NO emission. Therefore, in order to explain the reason further, the main purpose of this paper is to study the influence of the carboxyl (-COOH) group on the NO emission by injecting the acetic acid (CH_3COOH) at different locations into the VFBC. Additionally, the operating conditions including the stoichiometric oxygen in the combustion chamber and the bed temperature are also considered in experiments, and these operating conditions were determined by means of response surface methodology (RSM), which enables the examination of parameters with a moderate number of experiments. Based on the RSM, a mathematical model for the NO emission as a function of the operating conditions was empirically proposed. The model can be used to analyse the effect of the operating conditions on the NO emission in the VFBC.

EXPERIMENTAL

Experimental Apparatus

A process flowchart of the VFBC combustion system used in this study is shown in Fig. 1. The total primary gas is the sum of the primary air and the flue gas recirculation. The primary air is supplied by a 15 hp Root's blower, and the flue gas recirculation is supplied by a 7.5 hp blower. The 2nd air is supplied by a 7.5 hp turbo blower. Four equally spaced 2nd air injection nozzles with diameters of 30mm are installed tangentially at a level of 2.05m above the distributor to cause the swirling flow in the freeboard. A 20 hp compressor is used for transporting the feed through a pipe into the combustor. The acetic acid is added by the injecting tube. The injecting location of the acetic acid are 0.90m (A), 1.50m (B) and 2.05m (C) above the gas distributor, respectively.

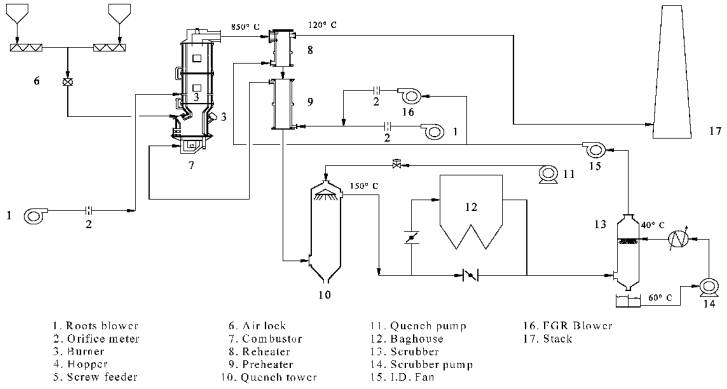

Fig. 1 Schematic diagram of VFBC system

Figure 2 shows the configuration of the VFBC used in this study. The VFBC is made up of four parts, i.e., the windbox, the distributor, the combustion chamber and the freeboard. The combustion chamber with cross section 0.8×0.4 m^2 is constructed of a 6 mm stainless steel covered with the ceramic fiber to limit the heat loss. A windbox with cross section 0.6×0.4 m^2, connected to the air supplied line, is fabricated of 6 mm stainless steel. Above the combustion chamber, the inner diameter of the freeboard is 0.75m. The static bed height is 0.35m. Twenty-seven nozzles with diameter of 5 mm and 3 mm mounted on a 6 mm thickness stainless steel plate are used as the gas distributor (the open area ratio is 0.516%).

The temperature in the VFBC are measured with the K type thermocouple installed in the combustor. The bed temperature is controlled by the heat-transfer tube immersed in bed. The flue gases are sampled at 0.9 m, 1.5 m, 2.05 m, 3.3 m and 4.45m above the gas distributor. The components of the flue gas, such as CO, CO_2, O_2 and

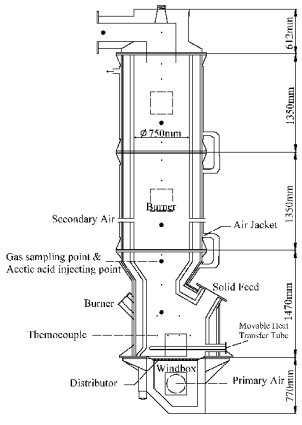

Fig. 2 Schematic diagram of the vortexing fluidized bed combustor

NO are analyzed by a TSI CA-6203. Gas samples are drawn out from the combustor and cooled, and then passed through the above analyzers. The dry process is carried out within the analyzers. The values of the concentrations reported in this study are all corrected to 6% residual oxygen on dry basis.

FUELS AND BED MATERIALS

The coal is used as the feeding material in this study. The total heat (wet base) feed is kept as 120000 kcal/hr. The proximate and ultimate analyses of feeding material are listed in Table 1.

Table 1 The Properties of Fuels

Proximate analysis (wt.%)		Ultimate analysis* (wt.%)	
Moisture	13.79	Carbon	60.83
Volatile	31.85	Hydrogen	7.54
Fixed carbon	41.02	Oxygen	20.45
Ash	13.34	Nitrogen	1.22
Low Heating value (kcal/kg)	5018	Sulphur	1.03

* Dry basis

Silica sand is employed as the bed material in this study. The sand particle size range is 177-840μm, and the mean size of the sand is 541 μm in diameter. The operating conditions for experiments are shown in Table 2. It should be noted that we change the stoichiometric oxygen in the combustion chamber by changing the ratio of the primary air to the flue gas recirculation in this experiment.

Table 2 Experimental conditions

Operating parameter	Range
Coal feeding rate (kg/h)	23.9
Acetic acid feeding rate (ml/min)	16.1
Bed temperature (°C)	810-890
Superficial velocity (m/s)	0.66-0.71
Stoichiometric oxygen in the combustion chamber (%)	80-120
Total primary gas flow rate (Nm^3/min)	3.5
Secondary air flow rate (Nm^3/min)	1.17
Excess oxygen ratio (%)	30-70
Bed material	silica sand
Average particle size of bed material (μm)	541
Density of bed material (kg/m^3)	2500
Static bed height above the gas distributor (cm)	35
Bed weight (kg)	175

MODEL SET-UP

Response surface methodology (RSM)

A quadratic polynomial model was used to describe the relationship between the objective function and the operating conditions in the response surface methodology. The general form of a quadratic model can be represented as:

$$Y = \sum_{i=1}^{n} \beta_{ii} X_i^2 + \sum_{i=1}^{n-1} \sum_{j=i+1}^{n} \beta_{ii} X_i X_j + \sum_{i=1}^{n} \beta_i X_i + \beta_0 \quad (1)$$

where Y is the objection function or response; X_i is the coded operating parameters of factors; n is the factor number. The coefficient values, β_0, β_i, β_{ii}, β_{ij} were chosen to fit the experimental data well using the least squares method.

In this study, the Box-Behnken design, which is a common experimental design for RSM, was used. A three-factor Box-Behnken design is illustrated in Fig. 3. It is a rotatable spherical design that contains no points at the vertices of the cubic region created by the upper and lower limits for each variable. This could be a great advantage when the points on the corners represent factor-level combinations that are cost-consuming of

impossible to execute due to the physical process constraints (Montgomery, 1997). A way to estimate the parameters of Eq. (1) is to study the response for all (combinations of) factors set at three different levels. This full factorial design would require $3^3 = 27$ different experiments. This set-up results in the Box-Behnken of three factors demanding only 15 experiments, which is a considered reduction compared to the three level factorial design.

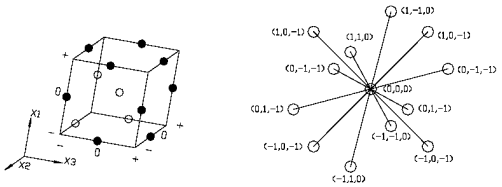

Fig. 3 A three-factor and three-level Box-Behnken design (Chyang et al., 2007)

Responses and factors

The operating conditions included the stoichiometric oxygen in the combustion chamber (S_b), the bed temperature (T_b) and the injecting location of acetic acid (L_i) in this paper. Three levels were chosen for each factor. The condition value was coded as the normalized values -1, 0, and +1. The coded factors, the coded levels and their corresponding operating conditions and values are summarized in Table 3. Analysis of variance (ANOVA) was carried out using the commercial package JMP4. The Student's t-test was used to examine the main effects, the quadratic effects and the interaction effects of the parameters. In this work, the NO emission concentration at the exit of the VFBC was assigned as the objective function, Y.

Table 3 Coded factors, coded levels, and corresponding operating conditions and values

Coded Factors	Corresponding Operating Conditions	Coded Levels		
		−1 (low)	0 (center)	+1(high)
		Corresponding Operating Value		
X_1	S_b/S_{b0}	1	1.25	1.5
X_2	T_b/T_{b0}	1	1.0494	1.0988
X_3	L_i/L_{i0}	1	1.6667	2.2778

S_{b0} =80%, T_{b0}=810°C and L_{i0}=0.9m

RESULTS AND DISCUSSION

Analysis of variance for the full model

Based on the Box-Behnken design, fifteen experimental sets were constructed into a fractional factorial experiment. The center point in the experimental design, i.e. the combination of all factors at the center-level, was replicated three times to estimate the experimental accuracy.

One obtains a second-order response surface model using multiple regressions, as follows:

$$Y = 126.33333 + 5.375X_1 + 32.75X_2 - 12.625X_3 + 2.9583333X_1^2 + 9.5\ X_2{*}X_1 + 1.7083333X_2^2 - 17.75\ X_3{*}X_1 + 5X_3{*}X_2 + 6.9583333X_3^2 \quad (2)$$

The corresponding analysis of variance is tabulated in Table 4. The small probability value indicates that the experimental data were fitted well by the regression model. The determination coefficient of the regression model, R^2, is 0.978.

Table 4 Analysis of variance for the whole quadratic model for NOx emission concentration

Source	DF	Sum of Squares	Mean Square	*F* Ratio	Prob.>*F*
Model	9	12012.317	1334.70	24.4078	0.0013
Error	5	273.417	54.68		
Total	14	12285.733			

$R^2 = 0.977745$, $R_{adj}^2 = 0.937687$

The effect examinations of the coded factors are tabulated in Table 5. The value of prob.>*t* increases with

the decreasing absolute t-ratio, or the coefficient to standard-error ratio. When the value of prob.>*t* for a factor is greater than 0.05, it means that the influential degree of the factor falls out of 95% confidence interval. For some factors, the standard error was even bigger than the coefficient, resulting in the value of prob.>*t* approaching 1, which means the factor is very uninfluential. Table 5 shows that the probability values of the regression model for those terms such as the intercept, X_2 (the main effect), X_3 (the main effect), and $X_1 X_3$ (the interaction effect), are lower than 0.05. This suggests that these factors have a significant influence on the objective function, *Y*. The combination of the both positive main effect and interaction effect leads to a polynomial dependence of *Y*.

Table 5 Effect examinations of the coded factors for the NO concentration

Factor	Coefficient	Standard Error	*t* Ratio	Prob.>*t*
Intercept	126.33333	4.2694	29.59	<0.0001
X_1	5.375	2.614463	2.06	0.0949
X_2	32.75	2.614463	12.53	<0.0001
X_3	-12.625	2.614463	-4.83	0.0048
X_1^2	2.9583333	3.848385	0.77	0.4768
X_2*X_1	9.5	3.697409	2.57	0.0501
X_2^2	1.7083333	3.848385	0.44	0.6757
X_3*X_1	-17.75	3.697409	-4.80	0.0049
X_3*X_2	5	3.697409	1.35	0.2342
X_3^2	6.9583333	3.848385	1.81	0.1304

The general dependency of *Y* on each factor is shown in Fig. 4, with the other two factors fixed at the center level. The short vertical bar on the curve represents the 95% confidence interval for the *Y* value. The influence of three factors on the *Y* value can be seen from Fig. 4, i.e., $X_2 > X_3 > X_1$. The NO emission concentration (*Y* value) increases with the bed temperature (X_2), which is consistent with other researchers' results.

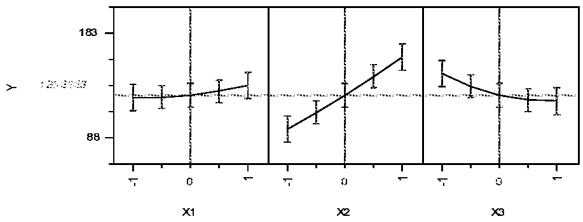

Fig. 4 Main effects of Y on each factor with any other two factors fixed at center level for NO emission

Figure 4 tell us that the NO emission concentration is decreased with increasing the height of the acetic acid injecting location above the gas distributor, i.e., when the acetic acid injecting location is higher (2.05m above the gas distributor), the NO emission concentration has the lowest value. The NO emission removal effect when injection the acetic acid can be seen in Table 6, which shows that the acetic acid can reduce the NO emission concentration. This phenomenon can be explained as follows: (1) Hämäläinen et al. (1994) has demonstrated that pyrrolic and pyridinic function groups are related to emission of nitric oxides. It was investigated that the formation of NO from 14 nitrogen-containing model compounds, and found that the -OH in the compound with the carboxyl (-COOH) hardly might convert HCN to NH_3. Therefore, the intermediate, ammonia (NH_3), hardly appears for the compounds with carboxyl and without phenolic during their combustion. It is generally thought that the conversion of fuel-N to nitric oxides is through the intermediates, hydrogen cyanide (HCN) and ammonia (NH_3), formed during fuel combustion. (2) Nimmo et al. (2004a, 2004b) found that Calcium Magnesium acetate ($CaMg_2(CH_3COO)_6$) could be decomposed to the reductive gas, CHi, which can be reacted with NO:

Table 6 Comparison of NO emission between before acetic acid injection and after acetic acid injection (Sb 100%, Tb=890℃)

Acetic acid injecting location		A	C
NO emission	Before acetic acid injection	177	198
	After acetic acid injection	171	154

$$CaMg_2\ (CH_3COO)_6 \longrightarrow CaO + MgO + CH_i \quad (3)$$

$$NO + CH_i \longrightarrow HCN \xrightarrow{LowO_2} N_2 \quad (4)$$

From these two points of view, the acetic acid can reduce the NO emission concentration. However, it should be noted that when the acetic acid injecting location is lower (0.90m above the gas distributor), the reductive reaction also occurs, but the O, H and OH radical liberated from the acetic acid at high temperature reacted with HCN and NH_3 liberated from the volatile, thus formed NO, and this effect is higher than the above reductive reaction. Therefore, the NO emission concentration is decreased with increasing the injection location of the acetic acid.

CONCLUSIONS

NO emission characteristics in a pilot scale vortexing fluidized bed combustor was studied using response surface methodology (RSM). The effects of the operating conditions on the NO emission in this vortexing fluidized bed were investigated comprehensively. The following results can be concluded:

(1) NO emission increases with the stoichiometric oxygen in the combustion chamber and the bed temperature.

(2) NO emissions can be decreased by injecting the acetic acid into the combustion chamber. The NO emission decreases with the height of the acetic acid injecting location above the distributor.

(3) The bed temperature has more important effect on the NO emission than the other two factors, and the effect order is X_2 (the bed temperature) > X_3 (the injecting location of acetic acid) > X_1 (the stoichiometric oxygen in the combustion chamber).

REFERENCES

Armesto, L., Boerrigter, H., Bahillo, A. and Otero, J.: Fuel. 82(2003), pp.1845-1850.
Chyang, C. S., Wu, K. T. and Lin, C. S.: Fuel 86(2007), pp. 234-243.
Chyang, C. S., Qian F. P., Lin Y. C. and Yang S. H.: Energy & Fuels. 22 (2008 a), pp.1004-1011.
Chyang, C. S., Qian F. P. and Huang K.S.: Energy & Fuels. Submitted (2008b).
Chyang, C. S., Qian F. P. and Chiou H. Y.: Chem. Eng. Technol. 30 (2007), pp.1700-1707.
Glarborg, P., Jensen, A. D. and Johnsson, J. E. Progr. Energy Combust. Sci. 29(2003), pp.89-113.
Hämäläinen, J. P., Aho M. J. and Tummavuori J. L.: Fuel. 73 (1994), pp.1894-1898.
Iwasaki, Y., Yamada, Y., Watanabe, N. US patent 4159000, 1979.
Korenberg, J. (1983). Proceedings of 4th International Conference on Fluidization.
Li, Z. W., Lu, Q. G. and Na, Y. J. Fuel Process. Technol. 85 (2004), pp.1539-1549.
Montgomery D.C. (1997). Design and Analysis of Experiments, 4th ed., New York, Wiley.
Nelson, P. F., Kelly, M. D.and Wornat, M. J. Fuel. 70 (1991), pp. 403-407.
Nieh, S.; Yang, G. *AIChE Annual Meeting*, Miami Beach, F: Paper No. 1986; pp 41.
Nimmo, W., Patsias, A.A., Hampartsoumian, E., Gibbs, B.M. and Williams, P.T.: Fuel. 83(2004a), pp.149-155.
Nimmo, W., Patsias, A. A., Hampartsoumian, E., Gibbs, B. M., Fairweather, M. and Williams, P. T.: Fuel. 83 (2004b), pp.1143-1150.
Permchart, W. and Kouprianov, V. I. Bioresour. Technol. 92 (2004), pp.83-91.
Shimizu, T., Toyono, M.and Ohsawa, H. Fuel. 86(2007), pp.957-964.
Svoboda, K. and Pohořely, M. Fuel. 83 (2004), pp.1095-1103.
Tarelho, L. A. C., Matos, Ma. A. A. and Pereira, F. J. M. A. Fuel Process. Technol. 86(2005), pp.925-940.
Zhao, W. et al. Bioresour. Technol. 99 (2008), pp.2956-2963.

A TRIAL TO SEPARATE FORMATION AND REDUCTION PROCESS DURING NO EMISSION IN FLUIDIZED BED COAL COMBUSTION

T. Murakami[1], Y. Suzuki[1], A. K. Durrani[2]

[1] *Energy Technology Research Institute, National Institute of Advanced Industrial Science and Technology (AIST), 16-1, Onogawa, Tsukuba, Ibaraki 305-8569, Japan*

[2] *University of the Punjab, Pakistan*

Abstract: A new approach to evaluate NO formation and reduction processes separately in fluidized bed coal combustion has been investigated. Sixteen different coals were burned in a lab-scale bubbling fluidized bed combustor with three different char loadings by changing the inlet oxygen concentration to 20 %, 15 % and 10 %. When O_2 consumption rate in the bed becomes zero, N conversion ratio to NO (X_{NO}) indicates a special value without contribution of NO reduction by char particles in the bed. We call it "ultimate NO conversion ratio (X_{NO}^*)". This imaginary NO conversion ratio, X_{NO}^*, expresses an NO conversion of a coal particle which burns singly in a fluidized bed combustor. Since there are no other char particles in the bed, X_{NO}^* should express a coal's original NO emission. X_{NO}^* can be determined by an extrapolation of a line, which is determined by a least-squares method, showing the relationship between X_{NO} and O_2 consumption rates for each tested coal. By this technique, the contribution of char particles to NO reduction and the original NO emission of the tested coals can be separated from each other.

X_{NO}^* depended on the N content and O/N molar ratio. Effect of the bed temperature on the sensitivity of X_{NO} on char loading, which expresses the effect of NO reduction by char particles, was very different among the different coals. On the other hand, the contribution of char particles on N_2O emission was affected little and experiments showed that a burning char particle cannot reduce N_2O. This result suggests that the reduction by the char particles involves the competitive reaction of NO and N_2O, and the effect of the N_2O reduction by burning char particles was less than NO reduction. Consequently, experiments showed that the effect of NO reduction by char particles was very important in the fluidized bed combustion when final NO_x emission is evaluated deeply.

Keywords: NO, coal, fluidized bed combustion, ultimate NO emission, char

INTRODUCTION

Fluidized bed combustion (FBC) is an excellent technique for coal combustion because the low operating temperature (~1123 K) and in-bed desufurization with limestone result in low NO_x and SO_x emissions. Therefore, FBC has been used for coals with a wide variety of properties. In previous studies, the relationships between NO_x emissions and FBC operating parameters such as temperature, pressure, air ratio, and coal properties have been experimentally elucidated (Åmand et al., 1991 and Johnsson, 1994). In addition, the effect of limestone on NO_x formation has been studied (Shimizu et al., 2002).

Several attempts have been made to predict NO_x emissions by using correlations obtained from fundamental studies. However, the predictions based on these correlations are not sufficiently accurate. The predictions for FBC of coal are usually less accurate than the predictions for pulverized coal combustion, and coals with the same analytical values frequent give very different NO_x emissions in FBC (Suganal et al., 2000). Therefore, combustion tests are still required for the accurate determination of NO_x emissions. For more accurate and reliable predictions, a better understanding of the factors relating to NO_x emissions under FBC conditions is required. Kunii et al. pointed out that char particles can reduce NO to N_2 under FBC conditions (Kunii et al., 1980). Since their pioneering study, many studies of the mechanisms of NO reduction by char have been done (Jensen et al., 1995 and Zhao et al., 2003). Researchers have developed mathematical models for these pathways and carried out kinetic calculations (Kunii et al., 1980; Miller et al., 1989; Jensen et al., 1995; Glarborg et al., 1998; and Shimizu et al., 2002).

Previous studies on the effect of different coals on NO_x emissions have dealt mainly with overall NO_x emissions. However, because of the existence of a dense particle phase containing char particles, which strongly reduce NO_x, the overall NO_x emissions will reflect both NO_x formation and NO_x reduction by char. Therefore, it is important that the contributions of these two processes be evaluated separately. In particular, more information about the contribution of char to NO reduction is required.

The objective of the current study was to evaluate the effect of different coals not on the overall NO emission but on NO formation and NO reduction individually. To separate the formation and reduction processes, a new experimental technique was employed. We carried out combustion experiments using 16 different coals in a lab-scale bubbling fluidized bed combustor with different char loadings in the bed. By using this methodology, the formation and reduction processes in the bed can be separately evaluated and the effect of different coals on NO emissions can be explained.

EXPERIMENTAL

The main components of the lab-scale bubbling fluidized bed combustor were a screw feeder, a reactor, an electric furnace, a cyclone, an ash pot and filters for dust and moisture removal (Fig. 1). The transparent quartz reactor was 32 mm in internal diameter and 450 mm in height, and the central part of the reactor was heated by the electric furnace. A sintered porous silica plate placed in the quartz tube served as a gas distributor. The bed temperature was measured with a type-K thermocouple immersed in the bed. Silica sand (mean diameter, 200 μm) was employed as the bed material; the static bed height was 30 mm. Fresh bed material was used in every experiment, to minimize the effect of the minerals in the ash.

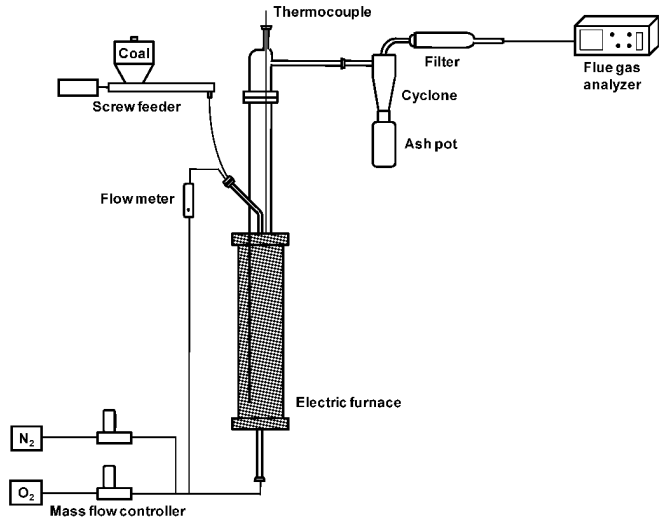

Fig. 1 Schematic diagram of a laboratory-scale bubbling fluidized bed combustor

Combustion air (a mixture of N_2 and O_2 in proportions controlled by means of mass flow controllers) was supplied to the bed through the gas distributor. Coal was pneumatically injected into the bed continuously by means of the screw feeder after the bed temperature exceeded a predetermined temperature. The coal supply point was a few millimeters above the gas distributor. The coal feed rate was maintained at 0.05-0.35 g/min, and the inlet gas flow rate was fixed at 2.50 L_N/min. Thus, the superficial gas velocity was about 0.21 m/s at 1123 K, and gas residence time in the reactor is about 2 sec. Experiments were conducted at three bed temperatures: 1093, 1123, and 1153 K. The O_2 concentration in the combustion air was 20, 15, or 10% by volume, and the O_2 concentration in the flue gas was adjusted to approximately 3.5 % by controlling the coal feed rate. Because the char loading in the bed was determined by the balance between the combustion rate and the coal feed rate, the char loading should decreased when the O_2 concentration difference between the inlet and the outlet of the bed becomes small, assuming that the average combustion rate of char was constant. Therefore, the experimental conditions described in this paragraph resulted in three different char loads in the bed.

The flue gas was analyzed after passing through the cyclone and the filters. The concentrations of O_2 and NO in the flue gas were analyzed with a continuous gas analyzer (NOA-7000 Shimadzu Corp., Kyoto, Japan), and the N_2O concentration was measured with a micro gas chromatograph (Q30L gas chromatograph, MTI Analytical Instruments, CA). Steady operation was continued for at least 15 minutes for each experimental condition.

The analytical values for the 16 different coals are listed in Table 1. The coals were selected to obtain a wide range of nitrogen contents (0.9-2.1 wt%) and a fixed carbon content of 42-60 wt%. The coals (particle diameter, <1.0 mm) were stored in N_2-filled aluminum-coated plastic bags to prevent low temperature oxidation by air. The coal samples were sieved to 0.25-0.50 mm diameter and dried in a vacuum oven at 353 K for 8 hours before the experiments.

Table 1 Coal properties

Sample No.	Proximate analysis [wt%]			Ultimate analysis [dry, wt%]		
	VM	FC	Ash	C	N	O
SS033	43.57	44.71	0.88	71.98	1.03	20.64
SS049	24.98	59.82	13.19	71.20	1.77	9.21
SS071	39.87	45.02	5.81	71.29	1.71	15.01
SS074	27.91	57.67	8.16	75.10	1.72	9.99
SS075	29.36	53.40	10.99	72.62	1.04	9.99
SS076	33.81	52.27	8.24	73.12	2.10	10.93
SS078	40.03	47.64	6.22	72.36	1.28	14.34
SS083	39.86	44.92	12.02	68.80	1.67	11.67
SS084	33.10	50.77	13.21	68.21	1.81	11.80
SS085	24.16	60.09	14.30	72.44	1.46	7.18
SS086	40.52	47.99	9.26	72.59	1.87	10.54
SS087	43.26	45.40	4.61	70.92	1.65	17.26
SS088	31.58	58.39	6.79	76.02	0.90	11.00
SS090	45.95	42.68	8.79	71.78	1.14	11.19
SS099	31.62	51.72	11.80	71.29	1.24	10.02
SS100	32.22	52.00	11.55	71.35	1.59	10.18

RESULTS AND DISCUSSION

Definition of ultimate NO conversion ratio (X_{NO}^*)

The NO conversion ratio of all the coals were determined. Figure 2 shows the relationship between NO conversion ratio (X_{NO}), which is the ratio of the mass of N atoms in the emitted NO to the mass of N atoms in the coal, and the O_2 consumption rate at 1123 K for all the tested coals. The O_2 consumption rate is defined as mass of moles of O_2 consumed per second per bed volume in the bed. The gas residence time in the bed was so short that X_{NO} values were higher than the values observed under the usual combustion conditions (Jensen et al., 1995 and Svoboda et al., 2004). For all the coals tested, the X_{NO} values increased linearly with decreasing O_2 consumption rate, because as the O_2 consumption rate decreased, the char loading in the bed, and thus NO reduction in the bed, decreased. At an O_2 consumption rate of zero, the corresponding X_{NO} value reflects the value that would be obtained in the absence of NO reduction by char particles in the bed, that is, the value for a single coal particle burning in the absence of char particles. We refer to this value as the "ultimate NO conversion ratio" (X_{NO}^*). Therefore, X_{NO}^* is a coal's intrinsic NO emission. X_{NO}^* for a given different coals can be determined by extrapolation of the lines (determined by a least-squares method) describing the relationship between X_{NO} and O_2 consumption rate for that coal to an O_2 consumption rate of zero. Figure 3 shows the results of extrapolation for several of the coals. This methodology was also applicable to data obtained under other temperature conditions (1093 and 1153 K).

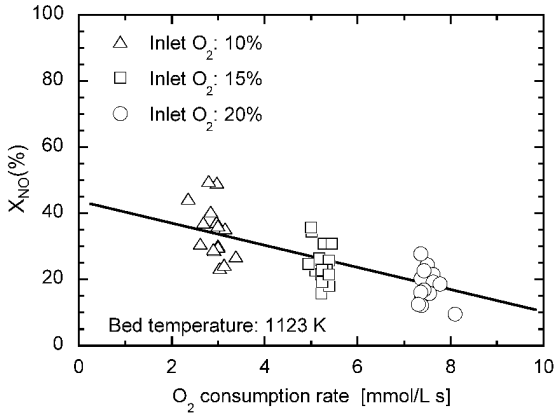

Fig. 2 Dependence of X_{NO} on O_2 consumption rates in the bed for all tested coals

The X_{NO}^* and X_{NO} values for all the tested coals at an O_2 consumption rate of 7.6 mmol/L s are shown in Fig. 4. The circle shows the ratio of X_{NO}^* and X_{NO} values at an O_2 consumption rate of 7.6 mmol/L s. The X_{NO}^*

values were remarkably higher than the X_{NO} values for all the coals, which clearly indicates that the contribution of NO reduction by char particles in the bed was large. In addition, the contribution of NO reduction differed substantially for the various coals. In other words, different coals affected not only NO formation but also NO reduction.

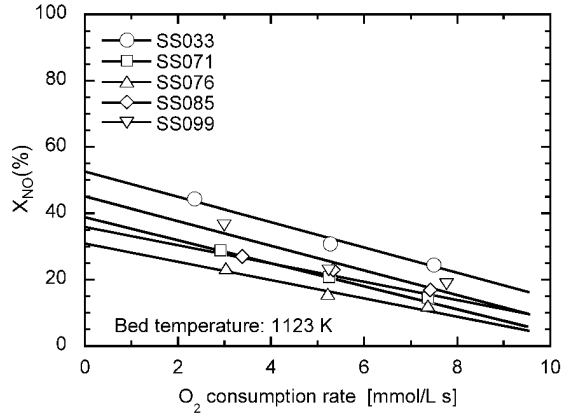

Fig. 3 Example of extrapolation method to determine ultimate X_{NO} in several coals

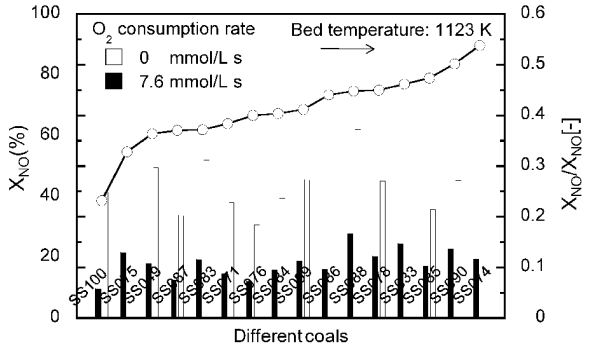

Fig. 4 Comparison of X_{NO} on O_2 consumption rates for all tested coals

Effect of different coals on X_{NO}^* values

Nitrogen content is one of the major factors that determine NO conversion during FBC, so the relationship between X_{NO} and N content for the tested coals was evaluated. X_{NO} increased with decreasing N content at all O_2 consumption rates (Fig. 5) (Winter, et al., 1999), and the dependence of X_{NO} on N content was almost the same for all O_2 consumption rates. We also found that X_{NO}^* increased with increasing O/N molar ratio in the coals (Fig. 6). NO emission can be expected to increase with O/N molar ratio because OH radicals tend to be generated at high O/N ratios, and OH radicals react with HCN to generate NH_3 (Hamalainen et al., 1995).

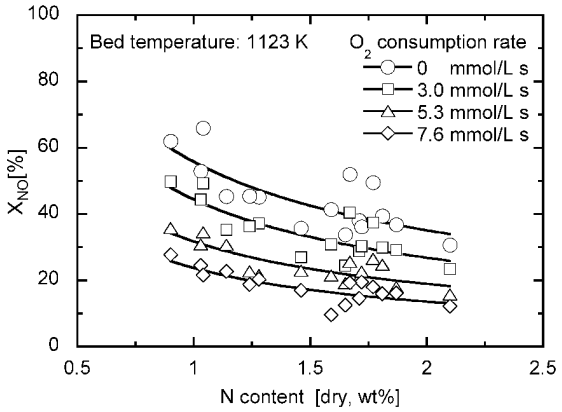

Fig. 5 Relationship between X_{NO} and N content in the coal

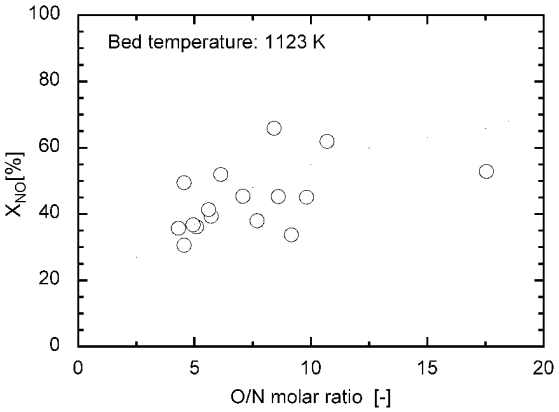

Fig. 6 Dependence of X_{NO}^* and O/N molar ratio in the coal

The dependence of the sensitivity, which corresponds to the slopes of the lines describing the relationship between X_{NO} and O_2 consumption rate for the different coals (Fig. 3), on the bed temperature differed substantially for the various different coals (Fig. 7). The coals fell into two categories. For some coals, the absolute value of the sensitivity increased with increasing bed temperature (Fig. 7(a)), whereas for other coals, the absolute value of the sensitivity decreased with increasing bed temperature (Fig. 7(b)). For coals in the first category, NO reduction by char particles was enhanced by increases in the bed temperature, and for coals in the second category, NO reduction by char particles decreased with increasing bed temperature. Typical coals in the first category were SS076, SS085, and SS099. These different behaviors of the two categories of coal may have been due to differences in char reactivity relating to the particle structures and mineral content in the ash. More research is required to clarify this issue.

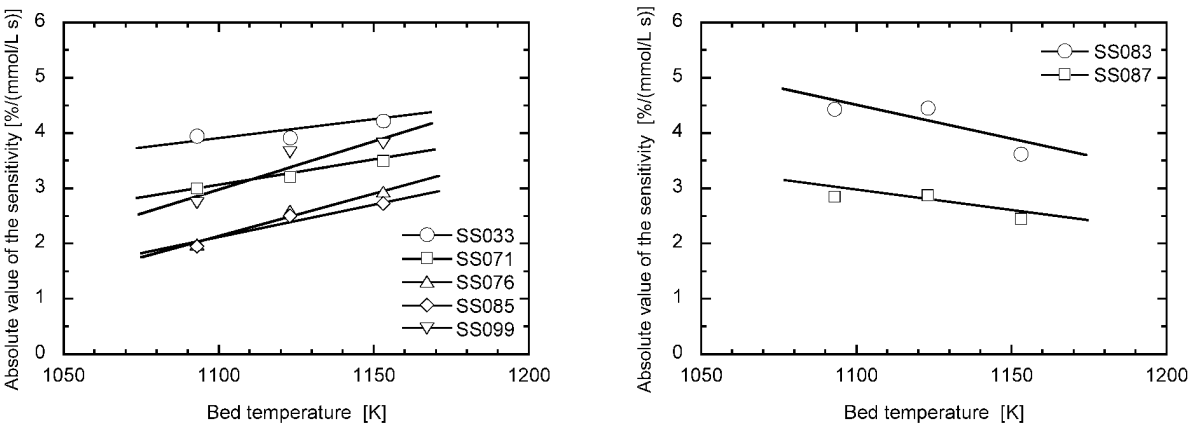

(a) Absolute value of sensitivity increasing with increasing bed temperature

(b) Absolute value of sensitivity decreasing with increasing bed temperature

Fig. 7 Relationship between sensitivity values and bed temperature

Effect of the different coals on N_2O emission

N_2O emissions were evaluated by the technique used to evaluate NO emissions. Figure 8 shows the relationship between N_2O conversion ratio (X_{N_2O}) and O_2 consumption rate at 1123 K for selected different coals. A slight increasing in X_{N_2O} with decreasing O_2 consumption rate was observed. However, the dependence was not nearly as strong as that observed for NO. This result indicates that X_{N_2O} was independent of char loading in the bed; that is, the contribution of N_2O reduction by char particles in the bed was small.

Previous studies have shown that char particles can reduce N_2O (Gulyurtlu et al., 1992). However, our experiments showed that actually burning char particles in the bed did not reduce N_2O. In previous studies, N_2O reduction by char particles was usually investigated in a packed bed reactor in the presence of N_2O/N_2 mixtures (Gulyurtlu et al., 1992); that is, N_2O reduction by char particles has not been investigated in actually burning char particle in the fluidized bed. According to standard two-phase theory, NO and N_2O generated in the bubble move to the emulsion phase by gas exchange between the bubble phase and emulsion phase, and the reduction reaction occurs on the surface of the char particles. The reduction by char particles involves the competitive reaction of NO and N_2O (Rodriguez et al., 1994). We have demonstrated experimentally that the effect of N_2O reduction by burning char particles was less than NO reduction. Consequently, burning char particles in the fluidized bed may not reduce N_2O. More detailed experiments may be required to verify these speculations.

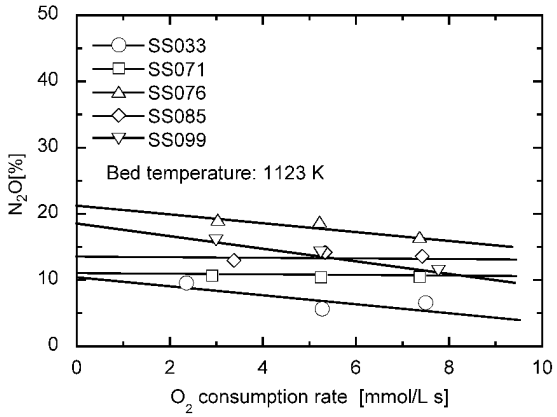

Fig. 8 Relationship between X_{N_2O} and O_2 consumption in the bed for different coals

The effect of different coals on N_2O emission was evaluated. Figure 9 shows the relationship between X_{N2O} and N content at an O_2 consumption rate of 7.6 mmol/L s. Coal having a higher N content greatly gave a higher X_{N_2O}. However, this trend was not as clear-cut as the trend observed for X_{NO}^* (Fig. 5). That is, the effect of N content on N_2O formation was not as strong as the effect on NO formation. X_{N2O} decreased with increasing O/N molar ratio (Fig. 10). This result can be explained by the fact that the mass of NH_3 (major substance of N_2O decreasing) released during devolatilization increased with increasing O/N molar ratio, as mentioned above (Hamalainen et al., 1995).

Therefore, our new approach to evaluating NO emissions indicates that under FBC conditions, char particles strongly affected NO emission but not N_2O emission.

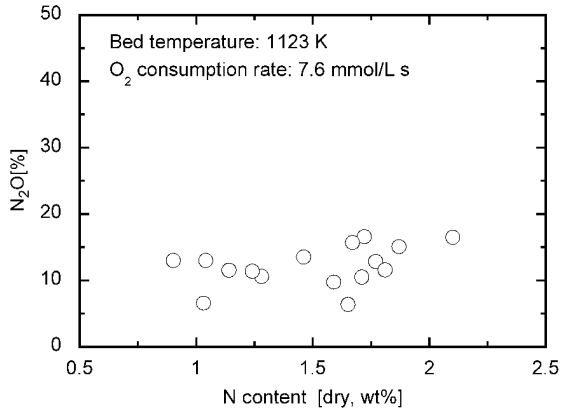

Fig. 9 Relationship between X_{N_2O} and N content in the coal

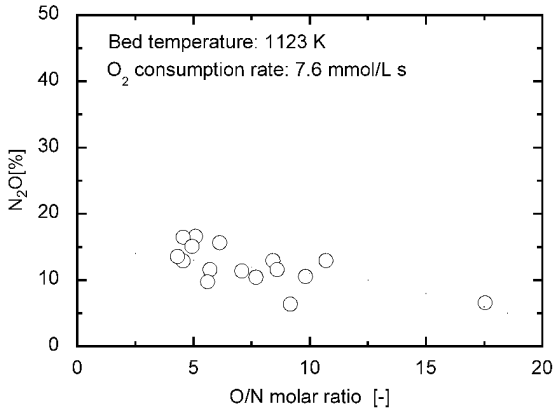

Fig. 10 Dependence of X_{N_2O} and O/N molar ratio in the coal

CONCLUSIONS

A method for separately evaluating NO formation and NO reduction by char during FBC of coal by changing the char loading in the bed was investigated. Following main conclusions were drawn from the experimental results:

It is found that as the O_2 consumption rate in the bed approached zero, the effect of char particles in the bed on NO emission became insignificant. The NO conversion ratio (X_{NO}) at a zero O_2 consumption rate, which we refer to as the "ultimate NO conversion ratio" (X_{NO}^*), was determined by extrapolation of the lines describing the correlation between X_{NO} and O_2 consumption rate for each tested coal to a zero O_2 consumption rate.

X_{NO}^* depended negatively on N content, and the dependence of X_{NO}^* on N content was almost the same as that of X_{NO} determined from NO emission in the flue gas. Additionally, X_{NO}^* depended positively on the O/N molar ratio.

Evaluating the reactivity of char particles is important for predicting overall NO emission, because the relationship between sensitivity and bed temperature varied widely with different coals.

The contribution of char particles to N_2O emission was small, and experiments suggest that N_2O cannot be reduced by burning char particles. Therefore, when both NO and N_2O exist around burning char particle, the effect of NO reduction by the char particles was considerably higher than N_2O reduction.

REFERENCES

Åmand, L.E. and Leckner, B.: Comb. & Flame **84** (1991), pp.181-196.
Glarborg, P., Alzueta, M. U., Johansen, K. D. and Miller, J.A.: Comb. & Flame **115** (1998), pp.1-27.
Gulyurtlu, I., Esparteiro, H. and Cabrita, I.: Proc. of the 5th Intl. Workshop on Mitrous Oxide Emissions Tsukuba. (1992), pp.255-265.
Hamalainen, J. P. and Aho, M. J.: Fuel **74** (1995), pp.1922-1924.
Jensen, A., Johnson, J. E., Andries, J., Laughlin, K., Read, G., Mayer, M., Baumann, H. and Bonn, B.: Fuel **74** (1995), pp.1555-1569.
Johnsson, J.E.: Fuel **80** (1994), pp.1398-1415.
Kunii, D., Wu, K. T. and Furusawa, T.: Chem. Eng. Sci. **35** (1980), pp.170-177.
Miller, J. A. and Bowman, C. T.: Prog. Energy Combust. Sci. **15** (1989), pp.287-338.
Rodriguez-M, J., Ooms, A. C., Pels, J. R., Kapteijn, F, Moulijn, J. A.: Comb. & Flame. **99** (1994), pp.499-507.
Shimizu, T., Satoh, M., Sato, K., Tonsho, M. and Inagaki, M.: Energy & Fuels **16** (2002), pp.161-165.
Suganal, D. D., Hosoda, H. and Hirama, T.: Proc. of the Coal Tech 2000 Jakarta. (2000), pp.281-289.
Svoboda, K. and Pohorely, M.: Fuel **83** (2004), 1095-1103.
Zhao, Z., Qiu, J., Li, W., Chen, H. and Li, B.: Fuel **82** (2003), pp.949-957.
Winter, F., Wartha, C. and Hofbauer, H.: Bioresource Tech. **70** (1999), pp.39-49.

EXPERIMENTAL STUDY OF NITROGEN OXIDE EMISSIONS IN A CIRCULATING FLUIDIZED BED

R. W. Liu, Q. L. Zhou, S. E. Hui, T. M. Xu

The State Key Laboratory of Power Engineering Multiphase Flow, Department of Energy and Power Engineering, Xi'an Jiaotong University, Xi'an, Shaanxi, 710049, China

Abstract: The experimental study was carried out on the emission characteristics of nitrogen oxide in a 0.3MW circulating fluidized bed as well as analysis of the formation and destruction mechanism of nitrogen oxide. Several variables associated with the combustion system were investigated in the experiment, which include bed temperature, excess air, primary-to-secondary air ratio, and coal species. It is found that the NO_x emissions decrease along the height of the furnace, while the N_2O emissions increase continuously. More NO_x emissions and less N_2O emissions are generated as the bed temperature increases. It is also illustrated that an increase of air stoichiometry leads to a significant NO_x increase and an obvious N_2O increase. And air staging is proved to be an effective way to control the nitrogen oxide emissions in the fluid bed. Besides, it is also shown in the experiment that the concentration of NO_x and N_2O is higher during the combustion of anthracite than that during the combustion of bituminous.

Keywords: CFB, nitrogen oxide, experiment

INTRODUCTION

Coal combustion generates quantities of nitrogen oxide emissions which contribute significantly to ozone decomposition and acid rain, and can react with volatile organic compounds to form photo-chemical smog. Nowadays, more and more attention has been paid to the NO_x emissions control technologies. It is well known that there are primarily three nitrogen oxide species emitted from fluidized bed combustors: nitric oxide (NO), nitrogen dioxide (NO_2) and nitrous oxide (N_2O). The first two is called NO_x selectively in many countries. As a greenhouse gas, N_2O is many times more powerful than CO_2 as an absorber of infrared radiation. And the N_2O emissions are much higher in fluidized beds than in other combustion equipments, such as pulverized coal combustion equipment (Grace et al., 1997).

In recent years, considerable research has been done upon NO_x /N_2O formation and potential methods for their destruction in fluidized bed environments. Pathways for NO_x formation illustrating typical fractional conversions at each step were presented by Johnsson in 1989, and Amand proposed the general pathways for NO and N_2O formation and destruction in FBC in 1994. Besides, effects of bed temperature, excess air, volatiles, limestone and ammonia on nitrogen oxide emissions have been studied by many researchers and some valuable conclusions were drawn (Harada, 1992; Braun, 1990, 1991; Leckner and Amand, 1987). However, there have been still many controversies over the formation and conversion mechanism of nitrogen oxide emissions, especially the formation and destruction mechanism of N_2O.

In the experiment presented in this paper, nitrogen oxide emissions were tested along the furnace height and several variables associated with the nitrogen oxide emissions were investigated, including the bed temperature, secondary air ratio, excess air and coal species, etc. The experiment data verifies the previous understanding about the formation and destruction mechanism of nitrogen oxide emissions and makes the experiment data in this area more sufficient. Also, some analysis of the results is presented in this paper.

TEST FACILITY

Figure 1 is the scheme of the test facility for a 0.3MW circulating fluidized bed. The furnace of the test facility is 7.75m in height, 0.245m in width and 0.245m in depth. On the wall of the furnace, two opposite secondary air nozzles were arranged symmetrically and two opposite membrane water walls of 1.6m in height were arranged symmetrically at a different height. The primary air is injected into the furnace through air distribution plate with 41 air caps.

There were 13 test points arranged along the height of the furnace for the central temperature measurement, as shown in Fig.1. NiCr-NiSi thermocouples were used in the measurement and temperature data were acquired by IMP (Isolated Measurement Pods). Besides, five test points along the height were set to measure the flue gas in the middle of the furnace. Amongst these points, the first one was set in the dense region, and the third one was set in the region of water wall, and the last one was set at the exit of the furnace. The concentration of gases was continuously tested by GASMET FTIR Dx4000 flue gas analyser, and the

measurement accuracy is 0.01%; O_2 concentration was tested by MSI compact flue gas analyser, and the measurement accuracy is 0.3%.

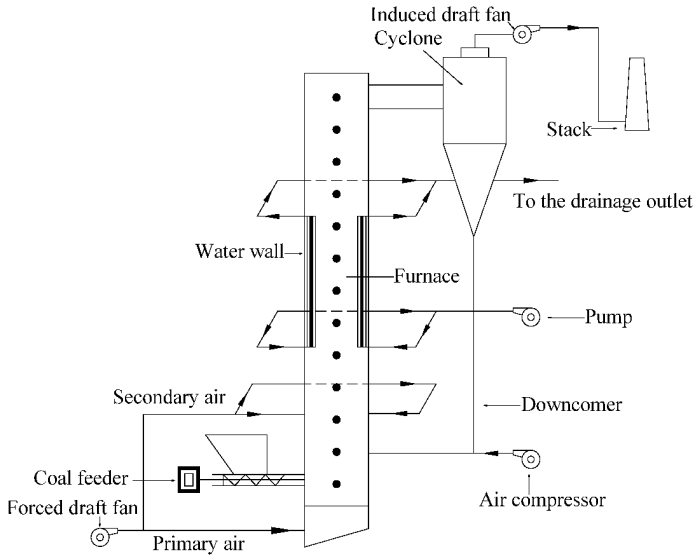

Fig.1 The scheme of the test facility for a circulating fluidized bed

PREPARATION OF COAL AND BED MATERIAL

River sand with the mean diameter of 274.6μm was constantly used as the bed material in the experiment. Two species of coal were investigated. One is bituminous coal with the mean diameter of 431μm, the other is anthracite coal with the mean diameter of 321μm.

The proximate and ultimate analysis data are given in Table 1.

Table 1 Proximate analysis and ultimate analysis of dry coal (%)

Proximate analysis, wt% (as air-dry)					
Specie	**Moisture**	**Ash**	**Volatile**	**Fixed carbon**	**Net heating(kJ/kg)**
Bituminous	3.34	17.53	29.21	49.92	24300
Anthracite	2.61	19.87	7.21	70.31	26950
Ultimate analysis, wt% (as air-dry)					
Specie	**Carbon**	**Hydrogen**	**Oxygen**	**Nitrogen**	**Sulphur**
Bituminous	60.14	5.07	12.51	0.56	0.85
Anthracite	71.75	2.81	1.78	0.8	0.38

RESULTS AND DISCUSSIONS

NO_x and N_2O emissions along the height of the furnace

Bituminous coal was utilized during this experiment. The volume of the primary air was 250m^3/h and no secondary air was involved. The air stoichiometry was 1.3.

Bed temperature in the dense region was kept at about 805℃ and temperature decreases along the height of the furnace as shown in Fig.2. It is also indicated in Fig.3 that the concentration of NO_x decreases along the height of the furnace, while the concentration of N_2O increases continuously.

NO_x decreases along the height of the furnace by reduction with char. During this process, N_2O and N_2 may be formed, as is evident from equation (1) and equation (2).

$$Char + 2NO \longrightarrow N_2O + CO \quad (1)$$

$$C + 2NO \longrightarrow N_2 + CO_2 \quad (2)$$

$$N - from\ char + O_2 \longrightarrow N_2O \quad (3)$$

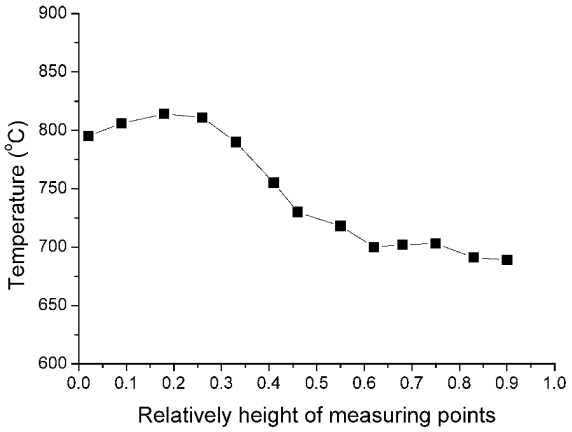

Fig.2 Temperature along the relative height of the furnace

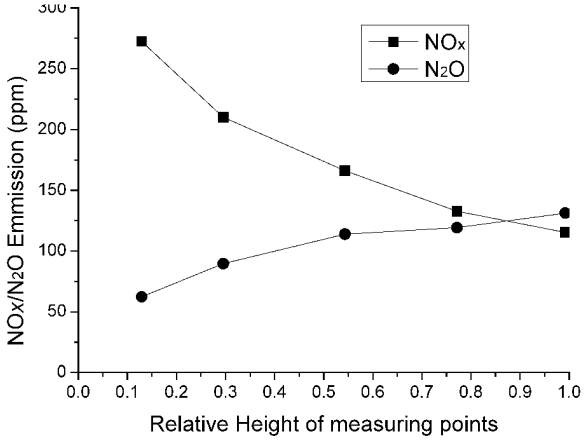

Fig.3 NO_x and N_2O emissions along the relative height of the furnace

On the other hand, formation of N_2O is primarily by the direct oxidation of char nitrogen as shown in equation (3) as well as the reduction reaction of char and NO. Besides, the reduction reaction of N_2O is very sensitive to the bed temperature, so the reduction rate decreases rapidly with the decrease of the bed temperature along the height of the furnace. Therefore, it is concluded that the concentration of N_2O increases along the height of the furnace.

Influences of bed temperature on the NO_x and N_2O emissions

The operation conditions were the same as specified above except the temperature.

Figures 4 and 5 show the relations between nitrogen oxide emissions and bed temperature in the dense region and exit region of the bed respectively. It is illustrated that NO_x increases with the bed temperature in dense region and the exit region, while N_2O decreases in contrast.

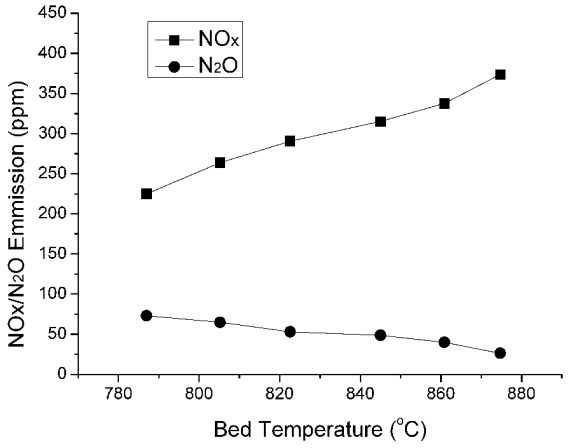

Fig.4 NO_x and N_2O emissions in the dense region

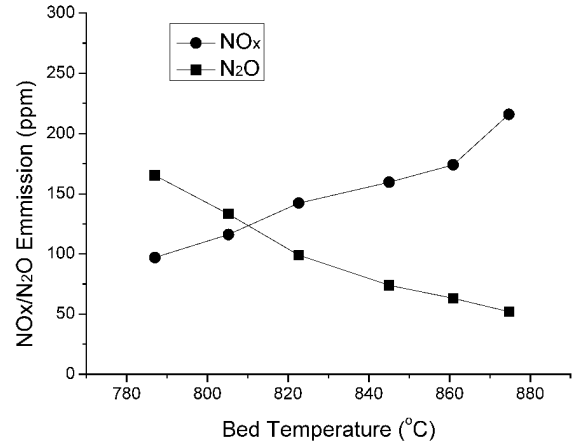

Fig.5 NO_x and N_2O emissions at the exit of the furnace

High temperature prompts the thermal decomposition of N_2O as shown in equation (5). On the other hand, more CO reacts with OH as the temperature increases, which leads to an increase of hydrogen atom concentration as shown in equation (6). According to equation (4), hydrogen atom helps the reduction of N_2O. Besides, as the bed temperature increases, more volatile nitrogen is released or decomposes from coal to form HCN and NH_3 which are converted homogeneously to NO_x and N_2O as shown in equations (7)-(11).

$$N_2O + H \Leftrightarrow N_2 + OH \quad (4)$$

$$N_2O + O \Leftrightarrow N_2 + O_2 \quad (5)$$

$$CO + OH \Leftrightarrow CO_2 + H \quad (6)$$

$$HCN + O \Leftrightarrow NCO + H \quad (7)$$

$$NCO + NO \Leftrightarrow N_2O + CO \quad (8)$$

$$NCO + OH \Leftrightarrow NO + CO + H \quad (9)$$

$$NCO + O \Leftrightarrow NO + CO \quad (10)$$

$$NH_3 + \tfrac{5}{4}O_2 \Leftrightarrow NO + \tfrac{3}{2}H_2O \quad (11)$$

Amongst these reactions, equation (8) has the negative activation energy, so this reaction is abated and the concentration of N_2O decreases with the increase of bed temperature.

However, reactions as shown in equation (7), (9), (10) and (11) are accelerated as the temperature increases. Therefore, more NO will be formed due to more volatile nitrogen released in this process. And it is also indicated that combustion of volatile nitrogen is dominant for the formation of NO.

Influences of the excess air on the NO_x and N_2O emissions

All operation parameters were kept unchanged in the experiment except the air stoichiometry and bed temperature.

Figures 6 and 7 show the relations between nitrogen oxide emissions and excess air in the dense region

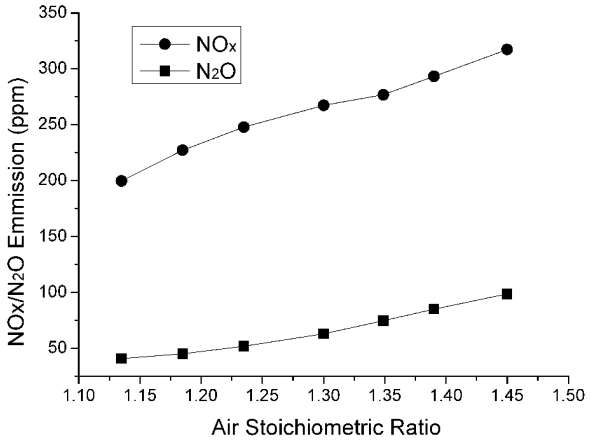

Fig.6 NO_x and N_2O emissions in the dense region

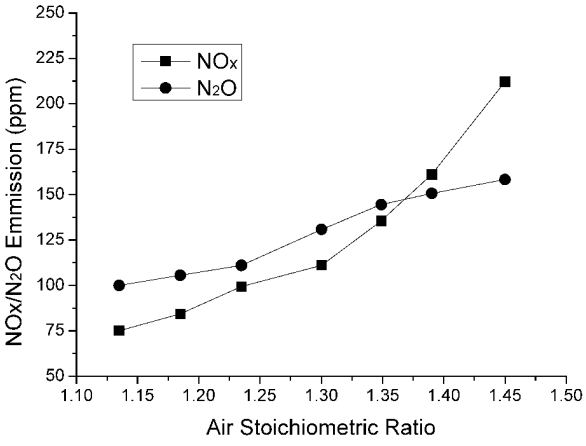

Fig.7 NO_x and N_2O emissions at the exit of the furnace

and exit region of the bed respectively. The relations between air stoichiometry ratio and bed temperature are shown in Fig.8.

It is illustrated that an increase of air stoichiometry leads to a significant NO_x increase and an evident N_2O increase. At the same time, the temperature in the dense region decreases smoothly, while the temperature at the furnace exit increases.

Increased excess air is beneficial to the oxidation of nitrogen species and reduces the amount of carbon which can react with the NO formed during the combustion. As the concentration of oxygen increases, more HCN is converted to NCO (equation (7)) which is helpful for the formation of NO (equations (9), (10)). Meanwhile, the excess oxygen helps more NH_3 convert into NO directly, as shown in equation (11). Therefore, the concentration of NO_x increases significantly due to the increased excess air.

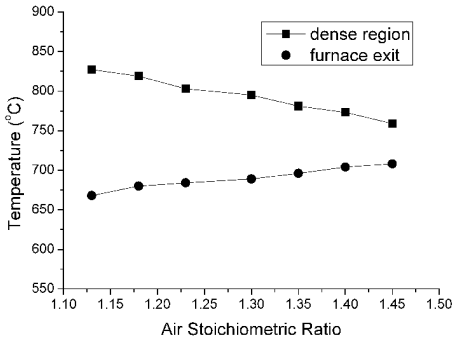

Fig.8 Effect of air stoichiometric ratio on temperature

The excess air has opposite influences on the N_2O formation. Despite more N_2O is formed due to the oxidation of nitrogen, part of N_2O will decrease by reactions with oxygen atoms. And the importance of these two processes is nearly the same.

Besides, as a result of the excess air, the bed temperature in the dense region actually decreases in some extent, which prompts the formation of N_2O as we discussed above. Therefore, less N_2O emissions should be obtained than what we observed in the experiment if the bed temperature is kept constant. That is to say, the influence of air stoichiometry on the N_2O emissions is not noticeably actually.

Influences of primary-to-secondary air ratio on the nitrogen oxide emissions and temperature distribution

It is widely accepted that air staging is an effective method of reducing nitrogen oxide emissions. In the experiment, the effects of primary-to-secondary air ratio on nitrogen oxide emissions were determined on condition that the total air volume was kept constant and the air stoichoimetry was 1.3.

Fig.9 shows that concentration of NO_x and N_2O at the exit of the furnace decreases along with the increase of the secondary air ratio. It is illustrated in Fig.10 that the temperature level in the dense region increases apparently but the temperature at the exit of the furnace is nearly unchanged until the secondary air ratio arrives

at 40%. After the secondary air ratio exceeds 40%, the temperature level in the dense region as well as that at the exit of the furnace decreases as the secondary air ratio increases. The reasons for the phenomena observed in the experiment are mainly as follows:

As secondary air ratio increases, Char holdup and CO concentration significantly increase in the bottom of the furnace because of the lack of O_2. Therefore, reducing atmosphere is created during the substoichiometrc combustion which helps NO_x reduction into molecular nitrogen over char. At the same time, it is difficult for the nitrogenous compounds released as volatiles (for example NH_3, HCN and so on) to be converted into NO_x as a result of insufficient oxygen although the quantity of these nitrogenous compounds increases. And these nitrogenous compounds can later contribute to further reduction of NO_x in the freeboard.

Besides, as the secondary air ratio increases, the formation of N_2O by reactions of char nitrogen oxidation as well as volatile nitrogen oxidation in the dense region is limited due to the lack of oxygen. Meantime, the temperature of the substoichiometric combustion region increases, so the decomposition reaction of N_2O is prompted and the concentration of N_2O decreases.

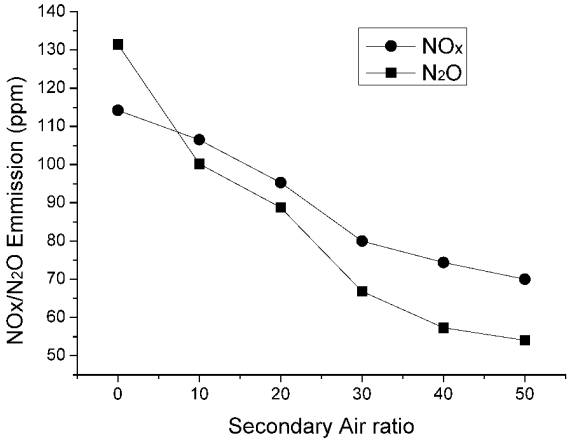

Fig.9 NO_x and N_2O emissions at the exit of the furnace

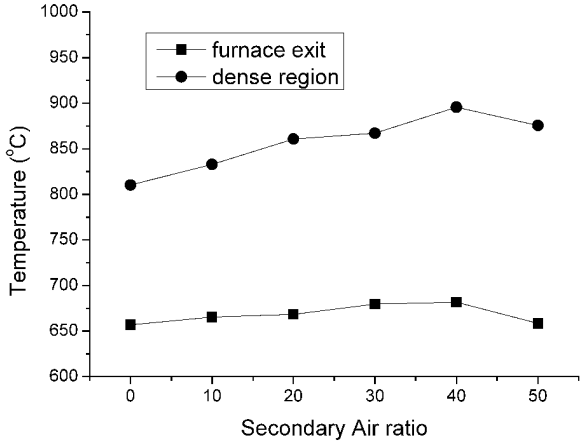

Fig.10 Temperature distributions in the furnace

Influences of coal species on the nitrogen oxide emissions

Anthracite coal was utilized instead of bituminous coal in the experiment. The volume of the primary air was 250m^3/h and no secondary air was involved. The air stoichiometry was 1.3.

It is shown in Fig.11 that the temperature decreases along the height of the furnace and the temperature in the dense region is higher than that during the combustion of bituminous as shown in Fig.2, while the temperature at the exit of the furnace is lower. It is also illustrated that both NO_x concentration and N_2O concentration are higher either in the dense region or at the exit of the furnace in contrast with that in Fig.3. This result is different from conclusions obtained from many investigations on the combustion of different coal species which indicate that high volatile coals produce considerably lower N_2O concentration and considerably higher NO_x concentration (Moritomi, H, et al., 1990, 1991). The main reason for this behavior is believed in this paper that both the bed temperature and the combustion rate of carbon in the dense region are higher during the

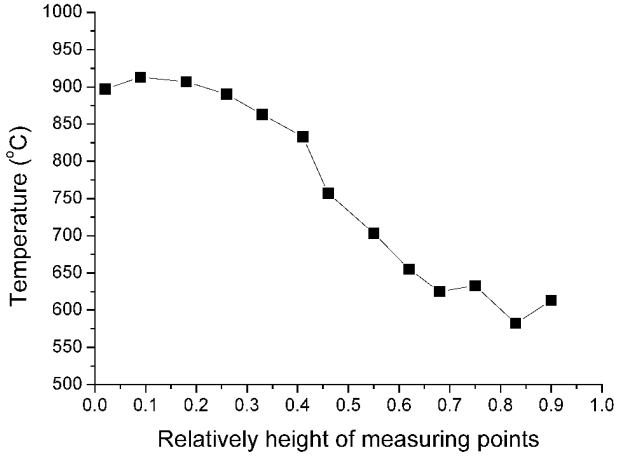

Fig.11 Temperature along the relative height of the furnace

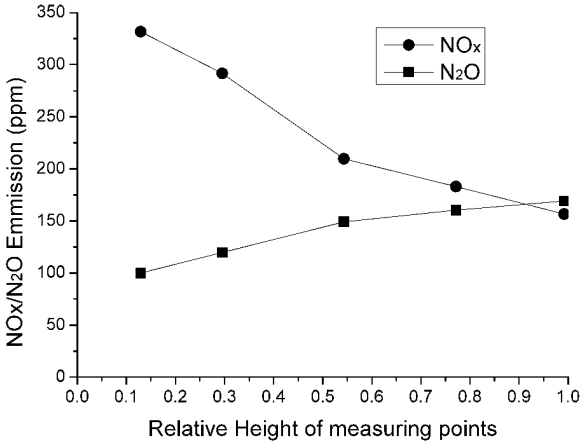

Fig.12 NO_x and N_2O emissions along the relative height of the furnace

combustion of anthracite. This explanation is based on some assumptions that the nitrous oxide is mainly produced from combustion of char nitrogen while the nitric oxide is mainly from the combustion of volatile nitrogen. In this case, the combustion rate of carbon in the dense region is higher and more volatile nitrogen is released as a result of higher bed temperature, so both NO_x and N_2O concentration is higher. If the bed temperature is kept constant, more volatile is released and burned in the combustion of bituminous compared with combustion of anthracite, which means lower combustion rate of carbon because the temperature level of these two combustions is kept the same. Therefore, less N_2O but more NO_x is produced. Along the height of the furnace, N_2O increases because of the combustion with the rest char volatile and conversion from NO, while NO_x decreases because of the conversion into N_2O and reduction by carbon.

CONCLUSIONS

The experiment of nitrogen oxide emissions in a circulating fluidized bed shows that the concentration of NO_x decreases along the height of the furnace, while the concentration of N_2O increases continuously. Combustion temperature has the dominant effect on nitrogen oxide emissions. It is clearly observed that the concentration of NO_x rises with bed temperature while the concentration of N_2O drops. It is also illustrated that an increase of air stoichiometry leads to a significant NO_x increase and an obvious N_2O increase. Therefore, reducing atmosphere is necessary in order to control the nitrogen oxide. And it is well interpreted that air staging is an effective way to reduce the nitrogen oxide emissions, which is strongly supported by the experiment data.

It is also shown in the experiment that the concentration of nitrogen oxide including NO_x and N_2O is higher during the combustion of anthracite than that during the combustion of bituminous. It is believed in this paper that this difference is generated from higher bed temperature and higher combustion rate of carbon during the combustion of anthracite because combustion of carbon is a dominant process for the formation of N_2O but the combustion of volatile is a primary reaction for the formation of NO_x.

REFERENCES

Amand, L.-E. Nitrous oxide emission from circulating fluidized bed combustion. PhD Dissertation, Chalmers University, Sweden, 1994.

Braun, A. Emission of NO and N_2O from a 4 MW fluidized bed combustor. 21st IEA-AFBC Technical Meeting, Belgrade, 1990.

Braun, A. (1991). Emission of NO and N_2O from a 4 MW fluidized bed combustor with NO reduction. 11th Int. CFB Conference, Vol. 2, pp. 709–717.

Grace, et al. Circulating Fluidized beds, Chapman & Hall, London, pp. 402, 1997.

Harada, M. N_2O emissions from FBC (1992). 24th IEA-FBC Technical Meeting.

Johnsson, J.E (1989). A kinetic model for NO_x formation in fluidized bed combustion.10th Int. CFB Conference. pp.1111-1118.

Leckner, B and Amand, L.-E (1987). Emissions from a circulating and a stationary fluidized bed boiler a comparison. 9th Int.CFB Conference. pp.891-897.

Moritomi, H, Suzuki, Y, Kido, N, Ogisu, Y. (1990). NO_x emission and reduction from CFB. 3th Int. CFB Conference.

Moritomi, H, Suzuki, Y, Kido, N. (1991). NO_x formation mechanism of circulating fluidized bed combustion. 11th Int. CFB Conference , Vol. 2, pp.1005–1011.

EFFECT OF METAL OXIDE ON THE EMISSION OF N_2O AND NO IN FLUIDIZED BED TEMPERATURE RANGE USING PYRIDINE AS A NITROGENOUS MODEL FUEL

X. B. Wang, H. Z. Tan , C. L. Wang, Q. X. Zhao, T. M. Xu, S. E. Hui

Key Laboratory for Thermal Science and Power Engineering of Ministry of Education, Department of Thermal Engineering, Tsinghua University, Beijing, 100084, China

Abstract: Pyridine has been chosen as the nitrogenous model fuel to research the effect of metal oxide (CaO, MgO and Fe_2O_3) on the emission of nitrogen oxides in the range of fluidized bed combustion temperature. The experiment was presented in a fixed bed reactor with metal oxide layer, and FT-IR gas analyzer was used to monitor the emission of N_2O and NO. When there is no metal oxide loaded, results show that the maximum peak of N_2O is at 725℃. Under the rich oxygen condition, NO increases monotonically with temperature increasing, however, under the lean oxygen condition there is a maximum peak of NO at 675℃, NO decreases to a minimum value at 725℃, and then increases slowly. With the addition of metal oxide, the loaded experimental results show that the addition will not change the general trend of nitrogen oxides, but it affects the emission in a certain extent and the effect has relation to temperature, oxygen atmosphere and metal oxide added. Under the lean oxygen condition, both CaO and Fe_2O_3 inhibit the formation of N_2O and NO in all temperature range; the effect of Fe_2O_3 on NO is negligible above 900℃; MgO inhibits N_2O at temperature higher than 725℃, and inhibits NO only from 625℃ to 700℃. Under the rich oxygen condition, CaO and MgO decrease the N_2O emission efficiently, but Fe_2O_3 can only act at the temperature higher than 700℃. For the NO emission, CaO and MgO inhibit NO just above 775℃, however, Fe_2O_3 promotes NO greatly especially below 700℃, and it even promotes NO_2 to 122.65ppm at 625℃. The results and discussion are helpful to demonstrate the effect of metal elements on the emission of nitrogen oxides in fluidized bed combustion.

Keywords: metal oxide, N_2O, NO, fluidized bed, pyridine

INTRODUCTION

Emission of nitrogen oxides and sulfur oxides from the coal combustion system continues to be a significant threat to the environment (Beer, 2000). Calcium-based materials are commonly proposed and applied to realize the high efficiency desulphurization in fluidized-bed combustion as well as in pulverized coal combustion (Hu et al., 2006). Meanwhile, considerable investigations have indicated that the metal elements also play some role in forming nitrogen oxides (Hayhurst and Lawrence, 1996; Li et al., 2002; Patsias et al., 2005; Zhong and Tang, 2007; Nimmo et al., 2005; Guo and Hecker, 1996). Experimental researches have found that calcium causes a significant N_2O decrease in fluidized bed combustion (Sasaoka et al., 1999; Shen et al., 2003), while others argue that the influence is little (Hayhurst and Lawrence, 1996; Wójtowicz et al., 1993). Despite considerable investigations, the effect of metal elements on the emission of nitrogen oxides from coal combustion is still confusing, and is generally explained to stem from the catalysis of metal elements while the mechanism is not fully demonstrated.

In this paper, the effect of metal oxide (CaO, MgO and Fe_2O_3) on the emission of N_2O, NO and NO_2 is investigated in the range of fluidized bed combustion temperature. Pyridine has been chosen as the nitrogen-containing model compound of coal. Fourier transform infrared spectroscopy (FT-IR) gas analyzer is used to on-line monitor the concentration of N_2O, NO and NO_2. The results will be helpful to elucidating the affect of different metal element on the emission of N_2O and NO in the fluidized bed combustion.

EXPERIMENTAL

It has been proved that the conversion of fuel nitrogen to nitrogen-containing species depends on nitrogenous functional groups in coal (Kambara et al., 1995). Investigations by X-ray photoelectron spectroscopy (XPS) established that the nitrogen of coal mainly exists in structures of heterocyclic rings and aliphatic nitrogen , and the predominant are the structures of heterocyclic rings, including pyridinic and pyrrolic structures (Fig.1) (Glarborg et al., 2003; Liu and Che, 2006).

Restricted by complex structures of coal and catalysis of mineral matters, it is difficult to obtain precise transformation mechanism of coal nitrogen directly, thus many works have been presented with model

compounds, including pyridine (Axworthy et al., 1978; Ninomiya et al., 2000; H. U. R. Memon, 2000; Mackie et al., 1990; Kiefer et al., 1997), pyrrole (John C. Mackie, 1991; Lifshitz et al., 1989; Zhai et al., 1999; Martoprawiro et al., 1999), quinoline (Laskin and Lifshitz, 1998) and picoline (Terentis et al., 1992). In present experiments, pyridine has been chosen as the model compounds to produce the nitrogen oxides.

As shown in Fig.2, volatile pyridine in vessel was taken out by the blowing of high-purity argon (>99.999%). In order to guarantee a constant sample quantity, the flow rate of argon was kept constant at 600ml • min^{-1} by a mass flow meter. The flow rate of oxygen was kept at 10mm • min^{-1} under the lean-oxygen condition, and 50ml • min^{-1} under the rich-oxygen condition. After passing through the mixer, pyridine reacted with oxygen in the reactor, which was 20mm in inner diameter and 1000mm in length. An electric furnace with a SiC tube as electrothermal element supplied heat to the reactor and could continuously work at a temperature as high as 1473K, and the constant-temperature heating zone was longer than 600mm. A Ni-Cr/Ni-Si thermocouple was used to measure the reaction zone temperature controlled by a SHIMADEN FP93 PID regulator. The precision of temperature control was ±2K. Analytically pure metal-oxide (CaO, MgO and Fe_2O_3) powder, which was squeezed in the mold at 5MPa for 5min, then crushed and sieved to 1-1.7mm, was placed onto an orifice in the middle of the reactor. The height of the solid layer was 12mm, and the stacking density was kept constant 680kg • m^3.

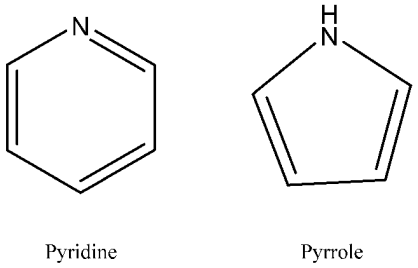

Fig. 1 Chemical structures of pyridinic-N and pyrrolic-N

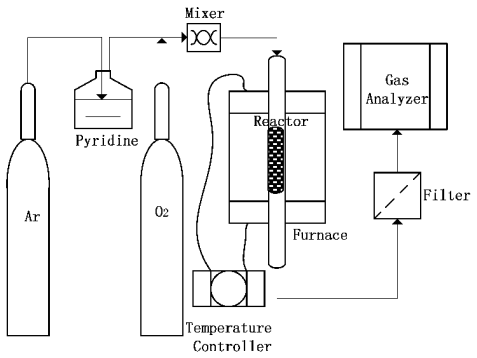

Fig. 2 Schematic diagram of experimental system for HCN formation and removal

The concentration of nitrogen oxides in flue gas were detected on-line by a Helsinki made DX-4000 FT-IR gas analyzer, which had a 1.07L gas analysis cell with a path of 5m, resolution of 8cm^{-1}, response time <120s, wave-number range of 900-4200^{-1} and scan frequency of 10 spectra • s^{-1}. The lowest detectable concentration was 1ppm and the estimated uncertainty limits of measurements were estimated to be within ±2%.

RESULTS AND DISCUSSION

Emission of nitrogen oxides without metal oxides loaded

Figure 3 illustrates the emission of nitrogen oxides (N_2O, NO and NO_2) without metal-oxide loaded under the lean-oxygen condition or rich-oxygen condition.

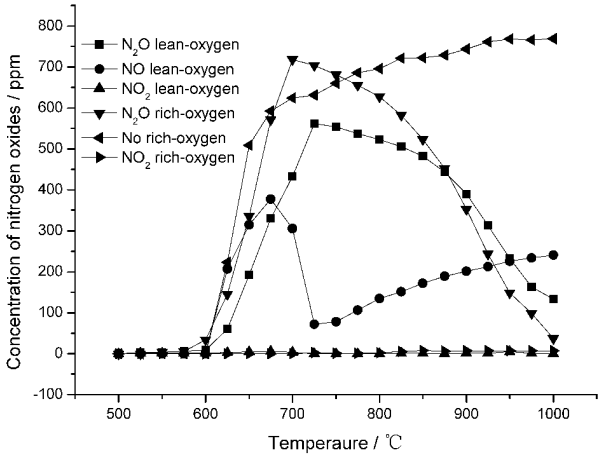

Fig. 3 Relationship of nitrogen oxides and temperature without metal oxides loaded

It can be seen that under the condition of lean-oxygen,

With the increase of temperature, NO and N_2O is formed initially at 600℃. NO reaches up to maximum at 675℃, and then decreases until 725℃, after that increases continually with temperature increasing; N_2O reaches up to maximum at 725℃, and then decreases. The maximum of NO is corresponding to the minimum of N_2O.

Under the condition of rich-oxygen, NO increases sharply to 600ppm at 675℃, and then increases slowly; N_2O reaches the maximum at 700℃. There is no NO_2 detected under lean-oxygen condition or rich-oxygen condition.

Compared the lean-oxygen and rich-oxygen condition, it can be seen that in the process of pyridine combustion, the temperature zone of N_2O existing is mainly between 650℃-900℃, which is corresponding to the zone in fluidized bed combustion. The concentration of NO and N_2O under oxygen condition is higher than that under lean-oxygen condition.

EFFECT OF CAO ON N_2O AND NO

The effect of CaO on the emission of nitrogen oxides is shown in Fig.4 (lean-oxygen) and Fig.5 (rich-oxygen). Under lean-oxygen condition, it can be seen from Fig.4 that CaO-loading can decrease the concentration of NO and N_2O at all temperatures.

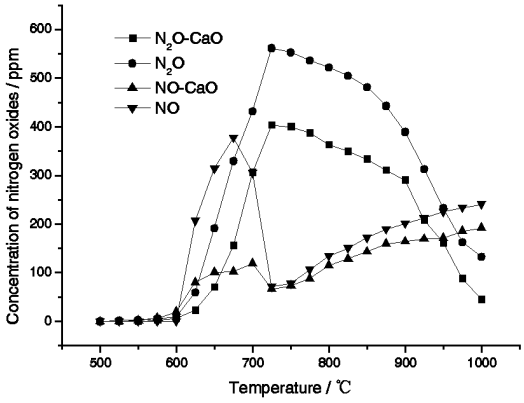

Fig. 4 Effect of CaO in lean-oxygen environment

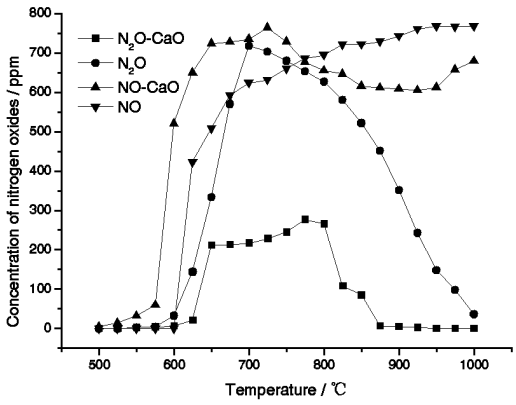

Fig. 5 Effect of CaO in rich-oxygen environment

Under the condition of rich-oxygen, CaO also inhibits N_2O high efficiently; however for NO, when temperature is lower than 775℃, CaO-loading improves the forming of NO, and only inhibits NO formation at temperature higher than 775℃. NO will reach a minimum value at 925℃, when CaO is loaded. It has been interpreted that CO and H_2 can react with nitrogen oxides to form N_2 through the catalysis reaction of CaO:

$$CO+N_2O \xrightarrow{CaO} N_2+CO_2 \quad (1)$$

$$CO+NO \xrightarrow{CaO} \frac{1}{2}N_2+CO_2 \quad (2)$$

$$NO+H_2 \xrightarrow{CaO} \frac{1}{2}N_2+H_2O \quad (3)$$

EFFECT OF MGO ON N_2O AND NO

The effect of MgO on the nitrogen oxides is shown in Fig.6 (lean-oxygen) and Fig.7 (rich-oxygen). Under the lean-oxygen condition, when temperature is higher than 725℃, MgO-loading inhibits the formation of N_2O, and decreases the temperature of NO formation. It implies that MgO can supply the activity site on its surface to catch the oxygen atom and nitrogen atom, improving the gas reactions.

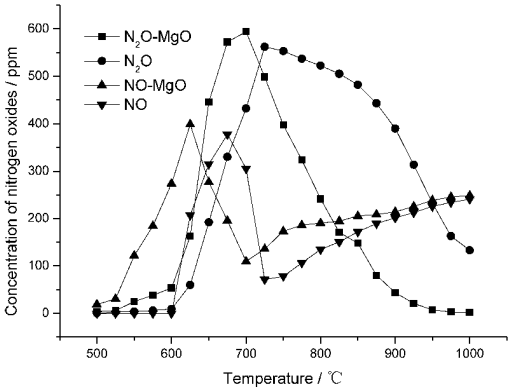

Fig. 6 Effect of MgO in lean-oxygen environment

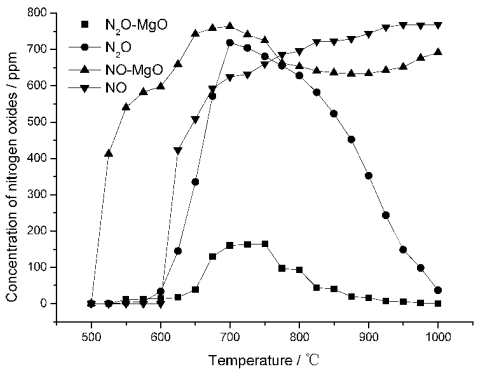

Fig. 7 Effect of MgO in rich-oxygen environment

Under the condition of rich-oxygen, compared with the effect of CaO, MgO decreases the concentration of N_2O more efficiently, and the lowest concentration of NO is also at 925℃.

EFFECT OF Fe_2O_3 ON N_2O, NO AND NO_2

Figues 8,9 illustrates the influence of Fe_2O_3 on the nitrogen oxides. Compared with CaO and MgO, the effect of Fe_2O_3 is different apparently.

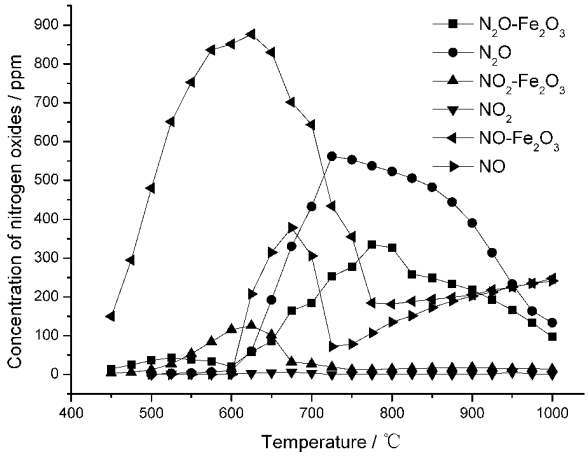

Fig. 8 Effect of Fe_2O_3 in lean-oxygen environment

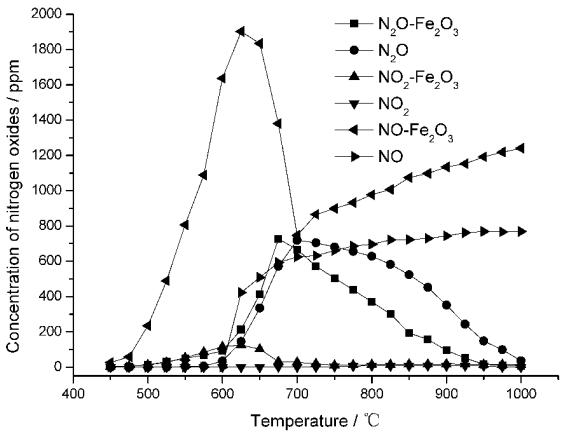

Fig. 9 Effect of Fe_2O_3 in rich-oxygen environment

Under the condition of lean-oxygen, Fe_2O_3 inhibits N_2O formation at temperature higher than 625℃, however, Fe_2O_3-loading greatly improves the NO formation. When Fe_2O_3 is loaded, NO_2 begins to form at 525℃, and reaches up to maximum at 625℃.

Under the condition of rich-oxygen with Fe_2O_3 loaded, when temperature is higher than 700℃, N_2O is inhibited by Fe_2O_3; NO formation is always enhanced.

CONCLUSIONS

In this paper, pyridine has been chosen as the nitrogenous model fuel to research the effect of metal oxide on the emission of nitrogen oxides in the range of fluidized bed combustion temperature. The conclusions are summarized as follows:

When there is no metal oxide loaded, the maximum peak of N_2O is at 725℃. Under the rich oxygen condition, NO increases monotonically with temperature increasing; under the lean oxygen condition there is a maximum peak of NO at 675℃, NO decreases to a minimum value at 725℃.

Under the lean oxygen condition, both CaO and Fe_2O_3 inhibit the formation of N_2O and NO; the effect of Fe_2O_3 on NO is negligible above 900℃; MgO inhibits N_2O at temperature higher than 725℃, and inhibits NO only from 625℃ to 700℃.

Under the rich oxygen condition, CaO and MgO decrease the N_2O emission efficiently, but Fe_2O_3 can only act at the temperature higher than 700℃. For the NO emission, CaO and MgO inhibit NO just above

775℃, however, Fe_2O_3 promotes NO greatly especially below 700℃, and it even promotes NO_2 to 122.65ppm at 625℃.

ACKNOWLEDGEMENTS

The present work was supported by the State Basic Research Development Program (No. 2005CB 221206) and National Key Technology R&D Program in the 11th Five-Year Plan of China (No. 2006BAK02B03).

REFERENCES

Axworthy, A. E., Dayan, V. H. and Martin, G. B: Fuel **57** (1978), pp. 29-35.
Beer, J. M.: Progress in Energy and Combustion Science **26** (2000), pp. 301-327.
Glarborg, P., Jensen, A. D.: Progress in Energy and Combustion Science **29** (2003), pp. 89-113.
Guo, F. and Hecker, W. C.: Symposium (International) on Combustion **26** (1996), pp. 2251-2257.
H. U. R. Memon; K. D. Bartle.: International Journal of Energy Research **24** (2000), pp. 1141-1159.
Hayhurst, A. N. and Lawrence, A. D.: Combustion and Flame **105** (1996), pp. 511-527.
Hu, G., Dam-Johansen, K., Wedel, S.: Progress in Energy and Combustion Science **32** (2006), pp. 386-407.
John C. Mackie, Meredith B. Colket III.: International Journal of Chemical Kinetics **23** (1991), pp. 733-760.
Kambara, S., Takarada, T., Toyoshima, M. and Kato, K.: Fuel **74** (1995), pp. 1247-1253.
Kiefer, J. H., Zhang, Q., Kern, R. D., Yao, J. and Jursic, B.: J. Phys. Chem. A **101** (1997), pp. 7061-7073.
Laskin, A. and Lifshitz, A.: J. Phys. Chem. A **102** (1998), pp. 928-946.
Li, Y., Loh, B. C., Matsushima, N., Nishioka, M. and Sadakata, M.:Energy Fuels **16** (2002), pp. 155-160.
Lifshitz, A., Tamburu, C. and Suslensky, A.: J. Phys. Chem. **93** (1989), pp. 5802-5808.
Liu, Y. and Che, D.: Fuel Processing Technology **87** (2006), pp. 355-362.
Mackie, J. C., Colket, M. B. and Nelson, P. F.:J. Phys. Chem. **94** (1990), pp. 4099-4106.
Martoprawiro, M., Bacskay, G. B. and Mackie, J. C.: J. Phys. Chem. A **103** (1999), pp. 3923-3934.
Nimmo, W., Patsias, A. A., Hall, W. J. and Williams, P. T.:Ind. Eng. Chem. Res. **44** (2005), pp. 4484-4494.
Ninomiya, Y., Dong, Z., Suzuki, Y. and Koketsu, J.: Fuel **79** (2000), pp. 449-457.
Patsias, A. A., Nimmo, W., Gibbs, B. M. and Williams, P. T.:Fuel **84** (2005), pp. 1864-1873.
Sasaoka, E., Sada, N., Hara, K. i., and Uddin, M. A.: Ind. Eng. Chem. Res. **38** (1999), pp. 1335-1340.
Shen, B. X., Mi, T., Liu, D. C. and Feng, B.: Fuel Processing Technology **84** (2003), pp. 13-21.
Terentis, A., Doughty, A. and Mackie, J. C.: J. Phys. Chem. **96** (1992), pp. 10334-10339.
Wójtowicz, M. A., Pels, J. R. and Moulijn, J. A.: Fuel Processing Technology **34** (1993), pp. 1-71.
Zhai, L., Zhou, X. and Liu, R. J.: Phys. Chem. A **103** (1999), pp. 3917-3922.
Zhong, B. J. and Tang, H.: Combustion and Flame **149** (2007), pp. 234-243.

WASTE TO ENERGY IFBC-PLANT IN FRANKFURT, GERMANY

Dipl. Ing. Paul Ludwig

Infraserv GmbH & Co. Höchst KG, Frankfurt am Main, Germany

Abstract: Infraserv Höchst, located in the Industrial Park Höchst, has longstanding experience with the operation and development of large scale FBC plants.
In previous conferences we provided information about the "Reduction of NO_x-Emissions by taking primary measures" and the "Debottlenecking of FBC furnaces with incineration by oxygen".
We are now able to provide information on the preparatory processes we are involved in as operators of our newest IFBC plant with an incineration capacity of 700,000 t/a RDF (Refuse Derived Fuel) and 270 MW combustion heat output.
Keywords: waste-to-energy, refuse derived fuel (RDF), FBC-technology, IFBC-technology, semi-dry-fluegas-cleaning

INTRODUCTION

The company Thermal Conversion Compound Industriepark Höchst GmbH, a subsidiary of Infraserv Höchst, builds and intends to operate at Industrial Park Höchst an incineration plant for thermal utilization of treated waste (refuse rerived fuel, RDF). Construction of the RDF-plant is a central component of the comprehensive energy concept for the Industrial Park Höchst. In the interest of its local customers, Infraserv wants to expand its own energy generation capacities to become more independent of the developments on the energy market. In so doing, Infraserv Höchst relies on resource-friendly and cost-efficient production plants. For the producing companies on location, energy costs are a decisive success factor. ISH has extensive experience in the operation of technically complex infrastructure facilities. And this is one of the many reasons why Industrial Park Höchst is the ideal location for such a plant.

The incineration plant (Fig. 1) generates energy – in this case, steam and electric power – with a maximum thermal output of 270 MW. The plant is being constructed in the south-west corner of Industrial Park Höchst. The future Industrial Park silhouette will be characterized by the plant's boiler house of a height of about 50 to 60 meters and its close to 80-meter high chimneys. The actual power station unit will be about 30 meters high. As general contractor, company Ebara will take over the complete construction of the plant including plant engineering. Ebara is a world-wide operating enterprise headquartered in Japan with extensive experience in the field of circulating fluidized bed technology and has already realized numerous plants of this type. The technical design of the RDF plant allows a broad acceptance range in terms of fuels.

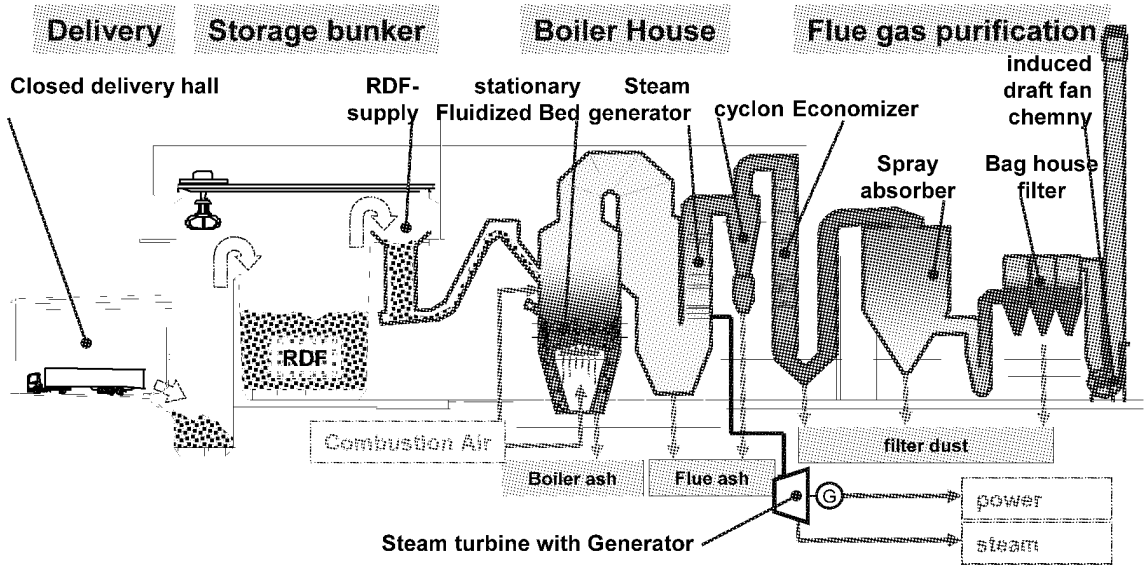

Fig. 1 Flow Chart Waste to Energy IFBC- Plant, 3-lines

As its regular fuel, the plant will use "refuse derived fuel" (RDF) with a high energy content ranging from 10 000 to 27 000 kJ/kg. The so-called refuse derived fuels are pre-sorted and processed, dry and high-calorific fractions of household and industrial waste which are no longer allowed to be dumped since June 1, 2005

according to the "Technische Anleitung Siedlungsabfall" (TASi – Technical Instruction Settlement Waste). Only those materials are to be used which the suppliers beforehand have disenriched, sorted and processed on the basis of a detailed quality specification. Quality controls in several steps will be additionally carried out at the plant.

The plant's construction at Industrial Park Höchst will increase, in the Rhine/Main area, the utilization capacities for refuse derived fuels which can be used for environmentally-friendly energy production by replacing fossil fuels such as hard coal and natural gas.

The design calorific value will be 13 400 kJ/kg with a mean RDF input of approx. 72.6 t/h for all incineration lines combined, equivalent to approx. 1 750 t/d. This will provide up to about 68 MWel electrical energy (full condensation operation) and up to about 173 MWtherm of steam for heat supply.

At the design calorific value, a throughput of approx. 675 000 t/a will result for the total plant with an availability of 8 760 h per year. The indicated operating period takes the assumption into account that operation of the plant may be possible on 365 days in the calendar year if revision and maintenance work is cleverly scheduled.

As a rule, up to about 6 000 m³ (1 800 t) of refuse derived fuel (RDF) are to be accepted per day. (Stocking up of raw material for a maximum of 5 days; acceptance only on weekdays during the day and one truck per hour at night). This volume can also increase to triple the amount on a few days of a year in case of special delivery situations before holidays.

Refuse derived fuels are to be preferably supplied by truck transports. This will require, on average, up to about 160 truck transports on weekdays for a volume of up to about 675 000 t (max. approx. 700 000 t). The supply of auxiliary materials/additives and the removal of wastes will additionally require up to about 40 truck transports per weekday. For any transports to and from Industrial Park Höchst, only such roads will be used in a perimeter of 1 km outside of the Industrial Park which do not run through residential areas.

In the delivery area, facilities are to be found for RDF sampling and for pre-crushing of small amounts of material within the course of RDF sampling.

Natural gas is to be used for start-up and shutdown, as well as for the support firing in continuous operation. In case of temporary transport problems for RDF within the RDF incineration plant, these fuels are to be used additionally to the RDF or up to 12 hours without RDF as the fuel – to continue operation of the boilers at minimum load in conformity with the permit and thus keeping the plant hot. In these cases, at least one incineration line is to be operated, if necessary at reduced output, for up to 12 h (duration of one shift) using up to 100 % EL fuel oil or natural gas as the fuel.

The incineration lines to be operated independently from each other are connected to joint peripheral plant parts which are used for charging raw and auxiliary materials and additives, and for the disposal of wastes such as ashes and filter dust. These joint peripheral plant parts are also used for the generation and distribution of electrical energy and steam, or they are otherwise required for the operation of the incineration plant. Such peripheral plant parts include, for example, systems for cooling water conditioning, condensate processing, facilities for the logistics of raw materials, auxiliary materials/additives and residual materials; also including electrical supply facilities, piping for supply and disposal, sewage lines for disposal, as well as facilities and equipment for the control of the plants.

Incineration at a temperature of 850 – 950 °C is to guarantee a complete burn-up of the materials used.

Waste gases are to be purified with a quasi-dry process in which no waste water will result. An SNCR method is to be used for the denitrification of waste gases (reduction of NOx in waste gases). Ammonia water (alternatively: urea solution) is to be injected at the outlet of the combustion chamber to reduce to nitrogen and water the nitrogen oxides which developed in the combustion process. Cyclones are to be preferably used for waste gas dust separation. A downstream spray absorber is to be used to neutralize acid, gaseous waste gas components – such as SO_2, SO_3, HCl and HF – by the injection of aqueous burnt lime or lime hydrate ($Ca(OH)_2$). HOK lignite coke or activated carbon, respectively, will be used for the separation of heavy metals, dioxins and furans. The optimum operating temperature for it is to be adjusted by the injection of water. Any dusts still remaining in the flue gas after this are to be separated in a downstream fabric filter.

MORE DETAILED PRESENTATION OF THE EVA HÖCHST PROJECT

RDF delivery and sampling area

The RDF is to be delivered by means of vehicles which normally unload the fuel directly into the RDF bunker in a delivery building. Main delivery times will be Mondays to Saturdays between 06:00 and 22:00; in isolated cases also at night, between 22:00 hours and 06:00 hours. In exceptional cases, delivery will also be possible on Sunday. Delivery is to be primarily by truck. Additionally, delivery by rail and ship will also be

possible via the container terminal of Industrial Park Höchst. From there, the corresponding container is to be taken by truck over works roads to the plant so that the RDF bunker will be exclusively charged by truck.

RDF bunker

The RDF bunker is to be used for the acceptance and intermediate storage of the delivered fuels. It will be designed for a storage capacity of approx. 5 days. The RDF bunker is to be designed as a deep bunker with a tipping area and with cranes which are used for the distribution and charging of the fuel. The cranes are to charge the individual furnace lines via a corresponding filling hopper.

For delivery, 10 tipping points are to be provided in the tipping area.

For the examination of RDF qualities, the steam generator is to be run in batch operation. In this case, only fuel from one supplier will be burnt. Upon RDF delivery, this fuel is to be stored in a separated bunker next to the tipping area.

Sampling area

In a separate area, the delivered RDF can be subjected to a classification (quality control) and crushed within the process of sampling. Quality controls are to be made, in particular, for new or recurrently conspicuous suppliers.

A separate entrance gate (gate 11) will be available for this. The RDF is here to be dumped onto a batch bottom, inspected and sampled there already, as needed. Two inspection catwalks are to be provided for this purpose. The tipped RDF material will thereafter be passed into the auxiliary bunker and supplied for sampling to the shredders – by means of an auxiliary crane.

After shredding and sampling, the remaining RDF material is conveyed into the bunker area by means of a conveyor. Batches which are rejected can again be loaded into the delivering truck. In this area, an additional gate (gate 12) is to be provided which will be used only in rare cases (maintenance case) for the transport of a gripper of the bunker crane system.

RDF charging to combustion

By means of crane systems, the RDF is to be charged from the storage bunker to the fuel filling hopper of the corresponding incineration line. From there, the RDF is to be passed to the combustion chamber by means of conveyor equipment (belts, slope conveyors, conveyor screws) and via rotary seals. Filling level monitoring will be provided in the seal of the dosing screws which is to regulate the fuel supply through access to the speed of the upstream conveyor equipment. Actual RDF charging into the combustion chamber is to be effected by rotary seals cooled with sealing air or, depending on the supplier's concept, with air.

Ignition and support burners

The start-up/support burners are to guarantee the start-up from cold conditions, as well as the complete combustion of waste material of very low calorific values. Thermal output, combustion end temperature, excess air and arrangement of the burners are to be selected such that the softening point of ash particles will be safely fallen short of even in continuous operation. Ignition and support burners are to be operated with natural gas. Ignition and support burners are to be dimensioned to approx. 60% of thermal output.

Ignition and support fuels

For start-up and for maintaining the minimum temperature in the combustion chamber of the RDF incineration plant, ignition and support burners are to be provided which are operated with natural gas. Natural gas for the RDF incineration plant is supplied via the natural gas grid at Industrial Park Höchst. After possibly required pressure reduction (natural gas reducing station with outdoor setup), natural gas will be supplied to the natural gas burners of the ignition and support burners.

Furnace and steam generation

The furnace is designed as an internally circulating fluidized bed which is integrated in a boiler for steam generation. The fluidized bed and the furnace arranged above (with a suitable furnace geometry) are to be precisely matched for optimizing the combustion. In terms of design and construction, any and all measures will be provided to prevent or quickly clear up any temperature fluctuations and CO development. The furnace is to be designed such that virtually complete burn-up of the fuels will be ensured in terms of pollutant-minimizing aspects. After the fuels have been charged, retention in the fluidized bed as well as good mixing through/cross-mixing will be ensured. Moreover, the tuyère or nozzle bottom will be able to quickly discharge the agglomeration-prone materials from the hot combustion chamber area. Selecting the appropriate nozzle forms and materials will minimize wear.

The furnace consists of tubular evaporator walls in the area of the fluidized bed and the combustion chamber (free space). An internally horizontal fluidized bed cooler is to be integrated in the control of the bed temperature. The evaporator bundles arranged in the fluidized bed cooler present a separate circulation system and are operated in forced circulation. As a protection against erosion and corrosion, the evaporators are to be provided with a thermal spraying layer.

The minimum temperature of the combustion gases in the combustion chamber after the last combustion air supply is to amount to at least 850 °C – according to § 4 para. 2 of the 17th BImSchV (Ordinance on Emissions Protection). After the last combustion air supply, the dwell time of the flue gases in the afterburner chamber will be more than 2s. The temperature is to be controlled during operation. Dimensioning and positioning of temperature measuring points during installation and during operation will ensure that the specifications of § 4 para. 2 of the 17th BImSchV are complied with.

Upon the start-up of every incineration line, charging the combustion chamber with refuse derived fuels will only be released if the above mentioned minimum temperature has been reached upon start-up by means of auxiliary burners. Furthermore, the auxiliary burners are used to maintain the minimum temperature in the event of the temperature foreseeably falling below (support firing). The burners for the additional or, respectively, support firing are to be operated with natural gas or EL fuel oil (DIN 51603-1).

The refuse derived fuel is supplied to the fluidized bed furnace by means of a crane from the bunker via filling hoppers (with large filling volume) and mixed in the combustion chamber with the hot fluidized bed material (sand). The fluidized bed is fluidized through the combustion air which is supplied via the nozzle or tuyère bottom to the combustion chamber as so-called primary air. Above the refuse derived fuel supply into the fluidized bed, the combustion chamber is to be supplied with secondary air for better mixing through and for a reduction of the pollutant concentrations.

One part of the bed material included in the fluidized bed is to be continuously discharged, cooled in conveyor screws, mechanically filtered in hot condition (freed from coarse parts) and – also in hot condition – conveyed for intermediate storage into the bed material silos.

One part of the bed material is used, within the combustion furnace/incinerator, for steam generation and steam heating with the aid of the built-in fluidized bed cooler.

The fluidized bed sand to be continuously replaced in the process will be delivered by truck and pneumatically blown via a conveyor device into the corresponding sand silo. The conveyor air flow incurred over the year during filling will be cleaned off via silo top filters to a residual dust concentration and passed into the ambient atmosphere via the emissions sources E 10 a – c.

A DeNOx plant according to the SNCR process is to be provided in the area of the combustion chamber for the reduction of nitrogen oxides contained in the flue gases. In the combustion chamber, a 25% aqueous ammonia solution (ammonia water) or a corresponding urea solution will be injected for the reduction of NOx. In the gas phase, a catalytic reduction of NOx to elementary nitrogen takes place at a temperature from 850 °C to 950 °C.

The corresponding ammonia water tank is to be filled directly from the ammonia water supply at Industrial Park Höchst. The displaced tank air is to be discharged into the surrounding atmosphere after the precipitation of gaseous ammonia by means of water and filtration via activated carbon (emissions sources E 18 a, E 18 b).

For a utilization of the combustion heat comprised in the waste gas, the hot waste gas flows developing during combustion are supplied via radiation passes into multi-stage superheaters and subsequently into the downstream economizer. The energy contained in the hot waste gases is to be used for steam generation. The fly ash collecting in the baffles of the steam generator is to be withdrawn from the steam generator; it is to be cooled down and pneumatically conveyed into the fly ash silo for solid wastes from the corresponding boiler.

The air to be discharged – upon filling the fly ash silo – by means of pneumatic conveyance with compressed air and filling level change is to be returned into the incineration lines.

Heat recovery boiler with steam generator

The flue gases from the fluidized bed developing during combustion first reach the area of the furnace located above the fluidized bed. The furnace walls are made of water-cooled membrane walls and, to control the heat loss, the membrane walls are covered with castable refractory over large parts of the furnace up to the entry into the radiation pass. The objective of this measure is, on the one hand, to comply with the statutory requirements regarding the dwell period of flue gases ($t > 2$ s at > 850 °C) and, on the other hand, to optimize the combustion of CxHy, CO as well as the burn-up rate, i.e. to minimize the C-concentration in the ash.

The furnace geometry here results from the requirements of how the fluidized material can fall back again into the fluidized bed.

In the steam generator, the flue gases are cooled down in steps, simultaneously using the energy contained

in the flue gases for steam generation. To this end, the flue gases first flow through a radiation pass and enter then into a boiler part with convective heat transmission.

The superheater is followed by the economizer. Still in liquid condition, the feed water is here heated up according to the boiler pressure stage. Demineralized water is taken from the Infraserv works system to provide the boiler feed water used in water/steam circulation. Soda lye and ammonia are added to the water/steam circulation system according to the requirements of the system's chemical operation (pH value adjustment). The fly ash collecting in the baffles of the boiler is to be removed from the boiler, cooled down and returned into the furnace after magnetic separation.

Afterburning

The secondary air supply is arranged above the bed surface in the furnace. Air is to be blown in by means of large nozzles distributed on the circumference of the furnace cross-section. On the one hand, the air still supplies oxygen for the combustion and, on the other hand, it also provides an improvement for the thorough mixing of flue gases. The concentrations of CxHy and CO can be reduced thereby. Due to the volatile components in the fuel, more or less pronounced afterburning can be detected above the bed. This predominantly concerns the outgassing which cannot dwell in the fluidized bed and is entrained with the flue gas. This afterburning increases the temperature of the flue gases by approx. 50 to 100 K as compared to the fluidized bed. Thus, temperatures can be controlled with the aid of secondary air regulation.

STEAM GENERATION

Design of the steam generators

For utilization of the heat, a steam generator will be used which is specifically designed for the requirements of waste incineration. The generator essentially works with natural water circulation. The circulation system is designed such that perfect water circulation will be ensured over the entire load range. The boiler concept to be used has proved to be excellent in numerous waste incineration plants.

The steam generator design is particularly characterized by the following:

- –Radiant heating surfaces in the combustion chamber down to the nozzle or tuyère bottom;
- –Submerged heating surfaces in the boiler-integrated fluidized bed cooler;
- –Boiler pass as an open pass exclusively with radiant heating surfaces;
- –Boiler pass with convection heating surfaces; inter alia protective evaporator, protective superheater;
- –Boiler pass with economizer housing and economizer heating surfaces, as well as cleaning system by means of soot blowers.

SNCR PROCESS

The development of NOX in the combustion process cannot be essentially influenced by regulating the air and the temperature. For this reason, the SNCR process as a NOX reduction measure is to be also integrated into the process engineering concept. The SNCR process is based on the principle of non-catalytic reduction of NOX in the gas phase with ammonia. The reduction takes place at temperatures ranging from 850 to 950 °C existing in the boiler in a specific temperature window of the combustion chamber. In this area of the boiler, ammonia is injected into the waste gas in the form of a 25% aqueous solution.

Flue Gas Purification Plant

After leaving the steam generator, the flue gas is supplied to the flue gas purification plant which consists of the following components per line:

- –Spray-type absorber for cooling and conditioning of the flue gases with a simultaneous separation of acid flue gas components (in particular HCI, HF and SO_x) through the injection of milk of lime or by the introduction of lime hydrate ($Ca(OH)_2$).
- –Dry injection of an adsorbent (e.g. activated coke, HOK lignite coke) for the effective separation of volatile heavy metals (mercury in particular) and toxic organic components (PCDD/F in particular).
- –Fabric filter for the separation of particulate contaminations in the flue gas, essentially consisting of fly dust, reaction salts and laden adsorbent.

The separation of acid flue gas components takes place in the absorber according to a quasi-dry spray absorption method. Milk of lime as a finely dispersed mist or lime hydrate is to be introduced into the flue gas flow, and the acid noxious gas components, such as SO_3, SO_2, HCI and HF, will be separated.

The alkaline calcium components of milk of lime or of lime hydrate will react with the acid noxious gas

components to form the corresponding calcium salts.

The aqueous portion of the adsorption agent here evaporates with a corresponding reduction of the flue gas temperature and with a continuous reaction of the acid flue gas components with the alkaline components of the milk of lime or the lime hydrate, respectively. The thus retained noxious substances occur in the form of their dry reaction salts and are discharged, together with the flue gas flow, in the form of a fly flow route from the spray absorber housing and transported to the subsequent components of the flue gas purification plant. A small part of the solid particles collects in the spray absorber and will be discharged into the filter dust silo which also takes up the separated solid particles from the fabric filter.

The purification of acid gases from the combustion gases will use either aqueous burnt lime (milk of lime) or moistened lime hydrate. The burnt lime or the lime hydrate/calcium hydroxide is to be delivered by a bulk trailer and pneumatically conveyed into a storage silo. For the production of the absorption agent required in the flue gas purification plant, burnt lime is withdrawn from the burnt lime silo according to the plant's consumption; it is supplied to a milk of lime mixing vessel, and water will be added. The sludge water from feed water processing and river water are to be used for it. The absorption agent is to be conveyed to the spray absorber via a lime of milk dosing vessel. Lime hydrate is withdrawn from the lime hydrate silo according to the plant's consumption; it is supplied to a moisturizer (here a screw conveyor with water dosing) where water is added to it; and it is then conveyed to the spray absorber.

In the further course of flue gas purification, the adsorbent is added and pneumatically dosed in the flue gas duct between spray absorber and fabric filter. Generally, HOK lignite coke or activated coke will be used as the adsorbent. It is also thoroughly mixed through with the flue gas so that volatile heavy metals and toxic organic components will be adsorptively bound; in particular, volatile mercury and dioxins as well as furans (PCDD/PCDF) will be removed from the flue gas.

In the downstream fabric filter, virtually all solid particles are filtered out of the flue gas flow while passing through the filtering bags, and they will be carried out as residual material. The residual fabric filter materials (RGR residual materials) consist of a small rest of fly ash, the reaction salts from the spray drier together with unspent calcium hydroxide and calcium oxide as well as small parts of laden adsorbent. The purified waste gas is to be given off into the atmosphere via an induced draft fan and an 80-meter high chimney per incineration line.

CHIMNEYS FOR COMBUSTION GASES

The waste gas from every incineration line exiting from the fabric filter is to be aspirated via an induced draft fan and subsequently passed via a waste gas duct to the corresponding chimney. Thus, at full load, approx. 217 000 m³/h dry under normal conditions, with 11 % O_2 will be discharged into the surrounding atmosphere at a height of approx. 80 m above ground level – from each incineration line via the emissions sources E 01, E 02 and E 03. With a height of approx. 80 m and a diameter of approx. 2.5 m, each chimney of the incineration lines complies with the requirements no. 5.5 of the TA Luft (Technical Instruction, Air). The minimum height of 70 m will not be used in construction for technical reasons so that any mutual influence of currents will be avoided (e.g. icing up of chimney E 14 in case of east or northeast wind conditions). Additionally, four chimneys of the same height will be able to provide a homogenous appearance for the RDF incineration plant. The remaining emissions sources (cold sources) are at least 3 m above the roof and at least 10 m above ground. Emissions from the incineration lines 1, 2 and 3 are to be provided with measuring equipment to monitor those emissions which are to be continuously monitored according to § 5 para. 1 no. 1 and 2 of the 17th BImSchV. The measuring results are to be recorded and analyzed by means of an analyzer system.

PERIPHERAL PLANT PARTS

Steam turbine with generator

The steam turbine with generator comprises all components which are necessary for the operation of the turbine, for the generation and decoupling of electrical energy, and for the decoupling of steam with different pressure stages. The steam turbine is to be operated with high-pressure steam from the operating units 1, 2 and 11 and will be able to take over up to about 227 t steam per hour for power generation. Steam flashing in the turbine is provided at two pressure stages, 17 bar(a) and 4.2 bar(a). With the pressure stages 17 bar(a) and 4.2 bar(a), part of the steam mass flow can be decoupled via extraction stations and supplied into the external steam grid (up to approx. 173 MWth). The remaining steam mass flow is flashed down to a condensation pressure of approx. 0.05 bar(a) and passes as wet steam into the cooling system (see operating unit 3).

OPTIMIZATION OF LIMESTONE FEED SIZE OF A PRESSURIZED FLUIDIZED BED COMBUSTOR

Tadaaki Shimizu[1], Jaakko Saastamoinen[2]

1 Department of Chemistry and Chemical Engineering, Niigata University, 2-8050, Ikarashi, Niigata, 950-2181, Japan, tshimizu@eng.niigata-u.ac.jp

2 VTT Technical Research Centre of Finland, P.O.Box 1603, FIN-40101, Jyväskylä, Finland,jaakko.saastamoinen@vtt.fi

Abstract: Limestone attrition is a major cause of loss of limestone during pressurized fluidized bed combustion. In the authors' previous works, the analysis of published results of solid attrition and desulfurization was conducted to determine the attrition rate expression. The specific attrition rate (rate of decrease in diameter) was estimated to be second order with respect to particle diameter in the previous work. This rate expression implies that reduction of feed size of limestone is effective for suppression of loss of limestone by attrition. However, too much grinding of raw limestone will increase the content of fine particles that are readily elutriated by gas stream and do not contribute to the sulfur capture. In this work, modeling works are conducted for particle attrition and desulfurization in order to predict the effect of feed size of limestone on total consumption of limestone and desulfurization is discussed. Optimum particle size to suppress limestone consumption was approximately 0.7 mm (as D_{p50}). However, the control of solid drain rate from the bottom was found to have more influence on total limestone consumption rate. Emissions of SO_2 from low sulfur coal (S=0.33%) could be sufficiently low irrespective of limestone feed size but SO_2 emissions from coals with higher sulfur content than 0.5% were anticipated to increase drastically. Such drastic change in SO_2 emissions with the change in sulfur content is attributable to non-linear nature of reaction rate for attrition-enhanced desulfurization by limestone.

Keywords: pressurized fluidized bed combustion, desulfurization, limestone, attrition

INTRODUCTION

Pressurized fluidized bed combustors (PFBCs) have been developed as a high-efficiency power generation technology. In Japan, two large-scale commercial plants, Karita 360 MWe plant and Osaki 250 MWe plant, are now working successfully. One feature of PFBCs is *in-situ* SO_2 capture by uncalcined limestone ($CaCO_3$) as follows:

$$CaCO_3+SO_2+(1/2)O_2 \longrightarrow CaSO_4+CO_2 \quad (1)$$

The uncalcined limestone is non-porous. Therefore, the reaction takes place at the external surface of the particle, thereby forming a product ($CaSO_4$) layer. The rate of reaction was investigated mainly using thermogravimetric analysis (Snow et al., 1988; Hajaligol et al., 1988; Iisa and Hupa, 1992; Krishnan and Sotirchos, 1993a; Krishnan and Sotirchos, 1993b; Zevenhoven et al., 1998; Qui and Lindqvist, 2000). Both chemical kinetics and SO_2 diffusion through the product layer govern the reaction rate.

An important feature of desulphurization in actual PFBC systems is attrition of limestone particles. Particle size decreases gradually due to surface removal by attrition. Attrition affects not only the particle size distribution (PSD) of the bed material, but also the SO_2 capture because it removes the $CaSO_4$ layer to reduce the diffusion resistance. Alternatively, it reduces limestone utilization if the unreacted part of limestone is lost. Sakuno et al. (2001a) and Shimizu et al. (2001) evaluated the attrition rate of limestone in a large-scale (71 MW electricity output) PFBC. The 71 MWe PFBC was operated with fly ash recycling (Phase-2 configuration) and without fly ash recycling (Phase-1 configuration). They reported that 70% or more of limestone was carried over and drained from the system as fly ash.

Based on the experimental results of 71 MWe PFBC, a model of attrition was proposed. Attrition of a limestone particle can be described by the rate of decrease in particle diameter (D_p) as a function of D_p as follows:

$$dD_p/dt = -k_n D_p^n \quad (2)$$

The exponent, n, was estimated by comparing PSD of bed material between experimental results and model calculation, and by analyzing the relationship between fine formation rate and bed condition (bed material mass and particle size distribution). The estimated value of n was 2 (Saastamoinen and Shimizu, 2007)

Models of desulfurization by limestone particles under solid attrition conditions have also been proposed. There are two modes of attrition models to be implemented in the model, namely, continuous attrition and

intermittent attrition. The latter assumes that the removal of surface layer takes place intermittently. Desulfurization rate under solid attrition condition has been reported to be strongly affected by the mode of attrition (Shimizu et al., 2001; Shimizu et al., 2002a; Shimizu et al., 2002b; Shimizu et al., 2003a; Shimizu et al., 2003b; Saastamoinen and Shimizu 2007). The continuous attrition model gives higher reaction rate and higher solid utilization than those of intermittent attrition. Finally, Saastamoinen and Shimizu (2007) found that the combination of the exponent of n=2 and continuous attrition or intermittent attrition with very short attrition interval (approximately 600 s) gave account for the experimental results of attrition rate, PSD of bed material, and desulfurization during combustion of wide variety of fuels from low-sulfur coal to high-sulfur petroleum coke.

The value of the exponent of n=2 implies that the loss of limestone by attrition can be reduced by decreasing the size of fed limestone. However, the reduction of feed size will increase the content of fine particles, which will be entrained by gas stream and do not contribute to the desulfurization. Therefore, it is conceivable that there exist an optimal feed size of limestone that can minimize the limestone consumption. Besides the loss of limestone by attrition, it is possible that the reduction of particle size will inhibit the desulfurization reaction since too low attrition rate will increase the thickness of the product layer ($CaSO_4$) at the particles' surface that will inhibit the diffusion of SO_2 towards the unreacted core.

In the present work, a theoretical work is conducted to find out the optimum feed size of limestone that minimizes the loss of attrition. In addition, SO_2 emission is calculated to find as to whether the decrease in feed size inhibits the removal of SO_2. At first, the type of particle size distribution of the feed is determined from the literature data. Then the effects of feed particle size on limestone consumption, the size of bed material, and desulfurization were calculated.

PARTICLE SIZE DISTRIBUTION OF FED LIMESTONE

The type of PSD of fed limestone was determined from the literature data of 71 MWe PFBC (Shimizu et al., 2001). Figure 1 shows Rosin-Rammler-Sperling of size of fed limestone. The relationship between $\ln(D_p)$ and $\ln(\ln(100/R))$ was well approximated by straight lines, thus the type of PSD was Rosin- Rammler distribution expressed as follows:

$$R(D_p)=100\exp(-bD_p^m) \tag{3}$$

The slope of the line, m, was nearly unity. By giving a value of m, the parameter of size distribution, b, is given by the size of particle whose cumulative weight fraction is 50 %, D_{p50}, as follows:

$$b=\ln(2)/D_{p50}^m \tag{4}$$

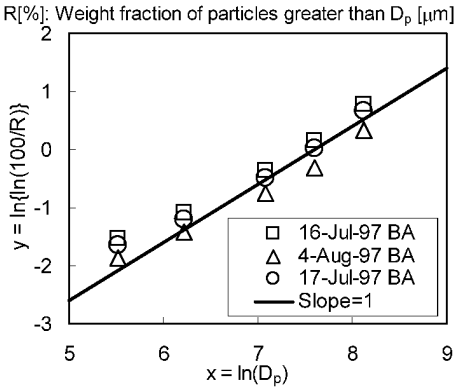

Fig.1 Rosin-Rammler-Sperling of fed limestone (Experimental results: Shimizu et al., 2001)

ATTRITION AND DESULFURIZATION MODEL

The model of attrition to calculate the PSD is illustrated in Fig.2. The detailed description of the attrition model is given elsewhere (Saastamoinen and Shimizu, 2007). In this work, a full-load condition was assumed. The calculation condition is summarized in Table 1. The total mass of bed material is assumed to be 60×10^3 kg. The drain rates of bed material from the bottom and the feed rate of limestone were given as input variables. The total mass of bed material decreases with time by solid attrition whereas the bed mass increases with limestone feed. If the total bed mass after attrition and feed is greater than the required bed mass, the excess was drained from the bottom. The calculation was repeated until steady state was attained. The feed rate was changed to attain desired drain rate from the bottom. It is clear that the minimum feed rate can be attained by minimizing the drain rate of the bottom (i.e. drain = 0), but such operation is not realistic because it is necessary

to remove coarse ash particles or clinker particles formed in the combustor. Thus several drain rates are assumed. The attrition rate constant was assumed to be k_2 =0.00087 $m^{-1}s^{-1}$ because this value gave the best fit of D_{p50} of bed material between experimental results and calculation.

For desulfurization, intermittent attrition-sulfation model presupposed by Shimizu et al. (2002a) was employed. The surface was treated as a flat plane because the thickness of product layer is sufficiently smaller than the solid radius. The surface area is intermittently removed by attrition with an interval of τ. At the same time, chemical reaction proceeds according to the shrinking core model with product layer diffusion control. The average specific rate is dependent upon whether fresh $CaCO_3$ surface appears when attrition occurs. The criterion of fresh surface exposure is given as follows:

$$(2D_eCM\tau/\rho)^{1/2} < (1/2)k_2D_p^2\tau \quad (5)$$

where C, M, and ρ are SO_2 concentration, molecular weight of $CaCO_3$, and limestone density, respectively. Effective diffusivity through the product layer, D_e, was 1.5×10^{-9} m^2/s (Qui and Lindqvist, 2000). When a fresh $CaCO_3$ surface appears with intermittent attrition, the average SO_2 capture rate per unit surface area under a steady condition is given as

$$r_{steady} = (2D_e\rho C/M\tau)^{1/2} \quad (6)$$

When only product layer is removed by attrition, i.e., $CaSO_4$ is exposed to the gas after attrition, the sulfation rate is governed by removal of $CaSO_4$ by attrition.

$$r_{steady} = (\rho/2M)k_2D_p^2 \quad (7)$$

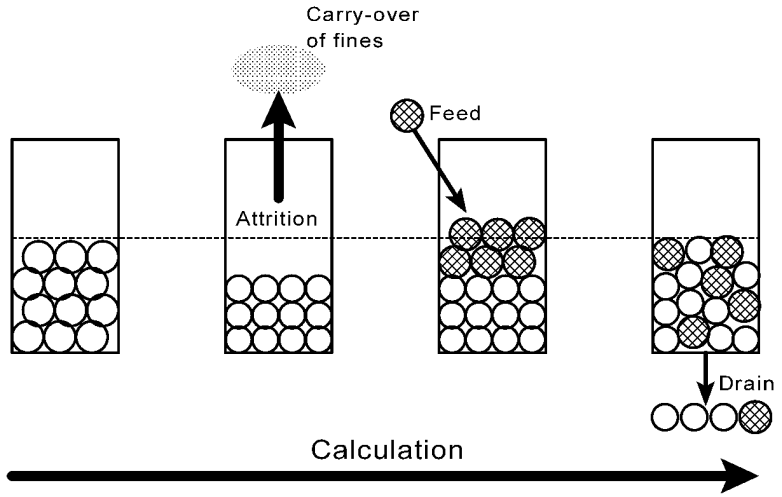

Fig.2 Model of attrition to calculate particle size distribution

Table 1 Calculation condition

Bed material mass	Pressure	Coal feed rate	Sulfur in coal	Gas flow rate
60×10^3 kg	1.065 MPa	23.5 t/h (dry)	0.33 %	2.49×10^5 m^3N/h

RESULTS AND DISCUSSION

Figure 3(a) shows the effect of limestone feed size on required feed rate of limestone. The minimum feed requirement of limestone was attained at D_{p50} of feed of approximately 0.5 – 0.7 mm. The optimum size decreased with decreasing drain rate. With increasing feed size, loss by attrition increased. With decreasing size, the content of finer particles in the feed increased. Not only the feed size but also drain rate affect the required feed rate. With increasing (Drain)/(Feed) ratio from 0 to 0.3, the required feed became double. This shows that the control of drain from the bottom is an important operating parameter to reduce limestone consumption. However, it should be noted that the reduction of drain may result in the accumulation of coarse solids in the bed, thus the monitoring of fluidization behavior will be necessary. The experimental results which were obtained under conditions of drain/feed = 0 – 0.3 during Phase-1 test series burning BA coal (Shimizu et al., 2001) agreed with the calculation.

Figure 3(b) shows the effect of particle size of fed limestone on bed material size. With decreasing feed size and drain/feed ratio, bed material size decreased. For bed material size, drain rate is found to play a significant role.

Figure 3(c) shows the effect of particle size of fed limestone on SO_2 emissions. SO_2 emissions increased with decreasing feed size when feed size is smaller than 0.7 – 1.0 mm, depending on drain/feed ratio. This

increase in SO_2 emission is attributable to lower attrition rate. Product layer is formed on the particle surface when attrition rate is low and it inhibits the SO_2 capture. On the other hand, too large feed size is not favorable to the desulfurization because of less external surface area of bed material.

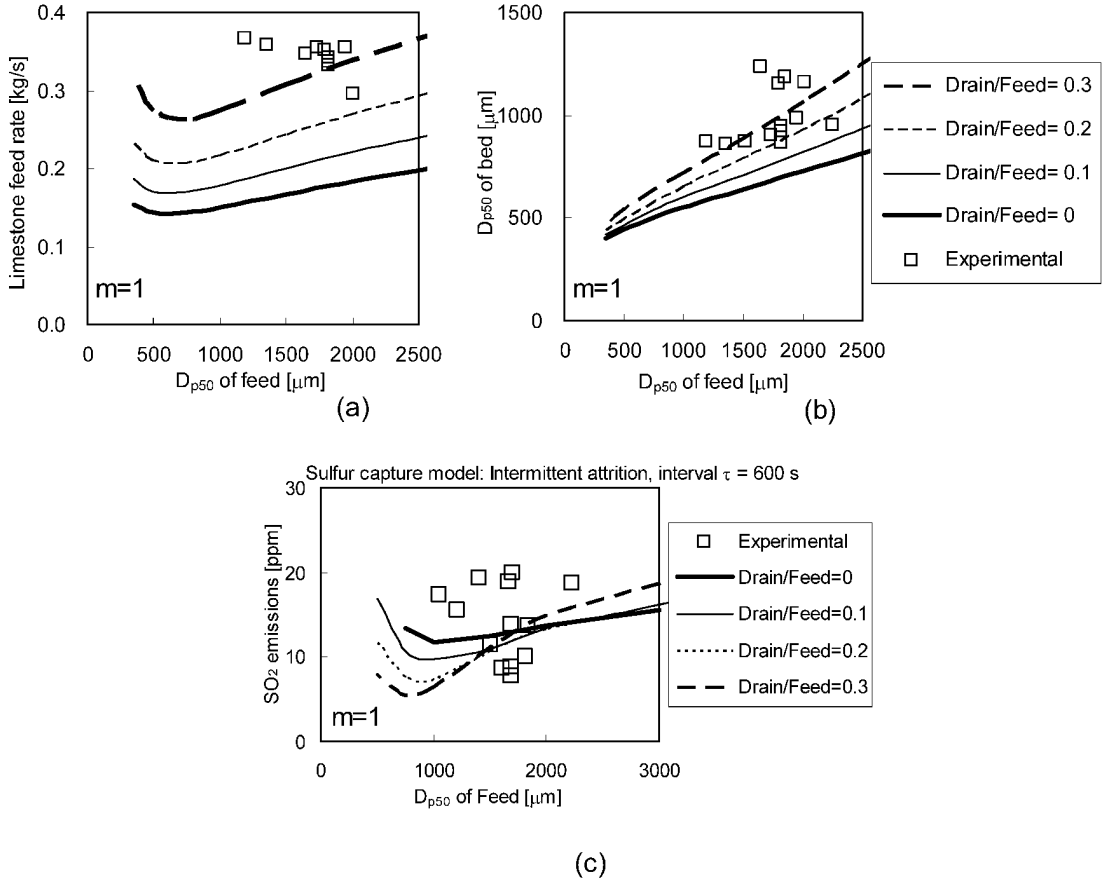

Fig. 3 Effect of limestone feed size on (a) required feed rate of limestone, (b) bed material size, and (c) SO_2 emissions (Experimental results: Shimizu et al., 2001)

Figure 4 shows the effect of sulfur content of coal on SO_2 emissions. The base case is for bituminous coal with low sulfur content (S=0.33%). With increasing sulfur content of coal, SO_2 emissions increased drastically; for a sulfur content of 0.66 % SO_2 emission is estimated to exceed 160 ppm whereas those for low sulfur content of 0.33 % were less than 25 ppm. This drastic increase is attributable to desulfurization nature under solid attrition conditions. At high SO_2 concentration conditions, overall sulfur removal rate is considered to be governed by the removal of product ($CaSO_4$) layer by attrition. This implies that the sulfur capture rate is nearly zero order with respect to SO_2 concentration. For zero-order dependency, emissions of SO_2 are considered to drastically increase with increasing sulfur content above a threshold value.

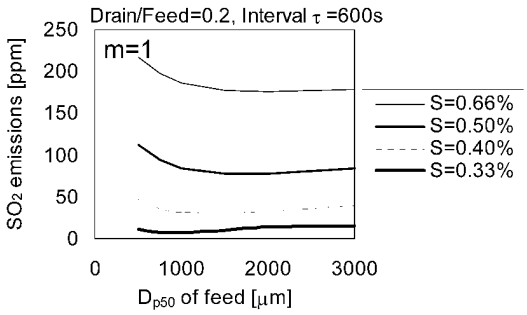

Fig. 4 Effect of sulfur content of coal on SO_2 emissions

In the above discussion, a value of m=1, which had been determined from the experimental PSD of fed limestone, was employed. However, by employing limestone with narrower side distribution is expected to improve limestone utilization efficiency because such limestone includes less coarse particles and less fine

particles; the coarse particles lost by attrition and the fine particles are carried over. The narrower size distribution corresponds to larger value of m. In Fig.5, calculated results for m=2 are shown compared with those for m=1. Limestone consumption is expected to be reduced by increasing m from 1 to 2 (Fig.5(a)). The bed material size is not remarkably affected by m (Fig.5(b)). The sulfur capture for m=2 at D_{p50} of feed between 0.8 - 1.5mm is expected to be better than that for m=1 (Fig.5(c)). However, too small feed size (D_{p50} of feed < 0.7 mm) will result in remarkably higher SO_2 emissions for m=2 than m=1.

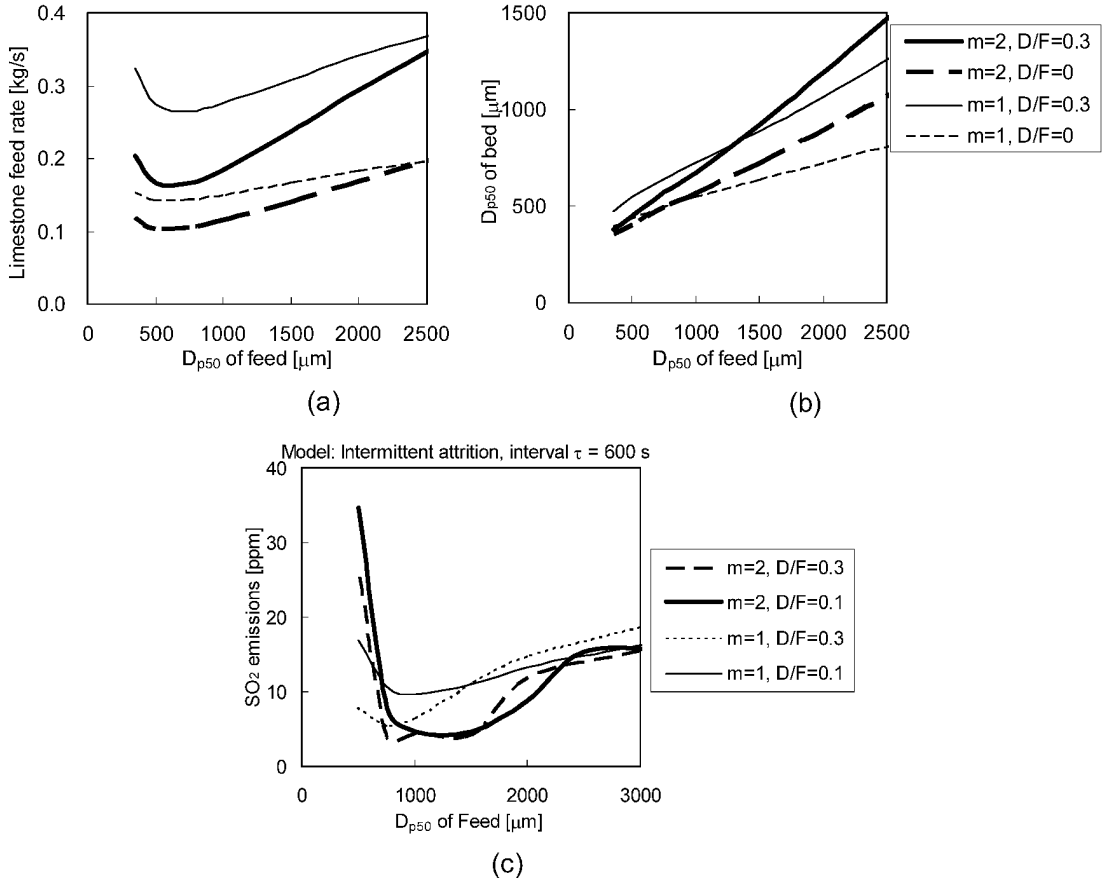

Fig.5 Effect of limestone feed size on (a) required feed rate of limestone, (b) bed material size, and (c) SO_2 emissions for different value of m

An approach to attain narrower size distribution of fed limestone is size classification by sieving, for example. Figure 6 shows an example of particle size distribution for m=1, m=2, and m=1 followed by "sieving" with bottom sieve size of 0.25 mm and top sieve size of 2.7 mm, for particles with D_{p50} = 1.0mm. By removing coarse and fine particles, whose total amount was about 1/3 of fed limestone of m=1, the size distribution after "sieving" is nearly the same as that of m=2. However, the reduction of limestone consumption by employing m=2 instead of m=1 is about 1/3 for D/F=0.3 (Fig.5(a)). So the overall consumption, even if removed coarse and fine particles are to be taken into account, will not increase by size classification. In addition, the removed limestone particles are not contaminated by $CaSO_4$ and coal ash, thus they can be used in other purposes.

Another approach to attain narrower size distribution of fed limestone is to improvement of crusher to obtain narrower size distribution. However, this topic is beyond the scope of this work and remained as a subject of future work.

It should be emphasized that the above results are applicable for attrition rate expression with a value of exponent of n=2. It is possible that the value of exponent differs for different limestone. With different value of n, the optimum size of limestone will be different. The mass attrition rate (dW/dt) per unit solid mass (W) is given as a function of particle size as follows:

$$(1/W)dW/dt = -3k_n D_p^{n-1} \quad (8)$$

For the case of n=1, the mass attrition rate is proportional to solid mass and is independent of the particle size as:

$$dW/dt = -3k_1 W \quad (9)$$

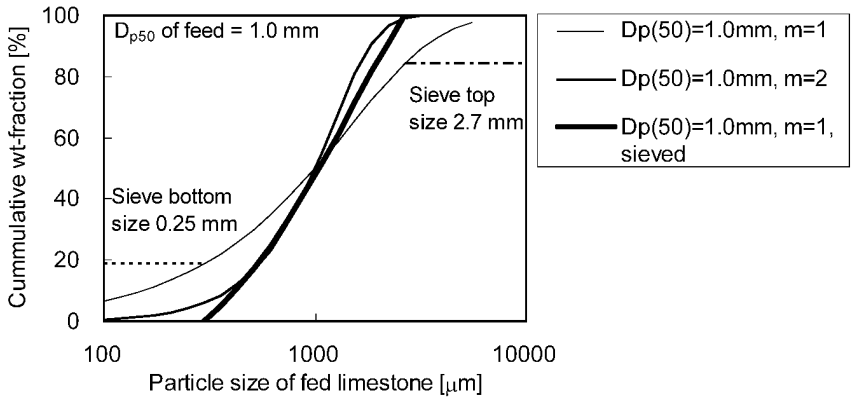

Fig. 6 An example of particle size distribution for m=1, m=2, and m=1 followed by "sieving"

Thus it is impossible to reduce the attrition rate by controlling the particle size of fed limestone. Coarser feed size is favorable to suppress the energy consumption but it will increase the bed material size, thus SO_2 capture rate will be lower and fluidization will be worse. When the fluidization becomes worse, dispersion of heat from the fuel feed points will be worse and problem with solid agglomeration caused by hot spot will occur. The feed size is then determined to attain the desired SO_2 capture and good fluidization. For the case of n<1, coarser size is favorable to suppress the attrition. The maximum feed size is then determined to attain the desired SO_2 capture and good fluidization, as discussed above. For the case of n>1, smaller size is favorable to suppress the attrition, to enhance SO_2 capture, and to attain good fluidization. As indicated in this article, there exists optimum size to suppress the loss caused by attrition and grinding process.

CONCLUSIONS

Effects of limestone feed size of on limestone consumption, bed material size, and desulfurization were calculated using a model that had been proposed by the present authors. The optimum limestone feed size was determined. Drain rate from the bottom was found to affect limestone consumption, bed material size, and desulfurization. Narrower size distribution of limestone is favorable to reduce limestone consumption.

NOTATIONS

b parameter defined in Eq.(3), m^{-m}
C SO_2 concentration, mol/m^3
D_e Effective diffusivity, m^2/s
D_p particle diameter, m
D_{p50} size of particle whose cumulative weight fraction is 50 %, m
k_n attrition rate constant, $1/(m^{m-1}s)$
M molecular weight of $CaCO_3$, kg/mol
m parameter of PSD defined in Eq.(3)
n order of attrition rate, -
$R(D_p)$ weight fraction of particles greater than D_p, %
r_{steady} SO_2 capture rate at steady state, $mol/(m^2s)$
W mass of a particle, kg

Greek symbols
ρ Particle density, kg/m^3
τ Interval of attrition when intermittent attrition occurs, s

ACKNOWLEDGEMENTS

This work was done as a part of Finland-Japan Co-operation Research Plan. The financial support from National Technology Agency of Finland (Tekes) is acknowledged.

REFERENCES

Hajaligol, M.R., Longwell, J.P., Sarofim, A.F.: Ind. Eng. Chem. Res., **27** (1988), pp.2203-2210.
Iisa, K., Hupa, M.: J. Inst. Energy **65** (1992), pp.201-205.
Krishnan, S.V., Sotirchos, S.V.: Canadian J. Chem. Eng. **71** (1993a), pp.244-255.
Krishnan, S.V., Sotirchos, S.V.: Canadian J. Chem. Eng. **71** (1993b), pp.734-745.
Qui, K., Lindqvist, O.: Chem. Eng. Sci. **55** (2000), 3091-3100.
Saastamoinen, J., Shimizu, T.: Chem. Eng. Sci. **62** (2007), pp.574 - 583.
Sakuno, S., Shimizu, T., Misawa, N., Suzuki, N., Ueda, H., Sasatsu, H., Gotou, H.: Nihon- Energy-Gakkai-Shi (J. Jpn. Inst. Energy) **80** (2001a), pp.747-757.

Sakuno, S., Misawa, N., Suzuki, N., Ueda, H., Sasatsu, H., Gotou, H. Shimizu, T.: Nihon-Energy-Gakkai-Shi, (J. Jpn. Inst. Energy) **80** (2001b), pp.758-764.

Shimizu, T., Peglow, M., Sakuno, S., Misawa, N., Suzuki, N., Ueda, H., Sasatsu, H., Gotou, H.: Chem. Eng. Sci. **56** (2001), pp.6719-6728.

Shimizu, T., Peglow, M., Yamagiwa, K., Tanaka, M., Sakuno, S., Misawa, N., Suzuki, N., Ueda, H., Sasatsu, H., Gotou, H.: Chem. Eng. Sci., **57** (2002a), pp.4117-4128.

Shimizu, T., Peglow, M., Yamagiwa, K., Tanaka, M.: Nihon-Energy-Gakkai-Shi(J. Jpn. Inst. Energy) **81** (2002b), pp.206-215.

Shimizu, T., Peglow, M., Yamagiwa, K., Tanaka, M.: Chem. Eng. Sci. **58** (2003a), pp.3053-3057.

Shimizu, T., Peglow, M., Yamagiwa, K., Tanaka, M., Sakuno, S., Misawa, N., Suzuki, N., Ueda, H., Sasatsu, H., Gotou, H.: Thermal Science **VII** (2003b), pp.17-31.

Snow, M.J.H., Longwell, J.P., Sarofim, A.F.: Ind. Eng. Chem. Res. **27** (1988), pp.268-273.

Zevenhoven, R., Yrjas, P., Hupa, M.: Fuel **77** (1998), pp.285-292.

ZERO EMISSIONS HYDROGEN PRODUCTION BY FLUIDIZED BED CATALYTIC DECOMPOSITION OF METHANE

Ammendola P.[1], Chirone R.[1], Ruoppolo G.[1], Russo G.[2]

1 Istituto di Ricerche sulla Combustione – CNR - P.le V. Tecchio, 80 – 80125 Napoli, Italy
2 Dipartimento di Ingegneria Chimica – Università degli Studi di Napoli Federico II
P.le V. Tecchio, 80 – 80125 Napoli, Italy

Abstract: The present paper deals with the strategic field of production of clean fuels with very low to zero emissions. A two stage fluidized bed process for catalytic decomposition of methane has been investigated. Firstly, the fluidized bed has been operated for the thermo-catalytic decomposition (TCD) of methane to produce hydrogen and solid carbon, which deposited on the catalyst. Secondly, the carbon oxy-combustion has been carried out to regenerate the catalyst producing a separated CO_2 stream candidate to be directly fed to a sequestration unit. Experiments have been carried out in a laboratory scale bubbling fluidized bed reactor (26mm ID) using a home-made copper dispersed on γ-alumina as catalyst operated at 800°C. The carbon oxy-combustion regeneration strategy have been compared to the carbon combustion one on the basis of the efficiency of carbon removal and the performance of regenerated catalyst with respect to the TCD process. The effect of multiple cycles of decomposition and regeneration steps has been also quantified. A reasonable cyclic process has been simulated switching between two different feeds, the first containing CH_4 and the second containing the regeneration stream. Experimental activity confirmed the possibility of producing a CO_2 stream that can be finalized to a sequestration unit but also indicated some drawbacks related to the oxy-combustion regeneration strategy which affect the production of CO_x species during the methane decomposition stage.
Keywords: methane decomposition, catalyst regeneration, carbon oxy-combustion, carbon combustion, fluidized bed

INTRODUCTION

The thermo-catalytic decomposition of methane is an attractive and promising process towards the production of hydrogen with reduced CO_2 emissions (Muradov et al., 2006; Muradov and Veziroğlu, 2005) and it could be an important step towards the realization of more and more effective and environmental friendly processes for hydrogen production. In this framework, fluidized bed reactors have been recently proposed (Muradov et al., 2005; Lee et al., 2004; Dunker et al., 2006) as a useful alternative solution to fixed bed reactors to operate with lower pressure drops, to optimize the energy balance due to the relatively high efficiency in heat transfer mechanism but not a real possibility of a continuous hydrogen production as a result of a continuous catalyst regeneration due to deposited carbon attrition (Ammendola et al., 2006). Previous works examined different regeneration strategies of the deactivated catalyst based on combustion or gasification by steam or CO_2 of the deposited carbon (Ammendola et al., 2008). Both processes, carbon combustion or gasification, present advantages and drawbacks. In the combustion case positive aspects are: i) CO_x are in principle only formed during the carbon removal from the catalyst in the regeneration phase and, as a consequence, they are separated in time from H_2; ii) the heat released during carbon oxidation can be used in situ to sustain the decomposition reaction. On the other hand, in the gasification case the use of steam or CO_2 as regeneration agent results in the prevention of catalyst re-oxidation and thermal shocks; an additional H_2 (not CO_x-free) production can be obtained also during the catalyst regeneration by steam. Authors indicated the possibility of adopting a periodic operation strategy in a bubbling fluidized bed reactor based on a two stage operation for hydrogen production by methane TCD followed by re-activation of catalyst by combustion with air. However, this regeneration strategy further requires a separation step of CO_2 produced during the carbon combustion stage from the N_2 present in the fed air before the CO_2 sequestration unit.

The present paper moves further to address a concrete and innovative contribution to the strategic field of production of clean fuels with very low to zero emissions. A two stage fluidized bed process for H_2 production has been analyzed. Firstly, the fluidized bed has been operated for the catalytic decomposition of methane to produce hydrogen. Secondly, the regeneration of catalyst, de-activated due to carbon deposition, has been achieved by adopting an oxy-combustion stage. The advantage of this regeneration strategy is the production of a separated CO_2 stream that can be directly fed to a CO_2 sequestration unit. Experiments have been carried out in a laboratory scale bubbling fluidized bed reactor (26mm ID) using a home-made copper dispersed on γ-alumina catalyst. The same reactor has been alternatively used for both methane decomposition and catalyst

regeneration steps. The carbon oxy-combustion regeneration strategy have been compared to the carbon combustion one on the basis of the efficiency of carbon removal and the performance of regenerated catalyst with respect to the TCD process. The effect of multiple cycles of decomposition and regeneration steps has been also quantified. A reasonable cyclic process has been simulated switching between two different feeds, the first containing CH_4 and the second containing the regeneration stream.

EXPERIMENTAL

The fluidized bed apparatus used for experiments is reported in Fig. 1. It consists of a 2.6 cm ID stainless steel reactor, equipped with a gauze type gas distributor, an electrical oven surrounding the reactor employed to heat up the reactor at the reaction temperature and to provide enough heat for methane decomposition, a device for collecting fine particles larger than 300nm escaping from the reactor in the exit gases. Temperature and pressure were measured by means of thermocouples horizontally inserted in the reactor and pressure transducers respectively. The inlet and outlet streams were analyzed by an on line continuous analyzer for CO, CO_2, CH_4, H_2 and O_2. The experimental apparatus has been alternatively used for both methane decomposition and catalyst regeneration step. A home-made Cu based catalyst, prepared by wet impregnation by dissolving the required amount of copper acetate in aqueous solution and adding a suitable amount of γ-Al_2O_3, has been used. Details of the catalyst properties are reported elsewhere (Ammendola et al., 2007). The catalyst has been characterized in terms of mechanical attrition (Ammendola et al., 2006). The Table 1 reports the main characteristics of the catalyst.

Table 1 Catalyst properties

Active phase	$CuAl_2O_4$*
Copper content (%wt)	8.4
Specific surface area (m^2/g)	156
Geldart's classification (Geldart, 1973)	B group
Particle size (μm)	300-400
Particle density (kg/m^3)	1900
Minimum fluidization velocity, U_{mf} (cm/s)**	2.9
Mechanical attrition rate (g/g·min)**	3×10^{-7}

*surface compound; **evaluated at 800°C.

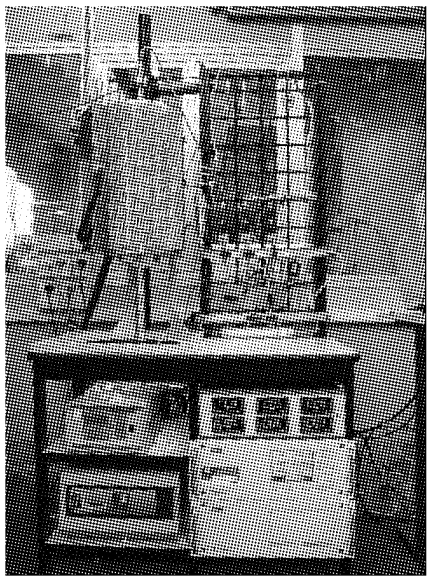

Fig. 1 Experimental rig

Methane decomposition experiments were carried out at 800°C and with an inlet gas made of methane (5%vol.) in nitrogen flow. Operative temperature (800°C) has been fixed as a compromise between the thermal stability of the catalyst and the thermodynamic limitations of methane decomposition process. As combustion agent, undiluted air or 20% O_2 in a CO_2 stream have been used at 800°C (the effect of oxygen concentration has been previously investigated (Ruoppolo and Ammendola, 2009).

Methane decomposition and catalyst regeneration tests were carried out using 25g of catalyst at a superficial gas velocities of 8.7cm/s. During each test the time resolved profiles of pressure drops, bed temperature and concentrations of different species analyzed have been recorded.

The absence of catalytic effects due to the stainless steel components of the reactor or due to the catalyst support have been verified by means of preliminary tests carried out operating the apparatus with an inert bed made of quartz or alumina particles respectively.

The fluidized bed reactor has been operated under repeated cycles of decomposition and regeneration steps using the same batch of catalyst. For each cycle, several methane decomposition stages have been carried out; each decomposition step is followed by a catalyst regeneration stage by carbon removal. N_2 is fluxed to wash the reactor between the two phases. The different operative conditions used for catalyst regeneration have been analyzed on the basis of the efficiency of carbon removal and of the performances of regenerated catalyst with respect to the operation in the TCD process.

RESULTS AND DISCUSSION

Methane decomposition stage

Typical curves of CH_4 conversion and of H_2 production obtained during a TCD test carried out in the fluidized bed reactor are reported in Fig. 2(a). Details are reported elsewhere (Ammendola et al., 2006).

Analysis of the curves shows that there are two main stages. During the first stage the catalyst acts as an oxygen carrier, due to its. This is the same phenomena occurring during a chemical-looping combustion (Chuang et al., 2008; de Diego et al., 2005) In particular, firstly the methane reacts with the oxygen linked to the copper producing CO_2 and CO. It is to note that the occurrence of this first stage is strictly related to the fact that a not pre-reduced the catalyst has been used (Ammendola et al., 2007) When the oxygen availability is depressed the methane decomposition reaction starts and H_2 is produced (second stage).

Catalyst regeneration stage

Figure 2(b) and 2(c) reports the concentration curves of products obtained during the regeneration treatment carried out on the deactivated catalyst after the decomposition phase at a operative temperature of 800°C and using air (Fig. 2(b)) and 20% O_2 in CO_2 (Fig. 2(c)). Curves reported in Fig. 2(b) show that O_2 reacts with the deposited carbon, producing initially CO and then CO_2. The complete regeneration of catalyst with air required about 15min. The total amount of carbon removed, evaluated from the amounts of CO_x produced, is in agreement with the carbon deposited on the catalyst during the previous decomposition step. An additional confirmation of the ability of combustion process to remove all the deposited carbon derives from the elemental analysis performed on the regenerated catalyst, which indicated that the catalyst is completely clean from carbon. A balance on oxygen consumed in the regeneration stage (evaluated from O_2 curve not reported in the figure) indicates that, in addition to the oxygen used for carbon oxidation, related to CO_x formation, a further amount of oxygen (26-28mmol) is consumed for the re-oxidation of the catalyst, already reduced by methane during the previous decomposition test. An increase of bed temperature of only 10°C has been measured during catalyst regeneration with air. The good heat exchange mechanism of fluidized bed is responsible for preventing catalyst overheating, as instead observed under the same experimental conditions using a fixed bed reactor (Ruoppolo and Ammendola, 2009).

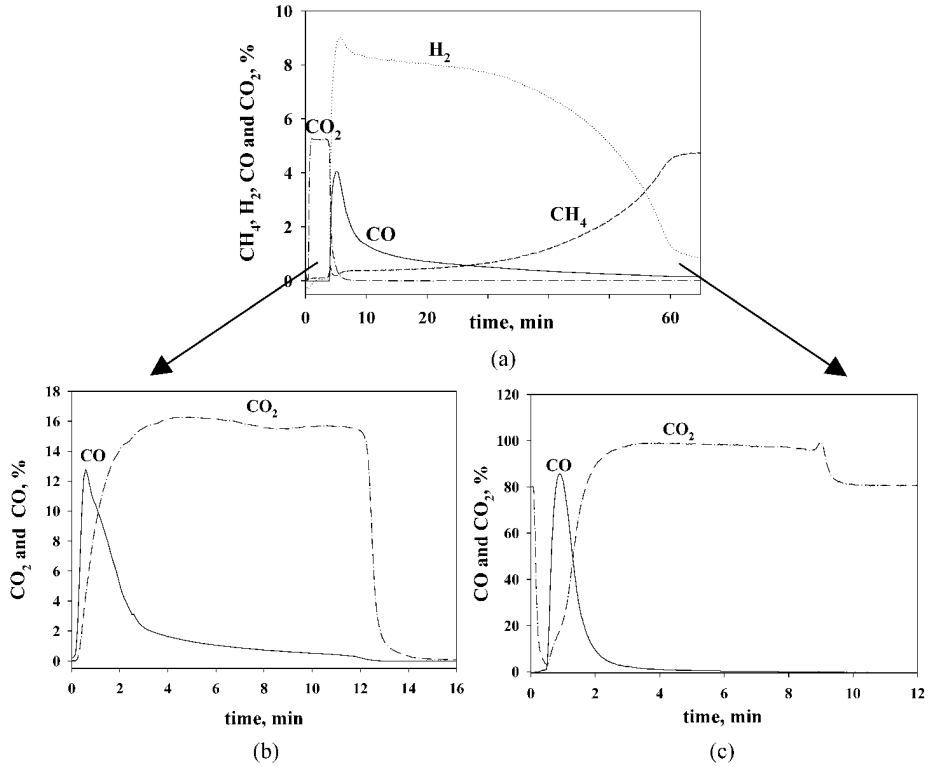

Fig. 2 (a) Typical methane catalytic decomposition test. Feed composition: CH_4 (5%vol.) in N_2; T=800°C; m_{cat}=25g; U=8.7cm/s; (b) Typical concentration curves obtained during regeneration by carbon combustion in air; T=800°C, m_{cat}=25g; U=8.7cm/s. Feed composition: air. (c) Typical concentration curves obtained during regeneration by carbon oxy-combustion; T=800°C, m_{cat}=25g; U=8.7cm/s. Feed composition: 20%vol. O_2 in CO_2

CO and CO_2 profiles obtained during the oxy-combustion stage are reported in Fig. 2(c). Analysis of the figure shows that there are two stages In particular, initially not only O_2 but also CO_2 react with the deposited carbon producing CO; then the CO production gradually lowers to zero and the CO_2 production is observed due to reaction of O_2 with the residual deposited carbon. Also this regeneration treatment is able to remove all the carbon deposited on the catalyst during the previous decomposition step. The complete regeneration of catalyst required about 10min. The presence of oxygen in the regeneration stream also involve the complete re-oxidation of the catalyst. Also in this case an increase of bed temperature of only 10°C has been measured during catalyst regeneration by carbon oxy-combustion.

The comparison between performances of fresh and regenerated catalyst has been reported in Fig. 3 in terms of hydrogen concentration curves obtained during successive methane decomposition/catalyst regeneration cycles for both air (A) and O_2-CO_2 mixture (B).

The perfect overlapping of the curves obtained after different cycles suggests that: i) the activity of catalyst is completely restored as a result of the complete removal of carbon by the regeneration treatment; ii) the catalyst is stable under repeated decomposition-regeneration cycles, as expected on the basis of the ability of fluidized bed configuration in reducing the increase of temperature during the regeneration phase and, in turn, in preventing the catalyst thermal deactivation (Ruoppolo and Ammendola, 2009). During the successive decomposition tests CO_x are also produced in the same amounts of those obtained on the fresh catalyst (Figure 2(a)), in agreement with the complete re-oxidation of the catalyst observed in the regeneration step. This finding confirms the role of oxygen carrier played by the catalyst during the first stage of methane decomposition.

A reasonable cyclic process has been simulated in fluidized conditions switching between two different feeds, the first containing CH_4 (5%vol.) in N_2 and the second containing the regeneration stream. In particular, the bubbling fluidized bed reactor has been operated for methane decomposition until a limit deactivation degree of catalyst is achieved and then as a combustor for catalyst regeneration by carbon removal. Between the two phases N_2 is fluxed for two minutes to wash the reactor.

The chosen decomposition time (about 25 min) corresponds to a not strong reduction of H_2 concentration of its maximum value (Fig. 2(a)). The regeneration time as been fixed at two minutes. The effect of different regeneration times on the performances in the decomposition step has been previously studied in the case of air (Ammendola et al., 2008). In particular, the regeneration time influences not only the catalyst re-oxidation, i.e. the CO_x production during the decomposition phase, but also the amount of carbon removed, i.e. the regenerated catalyst activity. In order to obtain a stable H_2 production a regeneration time larger than 2min is required. The periodic variation of the concentrations of different species at the reactor outlet is presented in Fig. 4.

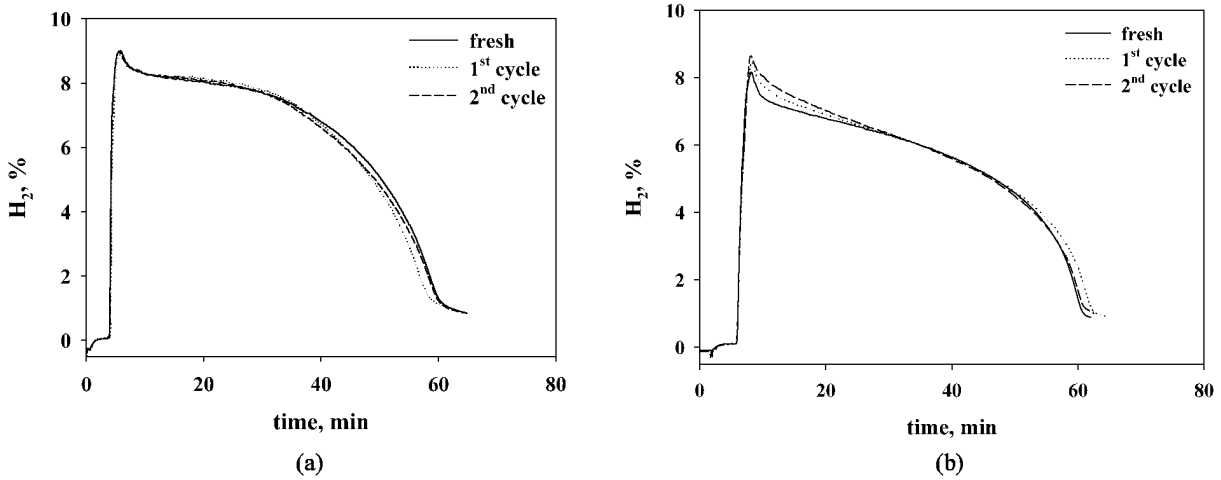

Fig. 3 H_2 concentration as function of time obtained on the fresh and regenerated catalyst. Feed composition: CH_4 (5% vol.) in N_2; T=800°C; m_{cat}=25g; U=8.7cm/s; regeneration agent: (a) air; (b) 20%vol. O_2 in CO_2

Comparison of decomposition curves reported in Fig. 4 shows that in both cases: i) the methane conversion, i.e. the hydrogen production, is quite stable during the different cycles; ii) after the first cycle the total amount of CO_x produced during the decomposition phase is reduced with respect to that obtained during the first one. The production of CO_2 is not totally suppressed during the decomposition phase (traces are present at the outlet). The quite stable CH_4 conversion indicates that 2min are enough to remove all the carbon deposited during 25min of previous decomposition. The production of traces of CO_2 during the decomposition

phase is probably due to the fact that the time of regeneration treatment of only two minutes is enough not only to restore the catalyst activity but also to re-oxidized the catalyst itself too much.

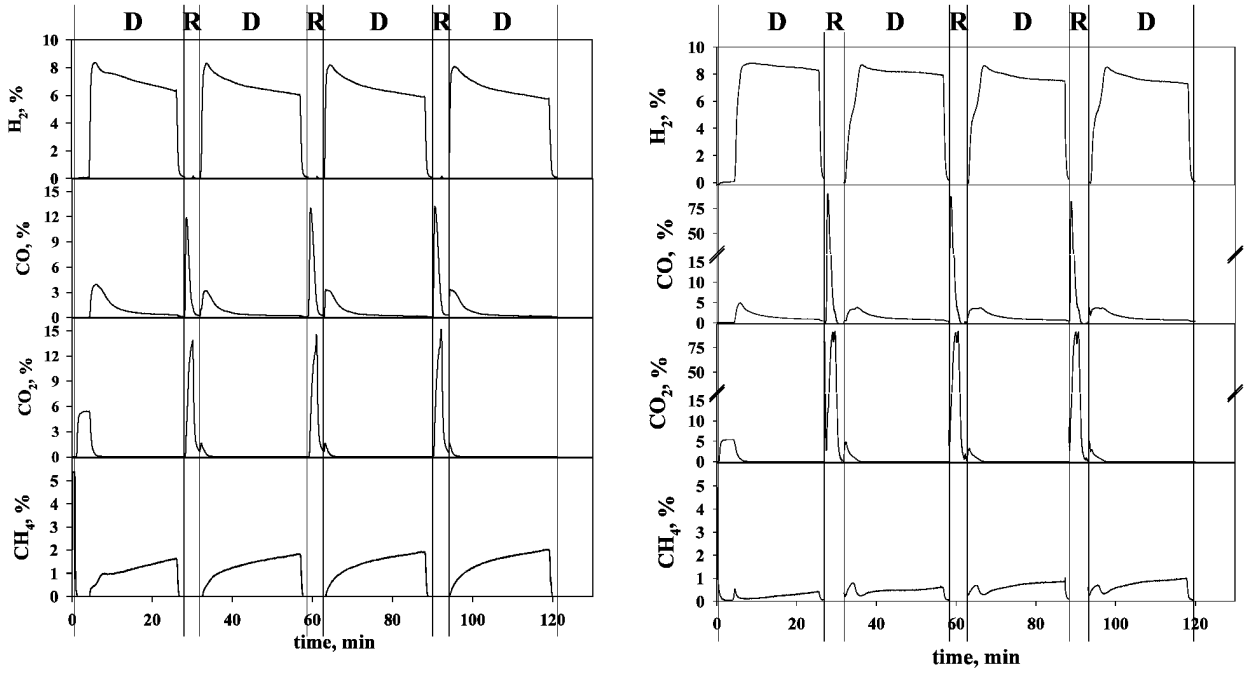

Fig. 4 Concentrations profiles during the cyclic process in fluidized bed. D=decomposition, R=regeneration; decomposition time=25min; regeneration time=2min; N_2 washing time=2min. Feed composition in the decomposition phase: CH_4 (5%vol.) in N_2; feeds composition in the regeneration phase: air (A) and 20% O_2 in CO_2 (B); T=800°C, m_{cat}=25g; U=8.7cm/s

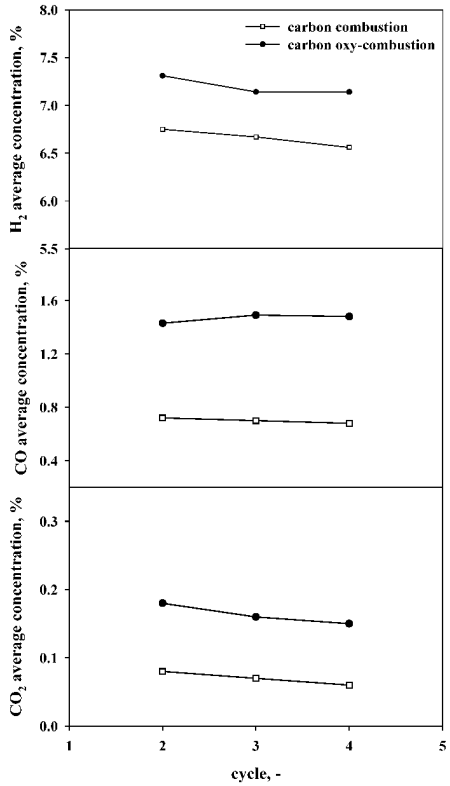

Fig. 5 H_2, CO and CO_2 average concentrations during the decomposition phase as a function of number of cycles. Feed composition: CH_4 (5%vol.) in N_2; T=800°C, m_{cat}=25g; U=8.7cm/s

With reference to the regeneration phase the comparison of curves reported in Fig. 4 shows that in both cases a mixture containing both CO and CO_2 is produced, even if it is diluted in N_2 during the carbon combustion treatment. In order to obtain a stream that can be fed to a CO_2 sequestration unit not only a post-combustion step (to convert the CO to CO_2) but also an additional separation step of CO_2 from N_2 would be required in the case of the carbon combustion treatment.

The influence of different regeneration streams on the performances of decomposition phase is reported in Fig. 5 in terms of concentration of products averaged on the decomposition time as a function of the number of cycles, except for the first cycle.

The comparison of the values of the average concentration shows that: i) the CO and CO_2 amounts produced during the decomposition step after the carbon oxy-combustion treatment are about two times higher than those obtained after the carbon combustion treatment; ii) the H_2 concentration obtained during the decomposition step after the carbon oxy-combustion treatment is slightly larger than that produced after the carbon combustion treatment. These results indicate that at a fixed regeneration time the oxy-combustion treatment is more effective not also in carbon removal but also in the catalyst re-oxidation due to a synergic effect of both O_2 and CO_2. Further investigations will be devoted to assess the effect of different regeneration time during the carbon oxy-combustion treatment, in order to reduce the CO_x production during the decomposition stage, keeping at the same time a stable hydrogen production.

CONCLUSIONS

The present paper deals with the strategic field of production of clean fuels with very low to zero emissions. The possibility of carrying out a two stage operation for hydrogen production from methane TCD in fluidized bed rectors, consisting into firstly operating the fluidized bed as a reactor for methane decomposition, until a defined catalyst deactivation degree is approached, and then operating the fluidized bed as a combustor or a oxy-combustor for catalyst regeneration by carbon removal, has been investigated. The carbon oxy-combustion regeneration strategy has been compared to the carbon combustion one on the basis of the efficiency of carbon removal and the performance of regenerated catalyst with respect to the TCD process. Both the regeneration strategies, even if re-oxidizing the catalyst, were able to remove all carbon species present on the catalyst, completely restoring the initial catalyst activity. On these basis they allowed to continuously produce H_2 by a cyclic dual step operation, without changing in the catalyst activity. On the other hand, at a fixed regeneration time (2 min), the oxy-combustion treatment is more effective not also in carbon removal but also in the catalyst re-oxidation due to a synergic effect of both O_2 and CO_2. With reference to the regeneration phase in both cases a mixture containing both CO and CO_2 is produced, even if it is diluted in N_2 during the carbon combustion treatment. In order to obtain a stream that can be fed to a CO_2 sequestration unit not only a post-combustion step (to convert the CO to CO_2) but also an additional separation step of CO_2 from N_2 would be required in the case of the carbon combustion treatment.

REFERENCES

Ammendola, P., Ruoppolo, G., Chirone, R., Russo, G.: Proc. 19th International Conference on Fluidized Bed Combustion (2006), Vienna, Austria.
Ammendola, P., Chirone, R., Lisi, L., Ruoppolo, G., Russo, G.: J. Mol. Catal. A-Chem. 266 (2007), pp. 31-39.
Ammendola, P., Ruoppolo, G., Chirone, R., Russo, G.: Combust. Sci. Technol. 180 (2008), pp. 869-882.
Chuang, S. Y., Dennis, J. S., Hayhurst, A. N., Scott, S. A.: Combust. Flame 154 (2008), pp. 109-121.
de Diego, L. F., Gayán, P., García-Labiano, F., Celaya, J., Abad, A., Adánez, J.: Energ. Fuel. 19 (2005), pp. 1850-1856.
Dunker, A. M., Kumar, S., Mulawa, P. A.: Int. J. Hydrogen Energ. 31 (2006), pp. 473-484.
Geldart, D.: Powder Technol. 7 (1973), pp. 285-292.
Lee, K. K., Han, G. Y., Yoon, K. J., Lee, B. K.: Catal. Today 93-95 (2004), pp. 81-86.
Muradov, N. Z. and Veziroğlu, T. N.: Int. J. Hydrogen Energ. 30 (2005), pp. 225-237.
Muradov, N., Chen, Z., Smith, F.: Int. J. Hydrogen Energ. 30 (2005), pp. 1149-1158.
Muradov, N., Smith, F., Huang, C. T-Raissi,A.: Catal. Today 116 (2006), pp. 281-288.
Ruoppolo, G., Ammendola, P.: Int. J. Nuclear Hydrogen Production and Applications 2 (2009), pp. 4-20.

CHARACTERIZATIONS OF DEPOSITED ASH DURING CO-FIRING OF WHITE PINE AND LIGNITE IN FLUIDIZED BED COMBUSTOR

Yuanyuan Shao[1,3], Jesse Zhu[3], Fernando Preto[2], Guy Tourigny[2], Jinsheng Wang[2], Chadi Badour[1], Hanning Li[1], Chunbao (Charles) Xu[1]

1 Department of Chemical Engineering, Lakehead University, Thunder Bay, Ontario
2 CANMET Energy Technology Centre , Ottawa, Ontario
3 Chemical and Biochemical Engineering Department, University of Western Ontario, London, Ontario

Abstract: Characterizations of ash deposits from co-firing/co-combusting of a woody biomass (i.e., white pine) and lignite coal were investigated in a fluidized-bed combustor using a custom designed air-cooled probe installed in the freeboard region of the reactor. Ash deposition behaviors on a heat transfer surface were comprehensively investigated and discussed under different conditions including fuel type, fuel blending ratios (20-80% biomass on a thermal basis), and moisture contents. For the combustion of 100% lignite, the compositions of the deposited ash were very similar to those of the fuel ash, while in the combustion of 100% white pine pellets or sawdust the deposited ash contained a much lower contents of CaO, SO_3, K_2O and P_2O_5 compared with the fuel ash, but the deposited ash was enriched with SiO_2, Al_2O_3 and MgO. A small addition of white pine (20% on a heat input basis) to the coal led to the highest ash deposition rates likely due to the strong interaction of the CaO and MgO (from the biomass ash) with the alumina and silica (from the lignite ash) during the co-combustion process, evidenced by the detection of high concentrations of calcium/magnesium sulfates, aluminates and silicates in the ash deposits. Interestingly, co-firing of white pine pellets and lignite at a 50% blending ratio led to the lowest ash deposition rates. Ash deposition rates in combustion of fuels as received with a higher moisture content was found to be much lower than those of oven-dried fuels.

Keywords: ash deposition, co-firing, wood pellet, sawdust, coal, chemical/mineralogical compositions, fluidized bed

INTRODUCTION

Biomass (wood, forestry/agricultural residues, energy crops, agro-industrial byproducts, etc.) can be used as renewable energy for heat and power generation by co-firing/co-combustion with coal. However, most biomass ash contains high concentrations of alkali metals and other ash-forming elements such as Ca, Mg and Si. Depending on the temperature of flue gas and fine particles during the firing/co-firing process, most of these elements may vaporize if they are formed in simple salts, but some of them may be in the form of the mineral grains, then these grains will adhere to each other and go through phase transformations to form fly ash particles. The abovementioned ash-forming matters, mostly in mobile forms, would generate the ash deposition problem during co-combustion of coal and biomass, potentially resulting in slagging and fouling of the biomass-fired boilers (Frandsen, 2005). The ash deposition problem is more severe firing/co-firing high-alkali herbaceous biomass fuels (e.g. switchgrass, crop residues), due to the lower melting points of the alkali/chorine -containing species in the ash such as NaCl, KCl, Na_2SO_4 and K_2SO_4 (Jenkins et al., 1998; Baxter et al., 1998; Jensen et al., 1997; Bryers, 1996). In comparison to the ash deposition characteristics of coal, only very limited data are available on the characteristics of the ash deposits from biomass fuels (Pronobis, 2006, Zheng and Koziński, 2000). The co-firing processes are not yet completely understood so that further investigation is needed.

When silica absorbs alkali/alkaline earth metals in the fuel, alkali silicates are formed and easily melt or sinter at low temperatures, 800-900°C, which can take place either in the solid phase during the combustion or more commonly in the vapour phase via fly ash (Baxter, 1993). The produced alkali silicates and/or mixed alkali and/or calcium chlorides/sulphates tend to deposit on the reactor wall or heat-exchanger surface causing fouling/corrosion with a low fusion temperature (typical < 700°C). In the case of fluidized bed reactors, these low boiling point species would cause slagging, sintering and de-fluidization of the bed materials (Arvelakis et al., 2005). Additionally, although calcium sulfates ($CaSO_4$) have lower mobility and vapour pressure of calcium than those of K_2SO_4, they still trend to deposit on the reactor walls or on the heat exchange surfaces (Baxter et al., 1998; Arvelakis et al., 2005).

Chlorine presenting in the biomass feedstock plays an important role in deposit formation and facilitates the mobility of K (predominant alkali in most biomass fuels) by forming KCl which is among the most stable vapour-phase alkali-containing species at a high temperature (Baxter et al., 1998). Chlorine compounds in

volatile ash may also result in corrosion of heat transfer surfaces inside the boiler at high temperature (Frandsen, 2005; Robinson et al., 2002). As such, the steam temperature for the biomass units is traditionally kept below 450°C in order to reduce the corrosion damage of the super-heater tubes. The low temperature, however, leads to negative effect on economic (Michelsen et al., 1998; Nielsen et al., 2000).

Recently, the ash-related studies during co-combustion or gasification of biomass fuels have attracted increasing interest worldwide. Air-cooled ash-deposition probes have been very commonly used in these studies to simulate the heat transfer surfaces in a boiler. For instance, using ash deposition probes the deposit formation mechanisms (Aho et al., 2008; Kupka et al., 2008; Theis et al., 2006a-c; Andersen et al., 2000), and the issues of slagging/fouling (Skrifvars et al., 2005) and high-temperature corrosion (Jensen et al., 2001a) during biomass co-firing were studied. Tackling technologies for reducing the ash deposition rates were also investigated. These include addition of combustion additives such as sulphur or SO_2 and SiO_2 (Overgaard et al., 2005; Aho and Silvennoinen, 2004; Andersson and Vattenfall, 2002), pretreatment of feedstocks to reduce the alkali metals (Arvelakis et al., 2005; Jensen et al., 2001a-b) and co-firing biomass fuels with fuels of low fouling-tendency (Theis et al., 2006a) as well as modification of the boiler internals (e.g. modification of the re-heater and super-heater in order to allow for larger spacing) and control of operating conditions (e.g., increasing soot-blowing and decreasing the live steam temperature to less than 500°C, etc.) (Overgaard et al., 2005). However, more research work is needed to enhance the knowledge on the interaction between ashes from different types of biomass feedstock, to understand the mechanism of ash deposition, and to develop effective measures to tackle the ash deposition problem for biomass co-firing.

The main objective of this work is to investigate on the ash deposition behaviors, the possible interactions between ashes from a woody biomass and lignite, and to chemically characterize the ash deposits collected during co-firing white pine pellets/sawdust and lignite with a pilot-scale fluidized bed combustor at CANMET Energy Technology Centre – Ottawa. Effects of fuel types, fuel blending ratios (20-80% biomass on a thermal basis), and moisture contents on the deposition rates and characteristics of deposited ash were comprehensively studied and discussed.

EXPERIMENTAL

Analyses of fuels and feedstock preparation

The lignite coal and the woody biomass fuel (white pine) used in this study for combustion/co-combustion tests were supplied by Ontario Power Generation (OPG) and a sawmill in South Ontario. Lignite has an ash content as high as 22 wt% db and a very content of volatile matters (54 wt% db), while the white pine contains an extremely low ash amount (0.4 wt% db) but very high amount of volatile matters (84.5 wt% db). In addition, pelletized form of the pine sawdust (5 mm OD, 40 mm long) was also used in the tests. The pellets were prepared using less than 1 wt% of the binding agent Ameribond 2x (Ammonium Lignosulfonate), designed as "white pine pellets" (WPP). The detailed proximate and ultimate analyses of these three fuels and their ash compositions are given in Table 1. As shown in the Table, as expected, the woody biomass contains significantly high concentrations of alkali and alkaline-earth metals (K, Na, Ca and Mg) in their ashes.

Table 1 Proximate and ultimate analyses of the fuels and their ash compositions

	CL	WPS	WPP
Moisture, wt% as received	30.0	38.0	5.3
Proximate analysis, wt% d.b.			
Ash[1]	22.0	0.4	3.13
Volatile matters (VM)	54.0	84.5	80.75
Fixed carbon	24.0	15.1	16.12
HHV (MJ/ kg dry)	21.8	20.6	
Ultimate analysis, wt% d.b.			
Carbon	58.8	52.5	47.99
Hydrogen	4.2	6.3	6.25
Nitrogen	0.9	0.1	1.31
Sulphur	0.5	<0.1	0.58
Oxygen[2]	13.6	40.6	40.73
Chlorine[3], μg/g	25	39	312
Bromine[3], μg/g	< 21	< 29	203
Fluorine[3], μg/g	100	< 29	<18

Continued

	CL	WPS	WPP
Dry ash analysis[4], wt% d.b.			
SiO_2	49.76	6.70	3.80
Al_2O_3	19.71	1.97	0.49
Fe_2O_3	3.82	1.46	0.58
TiO_2	0.86	0.09	<0.03
P_2O_5	0.30	3.52	23.13
CaO	9.91	31.10	23.36
MgO	2.11	4.34	6.86
SO_3	6.09	2.80	17.98
Na_2O	4.20	0.36	1.29
K_2O	1.04	15.45	16.46

1 The ashing temperature was 750°C for lignite and 500°C for white pine;
[2] By difference; [3]By Pyrohydrolysis and IC; [4]By XRF of the ashes from the feedstocks.

As for the feedstock preparation for the tests, the received lignite was crushed and screened into particles (<4 mm), designed as "crushed lignite" (CL) that was used throughout the tests. The white pine sawdust, after being sieved to particles (<2-6 mm), was used as "white pine sawdust" (WPS) for the tests. Generally, all the feedstock were used either as received or by air-drying, with a moisture content of 20-30 wt%. For investigating on the effects of moisture content, oven dried feedstocks (<5 wt% moisture content) were prepared. Prior to each test, the actual moisture contents of the feedstock used were accurately measured.

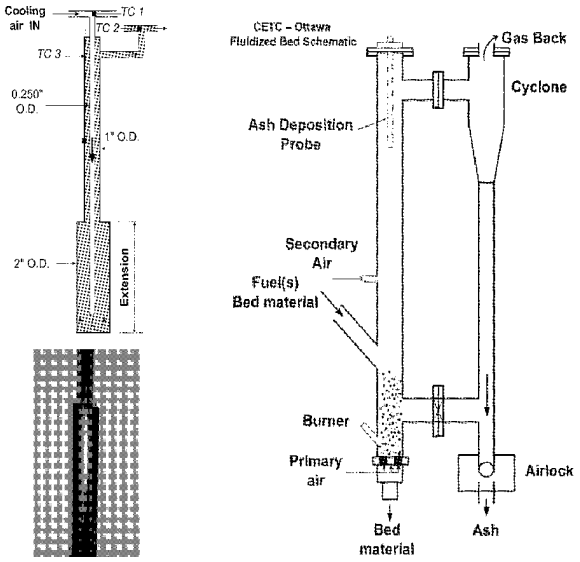

Fig. 1 Schematic diagrams of the ash deposition probe (left) and the fluidized bed facility at CETC-Ottawa (right)

Combustion facility

The co-firing tests were conducted with a pilot-scale fluidized bed combustor at CANMET Energy Technology Centre-Ottawa. The testing facility is a circulating fluidized bed reactor with a SS 316L column (4-in ID and 236-in total height) as illustrated in Fig. 1. while it was operated in a bubbling bed mode during the tests. The facility has a feeding capacity of about 15-20 kg/h, and is equipped with a belt feeder and a cyclone for bottom ash collection, and a water-cooled condenser for tar removal, as well as temperature sampling ports at different heights on the column and the flue gas sampling port in the flue gas pipe. On-line analyses of temperature distribution along the bed heights and flue gas compositions (CO, CO_2, O_2, NO_x, and SO_2) are available. An air-cooled probe, as also pictured in Fig. 1, is custom designed and installed in the freeboard region of the fluidized bed combustor using a flange. The probe is made of SS 316L with the following dimensions: 2-ft long and 1-in outer diameter (OD) with an extension of 1-ft long and 2-in OD. During the steady operation in all the tests, the surface temperature of the probe was maintained at 430±10 °C by carefully controlling the flow rate of the cooling air.

Testing methodologies and parameters

A cleaned probe was installed in the freeboard of the reactor before each test as illustrated in Fig. 1. The reactor was filled with 13 kg of olivine sand as bed materials in each test, and was heated up to above 700°C using propane gas before introducing the solid fuels. For all the tests reported in this work, a constant heat input as 58.3 MJ/h was used. By adjusting the secondary air and first air ratios (while maintaining a constant total air flow rate, determined by the excess air ratio and fuel compositions), a stable temperature profile along the bed height was achieved. In the present study, the excess air ratio was fixed at 40%, the average flue gas temperature was in the range of 650-700°C, and the deposition probe temperature was controlled at about 430°C for all runs. In each run, at least 3-4 hours of stable operation was performed before cooling down the reactor to room temperature. When the whole unit was cooled to room temperature, the ash deposition probe was carefully removed from the freeboard and the deposited ash was completely recovered for weighing for the calculation of superficial deposition rate (D_A, g/m^2/h) and the relative deposition rate (RD_A, g/m^2/h), as defined below respectively:

$$D_A = \frac{\text{Mass of collected ash deposit (g)}}{\text{Surface area of the probe (m}^2\text{)} \times \text{Duration (h)}} \quad (1)$$

$$RD_A = D_A \times \frac{\text{Ash feeding rate of crushed lignite (g/h)}}{\text{Ash feeding rate of the fuel (g/h)}} \quad (2)$$

Here, RD_A was proposed for the first time in order to bring into account the fact that a biomass fuel has ash content (normally < 1-5 wt%) much less than the lignite coal (22 wt% in this study from Table 1). Compared to D_A, RD_A will be a more effective variable to evaluate the deposition tendency of combustion of different biomass fuels (with different ash contents) or different biomass-coal blends in relation to that of the combustion of 100% coal. The collected deposited ashes were also submitted for characterizations using scanning electron microscopy (SEM) for morphology, ion chromatography (IC) for chlorine content, X-ray fluorescence (XRF) for chemical compositions and X-ray diffraction (XRD) for mineralogical compositions.

RESULTS AND DISCUSSION

Chemical compositions of the fuel ash versus chemical compositions of the ash deposits

Chemical compositions of the fuel ash and chemical compositions of the deposited ash during combustion of each individual fuel were compared. All deposits have an enrichment of Fe, which may be explained by the Fe-rich corrosion contaminants on the steel probe surface (Theis et al. 2006b). For the combustion of 100% lignite, the compositions of the deposited ash were very similar to those of the fuel ash. On the contrary, in the combustion of 100% white pine pellets or sawdust, the compositions of the deposited ash significantly differed from those of the fuel ash. In the combustion of white pine pellets or sawdust the deposited ash contained a much lower contents of CaO, SO_3, K_2O and P_2O_5 compared with the fuel ash, but the deposited ash was enriched with SiO_2, Al_2O_3 and MgO. These results may suggest that in combustion of white pine pellets or sawdust, the elements of Ca, S, P and K in the fuel ash tend to be captured in the bottom ash, while the Mg, Si and Al in the fuel ash easily evolved into fly ash and deposited on the probe.

Effect of fuel blending ratio

Effects of fuel blending ratios (0 -100% WPP on a thermal or heat input basis) on ash deposition behaviors for co-firing WPP and CL were investigated at fixed combustion parameters, i.e., constant 40% excess air and heat input of 58.3 MJ/h and carefully controlled probe surface temperature (430±10°C). All ash deposit samples were analyzed by XRF and XRD for the chemical compositions and the mineralogical compositions, and the corresponding results are shown in Fig. 2(a) and Fig. 2(b), respectively. The obvious difference in the compositions of some major metal elements in the deposited ashes from the co-firing of WPP-CL blends suggested the interactions between these fuel ashes during the co-combustion. For instance, co-combustion of the 20%WPP-80%CL or 50%WPP-50%CL bends resulted in increased concentrations of Al_2O_3, P_2O_5, N_2O and K_2O, and reduced concentrations of Fe_2O_3, MgO and SO_3 in the deposits. The similar phenomena were observed by many other researchers (Baxter, 1998, Kupka et al., 2008; Hansen et al., 1999). The analysis results of mineralogical compositions for the ash deposits from the combustion of 100% WPP and 20%WPP-80%CL are shown in Fig. 2(b). As clearly shown in Fig. 2(b), the Ca, Mg, Al and Si elements (the most abundant elements in the deposits as identified by XRF in Fig. 2(a)) were present in the deposited ashes mostly in the forms of calcium and magnesium sulfates, aluminates and silicates. $CaSO_4$ and Ca-related silicates were commonly regarded as ash-formation matters due to their low fusion temperature which can enhance the adhesion of ash deposits. In this work, these silicates refer to Ca-Al-Silicate, Ca-Mg-Silicate and

Magnesium silicate whose fusion temperature can be lower than 800-900°C (Baxter et al., 1998; Frandsen, 2005).

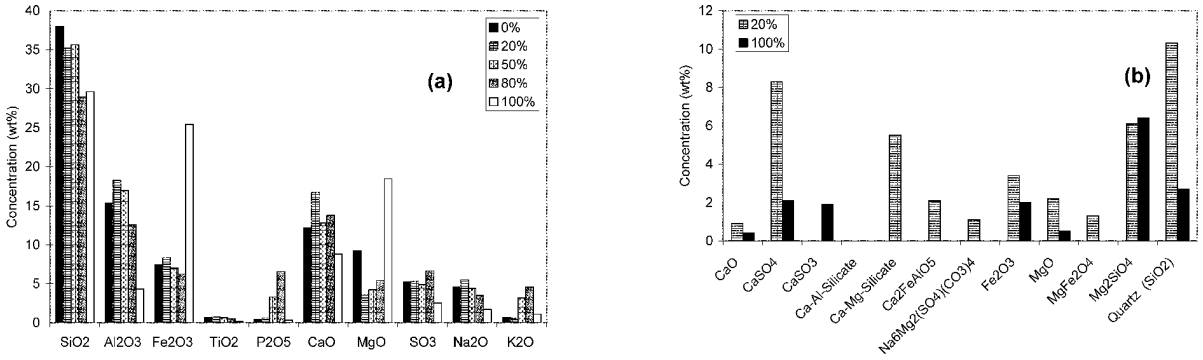

Fig. 2 Chemical compositions (a) and mineralogical compositions (b) of the deposited ashes from co-firing coal and white pine with different blending ratios

Figure 3 shows the superficial and relative ash deposition rates, D_A and DR_A, during co-combustion of white pine pellets (WPP) and crushed lignite (CL) at different blending ratios ranging from 0% WPP (or 100% CL) to 100% WPP. In terms of the results of D_A, an increase in the ratio of WPP in the WPP-CL blend fuel resulted in a lower ash deposition ratio. A conclusion is however difficult to be drawn from the D_A results only since the causes of the lower ash deposition could be either the lower total ash content in the feed or the positive interaction (to suppress the ash deposition) between the ash elements from the component fuels in the fuel blends. Woody biomass as a fuel in power plants co-firied with coal commonly produces relatively low ash deposits on heat transfer surface due to its extremely low ash content (Skrifvars et al., 2004). To rule out the effects of the former cause related to the total ash content in the feed and to evaluate the deposition tendency of combustion of different biomass fuels or different biomass-coal blends in relation to that of the combustion of 100% coal, it would be advantageous to compare the results of relative deposition rate (RD_A), as shown in Fig. 3. From the figure, combustion of 100% WPP has a greater tendency of ash deposition than of 100% CL, leading to a RD_A of about 11 $g/m_2/h$ for 100%WPP compared with 9.5 $g/m_2/h$ for 100% CL. This might be explained by the much higher contents of alkali and alkaline earth metals and halogens elements (Cl and Br), and much lower SiO_2 and Al_2O_3 contents in the WPP ash, as shown in Table 1. Interestingly, co-firing WPP and CL at a small blending ratio (20%) resulted in a significant increase in the RD_A, implying that negative interaction occurred (to enhance the ash deposition) between the ash elements from the component fuels in the fuel blends, which is coincident with the enhanced formation of calcium and magnesium sulfates, aluminates and silicates as indicated in Fig. 3(b). More interestingly, co-firing WPP and CL at 50% blending ratio produced a greatly reduced RD_A, suggesting that positive interaction occurred (to suppress the ash deposition) between the ash elements from the component fuels in the fuel blends. The reasons and mechanisms for the positive effects if co-firing 50%WPP and 50% CL on ash deposition are not clearly, but they will be further investigated in our future studies.

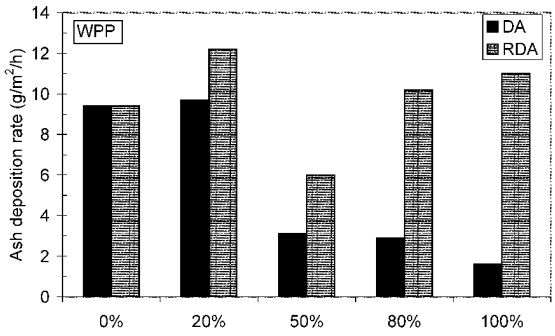

Fig. 3 Ash deposition rates during co-combustion of white pine pellets (WPP) and crushed lignite (CL) at different blending ratios

Effects of moisture

Some researchers tried some pretreatment methods including using water to wash fuel (Jenkins et al., 1996, Knudsen et al., 1998) or fuel char (Jensen et al., 2001a,b) to reduce the amount of potassium and chlorine in biomass, then achieved a slow fouling/slagging and corrosion process on the heat transfer surface in boiler.

Dewatering and drying of the washed fuels is an energy costly process, and the process would produce fuels of various moisture contents depending on the drying conditions. Moreover, many kinds of waste biomass feedstock, such as sawmill residues, crop residues and pulp/paper mill sludges and municipal sewage sludges, contains a very high moisture content up to 98 wt%. Of no question, fuel with lower moisture content would yield a higher thermal efficiency from the standpoint of fuel combustion. From the available literature, there is no research work reported so far on the effects of fuel moisture contents on the ash deposition behaviors in co-firing lignite and wood pellets. In this study, we performed combustion tests with fuels as received (or air-dried fuels) and the oven-dried fuels, in order to examine the influence of moisture content in the fuel or fuel blends on the ash deposits' compositions and the deposition rate. the lignite fuels and the white pine sawdust as received had very high moisture (30-40 wt%), while the wood pellets were received with relatively low moisture content (5.6 wt%), as shown in Table 1. After oven drying of the fuels at 105°C for 12 hours, the moisture content of all the fuels was ensured to be less than 5 wt%. For both tests with CL alone and 50%WPP-50%CL blend, the difference in moisture content did not result in noticeable differences in the compositions of the ash deposits. In contrast, the moisture content significantly influenced the compositions of the ash deposit in combustion of WPP alone. Compared with the ash compositions of the ash deposit from the oven-dried WPP, the ash deposit from the wet feed contained much higher concentrations of SiO_2, Al_2O_3, Fe_2O_3, MgO, and much lower concentrations of K_2O, CaO, SO_3 and P_2O_5. More interestingly, the moisture content in the feed did play an important role in varying the ash deposition rates for all the fuels or fuel blend tested. The combustion of an oven-dried fuel consistently produced a higher deposition rate (D_A or RD_A) compared with the wet fuel as received. This result may suggest that a higher content of moisture in the fuel could effectively reduce the ash deposition rate during the combustion or co-combustion process. It might be explained by the lower reactor temperature due to the presence of a high content of moisture in the fuel. More research is needed to clarify the roles of moisture in the process of ash deposition during co-firing biomass and coal.

CONCLUSIONS

(1) For the combustion of lignite alone, the compositions of the deposited ash were very similar to those of the fuel ash, while in the combustion of white pine pellets or sawdust alone the compositions of the deposited ash significantly differed from those of the fuel ash. In combustion of the woody biomass, the elements of Ca, S, P and K in the fuel ash tend to be captured in the bottom ash, while the Mg, Si and Al in the fuel ash easily evolved into fly ash and deposited on the probe.

(2) The analysis results of mineralogical compositions for the ash deposits demonstrated that the Ca, Mg, Al and Si elements (the most abundant elements in the deposits) were present in the deposited ashes mostly in the forms of calcium and magnesium sulfates, aluminates and silicates.

(3) An increase in the ratio of WPP in the WPP-CL blend fuel resulted in a lower superficial ash deposition ratio simply explained by the lower total ash content in the feed.). To evaluate the deposition tendency of combustion of different biomass fuels or different biomass-coal blends in relation to that of the combustion of 100% coal, the relative deposition rate (RD_A) was proposed for the first time in this work. In terms of RD_A, co-firing WPP and CL at a small blending ratio (20%) resulted in a significant increase in the deposition rate, while co-firing WPP and CL at 50% blending ratio produced a greatly reduced deposition rate.

(4) The moisture content in the feed play an important role in varying the ash deposition rates for all the fuels or fuel blend tested. The combustion of an oven-dried fuel consistently produced a higher deposition rate compared with the wet fuel as received.

ACKNOWLEDGEMENTS

The authors are grateful for the financial support from the Ontario Ministry of Energy and Ontario Centres of Excellence, through the Atikokan Bioenergy Research Center (ABRC) program. Ontario Power Generation is also gratefully acknowledged for supplying and donating the lignite for the tests. Special thanks are also extended to Dave Wambolt, Benjenmin Bronson and Bart Young for their participation and great assistance on the tests.

REFERENCES

Aho, M., Gil, A., Taipale, R., Vainikka, P. and Vesala, H.. Fuel 87(1) (2008), pp. 58-69.

Aho, M. and Silvennoinen, J. Fuel 83 (2004), pp. 1299-1305.

Andersson, C and Vattenfall, A.B.. Patent Number: WO 02059526 (2002).

Andersen, K.H., Frsen, F.J., Hansen, P.F.B., Wieck-Hansen, K., Rasmussen, I., Overgaard, P. and Dam-Johansen, K.. Biomass Bioenergy 19(4) (2000), pp. 765-780.

Arvelakis, S., Gehrmann, H., Beckmann, M. and Koukios, E.G.. Biomass and Bioenergy 28 (2005), pp. 331-338.
Baxter, L.L , Miles, T.R., Miles Jr., T.R., Jenkins, B.M., Milne, T., Dayton, D., Bryers, R.W. and Oden, L.L.. Fuel Processing Technology 54(1-3) (1998), pp. 47-78.
Baxter, L.L.. Biomass and Bioenergy 4(2) (1993), pp. 85-102.
Bryers, R.W.. Progress in Energy and Combustion Science 22 (1) (1996), pp. 29-120.
Frandsen, F.J..Fuel 84 (2005), pp. 1277-1294.
Hansen, L.A.. Energy and Fuels 13(4) (1999), pp. 803-816.
Jenkins, B.M., Baxter, L.L., Miles Jr, T.R. and Miles, T.R.. Fuel Process. Technol. 54 (1998), pp. 17-46.
Jenkins, B.M., Bakker, R.R. and Wei, J.B.. Biomass and Bioenergy 10 (4) (1996), pp. 177-200.
Jensen, P.A., Sander, B. and Dam-Johansen, K.. Biomass and Bioenergy, 20(6) (2001a), pp. 431-446.
Jensen, P.A.; Sander, B.; Dam-Johansen, K.. Biomass and Bioenergy 20(6) (2001b), pp. 447-457.
Jensen, P.A., Stenholm, M. and Hald, P.. Energy & Fuels 11(5) (1997), pp.1048-1055.
Knudsen, N.O., Jensen, P.A., Sander, B. and Dam-Johansen, K.. Biomass for Energy and Industry. Tenth European Conference and Technology Exhibition. Wurzburg, Germany (1998), pp.224.
Kupka, T., Mancini, M., Irmer, M. and Weber, R.. Fuel 87(12) (2008), pp. 2824-2837.
Michelsen, H.P., Frandsen, F., Dam-Johansen, K. and Larsen, O.H.. Fuel Processing Technology 54 (1998), pp. 95-108.
Nielsen, H., Frandsen, F., Dam-Johansen, K. and Baxter, L.. Process in Energy and Combustion Science 26 (2000), pp. 283-298.
Robinson, A.L., Junker, H. and Baxter, L.L.. Energy and Fuels 16(2) (2002), pp. 343-355.
Skrifvars, B.J., Yrjas, P., Laurén, T., Kinni, J., Tran, H. and Hupa, M.. Energy Fuels 19 (2005), pp. 1512-1519.
Skrifvars, B.J., Laurén, T., Hupa, M., Korbee, R. and Ljung, P.. Fuel 83 (2004), pp. 1371-1379.
Theis, M., Skrifvars, B.J., Hupa, M. and Tran, H.. Fuel 85 (7-8) (2006a), 1125-1130.
Theis, M., Skrifvars, B.J., Zevenhoven, M., Hupa, M. and Tran, H.. Fuel 85 (14-15) (2006b), pp. 1992-2001.
Theis, M., Skrifvars, B.J., Zevenhoven, M., Hupa, M. and Tran, H.. Fuel 85(14-15) (2006c), pp. 2002-2011.
Overgaard, P., Larsen, E., Friborg, K., Hille, T., Jensen, P.A. and Knudsen, S.. (2005).
Pronobis, M.. Fuel 85(4) (2006), pp. 474-480.
Zheng, G and Koziński, J.A.. Fuel 79(2) (2000), pp. 181-192.

THE EMISSIONS OF PAHS AND HEAVY METALS FROM CO-COMBUSTION OF PETROCHEMICAL SLUDGE WITH COAL IN CFB INCINERATOR

Ge Zhu, Changsui Zhao*, Huichao Chen, Xiaoping Chen, Cai Liang

School of Energy and Environment, Southeast University, Nanjing, 210096, China

Abstract: The polycyclic aromatic hydrocarbons (PAHs) and heavy metals (Hg, Pb, Ni, Cr, Cu, Zn) emission characteristics in flue gas from co-combustion of petrochemical sludge and coal were investigated in a pilot-scale circulating fluidized bed (CFB) incinerator with a thermal input of 0.2 MW. Experimental results show that when mass ratio of petrochemical sludge/coal increases from 10% to 40%, PAHs, Hg and Zn emissions increase, while Pb and Ni emissions decrease. Mass mixing ratio has no obvious effect on the emissions of Cr and Cu. As combustion temperature increases, PAHs emission decreases at first and then increases, there is an optimum combustion temperature inhibiting PAHs formation, while emissions of Hg, Pb, Cu, Zn increase relatively rapidly. With Ca/S molar ratio increasing, PAHs, Hg, Pb, Ni, and Cu emissions decrease due to adsorption by calcium sorbents. Limestone is effective in adsorbing Pb and Ni, while lime is suitable to adsorb Hg and Cu. However, Ca/S molar ratio doesn't have much influence on the emissions of Cr and Zn. Some combustion parameters are recommended based on stable combustion and low pollutant emission.

Keywords: petrochemical sludge, circulating fluidized bed (CFB), polycyclic aromatic hydrocarbons (PAHs), heavy metals

INTRODUCTION

Sludge generated during wastewater treatment is a problematic but unavoidable by-product (Oleszkiewicz and Mavinic, 2001). It is difficult to dispose owing to its increasing production and more restrictive policies.

Many novel technologies for sewage sludge treatment have been deeply studied (Suzuki et al., 1990; Goto et al., 1997; Lee et al.,2001; Gupta and Garg, 2008; Samaras et al., 2008; Yang et al.,2008). Recently, some published works have shown that the co-combustion of sludge and coal may be viable from an energetic, economic and environmental point of view, especially when it is carried out in existing infrastructures (Werther and Ogada, 1999; Folgueras et al.,2003; Yao and Naruse, 2005; Cartmell et al.,2006; Stasta et al.,2006). Although incineration has been chosen as a primary technique for its advantage of volume reduction and ability to recover energy from sludge, a lot of carcinogenic and mutagenic organic compounds, such as polycyclic aromatic hydrocarbons (PAHs), polychlorinated dibenzo-p-dioxin (PCDDs) and polychlorinated dibenzofurans (PCDFs), are produced during sludge incineration, together with inorganic pollutants, such as heavy metals, CO_x, SO_2, NO_x and particulate matter (Lee et al.,1993a, 1993b; Wang and Lin, 1998; Werther and Saenger, 2000; Sanger et al.,2001; Kim et al.,2005; Velden et al.,2008).

Polycyclic aromatic hydrocarbons (PAHs) are of great scientific interest in recent years because of their hazardous effects. Concerning the emission of PAHs, several of these compounds are known carcinogens and/or mutagens, very hazardous to human health. The environmental concerns has motivated regulatory agencies around the world, such as the US Environmental Protection Agency (EPA), to pass legislative restrictions over the release of PAHs into our environment, especially for 16 priority-controlled PAHs. Theoretically, organic compounds may be formed and/or released during inefficient combustion of any fuel containing carbon and hydrogen. Many organic materials with chemical structures are able to form PAHs during pyrolysis and combustion process, undergoing a series of reactions such as breakdown reactions, cyclization reactions and oxidation reactions. With great concerns about PAHs (Johansson and Bavel, 2003; Zhou et al.,2005; Wey et al.,2006; You, 2007), a great volume of research works on polycyclic aromatic hydrocarbons (PAHs) emission from coal combustion or MSW incineration in fluidized bed has been carried out. The influence of combustion parameters, such as combustion temperature, residence time, Ca/S molar ratio, sulfur and chlorine contents on PAHs emission has been wildly studied (Mastral et al.,1996, 1998, 1999, 2008; Liu et al.,2000, 2001; You, 2007).

Another major problem associated with the combustion of sludge is the possible release of heavy metals to the environment, as their volatility is enhanced at high temperature. This concern about the formation of fine inhalable particles enriched in toxic metals or gaseous emissions has been the focus on many research programs

* Corresponding author: Changsui Zhao (E-mail address: cszhao@seu.edu.cn).

performed all over the world (Linak and Wendt, 1993; Fernandez et al., 1992; Weissman et al., 1983) and is now being an issue for a stringent control. Sludge may present significant concentrations of potential toxic metals, depending on their origin and wastewater treatment technology used. Hence, their incineration must include measures in order to prevent their release and their transport over long distances.

So far, PAHs and heavy metals emissions from co-combustion of petrochemical sludge and coal in circulating fluidized bed incinerator have rarely been studied. The main objective of this paper is to investigate how operating combustion variables influence the emissions of PAHs and heavy metals in flue gas from co-combustion of petrochemical sludge and coal in circulating fluidized bed incinerator.

EXPERIMENTAL

Petrochemical sludge and coal

The petrochemical sludge used in the experiments was collected from refinery, chemical plants and sewage plants of Fushun Petrochemical Corporation in Liaoning, China. The coal used was also from Fushun. Table 1 shows the properties of fuels from the aspect of proximate analysis and ultimate analysis in the form of average values from several samples. According to the ultimate analysis and proximate analysis of petrochemical sludge, it can be seen that its fixed carbon and heat value are relatively low, whereas contents of sulfur, nitrogen and moisture are comparatively high. Table 2 shows the contents of 6 kinds of heavy metals in coal and sludge including Hg, Pb, Ni and so on. It can be seen that zinc is high in petrochemical sludge because transportation pipes of wastewater are covered with zinc. Nickel and zinc are high in coal. The contents of sixteen PAHs in coal and petrochemical sludge, specified by US EPA as preferentially controlled pollutants, are shown in Fig 1. It is clear that the contents of PAHs in petrochemical sludge are far more than those in coal. Moreover, PAHs in coal are mainly dominated by 2-ringed, 3-ringed and 5-ringed PAH, while PAHs in sludge are mainly dominated by 5-ringed PAH.

Table 1 Coal and petrochemical sludge properties

	Proximate analysis /%(mass, ar)				Ultimate analysis/%(mass, ar)					$Q_{net,ad}$ /MJ·kg^{-1}
	M	A	V	FC	C	H	O	N	S	
Sludge	50.37	14.59	24.10	6.05	19.11	2.79	11.04	1.41	0.73	7.58
Coal	6.50	37.62	27.87	32.51	42.67	3.44	8.54	0.77	0.46	18.86

Table 2 The content distribution of heavy metals in coal and petrochemical sludge (ppm)

	Hg	Pb	Ni	Cr	Cu	Zn
Sludge	0.24	31.56	78.03	64.81	64.73	857.77
Coal	0.10	45.85	103.69	71.12	60.18	229.13

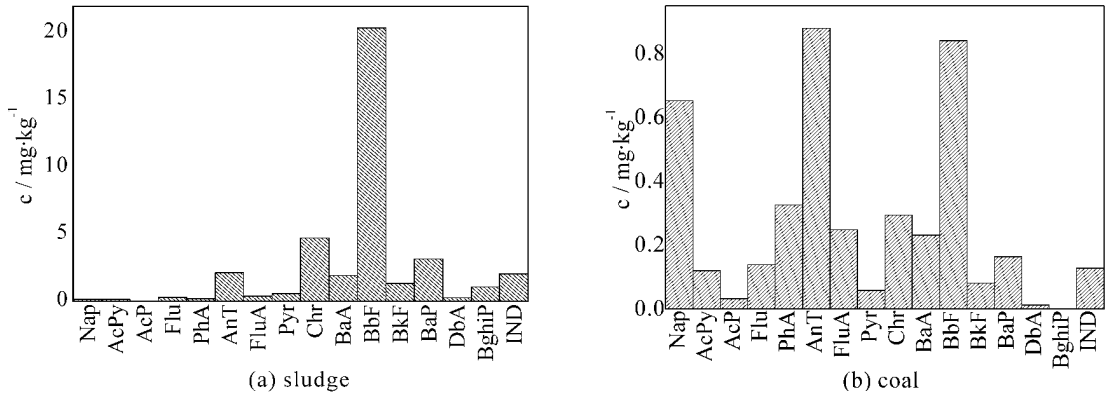

Fig. 1 The content distribution of sixteen PAHs in coal and petrochemical sludge

Test facility

The tests were conducted in a 0.2 MWth CFB incinerator (shown in Fig. 2). The experimental system is composed of a riser of 0.23 m I.D. and 7 m high, fuel (sludge, coal), feeding systems, a fly ash circulation loop and a flue gas cooling and clean-up system. A start-up burner is used to preheat CFB to the coal ignition temperature, and coal is fed into the bed by a screw feeder, while sludge is by a rotary feeder. Two streams of air are injected into the CFB; one is preheated to about 400℃ and distributed at the bottom of the bed; the other is injected through the airtight end of the sludge feeding path-way to prevent sludge from blocking. At the top

of the riser, a cyclone separates and recirculates the entrained particles.

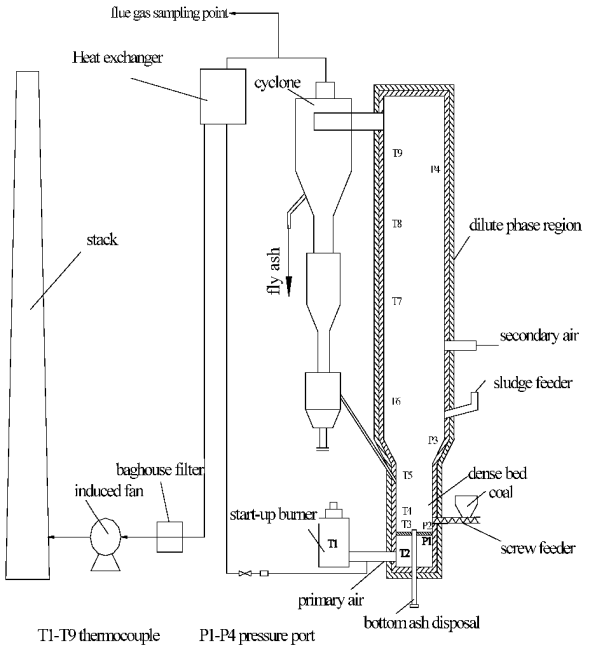

Fig. 2 Schematic diagram of circulating fluidized bed incinerator

The CFB incinerator is equipped for continuous measurement of temperature and pressure drops at different heights along the reactor. In the study, SAE-19 multi-function flue gas analyzer was employed to determinate the concentration of major components in exhaust gas sampled, such as SO_2 and NO_x. The sixteen PAHs in flue gas were measured with Gas Chromatograph and Mass Spectrometer (GC/MS after) they were extracted in a Soxhlet extractor, concentrated in a K-D apparatus, and separated in a silica gel clean-up column.

RESULTS AND DISCUSSION

Effect of mass mixing ratio

In this paper, mass mixing ratio represents the mass proportion of the petrochemical sludge in blended fuel. Figure 3 shows the effect of mass mixing ratio on PAHs emission concentration in flue gas. With the mass mixing ratio increasing, total PAHs emissions show an increase tendency, especially lower molecular weight (LMW) PAHs emission increases significantly. As shown in Fig.1, the content of PAHs in sludge is much more than that in coal. Furthermore, combustion efficiency decreases from 97.84% to 92.82% and carbon monoxide concentration increases from 85 mg/m^3 to 98 mg/m^3 with mass mixing ratio increases from 10% to 40%, because of high moisture in the sludge. Thus, more PAHs are generated owing to incomplete combustion for higher mass mixing ratio. Additionally, with the increase in mass mixing ratio, the heat balance of combustion was disturbed and the combustion of volatiles was delayed to form a possible local fuel-rich atmosphere. Therefore, that could enhance the formation of PAHs under higher sludge feeding rate.

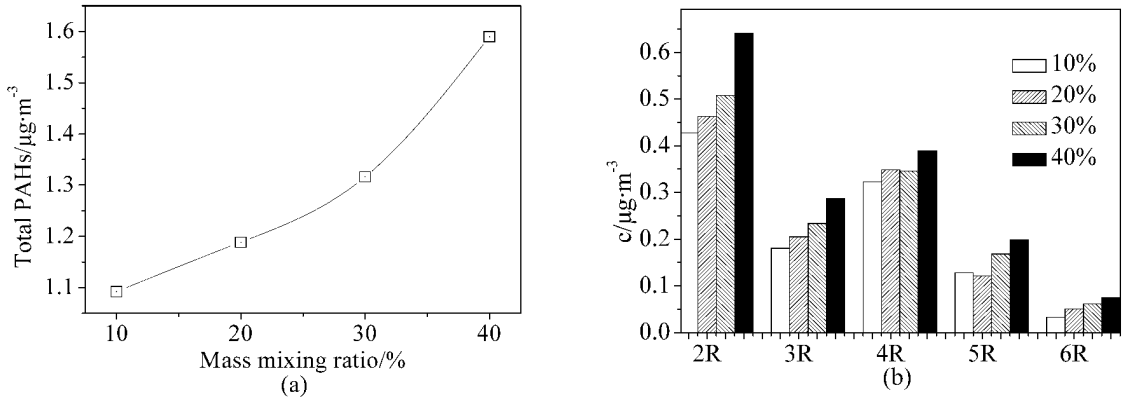

Fig.3 Effect of mass mixing ratio on PAHs emissions1

When the mass mixing ratio is 30%, combustion efficiency is 95.67% and CO concentration is 91 mg/m^3. Therefore, mass mixing ratio less than 30% is feasible for the co-combustion. Combustion efficiency increases to 97.03% and CO concentration decreases to 87 mg/m^3 when mass mixing ratio decreases from 30% to 20%. Considering all these factors, the mass mixing ratio of 20% is recommended because of better combustion efficiency and lower pollutants emissions.

Figure 4 shows the effect of mass mixing ratio on the emission of heavy metals in flue gas. With the increase in mass mixing ratio from 10% to 40%, Hg and Zn emissions increase gradually. Whereas, emissions of Pb and Ni show a tendency of decline. Moreover, mass mixing ratio doesn't show much impact on the emission of Cr and Cu.

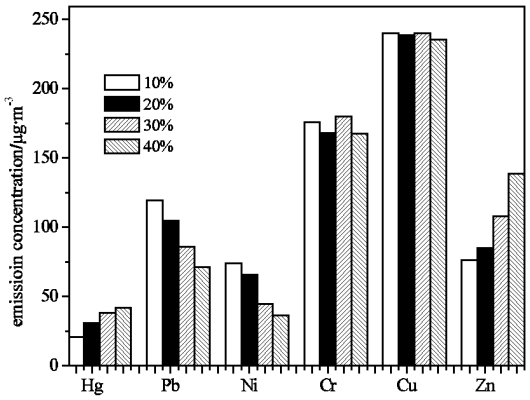

Fig.4 Effect of mass mixing ratio on heavy metals emissions

The content of Zn in the sludge is very high because the wastewater pipe is covered with zinc. Moreover, the content of Hg is much higher than that in coal. Thus, emissions of Hg and Zn in flue gas increase with the mass mixing ratio increasing. The contents of Ni and Pb in sludge are lower than those in coal. Furthermore, the content of moisture in petrochemical sludge is very high which decreases the Pb emission. Therefore, emissions of Pb and Ni declines with the increase in mass mixing ratio from 10% to 40%.

Effect of combustion temperature

Combustion temperature is one of the most important parameters influencing pollutants emissions in circulating fluidized bed. With combustion temperature increasing from 830℃ to 897℃, SO_2 concentration increases from 136 mg/m^3 to 147 mg/m^3 and NO_x concentration increases from 211 mg/m^3 to 270 mg/m^3. Figure 5 shows the influence of combustion temperature on PAHs emissions. The PAHs emissions decrease first and then increase with temperature rising.

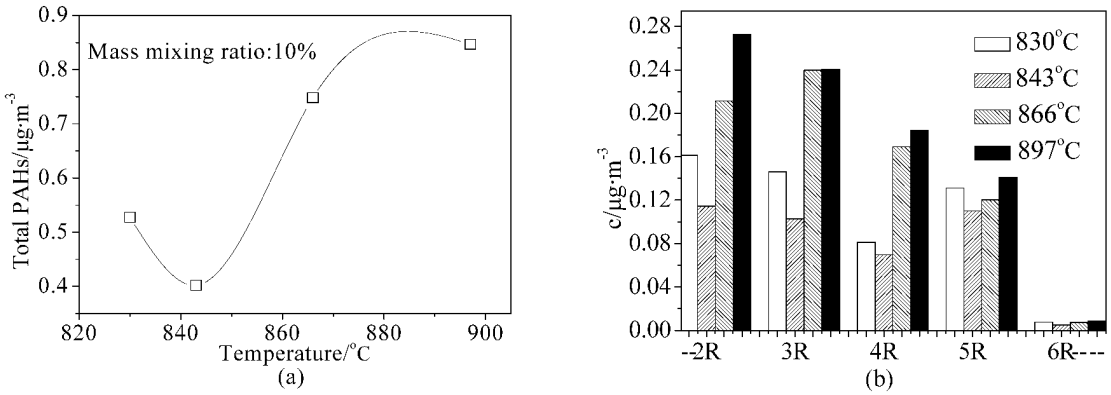

Fig.5 Effect of combustion temperature on PAHs emissions

Generally, large molecules break up into small fragments during pyrolysis at combustion temperature in circulating fluidized bed, but those lower hydrocarbons yield higher molecular mass products. The PAHs generated may be mainly due to incomplete combustion with low combustion temperature. With the increase in combustion temperature, more energy is supplied to destruct the chemical bonds of PAHs. Therefore, a great deal of low molecular hydrocarbons is produced owing to the pyrolysis of PAHs. However, synthesis reactions of PAHs are endothermic reactions, more PAHs can be formed at higher temperature. Consequently, the PAHs may be synthesized in dense zone or freeboard region of fluidized bed at higher temperature. Moreover, metals such as Fe, Cu in particles may also act as catalysts for the synthesis reactions. Considering all these factors above, the amount of PAHs generated decreases at first and then increases with combustion temperature increasing. After taking other factors such as stable combustion and pollutants emissions into account, the combustion temperature range between 850℃ and 860℃ is recommended.

The emission of heavy metals in the combustion process is mainly determined by the characteristics of heavy metals, the composition of fuel and combustion circumstance. The boiling point of heavy metals is one of the most important factors influencing their emission in flue gas. It can be seen from Fig.6 that emissions of

Hg, Pb and Zn increase with the combustion temperature increasing from 830℃ to 897℃. Ni, Cu and Cr are heavy metals with difficult volatilization and the boiling point of their elemental state and combined state is relatively high. Therefore, combustion temperature doesn't show much influence on the emissions of Ni, Cu and Cr.

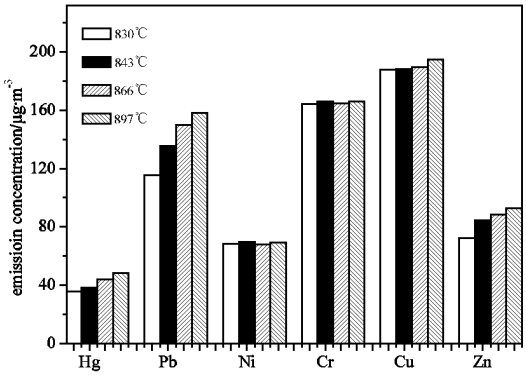

Fig. 6 Effect of combustion temperature on heavy metals emissions

Effect of Ca/S molar ratio

Ca/S molar ratio is another important parameter influencing the emission of pollutants in circulating fluidized bed. With Ca/S molar ratio increasing from 1.5 to 3.0, SO_2 concentration decreases from 213 mg/m^3 to 16 mg/m^3 and NO_x concentration increases from 224 mg/m^3 to 245 mg/m^3. It can be seen from Fig.7 that total PAHs emissions decline obviously with the increase in Ca/S molar ratio from 1.5 to 3.0. Moreover, aforementioned PAHs are dominated by 2-ringed and 4-ringed PAH.

The absorption effect of calcium-based sorbents and degradation effect of its microstructure may decrease PAHs emissions. The contents of sulfur and chlorine decrease with the limestone feeding increasing, which may inhibit the formation of PAHs. Moreover, the decomposition of limestone may absorb heat and combustion temperature decreases to where PAHs are unlikely to be formed from combustion and pyrolysis.

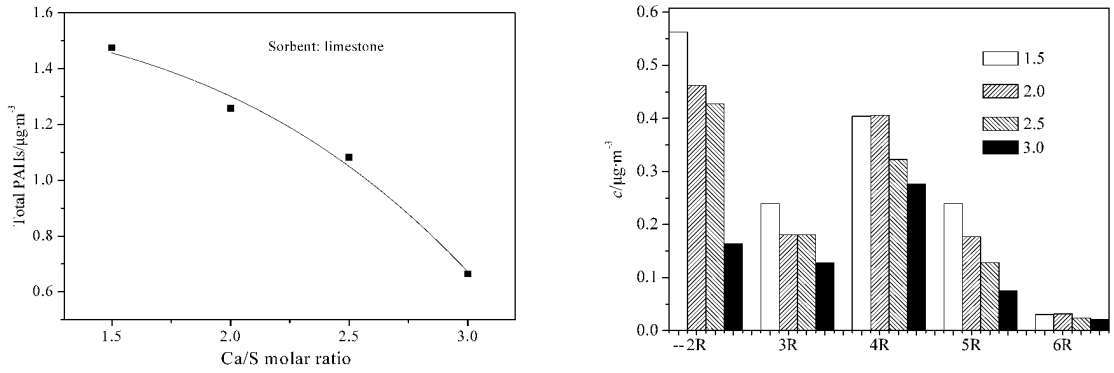

Fig. 7 Effect of Ca/S molar ratio on PAHs emissions

The effect of sorbent on the emission of heavy metals has rarely been studied. Experimental test has shown that sorbents (limestone, lime) play an important role in the emission of heavy metals. Figure 8 shows effect of Ca/S molar ratio of limestone and lime on the emission of heavy metals. With the increase in Ca/S molar ratio, emissions of Hg, Pb, Ni and Cu show a tendency of decline. Moreover, it is clearly seen that limestone is effective in the adsorption of Pb and Ni, whereas lime is suitable to adsorb Hg and Cu.

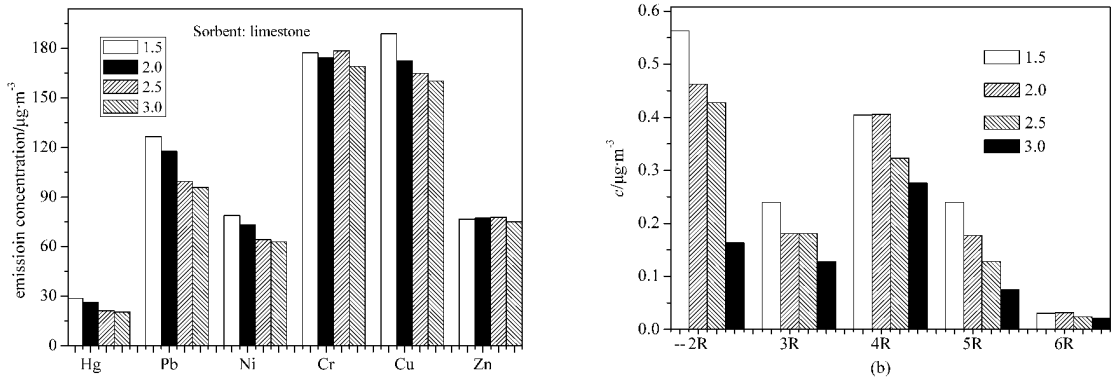

Fig. 8 Effect of Ca/S molar ratio of limestone and lime on heavy metals emissions

However, Ca/S molar ratio doesn't have much influence on the emissions of Cr and Zn. The emission concentration of Hg declines from 28.6 μg/m^3 to 20.5μg/m^3, with the Ca/S molar ratio of limestone increasing

from 1.5 to 3.0. Comparatively, the emission concentration of Hg declines from 24.2 μg/m^3 to 18.5μg/m^3, when the Ca/S molar ratio of lime increases from 2.0 to 3.0.

CONCLUSIONS

PAHs, Hg and Zn emissions increase, while Pb and Ni emissions decrease, when the mass mixing ratio increases from 10% to 40%. Mass mixing ratio has no obvious effect on the emissions of Cr and Cu. As combustion temperature increases, PAHs emission decreases at first and then increases, and there is an optimum combustion temperature inhibiting PAHs formation. The emissions of Hg, Pb, Cu, Zn increase relatively obviously. With the increase in Ca/S molar ratio, PAHs, Hg, Pb, Ni, and Cu emissions decrease due to adsorption by calcium sorbents. Moreover, limestone is effective in the adsorption of Pb and Ni, whereas lime is suitable to adsorb Hg and Cu. However, Ca/S molar ratio doesn't have much influence on the emissions of Cr and Zn. The mass mixing ratio of 20% and the combustion temperature range between 850 and 860℃ are recommended, when taking stable combustion and low pollutants emission into consideration.

REFERENCES

Cartmell, E., Gostelow, P., Riddell-Black, D., Simms, N., Oakey, J., Morris, J., Jeffrey, P., Howsam, P., and Pollard S. J.: Environ. Sci. Technol. **40**, (2006), pp.649-658.
Fernandez, M. A., Martinez, L., Segarra, M., Garcia, J.C., and Espiell, F.: Environ. Sci. Technol., **26**, (1992), pp.1040-1047.
Folgueras, M. B., Diaz, R. M., Xiberta J. and Prieto, I.: Fuel, **82**, (2003), pp. 2051-2055.
Goto, M., Nada, T., Kawajiri, S., Kodama, A., and Hirose, T.: J. Chem. Eng. Japan, **30**, (1997), pp. 813-818.
Gupta, R. and Garg, V. K.: J. Hazard Mater, **153**, (2008), pp. 1023-1030.
Johansson, I., and Bavel, B. V.: Chemosphere, **53**, (2003), pp. 123-128.
Kim, M. R., Jang, J. G., Yoa, S. J., Kim, I. K., and Lee, J. K.: J. Chem. Eng. Japan, **38**, (2005), pp. 883-886.
Lee, J. K., Lee, K. H., and Chun, H. S.: J. Chem. Eng. Japan, **26**, (1993a), pp.179-182.
Lee, J. K., Lee, K. H. , Jang, J. G., and Chun, H. S.: J. Chem. Eng. Japan, **26**, (1993b), pp. 368-373.
Lee, J. K., Gu, J. H., Kim, M. R., and Chun, H. S.: J. Chem. Eng. Japan, **34**, (2001), pp. 171-175.
Linak, W. P., and Wendt, J, O, L.: Prog. Energ. Combust., **19**, (1993), pp.145-185.
Liu, K. L., Xie, W. , Zhao, Z. B., Pan W. P., and Riley J. T.: Environ. Sci. Technol., **34**, (2000), pp. 2273-2279.
Liu, K. L., Han, W. J., Pan, W. P., and Riley, J. T.: J. Hazard Mater., B84, (2001), pp. 175-188.
Mastral, A. M., Callen, M. S., and Murillo, R.: Fuel, **75**, (1996), pp. 1533-1536.
Mastral, A. M., Callen, M. S., Murillo, R., and Garcia, T.: Fuel, **77**, (1998), pp. 1513-1516.
Mastral, A. M., Callen, M. S., and Garcia, T.: Environ. Sci. Technol., **33**, (1999), pp. 3177-3184.
Mastral, A. M., Garcia, T., Callen, M. S., Murillo, R., Navarro, M. V., and Lopez, J. M.: Fuel Process. Technol., 77-78, (2002), pp. 373-379.
Oleszkiewicz, J. A., and D. S. Mavinic.: Can. J. Civ. Eng, **28**, (2001), pp. 102-114.
Samaras, P., Papadimitriou, C. A., Haritou I., and A. I. Zouboulis.: J. Hazard. Mater., **154**, (2008), pp. 1052-1052.
Sanger, M., Werther, J., and Ogada, T.: Fuel, **80**, (2001), pp.167-177.
Stasta, P., Boran, J., Bebar, L., Stehilk, P., and Oral, J.: Appl. Therm. Eng, **26**, (2006), pp. 1420-1426.
Suzuki, A., Nakamura, T., and Yokoyama S. Y.: J. Chem. Eng. Japan, **23**, (1990), pp.6-11.
Velden, M. V., Dewil, R., Baeyens, J., Josson, L., and Lanssens, P.: J. Hazard. Mater., 151, (2008), pp.96-102.
Wang, R. C. and Lin, W. C.: J. Chem. Eng. Japan, **31**, (1998), pp.897-902.
Weissman, S. H., Carpenter, R. L., and Newton, G. J., Environ. Sci. Technol., **17**, (1983), pp.65-71.
Werther, J. and Ogada, T.: Prog. Energy Combust. Sci., **25**, (1999), pp.55-116.
Werther, J. and Saenger, M.: J. Chem. Eng. Japan, **33**, (2000), pp. 1-11.
Wey, M. Y., Chen, J. C., Wu, H. Y., Yu, W. J., and Tsai, T. H.: Fuel, **85**, (2006), pp. 755-763.
Yang, Y. B., Sliwinski, L., Sharifi, V., and Swithenbank, J.: Fuel, **87**, (2008), pp. 1552-1563.
Yao, H., and Naruse, I.: Energy Fuels, **19**, (2005), 2298-2303.
You, X. F.: Waste Manage., **28**, (2008), pp.1543-1551.
Zhou, H. C., Zhong, Z. P., Jin, B. S., Huang, Y. J., and Xiao, R.: Chemosphere, **59**, (2005), pp. 861-869.

COMPARISON OF ASH FROM PF AND CFB BOILERS AND BEHAVIOUR OF ASH IN ASH FIELDS

H. Arro, T. Pihu, A. Prikk, R. Rootamm, A. Konist

Department of Thermal Engineering, Tallinn University of Technology, 116 Kopli St., 11712 Tallinn, Estonia

Abstract: Over 90% of electricity produced in Estonia is made by power plants firing local oil shale and 25% of the boilers are of the circulating fluidised bed (CFB) variety. In 2007 approximately 6.5 million tons of ash was acquired as a byproduct of using oil shale for energy production. Approximately 1.5 million tons of that was ash from CFB boilers. Such ash is deposited in ash fields by means of hydro ash removal.

Ash field material properties have undergone changes as a result of CFB ash deposition – the ash field surface is not stabilising, the ash is not becoming petrified and is unsuitable for building dams needed for the hydro technology application.

The analytical research was dedicated to determining the reasons for this different ash field behaviour of ash from CFB and pulverised firing (PF) boilers based on changes of ash properties. Comparative CFB and PF ash studies were conducted: chemical analysis, surveys with X-ray diffractometers (XRD) and scanning electron microscopes (SEM), study of binding properties. Bottom and electrostatic precipitator ash was scrutinised, with its typical rougher and finer particles, accordingly. Such ash types comprise the predominant current ash deposit content in ash fields. The ash samples were taken from boilers of the Balti Power Plant.

The Estonian oil shale mineral part consists mainly of the following minerals: calcite 44.0%, dolomite 19.5%, quartz 8.7%, orthoclase 10.5%, hydromuscovite 8.6%. These minerals comprise 91.3% of the mineral part and it should be noted that 63.5% of that are minerals in the carbonaceous part and 27.8% – in the terrigeneous part. When oil shale is fired, thermal decomposition of these minerals occur into simpler compounds, coupled with volatilisation of some compounds and formation of novel minerals, and there are changes in the mineral phase state as well. The ash binding properties and behaviour in ash fields depend on these changes, the extent of which is determined by the firing temperature in the boiler furnace.

The comparative studies indicate that the introduction of the CFB method of firing has caused several important changes in the mineralogical composition and properties of oil shale ash. The reason behind this is that the CFB boiler furnace firing temperature is approximately 600°C lower than in the PF counterpart, resulting in weaker fuel mineral decomposition and lower novel mineral formation intensity during combustion. The ash solidification tendency is in this instance substantially less than that observed in PF ash. The compressive strength of the electrostatic precipitator ash test samples from CFB boilers was 4.4 N/mm^2; from PF boilers – 15.3 N/mm^2, the corresponding specific surface area: 4 533-9 806 cm^2/g and 707-3 966 cm^2/g.

The obtained data confirms the need to alter the ash storage technology.

Keywords: estonian oil shale ash, pulverised firing, circulating fluidised bed combustion

INTRODUCTION

The essential change in properties of ash field material while the CFB oil shale ash is stored, caused the demand to analyze the different behavior of stored PF and CFB ashes. The chemistry and mineralogy of CFB coal ashes and the behavior of coal ash-water system while deposited are thoroughly investigated (Anthony et al., 2002; Anthony et al., 2003).

The properties of PF ashes stored at ash fields are earlier investigated (Arro et al., 2002; Kespre, 2004). The change in properties of moistened PF ashes in laboratory conditions are also investigated (Kuusik et al., 2004). The results of XRD analyses show at X-ray spectra the peaks belonging to the portlantite, α-quartz, calcite and ettringite. The ash field material contains also in small extents: several silicates, Ca-aluminates and other minerals.

The short overview about behavior of fuel minerals in combustion process and formation of novel minerals and binding properties of ash is given below (Butt et al., 1967; Boikova, 1974; Budnikov et al., 1971).

Carbonate minerals. The decomposition processes start at temperatures below 800°C and depend on CO_2 partial pressure in flue gas. Formed (CaO, MgO ja FeO) stay in ash free oxides and CO_2 volatilize. Decomposition of dolomite ($CaMg(CO_3)_2$) occurs in two steps: $Mg(CO_3)$ decompose at lower temperatures and

$Ca(CO_3)$ at higher temperatures. The extent of carbonate decomposition (ECD) k_{CO2} is 0.97 in PF boilers, and 0.60 in CFB boilers because of lower temperatures in furnace (Arro et al., 2006).

Quartz (SiO_2) does not decompose in furnace processes, but may undergo polymorphic changes in crystal structure – β-quartz changes to the α-quartz at 573°C. SiO_2 mainly appears in oil shale ash in form of α- quartz.

Orthoclase ($K_2O{\cdot}Al_2O_3{\cdot}6SiO_2$) changes to the sanidine at ~900°C, in decomposition process it forms leucite ($K_2O{\cdot}Al_2O_3{\cdot}4SiO_2$), while SiO_2 separates in form of amorphous SiO_2 or cristobalite. The presence of lime accelerates the thermal decomposition of orthoclase.

Micas are presented in oil shale as muscovite. At 120°C, absorbed water and, between 450 and 700°C, crystal water are released. In the temperature range 850 to 1,200°C (depending on the composition of micas), novel crystals are formed. Between 1,000 and 1,300°C, the liquid phase begins. At higher temperatures, corundum (Al_2O_3), mullite ($3Al_2O_3{\cdot}2SiO_2$), and glassy substance form.

Novel minerals and binding properties of ash. One of more active oil shale mineral part decomposition component is CaO, which reacts with SiO_2 and other minerals decomposition components.

The binding properties of ash are basically caused by β-$2CaO{\cdot}SiO_2$ and CaO, but also Ca, Al, Fe ja SiO_2 classy phase content in ash (~30%). In addition, the non soluble residue of ash in hydrochloric acid contains compounds having no binding properties, but in presence of $Ca(OH)_2$ and water behave like binding material.

The hardening process of ash containing free CaO is associated with formation of $CaCO_3$. The CaO having contact with water (hydration) gives the $Ca(OH)_2$ and reaction with CO_2 from air gives $CaCO_3$.

The other binding materials in ash have water binding properties while petrified (hydro binding materials). These materials may petrify having no contact with air, also under the water.

The slackening factor of ash minerals hydration is high content of $Ca(OH)_2$ and $CaSO_4$ in water, which is specific to the ash transport water (Kespre, 2004).

The differences in CFB and PF ash properties are investigated earlier (Kuusik et al, 2005). The methods used to determine ash properties were chemical analyses, XRD, SEM and BET method for determination of the specific surface area (SSA).

The ash properties and behavior at ash fields has been changed because of low combustion temperatures in CFB boiler (~600°C lower comparing PF). Formation of novel minerals with binding properties in CFB ash is much lower comparing to PF ash – solidification is low.

Because of lower temperatures compare to PF boilers, presumably the fuel minerals decomposition and novel minerals formation proceeds at lower rate in CFB boilers. Presumably the CFB ash contains less β-$2CaO{\cdot}SiO_2$, also CaO in free form and less classy phase. Lower activity of CFB ash might be the main reason for inefficient solidification processes in ash fields.

MATERIALS AND METHODS

The ash samples were taken from boiler ash flows at nominal load: PF boiler – furnace, superheater, economizer, cyclone, ESP fields (I – IV); CFB boiler – bottom ash, FB heat exchanger of ash, superheater, economizer, air preheater, ESP fields (I – IV).

The furnace/bottom- and ESP I field ashes were chosen as main investigation objects, as they represent 80 – 85% of whole ash stored on ash fields and these are also coarse and fine ash fractions. The composition and properties of the rest ashes are between these two ash types mentioned before. The relative amount of these ashes is small and their role is not decisive in ash solidification process on ash field.

Following investigation methods were used: chemical analysis, X-ray diffractometry, scanning electron microscopy, determination of binding properties and specific surface area.

In XRD analysis the following parameters were used: step size 0.04°, time per step 5.0 s, tube current 40mA, tube voltage 40kV, 2Θ 20-40°. In data processing the software package *DIFFRAC^{plus}* was used. In crystal phase identification the software package *Powder Diffraction Database – 2 (PDF-2)* was used.

In furnace/bottom ash XRD and SEM analyses the ash with dimension <500 μm was used. The larger particles were separated by sieving. It was presumed that the large ash particles behave like filler in ash mortar.

To investigate the binding properties and solidification kinetics of ashes, the cubes with dimensions $40\times40\times40mm^3$ were made from the paste-water mix. The compressive strength of specimens was determined after 7, 14, 21, 28 and 56 days ageing in humid environment.

Ash specimen's bulking (volume stableness) was determined using Le Chatelier cylinders. The expansion of petrified specimens was measured in water and in humid environment up to 28 days.

Specific surface area of ash was determined using Blaine method.

RESULTES AND DISCUSSION

Chemical analysis

The CO_2 content and heating residue was determined in ash samples. As the PF and CFB boiler ashes were investigated earlier (Arro et al., 2005), these results can be used in this investigation to figure out the differences in ash composition from different combustion technologies. The chemical analyses data of bottom- and ESP I field ashes were represented in Table 1.

Table 1 Chemical analyze of CFB- ja PF-ashes, %

Description	Bottom ash		Ash from EP field I	
	PF-boiler	CFB-boiler	PF-boiler	CFB-boiler
Chemical analyse				
SiO_2	18.90	11.26	22.79	38.58
Fe_2O_3	5.28	3.12	4.11	4.88
Al_2O_3	4.59	4.38	10.45	11.86
CaO	55.35	48.90	39.60	27.98
CaO_v	26.63	13.88	14.75	8.36
MgO	7.77	6.37	4.69	4.53
K_2O	1.36	1.15	4.58	4.47
Na_2O	0.12	0.10	0.13	0.24
$SO_{3\ total}$	2.43	13.88	7.65	4.10
CO_2	2.70	11.90	1.91	5.28
Calculated extent of carbonates decomposition				
$CO_{2\ CaO}$	43.09	38.07	30.83	21.78
$CO_{2\ MgO}$	8.20	6.72	4.95	4.78
$CO_{2\ total}$	51.29	44.79	35.78	26.56
k_{CO2}	0.95	0.73	0.95	0.80
Distribution of CaO between ash minerals				
CaO_{carb}	3.44	15.15	2.43	6.72
CaO_{sulf}	1.70	9.72	5.36	2.87
CaO_{free}	26.63	13.88	14.75	8.36
$\sum CaO_{carb+sulf+free}$	31.77	38.75	22.54	17.95
CaO_{tm}	23.58	10.15	17.06	10.03

In calculations of extent of carbonates decomposition (k_{CO_2}) proceeded from fact, that in oil shale 99.2% from CaO and 96.7% from MgO are in composition of $CaCO_3$ and $MgCO_3$ respectively (Arro et al., 2006). On base of CaO and MgO content in ash it is possible to calculate CO_2 content in initial fuel. The content of Fe_2CO_3 is frivolous (Ots, 2006) and may be not excepted here. To estimate the formation of novel minerals in combustion process the distribution of CaO in ash minerals – CaO_{carb} and CaO_{sulf} are given in Table 1. Adding CaO_{free} (free lime) to them and subtracting acquired sum $\sum CaO_{carb+sulf+free}$ from overall CaO content, the result shows the portion of CaO bonded into the novel minerals – CaO_{tm}.

Comparing the ashes from different combustion technologies, proceeding from factors influenced the ash binding properties, significantly different ECD and CO_2 free lime content in PF and CFB ash samples can be observed. There is also significant difference in CaO content which bound into several novel minerals. The CaO_{tm} content in PF ashes is significantly higher than in CFB ashes. At considerably higher furnace temperatures approximately more than two times of CaO bound into different ash minerals. The novel minerals are mainly with binding properties.

On the basis of chemical analysis the PF ashes are significantly active in binding processes compare to CFB ashes.

X-ray diffractometry (XRD) analysis

To estimate the influence of furnace processes of different combustion technologies to the mineral content of ash, the content of components in crystal phase in ash samples were determined by XRD analyses.

On the basis of X-ray spectra the main minerals in ash samples are: α-quartz (SiO_2), free lime (CaO),

calcite ($CaCO_3$), anhydrite ($CaSO_4$) and periclase (MgO). Low intensity peaks in X-ray spectra refer to the content of different Ca-silicates, aluminates and ferrites.

Bottom ash (Fig. 1). The peaks in X-ray spectra of CFB ash are more intensive compare to PF ash. Because of lower furnace temperatures the binding of SiO_2 and CaO into novel minerals proceeded on lower rate than in PF boiler. The binding decreases CaO and SiO_2 content in sample and intensity of peaks. The content of $CaSO_4$ ja $CaCO_3$ in CFB ash is higher compare to PF ash.

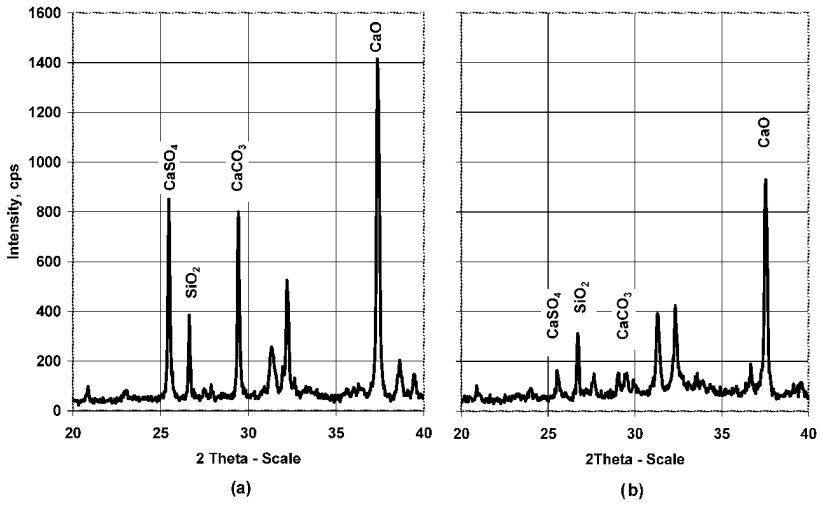

Fig. 1 XRD of bottom/furnace ashes. (a) CFB-boiler, (b) PF-boiler

ESP ash (Fig. 2). The peaks in X-ray spectra show that content of SiO_2 in form of α-quartz in CFB ash is substantially higher than in PF boiler ash. The free lime content in PF boiler ash is significantly higher compare to PF boiler ash.

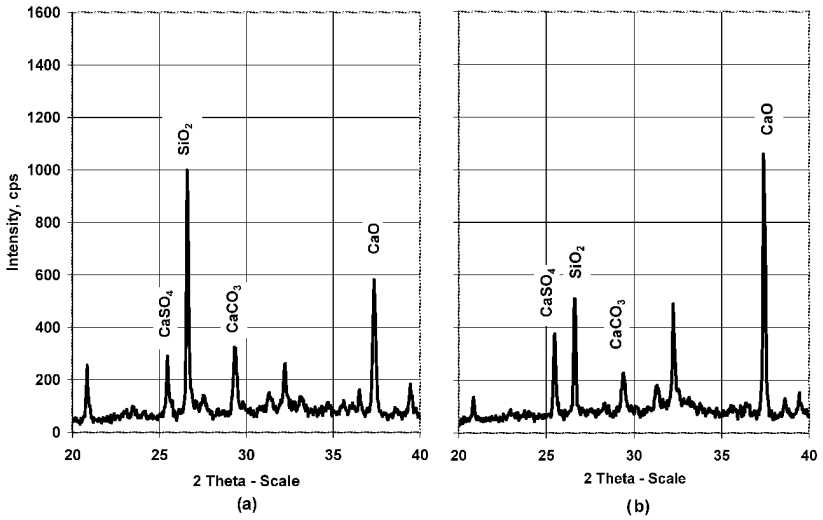

Fig. 2 XRD of ESP first field ashes. (a) CFB-boiler, (b) PF-boiler

Specific surface area of ash (blaine method)

The specific surface area (SSA) of CFB boiler ESP ashes is substantially bigger than PF boiler ashes – 4 533-9 806 cm^2/g and 707-3 966 cm^2/g correspondingly. The SSA of powder-like materials with same density depends of material fineness and shape as well. Finer material has bigger the SSA. It explains why the ESP last fields' ashes have bigger SSA. The SSA is smaller when the particles are regular shape (spherical).

Ash binding properties

Ash specimen's bulking (volume stableness), compressive strength and solidification kinetics were measured. The specimens were made of ash and water, without adding any filler. This method was chosen due to the interest of ash behavior in ash field. In comparison the binding activity of ash mortar were also determined.

The solidification data show that the specimens made of PF boiler ESP ash and cyclone ash expand in

water and in humid air a lot more than specimens made of CFB boiler ESP ash. The bottom ashes from CFB and PF boilers have no significant difference. During the test of solidification in water almost all the specimens resolved in water except specimens made of CFB boiler ESP ash, which stood the test for 28 days. Their bulking (expansion) did not exceed 3 mm in water and 2 mm in humid air. At the same time specimens made of PF boiler ESP ash and cyclone ash expanded 9 mm and 15 mm.

Data of ash solidification kinetics and compressive strength show that almost all specimens that were put into water resolved. Strength properties were only received from specimens that were petrified in humid air. The obtained data show that CFB and PF boiler bottom ash binding properties are significantly low (compressive strength after 56 days were only 1.9 N/mm^2 and 1.8 N/mm^2). The difference between CFB and PF boiler ESP ash compressive strength is approximately three times (4.4 N/mm^2 and 15.3 N/mm^2 accordingly).

Solidification kinetics is described with compressive strength change in time (Fig. 3).

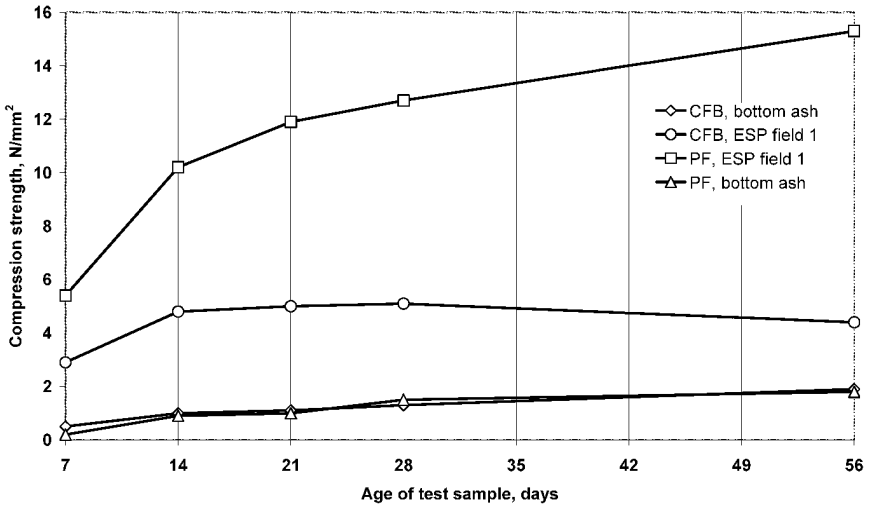

Fig. 3 Solidification kinetics of CFB and PF ash specimens

The CFB boiler ESP ash reaches the maximum compressive strength in 14 days. From there the compressive strength increase is extremely slow. The compressive strength of PF boiler ESP ash does not stabilize even in 56 days and continues increasing.

Better binding properties of PF boiler ESP ash are also seen on 28 day old specimens that are made of ash mortar. Even though the compressive strength difference between CFB and PF boiler ESP ashes is not as big they are for specimens that are made of ash only.

The test results allow to state that the main binder in ash solidification process in ash fields is ESP ash. Moreover, comparing binding properties of PF and CFB boiler ESP ashes, the first one is significantly better. The binding properties of PF and CFB boiler bottom ashes are relatively low and similar.

Scanning electron microscopy of ash

The results of SEM analyses with CFB and PF boiler ashes confirm previous research results with other methods.

Attached four photos in couple indicate expressively that CFB and PF boiler ash particles differ from each other substantially. CFB boiler ash particles have irregular shape; the percentage of melted spherical particles is irrelevant even in finest fractions of the ESP ash. In PF boiler ash the majority of particles have melted to sphere and their relative importance grows when it becomes finer. This confirms that in PF boiler (furnace temperature above 1400°C) the minerals decomposition process and formation of novel minerals takes place in relatively higher rate than in CFB boiler (furnace temperature around 800°C).

Last couple of photos illustrates the finest ash which has passed the ESP (particle size below 2.5 μm).

PF-BOILER **CFB-BOILER**

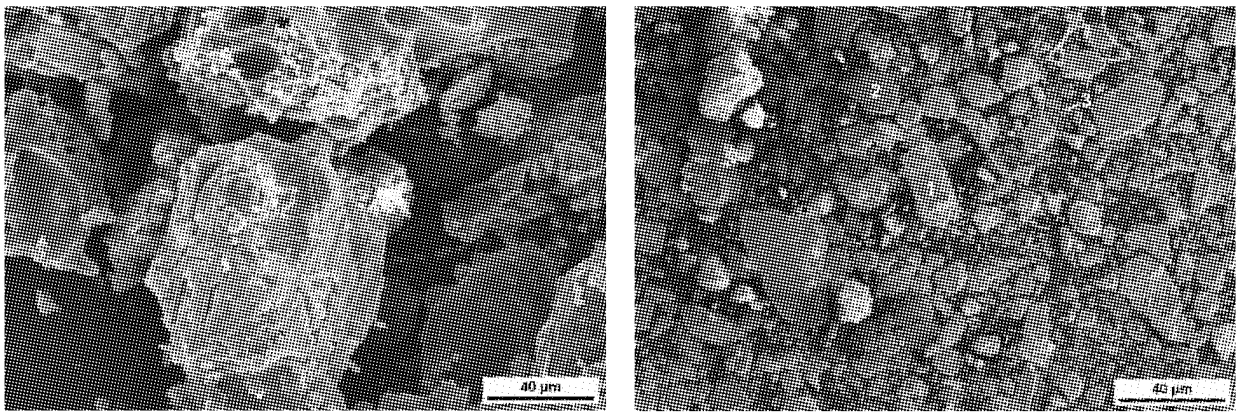

Bottom ash , ×500

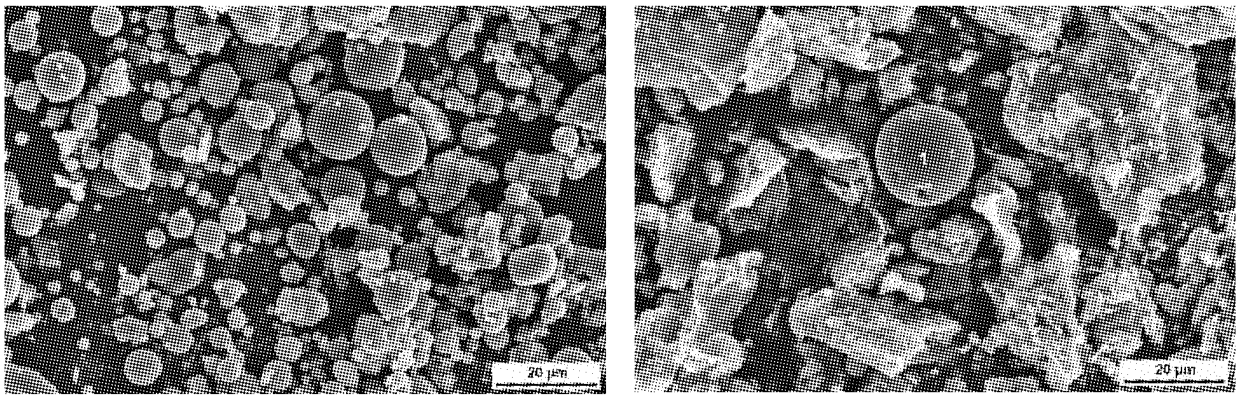

ESP field I, ×1000

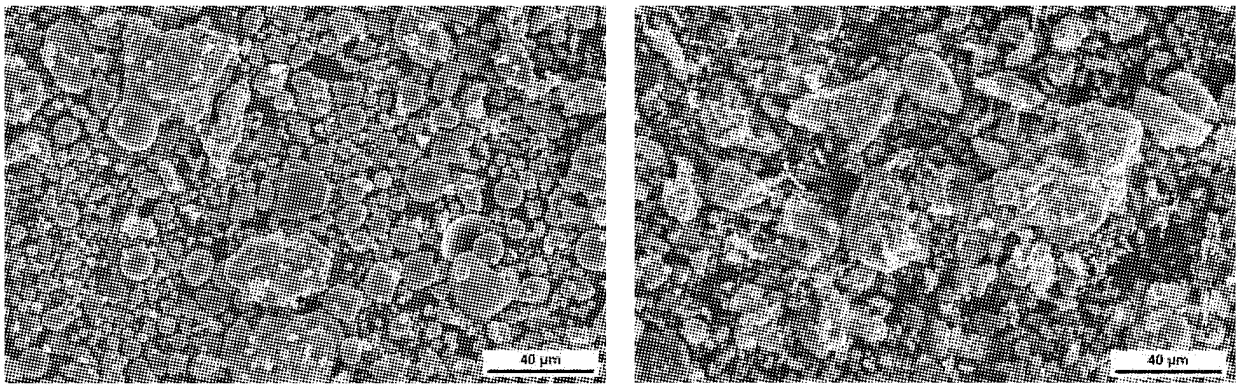

ESP field II, ×500

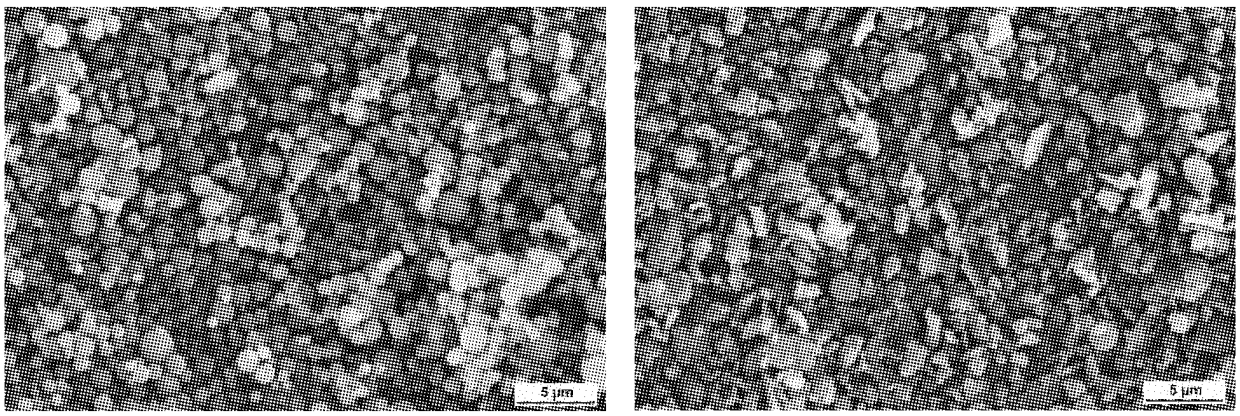

Ash sample after ESP, ×3000

CONCLUSIONS

Submitted data about behaviour of oil shale fuel minerals in combustion process and research works that have been done, indicate that CFB burning technology cause a lot of changes in oil shale ash mineralogical composition and properties. Reason for this is significantly lower burning temperature, which therefore cause lower fuel minerals decomposition and novel minerals formation. Ash is formed with the lowest binding properties and the solidification tendency in ash field is significantly lower than it is for PF boiler ash.

Research results raise a number of points, which determine the oil shale ash solidification tendency in ash field:

(1) The main binding material is ESP ash, which properties determine the solidification tendency and strength of ash field material.

(2) According to chemical analysis the free lime content in CFB boiler ESP and bottom ashes is twice lower from PF boiler ash.

(3) The most of CaO in PF ash is bonded into novel minerals than in CFB ash. As the novel minerals have binding properties, then the PF ash is more active in binding processes than CFB ash.

(4) Ash specimen XRD analyses show that PF boiler ESP ash contains more free lime and novel minerals than CFB boiler ESP ash.

(5) The comparison of specific surface area shows deeper thermal treatment of PF ash. The large specific surface area of CFB ESP ash show that the ash particles are not melted in burning process. Melting of ash particles generate classy phase which is active binder.

(6) Whole picture of ash binding properties is given by ash sample solidification kinetics, which shows that PF boiler ESP ash as binder is a lot better than CFB boiler ash and PF boiler bottom ash. PF boiler cyclone ash specimen compressive strength gains almost the strength of CFB boilers ESP ash specimen compressive strength within 56 days.

Above mentioned facts are confirmed by SEM analysis. SEM photos show that PF boiler ash has passed a lot deeper thermal processing than CFB boiler ash.

REFERENCES

Anthony E.J., Bulewicz E.M., Dudek K., Kozak A. The long term behaviour of CFBC ash–water systems. Waste Management 22 (2002) pp. 99–111.

Anthony E.J., Berry E.E., Blondin J., Bulewicz E.M., Burwell S. Advanced ash management technologies for CFBC ash. Waste Management 23 (2003) pp. 503–516.

Arro, H., Prikk, A., Pihu T. et al. Research of Balti Power Plant`s ash fields. Research report, Tallinn University of Technology (TUT), 2002, 84 p. In Estonian.

Arro, H., Prikk, A., Pihu T. et al. Results of investigations related to CFB boilers and ash fields (2004-2005). Research report, TUT, 2005, 41 p. In Estonian.

Arro, H., Prikk, A., Pihu T. CO_2 emission from CFB boilers of oil shale power plants. Research report, TUT, 2006, 18 p. In Estonian.

Arro, H., Prikk, A., Pihu, T. Calculation of CO_2 emission from CFB boilers of oil shale power plants. // Oil Shale, 2006, Vol. 23. No. 4 Special, pp. 356-365.

Boikova, A. Solid solutions of cement minerals. Leningrad, 1974, 100 p. In Russian.

Budnikov, P., Ginstling, A. Reactions in mixtures of solid materials. Moscow, 1971, 488 p. In Russian.

Butt, Y., Timashev, V. Portland Cement clinker. Moscow, 1967, 304 p. In Russian.

Kespre, T. Mineralogy of Eesti Power Plant`s oil shale ash plateau sediments. Master`s degree thesis. Tartu University, Tartu, 2004, 46 p. In Estonian.

Kuusik, R., Paat, A., Veskimäe, H., Uibu, M., Transformations in oil shale ash at wet deposition. // Oil Shale, 2004, Vol. 21. No. 1, pp. 27-42.

Kuusik, R., Uibu, M., Kirsimäe, K. Characterization of oil shale ashes formed at industrial-scale CFBC boilers. // Oil Shale, 2005, Vol. 22. No. 4 Special, pp. 407-419.

Ots, A. Oil Shale Fuel Combustion. Tallinn, 2006, 833 p.

BROMINE AND CHLORINE IN AEROSOLS AND FLY ASH WHEN CO-FIRING SOLID RECOVERED FUEL, SPRUCE BARK AND PAPER MILL SLUDGE IN A 80MWth BFB BOILER

P. Vainikka[1], J. Silvennoinen[2], P. Yrjas[1], A. Frantsi[3], L. Hietanen[4], M. Hupa[1], R. Taipale[5]

1 Åbo Akademi Process Chemistry Centre, Piispankatu 8, FIN-20500 Turku, Finland
2 Metso Power, Kelloportinkatu 1, FIN-33101 Tampere, Finland
3 Stora Enso Newsprint & Book Paper, Anjalankoski mills, FIN-46900 Anjalankoski, Finland
4 Lassila&Tikanoja, Sepelitie 6, FIN-40320 Jyväskylä, Finland
5 VTT, Koivurannantie 1, FIN-40101 Jyväskylä, Finland

Abstract: Aerosol and fly ash sampling was carried out at a 80MWth bubbling fluidised bed (BFB) boiler plant co-firing solid recovered fuel (SRF), spruce bark and paper mill wastewater sludge in two experimental conditions. The SRF-Bark ratio in the fuel mix was kept constant at 50%-50% on dry mass basis in both experiments but two sludge proportions were used: 15% and 4% on dry mass basis. Aerosol samples were collected from the superheater region of the boiler furnace and fly ash from the electrostatic precipitator (ESP). Na, K, Cl and S were found to be in mainly water soluble compounds in the aerosols sampled by means of a Dekati type Low Pressure Impactor (DLPI). Bromine was found in several weight percentages in aerosols and it was amongst the main elements in some of the samples collected. Bromine is assumed to mainly originate from flame retarded plastics and textiles in the SRF. According to the measurements, the fate of Br seems to be analogous to the other main halogen, Cl, and its conversion from fuel to aerosols was high, indicating a strong tendency to form bromine salts.

Keywords: fluidized bed combustion, co-incineration, aerosols, fine particles, halogens

INTRODUCTION

The Anjalankoski BFB plant

Stora Enso Anjalankoski co-firing plant started as a pulverized coal boiler in 1971 with a small fixed grate for bark combustion. The first commercial size BFB boiler in Finland was connected to the coal fired boiler in 1983 to combust wet sludge from the adjacent paper mill's wastewater treatment. In 1995 the whole coal fired unit was converted to BFB. Simultaneously, a wet scrubber was installed after the ESP to improve flue gas cleaning and establish heat recovery to scrubber water.

After the start-up of the BFB co-firing of SRF initiated in order to solve paper mill's waste treatment, and the fuel range was further broadened to include non-recyclable package wastes collected from commerce and industry. Simultaneously the live steam values were reduced to 500°C/80bar from 525°C/87bar in order to allow a safety margin for more corrosive combustion gases. In 2000 an indirect thermal sludge dryer was installed in order to combust all paper mill's sludge with a dry matter content of about 70-80 wt-%. This also made it possible to increase the amount of SRF in the fuel mix due to apparent ash chemistry synergies in co-firing. In 2006 the boiler received a new environmental permit according to the European Waste Incineration Directive (WID) with a SRF capacity of 50 000 tonnes per year. The share of SRF was later increased to 60 % (on energy basis) after long term tests and investigations.

Objectives

A suspension of solid fine particles or liquid droplets in a gas is called aerosol. In this paper the term aerosol is specifically used for the suspension particles less than 1 µm in aerodynamic diameter. Particles in this size range collected with the aerosol sampling system applied in this research were assumed to be mainly formed from compounds that were vaporized at fluidized bed combustion temperatures (Valmari, et al., 1998; Pyykönen et al., 2007; Sippula et al., 2008). The objective of this study was to take samples of aerosols in the superheater area of the boiler and determine the concentration together with chemical composition and compare the results to the fuel and ESP ash compositions in order to characterize the fate of chlorine and bromine in the combustion gases. It is widely known that alkali chlorides induce hot corrosion of boiler superheaters. One of the questions for the experimental work was that if bromine, analogously to the other halogen, chlorine, can be found as vaporised water soluble salts in the furnace superheater region.

In the experiments two experimental trials were carried out: day one was a business-as-usual situation with

the normal fuel ratios, and, on day two the share of the paper mill sludge was reduced to one third (on dry mass basis) from the normal operating conditions. The objective was to find out if any change in the composition or concentration of aerosols could be seen. As the sludge was a high sulphur, high kaolinite fuel it was postulated that varying the proportion in the fuel mix would influence the alkali halogen chemistry according to Reactions 1 and 2.

$$Al_2O_3 \cdot 2SiO_2(s) + 2KCl(g) + H_2O(g) \rightarrow K_2O \cdot Al_2O_3 \cdot 2SiO_2(s) + 2HCl(g) \quad (1)$$

$$2KCl(g) + SO_2(g) + \tfrac{1}{2} O_2(g) + H_2O(g) \rightarrow K_2SO_4(s) + HCl(g) \quad (2)$$

Bromine and chlorine sources

The Cl in SRF originates mainly from chlorinated plastics such as PVC or food residues which contain dietary salt (Ajanko et al., 2005). In addition, chlorine is used in flame retardants (Hornung et al., 2005). A commonly referred source of Br is flame retarded plastics and particularly Waste Electrical and Electronic Equipment (WEEE). Flame retarded plastics can contain several weight percentages of halogens, some examples are given in Table 1. They also contain significant amounts antimony (Sb) and lead (Pb). On top of these, circuit boards have many other metallic impurities. Halogenated flame retardants have traditionally been used because of their efficiency and suitability with various types of plastics. Bromine is generally preferred over chlorine because it requires lower quantities of flame retardant and minimizes the impact of the additive on the polymer's characteristics. The high content of bromine, chlorine and heavy metals in WEEE has led to the need for establishing separate collection and recycling scheme for this type of waste, in order to reduce environmental impacts (Hornung et al., 2005). For this reason, this type of material is not found in large quantities in SRF. However, flame retarded plastics can be found everywhere where thermal stability is required, also in waste fractions commonly found in SRF. These could be: polystyrene foams in construction; textiles in sofas, chairs and upholstery; decorative profiles; construction and protective films; polyamide or nylon based heat protective hoods and pipes; different types of polypropylene (lamp, gadget) holders, sockets and kitchen hoods, etc. The use of brominated compounds has also drawbacks because of the possible formation of polybrominated dibenzo-p-dioxins and -furans and the evolution of very corrosive bromine-containing gases in case of fire, incineration or recycling (Balabanovich et al., 2004).

Table 1 Concentration (mg/kg dry basis) of Cl, Br and selected other elements in some plastic fractions (Vehlow, Bergfeldt et al.)

	WEEE	TV housings	Circuit boards
Cl	56 400	19 040	23 000
K	70	<20	720
Cr	6	<1	220
Fe	80	<2	3 095
Ni	8	<1	470
Cu	80	<1	66 200
Zn	40	<1	1 310
Br	17 400	34 900	18 540
Sr	4	<1	160
Sb	7 190	23 980	5 730
Sn	935	170	5 550
Ba	<25	<20	770
Pb	1 010	220	4 960

EXPERIMENTAL

Anjalankoski BFB utilizes three main fuels: SRF, spruce bark and dried paper mill sludge. SRF and bark samples were collected during the experiments from the conveyor belts and sludge from the thermal dryer drum. Proximate and ultimate analyses were carried out according to standards: CEN/TS 14774-2 (mod.), ISO 1171:1997 (mod.), CEN/TS 14775 (mod.), ASTM D 4239 - 05 (mod.), CEN/TS 14918 (mod.), ISO 1928 (mod.), CEN/TS 15104, ISO/TS 12902, CEN/TS 15289/15408 (mod.) and SFS-EN ISO 10304-1:1995 (mod.).

Aerosols were sampled at two locations in the furnace at a depth of 1.5 m from the furnace walls within the superheater area (Fig. 1). The sampling system has been described by Aho et al. (2008a) and Aho et al. (2008b). The corresponding combustion gas temperatures were measured by k-type thermocouples, also approximately at a depth of 1.5 m from the furnace wall (Table in Fig. 1).

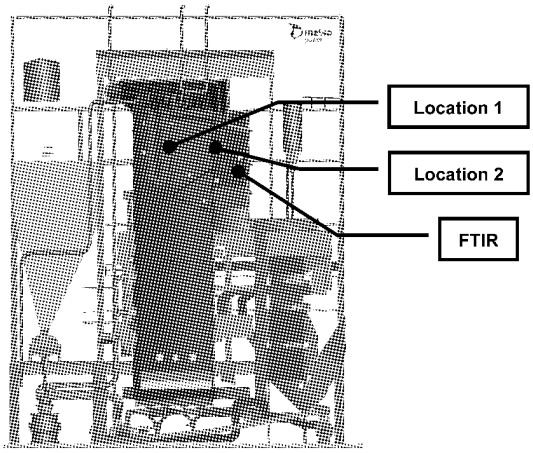

	Location 1	Location 2	FTIR
Experiment 1	724±20	555±11	477±5
Experiment 2	758±25	604±16	No data

Fig. 1 Schematic picture of the Anjalankoski BFB boiler indicating the aerosol, FTIR and temperature measurement locations. Gas temperatures and standard deviations at the measurement points are shown in the table in °C

Fly ash samples were collected from the ESP during both experiments. Leaching tests of the ESP ashes were carried out according to the principles of (Zevenhoven-Onderwater et al., 2000; Pettersson et al., 2008).

RESULTS AND DISCUSSION

Fuels and fuel properties

The SRF utilized at the Anjalankoski plant originates from wholesale business and small and middle scale industry from southern Finland. Suitable wastes are source-separated package and other solid industrial non-recyclable wastes which are separately collected by the SRF supplier. In the fuel preparation stage the material is crushed and hazardous materials are removed (by magnets, screens and eddy current). The spruce bark originates from the adjacent paper mill where stem wood is used for mechanical pulping. The wastewater sludge consists of wood fibre and paper filler and coating rejects which are mainly kaoline and calcium carbonate. In the treatment some 30-40 kg of ferric sulphate per ton of dry sludge is added to the wastewater stream as a flocking agent. In addition aluminium sulphate is used at the paper machines which may entrain in the wastewater. Proximate and ultimate analysis results of the fuels are shown in Table 2.

Table 2 Proximate and ultimate analysis results of the fuels and of the fuel mixtures used in the Experiments

	SRF I	SRF II	Bark	Sludge	Exp. I	Exp. II
Moisture (wt-%, ar)	18.3	18.1	54.8	8.3 (67*)	38.6	42.7
Ash (wt-%, db)	7.5	7.5	2.1	21	7.2	5.6
ULTIMATE ANALYSIS OF DRY SOLIDS (wt-%, db)						
C	54.9	55.1	50.4	41.7	51.0	52.4
H	7.6	7.6	5.9	5.2	6.5	6.7
S	0.15	0.15	0.02	0.73	0.18	0.12
O	29.06	29.06	41.31	29.74	34.4	34.6
N	0.79	0.48	0.27	1.63	0.69	0.43
Cl	0.46	0.44	0.015	0.021	0.21	0.23
Br**	0.001-0.026	0.001-0.026	NA	NA	0.011	0.013
HEATING VALUE (MJ/kg)						
LHV, db	23.56	23.51	19.00	16.33	20.54	21.17
LHV, ar	18.80	18.81	7.25	14.77	11.68	11.08

ar, As received; db, Dry basis; NA, Not applicable; * For wet sludge in Experiment II;
** MIN-MAX values from SRF supplier's long term follow-up.

The shares of fuels on energy basis were: in Experiment I 51%-36%-13%; and Experiment II 60%-38%-2% for SRF, bark and sludge, respectively. On energy basis the ratio of the SRF and bark in relation

to each other was close to 60%-40% in both experiments (59-41%, 61-39%). In Experiment I the plant was run as usual, but for the reduced sludge flow case the sludge dryer was shut down, as it can not be run in partial loads, and wet sludge was mixed with bark. In normal operating situation dried sludge is injected pneumatically into the furnace in a separate feeding line.

SRF samples were collected separately for both test trials, although they were quite similar in composition, and the analyses results of Br and Cl are treated separately. The bromine minimum and maximum contents are shown in Table 2 as they were analysed by the supplier during a several month follow-up, while Fig. 2 shows the Br content during the experiments for four separate samples collected each day. The Br content fluctuated considerably, which may indicate that there are specific sources of flame retarded materials in the SRF which are not supplied to the SRF preparation in a continuous manner. The Br content was higher in Experiment II, reaching a maximum value of 0.052 wt-%. The average Br content for the two days were 0.004 and 0.021 wt-%, for Experiment I and II, respectively.

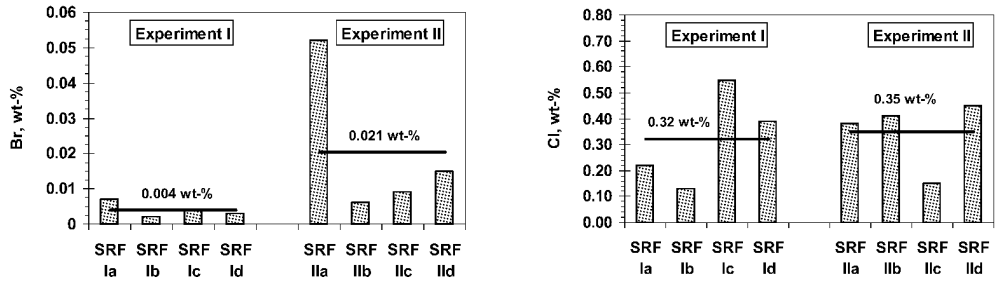

Fig. 2 Variation of Br (left) and Cl (right) concentrations in the SRF

The Cl content of the SRFs was 0.46 and 0.44 wt-% for Experiment I and II, respectively. Figure 2 shows the Cl content variations for the same five SRF samples as for Br from each experiment. The average values for Cl content based on the individual five samples are 0.32 and 0.35 wt-% for Experiments I and II, respectively.

ESP ash samples

From co-combustion experiments of flame retarded TV housing plastics with organic waste it has been found out that some 25 to 40% of bromine ended up in fly ash (Vehlow et al.). Some 5 to 10% was retained in the bottom slag of the grate fired unit and the rest was found in the gas phase mainly as HBr or in some cases Br_2. In the experimental work presented in this paper HBr was included in the FTIR gas analyses but it was not detected, with the exception of some occasional 1-2 ppm peaks. Vehlow et al. 1998 conclude from their experiments in a grate fired incinerator that Br had higher tendency to form alkali salts than Cl which is explained with HBr being a stronger acid than HCl. It was also observed that the volatilization of Zn and Pb increased with increased inventory of Cl and Br in the feedstock. (Vehlow and Mark, 2000)

Fly ash samples were collected from the ESP during both experiments. Leaching tests of the ESP ashes were carried out according to the principles of (Zevenhoven-Onderwater et al., 2000; Pettersson et al., 2008) and Fig. 3 shows the results for both the total content of Cl, K, Na, S and Br and the water soluble fractions.

The characters of the two halogens, Cl and Br, were similar in terms of solubility. They were, to a large extent, forming compounds that were water soluble. K, Na and S also formed compounds that were insoluble in water. Figure 3 also shows that the concentrations of all these elements were higher in Experiment II and their water soluble fractions were at least doubled, with the exception of S. This indicates higher concentrations of alkali halogen compounds in the furnace during Experiment II. If this is the case, it should show through also in the in-furnace aerosol sampling for vaporised ash forming compounds.

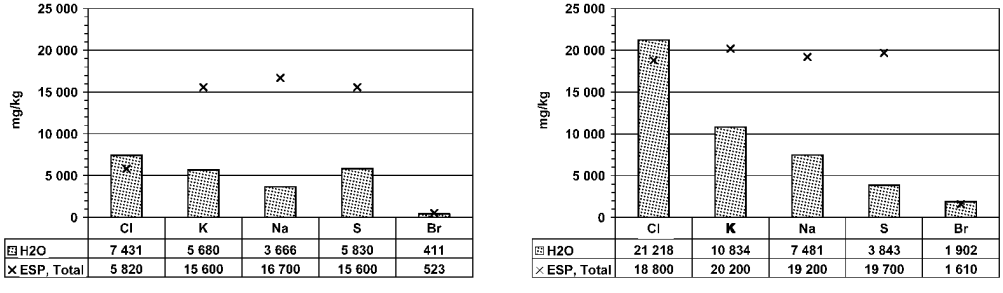

(a) (b)

Fig. 3 Total concentrations and water soluble fractions of Cl, K, Na, S and Br in the ESP ashes for Experiment I (a) and II (b).

Aerosol samples

Water soluble Br^-, SO_4^{2-}, Na^+, K^+, Cl^- were analysed from the aerosol samples by Ion Chromatography (IC) and Flame Atomic Absorption (FAAS). The fine mode, i.e. particles with aerodynamic diameter less than 1μm, consisted mainly of Cl, K, Na and SO_4 (Fig. 4). Sulphate was found in higher concentration in Experiment I. This was expected, as the sulphur content of the fuel mix was higher due to the higher sludge proportion in the fuel mix. As it was shown in Fig 3, the Br content in the fly ash was significantly higher in Experiment II, which seems to be the case also in the aerosol samples as water soluble Br was found in several weight percentages, particularly in samples from Location 2. In this case it can be stated that Br is becoming one of the major elements in the aerosols.

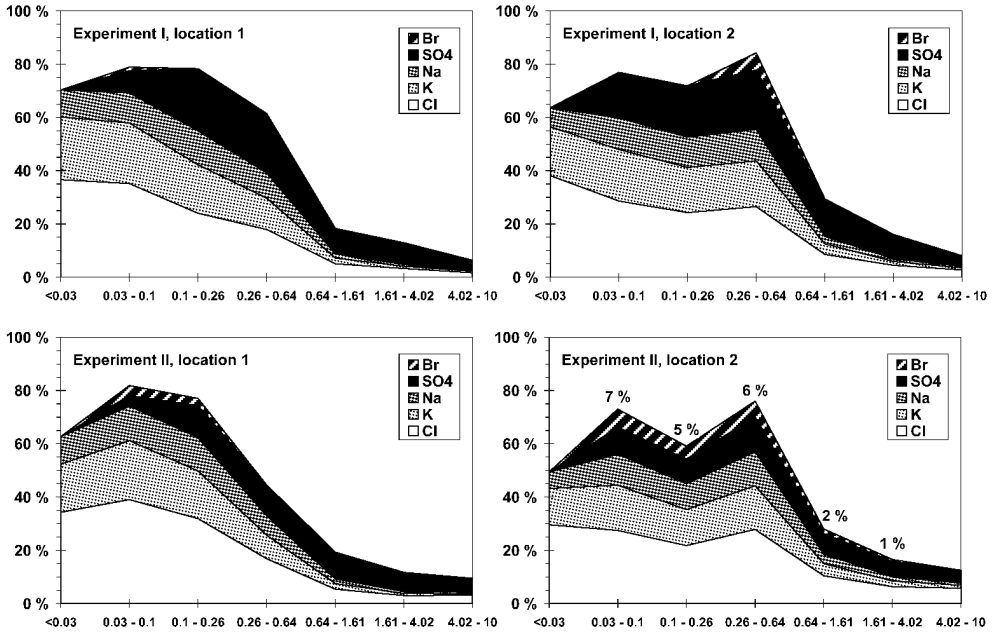

Fig. 4 Composition (wt-% on vertical axis) of different particle size fractions (μm on horizontal axis) collected by DLPI. In the lower right chart the numbers indicate the weight percentage for Br in the corresponding particle size sample.

Based on the mass fraction values at Location 2 in Experiment II it can be calculated that 9% on molar basis of the halogens in submicron particles were bromides. The amount of Br bound in the submicron fraction corresponded to 65% of the maximum, assuming that the SRF contained the maximum amount of Br according to Table 2 and that the Br content in the other fuels was negligible. If also the larger particulates, up to 10 μm, collected with the impactor are accounted for, the corresponding gain is 80%.

For the other halogen, Cl, it was easier to close the mass balance in the furnace, as its concentration was significantly higher. Figure 5 shows the split of Cl between the aerosols and the HCl gas measured by FTIR. The 'Cl MAX' lines indicate the theoretical maximum of Cl concentration in the combustion gases based on the Cl content in the fuel mixtures shown in Table 2. The conversion of fuel bound Cl to HCl was calculated to be 90% and 78% for Experiment I and Experiment II, respectively.

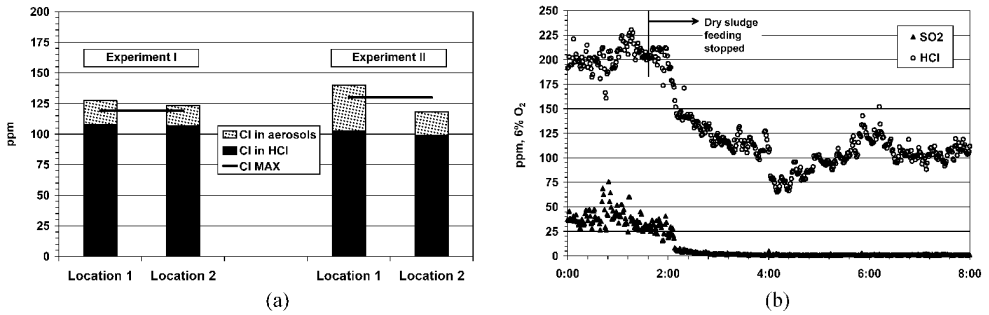

Fig. 5 The split of Cl between HCl and submicron aerosols (a) and HCl & SO_2 concentrations in combustion gases (b) as a function of time (in hours)

On the right in Fig. 5 is the FTIR data on HCl and SO_2 during the transition period when feeding of the

fuel proportions were changed from Experiment I to Experiment II. There are fluctuations in the SRF feeding during this period which is seen in the HCl concentration fluctuations in the gas. Nevertheless, HCl concentration of the gas decreased when shifting to Experiment II operation mode and all sulphur was bound in the ash.

CONCLUSIONS

The aerosol and ESP ash elemental analyses show that Br can be present in significant amounts. Alongside Cl, also Br should be included in the alkali halogen related studies regarding SRF co-firing. This can also be justified by the Br content found in SRF, which can be several hundreds of ppm. Both Br and Cl were found to form in large extent water soluble ash compounds, while K, Na, and S compounds were partly insoluble in water. The yield of Br in aerosols can be high, and based on these results it can sometimes be even higher than Cl.

Higher concentration of sulphates was found in the aerosols when increasing the share of sludge. Yet, alkali halogens were present in the aerosol and in the ESP samples in both experiments.

The alkali and halogen concentrations increased in the ESP-ashes with decreasing share of sludge. In the test with a lower sludge share the highest concentration of Cl bound in aerosols was reached and conversion of Cl from fuel to HCl gas was lower compared to the case with a higher proportion of sludge. The reasons for this and the role of sulphur and kaoline in alkali capture should be assessed.

ACKNOWLEDGEMENTS

Financial support from the Finnish Funding Agency for Technology and Innovation (Tekes), Metso Power Oy, Lassila&Tikanoja Oyj, UPM-Kymmene Oyj and Bioenergy NoE (through contract SES6-CT-2003-502788) is gratefully acknowledged. We are grateful to Stora Enso for providing the Anjalankoski BFB plant available for the experimental work. We thank Hannu Vesala, Marko Räsänen, Tor Laurén, Raili Taipale, Kauko Tormonen and Sari Kauppinen for their comments, hard work and commitment.

REFERENCES

[a]AHO, M., GIL, A., TAIPALE, R., VAINIKKA, P. and VESALA, H., 2008. A pilot-scale fireside deposit study of co-firing Cynara with two coals in a fluidised bed. *Fuel,* **87**(1), pp. 58-69.

[b]AHO, M., VAINIKKA, P., TAIPALE, R. and YRJAS, P., 2008. Effective new chemicals to prevent corrosion due to chlorine in power plant superheaters. *Fuel,* **87**(6), pp. 647-654.

AJANKO, S., MOILANEN, A. and JUVONEN, J., 2005. *Kierrätyspolttoaineiden laadunvalvonta.* VTT Publications: 587.

BALABANOVICH, A.I., HORNUNG, A., MERZ, D. and SEIFERT, H., 2004. The effect of a curing agent on the thermal degradation of fire retardant brominated epoxy resins. *Polymer Degradation and Stability,* **85**(1), pp. 713-723.

HORNUNG, A., DONNER, S., BALABANOVICH, A. and SEIFERT, H., 2005. Polypropylene as a reductive agent for dehalogenation of brominated organic compounds. *Journal of Cleaner Production,* **13**(5), pp. 525-530.

PETTERSSON, A., ZEVENHOVEN, M., STEENARI, B. and ÅMAND, L., 2008. Application of chemical fractionation methods for characterisation of biofuels, waste derived fuels and CFB co-combustion fly ashes. *Fuel,* **87**(15-16), pp. 3183-3193.

PYYKÖNEN, J., MIETTINEN, M., SIPPULA, O., LESKINEN, A., RAUNEMAA, T. and JOKINIEMI, J., 2007. Nucleation in a perforated tube diluter. *Journal of Aerosol Science,* **38**(2), pp. 172-191.

SIPPULA, O., LIND, T. and JOKINIEMI, J., 2008. Effects of chlorine and sulphur on particle formation in wood combustion performed in a laboratory scale reactor. *Fuel,* **87**(12), pp. 2425-2436.

VALMARI, T., KAUPPINEN, E.I., KURKELA, J., JOKINIEMI, J.K., SFIRIS, G. and REVITZER, H., 1998. Fly ash formation and deposition during fluidized bed combustion of willow. *Journal of Aerosol Science,* **29**(4), pp. 445-459.

VEHLOW, J., WANKE, T., SEIFERT, H., JAY, K. and MARK, F.E., 1998. *Chlor- und bromhaltige Kunststoffe in der Abfallverbrennung.* Nachrichten - Forschungszentrum Karlsruhe v. 29(2).

VEHLOW, J., BERGFELDT, B., HUNSINGER, H., JAY, K., MARK, F.E., TANGE, L., DROHMANN, D. and FISCH, H., *Recycling of bromine from plastics containing brominated flame retardants in state-ofthe-art combustion facilities.* Available at: http://www.bsef.com/. Association of Plastics Manufacturers in Europe (APME), FZK Forschungszentrum Karlsruhe (FZK), European Brominated Flame Retardant Industry Panel (EBFRIP).

VEHLOW, J. and MARK, F.E., 2000. Influence of bromine on metal volatilization in waste combustion. *Journal of Material Cycles and Waste Management,* **2**(2), pp. 89-99.

ZEVENHOVEN-ONDERWATER, M., BLOMQUIST, J.-., SKRIFVARS, B.-., BACKMAN, R. and HUPA, M., 2000. The prediction of behaviour of ashes from five different solid fuels in fluidised bed combustion. *Fuel,* **79**(11), pp. 1353-1361.

REBURNING CHARACTERISTICS OF RESIDUAL CARBON IN FLY ASH FROM CFB BOILERS

S.H. Zhang, H.H. Luo, H.P. Chen, H.P. Yang, X.H. Wang

State Key Laboratory of Coal Combustion(SKLCC)
Huazhong University of Science and Technology, Wuhan, 430074, China

Abstract: The content of residual carbon in fly ash of CFB boilers is a litter high especially when low-grade coal, such as lean coal, anthracite coal, gangue, etc. is in service, which greatly influences the efficiency of boilers and fly ash further disposal. Reburn of fly ash through collection, recirculation in CFB furnace or external combustor is a possibly effective strategy to decrease the carbon content, mainly depending on the residual carbon reactivity. In this work, the combustion properties of residual carbon in fly ash and corresponding original coal from large commercial CFB boilers (Kaifeng (440t/h), and Fenyi (410t/h), all in china) are comparably investigated through experiments. The residual carbon involved was firstly extracted and enriched from fly ash by means of floating elutriation to mitigate the influence of ash and minerals on the combustion behavior of residual carbon. Then, the combustion characteristic of two residual carbons and the original coal particles was analyzed with thermogravimetric analyzer (TGA, STA409C from Nestch, Germany). It was observed that the ignition temperature of the residual carbon is much higher than that of original coal sample, and the combustion reactivity of residual carbon is not only dependent on the original coal property, but also the operating conditions. The influence of oxygen content and heating rate was also studied in TGA. The O_2 concentration is set as 20%, 30%, 40% and 70% respectively in O_2/N_2 gas mixture with the flow rate of 100ml/min. It was found that higher oxygen content is favor for decreasing ignition temperature, accelerating the combustion rate of residual carbon. And about 40% of oxygen concentration is experimentally suggested as an optimal value when oxygen-enriched combustion is put into practice for decreasing residual carbon content of fly ash in CFB boilers.

Keywords: CFB boiler, residual carbon, reburning

INTRODUCTION

Circulating fluidized bed (CFB) boiler has being quickly developed with the flexibility of fuel and low level pollutant emissions. However, the carbon content of fly ash is a little high when low activity coal, such as anthracite coal, lean coal and coal gangue is served as mainly constituent feedings, especially for small to medium capacity CFB boilers, despite of a lot of combustion-intensified measures being made, including the improvement of separation efficiency of gas-solid separators, enhancement the penetration of secondary air into furnace, and etc.. As a result of the situations, the thermal efficiency can not get a desired high level, leading more fuel consumptions (Lu et al., 2004; Xiao et al., 2005). Simultaneously, high carbon content in fly ash has also inversely impacts on ash subsequent serviceable disposal as it will degrade the cement strength when fly ash is applied as additives of cement or load construction materials (Blackstock and Tyson, 1996).

Reburn of fly ash through collection, recirculation in CFB furnace or external combustor is a possibly effective strategy to decrease the carbon content, mainly depending on the residual carbon reactivity. The aim of this study is to catch the combustion characteristic of residual carbon in fly ash from CFB boilers. The residual carbon involved was firstly extracted and enriched from fly ash by means of floating elutriation to mitigate the influence of ash and minerals on the combustion behavior of residual carbon. Then, the combustion characteristic of two residual carbons and the original coal particles was analyzed with thermogravimetric analyzer (TGA, STA409C from Nestch, Germany). It was observed that the ignition temperature of the residual carbon is much higher than that of original coal sample, and the combustion reactivity of residual carbon is not only dependent on the original coal property, but also the operating conditions. The influence of oxygen content and heating rate was also studied in TGA. The O_2 concentration is set as 20%, 30%, 40% and 70% respectively in O_2/N_2 gas mixture with the flow rate of 100ml/min. It was found that higher oxygen content is favor for decreasing ignition temperature, accelerating the combustion rate of residual carbon. And about 40% of oxygen concentration is experimentally suggested as an optimal value when oxygen-enriched combustion is put into practice for decreasing residual carbon content of fly ash in CFB boilers.

EXPERIMENTAL

The original examples of fly ash were obtained at electrostatic precipitator dust outlets from Kaifeng and Fenyi CFB boilers of 440 and 410 tone high pressure superheat steam per hour respectively. The two boilers all burn its local anthracite coal. The residual carbon examples involved in following experiments were extracted and enriched from the fly ashes by means of floating elutriation (Hurt and Gibbins, 1995; Yu, 2001) to mitigate the influence of ash and minerals on their combustion behaviors. The particle size is centered on 45 to 65 μm .The proximate analysis of residue carbon (RC) and corresponding original coal is listed in Table 1.

Table 1 The proximate analysis of coal sample

Sample	KF		FY	
	coal	RC	coal	RC
Moisture ad (wt%)	1.21	1.08	1.33	0.92
Ash ad (wt%)	25.39	31.10	36.07	25.05
Volatile daf (wt%)	9.22	1.62	9.62	1.30
Fixed carbon ad (wt%)	66.63	66.72	56.58	73.07

The combustion of residue carbon was performed with a thermo balance (TGA, STA 409C, Netsch Germany) in O_2/N_2 with program controlled temperature. Sample size is (10 ±0.5)mg. The furnace was heated to 1000 ℃ at 20 ℃ per minute of temperature rise, and the flow rate of reaction gas was 100 milliliter per minute (40ml/min. O_2 and 60ml/min. N_2). Simultaneously, the influence of O_2 content on the combustion characteristics of residue carbon were analyzed with the ratio of O_2/N_2 variation at 20/80，30/70，40/60，70/30 as the total flow rate kept a constant of 100 ml/min.

RESULTS AND DISCUSSION

Combustion characteristic of remnant carbon

The TG and DTG curves of two kinds of remnant carbon and original coal are plotted in Figs. 1 and 2. The TGA characteristic temperatures of original coal and residual carbon are listed in Table 2.

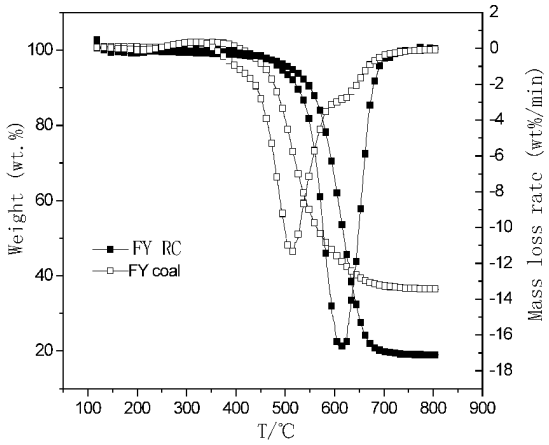

Fig.1 TG and DTG of FY coal combustion

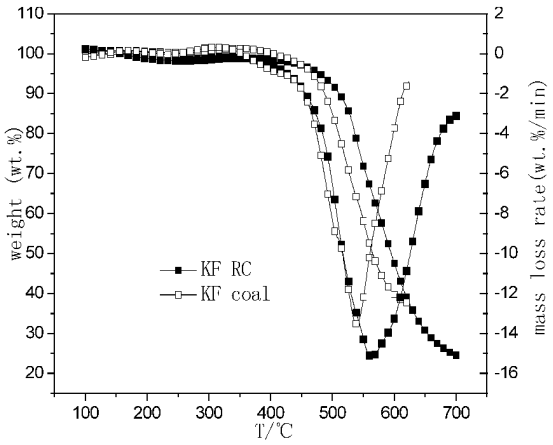

Fig. 2 TG and DTG of KF coal combustion

Table 2 Characteristic temperature of original coal and remnant carbon combustion

Sample	T_i(°C)	T_{cr}(°C)	T_{max}(°C)	T_f(°C)	dw/dt_{max}(%/min)	dw/dt_{mean}(%/min)
FY coal	462.3	475.2	518.7	583.6	11.1	7.8
FY RC	560.2	570.3	604.7	659.1	17.1	12.8
KF coal	495.3	520.6	538.8	599.6	12.4	9.6
KF RC	508.7	527.3	549.4	627.8	15.6	10.1

Ti: ignition temperature of sample combustion in TGA, T_f: final temperature of sample combustion in TGA, T_{max} : temperature of dw/dt_{max}.

The combustion reactivity (R) was chose to analyze the combustion characteristics of different samples, R can be defined as follows (Blake et al., 1967):

$$R=-1/w \times dw/dt \quad (1)$$

Where w is weight of sample, so temperature at R=0.11/min was defined as reaction characteristic token temperature (T_{cr}). The smaller T_{cr} is, the better material reaction characteristic is.

From Table 2, it can be known that T_i and T_{cr} of the two remnant carbon samples were higher than that of its original coal. It indicated that the combustion characteristic of remnant carbon was relatively worse than that of original coal. From Figs. 1 and 2, the maximum mass loss rate (dw/dt_{max}) of the remnant carbon samples were higher than that of the two original coals, and the average combustion rate (dw/dt_{mean}) of the whole burning process was also higher than that of original coal. It might be attributed to that the remnant carbon showed much higher surface area than the original coal, so the oxygen diffusivity compared to the stove coal is stronger, hence the combustion rate of the remnant carbon is much higher. However, T_i and T_f of remnant carbons are higher; some improvement should be made to keep it burn out steady and quickly.

It can also be known from Table 2 that the remnant carbon reaction activity not only depends on its original coal, but also relates with the combustion condition of CFB boiler. FenYi boiler operates with fly ash recycle to make the remnant carbon stay in furnace for much longer time than Kaifeng remnant carbon, and hence, T_i, T_{cr} and T_f of FY remnant carbon were much higher than that of KF remnant char, leading to much poor combustion characteristic although FY origin coal showed better combustion characteristics than KF coal in above TGA experiments.

Influence of oxygen content on RC combustion

The TG and DTG curves of remnant carbon combustion under variant O_2 inputting are shown in Figs. 3 to 6. From the four figures, similar trend can be observed with O_2 input increasing. The ignition of remnant carbon was shifted to 40 to 60 °C lower temperature with O_2 content increasing from 20% to 70%, while mass loss rate was greatly enhanced. It indicated that the ignition and combustion property can be upgraded with enriched O_2 inputting. However, the extent of changing depends on the property of solid samples served in experiments because KF RC showed more obvious changing. It might be attributed to that FY coal stayed in

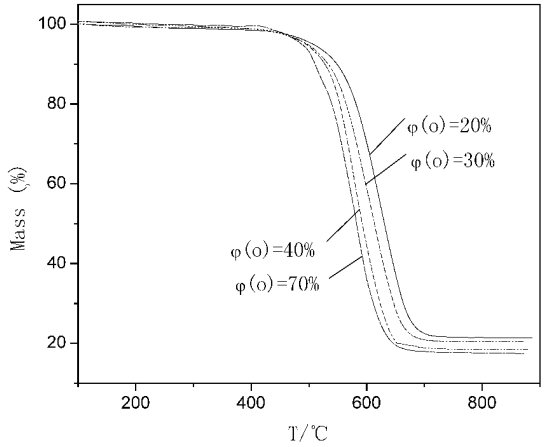

Fig. 3 TG of FY RC combustion

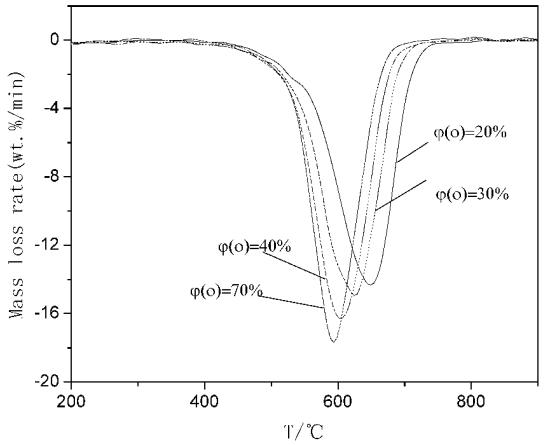

Fig. 4 DTG of FY RC combustion

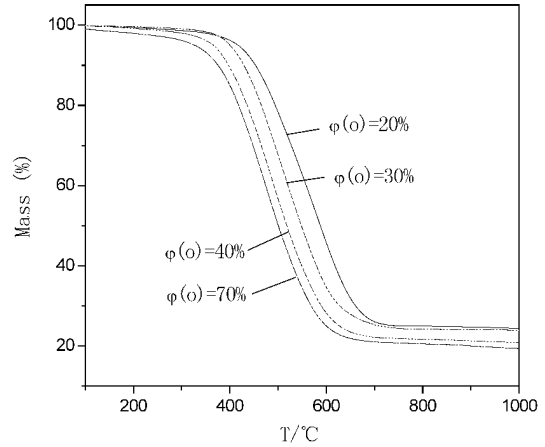

Fig. 5 TG of KF RC combustion

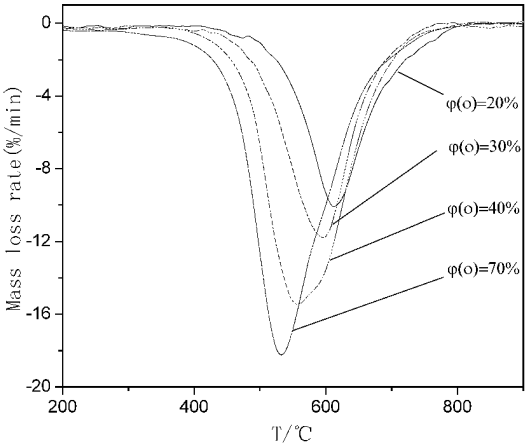

Fig. 6 DTG of KF RC combustion

furnace for longer time, and the physical structure of FY RC is much compact than that of KF RC.

In comparison with different O_2 inputting, T_i and dw/dt_{max} showed variant trend of RC combustion (refer to Fig. 7 and Fig. 8). For KF and FY RC combustion, Ti decreased 47°C and 32 °C respectively when O_2 input concentration increased from 20% to 40%. However, when O_2 input concentration further increased above 40% till to 70%, no obvious change of T_i was observed, suggesting extra high O_2 input concentration has no obvious influence on the ignition of RC, which is consistent with Dr. Fan's results about Shenmu coal (Fan et al.,2006).

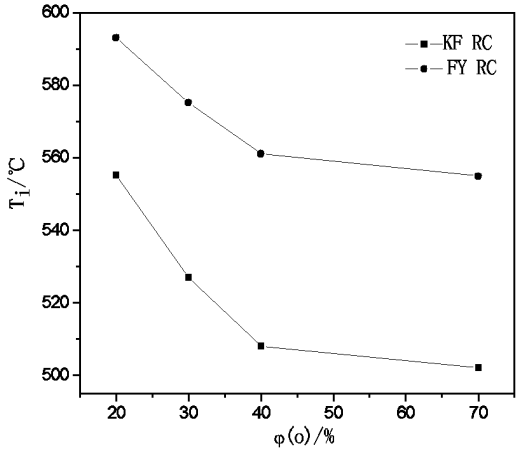

Fig. 7 T_i of KF and FY RC combustion

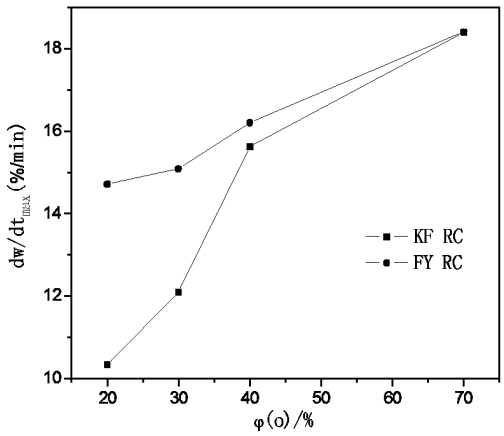

Fig. 8 dw/dt_{max} of KF and FY RC combustion

The maximum mass loss rate (dw/dt_{max}) of RC combustion showed similar tendency with ignition temperature. As O_2 content is 20%, dw/dt_{max} of FY was higher than KF coal by 5%/min, while the difference gradually diminished with O_2 content still increasing, and finally no obvious discrepancy was found at 70% O_2 content. The effect of O_2 content on RC combustion in above experiments reflects that O_2 content is one of key factors which determine RC combustion behavior. As O_2 input concentration increases, the transportation of oxygen to RC particle surface is enhanced and so the combustion rate improves. However, the fact that the augment effect is gradually poor with O_2 content continual increasing suggests that RC combustion is also controlled by other factors.

The index of combustion stability (R_w) is an important factor to describe the combustion property (Sun, 2002).

$$Rw = 560/T_i + 650/T_{max} + 0.27(dw/dt)_{max} \tag{2}$$

The index of combustion characteristics (P) is also introduced to comprehensively analyze the combustion behavior (Jiang, Li and Qiu, 2000).

$$P = \frac{(dw/dt)_{max}(dw/dt)_{mean}}{T_i^2 T_f} \tag{3}$$

The larger the value of R_w, the more stable RC combustion is. And so does the value P for RC combustion effect.

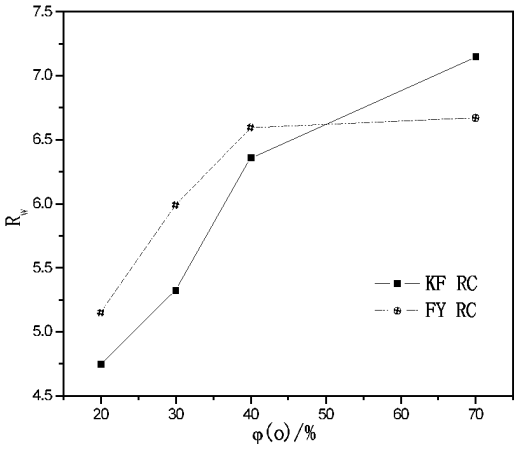

Fig. 9 R_w of KF and RC combustion

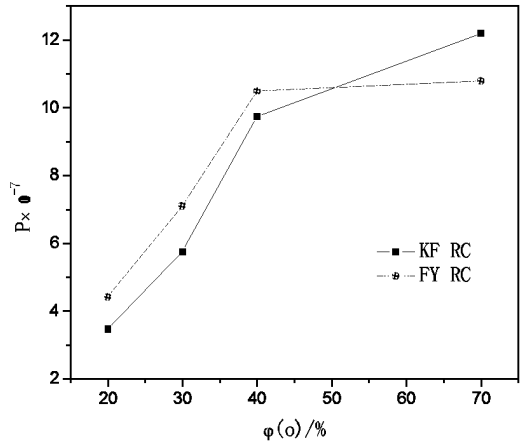

Fig. 10 P of KF and RC combustion

R_w and P of two remnant carbon combustion at variant O_2 input are plotted in Fig. 9 and Fig. 10. From the two figures, it can be observed that the indexes of combustion stability of two fly ash remnant carbons both gradually increase with O_2 content increasing. However the increasing extent for O_2 lower than 40% is much higher than that of O_2 content is higher than 40%. The combustion characteristics index(P) shows a similar trend with the index of combustion stability. Enriched O_2 input is favorable for the upgrading of remnant carbon combustion, and 40% content of O_2 might be an optimal value.

CONCLUSIONS

The combustion property of remnant carbon in fly ash from Kaifeng and Fengyi power plant of fluidized bed boilers was investigated through thermal analysis. Following two conclusions could be drawn from the experiments:

The typical temperatures T_i, T_{max}, T_{cr} and T_f of remnant carbon combustion are much higher than that of its original coal, which suggests that the combustion property of remnant carbon is poorer than that of the corresponding original coal and the combustion property is not only depended on original coal, but also on burning condition in CFB boilers.

Oxygen input concentration shows great influence on performance of remnant carbon combustion. As O_2 content increases from 20% to 40%, the combustion property of remnant carbon is greatly upgraded. However, after that, the influence is not obvious with its further increasing. The optimal O_2 content for remnant carbon combustion is 30%~40%.

ACKNOWLEDGEMENTS

The author wishes to express the great appreciation of financial support from "Key Projects of National Fundamental Research Planning" (National 973 project: 2007CB210202) and National Nature Science Foundation of China (No. 50676037 and No. 50721005).

REFERENCES

Blackstock, T. H. and Tyson, S. S. (1996).Present status and future initiatives regarding coal ash utilization in the United States [C]. Pro. of the American Power Con. 2.

Blake, J. H., Bopp, G. R. and Jones, J. F. : Fuel 46 (1967),pp.115-125.

Fan, Y.S., Zou, Z. and Gao, J.B.: J. of Xi' An Jiaotong Uni. 40 (2006), pp.19-20.

Hurt, R. and Gibbins, J.: Fuel 74 (1995), pp. 471-480.

Jiang, X.M., Li, J.B. and Qiu, J.R. (2000).Study on combustion characteristics of Micro pulverized coal [J]. Proc. of the CSEE.

Lu, J. F., Zhang, S.Y. and Liu, Q.: Power Eng.24 (2004), pp. 170-175.

Sun, X.X.(2002). Experiment technology and method of coal combustion in pulverized coal boiler. Beijing, Press of CEPP China Publ.

Xiao, X. and Yan. G. H.: Energy&Fuels.19 (2005), pp.1520-1525.

Yu, Q. M.: J. of Nanchang Uni. 23 (2001),pp. 82-85.

USE OF FLUIDIZED BED COMBUSTION ASH AND OTHER INDUSTRIAL WASTES AS RAW MATERIALS FOR THE MANUFACTURE OF CALCIUM SULPHOALUMINATE CEMENTS

M. Marroccoli[1], F. Montagnaro[2], M. L. Pace[1], A. Telesca[1], G. L. Valenti[1]

1 Dipartimento di Ingegneria e Fisica dell'Ambiente, Università degli Studi della Basilicata, Potenza, 85100, Italy

2 Dipartimento di Chimica, Università degli Studi di Napoli Federico II, Napoli, 80126, Italy

Abstract: Calcium sulphoaluminate cements, mainly composed by $4CaO{\cdot}3Al_2O_3{\cdot}SO_3$ and $2CaO{\cdot}SiO_2$, are special hydraulic binders which require limestone, bauxite and gypsum as natural raw materials for their manufacture. In order to save bauxite and natural gypsum, it has been explored the possibility of using, among the raw mix components, FBC waste together with pulverised coal fly ash or anodization mud and, when necessary, flue gas desulphurization gypsum. Mixtures containing limestone (29-39%), FBC waste (30-44%), pulverised coal fly ash (0-13%) or anodization mud (0-32%), bauxite (0-18%) and flue gas desulphurization gypsum (0-8%) were heated for 2 hours in a laboratory electric oven at temperatures ranging from 1150° to 1300°C. The X-ray diffraction patterns on the burnt products generally showed a good conversion of the reactants and a high selectivity degree towards $4CaO{\cdot}3Al_2O_3{\cdot}SO_3$, particularly at 1250°C.

Keywords: waste utilization, raw materials, cement manufacture, calcium sulphoaluminate cements

INTRODUCTION

Calcium sulphoaluminate (CSA)-based binders are non Portland cements containing calcium sulphoaluminate ($4CaO{\cdot}3Al_2O_3{\cdot}SO_3$) and dicalcium silicate ($2CaO{\cdot}SiO_2$) as major components (Klein and Troxell, 1986). Upon reaction with water, lime and/or calcium sulphate, calcium sulphoaluminate quickly generates ettringite ($6CaO{\cdot}Al_2O_3{\cdot}3SO_3{\cdot}32H_2O$) which regulates the technical behaviour of CSA cements, especially at early ages; on the other hand, through the formation of calcium silicate hydrate, dicalcium silicate contributes to strength and durability at longer ages.

According to its formation rate and microstructure, ettringite can promote an expansive behaviour or a rapid hardening (associated with dimensional stability). These properties can be usefully exploited by shrinkage-compensating and self-stressing cements (Mehta, 1973; Kurdowski et al., 1986; Muzhen et al., 1992) or by high performance cements (Muzhen et al., 1997; Glasser and Zhang, 2001; Bernardo et al., 2007; Marroccoli et al., 2007 a) like those manufactured in China since the decade 1970-1980, according to formulations first developed by the China Building Materials Academy.

CSA cements, depending on both proportioning of raw materials and synthesis temperature, may also contain various calcium silicates and aluminates which generally influence the technical behaviour to a limited extent.

Moreover CSA cements, compared to Portland cements, give a pronounced environment-friendly character to their manufacturing process (Mehta, 1980; Beretka et al., 1992; Beretka et al., 1993; Marroccoli et al., 2007b). In this regard, important features are: a) CSA clinkers can be synthesized at temperatures (1250-1350°C) lower than those requested by Portland clinkers (1450-1500°C); b) there is a reduction of both thermal input to the kiln and CO_2 generation due to the lower limestone concentration in the raw mix, since $4CaO{\cdot}3Al_2O_3{\cdot}SO_3$ requires less CaO for its synthesis; c) CSA clinkers are easier to grind; d) hardly recoverable wastes and by-products can be utilised.

FBC waste is mainly composed by coal ash and exhausted sulphur sorbent (major oxides=CaO, SiO_2, Al_2O_3 and SO_3). Both the disposal in landfill and the re-use of FBC waste is generally made difficult by its chemical and mineralogical composition. Upon hydration, exothermal and expansive phenomena occur and the utilization of FBC ash in the ordinary cement and concrete industries is furthermore hindered by its poor pozzolanic activity. Suitable application fields for FBC waste have to be therefore searched for (Julien et al., 1995; Weinberg and Hemmings, 1997; Bland, 1999; Kim et al., 2001; Montagnaro et al., 2005; Barone et al., 2006; Montagnaro et al., 2006; Fu et al., 2008; Liira et al., 2009; Montagnaro et al., 2009).

FBC waste can be a very useful raw material for the synthesis of CSA cements (Bernardo et al., 2003; Marroccoli et al., 2008): limestone, bauxite and gypsum are the main natural materials involved in their manufacturing process and the use of FBC waste as raw mix component can enable a saving of limestone and

bauxite as well as a full replacement of gypsum. In order to enhance the saving of an expensive natural material like bauxite, the further addition of industrial wastes with a relatively high Al_2O_3 content must be taken into consideration.

In this paper the combined use of FBC waste (fly- and bottom-ash) with a pulverized coal fly ash (PFA) or an anodization mud (AM) was investigated through the X-ray study on the synthesis behaviour of several CSA clinker generating raw mixes heated at various temperatures. When necessary, flue gas desulphurization (FGD) gypsum was used as a source of calcium sulphate.

EXPERIMENTAL

Table 1 lists the chemical composition of natural materials (limestone, bauxite and gypsum) as well as industrial wastes (FBC waste, PFA, AM and FGD gypsum) used in this investigation. It was evaluated through XRF analysis by using a BRUKER Explorer S4.

Table 1 Chemical composition of natural materials and industrial wastes, mass %

	limestone	bauxite	gypsum	FBC fly ash	FBC bottom ash	PFA	AM	FGD gypsum
CaO	54.70	1.69	10.20	24.20	43.12	4.30	7.71	32.04
SO_3	-	0.03	63.53	12.80	25.89	0.04	8.34	45.77
Al_2O_3	-	55.22	-	13.71	5.85	22.80	45.29	0.08
SiO_2	-	6.48	-	23.23	18.45	35.08	2.90	0.10
MgO	0.30	-	-	1.04	1.00	1.13	2.72	0.37
SrO	-	0.03	-	-	-	0.11	-	-
P_2O_5	-	0.01	-	-	-	0.10	-	-
TiO_2	-	2.34	-	0.82	0.48	1.52	-	-
Fe_2O_3	-	6.25	-	6.74	3.15	8.20	2.79	-
Mn_3O_4	-	-	-	0.07	0.08	0.10	-	-
Na_2O	-	-	-	-	-	-	-	0.03
l.o.i.*	42.61	27.68	23.70	16.26	1.39	25.85	30.25	20.59
Total	97.61	99.73	97.43	98.87	99.41	99.23	100.00	98.98

*loss on ignition at 950°C, according to EN 196-2 Standard for cements.

All the mixtures were heated in a laboratory electric oven for 2 hours in the temperature range 1150-1300°C, then submitted to X-ray diffraction (XRD) analysis in order to assess both conversion and selectivity of the reacting systems. A PHILIPS PW1710 diffractometer, operating between 5° and 60°2θ (Cu Kα radiation), was used.

RESULTS AND DISCUSSION

Proportioning of raw mixtures

Six mixtures (M1-M6), having the chemical composition shown in Table 2, were investigated: the first, M1, used as a reference term, was based only on natural materials; the others contained FBC waste (fly/bottom mass ratio equal to 1.5). M2-M3 and M4-M5-M6 contained also PFA and AM as supplementary sources of alumina, respectively. In the mixtures M2, M3, M5 and M6, FGD gypsum integrated the sulphate content.

Table 2 Composition of raw mixtures, mass %

Mixture	M1	M2	M3	M4	M5	M6
limestone	25.27	38.75	41.46	32.35	30.62	29.12
bauxite	42.14	18.32	12.71	-	-	-
gypsum	32.59	-	-	-	-	-
FBC fly and bottom ash	-	33.14	29.80	44.37	37.04	30.70
PFA	-	6.11	12.71	-	-	-
AM	-	-	-	23.28	28.22	32.50
FGD gypsum	-	3.68	3.32	-	4.12	7.68

The proportioning of all the raw mixtures was made by assuming that SO_3 and Al_2O_3 on the one hand, and

SiO_2, on the other, reacted to give only $4CaO{\cdot}3Al_2O_3{\cdot}SO_3$ and $2CaO{\cdot}SiO_2$, respectively, and supposing also that solid solution effects were absent.

The alumina and silica contents were the stoichiometric amounts needed for the synthesis of the above mentioned phases. In order to avoid the decomposition of calcium sulphoaluminate, the sulphur content was twice the stoichiometric amount required by its formation; the residual calcium sulphate was therefore available for CSA cement hydration. Table 3 shows the potential concentration values of $4CaO{\cdot}3Al_2O_3{\cdot}SO_3$, $2CaO{\cdot}SiO_2$ and $CaSO_4$ in the burning products of the six mixtures.

Table 3 Potential concentration of $4CaO{\cdot}3Al_2O_3{\cdot}SO_3$, $2CaO{\cdot}SiO_2$ and $CaSO_4$ in the burning products of mixtures M1-M6, mass %

Mixture	M1	M2	M3	M4	M5	M6
$4CaO{\cdot}3Al_2O_3{\cdot}SO_3$	66.58	41.19	36.42	43.41	46.83	49.72
$2CaO{\cdot}SiO_2$	11.23	41.58	47.13	42.14	35.66	30.24
$CaSO_4$	14.85	9.21	8.14	7.61	9.00	9.00

Burning of raw mixtures

At all the investigated temperatures the conversion of reactants was complete. In terms of selectivity towards calcium sulphoaluminate, the best results were obtained at 1300°C for the reference mixture and at 1250°C for the others, according to the following sequence: M1>M6>M5>M4>M2>M3. Figs. 1-6 show the XRD patterns of the Mixtures 1 – 6 heated at the best synthesis temperatures; the peak intensity is measured in counts per second (cps).

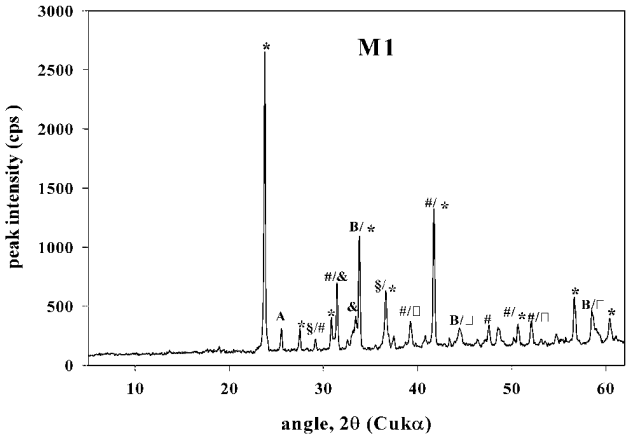

Fig. 1 XRD pattern of mixture M1 burnt at 1300°C: *=$4CaO{\cdot}3Al_2O_3{\cdot}SO_3$, A=$CaSO_4$, #=$5CaO{\cdot}2SiO_2{\cdot}SO_3$, §=$2CaO{\cdot}SiO_2$, &=$3CaO{\cdot}Al_2O_3$, B=$4CaO{\cdot}Al_2O_3{\cdot}Fe_2O_3$

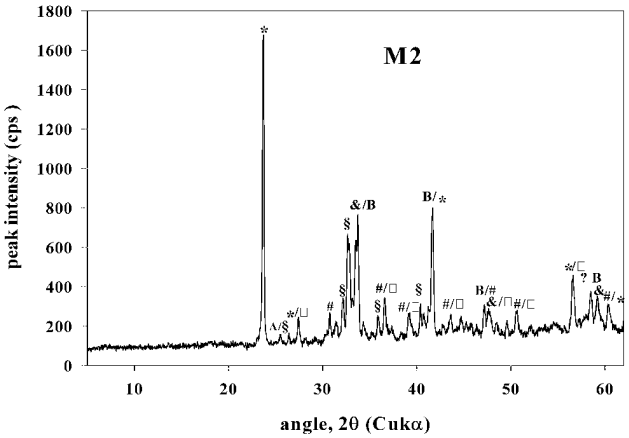

Fig. 2 XRD pattern of mixture M2 burnt at 1250°C: *=$4CaO{\cdot}3Al_2O_3{\cdot}SO_3$, A=$CaSO_4$, #=$5CaO{\cdot}2SiO_2{\cdot}SO_3$, §=$2CaO{\cdot}SiO_2$, &=$3CaO{\cdot}Al_2O_3$, B=$4CaO{\cdot}Al_2O_3{\cdot}Fe_2O_3$

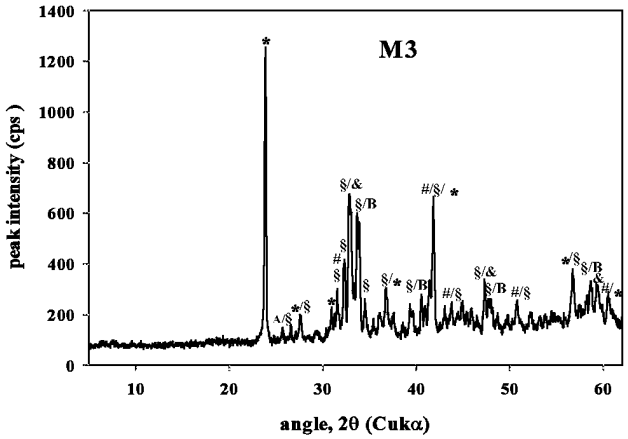

Fig. 3 XRD pattern of mixture M3 burnt at 1250°C: *=$4CaO \cdot 3Al_2O_3 \cdot SO_3$, A=$CaSO_4$, #=$5CaO \cdot 2SiO_2 \cdot SO_3$, §=$2CaO \cdot SiO_2$, &=$3CaO \cdot Al_2O_3$, B=$4CaO \cdot Al_2O_3 \cdot Fe_2O_3$

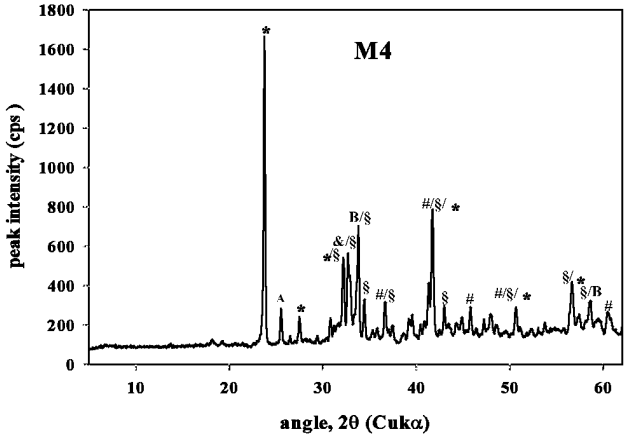

Fig. 4 XRD pattern of mixture M4 burnt at 1250°C: *=$4CaO \cdot 3Al_2O_3 \cdot SO_3$, A=$CaSO_4$, #=$5CaO \cdot 2SiO_2 \cdot SO_3$, §=$2CaO \cdot SiO_2$, &=$3CaO \cdot Al_2O_3$, B=$4CaO \cdot Al_2O_3 \cdot Fe_2O_3$

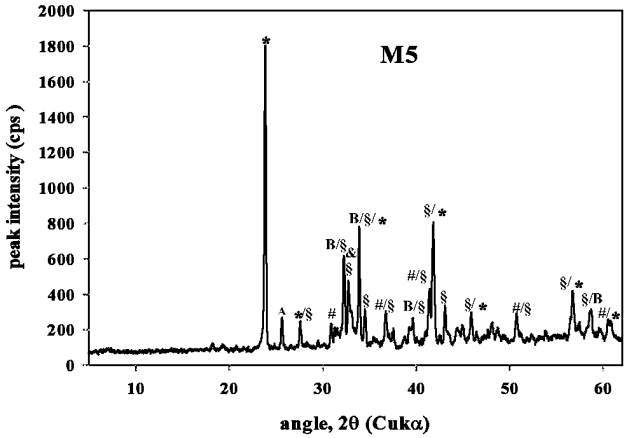

Fig. 5 XRD pattern of mixture M5 burnt at 1250°C: *=$4CaO \cdot 3Al_2O_3 \cdot SO_3$, A=$CaSO_4$, #=$5CaO \cdot 2SiO_2 \cdot SO_3$, §=$2CaO \cdot SiO_2$, &=$3CaO \cdot Al_2O_3$, B=$4CaO \cdot Al_2O_3 \cdot Fe_2O_3$

Mixture M1 - Calcium sulphoaluminate was the main mineralogical phase at all the investigated temperatures; furthermore, a significant presence of secondary phases like $4CaO \cdot Al_2O_3 \cdot Fe_2O_3$, $5CaO \cdot 2SiO_2 \cdot SO_3$, $CaSO_4$, $2CaO \cdot SiO_2$ and $3CaO \cdot Al_2O_3$ was generally observed.

Mixture M2 - $4CaO \cdot 3Al_2O_3 \cdot SO_3$ was always the main component. $2CaO \cdot SiO_2$, $4CaO \cdot Al_2O_3 \cdot Fe_2O_3$ and $5CaO \cdot 2SiO_2 \cdot SO_3$ were detected as secondary phases at 1250-1300°C, 1200-1250°C and 1150-1200°C, respectively; at the other burning temperatures they were present only in traces together with $3CaO \cdot Al_2O_3$.

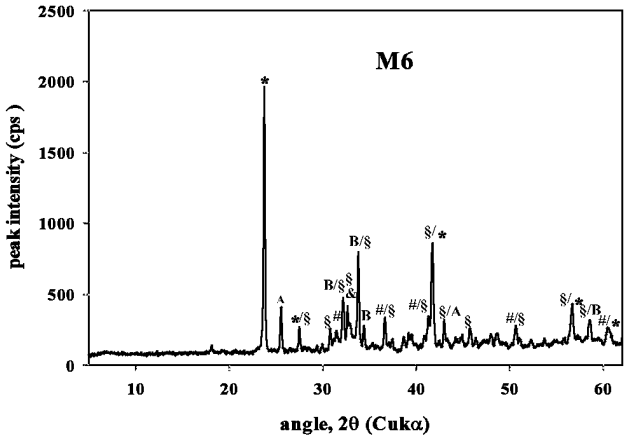

Fig. 6 XRD pattern of mixture M6 burnt at 1250°C: *=$4CaO{\cdot}3Al_2O_3{\cdot}SO_3$, A=$CaSO_4$, #=$5CaO{\cdot}2SiO_2{\cdot}SO_3$, §=$2CaO{\cdot}SiO_2$, &=$3CaO{\cdot}Al_2O_3$, B=$4CaO{\cdot}Al_2O_3{\cdot}Fe_2O_3$

Mixture M3 - The main component was $2CaO{\cdot}SiO_2$ at 1300°C and $4CaO{\cdot}3Al_2O_3{\cdot}SO_3$ (followed by $2CaO{\cdot}SiO_2$) at the other temperatures. Secondary phases were: $5CaO{\cdot}2SiO_2{\cdot}SO_3$, $4CaO{\cdot}Al_2O_3{\cdot}Fe_2O_3$ and $3CaO{\cdot}Al_2O_3$ (in traces) at every synthesis temperature; $CaSO_4$ was present in traces at 1200°C, 1250°C, 1300°C and in a higher amount at 1150°C.

Mixture M4 - The main component was $4CaO{\cdot}3Al_2O_3{\cdot}SO_3$ at every synthesis temperature. Secondary constituents were $5CaO{\cdot}2SiO_2{\cdot}SO_3$, $4CaO{\cdot}Al_2O_3{\cdot}Fe_2O_3$, $CaSO_4$, $2CaO{\cdot}SiO_2$ and $3CaO{\cdot}Al_2O_3$.

Mixture M5 - The main mineralogical phase was $4CaO{\cdot}3Al_2O_3{\cdot}SO_3$ followed by $4CaO{\cdot}Al_2O_3{\cdot}Fe_2O_3$. Secondary components were: $3CaO{\cdot}Al_2O_3$, $2CaO{\cdot}SiO_2$, $5CaO{\cdot}2SiO_2{\cdot}SO_3$ and $CaSO_4$.

Mixture M6 - The main mineralogical phase was $4CaO{\cdot}3Al_2O_3{\cdot}SO_3$ followed by $4CaO{\cdot}Al_2O_3{\cdot}Fe_2O_3$. The most important secondary constituent was $2CaO{\cdot}SiO_2$ at 1300°C and $CaSO_4$ (followed by $3CaO{\cdot}Al_2O_3$) at lower temperatures.

CONCLUSIONS

Calcium sulphoaluminate cements, based on $4CaO{\cdot}3Al_2O_3{\cdot}SO_3$ and $2CaO{\cdot}SiO_2$, are very interesting hydraulic binders due to both their technical properties useful for special applications and the environmental sustainability of their manufacturing process. It has been assessed that FBC waste can be used as raw mix component for the synthesis of calcium sulphoaluminate cements, enabling a substantial saving of natural materials like bauxite and gypsum. It has been also found that the use of supplementary sources of alumina like pulverised coal fly ash and anodization mud allow a further saving of bauxite. In particular, the addition of anodization mud enables a full replacement of bauxite and, at the optimum synthesis temperature (1250°C), gives better results in terms of selectivity towards $4CaO{\cdot}3Al_2O_3{\cdot}SO_3$. When necessary, flue gas desulphurization gypsum was successfully used as a source of calcium sulphate.

REFERENCES

Barone, G. A., Montagnaro, F., Nobili, M., Salatino, P., Telesca, A. and Valenti, G. L. (2006). The desulphurizing ability of ettringite formed during the hydration/reactivation of FBC coal fly ash. Proc. 19th Int. FBC Conf. (Vienna, Austria), paper number 84.

Beretka, J., Santoro, L., Sherman, N. and Valenti, G. L. (1992). Synthesis and properties of low energy cements based on C_4A_3S. Proc. 9th Int. Congr. Chem. Cem. (New Delhi, India) **3**, pp.195-200.

Beretka, J., de Vito, B., Santoro, L., Sherman, N. and Valenti, G. L.: Cem. Concr. Res. **23** (1993), pp.1205-1214.

Bernardo, G., Marroccoli, M., Montagnaro, F. and Valenti, G. L. (2003). Use of fluidized bed combustion wastes for the synthesis of low-energy cements. Proc. 11th Int. Congr. Chem. Cem. (Durban, South Africa), pp.1227-1236.

Bernardo, G., Buzzi, L., Canonico, F., Paris, M., Telesca, A. and Valenti, G. L. (2007). Microstructural investigations on hydrated high-performance cements based on calcium sulfoaluminate. Proc. 12th Int. Congr. Chem. Cem. (Montréal, Canada), paper number W3-11.4.

Bland, A. E. (1999). Effect of curing conditions on the geotechnical and geochemical properties of CFBC ashes. Proc. 15th Int. FBC Conf. (Savannah, GA-USA), paper number 99-0148.

Fu, X., Li, Q., Zhai, J., Sheng, G. and Li, F.: Cement Concrete Comp. **30** (2008), pp.220-226.

Glasser, F. P. and Zhang, L.: Cem. Concr. Res. **31** (2001), pp.1881-1886.

Julien, S., Brereton, C. M. H., Lim, C. J., Grace, J. R., Chiu, J. H., Skowyra, R. S. (1995). Spent sorbent reactivation using steam. Proc. 13th Int. FBC Conf. (Orlando, FL-USA), pp. 841-849.

Kim, A. G., Aljoe, W., Renninger, S. (2001). Wastes from the combustion of fossil fuels: research perspective on the regulatory determination. Proc. 16th Int. FBC Conf. (Reno, NV-USA), paper number 01-0156.

Klein, A. and Troxell, G. E. (1986). Studies of calcium sulfoaluminate admixtures for expansive cements. Proc. ASTM IV, pp.389-394.

Kurdowski, W., George, C. M. and Sorrentino, F. P. (1986). Special cements. Proc. 8th Int. Congr. Chem. Cem. (Rio de Janeiro, Brazil) **1**, pp.292-318.

Liira, M., Kirsimäe, K., Kuusik, R. and Mõtlep, R.: Fuel **88** (2009), pp.712-718.

Marroccoli, M., Nobili, M., Telesca, A. and Valenti, G. L. (2007a). Early hydration of calcium sulfoaluminate-based cements for structural applications. Proc. Congr. Sustainable Construction Materials and Technologies (Coventry, England), pp.389-395.

Marroccoli, M., Montagnaro, F., Nobili, M., Telesca, A. and Valenti, G. L. (2007b). Synthesis, hydration properties and environmentally friendly features of calcium sulfoaluminate cements. Proc. 12th Int. Congr. Chem. Cem. (Montréal, Canada), paper number W3-11.2.

Marroccoli, M., Nobili, M., Telesca, A. and Valenti, G. L. (2008). Use of wastes generated within coal-fired power stations for the synthesis of calcium sulphoaluminate cements. Proc. Congr. Role for Concrete in Global Development (Dundee, Scotland), pp.299-310.

Mehta, P. K.: Cem. Concr. Res. **3** (1973), pp.1-6.

Mehta, P. K.: World Cement Technol. **11** (1980), pp.166-177.

Montagnaro, F., Salatino, P., Bernardo, G., Telesca, A. and Valenti, G. L.: Energy Fuel. **43** (2005), pp.4054-4059.

Montagnaro, F., Salatino, P., Scala, F., Wu, Y., Anthony, E. J. and Jia, L.: J. Energy Resour. Technol. **128** (2006), pp.90-98.

Montagnaro, F., Nobili, M., Telesca, A., Valenti, G. L., Anthony, E. J. and Salatino, P.: Fuel **88** (2009), pp.1092-1098.

Muzhen, S., Kurdowski, W. and Sorrentino, F. P. (1992). Developments in non Portland-cements, Proc. 9th Int. Congr. Chem. Cem. (New Delhi, India) **1,** pp.317-354.

Muzhen, S., Wang, Y., Zhang, L. and Li, D. (1997). Preliminary study on the durability of sulfo/ferro-aluminate cements. Proc. 10th Int Congr. Chem. Cem. (Goteborg, Sweden) **4**, p.4iv029.

Weinberg, A. and Hemmings, R.: Fuel **76** (1997), pp.705-709.

EFFECT OF THE ADDITIVES ON THE DESULPHURIZATION RATE OF FLASH HYDRATED AND AGGLOMERATED CFB FLY ASH

D. X. Li[1], H. L. Li[1], M. Xu[2], J. F. Lu[2], Q. Liu[2], J. S. Zhang[2], G. X. Yue[2]

1 College of Environmental Science and Engineering, Donghua University, 2999 North Renmin Road, Songjiang District, Shanghai, 201620, China
2 Department of Thermal Engineering, Tsinghua University, Beijing, 100084, China

Abstract: CFB fly ash from separators was mixed with water or the mixture of water and additives under the temperature of 363K by use of a blender. Then, this compound of fly ash and water or additives was pumped into a CFB combustion chamber by a sludge pump. Because the temperature of flue gas was high in CFB, the fly ash was hydrated fast and agglomerated in the same time. Through this process, the size of agglomerating fly ash is larger than the original particle and the relative residence time of agglomerated fly ash in CFB becomes longer. Therefore, the rate of utility of calcium in fly ash improves and the content of carbon in fly ash decreases. This results in a low Ca/S and low operational cost for CFB boiler. The additive is one key factor, which affects the rate of desulfurization of agglomerated fly ash. Effect of different additives on rate of desulfurization is not same. Cement and limestone are beneficiated to sulfur removal of agglomerated fly ash, but sodium silicate does not devote to the rate of sulfur removal of agglomerated fly ash.
Keywords: fly ash, CFB, hydration, agglomeration, rate of wear

INTRODUCTION

Although the content of calcium oxide in CFB fly ashes is high, activity calcium oxide content is not high, and carbon content in some CFB fly ashes is over 20%. In order to improve the utilization of calcium and the rate of burnout of carbon in fly ashes, traditional hydration and activation technology of fly ashes include: flash hydration, steam activation process and agglomeration (Marquis, 1992; Sheerer and Smith, 1980; Jozewicz and Brown, 1986; Behr and Christina, 1994). Hydration processes need to be established as an independent process, and need a long active time or under a higher temperature (623-723K). Water activation and CFB combustion process are discontinuous. Thus, these processes are difficult to operate. In the same time, size of hydrated fly ash is smaller than original fly ash. This shall decrease the resident time of the re-injected fly ash. Thus, the improvement on the calcium utilization and carbon burnout is limited (Anthony, 2000).

Agglomeration process is complicated. On one hand, the process and CFB operation are discontinuous. On the other hand, the rate of combustion of hard fly ash carbon and absorption sulfur is low (Huang and Zhang, 1992). In order to improve the sulfur capture of calcium oxide and burnout of carbon in fly ash from a CFB boiler, flash hydration and agglomeration of CFB fly ash is suggested. The process is as following: The CFB fly ash is mixed with water in a blender to form sludge. Then, the sludge is directly injected into the combustor by sludge pump. Because the temperature in furnace is higher than 1123K, the fly ash would be rapidly hydrated, dehydrated and agglomerated. The size of agglomerated fly ash is larger than that of the original particle, and the residence time of agglomerates should be longer. Besides, the hydrated free calcium is more active than before. These result in a low Ca/S, low carbon content in fly ash and low operating cost for CFB. In order to increase the strength and reduce the rate of hot wear of agglomerated particles, additives are added into rapid hydrating and agglomerating process with fly ash and water. In this paper, the effect of the additives on the rate of desulphurization of hydrated and agglomerated flash was studied (Li, 2002).

EXPERIMENTAL

System and equipment

In this test, fly ash samples were taken from a CFB boiler in Suzhou paper mill (carbon content: 3.7%; total calcium: 4.6%; free calcium: 0.98%; average grain size: 12μm) and Hebei electricity –thermal plant (carbon content: 24%; total calcium: 3.7%; free calcium: 0.16%; average grain size: 53μm).

The schematic diagram of test facility for the flash hydration and agglomeration of CFB fly ash is shown in Fig. 1. The system mainly consists of a fluidized bed, a temperature-control system, a cyclone, a hydrator and a sludge injection system. The fluidized bed is a quartz cylinder with 40mm ID and 1000mm height. In the bottom of the fluidized bed, there is a gas distributor, a perforated plate with 55 holes of 0.55mm in a triangular pitch. The hydrator is a simple stirring reactor for fly ash hydration.

Before starting an experiment, the bed material was fluidized by nitrogen and preheated to the desired operational temperature. The superficial velocity was kept at the desired value. CFB fly ash was mixed with certain amount of hot water (363K) or the mixture of additives (such as waste water, cement, sodium silicate) with water and stirred about 10min. Then, the sludge was sprayed into hot fluidized bed reactor. Because the temperature in bed is higher than 1123K, the droplets of sludge were rapidly dehydrated and agglomerated in the same time. After agglomeration, the agglomerated particles were taken out for measurement.

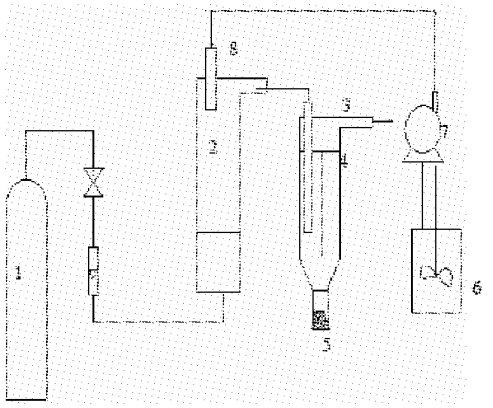

Fig. 1 Schematic experimental system for agglomeration and fast hydration of fly ash
1.Nitrogen bottle; 2. CFB; 3. separator; 4.filter plate; 5.cork plug; 6. Mortar pool; 7.sludge pump; 8. Sprayer

Flash hydrated and agglomerated of fly ash

A certain amount of fly ash or a certain amount of additives (one or more percentage) and a certain percentage of hot water (90 ℃) were added into mortar pond and mixed by a blender evenly. Then, the mixture was sprayed into combustion chamber of fluidized bed by sludge pump with the pipeline and nozzle set up in the combustion chamber (Figure 1). Nitrogen was chosen as the fluidized media, the above-mentioned mixture was flash hydrated at the temperature of 850 ℃ and the selected flow velocity. The water of the mixture was taken away by hot Nitrogen. In the same, the fine fly ash agglomerated.

Desulphurization test of agglomerated fly ash particles

Hot agglomerated fly ash particles were cooled down below 100 ℃ with nitrogen in fluidized bed. Then they were taken out from the bed and were grinded smaller than 100 meshes in order to study the desulphurization characteristics by thermal balance of DuPont-TA2100. The reaction medium includes air or 1200ppm SO_2 and 8.5% oxygen in nitrogen. 1123K was selected as the reaction temperature. Rate of weight change of agglomerated fly ash was used to analyze its reactivity of absorption. Under the center conditions, study desulphurization characteristics of agglomerated particles and compare effects of different additives on agglomerated particles desulphurization.

RESULTS AND DISCUSSION

Apparent characteristics of the agglomerated particles prepared by different additives

Agglomerated particles prepared with different additives have different roughness of the agglomerated particles surface (as shown in Fig. 2). Under the above-mentioned conditions, Suzhou agglomerated particles (A) prepared with the mixture of sodium silicate and calcium oxide are round with smooth surface, while Hebei agglomerated particles (B) prepared under same conditions are with a rough surface and cracks. The effect of test conditions on agglomerated particle size is shown in Table 1.

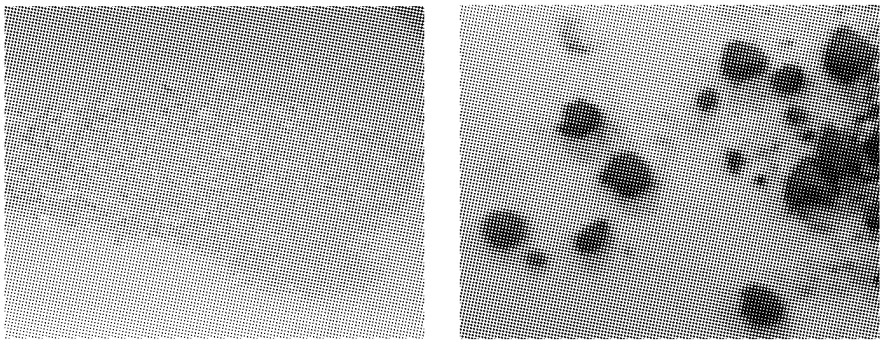

(a) (b)

Fig. 2 Agglomerated particles of fly ash
A—Suzhou Agglomerated particles was made of sodium silicate and calcium oxide
B—Hebei Agglomerated particles was made of Sodium silicate and calcium carbonate

As shown in Table 1, the agglomerated particles of fly ash with larger size can gained under low

temperature and low flow velocity. Under 1123K and the flow rate of 0.03m/s, average size of the agglomerated particles is 0.5 mm, while flow velocity is up to 0.07m/s, it is 0.1mm. If fly ash was hydrated and agglomerated with additives such as sodium silicate, smooth and strength of agglomerated particles increased.

Table 1 Effect of the additives on the size of agglomerated particles

additives	Sodium silicate (%)				Sodium silicate (%) and calcium carbonate (%)			Cement (%)		
average size(mm)	1	3	5	10	3:10	3:5	3:1	5	10	15
	0.5	0.1	3	1	10	4	Piece	11	Piece	11

Effect of the additives on the rate of desulfurization

Under temperature of 850 ℃ and flow rate of 300L/h, different agglomerated particles can be prepared by use of fly ash with 1-10% (relative weight of fly ash) sodium silicate and 60% water. It was found that sodium silicate is conducive for fly ash agglomerating, and the average size of agglomerated particle is larger. The reactivity of sulfur absorption of original and agglomerated fly ash (Shuzhou fly ash) had been studied by TGA. It is obvious that the activity of sulfur absorption of original fly ash is very low. The enhancement of the activity on SO_2 absorption by flash hydration is needed. As shown in Fig. 3, if fly ash is hydrated by water, higher reactivity of the agglomerates can be achieved, as shown in. Moreover, the desulphurization capability of the agglomerated fly ash is almost no change under the conditions of the change in the amount of sodium silicate is less than 10%. It also indicates that sodium silicate does not affect the desulphurization rate of fly ash. Desulphurization capability of hydration fly ash increases more than that of the original fly ash, because the inactivation calcium oxide becomes active calcium oxide and removes the shell of calcium sulfate outside of the calcium oxide in the package.

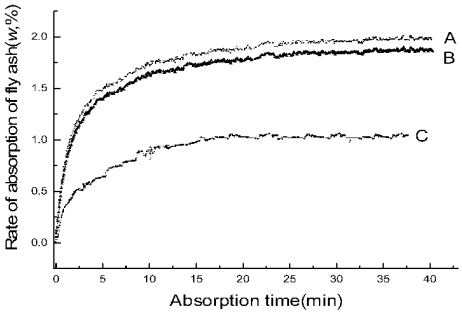

Fig. 3 Effect of sodium silicate on the rate of desulfurization of agglomerated
A-3% sodium silicate; B-water; C-original fly ash

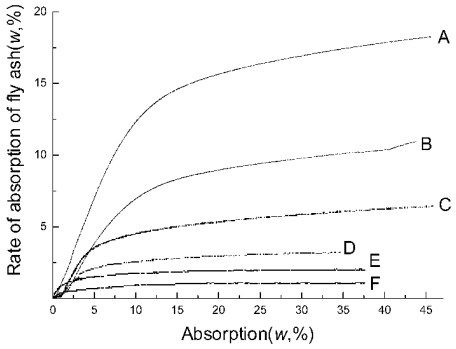

Fig. 4 Effect of the mixture of sodium silicate (3%) and calcium carbonate on the rate of desulphurization of agglomerated
A–20% limestone; B–10% limestone; C– 5% limestone; D–1% limestone; E–water; F– original fly ash

Effect of the mixture of sodium silicate and limestone on the rate of desulphurization

Under temperature of 850 ℃ and flow rate of 300L/h, different agglomerated particles can be prepared by use of fly ash with 0-20% (relative weight of fly ash) limestone, sodium silicate (3%) and 60% water . The effect of limestone on the desulphurization of fly ash is shown in Fig. 4. Figure 4 shows that the higher of the amount of calcium carbonate, the stronger of the desulphurization effect. The results agree with the reported in the literature. However, the higher the amount of calcium carbonates is, the smaller and more fragile fly ash agglomerated particles is. Agglomerated fly ash particles become less conducive and their the residence time in CFB boiler is shorter. Thus, it is suggest to use a moderate mount of calcium carbonate or replace calcium carbonate by calcium oxide to enhance the capacity of desulfurization.

Effect of cement on the rate of absorption of desulphurization

In order to enhance the strength of agglomerated particles, cement as additives was used to make fine agglomerated particles. Under temperature of 850 ℃ and flow rate of 300L/h, different agglomerated particles can be prepared by use of fly ash with 0-10% (relative weight of fly ash) cement and 60% water. The amount of cement influence on desulphurization capacity of fly ash is shown in Fig. 5. Figure 5 show the change of desulphurization capability of agglomerated particles with amount of cement. It indicates that the greater the

amount of cement, the greater desulphurization capability of fly ash agglomerated particles. In the same time, cement is useful for fly ash to agglomerate.

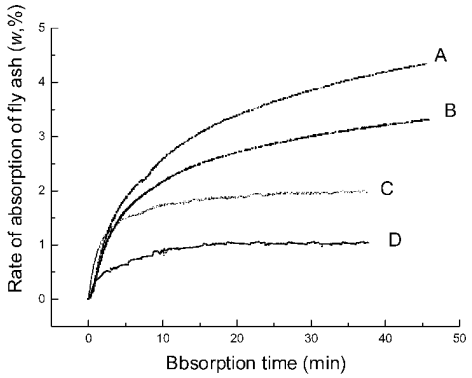

Fig.5 Effect of cement on the rate of absorption of agglomerated fly ash
A—10% cement; B—5% cement; C— Hydration of fly ash; D—original fly ash

CONCLUSIONS

The effect of sodium silicate as additives on the rate of desulphurization of fly ash agglomerated particles is low. Limestone can increase the capacity of desulphurization of fly ash greatly, under the condition of existence of sodium silicate.

Cement in favor of desulphurization of fly ash.

ACKNOWLEDGEMENTS

Financial support of this work by National Key fundamental research program of China (2004CB217705) and Key Project of the National eleventh-Five Year Research Program of China (2006BAA03B05) are gratefully acknowledged.

REFERENCES

Anthony, E. J.: Agglomeration and Strength Development of Deposits in CFBC Boilers Firing High-sulfur Fuels, Fuel 79(15), (2000), PP. 1933-1942.

Behr, A., Christina, B.: Characterization and Use of Fluidized Bed Combustion Coal Ash, Journal of Environmental Engineering 120 (6), (1994), PP. 1488-1506.

Huang, X. Y., Zhang, X.: One kind of fluidized bed boiler with re-burning and desulphurization functions. China patent: CN92233887, (1992), PP. 9-24.

Marquis, D.L.: Reactivation of Spent CFB Limestone by Hydration, New Brunswick: University of New Brunswick, (1992), pp. 45-99.

Li, D. X.: Study on flash hydrated and agglomerated fly ash and its activity reaction, The Chinese Journal of Process Engineering, Vol 2 (supplement), (2002), PP. 345-348.

Jozewicz, L.R., Brown, C.A.: Fly Ash Recycle in Dry Scrubbing, Environment progress, 5, (1986), PP. 234-243.

Sheerer, J.A., Smith, G.W.: Hydration Process for Reactive Spent Limestone and Dolomite Sorbents for Reuse in Fluidized Bed Coal Combustion, 6th International Conference on Fluidization Combustion, Atlanta: ASME, (1980), PP. 1135-1140.

EXPERIMENTAL STUDY ON PM_{10} FEATURE DURING CAOL COMBUSTION

Y.G. Du[1,2], J.C. Sui[2], G.Z. Yin[1]

1 College of Resources and Environmental Science, Chongqing University, Chongqing 400044, China;
2 CPI Yuanda Environmental-Protection Engineering CO. LTD., Chongqing, 400060, China

Abstract: By using Low Pressure Impactor, fly ash is sampled at the ESP inlet and outlet of a 300MW utility boiler. The composition, mass and element size distribution of fly ash was measured by X-ray fluorescence and 0.001mg precision microbalance, respectively. Mass and element size distribution of Si, Al, Fe, Ca, Mg, S, Cu, Pb, Zn and Mn is of bimodal. Fly ash diameters of the fine and the coarse are about 0.1μm and 2.36-3.95μm, respectively. Efficiency of ESP for submicron ash is lower than that for normal variables ranging 62～83%, while for ash bigger than 10μm it is almost 100%. Mg, S, Cu, Zn and Pb are obviously enriched in fine ash, especially Cu, Zn and Pb. They are found in $PM_{2.5}$ accounting for 50～60%. The relative enrichment coefficient of Cu, Zn and Pb is about 30～40. The relative enrichment coefficient of Si, Al and Ca decreases with the ash size decreasing. No direct connection is found between the change of relative enrichment coefficient of Fe, Mn and their ash size.

Keywords: coal combustion, PM_{10}, particulate matter, trace elements

INTRODUCTION

At present, the pollution caused by coal-fired power plant has become an important factor to restrict the national economic and social sustainable development in China. Also it (especially the particulate matter pollution PM_{10}) has become a focus of attention in the world, especially by neighboring countries and regions. According to the statistics 1996, the total particulate matter emissions from the whole domestic 6MW-and-above power plant to the atmosphere is 3.97Mt, accounting for 28%[1] of the total amount of various sources of particulate matter emissions (14.4Mt). As thermal efficiency of coal-fired boiler is low and coal quality is poor at the same time, particulate matter emissions from power plants is probably 1.2% -1.5% of the coal combustion. The coal consumption of the power stations in China now is about 800,000,000 tons per year. The annual emissions of particulate matter to the atmosphere is about 0.1 million tons[2] in total. These particles affect not only climate and air quality, damage the ecological environment and historical heritage, but also seriously endanger human health, particularly to children, mainly lead to heart and lung function hurt and respiratory diseases of children, such as asthma, and so on. These make it become a current hot spot in study.

The study on the generation of particulate matter and the emission characteristics of coal-fired power plant began in the world in the early 80's. Quann[3] and others have studied on the evaporation of minerals and trace elements in the coal; Mcnallan[4] and Helble[5] have studied the formation of particulate matter in the coal combustion process. As the particulate matter pollution caused in coal combustion is becoming increasingly serious, Japan, Australia and other countries have stepped up research in this area in recent years. In China, the experience on distribution characteristics of the metal elements in different size fly ash has considerably accumulated[6-8]. Study[9] has also been made on the particulate matter emission under different conditions in the coal combustion process; but so far the study of the application of Low Pressure Impactor(LPI), from the point of aerodynamic diameter, on the particulate matter emission characteristics in coal combustion has not yet started. Through sampling coal ash by Low Pressure Impactor(LPI), more detailed emission characteristics and chemical composition of the fine particles (especially sub-micron particles) is obtained. After having sampled coal ash from a 300MW coal-fired unit under a rated load, we have measured the weight and composition of different size fly ash, gained the PM_{10} mass size distribution as well as element distribution before and after the ESP, and provided the results to the environmental protection departments for reference.

EXPERIMENTAL

Characteristics of coal combustion and experimental conditions

The experiment is made in a 300MW coal-fired unit. It is a 1025t/h ultra-high pressure natural-cycle solid-state slag boiler. The hearth is in a square shape. CE WR burners are used, arranged in 4 corners. Four-electric-field ESP is used. The bituminous coal used is from Shanxi Province. The industrial and elemental analysis of the coal is given in Table 1. The chemical composition analysis of the ash is given in Table 2. The whole experiment is carried out under the rated load. The coal consumption of the boiler is

actually 136t/h. Coal fineness R_{90} = 24.31%, R_{200} = 2.24%. The hearth temperature is kept at about 1400℃. The temperature of the outlet is kept at about 150 ℃. Oxygen content at hearth outlet is 4.6%.

Table 1 Industrial and elemental analysis of studied coal

industrial analysis				elemental analysis			
Moisture M_{ar}(%)	Ash A_{ar}(%)	Volatile V_{ar}(%)	Fixed carbon C_{ar}(%)	C_{ar}(%)	H_{ar}(%)	N_{ar}(%)	S_{ar}(%)
0.86	34.99	13.51	50.65	50.87	2.34	0.73	2.49

Table 2 Composition of coal ash

SiO_2(%)	Al_2O_3(%)	Fe_2O_3(%)	CaO(%)	MgO(%)	Na_2O(%)	K_2O(%)
50.47	37.44	2.81	1.53	0.98	1.59	1.06

Sample collection

The experiment includes 3 times of sampling. Sampling of fly ash is collected at the inlet and outlet of ESP, as shown in Fig. 1. The sampling system consists of sampling gun, cyclone separator, Low Pressure Impactor and vacuum pump, as shown in Fig. 2. In order to prevent water vapor condensing in the flue gas sampling system, electric heating band is wrapped along sampling pipe and the temperature is controlled at about 150 ℃. The fly ash flows through the gun into the cyclone separator with a 10μm cut size, whose main role is to get rid of the particles larger than 10μm, so as to prevent the overweight of the particles on membrane; then, fly ash particles flow into LPI and are divided into 13 grades based on aerodynamic diameter size. Their size ranges are: 0-0.0281, 0.0281-0.0565, 0.0565-0.0944, 0.0944-0.154, 0.154-0.258, 0.258-0.377, 0.377-0.605, 0.605-0.936, 0.936-1.58, 1.58-2.36, 2.36-3.95, 3.95-6.6, 6.6-10μm. In the course of sampling, the pressure of the end membrane is kept at 10KPa around. Before sampling, a pitot tube is used for measurement of duct velocity. Then select sampling gun nozzle based on the vacuum pump flow and duct velocity, to ensure constant sampling.

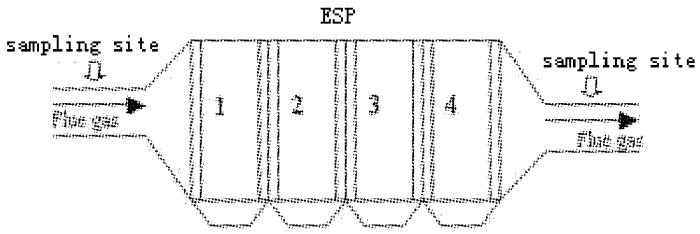

Fig. 1 Sampling position in experiment

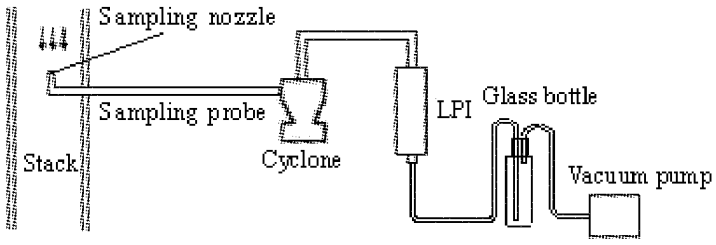

Fig. 2 Schematic diagram of sampling system

Method of analysis

In the experiment, organic film is used in the Impactor. In order to prevent particle rebound, Apiezon L vacuum grease diluted with carbon tetrachloride) is coated on the organic film. Organic membranes before sampling and organic membranes after sampling containing particles is baked and dried in the oven at 105 ℃ for 1 hour, then cooled to room temperature in the dryer, weighing by using a balance with sensitivity of 0.001mg.

After weighing, a determination of sample composition is made at Analysis and Testing Center of Huazhong University of Science and Technology. This paper explains the determination of the second elements Si, Al, Fe, Ca, Mg, S and trace elements Cu, Pb, Zn, Mn determined through an EAGLE III- Focus Scanning X-Ray Fluorescence Spectroscopy (XRF).

RESULTS AND DISCUSSION

PM_{10} mass size distribution at ESP inlet and outlet

Mass size distribution of fly ash particles produced in coal combustion generally follows log-normal distribution, so this article takes log*d* for abscissa and mass concentration (mg/m^3 gas) for longitudinal coordinate to show the mass size distribution of particles at inlet and outlet of the ESP. The advantage of this method is that a wide range of particle sizes may be analyzed at the same time, i.e. while the wide range of particulate mass size distribution is analyzed, the characteristics of sub-micron and ultra- micron particulate mass size distribution may also be analyzed. Figures 3 and 4 show the PM_{10} mass size distribution at ESP inlet and outlet. As can be seen from the figures, the PM_{10} mass size at the ESP inlet and outlet is in a bimodal distribution, but there exists little difference between their peaks, the inlet peak at about 0.1 and 3.95μm, the outlet peak at 0.1 and 2.36μm. The reason for this difference is not clear and needs further analysis of the sample. Bimodal distribution of PM_{10} is consistent with many reports and literatures[3-5,10], and such distribution of the PM_{10} in coal combustion process is formed following different mechanisms, i.e. fine particles following gasification - condensation mechanism, coarse particles following internal mineral coalescence, coke and external mineral breakdown.

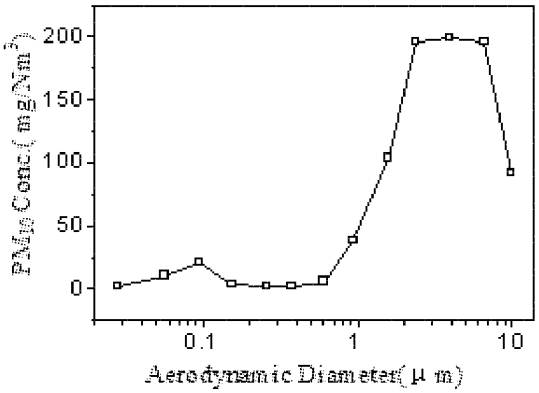

Fig. 3 Mass size distribution of PM_{10} at ESP inlet

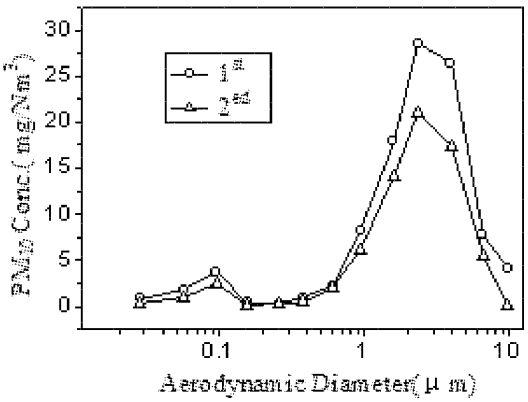

Fig. 4 Mass size distribution of PM_{10} at ESP outlet

Characteristics of particulate composition at ESP inlet and outlet

Table 3 gives the mass concentration of coal ash of different sizes and the mass percentage of coal ash at all levels of ESP inlet and outlet. From the table we can see an obvious difference of coal ash distribution characteristics. Before the ESP, ash particles with aerodynamic diameter greater than 10μm (PM_{10+}) account for about 96.07%, PM_{10} for about 3.92%, $PM_{2.5}$ about 0.84%; after the ESP, no PM_{10+} has been collected, PM_{10} accounts for 100%, $PM_{2.5}$ for 36.44%. This shows that the efficiency of ESP has great dial with coal ash size, i.e., the finer the ash size, the lower the collection efficiency. PM_{10+} collection efficiency is almost 100%.

Collection efficiency of ESP on different size coal ash particles

Collection efficiency is one of the important indexes of the ESP performance. In this paper, the following formula is used for the calculation of the collection efficiency:

$$\eta = (1 - C_2 / C_1) \times 100\% \quad (\%) \qquad (1)$$

Where: η for collection efficiency; C_1、C_2 for particle mass concentration at ESP inlet and outlet, mg/m^3.

Take the corresponding concentration value of the same size at ESP inlet and outlet into the equation (1), ash collection efficiency of different size coal ash particles may be found out. In this paper, the mean of 2 sample values is taken as the mass concentration of the particles at the ESP outlet. Figure 5 gives the ash collection efficiency on PM_{10} of different sizes. It is obvious that the smaller the ash size, the lower the collection efficiency. This is the overall trend for collection efficiency in general. The collection efficiency of ESP is relatively low on particles sized within 0.1-1μm. This is because: coarse particles (greater than 1μm) mainly going through electric-field charging collection, and fine particles (less than 0.1μm) mainly through diffusion charging, the size of about 0.1-1μm particles being at the transition zone, with the lowest collection efficiency. From Fig. 5 it is also clear that the collection efficiency is not very good. Its collection efficiency for size slightly smaller than 10μm particle is only about 96%. With the decreasing of the size down to 1μm, the collection efficiency decreases down to about 80%. The collection efficiency of the sub-micron particles is

Table 3 Distribution of different particle sizes

size (μm)	ESP inlet			ESP outlet 1st			ESP outlet 2nd		
	concentration (mg/m^3)	weight(%)	total(%)	concentration (mg/m^3)	weight (%)	total (%)	concentration (mg/m^3)	weight (%)	total (%)
0.0281	2.2	0.0099	0.0099	0.8	0.775	0.775	0.343	0.486	0.486
0.0565	10.8	0.048	0.0579	1.76	1.706	2.481	0.943	1.337	1.823
0.0944	21.6	0.097	0.1549	3.76	3.645	6.126	2.429	3.443	5.266
0.154	3.2	0.014	0.1689	0.36	0.349	6.475	0.057	0.081	5.347
0.258	1.6	0.007	0.1759	0.32	0.310	6.785	0.257	0.365	5.712
0.377	2.4	0.011	0.1869	0.92	0.892	7.677	0.429	0.608	6.320
0.605	6	0.027	0.2139	2.28	2.210	9.887	2	2.835	9.155
0.936	38.6	0.173	0.3869	8.2	7.945	17.832	6.057	8.586	17.741
1.58	103.8	0.456	0.8429	17.88	17.332	35.164	14.086	19.968	37.709
2.36	197.6	0.887	1.7299	28.52	27.646	62.810	21.029	29.810	67.519
3.95	199.4	0.895	2.6259	26.4	25.591	88.401	17.314	24.544	92.063
6.6	196.4	0.882	3.5079	7.76	7.522	95.923	5.543	7.857	99.920
10	91.8	0.412	3.9199	4.2	4.071	100	0.057	0.081	100
>10	21400	96.07	100	NC[1]	0	100	NC[1]	0	100

[1]NC for no ash collected.

62-83%.To illustrate the total particulate mass emission of the boiler into the atmosphere, further calculation is made using values given in Table 3. Taking boiler flue gas volume under rated load operation of 900,000 m^3/h, and LPI emission of 10L/min, we get the total particulate mass emission of 78.21kg/h and mass concentration of 86.85mg/m^3. Although the mass concentration in the gas is lower than China's current power plant emission standards, the whole emission is rather enormous. As a result, it is particularly important to develop new types of collection equipment for power station and take effective measures to control coal-fired power plant against a large number of respirable particulate matter (PM_{10}) emission, which is an effective way in controlling the respirable particulate matter pollution in atmosphere in China.

Distribution of minor, trace elements in PM_{10}

XRF is used for measuring the element of each level of particulate matter, collected by LPI at ESP outlet. The mass size distribution of the element of each level is gained after calculation. This article only discusses on samples taken from first sampling at ESP outlet. For the mass size distribution of minor elements Mg, S, Ca, Fe and Al, Si, and trace elements Mn, Cu, Zn, Pb, see Figs. 6(a) to 6(c). From the figures it is clear that the element mass size distribution is similar to that of PM_{10}, i.e. there is a peak in sub-micron size and ultra -micron size respectively. However the mass size distribution of elements is quite different from one another. Elements of Al, Si, Ca, Mn and Fe are mainly located in the ultra- micron particles. The concentration distribution of elements of Mg, S, Cu, Zn and Pb in the sub-micron and the ultra- micron is quite similar. The calculation result, in Table 4, of the mass fraction of elements in different size range, gives more explanation on this point that the elements of Al, Si, Ca, Fe and Mn in PM2.5 account for only about 30%, while the elements of Mg, S, Cu, Zn and Pb in PM2.5 account for about 50 to 60%. This is due to different enrichment characteristics of different size fly ash particles of elements[7].

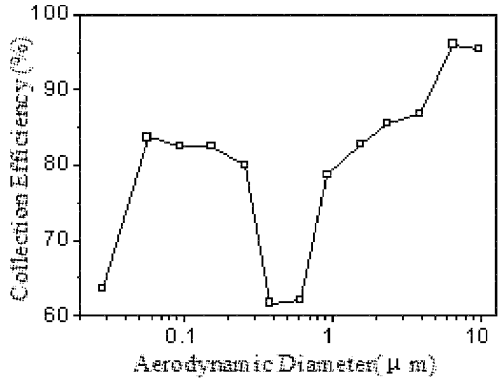

Fig. 5 Collection efficiency of PM_{10}

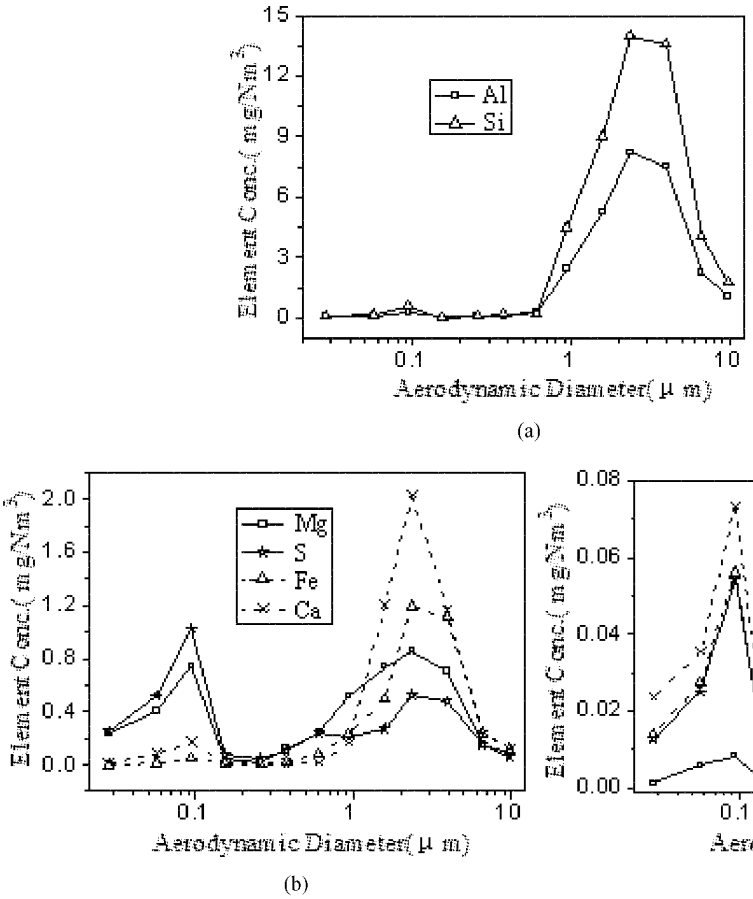

Fig. 6 (a) Mass size distributions of Al and Si, (b) Mass size distributions of Mg, S, Ca and Fe and (c) Mass size distributions of Mn, Cu, Zn and Pb

Table 4 Elemental mass fraction in fly ash with different sizes

size	percentage of element(%)									
	Mg	Al	Si	S	Ca	Fe	Mn	Cu	Zn	Pb
PM_1	58.98	4.32	2.72	36.67	4.42	7.89	21.32	42.63	49.38	39.83
$PM_{2.5}$	70	31.79	30.77	51.7	25.11	33.92	27.79	54.88	63.95	59.24

In order to further study the distribution of different size particles of elements, we define the relative enrichment coefficient formula as follows:

$$R_{ij} = C_{ij} / C_{i13} \quad (2)$$

Where: R_{ij} for the relative enrichment coefficient of element i in the j size fly ash particles; C_{ij} for the mass fraction of element i in the j size fly ash particles, μg/g; C_{i13} for mass fraction of element i in the 13th level of particles in LPI, μg/g. The relative enrichment coefficient means the ratio of the mass fraction of an element in the fly ash particles of j size to the mass fraction of particles in maximum size. The implication is that: to the biggest particles in the 13th level, if the ratio is larger than 1, the element in j size is in enrichment; On the other hand, there is no trend in enrichment. The relative enrichment coefficient of different elements is calculated by using the formula (2), see Fig. 7(a) and 7(b). From the figures we can see that, with the fly ash particle size decreasing, the relative enrichment coefficient of elements Mg, S, Cu, Zn, Pb significantly increases; the relative concentration coefficient of elements Al, Si, Ca significantly decreases; the relative concentration coefficient of elements Fe and Mn shows no regular changes. This means that the elements of Mg, S, Cu, Zn, Pb have a clear trend of enrichment in small size fly ash particles, especially the elements of Cu, Zn, Pb, whose relative concentration coefficient reaches 30 to 40; Elements of Al, Si, Ca in the coal are in the form of compounds with high melting point. In pulverized-coal combustion process it is difficult for these compounds following gasification- condensation mechanism to form fine particles, which led to the result that the mass fraction of these elements decreases as the size decreases; the enrichment coefficient of

element Mn varies little in fine and coarse particles. Literature[7] says that Mn is a nonvolatile metal. Its element and compounds will not volatile in combustion process, no clear enrichment in ash particles; many of the documents say that element Fe is easy of enrichment in small particles. However in this experiment it is difficult to find a regular result, so an in-depth study is in need.

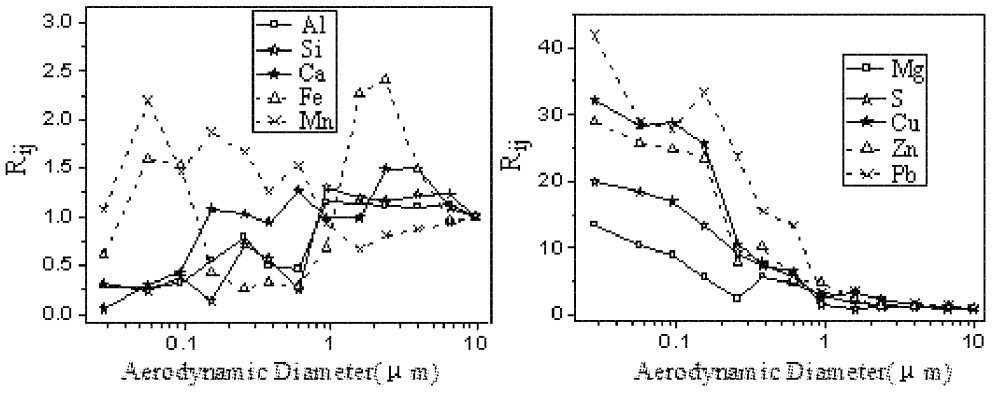

(a) (b)

Fig. 7 (a) Relative enrichment coefficient of Al, Si, Ca, Fe and Mn. (b) Relative enrichment coefficient of Mg, S, Cu, Zn and P

CONCLUSIONS

(1) The PM_{10} mass size at EPS inlet and outlet of the power station is in a bimodal distribution, with its peak at 0.1μm and 2.36-3.95μm around respectively. The characteristic of the fly ash at ESP inlet and outlet is obviously different. Before EPS, PM_{10+} accounts for about 96.07%, PM_{10} for 3.92%, $PM_{2.5}$ about 0.84%; after ESP no PM_{10+} has been collected, PM_{10} accounts for 100%, $PM_{2.5}$ about 36.44%.

(2) EPS has different collection efficiency over different size particles: collection efficiency over particle with the diameter slightly smaller than of 10μm is 96% or so, when the particle size decreases to 1μm, its collection efficiency decreases to about 80% or so, the collection efficiency over sub-micron particles is in the range of 62-83%.

(3) Elements of Al, Si, Ca, Fe and Mn account for only about 30% in $PM_{2.5}$, elements of Mg, S, Cu, Zn and Pb for about 50 to 60% in $PM_{2.5}$. Elements of Mg, S, Cu, Zn, Pb has a clear trend of enrichment in the small size fly ash particles, especially elements of Cu, Zn, Pb, the relative enrichment efficiency is about 30 to 40.

ACKNOWLEDGEMENTS

This work was sponsored by the Key Technologies R&D Program of China (2007BAC24B00).

REFERENCES

Bart B., Jim H., Raj G.T., Peter N., Terry W. (2004). 21st International Pittsburgh Coal Conference, 2004
Huang Y.J., Jin Z.S., Zhong Z.P.: *Proceedings of the CSEE* **23** (2003), pp. 205-210
Mcnallan M.J.: *Combustion and Flame* **42** (1981), pp. 45-60
Liu J.Z., Fan H.Y., Zhou J.H., Cao X.Y, Cen K.F.: *Proceedings of the CSEE* **23** (2003), pp. 145-149
Helble J.J. (1987). Massachusetts: Massachusetts Institute of Technology, Department of Chemical Engineering
Quann R.J., Neville M., Janghorbanl M., Mims C.A. and Sarofim F.: *Environmental Science Technology* **16** (1982), pp. 776-781
Qi L. Q., Yuan Y.T., Ji Y.X.: *Coal Conversion* **26** (2003), pp. 87-90
Soud H.N., Wu Z. (1998). *IEA Coal Research*, London, UK
Tao S., Ma Y. (1996). *Proceedings of International Conference on Environmental Protection of Electric Power*, Nanjing, China
Zhu Z.J., Tan Y., Zheng J.: *Proceedings of the CSEE* **23** (2003), pp. 167-171

STUDY ON THE CHARACTERISTICS OF GASEOUS POLLUTANT ABSORBED BY A MOVING LIQUID AEROSOL

Y.G. Du[1], J.J. Deng[2], F. He[2], Y. Yu[2]

1 College of Resources and Environmental Science, Chongqing University, Chongqing, 400044, China
2 R & D Center of China Power Investment Corporation Yuanda Environmental Protection Engineering Co., Ltd., Chongqing, 400060, China

Abstract: In order to study atmosphere chemical component, a model to depict the characteristic of the absorption process of gaseous pollutant by a liquid aerosol with internal circulation and chemical reaction was established. Based on the finite volume method, SIMPLE algorithm was employed to numerically study the experimental works of Walcek, which indicates that the present models and method are feasible. Then, the transient momentum and mass transfer characteristics of SO_2 into a droplet which radius is 5μm were evaluated numerically, and the results indicate that the chemical reaction increases the rate of mass transfer and the quasi-saturated time of aerosols, which provided theory basis for the heterogeneous reaction of liquid aerosols.

Keywords: liquid aerosol, gaseous pollutant, heterogeneous reaction, mass transfer, absorption

INTRODUCTION

In recent years, atmosphere pollution problem is more and more severe. Specially, the main pollutant—aerosols get people's attentions. Since the aerosols have small sizes, but big surfaces, they provide a large place for atmosphere chemical reactions. For example, the liquid aerosols in the air can absorb gaseous pollutants. As a result, the gaseous pollutants are enrichment excessively in the aerosols, and gaseous pollutants will be contained and suspended in the air with aerosols for a long time, it is so dangerous to the people's health and have a badly affect to atmosphere quality. So it is necessary to study the characteristic of the liquid aerosols and the absorption process of gaseous pollutants.

According to literatures, few numerical researches on the process of aerosols' movement and absorption of gaseous pollutant, but many investigations have been performed on the formation of acid rain (Walcek et al.,1981). Furthermore, not both the internal circulation and chemical reaction are considered in their works, which have an important role in increasing the mass transfer rate of gaseous pollutant. So, in this paper the models are established and the fully numerical simulation is conducted with considering the internal circulation and the chemical reaction, which are the basal works for study the process and mechanism of aerosols heterogeneous reactions.

The configuration of the model is sketched in Fig. 1, where a liquid aerosol of pure water is moving in environment that there are filled with the SO_2.

FORMULATION

In this paper, it supposes that the aerosol retains spherical shape during moving freely in air. According to paper (Hsu et al.,1994), the droplet whose diameter is 0.010mm used here can satisfy this requirement.

(1) The general controlling equations in polar coordinates

$$\frac{\partial}{\partial t}(\rho\phi r)+\frac{\partial}{\partial\theta}(\rho\phi u_\theta)+\frac{\partial}{\partial r}(\rho r\phi u_r)=sr+\frac{\partial}{\partial r}\left(\tau r\frac{\partial\phi}{\partial r}\right)+\frac{\partial}{\partial\theta}\left(\frac{\tau}{r}\frac{\partial\phi}{\partial\theta}\right) \tag{1}$$

Where ϕ is the general variables (u, v -velocity; c-concentration); τ is the generalized diffusion coefficient; s is the generalized source item.

(2) Chemical reaction

When SO_2 is absorbed by a liquid aerosol, the hydration happens, then it dissociates to HSO_3^- and SO_3^{2-}. The process is described as follow (oxidation is not considered here) (Hsu et al.,1994).

$$SO_2(g)+H_2O(l)\leftrightarrow SO_2\bullet H_2O(aq) \tag{2}$$

$$SO_2\bullet H_2O\leftrightarrow HSO_3^-+H^+ \tag{3}$$

$$HSO_3^-\leftrightarrow SO_3^{2-}+H^+ \tag{4}$$

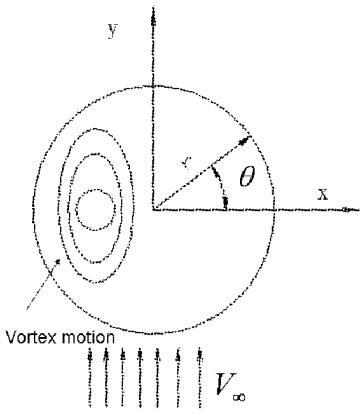

Fig. 1 Schematic diagram of an aerosol In polar coordinate systems

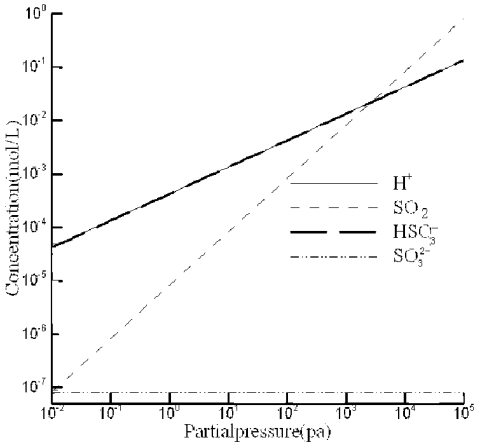

Fig. 2 Equilibrium concentrations of species in an aerosol versus SO_2 partial pressure (at 25℃, pH_0=6)

(3) Initial and boundary conditions

The gas phase initial conditions corresponding to the sudden exposure of a water droplet into a uniform flow are

$$v = v_\infty, u = 0, \quad p = p_\infty, \quad C_g = C_{ini}, \quad C_l = 0 \tag{5}$$

The boundary conditions have been transformed into the polar coordinates before calculation. They are expressed as follows.

(i) Upstream inflow and downstream outflow ($r_n = r_\infty$, $-\pi/2 \leqslant \theta \leqslant \pi/2$)

$$v = v_\infty, u = 0, \quad p = p_\infty, \quad C_g = C_{ini}, \quad C_l = 0 \tag{6}$$

(ii) Axis of symmetry($0 \leqslant r \leqslant r_\infty$, $\theta = -\pi/2 or \theta = \pi/2$)

$$u = \frac{\partial v}{\partial \theta} = \frac{\partial p}{\partial \theta} = \frac{\partial c}{\partial \theta} = 0 \tag{7}$$

(iii) Droplet surfaces ($r_n = r_s$)

$$u_{gs} = u_{ls}, \quad v_{ns} = 0, \mu_g \left(\frac{\partial u_\theta}{\partial r_n} - \frac{v_\theta}{r_s} \right)_g = \mu_l \left(\frac{\partial u_\theta}{\partial r_n} - \frac{v_\theta}{r_s} \right)_l \text{ and } [SO_2 \bullet H_2O] = H_{SO2} P_{SO2} \tag{8}$$

The phase equilibrium is assumed at gas-liquid interface, and the Henry's law is applied. In the equation (8), P_{SO2} stands for the partial pressure of SO_2 at the gas phase, while H_{SO2} represents constant of Henry's law ($1.26 Matm^{-1}$, Chen et al., 2001).

RESULTS AND DICUSSION

The computed results show the equilibrium concentrations of H^+ and sulfur species at 25℃, pH_0=6 versus various SO_2 partial pressure in Fig. 2. It indicates that the concentration of SO_3^{2-} is too small when $P_{so2} > 10^{-2}$, so the equation (4) can be ignored.

The SO_2 concentration and mass accumulation in following figures are nondimensionalized.

$$Y'_{SO2} = [SO_2.H_2O] / k_H P_{SO_2} \tag{9}$$

$$m'_{so2} = \int_0^1 \int_{-\pi/2}^{\pi/2} Y'_{1,so2} (r_n / r_s)^2 \cos\theta d\theta dr' \tag{10}$$

$$\Delta Y'_{SO2} = Y'_{SO2}(\max) - Y'_{SO2}(\min) \tag{11}$$

Moreover, Quasi-saturated time is the time when the mass accumulation reaches 0.66(Chen et al., 2001).

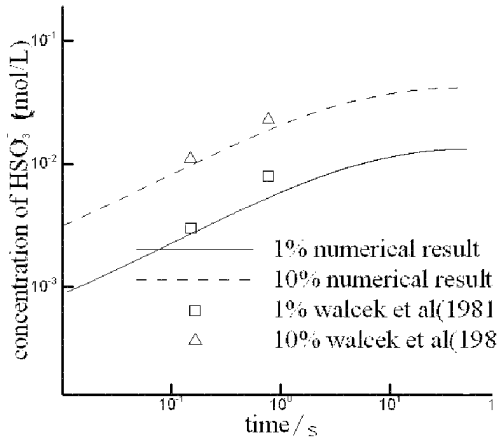

Fig. 3 Comparison of model predictions with the data of experiment

The experiment results and the model predictions for the concentration of HSO_3^- in a liquid aerosol are compared in Fig. 3, which indicates agreement between the experiment and the model is good. Consequently, the above established models and numerical methods are feasible for predicting this problem.

Figure 4 shows The transient momentum and mass transfer characteristics of SO_2 into a droplet of 5μm radius are evaluated at 25℃, P_{so2} =1%, pH_0= 6, which depicts that the quasi-saturate time is 0.01s without considering chemical reaction and 0.012s with considering chemical reaction.

Figure 5 shows that the rate of SO_2 mass transfer is larger when chemical reaction is considered, and it need more time to reach quasi-saturated state.

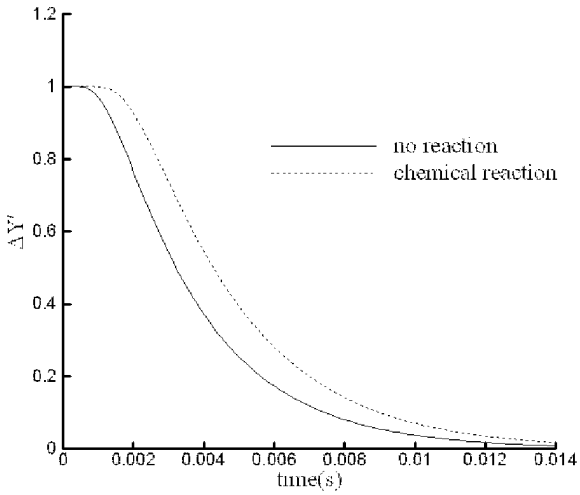

Fig. 4 Comparison of the time variation of the $\Delta Y'_{so2}$ inside the droplet

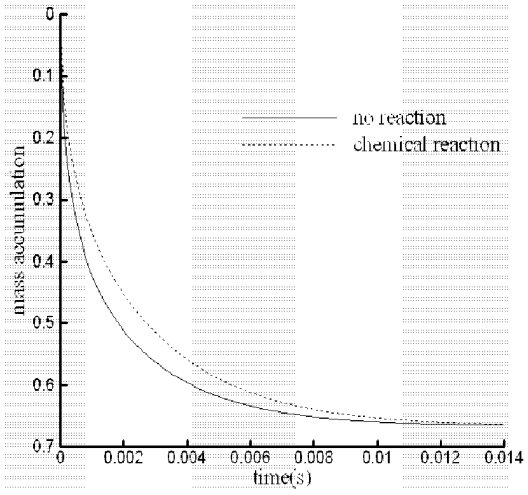

Fig. 5 Comparison of the time variation of SO_2 mass accumulation inside the droplet

CONCLUSIONS

In this paper, the models were established for hydration of gas pollutant (SO_2) and its dissociation. Based on the Simple scheme the numerical study was conducted with the internal circulation and the chemical reaction of aerosols by the finite volume method. Some predicted results had been obtained, which indicate that the chemical reaction in aerosols increases the mass transfer rate of gaseous pollutant and the quasi-saturated time markedly. So, it's necessary to include internal circulation and the chemical reaction of aerosols when study the characteristics of the absorption, which provides theory basis for accurately numerical investigate on heterogeneous reaction process of aerosols.

ACKNOWLEDGEMENTS

This work was sponsored by the Key Technologies R&D Program of China (2007BAC24B00).

REFERENCES

Chen W.H.:Atmospheric Environment **35**(2001), pp.2375-2393
Hsu C.T., Shih S.M., Chang C.Y.: Canadian Journal of Chemical Engineering **72**(1994), pp.256-261
Walcek C, Wang P.K., Topalia J.H., et al.:Journal of the Atmospheric Sciences **38**(1981), pp.871-876

Sustainable Fuels-Combustion and New Concept

CHARACTERIZATION OF COMBUSTION AND EMISSION OF SEVERAL KINDS OF HERBACEOUS BIOMASS PELLETS IN A CIRCULATING FLUIDIZED BED COMBUSTOR

S.Y. Li, H. P. Teng, W. H. Jiao, L. L. Shang, Q. G. Lu

Institute of Engineering Thermophysics, Chinese Academy of Sciences, Beijing,100190, China

Abstract: Characterizations of combustion and emission of four kinds of herbaceous biomass pellets were investigated in a 0.15 MWt circulating fluidized bed. Corn stalk, wheat stalk, cotton stalk and king grass, which are typical herbaceous biomass in China, were chosen for this study. Temperature profile, emission in flue gas and agglomeration were studied by changing the combustion temperature between 750℃ and 880℃. The combustion efficiencies are in the range from 97.4% to 99.4%, which are relatively high due to the homogeneous temperature profiles and good circulating fluidization of bed material. Suitable combustion temperatures for the different herbaceous biomass are mainly depended on the emission and bed agglomeration. SO_2 and HCl concentrations in flue gas are in direct proportion to the sulfur and chlorine contents of the herbaceous biomass. Agglomeration at the cyclone leg and the loop seal is the main reason for defluidization in the CFB combustor.

Keywords: combustion, biomass, circulating fluidized bed, agglomeration

INTRODUCTION

Biomass as an alternative fuel is a potentially CO_2-neutral and renewable energy resource. Biomass was defined as organic non-fossil material of biological origin, a part of which constitutes an exploitable energy resource (Gustavsson et al., 1995). Biomass can be grouped into the following categories: wood residues, agricultural residues, dedicated energy crops and industrial and municipal waste of plant origin (Lin et al., 2003). At present, biomass is converted into heat and electricity most often by combustion. Fluidized beds are used for a broad variety of fuels and significant economic importance; this flexibility with respect to different fuels is actually the stronghold of fluidized bed compared to other combustion technologies. In terms of the utilized fuels, coal has been most often applied so far, but also waste and biomass have been utilized and forecast to play a more important role in the future.

In China, fluidized bed combustion technology is developed very quickly in the last decade. More than 3000 commercial circulating fluidized bed (CFB) boilers have been put into operation since 1988 and about 100 CFB boilers (300MWe) were in operation and in planning or construction stages in 2008. Because of the CO_2-neutrality and low sulfur content of sustainable cultivated biomass, firing and co-firing biomass with coal in CFB boilers have recently intensified, to reduce the negative environmental impacts of coal combustion. In China, agricultural biomass is very rich, which will play an important role in the heat and electricity generation by circulating fluidized bed combustion.

However, some biomass, especially the herbaceous biomass has a high alkali content, which is released from the fuel during thermal conversion. It may thereafter be transported to the surface of the bed particles forming a sticky layer, which favors agglomeration (Davidsson et al., 2008; Fryda et al., 2008). This is often the case when the usual silica-rich sand is used as bed material, since alkali silicates with low melting points are formed. In severe cases, defluidization occurs (Fabrizio and Riccardo, 2008; Zheng et al., 2007; Wang et al., 2008; Lin et al., 2003; Weber et al., 2008). In the literatures many studies have been reported on the firing and co-firing of different biomasses with coal by using fluidized bed technology. The biomass types mainly used in the previous are olive oil industry waste, rice husk, peach, wheat straw, wood chips, mixed sawdust, forest residue, Salix (willow), vegetable waste, fruit juice industry waste and municipal solid waste (MSW) (Armesto et al., 2002, 2003; Cliffe and Patumsawad, 2001; Arvelakis et al., 2001; Bakker et al., 2002; Shen et al., 2003; Liu et al., 2002; Atimtay and Kaynak, 2008; Chirone et al., 2008). However, there was little work conduced to investigate the characterization of combustion and emission for biomass, especially typical agricultural biomasses of China, in a CFB combustor.

The objective of this study is to improve the level of understanding about China typical herbaceous biomass combustion in a CFB combustor. The characterization of combustion and emission for four kinds of herbaceous biomass, corn stalk, wheat straw, cotton stalk and king grass (a dedicated energy crops), were studied to determine the optimum combustion conditions with reduced emissions.

EXPERIMENTAL APPARATUS AND PROCEDURE

Apparatus

The work described in this paper was performed in a circulating fluidized bed combustor shown schematically in Fig. 1, which consists of a combustor section, a feeding section, a gas analysis section and a data acquisition section. The furnace has a height of 7.5 m and an inside diameter of 0.3 m.

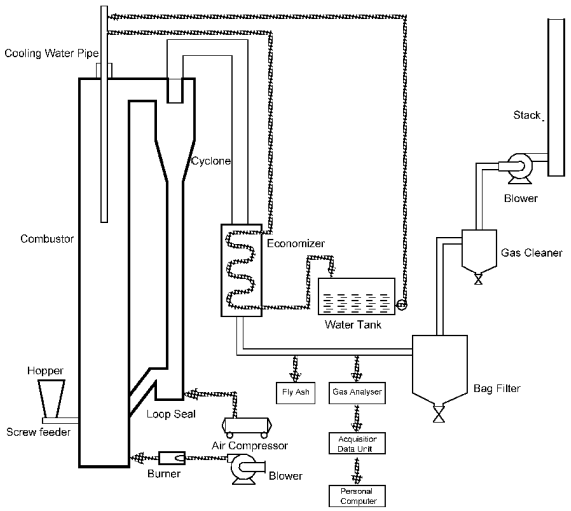

Fig.1 Schematic diagram of the circulating fluidized bed

Biomass fuel is stored in a hopper and can be continuously fed to the combustor at 0.82 m above the air distributor by a screw feeder with various feeding rates. Primary air is supplied without preheating and no secondary air is provided. The temperatures and pressures in the CFB combustor are measured at the locations of 0.26 m, 0.82 m, 1.52 m, 2.52 m, 5.85 m and 7.42 m above the distributor, and at the cyclone and the loop seal. The data is logged to a computer by Agilent 34970A Data Acquisition Switch Unit. The concentrations of O_2, CO, CO_2, NO_x, SO_2 and HCl in flue gas are continuously monitored on line by a FTIR analyzer (DX4000) before the bag filter.

Fuel and bed material

The four biomass fuels were corn stalk, wheat stalk, cotton stalk and king grass pelletized to a size range of 5-15 mm, which were purchased in the bio-fuel market. They are typical herbaceous biomasses in China. The proximate and ultimate analyses are shown in Table 1. The chemical analysis for biomass pellets by inductively coupled plasma-optical emission spectroscopy (ICP-OES) (IRIS Intrepid II XSP, Thermo Fisher Scientific Inc.) is also shown in Table 1.

Table 1 Composition of fuels

	corn stalk	wheat stalk	cotton stalk	king grass
Proximate analysis				
Moisture (wt% as received)	9.0	10.1	10.5	10.0
Ash (wt% dry)	22.28	6.97	11.79	7.45
Fixed carbon (wt% dry)	15.60	19.74	18.74	18.43
Volatile (wt% dry)	62.12	73.30	69.47	74.12
Ultimate analysis (wt% dry)				
C	38.47	45.10	44.03	44.98
H	4.70	5.6	5.23	5.65
N	1.11	0.57	0.94	0.67
O	33.27	41.56	37.88	41.06
S	0.16	0.20	0.14	0.18
Cl	0.515	1.137	0.226	0.295

Continuld

	corn stalk	wheat stalk	cotton stalk	king grass
Fuels composition (ug/g)				
Al	2920	324.9	692.4	348
Ca	12479	3375	8162	6003
Fe	4766	732.9	1205	863.5
K	10231	17962	8529	12043
Mg	7021	1773	2442	2157
Na	296.7	1016	1175	110.8
P	1548	487.6	1186	1222
Si	500.7	237.4	103.4	454.1
Heating value (MJ/kg)				
LHV, as received	14.10	16.46	16.02	16.43

Discharged bottom ash of combustion for stone coal (78.34% SiO_2) with size in the range of 0-2 mm was used as bed material in the experiments. The same quantity of the bed material was used in all the experiments with a bed height of approximately 400 mm in the stationary state in the combustor.

Experiment procedure

The CFB combustor was heated up to 400℃ by an oil gun, biomass stored in a hopper was then fed gradually into the combustor and shut down the oil gun. The tests started when the bed temperatures reached the defined values. Bed temperature was roughly fixed at 750℃, 800℃, 850℃ and 880℃. The CFB combustor was operated according to the parameters in Table 2. During the runs, the fly ash was collected continuously after the economizer during the experiments. The test ended once the defluidization occurred.

Table 2 Operating parameters

Parameter	Range
Thermal load (MW)	0.12-0.16
Biomass pellets feeding rate (kg/h)	22.39-47.95
Fluidization velocity (m/s)	2.9-4.6
Average temperature along the furnace T_a (℃)	735-890
Average temperature of the loop seal T_s (℃)	705-875
Excess air ratio	1.58-1.93

RESULTS AND DISCUSSION

Temperature profiles

The axial temperatures vs. height along the furnace for the stable combustion of the four kinds of biomasses are shown in Fig. 2. The arithmetic average temperatures along the furnace (T_a), the average temperatures of the loop seal (T_s), the fluidization velocities (U), the excess air ratio (e) and the operation time of the different tests (t) are shown in Table 3. For the four kinds of biomass fuels, the temperature profiles of stable combustion are similar. The temperatures along the height of the furnace are uniform except that at the point 0.82 m, it is lowest owing to the fuel pellets feeding. The good circulation of bed material is contributed to the content of ash in the biomass pellets which is higher than that in the original biomass, because a lot of dust or impurity is maybe brought into biomass pellets during the processing.

Flue gas emission

The reliance of CO emissions on combustion temperatures (T_a) is depicted in Fig. 3. For the four biomasses, the CO concentrations decrease rapidly with the increasing of combustion temperatures. At 750 ℃, the maximum of CO concentration reaches 1426 mg/m^3 for wheat stalk; the minimum is 330 mg/ m^3 for cotton stalk. However, when the combustion temperatures exceed 850 ℃, the CO concentrations are all under 98 mg/ m^3. CO emissions are essentially the result of incomplete combustion and belong to the category of unburnt pollutants. High CO emission was produced due to a shorter freeboard characterized by smaller residence times for the relatively low combustion temperatures (Grass et al., 1994). Another reason is also related to fuel composition. The biomass combustion do not follow shrinking core model but rather a shrinking sphere model,

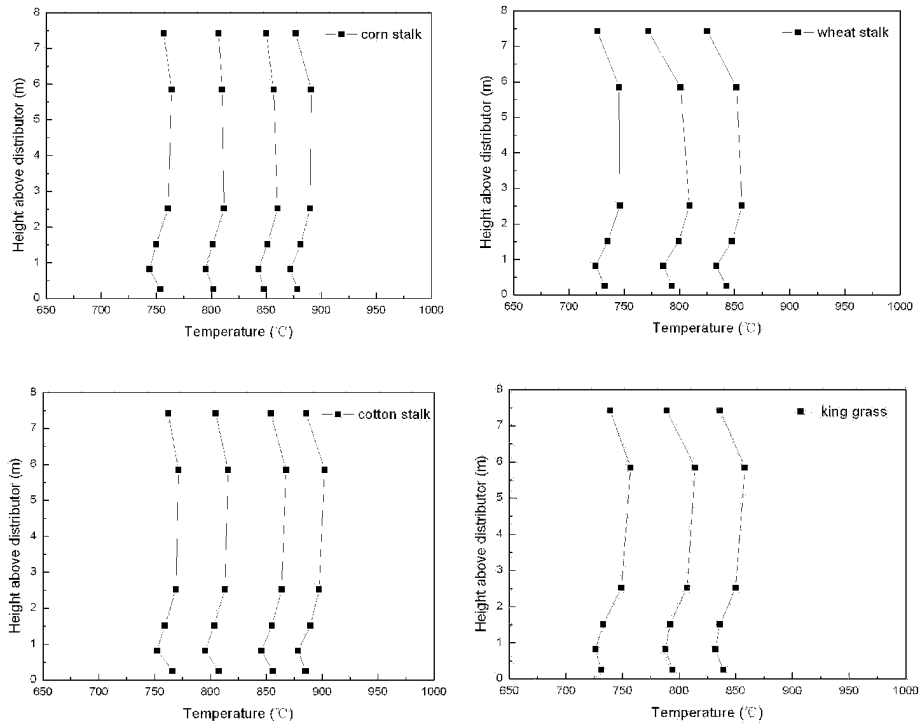

Fig. 2 Axial temperature profiles for the combustion of the four biomasses

which results in an ash layer surrounding the fuel particle and makes the oxygen diffusion difficult (Khan et al., 2005). The suitable combustion temperature mainly depends on the emission and agglomeration for different biomass. Considering the CO emission, the suitable combustion temperature should exceed 800 ℃.

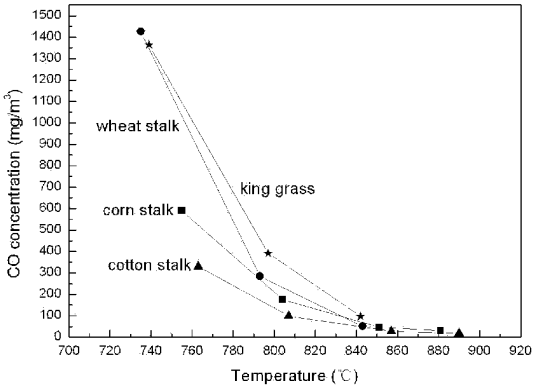

Fig. 3 Effect of combustion temperatures on the emissions of CO for the four biomasses

Table 3 Summary of operating parameters

Run	Fuel	T_a (℃)	T_s (℃)	U (m s^{-1})	e (-)	t (min)
1	corn stalk	755	743	3.2	1.93	50
2	corn stalk	804	794	3.3	1.82	60
3	corn stalk	851	838	3.7	1.69	60
4	corn stalk	881	866	4.6	1.68	50
5	wheat stalk	735	705	3.3	1.87	60
6	wheat stalk	793	733	3.4	1.74	100
7	wheat stalk	843	795	3.4	1.72	130
8	cotton stalk	763	748	2.9	1.86	40
9	cotton stalk	807	794	3.2	1.81	60

Continued

Run	Fuel	T_a (℃)	T_s (℃)	U (m s^{-1})	e (-)	t (min)
10	cotton stalk	857	842	3.4	1.68	60
11	cotton stalk	890	875	3.7	1.58	68
12	king grass	739	714	3.6	1.91	150
13	king grass	797	768	4.0	1.82	150
14	king grass	842	814	4.2	1.67	90

NO_x concentrations at different combustion temperatures for the four biomasses are shown in Fig. 4, the concentrations of NO, NO_2, N_2O, NH_3 and HCN vs. combustion temperatures for corn stalk are given in Fig. 5. With the combustion temperature increasing, NO concentration gradually increases and NO_2 decreases. At the same time, the concentrations of NH_3 and HCN are very low. NO_x produced from high nitrogen content biomass is high because the fuel nitrogen dominates at the temperature range of 750−900 ℃ in a circulating fluidized bed (Demirbas et al., 2004), as shown in Fig. 5. Contrary to NO_x, N_2O emission shown in Fig. 6 is a strong function of the operating temperatures (T_a), increasing the temperature results in the formation of more O and OH radicals and thus destruction of N_2O.

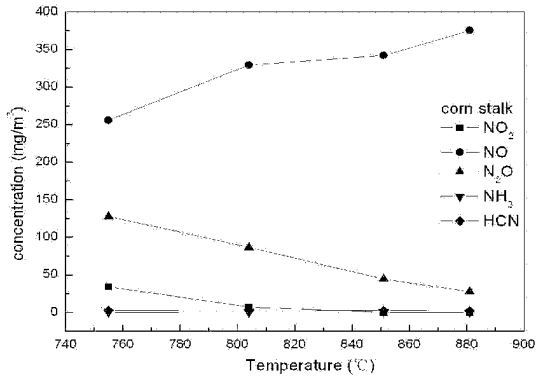

Fig. 4. Concentrations of NO, NO_2, N_2O, NH_3 and HCN vs combustion temperature for corn stalk

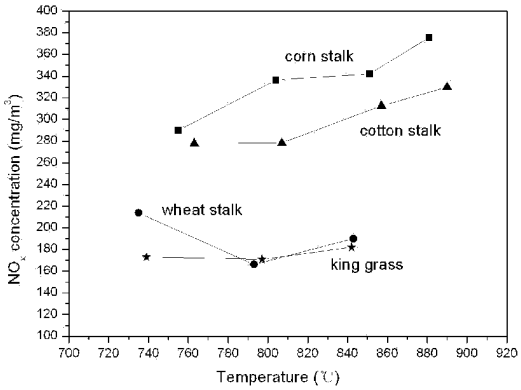

Fig. 5. Effect of combustion temperature on the emissions of NO_x for four biomasses

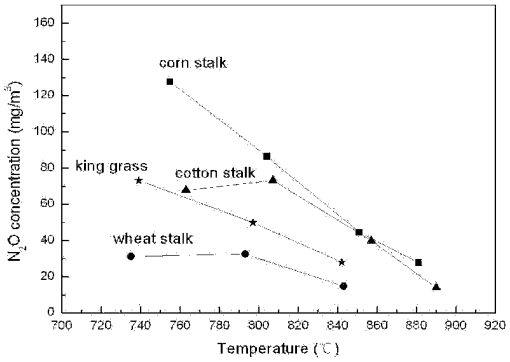

Fig. 6 Effect of combustion temperature on the emissions of N_2O for four biomasses

Figure. 7 and Fig. 8 shows the concentrations of SO_2 and HCl in flue gas for the four biomasses at different combustion temperatures. For the wheat stalk, no SO_2 is observed in flue gas at all runs. For the other three biomasses, the SO_2 concentration is nearly zero when the combustion temperature is under 850 ℃. SO_2 appears until the temperature exceeds 850 ℃, and the concentration is in direct proportion to the sulfur content of the biomass. The SO_2 concentrations are not high mainly due to low inherent sulfur content of the biomass (0.14% - 0.20% on dry basis). Another reason for low SO_2 emission is the change of the conversion rate. As the biomass ash contains relatively high CaO and MgO, the SO_2 may be absorbed to a certain extent. Higher alkaline earth content in the ash seems to result in higher SO_2 capture (Fuertes et al, 1992). On the other hand, for herbaceous biomass, as the chlorine content is higher (0.226% - 1.137% on dry basis) than other biomass, the HCl concentration is high at the temperature range of 750-900 ℃, shown in Fig. 8. However, it is shown that the presence of HCl will promote SO_2 capture by the bed material and fly ash particles (Xie et al., 1999).

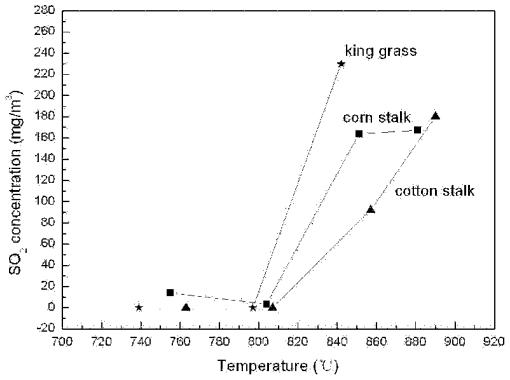

Fig.7 Effect of combustion temperature on the emissions of SO_2 for four biomasses

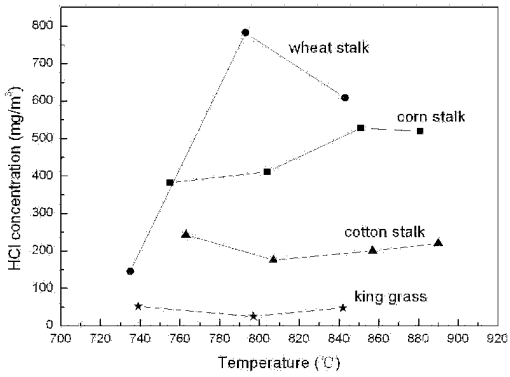

Fig. 8 Effect of combustion temperature on the emissions of HCl for four biomasses

Combustion efficiency

While combustion losses are a combination of energy losses due to CO and hydrocarbons in flue gases, and unburned carbon in fly ash. The loss from unburned carbon, ranging 2-12 wt% of fly ash, was much more important than from CO, especially at higher temperatures. Bottom ash loss was not a part in the calculation because no bottom ash was drained out during combustion. The change of the combustion efficiencies for the four biomasses at different combustion temperatures is shown in Fig. 9. At the same operation conditions, the combustion efficiency of cotton stalk ranged between 98.7% and 99.4% is the highest, while that of corn is the lowest, ranged between 97.6% and 98.5%. However, for larger commercial CFB boilers, the combustion efficiencies would certainly be higher because of longer residence time.

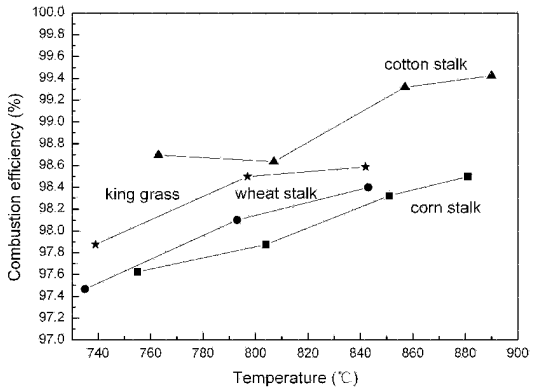

Fig. 9 Effect of combustion temperature on combustion efficiency for four biomasses

Defluidization analysis

Combustion processes with biomasses, especially with herbaceous biomasses which have a high content of alkaline elements, are prone to experience severe agglomeration problems. In our experiments, defluidization phenomenon caused by agglomeration only occurred in the experiments for wheat stalk and king grass. Figure 10 shows the profile of temperatures monitoring during the test for wheat stalk. The typical differential pressure and temperature monitoring during defluidization are shown in Fig.11. ΔP for the dense section is the differential pressure between 0.26 m and 0.82 m above the air distributor; and ΔP for the suspension section is the differential pressure between 0.82 m and 1.52 m above the air distributor. In the test for wheat stalk, defluidization took place twice. Defluidization generally occurred with a sudden bed differential pressure decrease. Once such decrease took place, the normal ash circulation had already been destroyed. Accompanied by the sudden differential pressure decrease, the temperature at the combustor bottom rose rapidly, at the same time, the temperature at the loop seal fell almost with the same rate. In addition, temperature differences between different locations in the CFB combustor also increased. In this case, the stop of fuel feeding had to be chosen. From the analysis of the temperatures and differential pressures at the onset of defluidization, it can be indicated that agglomeration of bed material at the cyclone leg and the loop seal, not first in the bed, is the main reason for defluidization in the CFB combustor, which is different from that in bubbling fluidized bed (Gluckman et al., 1976; Dawson et al., 1992). In this case, unless a mechanical outside force was given to the

ash sticky in the cyclone leg for good returning, the circulation of bed material couldn't be rebuilt.

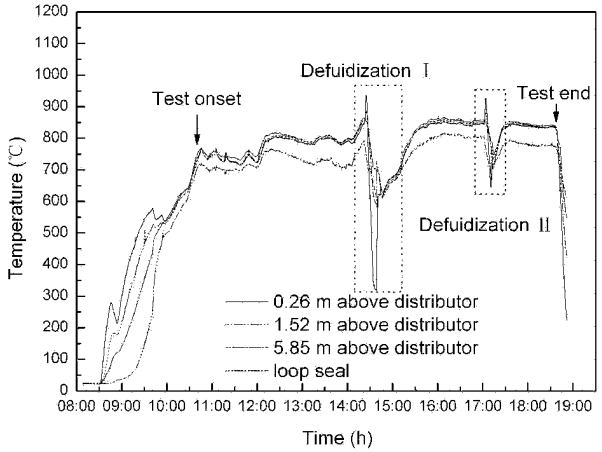

Fig. 10 Temperatures profiles monitoring during the test for wheat stalk

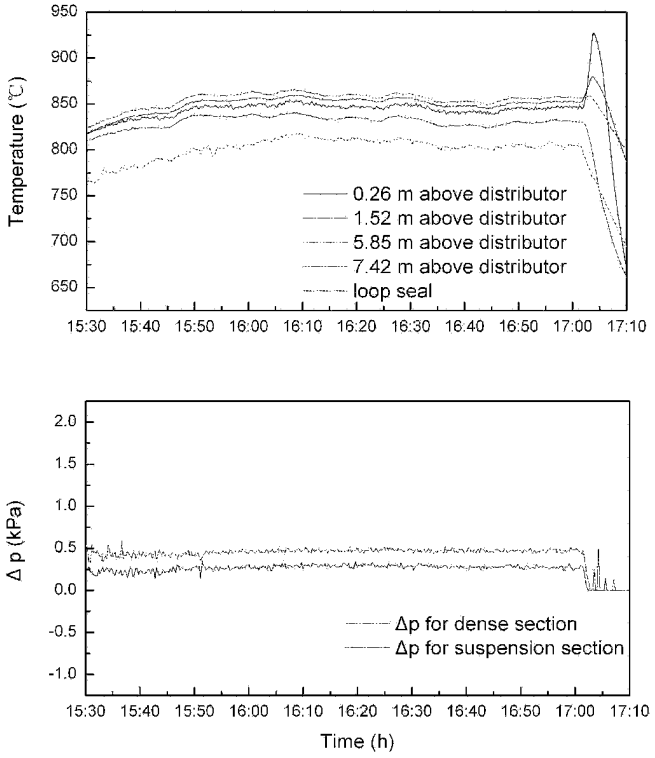

Fig. 11 The typical differential pressure and temperature monitoring during defluidization in the test for wheat stalk

CONCLUSIONS

An experimental study of the CFB combustion characterization for the four kinds of herbaceous biomass pellets, corn stalk, wheat stalk, cotton stalk and king grass, has been carried out to investigate the effect of the combustion temperature on the flue gas emission and combustion efficiency. Agglomeration phenomenon in circulating fluidized bed was also studied. The following conclusions resultd from the experiments:

The combustion efficiencies are in the range from 97.4% to 99.4%, which are relatively high due to the homogeneous temperatures and good ash circulation. The suitable combustion temperature mainly depends on the CO, NO_x, SO_2 and HCl emission and agglomeration for different biomass. However, considering the CO emission, the suitable combustion temperature should exceed 800℃.

With the combustion temperature increasing, the CO and N_2O concentrations decrease rapidly, and the NO concentration increase. SO_2 appears until the combustion temperature exceeds 850 ℃ except wheat stalk. The concentrations of SO_2 and HCl in flue gas are in direct proportion to the sulfur and chlorine content of the biomass.

Agglomeration of bed material at the cyclone leg and the loop seal is the main reason for defluidization in the CFB combustor, which is different from that in bubbling fluidized beds.

ACKNOWLEDGEMENTS

The authors gratefully acknowledge the support of National Natural Science Foundation of China (Project Code: 50706055).

REFERENCES

Armesto, L., Bahillo, A., Veijinen, K., Cabanillas, A., and Otero, J.: Biomass and Bioenergy. 23 (2002), pp. 171-179.
Armesto, L., Bahillo, A., Cabanillas, A., Veijinen, K., Otero, J., Plumed, A., Salvador, L.: Fuel. 82 (2003), pp. 993-1000.
Arvelakis, S., Vourliotis, P., Kakaras, E., Koukios, E. G.: Biomass and Bioenergy. 20 (2001), pp. 459-470.
Atimtay, A., Kurcak, K.: Fuel Procession Technology. 89 (2008), pp. 183-197.
Bakker, R. R., Jenkins, B. M., Williams, R. B.: Energy and Fuels. 16 (2002), pp. 356-365.
Chirone, R., Salatino, P., Scala, F., Solimene, R., Urciuolo, M.: Combustion and Flame. 155 (2008), pp. 21-36.
Cliffe, K. R., Patumsawad, S.: Waste Management. 21 (2001), pp. 49-53.
Davidsson, K. O., Amand, L. E., Steenari, B. M., Elled, A. L., Eskilsson, D., Leckner, B.: Chemical Engineering Science. 63 (2008), pp. 5314-5329.
Dawson, M. R., Brown, C. R.: Fuel. 71 (1992), pp. 585-592.
Demirbas, A.: Progress in Energy and Combustion Science. 30 (2) (2004), pp. 219-230.
Fryda, L. E., Panopoulos, K. D., Kakaras, E.: Powder Technology. 181 (2008), pp. 307-320.
Fuertes, A. B., Artos, V., Pis, J. J., Marban, G., Palacios, J. M.: Fuel. 71 (5) (1992), pp. 507-511.
Gluckman, M. J., Yerushalmi, J., Squires, A. M.: Fluidization Technology. 2 (1976), pp. 395-422.
Grass, S. W., Jenkins, B. M.: Biomass and Bioenergy. 6(4) (1994), pp. 243-260.
Gustavsson, L., Börjesson, B., Johansson, B., Svenningsson, P.: Energy. 20 (1995), pp. 1097-1113.
Khan, A. A., de Jong, W., Spliethoff, H.: Bioenergy for Wood Industry, Jyväskylä, Finland. (2005), pp. 365-370.
Lin, W., Dam-Johansen, K., Frandsen, F.: Chemical Engineering Journal. 96 (2003), pp. 171-185.
Liu, D. C., Mi, T., Shen, B. X., Feng, B.: Energy and Fuels. 16 (2002), pp. 525-526.
Scala, F., Chirone, R.: Biomass and Bioenergy. 32 (2008), pp. 252-266.
Shen, B. X., Mi, T., Liu, D. C., Feng, B., Yao, Q., Winter, F.: Fuel Processing Technology 84 (2003), pp. 13-21.
Wang, S., Baxter, L., Fonseca, F.: Fuel. 87 (2008), pp, 372-379.
Weber, S., Briens, C., Berruti, F., Chan, E. Gray, M.: Chemical Engineering Science. 63 (2008), pp. 4245-4256.
Xie, W., Liu, K., Pan, W. P., Riley, J. T.: Fuel. 78 (1999), pp. 1425-1436.
Zheng, Y., Jensen, P. A., Jensen, A. D., Sander, B., Junker, H.: Fuel. 86 (2007), pp. 1008-1020.

CHEMICAL CHARACTERIZATION OF BED MATERIAL COATINGSBY LA-ICP-MS AND SEM-EDS

M. H. Piispanen, A. J. Mustonen, M. S. Tiainen, R. S. Laitinen

Department of Chemistry, P.O.Box 3000, 90014 University of Oulu, Finland, Fax +358 8 553 1608
Risto.Laitinen@oulu.fi

Abstract: Bed material coatings and the consequent agglomeration of bed material are main ash-related problems in FB-boilers. The bed agglomeration is a particular problem when combusting biofuels and waste materials. Whereas SEM-EDS together with automated image processing has proven to be a convenient method to study compositional distribution in coating layers and agglomerates, it is a relatively expensive technique and is not necessarily widely available. In this contribution, we explore the suitability of LA-ICP-MS to provide analogous information of the bed.

Keywords: LA-ICP-MS, agglomeration, SEM-EDS, manganese

INTRODUCTION

The environmental and climate issues are important in the energy production. In the future the use of biofuels will be increased and amount of CO_2-emission should be minimized. The combustion of biofuels is not always trouble-free because the fuels contain alkali metals and halogens such as chlorine. Therefore the process of combustion should be optimal in order that the problems in the boiler would be avoided. It has been reported that the trace elements barium, manganese, nickel, strontium and vanadium play a role in ash melting, deposit formation, fly ash, aerosol emissions and corrosion (Obernberger et al.,2006; Fernándes Llorente and Escalda Cuadrado.,2007), as well as in the agglomeration of the bed particles in FB-boilers. These ash-related problems often result in high maintenance costs of power plants.

Bed agglomeration involves complex processes and the mechanism of agglomeration is not yet fully understood (Öhman and Nordin.,2000; Arvelakis et al.,2002; Lin et al.,2003; Visser,2004; Brus et al.,2005; De Geyter.,2006). Two main routes are suggested: melt-induced and coating induced. In the former case, the bed material particles are glued together by a molten phase. The latter type is typical for wood-based fuel in FB-combustors. The coating is formed on the surface of the bed particles and at the certain conditions the neck formation occurs between coatings of individual particles. Bed material and its particle size, fuel, combustion time and, the conditions in the boiler have an effect in the agglomeration formation (Grubor et al.,1995; Lin et al.,1997; Zhang et al.,1999; Vuthaluru and Zhang,2001).

The role of manganese in combustion and the agglomeration process has recently been reported (Thompson and Argend,2002; Kouvo and Backman,2003; Fernándes Llorente and Escalda Cuadrado,2007; Kalembkiewicz et al,2008). Manganese is harmful for an environment and has an effect in the human health (Kalembkiewicz et al.,2008; Erikson et al.,2008). Most of manganese would seem to be accumulating in the bed material rather than in economizer or multicyclone. The amount of silica in bed material correlates with the bed retention of elements. The degree of agglomeration also depends on the volatility of the material.

In this study the agglomeration of the bed particles was investigated in by Laser Ablation Inductively Coupled Plasma Mass Spectrometry (LA-ICP-MS) and Scanning Electron Microscope with an Energy Dispersive Spectrometer (SEM-EDS). LA-ICP-MS is a suitable alternative to SEM-EDS for the characterization of bed particles. LA-ICP-MS has also been applied for the fly ash and probe samples when combusting biofuels (Spears, 2004; Spears and Martinez-Tarrazona, 2004; Piispanen et al., 2008a; Piispanen et al.,2008b).

EXPERIMENTAL

Samples

Bed samples were collected from the full-scale power plants. The fuel in samples I and II was the pine sawdust and plywood and pure plywood in the sample III. GR-granule was used as bed material. A mixture of bark, wood ships and sawdust (not salix) was used as fuel in samples IV and V. GR-granule was used as a bed material in sample IV and sand in V. Olive stones and forest residue were combusted in the case of bed samples VI and VII. Kaolin was added to the bed in case of sample VIII. Sand was used as bed material in all three last samples.

Fusion with $Li_2B_4O_7$

The bulk analytical composition of the bed samples determined by fusion method by employing modified the ASTM-standard method (3682-87) (Annual Book of ASTM Standards,1989). The melts were dissolved in 5% HNO_3 and diluted with 5% HNO_3 to 100 ml. The samples were analyzed with a sequential Pye Unicam 7000 inductively coupled-plasma optical emission spectrometer.

Samples for LA-ICP-MS and SEM-EDS

Struers Epofix resin was used for the preparation of samples and standards (Nuutinen et al.,2004). Epofix resin and the hardener were mixed in a ratio of 15:2. The bed sample was cast and put in a vacuum desiccator to make sure to remove air bubbles from the sample. All mounted samples were ground by using 240 and 600 Mesh SiC-paper and polished by use 1200 Mesh SiC-paper. Both LA-ICP-MS and SEM-EDS were used for analysis of the same samples. The samples for SEM-analysis were coated with carbon to eliminate the electrostatic effects.

INSTRUMENTATION

LA-ICP-MS

A Thermo Elemental X7 ICP-MS with the laser unit Thermo New Wave UP/213 was used for the multielement analyses of the bed samples. The performance of the laser unit was verified daily with the glass standard (NIST 612) before analyses. ICP-MS operational conditions were optimized and a short term stability test was measured every day to assure the sensitivity of the instrument. The instrument should also be optimized by using the collision and reaction cell technology to ensure for analysis for maximum sensitivity. The operating conditions of LA-ICP-MS and the laser parameters are given in (Table 1). Manganese was analyzed without collision and reaction cell techniques.

SEM-EDS

SEM-EDS analyses were carried out with a JEOL JSM-6400 scanning electron microscope equipped with an Inca energy dispersive X-ray analyzer and Feature image processing software. An acceleration voltage of 15 kV and a beam current of 120×10^{-8} A were used for the SEM-EDS-analysis (Virtanen et al.,2000). The sample distance was 15 mm. The compositional distribution of the bed samples were determined with randomly selected areas. The chosen area of the sample surface was at least 10% and contained over one thousand analytical points. The domain analysis was performed with a Feature software.

Table 1 The operating conditions for the determination of eleven elements with LA-ICP-MS in point and bulk analyses

^{24}Mg, ^{48}Ti, ^{56}Fe, ^{27}Al, ^{28}Si, ^{31}P, ^{34}S, ^{40}Ca	^{23}Na, ^{39}K	^{55}Mn
Instrument parameters:		
Forward power (W)	1100	
1100		
1000		
Nebulizer (ml/min)	1.07	
1.07		
1.1		
Auxiliary gas (ml/min)	0.78	
0.78		1.01
Cooling gas (ml/min)	12.0	
12.0		
12.0		
Pole bias (V)	-1.2	
-10.0		
-2.4		
Hexapole bias (V)	1.3	
-8.0		

Continued

^{24}Mg, ^{48}Ti, ^{56}Fe, ^{27}Al, ^{28}Si, ^{31}P, ^{34}S, ^{40}Ca	^{23}Na, ^{39}K	^{55}Mn
-2.0		
Focus		8.0
	5.0	
16.0		
Reaction gas:	7 % H_2/He 7 ml/min	
H_2 2-2.4 ml/min	none	
Analytical parameters:		
Dwell time (main) ms	12[a], 15[a], 40[b]	
20[a], 40[b]		20
Sweep		150[a], 200[a], 400[b]
400		
400		
Main run		1[a], 10[b]
	1[a], 10[b]	
1		
Laser parameters:		
Depth (µm)	5	
5		
5		
Scan speed (µm/sec)	40[b]	
40[b]		
40[b]		
Energy (%)	70,100	
100		
55[a], 60[b], 75[a]		
Frequency (Hz)	20	
20		
10		
Spot size (µm)	60[a], 80[a], 120[b], 160[b]	
40[a], 60[a], 80[a], 95[a], 160[b]	12, 16, 40[b]	
Dwell (s)		60[a], 70[a]
	19[a]	
19[a]		

a = point analysis. b = bulk analysis.

RESULTS AND DISCUSSION

LA-ICP-MS has turned out to be suitable for the characterization of fly ash and deposit samples (Spears 2004; Spears and Martinez-Tarrazona 2004; Piispanen et al. 2008a; Piispanen et al. 2008b). In this study, we extend the method to bed particles using bulk and point analysis. The results case of sample I are compared to SEM-EDS and ICP-OES (see Fig. 1). The determination of phosphorous and sulfur is challenging with both LA-ICP-MS and SEM-EDS. The bulk analyses as determined with these three methods agree well with each other.

Comparison the results of samples I, II, IV, and V the point analyses for the most interesting elements present in agglomerates are shown in Fig. 2. Both LA-ICP-MS and SEM-EDS data were collected from the same points. Although manganese appears only a small amount in the sample it is easily detectable with LA-ICP-MS. On this account it was possible to use smaller spot size for manganese than for other elements. The results were comparable with those determined by SEM-EDS. LA-ICP-MS and SEM-EDS determinations showed more deviation for silicon than other elements.

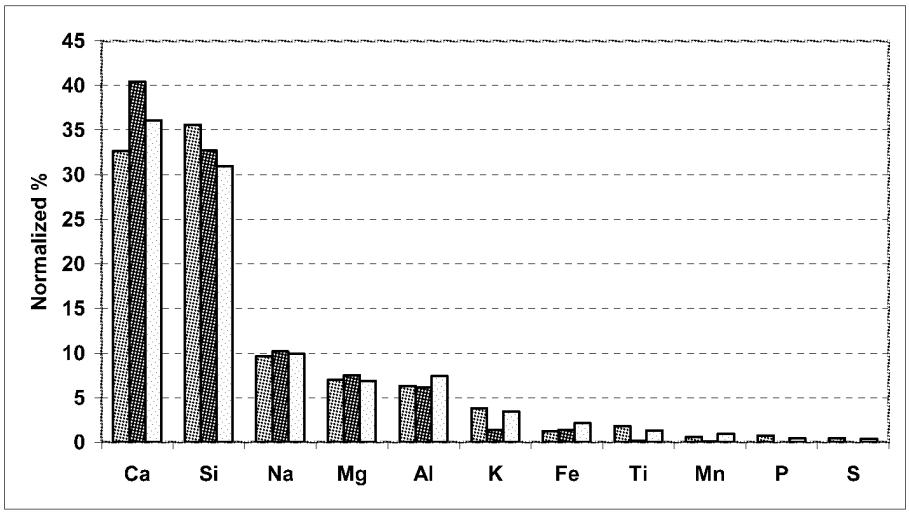

Fig.1 The chemical composition of bed sample I

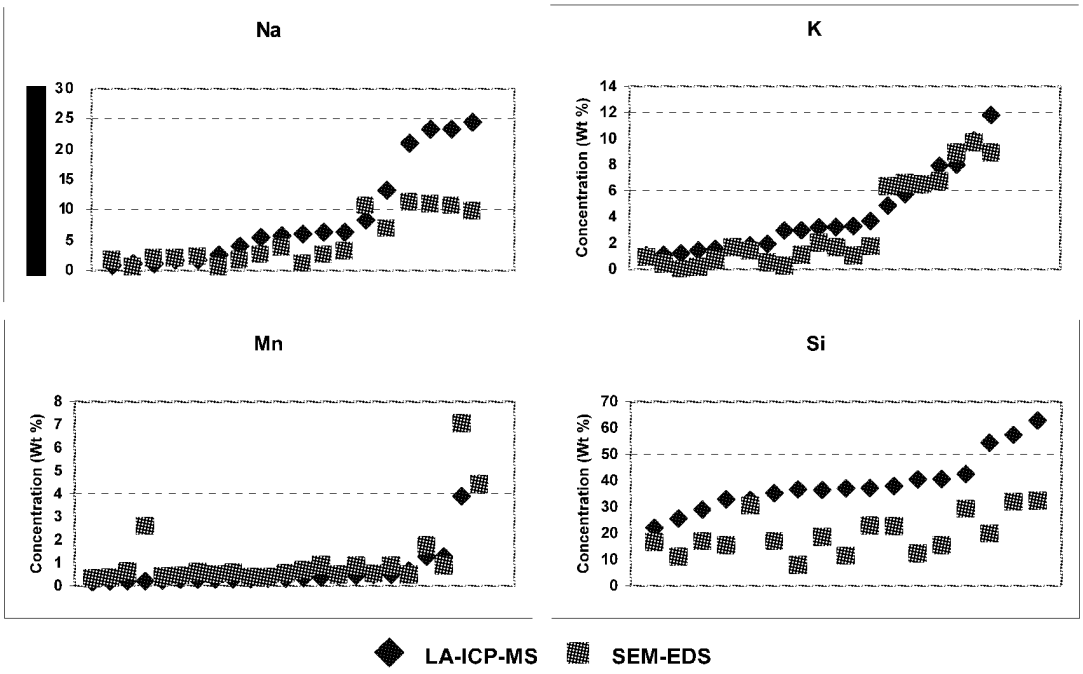

Fig. 2 The results of point analyses of the bed samples I, II, IV, and V for sodium, potassium, manganese, and silicon

With silicon sodium and potassium can form a low melting phase in bed and they can act as adhering material between bed particles leading to agglomeration. X-ray maps clearly show the agglomeration of bed particles, as exemplified in Fig. 3 for the sample II. The elemental distribution of adhesive material is presented on the quasiternary diagram. Manganese occurs as a minor element in solid biofuels. In addition to the coating layers of the bed particles was also enclosed in the agglomerate (Fig. 3). Manganese seems to occur together with calcium, magnesium, phosphorous, titanium and, iron. The content of manganese ranges between 0.5 and 5 % being higher in the outer layer than in the inner layer. If the combustion temperature is about 700 ˚C manganese occurs as oxides or sulfides. When the temperature of the bed is between 800-900 ˚C manganese occurs mainly as oxides. The formation of $MnSO_4$ is not possible because it is unstable temperatures (800-900 ˚C) (Gilewicz-Wolter et al.,2004). Manganese are found in the bed material, especially, when the pine sawdust and/or plywood was used as a fuel (samples I-V). Smaller contents of manganese were found in samples VI-VIII that were produced by combusting olive stones and forest residue.

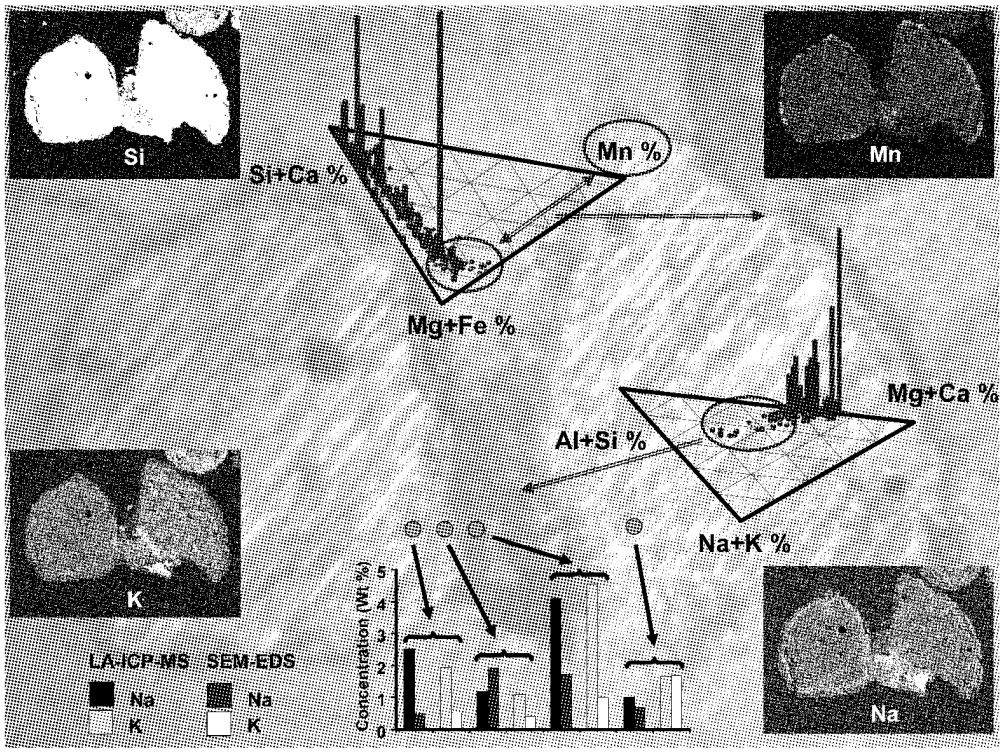

Fig. 3 Sticky material is formed between two silicate particles in sample II. Main components of the material are alkali metal silicates which can be seen in the X-ray maps and the quasiternary diagram on the right. The contents of sodium and potassium are higher between particles than inside the particles as the bar graph indicates. Manganese has mainly been gathered on the surface of bed particles as the X-ray map illustrates. Manganese seems to be linked with magnesium and iron and to a lesser extent with calcium

CONCLUSIONS

The scope of this study has been to apply LA-ICP-MS for the chemical characterization of bed material. Both bulk and point analyses were tested and the results were compared with those of SEM-EDS and ICP-OES. According to these results, LA-ICP-MS can be applied also in the investigations of bed particle coatings.

Eight bed samples were investigated in this study. Main components of the melt material between the bed particles seem to be alkali metal silicates. These compounds are sticky and induce agglomeration of the bed particles. The behavior of manganese is similar to that of calcium, magnesium, phosphorous, titanium, and iron. They are enclosed in the outer layer of the particles. The significance of manganese seems to be more an inhibitor than an accelerator in agglomeration.

ACKNOWLEDGEMENTS

This work was supported financially by Academy of Finland and Fortum foundation.

REFERENCES

Arvelakis, S., Gehrmann, H., Beckmann, M. and Koukios, E. G.: Biomass Bioenerg. **22** (2002), pp.55-69.
Brus, E., Öhman, M. and Nordin, A.: Energ. Fuel. **19** (2005), pp.825-832.
De Geyter, S. (2006). Master Thesis, University of Umeå.
Erikson, K. M., Thompson, K., Aschner, J. and Aschner, M.: Pharmacol. Therapeut. **113** (2008), pp.369-377.
Fernándes Llorente, M. J. and Escalda Cuadrado, R.: Fuel **86** (2007), pp.867-876.
Gilewicz-Wolter, J., Żurek, Z. and Dudała, J.: Solid State Ionics **170** (2004), pp.287-295.
Grubor, B. D., Oka, S. N., Ilić, M. S., Dakić, D. V. and Arsić, B. T. (1995). Proceedings 13th of the International Conference on Fluidized Bed Combustion. FBC Conference. pp.515-522.
Kalembkiewicz, J., Sitarz-Palczak, E. and Zapala, L.: Microchem. J. **90** (2008), pp.37-43.
Kouvo, P. and Backman R.: Fuel **82** (2003), pp.741-753.
Lin, C. H., Teng, J. T. and Chyang, C. S.: Combust. Flame **110** (1997), pp.163-172.
Lin, W., Dam-Johansen, K. and Frandsen, F.: Chem. Eng. J. **96** (2003), pp.171-185.
Nuutinen, L. H., Tiainen, M. S., Virtanen, M. E., Enestam, S. H. and Laitinen, R. S.: Energ. Fuel **18** (2004), pp.127-139.
Obernberger, I., Brunner, T. and Bärnthaler, G.: Biomass Bioenerg. **30** (2006), pp.973-982.
Piispanen, M. H., Arvilommi, S. A., Van den Broeck, B., Nuutinen, L. H., Tiainen, M.S., Perämäki, P. J. and Laitinen, R. S.: Energ.

Fuel., submitted (2008a).
Piispanen, M. H., Tiainen, M.S. and Laitinen, R. S.: Energ. Fuel., submitted (2008b).
Spears D. A.: Fuel **83** (2004), pp.1765-1770.
Spears, D. A. and Martinez-Tarrazona, M. R.: Fuel **83** (2004), pp.2265-2270.
Standard Test Method for Major and Minor Elements in Coal and Coke Ash by Atomic Absorption, D 3682-87, Annual Book of ASTM Standards, Gaseous Fuels; Coal and Coke, Ed.; (1989), pp.345-350.
Thompson, D. and Argend, B. B.: Fuel **81** (2002), pp.345-361.
Virtanen, M. E., Tiainen, M. S. and Laitinen, R. S.: (2000), In 5th European Conference on Industrial Furnaces and Boilers, INFUD, Ed., INFUD: Porto, Portucal, Vol. II, pp.117-126.
Visser, H. J. M. (2004). Energy Research Center of the Netherlands, ECN-C—04-054.
Vuthaluru, H. B. and Zhang, D. K.: Fuel **80** (2001), pp.583-598.
Zhang, D-k., Jackson, P. J. and Vuthaluru H. B. (1999) Impacts of Mineral Impurities in Solid Fuel Combustion.
Öhman, M. and Nordin A.: Energ. Fuel. **14** (2000), pp.169-178.

INVESTIGATION ON AGROPELLET COMBUSTION IN THE FLUIDIZED BED

Isemin R.L., Konayahin V.V., Kuzmin S.N., Zorin A.T., Mikhalev A.V.

Biocenter, Tambov State Technical University, Tambov, 392000, Russia

Abstract: Agricultural wastes (straw, sunflower or millet husk, etc.) are difficult to use as fuel because of low bulk density and relatively big ash content with a low melting point. It is possible to produce agropellets of agricultural wastes which are suggested to combust in a fluidized bed of pellets alone, their char particles and ash. The characteristics of the process of fluidization of agropellets are investigated at room temperature. The experiments on agropellet combustion in a fluidized bed are carried out in an experimental set-up. The results of the experiments have shown that in such a bed the pellets produced of straw and millet husk combust with the same rate as those of wood though the latter contain 8.76 – 19.4 times less ash. The duration of combustion of the same portion of straw pellets in a fluidized bed is 3.74 – 7.01 times less than the duration of combustion of cut straw in a fixed bed. Besides, the movement of agropellets prevents agglomeration and slagging of a boiler furnace.

Keywords: agropellets, fluidized bed, combustion rate, ash

INTRODUCTION

About 33 million tons of agricultural wastes (straw, sunflower and millet husk, etc.) is produced in Russia every year. About $4 \cdot 10^8$ MJ of thermal energy can be obtained during the combustion of agricultural wastes. However, the use of these wastes as fuel in their natural kind is economically reasonable only in rare cases due to their low bulk density (30 – 85 kg/m^3). The reprocessing of agricultural wastes into pellets allows to raise bulk density up to 630 – 670 kg/m^3. Pellets are homogeneous fuel, which feeding into a boiler furnace is rather easy to mechanize and to make automatic. However, the ash content in straw varies from 4.5 % in rye to 6.5 % in wheat, and the ash content in wood is usually about 0.5 % (Vares, 2005). The softening of straw ash can begin at 735 °C, and the melting of fluidized straw ash began at 1175 °C (Vares, 2005). As for wood, for example pine chip, the melting of fluidized ash begins at 1275 °C (Vares, 2005). All these make the work of boilers and furnace plants of known designs unreliable for agropellet combustion (Andreasen and Larsen, 1996). The combustion of agricultural wastes in most cases is carried out in a dense bed on a moving grate (Andreasen and Larsen, 1996; Yang et al., 2007). This method of agricultural waste combustion has a number of disadvantages (Khor, 2007): 1) the combustion rate of these fuel materials is low and does not exceed 250 (kg/m^2 hour); 2) the extreme dependence of the combustion rate on the blast air flow rate is observed. It requires substantial enlargement of sizes of furnaces and boilers when designing the boilers of greater productivity; 3) slag agglomerate, obstructing the work of furnaces and boilers, is formed. We have suggested combusting agropellets in a fluidized bed which consists of pellets alone, char particles formed after the emission of volatile matter and ash from pellet combustion. Pellets are large particles and their fluidization is possible at high gas velocity. Pellets are heavy particles which while moving can destroy formed agglomerate. Because of high gas velocity and exposed to pellet blows, the ash formed at pellet combustion will be crushed and taken out of a bed with smoke fumes, i.e. there will be no accumulation of potassium compounds in a bed.

EXPERIMENTAL

Agropellets are large particles of a cylindrical shape. The organization of the process of pellet combustion in a bed formed by pellets and solid products of their combustion presupposes the preliminary determination of the value of the minimum velocity of fluidization and the study of other characteristics of fluidization of such a bed, because particles of such a size as pellets are seldom used in the technology of fluidization. It is much more difficult to determine the minimum velocity of fluidization of a bed consisting of large particles of an irregular shape using the pressure drop in a bed versus velocity of gas passing through a gas bed diagram. (Abdullah M.Z. et al., 2003; Reina J et al., 2000). Therefore the present work is divided into two stages. At the first stage the processes of agropellet fluidization at room temperature were investigated. The characteristics of these processes are given in Table 1. The experiments were carried out in the apparatus with transparent walls which section was 483×195 mm and the height was 1500 mm. The apparatus was arranged upon a grill with 5 % fraction of an open area. The pressure drop in a bed was measured by a differential micromanometer «Testo 525», and the air flow rate on the outlet of the apparatus was measured by a heat-loss anemometer «Testo 405

V1». The micromanometer «Testo 525» allowed to register 12000 values of pressure drop in a bed in every 50 microseconds. The pressure drop measurements in a bed were carried out at increase (fluidization) and decrease (defluidisation) of the air flow rate feeding under the bed. The height of the bed of motionless particles varied from 44 to 230 mm. Using the results of the experiments the following values were calculated for each experiment by known methods (Leo and Lan, 1990): mean value of pressure drop through the bed (ΔP), root-mean-square deviation of pressure fluctuations (σ),dimensionless pressure fluctuation amplitude (δ) and absolute value of dimensionless pressure fluctuation amplitude ($|\Delta\delta| = \delta_i - \delta_{i-1}$). For the recording of the visual examination the video shooting of a bed in each experiment with a high-speed video camera was applied.

Table 1 Characteristic of agropellets

Name of an index	Wood wastes pellets (type 1)	Millet shell pellets (type 2)	Winter wheat straw pellets (type 3)
Diameter, mm	8.0	8.0	7.0
Ratio diameter of pellets to their average length	1:3	1:3	1:3
Density, kg/m^3	1050	1250	1110
Ash content, %, %	0.5	9.7	4.38
Emission of volatile matter, %	75.0	82.0	68.67
Heating value, MJ/kg	20.73	18.38	15.42

An experimental set-up was made for the research of the combustion processes of a portion of pellets. It was a fire-tube boiler (Kuzmin et al., 2006). A grill with 5 % fraction of an open area was placed on the bottom of a fire tube. The diameter of the fire tube of the experimental set-up was 1000 mm, the length was 600 mm. In the course of the experiments, a fresh pellet portion with the weight of 4.2 kg was fed intermittently on the bed of the hot ash remained from the combustion of the previous portion of pellets of the same type. Then a forced draft fan was turned on and the portion of pellets ignited. At the same time the temperature of gases over the bed of the combusting fuel was measured in every second by a Ni/Cr thermocouple of type (K) connected to the device «Center – 306» and to the computer. The air flow rate (U) on the outlet of a forced draft fan was measured by a heat-loss anemometer and was measured within the range from 0.065 to 0.25 kg/s. After the ending of the combustion of each portion of fuel, the sample was taken out of the furnace and exposed to the analysis for the identification of char content. Five experiments were carried out with each value of mass flow rate of air and for each type of pellets.

RESULTS AND DISCUSSION

Investigation on the processes of agropellet fluidization at room temperature

Figure 1 shows the dependence of a mathematical expectation of pressure drop through the bed on the air velocity passing through the bed. According to Fig. 1, it can be said that for a straw pellet bed the complete fluidization becomes possible at the air velocity of 2.4 m/s. For a millet husk bed the complete fluidization becomes possible at the air velocity of 2.6 m/s.

However, the visual examination shows that at the air velocity of 2.37 m/s in a bed of straw pellets, there are two heterogeneous streams which emit of the bed surface, thus the remained bed is motionless (Fig. 1(a)). The same as for straw pellets at the air velocity of approximately 2.6 m/s, at which according to Fig.1(b) complete fluidization of a millet husk pellet bed should take place, a heterogeneous stream, emitting of the surface of a bed, is formed at the air velocity of 2.56 m/s. Pellets out of a zone of the influence of this stream are motionless (Fig. 1).

Complete fluidization of a straw pellet bed occurs at the air velocity of 3.09 m/s. There is a formation of an air bubble (Figs.2(a)–(d)). Then the air bubble bursts upwards and the bed starts to expand (Figs.2(e)–(h)). After that the bed subsides, but the formation of a new air bubble begins.

A millet husk pellet bed becomes completely fluidized at the air velocity of 3.24 m/s. At the air velocity of 3.24 m/s the formation of a big air bubble occupying the whole open area of the apparatus is clearly seen (Figs.3(a),(b)). Then the bubble bursts (Figs.3(c)–(d)). Simultaneously with it there is a formation of a new bubble (Figs.3(e),(f)) and its bursting (Figs.3(g)–(h)).

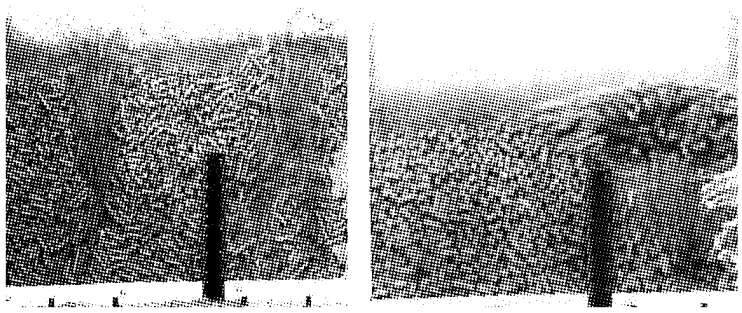

(a) (b)

Fig. 1 Condition of a straw pellet bed (air velocity of U=2.37 m/s) (a) and condition of a millet husk pellet bed (air velocity = 2.56 m/s) (b)

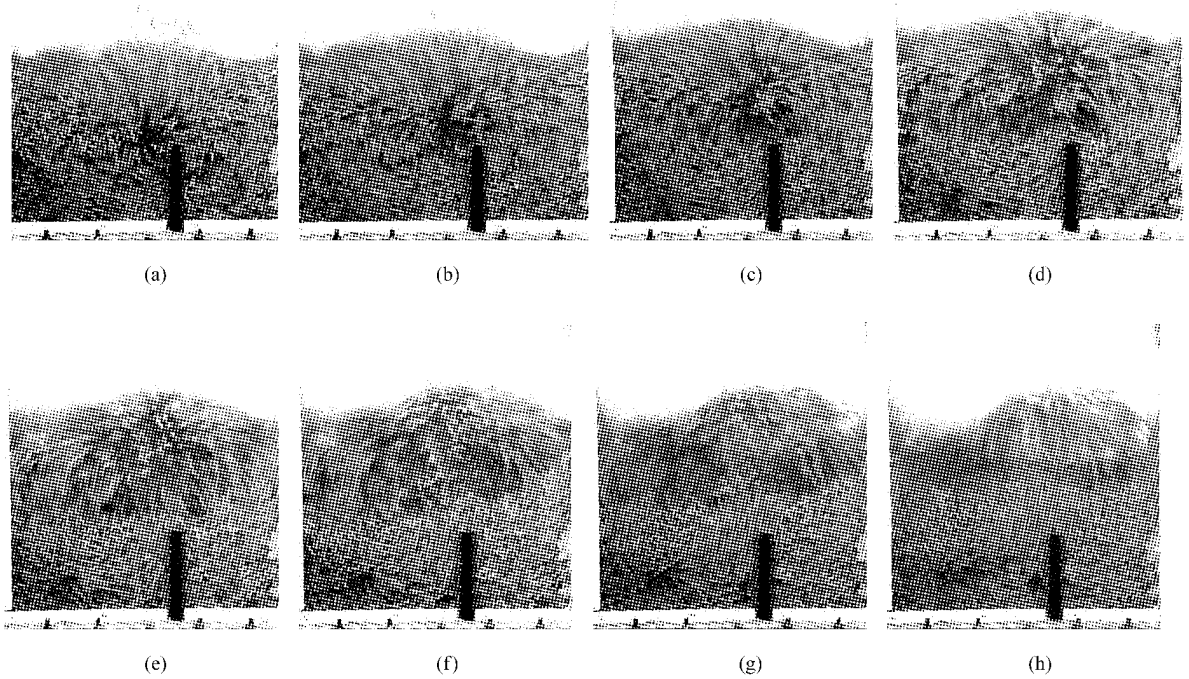

(a) (b) (c) (d)

(e) (f) (g) (h)

Fig. 2 Sequence of pictures of a physical form of straw granules. Air velocity = 3.09 m/s.

Thus, for a bed of particles of such a size and shape as pellets, the determination of the value of minimum combustion rate according to the pressure drop through the bed versus velocity of gas passing through the bed diagram is impossible. According to the diagram, at the value of the rate, determined in it, the pellet bed should completely become fluidized, but in fact the conversion only begins. Complete fluidization of a pellet bed occurs under the influence of formation and bursting of air bubbles. The frequency of formation and bursting of air bubbles at the stage of conversion from the initial fluidization to the complete fluidization increases with the increase of the air velocity passing through the bed at from 4.17 Hz for straw pellets and 5.0 for millet husk pellets to 6.25 Hz and 12.5 Hz for straw pellets and millet husk pellets respectively. After the complete conversion of a pellet bed into a fluidized condition, the frequency of formation and bursting of air bubbles doesn't change within the studied range of changes of the air velocity passing through the bed.

The method of the determination of the initial velocity of fluidization according to the change of a root-mean-square deviation of a random value of pressure drop fluctuations is also improper (Li et al., 2002, Puncochar et al., 1985; Leu and Lan, 1990). The curves of σ versus air velocity passing through the bed are given in Fig. 4. Using Fig. 4 it is impossible to determine the value of air velocity at which the bed becomes completely fluidized.

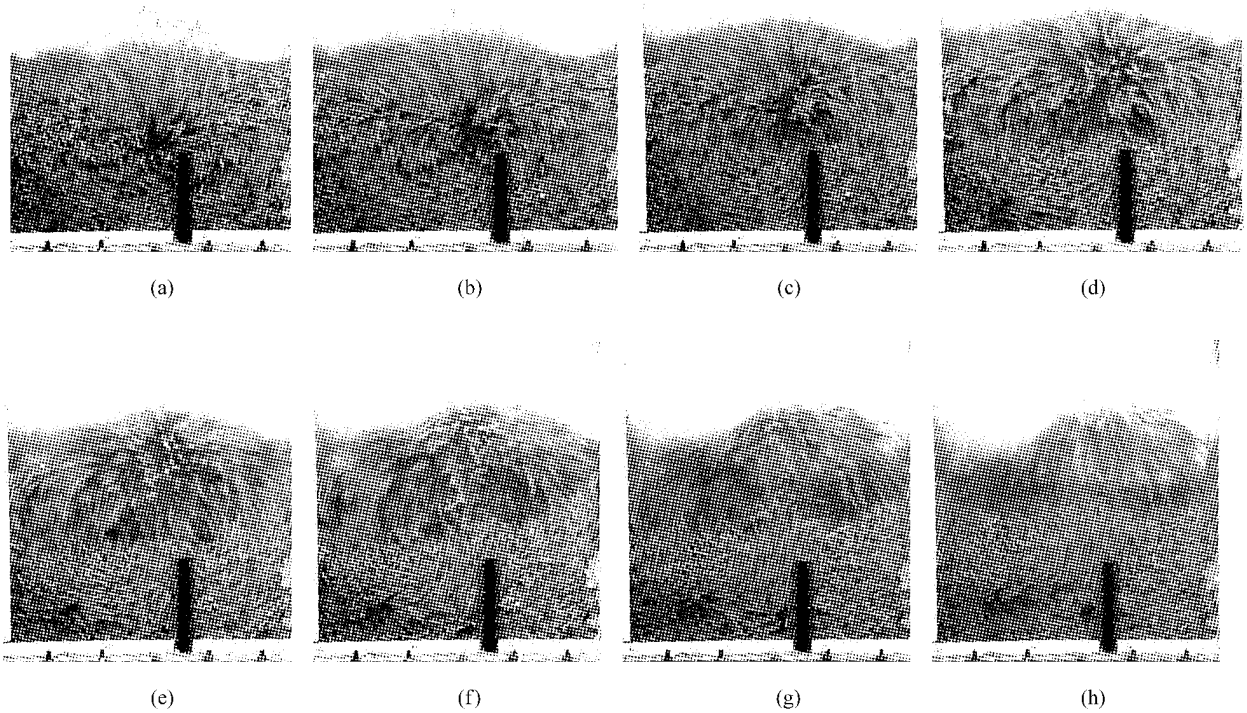

Fig. 3 Sequence of pictures of a physical form of a millet husk pellet bed. Air velocity = 3.24 m/s

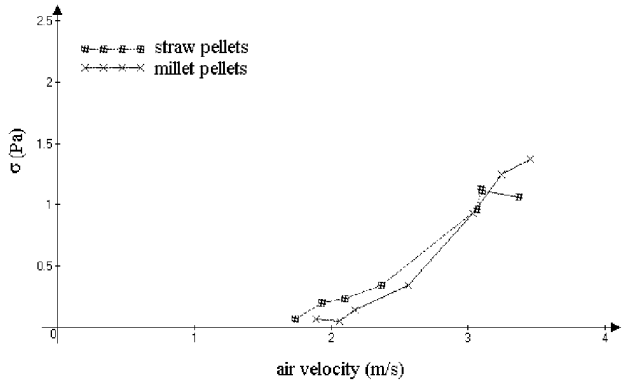

Fig. 4 Effect of σ on air velocity

However it turned out that the diagrams of $|\Delta\delta|$ versus air velocity can be used for the determination of values of minimum velocity of fluidization of a pellet bed (Fig. 5). That is really so that for a pellet bed a monotonous growth of $|\Delta\delta|$ is observed until the bed has become completely fluidized. The value $|\Delta\delta|$ sharply drops at the complete fluidization of a bed. Such drop for a millet husk pellet bed is observed at the air velocity of 3.24 m/s. For straw pellet the air velocity is 3.09 m/s. All these values exactly correspond to the results of the visual examination. As it has been shown earlier, after the conversion of a pellet bed into a fluidized condition, the frequency of formation and bursting of air bubbles which provides circulation of particles in a bed and causes pressure drop fluctuations, does not change. Therefore $|\Delta\delta|$ tends to zero.

The study of the process of fluidization of beds consisting of cylindrical pellets on a cold flow fluidization model has shown:

1) Fluidization of a pellet bed is provided due to the formation and bursting of air bubbles in a bed.

2) Air bubbles accumulate streams of fluidizing gas.

3) Therefore there is no necessity in even distribution of fluidizing gas on an input of a bed, for example, by means of cap gas-distributing grills.

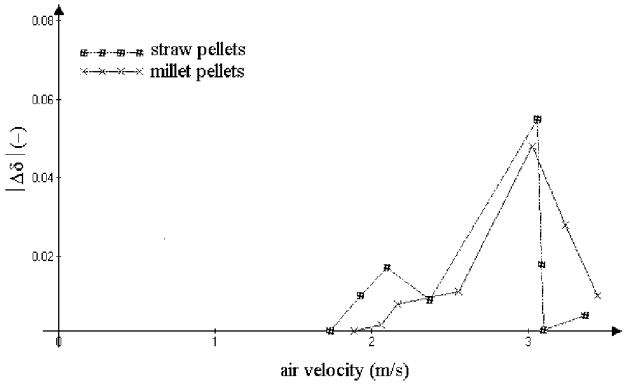

Fig. 5 Effect of |Δδ| on air velocity

Change of gas temperature over a bed of combusting fuel, the rate of fuel combustion

During the combustion of wood pellets, the gas temperature curve (Figs. 6 (a), (b)) has two clearly defined upper limits. By analogy with (Khor et al., 2007), it is possible to explain the left upper limit by the achievement of the maximum temperature at the combustion of volatile matter, and the right upper limit – at the combustion of char. With the increase of the gas velocity in 3.85 times the duration of combustion of a wood pellet portion decreases 2.61 times. At the gas velocity equal to 0.065 kg/s, the maximum temperature of gases over a bed of combusting fuel (1020 °C) is achieved at the combustion of char of wood pellets; and at the air flow rate of 0.25 kg/s, the maximum temperature is achieved during the combustion of volatile matter (980 °C).

During the combustion of straw pellets at the air flow rate of 0.065 kg/s two upper limits are also determined on a gas temperature curve (Fig. 6(c)). The maximum temperature of gases over a bed of fuel does not exceed 920 °C. The duration of combustion of a straw pellet portion at this air flow rate is 133.8 s. At the air flow rate of 0.25 kg/s only a weak maximum related to the combustion of char of pellets is determined on a gas temperature curve over a bed of combusting fuel (Fig. 6 (d)). The maximum temperature of gases over a bed of combusting pellets does not exceed 980 °C, and the duration of combustion of a portion of fuel is 71.3 s. The combustion rate of straw pellets in a fluidized bed is almost equal to the combustion rate of wood pellets in the same bed. The recalculation of the experimental data presented in the work (Khor et al.,2007) has shown that the portion of cut straw in a dense bed would combust at least 500 s (Khor et al.,2007) and it is 3.74 – 7.01 times more than the duration of straw pellet combustion in a fluidized bed.

While combusting millet husk pellets at the air flow rate of 0.065 kg/s (Fig.6 (e)) a diffuse maximum, corresponding to the maximum temperature, achieved during the combustion of volatile matter (1000 °C), and a sharp maximum corresponding to the maximum value of temperature, achieved during the combustion of char (also 1000 °C) are determined on a gas temperature curve. The duration of combustion of a portion of millet husk pellets at the air flow rate of 0.065 kg/s is 141.4 s. Two upper limits are also determined on a gas

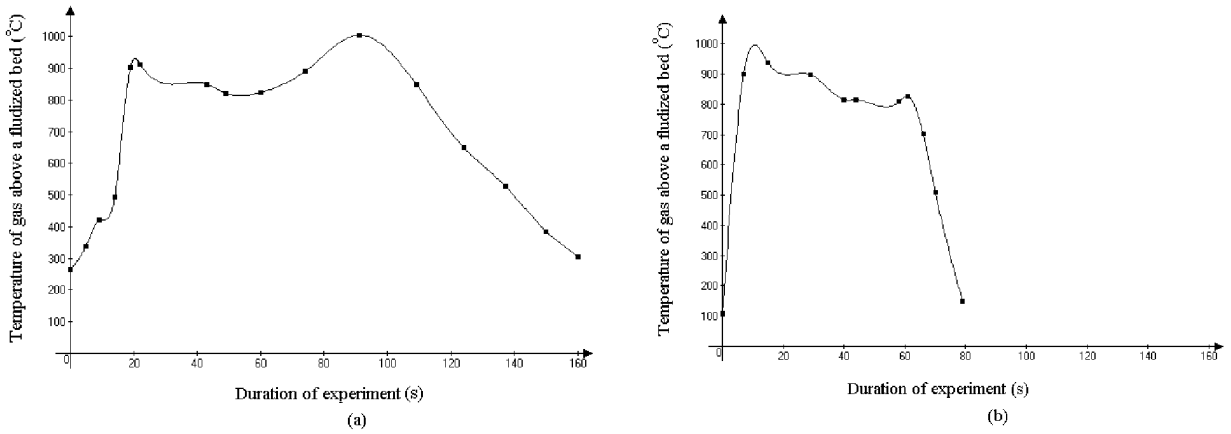

Fig. 6 Gases temperature curve over a bed of combusting pellets (a, b – wood pellets 1, a – mass flow rate of air is 0.065 kg/s, b – mass flow rate of air is 0.25 kg/s; c,d – straw pellets, c – mass flow rate of air is 0.065 kg/s, d – mass flow rate of air is 0.25 kg/s; e, f – agropellets of millet husk, e – mass flow rate of air is 0.065 kg/s, f – mass flow rate of air is 0,25 kg/s)

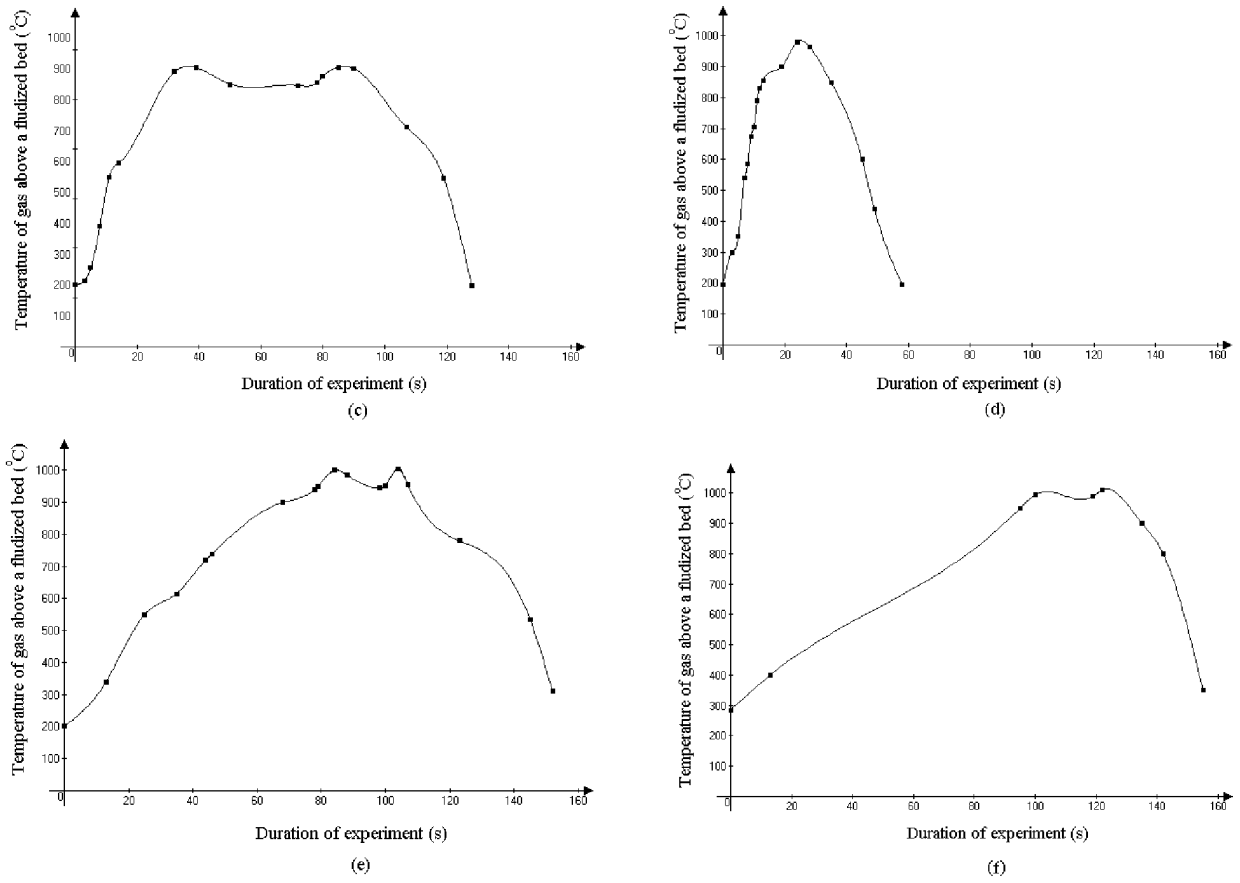

Fig. 6(Continued)

temperature curve over a bed of combusting fuel at the air flow rate of 0.25 kg/s (Fig. 3（f）): 1000 °C – at the combustion of volatile matter, 1020 °C – at the combustion of char. The duration of combustion of the same portions of millet husk pellets and wood pellets in a fluidized bed is similar, though millet husk pellets contain 19,4 times more ash, than wood pellets.

In the course of the visual examination it has been ascertained that moving in a bed agropellets and their char particles prevent slagging and agglomeration. The furnace refuse of agropellet combustion, carried out in the present research, was powder-like, without slag agglomerate.

CONCLUSIONS

In the course of the investigation the following results have been ascertained:

（1）The agropellet combustion in the fluidized bed formed by pellets alone, char particles and ash is possible. The duration of combustion of agropellet portions and the duration of combustion of wood pellets with identical weight in such a bed are almost equal, though the latter contain 8.76 – 19.4 times less ash. The duration of combustion of a straw pellet portion in a fluidized bed is 3.74 – 7.01 times less than the minimum duration of combustion of a cut straw portion which weight is equal to the weight of a straw pellet portion.

（2）The determination of the minimum velocity of agropellet fluidization on a pressure drop versus gas velocity curve in a bed of pellets is impossible. The minimum velocity of fluidization of agropellets may be determined by the pressure fluctuation method only.

（3）In the course of agropellet combustion the furnace refuse has a powder-like structure; there is no sintered ash and slag agglomerate in it.

NOTATIONS

U_i – initial fluidization velocity, m/s,
U_c – complete fluidization velocity, m/s
ΔP –pressure drop through the bed, Pa
σ –root-mean-square deviation of pressure fluctuations, Pa

δ– dimensionless pressure fluctuation amplitude, (-)

$|\Delta\delta|$ - the absolute value of dimensionless pressure fluctuation amplitude, (-)

REFERENCES

Vares V. (2005) Handbook of the consumer of biofuel, Tallinn, TPU.

Andreasen P., Larsen M.G. (1996) Straw Pellets as Fuel in Biomass Combustion Units. 9th European Conference in Copenhagen.

Yang Y. B., Newman R., Sharifi V., Swithenbank J., Ariss J.: Fuel. **86** (2007), pp. 129-142.

Khor A., Ryu Ch., Yang Y.B., Sharifi V. N., Swithenbank J.: Fuel. **87** (2007), pp. 152-160.

Leo L.-P., Lan Ch.-W.: J. of Chem. Eng. of Japan. **23** (1990), pp. 555 – 562.

Kuzmin S. N., Isemin R.L., Konjakhin V.V., Mikhalev A.V., Panfilova O.V., Zorin A.T. (2006) Co – combustion of coal and bio – pellets in the high temperature fluidized bed. 19th Int. FBC conference.

Li Z., Kobayashi N., Nashimura A., Hasatani M.: Drying Technology. **20** (2002), pp. 1193-1213.

Abdullah M.Z., Husain Z., Yin Pong S.L.: Biomass and Bioenergy **24** (2003), pp. 487-494.

Reina J., Velo E., Puigjaner L.:Powder Technology **111** (2000), pp. 245 – 251.

Puncochar M., Drahos J., Cermak J., Selucky K.: Chemical Engineering Communications, **35** (1985), pp. 81-87.

Leu L.P., Lan Ch-W.: Journal of Chemical Engineering of Japan, **23** (1990), pp. 555 – 562.

CHEMICAL CHARACTERIZATION OF WASTE FUEL FOR FLUIDIZED BED COMBUSTION

F. Claesson [1,2,3], B-J. Skrifvars[1], A-L. Elled[2], A. Johansson[2,3]

1 Åbo Akademi Process Chemistry Centre, Biskopsgatan 8, FIN-20500 ÅBO, Finland

2 University of Borås, SE-50190 Borås, Sweden

3 SP Technical Research Institute of Sweden, SE-501 15 Borås, Sweden

Abstract: Combustible waste is very heterogeneous and the variation in chemical composition is of great significance for the performance of the combustors in terms of boiler availability and power efficiency. For example, the content of alkali, Chlorine and sulfur affect agglomeration, fouling and corrosion mechanisms, which often limits the steam data and requires counteracts such as soot blowing and outages. An increased knowledge on favorable levels and ratios of fuel components are therefore highly important when developing waste combustors, both existing and future. However, to be able to make good predictions of reactions, reliable fuel analyses are a necessity and they are difficult to perform because of the heterogeneity of waste. As a consequence, it is also difficult to complete pro-active measure to reduce unwanted reactions.

This work has investigated the composition of the fuel during one year in a 40 MW commercial BFB waste plant. Twelve samples have been performed in order to estimate the variation of key components. The fuel samples were analyzed chemically for alkali and several other components of interest, such as Cl and S. Moreover, thermo-chemical multi-phase equilibrium calculations were performed for prediction of the chemical composition of the furnace in the temperature range 400-1000 °C. In this temperature range NaCl and $PbCl_x$ are formed as well as gas phase HCl and solid silicates. Furthermore, the calculations show that the chemistry is very sensitive to the input chemical composition, suggesting that already a minor shift in fuel mineral matter may change the behavior of the fuel radically in terms of its fouling and corrosion tendency.

Keywords: BFB, Waste combustion, chemical characterization, thermodynamic equilibrium calculations

INTRODUCTION

Landfilling of waste significantly contributes to release of methane gas (e.g. Zhang et al.,2008), which is a known green house gas, with a warming potential 21 times more powerful than carbon dioxide (IPCC, 2001). Furthermore, natural caused leaching of landfills leaks environmentally hazardous compounds into the nature. At the same time there is an increasing demand for raw material for production of heat, power, steam and vehicle fuels. Combustion of waste can therefore serve two purposes; production of heat and power and reduction of emission of methane. As a consequence, more and more countries are nowadays prohibiting landfilling of organic and combustible waste. In Sweden it has been prohibited to landfill combustible waste since 2002 and there are now about 30 operating waste combustion plants, contributing to district heating networks and supplying electricity. Less than 5 % of the MSW in Sweden is landfilled (Naturvårdsverket, 2008). A decreased landfilling in favor for an increased energy recovery from waste is expected in many countries, with combustion as a major conversion technology. The potential for waste combustion is vast. Many European countries still use landfill as the major method for treatment of MSW, which also globally is the dominating treatment method (Eurostat, 2007).

Waste as a fuel is, however, more complicated than other fuels due to the heterogeneous composition the high content of inorganic components. Several studies made over the last decades like Uberoi (1990) and van Lith (2006) have pointed out that the fuel composition is a determining factor considering combustion conditions and it highly affects the occurrence of fouling and corrosion. Compared to other biomass, waste contains a high amount of ash forming elements, which also contributes to the high risk of fouling. Furthermore, elements like alkali metals, Chlorine and Sulfur, which in high levels are present in waste, governs the formation of deposits, causing lower boiler efficiency, shorter boiler lifetimes and an increased need of maintenance. Induced by a high temperature, Chlorine-containing deposits are also known to cause severe corrosion on super heaters. To minimize these problems today, waste boilers are operated at a significant lower steam temperature than fossil fuel boilers (Nielsen, 2000).

During combustion, alkali metals are partly released from the fuel and once released the elements are easily available for chemical reaction. The main pathways are determined by the access of Sulfur and Chlorine,

but also by the other ash composition. Potassium in combination with Chlorine and / or silica is known to contribute to combustion problems in biomass combustion (Baxter, 1998). In waste combustion, the high share of sodium amplifies the alkali reactions with Chlorine, enhancing the possibility of corrosive deposits and reduced heat exchange. Alkali can be removed from the flue gas by ash components such as aluminum silicates (Uberoi,1990) and phosphates (Lindström,2007).

The trace elements zinc and lead have gained attention lately, due to their possibility to form corrosive deposits with Chlorine and Sulfur (Bøjer 2008 and Yao,2009). Moreover, Niemi et al. (2005) show that both lead and zinc chlorides melts at lower temperatures than alkali chlorides, creating an even more corrosive environment. Lead and zinc are often present in waste and should be considered as possible participants in deposit formation and contributors to boiler wear.

From an environmental, as well as an economical point of view, it is a necessity to enhance the knowledge regarding waste fuel mixtures. A better understanding of the chemical behavior in the boiler is helpful and of great importance when improving existing waste combustors, as well as designing for the future. A retrofit of present combustors based on the knowledge of origin of the problems could increase the boiler lifetimes and hence be of economical interest. Fewer boiler shut downs and increased durability are other motivations for studying parameters related to the main problems, fouling and corrosion.

The purpose of this work was to characterize the chemical composition of the ash forming material in waste. Sampling of waste is a complicated process due to the uncertainty of accuracy when taking just a few samples. The heterogeneous composition of waste gives great variation from time to time and therefore a single waste sample is not regarded as a general version of a whole waste bunker in terms of ash forming species and trace elements. One sample could be used but with the consideration that it only represents that particular waste and its unique composition. By performing repeated samplings over a long period of time a better overview of the fuel is gained and the scattering of different species can be correlated to for example, seasonal variation, large batches of a special industrial waste of a particular month or problems that arise in the boiler. Inorganic reactions during waste combustion differ somewhat from the ones in biomass combustion since a more varied fuel composition leads to more possible outcomes. Furthermore, the fuel characterization gives opportunities to perform reliable thermodynamic chemical calculations predicting possible outcomes of reactions during combustion. These calculations are helpful when estimating potential fouling or corrosion situations in the boiler, and are also a useful tool to investigate changes in the fuel mixtures to reduce these problems. In addition, the project investigates how variances in the fuel have different possible influences on combustion problems originating from the alkali, Chlorine and Sulfur content in the fuel. In 1976 Warnqvist and Norrström published results on removal of Chlorides from combustion. Another example is Pettersson et al. (2006) that showed in their work that alkali deposits in the super heater region can be suppressed by adding Sulfur to the combustion, forming the less corrosive Na_2SO_4 instead of NaCl.

EXPERIMENTAL

A commercial 40 MW plant with two 20 MW Bubbling Fluidized Bed (BFB) waste boilers (10 MW_e) designed by Metso Power operating at 49 bar and 405 °C, combusting 100 000 tonnes of waste per year was used for this project. The fuel flow is approximately fourteen tonnes per hour and this result in an ash flow of approximately 1.4 tonnes per hour. Four different ashes are produced, bottom ash, cyclone ash, ash from the empty gas pass and filter ash. The cyclone ash and the ash from the empty gas pass are collected in the same silo. Johansson et al. (2006) explains that the main part of the discharged bed ash is re-used as bed material in the furnace, reducing the consumption of fresh sand, while the coarse material is separated and fed to containers as bottom ash. The filter ash originates to a large extent from the lime added to the flue gas treatment plant. The waste burned in this BFB normally consists of 30 % MSW and 70 % industrial waste. During the summer months the industrial waste is baled and the combusted fuel is 100 % MSW. Figure 1 shows a schematic diagram of the BFB-system.

The MSW is initially sorted at household level, separating combustibles from for example, biodegradable waste, metals, glass, ceramics, and paper. The MSW is then taken to a preparation site where it is mixed with industrial waste, further separated from metals, and grinded into a particle size of around 100 mm. After this preparation process the waste fuel is transported to the boiler. From the dumping hall the fuel is fed to a conveyor by a large mechanical arm and via a screw feeder. The waste is then again passing a magnetic separator on its way to the combustion bed. A hatch is placed where the fuel falls down toward the last pass to the bed. At this point the waste fuel samples were collected from the falling stream of prepared waste. This was carried out by repentantly inserting a shovel into the falling waste stream in a certain pattern until a sample of circa 30 kg was collected. The fuel sampling was carried out during a one year period (September 2007 to August 2008) with twelve samples in total (one/month).

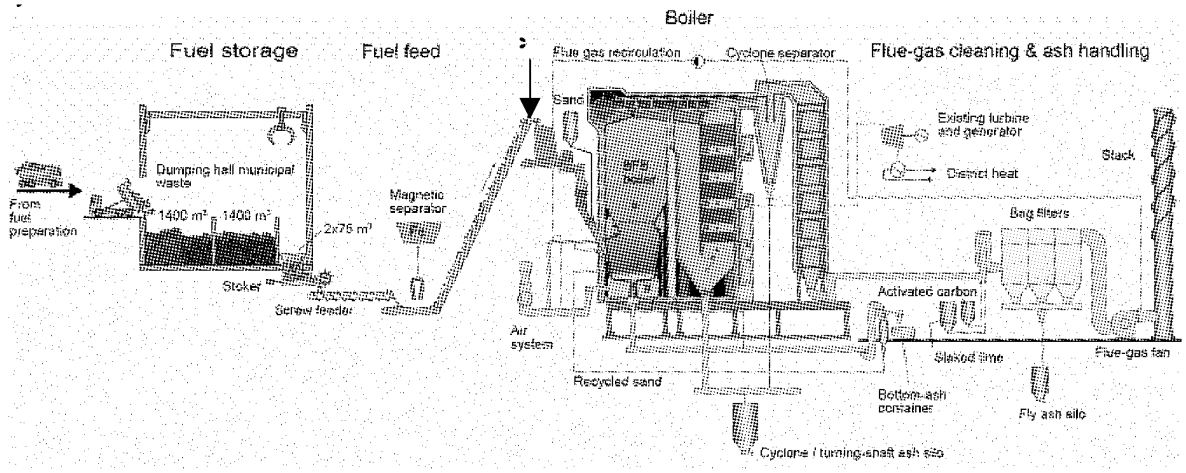

Fig.1 A schematic diagram of the BFB-system. Waste fuel is sampled in a falling stream after the magnetic separator. Sampling point is marked with * (Johansson, 2006)

Before analysis, the samples were fractioned and milled in a laboratory as preparation for the following chemical analysis process. Then the samples were chemically analyzed with ICP-OES (Inductively Coupled Plasma-Optical Emission Spectroscopy) for metal content and IC (Ion Chromatography) for Chlorine and Sulfur. The samples were also analyzed for moisture and heat value. The results from the analyses were used as input data to the chemical equilibrium calculations. Three different cases were analyzed; a reference case (#1) with normal combustion environment (oxidizing) where the average values from all fuel samples was used as input data. Case two (#2) is the same average values on all species except Chlorine, which has been decreased to the lowest measured value from the samples to investigate how the Chlorine content affect the reactions. In the third case (#3) the content of Sulfur was increased to a Chlorine-to-Sulfur ratio of 1:4 to simulate the influence of a Sulfur additive. All other values were kept at average for the samples. The program used was Factsage and the databases FToxid, FTsalt and Fact53 were used at an oxygen level of 5 %.

RESULTS AND DISCUSSION

Chemical characterization of waste fuel

In Table 1, the average values from the twelve waste fuel samples are compared with average values for coal and a woody fuel. Presented in the table are the main components and ash forming species of interest as well as two trace elements noted to vary in the fuel. The main differences in the chemical composition of these fuels are the moisture content and the ash content. High ash content implies a high share of metals, which often are troublesome in combustion processes. The lower effective heating value relates to the high moisture content in the waste. Compared to wood pellets, a commonly use fuel in Sweden, waste contains a higher share of Chlorine which is a potentially corrosive specie, especially in combination with high alkali content.

In Fig. 2 the variation of species are presented. Each sample of each species is normalized against its mean value. The y-axis represents thus the normalized value of each sample. Figure 2 is evidence of how heterogeneous waste are and that it is crucial to perform many fuel samplings over a long time period to characterize the fuel for a particular boiler. Taking only one fuel sample would not be representable since large differences occur over time.

For some species there is an upper and/or lower value represented with a black and grey line, respectively. These lines are guidelines for the fuel composition given by the boiler manufacturer. Sample 6 and 7 exceed the ash guideline and sample 6 also contains more Sulfur than recommended. In general carbon and hydrogen is not as scattered as the more varying ash forming species. This is natural since these species are main components in combustible waste and it is also a measure of the sampling method, giving the same result in main species but varying in ash forming species, such as Iron (Fe), Aluminum (Al), Silica (Si) and Potassium (K), like expected for a heterogeneous fuel. The largest scattering in the analysis results is found for Lead (Pb). In most months the Lead content in the fuel has been around 120 mg/kg ds. Two months are considerably separated from this number (6 and 4) and significantly increases the average.

The sample that diverts the most from the average is sample number six, taken in March 2008. This seems to be a consequence of an in general high share of ash in this sample. However, sample number 6 contains the least amount of Chlorine of all samples.

Table 1 Fuel analysis comparison. (Coal values taken from Pettersson, 2008)

	Coal	Wood pellets	Waste
Effective Heating Value (MJ/kg)	26.3	19.1	10.6
Moisture content (w-%)	9.4	7.6	35.3
Elemental analysis (wt-% ds*)			
Ash content	8.9	0.4	19.0
C	82.1	49.9	44.9
H	4.9	6.2	5.8
N	1.4	0.05	1.2
Cl	0.3	<0.01	0.5
S	0.6	<0.01	0.4
O**	10.7	43.4	28.2
Ash forming species (wt-% ds)			
Fe	0.06	0.007	0.5
Al	0.08	0.003	1.2
Si	2.1	0.02	3.7
Mg	0.04	0.01	0.3
Ca	0.07	0.09	2.6
Na	0.01	0.002	0.6
K	0.01	0.04	0.36
P	0.002	0.006	0.09
Trace elements (wt-% ds)			
Zn	-	0.001	0.06
Pb	-	-	0.02

* ds = dry substance, ** Oxygen is calculated as a percentage difference

The fuel samples were taken from September 2007 (1) to August (12) 2008. During the summer months, June, July and August (JJA), the industrial waste is baled and only household waste is combusted. JJA in this plot is represented by sample number 10 to 12 and as seen in the Fig., the amounts of almost all species are on or below average. Lower moisture content during JJA also gives a higher effective heating value during these months. The low ash content throughout JJA indicates that the MSW is of better quality and more sorted than the industrial waste. When the industrial waste is added in the fuel, a wider scattering range is noted.

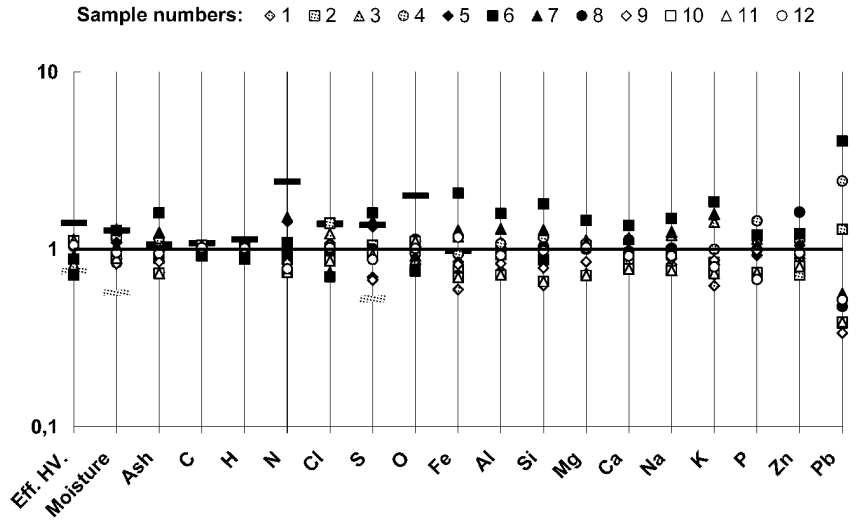

Fig. 2 Variation of species in the analyzed waste fuel

Chemical thermodynamic equilibrium calculations

The chemical thermodynamic equilibrium calculations were performed with the average values from the twelve fuel samples used as input data. Equilibrium calculations like these are to be used as plausible scenarios, and are only implying possible outcomes in equilibrium at each temperature, which is not always the true scenario. In addition to this, the calculated reactions do not take any consideration to kinetics or mixing.

Figure 3（a） shows the predicted sodium compounds at temperatures between 400 °C and 1000 °C. Most of the sodium is at these given conditions bound in silicates but with increasing temperature, there is a formation of Na_2SO_4 and NaCl that starts forming at 560 °C and increases with temperature. Figure 3(b) suggests that Chlorine is mostly found in the form of gaseous HCl but the share of alkali chlorides increases with the temperature. It is evident from the calculations that in the formation of corrosive alkali chlorides, sodium chloride is the favored compound rather than potassium chloride, showing sodium's importance in waste. The super heater temperature is just above 400 °C and it is at this point the fouling and corrosion is problematic when gaseous NaCl formed in higher temperatures can deposit on the colder heat exchanging surfaces.

Of the twelve fuel samples taken, the sample with the least amount of Chlorine (sample 6) contained 0.35 wt-% ds compared to the average of all samples, 0.5 wt-% ds. One calculation was performed with all values kept at their average but with the lower Chlorine content of 0.35 wt-% ds (a 30 % decrease). The results are shown in Figs. 4(a) and 4(b). As seen, this minor shift in Chlorine content in the fuel, changes some of the outcomes of the inorganic reactions in the boiler, like the formation of NaCl. Figure 4(a) shows that an average of 0.12 mole-% of sodium reacts to NaCl compared to 6.4 mole-% in the reference case. Fig. 4(b) shows that NaCl is formed but with approximately 40 % less Chlorine participating in the formation of NaCl at each temperature step compared to the reference case (Fig. 3(a)). Instead there is an increased formation of sodium calcium silicates. Furthermore, another trend in this calculation is that there is a 60 % increase in the formation of $PbCl_x$ between 400 °C and 900 °C.

Since 30 mole-% of the sodium is bound in the less corrosive form Na_2SO_4(s) it could be possible that Sulfur contributes to a lower amount of NaCl by reacting with the sodium. An increase of Sulfur was performed in case 3 and the results are presented in Figs. 5(a) and 5(b). The graph in Fig. 5(a) shows that the share of Chlorine bound in sodium chloride has decreased. Instead of forming NaCl, almost all sodium is found in the solid sodium aluminum silicates in the lower temperature range, but no significant increase of Na_2SO_4 was noticed in this case. Instead a considerable increase of $CaSO_4$ occurred, leaving the sodium accessible for reaction with Chlorine. Figure 5(b) shows that the formation of NaCl takes place at higher temperatures, starting to form at approximately 880 °C. Moreover, a minor increase in the formation of $PbCl_x$ can be seen in this case.

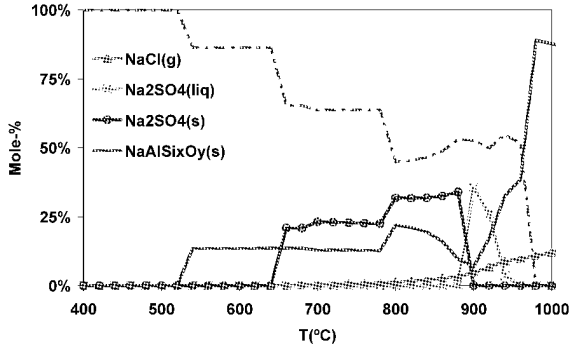

(a) Mole-% of Sodium

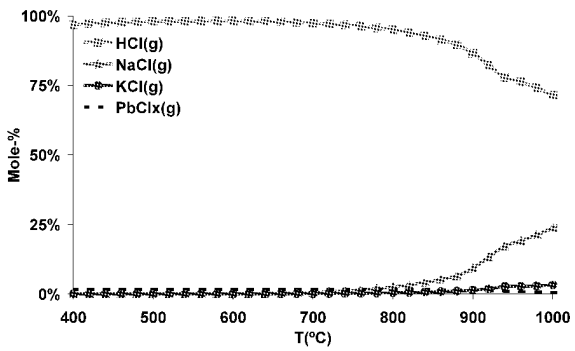

(b) Mole-% of Chlorin

Fig. 3 # 1 reference case

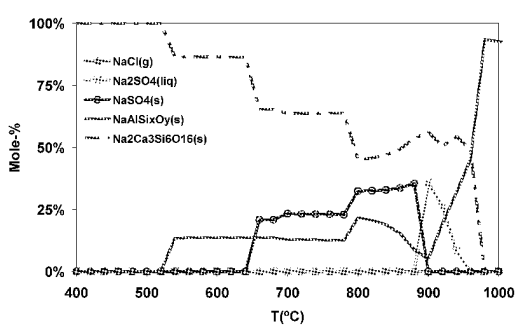

(a) Mole-% of Sodium

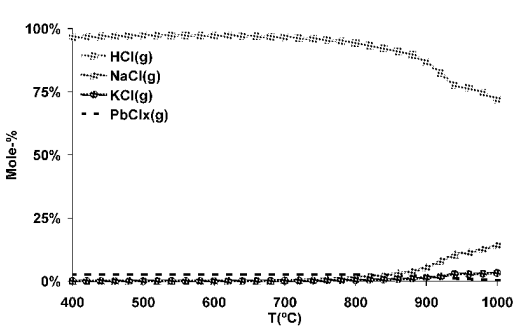

(b) Mole-% of Chlorine

Fig.4 # 2 low Chlorine content

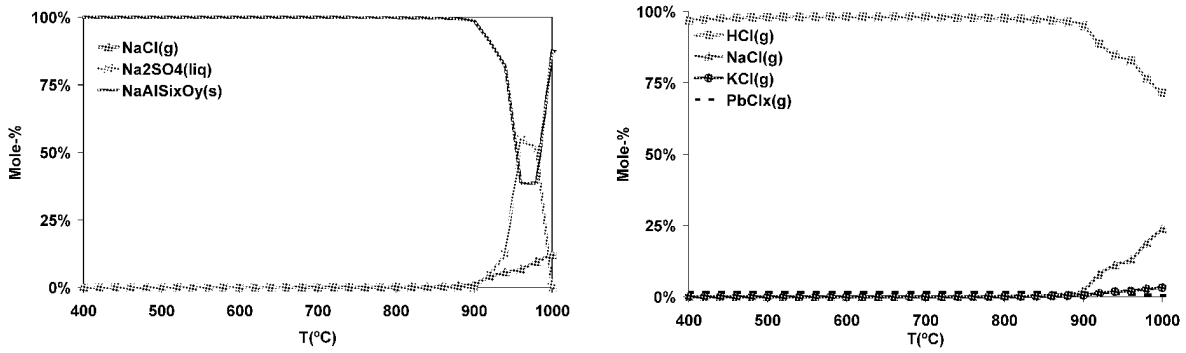

(a) Mole-% of Sodium (b) Mole-% of Chlorine

Fig. 5 # 3 high Sulfur case

CONCLUSIONS

Waste for a commercial 40 MW BFB plant has been chemically characterized and the result has been used as input data to thermodynamic equilibrium calculations.

Twelve months of sampling confirms that waste is very heterogeneous, with some of the samples diverting significantly from the period-average for several species.

The characterization shows that during the summer months, when only MSW is being combusted, the fuel contains less ash, and hence, less ash forming species like Ca, Si, K, Na and lower amounts of the trace elements Zn and Pb. Proposing that the MSW is better sorted and have less scattering in its composition than the industrial waste.

Thermodynamic equilibrium calculations suggest that Chlorine mainly form gaseous HCl but also the corrosive compound NaCl and the less corrosive Na_2SO_4.

Decreased amount of Chlorine in the input data results in reduced formation of NaCl. This case also increased the formation of $PbCl_x$. Calculations with the Cl:S ratio 1:4, reduced the formation of NaCl but not in the favour of Na_2SO_4, instead Sulfur forms $CaSO_4$. In addition, a minor increase of $PbCl_x$ was noticed in this case.

ACKNOWLEDGEMENTS

Financial support for this project is given by The Swedish Knowledge Foundation (KK-Stiftelsen), SP Technical Research Institute of Sweden, Borås Energi och Miljö and Dalkia. This is gratefully acknowledged.

REFERENCES

Backman, R., Hupa, M., Hiltunen, M., Peltola, K.: Proceedings of the 18th International Conference on Fluidized Bed Combustion , Toronto 2005

Baxter, L.L., Miles Jr., T.R., Jenkins, B.M., Milne T., Dayton, D., Bryers, R.W., Oden, L.L., Fuel Processing Technology 54 (1998) pp. 47-78

Bøjer, M., Arendt Jensen,P., Frandsen, F.J., Kim Dam-Johansen, K., Hedegaard Madsen, O., Lundtorp, K.: Fuelprocessing technology 89 (2008) pp. 528-539

EUROSTAT: www.epp.eurostat.ec.europa.eu

IPCC (Intergovernmental Panel on Climate Change), 2001. Climate Change 2001: Working Group I:

The Scientific Basis. Cambridge University Press, Cambridge, UK.

Johansson, A., Wikström, E.-L., Johansson L., Eskilsson, D., Tullin, C., Andersson, B.-Å., Victorén, Johnsson, A., Peters, G.: Proceeding of the 19th International Conference on Fluidized

Bed Combustion, Vienna 2006

Lindström, E., Sandström, M., Boström, D., Öhman, M.: Energy & Fuels 21 (2007) pp.710-717

Naturvårdsverket, report 5868 (2008)

Nielsen, H.P. Frandsen, F.J., Dam-Johansen, K., Baxter, L.L.: Progress in Energy and Combustion Science 26 (2000), 283–298

Niemi, J., Enestam, S., Mäkelä, K Proceeding of the 19th International Conference on Fluidized Bed Combustion, Vienna 2006

Pettersson, A., Zevenhoven, M., Steenari, B.M., Åmand, L.E.: Fuel 87 (2008) pp. 3183-3193

Pettersson, J., Pettersson, C., Folkeson, N., Johansson, L.G., Skog, E., Svensson, J.E.: Material Science Forum, (2006) 522-523:563-571

Skrifvars, B.J., Backman, R., Hupa, M., Salmenoja, K., Vakkilainen, E.: Corrosion Science 50 (2008) pp. 1274-1282

Uberoi, M., Punjak, W.A., Shadman, F.: Prog. Energy Combust. Sci. 16 1990 pp. 205-211
van Lith, S.C., Jensen, P.A., Frandsen, F.J, Glarborg, P.: Energy & Fuels 22 (2008), pp. 1598-1609
Warnqvist, B., Norrström, H.: Tappi Journal Vol 59, No 11 (1976) pp 89-91
Yao, H., Naruse, I.: Proceedings of the Combustion Institute (2009) doi:10.1016/j.proci.2008.07.026
Zhang, H., He, P.,Shao, L.: Atmospheric Environment 42 (2008), pp. 5579-5588

CO_2 REBINDING BY OIL SHALE CFBC ASHES: EFFECT OF PRE-TREATMENT

Andres Trikkel, Merli Keelmann, Aljona Aranson, Rein Kuusik

Laboratory of Inorganic Materials, Tallinn University of Technology, Ehitajate 5, 19086 Tallinn, Estonia

Abstract: Power production in Estonia is predominantly based on combustion of a local low-grade fossil fuel Estonian oil shale. Due to the high content of carbonaceous mineral matter in oil shale, its combustion is related to formation of lime-containing ashes (content of free CaO 10-30%) which could be utilized as sorbents for CO_2. In the present research CO_2 uptake by circulating fluidized bed and pulverized firing ashes from different technological devices (furnace, cyclones etc) of an operating power plant was studied and the effect of pre-treatment (grinding, calcination at different temperatures) of these ashes on their capture capacity was estimated using thermogravimetric, SEM, X-Ray and EDX analysis methods. It was found that capture capacities were determined mainly by free CaO content in the ashes, thereby, fluidized bed ashes showed higher CaO conversion levels (19.2-74.2%) as compared to pulverized firing ones (8.7-51.8%). Pre-treatment conditions influenced noticeably CO_2 uptake. Grinding decreased CO_2 capture capacity of fluidized bed ashes, calcination at higher temperatures decreased capture capacity of both types of ashes. Clarification of this phenomenon was given. Kinetic analysis of the process has been carried out, mechanism of the reactions and respective kinetic constants have been estimated.

Keywords: CFBC ashes, oil shale, CO_2 capture

INTRODUCTION

Circulating fluidized bed combustion (CFBC) is becoming a common technology for power production in Estonia, whose energy sector is predominantly based on combustion of a local low-grade fossil fuel – Estonian oil shale. Due to the high content of mineral matter in oil shale and its carbonaceous origin, combustion is related to the formation of lime-containing ashes (5-6 million tons annually, content of free CaO 10-30%) which could be utilized as sorbents for abatement of CO_2 emissions.

Data about CO_2 uptake by CFBC ashes, especially, oil shale ashes is quite limited (Jia and Anthony, 2000; Kaljuvee and Kuusik et al., 2004; Kuusik and Türn et al., 2002; Kuusik and Uibu et al., 2005a), more information can be found about limestone decarbonization and recarbonization (Abanades, 2002; Beruto and Vecchiattini et al., 2003; Lee, 2004; Salvador and Lu et al., 2003; Stanmore and Gilot, 2005).

At lower temperatures CO_2 is bound by calcium oxide according to the following reaction:

$$CaO(s) + CO_2(g) \rightarrow CaCO_3(s) \quad \Delta H = -182.1 \text{ kJ/mol} \qquad (1)$$

However, this reaction is far from reversibility as described by Abanades (2002). The process is initially controlled by chemical kinetics, but the end of this fast stage is determined already by the formation of 0.1 μm of product layer (Abanades, 2002; Salvador and Lu et al., 2003). The rates of carbonation are rapid at low conversion levels, with the initial rates depending notably on temperature in the range of 550-725°C. At higher temperatures almost up to the ultimate conversion levels, carbonation is controlled by the chemical reaction in combination with less effect of diffusion limitation. Conversion levels at which diffusion becomes rate limiting are lowered as temperature decreases (Lee, 2004).

Additives in limestone – belite, aluminum silicates and aluminum ferrates can react with CaO and up to 50% of the capture capacity might be lost in the fluidized bed boilers (Stanmore and Gilot, 2005).

The reaction of fly ash with CO_2 starts at 640-645°C and achieves its maximum rate at 725°C (Jia and Anthony, 2000). CaO conversion level remains in between 9-23%. It has been shown that grinding enhances CO_2 uptake by high temperature oil shale ash up to 40% (Kaljuvee and Kuusik et al., 2004), however, limestone can bind 3 times more CO_2 as compared to ash.

The aim of the present research was to study CO_2 uptake by different oil shale ashes formed at CFBC in comparison with some PF ashes and clarify the effect of pre-treatment (grinding, decarbonization temperature) on the process.

EXPERIMENTAL

The ash samples used were collected from different points of the ash separation systems of CFBC and pulverized firing (PF) boilers at Estonian Thermal Power Plant. The CFBC ashes studied were bottom ash (BA), intrex ash (IXA), economizer ash (ECO), air pre-heater ash (APHA) and electrostatic precipitator ash from fields 1 and 4 (EPA 1 and EPA 4). The PF ashes used were bottom ash (PBA), cyclone ash (PCA) and electrostatic precipitator ash from field 1 (PEPA 1). The chemical composition and physical properties of these ashes are presented in Table 1 and discussed in more detail in paper written by Kuusik and Uibu et al. (2005b).

Table 1 Characterization of the CFBC and PF ash samples

Sample	Content, %							SSA, m^2/g		
	CaO^t	CaO^f	CaO^{fc}	MgO	CO_2	I.r.	S sulfate	initial	ground	d_{mean}, μm
BA	49.4	12.5	31.7	9.3	15.1	8.9	4.3	2.1	4.8	197.0
IXA	47.6	18.9	20.4	13.7	1.2	13.3	7.7	2.6	4.2	95.0
ECOA	32.8	10.4	17.4	9.5	5.5	34.0	2.2	6.9	7.5	27.0
APHA	35.2	12.3	17.7	10.8	4.3	29.3	3.3	5.4	5.9	32.0
EPA1	29.5	8.5	14.3	8.3	4.6	42.5	1.7	8.0	8.6	25.0
EPA4	28.9	2.8	7.7	9.4	3.8	32.7	2.2	7.9	8.4	23.0
PBA	50.8	24.8	28.3	15.2	2.8	18.2	4.3	1.8	2.6	114.0
PCA	49.4	22.5	23.4	14.2	0.7	20.3	7.7	0.4	1.5	48.0
PEPA1	36.1	13.6	15.0	11.4	1.2	26.1	2.2	0.6	1.6	24.0

CaO^t total CaO

CaO^f free CaO

CaO^{fc} free CaO and CaO from $CaCO_3$

I.r. insoluble in *aqua regia* residue

d_{mean} mean particle diameter

The experiments for testing the reactivity of ashes with CO_2 in heterogeneous system gas – solid were performed with thermogravimetric equipment (MOM and Setaram Labsys) under isothermal conditions, mainly at 700°C in the mixture of air and CO_2 with partial pressure of CO_2 15.2 kPa. The samples (100 ± 5 mg) were heated up to 700°C in air with the heating rate of 10 K/min and kept until most part of the carbonates present in the sample was decomposed (about 10 minutes). After that 4.5 cm^3/s of the gas mixture was led into the furnace, duration of the experiments was 30 minutes. Multiplate Pt crucibles were used to diminish diffusion in sample-bed, thickness of the sample layer being about 0.2-0.3 mm.

To study the effect of grinding on CO_2 uptake, the initial samples were ground in an one-ball vibrational mill until most of the sample (at least 95%) passed the 45 μm sieve. In some experiments the samples were heated up to 900°C (marked as dc 900°C) to achieve complete decomposition of carbonates and to estimate the effect of decarbonization temperature. After that the samples were cooled quickly to 700°C (or any other experiment temperature) to perform isothermal binding.

The main parameters used to characterize the gas – solid interaction were the CO_2 capture capacity *CC* (mass of CO_2 bound by 100 mg of sample, mg CO_2/100 mg) and CaO conversion level *X* per free calcium oxide – $X(CaO^f)$ or per free and formed during decarbonization stage calcium oxide – $X(CaO^{fc})$ calculated on the basis of experiment data, analytically determined CaO^f and mineral CO_2 content in the ash and the summary binding reaction (Eq. (1)). Under the experiment conditions MgO does not take part in CO_2 binding, although it has a certain role in SO_2 capture forming $CaMg_3(SO_4)_4$ and β-$MgSO_4$ as clarified by Kaljuvee and Trikkel et al. (2005).

RESULTS AND DISCUSSION

The main binder of CO_2 in the ashes is free CaO. Pulverized firing ashes PBA and PCA are characterized by quite high content of free CaO (23-25%), but they differ noticeably in their specific surface area *SSA* (Table 1), besides, their *SSA* is lower as compared to CFBC ashes. Generally, PF ashes have higher free CaO content as compared to CFBC ashes due to higher combustion temperature and almost full decomposition of carbonates. The negative influence of coarser fractional composition of BA and IXA among CFBC ashes and, respectively, the lower level of *SSA* (2.1-2.6 m^2/g), should be compensated by higher content of free CaO (12.5-18.9%) or CaO^{fc} (20.4-31.7%). Grinding increased *SSA* noticeably for BA, IXA, PCA and PBA (1.6-4 times). For the

other ashes the increase was about 10%.

The CO_2 capture capacity *CC* of the ashes at 700°C remained in between 1.3 and 12.5 mg CO_2/100 mg in 30 minutes (Fig. 1). The highest *CC* values – about 12 mg CO_2/100 mg were calculated for the bottom ashes BA and PBA, having the highest free CaO content. Capture capacities of ECOA and APHA were 6.0-7.5 mg CO_2/100 mg, the lowest *CC* values belonged to the ashes collected from electrostatic precipitator. BA differs from the other ashes in quite high CO_2 content (undecomposed carbonates due to lower combustion temperature at CFBC), though its CaO^{fc} content is similar to PBA.

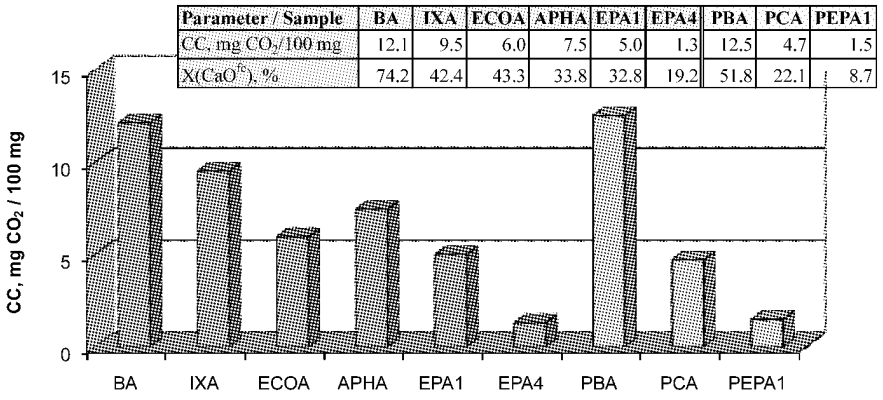

Fig. 1 CO_2 binding parameters of different ashes at 700°C in 30 minutes

Analysis of the experiment results showed that the CO_2 capture capacity was determined mainly by CaO^{fc} content in the ashes, the correlation was more evident in the case of CFBC ashes (Fig. 2). IXA and PCA have close CaO^{fc} values, but specific surface area of PCA is significantly lower (possible formation of liquid phases during high temperature combustion) and their capture capacities were also different – 9.5 and 4.7 mg CO_2/100 mg for IXA and PCA, respectively. CaO conversion level $X(CaO^{fc})$ of CFBC ashes was in between 19.2-74.2% and of PF ashes 8.7-51.8%. There was no clear correlation between *SSA* values of the initial ash samples and *CC*, yet a slight decrease in *CC* could be followed with the increase in *SSA*, especially, in the case of CFBC ashes.

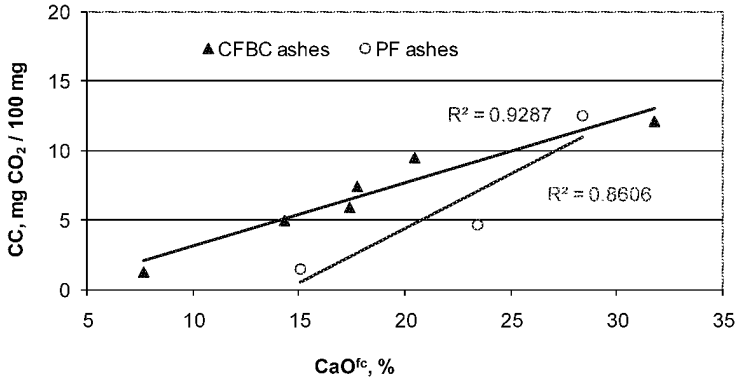

Fig. 2 Dependence of capture capacity on CaO^{fc} content

Effect of pre-treatment

To study the effect of grinding on the CO_2 uptake, some of the samples were ground to particle size < 45 μm. It was known from the experiments with SO_2 that grinding generally increased SO_2 uptake by the ashes as described by Kuusik and Uibu et al. (2005a).

The experiments showed that in contrary to SO_2 uptake, grinding decreased CO_2 capture capacity of all the CFBC ashes studied (Fig. 3). Although grinding increased *SSA* of the samples (e.g. 2.3 times for BA and 1.6 times for IXA), their *CC* decreased 1.3-2 times. Differently, capture capacity of PF ashes PBA and PCA increased in the result of grinding – 1.3 and 2.4 times, respectively, which is in correlation with the increase in their *SSA* (Table 1).

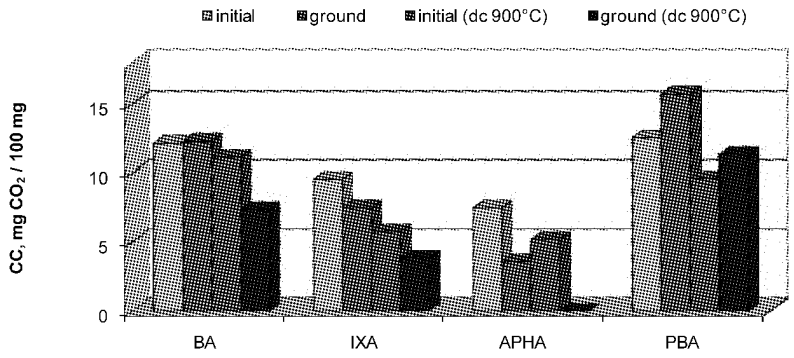

Fig. 3 Effect of pre-treatment on the capture capacity of selected ashes

The experiments also showed that decarbonization temperature had a noticeable effect on CO_2 uptake by the ashes (Fig. 3).

It was found that decarbonization at higher temperature decreased *CC* of the CFBC ashes 1.3-1.4 times. When the ground samples were used in these experiments, the decrease was even more severe – 2.1 to 5.5 times. At that, APHA lost its CO_2 binding ability at all. Also the ground and decarbonized at 900°C sample of PBA bound less CO_2 as compared to ground and decarbonized at 700°C sample (15.7 and 11.4 mg CO_2/100 mg, respectively).

To explain this phenomenon, some samples were heated in an electric tube furnace at different temperatures up to 1100°C during 30 minutes. The changes in their *SSA* were determined (Table 2). It can be seen that heating up to 700°C increased *SSA* of all the samples except of APHA. Increase in *SSA* can be explained by decomposition of carbonates and calcium hydroxide, present in small quantities due to quick hydration of the samples when exposed to air.

Table 2 Effect of decarbonization temperature on SSA (m^2/g)

Sample	initial	dc 700°C	dc 900°C	dc 1100°C
BA	4.7	5.1	2.4	0.7
IXA	4.3	4.7	2.3	0.5
APHA	5.8	5.5	2.4	0.6
PBA	2.9	4.1	3.2	0.6

The increase was the biggest for PBA – the pulverized firing ash, although it was expected to be bigger for BA due to its high CO_2 content. Heating at 900°C decreased *SSA* of all the samples noticeably and at 1100°C even up to 10 times. This kind of decrease indicates to possible formation of liquid phases inside and on the surface of the ash particles.

The products obtained were analyzed using quantitative X-Ray diffraction analysis method. It was found that the content of quartz (SiO_2) in the samples decreased significantly during heating at 1100°C – for BA from 6.9 to 1.8%, for APHA from 16.8 to 5.3% and for PBA from 5.8 to 1.3%. In parallel, also the content of CaO decreased – for BA from 37.2 to 32.6%, for PBA from 36.4 to 29.3% and for APHA from 25.6 to 8.5% (calculated on the basis of CO_2 and H_2O free composition). X-ray analysis also showed the increase in the content of wollastonite, belite and melilite in the heating products. It can be assumed that SiO_2 partly reacts with free and formed from $CaCO_3$ and $Ca(OH)_2$ calcium oxide and other ash constituents in secondary solid state processes according to the following simplified reactions:

$$CaO + SiO_2 \longrightarrow CaSiO_3 \quad (2)$$

$$2CaO + SiO_2 \longrightarrow Ca_2SiO_4 \quad (3)$$

giving different silicates. This, in case, can lead at enhanced temperatures to the reduction of *SSA* and the content of CaO which is the main binder of CO_2.

SEM-EDX analysis of the initial and treated samples showed that after heating at 900°C no essential changes were seen on the surface of the BA particles (Fig. 4). However, formation of liquid phases and partial shell can be seen on the surface and cross-section of APHA sample. Generally, during heating porosity slightly increased inside the particles, but outer surface became more dense and monolithic. Significant melting can take place during heating up to 1100°C as can be seen on the SEM picture of APHA sample (Fig. 4, bottom right).

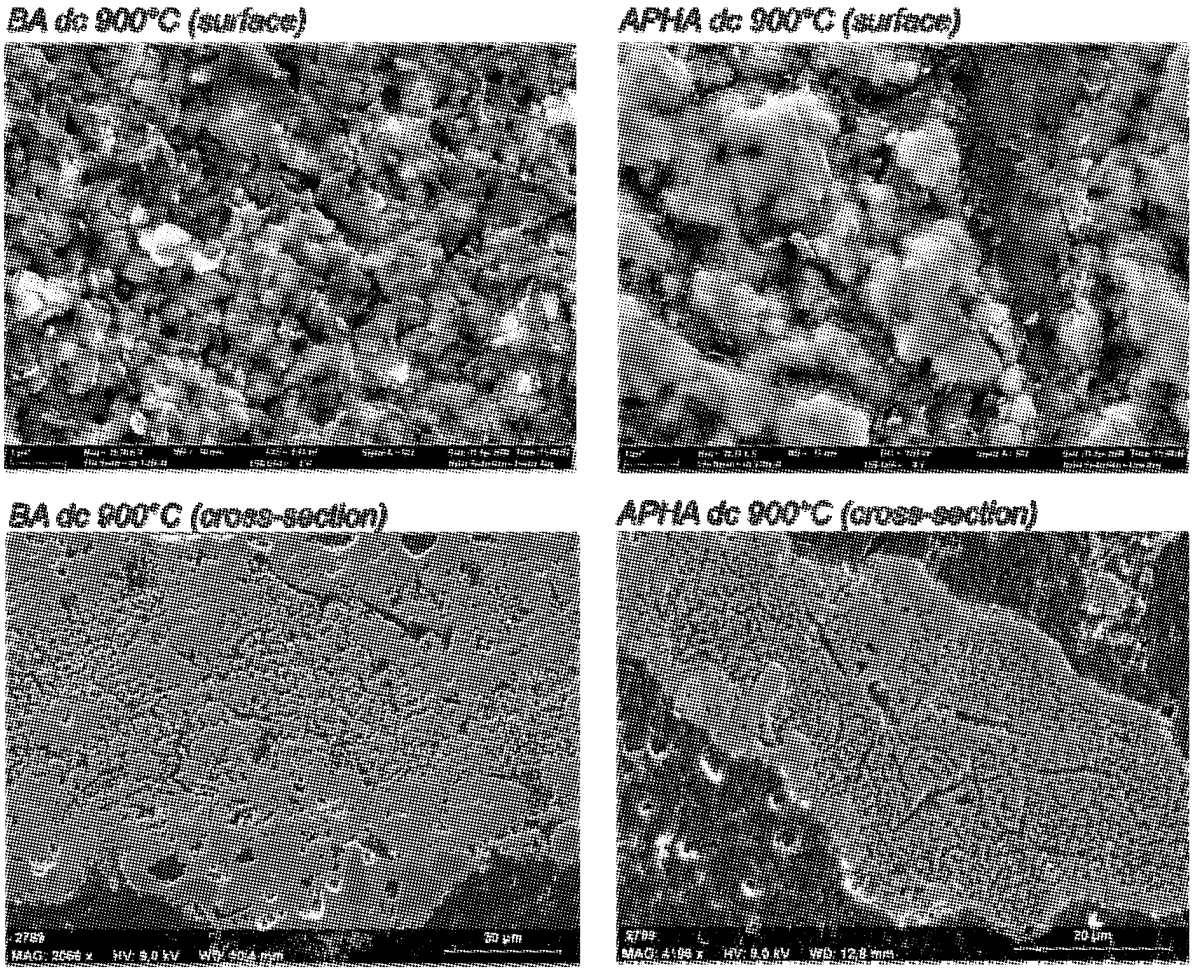

Fig. 4 SEM photos of the initial and decarbonized ash samples

EDX analysis of the cross-sections of the heated up to 900°C particles showed that Ca, Al and Si usually coexist, indicating to the presence of different Ca- Al- silicates. These silicates tend to concentrate on the surface of the particles in the areas where also melts can be seen. So, it can be assumed that at higher decarbonization temperatures dense core can form on the surface of ash particles through different silicate formation reactions. Accompanying melting phenomenon can reduce porosity and *SSA* and hinder diffusion of gaseous CO_2 through this shell. Besides, content of free CaO decreases in these solid-state processes which are accelerated in the case of ground samples and at higher temperatures reducing CO_2 uptake potential of the ash. In the particles of PF ashes these kinds of processes have partially taken place already in the boiler during combustion and grinding of them can favor CO_2 uptake, because the formed shell is crushed, *SSA* increases and more reactive CaO surface is freed. So, high temperatures should be avoided, especially, in the case of CFBC ashes which are obtained at lower temperature combustion regimes as compared to PF ashes.

Kinetic analysis

In the present research reaction mechanism was analyzed on the basis of the changes in the CaO conversion level $X(CaO^{fc})$ using different well-known reaction mechanisms presented e.g. in the paper of *Reich and Stivala,* (1984). It was found that the process is controlled by CO_2 diffusion into the ash particle.

(D3): $[1-(1-X)^{1/3}]^2 = k\,\tau$ (3-dimensional diffusion, spherical symmetry) (4)

k – rate constant, min^{-1}

τ – time, min

In the case of decarbonized at 700°C ash samples, a short kinetically controlled initial stage can be differentiated

(F1): $-ln(1-X) = k\,\tau$ (first order kinetics, random nucleation) (5)

having lower activation energy (E_A). This stage could not be distinguished for the samples decarbonized at 900°C. Activation energies for some samples have been presented in Table 3.

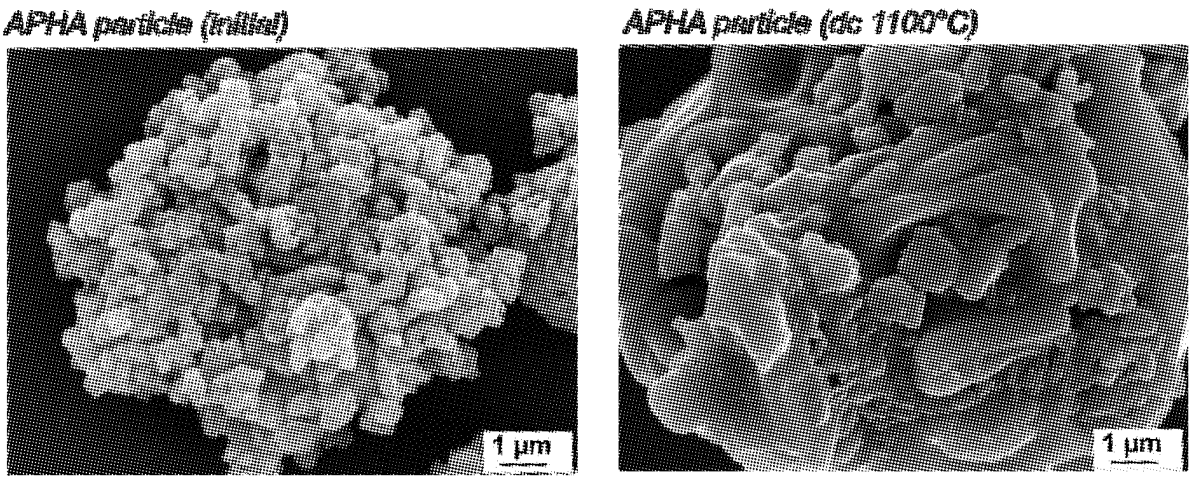

Fig. 4(Continued)

Table 3 Rate constants and activation energies of binding reaction

Sample	k at 700°C, min^{-1}	E_A, kJ/mol (Eq. (4))	E_A, kJ/mol (Eq. (5))*
BA initial	9×10^{-4}	47.7	33.8
BA ground	8×10^{-4}	101	44.0
APHA initial	1×10^{-3}	82.3	48.1
APHA ground	3×10^{-4}	112	49.0
PBA initial	1×10^{-3}	23.2	43.6
PBA ground	3×10^{-3}	50.2	47.8

* calculated for the initial stage of reaction.

Activation energies of CFBC ashes determined for the temperature range of 500-700°C for decarbonized at 700°C samples were generally higher as compared to pulverized firing ashes. Grinding of the samples increased E_A values noticeably, indicating to the increase in diffusion resistance.

CONCLUSIONS

CO_2 uptake by circulating fluidized bed oil shale ashes from different technological devices (furnace, cyclones etc) of an operating power plant was studied in comparison with some pulverized firing ashes and the effect of grinding and decarbonization temperature was estimated.

It was found that CO_2 capture capacities depend mainly on the free CaO content in the ashes, thereby, fluidized bed ashes showed higher levels of CaO conversion (19.2-74.2%) as compared to pulverized firing ones (8.7-51.8%).

It was shown that pre-treatment conditions influenced noticeably the CO_2 uptake. Grinding decreased CO_2 capture capacities of fluidized bed ashes, decarbonization at higher temperatures decreased capture capacities of both types of ashes. Clarification of this phenomenon was given.

Kinetic analysis of the process was carried out and respective kinetic constants were calculated.

ACKNOWLEDGEMENTS

Authors express their gratitude to Estonian Science Foundation (G7379) for financial support, to Dr Olga Volobujeva (TUT) for the help in carrying out SEM and EDX analysis and to Dr Kalle Kirsimäe (Tartu University, Estonia) for performing quantitative X-Ray analysis.

REFERENCES

Abanades, J. C.: Chem. Eng. J. Vol. 90 (2002), pp. 303-306.
Beruto, D. T., Vecchiattini, R., Giordani, M.: Thermochim. Acta Vol. 405 (2003), pp. 183-194.
Jia, L., Anthony, E. J.: Fuel Vol. 79 (2000), pp. 1109-1114.
Kaljuvee, T., Kuusik, R., Radin, M.: Oil Shale Vol. 21 (2004), pp. 13-26.
Kaljuvee, T., Trikkel, A., Kuusik, R. et al.: J. Therm. Anal. Cal. Vol. 80 (2005), pp. 591-597.

Kuusik, R., Türn, L., Trikkel, A. et al.: Oil Shale Vol. 19 (2002), pp. 143-160.
Kuusik, R., Uibu, M., Toom, M. et al.: Oil Shale Vol. 22 (2005a), pp. 421-434.
Kuusik, R., Uibu, M., Kirsimäe, K.: Oil Shale Vol. 22 (2005b), pp. 407-419.
Lee, D. K.: Chem. Eng. J. Vol. 100 (2004), pp. 71-77.
Reich, L., Stivala, S. S.: Thermochim. Acta Vol. 73 (1984), pp. 165-172.
Salvador, C., Lu, D., Anthony, E. J. et al.: Chem. Eng. J. Vol. 96 (2003), pp. 187-195.
Stanmore, B. R., Gilot, P.: Fuel Process. Technol. Vol. 86 (2005), pp. 1707-1743.

THE SUITABILITY OF THE FUEL MIXTURE OF HORSE MANURE AND BEDDING MATERIALS FOR COMBUSTION

Sanna K. Tyni, Minna S. Tiainen, Risto S. Laitinen

Department of Chemistry, University of Oulu, P.O. Box 3000, FI-90014 University of Oulu, Finland

Abstract: The mixture of horse manure and bedding materials (peat and sawdust) appear to be a potential biofuel. The chemical compositions of horse manure, bedding materials, and the mixture of these have been characterized by SEM-EDS and ICP-OES. In addition, the compositional distribution of ash of these materials has been determined and this facilitates the estimation of their propensity for ash-related problems in boilers. NO_x and SO_x emissions from the co-combustion are also discussed on the basis of the chemical composition of fuel mixtures. It seems that co-combustion of horse manure and bedding materials in FB boilers is suitable for small-scale energy production.

Keywords: ash, co-combustion, horse manure, peat, sawdust

INTRODUCTION

The interest in disposal of horse manure in Finland has increased recent years, since the number of horses is increasing year by year approximately by 2000 horses/year. In 2007 there were 68 000 horses and ponies in Finland. This has considerably increased the number of stables in urban areas. In 2005 there were ca. 15,000 horse stables and it is estimated to rise to 17,000 by 2012. This will cause difficulties in disposal of horse manure together with bedding material, especially when only a little or no farmland is found around the stables (Holopainen et al., 2002).

Bedding material is used in stables for keeping horses clean and reducing the content of manure gases such as ammonia indoors (Airaksinen, 2006). Good bedding material is essential for the well-being of the horses and workers. The optimal bedding material doesn't cause hygiene problems. The quality of the bedding material depends on the ammonia adsorption capacity, dustiness, and microbial quality of the material. Bedding material should also be economical in use and decompose quickly with manure.

Horse manure with bedding material is classified as a biowaste in EU. It should be utilized primarily as fertilizer and secondarily for energy use e.g. in composting or biogas production. Manure dumping in landfills has been prohibited in Finland since 2005, and therefore new ways to dispose horse manure with bedding materials should be found. The energy consumption of agriculture is mainly covered with fuel oils (65 %). The most significant renewable fuel in agriculture is wood, 12%. European Union has recommended that Finland should cover 35-40 % of energy consumption by renewable energy sources by 2020 (Haukkasalo, 2007). This is a challenging task and demands also re-estimation of the utilization of organic waste materials in energy production. Combustion of manure with bedding material could be one solution for the problem, but manure combustion is possible only at a plant with a license for waste combustion (Government Decree No.362/2003). On this account the production of bioenergy should be increased by utilizing old methods more efficiently and improving new methods for alternative energy sources such as manures.

Bedding materials such as peat, sawdust or straw are already utilized in energy production in boilers. The use of biomass fuels and waste materials in energy production has increased during the last decades, because their availability and the environmental issues have made them an alternative source of energy. Biomass fuels are considered CO_2-free, as they do not increase the CO_2 emissions into the atmosphere as much as fossil fuels. The inorganic compounds in biomass fuels form ashes and may cause problems during the combustion process, such as fouling, slagging, corrosion, and agglomeration of bed material. These problems are dependent on fuel, operating parameters, and the combustion technique. The utilization of new materials as a fuel demands study of combustion properties.

EXPERIMENTAL

The samples were collected from the Equine College Ypäjä. All samples are listed in Table 1.

Moisture content was determined from the fuel samples by the ISO-589 standard (ISO-589). The determination of ash content for the samples was done according to standard SS 18 71 71 (SS 18 71 71). Boxes made of steel were used for ashing instead of porcelain ships.

The ash samples were prepared for the ICP-OES determinations (Na, Mg, Al, Si, P, K, Ca, Ti, and Fe) according to the ASTM standard D 3682 by mixing the samples with $Li_2B_4O_7$ (ASTM D 3682). The ASTM standard was differed by using the 5 % H_2SO_4 instead of 5 % HCl. The determination of C, H, N, and S content

in the fuel samples were determined with a Perkin- Elmer 2400 series II CHNS/O analyzer.

Table 1 The samples

	Peat	Sawdust	Manure	Mix1	Mix2	Mix3
Samples	Bedding material	Bedding material	Horse manure	Mixture of peat and horse manure	Mixture of sawdust and horse manure	Briquette made of mixture of sawdust and manure

Fuel and ash samples were characterized by using a Jeol JSM-6400 scanning electron microscope combined with INCA energy dispersive X-ray analyzer and Feature image processing sofware. The acceleration voltage was 15kV and a beam current was 12×10^{-8} A for the SEM-EDS-analyses. The sample distances for all samples were 15mm. Small amounts of crushed fuel samples were attached to a metal plate with carbon tape and ash samples were mounted with epoxy resin, Struers Epofix (15:2). Mounts were cross-sectioned by grinding with 250, 600, and 1200 mesh sandpapers. All the samples were coated with a thin carbon layer to eliminate the electrostatic effects.

The SEM-EDS analyses were carried out as described by Virtanen et al. (Virtanen et al., 2000). The SEM-EDS was used to take backscattered electron images (BE) and to make point and line analyses. X-ray maps and domain analyses were also made with SEM-EDS. The original image was smoothed digitally by adjusting the brightness and contrast in the image to facilitate further treatments. In the BE images the heavier elements are seen brighter than the lighter elements and the epoxy background in the samples is seen as black in the images. Magnification was between 50 to 600 depending on the sample and the part in the sample we were interested in. Point and line analyses were made for each sample with secondary electron images (SE) by using INCA program package. The number of points in point and line analyses was 5-10 with each sample. The point and line analyze results are qualitative or semi-quantitative. The elemental compositions of the samples were characterized with semiquantitative domain analyses. Due to possible variations in the elemental composition in the larger areas, these regions were divided in the smaller domains and the elemental compositions of ca. 1000 domains were determined for every sample. The X-ray maps and the phase relationship images (Mix image) were also created with INCA's Feature image processing software. In the mix images three colored X-ray maps (red, green, and blue) were combined in the same image with BE image to see how the elements occur in the particles. The results from the domain analyses were visualized by using two- and three-dimensional quasiternary diagrams constructed with a locally designed software package (Virtanen et al., 2000; Virtanen et al., 2001a; Virtanen et al., 2001b).

The results from the domain analyzes were visualized by using two- and three-dimensional quasiternary diagrams with a locally designed software package (Virtanen et al.,2000; Virtanen et al., 2001a; Virtanen et al., 2001b). The quasiternary diagram illustrates composition distribution of the sample and it is a logical extension of the conventional ternary diagrams. In the quasiternary diagram, each corner has been defined in terms of a content of a single element. The content of the elements are 100 % or the content is 100 % for one element if sample does not contain other elements defined in the corner. The content decreases towards the opposite wall of the corner, being 0 % at the opposite wall. The sum of the contents of the elements is 100 % at any point in the quasiternary diagram such as in the ternary diagrams. The height of the column illustrates the contents of the elements in the sample and the location of the column in the quasiternary diagram represents the proportion of the elements. Suitable composition of the elements defined in the corners depends about the sample. Software package utilizes the results from the domain analyzes to calculate the proportion of each element in the sample and illustrates it in percentages.

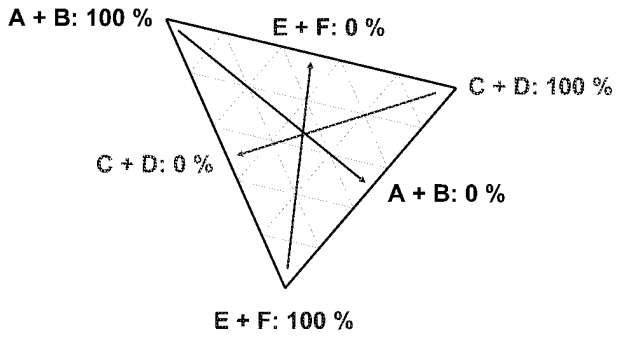

Fig.1 Two dimensional quasiternary diagram which illustrates the relation between *A + B, C + D, and E + F*

RESULTS AND DISCUSSION

The proximate methods were used to analyze moisture and ash content. The ultimate analyses determines the content of C, H, N and S in the samples. These analyses illustrate the major elemental composition of the dried fuel material. In addition, main ash forming elements were analyzed from the fuel and ash samples (Si, K, Ca, Mg, Na, P, S, Al, Fe, and Ti). Determination of some trace elements was also made, but contents were very low or under determination limits (As, Cd, Co, Cr, Cu, Mn, Mo, Ni, Pd, V, and Zn).

The moisture, ash content and the chemical composition of the fuel samples are given in Table 2. Peat samples have the lowest moisture content and the content was highest in the manure samples. Mix3 (briquettes) has very low moisture content due to prior drying of the mixture of sawdust and manure, before it was compressed to briquettes. The ash content of the samples varies between 0.20-7.84 %. Sawdust has low ash content, because it mainly contains organic compounds, whereas ash content from manure is higher. The mixture of peat and manure has the highest ash content. Sawdust has the highest carbon content. Nitrogen content is highest in the Mix1 (peat and manure), but the differences between the samples are small.

The chemical composition of the fuel samples was determined for the ten main ash-forming elements (Si, K, Ca, Mg, P, S, Na, Al, Fe, and Ti). Some trace elements were also analyzed. It is shown in Table 2 that the highest content of silicon was found in peat. Therefore, Mix1 (peat and manure) also shows high silicon content. Content of potassium and calcium was highest in the sawdust sample and also higher in Mix2 (sawdust and manure) and Mix3 (briquette) than in the Mix1 (peat and manure). Content of phosphorus was expectedly highest in manure and is therefore also seen in the mixture samples. Contents of the analyzed trace elements were under detection limits except for copper in the peat and manure samples.

Table 2 Chemical composition of the fuel samples

	Peat	Sawdust	Manure	Mix1	Mix2	Mix3
Moisture (% wt)	23.46	47.72	77.59	57.07	50.73	9.03
% ash (% wt db)	0.56	0.20	7.52	7.84	3.50	0.54
C (% wt db)	46.5	49	45	44.5	46.5	46.5
H	6	6	6	5.5	6	6
N	1	<0.5	1.5	2	0.85	1
S	<2	<2	<2	<2	<2	<2
SiO_2 (%. DM)	68.69	30.83	35.66	35.87	18.07	27.30
K_2O	4.00	39.16	19.15	34.32	51.86	36.00
CaO	7.81	20.16	4.60	5.07	7.64	14.84
MgO	2.75	0	3.93	3.79	4.22	2.72
P_2O_5	1.09	0	28.30	8.30	13.36	12.81
Na_2O	2.24	0	2.70	3.36	1.94	1.76
SO_3	0	0	0	0.5	1.22	0
Al_2O_3	10.08	0	2.57	6.11	1.71	3.39
Fe_2O_3	2.88	9.69	0.63	2.7	0	1.17
TiO_2	0	0	0	0	0	0
MnO	0	0	0	0	0	0
CuO	0.45	0	0.31	0	0	0
ZnO	0	0	0	0	0	0
As	*	*	*	*	*	*
Cd	*	*	*	*	*	*
Co	*	*	*	*	*	*
Cr	*	*	*	*	*	*
Mo	*	*	*	*	*	*
Ni	*	*	*	*	*	*
Pd	*	*	*	*	*	*
V	*	*	*	*	*	*

* under detection limits.

Table 3 Chemical composition of the ash samples

	Peat	Sawdust	Manure	Mix1	Mix2	Mix3
SiO_2 (%, DM)	52.71	11.48	48.80	38.41	22.84	40.17
K_2O	4.69	24.97	15.09	26.15	38.89	26.24
CaO	8.34	38.86	6.02	7.24	10.66	8.98
MgO	5.92	9.36	6.38	5.05	6.46	4.40
P_2O_5	5.60	4.31	14.24	5.27	6.23	6.32
Na_2O	2.84	1.75	4.04	3.92	3.28	2.91
SO_3	4.87	4.05	2.01	4.41	8.51	3.57
Al_2O_3	11.95	2.58	2.59	6.36	2.09	4.51
Fe_2O_3	5.32	2.82	0.80	3.01	1.07	2.68
TiO_2	0.51	0	0.03	0.19	0	0.24
MnO	0.34	7.92	0.39	0.28	0.46	0.89
CuO	0	0	0.05	0.05	0	0.07
ZnO	0.31	1.08	0.26	0.15	0.11	0.07
As	*	*	*	*	*	*
Cd	*	*	*	*	*	*
Co	*	*	*	*	*	*
Cr	*	*	*	*	*	*
Mo	*	*	*	*	*	*
Ni	*	*	*	*	*	*
Pd	*	*	*	*	*	*
V	*	*	*	*	*	*

* under detection limits

The chemical compositions of the ash samples are presented in the Table 3. Content of potassium and calcium is higher in the sawdust ash than peat or manure ash. This can also be seen in the contents of potassium and calcium in the ash of mixture samples. Potassium and phosphorus contents are lower in the ash samples than in the fuel samples, probably because they vaporize at low temperatures. Iron content is much lower in the ash sample from sawdust than in the fuel probably because of the heterogeneity of the fuel. The sulphur content is lower in the manure ash sample than in the peat and sawdust ash samples, which means that the SO_x-emission is not a serious problem during the combustion of manure.

Compositional distributions of the peat, manure, and mixture of peat and manure are shown in Fig. 2. All diagrams show that the main compounds in all samples are various aluminiumsilicates (red and green circles in the figures). Quasiternary diagram of the manure (Fig.2(b)) also has large maxima in the middle of the diagram (the blue circle). These maxima indicate phosphorus-rich material in manure. Maxima in the quasiternary diagram c) (blue circle) are lower due to a smaller amount of manure in the mixture. When manure is combusted with peat, phosphorus and magnesium are associates with potassium and calcium aluminiumsilicates. This can be seen as a shift of the maxima (blue circle) towards the Al+Si – K+Ca axis.

Potassium- and calcium-rich materials (blue circle) in the sawdust ash dominate in the quasiternary diagram (see Fig.3). This is also shown in the quasiternary diagram c). The diagram also indicates that manure has a larger effect on the compositional distribution of mixture with sawdust than with peat. Compositional distributions in the diagram c) and d) have minor differences. This may be a consequence of the processing of the sawdust manure mixture to the briquette.

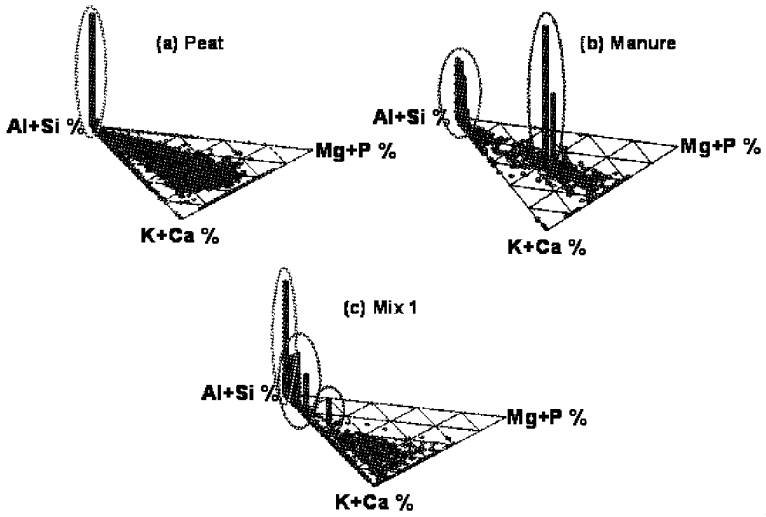

Fig. 2 Quasiternary diagrams from the ash samples of the peat, manure and mixture of peat and manure

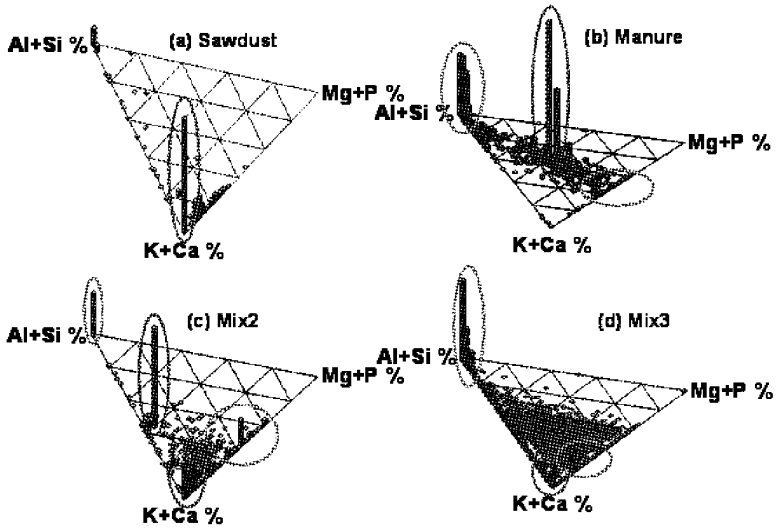

Fig. 3 Quasiternary diagrams from the ash samples of the sawdust, manure, mixture of sawdust and manure, and briquettes

CONCLUSIONS

Chemical compositions of the peat, sawdust, manure, and the mixture of these materials were determined. The moisture content was highest in the manure samples and lowest in the peat samples. Sawdust has lowest ash content and the mixture of peat and manure has the highest ash content.

Manure sample has the highest phosphorus content and this has an effect to the contents of phosphorus in the mixture samples. The analyzed trace elements were under detection limits.

According to this study it can be concluded that horse manure with bedding material (peat or sawdust) could be suitable material for co-combustion. Chemical composition of ashes indicates that ash could be exploited as a material for soil enrichment or fertilizer.

ACKNOWLEDGEMENTS

This work was supported by the Oulu University Scholarship Foundation, Academy of Finland, Equine College Ypäjä, The National Organization of Trotting and Horse Racing in Finland, Agrifood Research Finland, and The Equestrian Federation of Finland.

REFERENCES

Airaksinen, S. Bedding and Manure Management in Horse Stables, Kuopio Univ. Publ. C. Nat. and Envir. Sci., (2006), **190**, pp. 13.

ASTM D 3682: Major and Minor Elements in Coal and Coke Ash by Atomic Absorption, Annual Book of ASTM Standards, Section 5, **Vol. 05.05** (1989).

Council of State, 169/2000, (5.6.2008). (In Finnish)
Government Decree No.362/2003, (2003). (In Finnish)
Haukkasalo, A. Energia-lehti, Tekniikka &Talous, (27.4.2007), pp-1-3. (In Finnish)
ISO-589, Hard Coal - Determination of Total Moisture, International Organization for Standardization, (2003).
Holopainen, P., Airaksinen, S., Heinonen-Tanski, H., Heiskanen, M.-L., In: Schimilewski G, Rochefort L (Eds.): Peat In Horticulture- Quality and Environmental Challenges. Proceedings of the International Peat Symposium, Pärnu, Estonia 3-6 September (2002), pp. 154-160.
Paulrud, S.; Upgraded Biofuels- Effects of Quality on Processing Handling Characteristics, Combustion and Ash Melting, Swedish University of Agricultural Sciences, Umeå., (2004), pp.7.
SS 18 71 71, Biobränslen – Bestämning av askhalt, Sveriges Mekanstandardisering, (1984), pp. 1-3. (In Swedish)
Virtanen, M. E., Tiainen, M. S., Laitinen, R. S., SEM-EDS and image analysis in the characterisation of coatings and adhesive material in the quartz-bed. 5th European Conference on Industrial Furnaces and Boilers, Reis, A., Ed.; INFUB, Rio Tinto, Portugal: (2000); **Vol. II**, pp.117-126.
Virtanen, M., Tiainen, M., Nuutinen, L., Pudas, M., Laitinen, R., In Effects of coal quality on power plant performance: Ash problems, Management and Solutions; Metha, A. K., Benson, S. A.., Eds.; United Engineering Foundation Inc., New York, and EPRI, Palo Alto, CA: (2001a); 1001402; pp. 117-130.
Virtanen, M. E., Tiainen, M. S., Pudas, M., Laitinen, R. S., Visualization and analyses of SEM-EDS data of quartz-bed agglomerates Progress in Thermochemical Biomass Conversion, Bridgwater, A. V., Ed.; Blackwell Science: (2001b); Cornwall, **Vol. 1**, pp. 671-677.

FUEL-NITROGEN EVOLUTION DURING FLUIDIZED BED OXY-COAL COMBUSTION

Astrid Sanchez[1], Fanor Mondragon[1], Eric G. Eddings[2]

1Dept. of Chemistry, University of Antioquia, Medellín, Colombia

2Dept. of Chemical Engineering, University of Utah, Salt Lake City, Utah, USA

Abstract: FTIR, thermo-gravimetric analysis techniques and molecular modelling were employed to study the effect of CO_2 on fuel-nitrogen evolution under oxy-combustion conditions. The main objective is to compare NOx emissions at several molar fractions of O_2 using Ar or CO_2 as balance gas in a fluidized bed reactor. A char with about 16% N content was prepared by pyrolysis of polyacrylonitrile. This sample facilitated NOx evolution experiments due to the abundance of nitrogen complexes, and aided the identification and quantification of several N species by means of FTIR. Results indicate that the presence of CO_2 enhances NO_2 formation.
A complementary study was carried out by molecular modelling of the experimental reactions using the Gaussian 03 package. Different heterogeneous and homogeneous interactions between CO_2 and char N-species were simulated. The results thus obtained show that the presence of CO_2 during combustion can facilitate NCO formation which is a very reactive intermediate species that can be readily oxidized in the gaseous phase.
Keywords: CCS, oxy-coal combustion, NO_x evolution, Fuel-N, DFT modelling

INTRODUCTION

Around 85 % of the world's energy needs are supplied by fossil fuels (Davison,2007) causing a very significant increase in atmospheric CO_2 (Yang et al.,2008), which is considered one of the greenhouse gases. Several options have been proposed to try to diminish CO_2 emissions such as improving efficiencies of power plants, replacing use of fossil fuels by renewable sources; and, CO_2 capture and sequestration (CCS) (Wall 2007; Bejarano and Levendis,2008). The main disadvantage concerning application of CCS to conventional combustion is related to the low concentration of CO_2 in the flue gas, being usually lower than 15 % (Liu and Okazaki,2003; Chen et al., 2007); making it expensive and inefficient to separate and purify the CO_2. Several alternatives to address the issue have been proposed, such as post-combustion capture using sorbents, pre-combustion capture and oxy-fuel combustion (Wall,2007).

Oxy-fuel combustion is a combustion process carried out in high oxygen concentration environments relative to air; and produces higher concentrations of CO_2 (and water), making it easier to separate CO_2 from water by means of a condensation process (Buhre et al.,2005). However, the use of high partial pressures of O_2 causes higher temperatures inside the reactor (Buhre, Elliott et al.,2005) with deleterious consequences for the construction materials. One option to diminish the temperature consists of recirculation of flue gases whose main component is CO_2. In this way, the combustion environment is O_2/CO_2 instead of O_2/N_2, as in the case of conventional combustion. Chen, Liu et al. 2007 showed that average concentration of CO_2 in the flue gas for O_2/CO_2 coal combustion system can be higher than 90 %, while the maximum concentration of CO_2 in $50\%O_2/50\%N_2$ system is only 34 %, indicating oxy-fuel combustion offers an easier alternative for CO_2 recovery.

Several reports have shown that the presence of CO_2 affects combustion characteristics such as gas temperature (Andersson and Johnsson,2007), char burnout (Bejarano and Levendis,2008), ignition and devolatilization phenomena (Shaddix and Molina,2009) and evolution of pollutants (Chen, Liu et al.,2007).

In general, gas temperatures are lower when CO_2 is employed due to its higher heat capacity compared with N_2 (Andersson and Johnsson,2007; Bejarano and Levendis,2008), in that way it is necessary to employ a higher oxygen concentration to obtain similar temperatures to those observed for combustion with air. Shaddix and Molina 2009 have reported particle ignition and devolatilization properties in $30\%O_2/70\%CO_2$ are similar to those in air, and resulted in reduced NOx emissions and better coal burnout efficiency than coal combustion in air (see also Liu et al.,2005).However in a separate study, when similar O_2 concentration is used (in N_2 or CO_2), shorter combustion times are found for the O_2/N_2 cases (Bejarano and Levendis 2008).

Chen, Liu et al.(2007) and Croiset and Thambimuthu (2001) have also shown that NO_x emissions are higher under classical combustion (using air) than in oxy-fuel combustion. This behaviour has at least two possible explanations: in oxy-fuel combustion N_2 is eliminated by an air separation unit; therefore, thermal NOx formation is avoided under this process and this contribution to overall NO_x emissions is minimized and oxidation of fuel-N becomes the dominant source of nitrogen oxides in oxy-coal combustion systems.The

second explanation consists of reduction of NO into N_2 over the carbonaceous material when recirculation is employed (Liu, Zailani et al., 2005; Andersson et al., 2008). Chen, Liu et al. (2007) investigated the evolution of NO_x in a FBC and found that the formation of NO_x in conventional air combustion and oxygen-rich combustion is significant, but when recirculation of the flue gases (RFG) is applied, NO_x emission diminishes by 40-50 % due to reduction of NO into N_2 (Croiset and Thambimuthu,2001).

As mentioned previously, high CO_2 concentrations affect combustion properties as compared with those under conventional air combustion. Therefore, it is necessary to have a basic understanding of the oxycombustion process with the aim to optimize operational parameters and in this way to diminish emission of pollutants. Many studies are focused on evolution of NO_x (NO and NO_2: acid rain precursors and participants in photochemical smog (Glarborg et al.,2003)). However, less attention has been put into N_2O evolution, a very important greenhouse gas that is found in significant concentrations in fluidized bed combustion due to lower temperatures. The purpose of this study is to evaluate the behaviour of N_2O under fluidized bed oxy-coal combustion environments.

EXPERIMENTAL

High nitrogen model chars were obtained by pyrolysis of polyacrylonitrile. A heating ramp of 20 C/min was used with a final temperature of 800 C (PAN-8). An Ar atmosphere was used to avoid fixation of N_2 during the pyrolysis process (Zheng et al., 2009) was used.

For the combustion experiments a fluidized bed reactor that can be operated with a few fuel particles was assembled that allows the study of char oxidation rates and fuel nitrogen conversion as a function of temperature, P_{O2} and P_{CO2}. The reactor consists of an electrically heated furnace with a stainless steel tube, 2.6 cm internal diameter (Fig.1). Fluidization was reached with sea sand 0.1-0.2 mm diameter and the total flow rate is 500 mL/min in all cases. Reaction was carried out at 800 C.

Gases produced during oxidation are followed by FTIR spectroscopy using a gas cell. The reactor has an inner basket to allow extraction of the particles after specific reaction times, which allows for their characterization at different stages of the reaction.

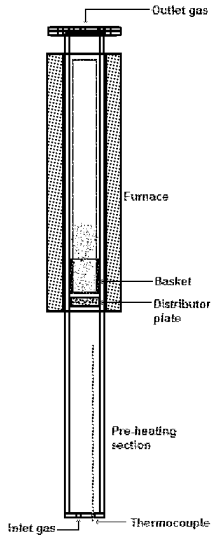

Fig.1 Schematic representation of the FBC reactor

COMPUTATIONAL

The computational work was focused on the interactions that can take place between the gaseous phase and the nitrogen functionalities in the solid char particles when there are high levels of CO_2. The calculations were performed using the Gaussian 03 package. The theory level and basis set employed were B3LYP/6-311G(d,p), respectively. Model chars were represented by five fused rings.

RESULTS AND DISCUSSION

Char characterization

Table 1 shows elemental and proximate analyses of the char obtained from PAN-8, and illustrates the high nitrogen content of this char.Fixed carbon was high as well, due to the pyrolysis conditions.

Table 1 Proximate and elemental analyses PAN-8 char

C%	H%	N%	O(diff) %	S%	VM%	Fixed C %
77.32	1.12	16.4	4.9	< 0.05	3.7	96.1

Species identification during char oxidation

Figure 2 shows the FTIR spectra for combustion gases of the PAN-8 char in 100% O_2. The most important species are NO, NO_2, N_2O, CO and CO_2. Some of these species have two absorption bands (I and II). In the case of CO_2 the signal II is more representative since signal I is very high and therefore the detector reaches saturation. In the case of N_2O, signal II was used to follow this compound since signal I is eclipsed by the CO_2 main absorption band. CO is a very important gas in oxy-fuel combustion, unfortunately, it was impossible to

clearly identify it because this signal is very close to CO_2 I and N_2O I; both of them with higher absorption bands.

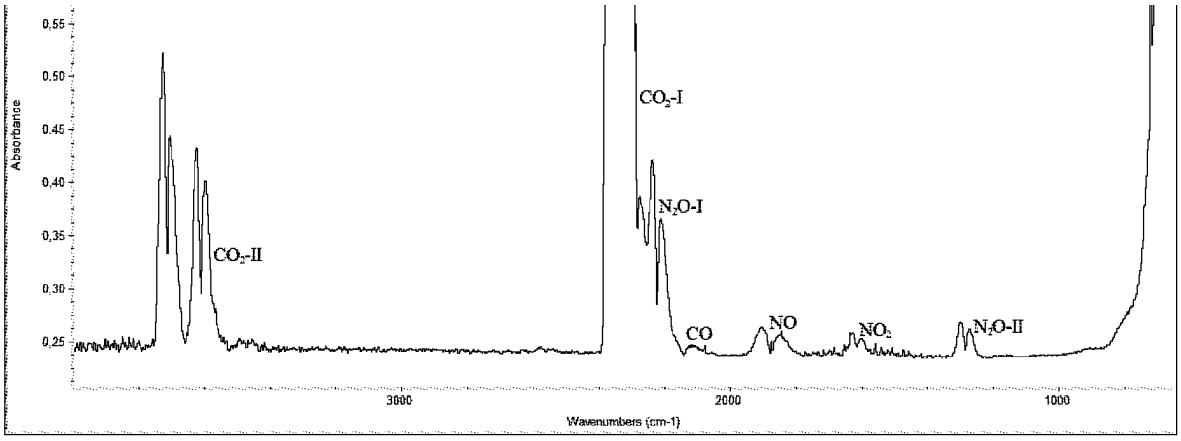

Fig.2 Species identification by means of FTIR during combustion experiments.
Data obtained in the PAN-8 char combustion under 100% O_2

With the experimental set-up used in this research it is possible to follow the evolution of the most important species as shown in Fig.3 for the combustion of PAN-8 char in 30%O_2/70%Ar. Figure 3 shows how, as time of reaction increases, the evolution of the different N-species is changing. For example, N_2O concentration is high at the beginning of the reaction; and, NO and NO_2 are not present. However, with the increase of conversion, NO_2 and especially NO are increasing. In Fig. 3 it is possible to identify when the reaction is over, since the CO_2 signal is drastically reduced (CO_2-signal II), offering a possibility to calculate burnout times in this transient fluidized bed combustion experiment.

FTIR spectra were taken every two seconds, and with this information we can create a "history" of PAN-8 char combustion and compare the behavior under O_2/Ar and O_2/CO_2 combustion. Fig. 4 shows the area under the peaks for N-species with respect to reaction time in the case 21%O_2/79%CO_2. It is possible to observe how N_2O is diminishing while, NO and NO_2 are increasing. Fig. shows the N-species evolution profile when the PAN-8 char was burned under 21%O_2/79%Ar. Comparison between Fig. 4 and Fig. 5 indicates that CO_2 presence modifies the kinetics of the evolution of NOx enhancing conversion to NO_2, probably by oxidation of N_2O.

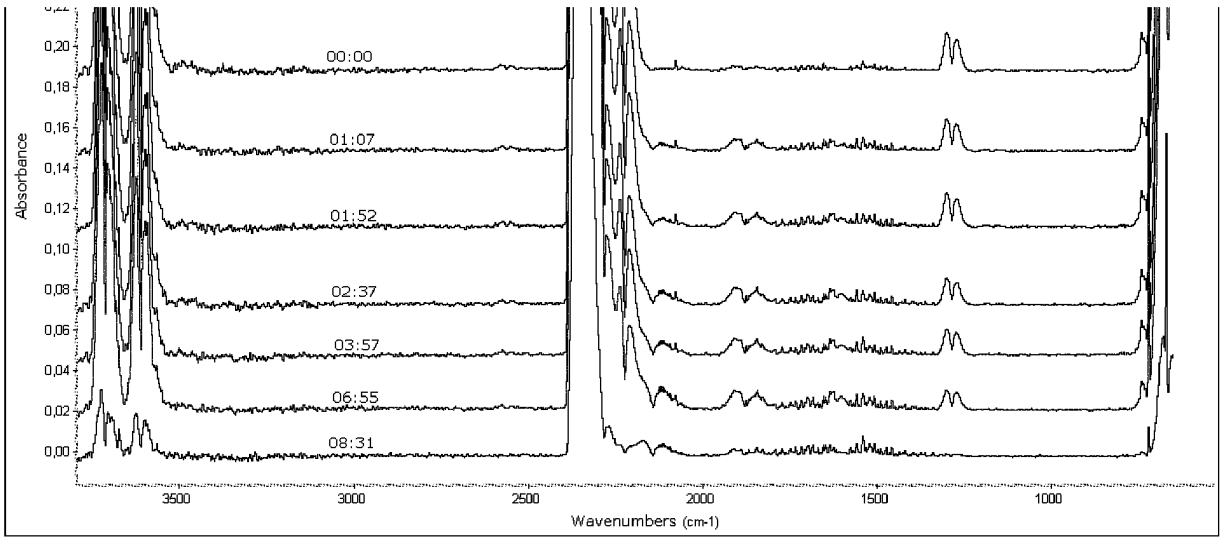

Fig.3 Sequence of combustion for PAN-8 char in 30%O_2/70%Ar

It is important to clarify how CO_2 affects N_xO_y evolution. Differences obtained in the above described FBC-FTIR results indicate that CO_2 is changing the mechanisms of the reaction. In order to understand this effect, electronic structure methods are a useful tool to be used. Heterogeneous interactions between CO_2 and N-complexes have been simulated offering a possible explanation for NO_2 formation under O_2/CO_2 combustion. Figure 6 shows a reaction path for the formation of NCO -very reactive specie – that can be easily oxidized.

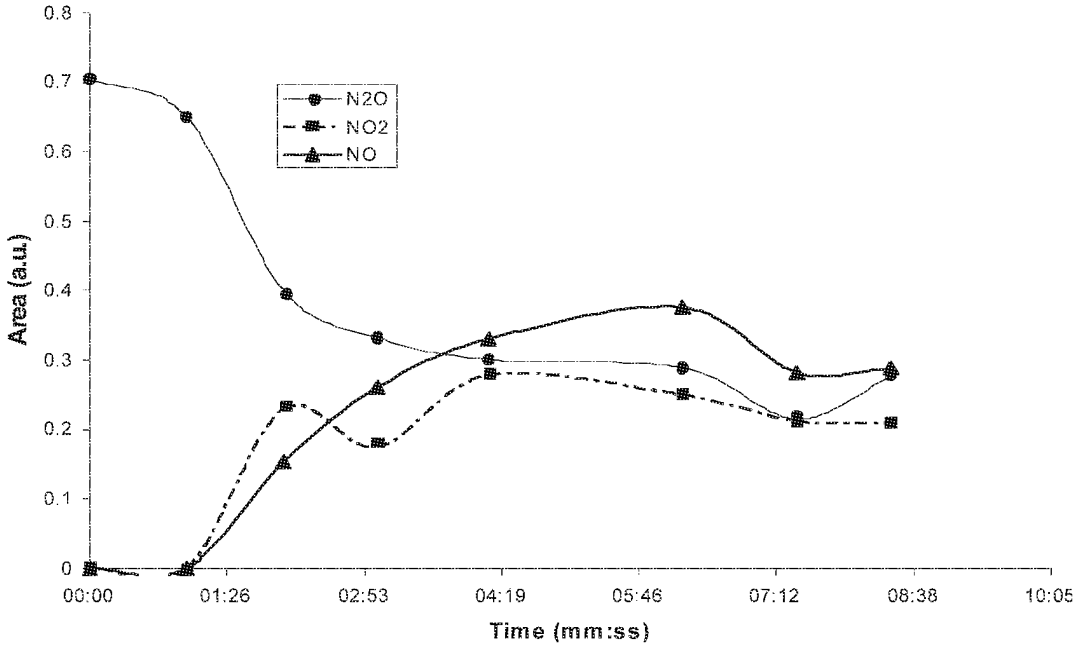

Fig. 4 Evolution of N_2O, NO_2 and NO in time for combustion of PAN-8 char in 21%O_2/79%CO_2

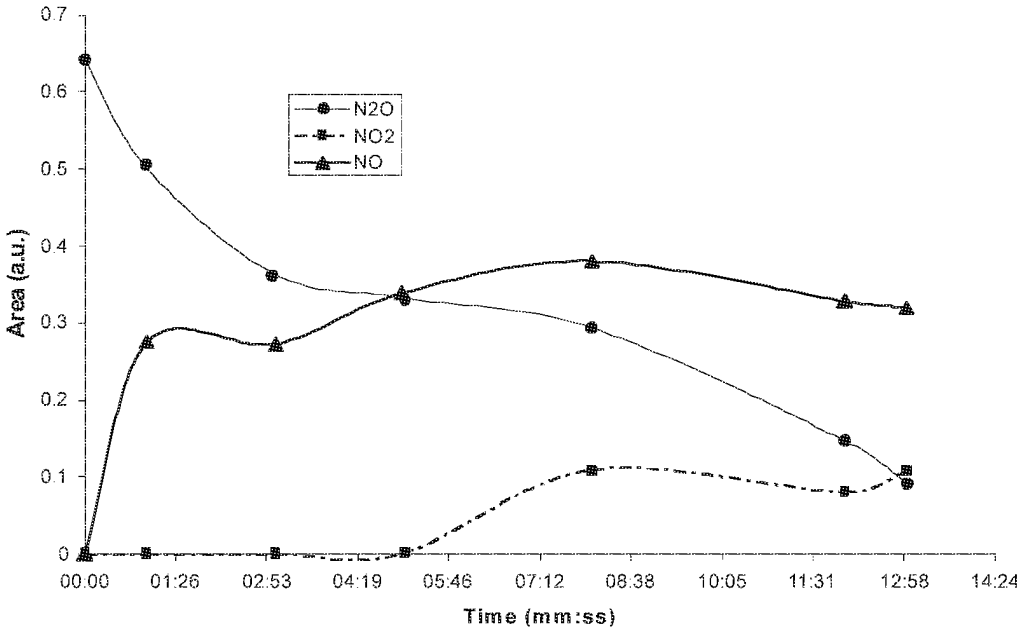

Fig. 5 Evolution of N_2O, NO_2 and NO in time for combustion of PAN-8 char in 21%O_2/79%Ar

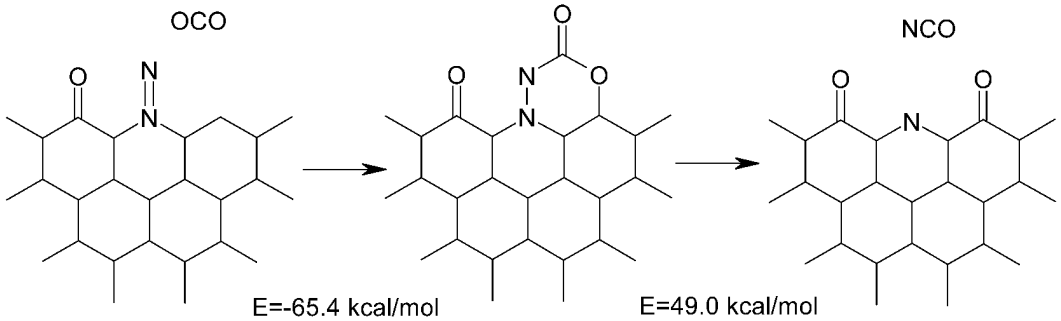

Fig. 6 NCO Formation NCO by CO_2 – N char interaction

Several homogeneous reactions can be explored for oxidation (or reduction) of this intermediate.Figure 7 shows formation of NO_2 and CO through NCO oxidation. It is important to note both of these gases are present in oxy-coal combustion experiments (Fig. 2).

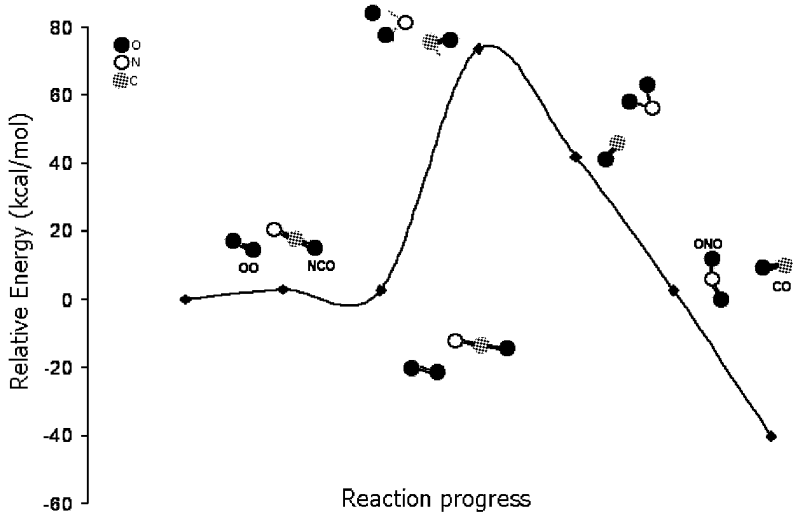

Fig. 7 Potential energy surface for the reaction NCO + O_2 ↔ NO_2 + CO

CONCLUSIONS

The results presented here indicate that CO_2 modifies the mechanisms for NO_x formation, favouring formation of NO_2, probably due to oxidation of N_2O or NO. At the initial time of the combustion reaction, the presence of high CO_2 concentrations does not have an important effect on the N_2O evolution. Under these conditions NO and NO_2 are evolved almost at the same time while under Ar these compounds are evolved at different times.

NCO is an energetically plausible intermediate that can be produced by the heterogeneous reaction between CO_2 and nitrogen complexes in the char during oxy-combustion.

N_2O formation under the experimental conditions used in this work is important. However, there is limited information on the formation mechanisms in heterogeneous systems and further research is needed.

ACKNOWLEDGEMENTS

The authors gratefully acknowledge support from the "Programa Sostenibilidad" of the "Universidad de Antioquia" and the "Utah Clean Coal Center". A.S. thanks Colciencias and the "Universidad de Antioquia" for her PhD scholarship.

REFERENCES

Andersson, K. and F. Johnsson. Fuel **86**(2007), pp. 656-668.
Andersson, K., F. Normann, et al. Industrial & Engineering Chemistry Research **47**(2008), pp. 1835-1845.
Bejarano, P. A. and Y. A. Levendis. Combustion and Flame,**153**(2008), pp. 270-287.
Buhre, B. J. P., L. K. Elliott, et al. Progress in Energy and Combustion Science **31**(2005), pp. 283-307.
Chen, J.-C., Z.-S. Liu, et al. Journal of Hazardous Materials **142**(2007), pp. 266-271.
Croiset, E. and K. V. Thambimuthu. Fuel **80**(2001), pp. 2117-2121.
Davison, J. Energy **32**(2007), pp. 1163-1176.
Glarborg, P., A. D. Jensen, et al. Progress in Energy and Combustion Science **29**(2003), pp. 89-113.
Li, Q., C. Zhao, et al. Journal of Analytical and Applied Pyrolysis **xxx**(2008), pp. xxx-xxx.
Liu, H. and K. Okazaki. Fuel **82**(2003), pp. 1427-1436.
Liu, H., R. Zailani, et al. Fuel **84**(2005), pp. 2109-2115.
Shaddix, C. R. and A. Molina. Proceedings of the Combustion Institute **32**(2009), pp. 2091-2098.
Wall, T. F. Proceedings of the Combustion Institute **31**(2007), pp. 31-47.
Yang, H., Z. Xu, et al. Journal of Environmental Sciences **20**(2008), pp. 14-27.
Zheng, Y., A. D. Jensen, et al. Proceedings of the Combustion Institute **32**(2009), pp. 1973-1980.

THE STUDY OF SAWDUST COMBUSTION IN A VORTEXING FLUIDIZED BED COMBUSTOR

Chien-Song Chyang[1],Kuo-Chao Lo[1],Kuan-Chang Su[1],Keng-Tung Wu[2]

1Department of Chemical Engineering, Chung Yuan Christian University, Chung-Li 320, Taiwan,China

2 Department of Forestry, Chung Hsing University,Taichung 40227, Taiwan,China

Abstract: In order to understand the combustion phenomena of woody material in a vortexing fluidized bed combustor (VFBC), a series sawdust combustion tests were carried out in a pilot scale VFBC. The sawdust is from the residuals of timber industry. The pilot VFBC consists of a 0.4m×0.8m×0.75m (W×L×H) of rectangular combustion chamber and a cylindrical freeboard with 0.75m I.D. The secondary air is injected at the position of 1.75m above distributor. The effects of operating parameters on the combustion efficiency, temperature distribution, and combustion proportion are investigated in this present work.

The results of this study indicate that as primary air increasing, more heat released in the splashing zone; however, more unburned carbon particles reduce combustion efficiency. Higher secondary air flow prolonged the residence time of the unburned carbon particles to make the heating release ratio rise on the second air zone and freeboard zone. The combustion efficiency and heating release ratio increase with excess air, because of more oxygen reacted with combustibles.

The features of the performance of sawdust combustion in VFBC reflect the specific fuel properties of high volatile biomass. The results of this study will help us to design a VFBC which can extract the biomass energy of woody biomass.

Keywords: vortexing fluidized bed combustor, biomass, combustion efficiency, combustion proportion.

INTRODUCTION

In the recent years, the interest in alternative energy source is increasing, because of the dramatically change of fossil fuels price. Since that, a sustainable energy resource and a credible combustion technology are needed to face the crisis of depletion of fossil fuel. Woody biomass is the oldest energy source since fire use appeared in human's history. It was the fourth largest source of total primary energy in the word in 2006 (International Energy Agency ,IEA, 2008). In Taiwan, biomass energy with a potential of 3.3 million kiloliters of oil equivalent is the most important renewable energy source at present (Industrial Technology Research Institute, 2006). Two reasons led us chose sawdust as biomass fuel in this present work. One is easily available and the other is that sawdust is residual of timber industry. Then a suitable and credible combustion technology is needed to treat this kind of high volatile fuels.

Fluidization technology was originated in 1920s last century. Nowadays, fluidization technology is considered as mature technology. It has been successfully applied in many fluid-solid two-phase operations in the past eighty years. Combustion is one of the most promising applications, because of its fuel flexibility, high combustion efficiency and low pollutants emission (Anthony, 1995). The advantage of fuel flexibility makes fluidized bed combustor appropriate for biomass combustion. Fluidized bed combustion chamber fills with solid bed materials and fluidizing gas. Two significant phases, bubble and emulsion phase, are defined in fluidized bed region. Generally, char particles combust in emulsion phase. And combustible gas combusts in both emulsion and bubble phase. Different from fluidized bed, freeboard characterizes as lean particles. The homogeneous gaseous combustion is violent in this region. Secondary or higher stages air provision in freeboard will increase combustion efficiency and decrease air pollutants emission (Varol and Atimtay, 2007). The positive effects of secondary air can be found when the secondary air is set as tangential injection (Zhu and Lee; 2005, Chyang et al., 2008).

Most of the applications of biomass combustion in fluidized bed are co-combustion with fossil fuel like coal. Less literature has been published on single biomass combustion in fluidized bed especially in vortexing fluidized bed combustor (VFBC). For both combustion applications, high volatile content of biomass dominants the temperature profiles in combustor. Biomass fuels release their volatile matter due to the rapid heating when they fed into combustor. Volatile matters mostly combust in the freeboard. Therefore, higher freeboard temperatures were found in many researches (Werther et al., 2000; Zhu and Lee, 2005; Varol and Atimtay, 2007). In few cases, lower combustion efficiency could be found during biomass combustion in fluidized bed combustor. It can be attributed to that more CO and hydrocarbons formed during volatile matters

combusted in freeboard (Varol and Atimtay, 2007). Therefore, VFBC was developed to improve the combustion proportion in freeboard. Vortex flow in freeboard acted like an internal cyclone which can trap more unburned carbon particles in combustor and provide excess air to improve combustion extent. Fluidization Research Laboratory (FRL) of department of chemical engineering of Chung Yuan Christian University (CYCU) has studied a lot of topics about various fuels combustion in VFBC. The advantages of fuel flexibility and low pollutants emission of VFBC have demonstrated (Lin et al.,1997; Teng et al., 1997; Chyang et al., 2001, 2005). Base on the experiences of VFBC's design and operation, a 150 kWth advanced VFBC was established by FRL in CYCU to obtain more practical data in such a pilot scale experimental system.

The objective of this work is to demonstrate the technical feasibility of a fluidized bed combustor as a clean technology for burning the sawdust. The effects of operating parameters (bed temperature, excess air ratio and air partition ratio) on combustion efficiency and combustion proportion in a pilot scale VFBC.

EXPERIMENTAL

A one-factor-at-a-time (OFAT) experimental design was conducted to study the effects of operating parameters on performances of biomass combustion in a VFBC. The VFBC performances were estimated by combustion efficiency (*CE*) and combustion proportion (*CP*). The tested operating parameters were bed temperature (*T*), excess air (*EA*) and air partition ratio (λ). OFAT experiment changes only one factor at one time while the other factors are kept fixed. A standard operating condition consisted of $T = 700^{\circ}C$, $EA = 0.6$ and $\lambda = Q_1/(Q_1+Q_2) = 0.625$. The tested factors increased and decreased based on the standard condition. The experimental array is listed in Table 1. The experiments were conducted in a pilot scale VFBC which consists of a 0.4m x 0.8m rectangular fluidized bed combustion chamber and a 0.75m diameter cylindrical freeboard. The combustor height is 4.5m. Secondary air is tangentially injected into freeboard by four nozzles at the position 1.75m above air distributor. Figure 1 shows the sketch of VFBC system. Biomass fuel fed into combustion chamber by a chute. The feed rate was controlled by switching rpm of screw feeder. A series of K-type thermocouples and five gas sampling probes detected temperature and $CO/CO_2/O_2$ concentration profiles along the height of VFBC combustor. Bed temperature was controlled by a tubular heat exchanger. The quantity of heat removal can be controlled by changing the area merged in bed. The flue gas from biomass combustion in VFBC goes into bag house filter after cooling. Dust materials in flue gas are separated in bag house. Then the flue gas will be induced into a wet scrubber to remove gaseous pollutants. Then the clean flue gas exhausts to the air.

Table 1 OFAT experimental array

T	*EA*	$\lambda = Q_1/(Q_1+Q_2)$
600	0.6	0.625
650	0.6	0.625
700	0.6	0.625
750	0.6	0.625
800	0.6	0.625
700	0.1	0.625
700	0.2	0.625
700	0.4	0.625
700	0.6	0.625
700	0.8	0.625
700	0.6	0.5
700	0.6	0.625
700	0.6	0.75
700	0.6	0.875
700	0.6	1

Table 2 The properties of pine sawdust

Proximate analysis	**wt.%**
Moisture	13.6
Volatile matters	72.18
Fixed carbon	13.82
Ash	0.4
Ultimate analysis	daf. wt.%
C	48.39
H	5.80
O	44.21
N	0.21
HHV	18.2 MJ/kg

The biomass fuel for this research was pine sawdust from the residuals of timber industry. The average particle size of sawdust is 490μm. The proximate and ultimate analyses are listed in Table 2.

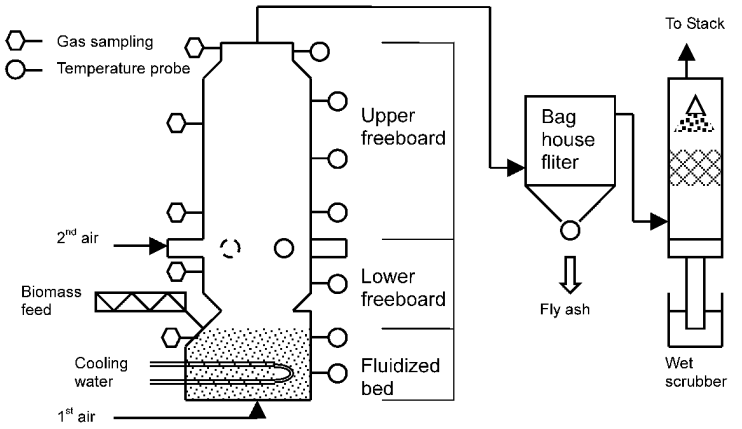

Fig. 1 The sketch of VFBC system

Five sampling points located at position of 0.6m (bed surface), 1.3m and 1.8m (lower freeboard), 3.2m (upper freeboard) and 4.3m (exit of combustor.) The gas samples were pumped into sample bags. MTI-M200 micro GC, China Chromatography 9800 and TSI CA-6230 flue gas analyzer were used to analyzed CO_2, CO and O_2 concentration, respectively. The unburned carbon contents in fly ash and bottom ash were detected with ASTM D6316-04.

DATA ANALYZING

Definition of combustion efficiency varies with different combustion systems. In this present work the combustion efficiency is defined as

$$CE = \frac{F_{feed} \times C_{feed} - [F_{fa} \times C_{fa} + F_{gas} \times x_{CO}]}{F_{feed} \times C_{feed}} \tag{1}$$

Where F_{feed}: feed rate of biomass fuel [kg/hr],
F_{fa}: production rate of fly ash [kg/hr],
F_{gas}: flow rate of flue gas [Nm^3/hr],
C_{feed}: wet based carbon content of feedstock [-],
C_{fa}: carbon content in fly ash [-],
x_{CO}: molar fraction of CO in flue gas [-].

Owing to the low fixed carbon of sawdust the unburned carbon in bottom ash is neglected. Combustion efficiency evaluates performance of a combustor. The higher *CE* the higher energy extracted from fuels.

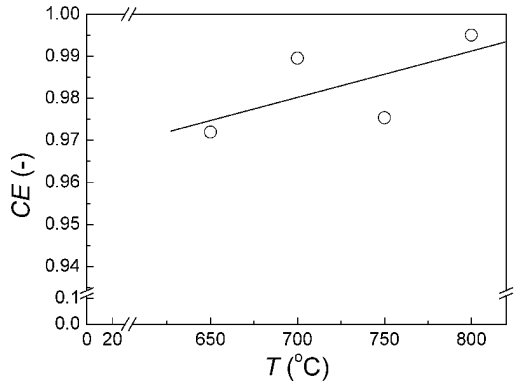

Fig. 2 Combustion efficiency vs. bed temperature

In addition, combustion proportion is adopted to define the ratio of combustion extent in a specific region of combustor. Combustion proportion marks the major region in fluidized bed combustor. It can help us to place the proper heat transfer area to gain more energy from biomass fuel. Before calculating of combustion proportion, the specific regions of combustor have to be defined by their flow features. The VFBC was divided into three sections as fluidized bed, lower freeboard and upper freeboard. Fluidized bed ranges from air distributor to the bed surface. Lower freeboard (splash zone included) ranges from bed surface to the injection point of secondary air. The rest part of combustor is upper freeboard from secondary air injection to the exit of combustor. The combustion proportion defined as the ratio of the oxygen consumption in a specific zone to the total oxygen consumption. It is formulated as

$$CP_i = \frac{Q_{O_2,i}}{Q_t} \tag{2}$$

where $Q_{O2,i}$: quantity of oxygen consumption in zone *i*,
Q_t: total oxygen consumption in whole combustor,
i: code of divided zone of combustor, $i = 1$ = bed, $i = 2$ = lower freeboard, $i = 3$ = upper freeboard.

RESULTS AND DISCUSSIONS

Combustion efficiency *CE*

Figure 2 shows the effect of bed temperature on combustion efficiency. Combustion efficiency increased with bed temperature. Because higher bed temperature enhanced faster combustion rates of not only gaseous combustibles but also char particles. Furthermore, the freeboard temperatures were high enough to ensure good combustion efficiency performances of VFBC even operated at low temperature e.g. 650°C.

The effect of excess air on combustion efficiency is shown in Fig. 3. In all the excess air tests, the primary (fluidizing) air were fixed at 100% stoichiometric O_2 demand i.e. all the excess air supplied by secondary air. The maximum combustion efficiency was taken place at EA = 0.4. The lowest unburned carbon in fly ash was observed in the case of EA = 0.4. It is attributed to the proper magnitude of secondary air that trapped most carbon particles in combustor to improve combustion efficiency. Less excess air leaded insufficient O_2 and weaker swirling flow; therefore, lower combustion efficiencies were observed at lower excess air cases. On the other hand, more excess air provides sufficient O_2 and more carbon particles were entrained with stronger secondary air. Therefore, lower combustion efficiencies were also found in higher excess air cases. Combustion efficiency of VFBC was highly dependent on secondary air. This phenomenon can be demonstrated in the following test that changed the air partition ratio (λ).

Air partition ratio is defined as the ratio of primary airflow rate to total flow rate. In air partition test, the total air supply was kept of 160% of stoichiometry. Higher λ means the VFBC operated for more primary air and less secondary air. Figure 4 shows the combustion efficiency varied with λ. In Fig. 4, we can find that there is an optimal condition of λ = 0.75. The features of sawdust are fine and lower density. Therefore, the devolatilization is almost completed when the sawdust fed into fluidized bed combustion chamber. After devolatilizing, part of char particles fell to bed, the volatile matters and the rest char particles were blown to freeboard. Less primary air blew less char particles to freeboard; meanwhile more char particles were carried out of combustor. In the case of λ = 1 all the combustion air was supplied via primary air through air distributor to bed. Greater amount of char particles were blown into freeboard but no swirling flow to trap carbon particles. Therefore, the lowest combustion efficiency was caused without secondary air.

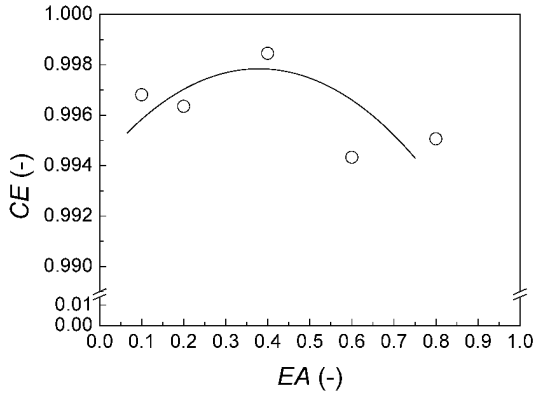

Fig. 3 CE vs. excess air

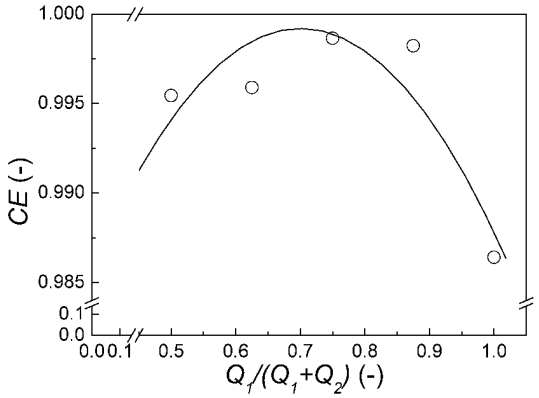

Fig. 4 CE vs. air partition ratio

Combustion proportion *CP*

Combustion proportion reflects the fate of sawdust combusted in a VFBC. Three regions of VFBC have different flow patterns and combustion environments. The effects of operating parameters on combustion proportion show in Figs. 5 to 7. The results revealed that combustion proportion of lower freeboard appears to be the greatest proportion. Figure 5 presents the effect of bed temperature on combustion proportion. According to the little char formation during devolatilization process, most combustibles combusted in freeboard. The combustion proportion of fluidized bed almost did not change with bed temperature. Higher bed temperature built higher temperature combustion environment in lower freeboard. Therefore, a little more combustion proportion was observed with bed temperature in lower freeboard. In general, as observed in Fig. 5, we can remark that combustion proportion is not sensitive to bed temperature.

As mention above, the performance of VFBC is highly dependent on tangentially secondary air injection. The swirling flow acted as an internal cyclone separator that traps unburned carbon particles to improve combustion efficiency. The increment of combustion efficiency can be attributed to the increasing of combustion proportion in lower freeboard. The effect of excess air on combustion proportion is illustrated in

Fig. 6. The combustion proportions of bed region in this test showed a little change with increasing of excess air. It is because excess air was entirely supplied by secondary air. Consequently, every combustion condition in bed region in this test was equivalent. The effect of excess air was exhibited on the increased combustion proportion of lower freeboard. Higher excess air implied more unburned carbon particles were trapped by swirling flow. However, stronger secondary does not always capture more particles. Surfeit secondary air will carry more carbon particles out of the combustor (see $EA = 0.8$ in Fig. 6).

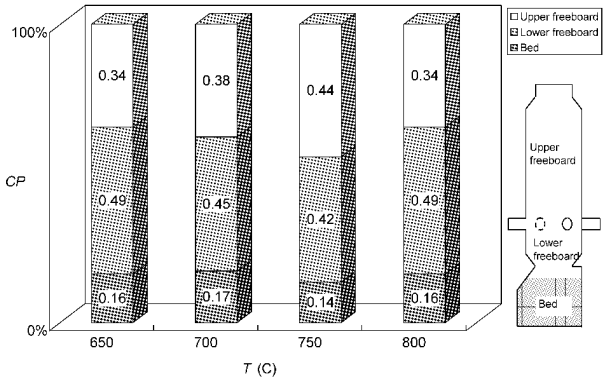

Fig. 5 Combustion proportion vs. bed temperature

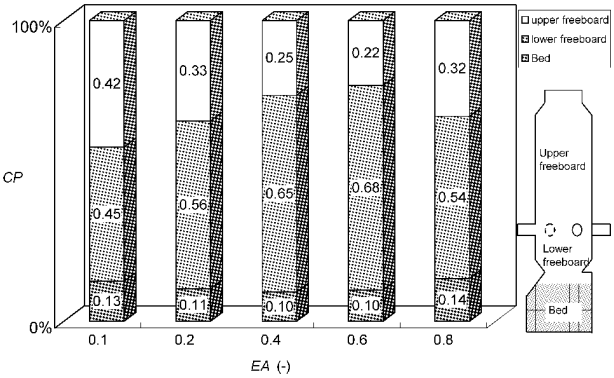

Fig. 6 Combustion proportion vs. excess air

Figure 7 presents the changes of combustion proportion corresponded to five air partition ratios. To contrast with the results of combustion efficiency test, an interesting finding has been found in the case of $\lambda = 0.75$. In this operating condition, the combustion proportion increased in lower freeboard. This phenomenon indicates that the effect of air partition ration is mainly reflected in lower freeboard region. The unchanged combustion proportion in bed region is attributed to the competition between carbon loading and oxygen supply in bed. In cases of lower primary air flow rate, less carbon particles were entrained to freeboard. Despite more carbon particles were combusted in bed, but oxygen supply was less correspondingly. In other cases of higher primary air flow rate, less carbon particles were combusted in bed, but the combustion was enhanced by more oxygen supply.

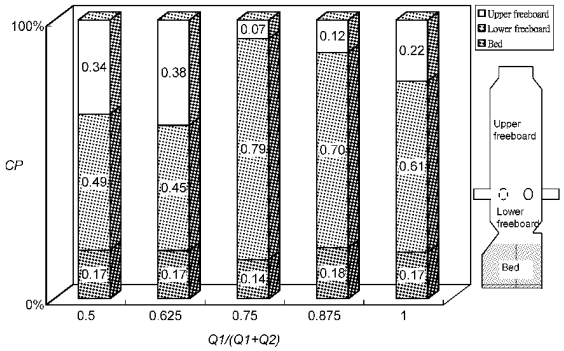

Fig. 7 Combustion proportion vs. air partition ratio

CONCLUSIONS

A series combustion tests were carried out to understand combustion phenomena of sawdust in a VFBC. Combustion efficiency and combustion proportion were evaluated in this work. Combustion efficiency assesses the performance of a combustor; combustion proportion helps us to determine the specific region where mainly combustion took place. The effects of typical operating parameters (bed temperature, excess air, air partition ratio) were investigated in this study.

Results indicated that combustion efficiency increased with bed temperature and had an optimal performance at excess air ratio = 0.6, air partition ratio = 0.75. Combustion proportions in lower freeboard were most affected by tangentially secondary air injection. Compare with the results combustion efficiency and combustion proportion, we can conclude that the effects of operating parameters on combustion efficiencies are mainly attributed to the increment of combustion proportion of lower freeboard. Secondary air plays an important role in high volatile fuel e.g. biomass combusted in VFBC. A proper secondary air supplied enough oxygen and acted as an internal cyclone to enhance the combustion efficiency. A condition of $T = 800^{\circ}C$, $EA = 0.4$ and $\lambda = 0.75$ is recommends operating on sawdust combustion in a VFBC.

REFFERENCES

Anthony, E. J.: Progress in Energy and Combustion Science 21 (1995), pp. 239-268.
Chyang, C. S., Liu, C. Y. and Chang, Y. D.: J. Air & Waste Mang. Assoc. 51 (2001), pp. 542-551.
Chyang, C. S., Lo, K. C. and Wang, K. L.: J. Chem. Eng. Korea 22 (2005), pp. 774-782.
Industrial Technology Research Institute, Taiwan renewable energy and conventional power market. Taipei: British Trade and Cultural Office; 2006.
International Energy Agency (IEA). Key world energy statistics 2008. Paris: IEA; 2008.
Lin, C. H., Teng, J. T. and Chyang, C. S.: Combustion and Flame 110 (1997), pp. 163-172.
Teng, H. S., Chyang, C. S., Shang, S. H. and Ho, J. A.: J. Air & Waste Mang. Assoc. 47 (1997), pp. 49-57.
Varol, M. and Atimtay, A. T.: Fuel 86 (2007), pp. 1430-1438.
Werther, J., Saenger, M., Hartge, E.-U., Ogada, T. And Siagi, Z.: Progress in Energy and Combustion Science 26 (2000), pp. 1-27.
Zhu, S. and Lee, S. W.: Waste Management **25** (2005), pp. 511-518.

EXPERIMENTAL STUDY ON HEAT TRANSFER IN A ROLLING ASH COOLER USED IN THE CFB BOILER

W. Wang, J. J. Li, S. Yang, X.D.Si, H. R. Yang, J. F. Lu, G. X. Yue

Key Laboratory for Thermal Science and Power Engineering of Ministry of Education
Department of Thermal Engineering, Tsinghua University, Beijing, 100084, China

Abstract: From the view of the reliability and the techno-economy, the rolling ash cooler is feasible for the large-scale CFB boilers. However, existing studies on heat transfer in rolling ash cooler mainly focused on heat balance calculation and cold, hot test on the ash cooler outputs. In the heat balance calculation, the value of the overall heat transfer coefficient (α) is usually estimated by the experience, lacking of the support of experimental data.

In this paper, a dynamic experimental system was built to measure the overall α in the rolling ash cooler and the influencing factors, including ash size, ash amount and rotational speed, using the orthogonal design. The results showed that the ash size has the greatest effect on α, and rotating speed has the least. The heat transfer in rolling ash cooler could be enhanced by increasing the rotating speed and decreasing the ash size. The α increased with ash amount when the ash amount is small, but keep nearly constant when ash amount exceeds a certain value.

Keywords: rolling ash cooler, heat transfer, CFB boiler, orthogonal experiment

INTRODUCTION

Ash coolers are auxiliary devices in a CFB (circulating fluidized bed) boiler, playing importance role in the long-term, safe, stable operation of the unit. During the operation of the large-scale CFB boilers, fluidization deterioration, plugging and slagging occur from time to time in the ash, resulting in forced turndown of boiler load or even outage. The problems on fluidization in an ash cooler were often caused by three kinds of bed materials: large pieces of ash, casting material and waste rock (Shu and Chen, 2007). Besides,, problems are also caused by such as plugging in the feed space, attrition of air cap, ash leakage in wind box, unreliable control on the amount of ash, complex operation and so on.

From a view of reliability and techno-economy, the rolling ash cooler is feasible for the large-scale CFB boiler (Liu and Du, 2006). Shown in Fig. 1, the ash cooler is consisted of the device of ash inlet and exhaust air, water-wind rolling rotating at low speed when working and bracket.

The ash is discharged from CFB boiler through the tube into the bucket of the ash cooler, then falls into the water-wind cooled ash roller and goes forward by the film spiral rows. For the time being, cold air continues to flow through the roller. The hot ash then exchanges heat with the cold air and water. After cooled to a lower temperature, the ash is discharged from the other side of roller. In order to prevent the surface from fouling, cooling water must be chemically desalinated and softened.

For rolling ash cooler, thermal conductivity, heat radiation and convection are three basic ways of heat transfer. The heat of hot ash in the rotating roller, on the one hand, will be transferred by thermal conduction to inner wall of outer sleeve, both side walls of inner sleeve, the blades welding on the wall of sleeve, and the air flowing through the surface of hot ash; on the other hand, will be transferred to the walls, blades and air by heat radiation. The radiation happens (1) from the surface of ash to the opposite wall and blades; (2) from the surface of bottom ash to the wall and blades close to it. All the heat transferred on the wall and blades is conducted to the other side of roller, and then is forcedly transferred to the water in the sleeve interlayer; and finally, the heat will be carried out of roller in air and water. Heat convection is the main mechanism for air cooling which is mainly affected by the ventilation and air temperature in practical operation. The water-cooling heat transfer is more complicated, not only affected by the water supply and water temperature, but also by ash amount, ash size, rotating speed of the roller and so on.

For rolling ash cooler, thermal conductivity, heat radiation and convection are three basic ways of heat transfer. The heat of hot ash in the rotating roller, on the one hand, will be transferred by thermal conduction to inner wall of outer sleeve, both side walls of inner sleeve, the blades welding on the wall of sleeve, and the air flowing through the surface of hot ash; on the other hand, will be transferred to the walls, blades and air by heat radiation. The radiation happens (1) from the surface of ash to the opposite wall and blades; (2) from the surface of bottom ash to the wall and blades close to it. All the heat transferred on the wall and blades is conducted to the other side of roller, and then is forcedly transferred to the water in the sleeve interlayer; and finally, the heat will be carried out of roller in air and water. Heat convection is the main mechanism for air cooling which is mainly affected by the ventilation and air temperature in practical operation. The

water-cooling heat transfer is more complicated, not only affected by the water supply and water temperature, but also by ash amount, ash size, rotating speed of the roller and so on.

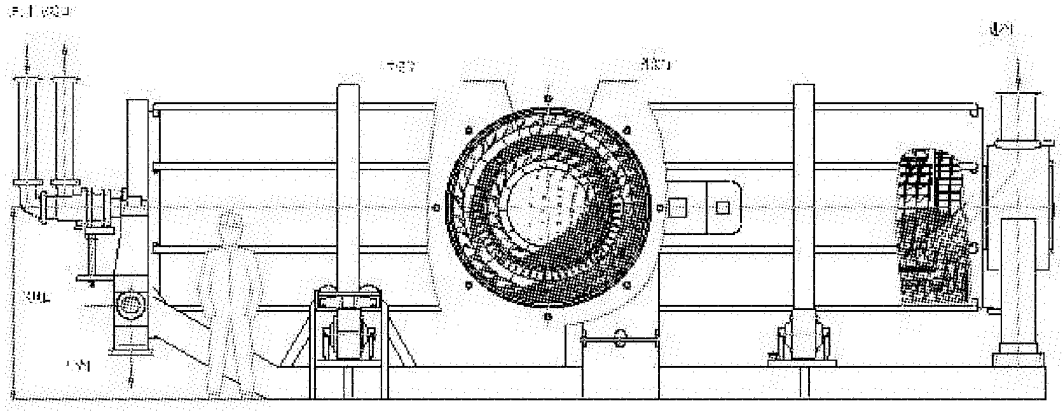

Fig.1 Structural diagram of rolling ash cooler

It is lack of maneuverability to measure local α in different parts of the ash cooler. Hence, the overall α ($W \cdot m^{-2} \cdot K^{-1}$) is measured instead. Obviously, the overall α is related with roller structure, material, rotating speed, ash size, and ash amount.

So far, the studies on heat transfer in the rolling ash cooler mainly limited in the heat balance calculation and cold, hot test on the slag cooler outputs. In the heat balance calculation, the value of overall α is usually estimated by the experience, lacking of the support of experimental data (Liu and Yi, 2006). In this paper, a dynamic experimental system was established to study the influencing factors, including ash size, ash amount and rotating speed, on the overall α in a rolling ash cooler, using the orthogonal design (Fang and Ma, 2001).

EXPERIMENTALS

According to the previous study on heat balance calculations of rolling ash cooler (Zhang and Zheng, 2003), 15% of ash heat is carried away by air, while the other 85% is carried away by cold water. Therefore, in present study, only one spiral length roller of actual ash cooler is used.

Shown in Fig.2, the experimental system mainly consists of three parts - roller, motor and spray equipment. Roller was one steel pipe of 148mm in diameter and 5mm in thickness, and its both ends were closed with flange. In order to reduce the heat loss from end covers, fiber glass gasket was used between the flange and the cover. The roller was driven by a motor with adjustable speed from 0 to 97r/min. Taking into account the experimental difficulties, sprays water was used to cool the outer wall instead of using a closed-loop water cycle outside the roller. The bed material used was the bottom ash from a CFB boiler. Both of the ash temperatures and water temperature of outer wall were measured by K-sheathed thermocouples. Due to rapid changes in temperature, real-time data acquisition was used.

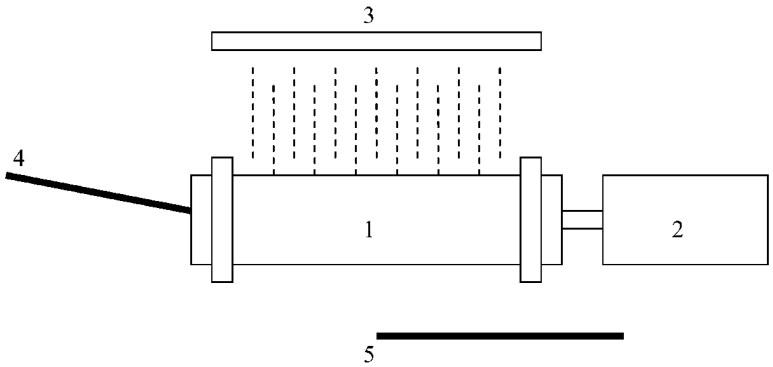

Fig.2 Experiment system of rolling ash cooler

1- roller; 2- adjustable speed motor; 3- spray equipment;

4- thermocouple to measure ash temperature; 5- thermocouple to measure water temperature

Experimental procedure were divided into three steps as: (1) Put the ash in line with the size conditions into the roller after weighing, and then set the roller into the muffle furnace to incandesce more than 700℃. (2) Placed the roller on the test rig connecting with the motor, and placed the thermocouples into the roller. (3)Adjusted the motor rotating speed to a desired value, and opened the spray water. Experimental data was acquired every 5-15 seconds, including the ash temperature, water temperature and time. The experiment ended when the temperature readings of the ash do not rise any more.

The factors studied in the experiments include ash size, ash amount and rotating speed of the roller. Each of the factors sets four levels, respectively recorded as the level of 0, 1, 2, 3, as seen in Table 1.

Table 1 Factors and levels for the experimental study

factors	Level 0	Level 1	Level 2	Level 3
Ash size (mm)	0-0.5	0.5-1	1-3.2	3.2-
Ash amount (kg)	1	1.45	2.35	1.9
Rotating speed (RPM)	20	40	60	80

In accordance with the conventional experimental method, the number of experiments of three factors and four levels must be 64. As each experiment takes 1-2 hours, the entire experimental period would be very long. It was found that the cooler could not last for more than 10 hours under such harsh experimental conditions. Thus, the orthogonal experimental method was chosen, and the orthogonal conditions for the experiments are listed in Table 2. Two tests are repeated at each experimental condition. At the same time, orthogonal method is used in main effect estimation of multiple factors. It shows that under the orthogonal design, the number of experimental conditions reduces to a quarter of the conventional method, saving much time and cost.

Table 2 Orthogonal design of experimental conditions

Condition number	Ash size(mm)	Ash amount(kg)	Rotating speed(RPM)
000	0-0.5	1	20
011	0-0.5	1.45	40
022	0-0.5	2.35	60
033	0-0.5	1.9	80
101	0.5-1	1	40
110	0.5-1	1.45	20
123	0.5-1	2.35	80
132	0.5-1	1.9	60
202	1-3.2	1	60
213	1-3.2	1.45	80
220	1-3.2	2.35	20
231	1-3.2	1.9	40
303	3.2-	1	80
312	3.2-	1.45	60
321	3.2-	2.35	40
330	3.2-	1.9	20

RESULTS AND DISSCUSIONS

Figure 3 shows the typical curve of heat transfer under the condition of #312, in which the enthalpy of ash was by the method purpose by Zhu et al. (2008). According to the heat transfer formula (1) of heat exchanger:

$$k = q / A \cdot \Delta T \tag{1}$$

Where heat transfer rate q is the slope of the curve of slag enthalpy changes, W; the inside surface area of roller A is 0.1953m^2; and ΔT is the temperature difference between the ash and cooling water, K. Thus, the overall α can be reversely derived. Figure 4 shows the relationship between overall α and ash temperature under experimental condition of #312. It can be seen that overall α nearly does not change with ash temperature. Due to the existence of measurement errors, the measurement value of α fluctuated in the vicinity of a certain value. Repeat experiments were conducted to obtain an average value.

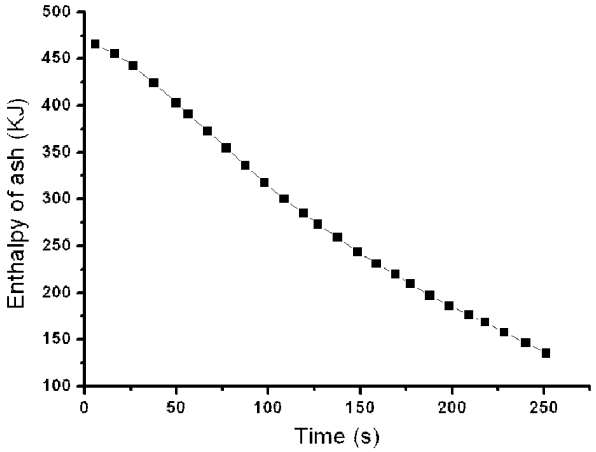

Fig.3 The curve of ash enthalpy changes

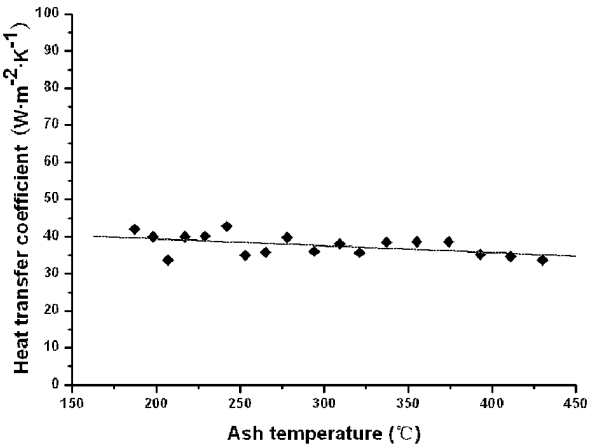

Fig.4 Relationship between heat transfer coefficient and ash temperature

Under the condition of water cooling, the overall α with the order of magnitude of 10-100 $W \cdot m^{-2} \cdot K^{-1}$ is impacted by operating parameters, and the ratio of the maximum to the minimum is nearly 4. Furthermore, the measurement standard error is with 4-11%. This is because of the low dynamic response of the thermocouple. Particularly in the condition of small ash amount and high ash temperature, ash temperature changes rapidly, introducing large deviation in the transient measurement.

Figure 5 shows the effect curve of the three factors. It is not difficult to see that the smaller is the ash size, the greater the overall α is. Therefore, in the view of increasing heat transfer capacity and ensuring the ash cooler effort, it is necessary to reduce the average size of the ash in a CFB boiler. The relationship between the rotating speed and the overall α is also monotonous, i.e., the overall α increases with the rotating speed. However, in the actual operation, the rotating speed of rolling ash cooler is also subjected to wear rate, operation stability and power cost.

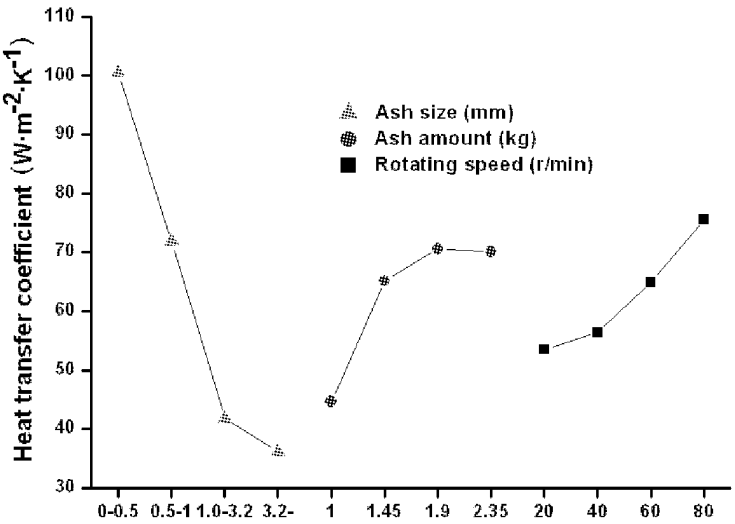

Fig.5 The corresponding curve of three factors

When ash amount is less than 1.9kg, the overall α increases as the ash amount increases; when the ash amount is more than 1.9kg, the overall α almost does not change with the ash amount. Thus, in actual operation, when ash amount is small, the ash amount increasing will be favor of heat transfer enhancement. Consequently, the boiler in the low-load operation should minimize the number of ash coolers to ensure that a single ash cooler has a larger amount of ash.

From the variation range of influencing factors listed in Table 3, we can see that ash size is the most sensitive and the rotating speed is the least sensitive; the factor of ash amount is close to the one of the rotating speed. The results indicate that the control of coal size and ash size are more effective in the actual operation compared to the rotating speed and ash amount increase.

Table.3 Variation ranges of the influencing factors

Factor	Ash size	Ash amount	Rotating speed
Range	64.536	26.088	21.952

CONCLUSIONS

Based on the experimental and the analysis above, we can draw the following conclusions:

Dynamic experimental method to measure the overall α in the rolling ash cooler is effective. For data accuracy, repeat experiments are needed to obtain average α due to the temperature fluctuation.

Among influential factors of ash size, ash amount and roller rotation speed, ash size is the most sensitive and the rotating speed is the least sensitive. The effect of ash amount is close to that of rotating speed.

The smaller is the ash size, the greater the overall α will be. To enlarge heat transfer capacity of the ash cooler, it is necessary to control the size distribution of the ash.

The overall α increases with the rotating speed, but at the same time, the wear rate, operation stability and power cost would also increase.

When ash amount is less than a certain value, the overall α increases with the ash amount. When ash amount exceeds the value, however, the overall α becomes insensitive to the ash amount. It is suggested that the boiler operating in low turndown ratio should keep the least ash coolers running to ensure that the amount of ash in the operating ones is large enough.

ACKNOWLEDGEMENTS

Financial supports of this work by Key Project of the National Eleventh-Five Year Research Program of China (2006BAA03B05) and National Science Fund Committee (50576041) are gratefully acknowledged.

REFERENCES

Fang, K. T., Ma, C. X., Uniformly orthogonal test designs. Beijing: Science Press, 2001.
Liu, L. Z., Du, S. G., Power System Engineering, 22 (2006), pp. 33-37.
Liu ,Y. C., Yin, H. C., Liu, Z. P., Power System Engineering, 22 (2006), pp. 35-38.
Shu, M. L., Chen, J. H., Lu, X. F., Liu, H. Z. Power System Engineering, 22 (2007), pp. 29-33.
Zhang, Z. L., Zheng, L. G. Coal Engineering, 12 (2003), pp. 55-56.
Zhu, A. Q., Rui X. H., Systems and equipments of circulating fluidized bed boiler. Beijing: China Electric Power Press, 2008.

3D UNSTEADY MULTIPHASE SIMULATION OF URANIUM TETRAFLUORIDE PARTICLE FLUORINATION IN FLUIDIZED BED PILOT

N. A. Konan[1], H. Neau[1], O. Simonin[1], M. Dupoizat[2], T. Le Goaziou[2]

1 Université de Toulouse, IMFT, UMR 5502 CNRS/INPT/UPS, France

2 Areva NC BU-Chimie, Pierrelatte, France

Abstract: This paper investigates Eulerian simulation approach of uranium hexafluoride production in fluidized bed pilot. Mass transfer is modeled by using the shrinking particle model. The model successfully predicts expected amount of uranium hexafluoride. As heat transfers with wall are neglected, temperature increases within the reactor and there is no gradient in wall-normal direction of reactor. External diffusion model of reactive gas around particle is developed. Effect of fluorine diffusion within nitrogen is found to be negligible under the simulation conditions. Moreover, inter-particle radiative heat transfer between particles of dense phase in the bed is investigated in the frame of Rosseland approximation.

Keywords: uranium fluorination, shrinking core model, diffusion, radiative heat transfer

INTRODUCTION

Adequate sources of energy remain one of the crucial challenges to ensure sustainability welfare of societies. Nuclear energy constitutes reliable component with the other alternative and renewable energies. However, natural uranium is 99.3% of 238-U whereas the 235-U needed as the combustible of the nuclear reactors is about 0.7%. Furthermore, as enriched uranium is commonly used for the manufacturing of reactor combustible, gaseous uranium hexafluoride (UF_6) production step is required. The fluorination of uranium tetrafluoride (UF_4) with fluorine (F_2) is performed in fluidized bed, beside the limitation of gas/solid contact due to the presence of gas bubbles. Advantages are excellent mass transfer, efficiency of heat transfers between phases in the bed and better control of the temperature. Although the fluorination reaction is exothermic, the process starts with prior pre-heating of the bed at 400°C with nitrogen (N_2). That would ensure the optimum conditions of a significant reaction rate of UF_4 particles. The bed is comprised of two particle phases: uranium tetrafluoride of Geldart A-type and B-type inert alumina particles (Al_2O_3) used as fluidizing agent. The second stage of the process consists of the injection of mixing gaseous of fluorine and nitrogen within the inlet of the reactor at a temperature lower than the pre-heating temperature.

The paper focuses on the simulation of gaseous hexafluoride production with Euler/Euler approach based on transport equations of mass, momentum and enthalpy of each phases in the bed, coupled through inter-phase transfer terms. The chemical reaction between reactive particles and surrounding fluorine arises from a source term modeled according to the shrinking particle model. Although UF_6 may react with UF_4 to yield some intermediate products such as U_4F_{17}, U_2F_9 and UF_5 in absence of fluorine and at low temperatures, only the reaction of the F_2 with UF_4 is assumed. The species of the gaseous mixture modified as reaction proceeds, are followed by solving mass fraction equations in which source terms are provided by the chemical reaction kinetic.

SYNOPTIC OF THE INTERACTIONS IN THE BED

Transfers of momentum and turbulent energy agitation due to inter-particle collisions control hydrodynamics in the bed. Basically, gaseous mixture surrounding both particle phases (Al_2O_3 and UF_4) imposes both Archimede's forces which ensure the suspension of the particles and drag that plays significant role in the dispersion mechanisms. Regarding the particulate phases, inter-particle collisions in each dispersed phase or/and between particles of both separated phases have crucial influence on their behavior in the bed.

Exothermic fluorination reaction of UF_4 with F_2 that occurs in the bed yields UF_6 according to:

$$UF_4\ (\text{solid}) + F_2\ (\text{gas}) \rightarrow UF_6\ (\text{gas}) \qquad (1)$$

with reaction enthalpy $\Delta H = -234.4$ kJ/mol .

Then as reaction proceeds, mass transfer continuously arises between gas and reactive UF_4 phases. Inter-phase mass exchange induces at the same time momentum and enthalpy transfer between phases. Furthermore, UF_4 and Al_2O_3 particles experience convection/diffusion heat transfers with the surrounding gas.

Besides heat exchanges with wall and intermediate reactions that may arise, the main interactions occurring between the three phases described above are summarized in Fig. 1.

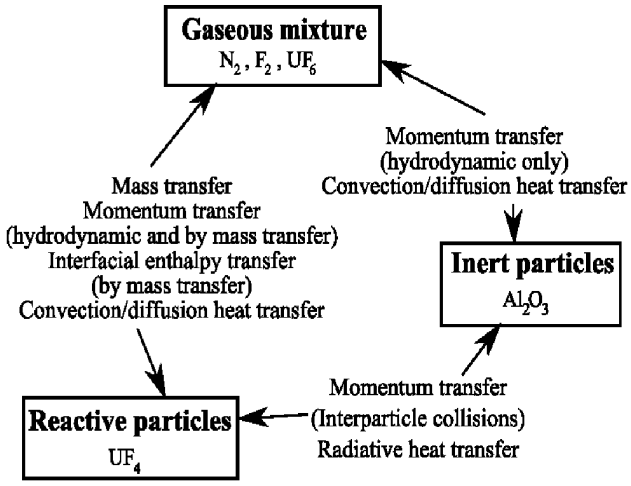

Fig.1 Simplified sketch of main interactions between phases in the bed

MODELING OF THE FLUORINATION PROCESS

N-fluid Eulerian approach, derived from Boltzmann type equation for particle mixture by analogy with the statistical formalism of the description of molecules in gas, is used to investigate the behavior of the cloud of particles moving within a reactive turbulent gas flow (Gobin et al., 2003; Ciais et al., 2007). Classical mass and momentum balance equations are modified by additional terms that depend on the interphase mass transfer rate (Γ_k for the *kth* phase in the bed, such as $\sum_k \Gamma_k = 0$) due to the chemical reaction between gas and reactive particles (see Randrianarivelo et al., 2007). Accordingly, the modeling of the reactive flow will be focused on the heat exchange and the chemical interactions that arise in the bed. In the following the subscripts f/g and p refer to the properties associated to the gas and particles (reactive: UF_4 and inert: Al_2O_3), respectively. $\langle \, . \, \rangle_k$ denotes the averaging for the *kth* phase.

Eulerian modeling of the reactive flow

Without external heat sources and neglecting the radiative transfer, the enthalpy H_k of a phase *k* satisfies the following balance equation:

$$\alpha_k \rho_k \frac{\partial H_k}{\partial t} + \alpha_k \rho_k U_{k,j} \frac{\partial H_k}{\partial x_j} = \frac{\partial}{\partial x_i}\left(\alpha_k \rho_k K_k^t \frac{\partial H_k}{\partial x_i}\right) - H_k \Gamma_k + H_\sigma \Gamma_k + \Pi_k' \tag{2}$$

K_k^t represents the diffusivity coefficient due to fluid turbulence ($k = f$) and particle agitation ($k = p$). H_σ is the averaged enthalpy of the mass flux crossing the reactive particle and directly released in the surrounding gas, as the chemical reaction proceeds. Therefore, one may reasonably assume that $H_\sigma = H_{UF_4}$. Furthermore, the heat exchange between dispersed phases and surrounding gas accounted for through Π_k' such as $\sum_k \Pi_k' = 0$, is modeled as convection/diffusion transfer of heat by:

$\Pi_{g\to p}' = -\dfrac{\alpha_p \rho_p C_{p_p}}{\tau_{g\to p}^T}\left(T_p - T_g\right)$ for the solid phases. As $\sum_k \Pi_k' = 0$, one obtains that $\Pi_g' = -\sum_k \Pi_{g\to k}'$ for the gaseous mixture. Note that the inter-particle heat exchange that may occur during inter-particle collisions is neglected because the collisions are assumed to be instantaneous. C_{p_k} is the specific heat of the phase *k*. The characteristic time $\tau_{g\to p}^T$ of the convection/diffusion heat transfer between gas and dispersed phases is approximated by:

$$\frac{1}{\tau_{g\to p}^T} = \frac{6\lambda_g}{\rho_p C_{p_p}} \frac{\langle Nu \rangle_p}{d_p^2} \quad \text{with} \quad \langle Nu \rangle_p = 2 + 0.55 Re_p^{1/2} Pr^{1/3} \quad , \quad Pr = \frac{\rho_g \nu_g}{\lambda_g} C_{p_g} \tag{3}$$

λ_g is the thermal conductivity of the gas phase and $\langle Nu \rangle_p$ represents the Nusselt number of the p-phase.

As the reaction proceeds, the diameter of the reactive UF_4 particles decreases. Assuming, furthermore, that the UF_4 particles do not agglomerate and also that no attrition occurs despite their friction, the number of particles per unit mass $\chi^d_{UF_4}$ obeys the following equation:

$$\alpha_{UF_4}\rho_{UF_4}\frac{\partial \chi^d_{UF_4}}{\partial t}+\alpha_{UF_4}\rho_{UF_4}U_{UF_4,i}\frac{\partial \chi^d_{UF_4}}{\partial x_i}=\frac{\partial}{\partial x_i}\left(\alpha_{UF_4}\rho_{UF_4}D^t_{k,ij}\frac{\partial \chi^d_{UF_4}}{\partial x_j}\right)-\chi^d_{UF_4}\Gamma_{UF_4} \tag{4}$$

where $D^t_{k,ij}$ denotes the diffusivity tensor.

Then, the local instantaneous mean diameter of the reactive particles may be written:

$$d_{UF_4}=d_{UF_4,0}\left(\frac{\chi^d_{UF_4,0}}{\chi^d_{UF_4}}\right)^{1/3} \tag{5}$$

where $d_{UF_4,0}$ and $\chi^d_{UF_4,0}$ are the initial mean diameter and the corresponding number of particles per unit mass, respectively,

Chemical reaction modifies the mass fractions of the species of the gaseous mixture which obey the following balance equation:

$$\alpha_g\rho_g\frac{\partial Y_\alpha}{\partial t}+\alpha_g\rho_g U_{g,j}\frac{\partial Y_\alpha}{\partial x_j}=\frac{\partial}{\partial x_i}\left(\alpha_g\rho_g\frac{\nu^t_g}{\sigma_g}\frac{\partial Y_\alpha}{\partial x_i}\right)-Y_\alpha\Gamma_g+\Psi_\alpha \tag{6}$$

where ν^t_g and σ_g are viscosity and Schmidt turbulent number of the gas mixture, respectively.

Ψ_{F_2} represents to the vanishing rate of fluorine as whereas Ψ_{UF_6} represents the apparition rate of uranium hexafluoride and according to chemical reaction equation (1) they may written as follows:

$$\Psi_{F_2}=\frac{W_{F_2}}{W_{UF_4}}\Gamma_{UF_4}\ ,\qquad \Psi_{UF_6}=-\frac{W_{UF_6}}{W_{UF_4}}\Gamma_{UF_4} \tag{7}$$

where W_{F_2}, W_{N_2}, W_{UF_4} and W_{UF_6} are molar mass of fluorine, nitrogen, uranium tetrafluoride and uranium hexafluoride, respectively. However, as nitrogen does not react: $\Psi_{N_2}=0$.

Finally, according to perfect gaseous mixture assumption, the density of the gaseous mixture is given by:

$$\rho_g=\frac{P_{ref}}{R_{gas}T_g}\left[\frac{Y_{N_2}}{W_{N_2}}+\frac{Y_{F_2}}{W_{F_2}}+\frac{Y_{UF_6}}{W_{UF_6}}\right]^{-1} \tag{8}$$

where P_{ref} is the mean reactor pressure and R_{gas} is the gas constant.

Modeling of the reaction rate

Reactive uranium particles are assumed nonporous. Accordingly, the reaction front is located at the surface of the particle. Furthermore, reaction is assumed uniform at the surface of the particles, so that they shrink uniformly. According to Randrianarivelo et al. (2007), by using the shrinking particle model describing the decrease of the particle radius in terms of the reaction velocity, the mass loss of single reactive particle is modeled by:

$$\frac{dm^{(1)}_{UF_4}}{dt}=-\pi d^2_{UF_4}\frac{W_{UF_4}P^S_{F_2}}{R_{gas}T^S_{UF_4}}f_c\exp\left(-\frac{E_a}{R_{gas}T^S_{UF_4}}\right) \tag{9}$$

where d_{UF_4}, W_{UF_4} and $T^S_{UF_4}$ represent the UF_4 particle diameter, molar mass and surface temperature, respectively. E_a is the activation energy and f_c the kinetic constant of the reaction. $P^S_{F_2}(=X^S_{F_2}P_{ref})$ and $X^S_{F_2}$ refer to the fluorine partial pressure and the mole fraction of fluorine at the surface of the particle, respectively. We will assume that the particle temperature is uniform ($T^S_{UF_4}=T_{UF_4}$).

Furthermore, the particle-shrinking rate given by (9) may be limited by the concentration of the reactive gas at the UF_4 particle surface that differs from the average concentration of fluorine in the gaseous mixture

(see e.g Homma et al., 2005). That effect is due to the diffusion mechanism of the fluorine in the nitrogen towards the particle surface. As the particles are assumed nonporous, the fluorine diffusion effect does not include pore diffusion effect. Therefore only the external diffusion is taken into account in the following analysis. Considering the diffusion process of fluorine around single particle, the mass loss as reaction proceeds can be written in the general form:

$$\frac{dm_{UF_4}^{(1)}}{dt} = -\pi \rho_g d_{UF_4} D_{F_2} Sh\left[Y_{F_2} - Y_{F_2}^S\right] \tag{10}$$

where D_{F_2} refers to the diffusion coefficient of fluorine in nitrogen, while $Y_{F_2}^S$ denotes the mass fraction of fluorine at the surface of the particle. *Sh* is the Sherwood number given by the empirical relation of Ranz and Marshall (1952):

$$Sh = 2 + 0.55 Re_p^{1/2} Sc^{1/3} \quad \text{with} \quad Sc = \frac{\nu_g}{D_{F_2}} \tag{11}$$

From (9) and (10), the mass fraction of fluorine at the surface of the reactive particle becomes:

$$Y_{F_2}^S = Y_{F_2}\left[1 + \frac{d_{UF_4}}{D_{F_2} Sh}\frac{T_g}{T_{UF_4}} f_c \exp\left(-\frac{E_a}{R_{gas} T_{UF_4}}\right)\right]^{-1} \tag{12}$$

Finally, considering the particle number density n_{UF_4} of the reactive particles, the interfacial mass transfer rate Γ_{UF_4} due to the reaction is written:

$$\Gamma_{UF_4} = n_{UF_4}\left\langle \frac{dm_{UF_4}^{(1)}}{dt}\right\rangle_p = \frac{6\alpha_{UF_4}}{\pi d_{UF_4}^3}\left\langle \frac{dm_{UF_4}^{(1)}}{dt}\right\rangle_p = -\frac{6\alpha_{UF_4}}{d_{UF_4}}\frac{W_{UF_4} X_{F_2}^S P_{ref}}{R_{gas} T_{UF_4}} f_c \exp\left(-\frac{E_a}{R_{gas} T_{UF_4}}\right) \tag{13}$$

where $X_{F_2}^S$ is the molar fraction of fluorine at the surface of UF_4 particles assessed from $Y_{F_2}^S$.

Modeling of inter-particle radiative heat transfer

With the dense alumina phase, inter-particle radiative heat exchange may turn out to be efficient. That obviously depends on the radiative characteristics of the particles. According to the Rosseland approximation that characterizes the radiative heat transfers as diffusion process, the total emitted flux is proportional to the temperature gradient. Therefore, the thermal diffusivity coefficient *D* required to account for the radiative heat transfers is given by:

$$D = \frac{\lambda_r^p}{\rho_p C_{p_p}} \tag{14}$$

where λ_r^p is the particle radiative thermal conductivity modeled as:

$$\lambda_r^p = \frac{4\pi}{3k_a + (1-g)k_d}\frac{dL^0}{dT_p} \tag{15}$$

T_p is the particle temperature and *g* is an asymmetry factor describing the asymmetry of radiation within the particle. k_a and k_d are absorption and diffusion coefficients, respectively. L^0 represents blackbody luminance at thermodynamic equilibrium. Furthermore, absorption and luminance are modeled by:

$$k_a = \frac{1}{\Lambda} = \frac{3\varepsilon_\lambda \alpha_p}{2d_p} \quad \text{and} \quad L^0 = \frac{\sigma T_p^4}{\pi} \tag{16}$$

where Λ is the mean free path of photons and σ the Stefan-Boltzmann constant. ε_λ is the emissivity of the particles . Assuming the alumina particles in the bed as blackbodies, $\varepsilon_\lambda = 1$ and $k_d = 0$.

Therefore:

$$D = \frac{32\sigma}{9\alpha_p}\frac{d_p T_p^3}{\rho_p C_{p_p}} \tag{17}$$

SIMULATION OVERVIEW

Computational case

The simulated reactor is an experimental pilot conducted by *AREVA-NC* to investigate the hexafluoride production process in fluidized bed. Experimental conditions used in the simulations are summarized in Table 1. The bed is preheated during 10s to 400°C using nitrogen, before injection of the gaseous mixture comprised of 10% and 90% of mole fraction of fluorine and nitrogen, respectively. The set of modeling equations and closure assumptions implemented in *NEPTUNE_CFD*, a French industrial consortium (EDF/CEA/AREVA_NP/IRSN) CFD code that solves unsteady n-fluid Eulerian equations, is used to simulate the UF_6 production in the bed. Unstructured finite volume method is employed in *NEPTUNE_CFD* and further informations about the numerical resolution method can be found in Méchitoua et al. (2003). The reactor is meshed using a uniform grid in the streamwise direction ($\Delta y \approx 19.0 \times 10^{-3}$ m). Initial simulation time step is $\Delta t = 10^{-3}$ s. However, further difficulties due to the characteristic transfer time scales that strongly decrease as reaction proceeds; require coupled solving of enthalpy and efficient implicit method to account for the different source terms. For example according to equation (3), the convection/diffusion heat transfer characteristic time $\tau^{T}_{g \to p}$ is proportional to the square of the particle diameter that obviously decreases for UF_4 particles as reaction proceeds. In first approximation, reactor wall is assumed adiabatic in the following simulations.

Table 1 Simulation parameters

Parameter	Data	Parameter	Data
Bed column height (m)	1.7	Bed height (m)	0.6
Bed section diameter (m)	0.108	Particle diameter (μm)	Al_2O_3: 150; UF_4: 250
Bed initial temperature (°C)	400	Particle density (kg • m^{-3})	Al_2O_3: 3790; UF_4: 3500
Pressure (Pa)	0.8x10^5	Particle mass in bed (kg)	Al_2O_3: 0.37; UF_4: 4.28x10^{-2}
Gas inlet temperature (°C)	100	Gas species specific heat (J • kg^{-1} • K^{-1})	$C_{p_{N_2}} = 1040$, $C_{p_{F_2}} = 926$ $C_{p_{UF_6}} = 426$
Gas inlet velocity (m • s^{-1})	0.26	Particle specific heat (J •kg^{-1} •K^{-1})	$C_{p_{UF_4}} = 405$, $C_{p_{Al_2O_3}} = 1100$

Results and discussion

Simulations are performed until complete consumption of uranium by fluorine in the bed. A priori benchmark simulation was carried out without fluorine diffusion within nitrogen around uranium particle and inter-particle heat transfer.

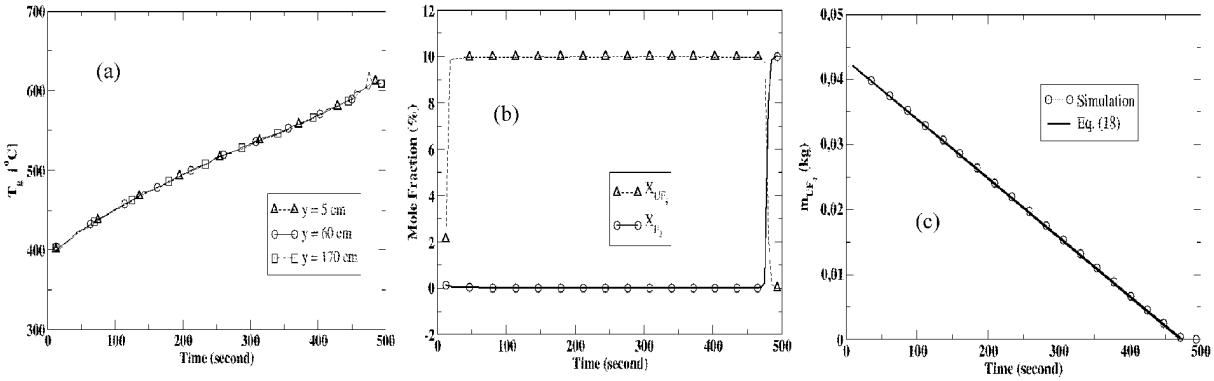

Fig. 2 a) Gaseous mixture temperature along the reactor for three locations (y=5 cm, 60 cm and 170 cm);
b) Mole fraction of fluorine and uranium hexafluoride at the outlet of the reactor (at y=170 cm);
c) Evolution of the total mass of UF_4 within the reactor during fluorination process

Fig. 2(a) depicts gas temperature change at the wall of the reactor for three locations: close to reactor inlet (at $y = 5$ cm), in the center (at $y = 60$ cm) and at the reactor outlet ($y = 170$ cm). Results indicate that the

temperature progressively increases throughout the reactor. That is obvious, since the reaction occurs by yielding heat and no heat transfer arises with adiabatic walls. In Fig. 3, the temperature in the wall-normal direction is plotted for three locations (y = 5cm, 30cm and 60cm) at three different times (t = 135s, 260s and 494s). For t = 135s and t = 260s during the fluorination (Figs. 3(a) & 3(b)), gaseous mixture temperature shows some fluctuations at y=5cm. That is due to both heat yielded by reaction that occurs in the inlet region just below y = 5cm and the cold mixing gas injected at the inlet. However there is not significant temperature gradient in the wall-normal direction at this inlet region. At y = 30 cm, wall-normal direction temperature presents weak fluctuation whereas at y = 60 cm it appears to be constant. Moreover, Figure 2(a) shows also that the gaseous mixture temperature is roughly uniform in the fluidized bed.

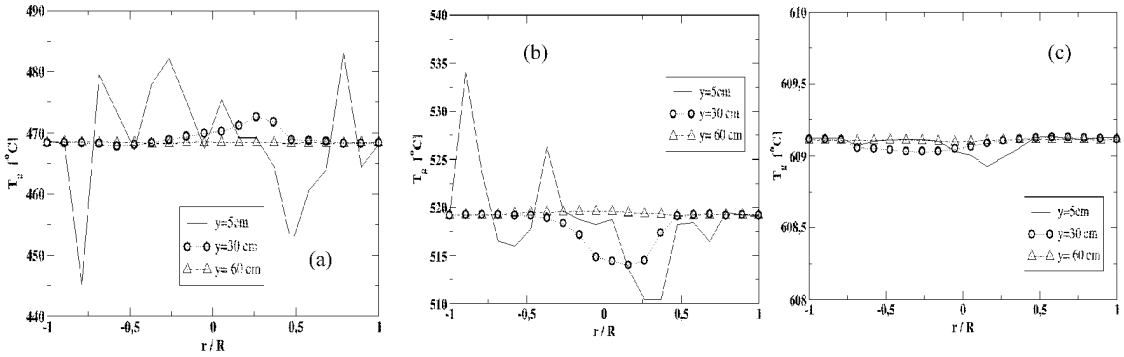

Fig.3 Horizontal profiles of the gaseous mixture temperature at different instant and three vertical locations in the reactor: y=5 cm, 60 cm and 170 cm (R denotes the radius of the reactor) (a) at t=135 s;(b) at t=260 s and; (c) at the end of simulation (t=494 s)

Figure 2(b), exhibiting the mole fractions of F_2 and UF_6 at the reactor outlet, shows opposite molar fraction amount of UF_6 and F_2 characterized by 10% of produced UF_6 that correspond to the amount of injected F_2 whereas F_2 at the outlet remains null. This demonstrates that all the injected F_2 reacts. In other words, there is not fluorine leak. That is consistent with linear decrease of the uranium mass in the reactor (Fig.2(c)). Basically, whole injected fluorine reacts with uranium tetrafluoride means that the mass variation of reactive particles according to the time is equal to the injected mass flow rate of fluorine:

$$\frac{dm_{UF_4}}{dt} = -\frac{W_{UF_4}}{W_{F_2}} Y_{F_2}^e Q_g^e \tag{18}$$

where $Y_{F_2}^e$ and Q_g^e are the mass fraction of fluorine and the gas debit at the inlet of the reactor, respectively.

However, one should note that expected amount of mole fraction of hexafluoride is abruptly reached contrary to what is observed in measurement. This indicates that the reaction between reactive particles and fluorine arises instantaneously at the moment the fluorine is injected. That could result either in omission of intermediate chemical reactions that might occur or other mechanisms that could limit the reaction rate.

Effect of fluorine diffusion in nitrogen around reactive particles

Accordingly, fluorine diffusion coefficient in nitrogen used to investigate diffusion mechanism around the particle is $D_{F_2} = 5.0\times10^{-5}$ m^2s^{-1}. Figure 4 compares the amount of uranium hexafluoride between simulations with and without fluorine diffusion in nitrogen. It may be observed a similar amount of UF_6 at the outlet of the reactor. This demonstrates that the diffusion does limit the reaction rate in the current simulation conditions. Similar simulation conditions of Khani et al. (2008) also show a negligible influence of the external diffusion of fluorine around uranium particle.

Influence of inter-particle radiative heat transfer

Regarding the radiative heat exchange between particles, Figure 5 reveals that there is no change occurred on the temperature in the reactor. This indicates a non-existent effect of the radiative heat transfer within the particles of the alumina phase. That could be expected because all the particles in the bed have the same temperature since temperature gradient was not observed in the reactor, in both wall-normal and streamwise directions. Influence of the inter-particle radiative heat transfers or between particles and wall might be efficient in the situation of cooled or heated wall, especially with particles fluidizing in the near wall region, in the thermal boundary layer thickness (Yamada et al., 2001).

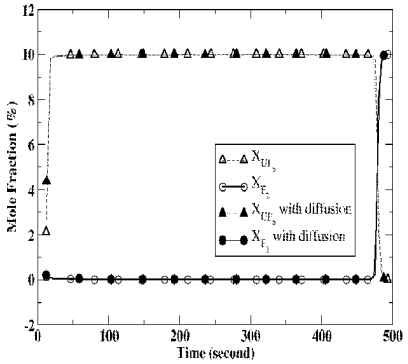

Fig. 4 Effect of fluorine diffusion within nitrogen on amount of mole fraction of both UF_6 and F_2 at reactor outlet

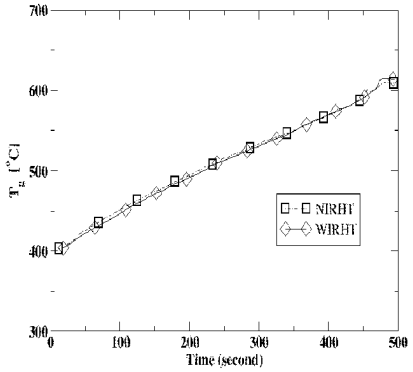

Fig. 5 Effect of inter-particle radiative heat transfer between alumina particles on the temperature in the adiabatic reactor (NIRHT: no inter-particle radiative heat transfer, WIRHT: with inter-particle radiative heat transfer)

CONCLUSIONS

Simulation of uranium hexafluoride production from experimental fluidized bed pilot is dealt with *NEPTUNE_CFD V1.07@Tlse*. Reactive flow in the bed is modeled according to n-fluid Eulerian approach. Uranium particles assumed nonporous reacted with fluorine according to the shrinking core model. As the reactor wall was adiabatic, simulations show expected increasing temperature in the reactor. Furthermore, no temperature gradient is predicted in the reactor. Amount of uranium hexafluoride found at the reactor outlet indicated complete reaction of injected fluorine in the bed. Influence of fluorine diffusion within nitrogen did not modify the reaction rate appreciably. Furthermore, as no temperature gradient was obtained in the reactor, effects of radiative heat transfer between particles of dense phase (alumina) appeared to be negligible.

Next step of fluorination simulation will account for the initial polydispersion of uranium tetrafluoride particles to estimate the influence on uranium hexafluoride amount. Furthermore, full three-dimensional simulations with convective gas/wall heat transfer would obviously ensure a better representation of the temperature distribution in the bed and a probable influence of the particle-to-particle radiative transfer.

REFERENCES

Ciais, V., Martin, R., Neau, H., Simonin, O. (2007): 6th ICMF, Leipzig (Germany), paper S7_Mon_D_10.

Gobin, A., Neau H., Simonin, O., Llinas, J. R., Reiling, V., Selo, J. L. (2003): Int. J. Num. Meth. In Fluids 43, pp. 1199-1220.

Homma, S, Ogata, S., Koga, J., Matsumoto, S. (2005): Chemical Engineering Science 60, pp. 4971- 4980.

Khani, M. H., Pahlavanzadeh, H., Ghannadi, M. (2008): Annals of Nuclear Energy 35, pp. 704-707.

Méchitoua, N., Boucker, M., Laviéville, J., Pigny, S., Serre, G. (2003): Int. Conf. on Supercomputing in Nuclear Applications, SNA'2003, Paris (France).

Randrianarivelo, T. N., Neau, H., Simonin, O., Nicolas, F. (2007): 6th ICMF, Leipzig (Germany), paper S6_Thu_A_46.

Yamada, J., Kurosaki, Y., Morikawa, T. (2001): Int. J. Therm. Sci. 40, pp. 104-113.

AN IDEA OF STAGED AND LARGE VELOCITY DIFFERENTIAL SECONDARY AIR FOR WATERWALL EROSION PROTECTION AND OXYGEN COMPLEMENTARITY

B. Q. Liu, X.H. Zhang

Department of Thermal Energy Engineering, University of Science and Technology Beijing, Beijing, 100083, China

Abstract: A successful design of circulating fluidized bed (CFB) boiler should have the highest combustion efficiency, economic operation, and optimum availability. There is a coupled phenomenon of an oxygen lean zone existing in the CFB boiler furnace which depresses combustion efficiency and particle (group) falling down faster and faster when it falls along the waterwall, abrading the tube metal effectively. A new secondary air design for the oxygen lean zone and erosion protection is conceived by using staged and large velocity differential secondary air. For example, a part of concentrate supplied secondary air has been divided into two parts: a low velocity part and a high velocity part. The low velocity part is used for rigid gas layer to reduce the particle falling velocity, and the high velocity part is used for oxygen supply. It is believed that 40~60m/s projecting air velocity could send new oxygen to at least half furnace depth in a short projecting lift as shown in calculation. In another view point, operational superficial gas velocity has an obvious effect on waterwall metal erosion, with a lower operation velocity having lower erosion.

Keywords: circulating fluidized bed (CFB), boiler, secondary air, combustion

INTRODUCTION

Circulating fluidized bed (CFB) combustion technology has obtained a new altitude in China since Baima (Sichuan province) 300MW unit CFB boiler had been put into operation in recent years. Many practices including laboratory, design considerations and operations show that erosion is still a heavy trouble to be solved for waterwall (Zhang et al., 2001;You et al.,2007; Fang et al.,2007; Hou et al.,2007).

Another fault in CFB boilers is the large oxygen lean zone in the furnace (Davis P.,2006;Joris K.,2006,2007). Due to the lack of oxygen, suspended combustibles cannot burn out perfectly. Even though combustion could be enhanced through particle circulation, this is a compensating process that requires additional power consumption.

Several methods are available to reduce waterwall erosion, such as bend tube(Luc L. and Louis J.,1995;Li and Rao,2007; Zhou and Zhang,2007) and circle beam(Li and Zhou,2007;Meng et al.,2007;Shao et al.,2007;Sun et al.,2007). The main idea for bend tube is to avoid the falling impact of particles in the furnace and possible swirl movement of the particles, which is well accepted in large CFB boilers. Circle beam is another idea for waterwall erosion protection and is arranged at different elevations of the furnace. Since it covers some heating surfaces, an obvious increase in furnace exit temperature is always present, sometime more than 100℃.

The main air supplied, except for coal spread and circulating particle feedback, is primary air and secondary air. Primary air from the distributor conducts dense phase fluidization and secondary air is used for suspension combustion organization.

It is becoming increasingly difficult to supply enough oxygen to the center of the furnace as boiler capacities are becoming larger and larger. The Lean oxygen zone could waste combustion time and space for suspended combustibles, so it is important to address how to send oxygen to that zone efficiently and economically. The pressure head providing fresh air to the oxygen lean zone needs overcome the resistance from falling down particles compared with other large space gas projections.

Falling particles scrape the waterwall tube metal when they contact it, and their effect is proportional to the falling velocity. If there is a force which could slow down the falling speed, there must be two benefits: one is to improve suspension combustion and another is reduction of waterwall erosion.

The aim of this paper is try to provide a prediction of staged and large velocity differential secondary air in basic physics connotation.

THE IDEA AND ITS RESOURCE

The quantity and speed of falling particles is enhanced with its falling distance, as seen in Fig.1,and can get as high as 8m/s velocity when furnace height is 35m. Erosion or metal consumption velocity is 3.3 power of gas velocity in traditional theory, or in other words, doubling the velocity results in 10 times the erosion.

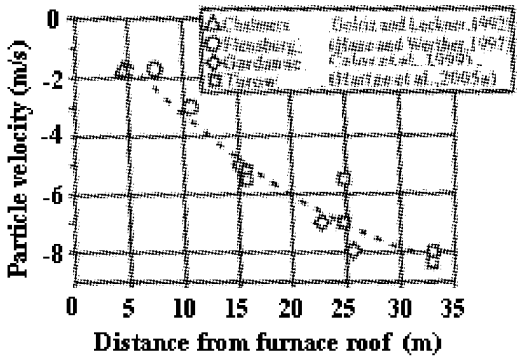

(a) Falling velocity distribution

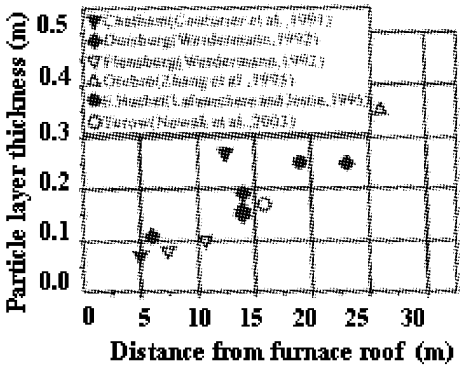

(b) Particle layer thickness distribution

Fig.1 Basic features of falling down particles

Circle beam can slow down the falling particle velocity, therefore reducing erosion of waterwall metal. The shortage of circle beam is that it covers heating surfaces, and for this shortage, the temperature of the furnace exit increases.

The immediate method to eliminate the lean oxygen zone is using high speed secondary air projection. Traditional secondary air in the CFB boiler is arranged at the dividing line between the dilute phase and dense phase, and this might be the reason for the lean oxygen zone. Gas or two phase flow projection is a mature technology in pulverized coal boilers, where projection depth and stream expansion can be calculated according to semi-empirical formula. Figure 2 provides an example of this calculation.

This paper is aimed at secondary air design with which can limit erosion and the lean oxygen zone.

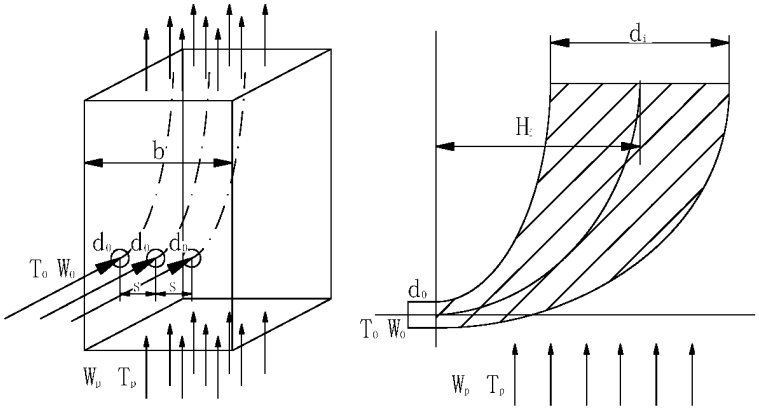

Fig.2 Gas projection in a large space flow stream

STAGED SECONDARY AIR AND LARGE VELOCITY DIFFERENTIAL PROJECTION

The secondary air is divided into two parts, the slow velocity part for slowing down falling particles and the high velocity part for supplying fresh air to the center of the furnace.

Staged secondary air

A part of the secondary air will be taken out from traditional design and rearranged along the height of furnace. One aim of this design is to slow down falling particles to protect the waterwall metal. Figure 3 illustrates the main thought of the idea.

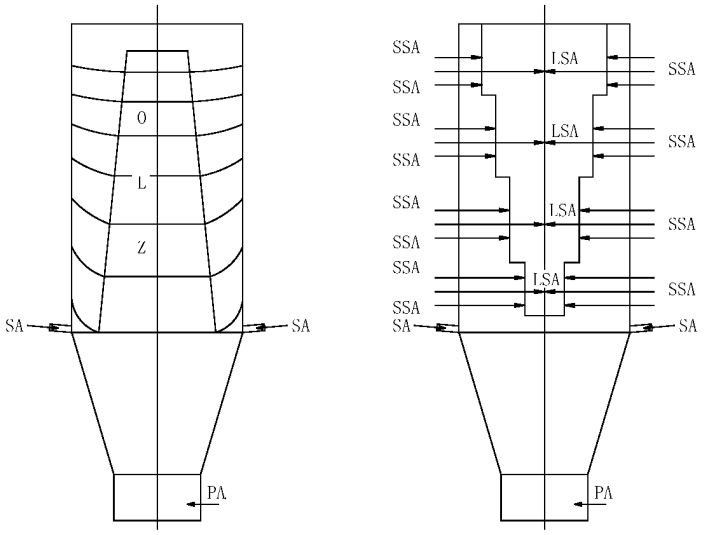

Fig.3 Scheme of staged secondary air
OLZ=Oxygen Lean Zone; AS=secondary Air; SSA=Staged secondary Air;
LSA=Large differential velocity secondary Air; PA=Pprimary Air

Large velocity differential projection

Another aim is to increase oxygen in the large oxygen lean zone in furnace. Even though there are many theories and empirical formulae in gas projection, projecting jets through falling particles is still in research. In this prediction, the main gas density was considered as:

$$\rho_w = \rho_y + \frac{a+0.1}{Q_{bs}(1+T/273)} \cdot B \tag{1}$$

where: Q_{bs} is flow quantity of primary air and B is fuel consumption.

RESULT AND DISCUSSION

Depth of air projection

Air Projection tracking curves were calculated for a CFB boiler. For these calculations, main stream gas velocity was set as 4m/s, 5m/s and 6m/s according to operational experience of CFB boilers and the projecting air velocity was set as 30m/s, 40m/s and 50m/s as seen in Fig.4.

In Fig.4a, projection lift height was 2.2m, 4.15m and 8.2m at 10m projection distance when the main gas stream took a velocity of 4m/s. At 5m/s and the same projection distance, the lift height became 4.1m, 7.4m, 14m, and at 6m/s the lift height became 7m, 11m, 20m, as shown in Fig.4b and Fig.4c respectively. Also shown in Fig.4, the lift height was lower than 2m, 3m and 4m in Figs.4(a), (b) and (c) at 5m projection distance, which is about half furnace depth.

The cross sectional dimensions of CFB boilers ranging from 300MW to 800MW are provided in Tables 1 and 2. It can be seen that the furnace depth ranges between 6m and 17m. This means that air projection track calculations above have an ability to supply fresh air to the center of the oxygen lean zone even if falling down particles are considered.

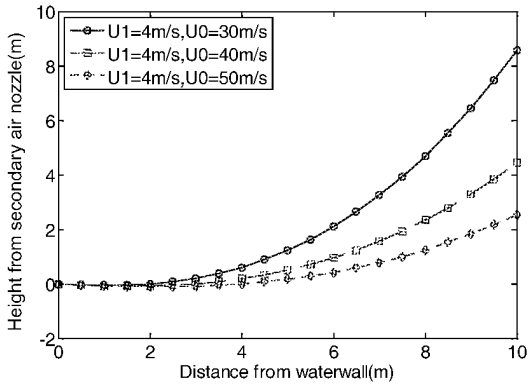

(a) Projection ability in 4m/s main stream

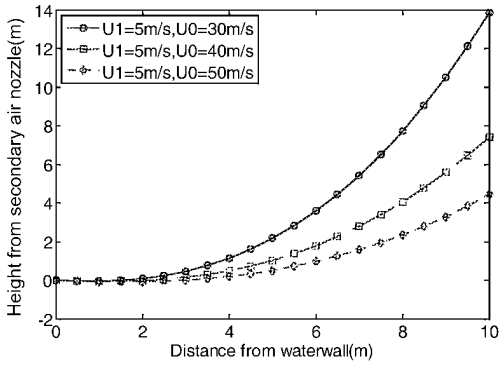

(b) Projection ability in 5m/s main stream

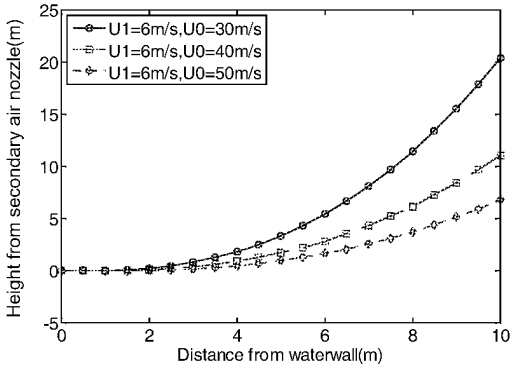

(c) Projection ability in 6m/s main stream

Fig.4 Projection track in different main gas streams

Table 1 Cross section of some large CFB boiler

Power plant	JEA 300MW	CLECO 330MW	Baima 300MW	600MW super critical In design
Furnace type	Single distributor	Single distributor	Two distributors	Two distributors
Cross section (m×m)	6.7×25.9	8.92×26.06	12.615 ×15.051	16.952 ×25.736
Distributor size(m×m)	3.4×25.9	4.5×26.06	3.5 ×15.051	4.3 ×25.736

Table 2 Cross section of FWs CFB boiler

Super critical CFB boiler	400MW	800MW
Depth × breadth × height (m×m×m)	10.185×26.377.9×47.600	11.5284×39.5224×49.3776

Effect of secondary air velocity

Impact erosion of falling particles can be divided in to two categories. One is fatigue erosion and another is metal cutting erosion, which is similar to what happens in pulverized boiler convection tube bundles. In general, most erosion is caused by the metal cutting mechanism in CFBs.

When metal cutting erosion occurs by a particle group of mass M (particle number n), there is a maximum impact angle ∂_0. The effect of impact can be written as:

$$V_{\mathrm{I}} = \frac{Mv^2}{2\sigma_y}\left(\frac{\sin 2\partial - 3\sin^2 \partial}{2}\right) \qquad 0 < \partial \le \partial_0 \tag{2}$$

$$V_{\mathrm{II}} = \frac{Mv^2}{2\sigma_y}\left(\frac{\cos^2 \partial}{6}\right) \qquad \partial_0 < \partial < 90^\circ \tag{3}$$

In CFB furnaces, the impact angle is always less than ∂_0, so equation (3) becomes meaningless here. The direction of falling of particles can be considered parallel with waterwall tube, so variation of falling particle velocity can change the effect of impact as the following.

$$\frac{V_1}{V_2}=\frac{M_1 v_1^2}{M_2 v_2^2}\frac{\frac{\sin 2\partial_1-3\sin^2\partial_1}{2}}{\frac{\sin 2\partial_2-3\sin^2\partial_2}{2}}=const. \tag{4}$$

Therefore, the erosion can be decreased effectively.

Staged secondary air design

Erosion of the waterwall depends on the characteristics of falling particles, including velocity and thickness, i.e. falling rate. As a result, the staged secondary air design should consider:

(1) A lower operating superficial velocity.

(2) A reduced falling velocity of particles (group).

(3) Minimized effect on heat transfer of waterwall.

For example, taking 2m/s as the maximum particle falling velocity, we can first arrange low speed projection air 5m from the furnace top according to Fig.1. Given that a 300MW CFB furnace has an approximate height of 35m, 6-7 layers could be considered for low speed project air, as illustrated in Fig.5.

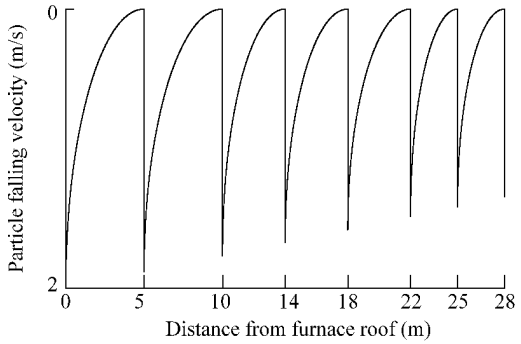

Fig.5 A prediction of projection air effect for a 300MW CFB

CONCLUSIONS

An arrangement of secondary air has been conceived for waterwall metal protection and oxygen complementarity in the furnace center. This prediction shows that high speed projection velocities of 40~60m/s could send fresh air to the furnace center and particle falling velocity might be reduced with low speed projection air.

NOTATIONS

a	-	elutriate particle fraction	V	m/s	Velocity of falling particle
B	kg/h	Fuel consumption	W_0	m/s	Velocity of projection stream
d_0	mm	Diameter of projection nozzle	W_p	m/s	Velocity of main stream
d_i	mm	Width of projection	Greece letter		
H_i	m	Projection distance	ρ_{ww}	kg/m^3	Density of main stream projected
M	kg	Particle mass	ρ_y	kg/m^3	Density of main stream
Q_{bs}	Nm^3/h	Primary air flow rate	δ_0		Impact angle
T_0	K	Temperature of projection air	v	m/s	Particle velocity
T_p	K	Temperature of main stream	σ_y		Plastic stress

REFERENCES

David P.: Progress in Energy and Combustion Science **32**(2006), pp.539-569
Fang L., Sun S. K.: Hydropower machinery,**9**(2007),pp.81-93
Hou X.S., Zhang J. S.,Wang J. W. et al: Boiler Technology **7**(2007), pp.19-14
Joris K.: Progress in Energy and Combustion Science **33** (2007), pp. 19-55

Li H.B.,Zhou Q.(2007).The erosion preventing technology of the water cooled wall in a circulating fluidized bed boiler, 1st conference of Circulating Fluidized Bed Combustion of Chinese.
Li Y., Rao J.(2007).Theoretic analysis of erosion of a 130t/h circulating fluidized bed Boiler and its solution, 1st conference of Circulating Fluidized Bed Combustion of Chinese.
Luc L., Louis J., Study of a circulating fluidized bed furnace behavior in order to scale it up to 600MWe, The 3rd international symposium on coal combustion, Beijing 18-21,1995.
Meng L.W., Xu Z.Q., Lv H.S.(2007). The practice and its analysis of the anti-erosion of the surface in a 480t/h circulating fluidized bed boiler,1st conference of Circulating Fluidized Bed Combustion of Chinese.
Shao Y.F., Song Z.B., Zhou C.M.(2007). Retrofitting of Superheater Wing Wall and Anti-erosion of Waterwall in a Circulating Fluidized Bed Boiler,1st conference of Circulating Fluidized Bed Combustion of Chinese.
Sun J.T., Li W.B., Ding Y.X.(2007). The water wall corrosion of circulating fluidized bed boiler and its protecting,1st conference of Circulating Fluidized Bed Combustion of Chinese.
You J. K., Wang C. W. and Wang S.H.: Energy research and Information, 2(2007),pp.91-94.
Zhang T., Chen Y.S., Zhang B. H.: Energy technology, 4(2001),pp.77-78
Zhou S., Zhang H.Y.(2007). Investigation and application of the anti-erosion technology in a circulating fluidized bed boiler, 1st conference of Circulating Fluidized Bed Combustion of Chinese.

APPENDIX PROJECTION CALCULATION

Main gas stream in boiler furnace goes up and secondary air stream projected at perpendicular direction with a nozzle dimension of $2b_0 \times h_0$ (breadth × height). Project gas track will be (when $h_0/(2b_0) = 5 \sim 12$):

$$y = 1.9\left(\frac{\rho_1 U_1^2}{\rho_0 U_0^2}\right)\left(\frac{a}{b_0}\right)^{1.5} x^{2.5} + \frac{\delta y}{\delta x} x \cot\alpha \tag{A1}$$

Where ρ_0, ρ_1 ——densities of main stream and project stream;

U_0, U_1 ——velocities of main stream and project stream;

α ——angle of main stream and project stream.

Project depth H_t is defined as a distance of project stream getting parallel with main stream. it was calculated as follow.

$$\frac{H_t}{d_0} = k_s k_\partial \frac{U_0}{U_1}\sqrt{\frac{\rho_0}{\rho_1}} \tag{A2}$$

Where d_0 is equivalent diameter, k_s is a factor considering the ratio of $\frac{s}{d_0}$ and k_∂ is also a factor considering angle between the streams.

Breadth at depth of H_t is

$$d_i = 0.75 H_t \tag{A3}$$

For rectangle secondary projector, it can be calculated as equation (4).

$$\frac{aH}{d_0} = k_\partial'' \frac{U_0}{U_1}\sqrt{\frac{\rho_0}{\rho_1}} \tag{A4}$$

Where a=0.08−0.12; k_∂'' is also a factor considering angle α between the two streams.

CFD MODELLING APPLIED TO THE CO-COMBUSTION OF PAPER SLUDGE AND COAL IN A 130 T/H CFB BOILER

Z. S. Yu, X. Q. Ma, Z. Y. Lai, H. M. Xiao

School of Electric Power, South China University of Technology, Guangzhou, 510640, China

Abstract: Three-dimensional mathematical model has been developed as a tool for co-combustion of paper sludge and coal in a 130 t/h Circulating Fluidized Bed (CFB) boiler. Mathematical methods had been used based on a commercial software FLUENT for combustion. The predicted results of CFB furnace show that the co-combustion of paper sludge/coal is initially intensively at the bottom of bed; the temperature reaches its maximum in the dense-phase zone, around 1400K. It indicates that paper sludge spout into furnace from the recycle inlet can increase the furnace maximum temperature (1396.3K), area-weighted average temperature (1109.6K) and the furnace gas outlet area-weighted average temperature(996.8K).The mathematical modeling also predicts that 15 mass% paper sludge co-combustion is the highest temperature at the flue gas outlet, it is 1000.8K. Moreover, it is proved that mathematical models can serve as a tool for detailed analysis of co-combustion of paper sludge and coal processes in a circulating fluidized bed furnace when in view of its convenience. The results gained from numerical simulation show that paper sludge enter into furnace from the recycle inlet excelled than mixing with coal and at the underside of phase interface.

Keywords: CFD, circulation fluidized bed, paper sludge, co-combustion

INTRODUCTION

China produces around 65 million tones of paper and paper plate in 2006. The paper sludge is a terminal product of waste water disposal in paper-making process, it contains not only the short-fiber, but also contains the compositions which are harmful to health, such as a lot of organic matter, nitrogen, phosphorus, chlorine, heavy metal, parasitic worm's ovum and pathogenic germs, etc. (Caputo and Pelagagge,2001). Incineration is a kind of very effective, reliable harmless and resource utilization treatment methods for paper sludge. The significant advantages using circulating fluidized bed (CFB) coal combustion technology are wide range fuel application and low pollution emissions (Lyngfelt, and Leckner 1999; Mukadi et al.,1999; Tsai et al., 2002).

Tsai et al. (2002) showed that co-combustion of coal and paper mill sludge is an appropriate technology to reduce SO_x and NO_x in a commercial circulating fluidized bed coal combustor. Shin et al. (2005) investigate the combustion characteristics of paper mill sludge in a lab-scale combustor with internally cycloned circulating fluidized bed. Lee et al. (2003) co-fire paper sludge with high-calorific industrial wastes in a pilot-scale nozzle-grate incinerator. Vamvuka et al. (2008) investigate the possibility of using paper sludge in co-firing applications, he found that if the mineral matter of paper sludge is partly removed before use, then the combustion behavior of the mixture could resemble that of coal alone and the overall efficiency of the process would increase.

Lopes and Quinta-Ferreira (2008) modeled a computational fluid dynamic (CFD) Modelling of Multiphase flow distribution in the trickle beds. Wang et al. (2008) investigate the mass transfer of air to naphthalene particle cluster in a circulating fluidized bed (CFB) via a CFD approach. The hydrodynamics of a gas-solid fluidized bed was studied using a combination of experiments and CFD simulations (Ahuja and Patwardhan 2008), the experimental data and comparison with CFD predictions provide useful basis for understanding bubbling fluidized beds. In the CCDM, the motion of discrete particles phase is obtained by Discrete Element Method (DEM) which applies Newton's laws of motion to every particle and the flow of continuum fluid is described by the local averaged Navier–Stokes equations that can be solved by the traditional CFD (Chu and Yu 2008). A CFD modeling of air and fluid catalytic cracking (FCC) particles in the riser of a high-density circulating fluidized bed (HDCFB) has been performed (Almuttahar and Taghipour,2008). A three-dimensional CFD model has been used for fuel mixing in fluidized bed combustors, the predictions yielding a reasonable agreement with experimental data(Pallarès and Johnsson,2008). The hydrodynamics of gas-solid flow was modeled by CFD in a CFB riser at various fluidization conditions using the Eulerian-Granular multiphase model (Almuttahar and Taghipour 2008).

The CFD Modelling has been used to study a 130 t/h circulating fluidized bed (CFB) boiler co-combustion characteristic of paper sludge (contains about 55% free water) and coal in this paper.

CIRCULATION FLUIDIZED BED BOILER AND FUEL

Table 1 The ultimate and proximate analyses used in the predictions

Ultimate analysis	Paper sludge (wt.%)	Coal (wt.%)	Proximate analysis	Paper sludge (wt.%)	Coal (wt.%)
Carbon	43.64	93.52	Moisture	55	10
Hydrogen	5.98	3.16	Ash	22.74	23
Oxygen	44.22	1.26	Volatile	20.01	18.2
Nitrogen	5.93	1.26	Fixed carbon	2.25	48.8
Sulphur	0.22	0.79	LHV as received	1497.8kJ/kg	22162.48kJ/kg

The CFB under design burns coal at a rate of 4.41 kg/s. Typical fuel analysis is shown in Table 1. The CFB employs two cyclone separators system as shown in Fig. 1. Primary air and secondary air is preheated about 483K, and is provided to the bottom of the CFB, in addition, supplied from the front wall and rear wall of the furnace, the velocity of primary and second air is 6.5m/s and 10.4 m/s respectively. Once fuels spouted into the furnace at normal temperature with a speed of 2m/s, it forming a dense-phase zone, which blown up by primary air. The furnace operates at an air to fuel stoichiometric ratio is around 1.4.

The mass percent of different ratio between paper sludge and coal based on energy balances, by varying mass percentage of paper sludge from 5% to 20%, the detail listed in Table 2.

Table 2 Various mass and weight percent of paper sludge and coal

paper sludge		coal	
mass%	kg/s	mass%	kg/s
0	0	100	4.413178
5	0.231449	95	4.397536
10	0.486698	90	4.380286
15	0.769617	85	4.361165
20	1.084963	80	4.339853

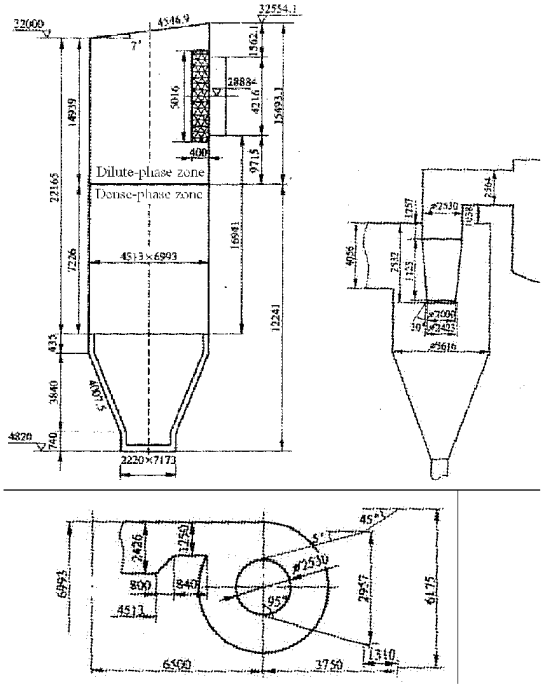

Fig. 1 Schematic of 130t/h circulation fluidized bed

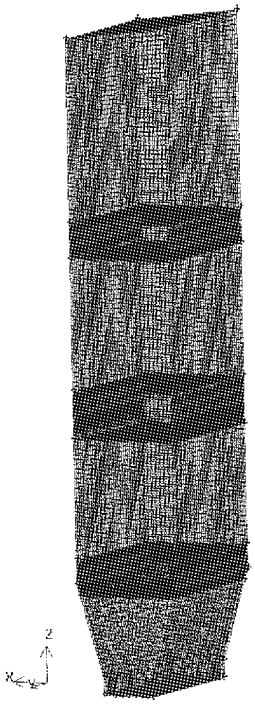

Fig. 2 Schematic of mesh scheme employed in the 3D numerical calculations in the circulation fluidized bed

SOLUTIONS AND MESH

FLUENT version 6.2.1 is used and a total of 436,585 volume meshes are employed for the whole 3D computation space as shown in Fig. 2. The steady-state governing equations are solved using the SIMPLE algorithm and the effect of turbulence on the mean flow field is accounted for using the RNG k-ε model. Discrete Phase Model (DPM) is employed to simulate the combustion of coal and paper sludge particles, the track field of the coal and paper sludge particle adopts the random particle track method based on Lagrange. Two Competing Rates Model is used to model the devolatilization of coal and paper sludge. The gas phase turbulent combustion model employs a Non-Premixed Combustion, and the mixture-fraction/PDF is used, the PDF file was defined by prePDF 4.1, for calculation of two kind of different fuels, coal is fuel steam, secondary stream was define as paper sludge. The fixed carbon combustion model is kinetic/diffusion-limited. Radiative heat transfer was modeled using the discrete transfer model(FLUENT 2005).

For the computer resource is limited, the whole boiler cannot be calculated at the same time, so that the boiler was divided into two parts, one is the CFB furnace, the other is cyclone separators. CFB furnace simulation provides the profiles of gas temperature, velocity, chemical species concentrations and particles amount at the gas outlet of CFB furnace, which are used as boundary conditions for the cyclone separators simulation. In conversation, the cyclone separators simulation provides the profile of the furnace recycle inlet. The two simulations iterate again, until convergence criteria is reached.

RESULTS AND DISCUSSION

The coal combustion and paper sludge/coal co-combustion processes in the CFB furnace

When oxygen concentration is 21 vol% in conventional operational condition, Air to fuel stoichiometric ratio is 1.4, the ratio of primary air and the second air is 6:4, coal combustion and coal/paper sludge co-combustion processes in the furnace. The mass percent of paper sludge is 20% in the fuel when it is co-combustion, the paper sludge adds into furnace by the inlet of recycle.

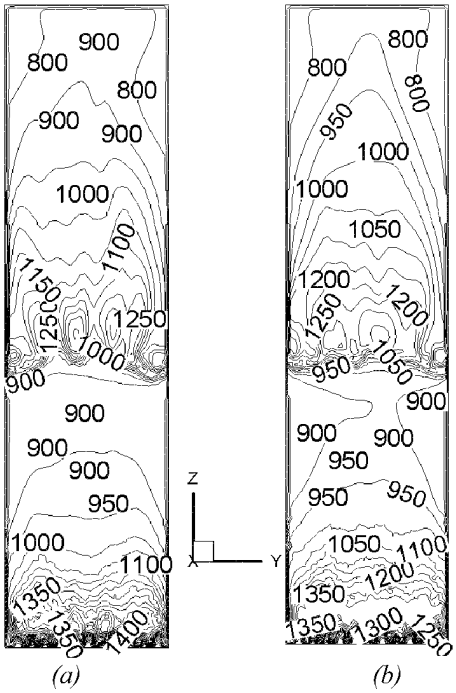

Fig. 3 The temperature profiles of coal combustion (a) and co-combustion of paper sludge/coal (b). (x=0mm, range from -2256.5mm to 2265.5mm)

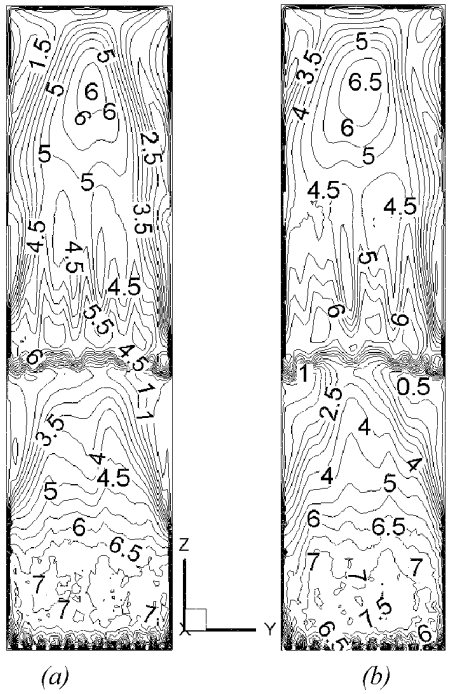

Fig. 4 The velocity magnitude profiles of coal combustion (a) and co-combustion of paper sludge/coal (b). (x=0mm, range from -2256.5mm to 2265.5mm)

Temperature profile inside the bed is illustrated in Fig. 3. As the fresh fuel feed spout into the furnace, it forms a dense-phase zone at the underside of phase interface. The fresh fuel is heated up at four fronts: in the CFB furnace, a strong heat transfer from the collision of bed material, heat convection of primary air, the radiation from the flame and furnace wall, quickly heats up the fuel particles to the ignition point and combustion processes ensue. The combustion intensifies and temperature reaches its maximum in the bed

bottom, around 1400 K. As it flows upward, the temperature drops as heat is lost to the cooler walls. With the addition of secondary air as the flame passes the phase interface of the furnace, temperature rises again due to continued combustion reactions of the left-over combustible species with the fresh secondary air, and maximum flame temperature reaches around 1350 K in the radiation shaft.

Figure 4 shows the velocity profile in furnace as x=0mm (range from -2256.5mm to 2265.5mm), it shows that the bulk of the flow out of the burning bed keeps close to the CFB bottom. The main flow slowly because the furnace passage section area is large than through hole of air distributor. However, There is a distinct difference in the second combustion region, because the fresh secondary air insufflate into the furnace and react intensively with gas which not burnout.

CO profile is shown in Fig. 5. High concentration CO comes from the dense-phase zone and that is consumed in both the fluidized particle combustion and the collision of bed material. The high CO region coincides with the main pass of the gas flow and is close to the secondary air inlet. In the volume space near the bed bottom, there is only low concentration CO. In the dilute-phase zone, temperature reduces to a lower level and any further CO reaction is very slow.

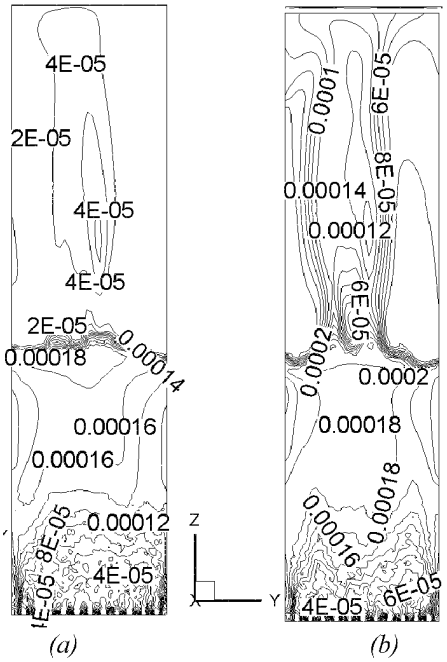

Fig.5 The CO concentrations profiles of coal combustion (a) and co-combustion of paper sludge/coal (b) (x=0mm, range from -2256.5mm to 2265.5mm)

The paper sludge enter into the furnace from the recycle inlet, brought a series number water and low caloric value fuel into the furnace, the temperature of co-combustion (about 1350K, see Fig. 3(b)) is low than coal combustion (about 1400K, see Fig. 3 (a)) at the CFB bottom. At the same time, because of the water's evaporation and fuel mixture, there is much more CO in co-combustion of paper sludge and coal (0.00018 kmol/m^3, see Fig. 5(b)) produced than that in coal combustion (0.00012 kmol/m^3, see Fig. 5 (b)) at the CFB bottom. It is result in the second combustion of co-combustion is intensively, so that the second combustion temperature (about 1300K) of paper sludge/coal is high than coal combustion temperature (about 1250K).

Table 3 The influences of various paper sludge inlet position on the co-combustion of paper sludge and coal in the CFB furnace

The position of paper sludge inlet	Furnace Temperature (K)		Gas outlet Area-Weighted Average	
	Maximum	Area-Weighted Average	Temperature(K)	velocity (m/s)
Mixing with coal	1379.2	1078.2	986.4	9.00
Enter in by the recycle inlet	1396.3	1109.6	996.8	9.17
Underside of phase interface	1394.4	1097.4	985.1	9.06

The influences of different paper sludge inlet position on the co-combustion of paper sludge and coal in the CFB furnace

Usually, paper sludge contains a large number of water; it is hard to guarantee steady-going combustion of paper sludge with no additional high caloric value fuel. When it co-combust with coal, the evaporation and devolatilization of paper sludge processes is different with of coal. Therefore, it is necessary to investigate clearly that when and how to put paper sludge into furnace.

Assume it enter into the CFB by three different mean, for instance mix with coal, enter in through the recycle inlet and spout into at underside of phase interface.

Take co-combustion of 20 mass% paper sludge and 80 mass% coal as an example; to simulate the three kinds of co-combustion as which mentioned. The influences of different paper sludge inlet position on the co-combustion paper and coal in the CFB is shown as Table 3, the predictions indicate that paper sludge spout

into furnace from the recycle inlet can increase the furnace maximum temperature (1396.3K), area-weighted average temperature (1109.6K) and the furnace gas outlet area-weighted average temperature(996.8K). Mainly, it is decided by the combustion characters of coal and paper sludge, paper sludge need more time and energy to guarantee the evaporation of water, too early and too late can influence the combustion efficiency of paper sludge. The gas outlet area-weighted average velocity was determined by the co-combustion efficiency of paper sludge and coal, there is different flue gas species in the furnace.

Table 4 The influences of mass percentage of paper sludge on the co-combustion of paper sludge and coal in the CFB furnace

Paper sludge mass fraction (%)	Furnace Temperature (K)		Gas outlet Area-Weighted Average	
	Maximum	Area-Weighted Average	Temperature(K)	velocity (m/s)
0	1371.6	1148.05	998.1	8.91
5	1361.0	1124.75	982.8	8.97
10	1347.8	1134.65	994.2	9.07
15	1361.8	1121.85	1000.8	9.12
20	1396.3	1109.65	996.8	9.17

The influences of mass percentage of paper sludge on the co-combustion of paper sludge and coal in the CFB furnace

Normally, the more paper sludge is disposed, the more energy needs to spend. To improve conventional existing CFB, make sure that it is feasible to co-combust with paper sludge. But how much paper sludge co-combustion with coal is reasonable? By varying mass percentage of paper sludge from 5% to 20% by mass fraction, and plunge it into furnace at the recycle inlet. The predictions result is shown as Table 4. The mathematical modeling predicts that 15 mass% paper sludge co-combustion is the highest temperature at the flue gas outlet, it is 1000.8K.

CONCLUSIONS

The following conclusions have been drawn as results of this study:

（1）Mathematical methods based on a commercial software FIUENT for DPM combustion was validated for detailed analysis of paper sludge/coal co-combustion processes in the CFB furnace;

（2）The predicted results of CFB furnace show that the co-combustion of paper sludge/coal is initially intensively at the bottom of bed; the temperature reaches its maximum in the dense-phase zone, around 1400K;

（3）The predictions indicate that paper sludge spout into furnace from the recycle inlet can increase the furnace maximum temperature (1396.3K), area-weighted average temperature (1109.6K) and the furnace gas outlet area-weighted average temperature(996.8K).

（4）The mathematical modeling predicts that 15 mass% paper sludge co-combustion is the highest temperature at the flue gas outlet, it is 1000.8K.

ACKNOWLEDGMENTS

This work was supported by Natural Science Foundation of Guangdong Province (China) Research Team (No. 003045) and the Doctorate Foundation of South China University of Technology.

REFERENCES

Ahuja, G. N. and Patwardhan A. W.: Chemical Engineering Journal **143** (2008), pp.147-160.
Almuttahar, A. and Fariborz T.: Chemical Engineering Science **63** (2008), pp.1696-1709.
Almuttahar, A. and Fariborz T.: Powder Technology **185** (2008), pp.11-23.
Caputo, A. C. and Pacifico M. P.: Journal of Hazardous Materials **81** (2001), pp.265-283.
Chu, K. W. and Yu, A. B.: Powder Technology **179** (2008), pp.104-114.
FLUENT, 6.2 Manual Fluent Inc USA(2005).
Lee, G. W., Sung J. L., Jurng, J. and Hwang, J.: Journal of Hazardous Materials **101** (2003), pp.273-283.
Lopes, Rodrigo, J. G. and Quinta-Ferreira, R. M.: Chemical Engineering Journal (2008), doi:10.1016/j.cej.2008.11.048.
Lyngfelt, A. and B. Leckner: Fuel **78** (1999), pp.1065-1072.
Mukadi, L., Guy, C. and Robert, L.: Chemical Engineering Science **54** (1999), pp.3071-3078.

Pallarès, D and Filip J.: Chemical Engineering Science **63** (2008), pp.5663-5671.
Shin, D., Jang, S. and Hwang, J.: Waste Management **25** (2005), pp.680-685.
Tsai, M. Y., Wu,K. T. Huang C. C. and Lee, H. T.: Waste Management **22** (2002), pp.439-442.
Vamvuka, D., Salpigido, N. U., Kastanaki, E. and Sfakiotakis, S.: Fuel (2008), doi: DOI: 10.1016/j.fuel.2008.09.029.
Wang, S., Xu, Y, Lu, H., Yu, L., Wan, S., and Ding Y.: Computers & Chemical Engineering(2008), doi: DOI: 10.1016/j.compchemeng.2008.10.020.

A NEW DRY FLUE GAS DESULFURIZATION PROCESS-UNDERFEED CIRCULATING SPOUTED BED

M. Tao, B. S. Jin, Y. P. Yang

School of Energy and Environment, Southeast University, Nanjing,210096, China

Abstract: Applying an underfeed system, the underfeed circulating spouted bed was designed as a desulfurization reactor. The main objective of the technology is to improve the mixing effect and distribution uniformity of solid particles, and therefore to advance the desulfurization efficiency and calcium utility. In this article, a series of experimental studies were conducted to investigate the fluidization behavior of the solid-gas two-phase flow in the riser. The results show that the technology can distinctly improve the distribution of gas velocity and particle flux on sections compared with the facefeed style. Analysis of pressure fluctuation signals indicates that the operation parameters have significant influence on the flow field in the reaction bed. The existence of injecting flow near the underfeed nozzle has an evident effect on strengthening the particle mixing.

Keywords: underfeed circulating spouted bed, desulfurization, solid-gas flow, solid flux, pressure fluctuation

INTRODUCTION

The underfeed circulating spouted bed is designed as a flue gas desulfurization reactor on the base of conventional circulating fluidizing bed. One of the main features of the technology is the uniform solid distribution and intense particles mixing in the riser. For the bottom humidifying area is the main zone where desulfurization reaction takes place (Li et al., 2002), the distribution uniformity of agent particles in the area would greatly affect the desulfurization efficiency and calcium utility. As the fresh agent is fed to the reactor by the underfeed nozzle, high speed injecting flow exists in the bottom bed and the gas-solid turbulence can be distinctly strengthened. This will be of great benefit to physical operation and chemical reaction.

In this article, the radical distribution of gas velocity was investigated and the solid upflow fluxes were acquired by means of isokinetic sampling with a suction probe (Herb et al., 1992; Aguillon et al., 1996; Zhang et al., 1997; Coronella and Deng, 1998). The sectional distribution of particle fluxes was compared between the two feed styles. In order to study the influential factors of the flow characteristic, a wide investment was made on pressure fluctuations at different operation parameters. The results have important value and instruction on the optimal design and operation of the underfeed circulating spouted bed.

EXPERIMENTAL

Experimental facility

The experiments were conducted in an underfeed circulating spouted bed-flue gas desulfurization (UCSB-FGD) system as shown in Fig.1. The height of the bed is 19m, with diameter of 0.6m. The whole facility consists of reaction bed, humidifying system, solid-gas separation system, underfeed system, recycling system and measure system.

For the facefeed style, the fresh agent is added by the screw feeder connected to the loop seal. For the underfeed style, the underfeed system is applied. The underfeed system includes barrel hopper, upright tube, injector, underfeed nozzle and propeller fan. The fresh agent in the barrel hopper was first translated to the injector and then pushed by high speed gas along the pipeline. Finally the agent was injected into the bottom bed from the underfeed nozzle and mixed with recycling materiel intensely.

Figure 2 illustrates the configuration of underfeed system. The nozzle served to this investigation contains four orifices of Φ10 mm. The distance from the centre of nozzle to the bottom of divergent cone can be adjusted at 0.4m or 0.5 m for the pipeline is connected by the pipe unions which can be taken down and set up easily. In this study, the nozzle was located at the height of 0.4m from the bottom of divergent cone.

Test content

In order to study the distribution uniformity of solid particles, the mass fluxes in the upflow were acquired by particle collection at each point using a sampling probe. Hetero-diameter configuration was applied within the probe in order to advance the velocity of the sampling gas and avoid particle aggradations (Duan et al., 2001). Before solid sampling the rotameter was adjusted by a valve to keep the gas velocity of the probe inlet

equal to the local position. The sampling period at each point was 60s. The underfeed material used in the experiment was silica sand, with an average diameter of 75μm and the density of 2600kg/m^3. The measuring system of the suction probe is as shown in Fig.3.

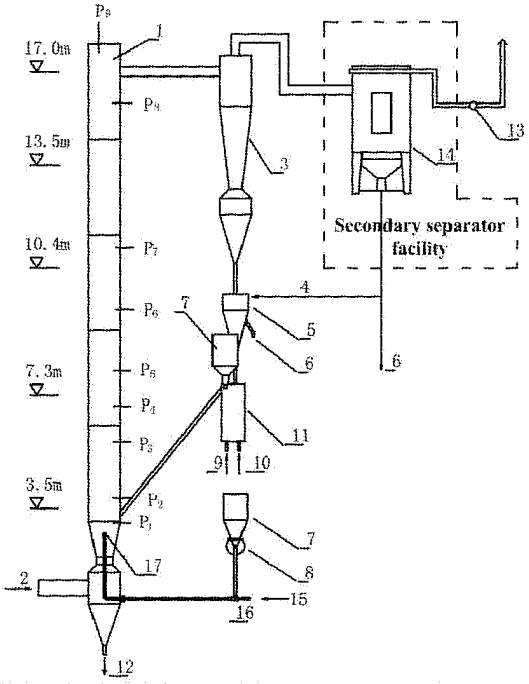

1. Reaction bed 2. Flue gas 3. Cyclone separator 4. Recycling material 5. Relay hopper 6. Exit 7. Barrel hopper 8. Screw feeder 9. Feeding air 10. Fluidizing air 11. Loop seal 12. Residual 13. Fan 14. Bag separator 15. Injecting gas 16. Injector 17. Underfeed nozzle Pi. Pressure Probes

Fig.1 Schematic diagram of the underfeed circulating spouted bed

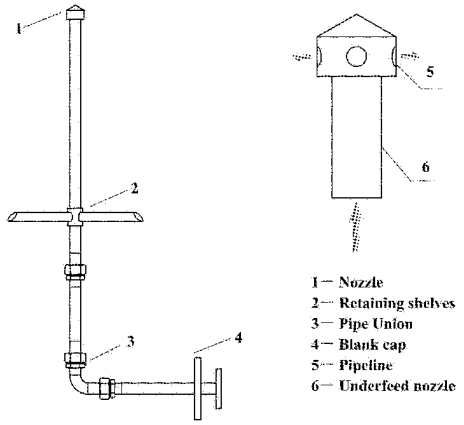

Fig.2 Configuration of the underfeed system

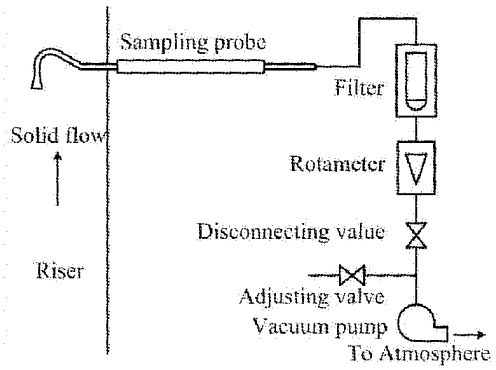

Fig.3 System of iso-kinetic suction probe

There are three sampling positions along the axial direction, at the height of 1.17m, 4.87m, and 7.95m from the bottom of divergent cone respectively. The sampling points are distributed by method of equiareal annulus. The distribution of radical positions and corresponding non-dimensional radius is listed in Table.1.

Pressure signals of eight positions were measured across the length of the riser. The arrangement of the pressure taps is as shown in Fig.1. The pressure fluctuations of the apparatus were monitored by rapid-response pressure transducers. To prevent blockage by fine particles, each port was filled by a filter tip. The probe was inserted at the apparatus wall to measure the fluid pressure signals. PFS signals were collected by an AD/DA board at a sampling rate of 50Hz. The acquisition time was 30s at each point and thus the maximum length of the time series is 1500 points.

Table 1 Disparity of solid upward fluxes in each annulus with facefeed style

Point	5'	4'	3'	2'	1'	0	1	2	3	4	5
r	-0.284	-0.250	-0.211	-0.162	-0.067	0	0.067	0.162	0.211	0.250	0.284
r/R	-0.947	-0.833	-0.703	-0.540	-0.223	0	0.233	0.540	0.703	0.833	0.947

RESULTS AND DISCUSSION

The influence of feed styles on gas velocity

Distribution of gas velocities in the X-axis direction was measured by a thermal anemoscope at different heights of the riser. The fluidizing velocity was 1.2m/s. Figure 4(a) shows that the gas velocity is lopsided at the height of 1.17m with facefeed style on account of the existence of recycling system. The material returned from the recycling tube on the right side disturbed the gas flow and resulted in the reduction of the gas velocity.

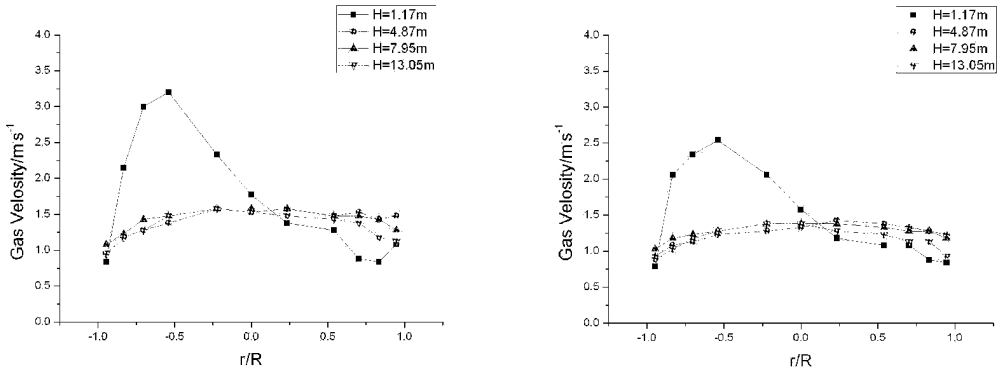

(a) facefeed style (b) underfeed style

Fig.4 Radial distribution of gas velocity with different feed styles

The radial distribution of gas velocities with underfeed style is as shown in Fig.4b. Compared with the facefeed style, the gas velocity distribution is more symmetrical and the disparity between the two sides is not that distinct at the height of 1.17m. This illuminates that the existence of spouting flow can reform and optimize the gas flow especially in the bottom area.

Influence of feed styles on solid upwards flux distribution

The distribution of solid upwards fluxes on the section of H=4.87m with facefeed style is as shown in Fig.5a. The fluidizing and spouting velocity were 1.2m/s and 17.5m/s respectively. It shows that the solid upwards flux, G_{up}, is lopsided on the section, with much higher value on the right side. This might be caused by the uneven distribution of solid concentration in the bottom bed. As the circulating material enters the bed from the right side, the solid concentration is much greater at that side along the bed. With the underfeed style, the G_{up} on the section also had an unbalanced distribution on the section (shown in Fig.5(b)). But the uniformity is evidently advanced comparing with the facefeed style. The contrast between the two sides gets smaller at each annulus area.

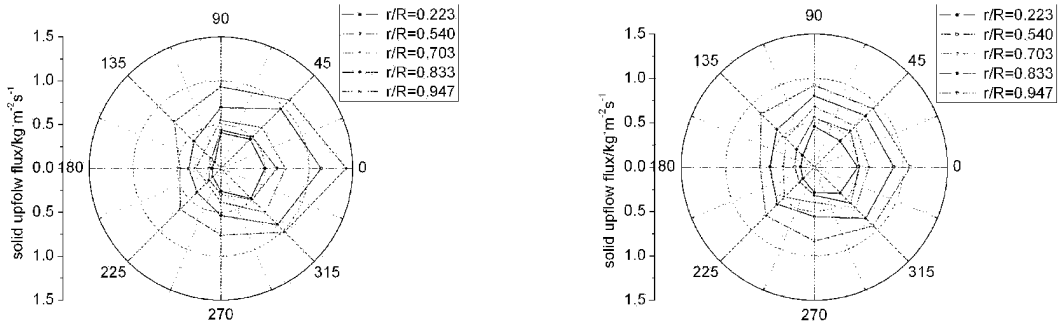

(a) facefeed style (b) underfeed style

Fig.5 Solid upwards flux distribution on section of H=4.87m with different feed styles

The disparity at each annulus area is measured by the relative standard deviation, σ_r, which is expressed by the standard deviation, σ, divided by the mean value of G_{up} on the annulus. It is illuminated in Tables 2-3 that the mean value of G_{up} in each annulus advances with the decreasing r/R with both feed styles. The standard deviation of the G_{up} is greater with lower r/R while the relative standard deviation gets smaller. It can also be observed that the σ_r with underfeed style is evidently smaller than that with facefeed style. This validates the improvement of solid distribution uniformity by the underfeed style.

Table.2 Disparity of solid upward fluxes in each annulus with facefeed style

r/R	0.223	0.540	0.703	0.833	0.947
standard deviation	0.178	0.190	0.210	0.294	0.298
mean value/kg • $m^{-2}s^{-1}$	0.307	0.357	0.478	0.678	0.891
relative deviation	0.580	0.531	0.438	0.434	0.334

Table.3 Disparity of solid upward fluxes in each annulus with underfeed style

r/R	0.223	0.540	0.703	0.833	0.947
standard deviation	0.136	0.158	0.129	0.150	0.139
mean value/kg • $m^{-2}s^{-1}$	0.322	0.408	0.536	0.697	0.867
relative deviation	0.423	0.387	0.241	0.216	0.160

Influence of fluidizing velocity

Figure 6 shows typical example of pressure fluctuation signals over the fluidizing velocity from 0.8m/s to 1.4m/s. The selected curves show the following bed behavior: The change of pressure fluctuations along the axial direction in the riser expresses the similar trend at different fluidizing velocities. In the bottom of the bed, the particles are thick and the solid mixing is intense, so the pressure fluctuations are very obvious. While in the upper bed, the solid is dilute and the particle movement becomes less complicated, thus the fluctuation signals are much more equable. At the height of 13.2m, the pressure fluctuations increase again. This is caused by the influence of the outlet. In the vicinity of the outlet, the particles accumulate and congregate and thus the pressure becomes more unstable (Ulrike and Joachim, 2002).

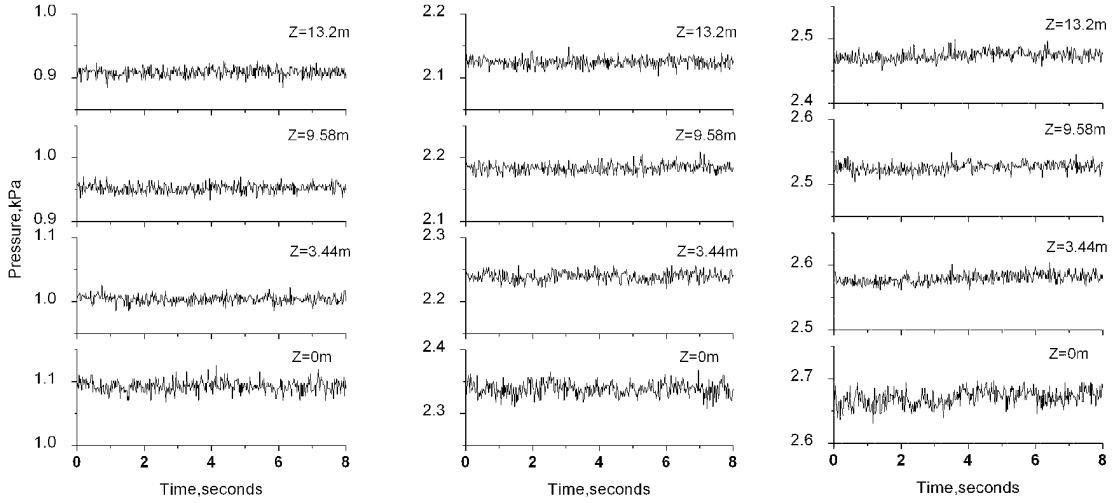

(a) V_f=0.8m/s (b) V_f=1.1m/s (c) V_f=1.4m/s

Fig.6 The time-series of pressure fluctuations at different fluidizing velocity (V_s=17.5m/s)

As the superficial velocity advances, more particles are elutriated and entrained. As a result, the circulating ratio increases and the particle concentration gets higher in the riser. Therefore, the fluctuations become more intense and this contributes to the change of pressure signals as shown in Fig.6.

Figure 7 shows the standard deviation of the pressure fluctuations for different fluidizing velocity. The standard deviation descends along the axial direction and then ascends near the outlet. The figure also illustrates that the standard deviations increase along the whole bed as the fluidizing velocity advances. The results correspond to the above analysis of the fluctuation signals very well.

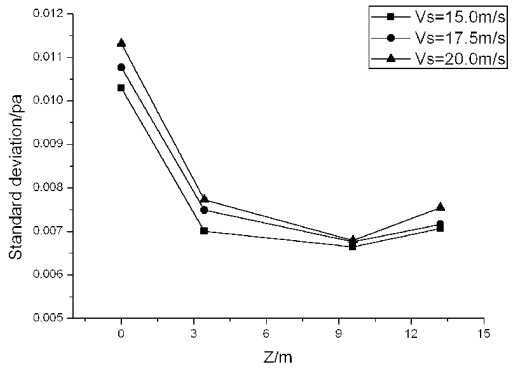

Fig.7 Influence of V_f on standard deviation of pressure fluctuations

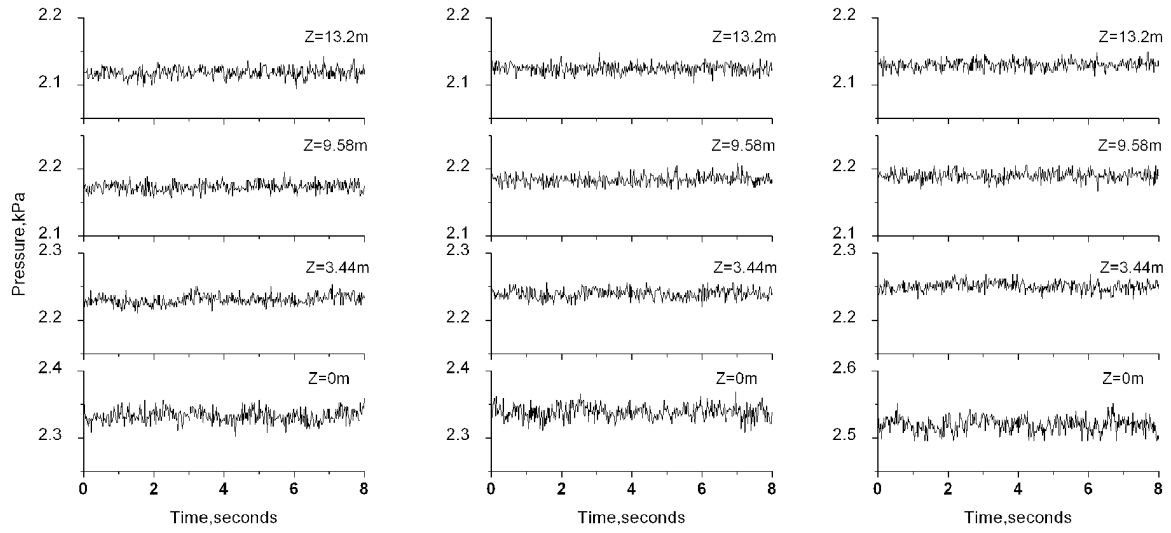

(a) V_s=15.0m/s (b) V_s=17.5m/s (c) V_s=20.0m/s

Fig.8 The time-series of pressure fluctuations at different spouting velocity (V_f=1.1m/s)

Influence of spouting velocity

The effect of the spouting velocity on the pressure fluctuation signals is as shown in Fig.8. The fluctuation amplitude seems to have inconspicuous change with the increasing spouting velocity. This is because the spouting flux is very few compared to the fluidizing flux. The influence of spouting velocity on the particle movement is mainly located in the bottom area, where the particles are fed by the underfeed nozzle. Fan et al (1984) divided a fluidized bed into three regions. The region close to the distributor is found to be affected mostly by the gas distribution and jet penetration. The central section is dominated by bubble dynamics while the upper bed is affected by pressure changes due to bubble breakage and bed height fluctuations.

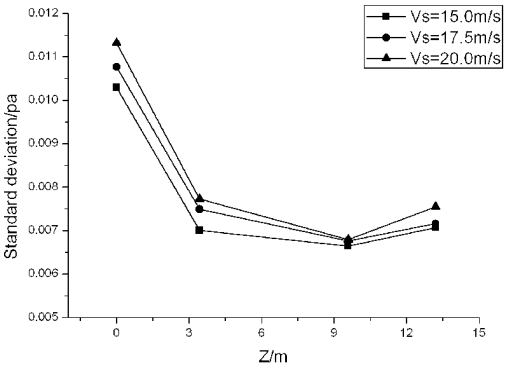

Fig.9 Influence of V_s on standard deviation of pressure fluctuations

The standard deviations of the pressure fluctuations for different spouting velocity are shown in Fig.9. As the spouting velocity advances, the standard deviations increase along the whole bed. With higher spouting velocity, the solid collides and mixes more intensely in the bottom area. In the actual desulfurization process, the intense turbulent flow can not only enhance the mass and heat transport, but also remove the product layer of the recycling material and uncover the inner fresh reactant (Chu and Hwang, 2005). This will be of great benefit to advance the calcium utility.

Influence of circulating ratio

The change of circulating ratio can directly results in the change of the particle concentration in the reaction bed. So the influence of circulating ratio on the pressure fluctuations is obvious. The pressure fluctuation signals in the bed with different circulating ratio are shown in Fig.10. As the circulating ratio advances, the pressure ascends and the fluctuant extent increases. This is caused by the increasing solid concentration in the reaction bed.

Figure 11 shows the standard deviation of the pressure fluctuations for different circulating ratio. It can be seen that as the circulating ratio advances, the standard deviations increases obviously along the bed and the increased extent is more distinct in the bottom bed. This corresponds to the above analysis on the change of the solid concentration with the increasing circulating ratio.

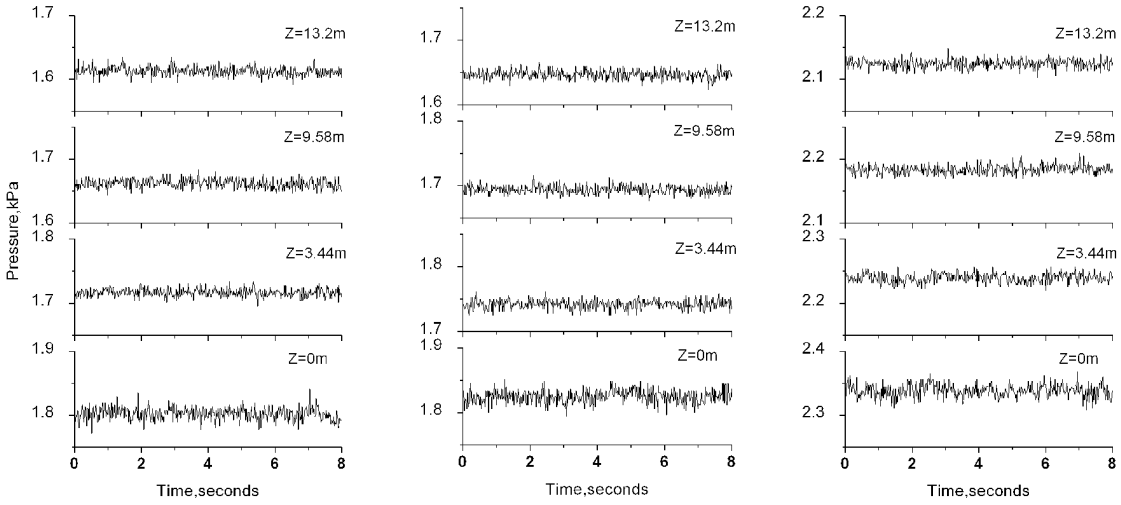

(a) G_b=524.31kg/h (b) G_b=602.96kg/h (c) G_b=728.21kg/h

Fig.10 The time-series of pressure fluctuations at different circulating ratio (V_f=1.1m/s, V_s=17.5m/s)

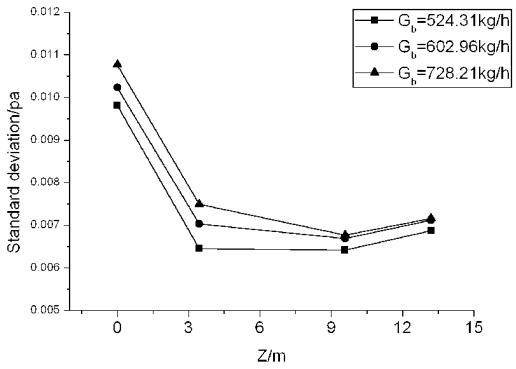

Fig.11 Influence of G_b on standard deviation of pressure fluctuations

CONCLUSIONS

The feed style has significant influence on the characteristic of solid-gas flow in the riser. As the fresh agent was fed by facefeed style in the conventional CFB-FGD facility, the gas field was quite lopsided especially in the bottom bed affected by the recycling flow. The abounding circulating material also caused serious asymmetry of the particle distribution on the section. The uneven flow field degraded the fluidization quality and made against the efficiency of the mass and heat transfer. The underfeed circulating spouted bed applied the underfeed system and fed the fresh agent with injecting flow from the center of bottom bed. The high speed injecting flow had a cutting and optimizing effect on the flow field and made the solid mixing more intense. This is of great benefits to the solid-gas contact and reaction efficiency.

As the fluidizing velocity or circulating ratio advances, the solid concentration along the axial direction increases obviously. This makes the solid-gas flow more turbulent and the pressure more fluctuant. Analysis of time traces of pressure fluctuation show that the fluidizing velocity and circulating ratio have great influence on the flow characteristic in the whole bed.

The solid-gas flow in the bottom bed can be greatly affected by the gas distribution and jet penetration. Advancing the spouting velocity makes the particles collide and mix more intensely and the flow becomes more turbulent. As a result, the pressure fluctuations get more unstable in the bottom of the reaction bed.

NOTATIONS

G_{up}	solid upward flux, kg/m^{2}s	V_f	fluidizing velocity, m/s
$\overline{G_{up}}$	mean value of G_{up}, kg/m^{2}s	r	radial position, m
G_b	mass flux of circulating material, kg/h	R	semi-diameter of the riser, m
H	axial height, m	σ	standard deviation of solid flux, kg/m^{2}s
V_s	spouting velocity, m/s	σ_r	relative standard deviation of solid flux

REFERENCES

Aguillon J., Shakourzadeh K., Guigon P.: Power Technol. **86**(1996), pp.251-255.
Chu C. Y. and Hwang S. J.: Power Technol. **154**(2005), pp.14-23.
Coronella C. J., Deng J. X.: Powder Technol. **99**(1998), pp.211-219.
Duan Y. F., Zhao C.S., Xu Y. Q.: Boiler Technol. **32**(2001), pp.1-4.
Herb B., Dou S. S., Tuzla K.: Power Technol. **70**(1992), pp.197-205.
Hiraoka S., Shin S. H., Fan L. T.: Powder Technol. **38**(1984), pp.125-143.
Li D. J., Feng B., Wu Y. H.: Journal of Engineering for Thermal Energy & Power. **17**(2002), pp.349-352.
Piskova E. and Morl L.: Chem. Eng. Sci. **63**(2008), pp.2307-2316.
Rhodes M. J.: Power Technol. **60**(1990), pp.27-38.
Ulrike L. and Joachim W.: Chem. Eng. Process. **41**(2002), pp.771-783.
Xu J., Bao X. J., Wei W. S.: Power Technol. **140**(2004), pp.141-154.
Zhang W, Johnson F, Leckner B: Chem. Eng. Sci. **52**(1997), pp.497-509.

Authors Index